WCAP-16996-NP-A
Revision 1

November 2016

Realistic LOCA Evaluation Methodology Applied to the Full Spectrum of Break Sizes (FULL SPECTRUM LOCA Methodology)

Volume II
WCOBRA/TRAC-TF2 Assessment

WCAP-16996-NP-A
Revision 1

Realistic LOCA Evaluation Methodology Applied to the Full Spectrum of Break Sizes (FULL SPECTRUM LOCA Methodology)

Jeffrey R. Kobelak	LOCA Integrated Services
Dr. Katsuhiro Ohkawa	LOCA Integrated Services
Dr. Liping Cao	LOCA Integrated Services
Aaron M. Everhard	LOCA Integrated Services
Dr. Jun Liao	LOCA Integrated Services
Nikolay P. Petkov	LOCA Integrated Services
Michael A. Shockling	LOCA Integrated Services

November 2016

Prepared by: Jeffrey R. Kobelak*
LOCA Integrated Services

Reviewer: Michael A. Shockling*
LOCA Integrated Services

Approved: Amy J. Colussy*, Manager
LOCA Integrated Services

*Electronically approved records are authenticated in the electronic document management system.

Westinghouse Electric Company LLC
1000 Westinghouse Drive
Cranberry Township, PA 16066, USA

TABLE OF CONTENTS

TABLE OF CONTENTS (cont.)

TABLE OF CONTENTS (cont.)

TABLE OF CONTENTS (cont.)

TABLE OF CONTENTS (cont.)

TABLE OF CONTENTS (cont.)

TABLE OF CONTENTS (cont.)

TABLE OF CONTENTS (cont.)

LIST OF TABLES

VOLUME II

LIST OF TABLES (cont.)

LIST OF TABLES (cont.)

LIST OF TABLES (cont.)

LIST OF TABLES (cont.)

LIST OF FIGURES

VOLUME II

LIST OF FIGURES (cont.)

LIST OF FIGURES (cont.)

LIST OF FIGURES (cont.)

LIST OF FIGURES (cont.)

LIST OF FIGURES (cont.)

LIST OF FIGURES (cont.)

LIST OF FIGURES (cont.)

LIST OF FIGURES (cont.)

LIST OF FIGURES (cont.)

LIST OF FIGURES (cont.)

LIST OF FIGURES (cont.)

LIST OF FIGURES (cont.)

LIST OF FIGURES (cont.)

LIST OF FIGURES (cont.)

LIST OF FIGURES (cont.)

LIST OF FIGURES (cont.)

LIST OF FIGURES (cont.)

LIST OF FIGURES (cont.)

LIST OF FIGURES (cont.)

LIST OF FIGURES (cont.)

LIST OF FIGURES (cont.)

LIST OF FIGURES (cont.)

LIST OF FIGURES (cont.)

LIST OF FIGURES (cont.)

LIST OF FIGURES (cont.)

LIST OF FIGURES (cont.)

LIST OF FIGURES (cont.)

LIST OF FIGURES (cont.)

LIST OF FIGURES (cont.)

LIST OF FIGURES (cont.)

LIST OF FIGURES (cont.)

LIST OF FIGURES (cont.)

LIST OF FIGURES (cont.)

LIST OF FIGURES (cont.)

LIST OF FIGURES (cont.)

LIST OF FIGURES (cont.)

LIST OF FIGURES (cont.)

LIST OF FIGURES (cont.)

LIST OF FIGURES (cont.)

LIST OF FIGURES (cont.)

LIST OF FIGURES (cont.)

LIST OF FIGURES (cont.)

LIST OF FIGURES (cont.)

LIST OF FIGURES (cont.)

LIST OF FIGURES (cont.)

LIST OF FIGURES (cont.)

LIST OF FIGURES (cont.)

LIST OF FIGURES (cont.)

LIST OF FIGURES (cont.)

LIST OF FIGURES (cont.)

LIST OF FIGURES (cont.)

LIST OF FIGURES (cont.)

LIST OF FIGURES (cont.)

LIST OF FIGURES (cont.)

LIST OF FIGURES (cont.)

LIST OF FIGURES (cont.)

LIST OF FIGURES (cont.)

LIST OF FIGURES (cont.)

LIST OF FIGURES (cont.)

LIST OF FIGURES (cont.)

LIST OF FIGURES (cont.)

LIST OF FIGURES (cont.)

LIST OF FIGURES (cont.)

LIST OF FIGURES (cont.)

LIST OF FIGURES (cont.)

LIST OF FIGURES (cont.)

LIST OF FIGURES (cont.)

LIST OF FIGURES (cont.)

LIST OF FIGURES (cont.)

LIST OF FIGURES (cont.)

LIST OF FIGURES (cont.)

LIST OF FIGURES (cont.)

LIST OF FIGURES (cont.)

LIST OF FIGURES (cont.)

LIST OF FIGURES (cont.)

LIST OF FIGURES (cont.)

LIST OF FIGURES (cont.)

LIST OF FIGURES (cont.)

LIST OF FIGURES (cont.)

LIST OF FIGURES (cont.)

LIST OF FIGURES (cont.)

12 ASSESSMENT OF BREAK FLOW MODEL

12.1 INTRODUCTION

During a Loss-of-Coolant Accident (LOCA), the break flow rate determines the depressurization rate as well as the mass inventory of the primary system of a pressurized water reactor (PWR). These parameters in turn influence the timing of various engineered safeguard system responses, such as reactor trip and safety injection, and the degree of core uncovery which is the major parameter determining the subsequent heatup and clad temperature. Although the size, location, and shape of the break are not known for the postulated LOCA, the best-estimate code needs to predict consistent responses given the break size and location over a range of pressure, subcooling, and upstream fluid states expected in LOCA.

In this section, an assessment is made of the critical flow model in the WCOBRA/TRAC-TF2 version described in Section 5.12.2, Volume 1, of this document. This section presents the following assessment results.

12.1.1 Critical Flow in LOCA (Relation to LOCA PIRT)

A fluid system contained in a reactor vessel with a pipe break is in communication with the containment atmosphere, which is at a lower pressure through the break flow path. Under critical flow conditions, the discharge flow rate from the high pressure system becomes independent of the containment conditions, which are at the lower pressure.

Since the break flow rate determines the depressurization and inventory and mass distribution in the vessel, it is easy to justify a high ranking of this phenomenon as discussed in Section 2, Volume 1. For Small Break LOCA (SBLOCA), because the Reactor Coolant System (RCS) pressure remains high enough to cause the break flow to be critical **[**

][a,c]

Early in a LOCA, the fluid condition upstream of the break location is subcooled. This results in a high discharge flow rate and a fast depressurization. As the pressure drops to the saturation pressure corresponding to the coolant liquid temperature upstream of the break, the discharge becomes two-phase and a relatively low discharge rate and a slow depressurization result. As the system mass depletes and the flow in the main pipe stratifies, the break location begins to uncover. The break quality under the stratified upstream is determined by the offtake phenomena and is the subject of Section 12.7.

12.1.2 Assessment Objective

In this section, the break flow model in WCOBRA/TRAC-TF2 is assessed relative to the following effects on the break flow in addition to the accuracy relative to data:

- Break path length
- Break flow area variation
- Upstream pressure variation
- Variation in degree of subcooling during liquid discharge
- Upstream void fraction/quality variation
- Break entrance geometry
- Non-condensable gas concentration in the Vapor phase

The critical flow model's bias and uncertainty will be determined by comparing the critical flow model prediction implemented in WCOBRA/TRAC-TF2 with selected data from the qualified break flow dataset. A selection of the model assessment dataset is described in the subsequent section.

12.2 CRITICAL FLOW DATA NEEDS FOR PWR LOCA MODEL VALIDATION

The requirements of a critical flow data base which would be suitable for use in validating critical flow models for the range of conditions occurring during PWR LOCAs is discussed in this section. The range of geometrical, and physical conditions, and the criteria for defining the necessary quality of the data were discussed by Holmes and Allen (1998).

Holmes and Allen (1998) identified the range of parameters, both geometrical and physical, which would cover the perceived need for the analytical model validation used in LOCA analyses as shown in Tables 12.2-1 through 12.2-3.

In LOCA scenarios, the worst break is postulated to occur in the cold leg of the primary coolant system. For bounding purposes, the size of the break is assumed to be as large as the full cross section of the primary loop pipes, and as small as the break size of ~0.5 in^2 below which the coolant makeup system is able to maintain the reactor coolant inventory by matching the injection to the leak rate from the break. Thus the scale requirement for the critical flow data for the purpose of PWR LOCA analyses is 0.5 in^2 to ~4.15 ft^2. The data requirement for the break upstream fluid conditions may be determined by examining LOCA experiment measurements/analyses and PWR LOCA simulations. Figures 12.2-1 and 12.2-2 show respectively the predicted temperature-pressure and the quality-pressure trajectories for LBLOCA transients and a 5% small break test. The blue line shows the predicted trajectory for the largest Double Ended Guillotine Break in a typical 3 loop PWR. The green line shows the predicted trajectory for the smallest (~1ft^2 break area) LBLOCA of a 3 loop PWR which could be considered the largest IBLOCA. The red line shows the predicted trajectory of SB-CL-05, a 5% cold leg break simulation performed at the Rig-of-Safety Assessment (ROSA) facility. The trajectory for IB and LBLOCA shows a rapid depressurization to saturation from the operating condition to saturation at around 1000~1200 psia where the initially subcooled liquid reaches saturation and the upstream of the break turns two-phase. The predicted SB-CL-05 small break trajectory reaches saturation at around 1200 psia and transitions from all liquid to all vapor due to loop-seal clearing. The upstream quality remains at or near 1.0 until accumulator injection at around 600 psia at which time the break becomes subcritical. The desired critical flow data should cover the range of fluid conditions indicated in these figures.

Table 12.2-1 Range of Geometrical Configurations[1]	
Component	**Ranges**
Straight Pipe	Diameter ≤ 0.7 m, 1 ≤ L/D ≤ 10 (This range of L/D is for large break LOCAs in PWRs, i.e., pipe length in the range of 0.5 m - 7 m, small break LOCAs will require a correspondingly wider range of L/D ratios)
Elbows	45°-90°, diameter ≤ 0.7 m, 1 ≤ r/d ≤ 4
Tees	Angle of offtake 45°-90°, main pipe diameter ≤ 0.7 m
Nozzles	Diameter ≤ 0.7 m, 0.3 ≤ L/D ≤ 10, round/square entry
Pumps	Pump Specific Geometry
Valves	All valve data
Orifices, flow meters, etc.	Where available
Note: 1. Holmes and Allen, 1998.	

Table 12.2-2 Break Configuration[1]	
Break Configuration	**Ranges**
Guillotine Breaks	Varying degree of off-set
Holes	10^{-4} m^2 ≤ Break Area ≤ 0.1 m^2
Splits	Horizontal/Circumferential, ~10^{-4} m^2 ≤ Break Area ≤ 1.0 m^2
Reactor Coolant Pump Seal Geometry	Pump design specific
Note: 1. Holmes and Allen, 1998.	

Table 12.2-3 Range of Physical Conditions Upstream of Discharge[1]		
Pressure (MPa)	**Temperature**	**Flow Condition**
0.1 – 20	~ Saturation	Single-phase steam/two-phase
0.1 – 15	≤ 200K subcooled/saturation	Single-phase liquid/two-phase
-	-	Single-phase vapor/two-phase with Non-condensable gas
Note: 1. Holmes and Allen, 1998.		

a,c

Figure 12.2-1 Upstream P-T in Small and Large Break LOCAs

a,c

Figure 12.2-2 Upstream Quality in Small and Large Break LOCAs

12.3 ASSESSMENT TEST MATRIX AND BASIS FOR SELECTION

The critical flow dataset compiled by Illic et al. (1986) was further examined for the purpose of the critical flow model validation and the bias/uncertainty evaluation in a similar screening discussed in Elias and Lellouche (1994), and Holmes and Allen (1998). Data without well-defined or stagnation condition or upstream condition were excluded for assessment. Datasets generated by Cruver (1963), Fauske (1962), Henry (1970), Isbin et al. (1957) and Zaloudek (1964) do not report the stagnation pressure. The dataset generated by Guizovarn et al. (1975) contains superheated liquid upstream of the nozzle, which is contrary to the description in Illic et al. (1986) which states a subcooled inlet condition. The dataset generated by Bryers et al. (1966) contains a highly subcooled stagnation condition contrary to the description. The dataset generated by Ogasawara (1969) did not contain the reservoir temperature or the quality. Datasets generated by Danforth (1941) and Schrock et al. (1977) are suspect with regard to achieving the critical condition according to Illic. The dataset generated by Morrison (1977) appears to be inconsistent with other similar data.

The datasets mentioned above need to be further investigated for the use in the model bias and uncertainty study since as-reported upstream condition is suspect. These subsections were discarded in much the same reasons as the previous work (pp. 117, Elias and Lellouche, 1994). The database was further expanded by including four additional sources. Marviken (1982) test data were added since this set is the only critical flow data for diameters above 200 mm and can be considered a full scale. While this is a transient experiment, necessary upstream conditions were reported at a 1 second interval which could be used to define the inlet condition. The offtake dataset taken at the two-phase flow loop (TPFL) (Anderson and Benedetti, 1986) was added which contains fluid condition measurements upstream of the break nozzle where the flow was critical. Amos and Schrock's (1983) data covers the pressure and subcooling range comparable to the PWR's operating condition. Celata's et al. (1988) subcooled data were included for the subsequent validation of the non-condensable gas capability. Table 12.3-1 is a summary of all selected datasets for this assessment. The subsection number in the table was assigned prior to the selection process. This is the reason why the dataset number seen in the table is not contiguous. The dataset represents 3199 points from 53 geometries containing data from 13 to 2300 psia. The geometry ranges from $1 < L < 2335$ mm, 0.464 mm $< D_H < 509$ mm.

Additionally, Celata's non-condensable gas data was selected for the validation of non-condensable gas effects as seen in Table 12.3-2.

Table 12.3-3, is the complete list of database in the assessment test matrix used to evaluate the accuracy of the WCOBRA-TRAC-TF2 break flow model; it describes in detail all 53 nozzle geometries and orientations. The comment section describes Diameter, D, as a function of axial distance, z.

Table 12.3-1 Selected Dataset and Input Variables

Reference	Pressure (psia)	Upstream Condition	No. of Data Points	Length (mm)	Dhyd (mm)
Ardron & Ackerman (1978)	22-54	Subcooled	32	1015	26.3
Boivin (1979)	284-1465	Subcooled	21	500-1700	12-50
Fincke & Collins (1981)	13-44	Subcooled	92	25	18.3
Jeandey (1981)	130-2030	Subcooled	88	463	20.13
Neusen (1962)	122-945	Saturated to X=0.23	37	Orifice (1 mm)	6.4-11.125
Reocreux (1974)	31-49	Subcooled	28	2335	20
Seynhaeve (1980)	41-147	Subcooled	57	221-306	12.5
Sozzi & Sutherland (1975)	440-1034	Subcooled and Saturated	667	1-1779	12.7-76.2
Amos & Schrock (1983)	600-2291	Subcooled	44	63.5	0.464, 0.748
Anderson & Benedetti (1986)	485-901	Saturated Liquid up to Saturated Vapor	109	54	16.2
Marviken (1982)	374-748	Subcooled and Saturated	1927	166-1809	200-509
Celata (1988)	73-228	Subcooled to Saturated	97	1500	4.6
	13-2300	Subcooled Liquid to Saturated Vapor	3199	1-2335	0.464-509

Table 12.3-2 Additional Dataset for Non-condensable Gas Model Validation and Input Variables

Reference	Pressure (psia)	Upstream Condition	No. of Data Points	Length (mm)	Dhyd (mm)
Celata (1988)	73-218	Data-41 with Non-C (Volume %): 0-80.	97	1500	4.6

Table 12.3-3 Critical Flow Data Considered for Model Evaluation

Reference	L (mm)	D (mm)	cosθ	N-Data	Comments
Ardron, K. H. & Ackerman, M. C. (1978)	1015	26.3	0	33	One measurement set indicating a superheated liquid upstream condition was not used.
Boivin (1979)	500	12	0	10	D=50 (z<0); 0<z<50 rounded entrance; D=12 (50<z<500); D=12+19(z-500) (500<z<700); D=50 (z>700 mm)
Boivin (1979)	1600	30	0	5	D=150 (z<0); 0<z<130 rounded entrance; D=30 (130<z<1730); D=30+0.12(z-1730) (1730<z<2305); D=100 (z>2305 mm)
Boivin (1979)	1700	50	0	6	D=150 (z<0); 0<z<130 rounded entrance; D=50 (130<z<1830); D=50+0.12(z-1830) (1830<z<2240); D=100 (z>2240 mm)
Fincke & Collins (1981)	25	18.3	0	92	D=18.28 (54.7<z<79.7); D=18.28+0.12(z-79.7), (z<215.9 mm)
Jeandey et al. (1981)	463	20	1	15	D=66.7-0.54z (0<z<86.9); D=20.1 (z>86.9 mm)
Jeandey et al. (1981)	463	20	1	73	see Appendix C.7.1 for (z<100); D=20.13 (100<z<463); D=20.13+0.12(z-463) (z<900); D=737 (z>900 mm)
Neusen (1962)	1	11	0	25	D=11.12 mm at throat; D=11.12+0.425z (0<z<35.91 mm)
Neusen (1962)	1	6	0	12	D=16.4 mm at throat; D=6.4+0.425z (0<z<59.81 mm)
Reocreux (1974)	2335	20	1	28	D=20 (0<z<2335); D=20+0.12(z-2335) (z<2662 mm)
Seynhaeve (1980)	306	13	1	26	D=12.5 (0<z<306); D=12.5+0.245(z-306) (z>541); D=70 (z>541 mm)
Seynhaeve (1980)	221	13	1	31	D=12.5 (0<z<221); D=12.5+0.245(z-221) (z>541); D=70 (z>541 mm)
Sozzi & Sutherland (1975)	1	12.7	0	129	D=43.2 (z=0); rounded convergent (0<z<44.5); D=12.7+0.105(z-44.5) (z<158.5 mm) (Nozzle 1)
Sozzi & Sutherland (1975)	1	12.7	0	13	D=43.2 (z=0); rounded convergent (0<z<44.5 mm) (Nozzle 2)
Sozzi & Sutherland (1975)	12.7	12.7	0	47	D=43.2 (z=0); rounded convergent (0<z<44.5 mm) (Nozzle 2)
Sozzi & Sutherland (1975)	318	12.7	0	19	D=43.2 (z=0); rounded convergent (0<z<44.5 mm) (Nozzle 2)

Table 12.3-3 Critical Flow Data Considered for Model Evaluation (cont.)

Reference	L (mm)	D (mm)	cosθ	N-Data	Comments
Sozzi & Sutherland (1975)	38.6	12.7	0	17	D=43.2 (z=0); rounded convergent (0<z<44.5 mm) (Nozzle 2)
Sozzi & Sutherland (1975)	508.5	12.7	0	13	D=43.2 (z=0); rounded convergent (0<z<44.5 mm) (Nozzle 2)
Sozzi & Sutherland (1975)	64	12.7	0	23	D=43.2 (z=0); rounded convergent (0<z<44.5 mm) (Nozzle 2)
Sozzi & Sutherland (1975)	635.5	12.7	0	96	D=43.2 (z=0); rounded convergent (0<z<44.5 mm) (Nozzle 2)
Sozzi & Sutherland (1975)	114.8	12.7	0	15	D=43.2 (z=0); rounded convergent (0<z<44.5 mm) (Nozzle 2)
Sozzi & Sutherland (1975)	1779	12.7	0	81	D=43.2 (z=0); rounded convergent (0<z<44.5 mm) (Nozzle 2)
Sozzi & Sutherland (1975)	191	12.7	0	12	D=43.2 (z=0); rounded convergent (0<z<44.5 mm) (Nozzle 2)
Sozzi & Sutherland (1975)	229	12.7	0	22	D=43.2 (z=0); rounded convergent (0<z<44.5 mm) (Nozzle 2)
Sozzi & Sutherland (1975)	4.7	12.7	0	58	Nozzle No. 3 (Sharp entrance)
Sozzi & Sutherland (1975)	322	12.7	0	24	Nozzle No. 3 (Sharp entrance)
Sozzi & Sutherland (1975)	513	12.7	0	24	Nozzle No. 3 (Sharp entrance)
Sozzi & Sutherland (1975)	639.7	12.7	0	17	Nozzle No. 3 (Sharp entrance)
Sozzi & Sutherland (1975)	195.2	12.7	0	23	Nozzle No. 3 (Sharp entrance)
Sozzi & Sutherland (1975)	1	19	0	23	D=43.2 (z=0); rounded convergent (0<z<44.5 mm)
Sozzi & Sutherland (1975)	1	54	0	4	D=260-0.39(z-202) (202<z<732); D=54+0.263(z-732) (z<1112 mm)
Sozzi & Sutherland (1975)	1	76.2	0	3	D=260-0.39(z-223) (223<z<696); D=54+0.263(z-696) (z<1076 mm)
Sozzi & Sutherland (1975)	1	28	0	5	D=72.6 (z=0); rounded elliptical sec. (0<z<63.5); D=28+0.246(z-63.5) (z<228.5)
Amos & Schrock (1983)	63.5	0.748	-1	18	Rec. Slit 0.381x63.5 mm with known entrance losses
Amos & Schrock (1983)	63.5	0.464	-1	26	Rec. Slit 0.254x63.5 mm with known entrance losses
Anderson & Benedetti (1986)	54	16.2	0	109	Rounded entrance (at 500, 640 and 900 psia)
Marviken Test 1 (1982)	895	300	-1	97	Rounded entrance, Nozzle I, Type III

Table 12.3-3 Critical Flow Data Considered for Model Evaluation (cont.)

Reference	L (mm)	D (mm)	cosθ	N-Data	Comments
Marviken Test 2 (1982)	895	300	-1	91	Rounded entrance, Nozzle II, Type II Exp.
Marviken Test 3 (1982)	1589	509	-1	40	Rounded entrance
Marviken Test 4 (1982)	1589	509	-1	39	Rounded entrance
Marviken Test 5 (1982)	1589	509	-1	43	Rounded entrance
Marviken Test 6 (1982)	300	300	-1	85	Rounded entrance
Marviken Test 7 (1982)	300	300	-1	84	Rounded entrance
Marviken Test 8 (1982)	1589	509	-1	40	Rounded entrance
Marviken Test 9 (1982)	1589	509	-1	58	Rounded entrance
Marviken Test 10 (1982)	1589	509	-1	57	Rounded entrance
Marviken Test 11 (1982)	1589	509	-1	41	Rounded entrance
Marviken Test 12 (1982)	895	300	-1	121	Rounded entrance
Marviken Test 13 (1982)	590	200	-1	139	Rounded entrance
Marviken Test 14 (1982)	590	200	-1	144	Rounded entrance
Marviken Test 15 (1982)	1809	500	-1	45	Rounded entrance
Marviken Test 16 (1982)	1809	500	-1	40	Rounded entrance
Marviken Test 17 (1982)	1110	300	-1	90	Rounded entrance
Marviken Test 18 (1982)	1110	300	-1	69	Rounded entrance
Marviken Test 19 (1982)	1110	300	-1	85	Rounded entrance
Marviken Test 20 (1982)	730	500	-1	50	Rounded entrance
Marviken Test 21 (1982)	730	500	-1	50	Rounded entrance
Marviken Test 22 (1982)	730	500	-1	37	Rounded entrance
Marviken Test 23 (1982)	166	500	-1	61	Rounded entrance
Marviken Test 24 (1982)	166	500	-1	44	Rounded entrance
Marviken Test 25 (1982)	510	300	-1	84	Rounded entrance
Marviken Test 26 (1982)	510	300	-1	134	Rounded entrance
Marviken Test 27 (1982)	730	500	-1	59	Rounded entrance
Celata et al. (1988)	1500	4.6	-1	97	Entrance loss calibrated using one single-phase flow test.

12.4 DESCRIPTION OF DATASETS

The stagnation condition of each dataset such as Pressure/Temperature and Pressure/Quality are shown graphically in the following figures. The Pressure/Temperature trajectories of the primary system of Loss-of-Fluid Test (LOFT) 2.5% cold leg break (Dao and Carpenter, 1980) and ROSA 5% cold break while the break is choked during small break LOCA experiments along with the saturation line are shown for comparison.

12.4.1 Ardron and Ackerman

Ardron and Ackerman conducted critical flow experiments by discharging subcooled water from a pressure vessel through a horizontal test section. The test section consisted of a straight cylindrical pipe 0.0263 m in diameter and 1.015 m long. Instrumentation included measurement of stagnation pressure and temperature with reported uncertainties of 7.0 kPa and 0.1°C, respectively, mass flux with uncertainty of 200 kg/m^2-s, and differential pressure measurements, the roughness of pipe was estimated to be 2.5E-06 m. As seen in Figures 12.4-1a and 12.4-1b, the range of stagnation pressure tested was from 150 to 370 kPa (21.8 to 53.7 psia) with subcooling from 0 to 7°C (quality of 0 to $-6x10^{-6}$). All tests were conducted with de-mineralized and degassed water.

a,c

Figure 12.4-1a Upstream P-T in Ardron-Ackerman

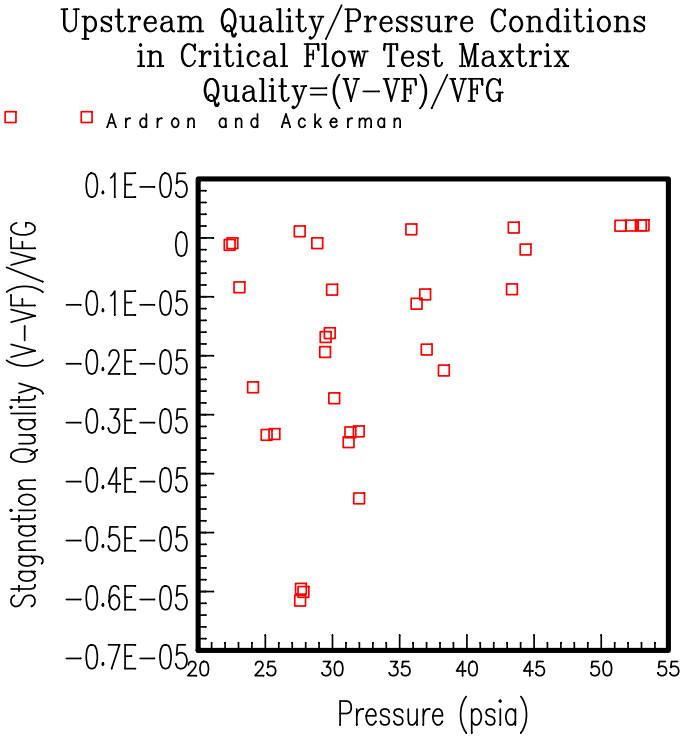

Figure 12.4-1b Upstream Quality in Ardron-Ackerman

12.4.2 Boivin

Boivin conducted critical flow experiments by discharging water through long, horizontal nozzles. Three nozzles were tested. Each nozzle had a rounded inlet, a long cylindrical smooth pipe, and a diffuser having a small expanding angle. In the three cases, the L/D ratio is greater than 30 to minimize 2D effects. The first nozzle had a pipe diameter of 0.012 m, 0.45 m long with a diffuser angle of 11 degrees. The second nozzle had a pipe diameter of 0.030 m, 1.6 m long with a 7 degree diffuser. The diameter of the third nozzle was 0.050 m, 1.7 m long with a diffuser of 7.7 degree.

Measurements reported include inlet (stagnation) pressure and temperature, mass flux, and throat pressure. No measurement uncertainties were reported. Stagnation pressure conditions ranged from 1960 to 10100 kPa (284.3 to 1464.9 psia) with inlet water somewhat subcooled.

The upstream conditions in Pressure/Temperature and Pressure/Quality planes, along with (P, T) trajectories observed in LOFT and ROSA small break tests, are shown in Figures 12.4-2a and 12.4-2b.

[a,c]

Figure 12.4-2a Upstream P-T in Boivin

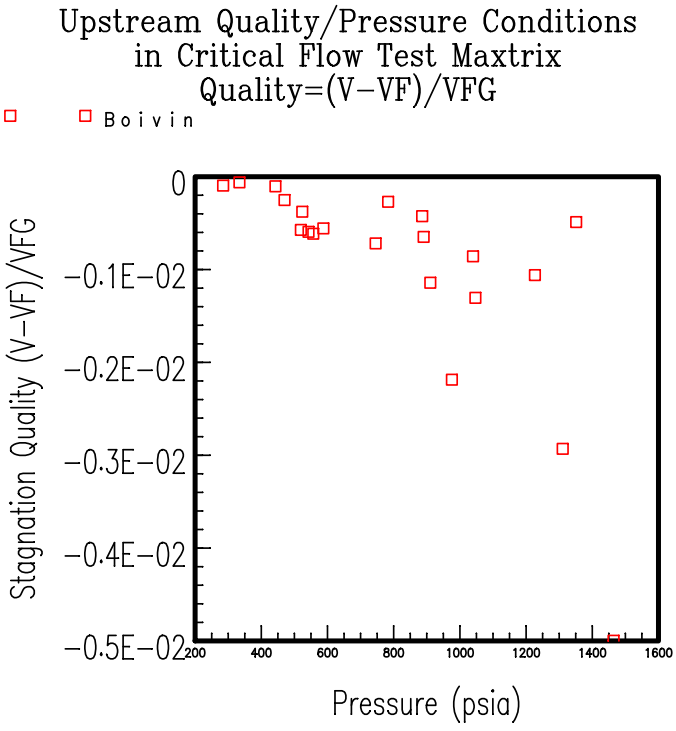

Figure 12.4-2b Upstream Quality in Boivin

12.4.3 Fincke and Collins

Fincke and Collins performed critical flow experiments by flowing subcooled water through a loop and test section. Mass flow rate was controlled by a flow control valve upstream of the test section and back pressure was controlled by a valve downstream of the test section. The test section consisted of a 1.8 m long, 0.0444 m diameter Lexan cylindrical tube followed by a convergent-divergent Lexan nozzle with a minimum diameter of 0.01828 m. Degassed water was used for all experiments. Instrumentation included upstream temperature (reported uncertainty of 0.1°C), volumetric flow rate (uncertainty of 0.1 l/s), pressure just upstream of the nozzle (no uncertainty given), and differential pressure measurements along the nozzle (uncertainty ranging from 0.5 to 2.5 kPa). The differential pressure measurements were used to determine the throat pressure that is included in this data base. The upstream pressure ranged from 90 to 300 kPa (13.1 to 43.5 psia), inlet temperatures were 5° to 40°C subcooled (quality of -3×10^{-6} to -7×10^{-5}).

The upstream conditions in Pressure/Temperature and Pressure/Quality planes, along with (P, T) trajectories from LOFT and ROSA small break tests are shown in Figures 12.4-3a and 12.4-3b.

a,c

Figure 12.4-3a Upstream P-T in Fincke-Collins

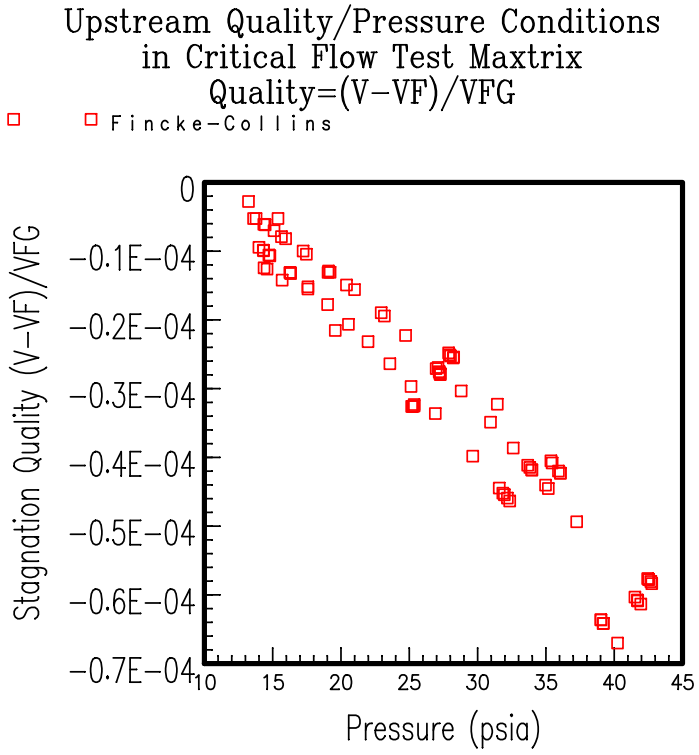

Figure 12.4-3b Upstream Quality in Fincke-Collins

12.4.4 Jeandey

Jeandey et al. performed critical flow experiments by flowing subcooled, demineralized and degassed water through a vertical test section. The test section consisted of a smoothly convergent entrance followed by a straight cylindrical pipe 0.02013 m in diameter followed by a diverging section with a divergent angle of 7 degrees. Flow was vertically upward for all the experiments. Stagnation conditions ranged from pressures of 900 to 14000 kPa (130.5 to 2030.5 psia) and temperatures of 148.5 to 324.6 C (quality of 0 to -0.01). The resulting critical mass fluxes ranged from 14500 to 62000 kg/m^2-s.

The throat pressure was measured along with many other pressures along the test section. In addition, for 21 of the experiments, axial and radial void fraction profiles were obtained using an X-ray densitometer.

The upstream conditions in Pressure/Temperature and Pressure/Quality planes, along with (P, T) trajectories observed in LOFT and ROSA small break tests, are shown in Figures 12.4-4a and 12.4-4b.

a,c

Figure 12.4-4a Upstream P-T in Jeandey et al.

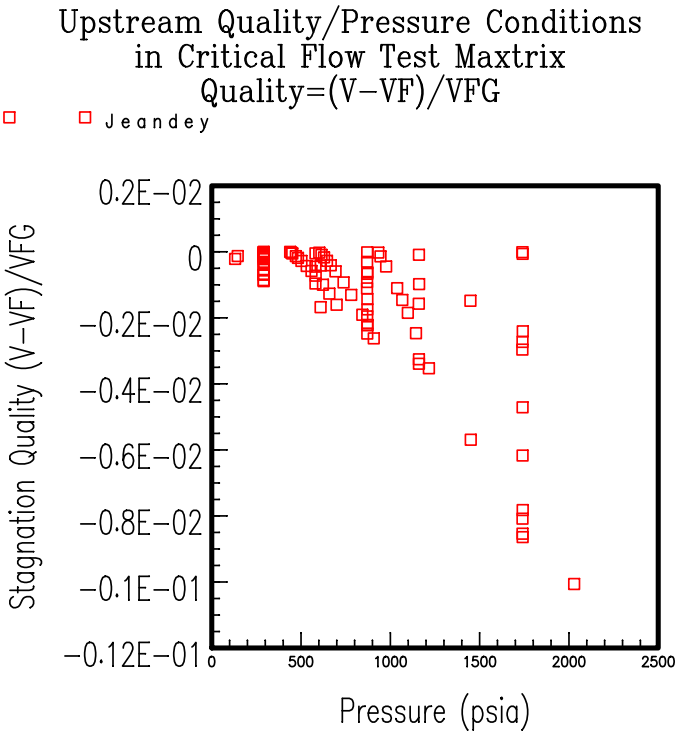

Figure 12.4-4b Upstream Quality in Jeandey et al.

12.4.5 Neusen

Neusen performed experiments to determine design criteria for convergent-divergent nozzles. Critical flow occurred during these experiments, and the data are included in this data base. Neusen ran the saturated water through two convergent-divergent nozzles with minimum diameters of 0.0064 and 0.011 m. Reported stagnation conditions ranged from pressures of 841 to 6516 kPa (122 to 945 psia) and qualities of 0.0028 and 0.228.

Stagnation conditions for these experiments were determined by measuring subcooled temperature and pressure upstream of a throttling valve. The throttling process was assumed to be isentropic, and pressure was measured downstream of the throttling valve (reported uncertainty of 1%). Reported uncertainties for mass flux and calculated enthalpy were less than 2.5% and 0.5%, respectively.

The upstream conditions in Pressure/Temperature and Pressure/Quality planes, along with (P, T) trajectories observed in LOFT and ROSA small breaks, are shown in Figures 12.4-5a and 12.4-5b.

a,c

Figure 12.4-5a Upstream P-T in Neusen

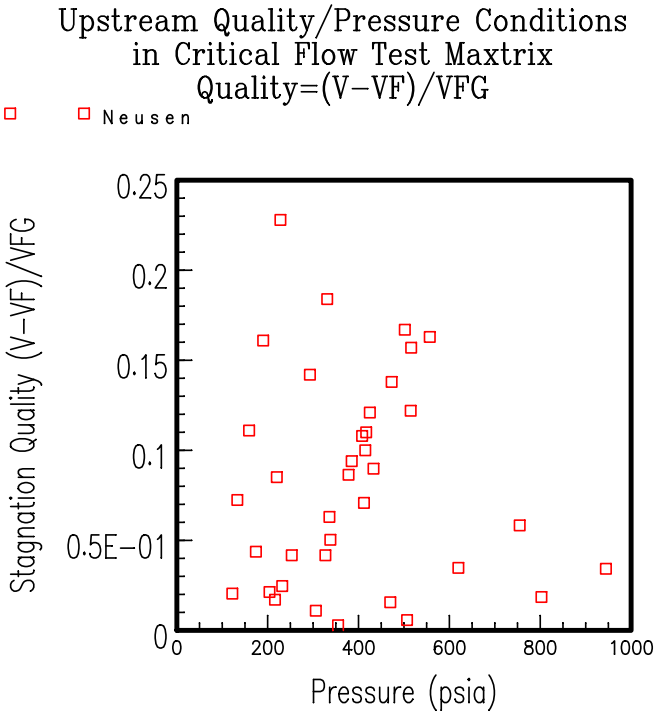

Figure 12.4-5b Upstream Quality in Neusen

12.4.6 Reocreux

Reocreux performed critical flow experiments by flowing subcooled degassed, demineralized water upwards through a vertical test section. The test section consisted of a straight, cylindrical section 2.335 m long and 0.020 m in diameter, followed by a divergent section 0.327 m long. Stagnation pressures ranged from 212 to 340 kPa (30.7 to 49.3 psia), and stagnation temperatures ranged from 115.9 to 121.8 C (quality of -5×10^{-6} to -3.5×10^{-5}). Pressures were measured along the test section at many locations, most concentrated near the choking point (at the entrance to the divergent section). The critical or throat pressures were determined from these measurements. In addition, the void fraction at the choking point was measured for most of the tests using X-ray attenuation method.

The upstream conditions in Pressure/Temperature and Pressure/Quality planes, along with (P, T) trajectories observed in LOFT and ROSA small break tests, are shown in Figures 12.4-6a and 12.4-6b.

a,c

Figure 12.4-6a Upstream P-T in Reocreux

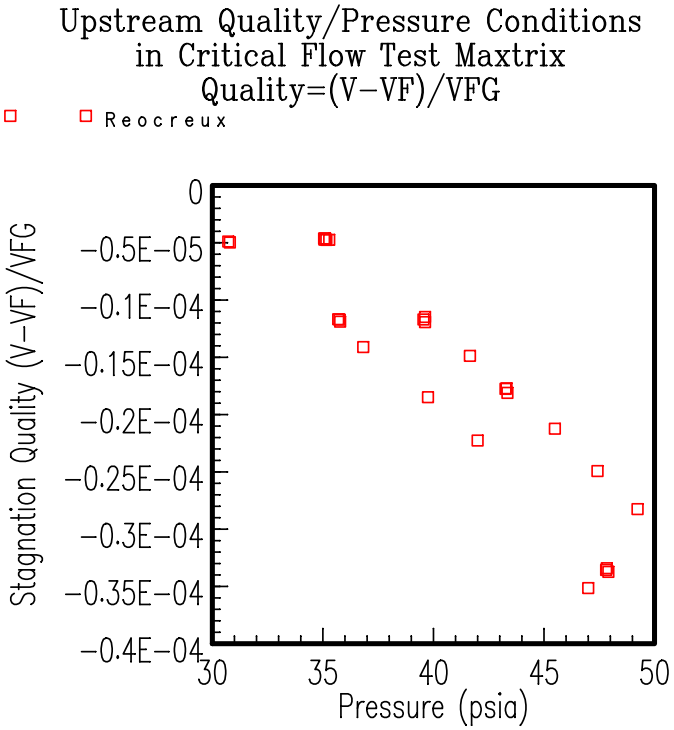

Figure 12.4-6b Upstream Quality in Reocreux

12.4.7 Seynhaeve

Seynhaeve performed critical flow experiments by flowing subcooled, demineralized water upwards in vertical test sections. Two test sections were employed. Each section consisted of a straight, cylindrical pipe 0.0125 m in diameter followed by a divergent section. One section had the straight pipe 0.306 m long, and the other 0.221 m long. Stagnation conditions for these experiments range from 280 to 1015 kPa (40.6 to 147.2 psia) in pressure and 111 to 166.8 C in temperature (quality of -9×10^{-6} to -8.9×10^{-5}). Critical pressure was measured near the choking plane. Measurement uncertainties are not known.

The upstream conditions in Pressure/Temperature and Pressure/Quality planes, along with (P, T) trajectories observed in LOFT and ROSA small break tests, are shown in Figures 12.4-7a and 12.4-7b.

a,c

Figure 12.4-7a Upstream P-T in Seynhaeve

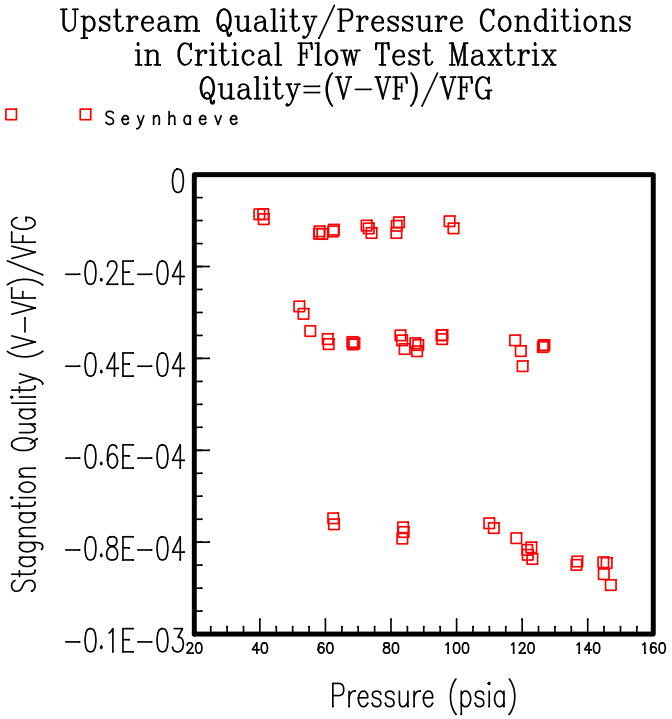

Figure 12.4-7b Upstream Quality in Seynhaeve

12.4.8 Sozzi and Sutherland

Sozzi and Sutherland conducted a series of critical flow experiments with subcooled and low quality water. The water for each experiment was demineralized and degassed. Water from a large vessel was blown down through test nozzles. Data from 21 different nozzle shapes and configurations have been taken with more than 650 individual data points. Stagnation pressure ranged from approximately 3000 to 7000 kPa (435 to 1015.3 psia), and stagnation qualities ranged from approximately -0.006 to 0.01 (based on the specific volume).

The upstream conditions in Pressure/Temperature and Pressure/Quality planes, along with (P, T) trajectories observed in LOFT and ROSA small break tests, are shown in Figures 12.4-8a and 12.4-8b.

a,c

Figure 12.4-8a Upstream P-T in Sozzi-Sutherland

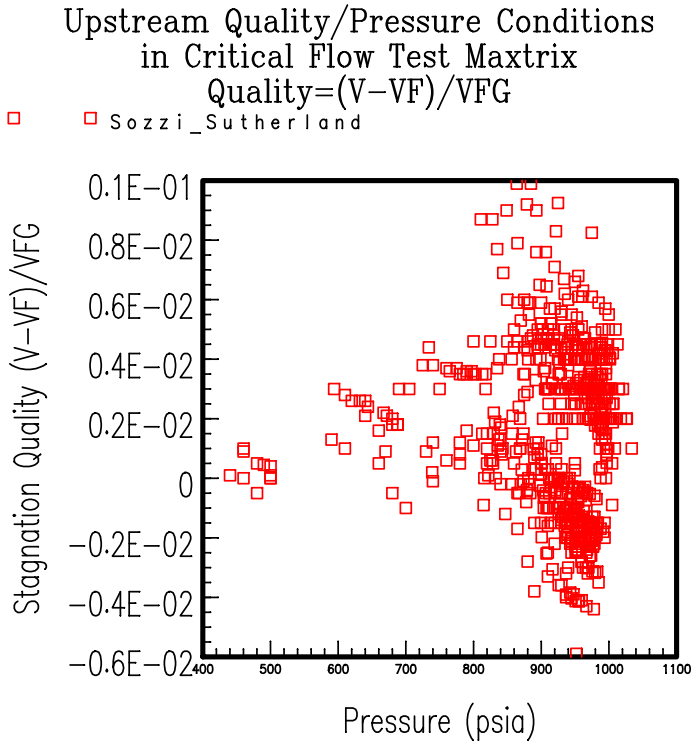

Figure 12.4-8b Upstream Quality in Sozzi-Sutherland

12.4.9 Marviken Tests 1 through 27

The Marviken tests provide very large diameter downflow data typically considered full scale. The Marviken facility was used for full-scale critical flow tests between mid-1977 and December 1979. During this time, 27 tests were conducted by a downward discharge of water and steam mixtures from a full-sized reactor vessel through a large diameter vertical discharge pipe that supplied the flow to a test nozzle. There were 9 nozzles tested; all had rounded entrances followed by a nominal 20, 30 and 50 cm constant diameter straight section. Table 12.4-1 shows the characteristic dimensions for the tests. As seen in the table, the entire test series (Tests 1 through 27) were selected for the model validation.

The discharge pipe that connects the vessel to the nozzle is 6283 mm long and is geometrically complex. It is made up of several pieces: nozzle, permanently attached to the vessel with a 752 mm diameter, a 1980 mm long drift tube of the same diameter, a 1778 mm long global valve with a 780 mm diameter and a 1000 mm long with 752 mm diameter section to which the nozzle is attached. Besides these there were two 120 mm long instrument rings inserted on either end of the 1980 mm drift tube. It is quite clear that with this degree of geometric complexity, the question of establishing a consistent set of complete inlet conditions is not simple.

For assessment, only the nozzle is modeled by the critical flow model. Thus the inlet condition to the nozzle was taken from 004M109 for pressure (0.7 m upstream of the nozzle entrance) ranging from 2580 to 5160 kPa (374 to 748 psia) and 003M404 for temperature (2.8 m upstream of the nozzle entrance) ranging from 469 to 535 K (quality of -0.0036 to 0.005).

Probable measurement error is stated as: Pressure – 7 kPa, Temperature – 0.6°C.

The upstream conditions in Pressure/Temperature and Pressure/Quality planes, along with (P, T) trajectories observed in LOFT and ROSA small break tests, are shown in Figures 12.4-9a and 12.4-9b.

Table 12.4-1 Marviken Test Nozzles (from pp. 51, MXC-101, EPRI/NP-2370)			
Nozzle Number	**Diameter (mm)**	**Length (mm)**	**Used in Tests**
1	200	590	13, 14
2	300	300	6, 7
3	300	511	25, 26
4	300	895	1, 2, 12
5	300	1116	17, 18, 19
6	500	166	23, 24
7	500	730	20, 21, 22, 27
8	500	1809	15, 16
9	509	1589	3, 4, 5, 8, 9, 10, 11

a,c

Figure 12.4-9a Upstream P-T in Marviken Tests 1 through 27

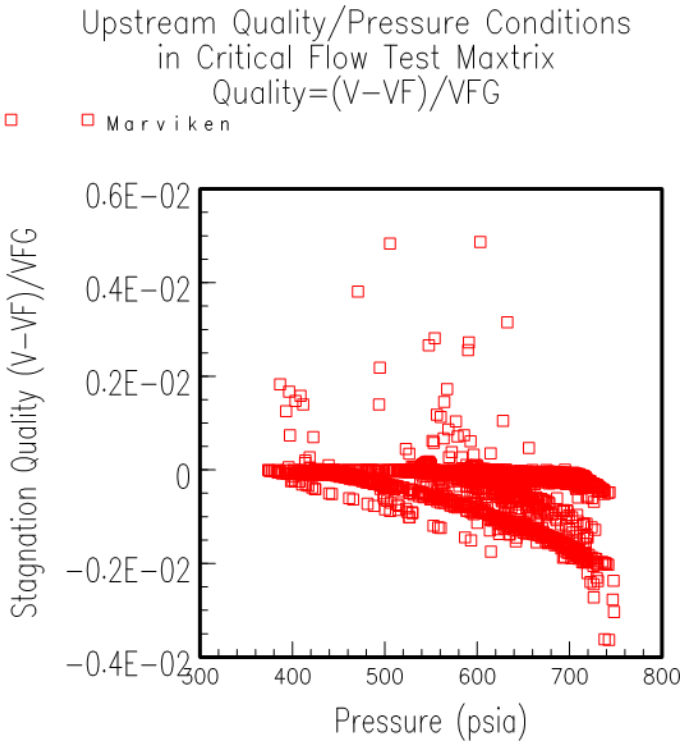

Figure 12.4-9b Upstream Quality in Marviken Tests 1 through 27

12.4.10 Amos and Schrock

Amos and Schrock's break flow data cover a wide range of pressure from approximately 4000 to 15500 kPa (580 to 2248 psia), and subcooling from 0 to 60°C (quality of $8x10^{-6}$ to -0.043) which is suited for evaluating a performance of the break model for small break LOCA analyses. The configuration of the break is a thin rectangular slit with the nominal width of 0.381 and 0.254 mm. These set of tests are two of larger slit size of the three of their experiments. Although the break flow area is rectangular and small (equivalent hydraulic diameter = 0.748 and 0.464 mm), the data is valuable since the phenomena which governs the critical condition appeared to be the same for breaks of all sizes. This may be why the 1D flow model is sufficiently accurate to describe the break flows.

The upstream conditions in Pressure/Temperature and Pressure/Quality planes, along with (P, T) trajectories observed in LOFT and ROSA small break tests, are shown in Figures 12.4-10a and 12.4-10b.

a,c

Figure 12.4-10a Upstream P-T in Amos-Schrock

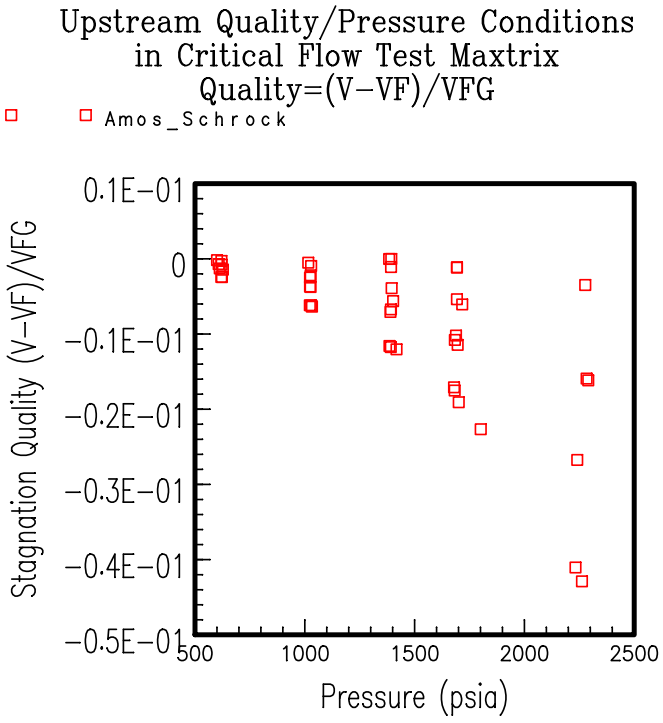

Figure 12.4-10b Upstream Quality in Amos-Schrock

12.4.11 Anderson and Benedetti (TPFL)

Anderson and Benedetti conducted critical flow tests at the TPFL located in Idaho National Engineering Laboratory (INEL), for purpose of investigating the entrainment at the break off the stratified upstream flow under saturated condition. A two-phase mixture of known phasic mass flow rate flowed through a branch line pipe of 1.63 m long, 34 mm diameter attached to a simulated cold leg pipe, to the nozzle which is 54 mm long and has a diameter of 16.2 mm. The pressure just upstream of the rounded entrance nozzle as well as the void fraction was measured by a gamma attenuation method. Their experiments are well instrumented critical flow tests with saturated upstream conditions at 900, 640 and 500 psia. The flow qualities in the tests were varied from 0 to 1 at all three pressures.

The upstream conditions in Pressure/Temperature and Pressure/Quality planes, along with (P, T) trajectories observed in LOFT and ROSA small break tests, are shown in Figures 12.4-11a and 12.4-11b.

a,c

Figure 12.4-11a Upstream P-T in TPFL

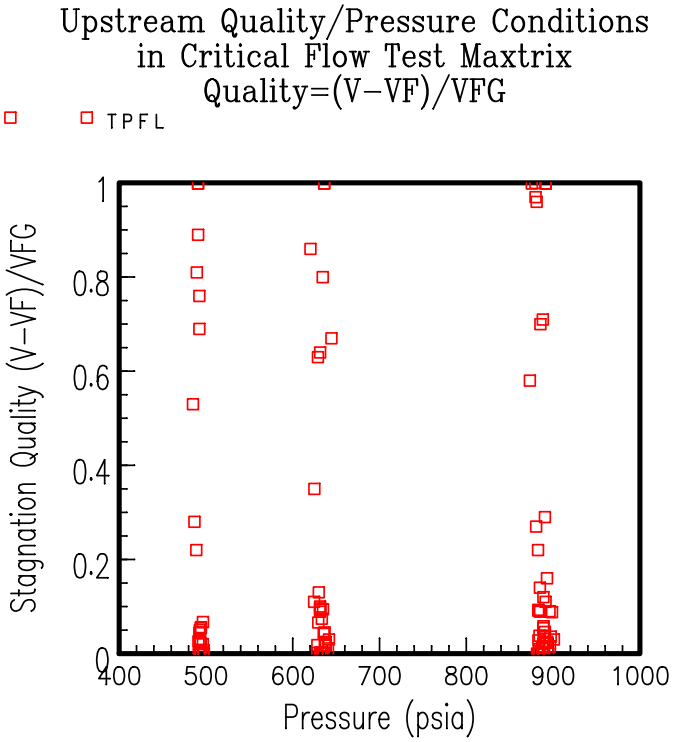

Figure 12.4-11b Upstream Quality in TPFL

12.4.12 Celata

Celata et al. conducted a set of flow rate critical flow experiments with and without non-condensable using a 1.5 m long 4.6 mm id vertical downward pipe. The experiments were conducted at the pressure of 0.5, 1.0, and 1.5 MPa, and the subcooling of 0, 20, 40, and 60°C (-5.5×10^{-5} to -6.3×10^{-4}). Figure 12.4-12a shows the stagnation pressure and the inlet subcooling of Celata's data. As seen in the figure data were taken at three roughly discrete pressures, namely 0.5 MPa (72.5 psia), 1.0 MPa (145 psia), and 1.5 MPa (217.5 psia). They have reported the un-reliability and a lack of reproducibility associated with the saturated water data. Figure 12.4-12b shows the measured critical mass flux vs. subcooling at all three pressures. It is noted that the critical mass flux data near saturation are higher than that at the higher subcooling condition which is inconsistent and is due to difficulty with this particular set of data as stated by Celata et al. (1988). Therefore the validation will use Celata's subcooled dataset (subcooling greater than 10°C). This represents 97 out of 132 test runs.

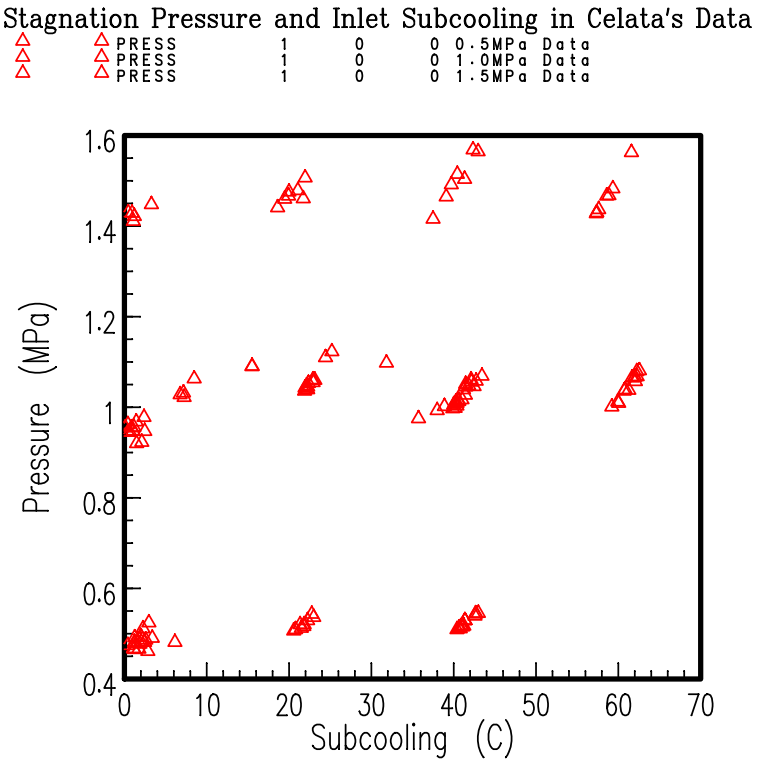

Figure 12.4-12a Stagnation (P,DTsub) in Celata et al.

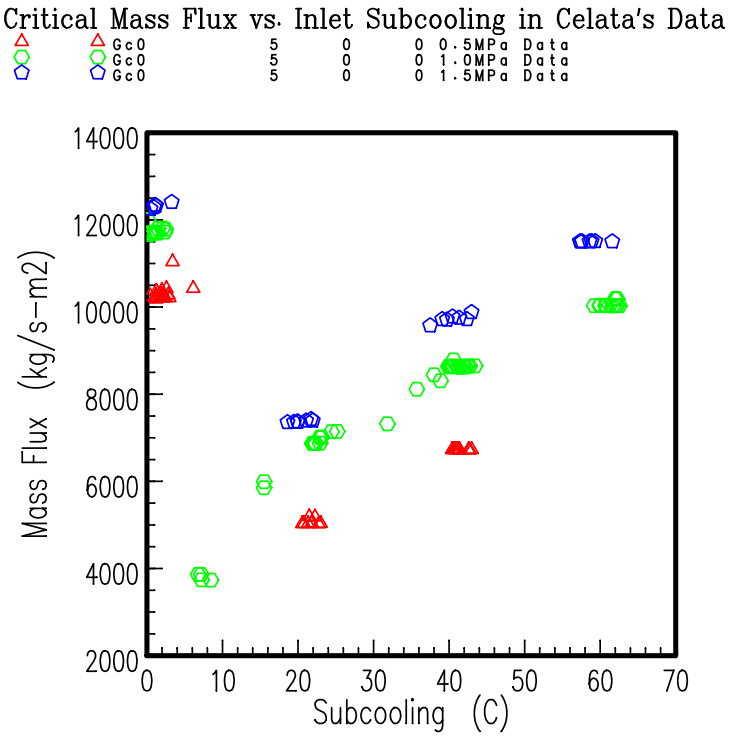

Figure 12.4-12b Critical Mass Flux in Celata et al.

For each test point, two paired runs were made, i.e., a reference run without non-condensable gas and with non-condensable gas, and the following data were recorded,

- Stagnation pressure, P_0 (MPa),
- Temperature, T_0 (°C),
- Inlet subcooling, ΔT_{sub} (°C)
- Outlet critical pressure, P_c (MPa)
- Reference Critical Mass Flux without non-condensable gas, G_{c0} (kg/s-m^2)
- Critical Mass Flux with non-condensable gas, G_c (kg/s-m^2)
- Air Mass Flux, G_a (kg/s-m^2)
- Ratio of Critical Mass Flux with non-condensable gas to the reference Critical Mass Flux, G_c/G_{c0}

In addition to the above data, pressure and temperature were measured at 6 locations in the test section for selected test runs.

The upstream conditions in Pressure/Temperature and Pressure/Quality planes, along with (P,T) trajectories observed in LOFT and ROSA small break tests, are shown in Figures 12.4-12c and 12.4-12d.

[a,c]

Figure 12.4-12c Upstream P-T in Celata et al.

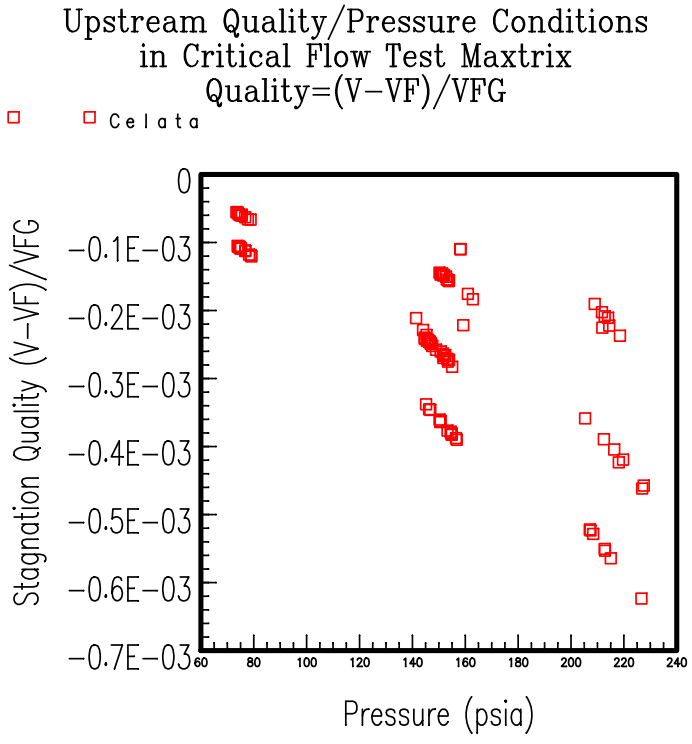

Figure 12.4-12d Upstream Quality in Celata et al.

12.4.13 Overall

The test matrix selected covers from 13 psia to 2300 psia, and quality of -0.0429 to 1.0. The coverage of the upstream condition is graphically shown in Figure 12.4-13a and Figure 12.4-13b below. The figures show the upstream fluid condition found in the critical flow database for the validation as well as the predicted trajectories of temperature-pressure and quality-pressure for small and large break LOCAs. It is noted that while more dataset with the two-phase inlet condition and high pressure-high subcooling are desirable, the validation database adequately covers the range of upstream conditions expected during PWR LOCAs.

a,c

Figure 12.4-13a Upstream Condition in Test Matrix

a,c

Figure 12.4-13b Upstream Condition in Test Matrix

12.5 ASSESSMENT RESULTS

12.5.1 Assessment Method

A stand-alone model of the WCOBRA/TRAC-TF2 critical flow module was used for the prediction-data comparison. The consistency between the stand-alone code results and the WCOBRA/TRAC-TF2 results was confirmed by comparing the prediction for a subset of critical flow data points in Section 12.5.4.1.

12.5.1.1 Calculation

As described in Section 5.12.4, in Volume 1 of this document, the inlet flow is iterated until either the exit pressure gradient becomes **[**

][a,c]. At this point the pressure along the break path becomes what is shown in Figure 12.5-1. The figure shows the pressure along the break path with the measured pressures for Celata's et al. Run 020 data.

[**]**[a,c] and compared to the measured critical mass flux, G_c value.

a,c

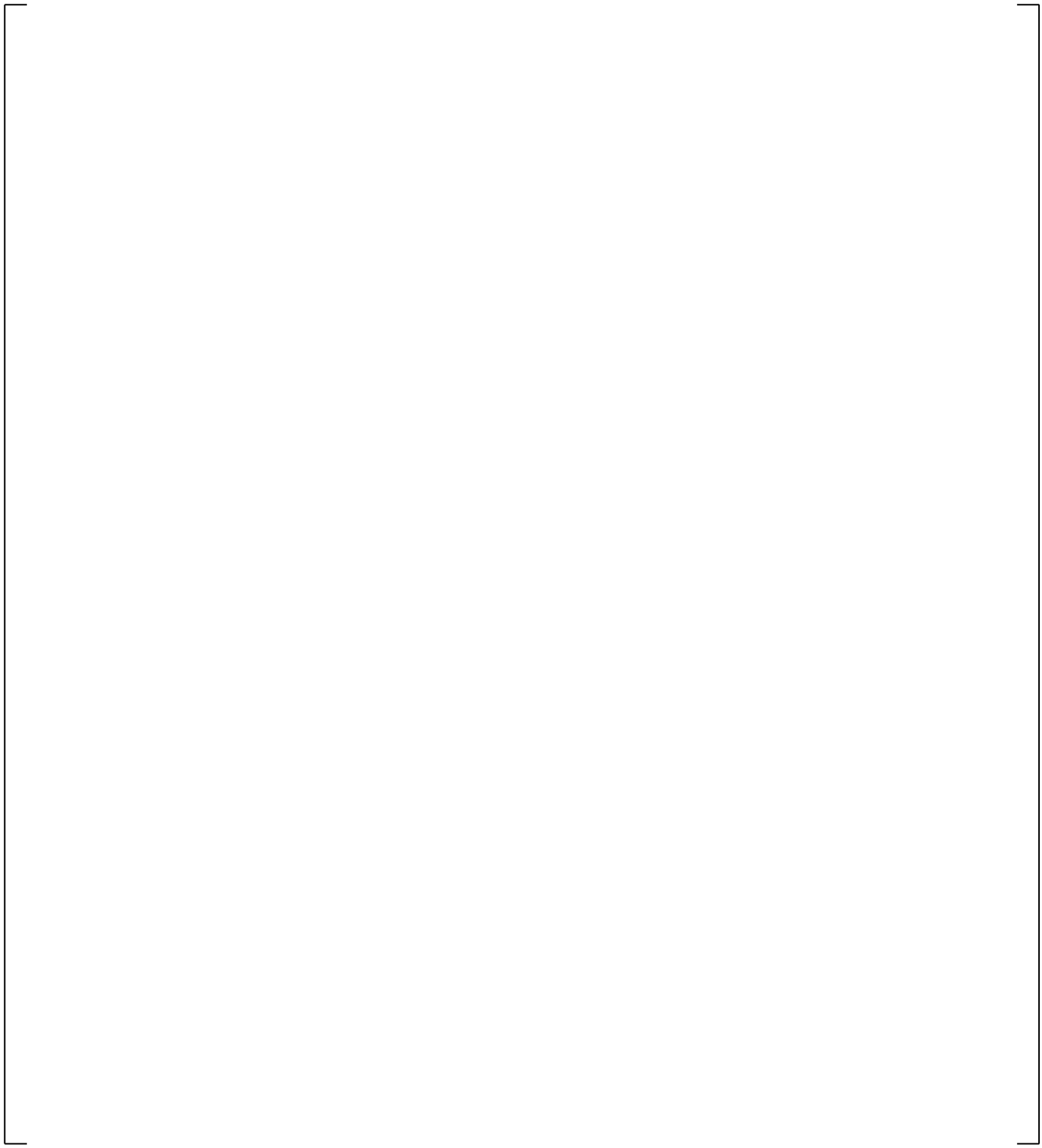

Figure 12.5-1 Pressure Profile along the Break Path

12.5.2 Data Comparison

The critical mass flux prediction is compared with the measured critical mass flux. This comparison is performed for a total of 3199 data points with no non-condensable gas and 96 data points with non-condensable gas.

12.5.2.1 Bias and Uncertainty Results

A total of 3199 data points from 53 nozzle geometries were used for the determination of bias and uncertainty associated with the critical flow model prediction used in WCOBRA/TRAC-TF2. The prediction error was calculated as, $\varepsilon = \frac{G_{meas} - G_{pred}}{G_{preds}}$. This is not a usual definition of the deviation from the measurement, $\frac{G_{pred} - G_{meas}}{G_{meas}}$, but the one convenient for the purpose of ranging the break flow for the statistical sampling process since the quantity (1 + ε) can be used as the multiplier to the model prediction (or C_D, the discharge coefficient) to recover the measured value.

The following results were obtained through the comparison to data. Note that the uncertainty associated with many of the measurements was unknown. Others have reported the uncertainty. The reported uncertainty was much smaller than the prediction error and thus the contribution of measurement error on the prediction error is neglected.

A valid range of the bias and uncertainty estimate given here is based on selected experimental data. A comparison was made for 1 (Orifice) < L ≤ 2335 mm, and 0.464 ≤ D_H ≤ 509 mm.

Overall (-0.0429 ≤ Quality ≤ 1.0)

Predictions for all selected data are shown in Table 12.5-1. Appendix A contains all output and the comparison of predicted and measured critical mass flux for all individual test series.

The mean error (or the bias) for the entire dataset,

$\bar{\varepsilon} = \frac{\sum_{i}^{N}\left(\frac{G_{meas} - G_{pred}}{G_{preds}}\right)}{N}$ was found to be **[ ]**[a,c],

and the standard deviation,

$\sigma(\varepsilon) = \sqrt{\frac{\sum_{i}^{N}(\varepsilon_i - \bar{\varepsilon})}{N-1}}$ was found to be **[ ]**[a,c].

The bias and standard deviation based on the upstream fluid state are;

- For Subcooled Liquid Region (-0.043 ≤ Quality ≤ 0)
  - Bias = **[ ]**[a,c]
  - Standard Deviation = **[ ]**[a,c]
- For Saturated Flow rate including Single Phase Vapor Region (0 < Quality ≤ 1.0)
  - Bias = **[ ]**[a,c]
  - Standard Deviation = **[ ]**[a,c]

Table 12.5-1 Critical Flow Data Comparison for WCOBRA/TRAC Critical Flow Model

Reference	L (mm)	D (mm)	cosθ	N-Data	Mean Error ε (%) $(\frac{G_{meas} - G_{calc}}{G_{meas}})$	σ(ε) (%)
Ardron, K. H. & Ackerman, M. C. (1978)	1015	26.3	0	32	[	] a,c
Boivin (1979)	500	12	0	10		
Boivin (1979)	1600	30	0	5		
Boivin (1979)	1700	50	0	6		
Fincke & Collins (1981)	25	18.3	0	92		
Jeandey et al. (1981)	463	20	1	15		
Jeandey et al. (1981)	463	20	1	73		
Neusen (1962)	1	11	0	25		
Neusen (1962)	1	6	0	12		
Reocreux (1974)	2335	20	1	28		
Seynhaeve (1980)	306	13	1	26		
Seynhaeve (1980)	221	13	1	31		
Sozzi & Sutherland (1975)	1	12.7	0	128		
Sozzi & Sutherland (1975)	1	12.7	0	13		
Sozzi & Sutherland (1975)	12.7	12.7	0	47		
Sozzi & Sutherland (1975)	318	12.7	0	19		
Sozzi & Sutherland (1975)	38.6	12.7	0	17		
Sozzi & Sutherland (1975)	508.5	12.7	0	13		
Sozzi & Sutherland (1975)	64	12.7	0	23		
Sozzi & Sutherland (1975)	635.5	12.7	0	96		
Sozzi & Sutherland (1975)	114.8	12.7	0	15		
Sozzi & Sutherland (1975)	1779	12.7	0	81		
Sozzi & Sutherland (1975)	191	12.7	0	12		
Sozzi & Sutherland (1975)	229	12.7	0	22		
Sozzi & Sutherland (1975)	4.7	12.7	0	58		.
Sozzi & Sutherland (1975)	322	12.7	0	24		
Sozzi & Sutherland (1975)	513	12.7	0	24		
Sozzi & Sutherland (1975)	639.7	12.7	0	17		]

Table 12.5-1 Critical Flow Data Comparison for WCOBRA/TRAC Critical Flow Model (cont.)

Reference	L (mm)	D (mm)	cosθ	N-Data	Mean Error ε (%) $(\frac{G_{meas} - G_{calc}}{G_{meas}})$	σ(ε) (%)
Sozzi & Sutherland (1975)	195.2	12.7	0	23	[	] a,c
Sozzi & Sutherland (1975)	1	19	0	23		
Sozzi & Sutherland (1975)	1	54	0	4		
Sozzi & Sutherland (1975)	1	76.2	0	3		
Sozzi & Sutherland (1975)	1	28	0	5		
Amos & Schrock (1983)	63.5	0.748	-1	18		
Amos & Schrock (1983)	63.5	0.464	-1	26		
Anderson & Benedetti (1986)	54	16.2	0	109		
Marviken Test 1 (1982)	895	300	-1	97		
Marviken Test 2 (1982)	895	300	-1	91		
Marviken Test 3 (1982)	1589	509	-1	40		
Marviken Test 4 (1982)	1589	509	-1	39		
Marviken Test 5 (1982)	1589	509	-1	43		
Marviken Test 6 (1982)	300	300	-1	85		
Marviken Test 7 (1982)	300	300	-1	84		
Marviken Test 8 (1982)	1589	509	-1	40		
Marviken Test 9 (1982)	1589	509	-1	58		
Marviken Test 10 (1982)	1589	509	-1	57		
Marviken Test 11 (1982)	1589	509	-1	41		
Marviken Test 12 (1982)	895	300	-1	121		
Marviken Test 13 (1982)	590	200	-1	139		
Marviken Test 14 (1982)	590	200	-1	144		
Marviken Test 15 (1982)	1809	500	-1	45		
Marviken Test 16 (1982)	1809	500	-1	40		
Marviken Test 17 (1982)	1110	300	-1	90		
Marviken Test 18 (1982)	1110	300	-1	69		]

Table 12.5-1 Critical Flow Data Comparison for WCOBRA/TRAC Critical Flow Model (cont.)

Reference	L (mm)	D (mm)	cosθ	N-Data	Mean Error ε (%) $(\frac{G_{meas} - G_{calc}}{G_{meas}})$	σ(ε) (%)
Marviken Test 19 (1982)	1110	300	-1	85		
Marviken Test 20 (1982)	730	500	-1	50		
Marviken Test 21 (1982)	730	500	-1	50		
Marviken Test 22 (1982)	730	500	-1	37		
Marviken Test 23 (1982)	166	500	-1	61		
Marviken Test 24 (1982)	166	500	-1	44		
Marviken Test 25 (1982)	510	300	-1	84		
Marviken Test 26 (1982)	510	300	-1	134		
Marviken Test 27 (1982)	730	500	-1	59		
Celata et al. (1988)	1500	4.6	-1	97		
Total				3199		

a,c

Figure 12.5-2 below shows the comparison of all points in the test matrix with ±1σ lines above and below the 45° line.

a,c

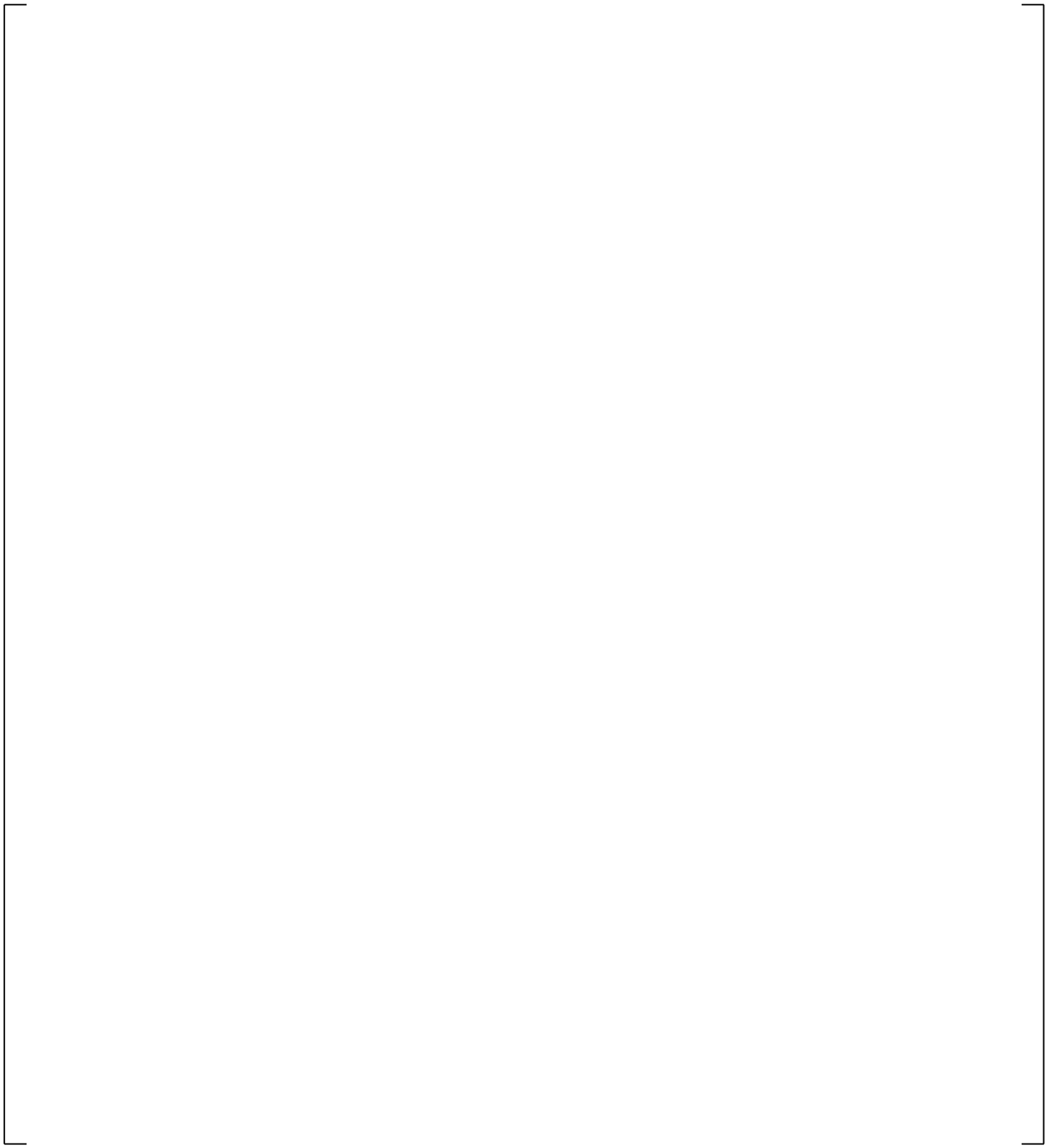

Figure 12.5-2 Comparison of Predicted and Measured Critical Flows

12.5.2.2 Non-condensable Effect

Figure 12.5-3a shows the predicted critical flow mass flux vs. the measured critical flow mass flux for cases with non-condensable gas.

To check for a consistency relative to the effect of non-condensable gas, the ratio of critical mass flux with non-condensable to that with no-non-condensable gas cases was reported from the paired experiment by Celata et al. (1988). The predicted ratios were calculated and compared with the measured values. This ratio as a function of the non-condensable gas concentration was examined. Figure 12.5-3b shows the comparison of measured effect of the non-condensable on the critical flow rate and the predicted effect of the non-condensable gas.

Considering the fact that the thermal equilibrium between the non-condensable gas (air) and the steam/water mixture at the inlet was not well established in the experiment, the agreement between the data and the prediction is considered to be adequate. Although there is a tendency to over-predict the impact of non-condensable gas as the fraction of non-condensable gas increases, the deviation is below the saturated two-phase upstream cases. Thus a separate uncertainty value for the two-phase upstream with non-condensable gas would not be applied. The saturated upstream values **[ ]**[a,c] will be used for two-phase regardless of the presence of non-condensable.

a,c

Figure 12.5-3a Comparison of Predicted and Measured Critical Mass Flux with Non-condensable Gas

a,c

Figure 12.5-3b Comparison of Predicted and Measured effect of Non-condensable Gas on Critical Mass Flux

12.5.3 Parametric Trend of Prediction

This section examines the presence of bias in the major parameters such as pressure, quality, break area and break path length. For the purpose of examining the model trend in this subsection, the error is defined in the usual way, (as the deviation from the measurement), $\frac{G_{pred} - G_{meas}}{G_{meas}}$.

12.5.3.1 Trend with Respect to Pressure Variation

In this section, a possible model trend with respect to the upstream pressure is examined. Figure 12.5-4 shows the error vs. pressure of all data points. The figure does not show any global trend relative to the upstream pressure, although it does show that there is a larger spread in the lower pressure points ($p < 1000$ psia).

a,c

Figure 12.5-4 Prediction Trend in Pressure Variation

12.5.3.2 Trend with Respect to Quality Variation

In this section, a possible model trend with respect to the upstream quality is examined. Figure 12.5-5a shows the error vs. quality of all data points. The figure shows a global trend relative to the upstream quality. The model **[**

][a,c]

a,c

Figure 12.5-5a Prediction Trend in Quality Variation

a,c

Figure 12.5-5b Prediction Trend in Quality Variation Near Saturation Quality

12.5.3.3 Trend with Respect to Channel Length Variation

In this section, a possible model trend with respect to the channel length is examined. Figures 12.5-6a and 12.5-6b show the error vs. channel length of all data points. The figures **[**

][a,c]

a,c

Figure 12.5-6a Prediction Trend in Channel Length Variation with Linear Scale

a,c

Figure 12.5-6b Prediction Trend in Channel Length Variation with Log Scale

12.5.3.4 Trend with Respect to Hydraulic Diameter Variation

In this section, a possible model trend with respect to the hydraulic diameter is examined. Figure 12.5-7a shows the error vs. hydraulic diameter of all data points. The figure **[**

][a,c]

a,c

Figure 12.5-7a Prediction Trend in Channel Diameter with Linear Scale

a,c

Figure 12.5-7b Prediction Trend in Channel Diameter with Log Scale

12.5.3.5 Trend with Respect to L/D Variation

In this section, a possible model trend with respect to the break path L/D is examined. Figures 12.5-8a and 12.5-8b show the relative errors vs. L/D of the break path in linear and log scale. **[**

][a,c]

a,c

Figure 12.5-8a Prediction Trend in Channel L/D Variation with Linear Scale

a,c

Figure 12.5-8b Prediction Trend in Channel L/D Variation with Log Scale

12.5.4 Model Performance as Implemented in WCOBRA/TRAC-TF2

12.5.4.1 Impact of Transient

The assessment presented in the previous section was performed with the stand-alone program extracted from WCOBRA/TRAC-TF2. Therefore, the model prediction as an integral part of WCOBRA/TRAC-TF2 was examined by repeating Marviken Test 6 to see the impact of coupling. Figure 12.5-9 shows the noding diagram used for Marviken Test 6 simulation. PIPE-26 models the discharge pipe with the homogeneous relaxation model (HRM) modeling the nozzle. The HRM break model is explicitly shown to be attached to the right most cell of PIPE-26. The input parameters for the nozzle, namely nozzle hydraulic diameter (HRMOFD), nozzle length (HRMOFL), the flow multiplier for single phase liquid (HRM1PM) and two-phase/single phase vapor (HRM2PM) are shown below the noding diagram. These parameters will be discussed in detail in Section 29, Volume 3. Figure 12.5-10 shows the Mass Flow comparison with the stand-alone prediction for Marviken Test 6 given in Appendix A.11.6. Predictions are equivalent. The differences are caused by the sparser boundary condition specification used in the WCOBRA/TRAC-TF2 model compared to the stand-alone input as seen in Figures 12.5-11a (Pressure) and 12.5-11b (Temperature).


a,c

Figure 12.5-9 Test 6 Noding Scheme


a,c

Figure 12.5-10 Test 6 Prediction of WCOBRA/TRAC-TF2 vs. Stand-Alone Model

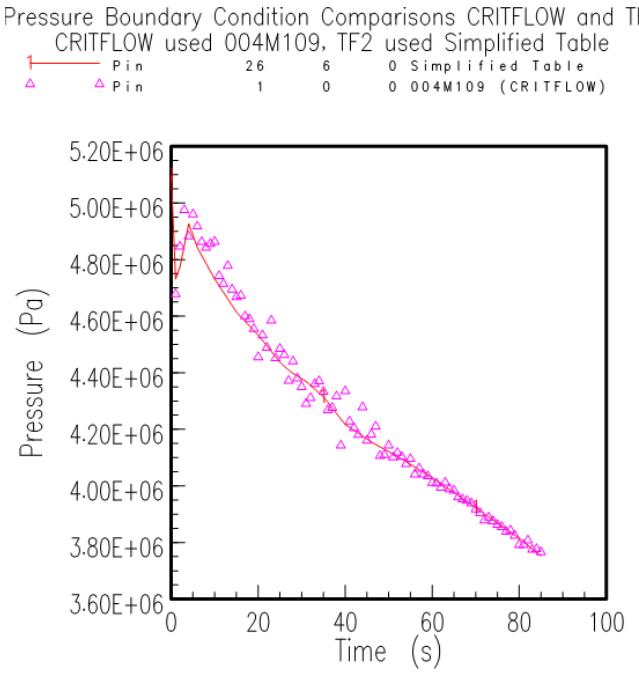

Figure 12.5-11a P(t) Boundary Condition Comparison

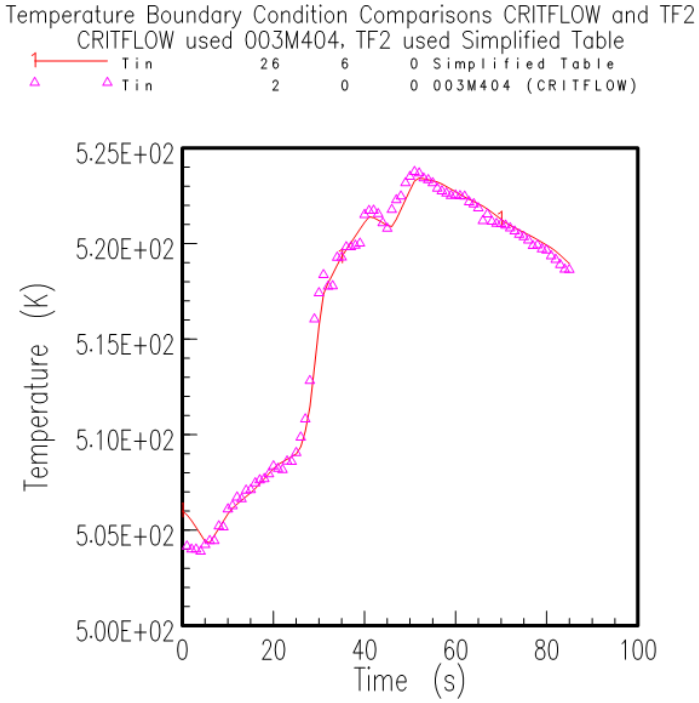

Figure 12.5-11b T(t) Boundary Condition Comparison

12.5.4.2 Influence of Mesh Size

The model prediction's sensitivity to a number of axial nodes used within the critical flow module, HRM, was investigated using a subset of the validation test cases. The number of axial nodes is set **[**

][a,c]

12.5.4.3 Influence of Friction Factor/Entrance Effect

The entrance and friction factors were found to be very important for predicting the low pressure experiments such as those of Ardron and Ackerman (1978). For very low pressure cases such as these, an inaccurate prediction of entrance and pipe friction pressure loss may cause significant mis-prediction of the pressure in the pipe and subsequent mis-prediction of critical flow rates. This is the reason the reported friction factors were used for simulation of Ardron and Ackerman. For higher pressures where the upstream of the break in PWR LOCAs are expected, the entrance loss and friction factors play an insignificant role.

12.5.4.4 Application of Multiplier (or Discharge Coefficient, CD)

Two sensitivity runs with CD=0.8 and 1.2 were performed to validate the method of applying the discharge coefficient. The results show that the discharge coefficient application via WCOBRA/TRAC-TF2 input parameters, HRM1PM and HRM2PM yields desired break flows as seen in Figure 12.5-9. These input parameters will be discussed in detail in Section 29, Volume 3. Figure 12.5-12a shows the impact of CD on the predicted break flows. Figure 12.5-12b shows the effective multiplier observed in this simulation. They are close to 0.8 and 1.2 but because of the feedback of the flow on the nozzle inlet pressure (Figure 12.5-12c), the multipliers are slightly deviated from CD values, which is expected.

a,c

Figure 12.5-12a Impact of CD on Predicted Flow

a,c

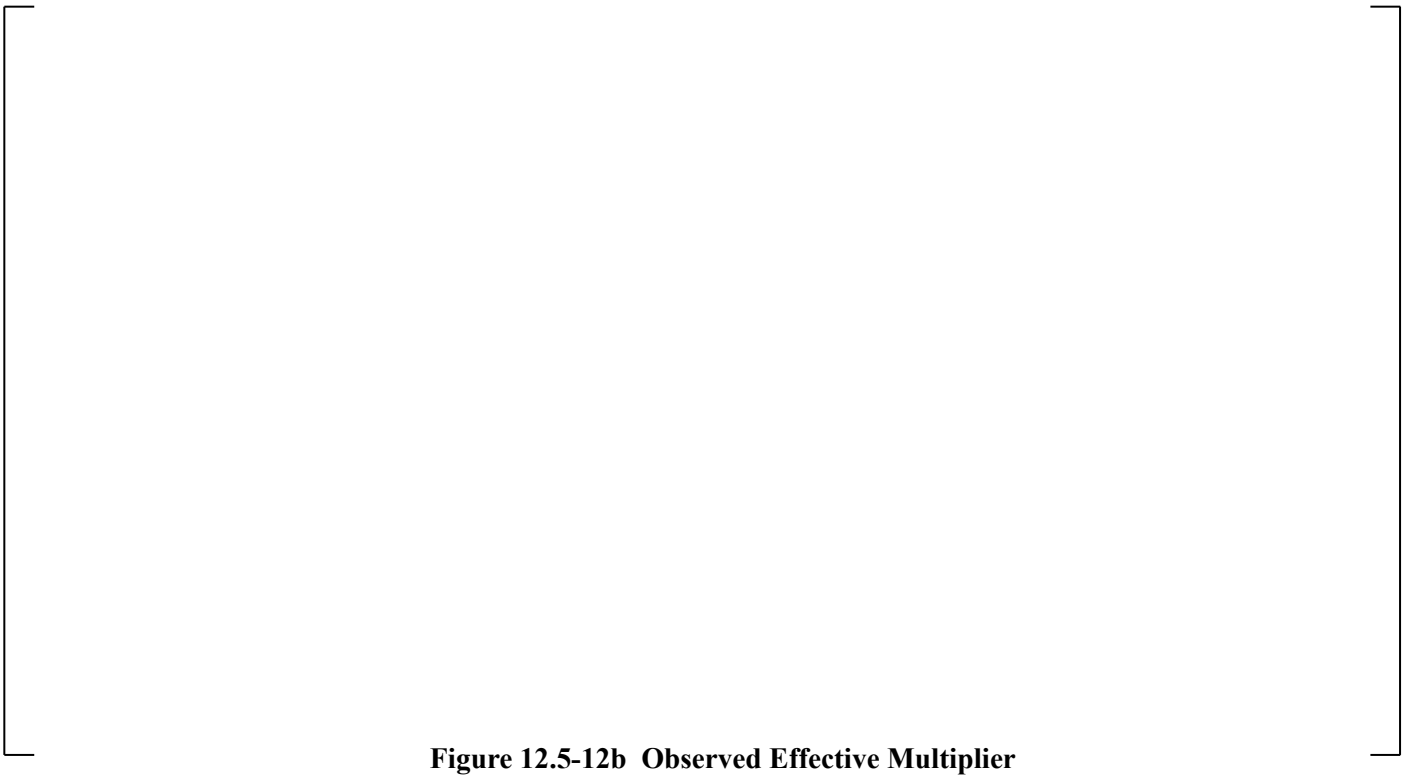

Figure 12.5-12b Observed Effective Multiplier

a,c

Figure 12.5-12c Nozzle Upstream Pressure

12.6 CRITICAL FLOW ASSESSMENT CONCLUSIONS

The critical flow comparisons showed that the present model predicted both small diameter tests such as Amos and Schrock at 0.0295 inch, and Sozzi and Sutherland at 0.5-inch as well as the large diameter (19.7-inch) data obtained in the Marviken (1982) tests with acceptable accuracy.

12.6.1 Scaling Consideration

An observation relative to the scalability of the model is addressed in this section.

12.6.1.1 Pressure, Subcooling, and Quality

For the subcooled break flow model, a pressure range of 13 to 2300 psia and a quality range of -0.0429 to 1.0 were examined. The results indicated that the model is scalable relative to pressure and subcooling with reasonable accuracy. The results showed that the model adequately accounts for the pressure and the quality variations.

12.6.1.2 Break Flow Area

The break flow comparisons showed that the present model predicted both small diameter tests such as Amos and Schrock for 0.0295 inch (Amos and Schrock, 1983), and Sozzi and Sutherland for 0.5-inch (Sozzi and Sutherland, 1975), as well as the large diameter (19.7-inch) data obtained in the Marviken (1982) tests with adequate accuracy. The WCOBRA/TRAC-TF2 break model was able to simulate both small and large diameter nozzles adequately.

12.6.2 Break Path Geometry and Application to PWR LOCA

The entrance effects, such as the roundness/sharpness of the orifice are accounted for in the present model when they are known and reported for simulation. However, roughness, and sharpness are not known in the PWR LOCA application **[**

][a,c]

12.7 OFFTAKE ENTRAINMENT MODEL

12.7.1 Introduction

During a small break LOCA, the break flow rate determines the depressurization rate as well as the mass inventory of the primary system of a PWR. These parameters in turn influence the timing of various engineered safeguard system responses, such as reactor trip and safety injection.

Early in a small break LOCA, the fluid condition upstream of the break location is subcooled. This results in a high discharge flow rate and a fast depressurization. As the pressure drops to the saturation pressure corresponding to the coolant liquid temperature upstream of the break, the discharge becomes two-phase and a relatively low discharge rate and a slow depressurization result. The flow in the cold leg is expected to be horizontally stratified. Under those conditions the void fraction upstream of the break changes from primarily liquid to primarily vapor as the liquid level in the main pipe decreases. As the stratified surface lowers in the vicinity of the break, the quality at the break is greatly influenced by the entrainment of vapor/liquid off the stratified surface upstream of the break.

Although the size, location, and shape of the break are not known for the postulated small break LOCA, the best-estimate code needs to predict consistent responses relative to experimental data over a range of pressure, subcooling, and upstream fluid states, as well as the break flow area variations, so that accurate sensitivity to small break LOCA responses can be obtained.

12.7.2 Offtake Phenomenon

The vapor pull through and liquid entrainment phenomenon are especially important in the analysis of the small break LOCA accident. For a portion of the small break LOCA accident, one would envision a stratified flow regime in the broken cold leg, where liquid would flow along the bottom of the pipe and vapor flow at the top of the pipe due to the effect of gravity. If the break in the pipe is located in the side of the pipe below the interface, or at the bottom of the pipe, then the quality of the flow through the break will be low. However, certain conditions will lead to a two-phase break flow as opposed to single phase liquid. This phenomenon is known as vapor pull-through, or also as vapor entrainment.

Vapor pull through can occur in the form of vortex or vortex free flow. Figure 12.7.2-1 contains a diagram of each of these flow mechanisms. Vortices tend to be unstable at low flow conditions, and are unable to form at high flow conditions. Vortex flow will also tend to transition into vortex free flow as the distance from the interface to the break decreases. While it is possible for a vortex to form for a break in the side of the pipe, the effect of the pipe wall tends to stunt vortex formation.

Again considering the condition of stratified flow in a pipe, if the break in the pipe is located in the side of the pipe above the interface, or at the top of the pipe, then the quality of the flow through the break will be high. However, certain conditions will lead to a two-phase break flow as opposed to single phase vapor. This phenomenon is known as liquid entrainment. A diagram of the liquid entrainment mechanism is given in Figure 12.7.2-2. The vapor velocity tends to increase near the break due to the Bernoulli effect. As the vapor velocity increases, waves will tend to form at the stratified interface. Some amount of liquid may be entrained from this surface, and carried into the break by the vapor.

Under certain conditions, the size of the wave formed at the break will increase until the wave reaches the top of the pipe. This behavior will propagate through the pipe, and the flow regime will undergo a transition from stratified flow into slug flow. The quality of the break flow will decrease significantly with a transition from a stratified flow regime into a slug flow regime. This transition to slug flow is observed in the experimental data for an upward break orientation presented later in this section. The offtake model is not applicable once transition to slugging occurs.

Some of the key factors which impact the quality of the break flow are the break orientation, flow regime, distance from the interface to the break (for stratified flow), vapor velocity (for liquid entrainment), liquid velocity (for vapor pull through), and the differential pressure across the break.

12.7.3 Relationship to PIRT

The ability of a code to accurately calculate the break flow quality is very important to the analysis of the small break LOCA accident. **[**

][a,c] Since the break flow rate has a significant effect on the system inventory during a SBLOCA, this process is important throughout the entire SBLOCA transient (except for blowdown where the break flow is primarily single-phase liquid).

12.7.4 Section Objectives

In this section, an assessment is made of the offtake model in the WCOBRA/TRAC-TF2 version described in Section 5.13, Volume 1 of this document. The model was validated against test data from the TPFL facility, as well as other additional data as discussed in Section 12.7.6. A description of all the tests performed at the TPFL is given in EPRI NP-4532 (1986).

12.7.5 Two-Phase Flow Loop Offtake Entrainment Tests

12.7.5.1 TPFL Test Facility Description

The tee/critical flow experiments were performed in the TPFL at the INEL Thermal Hydraulics Laboratory (Figure 12.7.5-1). **[**

][b] The schematic view of the facility is shown in Figure 12.7.5-2.

[

][b]

This facility is the largest scale facility with experimental data which can be used to validate the offtake model within WCOBRA/TRAC-TF2.

12.7.5.2 Test Matrix for TPFL Offtake Simulations

[

]b Table 12.7.5-1 summarizes the tests selected for simulation using WCOBRA/TRAC-TF2.

[

]a,c

12.7.5.3 Test Procedure for TPFL Offtake Simulations

[

]b

The intent of the test data was to correlate the flow quality in the branch pipe against the mainline liquid level for different pressures and break orientations.

12.7.5.4 WCOBRA/TRAC-TF2 Model for TPFL Offtake Tests

[

]a,c

[

][a,c]

12.7.5.5 Simulation of TPFL Offtake Tests

[

][b]

12.7.5.6 Summary and Conclusions

12.7.5.6.1 Comparison of WCOBRA/TRAC-TF2 Prediction to Horizontal Data

Figure 12.7.5-4 shows the comparison of the WCOBRA/TRAC-TF2 prediction for the branchline quality as a function of the mainline liquid level for the horizontal configuration. **[**

][a,c]

12.7.5.6.2 Comparison of WCOBRA/TRAC-TF2 Prediction to Downward-Vertical Data

Figure 12.7.5-5 shows the comparison of the WCOBRA/TRAC-TF2 prediction and the experimental data of the branchline quality as a function of the mainline liquid level for the downward-vertical configuration. **[**

][a,c]

[

]a,c

12.7.6 Additional Offtake Model Validation

The TPFL facility tests address the vertical downward and horizontal break orientations, but provide no data for an upward vertical break. As such, additional validation was performed to ensure that the WCOBRA/TRAC-TF2 code reasonably predicts the offtake phenomenon for an upward oriented break.

Using the TPFL facility geometry, the offtake model was exercised for vertical upward breaks across a range of boundary conditions. The model was exercised at pressures of [

]a,c The code results are compared to [

]a,c to assess the capability of the model.

12.7.6.1 Comparison of WCOBRA/TRAC-TF2 Prediction to Upward-Vertical Data

Figure 12.7.6-1 shows the comparison of the WCOBRA/TRAC-TF2 prediction for the branchline quality as a function of the mainline liquid level divided by the critical height for onset of offtake (hereafter referred to as the level ratio) for the upward-vertical configuration versus experimental data. [

]a,c

Table 12.7.5-1 Summary of Test Parameters for Two-Phase Flow Loop Offtake Tests

b

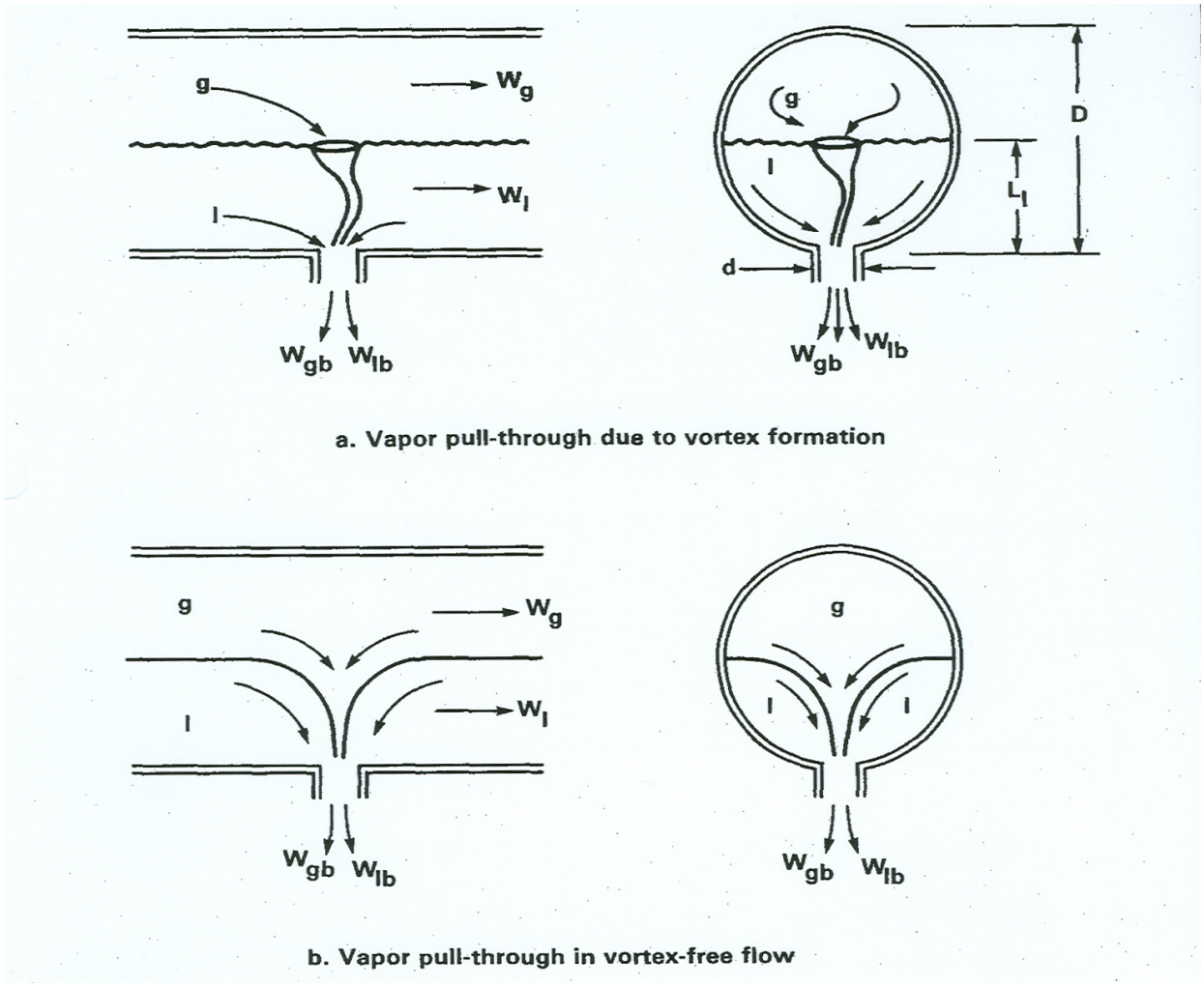

Figure 12.7.2-1 Vapor Pull Through Mechanisms (Figure 4-1 from Zuber, 1980)

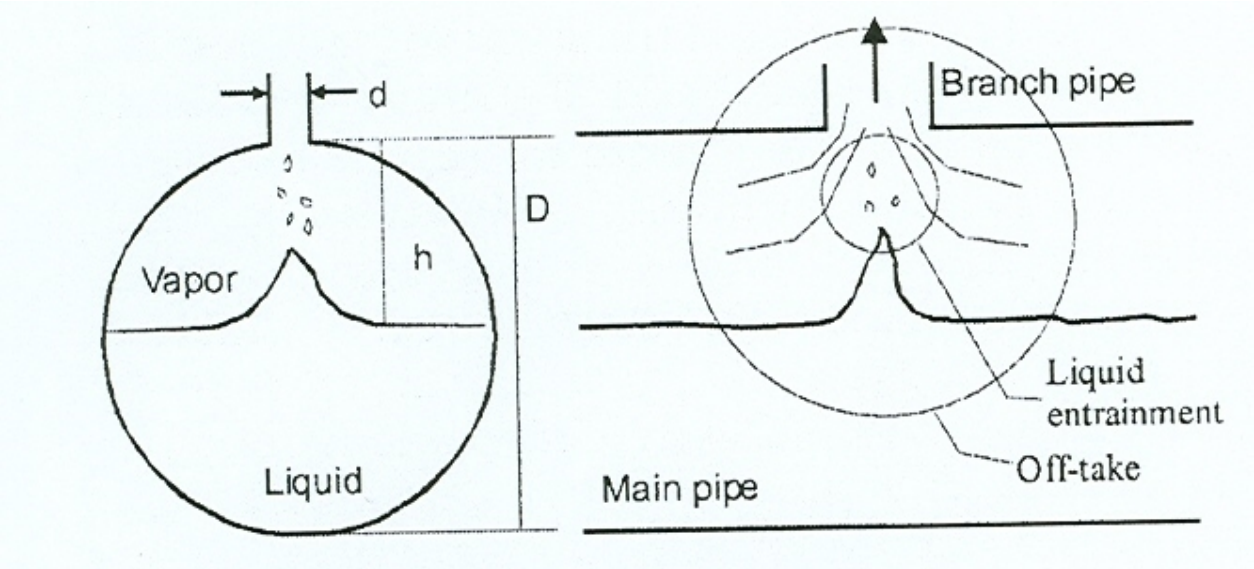

Figure 12.7.2-2 Liquid Entrainment Mechanism (Figure 1 from Moon and No, 2003)

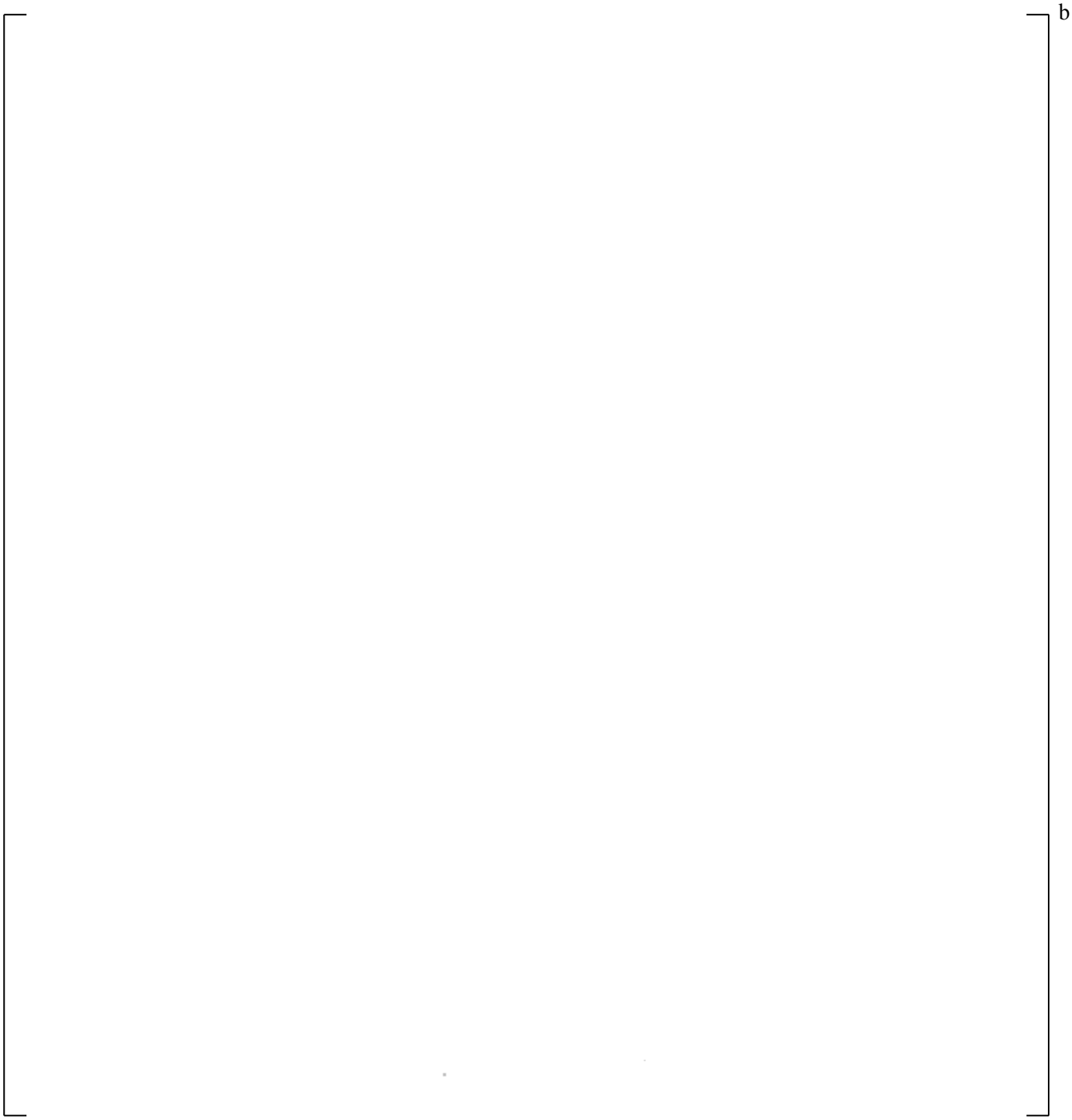

Figure 12.7.5-1 Diagram of the Two-Phase Flow Loop Facility

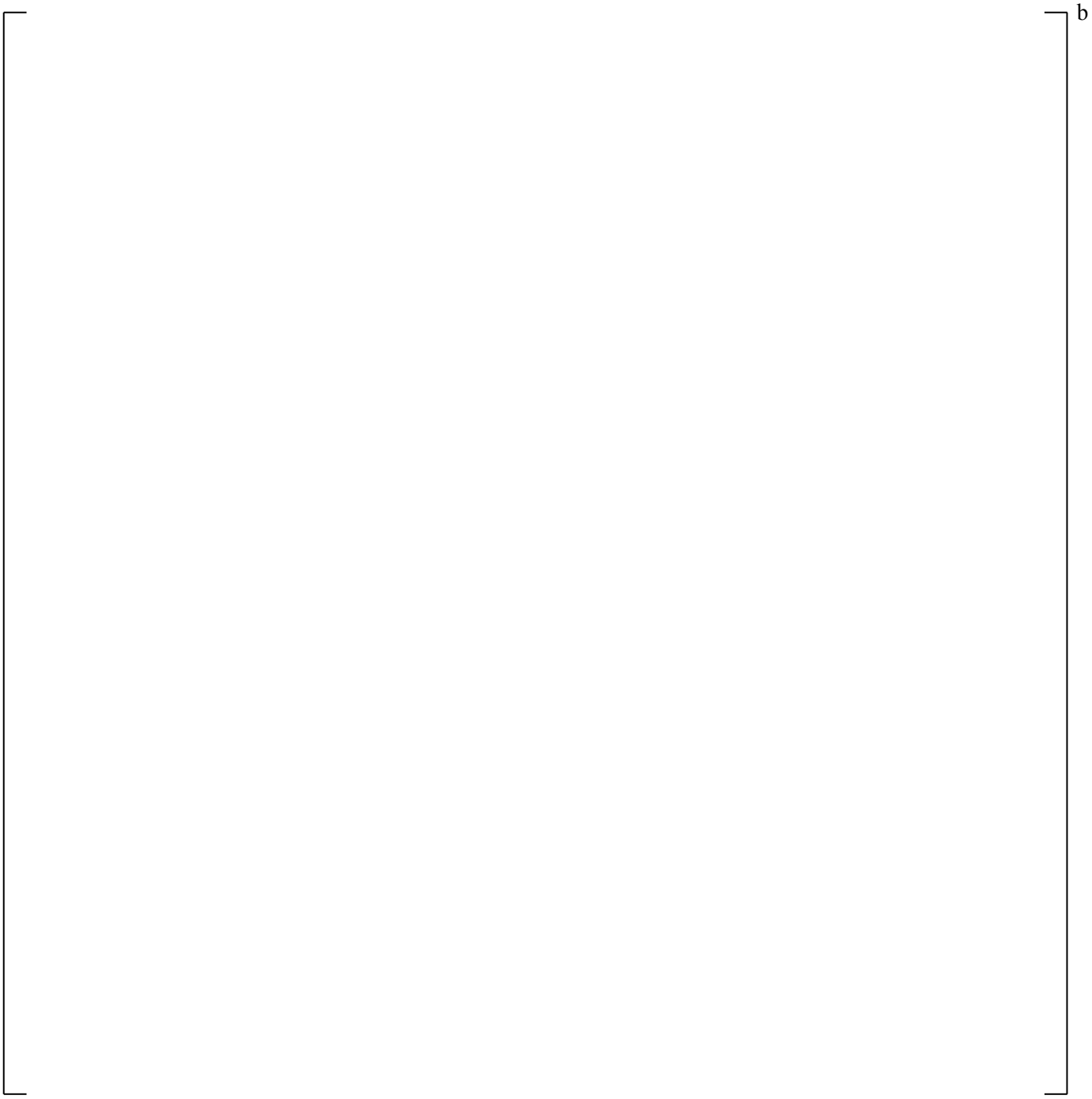

Figure 12.7.5-2 Schematic View of the Two-Phase Flow Loop Test Section

a,c

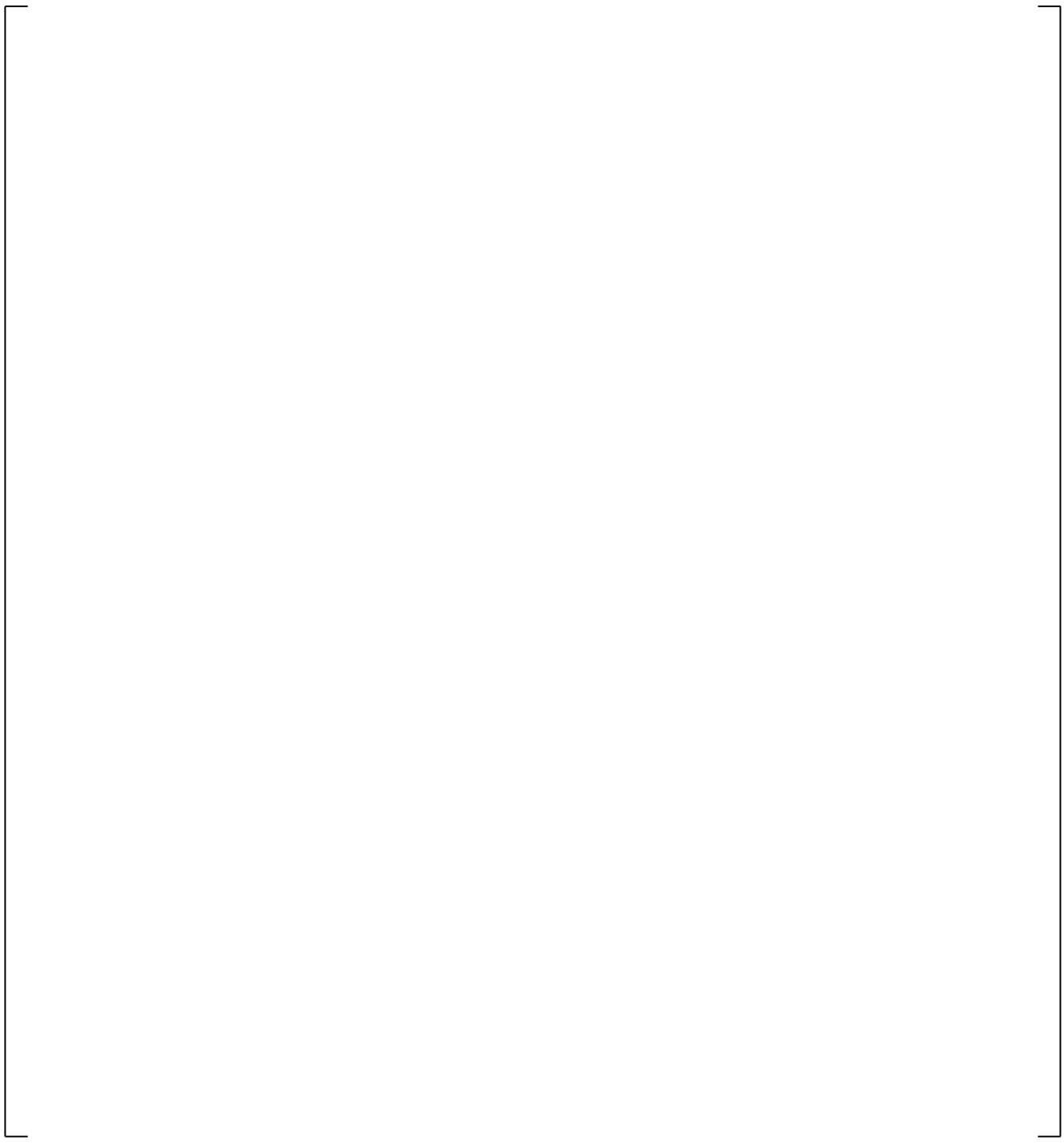

Figure 12.7.5-3 WCOBRA/TRAC-TF2 Noding Diagram of the Two-Phase Flow Loop

a,c

Figure 12.7.5-4 Branchline Quality Versus Mainline Liquid Level for Horizontal Configuration

a,c

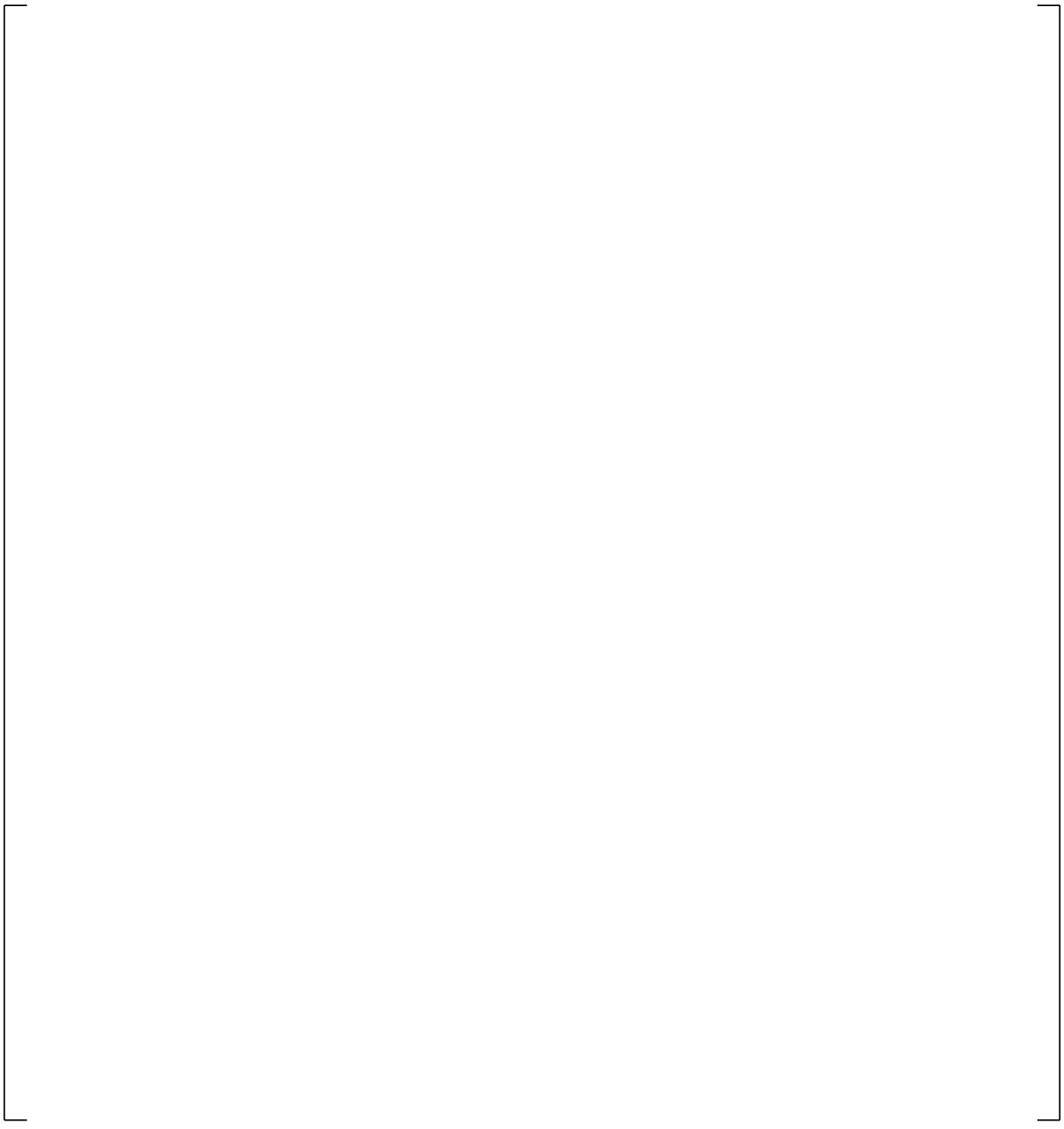

Figure 12.7.5-5 Branchline Quality Versus Mainline Liquid Level for Downward-Vertical Configuration

a,c

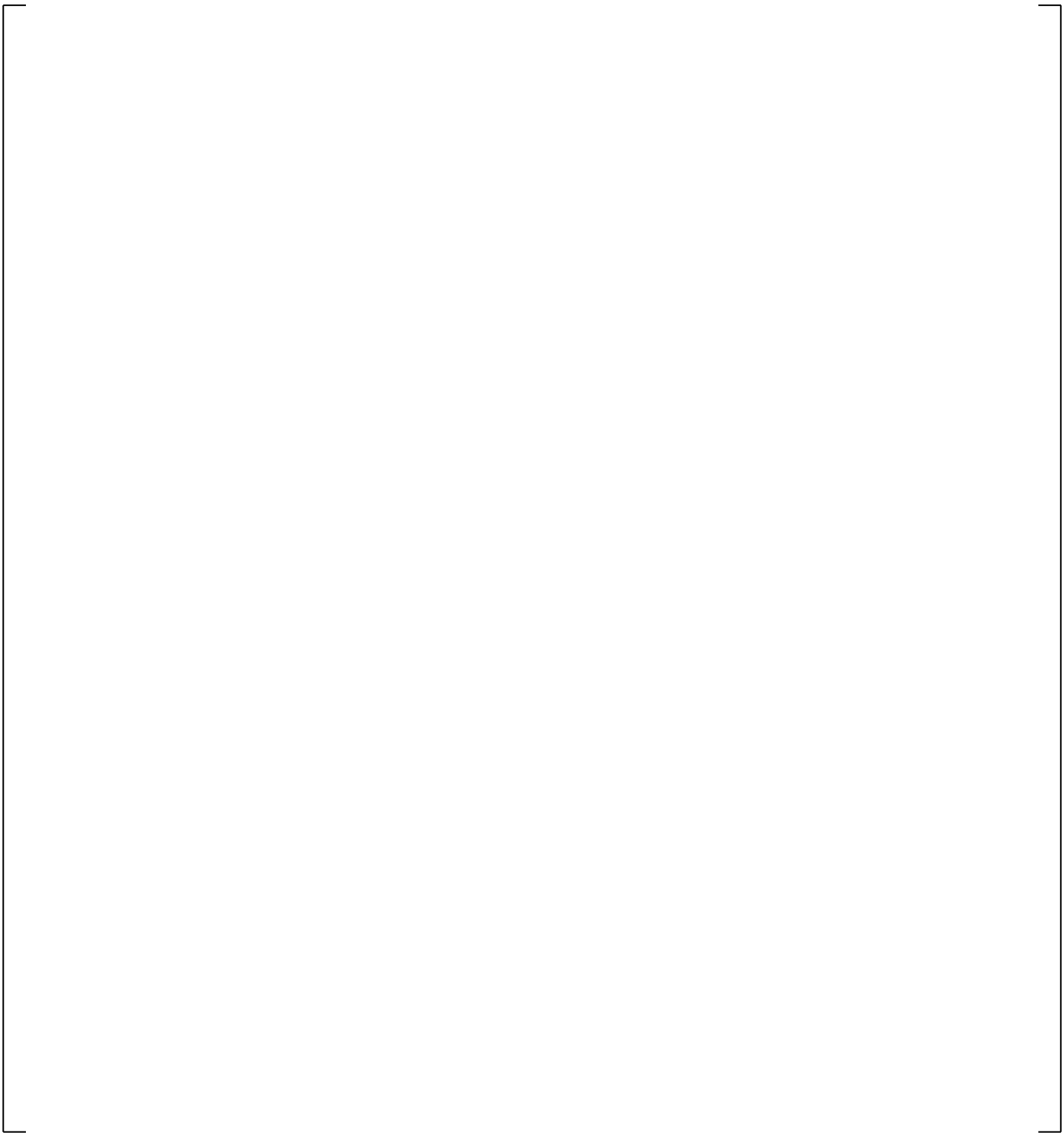

Figure 12.7.6-1 Branchline Quality Versus Mainline Liquid Level for Upward-Vertical Configuration

a,c

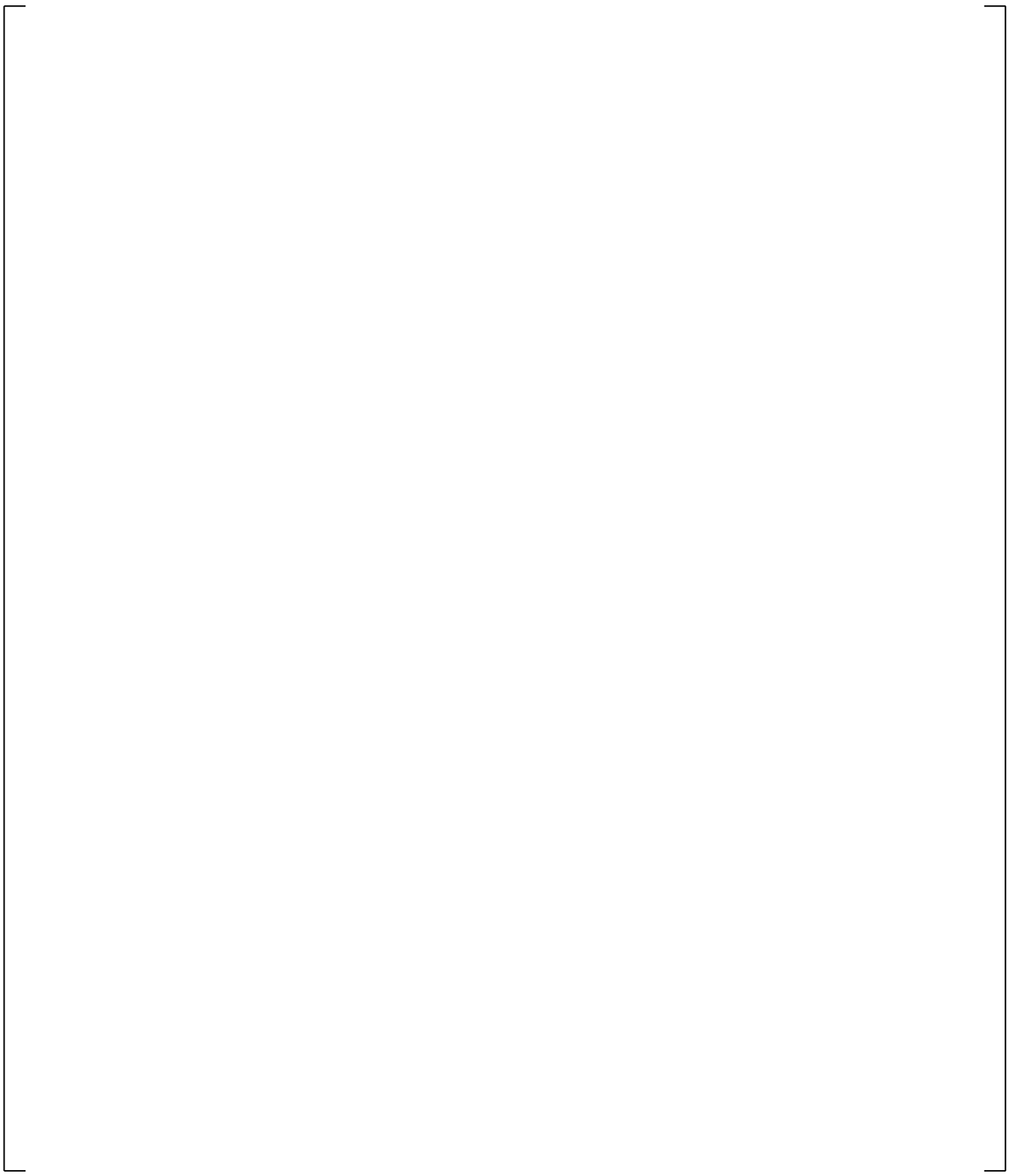

Figure 12.7.6-2 [

]a,c

12.8 REFERENCES

1. Amos, C. N. and Schrock, V. E., 1983, "Critical Discharge of Initially Subcooled Water Through Slits," NUREG/CR-3475.

2. Anderson, J. L. and Benedetti, R. L., 1986, "Critical Flow Through Small Pipe Break," EPRI NP-4532.

3. Ardron, K. H. & Ackerman, M. C., 1978, "Studies of the Critical Flow of Subcooled Water in a Pipe," CEGB Report: RD/B/N4299.

4. Boivin, J. V., 1979, "Two-phase Critical Flow in Long Nozzles," *Nuclear Technology*, 46, pages 540-545.

5. Bryers, R. W., Hsieh, W. W., Hunter, J. A. and Sieder, E. N., 1966, "Study of Two-phase Metastable Flow," U. S. Department of Interior, Office of Saline Water, R&D Progress Report No. 234, November, 1966.

6. Celata, G. P., Cumo, M., D'Annibale, F., and Farello, G. E., 1988, "THE INFLUENCE OF NON-CONDENSIBLE GAS ON TWO-PHASE CRITICAL FLOW," *International Journal of Multiphase Flow*, Volume 14, No. 2, pages 175-187.

7. Cruver, J. E., 1963, "Metastable Critical Flow of Steam Water Mixtures," Ph.D. Dissertation, Department of Chemical Engineering, University of Washington, (University Microfilms Inc., Ann Arbor, Michigan).

8. Danforth, J. L., 1941, "Flow of Hot Water Through a Rounded Orifice," M. S. Dissertation, Department of Mechanical Engineering, Massachusetts Institute of Technology.

9. Dao, L. T. L. and Carpenter, J. M., 1980, "Experiment Data Report for LOFT Nuclear Small-Break Experiment L3-5/L3-5A," NUREG/CR-1695, EGG-2060.

10. Elias, E., and Lellouche, G. S., 1994, "TWO-PHASE CRITICAL FLOW," *International Journal of Multiphase Flow*, Vol. 20, Supplement, pp. 91-168.

11. Fauske, H. K., 1962, "Contribution to the Theory of Two-phase, One Component Critical Flow," Argonne National Laboratory Report ANL-6633.

12. Fincke, J. R. and Collins, D. R., 1981, "The Correlation of Two-Dimensional and Nonequilibrium Effects in Subcooled Choked Nozzle Flow," NUREG/CR-1907, EGG-2081.

13. Guizovarn, L., Pinet, B., Barriere, G. and Pietri, D., 1975, "Etude Expermentale des Debits Critiques en Ecoulement Diphasiques eau Vapeur a Faible Titre Dans un Canal Avec Divergent de 7° a des Transports Thermiques," Note TT No. 501.

14. Henry, R. E., 1970, "An Experimental Study of Low Quality, Steam-Water Critical Flow at Moderate Pressures," Argonne National Laboratory Report ANL-7740.

15. Holmes, B. J., and Allen, E. J., 1998, "A REVIEW OF CRITICAL FLOW DATA FOR PRESSURISED WATER REACTOR SAFETY STUDIES," *Multiphase Science and Technology*, Vol. 10, pp. 141-302.

16. Illic, V., Banerjee S. and Behling S., 1986, "A Qualified Database for the Critical Flow of Water," EPRI-NP-4556.

17. Isbin, H. S., Moy, J. E. and Da Cruz, A. J. R., 1957, "Two-Phase Steam-Water Critical Flow," *AIChE Journal*, Vol. 3, Issue 3, pp. 361-365.

18. Jeandey, C., Gros D'Aillon, L., Bourgin, R. and Barriere, G., 1981, "Auto Vaporisation d'Ecoulements Eau/Vapeur," Departement des Reacteurs a Eau Service des Transferts Thermiques (Centre D'Etudes Nucleaires de Grenoble) Report T. T. No. 163.

19. Marviken Project, 1982, "The Marviken Full-Scale Critical-Flow Tests," EPRI-NP 2370, Vol. 1, Summary Report.

20. Moon, Y. M. and No, H. C., 2003, "Offtake and Slug Transition at T-junction of Vertical-up Branch in the Horizontal Pipe," *Journal of Nuclear Science and Technology*, Vol. 40, No. 5, pp. 317-324.

21. Morrison, A. F., 1977, "Blowdown Flow in the BWR BDHT Test Apparatus," GEAP-21656.

22. Neusen, K. F., 1962, "Optimizing of Flow Parameters for the Expansion of Very Low-quality Steam," University of California, Lawrence Radiation Laboratory, UCRL-6152.

23. Ogasawara, H., 1969, "A Theoretical Approach to Two-Phase Critical Flow," 4th Report, Experiments on Saturated Water Discharging through Long Tubes, *Bulletin of JSME*, Vol. 12, No. 52, pp. 837-846.

24. Ohkawa, K., 2007, "ASSESSMENT OF HOMOGENEOUS NON-EQUILIBRIUM RELAXATION CRITICAL FLOW MODEL," *15th International Conference on Nuclear Engineering*, ICONE15-10708, Nagoya, Japan, April 22-26.

25. Reocreux, M., 1974, "Contribution a l'Etude des Debits Critiques en Econlement Diphasique Eau-Vapeur," Ph.D. Thesis, Universite Scientifique et Medicale de Grenoble, France.

26. Schrock, V. E., et al., 1986, "Small Break Critical Discharge – The Roles of Vapor and Liquid Entrainment in a Stratified Two-phase Region Upstream of the Break," NUREG/CR-4761.

27. Schrock, V. E., Starkman, E. S. and Brown, R. A., 1977, "Flashing Flow of Initially Subcooled Water in Convergent-divergent Nozzles," *Journal of Heat Transfer* 99 (2).

28. Seynhaeve, J. M., 1980, "Etude Experimentale des Ecoulements Diphasiques Critiques a Faible Titre," Doctoral thesis, Department Thermodynamique et Turbomachines, Universite Catholique de Louvain.

29. Smoglie, C. and Reimann, J., 1986, "Two-phase Flow Through Small Branches in a Horizontal Pipe with Stratified Flow," *International Journal of Multi-Phase Flow*, pp. 609-626.

30. Sozzi, G. L. and Sutherland, W. A., 1975, "Critical Flow of Saturated and Subcooled Water at High Pressure," NEDO-13418.

31. Zaloudek, F. R., 1964, "Steam-Water Critical Flow From High Pressure Systems," HW-80535.

32. Zuber, N., 1980, "Problems in Modeling of Small Break LOCA," NUREG-0724.

APPENDIX A
RESULTS OF CRITICAL FLOW ASSESSMENT FOR INDIVIDUAL DATASET

In this appendix, the output for each dataset is given, and comparisons of predicted and measured mass flux for individual test subsection are presented graphically.

A.1 ARDRON & ACKERMAN

a,c

A.2 BOIVIN

a,c

A.3 FINCKE & COLLINS

a,c

A.4 JEANDEY

a,c

A.5 NEUSEN

a,c

A.6 REOCREUX

a,c

A.7 SEYNHAEVE

a,c

A.8 SOZZI-SUTHERLAND

a,c

A.9 AMOS & SCHROCK

a,c

A.10 TPFL (ANDERSON & BENEDETTI)

a,c

A.11 MARVIKEN

a,c

A.11.1 MARVIKEN TEST 1

a,c

A.11.2 MARVIKEN TEST 2

a,c

A.11.3 MARVIKEN TEST 3

a,c

A.11.4 MARVIKEN TEST 4

a,c

A.11.5 MARVIKEN TEST 5

a,c

A.11.6 MARVIKEN TEST 6

a,c

A.11.7 MARVIKEN TEST 7

a,c

A.11.8 MARVIKEN TEST 8

a,c

A.11.9 MARVIKEN TEST 9

a,c

A.11.10 MARVIKEN TEST 10

a,c

A.11.11 MARVIKEN TEST 11

a,c

A.11.12 MARVIKEN TEST 12

a,c

A.11.13 MARVIKEN TEST 13

a,c

A.11.14 MARVIKEN TEST 14

a,c

A.11.15 MARVIKEN TEST 15

a,c

A.11.16 MARVIKEN TEST 16

a,c

A.11.17 MARVIKEN TEST 17

a,c

A.11.18 MARVIKEN TEST 18

a,c

A.11.19 MARVIKEN TEST 19

a,c

A.11.20 MARVIKEN TEST 20

a,c

A.11.21 MARVIKEN TEST 21

a,c

A.11.22 MARVIKEN TEST 22

a,c

A.11.23 MARVIKEN TEST 23

a,c

A.11.24 MARVIKEN TEST 24

a,c

A.11.25 MARVIKEN TEST 25

a,c

A.11.26 MARVIKEN TEST 26

a,c

A.11.27 MARVIKEN TEST 27

a,c

A.12 CELATA

a,c

13 CORE VOID DISTRIBUTION AND MIXTURE LEVEL SWELL

13.1 INTRODUCTION

Early in a small break Loss-of-Coolant Accident (LOCA), voids are generated in the primary reactor coolant system (RCS) by flashing and boiling in the core. Because of the small break size, flows in the RCS are primarily gravity-driven. Following the initial rapid depressurization stage of the LOCA, distinct liquid levels are formed at several locations, and most significantly in the core. Below this liquid or two-phase mixture level, the fluid is a low quality two-phase mixture; while above the level, it is primarily single-phase vapor. Liquid levels initially occur in the pressurizer, in the upper head, and in the uphill and downhill steam generator tubing. Eventually, the RCS drains so that the level in the reactor vessel reaches the hot leg. At this point, the rate of system depressurization is low and vapor generation results from boiling in the core, from power produced by decay heat. Because the vapor generation rate resulting from this decay heat can be high, regions in the vessel can achieve a significant void fraction. The two-phase mixture level depends on the interfacial shear exerted by the vapor on the liquid, and as a result, the mixture level can be significantly higher than the collapsed liquid level. The difference between the two-phase mixture level and the collapsed level is a measure of the "mixture level swell," which is defined as:

$$S = \frac{\left(Z_{2\Phi} - Z_{SAT}\right) - \left(Z_{CLL} - Z_{SAT}\right)}{Z_{CLL} - Z_{SAT}} \tag{13-1}$$

where Z_{CLL} is the collapsed liquid level, $Z_{2\Phi}$ is the two-phase mixture level, and Z_{SAT} is the elevation where the liquid reaches the saturation point. Using this definition, a swell of zero corresponds to a two-phase mixture level which is the same as the collapsed liquid level.

Prediction of the mixture level swell and tracking of the mixture level are important **[**

][a,c] As more liquid is boiled away, the mixture level can eventually drop into the core. While good cooling can be maintained below the mixture level, dryout occurs above the mixture level. Heat transfer above the mixture level is by convection and thermal radiation to steam. These relatively poor modes of heat transfer cause the cladding temperature above the mixture level to increase rapidly. Thus, prediction of the two-phase mixture level in the active core is vital to an accurate prediction of the cladding behavior in a small break or intermediate break LOCA.

13.2 PHYSICAL PROCESSES

As described in Section 13.1, mixture level swell is the process that determines the vertical position of the two-phase interfaces in the system; above the interface the mixture is essentially single-phase vapor. **[**

][a,c]

[

]a,c

Several experimental tests have been run under small or intermediate break LOCA thermal-hydraulic conditions to measure the effects of various parameters on mixture level swell. [

]a,c

13.3 WCOBRA/TRAC-TF2 DETERMINATION OF THE MIXTURE LEVEL

The models and correlations for vessel wall and interfacial drag are described in Sections 5.2 through 5.4, Volume 1 of this document. Flow regime transitions are described in Section 4, Volume 1 of this document. These models are used to determine the void fraction distribution within a region. The models and correlations used to determine the critical heat flux elevation are detailed in Section 7.2.3, Volume 1, of this document.

[

]a,c

13.4 ASSESSMENT OF WCOBRA/TRAC-TF2 MIXTURE LEVEL PREDICTIONS

13.4.1 Introduction

There are several separate effects experimental tests that provide data on the mixture level and sometimes mass inventory distribution in a rod bundle under small break LOCA thermal-hydraulic conditions. Four such experimental facilities were modeled with WCOBRA/TRAC-TF2, and several experimental tests were simulated to determine the predictive capability of the code. The tests were as follows:

- The ORNL-THTF Uncovered Bundle Tests by Anklam (Anklam et al., 1982)
- The Westinghouse G-1 Core Uncovery Tests, WCAP-9764 (Anderson, 1980)
- The Westinghouse G-2 Core Uncovery Tests, EPRI NP-1692 (Andreychek, 1981)
- The JAERI-TPTF Critical Heat Flux Bundle Tests, JAERI-M 93-238 (Guo et al., 1993)

Each of these tests, **[** **]**[a,c] provides information on the cladding heatup elevation; and most provide the mass distribution in a vessel for various thermal-hydraulic conditions. The Oak Ridge National Laboratory (ORNL) Thermal-Hydraulic Test Facility (THTF), G-1, and G-2 tests provide mixture level and mass inventories for uncovered rod bundles, and the Japan Atomic Energy Research Institute (JAERI) Two-Phase Test Facility (TPTF) tests provide critical heat flux elevations for uncovered rod bundles. The following sections discuss each test, the WCOBRA/TRAC-TF2 simulation, and the comparisons between the measured and predicted results.

A comparison of the test conditions versus typical conditions expected in a pressurized water reactor (PWR) during the period(s) of interest is presented in Table 13.4.1-1.

The General Electric (GE) Vessel Blowdown Tests by Findlay and Sozzi (Findlay and Sozzi, 1981) provide mass inventory data in a vessel during rapid depressurization. These tests were also simulated with WCOBRA/TRAC-TF2, as described in Section 23.1.1 of this document. However, they are not included in this section as they are not prototypical of level swell under Small Break LOCA boiloff conditions.

Table 13.4.1-1 Comparison of Test Conditions with Typical PWR Conditions

[

]a,c

13.4.2 ORNL-THTF Small Break Tests

13.4.2.1 Introduction

A series of experimental tests pertinent to WCOBRA/TRAC-TF2 model validation were performed at the ORNL-THTF. Two types of experiments were conducted in the ORNL-THTF. One series consisted of several uncovered bundle heat transfer tests, and the other series consisted of level swell tests. These two different test series are fundamentally the same. In the bundle uncovery tests, the experiment was continued until a steady-state condition was reached in the uncovered part of the bundle and rods were heated to a high temperature. The second type of tests (level swell tests) either did not have bundle uncovery, or only a relatively short portion of the top of the bundle was uncovered. For these tests, a void profile over the entire axial length was obtained.

Additional information on the ORNL-THTF uncovered bundle heat transfer and two-phase mixture level swell tests is contained in NUREG/CR-2456 (Anklam et al., 1982).

13.4.2.2 ORNL-THTF Facility Description

The ORNL-THTF is a high pressure rod bundle thermal-hydraulics loop. Flow is pumped through the loop via a main coolant pump. After exiting the pump, the flow passes through a turbine meter and then enters the inlet manifold of the test section. The flow does not pass through a downcomer. The flow proceeds upward through the heated bundle and exits through the bundle outlet spool piece. The measurements taken at this spool piece include pressure, temperature, density, and volumetric flow. After leaving the orifice manifold, the flow passes through a heat exchanger and returns to the pump inlet.

The bundle is full height (12 ft) and contains 64 electrically heated rods with internal dimensions typical of a 17x17 PWR fuel bundle. The hydraulic diameter of the test section is consistent with a typical Westinghouse PWR. Figure 13.4.2-1 shows a cross section of the ORNL-THTF test bundle. Four of the rods were unheated to represent control rod guide tubes in a nuclear fuel assembly. Figure 13.4.2-2 shows an axial profile of the ORNL-THTF bundle. The rods have a flat power profile in both the axial and radial directions. The bundle had a heated length of 12 feet (3.66 m) and contained six spacer grids. Thermocouples were located at 25 different axial elevations.

13.4.2.3 Test Matrix for ORNL-THTF Simulations

Simulations of small break LOCAs in PWRs generally show that there are two periods in which the core can possibly be uncovered. The first occurs during the loop seal clearance period. During this uncovery, the primary system pressure **[ ]**[a,c] and the two-phase mixture level can drop below the top of the core. The second uncovery occurs if the break flow exceeds the pumped safety injection flow during the boiloff period. The system pressure during this uncovery is **[ ]**[a,c].

Table 13.4.2-1 lists tests selected for simulation by WCOBRA/TRAC-TF2. As previously discussed there were two different series of tests which were executed at ORNL; one series referred to as the bundle uncovery tests and one as the level swell tests.

Six of the tests are bundle uncovery tests. Three are at relatively low pressure (580 to 650 psia), and three are at high pressure (1010 to 1090 psia). All six had roughly one-half the bundle uncovered. Six other tests are from the level swell test series. Again, three were at low pressure (520 to 590 psia), and three were at high pressure (1090 to 1170 psia). **[**

][a,c]

13.4.2.4 Test Procedure for ORNL-THTF Simulations

All of the experiments in this test series were run within a 24 hour period, which minimized the amount of time required for preheating the facility, and enabled the use of a single instrumentation calibration. The facility was preheated using the accumulating pump heat in the primary flow circuit. Preheating continued until a stable loop temperature of 350°F to 400°F was obtained.

Once the base temperature and pressure were established, the flow was reduced to the pre-determined amount for each experiment. This was accomplished by closing the inlet flooding line and metering the flow through a 1/2 inch flow line.

After the loop was configured for each specific test, the bundle power was applied. Eventually, the test facility settled into a quasi-steady state condition, with the bundle partially uncovered and the inlet liquid mass flow equal to the exiting steam mass flow. The bundle power was then adjusted to produce a peak heater rod temperature of about 1,400°F, and the loop was again allowed to stabilize. Data acquisition was initiated after the loop stabilized, and then the pressure, flow, and power were adjusted for the next test in the series.

13.4.2.5 WCOBRA/TRAC-TF2 Model of the ORNL-THTF

Figure 13.4.2-3 shows the WCOBRA/TRAC-TF2 model of the ORNL-THTF. **[**

][a,c]

13.4.2.6 Simulation of ORNL-THTF Tests

[

][a,c]

[

]a,c

13.4.2.7 Summary and Conclusions

[

]^{a,c}

Table 13.4.2-1 ORNL-THTF Test Simulation Matrix

Test No.	Pressure (psia)	Rod Power (kW/ft)	Data Mixture Level (ft)	Data Collapsed Liquid Level (ft)
Bundle uncovery tests				
3.09.10I	650	0.68	8.60	4.39
3.09.10J	610	0.33	8.10	5.31
3.09.10K	580	0.10	6.98	5.31
3.09.10L	1090	0.66	9.02	5.77
3.09.10M	1010	0.31	8.60	6.20
3.09.10N	1030	0.14	6.98	6.10
Level swell tests				
3.09.10AA	590	0.39	11.23	6.56
3.09.10BB	560	0.20	10.85	7.61
3.09.10CC	520	0.10	11.80	9.45
3.09.10DD	1170	0.39	10.61	7.84
3.09.10EE	1120	0.19	11.40	9.35
3.09.10FF	1090	0.098	10.61	9.51

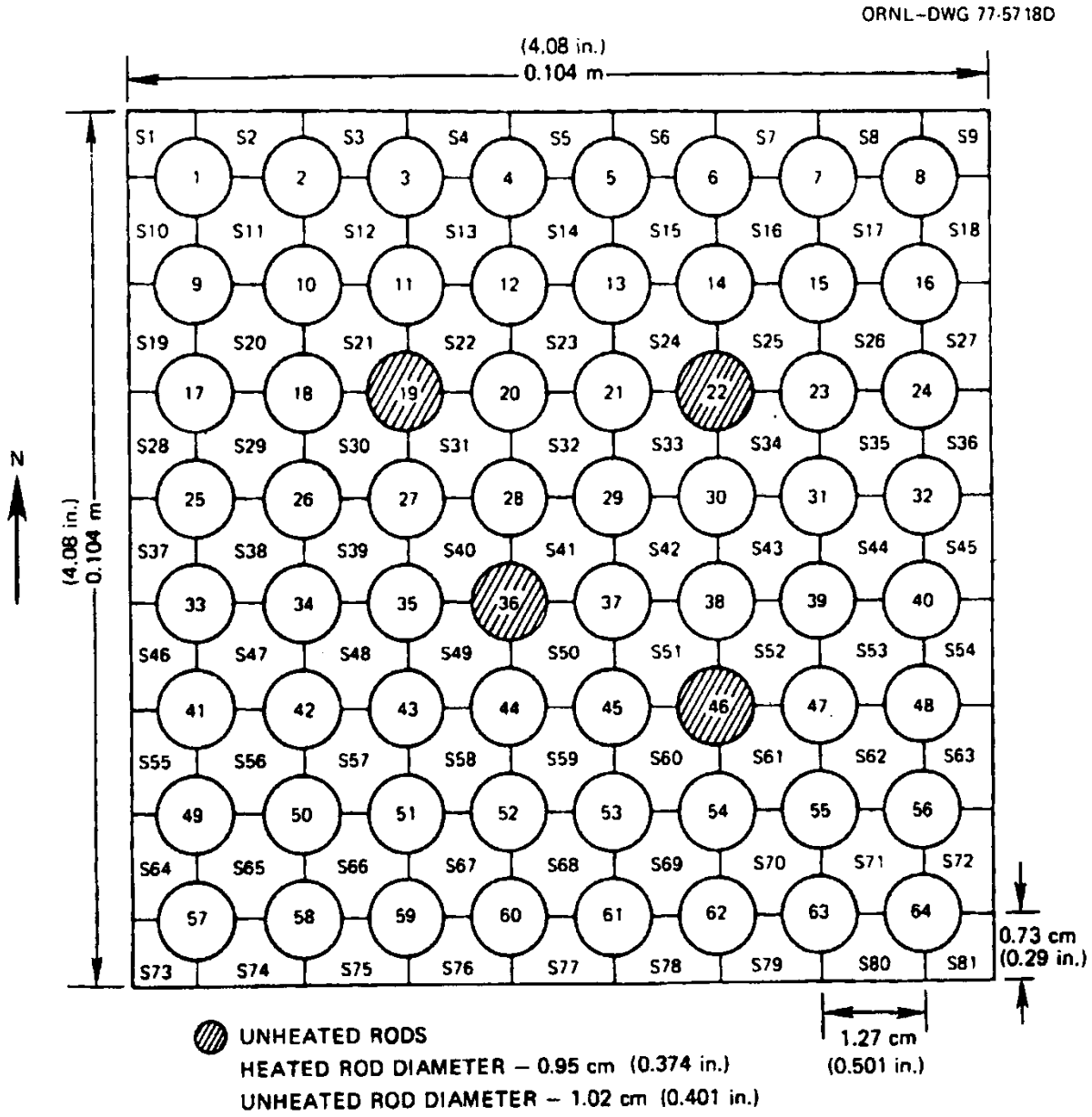

Figure 13.4.2-1 Cross Section of the ORNL-THTF Test Bundle

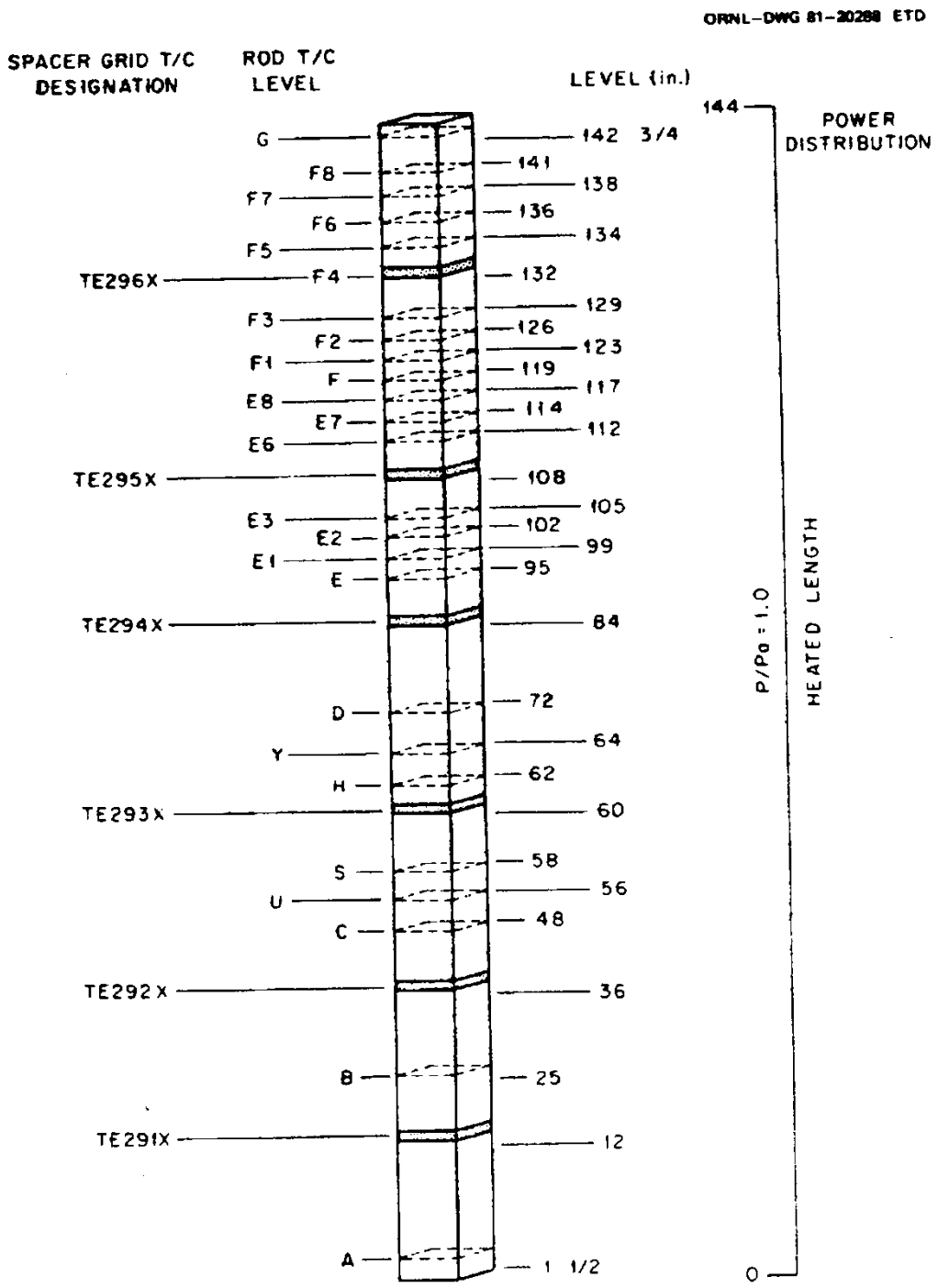

Figure 13.4.2-2 Axial View of the ORNL-THTF Test Bundle

a,c

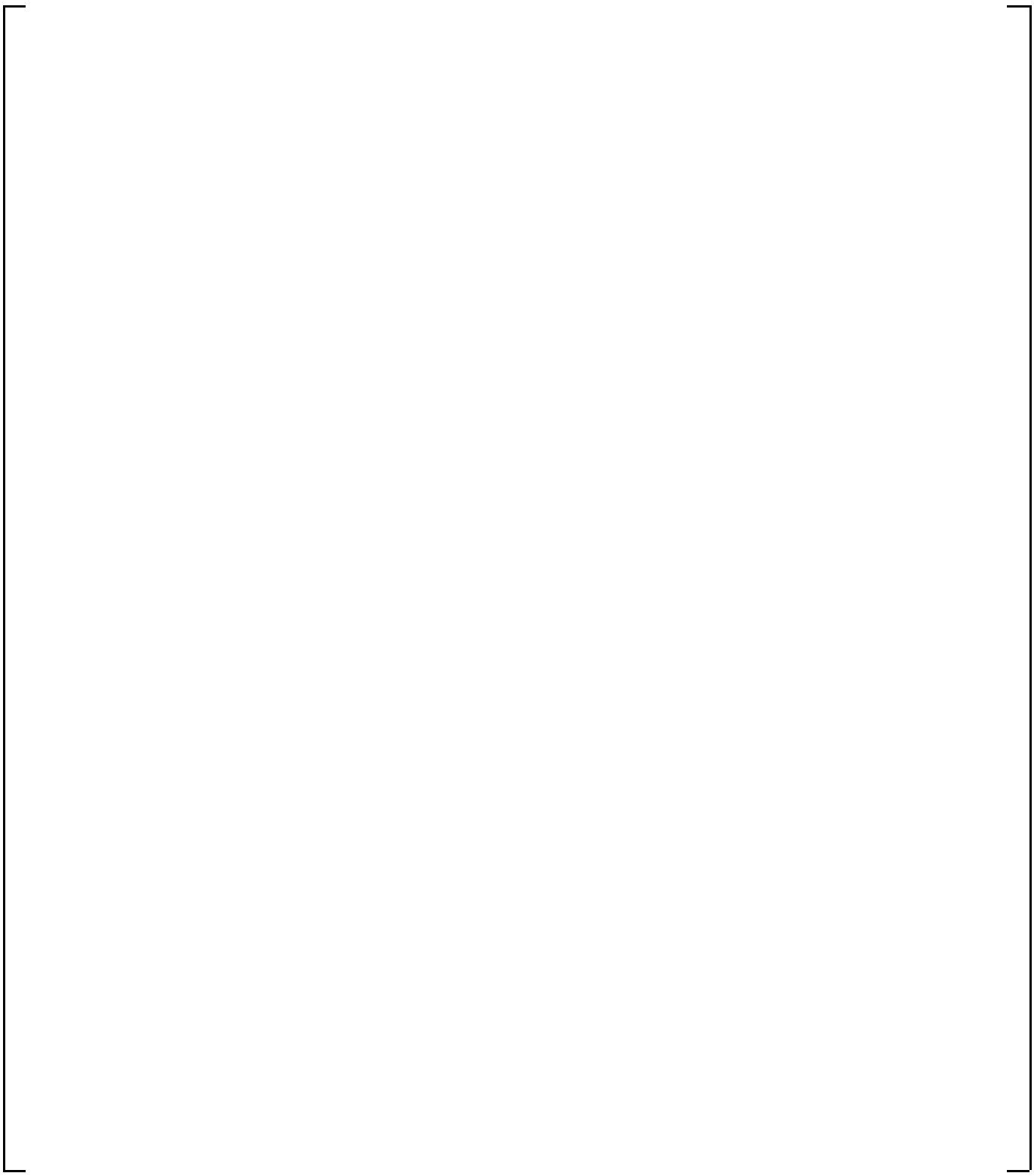

Figure 13.4.2-3 WCOBRA/TRAC-TF2 Model of the ORNL-THTF

a,c

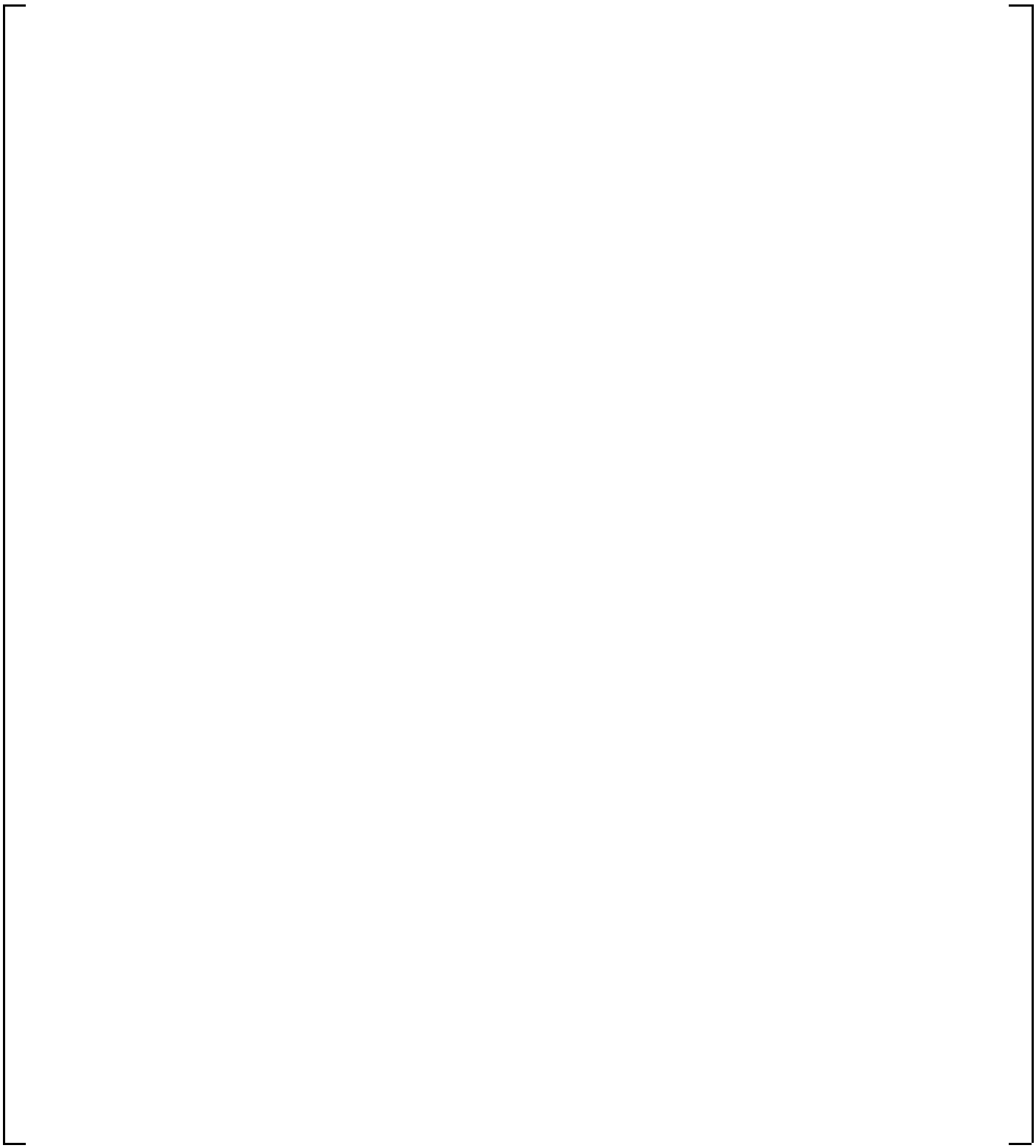

Figure 13.4.2-4 [

]a,c

a,c

Figure 13.4.2-5 [

][a,c]

a,c

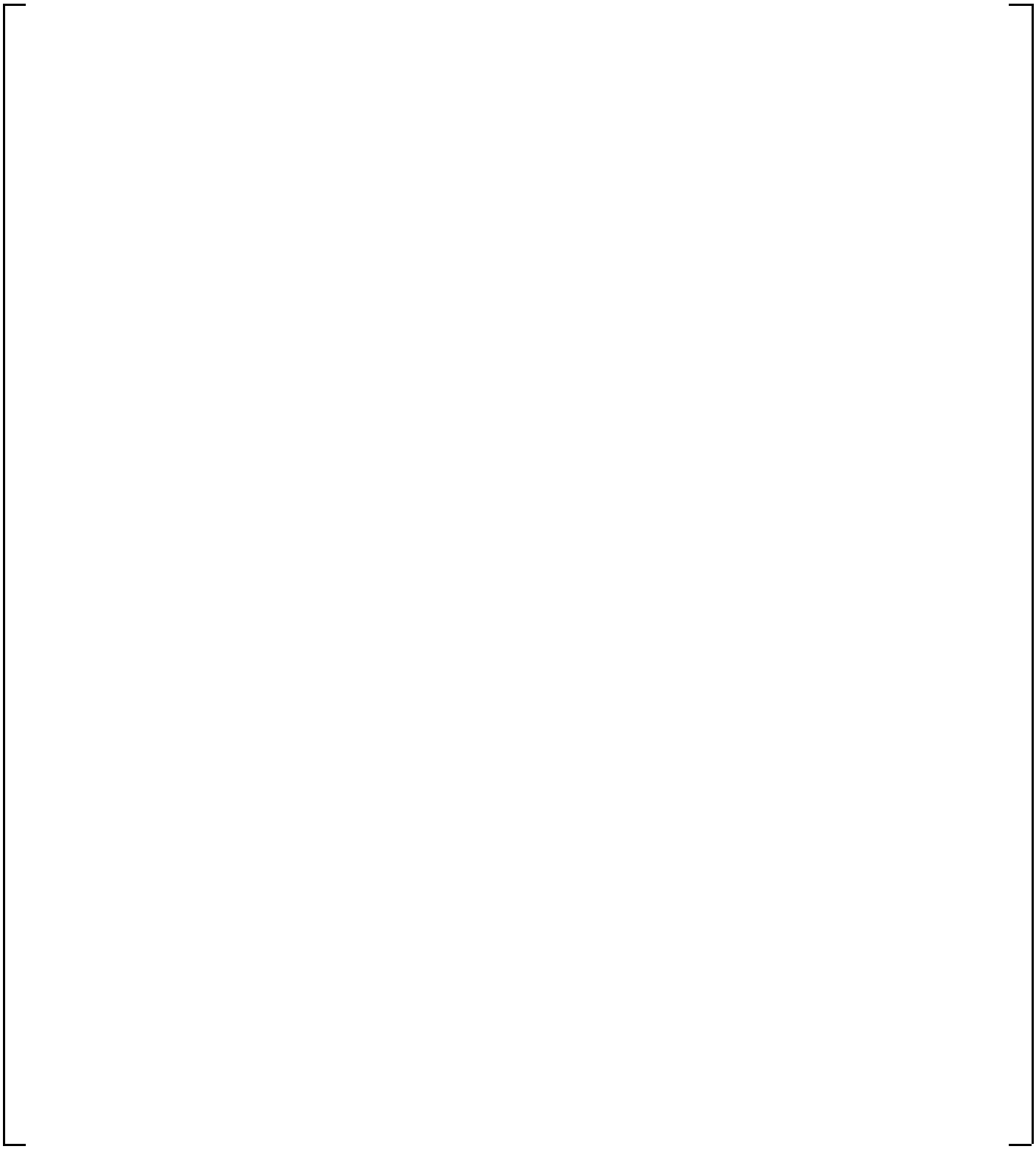

Figure 13.4.2-6 [

]a,c

a,c

Figure 13.4.2-7 [

]a,c

a,c

Figure 13.4.2-8 [

]a,c

a,c

Figure 13.4.2-9 [

]a,c

a,c

Figure 13.4.2-10 [

]a,c

a,c

Figure 13.4.2-11 [

]a,c

a,c

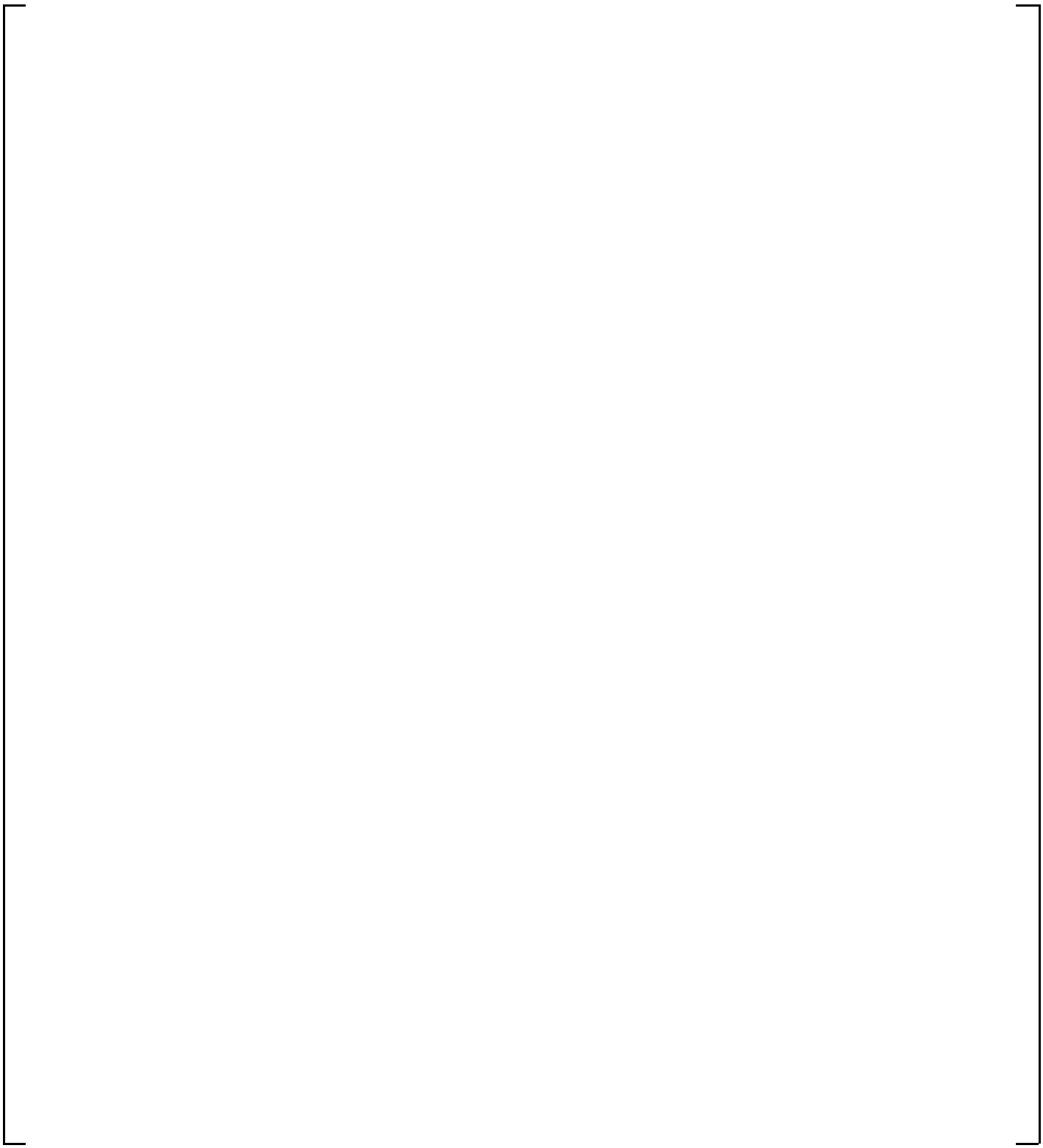

Figure 13.4.2-12 [

]a,c

a,c

Figure 13.4.2-13 [

]a,c

a,c

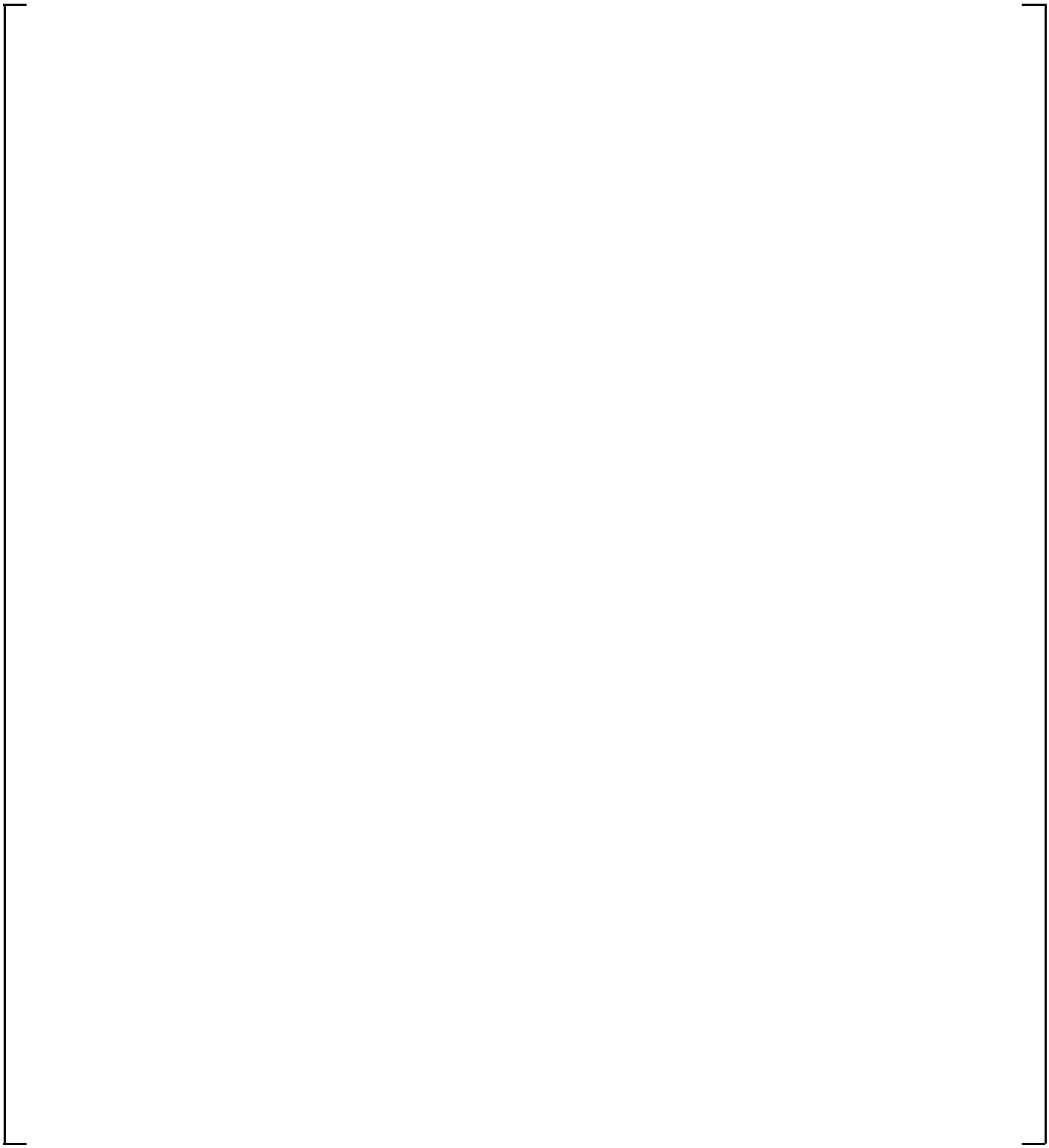

Figure 13.4.2-14 [

]a,c

a,c

Figure 13.4.2-15 [

]a,c

a,c

Figure 13.4.2-16 Comparison of Predicted and Measured Void Profiles for YDRAG Sensitivity Study, ORNL – THTF Test 3.09.10I

a,c

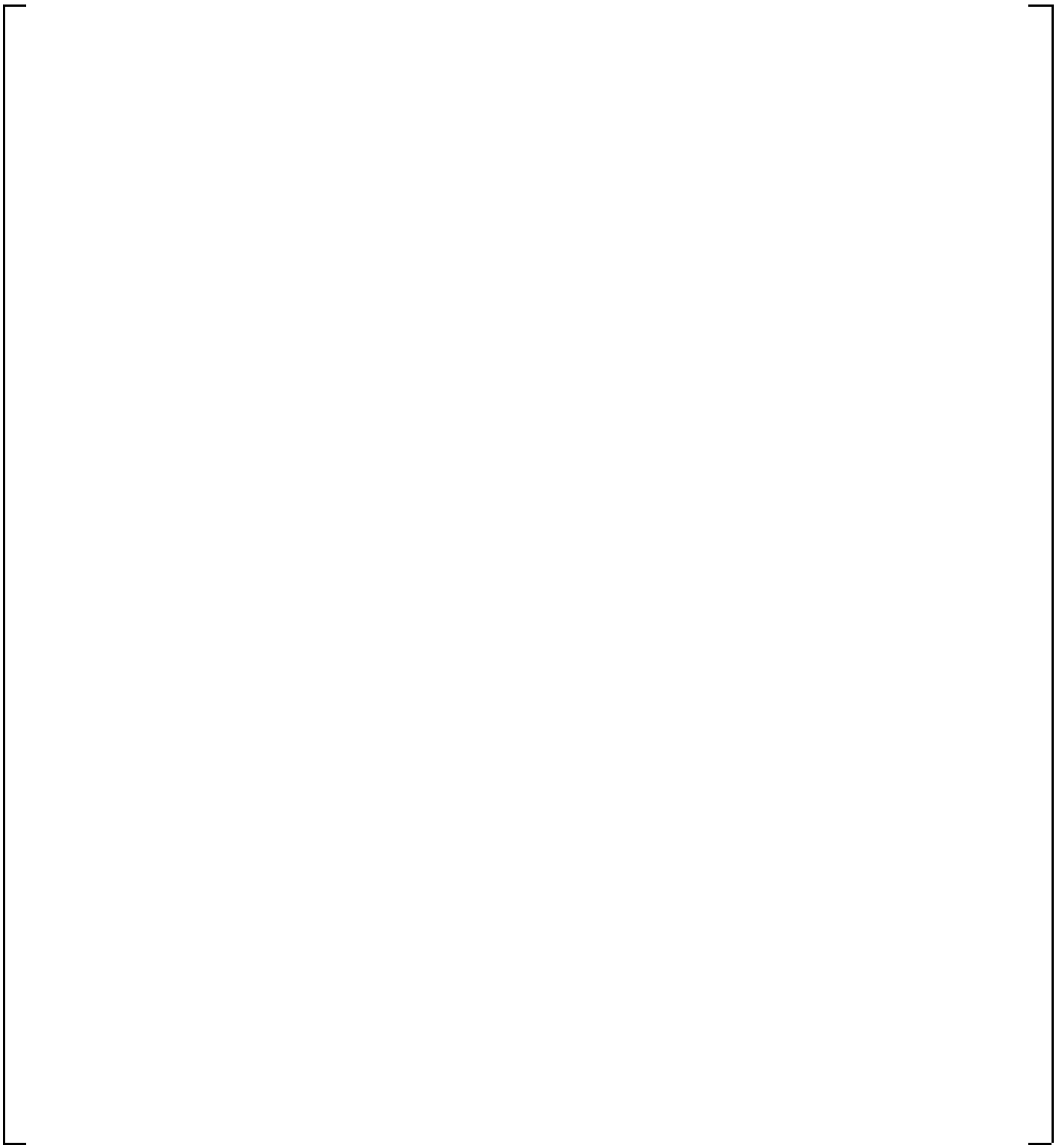

Figure 13.4.2-17 Comparison of Predicted and Measured Void Profiles for YDRAG Sensitivity Study, ORNL – THTF Test 3.09.10J

a,c

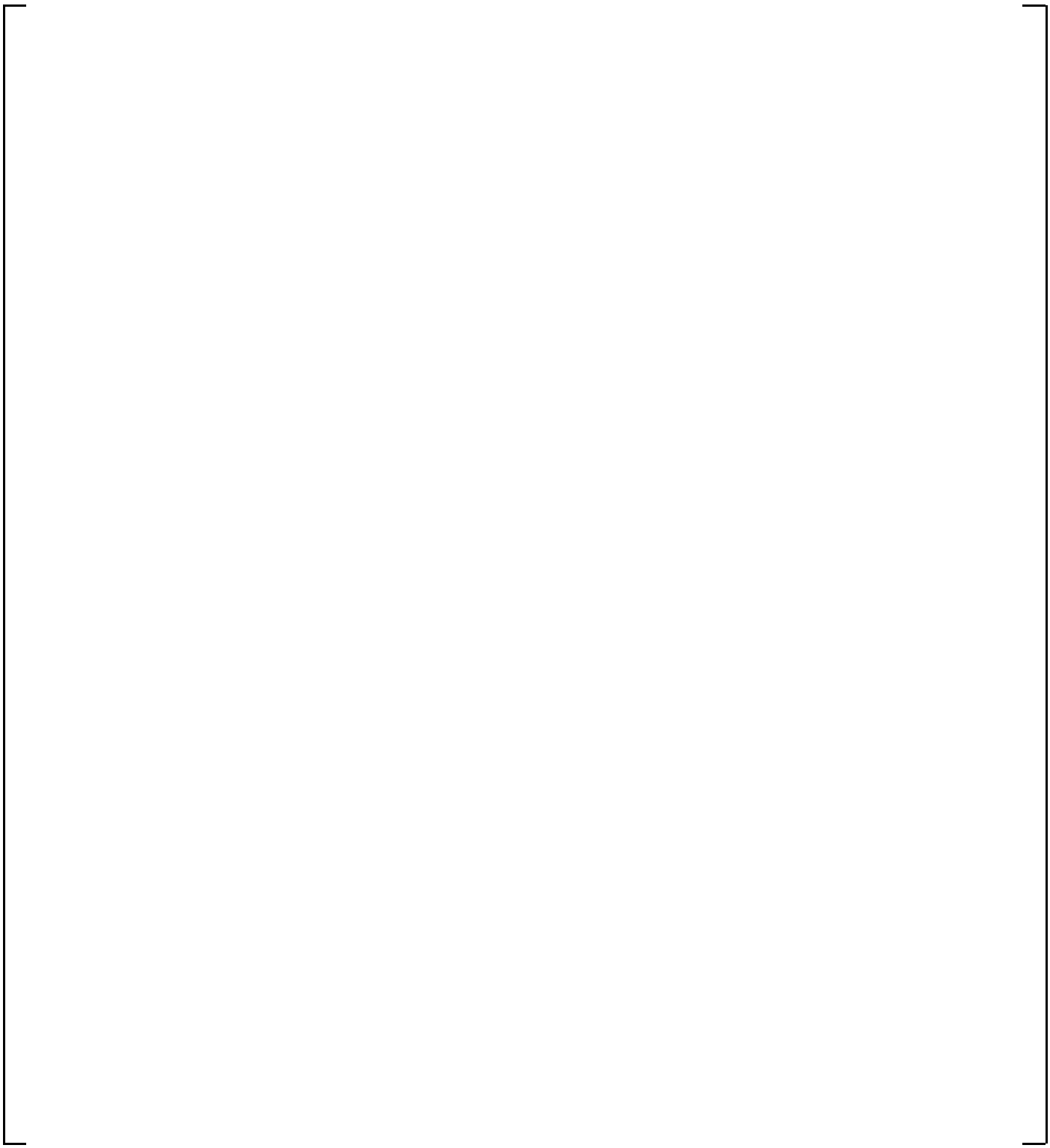

Figure 13.4.2-18 Comparison of Predicted and Measured Void Profiles for YDRAG Sensitivity Study, ORNL – THTF Test 3.09.10K

a,c

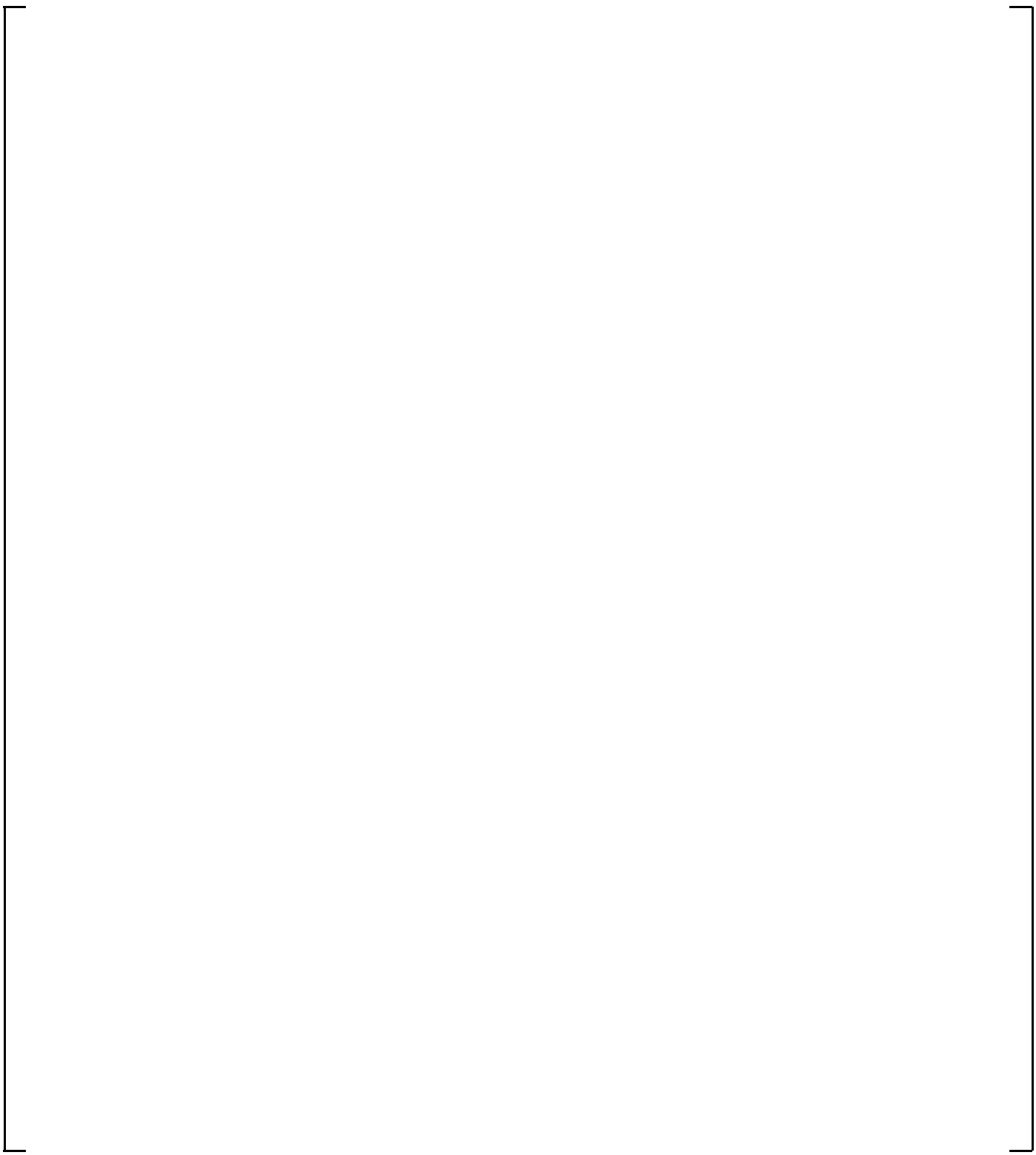

Figure 13.4.2-19 Comparison of Predicted and Measured Void Profiles for YDRAG Sensitivity Study, ORNL – THTF Test 3.09.10L

a,c

Figure 13.4.2-20 Comparison of Predicted and Measured Void Profiles for YDRAG Sensitivity Study, ORNL – THTF Test 3.09.10M

a,c

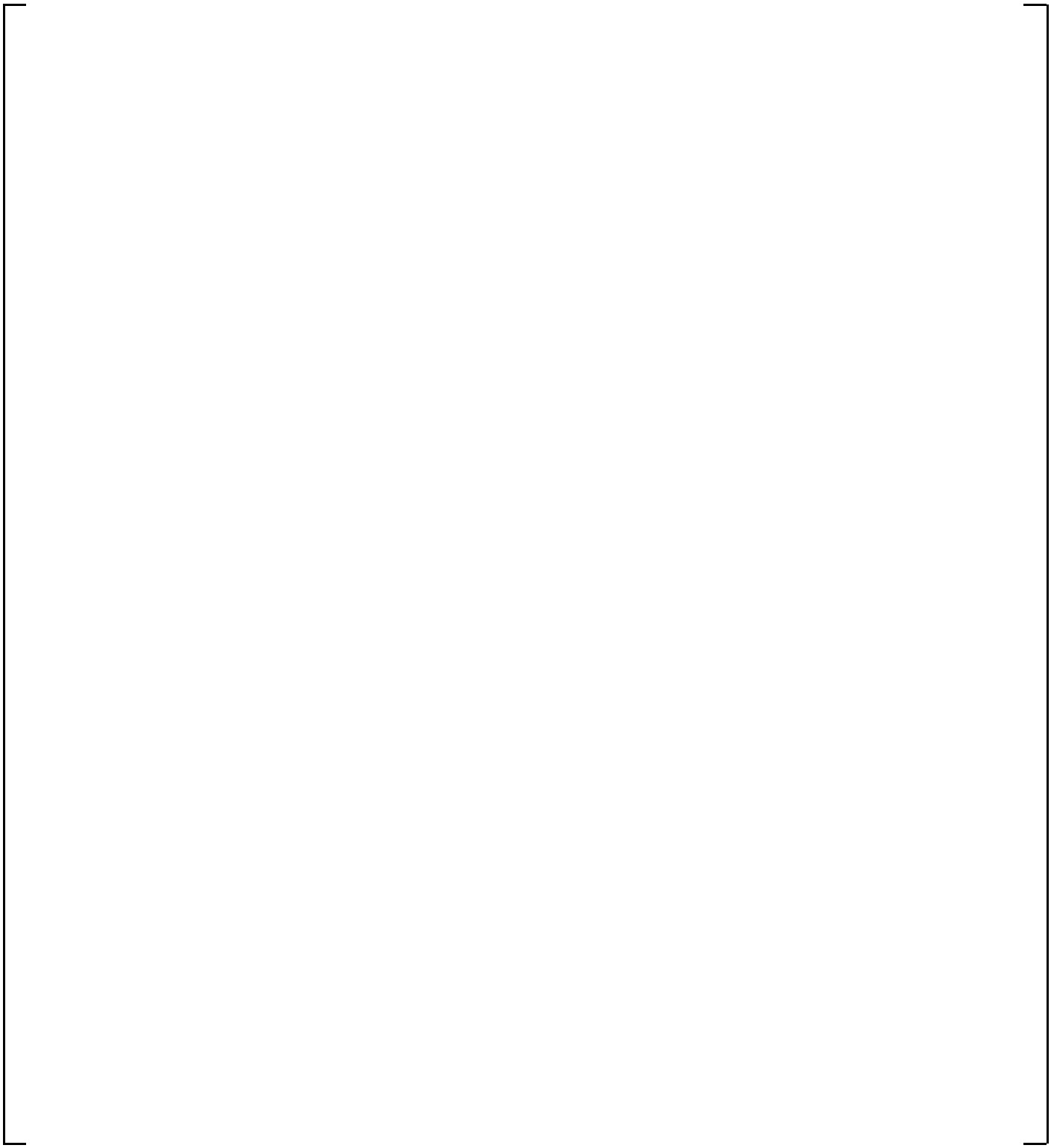

Figure 13.4.2-21 Comparison of Predicted and Measured Void Profiles for YDRAG Sensitivity Study, ORNL – THTF Test 3.09.10N

a,c

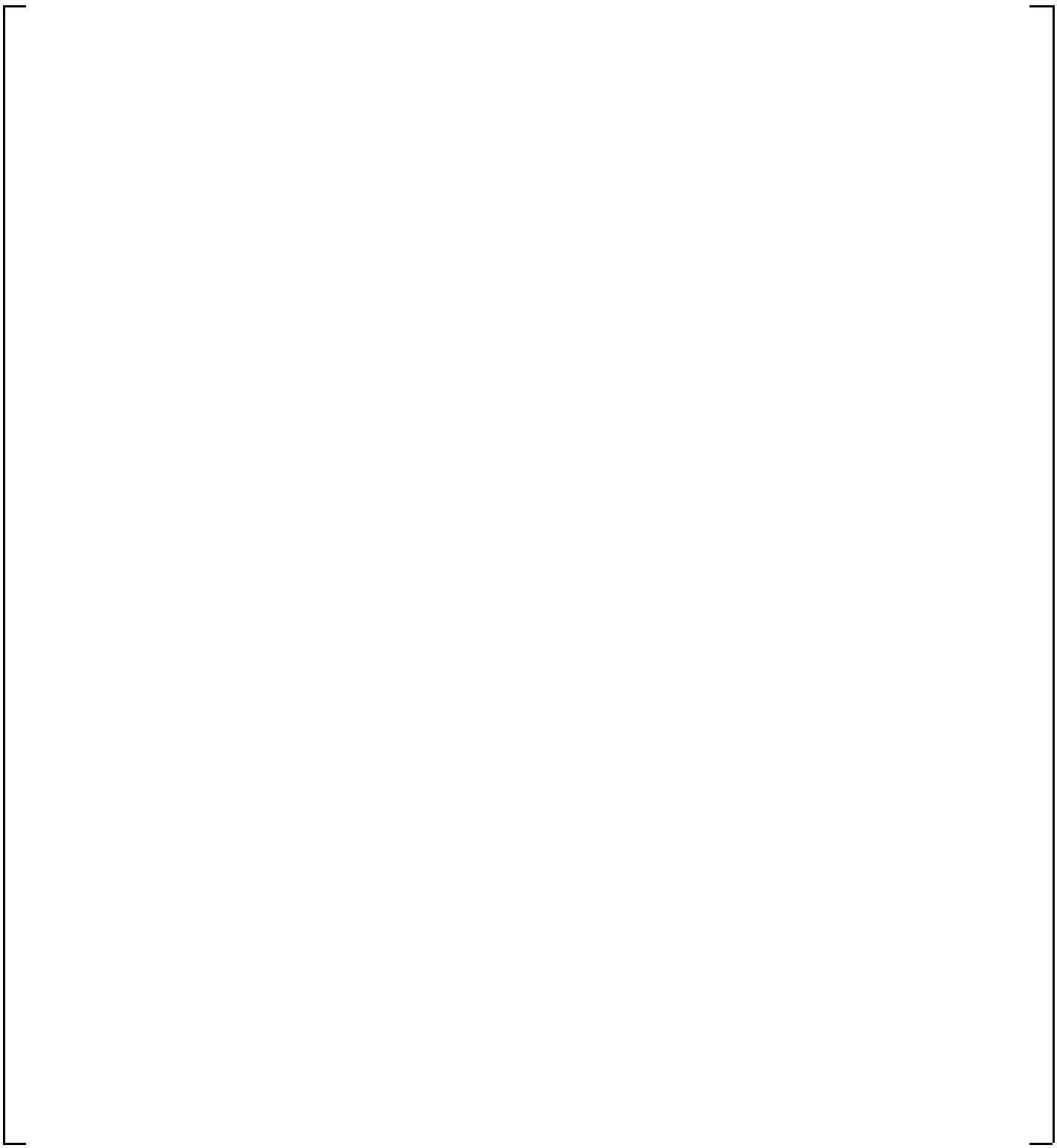

Figure 13.4.2-22 Comparison of Predicted and Measured Void Profiles for YDRAG Sensitivity Study, ORNL – THTF Test 3.09.10AA

a,c

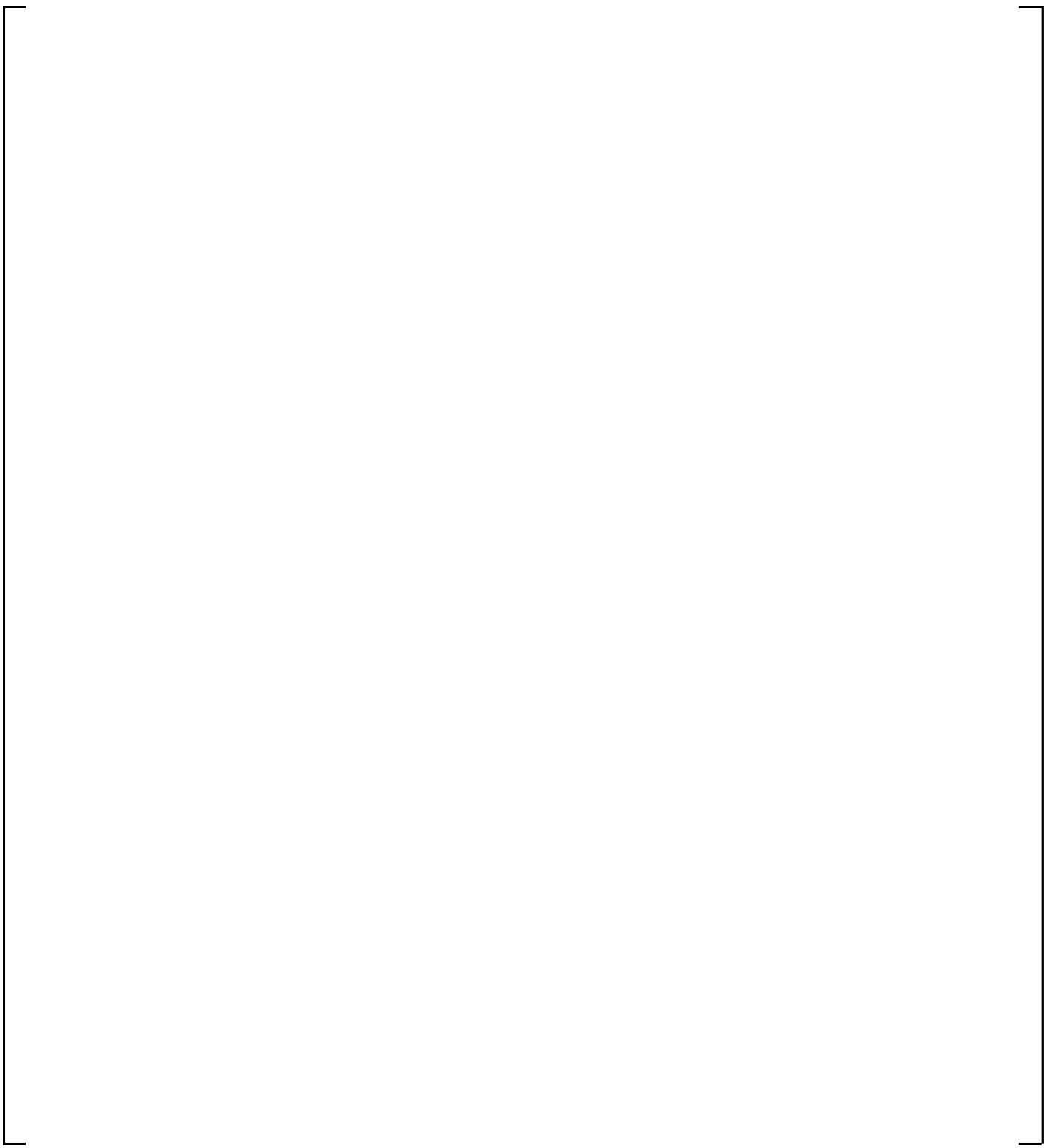

Figure 13.4.2-23 Comparison of Predicted and Measured Void Profiles for YDRAG Sensitivity Study, ORNL – THTF Test 3.09.10BB

a,c

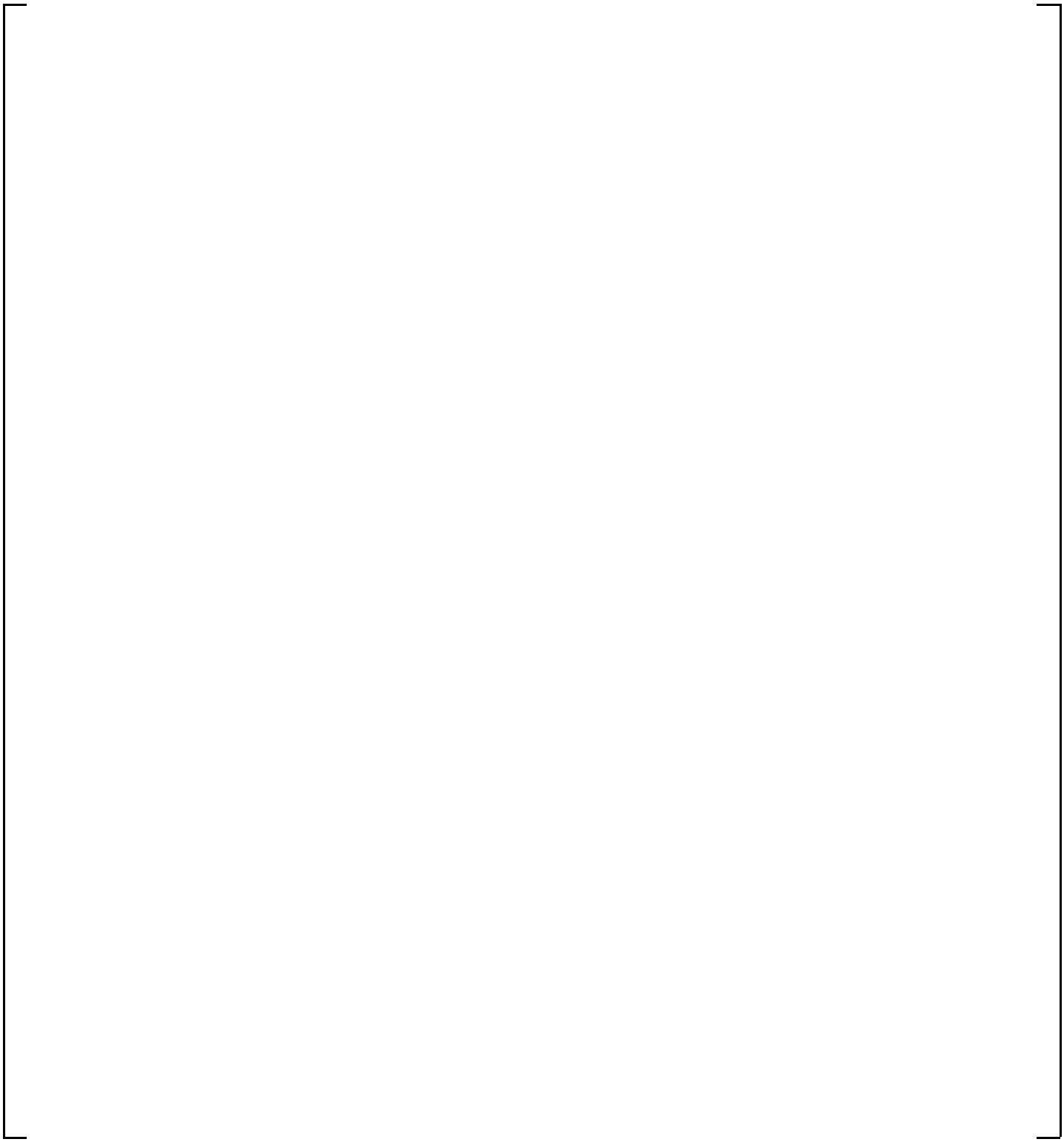

Figure 13.4.2-24 Comparison of Predicted and Measured Void Profiles for YDRAG Sensitivity Study, ORNL – THTF Test 3.09.10CC

a,c

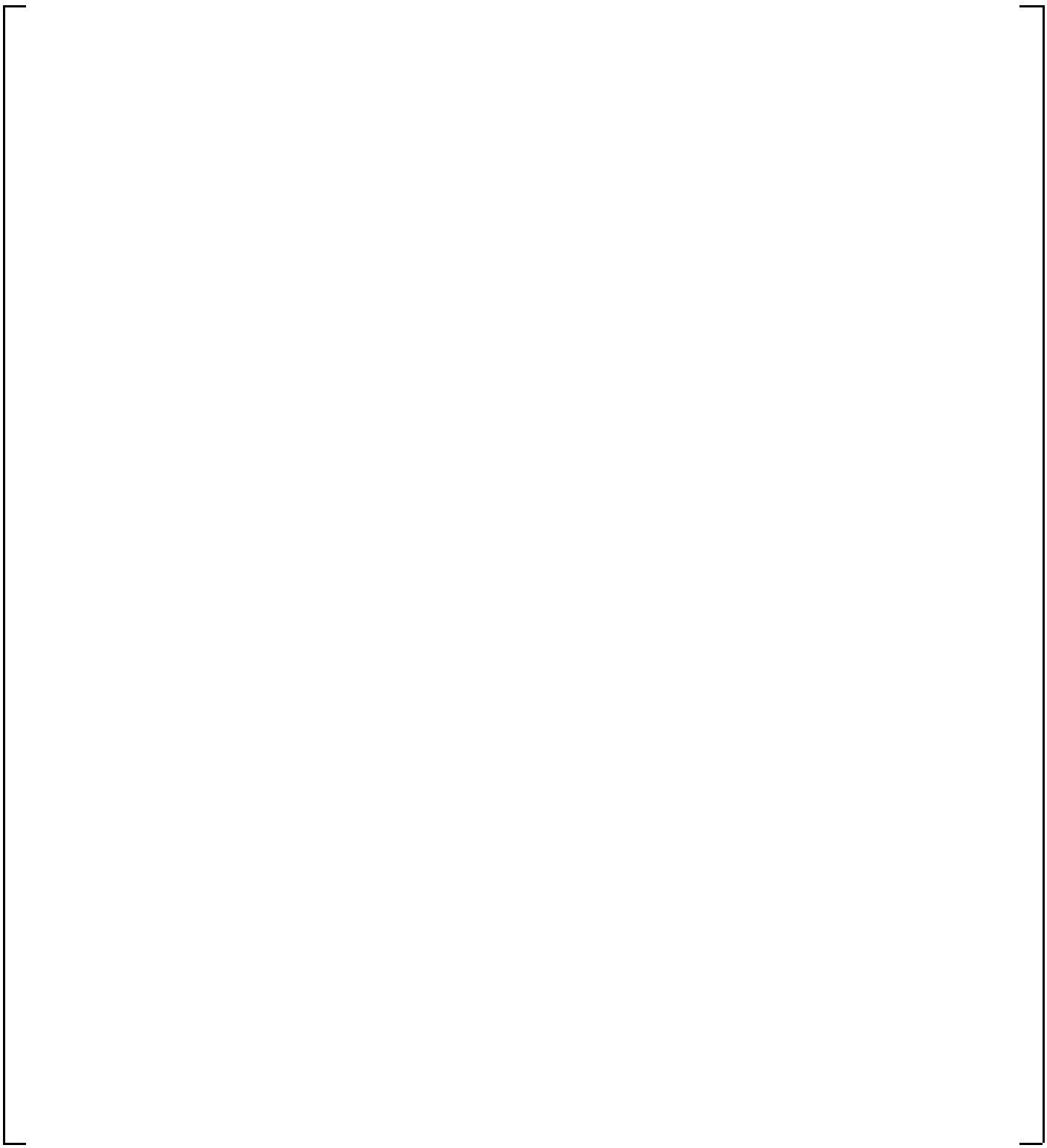

Figure 13.4.2-25 Comparison of Predicted and Measured Void Profiles for YDRAG Sensitivity Study, ORNL – THTF Test 3.09.10DD

a,c

Figure 13.4.2-26 Comparison of Predicted and Measured Void Profiles for YDRAG Sensitivity Study, ORNL – THTF Test 3.09.10EE

a,c

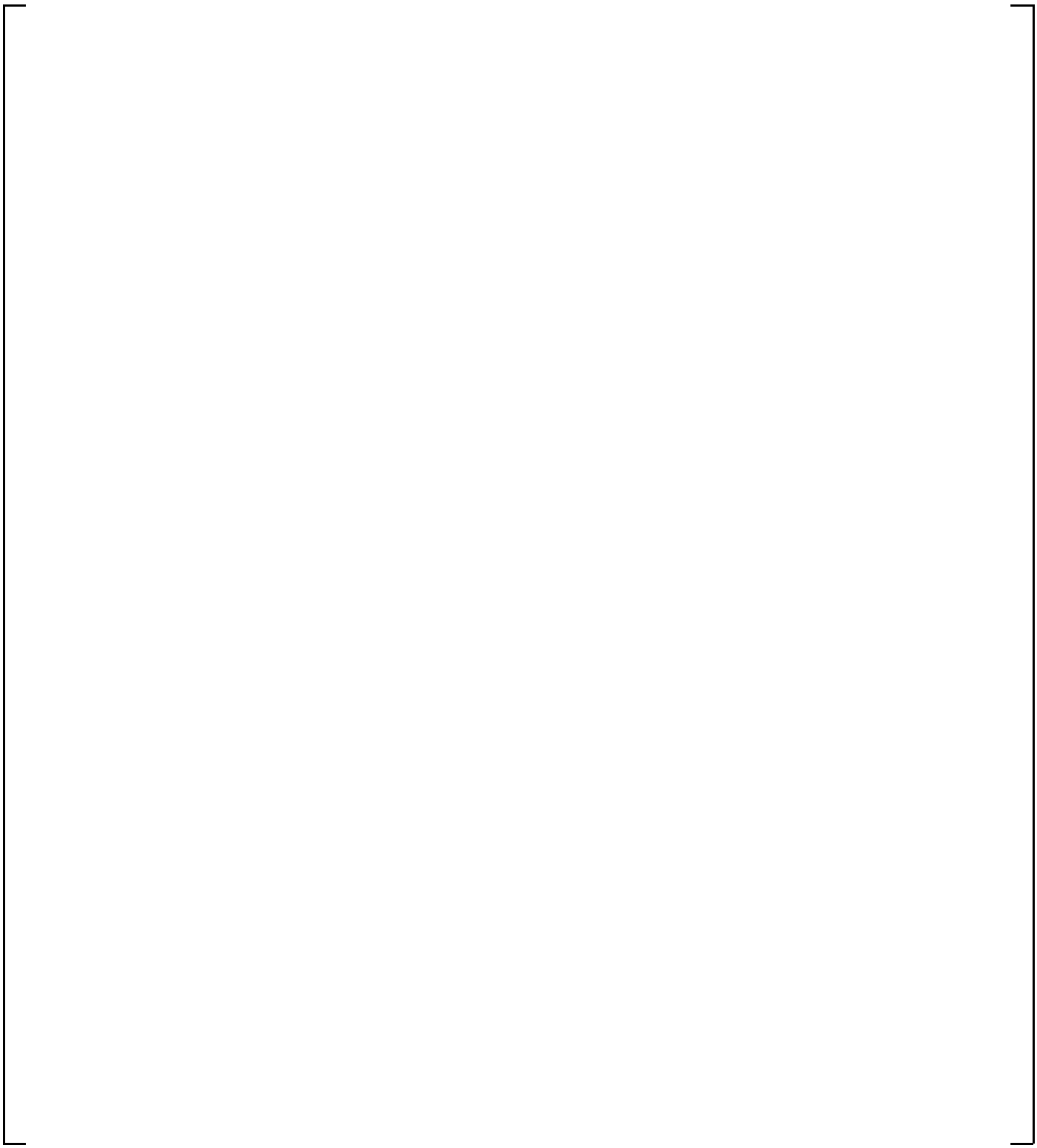

Figure 13.4.2-27 Comparison of Predicted and Measured Void Profiles for YDRAG Sensitivity Study, ORNL – THTF Test 3.09.10FF

13.4.3 Simulation of G-1 Core Uncovery Tests

13.4.3.1 Introduction

A series of core uncovery experiments was conducted in the Westinghouse Emergency Core Cooling System (ECCS) High Pressure Test Facility. These tests are pertinent to the validation of the WCOBRA/TRAC-TF2 models within the FULL SPECTRUM LOCA methodology. [

]^{b}

Additional information on the G-1 Core Uncovery Tests is contained in WCAP-9764 (Anderson, 1980).

13.4.3.2 G-1 Facility Description

[

]^{b}

[

]b

13.4.3.3 Test Matrix for G-1 Uncovery Tests

[

]b

13.4.3.4 Test Procedure for G-1 Uncovery Tests

[

]b

13.4.3.5 WCOBRA/TRAC-TF2 Model of G-1 Test Facility

[

]a,c

13.4.3.6 Simulation of G-1 Core Uncovery Tests

[

]a,b,c

13.4.3.7 Discussion of Results

[

]a,b,c

[

]a,b,c

13.4.3.8 Summary and Conclusions

[

]a,c

Table 13.4.3-1 Comparison of PWR Rod and G-1 Test Rod Bundle

a,b,c

Table 13.4.3-2 G-1 Core Uncovery Test Matrix

b

Table 13.4.3-3 G-1 Simulation Results Summary at Model Nominal YDRAG

a,b,c

Table 13.4.3-3 G-1 Simulation Results Summary at Model Nominal YDRAG (cont.)

[

a,b,c]

b

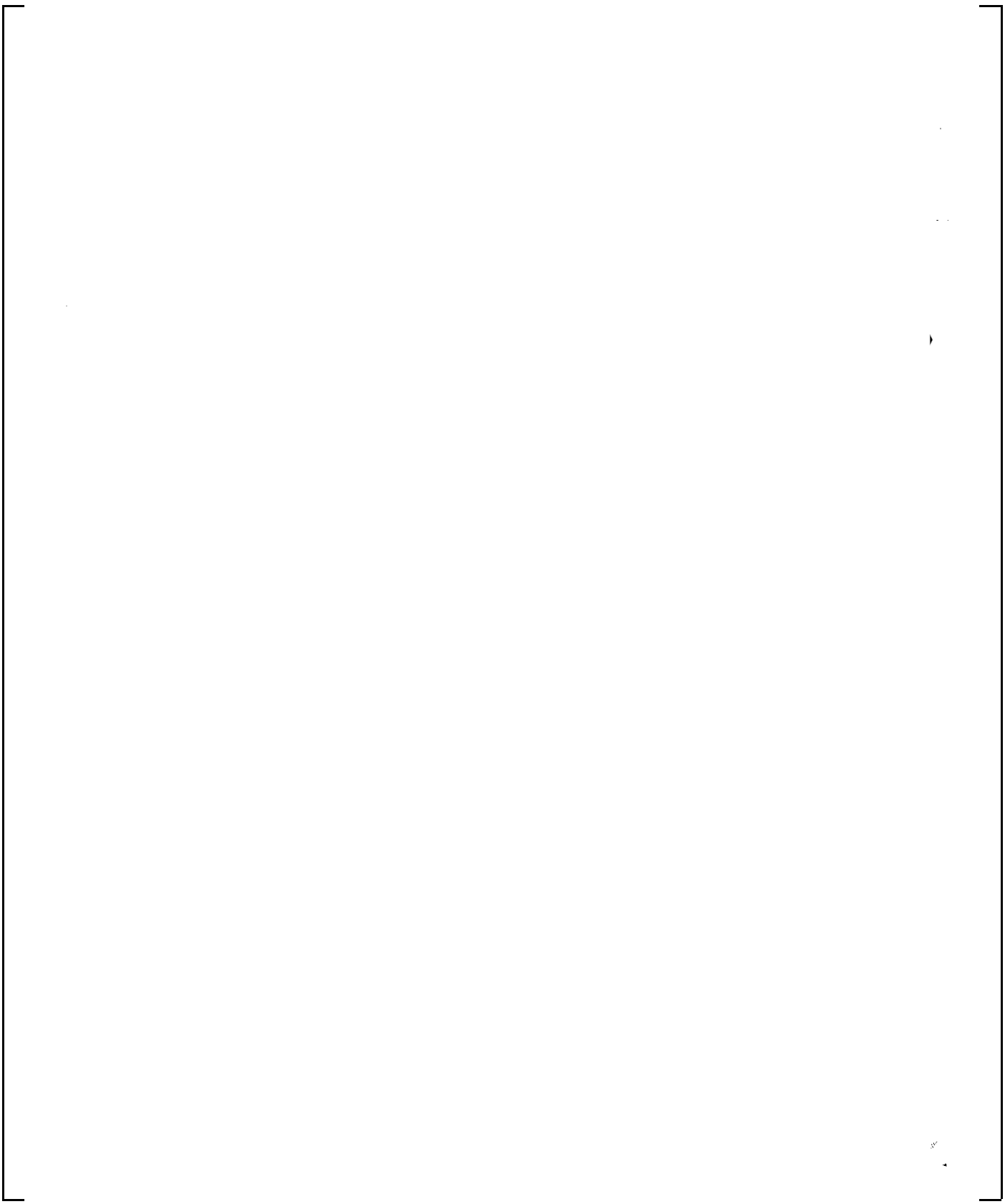

Figure 13.4.3-1 Westinghouse ECCS High Pressure Test Facility (G-1 Loop)

b

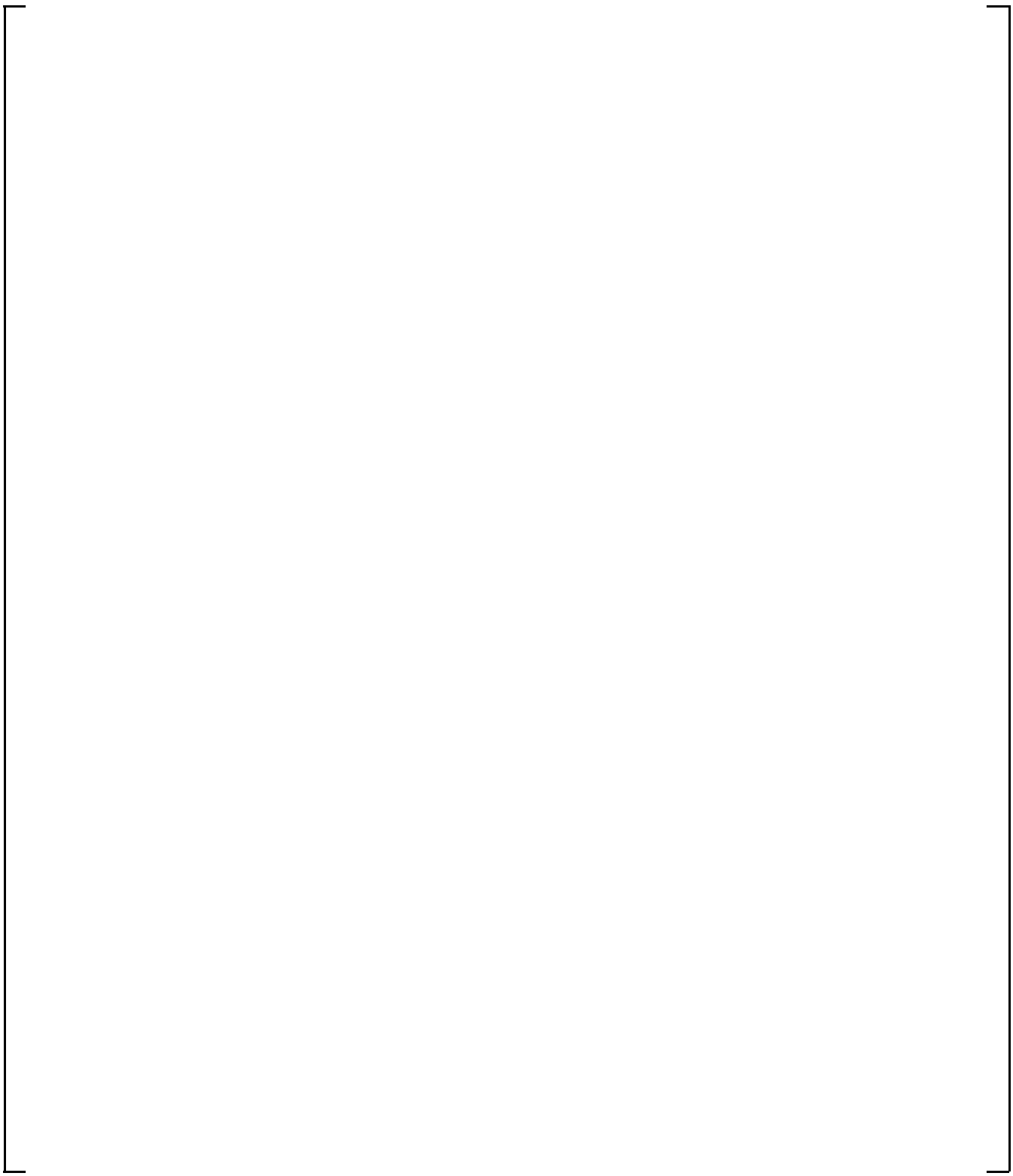

Figure 13.4.3-2 G-1 Test Vessel and Test Section

b

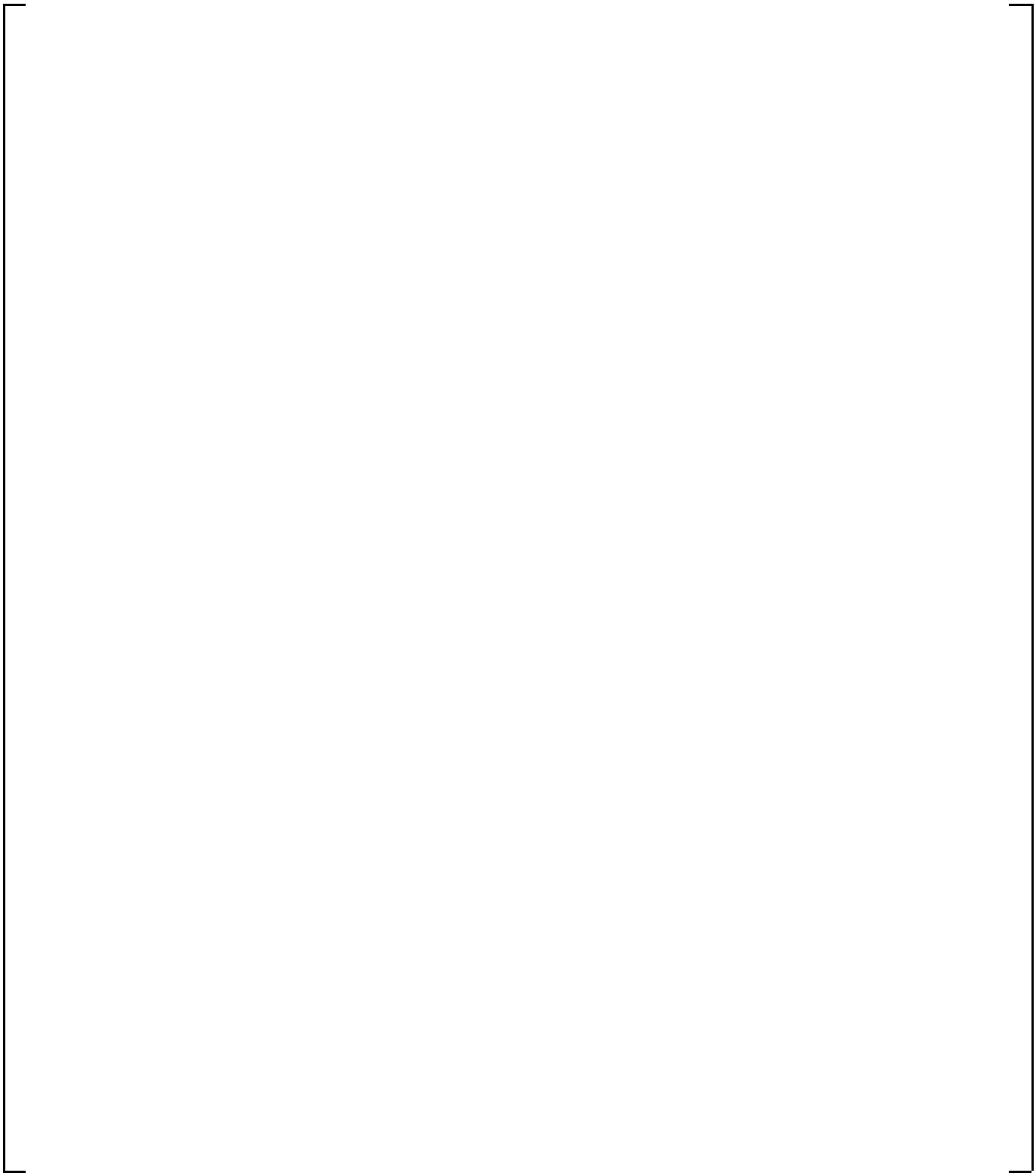

Figure 13.4.3-3A G-1 Uncovery Test Heater Rod Bundle Cross-Section

b

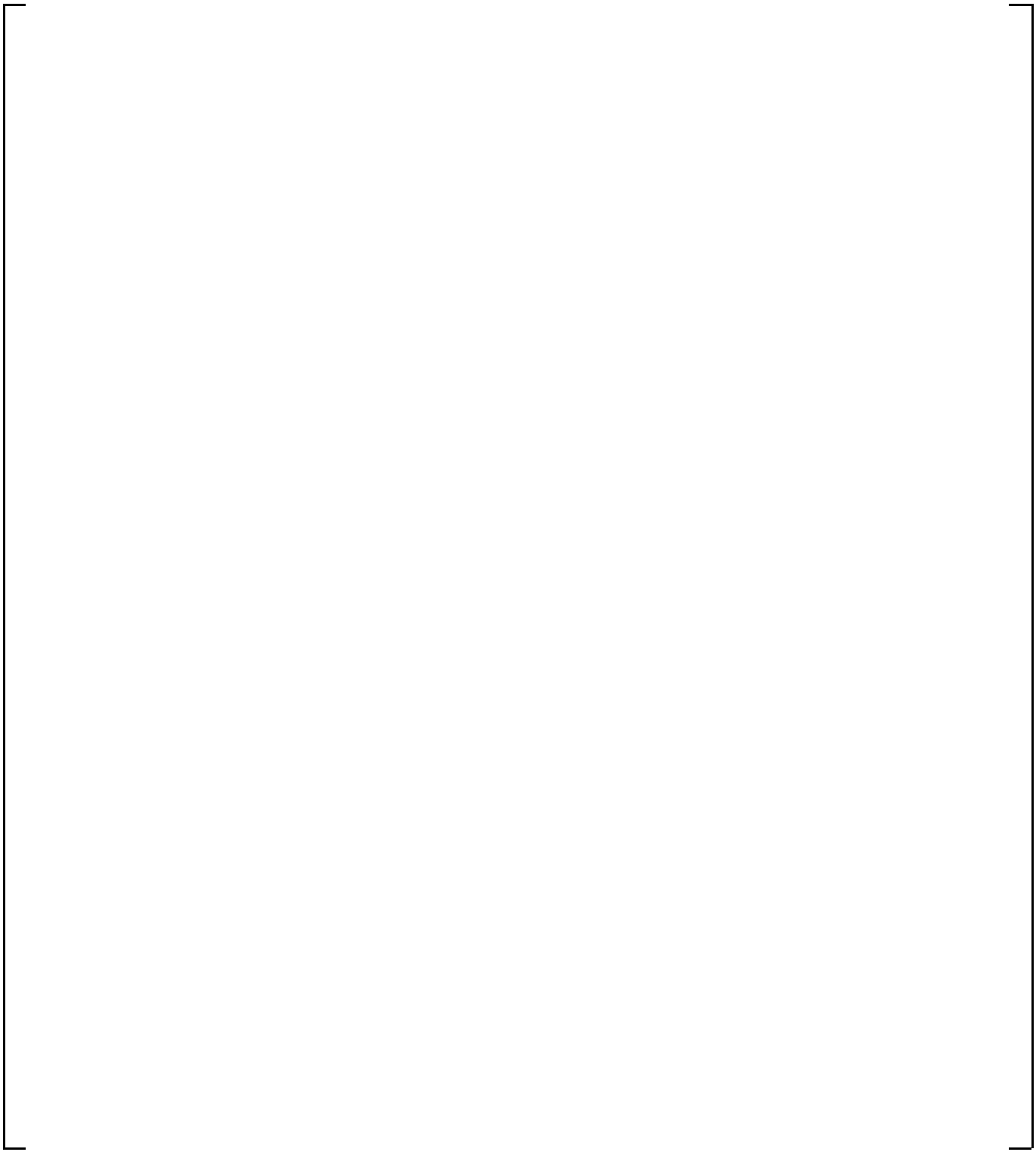

Figure 13.4.3-3B G-1 Uncovery Test Heater Rod Bundle Cross-Section

b

Figure 13.4.3-4 G-1 Facility Heater Rod

b

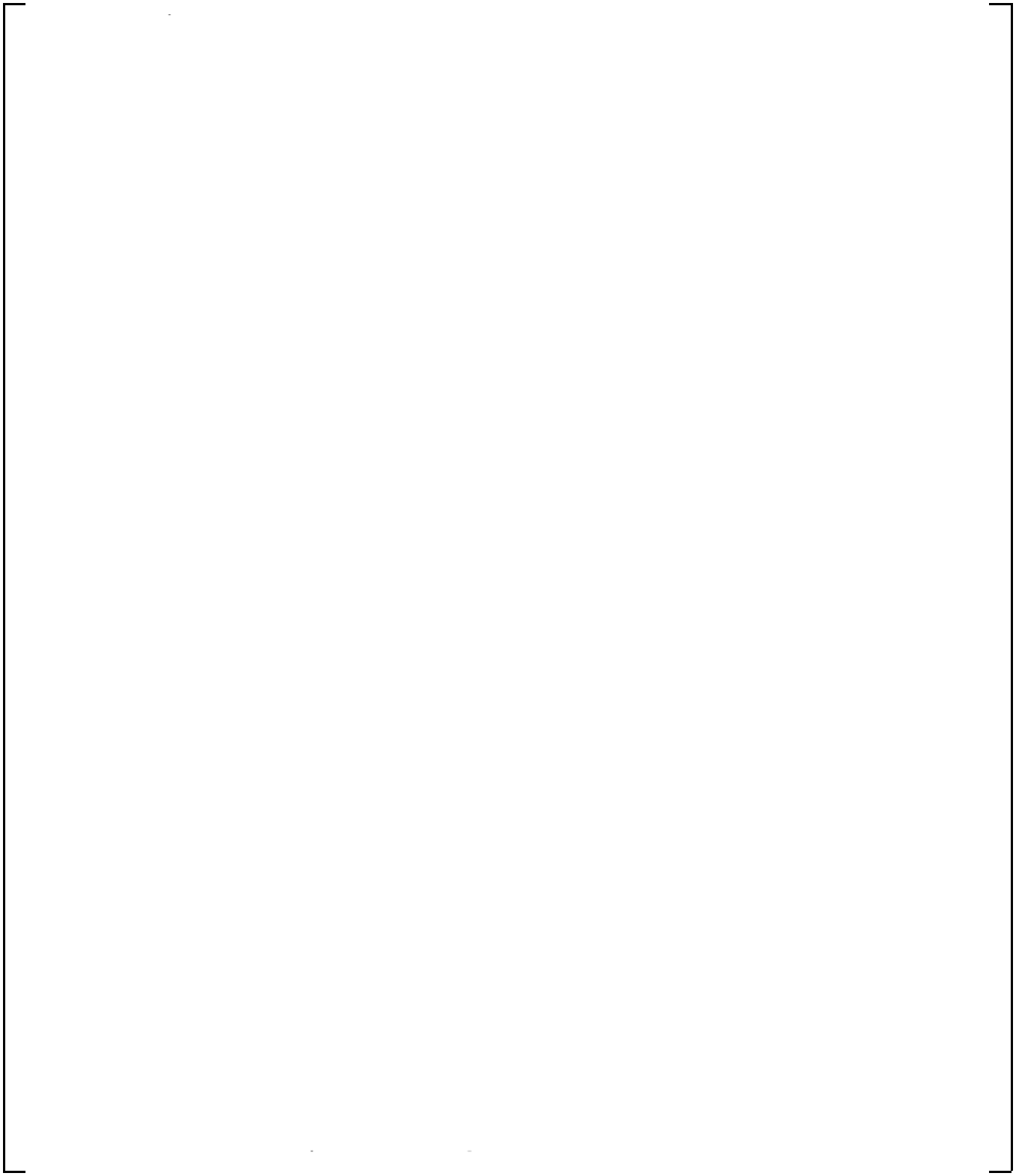

Figure 13.4.3-5 G-1 Axial Power Profile

a,c

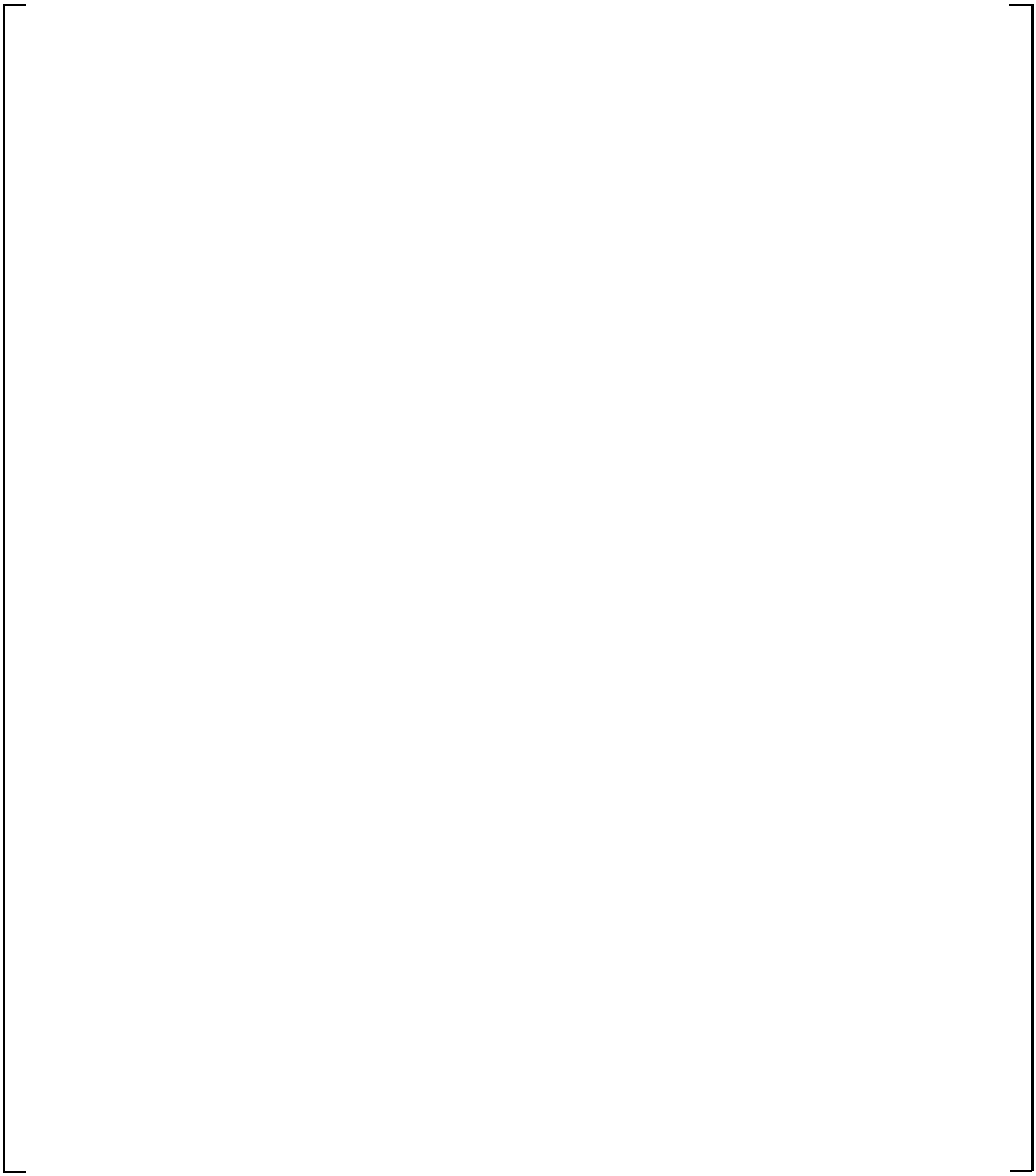

Figure 13.4.3-6 WCOBRA/TRAC-TF2 Model of the G-1 Test Bundle

a,c

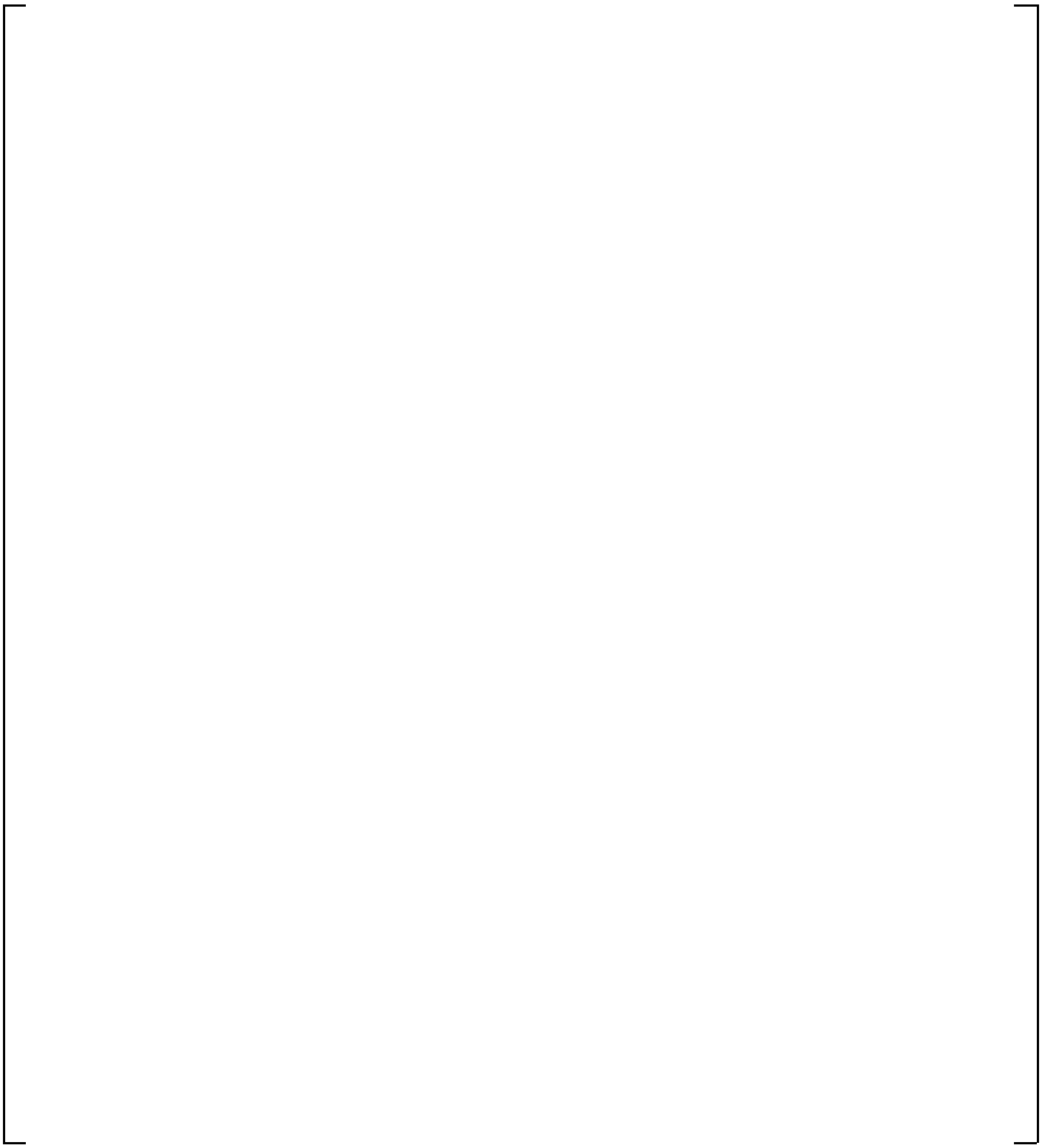

Figure 13.4.3-7 Collapsed Liquid Level and Predicted Cladding Temperatures at the 8- and 10- Foot Elevations, G-1 Test 62

a,c

Figure 13.4.3-8 Void Fraction and Predicted Cladding Temperature at the 10- Foot Elevation, G-1 Test 62

a,c

Figure 13.4.3-9 Comparison of Predicted and Measured Mixture Level Swell for G-1 Bundle Uncovery Tests at Model Nominal YDRAG

a,c

Figure 13.4.3-10 Predicted Over Measured Level Swell versus Bundle Power for G-1 Bundle Uncovery Tests

a,c

Figure 13.4.3-11 Predicted Over Measured Level Swell versus Pressure for G-1 Bundle Uncovery Tests

a,c

Figure 13.4.3-12 Predicted Over Measured Level Swell versus Bundle Elevation for G-1 Bundle Uncovery Tests

13.4.4 Simulation of G-2 Core Uncovery Tests

13.4.4.1 Introduction

The G-2 test facility is designed to provide data for downflow film boiling, reflood heat transfer, and core uncovery over a range of power, flow, temperature, and pressure conditions that simulate PWR large break and small break LOCAs. The core uncovery tests conducted at this facility are particularly relevant to the validation of the WCOBRA/TRAC-TF2 mixture level swell prediction; and are therefore the primary topic of this section.

Additional information on the G-2 Core Uncovery Tests is contained in EPRI NP-1692 (Andreychek, 1981).

13.4.4.2 G-2 Facility Description

[

]^{b}

[

]b

[

]b

13.4.4.3 Test Matrix for G-2 Uncovery Tests

[

]a,b,c

13.4.4.4 Test Procedure for G-2 Uncovery Tests

[

]b

[

]b

13.4.4.5 WCOBRA/TRAC-TF2 Model of G-2 Test Facility

Figure 13.4.4-6 shows the WCOBRA/TRAC-TF2 model for the G-2 test bundle. [

]a,b,c

[

]a,b,c

13.4.4.6 Simulation of G-2 Uncovery Tests

[

]a,b,c

13.4.4.7 Discussion of Results

[

]a,c

[

]a,c

13.4.4.8 Summary and Conclusions

[

]a,c

Table 13.4.4-1 Comparison of 17x17-XL PWR Rod and Test Rod Bundle

a,b,c

Table 13.4.4-2 G-2 Loop Core Uncovery Test Vessel Flow Areas

b

Table 13.4.4-3 G-2 Core Uncovery Test Matrix

b

Table 13.4.4-4 G-2 Simulation Results Summary at Model Nominal YDRAG

a,b,c

Table 13.4.4-4 G-2 Simulation Results Summary at Model Nominal YDRAG (cont.)

a,b,c

Table 13.4.4-5 YDRAG Values to Match G-2 Level Swell Data

a,b,c

b

Figure 13.4.4-1 G-2 Test Facility Flow Schematic

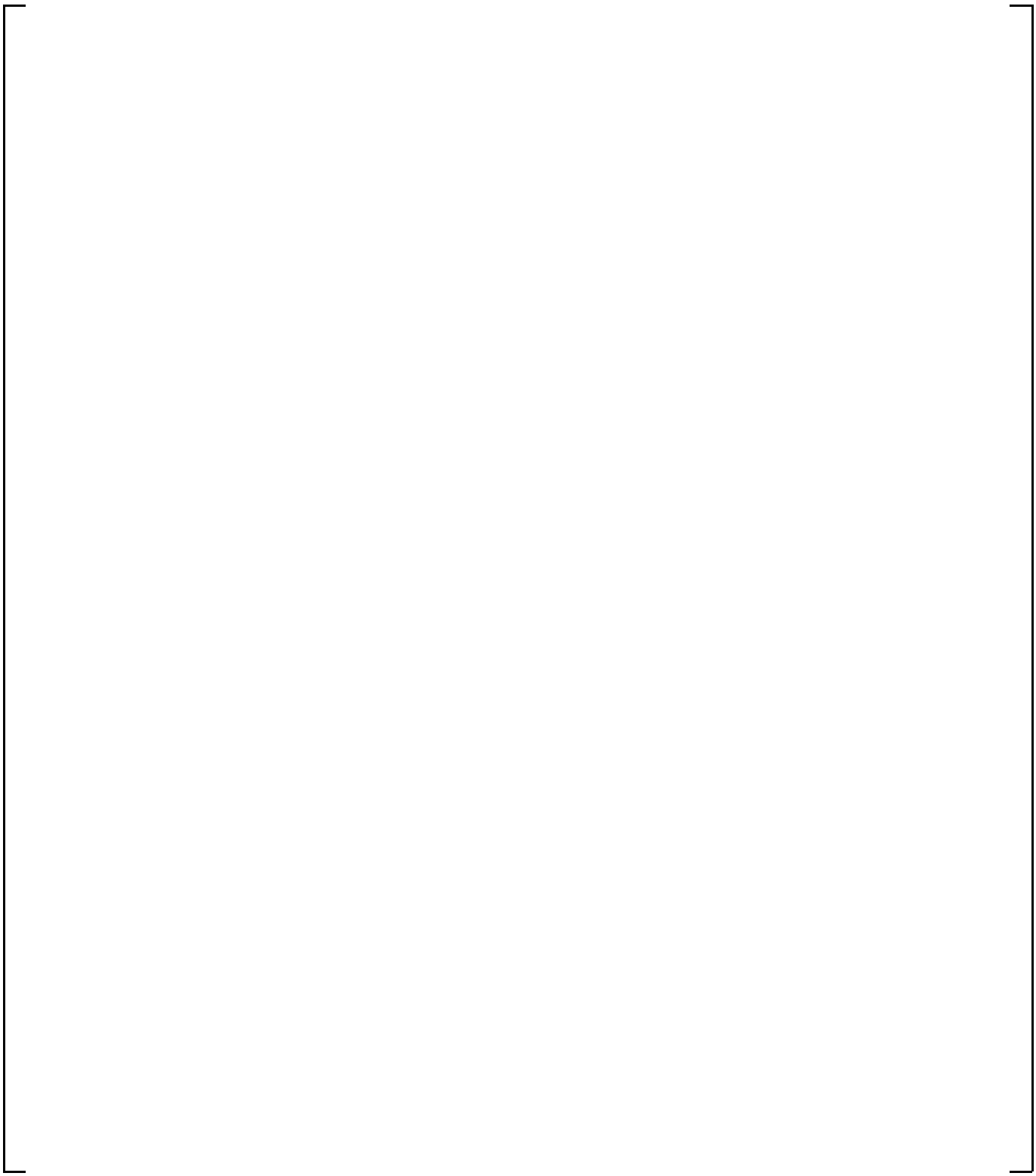

b

Figure 13.4.4-2 G-2 Test Vessel and Test Section

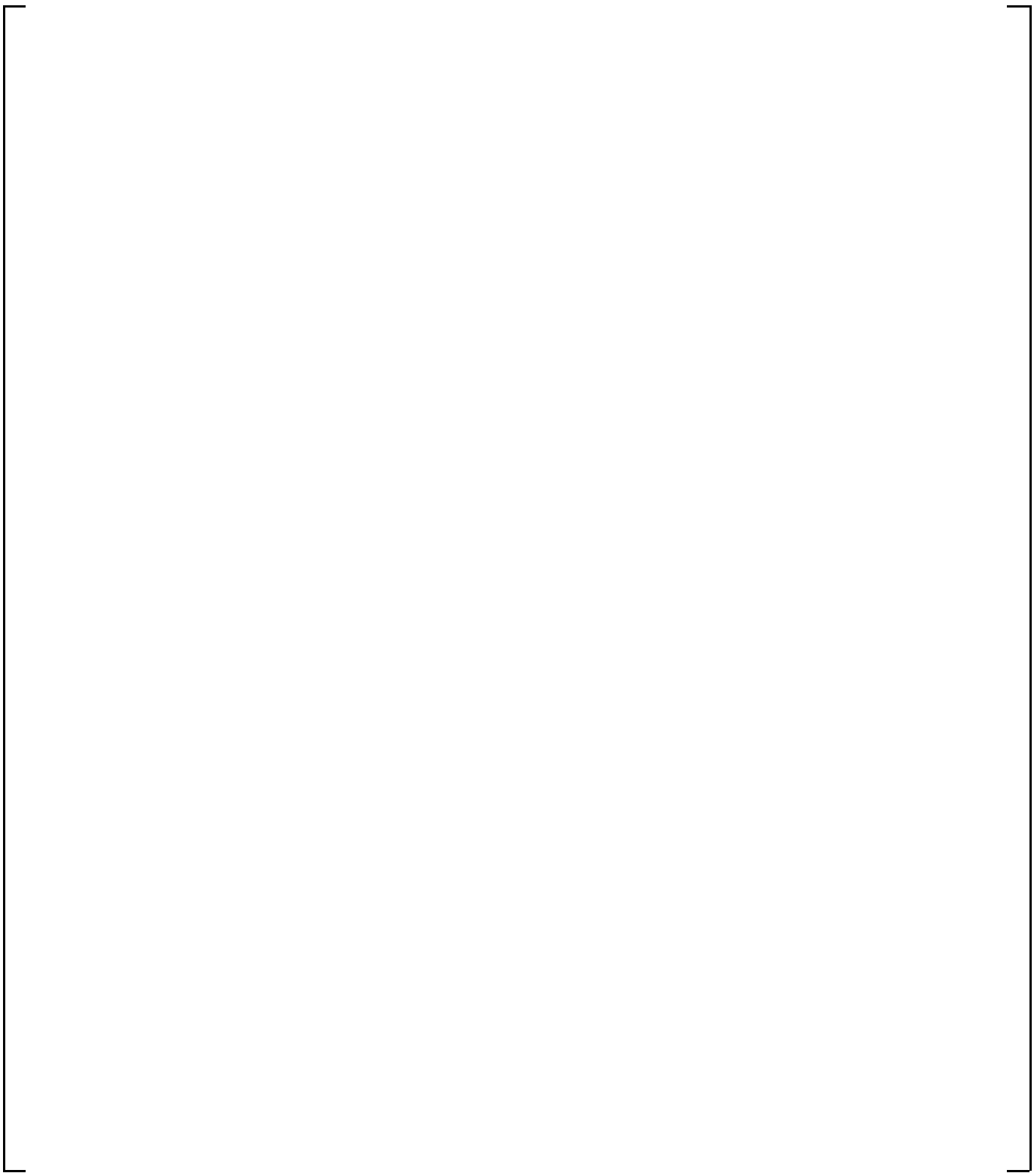

b

Figure 13.4.4-3 G-2 Rod Bundle, Baffle Cross Section, and Bundle Instrumentation

b

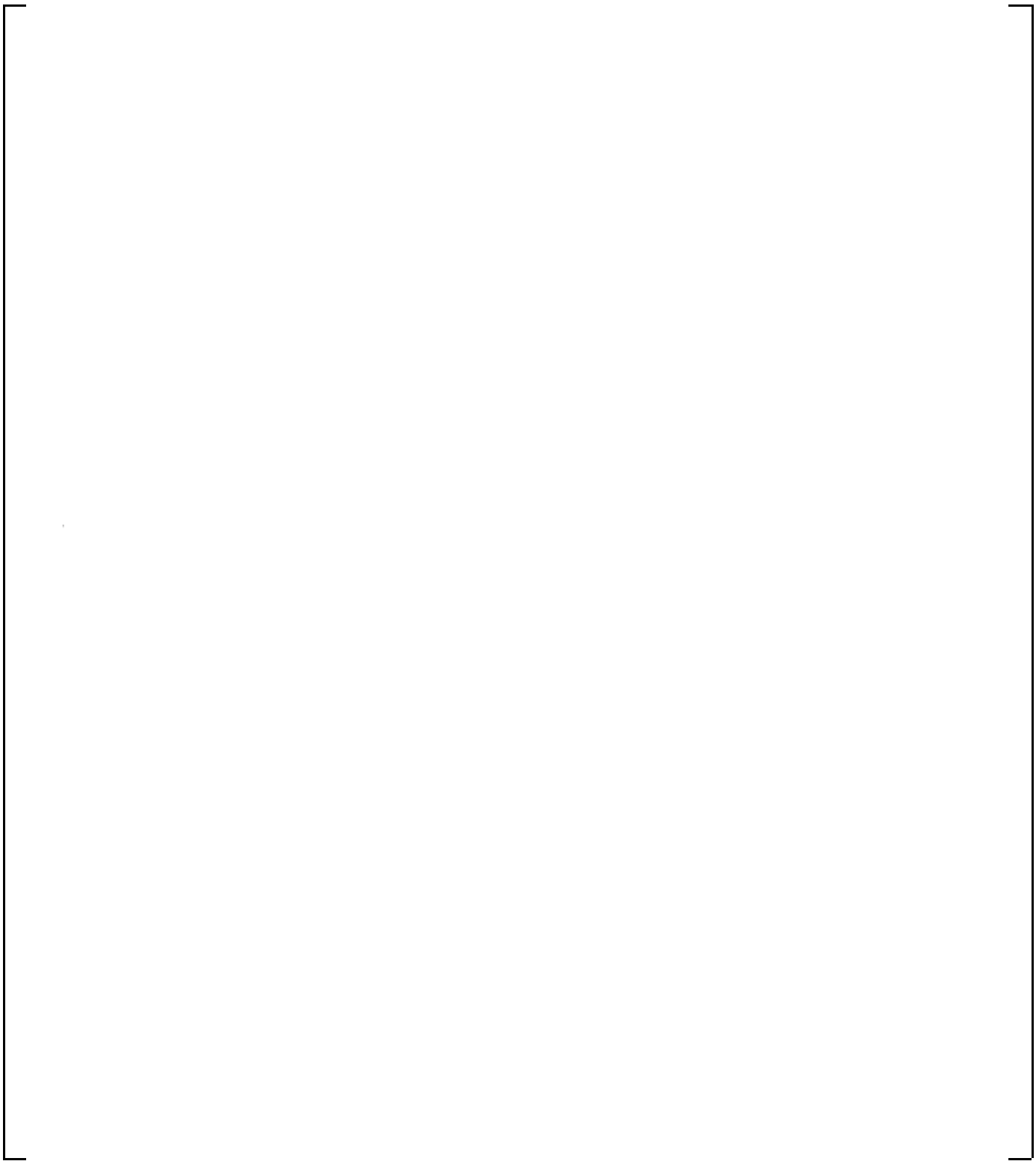

Figure 13.4.4-4 G-2 Facility Heater Rod

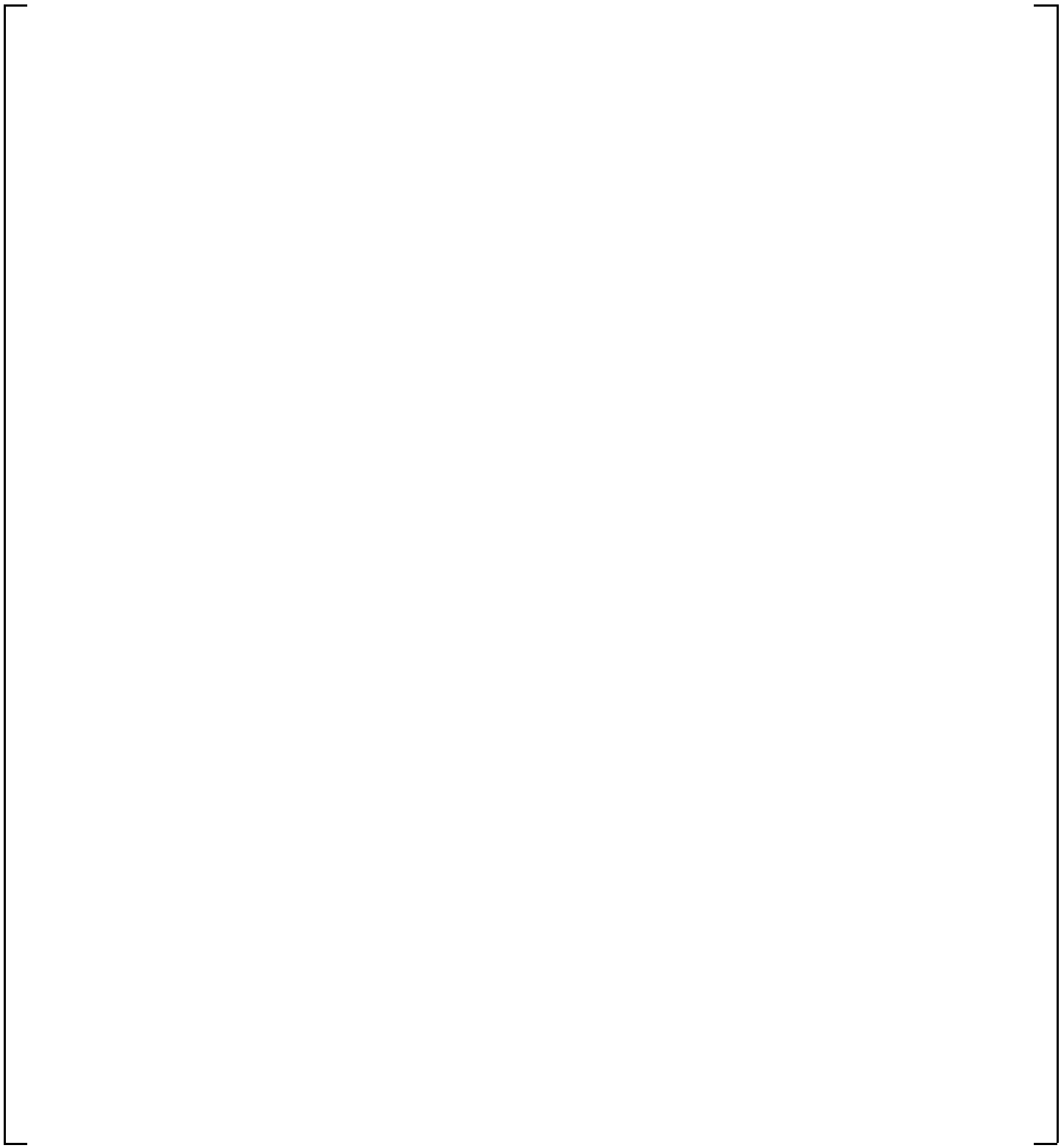

Figure 13.4.4-5 G-2 Facility Axial Power Profile

a,c

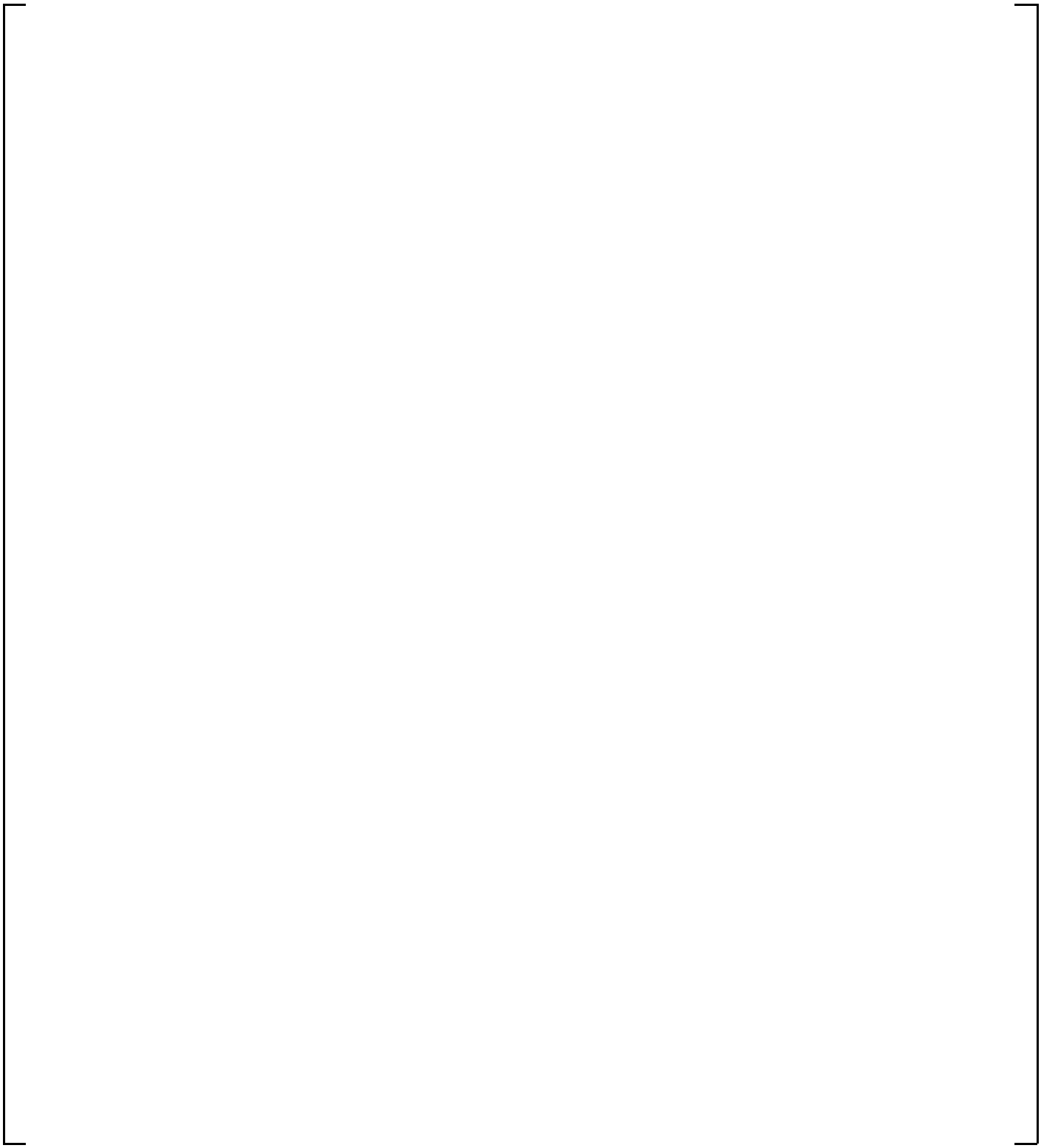

Figure 13.4.4-6 WCOBRA/TRAC-TF2 Model of the G-2 Test Bundle

a,c

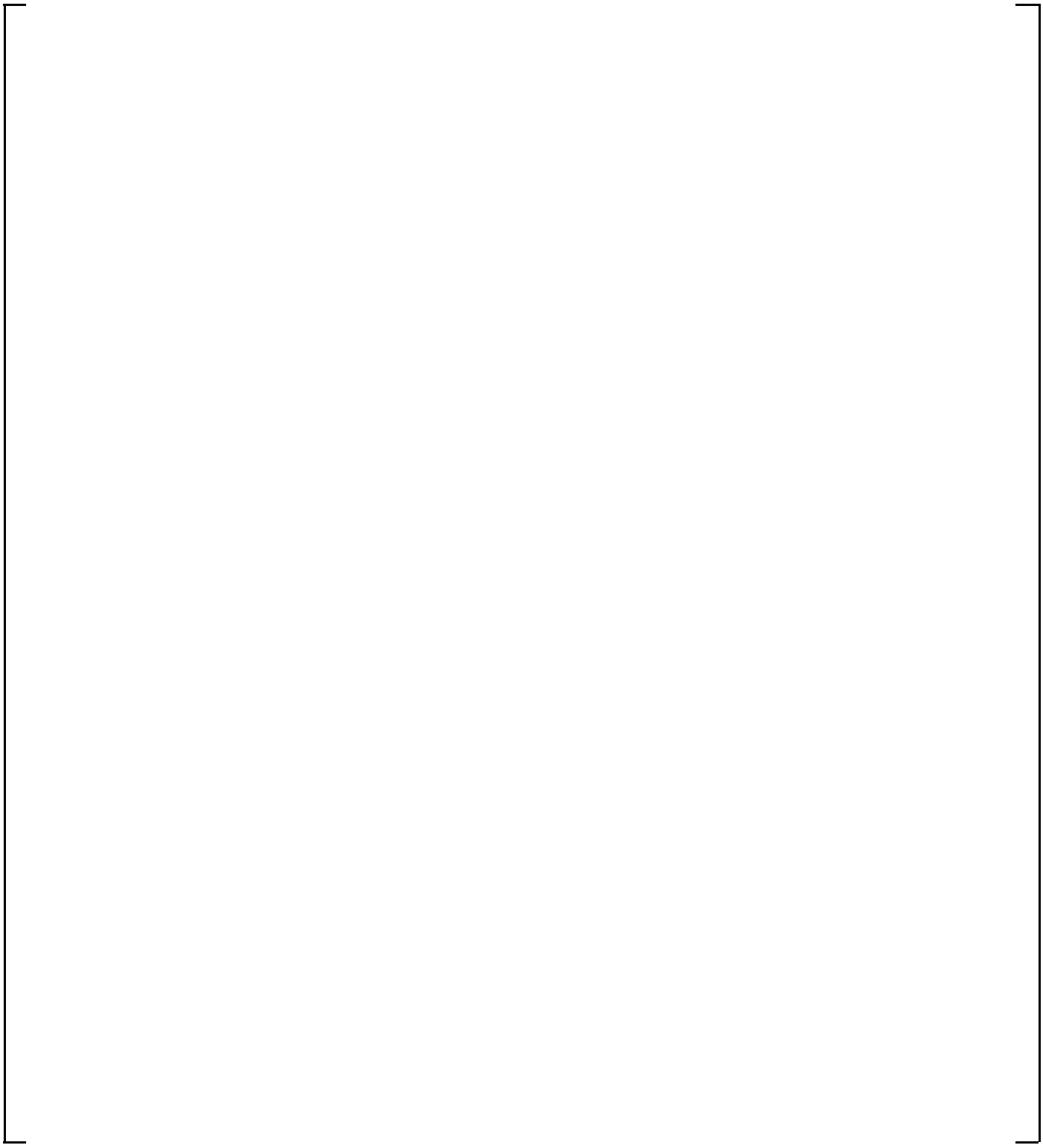

Figure 13.4.4-7 Collapsed Liquid Level and Predicted Cladding Temperatures at the 8- and 10- Foot Elevations, G-2 Test 716

a,c

Figure 13.4.4-8a Comparison of Predicted and Measured Mixture Level Swell for G-2 Bundle Uncovery Tests at Model Nominal YDRAG (All Cases)

a,c

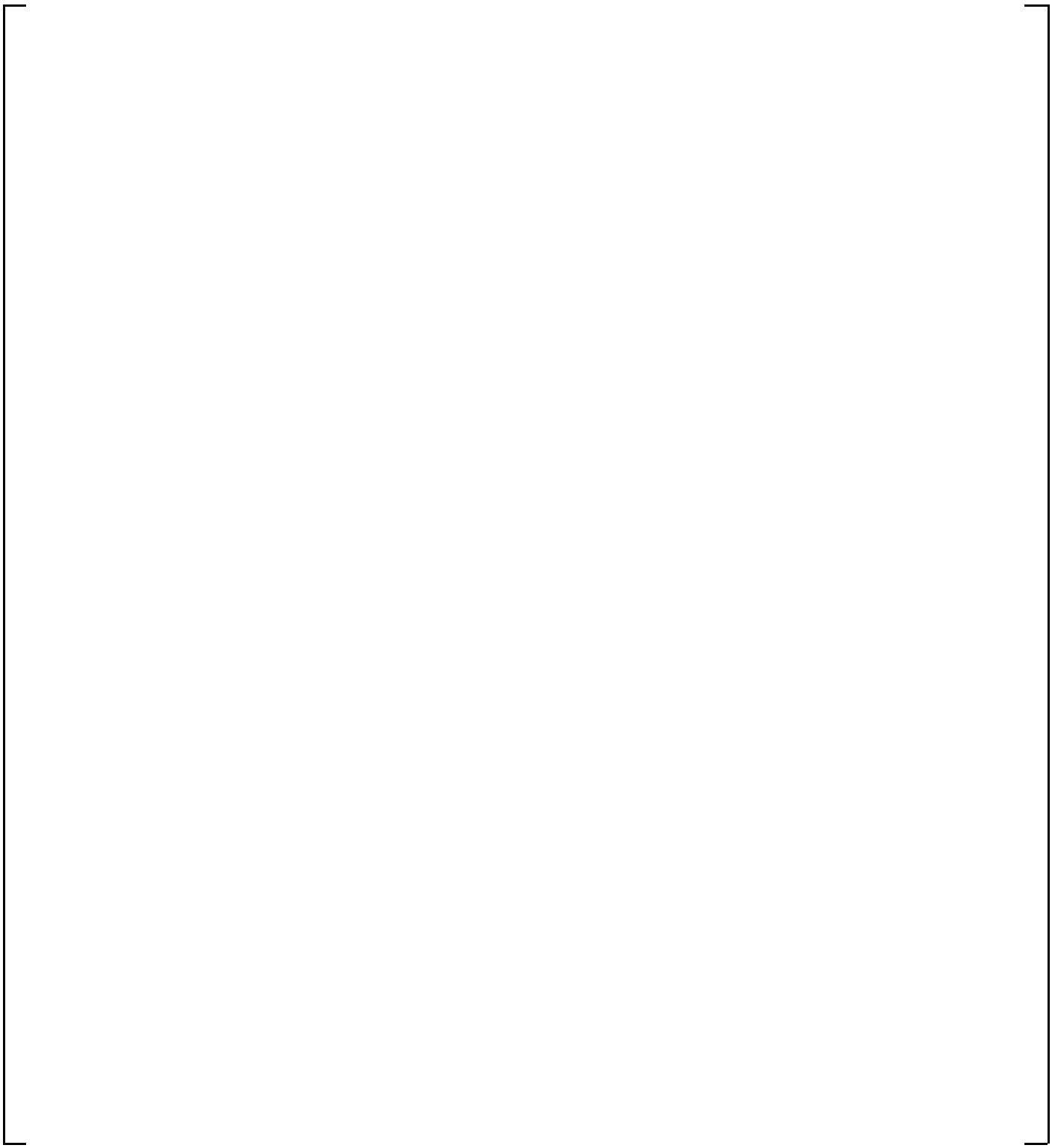

Figure 13.4.4-8b Comparison of Predicted and Measured Mixture Level Swell for G-2 Bundle Uncovery Tests at Model Nominal YDRAG (Higher Pressure Cases)

a,c

Figure 13.4.4-8c Comparison of Predicted and Measured Mixture Level Swell for G-2 Bundle Uncovery Tests at Model Nominal YDRAG (Lower Pressure Cases)

a,c

Figure 13.4.4-9 Predicted Over Measured Level Swell versus Peak Linear Heat Rate for G-2 Bundle Uncovery Tests

a,c

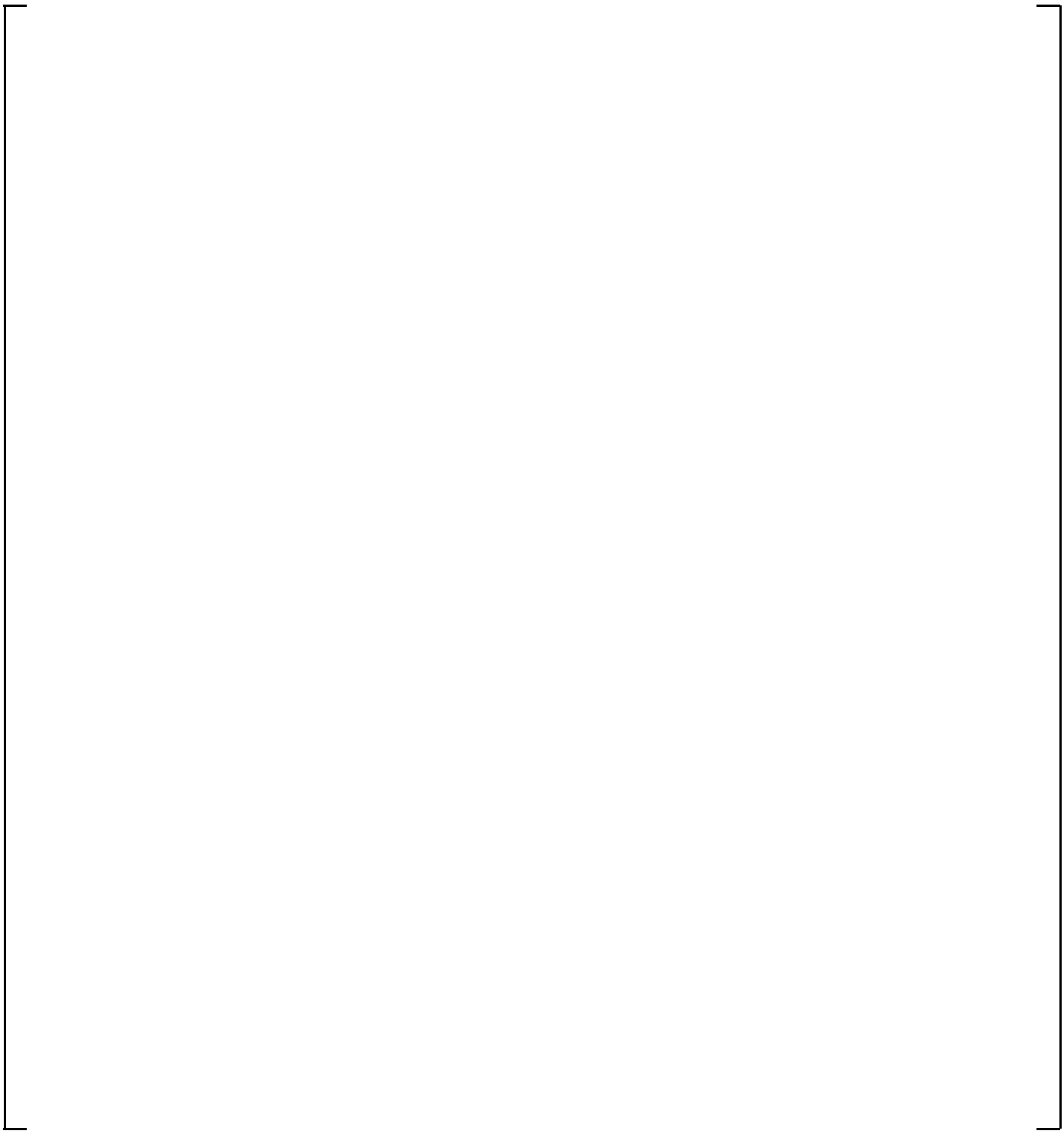

Figure 13.4.4-10a Predicted Over Measured Level Swell versus Pressure for G-2 Bundle Uncovery Tests (All Cases)

a,c

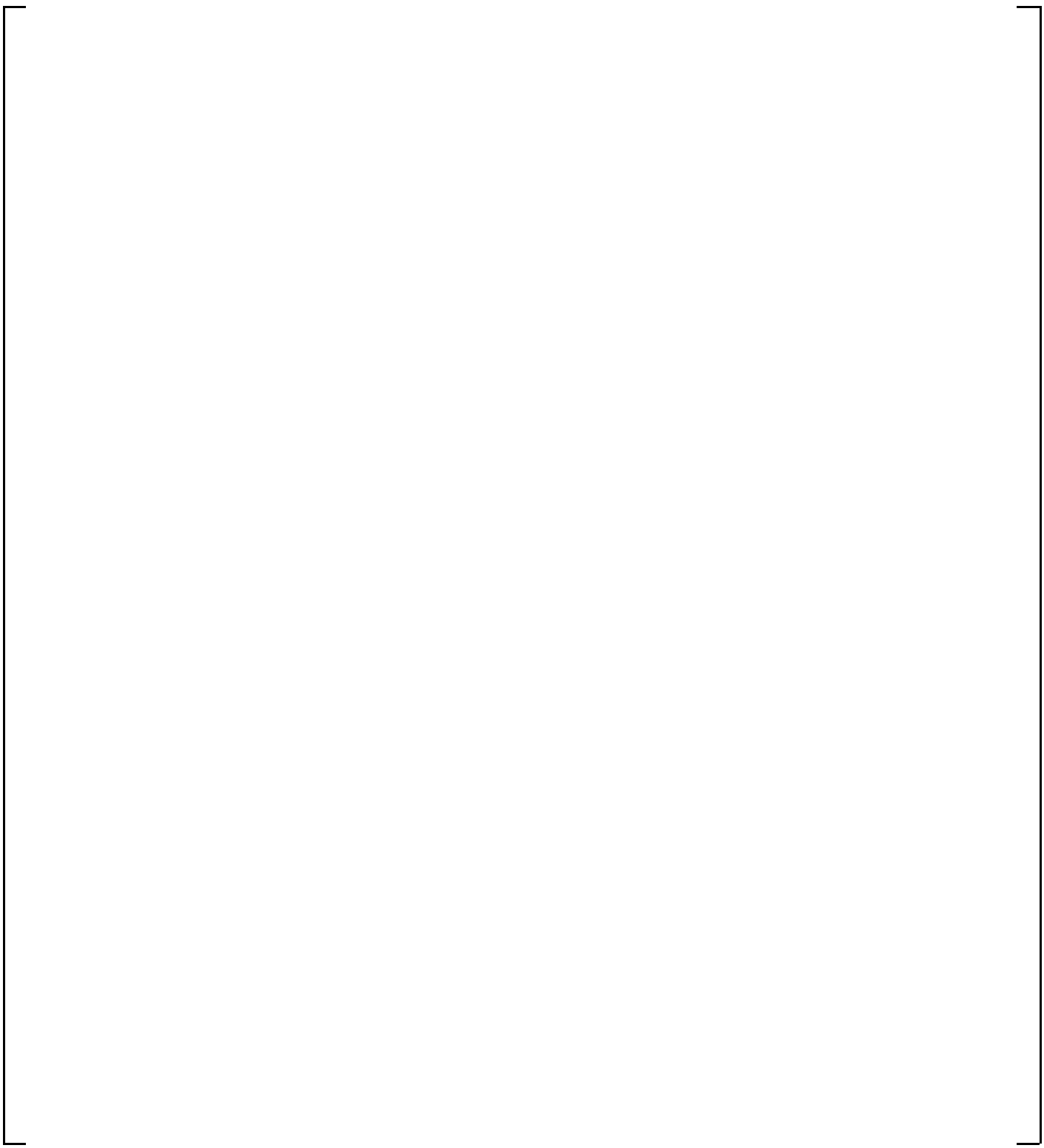

Figure 13.4.4-10b Predicted Over Measured Level Swell versus Pressure for G-2 Bundle Uncovery Tests (without 800 psia Cases)

a,c

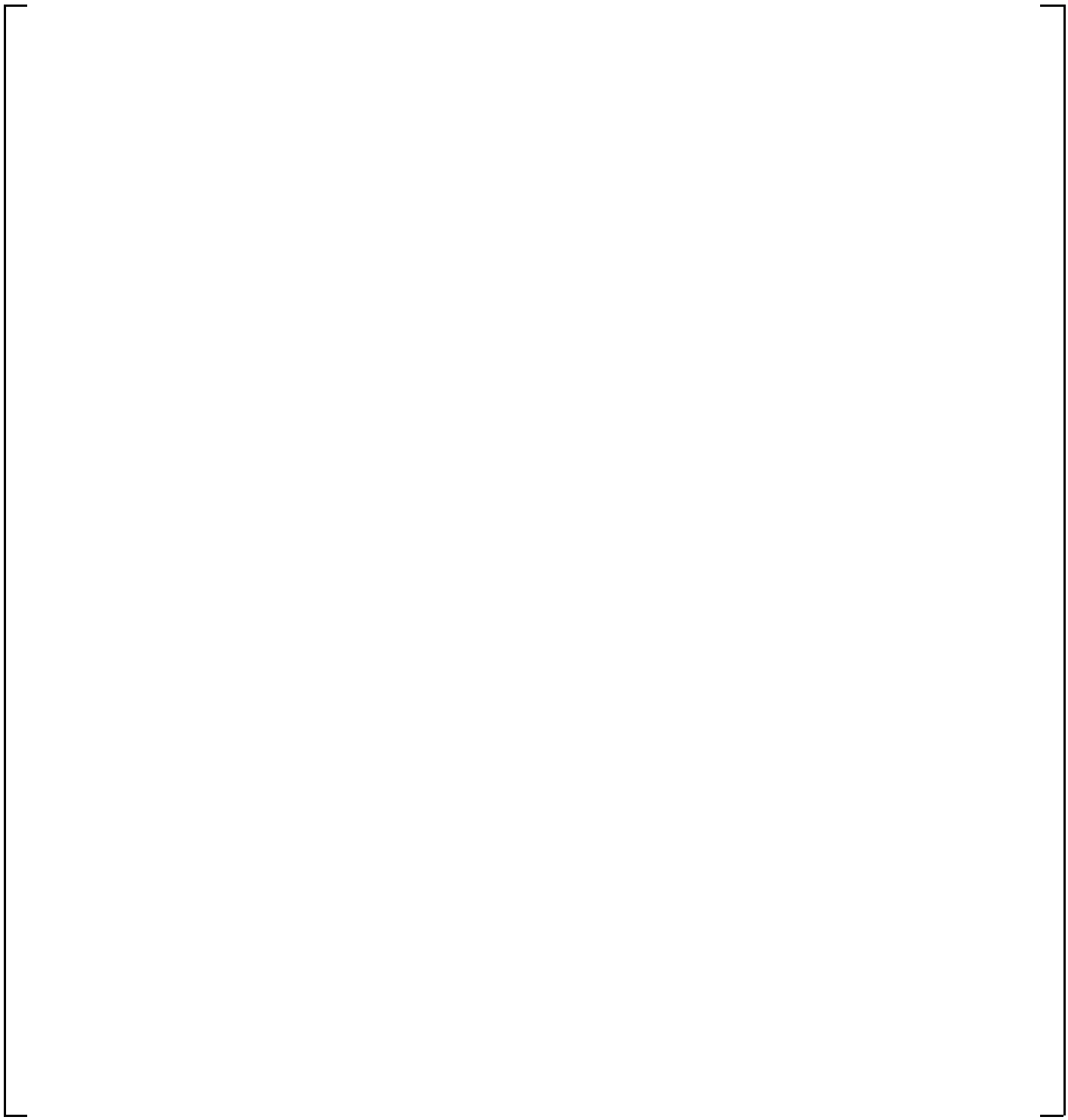

Figure 13.4.4-11 Predicted Over Measured Level Swell versus Bundle Elevation for G-2 Bundle Uncovery Tests

13.4.5 JAERI-TPTF Rod Bundle Tests

13.4.5.1 Introduction

The TPTF is a separate effect test facility built to study small break LOCA thermal-hydraulic behavior. In particular, the heat transfer and critical heat flux (CHF) point in typical SBLOCA conditions were studied. In these tests, the experiment was continued until a steady-state condition was reached in the uncovered part of the bundle and rods were heated to a high temperature. For these tests, the critical heat flux elevation was obtained.

Additional information on the JAERI-TPTF uncovered bundle heat transfer and critical heat flux elevation tests is contained in JAERI-M 93-238 (Guo et al., 1993).

The JAERI-TPTF rod bundle tests are CHF elevation tests, but cannot be considered level swell tests since no void fraction or collapsed liquid level information is available for these tests. However, the JAERI-TPTF tests are **[**

][a,c]

13.4.5.2 JAERI-TPTF Facility Description

The TPTF was a high pressure rod bundle thermal-hydraulics loop. The bundle was approximately full height for a typical PWR, and contained 25 heated rods in a 5x5 array.

Figure 13.4.5-1 contains a cross-section of the TPTF test bundle. The 25 heated rods were arranged in a square lattice with a pitch of 0.636 inches, and a rod outer diameter (OD) of 0.483 inches. The bundle had a heated length of 145.7 inches, which contained six spacer grids. Ninety-nine (99) thermocouples to measure rod surface temperature were located at 11 different axial elevations on 9 rods. Both the axial and lateral power profiles were uniform for the critical heat flux tests.

Figure 13.4.5-2 shows a flow diagram of the TPTF. The steam drum produces high-pressure saturated water and steam. The steam and water are pumped separately into a mixer at the inlet of the test section. The steam and water flow rates are measured using orifice flowmeters located upstream of the mixer. The pressure and temperature of the mixed fluid are measured at the test section inlet. This two-phase mixture flows into the test section, is heated by the rods, and then exits and returns to the steam drum.

13.4.5.3 Test Matrix for JAERI-TPTF Simulations

Eighteen critical heat flux experiments were conducted at the TPTF. These experiments spanned pressures from 464 to 1773 psia, mass fluxes from 3.49 to 19.18 lbm/ft^2-sec, and peak linear heat rates from 0.38 to 2.12 kW/ft. **[**

][a,c]

13.4.5.4 Test Procedure for JAERI-TPTF Simulations

These tests were conducted by supplying nearly saturated water to the test section. After a constant flow through the test section was achieved, the power to the bundle was turned on. The system was allowed to reach a quasi steady-state, where the inlet flow into the bundle was equal to the steam mass flow exiting the bundle. The bundle power was selected so that the maximum heater rod surface temperature was no more than 1,200°F.

Data was recorded after the steady-state condition was achieved. The dryout or critical heat flux elevation was defined as the average of the lowest thermocouple elevation where the temperature was 36°F above saturation and the adjacent upstream thermocouple. This exercise was performed for both the 5 instrumented rods in the middle of the assembly, as well as the 4 instrumented rods in the outside of the assembly. An average value for all 9 instrumented rods was also determined.

13.4.5.5 WCOBRA/TRAC-TF2 Model of the JAERI-TPTF

Figure 13.4.5-3 shows the WCOBRA/TRAC-TF2 model of the JAERI-TPTF. **[**

][a,c]

13.4.5.6 Simulation of JAERI-TPTF Tests

[

]a,c

13.4.5.7 Summary and Conclusions

[

]a,c

[

]^{a,c}

Table 13.4.5-1 JAERI-TPTF Rod Bundle Uncovery Test Matrix

Run No.	Pressure (psia)	Rod Power (kW/ft)
321	496	1.07
330	495	1.39
340	494	1.62
30	464	1.72
612	1064	0.87
620	1063	1.25
630	1060	1.54
640	1063	1.86
60	1035	2.12
910	1772	0.85
920	1773	1.25
930	1773	1.52
940	1772	1.82
90	1722	2.00

Table 13.4.5-2 JAERI-TPTF Rod Bundle Results Summary at Model Nominal YDRAG

a,c

a,c

Table 13.4.5-3 JAERI-TPTF Simulation Rod Bundle YDRAG Sensitivity Study Results

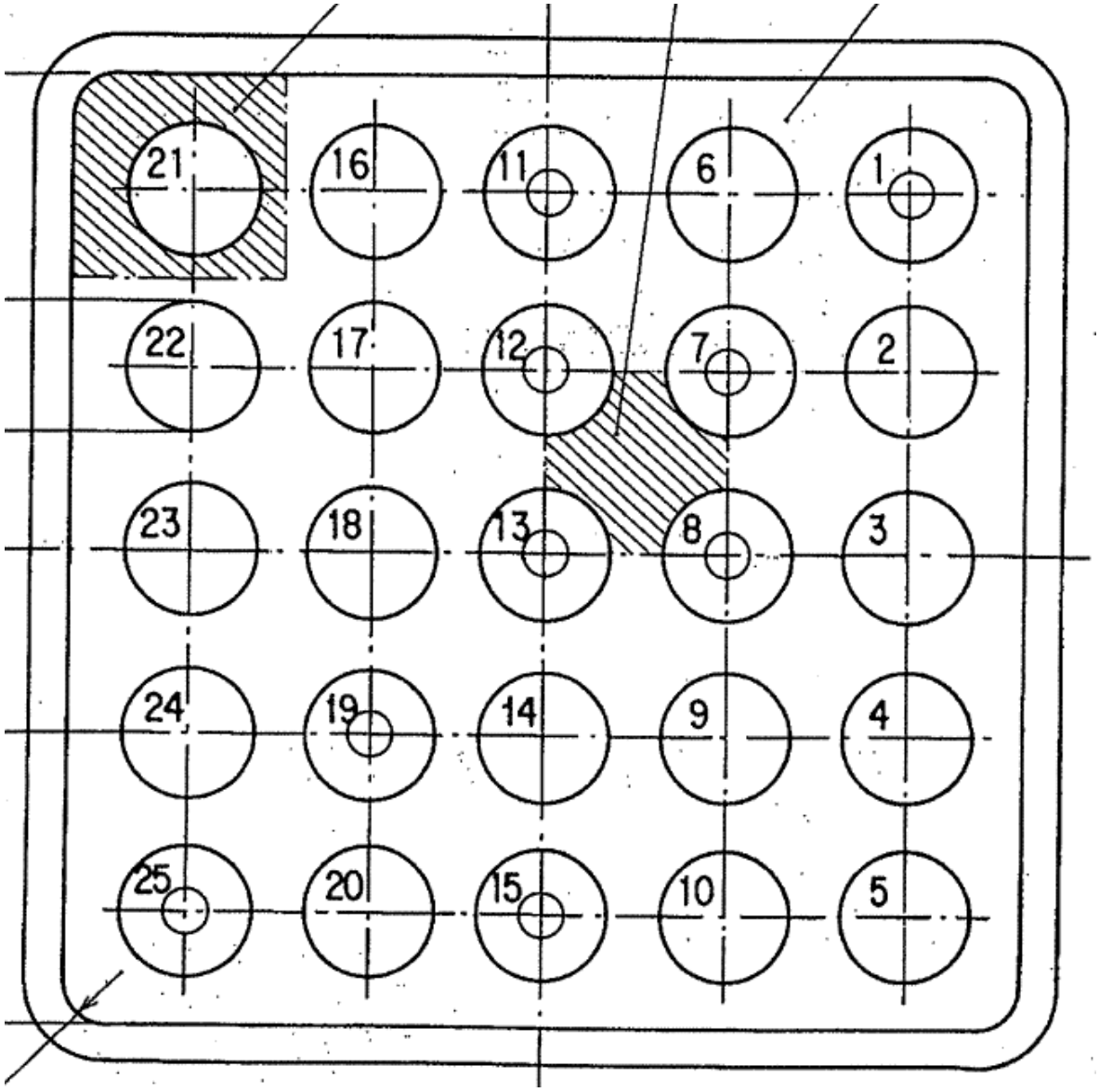

Figure 13.4.5-1 Cross Section of the JAERI-TPTF Test Bundle

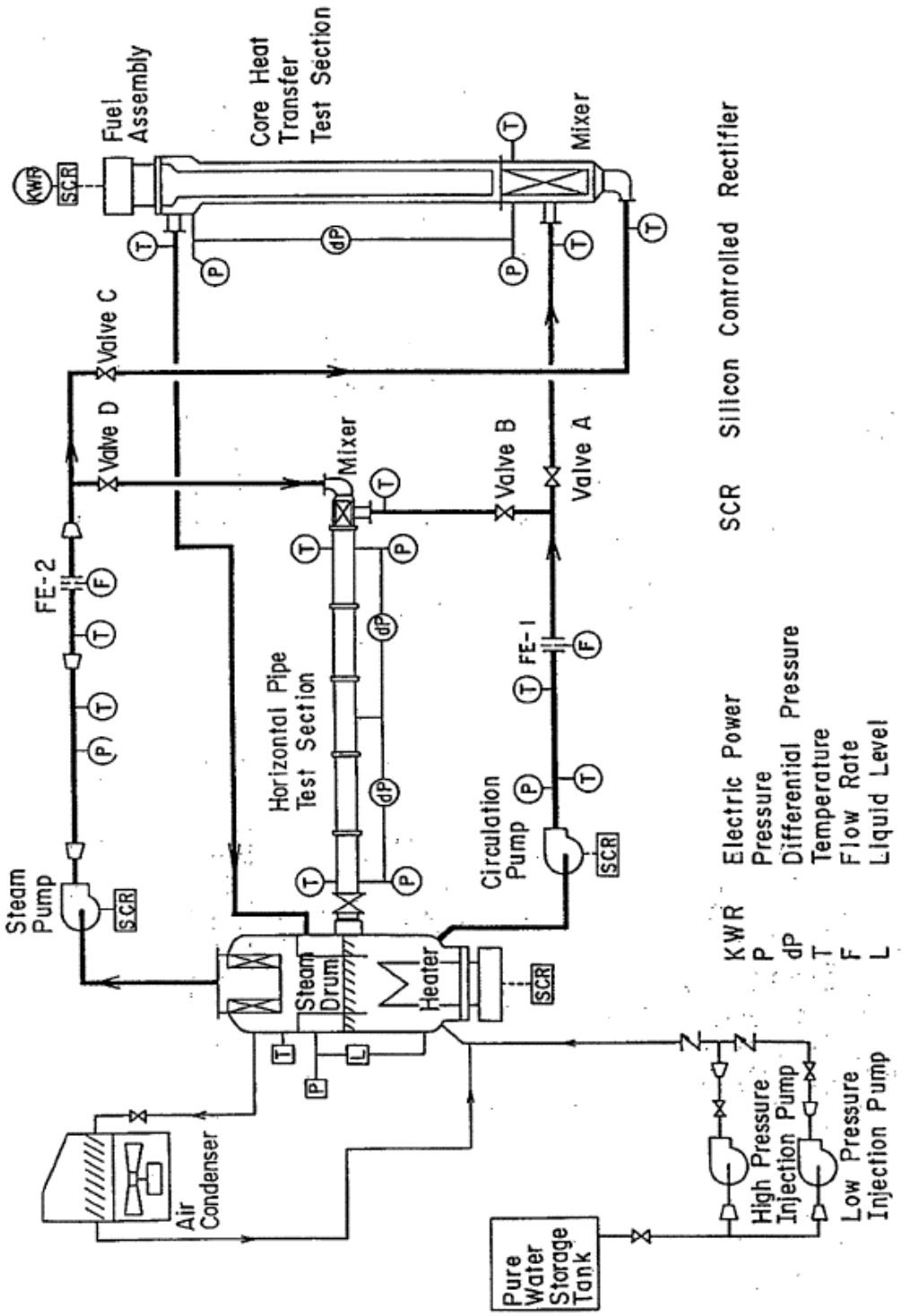

Figure 13.4.5-2 Flow Diagram of the JAERI-TPTF

a,c

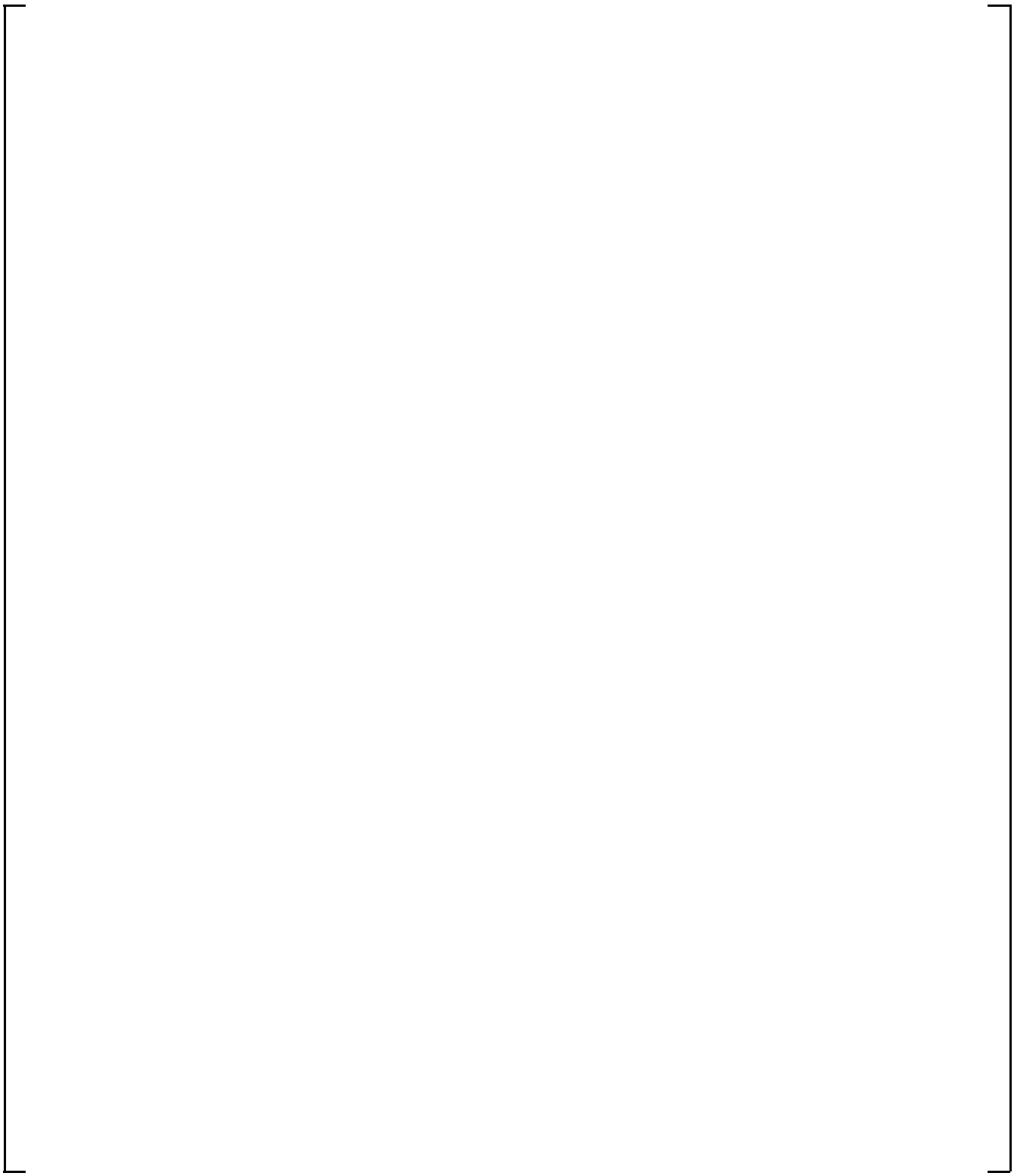

Figure 13.4.5-3 WCOBRA/TRAC-TF2 Model of the JAERI-TPTF

a,c

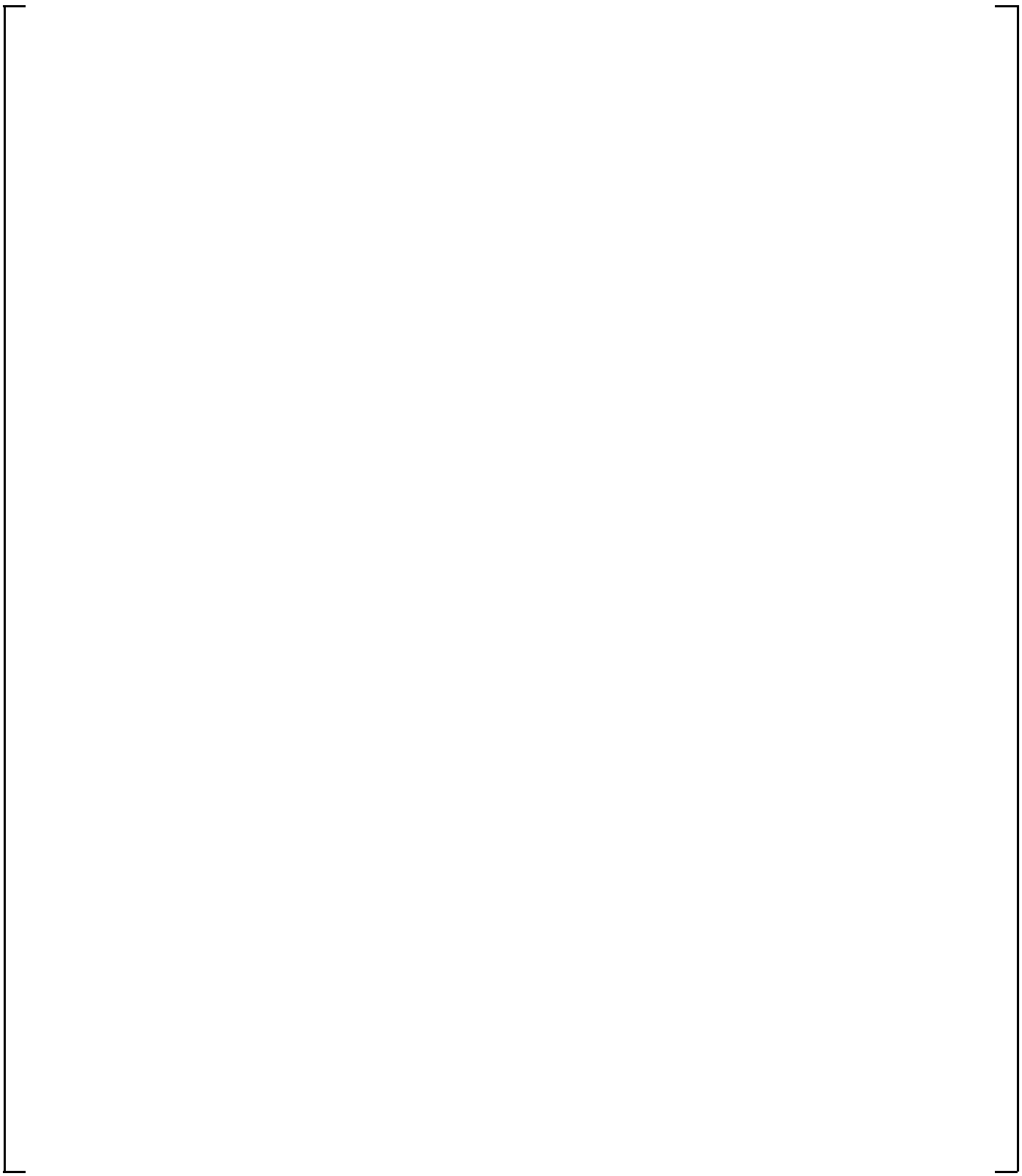

Figure 13.4.5-4 WCOBRA/TRAC-TF2 Predicted Void Fraction Profile, TPTF Test 321

a,c

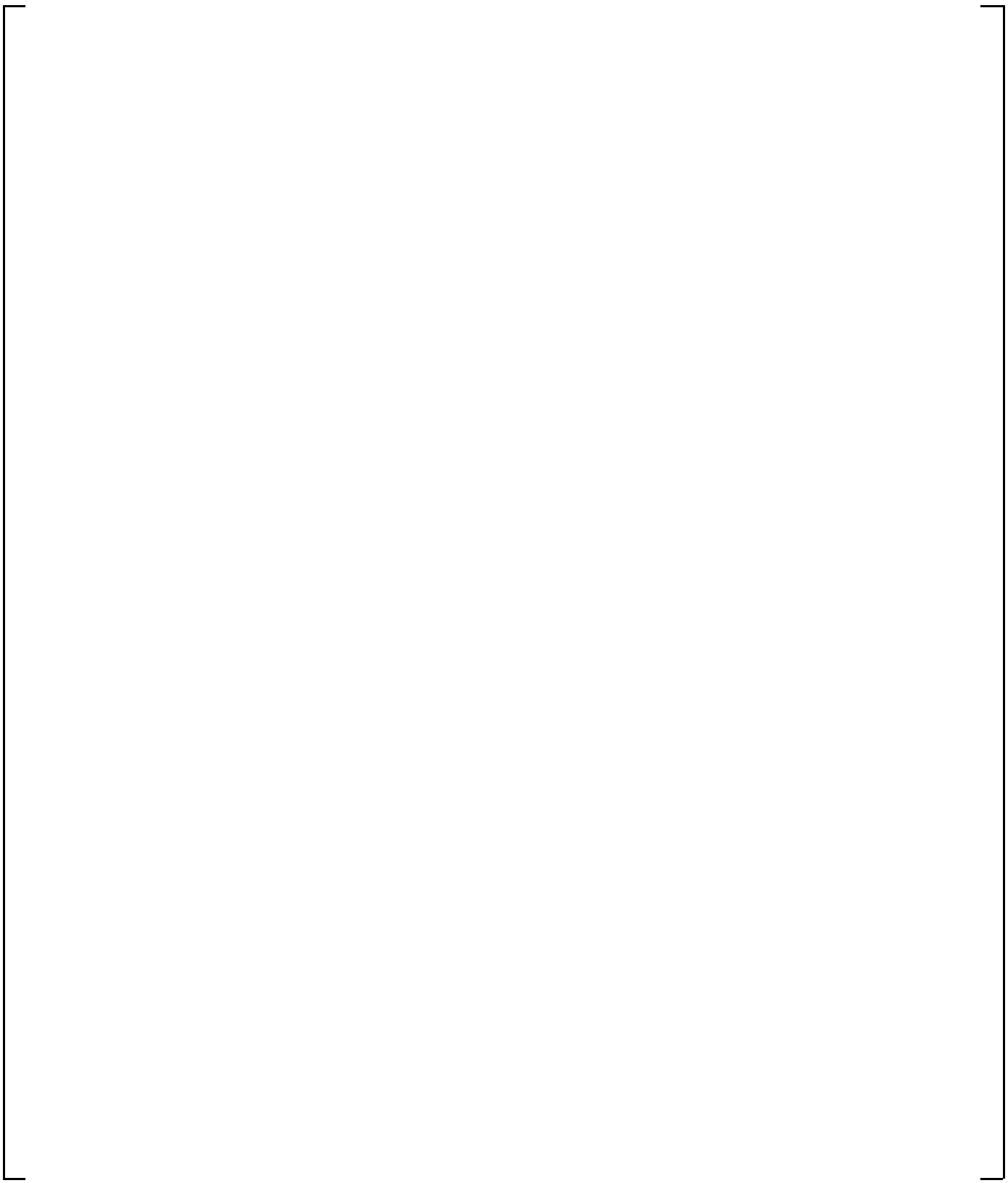

Figure 13.4.5-5 WCOBRA/TRAC-TF2 Predicted Clad Temperature Profile, TPTF Test 321

a,c

Figure 13.4.5-6 Predicted Versus Measured Dryout Elevation for JAERI-TPTF Rod Bundle Tests

a,c

Figure 13.4.5-7 Predicted Over Measured Dryout Elevation Versus Pressure for JAERI-TPTF Rod Bundle Tests

a,c

Figure 13.4.5-8 Predicted Over Measured Dryout Elevation Versus Linear Heat Rate for JAERI-TPTF Rod Bundle Tests

a,c

Figure 13.4.5-9 Predicted Over Measured Dryout Elevation Versus Mass Flux for JAERI-TPTF Rod Bundle Tests

13.5 SUMMARY AND CONCLUSIONS

[

]a,c

13.6 REFERENCES

1. Anderson, T. M., 1980, "Documentation of the Westinghouse Core Uncovery Tests and the Small Break Evaluation Model Core Mixture Level Model," WCAP-9764, Proprietary.

2. Andreychek, T. S., 1981, "Heat Transfer Above the two-Phase Mixture Level Under Core Uncovery Conditions in a 336-Rod Bundle," EPRI NP-1692, Volumes 1 and 2.

3. Anklam, T. M., et al., 1982, "Experimental Investigations of Uncovered Bundle Heat Transfer and Two-Phase Mixture Level Swell Under High Pressure Low Heat Flux Conditions," NUREG/CR-2456.

4. Findlay, J. A. and Sozzi, G. L., 1981, "BWR Refill-Reflood Program B Model Qualification Task Plan," NUREG/CR-1899.

5. Guo, Z., et al., 1993, "Critical Heat Flux for Rod Bundle Under High-Pressure Boiloff Conditions," JAERI-M 93-238.

14 SEPARATE EFFECT TESTS USED TO ASSESS CORE HEAT TRANSFER MODEL

14.1 INTRODUCTION

Section 7 in Volume 1 of the WCOBRA/TRAC-TF2 Code Qualification Document (CQD) described the VESSEL component heat transfer package. This package consists of a set of heat transfer correlations and selection logic to determine the appropriate correlation based on the local thermal-hydraulic conditions. The heat transfer package in WCOBRA/TRAC-TF2 produces a continuous boiling curve as a function of wall temperature and local fluid conditions. Figure 14.1-1 shows the heat transfer regime map used by the WCOBRA/TRAC-TF2 vessel component.

Heat transfer is modeled in WCOBRA/TRAC-TF2 as a regime dependent, three step process. Specific models and correlations are used for heat transfer from the wall to vapor field, heat transfer from the wall to the liquid fields, and interfacial heat transfer between the phases. Each of these processes is flow regime dependent and is based on the local hydrodynamic conditions in the computational cell. Section 7, Volume 1 described the wall to fluid heat transfer models, and Section 6, Volume 1 described those for interfacial heat transfer.

The same heat transfer package in WCOBRA/TRAC-TF2 is used for small, intermediate and large break phenomena. No specific logic is included that would result in a difference in small, intermediate and large break heat transfer models.

This section presents the tests used to assess the WCOBRA/TRAC-TF2 heat transfer package against the high ranked core heat transfer phenomena discussed in Section 2.3 and Table 2-1 in Volume 1. This includes **[**

][a,c].

Since the core heat transfer package is used for small, intermediate and large break phenomena, the focus of the core heat transfer assessment is heat transfer mode specific, rather than by transient phase. The assessment is broken into three areas: film boiling, single phase vapor and reflood heat transfer.
[

][a,c] Reflood is considered a special case, which encompasses many of the interactions and entanglements of the core heat transfer phenomena identification and ranking table (PIRT) phenomena, and as such will be assessed as a whole.

Single Phase Vapor (SPV)

SPV is predominant during refill and early reflood conditions of a large break, and boiloff/recovery of a small break. The experiments selected for the validation of the WCOBRA/TRAC-TF2 heat transfer package under SPV conditions were chosen from the following test series:

1. Oak Ridge National Laboratory (ORNL) Uncovered Bundle Heat Transfer tests (Anklam et al., 1982).

2. FLECHT-SEASET Unblocked Bundle Steam Cooling and Boiloff Tests (Lee et al., 1982).

These tests provide reasonable verification of the heat transfer package performance in the high and low pressure single phase vapor regimes. The tests chosen and their conditions are summarized in Table 14.1-1.

The ranges which these tests cover are compared to the typical pressurized water reactor (PWR) ranges in Table 14.1-2. **[**

][a,c]

Dispersed Flow Film Boiling (DFFB)

DFFB is predominant under blowdown and reflood conditions of a large break, and accumulator/safety injection phases of an intermediate break. The experiments selected for the validation of the WCOBRA/TRAC-TF2 heat transfer package under DFFB conditions were chosen from the following test series:

1. Oak Ridge National Laboratory High Pressure Film Boiling Tests (Yoder et al., 1982, Morris et al., 1982, and Mullins et al., 1982).

2. Westinghouse G-1 Intermediate Pressure Blowdown Tests (Cunningham et al., 1974).

3. Westinghouse G-2 Low Pressure Refill Tests (Hochreiter et al., 1976).

[

][a,c] The tests chosen and their conditions are summarized in Table 14.1-3.

[

]a,c

Reflood

The reflood phase of a large break LOCA is characterized by relatively constant, low pressure conditions, with two-phase film boiling and rewet under low flow conditions. As described in Section 2.3.1.2, Volume 1, characteristic features of the reflood transient are the interaction of cold ECCS water with hot fuel rods, and the oscillatory nature of the reflood process. In terms of basic thermal and hydraulic parameters, the reflood process in a typical fuel assembly takes place within the range of conditions depicted in Table 14.1-5.

Pressure, mass velocity, inlet subcooling and steam quality ranges are typically used to characterize the inlet fluid conditions applied to the test assemblies in experiments. Assembly maximum heat rate characterizes the peak power present in the test or fuel assembly, while the average linear heat rate is a measure of the total assembly power. The assembly maximum temperature, while actually a test or predicted result, is important because it identifies whether the tests were in the appropriate heat transfer regime for a sufficient period of time.

[

]a,c The experiments selected for the validation of the WCOBRA/TRAC-TF2 heat transfer package under reflood conditions were chosen from the following test series:

1. Westinghouse/NRC/EPRI FLECHT-SEASET Reflood Tests (Loftus et al., 1981).
2. Westinghouse/NRC FLECHT Low Flooding Rate Tests (Rosal et al., 1975).
3. Westinghouse/NRC FLECHT Skewed Power Reflood Tests (Rosal et al., 1977).
4. Westinghouse/Aerojet FLECHT Supplemental Tests (Cadek et al., 1972).
5. Westinghouse G-2 Reflood Tests (Cunningham et al., 1975).
6. FEBA Reflood Tests (Ihle and Rust, 1984).

The three Full-Length Emergency Core Heat Transfer (FLECHT) series of tests provide comprehensive coverage of heat transfer in rod bundles under constant flooding rate conditions. A broad range of possible assembly conditions, including power distribution, was tested, and detailed fluid and thermal data were obtained. The Flooding Experiment with Blocked Arrays (FEBA) tests allow the assessment of a different assembly power distribution from those tested in FLECHT, and the important contribution to heat transfer provided by the fuel assembly grids, since there are tests available with and without grids. The G-2 tests provide data in a bundle of different height, with prototypical mixing vane grids similar to those used in a PWR fuel assembly. The tests chosen and their conditions are summarized in Table 14.1-6.

[

]a,c

[

]a,c

Table 14.1-1 SPV Heat Transfer Test Conditions

Test Series	Test Number	Pressure psia	Vapor Reynolds Number	Steam Cooling Region ft	Power/Rod kW/ft	Comment
ORNL	3.09.10I	650	12,200 – 16,600	9.91-11.88	0.68	
	3.09.10J	620	5,000 – 6,700	9.91-11.88	0.33	
	3.09.10K	580	1,100 – 1,900	7.94-11.88	0.10	
	3.09.10L	1090	13,000 – 17,700	9.91-11.88	0.66	
	3.09.10M	1010	5,100 – 6,500	9.91-11.88	0.31	
	3.09.10N	1030	1,600 – 3,000	7.94-11.88	0.14	
FLECHT SEASET (Steam cooling)	32753	40	18,300 – 20,000	0.0 – 12.0	0.21	The listed rod powers for this test are the peak rod powers.
	36160	39	18,000 – 19,800	0.0 – 12.0	0.16	
	36261	39	14,700 – 16,100	0.0 – 12.0	0.13	
	36362	39	9,100 – 9,900	0.0 – 12.0	0.79	
	36463	40	5,600 – 6,100	0.0 – 12.0	0.48	
	36564	40	4.400 – 4,700	0.0 – 12.0	0.04	
	36766	40	2,800 – 3,000	0.0 – 12.0	0.02	
	36867	39	2,800 – 3,000	0.0 – 12.0	0.02	

Table 14.1-2 Typical Conditions in a PWR During SPV (Blowdown, Refill, Boiloff/Recovery, Reflood)

a,c

Table 14.1-3 DFFB Heat Transfer Test Conditions

Test Series	Test Number	Pressure psia	Mass Flux lbm/s-ft^2	Inlet Temperature °F	Peak Power kW/ft	Comment
ORNL	3.03.6AR	2040	467	513	5.6	
	3.07.9B	1849	146	590	8.3	
	3.07.9C	1805	68.4	559	5.1	
	3.07.9D	1847	10.6	577	6.3	
	3.07.9E	1908	121	579	6.5	
	3.07.9K	635	46.2	415	4.0	
	3.07.9L	1203	108	529	7.0	
	3.07.9M	1242	134	543	7.9	
	3.07.9P	874	107	513	7.4	
	3.07.9Q	947	66.6	502	5.1	
	3.07.9X	872	70.5	514	5.4	
	3.08.6C	1870	214	508	3.4	
[						] b

Table 14.1-4 Typical Conditions in a PWR During DFFB (Blowdown, Refill)

a,c

Table 14.1-5 Typical Conditions in a PWR During Reflood

a,c

Table 14.1-6 Reflood Heat Transfer Test Conditions

Test Series	Test Number	Pressure psia	Flooding Rate in/s	Inlet Subcooling °F	Peak Power kW/ft	Comment
FLECHT SEASET	31805 31203 31701 31504 32013	40 40 40 40 60	0.81 1.51 6.1 0.97 1.04	143 141 140 144 143	0.7 0.7 0.7 0.7 0.7	COSINE POWER SHAPE 17x17 PWR ROD ARRAY
FLECHT LOW FLOODING RATE	05029 05132 04641	40 40 20	0.85 1.0 1.0	141 140 139	0.73 0.95 0.95	COSINE POWER SHAPE 15x15 PWR ROD ARRAY
FLECHT SKEWED	15305 13812 15713 13914 13609	40 41 40 21 21	0.8 1.0 1.0 1.0 1.0	140 83 2 5 141	0.7 0.7 0.7 0.7 0.7	TOP SKEWED POWER SHAPE 15x15 PWR ROD ARRAY

b

a,c

Figure 14.1-1 WCOBRA/TRAC-TF2 Heat Transfer Regime Map (from Figure 7.2-3)

14.2 TEST FACILITIES DESCRIPTION

14.2.1 Test Facilities Used to Assess Single-Phase Vapor

14.2.1.1 Oak Ridge National Laboratory Thermal Hydraulic Test Facility Uncovered Bundle Heat Transfer Tests

A series of steady-state experiments investigating small break LOCA phenomena was performed in the ORNL Thermal-Hydraulic Test Facility (THTF) high pressure rod bundle thermal-hydraulics loop, as reported in NUREG/CR-2456 (Anklam, et al., 1982). The test facility, test procedure and test conditions are described in more detail in Section 13.4.2 of this report. The uncovered bundle tests provided local conditions for pressure, mass flow, quality, and steam temperature, which were used as input to a driver program containing the WCOBRA/TRAC-TF2 code heat transfer package for assessment. Table 14.1-1 lists the thermal-hydraulic conditions of the six selected ORNL-THTF uncovered bundle tests used to evaluate the WCOBRA/TRAC-TF2 single-phase vapor heat transfer models as part of the heat transfer driver program.

14.2.1.2 FLECHT-SEASET Steam Cooling Tests

The FLECHT Separate-Effects and System-Effects Tests (SEASET) series was conducted in order to provide an experimental data base at low flooding rates for simulated Westinghouse 17x17 fuel rods as described by Conway et al. (1977). The data from these tests were evaluated by Lee et al. (1982). The tests and experimental facility are described in more detail in Section 14.2.3.1 of this report. Local conditions from tests 32753, 36160, 36261, 36362, 36463, 36564, 36766, and 36867 were used as input to a driver program containing the WCOBRA/TRAC-TF2 code heat transfer package for assessment. Table 14.1-1 lists the thermal-hydraulic conditions of the eight selected FLECHT-SEASET steam cooling tests used to evaluate the WCOBRA/TRAC-TF2 single-phase vapor heat transfer models.

14.2.2 Test Facilities Used to Assess Dispersed Flow Film Boiling Heat Transfer

14.2.2.1 ORNL-THTF High Pressure Film Boiling Tests

The ORNL-THTF high pressure film boiling tests are one source of data for validating the heat transfer predictions of WCOBRA/TRAC-TF2 in the DFFB regimes of interest for LOCAs. A series of high-pressure steady-state upward DFFB tests in a rod bundle was performed in the ORNL-THTF and is discussed by Yoder (Yoder, et al., 1982). **[**

][a,c] The conditions for these tests are listed in Table 14.2.2.1-1. As seen in the table, these tests were conducted for pressures ranging from 23 bar (334 psia) to 132 bar (1908 psia) at flow rates from 226 kg/s-m^2 (46.3 lbm/s-ft^2) to 713 kg/s-m^2 (146 lbm/s-ft^2). These tests provided local conditions for pressure, mass flow, quality, and steam temperature at the tube exit, which were used as input to a driver program containing the WCOBRA/TRAC-TF2 code heat transfer package for assessment.

Additional ORNL-THTF tests were conducted to investigate heat transfer during dispersed flow film boiling (Morris et al., 1982). These tests simulate dryout and film boiling phenomena at high pressure in a transient condition. The initial conditions for these tests are listed in Table 14.2.2.1-2. To help validate the film boiling heat transfer models of WCOBRA/TRAC-TF2, two of the dispersed flow film boiling tests were simulated using WCOBRA/TRAC-TF2, as well as one of the steady-state tests.

14.2.2.1.1 Facility Description

The test facility is the same as that described in Section 13.4.2.

14.2.2.1.2 Test Procedure

During steady-state operation of the ORNL-THTF, the inlet flow at the bottom of the test section was established and the loop was adjusted to provide the desired inlet fluid temperature and inlet quality. The bundle power was then increased until the dryout (CHF) point was obtained. The steady-state point was assumed to be reached when both pressure and rod surface temperatures stabilized. The results of both rod surface conditions and local equilibrium fluid conditions were then reported as cross-sectional average values for each level. Table 14.2.2.1-1 lists the thermal-hydraulic conditions of the 10 selected ORNL-THTF steady-state film boiling tests used to evaluate the WCOBRA/TRAC-TF2 film boiling heat transfer models as part of the heat transfer driver program.

The following describes the tests used for full experiment simulation.

Steady-State Test – In the steady-state experiment (3.07.9B – Yoder et al., 1982), inlet flow at the bottom of the test section was established and adjusted such that the desired flow rate, temperature, and pressure was reached. The bundle power was increased until the dryout point was at the desired position in the bundle. When the operating pressure and rod surface temperature were stabilized, steady-state was assumed. The test conditions are listed in Table 14.2.2.1-2.

Transient Tests – The first step in the transient experiments (3.08.6C and 3.03.6AR – Mullins et al., 1982) was to establish steady-state conditions prior to the initiation of the transients. The initial conditions for the two selected transient tests are also listed in Table 14.2.2.1-2.

Once steady-state conditions were achieved, the transients were initiated by breaking the outlet rupture disk assembly. The outlet break areas were 0.486 square inches and 0.583 square inches for Tests 3.08.6C and 3.03.6AR, respectively. Following the breaking of the outlet rupture disk, bundle power was ramped up from the initial steady-state levels to near maximum power levels, over a period of time to prolong the film boiling. Then the power was ramped down slowly. The pump was turned off at transient initiation for Test 3.03.6AR, while the pump was left on during the first 20 seconds for Test 3.08.6C.

Figures 14.2.2.1-1 through 14.2.2.1-3 provide the inlet mass flow rates, outlet pressure and test section bundle power for Test 3.03.6AR. Figures 14.2.2.1-4 through 14.2.2.1-6 provide the inlet mass flow rates, outlet pressure and test section bundle power for Test 3.08.6C.

Table 14.2.2.1-1 ORNL-THTF Steady-State DFFB Initial Test Condition					
Test	**Pressure psia**	**Mass Flux lbm/s-ft^2**	**Inlet Quality**	**Inlet Temperature °F**	**Power kW/ft**
3.07.9B	1850	146	-0.107	624.7	8.3
3.07.9C	1806	68.4	-0.179	621.4	5.2
3.07.9D	1849	106	-0.154	624.5	6.3
3.07.9E	1908	121	-0.155	629.0	6.5
3.07.9K	635	46.3	-0.128	492.3	4.1
3.07.9L	334	108	-0.082	567.4	7.1
3.07.9M	1243	135	-0.061	571.4	8.1
3.07.9P	875	107	-0.029	528.4	7.4
3.07.9Q	947	66.6	-0.067	537.9	5.2
3.07.9X	872	70.5	-0.026	528.0	5.4

Table 14.2.2.1-2 ORNL-THTF Initial Test Conditions for WCOBRA/TRAC-TF2 Simulation				

a,c

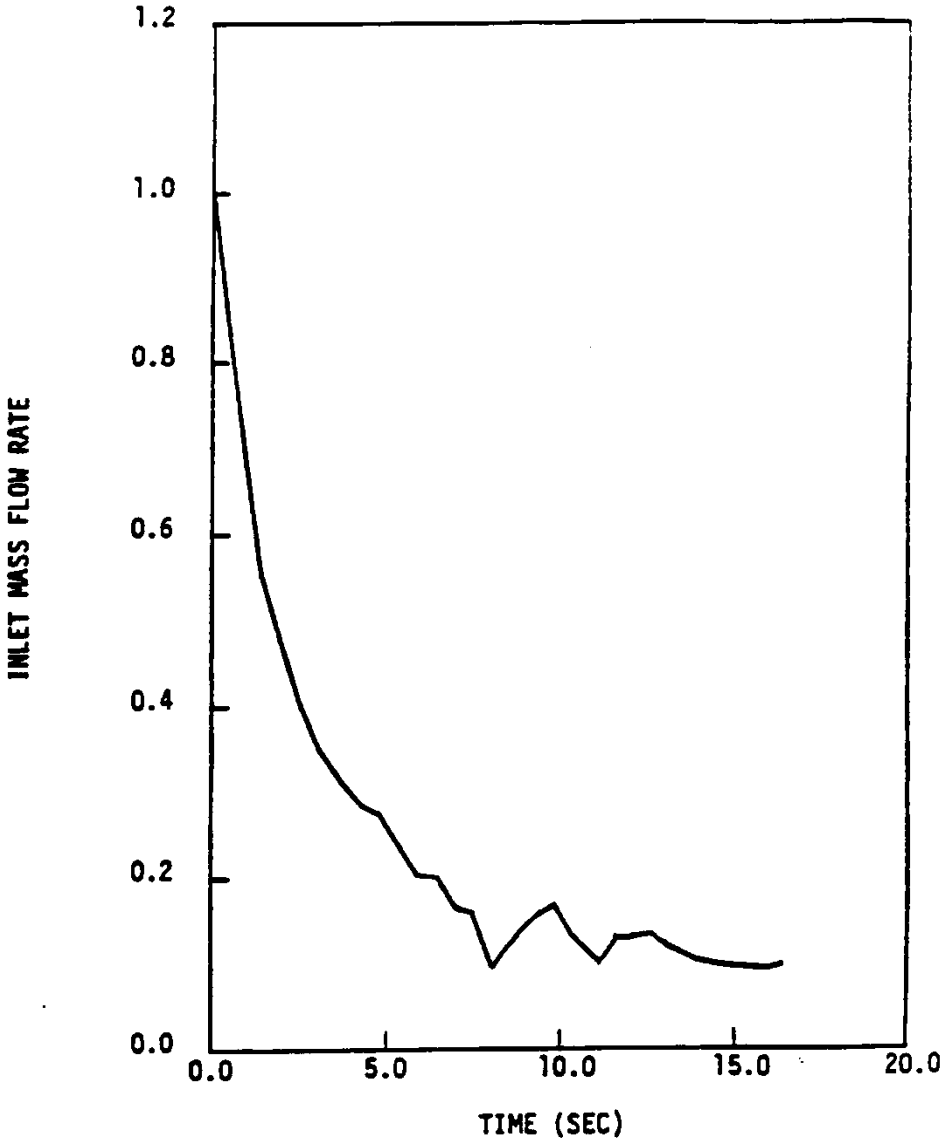

Figure 14.2.2.1-1 Inlet Mass Flow Rate Forcing Function Normalized to Initial Condition, Test 3.03.6AR

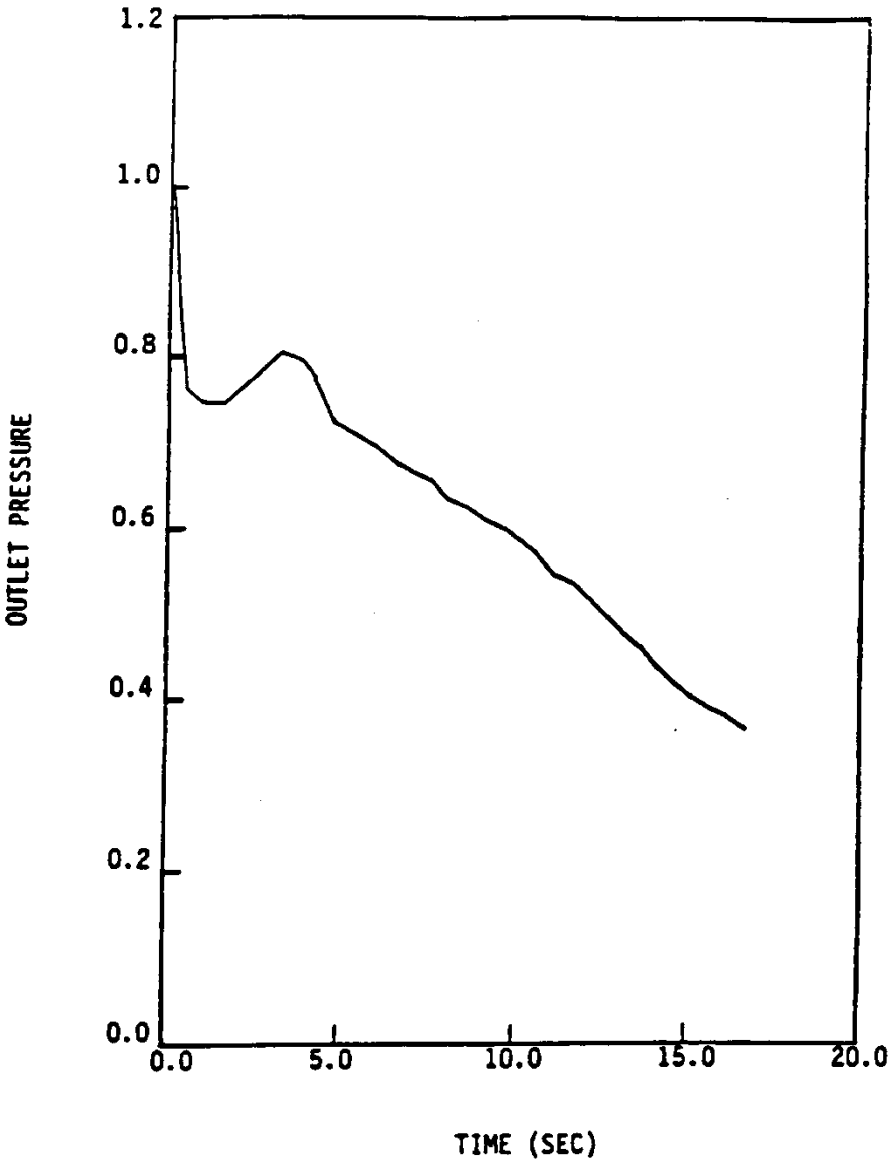

Figure 14.2.2.1-2 Outlet Pressure Forcing Function Normalized to Initial Condition, Test 3.03.6AR

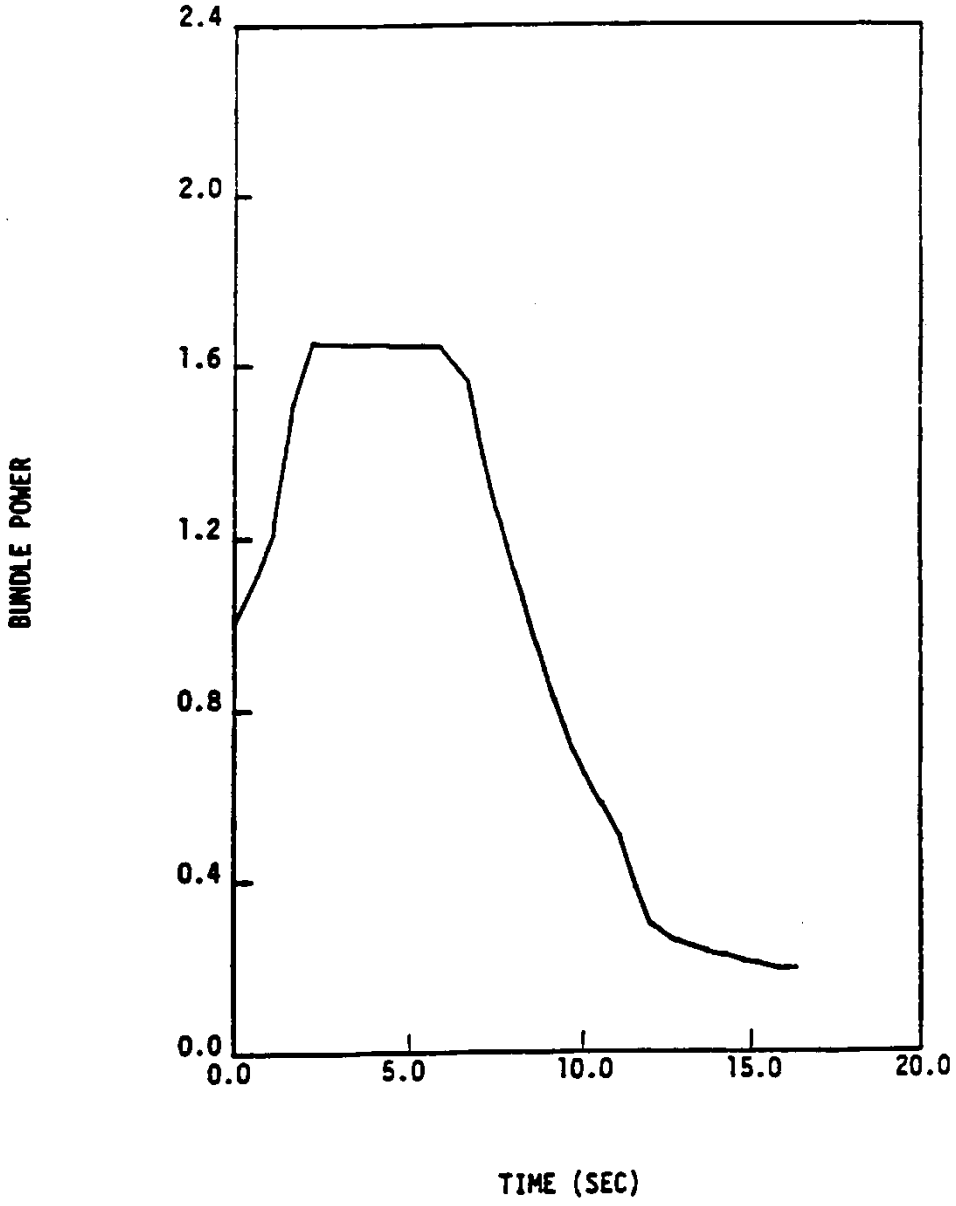

Figure 14.2.2.1-3 Test Section Bundle Power Forcing Function Normalized to Initial Condition, Test 3.03.6AR

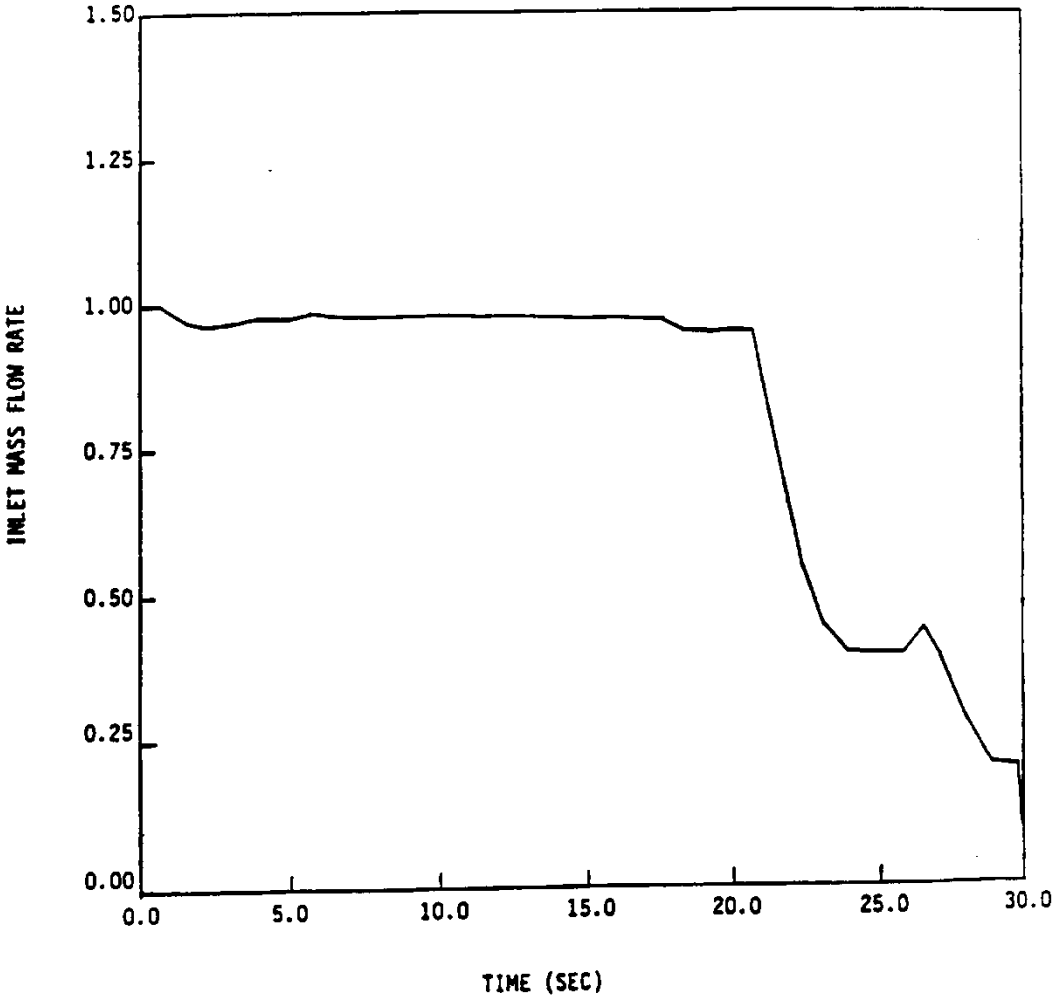

Figure 14.2.2.1-4 Inlet Mass Flow Rate Forcing Function Normalized to Initial Condition, Test 3.08.6C

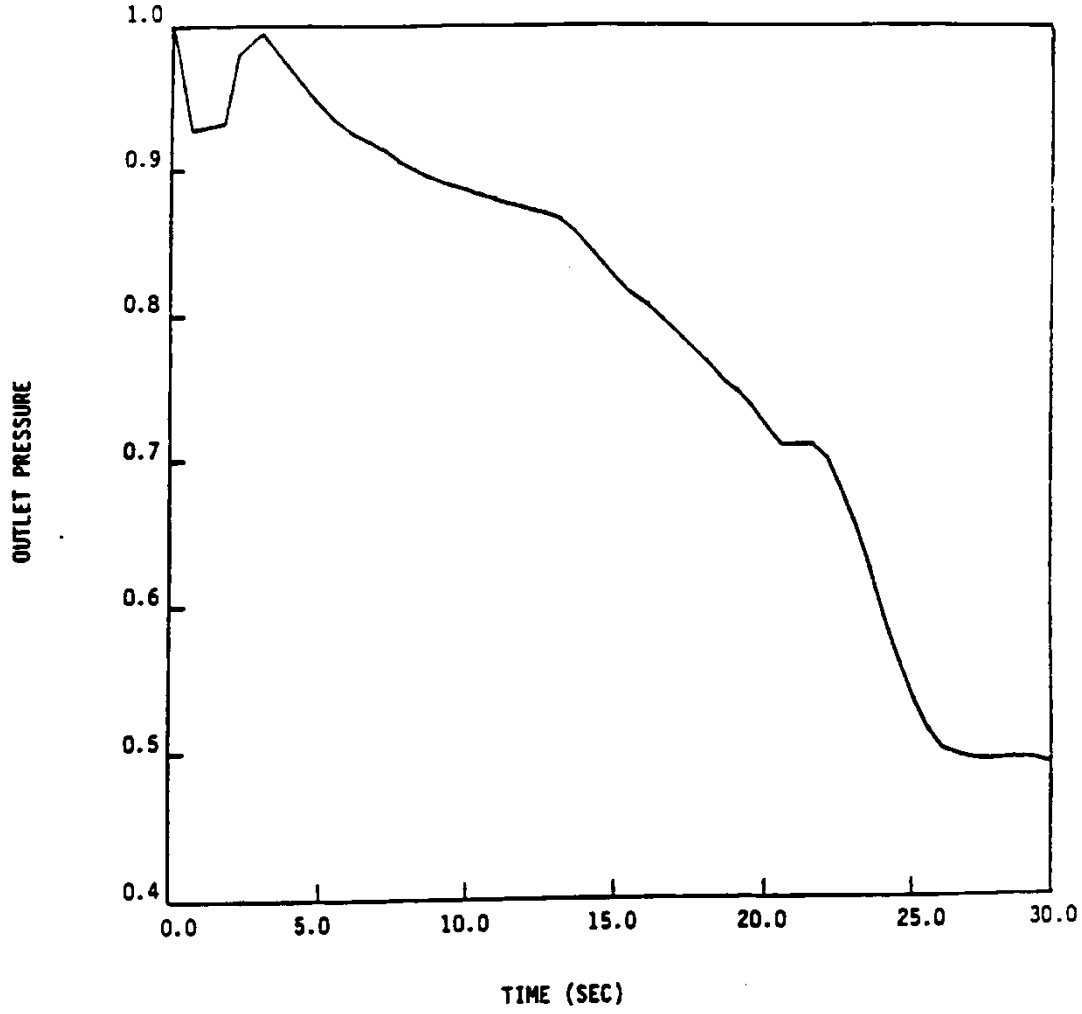

Figure 14.2.2.1-5 Outlet Pressure Forcing Function Normalized to Initial Condition, Test 3.08.6C

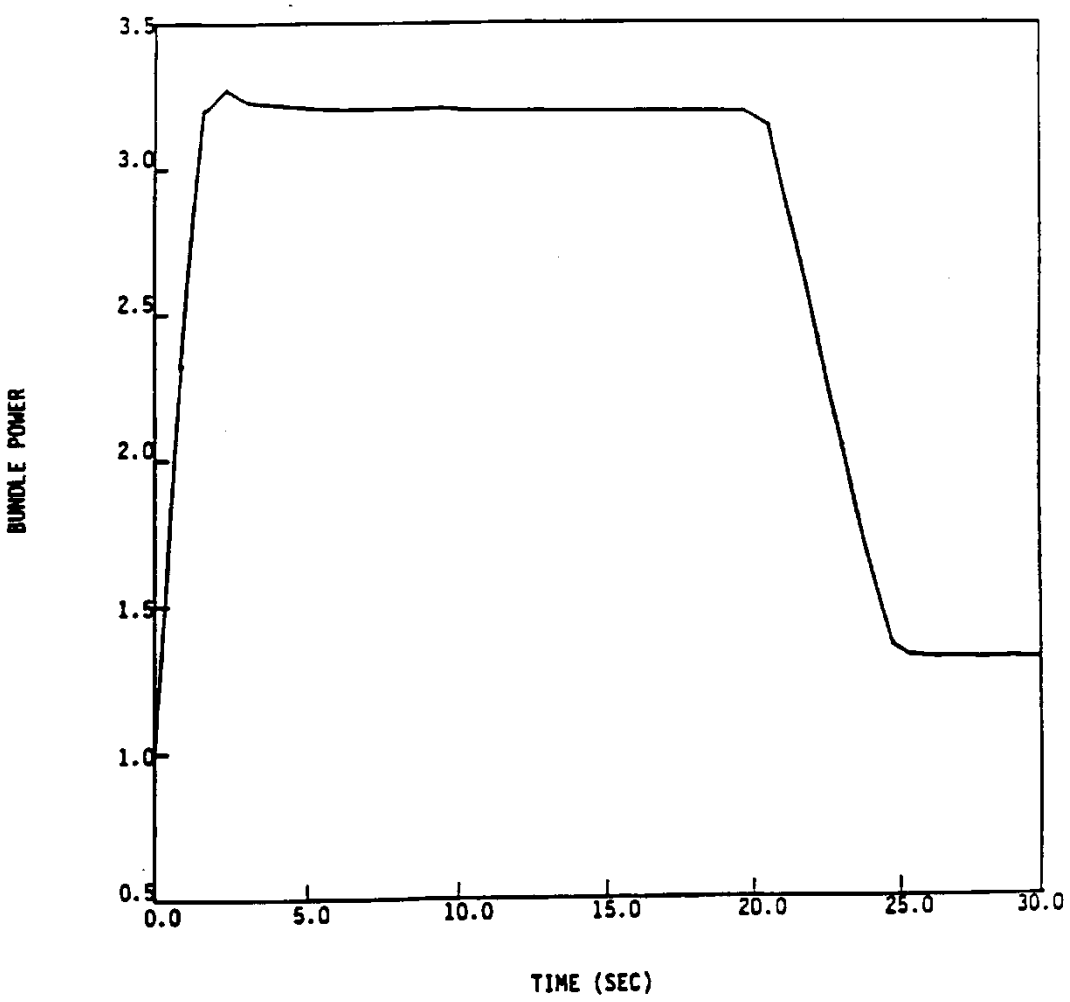

Figure 14.2.2.1-6 Test Section Bundle Power Forcing Function Normalized to Initial Condition, Test 3.08.6C

14.2.2.2 G-1 Intermediate Pressure Blowdown Heat Transfer Experiments

These experiments were designed to provide data which could be used to verify heat transfer models applicable to the analysis of heat transfer during the blowdown portion of a large break Loss-of-Coolant Accident in a PWR. They will be used to demonstrate the adequacy of the film boiling models in WCOBRA/TRAC-TF2.

14.2.2.2.1 Facility Description

The G-1 test facility, Figure 14.2.2.2-1, was designed to simulate thermal-hydraulic conditions calculated for a PWR during the blowdown portion of a LOCA. The facility could be operated at pressures up to 2000 psig and temperatures up to 650°F. The test facility's original purpose was to verify the performance of the Upper Head Injection (UHI) ECCS which was installed in some PWRs. The UHI system injected subcooled water into the top of the core during the blowdown phase of the LOCA. During the same time period, two-phase mixture from the upper plenum and reactor coolant loops was expected to flow into the core and provide additional cooling. Both of these processes were simulated in the test facility.

A detailed description of this facility is contained in Section 13.4.3.2 of this topical. However, a brief summary of the facility description is provided below.

[

]^{b}

14.2.2.2.2 Test Procedure

[

]b

Table 14.2.2.2-1 Comparison of PWR Rod and G-1 Test Rod Bundle

a,b,c

Table 14.2.2.2-2 G-1 Initial Test Conditions

b

b

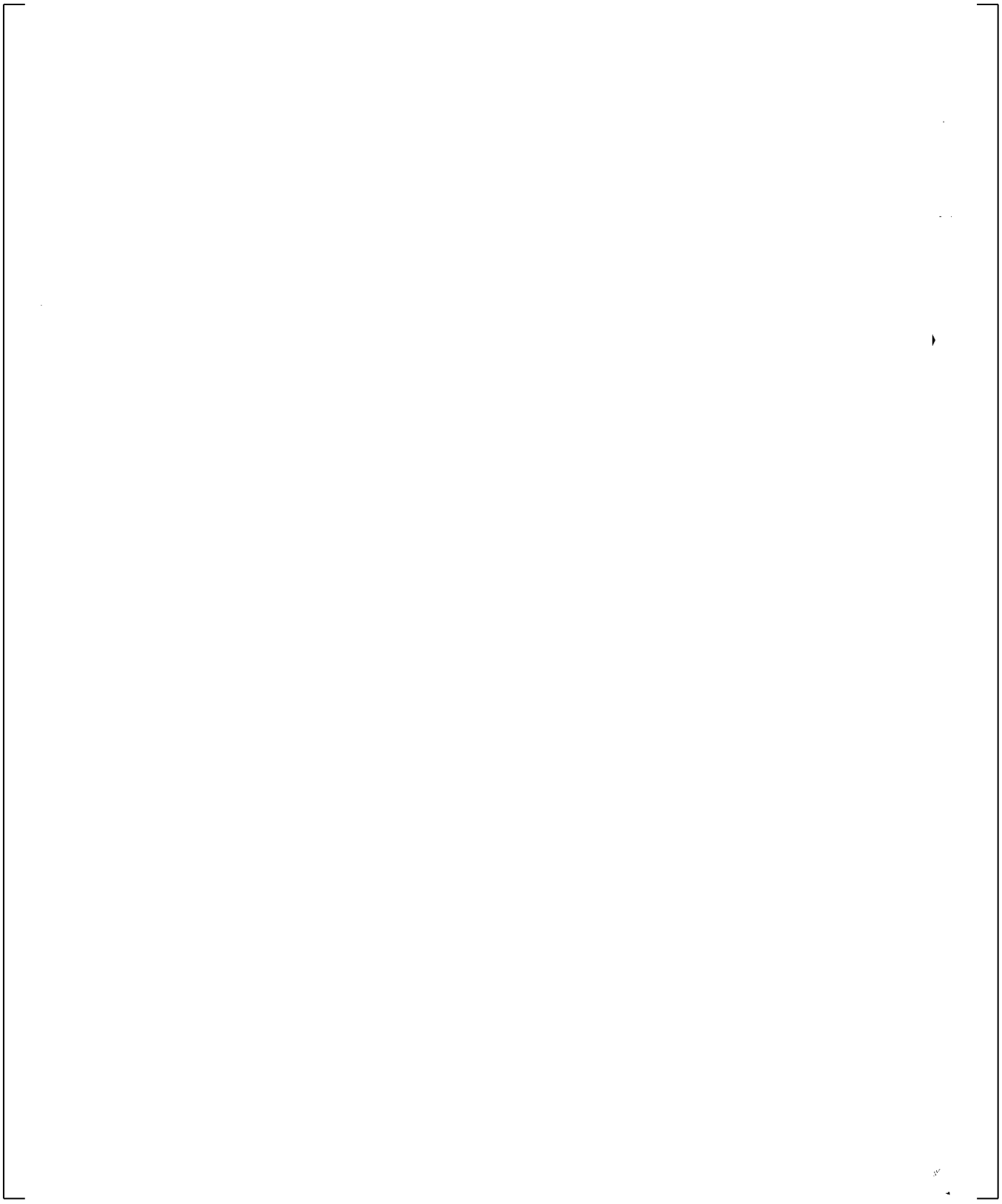

Figure 14.2.2.2-1 Diagram of G-1 Facility (from Cunningham, et al., 1974)

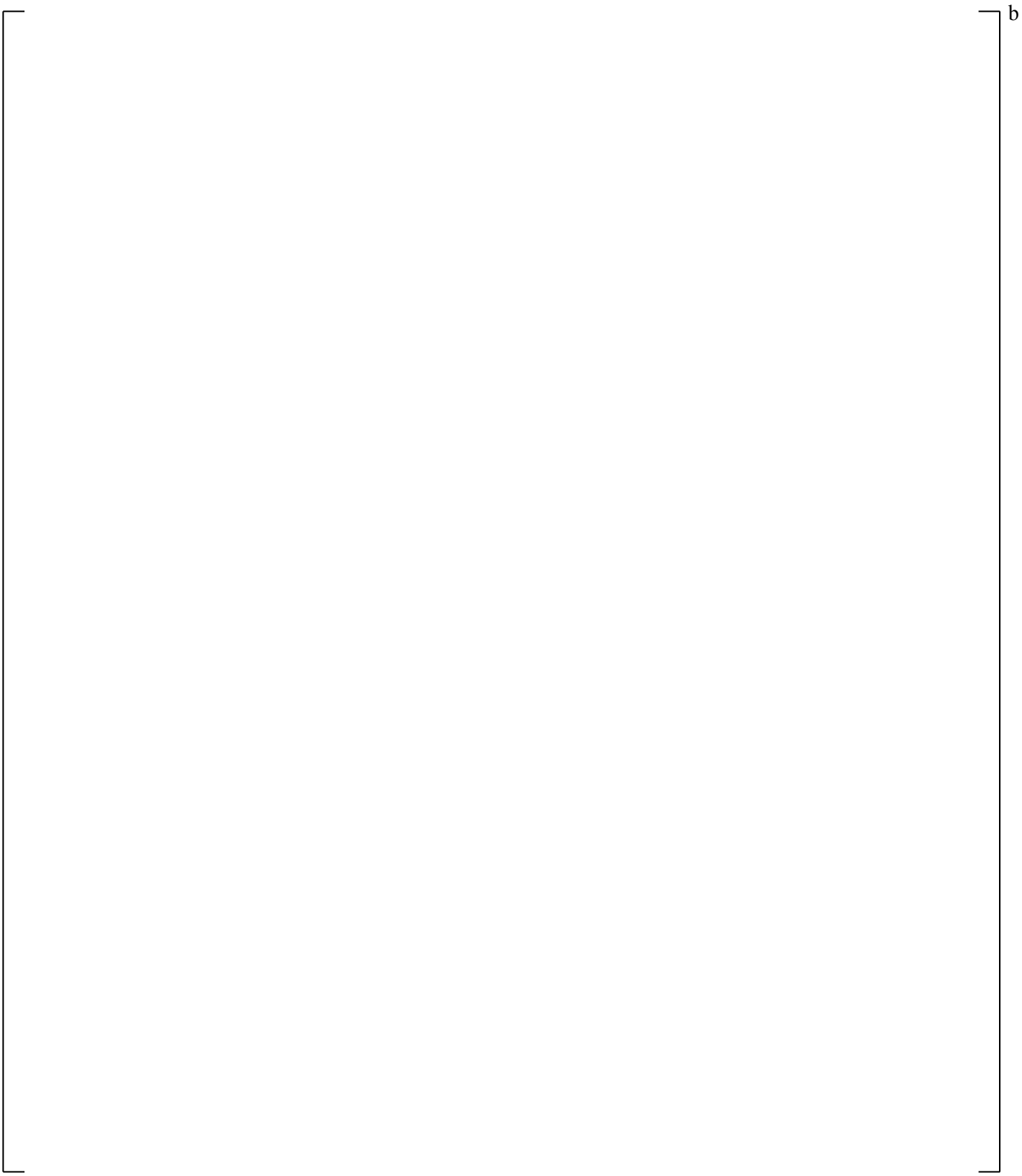

b

Figure 14.2.2.2-2 G-1 Test Vessel (from Cunningham, et al., 1974)

b

Figure 14.2.2.2-3 G-1 Heater Rod (from Cunningham, et al., 1974)

b

Figure 14.2.2.2-4 G-1 Heater Rod Axial Power Profile (from Cunningham, et al., 1974)

b

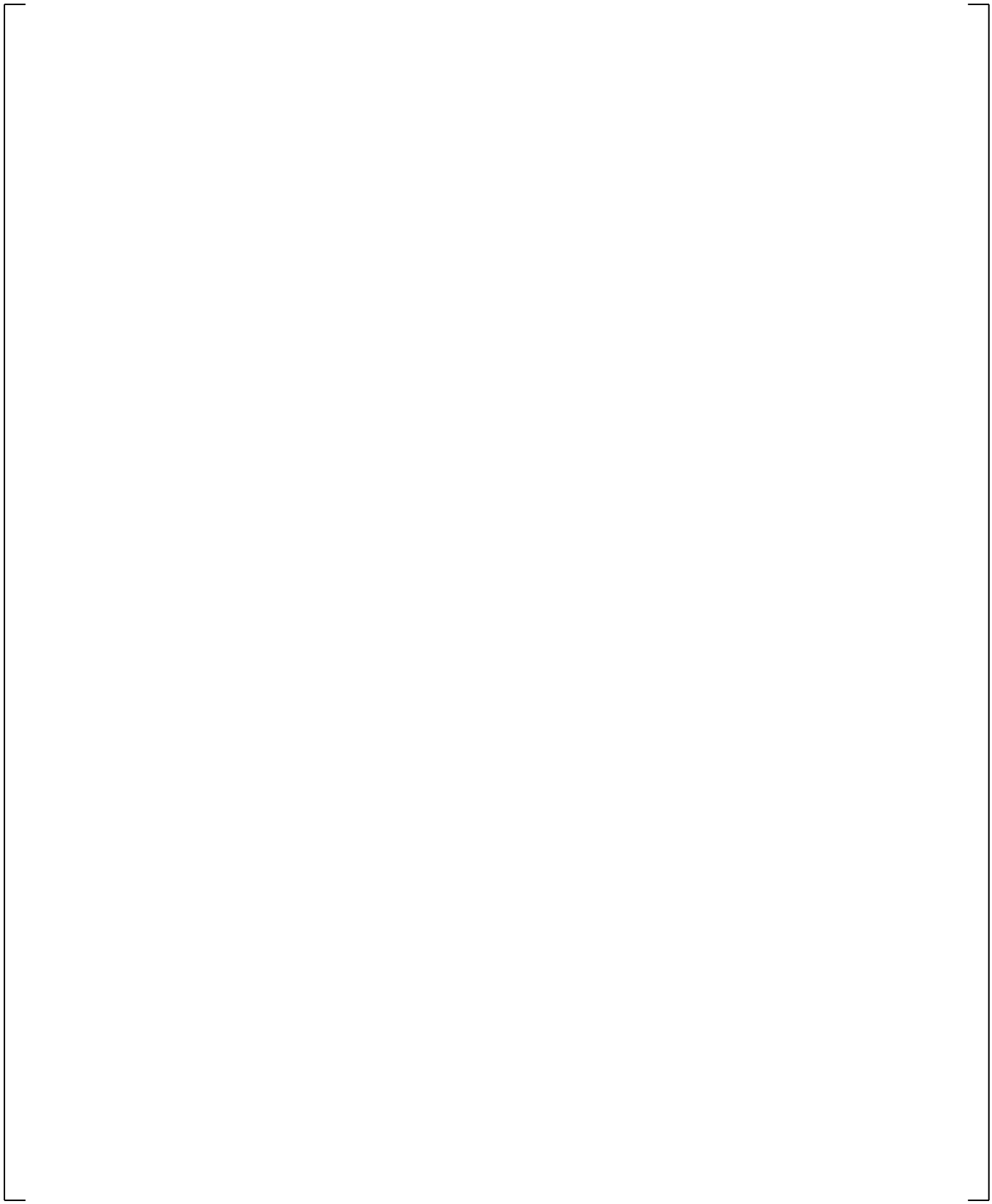

Figure 14.2.2.2-5 G-1 Bundle Cross Section and Instrumentation (from Cunningham, et al., 1974)

14.2.2.3 G-2 Low Pressure Refill Heat Transfer Experiments

Low pressure Upper Head Injection refill tests conducted at the Westinghouse G-2 test facility were simulated using the WCOBRA/TRAC-TF2 computer code. Comparisons of the WCOBRA/TRAC-TF2 results to the refill test experimental data can be used to help assess the capability of WCOBRA/TRAC-TF2 to accurately predict top-down quench phenomena, low pressure film boiling, and countercurrent film boiling heat transfer.

14.2.2.3.1 Facility Description

[

]^{b}

A detailed description of this facility is contained in Section 13.4.4.2 of this topical. However, a brief summary of the facility description is provided below.

[

]^{b}

14.2.2.3.2 Test Procedure

[

]^{b} Figure 14.2.2.3-6 shows the low pressure UHI refill test sequence of events. Table 14.2.2.3-2 summarizes the test conditions of the tests which were simulated with WCOBRA/TRAC-TF2.

Table 14.2.2.3-1 Comparison of 17x17 PWR Fuel Rod and G-2 Test Rod

a,b,c

Table 14.2.2.3-2 G-2 Refill Initial Test Conditions

a,b,c

b

Figure 14.2.2.3-1 G-2 Test Facility Flow Schematic (from Cunningham, et al., 1975)

b

Figure 14.2.2.3-2 G-2 Loop Heater Rod (from Cunningham, et al., 1975)

b

Figure 14.2.2.3-3 G-2 Loop Heater Rod Axial Power Profile (from Cunningham, et al., 1975)

Figure 14.2.2.3-4 Test Rod Bundle, Cross Section and Instrumentation (from Cunningham, et al., 1975)

b

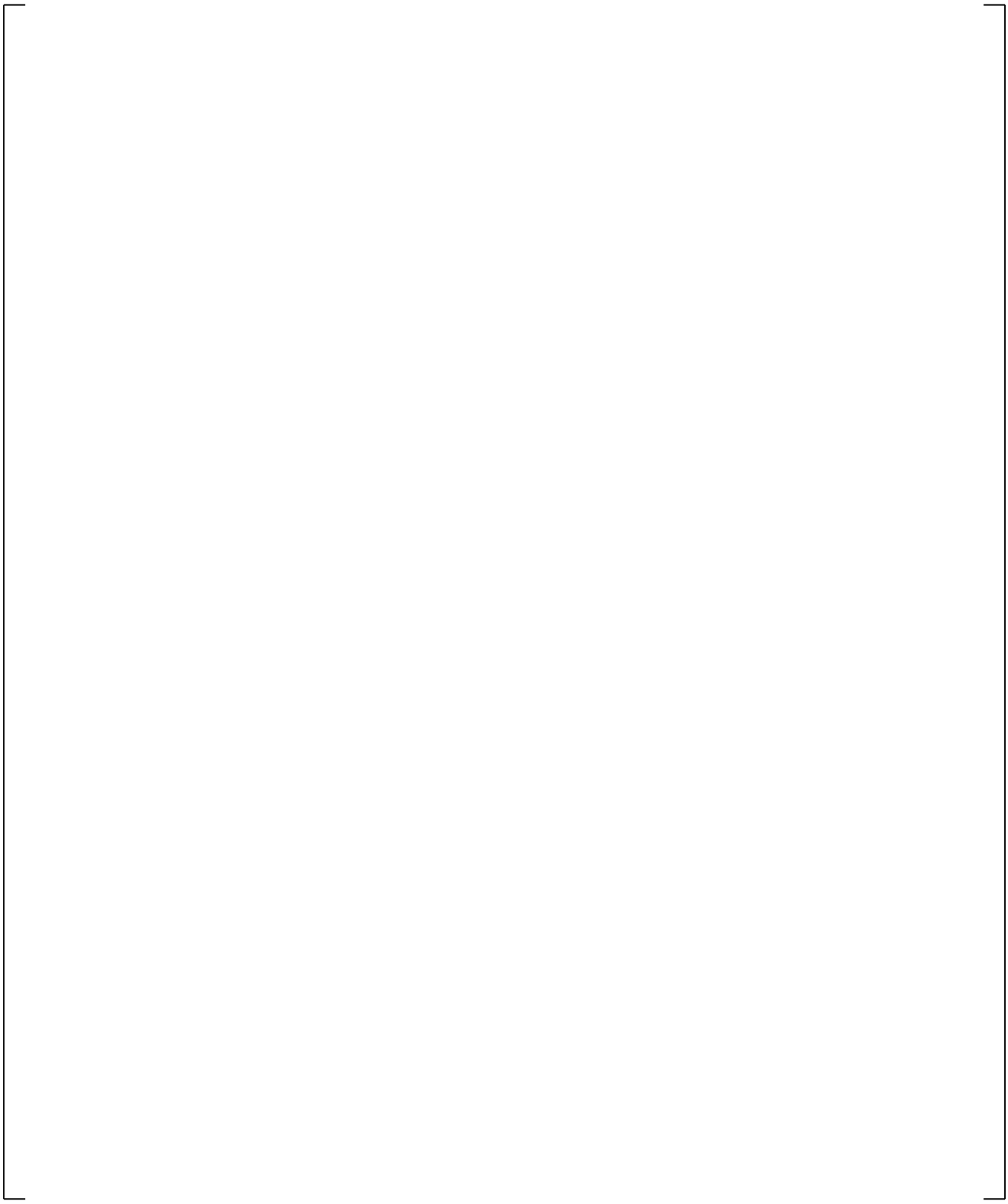

Figure 14.2.2.3-5 G-2 Loop Ground Plate (from Cunningham, et al., 1975)

b

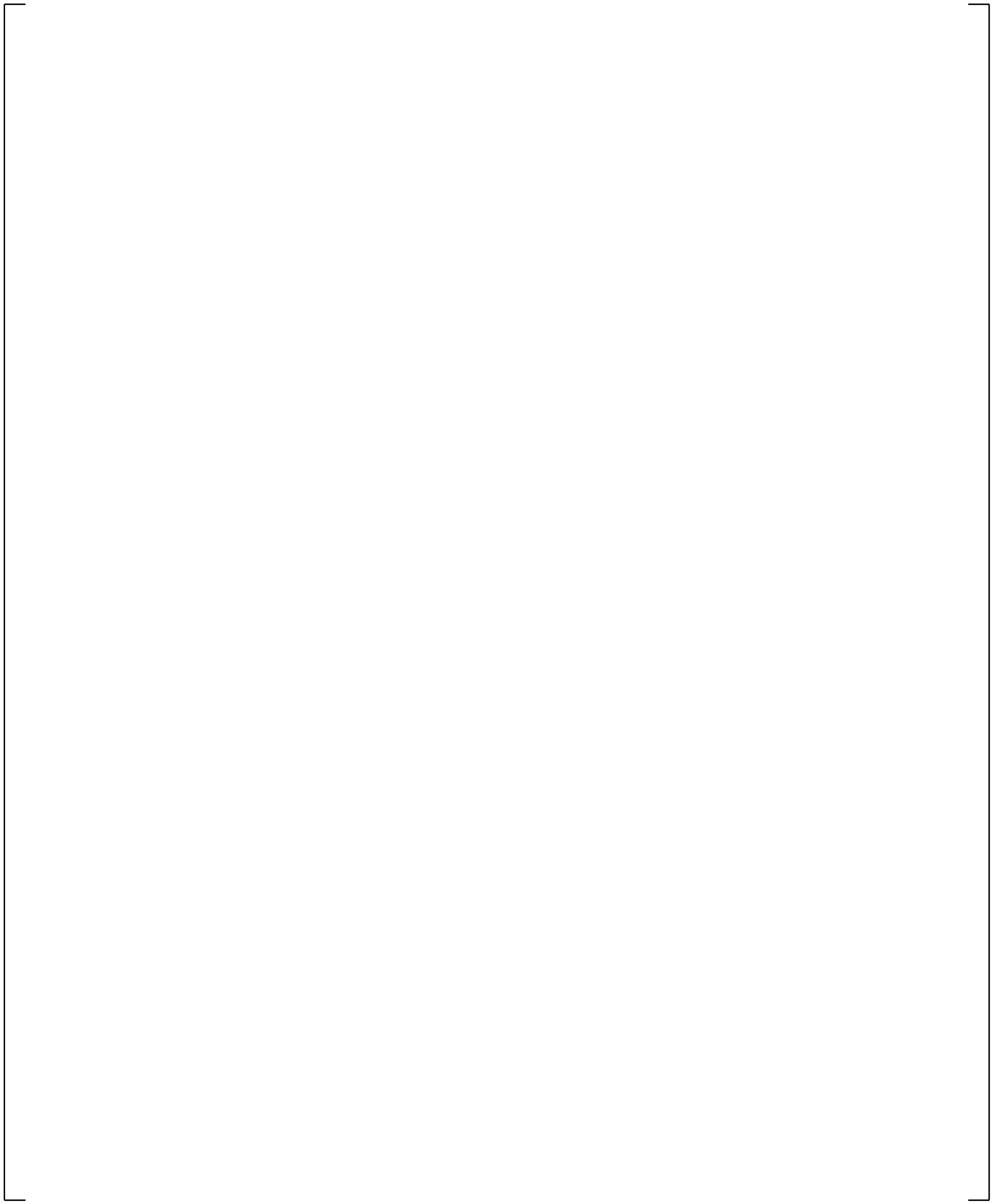

Figure 14.2.2.3-6 Low Pressure UHI Refill Test Sequence of Events (from Hochreiter, et al., 1976)

14.2.3 Test Facilities Used to Assess Reflood Heat Transfer

14.2.3.1 FLECHT-SEASET Reflood Tests

The FLECHT-SEASET test series was conducted in order to provide an experimental data base at low flooding rates for simulated Westinghouse 17x17 fuel rods. The tests and experimental facility are described by Conway et al. (1977) and the data from these tests were evaluated by Lee et al. (1982). Tests 31203, 31504, 31701, 31805, and 32013 were simulated in order to demonstrate the ability of WCOBRA/TRAC-TF2 to predict the thermal-hydraulic phenomena observed in each test and to verify the ability of the code to predict the parametric trends found in the tests. The test conditions for these experiments are shown in Table 14.2.3.1-1. Each of these tests had a peak rod power of 0.7 kW/ft and a uniform radial power shape.

14.2.3.1.1 Facility Description

A diagram of the FLECHT-SEASET test bundle is shown in Figure 14.2.3.1-1. The test section consisted of 161 electrical heater rods (93 non-instrumented and 68 instrumented) arranged in a square pitch with dimensions comparable to 17x17 PWR fuel rod arrays. The rod diameter was 0.374 inches and the rod pitch was 0.496 inches. The bundle also contained 16 control rod guide tubes of 0.484-inch diameter and eight solid filler rods. The triangular filler rods reduced the excess flow area to within 5 percent of the power/flow area ratio of a PWR fuel assembly. The test section was enclosed by a cylindrical stainless steel housing and was connected to an upper and lower plenum. The housing, with an inside diameter of 7.625 inches, was insulated from the outside air to reduce the heat loss to the environment. The bundle flow area was 24.1 square inches. The upper ends of both the housing and test rods were bolted to the top of the test assembly. The lower ends were allowed to hang free permitting axial movement. Horizontal movement and/or bowing of the heater rods was restricted by grid spacers located at 20.5-inch intervals, starting at the beginning of the heated length.

The electrical heater rods were constructed of a spiral-wound heating element embedded in a boron-nitride insulator. A chopped cosine power profile with a peak/average ratio of 1.66 was approximated by a seven-step power profile. The length of each power step and the peak-to-average power factors are shown in Figure 14.2.3.1-2 along with the location of six grid spacers. (Grids at the top and bottom of the bundle are not shown.)

Type K thermocouples were mounted in 68 of the heater rods and in four of the thimble tubes. Differential pressure cells were located every 12 inches along the test section and provided data used in determining mass balance and the bundle void fraction. Steam probes were placed in the bundle and in the test section outlet. The probes were located in the thimble tubes and were designed to separate moisture from the high temperature steam and then aspirate the steam across a thermocouple.

14.2.3.1.2 Test Procedure

The tests were conducted by first pressurizing the test section to the desired system pressure by valving steam from a boiler into the system and the exhaust line control valve. Water was then injected into the test section lower plenum until it reached the beginning of the heated length of the bundle heater rods. Power was next applied to the bundle and the rods were allowed to heatup. When the temperature of any two bundle thermocouples exceeded the pre-selected value of 1600°F, the bundle was reflooded at a specified rate and power was decreased to match the ANSI/ANS 5.1-1971 + 20 percent decay heat rate.

Table 14.2.3.1-1 Test Conditions for FLECHT-SEASET Tests

Test No.	Forced Injection Rate in/s	Upper Plenum Pressure psia	Injection Water Temperature °F
31805	0.81	40	124
31504	0.97	40	123
32013	1.04	60	150
31203	1.51	40	126
31701	6.1	40	127

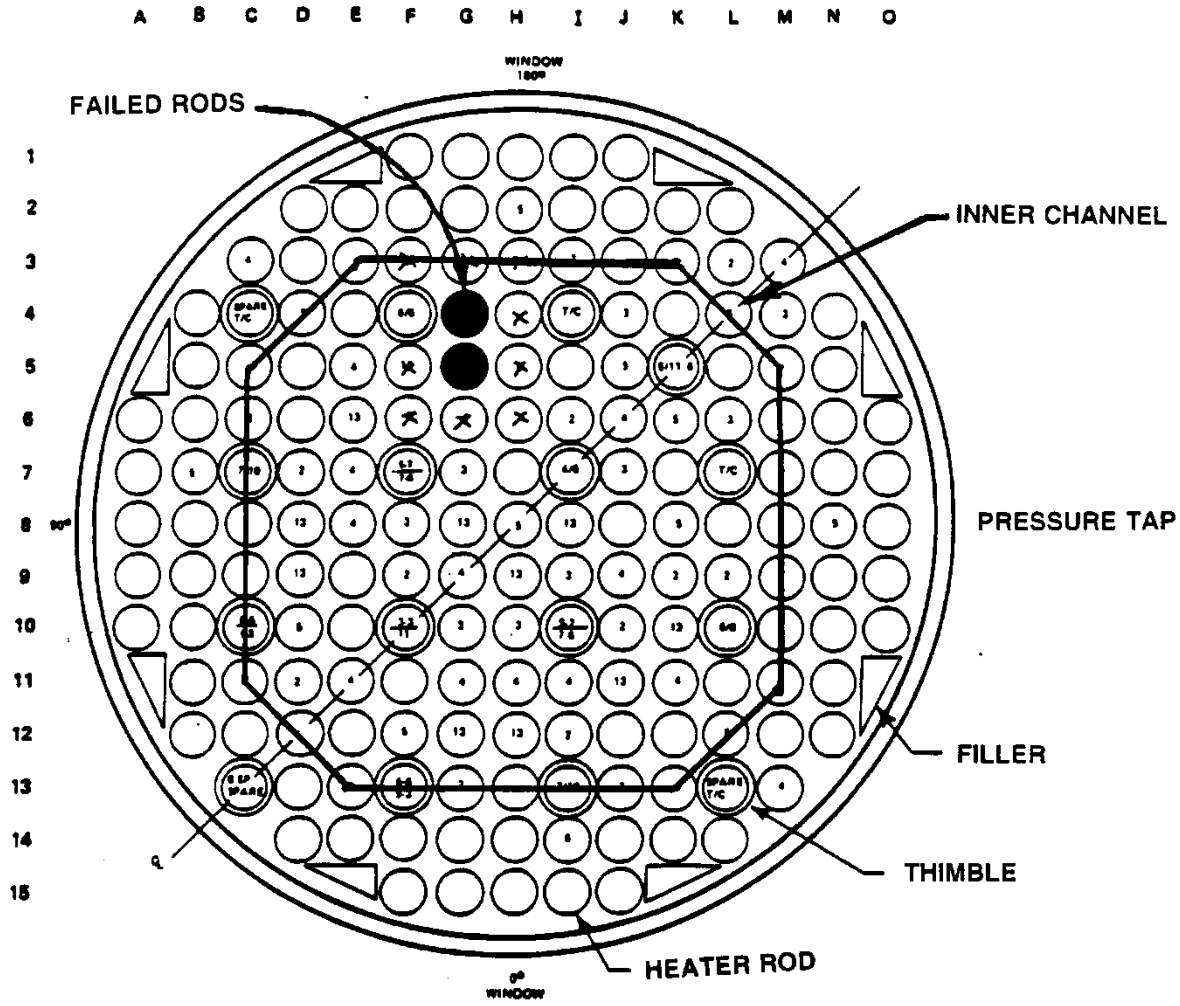

BUNDLE STATISTICS

HOUSING INSIDE DIAMETER	194.0 mm (7.625 in.)
HOUSING WALL THICKNESS	5.08 mm (0.200 in.)
ROD DIAMETER	9.50 mm (0.374 in.)
THIMBLE DIAMETER	12.0 mm (0.474 in.)
ROD PITCH	12.6 mm (0.496 in.)
CROSS-SECTIONAL FLOW AREA	15571 mm^2 (24.136 $in.^2$)
FILLER DIMENSIONS	18.8 x 8.43 mm (0.741 x 0.332 in.)
161 HEATER RODS	— —
16 THIMBLES	— —
8 FILLERS	— —

Figure 14.2.3.1-1 FLECHT-SEASET Rod Bundle Cross Section (from Loftus, et al., 1981)

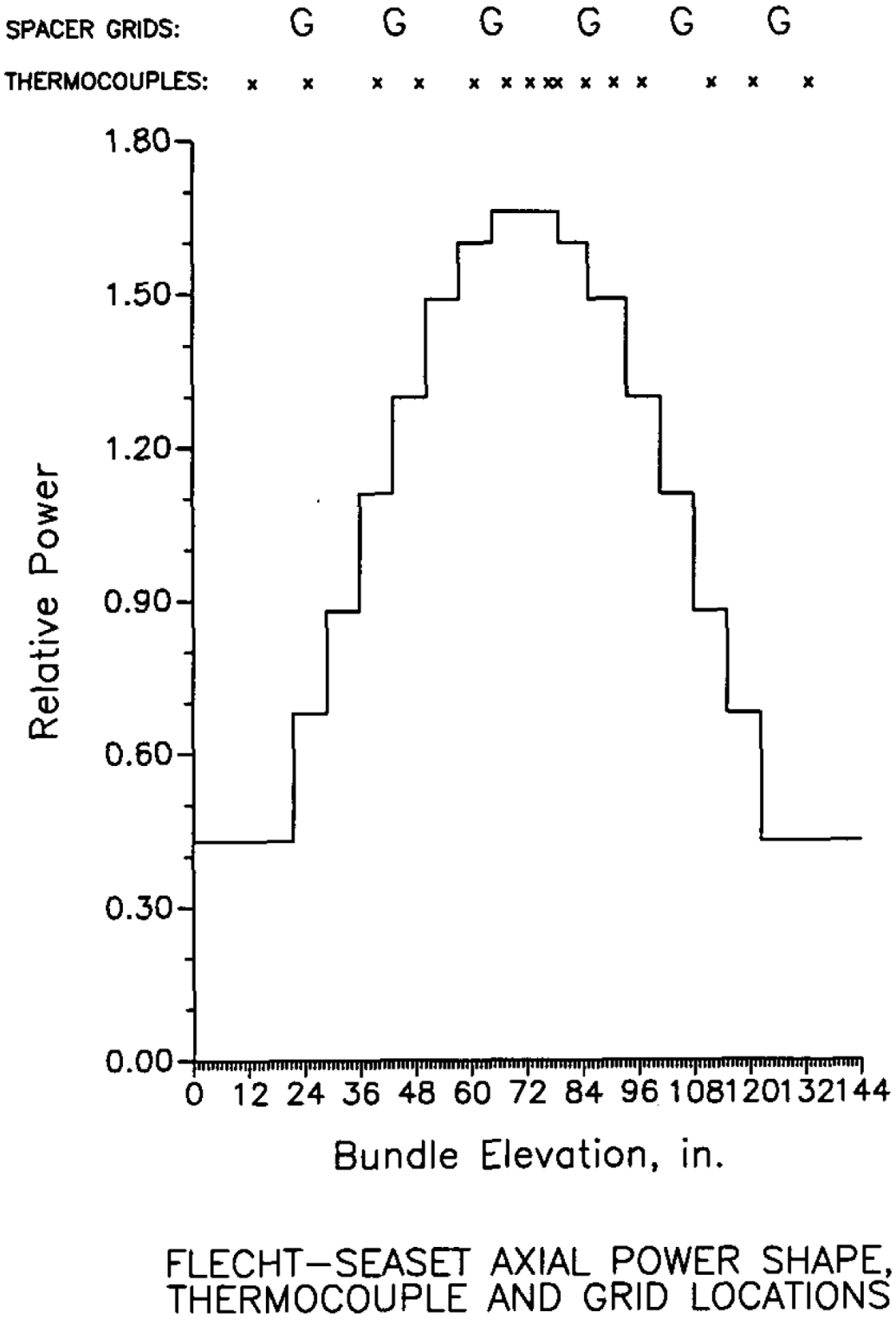

Figure 14.2.3.1-2 FLECHT-SEASET Axial Power Shape Profile and Grid Locations

14.2.3.2 FLECHT Low Flooding Rate Tests

The FLECHT Low Flooding Rate Cosine Power Shape Test series was conducted to provide experimental data for Westinghouse 15x15 fuel. The tests and the experimental facility are described by Rosal et al. (1975). Tests 05029, 05132, and 04641 were simulated to demonstrate the ability of WCOBRA/TRAC-TF2 to predict the thermal-hydraulic phenomena observed in these experiments. The test conditions for these tests are shown in Table 14.2.3.2-1. These tests had a cosine axial power shape with a peak to average power ratio of 1.66.

14.2.3.2.1 Facility Description

A diagram of the FLECHT test bundle is shown in Figure 14.2.3.2-1. The test section consisted of 91 electrical heater rods arranged in a square pitch with dimensions comparable to 15x15 PWR fuel rod arrays. The rod diameter was 0.422 inches and the rod pitch was 0.563 inches. The test bundle also contained eight control rod guide tubes and one instrument tube in a 10x10 square array. The test section was enclosed by a square, 0.7-inch thick carbon steel housing, and was connected to upper and lower plenums. The housing had internal dimensions of 5.889 inches x 5.889 inches, and was insulated from the outside air to reduce heat loss to the environment. Horizontal movement and/or bowing of the heater rods was restricted by eight grid spacers located at 20.5-inch intervals, starting at the beginning of the heated length.

The electrical heater rods were constructed of a spiral-wound heating element embedded in a boron-nitride insulator. A chopped cosine power profile with a peak/average ratio of 1.66 was approximated by a seven-step power profile. The length of each power step and the peak to average power factors are shown in Figure 14.2.3.2-2 along with the location of the grid spacers.

The bundle was assembled with 6 heater rods instrumented with 8 thermocouples, 15 rods with 5 thermocouples, 22 rods with 3 thermocouples and 48 un-instrumented rods.

Test section instrumentation also included fluid and wall thermocouples in the upper and lower plenums, differential pressure transducers which measured pressure drops every two feet along the heated length of the rod bundle, and an overall pressure drop across the entire bundle. A static pressure transducer connected to the upper plenum monitored the test section pressure.

14.2.3.2.2 Test Procedure

The tests were conducted by first pressurizing the test section to the desired system pressure by valving steam from a boiler into the system and the exhaust line control valve. Water was then injected into the test section lower plenum until it reached the beginning of the heated length of the bundle heater rods. Power was next applied to the bundle and the rods were allowed to heatup. When the temperature of any two bundle thermocouples exceeded a pre-selected value, the bundle reflood was initiated and power was decreased to match the ANSI/ANS 5.1-1971 + 20 percent decay heat rate.

Table 14.2.3.2-1 Test Conditions for FLECHT Low Flooding Rate Tests				
Test No.	**Forced Injection Rate in/s**	**Upper Plenum Pressure psia**	**Injection Water Temperature °F**	**Peak Rod Power kW/ft**
05029	0.85	40	126	0.73
05132	1.0	40	127	0.95
04641	1.0	20	89	0.95

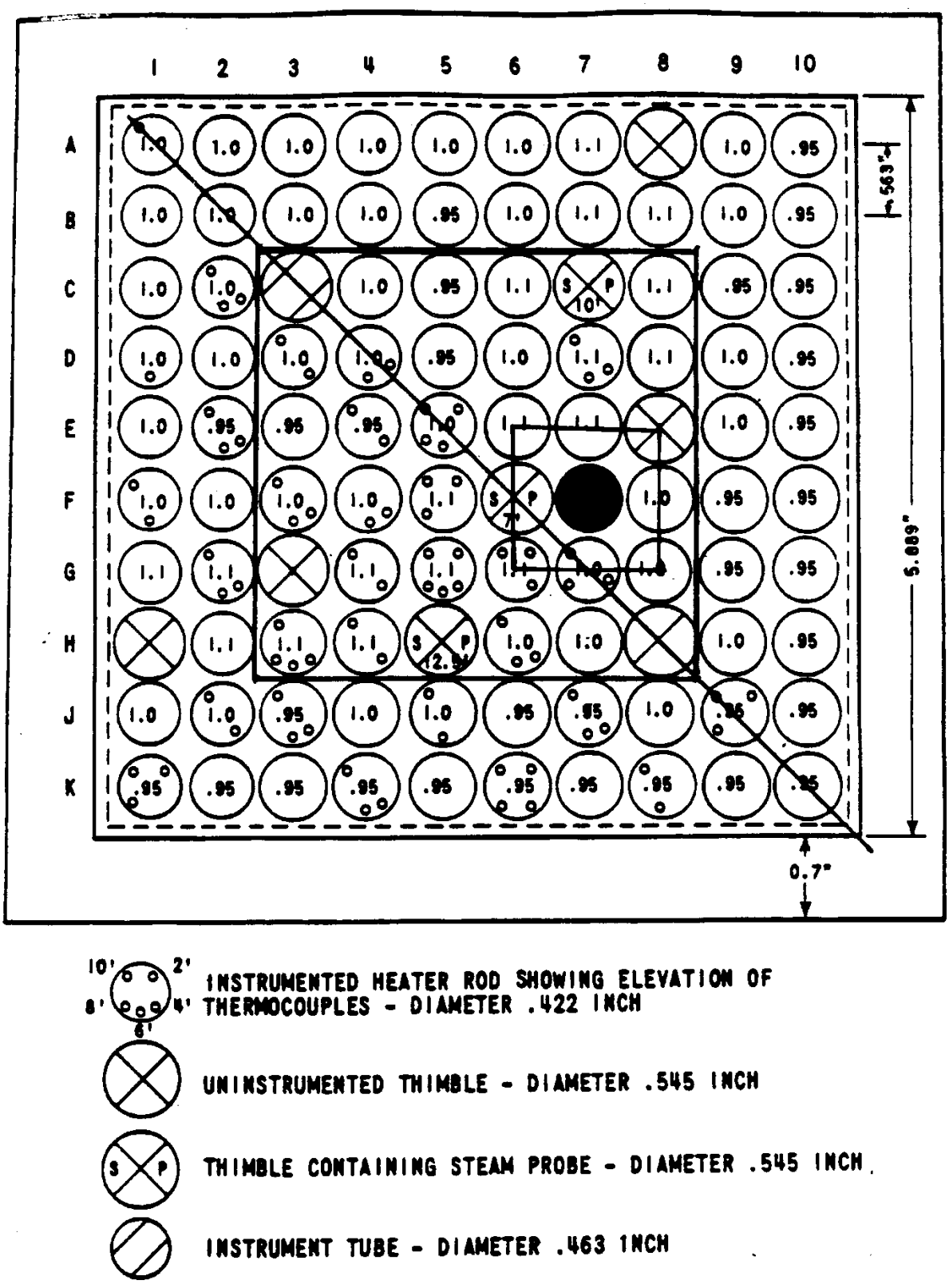

Figure 14.2.3.2-1 FLECHT Rod Bundle Cross Section (from Rosal, et al., 1975)

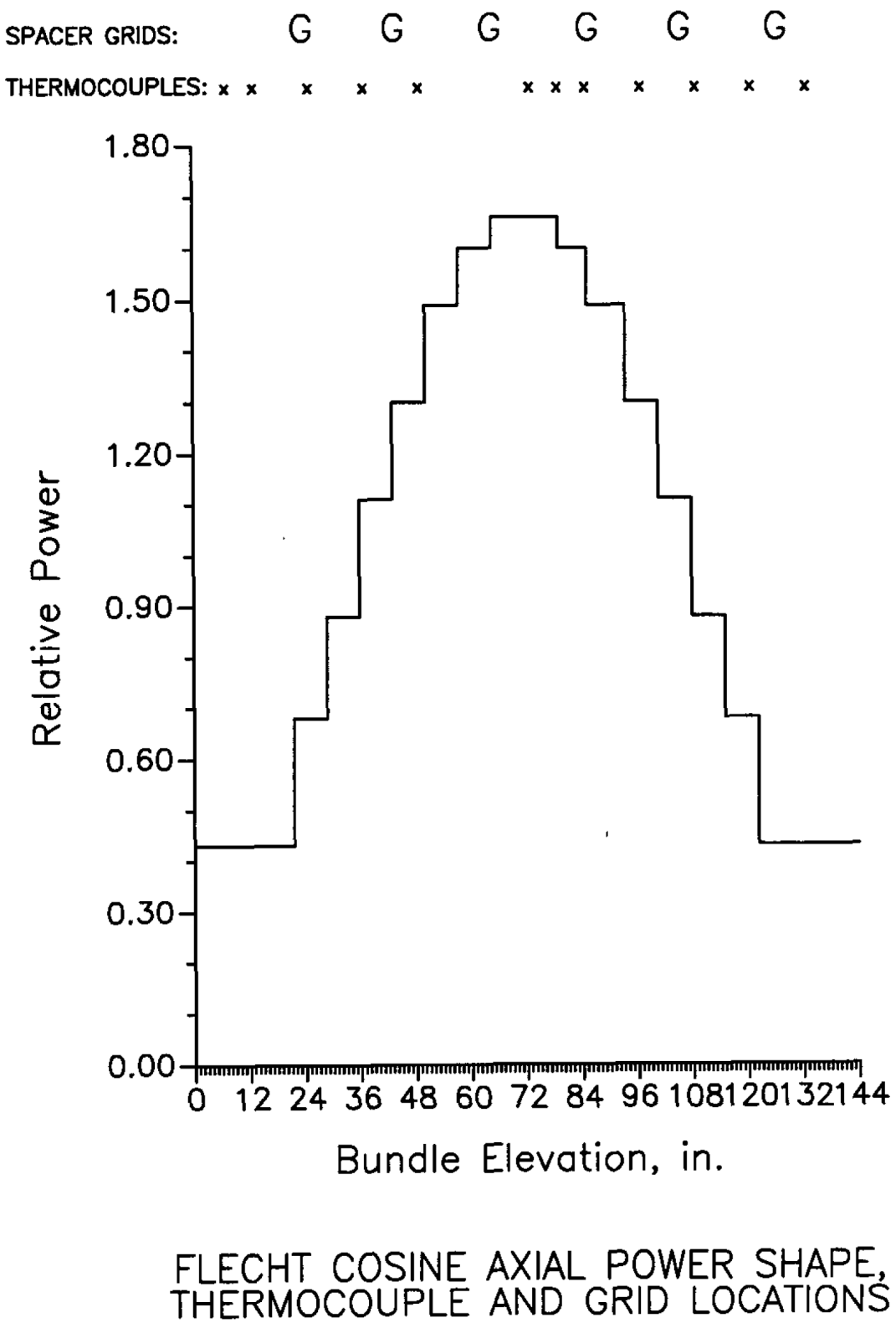

Figure 14.2.3.2-2 FLECHT Cosine Axial Power Shape Profile and Grid Locations

14.2.3.3 FLECHT Top-Skewed Power Tests

The FLECHT skewed power tests were run to provide experimental data at low flooding rates for simulated Westinghouse 15x15 fuel with a top-skewed axial power shape. These tests are described by Rosal et al. (1977). Tests 15305, 13812, 15713, 13914, and 13609 were simulated to demonstrate the ability of WCOBRA/TRAC-TF2 to predict the thermal-hydraulic phenomena observed in these experiments. Table 14.2.3.3-1 lists the conditions for each of these tests. These tests were simulated in order to demonstrate the ability of WCOBRA/TRAC-TF2 to predict the correct thermal-hydraulic response during reflood in a rod bundle with a top-skewed power shape.

14.2.3.3.1 Facility Description

A diagram of the FLECHT top-skewed power shape test bundle is shown in Figure 14.2.3.3-1. The test section consisted of 105 electrical heater rods arranged to simulate a quarter section of a 15x15 PWR fuel assembly. The rod diameter was 0.422 inches and the rod pitch was 0.563 inches. The test bundle also contained 7 simulated control rod thimble tubes and 12 solid filler rods. The triangular filler rods reduced the excess flow area to within 5 percent of the power/flow area ratio of a PWR fuel assembly. The test section was enclosed by a 0.188-inch thick cylindrical stainless steel housing that was connected to the upper and lower plenums. The housing, with an inside diameter of 7.0 inches, was insulated on the exterior to reduce heat loss to the environment. Horizontal movement and/or bowing of the heater rods was restricted by eight grid spacers located at 20.5-inch intervals starting at the beginning of the heated length.

The electrical heater rods were constructed of a spiral-wound heating element embedded in a boron-nitride insulator. The top-skewed power shape was peaked at 9.75 feet and had a maximum peak-to-average power ratio of 1.35. The power shape profile is shown in Figure 14.2.3.3-2.

Heater rod thermocouples were located at 14 elevations in the bundle including 4 thermocouple elevations downstream at the peak power location. Differential pressure transducers were spaced 12 inches apart along the test section. Steam probes were located in thimble tubes in the bundle and also in the test section outlet.

14.2.3.3.2 Test Procedure

The tests were conducted by first pressurizing the test section to the desired system pressure by valving steam from a boiler into the system and the exhaust line control valve. Water was then injected into the test section lower plenum until it reached the beginning of the heated length of the bundle heater rods. Power was next applied to the bundle and the rods were allowed to heatup. When the temperature of any two bundle thermocouples exceeded the pre-selected value of 1600°F, the bundle was reflooded at a specified rate and power was decreased to match the ANSI/ANS 5.1-1971 + 20 percent decay heat rate.

Table 14.2.3.3-1 Test Conditions for FLECHT Top-Skewed Power Tests				
Test No.	**Forced Injection Rate in/s**	**Upper Plenum Pressure psia**	**Injection Water Temperature °F**	**Peak Rod Power kW/ft**
15305	0.8	40	127	0.7
13812	1.0	41	184	0.7
15713	1.0	40	265	0.7
13914	1.0	21	223	0.7
13609	1.0	21	87	0.7

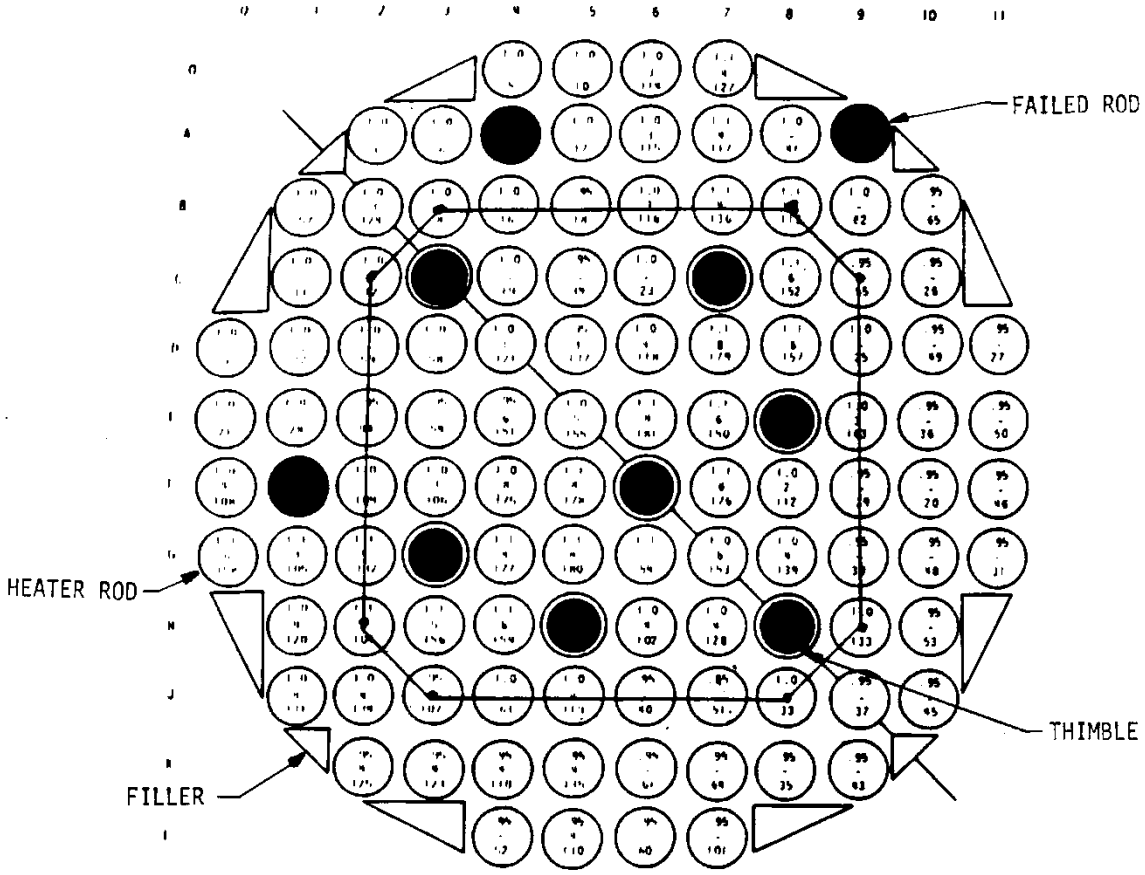

Figure 14.2.3.3-1 FLECHT Top-Skewed Power Shape Test Bundle (from Rosal, et al., 1977)

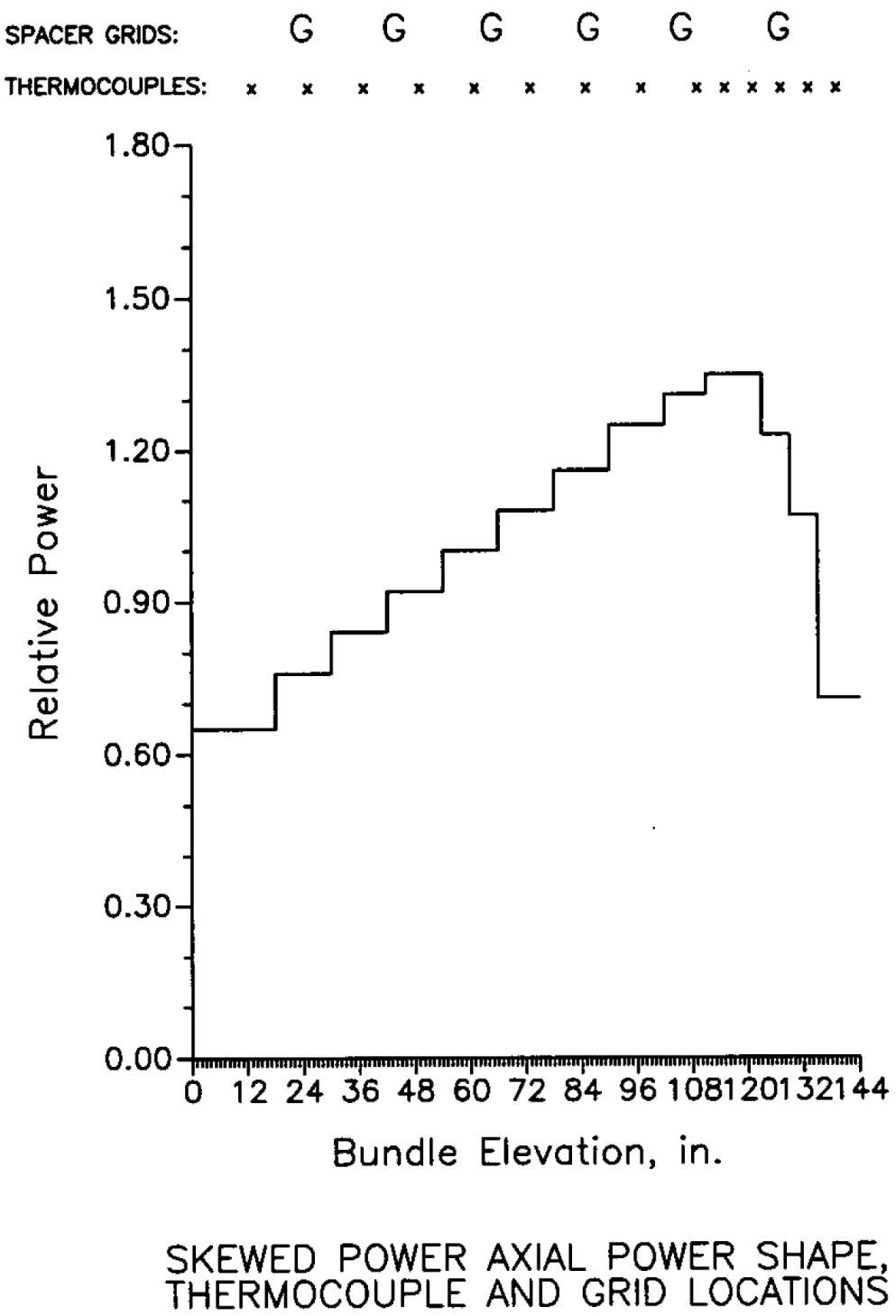

Figure 14.2.3.3-2 FLECHT Top-Skewed Axial Power Shape

14.2.3.4 FLECHT Supplemental Tests

The FLECHT Supplemental Test series was conducted to provide experimental data for Westinghouse 15x15 fuel. The tests and the experimental facility are described by (Cadek et al., 1972). Test 0791 was simulated to demonstrate the ability of WCOBRA/TRAC-TF2 to predict the thermal-hydraulic phenomena observed in this reflood experiment with a very low flooding rate. The test conditions for this test are shown in Table 14.2.3.4-1.

14.2.3.4.1 Facility Description

[

]b

14.2.3.4.2 Test Procedure

[

]b

Table 14.2.3.4-1 Test Conditions for FLECHT Supplemental Test

b

b

Figure 14.2.3.4-1 FLECHT Rod Bundle Cross Section (from Cadek et al., 1972)

b

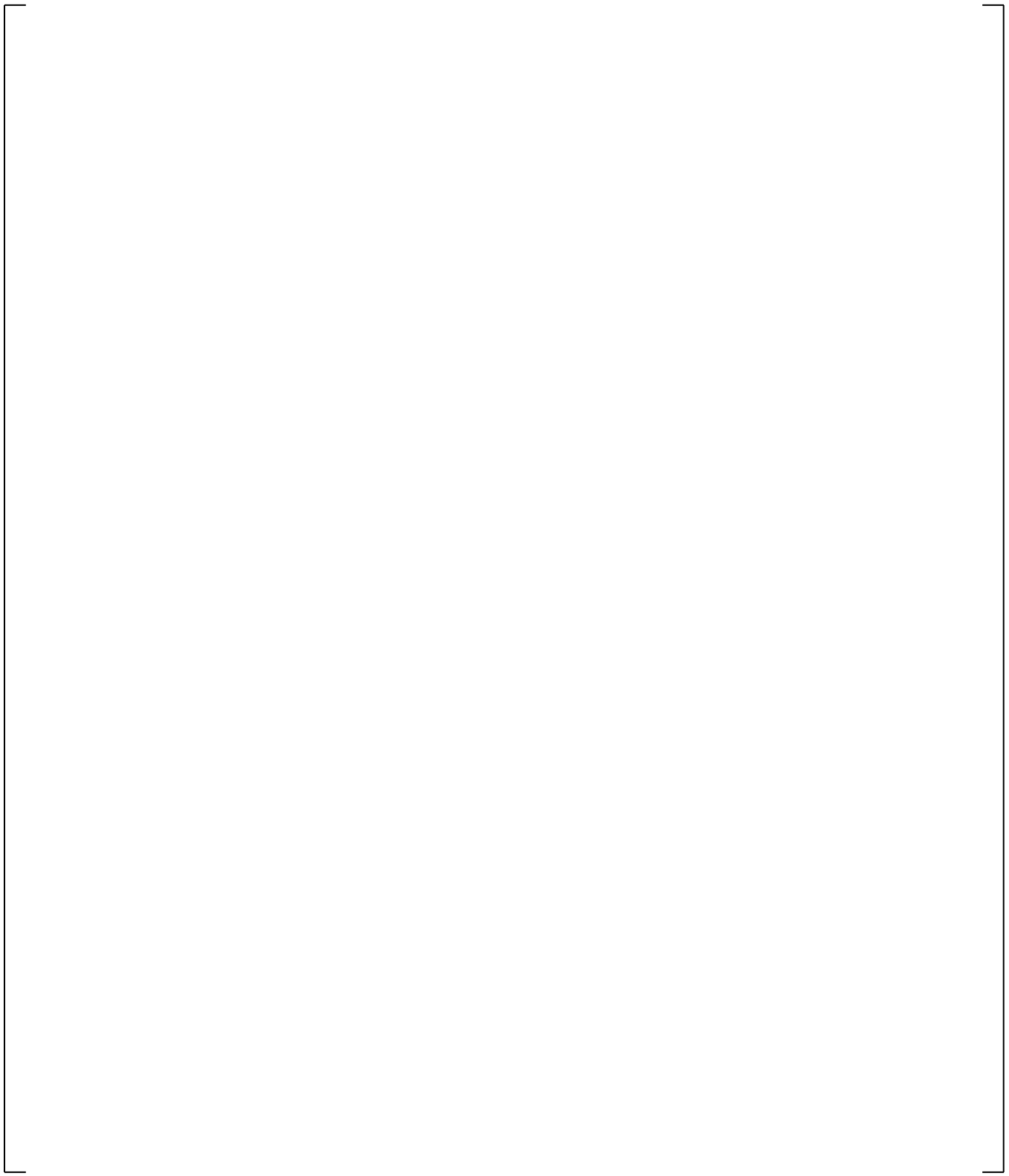

Figure 14.2.3.4-2 FLECHT Heater Rod Schematic Diagram

b

Figure 14.2.3.4-3 FLECHT Axial Power Shape Profile

14.2.3.5 G-2 Reflood Experiments

The low pressure, forced reflood tests performed at the Westinghouse G-2 test facility were simulated using the WCOBRA/TRAC-TF2 computer code. Comparisons of the WCOBRA/TRAC-TF2 results to the reflood test data can be used to help assess the capability of WCOBRA/TRAC-TF2 to accurately predict rod bundle reflood heat transfer behavior including spacer grid effects on dispersed flow film boiling heat transfer. **[**

][b]

14.2.3.5.1 Facility Description

The facility is the same as that described in Section 14.2.2.3.

14.2.3.5.2 Test Procedure

[

][b]

Table 14.2.3.5-1 G-2 Reflood Tests and Conditions

b

14.2.3.6 FEBA

The FEBA tests were a series of forced reflood tests conducted by the Karlsruhe Nuclear Research Center in West Germany and reported by Ihle and Rust (1984). The main purpose of these experiments was to investigate the effects of grid spacers and flow blockages on reflood heat transfer. However, FEBA tests also provided many typical results of a reflood transient.

In order to further verify WCOBRA/TRAC-TF2, four FEBA tests were simulated. **[**

][a,b,c] Table 14.2.3.6-1 summarizes the conditions for each test.

14.2.3.6.1 Facility Description

The FEBA test facility was originally designed to simulate typical forced reflood conditions in a KWU PWR core. **[**

][b]

14.2.3.6.2 Test Procedure

[

]**[b]**

Table 14.2.3.6-1 Conditions for FEBA Tests

b

b

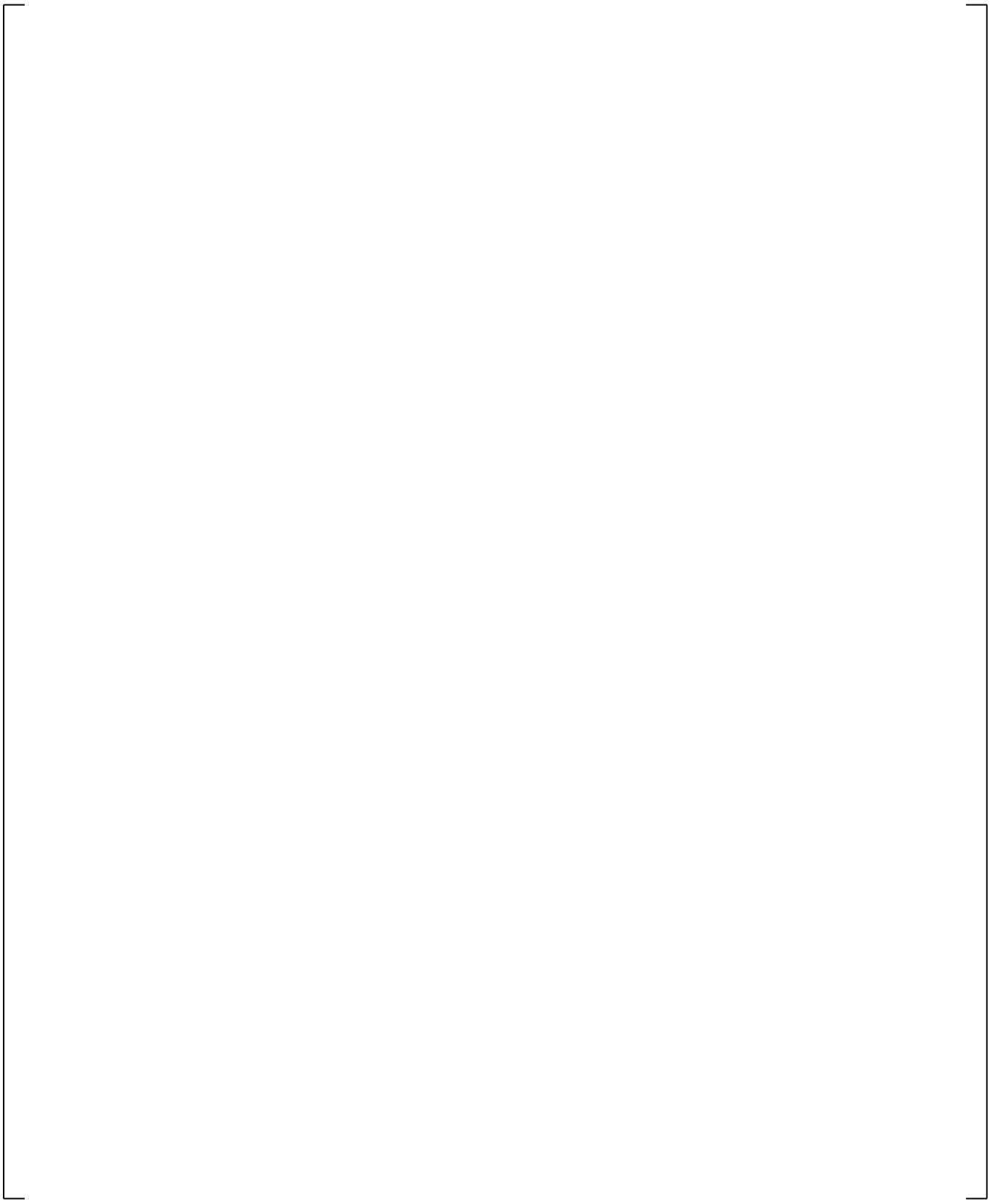

Figure 14.2.3.6-1 FEBA Test Bundle Cross Section (from Ihle and Rust, 1984)

b

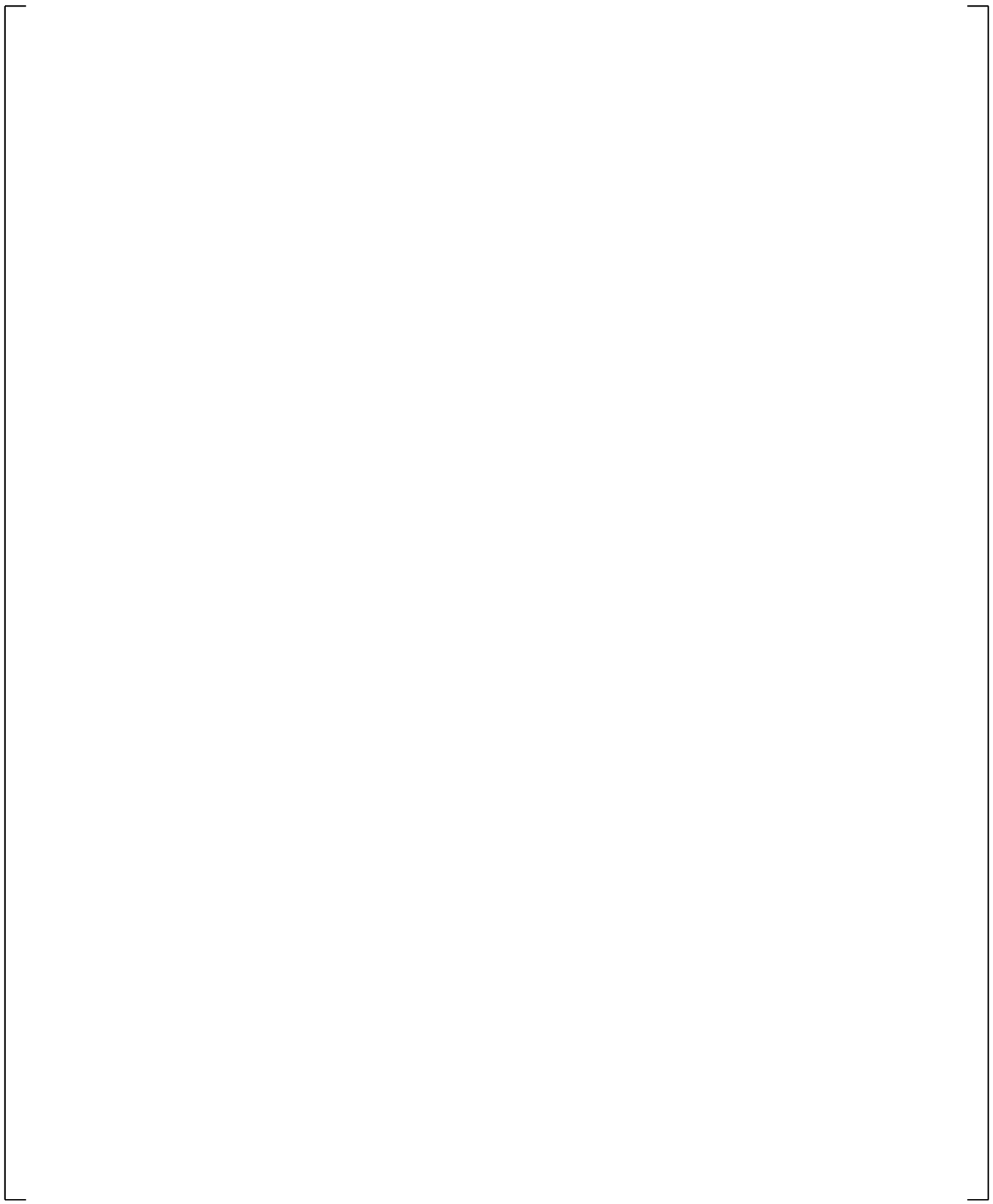

Figure 14.2.3.6-2 FEBA Power Shape and Grid Elevation (from Ihle and Rust, 1984)

14.3 REFERENCES

1. Anklam, T. M., et al., 1982, "Experimental Investigations of Uncovered Bundle Heat Transfer and Two-Phase Mixture Level Swell Under High Pressure Low Heat Flux Conditions," NUREG/CR-2456.

2. ANSI/ANS 5.1-1971, 1971, "Proposed ANS Standard Decay Energy Release Rates Following Shutdown of Uranium-Fueled Thermal Reactors," American Nuclear Society.

3. Cadek, F. F., et al., 1972, "PWR FLECHT Final Report Supplement," WCAP-7931.

4. Conway, C. E. et al., 1977, "PWR FLECHT Separate Effects and System Effects Test (SEASET) Program Plan," NRC/EPRI/Westinghouse-1.

5. Cunningham, J. P., et al., 1974, "ECCS Heat Transfer Experiments with Upper Head Injection, Volume 1: Test Facility, Procedures and Data," WCAP-8400.

6. Cunningham, J. P., Gray, A. D., Mendler, O. J., and Steer, R. W., 1975, "G-2 Facility Forced Flooding Tests with a 17x17 Rod Array – Volume 1: Test Facility, Procedures, and Data," WCAP-8551.

7. Hochreiter, L. E., et al., 1976, "G-2, 17x17 Refill Heat Transfer Test and Analysis," WCAP-8793.

8. Holowach, M. J., et al., 2003, "Scaling of quench front and entrainment-related phenomena," *Nuclear Engineering and Design*, 223, pp. 197-209.

9. Ihle, P., and Rust, K., 1984, "FEBA – Flooding Experiments with Blocked Arrays, Data Report 1, Test Series I through IV," Kernforschungszentrum Karlsruhe.

10. Lee, N., Wong, S., Yeh, H. C., and Hochreiter, L. E., 1982, "PWR FLECHT SEASET Unblocked Bundle, Forced and Gravity Reflood Task Data Evaluation and Analysis Report," NUREG/CR-2256, WCAP-9891.

11. Loftus, M. J. et al., 1981, "PWR FLECHT-SEASET Unblocked Bundle, Forced and Gravity Reflood Task Data Report," Volumes 1 and 2, NUREG/CR-1532, (WCAP-9699).

12. Morris D. G., et al., 1982, "An Analysis of Transient Film Boiling of High-Pressure Water in a Rod Bundle," NUREG/CR-2469.

13. Mullins, C. B., et al., 1982, "Thermal-Hydraulic Test Facility Experimental Data Report for Test 3.03.6AR and Test 308.6C – Transient Film Boiling in Upflow," NUREG/CR-2525, Volumes 2 and 5.

14. Rosal, E. R., Hochreiter, L. E., McGuire, M. F., and Krepinevich, M. C., 1975, "FLECHT Low Flooding Rate Cosine Test Series Data Report," WCAP-8651.

15. Rosal, E. R., Conway, C. E., and Krepinevich, M. C., 1977, "FLECHT Low Flooding Rate Skewed Test Series Data Report," WCAP-9108.

16. Yoder, et al., 1982, "Dispersed Flow Film Boiling in Rod Bundle Geometry-Steady State Heat Transfer Data and Correlation Comparisons," NUREG/CR-2435, ORNL-5822.

15 ASSESSMENT OF THE VESSEL POST-CHF HEAT TRANSFER

15.1 INTRODUCTION

Section 7, Volume 1 describes the VESSEL component heat transfer package. This package consists of a set of heat transfer correlations and selection logic to determine the appropriate correlation based on the local thermal-hydraulic conditions. The heat transfer package in WCOBRA/TRAC-TF2 produces a continuous boiling curve as a function of wall temperature and local fluid conditions. Figure 15.1-1 shows the heat transfer regime map used by the WCOBRA/TRAC-TF2 vessel component.

Heat transfer is modeled in WCOBRA/TRAC-TF2 as a regime dependent, three step process. Specific models and correlations are used for heat transfer from the wall to vapor field, heat transfer from the wall to the liquid fields (continuous and entrained liquid), and interfacial heat transfer between the phases. Each of these processes is flow regime dependent and is based on the local hydrodynamic conditions in the computational cell. Section 7 of Volume 1 described the wall to fluid heat transfer models, and Section 6 of Volume 1 described those for interfacial heat transfer.

The same heat transfer package in WCOBRA/TRAC-TF2 is used for small, intermediate and large break phenomena. No specific logic is included that would result in a difference in small, intermediate and large break heat transfer models.

Section 14 described the tests chosen to assess the WCOBRA/TRAC-TF2 heat transfer models. This section presents a summary of comparisons between test data and predictions of these tests based on the WCOBRA/TRAC-TF2 heat transfer package. Specific aspects of the heat transfer models and calculations will be compared to data where available, and specific calculated parameters are presented to show self-consistency of the WCOBRA/TRAC-TF2 heat transfer package.

a,c

Figure 15.1-1 WCOBRA/TRAC-TF2 Vessel Component Heat Transfer Regime Map (from Figure 7.2-3)

15.2 ROADMAP TO THE ASSESSMENT

The core heat transfer assessment is split into three main areas: single phase vapor (SPV), dispersed flow film boiling (DFFB), and reflood. Heat transfer to SPV is important for predicting cladding temperatures during the refill phase of a large break and the boiloff and recovery phases of a small break. Heat transfer in DFFB is important for predicting cladding temperatures during the blowdown phase of a large break and during the safety injection and accumulator injection phases of an intermediate break. Because of the complicated nature of the reflood phase of a large break which may involve all heat transfer regimes, it will be assessed separately.

One of the issues in quantifying the accuracy of heat transfer relations in a large thermal-hydraulic systems code such as WCOBRA/TRAC-TF2 is that few experimental tests provide a sufficient amount of simultaneous local information on void fraction, phasic flow rates, and phase temperatures. While modeling an entire separate effects test facility and simulating experiments can provide useful information on overall code performance, the predicted results are subject to compensating errors. That is, inaccuracies in one model package can compensate for the inaccuracies in another package producing a fortuitously correct result. An example is an accurate prediction of wall heat flux when heat transfer coefficients are under-predicted, while (T_{wall}-T_{vapor}) was over-predicted because of errors in the hydraulics package. If sufficient local information is available, it is possible to separate the calculation of the heat transfer coefficients from the calculation of the fluid conditions and provide an assessment of the heat transfer prediction alone.

Two types of calculations were used to assess the WCOBRA/TRAC-TF2 heat transfer package.
[

]^{a,c}

[

]a,c

[ ]a,c (15-1)

[

]a,c

a,c

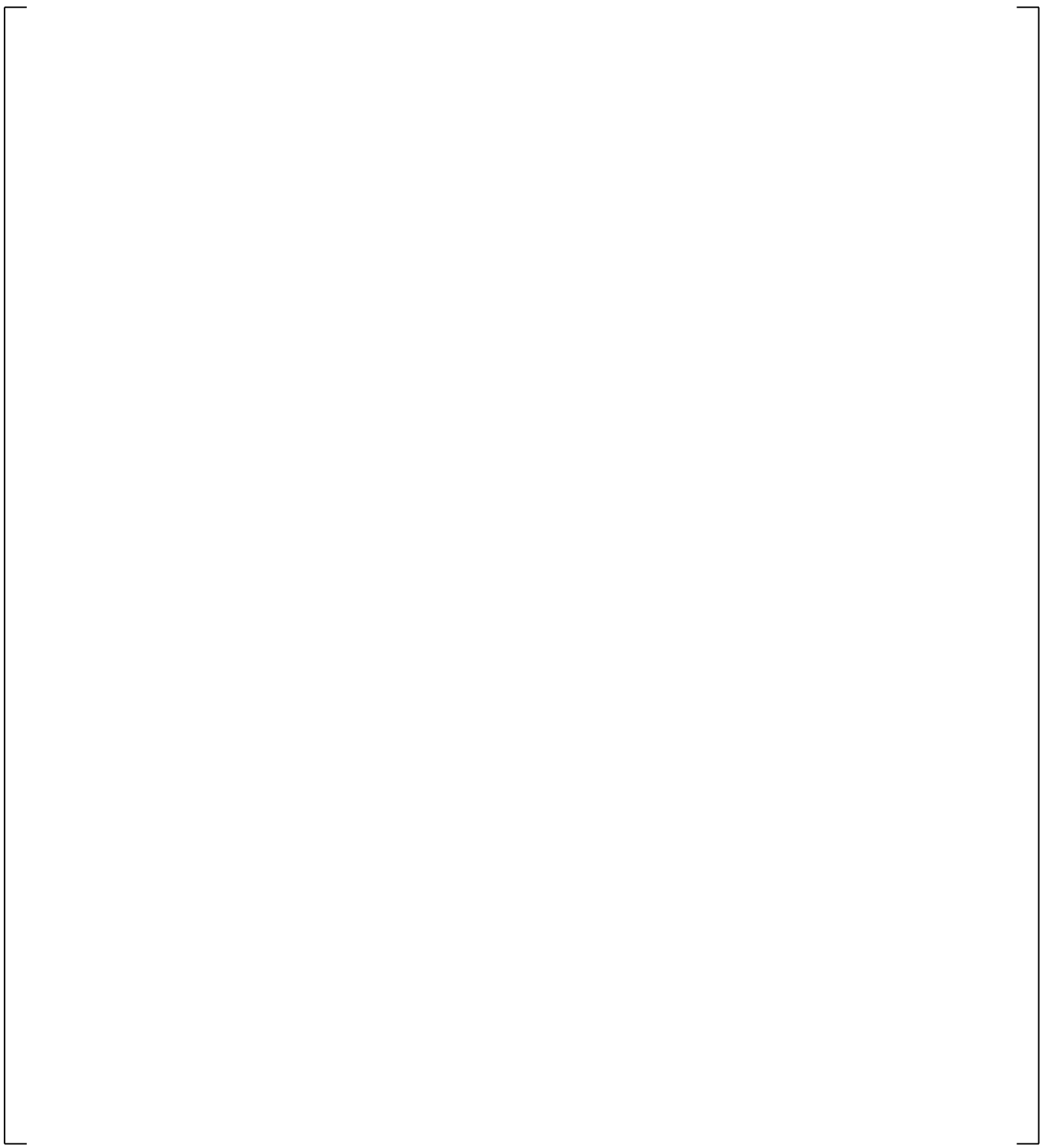

Figure 15.2-1 COBRAHT-TF2 Calculation Procedure

15.3 ASSESSMENT OF CRITICAL HEAT FLUX

Section 13 presents the level swell assessment with which predicting the dryout point is important for determining the location of the mixture level. Section 13.4.2 discusses the level swell assessment for the Oak Ridge National Laboratory (ORNL) Thermal-Hydraulic Test Facility (THTF) uncovered bundle heat transfer test simulations. These tests are assessed for heat transfer in Section 15.4.1. From the vapor temperature figures presented in Section 15.4.1 (Figures 15.4.1-9 to 15.4.1-14), the dryout point for the test simulations **[**

][a,c]

Section 13.4.5 presents an assessment of the critical heat flux (dryout point) for Japan Atomic Energy Research Institute (JAERI) Two-Phase Test Facility (TPTF) tests, and it was concluded that **[**

][a,c]

Tables 22-6 through 22-9 in Section 22.5.3 provide a comparison of measured vs. predicted critical heat flux (CHF) timing for the Loss-of-Fluid Test (LOFT) experiments and simulations, and concluded that **[**

][a,c]

WCOBRA/TRAC-TF2 models and correlations provide **[** **]**[a,c] of the ORNL dispersed flow film boiling tests (Section 15.5.2). There is a **[**

][a,c]

Based on the above, WCOBRA/TRAC-TF2 **[**

][a,c]

Table 15.3-1 LOFT Predicted vs. Measured CHF Timing

a,c

a,c

Figure 15.3-1 Predicted Versus Measured Critical Heat Flux Elevation from JAERI-TPTF Tests (from Figure 13.4.5-6)

15.4 SINGLE PHASE VAPOR HEAT TRANSFER ASSESSMENT

15.4.1 ORNL-THTF Uncovered Bundle Heat Transfer Test Simulations

The measured local heat flux and wall surface temperature were reported as a cross-sectional average value of all thermocouples at each level in (Anklam et al., 1982). In this validation, **[**

][a,c] Figure 15.4.1-1a shows a comparison of the predicted versus measured heat transfer coefficients for the ORNL-THTF uncovered bundle heat transfer tests. On average, the experimental heat transfer coefficients are **[**

][a,c] Figure 15.4.1-1b further shows this by comparing the ratio of the measured to the predicted heat transfer coefficients **[**

][a,c] versus vapor film Reynolds number. Figure 15.4.1-1b also shows that **[**

][a,c]

Section 13.4.2 describes the ORNL-THTF test facility and conditions as well as the WCOBRA/TRAC-TF2 simulations. In addition to void fraction, cladding temperature measurements were taken. Figures 15.4.1-2 through 15.4.1-7 provide a comparison of the measured cladding temperature profiles to the predicted temperature profiles from WCOBRA/TRAC-TF2.

In general, **[**

][a,c] This is further exemplified in Figure 15.4.1-8, which shows the predicted vs. measured cladding temperatures. Lastly, the code **[**

][a,c]

Figures 15.4.1-9 through 15.4.1-14 provide a comparison of the measured and predicted vapor temperatures profiles. As shown by the figures, **[**

][a,c]

a,c

Figure 15.4.1-1a Heat Transfer Coefficient Comparison for ORNL-THTF Uncovered Bundle Tests (from COBRAHT-TF2)

a,c

Figure 15.4.1-1b Ratio of Measured to Predicted Heat Transfer Coefficient vs. Vapor Film Reynolds Number for ORNL-THTF Uncovered Bundle Tests (from COBRAHT-TF2)

a,c

Figure 15.4.1-2 Cladding Temperature Profile Comparison for ORNL-THTF Uncovered Bundle Test I

a,c

Figure 15.4.1-3 Cladding Temperature Profile Comparison for ORNL-THTF Uncovered Bundle Test J

a,c

Figure 15.4.1-4 Cladding Temperature Profile Comparison for ORNL-THTF Uncovered Bundle Test K

a,c

Figure 15.4.1-5 Cladding Temperature Profile Comparison for ORNL-THTF Uncovered Bundle Test L

a,c

Figure 15.4.1-6 Cladding Temperature Profile Comparison for ORNL-THTF Uncovered Bundle Test M

a,c

Figure 15.4.1-7 Cladding Temperature Profile Comparison for ORNL-THTF Uncovered Bundle Test N

a,c

Figure 15.4.1-8 Comparison of Predicted vs. Measured Cladding Temperatures for ORNL-THTF Uncovered Bundle Tests

a,c

Figure 15.4.1-9 Vapor Temperature Profile Comparison for ORNL-THTF Uncovered Bundle Test I

a,c

Figure 15.4.1-10 Vapor Temperature Profile Comparison for ORNL-THTF Uncovered Bundle Test J

a,c

Figure 15.4.1-11 Vapor Temperature Profile Comparison for ORNL-THTF Uncovered Bundle Test K

a,c

Figure 15.4.1-12 Vapor Temperature Profile Comparison for ORNL-THTF Uncovered Bundle Test L

a,c

Figure 15.4.1-13 Vapor Temperature Profile Comparison for ORNL-THTF Uncovered Bundle Test M

a,c

Figure 15.4.1-14 Vapor Temperature Profile Comparison for ORNL-THTF Uncovered Bundle Test N

a,c

Figure 15.4.1-15 Conduction Node and Cell Vapor Temperature Profile Comparison for ORNL-THTF Uncovered Bundle Test I

15.4.2 FLECHT-SEASET Single Phase Vapor Heat Transfer Test Simulations

The measured local heat flux and wall surface temperature were reported for individual thermocouples at various elevations in Wong and Hochreiter (1981). In this validation, **[**

][a,c] Figure 15.4.2-1 shows a comparison of the predicted versus measured heat transfer coefficients for the Full-Length Emergency Core Heat Transfer (FLECHT) SPV heat transfer tests. On average, **[** **]**[a,c] Figure 15.4.2-2 shows a comparison of the ratio of the measured to the predicted heat transfer coefficients **[** **]**[a,c] versus vapor film Reynolds number. As the figure shows, **[**

][a,c]

a,c

Figure 15.4.2-1 Heat Transfer Coefficient Comparison for FLECHT SPV Tests (from COBRAHT-TF2)

a,c

Figure 15.4.2-2 Ratio of Predicted to Measured Heat Transfer Coefficient vs. Vapor Film Reynolds Number for FLECHT SPV Tests (from COBRAHT-TF2)

15.4.3 Single Phase Vapor Heat Transfer Summary and Conclusion

The heat transfer package in WCOBRA/TRAC-TF2 was "driven" with known local conditions from single-phase vapor experiments. The code predicted the heat transfer coefficient **[ ]**[a,c] for both data sets. The **[**

][a,c]

15.5 DISPERSED FLOW FILM BOILING

Dispersed flow film boiling was assessed using two methods. The first method **[**

][a,c] The second method **[**

][a,c]

15.5.1 Assessment Using COBRAHT-TF2

15.5.1.1 ORNL-THTF Steady-State Film Boiling Tests

In Yoder et al., 1982, the measured local heat flux and wall surface temperature were reported for each thermocouple at different levels for individual rods and as a cross-sectional average value of all thermocouples at each level. In this validation, the heat transfer coefficient data at **[**

][a,c]

Figure 15.5.1-1 compares the predicted and measured heat transfer coefficients, with **[**
][a,c]. On average, the experimental heat transfer coefficients are
[ ][a,c]. This is further exemplified with Figure 15.5.1-2, which also shows that **[**
][a,c].

a,c

Figure 15.5.1-1 Heat Transfer Coefficient Comparison for all Thermocouples at [ ]^{a,c} in ORNL Steady-State Film Boiling Tests (from COBRAHT-TF2)

a,c

Figure 15.5.1-2 Ratio of Measured to Predicted Heat Transfer Coefficient vs. Vapor Film Reynolds Number for all Thermocouples at [ ]^{a,c} in ORNL Steady-State Film Boiling Tests (from COBRAHT-TF2)

15.5.2 Assessment Using Test Simulations

15.5.2.1 ORNL-THTF Test Simulations

The WCOBRA/TRAC-TF2 model of the ORNL-THTF is shown in Figure 15.5.2.1-1. The test section is modeled using the vessel component of WCOBRA/TRAC-TF2. Section 1 of the vessel models the lower plenum of the test section. Section 2 models the heated length of the test section with two channels: **[ ]**[a,c]. In this model, the bottom of the heated test section begins 13.5 inches above the bottom of the test section. The measured outlet pressure is applied to the top of the vessel as a pressure boundary condition. Two other boundary conditions representing inlet mass flowrate and inlet flow enthalpy are applied to the bottom of the vessel. These boundary conditions are also derived from measured test data. Figures 14.2.2.1-1 to 14.2.2.1-6 provide the boundary conditions used for the transient tests, and Table 14.2.2.1-2 provides the boundary conditions for the steady-state test.

Two heater rod models are used to represent the 59 heater rods in the test section (one of the 60 heater rods failed during the test; therefore, only 59 heater rods are simulated). Two unheated structures are also used to simulate the shroud box of the test section. This is necessary since the stored energy in these structures is important in the transient experiments. The six grids of the assembly are explicitly modeled in the inner and outer portions of the rod bundle.

Two one-dimensional components are included in the model to satisfy WCOBRA/TRAC-TF2 input requirements. A PIPE component is attached to the last cell of Channel 4 of the VESSEL component. The volume of the pipe is set to a very small value (1.0×10^{-4} ft^3) such that negligible mass is contained in the pipe. A FILL component is attached to the other end of the PIPE to supply a zero velocity boundary condition. Such an arrangement ensures that the vessel component will not lose any fluid through the one-dimensional components.

15.5.2.1.1 Test 3.07.9B Simulation

The comparison of the axial heater rod surface temperature profile between the WCOBRA/TRAC-TF2 predictions and experimental data is shown in Figure 15.5.2.1-2. The experimental data are the averaged value of all the data at the same elevation as reported by Yoder et al., 1982. The local grid spacer effect on the rod temperature profile is clearly evident from the sharp temperature drop around the spacer grid locations. It can also be seen that the overall trend is a decrease in surface temperature with increasing distance above the dryout point. For this test, mass velocities remain high in the bundle, and the increased mixture velocity which results from increased steam quality, provides improved cooling.

The WCOBRA/TRAC-TF2 predictions are indicated by a solid line in the same figure. The dryout point is predicted between **[ ]**[a,c] from the bottom of the heated section. From the available data in the ORNL report, the actual dryout point is approximately 62 inches. Above the dryout point, the heater rod temperature increases during the test because the rod surface is in the transition and film boiling regime. The average peak cladding temperature (PCT) predicted by WCOBRA/TRAC-TF2 is **[ ]**[a,c] above the bottom of the heated test section. The

experimental data indicates an averaged PCT of 1374°F at 62 inches (Level H) with a minimum and maximum individual thermocouple temperature of 1036°F and 1417°F, respectively.

Calculated fluid conditions at the inner channel PCT location and time are presented in Table 15.5.2.1-1. **[**

][a,c]

15.5.2.1.2 Test 3.03.6AR Simulation

In Test 3.03.6AR, the axial temperature profile increases with increasing distance above the dryout point. In this test, low flowrates, increasing void fraction, and superheating of vapor decreases heat transfer, despite increased mixture velocity. The WCOBRA/TRAC-TF2 predictions and experimental data at the time the PCT occurred (11 seconds and 10 seconds from experimental data and WCOBRA/TRAC-TF2 predictions, respectively) are shown in Figure 15.5.2.1-3. The average PCT predicted by WCOBRA/TRAC-TF2 is **[** **]**[a,c] above the bottom of the heated test section, while the experimental data indicates an average PCT of 1217°F at 143 inches (near the top of the heated test section; based on Figure 4.22 of Morris, et al., 1982), with a minimum and maximum individual thermocouple temperature of 1200°F and 1247°F, respectively.

The WCOBRA/TRAC-TF2 prediction of the transient response of the ORNL-THTF bundle is compared to data at several locations (Figures 15.5.2.1-4 to 15.5.2.1-6). In these figures, averaged data and average predicted rod results are shown. These comparisons indicate that WCOBRA/TRAC-TF2 is **[**

][a,c] This test was characterized by relatively large uncertainties in measured inlet flow, as reported by Mullins et al., 1982.

Calculated fluid conditions at the inner channel PCT location and time are presented in Table 15.5.2.1-1. **[**

][a,c]

15.5.2.1.3 Test 3.08.6C Simulation

The axial rod surface temperature profile, at the time (20 seconds) when the PCT is predicted is shown in Figure 15.5.2.1-7. Because of the high inlet mass flowrate maintained during the first 20 seconds of this test, the temperature decreases with increasing distance above the dryout point. The average PCT predicted by WCOBRA/TRAC-TF2 is **[** **]**[a,c], while the available experimental data indicates an average PCT of 1510°F at 107 inches (based on Figure 4.34 of Morris, et al., 1982), with a minimum and maximum individual thermocouple temperature of 1490°F and 1520°F, respectively. Transient heater rod temperatures predicted by WCOBRA/TRAC-TF2 are compared to averaged data at three axial elevations in Figures 15.5.2.1-8 to 15.5.2.1-10. The predicted average cladding temperatures are **[** **]**[a,c].

Calculated fluid conditions at the inner channel PCT location and time are presented in Table 15.5.2.1-1.
[

]^{a,c}

15.5.2.1.4 Summary and Conclusions

The measured and predicted PCTs for all three ORNL tests are shown in Table 15.5.2.1-2 and in Figure 15.5.2.1-11. These results, along with the COBRAHT-TF2 results, indicate that:
[

]^{a,c}

Table 15.5.2.1-1 WCOBRA/TRAC-TF2 Calculated Fluid Conditions at Rod 1 PCT Time and Locations

Test Number	Time (s)	Location (in)	Fractions			Vapor Velocity (ft/s)	Entrained Liquid Velocity (ft/s)	Vapor Temperature (°F)	Droplet Size (ft)
			Liquid	Vapor	Entrained				

a,c

Table 15.5.2.1-2 WCOBRA/TRAC-TF2 PCT Comparisons

a,c

a,c

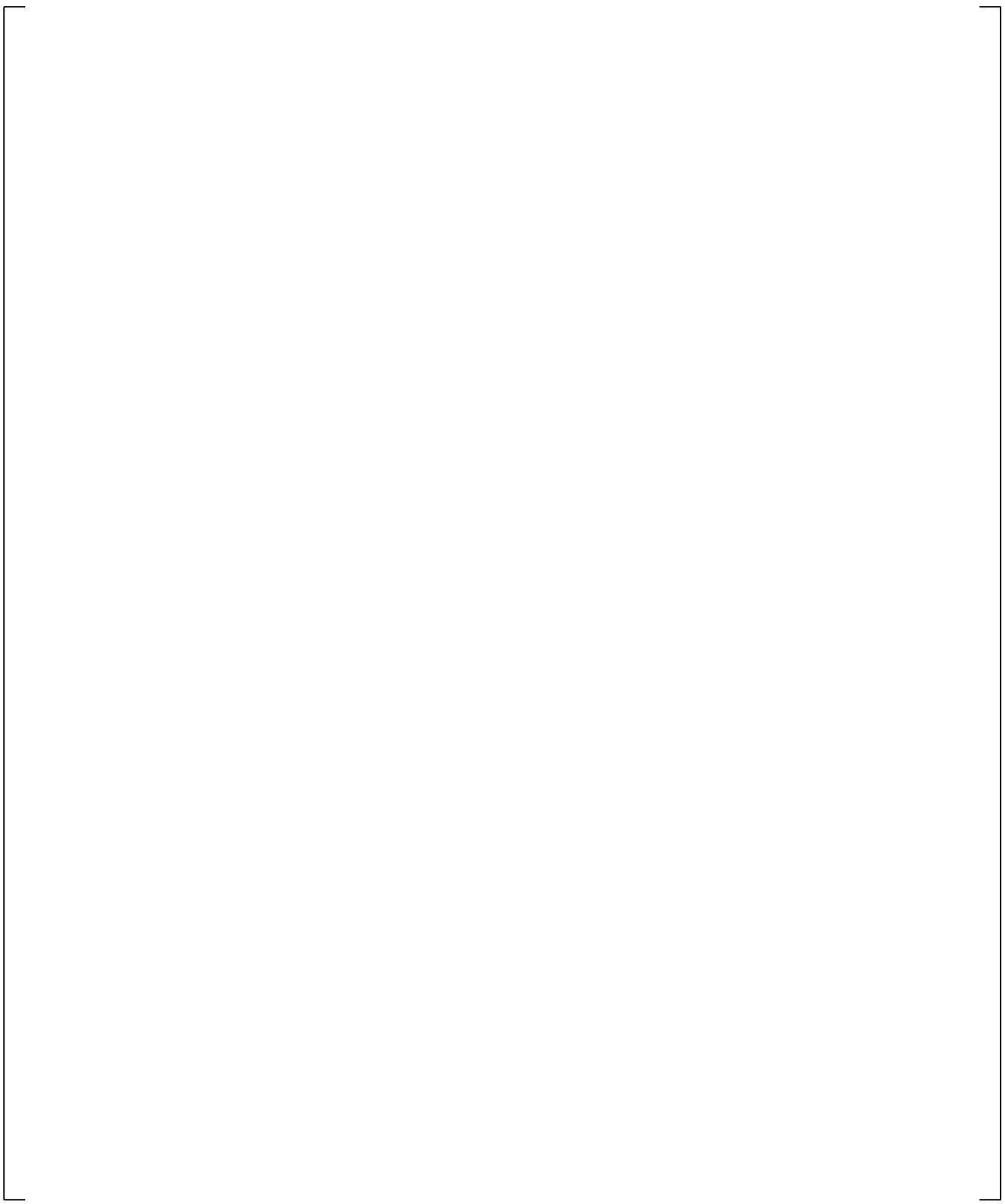

Figure 15.5.2.1-1 WCOBRA/TRAC-TF2 Model for the ORNL-THTF Simulations

[a,c]

Figure 15.5.2.1-2 ORNL-THTF 3.07.9B Axial Heater Rod Temperature Profile at 20 s of Transient

a,c

Figure 15.5.2.1-3 ORNL-THTF 3.03.6AR Axial Heater Rod Temperature Profile at 10 s of Transient

a,c

Figure 15.5.2.1-4 ORNL-THTF 3.03.6AR Transient Heater Rod Temperature at 96 in

a,c

Figure 15.5.2.1-5 ORNL-THTF 3.03.6AR Transient Heater Rod Temperature at 118 in

a,c

Figure 15.5.2.1-6 ORNL-THTF 3.03.6AR Transient Heater Rod Temperature at 143 in

a,c

Figure 15.5.2.1-7 ORNL-THTF 3.08.6C Axial Heater Rod Temperature Profile at 20 s of Transient

a,c

Figure 15.5.2.1-8 ORNL-THTF 3.08.6C Transient Heater Rod Temperature at 95 in

a,c

Figure 15.5.2.1-9 ORNL-THTF 3.08.6C Transient Heater Rod Temperature at 118 in

a,c

Figure 15.5.2.1-10 ORNL-THTF 3.08.6C Transient Heater Rod Temperature at 143 in

a,c

Figure 15.5.2.1-11 ORNL-THTF Predicted versus Measured Peak Cladding Temperature

15.5.2.2 G-1 Blowdown Test Simulations

The WCOBRA/TRAC-TF2 model of the G-1 bundle is comparable to the pressurized water reactor (PWR) core modeling, with similar core node heights. The G-1 model consists of three components: a vessel, a hot leg pipe, and a hot leg break. The vessel contains **[ ]**[a,c] in twelve channels. A schematic diagram of the model is shown in Figure 15.5.2.2-1.

Sections 1 and 2 of the vessel model the lower plenum of the vessel. Section 3 models the heated length of the test section with two channels: **[ ]**[a,c]. The fluid nodes are thermally connected to rods simulating the heater rods. Grids were explicitly modeled to simulate their effect on heat transfer. The inner channel represents the region **[ ]**[a,c] from the test section wall, as illustrated in Figure 14.2.2.2-5. Section 4 models the ground plate, which also has a loss coefficient. Section 5 of the vessel models the upper plenum. At the bottom of the vessel, a pressure boundary condition is used to model the pressure boundary condition imposed on the test section by the cold leg and downcomer. Section 6 models the elevation of the hot leg, and Section 7 models the upper plenum above the hot leg region. A flow and enthalpy boundary condition is used to model the flash chamber flow introduced into the test section through the hot leg (Channel 11). Upper head injection (UHI) flow (if specified) into the upper plenum (Channel 7) is also provided by a flow and enthalpy boundary condition.

15.5.2.2.1 Test 143 Simulation

Test 143 was designated the reference test. It was performed without UHI flow. Other initial conditions for this test are listed in Table 14.2.2.2-2 and repeated below.

[ ]a,c

[

][a,c]

[

]a,c

15.5.2.2.2 Test 148 Simulation

[

]a,c

15.5.2.2.3 Test 152 Simulation

[

]a,c

15.5.2.2.4 Test 146 Simulation

[

]a,c

15.5.2.2.5 Test 153 Simulation

[

]a,c

15.5.2.2.6 Test 154 Simulation

[

][a,c]

15.5.2.2.7 Summary and Conclusions

Overall, WCOBRA/TRAC-TF2 had a tendency to **[**

][a,c].

a,c

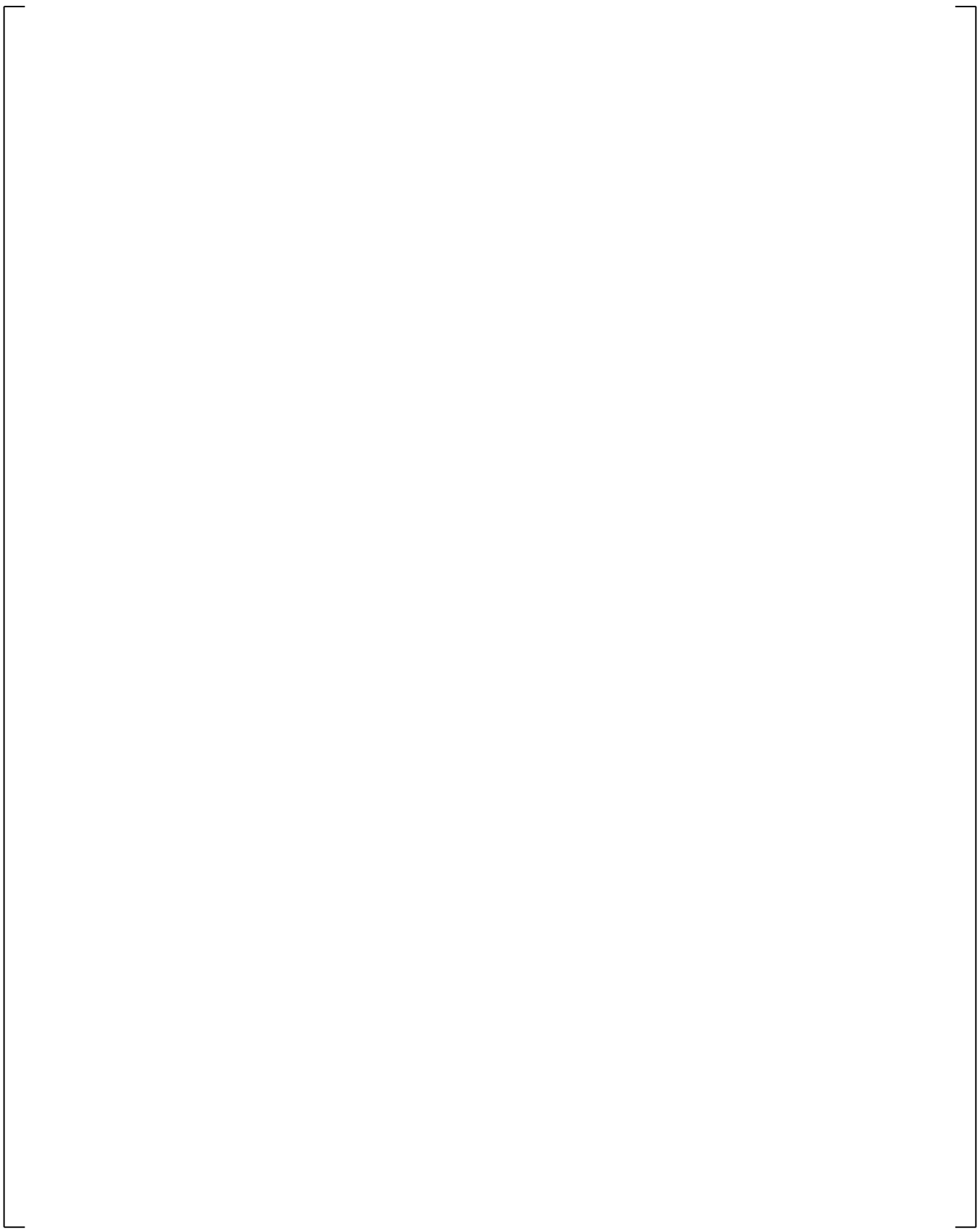

Figure 15.5.2.2-1 WCOBRA/TRAC-TF2 Model of the G-1 Blowdown Test Simulations

a,c

Figure 15.5.2.2-2 G-1 Blowdown Test 143 Cladding Temperature Time History Comparison (24-inch Elevation)

a,c

Figure 15.5.2.2-3 G-1 Blowdown Test 143 Cladding Temperature Time History Comparison (48-inch Elevation)

a,c

Figure 15.5.2.2-4 G-1 Blowdown Test 143 Cladding Temperature Time History Comparison (72-inch Elevation)

a,c

Figure 15.5.2.2-5 G-1 Blowdown Test 143 Cladding Temperature Time History Comparison (96-inch Elevation)

a,c

Figure 15.5.2.2-6 G-1 Blowdown Test 143 Cladding Temperature Time History Comparison (120-inch Elevation)

a,c

Figure 15.5.2.2-7 G-1 Blowdown Test 143 Axial Cladding Temperature Comparison (Time = 6 Seconds)

a,c

Figure 15.5.2.2-8 G-1 Blowdown Test 143 Axial Cladding Temperature Comparison (Time = 10 Seconds, PCT Time)

a,c

Figure 15.5.2.2-9 G-1 Blowdown Test 143 Axial Cladding Temperature Comparison (Time = 15 Seconds)

a,c

Figure 15.5.2.2-10 G-1 Blowdown Test 143 Axial Cladding Temperature Comparison (Time = 20 Seconds)

a,c

Figure 15.5.2.2-11 G-1 Blowdown Test 143 Axial Cladding Temperature Comparison (Time = 30 Seconds)

a,c

Figure 15.5.2.2-12 G-1 Blowdown Test 148 Cladding Temperature Time History Comparison (24-inch Elevation)

a,c

Figure 15.5.2.2-13 G-1 Blowdown Test 148 Cladding Temperature Time History Comparison (48-inch Elevation)

a,c

Figure 15.5.2.2-14 G-1 Blowdown Test 148 Cladding Temperature Time History Comparison (72-inch Elevation)

a,c

Figure 15.5.2.2-15 G-1 Blowdown Test 148 Cladding Temperature Time History Comparison (96-inch Elevation)

a,c

Figure 15.5.2.2-16 G-1 Blowdown Test 148 Cladding Temperature Time History Comparison (120-inch Elevation)

a,c

Figure 15.5.2.2-17 G-1 Blowdown Test 148 Axial Cladding Temperature Comparison (Time = 6 Seconds)

a,c

Figure 15.5.2.2-18 G-1 Blowdown Test 148 Axial Cladding Temperature Comparison (Time = 10 Seconds, PCT Time)

a,c

Figure 15.5.2.2-19 G-1 Blowdown Test 148 Axial Cladding Temperature Comparison (Time = 15 Seconds)

a,c

Figure 15.5.2.2-20 G-1 Blowdown Test 148 Axial Cladding Temperature Comparison (Time = 20 Seconds)

a,c

Figure 15.5.2.2-21 G-1 Blowdown Test 148 Axial Cladding Temperature Comparison (Time = 30 Seconds)

a,c

Figure 15.5.2.2-22 G-1 Blowdown Test 152 Cladding Temperature Time History Comparison (24-inch Elevation)

a,c

Figure 15.5.2.2-23 G-1 Blowdown Test 152 Cladding Temperature Time History Comparison (48-inch Elevation)

a,c

Figure 15.5.2.2-24 G-1 Blowdown Test 152 Cladding Temperature Time History Comparison (72-inch Elevation)

a,c

Figure 15.5.2.2-25 G-1 Blowdown Test 152 Cladding Temperature Time History Comparison (96-inch Elevation)

a,c

Figure 15.5.2.2-26 G-1 Blowdown Test 152 Cladding Temperature Time History Comparison (120-inch Elevation)

a,c

Figure 15.5.2.2-27 G-1 Blowdown Test 152 Axial Cladding Temperature Comparison (Time = 6 Seconds)

a,c

Figure 15.5.2.2-28 G-1 Blowdown Test 152 Axial Cladding Temperature Comparison (Time = 10 Seconds, PCT Time)

a,c

Figure 15.5.2.2-29 G-1 Blowdown Test 152 Axial Cladding Temperature Comparison (Time = 15 Seconds)

a,c

Figure 15.5.2.2-30 G-1 Blowdown Test 152 Axial Cladding Temperature Comparison (Time = 20 Seconds)

a,c

Figure 15.5.2.2-31 G-1 Blowdown Test 152 Axial Cladding Temperature Comparison (Time = 30 Seconds)

a,c

Figure 15.5.2.2-32 G-1 Blowdown Test 146 Cladding Temperature Time History Comparison (24-inch Elevation)

a,c

Figure 15.5.2.2-33 G-1 Blowdown Test 146 Cladding Temperature Time History Comparison (48-inch Elevation)

a,c

Figure 15.5.2.2-34 G-1 Blowdown Test 146 Cladding Temperature Time History Comparison (72-inch Elevation)

a,c

Figure 15.5.2.2-35 Blowdown Test 146 Cladding Temperature Time History Comparison (96-inch Elevation)

a,c

Figure 15.5.2.2-36 G-1 Blowdown Test 146 Cladding Temperature Time History Comparison (120-inch Elevation)

a,c

Figure 15.5.2.2-37 G-1 Blowdown Test 146 Axial Cladding Temperature Comparison (Time = 6 Seconds)

a,c

Figure 15.5.2.2-38 G-1 Blowdown Test 146 Axial Cladding Temperature Comparison (Time = 10 Seconds, PCT Time)

a,c

Figure 15.5.2.2-39 G-1 Blowdown Test 146 Axial Cladding Temperature Comparison (Time = 15 Seconds)

a,c

Figure 15.5.2.2-40 G-1 Blowdown Test 146 Axial Cladding Temperature Comparison (Time = 20 Seconds)

a,c

Figure 15.5.2.2-41 G-1 Blowdown Test 146 Axial Cladding Temperature Comparison (Time = 30 Seconds)

a,c

Figure 15.5.2.2-42 G-1 Blowdown Test 153 Cladding Temperature Time History Comparison (24-inch Elevation)

a,c

Figure 15.5.2.2-43 G-1 Blowdown Test 153 Cladding Temperature Time History Comparison (48-inch Elevation)

a,c

Figure 15.5.2.2-44 G-1 Blowdown Test 153 Cladding Temperature Time History Comparison (72-inch Elevation)

a,c

Figure 15.5.2.2-45 G-1 Blowdown Test 153 Cladding Temperature Time History Comparison (96-inch Elevation)

a,c

Figure 15.5.2.2-46 G-1 Blowdown Test 153 Cladding Temperature Time History Comparison (120-inch Elevation)

a,c

Figure 15.5.2.2-47 G-1 Blowdown Test 153 Axial Cladding Temperature Comparison (Time = 6 Seconds)

a,c

Figure 15.5.2.2-48 G-1 Blowdown Test 153 Axial Cladding Temperature Comparison (Time = 10 Seconds, PCT Time)

a,c

Figure 15.5.2.2-49 G-1 Blowdown Test 153 Axial Cladding Temperature Comparison (Time = 15 Seconds)

a,c

Figure 15.5.2.2-50 G-1 Blowdown Test 153 Axial Cladding Temperature Comparison (Time = 20 Seconds)

a,c

Figure 15.5.2.2-51 G-1 Blowdown Test 153 Axial Cladding Temperature Comparison (Time = 30 Seconds)

a,c

Figure 15.5.2.2-52 G-1 Blowdown Test 154 Cladding Temperature Time History Comparison (24-inch Elevation)

a,c

Figure 15.5.2.2-53 G-1 Blowdown Test 154 Cladding Temperature Time History Comparison (48-inch Elevation)

a,c

Figure 15.5.2.2-54 G-1 Blowdown Test 154 Cladding Temperature Time History Comparison (72-inch Elevation)

a,c

Figure 15.5.2.2-55 G-1 Blowdown Test 154 Cladding Temperature Time History Comparison (96-inch Elevation)

a,c

Figure 15.5.2.2-56 G-1 Blowdown Test 154 Cladding Temperature Time History Comparison (120-inch Elevation)

a,c

Figure 15.5.2.2-57 G-1 Blowdown Test 154 Axial Cladding Temperature Comparison (Time = 6 Seconds)

a,c

Figure 15.5.2.2-58 G-1 Blowdown Test 154 Axial Cladding Temperature Comparison (Time = 10 Seconds, PCT Time)

a,c

Figure 15.5.2.2-59 G-1 Blowdown Test 154 Axial Cladding Temperature Comparison (Time = 15 Seconds)

a,c

Figure 15.5.2.2-60 G-1 Blowdown Test 154 Axial Cladding Temperature Comparison (Time = 20 Seconds)

a,c

Figure 15.5.2.2-61 G-1 Blowdown Test 154 Axial Cladding Temperature Comparison (Time = 30 Seconds)

a,b,c

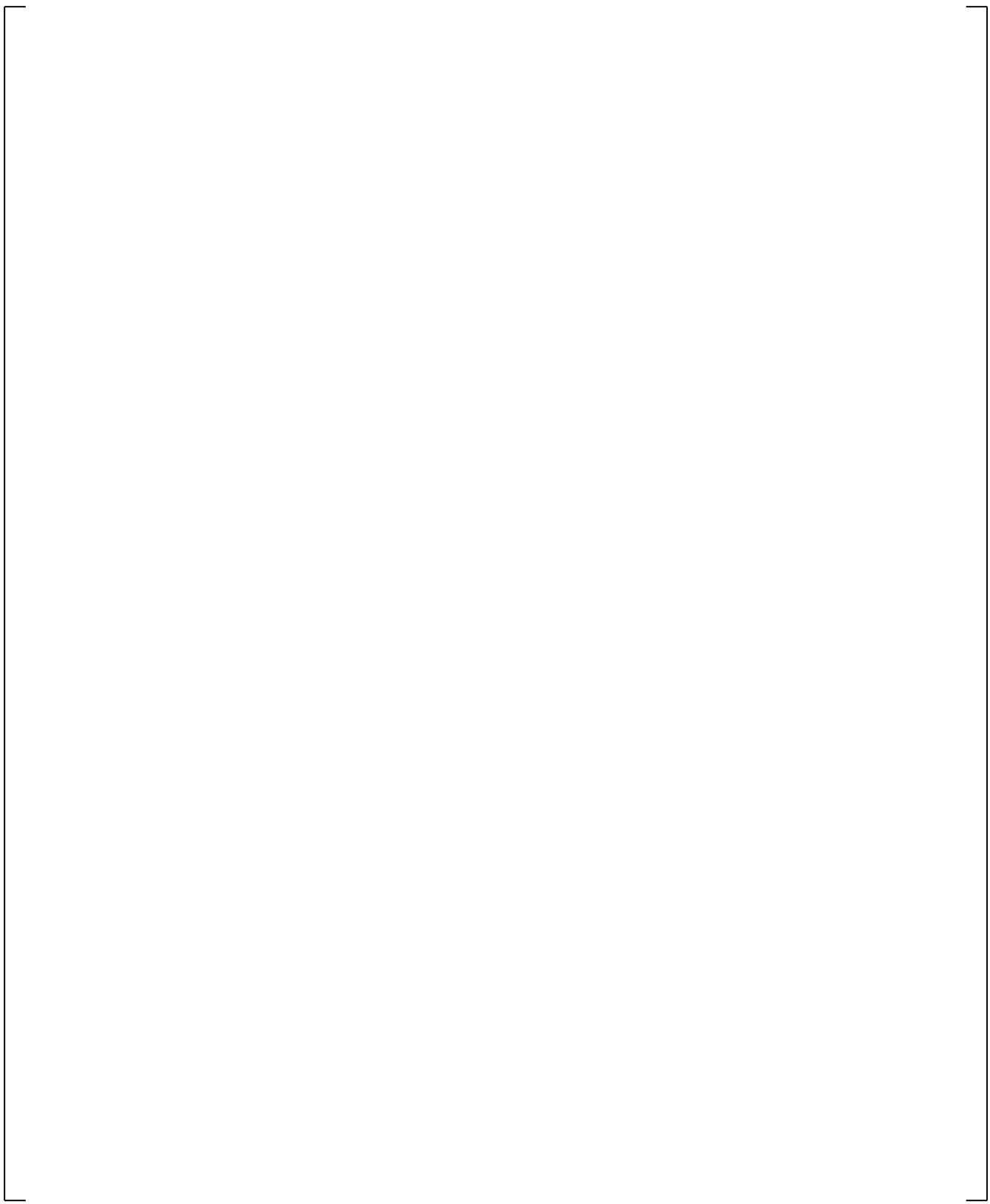

Figure 15.5.2.2-62 Measured Thermocouple Data from (Cunningham et al., 1974)

15.5.2.3 G-2 Refill Test Simulations

The WCOBRA/TRAC-TF2 model of the G-2 facility consisted of a vessel component, a pipe component, and a fill component. The vessel contained **[ ]**[a,c] in six channels. A schematic diagram of the model is shown in Figure 15.5.2.3-1.

Sections 1 and 2 of the vessel model the lower plenum of the vessel. Section 3 models the heated length of the test section with two channels: **[ ]**[a,c]. The fluid nodes are thermally connected to rods simulating the heater rods. Loss coefficients are used to model the nine grids of the fuel assembly in the inner and outer portions of the rod bundle. Section 4 models the ground plate region, and Section 5 of the vessel models the upper plenum. UHI flow into the upper plenum is provided by a vessel boundary condition. The boundary condition specifies the enthalpy and mass flow rate of water into the top of the vessel. At the bottom of the vessel, a pressure boundary condition is used to model the pressure boundary condition imposed on the test section by the cold leg and downcomer. Table 14.2.2.3-2 provides the initial conditions for these tests and is included here.

[ ] a,c

15.5.2.3.1 Test 743 Simulation

[

][a,c]

15.5.2.3.2 Test 750 Simulation

[

]a,c

15.5.2.3.3 Test 760 Simulation

[

]a,c

15.5.2.3.4 Test 761 Simulation

[

]a,c

15.5.2.3.5 Test 762 Simulation

[

]a,c

15.5.2.3.6 Test 767 Simulation

[

]^{a,c}

15.5.2.3.7 Summary and Conclusions

The capability of WCOBRA/TRAC-TF2 to accurately predict film boiling and rewet phenomena in the simulation of G-2 refill tests can be evaluated by comparisons with data of axial temperature profiles, cladding temperature transient histories at specific elevations, and the maximum cladding temperatures for the entire fuel assembly. [

]^{a,c}

Table 15.5.2.3-1 compares measured and predicted $\Delta TCLAD_Z$ (= $TCLAD_Z(t_{end}) - TCLAD_Z(0)$) at either 50 or 60 seconds (Data for some test is not available at 60 s) at several elevations Z. Table 15.5.2.3-2 compares measured and predicted ΔPCT (= $PCT(t_{end}) - PCT(0)$) at either 50 or 60 seconds (Data for some test is not available at 60 s). The average difference and standard deviations are also given in both tables. [

]^{a,c}

Table 15.5.2.3-1 WCOBRA/TRAC-TF2 Cladding Temperature Comparison with the Means of the G-2 Refill Experimental Data

a,c

Table 15.5.2.3-1 (cont.) WCOBRA/TRAC-TF2 Cladding Temperature Comparison with the Means of the G-2 Refill Experimental Data

a,c

Table 15.5.2.3-2 WCOBRA/TRAC-TF2 PCT Comparison with the Means of the G-2 Refill Experimental Data

a,c

a,c

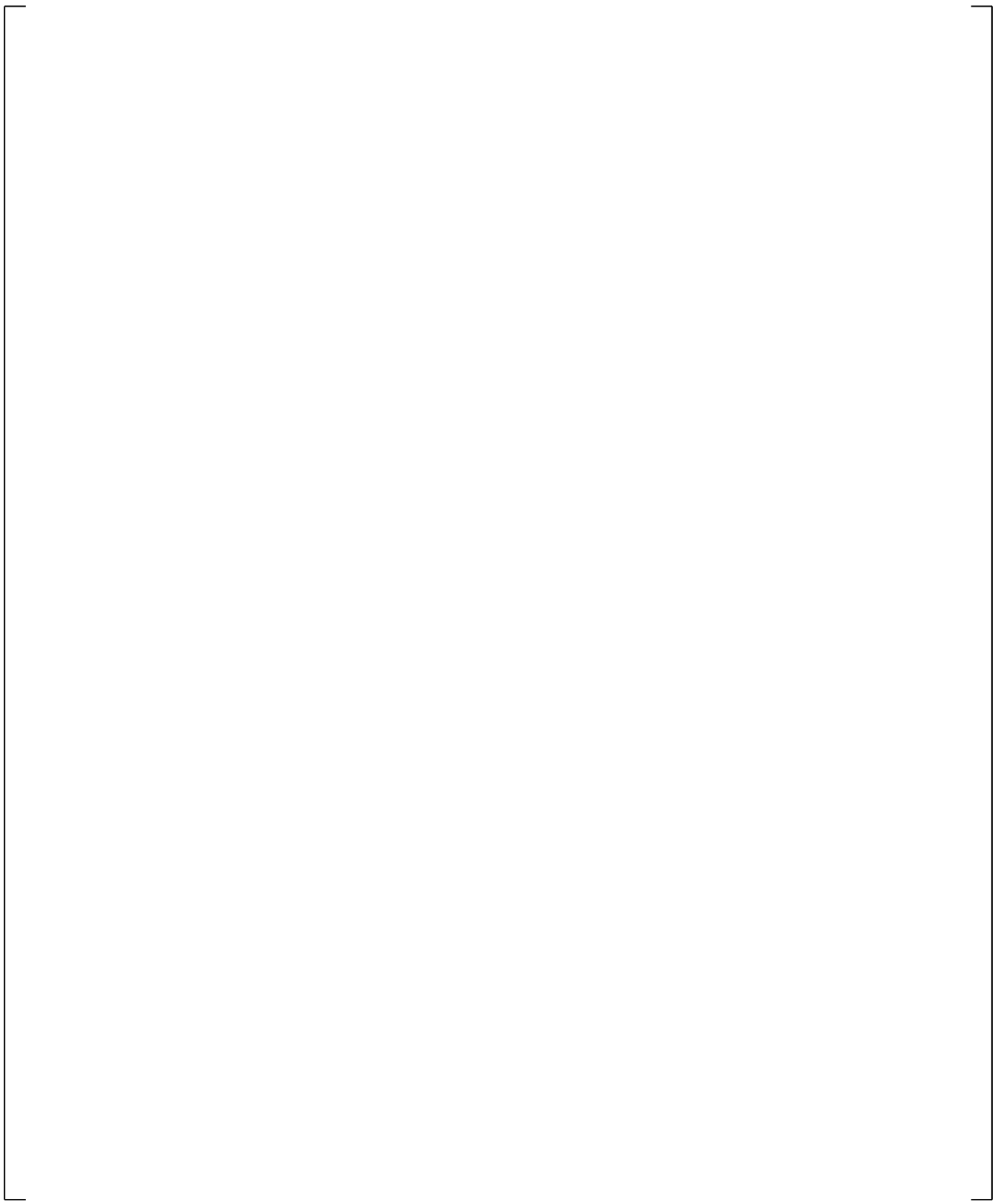

Figure 15.5.2.3-1 WCOBRA/TRAC-TF2 Model for the G-2 Refill Test Simulations

a,c

Figure 15.5.2.3-2 G-2 Refill Test 743 Cladding Temperature Time History Comparison (12.3-inch Elevation)

a,c

Figure 15.5.2.3-3 G-2 Refill Test 743 Cladding Temperature Time History Comparison (28.7-inch Elevation)

a,c

Figure 15.5.2.3-4 G-2 Refill Test 743 Cladding Temperature Time History Comparison (45.1-inch Elevation)

a,c

Figure 15.5.2.3-5 G-2 Refill Test 743 Cladding Temperature Time History Comparison (82.0-inch Elevation)

a,c

Figure 15.5.2.3-6 G-2 Refill Test 743 Cladding Temperature Time History Comparison (118.9-inch Elevation)

a,c

Figure 15.5.2.3-7 G-2 Refill Test 743 Axial Cladding Temperature at 60 s

a,c

Figure 15.5.2.3-8 G-2 Refill Test 750 Cladding Temperature Time History Comparison (12.3-inch Elevation)

a,c

Figure 15.5.2.3-9 G-2 Refill Test 750 Cladding Temperature Time History Comparison (28.7-inch Elevation)

a,c

Figure 15.5.2.3-10 G-2 Refill Test 750 Cladding Temperature Time History Comparison (45.1-inch Elevation)

a,c

Figure 15.5.2.3-11 G-2 Refill Test 750 Cladding Temperature Time History Comparison (82.0-inch Elevation)

a,c

Figure 15.5.2.3-12 G-2 Refill Test 750 Cladding Temperature Time History Comparison (118.9-inch Elevation)

a,c

Figure 15.5.2.3-13 G-2 Refill Test 750 Axial Cladding Temperature at 60 s

a,c

Figure 15.5.2.3-14 G-2 Refill Test 760 Cladding Temperature Time History Comparison (12.3-inch Elevation)

a,c

Figure 15.5.2.3-15 G-2 Refill Test 760 Cladding Temperature Time History Comparison (28.7-inch Elevation)

a,c

Figure 15.5.2.3-16 G-2 Refill Test 760 Cladding Temperature Time History Comparison (45.1-inch Elevation)

a,c

Figure 15.5.2.3-17 G-2 Refill Test 760 Cladding Temperature Time History Comparison (82.0-inch Elevation)

a,c

Figure 15.5.2.3-18 G-2 Refill Test 760 Cladding Temperature Time History Comparison (118.9-inch Elevation)

a,c

Figure 15.5.2.3-19 G-2 Refill Test 760 Axial Cladding Temperature at 50 s

a,c

Figure 15.5.2.3-20 G-2 Refill Test 761 Cladding Temperature Time History Comparison (12.3-inch Elevation)

a,c

Figure 15.5.2.3-21 G-2 Refill Test 761 Cladding Temperature Time History Comparison (28.7-inch Elevation)

a,c

Figure 15.5.2.3-22 G-2 Refill Test 761 Cladding Temperature Time History Comparison (45.1-inch Elevation)

a,c

Figure 15.5.2.3-23 G-2 Refill Test 761 Cladding Temperature Time History Comparison (82.0-inch Elevation)

a,c

Figure 15.5.2.3-24 G-2 Refill Test 761 Cladding Temperature Time History Comparison (118.9-inch Elevation)

a,c

Figure 15.5.2.3-25 G-2 Refill Test 761 Axial Cladding Temperature at 50 s

a,c

Figure 15.5.2.3-26 G-2 Refill Test 762 Cladding Temperature Time History Comparison (12.3-inch Elevation)

a,c

Figure 15.5.2.3-27 G-2 Refill Test 762 Cladding Temperature Time History Comparison (28.7-inch Elevation)

a,c

Figure 15.5.2.3-28 G-2 Refill Test 762 Cladding Temperature Time History Comparison (45.1-inch Elevation)

a,c

Figure 15.5.2.3-29 G-2 Refill Test 762 Cladding Temperature Time History Comparison (82.0-inch Elevation)

a,c

Figure 15.5.2.3-30 G-2 Refill Test 762 Cladding Temperature Time History Comparison (118.9-inch Elevation)

a,c

Figure 15.5.2.3-31 G-2 Refill Test 762 Axial Cladding Temperature at 50 s

a,c

Figure 15.5.2.3-32 G-2 Refill Test 767 Cladding Temperature Time History Comparison (12.3-inch Elevation)

a,c

Figure 15.5.2.3-33 G-2 Refill Test 767 Cladding Temperature Time History Comparison (28.7-inch Elevation)

a,c

Figure 15.5.2.3-34 G-2 Refill Test 767 Cladding Temperature Time History Comparison (45.1-inch Elevation)

a,c

Figure 15.5.2.3-35 G-2 Refill Test 767 Cladding Temperature Time History Comparison (82.0-inch Elevation)

a,c

Figure 15.5.2.3-36 G-2 Refill Test 767 Cladding Temperature Time History Comparison (118.9-inch Elevation)

a,c

Figure 15.5.2.3-37 G-2 Refill Test 767 Axial Cladding Temperature at 60 s

a,c

Figure 15.5.2.3-38 Comparison of G-2 Refill Test Predicted vs. Measured Peak Cladding Temperature

15.5.3 DFFB Heat Transfer Summary and Conclusions

WCOBRA/TRAC-TF2 simulations were performed for blowdown and refill DFFB heat transfer tests conducted in three different experimental programs using three different facilities. The heat transfer was assessed in two ways: 1) [ ]^{a,c}, as discussed in Section 15.5.1, and, 2) [ ]^{a,c}, as discussed in Section 15.5.2.

Using [ ]^{a,c}

Using [ ]^{a,c}

Six G-1 Blowdown test simulations were performed using WCOBRA/TRAC-TF2. In all six cases, the code [ ]^{a,c}.

Using WCOBRA/TRAC-TF2, simulations were performed for six G-2 Refill tests. In all six cases, the code [ ]^{a,c}.

It is concluded that WCOBRA/TRAC-TF2 [ ]^{a,c}.

Additional assessments for blowdown cooling rates, quench times and entrained droplets are performed in Section 15.9.

15.6 REFLOOD

15.6.1 WCOBRA/TRAC-TF2 Simulations of FLECHT-SEASET Test Series

The FLECHT Separate-Effects and System-Effects Tests (SEASET) assembly is modeled with three WCOBRA/TRAC-TF2 components. A VESSEL component is used to model the heated bundle, the upper plenum, and the top six inches of the lower plenum. Boundary conditions based on measured values were imposed on the top and the bottom of the VESSEL component. A PIPE component is attached at the top of the VESSEL, while a zero velocity FILL component is attached to the PIPE only to satisfy the WCOBRA/TRAC-TF2 requirement of at least one one-dimensional component.

The VESSEL component is composed of four channels. Two channels are used to model the test section, one for the inner region of the bundle and one for the outer region that includes the bundle housing. The transverse noding is shown in Figure 15.6.1-1. [ ]^{a,c} (The two rods that failed before testing were neglected.) These rods are each modeled with a single rod model having

the dimensions of the actual heater rods. The heat flux from the rod to the fluid is multiplied by the number of heater rods in the region represented by the channel to obtain the correct heat flux to the fluid. The test section housing is modeled with an unheated structure having a TUBE geometry, thermally connected to the outer channel on the inside surface and insulated on the outer surface. The WCOBRA/TRAC-TF2 vertical cell lengths for the vessel are shown in Figure 15.6.1-2.

The WCOBRA/TRAC-TF2 heater rods are initialized with axial temperature profiles determined by measured temperatures at the start of reflood for each individual test. The initial temperatures for all axial levels were computed by averaging the thermocouple temperatures within a radial boundary at a given elevation. Two heater rods were inoperative during the entire transient, therefore the rod temperatures in the immediate vicinity of the unpowered rods were eliminated from the initial temperature averaging. The housing is initialized with an axial temperature profile determined from thermocouples that were attached to the facility housing.

Both of the WCOBRA/TRAC-TF2 rods used the axial power profile shown in Figure 15.6.1-3. The housing had zero power generation.

The reflood transient was simulated using measured values of the injected flow as a boundary condition imposed on the bottom of the VESSEL component. A constant pressure boundary condition is imposed on the top node of the VESSEL. During the experiment, the heater rod power was decreased according to the ANS 1971 + 20 percent power decay curve, assuming a bottom of core recovery time of 30 seconds. The bundle power measurements were used as input for the simulated rods. The simulation was continued until quench was predicted at all elevations.

Additional initial conditions are provided in Table 14.1-6 for each test and are repeated here.

Test Series	Test Number	Pressure psia	Flooding Rate in/s	Inlet Sub-cooling °F	Peak Power kW/ft	Comment
FLECHT SEASET	31805	40	0.81	143	0.7	COSINE POWER SHAPE 17x17 PWR ROD ARRAY
	31203	40	1.51	141	0.7	
	31701	40	6.1	140	0.7	
	31504	40	0.97	144	0.7	
	32013	60	1.04	143	0.7	

15.6.1.1 FLECHT-SEASET Results

15.6.1.1.1 FLECHT-SEASET Test 31805

The reflood rate for Test 31805 was 0.81 in/sec. The test pressure was maintained at 40 psia and the injected coolant temperature was 124°F. The WCOBRA/TRAC-TF2 simulation of Test 31805 was run for the first 800 seconds of the experiment, by which time all heater rod elevations had quenched in both the prediction and the test. Figures 15.6.1-4 through 15.6.1-10 show the comparison of predicted and measured temperatures at elevations 24, 48, 72, 78, 84, 96, and 120 inches from the bottom of the heated length. The code prediction (the solid curve) is for simulated rod temperatures in the inner channel (rod no. 1 located in Channel 2 of Figure 15.6.1-2). The curves in these figures representing the data show individual thermocouples located within the boundary of the WCOBRA/TRAC-TF2 inner channel.

Figure 15.6.1-11 shows the prediction of the quench front elevation compared to the quench elevations deduced from temperature measurements. The code prediction shows **[**

][a,c]

Comparisons of the axial temperature profiles are shown in Figure 15.6.1-12 at 100 seconds, and in Figure 15.6.1-13 at 200 seconds. **[**

][a,c]

Figure 15.6.1-14 summarizes the comparisons of the maximum predicted cladding temperatures at elevations where thermocouples were located. The predicted and measured turn-around times for this test are compared in Figure 15.6.1-15. The code predicts **[**

][a,c].

Figures 15.6.1-16 through 15.6.1-18 provide comparisons of the predicted and measured axial pressure differentials in the bundle, which shows the distribution of liquid in the bundle. Figure 15.6.1-16 shows a comparison of the pressure differentials in the lower half (0 to 72 inches) of the bundle. The WCOBRA/TRAC-TF2 prediction is **[**

][a,c]

The FLECHT-SEASET facility included steam temperature probes located in the thimble tubes. Figures 15.6.1-19 through 15.6.1-23 show comparisons of the measured and predicted vapor temperatures at several locations in the bundle. Figure 15.6.1-19 shows a comparison low in the bundle, at the 48-inch elevation. Figure 15.6.1-20 shows the comparison near the bundle mid-height, just upstream of the peak temperature elevations, while Figure 15.6.1-21 shows the comparison just downstream of the peak temperatures. Figure 15.6.1-22 shows the comparison at the 120-inch elevation, and Figure 15.6.1-23 the comparison near the bundle exit. **[**

][a,c]

15.6.1.1.2 FLECHT-SEASET Test 31504

The reflood rate for Test 31504 was 0.97 in/sec. The test pressure was maintained at 40 psia and the injected coolant temperature was 123°F. The WCOBRA/TRAC-TF2 simulation of Test 31504 was run for the first 800 seconds of the experiment, by which time all heater rod elevations had reached their peak temperature and had started to decline. Figures 15.6.1-24 through 15.6.1-30 show the comparison of predicted and measured temperatures at elevations 24, 48, 72, 78, 84, 96, and 120 inches from the bottom of the heated length. The code prediction is for simulated rod temperatures in the inner channel (rod no. 1 located in Channel 2 of Figure 15.6.1-2). The curves in these figures that represent the data show the individual thermocouples located within the boundary of the WCOBRA/TRAC-TF2 inner channel.

Figure 15.6.1-31 shows the prediction of the quench front elevation compared to the quench elevations deduced from temperature measurements. Similar to Test 31805, the code prediction shows **[**

][a,c]

Comparisons of the axial temperature profiles are shown in Figure 15.6.1-32 at 50 seconds, and in Figure 15.6.1-33 at 100 seconds. The predicted temperature profiles are **[**

][a,c].

Figure 15.6.1-34 summarizes the comparisons of the maximum predicted cladding temperatures at each elevation where thermocouples were located. For this test, the WCOBRA/TRAC-TF2 predictions of the maximum cladding temperatures are **[** **]**[a,c]. The predicted and measured turn-around times are compared in Figure 15.6.1-35. This figure shows that for this test, **[**

][a,c]

Figures 15.6.1-36 through 15.6.1-38 show comparisons of the predicted and measured axial pressure differentials in the bundle. Figure 15.6.1-36 shows a comparison of the pressure differentials in the lower half (0 to 72 inches) of the bundle. The WCOBRA/TRAC-TF2 prediction is **[**

][a,c] The overall pressure differential comparison is shown in Figure 15.6.1-38.

The FLECHT-SEASET facility included steam temperature probes located in the thimble tubes. Figures 15.6.1-39 through 15.6.1-43 show comparisons of the measured and predicted vapor temperatures at several locations in the bundle. Figure 15.6.1-39 shows a comparison low in the bundle, at the 48-inch elevation. Figure 15.6.1-40 shows the comparison near the bundle mid-height, just upstream of the peak temperature elevations, while Figure 15.6.1-41 shows the comparison just downstream of the peak temperatures. Figure 15.6.1-42 shows the comparison at the 120-inch elevation, and Figure 15.6.1-43 the comparison near the bundle exit. **[**

][a,c]

15.6.1.1.3 FLECHT-SEASET Test 32013

The reflood rate for Test 32013 was 1.04 in/sec. The test pressure was maintained at 60 psia and the injected coolant temperature was 150°F which is approximately 143°F of sub-cooling, similar to the other tests in this series. The WCOBRA/TRAC-TF2 simulation of Test 32013 was run for 800 seconds, by which time all heater rod elevations had reached their maximum temperature and had quenched. Figures 15.6.1-44 through 15.6.1-50 show the comparison of predicted and measured temperatures at elevations 24, 48, 72, 78, 84, 96, and 120 inches from the bottom of the heated length. The code prediction is for simulated rod temperatures in the inner channel (rod no. 1 located in Channel 2 of

Figure 15.6.1-2). The curves in these figures that represent the data show the individual thermocouples located within the boundary of the WCOBRA/TRAC-TF2 inner channel. Figure 15.6.1-51 shows the prediction of the quench front elevation compared to the quench elevations deduced from temperature measurements. **[**

][a,c]

Comparisons of the axial temperature profiles are shown in Figure 15.6.1-52 at 50 seconds, and in Figure 15.6.1-53 at 100 seconds. The predicted temperature profiles are shown to be **[**

][a,c].

Figure 15.6.1-54 summarizes the comparisons of the maximum predicted peak cladding temperatures at each elevation where thermocouples were located. **[**

][a,c] The predicted and measured turn-around times are shown in Figure 15.6.1-55. For this test, **[**

][a,c]

Figures 15.6.1-56 through 15.6.1-58 show comparisons of the predicted and measured axial pressure differentials in the bundle. Figure 15.6.1-56 shows a comparison of the pressure differentials in the lower half (0 to 72 inches) of the bundle. **[**

][a,c]

Figure 15.6.1-57 shows the comparison for the upper half (72 to 144 inches) of the bundle, with **[**

][a,c].

The overall pressure differential comparison is shown in Figure 15.6.1-58, and generally shows **[**

][a,c].

The FLECHT-SEASET facility included steam temperature probes located in the thimble tubes. Figures 15.6.1-59 through 15.6.1-63 show comparisons of the measured and predicted vapor temperatures at several locations in the bundle. Figure 15.6.1-59 shows a comparison low in the bundle, at the 48-inch elevation. Figure 15.6.1-60 shows the comparison near the bundle mid-height, just upstream of the peak temperature elevations, while Figure 15.6.1-61 shows the comparison just downstream of the peak temperatures. Figure 15.6.1-62 shows the comparison at the 120-inch elevation, and Figure 15.6.1-63 the comparison near the bundle exit. Each elevation was found to **[**

][a,c].

15.6.1.1.4 FLECHT-SEASET Test 31203

The reflood rate for Test 31203 was 1.51 in/sec. The test pressure was maintained at 40 psia and the injected coolant temperature was 126°F (approximately 143°F of sub-cooling). The WCOBRA/TRAC-TF2 simulation of Test 31203 was run beyond the first 450 seconds of the experiment, by which time all heater rod elevations had reached their peak temperature and had quenched. Figures 15.6.1-64 through 15.6.1-70 show the comparison of predicted and measured temperatures at elevations 24, 48, 72, 78, 84, 96, and 120 inches from the bottom of the heated length. The code prediction is for simulated rod temperatures in the inner channel (rod no. 1 located in Channel 2 of

Figure 15.6.1-2). The curves in these figures that represent the data show the individual thermocouples located within the boundary of the WCOBRA/TRAC-TF2 inner channel. Figure 15.6.1-71 shows the prediction of the quench front elevation compared to the quench elevations deduced from temperature measurements. **[**

][a,c]

Comparisons of the axial temperature profiles are shown in Figure 15.6.1-72 at 50 seconds, and in Figure 15.6.1-73 at 100 seconds. **[**

][a,c]

Figure 15.6.1-74 summarizes the comparisons of the maximum predicted peak cladding temperatures at each elevation where thermocouples were located. For this test, the predicted maximum temperatures **[ ]**[a,c]. The predicted and measured turn-around times are shown in Figure 15.6.1-75. The temperatures at most elevations are predicted to **[ ]**[a,c] the data.

Figures 15.6.1-76 through 15.6.1-78 show comparisons of the predicted and measured axial pressure differentials in the bundle. Figure 15.6.1-76 shows a comparison of the pressure differentials in the lower half (0 to 72 inches) of the bundle. **[**

][a,c]

The FLECHT-SEASET facility included steam temperature probes located in the thimble tubes. Figures 15.6.1-79 through 15.6.1-83 show comparisons of the measured and predicted vapor temperatures at several locations in the bundle. Figure 15.6.1-79 shows a comparison low in the bundle, at the 48-inch elevation. Figure 15.6.1-80 shows the comparison near the bundle mid-height, just upstream of the peak temperature elevations, while Figure 15.6.1-81 shows the comparison just downstream of the peak temperatures. Figure 15.6.1-82 shows the comparison at the 120-inch elevation, and Figure 15.6.1-83 the comparison near the bundle exit. **[**

][a,c]

15.6.1.1.5 FLECHT-SEASET Test 31701

The reflood rate for Test 31701 was 6.1 in/sec. The test pressure was maintained at 40 psia and the injected coolant temperature was 127°F. The WCOBRA/TRAC-TF2 simulation of Test 31701 was run for the first 100 seconds of the experiment, by which time all heater rod elevations had reached their peak temperature and had quenched. Figures 15.6.1-84 through 15.6.1-90 show the comparison of predicted and measured temperatures at elevations 24, 48, 72, 78, 84, 96, and 120 inches from the bottom of the heated length. The code prediction is for simulated rod temperatures in the inner channel (rod no. 1 located in Channel 2 of Figure 15.6.1-2). The curves in these figures that represent the data show the individual thermocouples located within the boundary of the WCOBRA/TRAC-TF2 inner channel. Figure 15.6.1-91 shows the prediction of the quench front elevation compared to the quench elevations deduced from temperature measurements. **[**

][a,c]

Comparisons of the axial temperature profiles are shown in Figure 15.6.1-92 at 10 seconds, and in Figure 15.6.1-93 at 30 seconds. The predicted temperature profiles are shown to **[**

][a,c].

Figure 15.6.1-94 summarizes the comparisons of the maximum predicted peak cladding temperatures at each elevation where thermocouples were located. **[**

][a,c] The predicted and measured turn-around times for this test are summarized in Figure 15.6.1-95 and shows **[** **]**[a,c].

Figures 15.6.1-96 through 15.6.1-98 show comparisons of the predicted and measured axial pressure differentials in the bundle. Figure 15.6.1-96 shows a comparison of the pressure differentials in the lower half (0 to 72 inches) of the bundle. Figure 15.6.1-97 shows the comparison for the upper half (72 to 144 inches) of the bundle, and the overall pressure differential comparison is shown in Figure 15.6.1-98. **[**

][a,c]

The FLECHT-SEASET facility included steam temperature probes located in the thimble tubes. Figures 15.6.1-99 through 15.6.1-103 show comparisons of the measured and predicted vapor temperatures at several locations in the bundle. Figure 15.6.1-99 shows a comparison low in the bundle, at the 48-inch elevation. Figure 15.6.1-100 shows the comparison near the bundle mid-height, just upstream of the peak temperature elevations, while Figure 15.6.1-101 shows the comparison just downstream of the peak temperatures. Figure 15.6.1-102 shows the comparison at the 120-inch elevation, and Figure 15.6.1-103 the comparison near the bundle exit. **[**

][a,c]

15.6.1.2 FLECHT-SEASET Summary and Conclusions

The five FLECHT-SEASET tests simulated by WCOBRA/TRAC-TF2 cover a wide range of flooding rates. Test 31805 had a low flooding rate (0.81 in/sec) while Test 31701 had a very rapid flooding rate (6.1 inch/sec). Tests at 40 psia (31805, 31203, 31701, 31504) and 60 psia (32013) were simulated.
[

]^{a,c}

a,c

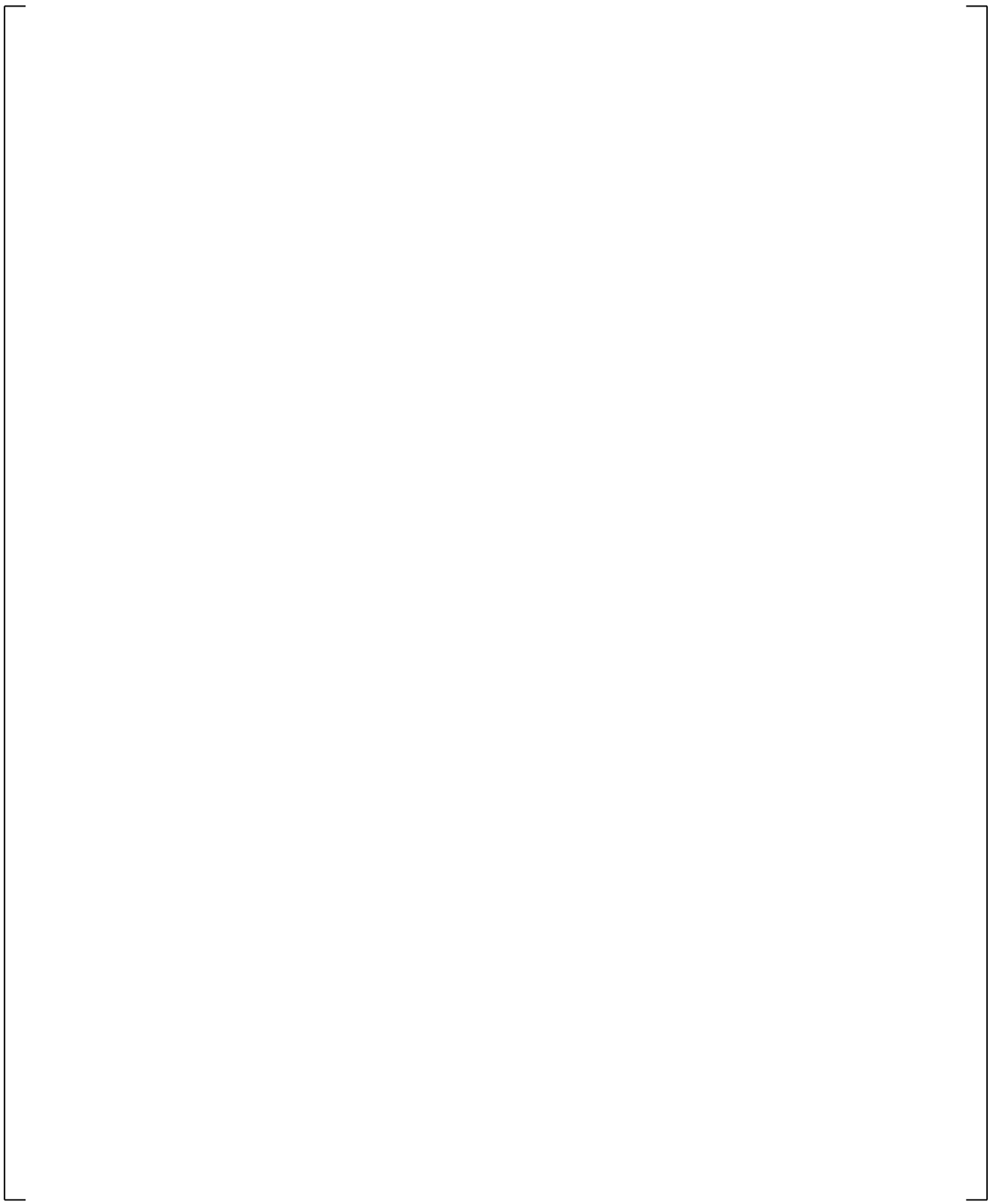

Figure 15.6.1-1 WCOBRA/TRAC-TF2 Transverse Noding for FLECHT-SEASET

a,c

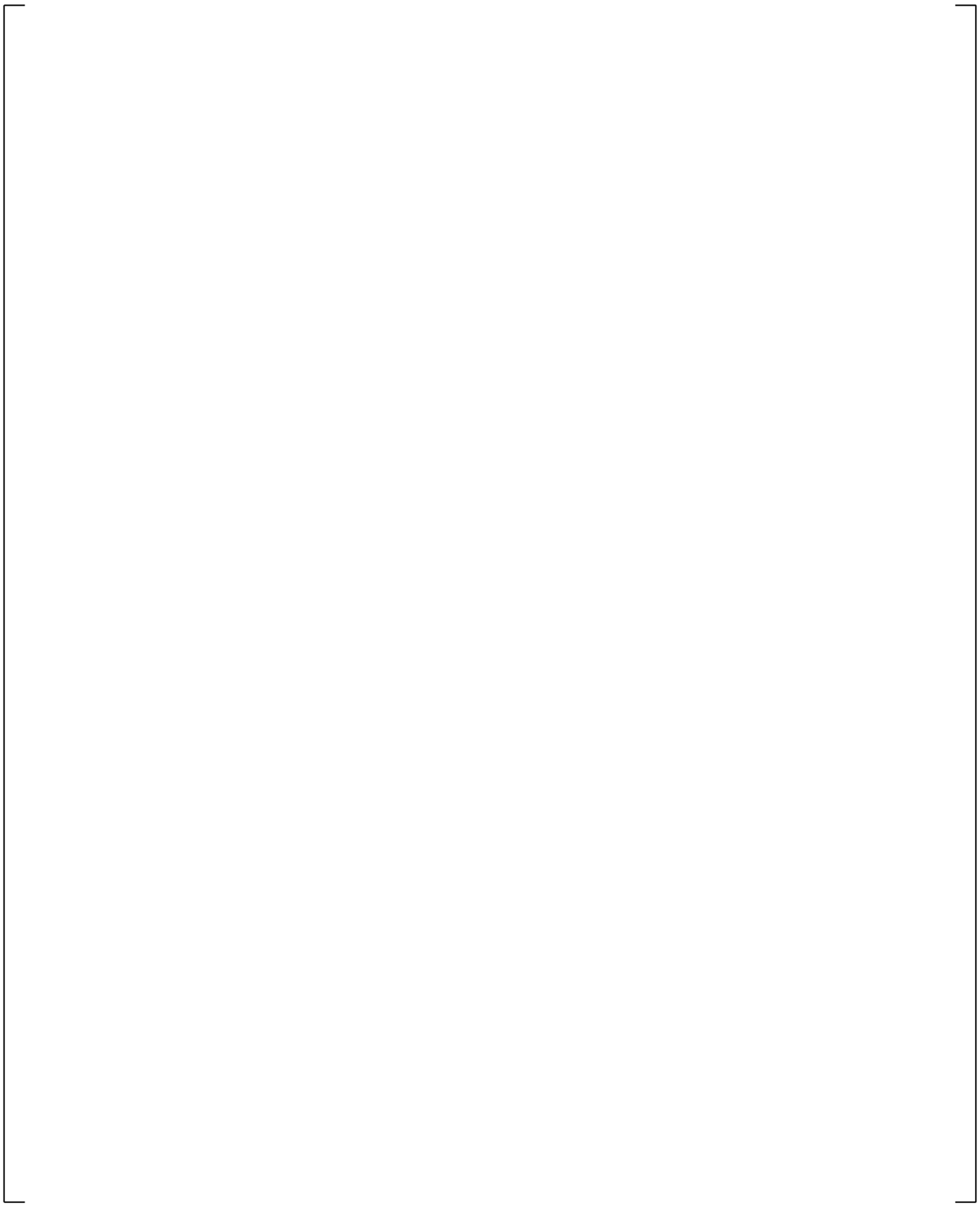

Figure 15.6.1-2 WCOBRA/TRAC-TF2 Axial Noding for FLECHT-SEASET

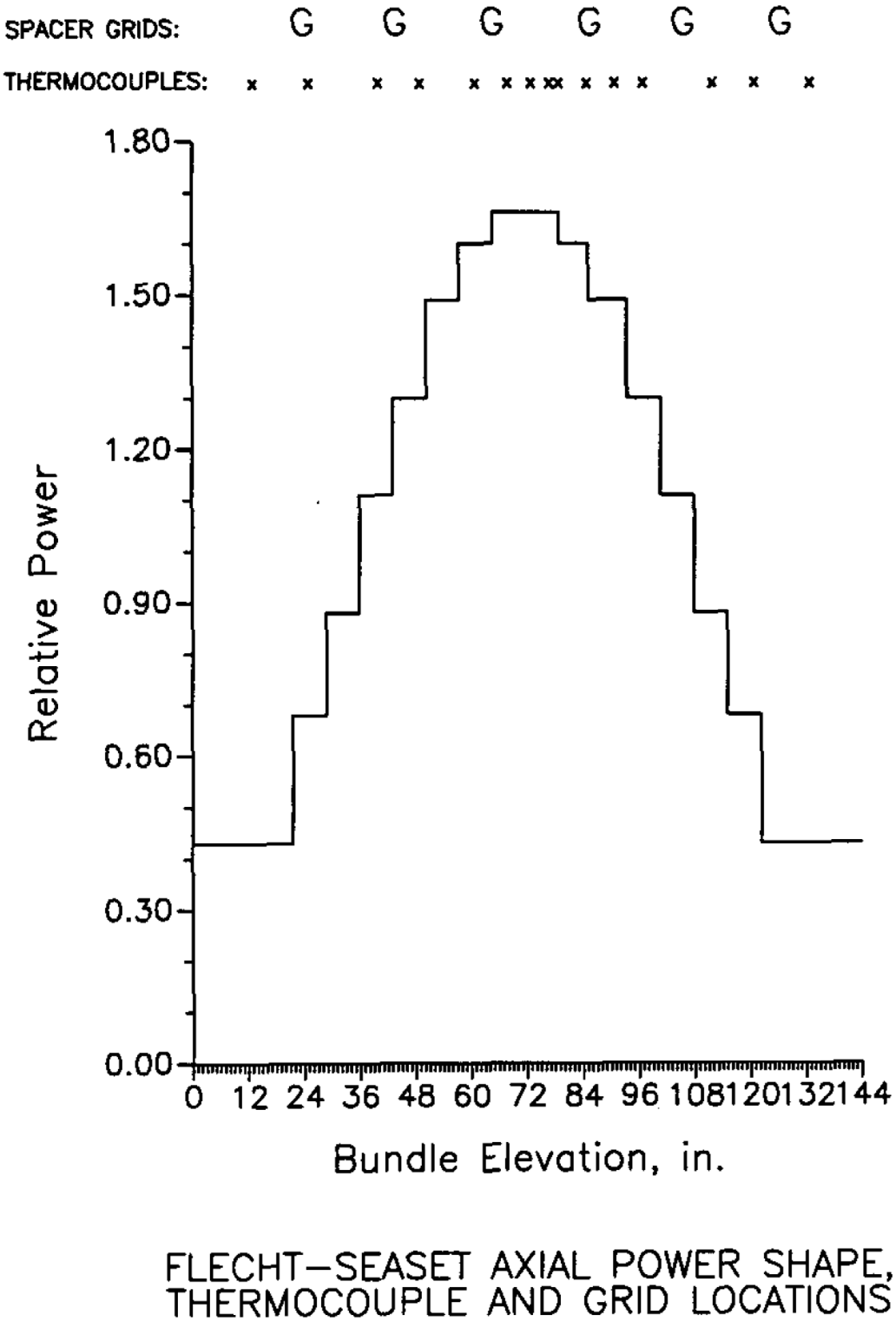

Figure 15.6.1-3 FLECHT-SEASET Axial Power Shape Profile

a,c

Figure 15.6.1-4 FLECHT-SEASET 31805 Rod Temperatures at 24-inch Elevation

a,c

Figure 15.6.1-5 FLECHT-SEASET 31805 Rod Temperatures at 48-inch Elevation

a,c

Figure 15.6.1-6 FLECHT-SEASET 31805 Rod Temperatures at 72-inch Elevation

a,c

Figure 15.6.1-7 FLECHT-SEASET 31805 Rod Temperatures at 78-inch Elevation

a,c

Figure 15.6.1-8 FLECHT-SEASET 31805 Rod Temperatures at 84-inch Elevation

a,c

Figure 15.6.1-9 FLECHT-SEASET 31805 Rod Temperatures at 96-inch Elevation

a,c

Figure 15.6.1-10 FLECHT-SEASET 31805 Rod Temperatures at 120-inch Elevation

a,c

Figure 15.6.1-11 Comparison of Predicted and Estimated Quench Front Elevations for FLECHT-SEASET 31805

a,c

Figure 15.6.1-12 Comparison of Predicted and Measured Axial Temperature Profile for FLECHT-SEASET 31805 at 100 Seconds

a,c

Figure 15.6.1-13 Comparison of Predicted and Measured Axial Temperature Profile for FLECHT-SEASET 31805 at 200 Seconds

a,c

Figure 15.6.1-14 Comparison of Predicted and Measured Maximum Cladding Temperatures at all Thermocouple Elevations for FLECHT-SEASET 31805

a,c

Figure 15.6.1-15 Comparison of Predicted and Measured Turn-Around Times for FLECHT-SEASET 31805

a,c

Figure 15.6.1-16 FLECHT-SEASET 31805 Bundle Lower Half ΔP

a,c

Figure 15.6.1-17 FLECHT-SEASET 31805 Bundle Upper Half ΔP

a,c

Figure 15.6.1-18 FLECHT-SEASET 31805 Overall ΔP

a,c

Figure 15.6.1-19 FLECHT-SEASET 31805 Vapor Temperatures at 48-inch Elevation

a,c

Figure 15.6.1-20 FLECHT-SEASET 31805 Vapor Temperatures near 72-inch Elevation

a,c

Figure 15.6.1-21 FLECHT-SEASET 31805 Vapor Temperatures near 90-inch Elevation

a,c

Figure 15.6.1-22 FLECHT-SEASET 31805 Vapor Temperatures near 120-inch Elevation

a,c

Figure 15.6.1-23 FLECHT-SEASET 31805 Vapor Temperatures near 138-inch Elevation

a,c

Figure 15.6.1-24 FLECHT-SEASET 31504 Rod Temperatures at 24-inch Elevation

a,c

Figure 15.6.1-25 FLECHT-SEASET 31504 Rod Temperatures at 48-inch Elevation

a,c

Figure 15.6.1-26 FLECHT-SEASET 31504 Rod Temperatures at 72-inch Elevation

a,c

Figure 15.6.1-27 FLECHT-SEASET 31504 Rod Temperatures at 78-inch Elevation

a,c

Figure 15.6.1-28 FLECHT-SEASET 31504 Rod Temperatures at 84-inch Elevation

a,c

Figure 15.6.1-29 FLECHT-SEASET 31504 Rod Temperatures at 96-inch Elevation

a,c

Figure 15.6.1-30 FLECHT-SEASET 31504 Rod Temperatures at 120-inch Elevation

a,c

Figure 15.6.1-31 Comparison of Predicted and Estimated Quench Front Elevations for FLECHT-SEASET 31504

a,c

Figure 15.6.1-32 Comparison of Predicted and Measured Axial Temperature Profile for FLECHT-SEASET 31504 at 50 Seconds

a,c

Figure 15.6.1-33 Comparison of Predicted and Measured Axial Temperature Profile for FLECHT-SEASET 31504 at 100 Seconds

a,c

Figure 15.6.1-34 Comparison of Predicted and Measured Maximum Cladding Temperatures at all Thermocouple Elevations for FLECHT-SEASET 31504

a,c

Figure 15.6.1-35 Comparison of Predicted and Measured Turn-Around Times for FLECHT-SEASET 31504

a,c

Figure 15.6.1-36 FLECHT-SEASET 31504 Bundle Lower Half ΔP

a,c

Figure 15.6.1-37 FLECHT-SEASET 31504 Bundle Upper Half ΔP

a,c

Figure 15.6.1-38 FLECHT-SEASET 31504 Overall ΔP

a,c

Figure 15.6.1-39 FLECHT-SEASET 31504 Vapor Temperatures at 48-inch Elevation

a,c

Figure 15.6.1-40 FLECHT-SEASET 31504 Vapor Temperatures near 72-inch Elevation

a,c

Figure 15.6.1-41 FLECHT-SEASET 31504 Vapor Temperatures near 90-inch Elevation

a,c

Figure 15.6.1-42 FLECHT-SEASET 31504 Vapor Temperatures at 120-inch Elevation

a,c

Figure 15.6.1-43 FLECHT-SEASET 31504 Vapor Temperatures at 138-inch Elevation

a,c

Figure 15.6.1-44 FLECHT-SEASET 32013 Rod Temperatures at 24-inch Elevation

a,c

Figure 15.6.1-45 FLECHT-SEASET 32013 Rod Temperatures at 48-inch Elevation

a,c

Figure 15.6.1-46 FLECHT-SEASET 32013 Rod Temperatures at 72-inch Elevation

a,c

Figure 15.6.1-47 FLECHT-SEASET 32013 Rod Temperatures at 78-inch Elevation

a,c

Figure 15.6.1-48 FLECHT-SEASET 32013 Rod Temperatures at 84-inch Elevation

a,c

Figure 15.6.1-49 FLECHT-SEASET 32013 Rod Temperatures at 96-inch Elevation

a,c

Figure 15.6.1-50 FLECHT-SEASET 32013 Rod Temperatures at 120-inch Elevation

a,c

Figure 15.6.1-51 Comparison of Predicted and Estimated Quench Front Elevations for FLECHT-SEASET 32013

a,c

Figure 15.6.1-52 Comparison of Predicted and Measured Axial Temperature Profile for FLECHT-SEASET 32013 at 50 Seconds

a,c

Figure 15.6.1-53 Comparison of Predicted and Measured Axial Temperature Profile for FLECHT-SEASET 32013 at 100 Seconds

a,c

Figure 15.6.1-54 Comparison of Predicted and Measured Maximum Cladding Temperatures at all Thermocouple Elevations for FLECHT-SEASET 32013

a,c

Figure 15.6.1-55 Comparison of Predicted and Measured Turn-Around Times for FLECHT-SEASET 32013

a,c

Figure 15.6.1-56 FLECHT-SEASET 32013 Bundle Lower Half ΔP

a,c

Figure 15.6.1-57 FLECHT-SEASET 32013 Bundle Upper Half ΔP

a,c

Figure 15.6.1-58 FLECHT-SEASET 32013 Overall ΔP

a,c

Figure 15.6.1-59 FLECHT-SEASET 32013 Vapor Temperatures at 48-inch Elevation

a,c

Figure 15.6.1-60 FLECHT-SEASET 32013 Vapor Temperatures near 72-inch Elevation

a,c

Figure 15.6.1-61 FLECHT-SEASET 32013 Vapor Temperatures near 90-inch Elevation

a,c

Figure 15.6.1-62 FLECHT-SEASET 32013 Vapor Temperatures at 120-inch Elevation

a,c

Figure 15.6.1-63 FLECHT-SEASET 32013 Vapor Temperatures at 138-inch Elevation

a,c

Figure 15.6.1-64 FLECHT-SEASET 31203 Rod Temperatures at 24-inch Elevation

a,c

Figure 15.6.1-65 FLECHT-SEASET 31203 Rod Temperatures at 48-inch Elevation

a,c

Figure 15.6.1-66 FLECHT-SEASET 31203 Rod Temperatures at 72-inch Elevation

a,c

Figure 15.6.1-67 FLECHT-SEASET 31203 Rod Temperatures at 78-inch Elevation

a,c

Figure 15.6.1-68 FLECHT-SEASET 31203 Rod Temperatures at 84-inch Elevation

a,c

Figure 15.6.1-69 FLECHT-SEASET 31203 Rod Temperatures at 96-inch Elevation

a,c

Figure 15.6.1-70 FLECHT-SEASET 31203 Rod Temperatures at 120-inch Elevation

a,c

Figure 15.6.1-71 Comparison of Predicted and Estimated Quench Front Elevations for FLECHT-SEASET 31203

a,c

Figure 15.6.1-72 Comparison of Predicted and Measured Axial Temperature Profile for FLECHT-SEASET 31203 at 50 Seconds

a,c

Figure 15.6.1-73 Comparison of Predicted and Measured Axial Temperature Profile for FLECHT-SEASET 31203 at 100 Seconds

a,c

Figure 15.6.1-74 Comparison of Predicted and Measured Maximum Cladding Temperatures at all Thermocouple Elevations for FLECHT-SEASET 31203

a,c

Figure 15.6.1-75 Comparison of Predicted and Measured Turn-Around Times for FLECHT-SEASET 31203

a,c

Figure 15.6.1-76 FLECHT-SEASET 31203 Bundle Lower Half ΔP

a,c

Figure 15.6.1-77 FLECHT-SEASET 31203 Bundle Upper Half ΔP

a,c

Figure 15.6.1-78 FLECHT-SEASET 31203 Overall ΔP

a,c

Figure 15.6.1-79 FLECHT-SEASET 31203 Vapor Temperatures at 48-inch Elevation

a,c

Figure 15.6.1-80 FLECHT-SEASET 31203 Vapor Temperatures near 72-inch Elevation

a,c

Figure 15.6.1-81 FLECHT-SEASET 31203 Vapor Temperatures near 90-inch Elevation

a,c

Figure 15.6.1-82 FLECHT-SEASET 31203 Vapor Temperatures at 120-inch Elevation

a,c

Figure 15.6.1-83 FLECHT-SEASET 31203 Vapor Temperatures at 138-inch Elevation

a,c

Figure 15.6.1-84 FLECHT-SEASET 31701 Rod Temperatures at 24-inch Elevation

a,c

Figure 15.6.1-85 FLECHT-SEASET 31701 Rod Temperatures at 48-inch Elevation

a,c

Figure 15.6.1-86 FLECHT-SEASET 31701 Rod Temperatures at 72-inch Elevation

a,c

Figure 15.6.1-87 FLECHT-SEASET 31701 Rod Temperatures at 78-inch Elevation

a,c

Figure 15.6.1-88 FLECHT-SEASET 31701 Rod Temperatures at 84-inch Elevation

a,c

Figure 15.6.1-89 FLECHT-SEASET 31701 Rod Temperatures at 96-inch Elevation

a,c

Figure 15.6.1-90 FLECHT-SEASET 31701 Rod Temperatures at 120-inch Elevation

a,c

Figure 15.6.1-91 Comparison of Predicted and Estimated Quench Front Elevations for FLECHT-SEASET 31701

a,c

Figure 15.6.1-92 Comparison of Predicted and Measured Axial Temperature Profile for FLECHT-SEASET 31701 at 10 Seconds

a,c

Figure 15.6.1-93 Comparison of Predicted and Measured Axial Temperature Profile for FLECHT-SEASET 31701 at 30 Seconds

a,c

Figure 15.6.1-94 Comparison of Predicted and Measured Maximum Cladding Temperatures at all Thermocouple Elevations for FLECHT-SEASET 31701

a,c

Figure 15.6.1-95 Comparison of Predicted and Measured Turn-Around Times for FLECHT-SEASET 31701

a,c

Figure 15.6.1-96 FLECHT-SEASET 31701 Bundle Lower Half ΔP

a,c

Figure 15.6.1-97 FLECHT-SEASET 31701 Bundle Upper Half ΔP

a,c

Figure 15.6.1-98 FLECHT-SEASET 31701 Overall ΔP

a,c

Figure 15.6.1-99 FLECHT-SEASET 31701 Vapor Temperatures at 48-inch Elevation

a,c

Figure 15.6.1-100 FLECHT-SEASET 31701 Vapor Temperatures near 72-inch Elevation

a,c

Figure 15.6.1-101 FLECHT-SEASET 31701 Vapor Temperatures near 90-inch Elevation

a,c

Figure 15.6.1-102 FLECHT-SEASET 31701 Vapor Temperatures at 120-inch Elevation

a,c

Figure 15.6.1-103 FLECHT-SEASET 31701 Vapor Temperatures at 138-inch Elevation

a,c

Figure 15.6.1-104 Comparison of Predicted and Measured Maximum Temperatures for FLECHT-SEASET Simulations

15.6.2 WCOBRA/TRAC-TF2 Simulations of FLECHT Low Flooding Rate Test Series and One Supplemental Test

The FLECHT low flooding rate (LFR) test assembly is modeled with three WCOBRA/TRAC-TF2 components. A VESSEL component is used to model the heated bundle, the upper plenum, and the top 6 inches of the lower plenum. Boundary conditions based on measured values were imposed on the top and the bottom of the VESSEL component. A PIPE component is attached to the top of the VESSEL, and a zero velocity FILL component is attached to the PIPE to satisfy the WCOBRA/TRAC-TF2 requirement of at least one one-dimensional component.

The VESSEL component is composed of four channels. Two channels are used to model the test section, one for the inner region of the bundle and one for the outer region that includes the bundle housing. The radial noding is shown in Figure 15.6.2-1. Channel 2 represents the inner channel. The remainder of the bundle is in the outer channel. **[**

][a,c] These rods are each modeled with a single rod model having the dimensions of the actual heater rods. The heat flux from the rod to the fluid is multiplied by the number of heater rods in the region represented by the channel to obtain the correct heat flux to the fluid. The test section housing is modeled with a wall geometry non-heated conductor that is thermally connected to the outer channel on the inside surface and is insulated on the outer surface. The WCOBRA/TRAC-TF2 vertical mesh lengths for the vessel are shown in Figure 15.6.2-2.

The WCOBRA/TRAC-TF2 heater rods are initialized with axial temperature profiles determined by measured temperature at the start of reflood for each individual test. The initial temperatures for all axial levels were computed by averaging the thermocouple temperature within a radial boundary at a given elevation. One heater rod was inoperative during the entire transient, therefore the thermocouples in the immediate vicinity of the unpowered rod were eliminated from the initial temperature averaging.

The housing is initialized with an axial temperature profile determined from thermocouples that were attached to the facility housing.

Both of the WCOBRA/TRAC-TF2 rods used the axial power profile shown in Figure 15.6.2-3. The housing had zero power generation.

The reflood transient is run by using measured values of the injected flow as a boundary condition imposed on the bottom of the VESSEL component. A constant pressure boundary condition is imposed on the top node of the VESSEL. During the transient, the heater rod power is decreased according to the ANS 1971 + 20 percent power decay curve. The simulations were continued until the entire bundle had quenched.

Additional initial conditions are provided in Table 14.1-6 for each test and are repeated here.

Test Series	Test Number	Pressure psia	Flooding Rate in/s	Inlet Sub-cooling °F	Peak Power kW/ft	Comment
FLECHT LOW FLOODING RATE	05029 05132 04641	40 40 20	0.85 1.0 1.0	141 140 139	0.73 0.95 0.95	COSINE POWER SHAPE 15x15 PWR ROD ARRAY
FLECHT SUPPLEMENTAL	0791	15	0.4	25	0.7	COSINE POWER SHAPE 15x15 PWR ROD ARRAY

15.6.2.1 FLECHT LFR Results

15.6.2.1.1 FLECHT Test 05029

The reflood rate for Test 05029 was 0.85 in/sec. The test pressure was maintained at 40 psia and the injected coolant temperature was 126°F. Conditions for this test are very similar to those for FLECHT-SEASET Test 31805. The WCOBRA/TRAC-TF2 simulation of Test 05029 was run past 500 seconds, by which time all heater rod elevations had reached their peak temperature and had started to decline. Figures 15.6.2-4 through 15.6.2-10 show the comparison of predicted and measured temperatures at elevations 24, 48, 72, 78, 84, 96, and 120 inches from the bottom of the heated length. The code prediction is for simulated rod temperatures in the inner channel (rod no. 1 located in Channel 2 of Figure 15.6.2-2). The curves in these figures that represent the data show the individual thermocouples located within the boundary of the WCOBRA/TRAC-TF2 inner channel. Figure 15.6.2-11 shows the prediction of the quench front elevation compared to the quench elevations deduced from temperature measurements. **[**

][a,c]

Comparisons of the axial temperature profiles are shown in Figure 15.6.2-12 at 50 seconds, and in Figure 15.6.2-13 at 100 seconds. The predicted temperature profiles are shown to **[**

][a,c].

Figure 15.6.2-14 summarizes the comparisons of the maximum predicted peak cladding temperatures at the thermocouple elevations presented in Figures 15.6.2-2 through 15.6.2-10. **[**

][a,c]

Figures 15.6.2-15 through 15.6.2-17 show comparisons of the predicted and measured axial pressure differentials in the bundle. Figure 15.6.2-15 shows a comparison of the pressure differentials in the lower half (0 to 72 inches) of the bundle. **[**

][a,c]

Figure 15.6.2-16 shows the comparison for the upper half (72 to 144 inches) of the bundle, **[**

][a,c]. The overall pressure differential comparison is shown in Figure 15.6.2-17 and shows **[** **]**[a,c].

The FLECHT facility included steam temperature probes located in the thimble tubes. Figure 15.6.2-18 shows the comparison at the 84-inch elevation, just downstream of the peak temperature location. Figure 15.6.2-19 shows the comparison at the 120-inch elevation, and Figure 15.6.2-20 the comparison near the bundle exit. **[**

][a,c]

15.6.2.1.2 FLECHT Test 05132

The reflood rate for Test 05132 was 1.0 in/sec. The test pressure was maintained at 40 psia and the injected coolant temperature was 127°F. The initial peak rod power for this test was 0.95 kW/ft. The WCOBRA/TRAC-TF2 simulation of Test 05132 was run past the 500 seconds of the experiment, by which time all heater rod elevations had reached their peak temperature and had quenched. Figures 15.6.2-21 through 15.6.2-27 show the comparison of predicted and measured temperatures at elevations 24, 48, 72, 78, 84, 96, and 120 inches from the bottom of the heated length. The code prediction is for simulated rod temperatures in the inner channel (rod no. 1 located in Channel 2 of Figure 15.6.2-2). The curves in these figures that represent the data show the individual thermocouples located within the boundary of the WCOBRA/TRAC-TF2 inner channel. Figure 15.6.2-28 shows the prediction of the quench front elevation compared to the quench elevations deduced from temperature measurements. **[**

][a,c]

Comparisons of the axial temperature profiles are shown in Figure 15.6.2-29 at 50 seconds, and in Figure 15.6.2-30 at 100 seconds. The predicted temperature profiles are shown to **[**

][a,c].

Figure 15.6.2-31 summarizes the comparisons of the maximum predicted peak cladding temperatures at the thermocouple elevations presented in Figures 15.6.2-21 through 15.6.2-27. **[**

][a,c]

Figures 15.6.2-32 through 15.6.2-34 show comparisons of the predicted and measured axial pressure differentials in the bundle. Figure 15.6.2-32 shows a comparison of the pressure differentials in the lower half (0 to 72 inches) of the bundle. The WCOBRA/TRAC-TF2 prediction is **[**

][a,c].

Figure 15.6.2-33 shows the comparison for the upper half (72 to 144 inches) of the bundle, where the code is **[**

][a,c]. The overall pressure differential comparison is shown in Figure 15.6.2-34 and shows **[**

][a,c].

The FLECHT facility included steam temperature probes located in the thimble tubes. Figure 15.6.2-35 shows the comparison at the 84-inch elevation, just downstream of the peak temperature location. Figure 15.6.2-36 shows the comparison at the 120-inch elevation, and Figure 15.6.2-37 the comparison near the bundle exit. **[**

][a,c]

15.6.2.1.3 FLECHT Test 04641

The reflood rate for Test 04641 was 1.0 in/sec. The test pressure was maintained at 20 psia and the injected coolant temperature was 89°F (139°F of sub-cooling). The initial peak rod power for this test was 0.95 kW/ft. The WCOBRA/TRAC-TF2 simulation of Test 04641 was run past 800 seconds, by which time all heater rod elevations had reached their peak temperature and had quenched. Figures 15.6.2-38 through 15.6.2-44 show the comparison of predicted and measured temperatures at elevations 24, 48, 72, 78, 84, 96, and 120 inches from the bottom of the heated length. The code prediction is for simulated rod temperatures in the inner channel (rod no. 1 located in Channel 2 of Figure 15.6.2-2). The curves in these figures that represent the data show the individual thermocouples located within the boundary of the WCOBRA/TRAC-TF2 inner channel. Figure 15.6.2-45 shows the prediction of the quench front elevation compared to the quench elevations deduced from temperature measurements. **[**

][a,c]

Comparisons of the axial temperature profiles are shown in Figure 15.6.2-46 at 50 seconds, and in Figure 15.6.2-47 at 100 seconds. The predicted temperature profiles are shown to **[**

][a,c].

Figure 15.6.2-48 summarizes the comparisons of the maximum predicted peak cladding temperatures at the thermocouple elevations presented in Figures 15.6.2-38 through 15.6.2-44. The code tends to **[**

][a,c].

Figures 15.6.2-49 through 15.6.2-51 show comparisons of the predicted and measured axial pressure differentials in the bundle. Figure 15.6.2-49 shows a comparison of the pressure differentials in the lower half (0 to 72 inches) of the bundle. **[**

][a,c] The overall pressure differential comparison is shown in Figure 15.6.2-51.

The FLECHT facility included steam temperature probes located in the thimble tubes. Figure 15.6.2-52 shows the comparison at the 84-inch elevation, just downstream of the peak temperature location. Figure 15.6.2-53 shows the comparison at the 120-inch elevation, and Figure 15.6.2-54 the comparison near the bundle exit. **[**

][a,c]

15.6.2.2 FLECHT Supplemental Results

15.6.2.2.1 FLECHT Test 0791

The reflood rate for Test 0791 was nominally set at 0.4 in/sec. The test pressure was maintained at 15 psia and the injected coolant temperature was 188°F (25°F of sub-cooling). The WCOBRA/TRAC-TF2 simulation of Test 0791 was run to 1500 seconds, by which time all of the heater rod elevations had reached their peak temperature and had started to decline. Figures 15.6.2-55 through 15.6.2-59 show the comparison of predicted and measured temperatures at elevations 24, 48, 72, 96 and 120 inches from the bottom of the heated length. The code prediction is for simulated rod temperatures in the inner channel (rod no. 1 located in Channel 2 of Figure 15.6.2-2). The curves in these figures that represent the data show the individual thermocouples located within the boundary of the WCOBRA/TRAC-TF2 inner channel. Figure 15.6.2-60 shows the prediction of the quench front elevation compared to the quench elevations deduced from temperature measurements. **[**

][a,c]

Figure 15.6.2-61 summarizes the comparisons of the maximum predicted peak cladding temperatures at the thermocouple elevations presented in Figures 15.6.2-55 through 15.6.2-59. **[**

][a,c]

Figures 15.6.2-62 through 15.6.2-65 show comparisons of the predicted and measured axial pressure differentials in the bundle. Figure 15.6.2-62 compares the pressure differentials at 0-2 ft and shows the code **[** **]**[a,c] in this region. Figures 15.6.2-63 and 15.6.2-64 compare the pressure differentials at 0-4 ft and 0-6 ft, respectively, and shows the code **[** **]**[a,c] in these regions. Figure 15.6.2-65 compares the pressure differentials at 0-8 ft, and shows **[**

][a,c].

15.6.2.3 FLECHT Cosine LFR and Supplemental Summary and Conclusions

Three FLECHT Low Flooding Rate Tests were simulated using WCOBRA/TRAC-TF2. These tests had a more limited range of flooding rates (0.4 to 1.00 in/sec), but included a test of low pressure (Test 04641 at 20 psia and Test 0791 at 15 psia) and two tests with a high initial rod peak power (Tests 04641 and 05132 at 0.95 kW/ft). In addition, the degree of sub-cooling ranged from 25°F to 140°F. Figure 15.6.2-66 presents a comparison of the predicted maximum cladding temperatures to the measured maximum cladding temperatures for all four test simulations. **[**

][a,c]

a,c

Figure 15.6.2-1 WCOBRA/TRAC-TF2 Transverse Noding for FLECHT-LFR

a,c

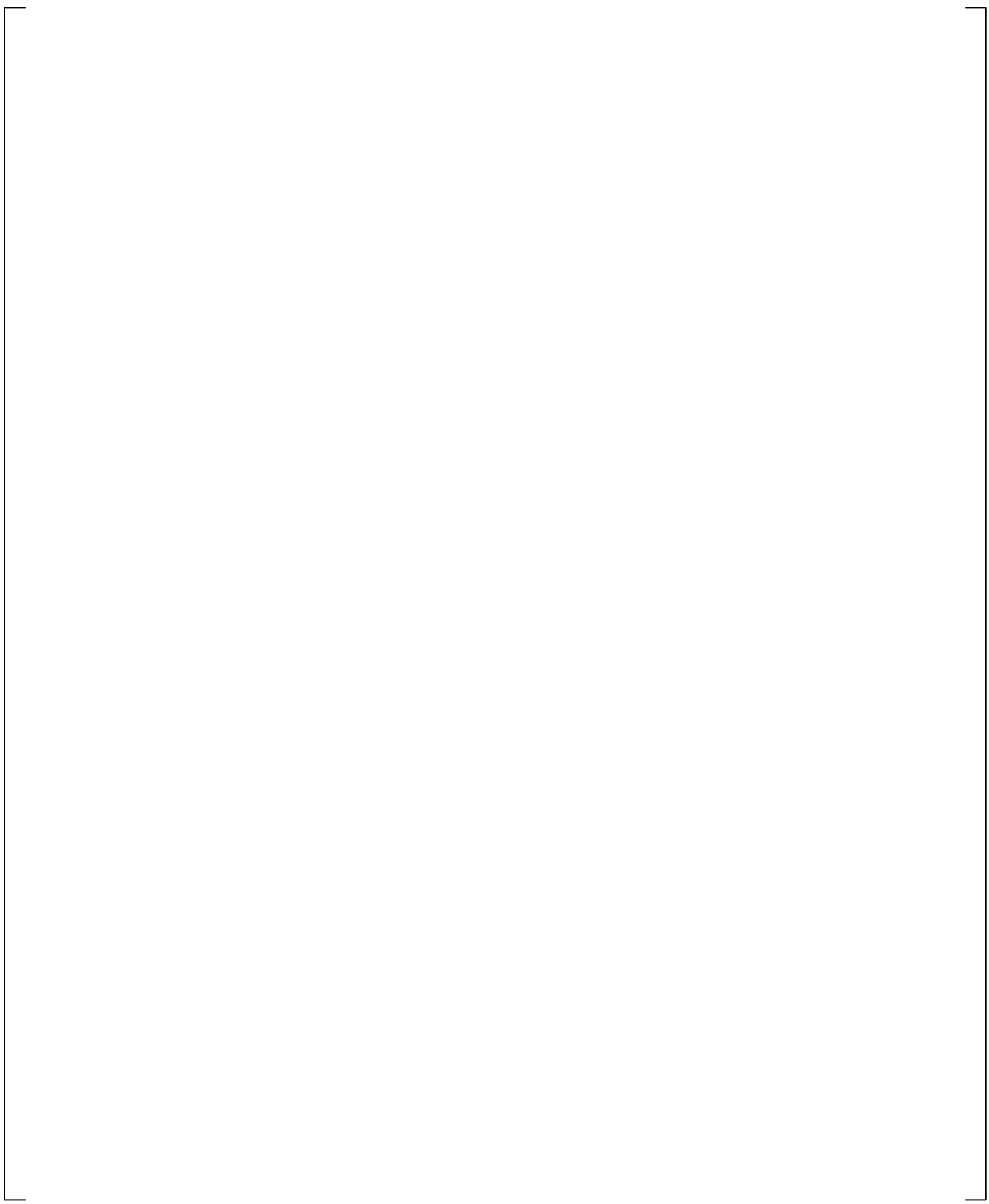

Figure 15.6.2-2 WCOBRA/TRAC-TF2 Axial Noding for FLECHT-LFR

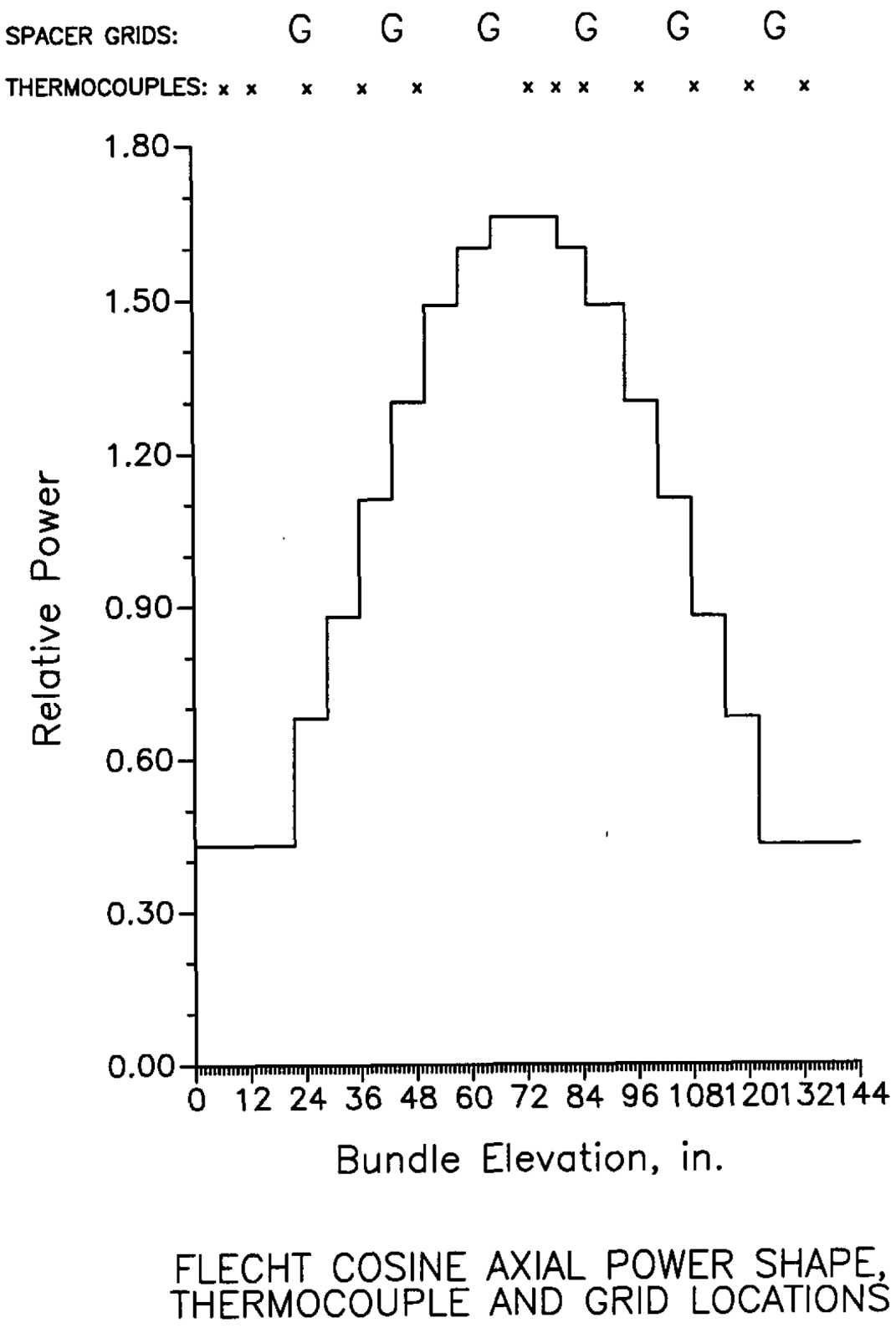

Figure 15.6.2-3 WCOBRA/TRAC-TF2 Axial Power Shape for FLECHT-LFR

a,c

Figure 15.6.2-4 FLECHT 05029 Rod Temperatures at 24-inch Elevation

a,c

Figure 15.6.2-5 FLECHT 05029 Rod Temperatures at 48-inch Elevation

Figure 15.6.2-6 FLECHT 05029 Rod Temperatures at 72-inch Elevation

Figure 15.6.2-7 FLECHT 05029 Rod Temperatures at 78-inch Elevation

a,c

Figure 15.6.2-8 FLECHT 05029 Rod Temperatures at 84-inch Elevation

a,c

Figure 15.6.2-9 FLECHT 05029 Rod Temperatures at 96-inch Elevation

a,c

Figure 15.6.2-10 FLECHT 05029 Rod Temperatures at 120-inch Elevation

a,c

Figure 15.6.2-11 Comparison of Predicted and Estimated Quench Front Elevations for FLECHT 05029

a,c

Figure 15.6.2-12 Comparison of Predicted and Measured Axial Temperature Profile for FLECHT 05029 at 50 Seconds

a,c

Figure 15.6.2-13 Comparison of Predicted and Measured Axial Temperature Profile for FLECHT 05029 at 100 Seconds

a,c

Figure 15.6.2-14 Comparison of Predicted and Measured Maximum Cladding Temperatures at all Thermocouple Elevations for FLECHT 05029

a,c

Figure 15.6.2-15 FLECHT 05029 Bundle Lower Half ΔP

a,c

Figure 15.6.2-16 FLECHT 05029 Bundle Upper Half ΔP

a,c

Figure 15.6.2-17 FLECHT 05029 Overall ΔP

a,c

Figure 15.6.2-18 FLECHT 05029 Vapor Temperatures at 84-inch Elevation

a,c

Figure 15.6.2-19 FLECHT 05029 Vapor Temperatures near 120-inch Elevation

a,c

Figure 15.6.2-20 FLECHT 05029 Vapor Temperatures near Bundle Exit

a,c

Figure 15.6.2-21 FLECHT 05132 Rod Temperatures at 24-inch Elevation

a,c

Figure 15.6.2-22 FLECHT 05132 Rod Temperatures at 48-inch Elevation

a,c

Figure 15.6.2-23 FLECHT 05132 Rod Temperatures at 72-inch Elevation

a,c

Figure 15.6.2-24 FLECHT 05132 Rod Temperatures at 78-inch Elevation

a,c

Figure 15.6.2-25 FLECHT 05132 Rod Temperatures at 84-inch Elevation

a,c

Figure 15.6.2-26 FLECHT 05132 Rod Temperatures at 96-inch Elevation

a,c

Figure 15.6.2-27 FLECHT 05132 Rod Temperatures at 120-inch Elevation

a,c

Figure 15.6.2-28 Comparison of Predicted and Estimated Quench Front Elevations for FLECHT 05132

a,c

Figure 15.6.2-29 Comparison of Predicted and Measured Axial Temperature Profile for FLECHT 05132 at 50 Seconds

a,c

Figure 15.6.2-30 Comparison of Predicted and Measured Axial Temperature Profile for FLECHT 05132 at 100 Seconds

a,c

Figure 15.6.2-31 Comparison of Predicted and Measured Maximum Cladding Temperatures at all Thermocouple Elevations for FLECHT 05132

a,c

Figure 15.6.2-32 FLECHT 05132 Bundle Lower Half ΔP

a,c

Figure 15.6.2-33 FLECHT 05132 Bundle Upper Half ΔP

a,c

Figure 15.6.2-34 FLECHT 05132 Overall ΔP

a,c

Figure 15.6.2-35 FLECHT 05132 Vapor Temperatures at 84-inch Elevation

a,c

Figure 15.6.2-36 FLECHT 05132 Vapor Temperatures near 120-inch Elevation

a,c

Figure 15.6.2-37 FLECHT 05132 Vapor Temperatures near Bundle Exit

a,c

Figure 15.6.2-38 FLECHT 04641 Rod Temperatures at 24-inch Elevation

a,c

Figure 15.6.2-39 FLECHT 04641 Rod Temperatures at 48-inch Elevation

a,c

Figure 15.6.2-40 FLECHT 04641 Rod Temperatures at 72-inch Elevation

a,c

Figure 15.6.2-41 FLECHT 04641 Rod Temperatures at 78-inch Elevation

a,c

Figure 15.6.2-42 FLECHT 04641 Rod Temperatures at 84-inch Elevation

a,c

Figure 15.6.2-43 FLECHT 04641 Rod Temperatures at 96-inch Elevation

a,c

Figure 15.6.2-44 FLECHT 04641 Rod Temperatures at 120-inch Elevation

a,c

Figure 15.6.2-45 Comparison of Predicted and Estimated Quench Front Elevations for FLECHT 04641

a,c

Figure 15.6.2-46 Comparison of Predicted and Measured Axial Temperature Profile for FLECHT 04641 at 50 Seconds

a,c

Figure 15.6.2-47 Comparison of Predicted and Measured Axial Temperature Profile for FLECHT 04641 at 100 Seconds

a,c

Figure 15.6.2-48 Comparison of Predicted and Measured Maximum Cladding Temperatures at all Thermocouple Elevations for FLECHT 04641

a,c

Figure 15.6.2-49 FLECHT 04641 Bundle Lower Half ΔP

a,c

Figure 15.6.2-50 FLECHT 04641 Bundle Upper Half ΔP

a,c

Figure 15.6.2-51 FLECHT 04641 Overall ΔP

a,c

Figure 15.6.2-52 FLECHT 04641 Vapor Temperatures at 84-inch Elevation

a,c

Figure 15.6.2-53 FLECHT 04641 Vapor Temperatures near 120-inch Elevation

a,c

Figure 15.6.2-54 FLECHT 04641 Vapor Temperatures near Bundle Exit

a,c

Figure 15.6.2-55 FLECHT 0791 Cladding Temperature at 24 inches

a,c

Figure 15.6.2-56 FLECHT 0791 Cladding Temperature at 48 inches

a,c

Figure 15.6.2-57 FLECHT 0791 Cladding Temperature at 72 inches

a,c

Figure 15.6.2-58 FLECHT 0791 Cladding Temperature at 96 inches

a,c

Figure 15.6.2-59 FLECHT 0791 Cladding Temperature at 120 inches

a,c

Figure 15.6.2-60 FLECHT 0791 Quench Front Progression

a,c

Figure 15.6.2-61 Maximum Cladding Temperature Comparison

a,c

Figure 15.6.2-62 FLECHT 0791 Differential Pressure 0-2 ft

a,c

Figure 15.6.2-63 FLECHT 0791 Differential Pressure 0-4 ft

a,c

Figure 15.6.2-64 FLECHT 0791 Differential Pressure 0-6 ft

a,c

Figure 15.6.2-65 FLECHT 0791 Differential Pressure 0-8 ft

a,c

Figure 15.6.2-66 Comparison of Predicted and Measured Cladding Temperatures for FLECHT Low Flooding Rate Simulations

15.6.3 WCOBRA/TRAC-TF2 Simulations of FLECHT Skewed Power Test Bundle

The FLECHT skewed power test assembly is modeled with three WCOBRA/TRAC-TF2 components. A VESSEL component is used to model the heated bundle, the upper plenum, and the top 6 inches of the lower plenum. Boundary conditions based on measured values were imposed on the top and the bottom of the VESSEL component. A PIPE component is attached to the top of the VESSEL, and a zero velocity FILL component is attached to the PIPE to satisfy the WCOBRA/TRAC-TF2 requirement of at least one one-dimensional component.

The VESSEL component is composed of four channels. Two channels are used to model the test section, one for the inner region (Channel 2) of the bundle and one for the outer region (Channel 3) that includes the bundle housing. The transverse noding is shown in Figure 15.6.3-1. Channel 2 is connected to Channel 3 by Gap 1. **[**

][a,c] These rods are each modeled with a single rod model having the dimensions of the actual heater rods. The heat flux from the rod to the fluid is multiplied by the number of heater rods in the region represented by the channel to obtain the correct heat flux to the fluid. The test section housing is modeled with a tube geometry non-heated conductor that is thermally connected to the outer channel on the inside surface and is insulated on the outer surface. The WCOBRA/TRAC-TF2 axial cell lengths for the vessel are shown in Figure 15.6.3-2.

The WCOBRA/TRAC-TF2 heater rods are initialized with axial temperature profiles determined by measured temperatures at the start of reflood for each individual test. The initial temperatures for all axial levels were computed by averaging the thermocouple temperatures within a radial boundary at a given elevation. Two heater rods were inoperative during the entire transient, therefore the rod temperatures in the immediate vicinity of the unpowered rods were eliminated from the initial temperature averaging.

The housing is initialized with an axial temperature profile determined from thermocouples that were attached to the facility housing.

Both of the WCOBRA/TRAC-TF2 rods used the axial power profile shown in Figure 15.6.3-3. The housing had zero power generation.

The reflood transient is run by using measured values of the injected flow as a boundary condition imposed on the bottom of the VESSEL component. A constant pressure boundary condition is imposed on the top node of the VESSEL. During the transient, the heater rod power is decreased according to the ANS 1971 + 20 percent power decay curve. The simulation is continued until the cladding temperatures have peaked and begin to decrease.

Additional initial conditions are provided in Table 14.1-6 for each test and are repeated here.

Test Series	Test Number	Pressure psia	Flooding Rate in/s	Inlet Sub-cooling °F	Peak Power kW/ft	Comment
FLECHT SKEWED	15305	40	0.8	140	0.7	TOP SKEWED POWER SHAPE 15x15 PWR ROD ARRAY
	13812	41	1.0	83	0.7	
	15713	40	1.0	2	0.7	
	13914	21	1.0	5	0.7	
	13609	21	1.0	141	0.7	

15.6.3.1 FLECHT Top-Skewed Power Results

15.6.3.1.1 FLECHT Top-Skewed Power Test 15305

The reflood rate for Test 15305 was 0.8 in/sec. The test pressure was maintained at 40 psia and the injected coolant temperature was 127°F (140°F of sub-cooling). The fluid conditions for this test are very similar to those for FLECHT-SEASET Test 31805, with the main difference being the power shape. The WCOBRA/TRAC–TF2 simulation of Test 15305 was run for 800 seconds, by which time all predicted heater rod elevations had reached their peak temperature and had quenched. Figures 15.6.3-4 through 15.6.3-10 show the comparison of predicted and measured temperatures at elevations 24, 48, 72, 96, 120, 126, and 132 inches from the bottom of the heated length. The code prediction is for simulated rod temperatures in the inner channel (rod no. 1 located in Channel 2 of Figure 15.6.3-2). The thermocouple temperature curves in these figures represent different radial positions on individual rods located within the boundary of the WCOBRA/TRAC-TF2 inner channel. Figure 15.6.3-11 shows the prediction of the quench front elevation compared to the quench elevations deduced from temperature measurements.
[

][a,c]

Comparisons of the axial temperature profiles are shown in Figure 15.6.3-12 at 100 seconds, and in Figure 15.6.3-13 at 300 seconds. **[**

][a,c]

Figures 15.6.3-15 through 15.6.3-17 show comparisons of the predicted and measured axial pressure differentials in the bundle. Figure 15.6.3-15 shows a comparison of the pressure differentials in the lower half (0 to 72 inches) of the bundle. WCOBRA/TRAC-TF2 tends to **[** **]**[a,c]. Figure 15.6.3-16 shows the comparison for the upper half (72 to 144 inches) of the bundle. WCOBRA/TRAC-TF2 tends to **[**

][a,c]. The overall pressure differential comparison is shown in Figure 15.6.3-17.

The FLECHT facility included steam temperature probes located in the thimble tubes. Figure 15.6.3-18 shows the comparison at the 84-inch elevation, just upstream of the peak temperature location. Figure 15.6.3-19 shows the comparison at the 120-inch elevation and Figure 15.6.3-20 the comparison at 132 inches, which is near the bundle exit. **[**

][a,c]

15.6.3.1.2 FLECHT Top-Skewed Power Test 13812

The reflood rate for Test 13812 was 1.0 in/sec. The test pressure was maintained at 41 psia and the injected coolant temperature was 184°F (83°F of sub-cooling). The WCOBRA/TRAC-TF2 simulation of Test 13812 was run for 800 seconds of the experiment, by which time all predicted heater rod elevations had reached their peak temperature and had quenched. Figures 15.6.3-21 through 15.6.3-27 show the comparison of predicted and measured temperatures at elevations 24, 48, 72, 96, 120, 126, and 132 inches from the bottom of the heated length. The code prediction is for simulated rod temperatures in the inner channel (rod no. 1 located in Channel 2 of Figure 15.6.3-2). The thermocouple temperature curves in these figures represent different radial positions on individual rods located within the boundary of the WCOBRA/TRAC-TF2 inner channel. Figure 15.6.3-28 shows the prediction of the quench front elevation compared to the quench elevations deduced from temperature measurements. **[**

][a,c]

Comparisons of the axial temperature profiles are shown in Figure 15.6.3-29 at 100 seconds, and in Figure 15.6.3-30 at 300 seconds. **[**

][a,c]

Figure 15.6.3-31 summarizes the comparisons of the maximum predicted peak cladding temperatures at several elevations where thermocouples were located. **[**

][a,c]

Figures 15.6.3-32 through 15.6.3-34 show comparisons of the predicted and measured axial pressure differentials in the bundle. Figure 15.6.3-32 shows a comparison of the pressure differentials in the lower half (0 to 72 inches) of the bundle. The WCOBRA/TRAC-TF2 prediction is **[**

][a,c]. Figure 15.6.3-33 shows the comparison for the upper half (72 to 144 inches) of the bundle. The figure shows **[**

][a,c]. The overall pressure differential comparison (Figure 15.6.3-34) is seen to **[** **]**[a,c]

The FLECHT top-skewed facility included steam temperature probes located in the thimble tubes. Figure 15.6.3-35 shows the comparison at the 84-inch elevation, just upstream of the peak temperature location. Figure 15.6.3-36 shows the comparison at the 120-inch elevation, and Figure 15.6.3-37 shows the comparison at 132 inches, which is near the bundle exit. **[**

][a,c]

15.6.3.1.3 FLECHT Top-Skewed Power Test 15713

The reflood rate for Test 15713 was 1.0 in/sec. The test pressure was maintained at 40 psia and the injected coolant temperature was 265°F (2°F of sub-cooling). The WCOBRA/TRAC-TF2 simulation of Test 15713 was run for 800 seconds of the experiment, by which time all heater rod elevations had reached their peak temperature and had quenched. Figures 15.6.3-38 through 15.6.3-44 show the comparison of predicted and measured temperatures at elevations 24, 48, 72, 96, 120, 126, and 132 inches from the bottom of the heated length. The code prediction is for simulated rod temperatures in the inner channel (rod no. 1 located in Channel 2 of Figure 15.6.3-2). The thermocouple temperature curves in these figures represent different radial positions on individual rods located within the boundary of the WCOBRA/TRAC-TF2 inner channel. Figure 15.6.3-45 shows the prediction of the quench front elevation compared to the quench elevations deduced from temperature measurements. **[**

][a,c]

Comparisons of the axial temperature profiles are shown in Figure 15.6.3-46 at 100 seconds, and in Figure 15.6.3-47 at 300 seconds. **[**

][a,c]

Figures 15.6.3-49 through 15.6.3-51 show comparisons of the predicted and measured axial pressure differentials in the bundle. Figure 15.6.3-49 shows a comparison of the pressure differentials in the lower half (0 to 72 inches) of the bundle. Figure 15.6.3-50 shows the comparison for the upper half (72 to 144 inches) of the bundle. **[**

][a,c] The overall pressure differential comparison is shown in Figure 15.6.3-51.

The FLECHT top-skewed facility included steam temperature probes located in the thimble tubes. Figure 15.6.3-52 shows the comparison at the 84-inch elevation, just upstream of the peak temperature location. Figure 15.6.3-53 shows the comparison at the 120-inch elevation, and Figure 15.6.3-54 the comparison at 132 inches, which is near the bundle exit. **[**

][a,c]

15.6.3.1.4 FLECHT Top-Skewed Power Test 13914

The reflood rate for Test 13914 was 1.0 in/sec. The test pressure was maintained at 21 psia and the injected coolant temperature was 223°F (5°F of sub-cooling). The WCOBRA/TRAC-TF2 simulation of Test 13914 was run past 1000 seconds, by which time all predicted heater rod elevations had reached their peak temperature and quenched. Figures 15.6.3-55 through 15.6.3-61 show the comparison of predicted and measured temperatures at elevations 24, 48, 72, 96, 120, 126, and 132 inches from the bottom of the heated length. The code prediction is for simulated rod temperatures in the inner channel (rod no. 1 located in Channel 2 of Figure 15.6.3-2). The thermocouple temperature curves in these figures represent different radial positions on individual rods located within the boundary of the WCOBRA/TRAC-TF2 inner channel. Figure 15.6.3-62 shows the prediction of the quench front elevation compared to the quench elevations deduced from temperature measurements. **[**

][a,c]

Comparisons of the axial temperature profiles are shown in Figure 15.6.3-63 at 100 seconds, and in Figure 15.6.3-64 at 300 seconds. **[**

][a,c]

Figures 15.6.3-66 through 15.6.3-68 show comparisons of the predicted and measured axial pressure differentials in the bundle. Figure 15.6.3-66 shows a comparison of the pressure differentials in the lower half (0 to 72 inches) of the bundle. **[**

][a,c] Figure 15.6.3-67 shows the comparison for the upper half (72 to 144 inches) of the bundle and shows **[**

][a,c]. The overall pressure differential comparison is shown in Figure 15.6.3-68. There are large oscillations in the code prediction.

The FLECHT top-skewed facility included steam temperature probes located in the thimble tubes. Figure 15.6.3-69 shows the comparison at the 84-inch elevation, just upstream of the peak temperature location. Figure 15.6.3-70 shows the comparison at the 120-inch elevation, and Figure 15.6.3-71 shows the comparison at the 132-inch elevation, which is near the bundle exit. **[**

][a,c]

15.6.3.1.5 FLECHT Top-Skewed Power Test 13609

The reflood rate for Test 13609 was 1.0 in/sec. The test pressure was maintained at 21 psia and the injected coolant temperature was 87°F (141°F of sub-cooling). The WCOBRA/TRAC-TF2 simulation of Test 13609 was run past 800 seconds, by which time all heater rod elevations had reached their peak

temperature and were approaching quench. Figures 15.6.3-72 through 15.6.3-78 show the comparison of predicted and measured temperatures at elevations 24, 48, 72, 96, 120, 126, and 132 inches from the bottom of the heated length. The code prediction is for simulated rod temperatures in the inner channel (rod no. 1 located in Channel 2 of Figure 15.6.3-2). The thermocouple temperature curves in these figures represent different radial positions on individual rods located within the boundary of the WCOBRA/TRAC-TF2 inner channel. Figure 15.6.3-79 shows the prediction of the quench front elevation compared to the quench elevations deduced from temperature measurements. **[**

][a,c]

Comparisons of the axial temperature profiles are shown in Figure 15.6.3-80 at 100 seconds and in Figure 15.6.3-81 at 300 seconds. **[**

][a,c]

Figure 15.6.3-82 summarizes the comparisons of the maximum predicted peak cladding temperatures at several elevations where thermocouples were located. **[**

][a,c]

Figures 15.6.3-83 through 15.6.3-85 show comparisons of the predicted and measured axial pressure differentials in the bundle. Figure 15.6.3-83 shows a comparison of the pressure differentials in the lower half (0 to 72 inches) of the bundle. **[**

][a,c] The overall pressure differential comparison is shown in Figure 15.6.3-85, with **[** **]**[a,c].

The FLECHT top-skewed facility included steam temperature probes located in the thimble tubes. Figure 15.6.3-86 shows the comparison at the 84-inch elevation, just upstream of the peak temperature location. Figure 15.6.3-87 shows the comparison at the 120-inch elevation, and Figure 15.6.3-88 shows the comparison at the 132-inch elevation, which is near the bundle exit. **[**

][a,c]

15.6.3.2 FLECHT Skewed Power Summary and Conclusions

Five FLECHT Top-Skewed Power Shape Tests were simulated using WCOBRA/TRAC-TF2. These tests had a power shape that was nearly 10 feet from the bottom of the heated length. This power shape is peaked at a higher elevation than most probable power shapes in an actual PWR. Thus, these tests are effectively an upper bound on the range of power shapes for analyses with the FULL SPECTRUM LOCA methodology. In addition, the tests had a range of inlet sub-cooling from 2°F to 141°F, a range of pressure from 20 to 40 psia, and a range of flooding rates from 0.8 in/s to 1.0 in/s.

[

]^{a,c}

a,c

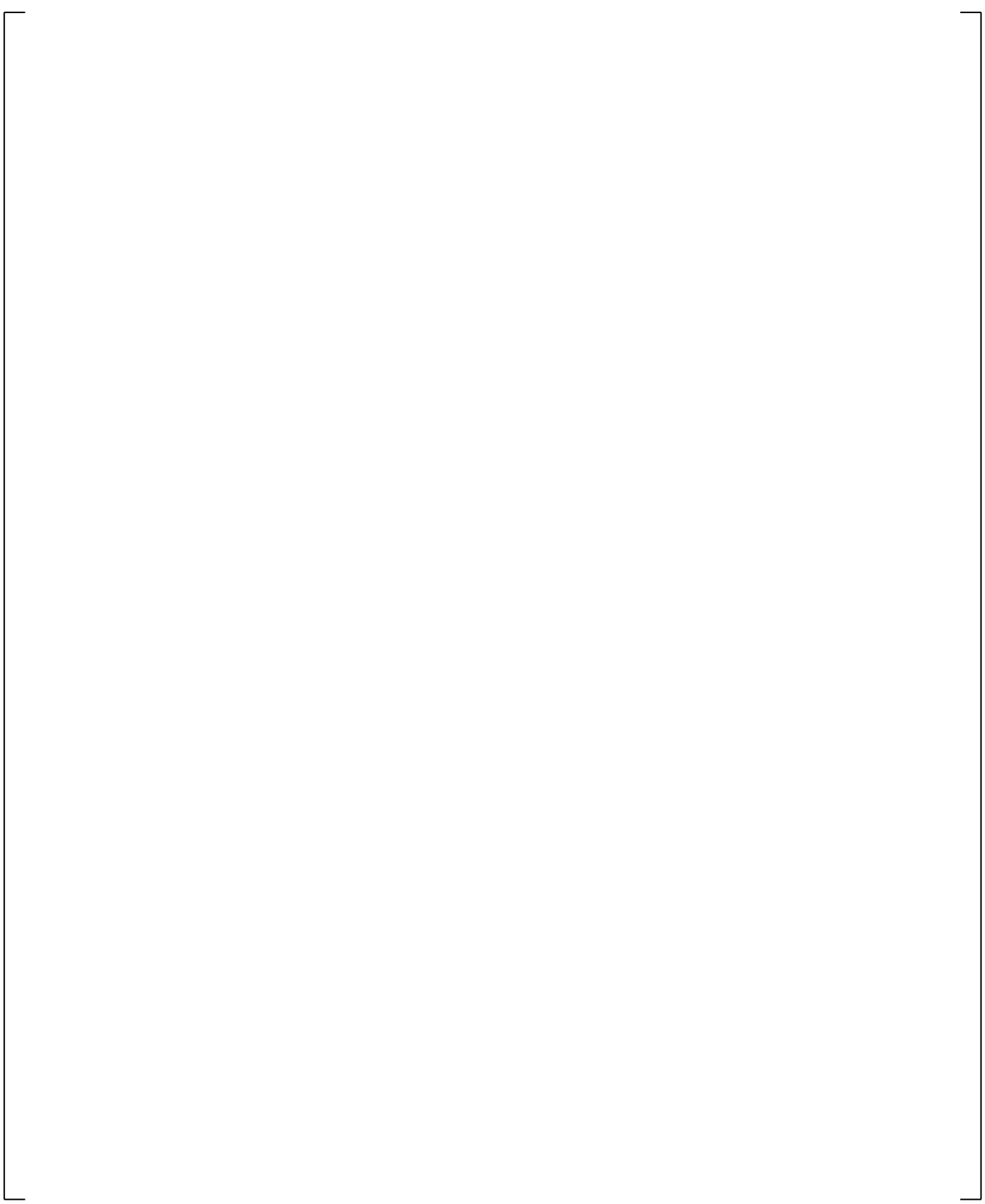

Figure 15.6.3-1 WCOBRA/TRAC-TF2 Transverse Noding for FLECHT Top-Skewed Test Bundle

a,c

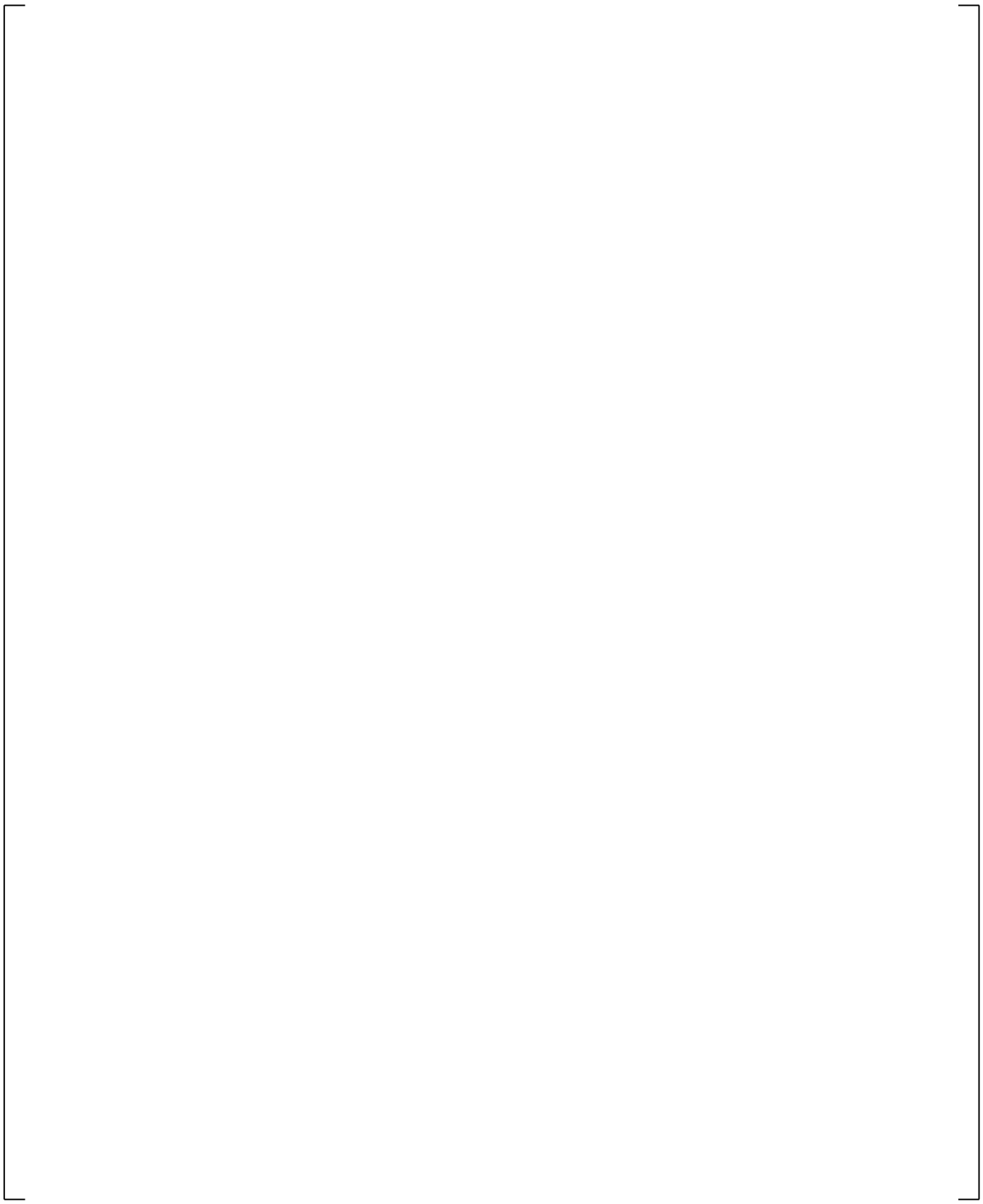

Figure 15.6.3-2 WCOBRA/TRAC-TF2 Axial Noding for FLECHT Top-Skewed Test Bundle

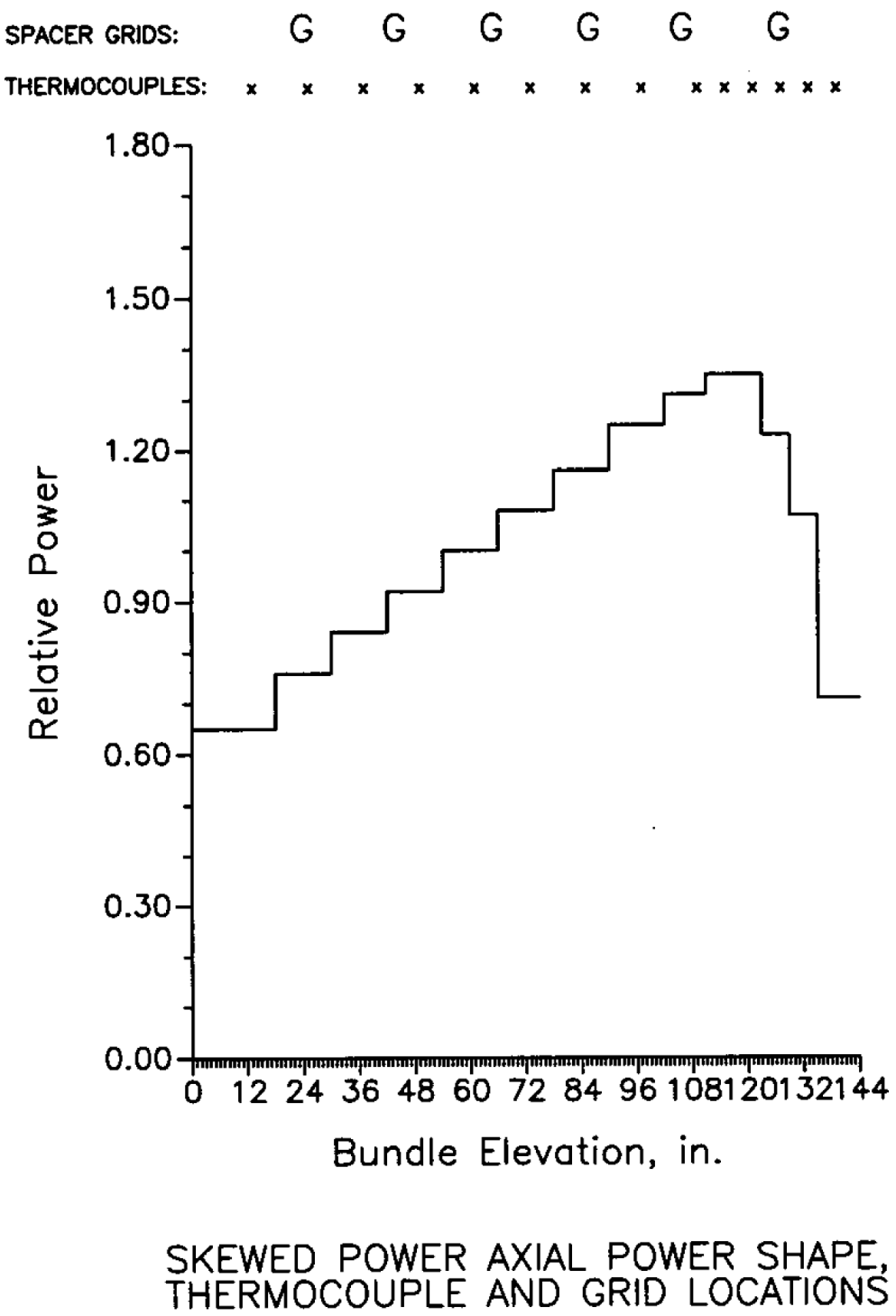

Figure 15.6.3-3 WCOBRA/TRAC-TF2 Axial Power Shape for FLECHT Top-Skewed Test Bundle

a,c

Figure 15.6.3-4 FLECHT 15305 Rod Temperatures at 24-inch Elevation

a,c

Figure 15.6.3-5 FLECHT 15305 Rod Temperatures at 48-inch Elevation

a,c

Figure 15.6.3-6 FLECHT 15305 Rod Temperatures at 72-inch Elevation

a,c

Figure 15.6.3-7 FLECHT 15305 Rod Temperatures at 96-inch Elevation

a,c

Figure 15.6.3-8 FLECHT 15305 Rod Temperatures at 120-inch Elevation

a,c

Figure 15.6.3-9 FLECHT 15305 Rod Temperatures at 126-inch Elevation

a,c

Figure 15.6.3-10 FLECHT 15305 Rod Temperatures at 132-inch Elevation

a,c

Figure 15.6.3-11 Comparison of Predicted and Estimated Quench Front Elevations for FLECHT 15305

a,c

Figure 15.6.3-12 Comparison of Predicted and Measured Axial Temperature Profile for FLECHT 15305 at 100 Seconds

a,c

Figure 15.6.3-13 Comparison of Predicted and Measured Axial Temperature Profile for FLECHT 15305 at 300 Seconds

a,c

Figure 15.6.3-14 Comparison of Predicted and Measured Maximum Cladding Temperatures at all Thermocouple Elevations for FLECHT 15305

a,c

Figure 15.6.3-15 FLECHT 15305 Bundle Lower Half ΔP

a,c

Figure 15.6.3-16 FLECHT 15305 Bundle Upper Half ΔP

a,c

Figure 15.6.3-17 FLECHT 15305 Overall ΔP

a,c

Figure 15.6.3-18 FLECHT 15305 Vapor Temperatures at 84-inch Elevation

a,c

Figure 15.6.3-19 FLECHT 15305 Vapor Temperatures at 120-inch Elevation

a,c

Figure 15.6.3-20 FLECHT 15305 Vapor Temperatures at 132-inch Elevation

a,c

Figure 15.6.3-21 FLECHT 13812 Rod Temperatures at 24-inch Elevation

a,c

Figure 15.6.3-22 FLECHT 13812 Rod Temperatures at 48-inch Elevation

a,c

Figure 15.6.3-23 FLECHT 13812 Rod Temperatures at 72-inch Elevation

a,c

Figure 15.6.3-24 FLECHT 13812 Rod Temperatures at 96-inch Elevation

a,c

Figure 15.6.3-25 FLECHT 13812 Rod Temperatures at 120-inch Elevation

a,c

Figure 15.6.3-26 FLECHT 13812 Rod Temperatures at 126-inch Elevation

a,c

Figure 15.6.3-27 FLECHT 13812 Rod Temperatures at 132-inch Elevation

a,c

Figure 15.6.3-28 Comparison of Predicted and Estimated Quench Front Elevations for FLECHT 13812

a,c

Figure 15.6.3-29 Comparison of Predicted and Measured Axial Temperature Profile for FLECHT 13812 at 100 Seconds

a,c

Figure 15.6.3-30 Comparison of Predicted and Measured Axial Temperature Profile for FLECHT 13812 at 300 Seconds

a,c

Figure 15.6.3-31 Comparison of Predicted and Measured Maximum Cladding Temperatures at all Thermocouple Elevations for FLECHT 13812

a,c

Figure 15.6.3-32 FLECHT 13812 Bundle Lower Half ΔP

a,c

Figure 15.6.3-33 FLECHT 13812 Bundle Upper Half ΔP

a,c

Figure 15.6.3-34 FLECHT 13812 Overall ΔP

a,c

Figure 15.6.3-35 FLECHT 13812 Vapor Temperatures at 84-inch Elevation

a,c

Figure 15.6.3-36 FLECHT 13812 Vapor Temperatures near 120-inch Elevation

a,c

Figure 15.6.3-37 FLECHT 13812 Vapor Temperatures at 132-inch Elevation

a,c

Figure 15.6.3-38 FLECHT 15713 Rod Temperatures at 24-inch Elevation

a,c

Figure 15.6.3-39 FLECHT 15713 Rod Temperatures at 48-inch Elevation

a,c

Figure 15.6.3-40 FLECHT 15713 Rod Temperatures at 72-inch Elevation

a,c

Figure 15.6.3-41 FLECHT 15713 Rod Temperatures at 96-inch Elevation

a,c

Figure 15.6.3-42 FLECHT 15713 Rod Temperatures at 120-inch Elevation

a,c

Figure 15.6.3-43 FLECHT 15713 Rod Temperatures at 126-inch Elevation

a,c

Figure 15.6.3-44 FLECHT 15713 Rod Temperatures at 132-inch Elevation

a,c

Figure 15.6.3-45 Comparison of Predicted and Estimated Quench Front Elevations for FLECHT 15713

a,c

Figure 15.6.3-46 Comparison of Predicted and Measured Axial Temperature Profile for FLECHT 15713 at 100 Seconds

a,c

Figure 15.6.3-47 Comparison of Predicted and Measured Axial Temperature Profile for FLECHT 15713 at 300 Seconds

a,c

Figure 15.6.3-48 Comparison of Predicted and Measured Maximum Cladding Temperatures at all Thermocouple Elevations for FLECHT 15713

a,c

Figure 15.6.3-49 FLECHT 15713 Bundle Lower Half ΔP

a,c

Figure 15.6.3-50 FLECHT 15713 Bundle Upper Half ΔP

a,c

Figure 15.6.3-51 FLECHT 15713 Overall ΔP

a,c

Figure 15.6.3-52 FLECHT: 15713 Vapor Temperatures at 84-inch Elevation

a,c

Figure 15.6.3-53 FLECHT 15713 Vapor Temperatures near 120-inch Elevation

a,c

Figure 15.6.3-54 FLECHT 15713 Vapor Temperatures at 132-inch Elevation

a,c

Figure 15.6.3-55 FLECHT 13914 Rod Temperatures at 24-inch Elevation

a,c

Figure 15.6.3-56 FLECHT 13914 Rod Temperatures at 48-inch Elevation

a,c

Figure 15.6.3-57 FLECHT 13914 Rod Temperatures at 72-inch Elevation

a,c

Figure 15.6.3-58 FLECHT 13914 Rod Temperatures at 96-inch Elevation

a,c

Figure 15.6.3-59 FLECHT 13914 Rod Temperatures at 120-inch Elevation

a,c

Figure 15.6.3-60 FLECHT 13914 Rod Temperatures at 126-inch Elevation

a,c

Figure 15.6.3-61 FLECHT 13914 Rod Temperatures at 132-inch Elevation

a,c

Figure 15.6.3-62 Comparison of Predicted and Estimated Quench Front Elevations for FLECHT 13914

a,c

Figure 15.6.3-63 Comparison of Predicted and Measured Axial Temperature Profile for FLECHT 13914 at 100 Seconds

a,c

Figure 15.6.3-64 Comparison of Predicted and Measured Axial Temperature Profile for FLECHT 13914 at 300 Seconds

a,c

Figure 15.6.3-65 Comparison of Predicted and Measured Maximum Cladding Temperatures at all Thermocouple Elevations for FLECHT 13914

a,c

Figure 15.6.3-66 FLECHT 13914 Bundle Lower Half ΔP

a,c

Figure 15.6.3-67 FLECHT 13914 Bundle Upper Half ΔP

a,c

Figure 15.6.3-68 FLECHT 13914 Overall ΔP

a,c

Figure 15.6.3-69 FLECHT 13914 Vapor Temperatures at 84-inch Elevation

a,c

Figure 15.6.3-70 FLECHT 13914 Vapor Temperatures at 120-inch Elevation

a,c

Figure 15.6.3-71 FLECHT 13914 Vapor Temperatures at 132-inch Elevation

a,c

Figure 15.6.3-72 FLECHT 13609 Rod Temperatures at 24-inch Elevation

a,c

Figure 15.6.3-73 FLECHT 13609 Rod Temperatures at 48-inch Elevation

a,c

Figure 15.6.3-74 FLECHT 13609 Rod Temperatures at 72-inch Elevation

a,c

Figure 15.6.3-75 FLECHT 13609 Rod Temperatures at 96-inch Elevation

a,c

Figure 15.6.3-76 FLECHT 13609 Rod Temperatures at 120-inch Elevation

a,c

Figure 15.6.3-77 FLECHT 13609 Rod Temperatures at 126-inch Elevation

a,c

Figure 15.6.3-78 FLECHT 13609 Rod Temperatures at 132-inch Elevation

a,c

Figure 15.6.3-79 Comparison of Predicted and Estimated Quench Front Elevations for FLECHT 13609

a,c

Figure 15.6.3-80 Comparison of Predicted and Measured Axial Temperature Profile for FLECHT 13609 at 100 Seconds

a,c

Figure 15.6.3-81 Comparison of Predicted and Measured Axial Temperature Profile for FLECHT 13609 at 300 Seconds

a,c

Figure 15.6.3-82 Comparison of Predicted and Measured Maximum Cladding Temperatures at all Thermocouple Elevations for FLECHT 13609

a,c

Figure 15.6.3-83 FLECHT 13609 Bundle Lower Half ΔP

a,c

Figure 15.6.3-84 FLECHT 13609 Bundle Upper Half ΔP

a,c

Figure 15.6.3-85 FLECHT 13609 Overall ΔP

a,c

Figure 15.6.3-86 FLECHT 13609 Vapor Temperatures at 84-inch Elevation

a,c

Figure 15.6.3-87 FLECHT 13609 Vapor Temperatures at 120-inch Elevation

a,c

Figure 15.6.3-88 FLECHT 13609 Vapor Temperatures at 132-inch Elevation

a,c

Figure 15.6.3-89 Comparison of Predicted and Measured Maximum Cladding Temperatures for FLECHT Top-Skewed Power Test Simulations

15.6.4 WCOBRA/TRAC-TF2 Simulations of G-2 Reflood Test Bundle

The WCOBRA/TRAC-TF2 model of the G-2 reflood test bundle used the same level of detail as was used for other separate effects test simulations. This model consisted of three components: a VESSEL, a PIPE component, and a zero velocity FILL component. A schematic diagram of the model is shown in Figures 15.6.4-1 and 15.6.4-2.

The reflood flow into the lower plenum is provided as a vessel boundary condition in Section 1 of the VESSEL component. Section 3, shown in Figure 15.6.4-1, models the heated length of the test section with two channels: Channel 4 represents the flow around the outer heater rods and Channel 3 represents the flow in the central portion of the rod bundle. (The bundle is representative of a 14-ft, 17x17 assembly in a PWR.) The G-2 reflood tests had a radial power distribution for these experiments. The outer channel grouped together the outer, lower power rods, while the region containing the higher power rods in the bundle center was modeled as the inner channel. Figure 15.6.4-3 shows the radial power zones for the bundle and the grouping of the heater rods for the two channels in WCOBRA/TRAC-TF2. The fluid nodes are thermally connected to rods simulating the heater rods. Loss coefficients are used to model the seven mixing vane grids of the fuel assembly in the inner and outer portions of the rod bundle which are representative of Westinghouse mixing vane grids. Section 4 (Channel 5) models the ground plate, which also has a loss coefficient. Section 5 (Channel 6) represented the upper plenum.

[

]^{a,c}

Additional initial conditions are provided in Table 14.1-6 for each test and are repeated here.

[

Test Series	Test Number	Pressure psia	Flooding Rate in/s	Inlet Sub-cooling °F	Peak Power kW/ft	Comment

]^{b}

15.6.4.1 G-2 Reflood Results

15.6.4.1.1 G-2 Reflood Test 550

The reflood rate for Test 550 was 1.0 in/sec. The test pressure was maintained at 40 psia and the injected coolant temperature was 150°F (116°F of sub-cooling). The WCOBRA/TRAC-TF2 simulation of Test 550 was run for the first 500 seconds of the experiment, by which time all heater rod elevations had reached their maximum temperatures and had started to decline.

Figures 15.6.4-4 through 15.6.4-10 show the comparison of predicted and measured temperature histories at elevations 29, 45, 70, 82, 95, 111, and 135 inches from the bottom of the heated length. The time is after the start of reflood and start of decrease of bundle power. The code prediction is for simulated cladding temperatures in the inner channel (rod no. 1 located in Channel 3 of Figure 15.6.4-1). The data curves in these figures are all of the valid thermocouples located within the boundary of the WCOBRA/TRAC-TF2 inner channel. **[**

][a,c]

Comparison of the axial temperature profiles are shown in Figures 15.6.4-11 through 15.6.4-13 at the **[**

][a,c]

Figures 15.6.4-14 through 15.6.4-16 show comparisons of the predicted and measured axial pressure differentials in the bundle. Figure 15.6.4-14 shows a comparison of the pressure differential in the lower half of the bundle (27.3 to 82 inches). **[**

][a,c] The overall bundle pressure differential comparison (27.3 to 136.7 inches) is shown in Figure 15.6.4-16.

The G-2 facility included steam temperature probes in the thimble tubes located at several elevations in the bundle. Figure 15.6.4-17 shows a comparison of predicted and measured steam temperatures at the 109-inch elevation. Figure 15.6.4-18 shows the comparison at the 136.7-inch elevation. **[**

][a,c]

Figure 15.6.4-19 shows a comparison of predicted and measured maximum cladding temperatures reached at all of the 12 elevations measured. The measured values are the maximum of all valid thermocouple temperatures in the inner region. **[**

][a,c]

15.6.4.1.2 G-2 Reflood Test 562

The reflood rate for Test 562 was 1.0 in/sec. The test pressure was maintained at 20 psia and the injected coolant temperature was 117°F (110°F of sub-cooling). The WCOBRA/TRAC-TF2 simulation of Test 562 was run for the first 500 seconds of the experiment, by which time all heater rod elevations had reached their peak and had started to decline.

Figures 15.6.4-20 through 15.6.4-26 show the comparison of predicted and measured temperature histories at elevations 29, 45, 70, 82, 95, 111, and 135 inches from the bottom of the heated length. The code prediction is for heater rods within the inner channel (rod no. 1 located in Channel 3 of Figure 15.6.4-1). The data curves in these figures are all valid thermocouples located within the boundary

of the WCOBRA/TRAC-TF2 inner channel. **[**

][a,c]

Comparison of the axial temperature profiles are shown in Figures 15.6.4-27 through 15.6.4-29 at times before, near, and after the occurrence of the peak average cladding temperature, respectively. **[**

][a,c]

Figures 15.6.4-30 through 15.6.4-32 show comparisons of the predicted and measured axial pressure differentials in the bundle. Figure 15.6.4-30 shows a comparison of the pressure differential in the lower half of the bundle (27.3 to 82 inches), where **[** **]**[a,c] Figure 15.6.4-31 shows the comparison for the upper half of the bundle (82 to 136.7 inches), which **[** **]**[a,c] The overall bundle pressure differential comparison (27.3 to 136.7 inches) is shown in Figure 15.6.4-32.

The G-2 facility included steam temperature probes in the thimble tubes located at several locations in the bundle. Figure 15.6.4-33 shows a comparison of predicted and measured steam temperatures at the 109-inch elevation. Figure 15.6.4-34 shows the comparison at the 136.7-inch elevation. **[**

][a,c]

Figure 15.6.4-35 shows a comparison of predicted and measured maximum cladding temperatures reached at all of the 12 elevations measured. The measured values are the maximum of all valid thermocouple temperatures in the inner region. **[**

][a,c]

15.6.4.1.3 G-2 Reflood Test 568

The reflood rate for Test 568 was 1.00 in/sec. The test pressure was maintained at 40 psia and the injected coolant temperature was 150°F (117°F of sub-cooling). The WCOBRA/TRAC-TF2 simulation of Test 568 was run for the first 500 seconds of the experiment, by which time all heater rod elevations had reached their peak and had started to decline.

Figures 15.6.4-36 through 15.6.4-42 show the comparison of predicted and measured temperature histories at elevations 29, 45, 70, 82, 95, 111, and 135 inches from the bottom of the heated length. The code prediction is for heater rods within the inner channel (rod no. 1 located in Channel 3 of Figure 15.6.4-1). The data curves in these figures are all of the valid thermocouples located within the boundary of the WCOBRA/TRAC-TF2 inner channel. **[**

][a,c]

Comparison of the axial temperature profiles are shown in Figures 15.6.4-43 through 15.6.4-45 at times before, near, and after the occurrence of the peak average cladding temperature, respectively. **[**

][a,c]

Figures 15.6.4-46 through 15.6.4-48 show comparisons of the predicted and measured axial pressure differentials in the bundle. Figure 15.6.4-46 shows a comparison of the pressure differential in the lower half of the bundle (27.3 to 82 inches) where **[** **]**[a,c]. Figure 15.6.4-47 shows the comparison for the upper half of the bundle (82 to 136.7 inches), which **[** **]**[a,c]. The overall bundle pressure differential comparison (27.3 to 136.7 inches) is shown in Figure 15.6.4-48.

The G-2 facility included steam temperature probes in the thimble tubes located at several locations in the bundle. Figure 15.6.4-49 shows a comparison of predicted and measured steam temperatures at the 109-inch elevation. Figure 15.6.4-50 shows the comparison at the 136.7-inch elevation. **[**

][a,c]

Figure 15.6.4-51 shows a comparison of predicted and measured maximum cladding temperatures reached at all of the 12 elevations measured. The measured values are the maximum of all valid thermocouple temperatures in the inner region. **[**

][a,c]

15.6.4.2 G-2 Reflood Tests Simulation Summary and Conclusions

Three G-2 reflood tests were simulated with WCOBRA/TRAC-TF2. **[**

][a,c]

The predicted maximum cladding temperatures were **[** **]**[a,c]. Figure 15.6.4-52 shows the comparison of predicted and measured maximum temperatures for all three G-2 test simulations. **[**

][a,c]

a,c

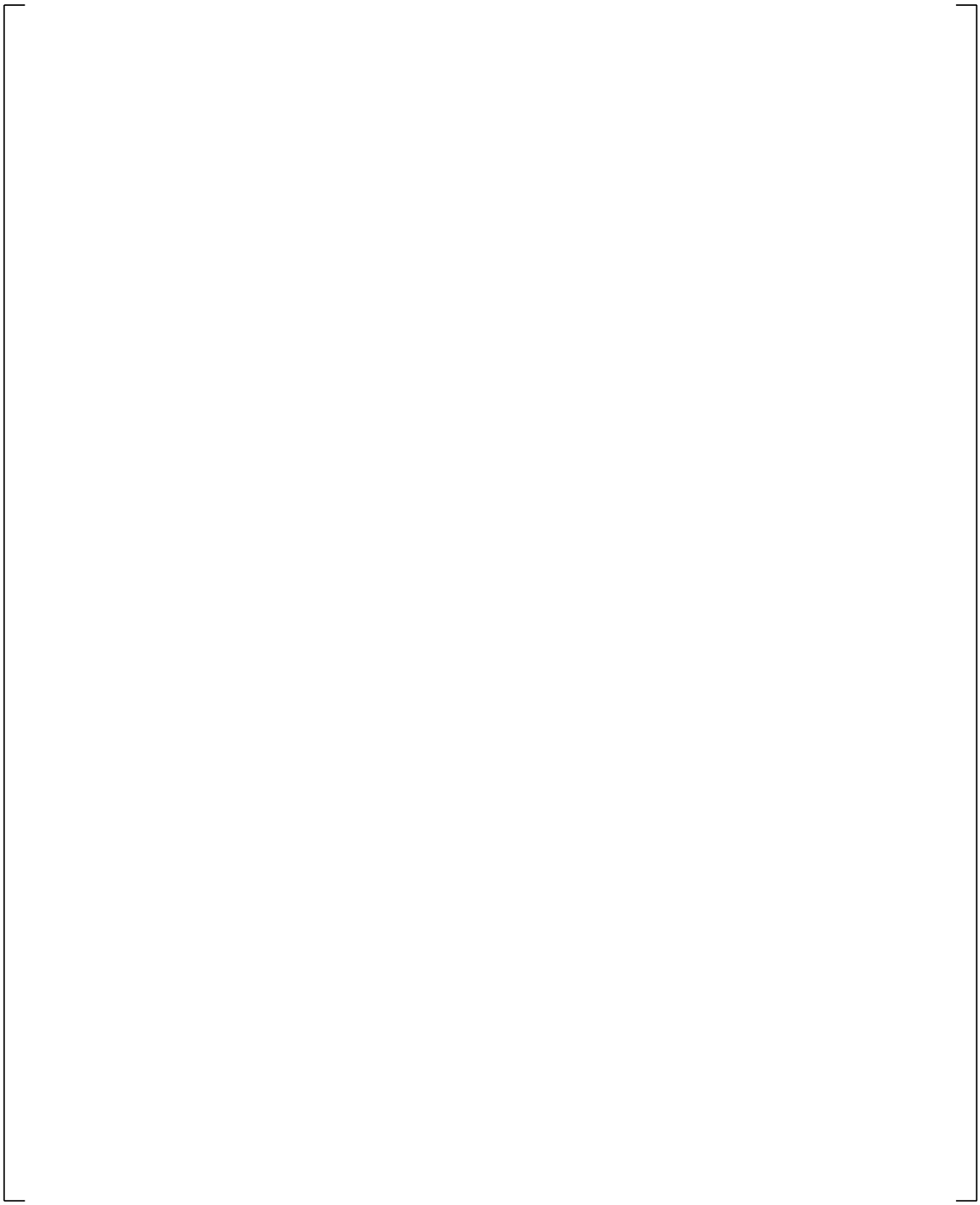

Figure 15.6.4-1 WCOBRA/TRAC-TF2 Axial Noding for G-2 Reflood Simulations

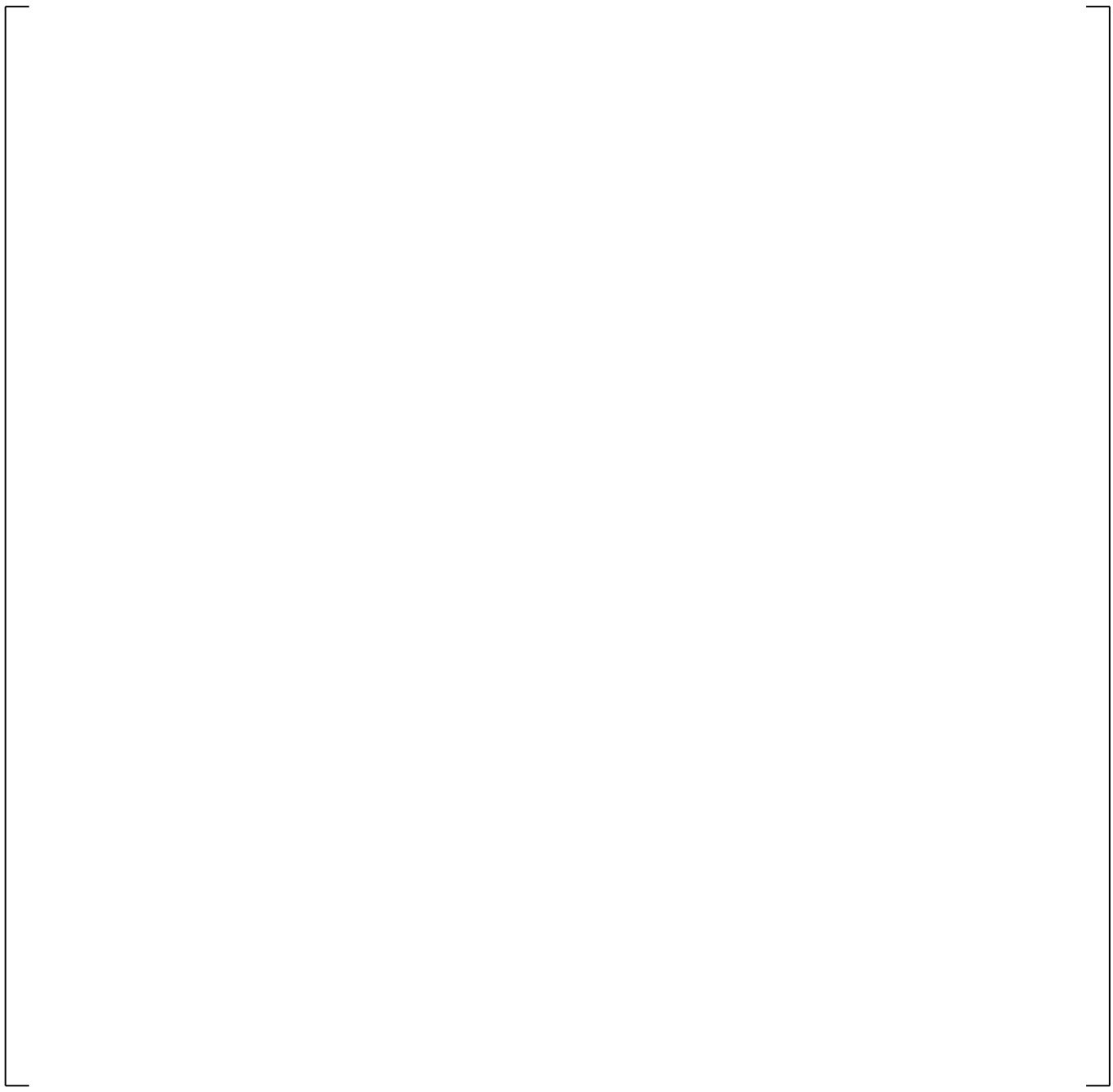

a,c

Figure 15.6.4-2 WCOBRA/TRAC-TF2 Transverse Noding for G-2 Reflood Simulations

a,c

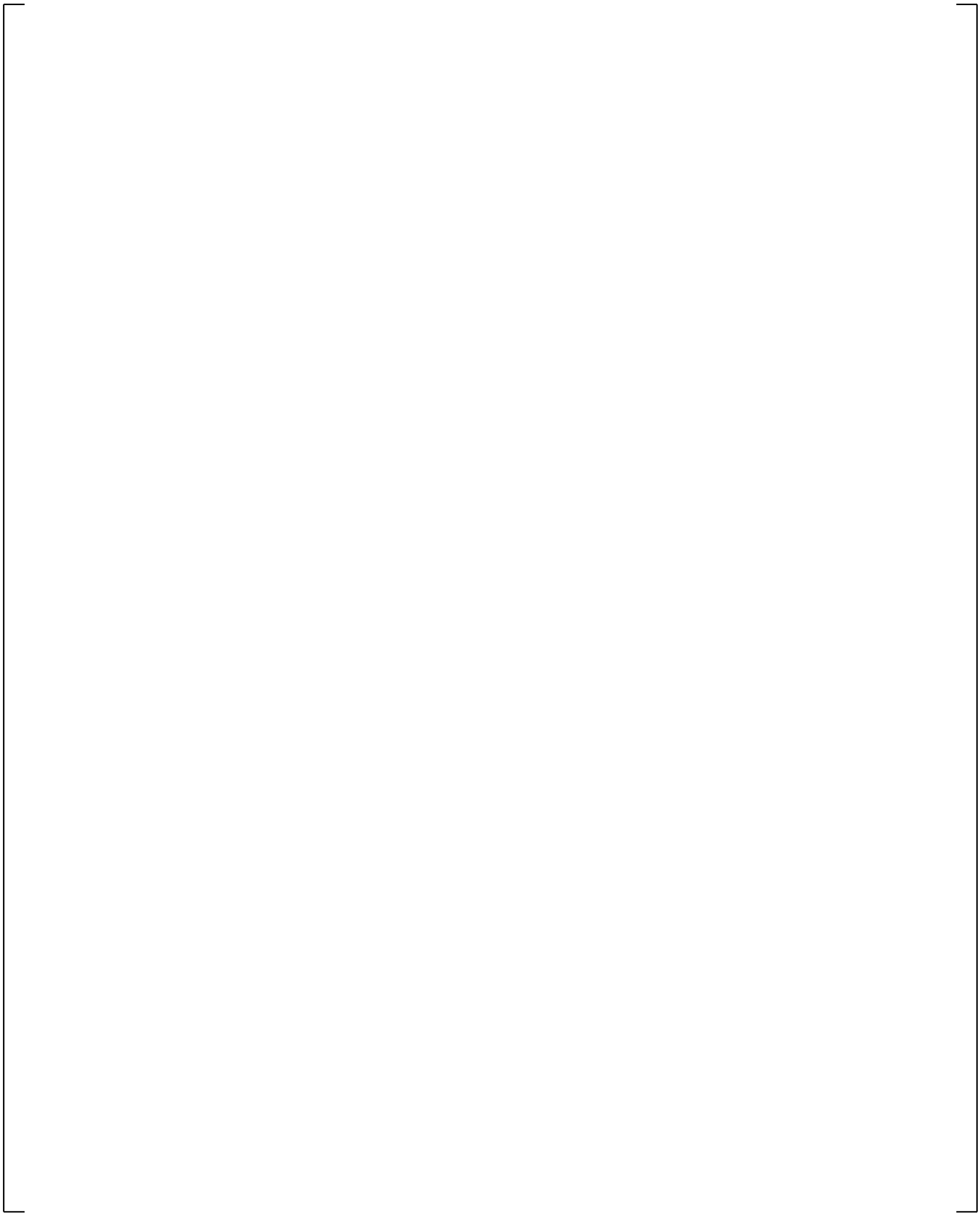

Figure 15.6.4-3 G-2 Bundle Cross Section

a,c

Figure 15.6.4-4 G-2 Reflood Test 550 Rod Temperatures at 29-inch Elevation

a,c

Figure 15.6.4-5 G-2 Reflood Test 550 Rod Temperatures at 45-inch Elevation

a,c

Figure 15.6.4-6 G-2 Reflood Test 550 Rod Temperatures at 70-inch Elevation

a,c

Figure 15.6.4-7 G-2 Reflood Test 550 Rod Temperatures at 82-inch Elevation

a,c

Figure 15.6.4-8 G-2 Reflood Test 550 Rod Temperatures at 95-inch Elevation

a,c

Figure 15.6.4-9 G-2 Reflood Test 550 Rod Temperatures at 111-inch Elevation

a,c

Figure 15.6.4-10 G-2 Reflood Test 550 Rod Temperatures at 135-inch Elevation

a,c

Figure 15.6.4-11 Axial Temperature Profile for G-2 Reflood Test 550 at 57 Seconds

a,c

Figure 15.6.4-12 Axial Temperature Profile for G-2 Reflood Test 550 at 87 Seconds

a,c

Figure 15.6.4-13 Axial Temperature Profile for G-2 Reflood Test 550 at 137 Seconds

a,c

Figure 15.6.4-14 G-2 Reflood Test 550 Bundle Lower Half ΔP

a,c

Figure 15.6.4-15 G-2 Reflood Test 550 Bundle Upper Half ΔP

a,c

Figure 15.6.4-16 G-2 Reflood Test 550 Overall ΔP

a,c

Figure 15.6.4-17 G-2 Reflood Test 550 Vapor Temperatures near 109-inch Elevation

a,c

Figure 15.6.4-18 G-2 Reflood Test 550 Vapor Temperatures at 136.7-inch Elevation

a,c

Figure 15.6.4-19 Maximum Cladding Temperatures for G-2 Reflood Test 550

a,c

Figure 15.6.4-20 G-2 Reflood Test 562 Rod Temperatures at 29-inch Elevation

a,c

Figure 15.6.4-21 G-2 Reflood Test 562 Rod Temperatures at 45-inch Elevation

a,c

Figure 15.6.4-22 G-2 Reflood Test 562 Rod Temperatures at 70-inch Elevation

a,c

Figure 15.6.4-23 G-2 Reflood Test 562 Rod Temperatures at 82-inch Elevation

a,c

Figure 15.6.4-24 G-2 Reflood Test 562 Rod Temperatures at 95-inch Elevation

a,c

Figure 15.6.4-25 G-2 Reflood Test 562 Rod Temperatures at 111-inch Elevation

a,c

Figure 15.6.4-26 G-2 Reflood Test 562 Rod Temperatures at 135-inch Elevation

a,c

Figure 15.6.4-27 Axial Temperature Profile for G-2 Reflood Test 562 at 34 Seconds

a,c

Figure 15.6.4-28 Axial Temperature Profile for G-2 Reflood Test 562 at 64 Seconds

a,c

Figure 15.6.4-29 Axial Temperature Profile for G-2 Reflood Test 562 at 114 Seconds

a,c

Figure 15.6.4-30 G-2 Reflood Test 562 Bundle Lower Half ΔP

a,c

Figure 15.6.4-31 G-2 Reflood Test 562 Bundle Upper Half ΔP

a,c

Figure 15.6.4-32 G-2 Reflood Test 562 Overall ΔP

a,c

Figure 15.6.4-33 G-2 Reflood Test 562 Vapor Temperatures near 109-inch Elevation

a,c

Figure 15.6.4-34 G-2 Reflood Test 562 Vapor Temperatures at 136.7-inch Elevation

a,c

Figure 15.6.4-35 Maximum Cladding Temperatures for G-2 Reflood Test 562

a,c

Figure 15.6.4-36 G-2 Reflood Test 568 Rod Temperatures at 29-inch Elevation

a,c

Figure 15.6.4-37 G-2 Reflood Test 568 Rod Temperatures at 45-inch Elevation

a,c

Figure 15.6.4-38 G-2 Reflood Test 568 Rod Temperatures at 70-inch Elevation

a,c

Figure 15.6.4-39 G-2 Reflood Test 568 Rod Temperatures at 82-inch Elevation

a,c

Figure 15.6.4-40 G-2 Reflood Test 568 Rod Temperatures at 95-inch Elevation

a,c

Figure 15.6.4-41 G-2 Reflood Test 568 Rod Temperatures at 111-inch Elevation

a,c

Figure 15.6.4-42 G-2 Reflood Test 568 Rod Temperatures at 135-inch Elevation

a,c

Figure 15.6.4-43 Axial Temperature Profile for G-2 Reflood Test 568 at 49 Seconds

a,c

Figure 15.6.4-44 Axial Temperature Profile for G-2 Reflood Test 568 at 79 Seconds

a,c

Figure 15.6.4-45 Axial Temperature Profile for G-2 Reflood Test 568 at 129 Seconds

a,c

Figure 15.6.4-46 G-2 Reflood Test 568 Bundle Lower Half ΔP

a,c

Figure 15.6.4-47 G-2 Reflood Test 568 Bundle Upper Half ΔP

a,c

Figure 15.6.4-48 G-2 Reflood Test 568 Overall ΔP

a,c

Figure 15.6.4-49 G-2 Reflood Test 568 Vapor Temperatures near 109-inch Elevation

a,c

Figure 15.6.4-50 G-2 Reflood Test 568 Vapor Temperatures at 136.7-inch Elevation

a,c

Figure 15.6.4-51 Maximum Cladding Temperatures for G-2 Reflood Test 568

a,c

Figure 15.6.4-52 Predicted and Measured Maximum Cladding Temperatures for G-2 Reflood Test Simulations

15.6.5 WCOBRA/TRAC-TF2 Simulations of FEBA

Figures 15.6.5-1 and 15.6.5-2 presents the noding scheme used to model the Flooding Experiment with Blocked Arrays (FEBA) test facility. A WCOBRA/TRAC-TF2 VESSEL component was used to represent the test bundle, and upper and lower plenums to the test bundle so that boundary conditions could be applied. The first section represents a lower plenum, where the flow boundary condition is applied to the bottom of Channel 1. The second section models the test bundle with two channels. **[**

][a,c] An unheated conductor was used to model the thick FEBA housing, since metal heat release to the fluid was expected to be significant. The third section contains a single channel (Channel 4) and serves as the upper plenum. A pressure boundary condition is applied to the top of Channel 4. A PIPE component with a zero velocity FILL is attached to Channel 4 which serves to satisfy the WCOBRA/TRAC-TF2 requirement of at least one one-dimensional component. The zero velocity FILL prevents flow through the PIPE.

The axial noding in the section modeling the test bundle is **[**

][a,c]

Measured values of heater rod temperature, housing temperature, injection flowrate, and bundle power were used to determine the initial temperatures and the time-dependent rod heat source in the simulation.

15.6.5.1 FEBA Results

15.6.5.1.1 Simulation of FEBA Test 223

Test 223 included the mid-plane spacer grid. The flooding rate was 1.5 in/sec, and the bundle pressure was maintained at 32 psia. The WCOBRA/TRAC-TF2 simulation was run for 500 transient seconds. Figures 15.6.5-3 through 15.6.5-9 compare the predicted cladding temperature with the average of the measured values at several elevations in the test bundle for **[**

][a,c]

Figures 15.6.5-10 and 15.6.5-11 show the predicted and measured axial temperature profiles at 75 and 150 seconds, respectively. The locations of the spacer grids are apparent in the axial profiles where there is a “dip” in temperature. **[**

][a,c]

15.6.5.1.2 Simulation of FEBA Test 234

Test 234 is similar to Test 223, except it did not include the mid-plane spacer grid. The flooding rate was 1.5 in/sec, and the bundle pressure was maintained at 29 psia. The WCOBRA/TRAC-TF2 simulation was run for 500 seconds. Figures 15.6.5-12 through 15.6.5-18 compare the predicted cladding temperature with the average of the measured values at several elevations in the test bundle for **[**

][a,c]

Figures 15.6.5-19 and 15.6.5-20 show the predicted and measured axial temperature profiles at 75 and 150 seconds, respectively. As can be observed, **[**

][a,c] due to the absence of the spacer grid. **[**

][a,c]

15.6.5.1.3 Simulation of FEBA Test 216

Test 216 included the mid-plane spacer grid. The flooding rate was 1.5 in/sec, and the bundle pressure was maintained at 60 psia. The WCOBRA/TRAC-TF2 simulation was run for 500 seconds. Figures 15.6.5-21 through 15.6.5-27 compare the predicted cladding temperature with the average of the measured values at several elevations in the test bundle for **[**

][a,c]

Figures 15.6.5-28 and 15.6.5-29 show the predicted and measured axial temperature profiles at 75 and 150 seconds, respectively, and show **[** **]**[a,c].

15.6.5.1.4 Simulation of FEBA Test 229

Test 229 is similar to Test 216, except it did not include the mid-plane spacer grid. The flooding rate was 1.5 in/sec, and the bundle pressure was maintained at 61 psia. The WCOBRA/TRAC-TF2 simulation was run for the first 500 seconds of the experiment. Figures 15.6.5-30 through 15.6.5-36 compare the predicted cladding temperature with the average of the measured values at several elevations in the test bundle for **[**

][a,c]

Figures 15.6.5-37 and 15.6.5-38 show the predicted and measured axial temperature profiles at 75 and 150 seconds, respectively. As can be observed, the dip at 76 inches in Figures 15.6.5-28 and 15.6.5-29 is not observed in Figures 15.6.5-37 and 15.6.5-38 due to the absence of the spacer grid.

15.6.5.2 Summary and Conclusions

Four FEBA tests were simulated using WCOBRA/TRAC-TF2. Two low pressure tests (Tests 223 and 234) were simulated as well as two at a higher pressure (Tests 216 and 229). Each pair of tests were run with similar thermal-hydraulic conditions, but in one of the two tests the mid-plane grid was removed.

[

]^{a,c}

a,c

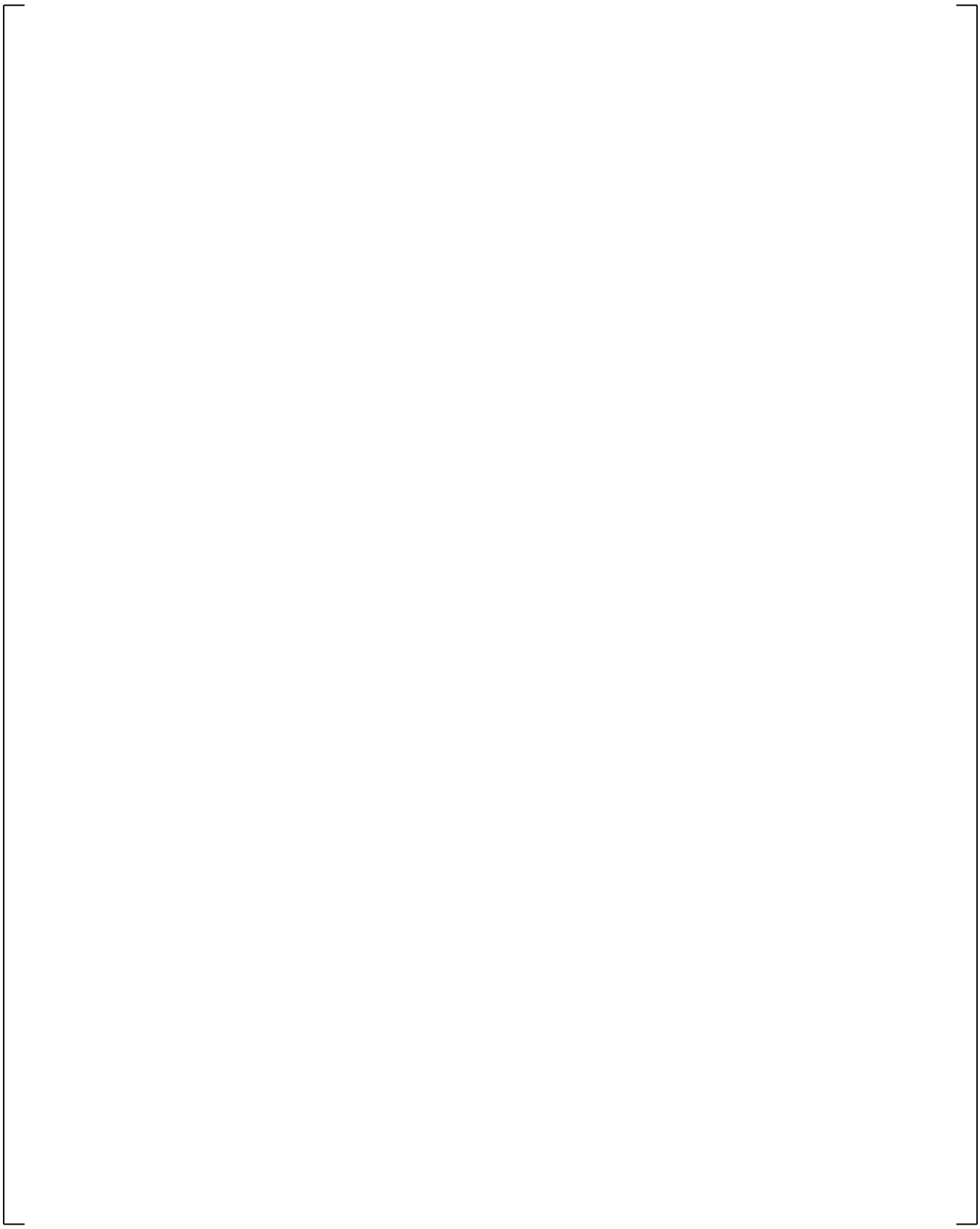

Figure 15.6.5-1 WCOBRA/TRAC-TF2 Transverse Noding for FEBA

a,c

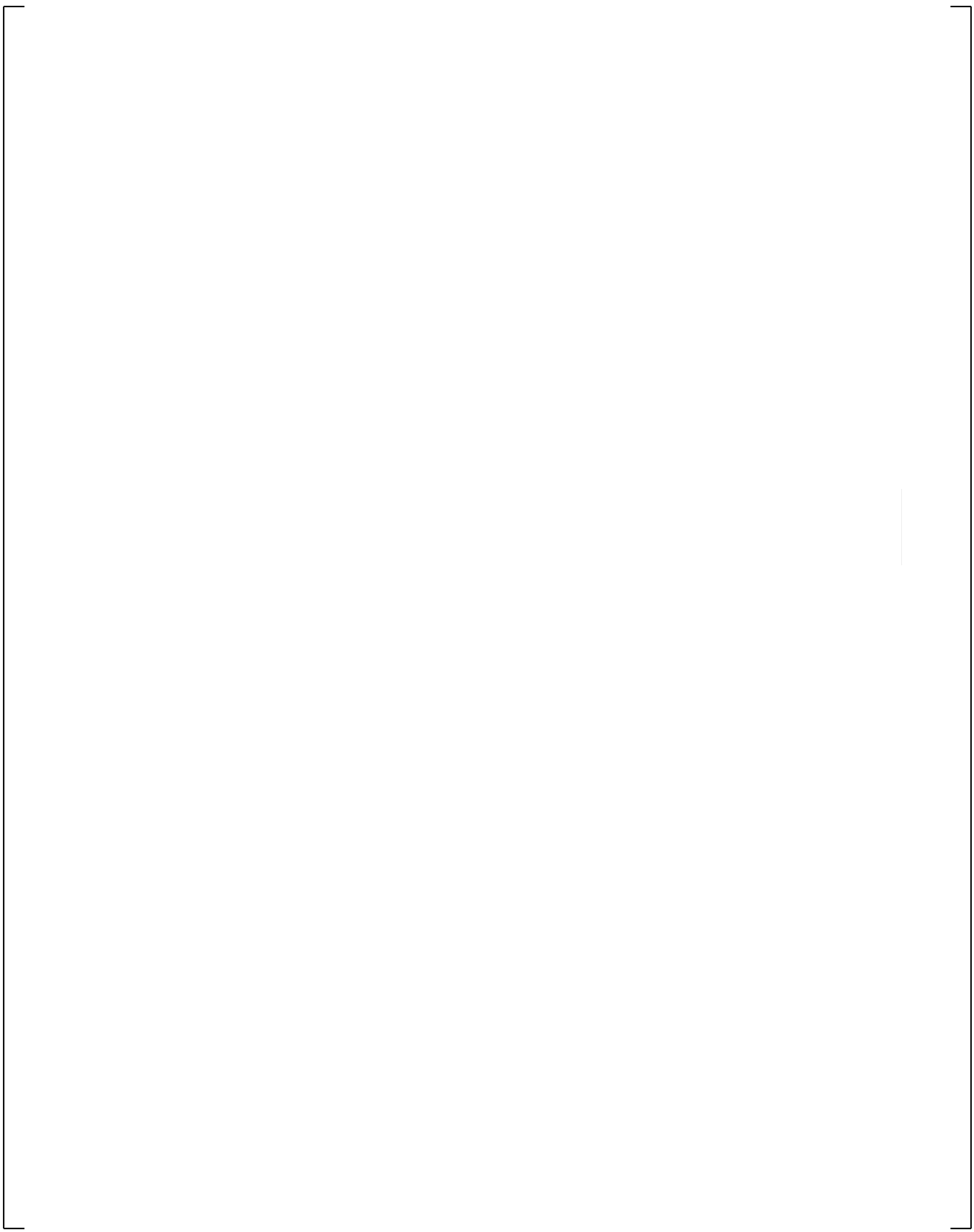

Figure 15.6.5-2 WCOBRA/TRAC-TF2 Axial Noding for FEBA

a,c

Figure 15.6.5-3 Rod Temperatures for FEBA Test 223 at 2770 mm Reference Elevation

a,c

Figure 15.6.5-4 Rod Temperatures for FEBA Test 223 at 2225 mm Reference Elevation

a,c

Figure 15.6.5-5 Rod Temperatures for FEBA Test 223 at 2125 mm Reference Elevation

a,c

Figure 15.6.5-6 Rod Temperatures for FEBA Test 223 at 2025 mm Reference Elevation

a,c

Figure 15.6.5-7 Rod Temperatures for FEBA Test 223 at 1925 mm Reference Elevation

a,c

Figure 15.6.5-8 Rod Temperatures for FEBA Test 223 at 1625 mm Reference Elevation

a,c

Figure 15.6.5-9 Rod Temperatures for FEBA Test 223 at 1135 mm Reference Elevation

a,c

Figure 15.6.5-10 Comparison of Predicted and Measured Axial Temperature Profiles for FEBA Test 223 at 75 Seconds

a,c

Figure 15.6.5-11 Comparison of Predicted and Measured Axial Temperature Profiles for FEBA Test 223 at 150 Seconds

a,c

Figure 15.6.5-12 Rod Temperatures for FEBA Test 234 at 2770 mm Reference Elevation

a,c

Figure 15.6.5-13 Rod Temperatures for FEBA Test 234 at 2225 mm Reference Elevation

a,c

Figure 15.6.5-14 Rod Temperatures for FEBA Test 234 at 2125 mm Reference Elevation

a,c

Figure 15.6.5-15 Rod Temperatures for FEBA Test 234 at 2025 mm Reference Elevation

a,c

Figure 15.6.5-16 Rod Temperatures for FEBA Test 234 at 1925 mm Reference Elevation

a,c

Figure 15.6.5-17 Rod Temperatures for FEBA Test 234 at 1625 mm Reference Elevation

a,c

Figure 15.6.5-18 Rod Temperatures for FEBA Test 234 at 1135 mm Reference Elevation

a,c

Figure 15.6.5-19 Comparison of Predicted and Measured Axial Temperature Profiles for FEBA Test 234 at 75 Seconds

a,c

Figure 15.6.5-20 Comparison of Predicted and Measured Axial Temperature Profiles for FEBA Test 234 at 150 Seconds

a,c

Figure 15.6.5-21 Rod Temperatures for FEBA Test 216 at 2770 mm Reference Elevation

a,c

Figure 15.6.5-22 Rod Temperatures for FEBA Test 216 at 2225 mm Reference Elevation

a,c

Figure 15.6.5-23 Rod Temperatures for FEBA Test 216 at 2125 mm Reference Elevation

a,c

Figure 15.6.5-24 Rod Temperatures for FEBA Test 216 at 2025 mm Reference Elevation

a,c

Figure 15.6.5-25 Rod Temperatures for FEBA Test 216 at 1925 mm Reference Elevation

a,c

Figure 15.6.5-26 Rod Temperatures for FEBA Test 216 at 1625 mm Reference Elevation

a,c

Figure 15.6.5-27 Rod Temperatures for FEBA Test 216 at 1135 mm Reference Elevation

a,c

Figure 15.6.5-28 Comparison of Predicted and Measured Axial Temperature Profiles for FEBA Test 216 at 75 Seconds

a,c

Figure 15.6.5-29 Comparison of Predicted and Measured Axial Temperature Profiles for FEBA Test 216 at 150 Seconds

a,c

Figure 15.6.5-30 Rod Temperatures for FEBA Test 229 at 2770 mm Reference Elevation

a,c

Figure 15.6.5-31 Rod Temperatures for FEBA Test 229 at 2225 mm Reference Elevation

a,c

Figure 15.6.5-32 Rod Temperatures for FEBA Test 229 at 2125 mm Reference Elevation

a,c

Figure 15.6.5-33 Rod Temperatures for FEBA Test 229 at 2025 mm Reference Elevation

a,c

Figure 15.6.5-34 Rod Temperatures for FEBA Test 229 at 1925 mm Reference Elevation

a,c

Figure 15.6.5-35 Rod Temperatures for FEBA Test 229 at 1625 mm Reference Elevation

a,c

Figure 15.6.5-36 Rod Temperatures for FEBA Test 229 at 1135 mm Reference Elevation

a,c

Figure 15.6.5-37 Comparison of Predicted and Measured Axial Temperature Profiles for FEBA Test 229 at 75 Seconds

a,c

Figure 15.6.5-38 Comparison of Predicted and Measured Axial Temperature Profiles for FEBA Test 229 at 150 Seconds

a,c

Figure 15.6.5-39 Comparison of Predicted and Measured Maximum Cladding Temperatures for FEBA Simulations

15.6.6 Reflood Heat Transfer Assessment Summary and Conclusions

Table 15.6.6-1 provides a summary of the test conditions from the 21 different reflood separate effects tests simulated using WCOBRA/TRAC-TF2 and presented in Sections 15.6.1 through 15.6.5. For the FLECHT-SEASET tests, the peak cladding temperatures were **[**

][a,c].

In general, the peak cladding temperatures are **[**

][a,c]

Additional assessments for pressure effects, inlet sub-cooling, inlet flow rate, grid effects and entrained droplets are performed in Section 15.9.

Table 15.6.6-1 Range of Reflood Heat Transfer Test Conditions

Parameter	Range of Conditions

a,c

15.7 GRID HEAT TRANSFER MODELS

Grid spacers are an integral part of all rod bundle designs, and have important effects on the local heat transfer. At a spacer grid, the assembly flow area is reduced. Flow approaching the grid first contracts, and then expands downstream of the grid. As the flow passes through the grid, the fluid and thermal boundary layers are disrupted resulting in a local increase in the rod to fluid heat transfer coefficient. In addition, the grids shatter incoming droplets, increasing the interfacial area and evaporation rate. Since the grids are unpowered, they can rewet before the local heater rod surface. Section 7, Volume 1 describes the WCOBRA/TRAC-TF2 models for heat transfer enhancement, grid droplet breakup and grid rewet. This section provides additional information on the calculated results near a grid spacer.

The effect of the grids on the results can be seen in nearly all of the SPV, DFFB and reflood test simulations presented in Sections 15.4 through 15.6. Figures showing the axial temperature profile of the heater rods typically indicate a sharp decrease in temperature at and immediately downstream of a spacer grid. In Figure 15.6.1-73 for example, the decrease in the rod temperature at the 83-inch elevation is due to the presence of the spacer grids. **[**

][a,c]

Most rod bundle tests did not include a sufficient number of thermocouples at grid locations to quantify the grid effect. The FEBA tests (Section 15.6.5) included a large number of thermocouples around the mid-plane grid, and the ORNL uncovered bundle tests (Section 15.4.1) included a large number of thermocouples around the upper grid. For FEBA, the mid-plane grid was at an elevation 76.77 inches from the bottom of the heated length. WCOBRA/TRAC-TF2 simulations of FEBA Tests 223 and 216, calculated a decrease in rod temperature downstream of the grid. In simulations of FEBA Tests 234 and 229, in which the mid-plane grid had been removed from the bundle, no decrease at the 76.77-inch elevation was predicted. For ORNL, the upper grid was at an elevation 131.25 inches from the bottom of the heated length. WCOBRA/TRAC-TF2 simulations of ORNL Test M calculated a decrease in rod temperature downstream of the grid. For ORNL Test N, which had a very low flow rate, the decrease in rod temperature downstream of the grid exists, but to a much lower extent.

Figure 15.7-4 shows **[**

][a,c]

[

]^{a,c}.

Figure 15.7-5 shows the calculated rod temperature profile and thermocouple measurements for ORNL Test M at 1500 seconds near the upper grid. Like the FEBA test, the measurements shown in this figure represent an average of all thermocouples at a given elevation. As seen in the figure, [

]^{a,c}

Figure 15.7-6 shows the calculated rod temperature profile and thermocouple measurements for ORNL Test N at 1500 seconds near the upper grid. Test N had a much lower flow rate, and shows the effect of flow rate on the grid enhancement. The measurements shown in this figure represent an average of all thermocouples at a given elevation. As seen in the figure, [

]^{a,c}.

The WCOBRA/TRAC-TF2 simulations indicate that the grids have an important effect on the local cladding temperatures. The predictions are [ ]^{a,c} with available experimental results. Therefore, the grid heat transfer models in WCOBRA/TRAC-TF2 can be expected to provide reasonable estimates of the grid effect in a LOCA transient, and the model is able to reasonably capture the impact of flow on the enhancement magnitude.

a,c

Figure 15.7-1 Comparison of Predicted and Measured Axial Temperature Profile for FLECHT-SEASET 31805 at 200 Seconds

a,c

Figure 15.7-2 Cladding Temperature Profile Comparison for ORNL-THTF Uncovered Bundle Test M

a,c

Figure 15.7-3 Comparison of Predicted and Measured Axial Temperature Profile for FLECHT-SEASET 31701 at 10 Seconds

a,c

Figure 15.7-4 Temperature Profile Near a Spacer Grid from FEBA 223 and 234

a,c

Figure 15.7-5 Temperature Profile Near a Spacer Grid from ORNL Test M

a,c

Figure 15.7-6 Temperature Profile Near a Spacer Grid from ORNL Test N

15.8 TIME STEP STUDY

Section 7 describes the WCOBRA/TRAC-TF2 models for the application of numerical damping to avoid rapid changes with time in the heat transfer models. To determine the impact of time-step size on the reflood heat transfer and numerical damping, the highest and lowest flooding rate cases from the FLECHT-SEASET series (Tests 31701 and 31805, respectively) are exercised with the following maximum time-step sizes (DTMAX):
[

][a,c]

Figure 15.8-1 compares the overall peak cladding temperatures for the Test 31701 transients, and Figure 15.8-2 compares the quench progression. As seen from the figures, the time-step sizes chosen here have **[**

][a,c].

Figure 15.8-3 compares the overall peak cladding temperatures for the Test 31805 transients, and Figure 15.8-4 compares the quench progression. As seen from the figures, the time-step sizes chosen here have **[**

][a,c].

Based on the above study, the changes in time step size up to **[**

][a,c] on the transient, and thus it is recommended that **[** **]**[a,c] is the largest maximum time-step to be used for the reflood portion of a large break LOCA transient.

a,c

Figure 15.8-1 Peak Cladding Temperature Comparison for FLECHT Test 31701

a,c

Figure 15.8-2 Quench Front Progression Comparison for FLECHT Test 31701

a,c

Figure 15.8-3 Peak Cladding Temperature Comparison for FLECHT Test 31805

a,c

Figure 15.8-4 Quench Front Progression Comparison for FLECHT Test 31805

15.9 HEAT TRANSFER COMPOSITE RESULTS

The simulations of separate effects tests which experienced single-phase vapor were described in Section 15.4; the dispersed-flow film boiling separate effects tests were described in Section 15.5; and, the reflood heat transfer separate effects tests were described in Section 15.6. Table 15.9-1 lists the major design features in these facilities that were modeled and simulated using WCOBRA/TRAC-TF2. Each of the test facilities was modeled in a consistent noding scheme. **[**

][a,c] Predicted and measured heater rod temperatures at several elevations in the test bundle were compared to demonstrate the ability of WCOBRA/TRAC-TF2 to simulate each transient.

This section summarizes additional comparisons to data for the core heat transfer separate effects tests. By using a consistent noding methodology, the models and correlations cannot be "tuned" to match any one particular test or test series, and the user effects are minimized. Thus, the composite summary of the results presented in this section provides evidence that when used with the noding scheme consistent with the validation cases, the WCOBRA/TRAC-TF2 heat transfer package is sufficiently general and accurate so that it can be used for a best-estimate PWR analysis with the FULL SPECTRUM LOCA methodology.

Table 15.9-1 Reflood Facilities Major Design Features

[a,c

]

15.9.1 Prediction of Cladding Temperatures and Quench Times

Blowdown Cooling Rates

The simulations of the G-1 Blowdown heat transfer tests were described in Section 15.5.2.2. In these tests, the maximum cladding temperatures at all elevations occurred at or very near the beginning of the test. To assess the WCOBRA/TRAC-TF2 heat transfer package with these tests, three parameters can be compared; the cooling rate prior to quench, the time of quench, and the average heat transfer coefficient during the blowdown cooling period. The cooling rate prior to quench, referred to as the blowdown cooling rate, provides information on the models and correlations for dispersed droplet heat transfer, as well as convective heat transfer to single-phase vapor. Comparisons of the time of quench provide information on the cumulative effects of the code's calculation of post-CHF heat transfer and the minimum film boiling temperature.

Figure 15.9.1-1 shows the comparison of blowdown cooling rates for the G-1 Blowdown tests. The blowdown cooling rates were calculated by subtracting the average bundle cladding temperature at a time t_1 from an initial temperature at time t_0. The times were chosen **[**

][a,c]. For some tests, at several locations, the cladding temperatures remained nearly constant before quenching. Both positive and negative axes are shown in the figure to identify elevations where the predicted and measured rates of temperature change were in opposite directions. In G-1 Blowdown Test 148, for example, the elevation 24 inches from the bottom of the heated length **[**

][a,c].

The predicted and estimated quench times for the G-1 Blowdown test are compared in Figure 15.9.1-2. At the upper- and lower-most elevations, WCOBRA/TRAC-TF2 is seen to **[**

][a,c].

Refill Heat Transfer

The simulations of the G-2 Refill heat transfer tests also provide a means of assessing the overall capability of the WCOBRA/TRAC-TF2 heat transfer package. The simulation of the G-2 Refill tests was described in Section 15.5.2.3. In the G-2 Refill experiments, the cladding temperatures at most elevations in the bundle did not quench. Cladding temperatures near the bundle mid-height increased steadily until termination of the test. These locations remained in post-CHF, two-phase flow throughout the test and simulations. Figure 15.9.1-3 compares the predicted and measured heater rod cladding temperatures at the end of the G-2 Refill tests. The figure shows that WCOBRA/TRAC-TF2 **[**

][a,c]

Reflood Heat Transfer

The simulations of the reflood separate effects tests were found to predict the peak temperatures in most tests **[ ]**[a,c]. Figure 15.9.1-4 shows the comparison of the predicted maximum cladding temperatures at the thermocouple elevations presented in Section 15.6 for each simulated reflood separate effects test. WCOBRA/TRAC-TF2 shows **[ ]**[a,c].

Figures 15.9.1-5 through 15.9.1-7 show a comparison of predicted versus measured quench times for the FLECHT forced reflood tests. The elevations are the same as those used in the PCT comparisons. WCOBRA/TRAC-TF2 is seen to **[ ]**[a,c]. Figure 15.9.1-8 compares the predicted and measured turn-around times for the thermocouple elevations presented in Section 15.6 for each simulated forced reflood separate effects test. There is a large scatter in the figure due to elevations in many of the tests that remained quasi-steady for a long period of time. This often occurs at upper elevations (for example, the points in the upper left corner of the figure are from the 135-inch and 150-inch elevations from G-2 Reflood Test 568). Overall, the code **[ ]**[a,c]. Figure 15.9.1-9 compares the time the cladding temperature at the peak power elevation is greater than 1600°F for the FLECHT forced reflood tests. This is the temperature at which the oxidation kinetic is significant enough to result in appreciable transient oxidation. As the figure shows, the code **[ ]**[a,c].

a,c

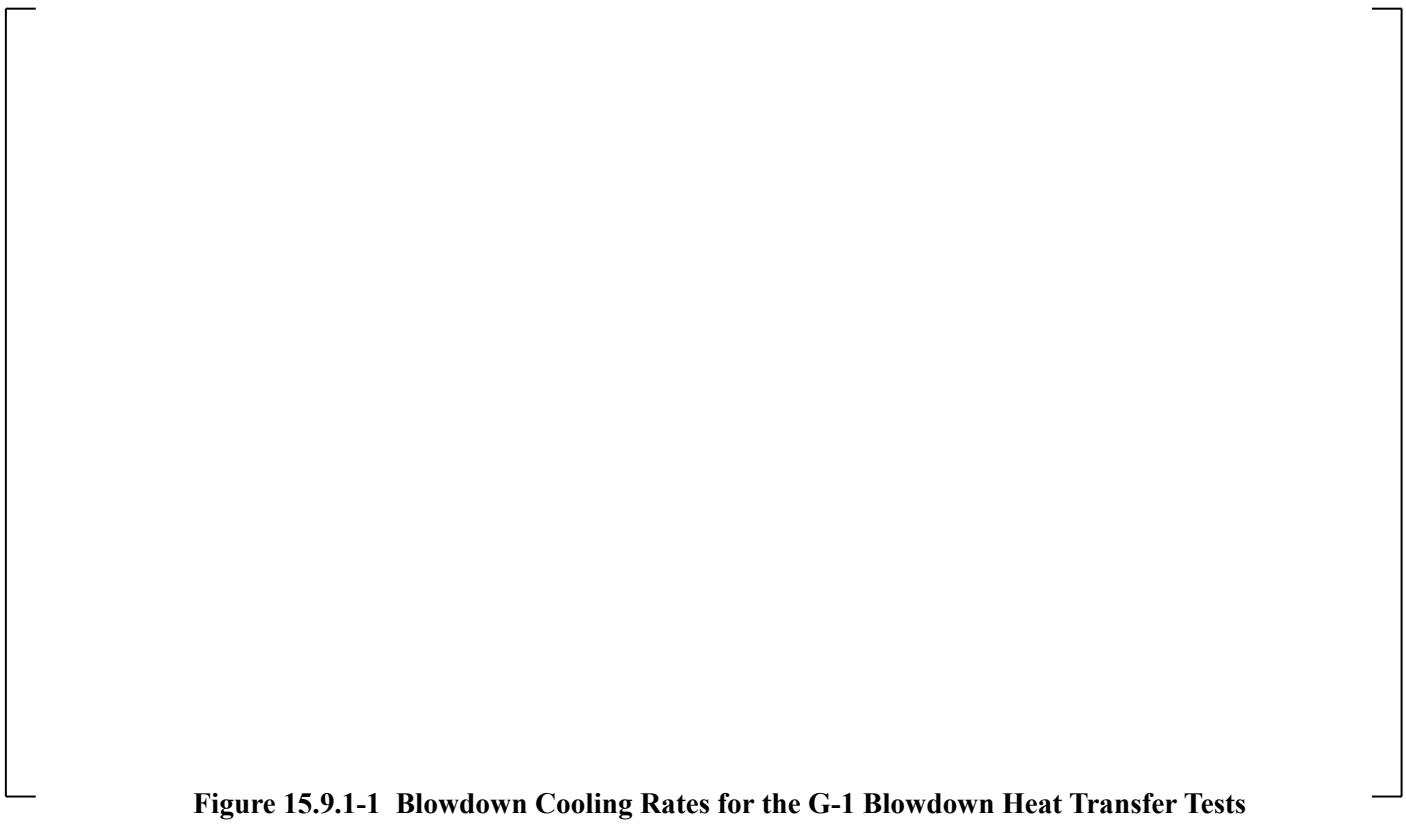

Figure 15.9.1-1 Blowdown Cooling Rates for the G-1 Blowdown Heat Transfer Tests

a,c

Figure 15.9.1-2 Comparison of Predicted and Measured Quench Times in the G-1 Blowdown Heat Transfer Tests

a,c

Figure 15.9.1-3 Comparison of Predicted and Measured Cladding Temperatures for the G-2 Refill Tests

a,c

Figure 15.9.1-4 Comparison of Predicted and Measured Maximum Cladding Temperatures for all Reflood Separate Effects Tests Simulated

a,c

Figure 15.9.1-5 Comparison of Predicted and Measured Quench Times for the FLECHT-SEASET Reflood Separate Effects Tests Simulated

a,c

Figure 15.9.1-6 Comparison of Predicted and Measured Quench Times for the FLECHT Low Flooding Rate Reflood Separate Effects Tests Simulated

a,c

Figure 15.9.1-7 Comparison of Predicted and Measured Quench Times for the FLECHT Skewed Reflood Separate Effects Tests Simulated

a,c

Figure 15.9.1-8 Comparison of Predicted and Measured Turn-Around Times for Each Reflood Separate Effects Tests Simulated

a,c

Figure 15.9.1-9 Comparison of Predicted and Measured Time above 1600°F for the FLECHT Reflood Separate Effects Tests Simulated

15.9.2 Droplet Assessment

Dispersed Flow Film Boiling

In Section 15.5 of this report, WCOBRA/TRAC-TF2 was used to simulate a range of blowdown film boiling heat transfer experiments. In this section, the calculations will be examined in more detail to assess whether variables such as droplet phase velocity and droplet size are predicted correctly. While data will usually not be available to assess these quantities directly, judgments can be made whether the magnitude of these variables are reasonable, based on evidence from other available measurements and by examining the consistency of the interaction among measureable quantities.

The details of the film boiling heat transfer models have been given in Section 7, Volume 1 and are summarized in Figure 15.9.2-1. The film boiling package consists of the Bromley correlation for film boiling at low void fractions, and a detailed dispersed flow film boiling model at high void fractions. The figure indicates that as the void fraction increases, the Bromley correlation contribution to the total film boiling heat flux decreases, and the dispersed flow film boiling models become dominant. The wall-to-vapor convective heat transfer component increases as the wall-to-vapor temperature difference increases. Thermal radiation from the wall-to-vapor and from the wall-to-droplets is also calculated.

Two blowdown heat transfer experiments are examined in detail in this section to examine the WCOBRA/TRAC-TF2 calculations. The first test examined is G-1 Blowdown Test 154, and the second test is ORNL 3.08.6C.

G-1 Blowdown Test 154

[

]^{a,c}

For a down-flow situation, the entrained drop size is determined by the models described in Section 4, Volume 1. The G-1 bundle included [

]^{a,c}

[

]a,c

The calculated cladding axial temperature distribution is shown in Figure 15.9.2-7 along with the calculated vapor temperature. As this figure indicates, [

]a,c The resulting heat flux, shown in Figure 15.9.2-8 for this case,

[

]a,c

Examining Figures 15.9.2-3 to 15.9.2-8 indicates that WCOBRA/TRAC-TF2 [

]a,c

ORNL Test 3.08.6C

ORNL Test 3.08.6C was an up-flow film boiling experiment in which the bundle was initially in single-phase liquid flow at high pressure. A break was initiated at the test section outlet. The inlet mass flux and pressure in this test are higher than in G-1 Test 154 such that lower void fractions are calculated, as well as less non-equilibrium in the vapor phase. Figure 15.9.2-9 shows the calculated mass flows along the test section and shows [

]a,c

The calculated droplet diameter for the center channel is given in Figure 15.9.2-12 and shows that the calculated drop sizes which are [ ]a,c. The entrained drops are being shattered by the spacer grids as described in Section 5, Volume 1. [

]a,c

[

]a,c

Figure 15.9.2-13 shows the calculated droplet interfacial area/volume which shows [

]a,c

Figure 15.9.2-14 presents the calculated rod surface temperature, the calculated vapor temperature, and indicates where CHF occurs. Because of the high flowrate and significant amount of entrained liquid, the vapor does not become greatly superheated.

The rod heat flux is presented in Figure 15.9.2-15 and shows the different heat transfer regimes calculated for these conditions. The spacer grid locations are shown at the bottom of Figures 15.9.2-12 to 15.9.2-15. The calculated heater rod surface temperatures and the vapor temperature show the heat transfer improvement caused by the grids. This improvement is also reflected in the calculated heater rod surface heat flux. The calculated grid temperatures are also shown in Figure 15.9.2-14. All grids rewet in this calculation due to the low heater rod temperatures and the high flows.

A review of Figures 15.9.2-10 to 15.9.2-15 indicates that for this high flow, high pressure test, WCOBRA/TRAC-TF2 calculates the two-phase heat transfer behavior in a self-consistent manner.

Reflood Assessment

Sections 15.6.1 through 15.6.5 described the simulations of 21 different reflood separate effects tests using WCOBRA/TRAC-TF2. This section presents additional details of the code calculations for two of these reflood tests. The two tests which are examined are FLECHT-SEASET Test 31701 and Test 31805, which bracket the range of flooding rates and cladding temperatures expected in a best-estimate large break LOCA reflood transient. These two tests were also designated as US Standard Problem 9 and were originally used as part of the COBRA/TRAC validations by Thurgood et al., 1983.

FLECHT Test 31701

Test 31701 is a 40 psia, 6.1 in/sec constant forced flooding rate test. The high inlet flow results in a low quality flow with little thermal non-equilibrium and higher heat transfer rates than in tests with lower flood rates. This test is initiated with the bundle heated in steam to 1600°F. When this temperature is reached, the flow into the bundle is initiated and the rod bundle power is decayed following the ANS 1971 plus 20 percent decay curve starting at 40 seconds after the accident.

Because of the large flooding rates, the heater rod temperatures in Test 31701 turn around quickly and quench as described in Section 15.6.1.1.5. For a detailed evaluation, a time of 10 seconds into the transient was chosen since high speed films of the flow patterns were available from the test and analysis reports given by Lee et al., 1982.

The mass flows of each phase at 10 seconds are shown in Figure 15.9.2-16 and indicate [

]a,c

[

]a,c

As Figure 15.9.2-20 indicates, [

]a,c

The calculated heater rod, spacer grid, and vapor temperatures are shown in Figure 15.9.2-19. Thepredicted heater rod temperatures have been compared to the test data in Section 15.6.1.1.5. The calculated spacer grid temperatures follow the calculated vapor temperatures for this test since the flows are high and the rod temperatures are relatively low. The center region of the bundle has [

]a,c.

For Test 31701, high speed movies were taken through the windows of the housing of the FLECHT-SEASET test facility. The movie data was reduced to obtain drop sizes and velocities for discrete times during the test. The movies were taken at the three-foot and nine-foot elevations (relative to the heated length) and drop velocities and sizes were estimated from the high speed movies (Lee et al., 1982). Figures 15.9.2-22 and 15.9.2-23 show the measured droplet data along with the drop sizes and velocities calculated by WCOBRA/TRAC-TF2 for the time period observed in the movies.
[

]a,c

Figure 15.9.2-24 shows the calculated droplet diameter plotted as a function of elevation at 10 seconds into the transient. [

]a,c

The calculated interfacial area for droplet-to-vapor heat transfer is shown in Figure 15.9.2-25 for Test 31701. As the figure indicates, the interfacial area significantly increases in the lower regions of the bundle where the spacer grids are shattering drops and decreases at the top of the bundle due to droplet evaporation. Figure 15.9.2-26 is a histogram indicating the percent of drops that are of a given size. WCOBRA/TRAC-TF2 predicts a single average drop size, which changed over the time periods sampled over the first 10 seconds. The predicted distribution **[**

][a,c].

FLECHT Test 31805

The second FLECHT-SEASET experiment examined in detail is Test 31805. This is a constant pressure, low flooding rate test with poor overall rod heat transfer compared to Test 31701. The nominal inlet flooding rate was 0.81 in/sec and the initial temperature was 1600°F. This test attained peak temperatures near 2200°F. The WCOBRA/TRAC-TF2 results at 100 seconds are examined to show the self-consistency in the heat transfer models. Figure 15.9.2-27 shows the mass flows for each phase along the bundle and indicates that continuous liquid flow is evaporated or entrained as droplets form at the quench front. The phase velocities are shown in Figure 15.9.2-28, the void fractions for each phase are given in Figure 15.9.2-29 and the net vapor generation is given in Figure 15.9.2-30. Unlike Test 31701, there is very little liquid sub-cooling at the quench front, so that the quench front energy release results primarily in steam generation.

The quench front heat release and subsequent steam generation result in a large vapor fraction change just above the quench front, as the flow regime transitions from a bubbly flow to a dispersed flow. The high heat release at the quench front and the low vapor void fraction gives rise to large local vapor velocities.

The calculated heater rod surface, spacer grid, and vapor temperatures along the bundle length for the inner channel are shown in Figure 15.9.2-31. Only the spacer grids **[**

][a,c]

The improvement in heat transfer downstream of a spacer grid can be seen in the calculated surface temperature at the grid locations in Figure 15.9.2-31. The rod surface heat flux is shown in Figure 15.9.2-32 and indicates the different heat transfer regimes along the rod surface. The majority of the heater rod is in DFFB.

Figure 15.9.2-33 shows the droplet diameter size along the test bundle at 100 seconds into the test. **[**

][a,c] The calculated interfacial area per unit volume for droplet-to-vapor heat transfer is presented in Figure 15.9.2.34 showing **[**

][a,c]. The interfacial area/volume is highest in **[** **]**[a,c]. Above this elevation the droplet Weber number becomes smaller, such that there is less breakup and the drops evaporate in the presence of the highly superheated vapor, resulting in a decreased drop diameter along the length of the bundle.

There was high speed movie data taken for Test 31805 at the bundle mid-plane (six-foot elevation) for an extended period of time. Although the precise time of the filming was not recorded, Test 31805 is a long quasi-steady-state test where the flow conditions change very slowly and the bundle is in dispersed flow film boiling for several minutes. Calculated drop sizes and velocities at the bundle mid-plane (six-foot elevation) at a time period of **[ ]**[a,c] was used to compare to the test data. Figure 15.9.2.35 shows the comparisons of the calculated droplet velocities and sizes with respect to the test data. The drop velocities are **[ ]**[a,c].

The WCOBRA/TRAC-TF2 droplet size model for bottom reflood is described in Section 5.6.3, Volume 1, and was based on earlier FLECHT reflood data. Therefore, it is not surprising that good agreement is achieved with the FLECHT-SEASET movie data.

As was concluded for the dispersed flow film boiling assessment described previously, the WCOBRA/TRAC-TF2 heat transfer package provides a self-consistent model which captures the complex non-equilibrium two-phase flow phenomena found in the reflood experiments.

a,c

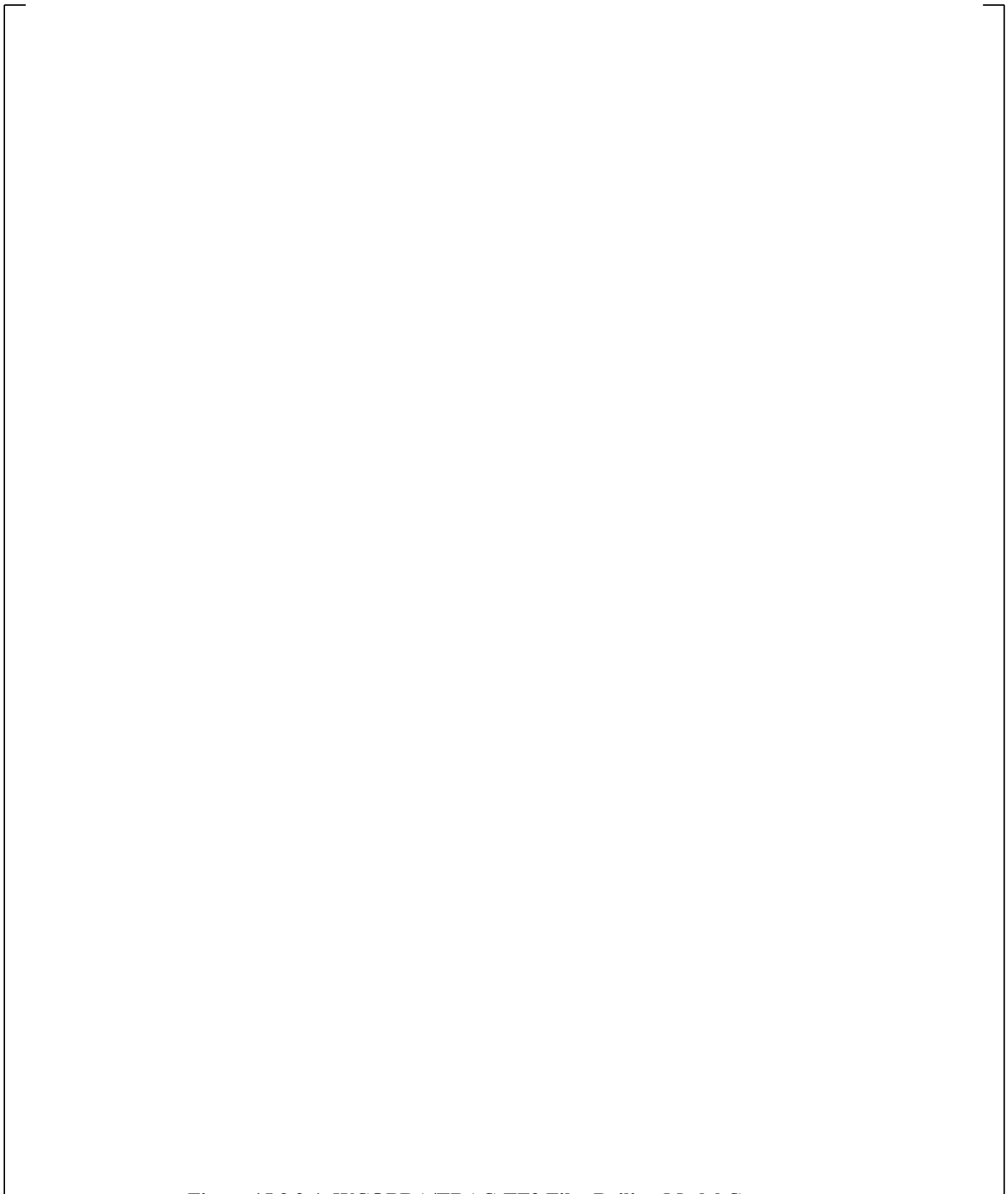

Figure 15.9.2-1 WCOBRA/TRAC-TF2 Film Boiling Model Components

a,c

Figure 15.9.2-2 Calculated Mass Flows as a Function of Elevation for G-1 Test 154 at 7 Seconds into the Test

a,c

Figure 15.9.2-3 Calculated Phase Velocities as a Function of Elevation for G-1 Test 154 at 7 Seconds into the Test

a,c

Figure 15.9.2-4 Calculated Volume Fraction as a Function of Elevation for G-1 Test 154 at 7 Seconds into the Test

a,c

Figure 15.9.2-5 Calculated Droplet Size as a Function of Elevation for G-1 Test 154 at 7 Seconds into the Test

a,c

Figure 15.9.2-6 Calculated Droplet (Entrained Phase) Interfacial Surface Area as a Function of Elevation for G-1 Test 154 at 7 Seconds into the Test

a,c

Figure 15.9.2-7 Calculated Heater Rod Surface Temperature, Spacer Grid Temperature, and Vapor Temperature as a Function of Elevation for G-1 Test 154 at 7 Seconds into the Test

a,c

Figure 15.9.2-8 Calculated Heater Rod Surface Heat Flux and Heat Transfer Mode as a Function of Elevation for G-1 Test 154 at 7 Seconds into the Test

a,c

Figure 15.9.2-9 Calculated Mass Flowrates as a Function of Elevation for ORNL Test 3.08.6C at 60.1 Seconds into the Test

a,c

Figure 15.9.2-10 Calculated Phase Velocities as a Function of Elevation for ORNL Test 3.08.6C at 60.1 Seconds into the Test

a,c

Figure 15.9.2-11 Calculated Phase Volume Fraction as a Function of Elevation for ORNL Test 3.08.6C at 60.1 Seconds into the Test

a,c

Figure 15.9.2-12 Calculated Droplet Diameter as a Function of Elevation for ORNL Test 3.08.6C at 60.1 Seconds into the Test

a,c

Figure 15.9.2-13 Calculated Droplet Interfacial Area as a Function of Elevation for ORNL Test 3.08.6C at 60.1 Seconds into the Test

a,c

Figure 15.9.2-14 Calculated Heater Rod Surface Temperature, Spacer Grid Temperature, and Vapor Temperature as a Function of Elevation for ORNL Test 3.08.6C at 60.1 Seconds into the Test

a,c

Figure 15.9.2-15 Calculated Heater Rod Surface Heat Flux and Heat Transfer Mode as a Function of Elevation for ORNL Test 3.08.6C at 60.1 Seconds into the Test

a,c

Figure 15.9.2-16 Calculated Mass Flowrate of Each Phase as a Function of Elevation for FLECHT-SEASET Test 31701 at 10 Seconds into the Test

a,c

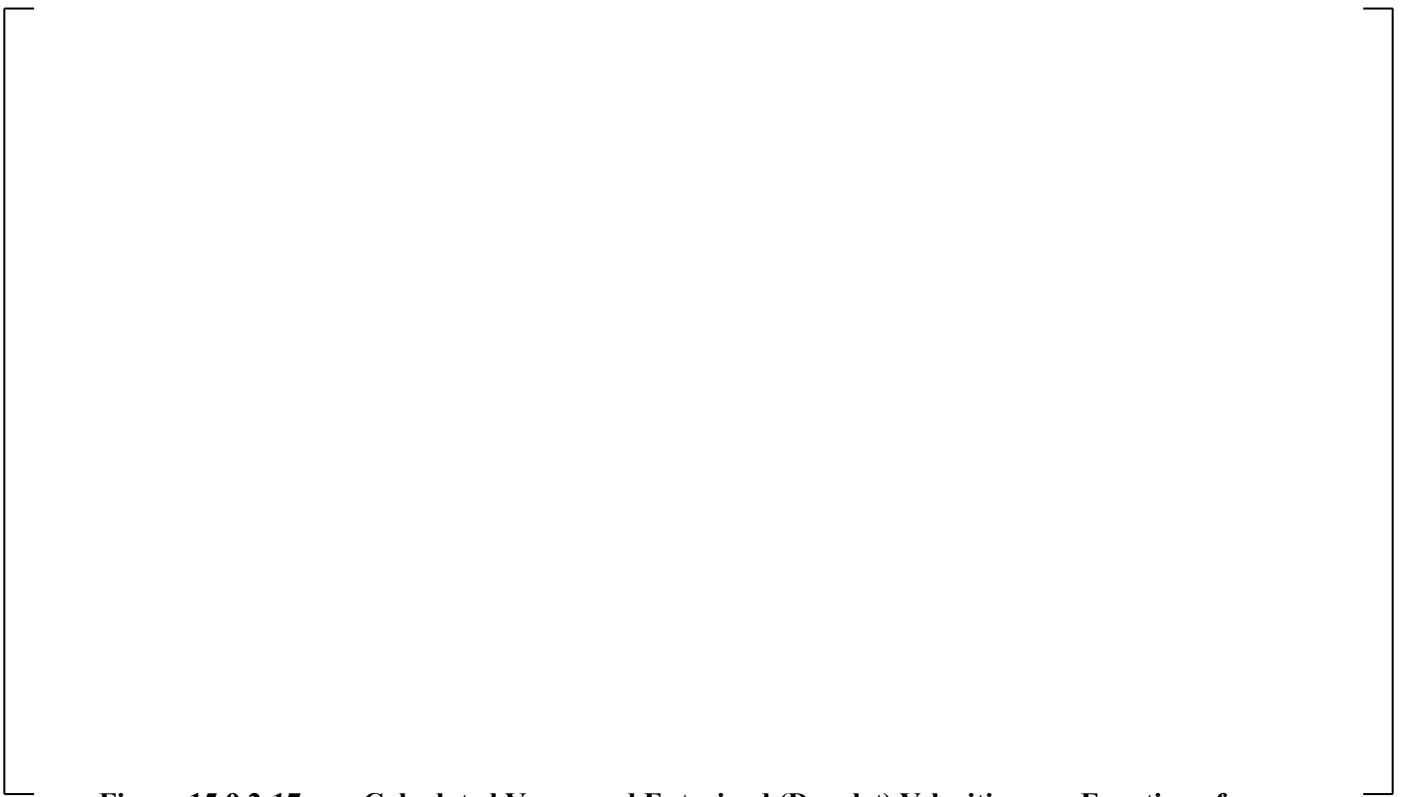

Figure 15.9.2-17 Calculated Vapor and Entrained (Droplet) Velocities as a Function of Elevation for FLECHT-SEASET Test 31701 at 10 Seconds into the Test

a,c

Figure 15.9.2-18 Calculated Phase Volume Fractions as a Function of Elevation for FLECHT-SEASET Test 31701 at 10 Seconds into the Test

a,c

Figure 15.9.2-19 Calculated Heater Rod Surface Temperature, Spacer Grid Temperature, and Vapor Temperature as a Function of Elevation for FLECHT-SEASET Test 31701 at 10 Seconds into the Test

a,c

Figure 15.9.2-20 Calculated Heater Rod Heat Flux as a Function of Elevation for FLECHT-SEASET Test 31701 at 10 Seconds into the Test

a,c

Figure 15.9.2-21 Calculated Net Vapor Generation Rate as a Function of Elevation for FLECHT-SEASET Test 31701 at 10 Seconds into the Test

a,c

Figure 15.9.2-22 Comparison of Calculated Droplet Size and Drop Velocity at the Three-Foot Elevation with FLECHT-SEASET Test Data for Test 31701 (2.5 – 9 s)

a,c

Figure 15.9.2-23 Comparison of Calculated Droplet Size and Drop Velocity at the Nine-Foot Elevation with FLECHT-SEASET Test Data for Test 31701 (7 – 15 s)

a,c

Figure 15.9.2-24 Calculated Droplet Diameter as a Function of Elevation for FLECHT-SEASET Test 31701 at 10 Seconds into the Transient

a,c

Figure 15.9.2-25 Calculated Droplet Interfacial Area/Volume as a Function of Elevation for FLECHT-SEASET Test 31701 at 10 Seconds into the Test

a,c

Figure 15.9.2-26 Comparison of Calculated Droplet Size Frequency for FLECHT-SEASET Test 31701 (Results are from the 9-foot Elevation for 7 to 15 Seconds)

a,c

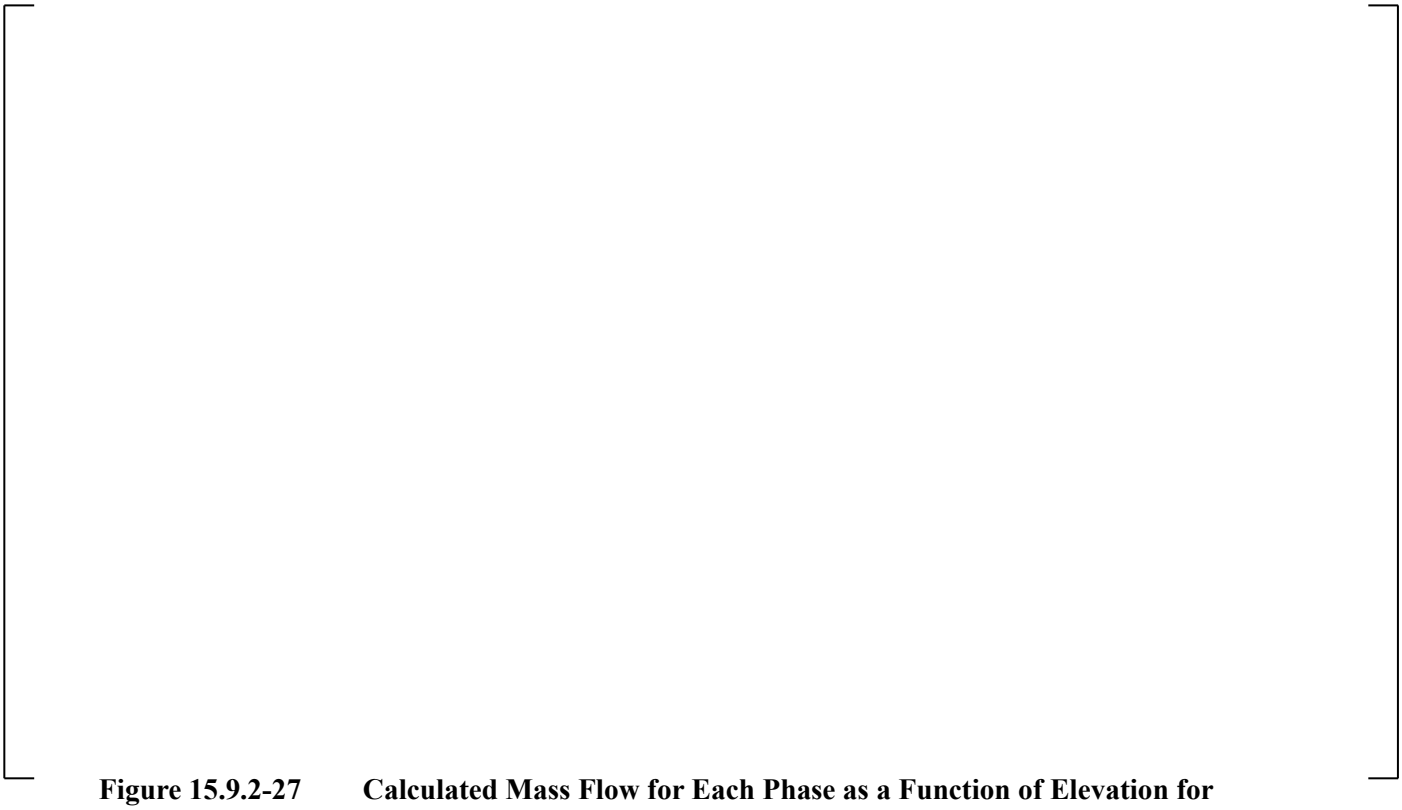

Figure 15.9.2-27 Calculated Mass Flow for Each Phase as a Function of Elevation for FLECHT-SEASET Test 31805 at 100 Seconds into the Test

a,c

Figure 15.9.2-28 Calculated Phase Velocities as a Function of Elevation for FLECHT-SEASET Test 31805 at 100 Seconds into the Test

a,c

Figure 15.9.2-29 Calculated Phase Void Fractions for Each Phase as a Function of Elevation for FLECHT-SEASET Test 31805 at 100 Seconds into the Transient

a,c

Figure 15.9.2-30 Calculated Net Vapor Generation as a Function of Elevation for FLECHT-SEASET Test 31805 at 100 Seconds into the Transient

a,c

Figure 15.9.2-31 Calculated Heater Rod Surface Temperature, Spacer Grid Temperature, and Vapor Temperature as a Function of Elevation for FLECHT-SEASET Test 31805 at 100 Seconds into the Test

a,c

Figure 15.9.2-32 Calculated Heater Rod Surface Heat Flux as a Function of Elevation for FLECHT-SEASET Test 31805 at 100 Seconds into the Test

a,c

Figure 15.9.2-33 Calculated Droplet Diameter as a Function of Elevation for FLECHT-SEASET Test 31805 at 100 Seconds into the Test

a,c

Figure 15.9.2-34 Calculated Droplet Interfacial Surface Area/Volume as a Function of Elevation for FLECHT-SEASET Test 31805 at 100 Seconds into the Test

a,c

Figure 15.9.2-35 Comparison of Calculated Drop Size and Velocities with FLECHT-SEASET Test Data for Test 31805 at 6 ft (44 – 51 s)

15.9.3 Simulation of Parametric Trends

This section provides a description of the effects of principle test parameters and demonstrates the ability of WCOBRA/TRAC-TF2 to simulate variations in those parameters. The test simulation matrix for WCOBRA/TRAC-TF2 validation includes a number of tests that varied only one parameter at a time. The parametric effects examined are flooding rate, pressure, and sub-cooling.

Flooding Rate Effect

The FLECHT-SEASET Tests 31805 (0.8 in/sec), 31504 (1.0 in/sec), 31203 (1.5 in/sec), and 31701 (6.1 in/sec) constitute a set of tests with the same test conditions except for the flooding rate. Figure 15.9.3-1 shows the experimental effect of flooding rate on heat transfer coefficient reported by Lee et al., 1982 for several FLECHT-SEASET tests. The WCOBRA/TRAC-TF2 prediction of this same trend is shown in Figure 15.9.3-2. A comparison of these two figures shows that WCOBRA/TRAC-TF2 **[ ]**[a,c].

The flooding rate effect on cladding temperature as determined experimentally is shown in Figure 15.9.3-3, and the WCOBRA/TRAC-TF2 predicted trend is shown in Figure 15.9.3-4. The code **[ ]**[a,c].

The quench front advance as a function of flooding rate is shown in Figure 15.9.3-5 for the data and in Figure 15.9.3-6 for the WCOBRA/TRAC-TF2 predictions. **[ ]**[a,c]

Pressure Effect

Several experimental reflood tests have shown that heat transfer improves at higher pressure. Figure 15.9.3-7 shows the observed experimental effect on the measured heat transfer coefficient for three FLECHT-SEASET tests. WCOBRA/TRAC-TF2 simulations for FLECHT-SEASET Tests 31504 (40 psia) and 32013 (60 psia) were run to evaluate the ability of the code to predict the pressure effect. Figure 15.9.3-8 shows the predicted heat transfer coefficients at the 72-inch elevation for Tests 31504 and 32013. **[ ]**[a,c]

Simulations of FLECHT Low Flooding Rate Tests 04641 (20 psia) and 05132 (40 psia) also test the ability of the code to predict the pressure effect. Heat transfer coefficients from these two simulations are compared in Figure 15.9.3-9. In this comparison, **[ ]**[a,c].

The experimental effect of pressure on cladding temperature is shown in Figure 15.9.3-10. The simulated effect for FLECHT-SEASET Tests 31504 and 32013 is shown in Figure 15.9.3-11 and for FLECHT Tests 05132 and 04641 in Figure 15.9.3-12. Figure 15.9.3-13 shows the effect of pressure on the quench front advance from the experiments, and Figures 15.9.3-14 and 15.9.3-15 show the code predicted effect. The experimental results show similar maximum cladding temperatures with an earlier quench within increasing pressure. The predictions **[ ]**[a,c].

Sub-cooling Effect

The effect of sub-cooling on cladding temperature has been investigated in the FLECHT-SEASET, FLECHT (Cosine) Low Flooding Rate, and the FLECHT Skewed Power test series with the results shown in Figure 15.9.3-16. Tests in each of these series demonstrated that sub-cooling has a fairly weak effect on the cladding temperature rise. Two of the test series showed that cladding temperature rise decreased with higher sub-cooling, while the skewed power tests indicated a slight increase in temperature rise with sub-cooling.

FLECHT-SEASET

To determine the code sensitivity to inlet sub-cooling for forced reflood tests, a series of calculations was performed using FLECHT-SEASET Test 31504 as a base case. This test was a 40 psia test, with a nominal inlet flooding rate of 1.0 in/sec and an initial peak rod power of 0.7 kW/ft. The inlet sub-cooling for Test 31504 was 144°F. This test matched conditions from the FLECHT-SEASET tests that composed the "SUB-COOLING" tests listed on page 2-15 of Lee et al., 1982.

The main parameters of interest of the sub-cooling tests are listed in Table 15.9.3-1. Test 31504 is included for comparison.

Lee et al., 1982 concluded that the sub-cooling effect was very weak and that temperature rise decreased slightly with higher inlet sub-cooling based on experimental results from Tests 35114 and 31504.

Figure 15.9.3-16 shows the trends in cladding temperature rise and quench time with inlet sub-cooling for FLECHT-SEASET, FLECHT Cosine, and Skewed Power Tests as reported by Lee et al., 1982. The FLECHT-SEASET points in the figure refer to Test 35114 (ΔTsub = 7.9°C = 14.2°F) and Test 31504 (ΔTsub = 80°C = 144°F). **[**

][a,c]

A WCOBRA/TRAC-TF2 sensitivity to inlet sub-cooling was obtained by making several calculations in which the inlet sub-cooling was the only boundary condition that was varied. The input deck for Test 31504 was used, and the calculations are summarized in Table 15.9.3-2. The column $PCT_{1,6}$ represents the Rod 1 PCT at the 6.08-foot elevation, and $TQ_{1,6}$ is the quench time for that elevation.

[

][a,c]

Figure 15.9.3-18 shows the predicted and measured trends with inlet sub-cooling on quench time at the 6-foot elevation. The data indicates a trend toward an earlier quench time as the inlet sub-cooling increases, **[ ]**[a,c]. Both show the effect to be weak. This is the same conclusion drawn by (Lee, et al., 1982) which reported that the effect of sub-cooling for these tests is very weak, as supported by Figure 3-18 in that report (Figure 15.9.3-16 here).

FLECHT LFR

In the FLECHT series of tests, two experiments were reported as being part of the "Sub-cooling" test series. Those tests were Tests 05342 and 05543. The conditions for these tests are listed in Table 15.9.3-4. Test 05132 data is listed for reference.

A similar sensitivity study was run for the FLECHT facility using Test 05132 as a base case. (This test was selected because it matched the rod power. The inlet flooding rate, however, is higher than that of the experimental tests composing the sub-cooling sensitivity study.) Table 15.9.3-5 lists results of that sensitivity study using WCOBRA/TRAC-TF2.

[

][a,c]

FLECHT Top Skewed Power

In the FLECHT Top Skewed Power Test series three tests are listed in the data report as being part of the sub-cooling effect tests. Tests 13812 and 15713 were both conducted at 40 psia. The third test (Test 13914) was run at 21 psia. All three of these tests were simulated as part of the WCOBRA/TRAC-TF2 assessment matrix. Figures 15.9.3-21 and 15.9.3-22 show comparisons of the effects of sub-cooling on skewed power facility results. Consistent with the other experimental results in the other facilities, the data peak temperatures increase with higher inlet sub-cooling. **[**

][a,c]

Conclusions

Sensitivity studies for the FLECHT-SEASET, FLECHT LFR, and FLECHT Top Skewed facility bundles using WCOBRA/TRAC-TF2 indicate that the code **[**

][a,c]

Table 15.9.3-1 FLECHT-SEASET Sub-cooling Test Series – Test Data

Test No.	Pressure (psia)	Rod Peak Power (kW/ft)	Flooding Rate (in/sec)	Coolant Temp (°F)	ΔTsub (°F)	Max Temp (°F)	Temp Rise (°F)
32114	40	0.70	1.0-1.22	257	10	2172	628
35114	40	0.74	0.98	253	14	2178	550
34815	20	0.74	0.98	221	7	2152	555
34316	40	0.74	0.97	124-246	143-21	2206	646
31504	40	0.70	0.97	123	144	2101	593

Table 15.9.3-2 FLECHT-SEASET Predicted Sub-cooling Sensitivity Study Results

[| | |]a,c

Table 15.9.3-3 Average PCT – Based on Data for Six-foot Thermocouples

Pressure (psia)	ΔTsub (°F)	Ave PCT (°F)	Ave TQ (°F)
40	10	1970	270
40	14	1947	356
20	7	1915	502
40	143-21	2041	302
40	144	1970	270

Table 15.9.3-4 FLECHT Low Flooding Rate Sub-cooling Test Series – Test Data

Test	Rod Peak Power (kW/ft)	Flooding Rate (in/sec)	Coolant Temp (°F)	ΔT_{sub} (°F)
05342	0.95	0.80	248	19
05543	0.95	0.81	188	79
05132	0.95	0.99	127	140

Table 15.9.3-5 FLECHT Low Flooding Rate Inlet Sub-cooling Sensitivity Using WCOBRA/TRAC-TF2

a,c

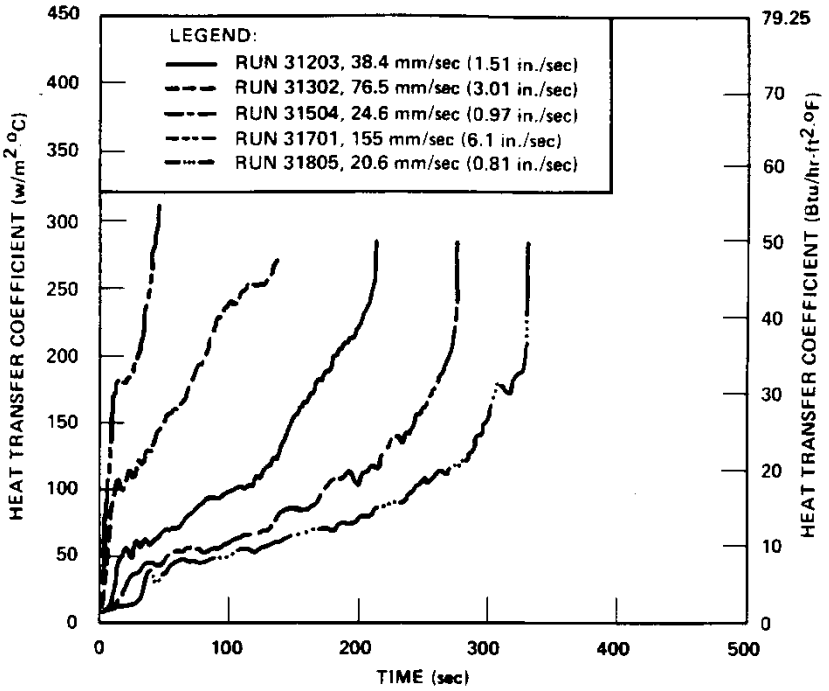

Figure 15.9.3-1 Effect of Flooding Rate on Heat Transfer Coefficient as Determined from Experimental Data (Lee et al., 1982)

a,c

Figure 15.9.3-2 Predicted Effect of Flooding Rate on Heat Transfer Coefficient

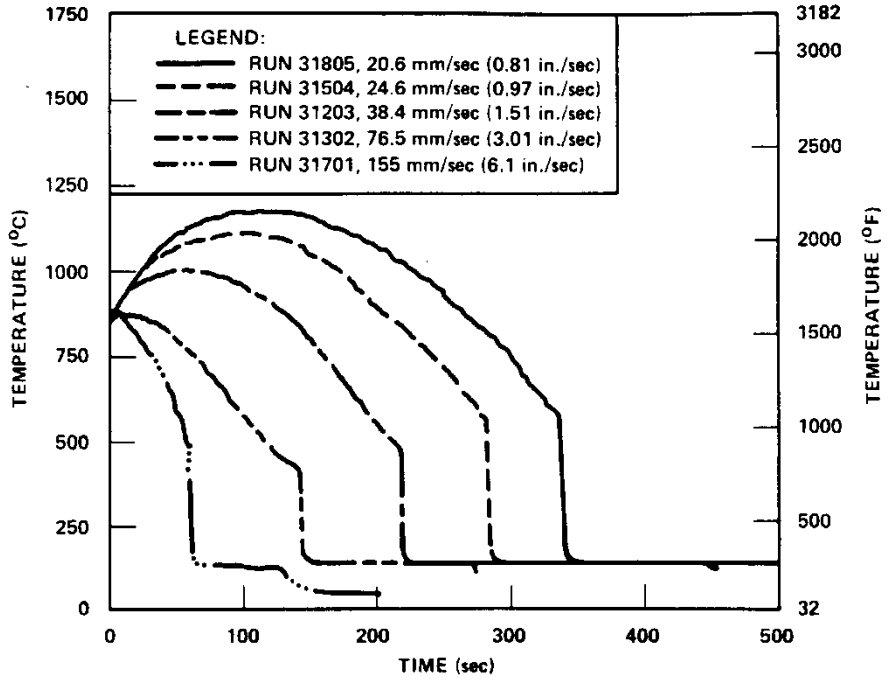

Figure 15.9.3-3 Effect of Flooding Rate on Cladding Temperature at the 72-inch Elevation as Determined from Experimental Data (Lee et al., 1982)

a,c

Figure 15.9.3-4 Predicted Effect of Flooding Rate on Cladding Temperature at the 72-inch Elevation

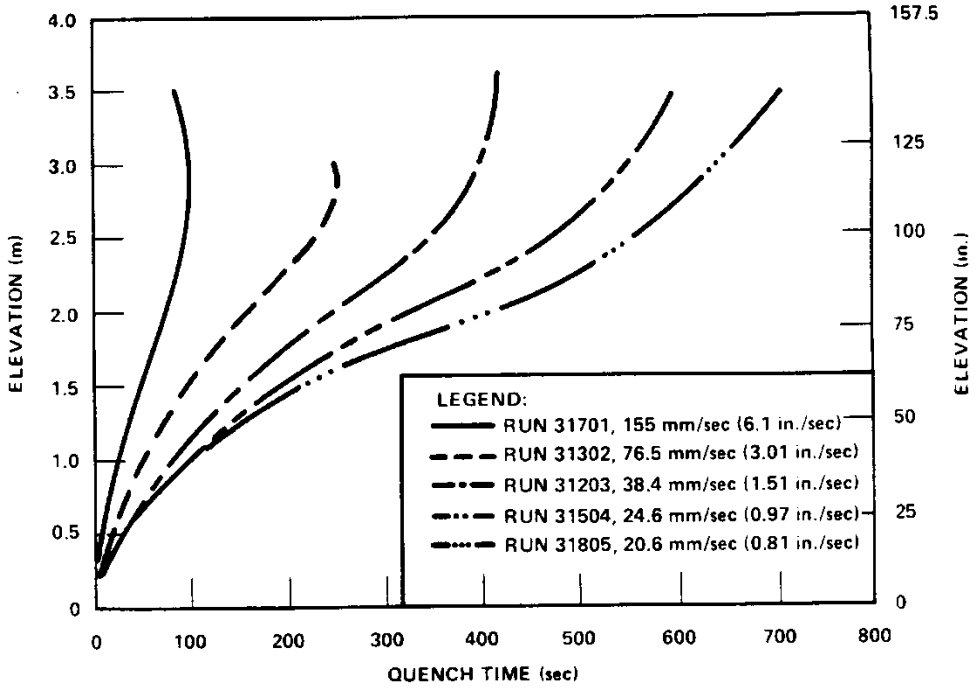

Figure 15.9.3-5 Effect of Flooding Rate on Quench Front Advance as Determined from Experimental Data (Lee et al., 1982)

a,c

Figure 15.9.3-6 Predicted Effect of Flooding Rate on Quench Front Advance

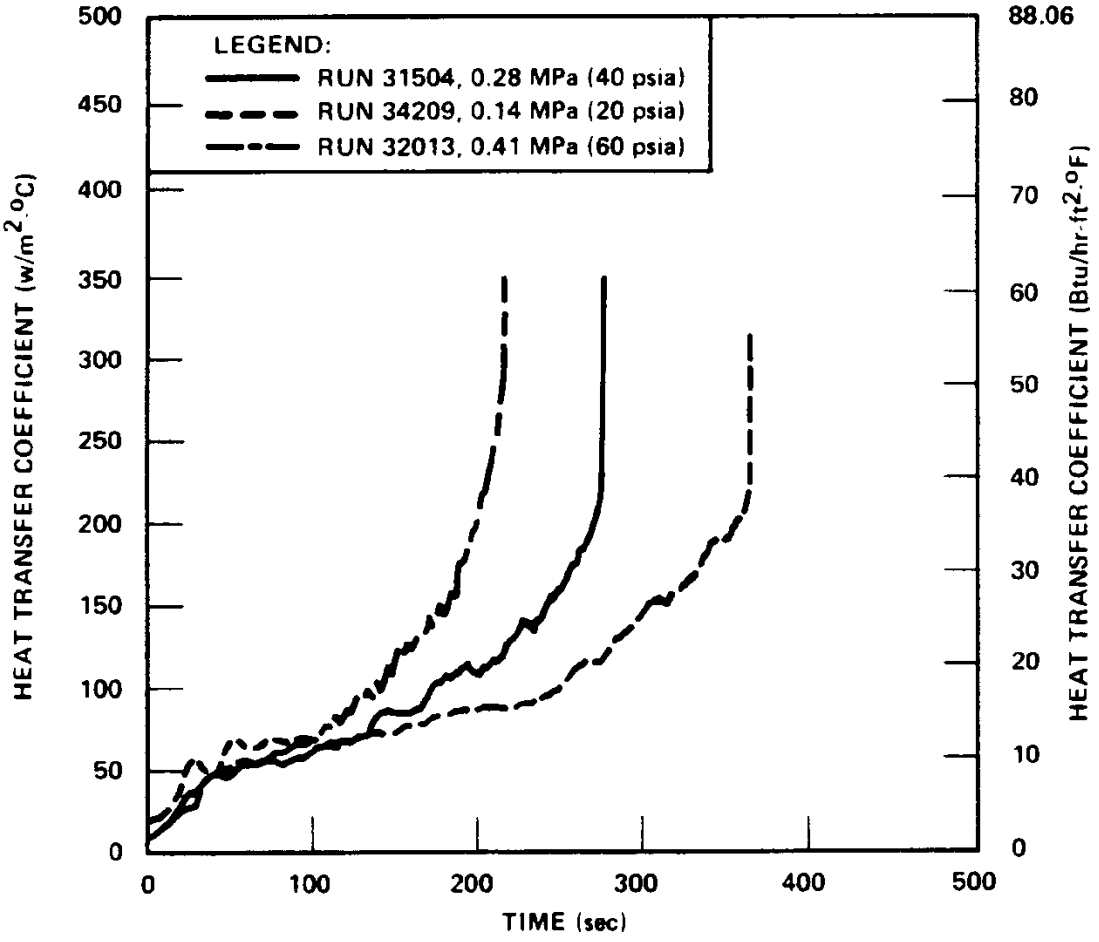

Figure 15.9.3-7 Effect of Pressure on Heat Transfer Coefficient as Determined from Experimental Data (Lee et al., 1982)

a,c

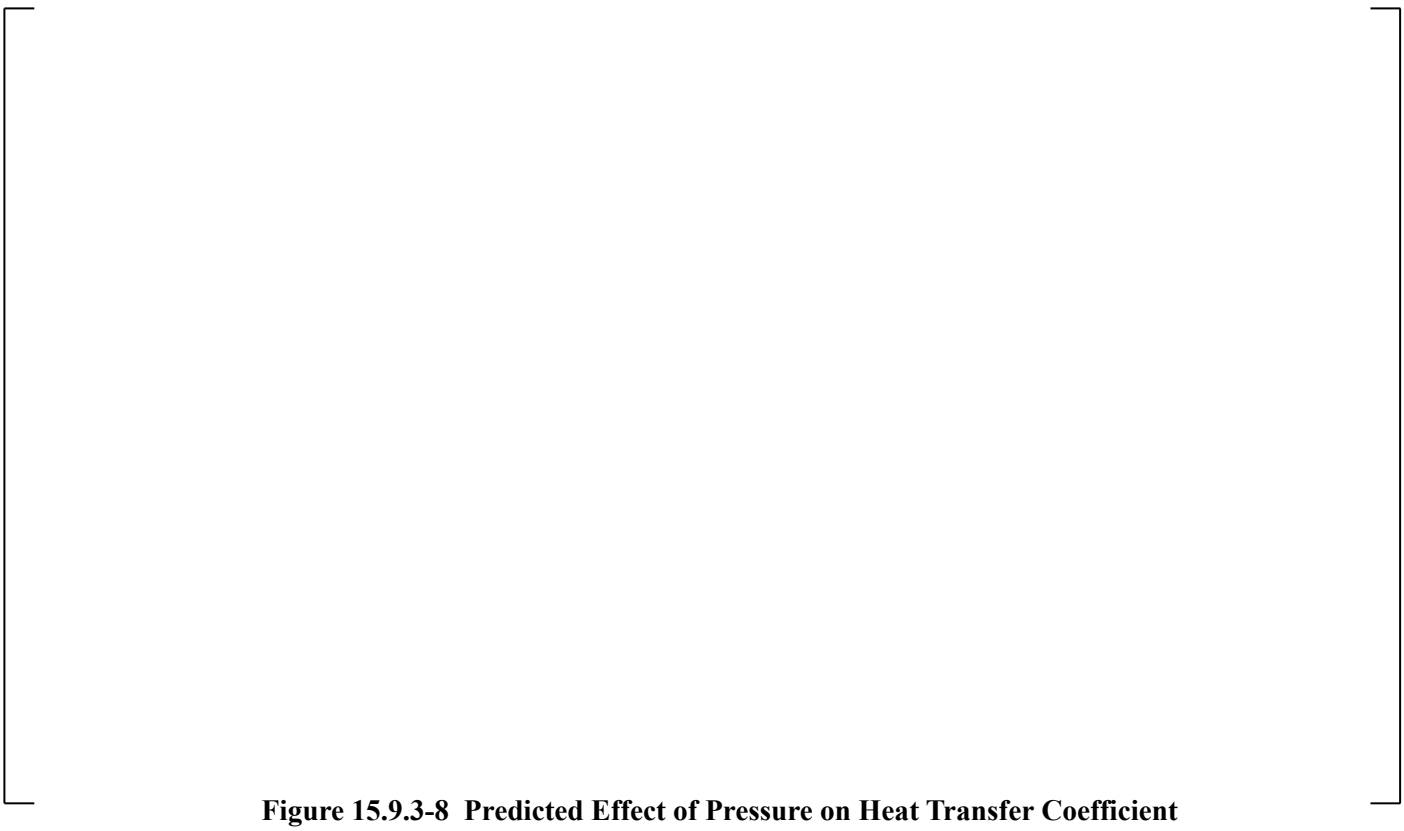

Figure 15.9.3-8 Predicted Effect of Pressure on Heat Transfer Coefficient

a,c

Figure 15.9.3-9 Predicted Effect of Pressure on Heat Transfer Coefficient (FLECHT Low Flooding Rate)

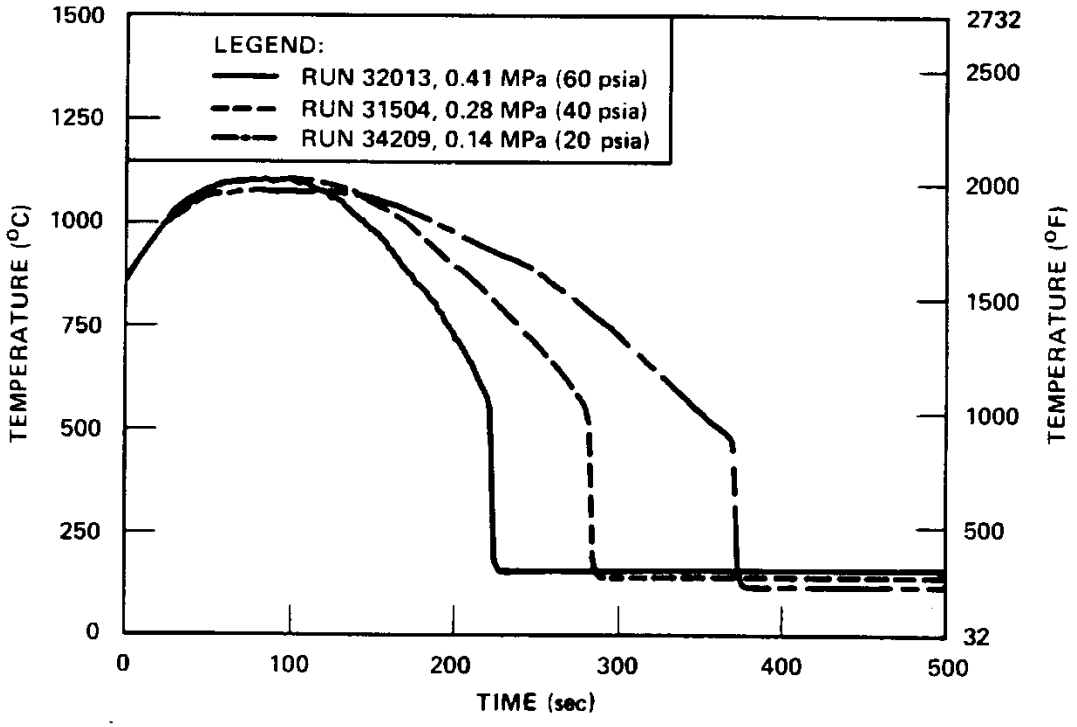

Figure 15.9.3-10 Effect of Pressure on Cladding Temperature at the 72-inch Elevation as Determined from Experimental Data (Lee et al., 1982)

a,c

Figure 15.9.3-11 Predicted Effect of Pressure on Cladding Temperature at the 72-inch Elevation (FLECHT-SEASET)

a,c

Figure 15.9.3-12 Predicted Effect of Pressure on Cladding Temperature at the 72-inch Elevation (FLECHT Low Flooding Rate)

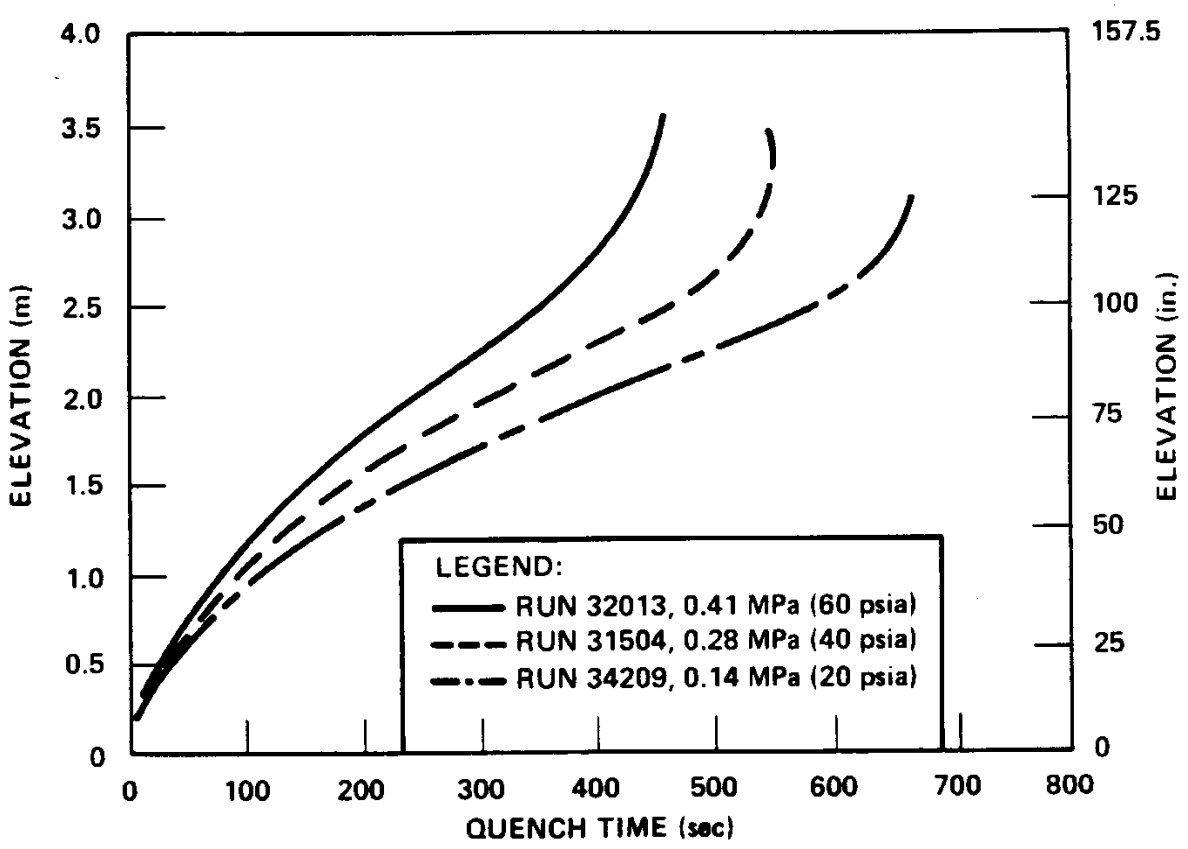

Figure 15.9.3-13 Effect of Pressure on Quench Front Advance as Determined from Experimental Data (Lee et al., 1982)

a,c

Figure 15.9.3-14 Predicted Effect of Pressure on Quench Front Advance (FLECHT-SEASET)

a,c

Figure 15.9.3-15 Effect of Pressure on Quench Front Advance (FLECHT Low Flooding Rate)

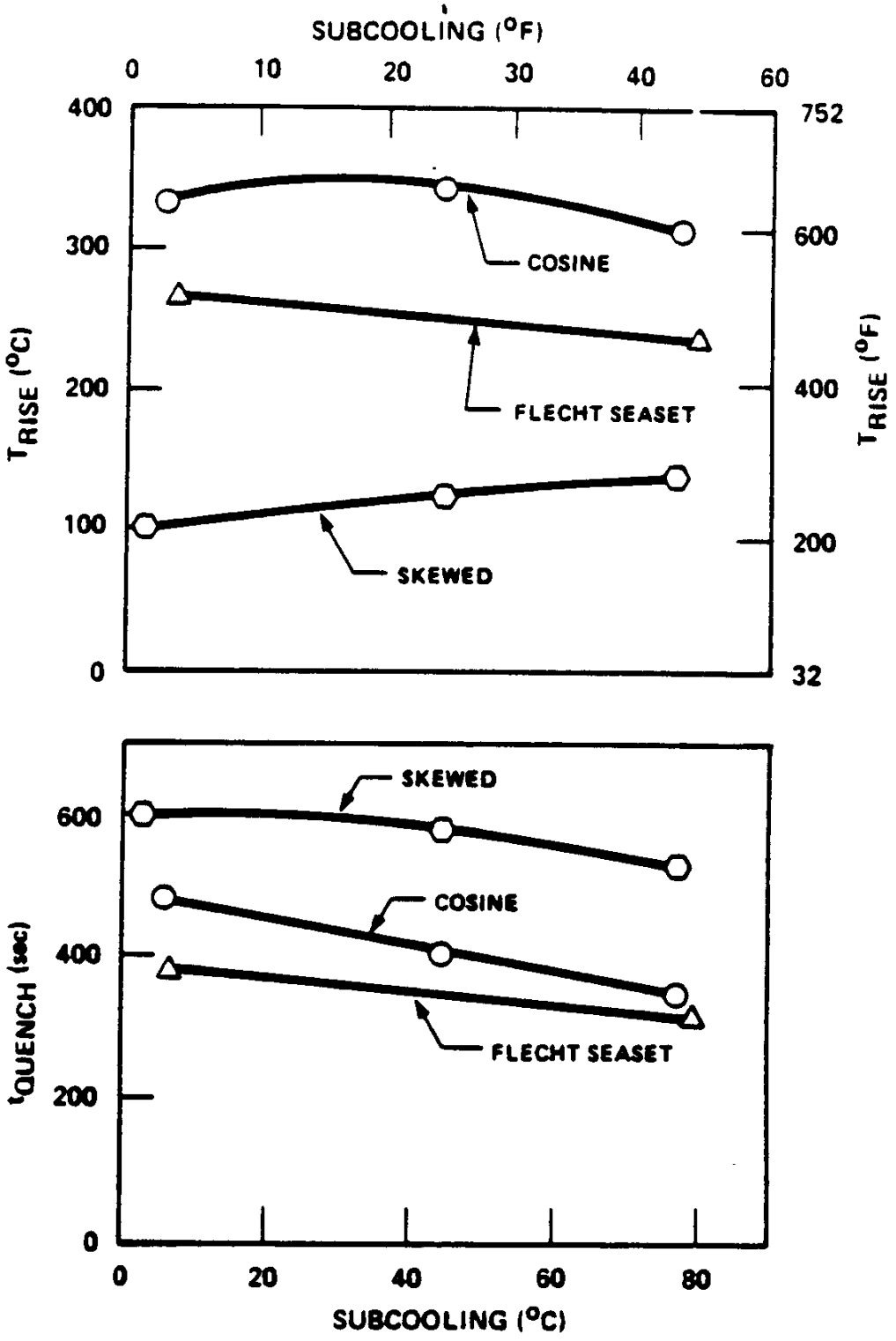

Figure 15.9.3-16 Effect of Sub-cooling on Temperature Rise and Quench Time as Determined from Experimental Data (Lee et al., 1982)

a,c

Figure 15.9.3-17 Comparison of Cladding Temperatures at 6-ft. and WCOBRA/TRAC-TF2 Prediction of Sensitivity to Inlet Sub-cooling in FLECHT-SEASET

a,c

Figure 15.9.3-18 Comparison of Quench Times at 6-ft. and WCOBRA/TRAC-TF2 Prediction of Sensitivity to Inlet Sub-cooling in FLECHT-SEASET

a,c

Figure 15.9.3-19 Comparison of Cladding Temperatures at 6-ft. and WCOBRA/TRAC-TF2 Prediction of Sensitivity to Inlet Sub-cooling in FLECHT LFR Facility

a,c

Figure 15.9.3-20 Comparison of Quench Times at 6-ft. and WCOBRA/TRAC-TF2 Prediction of Sensitivity to Inlet Sub-cooling in FLECHT LFR Facility

a,c

Figure 15.9.3-21 Comparison of Cladding Temperatures at 10-ft. and WCOBRA/TRAC-TF2 Prediction of Sensitivity to Inlet Sub-cooling in FLECHT Skewed Power Facility

a,c

Figure 15.9.3-22 Comparison of Quench Times at 10-ft. and WCOBRA/TRAC-TF2 Prediction of Sensitivity to Inlet Sub-cooling in FLECHT Skewed Power Facility

15.10 SUMMARY AND CONCLUSIONS

The heat transfer models in WCOBRA/TRAC-TF2 have been compared to a wide range of different rod bundle heat transfer experiments which include:

- A range of fluid conditions and bundle powers expected to occur during a LOCA.
- Different rod bundle arrays and geometries characteristic of different fuel assembly designs.
- A range of axial power shapes.
- Different spacer grid geometries (e.g., mixing vane grids vs. non-mixing vane grids) which can cause different sub-channel blockages due to different grid types within the rod bundle.

Experiments were also specifically modeled which tested the WCOBRA/TRAC-TF2 calculations for up-flow film boiling, down-flow film boiling, and counter-flow film boiling, all of which occur for a postulated LOCA.

The philosophy used in the WCOBRA/TRAC-TF2 validation was to select series from several facilities, and simulate tests over a wide range of conditions. The individual tests were selected to cover the range of thermal-fluid conditions expected in a LOCA, and to challenge particular models in the code. By analyzing different facilities with the same code, the possibility of successful comparisons by "tuning" to a particular test facility or set of experiments is reduced. By using this approach, the code has been demonstrated to be applicable to a wide range of PWR conditions and geometries.

The heat transfer and fluid flow package which has been described in Sections 5 to 7 in Volume 1 is a complex two-phase flow, non-equilibrium, flow regime dependent model. Experiments were chosen which provide data that can test several predicted quantities, thereby reducing the possibility of compensating error. The FLECHT-SEASET tests were used because they have reliable non-equilibrium vapor temperature data, axial void fraction or pressure drop data, as well as droplet diameter, velocity data, and heater rod temperature data. The FEBA reflood experiments had a different axial power shape as well as matching tests with and without the mid-plane spacer grid. The G-2 reflood experiments had prototypical spacer grid geometry.

For the DFFB assessment, down-flow and up-flow tests were examined. In the WCOBRA/TRAC-TF2 heat transfer logic there are differences in the entrained droplet size depending upon whether the flow is up or down since the entrainment mechanisms are different. This difference is observed in the tests, and represented in WCOBRA/TRAC-TF2. In addition, **[**

][a,c].

For the SPV assessment, high and low pressures and flows were examined, mainly **[**

][a,c].

Examining the composite blowdown and reflood results in Section 15.9, WCOBRA/TRAC-TF2 tends to **[**

][a,c]

[

]^{a,c}

The validation contained herein has examined the various aspects of a complex two-phase flow, non-equilibrium heat transfer model. The simulations presented in this section are intended to demonstrate that the heat transfer models in WCOBRA/TRAC-TF2 are reasonable over the intended ranges of application.

15.11 REFERENCES

1. Anklam, T. M., et al., 1982, "Experimental Investigations of Uncovered Bundle Heat Transfer and Two-Phase Mixture Level Swell Under High Pressure Low Heat Flux Conditions," NUREG/CR-2456.

2. Bajorek et al., 1998, "Code Qualification Document For Best Estimate LOCA Analysis," WCAP-12945-P-A.

3. Cunningham, J. P., et al., 1974, "ECCS Heat Transfer Experiments with Upper Head Injection, Volume 1: Test Facility, Procedures and Data," WCAP-8400.

4. Lee, N., Wong, S., Yeh, H. C., and Hochreiter, L. E., 1982, "PWR FLECHT SEASET Unblocked Bundle, Forced and Gravity Reflood Task Data Evaluation and Analysis Report," NUREG/CR-2256, WCAP-9891.

5. Loftus, M. J. et al., 1981, "PWR FLECHT-SEASET Unblocked Bundle, Forced and Gravity Reflood Task Data Report," Volumes 1 and 2, NUREG/CR-1532, (WCAP-9699).

6. Morris, D. G., et al., 1982, "An Analysis of Transient Film Boiling of High-Pressure Water in a Rod Bundle," NUREG/CR-2469, ORNL/NUREG-85.

7. Mullins, C. B., et al., 1982, "Thermal-Hydraulic Test Facility Experimental Data Report for Test 3.03.6AR and Test 308.6C – Transient Film Boiling in Upflow," NUREG/CR-2525, Volumes 2 and 5.

8. Thurgood, M. J., et al., 1983, "COBRA/TRAC – A Thermal-Hydraulics Code for Transient Analysis of Nuclear Reactor Vessels and Primary Coolant Systems," Volume 1, PNL-4385, NUREG/CR-3046.

9. Wong, S. and Hochreiter, L. E., 1981, "Analysis of the FLECHT SEASET Unblocked Bundle Steam Cooling and Boiloff Tests," WCAP-9729.

10. Yoder, et al., 1982, "Dispersed Flow Film Boiling in Rod Bundle Geometry-Steady State Heat Transfer Data and Correlation Comparisons," NUREG/CR-2435, ORNL-5822.

16 HORIZONTAL STRATIFIED FLOW AND WAVY-DISPERSED FLOW

16.1 INTRODUCTION

[

][a,c]

In general, the predicted performance of a pressurized water reactor (PWR) during a small break Loss-of-Coolant Accident (LOCA) transient is, to some extent, determined by the two-phase flow regime present in the horizontal pipes of the reactor coolant system (RCS). The duration of the **[**

][a,c] are a consequence of the flow regime(s) in the **[**

][a,c] respectively.

In the WCOBRA/TRAC-TF2 computer code, a hybrid transition criterion combining **[**

][a,c] is utilized to define the horizontal stratified flow regime. At the relatively low flow rates associated with the break size range of a small break LOCA, the horizontal two-phase flow is expected to be in the horizontal stratified or wavy-dispersed flow regimes most of the time. Once the flow regime is identified to be horizontal stratified or wavy-dispersed, the appropriate closure relations are selected for the interfacial area, the interfacial drag and the interfacial heat transfer. The interfacial drag and interfacial heat transfer, particularly condensation in the cold leg (Section 6, Volume 1), for the horizontal stratified and wavy-dispersed flow are the basic processes that are directly related to the high-ranked items in the LOCA PIRT. In addition, the offtake phenomenon (Section 5.13, Volume 1) affects the inlet boundary conditions (quality) at the inlet of the break flow. The offtake model in Section 5.13, Volume 1 is considered when the cold leg node connected to the break is calculated to be in the horizontal stratified flow regime or wavy-dispersed flow regime.

The selection criterion for either the horizontal stratified or wavy-dispersed flow regimes is discussed in Section 4, Volume 1, while Sections 5 (interfacial and wall drag) and 6 (interfacial heat transfer) of Volume 1 provide the closure relationships associated with these flow regimes. Scaling and applicability of those models were also discussed in these sections.

The objective of this section is to compare the void fraction prediction for horizontal stratified flow with relevant test data to assess the stratified flow interfacial drag model, wall drag model, and influence of inlet and outlet boundaries.

16.2 KEY PHYSICAL PROCESSES

The capability of the code in predicting the transition from the horizontal stratified or wavy-dispersed regimes to other intermittent flow regimes (bubbly slug, churn, and annular-mist) or interpolation region is very important because interface characteristics (interfacial drag and interfacial heat transfer) change by several orders of magnitude. This is an important mechanism because it affects the venting capability of the vessel from the upper plenum to the cold legs and finally to the break.

The transition criterion from stratified to non-stratified regimes in Section 4, Volume 1 is affected by the predicted void fraction, or water level, in a stratified pipe with the given liquid and gas superficial velocities. From the mass and momentum equations for the stratified flow in Section 5, Volume 1, the void fraction is determined by the interfacial drag, wall drag, and boundary condition (via gravitational water head term) for a horizontal pipe. **[**

][a,c]

The wavy-dispersed flow regime is a special horizontal stratified flow regime, which prevents intermittent flow in the high pressure conditions of a Small Break LOCA (SBLOCA) scenario. The relevance of the wavy-dispersed flow regime was discussed in Section 4, Volume 1. The wavy-dispersed regime is established **[**

][a,c]. Under these circumstances, **[**

][a,c]. The wavy-dispersed flow regime will prevent the formation of slug flow and departure from the separated flow regimes.

The four other processes in LOCA which are affected by the horizontal stratified flow regime are:
[

][a,c]

[

]a,c

In WCOBRA/TRAC-TF2 the transition criterion for stratification is a hybrid model based on [

]a,c The accuracy of the hybrid transition criterion was assessed against experimental data at various pressures, pipe diameters, and void fractions and an uncertainty range for the transition criterion was quantified. The adoption of a transition criterion as a function of [

]a,c. In this section, the assessment focuses on the accuracy of void fraction prediction by WCOBRA/TRAC-TF2.

The prediction of void fraction is controlled by the wall drag, the interfacial drag and the gravitational water head. The applicability of the wall drag model for stratified flow was addressed in Section 5, Volume 1. The gravitational water head term was implemented in the momentum equations as discussed in Section 3, Volume 1. Therefore, the assessment of this section focuses on the interfacial drag model together with the influence of the inlet and outlet boundaries.

The assessment is made against Two-Phase Flow Test Facility (TPTF) stratified flow data. TPTF is a Japan Atomic Energy Research Institute (JAERI) steam-water stratified flow test with a large scale pipe diameter, high pressure, and broad range of flow rates and void fractions. These characteristics render TPTF tests to be excellent benchmark tests for the stratification in small break LOCA. The interfacial and wall drag models for the stratified flow in WCOBRA/TRAC-TF2 are assessed via comparison between the measured void fraction and the predicted void fraction.

The wavy-dispersed flow regime was first reported by TPTF researchers as a relevant flow regime for SBLOCA (see Section 4, Volume 1). [

]a,c

16.3 TEST FACILITY DESCRIPTION

TPTF (Nakamura et al., 1983) was designed and built by JAERI to study the nature of SBLOCA. This facility was designed to perform various steam/water two-phase flow and heat transfer experiments at steady state and at pressures up to 12.8 MPa. These experiments were characterized by a high system pressure (3~12 MPa), a large test section diameter (0.18 m) and a wide range of mass flux (40 to 1000 kg/m^2-s) obtained in the test section for concurrent saturated two-phase flow. The test also simulated the pump effect at inlet, and the water level effect at outlet. These characteristics render TPTF to be an ideal test to assess SBLOCA safety evaluation codes.

Figure 16-1 shows the flow loop used in the TPTF, which consisted of an electrically heated boiler, separate pumps for steam and water lines, a mixer and a 10 m long, 180 mm inner diameter (ID) horizontal test section. The demineralized water was heated in the boiler to saturation conditions at a desired system pressure. Saturated steam was pumped from the top of the boiler through an orifice meter and into the mixer located at the entrance of the test section. The steam pump was a blower-type pump that was specially designed and manufactured for use at high pressure. The steam flowed through a demister located at the top of the boiler and became slightly superheated at the exit of the pump. Saturated liquid was drawn from the bottom of the boiler and similarly pumped through an orifice meter into the mixer. The piping for both the steam and liquid lines was well-insulated to minimize heat loss and prevented steam condensation or liquid subcooling.

The mixer was T-shaped and was connected to the steam and water lines such that steam was introduced horizontally and liquid from the bottom of the tee. There were two types of T shaped mixers used in TPTF experiments as schematically shown in Figure 16-2. Early series of tests used a “bubbly flow” type of mixer. The steam was introduced horizontally into a bundle of tubes and was forced out through numerous holes drilled along the side of each tube. Liquid introduced from the bottom of the tee flowed on the outside of the tube bundle, where the steam and liquid mixed with each other. A nearly homogeneous mixture of liquid and vapor was expected to enter the test section. This homogeneous mixture is similar to the two-phase flow condition in the cold leg after a rotating reactor coolant pump (RCP). The data of Kawaji et al. (1987) came from this “bubbly flow” type mixer. However, because of the homogeneous flow type inlet, the flow was far away from the equilibrium state horizontal stratified flow. The void fraction tended to be larger than the equilibrium state flow and the relative gas-liquid speed was lower than the relative speed in equilibrium state stratified flow. Thus, the non-equilibrium stratified flow due to the homogeneous flow inlet tended to be stable according to the horizontal stratification model. The length of cold leg pipe (L/D=56) was not long enough to allow flow to reach equilibrium state from the homogeneous mixture. Another problem associated with a “bubbly flow” mixer is that the entrained bubbles cannot be released rapidly from liquid if the speed of liquid is large. Those factors led to the observation that the separated to slug flow transition never appeared in the tests with a “bubbly-flow” mixer.

The later TPTF tests used a “separated-flow” type mixer, which contained a horizontal flat plate. Due to this flat plate, the two phases entered the test section as a separated two-phase flow. The height of the separator plate was either 0.3 or 0.7 in height-to-diameter ratio. Thus, there was essentially no bubble entrainment and the flow was not far away from the equilibrium state horizontal stratified flow. All the TPTF flow regime transition data by JAERI were obtained with a “separated flow” type mixer (Anoda et al., 1989). The TPTF data from the “separated-flow” mixer was utilized to verify the stratification transition criteria in Section 4, Volume 1. In this section, the data from the “bubbly-flow” mixer are applied to assess the interfacial drag and the prediction of void fraction.

The water level at the exit of the test section was controlled by the water level in the boiler. There were two water levels in the TPTF tests. In the case of high water level, the water level in the boiler was 0.4 m higher than the center of the test section pipe. In the case of low water level, the water level in the boiler was 0.4 m lower than the center of the test section pipe. The purpose of high or low water level was to simulate the effect of downcomer. The effect of full or empty downcomer was simulated in TPTF test.

The test section consisted of five sections of 180 mm ID stainless-steel piping, each 2 m long and joined by Grayloc connectors. The overall length was 10.0 m and the length-to-diameter ratio (L/D) was 56. The volumetric flow rates of vapor and liquid entering the test section were changed independently by adjusting the flow control valves and the pump speed. The maximum volumetric flow rates were 0.194 m^3/s for steam and 0.047 m^3/s for liquid. For the 180 mm ID test section, the maximum superficial liquid and vapor velocities were 1.9 and 7.6 m/s, respectively.

The horizontal test section was equipped with various two-phase flow instruments (Figure 16-3). In order to obtain detailed information about the flow structure, several of the instruments were attached to traversing devices which enabled measurement of mass and momentum distributions across the pipe cross section. To measure density (or void) distribution, two of the γ-densitometers with vertically-shot γ-ray beams were traversed across the pipe cross section horizontally, yielding a horizontal distribution of vertical chord-average void fractions at locations near the inlet (L/D=17) and outlet (L/D=48) of the test section. The third densitometer with a horizontal beam was traversed vertically across the pipe cross section at L/D=21, yielding a vertical distribution of horizontal chord-average void fractions. The fourth was a three-beam densitometer fixed to the pipe. To measure momentum flux, a water-purged Pitot tube was used. The Pitot tube was attached to a driving mechanism which moved the probe vertically along the centerline of the pipe at a speed of 0.22 mm/s to measure the momentum flux distribution. To further aid in flow pattern identification, five conductivity probes specially developed for use in high-temperature and high-pressure steam/water environments were attached to a rod which was situated along the vertical centerline of the test section.

A large matrix of tests was conducted by JAERI during 1980s. Part of the data is available in public literature (Kawaji et al., 1987). That data were digitized and provides the applicability for the validation of the flow regime and interfacial drag closure relation in WCOBRA/TRAC-TF2.

In summary, TPTF data are selected as the primary data source for the assessment because of the following reasons:

[

][a,c]

16.3.1 Test Selection and Basis

A large matrix of tests was conducted by JAERI during the 1980s. Part of data is available in the public literatures (Kawaji et al., 1987). TPTF experiment data are listed in Tables 2, 3, 4, and 5 in Kawaji et al. (1987). The void fraction information of the data in Table 2 (Kawaji et al., 1987) is missing, and thus could not be used here. The void fraction data in Table 5 (Kawaji et al., 1987) are in contradiction with Figure 11 in Kawaji et al. (1987). There is no other resource to verify those data, so data in Table 5 (Kawaji et al., 1987) are also excluded from the assessment. The remaining data in Tables 3 and 4 (Kawaji et al., 1987) are selected for the assessment. The data are reproduced in Table 16-1 for convenience. According to Kawaji et al. (1987), all those data were in the stratified flow regime based on visual inspections during experiments. The data points are also presented in the WCOBRA/TRAC-TF2 flow regime map in Figure 16-4. There is a substantial amount of data points beyond the horizontal stratification transition boundary of WCOBRA/TRAC-TF2. The discrepancy between the WCOBRA/TRAC-TF2 flow regime map and the observed stratified flow regime in the experiment is likely attributed to **[** **]**[a,c]. Nevertheless, the data with the homogenous inlet mixer are still applicable to assess the interfacial drag and the prediction of void fraction.

It is noted that the selected data are limited to the pressure range from 7.4 MPa to 8.0 MPa. **[**

][a,c]

There are two main aspects that are critical for an accurate prediction of the flow regime: a) the transition from stratified to non-stratified flow regimes; and b) the predicted void fraction in the stratified flow regime.

The adequacy of the transition criterion was discussed in Section 4, Volume 1. Here the focus is on the accuracy of the prediction of void fraction (level) in the pipe. The main objectives of the assessment are the following:

1. Confirm the capability of the code in predicting the transition from stratified flow to non-stratified flow.

2. Assess the interfacial drag model together with the effect of boundary conditions.

3. Identify the controlling parameters and associated biases and uncertainties.

16.4 WCOBRA/TRAC-TF2 MODEL DESCRIPTION

The WCOBRA/TRAC-TF2 model includes the TPTF pipe from the location of first void fraction measurement point (L/D=17) to the exit to the water tank. The pipe from the homogeneous mixer to the first void fraction measurement point at L/D=17 is neglected. The influence of the homogenous inlet mixer is removed to better assess the interfacial drag model and wall drag model for horizontal stratified flow. The inlet of the pipe is modeled with flow boundary conditions (FILL component) by providing the specific j_g and j_l for each test run. The **[** **]**[a,c] is used to evaluate the gas phase velocity and the liquid phase velocity for the FILL component. The water level in the tank is simulated by **[**

][a,c]

The noding diagram is shown in Figure 16-5. The cold leg in the TPTF test section is intended to represent the PWR's cold leg. However, the L/D of the TPTF pipe is longer than the L/D of the PWR's cold leg, but not long enough to develop an equilibrium state stratified flow. The boundary conditions of the TPTF tests have been incorporated into the input model. Thus, the non-equilibrium state stratified flow, as well as the influence from the boundary condition, is part of the simulation.

The diameter of the TPTF pipe is similar to that of the ROSA Integral Effects Test (Section 21) cold leg, but the L/D is much larger than that of ROSA. To preserve the **[**
][a,c] is adopted. The node length (DX) and the hydraulic diameter (HD) of the cold leg node in the ROSA IET are **[** **]**[a,c], respectively. The HD of the pipe in TPTF is 0.18 m (Figure 16-3). **[**

][a,c]

[

]a,c

[

]a,c

16.5 ASSESSMENT RESULTS

The simulation is carried out until a steady-state condition is reached. A typical void fraction profile in the pipe is shown in Figure 16-6 together with the flow regime numbers for TPTF Test 722. Per Table 16-1, Run 722 was a low mass flux case with a high water level in the boiler. The weighting factors W_{st} of the two measurement points in Run 722 were calculated as 1.0 and 0.95 using Equation 4-117 in Section 4.4.5, Volume 1. The parameters C_{stfru} and C_{hs_slug} default to [ ]a,c, respectively.

The weighting factors W_{st}=1 indicates stratified flow, while W_{st}=0 indicates a non-stratified flow in the basic flow regime map. In the interpolation region, $0 < W_{st} < 1$. The weighting factors indicate the flow in TPTF Test 722 is [ ]a,c per the WCOBRA/TRAC-TF2 flow regime map.

The code-predicted flow regime number of each node is marked with "N". A summary of flow regime numbers in a 1D component is given in Table 4.4-1. It is seen that the flow regime numbers are [ ]a,c in the nodes of the PIPE component, except [

]a,c

The WCOBRA/TRAC-TF2 predicted void profile is shown with the solid line in Figure 16-6. The squares represent the measured void fractions at L/D=17 and L/D=48. [

]a,c The dashed line represents the theoretical void fraction that would be obtained assuming the steady-state equilibrium in an infinitely long pipe [ ]a,c. Obviously in this case, [

]a,c

Figure 16-7 presents the void fraction distribution and the flow regime numbers for TPTF Test 845, which was a high mass flux case with a low water level in the boiler. The flow is [

]a,c

The measured void fractions and weighting factors at L/D=17 and L/D=48, together with the predicted void fractions and flow regime numbers at node 1 (L/D=18) and node 13 (L/D=48) are collected in Table 16-2. It is noted that the FILL component is a boundary node, so the flow regime is not evaluated by the code. Instead, **[**

][a,c].

The weighting factors in Table 16-2 confirm that **[**

][a,c].

Figure 16-8 compares the predicted void fraction at node 13 (L/D=48) with the measured void fraction at L/D=48 for the runs **[**

][a,c]

16.6 CONCLUSIONS

An improved horizontal flow regime map is included in the 1D module of WCOBRA/TRAC-TF2 to expand the applicability of the code to small break LOCA scenarios. The 1D module is based on the TRAC-P **[** **]**[a,c] formulation. TRAC-P **[** **]**[a,c] shortcomings are identified and corrected with a revised model which better describes the conditions expected in a PWR during postulated LOCA scenarios.

The improved model includes a hybrid transition criterion for the transition from horizontal stratified flow to non-horizontal stratified flow, **[**

][a,c]. A wavy-dispersed model, **[**

][a,c] which in TRAC-P **[** **]**[a,c] is applied generically regardless of the orientation of the pipe. A detailed discussion on the flow regime, transition criteria and applicability can be found in Section 4, Volume 1.

The purpose of this section is to assess the void fraction prediction for the horizontal stratified flow against relevant test data. **[**

][a,c]

16.7 REFERENCES

1. Anoda, Y., Kukita, Y., Nakamura, N., and Tasaka, K., 1989, "Flow Regime Transition in High-Pressure Large-Diameter Horizontal Two-Phase Flow," *Proc. of 26th ASME/AICHE/ANS National Heat Transfer Conference*, pp. 61-68, Philadelphia.

2. Asaka, H., Kukita, Y., Anoda, Y., Nakamura, H., and Tasaka, K., 1991, "Improvement of TRAC-PF1 Interfacial Drag Model for Analysis of High-Pressure Horizontally – Stratified Two-Phase Flow," *Journal of Nuclear Science and Technology*, Vol. 28, No. 1, pp. 33-44.

3. Barnea, D., and Taitel, Y., 1993, "Stability criteria for stratified flow: viscous versus non-viscous (Inviscid) approaches," *Int. J. Multiphase Flow*, Vol. 19, No. 4, pp. 639-649.

4. Crowley, C. J., Wallis, G. B., and Barry, J. J., 1992, "Validation of one–dimensional wave model for the stratified to slug flow regime transition with consequences for wave growth and slug frequency," *Int. J. Multiphase Flow*, Vol. 18, No. 2, pp. 249-271.

5. Kawaji, K., Anoda, Y., Nakamura, H., and Tasaka, T., 1987, "Phase and Velocity Distributions and Holdup in High-Pressure Steam/Water Stratified Flow in a Large Diameter Horizontal Pipe," *Int. J. Multiphase Flow*, Vol. 13, No. 2, pp. 145-159.

6. Kukita, Y., Asaka, H., Mimura, Y., Anoda, Y., Ishiguro, M., Nemoto, T., Tasaka, K., 1990, "Developmental Assessment of RELAP5/MOD3 Code Against ROSA-IV TPTF Horizontal Two-Phase Experiments," JAERI-M-90-053.

7. Nakamura, H., Tanaka, M., Tasaka, T., Koizumi, Y., and Murata, H., 1983, "System Description for ROSA IV Two Phase Flow Test Facility (TPTF)," JAERI-M-83-042.

8. Taitel, Y., and Dukler, A.E., 1976, "A Model for Predicting Flow Regime Transitions in Horizontal and Near Horizontal Gas-Liquid Flow," *AIChE Journal*, Vol. 22, No. 1, pp. 47-55.

9. Wallis, G. B., and Dobson, J.E., 1973, "The Onset of Slugging in Horizontal Stratified Air-Water Flow," *Int. J. Multiphase Flow*, Vol. 1, pp. 173-193.

Table 16-1 Selected TPTF Test Data from Kawaji et al. (1987)

Run	P(MPa)	Water Level[1]	G (kg/m^{2}s)	x (-) ; quality	j_l (m/s)	j_g (m/s)	Void Fraction	
							L/D=17	L/D=48
857	7.4	Low	1016	0.2	1.12	5.15	0.67	0.64
855	7.4	Low	1020	0.104	1.26	2.69	0.51	0.47
853	7.4	Low	1025	0.06	1.33	1.55	0.35	0.33
851	7.4	Low	1015	0.02	1.37	0.52	0.17	0.17
849	7.4	Low	1015	0.011	1.38	0.28	0.08	0.10
845	7.4	Low	440	0.374	0.38	4.17	0.76	0.77
843	7.4	Low	442	0.122	0.54	1.37	0.42	0.42
847	7.4	Low	426	0.022	0.57	0.23	0.16	0.22
836	7.5	Low	114	0.81	0.03	2.33	0.89	0.91
838	7.4	Low	112	0.634	0.056	1.79	0.83	0.87
1561	7.6	Low	116	0.153	0.14	0.45	0.67	0.68
1563	7.6	Low	114	0.093	0.14	0.27	0.65	0.66
1565	7.6	Low	115	0.052	0.15	0.15	0.64	0.65
1567	7.7	Low	116	0.038	0.16	0.11	0.64	0.67
834	7.5	Low	42.6	0.575	0.025	0.62	0.82	0.88
1555	8	Low	45.2	0.378	0.041	0.42	0.87	0.83
1557	7.8	Low	43.5	0.209	0.049	0.23	0.83	0.79
1559	7.7	Low	42.8	0.122	0.053	0.13	0.79	0.82
779	7.3	High	1011	0.003	1.38	0.085	0.06	0.09
781	7.3	High	1013	0.005	1.37	0.13	0.09	0.13
775	7.3	High	1010	0.01	1.37	0.26	0.13	0.15
751	7.4	High	1007	0.019	1.35	0.51	0.19	0.15
749	7.4	High	1004	0.048	1.31	1.28	0.38	0.29
747	7.4	High	1001	0.077	1.27	2.02	0.48	0.41
773	7.3	High	1010	0.101	1.24	2.58	0.57	0.50
743	7.4	High	1000	0.195	1.1	5.1	0.73	0.69
732	7.4	High	400	0.391	0.33	4.1	0.84	0.81
730	7.3	High	402	0.196	0.44	2.06	0.66	0.64
783	7.3	High	414	0.106	0.51	1.11	0.43	0.47

Table 16-1 (cont.) Selected TPTF Test Data from Kawaji et al. (1987)

Run	P(MPa)	Water Level[1]	G (kg/m^{2}s)	x (-) ; quality	j_l (m/s)	j_g (m/s)	Void Fraction	
							L/D=17	L/D=48
785	7.3	High	410	0.039	0.54	0.41	0.26	0.27
755	7.4	High	407	0.019	0.55	0.21	0.13	0.13
757	7.4	High	383	0.01	0.52	0.1	0.16	0.12
759	7.4	High	381	0.005	0.52	0.05	0.08	0.06
761	7.4	High	380	0.003	0.52	0.031	0.06	0.04
726	7.4	High	99.1	0.794	0.028	2.06	0.97	0.83
728	7.3	High	100	0.596	0.055	1.57	0.91	0.69
708	7.3	High	99.4	0.293	0.1	0.76	0.65	0.53
710	7.3	High	99.5	0.391	0.083	1.02	0.76	0.61
1545	7.4	High	106	0.164	0.12	0.44	0.32	0.31
1547	7.4	High	103	0.098	0.13	0.26	0.2	0.20
1549	7.4	High	105	0.05	0.14	0.13	0.12	0.11
763	7.4	High	102	0.01	0.14	0.027	0.05	0.04
720	7.3	High	39.6	0.691	0.017	0.72	0.63	0.48
722	7.3	High	39.7	0.59	0.022	0.61	0.57	0.44
712	7.3	High	39.9	0.392	0.033	0.41	0.48	0.38
714	7.3	High	40.2	0.196	0.044	0.21	0.31	0.24

Note:
1. High water level: water level in boiler is about 0.4 m above center of test section pipe. Low water level: water level in boiler is below center of test section pipe.

Table 16-2 [ ][a,c]

a,c

Table 16-2 [ ]^{a,c} (cont.)

a,c

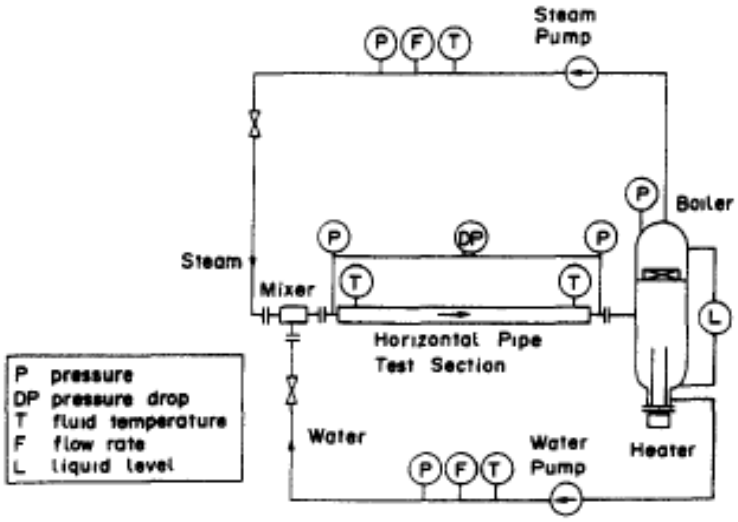

Figure 16-1 The Schematic of the TPTF Facility (Nakamura et al., 1983)

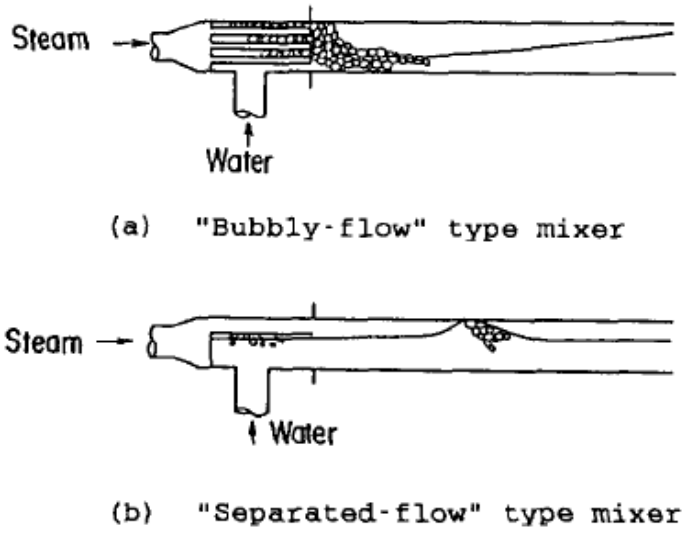

Figure 16-2 T Shaped Mixers used in TPTF (Anoda et al., 1989)

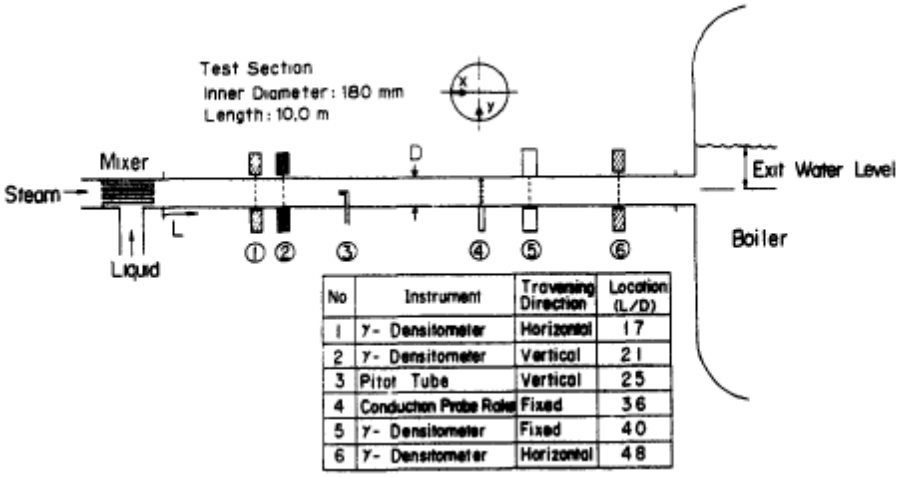

No	Instrument	Traversing Direction	Location (L/D)
1	γ- Densitometer	Horizontal	17
2	γ- Densitometer	Vertical	21
3	Pitot Tube	Vertical	25
4	Conduction Probe Rake	Fixed	36
5	γ- Densitometer	Fixed	40
6	γ- Densitometer	Horizontal	48

Figure 16-3 Test Section and Measurement Instruments (Kawaji et al., 1987)

a,c

Figure 16-4 TPTF Test Data on WCOBRA/TRAC-TF2 Flow Regime Map

a,c

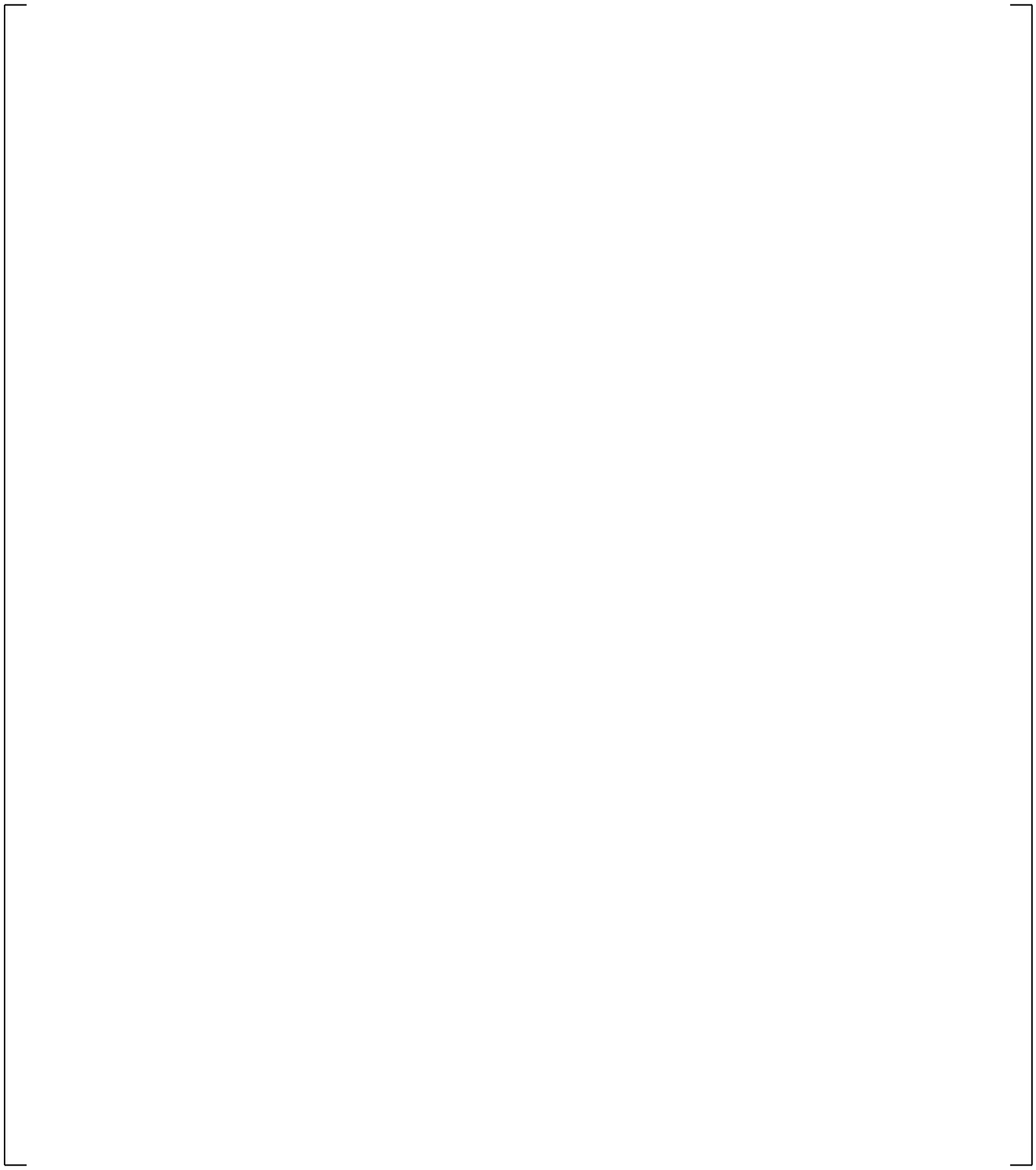

Figure 16-5 WCOBRA/TRAC-TF2 Input Models for TPTF. The Fill Component Corresponds to the Location of L/D=17 in the TPTF Facility

a,c

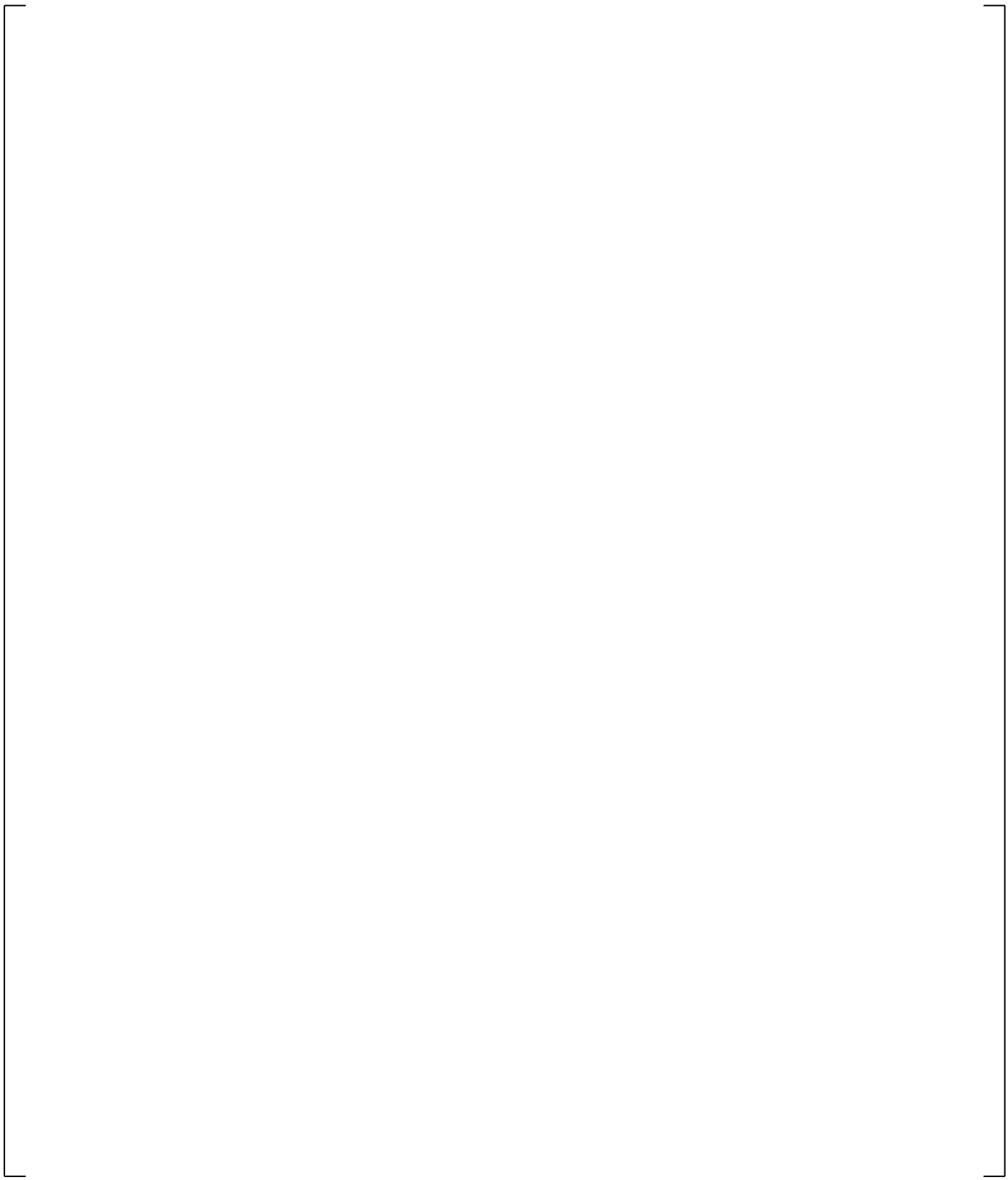

Figure 16-6 Comparison Between Measured Void Fraction in TPTF Run 722 and Predicted Void Fraction

a,c

Figure 16-7 Comparison Between Measured Void Fraction in TPTF Run 845 and Predicted Void Fraction

a,c

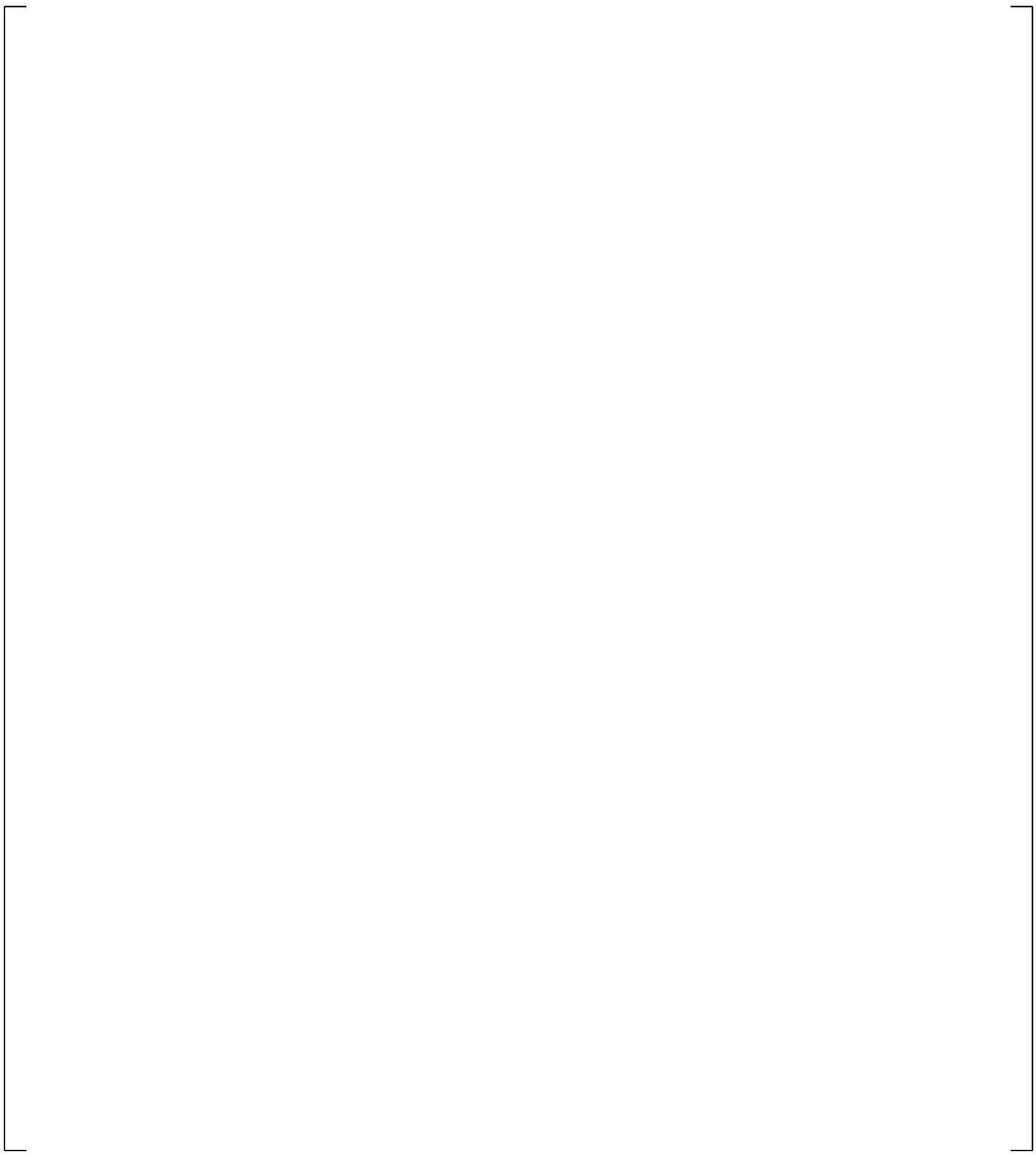

Figure 16-8 [

]a,c

17 COLD LEG CONDENSATION: COSI EXPERIMENTS, ROSA-IV SB-CL-05 EXPERIMENT, AND UPTF 8A EXPERIMENT

17.1 INTRODUCTION

The condensation of steam by the cold liquid injected from the emergency core cooling system (ECCS) by sources such as the accumulator (ACC), safety injection (SI), and residual heat removal (RHR) injection (also called low head safety injection (LHSI)) into the cold leg is an important phenomenon during both small and large break loss-of-coolant accidents (LOCAs) (see Phenomena Identification and Ranking Table (PIRT) in Section 2, Volume 1). Cold leg condensation is ranked high (H) during the boiloff period and the recovery period of a small break LOCA. During these periods, the flow in the cold leg is stratified flow which would lead to negligible condensation due to low interfacial heat transfer. However, the impingement of the SI jet into the layer of liquid in the cold leg enhances condensation greatly. As the break size increases, the effect of the accumulator injection and of the higher pumped SI flow rates leads to an increased importance of condensation in the jet region. For a large break LOCA (LBLOCA), the cold leg condensation is the highest (H) ranked phenomenon during the refill period when the condensation process in the cold leg helps to reduce bypass flow at the top of downcomer, promoting emergency core cooling (ECC) penetration. The condensation effects are reduced during the reflood period as the accumulators end their injection and the low head safety injection continues, but condensation still impacts the break flow rate, the downcomer and core water inventory, and the liquid subcooling in the downcomer. Thus, a ranking of medium (M) was assigned for the cold leg condensation in the reflood stage of a LBLOCA. For intermediate breaks, the cold leg condensation is ranked high (H) for both the accumulator injection period and (low head) safety injection period. More details on the cold leg direct contact condensation processes were also discussed in Section 6.3.6, Volume 1.

As discussed in Section 6.3.6 of Volume 1, a special cold leg condensation model was developed and implemented in WCOBRA/TRAC-TF2 to calculate the condensation heat transfer rate from cold water injection into the cold leg when the cold leg is expected to be in the horizontal stratified flow regime, wavy-dispersed flow regime, or annular-mist flow regime. The model basis, development and applicability are discussed in Section 6.3.6, Volume 1. The purpose of this section is to describe the assessment of the model against an independent dataset. The model is applied whenever the flow regime in the cold leg is predicted to be horizontal stratified, wavy-dispersed, or annular-mist, regardless of the break size or pressure. Therefore, it is important to assess the model performance, not only under conditions for which the model was developed (COSI experiments), but also under conditions at lower pressures and higher flow rates, more typical of intermediate and large break LOCA.

The assessments of small break LOCA and large break LOCA are given in Section 17.2 and Section 17.3, respectively. Section 17.2 covers condensation experiments designed for small break LOCA, such as Condensation On Safety Injection (COSI) and Rig-of-Safety Assessment Number 4 (ROSA-IV) SB-CL-05, which are high pressure and medium scale experiments, while Section 17.3 gives an assessment of the condensation in Upper Plenum Test Facility (UPTF) 8A experiments designed for large break LOCA (low pressure, full-scale experiments).

The focus of this section is to assess the WCOBRA/TRAC-TF2 performance in the analysis of condensation in the cold leg. Additional assessment of the condensation process, especially relative to condensation in the downcomer during the ECC bypass period of larger breaks, is provided in Section 19.

The cold leg condensation model uncertainty will be addressed in Section 29.1.6, Volume 3.

17.2 SMALL BREAK LOCA EXPERIMENTS – COSI AND ROSA SB-CL-05

To investigate the ability of the WCOBRA/TRAC-TF2 code to correctly predict condensation phenomena under conditions representative of small break scenarios, three different test facilities have been considered.

The Westinghouse COSI facility (Shimeck, 1988) is an approximately 1:100 scale model of the cold leg and safety injection lines of a Westinghouse-type pressurized water reactor (PWR), constructed specifically for investigating the interaction of steam and cold SI water in a prototypical PWR configuration and at typical PWR fluid conditions encountered during a small break LOCA.

The cold leg condensation correlation used in WCOBRA/TRAC-TF2 was fitted against a subset of Westinghouse COSI data. Therefore, an independent dataset is needed for the code assessment. The following tests were selected for this purpose.

1. The Westinghouse horizontal injection COSI experiment **[**

   ][a,c]

   The diameter of **[**

   ][a,c] The assessment of the Westinghouse horizontal injection COSI tests provides information on the capability of the WCOBRA/TRAC-TF2 code with the SI pipe running partially full.

2. The Framatome COSI experiments, which compared with the Westinghouse COSI experiments were performed at a lower pressure **[** **]**[a,c], higher SI water temperature **[** **]**[a,c], and with a **[** **]**[a,c] condition.

3. ROSA is an integral effects test (IET). The facility had volumes scaled at 1/48 of a typical Westinghouse 4-loop plant. Its layout was a 2-loop test facility. The diameter of the cold leg was 0.207 m. An extensive assessment of the ROSA integral effects test results is provided in Section 21. In this section, we are interested in the analysis of ROSA SB-CL-05 (Kawaji, M., et al., 1986), a 5% side break in the cold leg with high head safety injection, with respect to the assessment of the condensation process in the cold leg. In the assessment, only the **[** **]**[a,c] were modeled in the WCOBRA/TRAC-TF2 input decks. This makes it a type of **[** **]**[a,c] and this ROSA SB-CL-05 SET provides an SI condensation experiment in a cold leg larger than the COSI experiment. The effect of superheated steam on the cold leg condensation model is also assessed by the ROSA SB-CL-05 cases.

17.2.1 Test Facilities and Tests Description

As discussed above, there are three test facilities serving as the basis for the assessment plan for small break LOCA. Those are the Westinghouse COSI facility, Framatome COSI facility, and ROSA-IV SB-CL-05 test facility. Both the Westinghouse COSI and Framatome COSI tests are separate effects tests. ROSA-IV SB-CL-05 is an integral effects test, however separate effects test data was extracted for the purpose of the assessment of the condensation rate in the cold leg. The facilities are introduced separately in the following sections.

Westinghouse COSI Facility

In the 1980's, the COSI experiments were performed as a four party venture between Westinghouse, Framatome, the French Atomic Energy Commission (CEA), and Électricité de France (EDF). The objective of these experiments was to characterize the condensation phenomenon and develop an accurate condensation model which could be used to evaluate the condensation heat transfer in a PWR during a LOCA.

The Westinghouse COSI facility is a 1:100 scale model of the cold leg and safety injection ports of a Westinghouse-type PWR. It is capable of operating at pressures **[ ]**[a,c] and at appropriately scaled flow rates to cover nearly the entire range of injection conditions expected in a PWR small break transient, during which condensation on the safety injection water phenomenon was judged important. The main scaling philosophy followed in designing the system was to maintain similar **[ ]**[a,c] in the cold leg as would be encountered in a small break LOCA.

The main loop of the test facility **[**

][a,c]

A removable weir with a height **[ ]**[a,c] was incorporated into a spool piece at the outlet end of the main pipe to allow for varying of the water level retained within the cold leg pipe. Measurements were available for the steam and liquid flow rates in and out of the test

assembly, the temperature of fluid entering and exiting the test section, and the system pressure and differential pressures. Within the test section, a series of thermocouple rakes provided the temperature profile and the information concerning stratification of the liquid. Significant amounts of temperature stratification were observed and combined with examination of the actual temperatures the conclusion was that the overall behavior depicted in Figure 17-3 was taking place. Fluid temperatures upstream and downstream of the injection point were stable and indicated that a counter-current flow pattern was in place on the upstream side. On the downstream side, the flow pattern was co-current or counter-current depending on the steam flow configuration, but again stratification was noted. In the immediate vicinity of the injection port, the thermocouple measurements exhibited significant temperature oscillations, indicating turbulent conditions. The downward impingement of the safety injection jet, combined with the significant influx of steam to this point, supported a turbulent jet mixing zone, with rather complex flow and heat transfer patterns. The conclusion from analysis of the data was that most of the condensation mechanism occurs in the proximity of the jet mixing zone. The Westinghouse cold leg condensation model in Section 6.3.6 of Volume 1 was developed based on the assumption that the majority of condensation occurs near the safety injection point.

A large matrix of tests was conducted over the course of the program by both Westinghouse and Framatome (Gros d'Aillon, 1987), and some reconfigurations of the facility test section were performed with regard to the length of the main pipe in the test assembly and the angle and size of the injection piping. A core series of 15 tests, with 75 individual data, from Westinghouse configuration was conducted.

The COSI experimental data report only gives boiler power and heat loss for the entire test loop. The net condensation heat transfer rate Q_{cond} in the cold leg is calculated [

]^{a,c}

$$\left[\qquad\qquad\right]^{a,c} \tag{17-1}$$

[

]^{a,c}

The condensation heat transfer rate in the downcomer Q_{DC} is estimated by [

]^{a,c}

[

]^{a,c}

The process of the data reduction is listed below for the Westinghouse COSI tests.

1. The net condensation heat transfer rate, Q_{net}, in the test section (including downcomer) is **[ ]**[a,c]

2. The net condensation efficiency is calculated using Equation 17-2,

$$\eta_{net} = \frac{Q_{net}}{m_{SI}(h_f - h_{SI})} \quad (17\text{-}2)$$

   where Q_{net} is net condensation heat transfer in the test section, m_{SI} is the SI flow rate and h_f and h_{SI} are the enthalpy of saturated water and the SI water (at the test pressure and SI temperature).

3. The net condensation efficiency is **[ ]**[a,c] in several runs, for which the test report did not provide an explanation. In this data reduction process, the net condensation in those cases is **[ ]**[a,c].

4. The condensation heat transfer rate in the test section is split into two portions, the condensation in the cold leg (Q_{cond}) and the condensation in the downcomer (Q_{DC}). The condensation heat transfer rate in the downcomer is evaluated using 3 pairs of tests with the only differences being the **[ ]**[a,c]. There are 3 pairs of tests identified for different pressures, **[ ]**[a,c]. All 5 runs in each pair are used to establish the downcomer condensation efficiency at the particular pressure. The **[ ]**[a,c] is the nominal condensation efficiency at the pressure and the maximum and minimum values provide the uncertainty of the downcomer condensation efficiency.

5. The net condensation efficiency minus the efficiency caused by downcomer condensation is the cold leg condensation efficiency. **[ ]**[a,c]

6. The cold leg condensation heat transfer rate is evaluated using the cold leg condensation efficiency and the condensation potential with Equation 17-3.

$$Q_{cond} = \eta_{cond} m_{SI}(h_f - h_{SI}) \quad (17\text{-}3)$$

   [ ][a,c]

There were two types of Westinghouse COSI tests based on their SI angle relative to the direction of the cold leg. The tests with **[ ]**[a,c] are called “vertical” COSI test, and the tests with **[ ]**[a,c] injection angle are called “horizontal” COSI test. Section 6.3.6 in Volume 1 describes in detail how the vertical injection tests have been used to define the cold leg condensation model implemented in

WCOBRA/TRAC-TF2. The vertical injection COSI tests also serve as a part of the assessment documented in this section because the data will be used to validate the WCOBRA/TRAC-TF2 code with the cold leg condensation model, not only the cold leg condensation correlation itself. The Westinghouse vertical COSI data, which were utilized to define the safety injection condensation correlation, are listed in Table 17-1.

Compared with the vertical COSI tests, the horizontal COSI tests have a **[**

][a,c] Test data from the Westinghouse horizontal COSI tests are shown in Table 17-2.

Framatome COSI Facility

The Framatome COSI facility is similar to the Westinghouse COSI facility. The loop structure shown in Figure 17-1 is the same for the Framatome COSI facility, but the Westinghouse test section in Figure 17-2 was replaced with the Framatome test section, which is shown in Figure 17-5. The cold leg diameter of both test sections is 0.118 m, but the length of the Framatome test section (cold leg) is only **[** **]**[a,c] in the Westinghouse test section. Compared to the Westinghouse setup, this shorter test section is more appropriate from a scaling standpoint.

The Framatome test section had two injection points (Boileau, 1988). One injection was **[** **]**[a,c]. The diameter of this injection port was **[** **]**[a,c]. Another injection port was located in the horizontal plane with a diameter of **[** **]**[a,c]. Since there is no data reported for the larger horizontal pipe, that flow configuration is not considered in this report.

Another difference between the Westinghouse test section and the Framatome test section is steam flow. **[**

][a,c]

The Framatome test section had two weir heights, **[** **]**[a,c] cold leg diameters, and a case without a weir. In contrast to the two downcomer water levels **[** **]**[a,c] used in the Westinghouse COSI tests, the water level in the downcomer was consistently set to **[** **]**[a,c] relative to the cold leg. In the Framatome test, the water level in downcomer was always in the high position **[**

][a,c]

The system pressure in the Framatome COSI tests was either **[** **]**[a,c]. The pressure of **[** **]**[a,c] is lower than the lowest system pressure **[** **]**[a,c] in the Westinghouse COSI tests.

The range of SI water temperature in the Framatome COSI tests was **[** **]**[a,c], while the SI water temperature in the Westinghouse COSI tests was almost constant **[** **]**[a,c]. High SI

water temperature is possible during the later stages of a SBLOCA in some PWRs, when the SI water comes from the sump instead of the RWST and is not cooled by the component cooling water.

The calculation for the heat loss, downcomer condensation, and upper and lower bound of the Q_{cond} follows the same procedure used for the Westinghouse COSI data reduction.

The condensation in the downcomer is a function of the downcomer water level and the SI water mass flow rate. Both the Westinghouse and Framatome COSI experiments used the same downcomer (a structural difference only exists at the cold leg). The downcomer water level in the Framatome COSI tests was **[ ]**[a,c]. Therefore, the downcomer condensation can be evaluated using the same equation for the Westinghouse COSI test with a downcomer water level of **[ ]**[a,c]. However, it is noted that **[**

][a,c]. Thus, the downcomer condensation efficiency of **[**

][a,c]. It is also noted that the SI injection rate in the Framatome COSI tests is generally higher than those in the Westinghouse COSI tests. However, the downcomer condensation efficiencies **[ ]**[a,c].

The Framatome COSI experiments include both **[ ]**[a,c]. It is noted that the cold leg condensation model does not depend on the **[ ]**[a,c] flow configuration. The cold leg condensation model predicts the same condensation heat transfer rate if all the parameters in the correlation are the same. To validate the cold leg condensation model against the possible **[ ]**[a,c] in the broken cold leg, the Framatome inverse COSI tests are included in the assessment plan.

[

][a,c]

The qualified Framatome COSI test data with zero break flow are shown in the Table 17-3.

JAERI ROSA-IV/LSTF Facility

The ROSA-IV Large Scale Test Facility (LSTF) is a 1/48 volumetrically scaled facility discussed in Section 21. In this section, only the ROSA-IV SB-CL-05 test is considered. **[**

][a,c]

Table 17-4 provides the major dimensions and scaling factors of the ROSA facility in comparison to the COSI facilities and typical PWR dimensions. While the detailed ROSA-IV LSTF system description is

discussed in Section 21, some key features, specifically relative to the cold leg and SI injection, are reviewed here.

[

]^{a,c}

The test facility was very well instrumented and this allowed for the extraction of separate effects test data. The test SB-CL-05 was considered for the purpose of analyzing the cold leg condensation in detail. The cold leg condensation in the cold leg was in a slow transient state. However an accurate evaluation of the cold leg condensation was possible by assuming a quasi-steady state progression of the transient.

[

]^{a,c} in ROSA is modeled and simulated in the separate effects test.

[

]^{a,c}

[

][a,c]

To set up the steady state separate effects test, several instantaneous flow conditions in the cold leg are captured. **[**

][a,c] The flow conditions are given in Table 17-5.

In summary, the following key considerations are applied to select the tests for the assessment:

- The Westinghouse vertical injection COSI experiment (i.e., with injection angle of 90°) has been used, as documented in detail in Section 6.3.6, Volume 1 to define the cold leg condensation model implemented in WCOBRA/TRAC-TF2. The assessment of the vertical injection COSI tests is provided here to **verify** the WCOBRA/TRAC-TF2 code with the cold leg condensation model described in Section 6.3.6 of Volume 1, thus to confirm the correct code implementation of the model documented in Section 6.3.6, Volume 1.

- The Westinghouse horizontal injection COSI experiment had a **[** **]**[a,c] injection angle in the flow direction, different than the vertical injection experiments. The diameter of the horizontal injection port was larger than the diameters in vertical experiment. This larger diameter and the 45° injection angle cause the water to **[** **]**[a,c]. The assessment of WCOBRA/TRAC-TF2 against the Westinghouse horizontal injection serves the purpose of **validating** the cold leg condensation model.

- The Framatome COSI experiment provides the assessment of the code at lower pressure **[** **]**[a,c] and at higher SI water temperature **[** **]**[a,c] than the Westinghouse experiments.

- The ROSA SB-CL-05 separate effects test provides an SI condensation experiment with a larger diameter cold leg. The effect of superheated steam on the cold leg condensation model is also assessed by simulating ROSA SB-CL-05 cases.

17.2.2 Description of WCOBRA/TRAC-TF2 Models

Figure 17-9 shows the component layout of the WCOBRA/TRAC-TF2 model of the Westinghouse vertical COSI facility. **[**

][a,c]

[

]a,c

The cold leg condensation model is applied only [ ]a,c.
As discussed in Section 6.3.6 of Volume 1, [

]a,c The condensed water flows to the BREAK component. It is noted that the physical location of the vertical SI injection is not at the center of the cold leg in the Westinghouse COSI test facility. Only the scaled part of the cold leg (Figure 17-2) is simulated. The injection port is at the junction of the TEE component. This logic is applied to both the Westinghouse horizontal COSI and Framatome COSI test facilities.

The layouts of the Westinghouse horizontal COSI and Framatome COSI test facilities are similar to that of the Westinghouse vertical COSI facility. The major differences are the diameter of SI line and the angle of the SI line, which is [ ]a,c for the horizontal COSI.

The noding diagram for the ROSA SB-CL-05 safety injection tests is similar to that of the Westinghouse vertical COSI facility, which is given in Figure 17-9. However, the diameters and lengths of the cold leg and SI line are different, as are the system pressure, steam flow rate, and SI flow rate. The [ ]a,c of the ROSA facility is also simulated.

The noding diagram for the Framatome counter-current (Inverse) COSI tests is shown in Figure 17-10.
[

]a,c

17.2.3 WCOBRA/TRAC-TF2 Results

The condensation heat transfer rate is calculated from the heat transfer rate of the liquid, which is given as:

$$q_{i\ell} = h_{i\ell} A_i \left(T_{sat} - T_\ell \right) \tag{17-4}$$

where $q_{i\ell}$ is the heat transfer rate from the liquid to the gas-liquid interface, $h_{i\ell}$ is the heat transfer coefficient from the liquid to the interface, and A_i is the gas-liquid interfacial area. Because the cold leg condensation model is only applied to the junction cell of the TEE component, the heat transfer comparison is only on the junction cell. [ ]a,c

[

]a,c

The comparison between the calculated condensation heat transfer rate and the measured heat transfer rate for the Westinghouse COSI tests is shown in Figure 17-11a. [

]a,c

There are differences between the vertical COSI and horizontal COSI. [

]a,c

The comparison between the calculated condensation heat transfer rate and the measured heat transfer rate for Framatome COSI tests is shown in Figure 17-12. The test series at [

]a,c

The comparison between the calculated condensation heat transfer rate and the measured heat transfer rate for the ROSA SB-CL-05 cold leg condensation tests is shown in Figure 17-13. [

]a,c

The steam temperatures in the cold leg for ROSA SB-CL-05 are shown in Figures 17-14 to 17-17. Steam superheating is constant upstream of the safety injection. The steam superheating gradually decreases downstream of the safety injection. **[**

][a,c]

17.2.4 Small Break LOCA Experiments Conclusions

WCOBRA/TRAC-TF2 models for three test facilities (Westinghouse COSI, Framatome COSI, and ROSA SB-CL-05) are developed to assess the cold leg condensation model with focus on the small break LOCA scenario.

The overall assessment of code predictions against data from Westinghouse COSI, Framatome COSI, and ROSA-IV SB-CL-05 is summarized in Figure 17-18. **[**

][a,c]

The uncertainty range of the cold leg condensation model will be assessed in Section 29, Volume 3.

17.3 LARGE BREAK LOCA EXPERIMENTS: UPTF TEST 8A

17.3.1 Introduction

In Section 17.2, the assessment of the condensation process in the cold leg was focused on the small break LOCA scenario. For the large breaks, condensation is of the highest relative importance during the refill period. When the ECC water is no longer bypassed in the refill period, the condensation process at the top of the downcomer helps to induce downflow through the core, promoting cooling. In this scenario, the thermal hydraulic conditions are different from those analyzed in the previous sections, and the effect of the accumulator injection and the low head safety injection flow rates needs to be assessed.
[

][a,c]

As part of the UPTF test matrix, two cold leg flow regime separate effects tests, Tests 8 and 25, were run to investigate steam/water flow phenomena in the cold legs during the refill/reflood phase of a large break LOCA. These phenomena include steam condensation on subcooled ECC at different flow regimes (e.g., plug flow, stratified flow) in the cold leg. Test 8A (2D/3D Program Report, 1988) focused on the effect of ECC flow rate on cold leg flow phenomena. Test 25A (2D/3D Program Report, 1990) investigated the effects of steam flow rate and steam superheating. UPTF Test 25A provides the assessment basis for different hydrodynamic phenomena and is discussed in Section 19, but the

implication to the cold leg condensation model will be addressed in this section. The integral UPTF Test 8A model with the VESSEL and the loop structure is developed and assessed in Section 19. In this section, the UPTF Test 8A is modeled as a single TEE as discussed in Section 17.3.2.

UPTF Test 8A was performed to investigate the flow regimes that might arise in the intact cold legs of a PWR during a postulated LBLOCA, when subcooled ECC liquid mixes with superheated steam. During the blowdown and refill phases, the flow of accumulator water is of sufficient magnitude to theoretically condense all the steam flowing into the cold leg. During reflood the low head safety injection flow (LHSI/RHR), at its minimum levels, is typically insufficient to condense all the steam flowing into the cold leg.

Cold leg liquid slug formation and oscillations may occur when the subcooled injected ECC liquid causes condensation of the steam flowing in the cold leg. A liquid slug is a region in which the cold leg is completely filled with liquid. Steam flowing through the cold leg from the pump towards the downcomer condenses when in contact with subcooled injected ECC liquid. A liquid slug in the region between the injection point and the downcomer can form when the liquid subcooling and the interfacial heat transfer are sufficient to completely condense the flow of steam.

Once the liquid slug forms, further condensation of steam results in a reduction of pressure upstream of the liquid slug. A local reduction in pressure at the condensation point causes the slug to move back towards the ECC injection point. The movement may be expected to continue until the liquid slug completely covers the injection point.

Eventually, the pressure increase, due to the steam entering the cold leg, is sufficient to move the liquid slug towards the downcomer again. These conditions were experienced in UPTF Test 8.

17.3.2 WCOBRA/TRAC-TF2 Model Description

The WCOBRA/TRAC-TF2 model of UPTF Test 8A is documented in Section 19.3.7 with the full structure of the loop and the vessel. The single TEE model in this section serves as the base model for validating the cold leg condensation model and performing sensitivity studies. Unlike the integral UPTF Test 8A model in Section 19.3.7, which represents the entire facility, the TEE model only represents **[ ]**[a,c]. The advantage of the single TEE model is that **[ ]**[a,c]. The single TEE model development includes the following cases:

1. Base Model – **[ ]**[a,c]

2. Sensitivity Study on ECC Injection Angle – **[ ]**[a,c]

3. Sensitivity Study on Cold Leg Noding – **[**
][a,c]

4. Sensitivity Study on ECC Injection Node – **[**

][a,c]

5. Sensitivity Study on Ranging Cold Leg Condensation Rate Multiplier (KCOSI) – **[**

][a,c]

6. Sensitivity Study on Ranging Horizontal Stratification Criteria (HS_SLUG) – **[**

][a,c]

The noding diagram is shown in Figure 17-20. **[**

][a,c]

17.3.3 WCOBRA/TRAC-TF2 Results: Base Model

The WCOBRA/TRAC-TF2 simulation of UPTF Test 8A was run for the first 200 seconds of the test, which covered the period where flow was injected into the Loop 2 intact cold leg. The as-measured injection steam and ECC flow rates were used as boundary conditions in the WCOBRA/TRAC-TF2 model. The BREAK component was maintained at a constant pressure of 390 kPa (57 psia).

In Section 19, it is demonstrated that the WCOBRA/TRAC-TF2 simulation of UPTF Test 8A with the full vessel model and loop structure shows **[**
][a,c]. The TEE model for UPTF Test 8A provides additional validation on the cold leg condensation model with a fixed boundary condition. **[**

][a,c]

The measured and predicted temperatures in the Loop 2 cold leg are compared in Figures 17-21 through 17-24. At the pump exit (Figure 17-21), the single TEE model predicts a lower degree of oscillation with a shorter time period at the beginning of stage 1 than the integral model does (Figure 19.3-156). **[**

][a,c]

[

]a,c

The single TEE model predicted the water temperature near the injection point is shown in Figure 17-22. [

]a,c

Figure 17-23 shows the comparison between the measured temperature and the WCOBRA/TRAC-TF2 predicted water temperature at the downstream injection point. [

]a,c

Figure 17-24 shows the comparison between the measured temperature and the WCOBRA/TRAC-TF2 predicted water temperature at the cold leg near the vessel inlet. The overall effect of the cold leg condensation is shown in this figure. [

]a,c

17.3.4 WCOBRA/TRAC-TF2 Results: Sensitivity Studies

Sensitivity Study on ECC Injection Angle

This case studies the impact of the ECC injection angle on the cold leg condensation. [

]a,c

[

]a,c

[

]a,c

Sensitivity Study on Cold Leg Noding

Figure 17-28 shows the noding size sensitivity on the predicted water temperatures at the injection cell of the cold leg. The predicted temperatures are different from stage 3 to stage 6. Figures 17-29 and 17-30 show the same comparison downstream of the injection cell and at the outlet of the cold leg, respectively.

[

]a,c

Sensitivity Study on ECC Injection Node

This is a sensitivity study on the junction node to which ECC water is injected. [

]a,c

[

]a,c

Sensitivity Study on Cold Leg Condensation Rate Multiplier (KCOSI)

The uncertainty of the cold leg condensation model is ranged using the cold leg condensation rate multiplier, KCOSI. [

]a,c

Sensitivity Study on Horizontal Stratification Criteria

The cold leg condensation model requires the flow regime to be horizontal stratified flow, wavy-dispersed flow, or annular-mist flow. The transition from horizontal stratified flow to non-stratified flow is ranged by the multiplier HS_SLUG. [

]a,c

[

]a,c

17.3.5 Large Break LOCA Experiments Conclusions

UPTF Test 8A is utilized to assess the applicability of the cold leg condensation model in a large break LOCA. The simulation of UPTF Test 8A with the full vessel and loop structure in Section 19 shows [ ]a,c. The single TEE models for the UPTF Test 8A experiment were assessed in this section. [ ]a,c

The sensitivity studies give the following conclusions:

[

]a,c

UPTF Test 25A is another cold leg condensation test for the reflood stage of LBLOCA characterized with a variable steam flow rate and a substantial steam superheating. The simulation and results of UPTF Test 25A are discussed in Section 19.3.

17.4 OVERALL CONCLUSIONS

WCOBRA/TRAC-TF2 models for four test facilities (Westinghouse COSI, Framatome-COSI, ROSA SB-CL-05, and UPTF Test 8A) are developed to assess the cold leg condensation model over conditions representative of both small and large break LOCA scenarios.

The overall assessment documented in Sections 17.2 and 17.3, together with the LBLOCA assessment in Section 19, is summarized in Sections 17.2.4 and 17.3.5 for small and large break LOCA conditions, respectively. The comparison with experimental results shows that the WCOBRA/TRAC-TF2 code is able to predict condensation within a reasonable range of uncertainty. The WCOBRA/TRAC-TF2 predictions are judged to be acceptable for the purpose of analyzing a full spectrum of break sizes in a PWR LOCA.

Sensitivity analyses to key parameters using a single TEE model of UPTF Test 8A cold leg and ECC lines are also performed. The sensitivities considers the ECC branch line orientation relative to the cold leg, the noding size selected for modeling the cold leg, the condensation rate multiplier (KCOSI) and the horizontal stratified flow regime transition criterion (HS_SLUG). Results of the sensitivity studies are summarized in Section 17.3.5 to support methodology decisions for the purpose of modeling a PWR.

Additional validation of the cold leg condensation model is provided by the simulation of UPTF Test 25A in Section 19.3.

17.5 REFERENCES

1. 2D/3D Program Upper Plenum Test Facility Experimental Data Report, 1990, “Test No. 25, Downcomer/Cold Leg Steam/Water Interaction Test,” E314/90/11, KWU.

2. 2D/3D Program Upper Plenum Test Facility Experimental Data Report, 1988, “Test No. 8, Cold/Hot Leg Flow Pattern Test,” U9 316/88/12, KWU.

3. Boileau, H., 1988, “Condensation on Safety Injection, FRAMATOME Analysis Report,” EP/TA/DC.0771.

4. Emmerling, R., et al., 1988, “UPTF: Program and System Description,” Siemens U9 414/88/023.

5. Gros d’Aillon, M., 1987, “Essais De Condensation En Regime Permanent,” (COSI Report), SETh/LETC/87-45.

6. Kawaji, M., et al., 1986, “ROSA-IV/LSTF 5% Cold Leg Break LOCA Experiment Data Report, Run SB-CL-05,” JAERI-memo 61-056.

7. The ROSA IV Group, 1985, "ROSA-IV Large Scale Test Facility (LSTF) System Description," JAERI-M 84-237.

8. Shimeck, D. J., 1988, "COSI SI/Steam Condensation Experiment Analysis," WCAP-11767.

Table 17-1 Westinghouse Vertical COSI Tests Data

a,c

Table 17-1 Westinghouse Vertical COSI Tests Data (cont.)

a,c

Table 17-2 Westinghouse Horizontal COSI Tests Data

[a,c

]

Table 17-3 Selected Framatome COSI Tests Data and Calculation for Qcond

a,c

Table 17-4 Comparison of Facilities for Cold Leg Condensation Assessment

a,c

Table 17-5 ROSA SB-CL-05 SI Condensation Test Data for SETs

[

]a,c

a,c

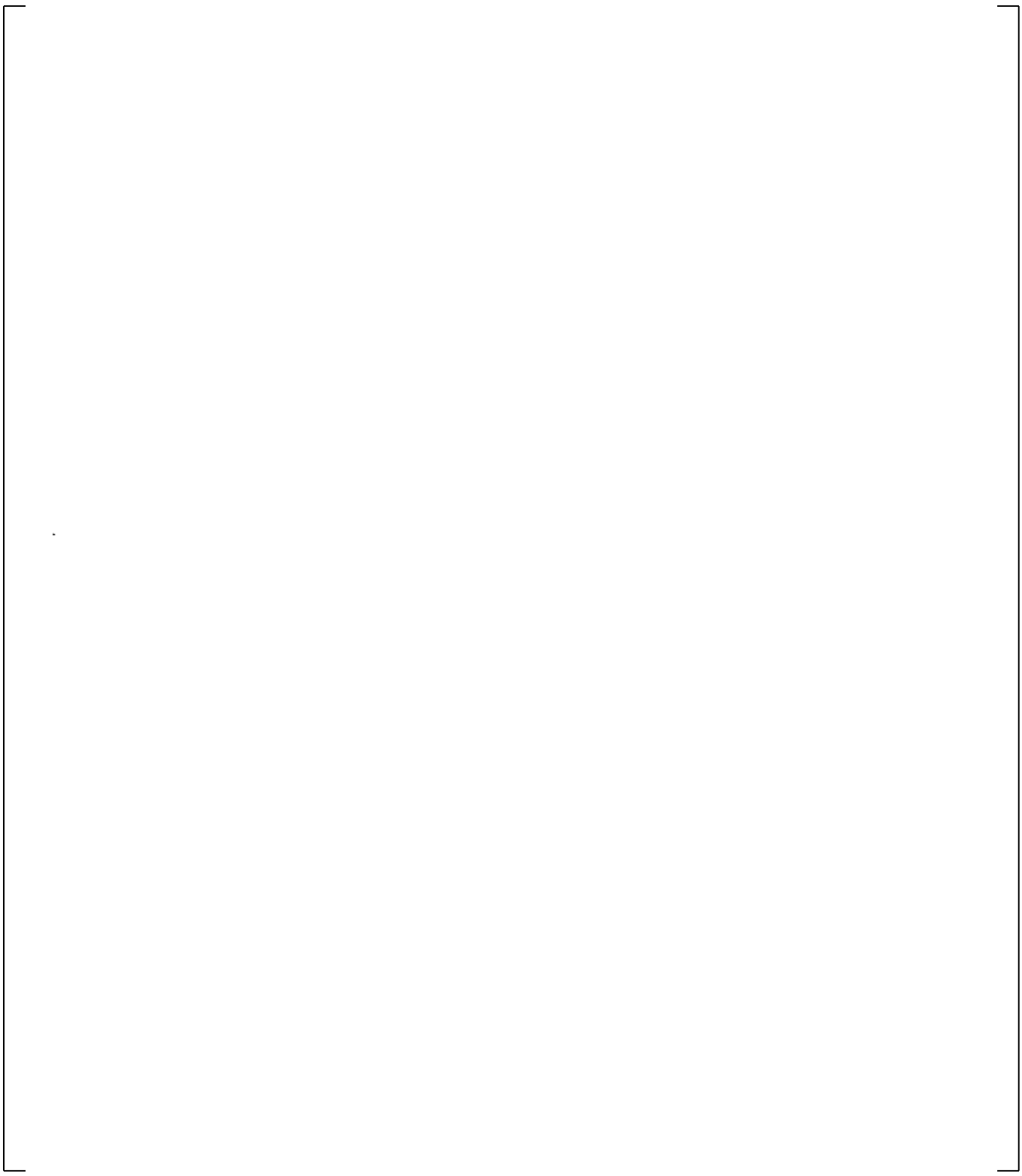

Figure 17-1 COSI Facility Arrangement

a,c

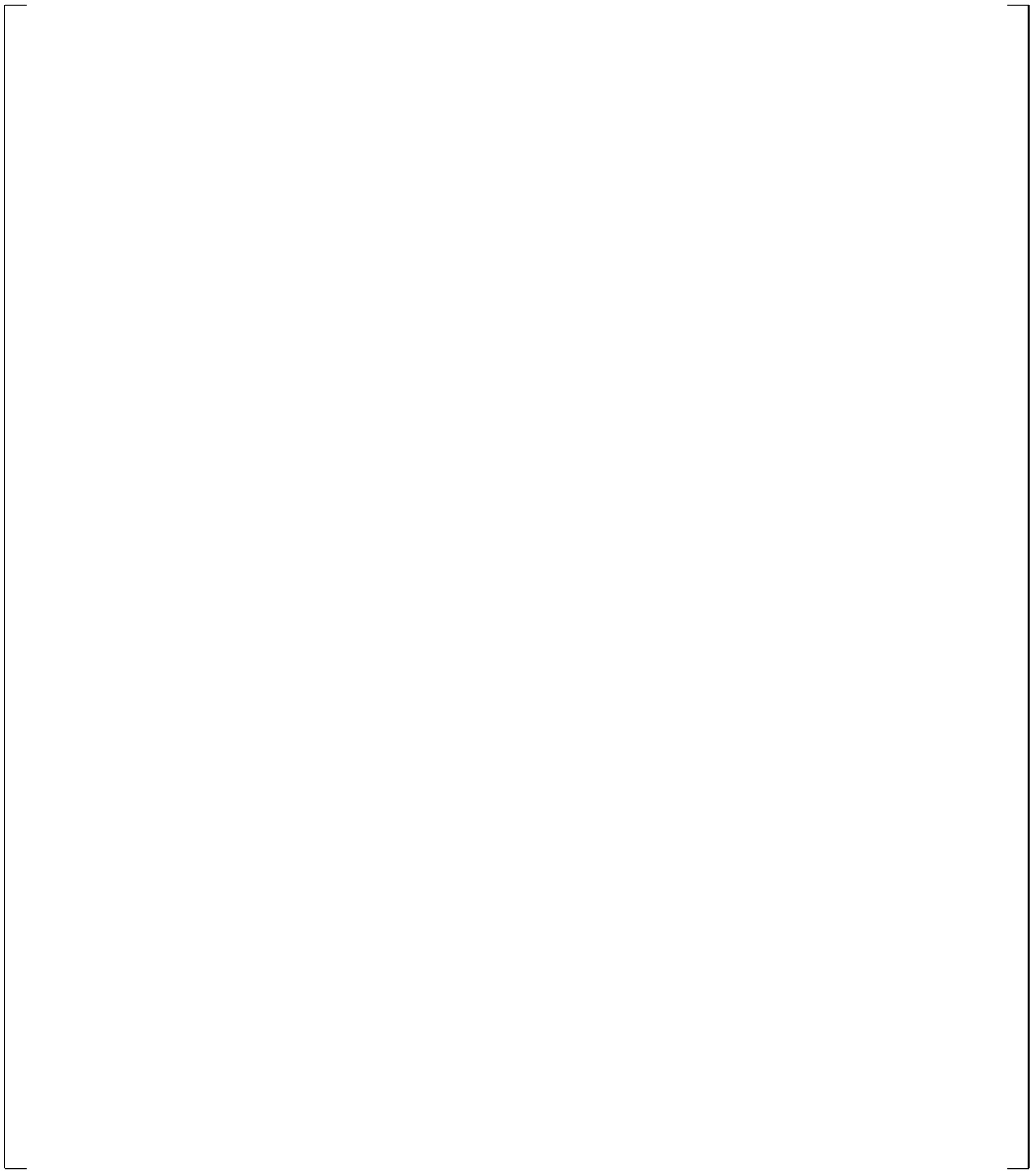

Figure 17-2 Westinghouse COSI Test Section Arrangement

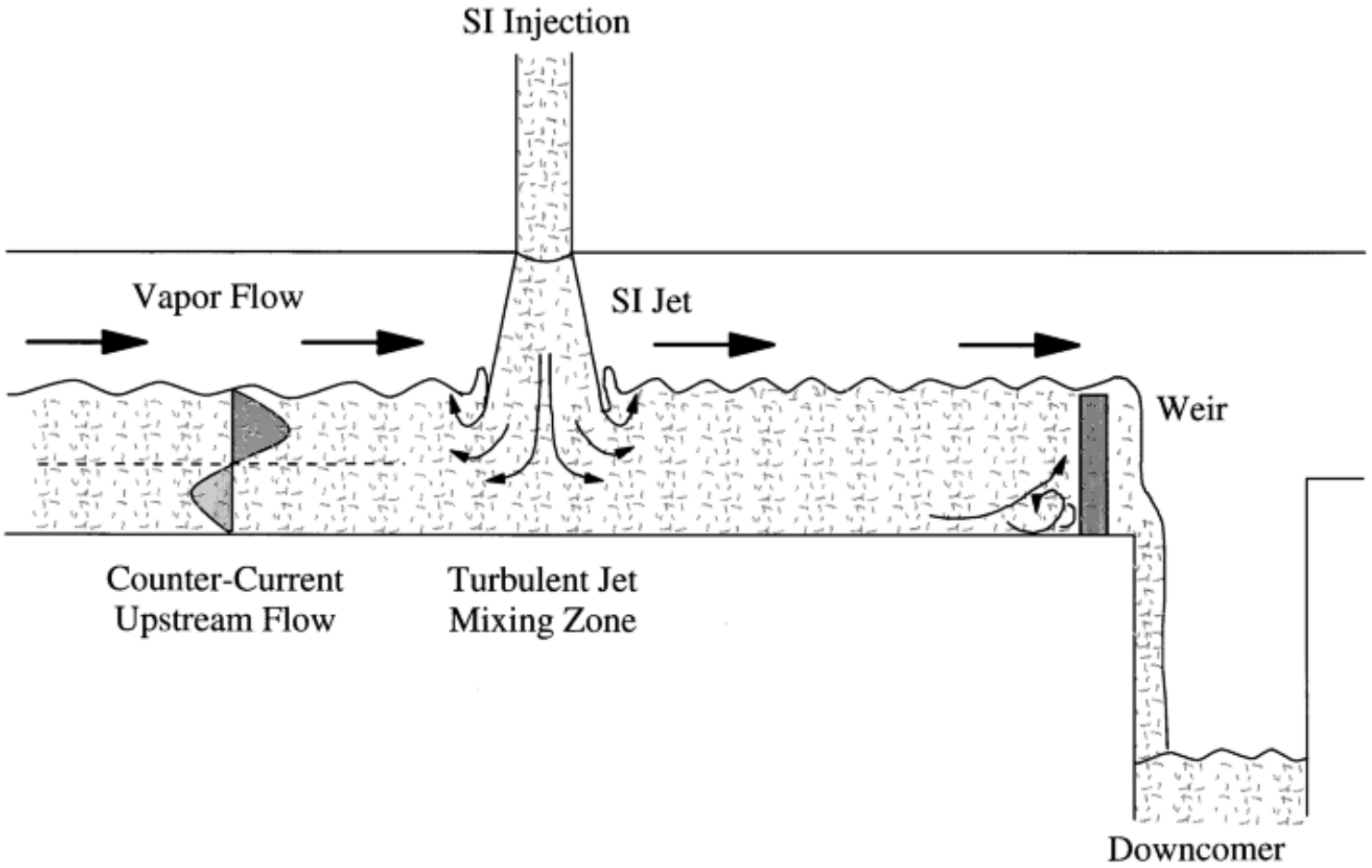

Figure 17-3 Depiction of Flow Patterns in the Test Section as Deduced from Data

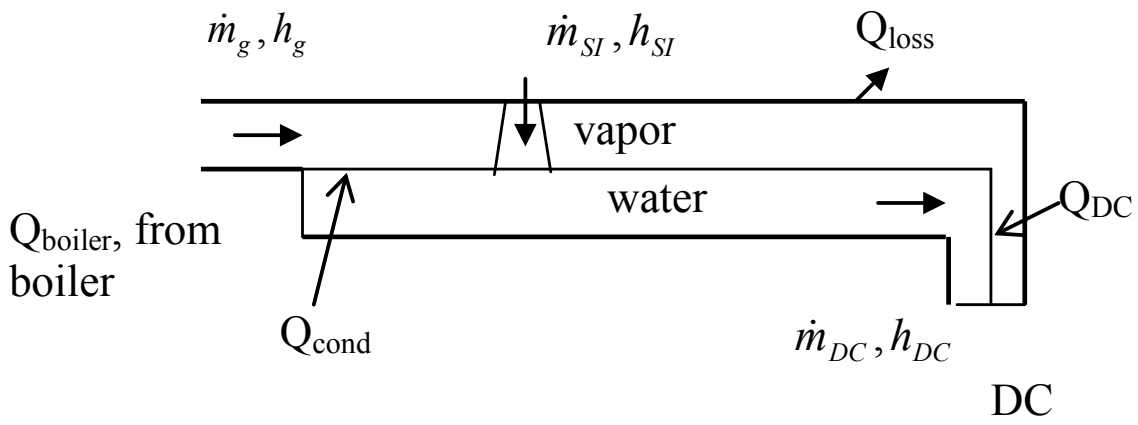

Figure 17-4 Illustration of Condensation in COSI Test Section

a,c

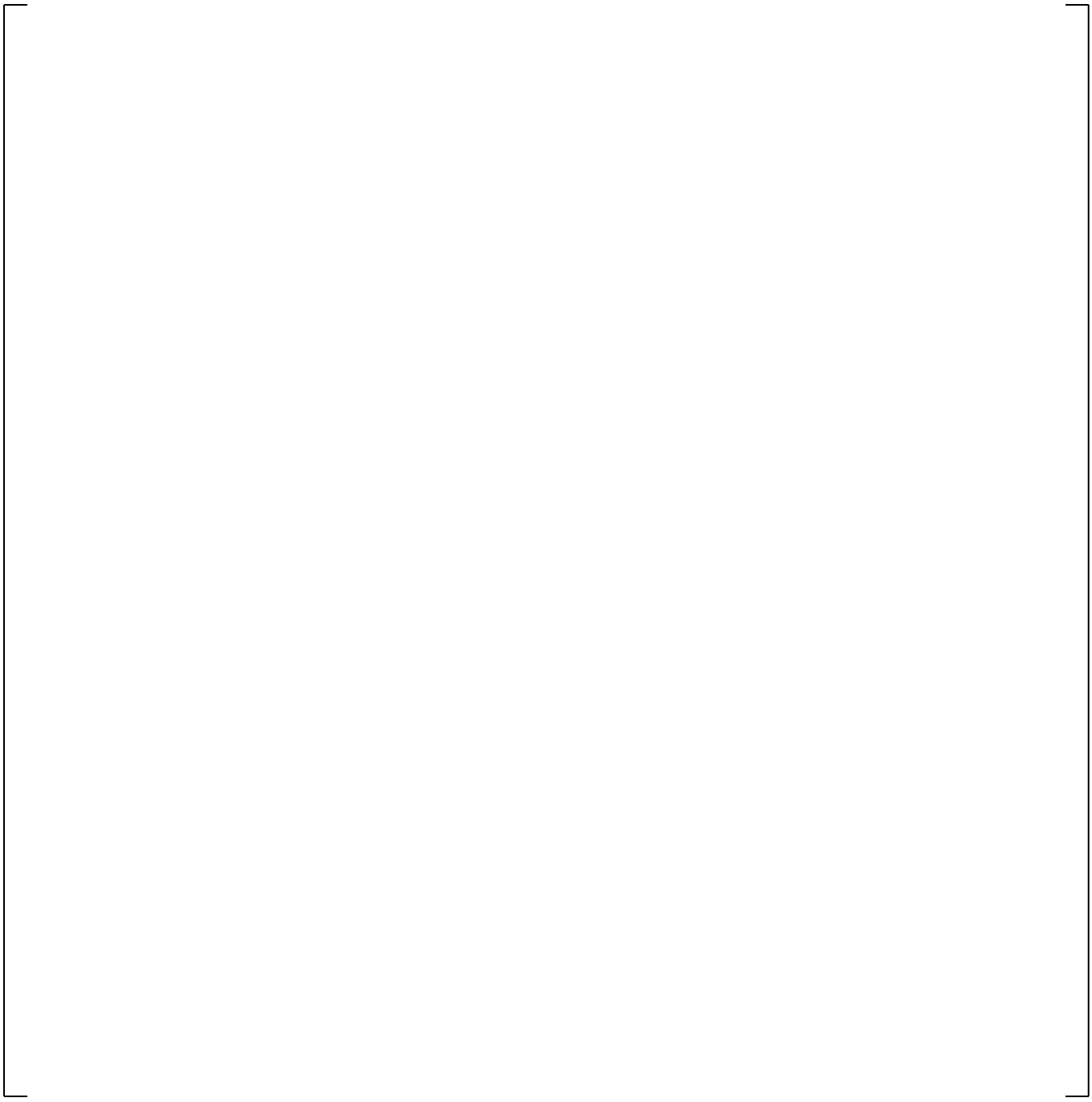

Figure 17-5 [

]a,c

a,c

Figure 17-6 Comparison of Westinghouse Test Section and Framatome Test Section in Cross Section of Cold Leg

a,c

Figure 17-7 General Structure of Cold Leg from Crossover Leg to Downcomer in the ROSA Facility

Figure 17-8 Schematics of ECCS Configuration in ROSA-IV SB-CL-05

a,c

Figure 17-9 WCOBRA/TRAC-TF2 Single TEE Noding Diagram for Westinghouse Vertical COSI, Framatome COSI, and ROSA-IV SB-CL-05; for Westinghouse Vertical COSI, the Inclination angle of SI Line is 45°

a,c

Figure 17-10 WCOBRA/TRAC-TF2 Two-TEE Noding Diagram for Framatome Inverse COSI Tests

a,c

Figure 17-11a Comparison between Measured Westinghouse COSI Condensation Heat Transfer Rate and WCOBRA/TRAC-TF2 Predicted Condensation Heat Transfer Rate

a,c

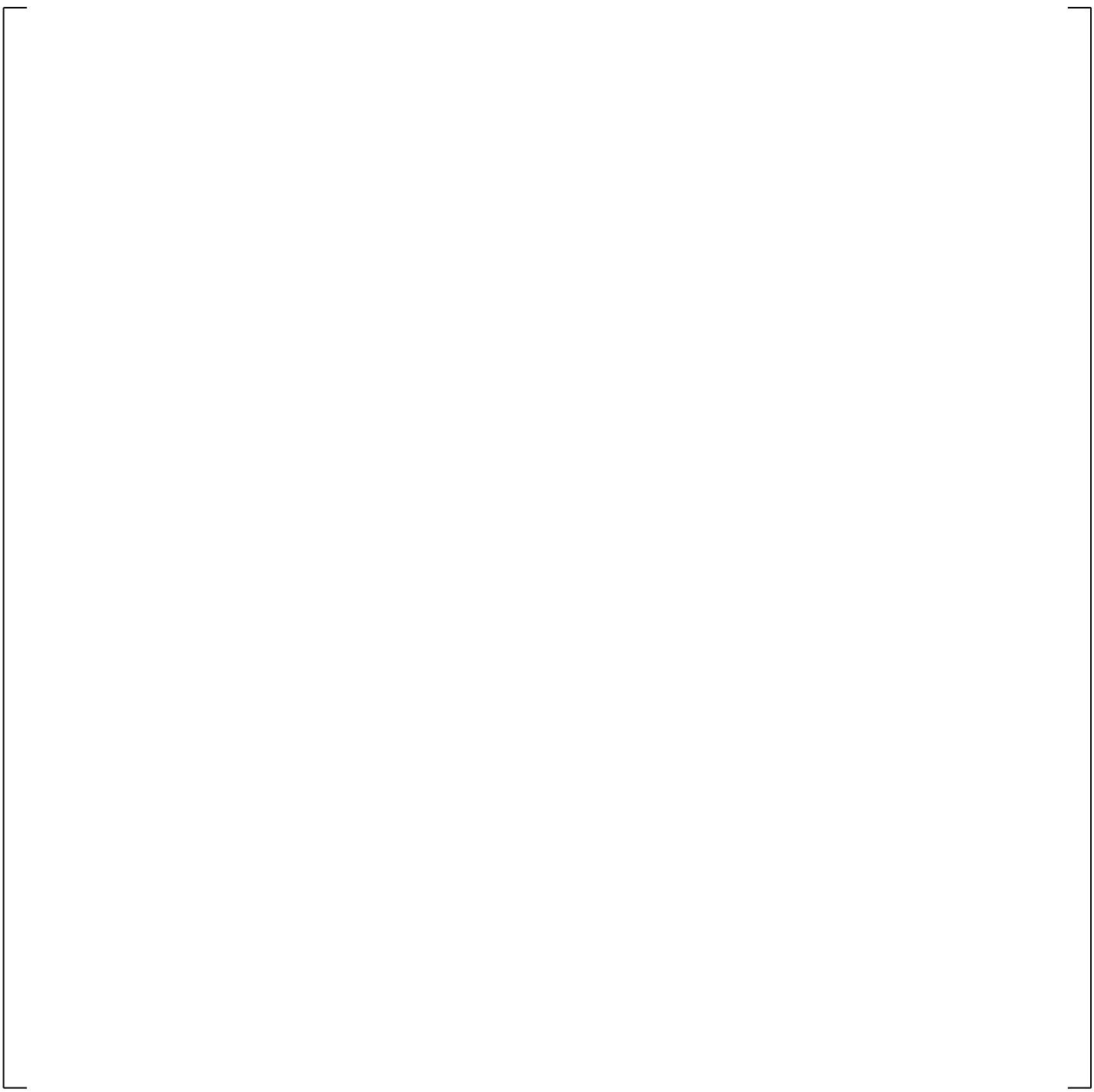

Figure 17-11b Predicted Heat Transfer Rate for Westinghouse COSI (TEE Junction Cell is Number 4)

a,c

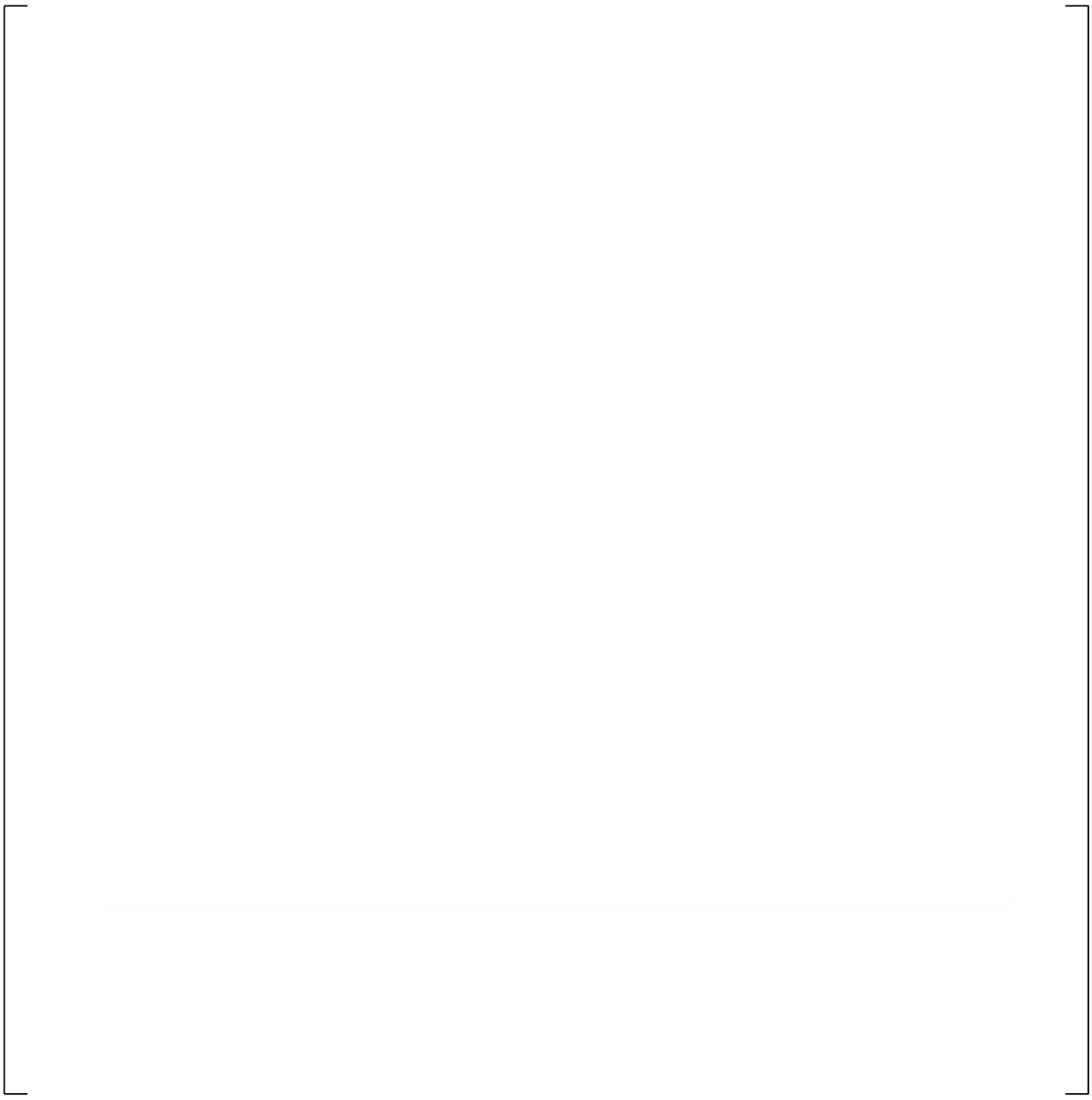

Figure 17-12 Comparison between Measured Framatome COSI Condensation Heat Transfer Rate and WCOBRA/TRAC-TF2 Predicted Condensation Heat Transfer Rate. Data in Circles are Tests with High SI Temperature (~80C)

a,c

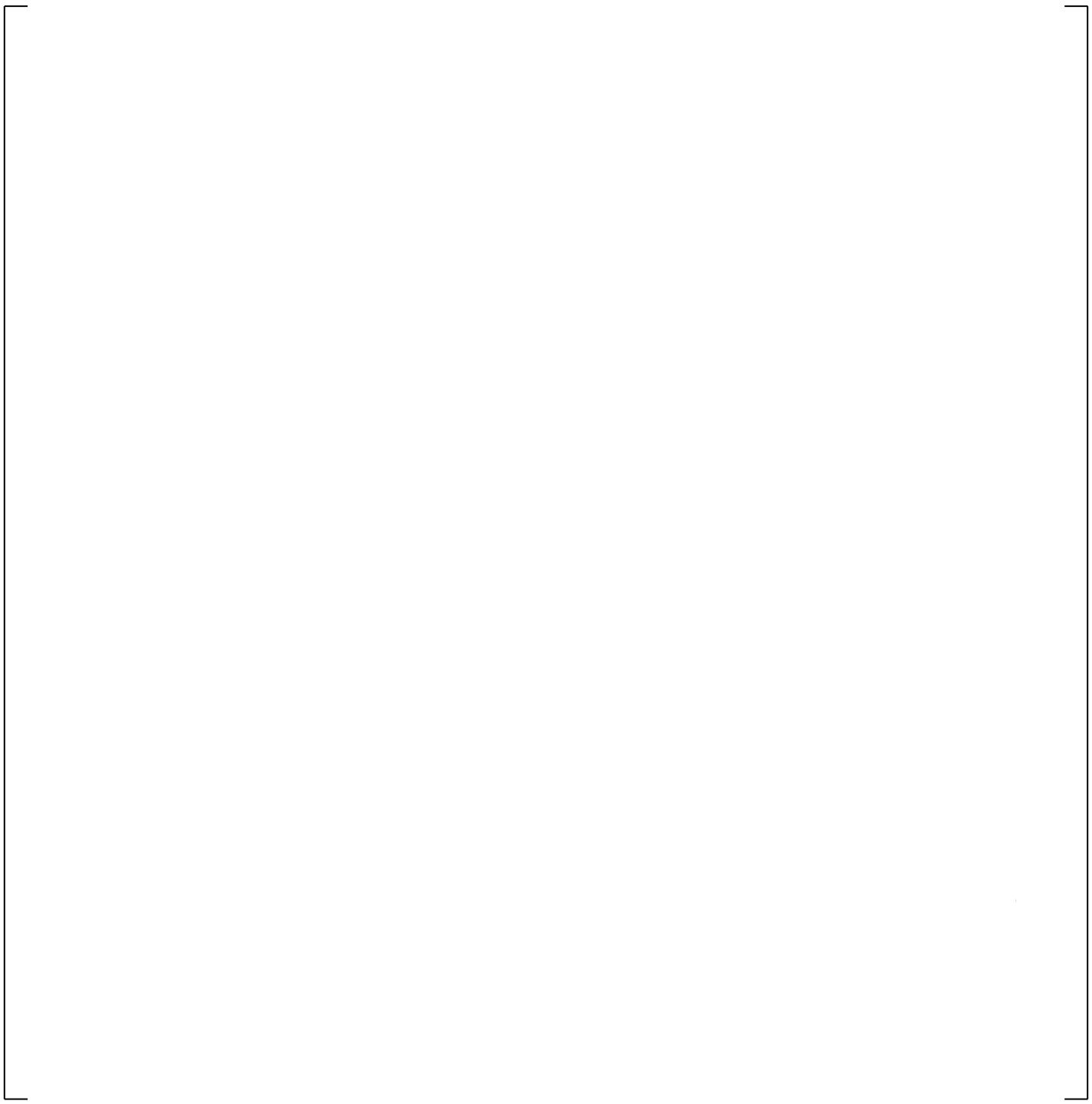

Figure 17-13 Comparison between Measured ROSA SB-CL-05 SI Condensation Heat Transfer Rate and WCOBRA/TRAC-TF2 Predicted Condensation Heat Transfer Rate

a,c

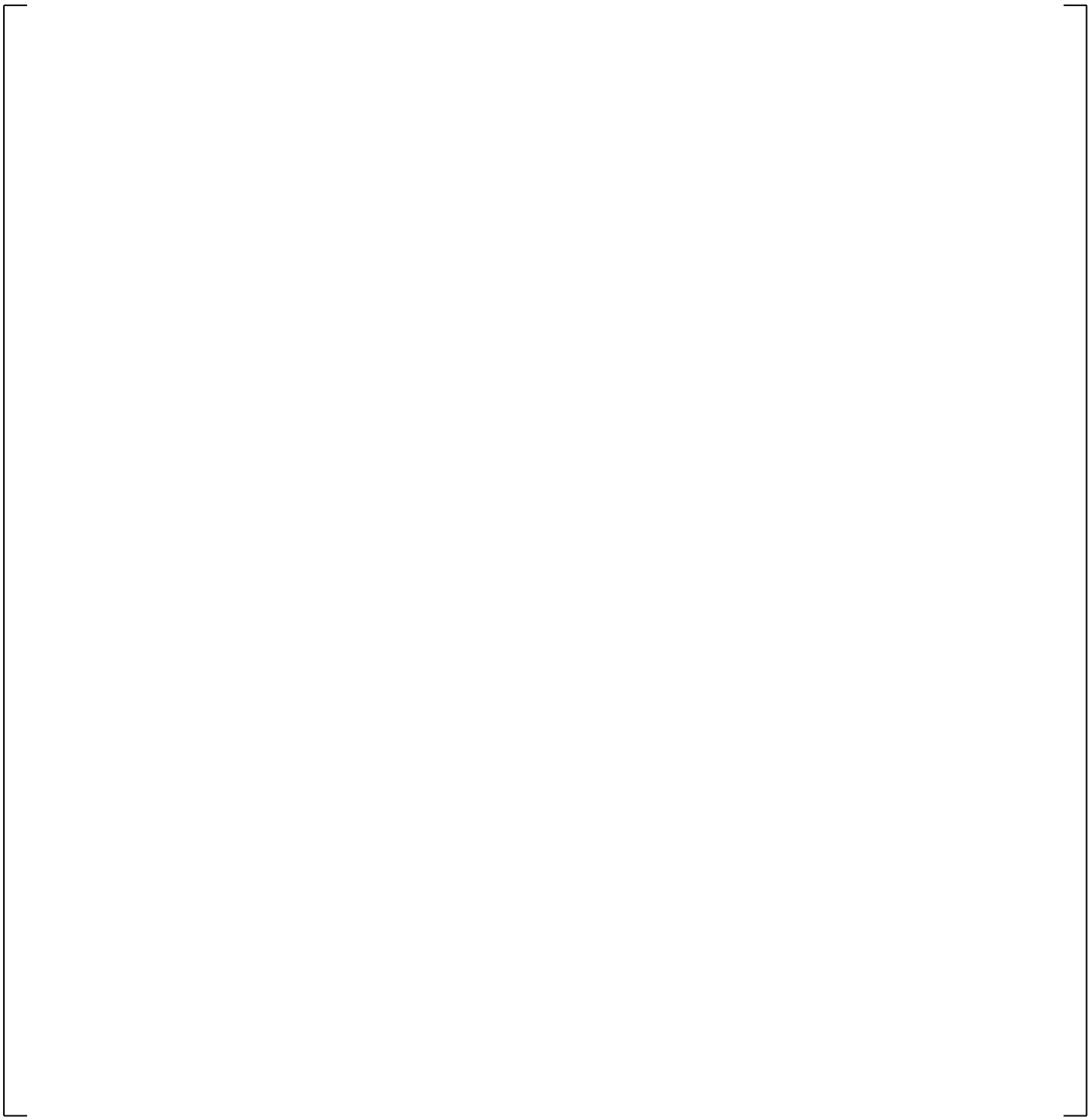

Figure 17-14 Steam Temperature Profile in Cold Leg in ROSA Test No. 1

a,c

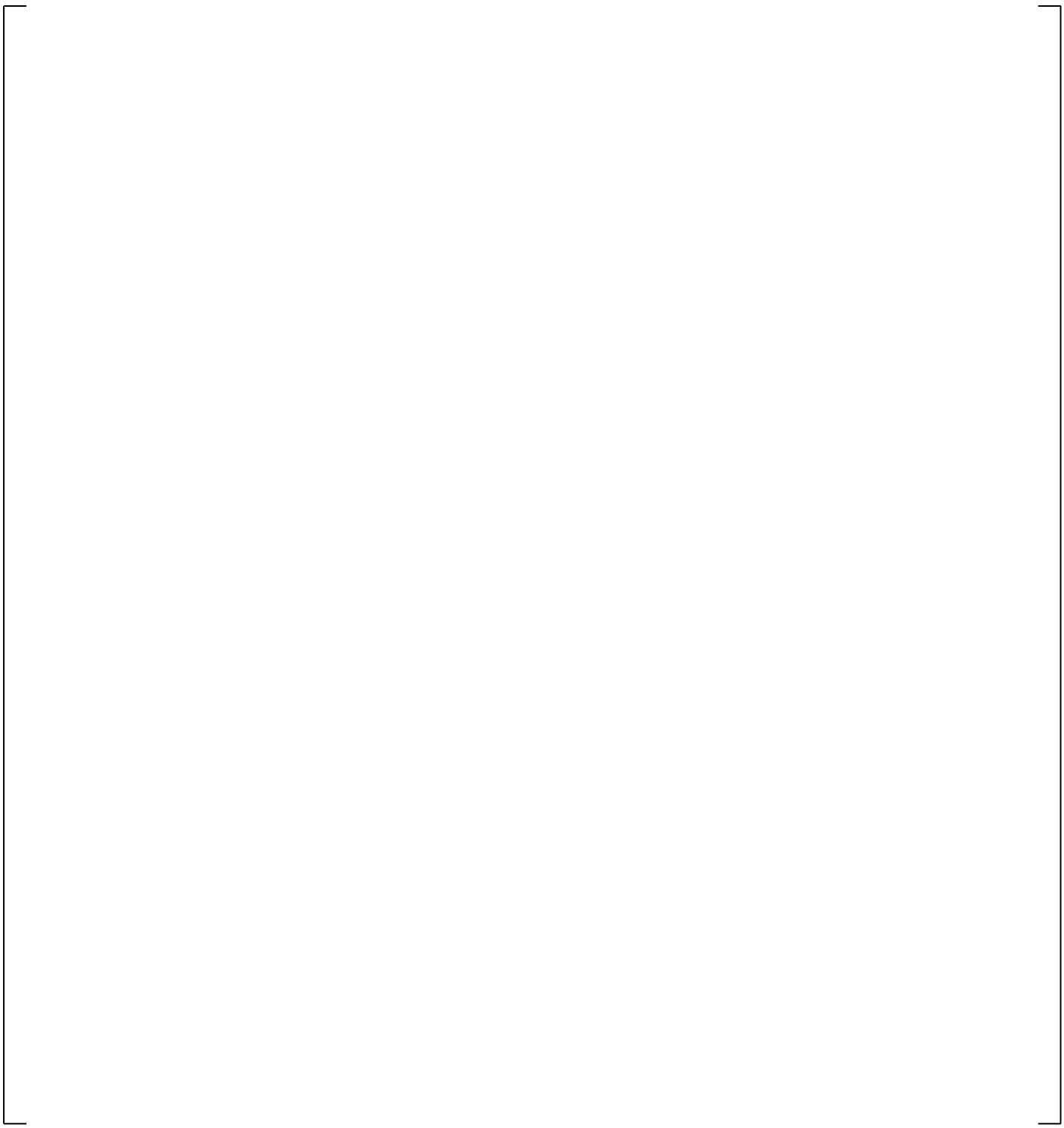

Figure 17-15 Steam Temperature Profile in Cold Leg in ROSA Test No. 2

a,c

Figure 17-16 Steam Temperature Profile in Cold Leg in ROSA Test No. 3

a,c

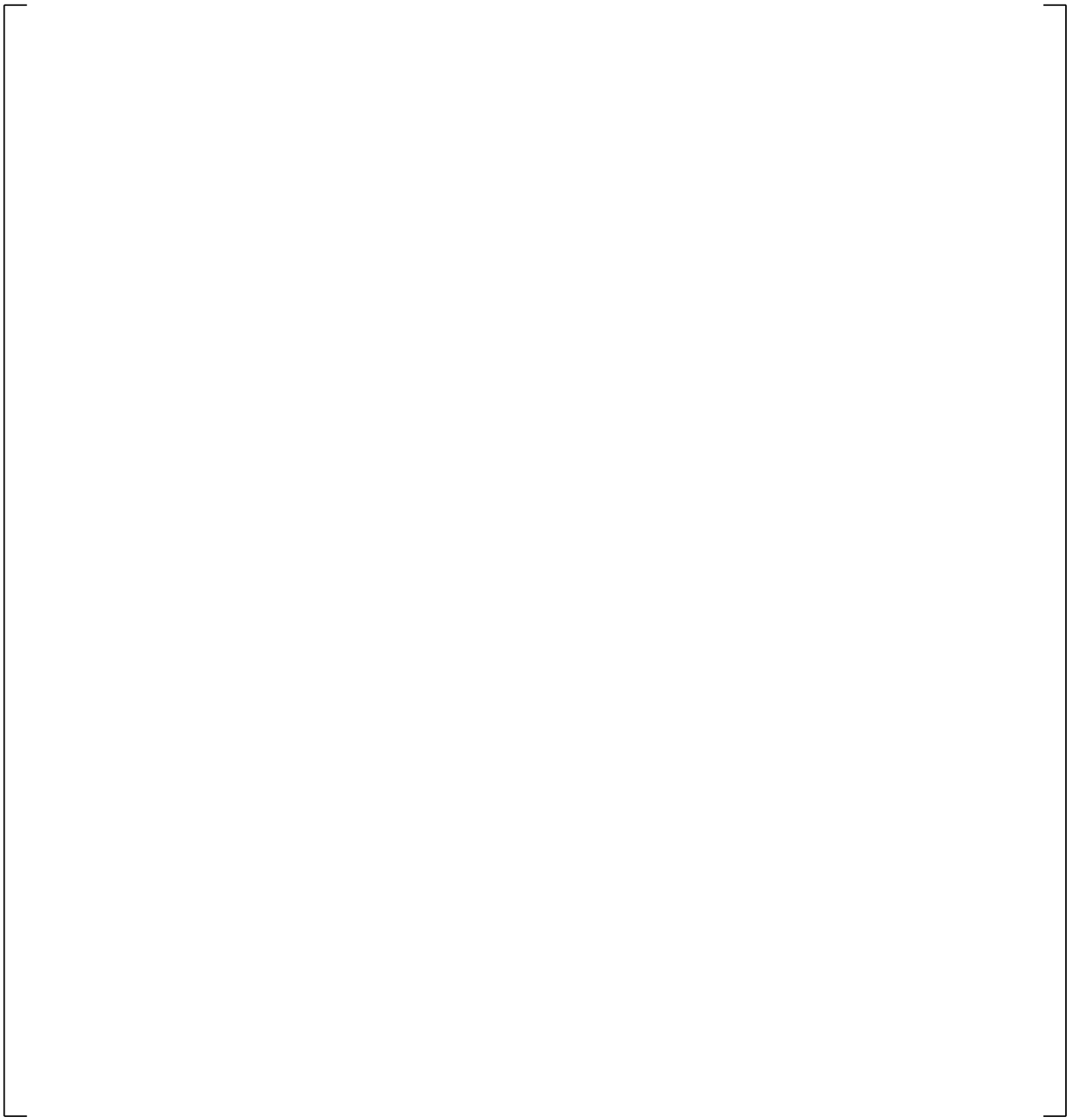

Figure 17-17 Steam Temperature Profile in Cold Leg in ROSA Test No. 4

a,c

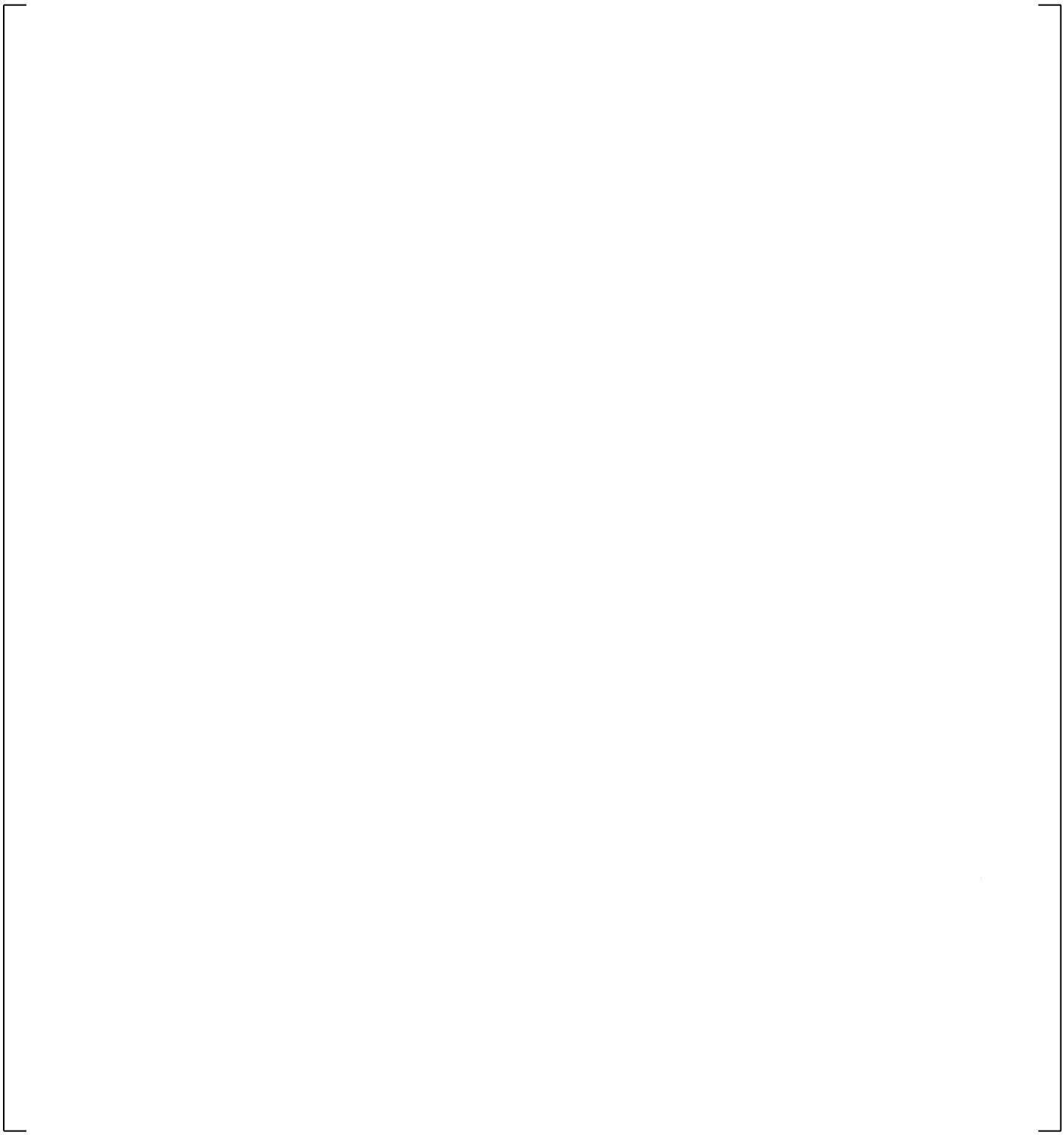

Figure 17-18 Comparison between Measured Condensation Heat Transfer Rate and WCOBRA/TRAC-TF2 Predicted Condensation Heat Transfer Rate for All Validation Cases

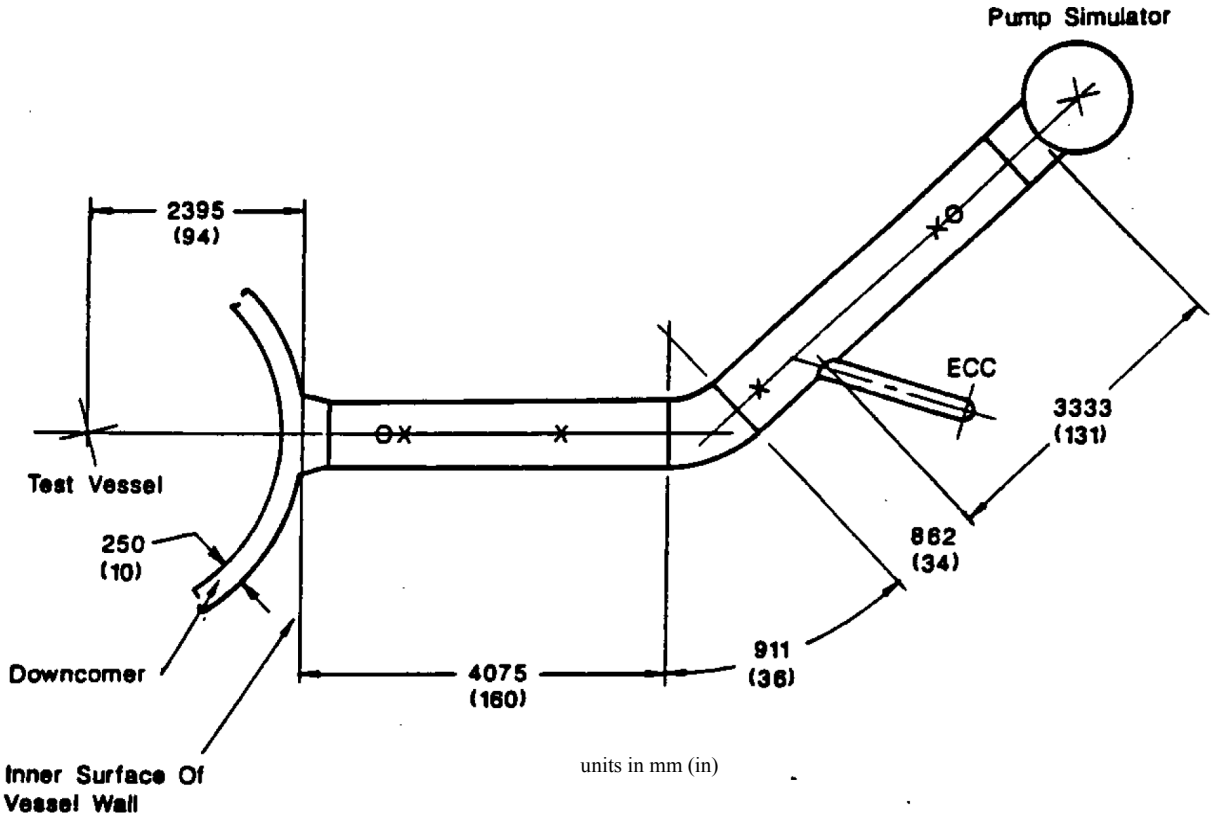

Figure 17-19 Cold Leg Piping Region of UPTF Test Facility

a,c

Figure 17-20 WCOBRA/TRAC-TF2 Single TEE Model for UPTF 8A

a,c

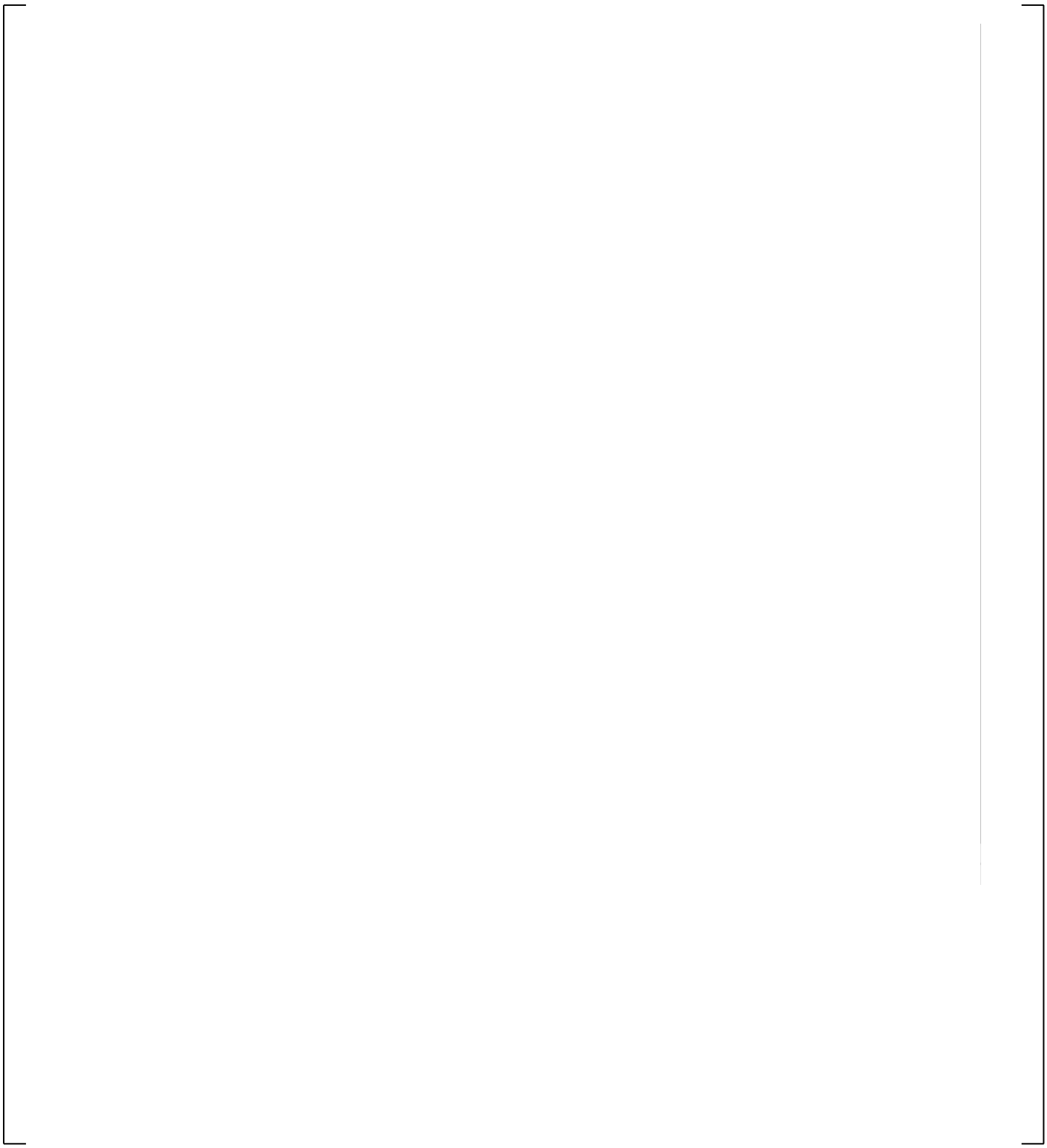

Figure 17-21 Comparison between Measured Fluid Temperature and WCOBRA/TRAC-TF2 Predicted Water Temperature at Pump Exit

a,c

Figure 17-22 Comparison between Measured Fluid Temperature and WCOBRA/TRAC-TF2 Predicted Water Temperature near Injection Point

a,c

Figure 17-23 Comparison between Measured Fluid Temperature and WCOBRA/TRAC-TF2 Predicted Water Temperature at Downstream of Injection Point

a,c

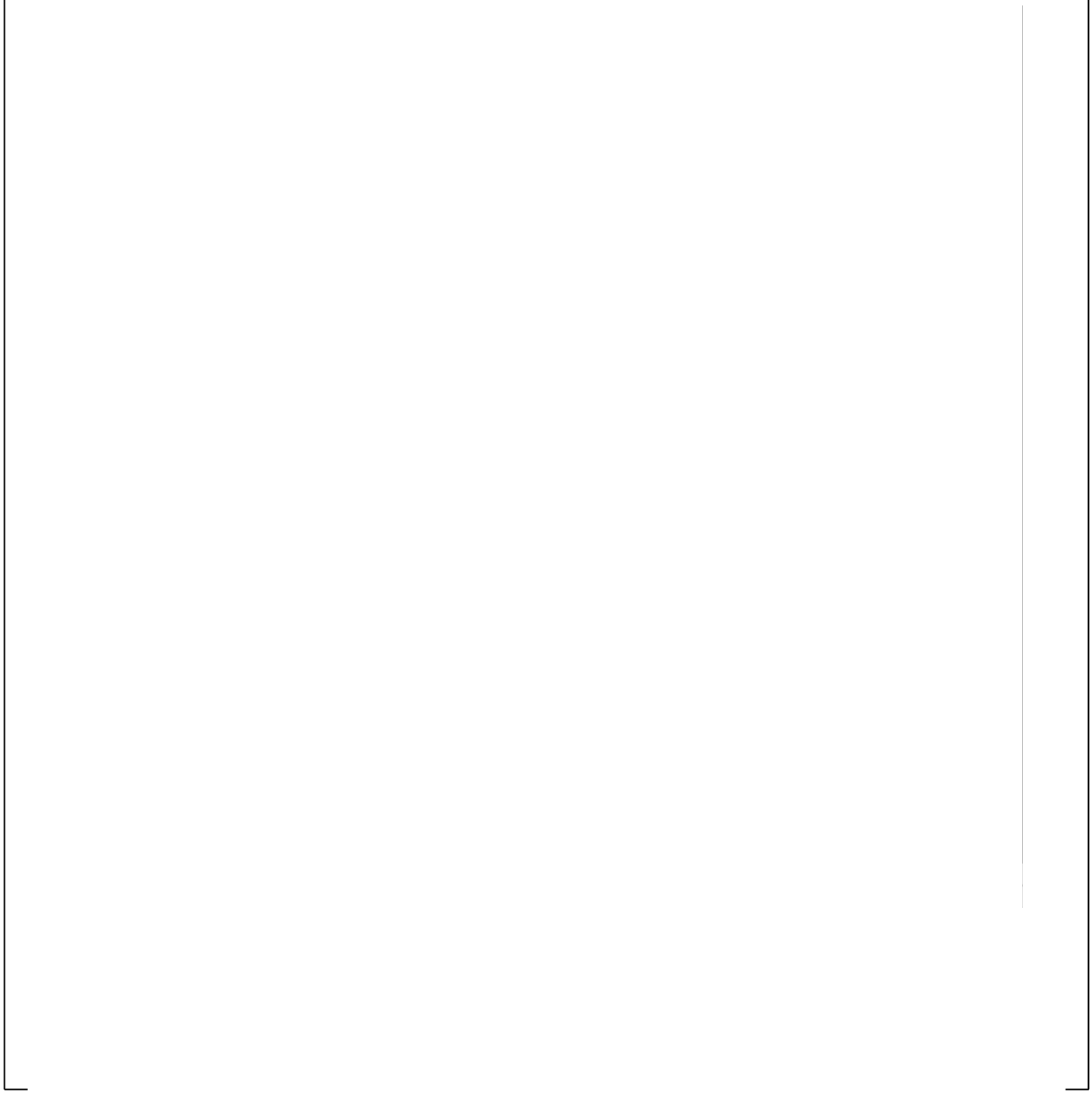

Figure 17-24 Comparison between Measured Fluid Temperature and WCOBRA/TRAC-TF2 Predicted Water Temperature at Outlet of Cold Leg

a,c

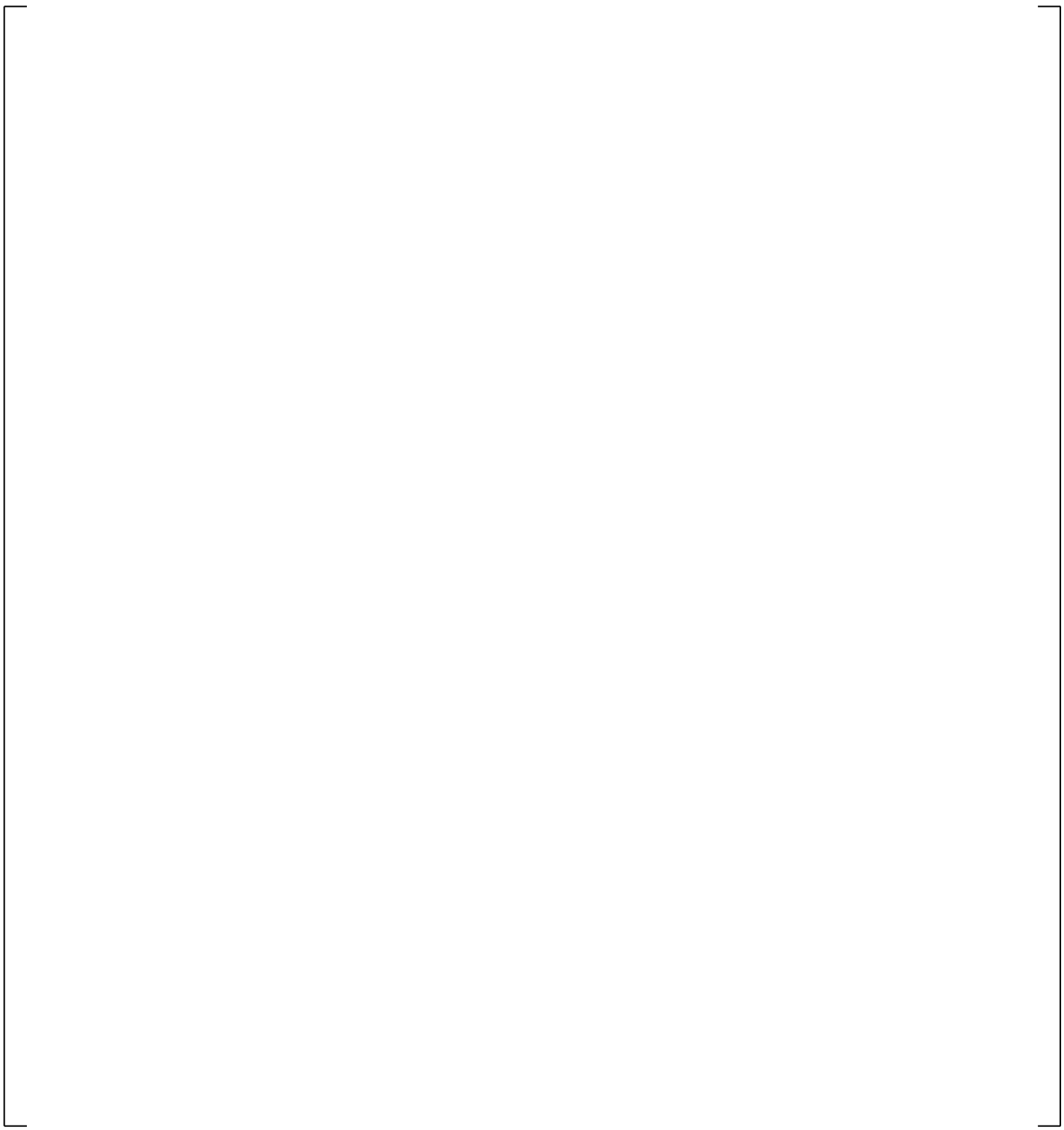

Figure 17-25 Comparison between the Predicted Water Temperatures at Injection Cell of Cold Leg in ECC Injection Angle Sensitivity Study

a,c

Figure 17-26 Comparison between the Predicted Water Temperatures at Downstream Cell of Cold Leg in ECC Injection Angle Sensitivity Study

a,c

Figure 17-27 Comparison between the Predicted Water Temperatures at Outlet of Cold Leg in ECC Injection Angle Sensitivity Study

a,c

Figure 17-28 Comparison between the Predicted Water Temperatures at Injection Cell of Cold Leg in Cold Leg Noding Sensitivity Study

a,c

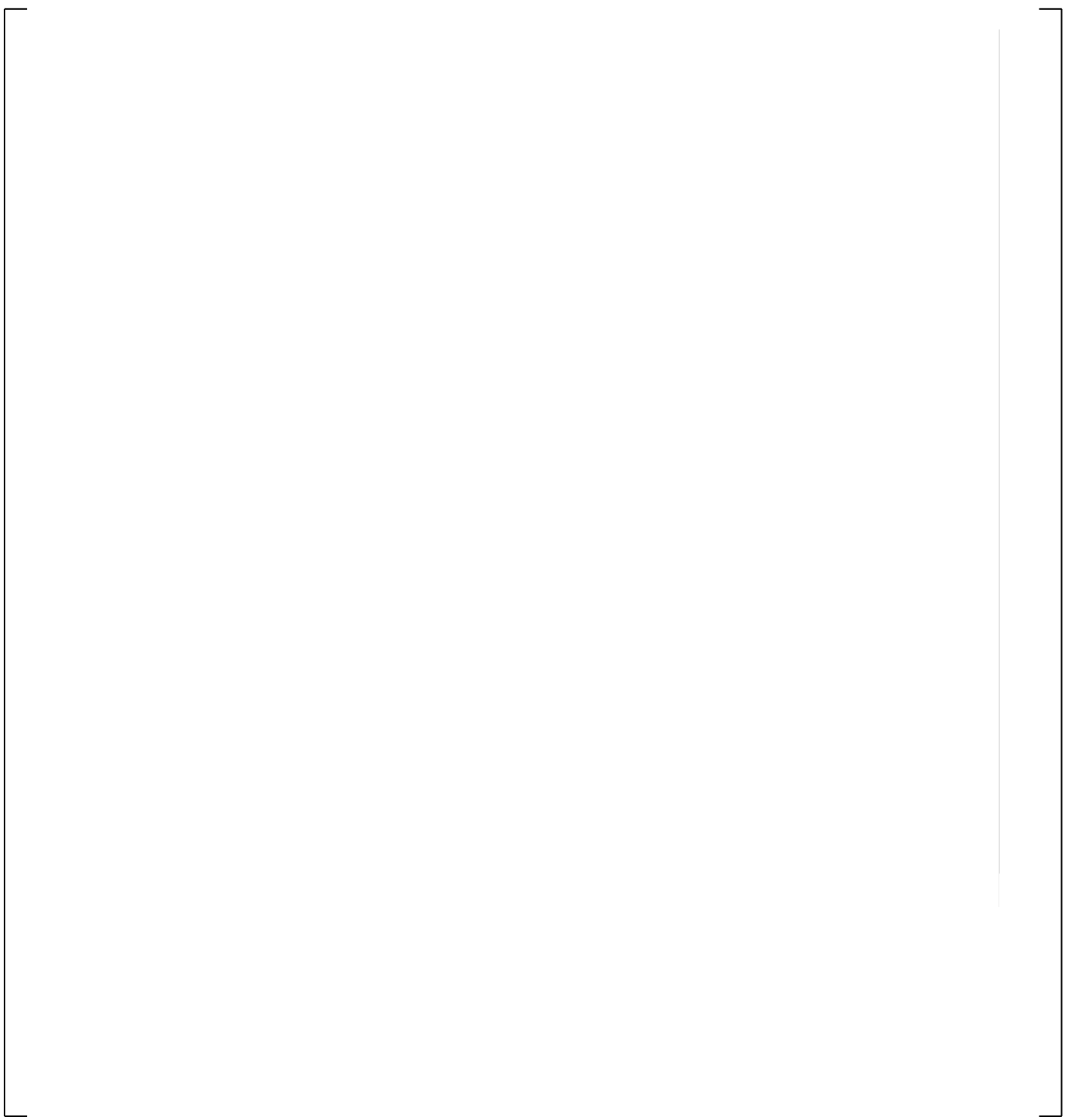

Figure 17-29 Comparison between the Predicted Water Temperatures at Downstream of Injection Cell in Cold Leg in Cold Leg Noding Sensitivity Study

a,c

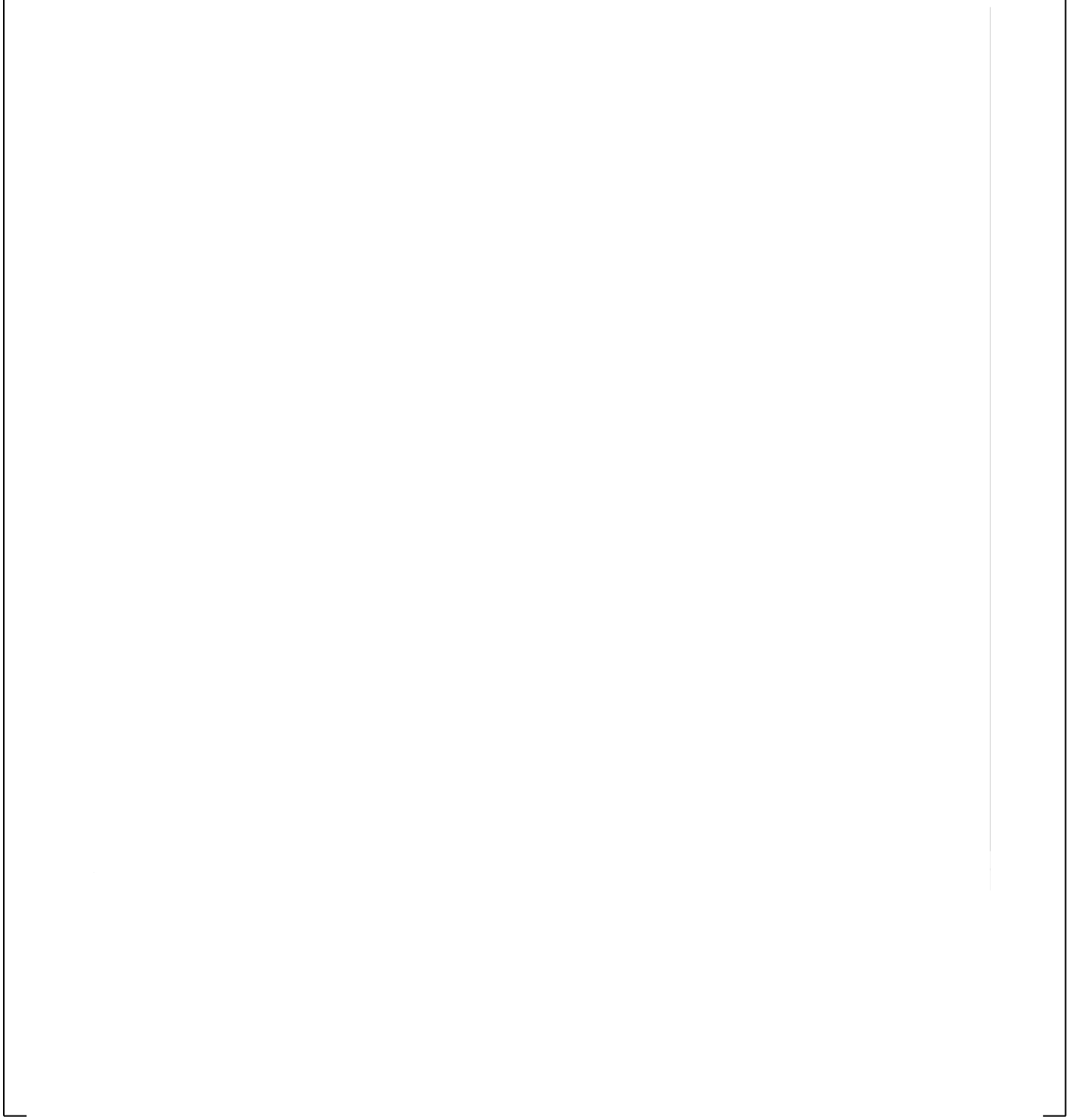

Figure 17-30 Comparison between the Predicted Water Temperatures at Outlet of Cold Leg in Cold Leg Noding Sensitivity Study

a,c

Figure 17-31 [

]a,c

a,c

Figure 17-32 [

][a,c]

a,c

Figure 17-33 [

]^{a,c}

a,c

Figure 17-34 [

]a,c

a,c

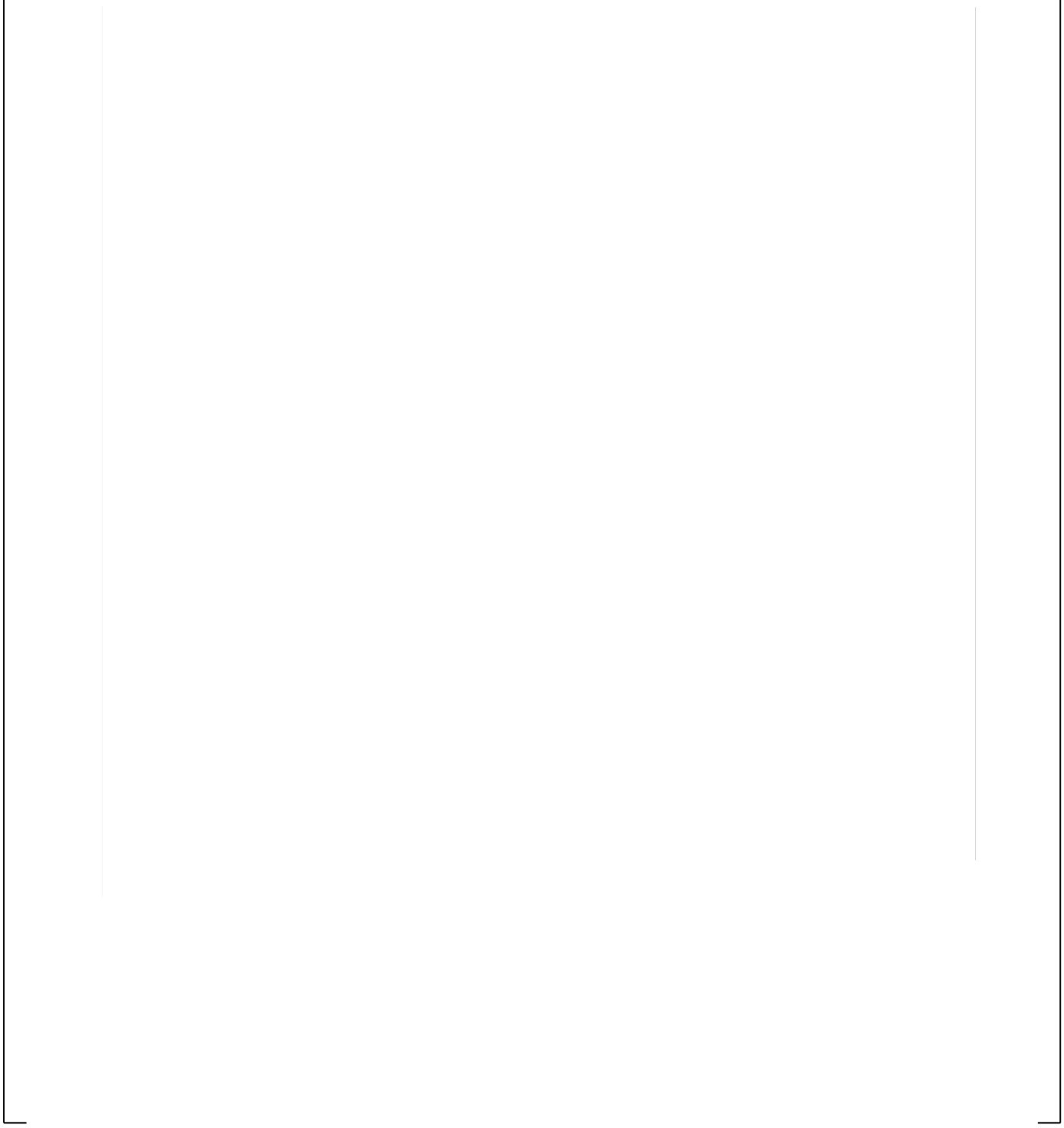

Figure 17-35 [

]a,c

a,c

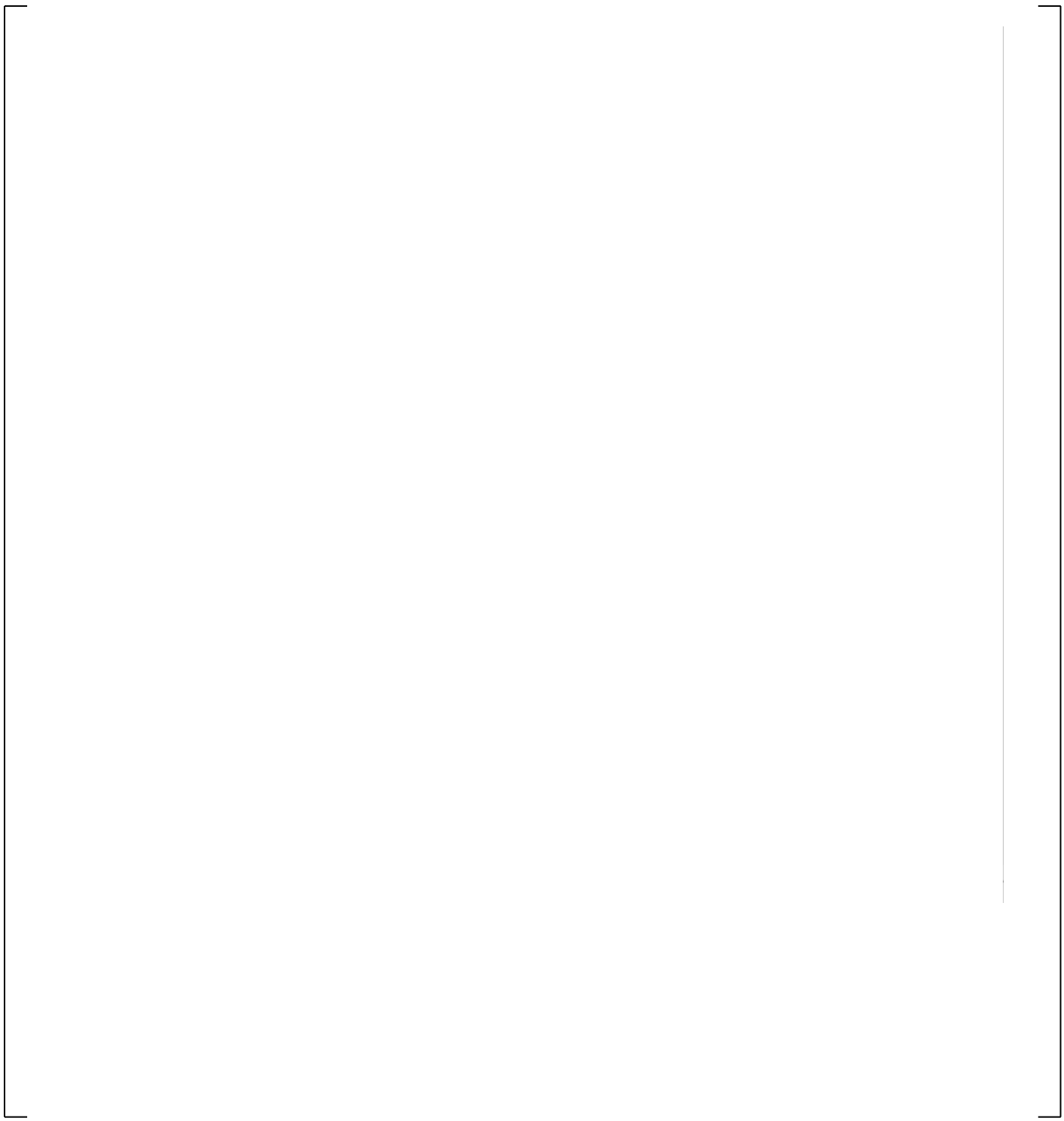

Figure 17-36 [

]a,c

a,c

Figure 17-37 [

]a,c

a,c

Figure 17-38 [

]a,c

18 LOOP SEAL CLEARANCE

18.1 INTRODUCTION

The FULL SPECTRUM LOCA (FSLOCA) methodology Phenomena Identification and Ranking Table (PIRT) in Section 2.3, Volume 1 of this document identifies the loop seal behavior as an important process affecting the evolution of a small break Loss-of-Coolant Accident (LOCA) transient. This component and its effect on the transient are discussed in more detail below. The following sections identify the important phenomena occurring in the loop seal and the available experiments to assess the performance of WCOBRA/TRAC-TF2 in predicting such phenomena.

During a small break LOCA, mass is slowly depleted from the system. Early in the transient, the pumps continue to run and the flow through the pump suction piping remains single-phase. After generation of a reactor trip signal, the reactor trips and subsequently the pumps trip either due to loss of offsite power or operator action. The system then enters a natural circulation phase. Pressures have fallen sufficiently to cause boiling in the fluid entering the hot leg, but the steam generator acts as a heat sink, and the fluid entering the pump suction pipe is still nearly single-phase. Any bubbles that enter the pump suction pipe are carried through by natural circulation as illustrated in Figure 18.1-1a.

When the primary pressure approaches the secondary pressure, voids remain in the fluid as it enters the steam generator. As the loop mass flow rate decreases further, liquid begins to drain down both the uphill and downhill sides of the steam generator tubes. Natural circulation is terminated, and mixture levels form on both the uphill and downhill sides of the tubes. The levels then move downward as liquid drains and vapor rises as shown in Figure 18.1-1b.

Because there is no escape path for the steam generated in the core, except for some small bypass paths such as the upper head, the pressure in the region above the core (the upper plenum, the hot legs, and the steam generator tubes) rises and depresses the level in both the core and the downhill sides of the pump suction pipe. Eventually, the downhill side level reaches the top of the horizontal portion of the pump suction pipe, as shown in Figure 18.1-1c, and vapor begins to escape into the pump and flow toward the break.

At the onset of clearing, the fluid pressure in the downhill leg of the loop seal is higher than on the uphill side, due to the column of liquid from the horizontal leg to the pump outlet as shown in Figure 18.1-1c. Because the volume of steam at this pressure is significant in the steam generator tubes, hot legs, vessel upper plenum and upper head, the steam flowing through the pump suction becomes significantly greater than the core steam generation rate for a period of time (Kukita, 1990). This causes the loop seal to clear completely, not resealing until much later in the transient.

As the steam flows through the pump suction, the flow regime is first a slug regime with significant amounts of liquid being entrained from the pump suction pipe as seen in Figure 18.1-2 and described by (Tuomisto and Kajanto, 1988). Eventually, a residual level of liquid will remain in the pump suction pipe.

As the pressure in the system is relieved, the steam flow decreases to the core steam generation level. If this steam flow is low enough, liquid in the cold leg may begin to drain back through the pump and begin to fill the pump suction again as shown in Figure 18.1-1d. Another potential source of loop seal refilling is the draining of condensed steam from the downhill side of the steam generators. Because there is no pressure driving force, the steam flow through the loop seal is quickly terminated when the liquid level reaches the top of the horizontal section and plugs the loop seal. The system pressure increases, and core and loop seal levels change once again as the loop seal plugging and clearing cycle is repeated (Kukita, 1990).

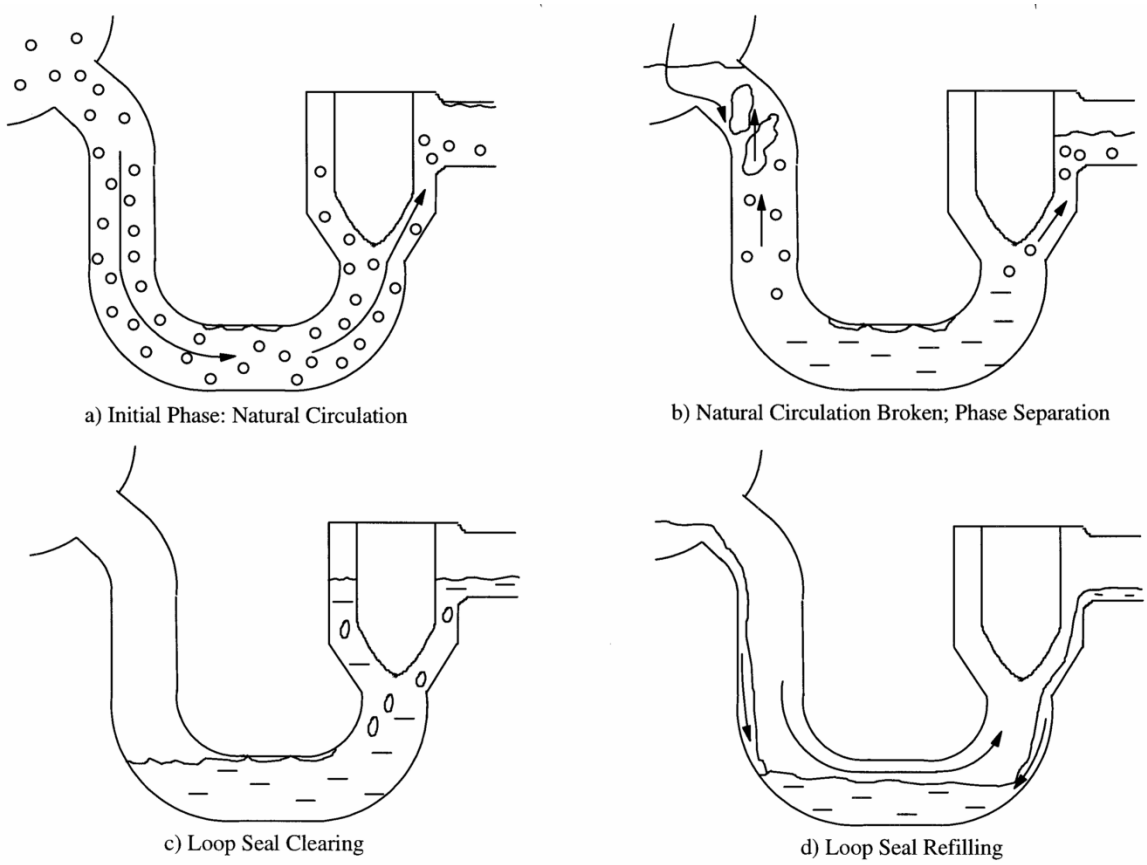

Figure 18.1-1 Loop Seal Clearing and Refilling

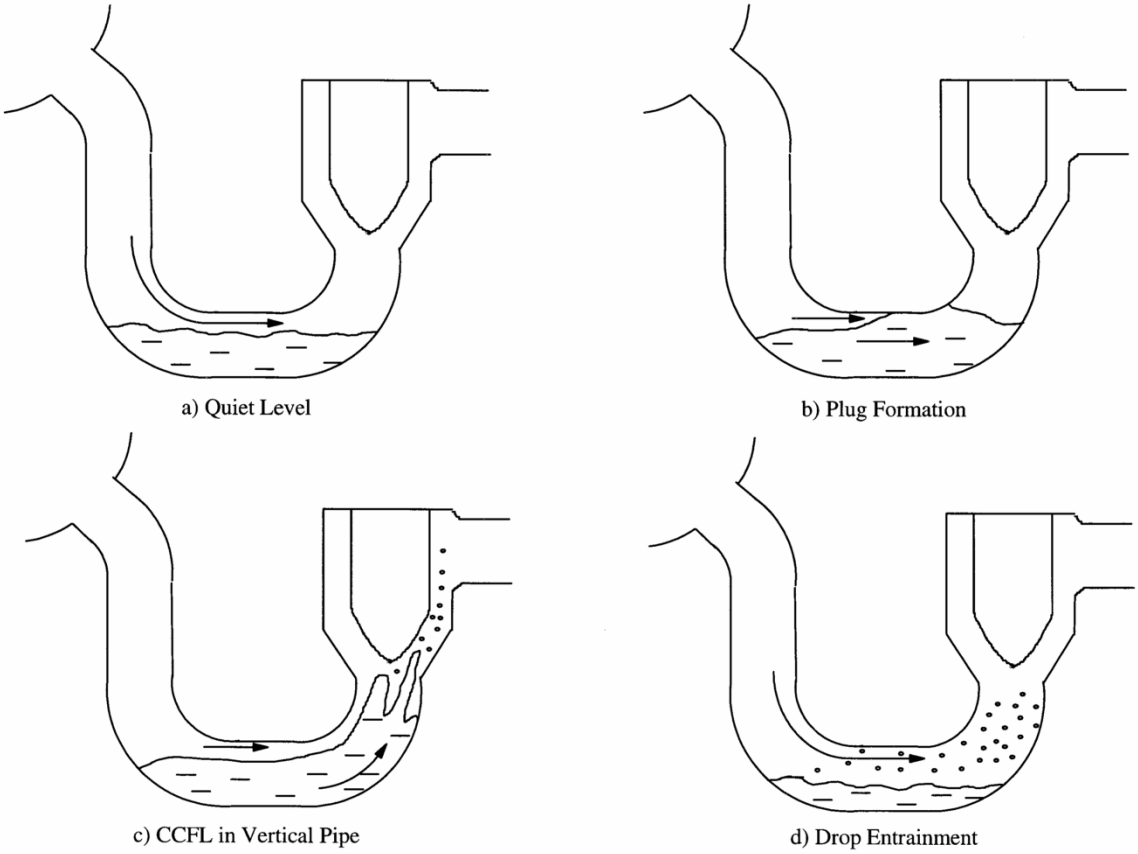

Figure 18.1-2 Loop Seal Clearing Process

18.2 IMPORTANT PHYSICAL PROCESSES AND SCALING LAWS

The onset of loop seal clearing is a function of the pressure difference across the loop seal, which depresses the level to the bottom of the loop seal and depends on the following factors:

- Core steam generation rate
- Bypass steam flow rate through vent paths
- Rate of accumulation of liquid in the pump suction pipe

These factors are the result of processes that occur elsewhere in the system and are accounted for in other components (for example, the core steam generation rate is accounted for by sampling the core power which directly influences the steam generation).

The loop seal clearing and refilling process is a function of the interfacial drag between the vapor and the liquid. The initial steam flow surge and the interfacial drag determine the rate at which liquid is expelled. The steam flow rate, in turn, depends on the loop pressure drop, of which the loop seal is a part. This determines how quickly the venting process takes place and the final liquid level in the horizontal section. The residual liquid and degree to which liquid is held up by steam flowing out of the pump suction pipe determine the rate at which the pump suction refills and replugs. Based on these considerations, the following factors are considered to be important in the assessment of predictions of loop seal behavior:

- Overall loop seal pressure drop as a function of steam flow
- Liquid distribution in the loop seal as a function of steam flow

Various experiments have shown that the basic physical process is controlled by two factors: the extent to which a stratified flow regime can be maintained in the horizontal leg of the loop seal, and the degree to which liquid pushed into the downstream vertical leg can be entrained out of the loop seal. Figure 18.1-2 illustrates these processes.

First, the Rig-of-Safety Assessment (ROSA) 5% and 10% break integral tests are examined for loop seal behavior. Then, scaled loop seal experiments are discussed in the following section to gain a better understanding of the loop seal behavior. These tests are used to highlight important physical and scaling features. The time period of interest is the steady-state, post clearing portion. Next, the scaled tests are compared with larger scale tests to confirm the indicated scaling trends. Finally, the larger scale tests are simulated using WCOBRA/TRAC-TF2 to assess the models and correlations in the code.

18.2.1 ROSA

Loop seal clearing behavior can be observed from the ROSA 5% and 10% break integral tests (Kumamaru, et al., 1989 and Koizumi and Tasaka, 1988; see Section 21 for test facility description). Figures 18.2.1-1a and 18.2.1-1b show the loop seal differential pressure behavior of the broken loop for the 5% and 10% breaks, respectively. As observed in the figures, **[**

][a,c].

a,b,c

Figure 18.2.1-1a Measured Pressure Drop in Broken Loop of ROSA 5% Break (Kumamaru, et al., 1989)

a,b,c

Figure 18.2.1-1b Measured Pressure Drop in Broken Loop of ROSA 10% Break (Koizumi and Tasaka, 1988)

18.2.2 PWS 2.3 Loop Seal Tests

Scaled U-tube experiments designed to examine the hydraulic behavior of a U-tube under conditions similar to those encountered during a small break LOCA were performed as part of the ECTHOR (an acronym from French "Ecoulements dans des Tuyauteries Horizontales en Eau-Air" which stands for Air-Water Flow in Horizontal Pipes) Program (Boileau and Bourteele, 1985). The vapor flow required to clear the U-tube was a specific focus of the tests.

18.2.2.1 Test Facility Description

The tests were run in a plexiglass facility with air and water at atmospheric pressure. The facility, illustrated schematically in Figure 18.2.2-1, consists of a blower, a run of horizontal piping from the blower, a U-tube, and a catch tank.

The pipe diameter chosen for the facility was **[ ]**[a,c]. This corresponds to approximately **[ ]**[a,c] scale compared with a pressurized water reactor (PWR), which has a pipe diameter of 2.58 feet. The air and water flow rates were scaled so that approximate similitude was maintained for the Froude number, shown to define the flow regime transition from stratified to intermittent and annular flow by (Taitel and Dukler, 1976). Figure 18.2.2-2 shows the predicted flow regime transition using the Taitel and Dukler flow regime map for atmospheric pressure, **[ ]**[a,c] scale, compared with the transition for steam at 1000 psia, full-scale geometry. This figure indicates that the transition from stratified to annular flow occurs at a higher vapor flux in the air-water tests. While better similitude could have been obtained with a smaller pipe, the chosen diameter also assures that the vertical pipes of the U-tube are sufficiently large so that any countercurrent flow limits (CCFL) that occur will not be affected by the pipe diameter. According to (Richter, 1981), the critical vapor flux for CCFL in pipes larger than approximately 2 inches in diameter depends only on pressure, not on pipe diameter.

Pressure drop across the U-tube was measured. In the horizontal and in the downstream vertical sections, several independent measurements of void fraction were made using pressure drops, optical probes, and gamma densitometers.

18.2.2.2 Test Procedures

Several test series were performed, as described below:

- Limit Line Tests

  These tests were designed to obtain the liquid level in the horizontal portion of the U-tube, which produces significant liquid entrainment for a given air flow rate. This is equivalent in some ways to the CCFL limit and is termed the U-tube limit line. The tests were performed as follows:
  [

][a,c]

[

]a,c

- Within Limit Line Tests

  These tests were performed at air and water flows inside the limit lines established in the first phase with little or no entrainment. The tests primarily examined the interaction, if any, between the gas and the liquid at non-limiting flows (i.e., no entrainment). The tests were run as follows:
  [

  ]a,c

- Optical Probe Tests

  These tests were performed similar to the Within Limit Line Tests. Optical probes were used to measure the liquid level. These tests confirmed the differential pressure measurements later used to derive vapor fraction.

- Complementary Tests

  In some of the tests with high initial liquid level, oscillatory flow was observed. These oscillations consisted of movements of water back and forth between the upstream and downstream elbows. Slugs of liquid momentarily filled the pipe, increasing the pressure drop across the U-tube. These slugs were then ejected from the U-tube. The tests were similar to the limit line tests except [
  ]a,c.

- Gamma Densitometer Tests

  These tests used a gamma densitometer to measure the mixture density inside the horizontal portion of the U-tube. The tests confirmed void fraction measurements based on differential pressure.

18.2.2.3 Analysis of PWS 2.3 Test Results

Figure 18.2.2-3 plots the normalized residual liquid level in the loop seal (H/D) as a function of the gas volumetric flux (j_g). The loop seal was completely cleared when gas velocities exceeded about **[ ]**[a,c]. At low gas flows **[**

][a,c]

The residual liquid level is an indication of the overall liquid mass contained in the loop seal as a function of gas flow, but does not represent the liquid distribution within the U-tube during the tests.
Figure 18.2.2-4 shows the average void fraction at the midpoint of the horizontal leg and in the downstream vertical leg during the test. At low gas flow rates, **[**

][a,c]

Figure 18.2.2-6 shows the measured pressure difference between the upstream and downstream exits of the U-tube. As liquid collects in the downstream vertical leg for the low gas flows, the pressure difference increases.

The basic processes occurring during these tests can be explained in terms of several hydrodynamic limits applied to both the horizontal and vertical legs. Figure 18.2.2-7 shows the horizontal leg average void fraction as a function of j_g^*, defined as:

$$j_g^* = \frac{j_g}{\left[\frac{(\rho_\ell - \rho_g) g D}{\rho_g}\right]^{0.5}} \tag{18-1}$$

where,

D is the pipe diameter, j_g is gas superficial velocity, g is the acceleration due to gravity, and ρ_ℓ and ρ_g are the liquid and gas densities, respectively.

Figure 18.2.2-8 shows the various flow regimes observed for the tests performed under the limit lines and that the liquid level in the horizontal leg was **[**

][a,c].

The loop seal behavior can be explained in terms of three regimes, bounded by the limit lines shown in Figure 18.2.2-7. The three regimes are described in the following paragraphs.

[

]a,c

[

]a,c

[

]a,c

18.2.2.4 Effect of Scale

An important question which must be answered is what distortions the scaled geometry and low pressure used in these tests have introduced relative to the PWR. Having explained the data in terms of the limit lines above, we can examine the effect of scale by seeing how these limit lines change with scale (Figure 18.2.2-10). [

]a,c

[

]a,c

a,c

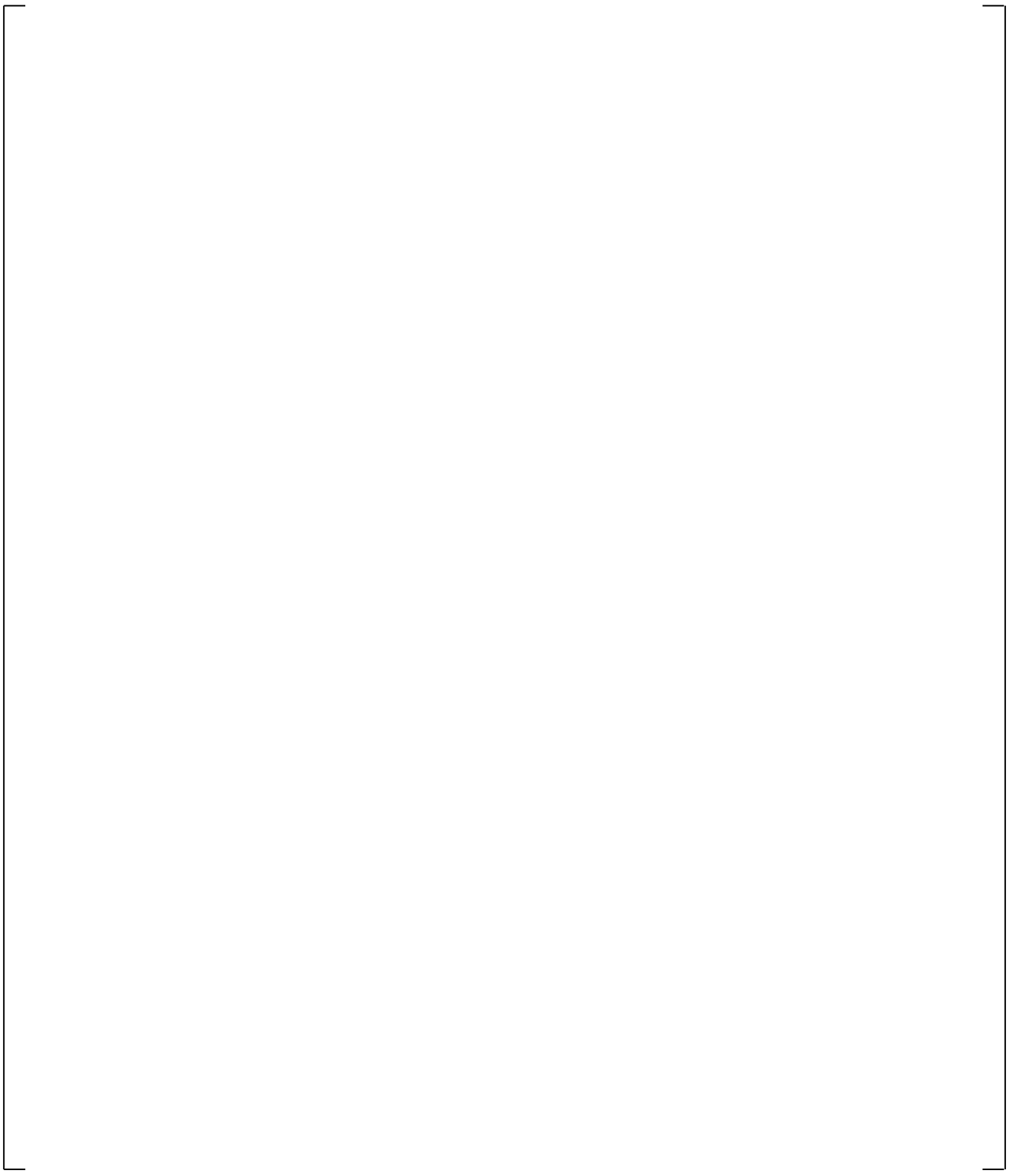

Figure 18.2.2-1 PWS 2.3 U-Tube Test Facility

a,c

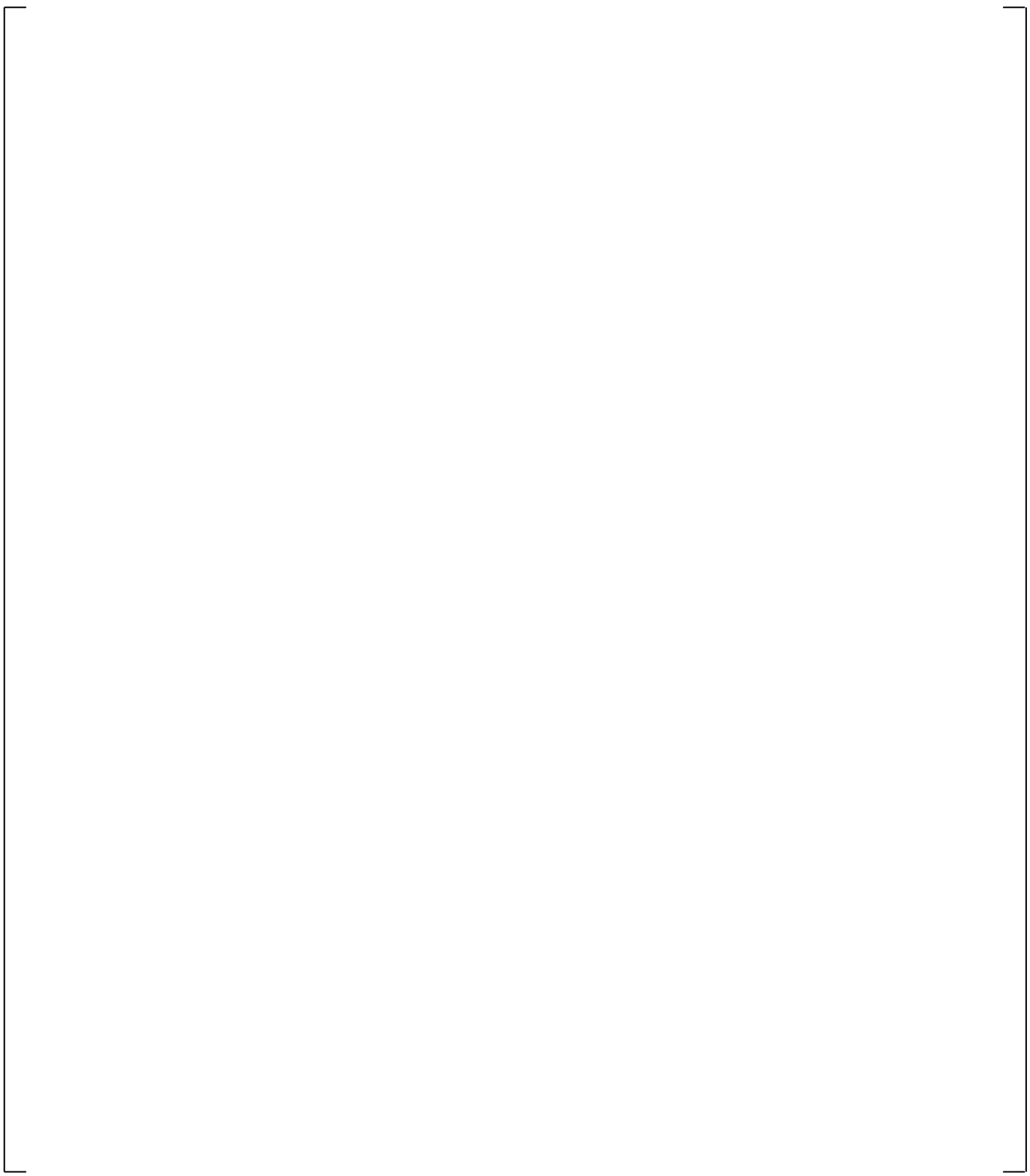

Figure 18.2.2-2 Taitel-Dukler Flow Regime Map, Comparing 1/3-Scale Pipe at 14.7 psia and Full-Scale Pipe at 1000 psia

a,b,c

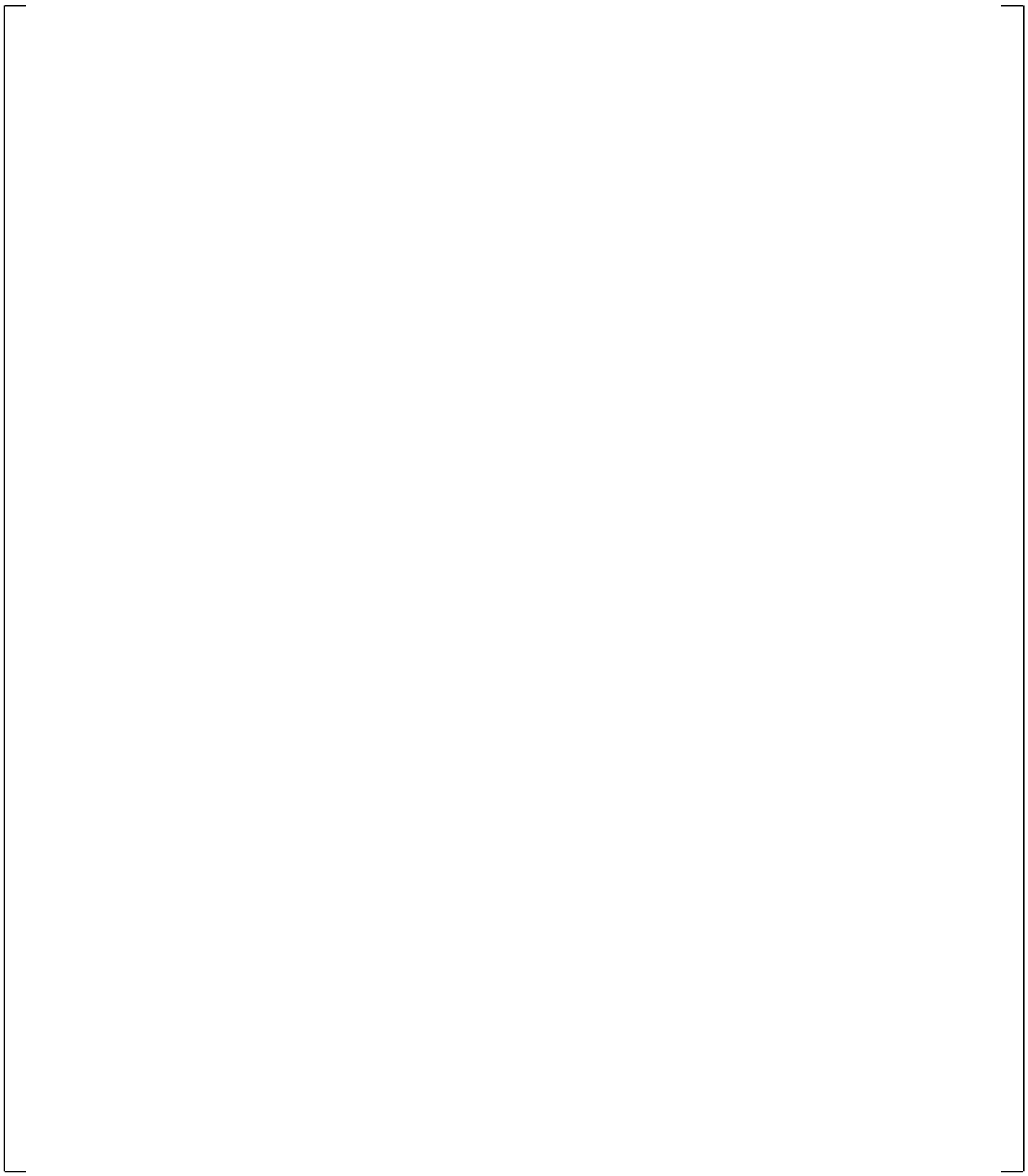

Figure 18.2.2-3 PWS 2.3 U-Tube Residual Liquid Level Remaining After Test as a Function of Test Gas Flow Rate

a,b,c

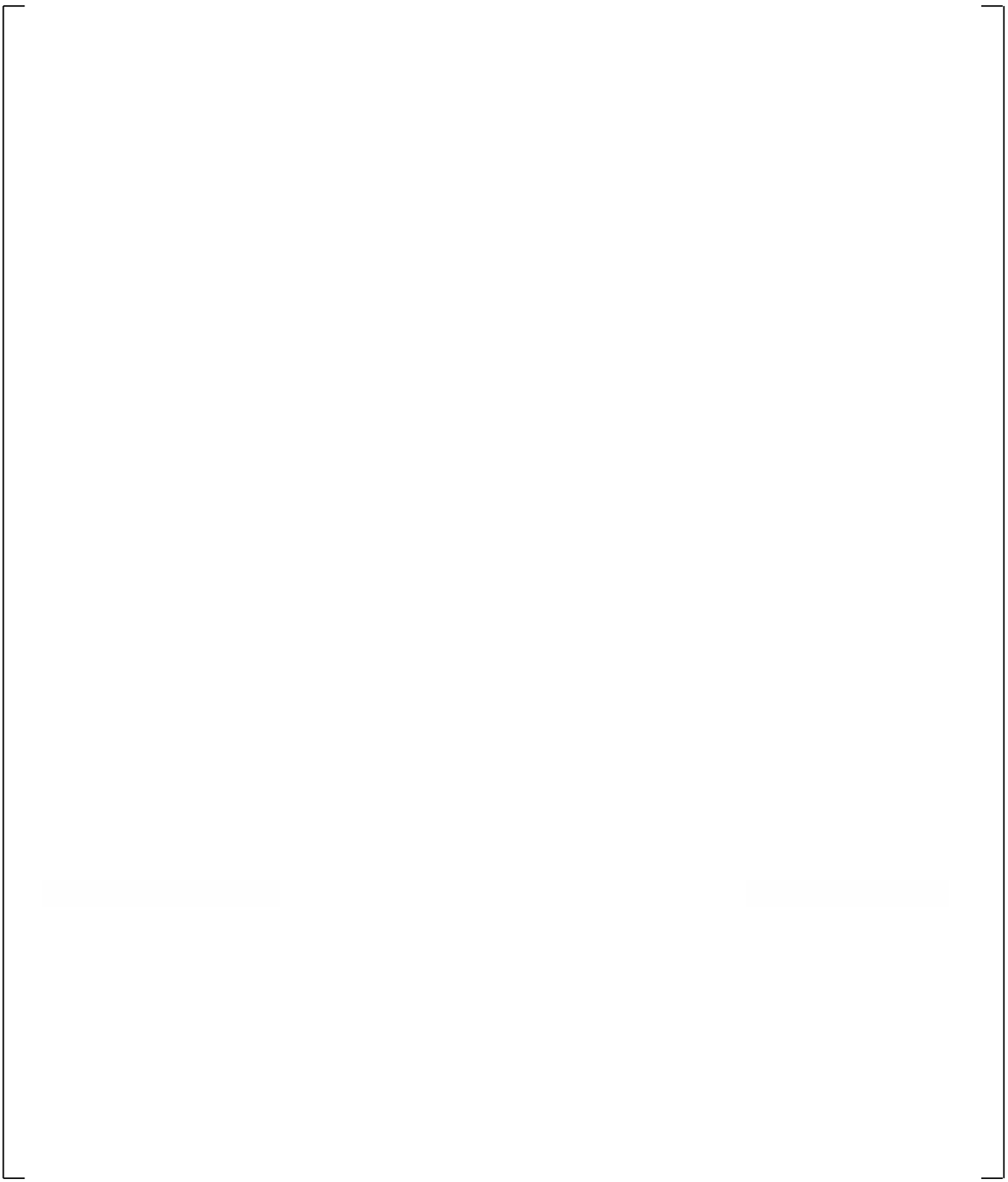

Figure 18.2.2-4 PWS 2.3 U-Tube Horizontal and Vertical Leg Average Void Fractions During Test

a,b,c

Figure 18.2.2-5 PWS 2.3 U-Tube Horizontal Average Void Fraction During Test Compared with Average Void Fraction after Test

a,b,c

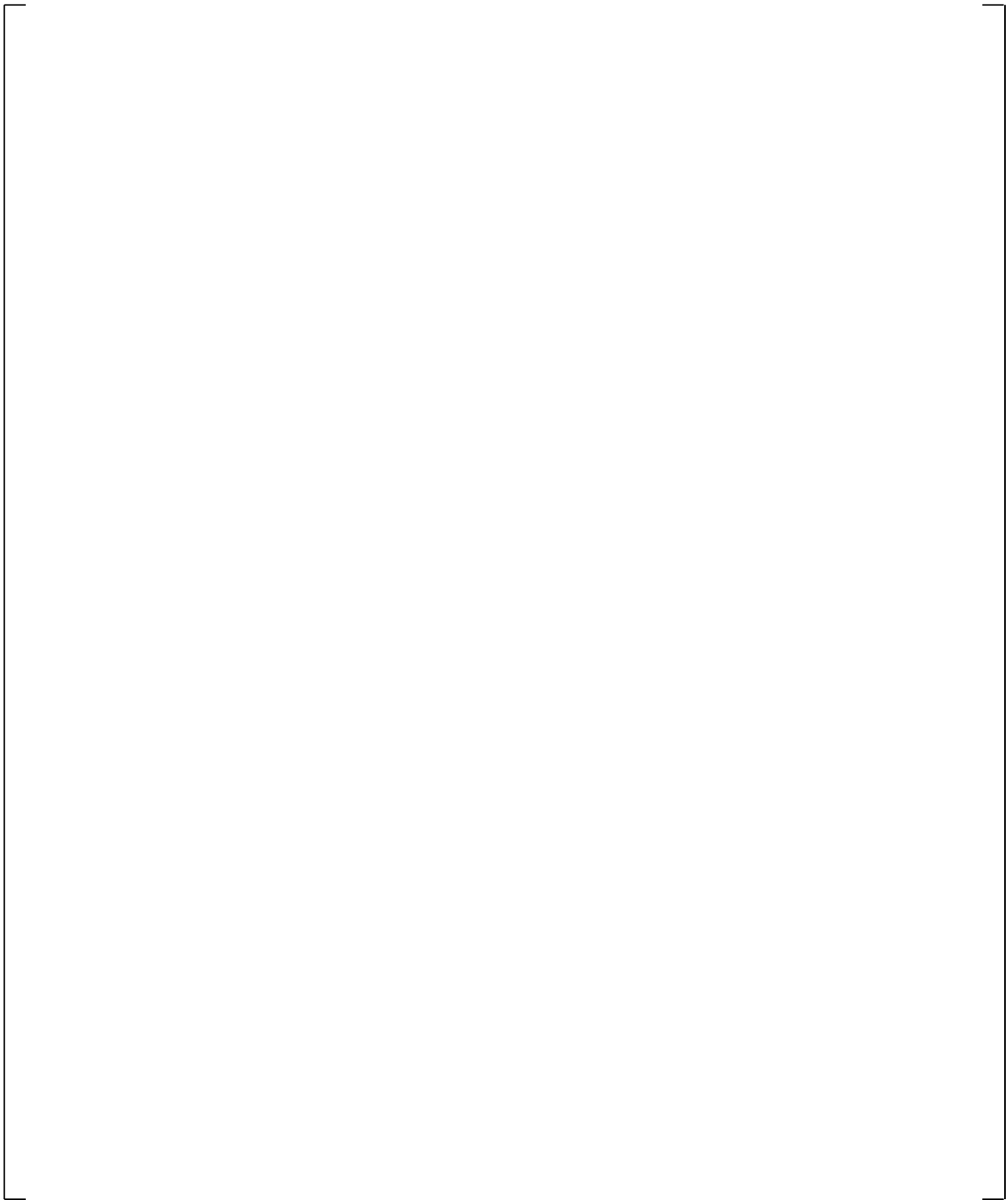

Figure 18.2.2-6 Pressure Difference Across the PWS 2.3 U-Tube

a,b,c

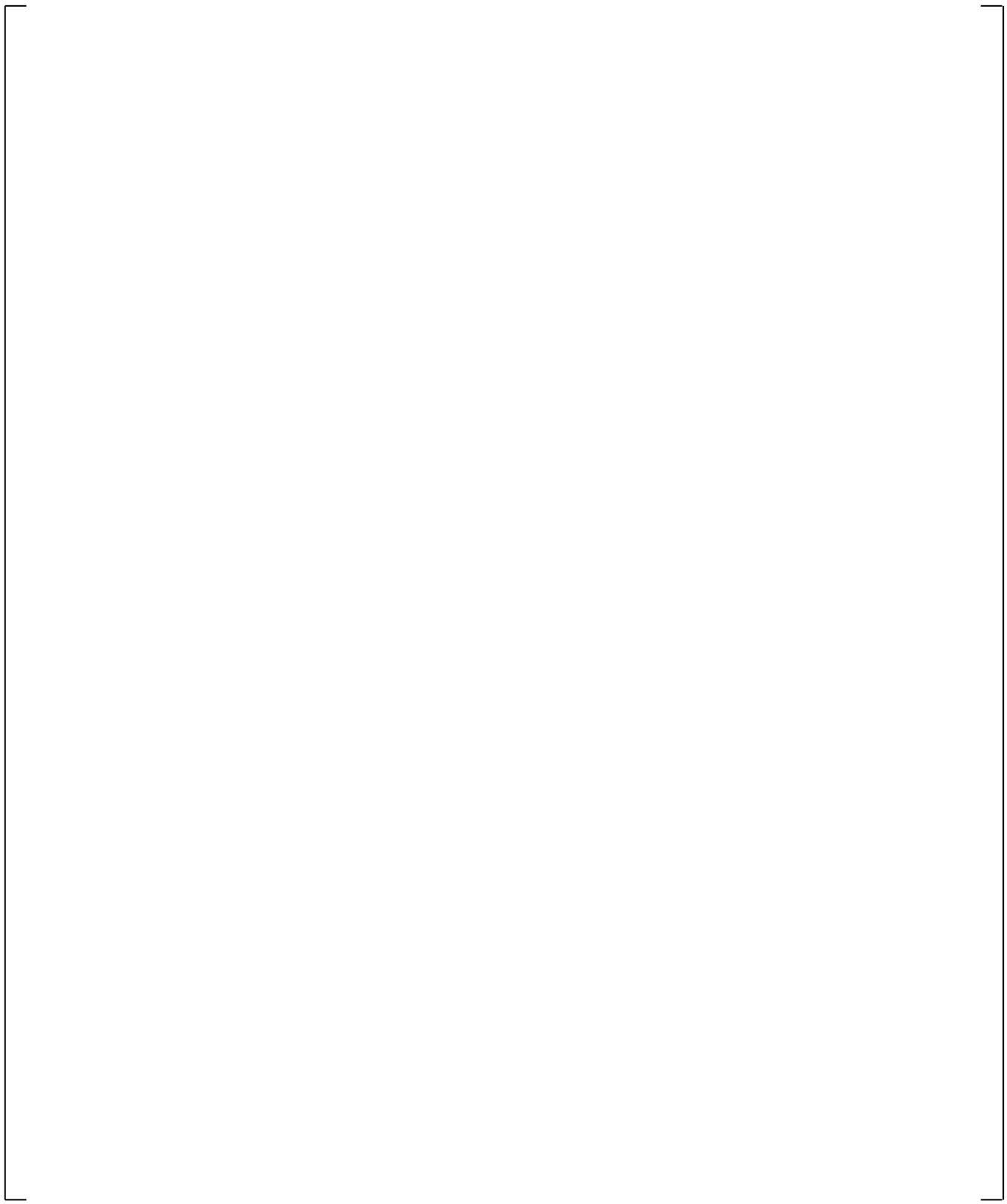

Figure 18.2.2-7 PWS 2.3 U-Tube Normalized Level and Limit Lines

a,b,c

Figure 18.2.2-8 PWS 2.3 U-Tube Flow Regimes Observed Under the Limit Line

a,b,c

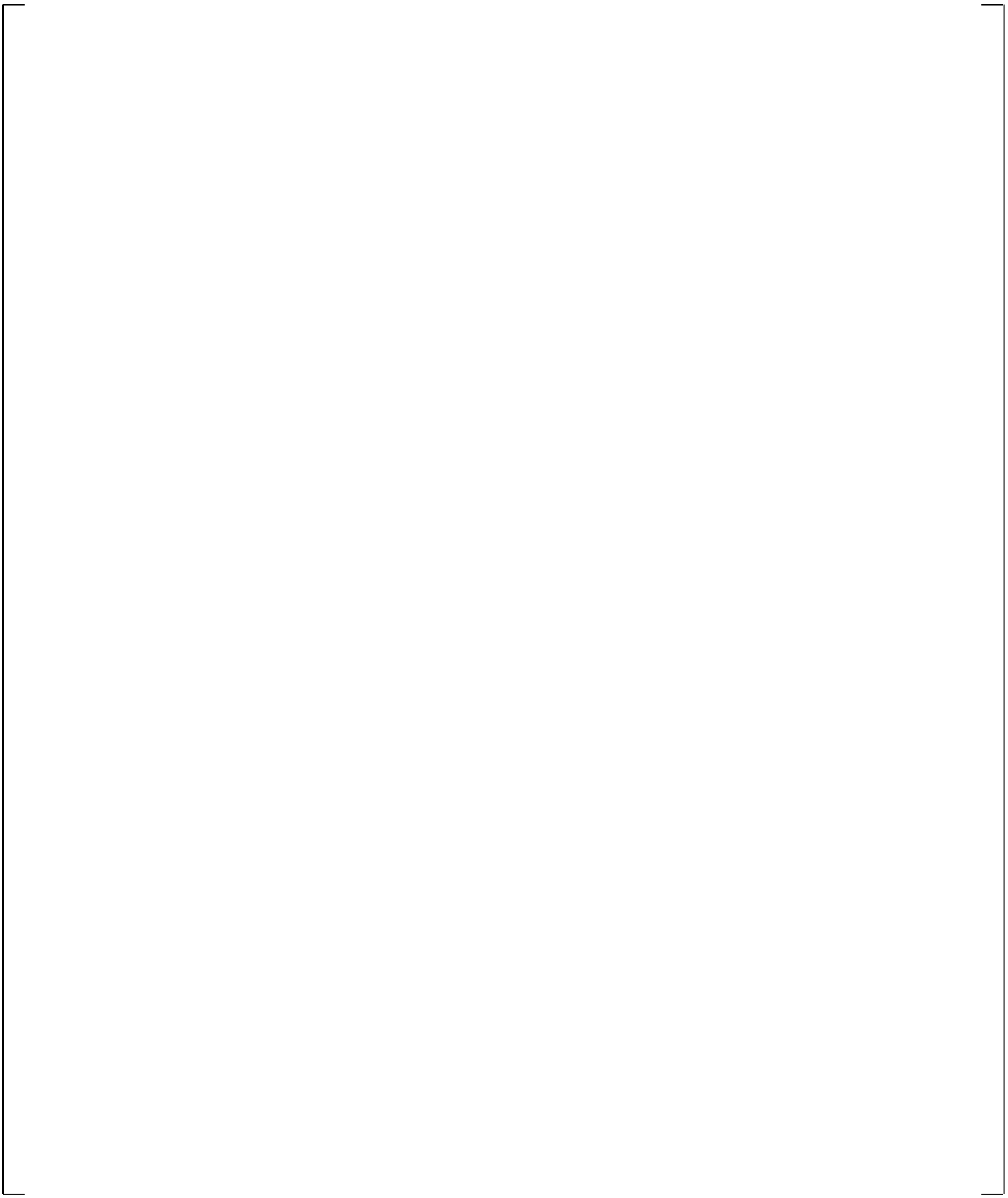

Figure 18.2.2-9 Hysteresis in Loop Seal Limit Line

a,c

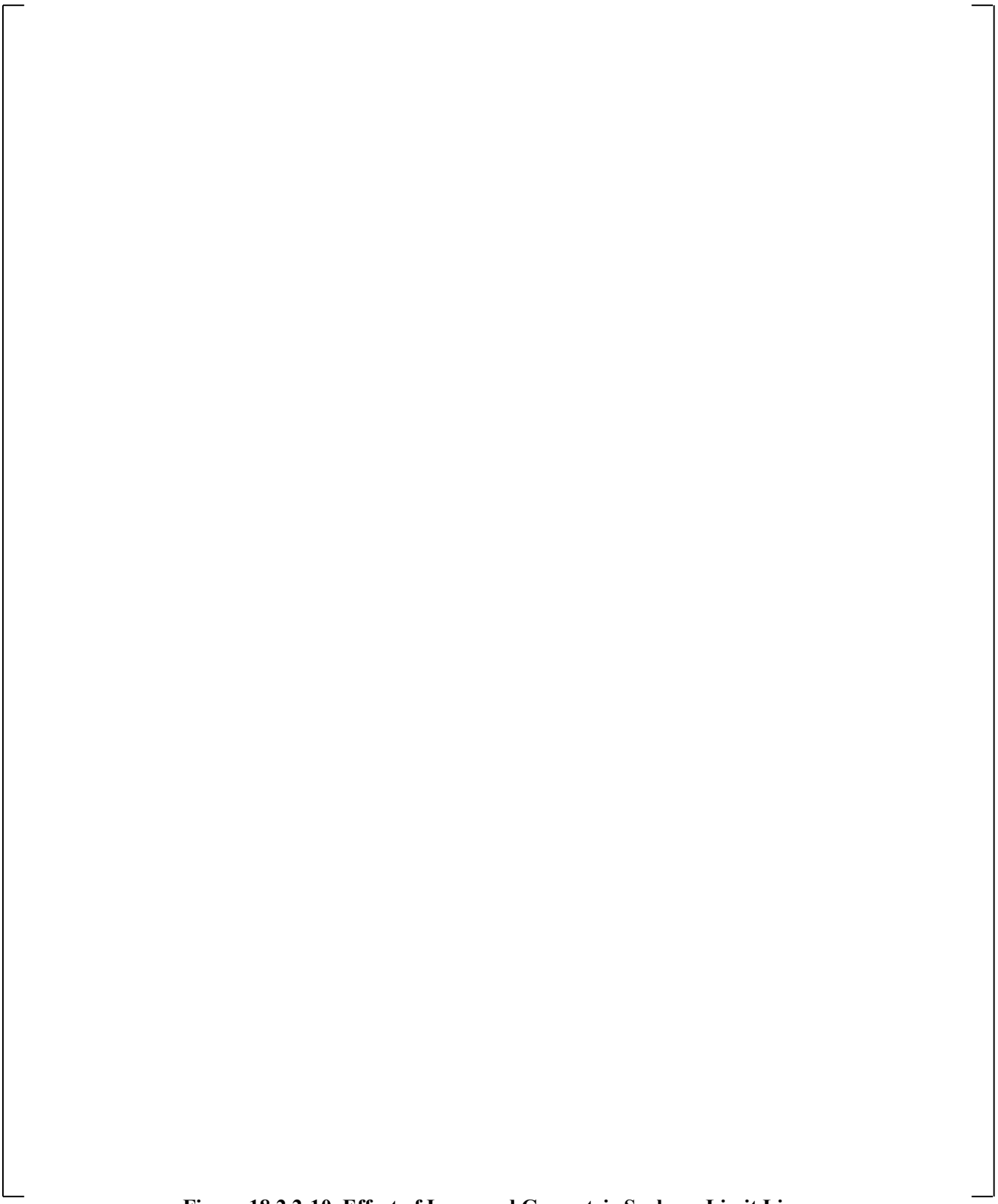

Figure 18.2.2-10 Effect of Increased Geometric Scale on Limit Lines

a,c

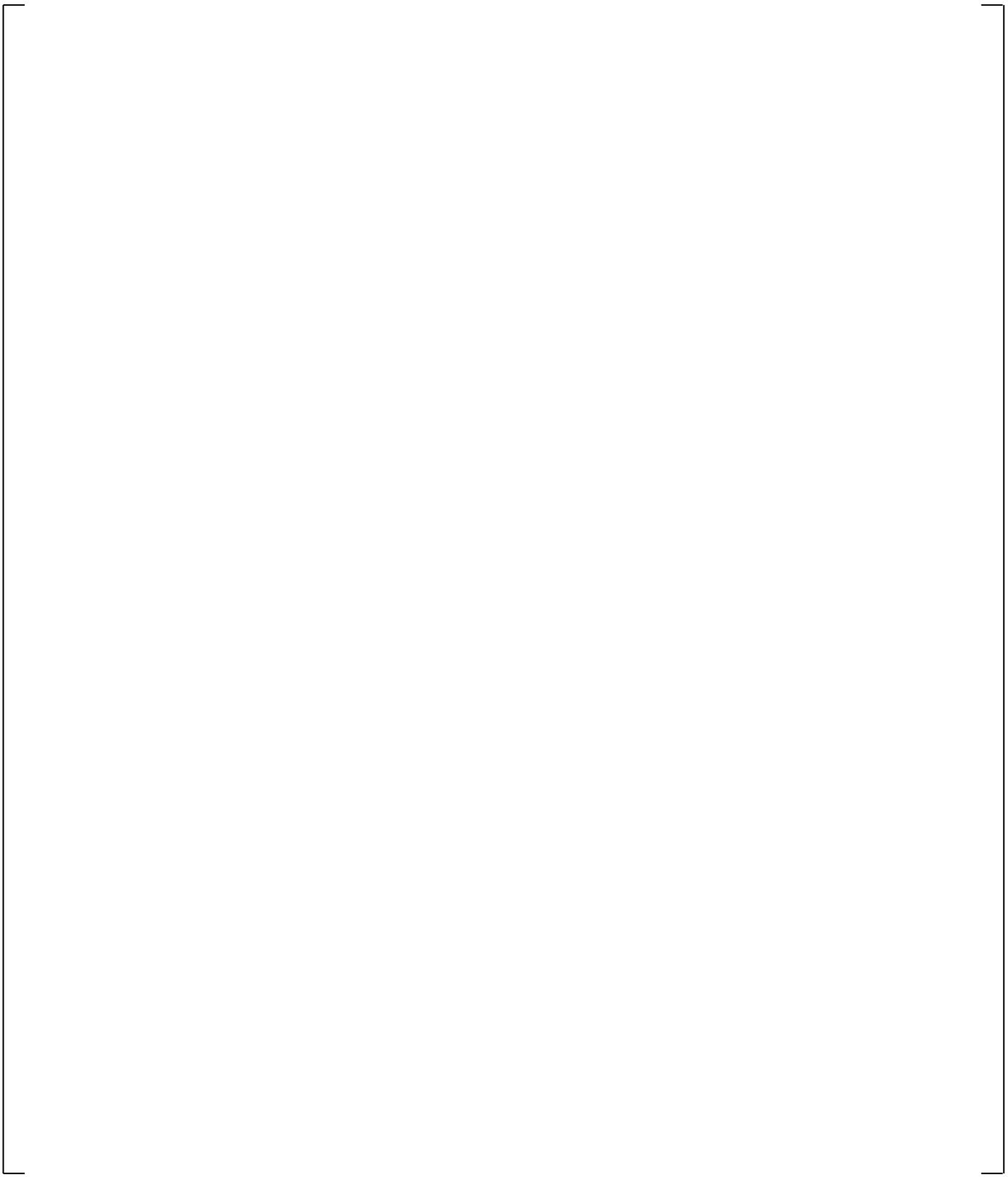

Figure 18.2.2-11 Effect of Increased Pressure and Scale on Limit Lines

a,c

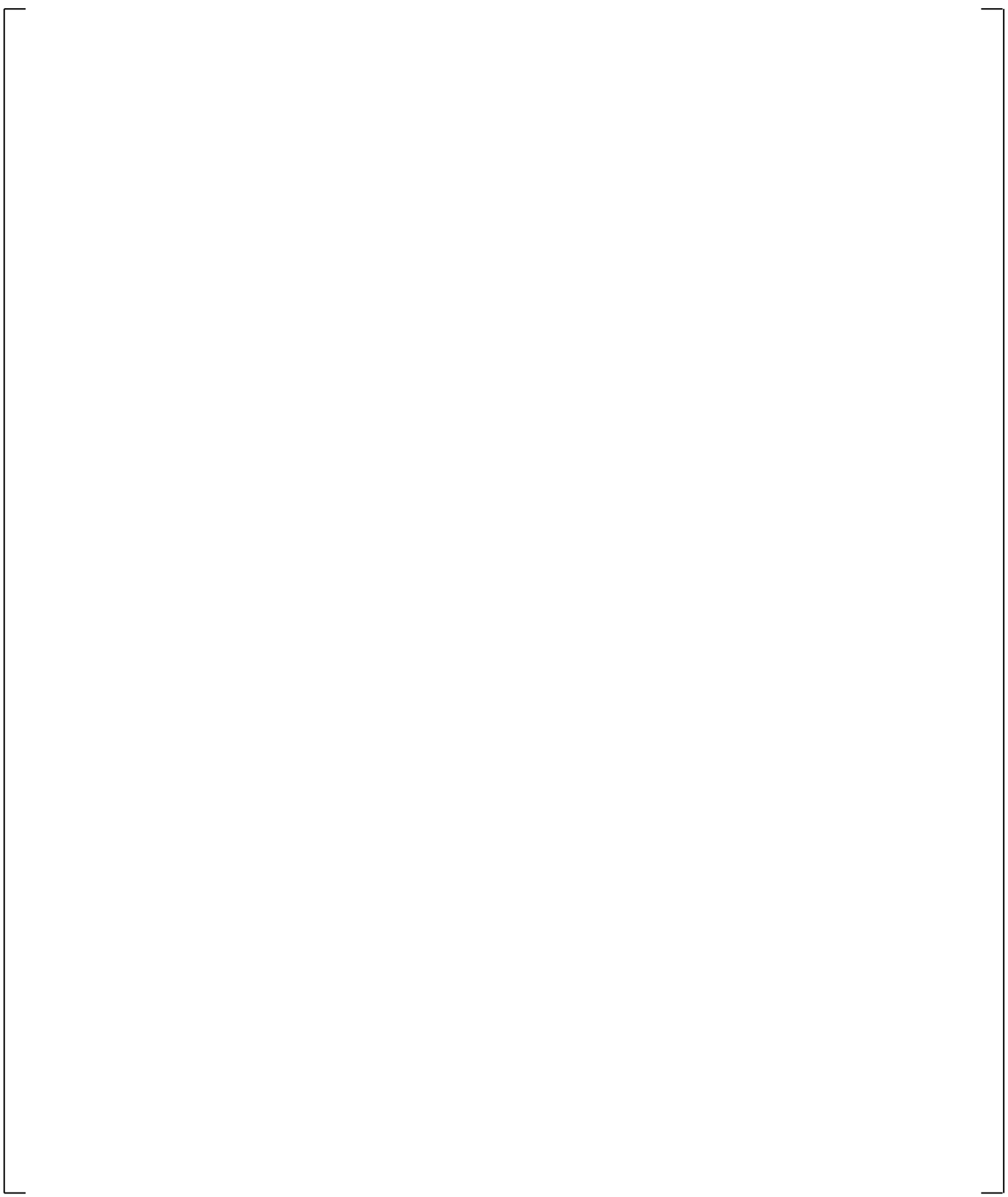

Figure 18.2.2-12 IVO Full-Scale Final Void Fraction and Limit Lines

18.2.3 Full-Scale Steam-Water Tests

Tests were performed at full-scale for a typical four-loop PWR in the Upper Plenum Test Facility (UPTF) at pressures of 3 bar (43.5 psia) and 15 bar (217.5 psia). The separate effects tests (Liebert and Emmerling, 1998) were conducted by blocking three of the four loops as seen in Figure 18.2.3-1, partially filling the loop seal in the open loop, injecting steam into the reactor vessel simulator, and measuring the residual level once entrainment had completed, but before the steam flow was terminated. The published data from the two test series are shown in Figure 18.2.3-2 (Liebert and Emmerling, 1998 and Ohvo, et al., 1998).

Lines are drawn through the data that represents a constant average gas velocity as seen in Figure 18.2.3-2. This velocity is the best-estimate of the minimum velocity at which entrainment from the liquid surface will take place within the horizontal section of the loop seal and is independent of the level in the horizontal run. Also shown is the Taitel-Dukler line for transition from slug to entrained flow. Liebert and Emmerling note that slugging was observed only at the lowest Froude number in each test series. Otherwise, the flow was observed to be stratified. The calculated critical gas velocities are 60 ft/s and 32 ft/s for the 3-bar and 15-bar test series, respectively.

Using the above critical velocities and calculated viscosity numbers and the critical velocity from the PWS 2.3 air-water tests (Figure 18.2.2-3), the results can be compared to Ishii's correlation as shown in Figure 18.2.3-3 (Ishii and Grolmes, 1975), where the Ishii parameter is calculated as:

$$\mathrm{Ish} = \frac{w_g \mu_g}{\sigma}\left(\frac{\rho_g}{\rho_w}\right)^{0.5} \tag{18-7}$$

The UPTF and PWS 2.3 data (diamonds in the figure) lie **[** **]**[a,c] the database upon which Ishii's correlation was constructed (triangles in figure). While the UPTF data lie **[** **]**[a,c]. As shown in Figure 18.2.3-3, the UPTF data lie **[**

][a,c]

Using an Ishii number of 0.0033, a Reynolds number of approximately **[** **]**[a,c] is obtained from Equation 18-3. Recalling that this is the approximate Reynolds number for **[**

][a,c]

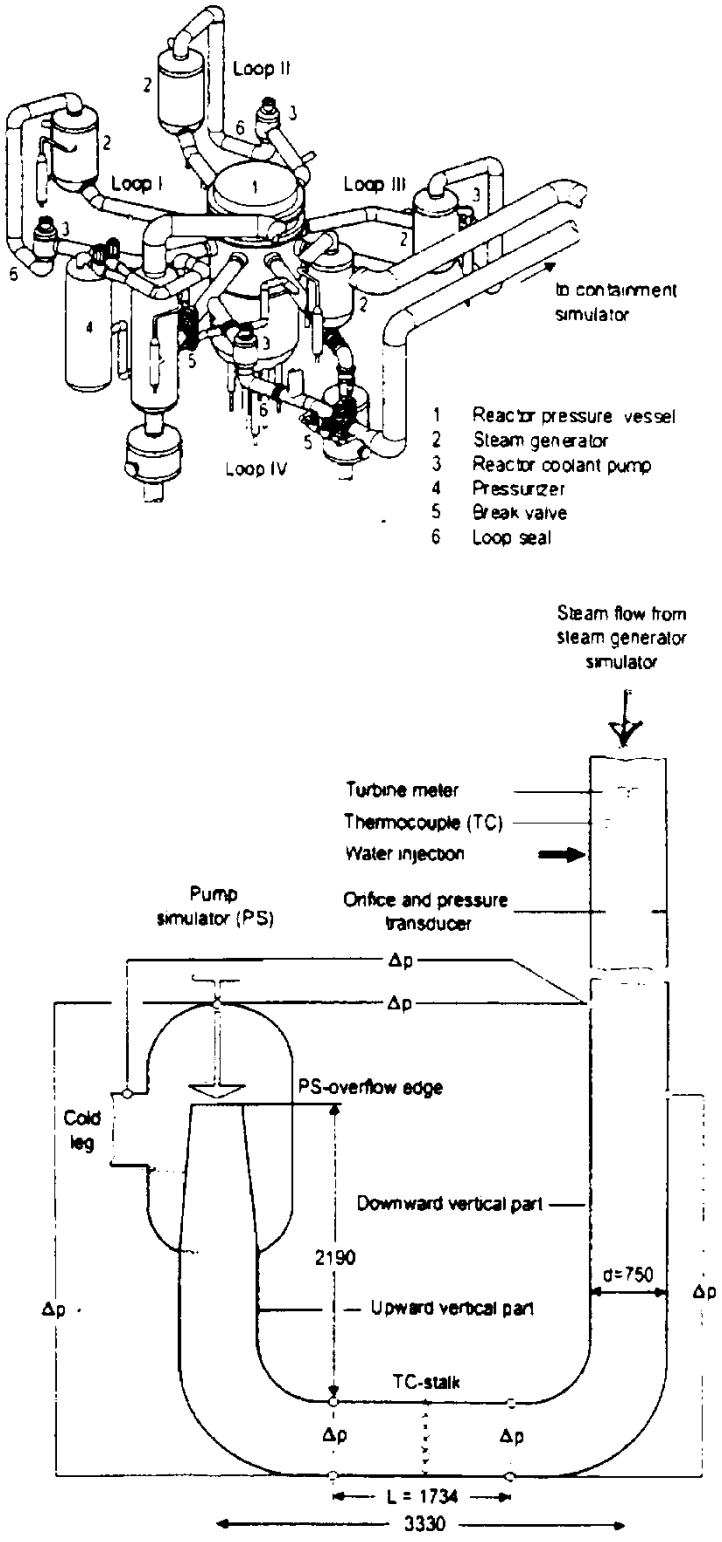

Figure 18.2.3-1 UPTF Facility and Single Loop Seal (Liebert and Emmerling, 1998)

a,c

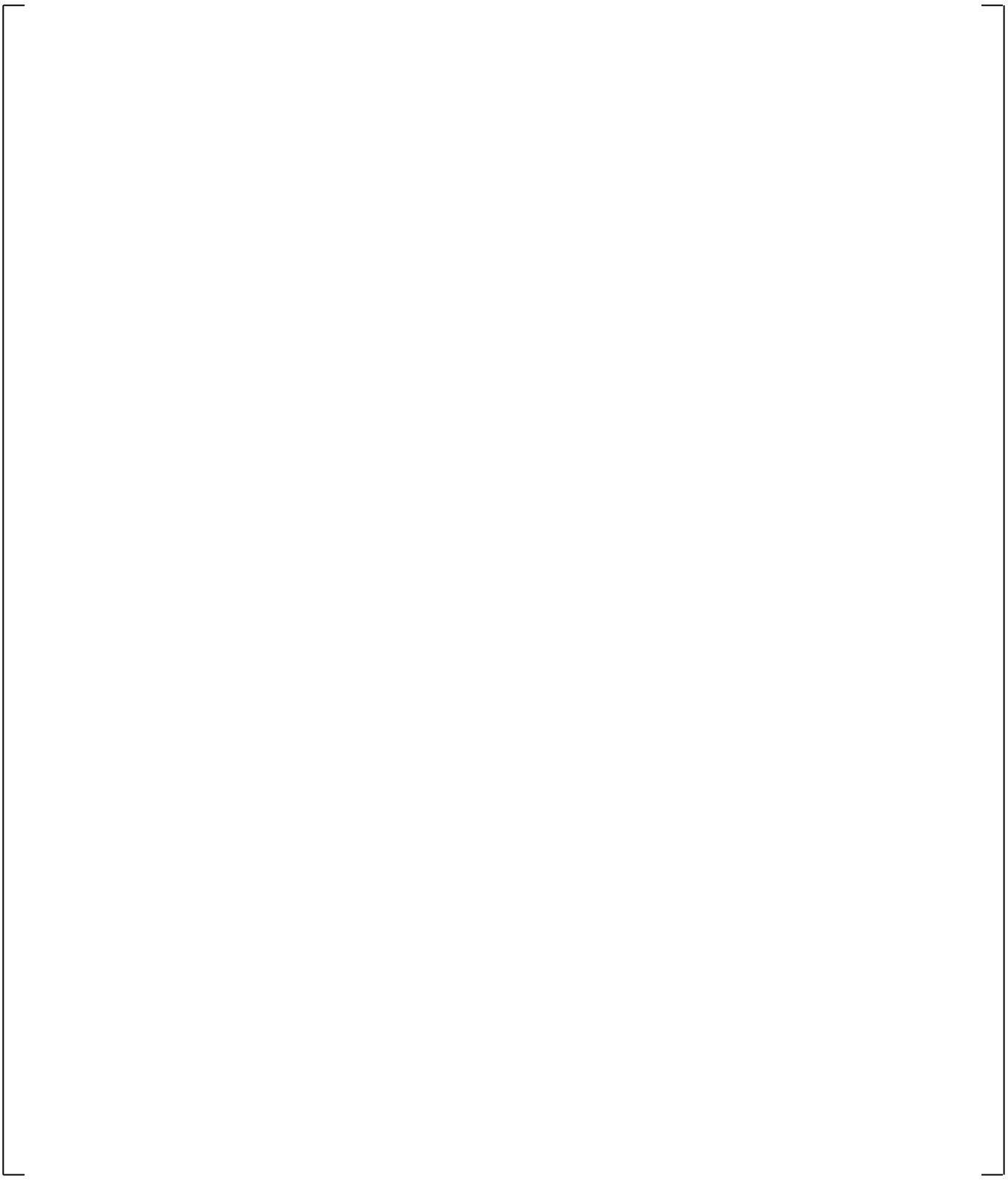

Figure 18.2.3-2 Lines of Constant Gas Velocity Compared to UPTF Data for 3-Bar and 15-Bar Loop Seal Tests

a,c

Figure 18.2.3-3 UPTF and PWS 2.3 Compared to the Ishii Correlation and Data Base

18.3 WCOBRA/TRAC-TF2 MODELING OF LOOP SEAL CLEARING PROCESS

The objective of this assessment is to confirm that WCOBRA/TRAC-TF2 adequately predicts the loop seal clearing phenomena for a PWR, namely, the residual liquid level in the loop seal and differential pressure across the loop seal post clearing. Discussions on the number of loop seals that clear and which loop seals clear are in Sections 28 and 31, Volume 3.

18.3.1 WCOBRA/TRAC-TF2 Simulation of the UPTF 3-Bar and 15-Bar Tests

The two UPTF full-scale steam-water tests were simulated with WCOBRA/TRAC-TF2. The separate effects tests were conducted by blocking three of the four loops and injecting steam into the reactor vessel simulator as shown in Figure 18.2.3-1 (Liebert and Emmerling, 1998). The WCOBRA/TRAC-TF2 model for the simulations has three components, as depicted in Figure 18.3-1; a FILL is used to supply the vapor; a PIPE is used to simulate loop 2 of the facility; and, a BREAK is used to maintain the test pressure. The PIPE has a total of **[** **]**[a,c] making up the actual loop seal. **[** **]**[a,c] The noding in this model is judged sufficient for simulation of the UPTF tests, and similar modeling (STRTX=1 at these cell faces) is expected to be used in the plant simulations.

The UPTF tests were run with a slightly superheated steam supply (Ohvo, et al., 1998). With the flow of superheated steam, liquid in the loop seal may be evaporated. However, it is expected that the amount of liquid evaporation is small compared to the amount of liquid lost due to slugs of liquid/entrained liquid being expelled out the loop seal. As such, the WCOBRA/TRAC-TF2 simulations were performed assuming **[** **]**[a,c].

Although the initial liquid level was varied in the tests, the calculations are initialized **[**

][a,c] Liebert noted that varying the initial level and liquid flow did not significantly affect the test results. For the 3-bar tests, the residual levels are lower for the cases with liquid injection for approximately the same Froude number. Thus, a set of initial conditions consistent with a hypothetical small break LOCA are used for the simulations.

Each of the test simulations is run separately, starting from the same initial conditions. The steam flow rate is increased from zero to the specified flow rate **[**

][a,c]

The results of the 3-bar simulations are shown in Figure 18.3-2. WCOBRA/TRAC-TF2 generally **[**

][a,c] Figure 18.3-3 shows the total mass in the system for the 3-bar and 15-bar cases with $j_g^* \approx 0.1$.

The predicted behavior for the 15-bar tests compared to the data is shown in Figure 18.3-4. WCOBRA/TRAC-TF2 **[**

][a,c].

Figure 18.3-5 shows a comparison of the predicted versus measured residual liquid levels for both tests. As observed in the figure, the **[** **]**[a,c] for both pressures.

Although no data are known to exist for full geometric and pressure scale, WCOBRA/TRAC-TF2 calculations were performed using the UPTF model at 1000 psia. Based on the pressure-scaling discussion in Section 18.2.2.4, it is expected that **[**

][a,c]

Measured pressure drops across the UPTF loop seal are shown in Figure 18.3-7a. The highest pressure drops occur for $j_g^* < 0.1$ and then become approximately constant with increasing steam velocity. Also the magnitude of the observed differential pressure oscillations is significantly greater for $j_g^* < 0.1$. The pressure drop calculated by WCOBRA/TRAC-TF2 is shown in Figure 18.3-7b. The calculated pressure drops shown in Figure 18.3-7b represent **[**

][a,c]

Figures 18.3-8a through 18.3-8c provide the pressure drop transient during the vapor injection period for three different 15-bar cases, which shows trends in pressure drop amplitude and frequency **[**

][a,c] (Figure 18.3-7a).

Figures 18.3-9a and 18.3-9b show smoothed pressure drop transients for the 3-bar and 15-bar $j_g^* \approx 0.05$ cases, respectively, and Figures 18.3-9c and 18.3-9d show smoothed pressure drop transients for the 3-bar and 15-bar $j_g^* \approx 0.22$ cases, respectively. For the 3-bar and 15-bar high vapor flow cases, **[**

][a,c]. For the 3-bar and 15-bar low vapor flow cases, **[**

][a,c].

a,c

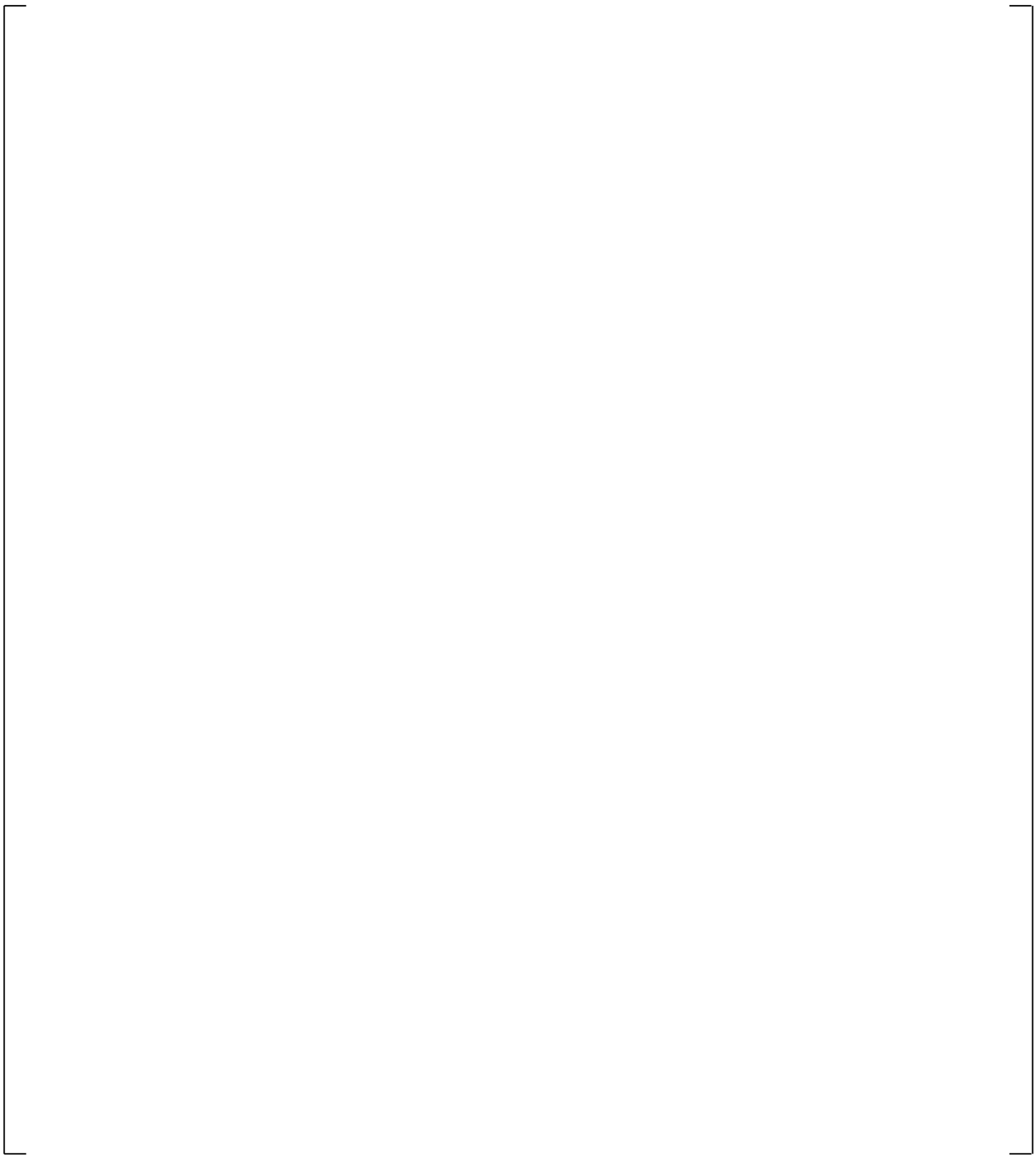

Figure 18.3-1 WCOBRA/TRAC-TF2 Model of the UPTF Separate Effects Loop Seal Clearing Tests

a,c

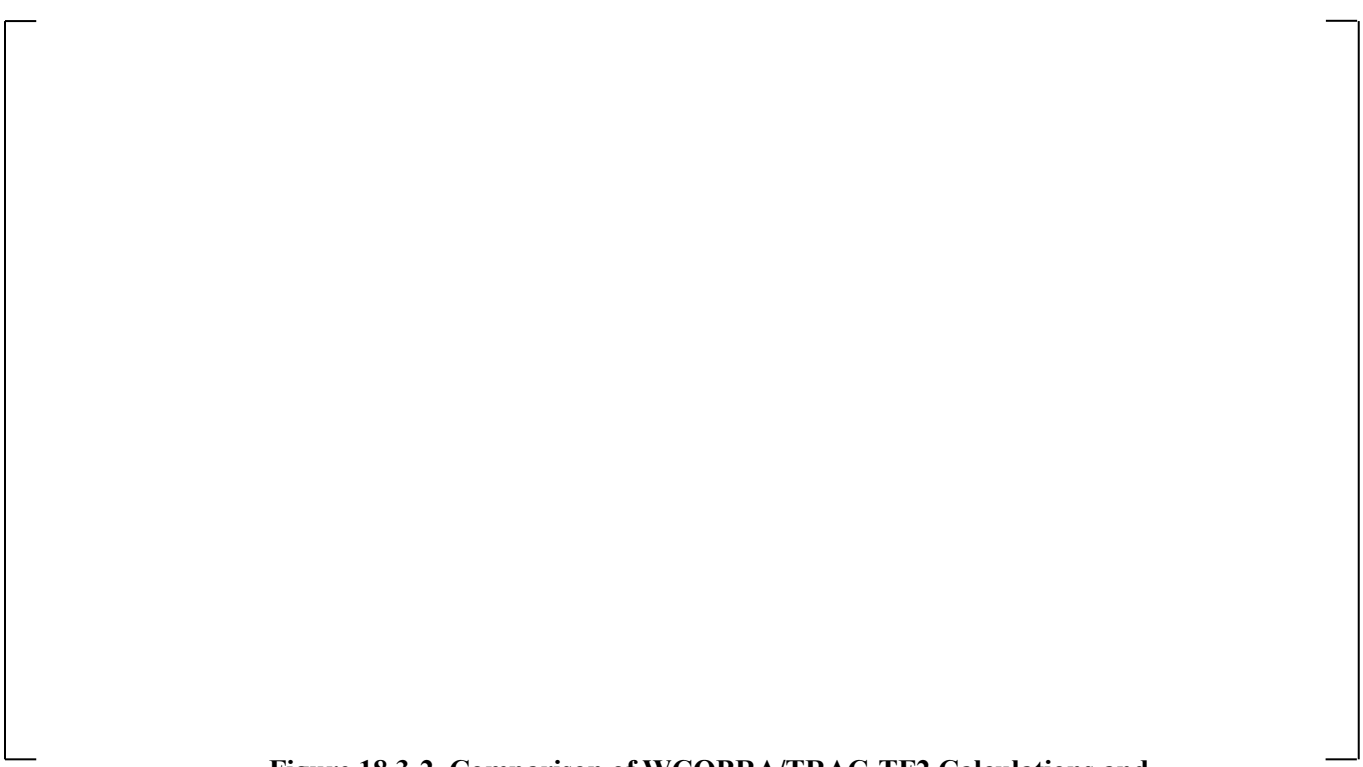

Figure 18.3-2 Comparison of WCOBRA/TRAC-TF2 Calculations and UPTF Data for the 3-Bar Tests

a,c

Figure 18.3-3 Comparison of WCOBRA/TRAC-TF2 Calculations Total System Mass for UPTF 3-bar and 15-bar $j_g^* \approx 0.1$ Cases

a,c

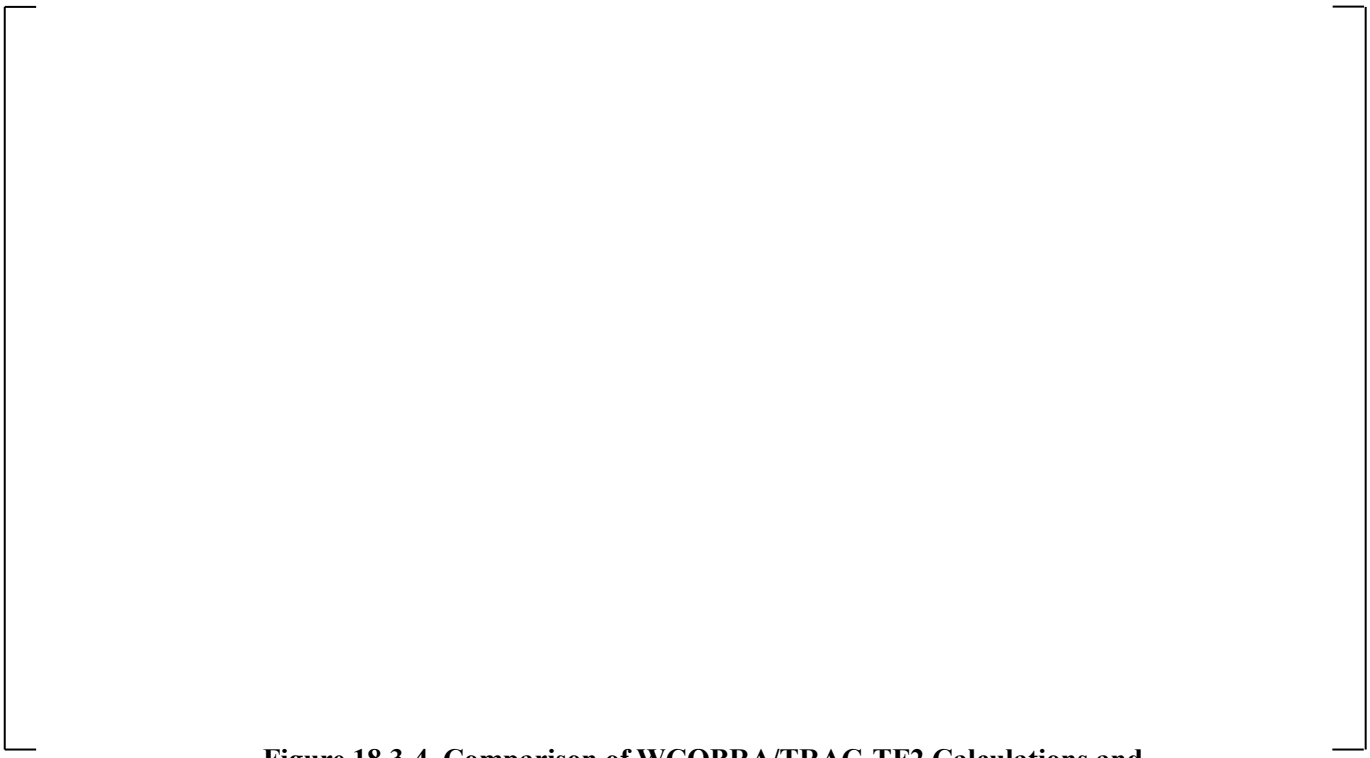

Figure 18.3-4 Comparison of WCOBRA/TRAC-TF2 Calculations and UPTF Data for the 15-Bar Tests

a,c

Figure 18.3-5 Comparison of Calculated vs. Measured Residual Liquid Levels

a,c

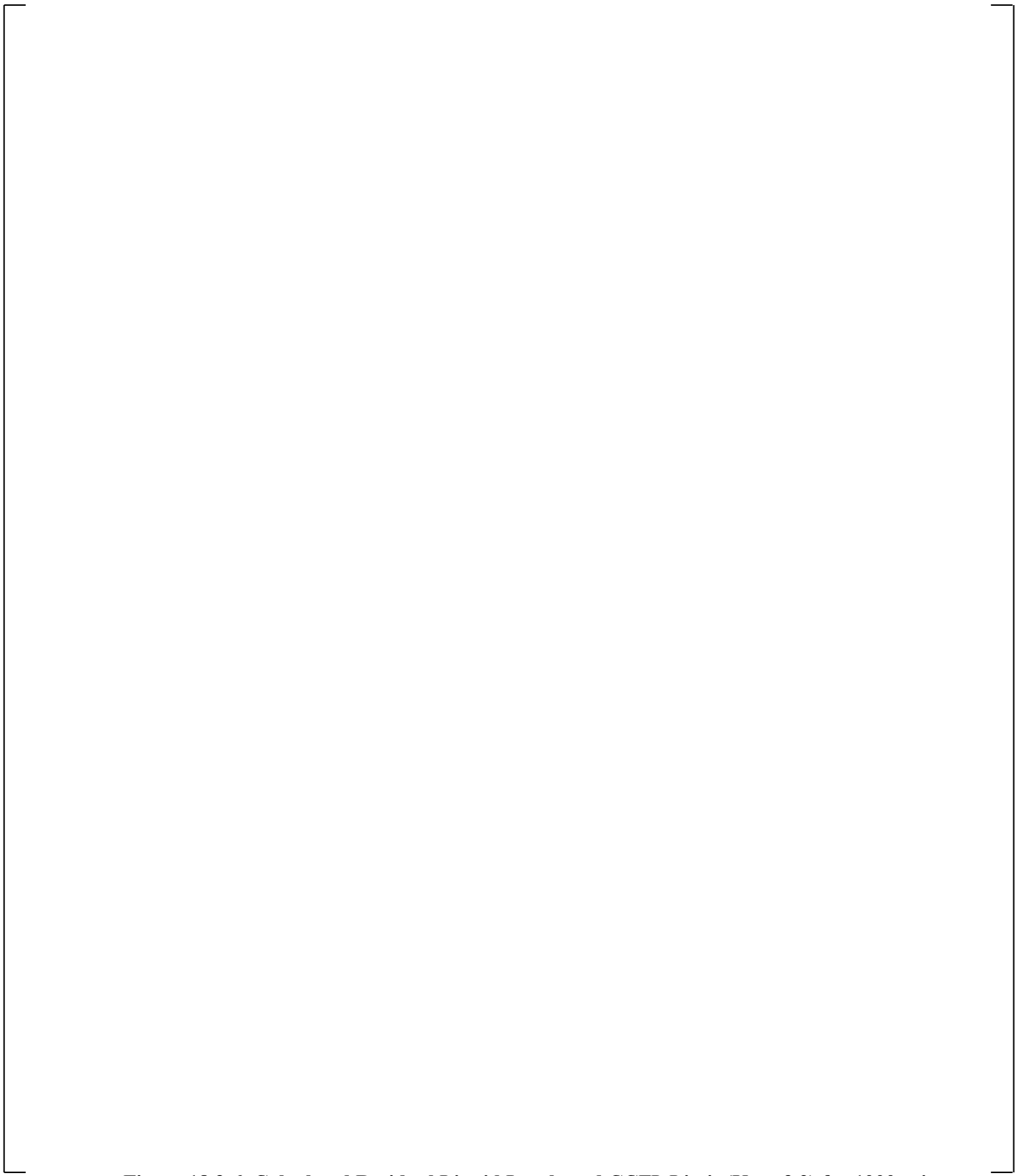

Figure 18.3-6 Calculated Residual Liquid Levels and CCFL Limit (Ku = 3.2) for 1000 psia

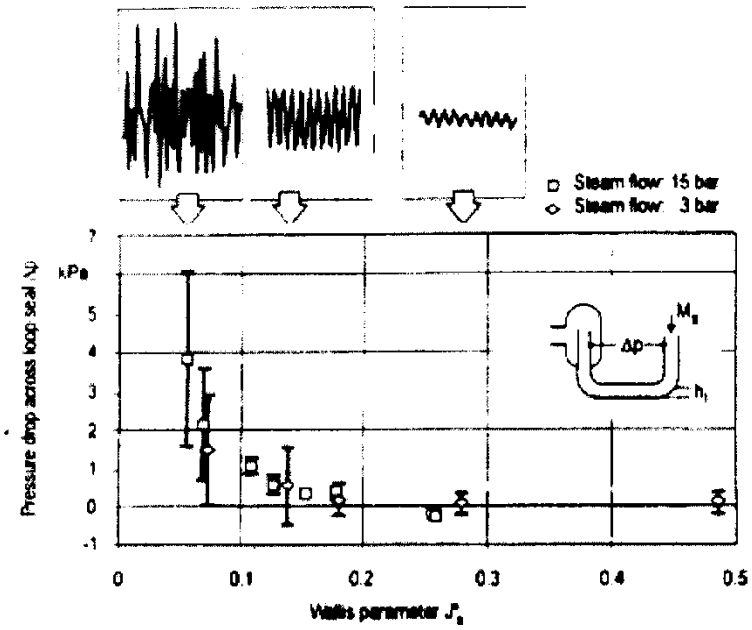

Figure 18.3-7a Measured Pressure Drop for UPTF 3-Bar and 15-Bar Loop Seal Tests (from Liebert and Emmerling, 1998)

a,c

Figure 18.3-7b Calculated Loop Seal Pressure Drop for 3-Bar, 15-Bar, and 1000 psia

a,c

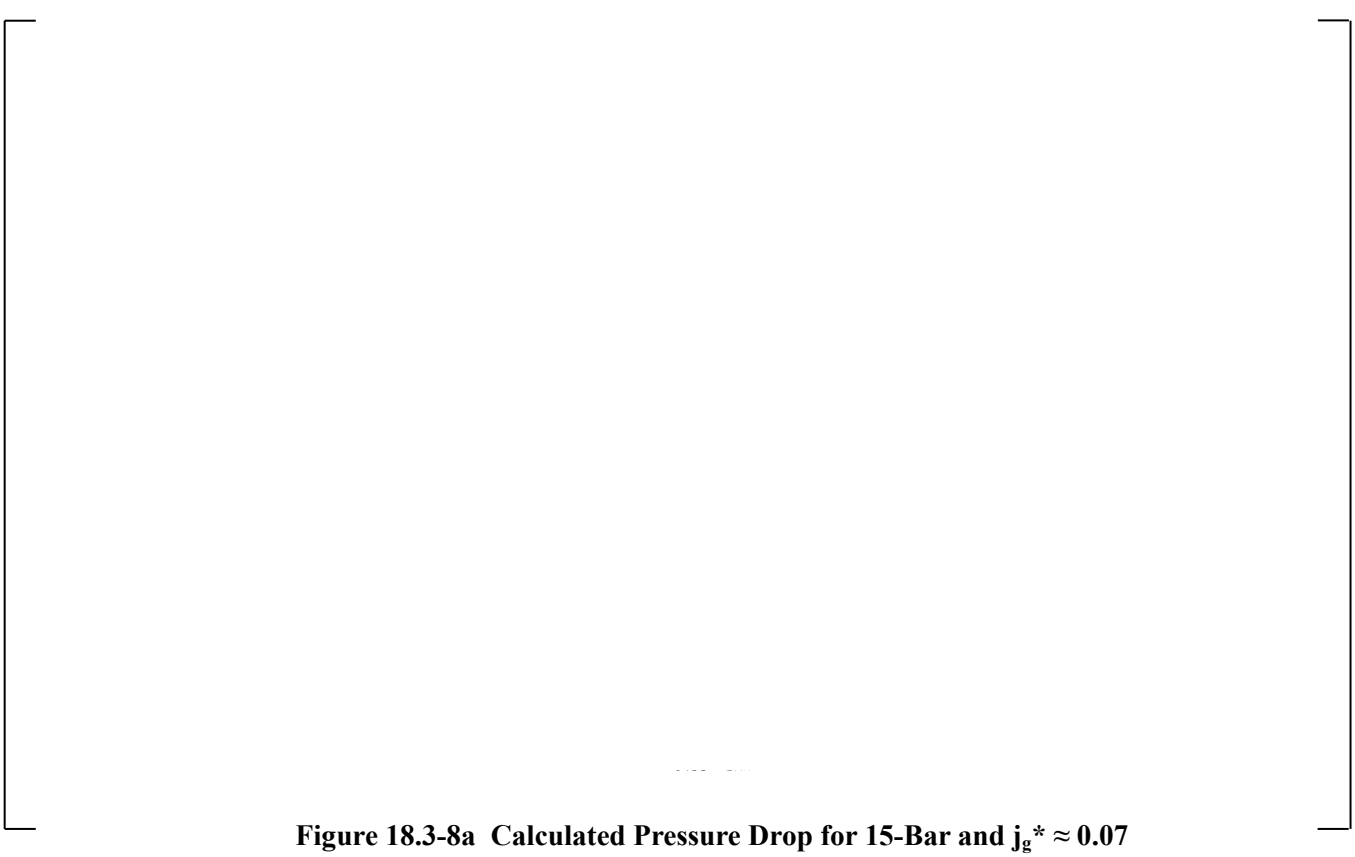

Figure 18.3-8a Calculated Pressure Drop for 15-Bar and $j_g^* \approx 0.07$

a,c

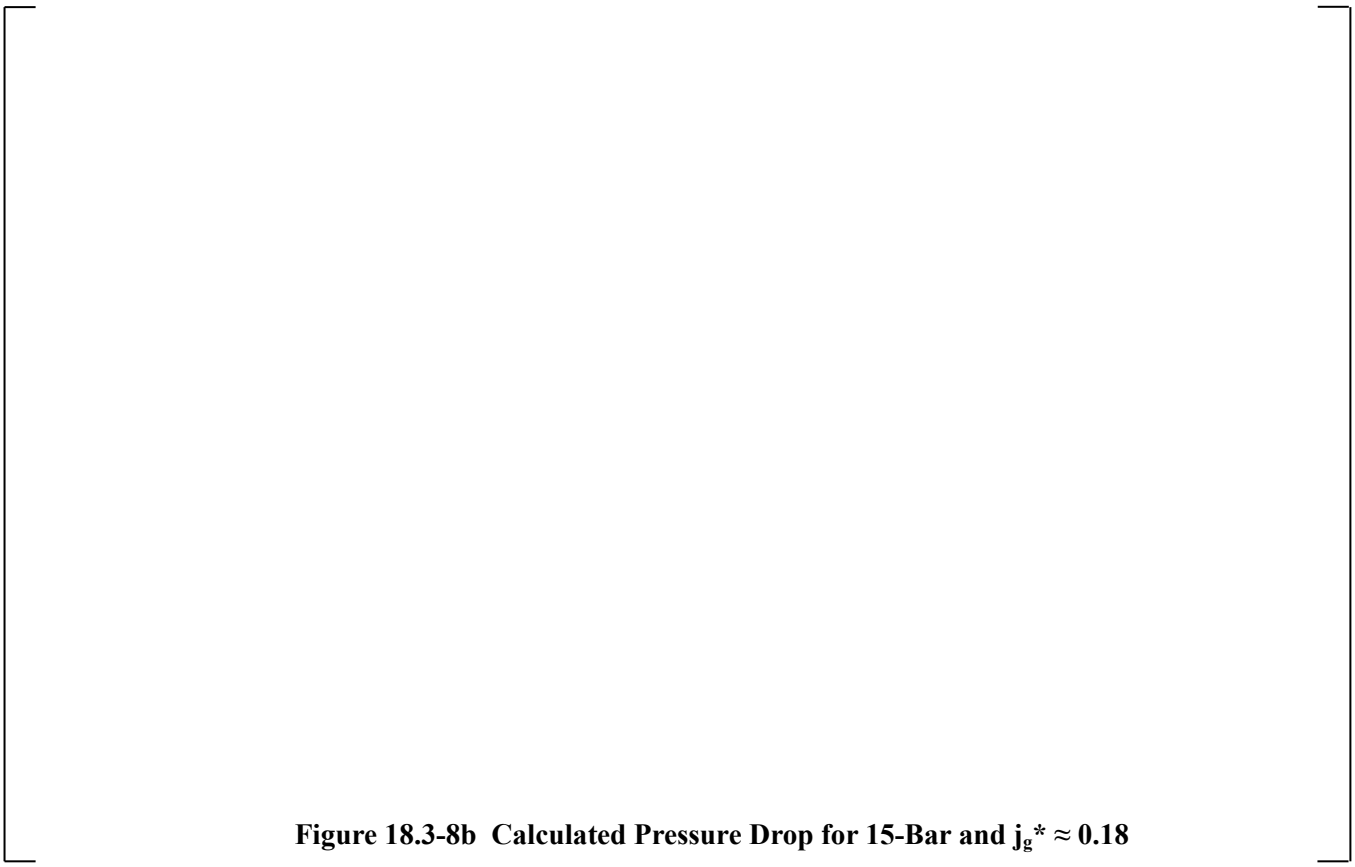

Figure 18.3-8b Calculated Pressure Drop for 15-Bar and $j_g^* \approx 0.18$

a,c

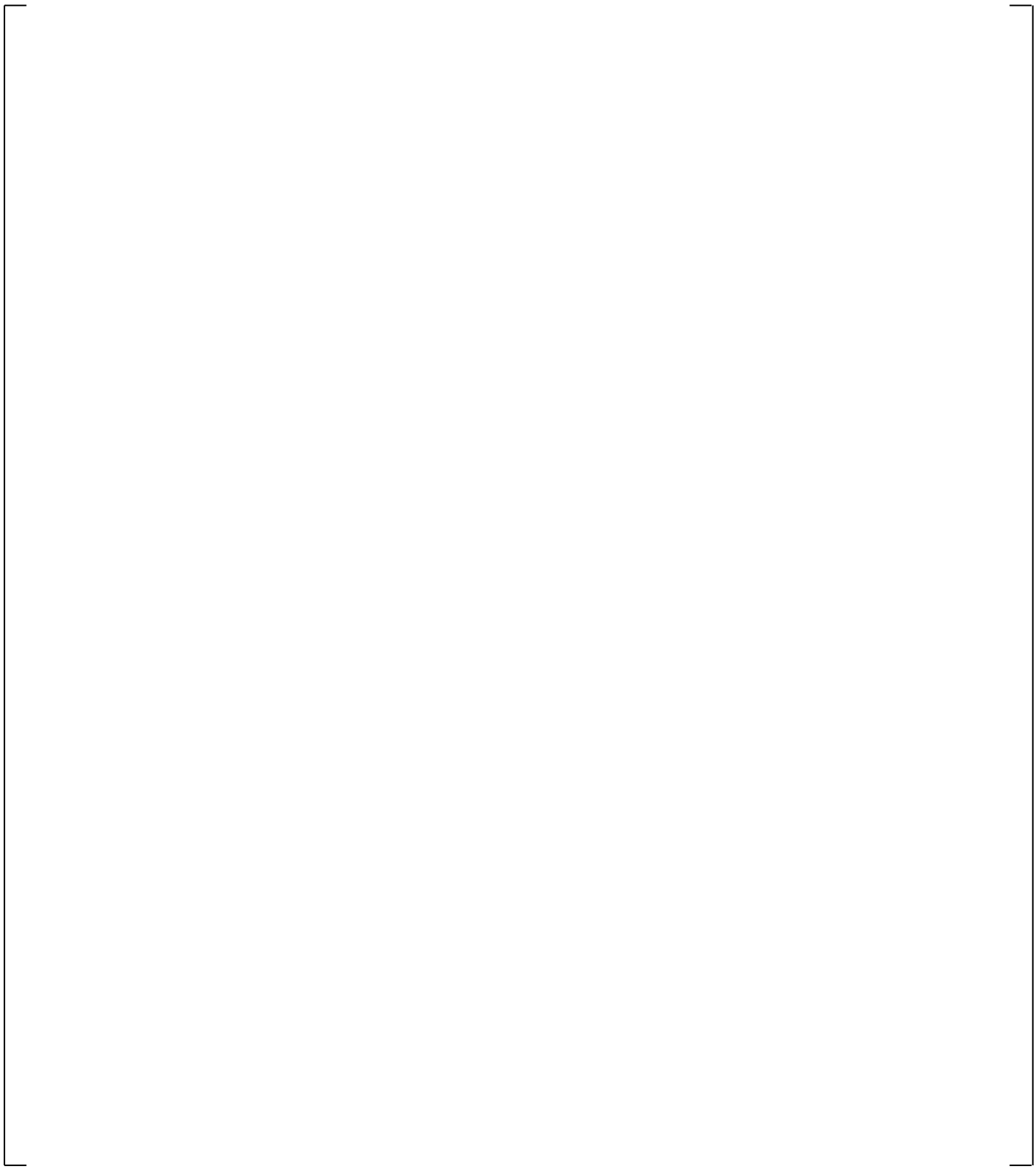

Figure 18.3-8c Calculated Pressure Drop for 15-Bar and $j_g^* \approx 0.32$

a,c

Figure 18.3-9a Comparison of Pressure Drop in Bends for $j_g^* \approx 0.05$ 3-bar Case

a,c

Figure 18.3-9b Comparison of Pressure Drop in Bends for $j_g^* \approx 0.05$ 15-bar Case

a,c

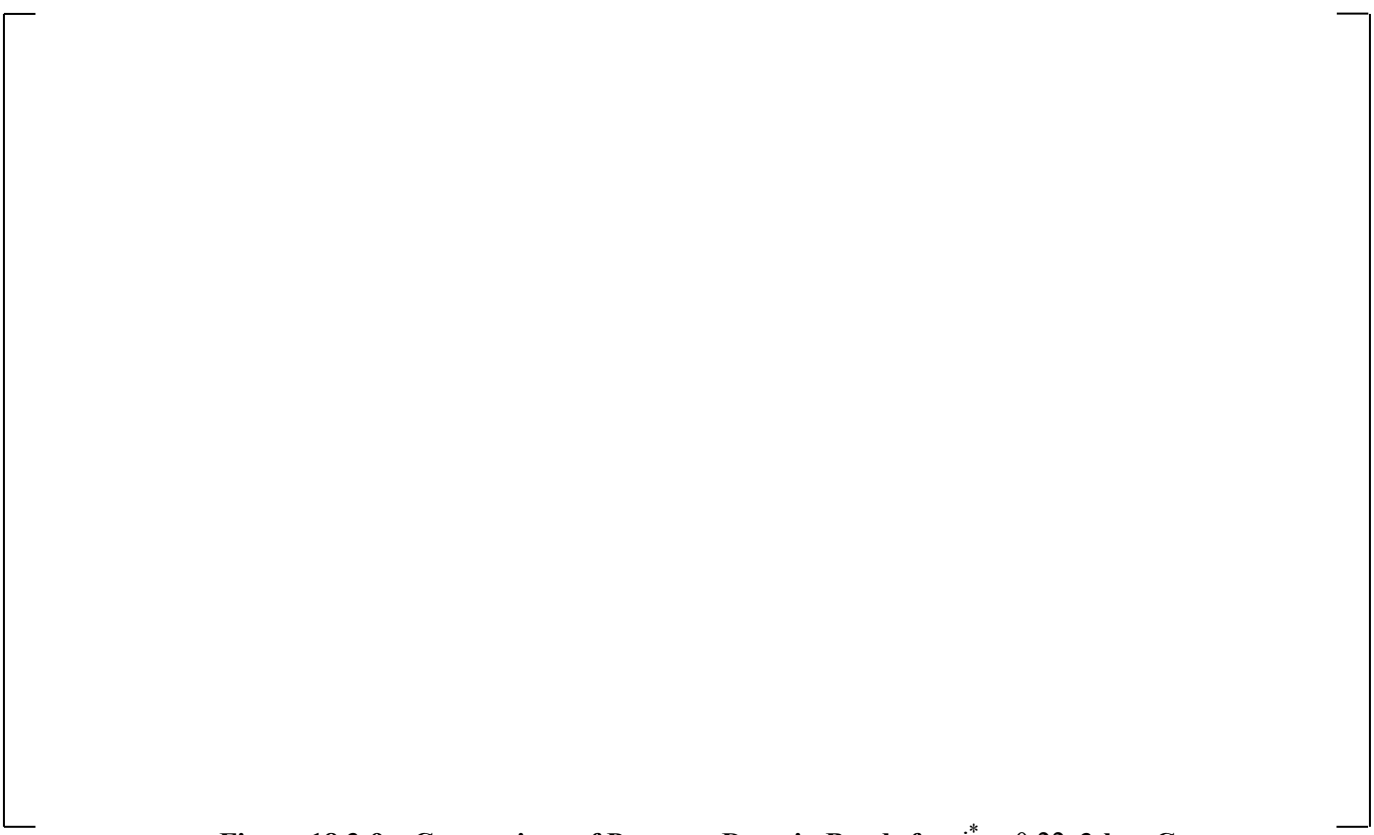

Figure 18.3-9c Comparison of Pressure Drop in Bends for $j_g^* \approx 0.22$ 3-bar Case

a,c

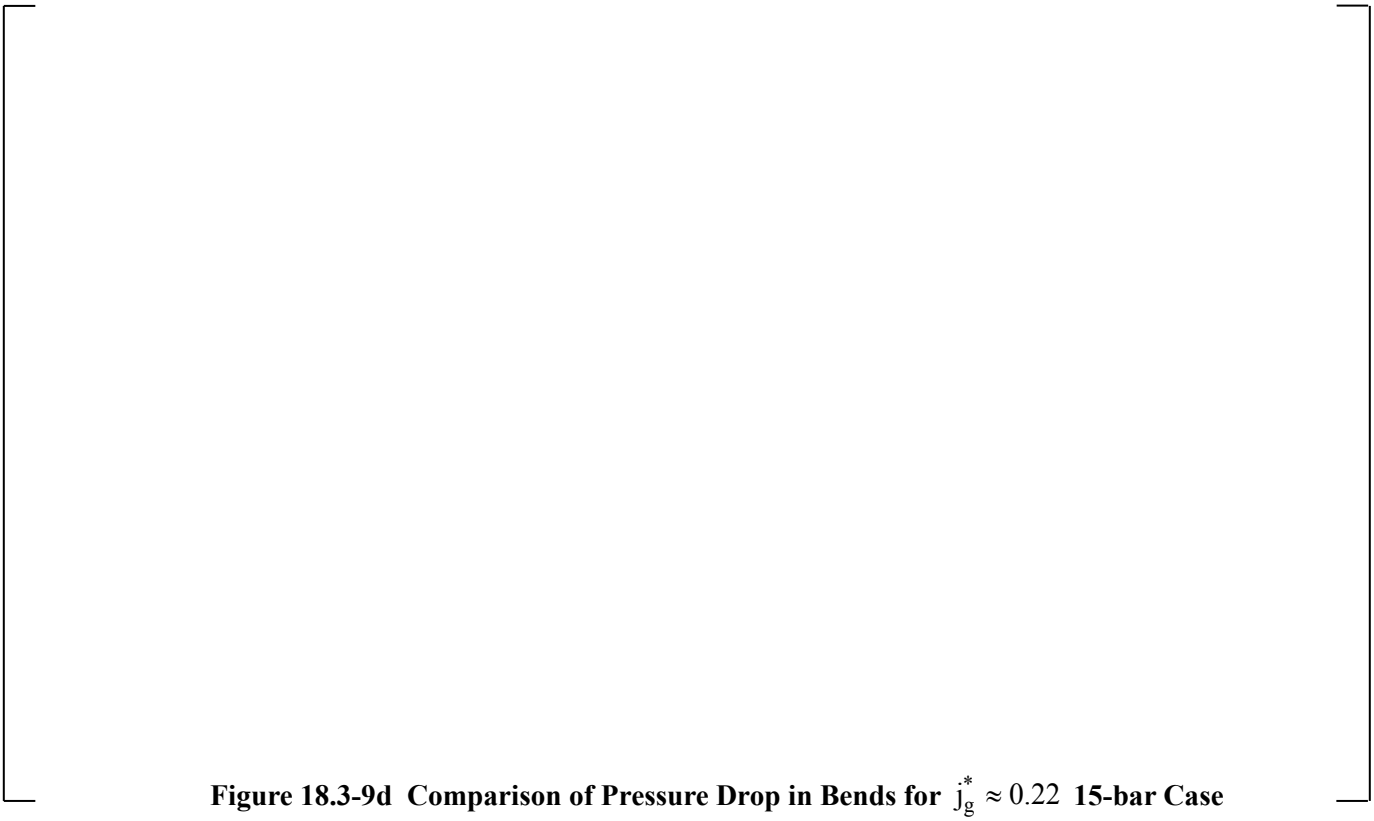

Figure 18.3-9d Comparison of Pressure Drop in Bends for $j_g^* \approx 0.22$ 15-bar Case

18.4 CONCLUSIONS

Assessment of the experimental data indicates the following:

[

]^{a,c}

Assessment of WCOBRA/TRAC-TF2 relative to the experiments indicates the following:

[

]^{a,c}

18.5 REFERENCES

1. Boileau, H., and Bourteele, J. P., 1985, "ECTHOR Program, PWS 2.3: Small Size Break, Final Report," EP/TA/DC 533.

2. Ishii, M. and Grolmes, M. A., 1975, "Inception Criteria for Droplet Entrainment in Two-Phase Concurrent Film Flow," *AIChE J.*, Vol. 21, No 2.

3. Koizumi, and Tasaka, K., 1988, "Quick Look Report for ROSA-IV/LSTF 10% Cold Leg Break LOCA Test, SB-CL-14," **[ ]**[b]

4. Kukita, Y. et al., 1990, "Loop Seal Clearing and Refilling During a PWR Small Break LOCA," *Nuclear Eng. and Design*, 121, 431-440.

5. Kumamaru, H. et al., 1989, "ROSA-IV/LSTF 5% Cold Leg Break LOCA Experiment Run SB-CL-18 Data Report," JAERI-M 89-027.

6. Liebert, J. and Emmerling, R., 1998, "UPTF Experiment Flow Phenomena During Full-Scale Loop Seal Clearing of a PWR," *Nuclear Engineering and Design*, Vol. 179, pp. 51-64.

7. Ohvo, J., et al., 1998, "Simulation of Full-Scale UPTF Loop Seal Experiments with APROS, CATHARE and RELAP," 6th International Conference on Nuclear Engineering, ICONE6-6090.

8. Pushkina, O. L. and Sorokin, Y. L., 1969, "Breakdown of Liquid Film Motion in Vertical Tubes," *Heat Transfer-Soviet Research*, Vol. 1, No. 5.

9. Richter, H. J., 1981, "Flooding in Tubes and Annuli," *Int. J. Multiphase Flow*, Vol. 7, No. 6, pp. 647-658.

10. Taitel, Y. and Dukler, A. E., 1976, "A Model for Predicting Flow Regime Transitions in Horizontal and Near Horizontal Gas-Liquid Flow," *AIChE J.*, Vol. 22, No 1.

11. Tuomisto, H. and Kajanto, P., 1988, "Two Phase Flow in a Full Scale Loop Seal Facility," *Nuclear Eng. and Design*, 107, 295-305.

19 ADDITIONAL LOCA HYDRODYNAMIC ASSESSMENT AGAINST LARGE SCALE EXPERIMENTS

19.1 INTRODUCTION

The phenomena identification and ranking table (PIRT) documented in Section 2, Volume 1 identified highly important hydrodynamic phenomena that occur during the Loss-of-Coolant Accident (LOCA) sub-scenarios. The objective of this section is to complete the assessment of specific WCOBRA/TRAC-TF2 models that were not addressed with the Separate Effects Test (SET) or Integral Effects Test (IET) evaluation presented in the other sections. The phenomena considered here are associated in particular with the Large Break LOCA (LBLOCA) scenario.

For previous WCOBRA/TRAC evaluation models, an extensive assessment was performed, and has been documented in Sections 14 and 15 of the Code Qualification Document, CQD (Bajorek et al., 1998). The most critical elements of this original assessment are repeated here to validate the performance of the new WCOBRA/TRAC-TF2 code, and confirm that the conclusions in terms of biases remain consistent with the already validated versions. The rational for the selection of the tests used in this assessment is discussed in Section 2, Volume 1.

The PIRT identified the following critical hydrodynamic models that can occur during a postulated LOCA transient.

Counter-Current Flow Limitation

The Counter-Current Flow Limitation (CCFL) is associated with the process of restricting liquid flow by counter-flowing vapor, due to interfacial drag forces. For example, liquid downflow in a pipe under the influence of gravity becomes unstable with increasing vapor upflow and eventually flows together with the vapor. Thus, stable counter-current conditions can exist only within a certain range. The boundary of this range is recognized as the CCFL.

CCFL can occur in several locations in a pressurized water reactor (PWR) during a LOCA. Emergency Core Cooling (ECC) bypass during the blow-down phase of a Large Break LOCA is an example of exceeding CCFL conditions in the downcomer annulus. CCFL is possible in other locations in the vessel. Liquid in the upper plenum may be held up at the upper core plate or tie plate by an upflow of steam from the core. Note, the upper core plate is the most flow restrictive area between the core and upper plenum. For Westinghouse PWRs, the tie plate corresponds to the fuel assembly top nozzle region. CCFL may also occur in the loops during some LOCA scenarios. CCFL may occur in the U-tubes of a steam generator or in the hot leg bend during a Small Break LOCA (SBLOCA) transient, affecting the depressurization of the system, and therefore, the overall progression of the transient. For larger breaks, the flow in the hot leg tends to stratify, and liquid is intermittently swept into the plenum of the steam generator. Any liquid swept into the steam generator tubes will tend to be evaporated, Section 1-3-3-3 of (Bajorek et al., 1998).

The predictive capability of WCOBRA/TRAC-TF2 for CCFL phenomena is assessed for different conditions, as follows:

1. CCFL in a Downcomer Annulus – **[**

][a,c]

2. CCFL in a Perforated Plate – **[**

][a,c]

3. CCFL in the Steam Generators – **[**

][a,c]

4. CCFL in the Hot Leg Bend – CCFL in the hot leg was **[**

][a,c]

Entrainment and De-Entrainment

Entrainment from liquid films and de-entrainment on structures are important processes that determine the mass distribution in the Reactor Coolant System (RCS) during a LOCA. Droplets leaving the core can be de-entrained by the upper plenum structures, forming a pool above the upper core plate. The de-entrainment and liquid accumulation in the upper plenum has two competing effects on the core flooding rate. Liquid that de-entrains in the upper plenum does not carryover into the steam generators and forms a pool in the upper plenum. The pool in the upper plenum creates a static pressure head that could decrease the flooding rate by some amount. A beneficial effect of the upper plenum pooling is the potential for draining of water into the core in the low power regions, where the steam flow is insufficient to prevent counter-current flow conditions. Liquid draining from the upper plenum can contribute to cooling by replenishing the core liquid inventory and providing topdown cooling. The entrained droplets that leave the upper plenum can be brought to the steam generator and evaporate inside the steam generator U-tubes, if the secondary side temperature is higher than the primary side temperature. The steam acceleration and the high speed of steam result in a large pressure drop in the steam generators. This high pressure loss in the steam generator caused by the evaporation of droplets, which is called steam binding effect, further contributes to additional pressure increase in the upper plenum.
[

][a,c]

Entrainment at the quench front has a strong effect on the net reflood rate and on the downstream heat transfer. Droplets entrained at the quench front readily evaporate, de-superheating the vapor, and can under certain conditions, impact on the fuel rods (though direct contact heat transfer is not modeled as discussed in Section 7.2.7, Volume 1). Lower downstream vapor temperatures and direct contact heat transfer increases the rate of heat transfer far ahead of the quench front, decreasing the peak cladding temperatures. **[**

][a,c]

Entrainment also occurs in the lower plenum during blowdown and the early part of refill. Droplets can be entrained from the liquid pool at the bottom of the vessel. During blowdown, these droplets are swept out of the vessel to the break through the voided downcomer. In the refill period, some of the droplets may enter the core and contribute to cooling, while most de-entrain on the lower core plate and remain in the lower plenum. **[** **]**[a,c]

Finally, entrainment/de-entrainment occurs in the downcomer during reflood. As the water level in the downcomer approaches the loop level, high steam or non-condensable flow from the intact loops may cause some water entrainment out the break. **[**

][a,c]

Therefore, the predictive capability of WCOBRA/TRAC-TF2 for entrainment and de-entrainment phenomena needs to be assessed for different conditions, as follows:**[**

][a,c]

Entrainment/de-entrainment models are relevant in various regions of plant analyzed. The capability of the code to model these processes together with the interaction with other process (e.g., the heat transfer) is a potential source of compensating errors. Section 24 provides an in-depth analysis of such compensating errors and the assessment presented in this section is the basis of such analysis.

Condensation

Condensation of steam by subcooled water will be initiated during a Large Break LOCA when accumulator water begins to flow into the cold leg piping. High head safety injection (HHSI) may begin earlier, but the flow rate is much lower than the accumulator (ACC) or low head safety injection (LHSI), and is therefore relevant only for the smaller breaks, where the time before accumulator or low head safety injection could be significant. Condensation of steam is of critical importance for both small and larger breaks, but the physical conditions differ significantly, and the Westinghouse cold leg condensation models introduced in Section 6 must be robust and generic enough to adequately address these different conditions. It is noted that the high head safety injection and low head safety injection are named as safety injection (SI) and residual heat removal (RHR) in Section 26, respectively.

For large breaks, the subcooled Emergency Core Cooling System (ECCS) water will flow from the cold legs into the upper downcomer and, later in the transient, into the lower plenum and core. During late blowdown and refill, the flow of accumulator water is of sufficient magnitude to theoretically condense all the steam flowing into the cold leg. During the reflood phase, the low head safety injection flow, at its minimum levels, is typically insufficient to condense all the steam flowing into the cold leg. Condensation of steam in the downcomer has been observed to strongly affect the counter-current flow behavior in the downcomer as ECCS water penetrates into the lower plenum. As discussed above, ECCS bypass and Counter-Current Flow are basic processes, of which the accurate prediction is a fundamental requirement for a best-estimate LOCA code.

Also, steam condensation affects steam velocity in the downcomer and as a result the sweep-out, entrainment of liquid toward the break. The higher steam flow rate, in turn, may entrain more water from the downcomer to the break, and may increase the pressure drop through the broken cold leg nozzle.

Condensation of steam by ECCS water was also observed to produce flow and pressure oscillations of sufficient magnitude to affect the flow through the intact loops during reflood. This led initially to a concern that condensation phenomena would induce resistance in the intact cold legs and impede the flow of steam from the core during reflood. Tests in which the injection of ECCS water into the cold leg was simulated indicated that, while the hydrodynamic behavior was highly oscillatory, the induced resistance was relatively small.

The degree to which condensation of steam occurs in the cold leg, usually indicated by the condensation efficiency, is also important in determining the steam flow rate and temperature of the water flowing into the vessel during reflood. If the condensation efficiency is high, the steam flow will be reduced, and the water temperature will be increased. The condensed water, if it is still subcooled, will reach saturation after it enters the vessel and begin to boil sooner in the downcomer and core. The lower steam flow may entrain less water from the downcomer out the break, and leads to more vessel inventory. It also may result in a smaller pressure drop across the broken cold leg nozzle. If the condensation efficiency is low, the colder water will contribute to maintain the subcooling of the water in the downcomer.

Condensation is known to be strongly affected by the presence of non-condensable gases. As the accumulator empties, nitrogen is discharged in the system and results in pressurization of the downcomer as well as reduction in steam condensation rate. During reflood, a large volume of nitrogen is injected into the cold legs when the accumulator runs out of water. During refill, the RCS pressure may momentarily drop below containment pressure because of condensation, allowing containment gases to flow into the RCS via the broken cold leg.

For larger breaks, the primary side system experiences a rapid depressurization so that most of the condensation phenomena take place at low pressure. For smaller breaks however, the system pressure transient is slower, as discussed in Section 2. In this case, condensation in the cold leg at the high head safety injection is of significant importance, as condensation of the steam from the cold high head safety injection can significantly impact the transient pressure and vessel inventory. The assessment of the cold leg condensation for the Small Break LOCA is addressed in Section 17, while this section focuses on the Large Break LOCA.

Therefore, the predictive capability of WCOBRA/TRAC-TF2 for the condensation phenomenon needs to be assessed for different conditions, as follows:**[**

][a,c]

The rest of this section discusses the performance of the models and correlations in WCOBRA/TRAC-TF2 used to simulate the processes discussed above.

The assessment roadmap is presented in Section 19.2. WCOBRA/TRAC-TF2 assessments are then documented in detail in Sections 19.3 through 19.6. Finally, Section 19.7 provides overall conclusions of the assessments documented in this Section.

19.2 HYDRODYNAMIC MODELS ASSESSMENT

Counter-Current Flow Limitation

Section 5.4 discusses the interfacial drag models that determine the existence of CCFL conditions in the vessel, Section 5.7 describes the corresponding interfacial drag models used for 1D components, and Section 5.15 describes the models available to enforce CCFL in the vessel and 1D components. As discussed in the previous Section 19.1, the predictive capability of WCOBRA/TRAC-TF2 for CCFL phenomena needs to be assessed for the following conditions:

1. CCFL in a Downcomer Annulus – CCFL/ECC bypass in the downcomer annulus of the full-scale Upper Plenum Test Facility (UPTF) is evaluated in Section 19.3, where WCOBRA/TRAC-TF2 results are compared to experimental data for the UPTF 6 tests.

2. CCFL in a Perforated Plate – CCFL could occur above the core at the top nozzle (tie plate) or upper core plate elevations. CCFL is **[**

   ][a,c] WCOBRA/TRAC-TF2 predictions of CCFL at a perforated plate are evaluated with saturated liquid and steam at 1000 psia, 35 psia, and 14.7 psia, and results are compared with Northwestern test data in air-water at atmospheric conditions (Hsieh et al., 1980) in Section 19.4. The geometry of the plate (perforation ratio and thickness) simulates, at small scale, a perforated plate in a PWR. **[**

   ][a,c]

3. CCFL in the Steam Generators – CCFL is **[**

   ][a,c] The CCFL in steam generator U-tubes is evaluated based on simulations of the Rig-of-Safety Assessment (ROSA) experiments in Section 21.10. **[**

   ][a,c]

4. CCFL in the Hot Leg Bend – CCFL is **[**

   ][a,c] The CCFL in the hot leg bend is also evaluated based on simulations of the ROSA experiments in Section 21.10. CCFL in the hot leg was **[**

   ][a,c]

CCFL is not enforced in the pump suction piping since any draining of liquid into the loop seal region would tend to increase the resistance to steam venting.

Entrainment and De-Entrainment

Section 5.6 of Volume 1 described the models and correlations in WCOBRA/TRAC-TF2 that are used to calculate the entrainment and de-entrainment processes. A summary of the applicable models in WCOBRA/TRAC-TF2 is provided for reader convenience in Section 19.2.1 herein.

As discussed in the previous Section 19.1, the predictive capability of WCOBRA/TRAC-TF2 for entrainment and de-entrainment phenomena needs to be assessed for the following conditions:

1. Upper Plenum Entrainment and Carryover – WCOBRA/TRAC-TF2 simulations were performed for tests that provided information on the net effects of entrainment/de-entrainment and carryover in the upper plenum. Applicable simulations include UPTF Test 29B, Cylindrical Core Test Facility (CCTF) 62 and Loss-of-Fluid Test (LOFT) experiments (LOFT analysis is presented in Section 22). UPTF Test 29B simulated the conditions in the upper plenum during reflood, and provided measurements of liquid level above the upper core plate. The UPTF upper plenum was full-scale in both height and cross section. The main purpose of Test 29B was to determine the amount of upper plenum de-entrainment and carryover. The WCOBRA/TRAC-TF2 simulation of this test is described in Section 19.3.

2. Downcomer Entrainment, during ECC Bypass Period and During Reflood – During the latter part of blowdown, ECC fluid injected into the cold legs begins to penetrate and fall into the downcomer. Partial penetration may occur, as liquid falls part way down the downcomer but is then swept back to the broken cold leg. As the steam flow rates in the downcomer decrease, liquid can eventually reach the lower plenum. Evaluations by Siemens of UPTF bypass tests showed that the ECC delivery to the lower plenum is multi-dimensional in nature. The fraction of ECC liquid reaching the lower plenum depended not only on the steam flow rate, but also on the relative location of the ECC downcomer entry point to the broken loop (Glaeser, 1992). In addition to determining the downcomer flooding limit, the five subphases of UPTF Test 6 are selected to evaluate the ability of WCOBRA/TRAC-TF2 to predict entrainment and de-entrainment phenomena that occur in a downcomer during the blowdown and early refill periods of a LOCA. These tests and the WCOBRA/TRAC-TF2 simulations of them are described in Section 19.3.

   Downcomer entrainment is also an important process during the reflood phase. During reflood, the liquid level in the downcomer can oscillate and reach up to the level of the bottom of the cold legs. Liquid can be swept from the downcomer out of the break during these oscillations. While the liquid level is below the cold legs, drops can be entrained from the liquid pool and carried out the break if high steam flows occur around the downcomer. UPTF Test 25A was conducted in order to investigate entrainment and downcomer level behavior during the reflood phase of a Large Break LOCA. The simulation of UPTF 25A using WCOBRA/TRAC-TF2 is described in Section 19.3.

3. Entrainment in the Core During Bottom Reflood – The correlation used to determine the entrainment rate at a quench front is described in Section 5.6 of Volume 1. The model is consistent with the work of Kataoka and Ishii (1983) and assumes the entrainment is due to vapor bubbling through a pool of liquid. The Full-Length Emergency Core Heat Transfer (FLECHT)

reflood test simulations provide a means of examining the performance of the entrainment model for bottom reflood. Mass balances were calculated from the test data so that carryout fraction and mass retention in the test bundle could be estimated. Section 19.5 compares the WCOBRA/TRAC-TF2 predictions of carryout fraction, total bundle mass, steam exit flow, and liquid outflow to estimates derived from the FLECHT test data. The comparisons provide a means of assessing the bottom reflood entrainment model.

Condensation

Section 6 of Volume 1 described the models and correlations in WCOBRA/TRAC-TF2 that are used to calculate the condensation processes (interfacial heat and mass transfer models). Section 6.2 describes the treatment of interfacial heat and mass transfer in the vessel component, while Section 6.3 addresses 1D components. The effect of non-condensable is described in Sections 6.2.11 and 6.3.7 for the respective vessel component and 1D components.

As discussed in the previous Section 19.1, the predictive capability of WCOBRA/TRAC-TF2 for condensation phenomena needs to be assessed for the following conditions:

1. Condensation in Downcomer Annulus – Condensation in the downcomer is an important contributor to the end of bypass/beginning of refill in a Large Break LOCA. Condensation in the downcomer of the full-scale UPTF is evaluated in Section 19.3, where WCOBRA/TRAC-TF2 results are compared to experimental data for the UPTF Test 6 series.

2. Condensation in Cold Legs, at both High and Low Pressure – Condensation in the cold legs was evaluated in Section 17. Condensation in the presence of safety injection at high pressures, representative of a Small Break LOCA, was assessed using data from the Westinghouse and Framatome Condensation on Safety Injection (COSI) configurations, and the ROSA facility. Condensation at low pressures, representative of a Large Break LOCA, was assessed using data from UPTF Test 8A. The effect of condensation in both the cold legs and downcomer is also examined with respect to the sweep-out phenomena during reflood by examining UPTF test 25A. The assessment of code predictions against UPTF 8A and UPTF 25A is presented in Section 19.3

3. Effect of Non-Condensable Gases on Condensation – Accumulator nitrogen injection was part of the LOFT and ACHILLES experiments, and the WCOBRA/TRAC-TF2 assessment results are discussed in Section 20. Additional assessment of the effect of non-condensables is provided via numerical “thought problems” in Section 23.

Integral Effects Assessment

CCTF is an integral effects test to evaluate the combined effect of CCFL in the tie plate, upper plenum de-entrainment, steam binding in steam generators, condensation in the cold leg and downcomer, entrainment/de-entrainment in the downcomer, and entrainment in the core, for the reflood phase of a Large Break LOCA. The modeling, simulation and assessment of CCTF 62 are presented in Section 19.6.

19.2.1 WCOBRA/TRAC-TF2 Models for Entrainment

Section 5.6 of Volume 1 described the models and correlations in WCOBRA/TRAC-TF2 that are used to calculate the entrainment and de-entrainment processes. Entrainment is the result of interfacial shear between vapor and liquid film. In WCOBRA/TRAC-TF2, liquid is moved from the continuous liquid field to the entrained field when the interfacial shear forces acting on the liquid are sufficient. In de-entrainment, liquid is moved from the entrained field to the continuous liquid field. A summary of the applicable models in WCOBRA/TRAC-TF2 is as follows:

1. Entrainment in Film Flow – WCOBRA/TRAC-TF2 determines film entrainment rates by comparing the entrainment rate based on a stable film flow to an empirical entrainment rate based on the work of Walley et al. (1973).

2. Entrainment in Bottom Reflood – The model for entrainment in the core near the quench front is based on a model by Kataoka and Ishii (1983) assuming vapor bubbling through a liquid pool.

3. Entrainment in Top Down Reflood – Models describing the transfer of liquid from the continuous liquid to the entrained drop field is described in Section 5.6.4 of Volume 1. The models account for the entrainment of liquid draining from pools and the entrainment of films from the rods at a top down quench front.

4. De-Entrainment in Film Flow – The model to estimate the de-entrainment of entrained drops into the continuous liquid field uses an empirical model by Cousins et al. (1965).

5. Crossflow De-Entrainment – Entrained liquid in the upper plenum can de-entrain on structures there as the two-phase mixture flows from the vessel into the hot legs. WCOBRA/TRAC-TF2 uses a model based on experiments by Dallman and Kirchner (1980) to determine the amount of de-entrainment in the upper plenum and other regions of the reactor vessel.

6. De-Entrainment at Area Changes – De-entrainment occurs as a two-phase mixture encounters a flow restriction such as a tie plate. WCOBRA/TRAC-TF2 uses a simple area ratio to de-entrain a fraction of the droplet field where an area reduction occurs in the reactor vessel.

7. De-Entrainment at Solid Surfaces and Liquid Pools – Drops are assumed to de-entrain when the drops flow into a cell with a solid surface at the opposite face, or when the drops flow into a cell which is in a bubbly flow regime.

19.3 UPPER PLENUM TEST FACILITY TESTS

19.3.1 Introduction

The UPTF was designed to obtain experimental data relative to the multi-dimensional flows expected in a PWR during a LOCA. The UPTF was the German contribution to the 2D/3D program established by the United States Nuclear Regulatory Commission (NRC), the Japan Atomic Energy Research Institute (JAERI) and the Federal Republic of Germany (BMFT). Tests conducted in the UPTF gave special consideration to:

1. Entrainment and de-entrainment in the upper plenum,
2. Co-current and counter-current two-phase flow in the upper core plate and tie plate region,
3. Co-current and counter-current flow and bypass in the downcomer, and
4. Condensation and steam/water mixing processes caused by ECC injection in the cold legs.

This section describes the modeling and simulation of several of the UPTF experiments using WCOBRA/TRAC-TF2. The simulations used were Tests 6 (to evaluate the ability of the code to predict ECC bypass), Test 25A (to evaluate entrainment of liquid out of the downcomer due to steam flow during reflood and condensation in cold leg and downcomer), Test 8A (to evaluate the models and correlations for condensation in the cold leg), and Test 29B (to validate the models for calculating de-entrainment in the upper plenum).

An overall facility description is provided in Section 19.3.2. The ECC bypass and entrainment/de-entrainment in downcomer and the simulations of UPTF 6 are described in Sections 19.3.3 to 19.3.5, while the cold leg condensation and the simulation of UPTF 8A are described in Sections 19.3.6 to 19.3.8. The downcomer entrainment/de-entrainment and cold leg condensation in UPTF 25A is described and simulated in Sections 19.3.9 to 19.3.11, and the upper plenum de-entrainment in UPTF 29B is described in Sections 19.3.12 to 19.3.14.

19.3.2 UPTF Facility Description

The UPTF simulated a full-scale 3900 MWt German PWR. The facility had four loops, each with a steam/water separator to simulate a steam generator and a variable resistance to simulate a reactor coolant pump. The upper plenum contained full size internals in an arrangement typical of a KWU PWR. Figures 19.3-1 and 19.3-2 show an overall diagram of the UPTF.

The upper plenum test facility was designed to investigate:

1. Water entrainment and separation processes in the upper plenum,

2. Co-current and counter-current steam/water flow phenomena in the upper core plate or tie plate region including water break-through into the core,

3. Co-current and counter-current steam/water flow in the downcomer and possible bypass of the ECC water injected into the cold legs of the loops to the break nozzle,

4. Condensation and mixing processes in the hot and cold legs of the loops, in the upper plenum and in the downcomer as a result of the injection of cold ECC water and,

5. Loop behavior with regard to possible water plug formation and oscillations in the hot and cold legs of the loops with ECC injection.

This range of investigation was achieved by varying the configuration of the facility. Full details of the facility and its instrumentation are given in Emmerling et al. (1988).

There were three intact loops and one loop with a break in the cold leg. The loop break was represented by gate valves and orifice plates to control the flow and a containment simulator gave the desired back pressure. The broken loop cold leg contained a water separator to prevent water from entering the containment simulator. The steam generators were simulated by four steam/water separators and adjustable passive resistances were used to simulate the four reactor coolant pumps. The facility did not contain a heated core, but the internals at the top of the core and in the upper plenum were full-scale replicas. The core itself was simulated by a steam/water injection system to set up the appropriate flow conditions in the vessel. The tubes that deliver the fluid to the core came up through the lower plenum.

The reactor vessel is shown in Figure 19.3-3. The upper plenum contained sixty-one guide tubes, eight support columns above the simulated fuel assemblies and eight support columns outside the periphery of the core (Figure 19.3-4). The downcomer gap width was 0.25 meters (9.8 inches) and the vessel internal diameter was 4.87 meters (191.7 inches).

The UPTF simulated the upflow of steam and droplets through the core during reflood by injection of steam and water into dummy fuel rods. The dummy fuel rods represented the upper quarter of a core with 193 assemblies of 16x16 array of fuel rods. Sixty-one of the assemblies were below guide tubes and had control rod spider simulators (Figure 19.3-5). The remaining assemblies were below flow restrictors in the upper core plate. The water and steam injection nozzles are shown in Figure 19.3-6. There were seventeen independently controlled injectors which divided to provide a separate nozzle for each dummy fuel rod assembly.

The dummy control rods terminated at the bottom of the guide tubes which were sealed to prevent flow from the upper plenum to the upper head. The upper head was thereby isolated from the rest of the vessel and had no effect on the facility.

The UPTF cold legs had an inner diameter of 750 millimeters. The ECC injection was at an angle of 60° to the cold leg centerline in UPTF and was 5822 millimeters (19.1 feet) from the inside wall of the vessel.

The steam generator simulators for the intact and broken loops and the broken cold leg water separator are shown in Figure 19.3-7. Flow entered an inlet plenum, which had the same volume as a PWR steam generator, and rose through cyclone tubes. The cyclones separated the water from the steam and the water was removed from the loop. The steam flowed through the steam generator upper plenum and returned to the cold leg.

The water drainage system removed the large quantities of water that accumulated during a test. Generally these quantities were found in the test vessel, the steam generator simulators, the broken cold leg water separator, and in the drainage vessels of the broken loops.

The raw data produced from the instrumentation was continuously recorded throughout a test, some of which was post-processed to give computed parameters. An example of a computed parameter derived from raw data is liquid level, which is derived from the measurement of differential pressure.

The downcomer was instrumented with fluid distribution grids, turbine meters, differential and absolute pressure transducers, and fluid and wall thermocouples. The lower plenum and core regions were instrumented with optical liquid level detectors, differential pressure transducers, and fluid and wall thermocouples. The instrumentation in the upper plenum included:

1. Wall and fluid thermocouples,
2. Fluid thermocouples in end boxes and below the tie plate,
3. Differential pressure transducers across the tie plate,
4. Differential pressure transducers and capacity liquid level detectors in upper plenum,
5. Optical liquid level detectors and fluid distribution grids,
6. Video probes in upper plenum,
7. Break-through detectors below tie plate,
8. Tie plate drag bodies in end boxes and,
9. Turbine meters in end boxes and in upper plenum.

19.3.2.1 Scaling Consideration and Applicability to PWR

The cold leg and the test vessel upper plenum, the lower plenum, and the downcomer of the UPTF are geometrically similar to a PWR. Table 19.3-1 compares the major dimensions of UPTF with a typical Westinghouse 4-loop PWR, which is referred to as typical PWR in the following discussions. Comparisons of the primary system components are summarized below.

Downcomer

The downcomer dimensions below the cold legs (e.g., gap, diameter, length, and flow area) are basically the same for UPTF and the typical PWR. The vessel wall of the UPTF is thinner than that of a typical PWR.

Cold Leg

The cold leg piping diameters are fairly similar between UPTF and the typical PWR (0.75 m vs. 0.70 m). The UPTF cold leg flow area is only 15% larger than that for the typical PWR. The distance from the ECC nozzle to the downcomer at UPTF is 30% longer than that at the typical PWR. A longer mixing region in the cold leg may result in more condensation at UPTF than at a PWR. The ECC nozzle diameters are comparable between UPTF and the typical PWR. For a PWR, the ECC nozzles are typically located on top of the cold leg with an injection angle of 90°. In UPTF, the nozzle lies in a horizontal plane at an angle of 60° from the cold leg piping.

Reactor Core

UPTF did not have an active core, but there were 193 16x16 dummy fuel assemblies on top of the core, which is similar to the core of a typical PWR (193 15x15 fuel assemblies). As for flow area, UPTF has a core flow area of 1.05 times the core flow area of a typical PWR.

Upper Plenum

The ratio of the UPTF upper plenum flow area to that of typical PWRs is around 1.2. It should be noted that the exact configuration and arrangement of the upper plenum structures are plant specific. The height of the upper plenum in the UPTF is only about 0.67 of that in a typical PWR because of the shorter distance from the hot leg nozzle to the upper support plate in UPTF. The height difference is not expected to be important for the assessment of the entrainment/de-entrainment in the upper plenum.

Hot Leg

The hot leg diameter at UPTF is slightly larger than that at typical PWRs, while the flow area of an UPTF hot leg is less than the flow area of a typical PWR hot leg. This is because the flow area of the UPTF hot leg is reduced by an internal ECC injection pipe (called Hutze in UPTF). The difference of the hot leg between UPTF and a typical PWR is judged inconsequential for the assessment.

UPTF 6, UPTF 8A, UPTF 25A, and UPTF 29B are utilized for the assessment in this section. The test conditions and the applicability of the test are analyzed below.

UPTF 6

[

]^{a,c}

UPTF 25A

[

]a,c

UPTF 8A

[

]a,c

UPTF 29B

[

]a,c

[

]a,c

19.3.3 UPTF 6 ECC Bypass and Downcomer Counter-Current Flow Test Descriptions

During the blowdown phase of a large cold leg break LOCA, the reactor vessel rapidly depressurizes, causing most of the liquid inventory to flash into steam. This steam and entrained water flow up the downcomer and out the broken cold leg. After the system has partially depressurized, ECC is injected into the intact cold legs. The resulting counter-current steam/water flow in the downcomer is important since it affects how quickly the reactor vessel refills. As the pressure in the reactor vessel begins to reach an equilibrium state with the containment pressure, the steam flow is reduced and the ECC starts to fill the vessel and reflood the core. The objective of UPTF Test 6 was to investigate ECC penetration and counter-current flow phenomena in the downcomer of a PWR during the end of blowdown and refill portions of a LOCA. In addition to determining the downcomer flooding limit, simulation of these tests also evaluates the ability of WCOBRA/TRAC-TF2 to predict entrainment and de-entrainment phenomena in a downcomer during blowdown and early refill. The assessment of the condensation efficiency in the downcomer is also part of the objective of UPTF 6 simulations.

The system configuration of UPTF Test 6 is shown in Figure 19.3-8; the pump simulators were closed and only the cold leg break valve was opened. Steam was injected in the core simulator and steam generator simulator. Because flow paths to the intact cold leg and broken hot leg were blocked, the steam was forced to flow downward through the lower plenum, up the downcomer, and out the vessel through the broken cold leg. ECC water was injected to each intact cold leg.

A summary of test boundary conditions for UPTF 6 is given in Table 19.3-2. In UPTF Test 6, five steady-state runs were conducted with steam flows of 102, 203, 295, 396, and 439 kg/s to establish points on a flooding curve for UPTF. Steam injection was to both the core and steam generator simulators except for the low steam flow run during which injection was only to the core. ECC water was injected at approximately 500 kg/s to each of the three intact cold legs. The subcooling of ECC water varied from 28 to 65 °C. The containment pressure was maintained around 2.5 bar except Test 135, where pressure was 3.4 bar.

19.3.4 WCOBRA/TRAC-TF2 Model for UPTF Test 6

The WCOBRA/TRAC-TF2 model VESSEL component for the calculations to compare to UPTF Test 6 simulations is shown in Figures 19.3-9 through 19.3-13. [

]a,c

The WCOBRA/TRAC-TF2 loop model used for the UPTF Test 6 transient calculations is shown in Figure 19.3-14. In the test facility, the broken loop is a piping system leading from the vessel to a steam water separator and then to the containment simulator (Figure 19.3-1). A simplified model was used to simulate UPTF Test 6. **[**

][a,c]

The intact cold legs were represented by PIPE components, and the ECC was modeled as a boundary condition applied through the FILL components. The broken loop was represented by one PIPE component. The pressure at the broken loop flowmeter was specified by a BREAK component.

19.3.5 Simulation of UPTF Test 6

UPTF Test 6 was run in five separate sub-phases, each sub-phase with a different combination of liquid and steam injection rates. The intact loops were blocked at the pump simulators, forcing all steam down through the lower plenum and up the downcomer to the broken cold leg.

The results of the five tests UPTF 6-131, 132, 133, 135, and 136 are presented in the following sections. As discussed in Section 19.2, the UPTF 6 simulation with WCOBRA/TRAC-TF2 is used specifically to assess the code capability with regards to three specific processes: (1) ECC Bypass in the downcomer (CCFL); (2) entrainment and de-entrainment in the downcomer during ECC Bypass and (3) condensation in the downcomer. The discussion of CCFL during ECC bypass, entrainment and de-entrainment during ECC bypass, and condensation efficiency in the UPTF 6 tests is also given in this section.

19.3.5.1 UPTF 6-131

The total core steam injection flow for Run 131 is shown in Figure 19.3-15, and the steam generator injection flows is shown in Figure 19.3-16. The ECC injection to each of the intact cold legs is shown in Figure 19.3-17. These as-measured injection flow rates were used as boundary conditions in the WCOBRA/TRAC-TF2 model for Run 131. The measured pressure at the pipe flow meter was applied to the BREAK component as the boundary condition.

The WCOBRA/TRAC-TF2 simulation was run for 100 seconds, which corresponds to the test time period of 30 to 130 seconds for Run 131. **[**

][a,c]

[

]a,c

19.3.5.2 UPTF 6-132

The total core steam injection flow for Run 132 is shown in Figure 19.3-33, and the steam generator injection flows in Figure 19.3-34. The ECC injection to each of the intact cold legs is shown in Figure 19.3-35. These as-measured injection flow rates were used as boundary conditions in the WCOBRA/TRAC-TF2 model for Run 132. The measured pressure at the pipe flow meter was applied to the BREAK component as the boundary condition.

The WCOBRA/TRAC-TF2 simulation was run for 100 seconds, which corresponds to the test time period of 31 to 131 seconds for Run 132. [

]a,c

[

]a,c

19.3.5.3 UPTF 6-133

The total core steam injection flow for Run 133 is shown in Figure 19.3-51, and the steam generator injection flows in Figure 19.3-52. The ECC injection to each of the intact cold legs is shown in Figure 19.3-53. These as-measured injection flow rates were used as boundary conditions in the WCOBRA/TRAC-TF2 model for Run 133. The measured pressure at the pipe flow meter was applied to the BREAK component as the boundary condition.

The WCOBRA/TRAC-TF2 simulation was run for 100 seconds, which corresponds to the test time period of 30 to 130 seconds for Run 133. [

]a,c

[

]a,c

19.3.5.4 UPTF 6-135

The total core steam injection flow for Run 135 is shown in Figure 19.3-69, and the steam generator injection flows in Figure 19.3-70. The ECC injection to each of the intact cold legs is shown in Figure 19.3-71. These as-measured injection flow rates were used as boundary conditions in the WCOBRA/TRAC-TF2 model for Run 135. The measured pressure at the pipe flow meter was applied to the BREAK component as the boundary condition.

The WCOBRA/TRAC-TF2 simulation was run for 100 seconds, which corresponds to the test time period of 30 to 130 seconds for Run 135. [

]a,c

[

][a,c]

19.3.5.5 UPTF 6-136

The total core steam injection flow for Run 136 is shown in Figure 19.3-87. The ECC injection to each of the intact cold legs is shown in Figure 19.3-88. No steam was injected through the steam generator simulators in this run. These as-measured injection flow rates were used as boundary conditions in the WCOBRA/TRAC-TF2 model for Run 136. The measured pressure at the pipe flow meter was applied to the BREAK component as the boundary condition.

The WCOBRA/TRAC-TF2 simulation was run for 100 seconds, which corresponds to the test time period of 30 to 130 seconds for Run 136. **[**

][a,c]

19.3.5.6 ECC Bypass in UPTF 6: CCFL in Downcomer Annulus

The amount of ECC water which penetrated into the lower plenum during the UPTF 6 tests was obtained by converting a pressure difference to the lower plenum inventory (2D/3D, 1989) or performing a mass balance on the lower plenum (2D/3D, 1989) or the vessel (MPR-1163, 1990a). Three different methods have been used to estimate the test ECC penetration flow rate:

- Method 1: Lower plenum refill rate converted from measured pressure difference between the bottom of lower plenum and the top of lower plenum (direct way), as determined by Siemens (2D/3D, 1989).

- Method 2: Lower plenum refill rate estimated from a mass balance (indirect way), as determined by Siemens (2D/3D, 1989).

- Method 3: Vessel refill rates estimated from vessel liquid accumulation (direct way) and mass balance (indirect way), as determined by MPR (MPR-1163, 1990a).

The ECC penetration rate was estimated for a certain period of time during the test, called the evaluation time period. The evaluation time period over which the pressure measurement or mass balance was taken extended from the point where full steam and water flow were established in the test, to the point where the lower plenum filled with liquid. The ECC penetration rate was then calculated as the average accumulation rate over this time period.

The evaluation period and refill rate of Method 1 are obtained from Table 4 in the UPTF 6 test report (2D/3D, 1989), and the lower plenum inventory of Runs 131, 132, 133, 135, and 136 are obtained from Tables 5, 6, 7, 8, 9, and 10 of the UPTF 6 test report (2D/3D, 1989), respectively. The evaluation period, lower plenum inventory, and refill rate of Method 1 are summarized in Table 19.3-3.

The evaluation period of Method 2 is the same as that of Method 1, and the refill rate of Method 2 is also obtained from Table 4 of the UPTF 6 test report (2D/3D, 1989). The evaluation period, lower plenum inventory, and refill rate of Method 2 are summarized in Table 19.3-4. It is noted that no refill rate of Method 2 is available for Run 135. There is no record of lower plenum inventory from Method 2. Instead, the lower plenum inventory at the beginning of the evaluation period is assumed the same as that from Method 1. The lower plenum inventory at the end of the evaluation period is evaluated from the inventory at the beginning, the length of the evaluation period, and the refill rate.

The difference between Method 1 and Method 2 is an indication that such estimates are affected by a large uncertainty.

The MPR report (MPR-1163, 1990a) gives estimated vessel inventories from both measured pressure difference (direct way) and mass balance (indirect way) using Method 3. For estimation of the ECC penetration rate, the lower plenum inventory and the lower plenum refill rate are clearer indicators than the vessel inventory, which includes the downcomer inventory. Therefore, this report focuses on the comparison between the lower plenum refill rate from Method 1 and Method 2 and the WCOBRA/TRAC-TF2 prediction.

[

]^{a,c}

The CCFL behavior calculated by WCOBRA/TRAC-TF2 for UPTF Test 6 was evaluated by comparing the scaled Kutateladze number (UPTF scale) to the published data (Glaeser, 1992) and the following CCFL flooding curve suggested for UPTF (Glaeser, 1992):

$$\sqrt{K_g^*} + m\sqrt{K_\ell^*} = C \tag{19.3-1}$$

where K^*_g is the UPTF-scaled Kutateladze number $K_g^* = \frac{K_g \nu_g^{2/3}}{g^{1/3}\left(\frac{l_2 + l_3}{2}\right)}$, m=0.011 and C=0.0245.

The Kutateladze numbers are expressed as:

$$K_g = \frac{\dot{m}_s}{\sqrt{\rho_g} A_{DC} \left(g\sigma\left(\rho_\ell - \rho_g\right)\right)^{1/4}} \tag{19.3-2}$$

$$K_\ell = \frac{\dot{m}_\ell}{\sqrt{\rho_\ell} A_{DC} \left(g\sigma\left(\rho_\ell - \rho_g\right)\right)^{1/4}} \tag{19.3-3}$$

The symbols $\dot{m}_s$ and $\dot{m}_\ell$ are the steam mass flow rate and liquid mass flow rate, respectively, the phasic density is ρ, the surface tension is σ, and g is the gravitational acceleration. The value A_{DC}, l_2, and l_3 are geometry information of UPTF.

Table 19.3-7 presents the results of the calculation of Kutateladze numbers for both the experimental data and the WCOBRA/TRAC-TF2 prediction. The steam flow rates in Table 19.3-7 are the actual steam flow rates of the UPTF 6 tests in Table 19.3-5. The actual steam flow rate also served as the boundary condition for the prediction. Therefore, the Kutateladze number of the steam flow is the same for both the experiment and the prediction.

[

]^{a,c}

19.3.5.7 Entrainment and De-Entrainment in the Downcomer During ECC Bypass

In the previous discussion, the lower plenum mass inventory was analyzed to assess the prediction of CCFL in a downcomer annulus during ECC bypass. In the following discussion, comparisons of the estimated and predicted mass distributions in the UPTF Test 6 series are used to assess the prediction of net entrainment/de-entrainment effects. The correctness of the prediction of net entrainment/de-entrainment requires the correct prediction of the vessel mass, and the correct prediction of the mass flow rate to the broken loop, with the condition of the same total ECC injection and steam injection.

In Run 131, steam was injected into the core simulators and the steam generator simulators at a combined initial rate of nearly 400 kg/sec. ECC was injected into each intact cold leg at a rate of 482 kg/sec. Figure 19.3-112 shows the estimated mass distribution for Run 131. Shortly after the start of ECC injection, fluid mass began to collect in the vessel. Later in time, after about 60 seconds, the rate of mass retention in the vessel increased. The vessel inventory leveled off, until after 65 seconds, when it began to increase more rapidly indicating that CCFL breakdown occurred. Figure 19.3-113 shows the WCOBRA/TRAC-TF2 prediction of the mass distribution during Run 131. For Run 131,
[

][a,c]

In Run 132, the steam was injected into the core simulators and the steam generator simulators at a combined initial rate of nearly 300 kg/sec. The ECC was injected into each intact cold leg at a rate of 490 kg/sec. Figure 19.3-114 shows the estimated mass distribution for Run 132. Shortly after the start of ECC injection, the fluid mass began to slowly collect in the vessel. Later in time, between 60 and 67 seconds, the rate of mass retention in the vessel increased but then leveled off through 80 seconds into the test. Figure 19.3-115 shows the WCOBRA/TRAC-TF2 prediction of the mass distribution during Run 132. **[**

][a,c]

Figures 19.3-116 and 19.3-117 compare the estimated and predicted mass distributions in Run 133. In this run, the steam was injected into the core simulators and the steam generator simulators at a combined initial rate of 203 kg/sec. ECC was injected into each intact cold leg at a rate of 491 kg/sec. **[**

][a,c]

The estimated and predicted mass distributions for Run 135 are shown in Figures 19.3-118 and 19.3-119, respectively. Shortly after the start of ECC injection, the fluid mass began to collect rapidly in the vessel in the experiment. The estimated vessel mass became erratic for a brief period, actually decreasing near 55 seconds. **[**

][a,c]

Figures 19.3-120 and 19.3-121 compare the estimated and predicted mass distributions in Run 136. In this subphase, steam was injected into the core simulator at an initial rate of 102 kg/sec. This was the lowest steam injection rate of the five runs. ECC was injected into each intact cold leg at a rate of 490 kg/sec. After 50 seconds, the vessel inventory was estimated to have increased steadily for the rest of the test.
[

][a,c]

19.3.5.8 Condensation Efficiency in UPTF 6

The UPTF Test 6 series also gave consideration to the steam-water interaction in the downcomer. The steam-water interaction calculation with WCOBRA/TRAC-TF2 is reflected by the condensation efficiency calculation.

Condensation efficiencies (f_c) were estimated by MPR (MPR-1163, 1990a) for the UPTF flooding test series using two methods. The condensation efficiency was calculated in two ways. In Method 1, the efficiency is defined as **[**

][a,c]

[a,c] (19.3-4)

[

][a,c]

The second method measured **[**

][a,c]

[a,c] (19.3-5)

[

][a,c]

[

]^{a,c}

The WCOBRA/TRAC-TF2 predicted condensation efficiencies for UPTF 6 Runs 131 to 136 were obtained from Equation 19.3-5, [

]^{a,c}

19.3.5.9 DTMAX Sensitivity Study for UPTF 6

[

]a,c

19.3.5.10 Cold Leg Nozzle Loss Coefficient of UPTF 6

[

]a,c

A detailed analysis of the pressure drops in the broken cold leg from CCTF tests was performed, and a nozzle loss coefficient of 0.5 was estimated (Akimoto et al., 1984). UPTF ECC bypass (Test 6) data were examined here in more detail to determine whether they could be used to better define the value to be used in the PWR. A short period of single-phase steam flow exists in UPTF before the ECC is injected into the cold legs. Using the measured steam flow, pressure, temperature, and measured differential pressure, a cold leg nozzle unrecoverable loss can be calculated from the extended Bernoulli Equation for a number of run points from UPTF Test 6.

19.3.5.10.1 Data Reduction for the Cold Leg Nozzle Loss Coefficient

The calculation approach used in this analysis was to write the extended Bernoulli Equation between the pressure taps for pressure cell **[ ]**[a,c] which is shown on Figure 19.3-131. This cell spans the broken cold leg nozzle from the upper downcomer region to a point **[ ]**[a,c] down the broken cold leg.

The extended Bernoulli Equation (or Mechanical Energy Equation) is written as:

$$\frac{P_2 - P_1}{\rho} + \frac{U_2^2 - U_1^2}{2g_c} + \frac{fL}{D}\frac{U_2^2}{2g_c} + k_N\frac{U_2^2}{2g_c} + \frac{(Z_2 - Z_1)g}{g_c} = 0 \qquad (19.3\text{-}6)$$

The first term is the static pressure change, the second term represents the kinetic energy change, the third term is the frictional drop in the cold leg, the fourth term represents the unrecoverable loss of the nozzle, both contraction and turning loss. The last term represents the potential energy change, and is set to zero since the flow is horizontal. Equation 19.3-6 assumes the flow to be incompressible, which is a reasonable approximation for the purpose of this analysis.

The steam flow, pressure drop, steam temperature, and absolute pressure were taken directly from the data, and were averaged over the single-phase period. The friction factor was taken from the Moody chart for smooth pipes using the cold leg Reynolds number (Figure 19.3-132). The single-phase friction was used over the length of the cold leg up to the pressure tap.

Solving Equation 19.3-6 for the nozzle cold leg loss coefficient, where state 2 is the cold leg (CL) and state 1 is the downcomer (DC) annulus, results in:

$$K_N = -\frac{\left[\left(\frac{P_{CL} - P_{DC}}{\rho}\right) + \frac{U_{CL}^2 - U_{DC}^2}{2g_c} + \frac{fL_{CL}}{D_{CL}}\frac{U_{CL}^2}{2g_c}\right]}{\frac{U_{CL}^2}{2g_c}} \qquad (19.3\text{-}7)$$

The data for the steam mass flow rate, downcomer pressure, and steam temperature were taken from the UPTF data report (2D/3D, 1989). The selected values of the measured parameters are given in Tables 19.3-12 and 19.3-13. The data which was used to obtain these values are shown in Figures 19.3-133 to 19.3-142, and the selected values are indicated on the figures. **[**

][a,c]

The steam mass flow values reflect the sum of the steam flow injected from the core simulator as well as the steam generator simulators. The measured broken cold leg steam flow was the measurement used to calculate the cold leg velocity in this analysis. The cold leg steam temperatures and the downcomer pressure minus one-half the pressure drop were used to calculate the effective density which was used in Equation 19.3-7.

Table 19.3-14 gives calculated thermal-hydraulic values for the different runs of Test 6. The broken cold leg velocity was calculated using the average density in Table 19.3-14 and the cold leg inside diameter D_{CL}=750 mm (2.46 ft). That is:

$$U_{CL} = \frac{\dot{m}}{\bar{\rho} A_{CL}} = \frac{\dot{m}}{\bar{\rho}\left(\frac{\pi D_{CL}^2}{4}\right)} \tag{19.3-8}$$

where,

$\dot{m}$ is the steam mass flow rate and the cold leg area is:

$$A_{CL} = \frac{\pi D_{CL}^2}{4} \tag{19.3-9}$$

The cold leg Reynolds number was calculated from the cold leg velocity, cold leg diameter and the average steam density and viscosity as:

$$Re_{CL} = \frac{U_{CL}\bar{\rho} D_{CL}}{\bar{\mu}_{CL}} \tag{19.3-10}$$

The cold leg Mach number was then calculated using the following value for the speed of sound,

$$C_{CL} = \sqrt{\gamma R\,(\bar{T}_{CL} + 460°R)} \tag{19.3-11}$$

where,

$\bar{T}_{CL}$ is cold leg steam temperature
$\gamma = 1.25$ for steam
$R = 85.7 \frac{ft\text{-}lb_f}{lbm\,°R}$ for steam

the Mach number is then:

$$M_{CL} = \frac{V_{CL}}{C_{CL}} \tag{19.3-12}$$

The cold leg friction factor was taken from the Moody chart shown in Figure 19.3-132. A value of roughness for commercial pipe (ε = 0.00015 ft) was used. The ε/D value for the UPTF cold leg is then:

[ ] a,c

The steam density values calculated using the average pressure between the cold leg and the downcomer, and the cold leg temperature were found to agree with the cold leg density values presented in the UPTF report (2D/3D, 1989).

The results of these calculations are summarized in Table 19.3-15. **[**

][a,c] The average loss coefficient is recommended for the broken cold leg nozzle of IETs, SETs and plant models (unless a more appropriate value is determined due to geometrical differences). The uncertainty of cold leg nozzle loss coefficient (KN) for plant models is discussed in Section 29.1.2.1, Volume 3.

19.3.5.10.2 Nozzle Loss Assessment

The estimated average loss coefficient 0.54 has been applied to the broken cold leg nozzle in UPTF 6 input models in Section 19.3.4. Next, the predicted pressure loss across the broken cold leg nozzle is compared with the measured pressure loss. **[**

][a,c]

In summary, an average broken cold leg nozzle loss coefficient of 0.54 is generated from UPTF 6 test data. The average loss coefficient 0.54 is applied to the broken cold leg nozzle in the UPTF 6 input models. **[**

][a,c]

19.3.6 UPTF 8A Cold Leg Condensation Test Descriptions

The UPTF test facility is discussed in detail in Section 19.3.2. The components relevant to condensation in the cold leg are discussed in more detail below.

The cold leg flow regime tests (2D/3D, 1988) focused on behavior in the cold legs in the region of ECC injection. This region is bounded by the reactor coolant pump simulator and the test vessel downcomer as shown in Figure 19.3-149. The cold leg piping has an internal diameter of 750 mm (29.5 inches) and each loop is 9181 mm (30.1 feet) long from the reactor coolant pump simulator outlet to the inner surface of the test vessel wall at the downcomer. The diameter of safety injection line is 222.5 mm.

The distance from the ECC nozzle to the downcomer is 30% longer at UPTF than at typical PWRs. The ECC nozzle diameters are comparable with the UPTF nozzle diameter slightly smaller (by no more than 16%). The most significant difference is that UPTF uses side injection whereas typical PWRs, generally use top injection.

Test Conditions

For UPTF Test 8A steam was injected only in the core simulator and flowed through the loops. ECC was injected into the cold leg of Loop 2. The steam injection rate was relatively constant while the ECC flow rate was decreased in steps. Each ECC flow rate was maintained for about 30 seconds to allow steady-state conditions to be established. The ECC flow rates covered the range of flows expected in a PWR during a Large Break LOCA. Test 8A had two phases with essentially the same conditions; the difference being that the pump simulator K-factor in Loop 2 was higher for Phase B than Phase A. This condition resulted in a slightly lower Loop 2 steam flow in Phase B compared to Phase A.

The steam flow in Loop 2 was held approximately constant due to Loop 3 being open to maintain a constant differential pressure across the reactor coolant loops. Loop 2 steam flow was maintained between 31 and 38 kg/sec throughout the test.

UPTF Test 8A was conducted in two major phases, each with two parts. In the first part of each phase ECC was injected to the Loop 2 cold leg, and in the second part the ECC injection went to the hot leg. Since there is not hot leg ECC injection to typical PWRs, and since the boundary conditions for Phase A (Run 112) and Phase B (Run 111) are similar, only the first part of Phase A was simulated with WCOBRA/TRAC-TF2. Figure 19.3-150 shows the system configuration for UPTF 8A. The configurations of specific components are as follows:

- A water seal was maintained in the lower plenum of the test vessel to ensure the steam from the core simulator flows through the loops.
- Steam was injected through the test vessel core simulator.
- Loop 1 was blocked at the pump simulator.
- The Loop 2 pump simulator was set to provide a K factor of 10 based on a pipe diameter of 750 mm (29.5 inches).
- The Loop 3 pump simulator was set to provide a K factor of 18 based on a pipe diameter of 750 mm (29.5 inches).
- ECC was injected into the Loop 2 cold leg. No nitrogen was injected into the ECC water.
- The broken loop hot leg and broken loop cold leg were open to the containment simulator. The broken loop hot leg break valve was set to provide a K factor of 18.2 based on a pipe diameter of 750 mm (29.5 inches).

A summary of test boundary conditions for UPTF 8A is given in Table 19.3-16.

Summary of Experimental Results

An observation on the temperature distribution in the cold leg in UPTF 8A is given in Figure 19.3-151. The flow regime and temperature stratification are clearly shown in Figure 19.3-151. The results of the UPTF cold leg flow regime separate effects tests indicate that plug flow only occurred when the condensation of the ECC exceeded the steam supply. At low steam flows, plug flow was unstable because the momentum of the steam flow was not sufficient to maintain the plug. The cyclic formation and decay of water plugs in unstable plug flow resulted in large pressure and flow oscillations. The test results also indicate that stratified flow always occurred when the steam supply exceeded the ECC condensation potential. In some cases, thermal stratification of the water layer in the bottom of the cold leg limited condensation to less than its maximum value and prevented total consumption of the steam.

The loop steam flow was completely condensed for plug conditions and only partially condensed for stratified flow conditions. The condensation efficiency (the ratio of condensation heat transfer rate to the condensation rate that would bring liquid to saturation temperature), during stratified flow conditions ranged from 80 to 100%. The efficiency was higher as ECC flow decreased or as steam flow increased.

19.3.7 WCOBRA/TRAC-TF2 Model for UPTF 8A

The validations against UPTF Test 8A serve as a separate effect test for the condensation in cold leg and downcomer during refill period and reflood period. The test is also part of validation for the cold leg condensation model discussed in Section 17. Two UPTF 8A models are developed. An integral UPTF 8A input model includes both vessel and loop structure of the UPTF. A simplified (separate effects) UPTF 8A TEE model documented in Section 17 only simulates the cold leg and the ECC line in UPTF 8A test. The UPTF 8A TEE model presented in Section 17 also serves as a base model for the sensitivity studies on the ECC line injection angle, the cold leg noding, the uncertainty of the cold leg condensation model and the uncertainty of the horizontal stratification model.

The integral UPTF 8A model presented here **[**

][a,c]

[

]a,c

19.3.8 Simulation of UPTF 8A

The WCOBRA/TRAC-TF2 simulation of UPTF Test 8A was run for the first 200 seconds of the test, which covered the period where flow was injected into the loop 2 intact cold leg. The as-measured injection flow rates were used as boundary conditions in the WCOBRA/TRAC-TF2 model. The containment simulator was maintained at a constant pressure of 400 kPa (58 psia).

Since most of ECC injections were turned-off for Test 8A, the condensation only exists in the intact loop 2. The WCOBRA/TRAC-TF2 simulation of Phase A (Run 112) modeled only the cold leg injection phase, so results after 200 seconds are not considered. The following comparison of WCOBRA/TRAC-TF2 results and UPTF Test 8A data considers the overall performance of the code and modeling of the facility. Note, the simulation of 200 seconds covers periods 1 through 6 in Table 19.3-16. The stage 7 is insignificant for the assessment because the ECC flow rate was too low related to the typical RHR flow.

[

]a,c

[

]^{a,c}

[

]a,c

19.3.9 UPTF 25A Downcomer Entrainment/De-Entrainment and Cold Leg Condensation Test Descriptions

UPTF Test 25A (2D/3D, 1990a) was a quasi-steady state experiment to investigate entrainment/de-entrainment in the downcomer and condensation in the cold leg and downcomer during the reflood phase of a PWR LBLOCA. The UPTF test facility is discussed in detail in Section 19.3.2. Figure 19.3-164 shows the system configuration of UPTF Test 25A.

The configurations of specific components are as follows:[

]a,c

[

]a,c

UPTF Test 25 Phase A simulated conditions expected during the reflood phase of a Large Break LOCA. ECC was injected to the cold legs, while the steam flow through the UPTF was established by injecting steam in the steam generator simulators. UPTF 25 Phase B was similar to Phase A, but the vessel walls were not superheated and there was no waiting period between phases. Since UPTF 25A is more representative for the reflood period of a LBLOCA, only Phase A was simulated using WCOBRA/TRAC-TF2.

Table 19.3-17 lists the conditions for each Phase A sub-phase of Test 25.

19.3.10 WCOBRA/TRAC-TF2 Model for UPTF Test 25A

The vessel model for UPTF 25A is also similar to the vessel model for UPTF 6. [

]a,c

19.3.11 Simulation of UPTF Test 25A

The WCOBRA/TRAC-TF2 calculated transient corresponding to the UPTF Test 25A simulation is run for nearly the entire 900 seconds of the test. [

]a,c

The downcomer fluid temperatures at Level 28 are compared in Figures 19.3-170 and 19.3-171, while the downcomer fluid temperatures at Level 24 are compared in Figures 19.3-172 and 19.3-173. **[**

][a,c]

Figure 19.3-175 shows the measured and predicted axial differential pressure from the bottom of the lower plenum to the middle of the downcomer **[ ]**[a,c] and the axial differential pressure from the bottom of the lower plenum to the top of the downcomer **[ ]**[a,c] for UPTF 25-Phase A. The axial pressure difference is an indicator of the water level in the downcomer. **[**

][a,c]

The measured and predicted axial differential pressures in the downcomer between the bottom of downcomer and the cold leg nozzle elevation are compared in Figure 19.3-176. In Figure 19.3-176, four WCOBRA/TRAC-TF2 curves are shown. Each curve represents the level in a different quadrant of the downcomer, each being adjacent to a loop connection. In the measured levels, the level was highest in the downcomer quadrant below the broken cold leg. **[**

][a,c]

[

]a,c

Figures 19.3-177 and 19.3-178 provide the steam and water flow rates to the broken loop. The vapor flow to the broken loop is shown in Figure 19.3-177. Figure 19.3-177 demonstrates that the vapor flow rate changes during each sub-phase with the change in steam injection rate. [

]a,c

One additional parameter of interest is the void height in the downcomer as a function of the steam flow rate. The void height is the distance from the average collapsed downcomer liquid level to the bottom of the cold leg nozzles. The distance from the bottom of the downcomer to the bottom of the cold leg nozzle is [ ]a,c. The WCOBRA/TRAC-TF2 calculated downcomer void height is determined for each of the four sub-phases, and then plotted against test data and estimates provided by MPR Associates (MPR-1346, 1993) in Figure 19.3-179.

[

]a,c

The measured and predicted fluid temperatures in the Loop 2 cold leg are compared in Figures 19.3-180 through 19.3-182. Figure 19.3-180 shows the comparison between the measured temperature and the WCOBRA/TRAC-TF2 predicted water temperature at the ECC injection point. The measured temperature profiles from the top of the cold leg to the bottom of the cold leg indicate a stratified flow pattern in all sub-phases, with superheated steam at the top and subcooled water at the bottom. The fluid temperature drops from sub-phase I to sub-phase IV as the steam flow rate reduces in a stepwise manner. **[**

][a,c]

Figure 19.3-181 shows the comparison between the measured temperature and the WCOBRA/TRAC-TF2 predicted water temperature downstream of the injection point. Thermocouples were wetted by the liquid during the experiment and showed saturated or subcooled temperature. The measured liquid temperature at the bottom of the cold leg increased substantially from measured temperature at the ECC injection point, which implies further condensation downstream of the ECC injection point. **[**

][a,c]

Figure 19.3-182 shows the comparison between the measured temperature and the WCOBRA/TRAC-TF2 predicted water temperature at the cold leg near the vessel inlet. It is shown that the water temperature rose further for all four sub-phases. **[**

][a,c]

[

][a,c]

Sensitivity Study with [ ]^{a,c}

[

]^{a,c}

Sensitivity Study with [ ]^{a,c}

[

]^{a,c}

[

]a,c

19.3.12 UPTF 29B Upper Plenum Entrainment/De-Entrainment Test Descriptions

During the reflood phase of a LBLOCA, water rises through the core. The hot fuel rods cause the water to boil and the steam produced entrains droplets which are carried through the core into the upper plenum. The droplets either fall back into the core, de-entrain on the internals in the upper plenum, or pass through into the hot legs towards the steam generators. The entrained droplets which enter the hot steam generator tubes are vaporized, causing an increase in loop pressure, which inhibits core reflood. This phenomenon is known as steam binding.

UPTF Test 29B (2D/3D, 1990b) was a quasi-steady state experiment to investigate upper plenum entrainment and steam binding during the reflood phase a PWR LBLOCA. The UPTF test facility is discussed in detail in Section 19.3.2. Figure 19.3-193 shows the system configuration of UPTF Test 29B.
[

]a,c

A summary of test boundary conditions for UPTF 29B (Run 212) is given in Table 19.3-19.

19.3.13 WCOBRA/TRAC-TF2 Model for UPTF Test 29B

The vessel model used in the simulation of the UPTF 29B is shown in Figure 19.3-195. Compared to the vessel models employed in the simulation of the UPTF 6, 8A, 25A tests, this model is more detailed above the tie plate and in the upper plenum region. The vessel model for the upper plenum tests used a coarser noding in the downcomer and the lower plenum regions because in these tests the flows into the downcomer were not significant. At the start of the tests, a liquid level was established in the bottom of the vessel to prevent the steam flow from the core to the downcomer through the lower plenum.

[

]^{a,c}

19.3.14 Simulation of UPTF Test 29B

Test 29B was performed to determine the amount of upper plenum de-entrainment and carryover. This test consists of six sub-phases. Each sub-phase consists of a period of steady core simulator injection followed by a "rest" period. During the "rest" period, water suspended in the upper plenum was allowed to drain back into the vessel. Table 19.3-19 lists the core simulator injection rates for Test 29B.

Phase B of Test 29 is simulated using WCOBRA/TRAC-TF2 over the entire 900 seconds of the test. For each phase of UPTF Test 29B, a mass balance is performed based on test measurements by MPR Associates (MPR-1213, 1990b), and the mass distribution estimated.

Figure 19.3-199 compares the estimated and predicted upper plenum water mass in sub-phase 1 of UPTF Test 29B. **[**

][a,c]

The estimated and predicted upper plenum mass for sub-phase 2 of UPTF Test 29B is shown in Figure 19.3-200. **[**

][a,c]

Figure 19.3-201 compares the estimated and predicted upper plenum mass for sub-phase 3.
[

][a,c]

The estimated and predicted upper plenum mass for sub-phase 5 of Test 29B are compared in Figure 19.3-203. **[**

][a,c]

Finally, Figure 19.3-204 compares the estimated and predicted upper plenum mass for sub-phase 6. In this case, **[**

][a,c]

[

]a,c

Table 19.3-1 [ ][a,c]

a,c

Table 19.3-2 [ ]a,c

a,c

Table 19.3-3 [ ]a,c

a,c

Table 19.3-4 [ ]a,c

a,c

Table 19.3-5 [ ]a,c

a,c

Table 19.3-6 [ ]a,c

a,c

Table 19.3-7 [ ]a,c

a,c

Table 19.3-8 [ ]^{a,c}

a,c

Table 19.3-9 [ ]^{a,c}

a,c

Table 19.3-10 [ ]a,c

a,c

Table 19.3-11 [ ]a,c

a,c

Table 19.3-12 Steam Mass Flows in UPTF Test 6 (all Values are in kg/sec)

a,c

Table 19.3-13 Selected Test Conditions from UPTF Test 6 (Single-Phase Steam Portion)

a,c

Table 19.3-14 Calculated Parameters for UPTF Test 6

a,c

Table 19.3-15 Calculated Cold Leg Nozzle K, $U_{DC} = 0$

a,c

Table 19.3-16 UPTF Test 8 Phase A Conditions							
	Subphase						
Conditions	**1**	**2**	**3**	**4**	**5**	**6**	**7**
Pressure (kPa)	405						
Saturation Temperature (°C)	144						
Core Simulator Steam Flow (kg/s)	110						
Loop Steam Flow Rate (kg/s)	31~38(1)						
Steam Temperature (°C)	145(2)						
ECC Flow (Parts 1-7) (kg/s)	600	400	250	200	150	90	15
ECC Subcooling (°C)	110						

Notes:
1. Estimated steam flow rate in loop 2.
2. This steam temperature is cold leg inlet steam temperature. The nominal temperature of steam injection to core simulator is 201°C.

Table 19.3-17 [[a,c] a,c

Table 19.3-18 [ ]a,c

a,c

Table 19.3-19 [ ]a,c

a,c

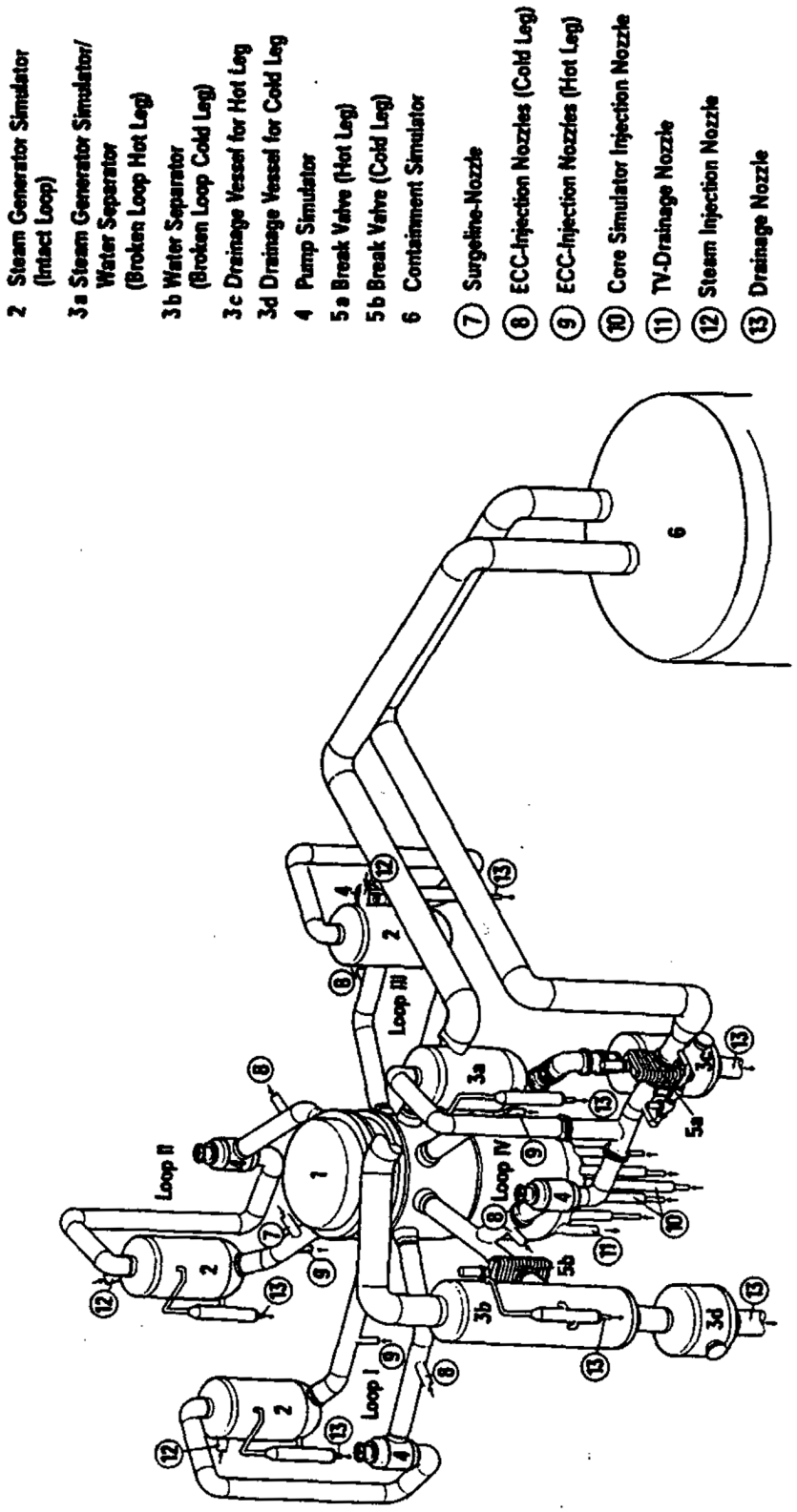

Figure 19.3-1 UPTF Plan View

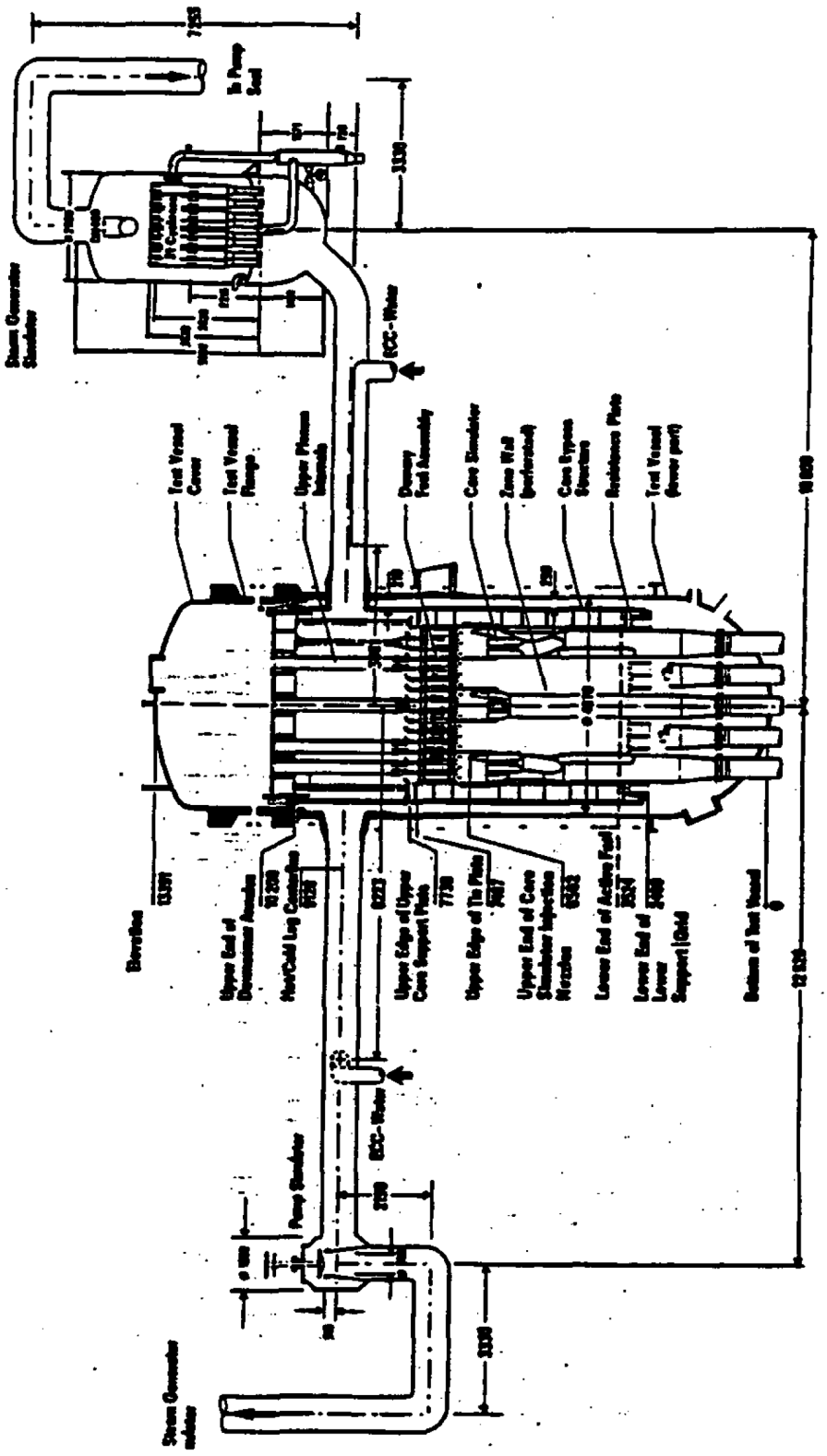

Figure 19.3-2 UPTF Test Vessel and Primary Loop

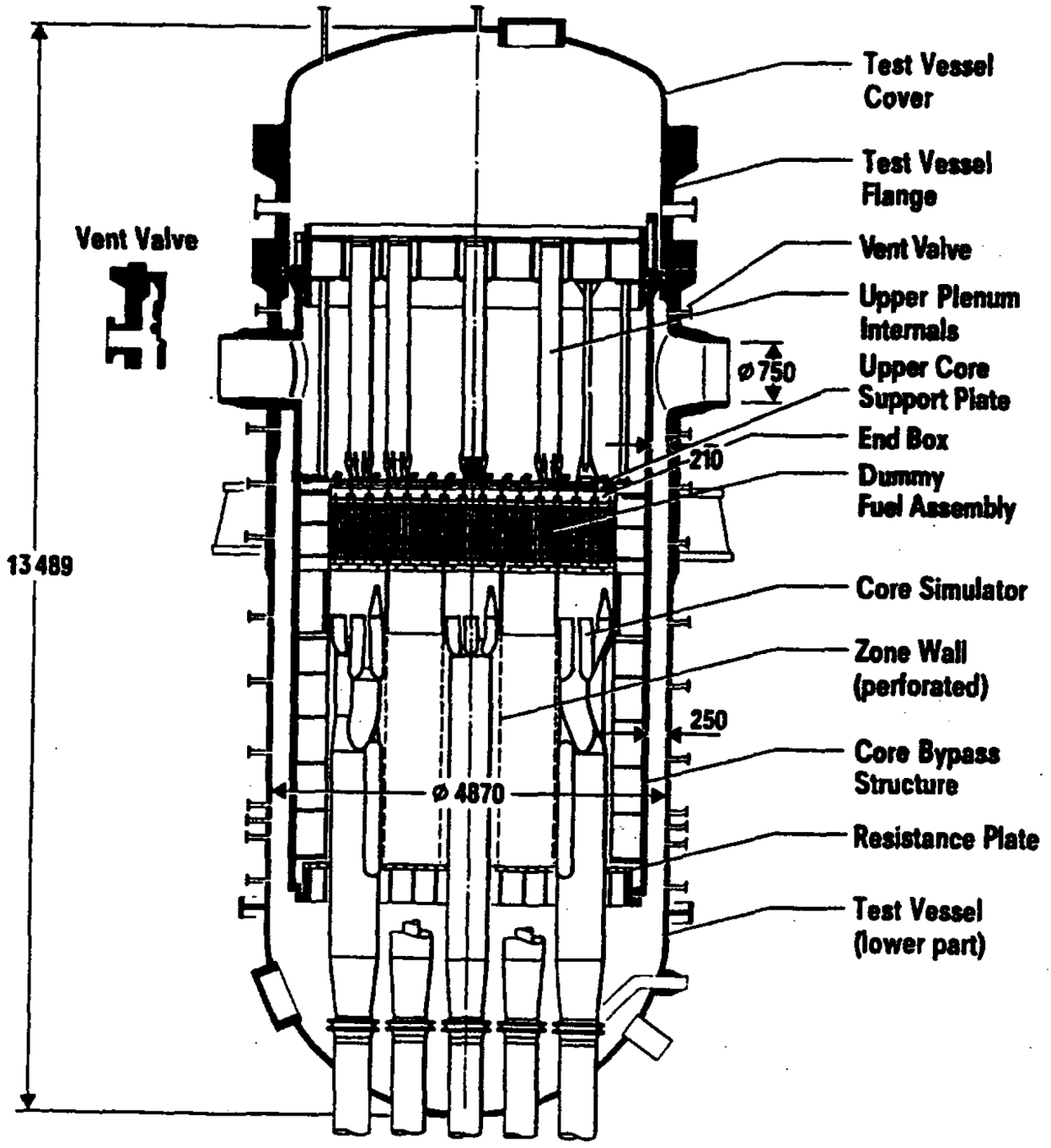

Figure 19.3-3 UPTF Reactor Vessel

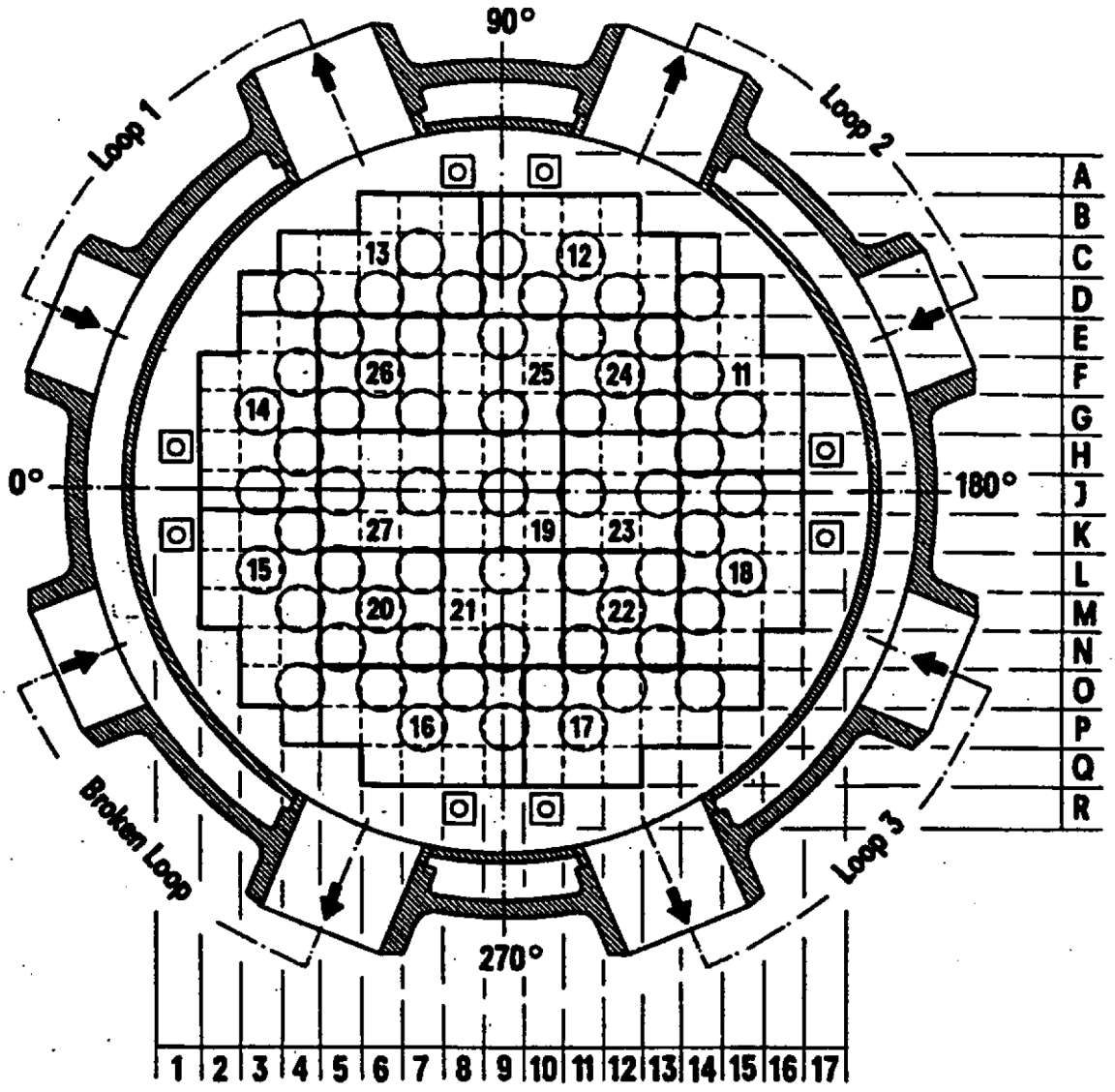

Figure 19.3-4 UPTF Upper Plenum Structures

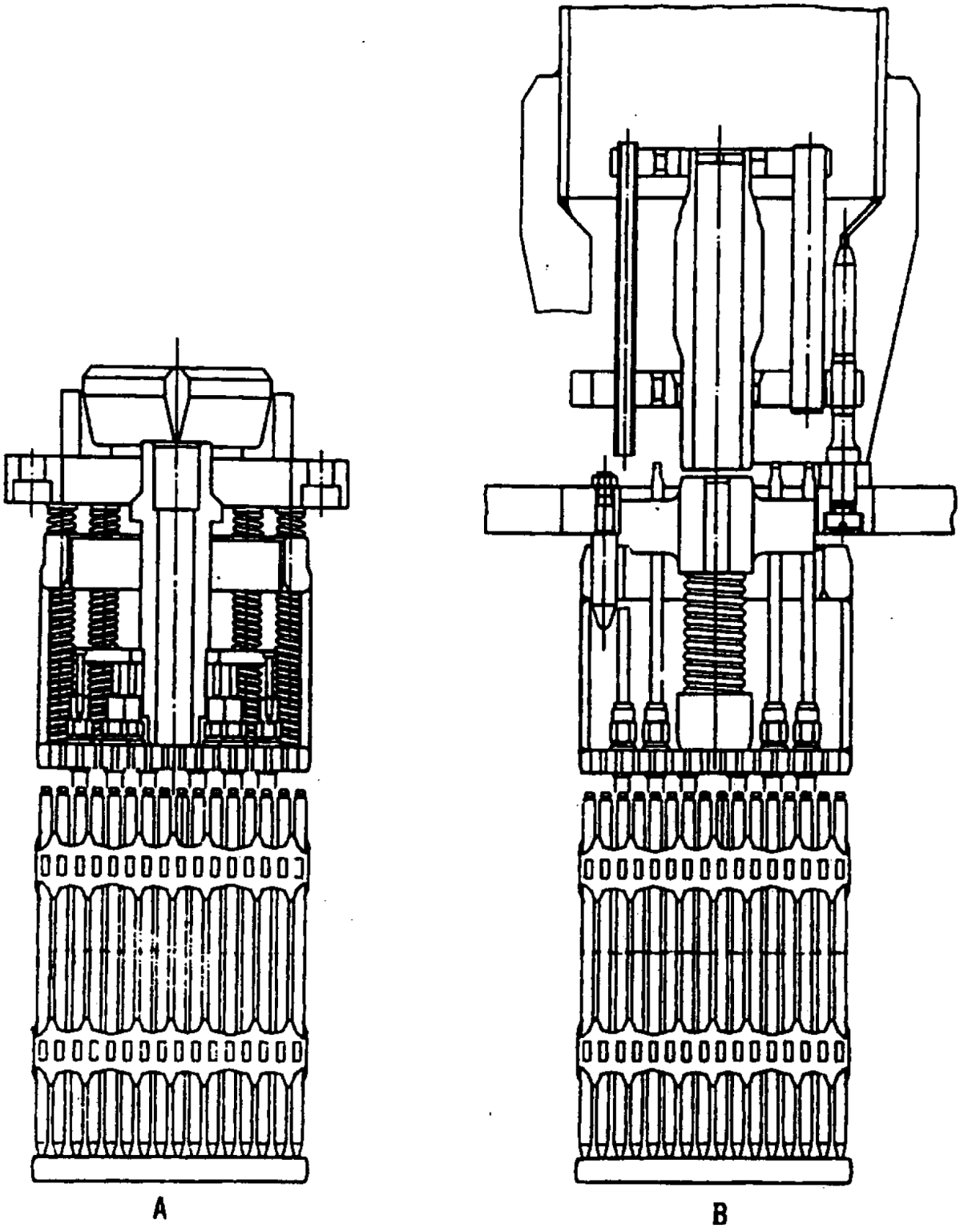

Figure 19.3-5 Dummy Fuel Assembly and End Box with Flow Restrictor (A) or Spider (B)

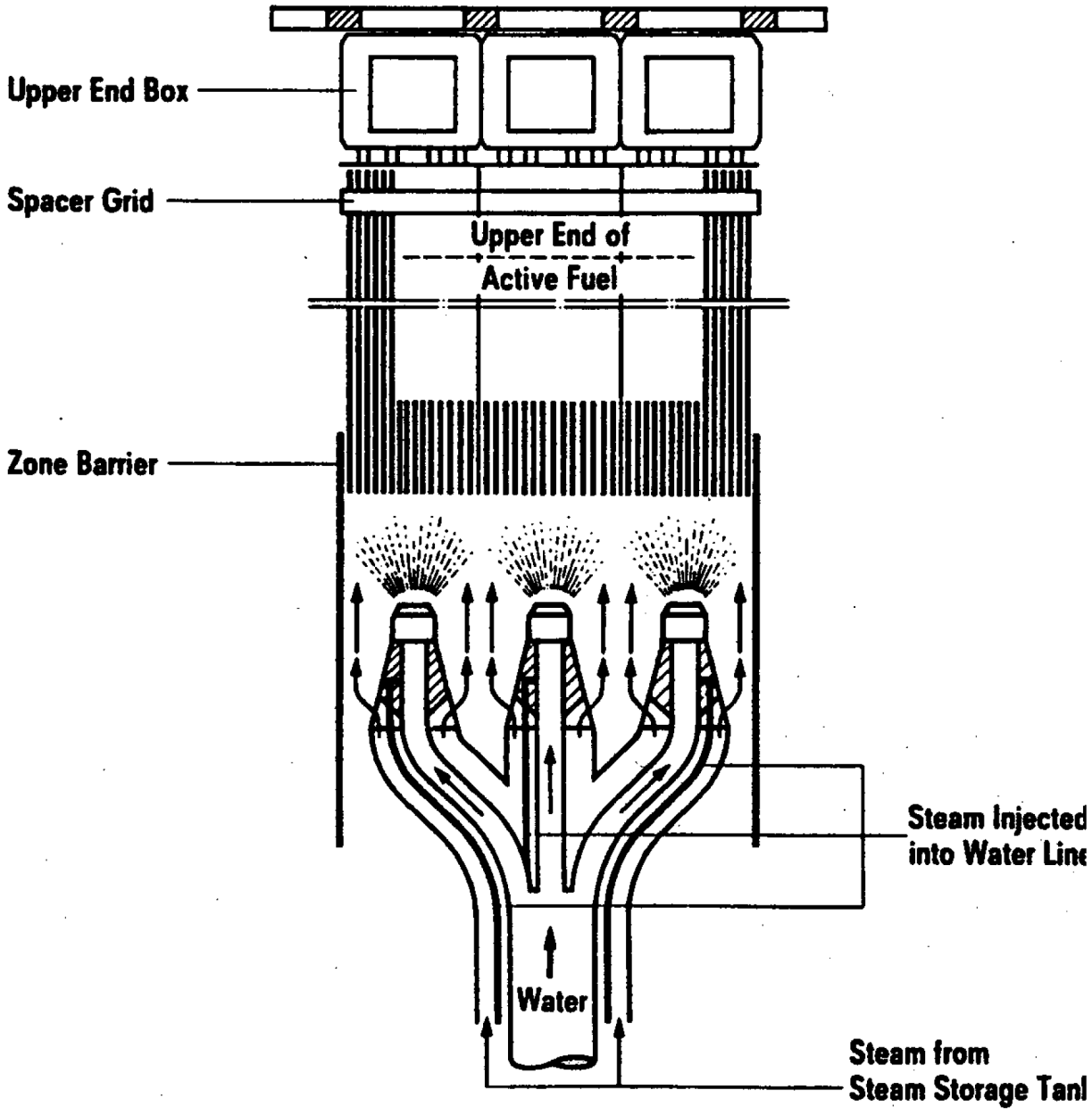

Figure 19.3-6 UPTF Core Simulator Injection Assembly

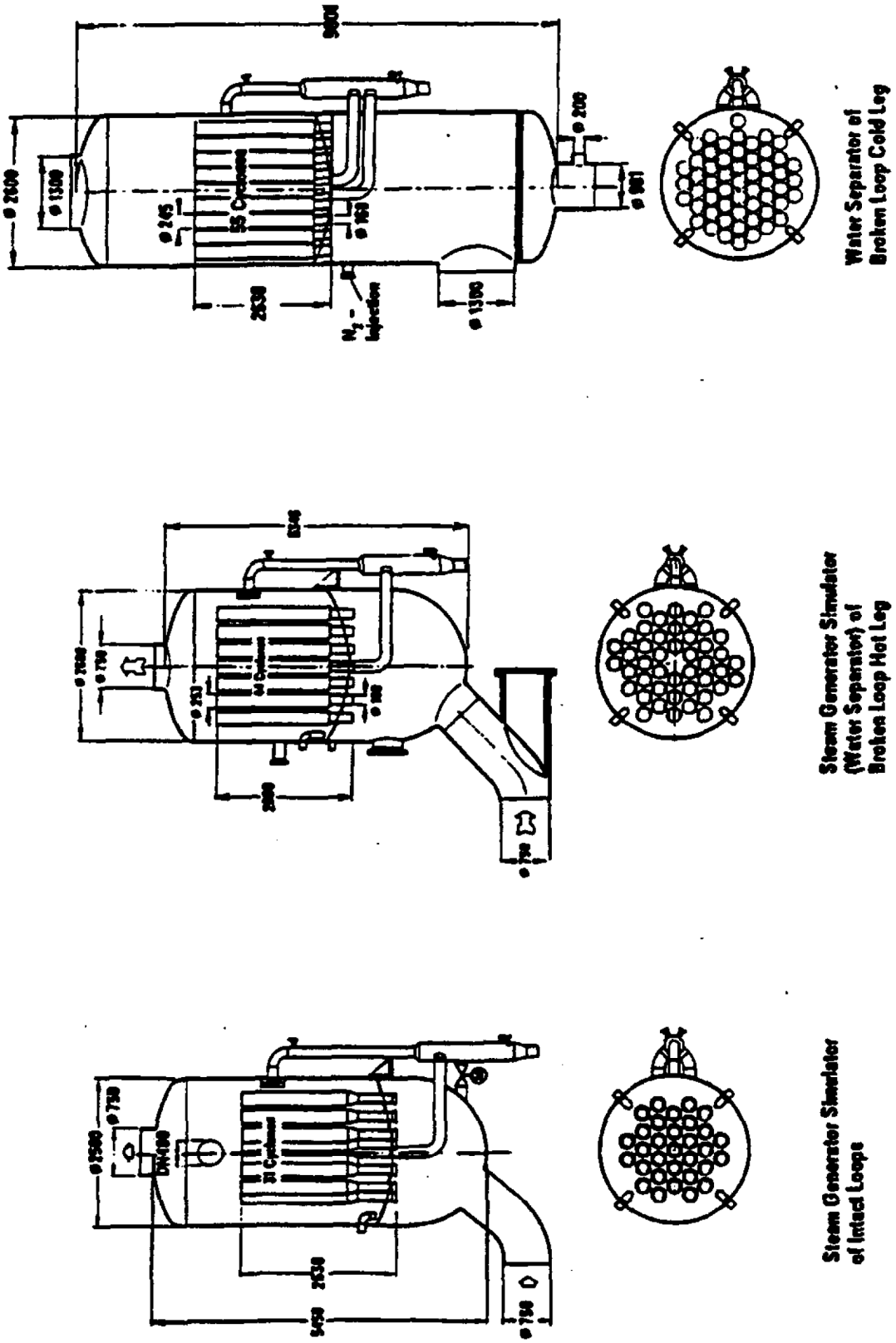

Figure 19.3-7 UPTF Steam Generator Simulators and Water Separators

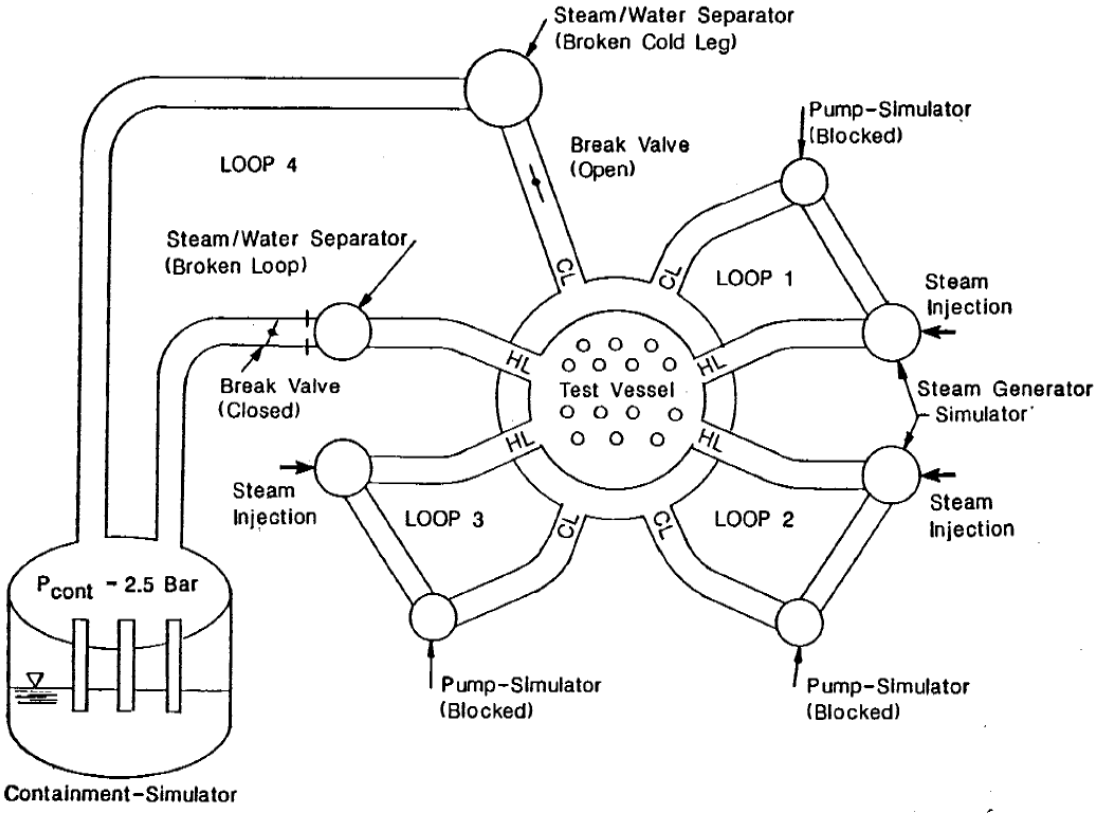

Figure 19.3-8 UPTF System Configuration for Test 6 (MPR-1163, 1990a)

a,c

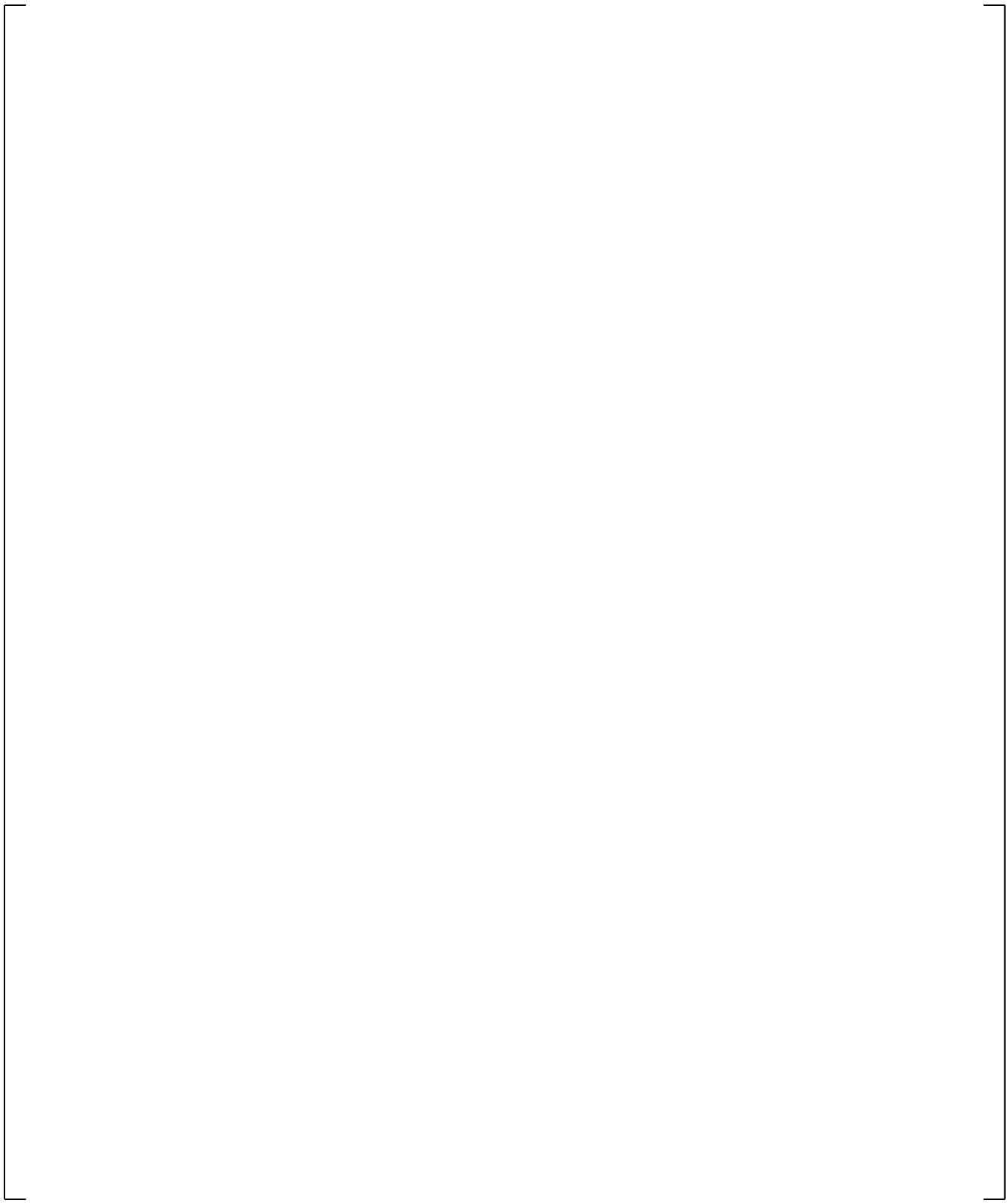

Figure 19.3-9 WCOBRA/TRAC-TF2 VESSEL Component Axial View for UPTF Bypass Tests

a,c

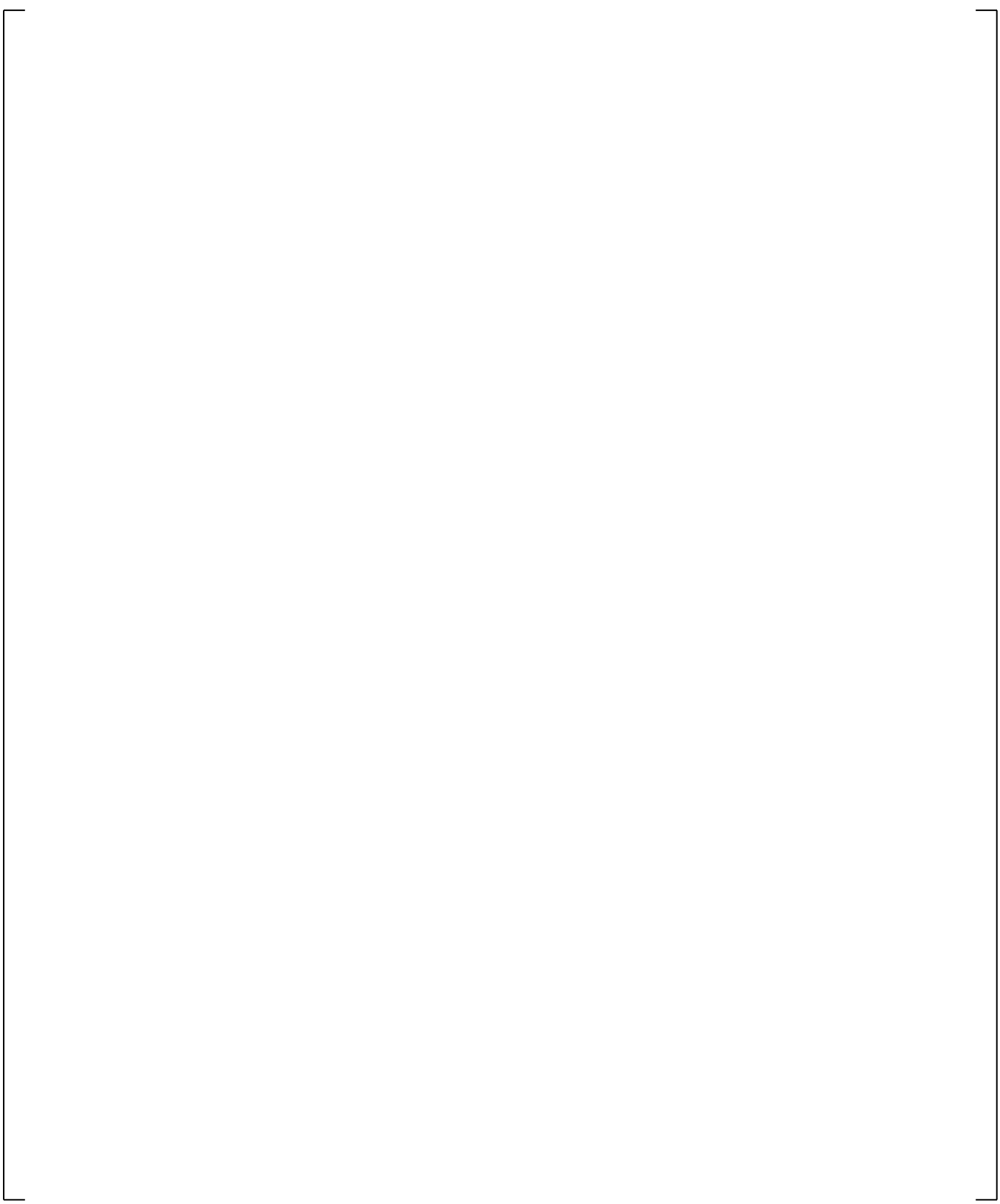

Figure 19.3-10 WCOBRA/TRAC-TF2 VESSEL Component Sections 1 and 2 for UPTF Bypass Tests

a,c

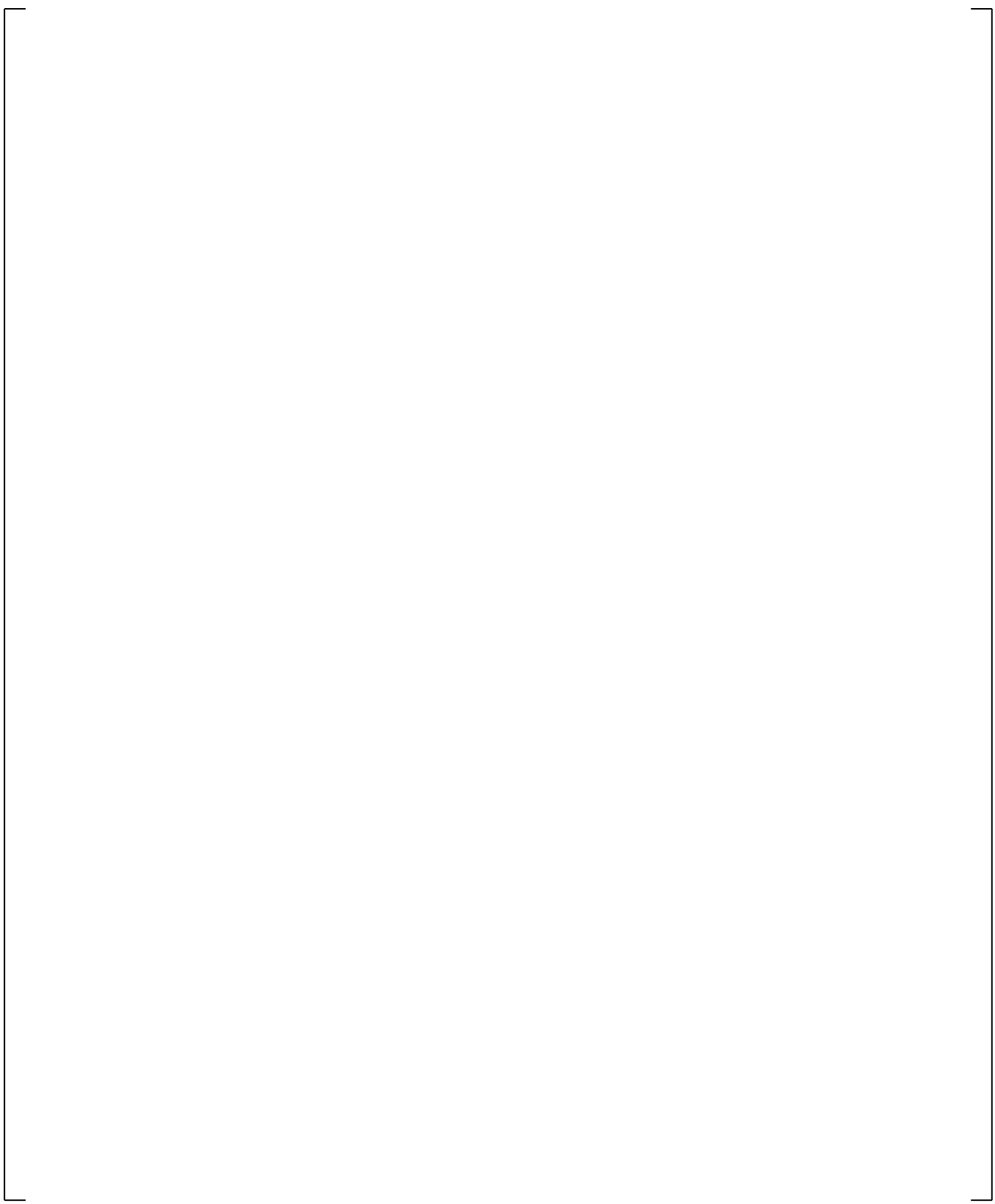

Figure 19.3-11 WCOBRA/TRAC-TF2 VESSEL Component Sections 3 and 4 for UPTF Bypass Tests

a,c

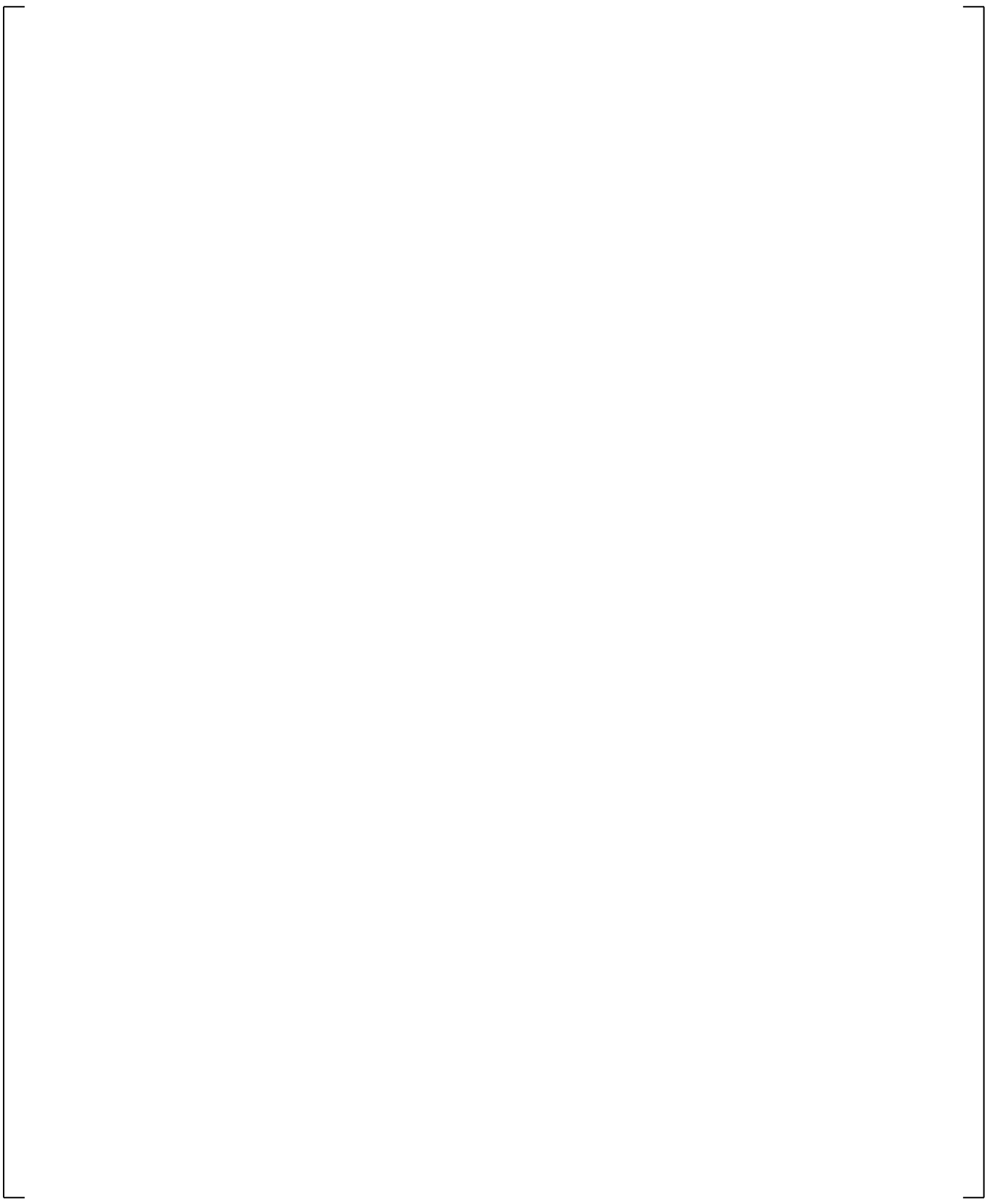

Figure 19.3-12 WCOBRA/TRAC-TF2 VESSEL Component Sections 5 and 6 for UPTF Bypass Tests

a,c

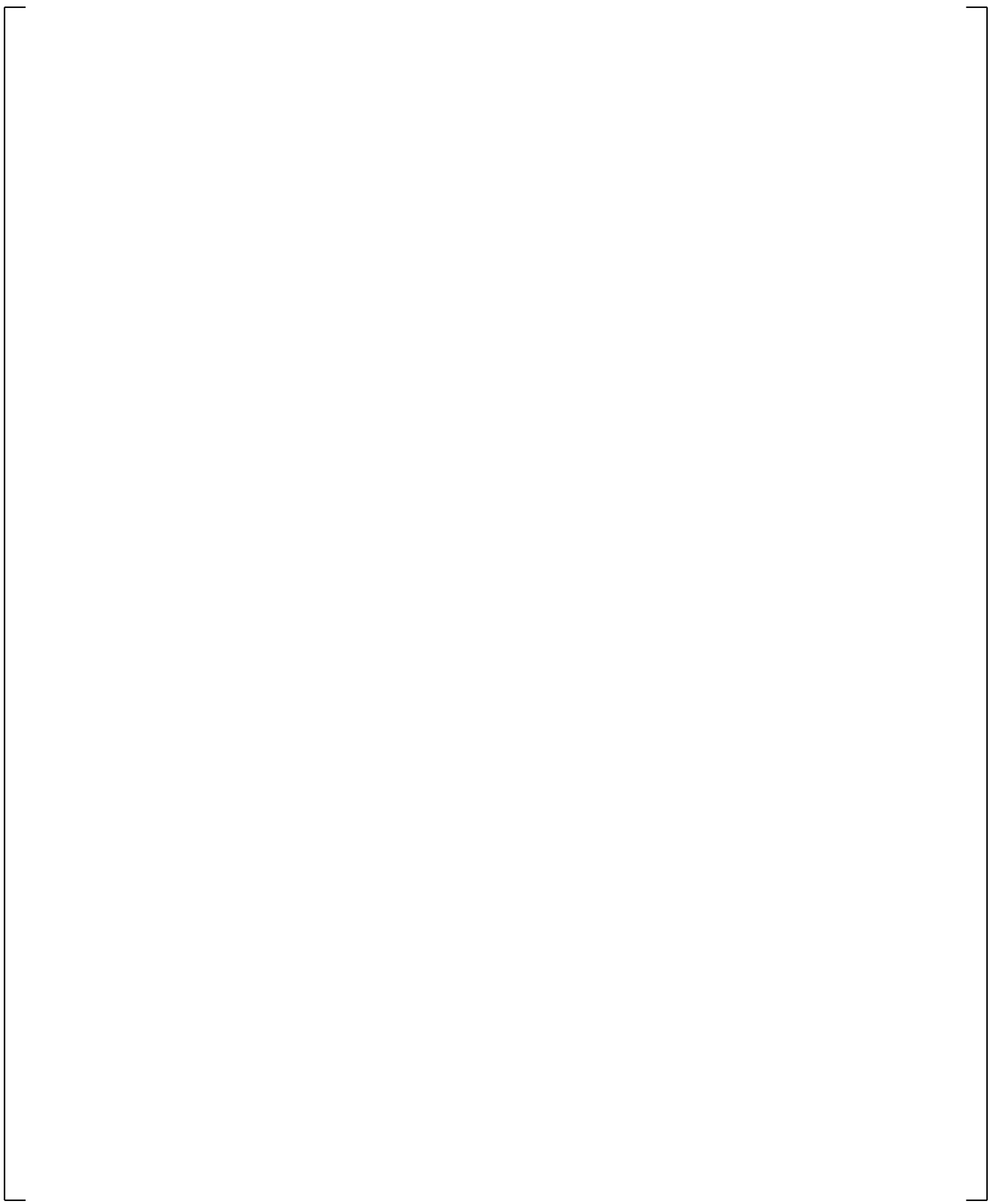

Figure 19.3-13 WCOBRA/TRAC-TF2 VESSEL Component Sections 7 and 8 for UPTF Bypass Tests

a,c

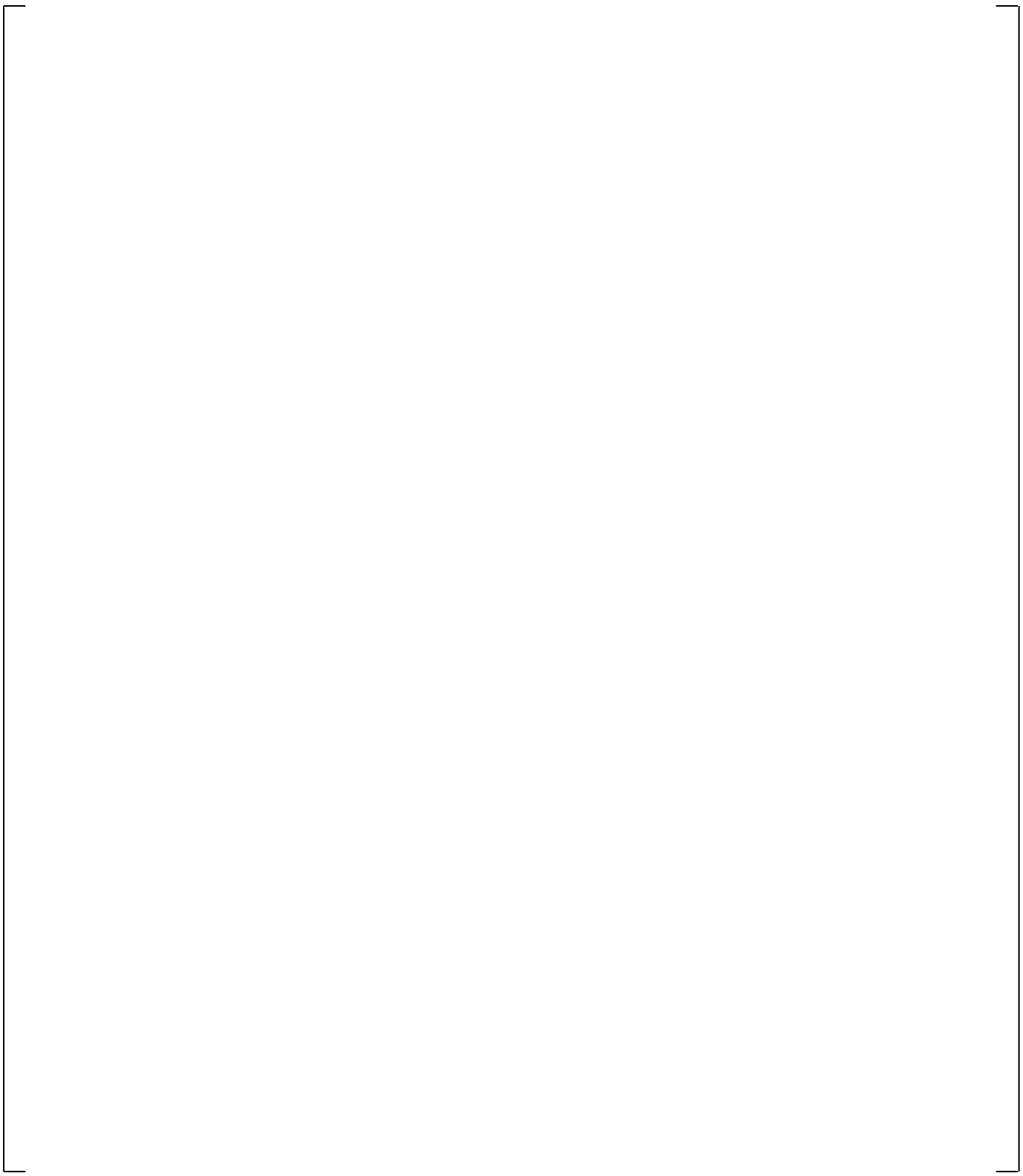

Figure 19.3-14 WCOBRA/TRAC-TF2 One-Dimensional Component Model for UPTF Test 6

a,c

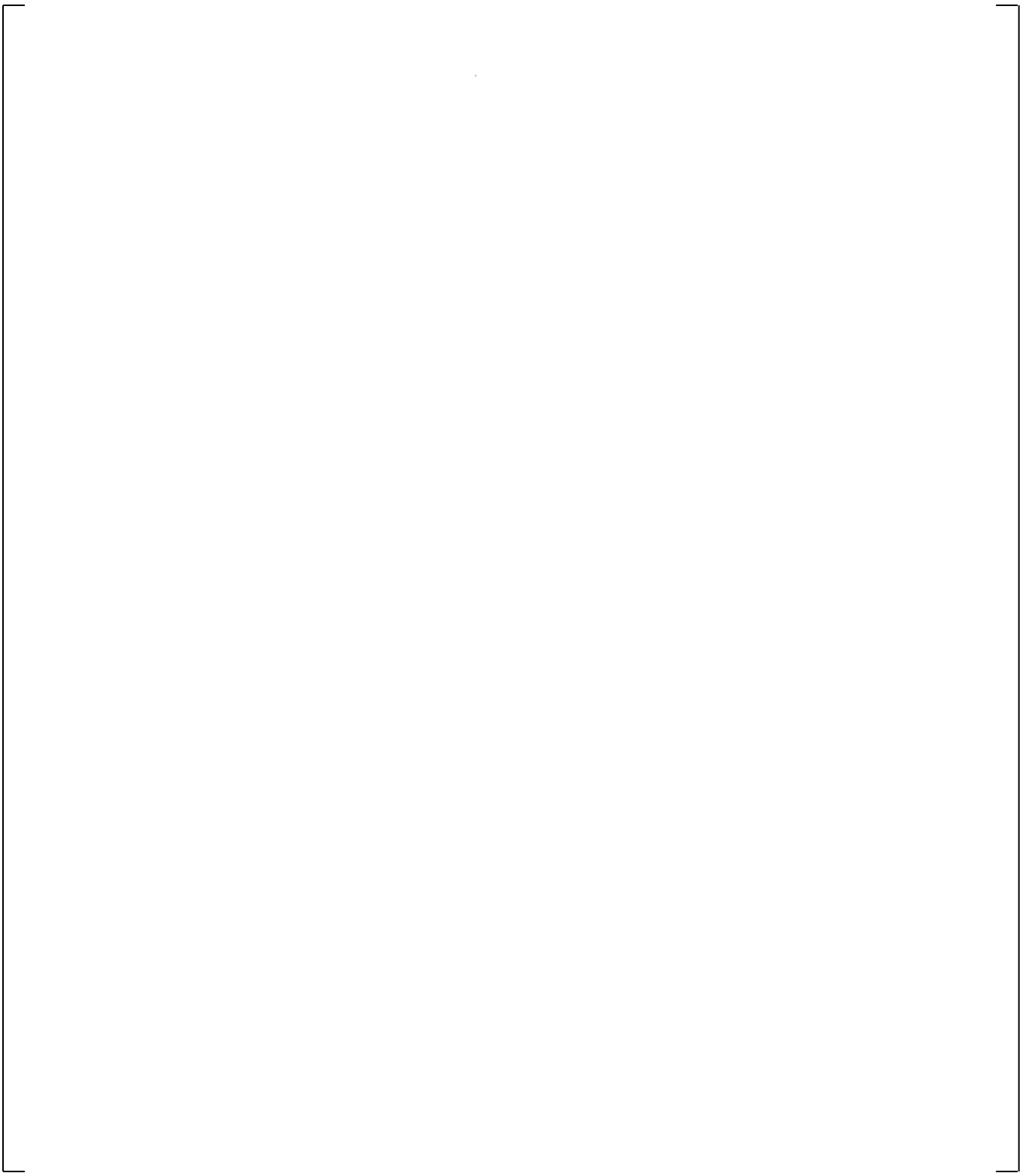

Figure 19.3-15 Total Core Steam Injection, UPTF Test 6 – Run 131

a,c

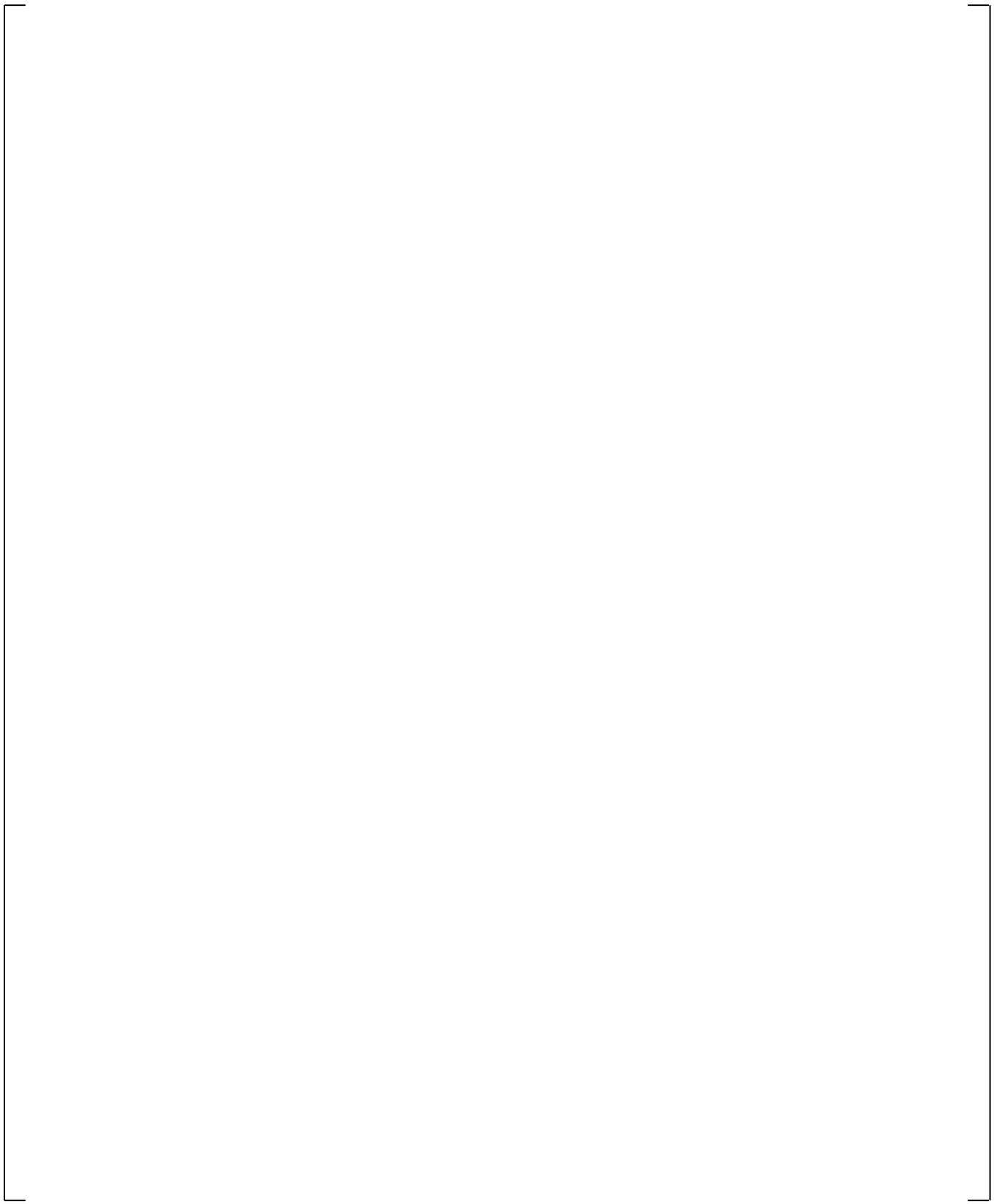

Figure 19.3-16 Steam Generator Simulator Steam Injection, UPTF Test 6 – Run 131

a,c

Figure 19.3-17 Intact Loop ECC Injection, UPTF Test 6 – Run 131

a,c

Figure 19.3-18 Measured Absolute Pressures in the Upper Plenum and Downcomer, UPTF Test 6 – Run 131

a,c

Figure 19.3-19 Predicted Absolute Pressures in the Upper Plenum and Downcomer, UPTF Test 6 – Run 131

a,c

Figure 19.3-20 Measured Downcomer Fluid Temperature at Level 21, UPTF Test 6 – Run 131

a,c

Figure 19.3-21 Predicted Downcomer Fluid Temperature at Level 21, UPTF Test 6 – Run 131

a,c

Figure 19.3-22 Measured Downcomer Fluid Temperature at Level 01, UPTF Test 6 – Run 131

a,c

Figure 19.3-23 Predicted Downcomer Fluid Temperature at Level 01, UPTF Test 6 – Run 131

a,c

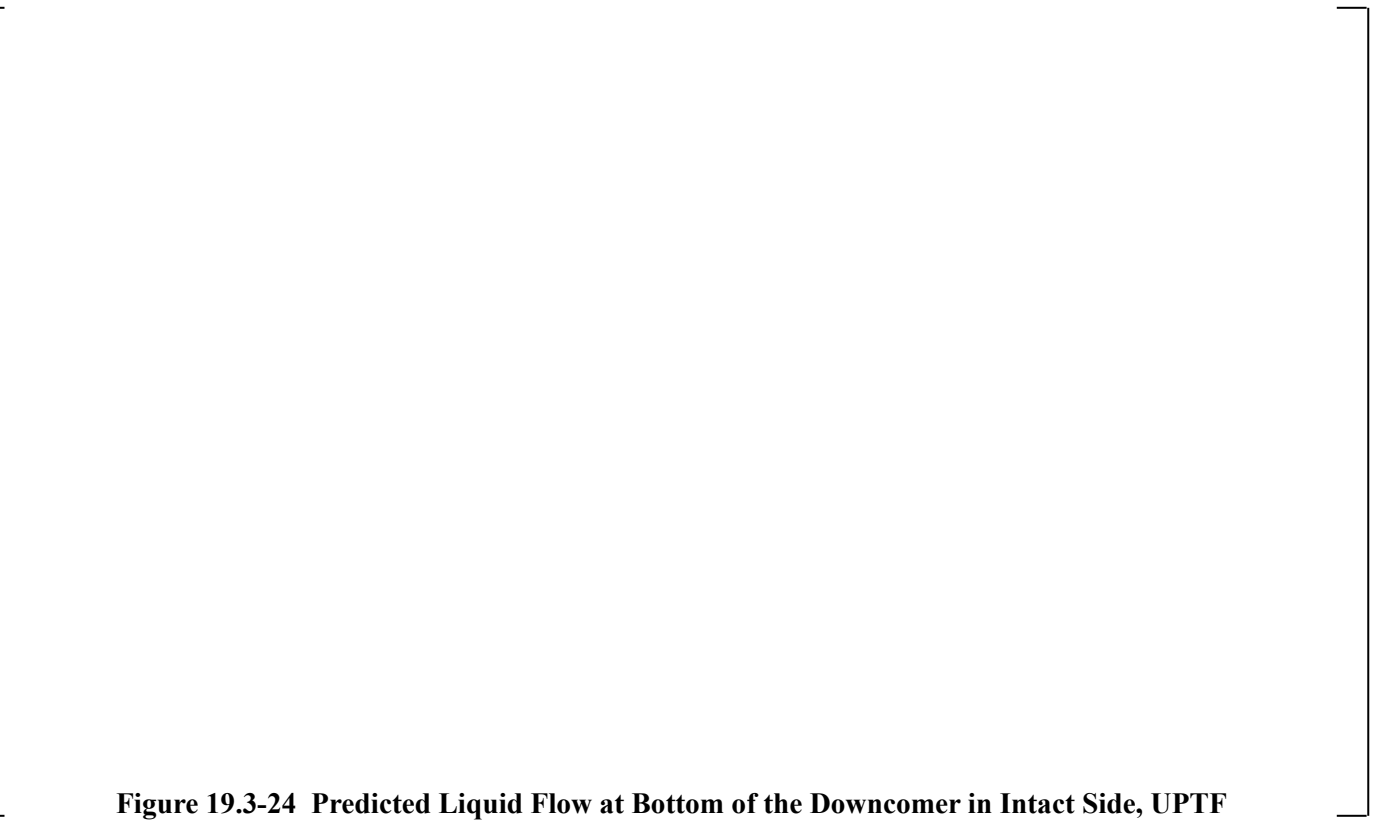

Figure 19.3-24 Predicted Liquid Flow at Bottom of the Downcomer in Intact Side, UPTF Test 6 – Run 131

a,c

Figure 19.3-25 Predicted Liquid Flow at Bottom of the Downcomer in Broken Side, UPTF Test 6 – Run 131

a,c

Figure 19.3-26 Measured Axial Differential Pressures in Downcomer, UPTF Test 6 – Run 131

a,c

Figure 19.3-27 Predicted Axial Differential Pressures in Downcomer, UPTF Test 6 – Run 131

a,c

Figure 19.3-28 Measured Azimuthal Differential Pressures in Downcomer at Level 06, UPTF Test 6 – Run 131

a,c

Figure 19.3-29 Predicted Azimuthal Differential Pressures in Downcomer at Level 06, UPTF Test 6 – Run 131

a,c

Figure 19.3-30 Measured Azimuthal Differential Pressures in Downcomer at Level 22, UPTF Test 6 – Run 131

a,c

Figure 19.3-31 Predicted Azimuthal Differential Pressures in Downcomer at Level 22, UPTF Test 6 – Run 131

a,c

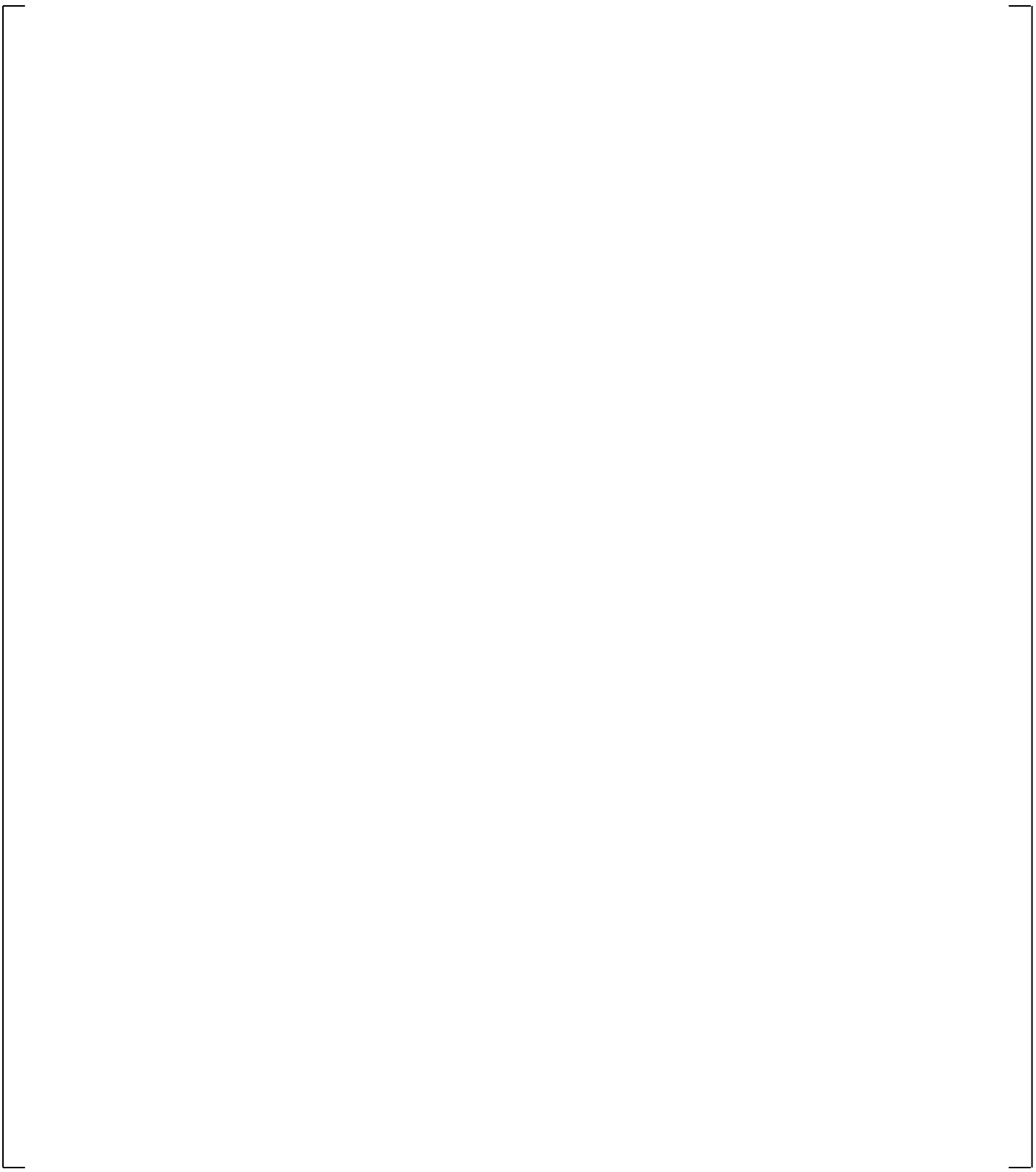

Figure 19.3-32 Comparison on Differential Pressure in Lower Plenum, UPTF Test 6 – Run 131

a,c

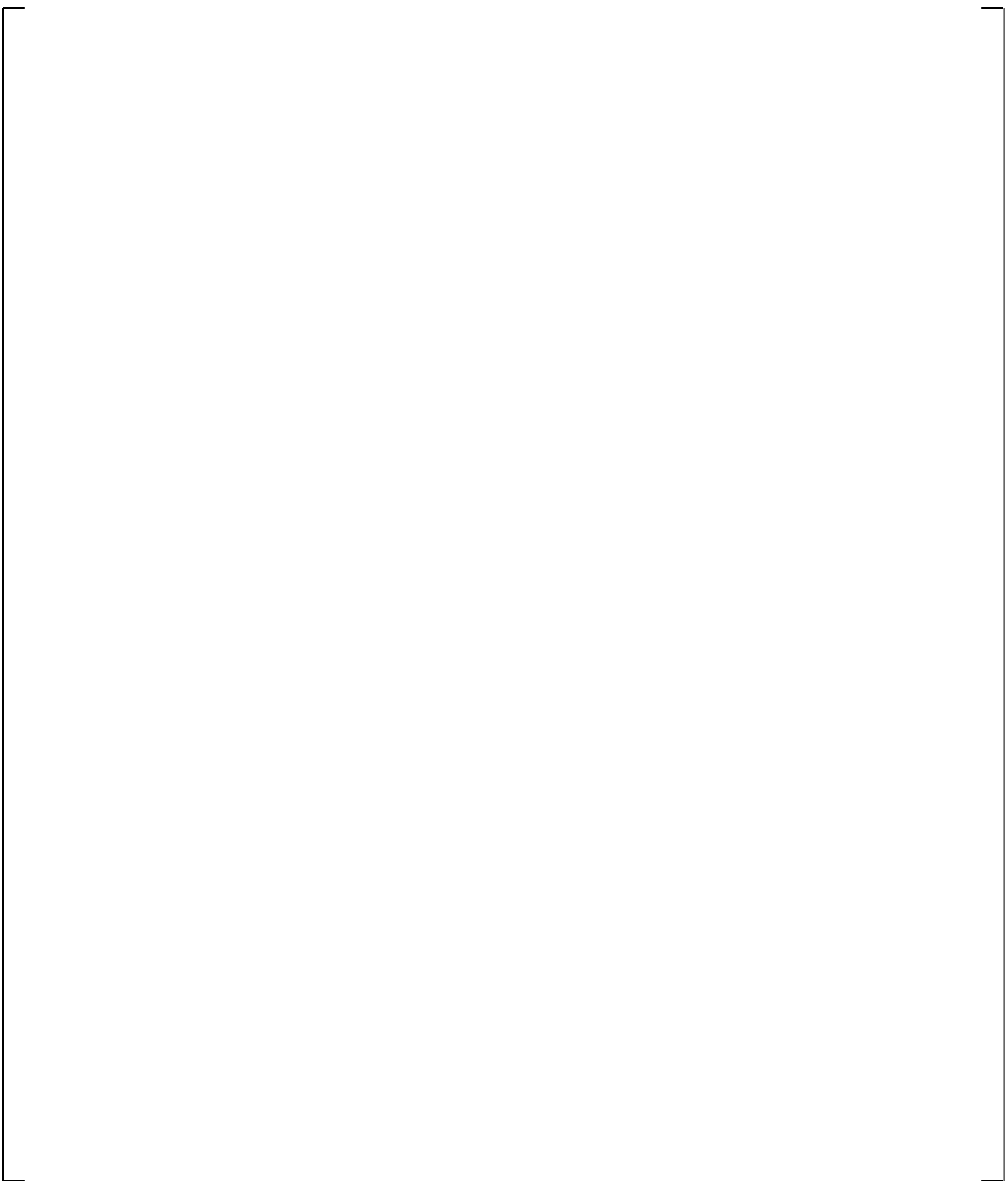

Figure 19.3-33 Total Core Steam Injection, UPTF Test 6 – Run 132

a,c

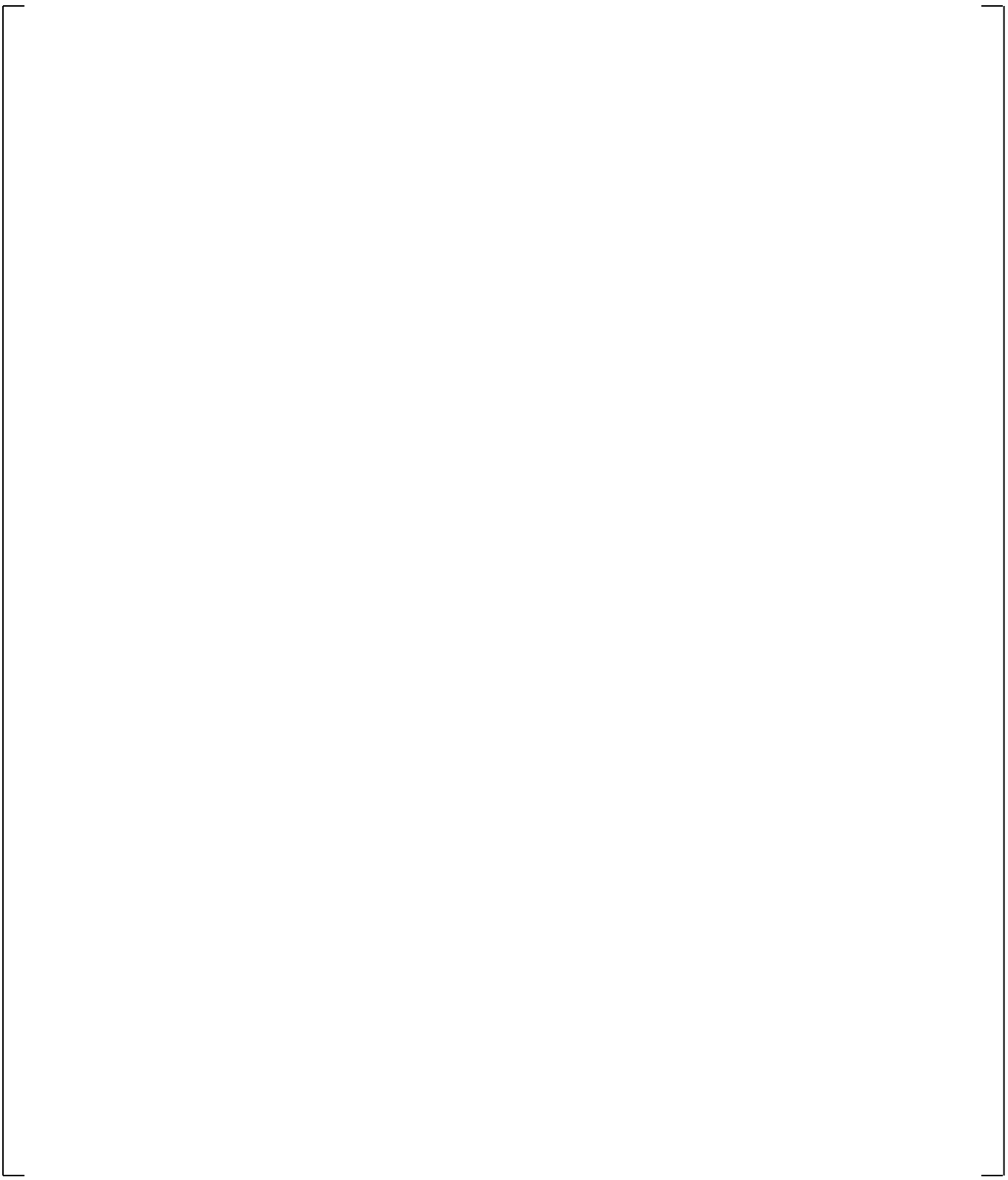

Figure 19.3-34 Steam Generator Simulator Steam Injection, UPTF Test 6 – Run 132

a,c

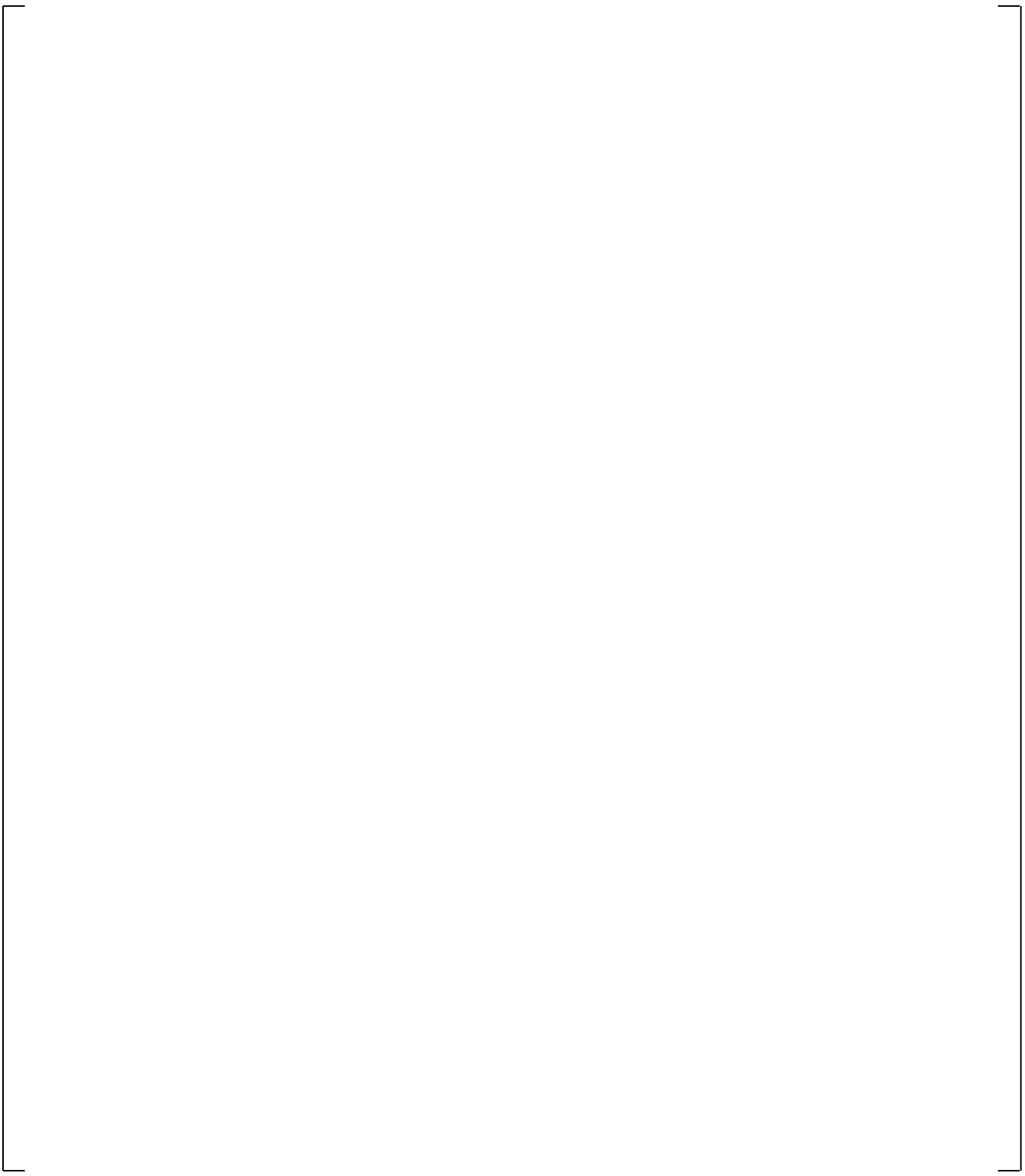

Figure 19.3-35 Intact Loop ECC Injection, UPTF Test 6 – Run 132

a,c

Figure 19.3-36 Measured Absolute Pressures in the Upper Plenum and Downcomer, UPTF Test 6 – Run 132

a,c

Figure 19.3-37 Predicted Absolute Pressures in the Upper Plenum and Downcomer, UPTF Test 6 – Run 132

a,c

Figure 19.3-38 Measured Downcomer Fluid Temperature at Level 21, UPTF Test 6 – Run 132

a,c

Figure 19.3-39 Predicted Downcomer Fluid Temperature at Level 21, UPTF Test 6 – Run 132

a,c

Figure 19.3-40 Measured Downcomer Fluid Temperature at Level 01, UPTF Test 6 – Run 132

a,c

Figure 19.3-41 Predicted Downcomer Fluid Temperature at Level 01, UPTF Test 6 – Run 132

a,c

Figure 19.3-42 Predicted Liquid Flow at Bottom of the Downcomer in Intact Side, UPTF Test 6 – Run 132

a,c

Figure 19.3-43 Predicted Liquid Flow at Bottom of the Downcomer in Broken Side, UPTF Test 6 – Run 132

a,c

Figure 19.3-44 Measured Axial Differential Pressures in Downcomer, UPTF Test 6 – Run 132

a,c

Figure 19.3-45 Predicted Axial Differential Pressures in Downcomer, UPTF Test 6 – Run 132

a,c

Figure 19.3-46 Measured Azimuthal Differential Pressures in Downcomer at Level 06, UPTF Test 6 – Run 132

a,c

Figure 19.3-47 Predicted Azimuthal Differential Pressures in Downcomer at Level 06, UPTF Test 6 – Run 132

a,c

Figure 19.3-48 Measured Azimuthal Differential Pressures in Downcomer at Level 22, UPTF Test 6 – Run 132

a,c

Figure 19.3-49 Predicted Azimuthal Differential Pressures in Downcomer at Level 22, UPTF Test 6 – Run 132

a,c

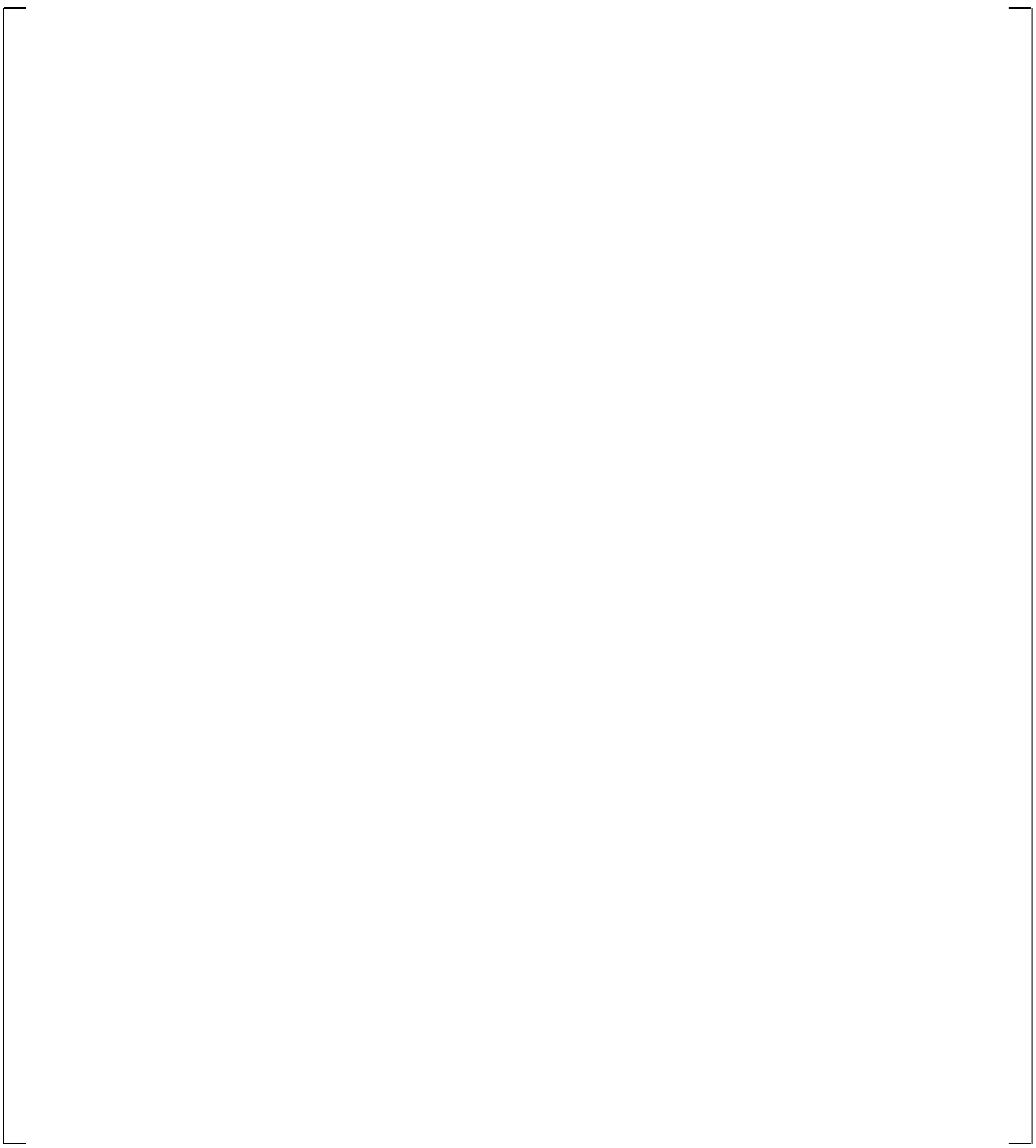

Figure 19.3-50 Comparison on Differential Pressure in Lower Plenum, UPTF Test 6 – Run 132

a,c

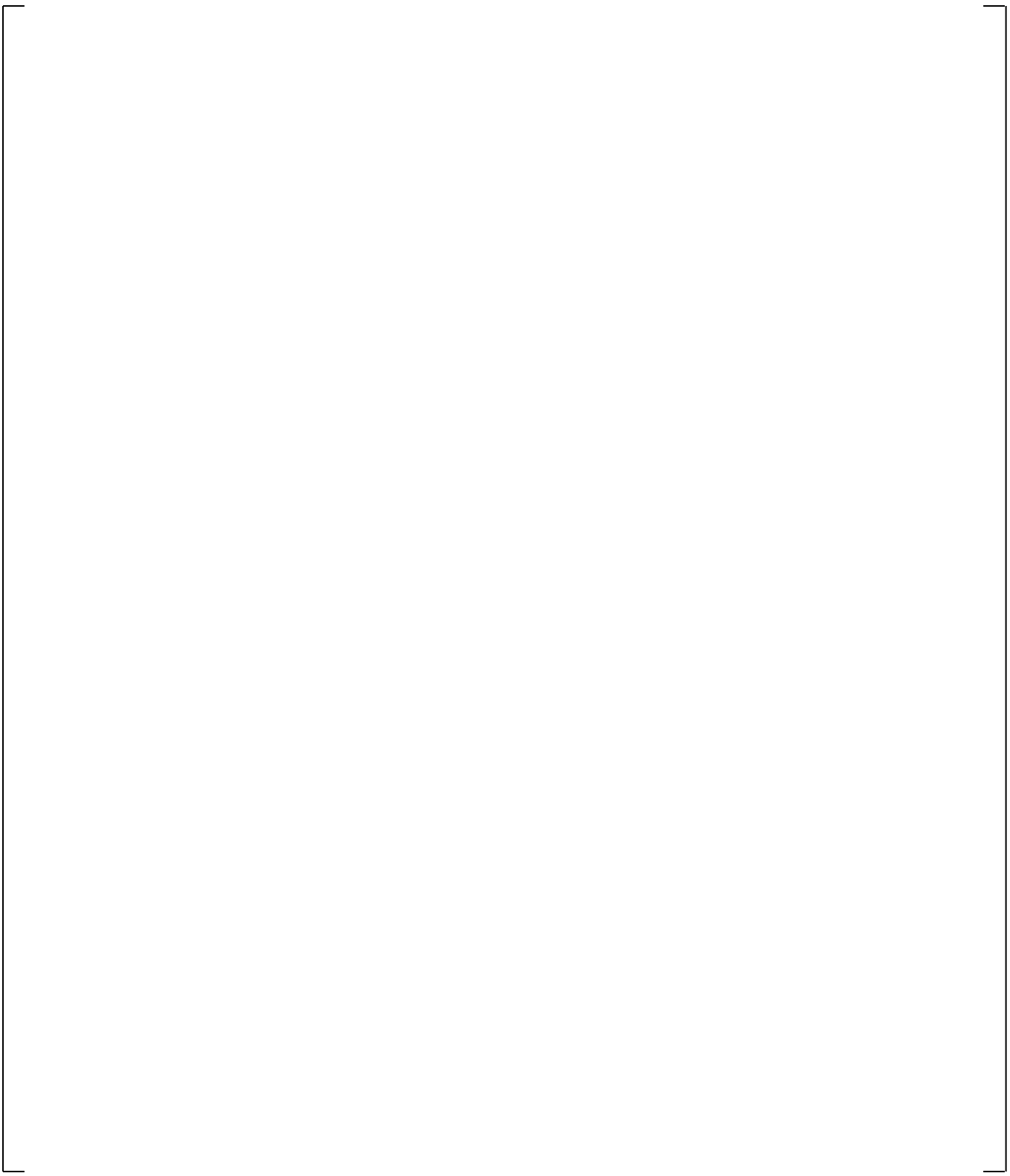

Figure 19.3-51 Total Core Steam Injection, UPTF Test 6 – Run 133

a,c

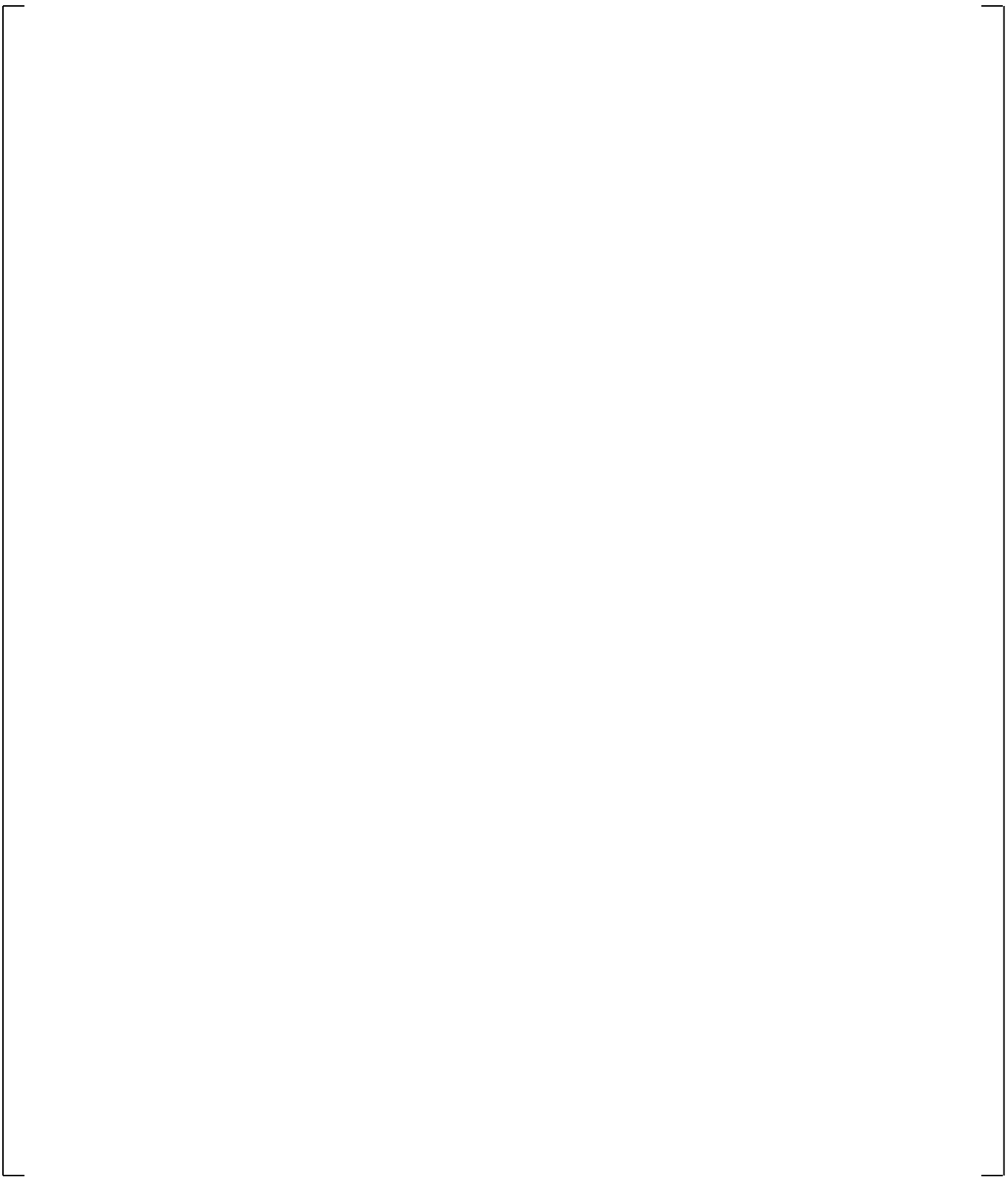

Figure 19.3-52 Steam Generator Simulator Steam Injection, UPTF Test 6 – Run 133

a,c

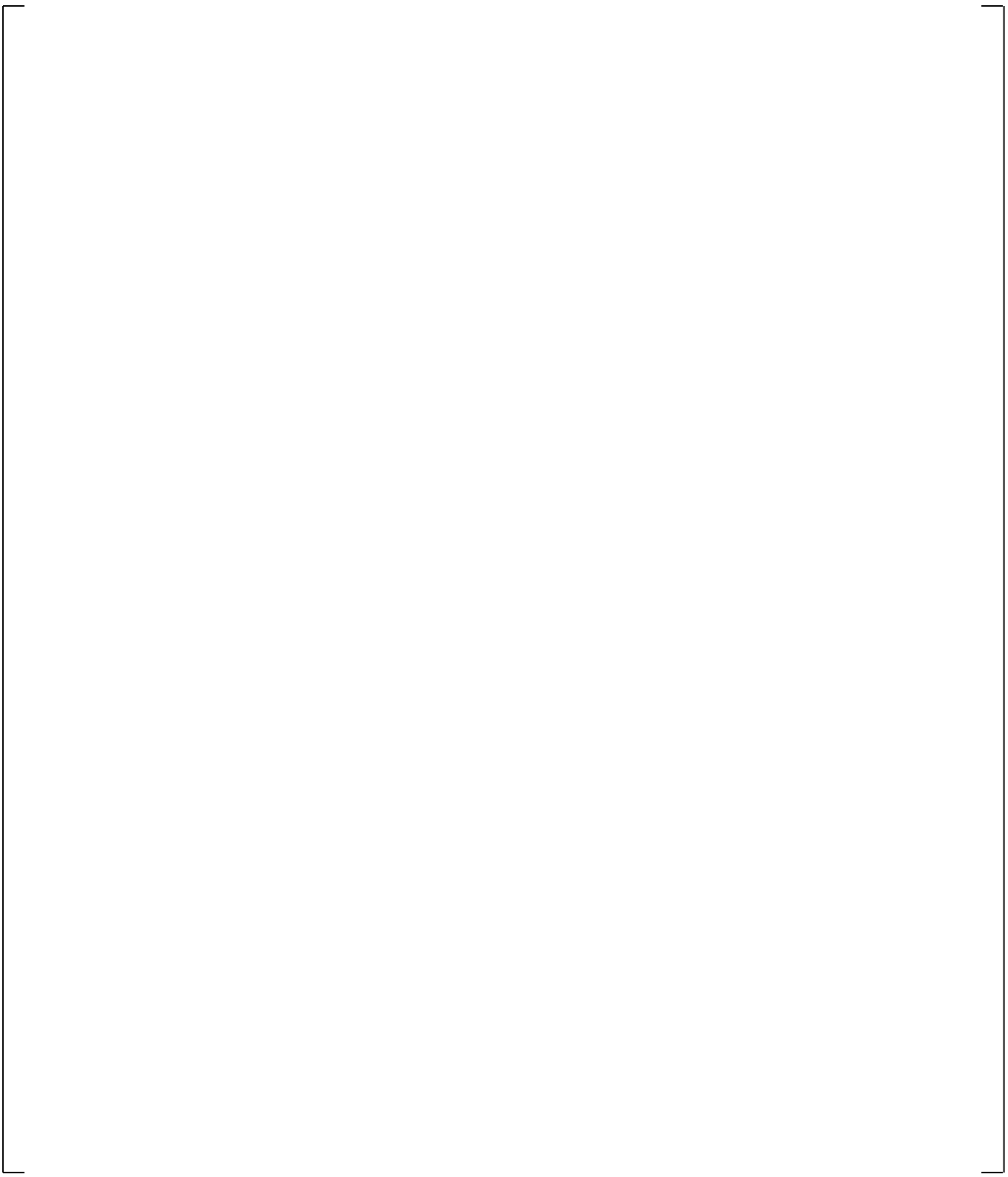

Figure 19.3-53 Intact Loop ECC Injection, UPTF Test 6 – Run 133

a,c

Figure 19.3-54 Measured Absolute Pressures in the Upper Plenum and Downcomer, UPTF Test 6 – Run 133

a,c

Figure 19.3-55 Predicted Absolute Pressures in the Upper Plenum and Downcomer, UPTF Test 6 – Run 133

a,c

Figure 19.3-56 Measured Downcomer Fluid Temperature at Level 21, UPTF Test 6 – Run 133

a,c

Figure 19.3-57 Predicted Downcomer Fluid Temperature at Level 21, UPTF Test 6 – Run 133

a,c

Figure 19.3-58 Measured Downcomer Fluid Temperature at Level 01, UPTF Test 6 – Run 133

a,c

Figure 19.3-59 Predicted Downcomer Fluid Temperature at Level 01, UPTF Test 6 – Run 133

a,c

Figure 19.3-60 Predicted Liquid Flow at Bottom of the Downcomer in Intact Side, UPTF Test 6 – Run 133

a,c

Figure 19.3-61 Predicted Liquid Flow at Bottom of the Downcomer in Broken Side, UPTF Test 6 – Run 133

a,c

Figure 19.3-62 Measured Axial Differential Pressures in Downcomer, UPTF Test 6 – Run 133

a,c

Figure 19.3-63 Predicted Axial Differential Pressures in Downcomer, UPTF Test 6 – Run 133

a,c

Figure 19.3-64 Measured Azimuthal Differential Pressures in Downcomer at Level 06, UPTF Test 6 – Run 133

a,c

Figure 19.3-65 Predicted Azimuthal Differential Pressures in Downcomer at Level 06, UPTF Test 6 – Run 133

a,c

Figure 19.3-66 Measured Azimuthal Differential Pressures in Downcomer at Level 22, UPTF Test 6 – Run 133

a,c

Figure 19.3-67 Predicted Azimuthal Differential Pressures in Downcomer at Level 22, UPTF Test 6 – Run 133

a,c

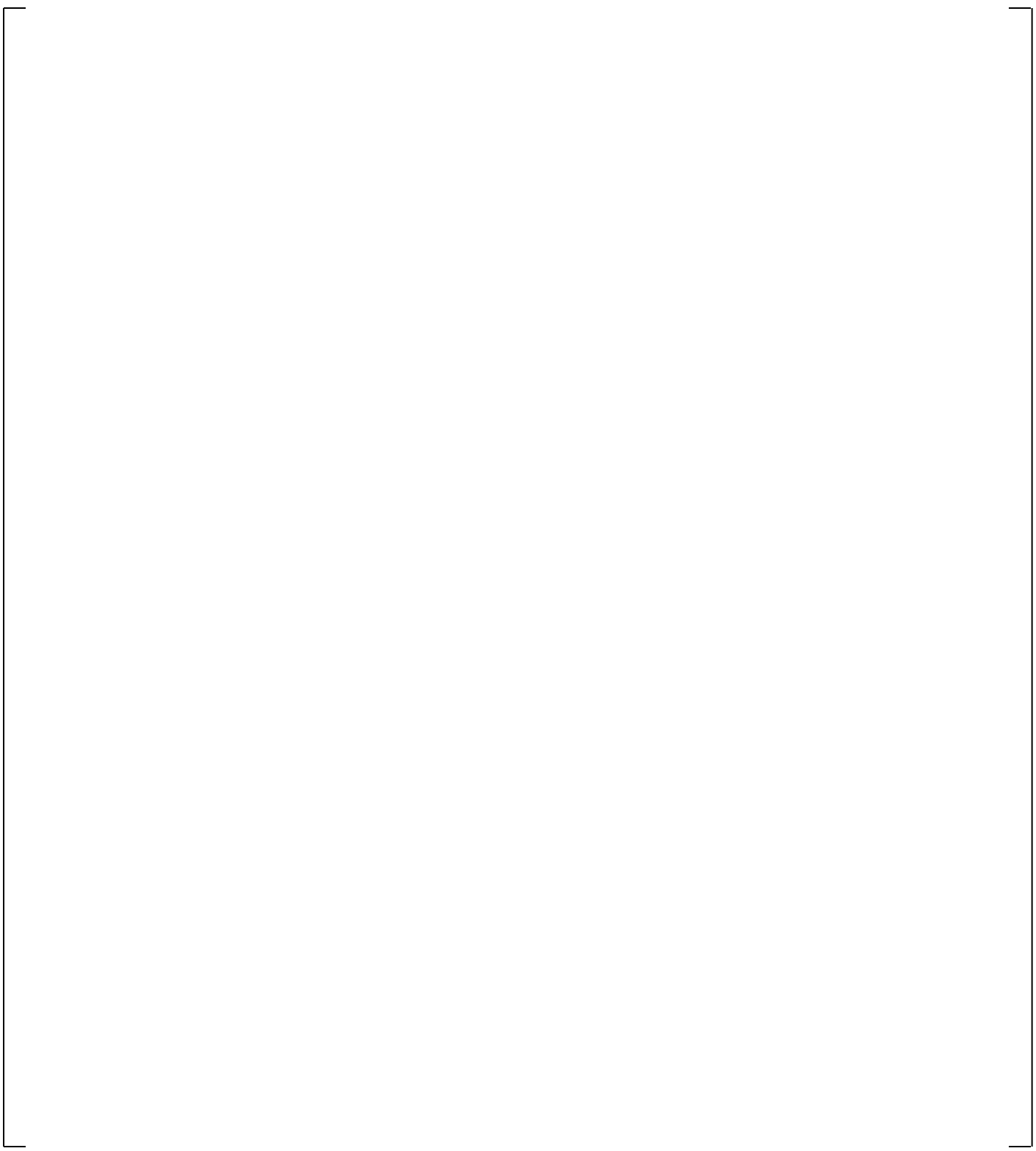

Figure 19.3-68 Comparison on Differential Pressure in Lower Plenum, UPTF Test 6 – Run 133

a,c

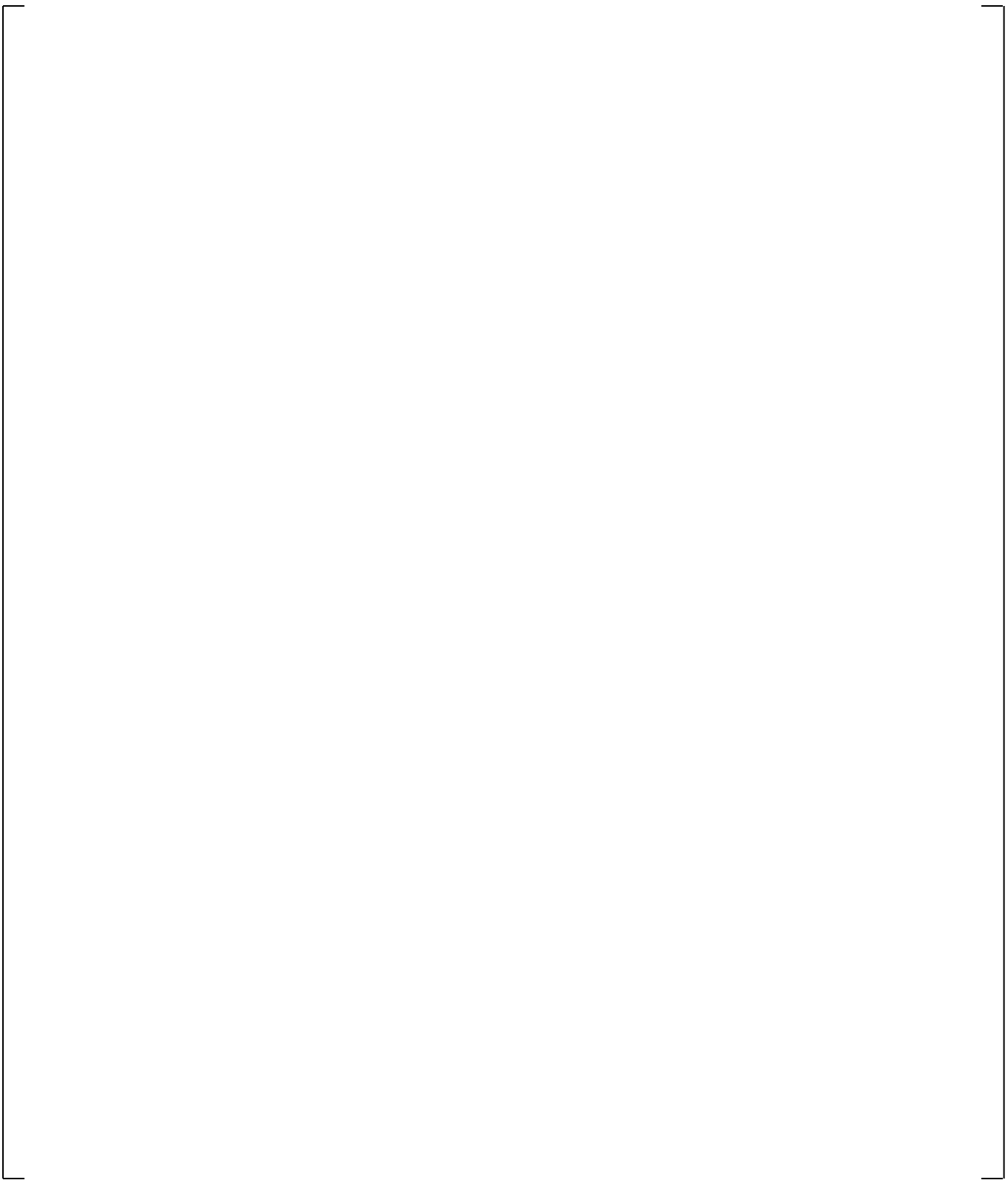

Figure 19.3-69 Total Core Steam Injection, UPTF Test 6 – Run 135

a,c

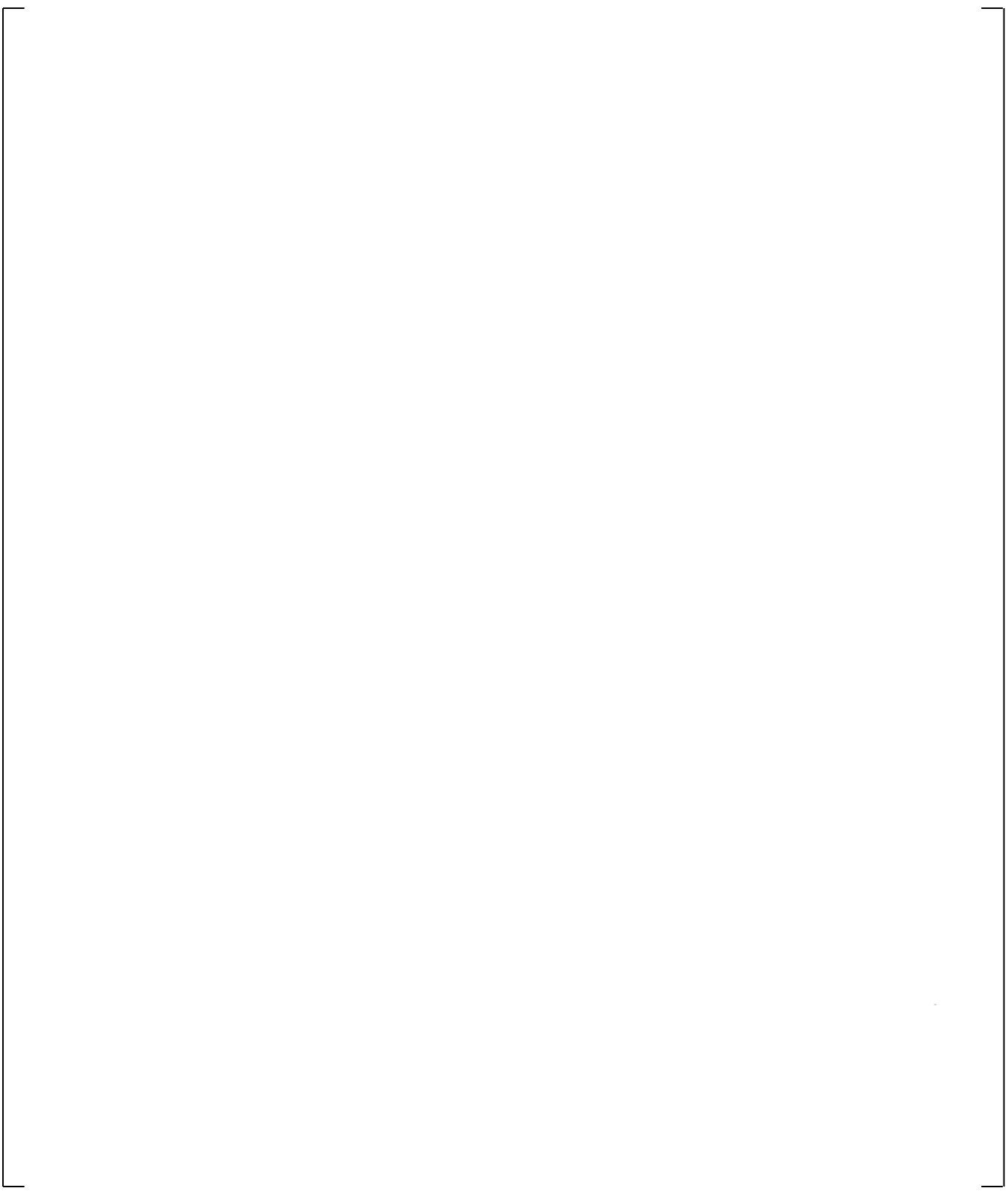

Figure 19.3-70 Steam Generator Simulator Steam Injection, UPTF Test 6 – Run 135

a,c

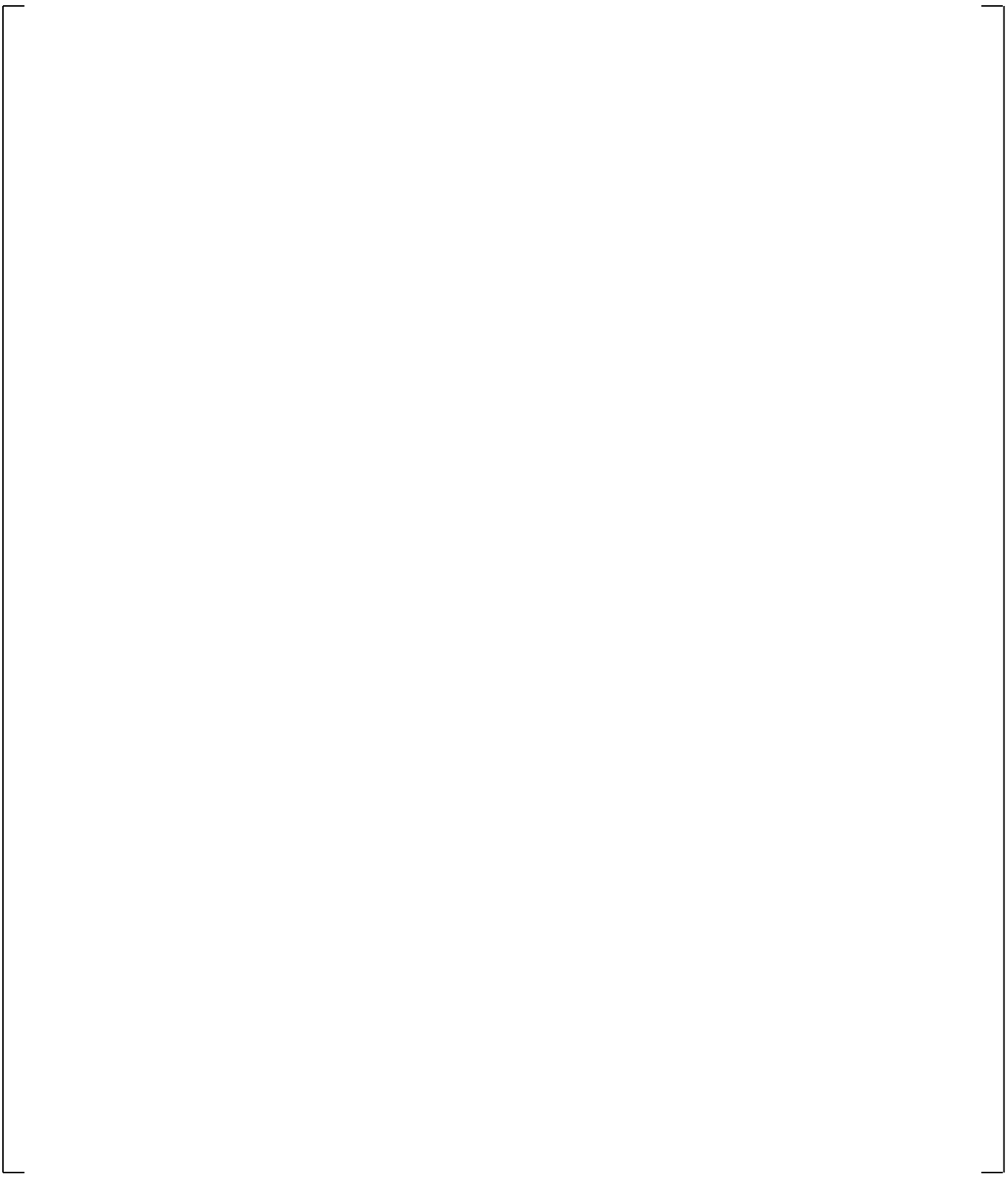

Figure 19.3-71 Intact Loop ECC Injection, UPTF Test 6 – Run 135

a,c

Figure 19.3-72 Measured Absolute Pressures in the Upper Plenum and Downcomer, UPTF Test 6 – Run 135

a,c

Figure 19.3-73 Predicted Absolute Pressures in the Upper Plenum and Downcomer, UPTF Test 6 – Run 135

a,c

Figure 19.3-74 Measured Downcomer Fluid Temperature at Level 21, UPTF Test 6 – Run 135

a,c

Figure 19.3-75 Predicted Downcomer Fluid Temperature at Level 21, UPTF Test 6 – Run 135

a,c

Figure 19.3-76 Measured Downcomer Fluid Temperature at Level 01, UPTF Test 6 – Run 135

a,c

Figure 19.3-77 Predicted Downcomer Fluid Temperature at Level 01, UPTF Test 6 – Run 135

a,c

Figure 19.3-78 Predicted Liquid Flow at Bottom of the Downcomer in Intact Side, UPTF Test 6 – Run 135

a,c

Figure 19.3-79 Predicted Liquid Flow at Bottom of the Downcomer in Broken Side, UPTF Test 6 – Run 135

a,c

Figure 19.3-80 Measured Axial Differential Pressures in Downcomer, UPTF Test 6 – Run 135

a,c

Figure 19.3-81 Predicted Axial Differential Pressures in Downcomer, UPTF Test 6 – Run 135

a,c

Figure 19.3-82 Measured Azimuthal Differential Pressures in Downcomer at Level 06, UPTF Test 6 – Run 135

a,c

Figure 19.3-83 Predicted Azimuthal Differential Pressures in Downcomer at Level 06, UPTF Test 6 – Run 135

a,c

Figure 19.3-84 Measured Azimuthal Differential Pressures in Downcomer at Level 22, UPTF Test 6 – Run 135

a,c

Figure 19.3-85 Predicted Azimuthal Differential Pressures in Downcomer at Level 22, UPTF Test 6 – Run 135

a,c

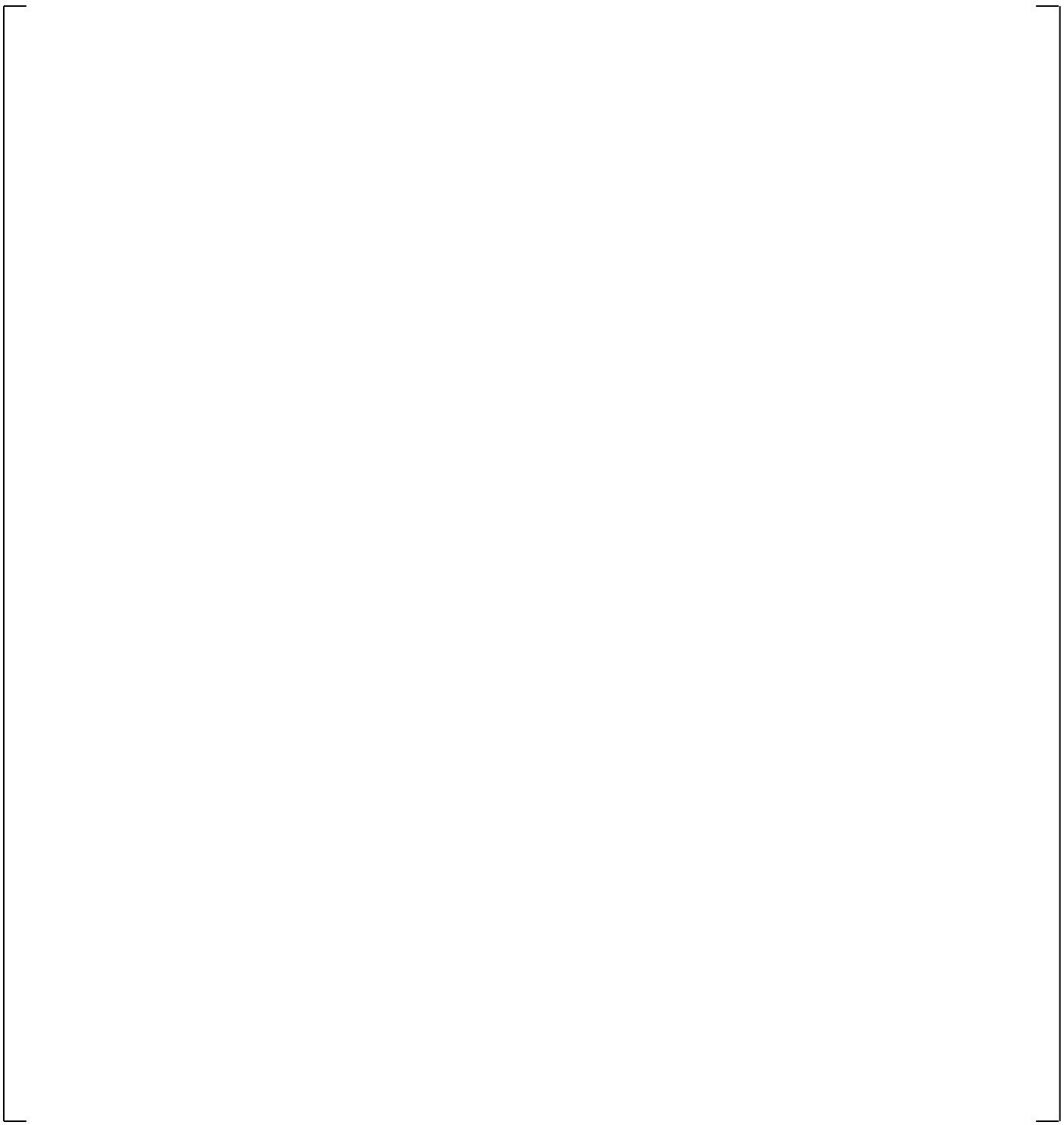

Figure 19.3-86 Comparison on Differential Pressure in Lower Plenum, UPTF Test 6 – Run 135

a,c

Figure 19.3-87 Total Core Steam Injection, UPTF Test 6 – Run 136

a,c

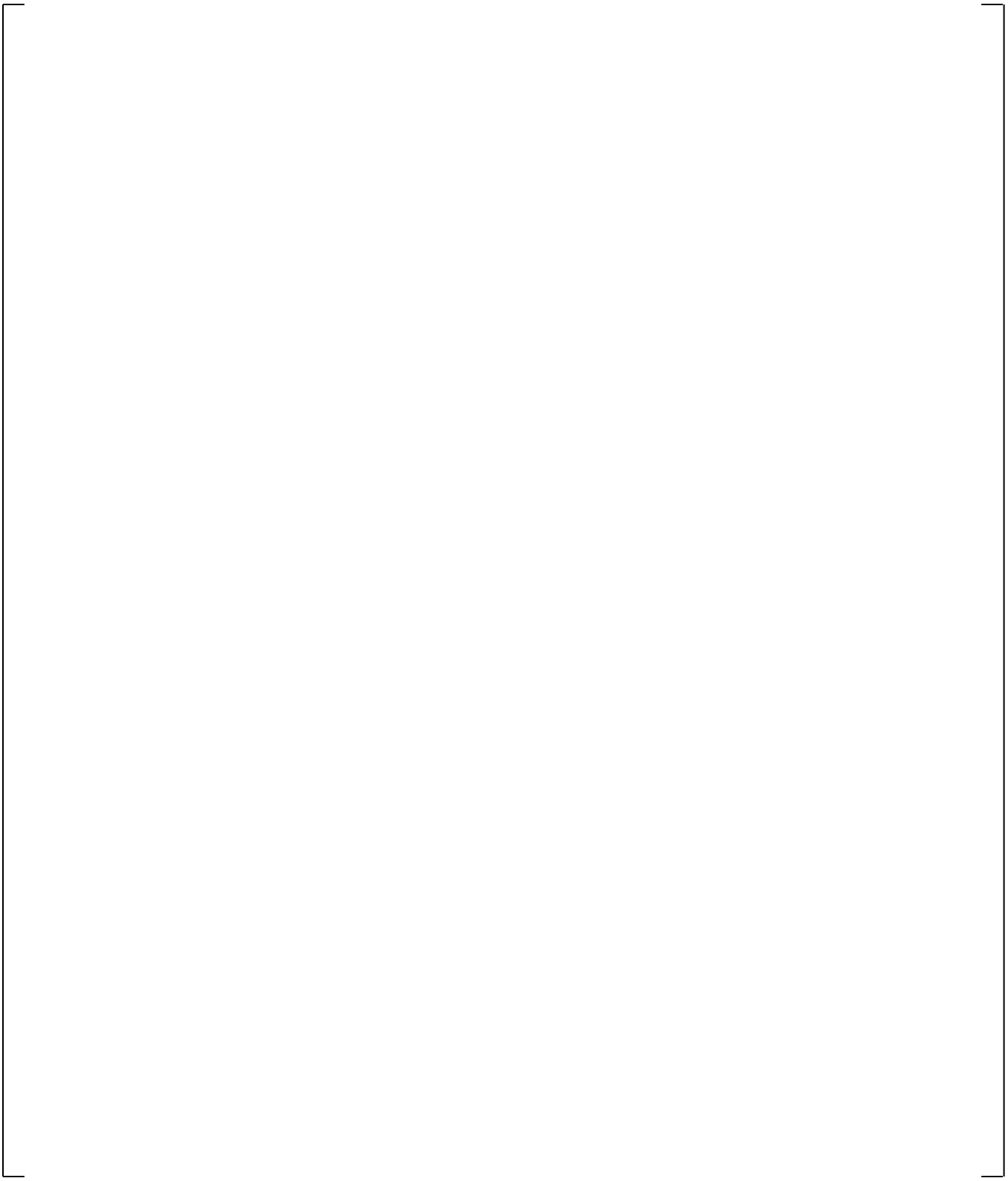

Figure 19.3-88 Intact Loop ECC Injection, UPTF Test 6 – Run 136

a,c

Figure 19.3-89 Measured Absolute Pressures in the Upper Plenum and Downcomer, UPTF Test 6 – Run 136

a,c

Figure 19.3-90 Predicted Absolute Pressures in the Upper Plenum and Downcomer, UPTF Test 6 – Run 136

a,c

Figure 19.3-91 Measured Downcomer Fluid Temperature at Level 21, UPTF Test 6 – Run 136

a,c

Figure 19.3-92 Predicted Downcomer Fluid Temperature at Level 21, UPTF Test 6 – Run 136

a,c

Figure 19.3-93 Measured Downcomer Fluid Temperature at Level 01, UPTF Test 6 – Run 136

a,c

Figure 19.3-94 Predicted Downcomer Fluid Temperature at Level 01, UPTF Test 6 – Run 136

a,c

Figure 19.3-95 Predicted Liquid Flow at Bottom of the Downcomer in Intact Side, UPTF Test 6 – Run 136

a,c

Figure 19.3-96 Predicted Liquid Flow at Bottom of the Downcomer in Broken Side, UPTF Test 6 – Run 136

a,c

Figure 19.3-97 Measured Axial Differential Pressures in Downcomer, UPTF Test 6 – Run 136

a,c

Figure 19.3-98 Predicted Axial Differential Pressures in Downcomer, UPTF Test 6 – Run 136

a,c

Figure 19.3-99 Measured Azimuthal Differential Pressures in Downcomer at Level 06, UPTF Test 6 – Run 136

a,c

Figure 19.3-100 Predicted Azimuthal Differential Pressures in Downcomer at Level 06, UPTF Test 6 – Run 136

a,c

Figure 19.3-101 Measured Azimuthal Differential Pressures in Downcomer at Level 22, UPTF Test 6 – Run 136

a,c

Figure 19.3-102 Predicted Azimuthal Differential Pressures in Downcomer at Level 22, UPTF Test 6 – Run 136

a,c

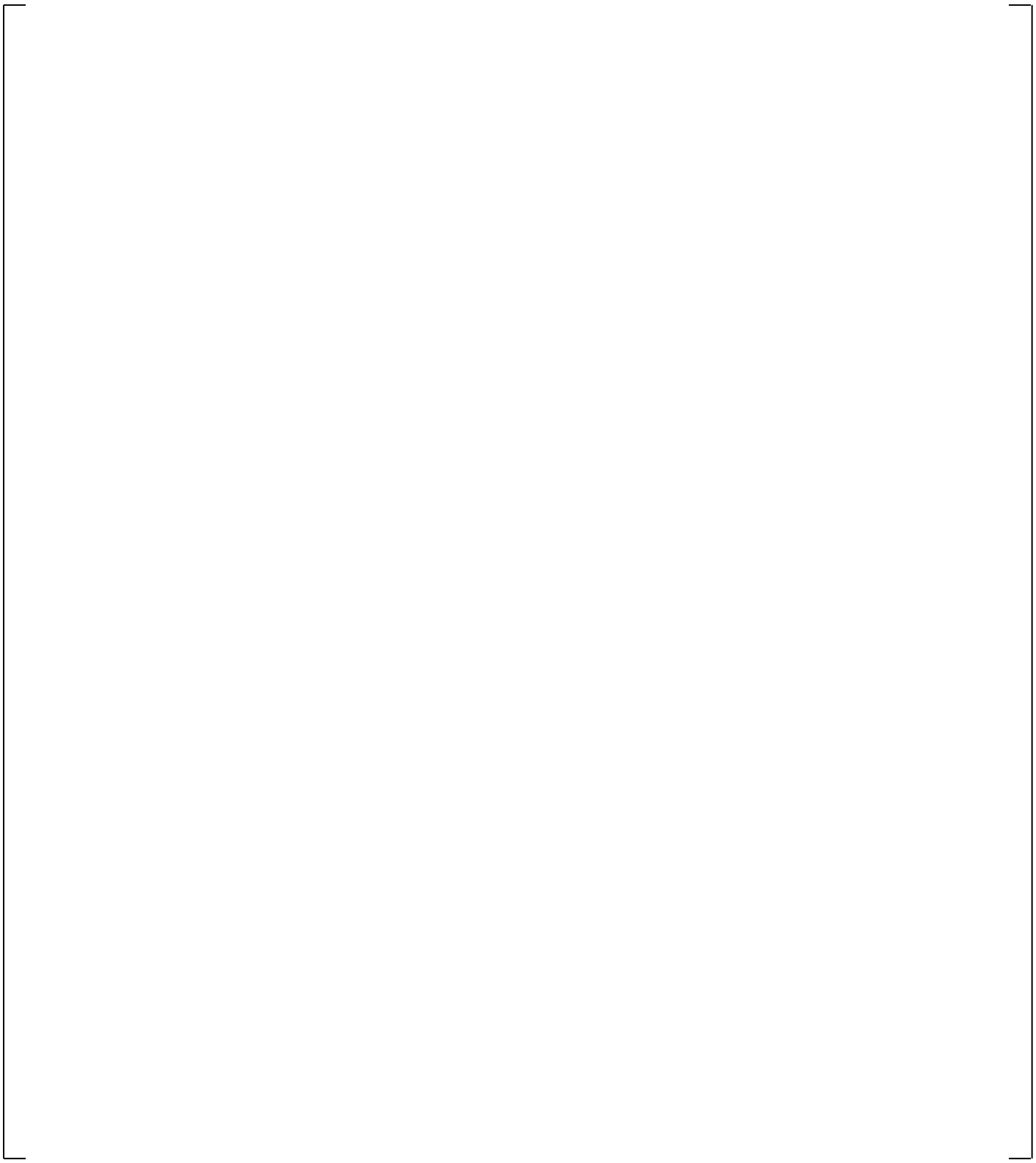

Figure 19.3-103 Comparison on Differential Pressure in Lower Plenum, UPTF Test 6 – Run 136

a,c

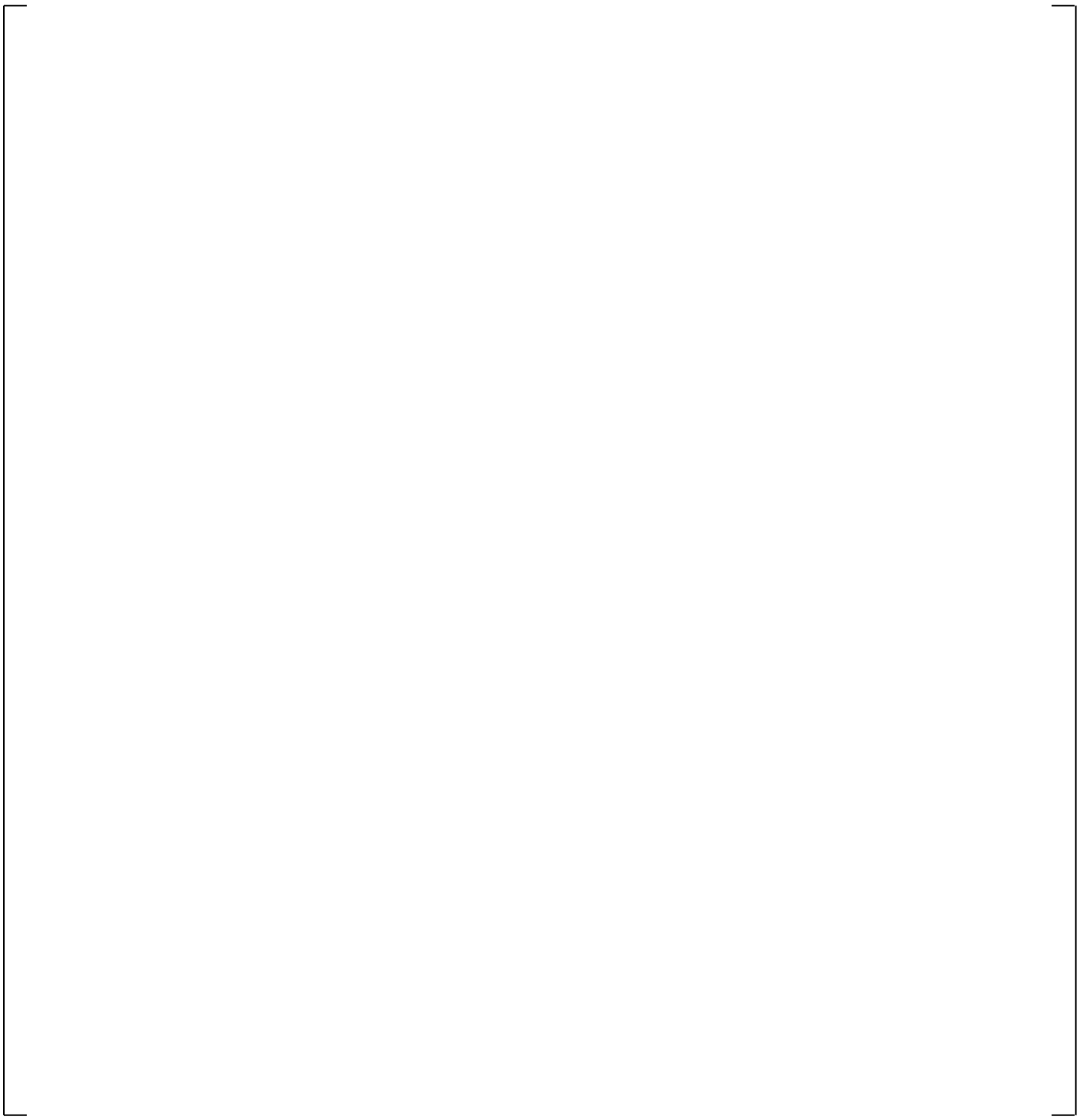

Figure 19.3-104 Lower Plenum Fluid Inventory, UPTF Test 6 – Run 131

a,c

Figure 19.3-105 Lower Plenum Fluid Inventory, UPTF Test 6 – Run 132

a,c

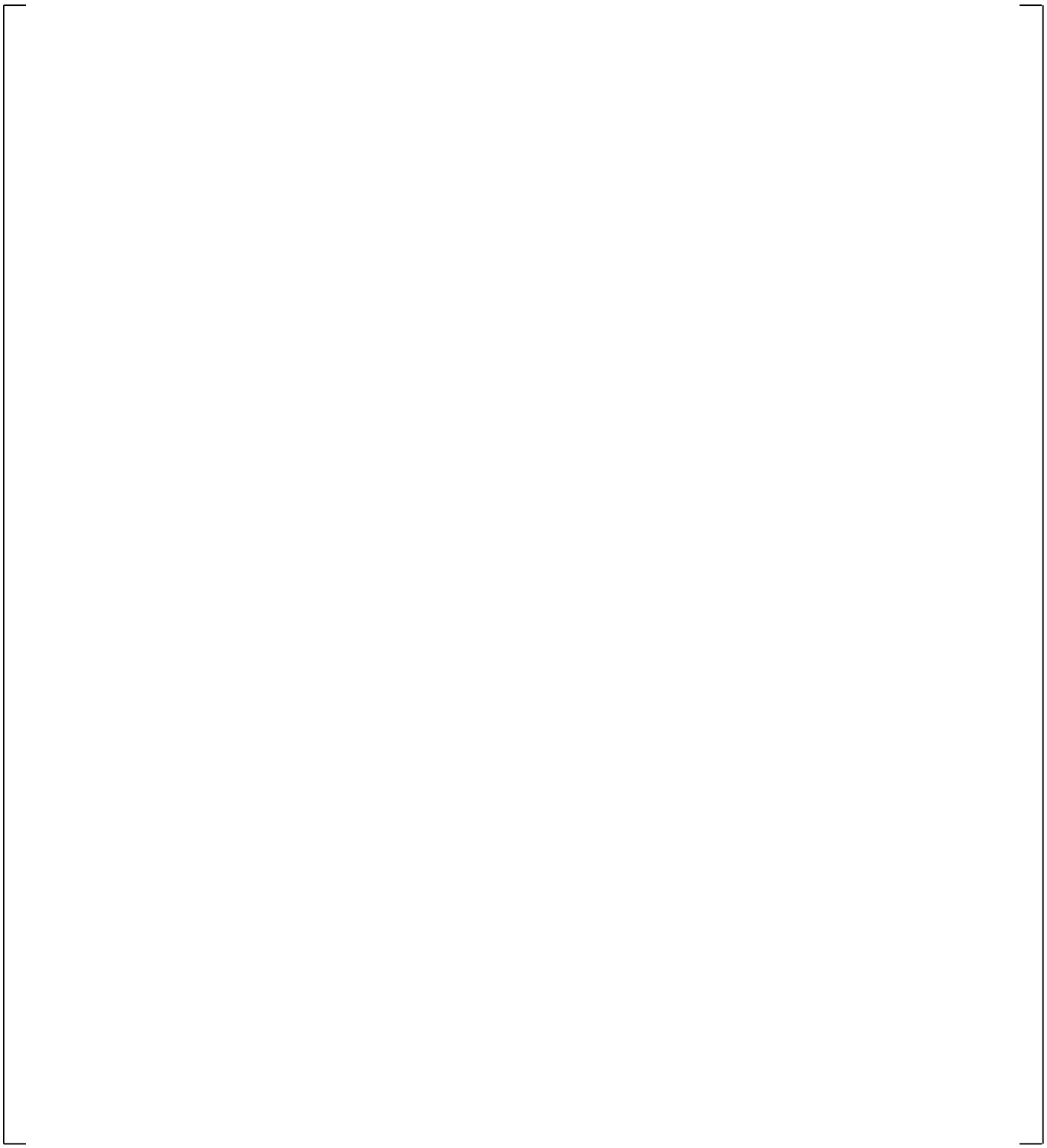

Figure 19.3-106 Lower Plenum Fluid Inventory, UPTF Test 6 – Run 133

a,c

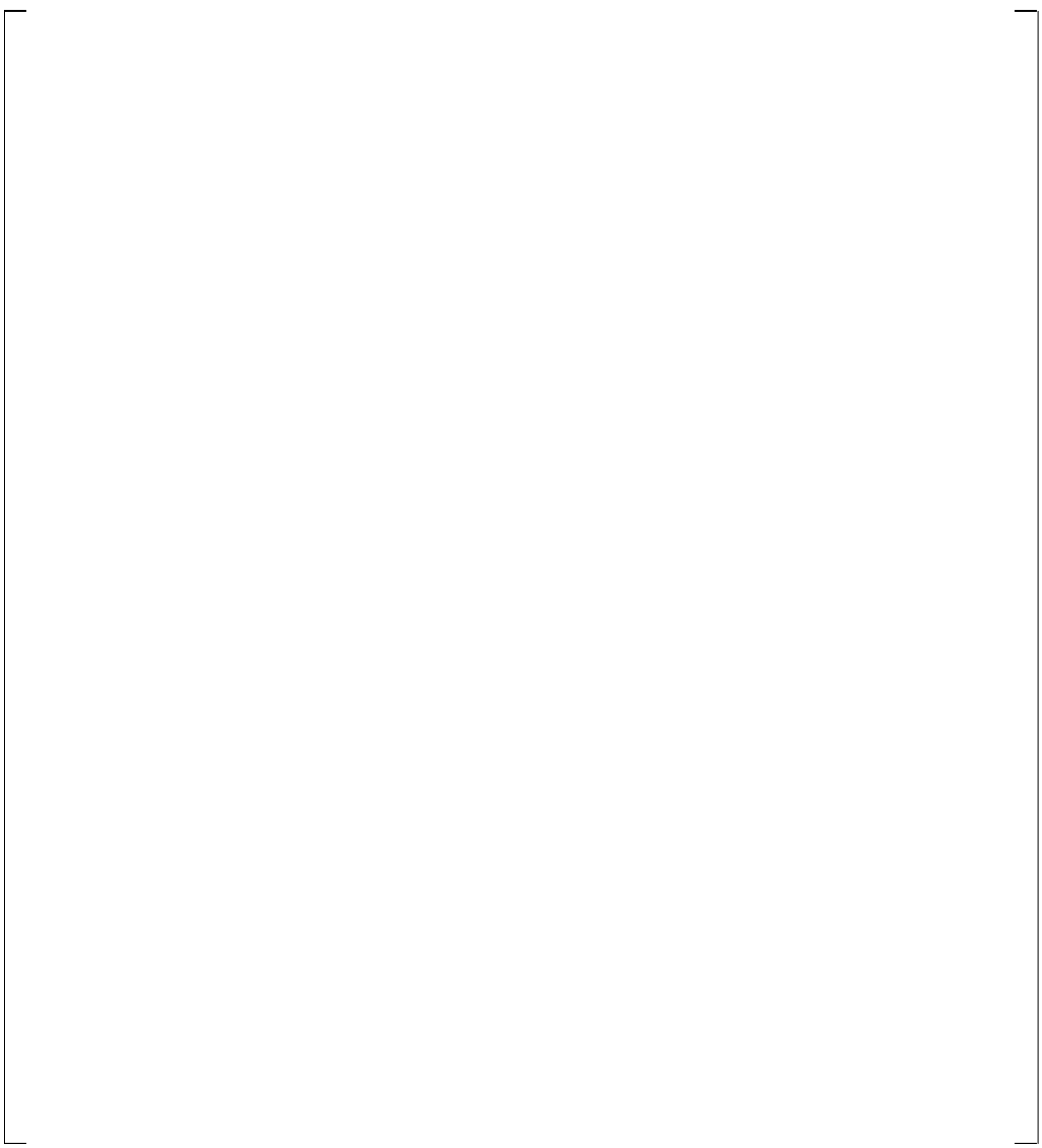

Figure 19.3-107 Lower Plenum Fluid Inventory, UPTF Test 6 – Run 135

a,c

Figure 19.3-108 Lower Plenum Fluid Inventory, UPTF Test 6 – Run 136

a,c

Figure 19.3-109 Comparison between Measured and Predicted Penetration Rates in UPTF Test 6

a,c

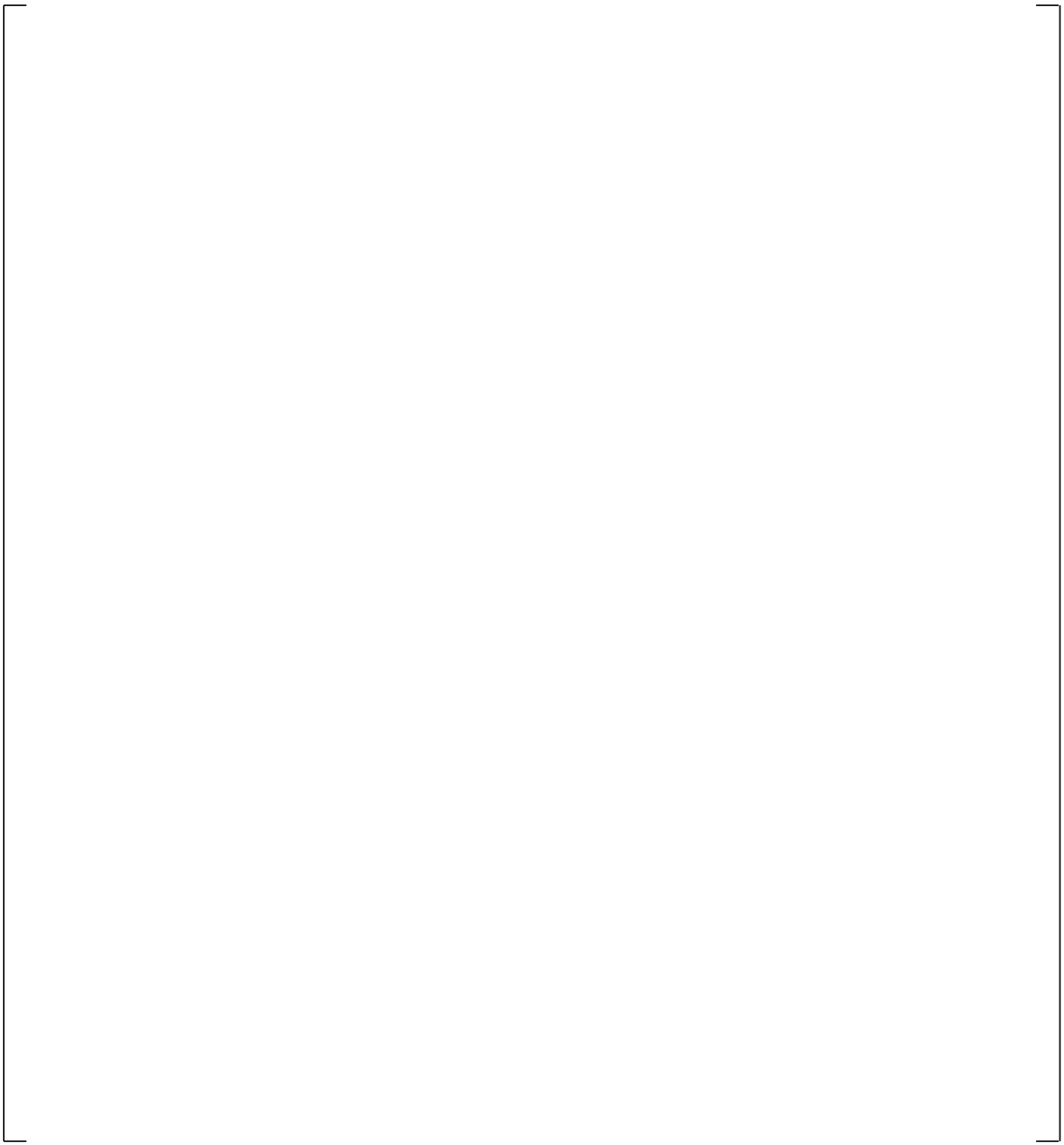

Figure 19.3-110 Comparison between Measured and Predicted Refill Periods versus Nominal Steam Flow Rate for Lower Plenum in UPTF Test 6

b

Figure 19.3-111 Downcomer CCFL Behavior for UPTF Test 6

a,c

Figure 19.3-112 Estimated Mass Distribution, UPTF Test 6 – Run 131

a,c

Figure 19.3-113 Predicted Mass Distribution, UPTF Test 6 – Run 131

a,c

Figure 19.3-114 Estimated Mass Distribution, UPTF Test 6 – Run 132

a,c

Figure 19.3-115 Predicted Mass Distribution, UPTF Test 6 – Run 132

a,c

Figure 19.3-116 Estimated Mass Distribution, UPTF Test 6 – Run 133

a,c

Figure 19.3-117 Predicted Mass Distribution, UPTF Test 6 – Run 133

a,c

Figure 19.3-118 Estimated Mass Distribution, UPTF Test 6 – Run 135

a,c

Figure 19.3-119 Predicted Mass Distribution, UPTF Test 6 – Run 135

a,c

Figure 19.3-120 Estimated Mass Distribution, UPTF Test 6 – Run 136

a,c

Figure 19.3-121 Predicted Mass Distribution, UPTF Test 6 – Run 136

a,c

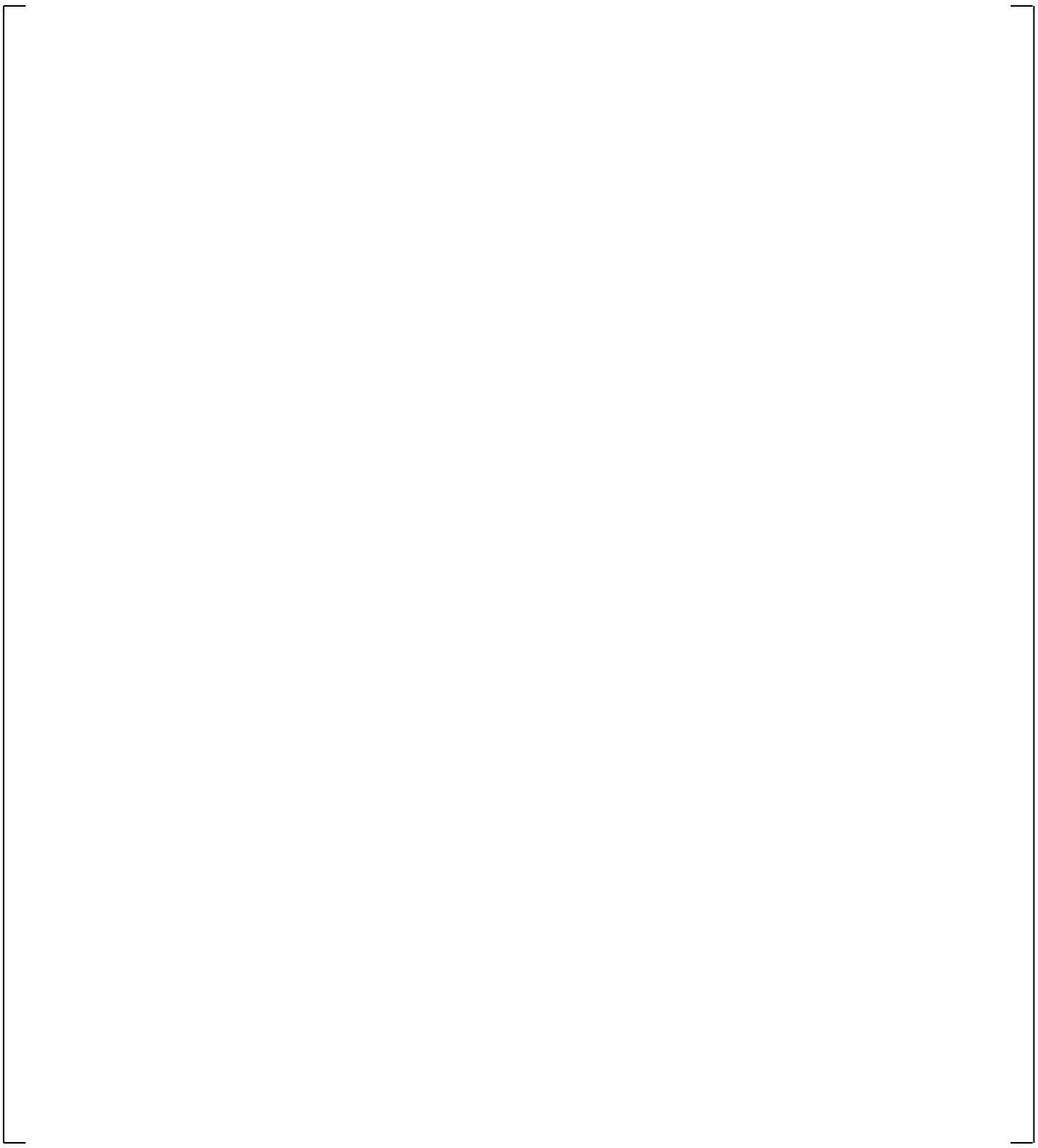

Figure 19.3-122 Vessel Condensation Efficiency, UPTF Test 6 – Run 131

a,c

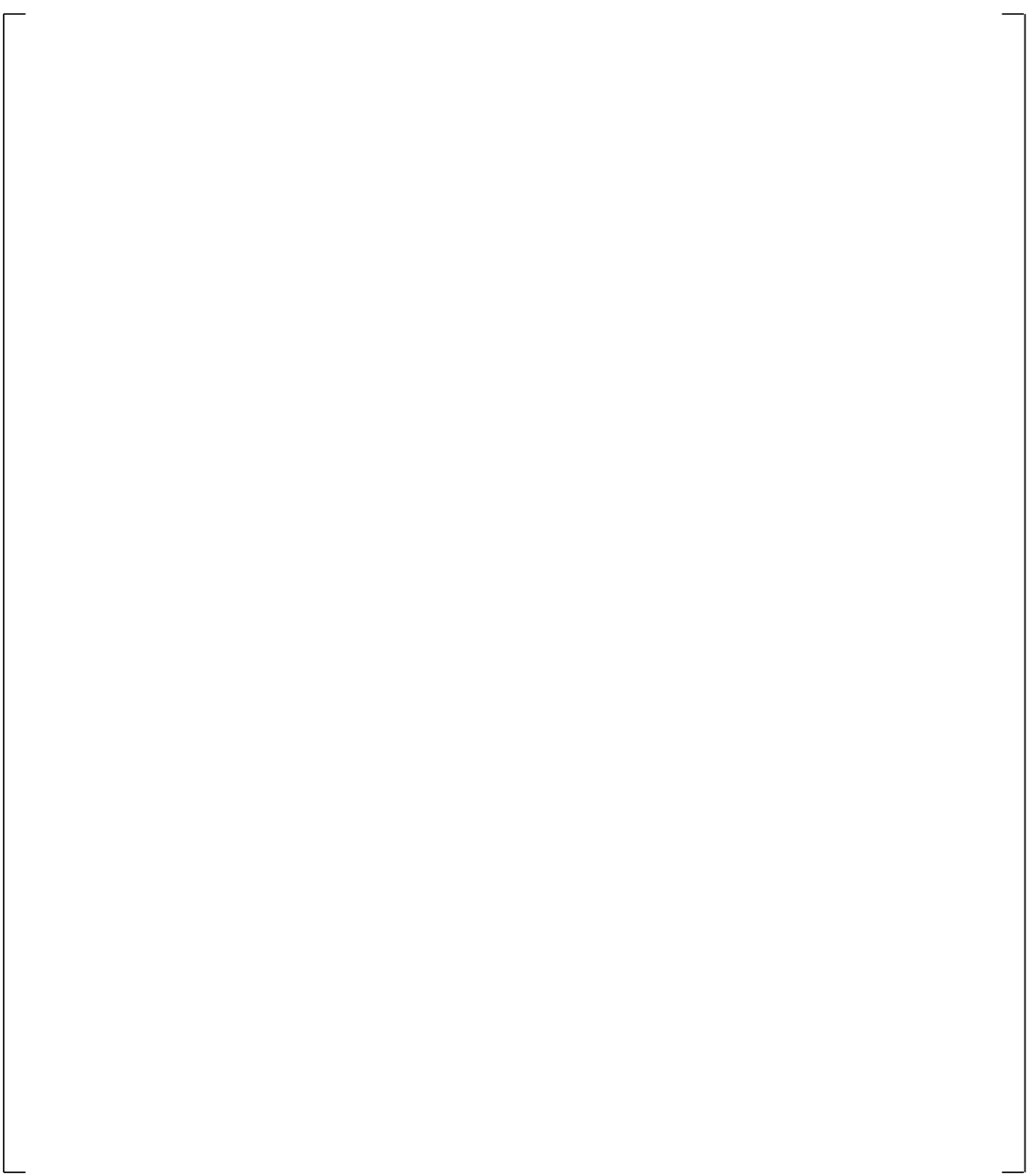

Figure 19.3-123 Vessel Condensation Efficiency, UPTF Test 6 – Run 132

a,c

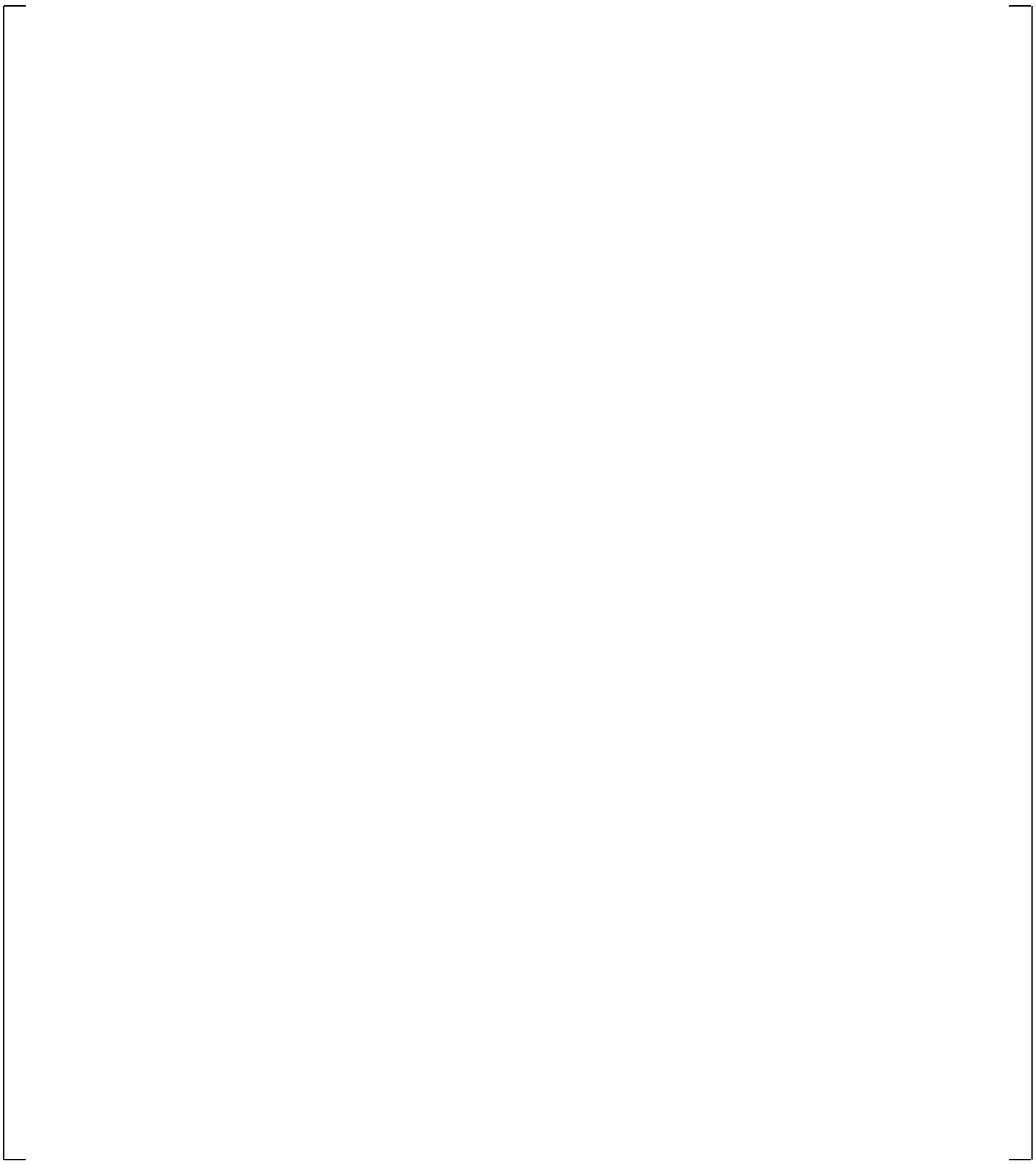

Figure 19.3-124 Vessel Condensation Efficiency, UPTF Test 6 – Run 133

a,c

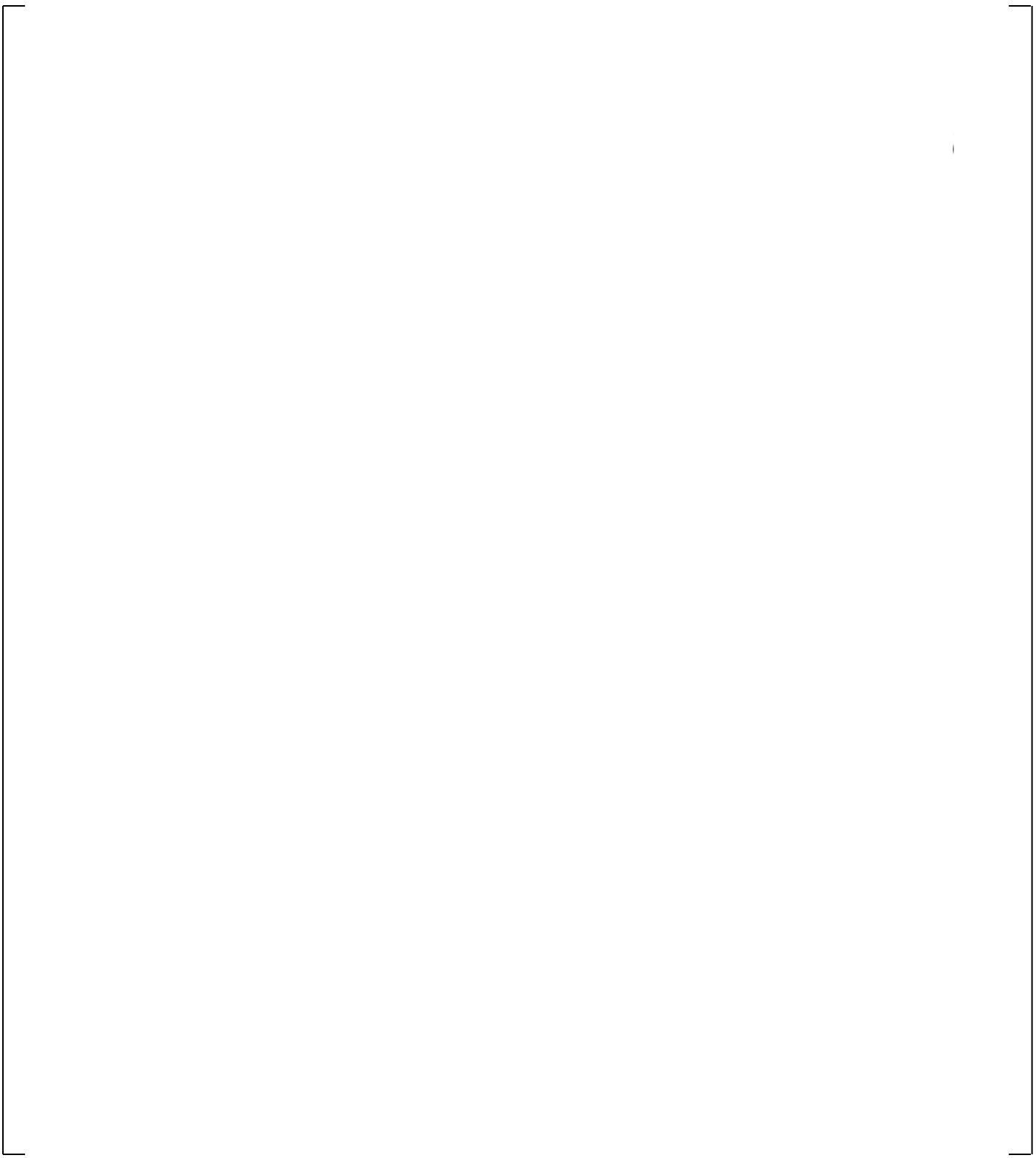

Figure 19.3-125 Vessel Condensation Efficiency, UPTF Test 6 – Run 135

a,c

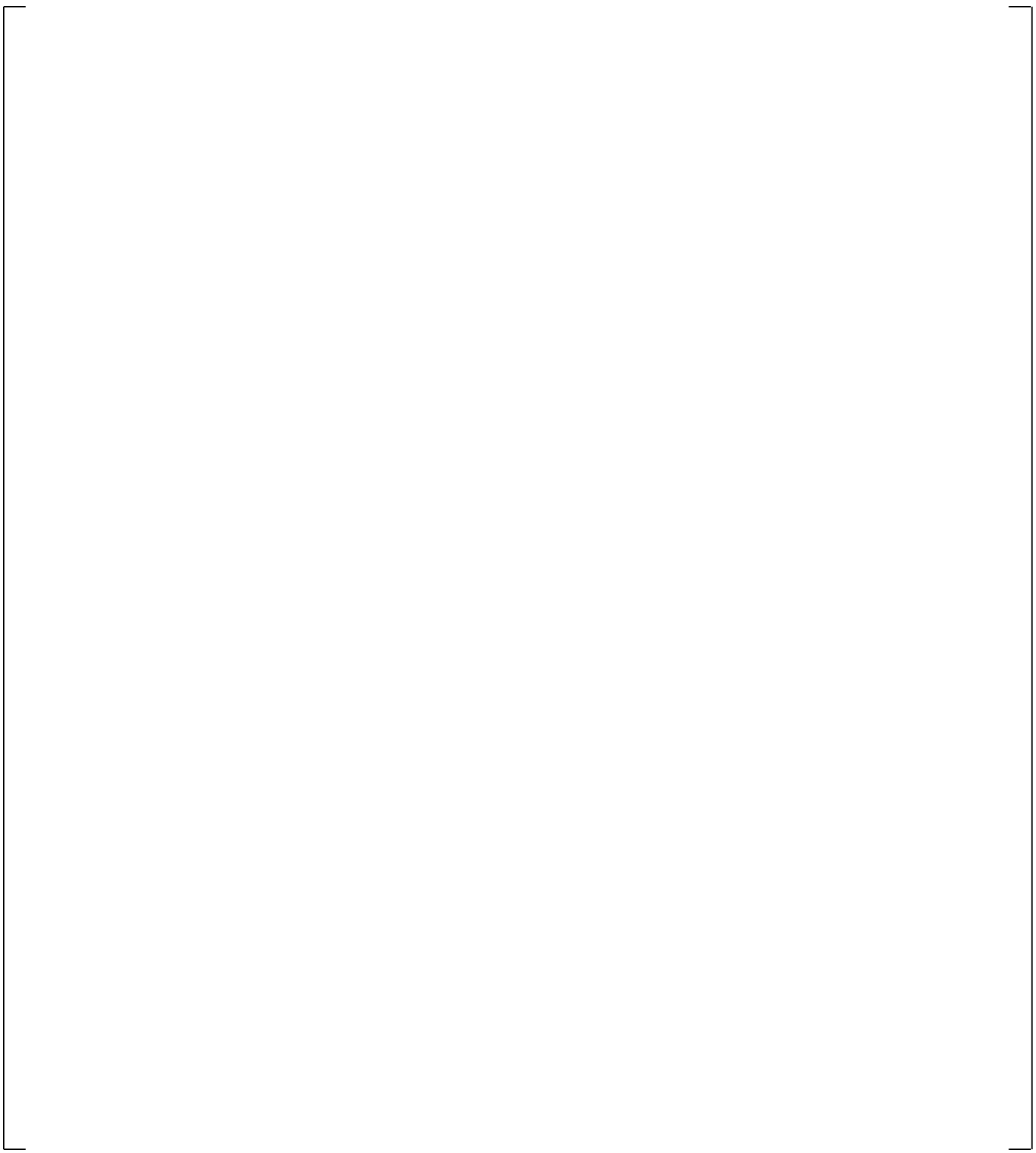

Figure 19.3-126 Vessel Condensation Efficiency, UPTF Test 6 – Run 136

a,c

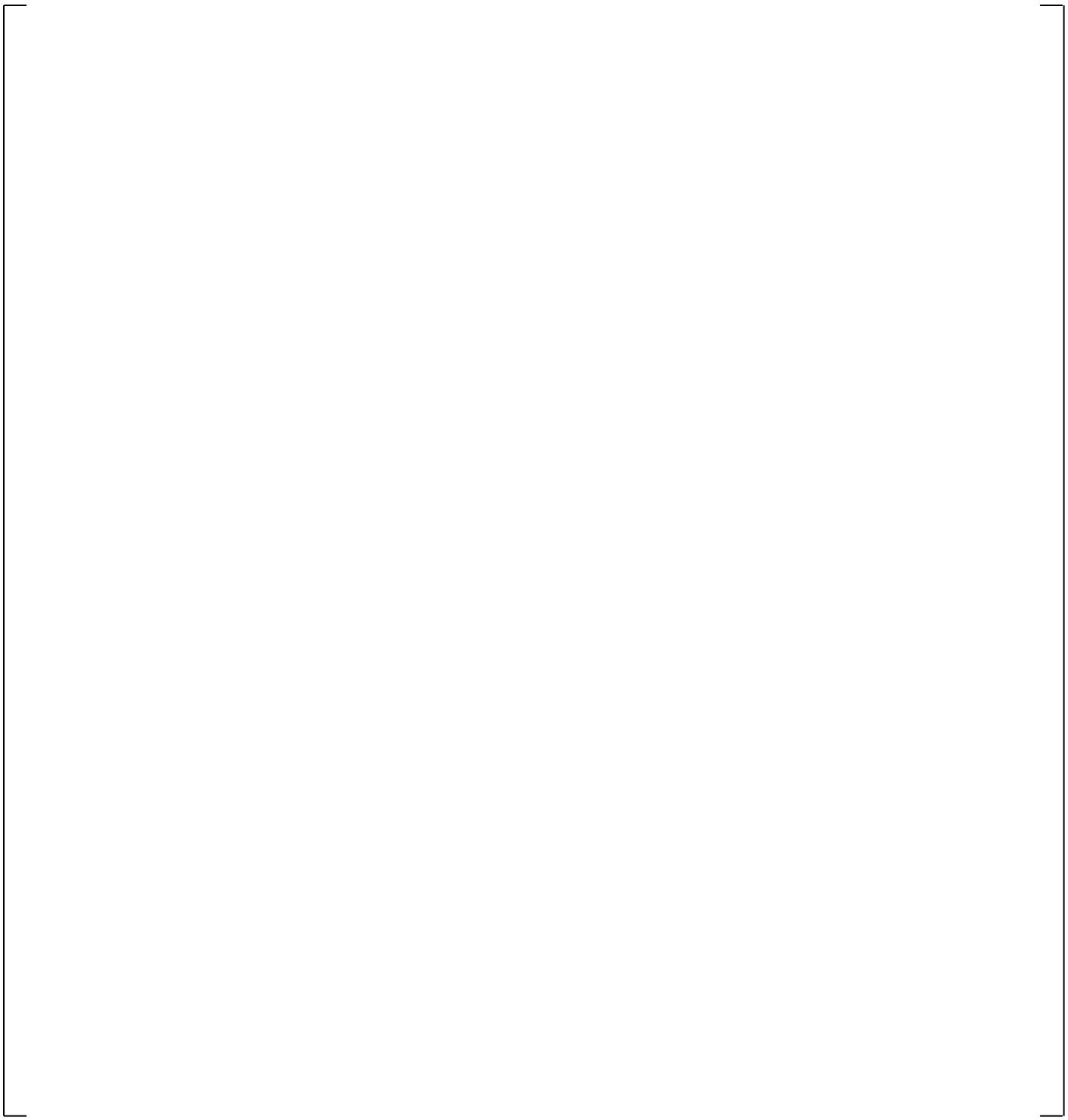

Figure 19.3-127 Comparison of Vessel Condensation Efficiency versus Nominal Steam Flow Rate, UPTF Test 6; Experimental Condensation Efficiency is Estimated by MPR (MPR-1163, 1990a); Predicted Condensation Efficiency is Evaluated Using Steam Flow Rate at Break

a,c

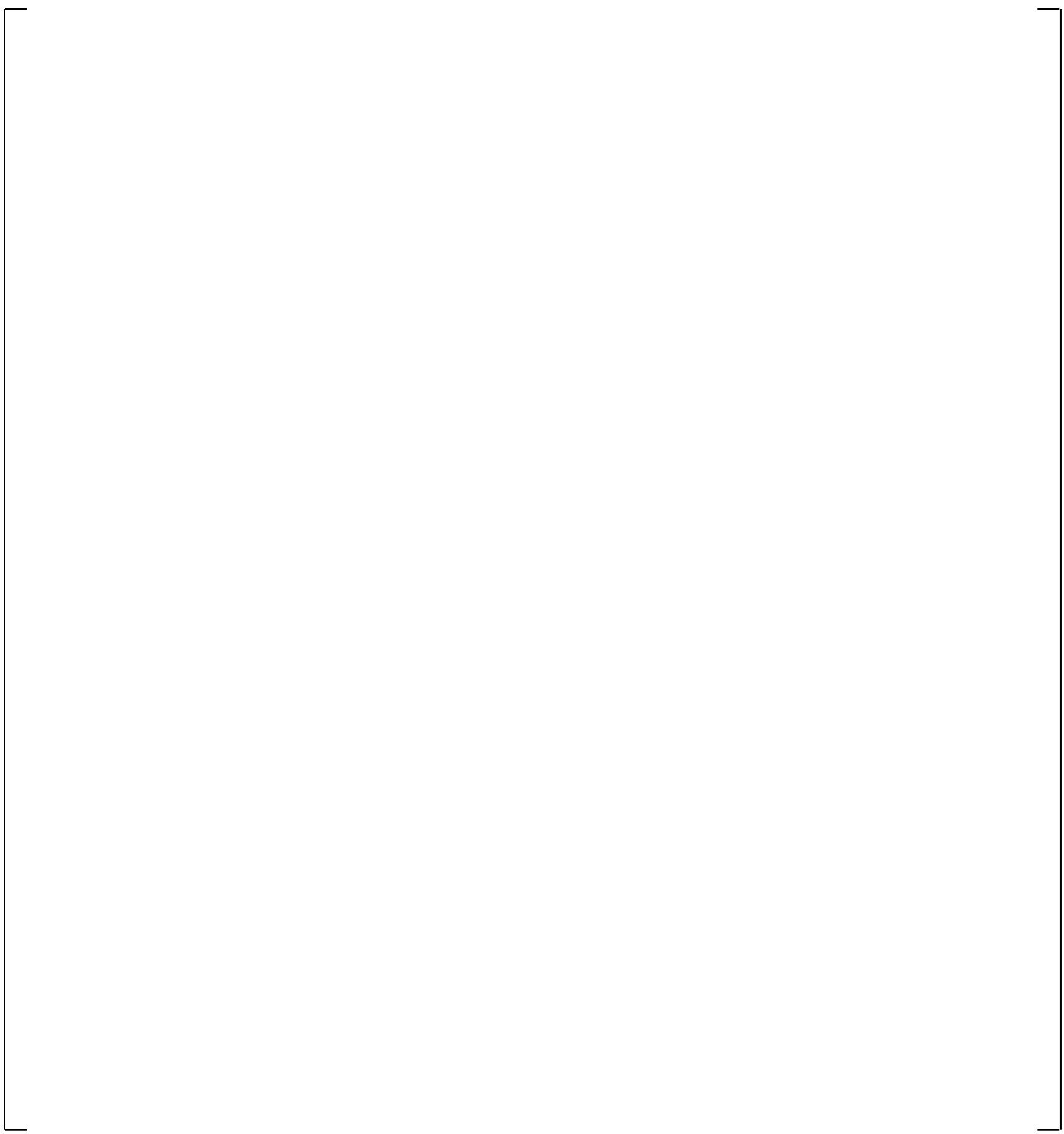

Figure 19.3-128 Comparison of Vessel Condensation Efficiency versus Nominal Steam Flow Rate with Various DC Condensation Multipliers, UPTF Test 6; Predicted Condensation Efficiency is Evaluated Using Steam Flow Rate at Inlet of Broken Cold Leg

a,c

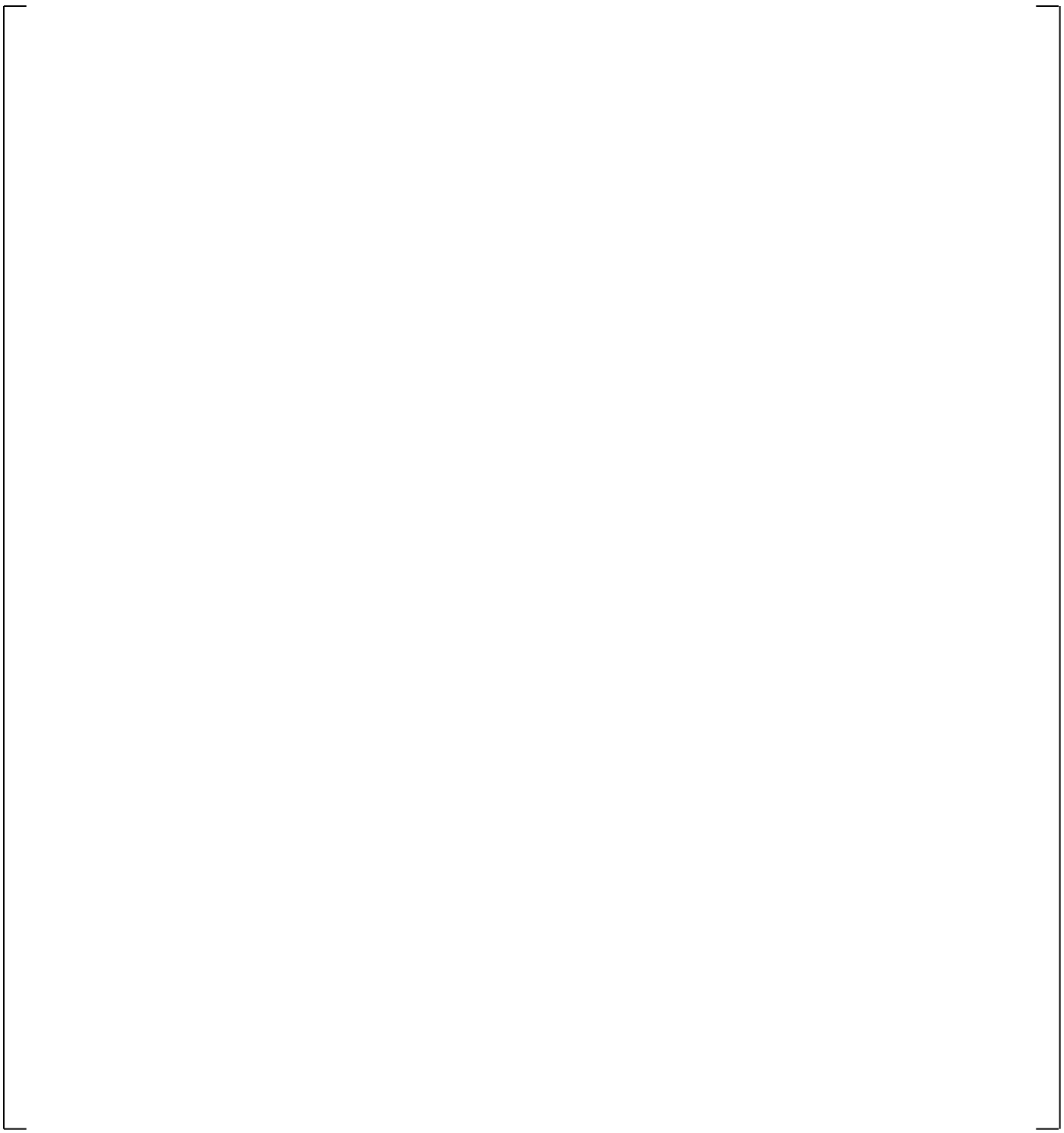

Figure 19.3-129 Comparison of Filling Period from Start of ECC Injection to End of Lower Plenum Filling with Various DC Condensation Multipliers versus Nominal Steam Flow Rate, UPTF Test 6. Note, Run 132 did not Fill the Lower Plenum at the End of the Calculation.

a,c

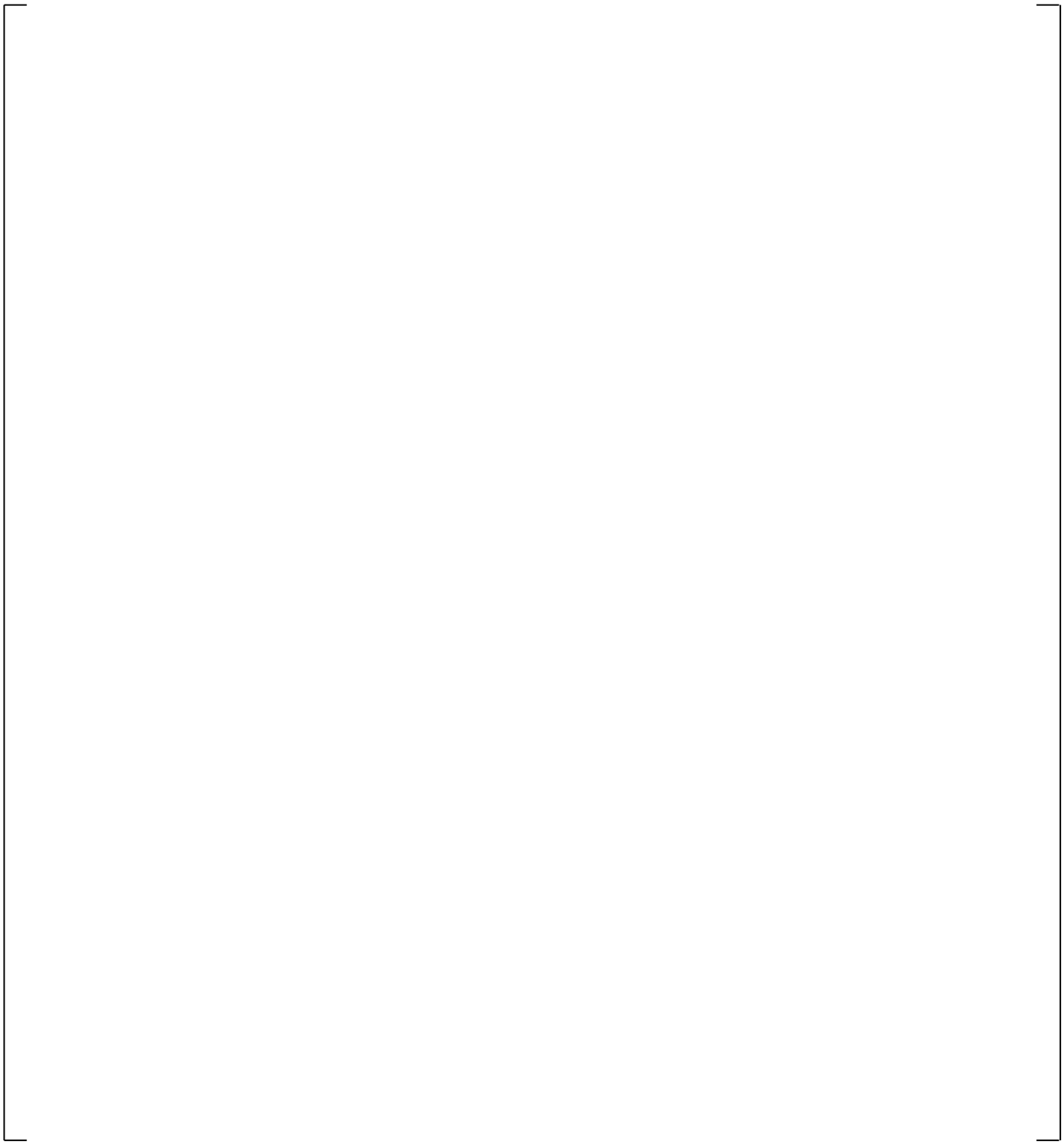

Figure 19.3-130 Comparison of Length of Refill Period from Start of ECC Injection to End of Lower Plenum Filling versus Nominal Steam Flow Rate with Various DTMAX, UPTF Test 6

a,c

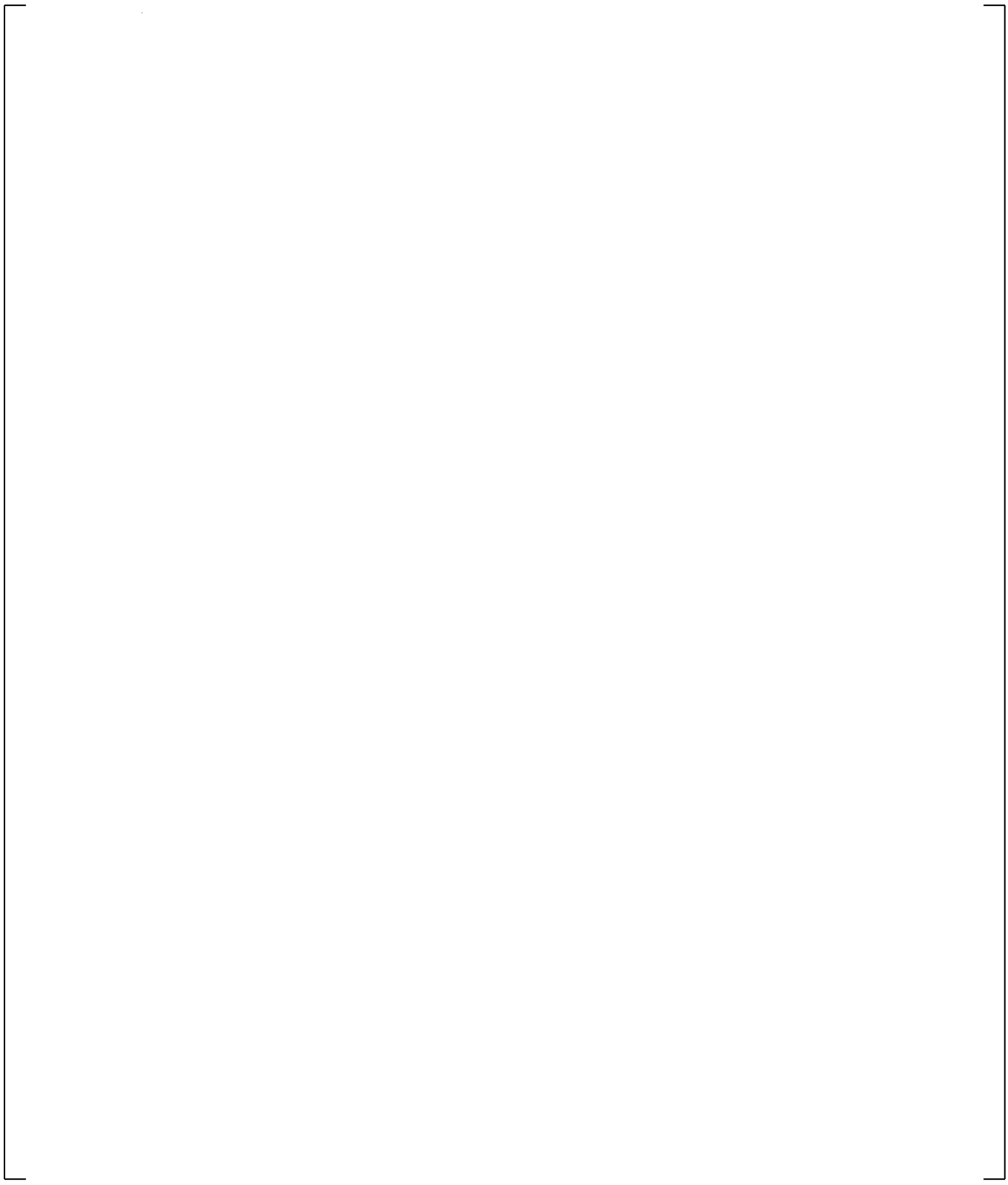

Figure 19.3-131 Location of Fluid Thermocouples, Differential and Absolute Pressure Measurements in Broken Cold Leg of Loop 04

a,c

Figure 19.3-132 Moody Diagram

a,c

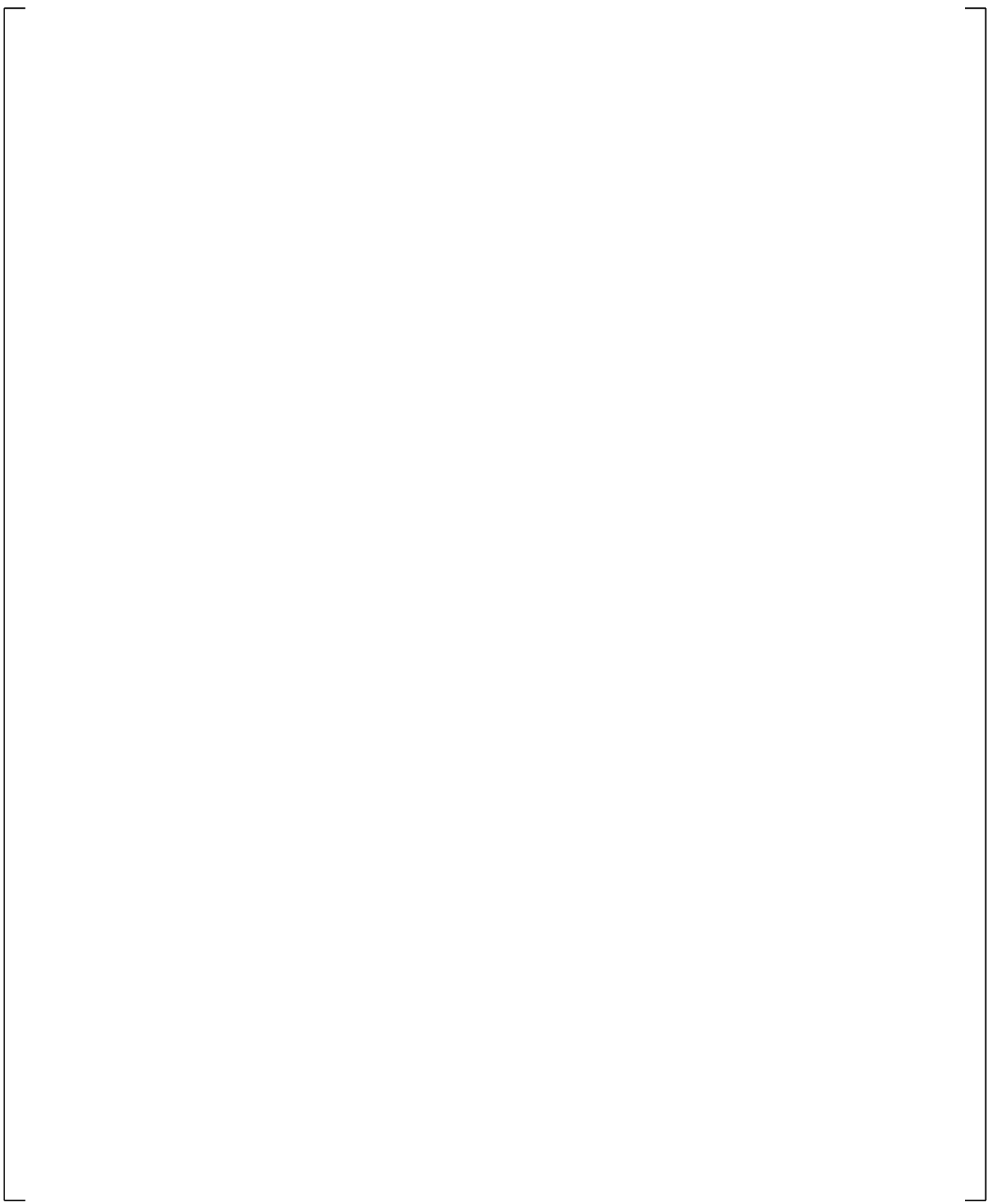

Figure 19.3-133 Cold Leg Steam Flow Rate (Top) and Downcomer Pressure (Bottom) for Test Run 131

a,c

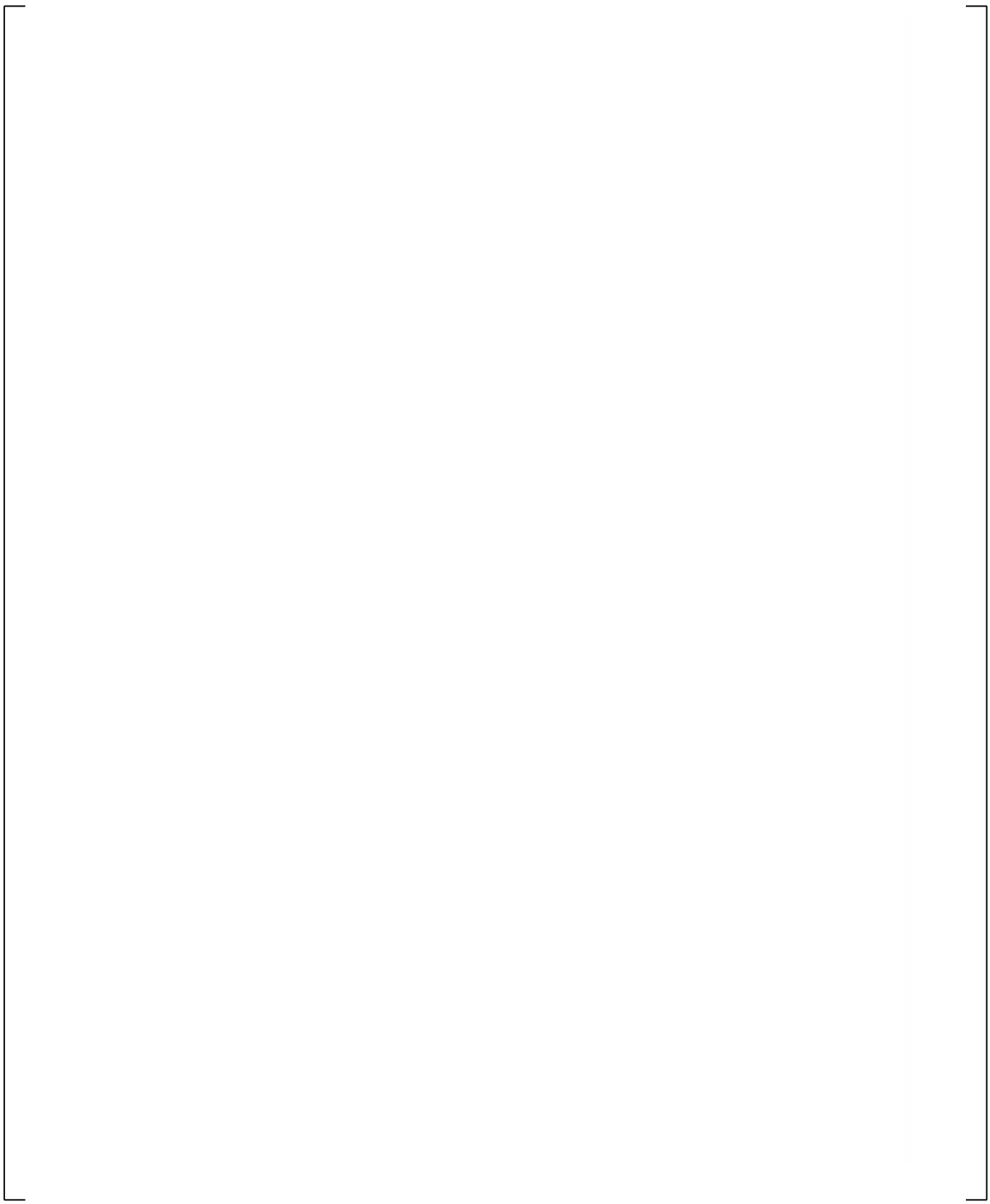

Figure 19.3-134 Cold Leg Fluid Temperature (Top) and Cold Leg to Downcomer Pressure Drop (Bottom) for Test Run 131

a,c

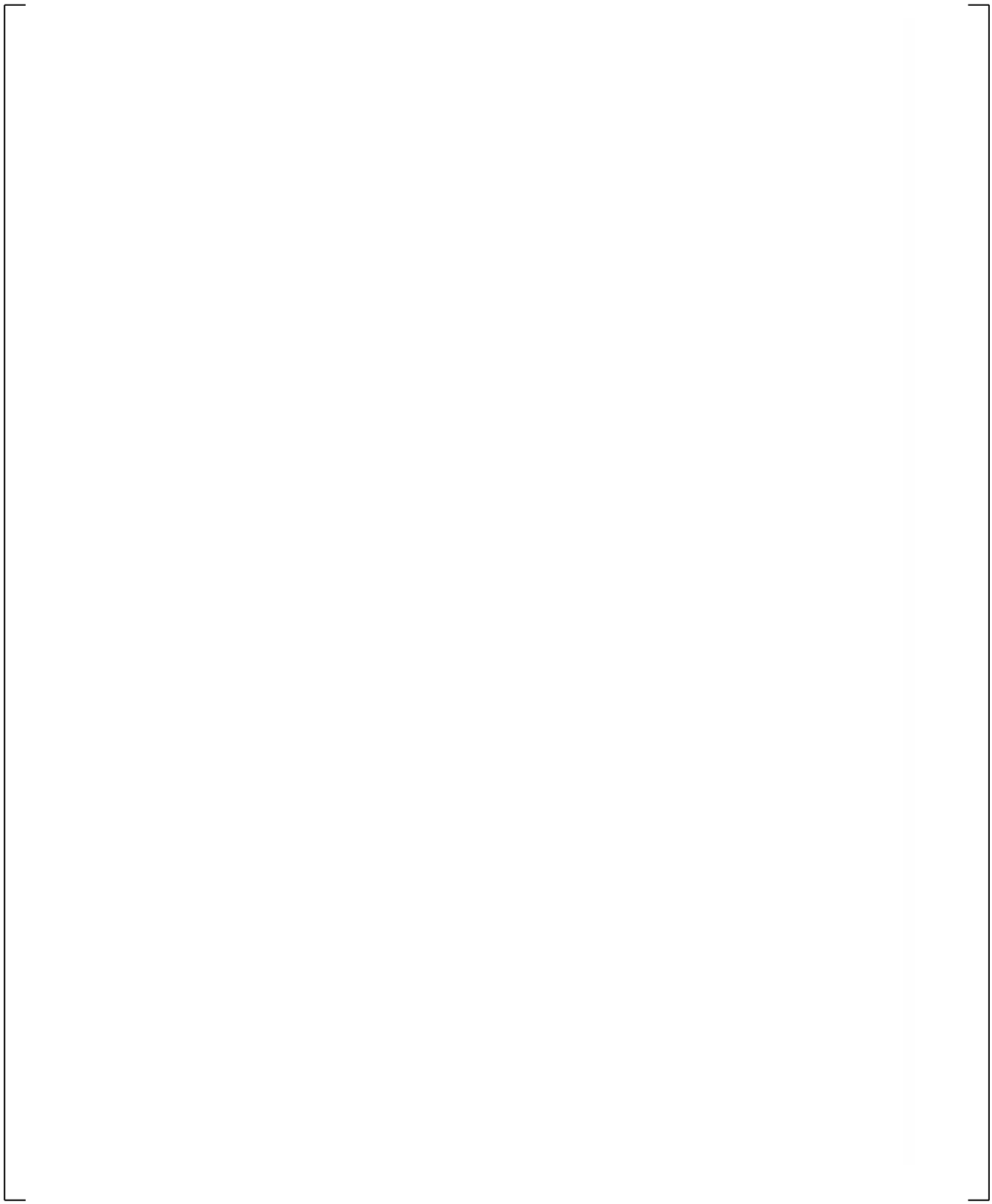

Figure 19.3-135 Cold Leg Steam Flow Rate (Top) and Downcomer Pressure (Bottom) for Test Run 132

a,c

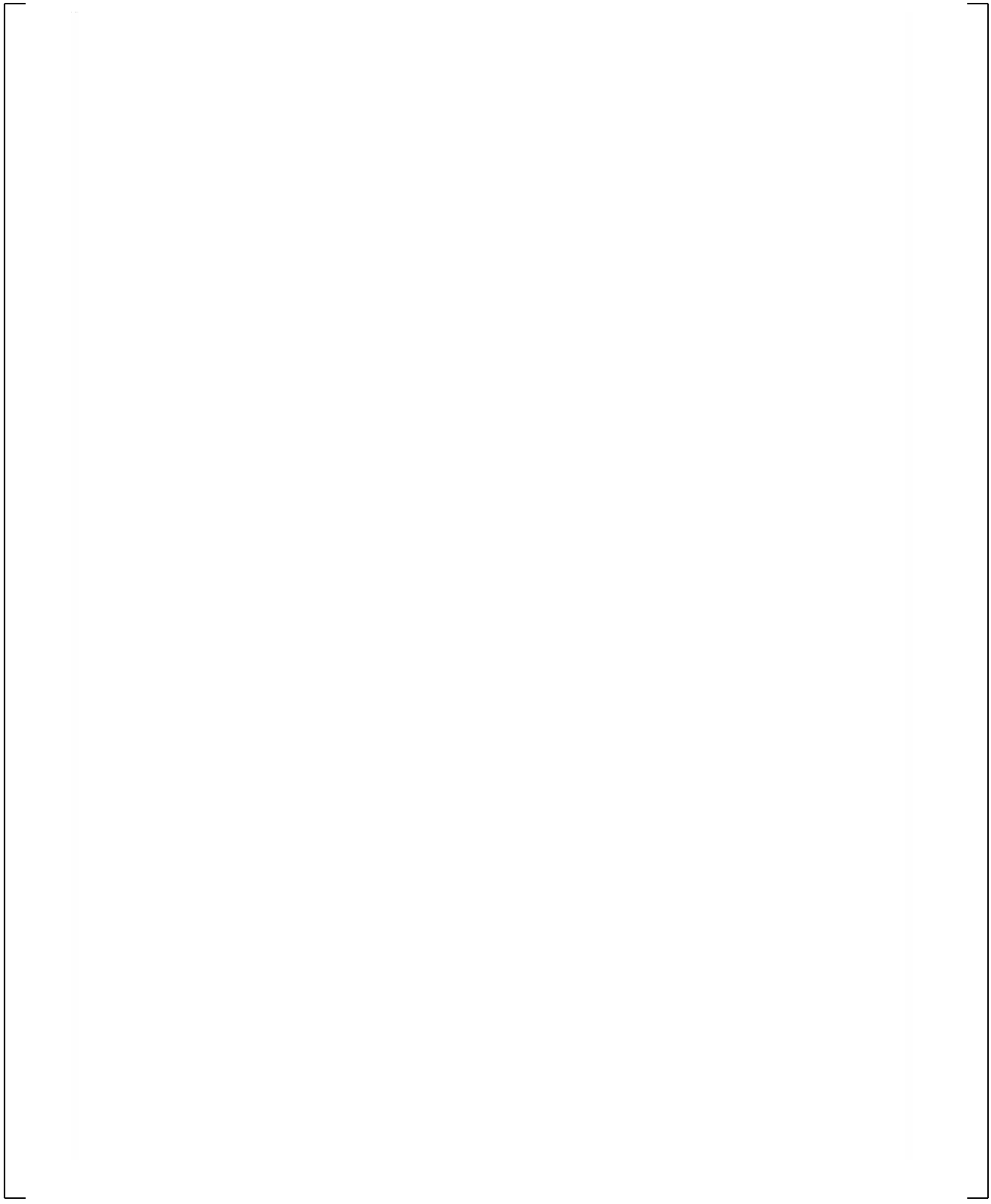

Figure 19.3-136 Cold Leg Fluid Temperature (Top) and Cold Leg to Downcomer Pressure Drop (Bottom) for Test Run 132

a,c

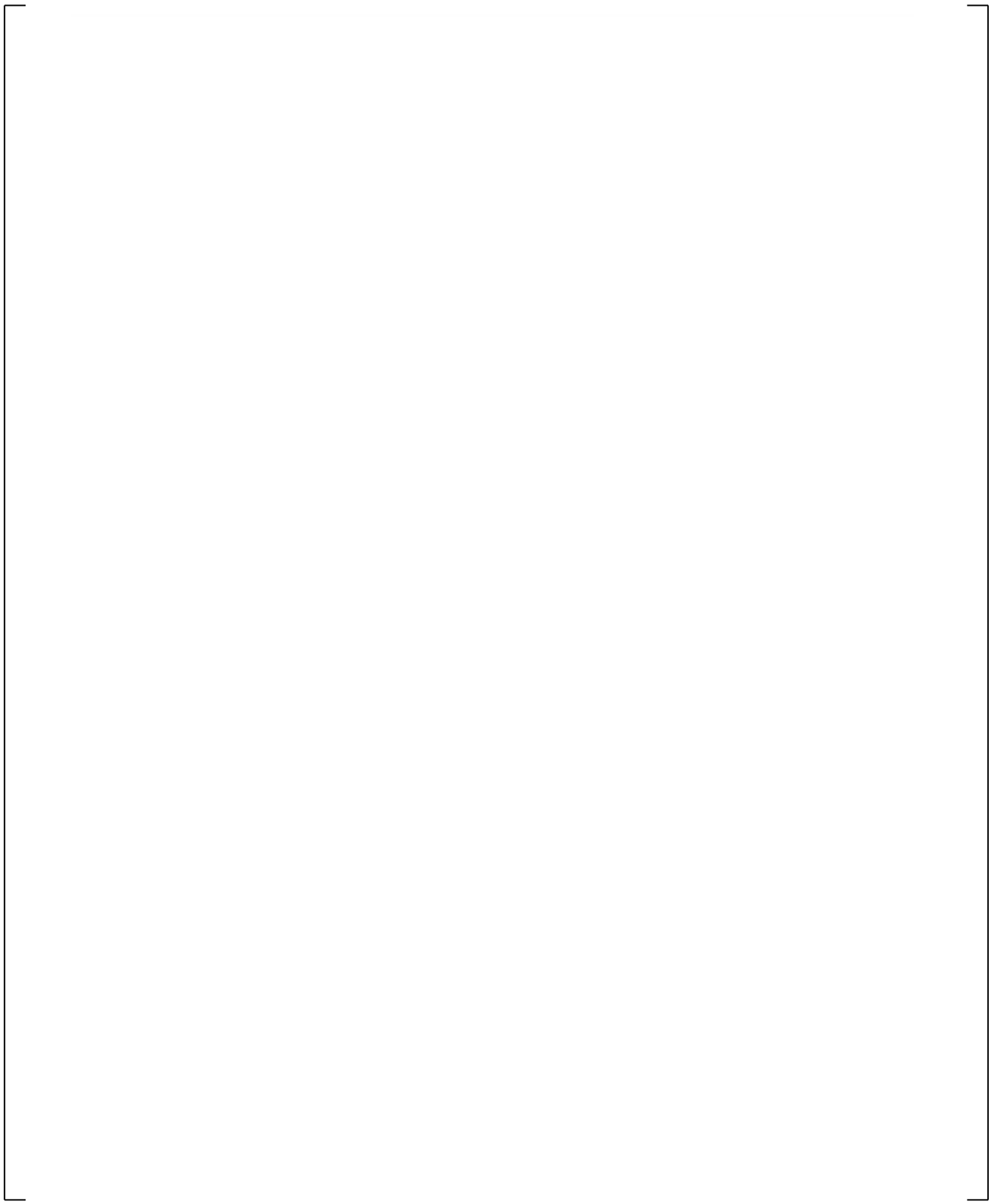

Figure 19.3-137 Cold Leg Steam Flow rate (Top) and Downcomer Pressure (Bottom) for Test Run 133

a,c

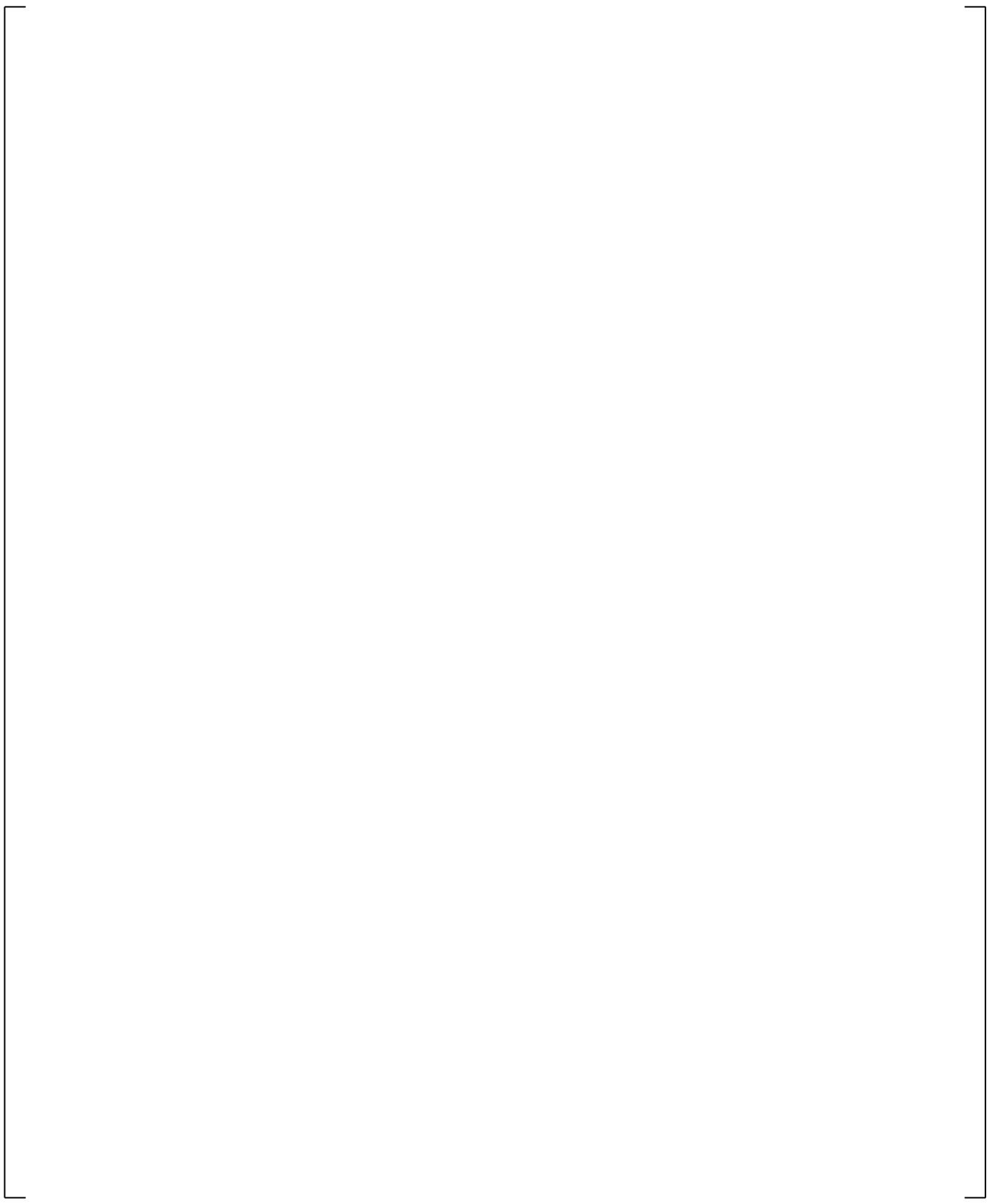

Figure 19.3-138 Cold Leg Fluid Temperature (Top) and Cold Leg to Downcomer Pressure Drop (Bottom) for Test Run 133

a,c

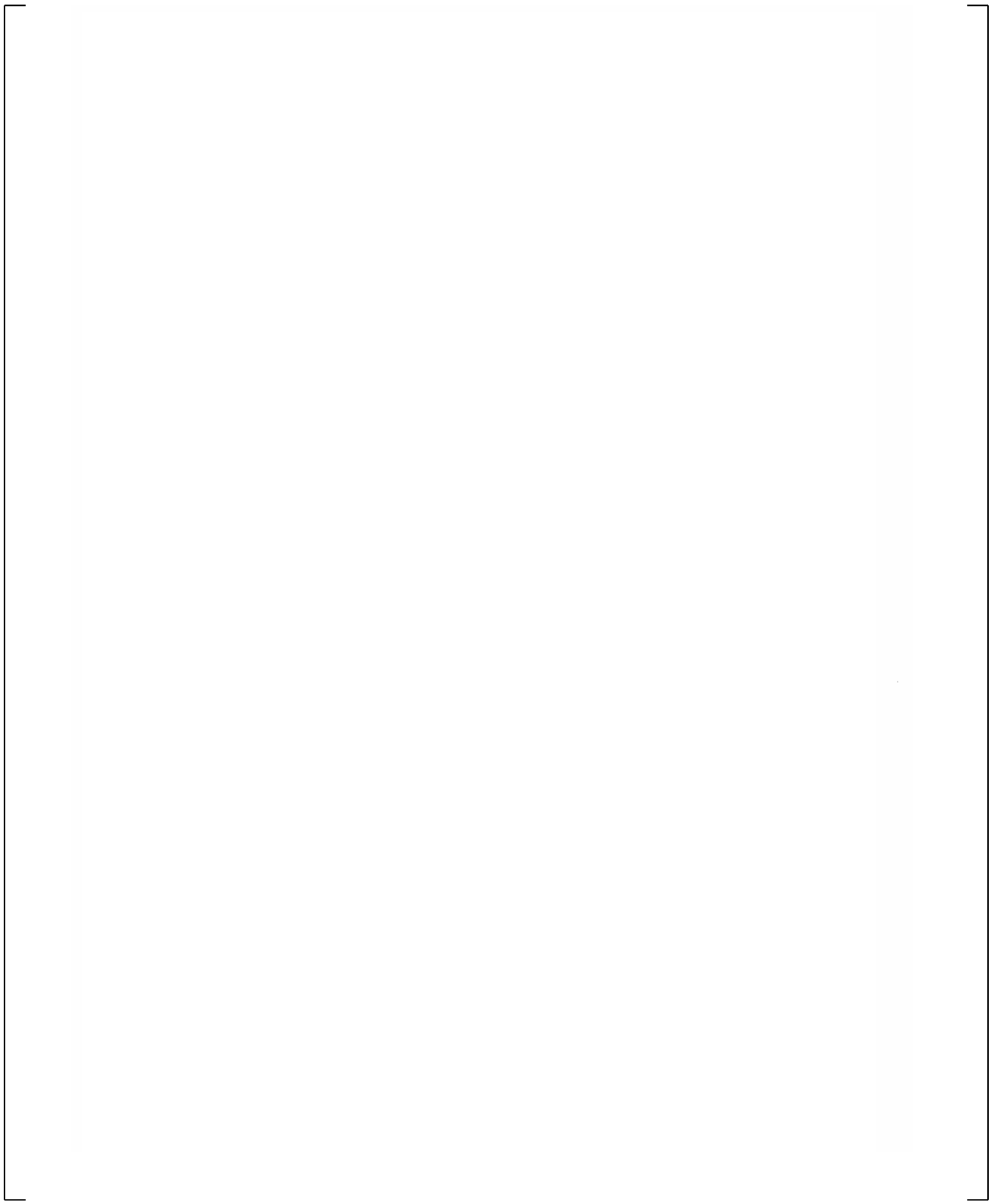

Figure 19.3-139 Cold Leg Steam Flow rate (Top) and Downcomer Pressure (Bottom) for Test Run 135

a,c

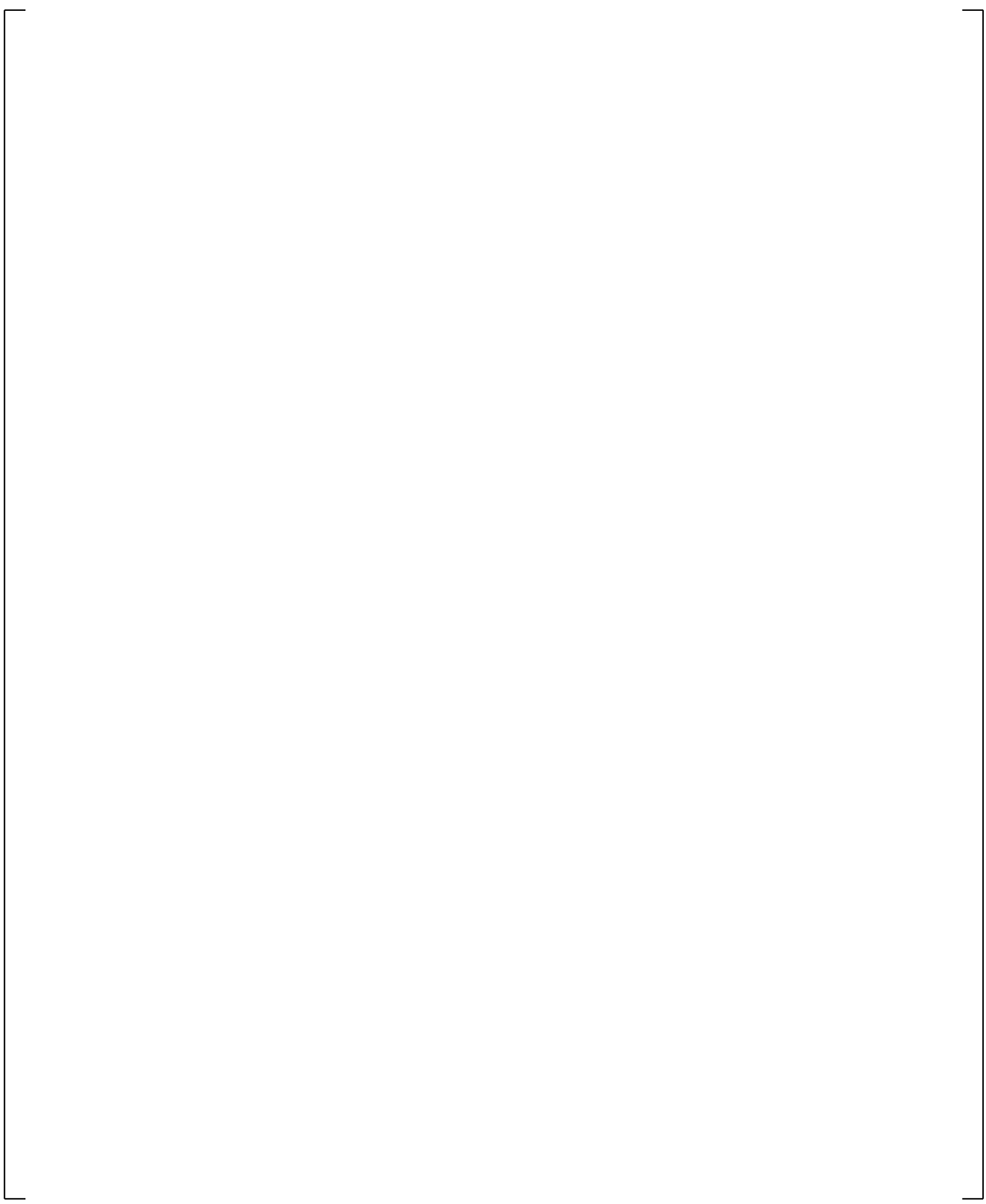

Figure 19.3-140 Cold Leg Fluid Temperature (Top) and Cold Leg to Downcomer Pressure Drop (Bottom) for Test Run 135

a,c

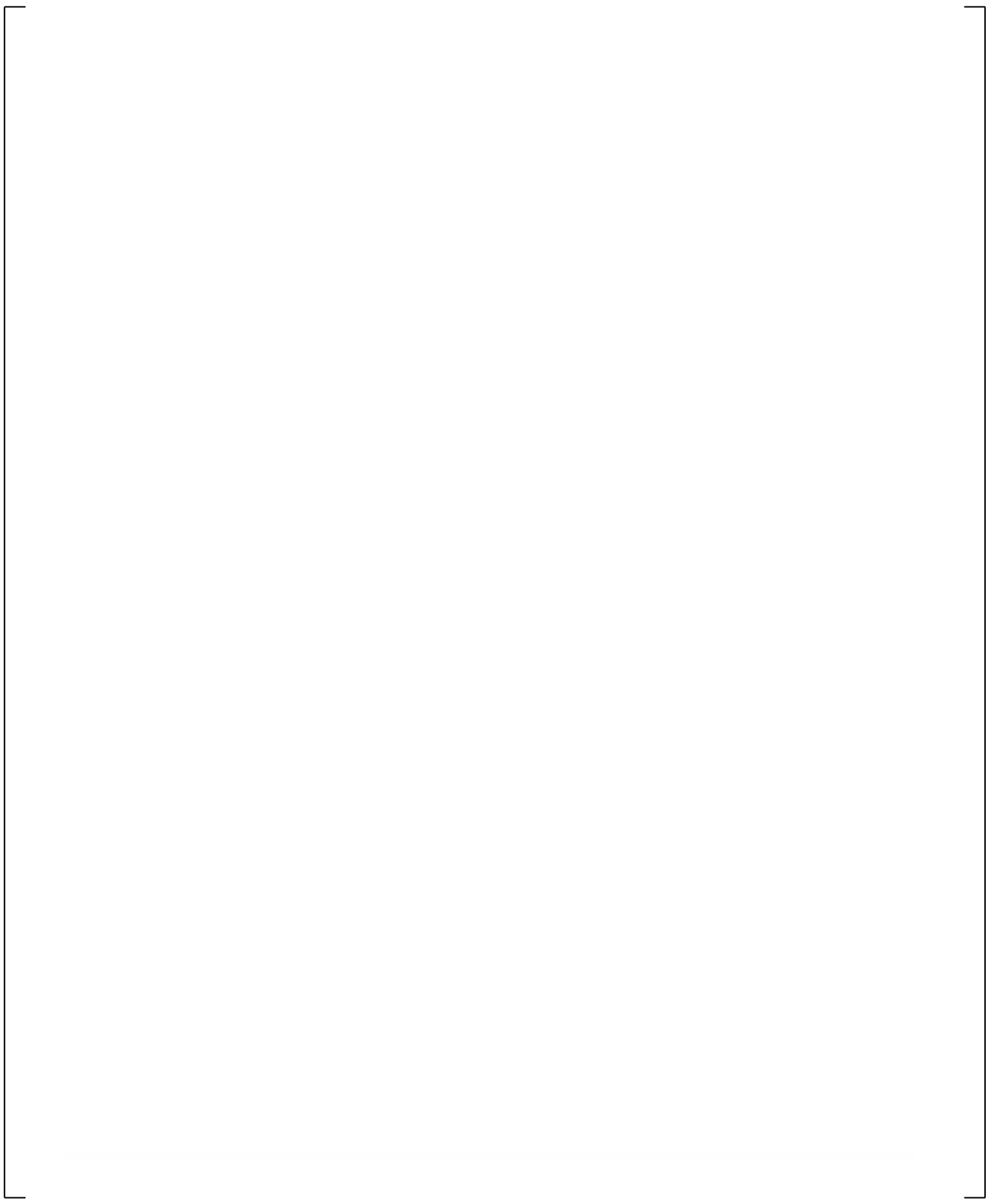

Figure 19.3-141 Cold Leg Steam Flow Rate (Top) and Downcomer Pressure (Bottom) for Test Run 136

a,c

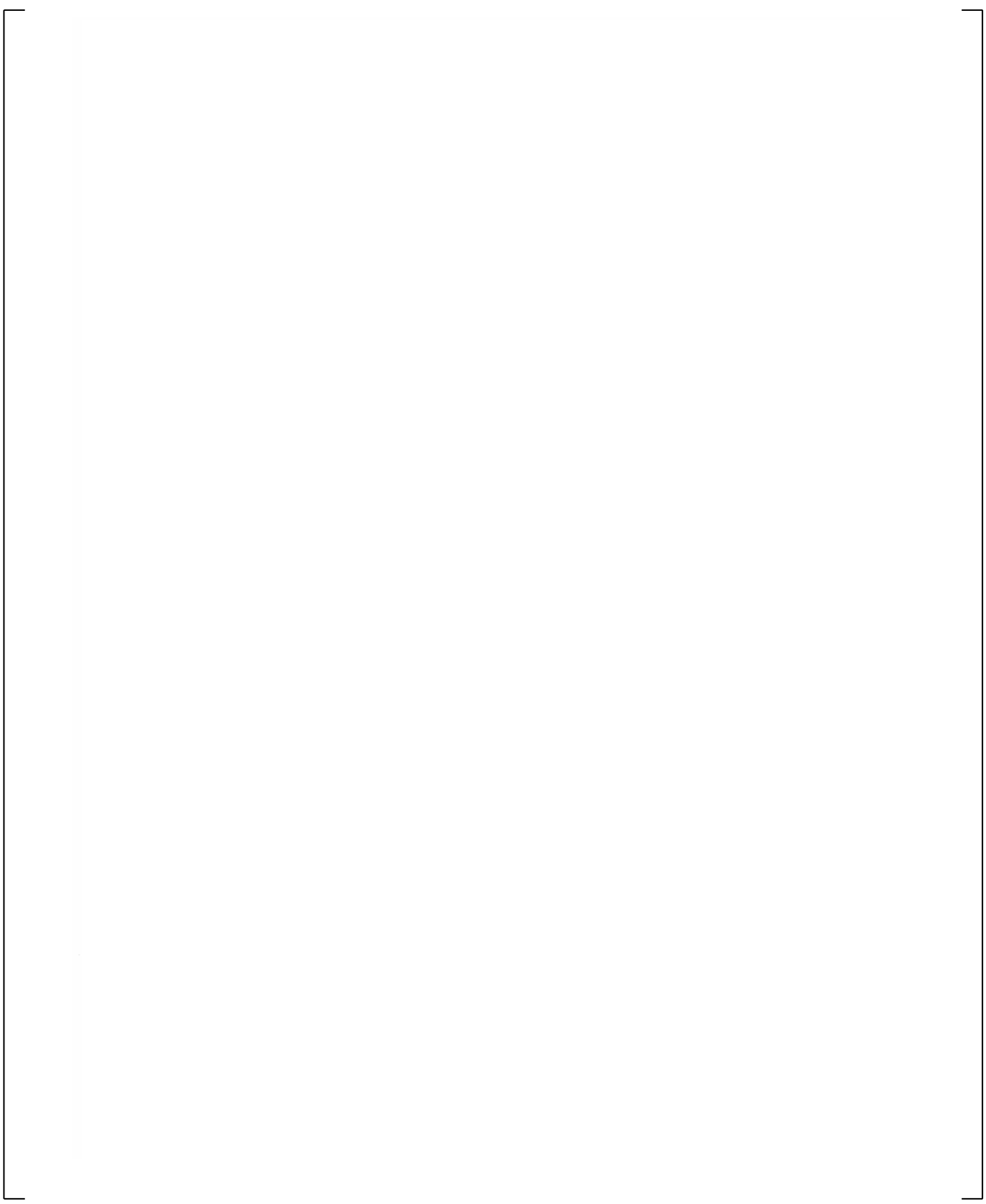

Figure 19.3-142 Cold Leg Fluid Temperature (Top) and Cold Leg to Downcomer Pressure Drop (Bottom) for Test Run 136

a,c

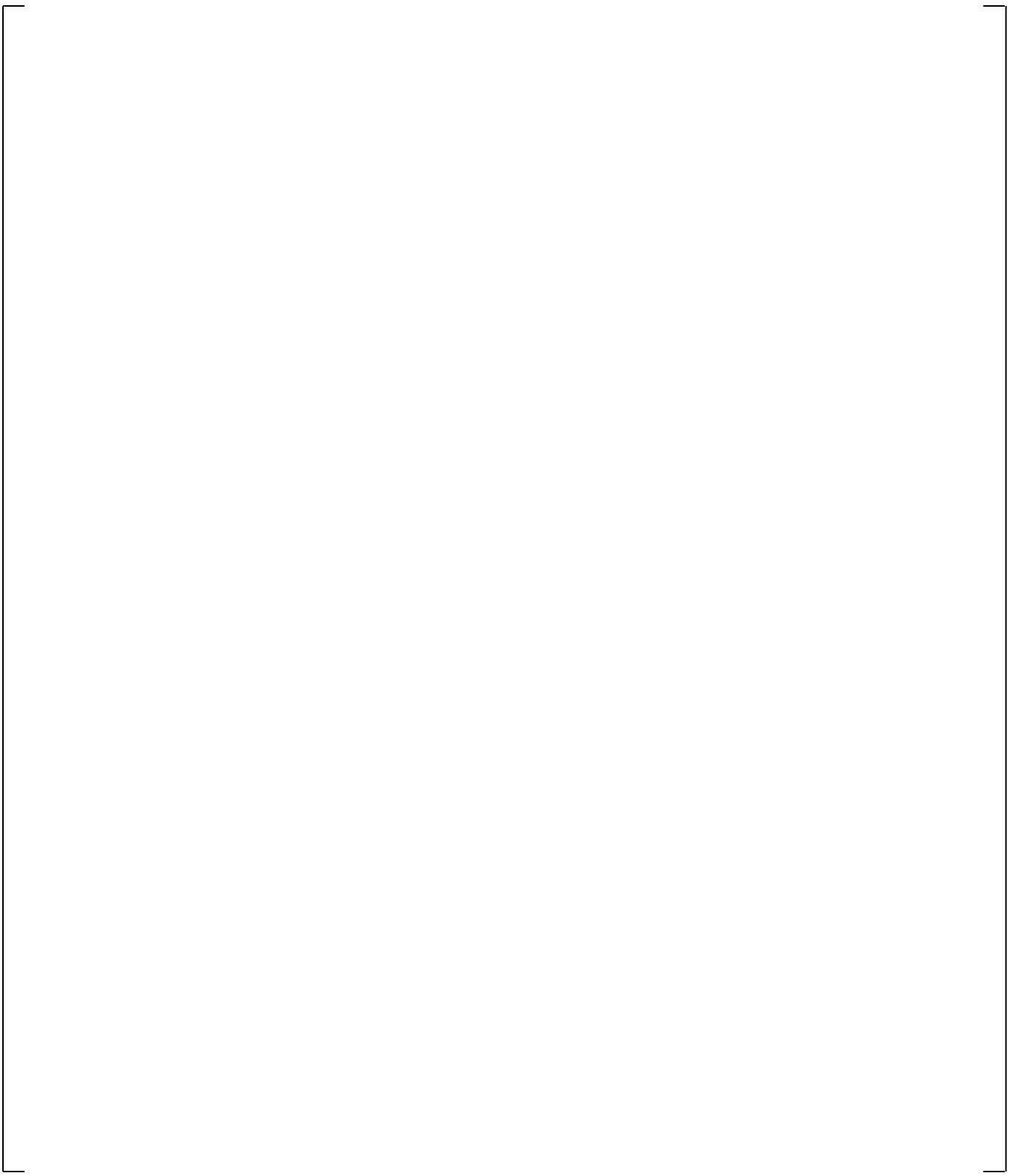

Figure 19.3-143 An Illustration of Downcomer and Broken Cold Leg Nozzle Noding

a,c

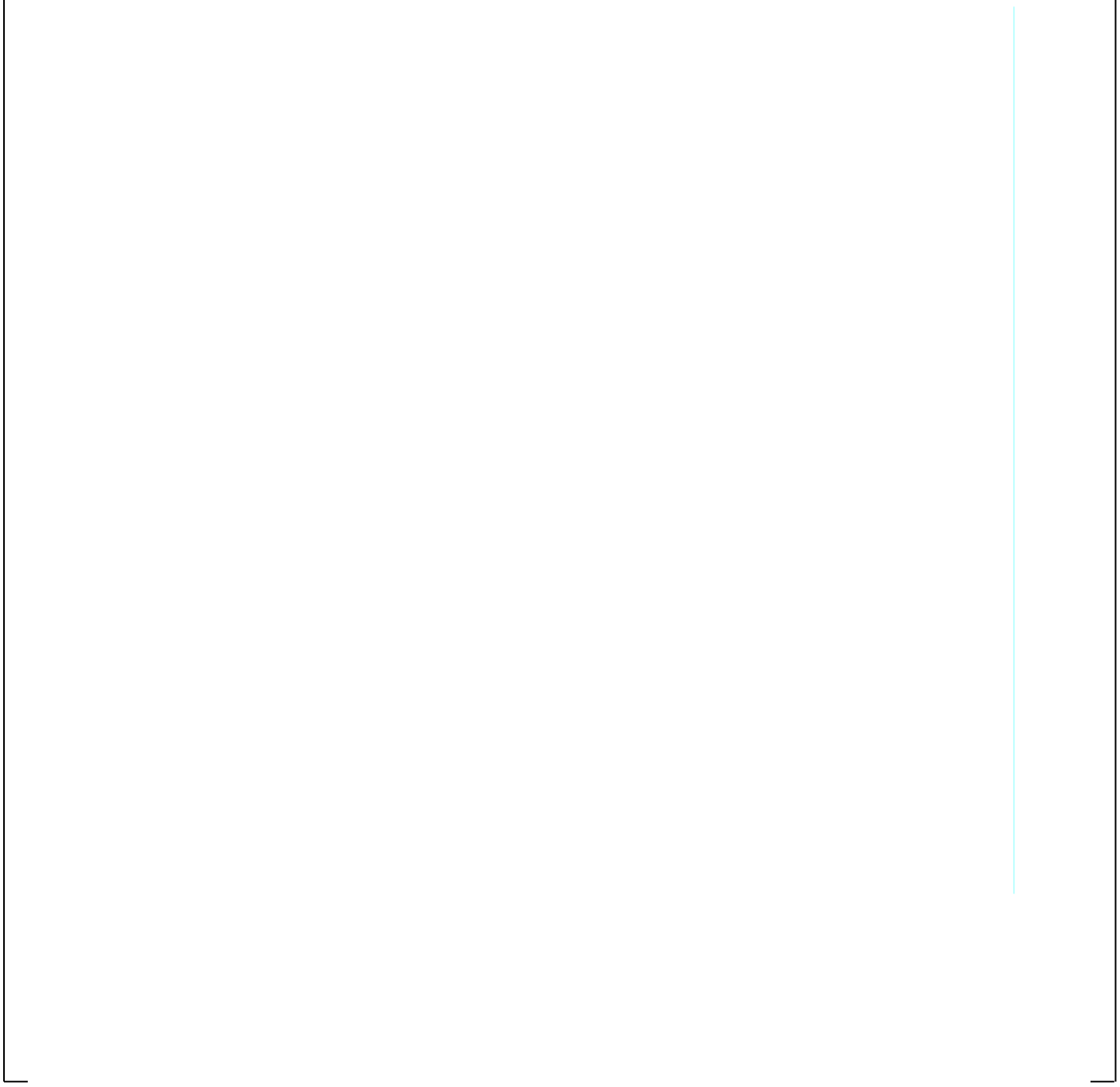

Figure 19.3-144 Comparison between Measured Pressure Loss and Predicted Pressure Loss across Broken Cold Leg Nozzle for UPTF 6-131

a,c

Figure 19.3-145 Comparison between Measured Pressure Loss and Predicted Pressure Loss across Broken Cold Leg Nozzle for UPTF 6-132

a,c

Figure 19.3-146 Comparison between Measured Pressure Loss and Predicted Pressure Loss across Broken Cold Leg Nozzle for UPTF 6-133

a,c

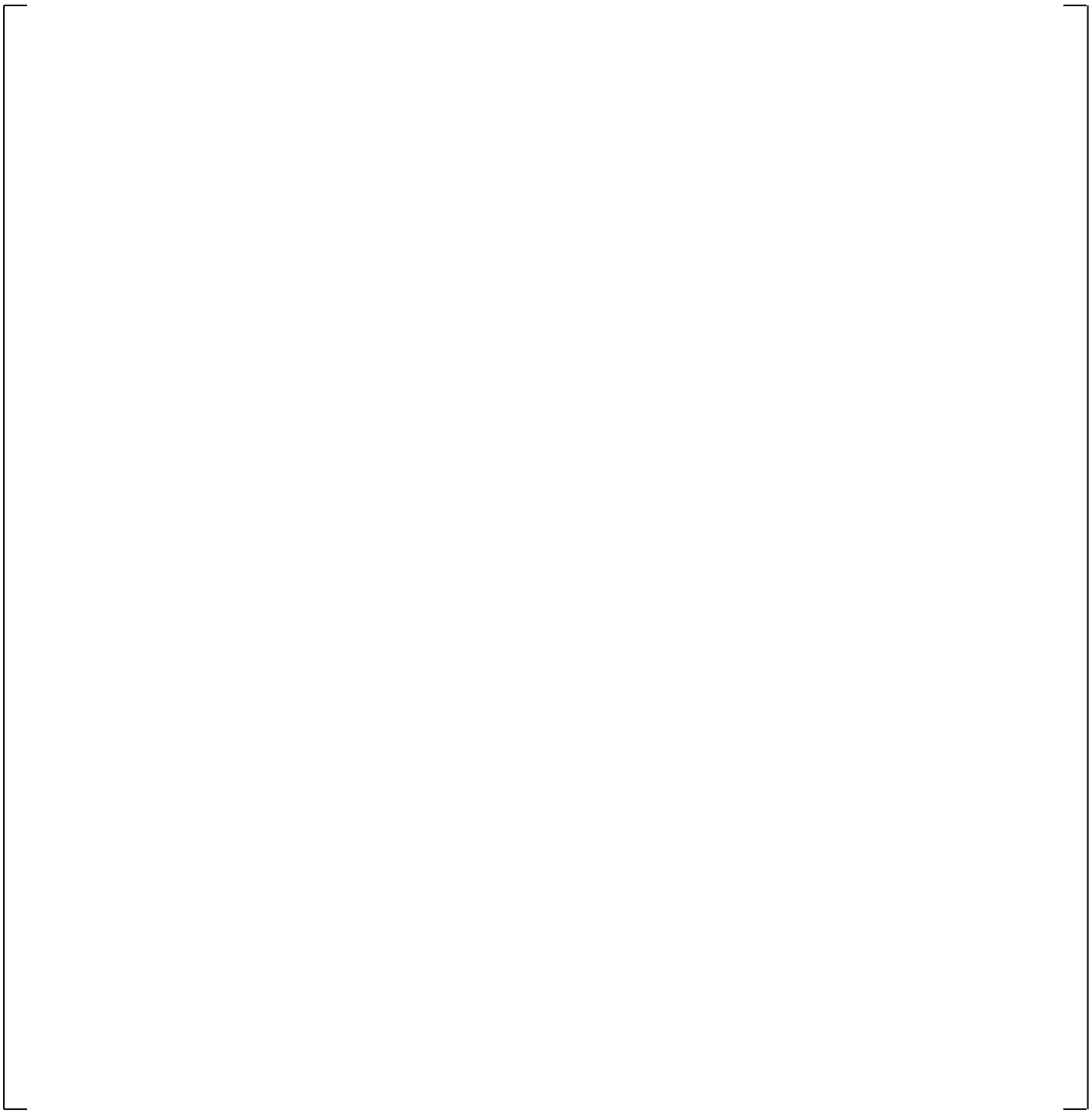

Figure 19.3-147 Comparison between Measured Pressure Loss and Predicted Pressure Loss across Broken Cold Leg Nozzle for UPTF 6-135

a,c

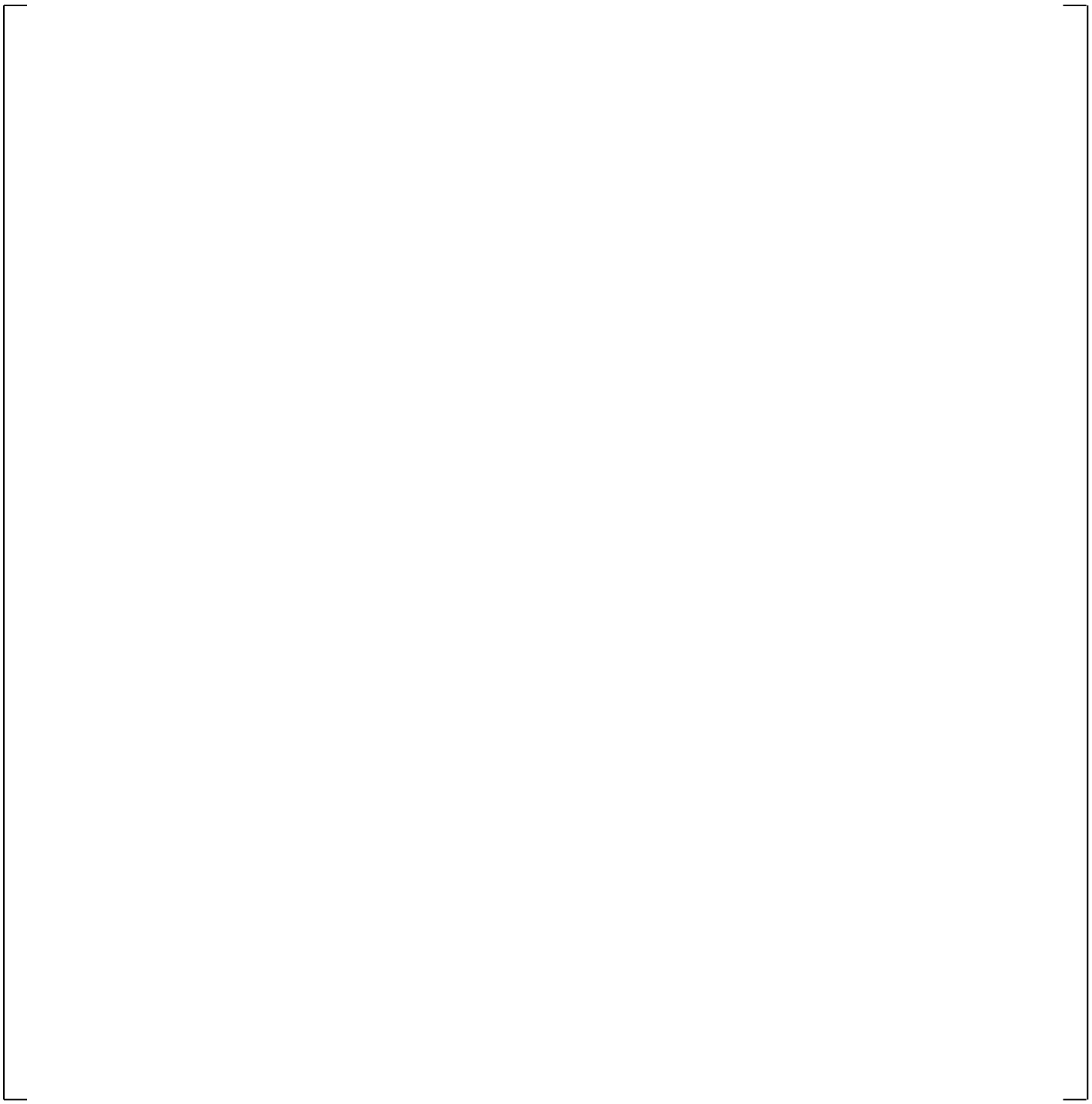

Figure 19.3-148 Comparison between Measured Pressure Loss and Predicted Pressure Loss across Broken Cold Leg Nozzle for UPTF 6-136

a,c

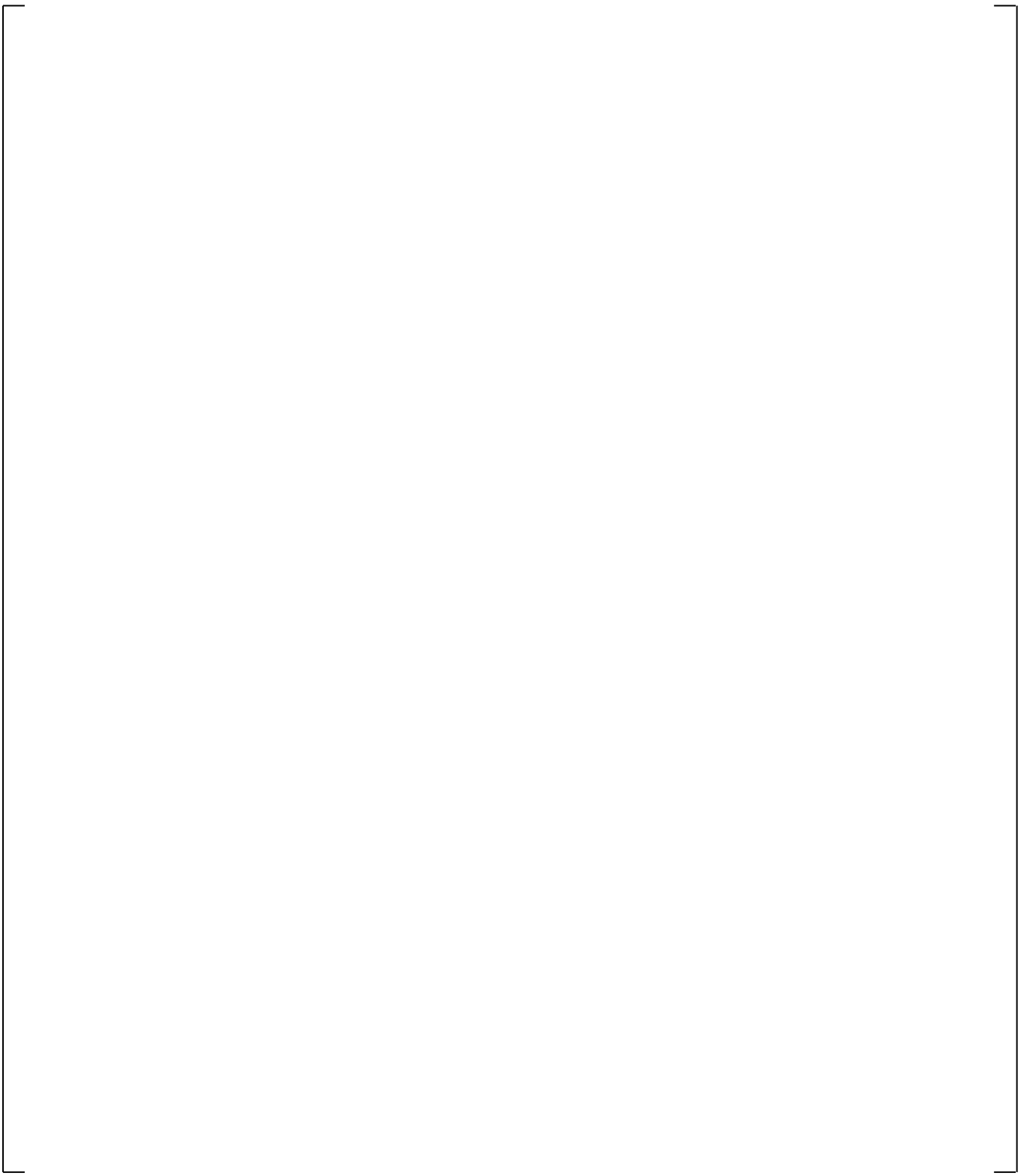

Figure 19.3-149 Cold Leg Piping Region of UPTF and Cold Leg Noding

a,c

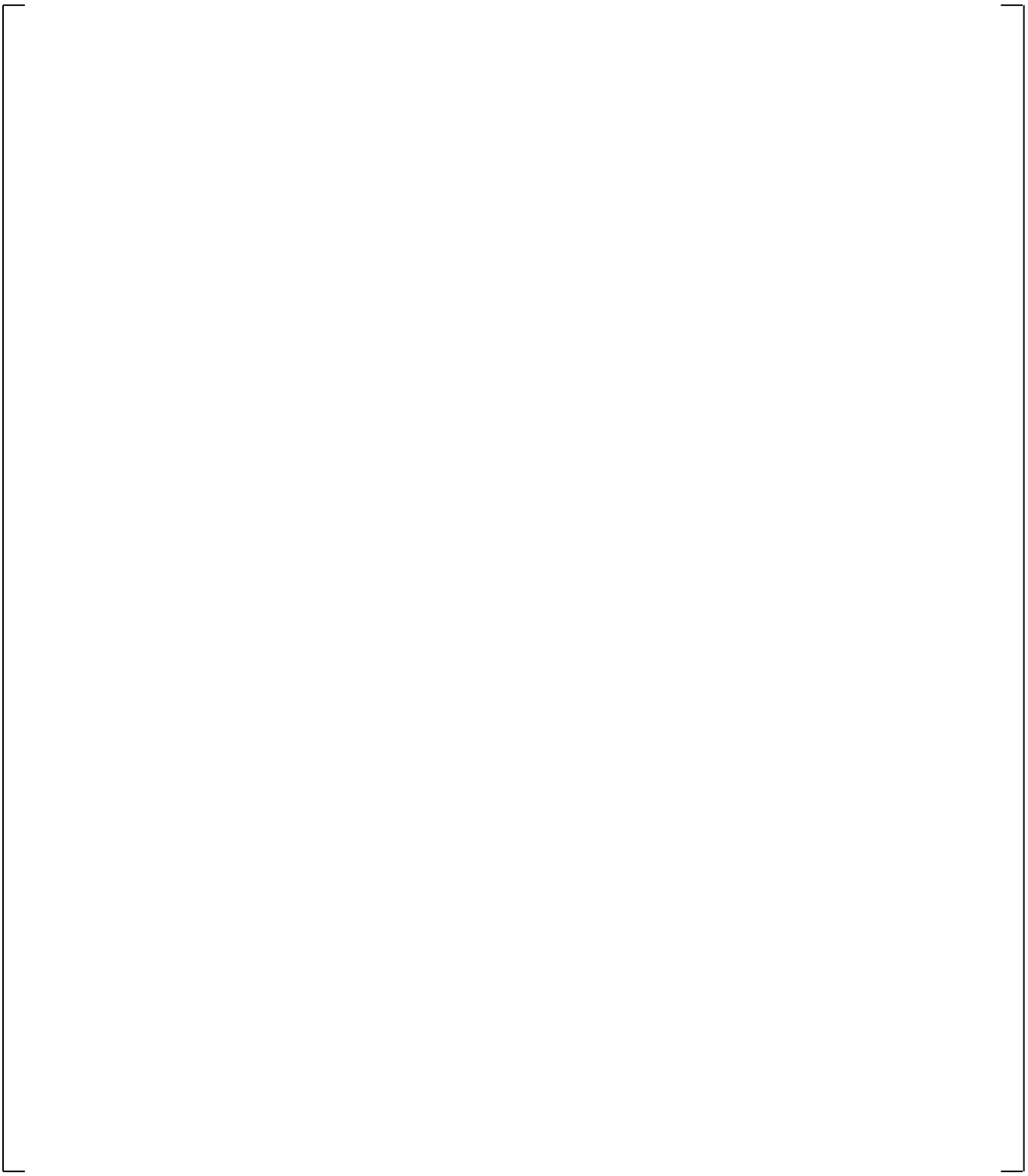

Figure 19.3-150 System Configuration for UPTF 8A

a,c

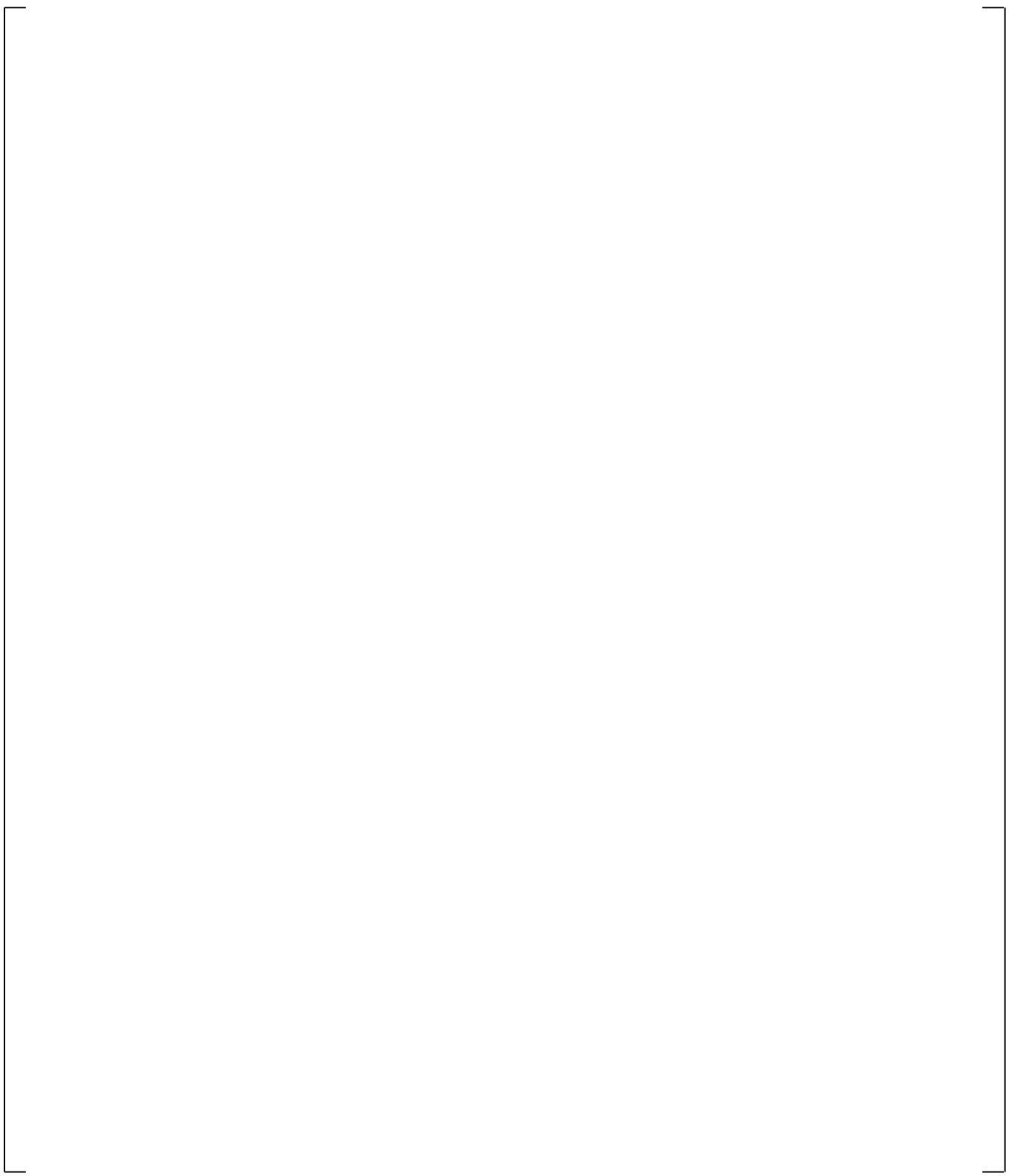

Figure 19.3-151 Observation on Temperature Distribution in UPTF 8A Experiments (MPR-1208, 1992) and Comparison with Predictions from WCOBRA/TRAC-TF2

a,c

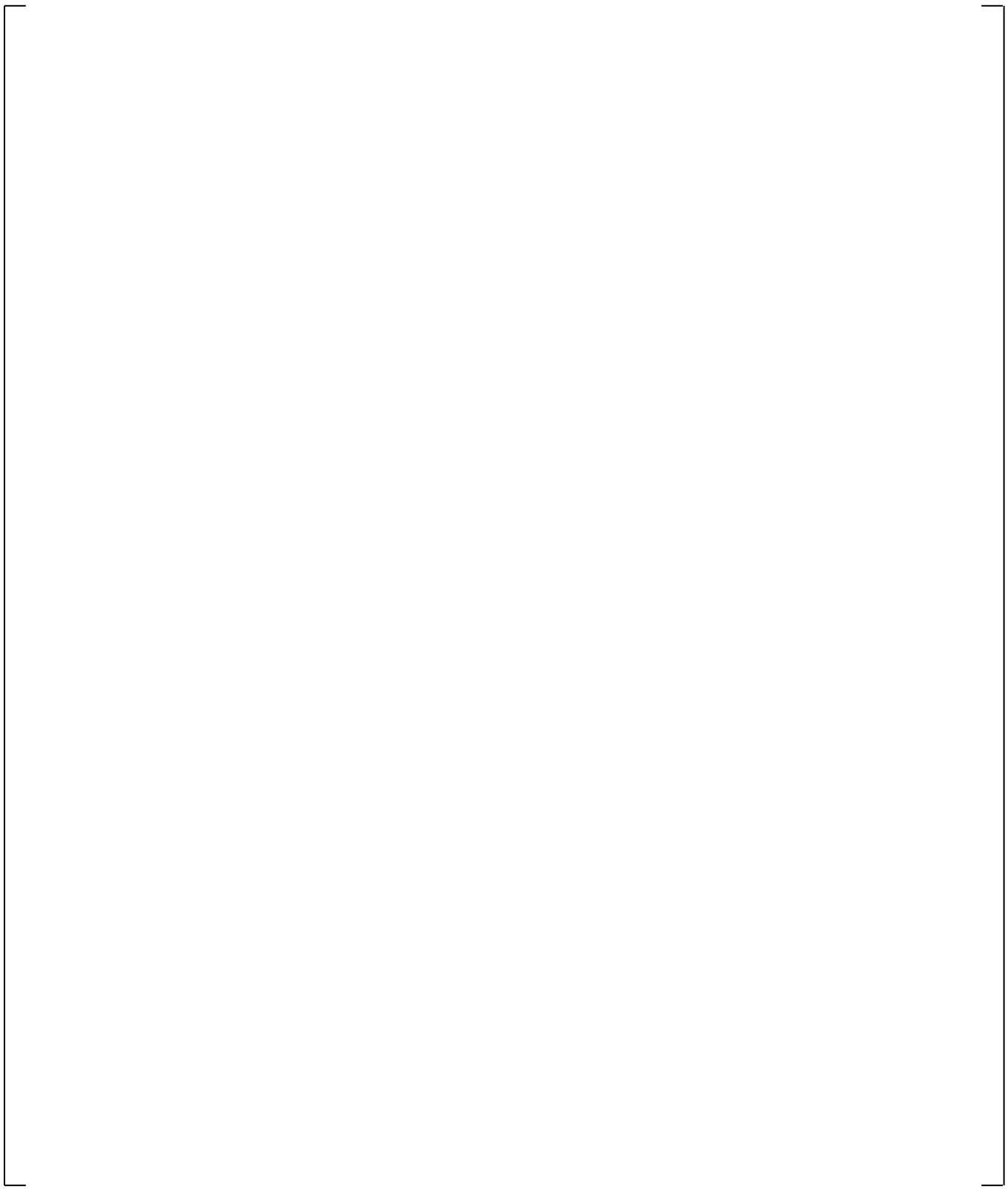

Figure 19.3-152 WCOBRA/TRAC-TF2 Vessel Model for UPTF Test 8A

a,c

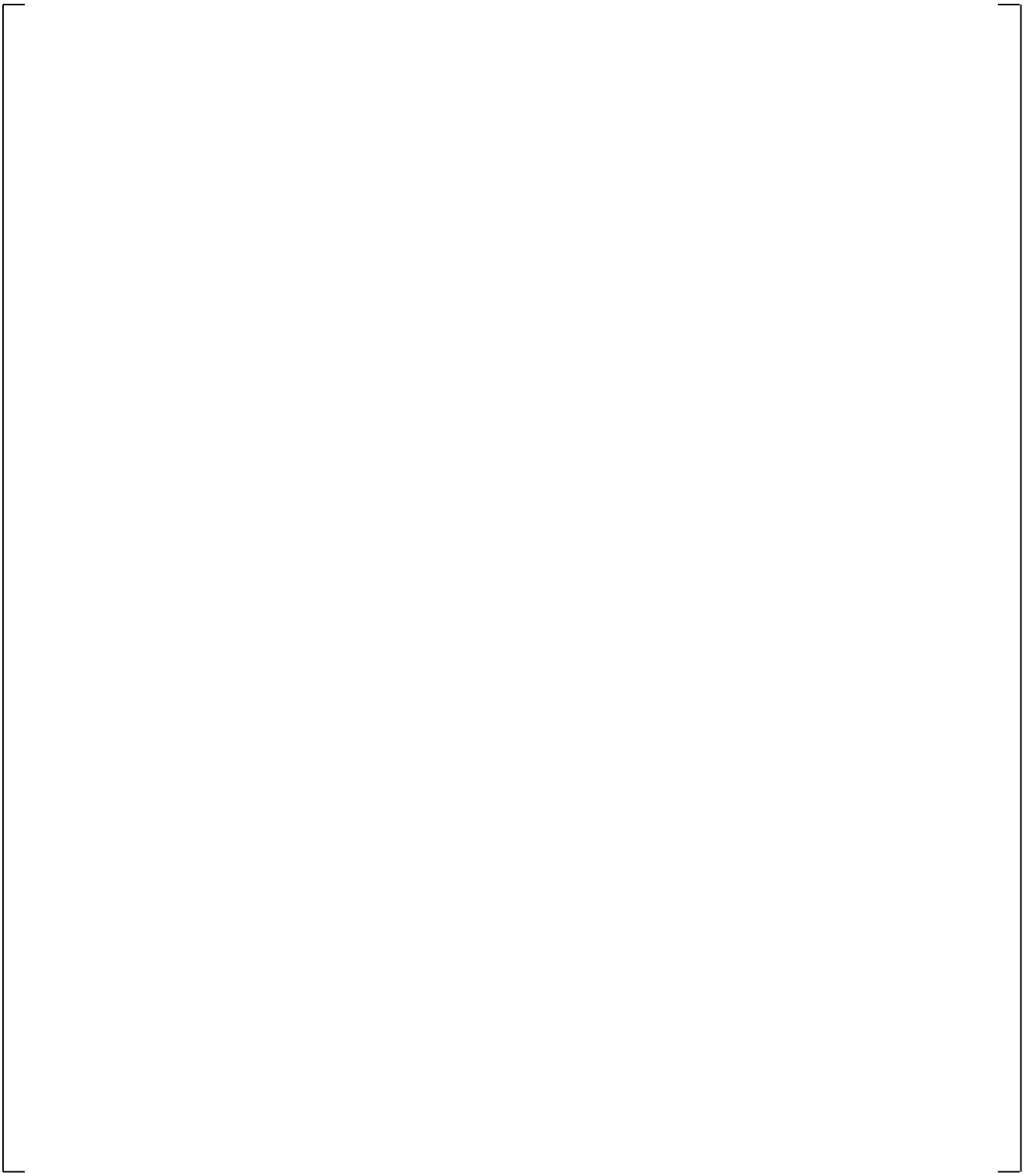

Figure 19.3-153 WCOBRA/TRAC-TF2 Loop Model for UPTF 8A

a,c

Figure 19.3-154 Comparison between the Measured Steam Flow Rates and the WCOBRA/TRAC-TF2 Predicted Steam Flow Rates in the Cold Leg of the Loop 2

a,c

Figure 19.3-155 ECC Injection Flow Rate to Cold Leg in Loop 2

a,c

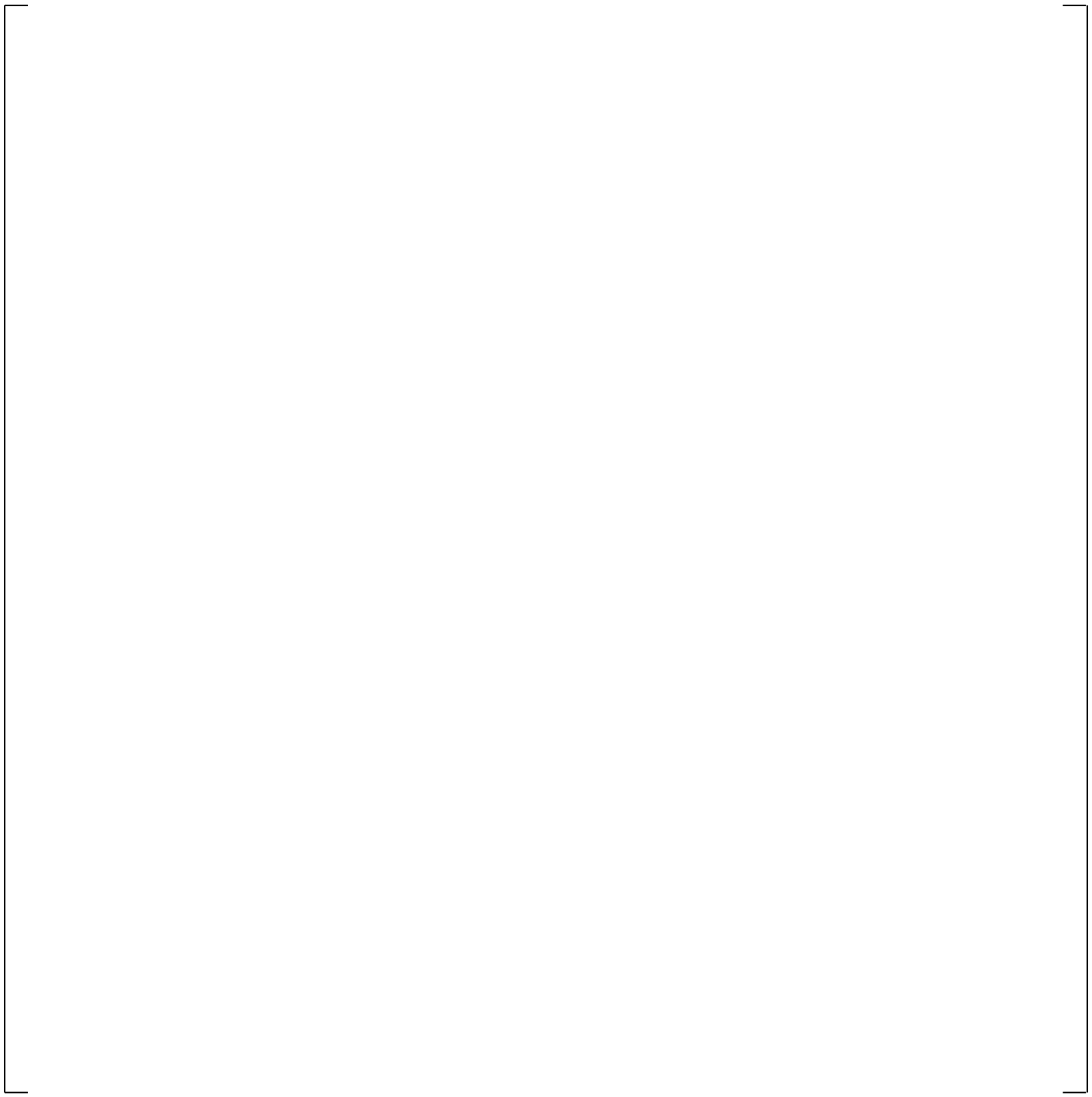

Figure 19.3-156 Comparison between Measured Fluid Temperature and WCOBRA/TRAC-TF2 Predicted Water Temperature at Pump Exit

a,c

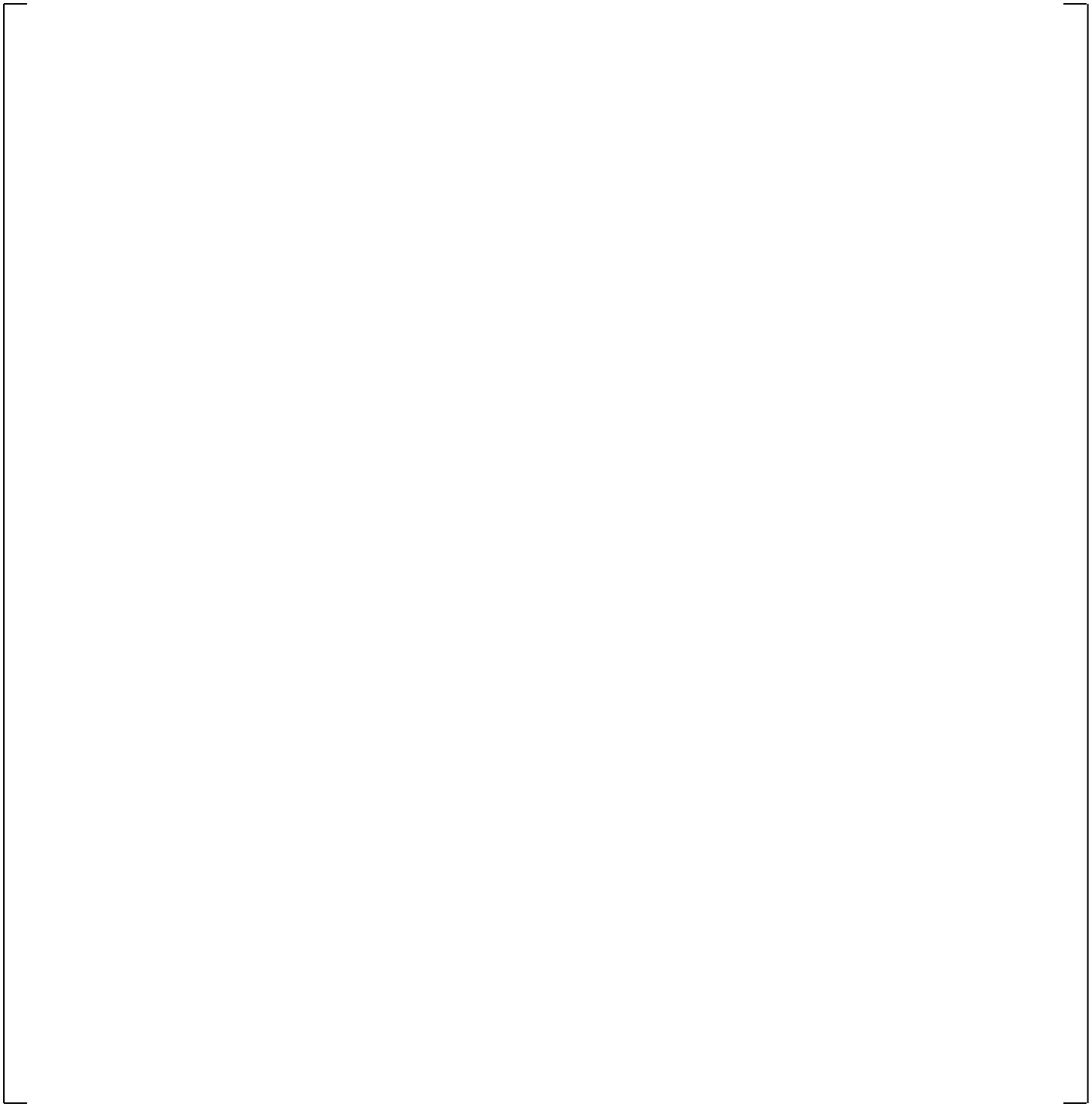

Figure 19.3-157 Comparison between Measured Fluid Temperature and WCOBRA/TRAC-TF2 Predicted Water Temperature near Injection Point

a,c

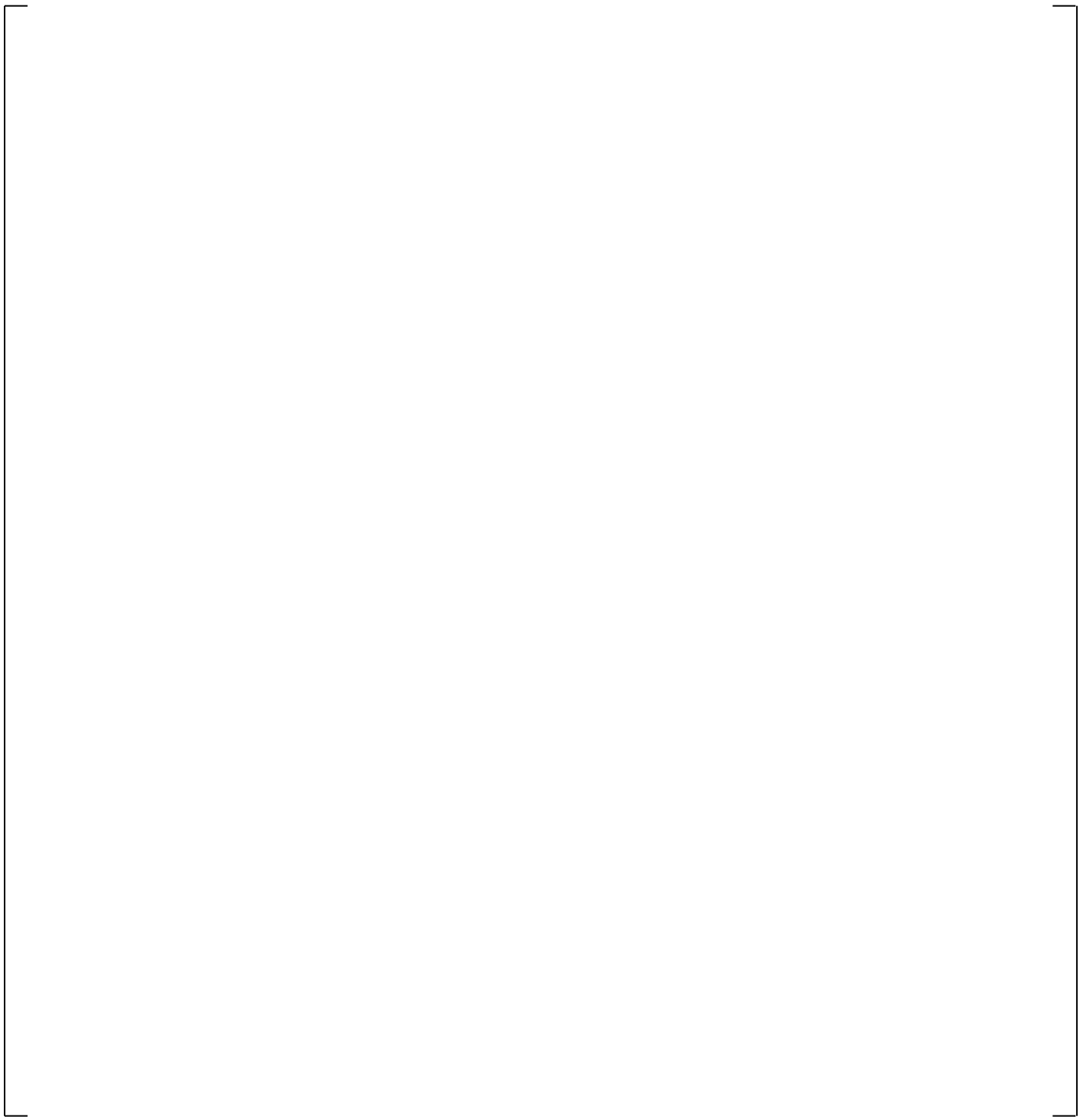

Figure 19.3-158 Comparison between Measured Fluid Temperature and WCOBRA/TRAC-TF2 Predicted Water Temperature at Downstream of Injection Point

a,c

Figure 19.3-159 Comparison between Measured Fluid Temperature and WCOBRA/TRAC-TF2 Predicted Water Temperature at Outlet of Cold Leg

a,c

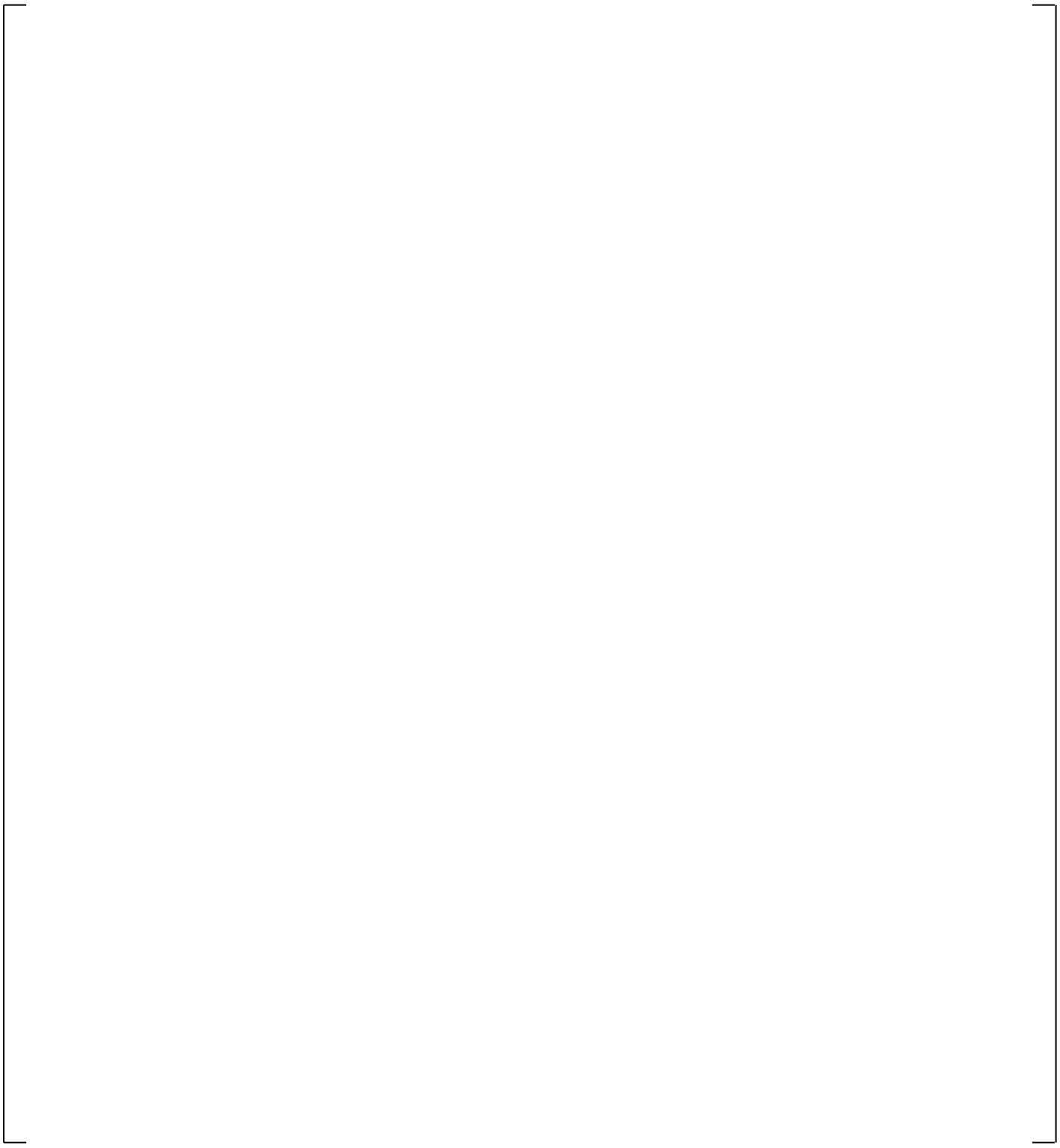

Figure 19.3-160 Predicted Flow Regime Number of Cell Face 4 of Cold Leg

a,c

Figure 19.3-161 Predicted Flow Regime Number of Cell Face 5 of Cold Leg

a,c

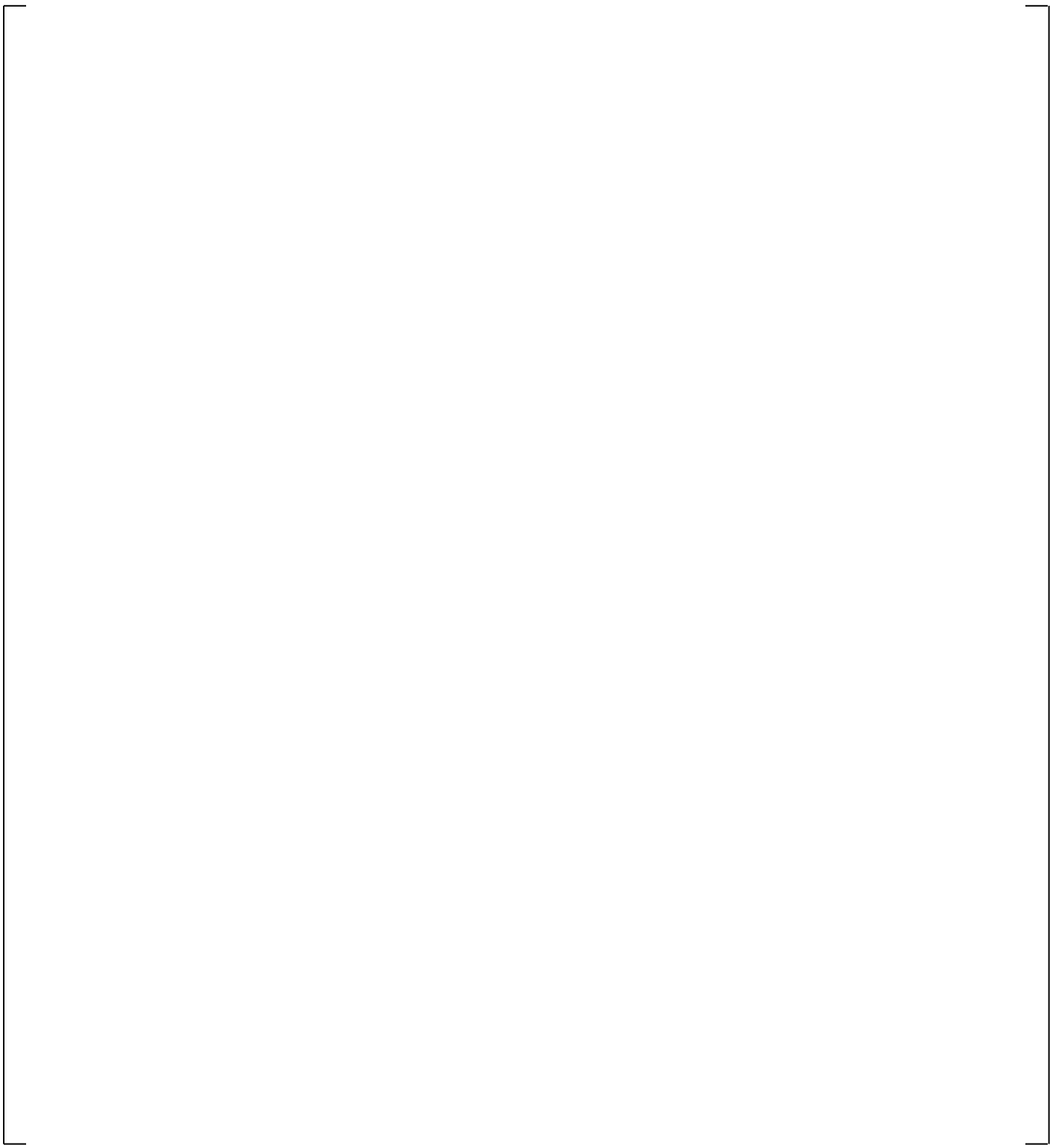

Figure 19.3-162 Predicted Flow Regime Number of Cell Face 6 of Cold Leg

a,c

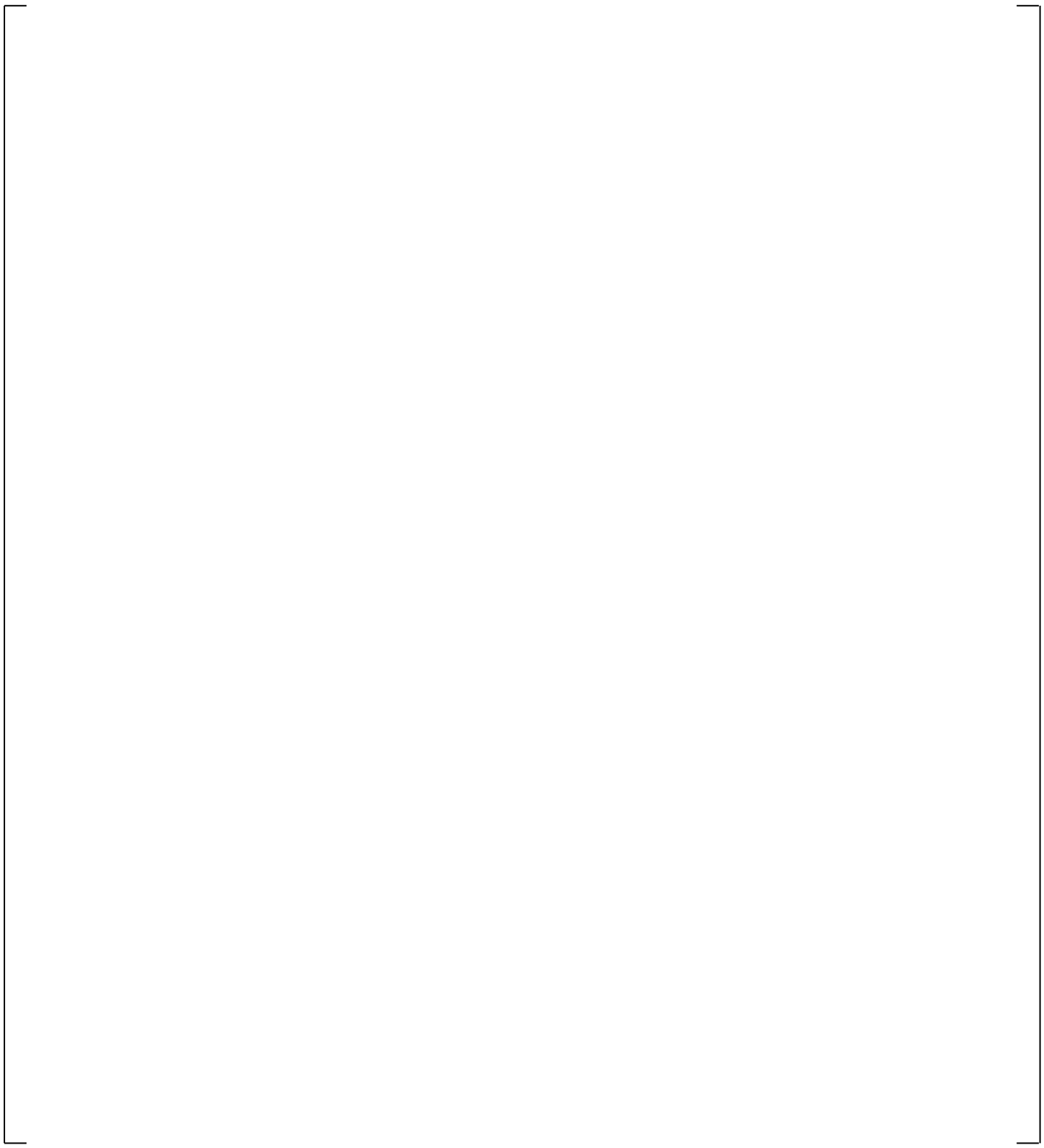

Figure 19.3-163 Predicted Flow Regime Number of Cell Face 7 of Cold Leg

a,c

Figure 19.3-164 System Configuration for UPTF Test 25, Phase A (Run 242) and Phase B (Run 241)

a,c

Figure 19.3-165 Steam Flow Rate for UPTF Test 25, Phase A (Run 242)

a,c

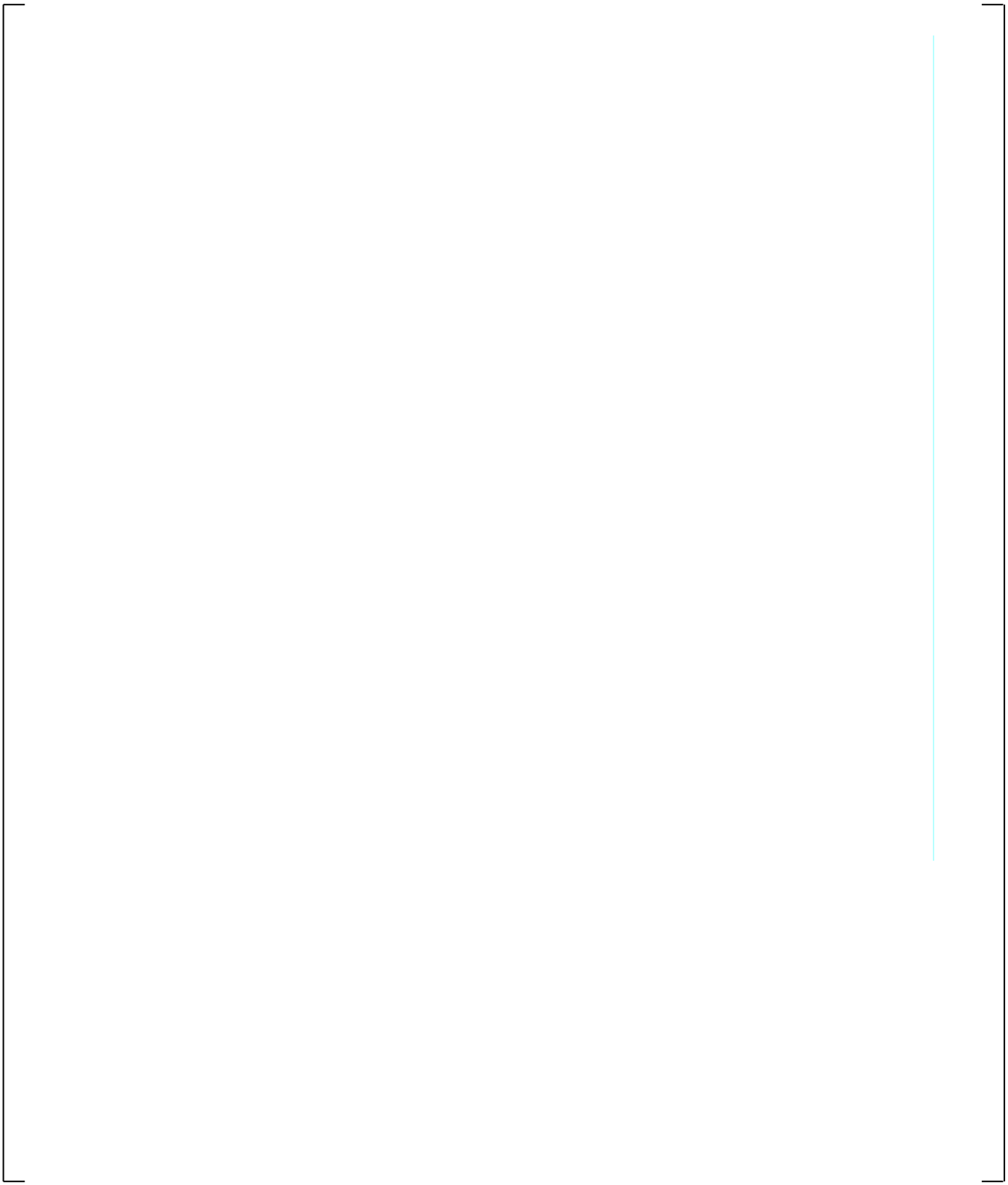

Figure 19.3-166 ECC Flow Rate for UPTF Test 25, Phase A (Run 242)

a,c

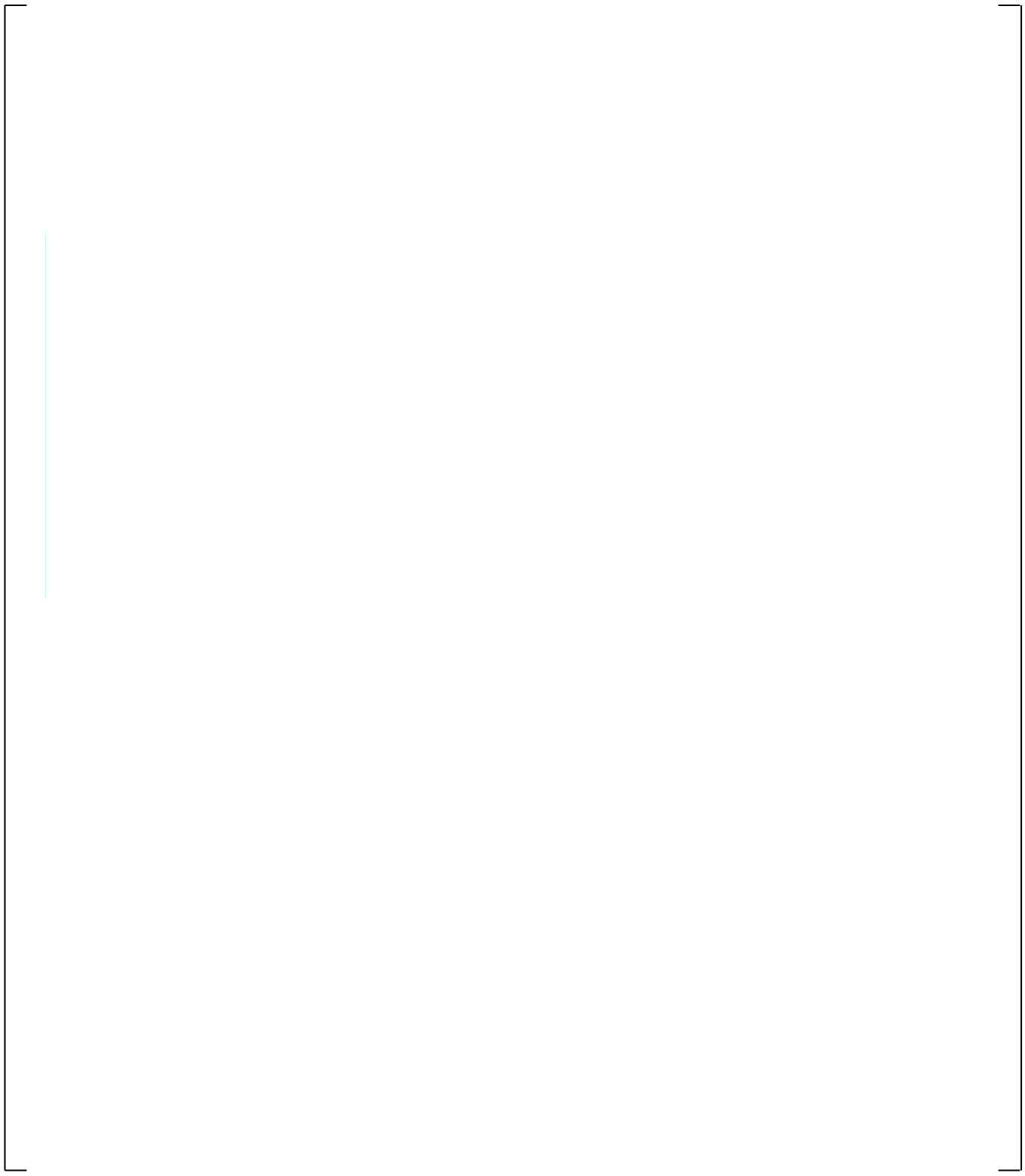

Figure 19.3-167 Drainage Flow Rate for UPTF Test 25, Phase A (Run 242)

a,c

Figure 19.3-168 WCOBRA/TRAC-TF2 Loop Model for UPTF Test 25A

a,c

Figure 19.3-169 Absolute Pressure in the Upper Plenum and Downcomer for UPTF Test 25A

a,c

Figure 19.3-170 Measured Downcomer Fluid Temperature at Level 28 for UPTF Test 25A

a,c

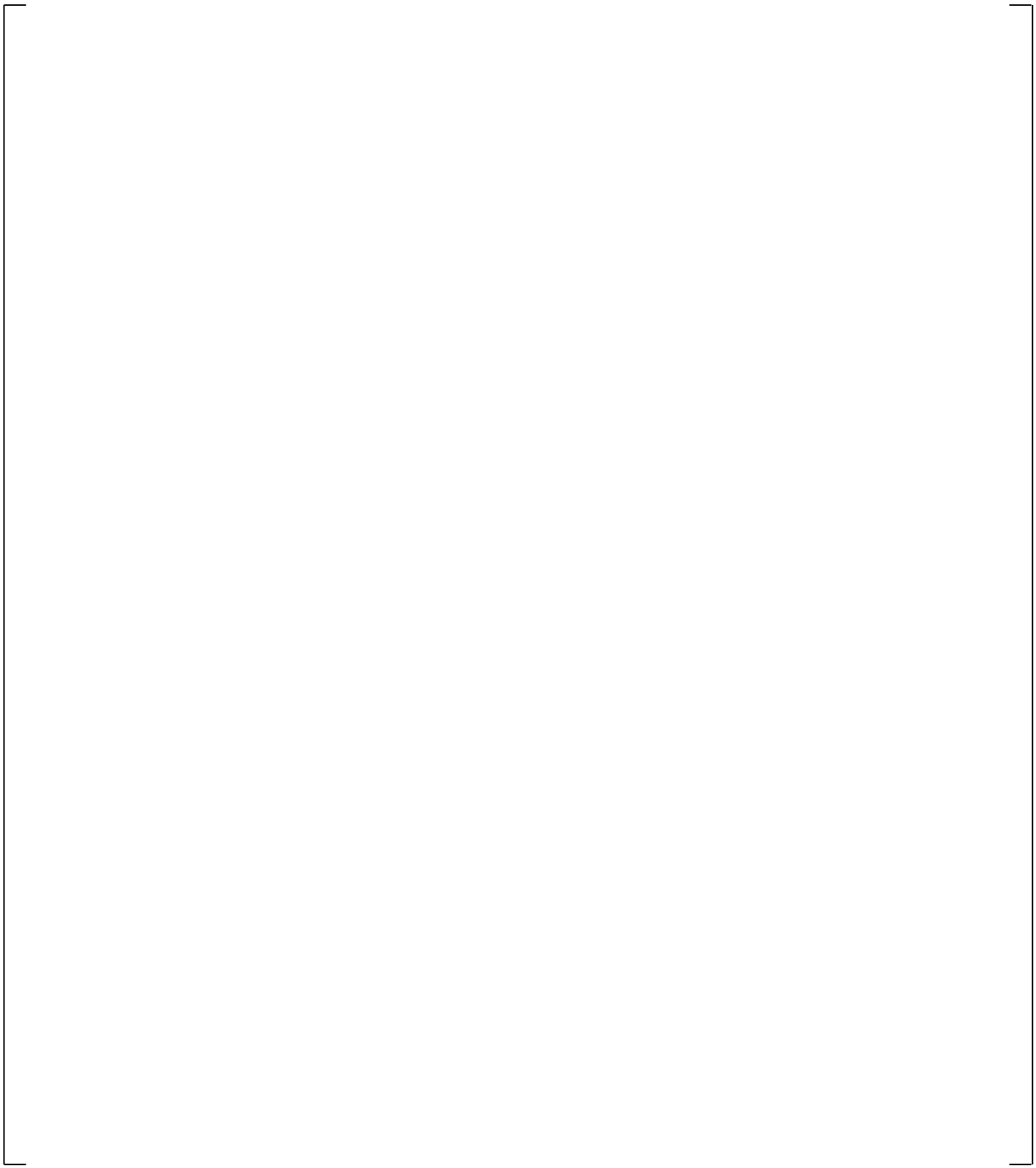

Figure 19.3-171 Predicted Downcomer Fluid (Vapor) Temperature at Level 28 for UPTF Test 25A

a,c

Figure 19.3-172 Measured Downcomer Fluid Temperature at Level 24 for UPTF Test 25A

a,c

Figure 19.3-173 Predicted Downcomer Fluid (Liquid) Temperature at Level 24 for UPTF Test 25A

a,c

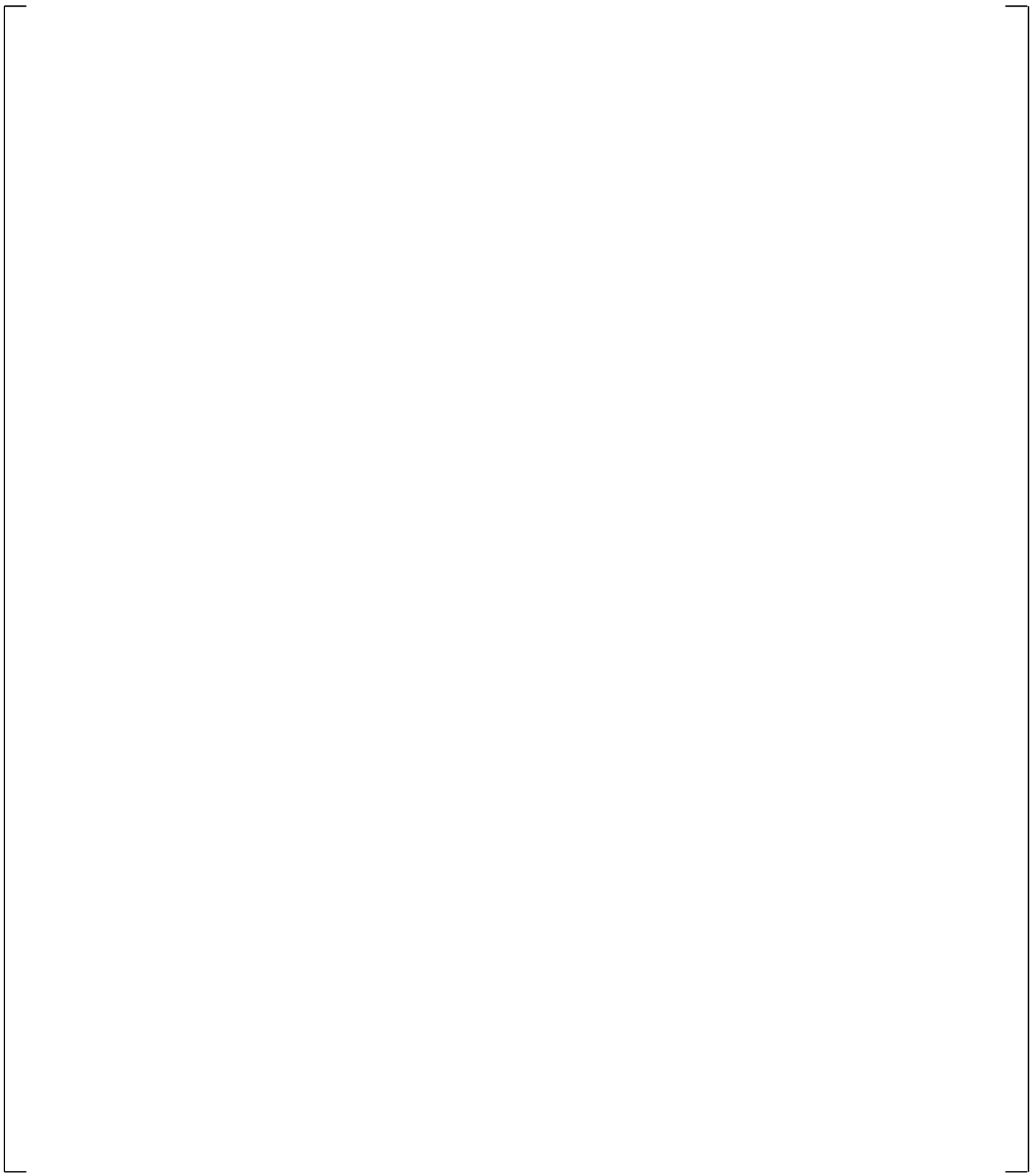

Figure 19.3-174 Differential Pressure between Upper Plenum and Downcomer for UPTF Test 25A

a,c

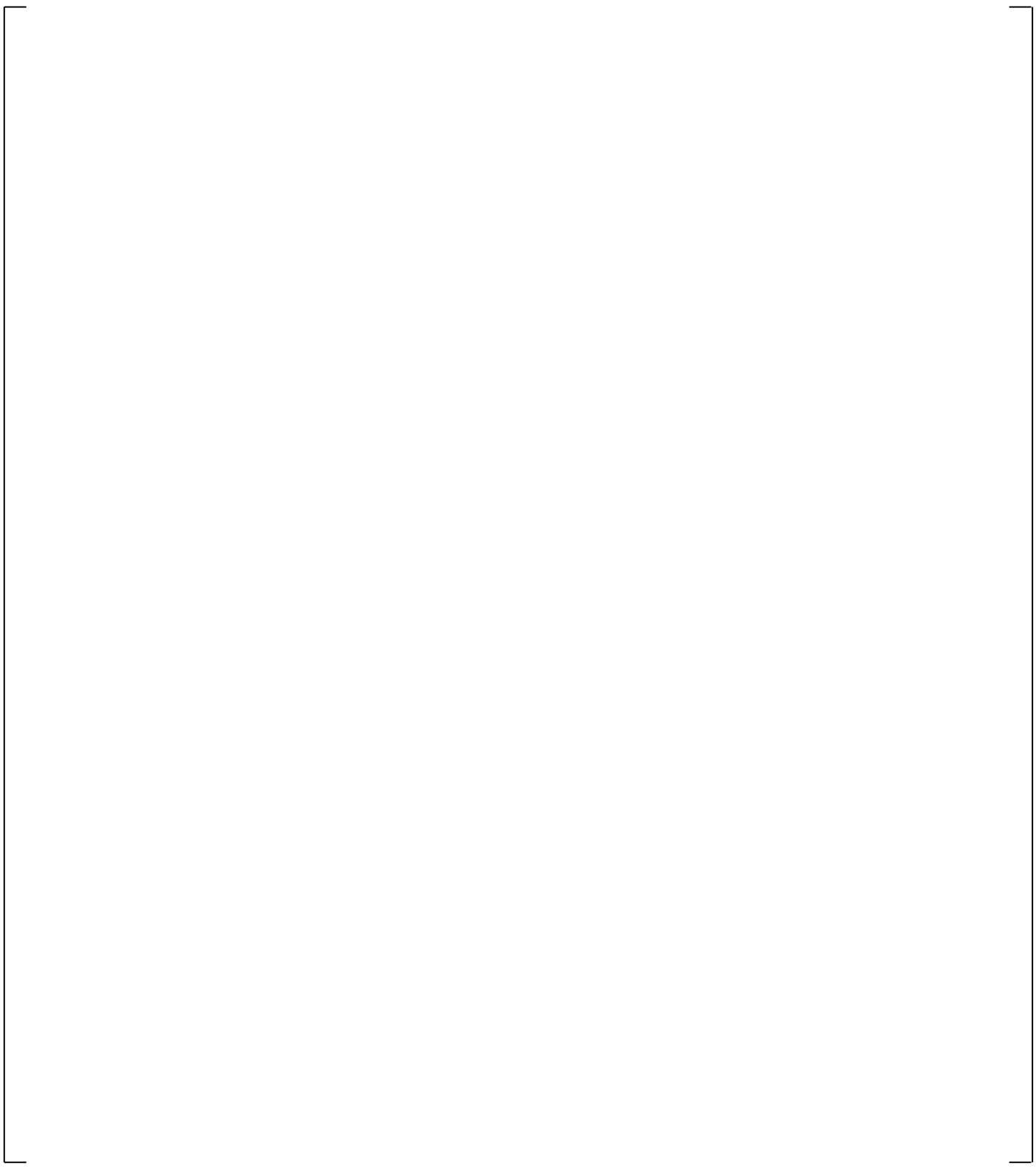

Figure 19.3-175 Axial Differential Pressure in Downcomer for UPTF Test 25A

a,c

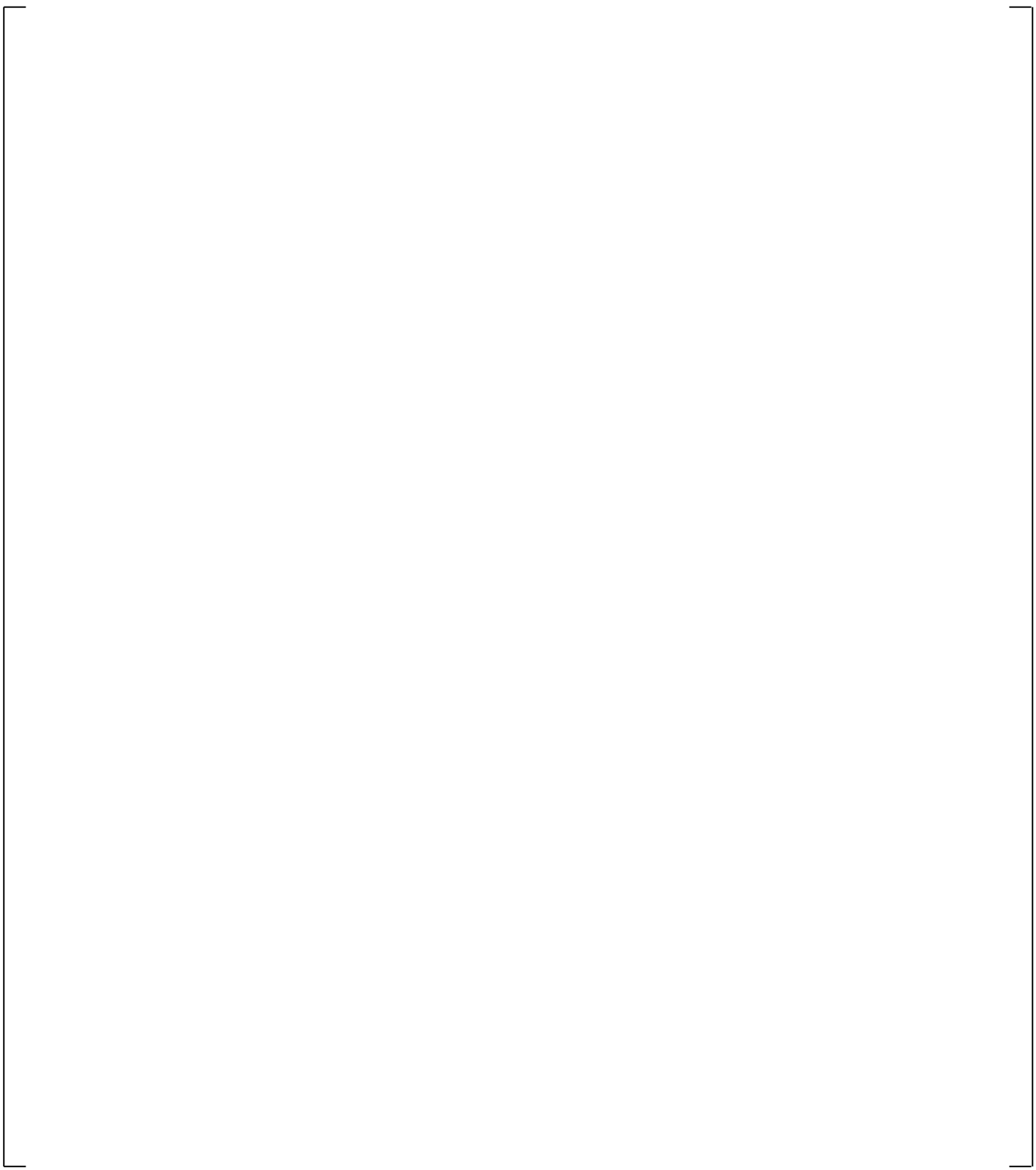

Figure 19.3-176 Axial Differential Pressures in Downcomer for UPTF Test 25A; Curve 2 is in Broken Quadrant and Curves 1, 3 and 4 are in Intact Quadrants

a,c

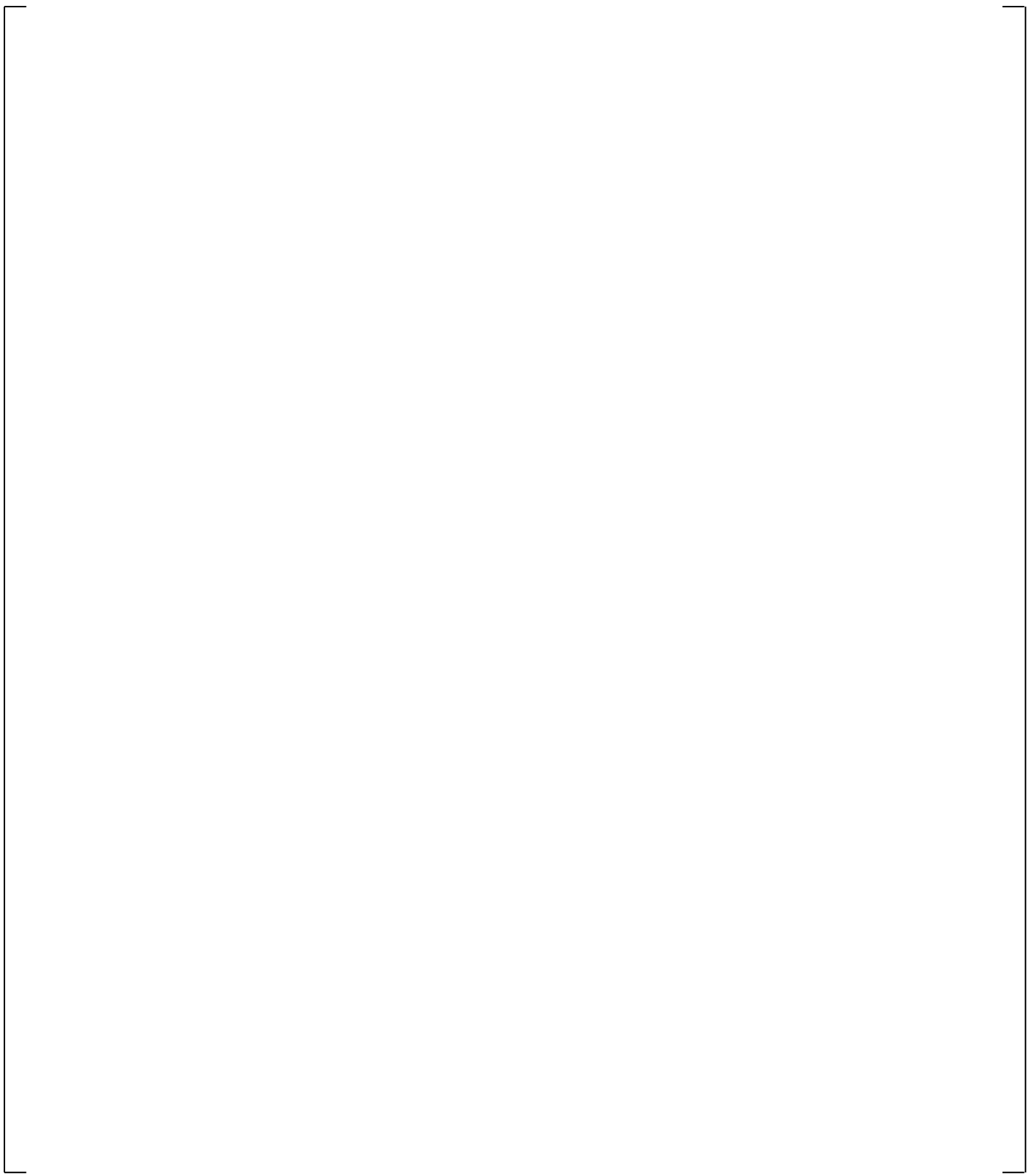

Figure 19.3-177 Broken Loop Steam Flow Rate for UPTF Test 25A

a,c

Figure 19.3-178 Broken Loop Liquid Flow Rate for UPTF Test 25A

a,c

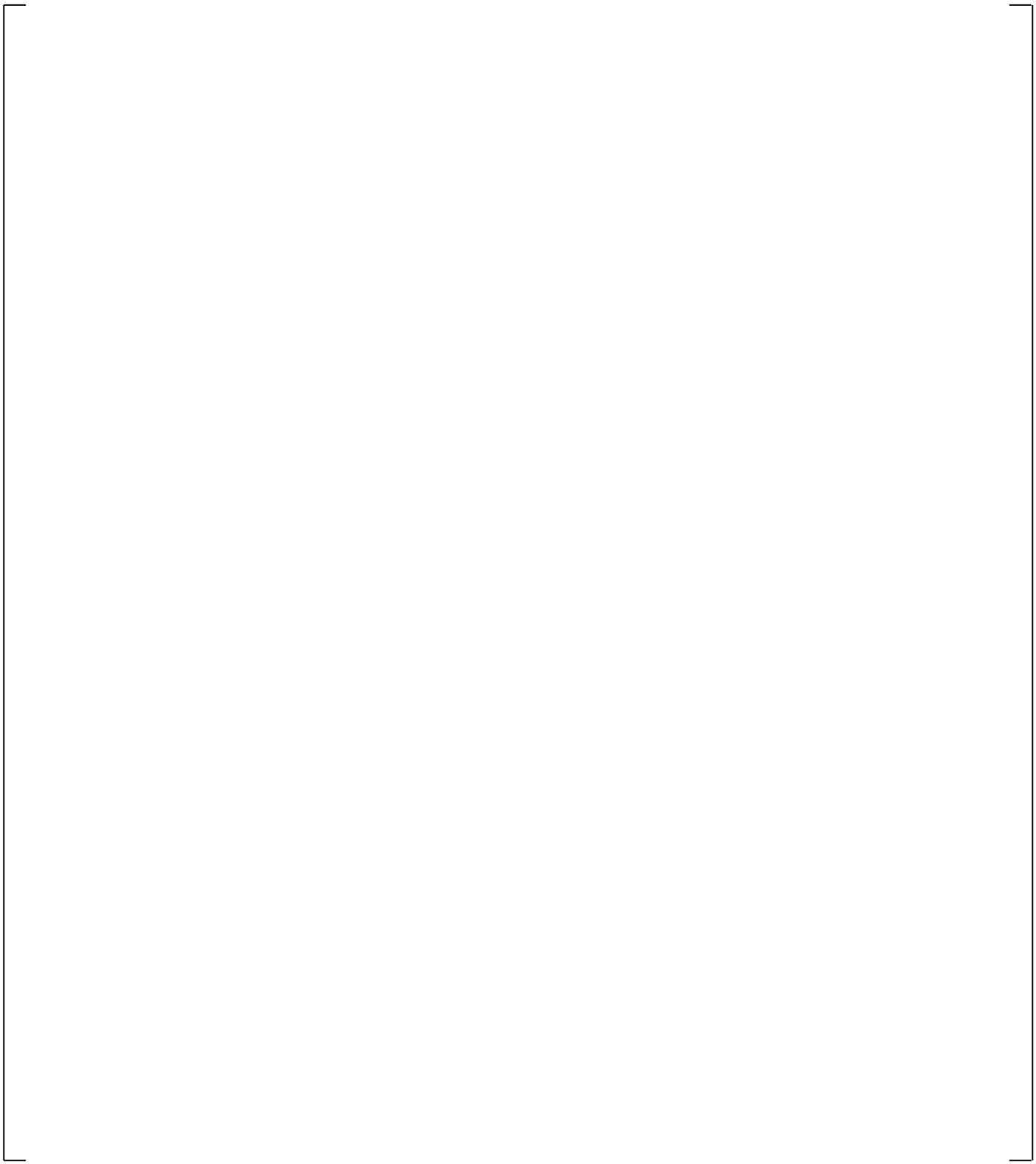

Figure 19.3-179 Void Height versus Steam Flow Rate for UPTF Test 25A

a,c

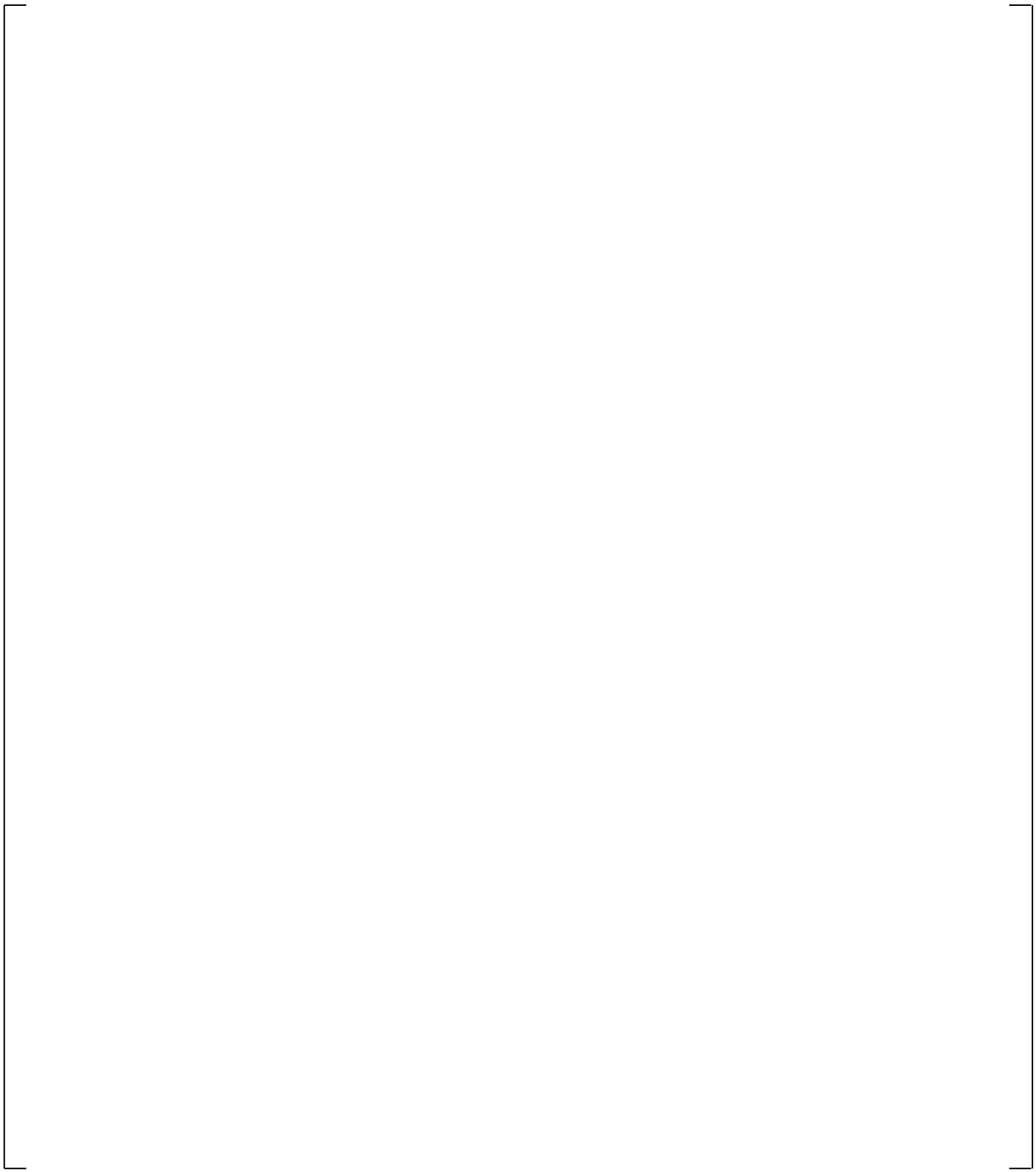

Figure 19.3-180 Cold Leg Temperature near ECC Injection for UPTF Test 25A

a,c

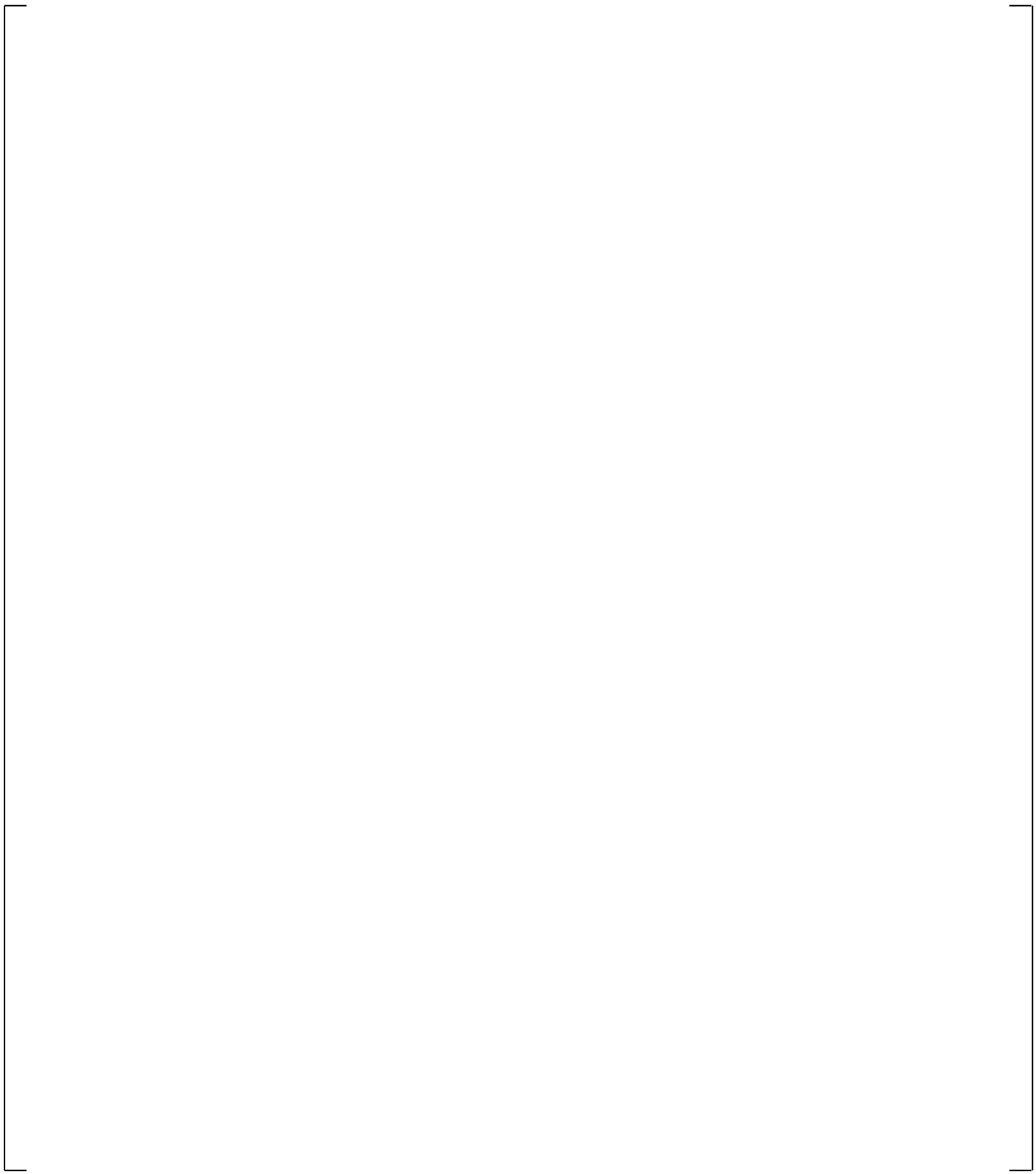

Figure 19.3-181 Cold Leg Temperature Downstream of ECC Injection for UPTF Test 25A

a,c

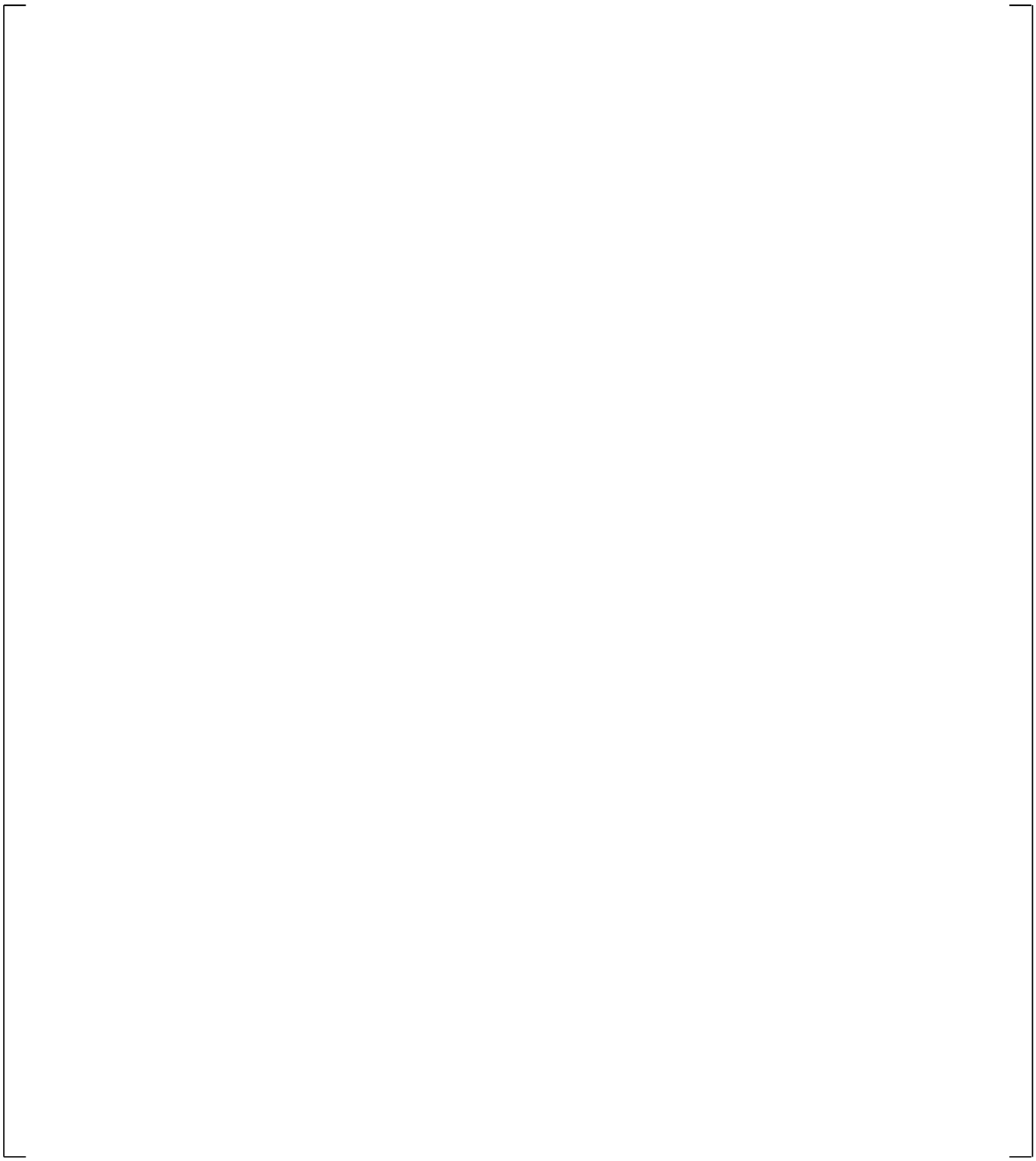

Figure 19.3-182 Cold Leg Temperature at Exit of Cold Leg for UPTF Test 25A

a,c

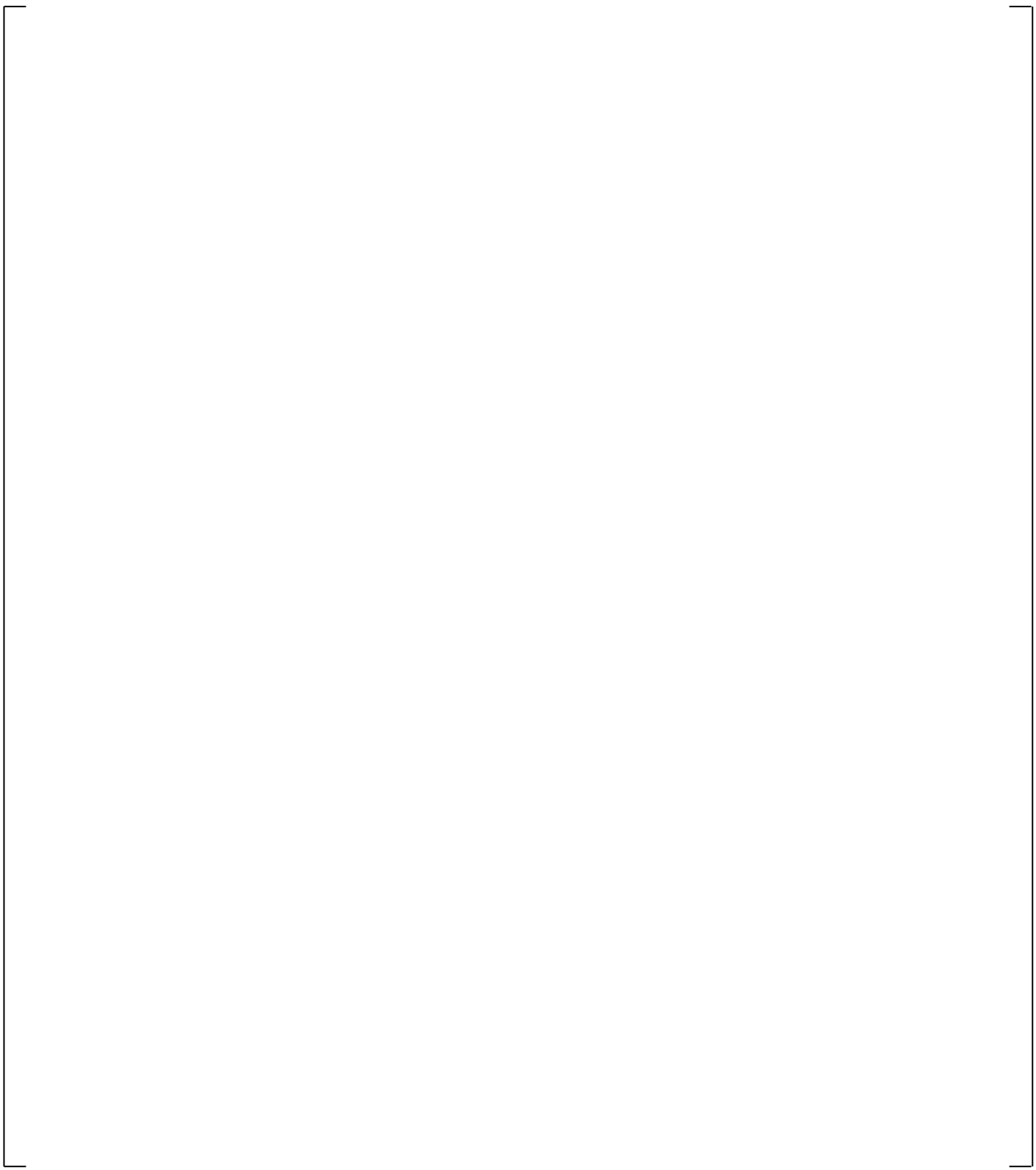

Figure 19.3-183 Cold Leg Temperature near ECC Injection for UPTF Test 25A with KCOSI=0.5

a,c

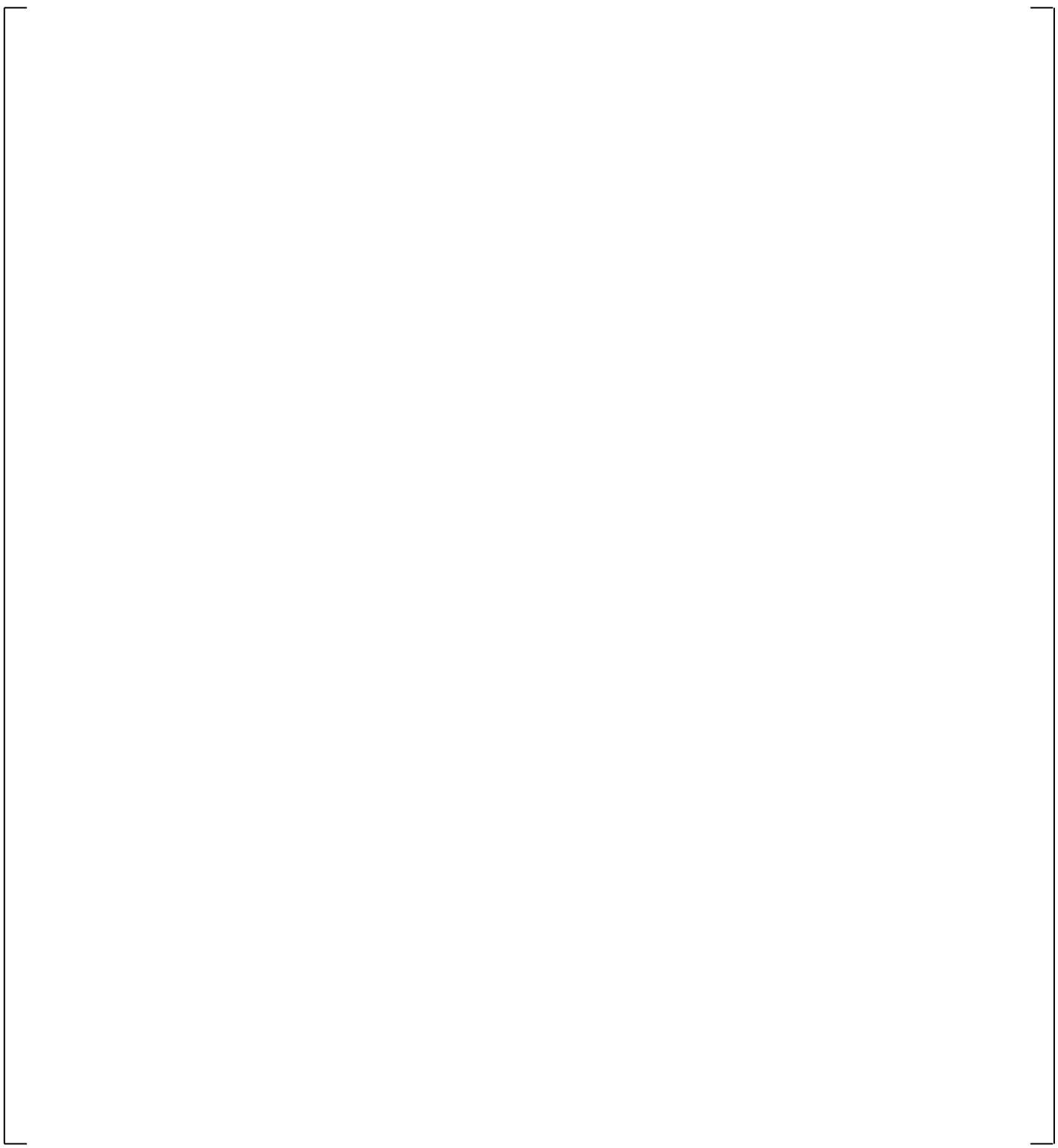

Figure 19.3-184 Cold Leg Temperature Downstream of ECC Injection for UPTF Test 25A with KCOSI=0.5

a,c

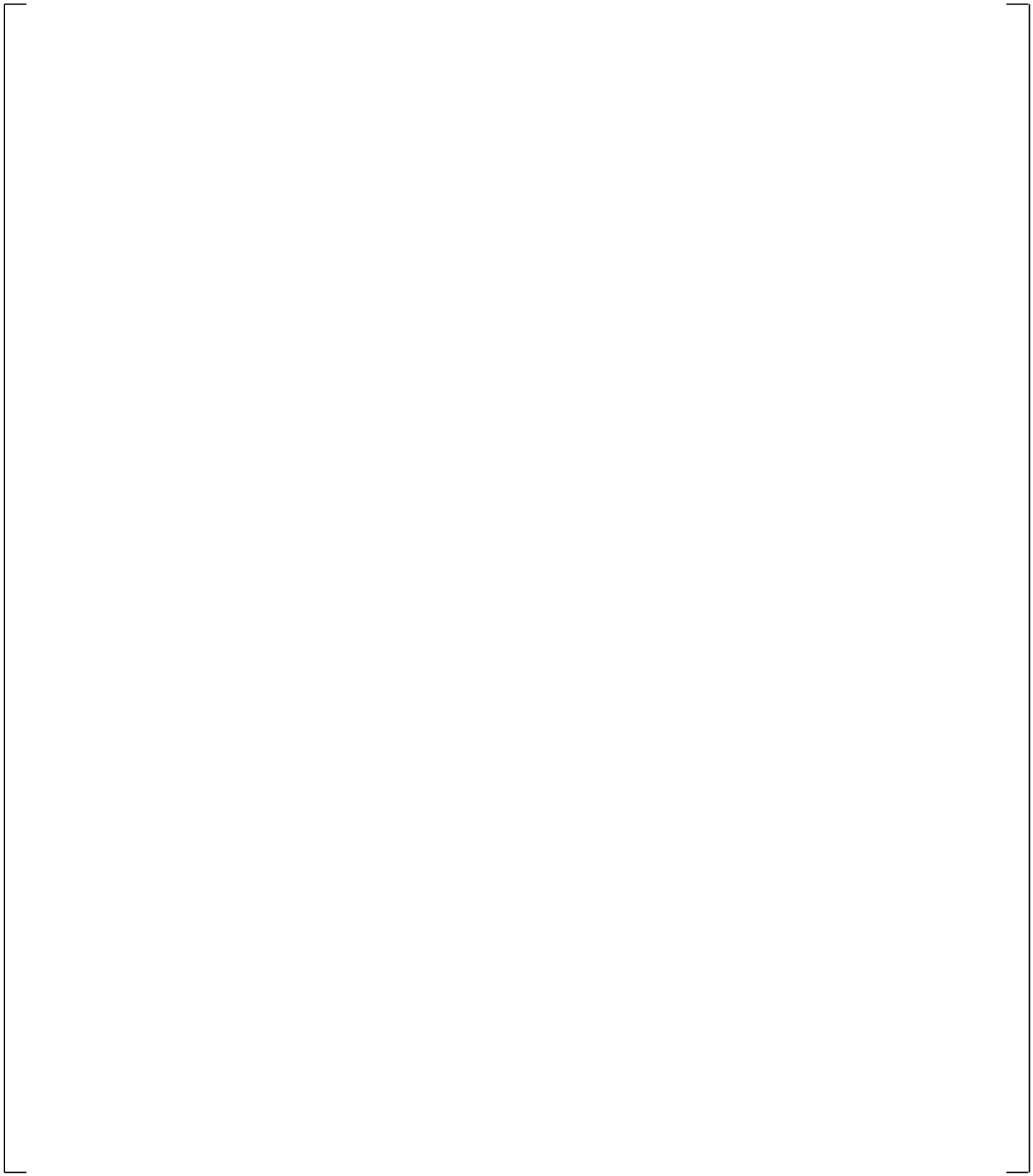

Figure 19.3-185 Cold Leg Temperature at Exit of Cold Leg for UPTF Test 25A with KCOSI=0.5

a,c

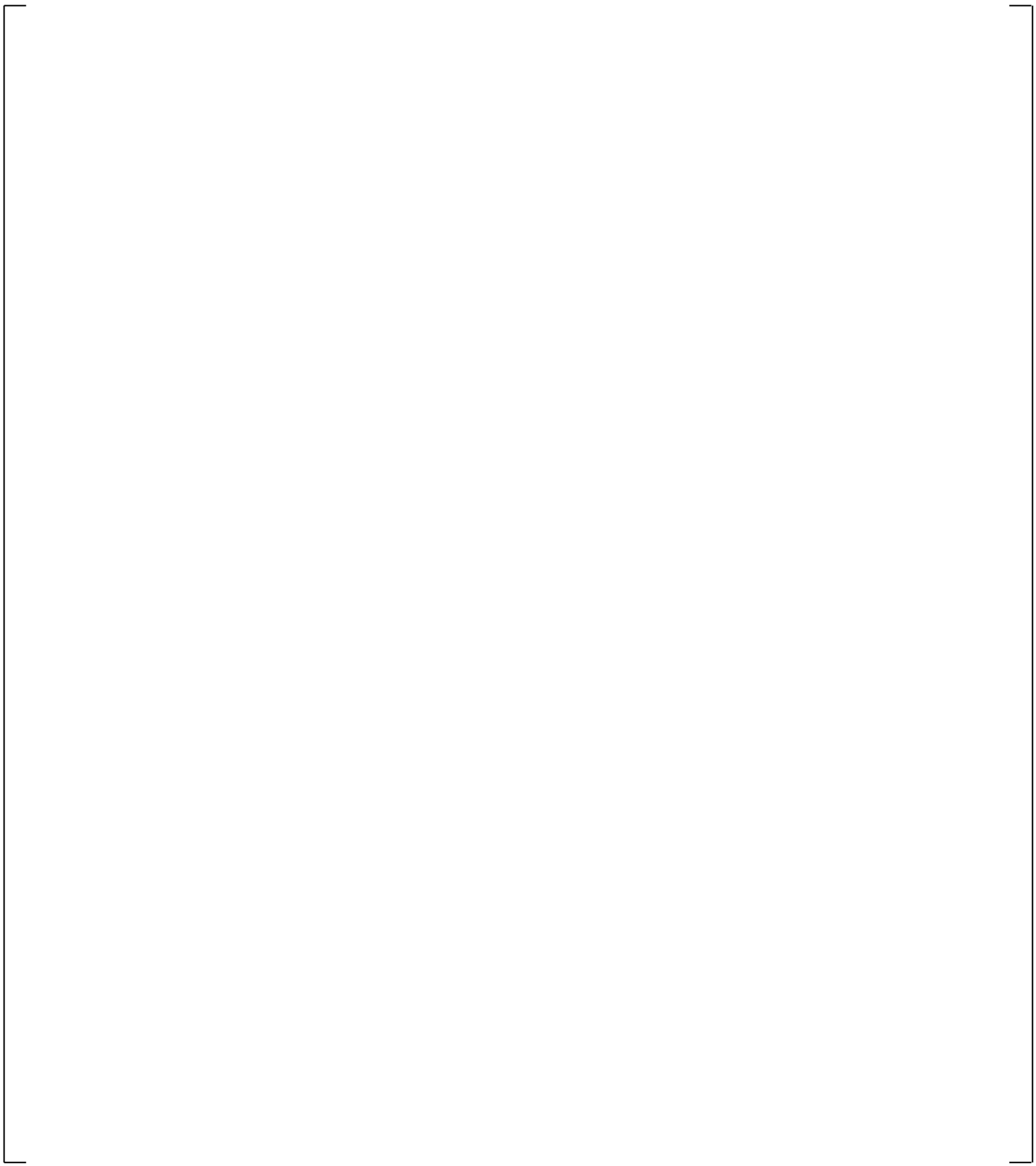

Figure 19.3-186 Axial Differential Pressures in Downcomer for UPTF Test 25A with KCOSI=0.5

a,c

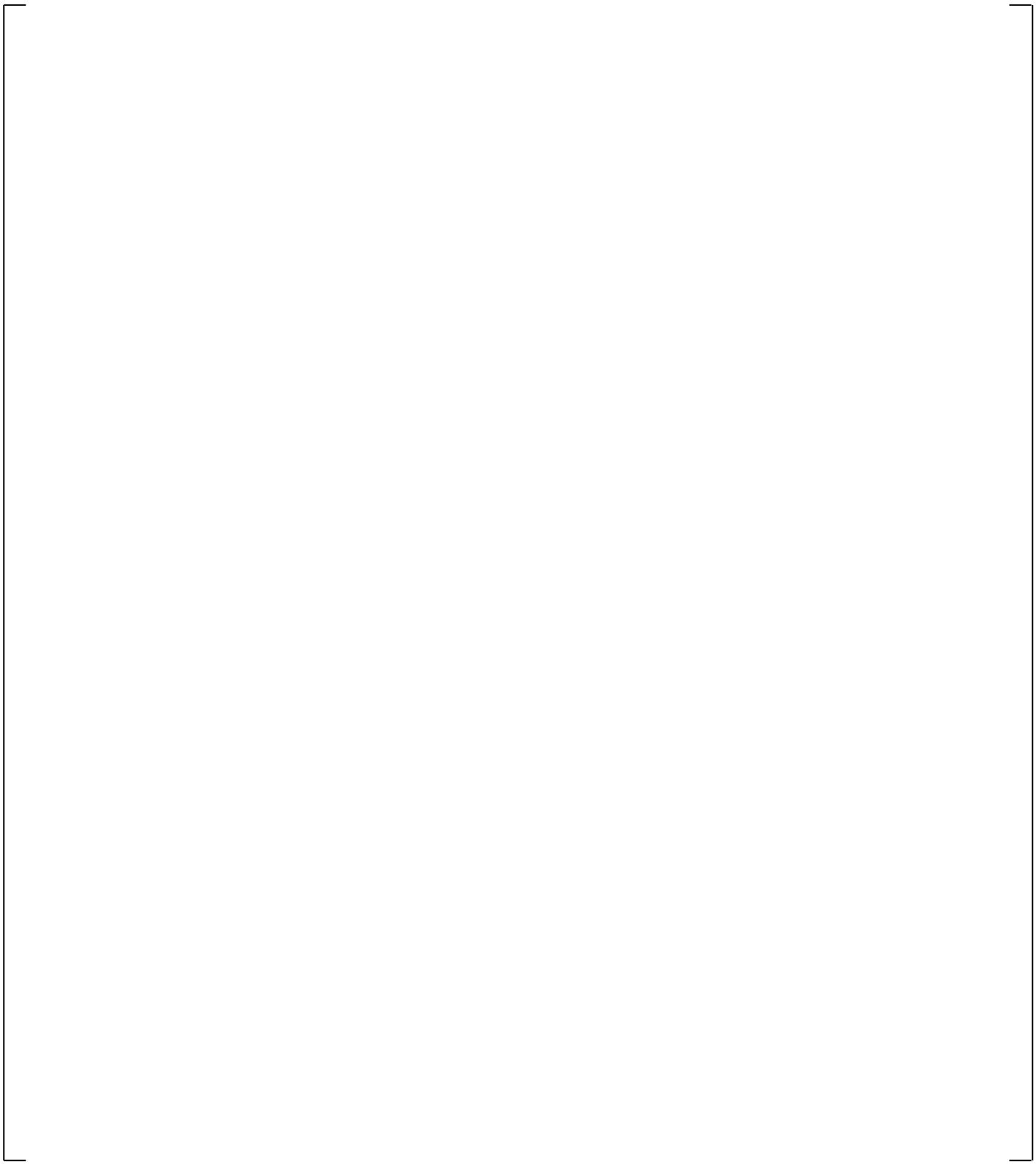

Figure 19.3-187 Broken Loop Steam Flow Rate for UPTF Test 25A with KCOSI=0.5

a,c

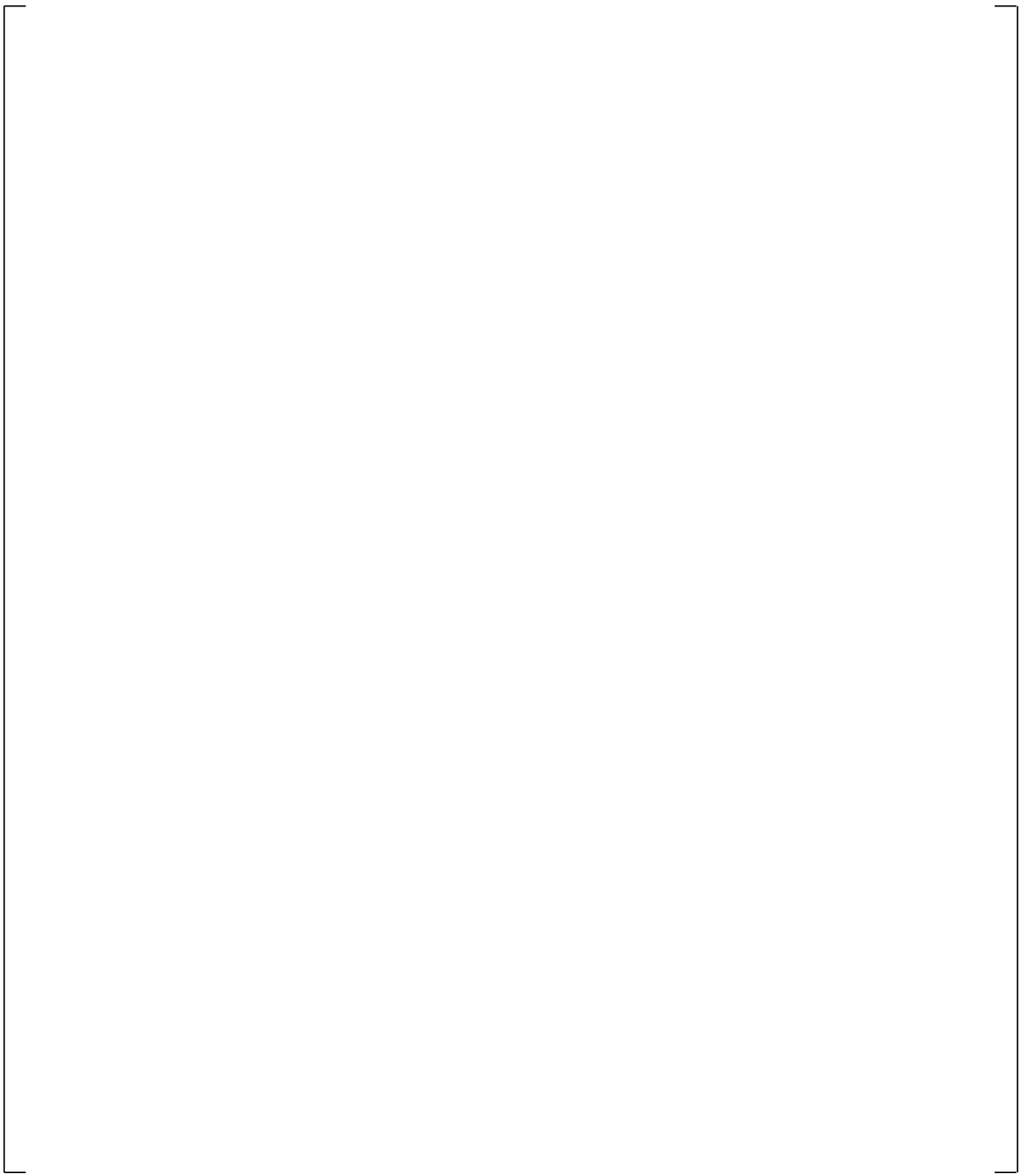

Figure 19.3-188 Broken Loop Liquid Flow Rate for UPTF Test 25A with KCOSI=0.5

a,c

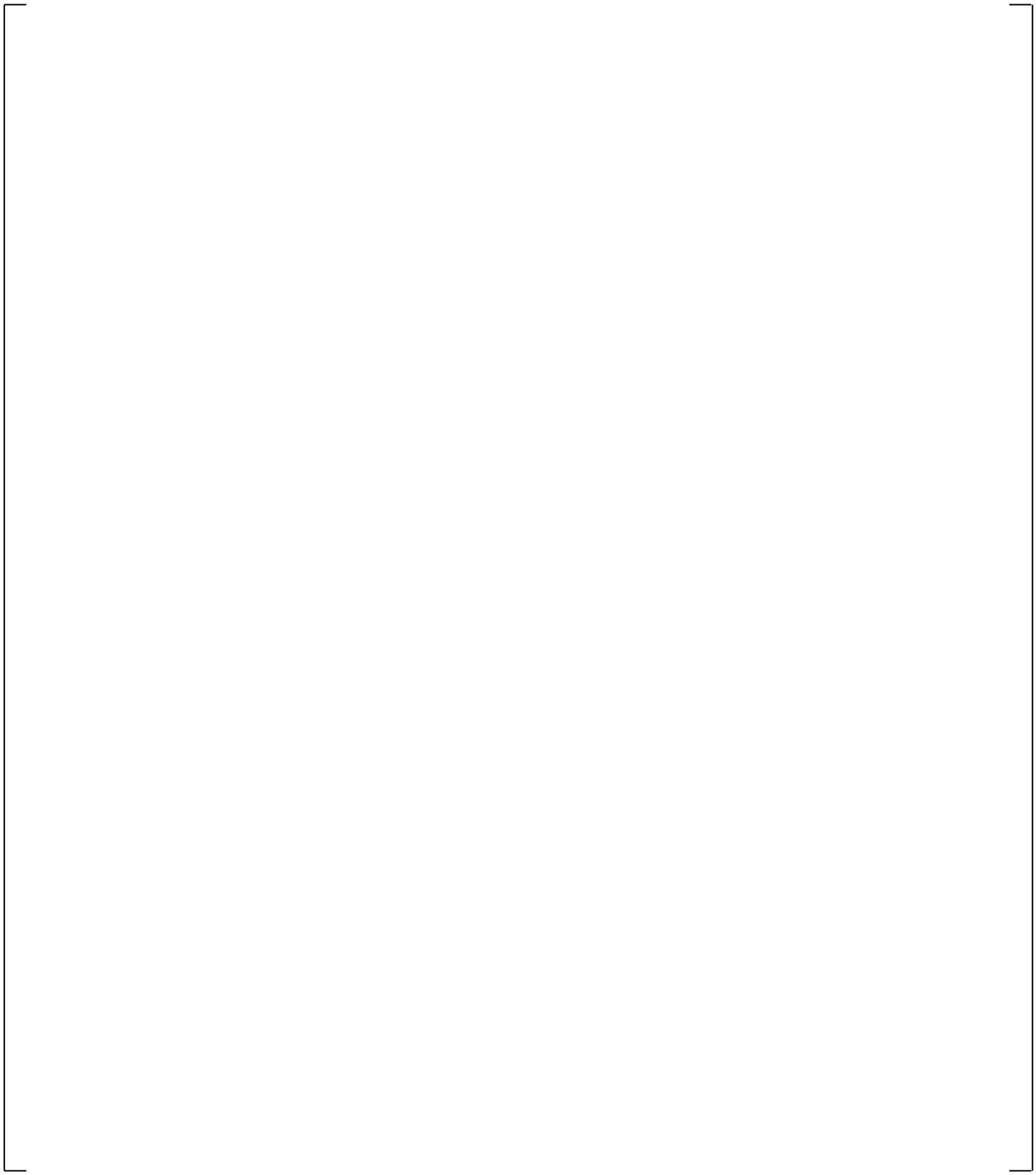

Figure 19.3-189 Differential Pressure between Upper Plenum and Downcomer for UPTF Test 25A with XC=0.4

a,c

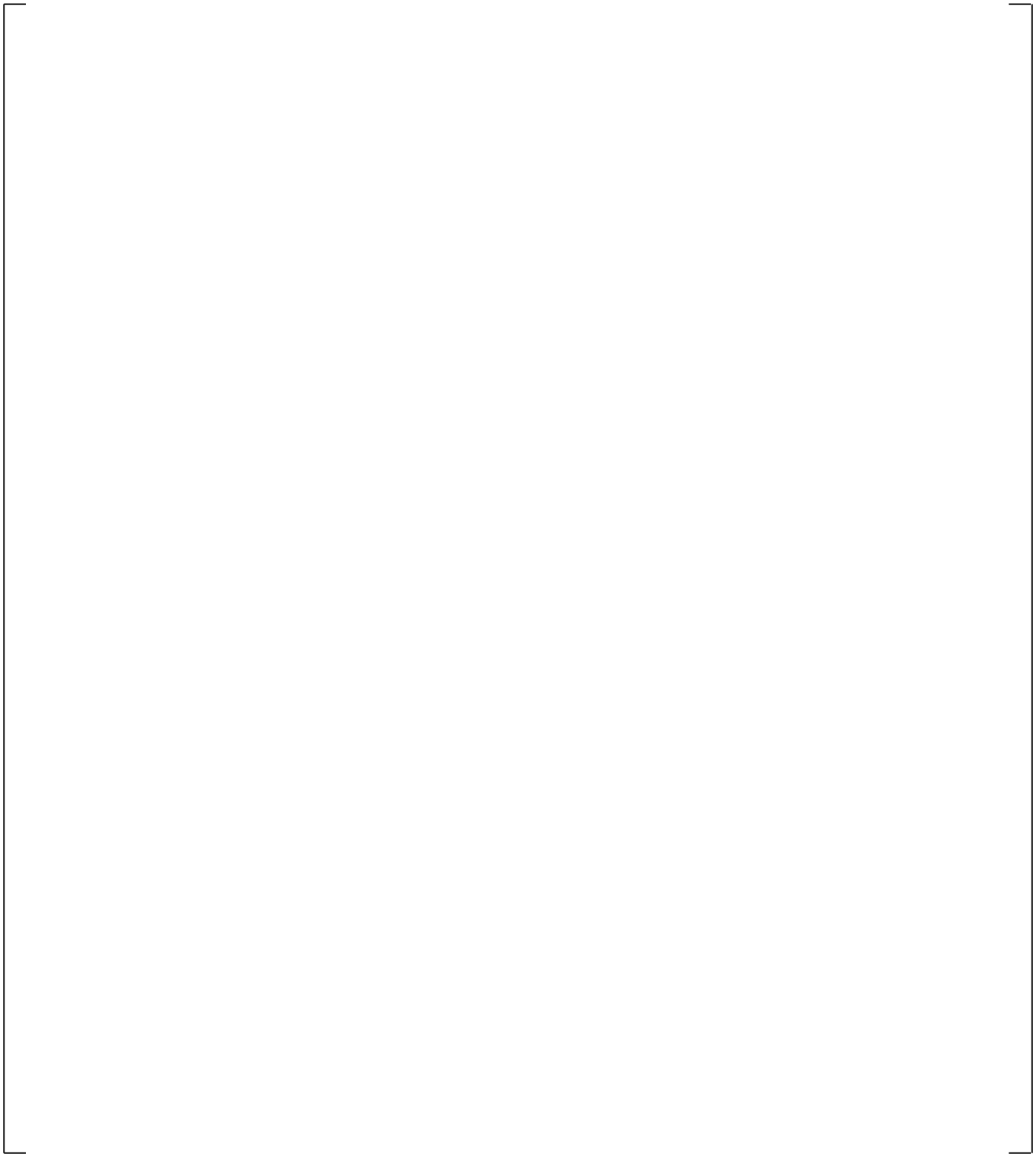

Figure 19.3-190 Axial Differential Pressure in Downcomer for UPTF Test 25A with XC=0.4

a,c

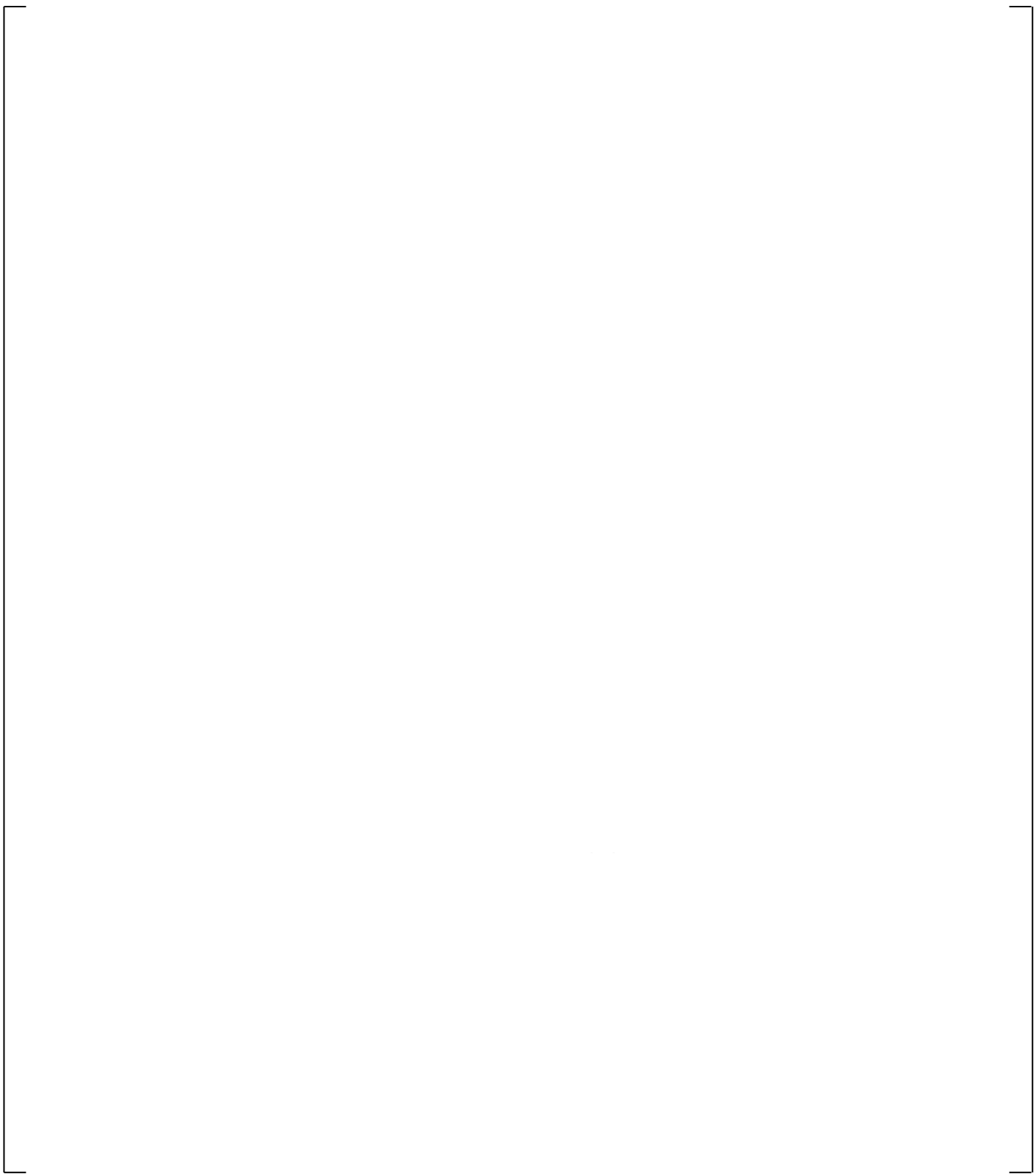

Figure 19.3-191 Axial Differential Pressures in Downcomer for UPTF Test 25A with XC=0.4

a,c

Figure 19.3-192 Void Height versus Steam Flow Rate for UPTF Test 25A with XC=0.4

a,c

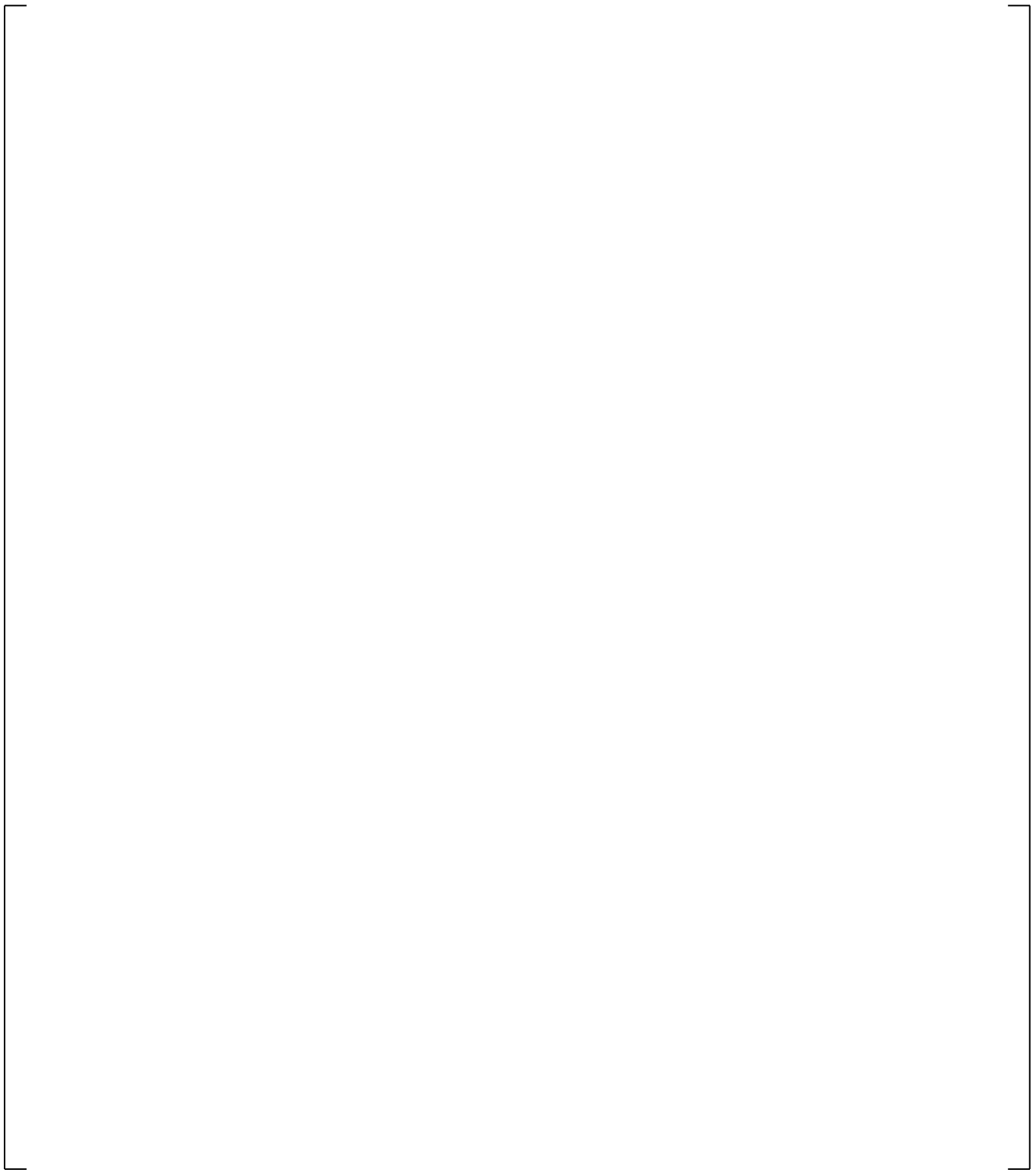

Figure 19.3-193 System Configuration for UPTF, Test 29 Phase B (Run 212) (MPR-1213, 1990b)

a,c

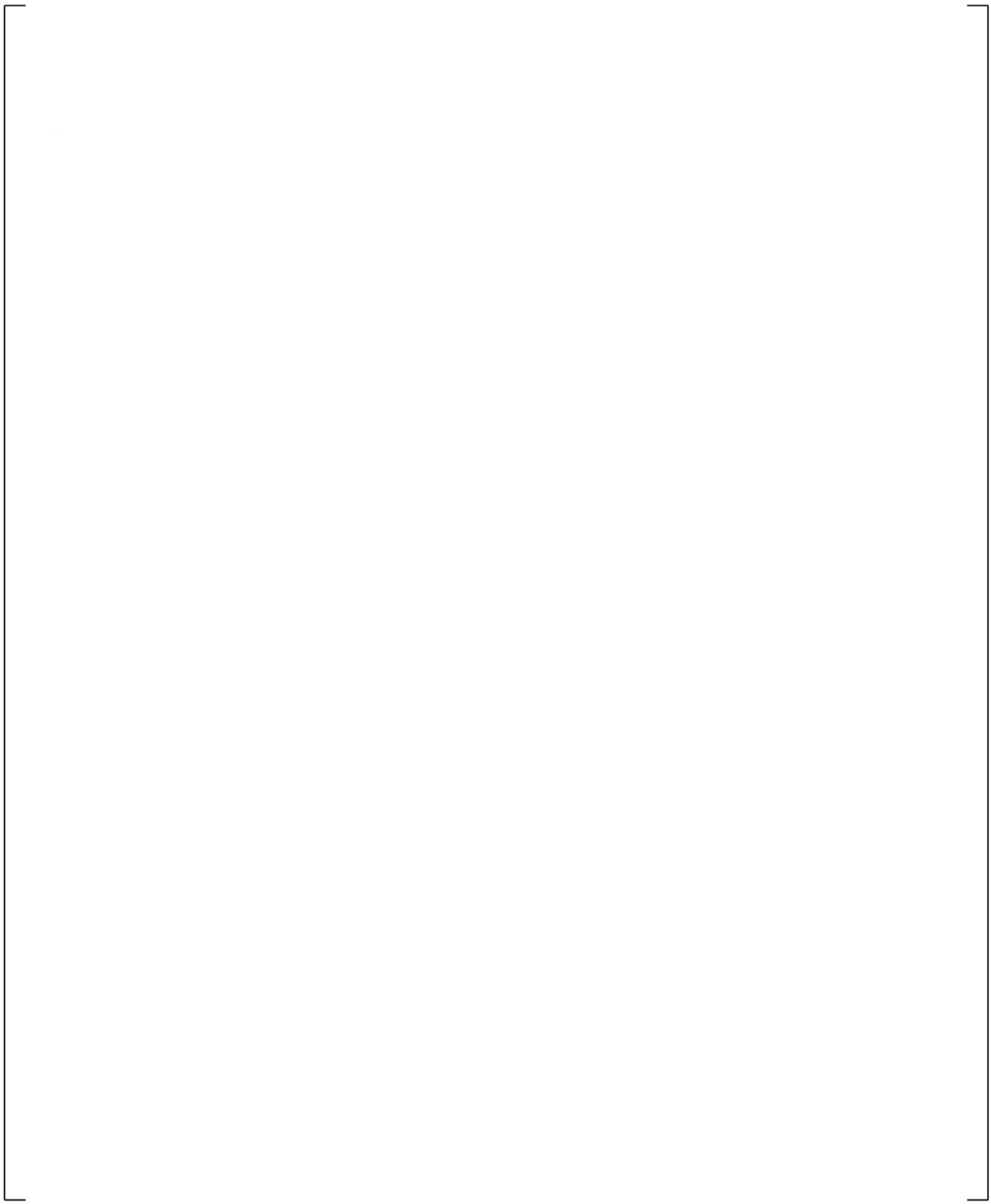

Figure 19.3-194 Injection Rates into Core Simulator, UPTF 29B

a,c

Figure 19.3-195 WCOBRA/TRAC-TF2 Vessel Component for UPTF Test 29B

a,c

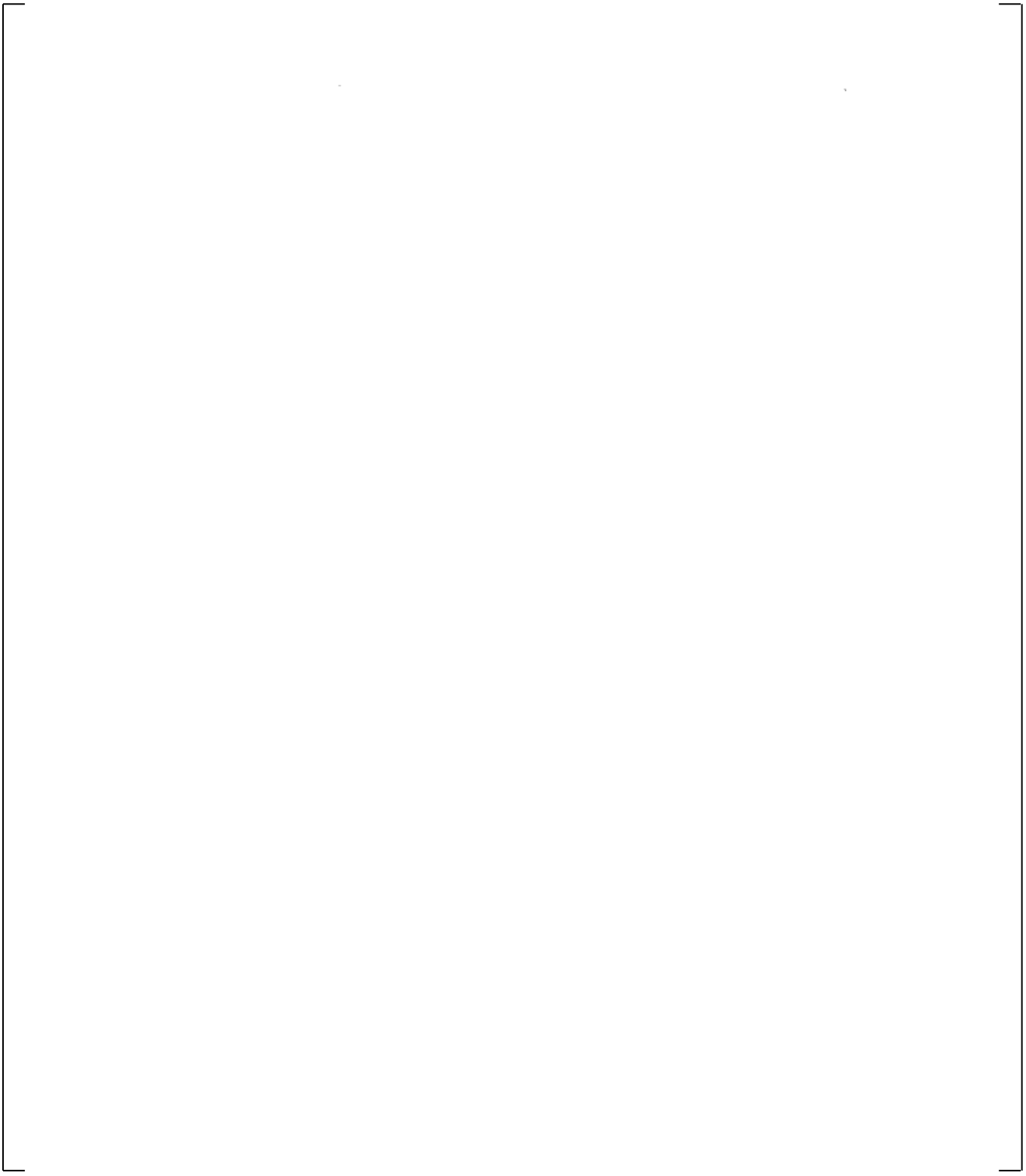

Figure 19.3-196 Illustration of Jet Channel and Global Channel in Upper Plenum

a,c

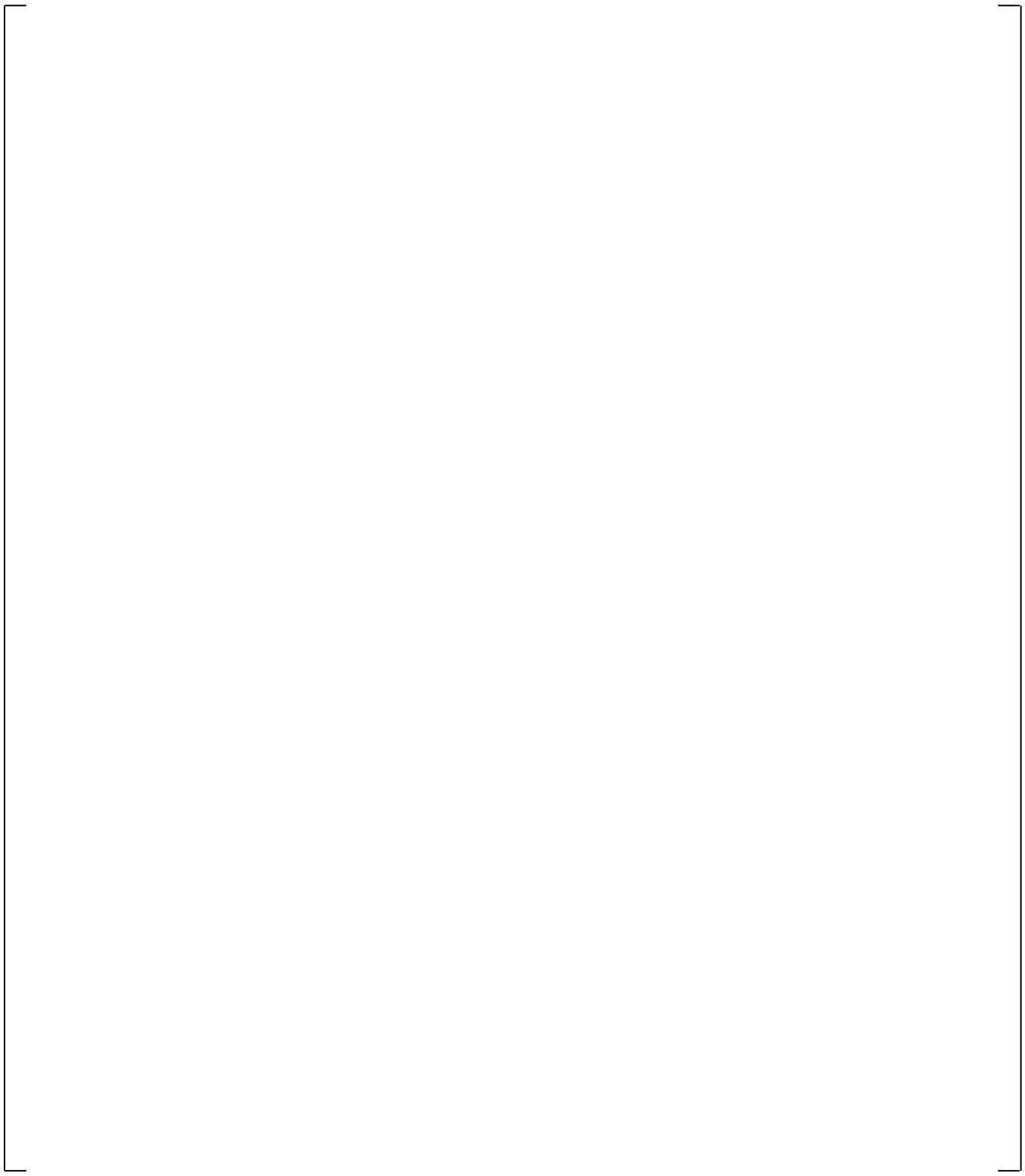

Figure 19.3-197 Section 5 of Upper Plenum Noding Model for UPTF Test 29B

a,c

Figure 19.3-198 WCOBRA/TRAC-TF2 Loop Model for UPTF Upper Plenum Test 29B

a,c

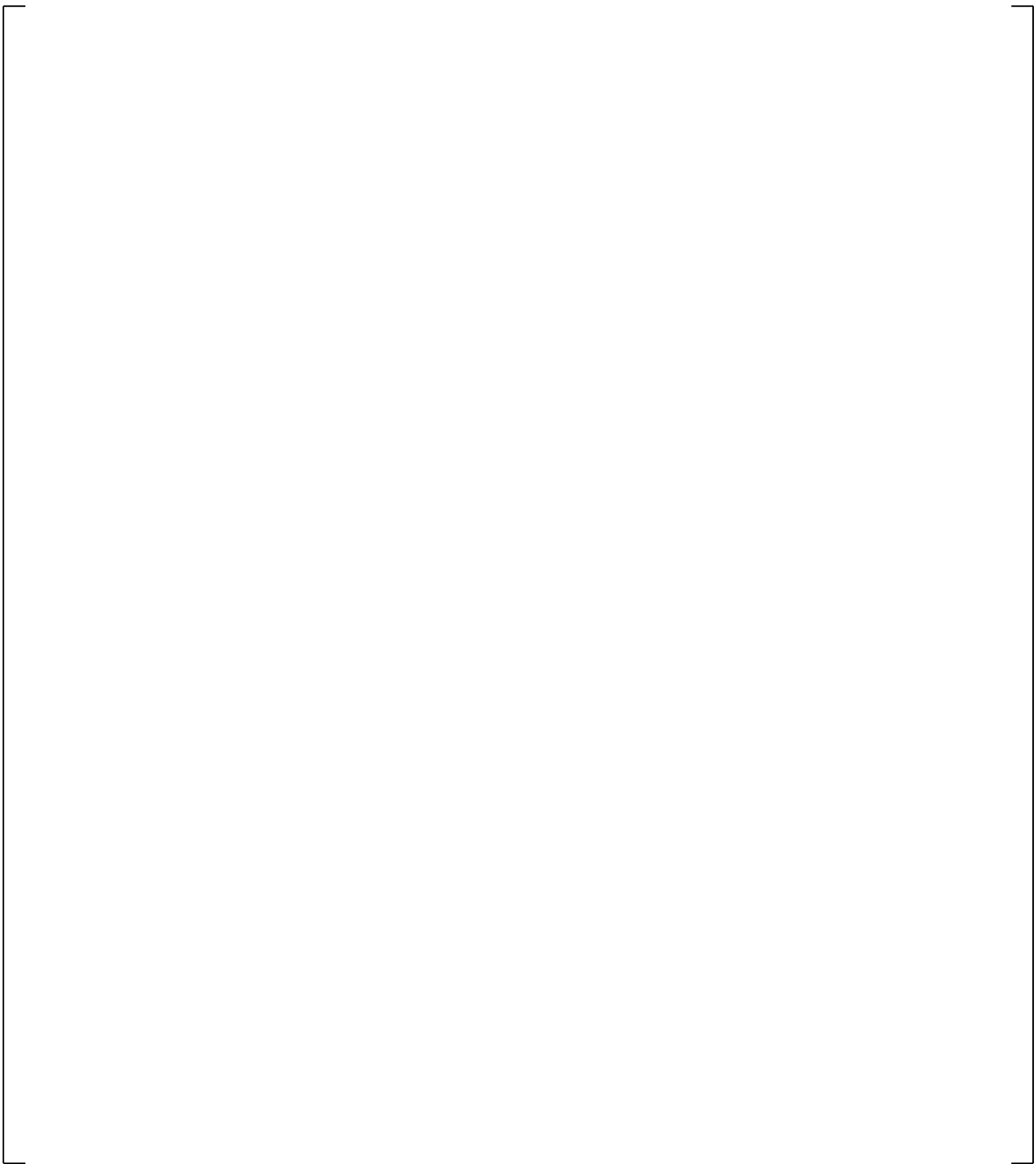

Figure 19.3-199 Quasi-Steady State Upper Plenum Mass for Phase I of UPTF Test 29B

a,c

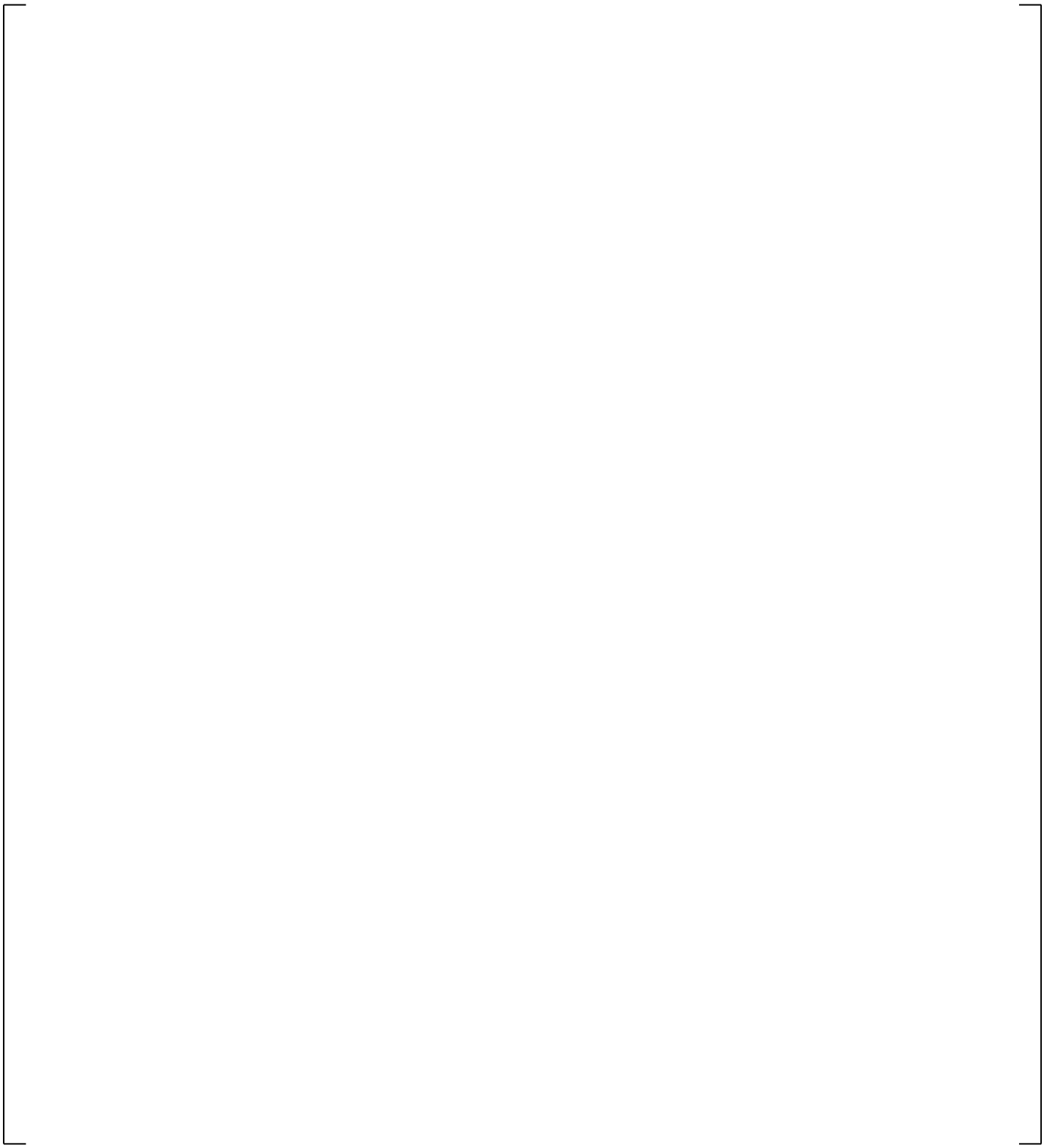

Figure 19.3-200 Quasi-Steady State Upper Plenum Mass for Phase II of UPTF Test 29B

a,c

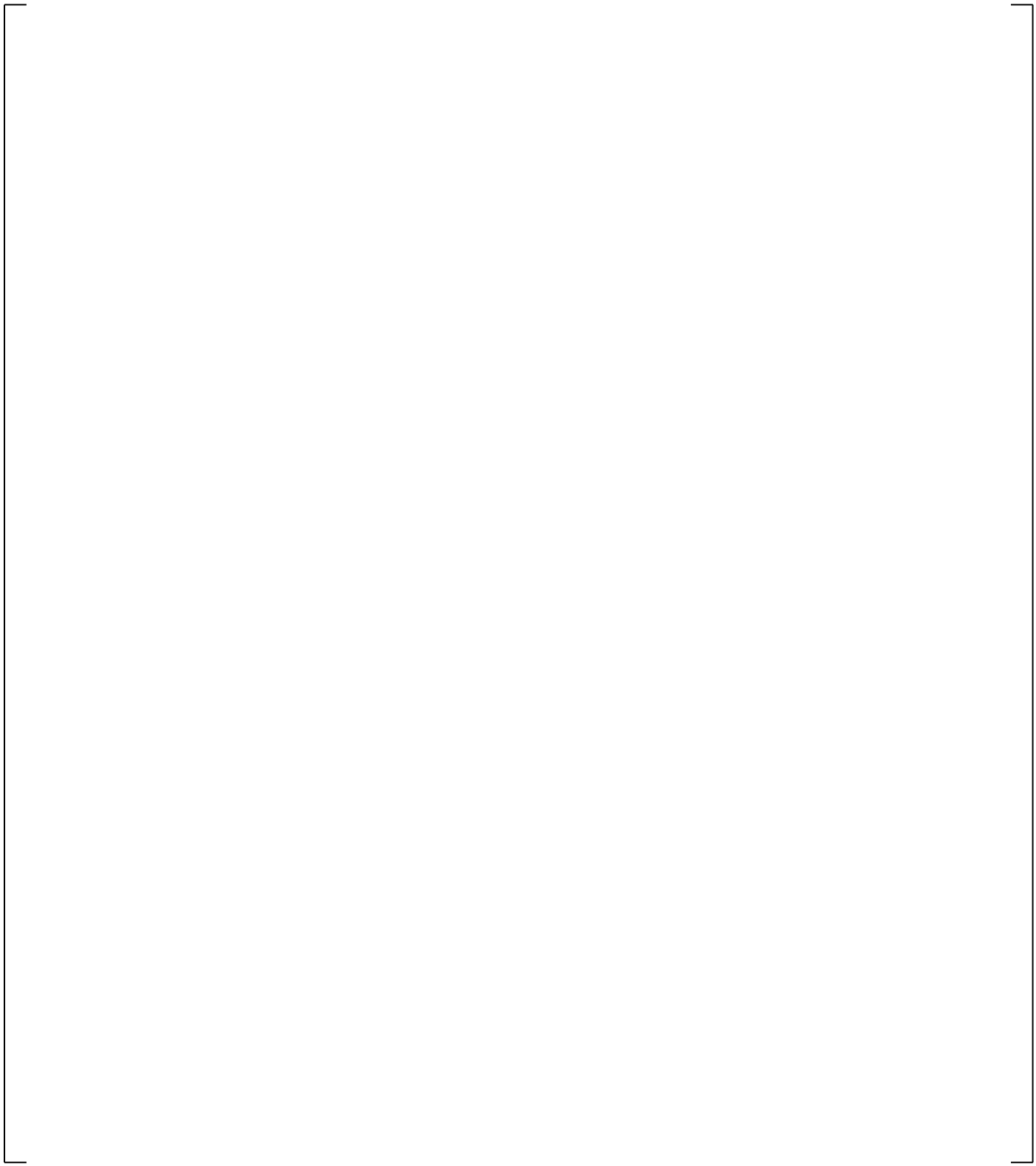

Figure 19.3-201 Quasi-Steady State Upper Plenum Mass for Phase III of UPTF Test 29B

a,c

Figure 19.3-202 Quasi-Steady State Upper Plenum Mass for Phase IV of UPTF Test 29B

a,c

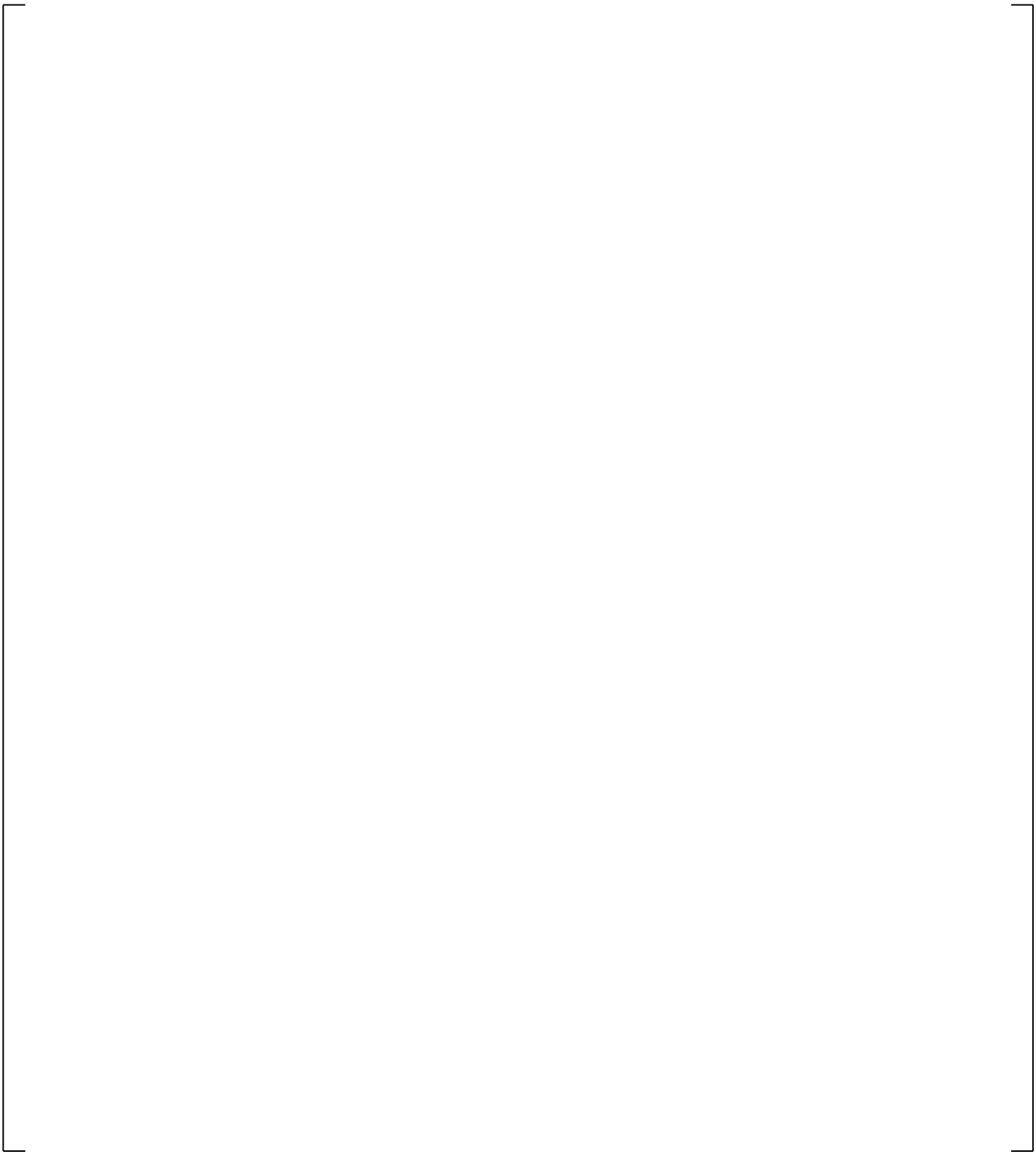

Figure 19.3-203 Quasi-Steady State Upper Plenum Mass for Phase V of UPTF Test 29B

a,c

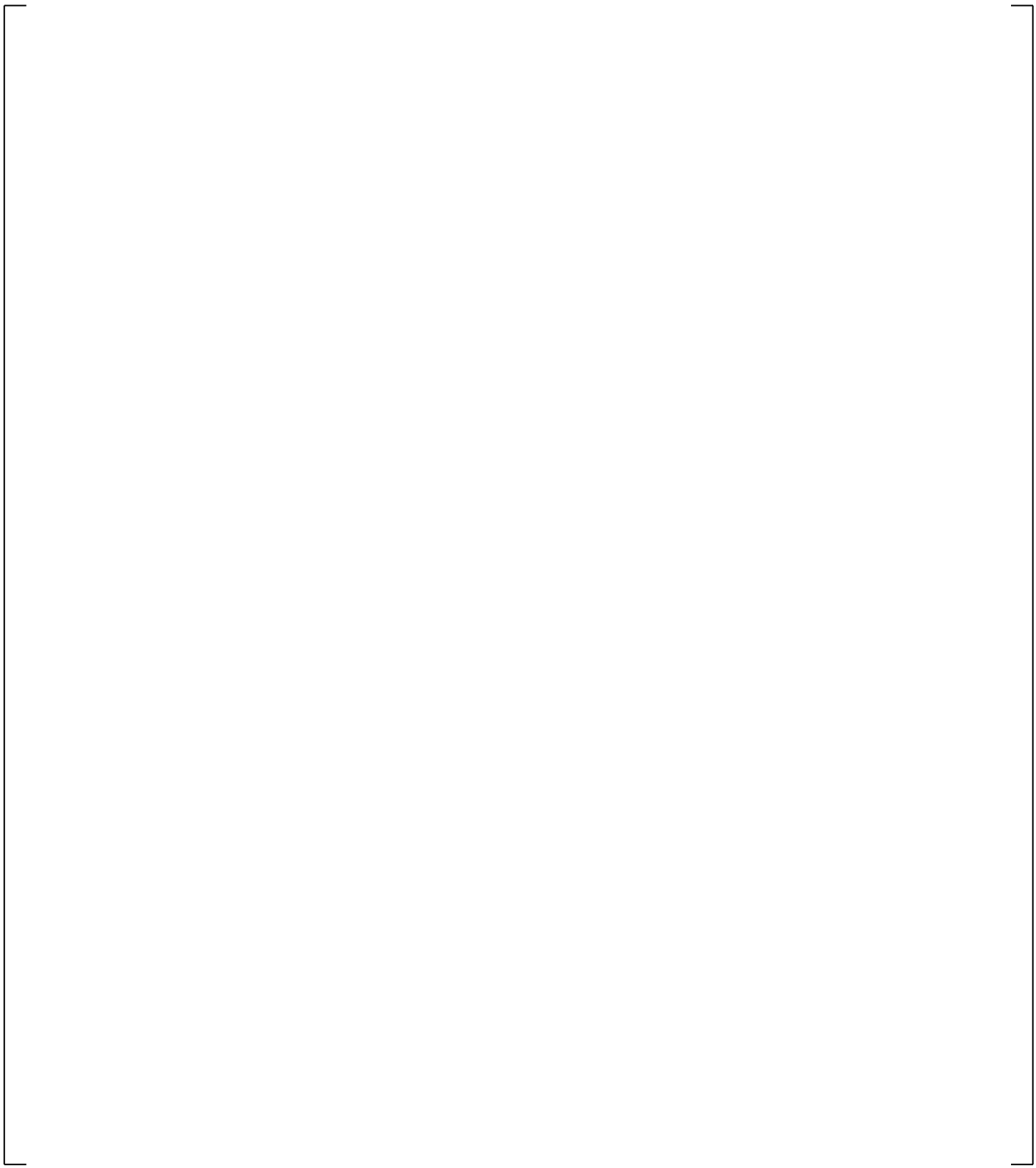

Figure 19.3-204 Quasi-Steady State Upper Plenum Mass for Phase VI of UPTF Test 29B

19.4 PERFORATED PLATE FLOODING ANALYSIS

CCFL in a perforated plate has been tested and analyzed by Hsieh et al. (1980). The tests were conducted with air/water and steam/water systems on perforated plates with different hole size and geometries. The air/water experiment was designed to investigate the effects of geometric factors on the rate of weeping. The steam/water tests investigated subcooling effects on the CCFL. To assess the capability of WCOBRA/TRAC-TF2 on modeling the CCFL phenomenon, the air/water tests performed by Hsieh et al. (1980) on their 15-hole perforated plate is simulated. The 15-hole plate tests were selected due to its similar geometry to a PWR fuel assembly top nozzle (or tie plate). As the steam/cold water CCFL on a perforated plate is not encountered in the LOCA transients of a typical PWR except for the upper plenum injection (UPI) plant which is currently not included in the FSLOCA methodology, the steam/cold water CCFL tests reported by Hsieh et al. (1980) were not used to assess WCOBRA/TRAC-TF2. Furthermore, the test data on the steam/water system are only limited to the boundaries of weeping and no-weeping and therefore insufficient to check the code on predicting the weeping liquid rate in the range between the 'no-weeping' and 'dumping' (all the inlet liquid falls down through the perforated plate). The obtained test data on the weeping rate in their air/water system are readily available to develop a test CCFL flooding limit which can then be checked against the applicable theoretical CCFL flooding limits based on the scaling factors developed, for example, by Hsieh et al. (1980) among others.

Based on the available and applicable test data, first, the air/water test with a 15-hole perforated plate was simulated by WCOBRA/TRAC-TF2 using nitrogen/water to compare with the test and the CCFL curve based on the Northwestern scaling factor (Hsieh et al., 1980). The computed results of the nitrogen/water system are compared with the test data since the pertinent properties to CCFL of the air and nitrogen are within the appropriate range for the WCOBRA/TRAC-TF2 assessment.

[

]^{a,c}

In Section 19.4.1, the different scaling factors used in the CCFL at a perforated plate are described. The WCOBRA/TRAC-TF2 input models for the perforated CCFL simulations are introduced in Section 19.4.2 for the nitrogen/water and high pressure and low pressure steam/water systems. The comparisons of the computed CCFL are presented and summarized in Section 19.4.3; [

]^{a,c}.

19.4.1 Correlations and Scaling for CCFL in a Perforated Plate

The various flooding models available within the code were discussed in Section 5.15, Volume 1. The Northwestern scaling is compared to other scaling methods in this section.

Northwestern (H*) Scaling

Hsieh et al. (1980) developed a scaling parameter similar to the one employed by Wallis (1969) to define a non-dimensional volumetric flux, which is referred to here as Northwestern scaling,

$$H_k^* = j_k\left[\frac{\rho_k}{gw\left(\rho_f - \rho_g\right)}\right]^{1/2} \tag{19.4-1}$$

$$w = d_h{}^{1-\alpha}L^{\alpha} \tag{19.4-2}$$

$$\alpha = \tanh\left(r \cdot k_c \cdot d_h\right) \tag{19.4-3}$$

where,

subscript k	=	g, f for gas and liquid phase, respectively
j_k	=	the superficial velocity of phase k
ρ_k	=	the density of phase k
d_h	=	the hole diameter
L	=	the Laplace capillary constant
r	=	A_h/A_T (hole area divided by total plate area)
k_c	=	the wave number defined by:

$$k_c = \frac{2\pi}{t_p} \tag{19.4-4}$$

in which t_p is the thickness of the plate.

With these dimensionless volumetric fluxes, the test data for CCFL in the perforated plates was correlated by Hsieh et al. (1980) to yield:

$$H_g^{*1/2} + H_f^{*1/2} = C \tag{19.4-5a}$$

where,

$$C = \min\begin{cases}1.07 + 4.32\times10^{-3}L^* \\ 2.0\end{cases} \tag{19.4-5b}$$

$$L^* = n\pi d_h\left[\frac{g(\rho_f - \rho_g)}{\sigma}\right]^{1/2} \tag{19.4-5c}$$

and n is the number of holes. One way to examine Northwestern scaling is to compare it to other scaling methods as discussed below.

Wallis (J*) Scaling

$$j_k^* = j_k\left[\frac{\rho_k}{gd_h(\rho_f - \rho_g)}\right]^{1/2} \tag{19.4-6}$$

Kutateladze (K*) Scaling

$$K_k^* = j_k\left[\frac{\rho_k}{g\left[\frac{\sigma}{g(\rho_f - \rho_g)}\right]^{1/2}(\rho_f - \rho_g)}\right]^{1/2} = j_k\left[\frac{\rho_k^2}{g\sigma(\rho_f - \rho_g)}\right]^{1/4} \tag{19.4-7}$$

or

$$K_k^* = j_k^*\left(D^*\right)^{1/2}$$

where use has been made of the dimensionless diameter,

$$D^* = d_h\left[\frac{g(\rho_f - \rho_g)}{\sigma}\right]^{1/2} \tag{19.4-8}$$

For a given plate thickness (t), the Northwestern scaling approaches the following limits:

For $d_h \to 0$, it approaches the Wallis number,

$$H_k^* \to j_k^*, \quad k = g, f \tag{19.4-9}$$

For $d_h \to \infty$, on the other hand,

$$H_k^* \to K_k^*, \quad k = g, f \tag{19.4-10}$$

19.4.2 WCOBRA/TRAC-TF2 Model

For WCOBRA/TRAC-TF2 analyses of the test data, the test case with the 15-hole plate that approximates the typical dimensions in a PWR or LOFT fuel assembly top nozzle (tie plate) is selected. The 15-hole plate has the following dimensions:

d_h = 0.413 in
t_p = 0.787 in
A_T = 4.754 in^2
A_h = 2.013 in^2
$r = A_h / A_T$ = 0.4260

With these dimensions, the C in Equation (19.4-5) is calculated to be 1.9 and 2.0 using Equations (19.4-5b) and (19.4-5c) for the nitrogen/water and steam/water systems, respectively. The WCOBRA/TRAC-TF2 model used to predict the CCFL for the perforated plate is shown in Figure 19.4-1.

[

]^{a,c}

For the steam/water or nitrogen/water system, the computational experiment is performed in the following manner. [

]^{a,c}

[

]a,c

[ ] a,c

[

]a,c

19.4.3 WCOBRA/TRAC-TF2 Simulation

The predicted nitrogen/water system CCFL by WCOBRA/TRAC-TF2 is compared with the air/water test data in Figure 19.4-2, covering the range of liquid flow rate tested in the experiment. The nitrogen/water and air/water systems at the room temperature and pressure are considered to be comparable with regard to the concerns of the CCFL phenomena. The Northwestern flooding limit is also shown in the comparison in Figure 19.4-2 [

]a,c

Figures 19.4-3 and 19.4-4 show the predicted steam/water system flooding curve under the system [

]a,c

For a higher [

]a,c

a,c

Figure 19.4-1 Flooding Model for a Perforated Plate

a,c

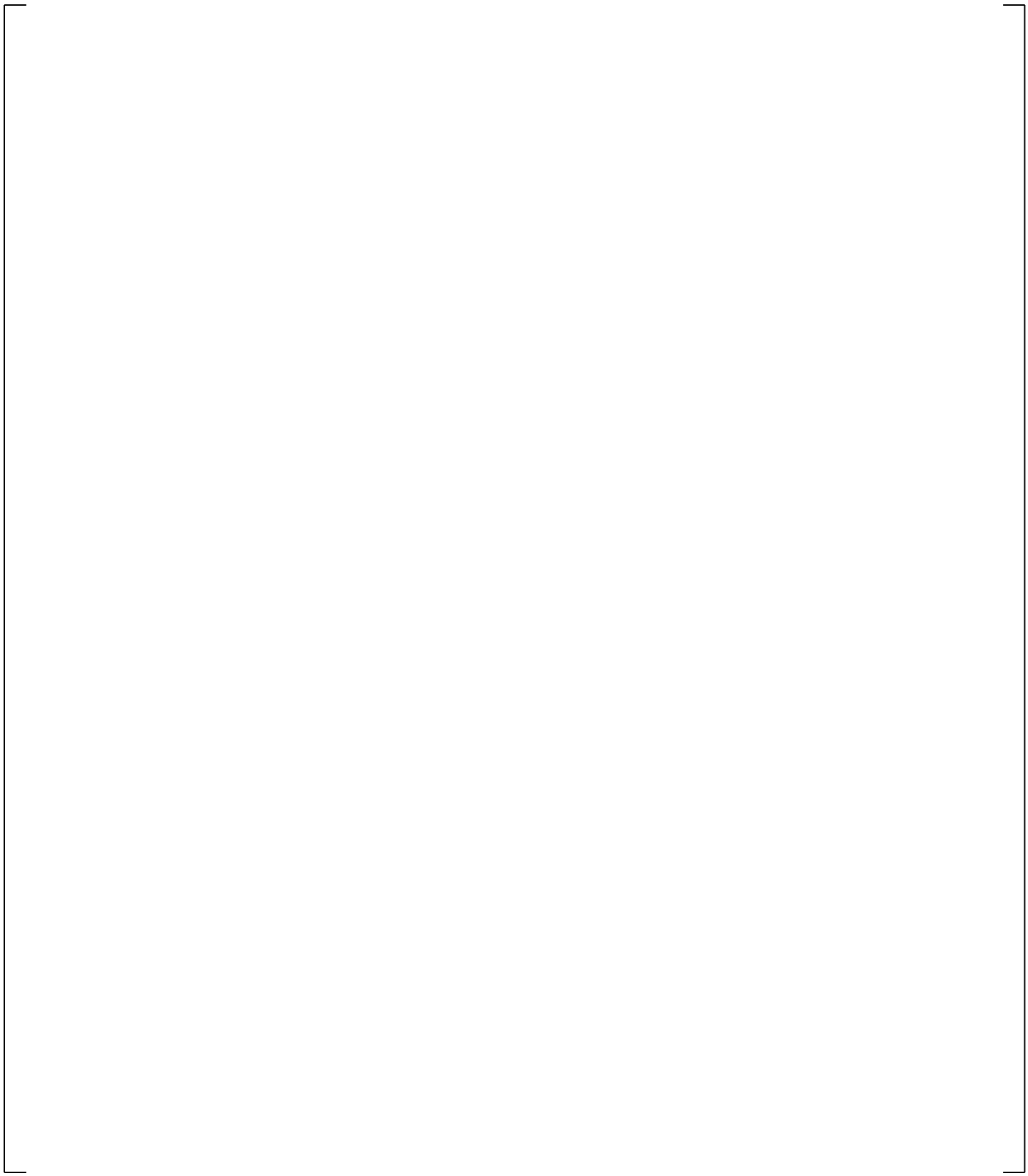

Figure 19.4-2 Flooding Velocities for the Nitrogen/Water System at [ ]^{a,c} Compared with the Air/Water Test (Hsieh et al., 1980) and Northwestern Flooding Limit

a,c

Figure 19.4-3 Flooding Velocities for Saturated Liquid and Vapor at [ ]^{a,c} Compared with Northwestern Flooding Limit (WCOBRA/TRAC-TF2)

a,c

Figure 19.4-4 Flooding Velocities for Saturated Liquid and Vapor at [ ]^{a,c} Compared with Northwestern Flooding Limit (WCOBRA/TRAC-TF2)

a,c

Figure 19.4-5 Liquid Mass Flow Rates through Perforated Plate at [ ]^{a,c} (WCOBRA/TRAC-TF2)

a,c

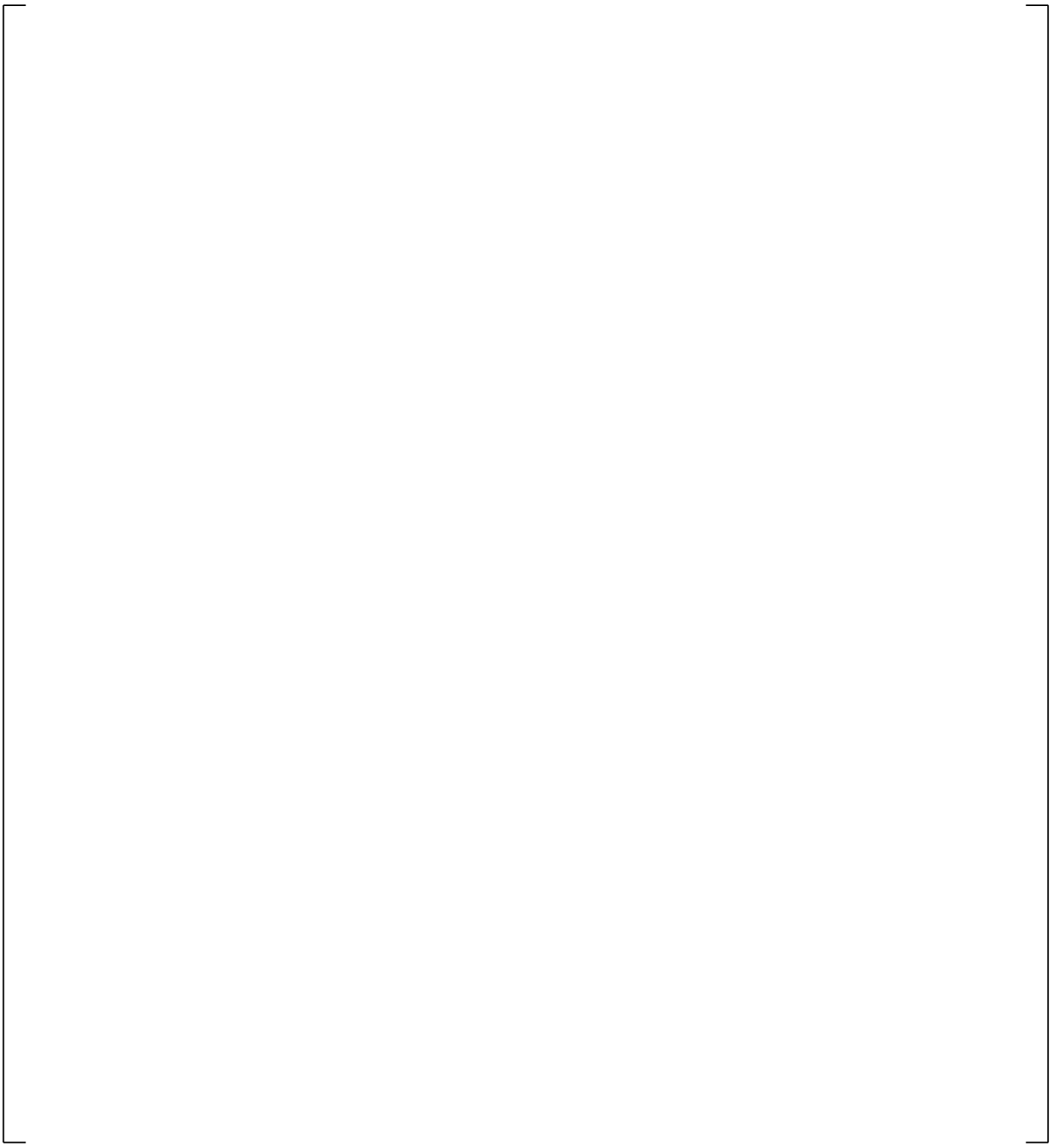

Figure 19.4-6 Vapor/Liquid Mass Flow Rates through Perforated Plate at [ ]^{a,c} (WCOBRA/TRAC-TF2)

a,c

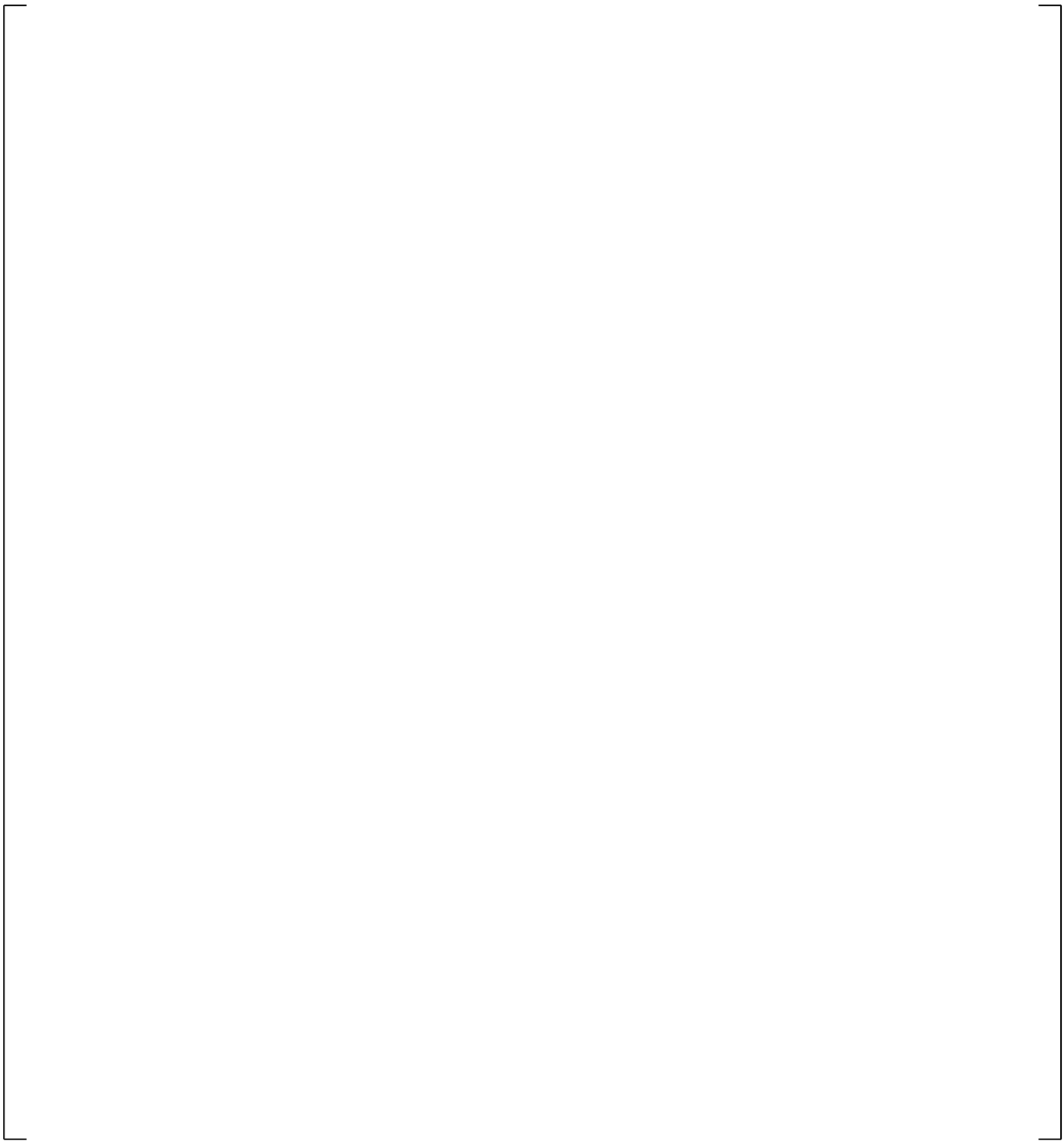

Figure 19.4-7 Liquid Mass Flow rates through Perforated Plate at [ ]^{a,c} (WCOBRA/TRAC-TF2)

a,c

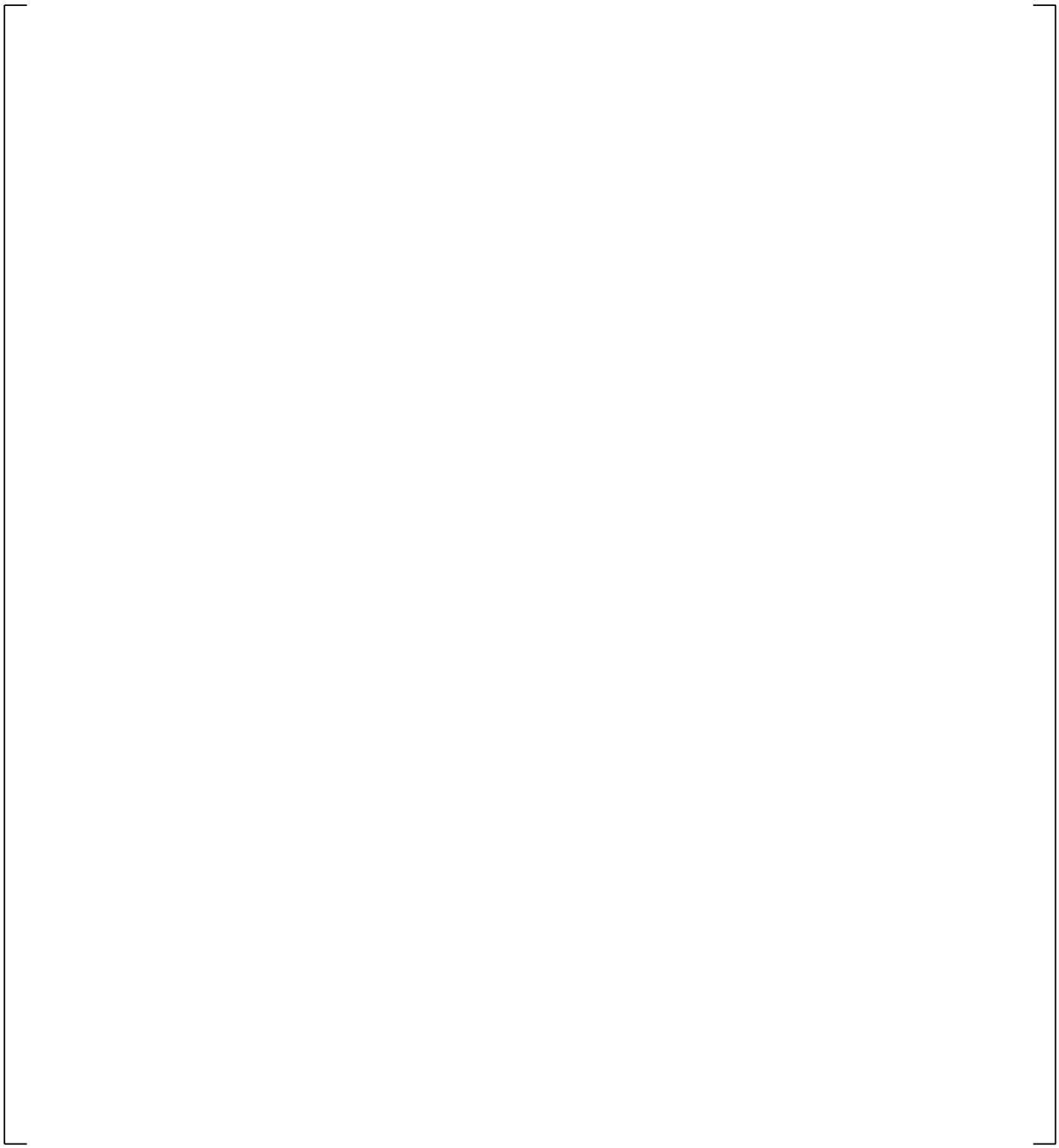

Figure 19.4-8 Vapor/Liquid Mass Flow rates through Perforated Plate at [ ]^{a,c} (WCOBRA/TRAC-TF2)

19.5 FULL-LENGTH EMERGENCY COOLING/CORE HEAT TRANSFER

The correlation used to determine the entrainment rate at a quench front is described in Section 5.6, Volume 1. The model is consistent with the work of (Kataoka and Ishii, 1983) and assumes the entrainment is due to vapor bubbling through a pool of liquid.

The reflood test simulations provide a means of examining the performance of the entrainment model for bottom reflood. Mass balances were calculated from the test data so that carryover fraction and mass retention in the test bundle could be estimated. This section compares the WCOBRA/TRAC-TF2 predictions of carryover fraction, total bundle mass, steam exit flow, and liquid outflow to estimates derived from the test data. The comparisons provide a means of assessing the bottom reflood entrainment model.

19.5.1 FLECHT Test Facility

First, it is important to describe the data collection methods used to estimate carryover which are not discussed in Section 14 for the FLECHT facility. Figure 19.5-1 shows a schematic of the FLECHT facility, identifying mass collection and flow rate measurements. These measurements were used to determine the mass inventory in the bundle, and the carryover fraction. Each of the FLECHT facilities, FLECHT Separate-Effects and System-Effects Tests (SEASET) (Loftus et al., 1981), FLECHT Low Flooding Rate (Rosal et al., 1975), and FLECHT Top Skewed Power (Rosal et al., 1977), used the same type of collection system. The difference between the facilities was the design of the test bundle itself, and in the number of differential pressure (DP) cells used in the test bundle.

Liquid was injected into the test bundle from an accumulator. The mass lost from this accumulator was reported in the test data and used as a check on the overall mass balance. Liquid leaving the accumulator was regulated, and the flow rate into the bundle was measured by a turbine meter. DP cells in the test bundle were used to estimate the bundle mass. The measurements were corrected for frictional effects.

The steam/droplet mixture leaving the heated bundle entered an upper plenum. In this plenum, the steam and most droplets were separated. The liquid went to a “Carryover Tank,” where the total mass and its rate of change were determined from a DP cell.

After leaving the upper plenum, the steam went through another separator to remove any remaining droplets. The liquid removed at this second removal point went into a “Steam Separator Tank” and was measured. In general, this amount of liquid was small compared to the mass retained in the Carryover Tank.

Finally steam, now assumed to be “dry,” was vented to the atmosphere through an exhaust orifice. The exhaust orifice provided the flow rate of steam from the facility. The data evaluation provided both the dry steam effluence rate, and the total mass of steam that exited the facility.

The instantaneous carryover fraction (CO) is defined as:

$$CO(t) = \frac{\dot{m}_{out}(t)}{\dot{m}_{inj}(t)} \tag{19.5-1}$$

where $\dot{m}_{out}(t)$ and $\dot{m}_{inj}(t)$ are the flow rate out of and into the bundle, respectively. Note that for forced injection reflood tests such as FLECHT-SEASET, the flow rate into the bundle is essentially constant.

The instrumentation in the facility allowed the carryover fraction to be determined in two different ways; from mass stored in the bundle and from mass flows exiting the bundle. The following forms were calculated:

1. From mass stored in the test bundle,

$$CO_1 = 1 - \frac{m_{TS}(t)}{\int \dot{m}_{inj}(t)\,dt} \tag{19.5-2}$$

2. From the (instantaneous) rate of storage in the test bundle,

$$CO_2 = 1 - \frac{\dot{m}_{TS}(t)}{\dot{m}_{inj}(t)} \tag{19.5-3}$$

3. From the total mass that exited the test section and was stored in the separator tanks or exited as dry steam,

$$CO_3 = \frac{m_{CO}(t) + m_{ss}(t) + \int \dot{m}_{steam}(t)\,dt}{\int \dot{m}_{inj}(t)\,dt} \tag{19.5-4}$$

4. From the rate of change of mass in the separator tanks and the exhaust orifice flow rate,

$$CO_4 = \frac{\dot{m}_{CO}(t) + \dot{m}_{ss}(t) + \dot{m}_{steam}(t)}{\dot{m}_{inj}(t)} \tag{19.5-5}$$

(Nomenclature is indicated in Figure 19.5-1.)

The carryover fractions CO_1 and CO_3 are essentially the instantaneous carryover fraction integrated over time period "t" and then averaged over that same time period (this is true for the FLECHT tests, since the tests are at a constant flooding rate), while CO_2 and CO_4 are based entirely on instantaneous measurements. Both instantaneous and averaged forms show the amount of carryover. **[**

][a,c]

The carryover fraction and bundle mass were calculated using WCOBRA/TRAC-TF2 predictions of several forced reflood tests. The carryover fraction for the WCOBRA/TRAC-TF2 results is based on the total integrated vapor mass flow (FGM), continuous liquid mass flow (FLM), and entrained liquid mass flow (FEM) entering and leaving the bundle. (Recall from Figures 15.6.1-2, 15.6.2-2 and 15.6.3-2, the channels representing the bundle are Channels 2 and 3, and there are a total of **[ ]**[a,c] cells in the channels of the bundle region.) Since subcooled liquid was injected for all the tests, the inlet mass flow is taken to be only the liquid mass flow. So, the WCOBRA/TRAC-TF2 predictions are calculated as:

[ ]a,c (19.5-6)

The carryover fraction thus calculated by Equation 19.5-6 is of integral form. The carryover fraction for the prediction CO_{WCT}, is equivalent to the CO_1 and CO_3 definitions in the data evaluation, since in the calculation there is no "lost mass" as there can be in the experiment due to measurement inaccuracy. This form for CO_{WCT} was chosen, because it provides a more clear comparison with the data. Instantaneous values are too oscillatory to provide a clear indication of the trends.

19.5.2 WCOBRA/TRAC-TF2 Simulation

The tests presented here are FLECHT-SEASET (Loftus et al., 1981) Tests 31805, 31701, and 31203; FLECHT Low Flooding Rate (Rosal et al., 1975) Tests 04641 and 05029; and, FLECHT Top Skewed (Rosal et al., 1977) Tests 15305, 13609, and 13812. Figures 19.5-2 through 19.5-9 show comparisons of predicted and measured carryover fraction. The most appropriate comparison to make in these figures is between the predicted carryover fraction and CO_1. **[**

][a,c]

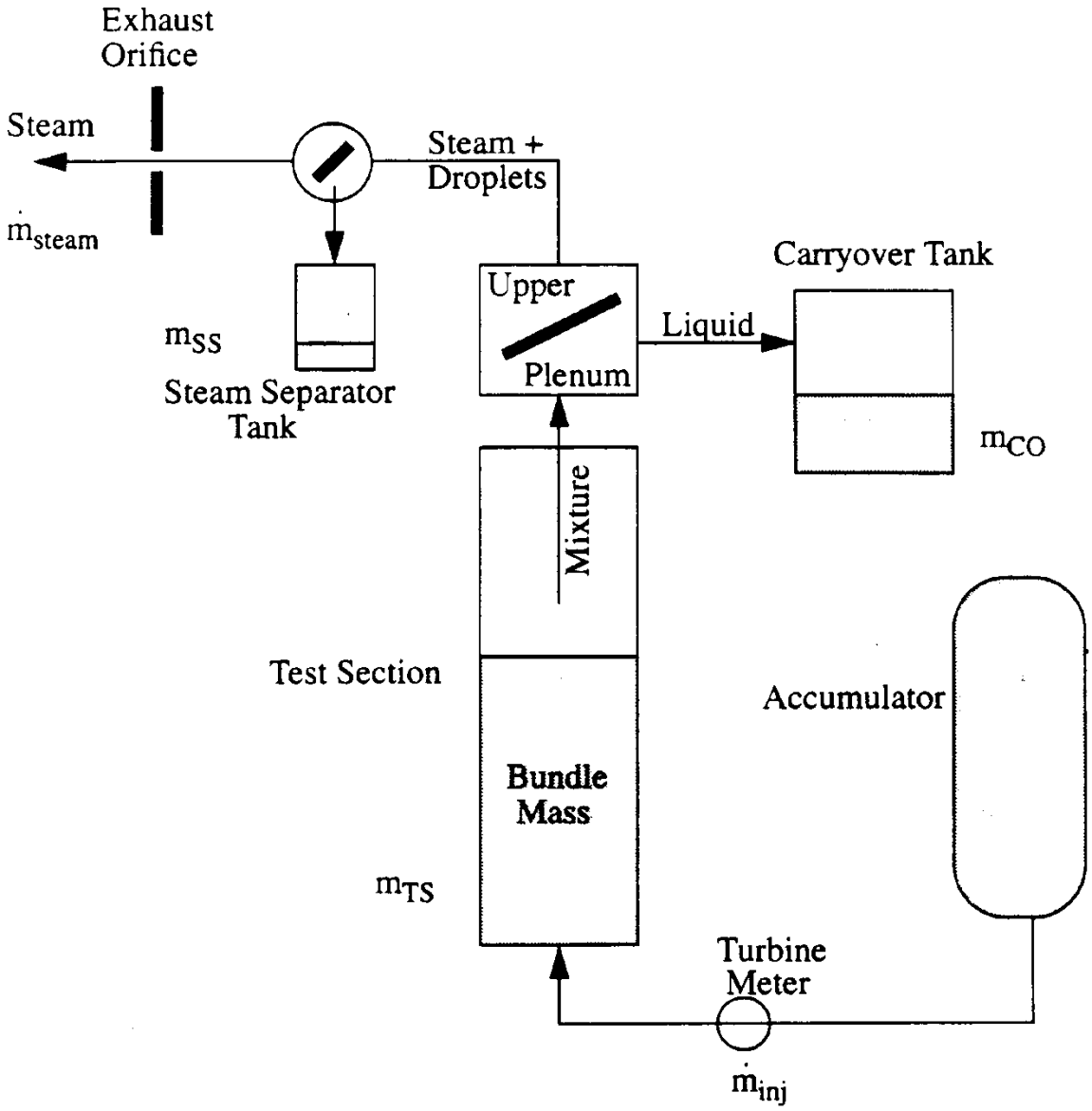

Figure 19.5-1 Mass Inventory Measurements in the FLECHT Facilities

a,c

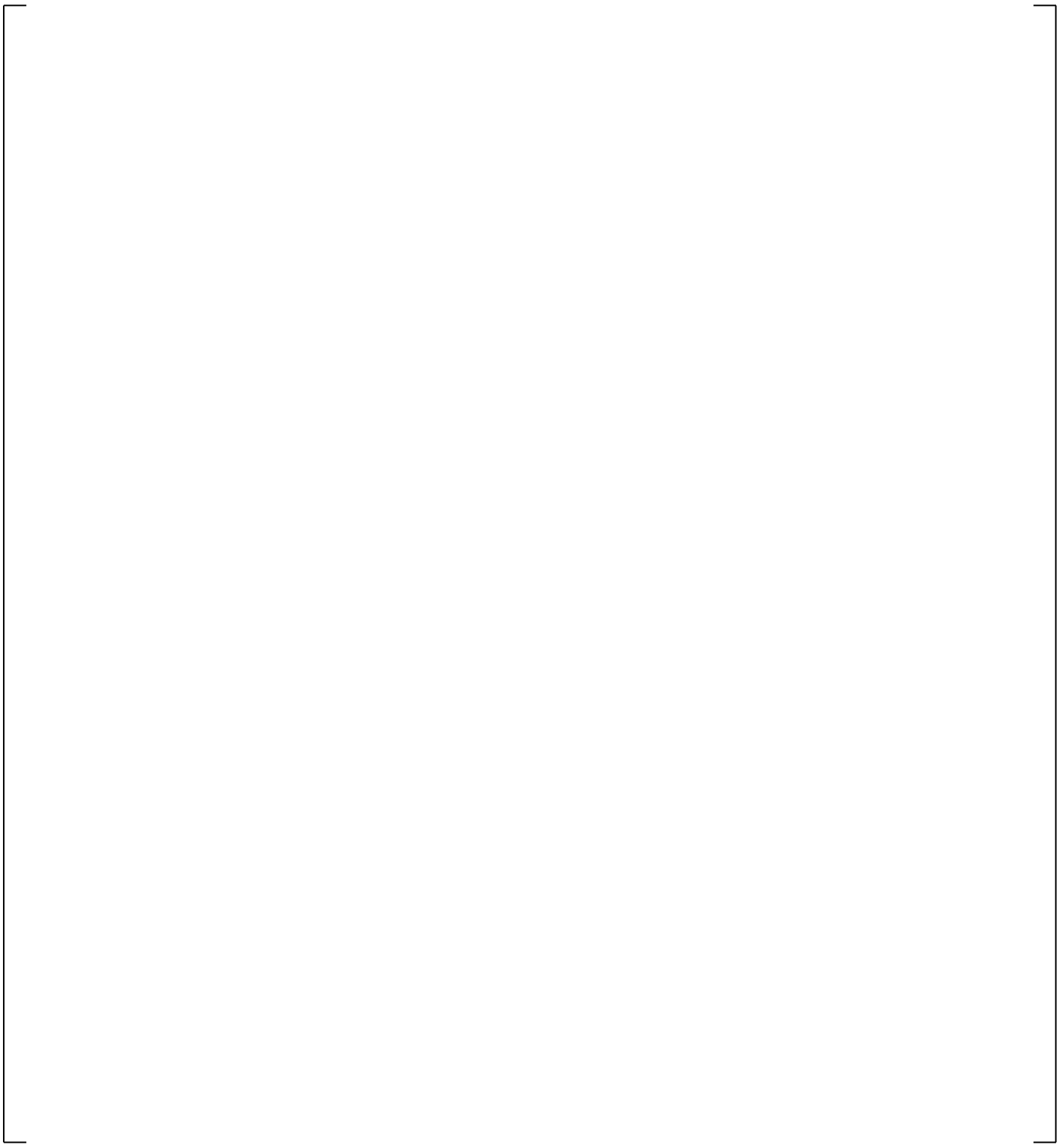

Figure 19.5-2 Predicted and Measured Carryover Fraction, FLECHT-SEASET Test 31805

a,c

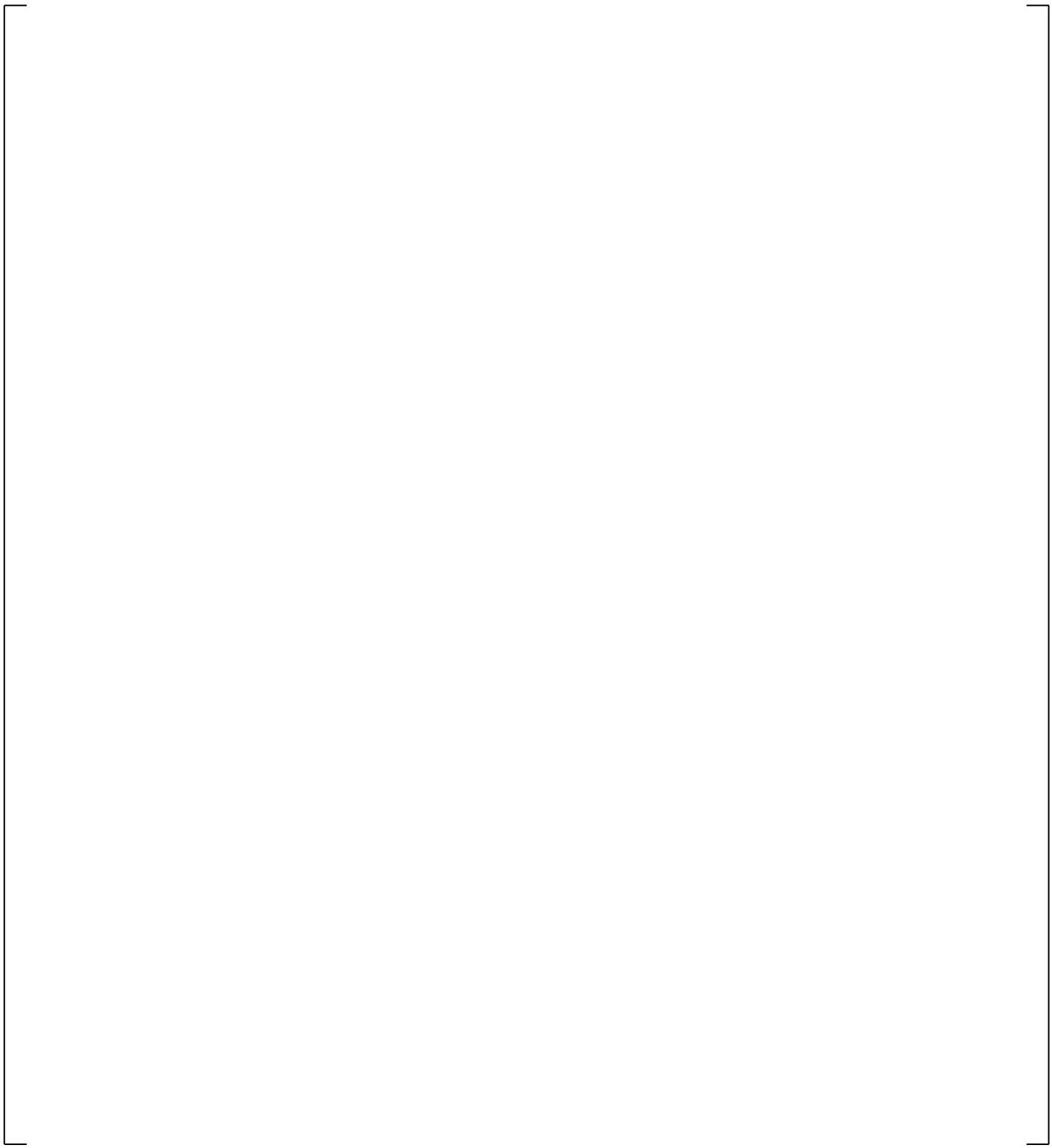

Figure 19.5-3 Predicted and Measured Carryover Fraction, FLECHT-SEASET Test 31701

a,c

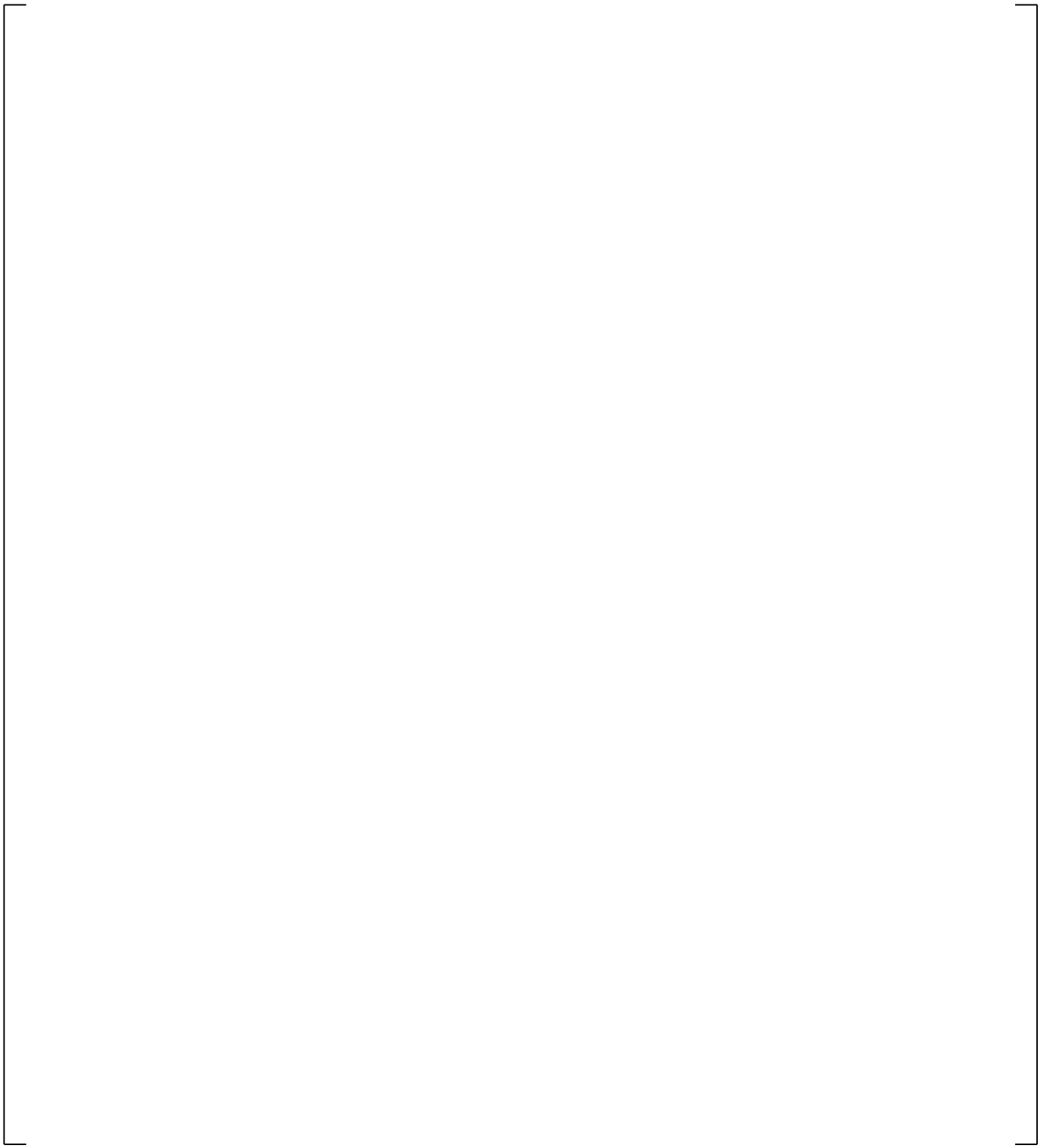

Figure 19.5-4 Predicted and Measured Carryover Fraction, FLECHT-SEASET Test 31203

a,c

Figure 19.5-5 Predicted and Measured Carryover Fraction, FLECHT Test 04641

a,c

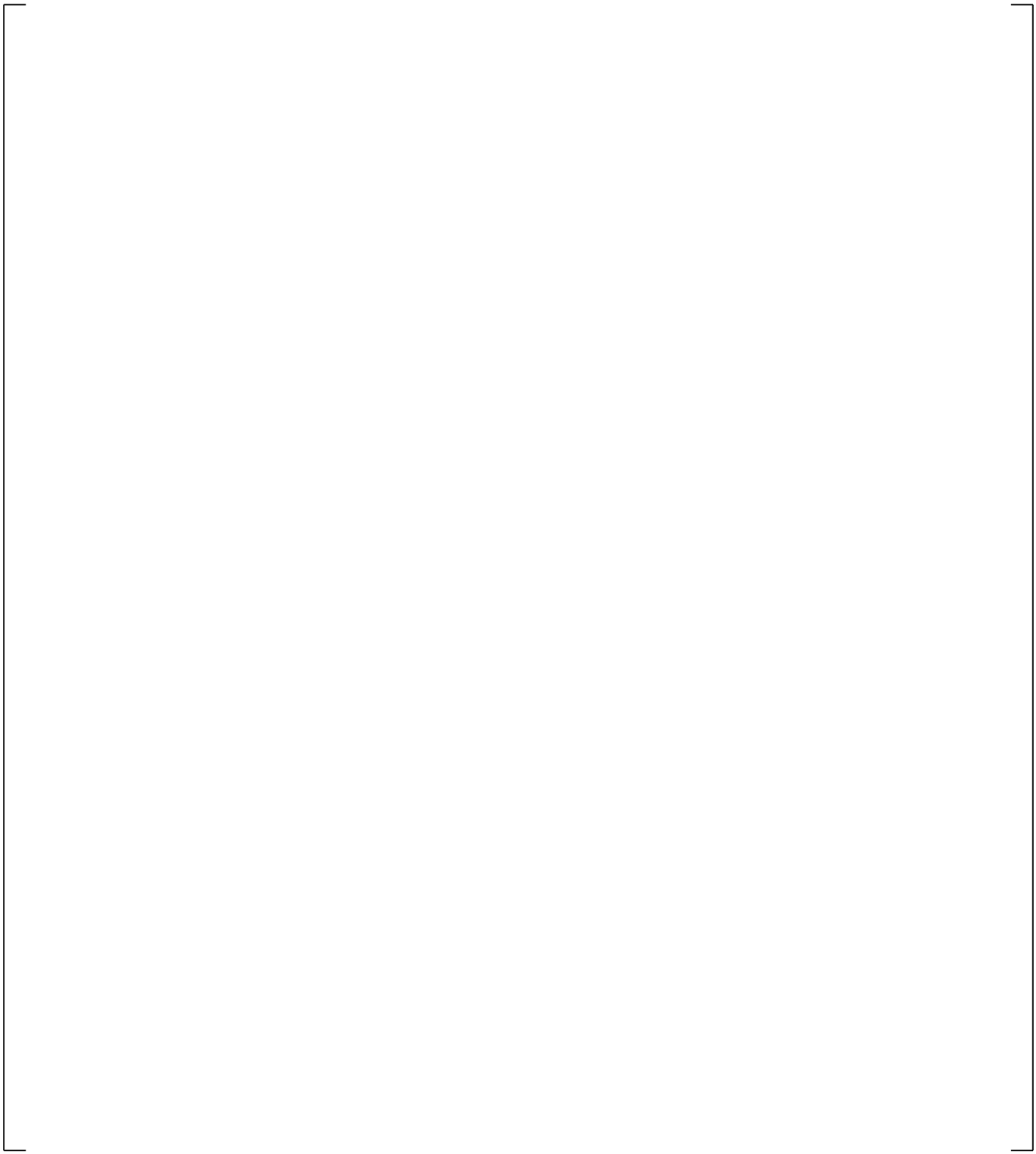

Figure 19.5-6 Predicted and Measured Carryover Fraction, FLECHT Test 05029

a,c

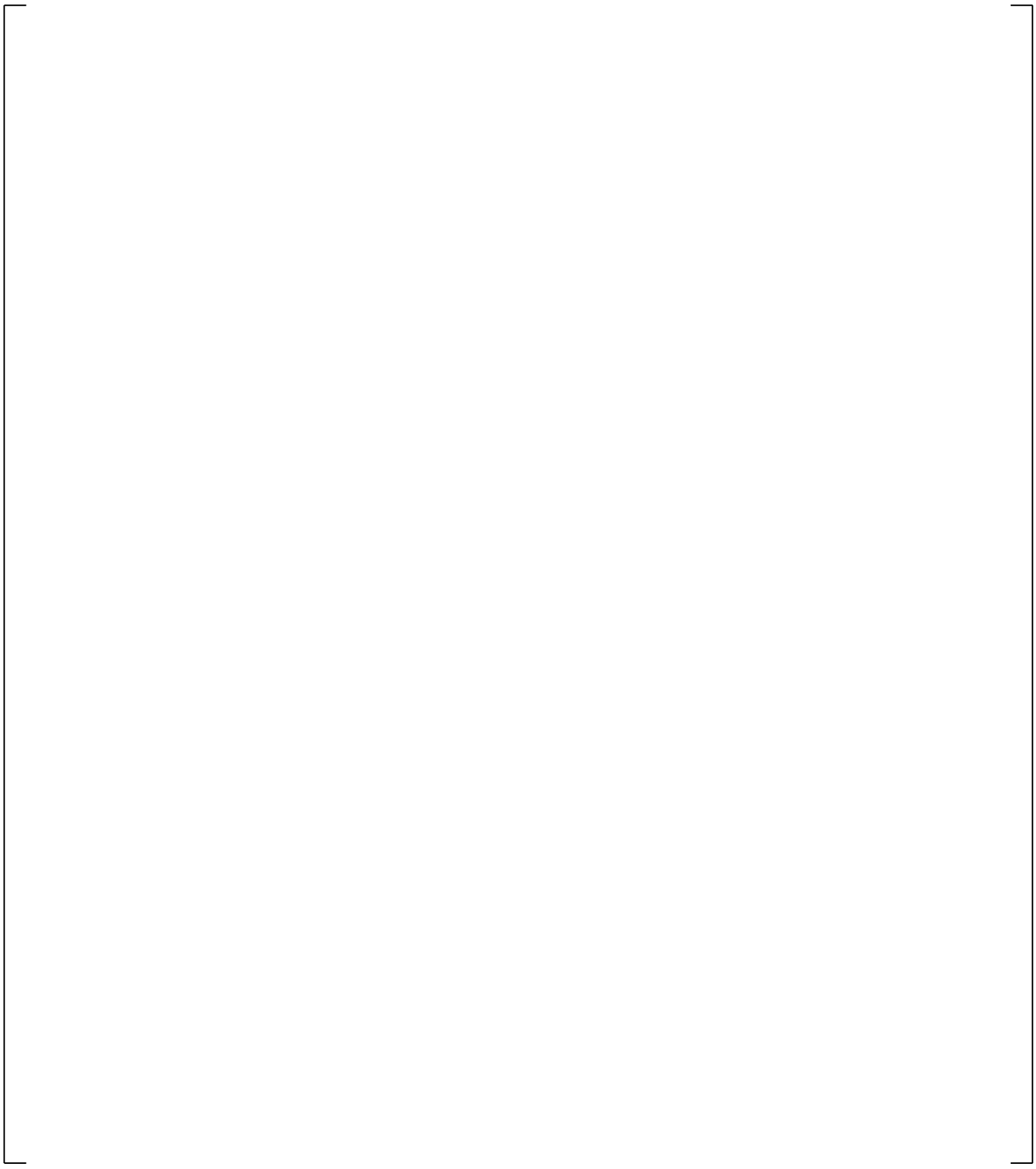

Figure 19.5-7 Predicted and Measured Carryover Fraction, FLECHT Top Skewed Test 15305

a,c

Figure 19.5-8 Predicted and Measured Carryover Fraction, FLECHT Top Skewed Test 13609

a,c

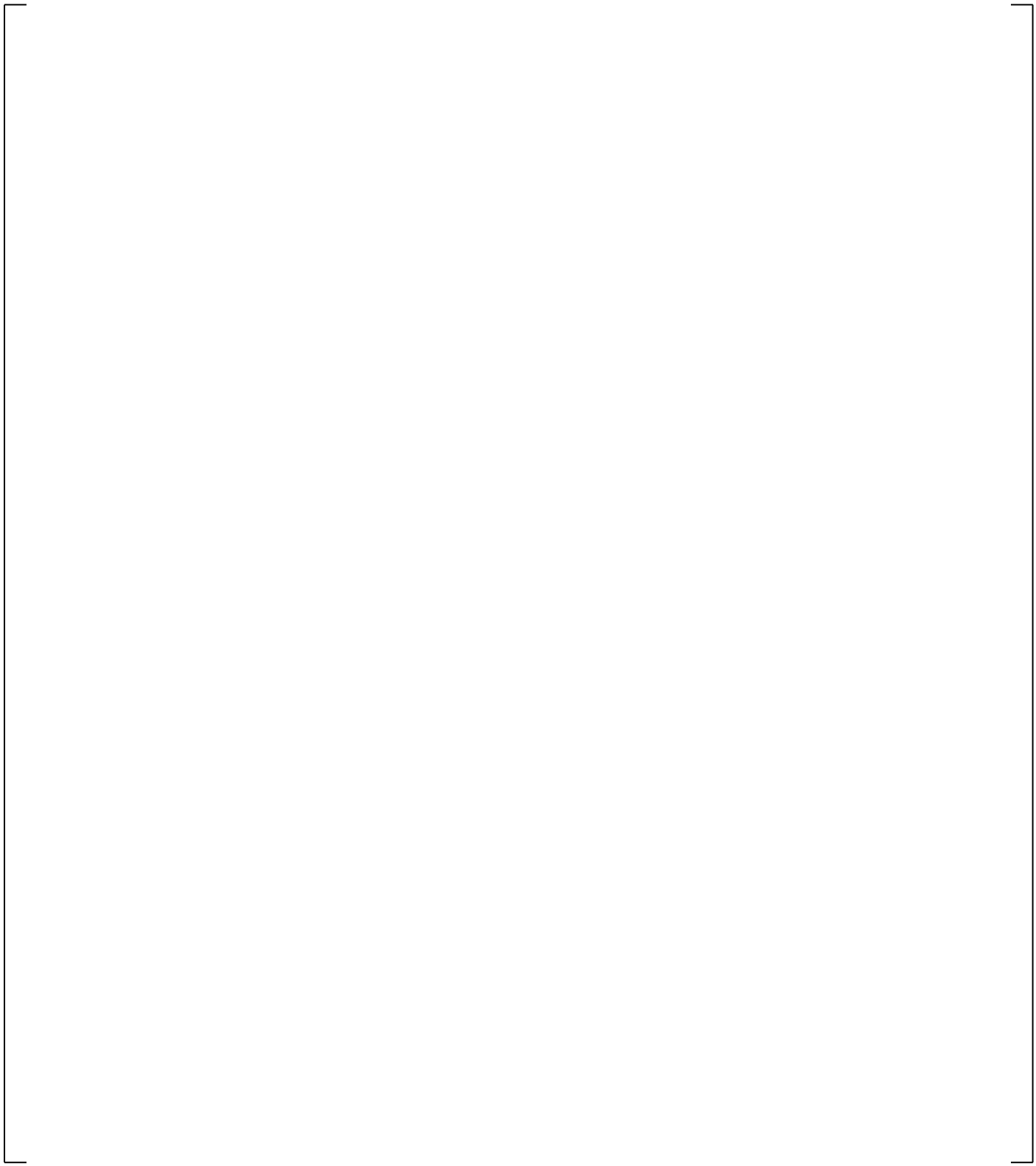

Figure 19.5-9 Predicted and Measured Carryover Fraction, FLECHT Top Skewed Test 13812

19.6 CYLINDRICAL CORE TEST FACILITY

To assess the capability of the WCOBRA/TRAC-TF2 computer code to predict the thermal-hydraulic core behavior in PWRs, specific code validation was performed using data from the Cylindrical Core Test Facility (Core II). The CCTF test program was conducted by JAERI and was used to investigate the thermal-hydraulic response of the plant during the refill and reflood phases associated with a postulated LBLOCA.

The objective of this section is to assess the ability of WCOBRA/TRAC-TF2 to predict the cladding temperature response, mass flows, and liquid distribution in CCTF. The important phenomena to be addressed by the CCTF 62 simulation are water accumulation in the upper plenum, the steam binding effect, and core quenching during gravity reflood. The facility and tests used for the prediction are summarized, the WCOBRA/TRAC-TF2 modeling is described in detail, and the predicted results are compared with data.

19.6.1 CCTF Tests

The CCTF tests are the largest scale integral tests available to investigate the phenomena important during the reflood phase of a PWR during a LBLOCA. CCTF has a flow area scaling of 1/21.4 of a four loop PWR. Their large scale makes them particularly suited as verification of the code's ability to handle the multi-dimensional thermal hydraulics in the core. In addition, the full-height scaling makes these tests important indicators on the extent to which core/downcomer oscillations affect the reflood transient.

The test chosen for simulation by WCOBRA/TRAC-TF2 is C2-4 (Run 62). Run 62 (Okubo et al., 1984) was taken as the reference test in the Code Qualification Document (Bajorek et al., 1998) CCTF Simulations; while other CCTF tests were examined in the CQD (63, 64, 67 and 75, as documented in Section 14-2-6-2 of the CQD), only this reference test is analyzed in detail herein.

The initial and boundary conditions for this test are given in Table 19.6-2. They are compared, where appropriate, with the range of conditions expected in a typical four-loop PWR at the beginning of reflood (scaled to CCTF).

19.6.2 CCTF Facility Description

The CCTF Core-II is a large scale experimental facility designed to study the system response of a typical four-loop PWR for loss-of-coolant transients (Figure 19.6-1). The facility is used to provide data on the thermal-hydraulic behavior in the primary system during the refill and reflood phases of a hypothetical LOCA in a PWR. Table 19.6-1 compares the scaled dimensions of the system components with those of a PWR.

The CCTF includes a full-height (12-foot heated length) core section with three intact loops, and a fourth loop simulating a full double-ended guillotine break. The test vessel includes a downcomer, lower plenum, core region, and upper plenum with associated internals (support columns and guide tubes). The dimensions for the vessel are shown in Figure 19.6-2. The configuration of the rods in the core and the upper plenum structure are shown in Figure 19.6-3. The core has 32 8x8 rod bundles each containing

57 electrically heated rods (0.421-inch OD) and 7 unheated/instrumented rods (0.543-inch OD). The rods have a pitch spacing of 0.563 inches. The geometry of these rods is equivalent to a typical PWR 15x15 fuel assembly. Each heated rod has a nichrome heating element and is packed with magnesium oxide and boron nitride. The sheath is made of Inconel-600. The rods are held together by six grids spaced at 26.18-inch intervals up the bundle.

The core is divided into the three main power zones: low, intermediate, and high. The lower power zone consists of 16 assemblies on the periphery of the core, as shown in Figure 19.6-3. The intermediate power zone consists of 12 assemblies, while the high power zone consists of the 4 central assemblies. Under guide tubes, there are 4 low power assemblies and 6 medium power assemblies. Under support columns, there are 8 low power assemblies and 2 high power assemblies. Under open holes, there are 4 low power assemblies, 6 medium power assemblies, and 2 high power assemblies. The axial power profile, along with the locations at the grid spacers, is shown in Figure 19.6-4.

The three intact loops and the broken loop each contain a steam generator and pump simulator. Flow from the broken loop enters two interconnected containment tanks via two blowdown valves, connected to each break. ECC water can be injected either from two accumulator tanks or by a low pressure coolant injection (LPCI) pump and its associated water storage tank. Water can be injected directly to injection ports positioned in the lower plenum or to the cold legs.

19.6.3 CCTF Test Procedure

The following is a general outline of the experimental test procedure. Figure 19.6-5 shows the sequence of events for the CCTF 62 test. The initial and boundary conditions for this test are given in Table 19.6-2. They are compared, where appropriate, with the range of conditions expected in a typical four-loop PWR at the beginning of reflood (scaled to CCTF).

The primary system was heated with pre-heaters to its specified temperatures and pressurized to a specified pressure using steam. The water in the LPCI tanks and accumulator tanks was heated to its specified temperature. LPCI water was circulated to ensure that the injection lines were at the same temperature. The accumulator tanks were pressurized with nitrogen to give sufficient head for the required injection flow. The steam generator secondary fluid was then heated and pressurized. The heaters were then turned off and the lower plenum was filled to the specified level with saturated water. When the initial conditions had been established, power was applied to the heater rods and data recording started (referred to as time zero.) The heater rods heated up under near adiabatic conditions until the cladding temperature reached a pre-specified value.

At this point accumulator injection to the lower plenum began. The containment tank pressure was maintained throughout the tests by controlling the outlet valve on the containment tanks. The heater rod power decay was initiated when the water reached the bottom of the heated length of the core (referred to as the BOCREC time). The water injection was changed from the lower plenum to the cold legs after a specified time. When the accumulator flow was coming to an end, LPCI flow was introduced to the cold legs and was maintained until the end of the test.

The generated steam and the entrained water flowed via broken and intact loops to the containment tanks. The steam was then vented to the atmosphere to maintain a constant pressure in the containment tanks. After all thermocouples on the surface of the heater rods indicated quench, the power supply to the heater rods and the ECC water injection were turned off. The recording system was then stopped, terminating the test.

19.6.4 WCOBRA/TRAC-TF2 CCTF Model

The WCOBRA/TRAC-TF2 model used for the CCTF simulations uses one-dimensional components for the intact loops (which models three CCTF loops) and for the broken loop, and employs a sub-channel formulated mesh for the vessel. First, the vessel component model is described. This is followed by a description of the loop model.

[

]^{a,c}

19.6.4.1 Vessel Component Model

The vessel component model is developed following the noding strategy in Section 26.1.1, Volume 3. A comparison between the CCTF and the PWR noding as presented in the FSLOCA methodology application is summarized in Table 19.6-3.

[

]^{a,c}

[

]^{a,c}

[

]^{a,c}

19.6.4.2 Loop Component Model

[

]^{a,c}

[

]a,c

19.6.5 CCTF Run 62 Transient Calculation

In the following sections, the WCOBRA/TRAC-TF2 predictions are examined. Predicted cladding temperatures are compared with data averages of all instrumented rods within the channel (excluding obviously bad data channels). Predicted vapor fractions are compared with vapor fractions estimated from differential pressure (delta-p) measurements. In the core, the delta-p between several one-foot spans is available. Collapsed water levels and masses in various components are also estimated from the delta-p measurements. In CCTF, the liquid and vapor mass flows in the loops were measured at instrument spool pieces containing turbine meters and drag discs. The locations of these measurements in the system are shown in Figure 19.6-1.

The discussion provided here is intended to assess key variables and identify important differences between the predictions and the data. This run has the nominal test conditions which are summarized in Table 19.6-2. It is noted the simulation of CCTF 62 starts from BOCREC (bottom of core recovery) which is 94s after the test initialized, and the comparisons in this section are based on time of BOCREC.

In general, peak cladding temperatures (PCTs) and quench times in the CCTF tests tend to be [ ]a,c (Figures 19.6-20 to 19.6-22 and Table 19.6-5). [

]a,c

There are two thermal couples at 6 ft. **[**

][a,c]

The core collapsed liquid level is shown in Figure 19.6-24. **[**

][a,c]

Figures 19.6-31 to 19.6-33 compare the predicted steam temperature rise and the measured temperature rise across the steam generators in 3 intact loops. **[**

][a,c]

Figures 19.6-34 and 19.6-35 compare the predicted and the measured total flow rates in the intact and broken hot legs. **[**

][a,c]

The integrated core inlet mass flow rates are shown in Figure 19.6-36. **[**

][a,c]

For the CCTF Test C2-4 Run 62 simulation, the WCOBRA/TRAC-TF2 calculated clad temperature is **[** **]**[a,c] the experimental data considering the same elevations.

The results from the CCTF 62 test show the code giving reasonable prediction of the various phenomena involved. **[**

][a,c]

19.6.6 DTMAX Sensitivity Study for CCTF 62

To support the time step sensitivity study in Section 28.1.3, Volume 3, the sensitivity studies for DTMAX are carried out for the CCTF 62 test. **[**

][a,c]

Those time step sizes are consistent with those used in the plant model in Section 26, Volume 3. In this sensitivity study, the relative **[** **]**[a,c] time step sizes are chosen to show the effect of time step sensitivity. For the initial surge stage, the time step size is increased from **[** **]**[a,c], while **[** **]**[a,c] are used for the remaining reflood period.

Figures 19.6.37 to 19.6.39 compare the predicted cladding temperatures at elevations of 6.0 ft, 8.0 ft, and 10.0 ft, respectively. **[**

][a,c]

In general, the time step sensitivity study shows the time step size effect is **[** **]**[a,c] for the CCTF 62 simulation, which covers the initial surge of the reflood period of a LBLOCA.

Table 19.6-1 [ ][a,c]

a,c

Table 19.6-2 [ ][a,c]

Run							

a,c

Table 19.6-3 [ ][a,c]

a,c

Table 19.6-4 [ ]a,c

a,c

Table 19.6-5 [ ]a,c

a,c

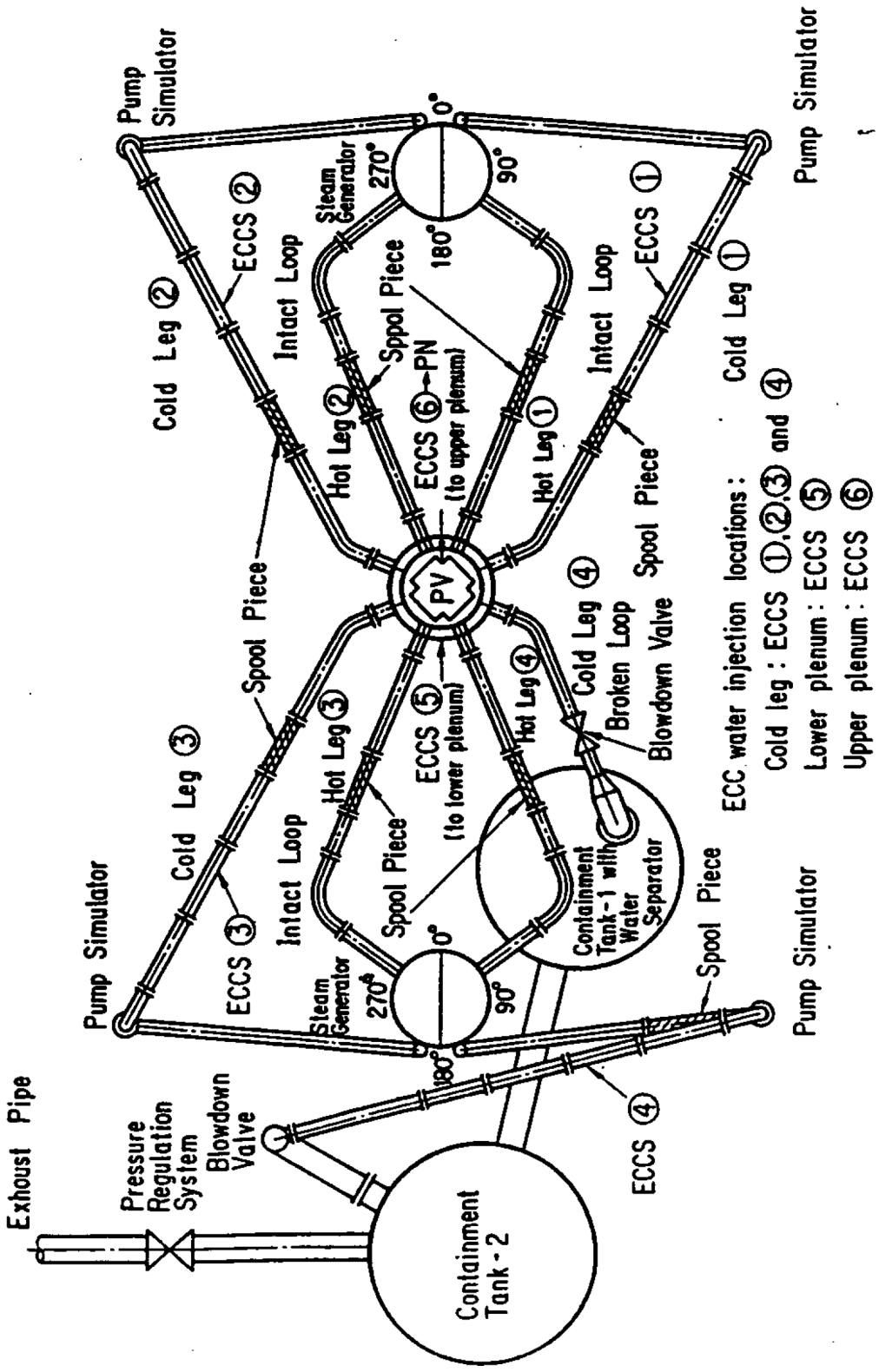

Figure 19.6-1 Top View of Primary Loop Piping

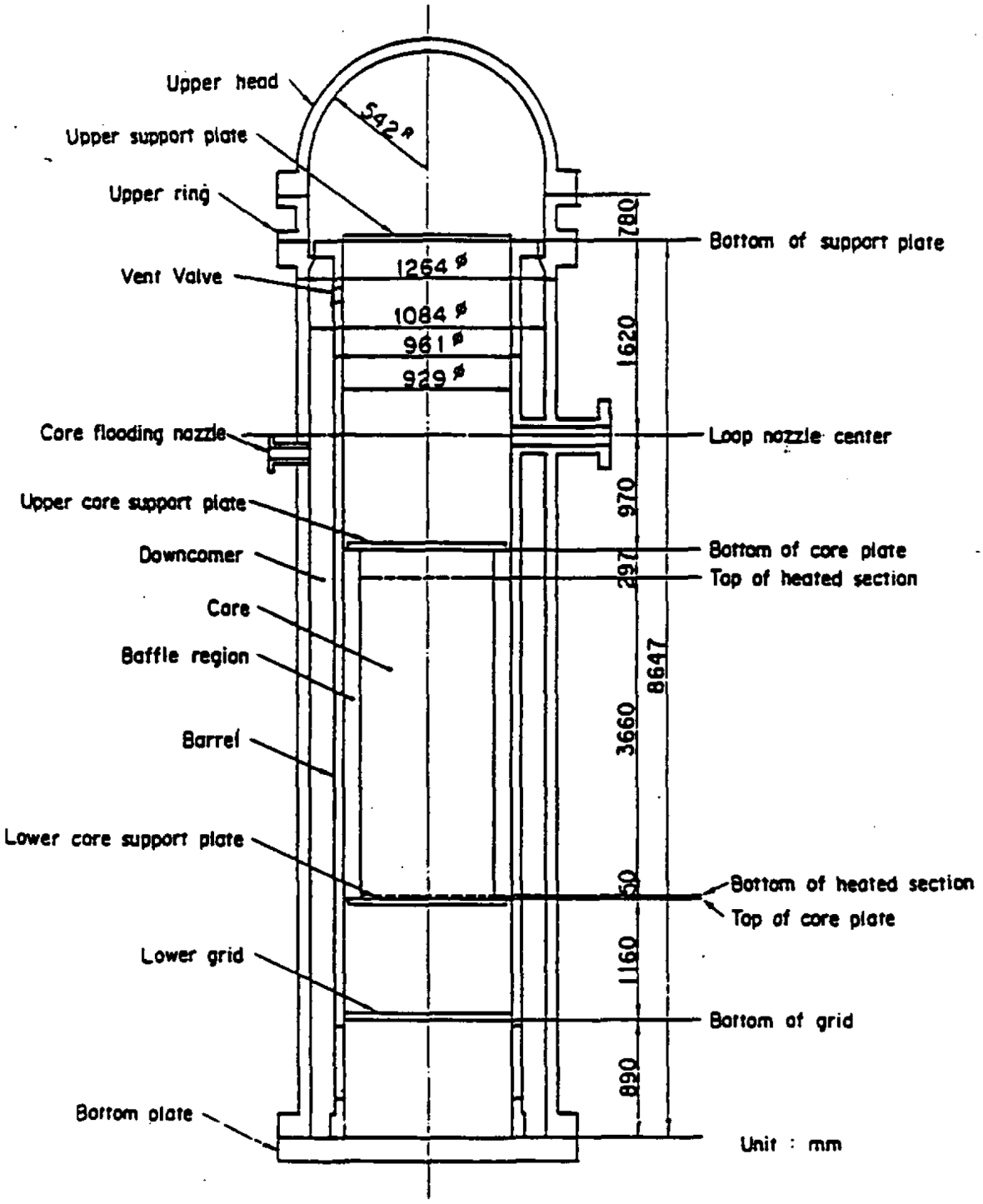

Figure 19.6-2 Diagram of CCTF Pressure Vessel

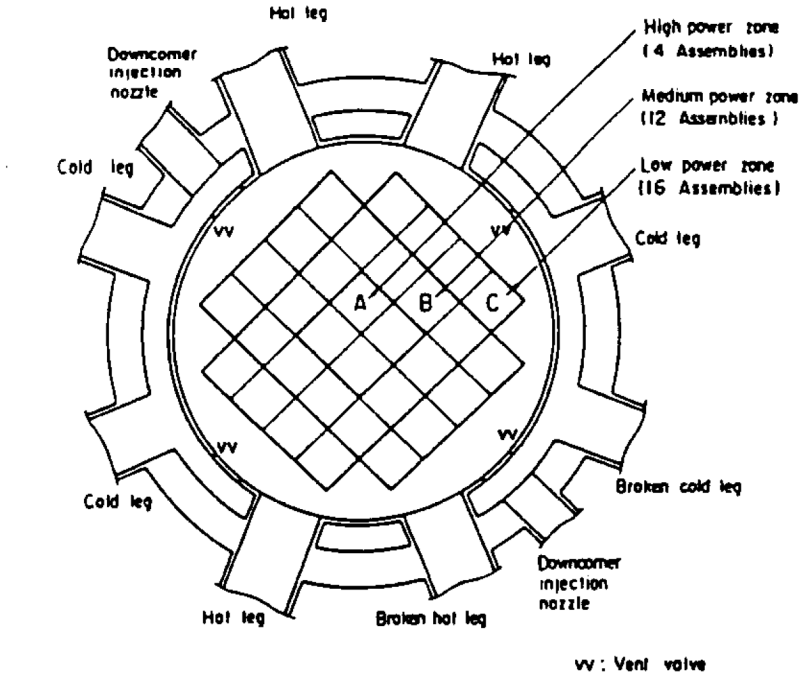

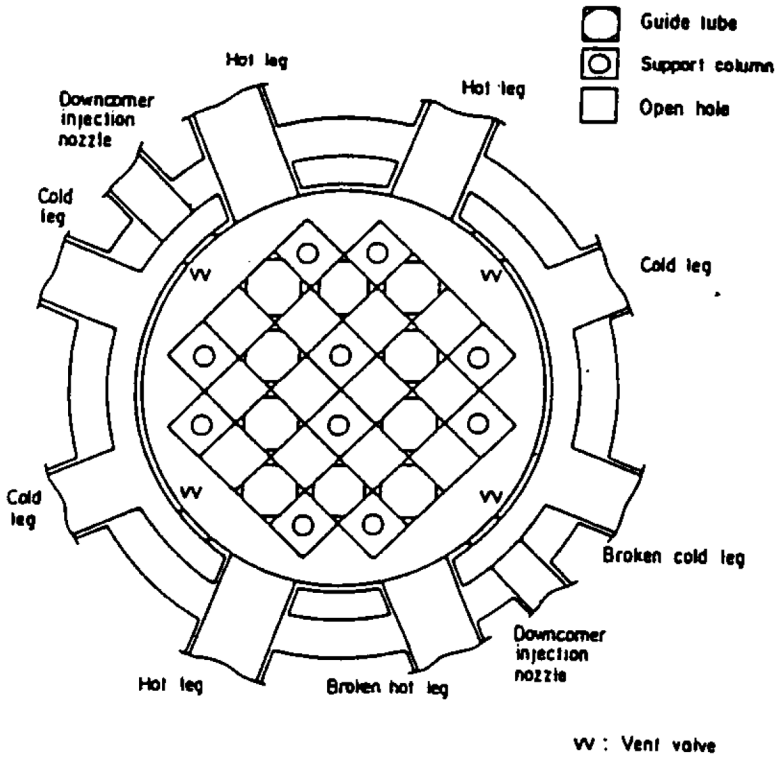

Figure 19.6-3 CCTF Cross Sections (a) Pressure Vessel (b) Upper Plenum Internals

e

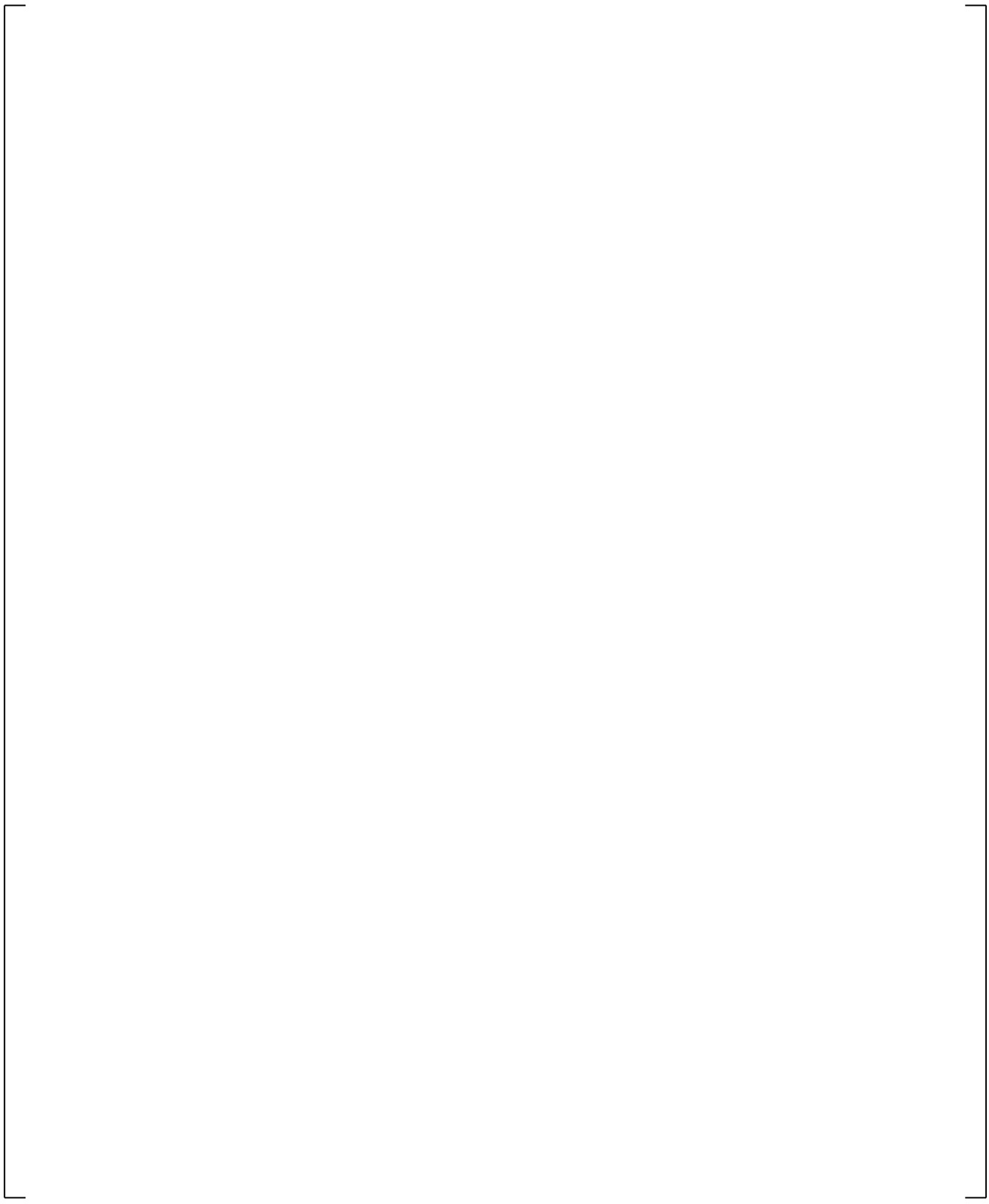

Figure 19.6-4 Axial Power Profile of Heated Rods in CCTF

e

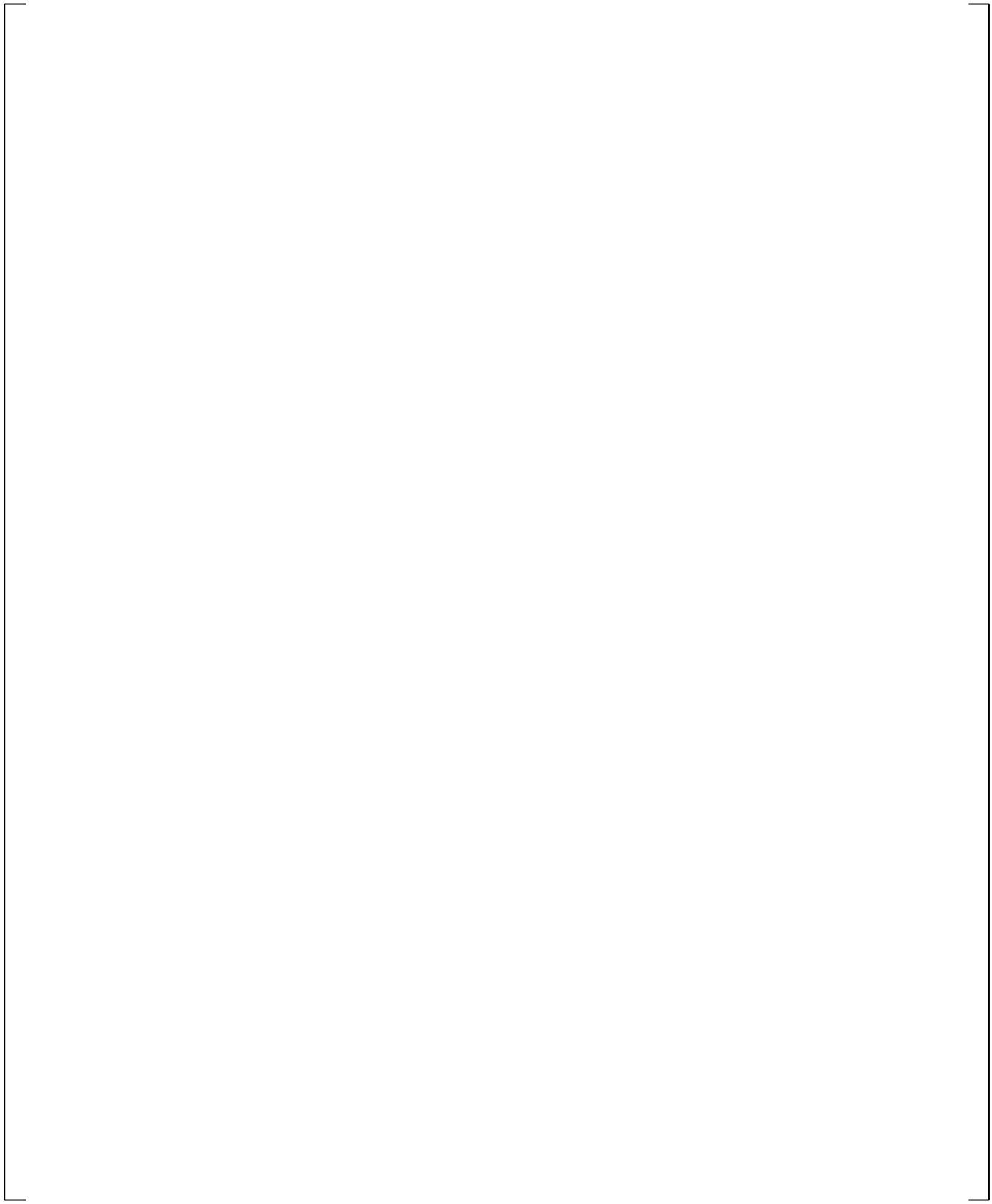

Figure 19.6-5 CCTF Test Sequence for Run 62

a,c

Figure 19.6-6 CCTF Vessel Noding Diagram

a,c

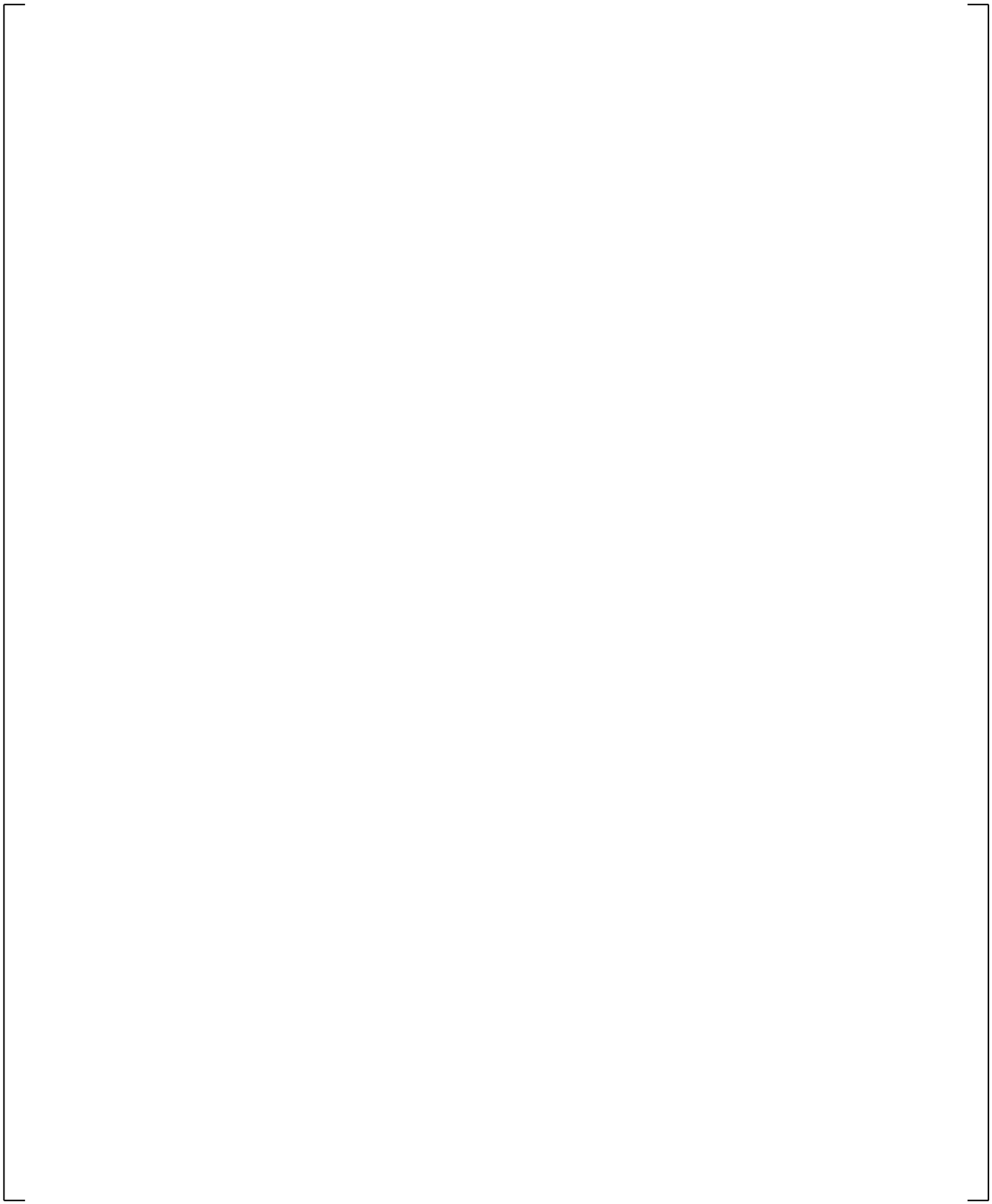

Figure 19.6-7 CCTF Section 1 Noding

a,c

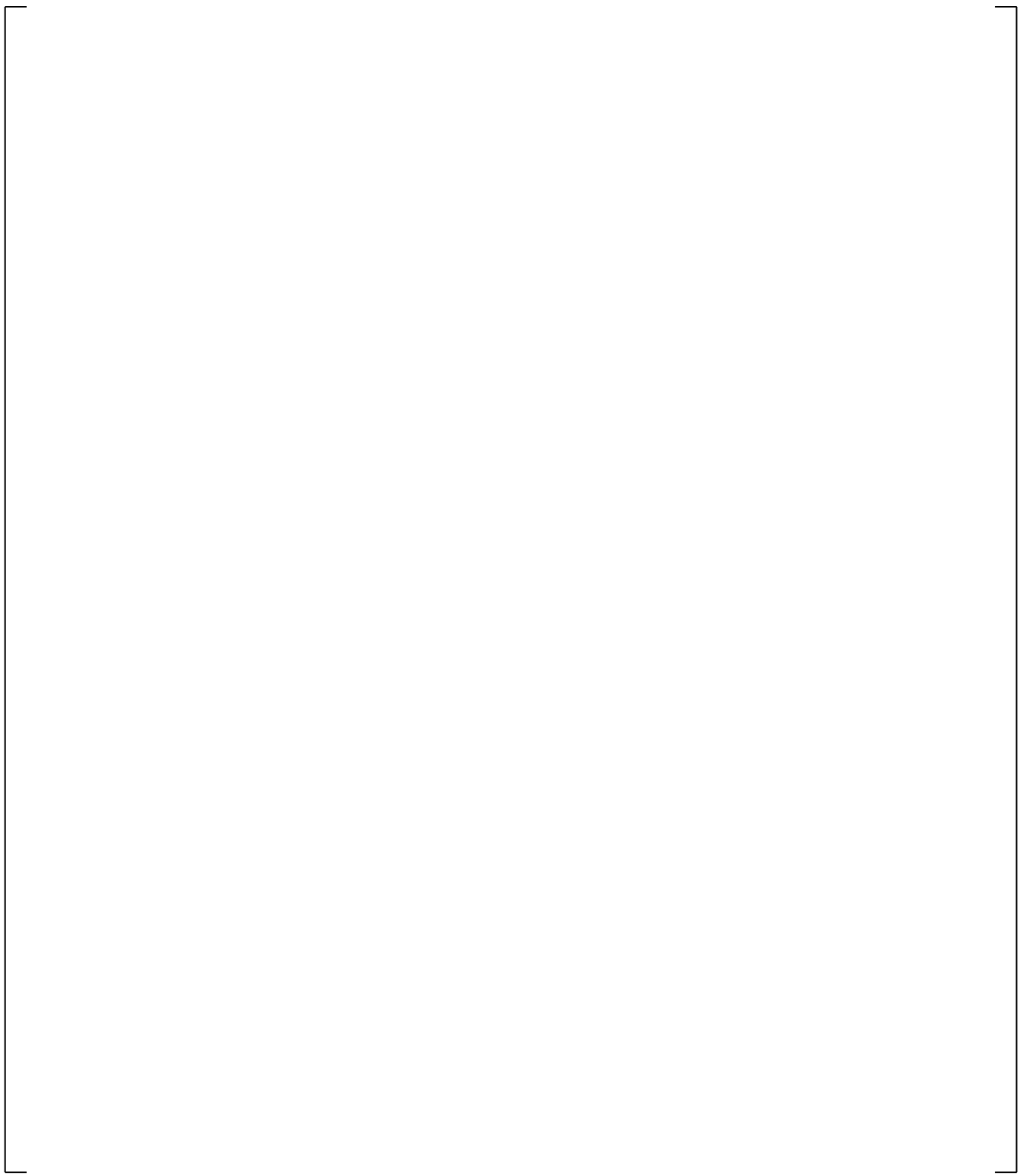

Figure 19.6-8 CCTF Section 2 Noding

a,c

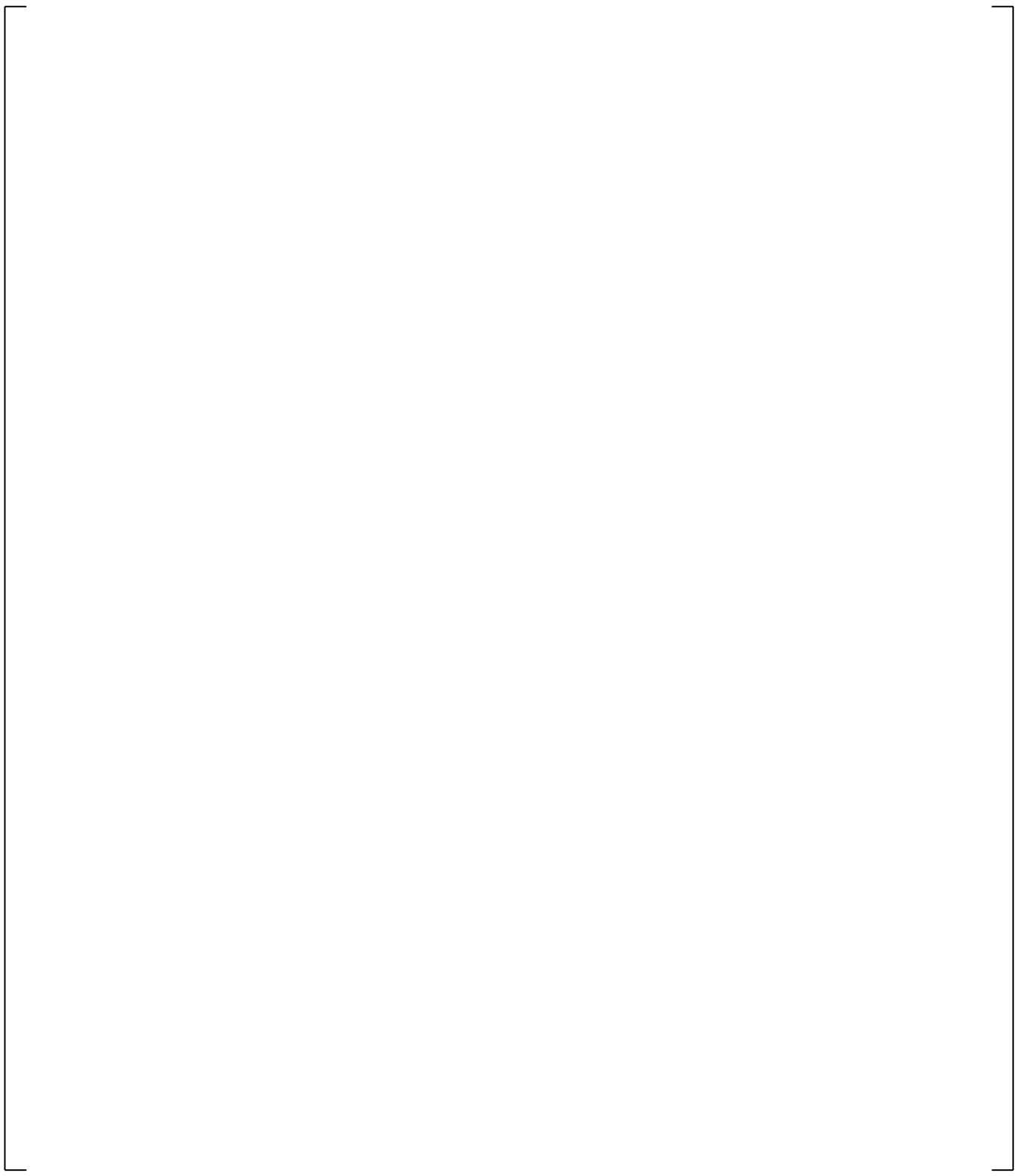

Figure 19.6-9 CCTF Section 3 Noding

a,c

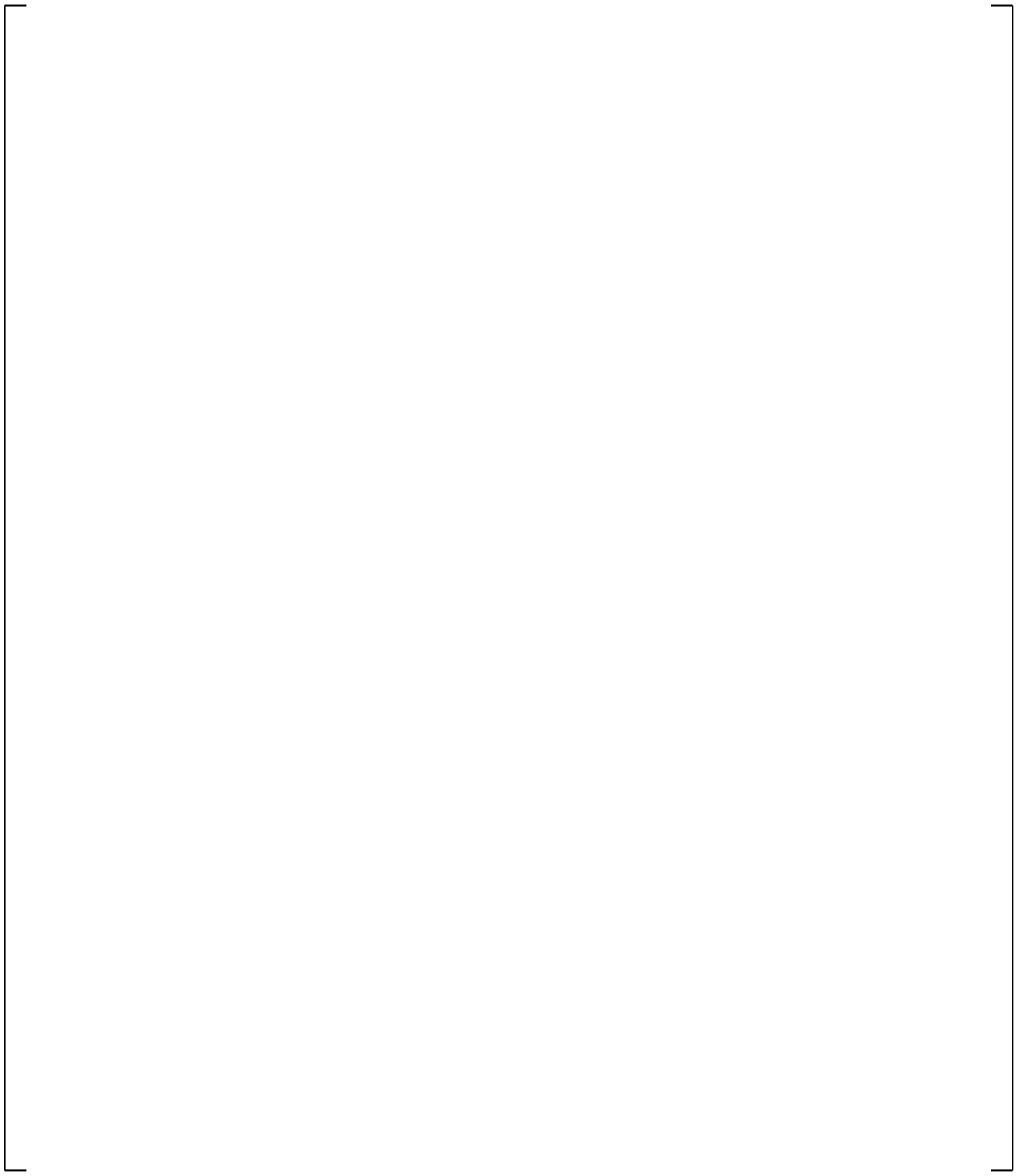

Figure 19.6-10 CCTF Section 4 Noding

a,c

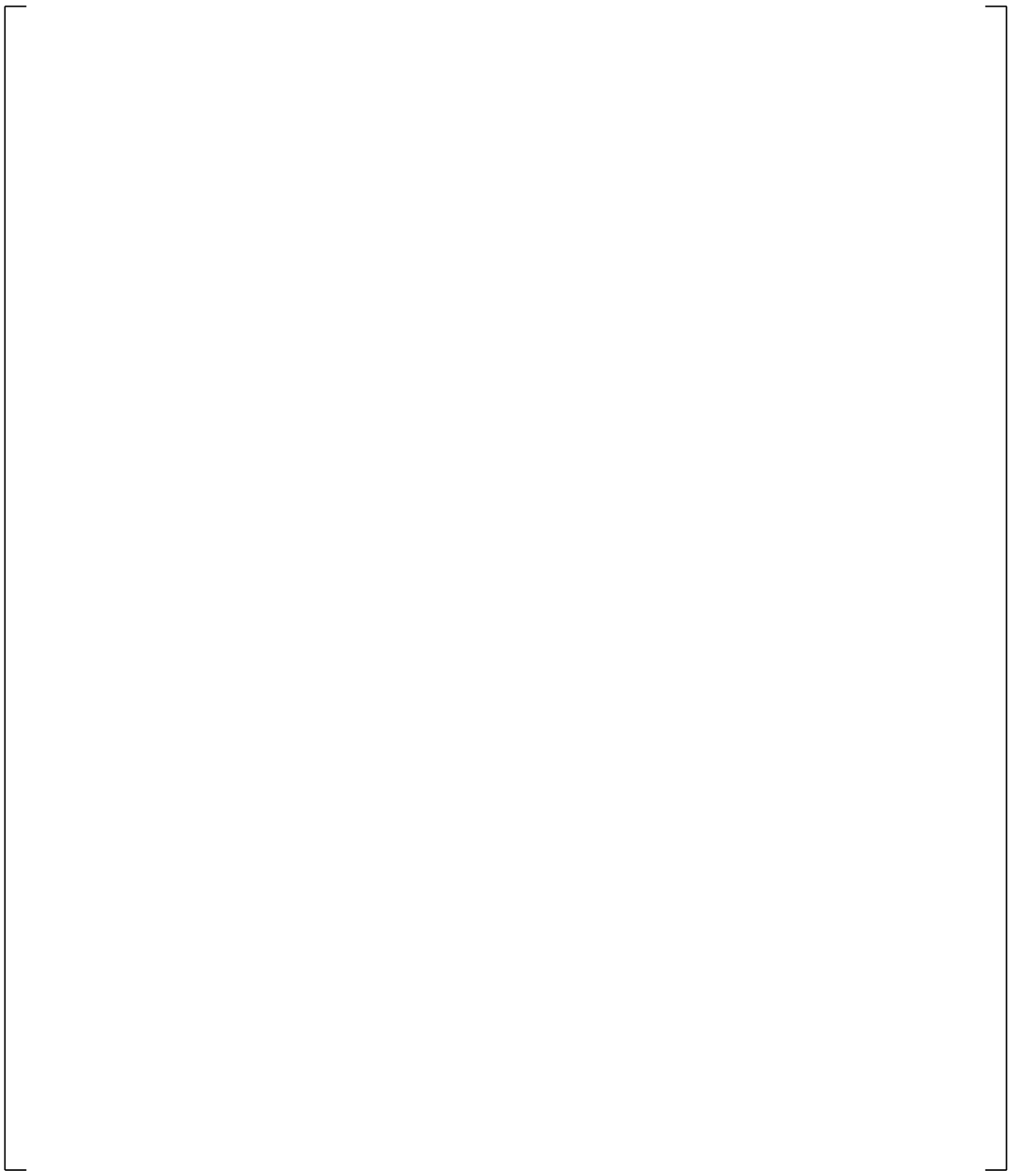

Figure 19.6-11 CCTF Section 5 Noding

a,c

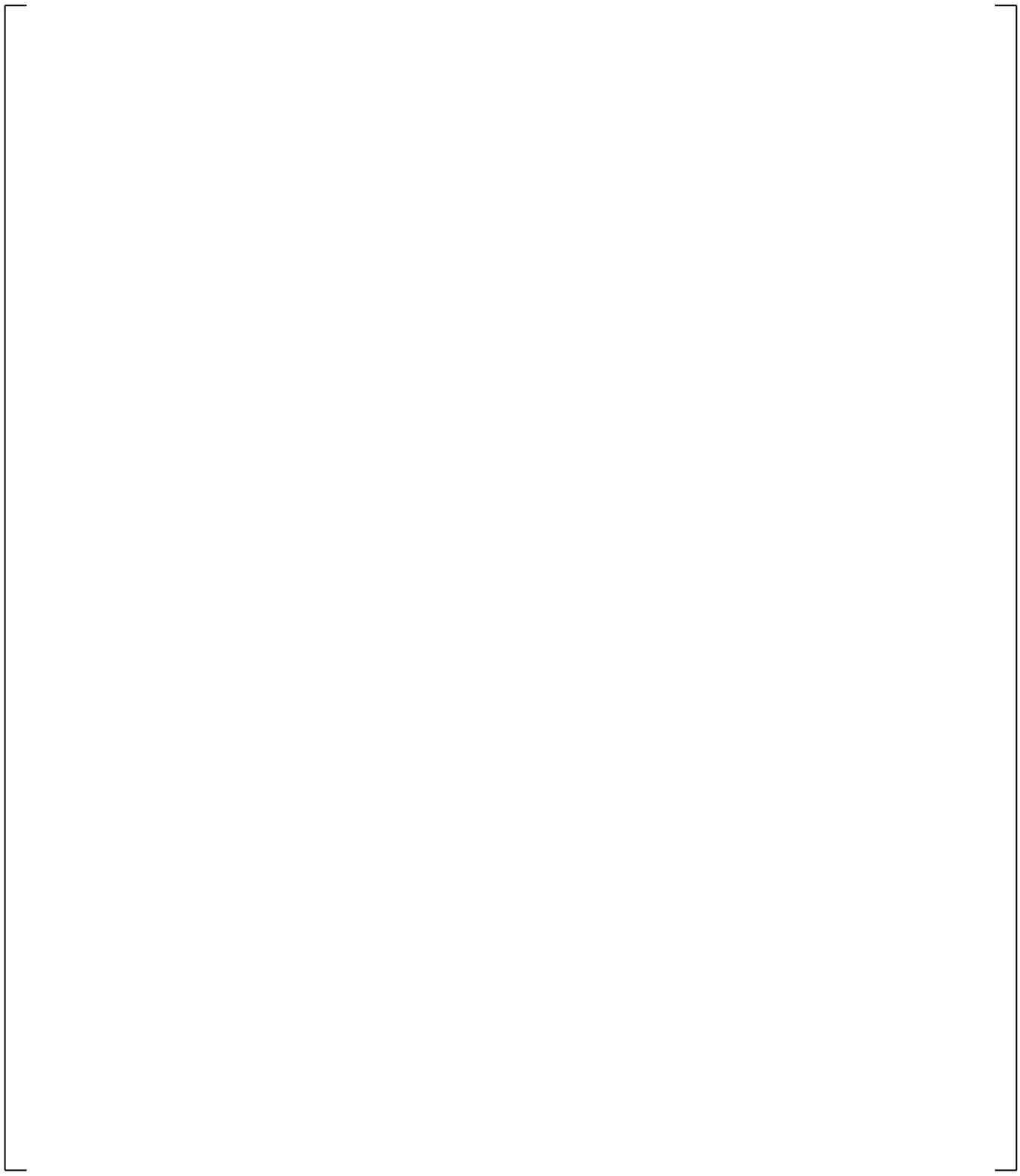

Figure 19.6-12 CCTF Section 6 Noding

a,c

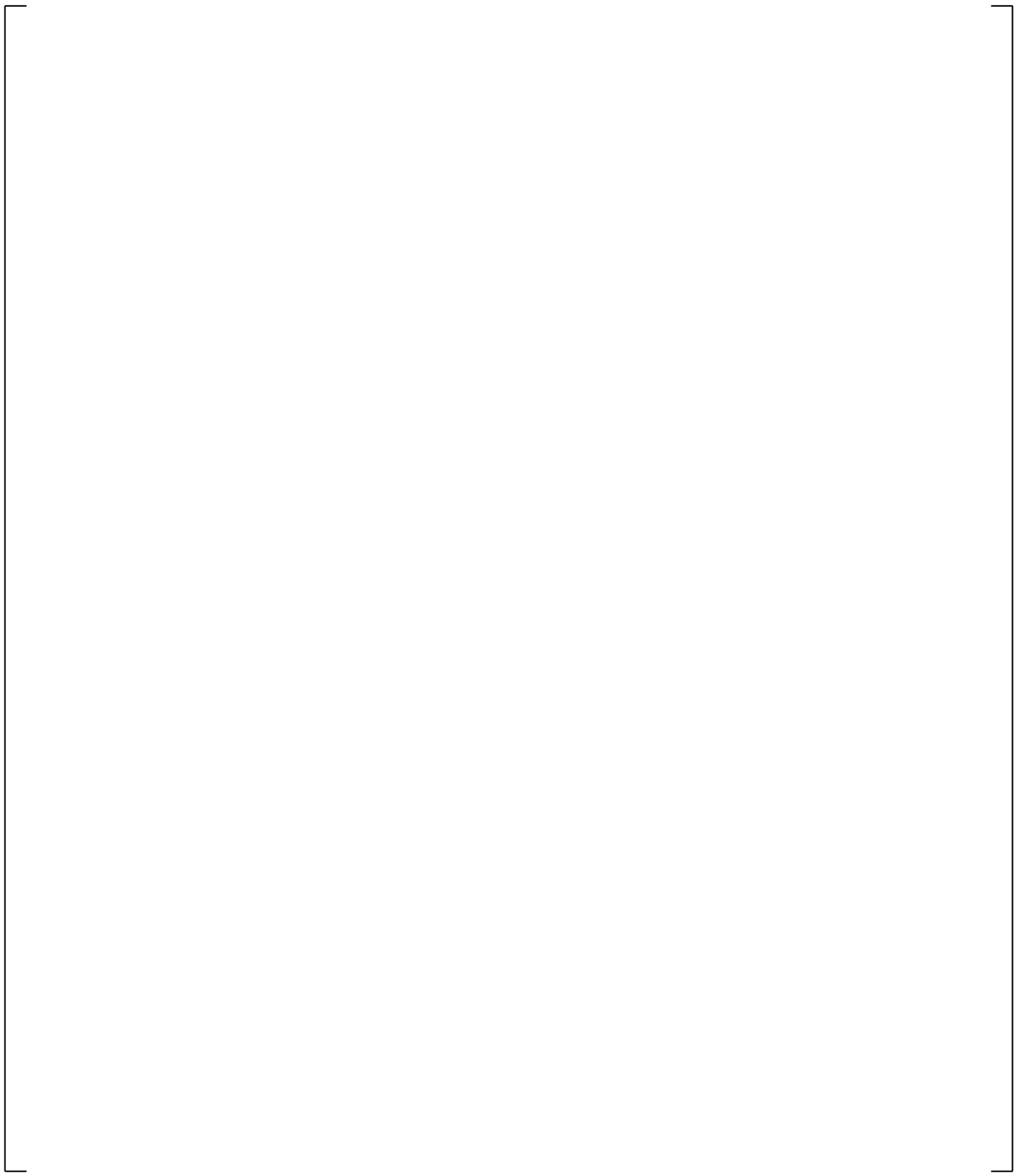

Figure 19.6-13 CCTF Section 7 Noding

a,c

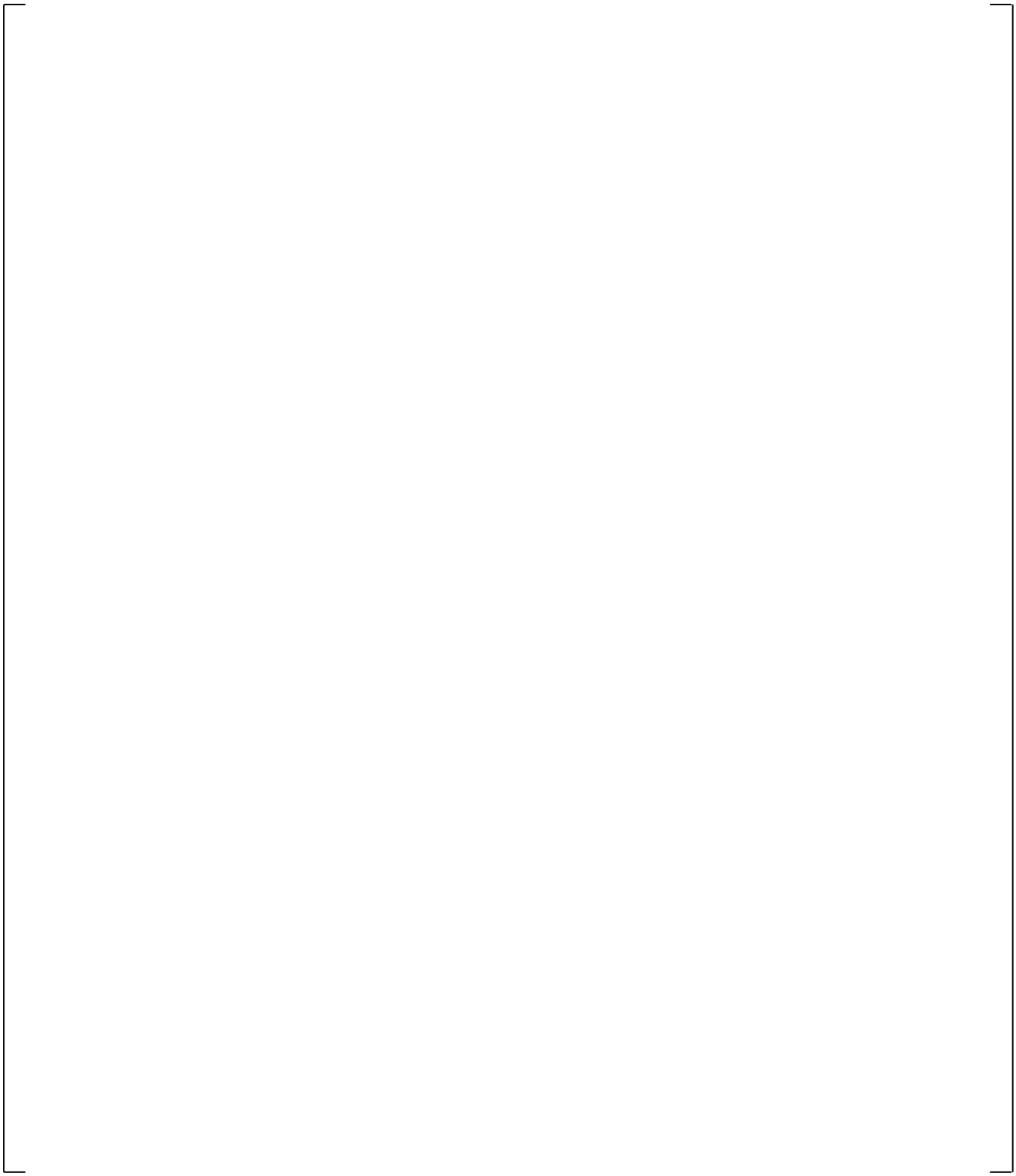

Figure 19.6-14 CCTF Loop Component Diagram

e

Figure 19.6-15 Dimensions of Hot Leg in CCTF

a,c

Figure 19.6-16 Noding Diagram of Hot Leg

e

Figure 19.6-17 Dimension of Crossover Leg, Pump Simulator, Cold Leg, and ECC Port in CCTF

a,c

Figure 19.6-18 Noding Diagram of Crossover Leg, Pump Simulator, Cold Leg, and ECC Port in Loop 1; Other Intact Loops are Identical to Loop 1

a,c

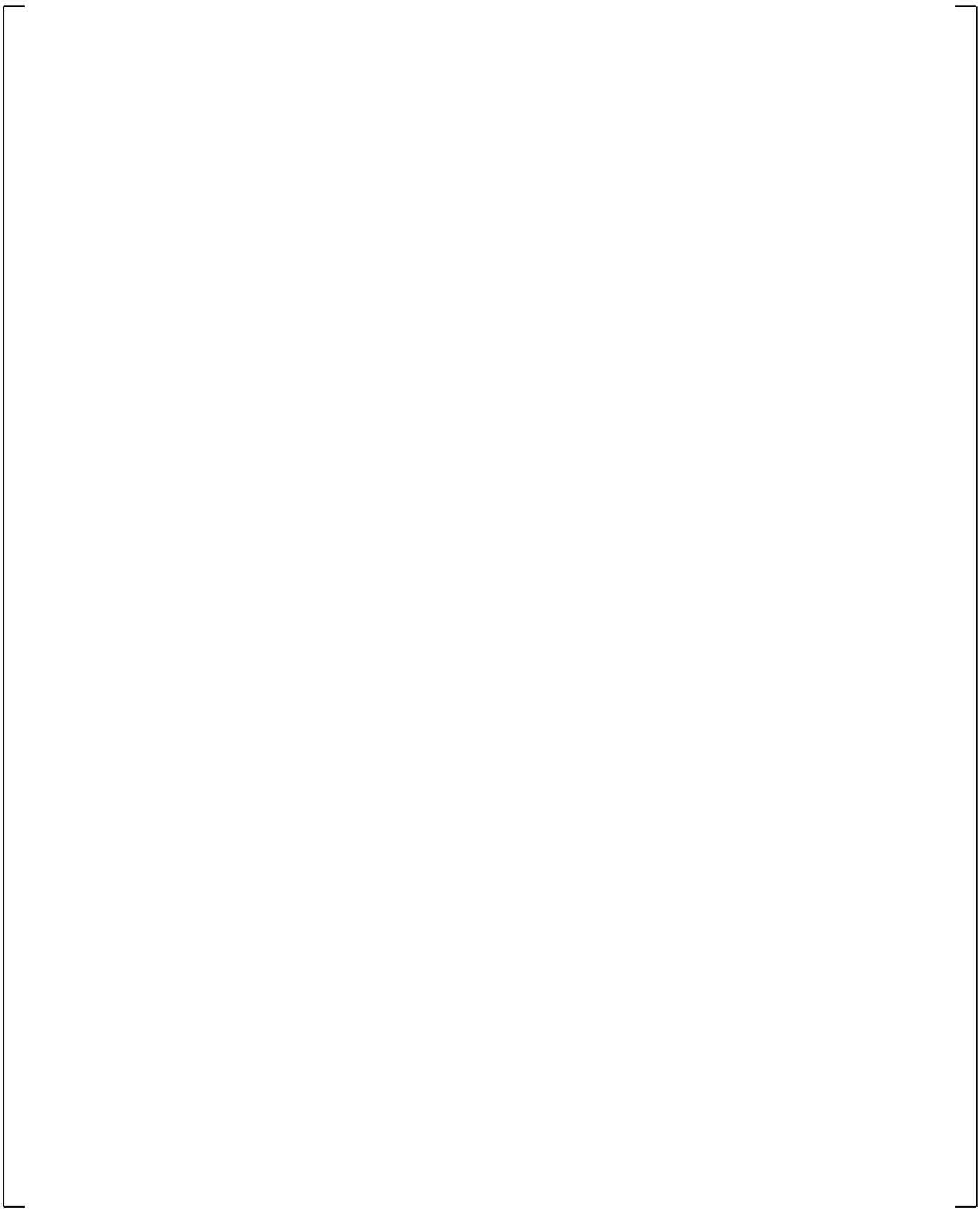

Figure 19.6-19 Steam Generator Component Diagram

a,c

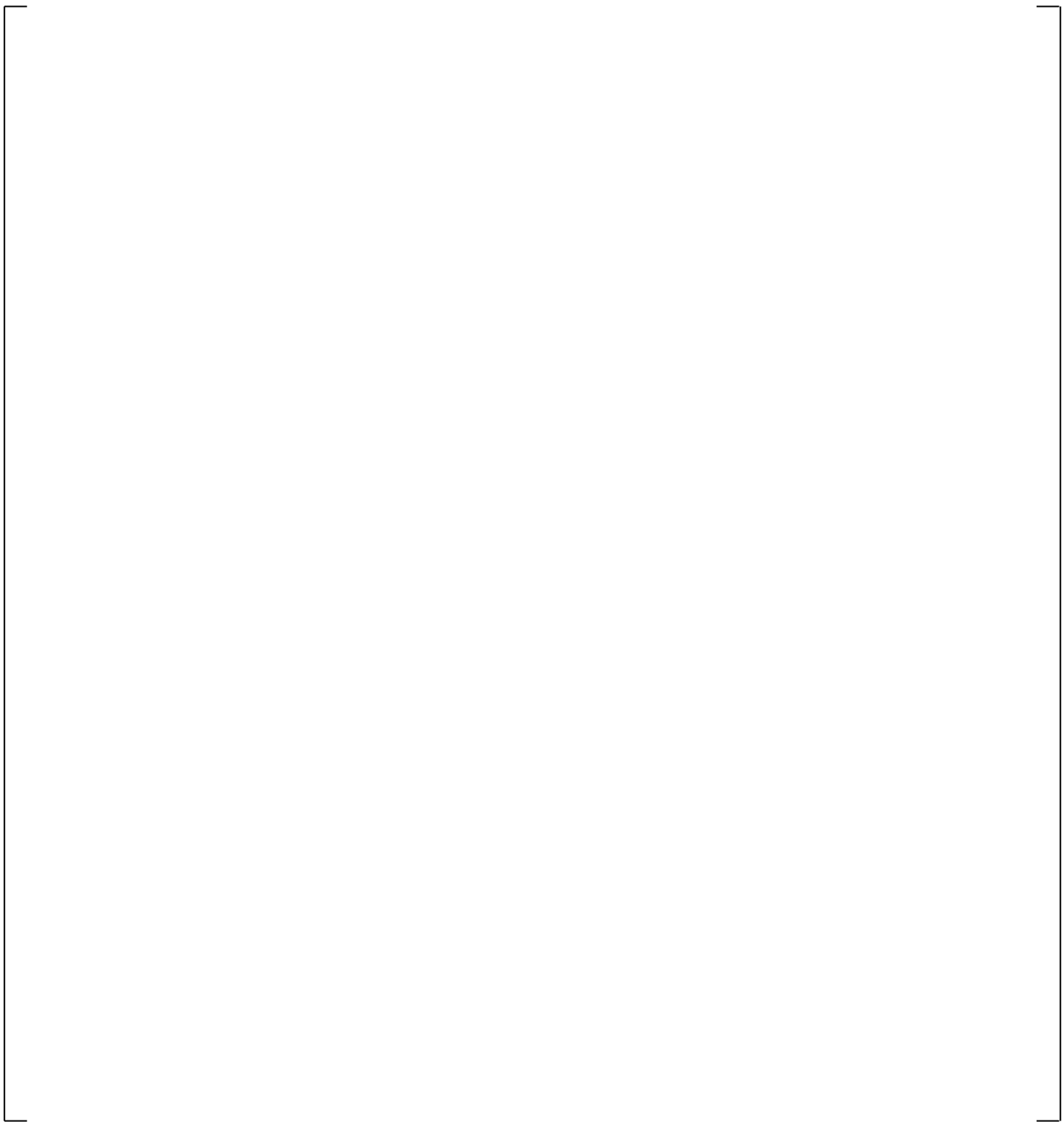

Figure 19.6-20 CCTF Run 62 Cladding Temperature at 6.0 ft for Channel 9 (Rod 6)

a,c

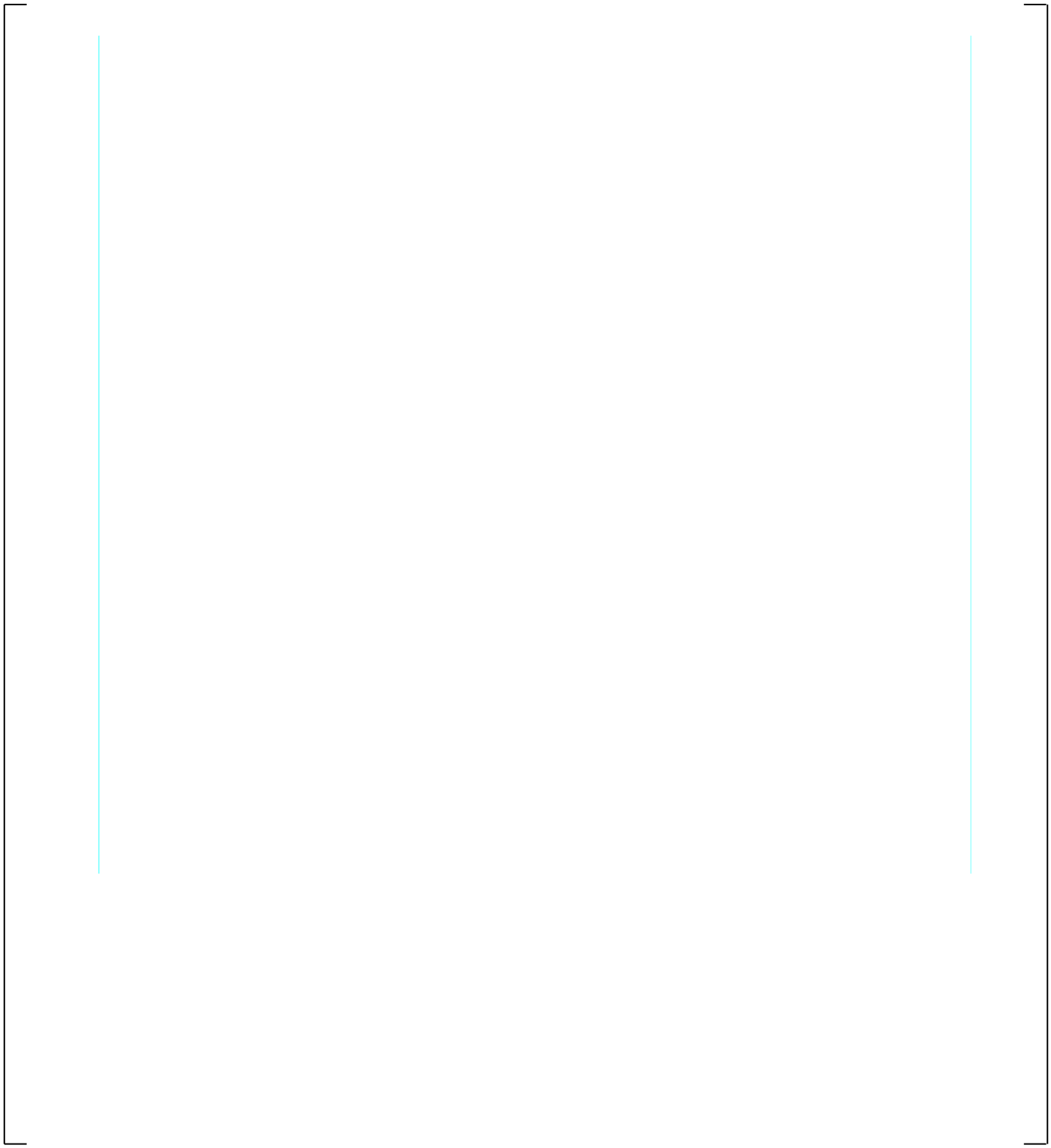

Figure 19.6-21 CCTF Run 62 Cladding Temperature at 8.0 ft for Channel 9 (Rod 6)

a,c

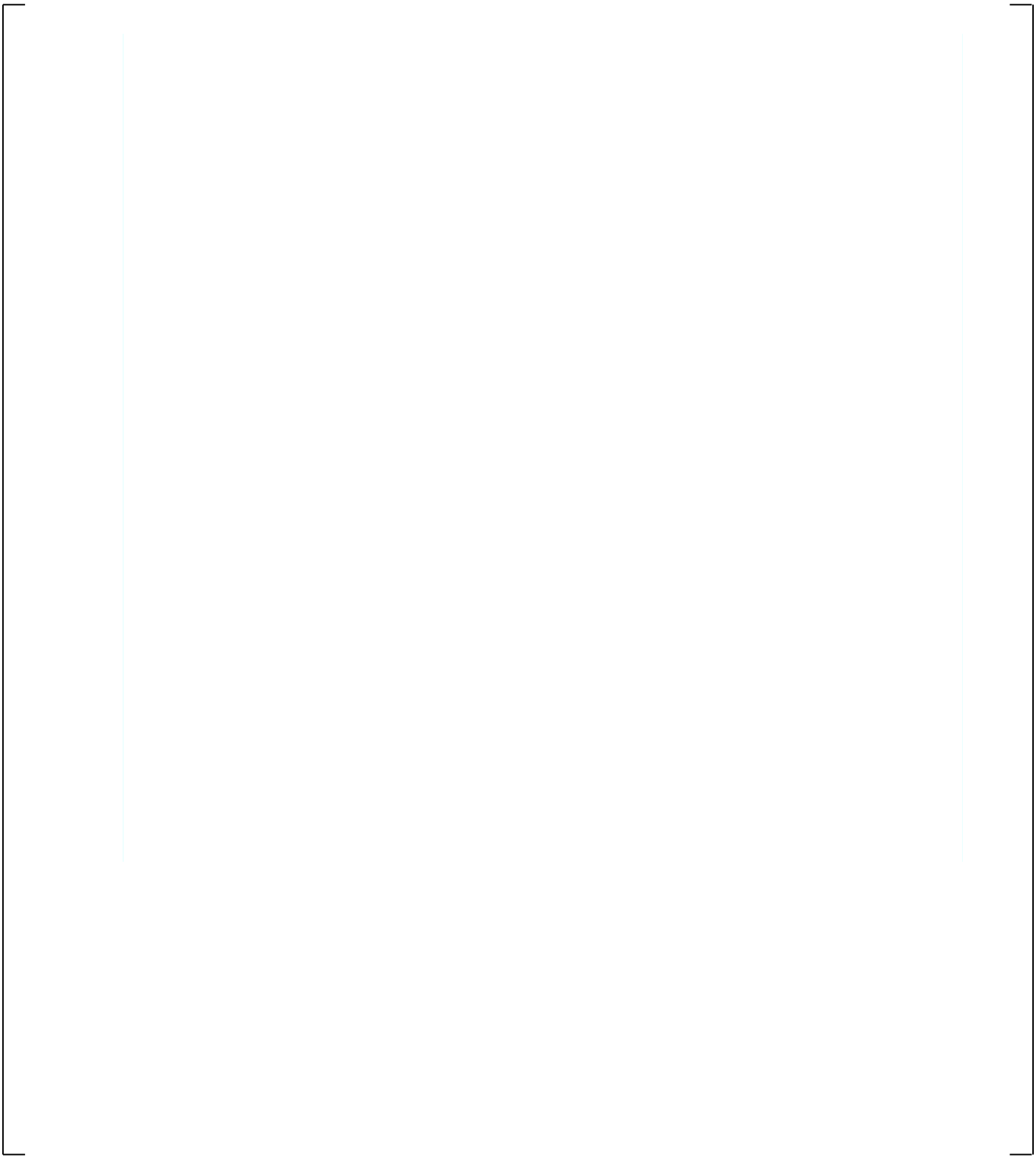

Figure 19.6-22 CCTF Run 62 Cladding Temperature at 10.0 ft for Channel 9 (Rod 6)

a,c

Figure 19.6-23 CCTF Run 62 Vapor Temperature at 6.0 ft for Channel 9

a,c

Figure 19.6-24 CCTF Run 62 Liquid Level in Core

a,c

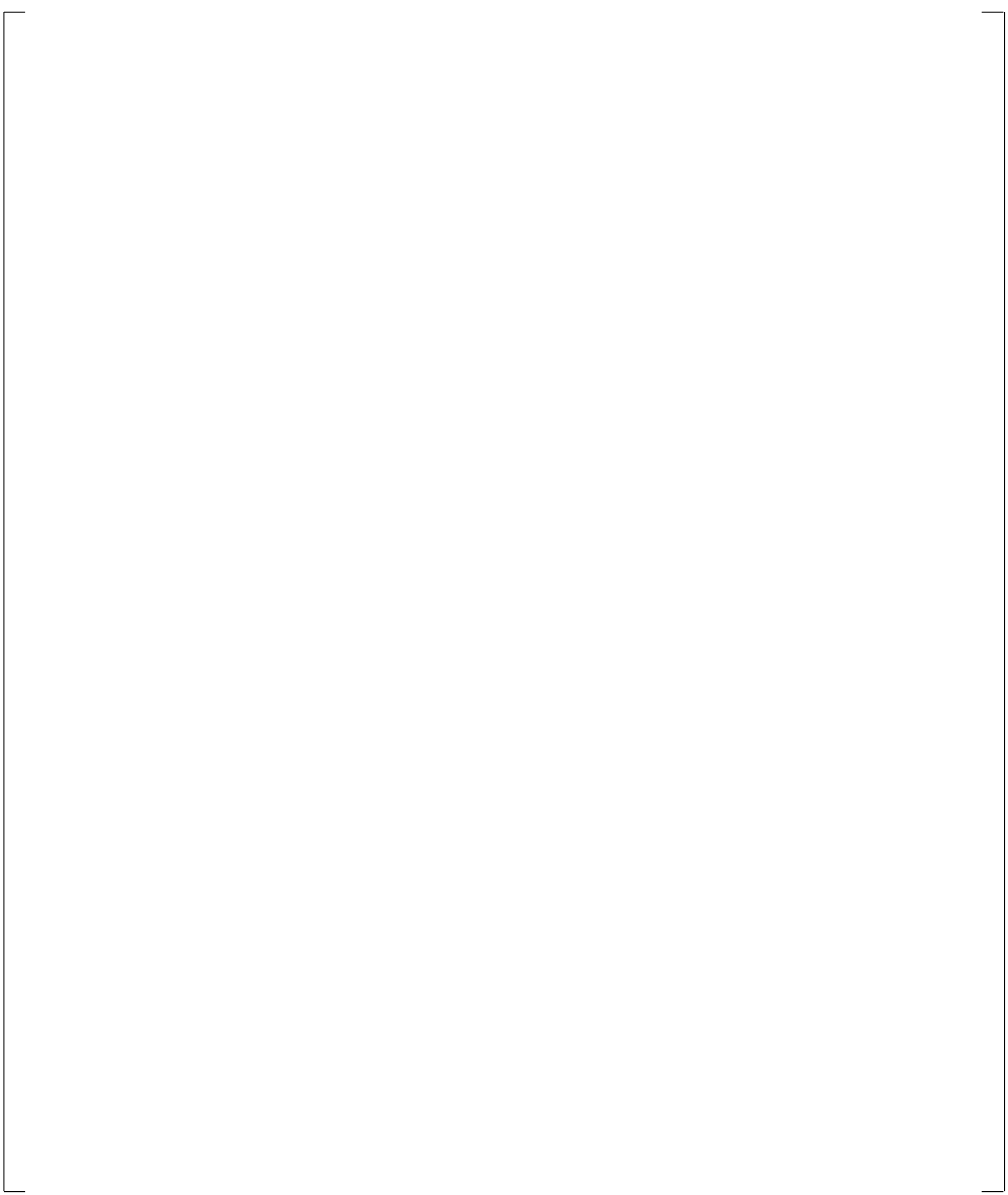

Figure 19.6-25a CCTF Run 62 Void Fraction in End Box (CCFL Region)

a,c

Figure 19.6-25b CCTF Run 62 Liquid Level in Upper Plenum

a,c

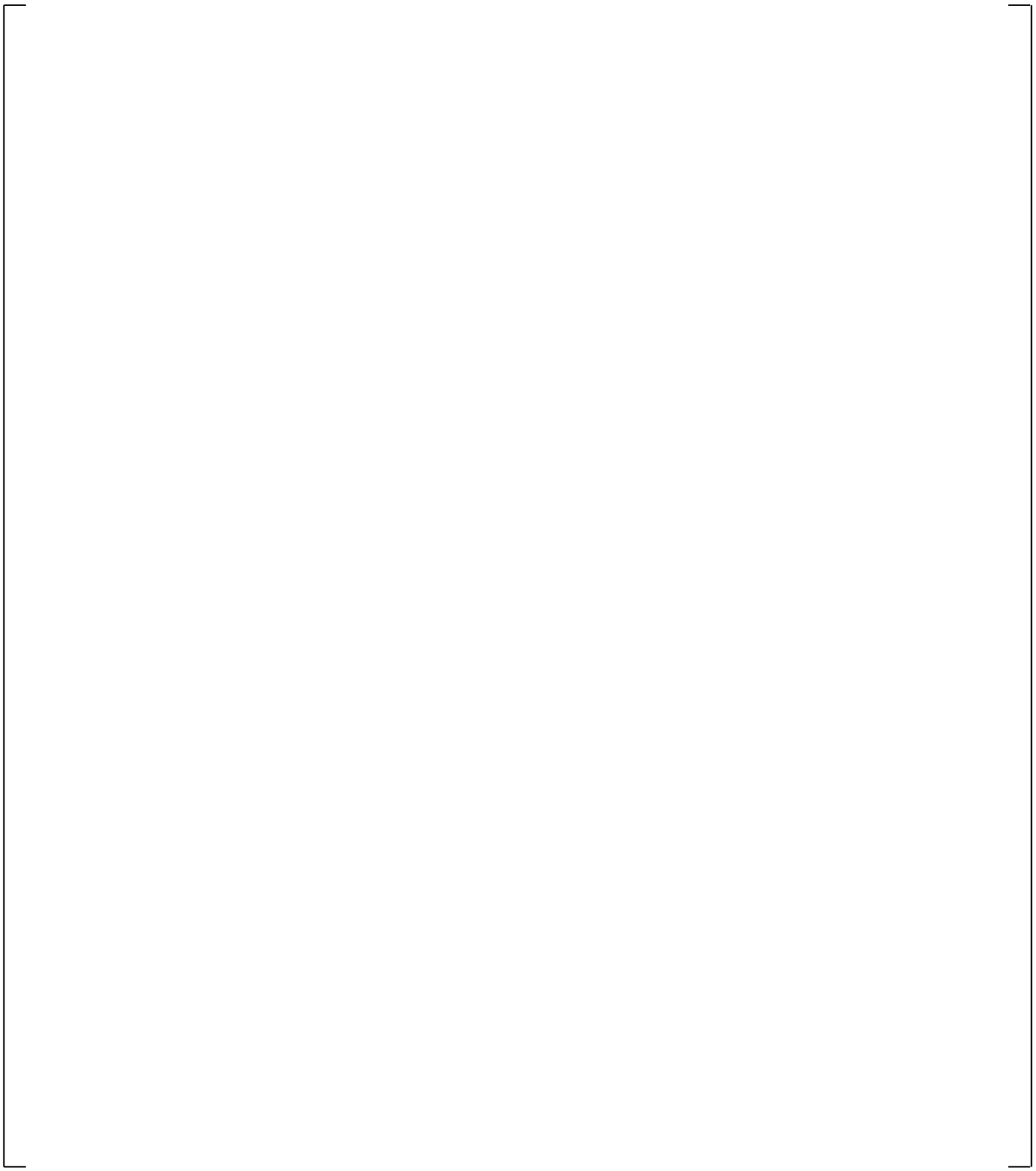

Figure 19.6-26 CCTF Run 62 Pressure Difference from Lower Plenum to Upper Plenum

a,c

Figure 19.6-27 CCTF Run 62 Pressure Difference from Lower Plenum to Top of Downcomer

a,c

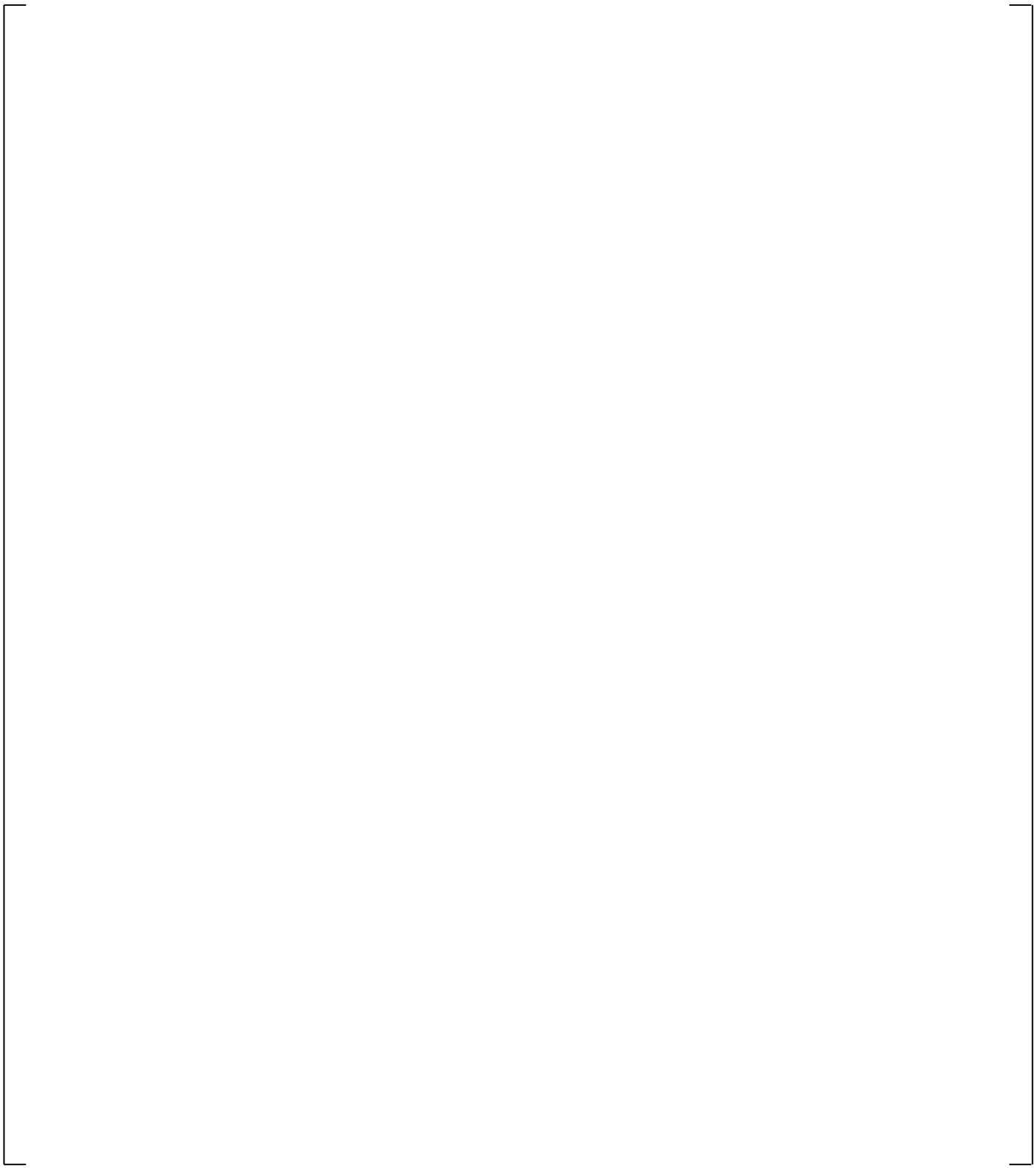

Figure 19.6-28 CCTF Run 62 Pressure Difference across Intact Loop

a,c

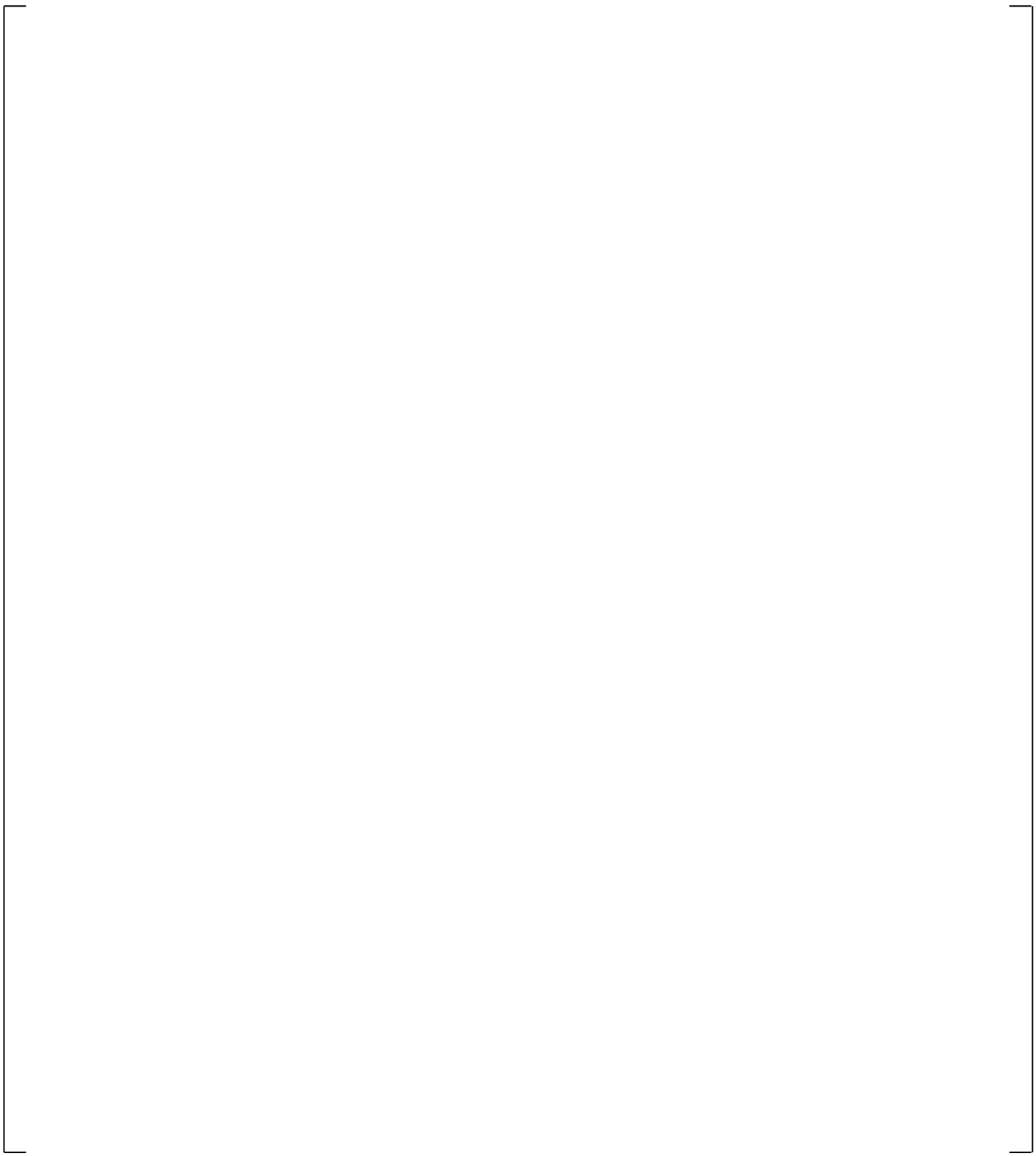

Figure 19.6-29 CCTF Run 62 Pressure Difference across Broken Loop

a,c

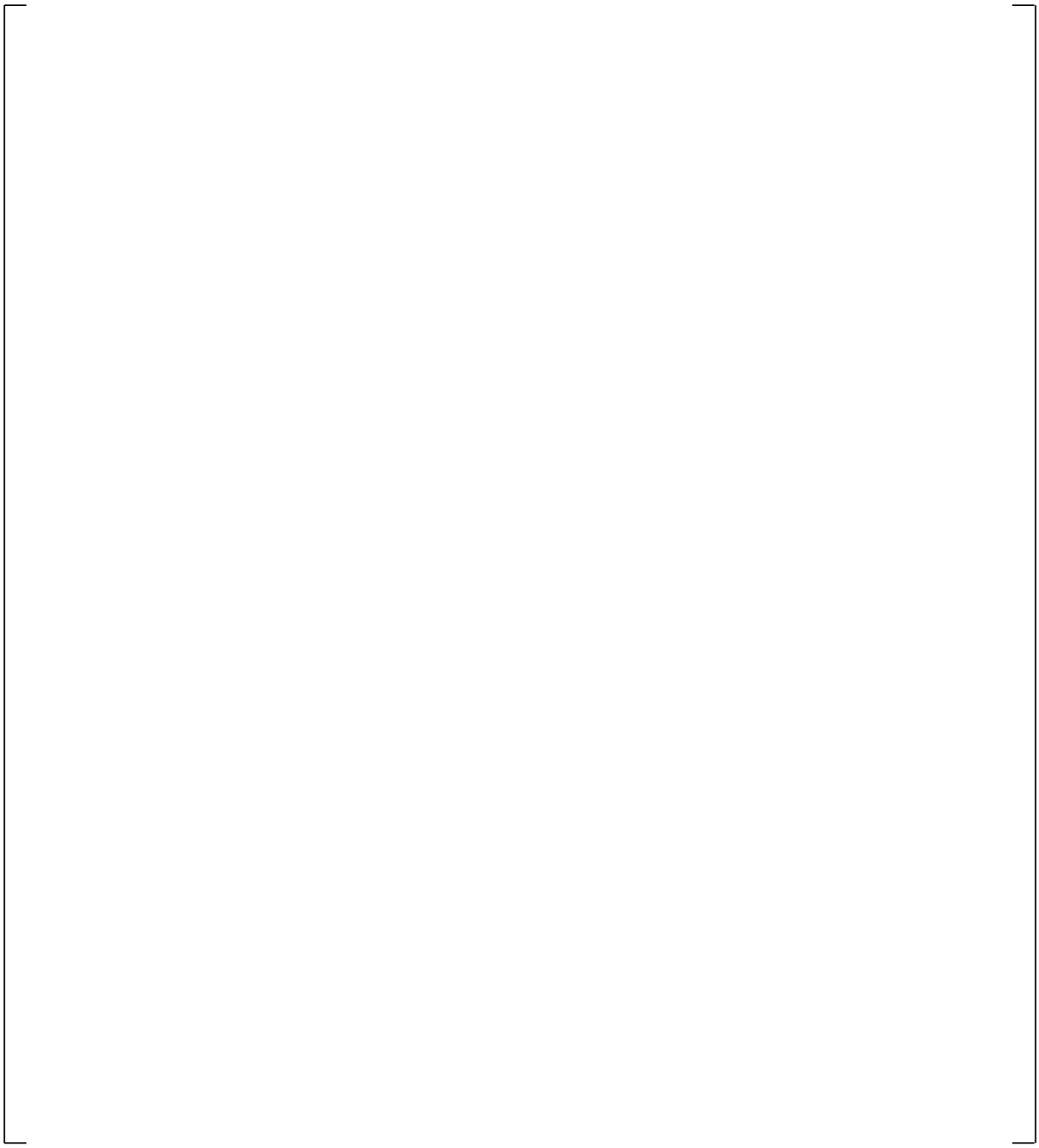

Figure 19.6-30 CCTF Run 62 Pressure Difference across Steam Generators; Averaged for 3 Intact Loops

a,c

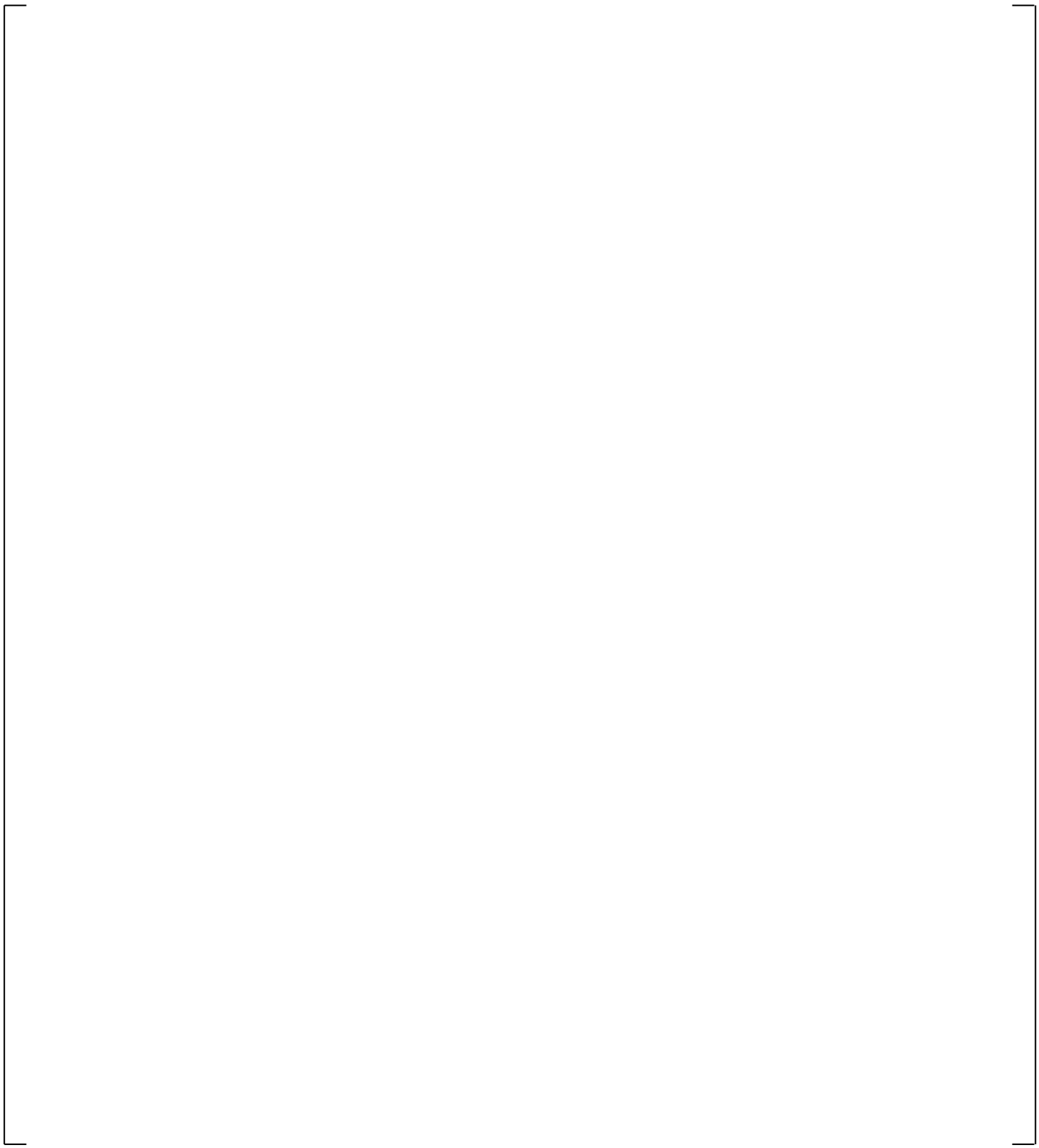

Figure 19.6-31 CCTF Run 62 Temperature Rise across Steam Generator of Loop 1

a,c

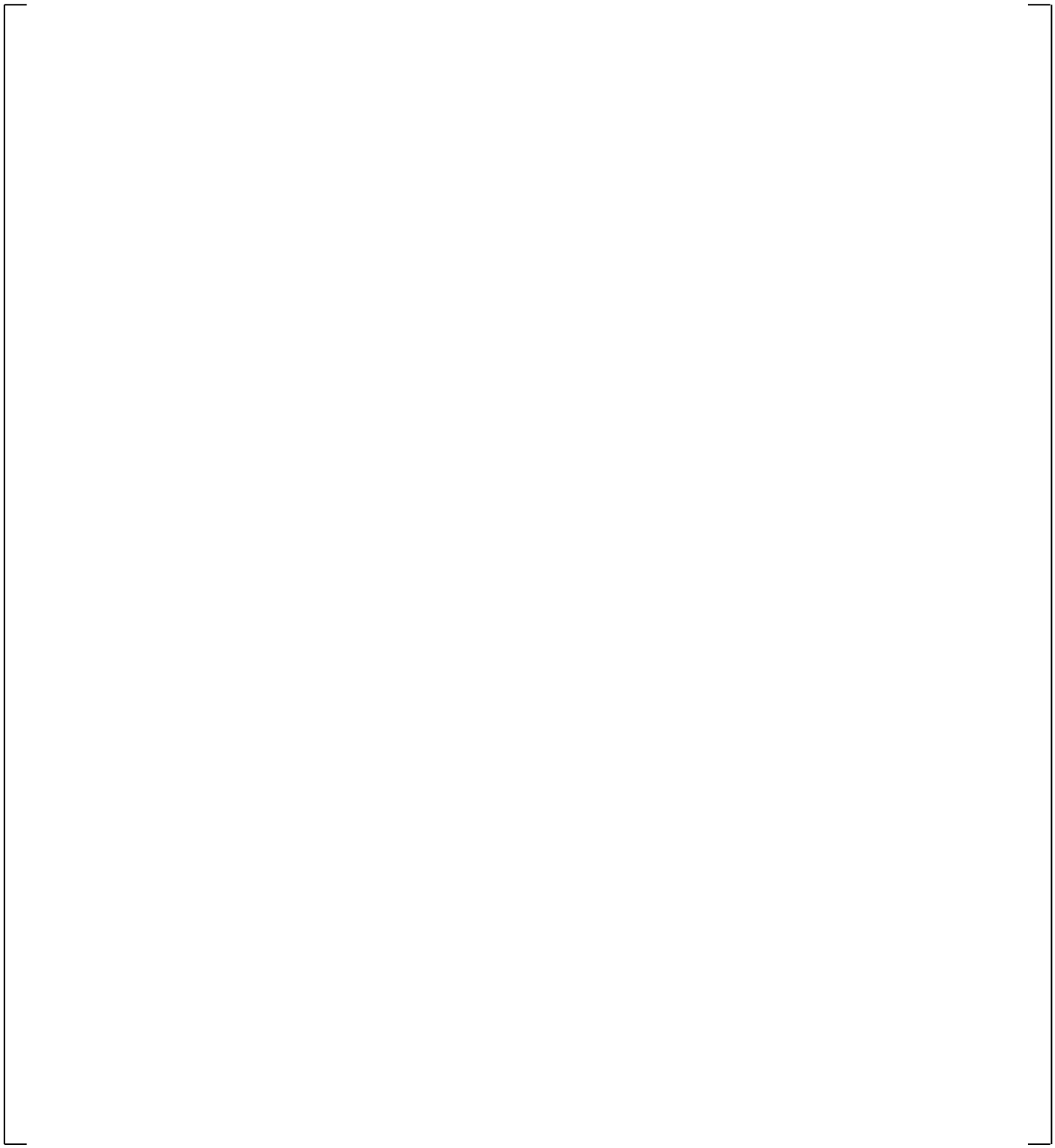

Figure 19.6-32 CCTF Run 62 Temperature Rise across Steam Generator of Loop 2

a,c

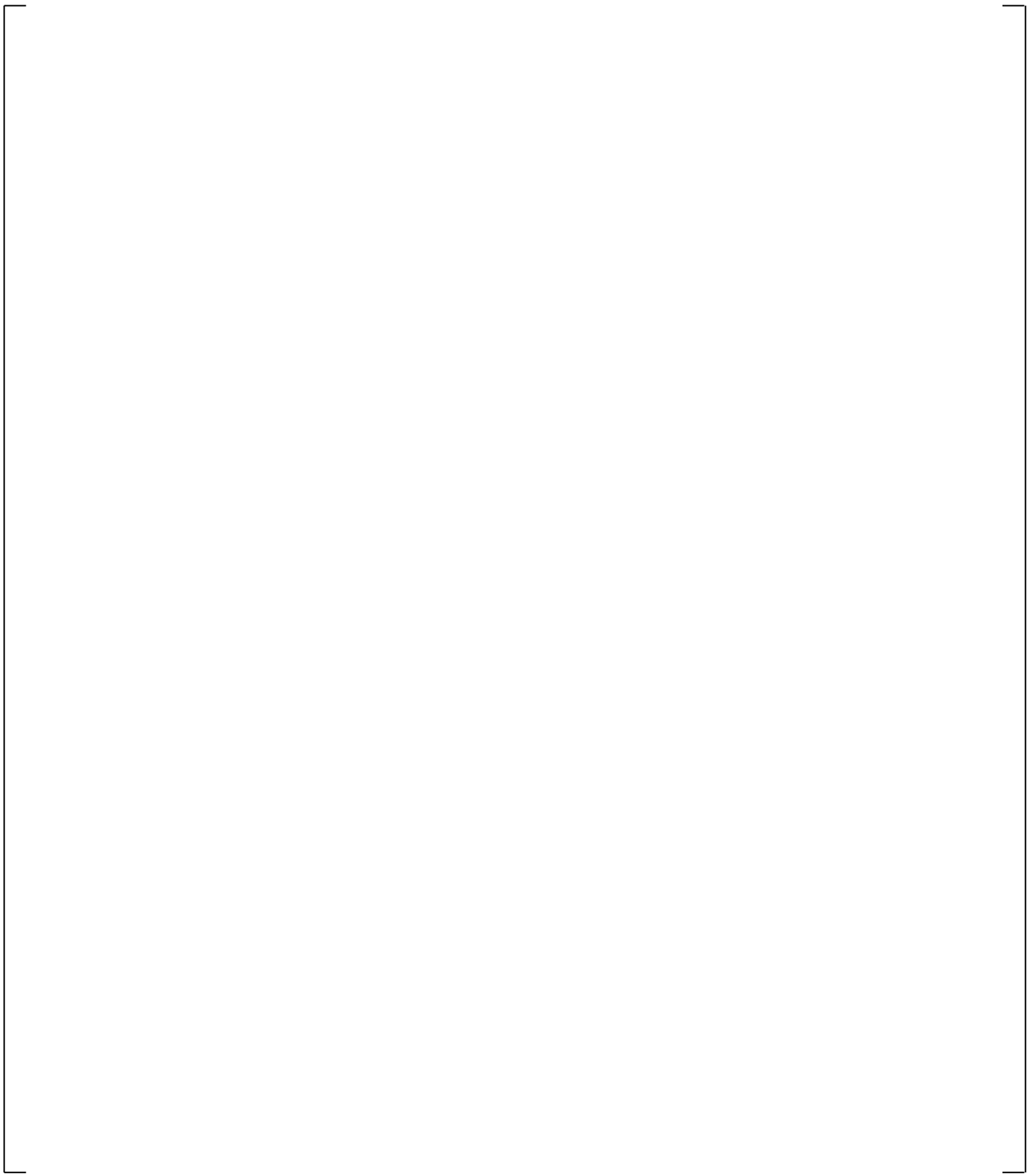

Figure 19.6-33 CCTF Run 62 Temperature Rise across Steam Generator of Loop 3

a,c

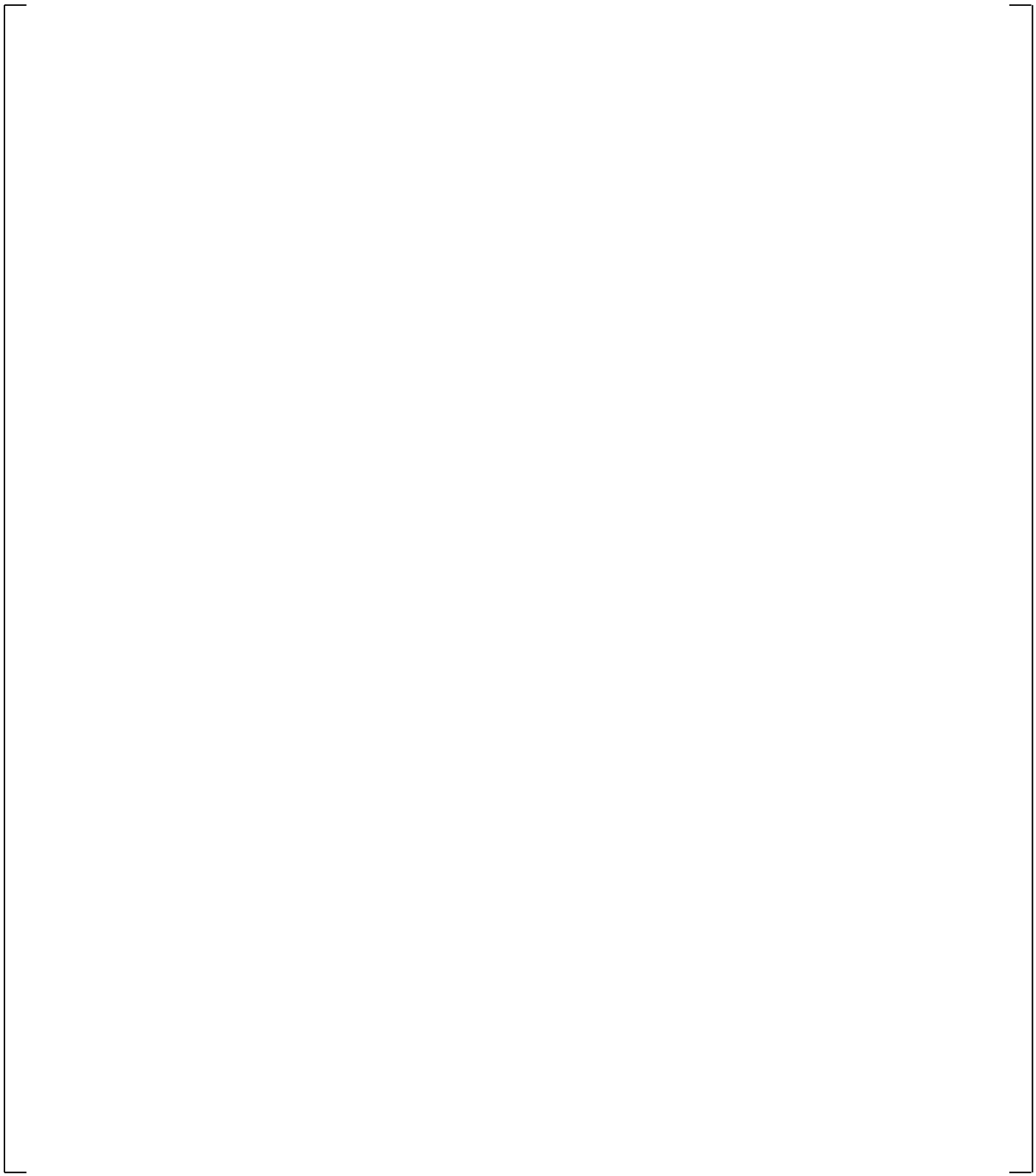

Figure 19.6-34 CCTF Run 62 Total (Liquid and Vapor) Mass Flow Rate in Intact Loop Hot Leg

a,c

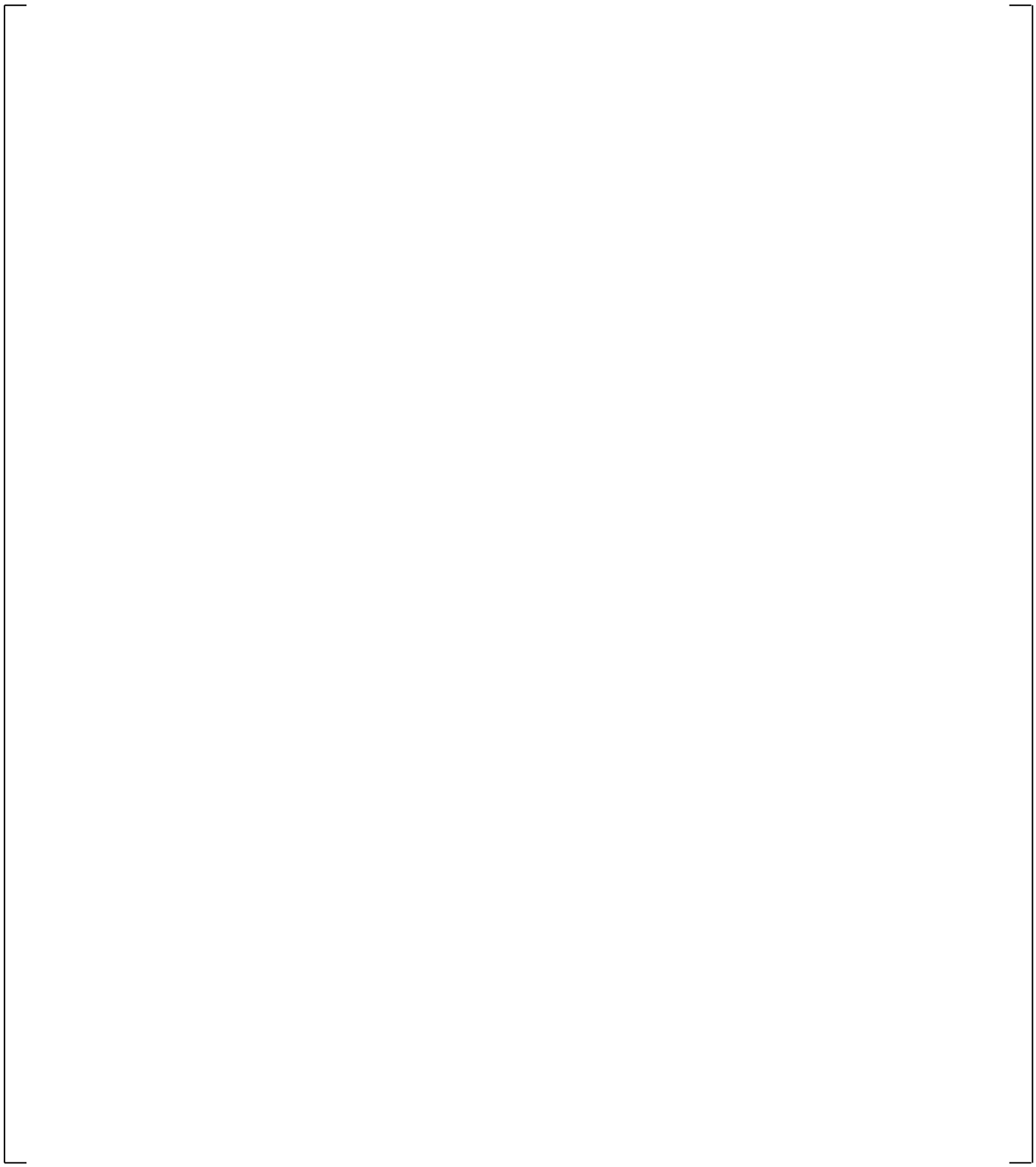

Figure 19.6-35 CCTF Run 62 Total (Liquid and Vapor) Mass Flow Rate in Broken Loop Hot Leg

a,c

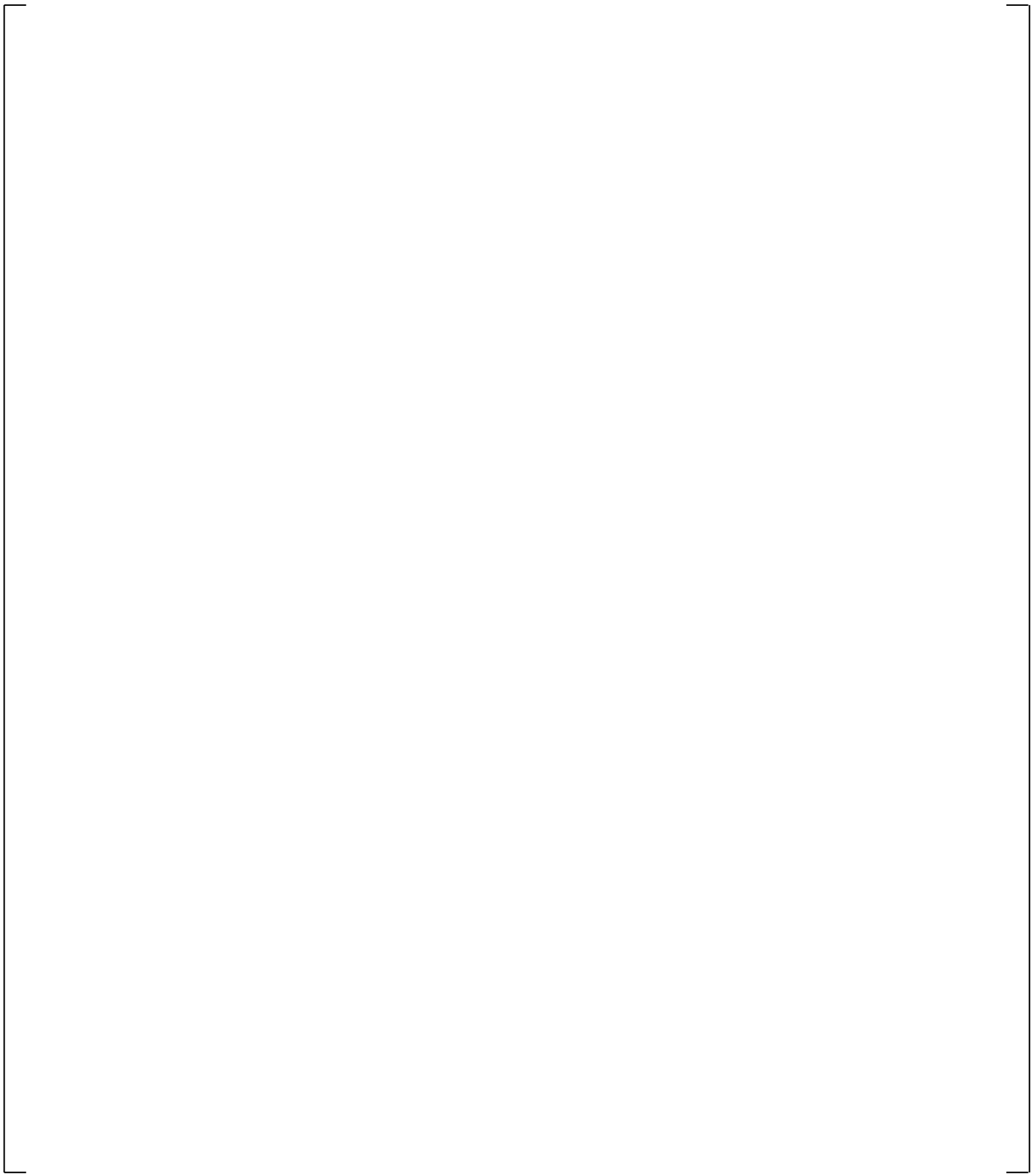

Figure 19.6-36 CCTF Run 62 Core Inlet Mass Flow Rate

a,c

Figure 19.6-37 CCTF Run 62 Time Step Sensitivity Study: Cladding Temperature at 6.0 ft.

a,c

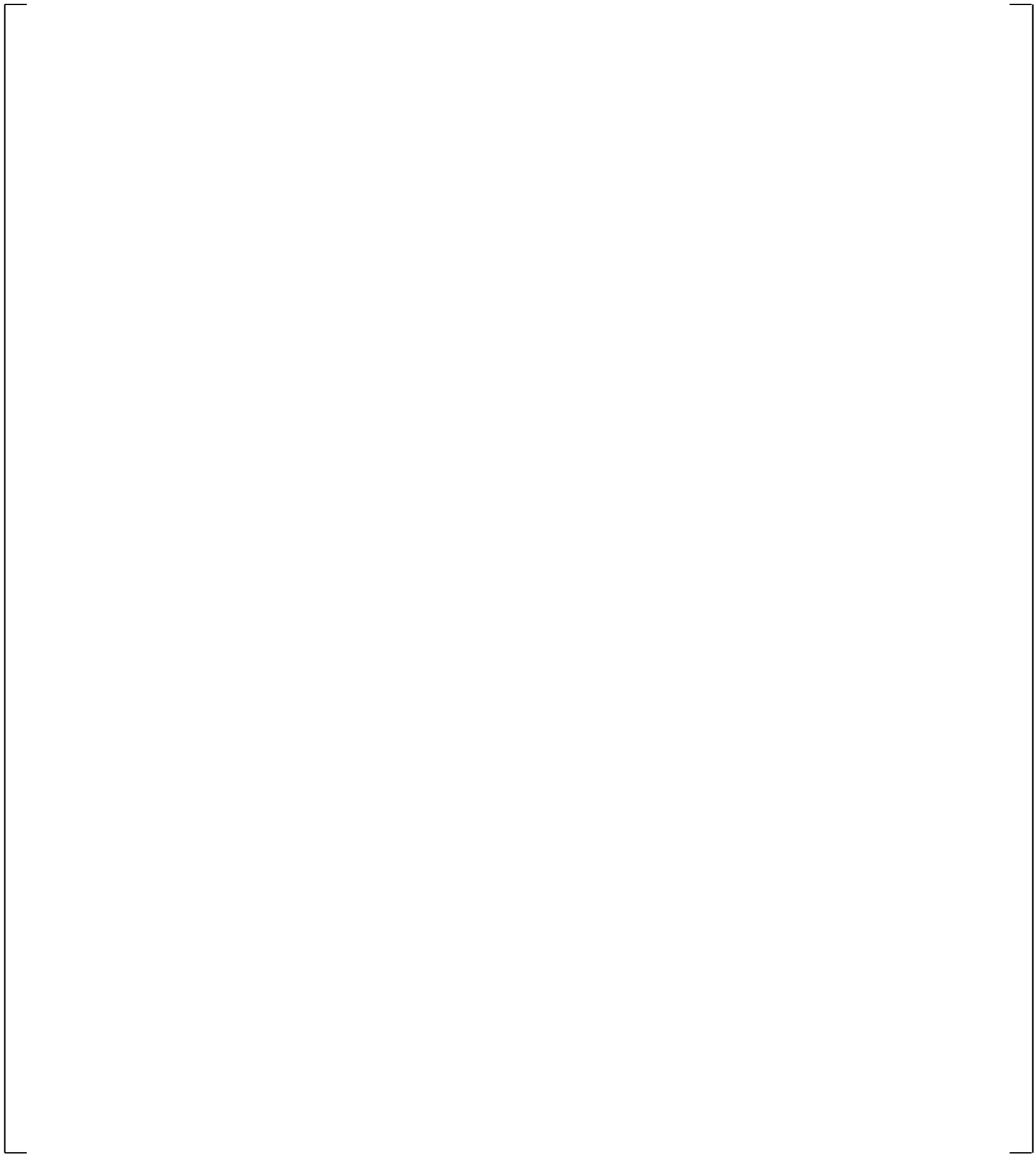

Figure 19.6-38 CCTF Run 62 Time Step Sensitivity Study: Cladding Temperature at 8.0 ft.

a,c

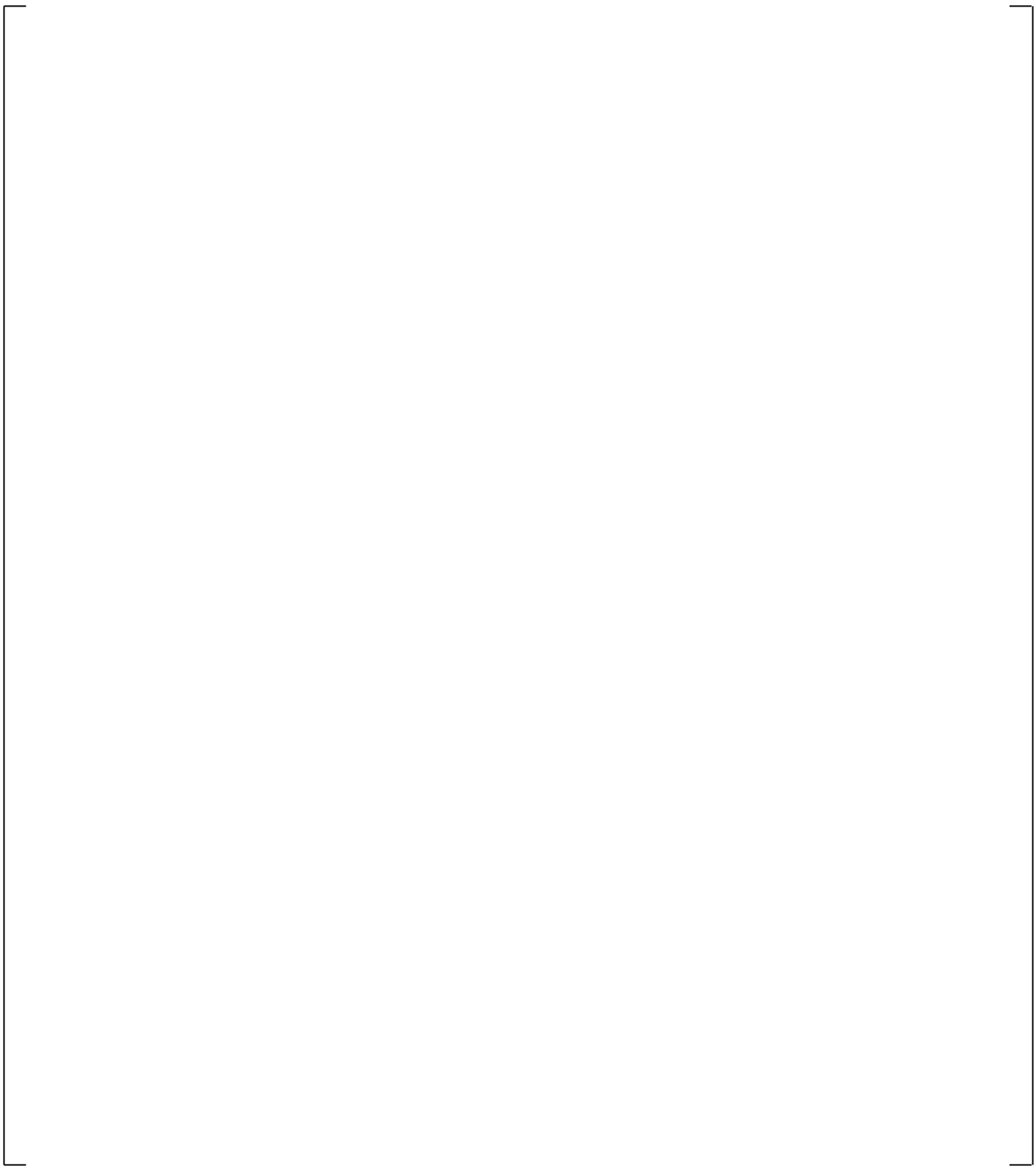

Figure 19.6-39 CCTF Run 62 Time Step Sensitivity Study: Cladding Temperature at 10.0 ft.

a,c

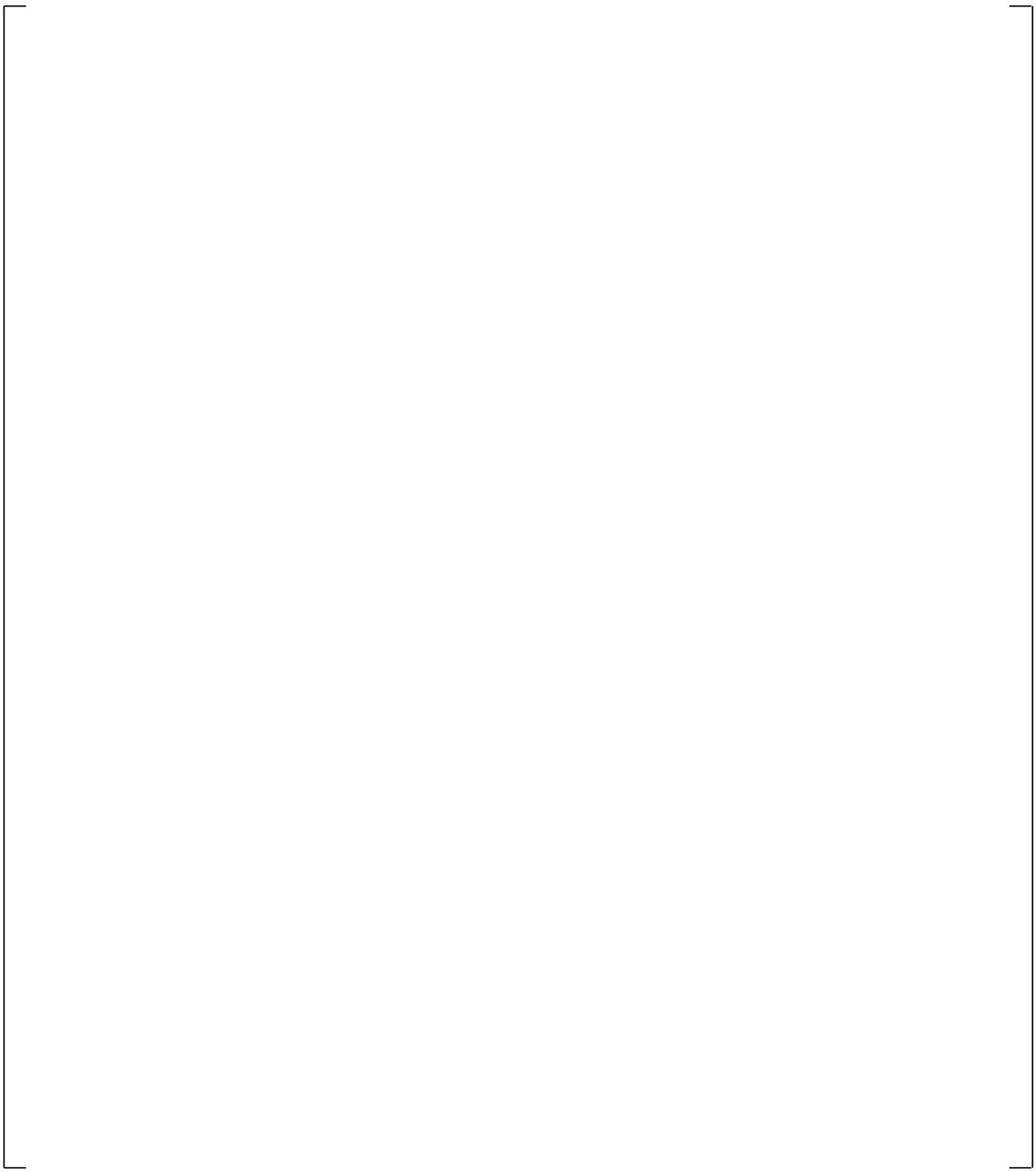

Figure 19.6-40 CCTF Run 62 Time Step Sensitivity Study: Collapsed Liquid Level in Core

a,c

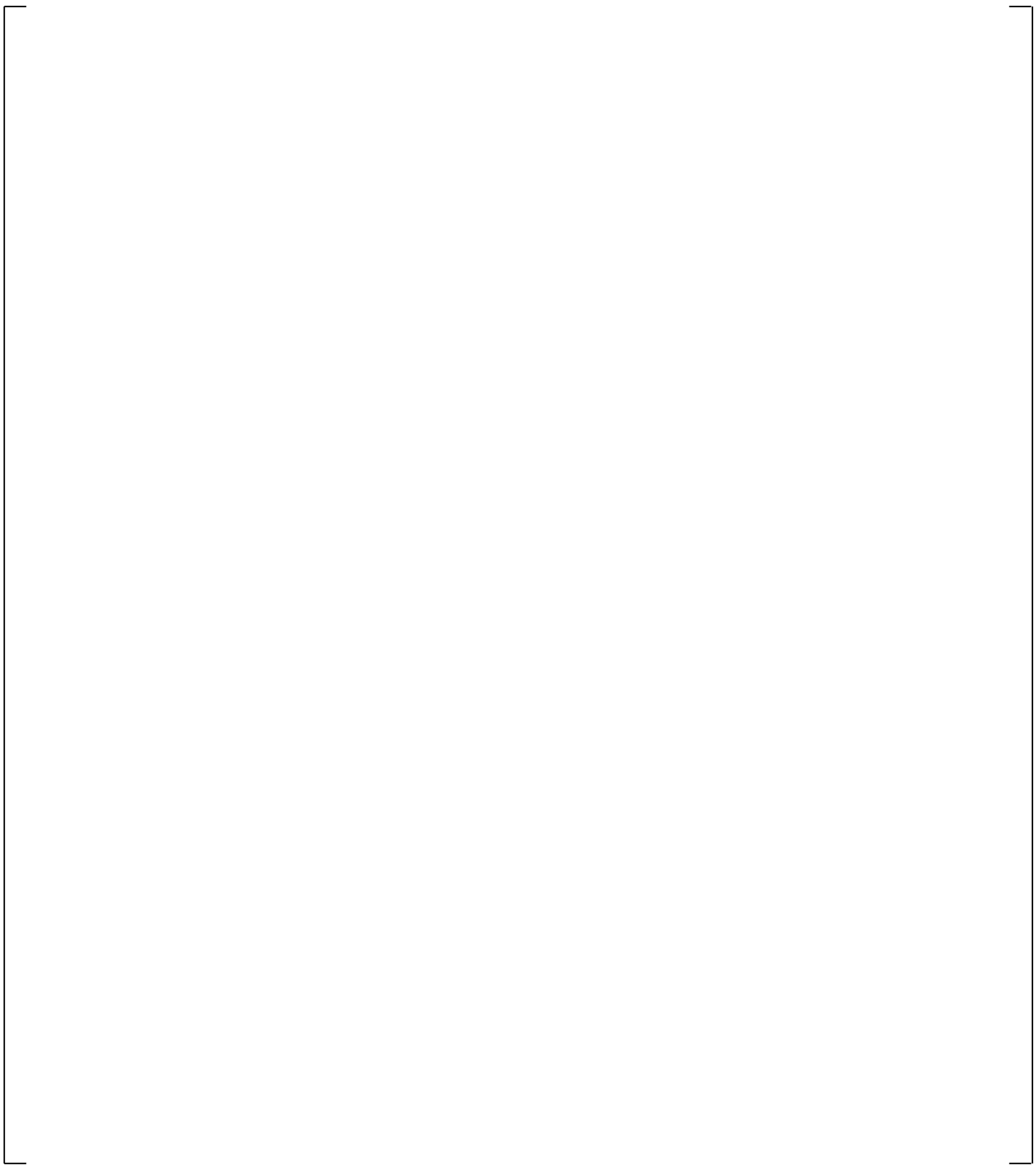

Figure 19.6-41 CCTF Run 62 Time Step Sensitivity Study: Collapsed Liquid Level in Upper Plenum

a,c

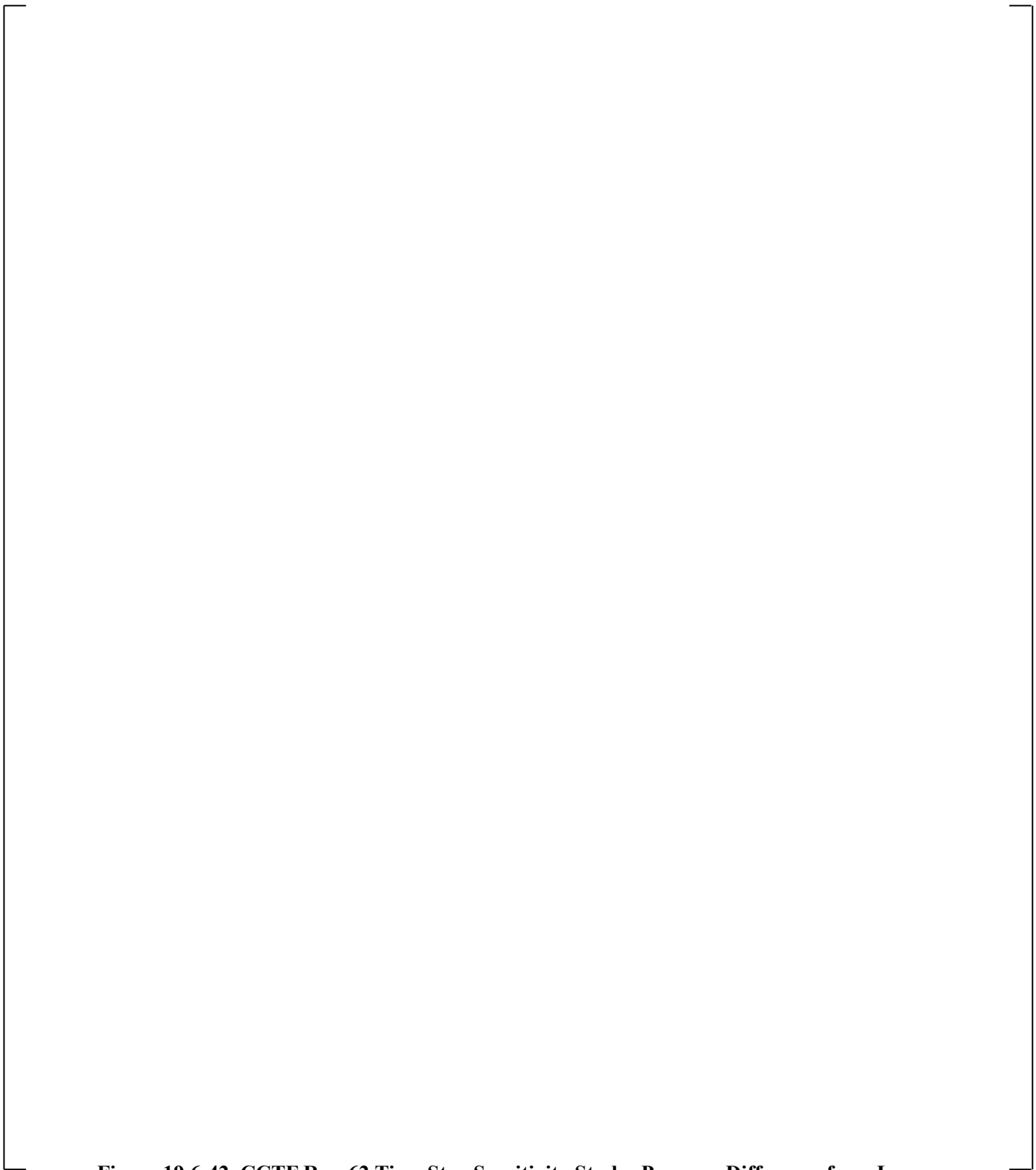

Figure 19.6-42 CCTF Run 62 Time Step Sensitivity Study: Pressure Difference from Lower Plenum to Upper Plenum

a,c

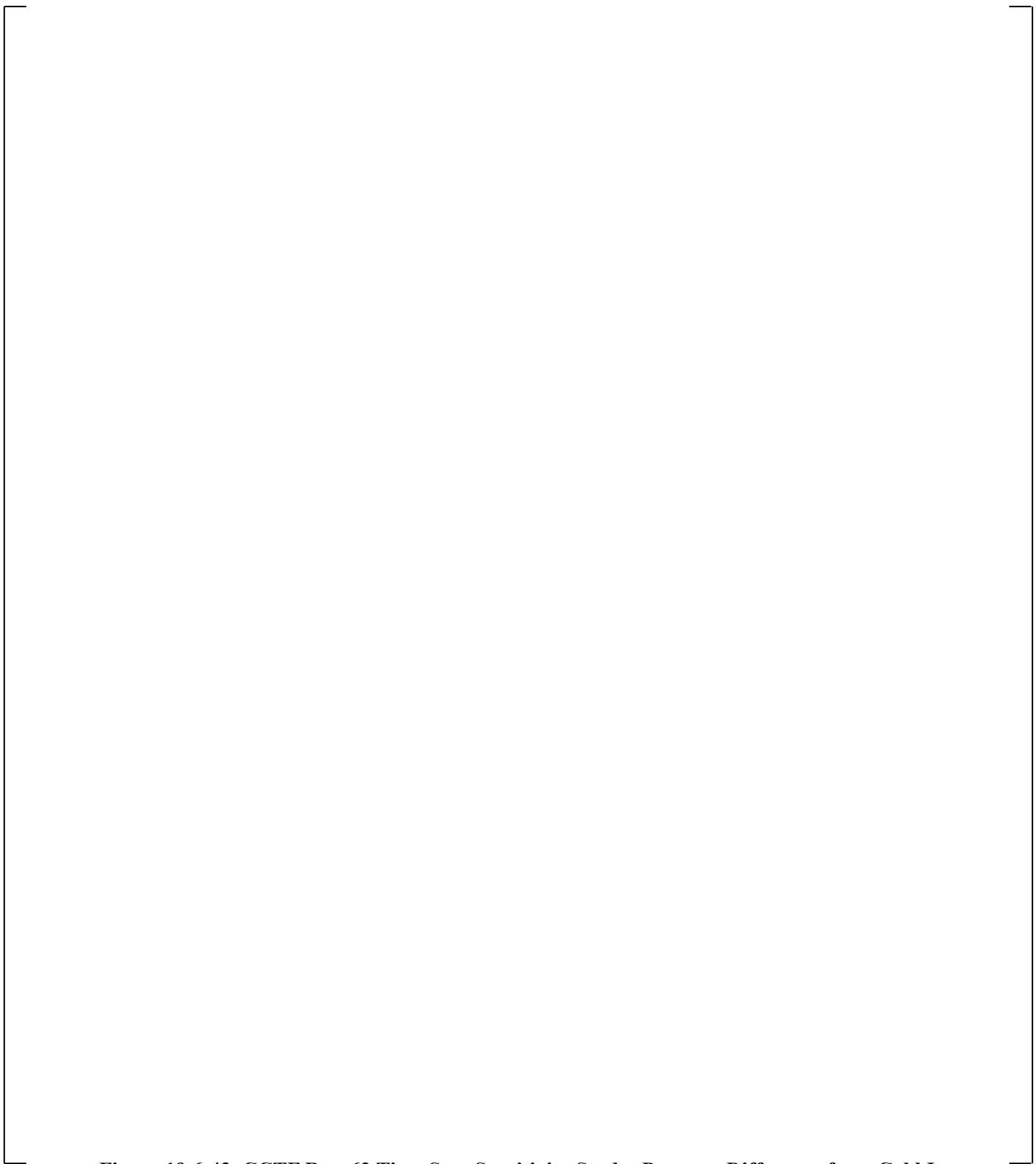

Figure 19.6-43 CCTF Run 62 Time Step Sensitivity Study: Pressure Difference from Cold Leg Nozzle to Upper Plenum

19.7 CONCLUSIONS

The results of the assessment of CCFL, entrainment and de-entrainment, and condensation documented in these sections are summarized as follows. The assessment includes Separate Effects Tests of UPTF 6, UPTF 8A, UPTF 25A, UPTF 29B, FLECHT, and perforated plate, and CCTF-62 Integral Effects Tests.

Counter-Current Flow Limitation

1. CCFL in a Downcomer Annulus – CCFL/ECC bypass in the downcomer annulus of the full-scale UPTF was evaluated in Section 19.3, where WCOBRA/TRAC-TF2 results were compared to experimental data for the UPTF 6 tests. **[**

][a,c]

2. CCFL in a Perforated Plate – The perforated plate analysis documented in Section 19.4 shows that the WCOBRA/TRAC-TF2 predictions **[**

][a,c]

3. CCFL in the Steam Generators – This is addressed in Section 21.10. **[**

][a,c]

4. CCFL in the Hot Leg Bend – This is addressed in Section 21.10. CCFL in the hot leg was **[**

][a,c]

Entrainment and De-Entrainment

As discussed in the previous Section 19.1, the predictive capability of WCOBRA/TRAC-TF2 for entrainment and de-entrainment phenomena needs to be assessed for the following conditions:

1. Upper Plenum Entrainment and Carryover – UPTF Test 29B has been simulated and the predicted upper plenum inventories were compared to test data in Section 19.3.14. **[**

][a,c]

2. Downcomer Entrainment, During ECC Bypass Period and During Reflood – UPTF Tests 6 and 25A were simulated and the results were used to examine the ability to model the entrainment process in the downcomer in Sections 19.3.5 and 19.3.11, respectively. **[**

][a,c]

3. Entrainment During Bottom Reflood – The ability of WCOBRA/TRAC-TF2 to calculate the entrainment rate at a quench front was evaluated by comparing the predicted bundle mass, carryout fraction and exit flows to experimental data from the FLECHT forced reflood facilities in Section 19.5, and by comparing the liquid distribution from the CCTF Run 62 simulation to the experimental data. **[**

][a,c]

Condensation

1. Condensation in Downcomer Annulus – Condensation, CCFL, and entrainment/de-entrainment in the downcomer are inter-related physical processes that affect the ability to predict end-of-bypass and beginning of reflood. **[**

][a,c]

2. Condensation in Cold Legs, at Low Pressure – **[**

][a,c]

3. Effect of Non-Condensable Gases on Condensation – Non-condensable effects on interfacial heat transfer in the 1D and 3D components were assessed in Section 20.

Integral Effects Assessment

The results from the CCTF 62 test show the code giving **[**

][a,c]. The comparisons between the prediction and the measurements show that WCOBRA/TRAC-TF2 predicts the overall thermal-hydraulics of a reflood transient properly. In particular, **[**

][a,c]

19.8 REFERENCES

1. 2D/3D Program Upper Plenum Test Facility Experimental Data Report, 1988, "Test No. 8, Cold/Hot Leg Flow Pattern Test," U9 316/88/12, KWU.

2. 2D/3D Program Upper Plenum Test Facility Quick Look Report, 1989, "Test No. 6; Downcomer Countercurrent Flow Test," Siemens/KWU U9 316/89/2.

3. 2D/3D Program Upper Plenum Test Facility Experimental Data Report, 1990a, "Test No. 25, Downcomer/Cold Leg Steam/Water Interaction Test," E314/90/11, KWU.

4. 2D/3D Program Upper Plenum Test Facility Experimental Data Report, 1990b, "Test No. 29, Entrainment/De-entrainment Test," E314/90/05, KWU.

5. Akimoto, H., et al., 1984, "Pressure Drop through Broken Cold Leg During Reflood Phase of Loss-of-Coolant Accident of PWR," *Journal of Nuclear Science and Technology*, 21 [6].

6. Bajorek, S. M., et al., 1998, "Code Qualification Document for Best Estimate LOCA Analysis," WCAP-12945-P-A, Volume 1, Revision 2, and Volumes 2 through 5, Revision 1, and WCAP-14747 (Non-Proprietary).

7. Cousins, L. B., et al., 1965, "Liquid Mass Transfer in Annular Two-Phase Flow," Paper C4 presented at the Symposium on Two-Phase Flow, Volume 2, Exeter, England, pp. 401-430.

8. Dallman, J. C., and Kirchner, W. L., 1980, Los Alamos Scientific Laboratory, "De-Entrainment Phenomena on Vertical Tubes in Droplet Cross Flow," USNRC Report, NUREG/CR-1421.

9. Emmerling, R., et al., 1988, "UPTF: Program and System Description," U9 414/88/023, KWU.

10. Glaeser, H., 1992, "Downcomer and Tie Plate Countercurrent Flow in the Upper Plenum Test Facility (UPTF)," *Nucl. Eng. Des.*, 133.

11. Glaeser, H. and Karwat, H., 1993, "The contribution of UPTF experiments to resolve some scale-up uncertainties in countercurrent two phase flow," *Nuclear Engineering and Design*, 145, pp. 63-84.

12. Hsieh, C., et al., 1980, "Countercurrent Air/Water and Steam/Water Flow above a Perforated Plate," NUREG/CR-1808.

13. Kataoka, I. and Ishii, M., 1983, "Mechanistic Modeling and Correlations for Pool Entrainment Phenomenon," Argonne National Laboratory Report ANL-83-37, NUREG/CR-3304.

14. Loftus, M. J. et al., 1981, "PWR FLECHT-SEASET Unblocked Bundle, Forced and Gravity Reflood Task Data Report," Volumes 1 and 2, NUREG/CR-1532, WCAP-9699.

15. MPR Associates, 1990a, "Summary of Results from the UPTF Downcomer Separate Effects Tests, Comparison to Previous Scaled Tests, and Application to U.S. PWRs," MPR-1163.

16. MPR Associates, 1990b, "Summary of Results from the UPTF Carryover/Steam Binding Separate Effects Tests, Comparison to Previous Scaled Tests, and Application to U.S. Pressurized Water Reactors," MPR-1213.

17. MPR Associates, 1992, "Summary of Results from the UPTF Cold Leg Flow Regime Separate Effects Tests, Comparison to Previous Scaled Tests, and Application to U.S. Pressurized Water Reactors," MPR-1208.

18. MPR Associates, 1993, "Reactor Safety Issues Resolved by the 2D/3D Program," MPR-1346.

19. Okubo, T., et al., 1984, "Data Report on Large Scale Reflood Test – 82 – CCTF CORE-II TEST C2-4 (RUN 062) –," Department of Nuclear Safety Research, Tokai Research Establishment, JAERI-memo 59-450.

20. Okubo, T., Iguchi, T., Okabe, K., Sugimoto, J., Akimoto, H., and Murao, Y., 1985, "Evaluation Report on CCTF Core-II Reflood Test C2-4 (Run 62)," JAERI-M 85-026.

21. Rosal, E. R., Hochreiter, L. E., McGuire, M. F., and Krepinevich, M. C., 1975, "FLECHT Low Flooding Rate Cosine Test Series Data Report," WCAP-8651.

22. Rosal, E. R., Conway, C. E., and Krepinevich, M. C., 1977, "FLECHT Low Flooding Rate Skewed Test Series Data Report," WCAP-9108.

23. USNRC, 1989, "Best-Estimate Calculations of Emergency Core Cooling System Performance," Regulatory Guide 1.157.

24. Walley, P. B., et al., 1973, "Experimental Wave and Entrainment Measurements in Vertical Annular Two-Phase Flow," AERE-R7521, Atomic Energy Research Establishment, Harwell, England.

25. Wallis, G. B., 1969, One-Dimensional Two-Phase Flow. McGraw-Hill Inc., NY

20 ADDITIONAL COMPONENT MODEL ASSESSMENTS

This section provides additional validation of components not individually addressed in previous sections. Section 20.1 examines the accumulator component, Section 20.2 examines the pump, and Section 20.3 presents a control-volume verification of mass and energy conservation at the 1D/3D junction. The momentum coupling treatment and assessment is discussed in Section 19.3.5.10 regarding the cold leg nozzle loss coefficient.

20.1 ACCUMULATOR COMPONENT

20.1.1 Introduction

The accumulator component model was described in Volume 1, Section 10.8. That section also described the phases of accumulator water injection, emptying, and accumulator nitrogen discharge.

The Phenomena Identification and Ranking Table (PIRT) identifies 3 highly ranked phenomena associated with the accumulator behavior during a loss-of-coolant accident (LOCA) transient:

1. Injection Flow Rate/Flow Resistance. The delivery flow rate of the accumulator is of high or medium importance for the whole spectrum of postulated LOCAs: for the smaller breaks, injection from the accumulator is responsible for terminating the transient and limiting the duration of clad heatup (medium rank). For intermediate and large breaks, injection from the accumulator is responsible for re-filling the downcomer and initiating reflood, and the flow rate/flow resistance is ranked high. The Indian Point Unit 2 (IPP) and Callaway Blowdown Tests, as described in Sections 20.1.2 and 20.1.3, document the capability of a simplified accumulator model in adequately predicting accumulator injection flow rate both under rapid discharge conditions (i.e., larger break scenarios) and gradual discharge conditions (i.e., smaller break scenarios). In addition to these separate effect tests, the accumulator discharge is analyzed in the Rig-of-Safety Assessment (ROSA) and Loss-of-Fluid Test (LOFT) integral effect tests, as documented in Sections 21 and 22. Finally, the accumulator discharge for the LOFT 2-5 and ACHILLES tests are documented in Section 20.1.4.

2. Nitrogen Discharge (Non-condensable effects). The accumulator nitrogen provides the main source of non-condensable gas in the system during the LOCA transient. While the potential effects of non-condensables are discussed elsewhere as applicable, it is recognized that the accumulator cover gas provides the main source of non-condensable gas in the system, and thus the discharge process and impact on the transient is discussed herein. In general, large amounts of non-condensable gas will be released from the accumulator only during the larger breaks (for the period of interest in the analysis), and thus the assessment is focused on these break sizes. The LOFT 2-5 and ACHILLES tests documented in Section 20.1.4 are used to assess the discharge of nitrogen from the accumulator and the effect on the pressurized water reactor (PWR) reflood transient.

3. Broken Loop Accumulator Treatment. The approach and justification for the treatment of the accumulator in the broken loop for different break sizes is discussed in Section 26.2.1.3 of Volume 3 and with plant scoping studies in Section 28.2.6, Volume 3.

This overall assessment demonstrates the adequacy of the accumulator model documented in Volume 1, Section 10.8.

20.1.2 IPP Accumulator Test

An accumulator blowdown test was performed at Indian Point Unit 2 in 1971 during startup testing. The initial gas pressure in the accumulator was about 100 psig, the gas volume was about 400 cubic feet and the water volume was 700 cubic feet. Test runs were performed at ambient temperature (80°F), with reactor coolant system (RCS) back pressure of 0 psig. The cold legs were empty and water level in the vessel was well below the cold leg nozzle elevation. The control valves used to initiate the test runs were set to open from 0 to 100 percent in 10 seconds. Test runs were performed for the four accumulators which had various accumulator line lengths. The test runs would terminate when the pressure in the accumulator reached approximately 20 psig while the accumulator line was still in single-phase liquid flow. The measured pressure responses of the four accumulators were all similar. Pressure response for one of the accumulators was selected for WCOBRA/TRAC-TF2 model verification. Figure 20.1-1 is a sketch showing the layout of the accumulator piping.

20.1.2.1 WCOBRA/TRAC-TF2 Model

A WCOBRA/TRAC-TF2 model was constructed to simulate the accumulator test. A typical PWR model of the accumulator and its piping consists of **[**

][a,c] as shown in Figure 20.1-2. **[**

][a,c] In this model, the RCS was simulated by a BREAK component, supplying a constant back pressure. The volume, length, and hydraulic diameter for the accumulator and the accumulator line were all preserved. **[**

][a,c] Section 28.1.5, Volume 3 presents a Large Break LOCA (LBLOCA) sensitivity study with an accumulator elevation varying **[**

][a,c]

The resistance in the accumulator line was simulated **[**

][a,c]. The initial and boundary conditions were the same as those used in the 1971 IPP test. Both the water and nitrogen cover gas were initially at 80°F. A steady-state run of 20 seconds was first performed, followed by a blowdown run initiated by opening a control valve in the accumulator line. The valve reached 100 percent opening within the first 10 seconds of the blowdown run.

20.1.2.2 WCOBRA/TRAC-TF2 Simulation Results

The accumulator pressure predicted by WCOBRA/TRAC-TF2 is compared to measured test data (the only data available) in Figure 20.1-3. It can be seen that WCOBRA/TRAC-TF2 prediction and test data are in good agreement **[**

][a,c]

20.1.3 Callaway Accumulator Test

In order to evaluate the Small Break LOCA (SBLOCA) emergency core cooling system (ECCS) model, Westinghouse, with the cooperation of the personnel of the Callaway Nuclear Plant, conducted a slow accumulator blowdown test at the plant in December 1982.

In order to simulate the accumulator discharge during a small break LOCA within constraints of the plant, the accumulators would discharge into an empty reactor vessel from normal pressure. The discharge was extended by using an orifice to restrict the flow so that the tank would empty at a prescribed time. An orifice plate was installed in the outlet nozzle of the accumulator. The **[**

][a,c] was calculated to result in a discharge time of approximately 15 minutes.

The test was conducted by opening the motor operated gate valve which would allow the tank to drain and the data to be recorded. The test was performed from an initial pressure of 600 psig and with initial water volume of 850 cubic feet.

The opening time of the accumulator isolation valve was 11 seconds. The time required for the water to discharge from the accumulator was 954 seconds.

20.1.3.1 WCOBRA/TRAC-TF2 Model

The Callaway small break accumulator blowdown was simulated **[**

][a,c]. Water and gas volumes, as well as the accumulator discharge nozzle diameter were preserved to accurately represent the test conditions. **[**

][a,c] Liquid and gas temperatures were set to 87°F, consistent with test data.

20.1.3.2 WCOBRA/TRAC-TF2 Simulation Results

Figure 20.1-6 shows a comparison of the accumulator pressure and the test data. **[**

][a,c]

20.1.4 Effect of Accumulator Nitrogen on PWR Reflood Transients

In Appendix K-based evaluation models, simple models were incorporated to simulate the effect of the nitrogen injecting from the accumulator into the cold legs and out the break for approximately 30 seconds during reflood. The effect of the nitrogen is to pressurize the downcomer and force water into the core, while promoting core cooling. Typically, the effect of nitrogen was ignored in these earlier evaluation models.

The previous Westinghouse Best-Estimate LOCA methodologies (Code Qualification Document (CQD) and Automated Statistical Treatment of Uncertainty Method (ASTRUM)) used experimental evidence to support the conclusion that the effect of accumulator nitrogen realistically improves reflood rates and heat transfer. A simplified method was developed for WCOBRA/TRAC MOD7A to treat the effects of accumulator discharge on the reflood transient, without considering an explicit transport of the non-condensable gases.

WCOBRA/TRAC-TF2 explicitly provides the capability of treating non-condensable gases, which allows more mechanistic treatment of the effects of the nitrogen discharge on the reflood transient, without the need of a simplified model. The experimental evidence that assesses the WCOBRA/TRAC-TF2 on modeling the effects of the nitrogen discharge on the reflood transient is discussed below.

20.1.4.1 LOFT Test L2-5

The description of the LOFT facility and tests are provided in Sections 22.2 and 22.3, and the WCOBRA/TRAC-TF2 input models and simulation results of the six simulated LOFT tests, including L2-5, are presented in Section 22.4.

The sequence of events for the LOFT large break Test L2-5 (Bayless et al., 1982) during the period of accumulator flow is similar to that calculated for a typical plant transient. The accumulator liquid flows down into the downcomer directly below the intact loop cold leg nozzle while steam and dispersed liquid flows up the opposite side and out of the cold leg break during the blowdown. Toward the end of the period of accumulator flow, the downcomer is partially full of subcooled liquid.

As the LOFT accumulator empties of liquid, the nitrogen contained in the accumulator begins to flow down the accumulator line and into the cold leg. Figures 20.1-10 and 20.1-11 show the accumulator liquid level and pressure for Test L2-5. From the density measurement in the intact loop cold leg, as shown in Figure 20.1-12, the nitrogen in the accumulator entered the RCS after the accumulator emptied at about 50 seconds (Figure 20.1-10).

It can be seen from the core bubble plot (Figure 20.1-13a) that there is an increase in core level beginning at about 43 seconds. By 60 seconds the core is completely covered. Figure 20.1-13b shows the cladding temperature in one of the central bundles at different elevations in the test, and indicates a progressive quenching at two lower elevations, 8 inches and 26 inches from the bottom of the core, from approximately 48 to 60 seconds, respectively. Therefore, the appearance of the nitrogen in the downcomer does not cause a simultaneous sudden quench at these two different elevations.

A more recent analysis of the LOFT Self-Power Neutron Detectors (SPNDs) (Mackley and Birchley, 1985) provides further qualitative evidence of the density of the fluid in the LOFT core. Figure 20.1-14 shows the fluid densities in the central fuel bundle for LOFT Test L2-5 at elevations of 27 and 44 inches above the bottom of the core, and the fuel clad temperature transients at the same elevations were also co-plotted with the fluid densities respectively. In this experiment, the peripheral low power regions of the core were quenched either during blowdown or by the liquid entering the core prior to 60 seconds, and the high power regions were quenched by 60 seconds.

Evidence of the effect of nitrogen on the downcomer pressure is shown in Figure 20.1-15. A sudden increase in pressure is observed in the suppression tank at 60 seconds, coincident with the time that nitrogen enters the cold leg from the accumulator.

20.1.4.2 WCOBRA/TRAC Prediction of LOFT Reflood Transient

In the simulation of the LOFT tests (Section 22.3), the accumulators were modeled as in a PWR, **[**

][a,c]

The simulation results show that the accumulator water is predicted to flow down into the downcomer after the check valve in its discharging line is opened by low RCS pressure and makes its way into the cold leg and vessel. **[**

][a,c]

20.1.4.3 ACHILLES Experiments

A series of reflood heat transfer experiments were conducted in the ACHILLES test facility, using boundary conditions based on best-estimate computer code calculations (Dore and Denham, 1990). Two types of tests were conducted; "forced" reflood experiments, in which the downcomer water was forced into the core by applying a high nitrogen overpressure, and "natural" reflood experiments, in which the nitrogen overpressure was created by nitrogen discharged from a scaled accumulator. In both types of tests, the initial surge of water resulted in significant cooling, and entrainment of water out of the top of the test bundle. This was followed by a period of poor cooling, until the downcomer driving head could be re-established by the continuation of pumped safety injection. However, the net result was a significant reduction in the maximum cladding temperatures attained, relative to comparable tests with no initial surge into the bundle.

20.1.4.4 WCOBRA/TRAC Prediction of ACHILLES International Standard Problem 25

Westinghouse has used WCOBRA/TRAC-TF2 to simulate International Standard Problem (ISP) number 25 (Holmes, 1991), an experiment which simulated the end of the accumulator discharge period in a postulated large break loss of coolant accident. The test was performed in the ACHILLES test facility at AEA Technology Winfrith. The test facility was described by Denham et al. (1989), and ISP 25 results were reported by Holmes (1991). The facility layout is shown in Figure 20.1-24.

The WCOBRA/TRAC-TF2 model of the ACHILLES test facility is shown in Figure 20.1-25.
[

]^{a,c}

The test section was modeled [

]^{a,c}

Comparisons of the WCOBRA/TRAC-TF2 simulation with the experimental data are shown in Figures 20.1-27 through 20.1-36. Figures 20.1-27 and 20.1-28 show the accumulator depressurization and mass flow rate through the injection line during the early part of the transient. **[**

][a,c]

The predicted pressure loss from the top of the downcomer to the break is compared with the measured pressure loss in Figure 20.1-30. **[**

][a,c] The predicted gas mass flow rates to the break are compared with the measured data in Figure 20.1-31. **[**

][a,c]

Downcomer and core collapsed liquid levels are shown in Figures 20.1-32 and 20.1-33. **[**

][a,c]

Figures 20.1-34 through 20.1-36 show the cladding temperature transients at 1.08m, 2.01m, and 2.65m.
[

]a,c

Broken Pipe Pressure Loss Sensitivity Study

[

]a,c

In general, the ACHILLES test simulation shows that [

]a,c

[

][a,c]

However, they do show that the effect of the initial surge on core cooling is reasonably predicted.

20.1.5 Conclusion

The accumulator model as used in the PWR, was assessed against both Separate Effect Tests (SETs) and Integral Effects Tests (IETs). The prediction of discharge of subcooled water into the RCS in both LBLOCA and SBLOCA conditions is **[**

][a,c] Therefore, based on the assessment it is concluded that the WCOBRA/TRAC-TF2 accumulator model **[**

][a,c]

20.1.6 References

1. Bayless, P. D., et al., 1982, "Experimental Data Report for LOFT Large-Break Loss-of-Coolant Experiment L2-5," NUREG/CR-2826, EGG-2210.

2. Denham, M. K., et al., 1989, "ACHILLES Unballooned Cluster Experiments Part 1: Description of the ACHILLES Rig, Test Section, and Experimental Procedures," AEEW-R2336.

3. Dore, P. and Denham, M. K., 1990, "ACHILLES Unballooned Cluster Experiments Part 5: Best Estimate Experiments," AEEW-R2412.

4. Holmes, B. J., 1991, "ISP 25 Comparison Report," AEA-TRS-1043.

5. Mackley, A. D. and Birchley, J. C., 1985, "Estimated Post-Scram Reactor Coolant Densities from Prompt Response Self Powered Neutron Detectors in Loss-of-Coolant Experiments," Instrumentation Society of America, 31st International Instrumentation Symposium, San Diego, California.

a,c

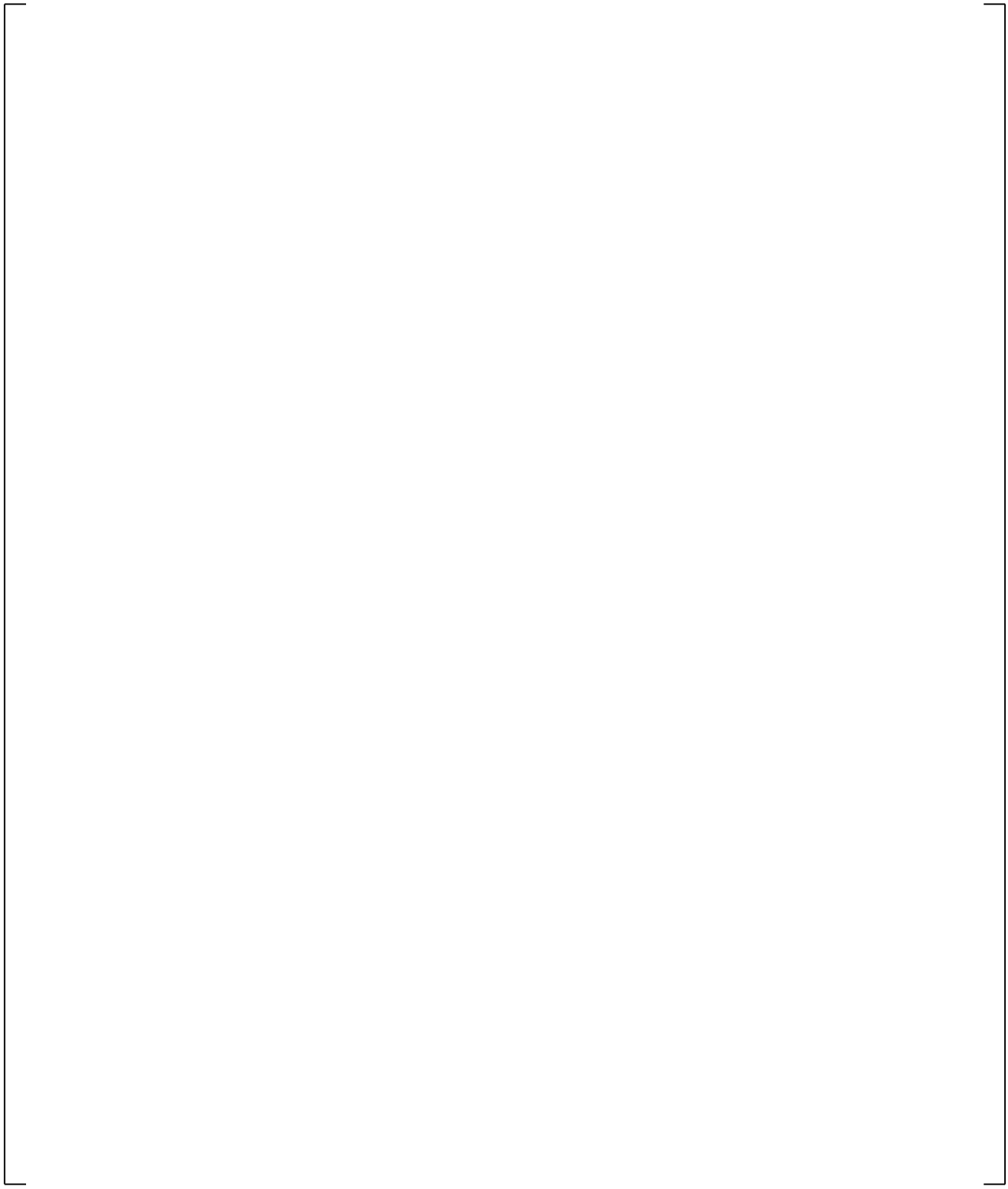

Figure 20.1-1 IPP Loop #2 Accumulator Line Schematic

a,c

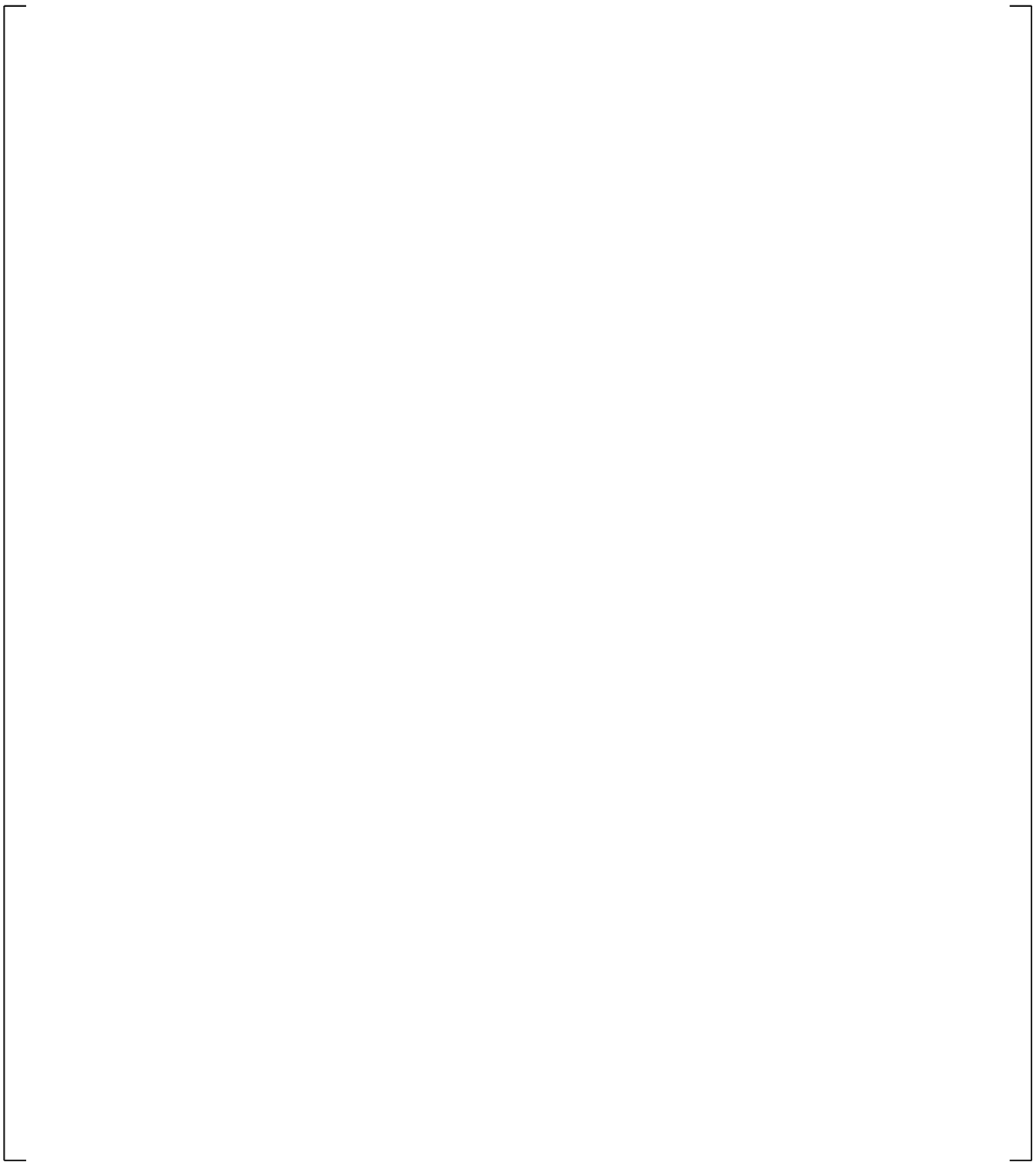

Figure 20.1-2 WCOBRA/TRAC-TF2 Model of Accumulator and SI Line in IPP and Callaway Test Models

a,c

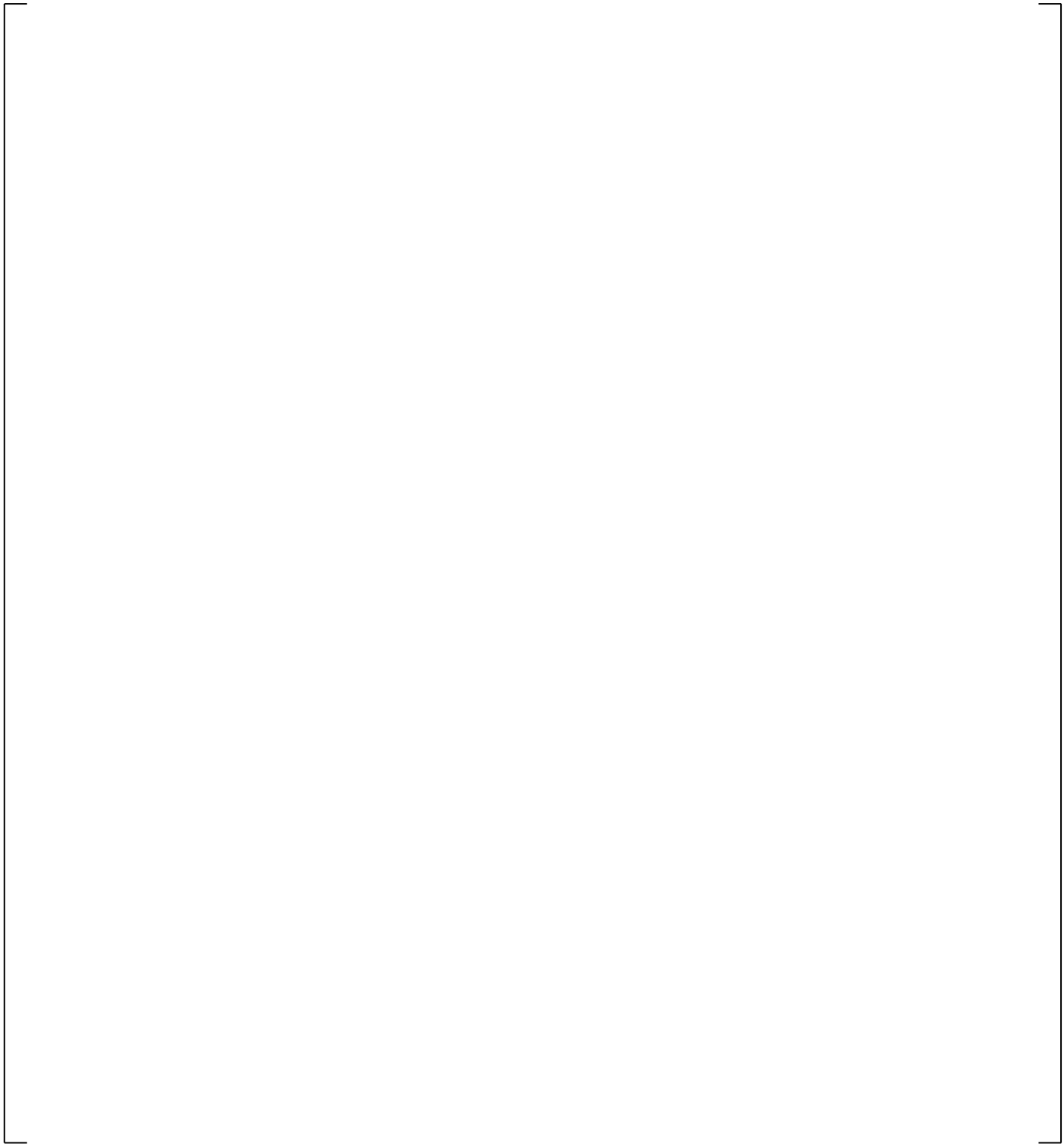

Figure 20.1-3 Predicted Accumulator Pressure (Solid Line) Compared with Measured Test Data (Dashed Line)

a,c

Figure 20.1-4 Predicted Accumulator Flow Rate

a,c

Figure 20.1-5 Predicted Gas Temperature at Top of Accumulator

a,c

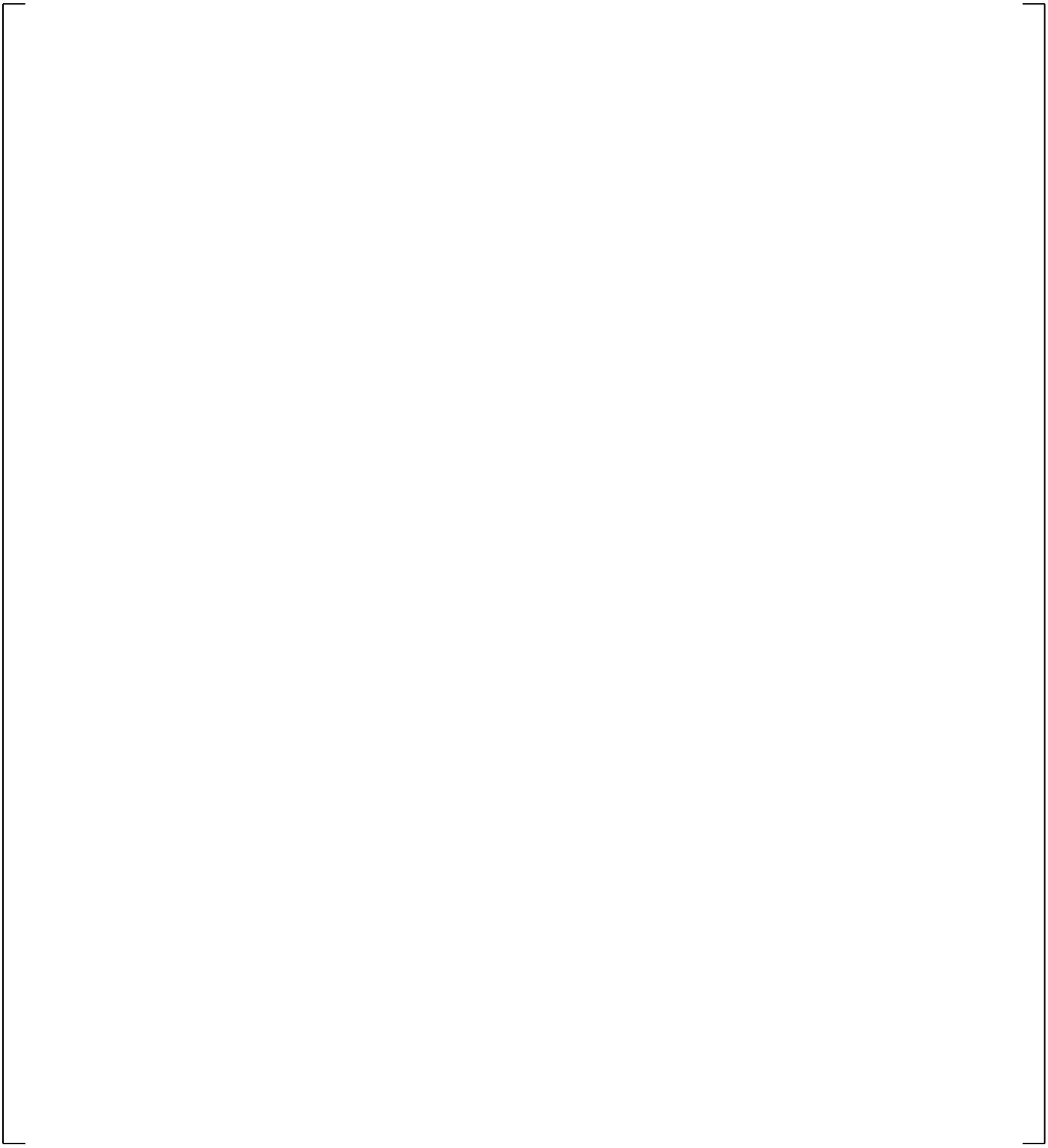

Figure 20.1-6 Comparison of Callaway Accumulator Blowdown Test Data and WCOBRA/TRAC-TF2 Prediction of Accumulator Pressure

a,c

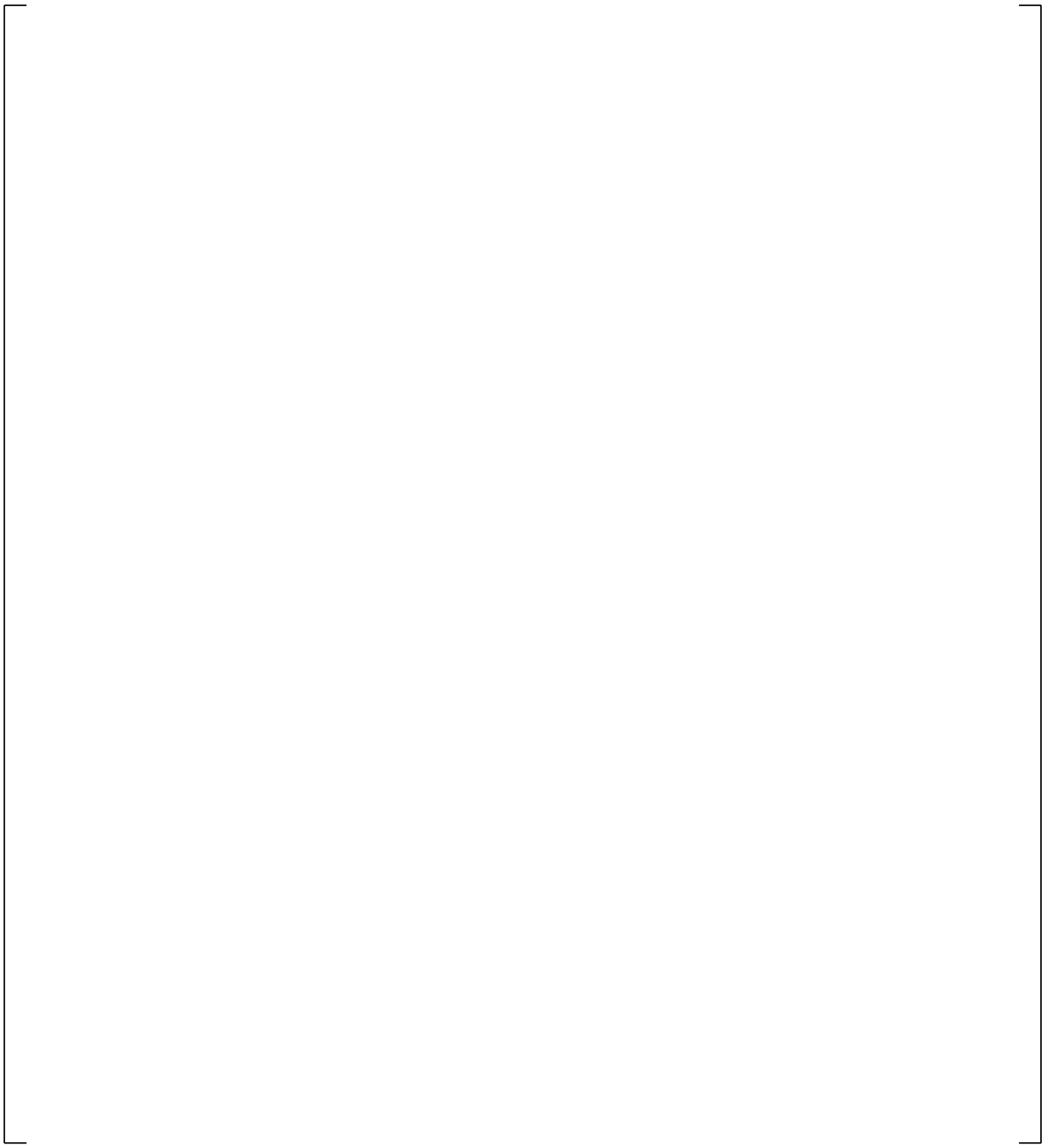

Figure 20.1-7 Comparison of Callaway Accumulator Blowdown Test Data and WCOBRA/TRAC-TF2 Prediction of Accumulator Gas Volume

a,c

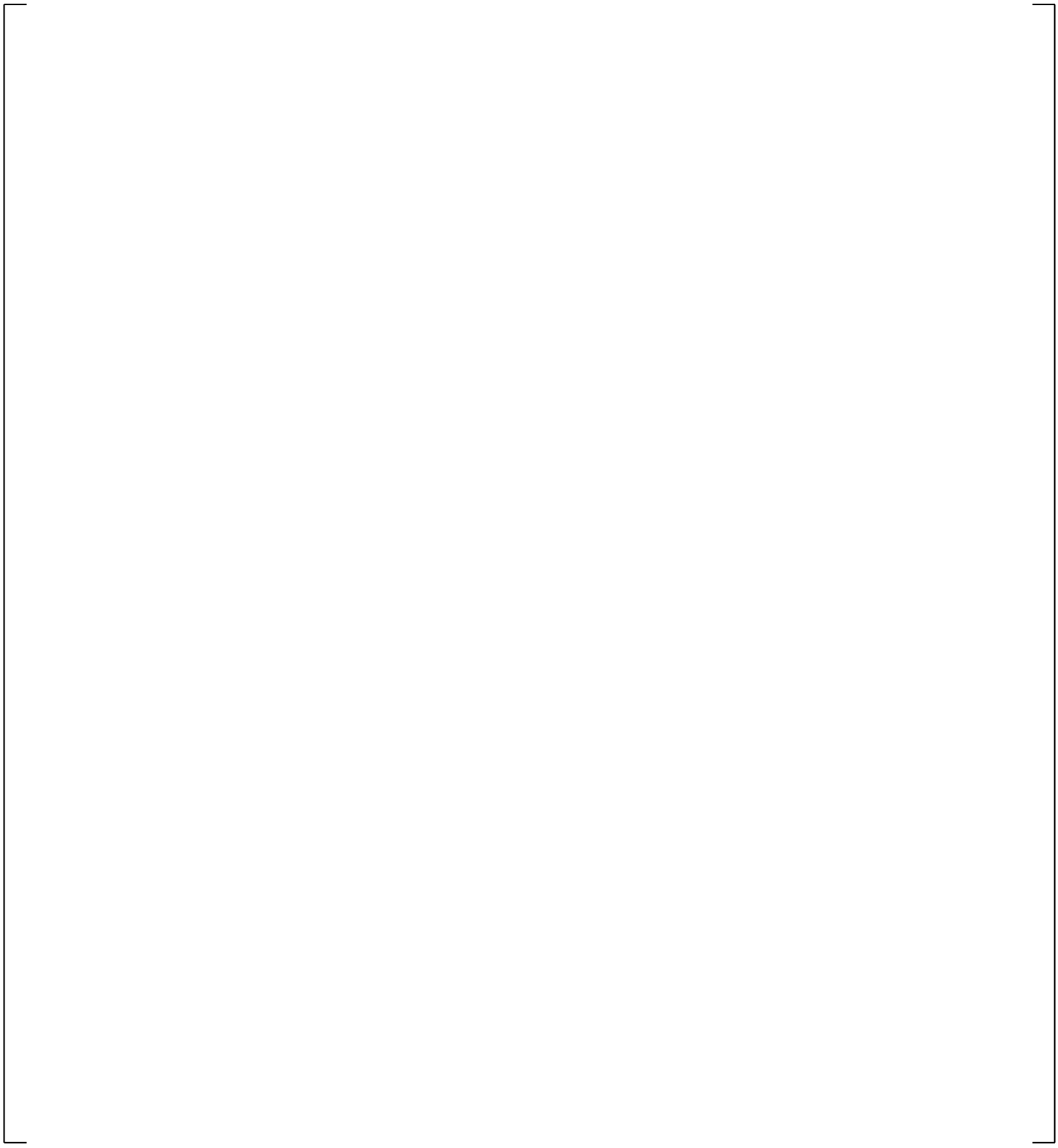

Figure 20.1-8 Comparison of Callaway Accumulator Blowdown Test Data and WCOBRA/TRAC-TF2 Prediction of Accumulator Gas Temperature

a,c

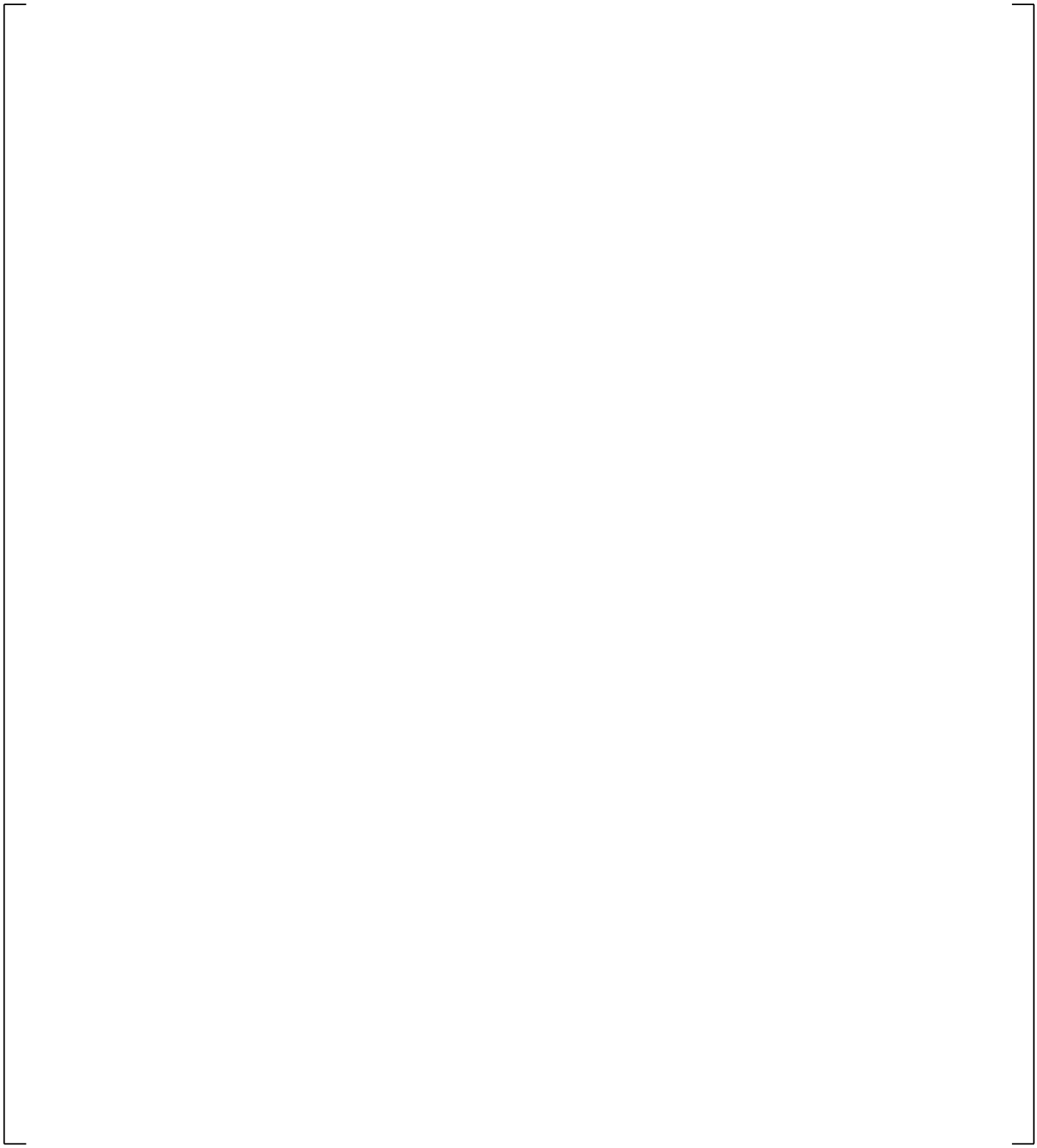

Figure 20.1-9 Best-fit Calculation of Polytropic Exponent from Callaway Accumulator Blowdown WCOBRA/TRAC-TF2 Prediction

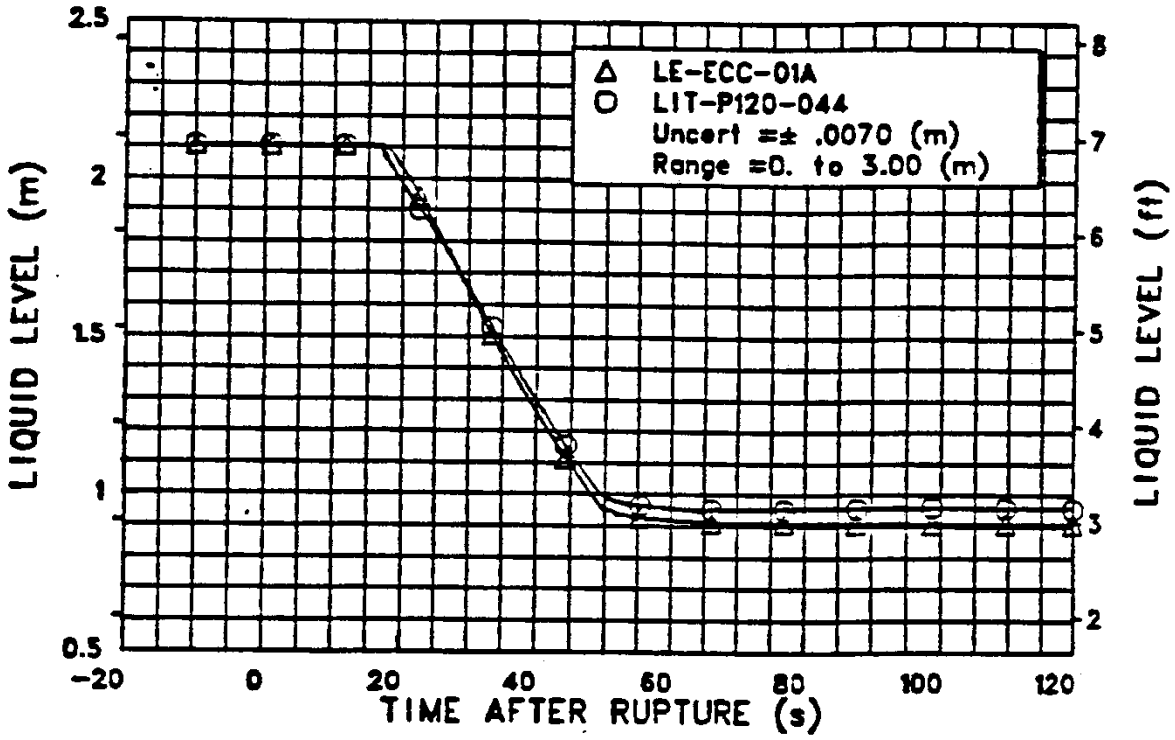

Figure 20.1-10 Accumulator Liquid Level for LOFT Test L2-5 (Bayless et al., 1982)

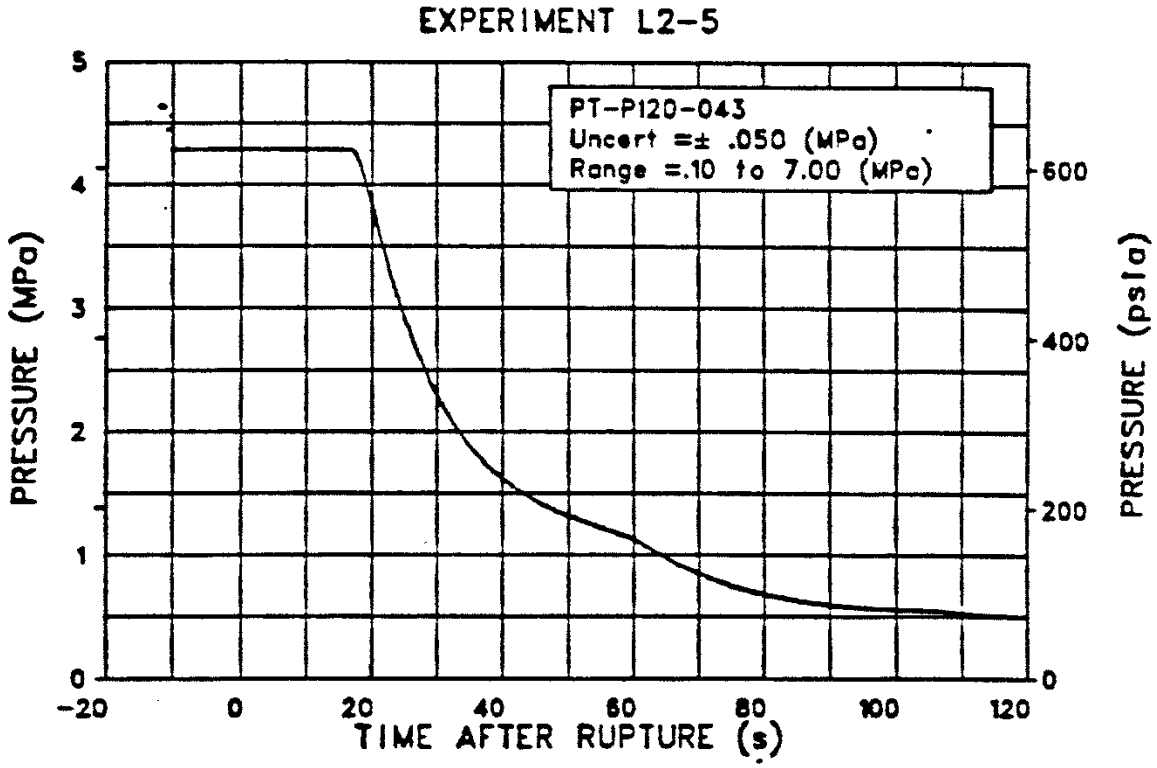

Figure 20.1-11 Accumulator Pressure for LOFT Test L2-5 (Bayless et al., 1982)

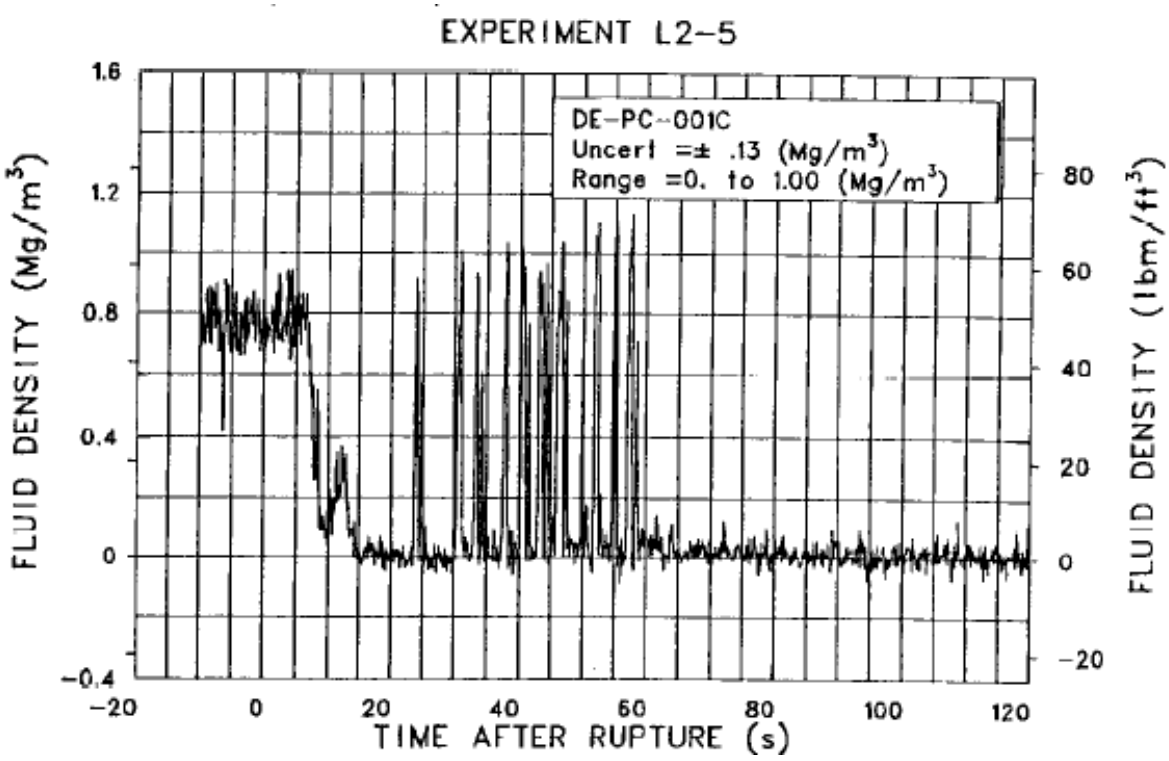

Figure 20.1-12 Intact Loop Cold Leg Density for LOFT Test L2-5 (Bayless et al., 1982)

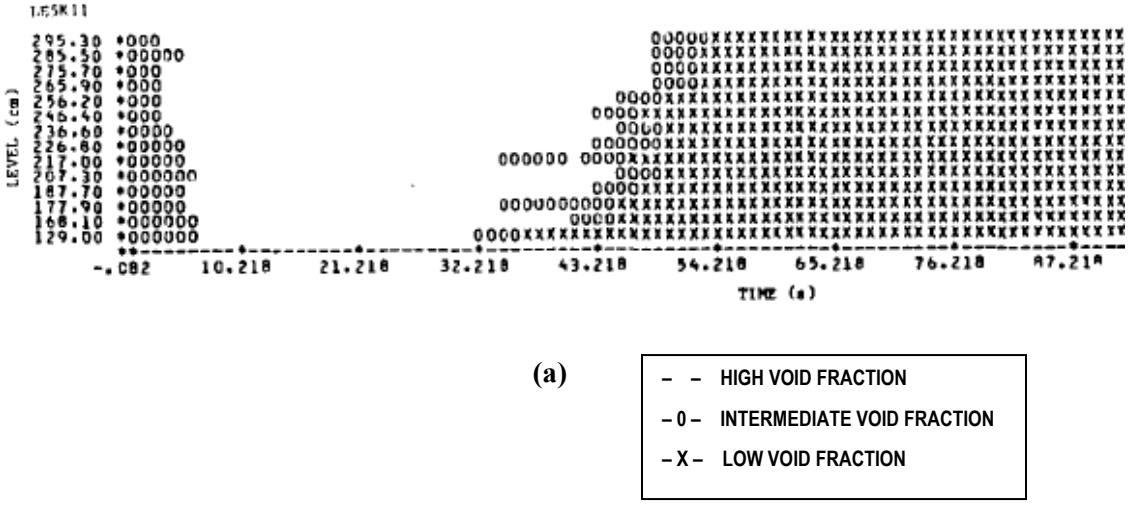

(a)

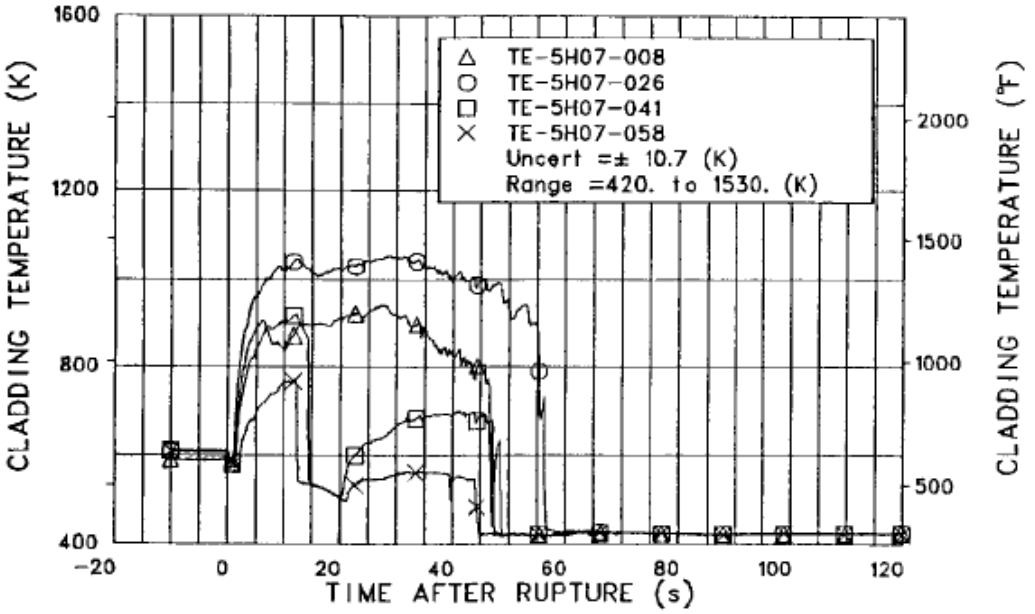

(b)

Figure 20.1-13 (a) Core Liquid Level Plots for LOFT Test L2-5 (Bayless et al., 1982)
(b) Fuel Rod Clad Temperatures (Bayless et al., 1982)

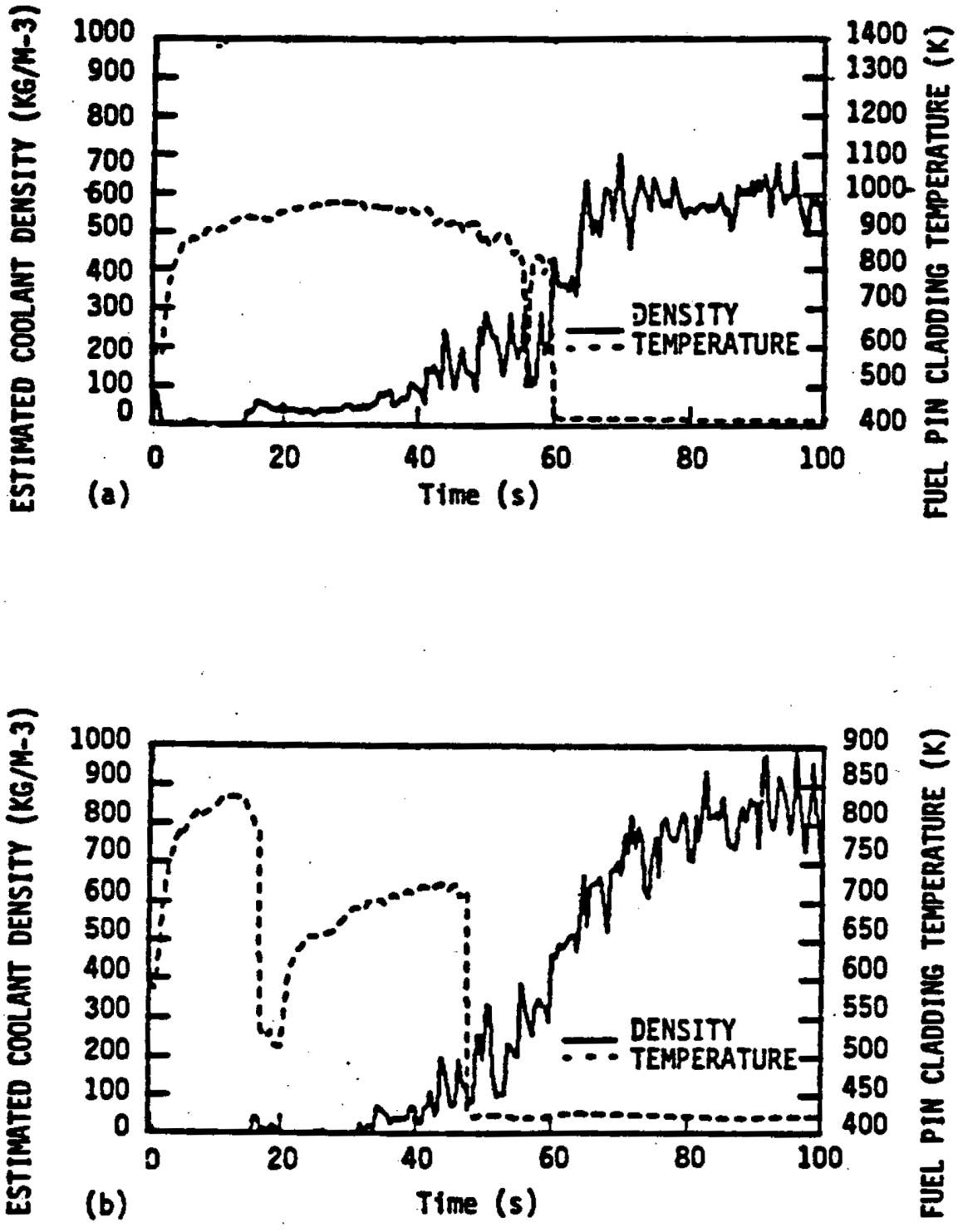

Figure 20.1-14 Fluid Density and Clad Temperature in Core at
a) 27 inches,
b) 44 inches Above Bottom of Core (Mackley and Birchley, 1985)

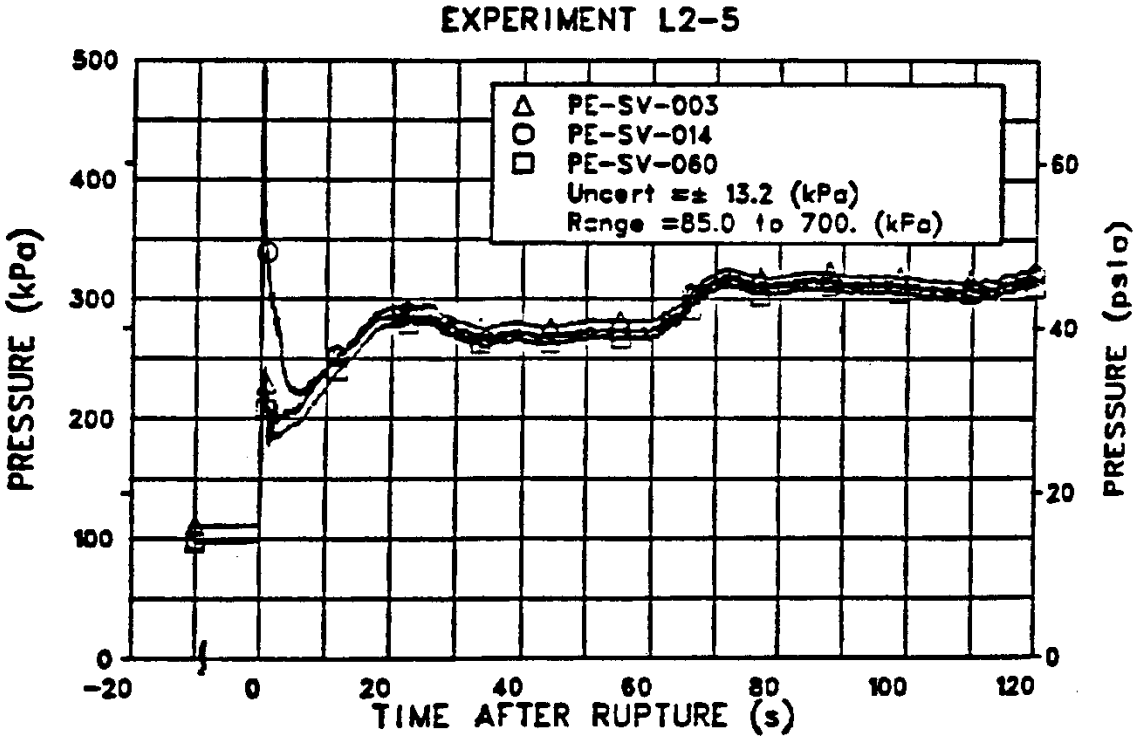

Figure 20.1-15 Suppression Tank Pressure for LOFT Test L2-5 (Bayless et al., 1982)

a,c

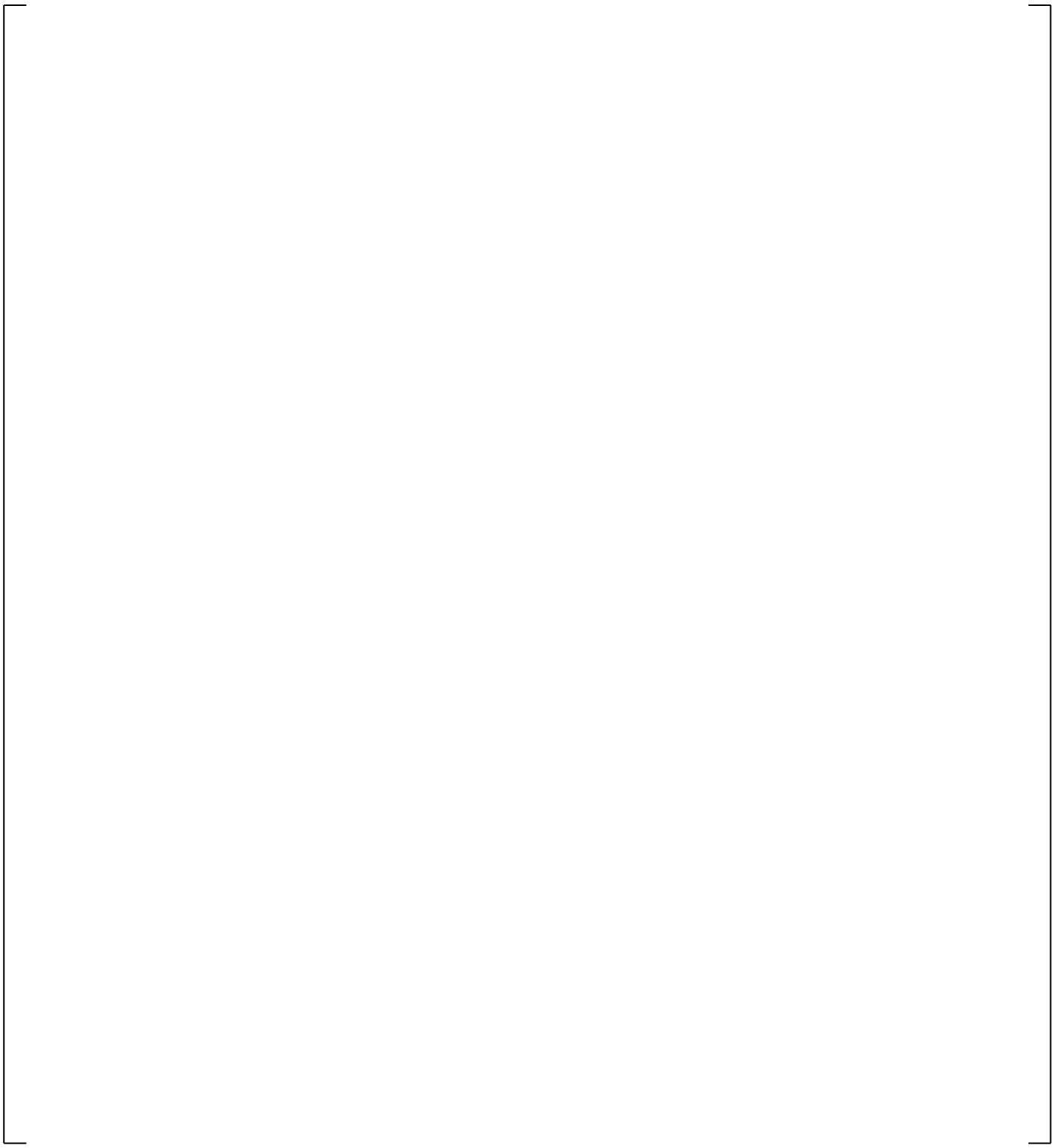

Figure 20.1-16 [

][a,c]

a,c

Figure 20.1-17 [ ]a,c

a,c

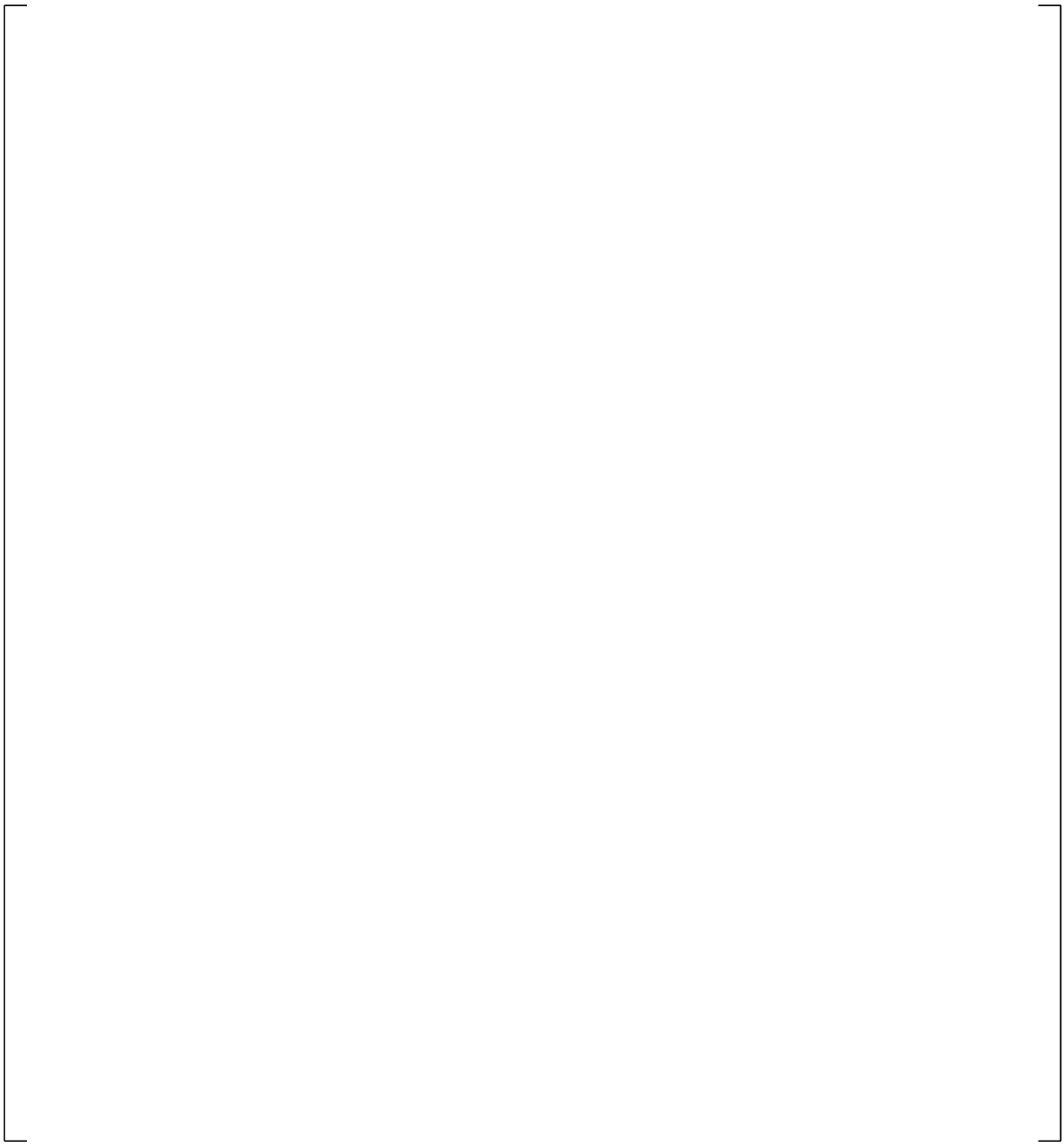

Figure 20.1-18 [ ][a,c]

a,c

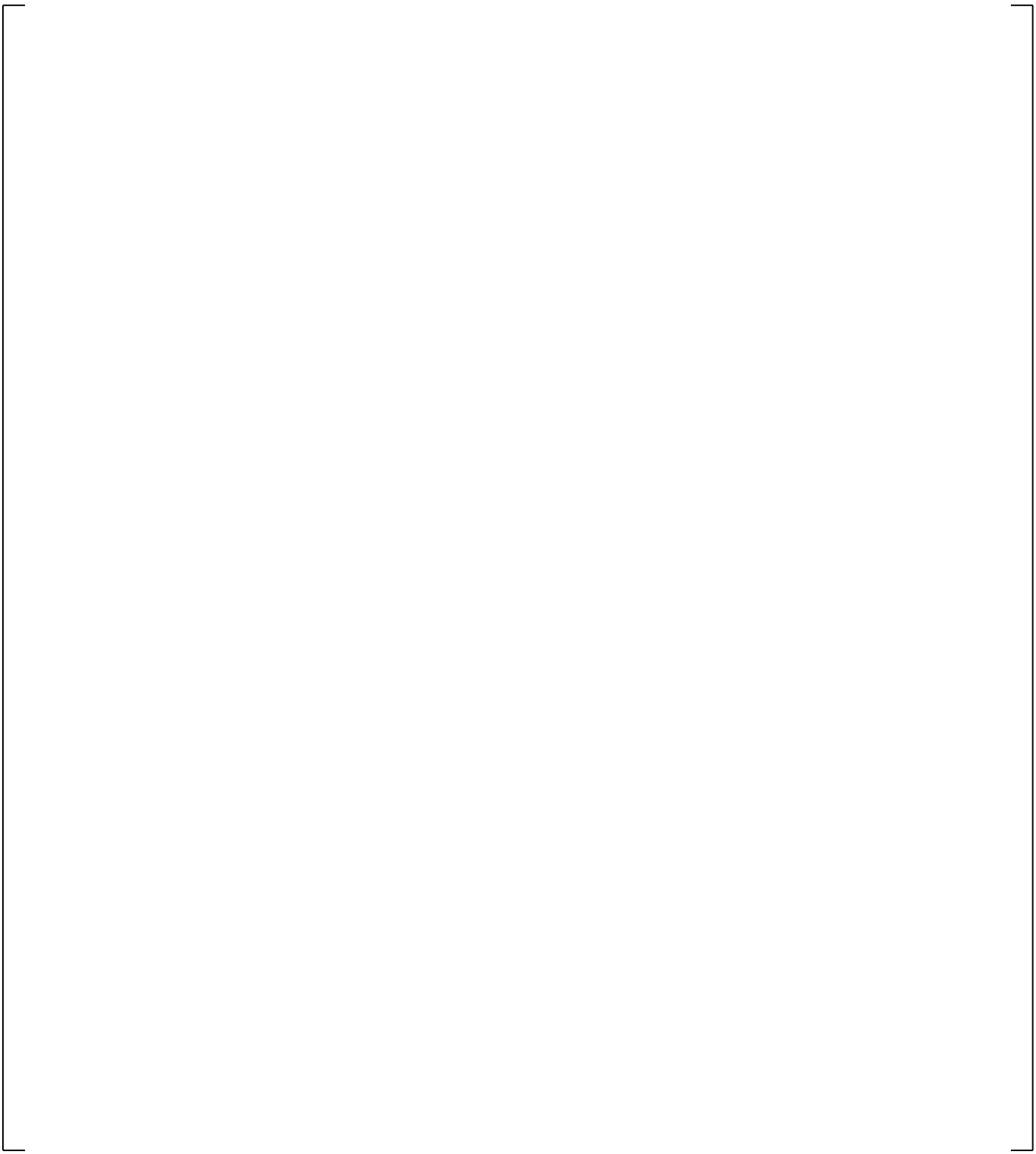

Figure 20.1-19 [

][a,c]

a,c

Figure 20.1-20 [

]a,c

a,c

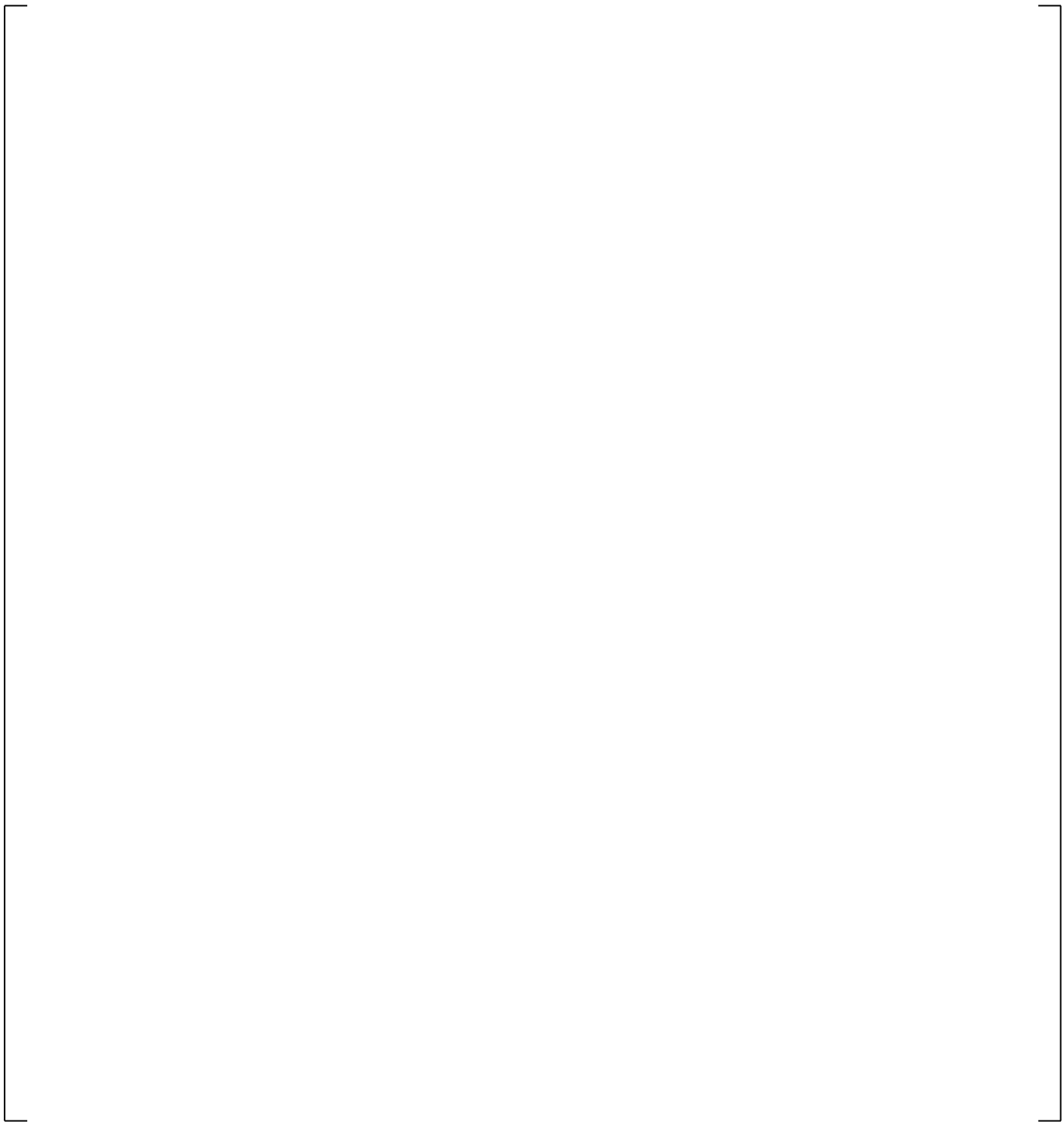

Figure 20.1-21 [

]a,c

a,c

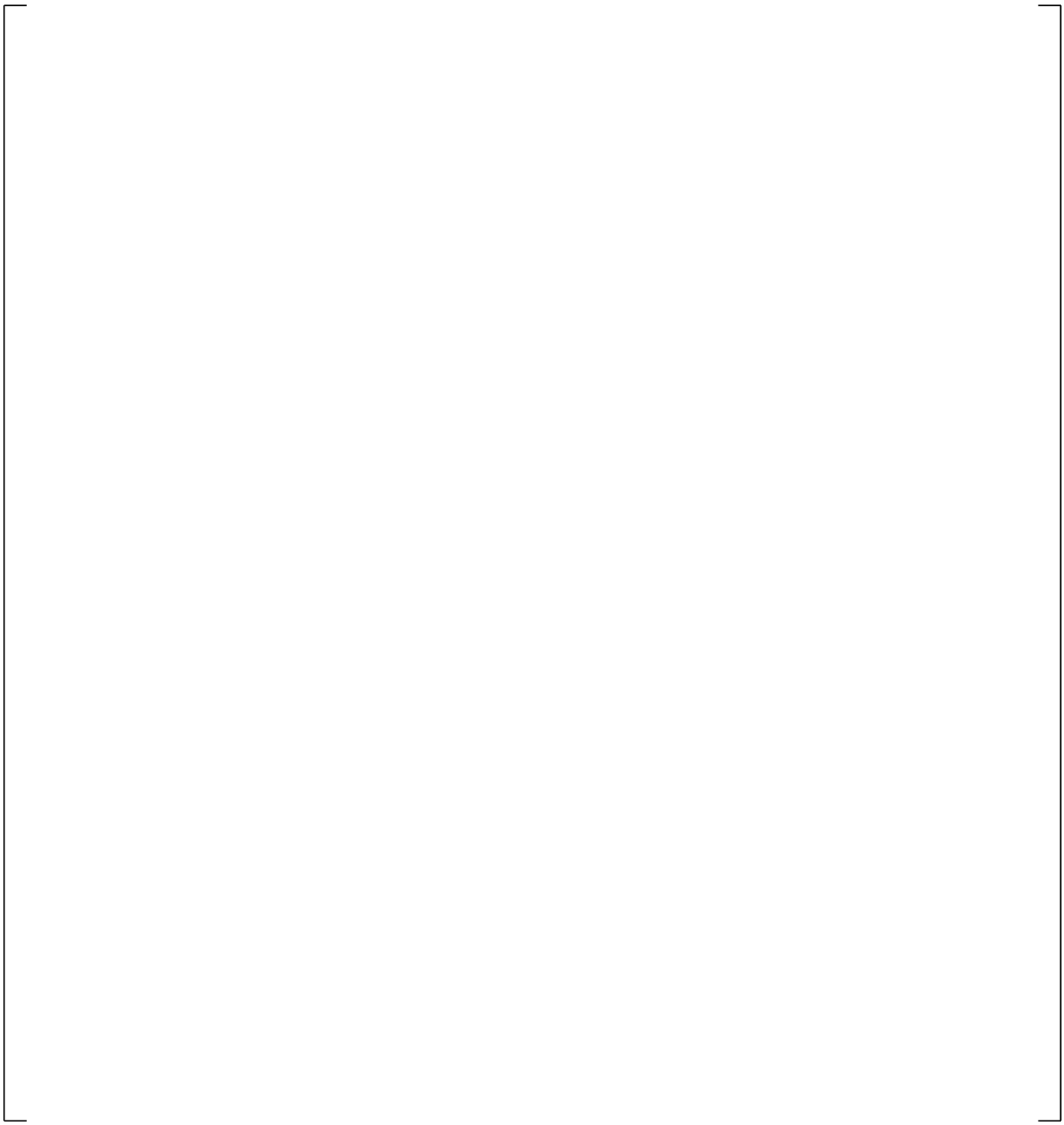

Figure 20.1-22 [

]a,c

a,c

Figure 20.1-23 [

]a,c

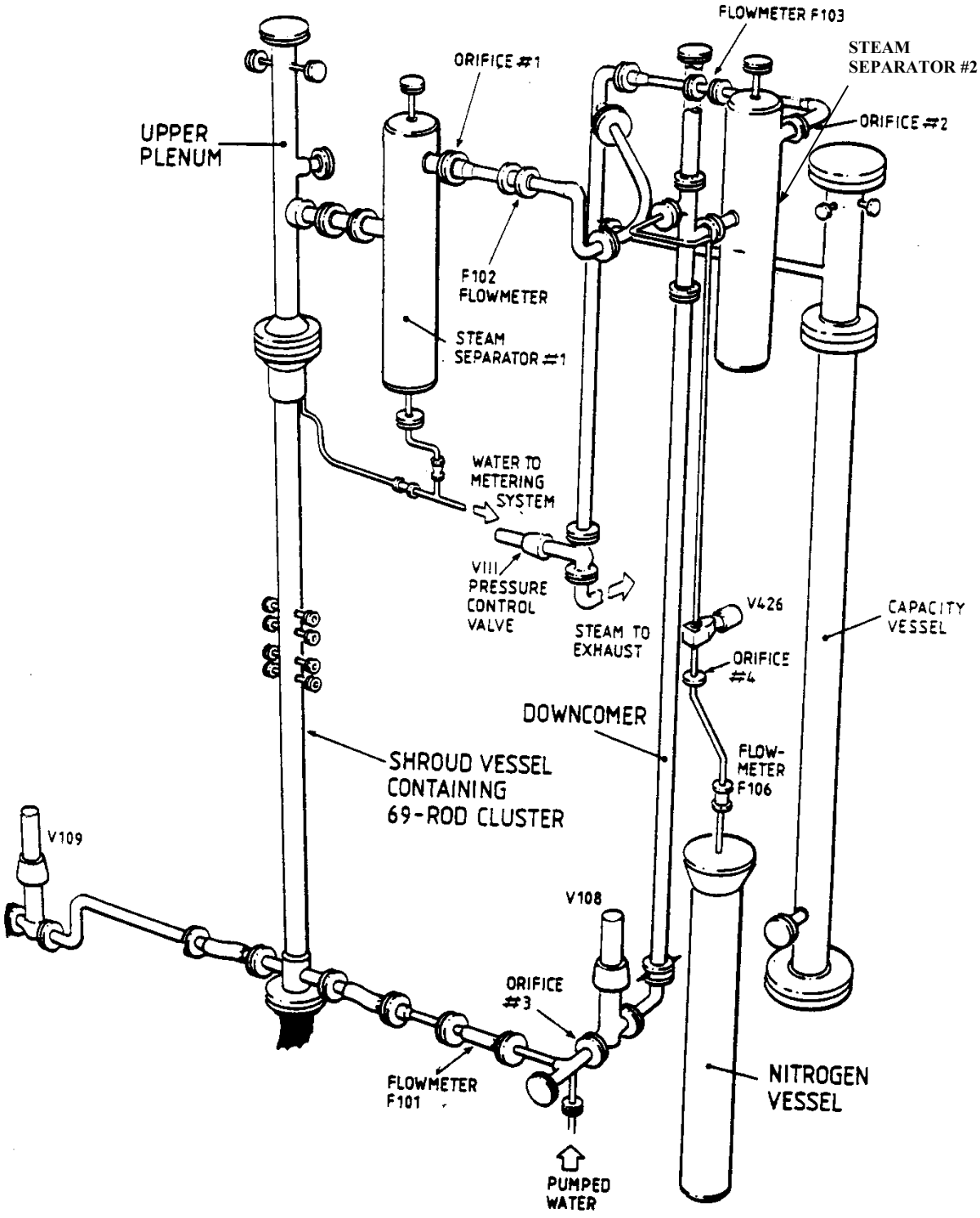

Figure 20.1-24 ACHILLES Rig Configured for Best-Estimate Transients

a,c

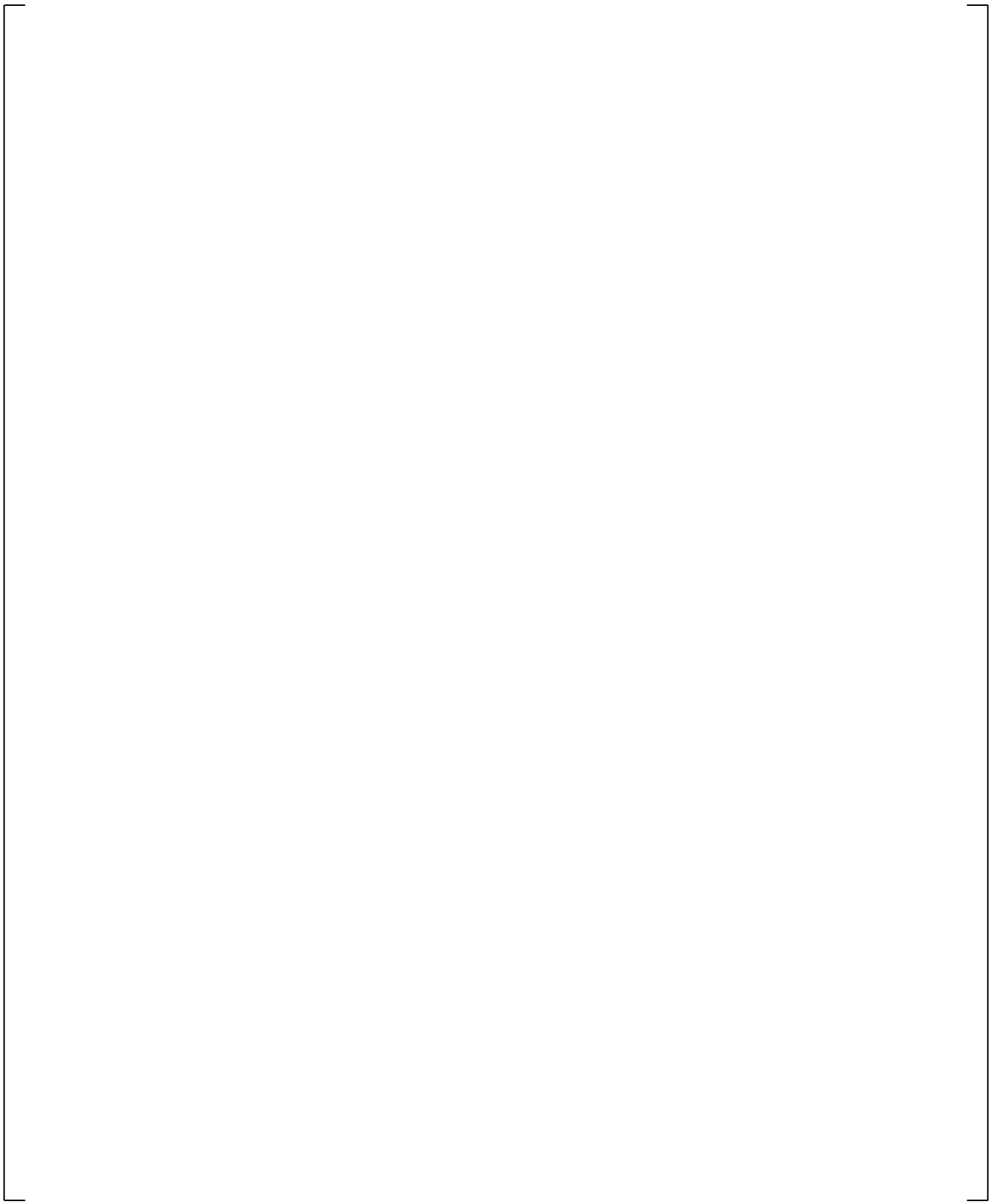

Figure 20.1-25 WCOBRA/TRAC-TF2 Model of ACHILLES Test

a,c

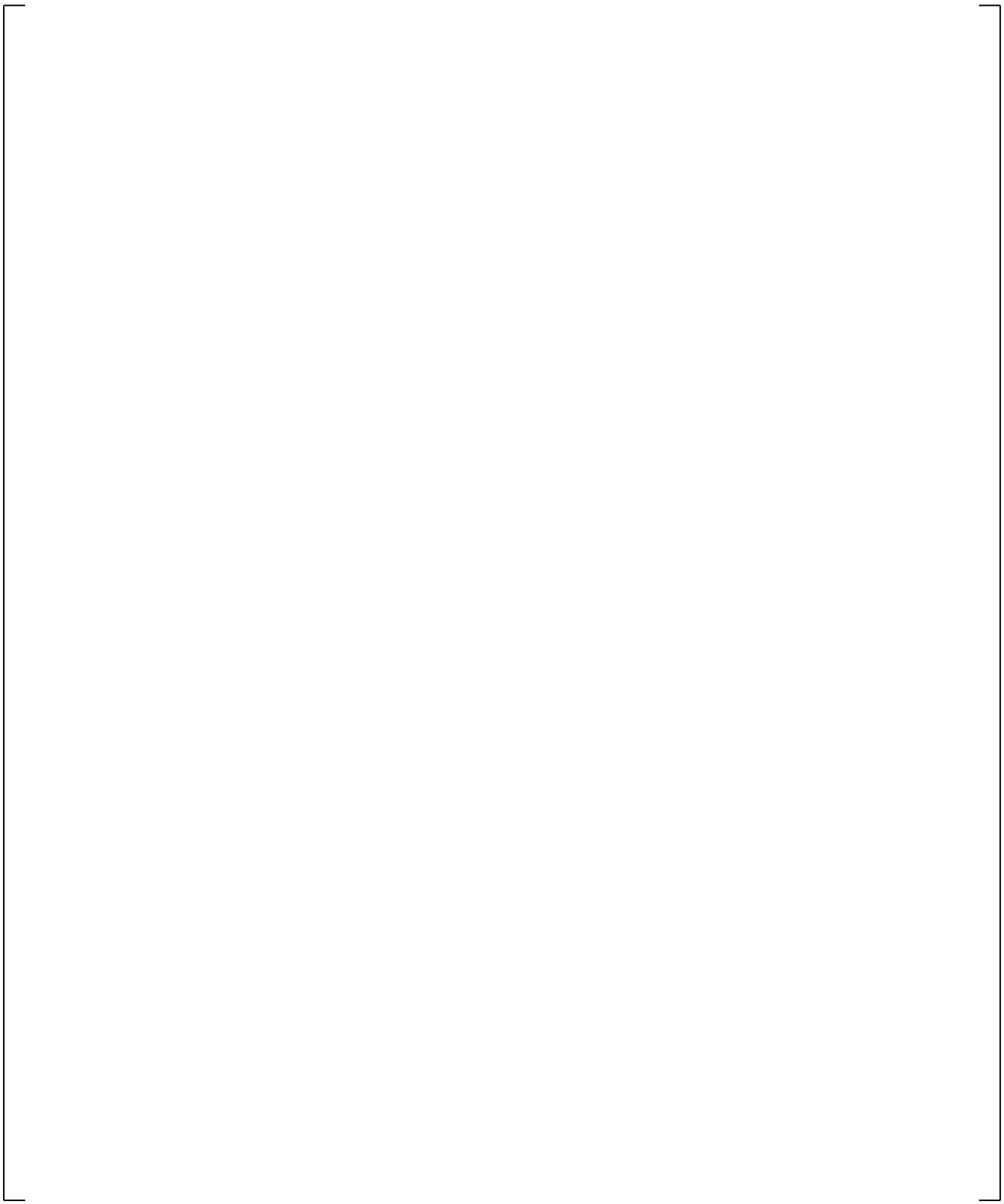

Figure 20.1-26 Cross Section of ACHILLES Cluster

a,c

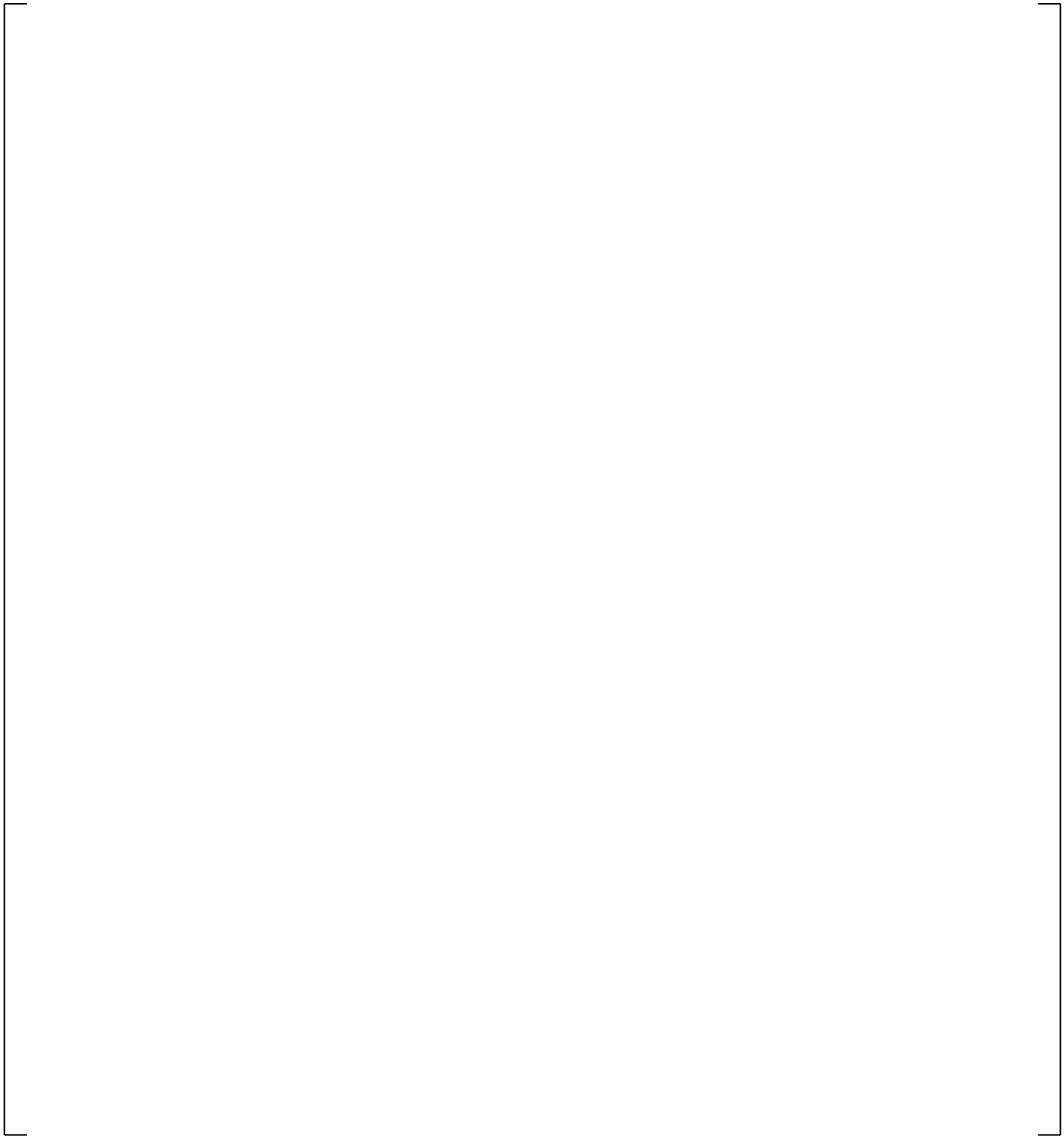

Figure 20.1-27 Measured and Predicted Accumulator Pressure

a,c

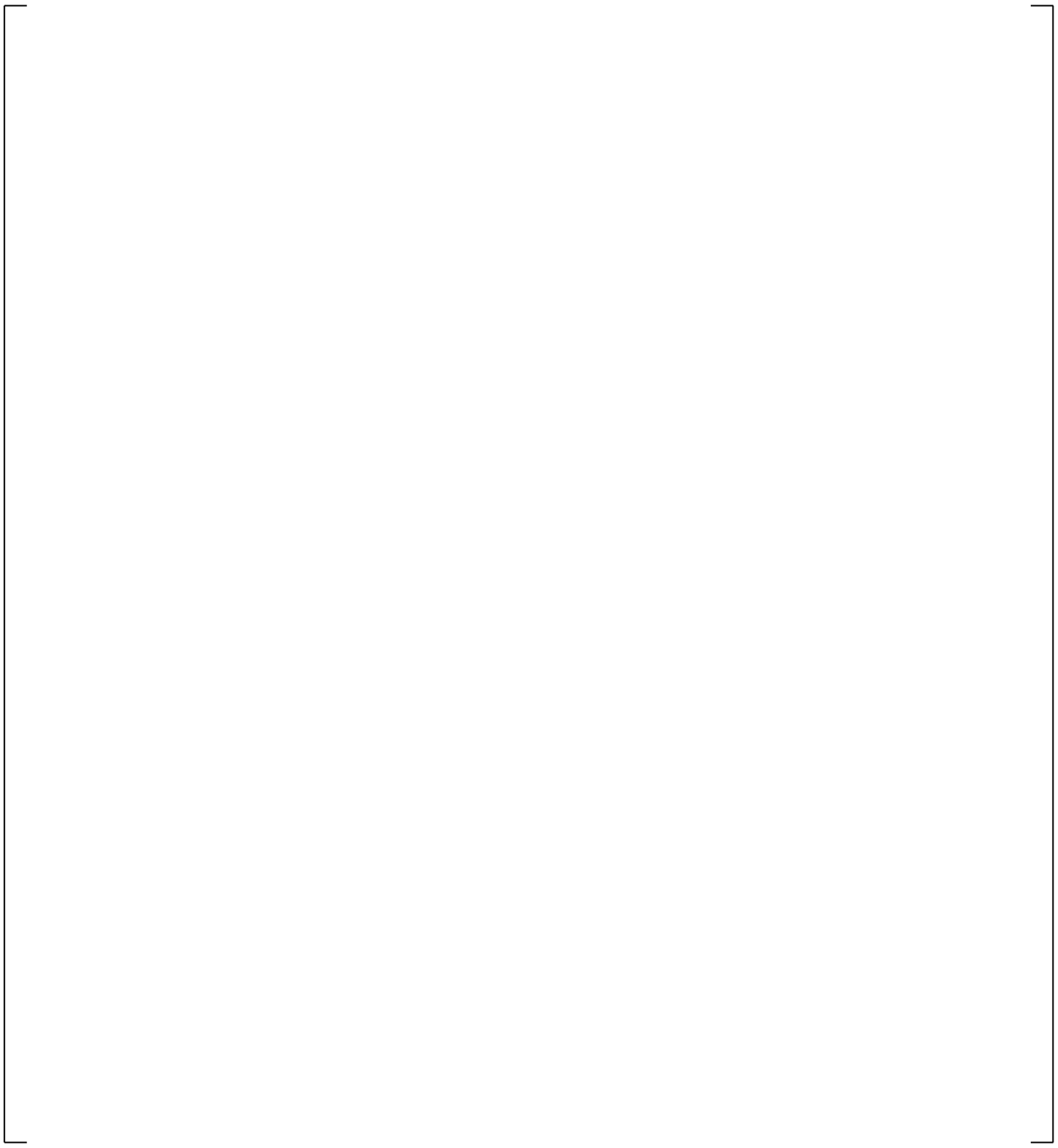

Figure 20.1-28 Measured and Predicted Accumulator Discharge Line Mass Flow Rate

a,c

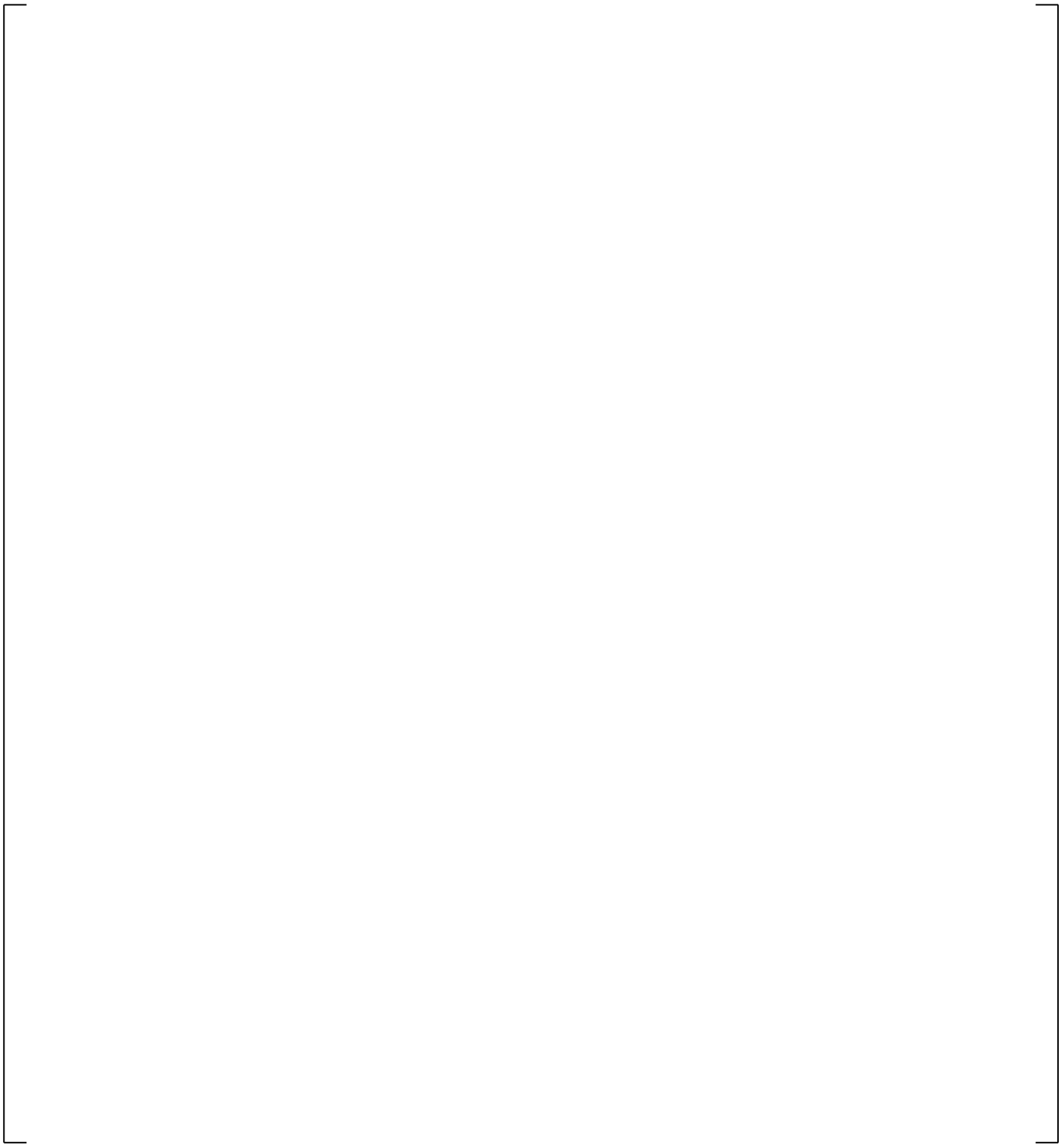

Figure 20.1-29 Measured and Predicted Pressure at Top of Downcomer

a,c

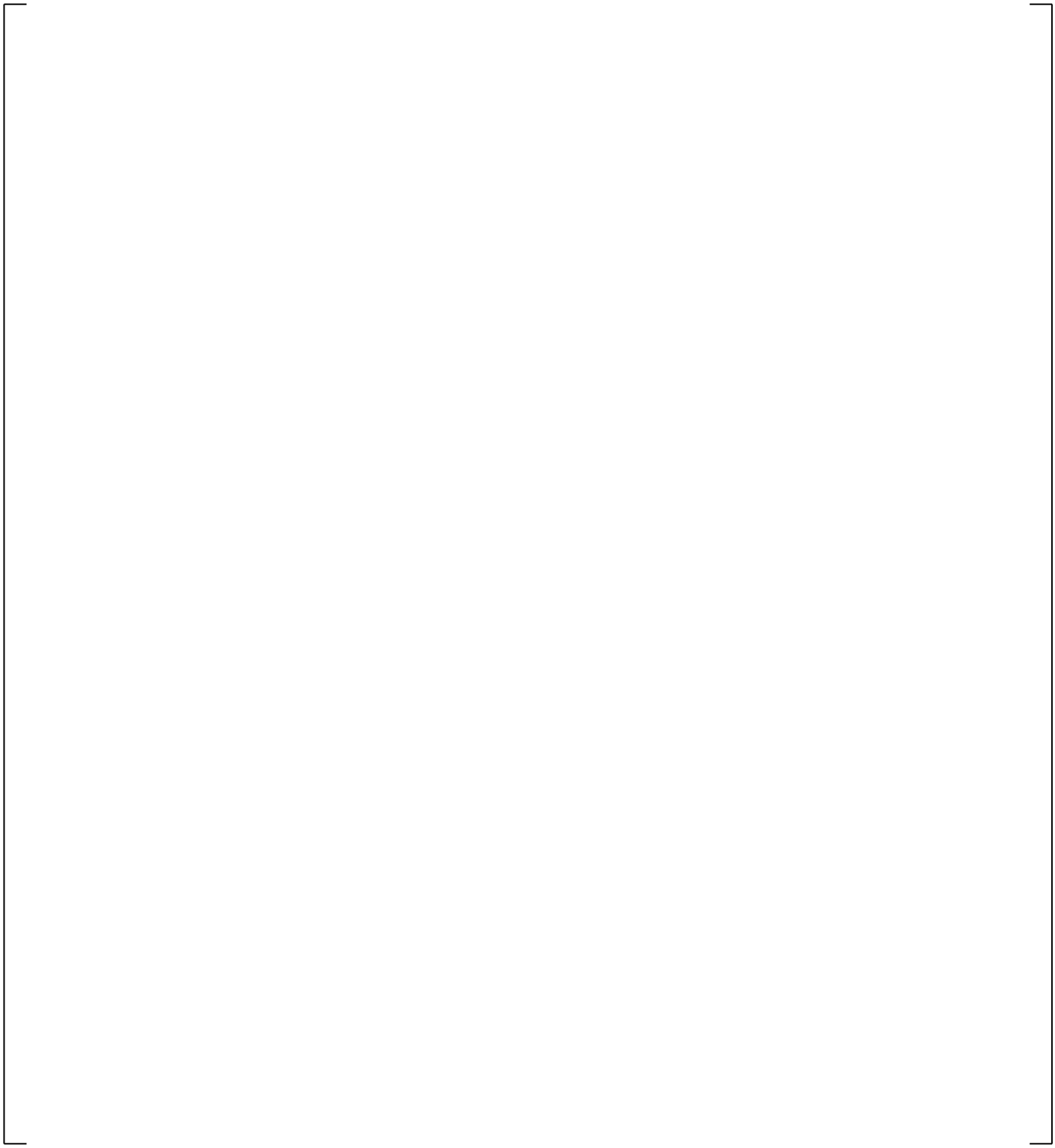

Figure 20.1-30 Measured and Predicted Pressure Loss from Top of Downcomer to Break

a,c

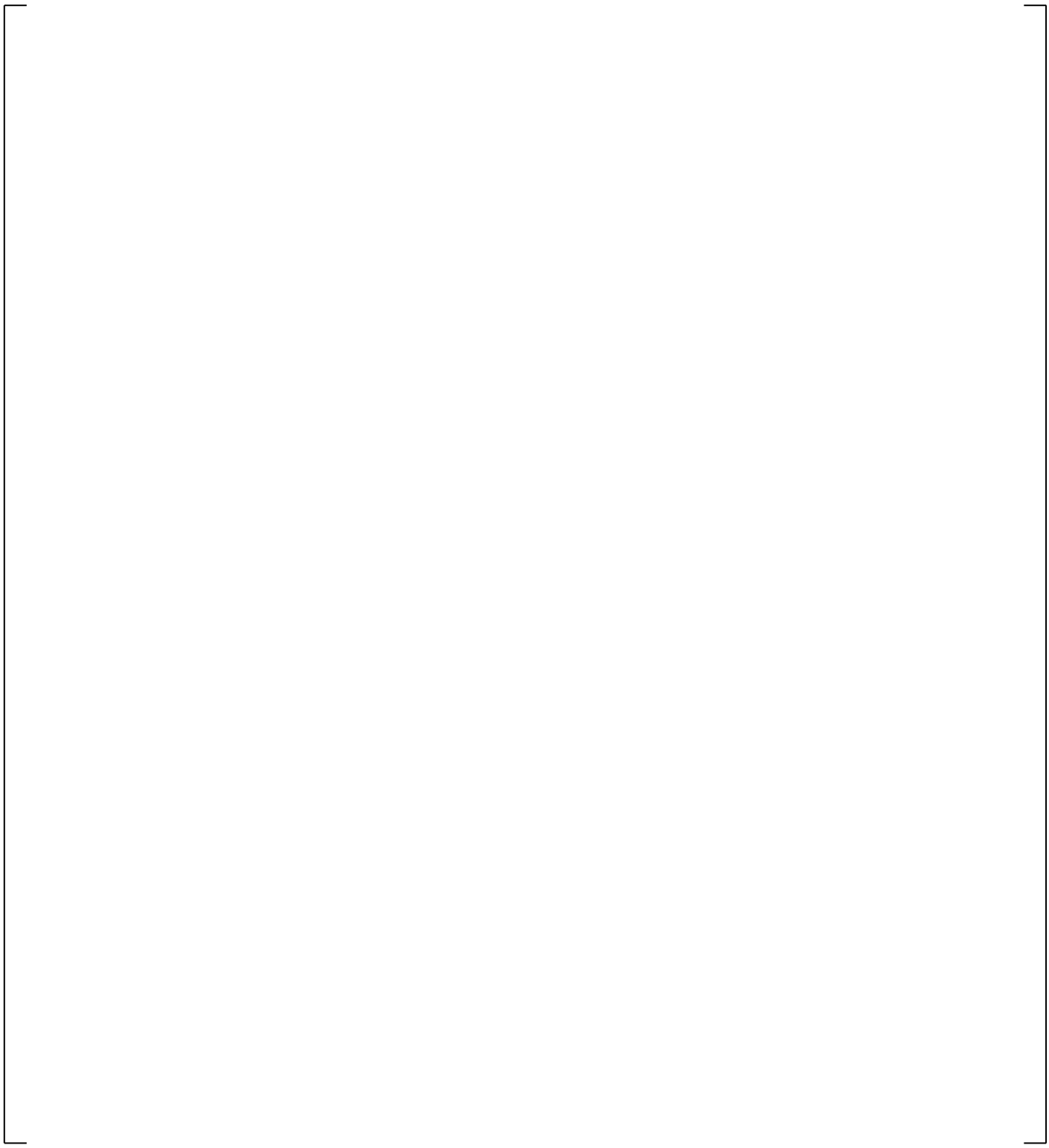

Figure 20.1-31 Measured and Predicted Gas Flow Rate from Top of Downcomer to Break

a,c

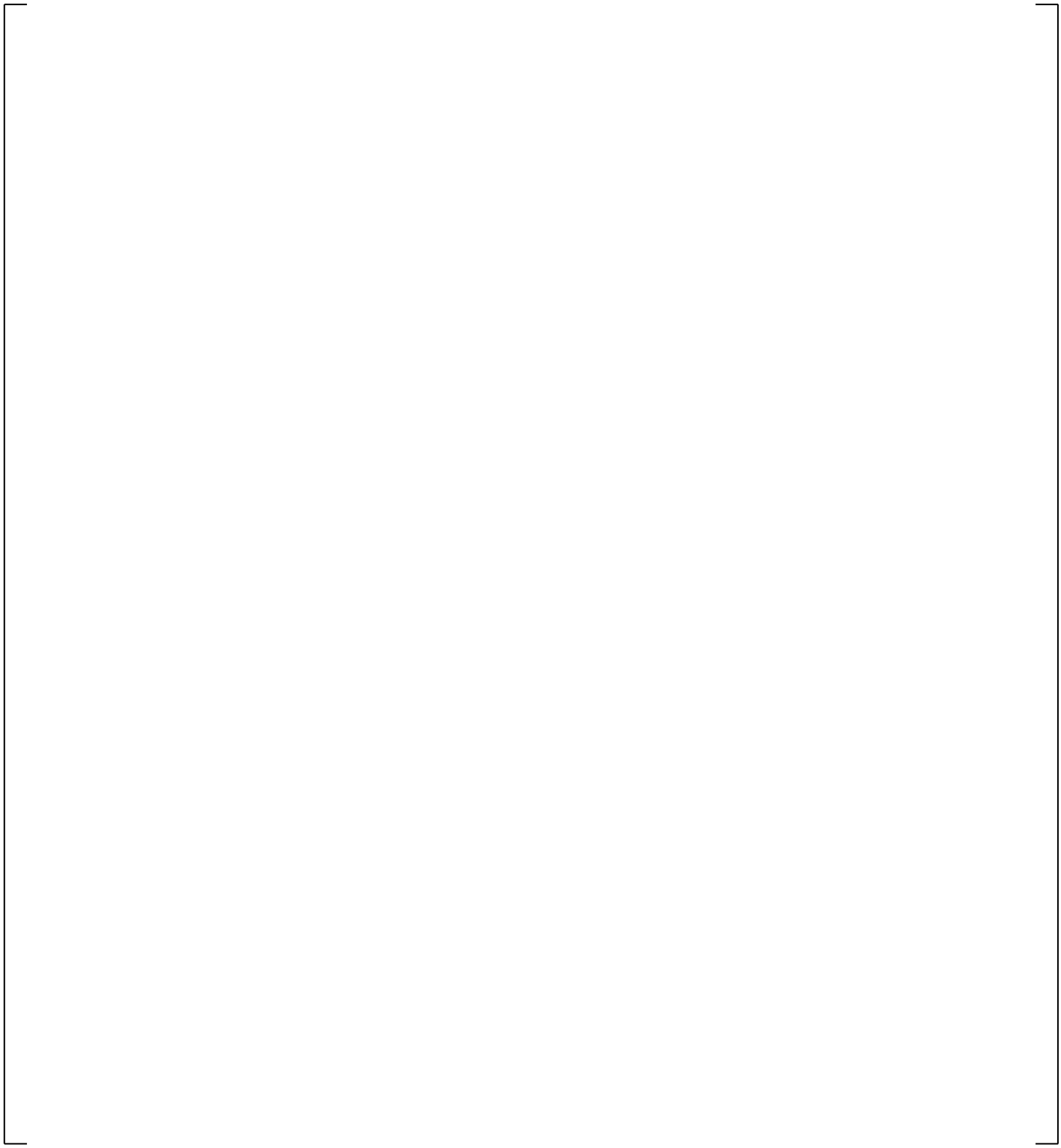

Figure 20.1-32 Measured and Predicted Downcomer Liquid Level

a,c

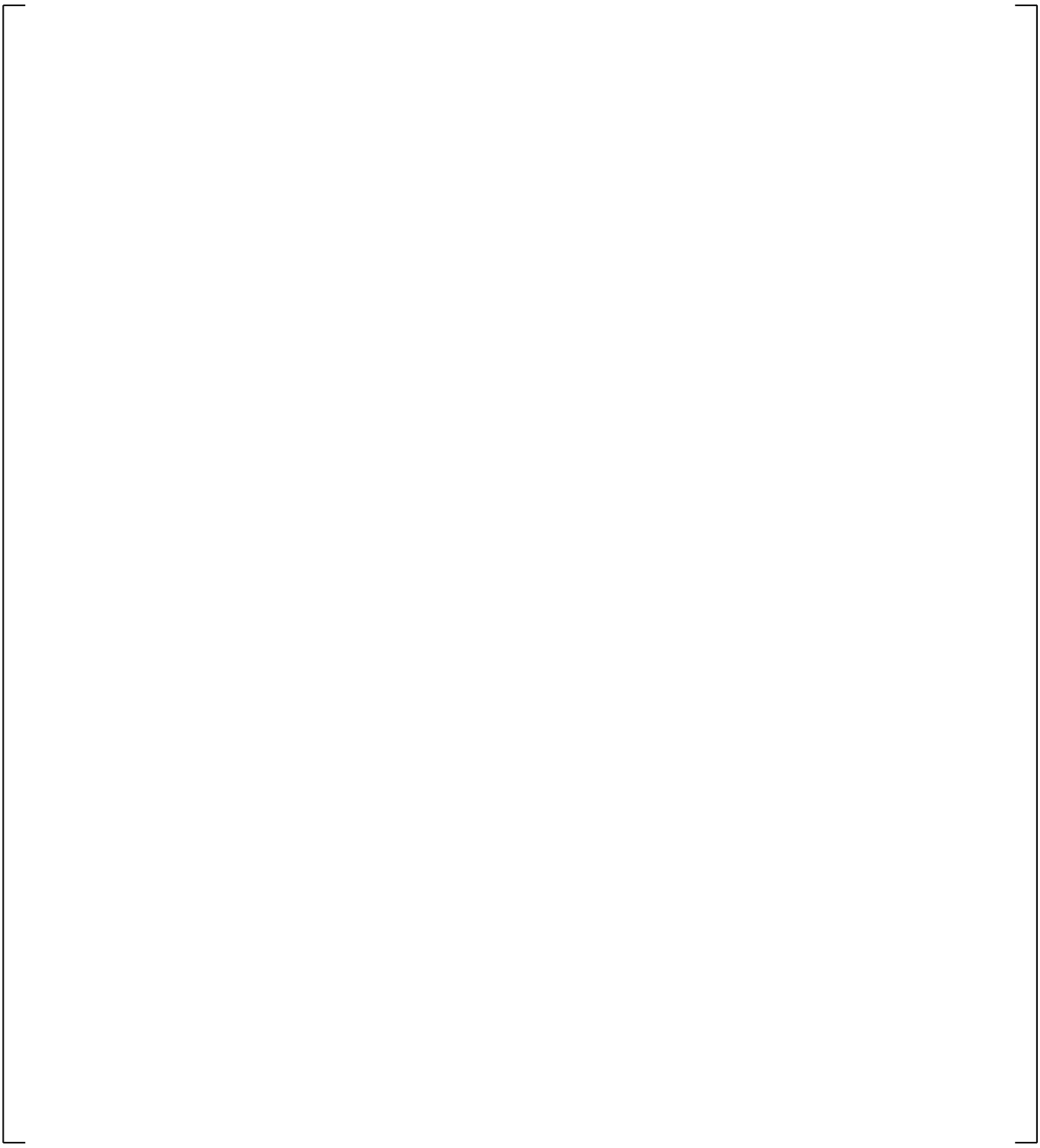

Figure 20.1-33 Measured and Predicted Test Section Liquid Level

a,c

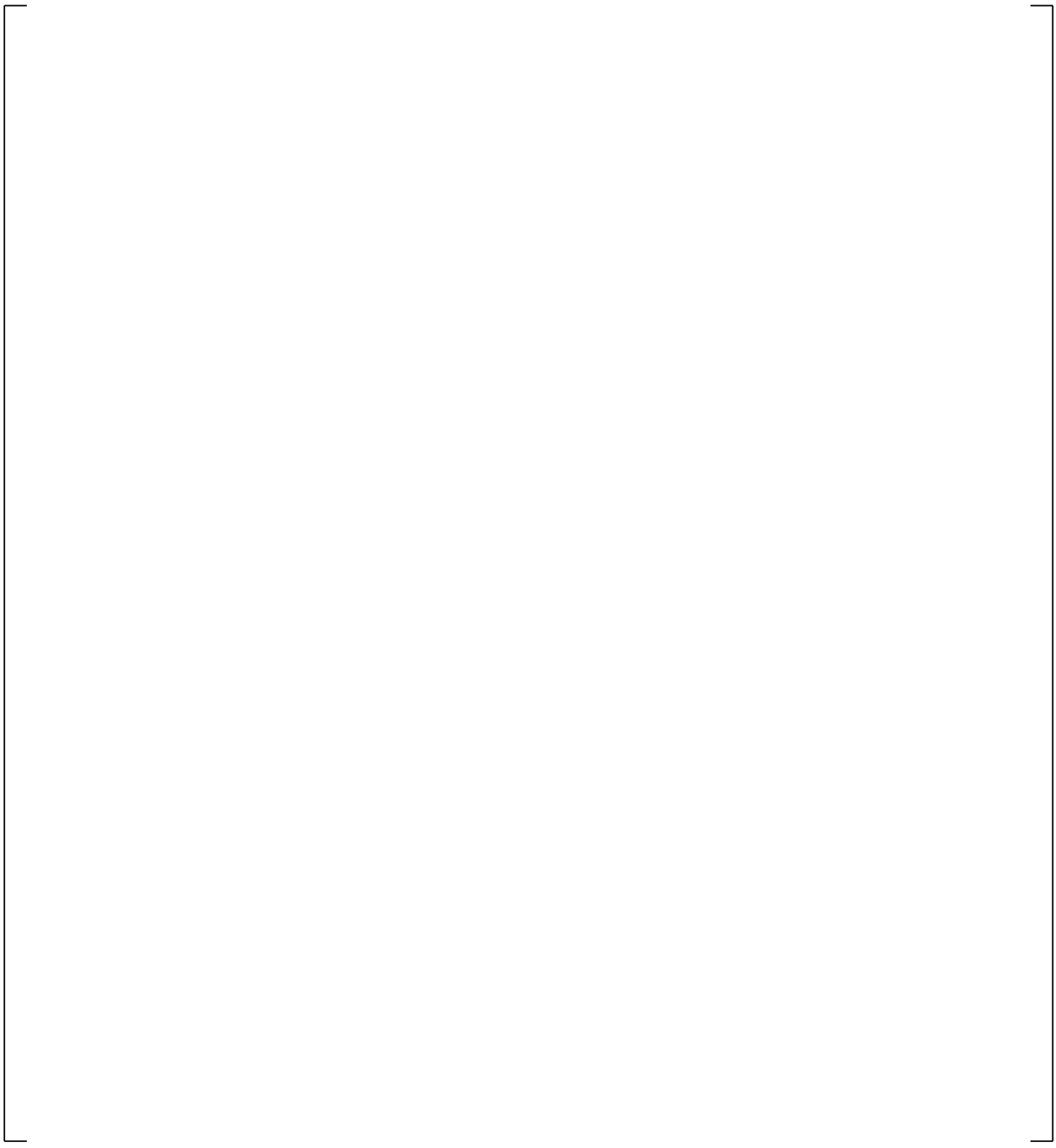

Figure 20.1-34 Measured and Predicted Cladding Temperature at 1.08m (3.54 ft)

a,c

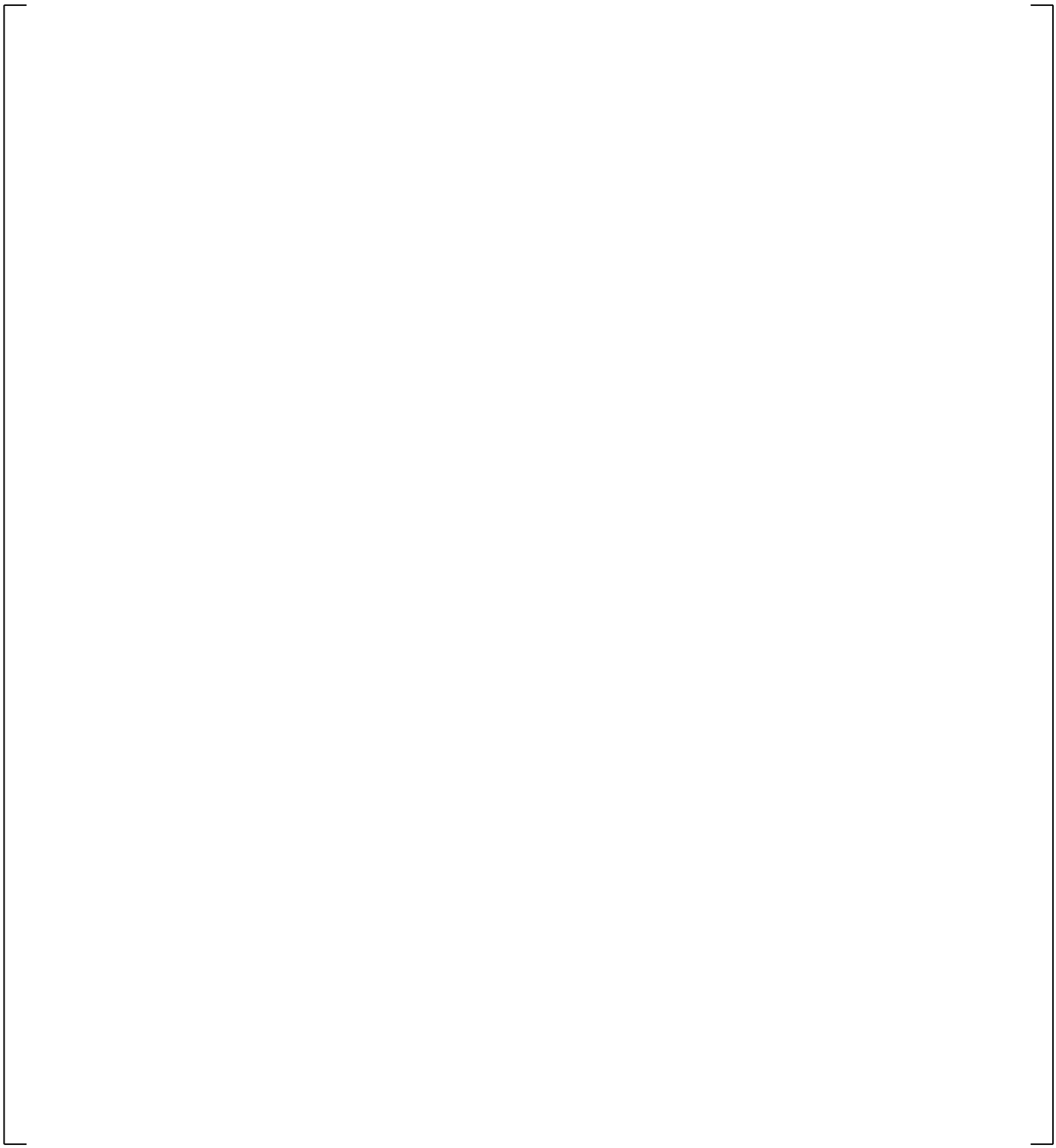

Figure 20.1-35 Measured and Predicted Cladding Temperature at 2.01m (6.59 ft)

a,c

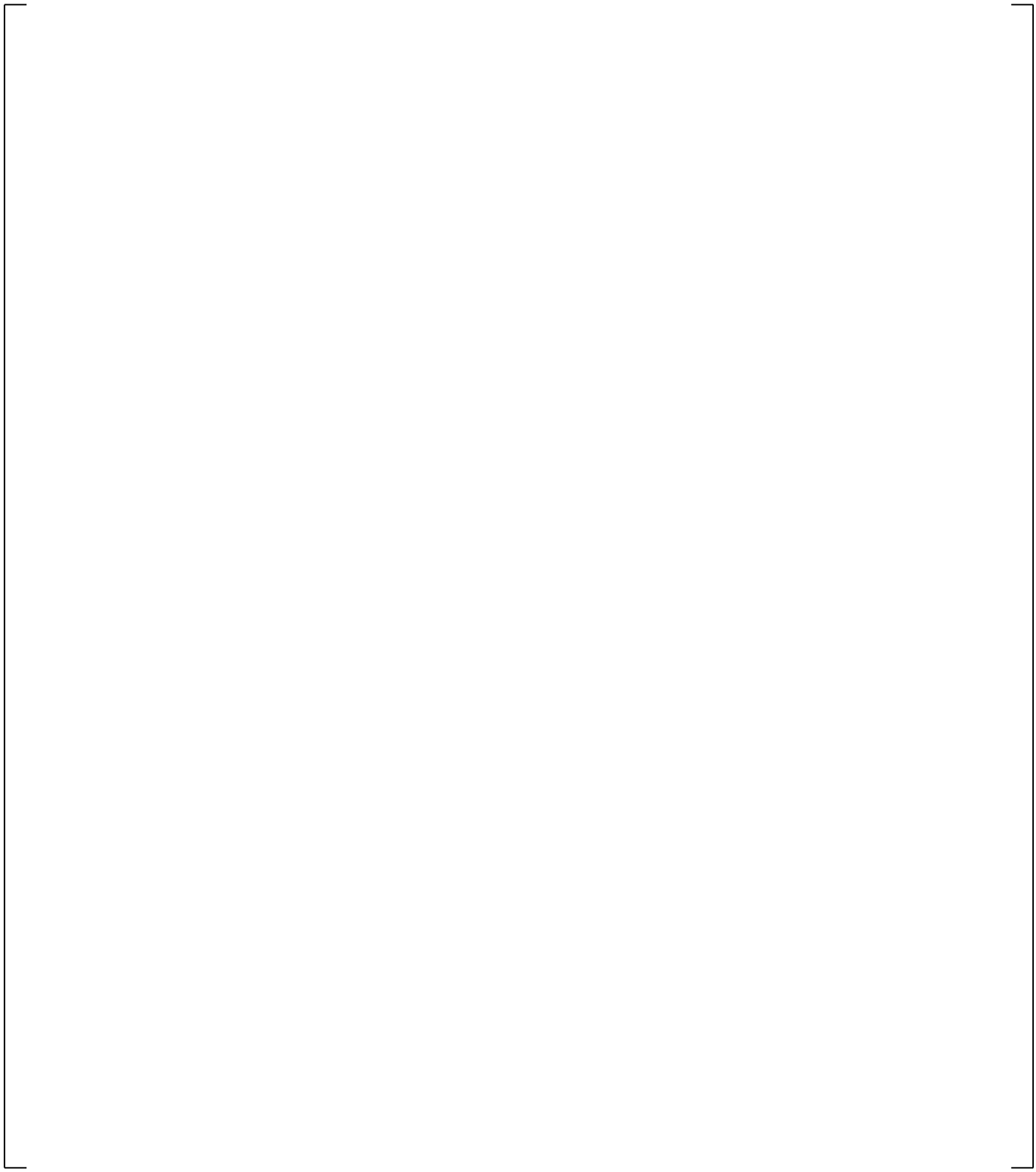

Figure 20.1-36 Measured and Predicted Cladding Temperature at 2.65m (8.69 ft)

a,c

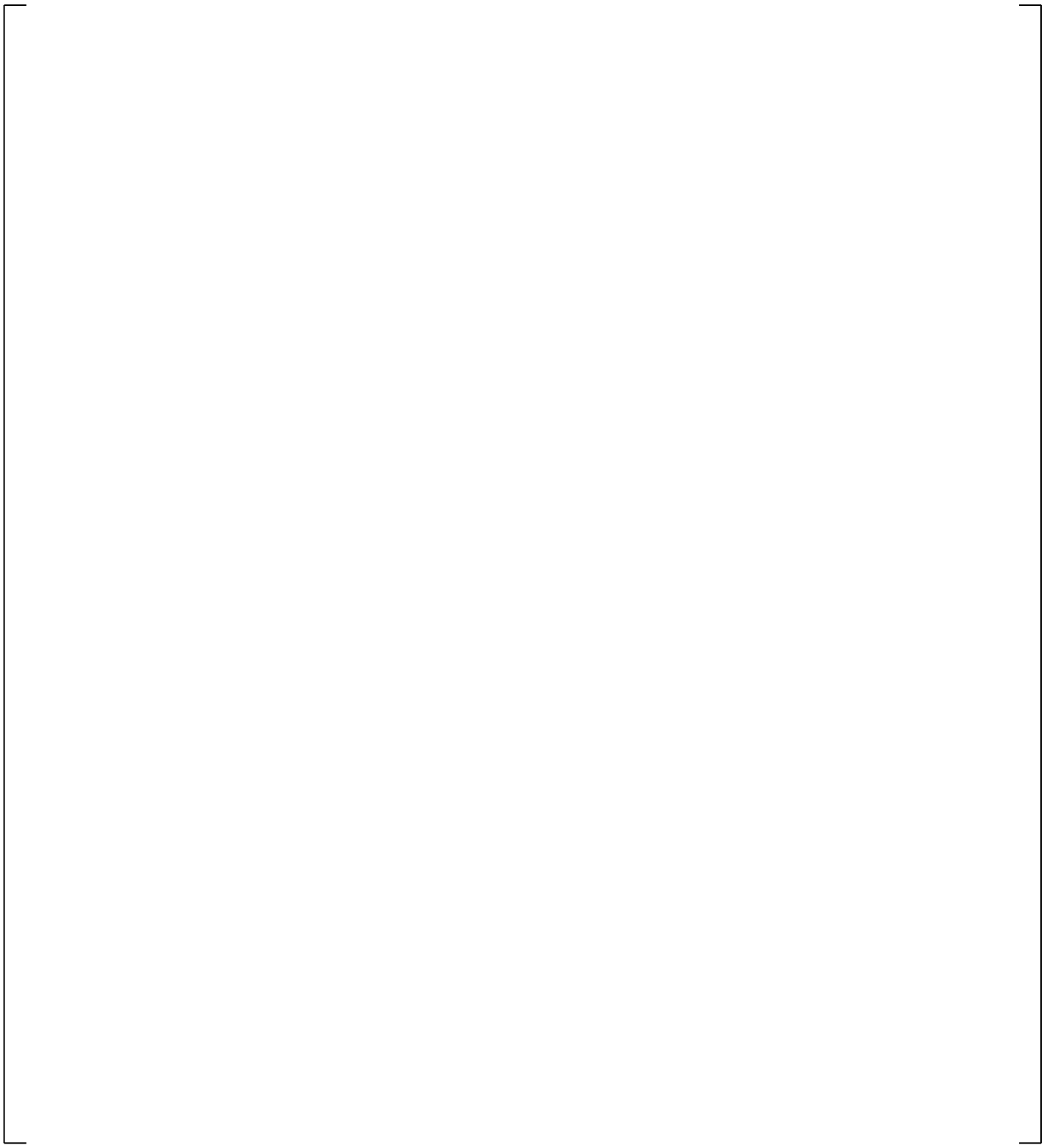

Figure 20.1-37 Measured and Predicted Accumulator Pressure (Broken Pipe Pressure Loss Sensitivity Study)

a,c

Figure 20.1-38 Measured and Predicted Accumulator Discharge Line Mass Flow Rate (Broken Pipe Pressure Loss Sensitivity Study)

a,c

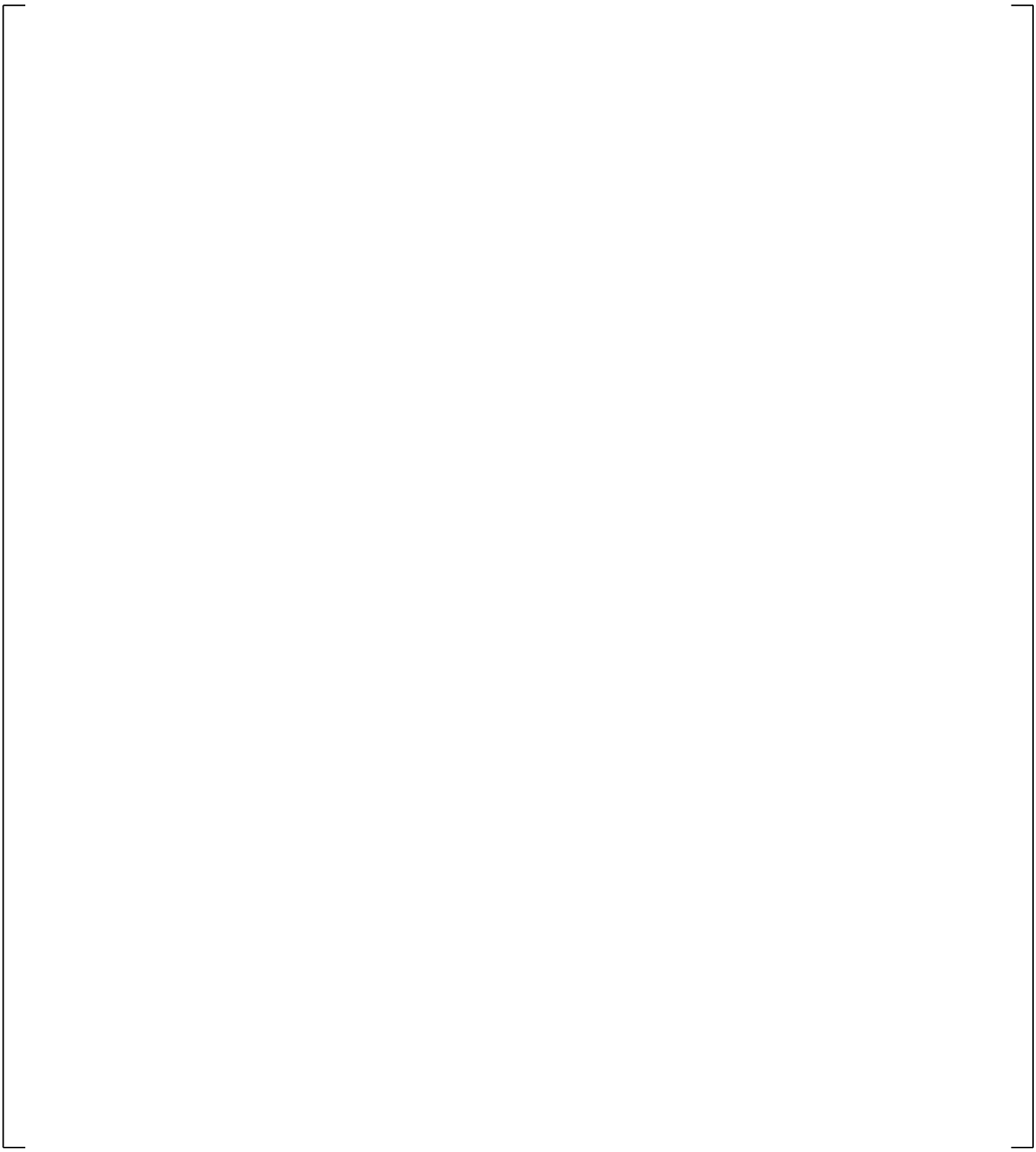

Figure 20.1-39 Measured and Predicted Pressure at Top of Downcomer (Broken Pipe Pressure Loss Sensitivity Study)

a,c

Figure 20.1-40 Measured and Predicted Downcomer Liquid Level (Broken Pipe Pressure Loss Sensitivity Study)

a,c

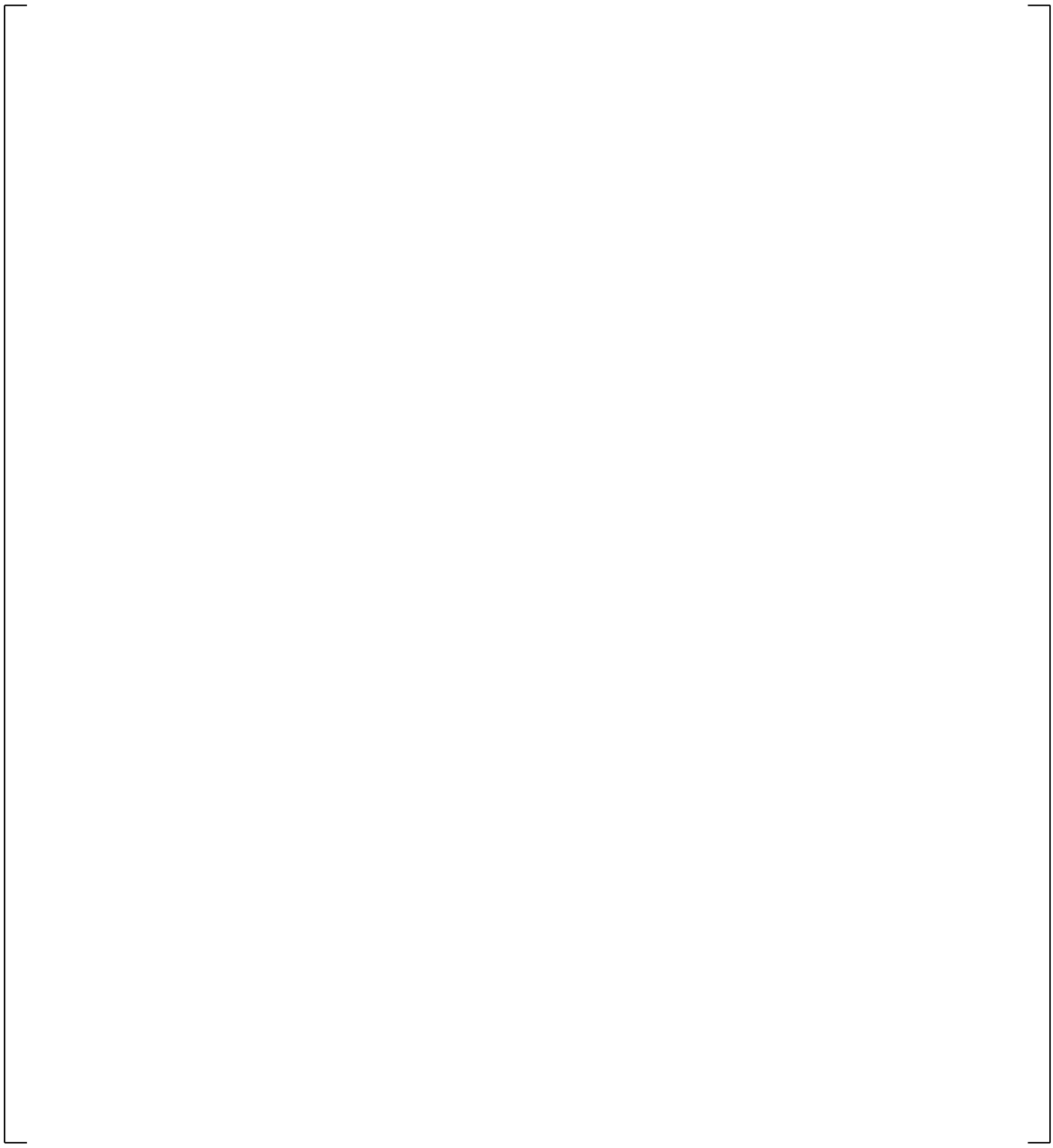

Figure 20.1-41 Measured and Predicted Test Section Liquid Level (Broken Pipe Pressure Loss Sensitivity Study)

a,c

Figure 20.1-42 Measured and Predicted Cladding Temperature at 1.08m (3.54 ft) (Broken Pipe Pressure Loss Sensitivity Study)

a,c

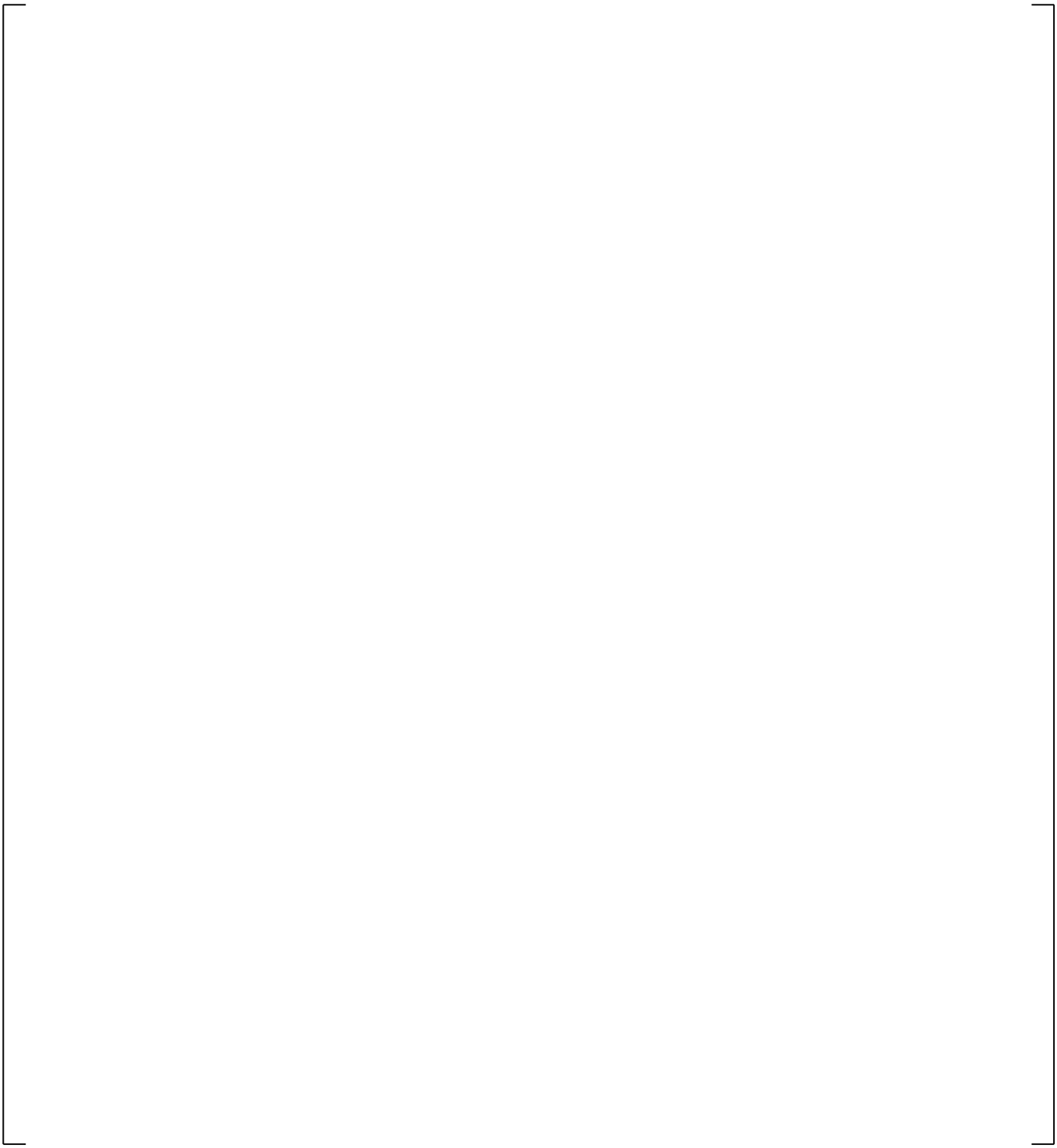

Figure 20.1-43 Measured and Predicted Cladding Temperature at 2.01m (6.59 ft) (Broken Pipe Pressure Loss Sensitivity Study)

a,c

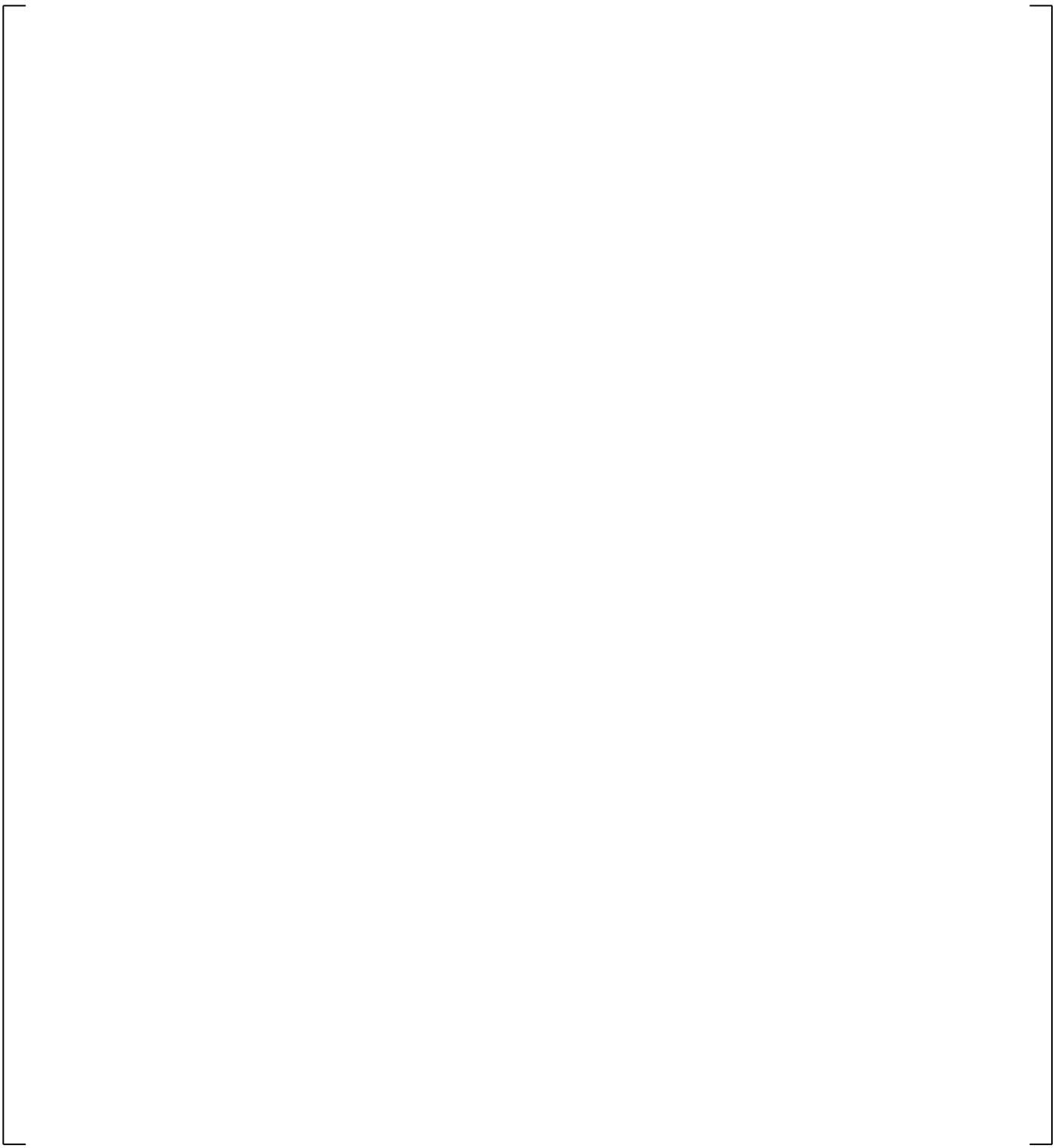

Figure 20.1-44 Measured and Predicted Cladding Temperature at 2.65m (8.69 ft) (Broken Pipe Pressure Loss Sensitivity Study)

20.2 PUMP COMPONENT MODEL

The pump component model was described in Section 10.4 of Volume 1. It is an empirical model in which the pressure differential generated by the pump, and the corresponding torque applied to the pump during single- and two-phase flow, is derived from single- and two-phase flow data in scaled pumps. In particular, the pump head and torque during two-phase flow is assumed to vary as a function of void fraction from the single-phase value to a "fully degraded," or minimum value which occurs at intermediate void fractions. For the pump head,

$$H = H_1 - M(\alpha) * (H_1 - H_2) \quad (20.2\text{-}1)$$

where,

H	=	pump head
H_1	=	single-phase pump head
H_2	=	fully degraded pump head
$M(\alpha)$	=	two-phase multiplier

A similar equation is used for the pump torque (Equation 10-9) with the multiplier defined as $N(\alpha)$.

This is clearly an approximate description of the actual variation of the pump head. As described by Rohatgi et al. (1989), the uncertainty associated with such a model is relatively large and needs to be considered in the code uncertainty. In Section 2.3.2.9 of Volume 1, the performance of the reactor coolant pump was included as part of the PIRT. For one- and two-phase performance, a medium (M) ranking was assigned during blowdown. Pump coastdown was ranked medium (M) during blowdown for intermediate breaks as well, and was ranked high (H) for large breaks. Flow resistance was ranked medium (M) for intermediate breaks and high (H) for large breaks during blowdown. The purpose of this section is to describe the basis for the empirical model used in the LOCA analysis of the PWR, establish the basis for its uncertainty, and relate it to the pump model used in LOFT. Comparisons with LOFT data of the predicted pump head then serve as validation that the empirical model adequately predicts pump head for both LOFT and a PWR.

20.2.1 Westinghouse Pump Data

The Westinghouse pump model is based on air/water data obtained from a scale model of a 93A model pump, designed to operate at a pump head of 92.6 feet, a flow of 7420 gpm, and an impeller speed of 1799 rpm. The scale model used to obtain single- and two-phase data is shown in Figure 20.2-1. It was designed to be geometrically similar to a full-scale Westinghouse model 93A pump, with an equivalent specific speed. The specific speed Ns of a centrifugal pump is defined as:

$$Ns = N\, Q^{1/2}/H^{3/4} \quad (20.2\text{-}2)$$

where,

N is in rpm
Q is in gpm

H is in feet of water

Specific speed has been found to be a convenient parameter distinguishing the performance characteristics of different pumps. The specific speeds of Westinghouse pumps range from approximately 5000 to 7000 rpm. In contrast, the specific speed of the LOFT pumps is 3300 rpm.

Single-Phase Data

Figures 20.2-2 and 20.2-3 show some of the test data used to determine the single-phase homologous curves for forward and reverse flow through the pump. The data consists of water data from the scale model of the 93A pump, as well as air data from the same scale model and test facility where two-phase data was obtained (Howland and Lamers, 1973). It can be seen that the air and water data agree well, indicating that the change in test fluid and test facility had little effect on the test results.

The uncertainty of the single-phase data was determined by evaluating two data sources. The first source was from the Westinghouse single-phase data cited above. A band can be drawn to bound the data in Figure 20.2-3 (the normalized head ratio h/υ^2 data is plotted against the inverse of the normalized flow ratio υ/α in this figure). **[**

][a,c]

The second source examined was from data developed by Cudlin (1977), where the normalized head ratio in the forward flow, dissipative quadrant for a 1/3-scale model pump is shown in Figure 20.2-4.
[**]**[a,c]

Two-Phase Data

The two-phase data were obtained by running air/water mixtures through the pump (Howland and Muench, 1975). The test facility is illustrated in Figure 20.2-5. Water was drawn from a large basin using a diesel powered pump, mixed with air in a mixing chamber, and pushed through the scale model pump. Inlet line venturi meters and orifices were used to measure inlet flow rates. Pump pressure differential, impeller speed, and impeller torque were also measured. The inlet void fraction was not measured but was inferred from the flow rates. A correlation was used to estimate the void fraction from the flow rates. In addition, a homogeneous void fraction was used. It was found that the basic nature of the data was not affected by the choice of void fraction. In the following discussion, the homogeneous (zero slip) void fraction is used.

Typically, homologous head data is plotted using two x-axes, normalized flow divided by normalized speed (υ/α as in Figure 20.2-2), and normalized speed divided by normalized flow (α/υ as in Figure 20.2-3). An alternative way to plot the head data is to show normalized head divided by normalized speed squared (h/α^2), versus normalized flow divided by normalized speed (υ/α), for all forward flow conditions. This results in Figure 20.2-6, which more clearly shows the transition, as flow increases, from a positive head or pumping mode, to a negative head or energy dissipation mode. The intact loop pumps are operating in the pumping mode during the initial stages of a cold leg break LOCA, while the broken loop pump is operating in an energy dissipation mode during the entire transient. The two-phase data is also shown on this figure, and indicates that the pumping mode data shows relatively little scatter, while the dissipation mode data shows more scatter. The increased scatter may be due to the fact that, when the downstream pressure is lower, the upstream conditions are no longer as accurate a

representation of conditions within the pump. Also plotted on this figure are the single-phase head curve and a fully degraded head curve drawn through the lower bound data.

The method for determining the two-phase multiplier M(α) and N(α) in Equations 10-8 and 10-9 from the pump data is as follows:

1. Determine single-phase homologous head and torque. The pressure difference across the pump, and the torque applied to the pump impeller, are measured under a variety of flow conditions. Homologous head and torque curves are derived by dividing these data by the appropriate quantities (rated flow, rated speed, etc.). Each pump model (designated 93, 93A, 100, etc.) designed by Westinghouse has a set of homologous curves derived from scale model single-phase tests using both air and water.

2. Measure the pump pressure difference and torque under two-phase conditions over a range of void fractions. The lower boundary of the data, when converted to homologous form, is defined as the "fully degraded" homologous head and torque. These data were obtained from a 1/3-scale model pump with the same specific speed as the model 93A pump. The pump head data are shown in Figure 20.2-7, and the pump torque data in Figure 20.2-8. The single-phase and "fully degraded" curves constructed from these data are also shown (they are also shown in Figures 10-4 to 10-7). In Figure 20.2-7, HSP1 and HTP1 are the single- and fully degraded two-phase head (h/α^2) curves presented as a function of υ/α, while HSP2 and HTP2 present the head (h/υ^2) as a function of α/υ. Note that the fully degraded curves are always drawn below the single-phase curves, and bound nearly all the data.

   The two-phase data indicate that the amount of full degradation in head or torque is approximately a constant. That is, the fully degraded curve is offset from the single-phase curve by a constant. This is more easily seen in Figure 20.2-6. This observation allows the fully degraded curve to be extended into areas where data is sparse or lacking.

3. Assume that the homologous head and torque go from single-phase to fully degraded back to single-phase values as the pump inlet void fraction ranges from 0 to 1.0. Use Equation 20.2-1 in the following form to calculate M(αi) for each pump head data point $H(\alpha_i)$:

$$M(\alpha_i) = \frac{H(\alpha_i) - H_1}{H_2 - H_1}$$

   Use the M(αi) data to define the appropriate shape of the M(α) function, as in Figures 20.2-9 and 20.2-10. Figure 20.2-9 includes only the pumping mode data, while Figure 20.2-10 includes all the data. Perform a similar exercise for the pump torque (Figure 20.2-11).

Data are lacking for void fractions greater than approximately 65 percent. **[**

][a,c] This assumption is supported by test data from other design pumps, for example, Figure 2.1 on page L-9 of the Code Scaling, Applicability, and Uncertainty (CSAU) report (Boyack et al., 1989).

The simple form of the M(α) function results in considerable scatter in the data in the dissipative, or turbine mode of pump operation. The effect of this uncertainty was examined by defining a new multiplier which was drawn below the lower bound of the data and was found to result in a relatively small effect for large breaks, due to the relatively short time that the pump is in the fully degraded low void fraction two-phase regime. This result is consistent with results obtained in the CSAU report (Boyack et al., 1989). For small breaks, the use of a multiplier representing the lower bound of the data has only a small effect when offsite power is available. In that case, because the pumps continue to rotate at fixed speed into the early portion of the natural circulation phase, differential pressure across the pumps is predicted differently when the flow is two-phase using the lower bound degradation curve. This effect subsides before loop seal clearance, however, so the effect on the transient is negligible. With a loss of offsite power, the effect on the small break transient is negligible due to the early coastdown of the pumps and the presence of primarily single phase flow in the loops.

[

]^{a,c}

20.2.2 Pump Model Comparison to Data

The only large break test which contains a powered pump is the LOFT test. Although the pumps in LOFT are of a different design than PWR pumps, they exhibit similar overall performance as can be seen from Figure 20.2-12. The pump model used in the LOFT simulations, described in Section 22 of this report, is the same as that used in the PWR, except that the homologous curves and the two-phase multiplier used were the LOFT specific curves, obtained from tests on the Semiscale pump (Reeder, 1978). Another difference was that the pump speed was input from the LOFT data, rather than calculated. This was done to examine specifically the pump head prediction, which will be shown later to be the more important parameter in the PWR calculation. The resulting prediction for LOFT Test L2-5 is shown in Figure 22-43.

These comparisons show that the predicted pressure difference across the pumps in the intact loops compares well with the measured pressure difference during blowdown.

The ROSA-IV test facility provides a means for comparison in the context of small breaks. Figure 21.5-2 shows that WCOBRA/TRAC-TF2 adequately predicts the pump speed throughout the SB-CL-05 test. Figure 21.6-1 shows the same for SB-CL-14. This, in conjunction with the reasonable prediction of pressures throughout the primary loops suggests that the pump model in WCOBRA/TRAC-TF2 is adequate.

These comparisons indicate that the relatively simple pump model in WCOBRA/TRAC adequately predicts pump behavior during LOCA. In addition, for the Westinghouse pump, the uncertainty in the data is most significant for a broken loop pump operating in the dissipative mode. Section 29.1.2.2, Volume 3 describes how this uncertainty will be treated in plant analyses.

20.2.3 References

1. Boyack, et al., 1989, "Quantifying Reactor Safety Margins," NUREG/CR-5249.

2. Cudlin, J. J., 1977, "1/3 Scale Air-Water Pump Program, Analytical Pump Performance Model," EPRI NP-160.

3. Howland, G. R. and Lamers, R. P., 1973, "Air Test Program to Establish the Complete Pump Characteristics of WEMD 93A Model Reactor Coolant Pump," Westinghouse Research Report 73-7E9-TAPSC-R1.

4. Howland, G. R. and Muench, R. A., 1975, "Air/Water Mixed Flow Testing of the WEMD 93A Model Reactor Coolant Pump," Westinghouse Research Report 75-7E9-CORCL-R1.

5. Reeder, D. L., 1978, "LOFT System and Test Description," NUREG/CR-0247.

6. Rohatgi, et al., 1989, "Quantifying Reactor Safety Margins," NUREG/CR-5249.

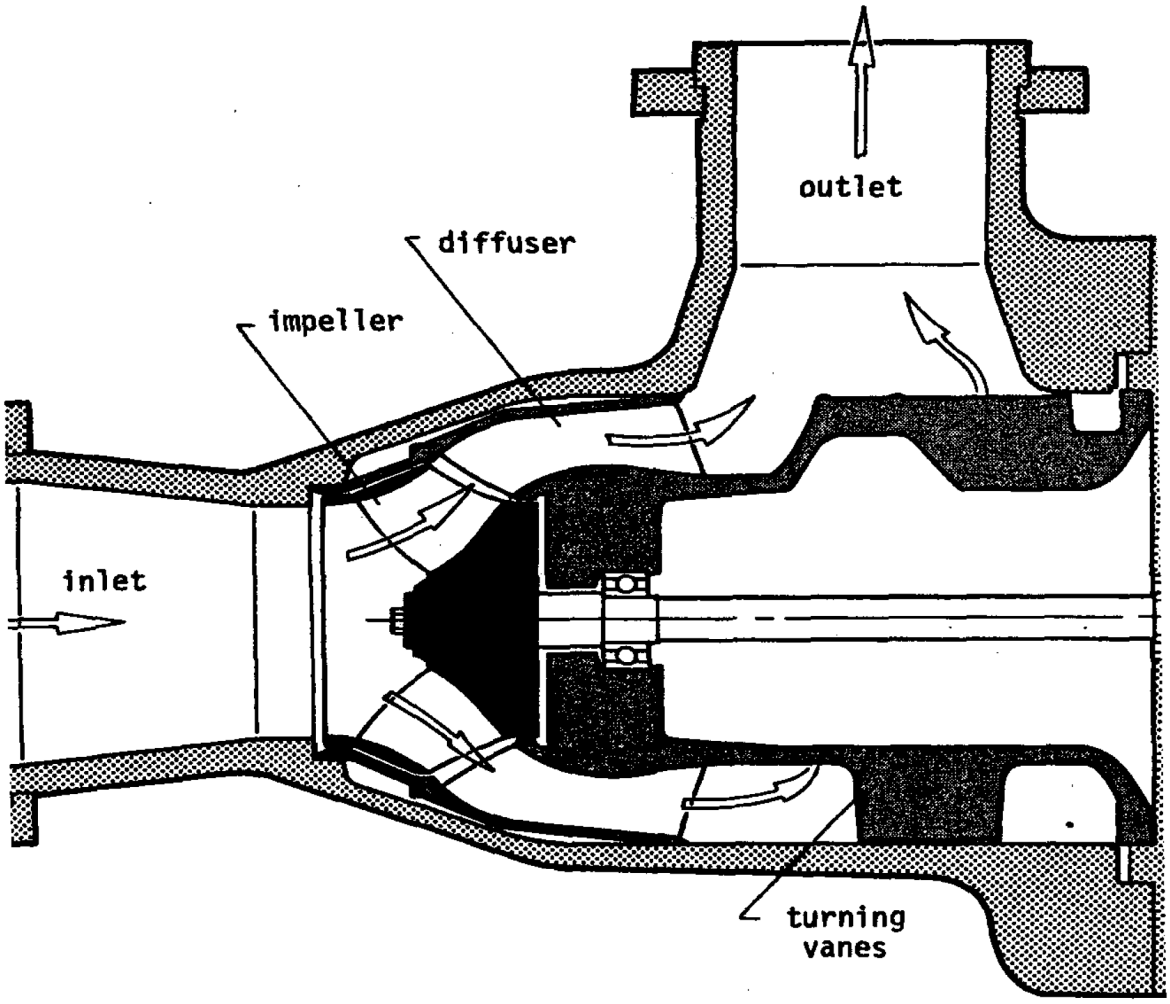

Figure 20.2-1 Cross-Sectional View of the Westinghouse Scale Model Pump

a,c

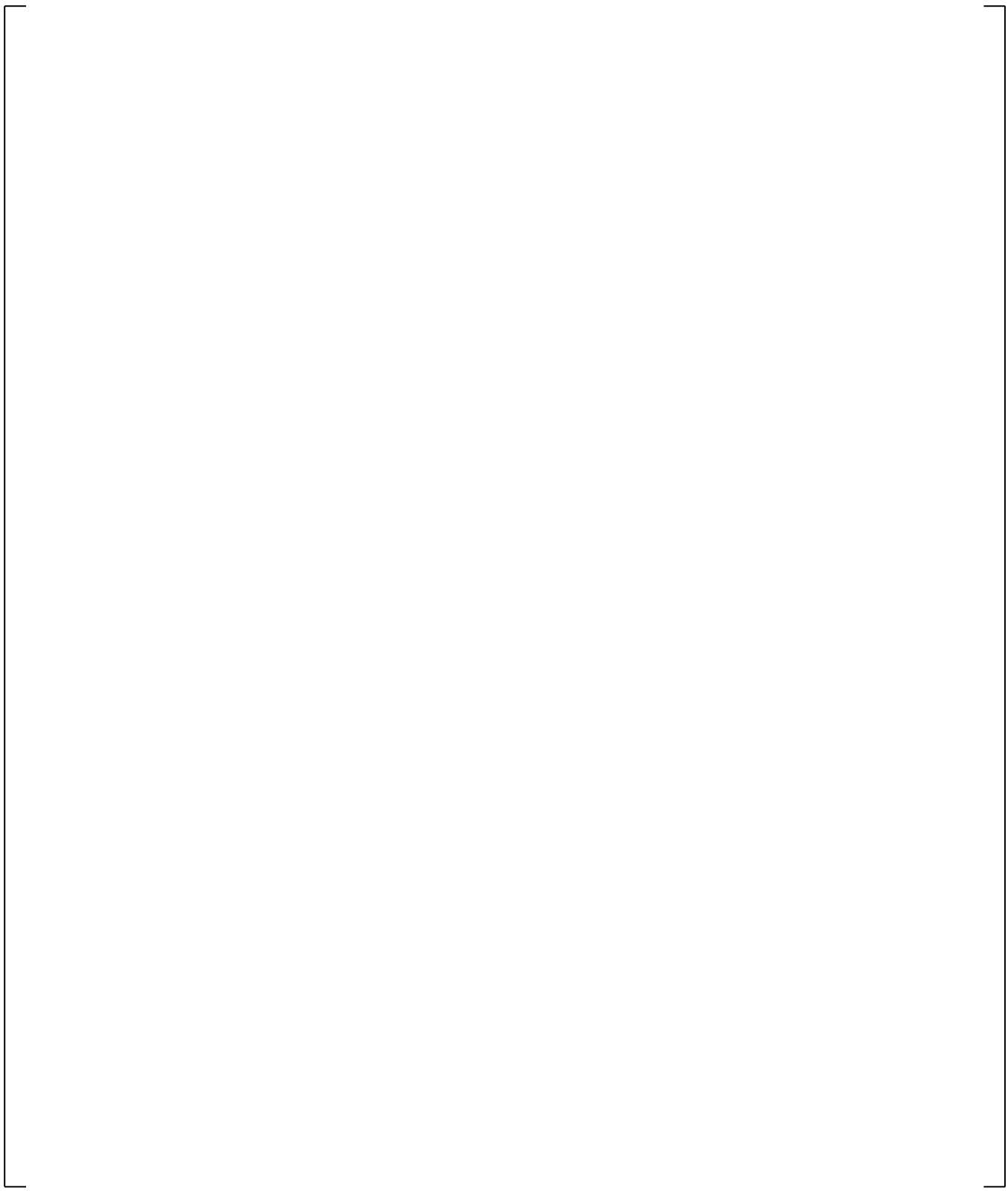

Figure 20.2-2 Scale Model Homologous Head Single-Phase Data in the Pumping Mode, Forward and Reverse Flow

a,c

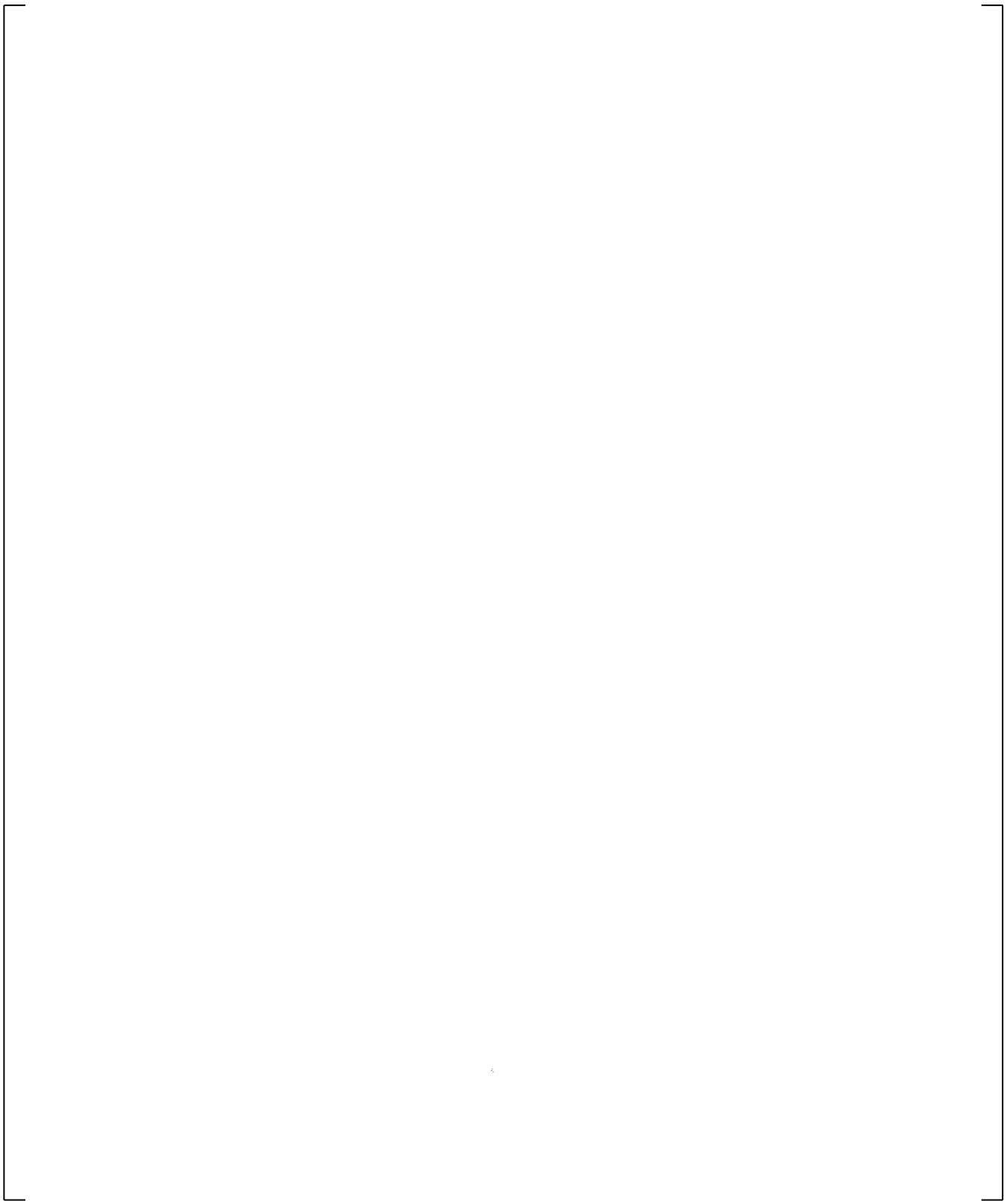

Figure 20.2-3 Scale Model Homologous Head Single-Phase Data in the Dissipation Mode, Forward Flow

a,c

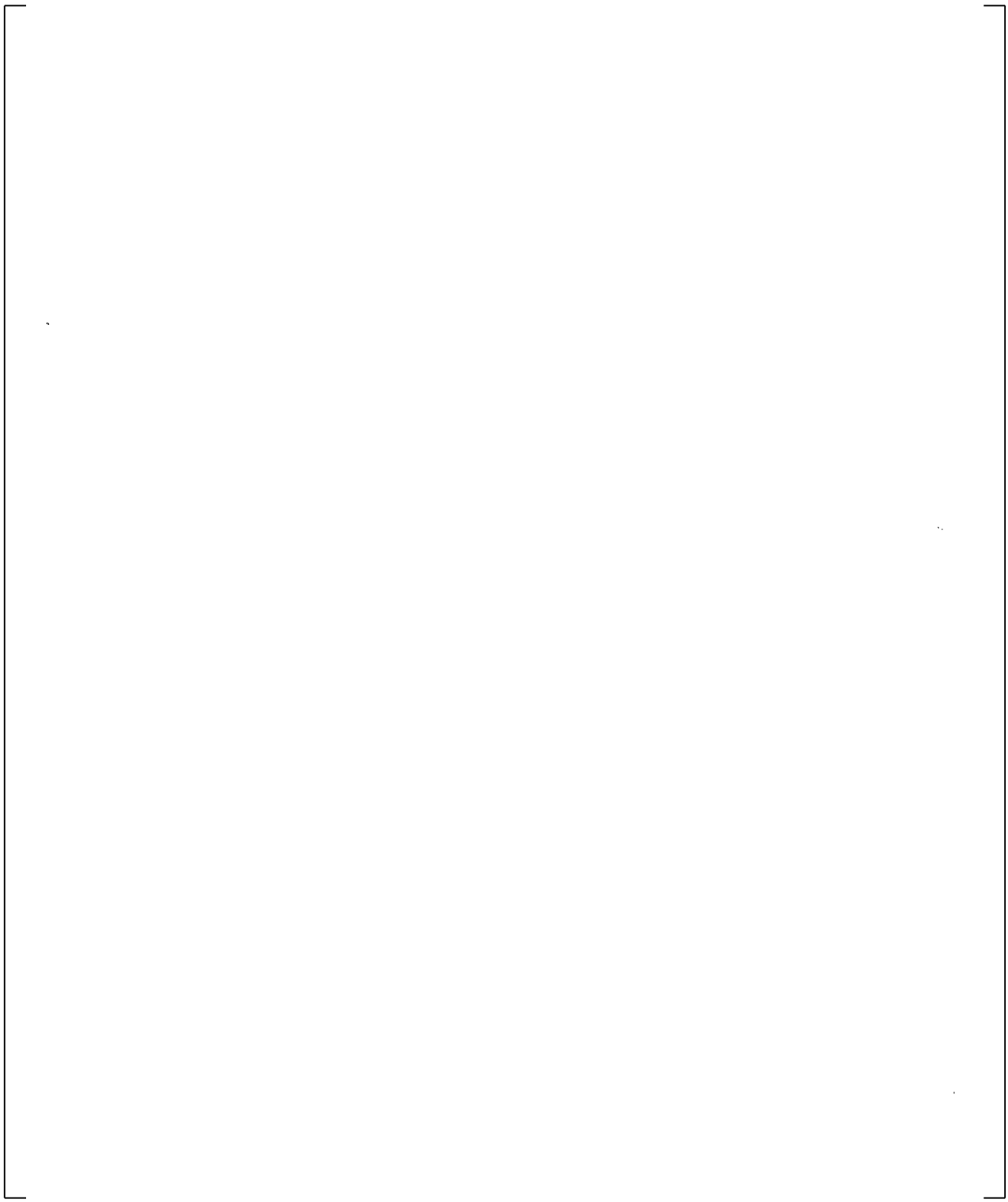

Figure 20.2-4 Data Scatter for Dissipative Mode 1/3-Scale Pump Data (Cudlin, 1977)

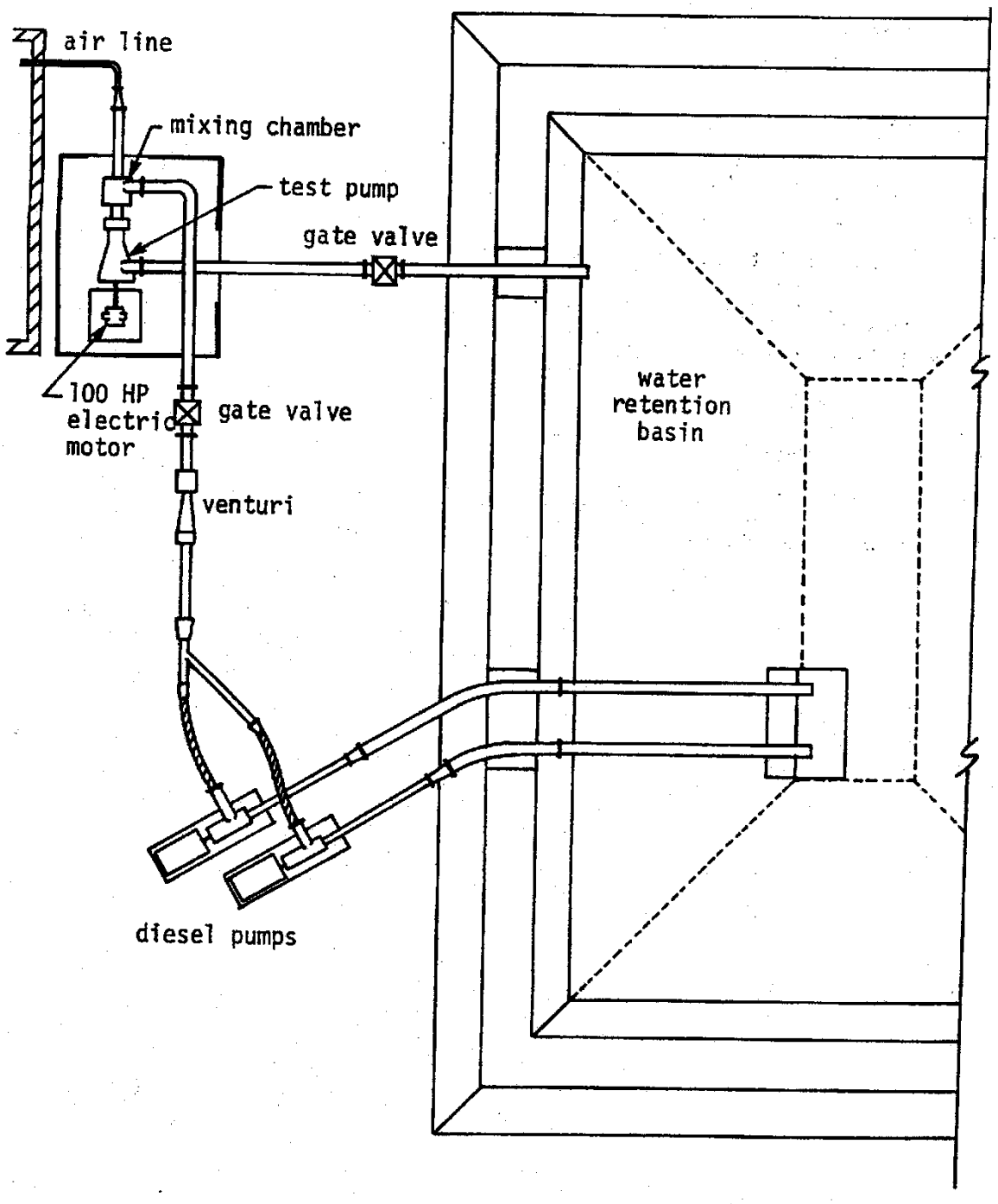

Figure 20.2-5 Schematic of the Air/Water Test Facility

a,c

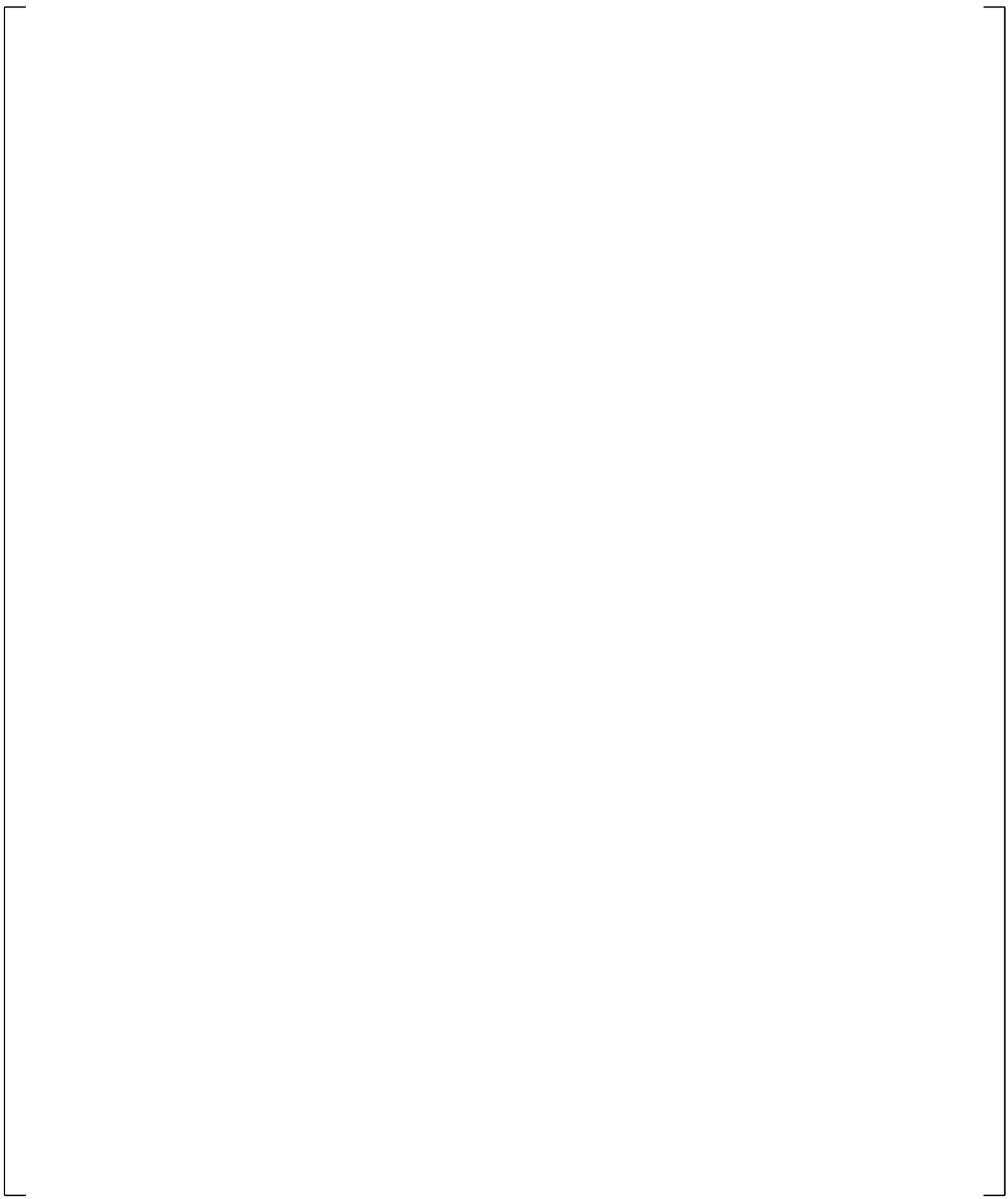

Figure 20.2-6 Homologous Head Curves and Westinghouse Air/Water Data

a,c

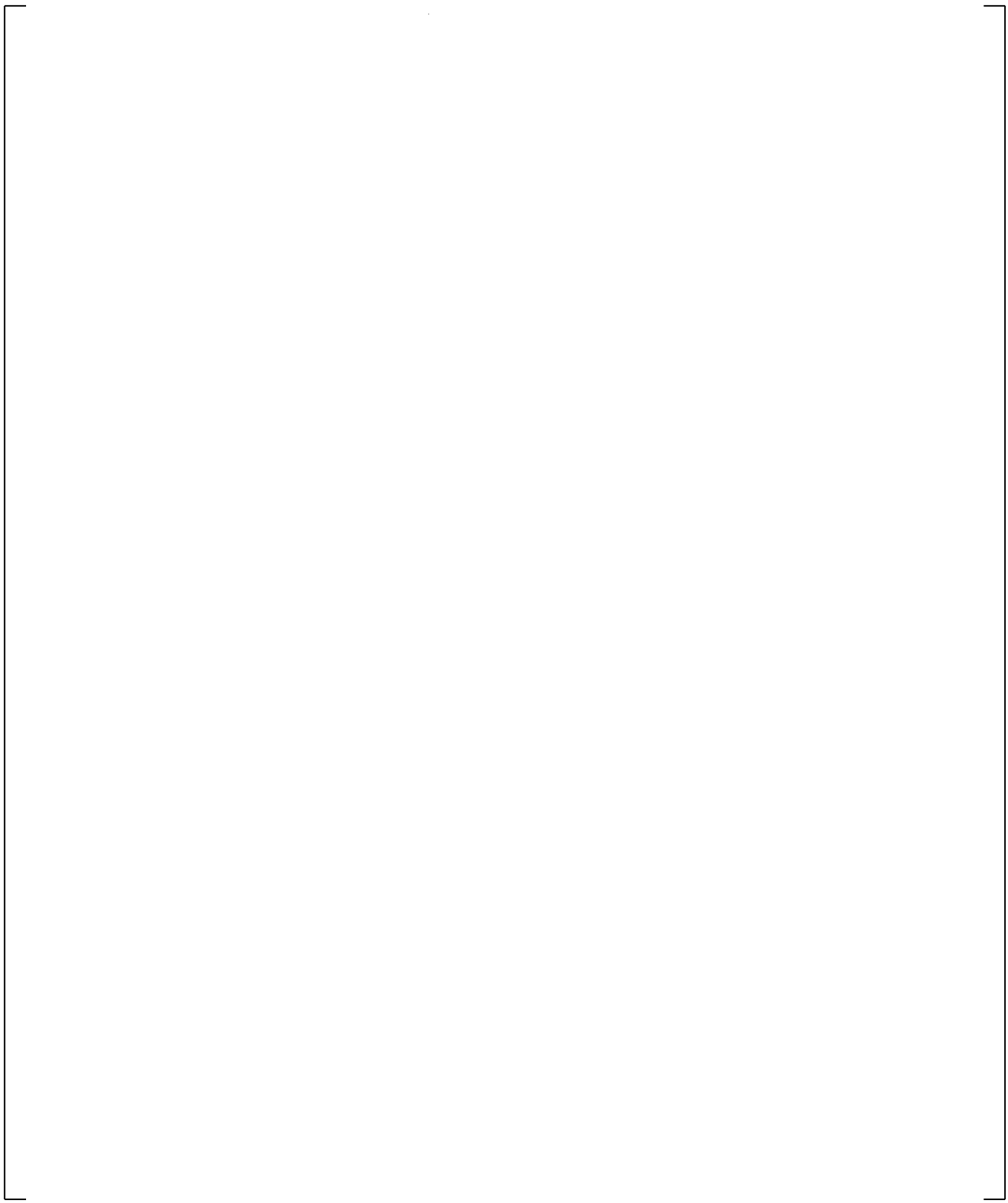

Figure 20.2-7 Single-Phase and Fully Degraded Pump Head Curves Compared With Two-Phase Data

a,c

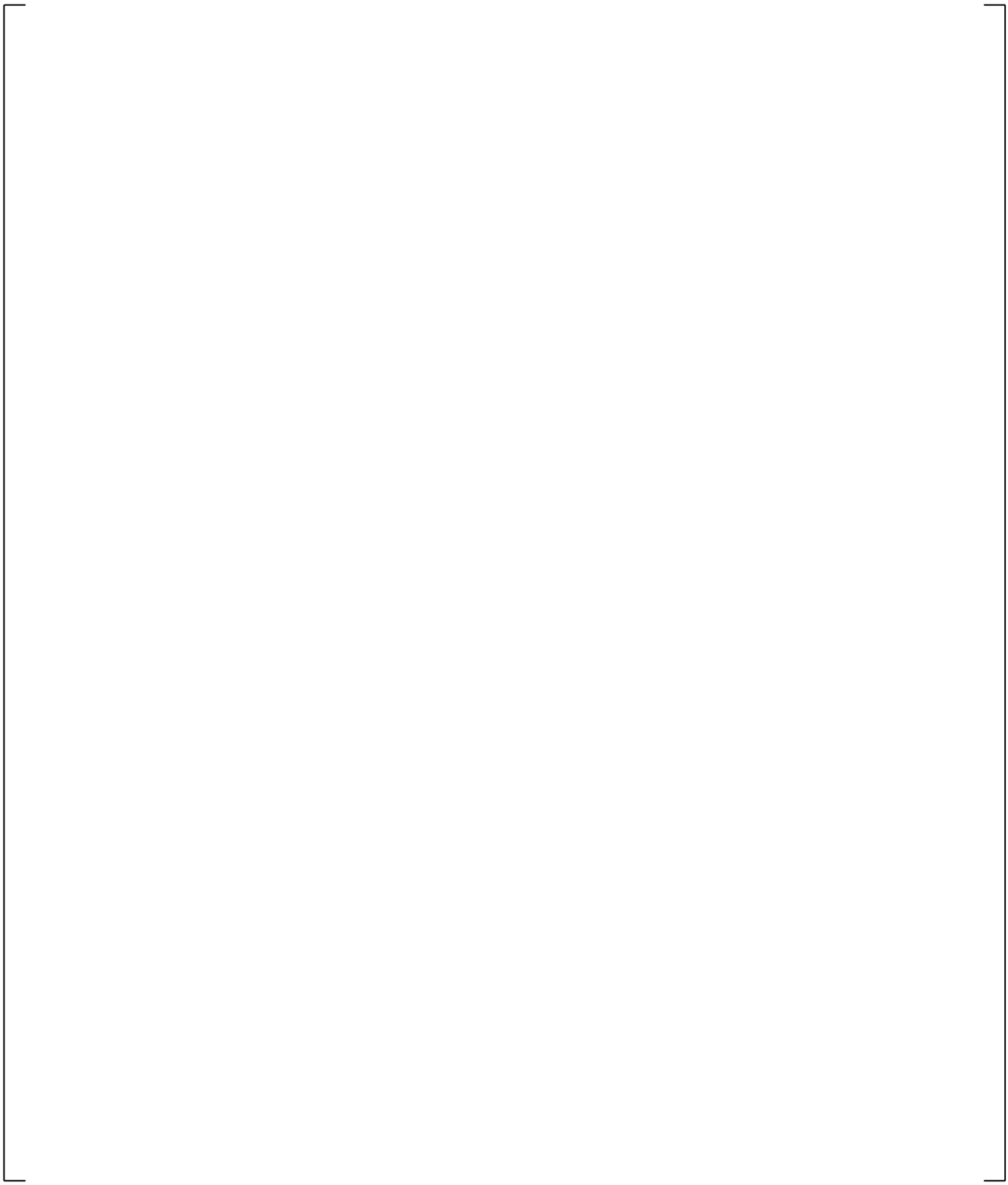

Figure 20.2-8 Pump Single-Phase and Fully Degraded Torque Curves, Compared With Two-Phase Data

a,c

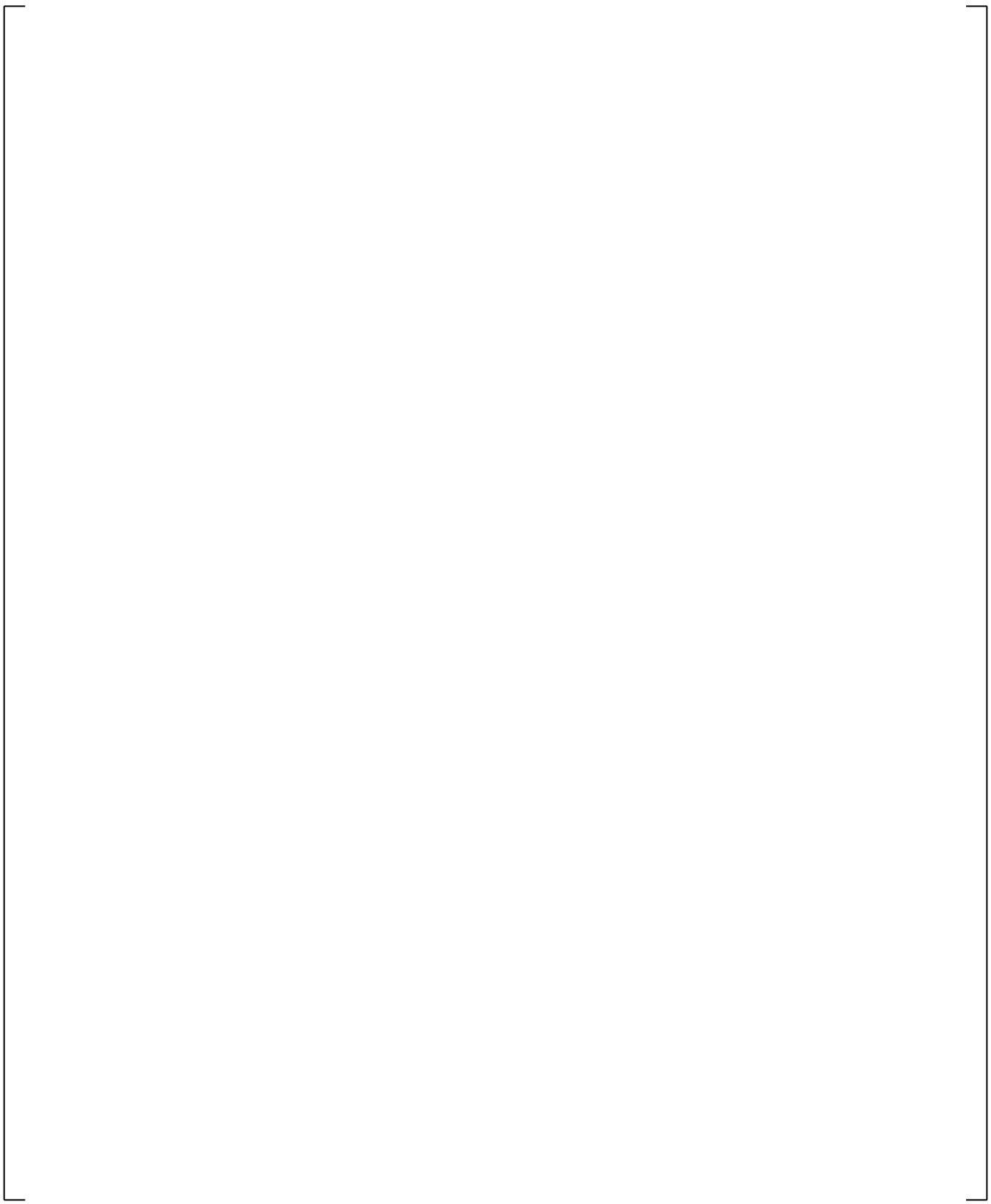

Figure 20.2-9 Two-Phase Multiplier and Pumping Mode Data

a,c

Figure 20.2-10 Two-Phase Multiplier and All Two-Phase Data

a,c

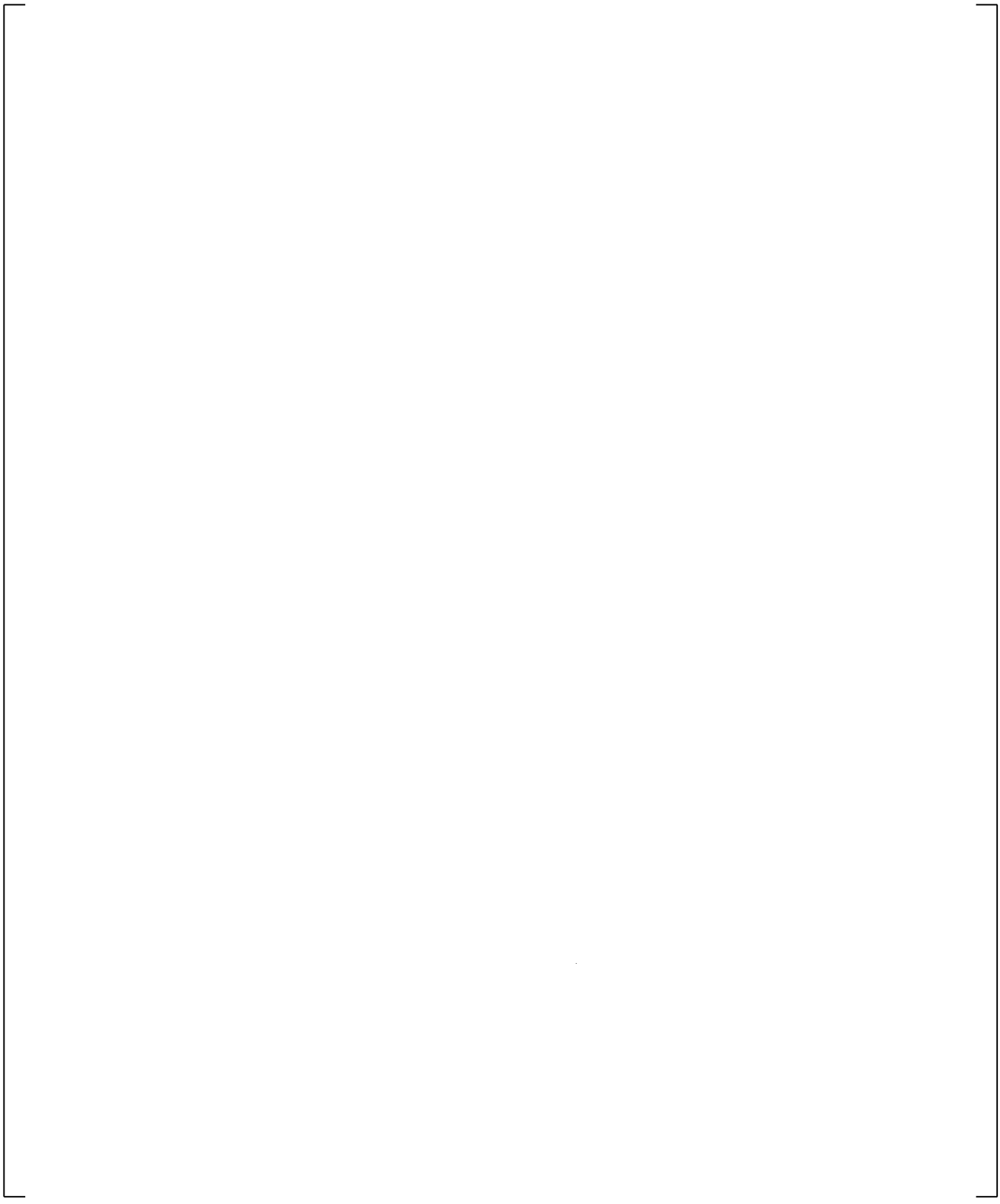

Figure 20.2-11 M(α) for Pump Torque (Referred to as N(α) in Equation 10-9)

a,c

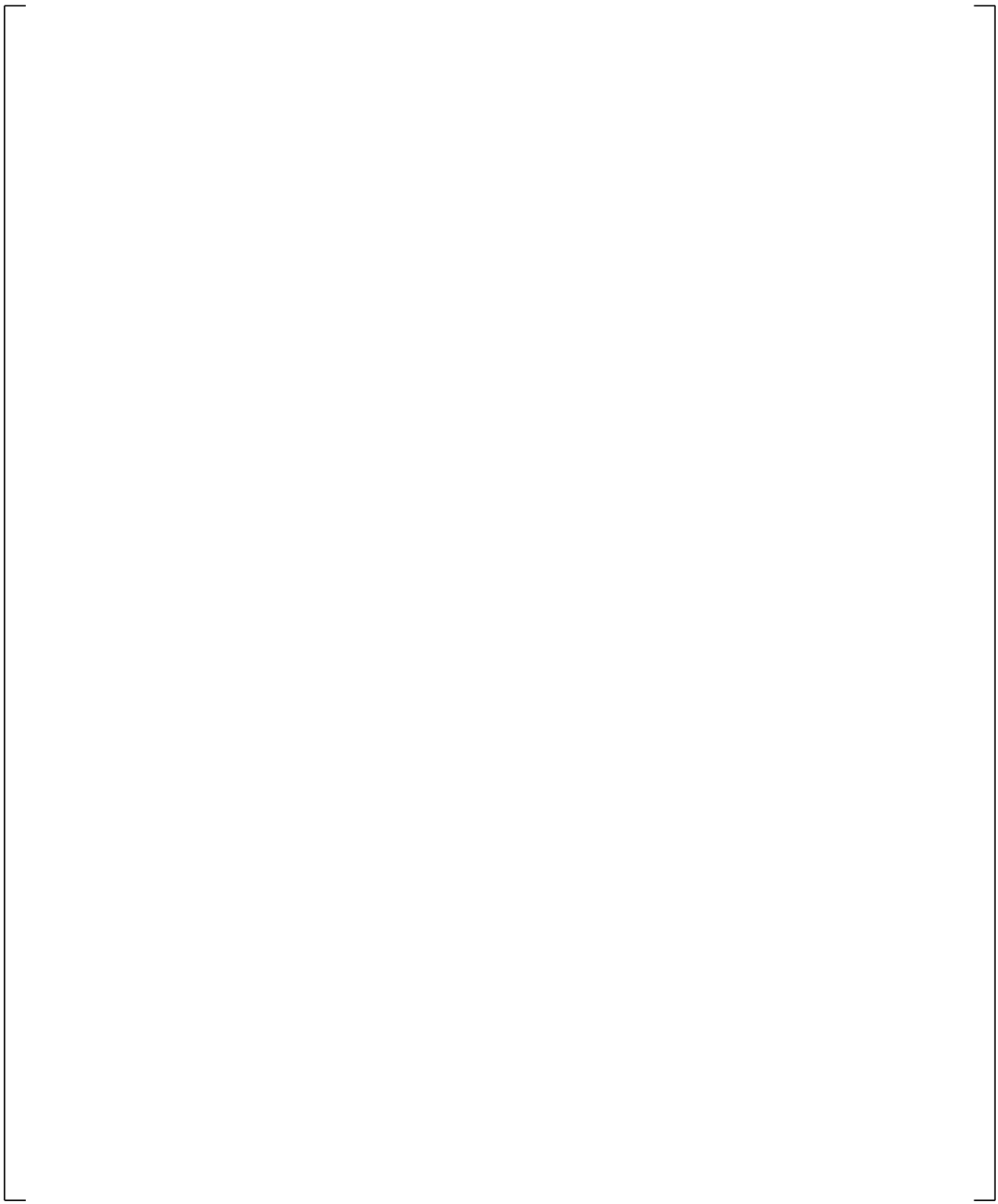

Figure 20.2-12 Westinghouse Pump Head Curves Compared With LOFT Pump Head Curves

20.3 MASS AND ENERGY CONSERVATION ACROSS 1D/3D JUNCTION

WCOBRA/TRAC-TF2, as described in Section 3 of Volume 1, is comprised of a two-fluid, three field representation of the vessel component (3D) and a two-phase, two-fluid representation for the one-dimensional components (1D). At the interfaces, such as cold and hot leg nozzles, are junctions coupling the numerical solution. This section serves to demonstrate the conservation of mass and energy across such a junction with the use of a simple numerical test problem. The momentum coupling treatment and assessment is discussed in Section 19.3.5.10 regarding the cold leg nozzle loss coefficient.

20.3.1 Scenario Description and WCOBRA/TRAC-TF2 Model Description

A single channel, 10 node vessel (node height = 1.0 ft, node diameter = 2 in.) is connected to PIPE components at junctions at the bottom and top nodes (Figure 20.3-1). A third pipe is connected to node 5. Each PIPE has a diameter of 0.2 ft. A liquid velocity ramping up to 5 ft/s in the first 10s of the transient and to 10 ft/s within the first 50s is supplied with FILL components connected through junctions at the top and middle node. Zero axial flow boundary conditions are prescribed at the top and bottom of the vessel such that both inlet flows must exit the vessel at the 1D junction at the bottom node, where a 100 psia pressure boundary condition is prescribed with a BREAK component. The assumed temperature is 60°F.

The solution requires mass and energy to be conserved for the control volume. Given that the problem considers single phase, quasi-steady flow, and there is no net mass or energy accumulation in the vessel component, the following equations must be satisfied at the junctions:

$$\dot{m}_{in} = \dot{m}_{out}$$
$$h_{in}\dot{m}_{in} = h_{out}\dot{m}_{out}$$

where,

h is the enthalpy of the mixture per unit mass and $\dot{m}$ is the mixture mass flow rate.

20.3.2 Results and Conclusions

Figure 20.3-2 shows that throughout the transient as the velocity of each of the FILL components ramps to 10 ft/s, the mass flow entering the vessel equals the mass flow exiting the vessel. After 100 seconds, the mass flow rate error is **[ ]**[a,c]. Figure 20.3-3 shows that the energy (enthalpy) flow rate into the vessel equals the energy flow out of the vessel throughout the transient. After 100 seconds, the error is **[ ]**[a,c].

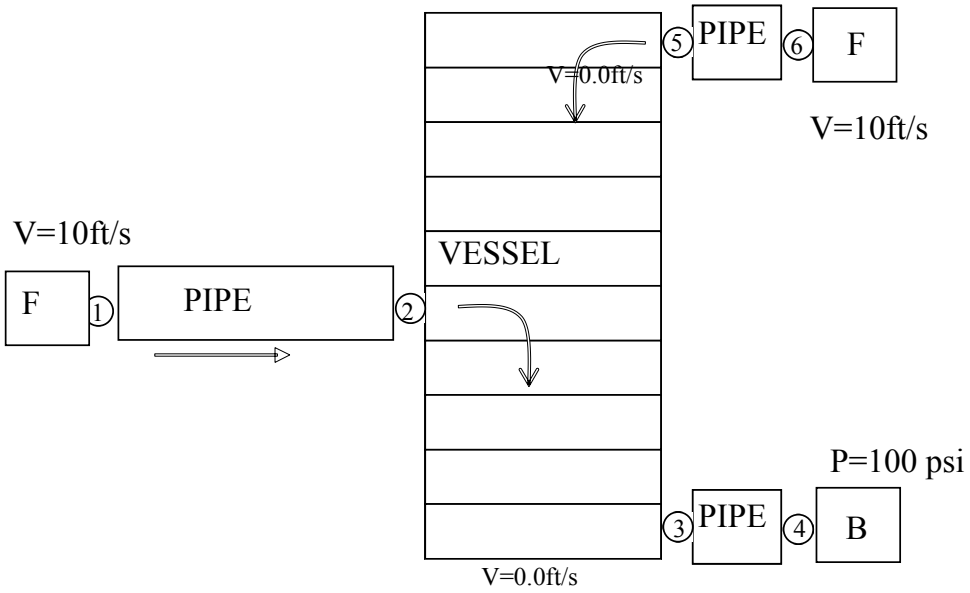

Figure 20.3-1 Scenario and Noding Diagram for 1D/3D Mass and Energy Test

a,c

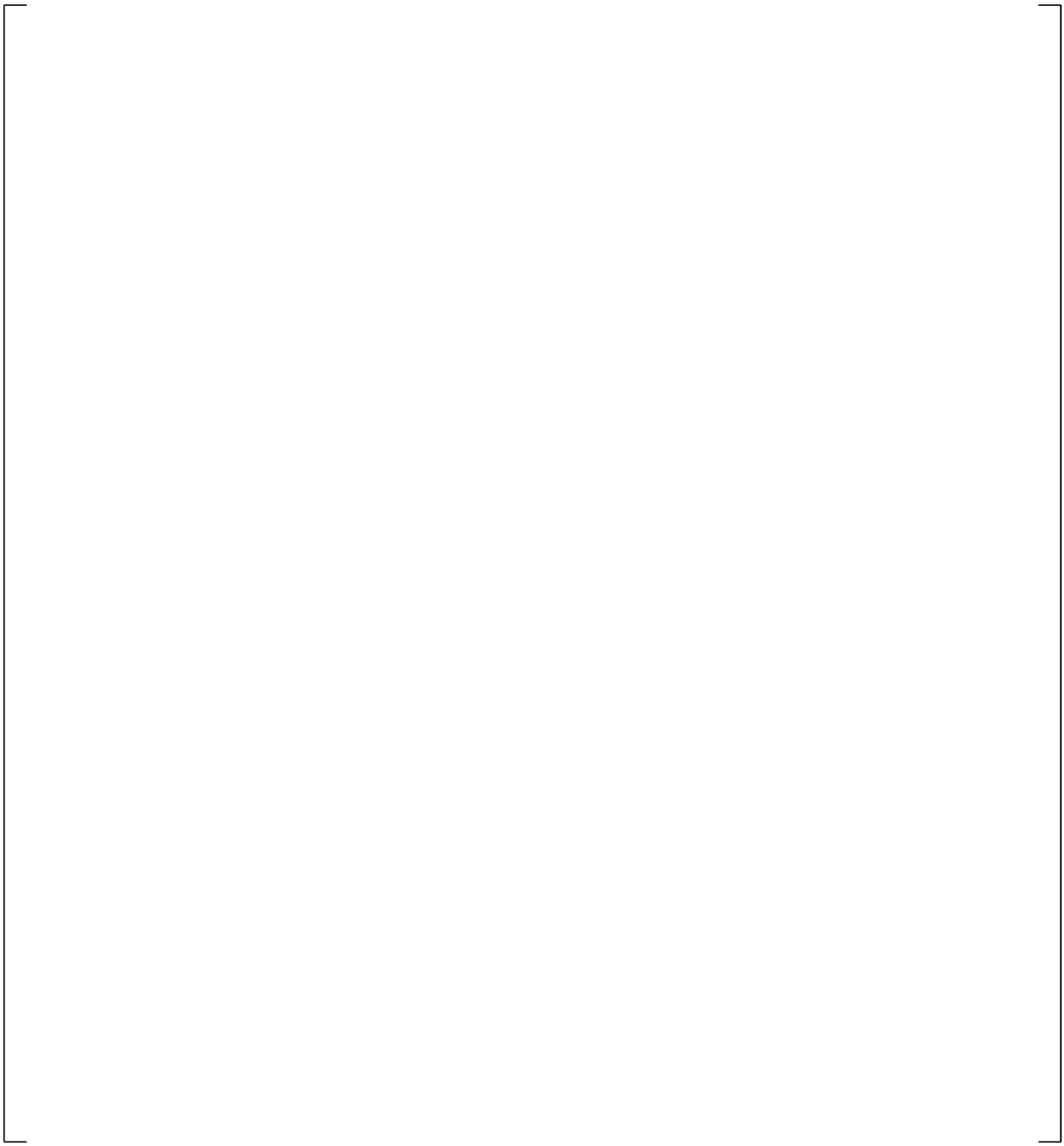

Figure 20.3-2 Mass Conservation for 1D/3D Mass and Energy Test

a,c

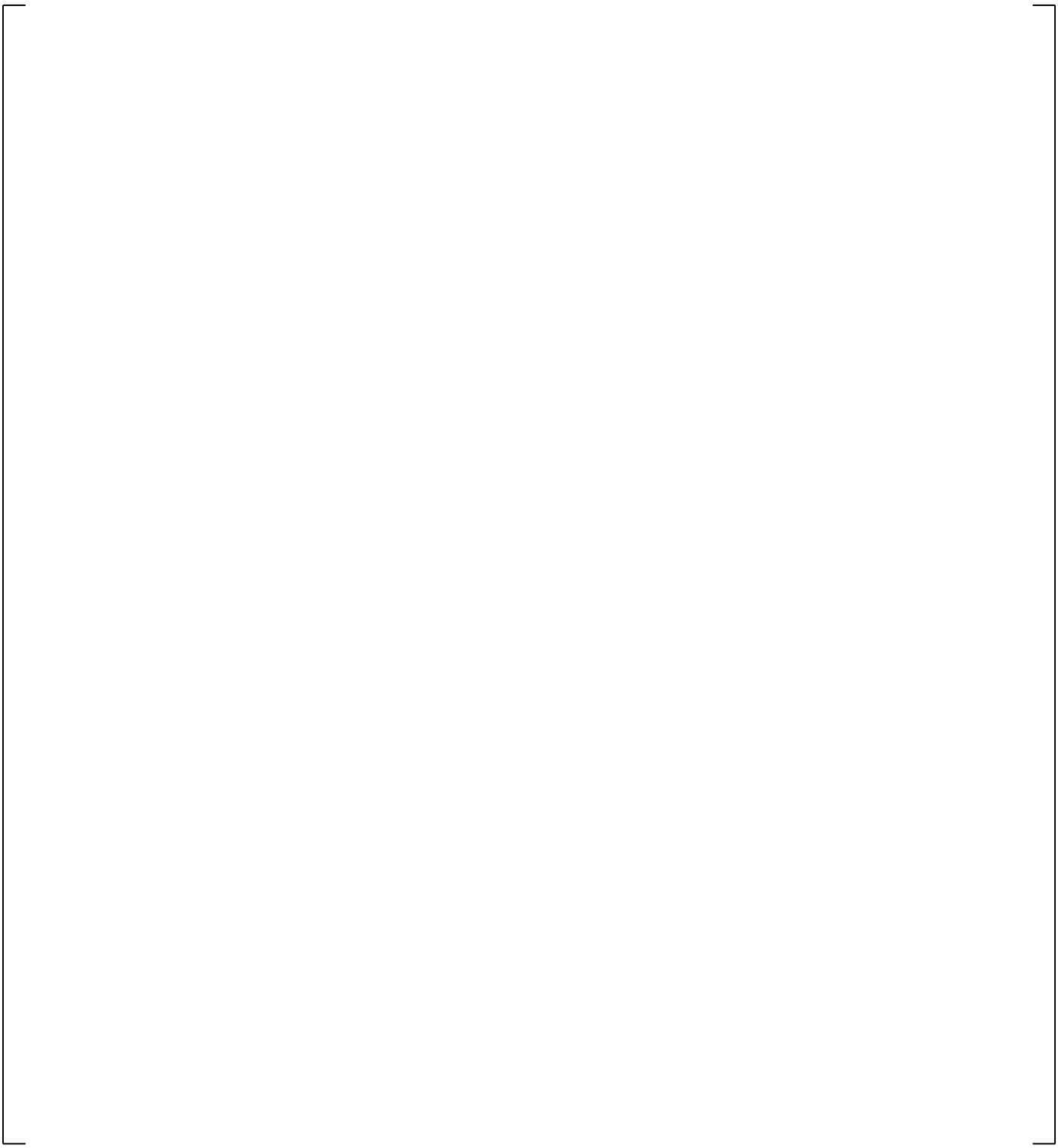

Figure 20.3-3 Energy Conservation for 1D/3D Mass and Energy Test

20.4 SUMMARY AND CONCLUSIONS

This section considered the WCOBRA/TRAC-TF2 component models that have special importance during the simulation of a LOCA in a PWR, and that have not been discussed in previous sections.

Section 20.1 documented the validation performed for the accumulator model. Accumulator blowdown tests performed at Indian Point Unit 2 and Callaway were modeled and simulated with WCOBRA/TRAC-TF2, and **[**

][a,c] Simulations of the LOFT experiments were made with accumulator modeling similar to that used in a PWR. The LOFT simulations showed that WCOBRA/TRAC-TF2 predicted **[**

][a,c]

The WCOBRA/TRAC-TF2 pump model was discussed in Section 20.2. The model was used in the simulation of the LOFT and ROSA tests, and the comparison of the predicted versus measured pressure difference across the pump was **[**

][a,c]

Finally, Section 20.3 provided **[**

][a,c].

21 ROSA-IV TEST SIMULATIONS

21.1 INTRODUCTION

The Rig-of-Safety Assessment Number 4 (ROSA-IV) program conducted a series of experiments to investigate the thermal-hydraulic behavior of a Westinghouse-designed four-loop pressurized water reactor (PWR) during small break loss-of-coolant accidents (LOCAs) and operational transients using the Large Scale Test Facility (LSTF). A number of phenomena that are of interest to the FULL SPECTRUM LOCA (FSLOCA) Methodology were investigated in the ROSA-IV test facility. Tests were well documented and many test reports are available in open literature or via the library of the Japan Atomic Energy Agency (JAEA), former Japan Atomic Energy Research Institute (JAERI).

The ROSA-IV LSTF is discussed in Section 21.2, and the WCOBRA/TRAC-TF2 model of the facility used for analysis of the full spectrum of breaks considered is presented in Section 21.3.

Sections 21.4 through 21.9 describe the simulations of a number of ROSA tests using WCOBRA/TRAC-TF2. The following test series were selected for the assessment of the WCOBRA/TRAC-TF2 code and the FSLOCA methodology. SB-CL-01, SB-CL-02, SB-CL-03, SB-CL-05, SB-CL-14, SB-CL-12, SB-CL-15, SB-CL-16, SB-CL-18, and ST-NC-02. SB-CL-18 is a 5% cold leg break test which is considered to be the reference transient and is the Organization for Economic Cooperation and Development (OECD) international standard problem No. 26 (ISP-26) (Kukita et al., 1992). SB-CL-01, SB-CL-02, and SB-CL-03 are 2.5% cold leg break tests with the break located at the side, bottom and top. SB-CL-12, SB-CL-15, and SB-CL-16 studied the same break orientation effect but at 0.5% break size. SB-CL-14 is a 10% break test. SB-CL-12, SB-CL-01, SB-CL-18, and SB-CL-14 form a break size sensitivity study covering a break range of 0.5% to 10%. SB-CL-05 is another 5% cold leg break test and it is the only test with the high-head safety injection (SI) activated. Comparison of SB-CL-05 and SB-CL-18 investigated the impact of having the pumped SI throughout the transient. Finally, ST-NC-02 is the 2% power natural circulation test.

Table 21.1-1 shows the list of tests used for the validation work. It contains relevant reports and articles related to the ROSA-IV LSTF and the different tests considered herein.

The analysis of the different tests is presented as follows in Sections 21.4 through 21.9. First, the reference transient, SB-CL-18, is discussed in Section 21.4. Section 21.5 documents the simulation of another 5% break test (SB-CL-05) which was conducted with actuation of pumped safety injection. The results of the simulation of the 10% break test SB-CL-14 (intermediate break size) are documented in Section 21.6. The effect of break orientation is discussed in Section 21.7, using simulation results from the top/side/bottom 0.5% (SB-CL-16/12/15) and 2.5% (SB-CL-03/01/02) cold leg break tests. In Section 21.8, a break spectrum study is documented, using the simulation results of the 0.5% (SB-CL-12), 2.5% (SB-CL-01), 5% (SB-CL-18) and 10% (SB-CL-14) break tests. Finally, the simulation of ST-NC-02, a 2% power natural circulation test is documented in Section 21.9.

Section 21.10 discusses the capability of the code to calculate counter-current flow at the upper core plate (UCP), in the vicinity of the hot leg elbow and steam generator inlet nozzle, and the steam generator U-tube bundle. The results presented in that section are based on the code calculation of the different break tests, described in the previous Sections 21.4 through 21.9.

Section 21.11 contains results of various sensitivity calculations performed with selected ROSA-IV tests that are needed to support conclusions made in other sections of this Topical report.

Table 21.1-1 Selected ROSA-IV Test Series Description and Related Technical Reports

Run ID	Date	Break	Condition	JAERI-Report/Article
SB-CL-01	5/30/85	2.5% CL	Cold Leg w/o high-pressure injection (HPI), (Orifice in branch pipe)	(Koizumi et al., 1987), (Koizumi et al., 1988), (Osakabe et al., 1987)
SB-CL-05	6/26/85	5% CL	Cold Leg w/HPI, w/o auxiliary feed water (AFW), **side break**, (Orifice in branch pipe)	(Kawaji et al., 1986), (Osakabe et al., 1987), (Osakabe et al., 1988)
SB-CL-02	7/18/85	2.5% CL	Cold Leg w/o HPI, **bottom break** (orifice in branch pipe)	(Koizumi et al, 1987), (Koizumi et al.,1988)
SB-CL-03	8/8/85	2.5% CL	Cold Leg w/o HPI, **top break** (orifice in branch pipe)	(Koizumi et al., 1987), (Koizumi et al., 1988)
ST-NC/SG-02	12/4/85	2% power nat. circ.	Reflux to core uncovery. Then stepwise secondary level drop.	(Tasaka et al., 1988), (Kukita et al., 1988), (Kukita et al., 1989), (Chauliac et al., 1988), (Stumpf et al., 1987), (Yonomoto, 2005)
SB-CL-14	8/28/86	10% CL	Cold Leg w/o HPI, **side break**, (orifice in branch pipe), realistic (low) power curve.	(Koizumi and Tasaka, 1988a)
SB-CL-12	7/29/87	0.5% CL	Cold leg w/o HPI, **side break** (orifice flush w/cold leg wall)	(Kukita et al., 1990a), (Kukita et al., 1990b)

Table 21.1-1 Selected ROSA-IV Test Series Description and Related Technical Reports (cont.)				
Run ID	**Date**	**Break**	**Condition**	**JAERI-Report/Article**
SB-CL-15	1/26/88	0.5% CL	Cold leg w/o HPI, w/o AFW, **bottom break,** (orifice flush w/cold leg wall)	(Koizumi and Tasaka, 1988b), (Asaka et al., 1990)
SB-CL-16	3/2/88	0.5% CL	Cold leg w/o HPI, w/o AFW, **top break**, (orifice flush w/ cold leg wall)	(Koizumi and Tasaka, 1988b), (Asaka et al., 1990)
SB-CL-18	5/25/88	5% CL	Cold leg w/o HPI, w/o AFW, **side break** (orifice in branch pipe), repeat of SB-CL-08 with improved SG ΔP measurements. **This is CSNI ISP-26.**	(Kumamaru et al., 1989), (Kukita et al., 1992), (Glaeser et al., 2000)

21.2 TEST FACILITY DESCRIPTION

The LSTF is a 1/48 volume scale representation of a Westinghouse four-loop 3423 MWt PWR. Figure 21.2-1 is a schematic diagram of the facility. The LSTF consists of two equal volume loops, A and B, with a pressurizer attached to the hot leg of loop A. Table 21.2-1 compares the major design characteristics of the LSTF and the PWR. The core simulator contains 16 square 7x7 and 8 semi-crescent heater rod assemblies. The heater rods are 9.5 mm (0.374 inches) in diameter and 3.66 m (12 feet) in length. To simulate possible effects of non-uniform radial power distribution there are low, average and high power assemblies. The core utilizes chopped cosine axial power distribution.

The maximum power in the facility at steady state is 10 MW, which is equivalent to 14 percent of the scaled steady state core power of the reference PWR.

The secondary coolant system consists of two steam generators, main and auxiliary feed water pumps, and condensing system. The height of the LSTF steam generator is the same as in the reference PWR. The downcomer of each steam generator consists of four pipes located outside the steam generator vessel. The pipes are sized to provide a representative volume and width of a typical steam generator downcomer. Each steam generator contains 141 U-tubes with 19.6 mm (0.772 inches) inside diameter (ID) and 25.4 mm (1.0 inches) outside diameter (OD). Primary and secondary steam separators are included in each steam generator vessel.

The LSTF Emergency Core Cooling System (ECCS) consists of a high pressure charging system, a high pressure injection system, a low pressure injection system, an accumulator system, and a residual heat removal system.

The operational setpoints of the LSTF are detailed in Table 21.2-2. A detailed description of the facility is available in the JAERI documents (The ROSA-IV Group, 1985) and (The ROSA-IV Group, 1989).

21.2.1 Important Physical Phenomena and Scaling Considerations

The ROSA-IV LSTF is designed to conduct tests which provide important information regarding the behavior of a Westinghouse PWR during a small break LOCA transient. The scaling, relative to the typical 4-loop PWR, is such that the tests conducted can reproduce realistically the most important small break thermo-hydraulic phenomena. Since it is practically impossible to design a small test facility that can reproduce all aspects of the behavior of a complex system like a PWR, proper scaling can be achieved for only a few key small break LOCA phenomena.

The key scaling ratios of the ROSA-IV LSTF against a typical PWR are presented in Table 21.2-1.

At steady state conditions the core simulator power is 10 MW, which is 14% of the 1:48 scaled power of the reference PWR, resulting in a 1:342 power ratio at steady state conditions. The core flow ratio at steady state is 1:342 in order to achieve initial primary side temperatures representative of a PWR. Under these conditions the steady state power-to-volume (power density) ratio is approximately 1:7.

Preserving power-to-volume ratio of 1:1 assures that the time scale of the simulated transient phenomena is prototypical of the PWR. To achieve this ratio during the important phases of the small break LOCA transient, the power of the LSTF core simulator is actively controlled and follows a predefined power-vs-time curve which assures that beyond 30 seconds after reactor trip the simulated decay heat is scaled 1:48 to that of the representative PWR. In the small break tests, immediately after the break the pump speed is briefly increased and then follows a predefined coastdown curve, which assures that fluid velocities typical of a PWR are achieved during the initial phase of the transient.

Since the elevations of the major components of the LSTF are full-scale and match those of the real PWR the height scaling ratio is 1:1. Preserving the same height and characteristic elevations assures that the natural circulation phenomena important to core cooling and the general system behavior are adequately simulated in the tests. Preserving the bottom elevation of the cross-over legs is of great importance to observing the effects of a realistic depth of core uncovery related to the loop seal clearance phenomenon.

Preservation of the same core height and fuel bundle geometry characteristics (square lattice, rod diameter, pitch, etc.) assures that important phenomena that might occur in the core during the different phases of the accident are simulated in a realistic manner. Some of these are void generation and distribution and related rod heatup during loop seal clearance, level swell and rod heatup during boiloff, etc.

With the height of key elevations preserved the same as the PWR, the scaling of each steam generator (volume and flow area ratios of 1:24 and U-tube surface area 1:25) assures that important thermo-hydraulic phenomena like primary-to-secondary heat transfer, natural circulation, reflux condensation and counter-current flow are simulated in a realistic manner. Note that one LSTF steam generator represents two PWR steam generators; therefore the total steam generator (SG) surface area scaling ratio is actually 1:48.

The diameter of the hot and cold leg pipes is large enough to allow the establishment of all possible flow regimes of significance that may develop in the real plant. This also allows investigating effects of break orientation on the small break LOCA (SBLOCA) transient.

The hot and cold legs, with a diameter of 207 mm (8.15 inches), are sized to conserve volume scaling and the ratio of length to the square root of the pipe diameter ($L/\sqrt{D}$) of the reference PWR. The ($L/\sqrt{D}$) ratio is in essence a Froude number and the 1:1 scaling relative to a PWR assures that flow regime transition would be manifested properly during the various tests, performed with the ROSA-IV LSTF.

The goal of preserving hot leg $L/\sqrt{D} = 1$ and volume ratio of 24 results in a hot leg flow area ratio of 12.68. Thus the flow area of the LSTF hot leg (and cold leg as well) is essentially twice the 1:24 scaled PWR hot leg area. This scaling distortion would create conditions where easier flow stratification in the hot and cold legs will be simulated during the tests compared to a real PWR small break transient.

As seen in Table 21.2-1, the scaling ratio of the upper core plate flow area is approximately 1:45, which is very close to the PWR/LSTF volume and power ratio of 1:48. This similarity creates the preconditions to simulate realistic fluid velocities and counter-current flow at the upper core plate during the SBLOCA tests.

Another phenomenon is the counter-current flow limitation (CCFL) that might occur at various locations of the primary system of a PWR. The importance of this phenomenon and its ranking with respect to its effect on the system behavior during the different phases of the LOCA transient have been discussed in Section 2.3.2, Volume 1. The design and scaling of the ROSA-IV LSTF allows for the effects of CCFL to be measured and observed at realistic PWR LOCA conditions. Detailed discussion of the CCFL considered at three key system locations (inlet of steam generator U-tubes, hot leg elbows and upper core plate) is provided in Section 21.10 and the ROSA-IV LSTF model described in Section 21.3.

Based on the discussion of the key scaling ratios presented above it is concluded that the tests conducted on the ROSA-IV LSTF can simulate the most important small break LOCA phenomena. Therefore, the available measurements and observations from various small break tests are appropriate for performing WCOBRA/TRAC-TF2 Model Assessments. Since the LSTF is a full height facility with exact representation of the key elevations of the individual PWR components, the modeling techniques developed, implemented and assessed in the LSTF test simulations can be adopted in the simulations of small break LOCA transients of the real PWR.

Table 21.2-1 Major Design Characteristics of LSTF and PWR

Characteristic	LSTF	PWR	PWR/LSTF
Pressure, MPa (psia)	15.5 (2250)	15.5 (2250)	1
Temperature, K (°F)	598 (617)	598 (617)	1
Number of fuel rods	1064	50,952	48
Core height, m (ft)	3.66 (12)	3.66 (12)	1
Total Primary Fluid volume, m^3 (ft^3)	7.23 (255.3)	374 (12,254.2)	48
Vessel Fluid Volume, m^3 (ft^3)	2.675 (94.47)	131.7 (4650.9)	49.24
Core Volume, m^3 (ft^3)	0.4078 (14.4)	17.5 (618.0)	42.91
Upper Plenum Volume (incl. end box), m^3 (ft^3)	0.5472 (19.32)	28.4 (1002.9)	51.9
Lower Plenum Volume, m^3 (ft^3)	0.5802 (20.49)	29.62 (1046.0)	51.05
Core power, MW	10	3423(t)	342[(2)]
Power density, kW/m^3 (kW/ft^3)	1383 (39.17)	9152.4 (279.33)	7.1
Core inlet flow, kg/sec (lbm/sec)	48.8 (97.6)	16700 (33,400)	342
Core Flow Area, m^2 (ft^2)	0.1134 (1.22)	4.75 (51.13)[(1)]	41.9
Upper Core Plate Area, m^2 (ft^2)	0.066 (0.71)	2.94 (31.65)[(1)]	44.5
Upper Plenum Area, m^2 (ft^2)	0.159 (1.71)	6.92 (74.48)[(1)]	43.5
Downcomer gap, m (in.)	0.053 (2.09)	0.26 (10.24)	4.9
Hot leg			
Diameter (D), m (ft)	0.207 (0.679)	0.737 (2.418)	3.56
Length (L), m (ft)	3.69 (12.1)	6.99 (22.93)	1.89
$L/\sqrt{D}$, $m^{1/2}$ ($ft^{1/2}$)	8.14 (14.68)	8.14 (14.68)	1.0
Volume $\left(\frac{\pi}{4}D^2L\right)$, m^3 (ft^3)	0.124 (4.38)	2.98 (105.2)	24.0
Area $\left(\frac{\pi}{4}D^2\right)$, m^2 (ft^2)	0.03365 (0.362)	0.4266 (4.59)	12.68
Number of loops	2	4	2
Number of tubes in steam generator	141	3382	24.0
Total Inner Surface Area of U-tubes, m^2 (ft^2)	171 (1840.6)	4214 (45359.1)	25
Length of steam generator tube (average), m (ft)	20.2 (66.3)	20.2 (66.3)	1.0

a,c

Table 21.2-2 Standard Operational Setpoints of the ROSA-IV Large Scale Test Facility	
Event	**Setpoint**
Reactor scram signal, MPa (psia)	12.97 (1881.1)
Initiation of pump coastdown	With reactor scram
Safety injection signal, MPa (psia)	12.27 (1779.6)
High pressure charging(1)	12 s after safety injection signal
Safety injection	17 s after safety injection signal
High pressure injection cutoff, MPa (psia)(2)	10.7 (1551.9)
Low pressure injection cutoff, MPa (psia)(3)	1.29 (187.1)
Accumulator injection, MPa (psia)	4.51 (654.1)
Main feedwater termination	With reactor scram
Turbine throttle valve closure	With reactor scram
Auxiliary feedwater initiation(4)	28 s after reactor scram

Notes:
1. High-pressure charging was not actuated during the SB-Cl-18 and SB-CL-14.
2. High-pressure injection was not actuated during the SB-CL-18 test and SB-CL-14.
3. The SB-CL-18 test was terminated prior to the actuation of low-pressure injection.
4. Auxiliary feedwater was not actuated during the SB-CL-18 test.

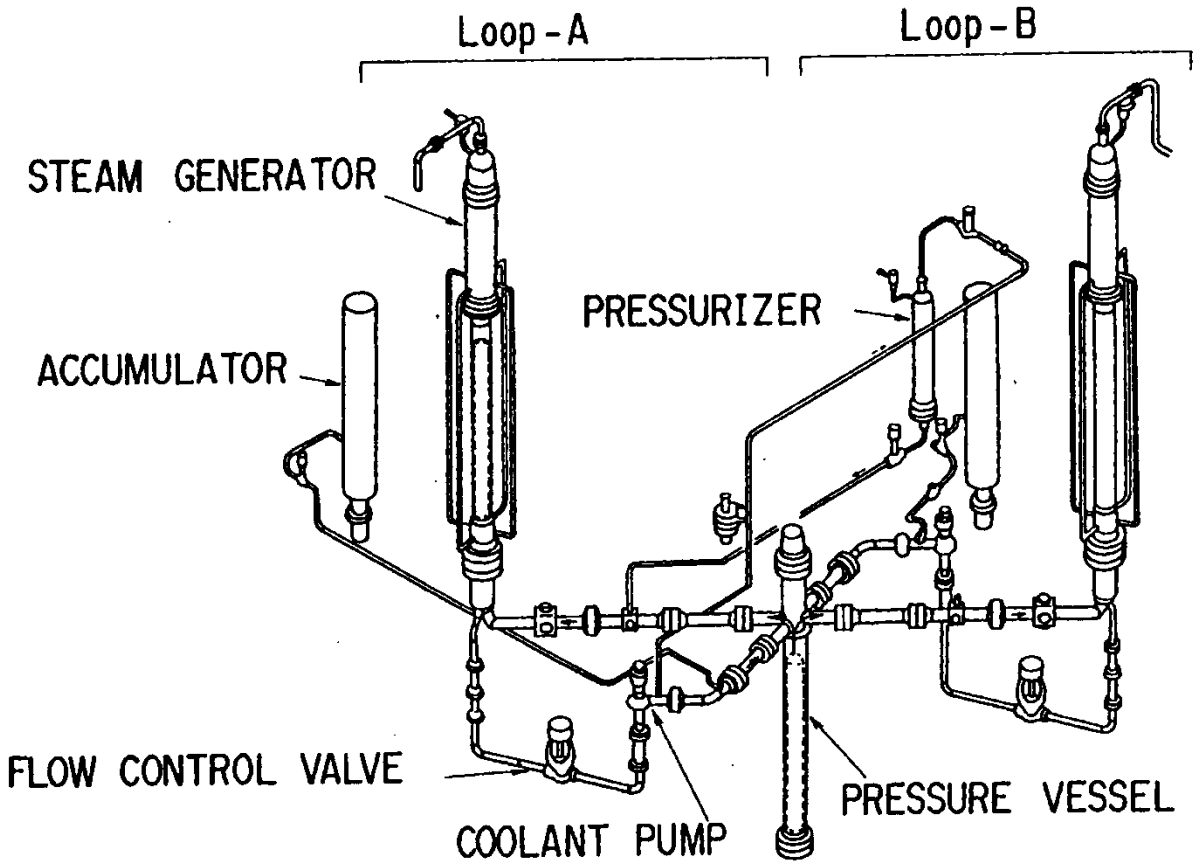

Figure 21.2-1 Schematic Diagram of LSTF

21.3 DESCRIPTION OF WCOBRA/TRAC-TF2 MODEL FOR ROSA/LSTF-IV

[

][a,c]

Vessel Model:

Figure 21.3-1 shows the WCOBRA/TRAC-TF2 noding of the LSTF pressure vessel. Figures 21.3-2 through 22.3-6 show the transverse channel connections in each of the vessel sections. Figure 21.3-7 shows the core simulator map of the LSTF. **[**

][a,c]

The upper plenum modeling of the LSTF facility includes **[**

][a,c]

[

]a,c

Loop Model:

The piping outside the LSTF pressure vessel is modeled by using 1-D components. Figure 21.3-8 shows the general 1-D loop noding diagram of the LSTF and Figure 21.3-9 provides more detail in the noding of the hot leg, steam generator and the loop seal regions.

Each hot leg, including the elbow at the inlet of the steam generator, is modeled [

]a,c

As seen from Figure 21.3-8 and the more detailed Figure 21.3-9, primary flow enters the steam generator [

]a,c

The steam generator secondary side includes sufficient detail to model recirculation in the downcomer and separation in the vapor dome region. [

]a,c

During steady state simulation, and prior to reactor trip, steam leaving the generators passes through a TEE component and VALVE component to a constant pressure BREAK. At reactor trip, the main steam isolation valve (MSIV) is closed and flow goes through a VALVE component representing the main steam safety valve (MSSV) to a second BREAK component that provides a constant pressure boundary condition at the MSSV setpoint pressure.

Figure 21.3-9 shows the loop seal nodalization. Flow from the steam generator outlet passes through **[**

][a,c]

The safety injection system is shown in Figure 21.3-8. Combined high pressure safety injection plus charging flows to each loop are modeled **[**

][a,c] accumulator setpoint of 4.51 MPa (654.1 psia). VALVE Components 216 and 226 are isolation valves. The combined safety injections from the pumps and accumulators enter each of the cold legs through the side pipes of TEE Components 15 and 25 to loops A and B, respectively.

The cold leg condensation model, described in Section 6.3.6 of Volume 1, is **[**
][a,c], consistent with the SI modeling approach and validation presented in Section 17.

a,c

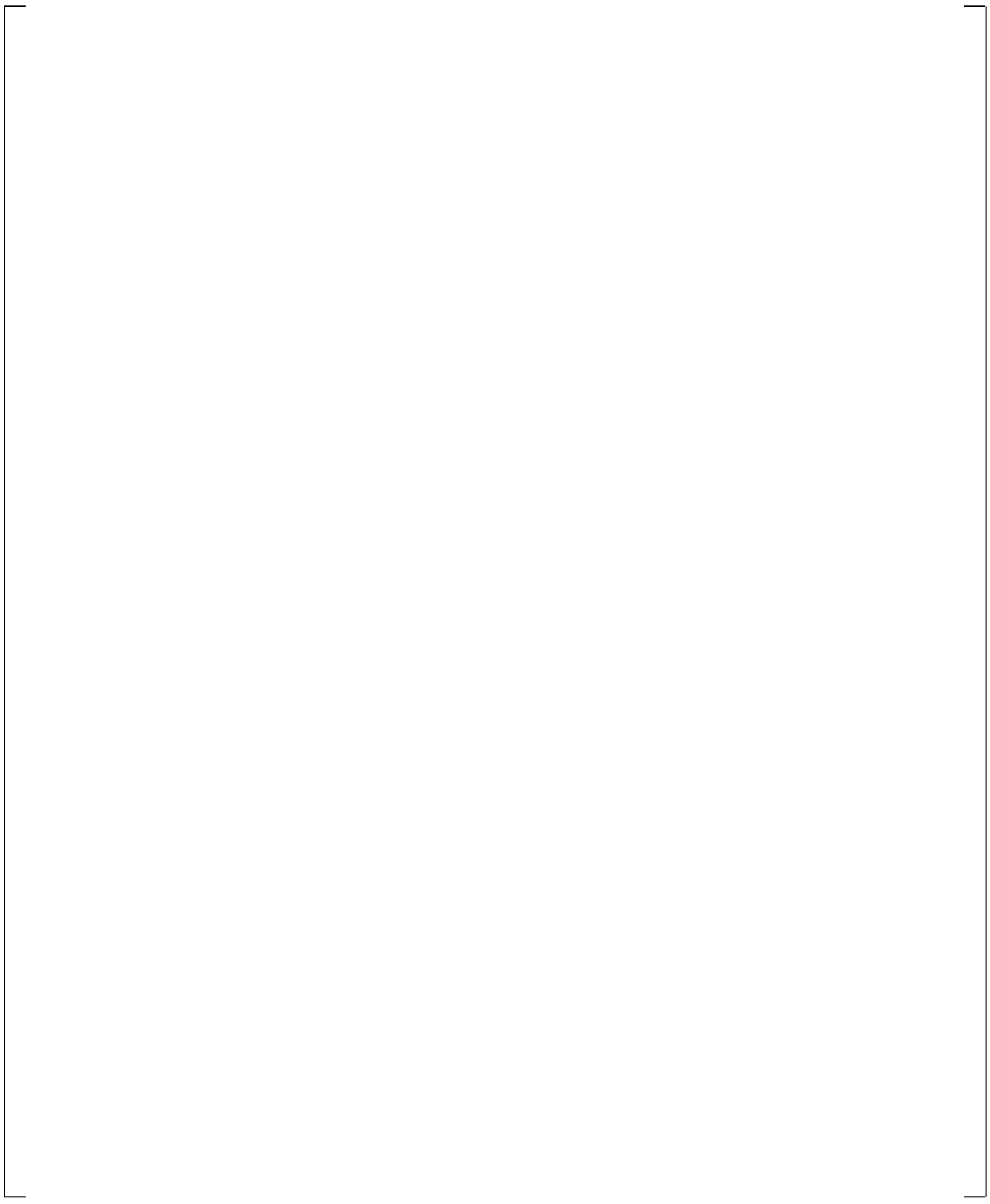

Figure 21.3-1 WCOBRA/TRAC-TF2 Model of LSTF Pressure Vessel

a,c

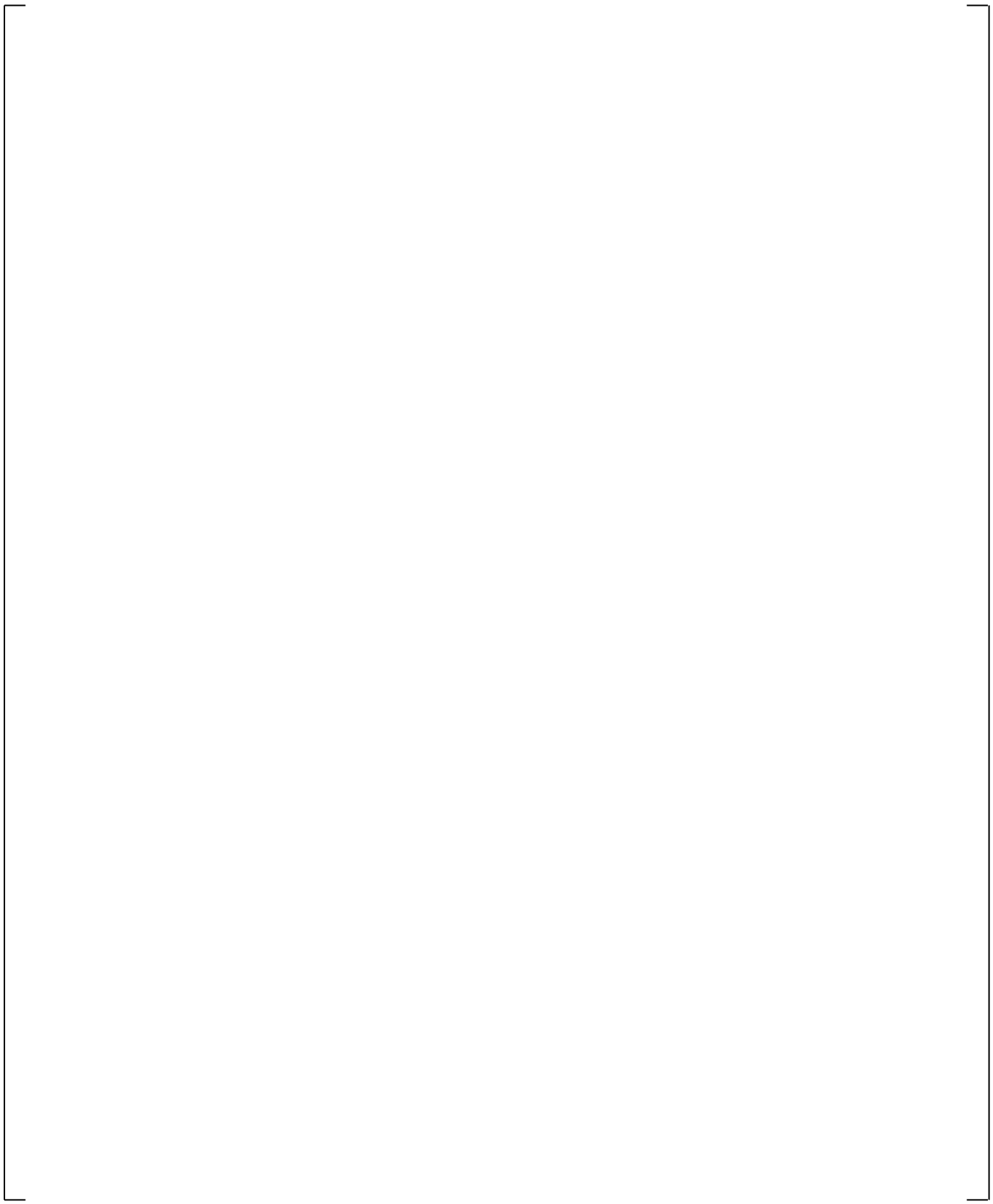

Figure 21.3-2 LSTF Pressure Vessel Sections 1 and 2

a,c

Figure 21.3-3 LSTF Pressure Vessel Sections 3 and 4

a,c

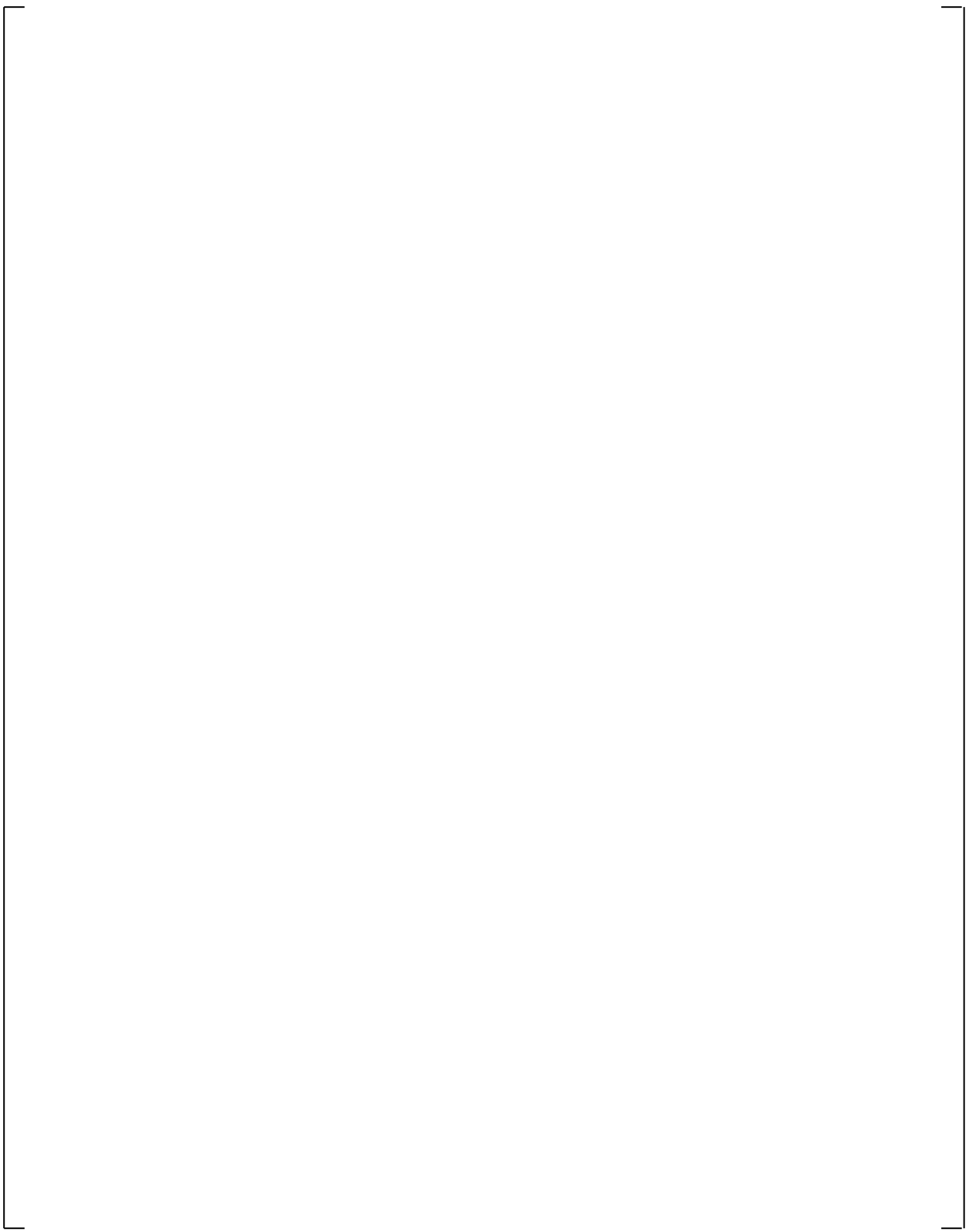

Figure 21.3-4 LSTF Pressure Vessel Sections 5 and 6

a,c

Figure 21.3-5 LSTF Pressure Vessel Sections 7 and 8

a,c

Figure 21.3-6 LSTF Pressure Vessel Sections 9 and 10

a,c

Figure 21.3-7 ROSA-IV LSTF Core Simulator Map

a,c

Figure 21.3-8 WCOBRA/TRAC-TF2 Loop Noding Diagram of LSTF

a,c

Figure 21.3-9 Hot Leg (Including Pressurizer), Steam Generator and Cross-Over Leg Noding

21.4 SIMULATION OF SB-CL-18, 5-PERCENT COLD LEG SIDE BREAK

21.4.1 Description of the SB-CL-18 Test Boundary and Initial Conditions

Experiments as part of ROSA-IV (LSTF-IV) were conducted for several different break areas. Test SB-CL-18 simulated a 5-percent cold leg break, which corresponds to approximately a 6-inch break in a PWR. The break was located in loop B and had a horizontal orientation. Unlike test SB-CL-05, high-head safety injection (HHSI) and low-head safety injection (LHSI) were not modeled in this test. The experimental results are available in the test data report JAERI-M 89-027 (Kumamaru et al., 1989). This test is also known as OECD/NEA/CSNI International Standard Problem No. 26 (Kukita et al., 1992).

For each of the break test simulations, verification that the WCOBRA/TRAC-TF2 model of the LSTF-IV adequately represented the facility was accomplished through a full-power, 300-seconds steady state simulation. Table 21.4-1 summarizes initial conditions achieved for the SB-CL-18 test at the end of the 300 seconds steady state calculation. At the end of this 300-seconds simulation, predicted and measured system parameters were compared to ensure reasonably good agreement.

The operational setpoints for this test are the same as the standard set implemented for all ROSA-IV tests, provided in Table 21.2-2. As described in the test report (Kumamaru et al., 1989), the high-pressure charging and high-pressure injection were not actuated for this test, since they were assumed to fail. Low-pressure safety injection did not occur since the test was terminated before the cut-off pressure of 1.29 MPa was reached. Auxiliary feed water was not actuated as well.

The core power was scrammed once the primary pressure decreased below 12.97 MPa (1881 psia). The core decay heat was simulated following a pre-programmed curve, which accounts for actinides and delayed neutron effects and gives a slower decrease than the American Nuclear Society (ANS) standard. The decay heat curve implemented during the test and used in the SB-CL-18 simulations is provided in Table 21.4-2.

On the LSTF, the initial conditions prior to the initiation of the test are established at pump speeds (respectively fluid velocities) that are much lower than those existing at the PWR at steady state conditions. This was done so that, with the reduced core power at the LSTF, the initial cold leg and hot leg temperatures are preserved similar to a PWR. Immediately following the break, the pump speed was increased to achieve loop flow rates similar to the reference PWR. Loss of offsite power is assumed and the reactor coolant pumps are tripped to begin coastdown coincident with reactor scram. In the transient simulation, the pumps followed a coastdown curve consistent with the test. The main feed water was stopped, and the secondary sides of the two steam generators were isolated by closure of their MSIVs coincident with reactor trip.

21.4.2 Steady State Calibration and Transient Calculation Procedures

Steady State Calculation

In the SB-CL-18 test simulation first a steady state calculation is performed (in this case 300 seconds) in order to achieve the desired primary and secondary side conditions, according to those measured at the test. The initial steady state conditions achieved for the SB-CL-18 test are presented in Table 21.4-1.

Transient Calculation Procedure

The WCOBRA/TRAC-TF2 simulation of the LSTF-IV 5-percent cold leg break test SB-CL-18 is initiated by **[**

][a,c]

The transient calculation procedure described above is implemented for all ROSA LSTF-IV cold leg break test simulations presented in this section. Depending on the break size being simulated, the appropriate set of HRM1PM, HRM2PM and HRMOFD multipliers is used, in accordance with the break modeling described in Section 12.5.4.

Transient Acceptance Criteria

The primary acceptance criterion for the simulations of the ROSA-IV test documented herein is achieving the best possible consistency with the available test data. Particular attention is given to the accurate prediction of key transient phenomena like system depressurization, timing and magnitude of loop seal clearance, boiloff, etc. **[**

][a,c]

[

][a,c]

21.4.3 Results and Conclusions From the SB-CL-18 Simulations

This section presents the results of two SB-CL-18 test transient simulations. Both simulations were performed with break flow discharge coefficients **[ ]**[a,c] One of the simulations was performed with CCFL enforced at the steam generator U-tubes **[ ]**[a,c], the hot leg elbows **[ ]**[a,c] and upper core plate (Bankoff correlation). To illustrate the degree of conservatism of the adopted CCFL modeling approach, the other simulation was performed without any CCFL limits enforced. In the remainder of this section, similar pairs of simulations will commonly be referred to as "CCFL on" and "CCFL off" simulations, or simulations "with and without CCFL," respectively. Note that CCFL may be predicted to occur even without enforcing the CCFL limits, as a result of the interfacial drag.

In this test, the primary system rapidly depressurized and equilibrated at a pressure slightly higher than the stream generator secondary pressure, at approximately 8.3 MPa (~1200 psia), Figure 21.4-1, until the loop seal cleared at about 140 seconds, (see DPE080-LSA in Figure 21.4-3 and DPE220-LSB in Figure 21.4-4).

After loop seal clearance, the break quality changed from a low quality mixture to primarily vapor and the primary system continued to depressurize.

As the primary system continued to drain, liquid is redistributed among the different regions; the core and downcomer, the upper plenum, hot legs and steam generator uphill and downhill side, and the uphill and downhill sides of the loop seal piping. A manometric (hydrostatic) balance is established between the liquid present in these regions during the transient. Prior to the loop seal clearance, the core collapsed level became depressed nearly to the bottom of the core, while liquid remained in the uphill side of the loop seal. At this time, the heater rods heated up rapidly. While most of the liquid had drained from the steam generator tubes, some of it remained in the steam generators' inlet plenums and the bottom of the uphill side. After steam slipped through the loop seals, the core level recovered and most of the water was pushed out of both loop seals through the cold legs and into the downcomer.

Test SB-CL-18 had a core depression during loop seal clearance that was considerably below the elevation of the bottom of the loop seal piping. Osakabe (Osakabe et al., 1987) attributed this to a significant liquid holdup in the uphill side of steam generator tubes. During this core level depression, the peak rod cladding temperature at the test increased by approximately 190K (342°F) reaching a maximum of approximately 740K (872°F), Figure 21.4-6. After loop seal clearance, the core level recovered quickly and the rods were quenched.

Figures 21.4-1 through 21.4-20 compare predicted and measured results for the 5-percent cold leg break test SB-CL-18. Each of the figures shows SB-CL-18 simulation results with and without CCFL. Figures 21.4-21 through 21.4-24 present calculated CCFL conditions at key system locations (steam generator U-tube inlets, hot leg elbows and upper core plate) extracted from the SB-CL-18 simulations with and without CCFL enforced. Figures 21.4-25 through 21.4-27 show the calculated cladding temperatures at the 7.33-ft core elevation compared to the test data.

System Depressurization and Break Flow

Figure 21.4-1 compares predicted and measured primary system pressure. **[**

][a,c]

Break flow is compared in Figure 21.4-2. Early in the transient, flow out of the break is sub-cooled single-phase liquid. **[**

][a,c]

Loop Seal Clearance and Core Uncovery

Figures 21.4-3 and 21.4-4 show a comparison of the calculated and measured loop seal differential pressures. In the test, loop seal venting occurs at approximately 140 seconds. **[**

][a,c] The test data and calculations also show that after the loop seals clear, steam venting is established through both cross-over legs.

Before the loop seals vent, the collapsed liquid level in the core is depressed. Figure 21.4-5 compares calculated and measured inner vessel differential pressure, which is an indicator of the inner vessel collapsed level. **[**

][a,c]

Core heat-up occurs during the loop seal clearance period as the core is temporarily uncovered. Figure 21.4-6 compares the PCT predicted by WCOBRA/TRAC-TF2 to the maximum cladding heat-up observed in the data. **[**

][a,c]

The depth of core uncovery during the loop seal clearance period depends upon the manometric balance between the core and downcomer, and the sum of pressure drops through the loop and uphill side of the loop seal piping. An important static head exists on the uphill side of the steam generator tubes, where water condensed in the tubes collects because of CCFL and flooding in the steam generator up-hill tubes. Figures 21.4-7 and 22.4-8 show a comparison of the predicted and measured differential pressures in the uphill steam generator tubes for SG-A and SG-B respectively. The calculation results in these two figures should be analyzed in conjunction with the calculated CCFL conditions at the steam generator U-tube inlets shown in Figures 21.4-21 and 21.4-22.

The calculated downcomer differential pressures, Figure 21.4-18, are in good agreement with the test.

Steam Generator U-tube and Inlet Plenum Draining

[

][a,c]

Figures 21.4-11 and 21.4-12 show a comparison of the calculated and measured differential pressures across the two steam generators. From those two figures, it is evident that during the loop seal clearance period (t>150 sec) in both simulations the code calculates steam generator resistance **[**

][a,c]

Figures 21.4-13 and 21.4-14 show the calculated and measured collapsed liquid levels in the steam generator inlet plenums. **[**

][a,c]

[

]a,c

Upper Plenum Draining

The upper plenum differential pressures (indicators of the liquid levels in the upper plenum) are shown in Figure 21.4-17. Until about 110 seconds the predictions are consistent with the test. Later on, the upper plenum level [

]a,c

The almost complete draining of the upper plenum, observed at the test between 125 and 160 seconds, Figure 21.4-17, is related to the significant core uncovery due to the loop seal clearance depression, Figure 21.4-5. The fast recovery of the upper plenum level between 160 and 170 seconds is caused by both the recovery of the core inventory and the draining of the steam generators, especially the draining surge from the steam generator inlet plenums, seen in Figures 21.4-13 and 21.4-14. Relatively constant liquid level is measured in the upper plenum until 330 seconds maintained by the gradual draining of the steam generator inlet plenums and the hot legs. As the system inventory is further depleted, due to the steam discharged through the break, the upper plenum drains completely by 400 seconds.

[

]a,c

Rod Cladding Heatup

Figures 21.4-25 through 21.4-27 show a comparison of measured (TW curves) and calculated rod cladding temperatures (TCLAD curves) at the 7.33-ft elevation in the core; the TCLAD curves are from the SB-CL-18 simulation with CCFL enforced . The period of interest for this discussion is between 124 and 320 seconds; this is the period when counter-current flow conditions are predicted to occur at the UCP. The 7.33-ft elevation is selected since it is one of the locations where significant rod heatup was measured at the test during this period of interest due to loop seal core uncovery.

Figure 21.4-25 shows the calculated and measured cladding temperatures of the low power rods. As seen in this figure, the test measurements show that only 4 out of 15 rods heated up briefly during the loop seal clearance period. The heatup of these (low power) rods was brief and the temperature increase did not exceed 50K. According to the measurements, the majority of the high-power rods heated up during the loop seal clearance period, Figure 21.4-26. Only 5 out of 13 rods in the inner average power region experienced heatup, according to Figure 21.4-27. In summary, the rod temperature measurements at the 7.33-ft elevation show that during the period of interest the peripheral (low power) region of the core simulator received and retained most of the fluid that was draining from the upper plenum. As a result, the inner average and high power regions tend to be depleted from coolant and experience more severe rod heatup.

[

]a,c

Accumulator Injection

Figures 21.4-19 and 21.4-20 show the calculated and measured accumulator injection flows. The calculated initiation of the accumulator injection and the timing of the turn-around of the boil-off PCT, Figure 21.4-6, are consistent with those observed at the test. **[**

][a,c]

Summary

[

][a,c]

Table 21.4-1 Steady-State Parameter Checklist (Initial Conditions) for the SB-CL-18 Test		
Parameter	**Target (Measured)**	[ ] a,c
Pressurizer pressure, MPa (psia)	15.5 (2248)	
Hot leg fluid temperature, K (°F)	599 (619)	
Cold leg fluid temperature, K (°F)	564(555)	
Core power, MW (MBTU/hr)	10	
Core inlet flow rate, kg/sec (lbm/s)	48.7 (107.3)	
HL-to-DC Leakage Flow Rate, kg/sec (% core flow)	0.124 (0.25%)	
DC-to-UH Bypass Flow Rate, kg/sec/sec (% core flow)	0.146 (0.3%)	
Pressurizer water level, m (ft)	2.6 (8.5)	
Pump speed, rad/sec (rpm) For Pump A For Pump B	 80.5 (769) 83.3 (796)	
Hot leg ΔP, kPa (psi) For Loop A For Loop B	 3.62 (0.53) 3.50 (0.50)	
Steam generator inlet to outlet, kPa (psi) For Loop A For Loop B	 1.35 (0.19) 1.46 (0.21)	
Cross-Over Leg Down ΔP, kPa (psi) For Loop A For Loop B	 -45.3 (-6.57) N/A	
Cross-Over Leg Up ΔP, kPa (psi) For Loop A For Loop B	 26.6 (3.86) 26.6 (3.86)	
Downcomer ΔP, kPa (psi)	61.5 (8.92)	
Downcomer to upper plenum ΔP, kPa (psi)	2.65 (0.38)	
Lower Plenum ΔP, kPa (psi)	12.9 (1.87)	
Core ΔP (including lower core plate), kPa (psi)	33.2 (4.8)	
Upper Plenum ΔP, kPa (psi)	13.5 (1.96)	
Steam generator secondary pressure, MPa (psia)	7.35 (1066)	
Steam generator secondary level, m (ft)	10.6 (34.8)	
Steam generator feedwater temperature, K (°F)	494 (429.5)	
Steam generator feedwater flow rate, kg/sec (lbm/s)	2.7 (5.95)	
Steam generator secondary circulation flow, kg/sec (lbm/s)	16.5 (36.3)	

Table 21.4-2 Decay Heat Power Curve Used in the SB-CL-18 Test Simulation			
Test Time	**WC/T Time**	**Test Power**	**Normalized Power**
sec	**sec**	**MW**	**-**
(1)	**(2)**	**(3)**	**(4)**
0	300.0	10.022	1.00000
46.6	346.6	10.025	1.00030
57.6	357.6	8.8175	0.87981
77.6	377.6	7.2675	0.72516
97.6	397.6	6.0925	0.60791
117.6	417.6	5.1775	0.51661
167.6	467.6	3.6325	0.36245
217.6	517.6	2.8650	0.28587
417.6	717.6	1.7925	0.17886
617.6	917.6	1.5800	0.15765
817.6	1117.6	1.5100	0.15067
899.6	1199.6	1.4750	0.14718

a,c

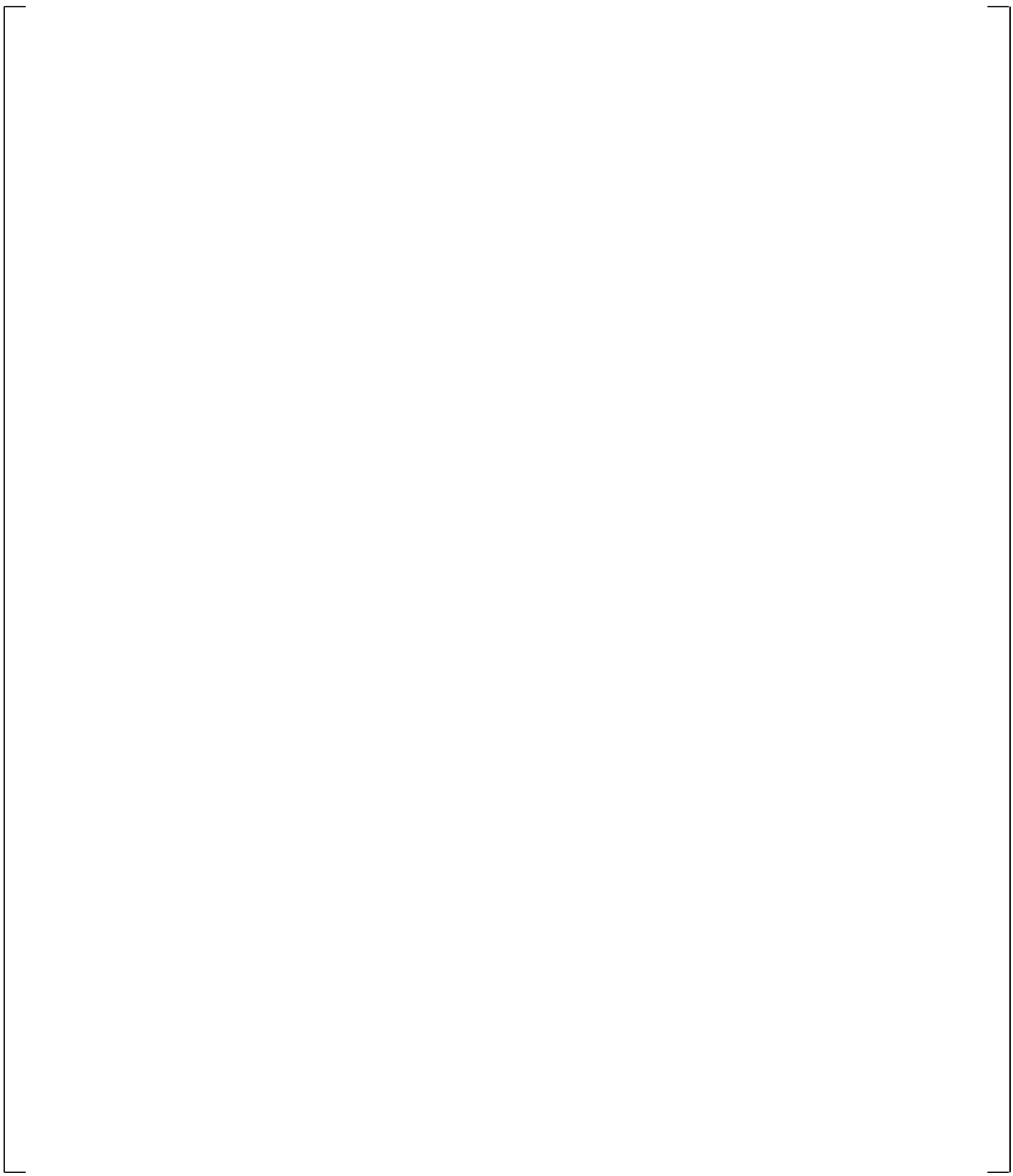

Figure 21.4-1 Pressurizer Pressure

a,c

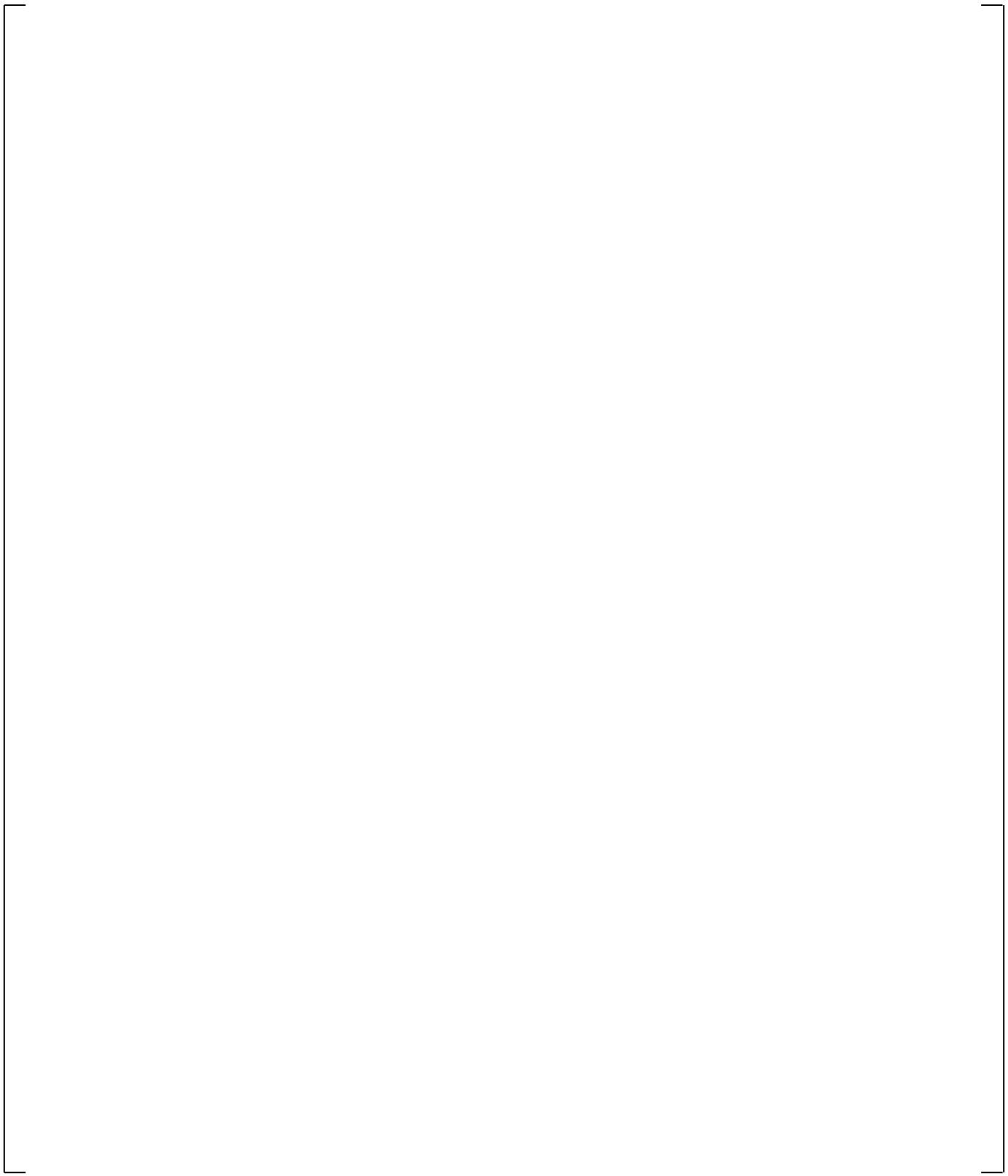

Figure 21.4-2 Break Flows

a,c

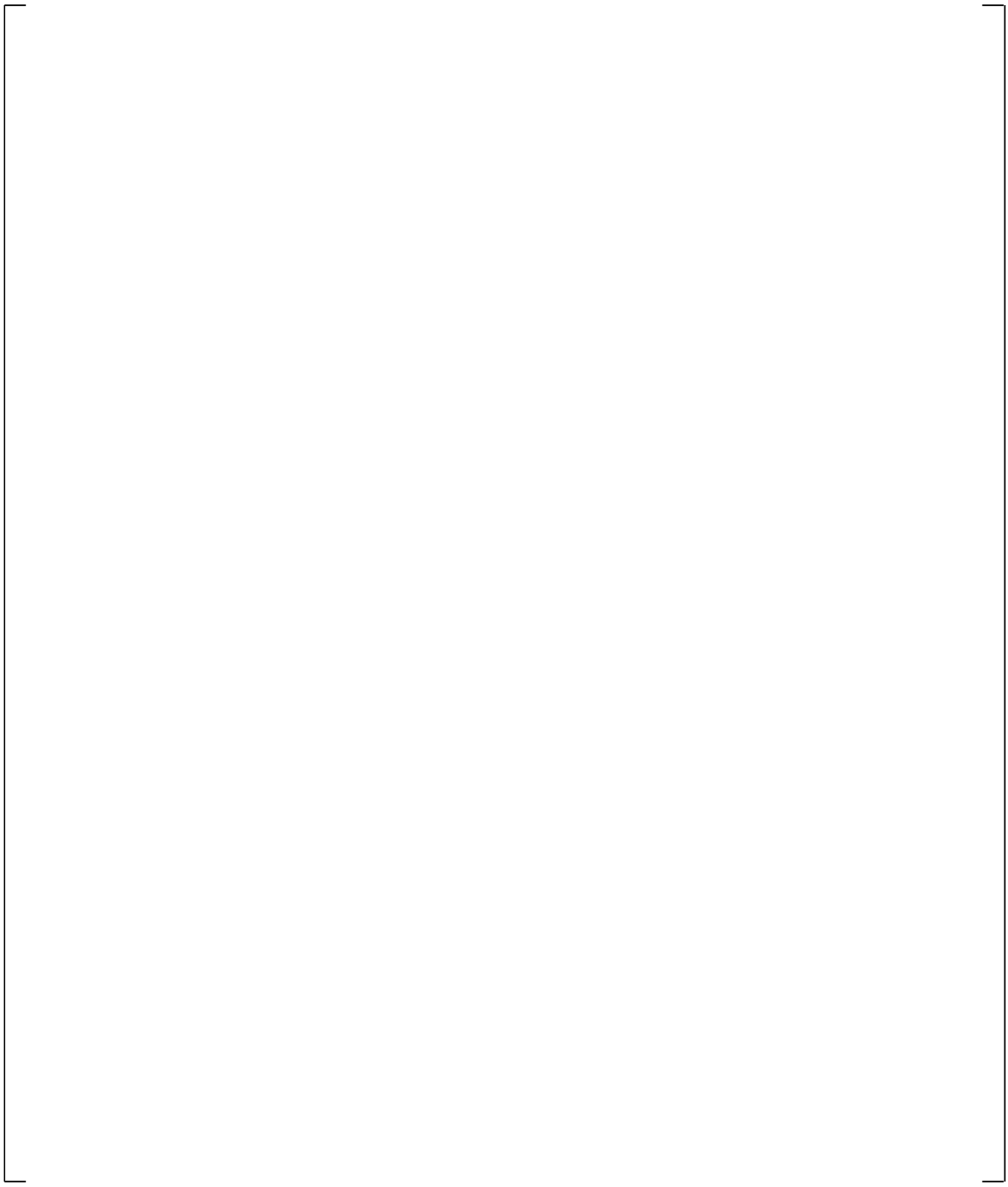

Figure 21.4-3 Cross-Over Leg A Differential Pressures

a,c

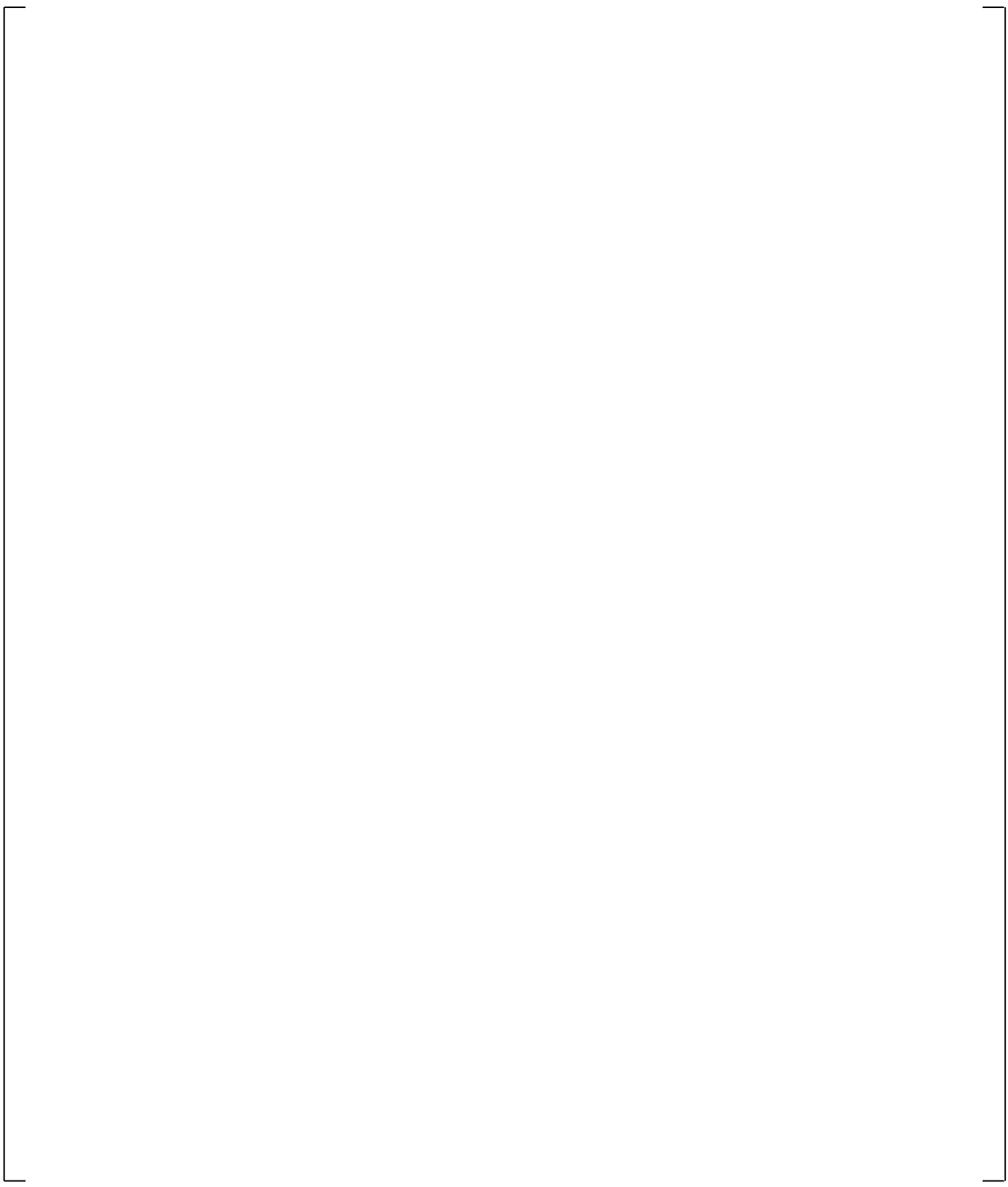

Figure 21.4-4 Cross-Over Leg B Differential Pressures

a,c

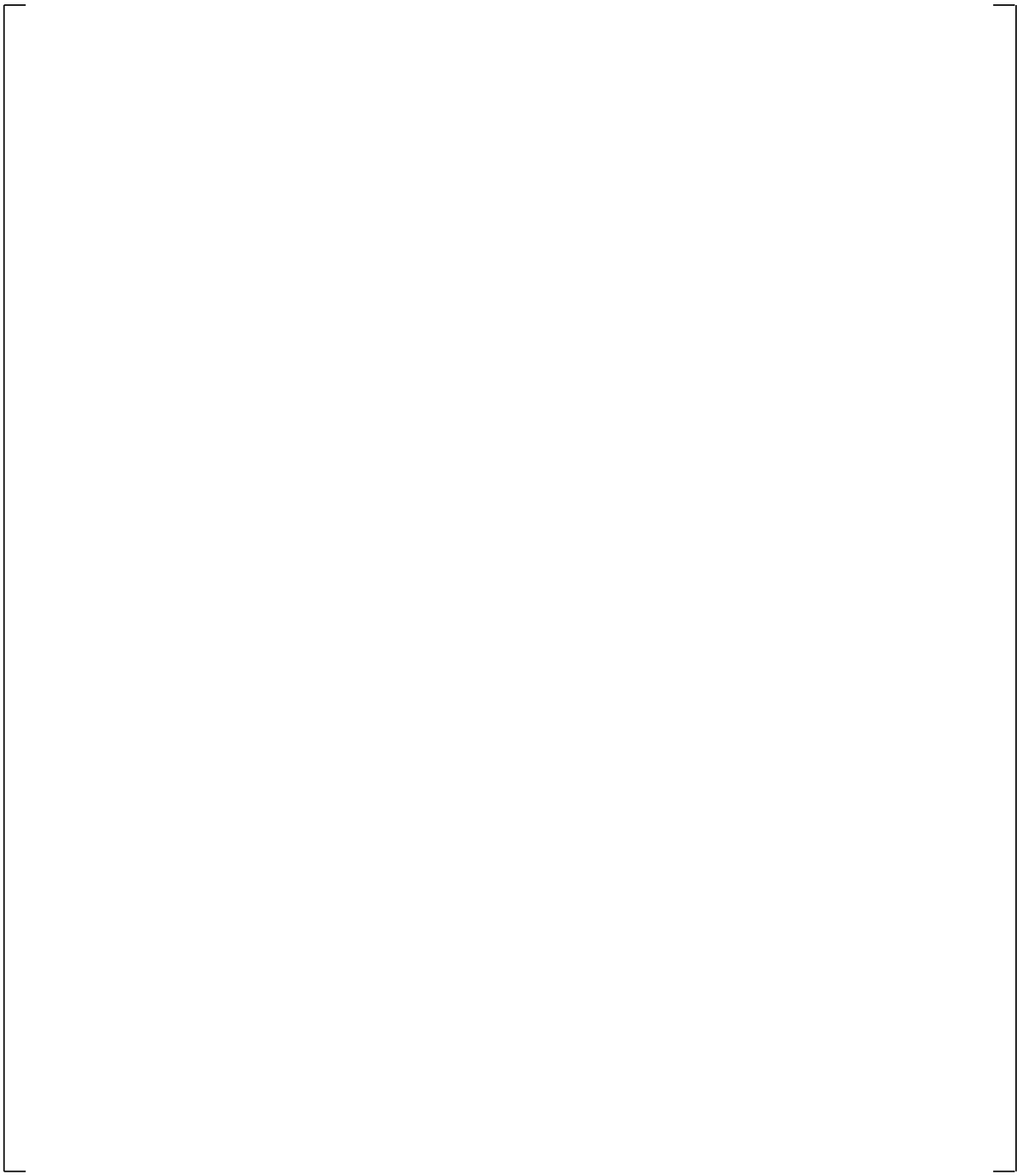

Figure 21.4-5 Inner Vessel Differential Pressures

a,c

Figure 21.4-6 Calculated and Measured Peak Cladding Temperatures

a,c

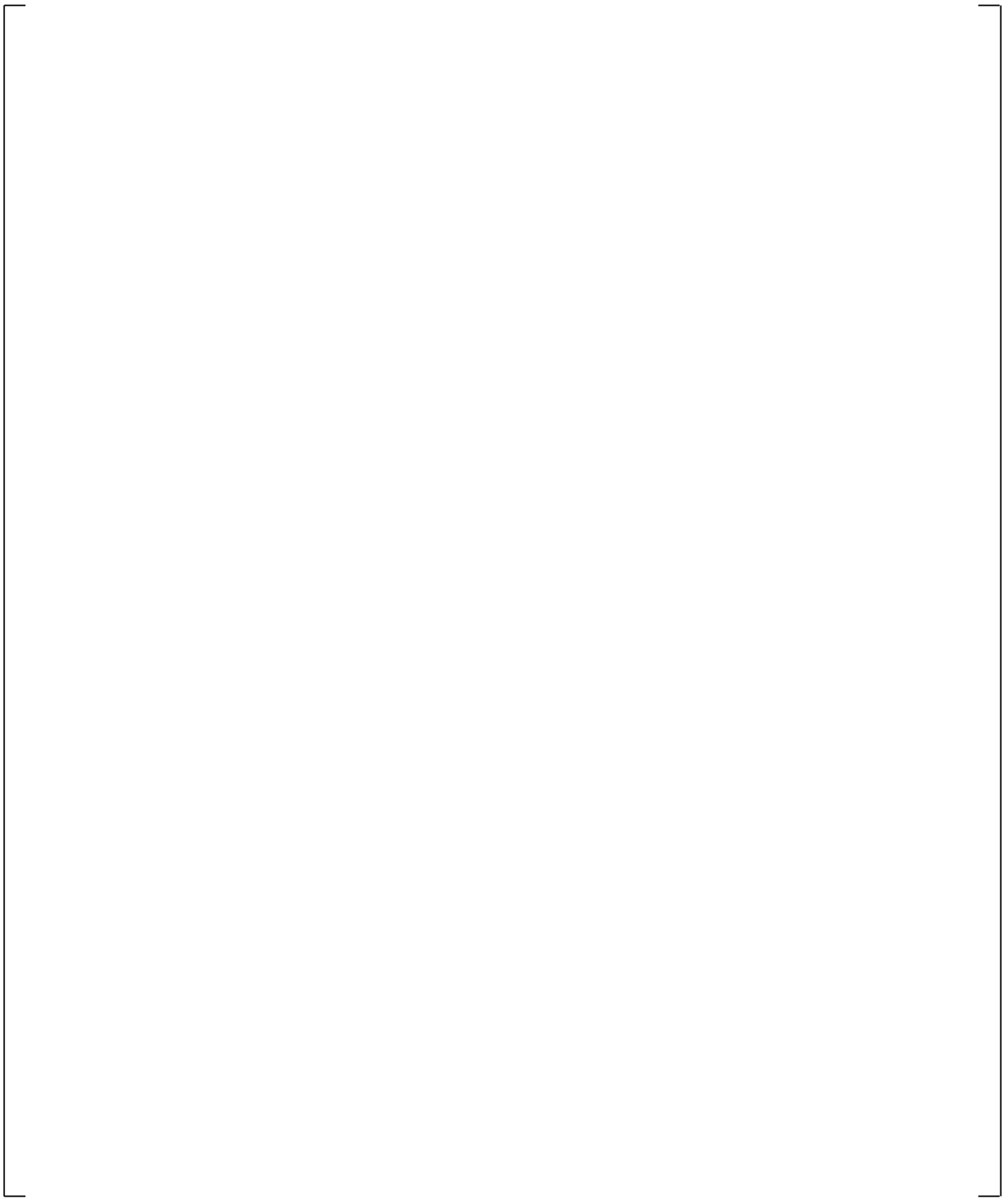

Figure 21.4-7 Steam Generator A U-tube Upflow Side Differential Pressures

a,c

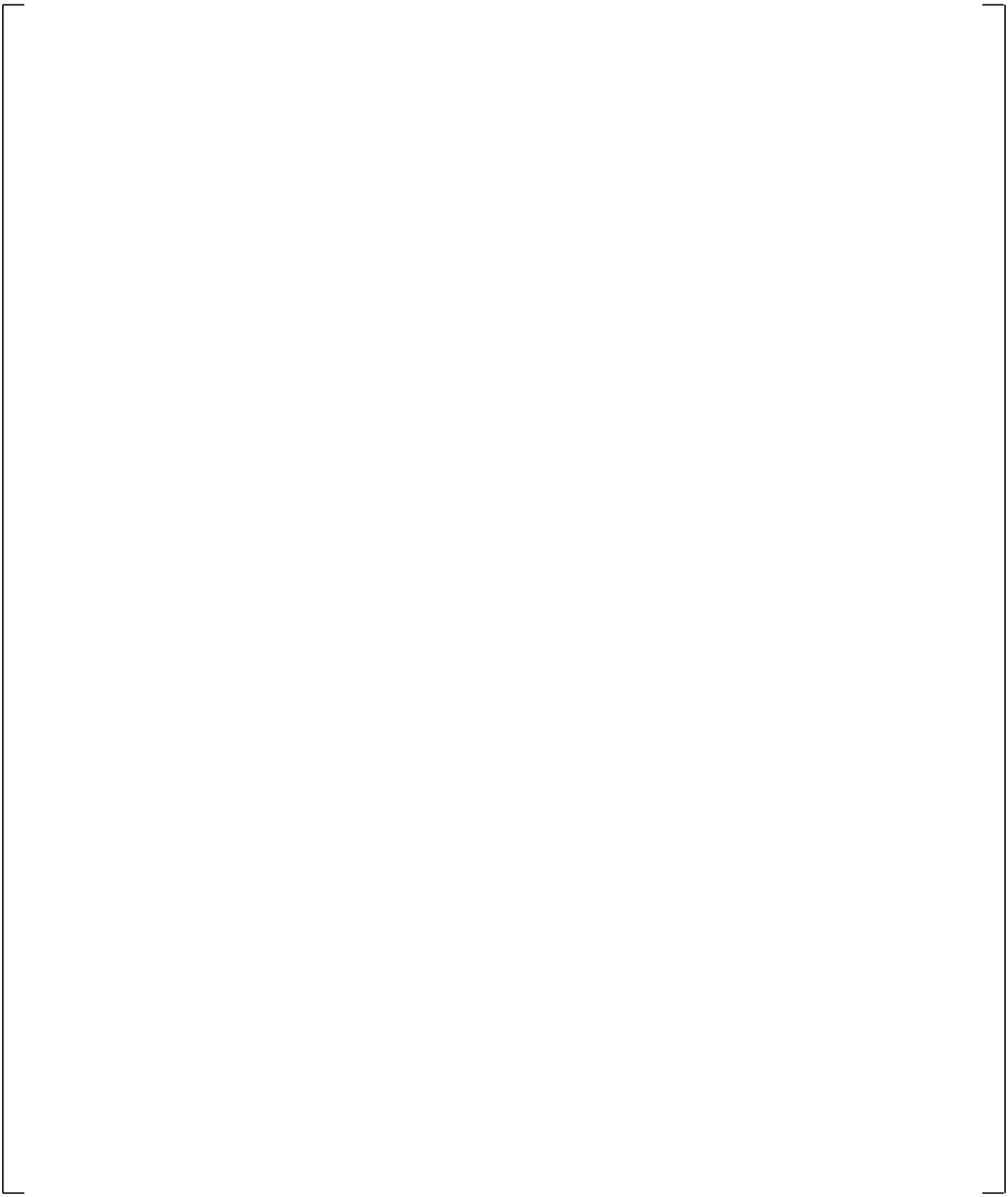

Figure 21.4-8 Steam Generator B U-tube Upflow Side Differential Pressures

a,c

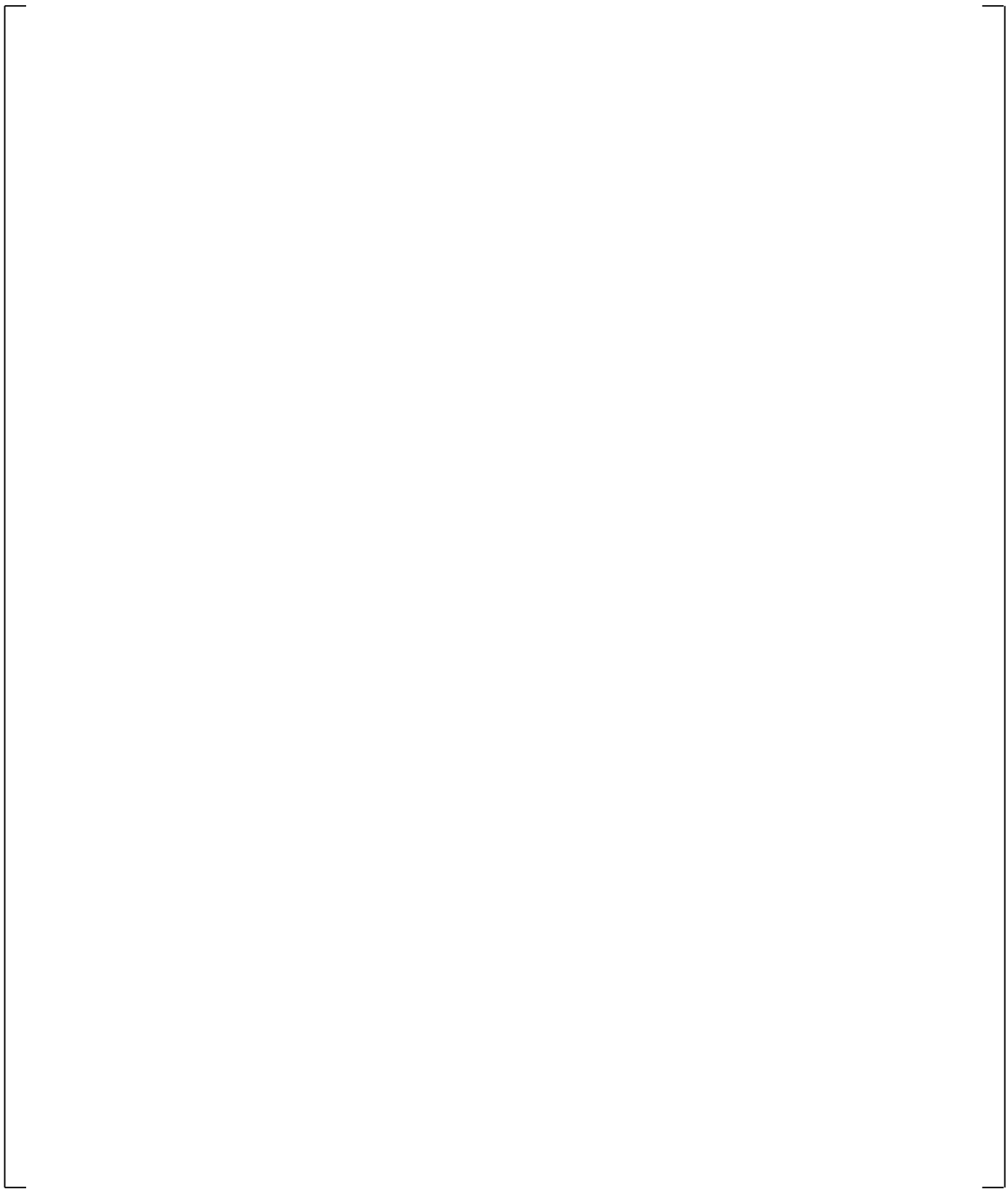

Figure 21.4-9 Steam Generator A U-tube Downflow Side Differential Pressures

a,c

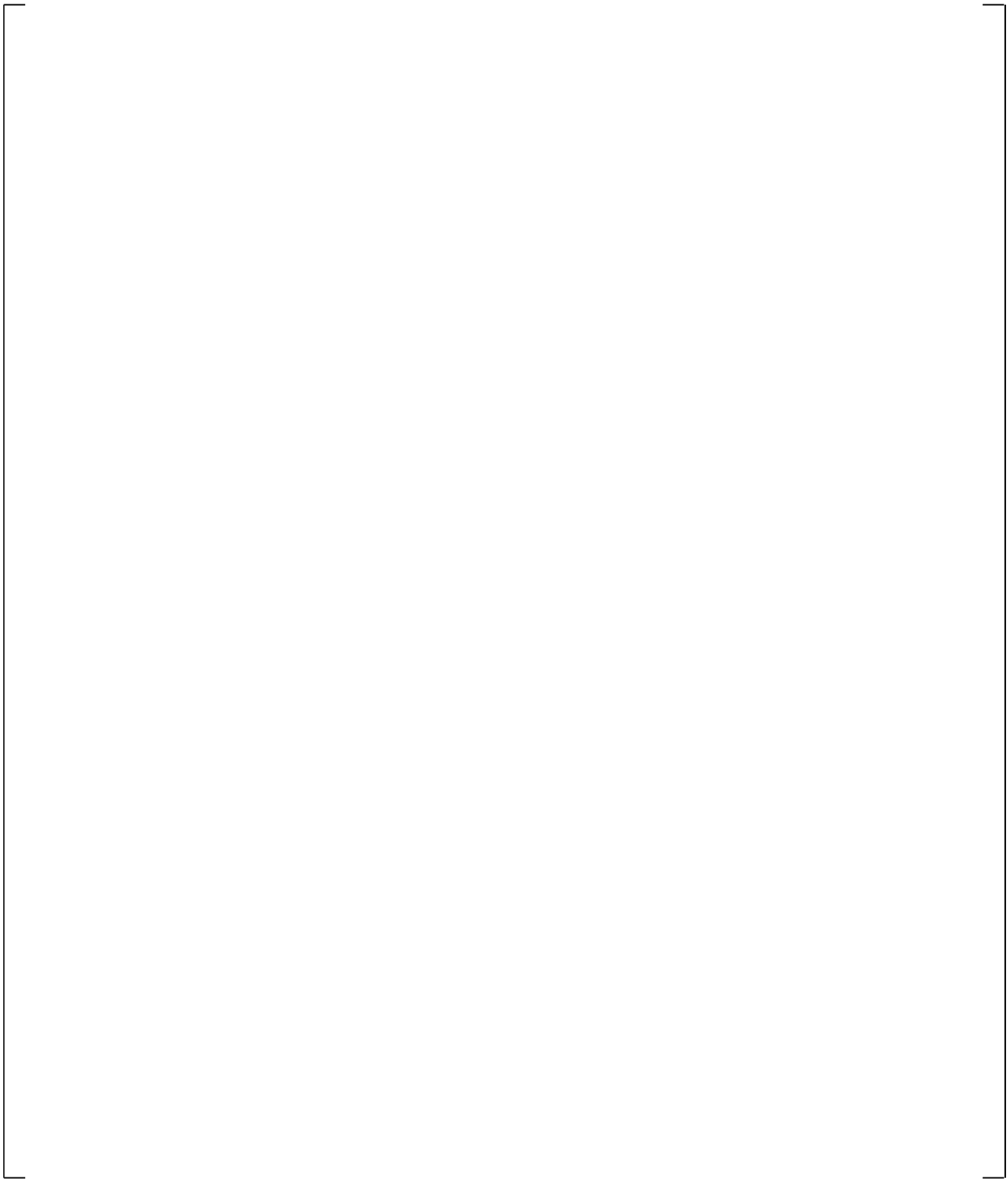

Figure 21.4-10 Steam Generator B U-tube Downflow Side Differential Pressures

a,c

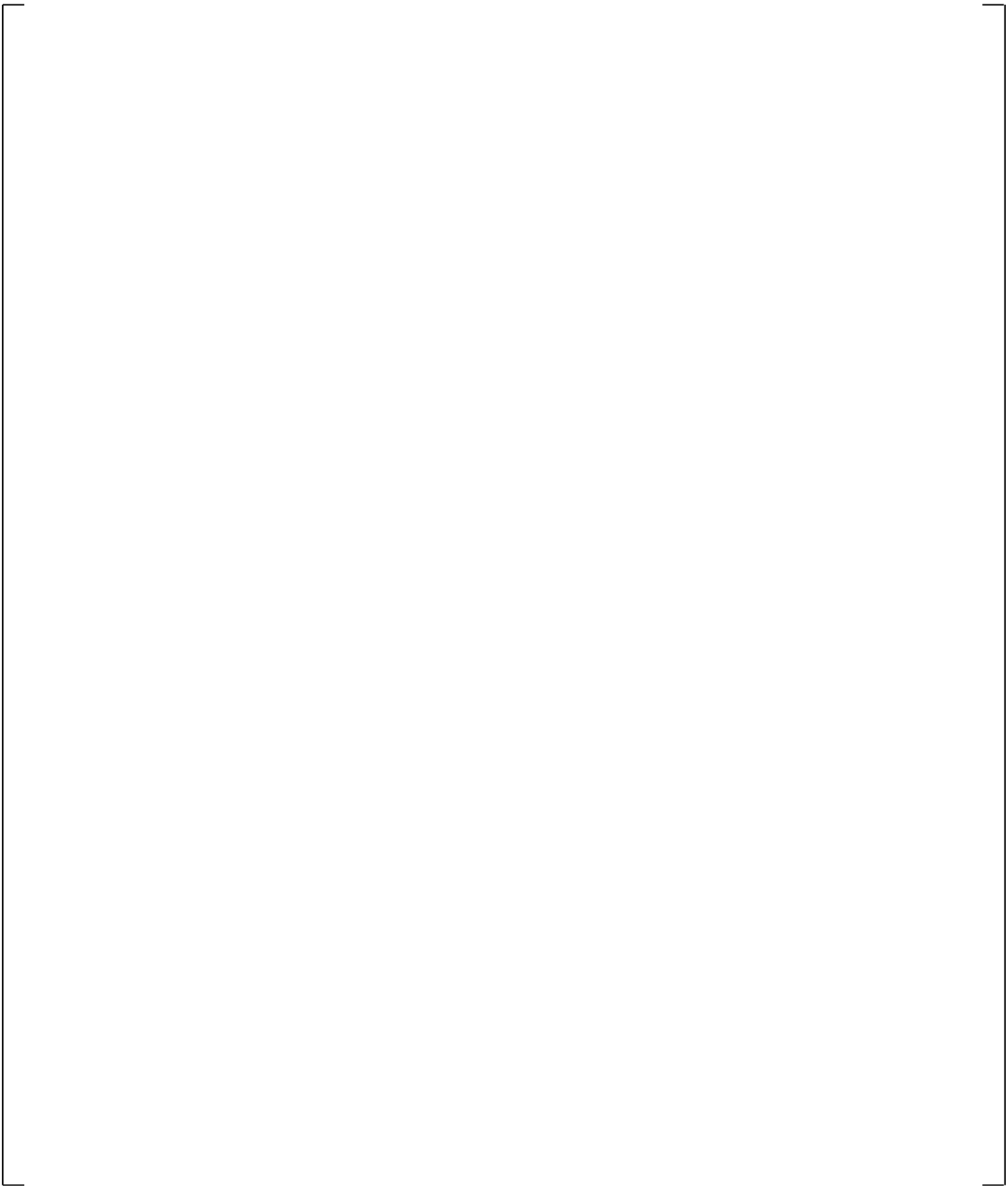

Figure 21.4-11 Steam Generator A Inlet-to-Outlet Differential Pressures

a,c

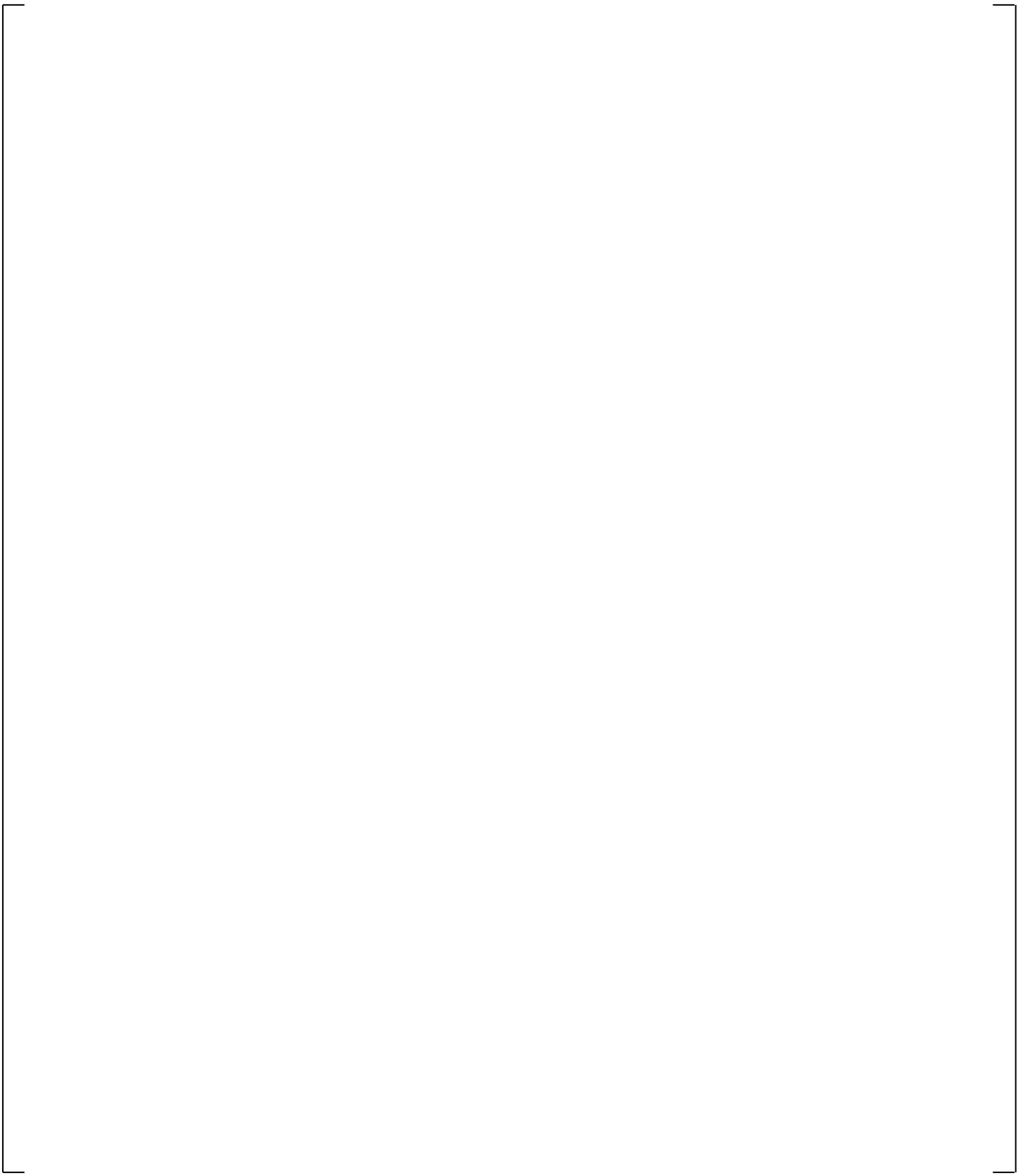

Figure 21.4-12 Steam Generator B Inlet-to-Outlet Differential Pressures

a,c

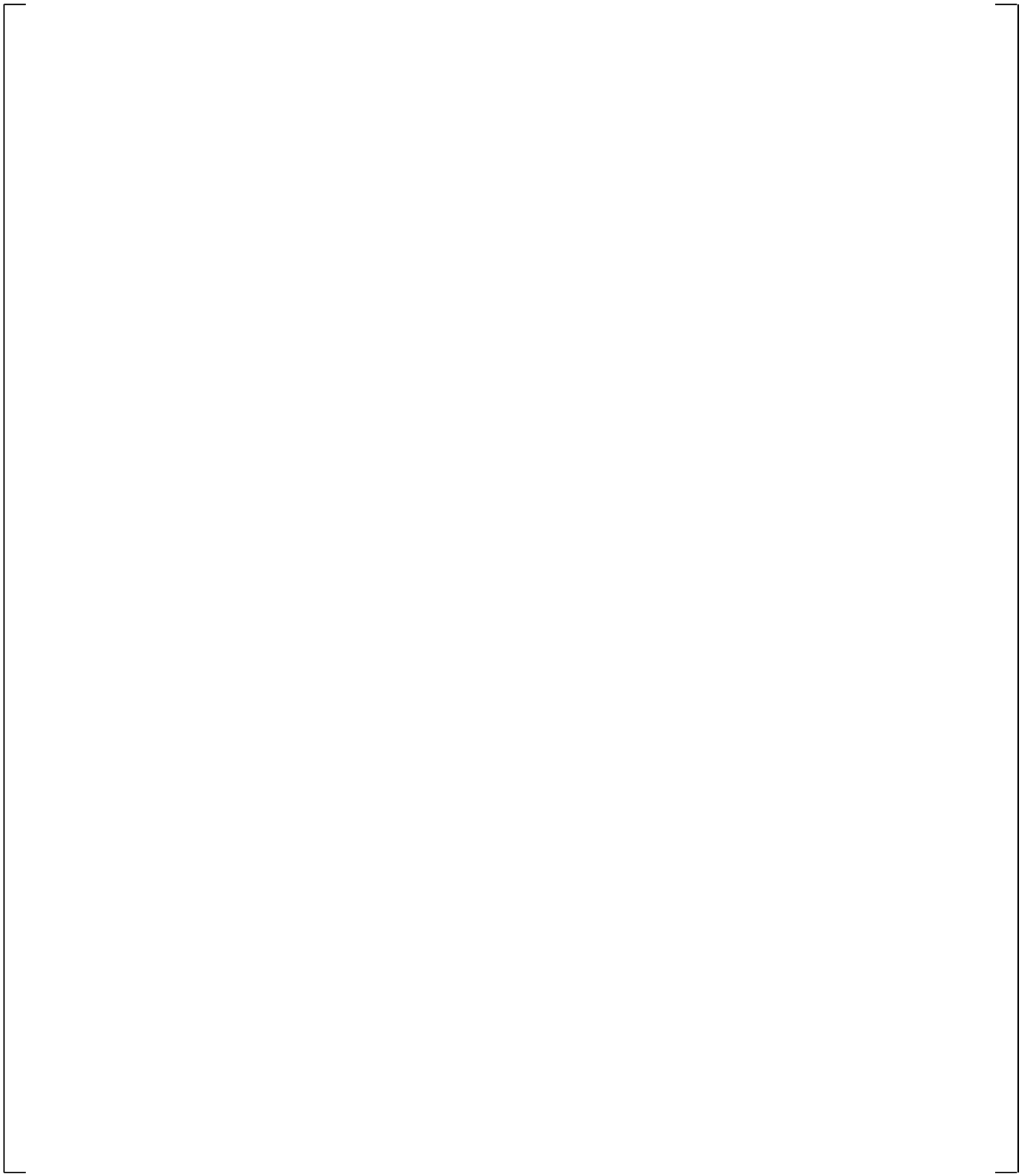

Figure 21.4-13 Steam Generator A Inlet Plenum Collapsed Liquid Levels

a,c

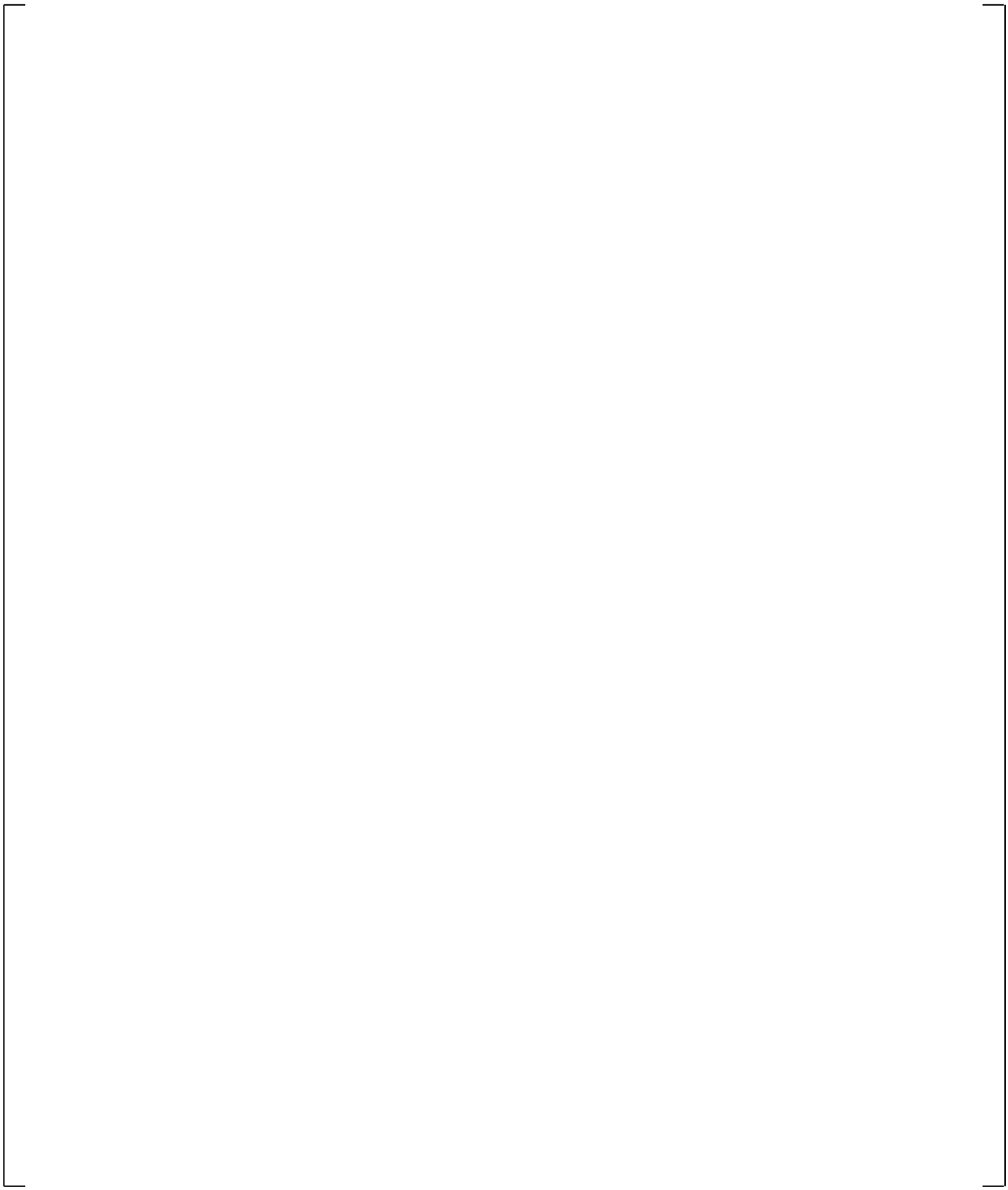

Figure 21.4-14 Steam Generator B Inlet Plenum Collapsed Liquid Levels

a,c

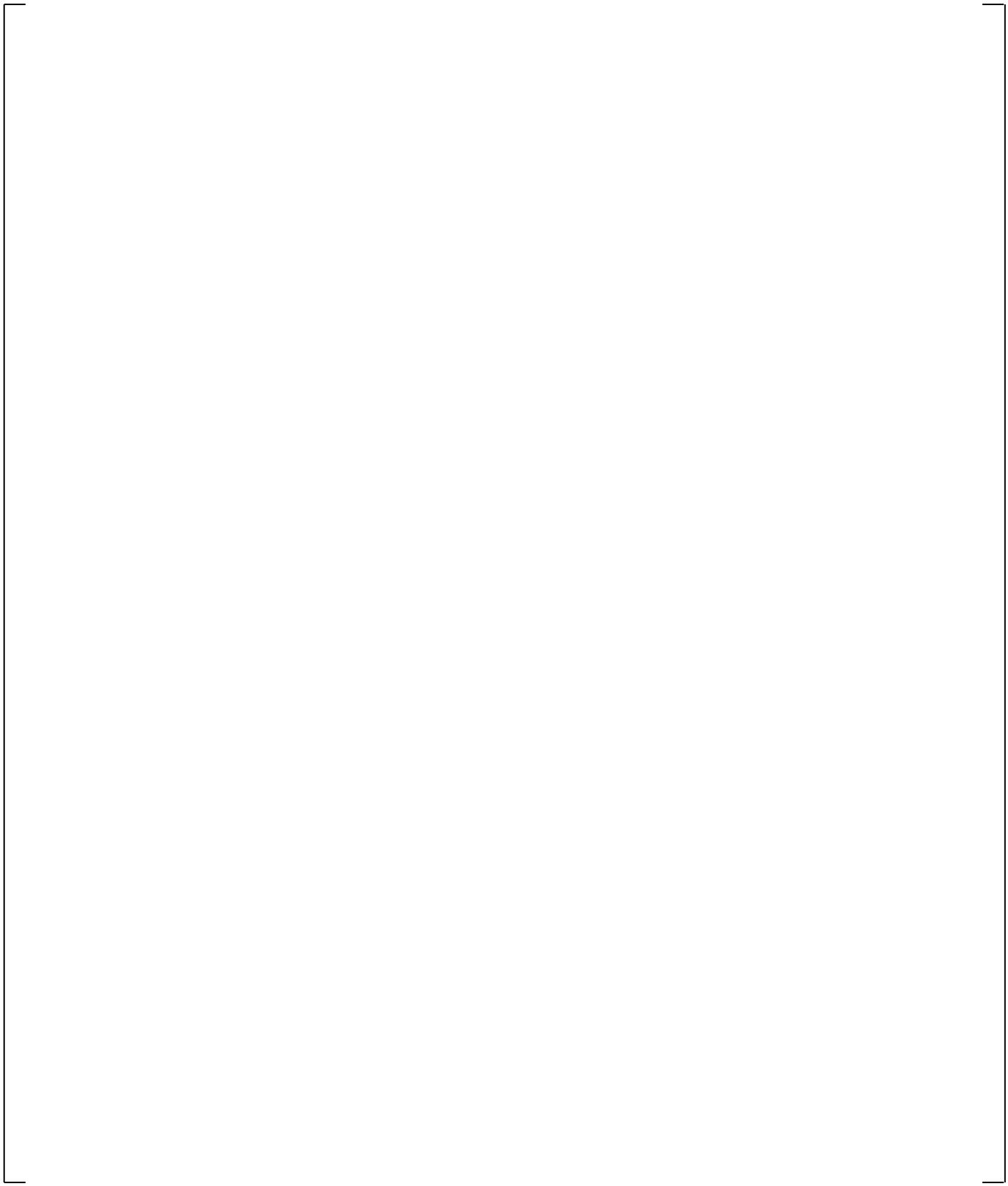

Figure 21.4-15 Upper Plenum to Steam Generator A Inlet Differential Pressures

a,c

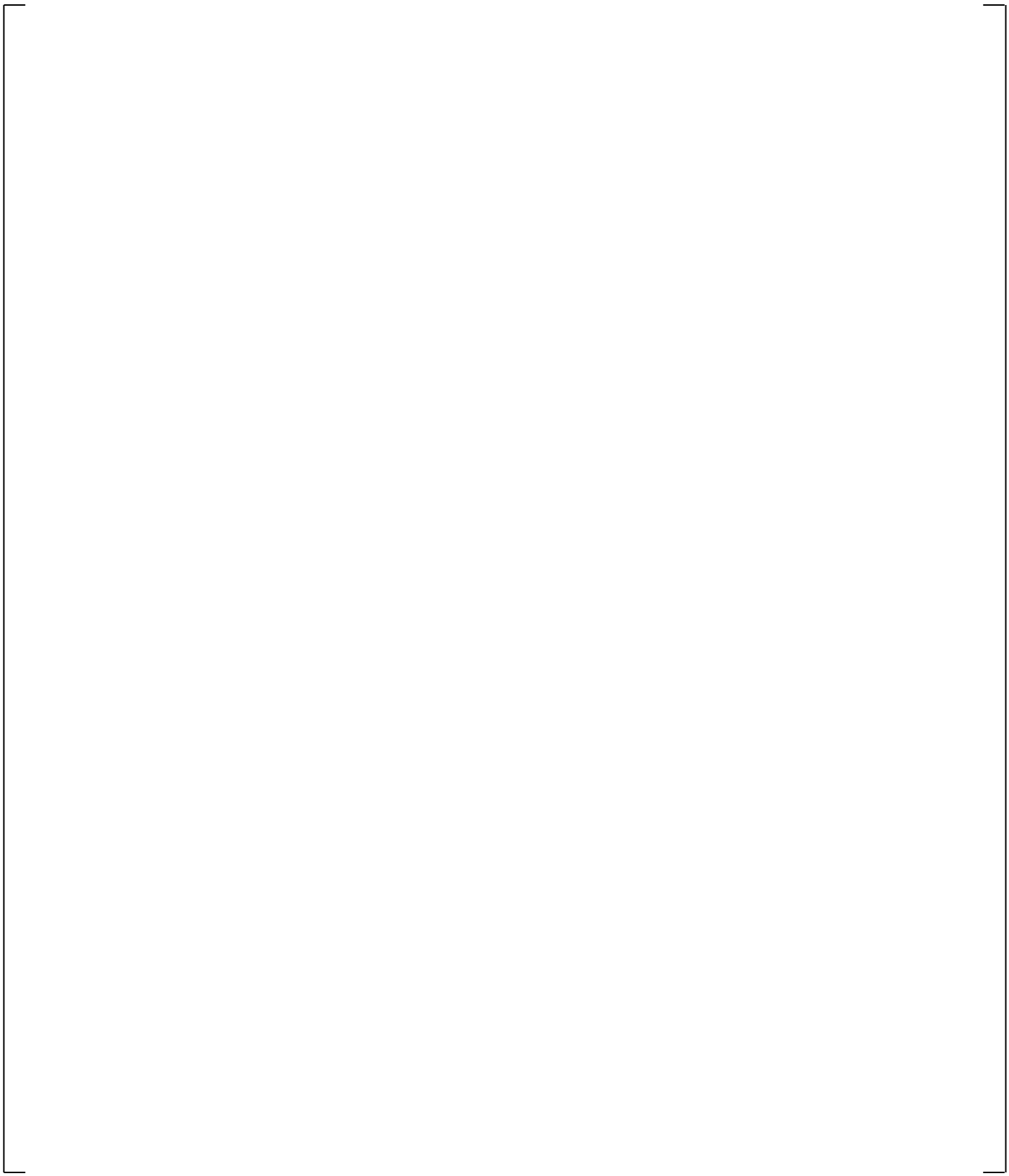

Figure 21.4-16 Upper Plenum to Steam Generator B Inlet Differential Pressures

a,c

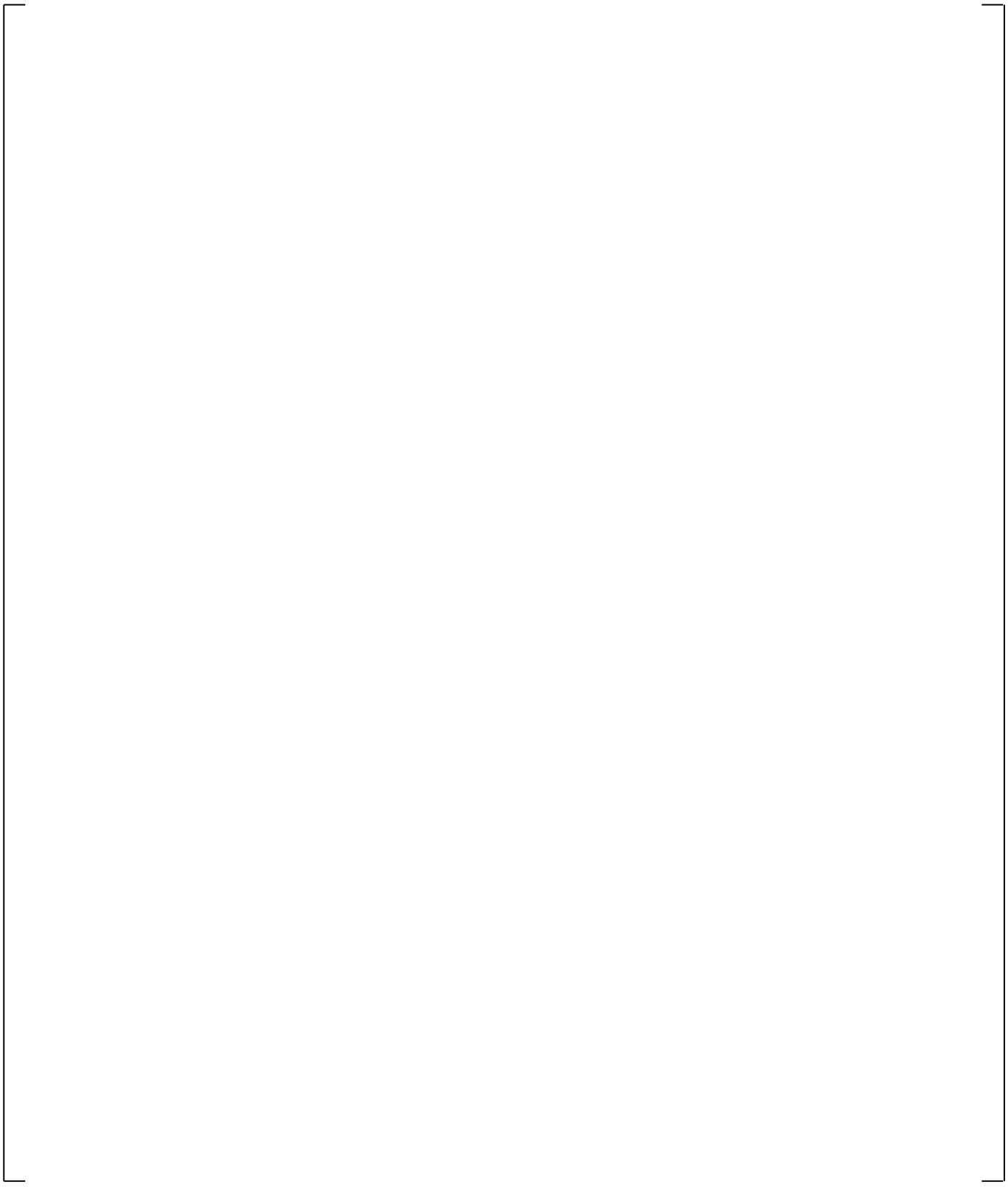

Figure 21.4-17 Upper Plenum Differential Pressures

a,c

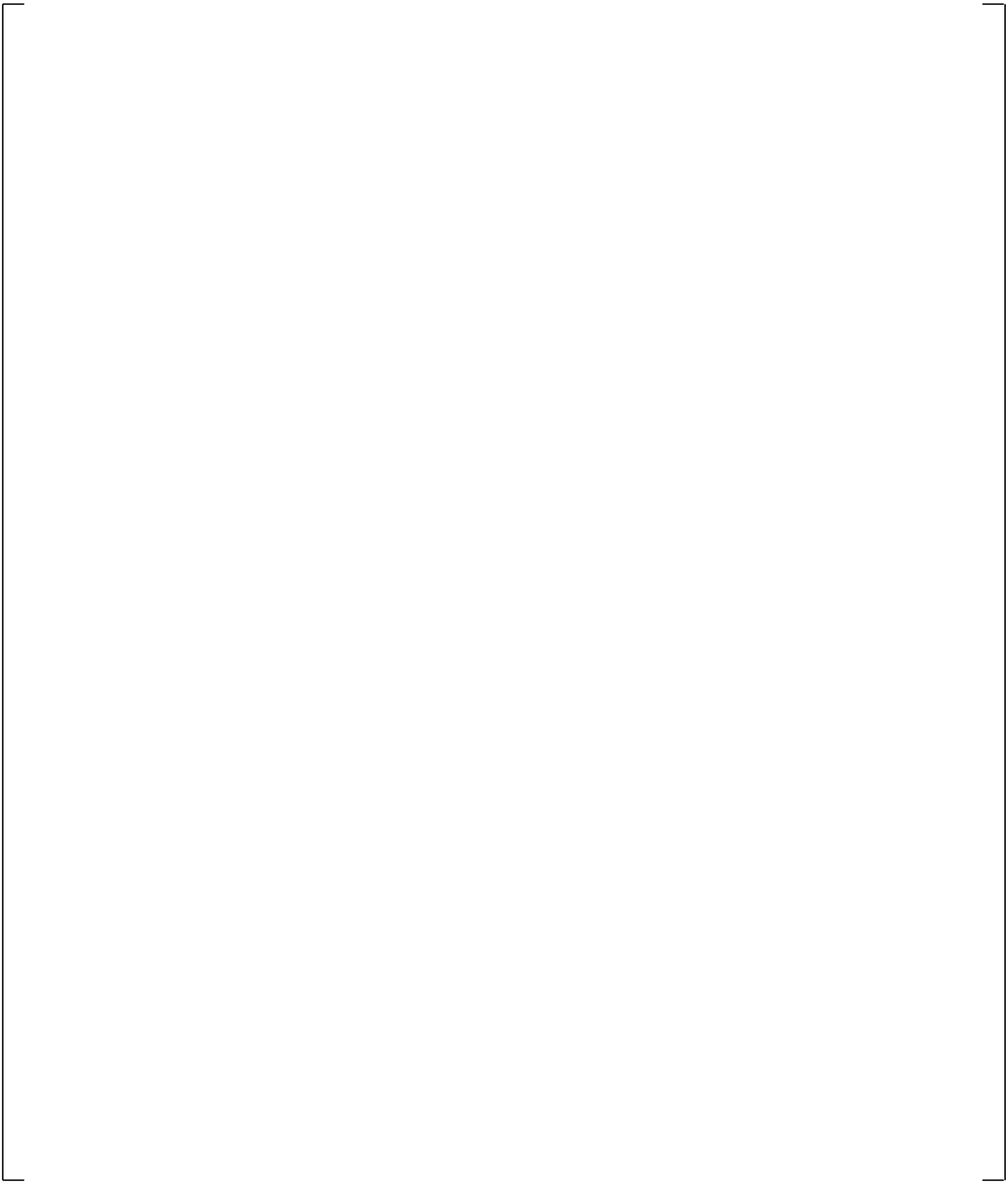

Figure 21.4-18 Downcomer Differential Pressures

a,c

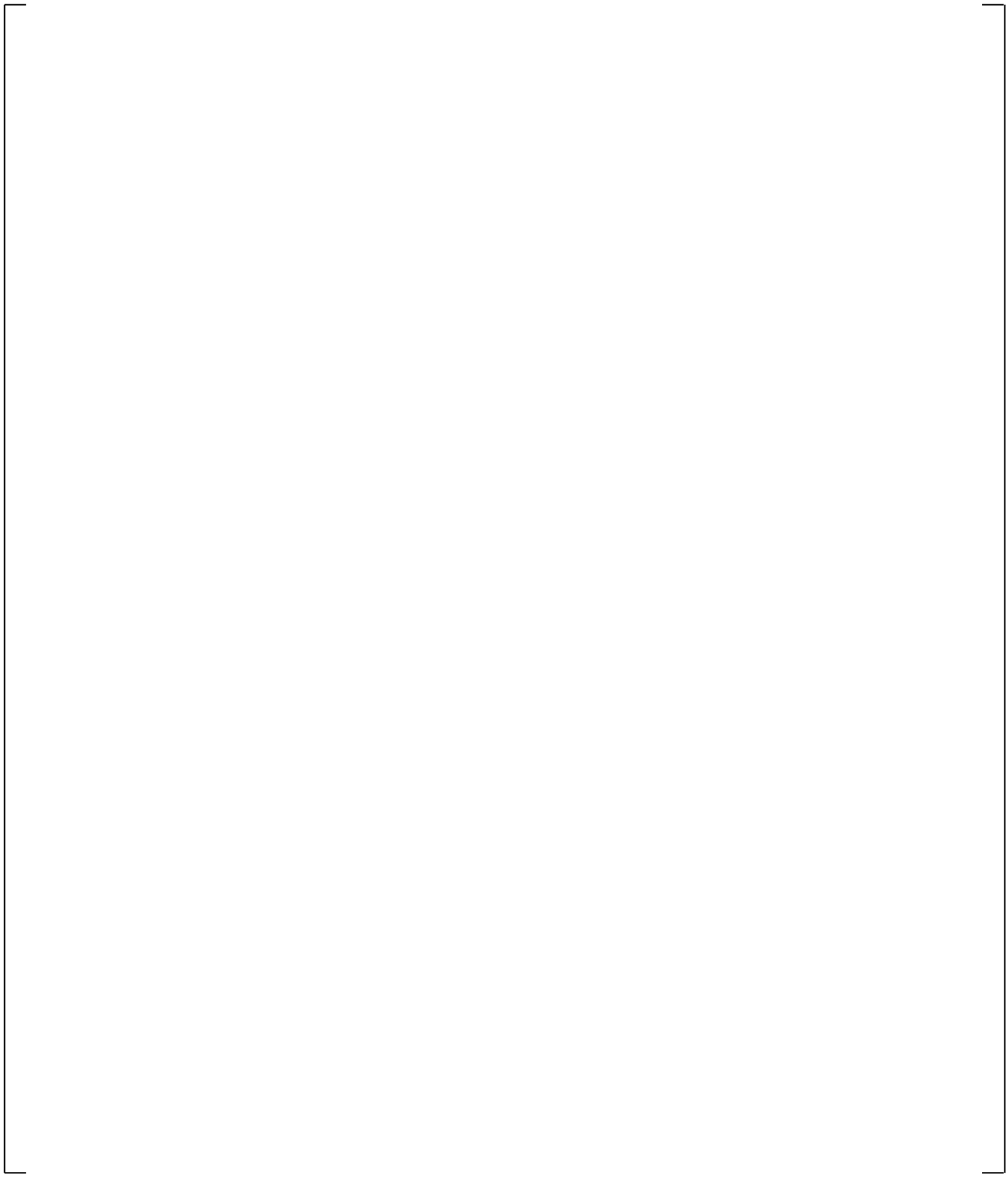

Figure 21.4-19 Comparison of Calculated and Measured Accumulator Injection Flows Loop A

a,c

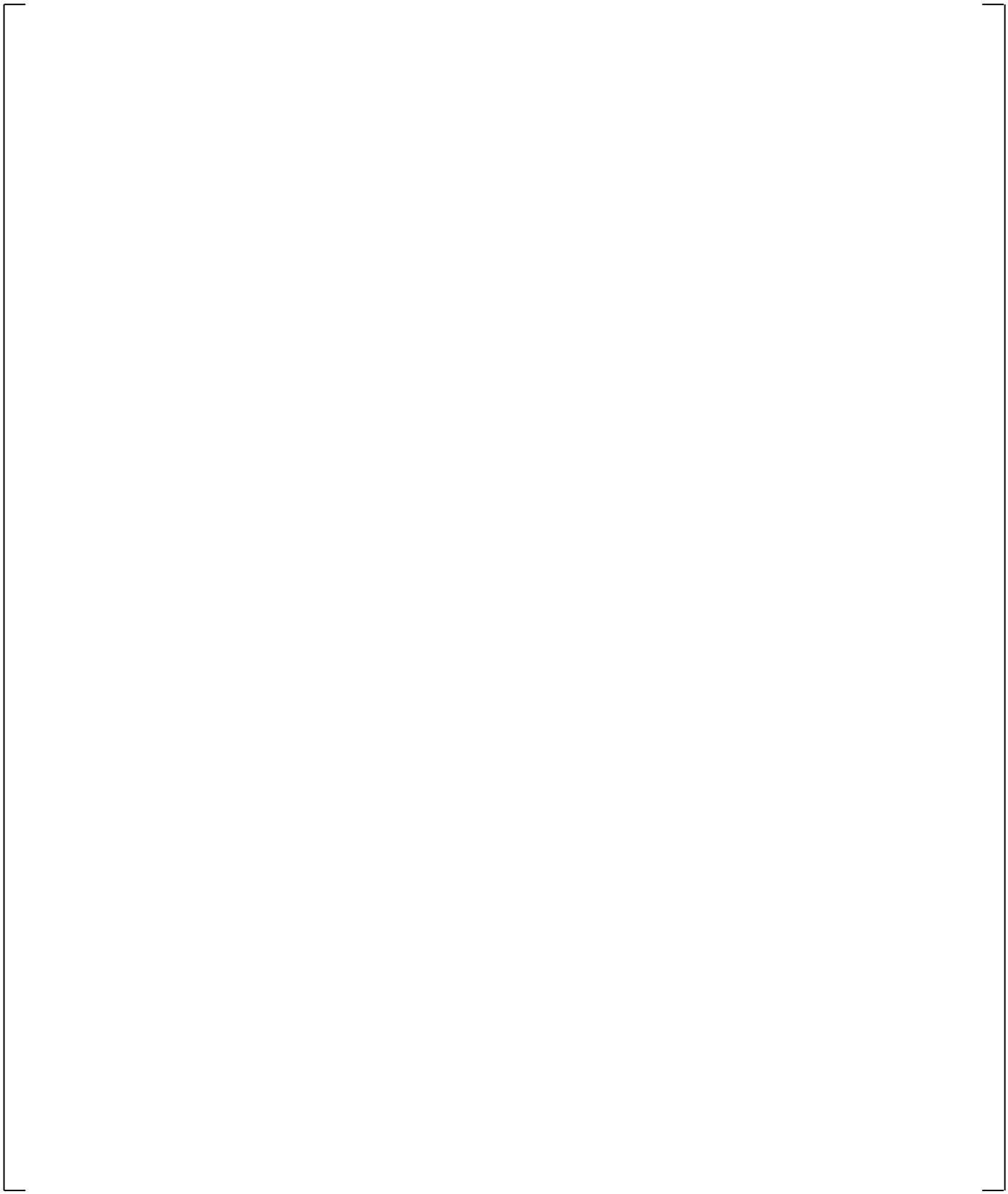

Figure 21.4-20 Comparison of Calculated and Measured Accumulator Injection Flows Loop B

a,c

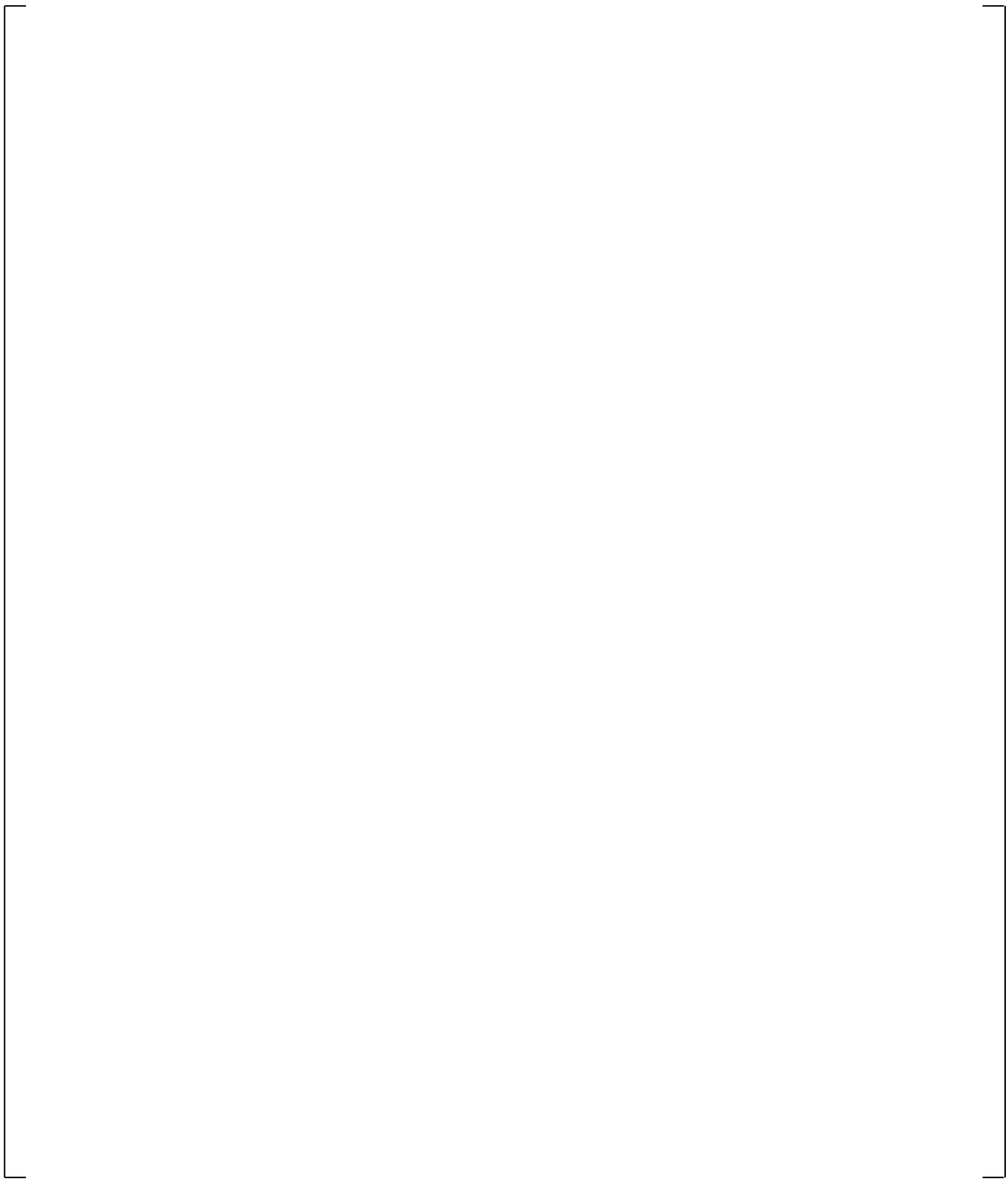

Figure 21.4-21 Calculated Counter-current Flow at Steam Generator A U-tube Inlet

a,c

Figure 21.4-22 Calculated Counter-current Flow at Steam Generator B U-tube Inlet

a,c

Figure 21.4-23 Calculated Counter-current Flow at Elbow of Hot Leg A

a,c

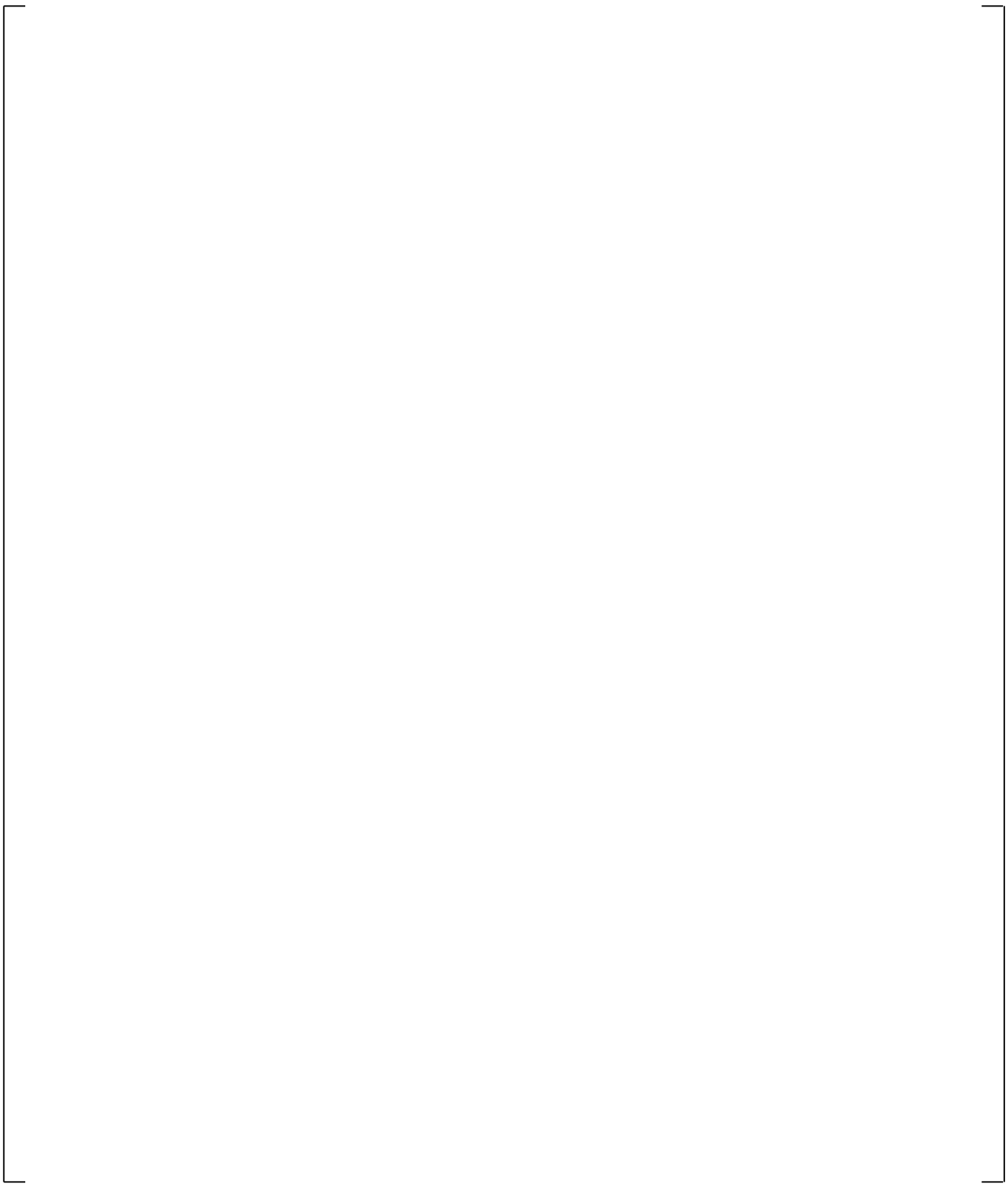

Figure 21.4-24 Calculated Counter-current Flow at Elbow of Hot Leg B

a,c

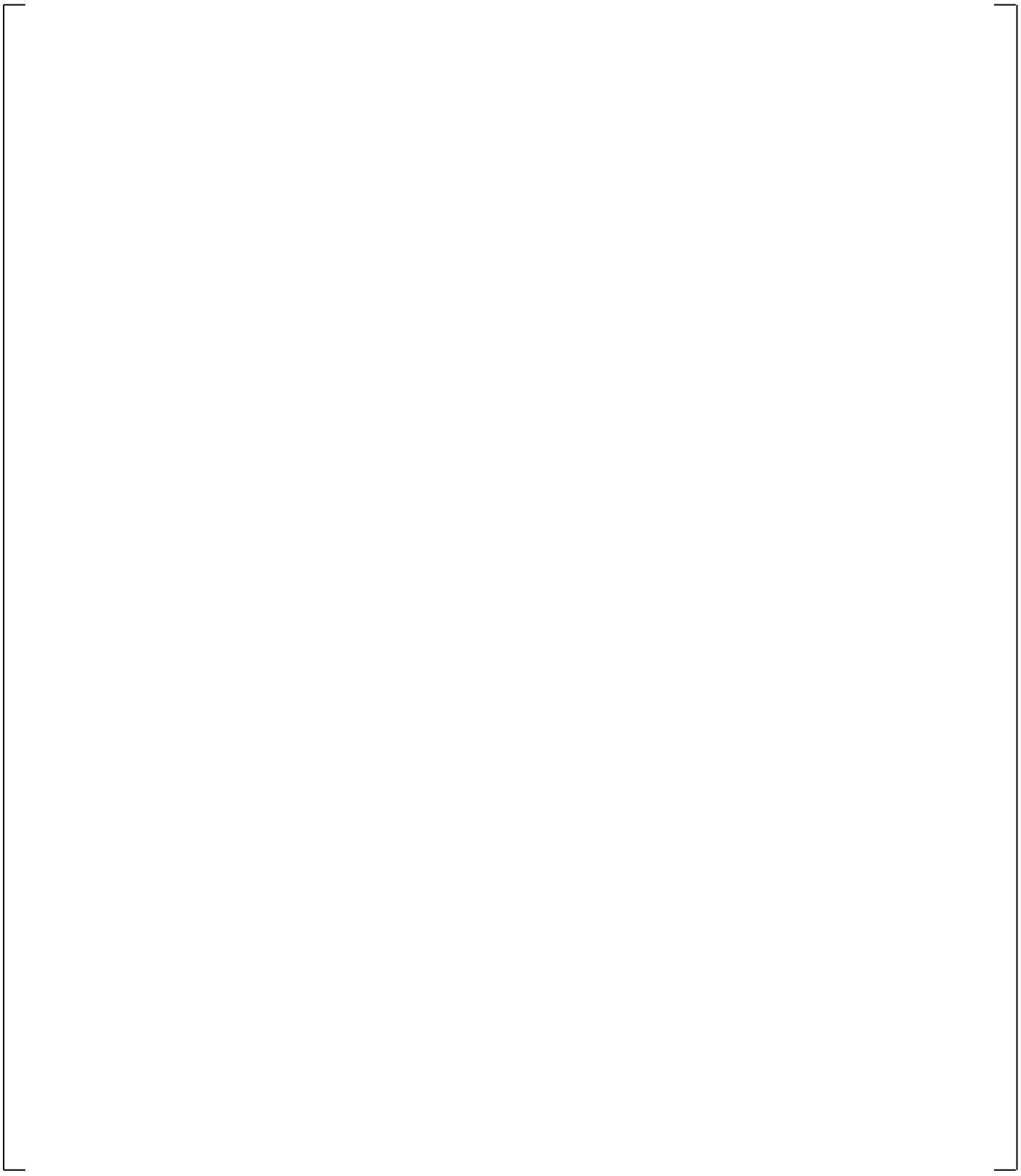

Figure 21.4-25 Calculated and Measured Cladding Temperatures of Low Power Rods at 7.33-ft Elevation

a,c

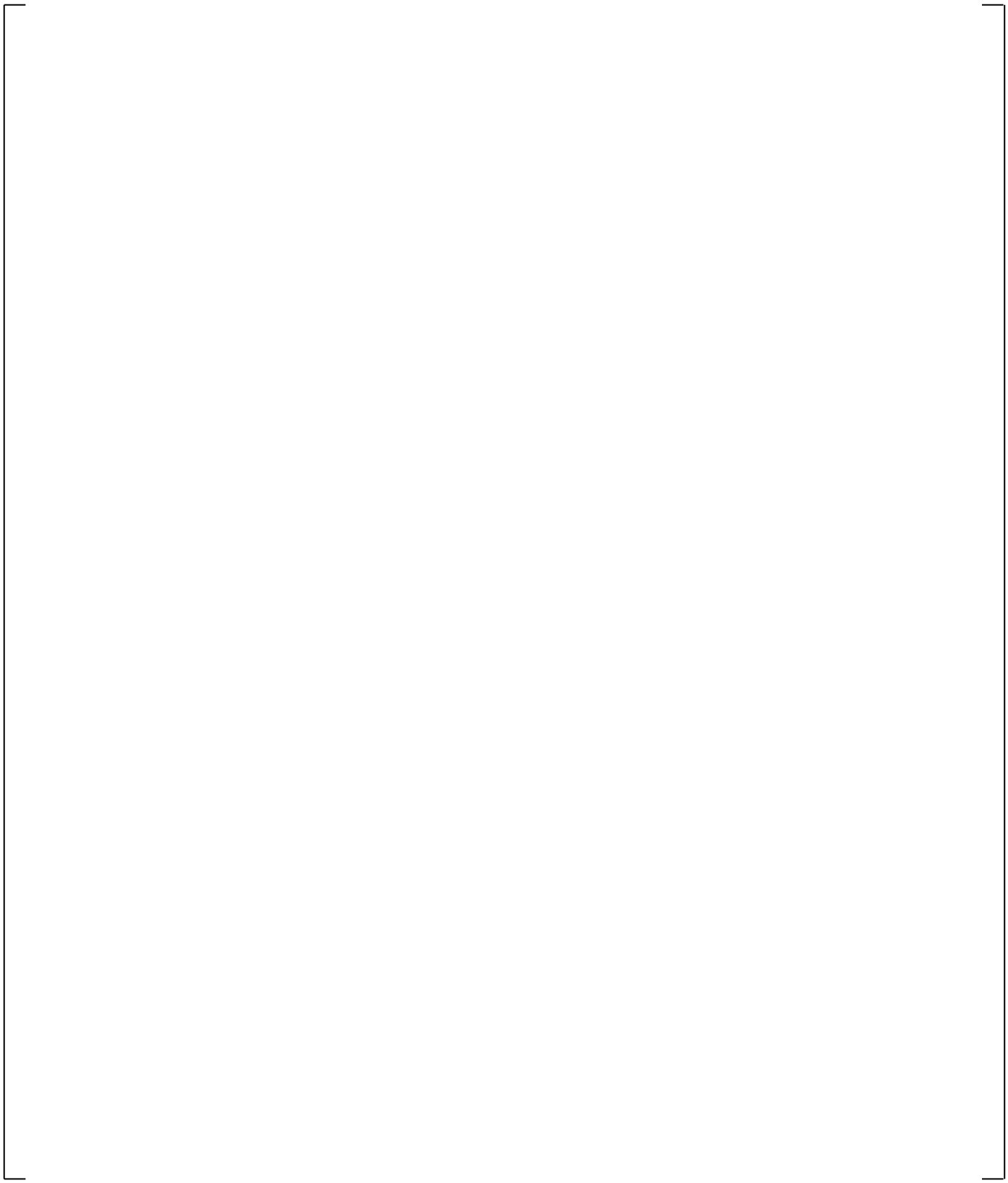

Figure 21.4-25 Calculated and Measured Cladding Temperatures of Low Power Rods at 7.33-ft Elevation

a,c

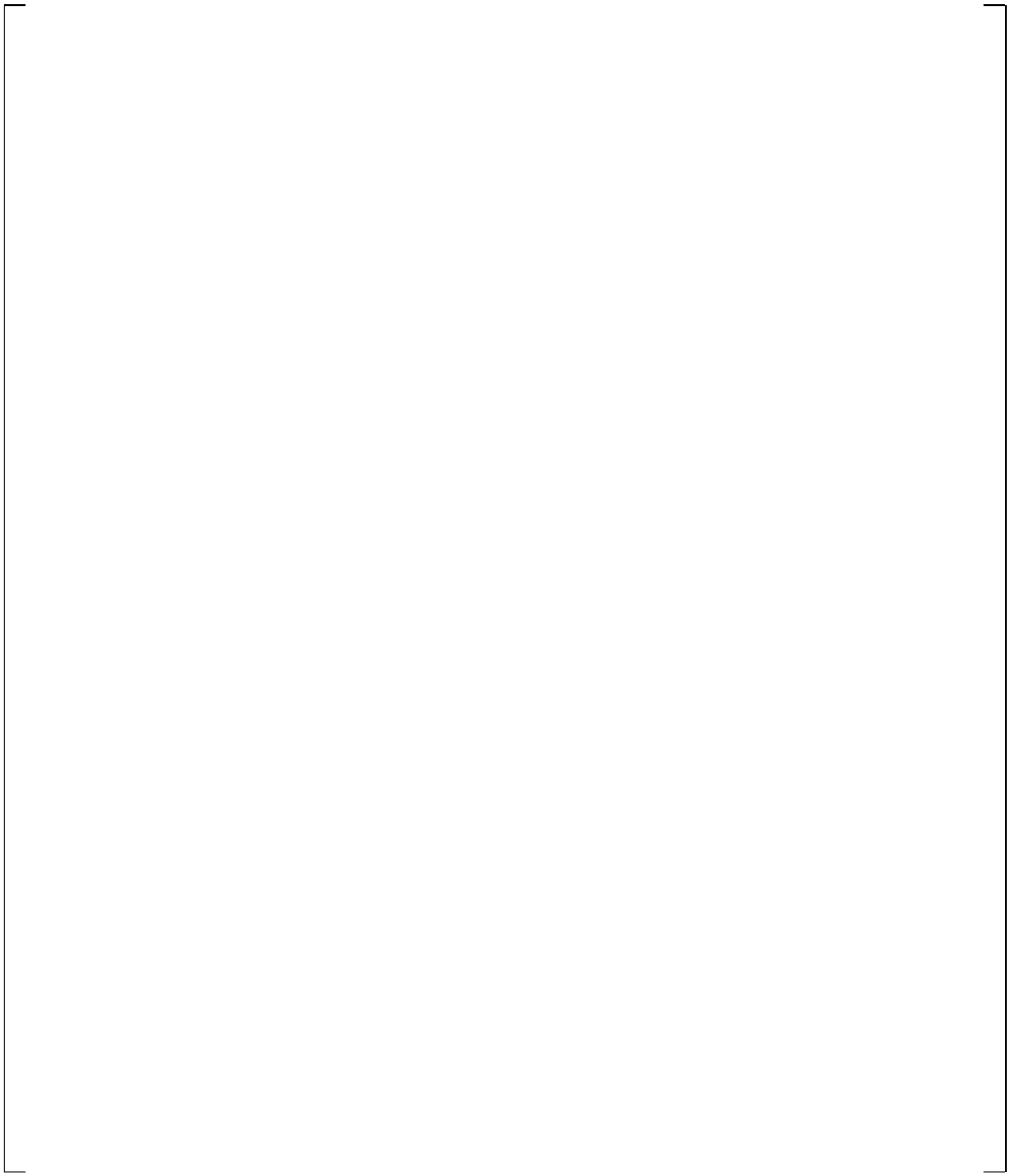

Figure 21.4-26 Calculated and Measured Cladding Temperatures of High Power Rods at 7.33-ft Elevation

a,c

Figure 21.4-26 Calculated and Measured Cladding Temperatures of High Power Rods at 7.33-ft Elevation

a,c

Figure 21.4-27 Calculated and Measured Cladding Temperatures of Average Power Rods at 7.33-ft Elevation

a,c

Figure 21.4-27 Calculated and Measured Cladding Temperatures of Average Power Rods at 7.33-ft Elevation

21.5 SI-INJECTION SENSITIVTY STUDY: SIMULATION OF SB-CL-05, 5-PERCENT COLD LEG SIDE BREAK

21.5.1 Description of the Boundary and Initial Conditions

Test SB-CL-05 simulated a 5-percent cold leg break (equivalent to a 6-inch break in a PWR). The test is one of the earliest of the ROSA-IV series. In terms of initial conditions, break size and decay heat curve this test is equivalent to the 5% break SB-CL-18, which is documented in the previous section. However, the SB-CL-05 test was conducted with charging and high-pressure injection available.

As in the SB-CL-18 test, the break was located in loop B and had a horizontal orientation. Safety injection flow rates corresponding to a single failure in the safety injection system were assumed. Experimental results are discussed by Kawaji (Kawaji et al., 1986) and Tasaka (Tasaka et al., 1988).

The operational setpoints for this test are the same as implemented in all ROSA-IV break tests, as listed in Table 21.2-2.

The core power was scrammed once the primary pressure decreased below 12.97 MPa (1881 psia). At scram, the primary coolant pumps began to coast down, the main feedwater was stopped, and the secondary sides of the two steam generators were isolated by closure of their main isolation valves.

In this test, the primary system rapidly depressurized to a pressure slightly higher than the secondary pressure, approximately 8 MPa (1160 psia), until the loop seal cleared at about 140 seconds.

After loop seal clearance, the break quality changed from a low quality mixture to primarily vapor and the primary system continued to depressurize. Primary pressure falls below secondary pressure at about 180 seconds after the break.

Test SB-CL-05 had a core depression during loop seal clearance that was considerably below the elevation of the bottom of the loop seal piping. Osakabe (Osakabe et al., 1987) attributed this to a large liquid holdup in the uphill steam generator tubes. During this core level depression, the cladding temperature increased by approximately 100K (180°F) reaching a maximum cladding temperature of approximately 720K (836°F). After loop seal clearance, the core level recovered quickly. Accumulator injection began at 417 seconds and prevented a second core uncovery.

21.5.2 Results and Conclusions from the SB-CL-05 Simulation

Table 21.5-1 shows a summary of the key initial parameters measured at the SB-CL-05 test and achieved at the end of the steady-state calculation. Table 21.5-2 summarizes the observed (data) and predicted results for the SB-CL-05 test simulation.

The simulation of the SB-CL-05, presented herein, was performed with break discharge coefficients **[ ]**[a,c] In addition, Wallis-type counter-current flow limits were enforced **[ ]**[a,c] The results from the simulation are presented in the

following Figures 21.5-1 through 21.5-21. In these figures, the WCOBRA/TRAC-TF2 calculation results are compared to measured SB-CL-05 test parameters.

As intended, the core power (Figure 21.5-1) and pump speed (Figure 21.5-2) were modeled to be consistent with the measurements. **[**

][a,c]

Figure 21.5-4 shows the calculated break flow compared against that measured by the high-range flow meter (FE560A-BU).

The break flow prediction is similar to the one observed in the SB-CL-18 test simulations. Early in the transient, flow out of the break is sub-cooled, that is, single-phase liquid. **[**

][a,c]

Beyond 100 seconds the conditions at the break transition from single-phase liquid to single-phase steam. The observed disparity relative to the FE560A-BU measurement is explained by the fact that the test break flow is outside the measurement accuracy of the FE560A flow meter. **[**

][a,c]

The pressurizer pressure calculation is fairly consistent with the measured (Figure 21.5-6). Initially, there is a small discrepancy in the depressurization which appears to be consistent with the break flow mismatch trend.

[

][a,c]

[

]a,c

[

]^{a,c}

The agreement between the calculated pumped ECCS flows and the measured during the test is good, Figures 21.5-18 and 21.5-19.

The comparison of the calculated and measured accumulator levels indicate inconsistency between the code calculation and the test, Figure 21.5-20. The inconsistency is not investigated in further detail due to the fact that the timing and magnitude of accumulator injection does not appear to be a contributor to the lack of boil-off. As discussed earlier in Section 21.4, possible reason of the under-prediction of accumulator injection is that the code tends to calculate nitrogen gas expansion following a polytropic exponent of 1.225, compared to 1.118 estimated from the test measurements, as evident from the Callaway small break accumulator discharge presented in Section 20.1.3.2. Overall, the predicted accumulator discharge is conservative and adequate for the purpose of the FSLOCA methodology.

[

]^{a,c}

Table 21.5-1 [ ][a,c]

a,c

Table 21.5-2 [ ]a,c

a,c

a.c

Figure 21.5-1 Core Power

a,c

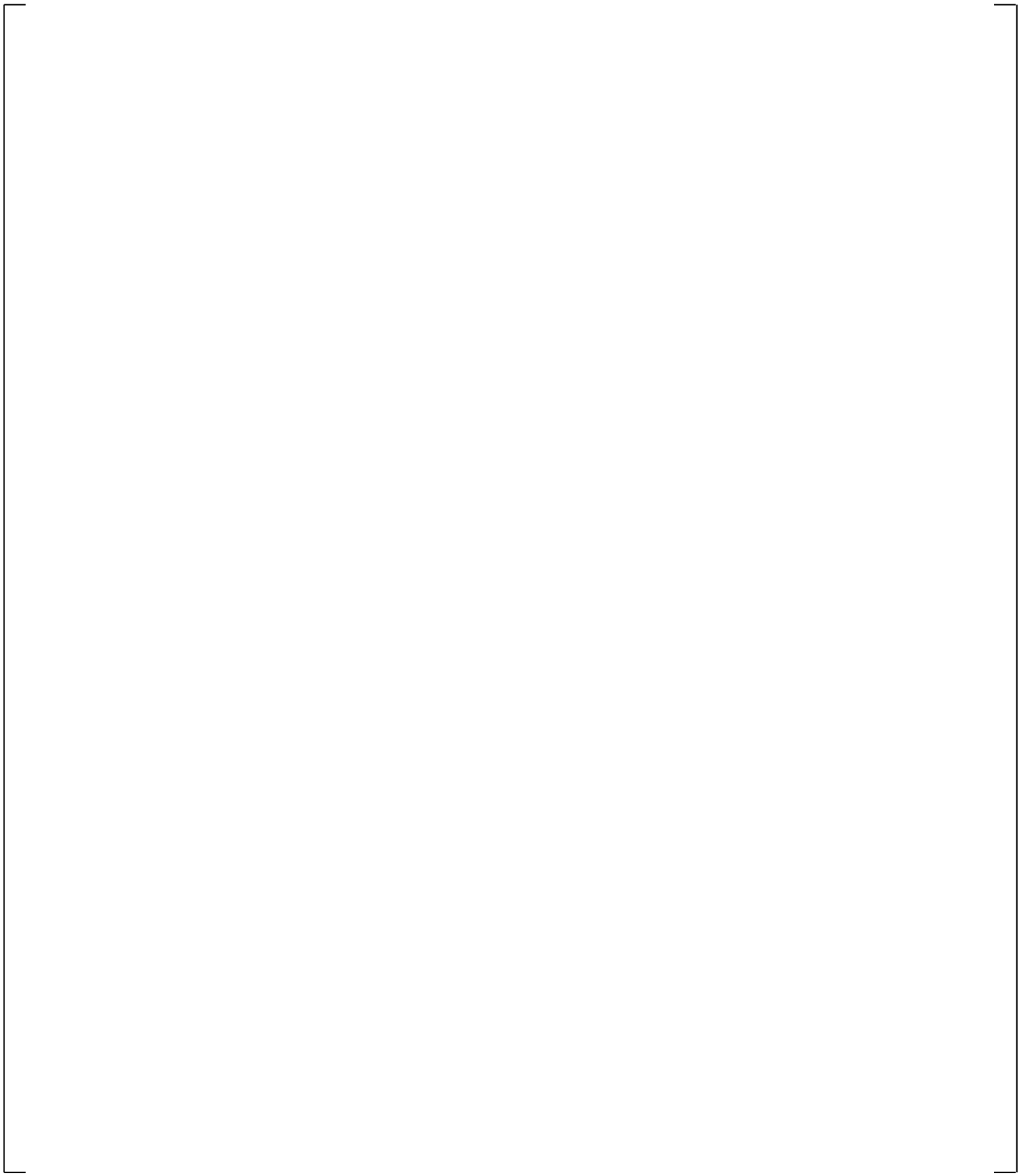

Figure 21.5-2 Pump Speed

a,c

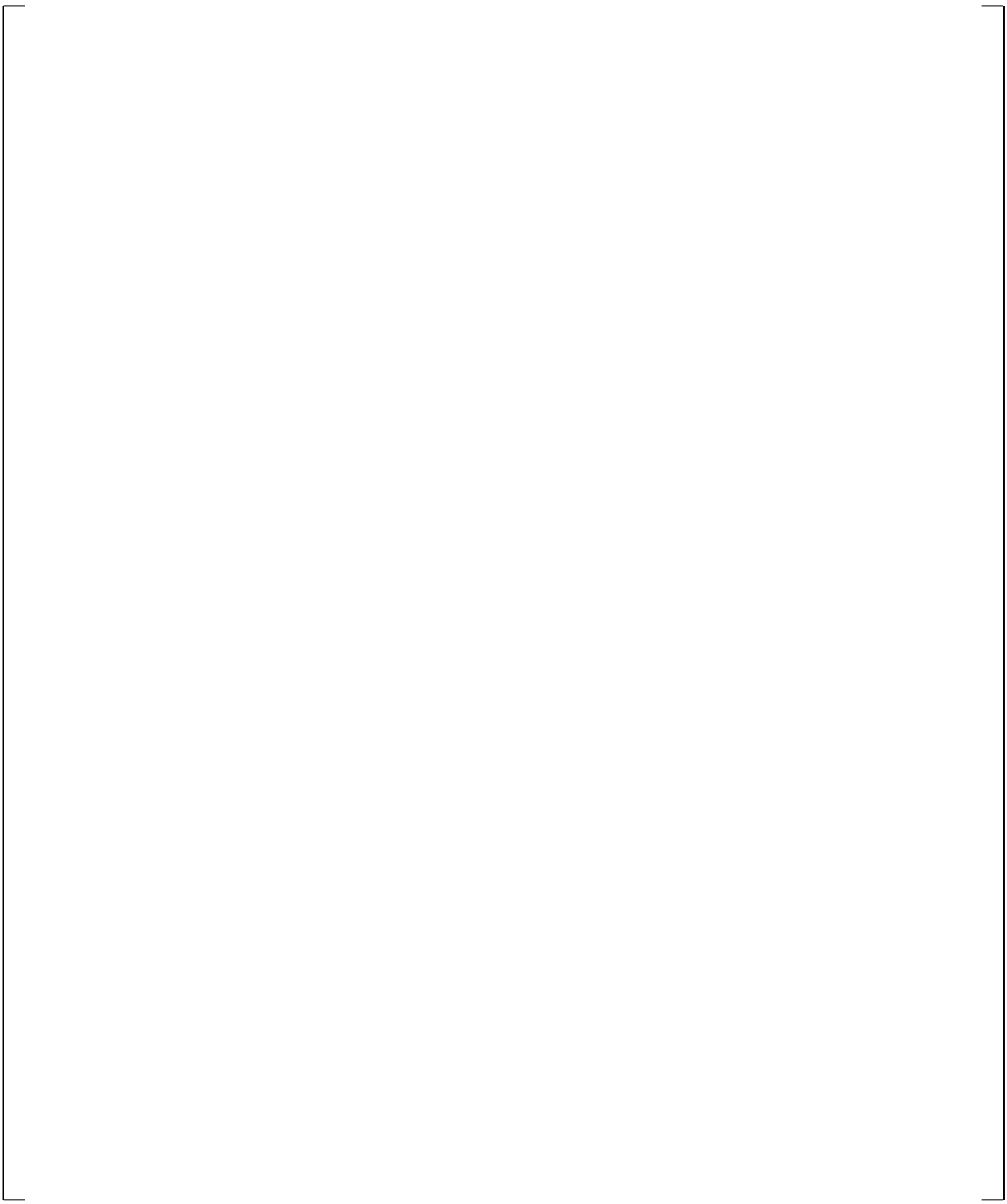

Figure 21.5-3 Loop Flow Rates

a,c

Figure 21.5-4 Break Flows

a,c

Figure 21.5-5 Calculated Break Spool Void Fraction

Note: This location is in the side pipe of the broken TEE#26, upstream of the break orifice location.

a,c

Figure 21.5-6 Pressurizer Pressures

a,c

Figure 21.5-7 Steam Generator Secondary Side Pressures

a,c

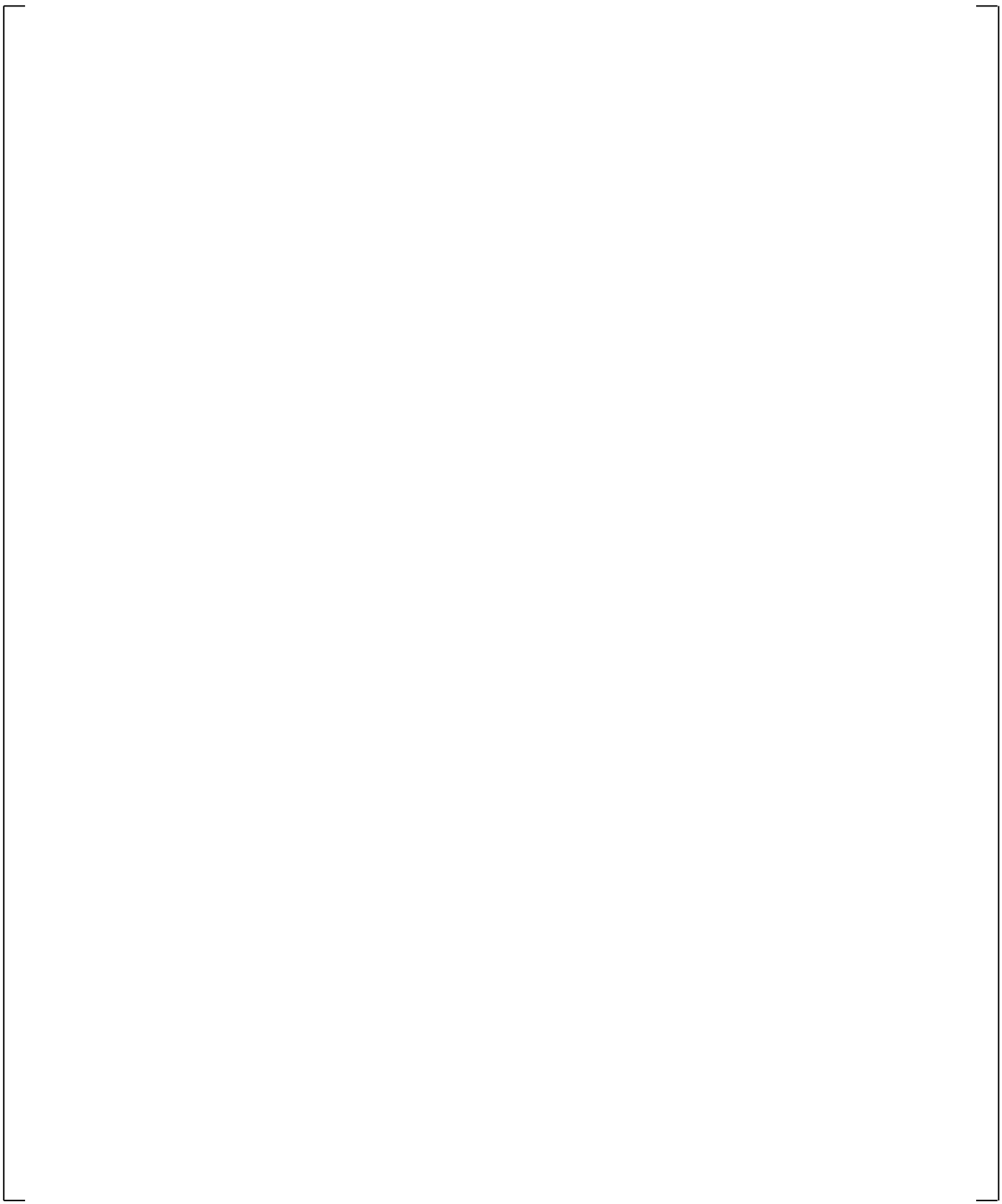

Figure 21.5-8 Steam Generator A U-tube Differential Pressures

a,c

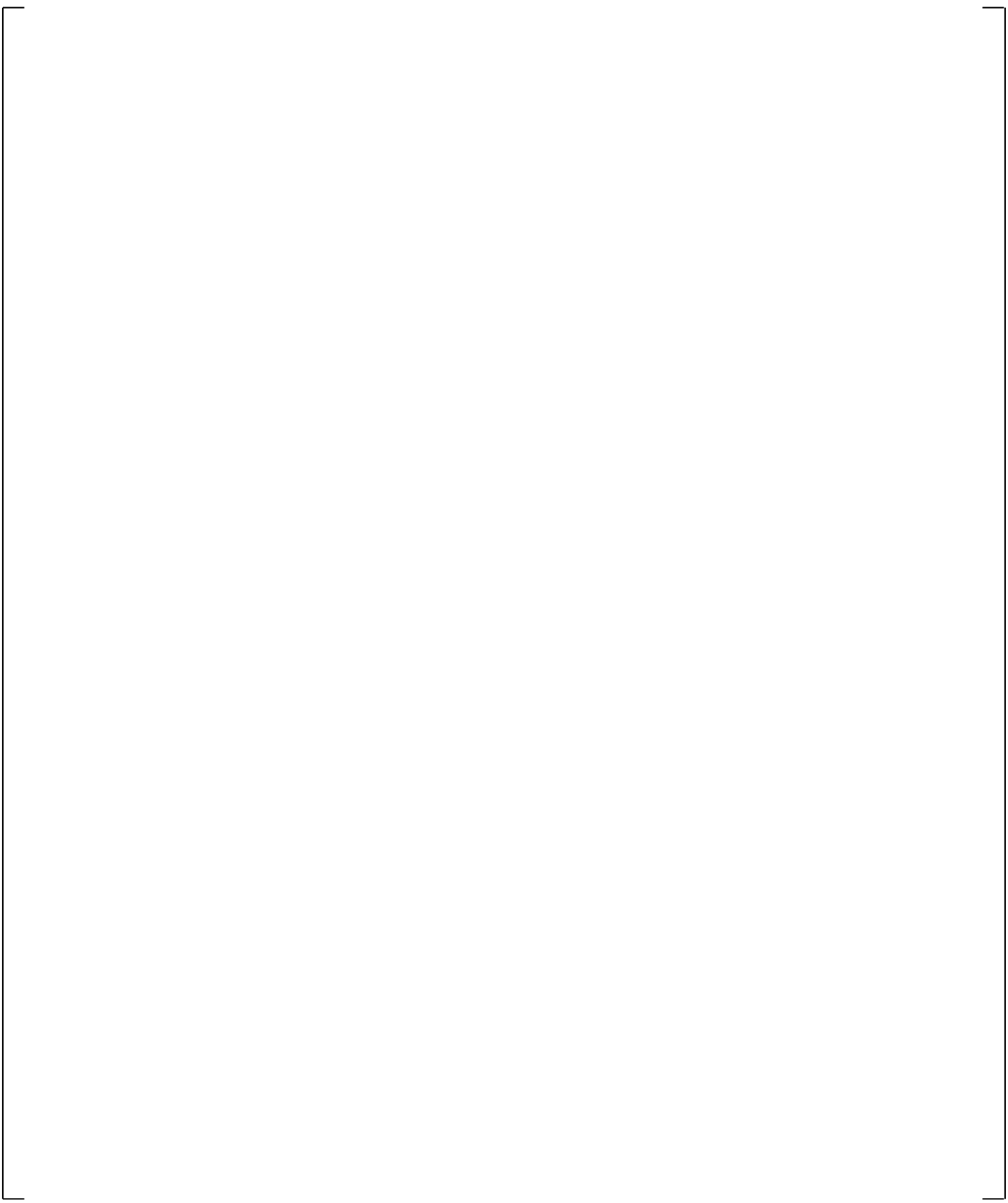

Figure 21.5-9 Steam Generator B U-tube Differential Pressures

a,c

Figure 21.5-10 Cross-Over Leg A Differential Pressures

a,c

Figure 21.5-11 Cross-Over Leg B Differential Pressures

a,c

Figure 21.5-12 Upper Plenum Differential Pressures

a,c

Figure 21.5-13 Upper Plenum to Steam Generator A Inlet Differential Pressures

a,c

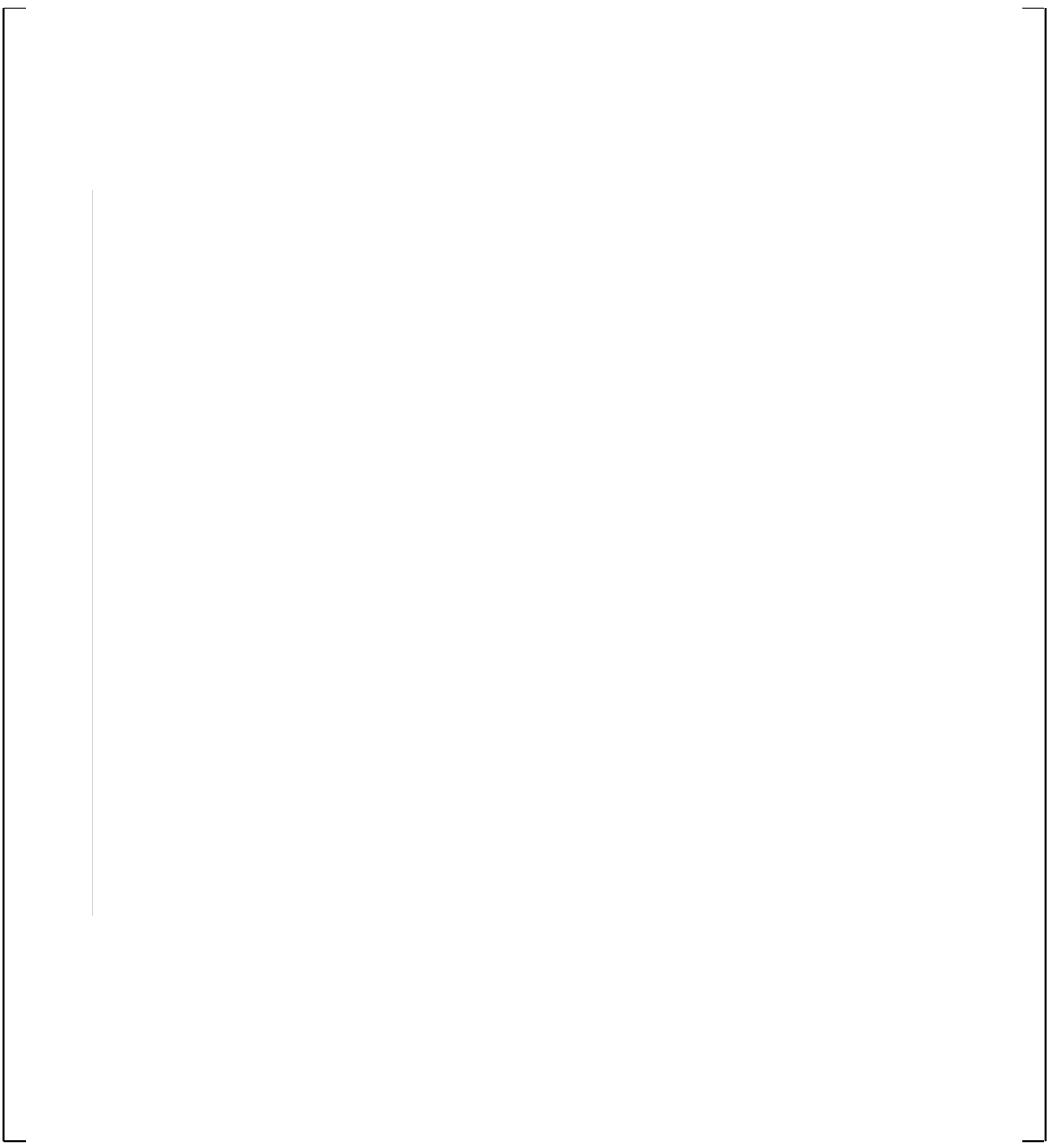

Figure 21.5-14 Upper Plenum to Steam Generator B Inlet Differential Pressures

a,c

Figure 21.5-15 Downcomer Differential Pressures

a,c

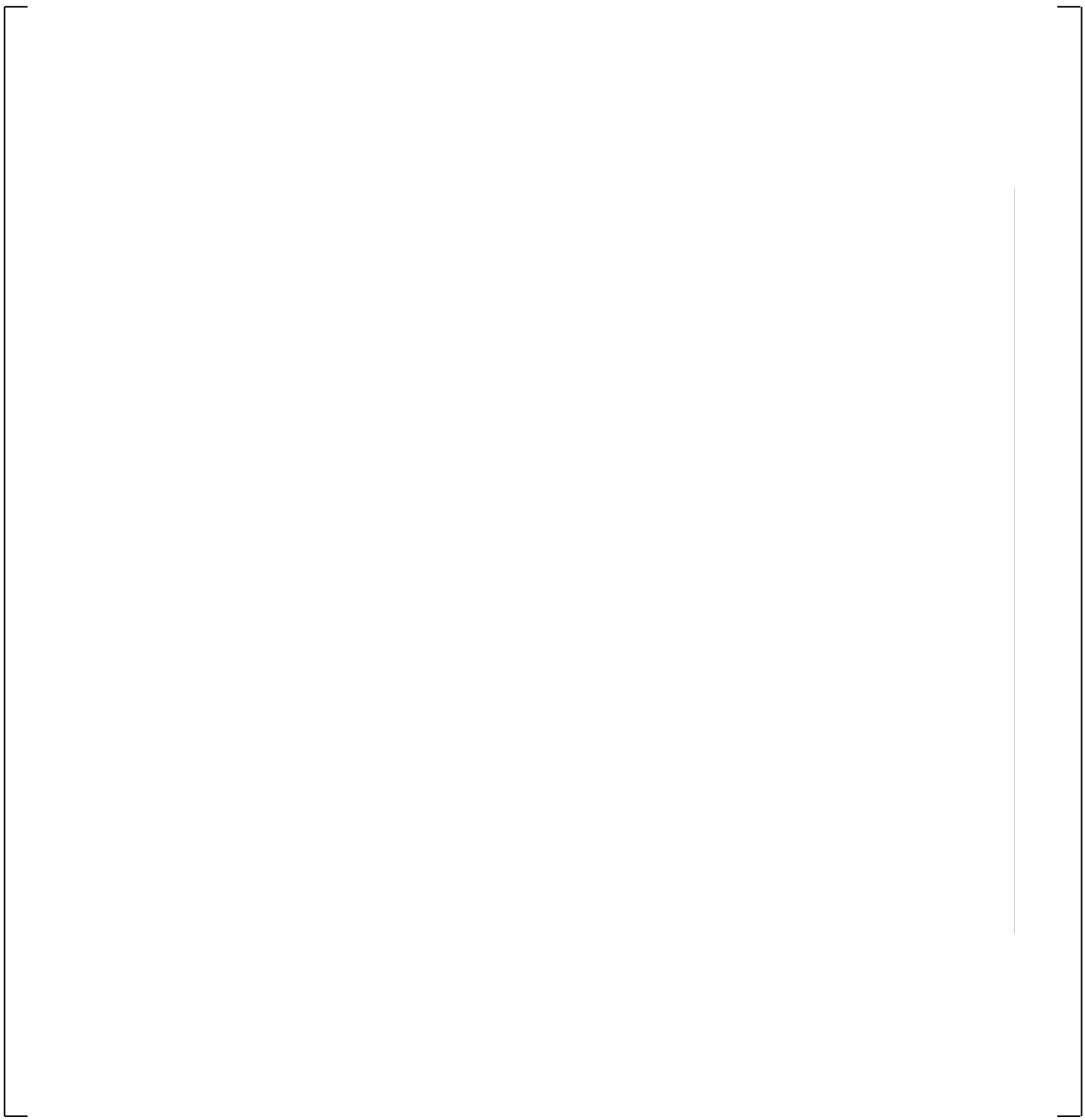

Figure 21.5-16 Core Differential Pressures

a,c

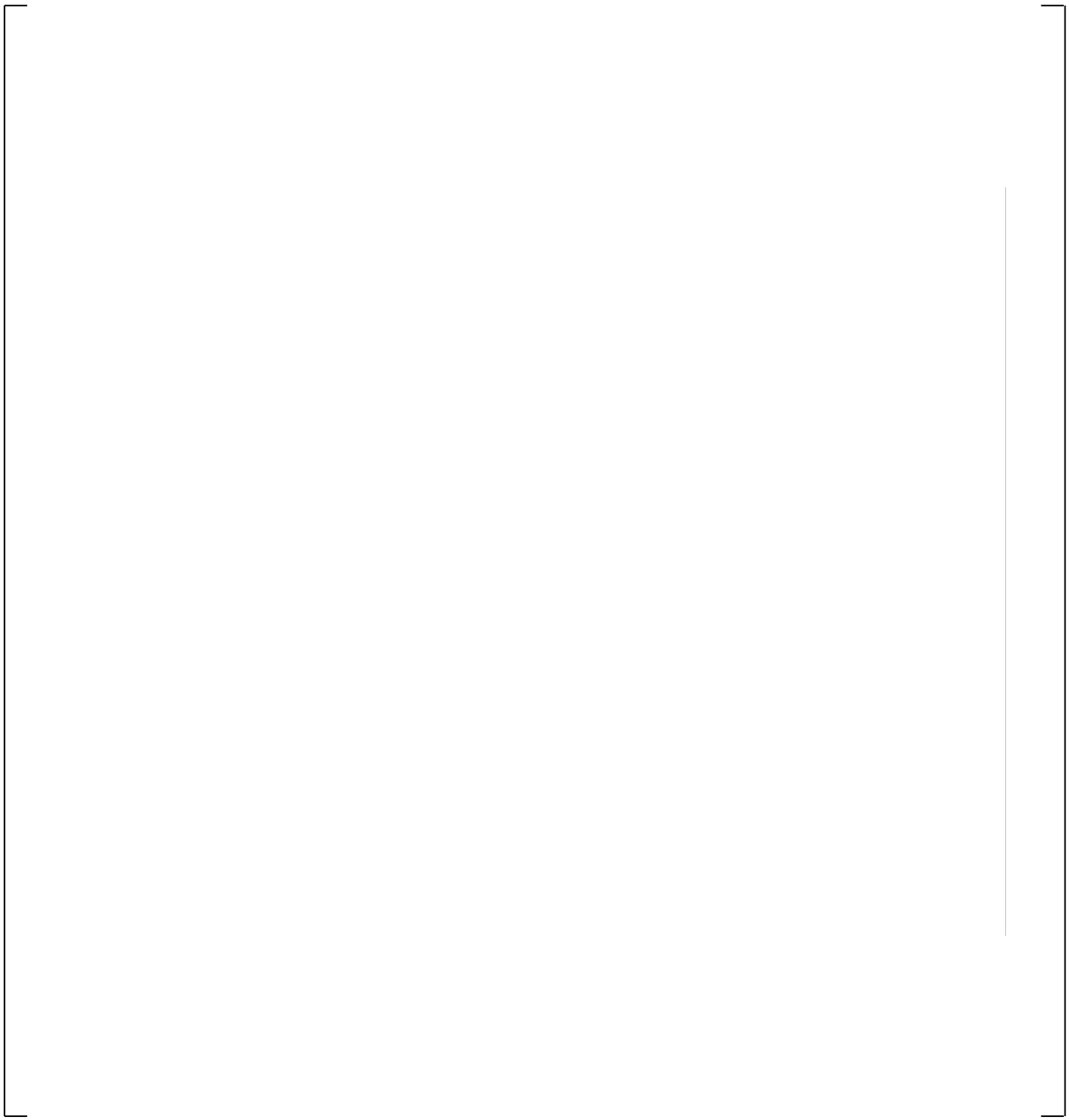

Figure 21.5-17 Core Differential Pressures for SB-CL-05 and SB-CL-18

a,c

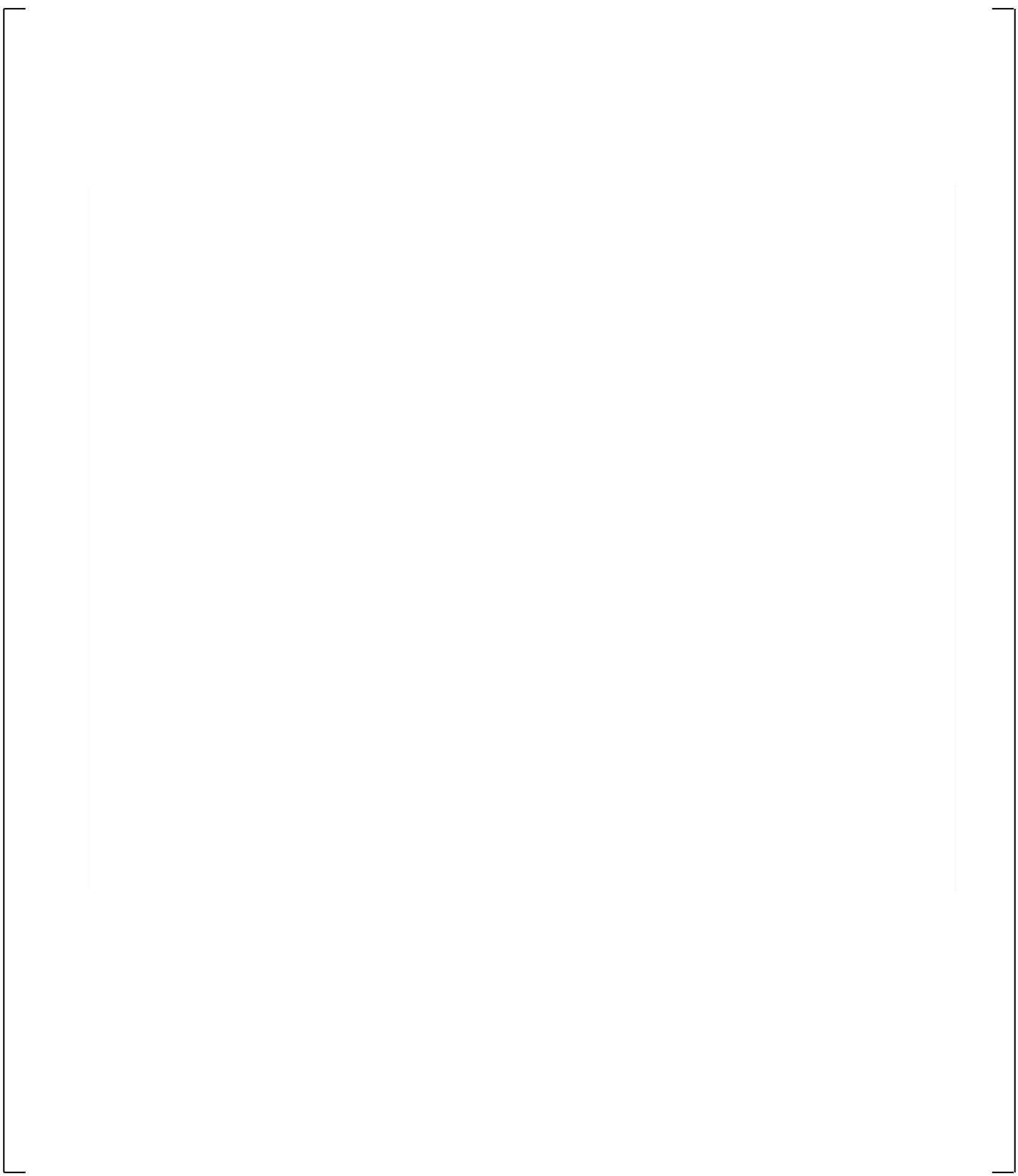

Figure 21.5-18 Cold Leg A Pumped ECCS Injection Flows (CLA)

a,c

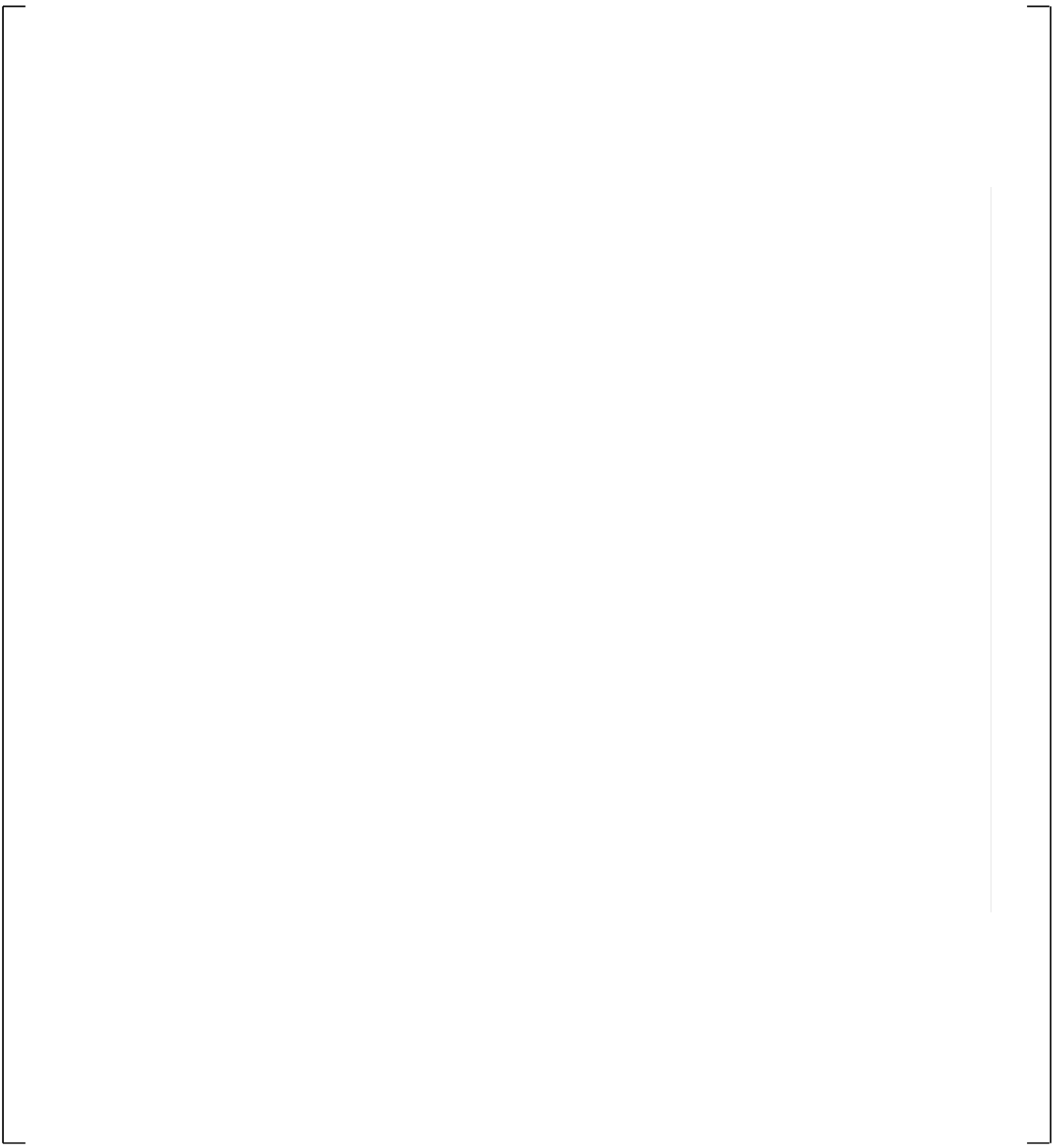

Figure 21.5-19 Total Pumped ECCS Injection Flows (Cold Leg A plus Cold Leg B)

a.c

Figure 21.5-20 Accumulator Hot (ACH) Liquid Level

a.c

Figure 21.5-21 Calculated and Measured Cladding Temperatures at Mid-Core Elevation

21.6 SIMULATION OF THE 10% SIDE BREAK TEST SB-CL-14

One of the integral shakedown tests performed in the LSTF is a 10-percent cold leg break, which was the maximum break size for the facility design. This is a relatively large break size, corresponding to approximately a 9-inch break in a PWR, which could be considered more of an intermediate break as opposed to a small break LOCA. This break size is considered in order to test the code capabilities and expand the break spectrum to include intermediate break sizes as well.

[

]^{a,c}

21.6.1 Description of the Boundary and Initial Conditions

The initial conditions for the 10% break test SB-CL-14 are summarized in Table 21.6-2.

The operational setpoints for this 10-percent break are consistent with the standard set used in all ROSA-IV tests, as summarized in Table 21.2-2. The charging and the high-pressure injection were not actuated in this test. The low-pressure injection system was active in this test, but was not modeled in the simulation, since during the test the injection initiated 862 seconds after the break, well beyond the period of interest in this calculation.

The break was located in loop B, the loop without the pressurizer, and was oriented horizontally from the middle of the cold leg. The 10% break size was simulated by using a break orifice with diameter of 31.9 mm (1.256 inch). The break was initiated by opening of a fast acting air operated valve that directed the break flow into the catch tank.

As mentioned earlier, this test used a realistic decay heat curve, as documented in Table 21.6-1. Initiated by the reactor scram signal, the core power was controlled by a test sequence controller according to the curve in Table 21.6-1.

The pump speed was controlled by the sequence controller to follow a preprogrammed coastdown curve. The pump speed was initially increased but then, triggered by the reactor scram signal, a coastdown was initiated at 13.2 seconds which followed a predefined curve.

21.6.2 Results and Conclusions for the SB-CL-14 Simulations

This section presents the results of two SB-CL-14 test transient simulations. Both simulations were performed with break flow discharge coefficients **[** **]**[a,c] Consistent with the adopted modeling approach with regards to counter-current flow, one of the simulations was performed with CCFL **[**

][a,c]

Table 21.6-3 summarizes the predicted and measured chronology of key events for the 10-percent cold leg test. Figures 21.6-1 through 21.6-16 present the SB-CL-14 test simulation results compared to the test measurements. With the exception of Figures 21.6-1 and 21.6-2, these figures show the results of both simulations, with and without CCFL enforced. Figures 21.6-17 through 21.6-20 show counter-current flow conditions at the steam generator U-tube inlet and the hot leg elbow locations, calculated for both test simulations.

Figures 21.6-1 and 21.6-2 show a comparison of the modeled vs. measured pump speed for the two pumps for the simulation with CCFL enforced; it is noted that the same pump coast-down curves were implemented for the simulation without CCFL enforced. As seen, there is a good match between the modeled and measured pump speed. Consequently, the calculated loop flows for the first minute of the transient are fairly consistent with the test measurements, as shown in Figures 21.6-3 and 21.6-4. Due to the two-phase conditions established at the flow meters following the onset of loop seal clearance, the measured (test) flow rates beyond 80 seconds are unreliable and cannot be used for validation of the calculated break flow.

The break flow comparison is shown in Figure 21.6-5, where the predicted break flow is compared against the test break flow as calculated from the measured level in the catch tank. **[**

][a,c]

[

]a,c

Table 21.6-1 [ ][a,c]

a,c

Table 21.6-2 [ ][a,c]

a,c

Table 21.6-3 [ ][a,c]

a,c

a,c

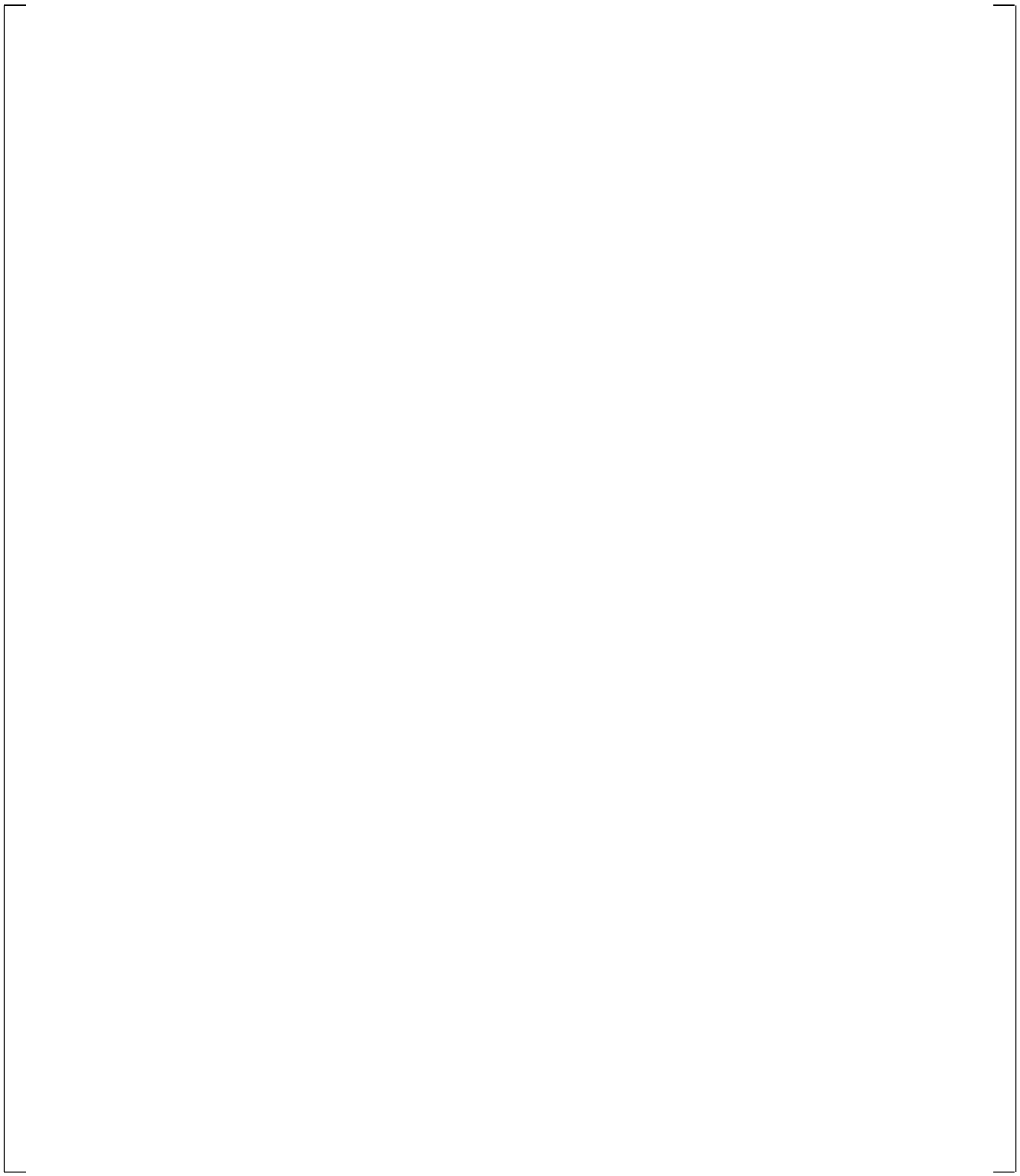

Figure 21.6-2 Loop-B Pump Speed Comparison

Note: 1 Hz=30 rpm=3.1415 rad/sec

a,c

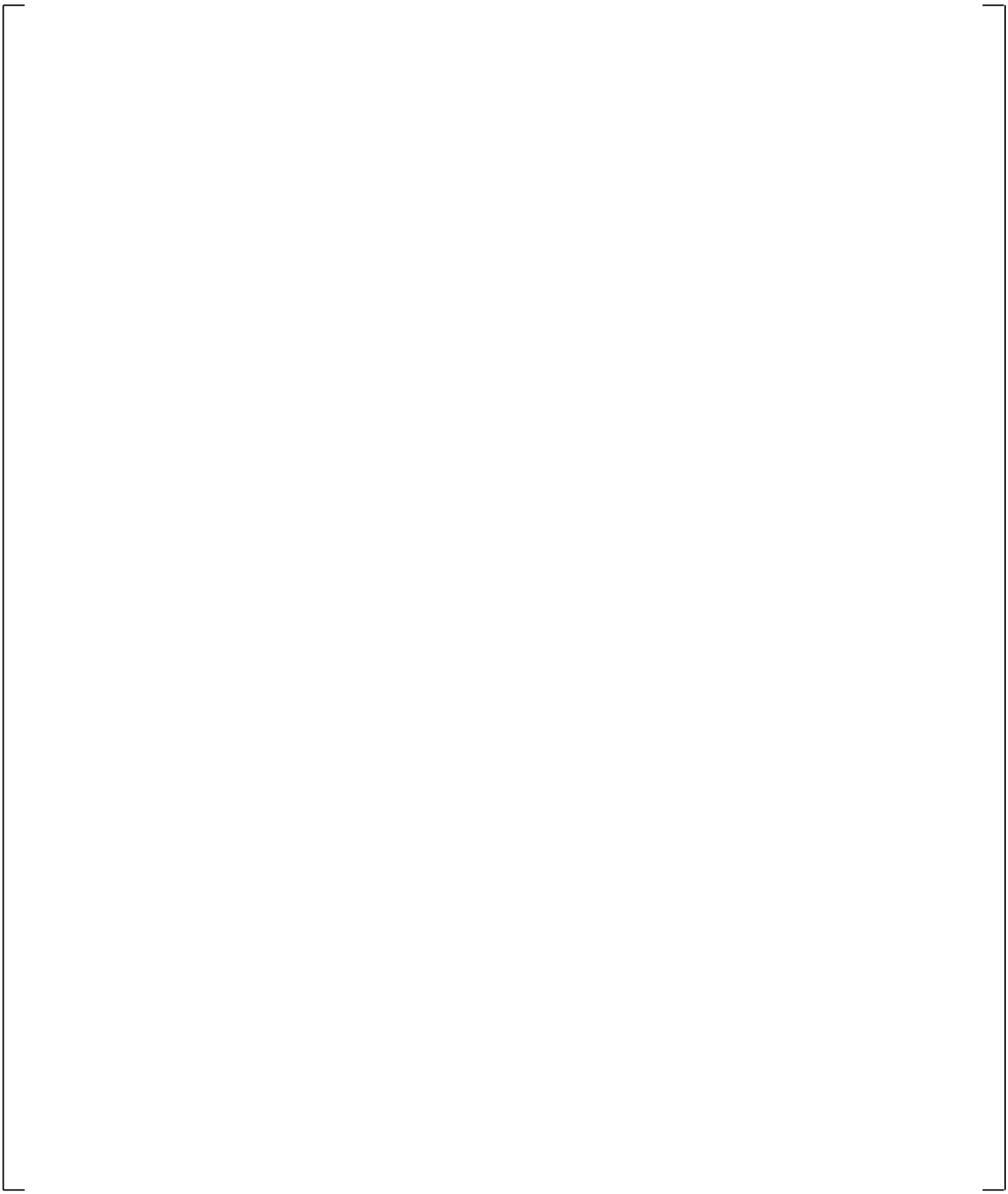

Figure 21.6-3 Comparison of Loop-A Flow Rates

a,c

Figure 21.6-4 Comparison of Loop-B Flow Rates

a,c

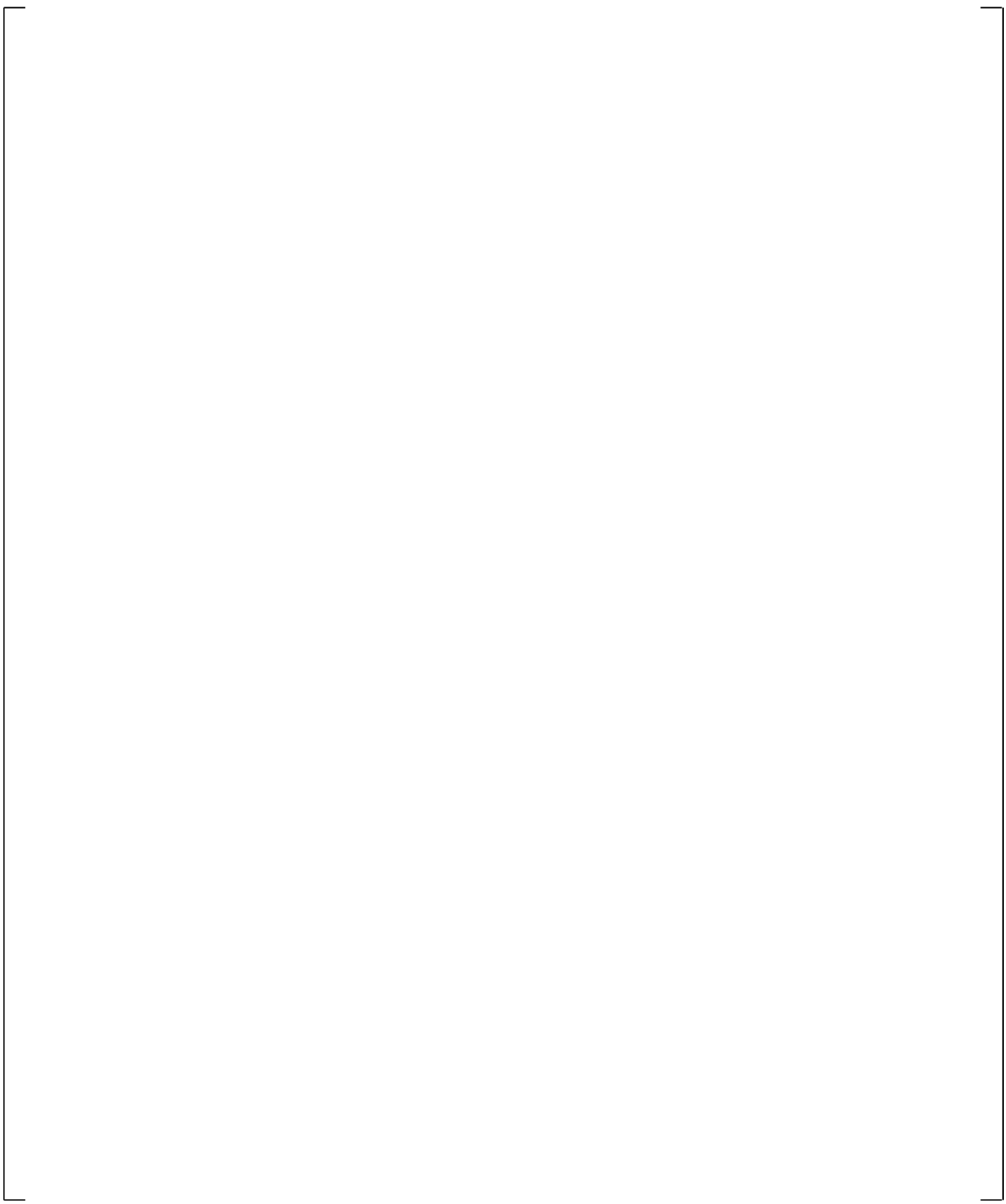

Figure 21.6-5 Comparison of Break Flows

a,c

Figure 21.6-6 Comparison of Fluid Density in the Break Spool

a,c

Figure 21.6-7A Comparison of Loop-A Cross-Over Leg Differential Pressures

a,c

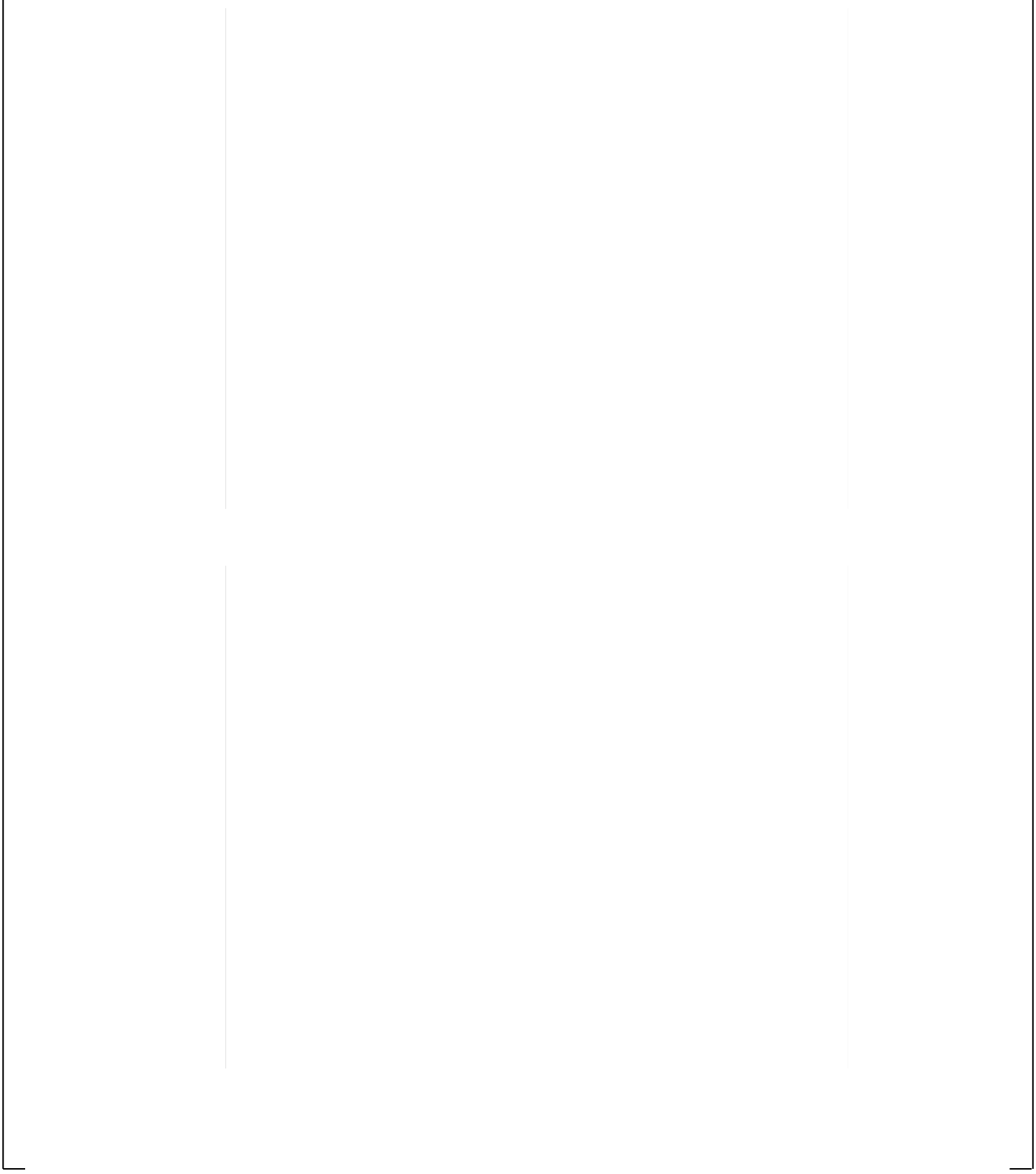

Figure 21.6-7B Comparison of Loop-B Cross-Over Leg Differential Pressures

a,c

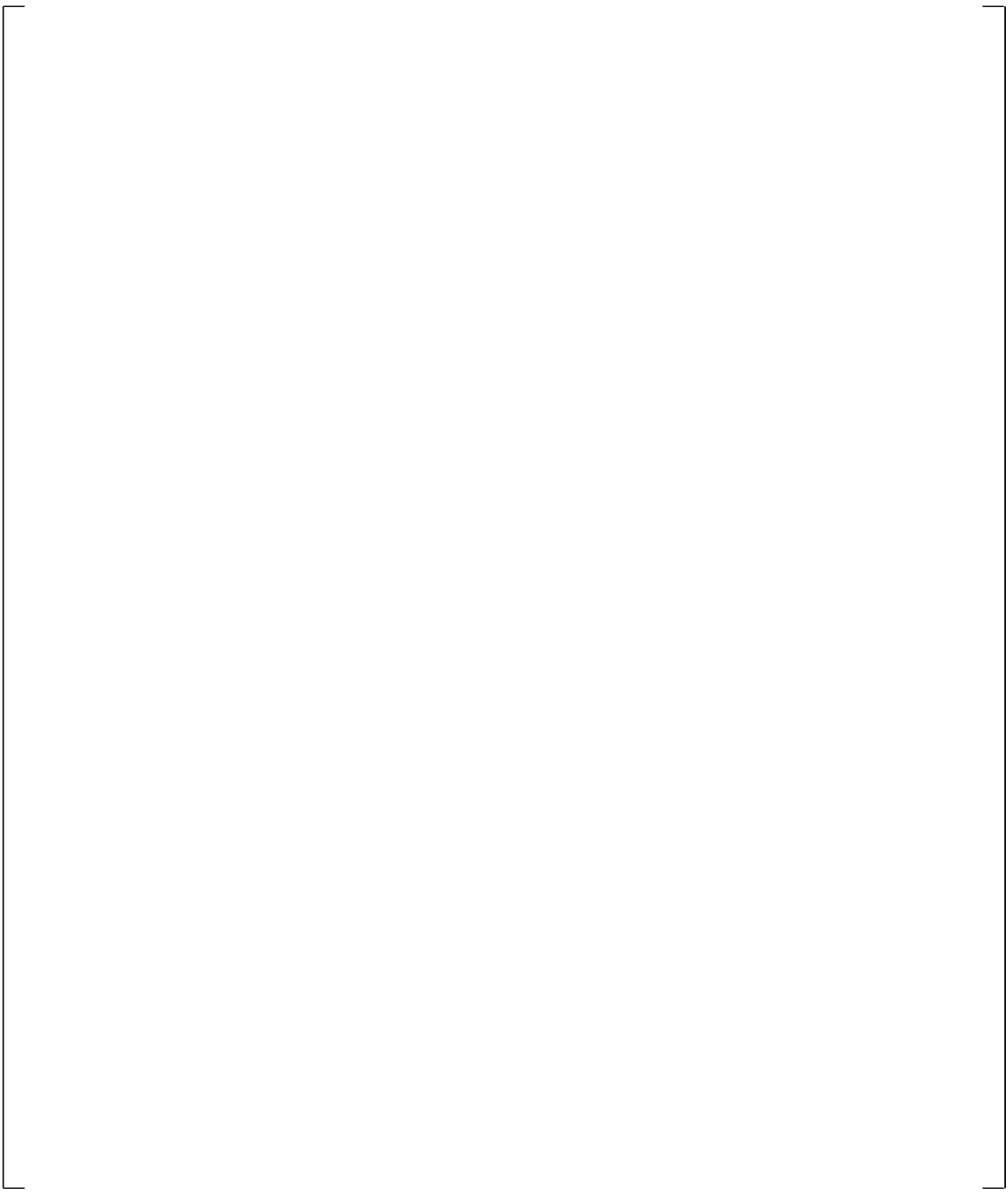

Figure 21.6-8 Comparison of System Pressures

a,c,e

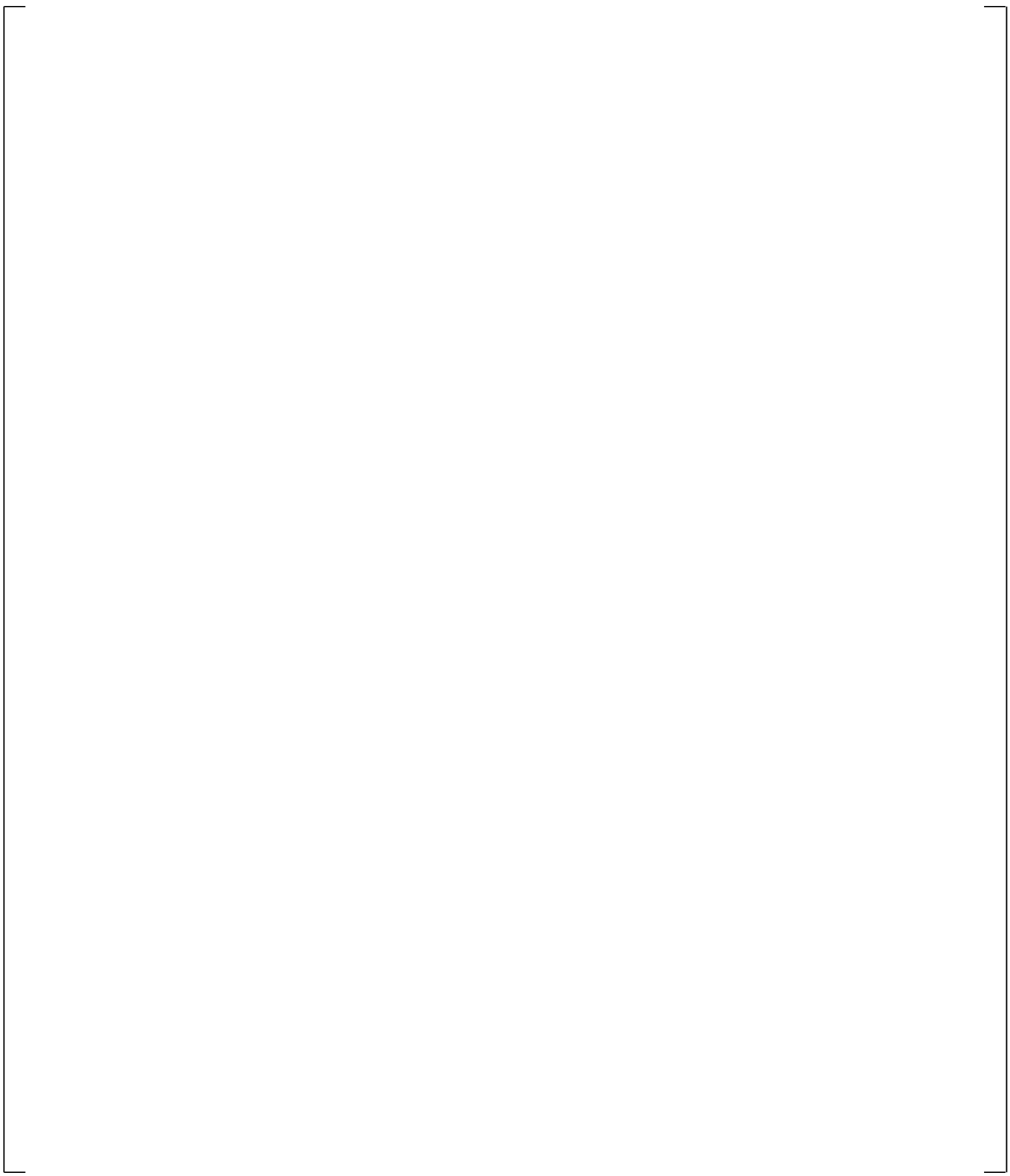

Figure 21.6-9 Comparison of Steam Generator A U-tube Inlet-to-top Differential Pressures

a,c,e

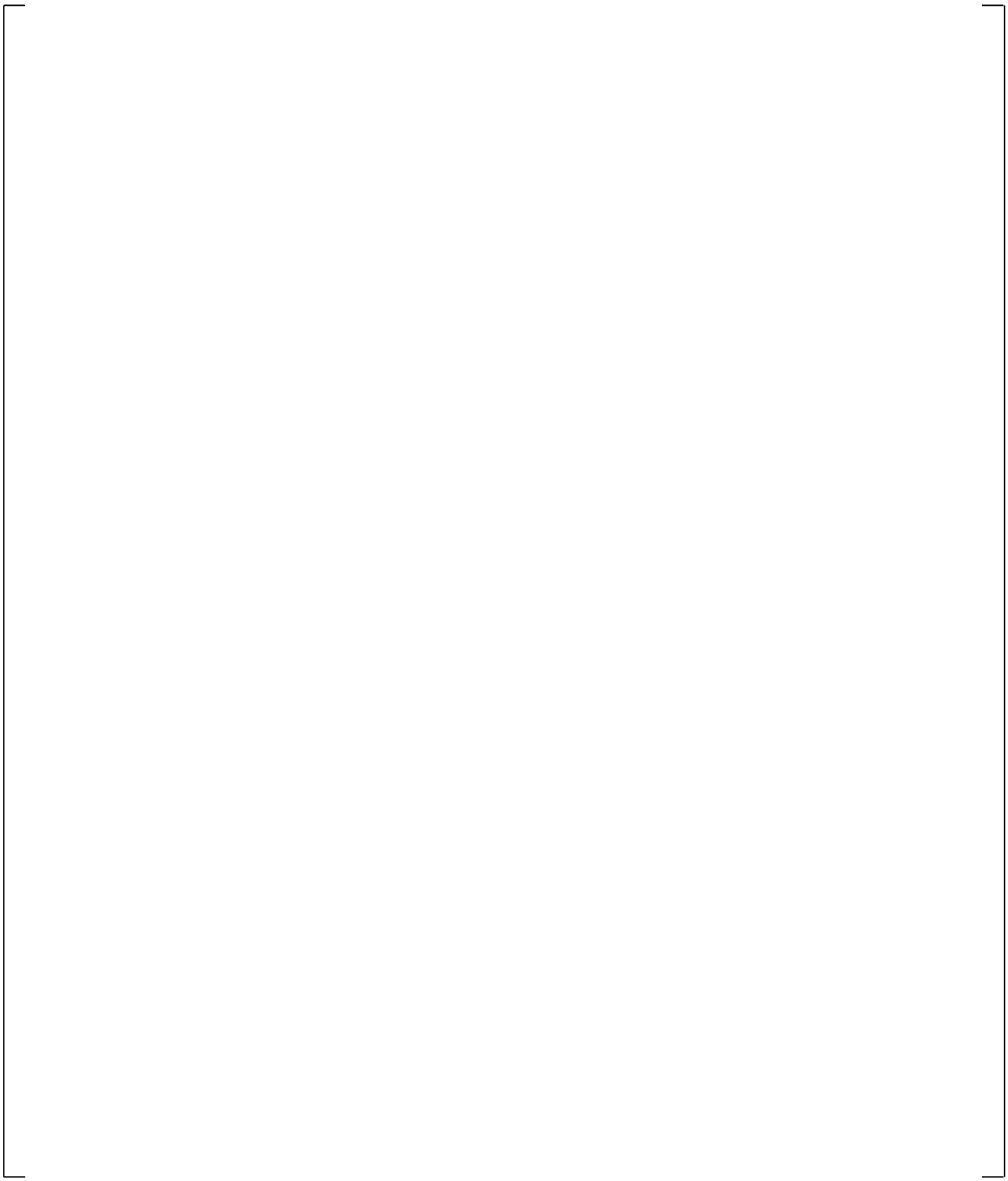

Figure 21.6-10 Comparison of Steam Generator B U-tube Inlet-to-top Differential Pressures

a,c,e

Figure 21.6-11 Comparison of Steam Generator A U-tube Outlet-to-top Differential Pressures

a,c,e

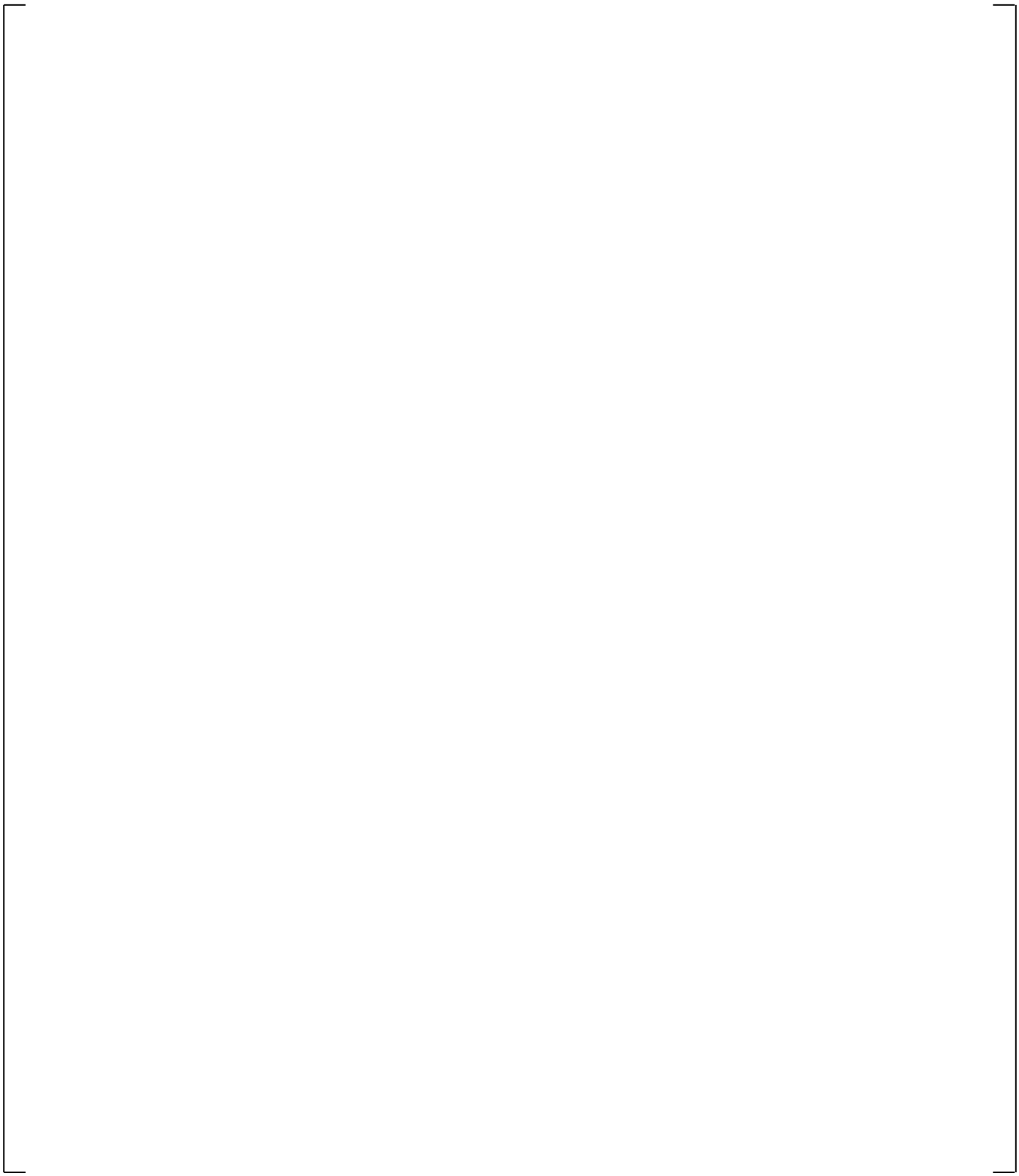

Figure 21.6-12 Comparison of Steam Generator B U-tube Outlet-to-top Differential Pressures

a,c,e

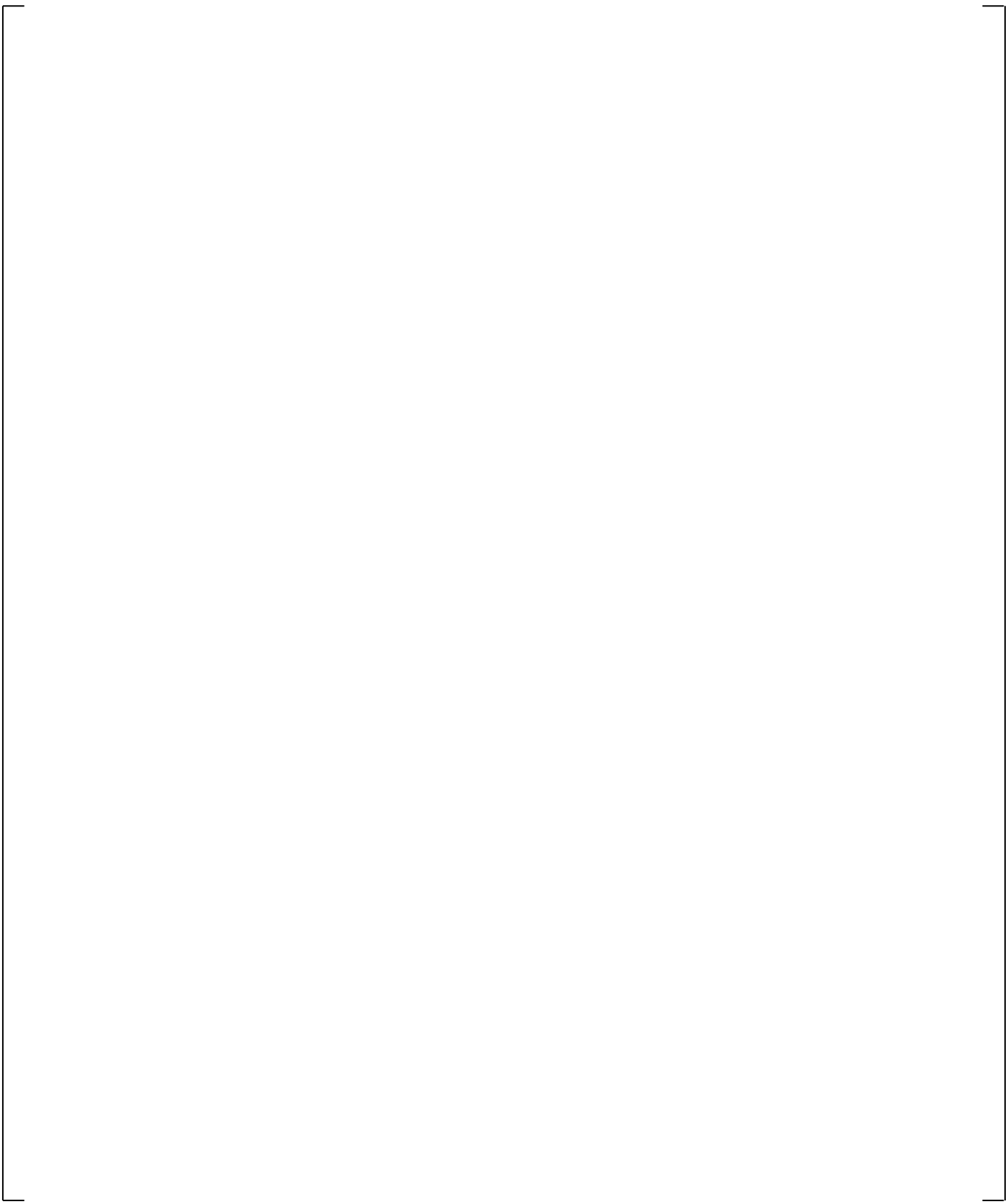

Figure 21.6-13A Comparison of Steam Generator A Inlet Plenum Draining

a,c

Figure 21.6-13B Comparison of Steam Generator B Inlet Plenum Draining

a,c,e

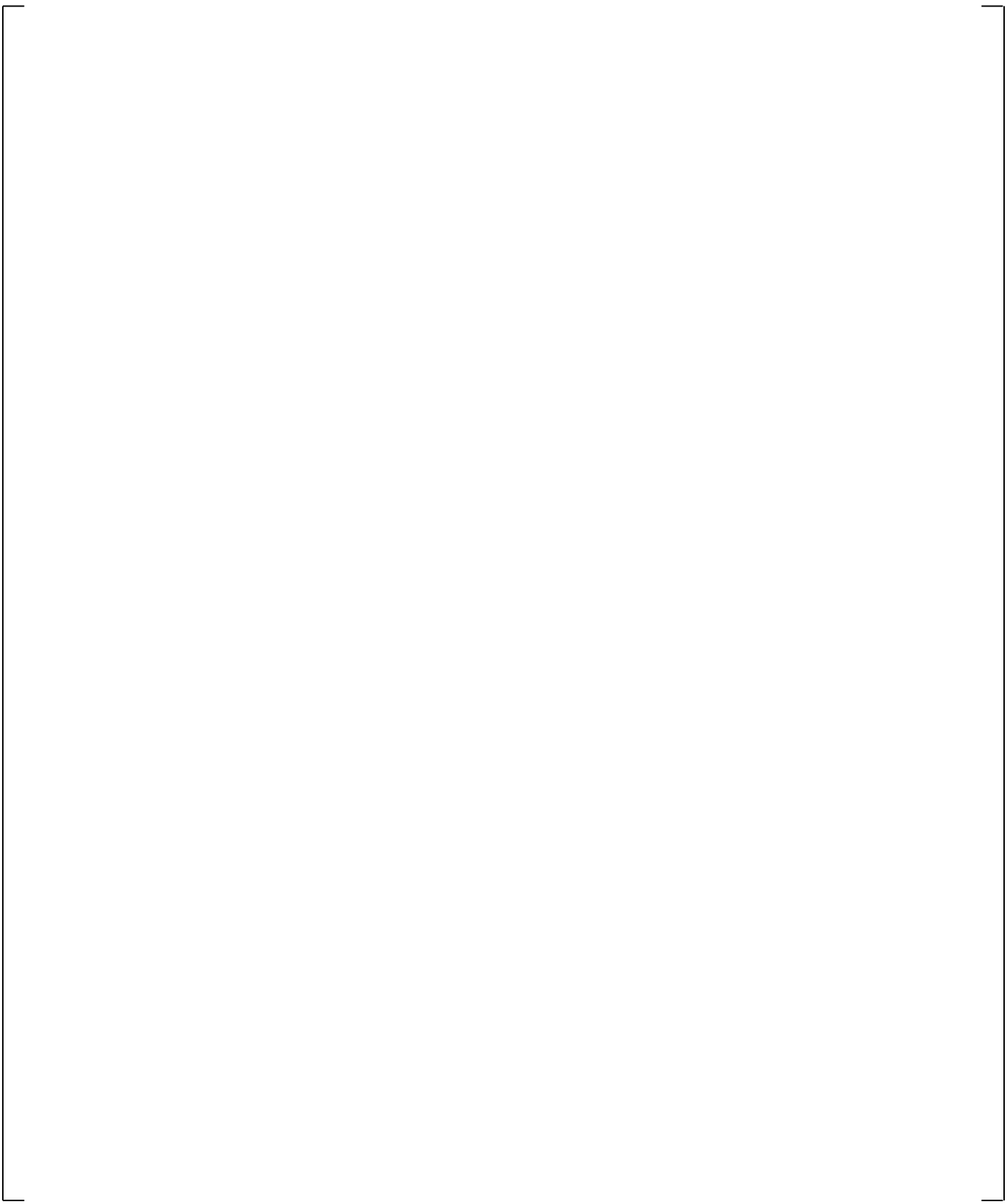

Figure 21.6-14 Comparison of Core Collapsed Liquid Levels

a,c

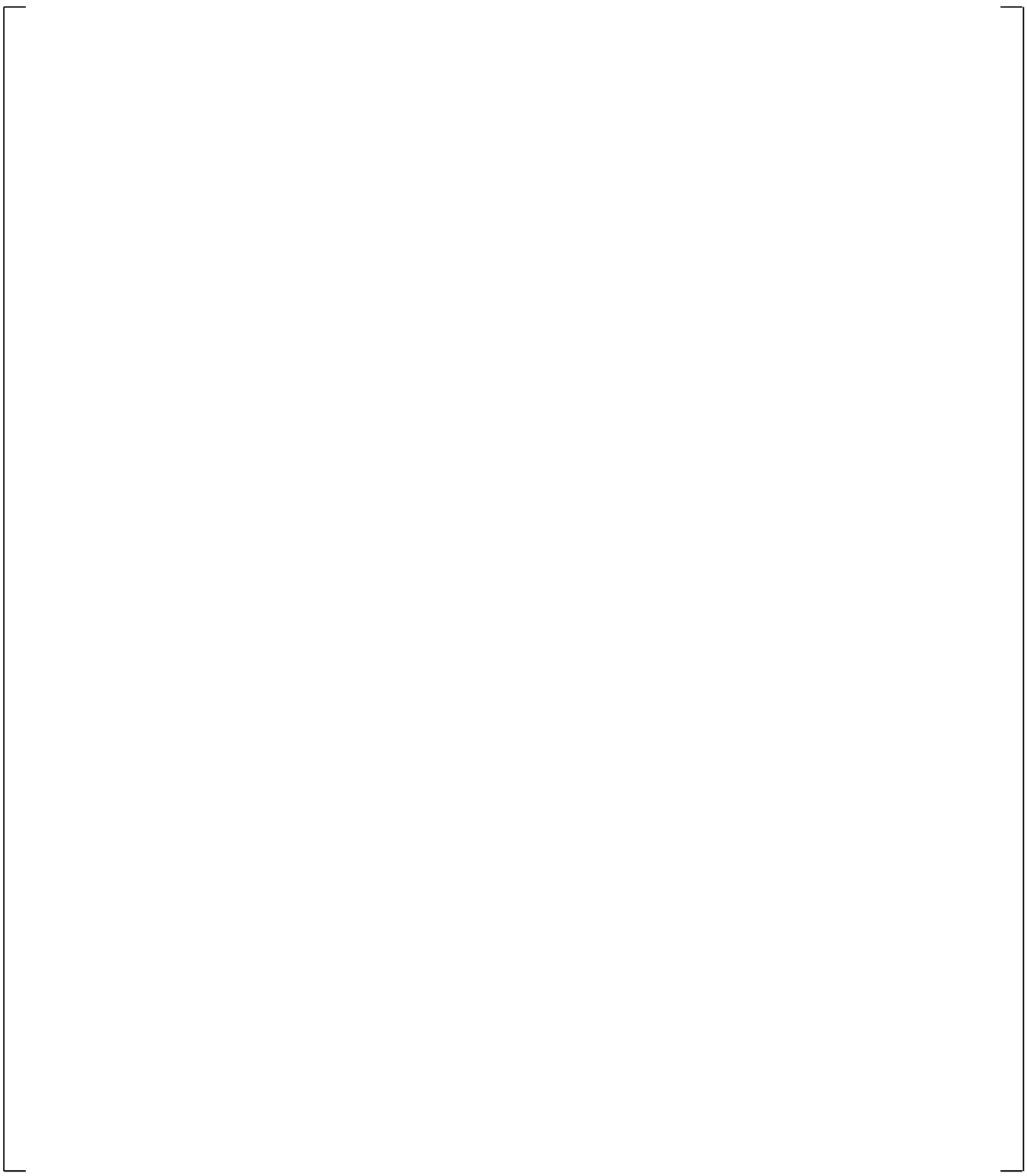

Figure 21.6-15A Calculated Accumulator Injection to Loop A

a,c

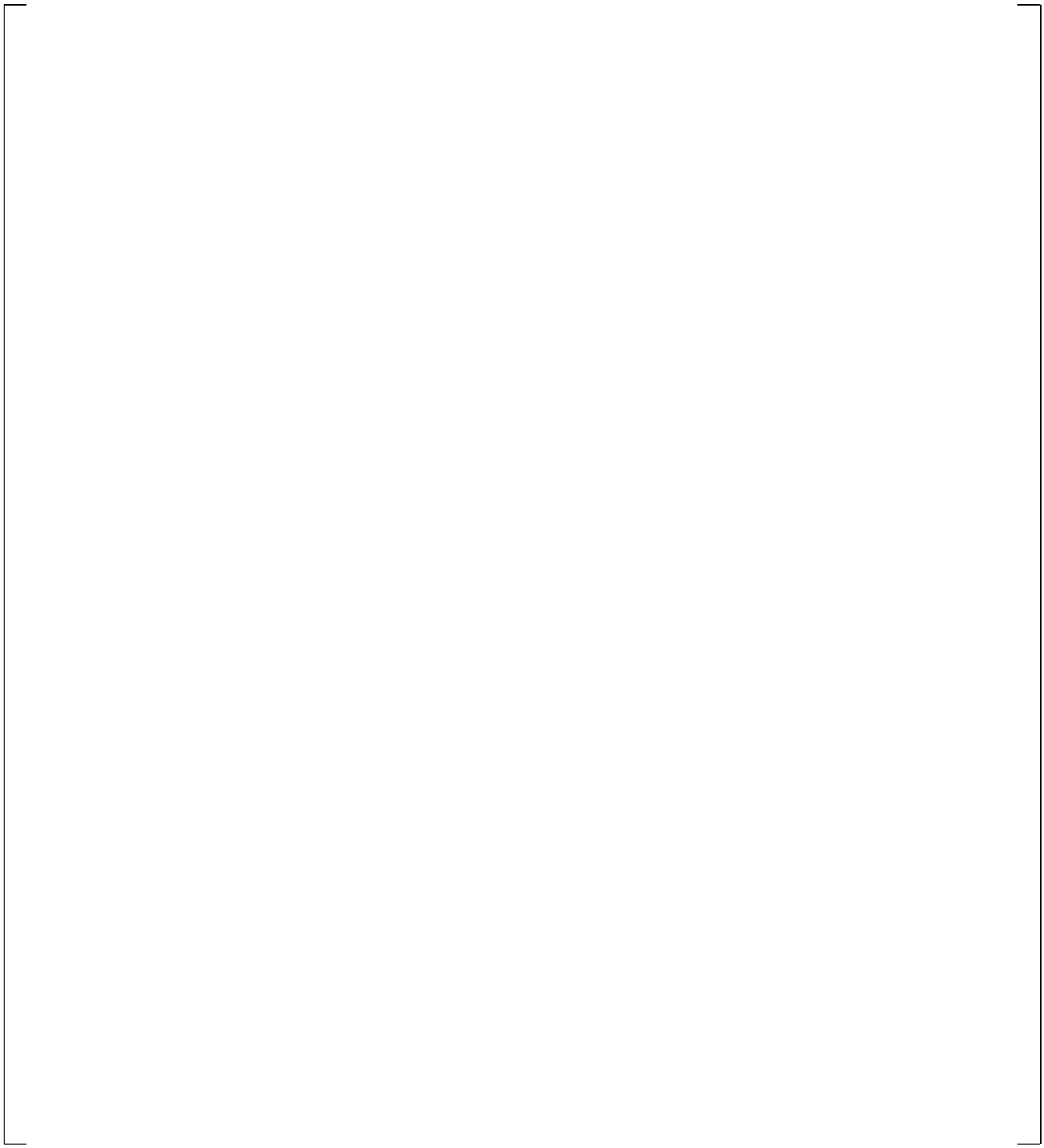

Figure 21.6-15B Calculated Accumulator Injection to Loop B

a,c

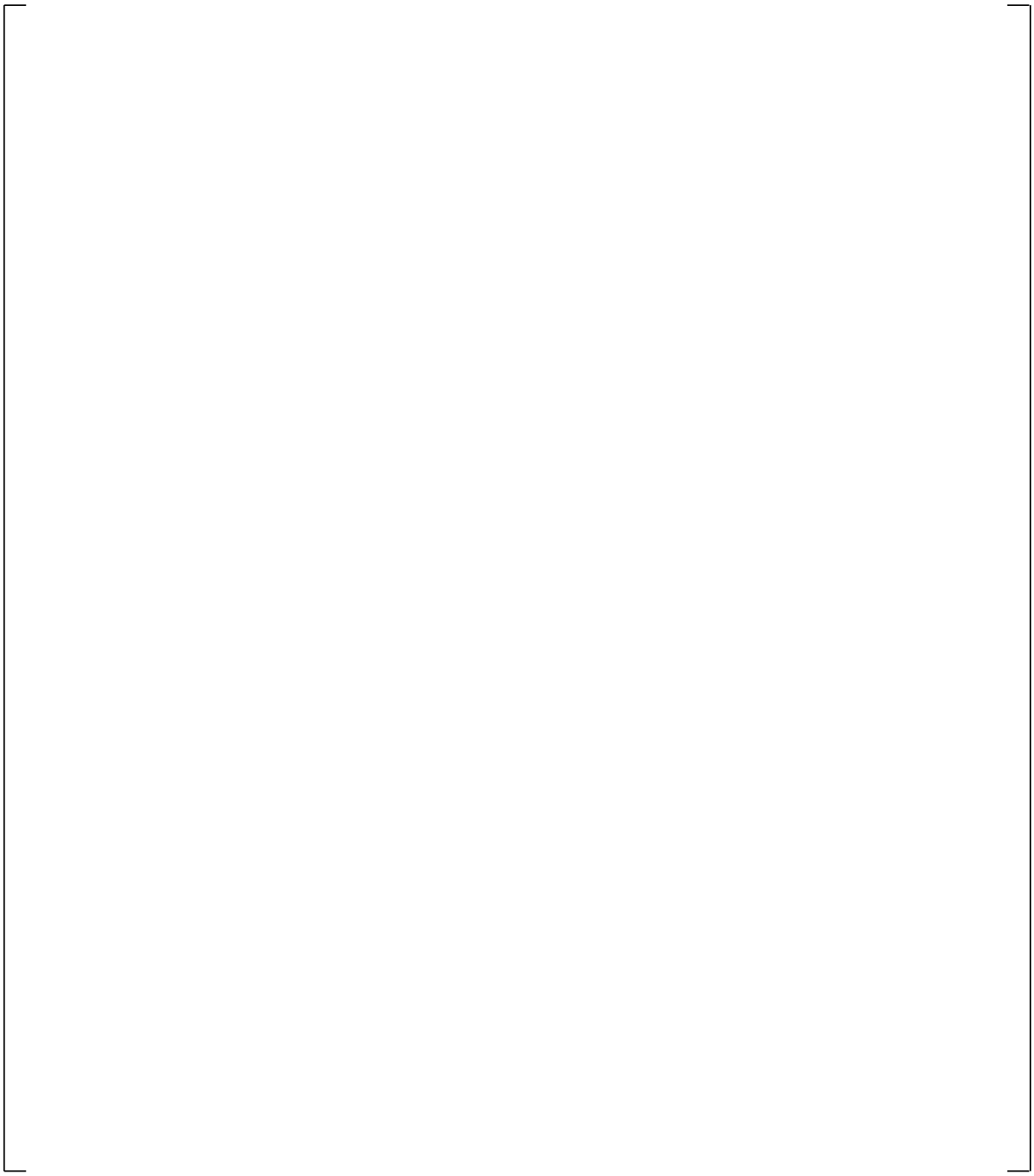

Figure 21.6-16 High Power Rod (Rod 1) Cladding Temperature at 6-ft (1830 mm) Core Axial Location (Measurement uncertainty is 6.4K)

a,c

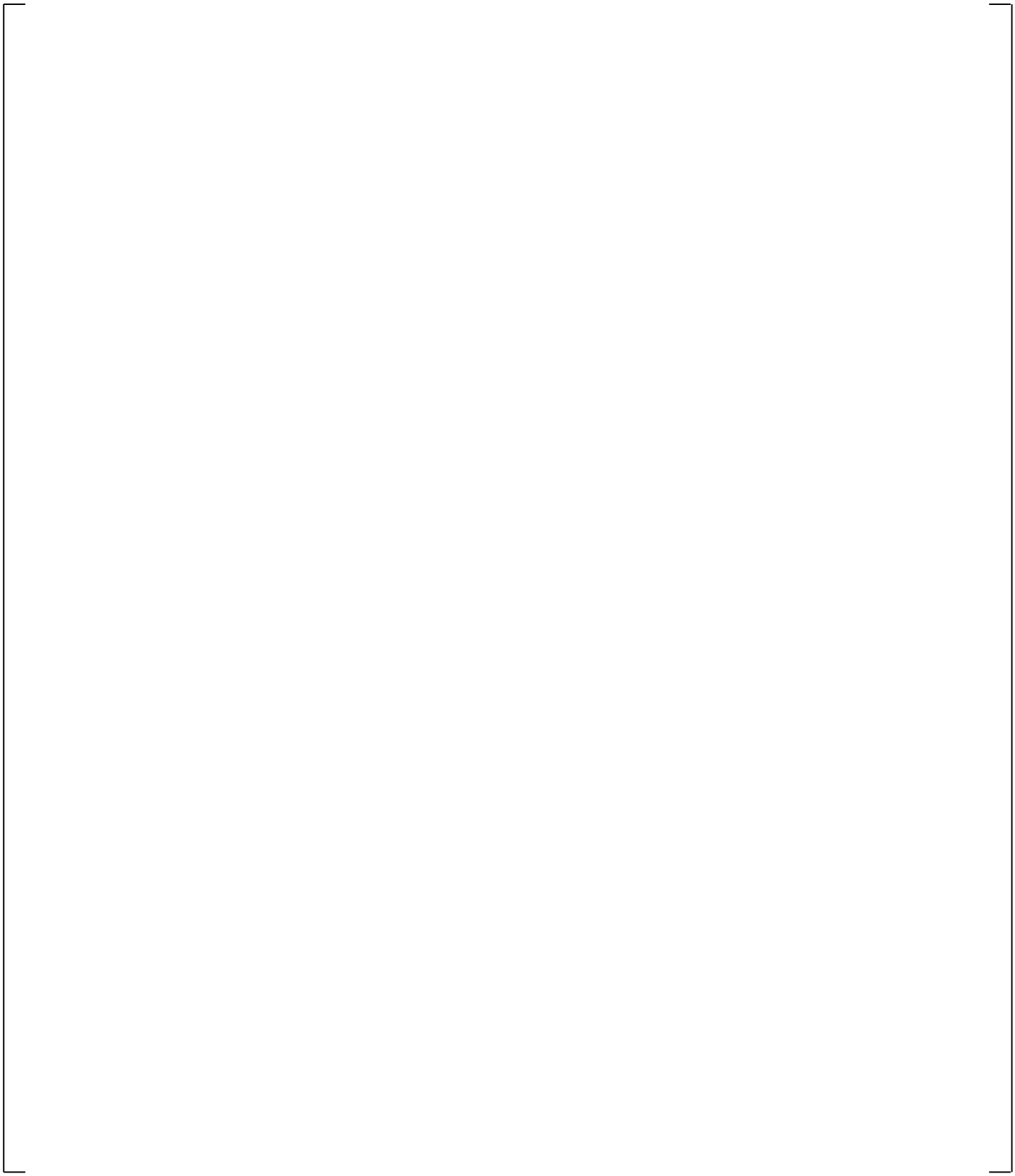

Figure 21.6-17 Calculated Counter-current Flow at Steam Generator A U-tube Inlet

a,c

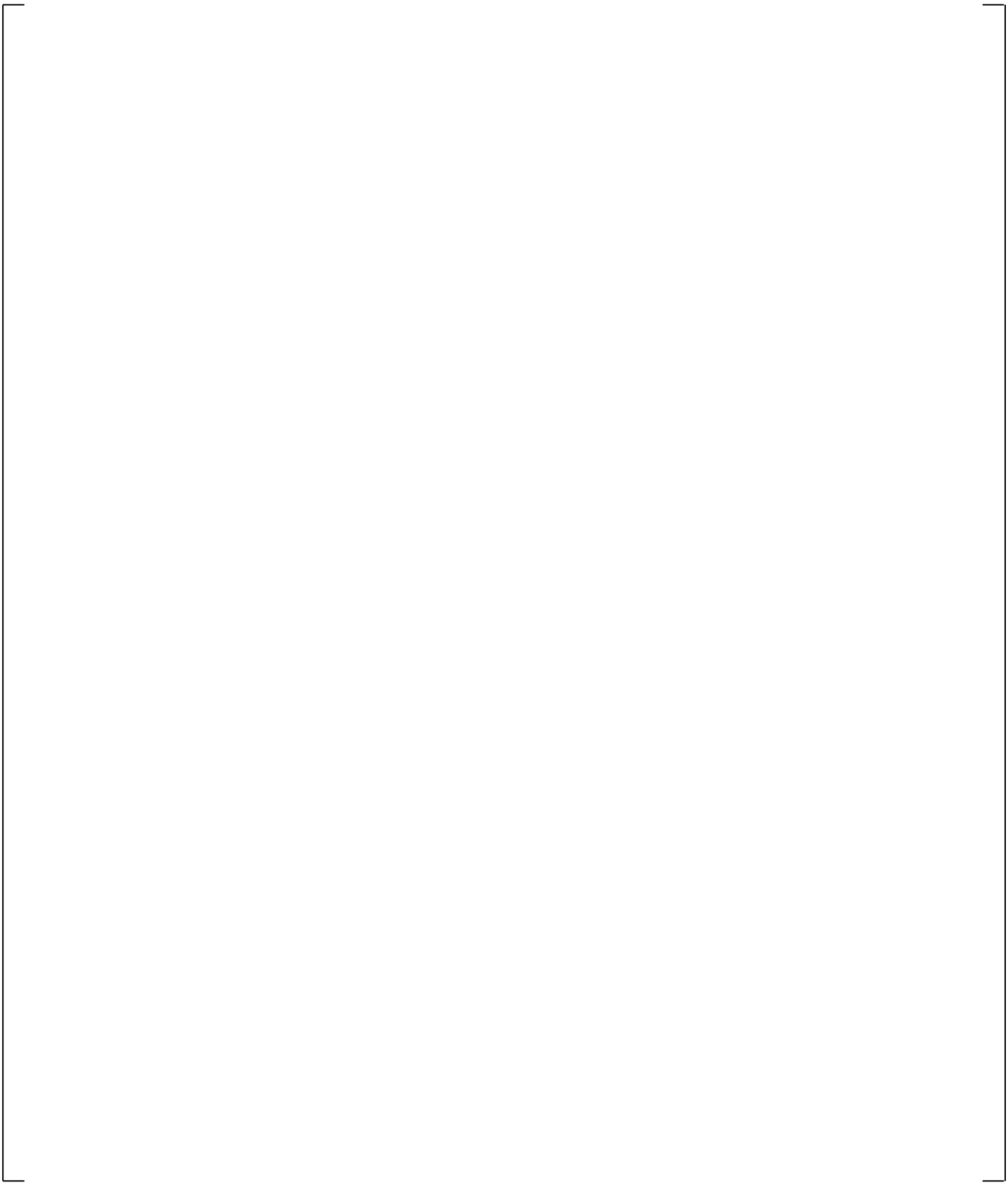

Figure 21.6-18 Calculated Counter-current Flow at Steam Generator B U-tube Inlet

a,c

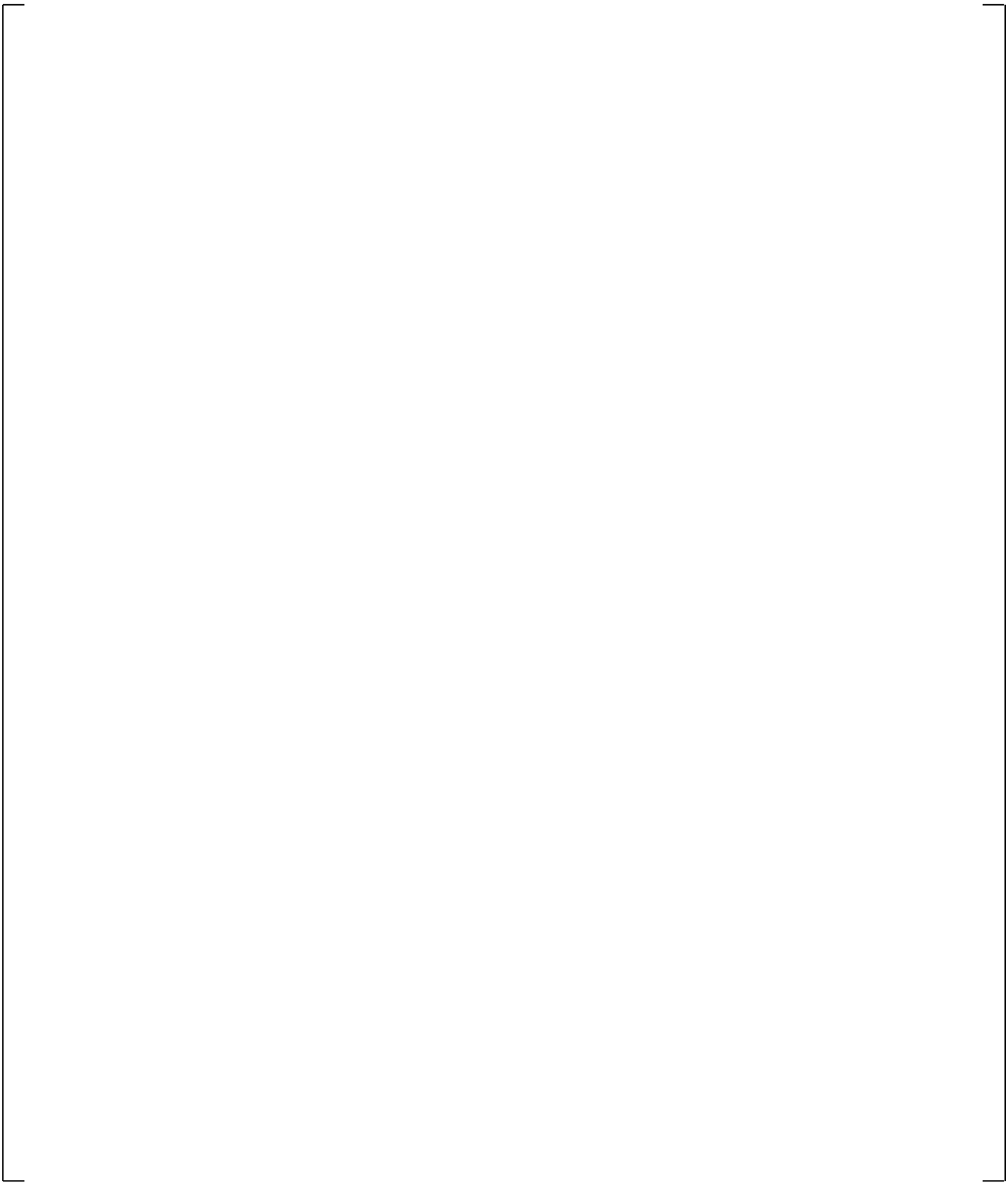

Figure 21.6-19 Calculated Counter-current Flow at Elbow of Hot Leg A

a,c

Figure 21.6-20 Calculated Counter-current Flow at Elbow of Hot Leg B

21.7 BREAK ORIENTATION STUDY: SIMULATION OF TOP/SIDE/BOTTOM 0.5% (SB-CL-16/12/15) AND 2.5% (SB-CL-03/01/02) COLD LEG BREAKS

[

]^{a,c} The purpose of the study, presented in this section, is to assess the ability of the WCOBRA/TRAC-TF2 code to predict break orientation effects.

21.7.1 Description of the Boundary and Initial Conditions

For each of the test simulations presented here a steady-state calculation is performed first to achieve the desired initial conditions according to the particular test being simulated. [

]^{a,c}

21.7.2 Discussion of Results

In LSTF, the break unit can be configured such that the break orientation effect can be studied. Two sets of three experiments were conducted in the LSTF to investigate the effect of break orientation. The first three tests (SB-CL-01, -02, and -03; side, bottom and top respectively), simulated a 2.5 % break in the cold leg. The second set of three tests (SB-CL-12, -15 and -16) simulated a 0.5% break in the cold leg. In this section these two sets of break orientation studies will be discussed.

21.7.2.1 2.5% Tests

In these experiments, the break was oriented at the side, bottom, and top of the loop B cold leg. Experimental results are summarized in the data report by Koizumi (Koizumi et al., 1988). The test results showed that break orientation had only a small effect on system parameters such as pressure and core collapsed liquid level. Figure 21.7-1 shows the break geometry and orientation for these tests. Together with 0.5% break orientation tests, which will be discussed later in this section, these tests provide a useful means of evaluating the break flow model in WCOBRA/TRAC-TF2 for the effects of vapor pull through and liquid entrainment near the break orifice.

Boundary Conditions

Operational setpoints for the 2.5 % cold leg break tests were the same as those implemented in all ROSA-IV small break tests, shown in Table 21.2-2, with the following two exceptions. [

]^{a,c}

All three tests were conducted, and modeled, using the same JAERI (full conservative) decay heat curve, Table 21.7-1.

Figure 21.7-2 shows the break modeling approach used in the 2.5 percent cold leg break simulations. Results for the 2.5 percent cold leg break runs are compared to data in Figures 21.7-3 through 21.7-9. Figure 21.7-10 shows just the calculated accumulator flows; no test data was available for comparison.

Pressure

[

]^{a,c}

Break Flow

Figure 21.7-4 shows the predicted and measured break flows. The test data for all three orientation breaks show no difference in the break flow rate until 150 seconds. Similar to the experimental data, the break orientation simulations showed only a small effect on the predicted break flow during the first 150 seconds as well. After the transition to two-phase, which occurs around 150 seconds, the flow in the cold legs becomes stratified. When the break flow quality turns to two-phase and the cold leg flow stratifies, the test data shows that the break flows diverge from each other, Figure 21.7-4(b). First, the top break and side break discharge becomes two-phase, and the discharge flow rate reduces abruptly. In the test, the transition of the bottom break to two-phase occurs about 50 seconds later. For the bottom break, it takes longer to become two-phase because the level in the cold leg needs to drop low enough in order for the vapor to be entrained into the break spool. In the simulations, the predicted timing of the break flow transition from single-phase sub-cooled discharge to high void two-phase discharge is predicted [

]^{a,c}

The comparison in Figure 21.7-5 indicates that the WCOBRA/TRAC-TF2 simulations predict relatively well the general two phase level characteristics of the experiments. Similar to the test, after the calculated brief period of 30 seconds instability following the transition to two-phase flow, the top and side breaks tend to maintain a higher mixture level in the broken cold leg compared to the bottom oriented break. However, the calculated mixture level for the bottom break is somewhat higher than that observed in the test. One possible explanation of this inconsistency might be that the code calculates downcomer level [

]^{a,c}

Core Collapsed Liquid Level

[

]^{a,c}

Core Heat-up

[

]^{a,c}

21.7.2.2 0.5% Breaks

Break orientation study was also conducted with the 0.5% break tests SB-CL-12, 15 and 16 (side, bottom and top break respectively). Figure 21.7-11 shows the break unit used in these tests. Unlike the SB-CL-01/02/03 tests, in these tests there is no break offtake pipe and the break hole (orifice) is located right at the cold leg wall.

As the 2.5% break tests, these three tests were conducted, and modeled, using the same JAERI (full conservative) decay heat curve, Table 21.7-1.

Liquid Level in Broken Cold Leg

[

]a,c

Core Collapsed Level

[

]a,c

Break Flow

[

]a,c

21.7.3 Conclusions

Comparison between the test data and the simulation runs performed using WCOBRA/TRAC-TF2 show that the break orientation effects exhibit similar trends in terms of the break flow, loop seal clearing timing, core depression, and the beginning of boil-off heat-up. **[**

][a,c]

Table 21.7-1 JAERI (Full Conservative) Decay Heat Curve		
Time After Rx Trip	**Test Power**	**Normalized Power**
sec	**MW**	**-**
(1)	**(2)**	**(3)**
-	10.000	1.00000
0	10.000	1.00000
29	10.000	1.00000
40	8.912	0.89120
60	7.344	0.73440
80	6.128	0.61280
100	5.200	0.52000
150	3.632	0.36320
200	2.848	0.28480
400	1.776	0.17760
600	1.568	0.15680
800	1.488	0.14880
1000	1.424	0.14240
1500	1.280	0.12800
2000	1.200	0.12000
4000	0.992	0.09920

a,c

Figure 21.7-1 Break Unit Configuration used in 2.5% Cold Leg Break Tests, SB-CL-01, 02, and 03 (Koizumi et al., 1987)

a,c

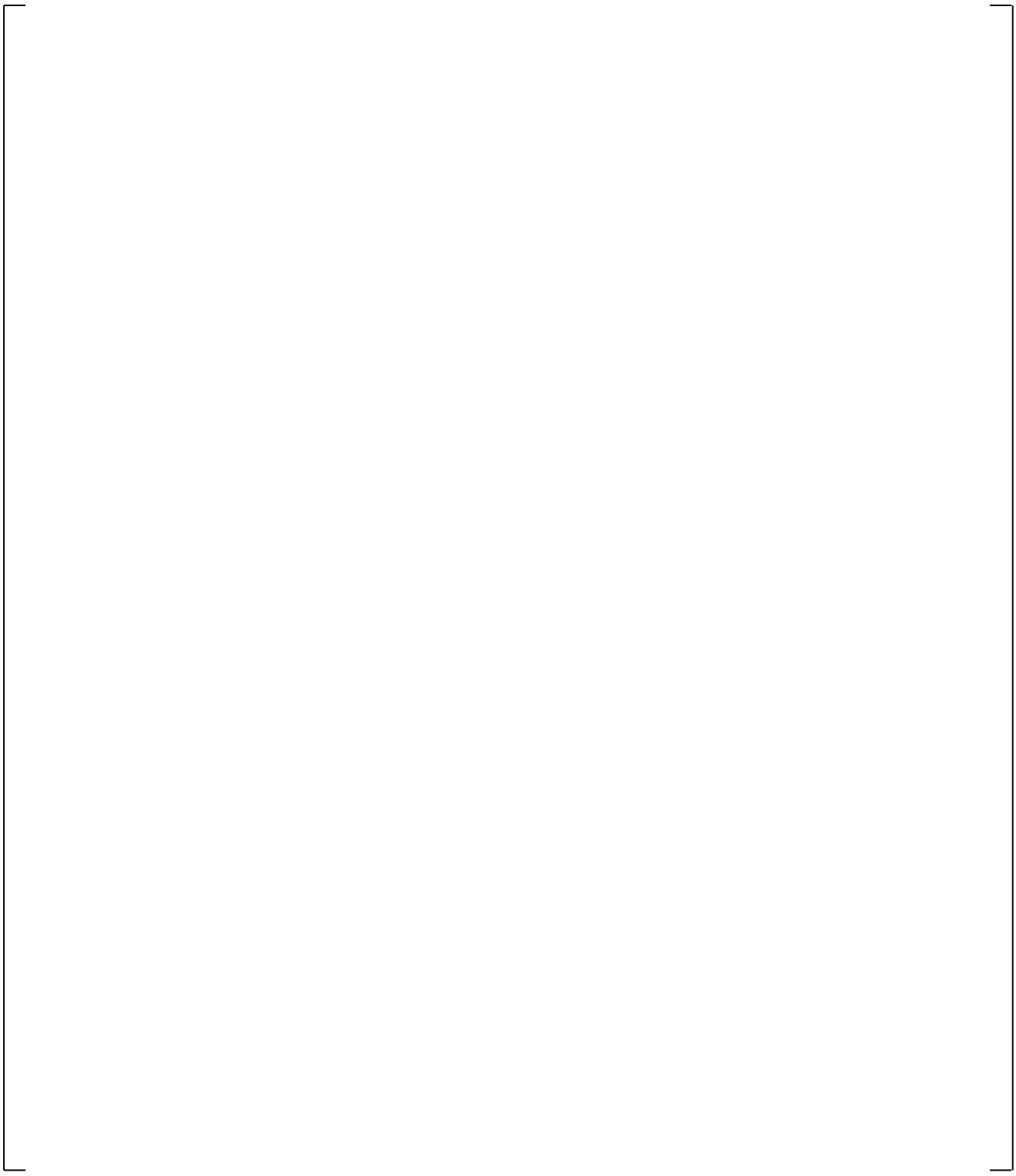

Figure 21.7-2 WCOBRA/TRAC-TF2 Nodalization of LSTF Break Unit

a,c,e

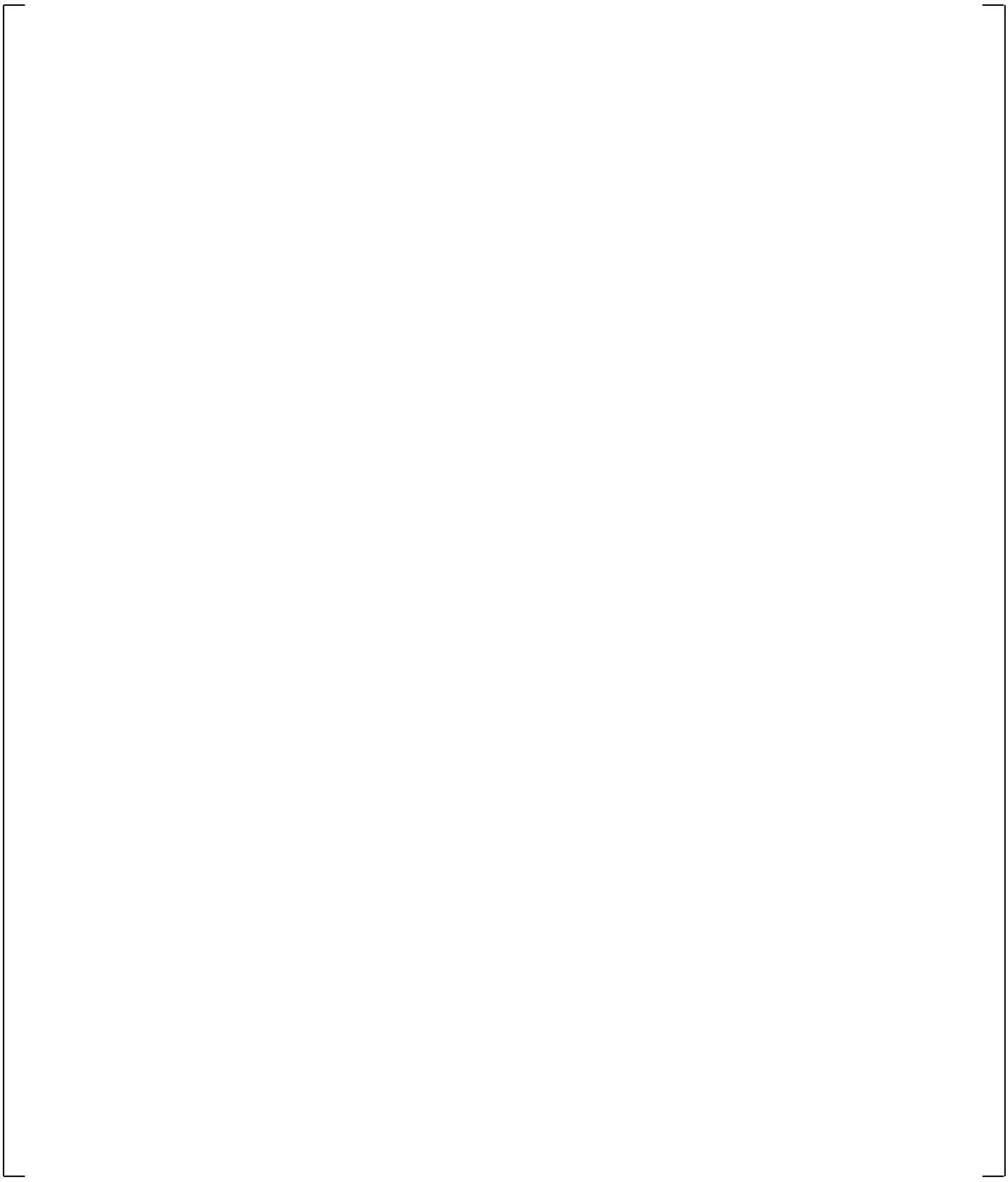

Figure 21.7-3 Comparison of Predicted and Measured Primary System Pressure (ROSA-IV 2.5-Percent Cold Leg Break)

a,c

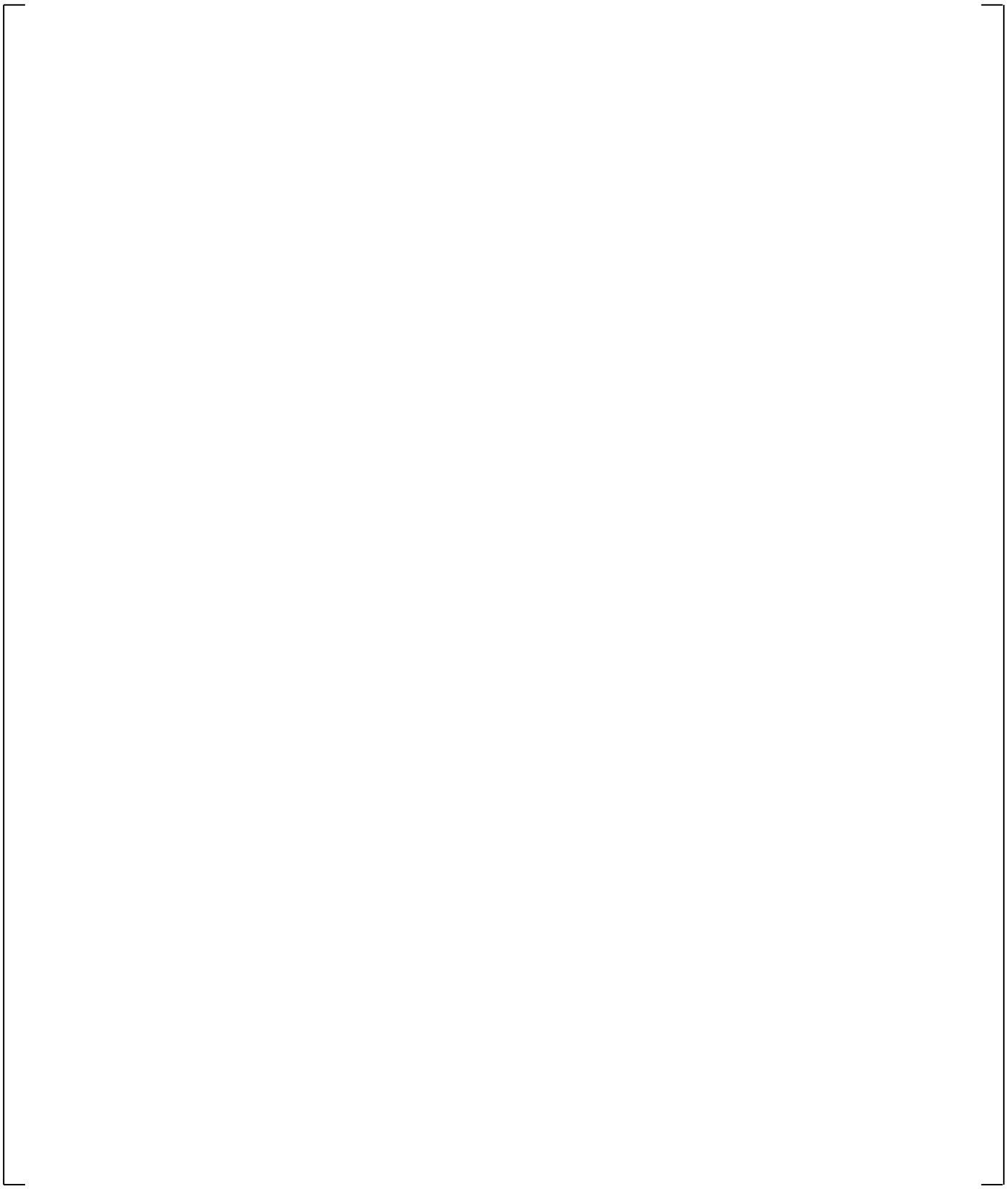

Figure 21.7-4 Comparison of Predicted and Measured Break Flow Rates (ROSA-IV 2.5-Percent Cold Leg Break)

a,c

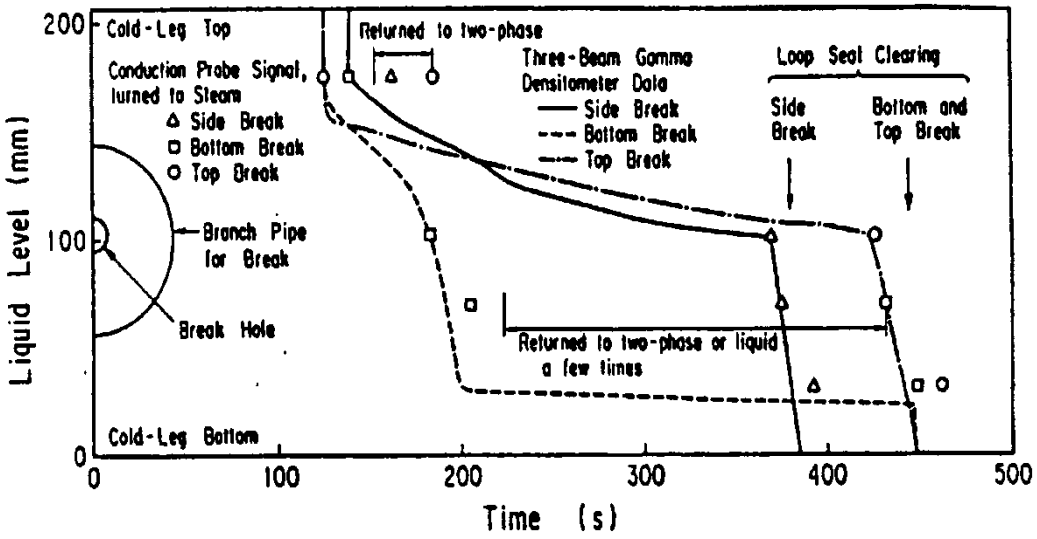

(b) Reported in (Koizumi et al., 1988)

Figure 21.7-5 Comparison of Predicted and Measured Mixture Levels in Broken Cold Leg (ROSA-IV 2.5-Percent Cold Leg Break Runs)

a,c

Figure 21.7-6 Comparison of Predicted and Measured Core Collapsed Liquid Levels (ROSA-IV 2.5-Percent Cold Leg Break Runs)

a,c,e

Figure 21.7-7 Cladding Temperature of B-20 Rod at Position 7 (8.67-ft Elevation) for Side, Bottom, and Top Break Experiments

a,c,e

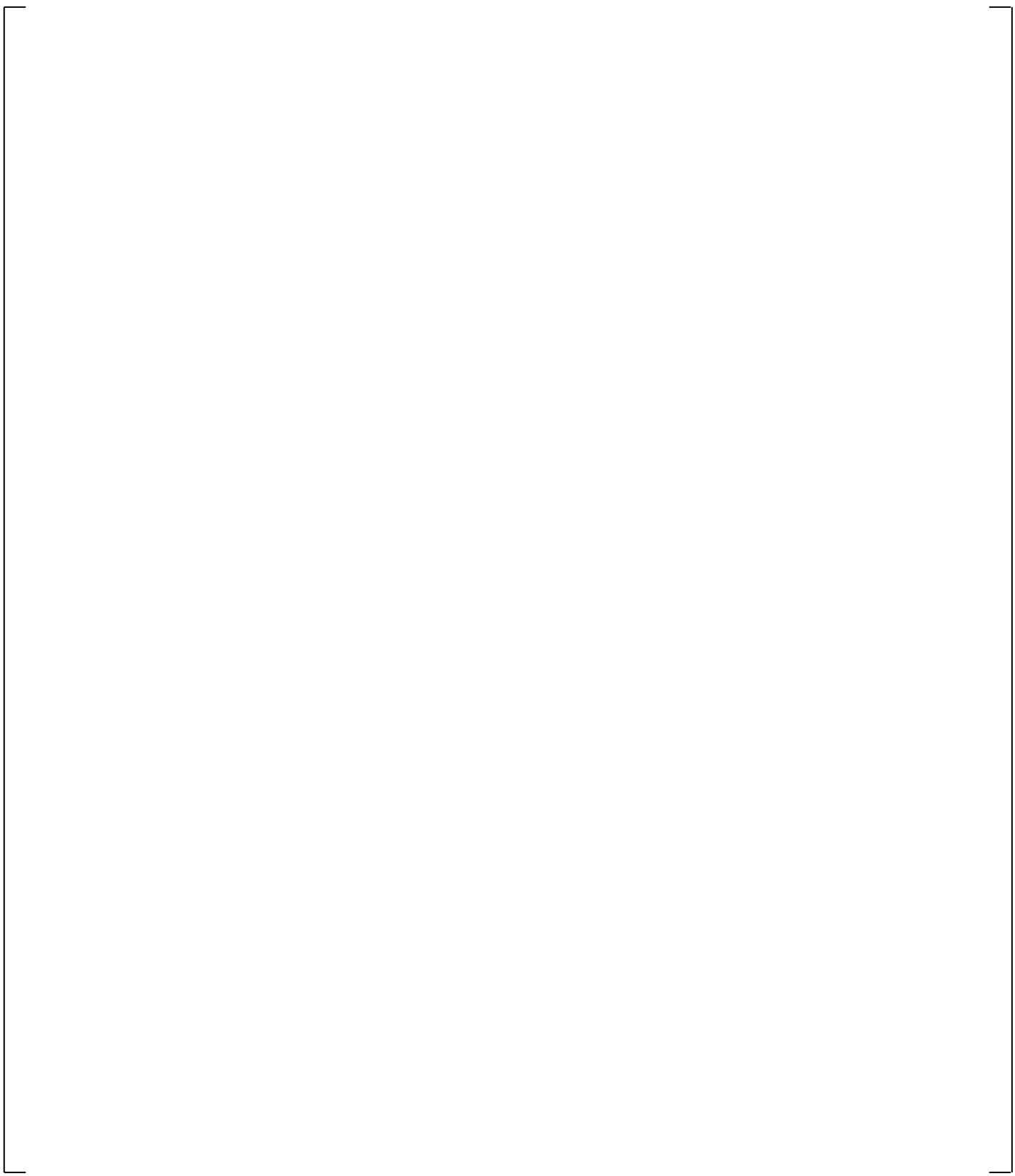

Figure 21.7-8 Predicted and Measured Differential Pressures in Steam Generator A Uphill Side

a,c,e

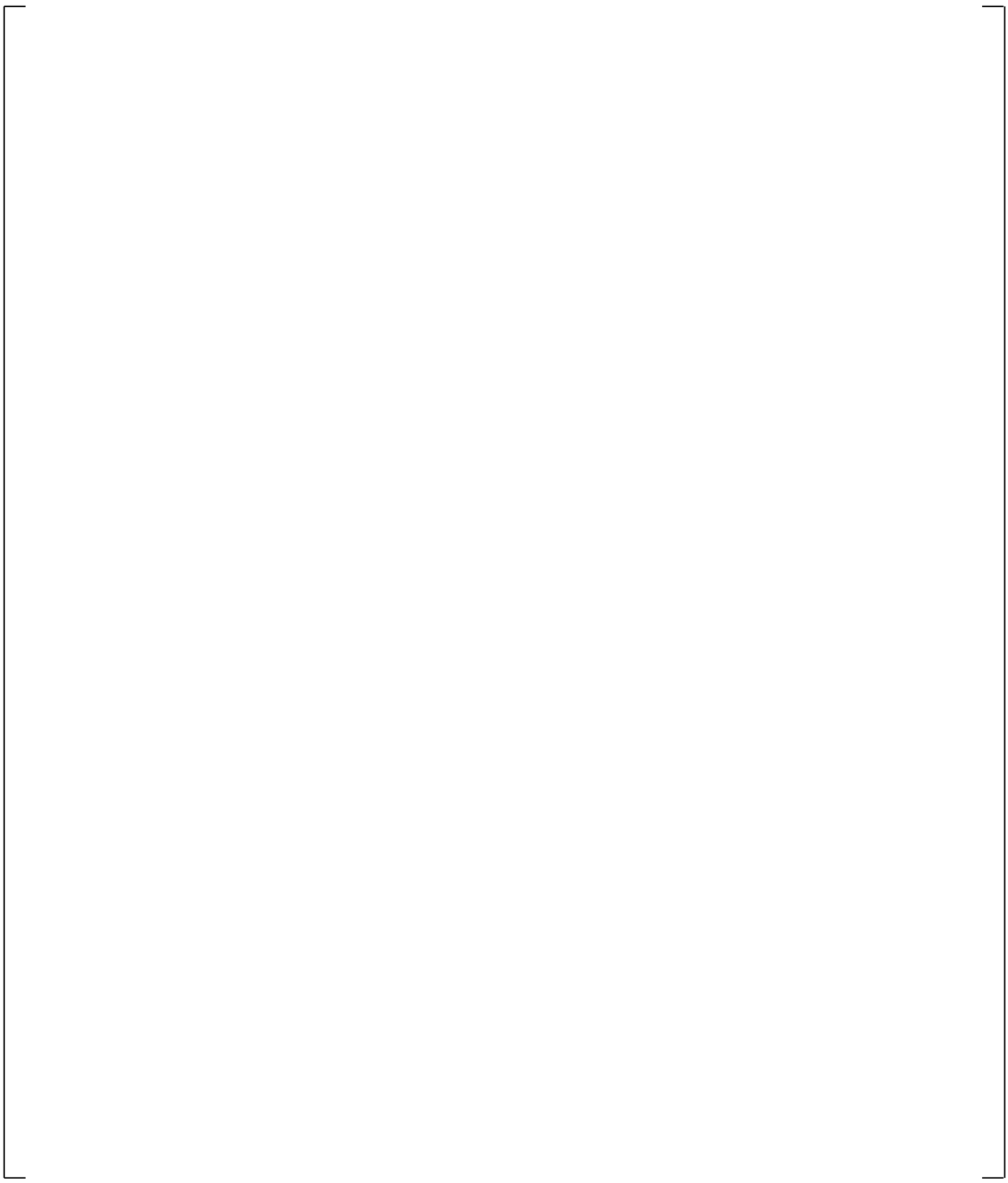

Figure 21.7-9 Predicted and Measured Differential Pressures in Steam Generator B Uphill Side

a,c

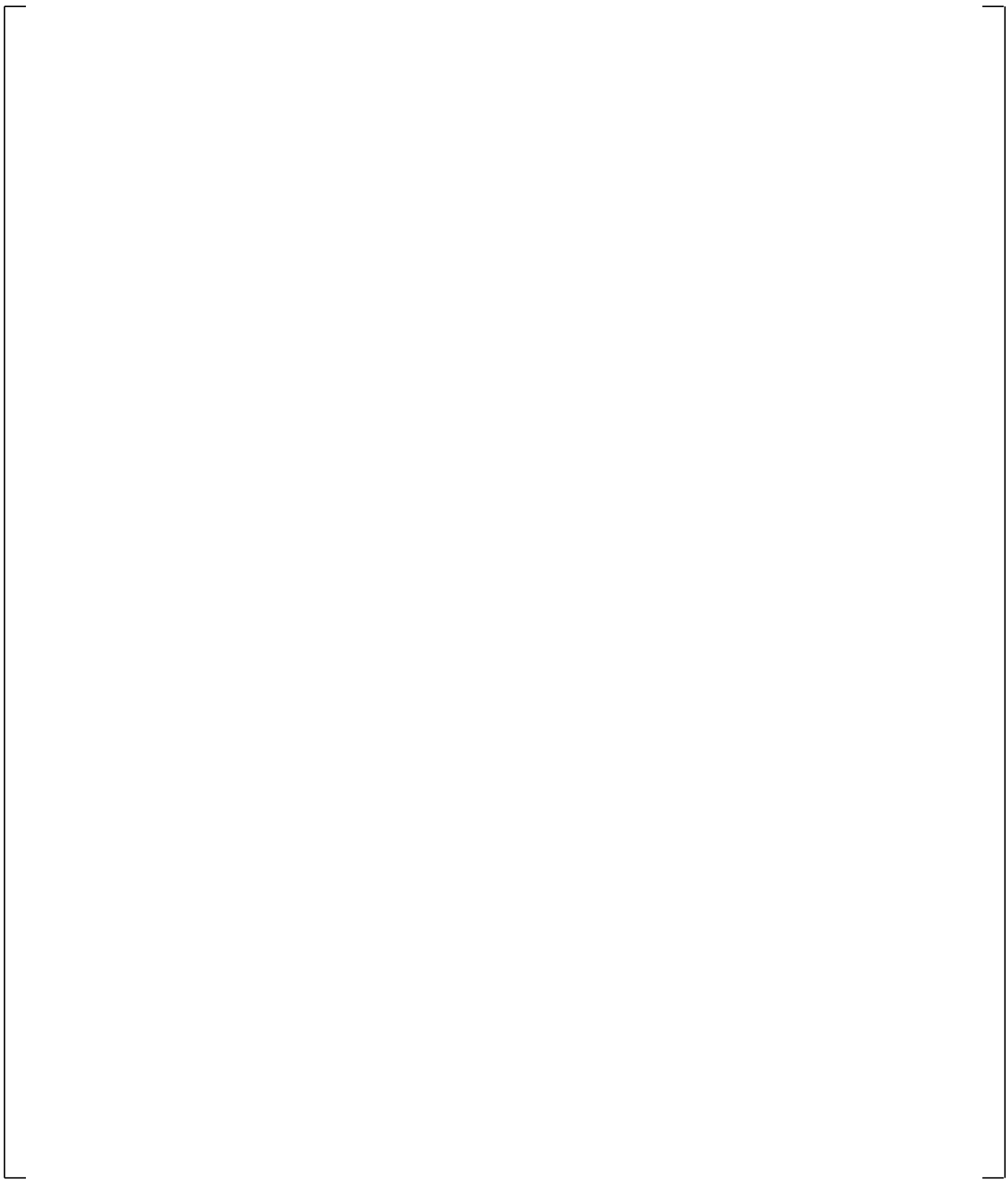

Figure 21.7-10 Calculated Accumulator Injection Flows

e

Figure 21.7-11 Break Unit Configuration used in the 0.5% Break Tests, SB-CL-12, -15, and -16

a,c,e

Figure 21.7-12 Comparison of Predicted and Measured Broken Cold Leg Liquid Levels, ROSA 0.5-Percent Cold Leg Break Runs

a,c,e

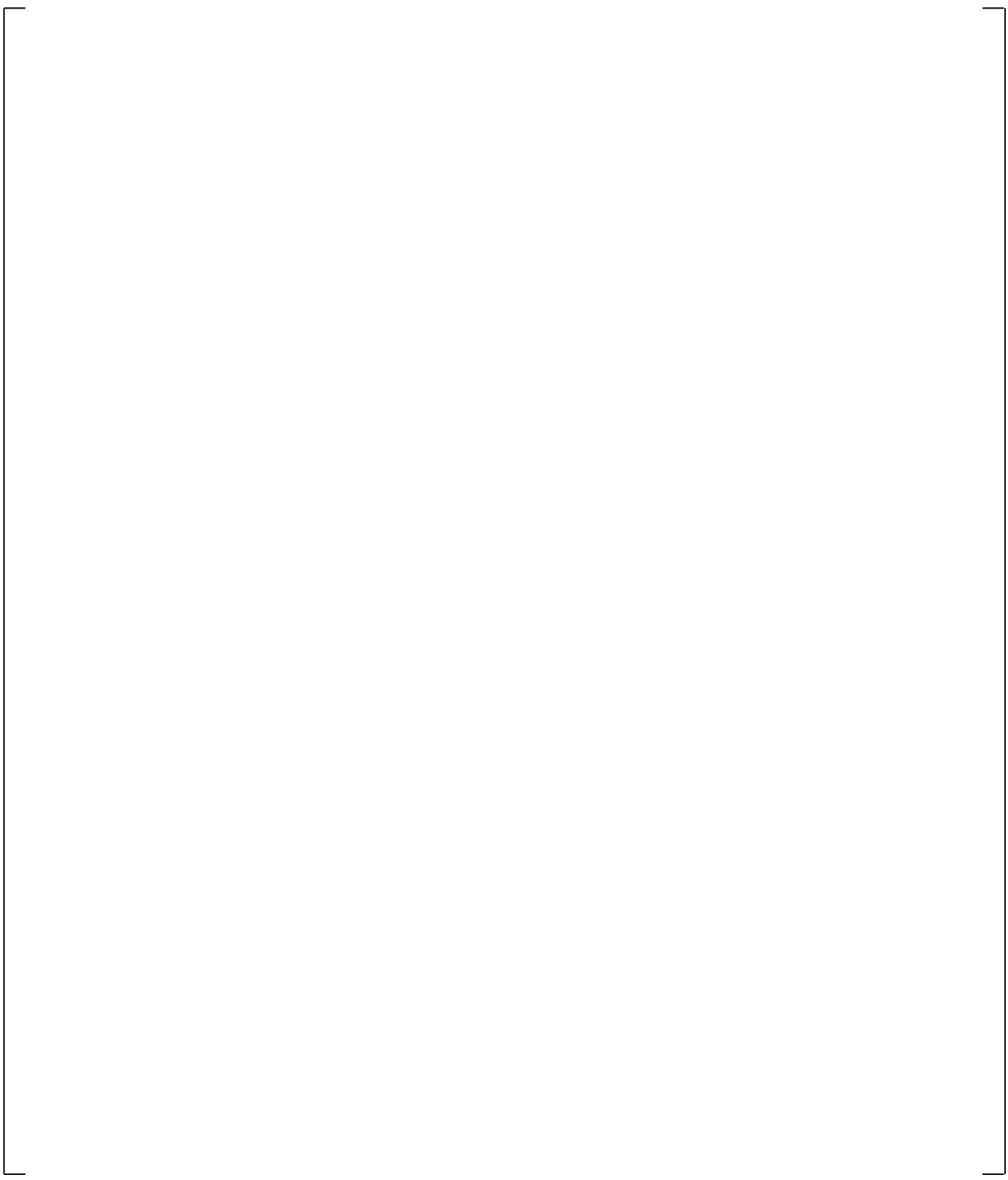

Figure 21.7-13 Comparison of Predicted and Measured Core Collapsed Liquid Levels, ROSA 0.5-Percent Cold Leg Break Runs

a,c,e

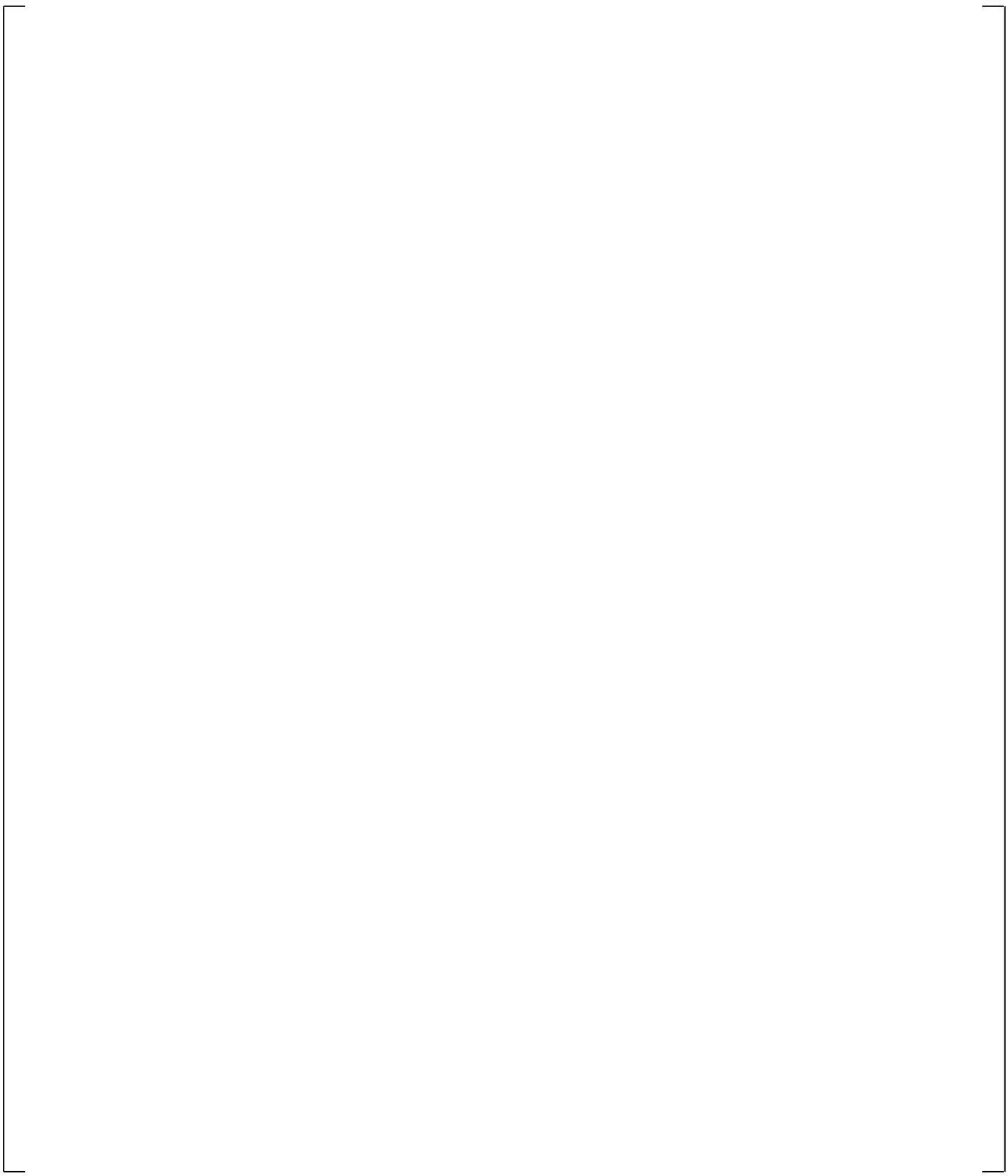

Figure 21.7-14 Comparison of Predicted and Measured Integrated Break Flows, ROSA 0.5-Percent Cold Leg Break Runs

21.8 BREAK SPECTRUM STUDY

The break spectrum study presented herein is compiled from simulations results of cold leg side break tests, documented in the previous sections. These are the 0.5% break (SB-CL-12), 2.5% break (SB-CL-01), 5% break (SB-CL-18), and 10% break test (SB-CL-14). The results of the break spectrum study are presented in Figures 21.8-1 through 21.8-5.

Figure 21.8-1 compares the calculated break flows. As seen from that figure, the initial values of the break flows are proportional to the break size. Larger break size results in a greater inventory loss at the beginning of the transient, and thus the initial depressurization rate is higher for the larger breaks, which is evident on the system pressure comparison provided on Figure 21.8-2. After the initial fast depressurization, a period of primary system pressure hold-up is observed slightly above 8 MPa, which is the secondary side pressure. The length of this holdup period depends on the break size with the smallest break having the longest hold-up period. During this period, the steam generators are a heat sink and remove heat from the primary side by natural circulation. The length of pressure hold-up (and natural circulation) period is decreasing with the increase of the break size, with the 10% size break exhibiting almost no pressure holdup.

Figures 21.8-3(a) and (b) and Figure 22.8-4 show the cross-over leg vapor flows and the core collapsed liquid levels respectively. Results in these figures show a correlation between the clearing of the loop seal (characterized by spike in loop vapor flow, Figure 21.8-3) and the depression of the core collapsed liquid level (Figure 21.8-4). As seen from those figures, the bigger the break size is, the sooner the loop seals are cleared. The smallest break size (0.5%) clears only one of the loop seals very late – about 1750 seconds into the transient.

And finally, Figures 21.8-5(a) and (b) show the calculated differential pressures in the uphill side of the steam generator U-tubes. The calculation results show that the smallest break size, which has the longest natural circulation period, retains liquid in the U-tubes much longer than the larger breaks.

a,c

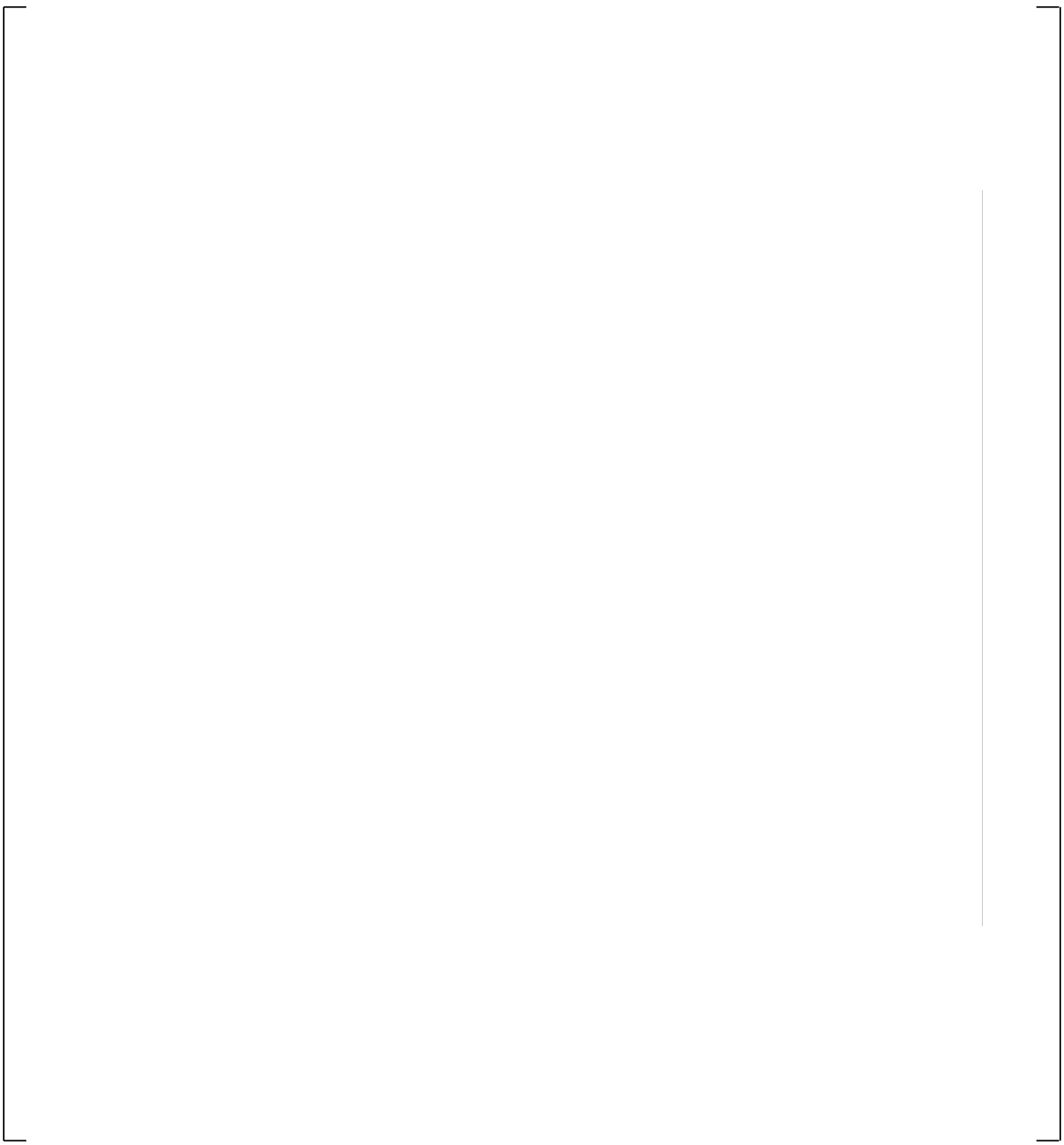

Figure 21.8-1 Break Flow Comparison

a,c

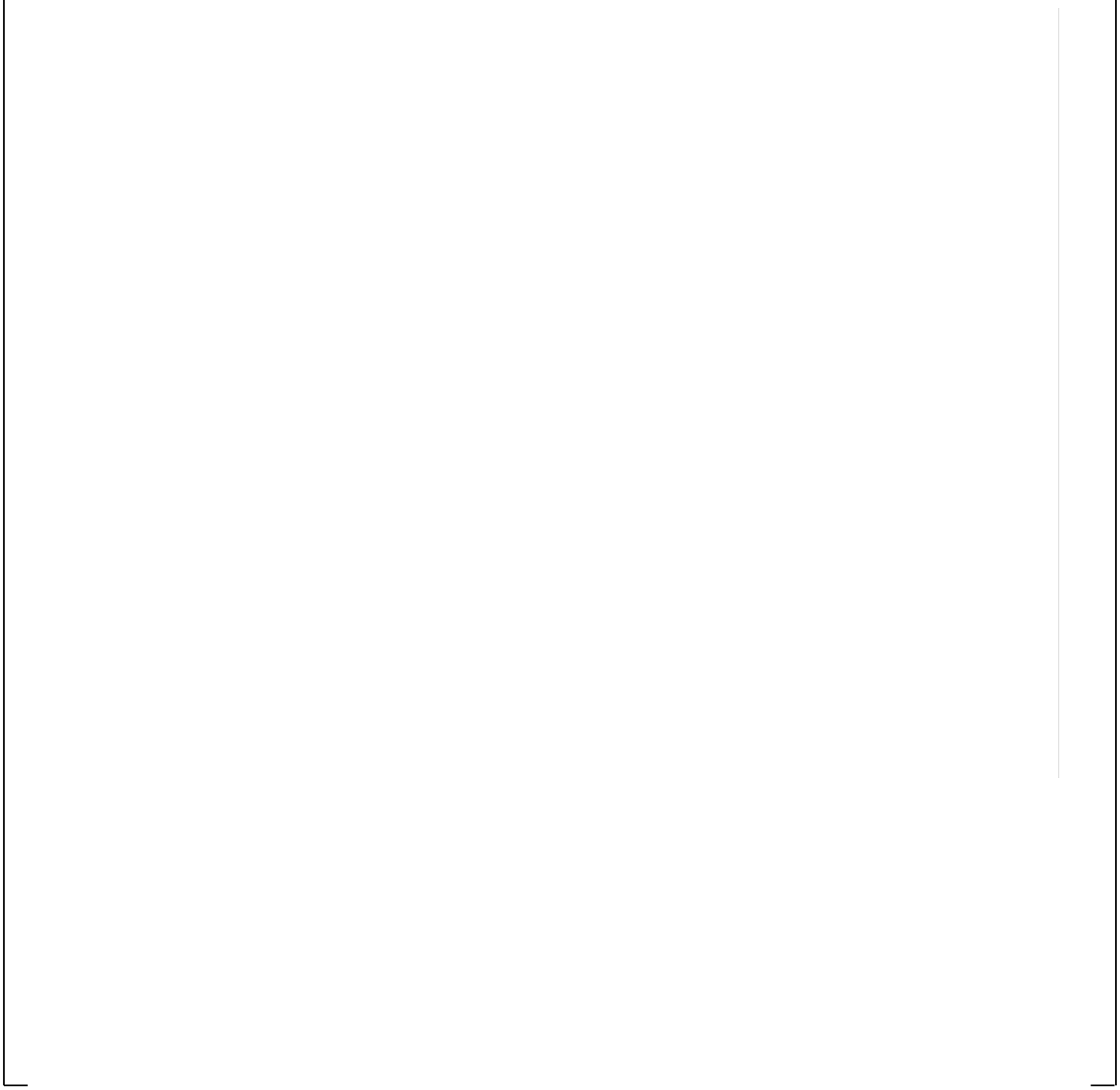

Figure 21.8-2 System Pressure Comparison

a,c

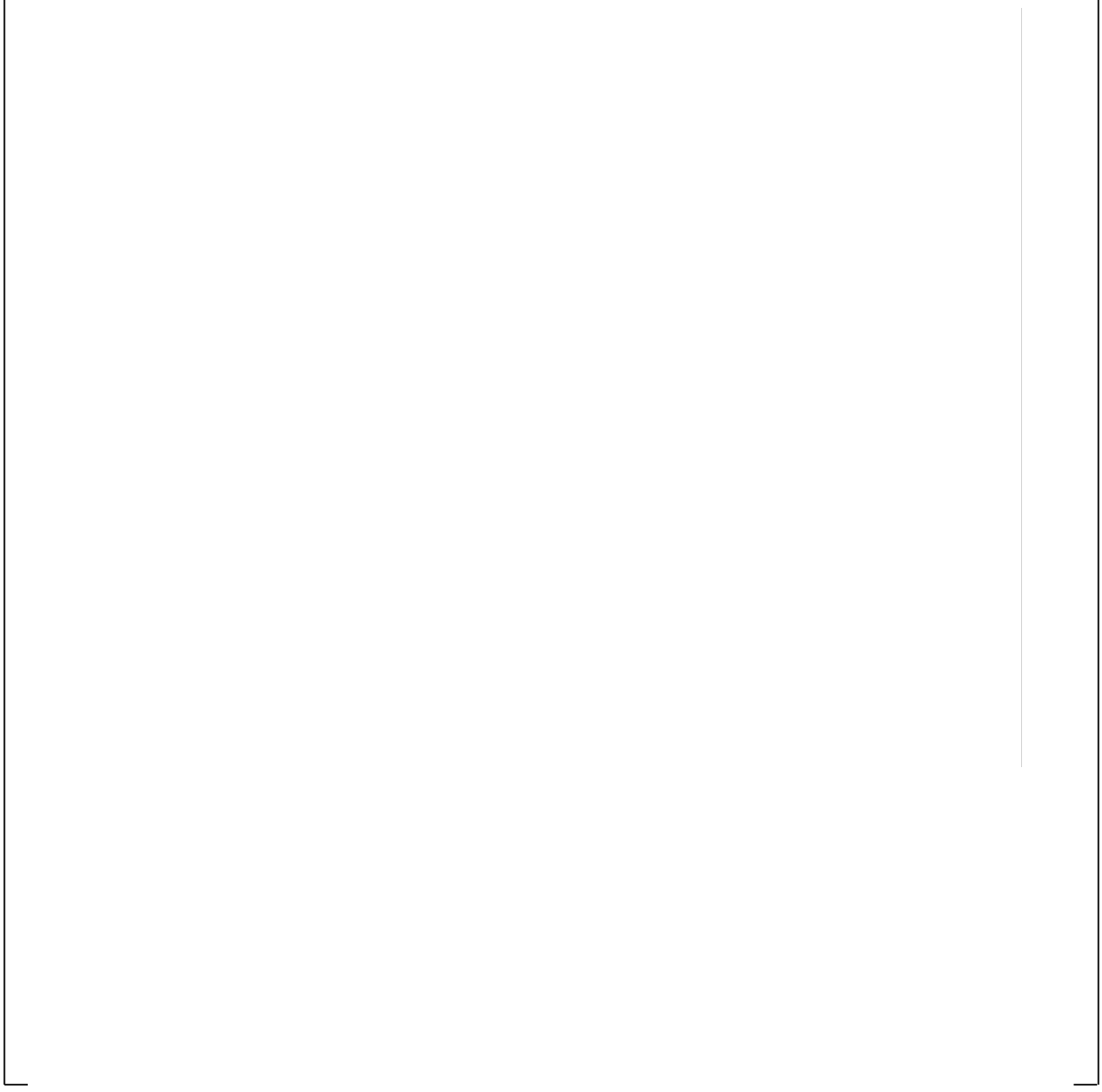

Figure 21.8-3(a) Cross-over Leg A Vapor Flows

a,c

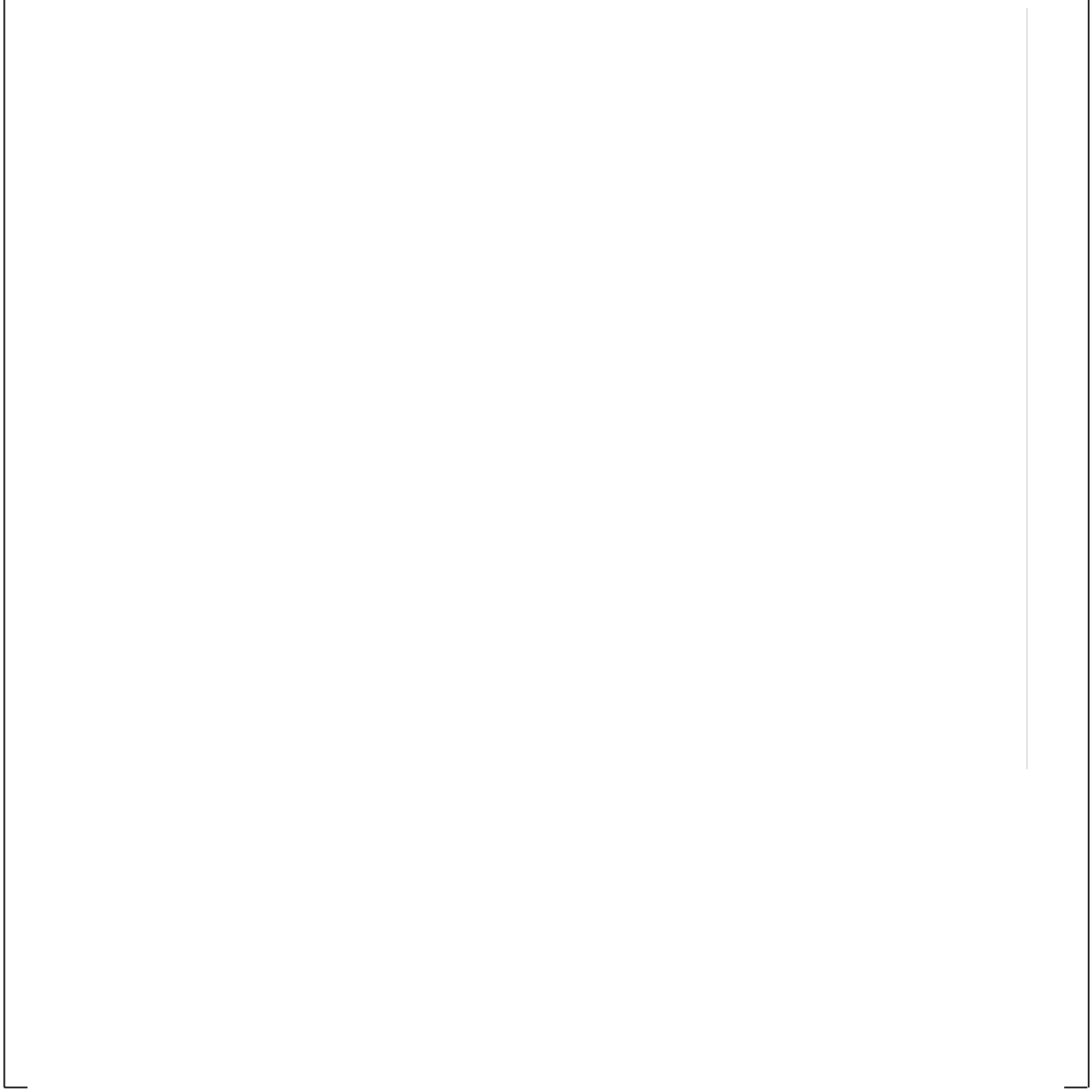

Figure 21.8-3(b) Cross-over Leg B Vapor Flows

a,c

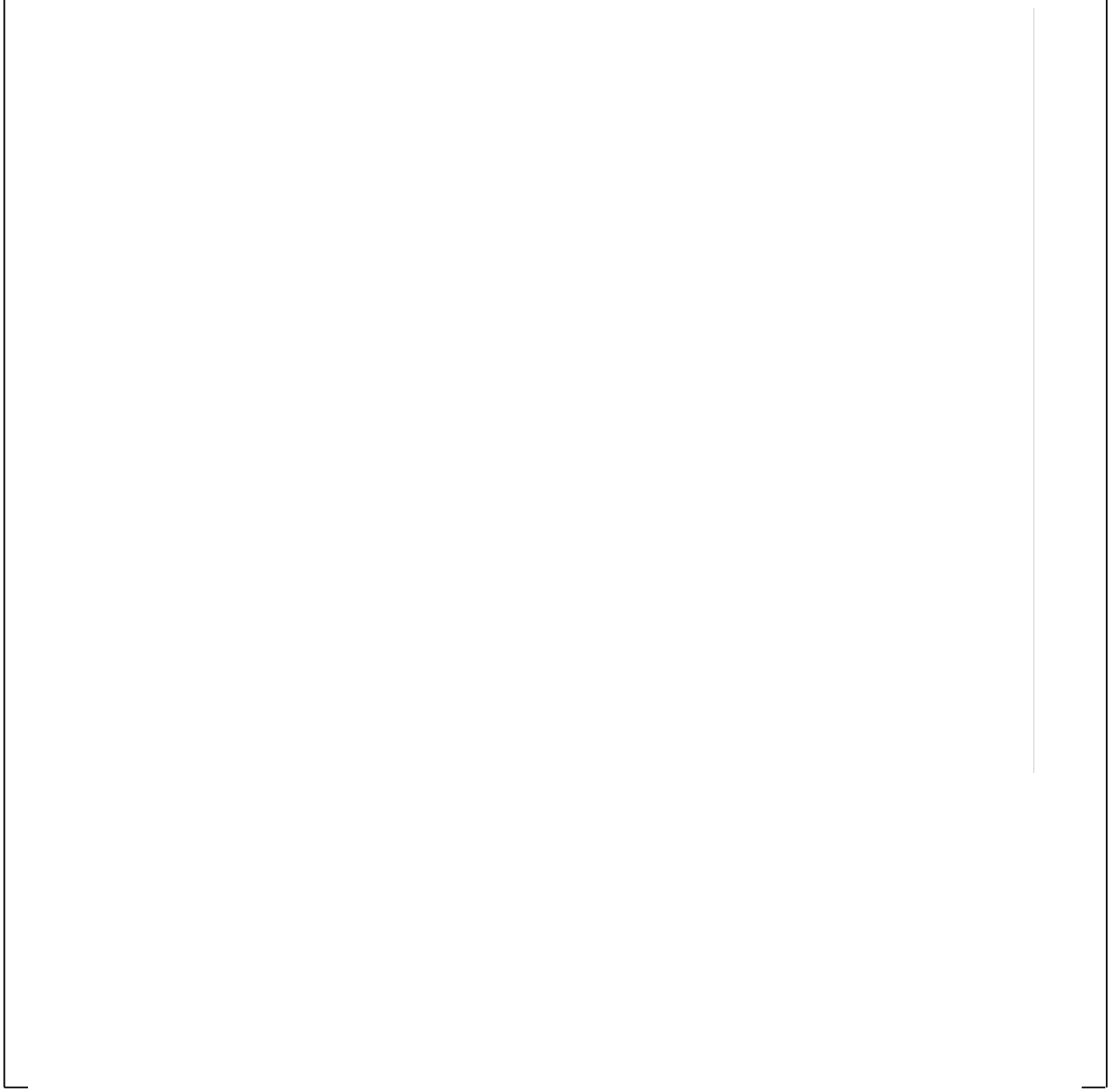

Figure 21.8-4 Core Collapsed Levels

a,c

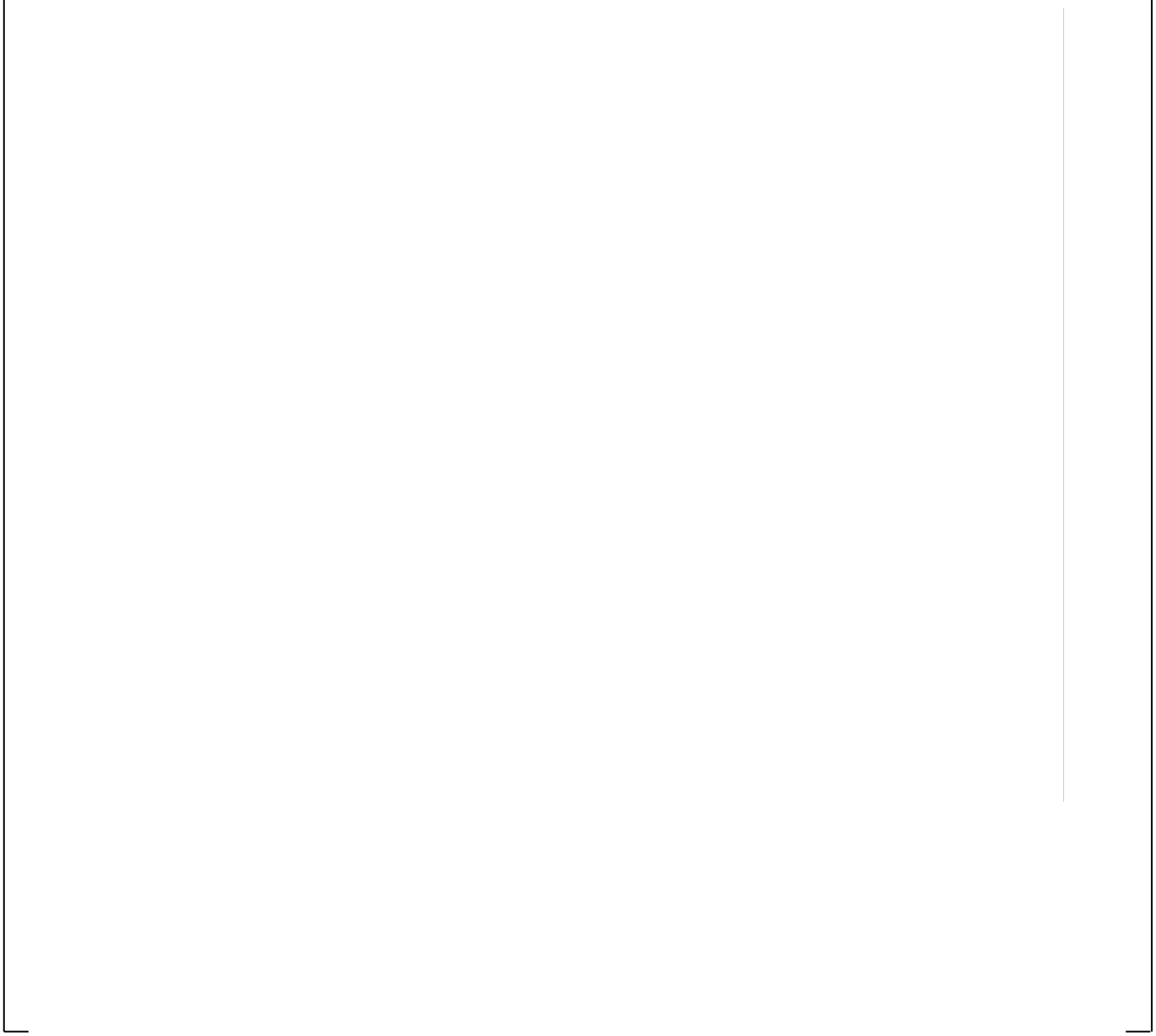

Figure 21.8-5(a) Steam Generator A U-tubes Uphill Differential Pressures

a,c

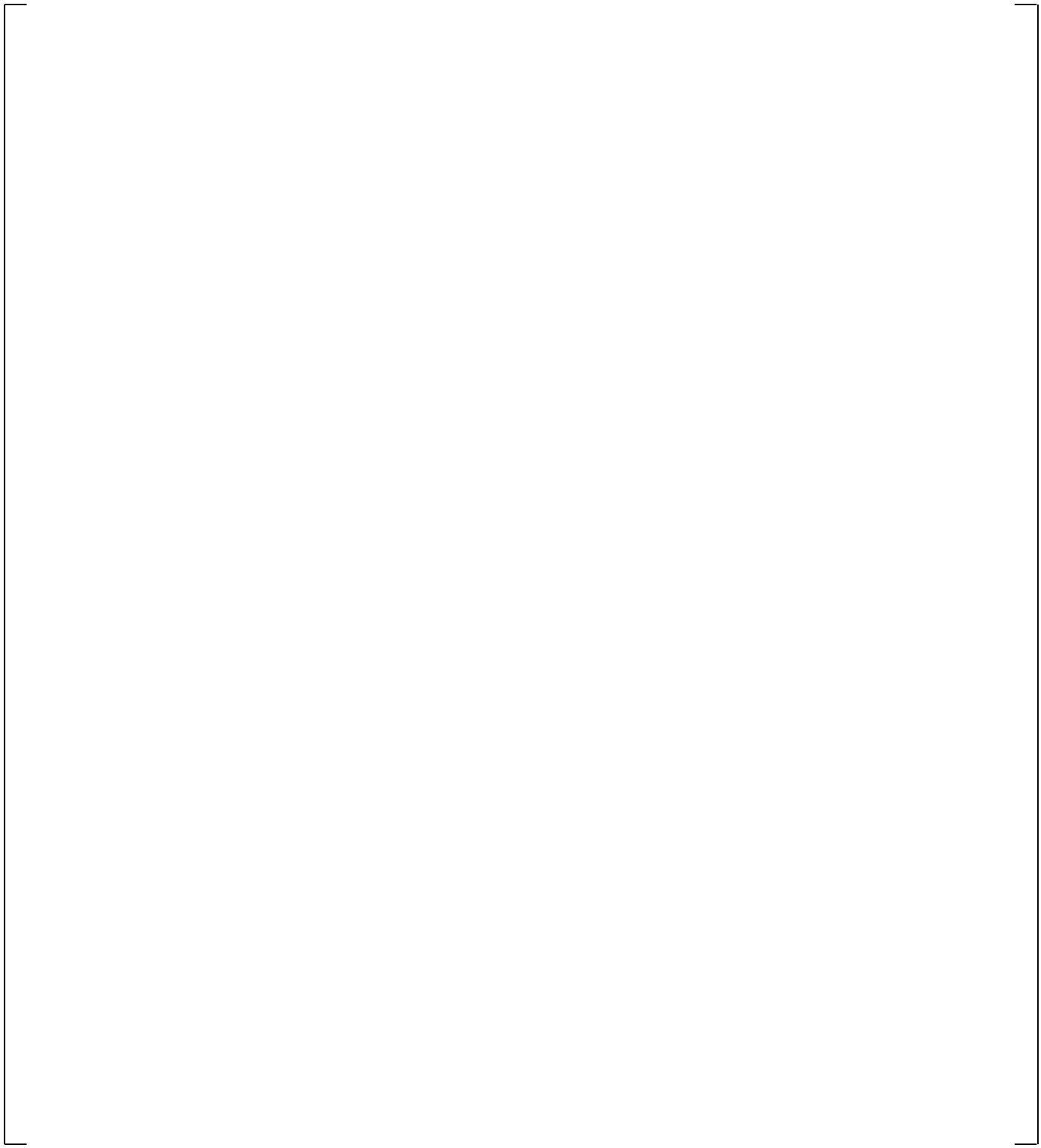

Figure 21.8-5(b) Steam Generator B U-tubes Uphill Differential Pressures

21.9 SIMULATION OF ST-NC-02, 2% POWER NATURAL CIRCULATION TEST

21.9.1 Natural Circulation Phenomena

The natural circulation is an important phenomenon and effective mechanism of heat removal from the primary to the secondary side of the steam generators during a small break LOCA.

One important phenomenon that might influence the severity of small break LOCA transients is liquid holdup in the steam generator U-tubes. This holdup phenomenon was first identified experimentally in the Semiscale small break LOCA experiments (Leonard, 1982a). It has since been duplicated in other facilities such as ROSA (Osakabe et al., 1987) and has been discussed extensively in the open literature (Leonard, 1982b) and (Loomis and Streit, 1985).

The liquid present in the steam generator tubes as a function of total system inventory is an important phenomenon in small break LOCA performance. During the initial phase of natural circulation, the system inventory is sufficient to maintain enough (two-phase bubbly) fluid present in both the uphill and downhill sides the steam generator U-tubes. At this stage, the interfacial drag is big enough to prevent draining of the SG tubes by gravity, and there is a continuous single-phase to bubbly flow established in the entire region of the steam generator tubes. As the primary system inventory is further depleted, voids are first developed at the top of the U-tubes, which then collapse and give way to a cyclic "fill-and-dump" phenomenon. The hydrostatic balance between the uphill and downhill side of the steam generator tubes becomes unstable and the fluid drains from the steam generator tubes – first the downhill side and later the uphill side.

In the later stages of natural circulation, when the inventory is depleted enough to expose the steam generator tubes to steam coming from the core, liquid that is caused by the condensation of that steam – a phenomenon called "reflux condensation," may be held up in the tubes. This holdup may not be able to drain by gravity back through the hot leg into the upper plenum if it is impeded by high upward steam flow rates; the pressure drop induced by this holdup affects the hydrostatic head balances throughout the RCS.

21.9.2 Description of the ST-NC-02 Natural Circulation Test

JAERI-M-88-215 (Chauliac et al., 1988) documents results of simulations of the ST-NC-02 test with RELAP5/MOD2, and contains a fair amount of detail related to the initialization and execution of the ST-NC-02 natural circulation test and RELAP5/MOD2 simulation results.

Unfortunately, JAERI did not issue the anticipated official Test Report for the ST-NC-02 natural circulation test, listed as Reference [1] in (Chauliac et al., 1988).

(Tasaka et al., 1988), (Kukita et al., 1988) and (Stumpf et al., 1987) present additional analyses of the ST-NC-02 test and provide valuable information that cannot be easily found in (or inferred from) (Chauliac et al., 1988).

As described in Section 2.2 of (Chauliac et al., 1988), the first stage of the experiment was performed at the LSTF nominal conditions: full power (10 MW), pumps on, temperature increase across the core as in the actual plant.

The second stage was designed to study the natural circulation at 100% primary side inventory. The core power was reduced down to 1.42 MW (this is 2% power of the reference PWR) and was kept at that level for the rest of the entire experiment. The pumps were turned off and the secondary side pressure was reduced to 6.6 MPa and kept constant until the end of the experiment. Figure 4 of (Kukita et al., 1988), presented here as Figure 21.9-1, illustrates the measured evolution of the primary side pressure and loop flow and sheds some light on the timing of the different stages of the experiment. As seen from that figure, at the end of the second stage of the experiment, when the pressurizer pressure was established at 12.2 MPa, the pressurizer surge line valve was closed and the pressurizer isolated prior to the drain of the primary side inventory.

During the rest of the experiment, the primary side water inventory was reduced step-wise by bleeding through the drain line at the bottom of the vessel. The drain valve at the bottom was closed when certain inventory reduction was reached and kept closed for some time until intermediate steady state primary pressure and loop flow was achieved at that inventory level.

As described in (Chauliac et al., 1988), constant secondary side water level was maintained throughout the experiment. Unfortunately, there is no ST-NC-02 test report that documents in detail the test execution, and Section 2.2 of (Chauliac et al., 1988) does not explain how the secondary side pressure reduction was achieved and maintained at 6.6 MPa. Most likely, the feed water flow rate was adjusted to keep the constant steam generator level and balance the primary-to-secondary side heat transfer at the reduced secondary side pressure. (Chauliac et al., 1988) (pg. 6) also states that feed water temperature fluctuation of 30K has been observed throughout the drain-down phase of the test as well. Since the test simulated the natural circulation at different primary side inventory levels, safety injection was not modeled by isolating the accumulators.

As seen on Figure 21.9-1, the duration of the experiment was almost 10 hours (35000 sec). Due to computational (CPU) time constraints, it is not reasonable to try and replicate the test in real time length. Moreover, as seen on that figure, the quasi-steady states at different stages could be achieved for time periods shorter than the ones implemented through the experiment, especially those of Stage 1 and 2. Therefore, shorter time periods are used to achieve the desired quasi-steady state conditions at each stage.

21.9.3 Description of the Test Simulation and Boundary and Initial Conditions

The system initial conditions achieved for the ST-NC-02 simulation are presented in Table 21.9-1. The test simulation followed the procedure implemented during the real test, except that shorter time periods were simulated to achieve a quasi-steady state during each drain period. The length of the individual drain periods and the drain flows used in the simulation were estimated from the information in Figure 21.9-1. The accumulators were isolated by closing the accumulator isolation valves. Prior to the beginning of the draining, the pressurizer was isolated by closing the PRZ isolation valve.

The following steps were implemented for the simulation of the natural circulation test ST-NC-02:
[

]a,c

21.9.4 Results and Conclusions

The results of the simulation of the ST-NC-02 natural circulation test (2% core power) are presented in Figure 21.9-2 through Figure 21.9-16.

Figure 21.9-2 compares the measured primary system loop circulation flow against that calculated by the code. During the single-phase natural circulation (primary side inventory from 100% to 90%) the circulation flow is predicted fairly well. [

]a,c

[

]^{a,c}

The comparison of the downcomer differential pressures, Figure 21.9-7, shows a good prediction of the amount of liquid in the downcomer.

[

]^{a,c}

Figures 21.9-11 and 21.9-12 show the calculated void fraction distributions in the uphill and downhill side of the steam generator A U-tubes. The same information is shown for steam generator B in Figures 21.9-13 and 21.9-14. The calculation shows that the downhill sides of the steam generators tends to drain first, while the uphill side retains liquid for a longer period of time; this is consistent with the steam generator draining sequence observed at the rest of the ROSA-IV tests considered here.

Figures 21.9-15 and 21.9-16 show the calculated vapor flows at the inlet and the top of the steam generator U-tube bundles for steam generator A and B respectively. The calculated vapor flow split indicates that the steam condensation would occur predominantly at the uphill section of the U-tubes.

The following major conclusions are made with respect to the ability of the code to calculate primary-to-secondary side heat transfer.

- For purely reflux condensation conditions in the steam generators, the code calculates overall effective heat transfer coefficient (normalized for the outside SG surface area) in the range of [

]^{a,c}

- The power is removed effectively to the steam generator secondary side even though one of the steam generators remains plugged for a prolonged time.

Based on the results documented in this section, it is concluded that when used with WCOBRA/TRAC-TF2, the ROSA-IV LSTF model developed for the purpose of the FSLOCA methodology produces simulation results that are in general consistent with those observed at the ST-NC-02 experiment.

Table 21.9-1 Initialization of the SB-CL-02 Natural Circulation Test Simulation

Parameter	End of Stage 1		End of Stage 2 (Prior to Drain)	
	Target	a.c	Target	a.c
Core Power, MW	10.0		1.42	
Pressurizer Pressure, MPa	15.47 ±0.06		12.2	
Hot Leg Temperature, K	598 ±5		N/A	
Cold Leg Temperature, K	565 ±5		N/A	
Pump Speed, rad/sec (rpm)	85.8/86.1 (819/822)		0.00/0.00	
Total Loop Flow Rate, kg/sec	51.0 (±0.6)		11.4	
DC-to-UH Bypass Flow Rate, % total loop flow (kg/sec)	0.9% (0.46)		N/A	
Core Inlet Flow Rate, kg/sec	50.54		N/A	
SG Secondary Pressure, MPa	7.38/7.42 (±0.03)		6.5	
SG Steam Flow Rate, kg/sec	2.6 (±0.1)		N/A	

a,c

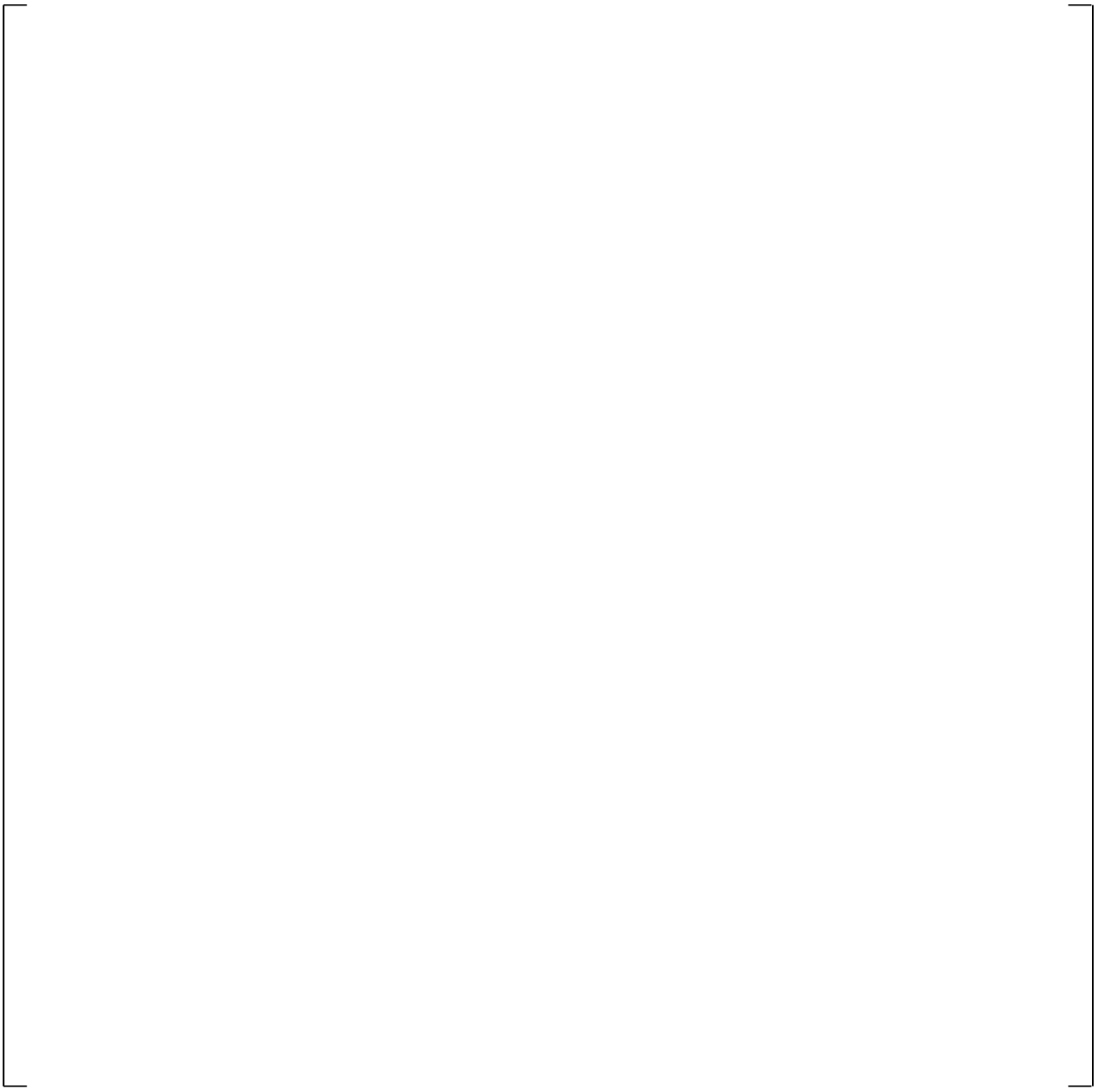

Figure 21.9-1 ST-NC-02 Primary Pressure and Loop Flow Rate (Kukita et al., 1988)

a,c

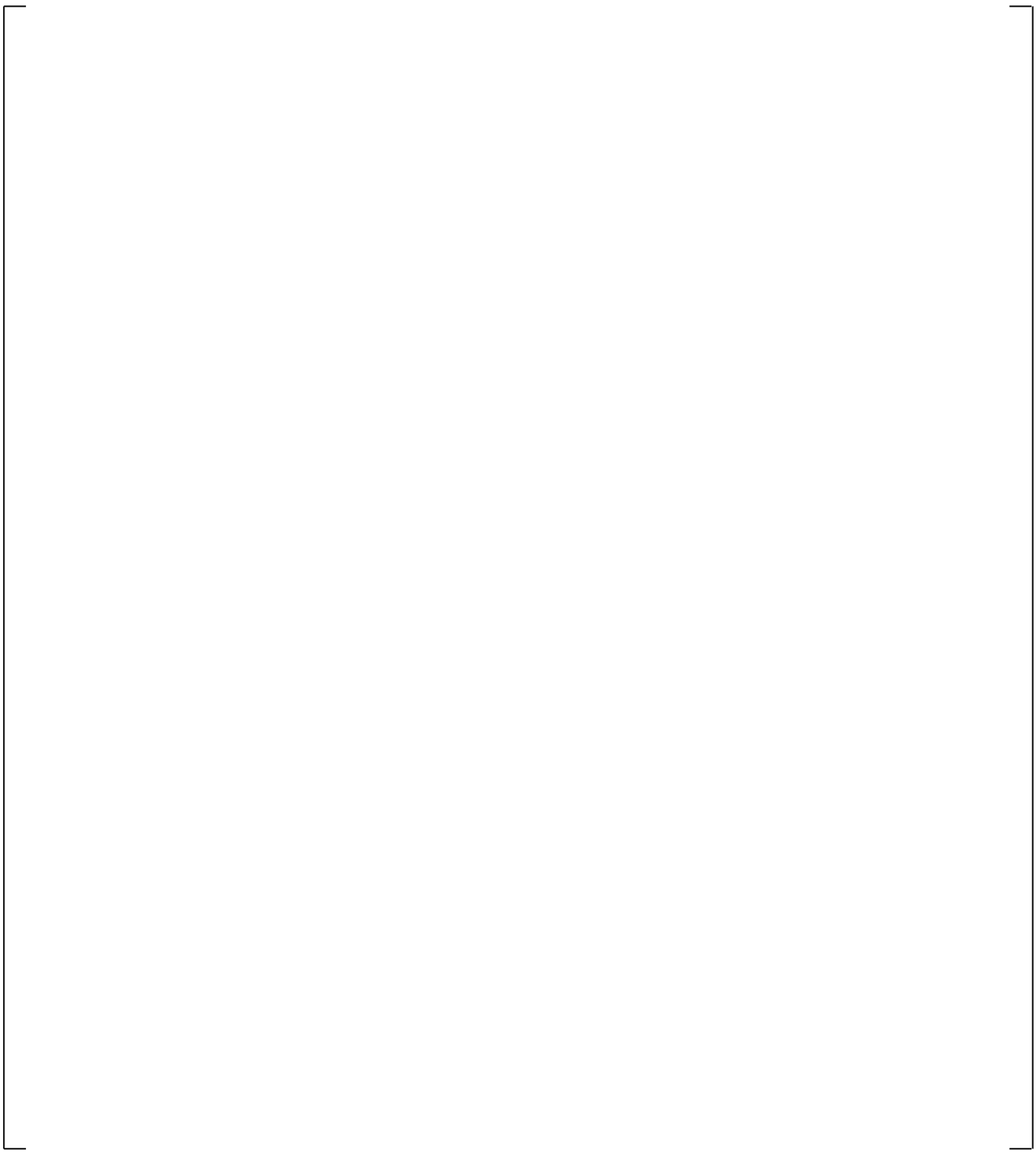

Figure 21.9-2 Primary Side Circulation Flow as a Function of Primary Side Inventory

a,c

Figure 21.9-3 ST-NC-02 Primary and Secondary System Pressures

a,c

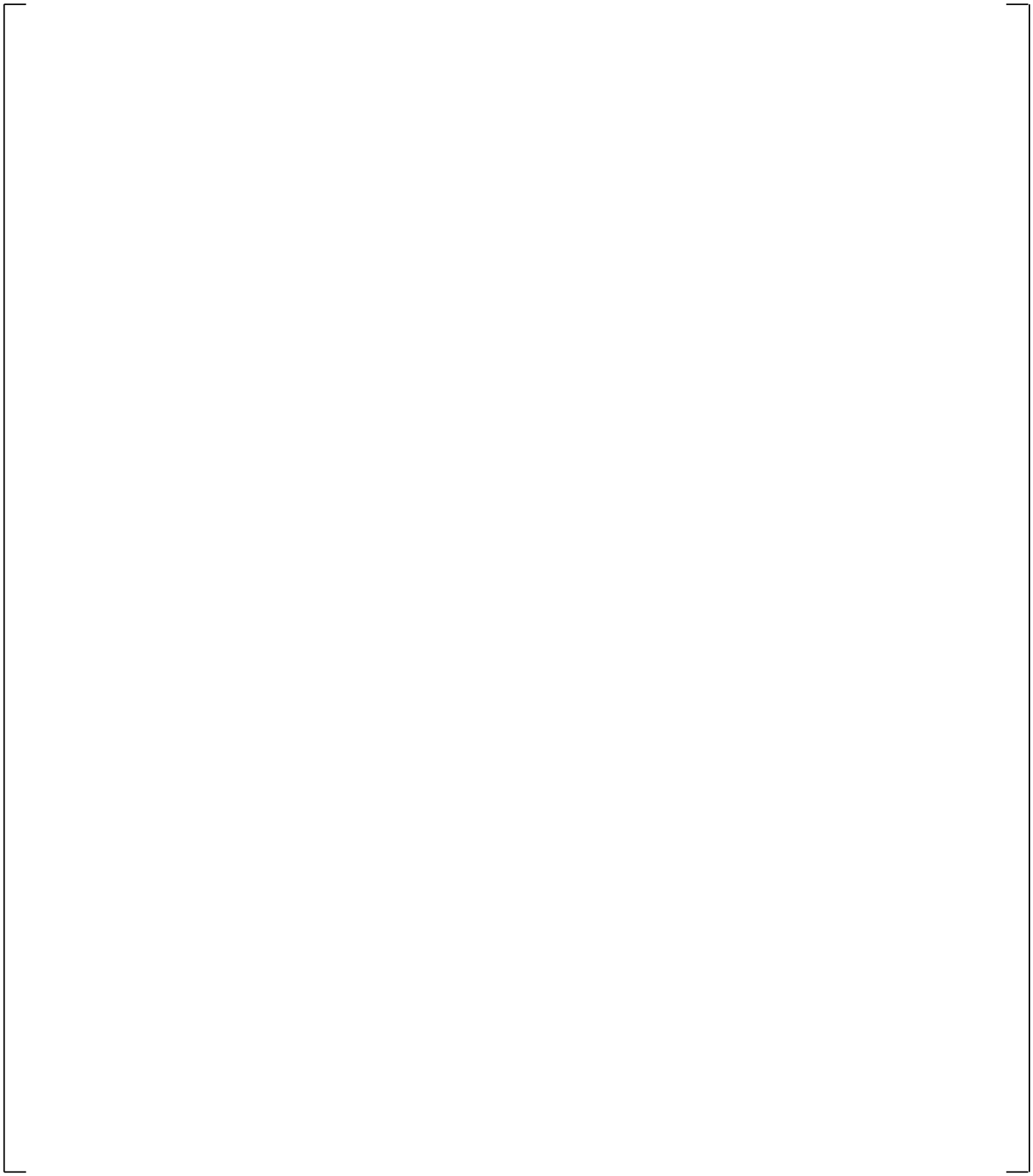

Figure 21.9-4 Steam Generator U-tube Uphill Side Differential Pressures

a,c

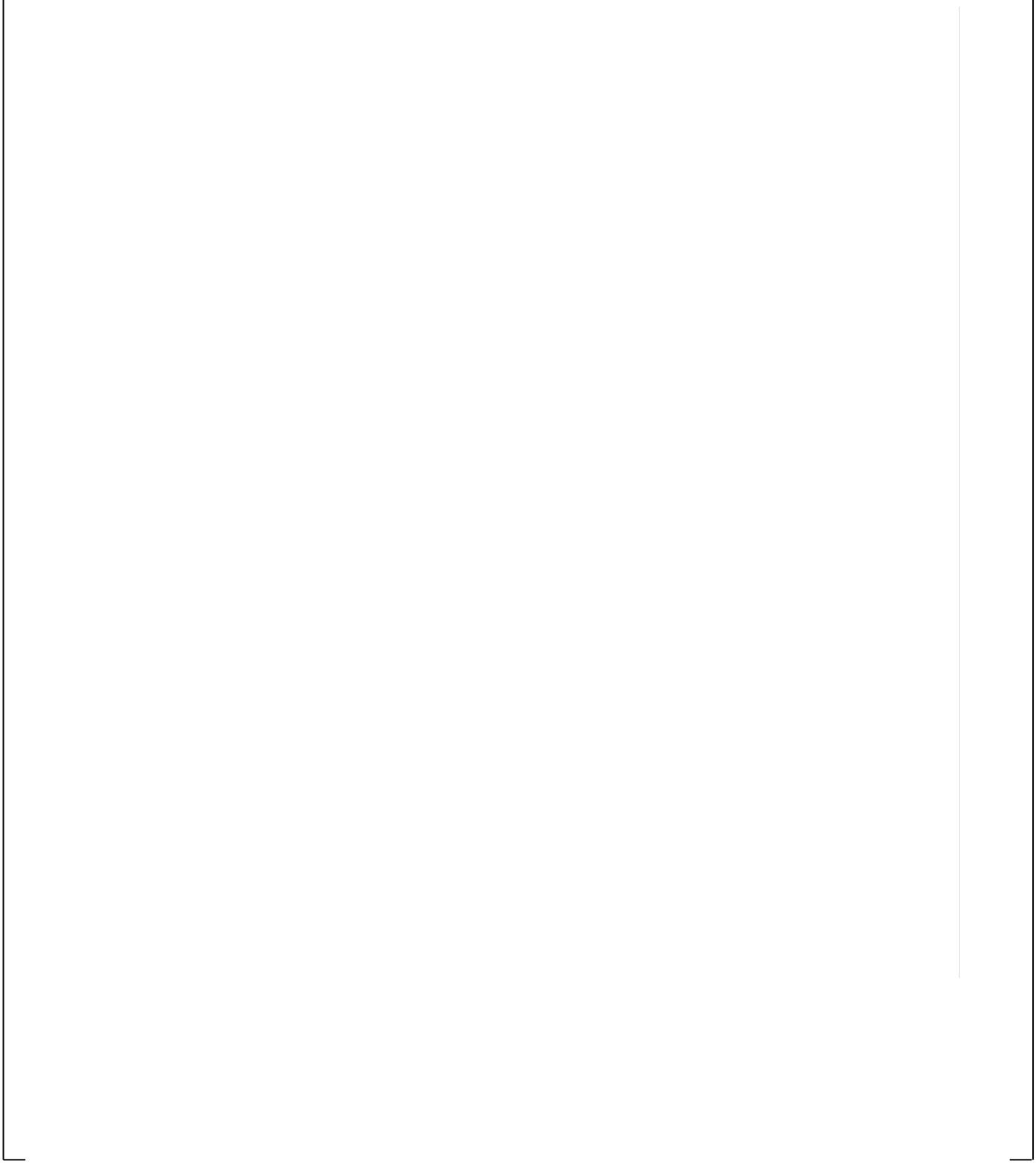

Figure 21.9-5 Core Differential Pressure

a,c

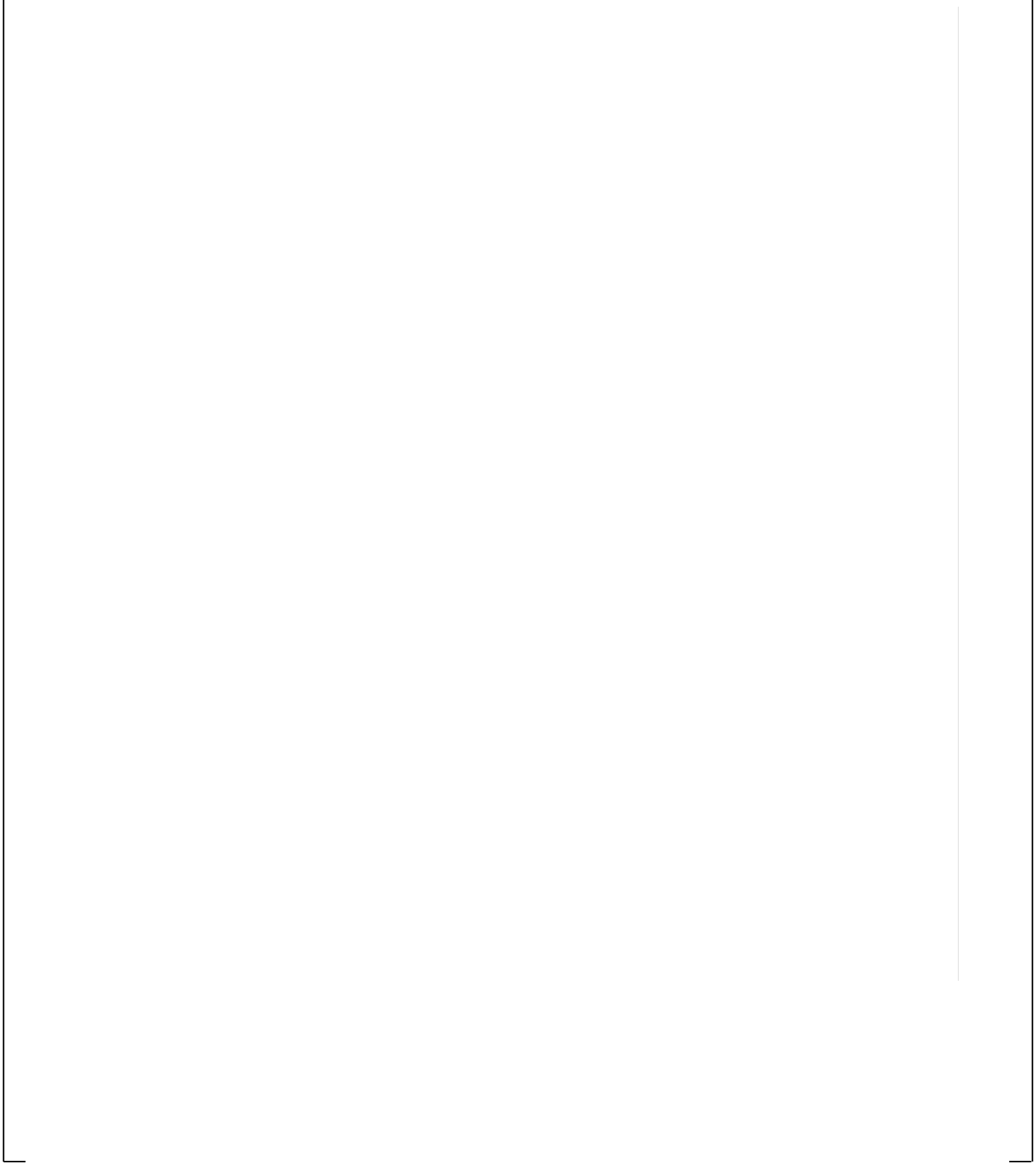

Figure 21.9-6 Upper Plenum Differential Pressure

a,c

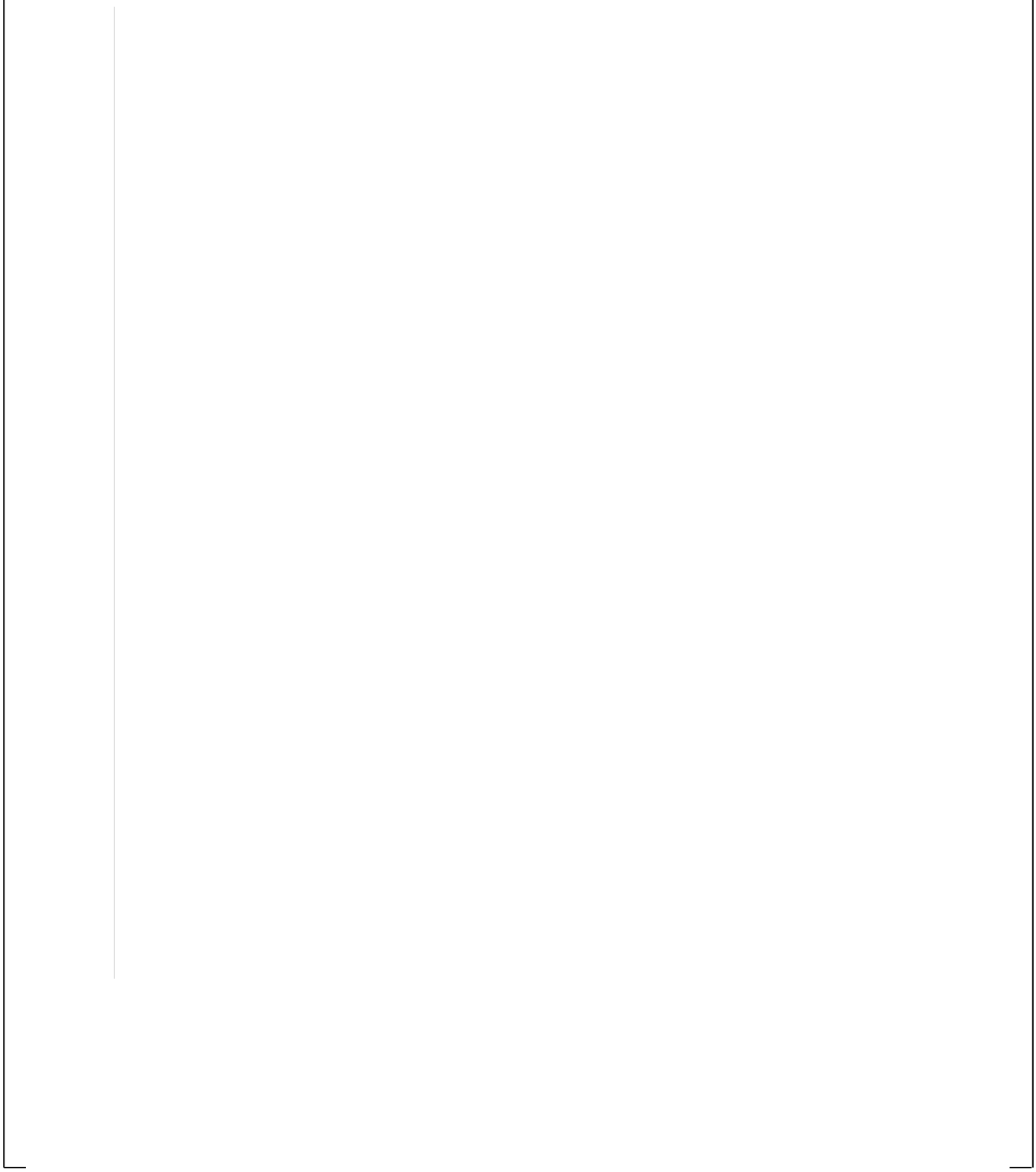

Figure 21.9-7 Downcomer Differential Pressure

a,c

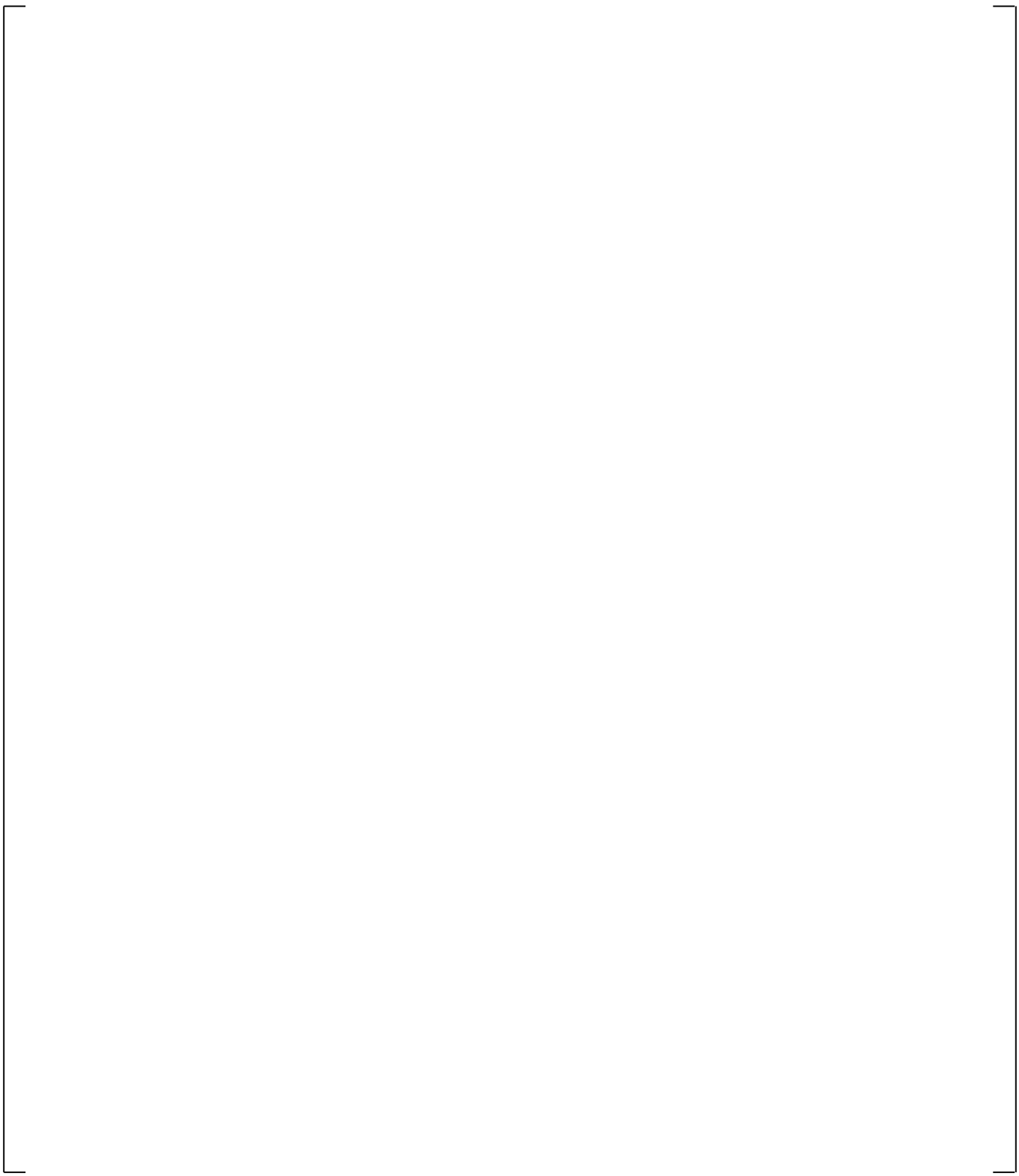

Figure 21.9-8 Downcomer-to-Upper Plenum Differential Pressure

a,c

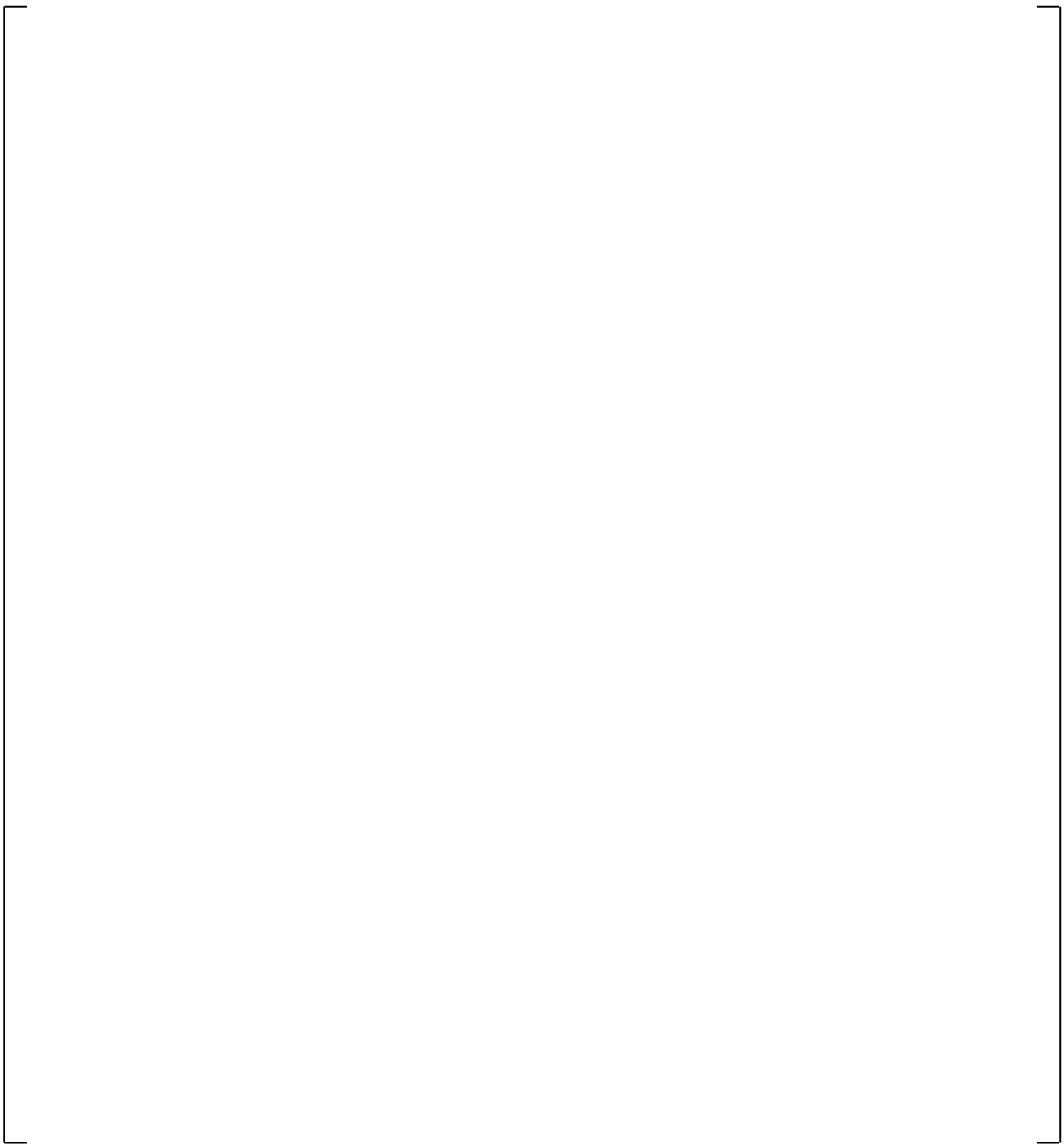

Figure 21.9-9 Calculated SG Primary-to-Secondary Side Heat Transfer Coefficients

Note: The SG heat transfer coefficient is calculated as $h_{SG} = \frac{Q_{SG,OUT}}{\left(FA_{SG,OUT} \times \Delta T_{SG}\right)}$

a,c

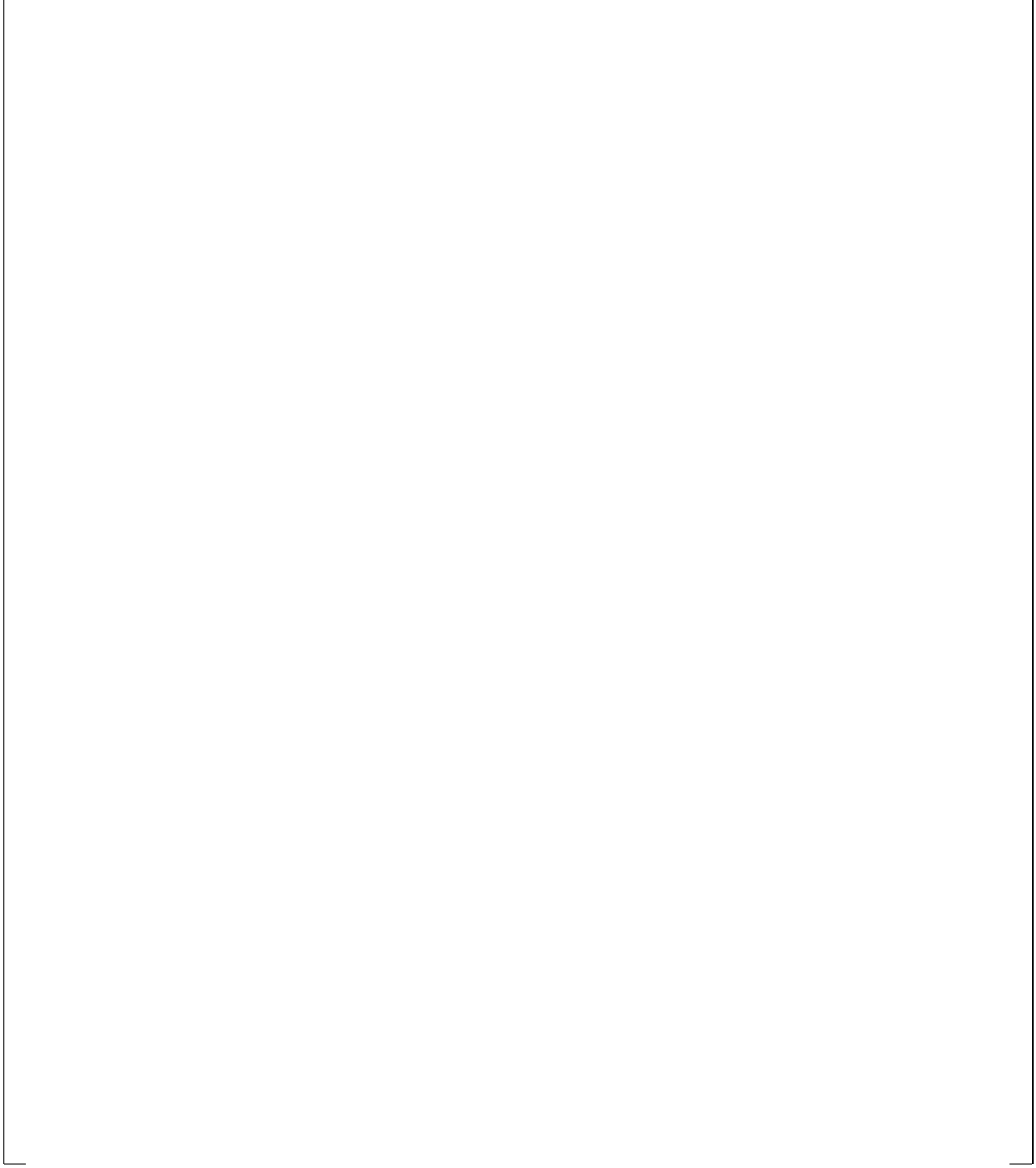

Figure 21.9-10 Calculated Steam Generator Primary-to-Secondary Side Temperature Difference

a,c

Figure 21.9-11 Calculated Steam Generator SGA U-tube Uphill Void Fraction

a,c

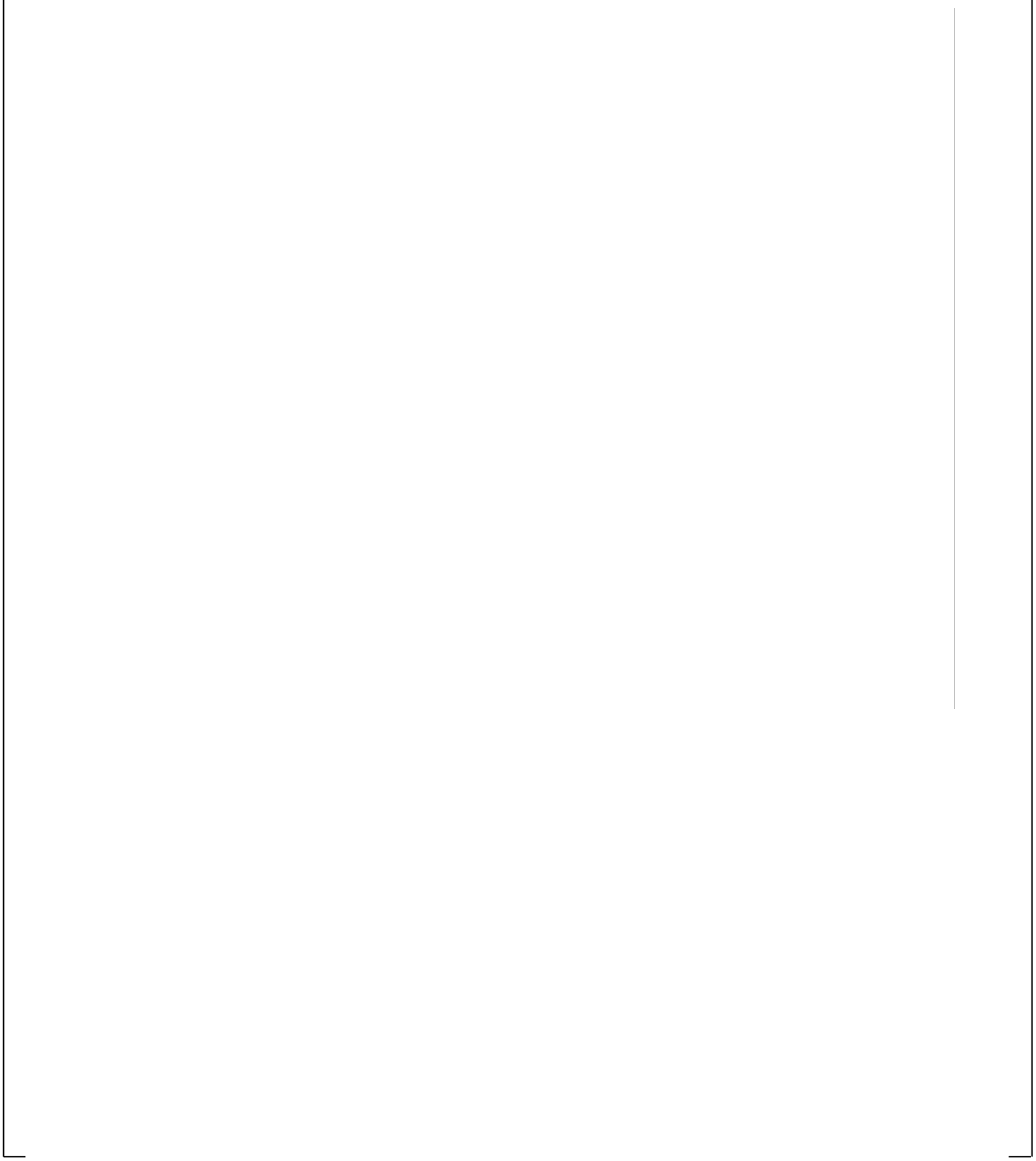

Figure 21.9-12 Calculated Steam Generator SGA U-tube Downhill Void Fraction

a,c

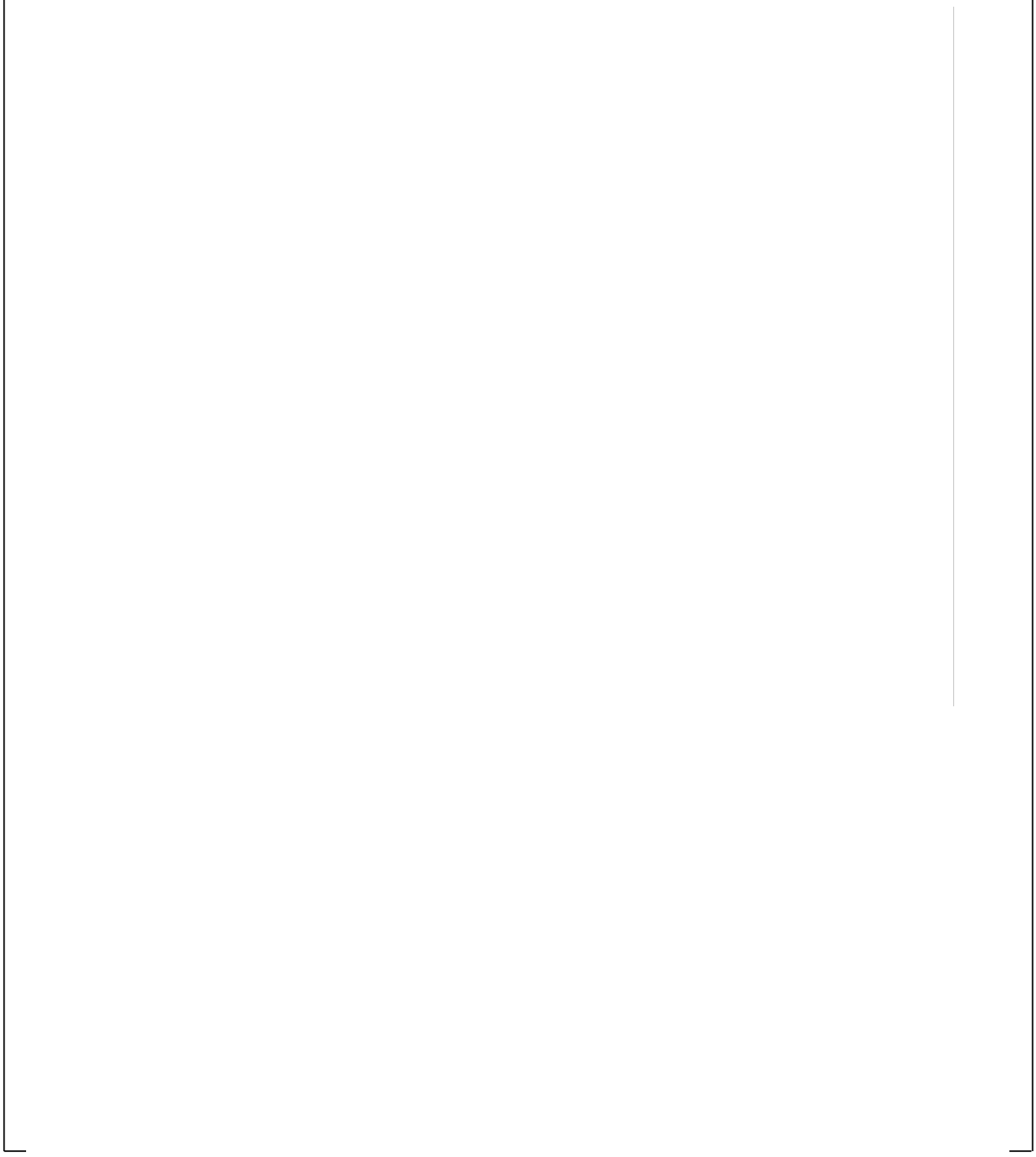

Figure 21.9-13 Calculated Steam Generator SGB U-tube Uphill Void Fraction

a,c

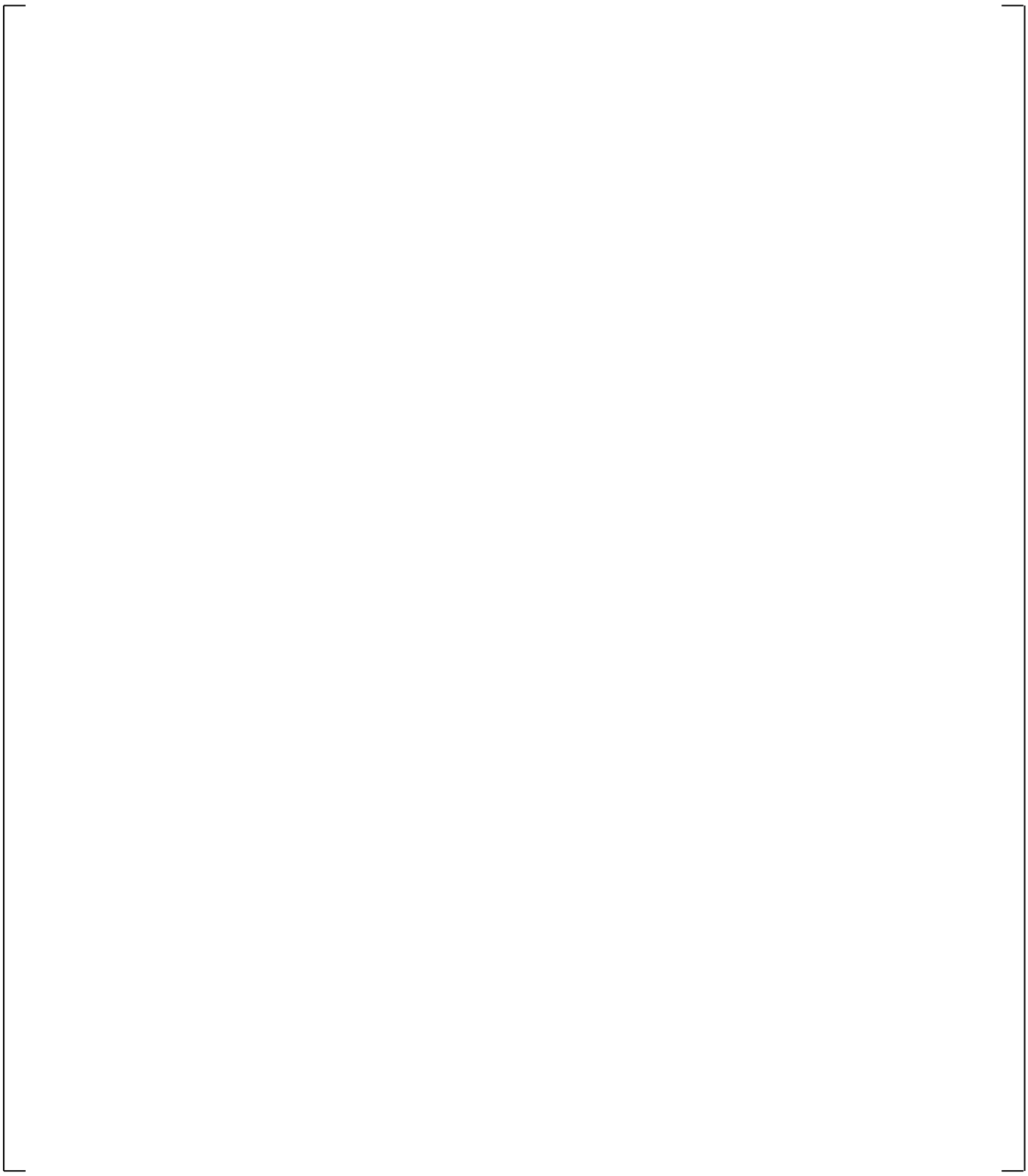

Figure 21.9-14 Calculated Steam Generator SGB U-tube Downhill Void Fraction

a,c

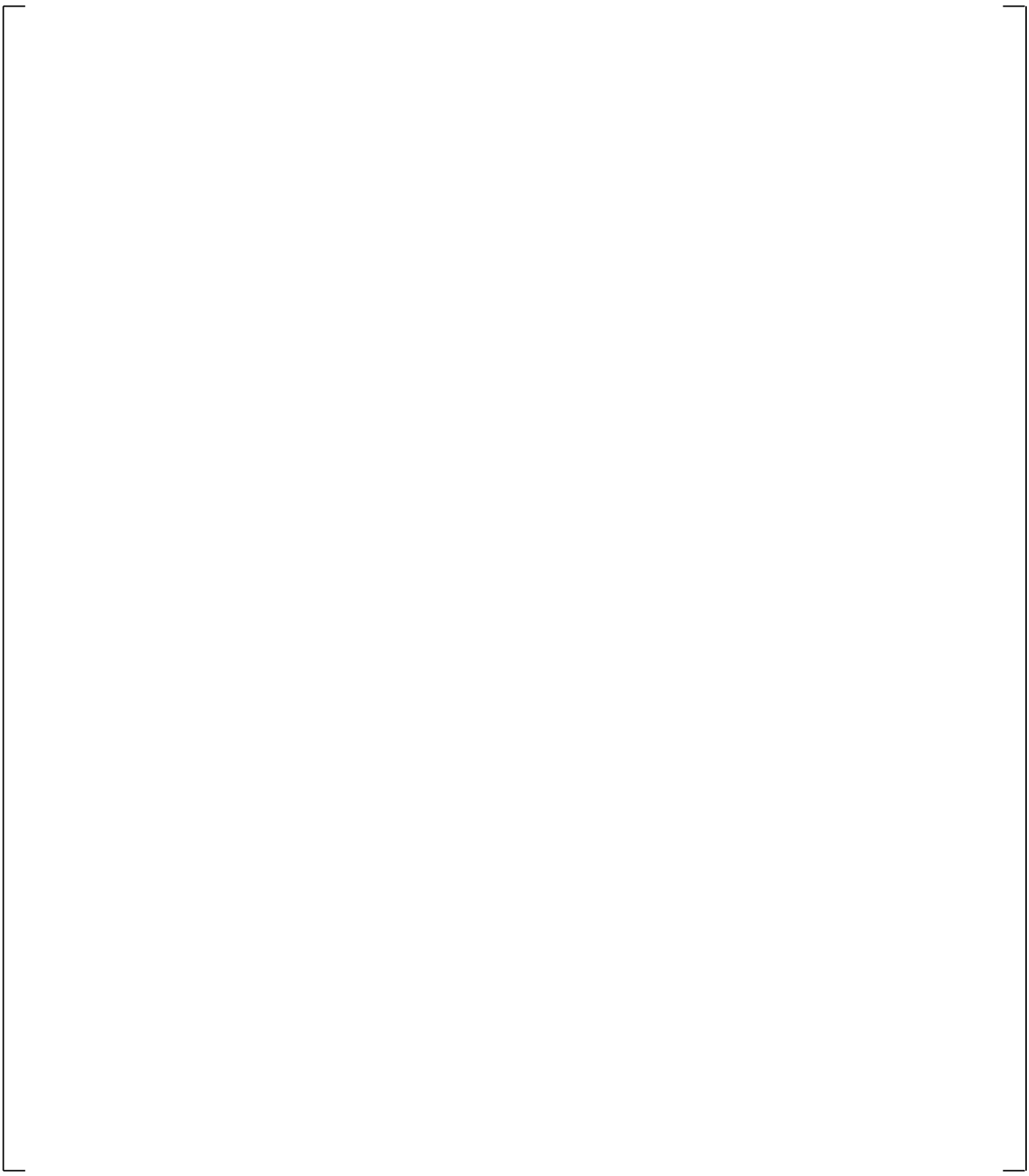

Figure 21.9-15 Calculated Steam Generator SGA Vapor Flows

a,c

Figure 21.9-16 Calculated Steam Generator SGB Vapor Flows

21.10 COUNTER-CURRENT FLOW LIMITATION RESULTS AND EVALUATION

The counter-current flow limitation phenomenon is a process where liquid flow, directed downward by the force of gravity, is restricted by vapor flowing in the opposite (upward) direction, due to interfacial drag forces. With increasing vapor velocity, at some point the downward flow of liquid becomes unstable, stagnates and is eventually reversed so that co-current flow is established. The boundary between the stable counter-current flow and the unstable co-current flow configuration is generally recognized as the so called Counter-current Flow Limitation (CCFL).

The importance of CCFL at different locations of the primary side during the different periods of the LOCA transient and its PIRT ranking are discussed in Section 2, Volume 1.

The liquid in the uphill and downhill side of the SG U-tubes drains into the hot leg and loop seal, respectively; CCFL is possible at the U-tube inlet, SG plenum inlet, and in the hot leg elbow. The potential for CCFL in these locations and the impact of CCFL predictions on the transient dictate that a high (H) ranking is assigned for the loop seal clearing period.

During the steam generator reflux phase of the small break LOCA, steam leaving the core enters the SG and condenses forming a liquid film inside the U-tubes. The condensate from the uphill side of the steam generator U-tubes would accumulate at the inlet of tube due to CCFL, and the resultant pressure increase would further depress the core mixture level. The condensate draining in to the SG plenum could again accumulate at the hot leg elbow causing additional pressure loss which would lower the core mixture level.

The liquid draining from the SG through the hot legs and into the upper plenum collects above the upper core plate (UCP). Water draining from the upper plenum region, or falling back after entrainment from the core, can contribute to core cooling. The amount of water that can drain may be limited by CCFL at the upper core plate, if the steam upflow is sufficient to limit or prevent draining.

Validation of the code capability to model CCFL in different regions of the primary system of a PWR is presented in Section 19. However, the large scale experiments considered therein are designed primarily for conditions developing in Large Break LOCA accidents. The purpose of the discussions included in this section is to complement the CCFL discussions in Section 19 and expand the CCFL considerations into the intermediate and small break LOCA space.

21.10.1 CCFL in the Steam Generator U-tubes

Counter-current flow in the steam generator U-tubes develops during the later stage of the two-phase natural circulation and continues into the reflux condensation phase of the Small Break LOCA transient. It is an important phenomenon since it is the major factor that controls the draining of the steam generator tubes especially during the reflux condensation phase of the loop seal clearing period.

One of the most widely used correlations to describe counter-current flow and flooding in U-tubes is a Wallis-type correlation in its general form $(j_g^*)^{1/2} + m \times (j_f^*)^{1/2} = C$, where m = 0.8-10 and C = 0.7 – 1.0 are empirically determined constants. In the case of turbulent flow m is close to 1.0.

Based on investigation of reflux condensation tests, performed at the ROSA-IV LSTF, it has been suggested by (Kukita et al., 1991) that the steam generator U-tube flooding (CCFL) line can be represented by the following Wallis-type correlation.

$$(j_g^*)^{1/2} + (j_f^*)^{1/2} = 0.88 \qquad (21.10\text{-}1)$$

It is however important to note that in the C=0.88 flooding line suggested in (Kukita et al., 1991) was determined based on the assumption that during reflux condensation phase the vapor entering the steam generator U-tube bundle condenses uniformly along the length of the bundle, so that there is a 1:1 split of the condensation; this is half of the vapor condenses in the uphill and drains back into the hot leg, while the rest condenses in the downhill side of the U-tubes and drains into the SG outlet plenum. However, there is no solid experimental evidence to support this assumption. **[**

][a,c]

The counter-current flow calculation results, presented in Figures 21.10.1-1 through 21.10.1-4, are extracted for the steam generator U-tube inlet locations from different ROSA-IV test simulations documented in the previous subsections. The CCFL results presented in these figures are from test simulations performed with the **[**

][a,c] In each of the figures, (a) shows all the counter-current points calculated at the U-tube inlet of Steam Generator A, and (b) shows the counter-current flow points at the U-tube inlet of Steam Generator B.

[

][a,c]

[

]^{a,c}

The counter-current flow calculated in the simulation of the natural circulation test ST-NC-02 is presented in Figure 21.10.1-5. The results show no CCFL points are on the flooding line during reflux conditions in the steam generators. The natural circulation test, ST-NC-02 was conducted at 2% of the nominal power. At this vapor generation level, very little CCFL was expected at the inlet of the U-tubes.

a,c

Figure 21.10.1-1 Calculated Counter-current Flow at the Inlet of Steam Generator U-tubes (Simulation of 10% Break Test SB-CL-14)

a,c

Figure 21.10.1-2 Calculated Counter-current Flow at the Inlet of Steam Generator U-tubes (Simulation of 5% Break Test SB-CL-18)

a,c

Figure 21.10.1-3 Calculated Counter-current Flow at the Inlet of Steam Generator U-tubes (Simulation of 2.5% Break Test SB-CL-01)

a,c

Figure 21.10.1-4 Calculated Counter-current Flow at the Inlet of Steam Generator U-tubes (Simulation of 0.5% Break Test SB-CL-12)

a,c

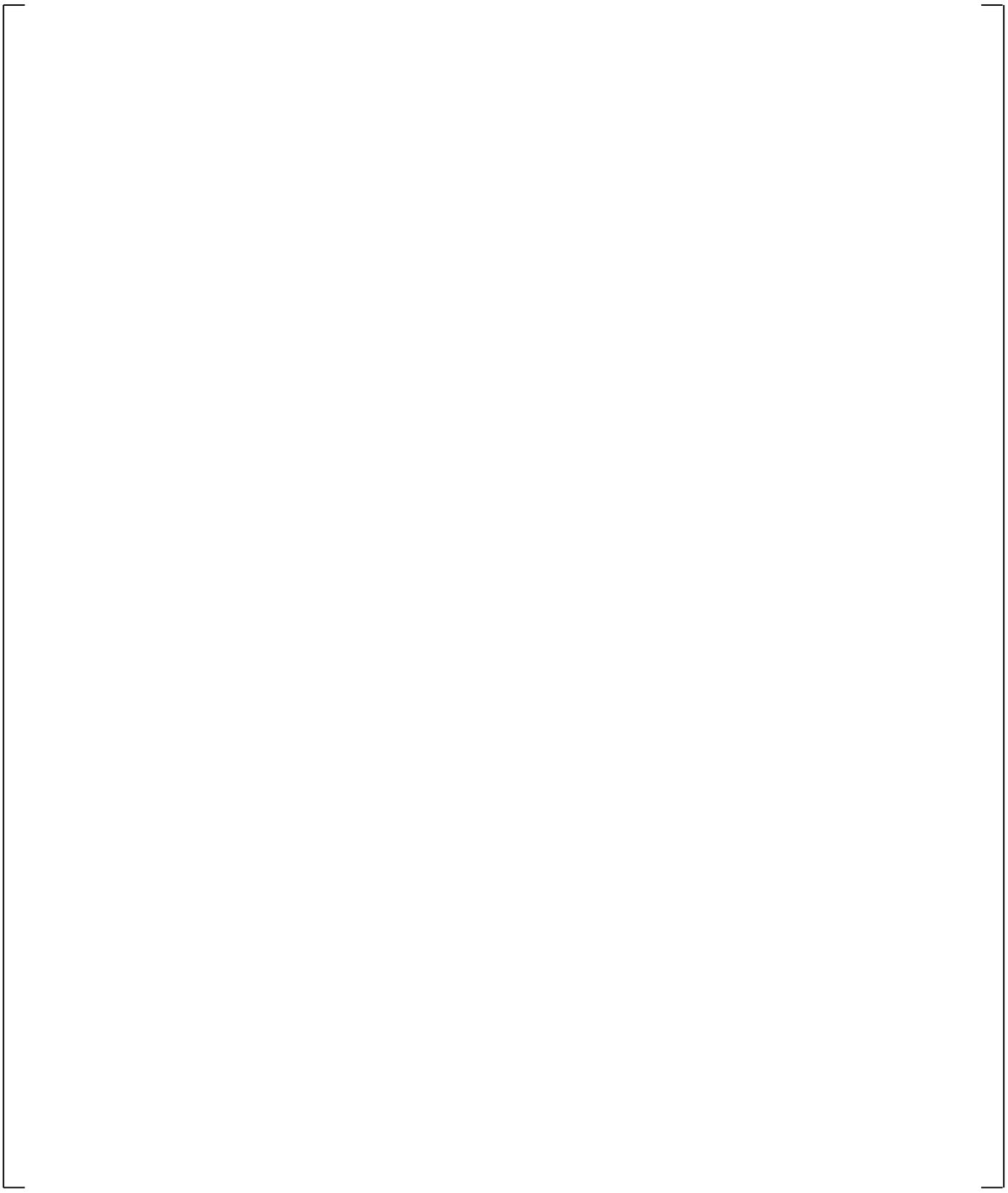

Figure 21.10.1-5 Calculated Counter-current Flow at the Inlet of Steam Generator U-tubes (Simulation of the Natural Circulation Test ST-NC-02)

21.10.2 CCFL in the Vicinity of the Hot Leg Elbow (Steam Generator Inlet)

Counter-current flow in the hot leg (HL), including the vicinity of the elbow and the inlet of the steam generator plenum, can develop during the period of two-phase natural circulation and is especially important during the subsequent reflux condensation phase. The ability of the code to properly calculate the counter-current flow at that location would affect the calculated draining of the SG inlet plenum and subsequently the draining of the U-tubes as well. Acceptable counter-current flow calculation in the hot leg is of critical importance for the correct prediction of the system behavior during the reflux condensation phase of the LOCA transient.

[

][a,c]

[a,c] (21.10-2)

The counter-current flow calculation results, presented in Figures 21.10.2-1 through 21.10.2-4, are extracted for the hot leg elbow and steam generator inlet locations from different ROSA-IV test simulations documented in the previous subsections. All of the simulations considered here were performed with a **[** **]**[a,c] In these figures, the calculated counter-current conditions (points) are plotted against the two limiting flooding lines, **[**

][a,c] In each of the figures, the hot leg elbow counter-current flow points are compared against Equation 21.10-2.

Figure 21.10.2-1 shows results extracted from the simulation of the 10% cold leg side break test SB-CL-14. The calculated counter-current flow points are mostly clustered onto the enforced **[** **]**[a,c] flooding limit without any CCFL violations.

Figure 21.10.2-2 shows the results extracted from the simulation of the 5% cold leg side break test SB-CL-18. **[**

][a,c]

The counter-current flow points, extracted from the simulations of the 2.5% break test SB-CL-01, Figure 21.10.2-3, and the 0.5% break test SB-CL-12, Figure 21.10.2-4, further confirm the conservative bias of the code with respect to counter-current flow at the hot leg and the steam generator inlet.
[

][a,c]

a,c

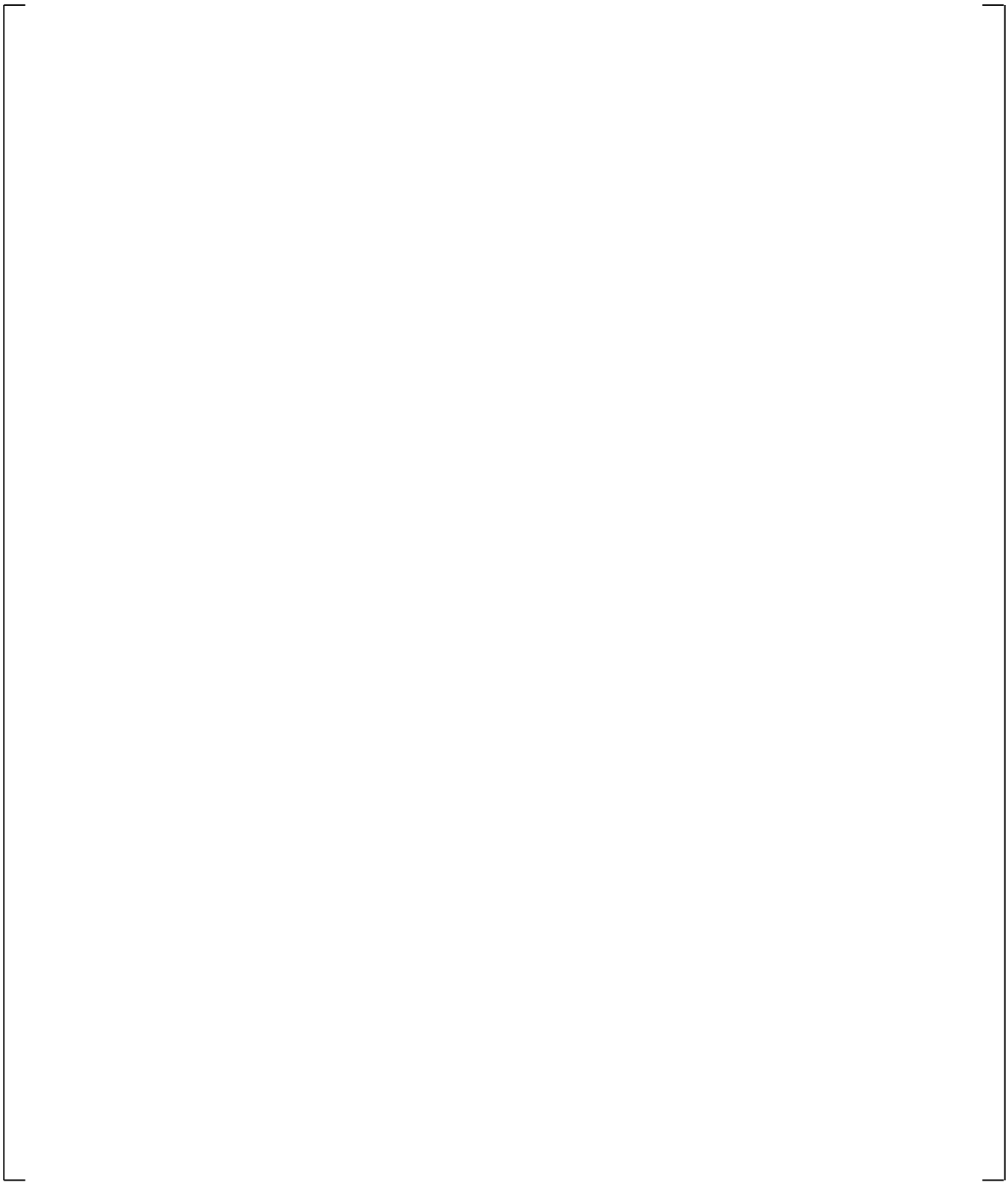

Figure 21.10.2-1 Calculated Counter-current Flow at the Hot Leg Elbows and SG Inlets (Simulation of 10% Break Test SB-CL-14)

a,c

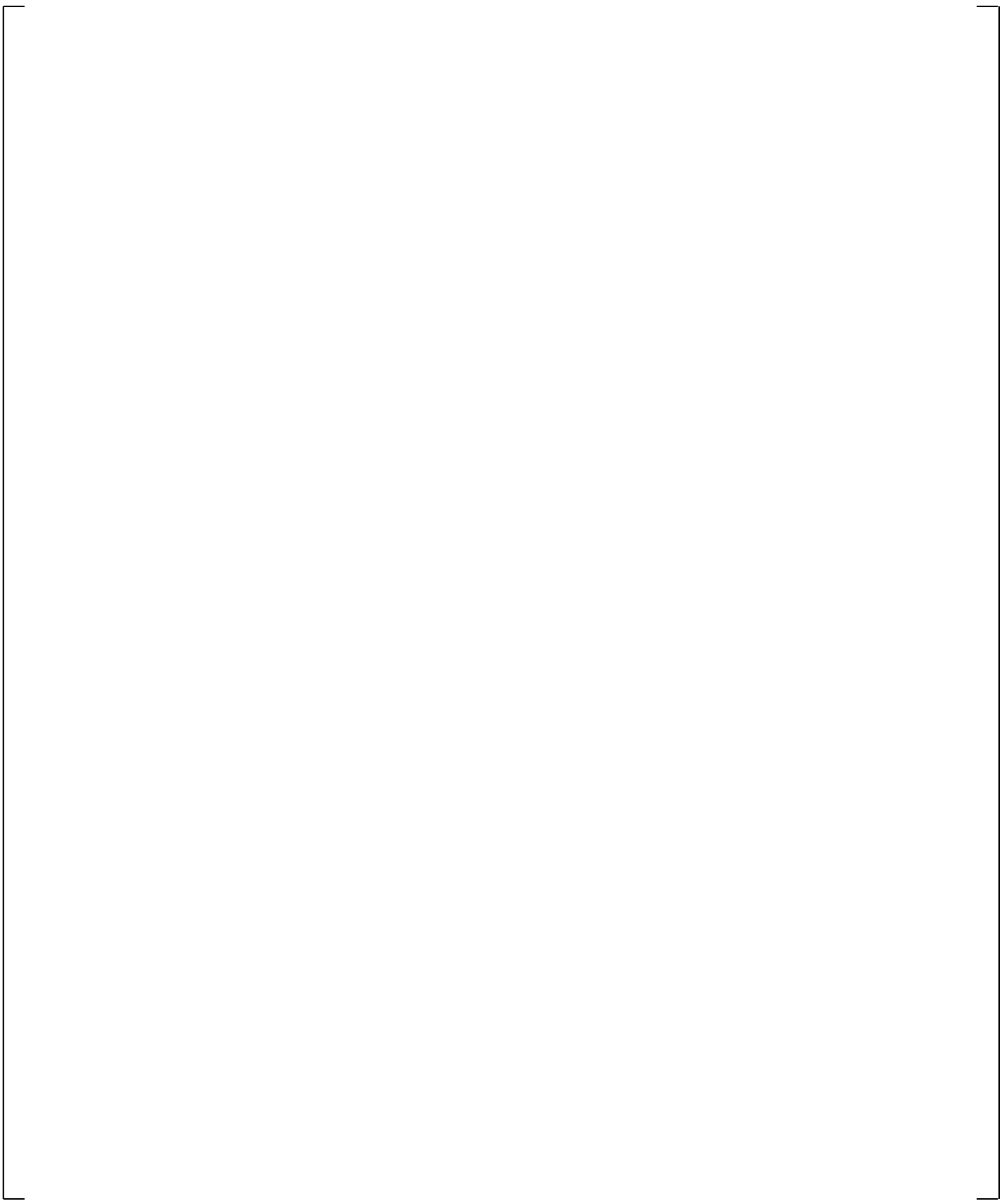

Figure 21.10.2-2 Calculated Counter-current Flow at the Hot Leg Elbows and SG Inlets (Simulation of 5% Break Test SB-CL-18)

a,c

Figure 21.10.2-3 Calculated Counter-current Flow at the Hot Leg Elbows and SG Inlets (Simulation of 2.5% Break Test SB-CL-01)

a,c

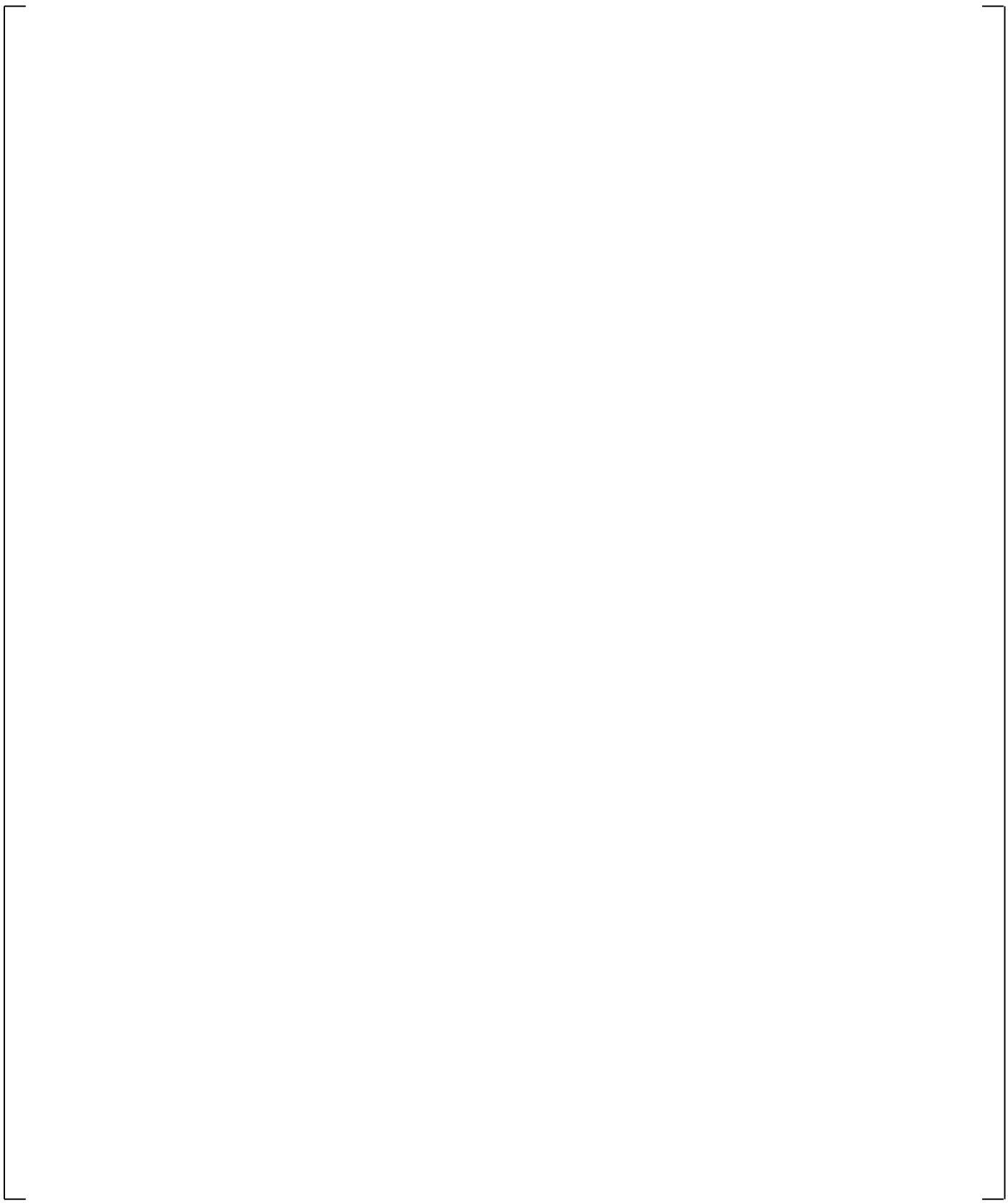

Figure 21.10.2-4 Calculated Counter-current Flow at the Hot Leg Elbows and SG Inlets (Simulation of 0.5% Break Test SB-CL-12)

21.10.3 CCFL at the Upper Core Plate (UCP)

Counter-current flow limitation at the upper core plate is an important phenomenon during both large-break and small-break loss-of coolant accidents. Steam-water counter-current flow condition at the top of UCP might occur during different phases of the LOCA accidents.

In large-break accidents CCFL can occur during the reflood phase when water is accumulated above the UCP as a result of de-entrainment or direct SI injection in the upper plenum. If the flow of vapor generated in the core is high enough, it may impede the penetration of the water accumulated in the upper plenum and reduce the effectiveness of the core cooling. Validation of the capability of the code to calculate CCFL in large break LOCA conditions is presented in Section 19.4, **[**

][a,c].

In Small-break LOCA, the accumulation of water in the upper plenum occurs primarily as a result of the draining of the hot legs and the uphill side of the steam generators during the later stages of the two-phase natural circulation period. A pool of water accumulated above the UCP can still exist during the reflux condensation period maintained by steam condensing on the surface of the steam generator U-tubes and draining back into the upper plenum. Irrespective of how the pool of water above the UCP is formed and maintained during the accident, the nature of the CCFL phenomenon is in essence similar in both Large-break and Small-break LOCA scenarios.

The results of calculated counter-current flow at the UCP, presented in this section, are extracted from the ROSA-IV LSTF simulations for the individual channels that are modeled in the **[**

][a,c] , see Figures 21.3-1 and 21.3-3. **[**

][a,c]

Figure 21.10.3-1 shows calculated counter-current flow at Channels 73 and 80, located above the peripheral (low-power) core region, extracted from the simulation of the SB-CL-18 test. Figures 21.10.3-2 and 21.10.3-3 show the counter-current flow calculated at the inner average and inner hot channels respectively.

[

][a,c]

Figures 21.10.3-4 through 21.10.3-6 show counter-current flow results that were extracted from other ROSA-IV test simulations documented in the previous sections. The CCFL results shown in these figures include all instances where counter-current flow is calculated to occur at the UCP location.

Figure 21.10.3-4 shows counter-current flow points extracted from the simulation of the 10% break test SB-CL-14. **[**

][a,c]

The few instances when the NW flooding line is violated (Figures 21.10.3-2, 21.10.3-4 and 21.10.3-5) are of short durations caused by the flow oscillations; they are found to have negligible consequences to the core heat up predictions.

In summary, the results presented in this section show that with the current ROSA-IV LSTF model, the code (WCOBRA/TRAC-TF2) calculates counter-current flow at the UCP location which is, for the most part, conservative with respect to the draining of the liquid pool that might exist above the upper core plate. This is especially true for the periods of significant core uncovery that may be predicted to occur during the loop seal clearance and core boiloff periods of the small-break transient simulations.

a,c

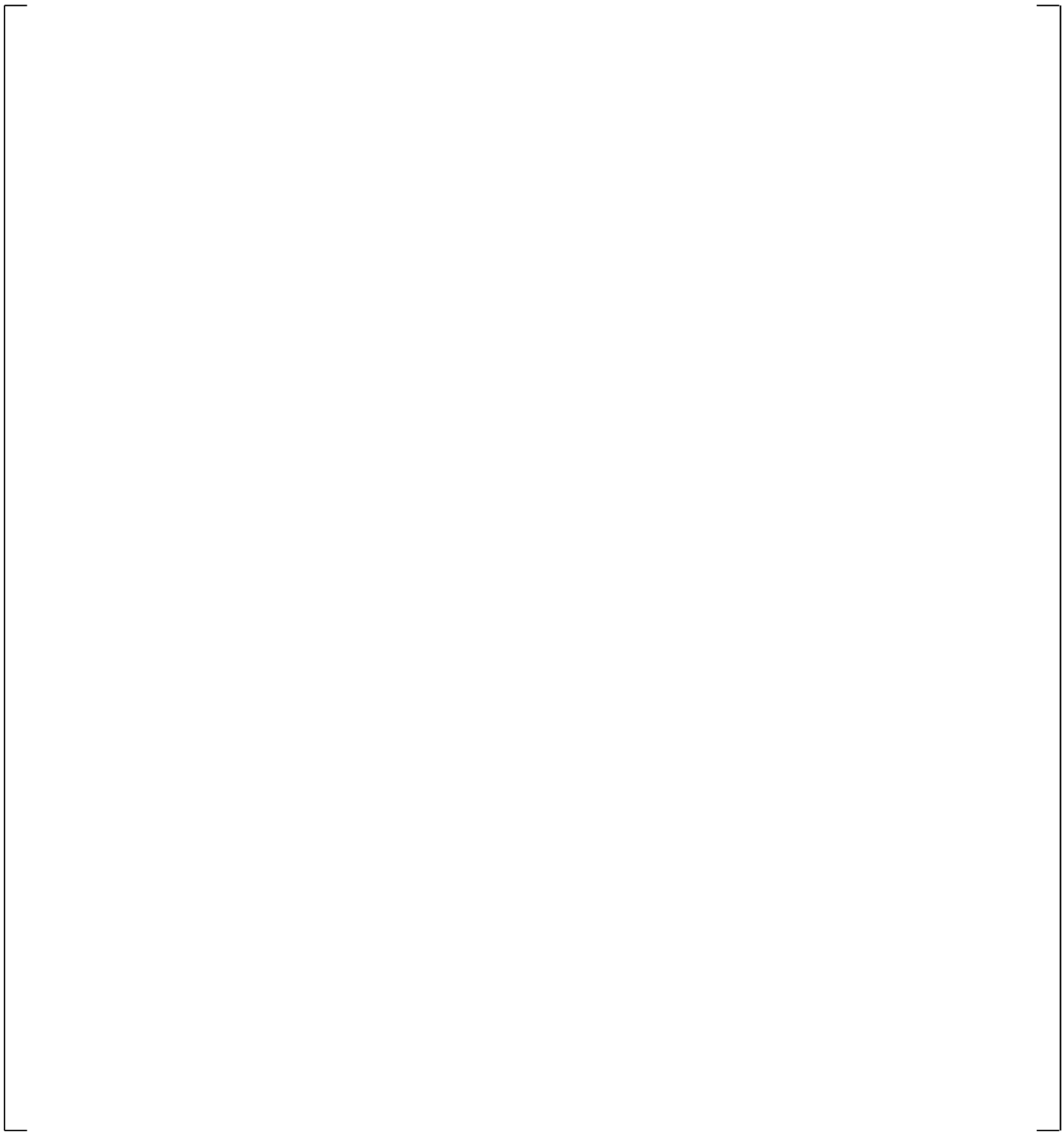

Figure 21.10.3-1 Calculated Counter-current Flow Conditions at the Bottom of Peripheral CCFL Channels 73 and 80

a,c

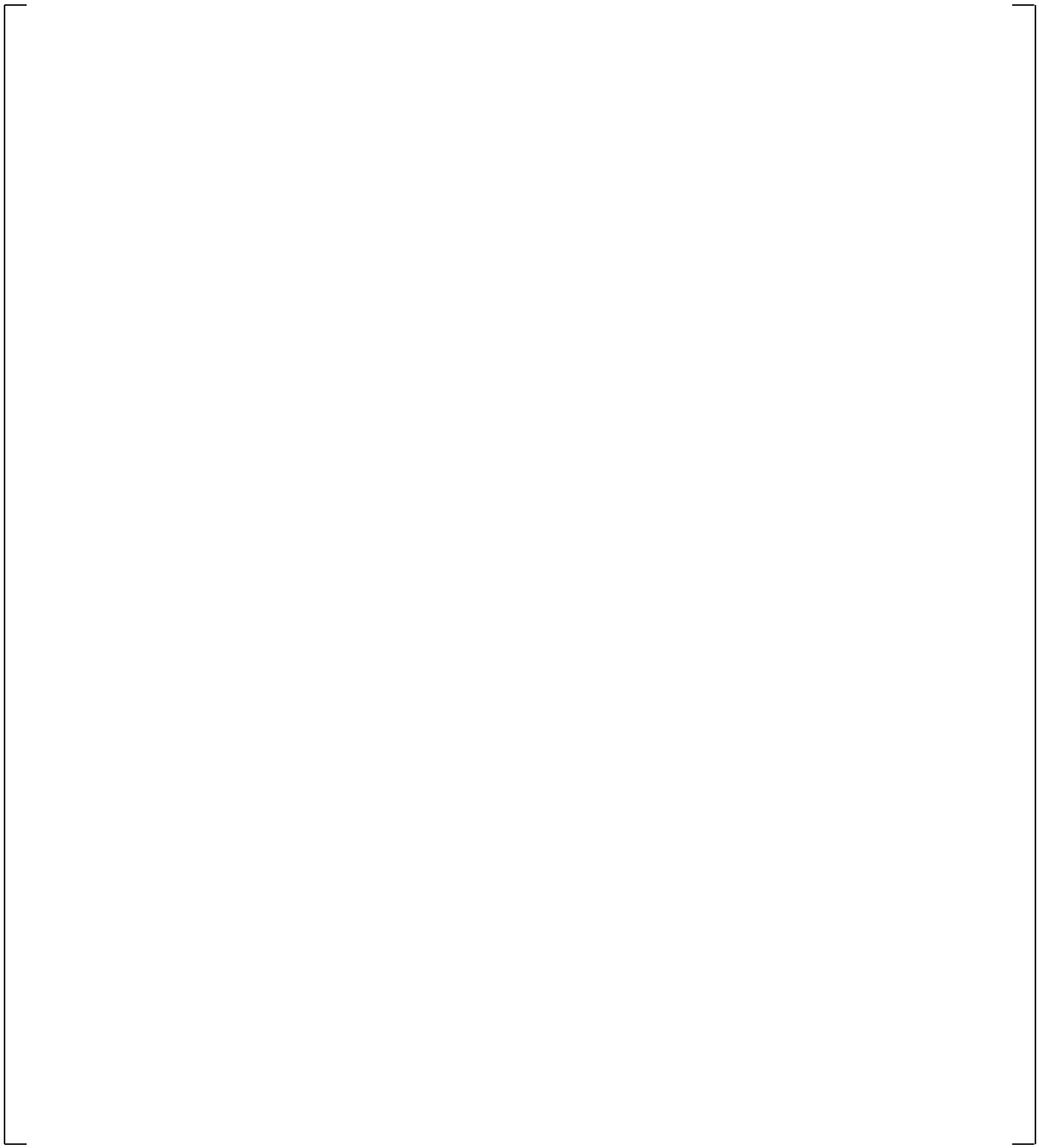

Figure 21.10.3-2 Calculated Counter-current Flow Conditions at the Top of the Inner Average CCFL Channels 13 and 14

a,c

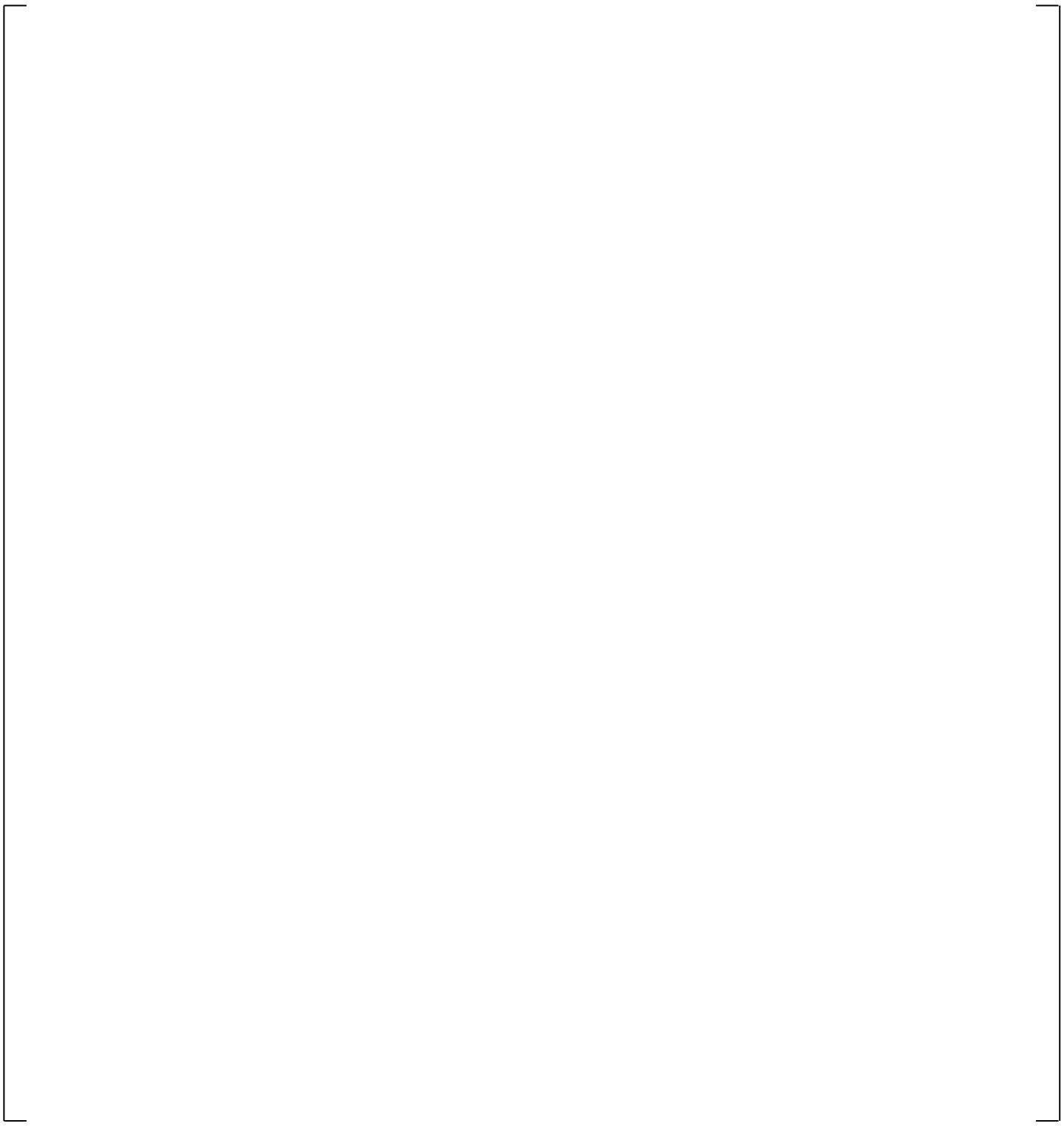

Figure 21.10.3-3 Calculated Counter-current Flow Conditions at the Top of the Inner Hot CCFL Channels 11 and 12

a,c

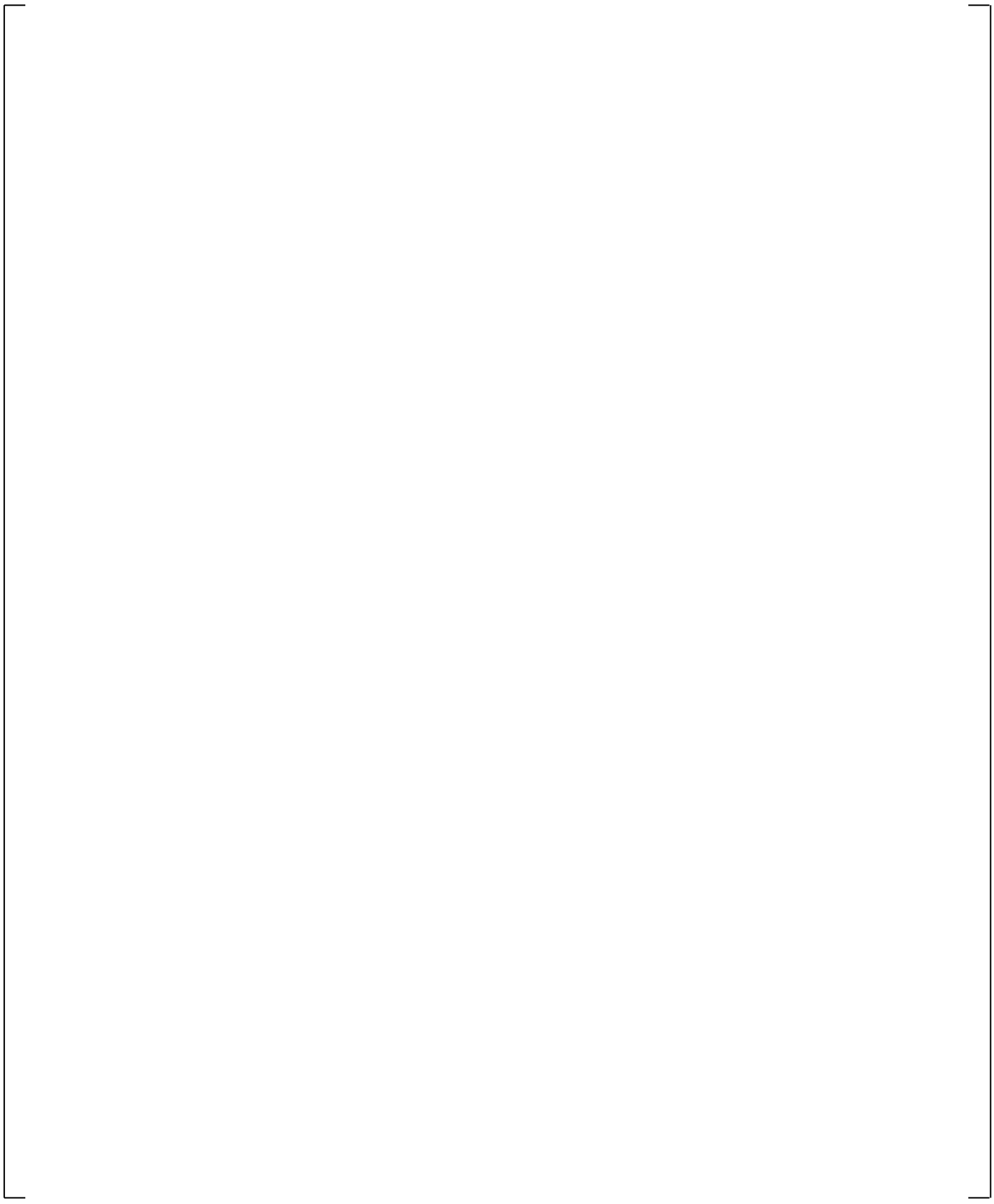

Figure 21.10.3-4 Calculated UCP Counter-current Flow Conditions (10% Break Test SB-CL-14).

a,c

Figure 21.10.3-5 Calculated UCP Counter-current Flow Conditions (2.5% Break Test SB-CL-01)

a,c

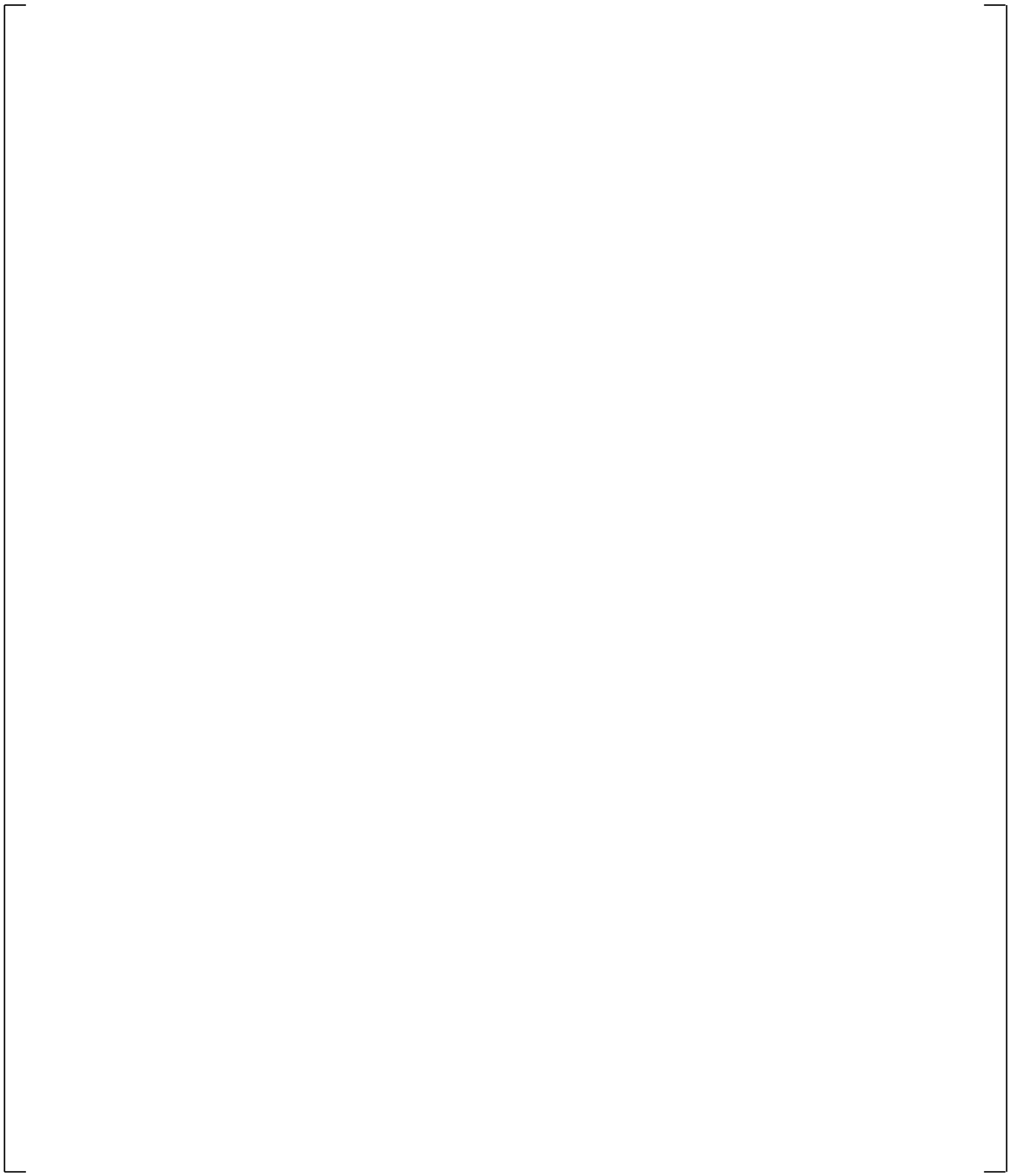

Figure 21.10.3-6 Calculated UCP Counter-current Flow Conditions (0.5% Break Test SB-CL-12)

21.11 BYPASS SENSITIVITY CALCULATIONS

This section documents results from various simulations of ROSA-IV tests performed with different modeling variations. These sensitivity calculations are needed to provide a basis for the treatment of the modeling uncertainty within the FSLOCA Methodology.

21.11.1 Hot Leg Nozzle Gap Modeling Sensitivity with the SB-CL-18 Test

As described in Section 21.3, the ROSA-IV LSTF vessel model used in the different break simulations documented in Section 21 implements a split bypass modeling where the spray nozzle flow path and the line that connects the hot leg outlet nozzles to the downcomer are modeled as separately.

The goal of this sensitivity calculation is to investigate the effect of a modeling approach where the bypass flow through the hot leg nozzle gaps (HL-to-DC) is lumped together with the spray nozzle and the flow link from hot leg nozzles to the downcomer is not explicitly modeled. A calculation with this revised "lumped" bypass modeling is performed with the SB-CL-18 test to investigate the effect of this modeling approach.

Figures 21.11.1-1 through 21.11.1-7 compare the simulation results with the lumped bypass modeling approach against the simulation results of the SB-CL-18 documented in the previous Section 21.4. In each of the figures, the reference SB-CL-18 simulation results (split bypass model) are at the top, while the simulation results obtained with the lumped bypass model are at the bottom.

[

]^{a,c}

a,c

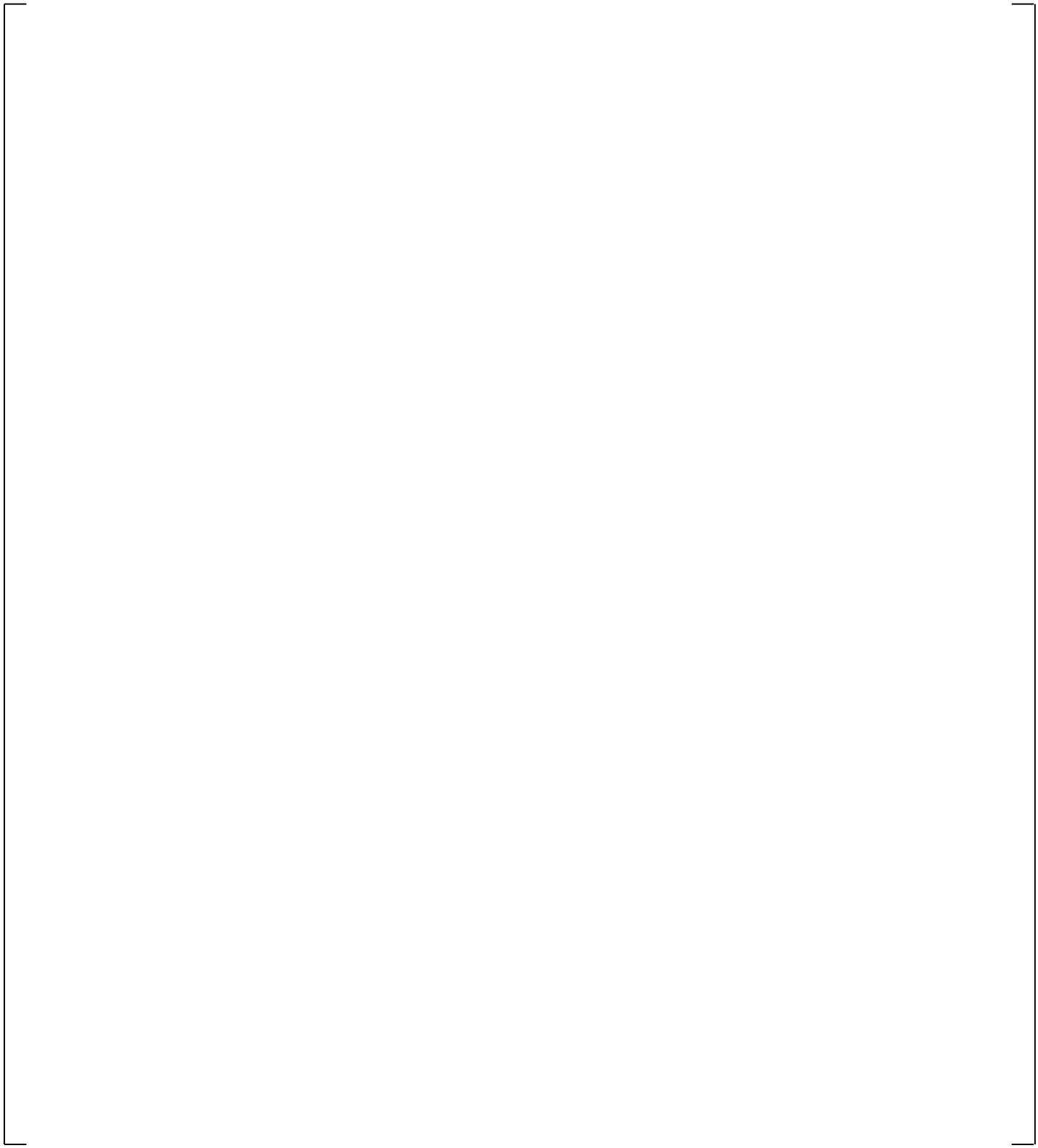

Figure 21.11.1-1 SB-CL-18 Cross-Over Leg A Differential Pressures

a,c

Figure 21.11.1-2 SB-CL-18 Cross-Over Leg B Differential Pressures

a,c

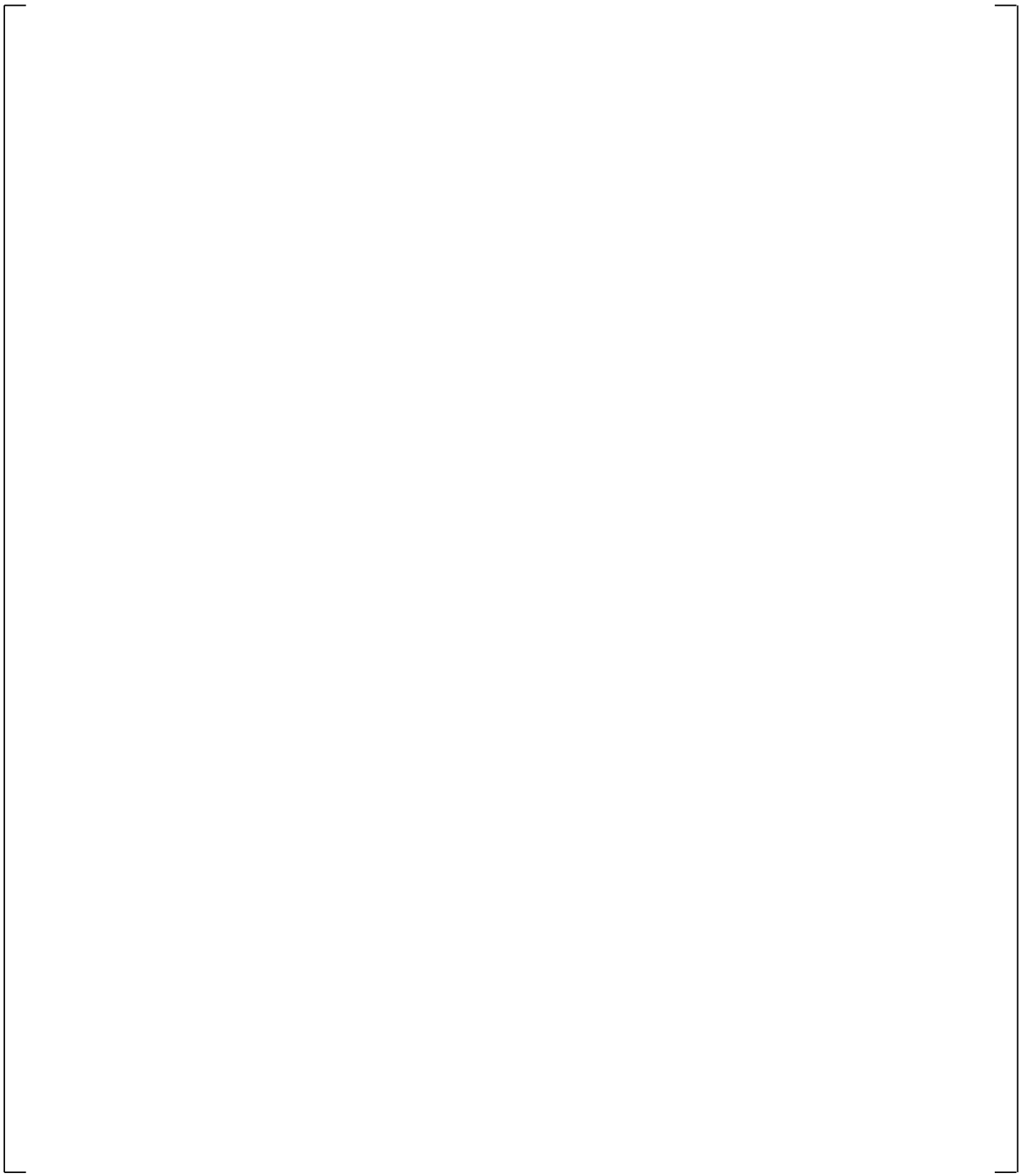

Figure 21.11.1-3 Inner Vessel Differential Pressures (LP+Core+UCP)

a,c

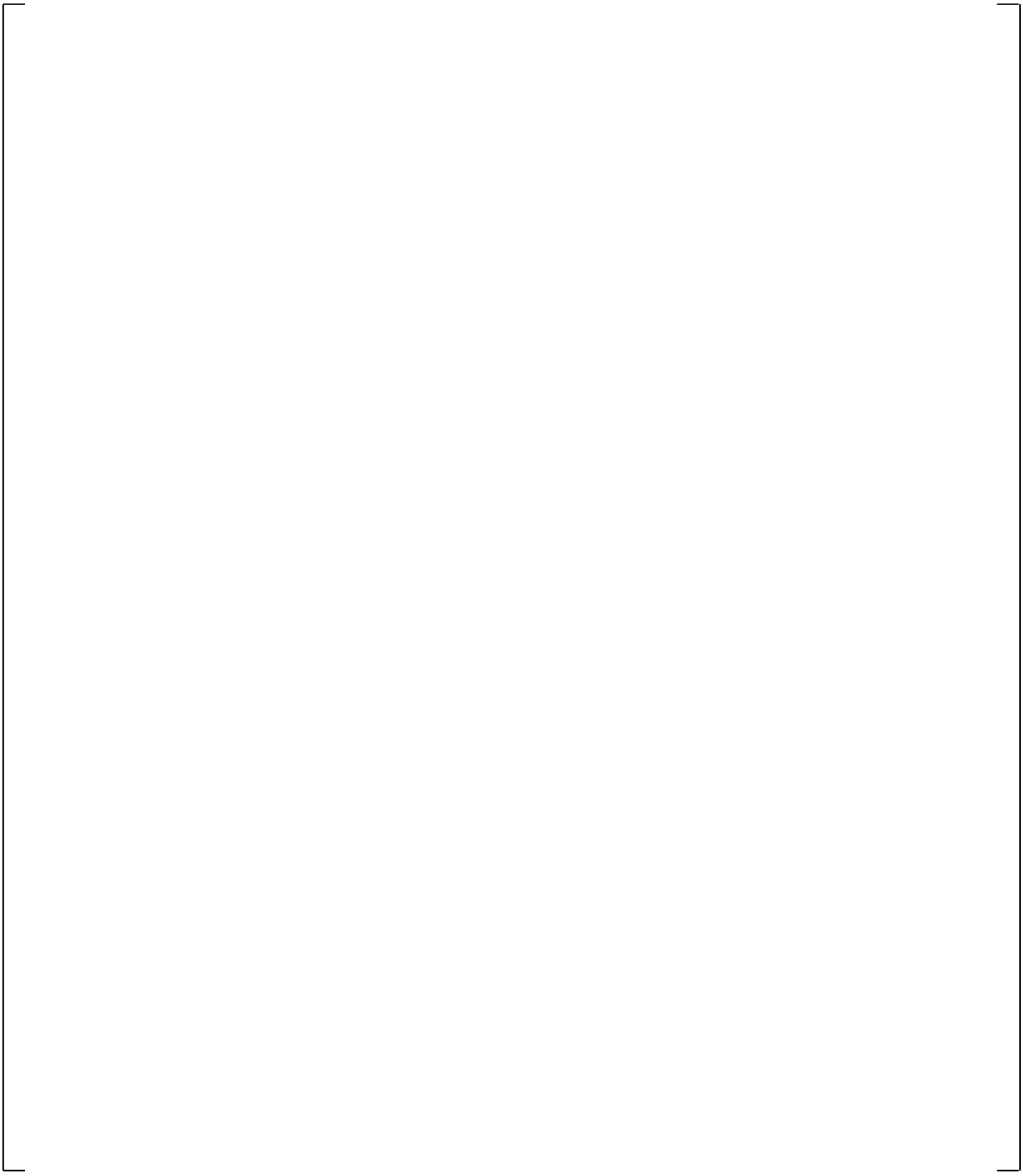

Figure 21.11.1-4 Downcomer Differential Pressures

a,c

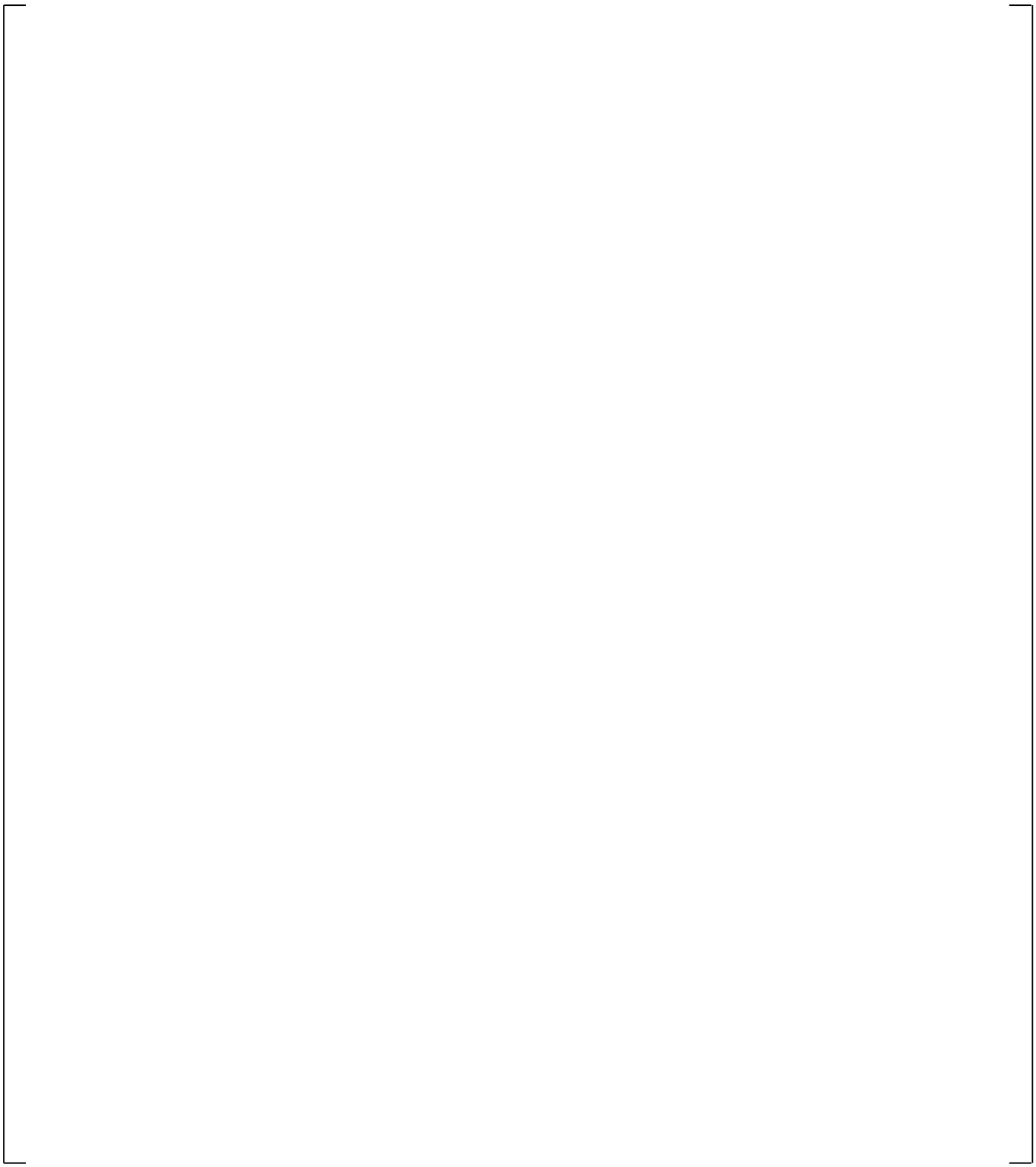

Figure 21.11.1-5 Lower Plenum Differential Pressures

a,c

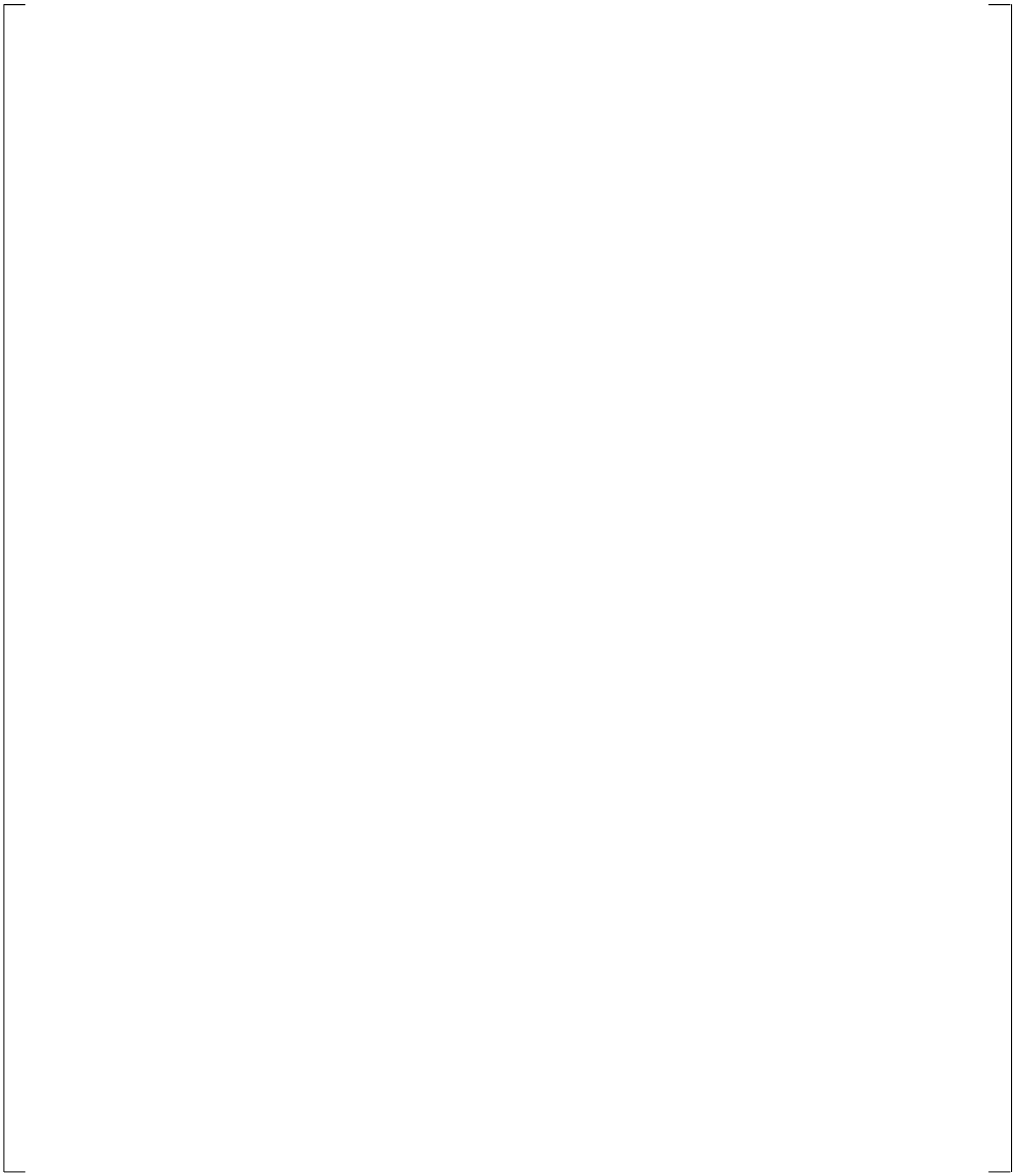

Figure 21.11.1-6 Upper Plenum Differential Pressures

a,c

Figure 21.11.1-7 Peak Cladding Temperatures

21.11.2 SB-CL-18 Simulation Without Hot Leg Nozzle Bypass Flow

In this calculation, the (spray) bypass flow is tuned to **[ ]**[a,c] of the total core flow. This is a case, where the **[ ]**[a,c] HL-to-DC gap bypass (modeled in the reference SB-CL-18 simulation in Section 21.4) is eliminated by blocking the HL-to-DC Gaps 21 and 22. The results of this sensitivity calculation are intended to provide a basis for judgment whether modeling HL-to-DC bypass flow has a big effect on the transient calculation. Establishing a direction of conservatism can support making a decision whether to model HL-to-DC bypass in addition to the spray nozzle bypass or not.

[

][a,c]

a,c

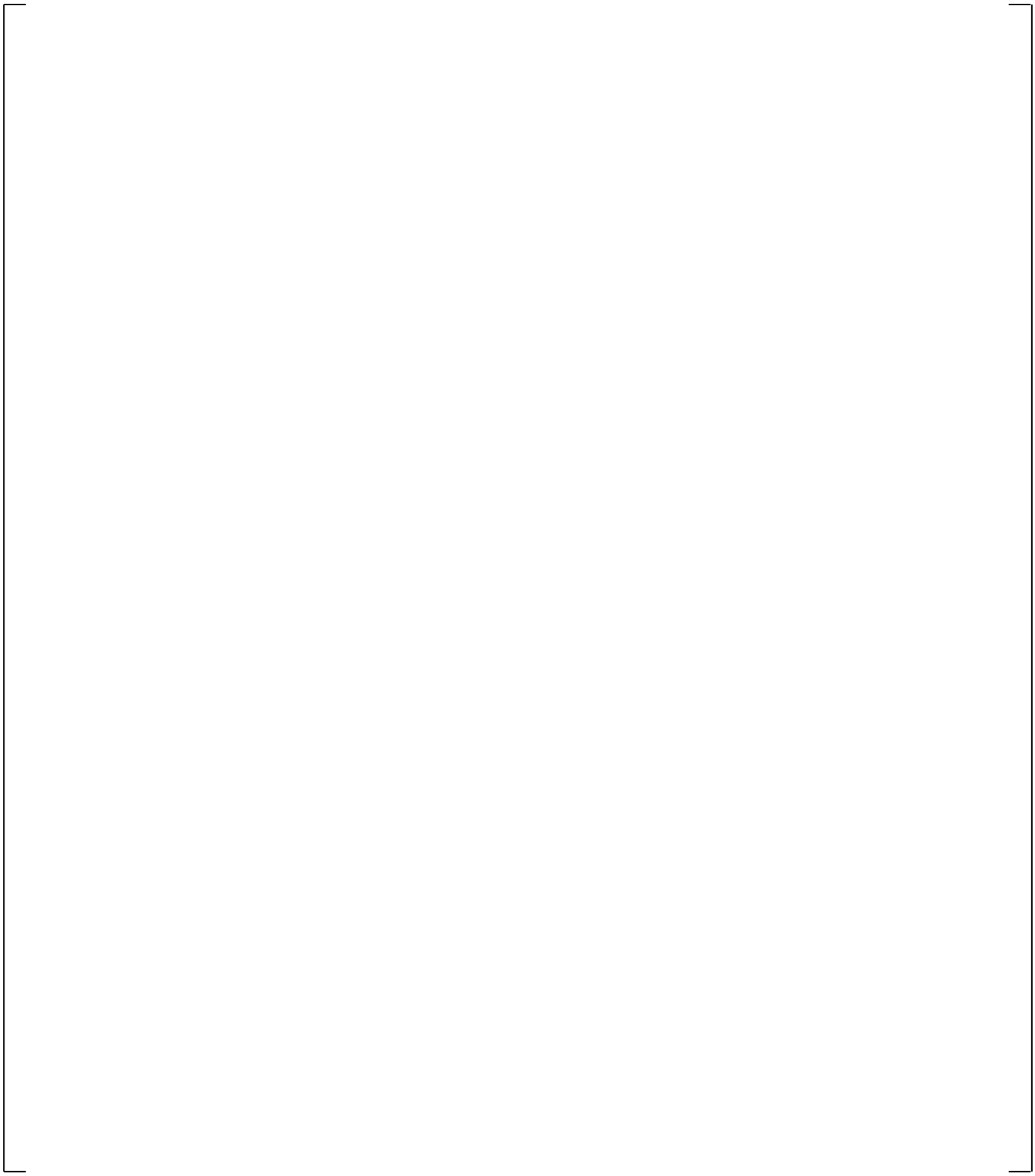

Figure 21.11.2-1 SB-CL-18 Cross-Over Leg A Differential Pressures

a,c

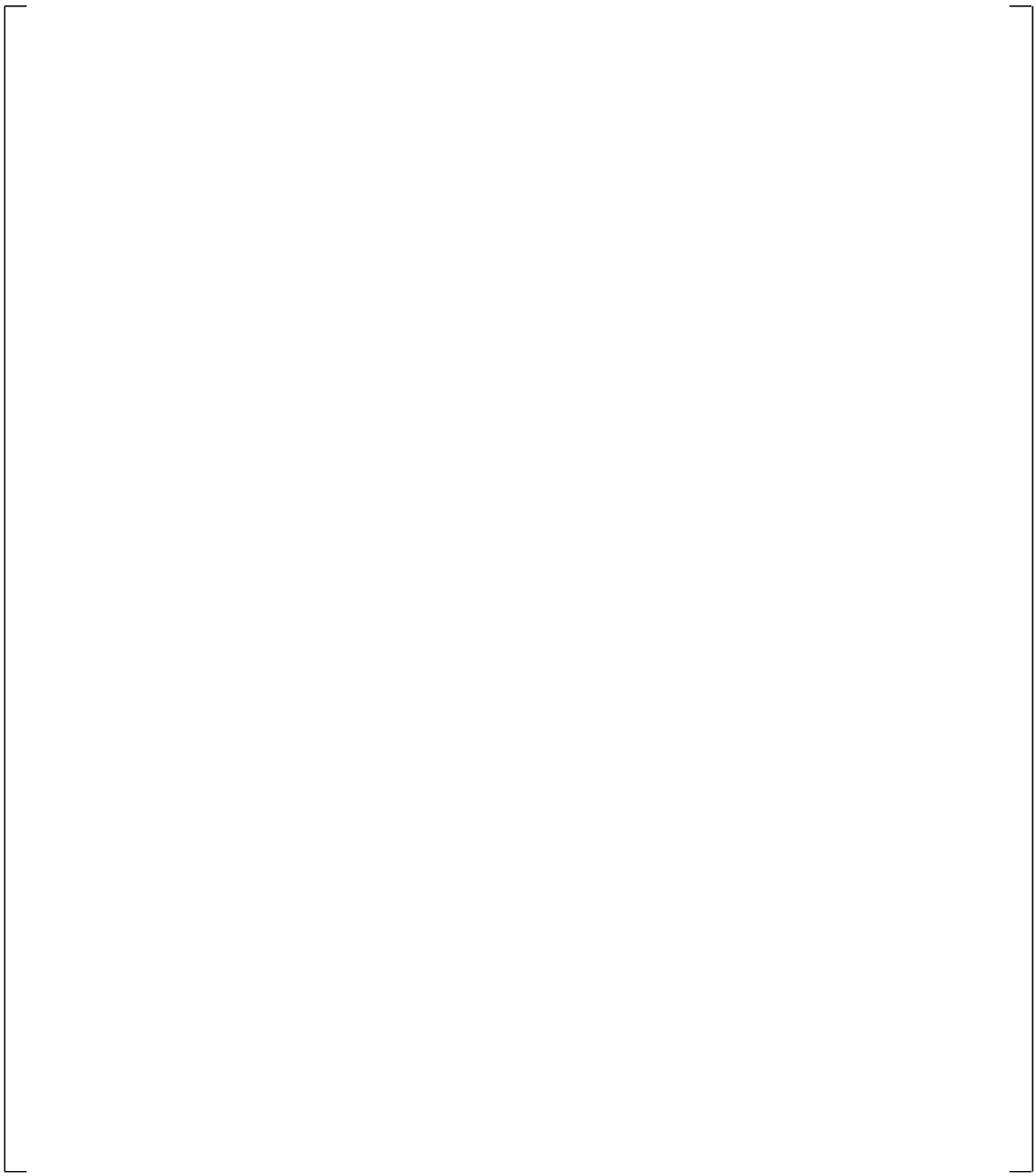

Figure 21.11.2-2 SB-CL-18 Cross-Over Leg B Differential Pressures

a,c

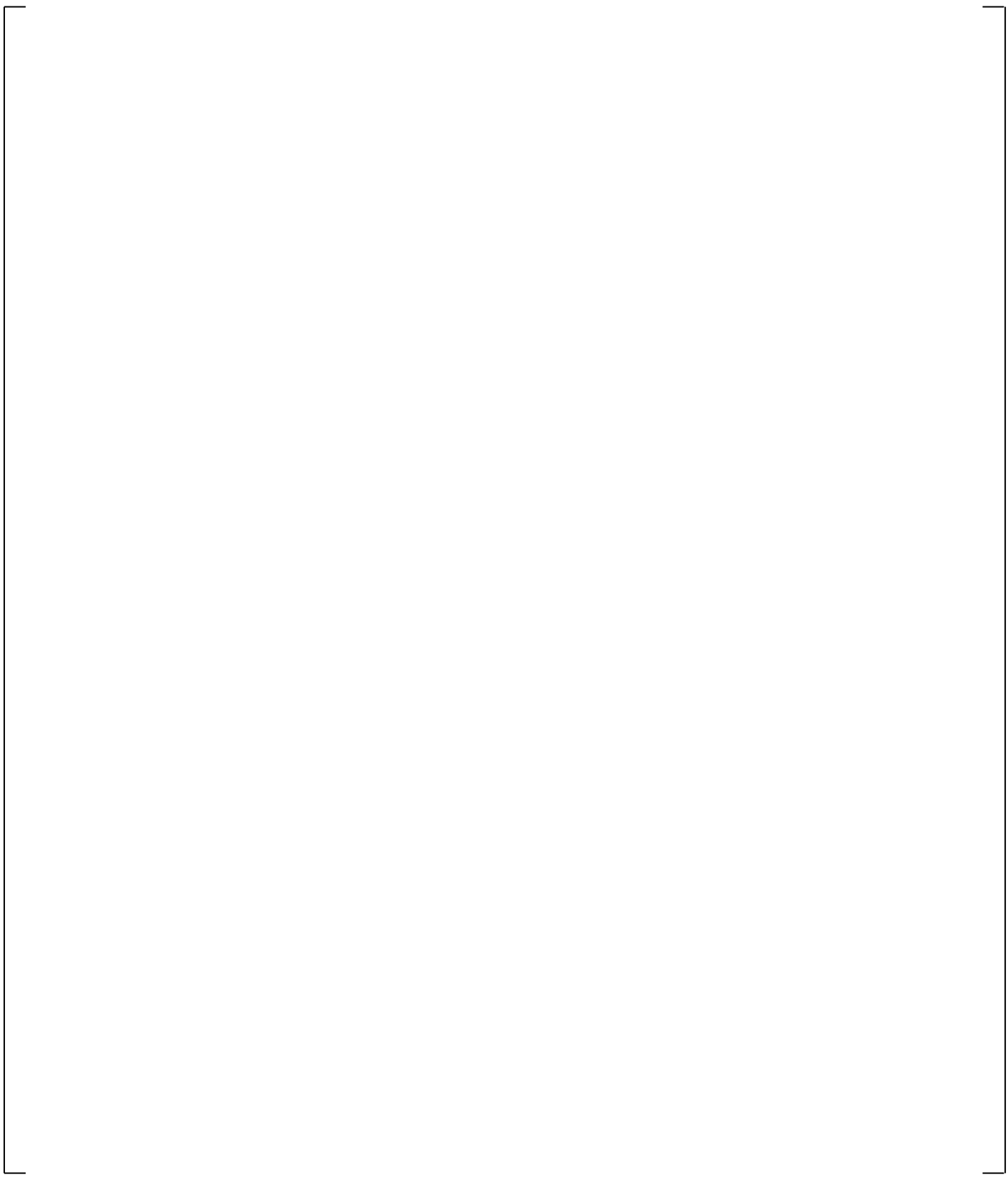

Figure 21.11.2-3 Inner Vessel Differential Pressures (LP+Core+UCP)

a,c

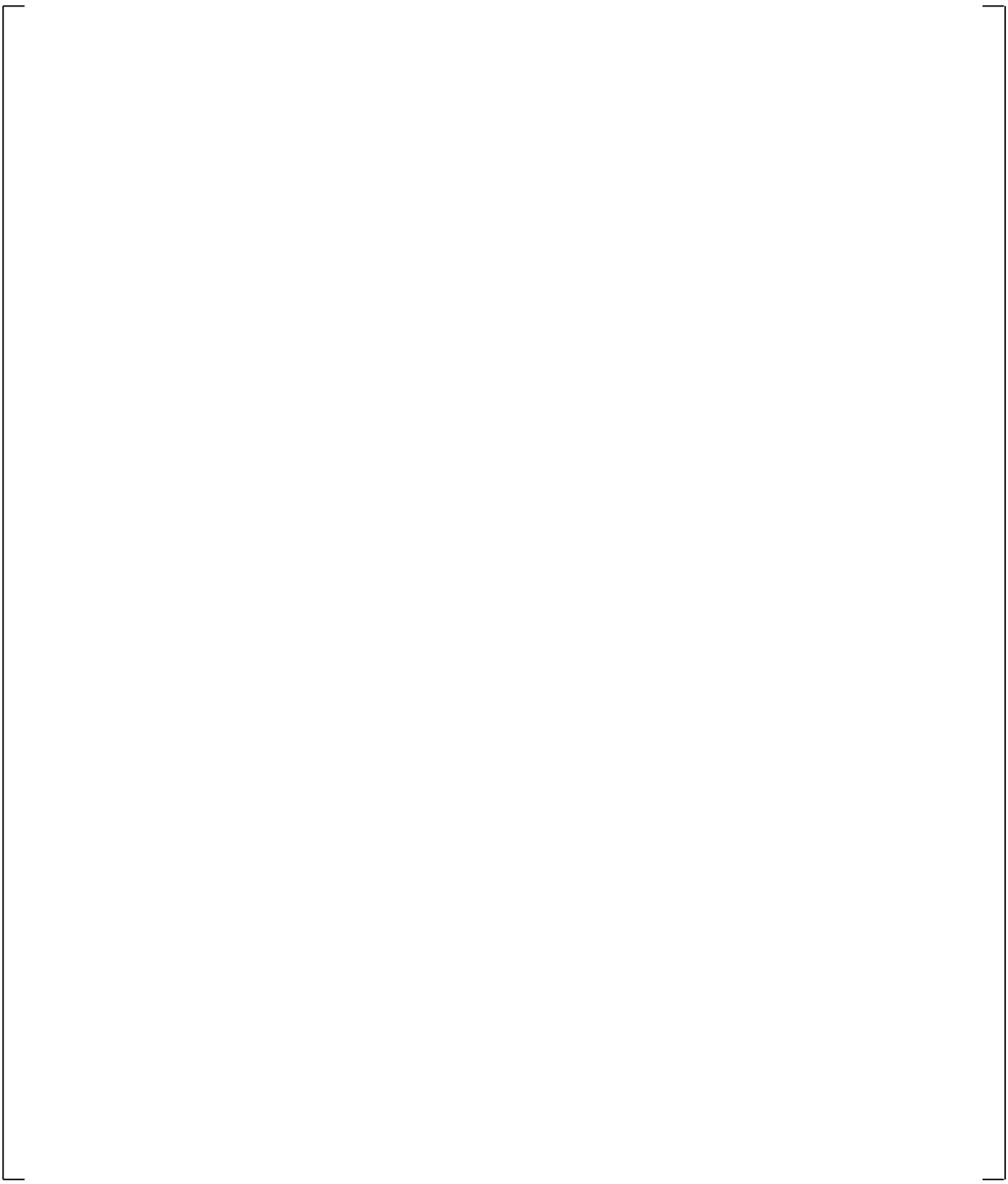

Figure 21.11.2-4 Downcomer Differential Pressures

a,c

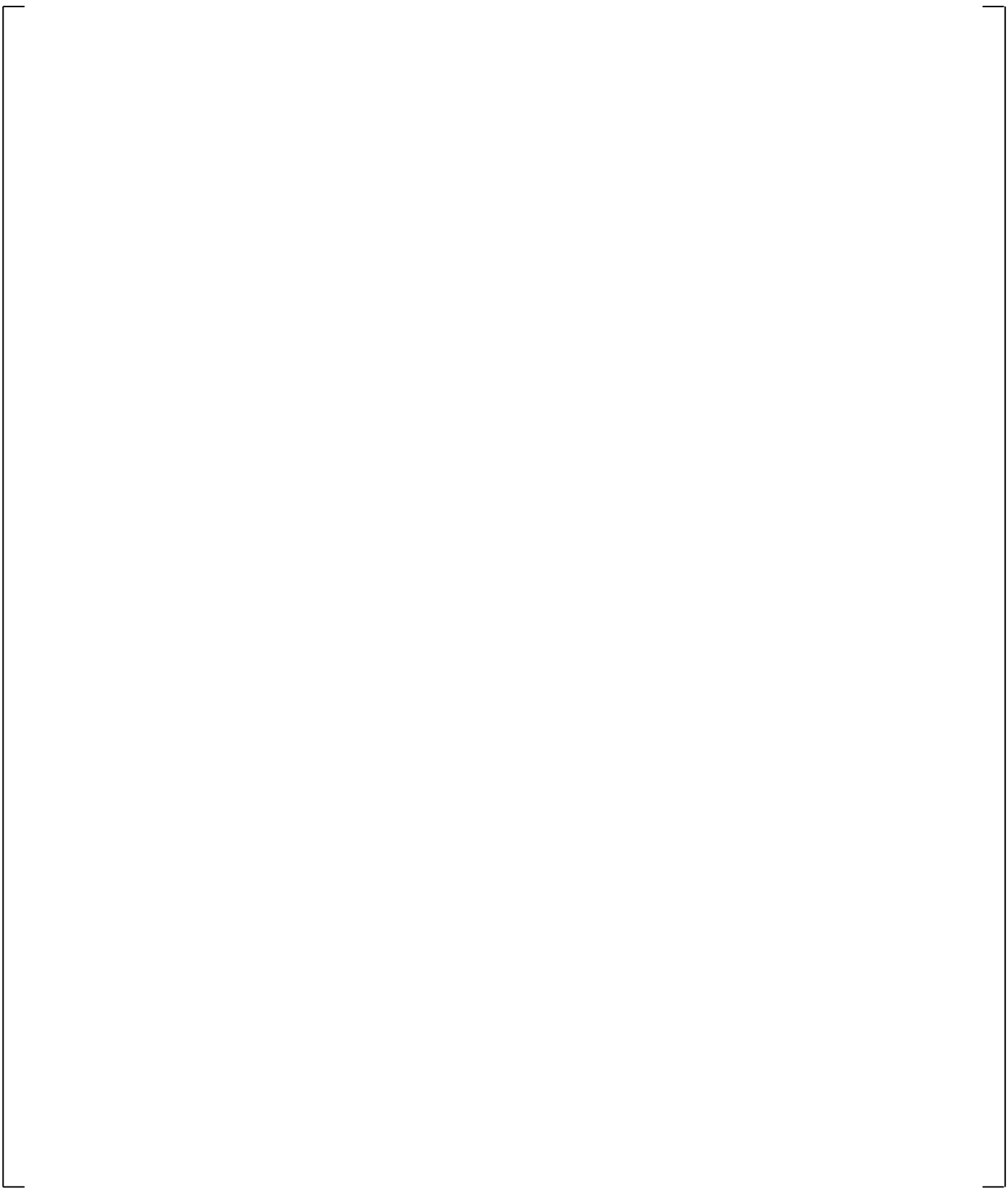

Figure 21.11.2-5 Lower Plenum Differential Pressures

a,c

Figure 21.11.2-6 Upper Plenum Differential Pressures

a,c

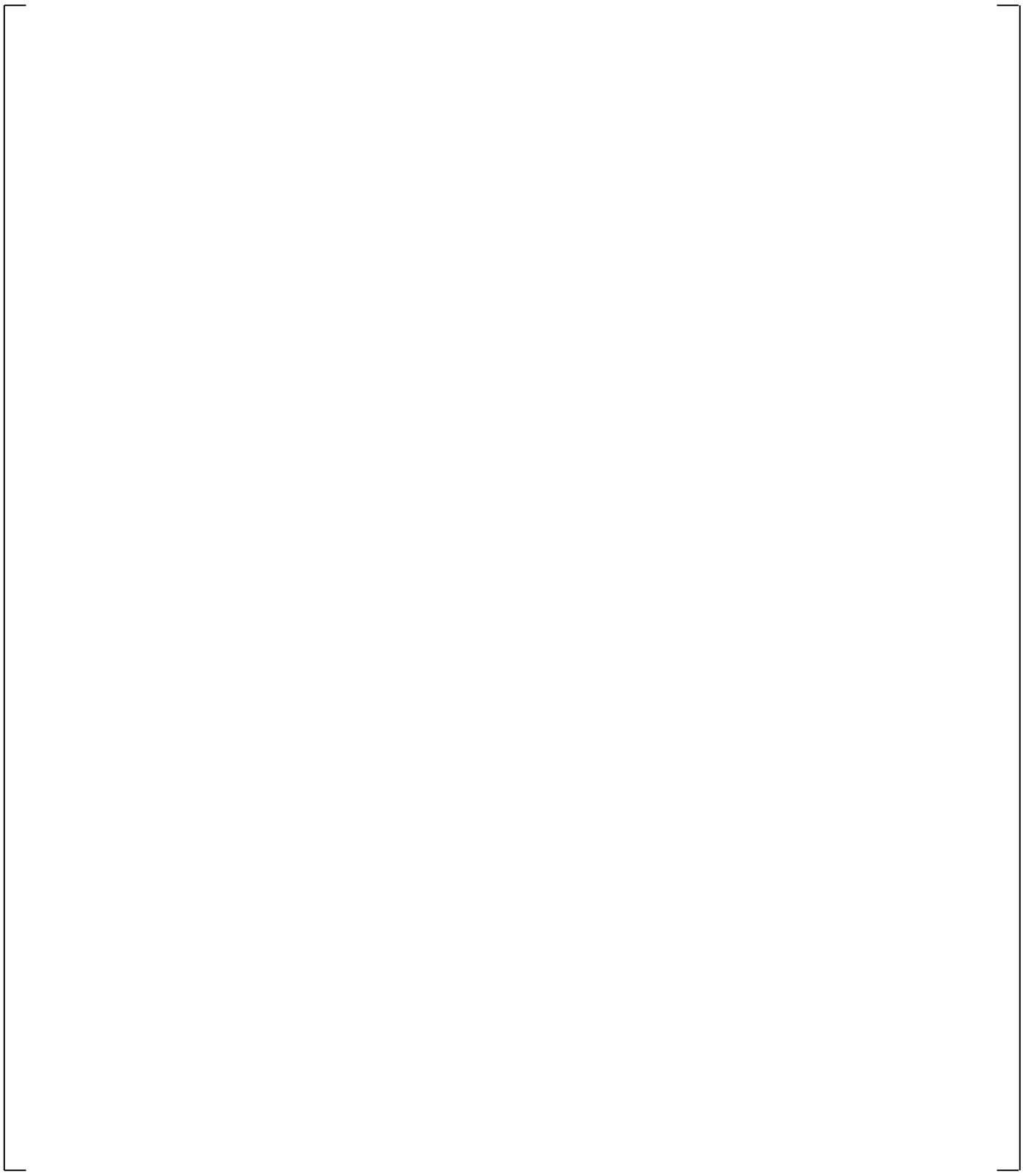

Figure 21.11.2-7 Peak Cladding Temperatures

21.11.3 Spray Nozzle Bypass Ranging Sensitivity with the SB-CL-18 Test

The purpose of this sensitivity is to investigate if ranging the spray bypass at **[ ]**[a,c] will have a significant effect on the transient.

The results of the sensitivity are presented in Figures 21.11.3-1 through 21.11.3-7. The top figure on each page is the high **[ ]**[a,c] bypass case and the bottom is the lower [ ]**[a,c] bypass case. The comparison of the calculation results, provided in this section shows that ranging the spray nozzle bypass [ ]**[a,c] of the desired steady state value has a small effect on the SB-CL-18 transient results.

Consistent with the trend established with the **[ ]**[a,c] bypass sensitivity presented in the previous Section 21.11.2, the loop seal clearance PCT is predicted to occur a little earlier with the smaller bypass case and the calculated boiloff PCT excursion is similar, Figure 21.11.3-7. In summary, ranging of the spray bypass **[ ]**[a,c] of the desired steady state value does not appear to have significant effect on the SBLOCA transient.

a,c

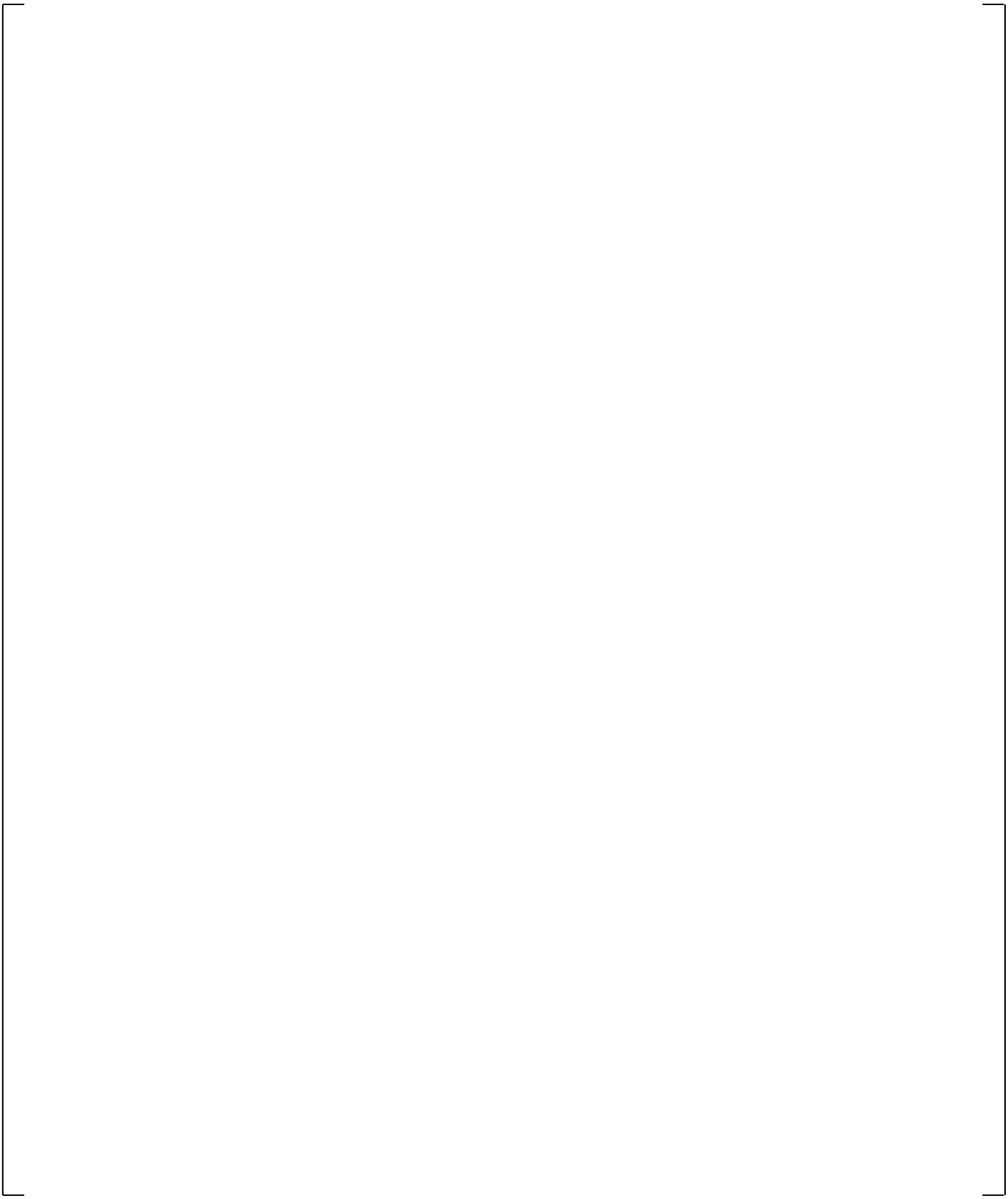

Figure 21.11.3-1 SB-CL-18 Cross-Over Leg A Differential Pressures

a,c

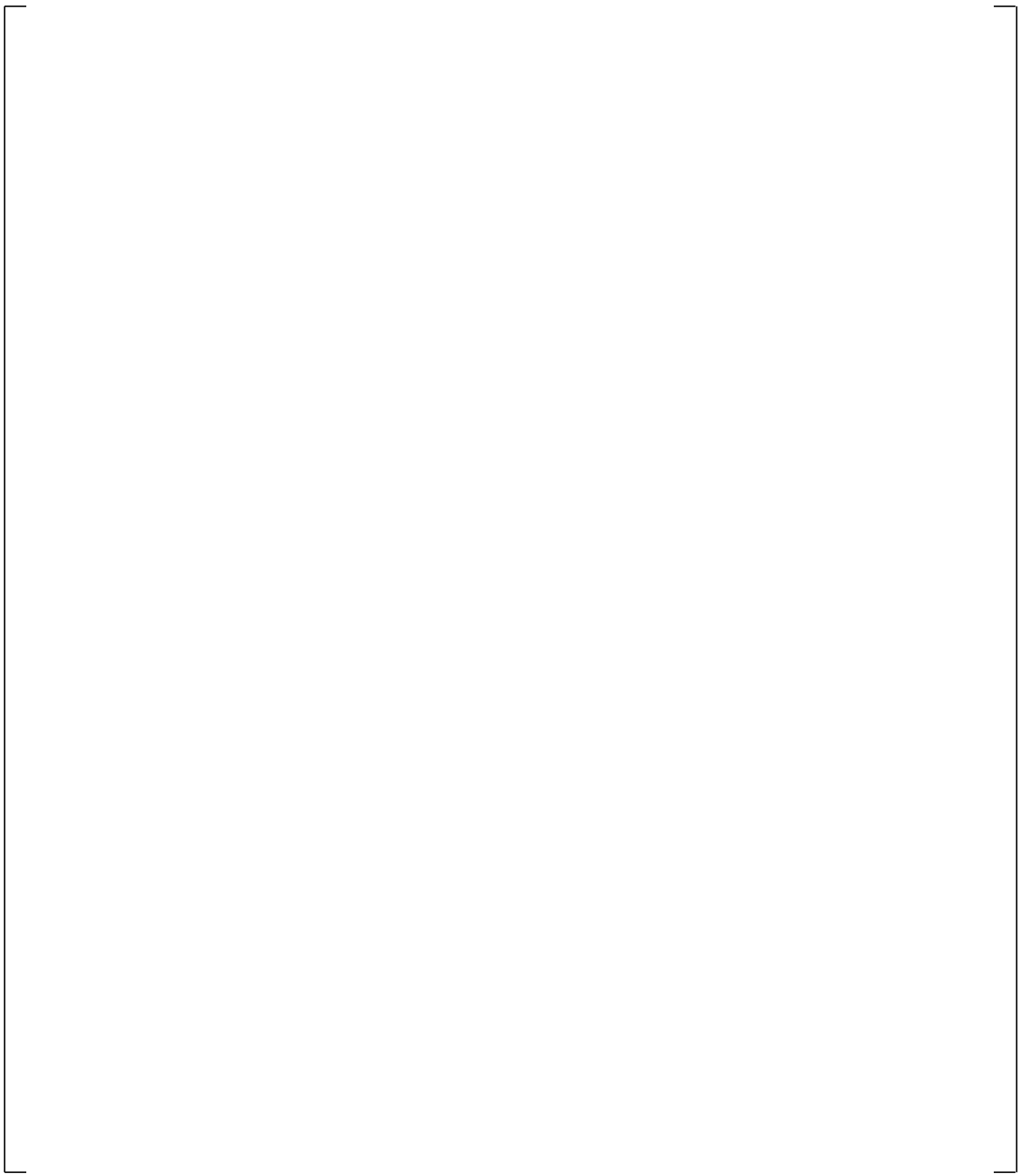

Figure 21.11.3-2 SB-CL-18 Cross-Over Leg B Differential Pressures

a,c

Figure 21.11.3-3 Inner Vessel Differential Pressures (LP+Core+UCP)

a,c

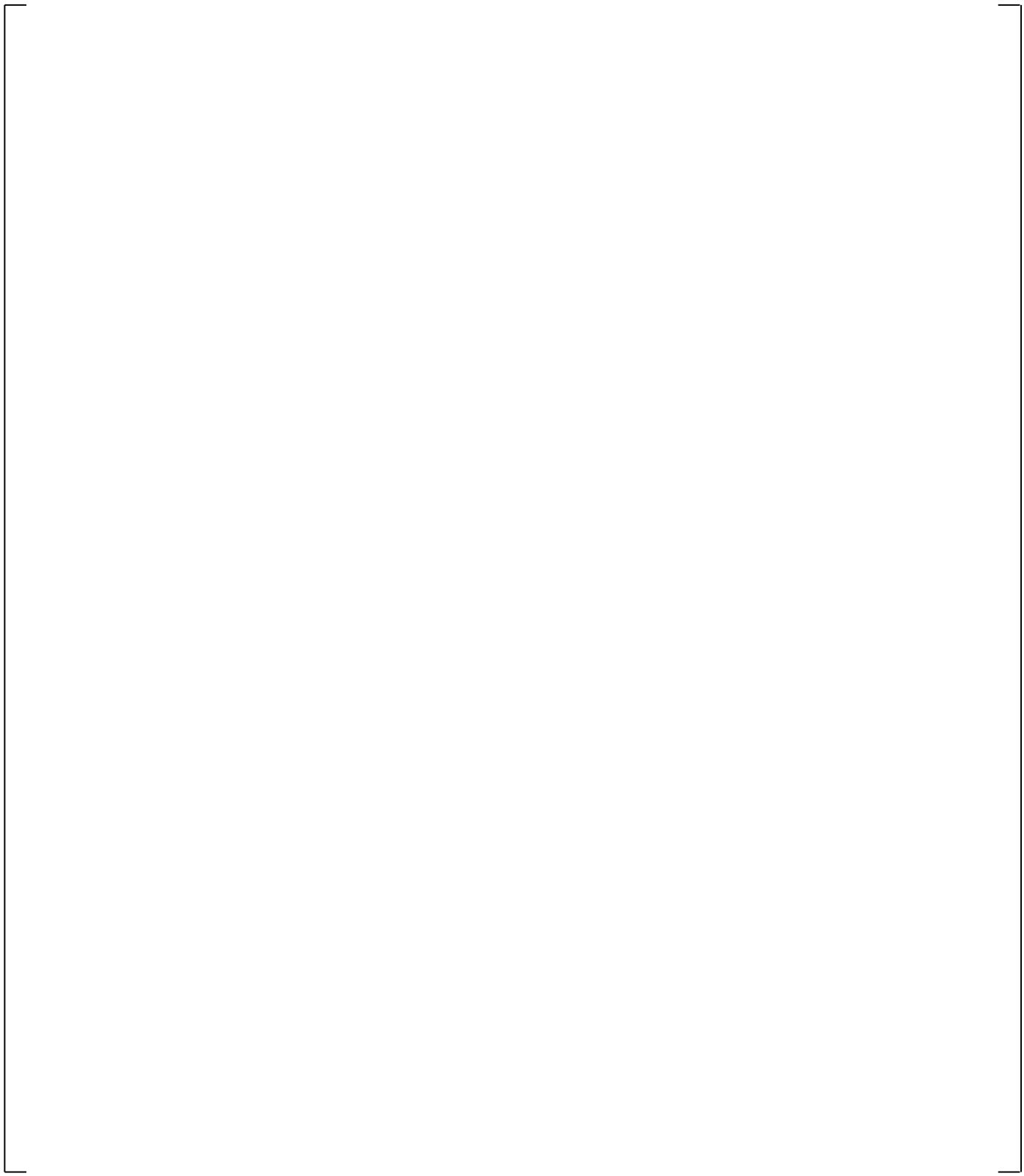

Figure 21.11.3-4 Downcomer Differential Pressures

a,c

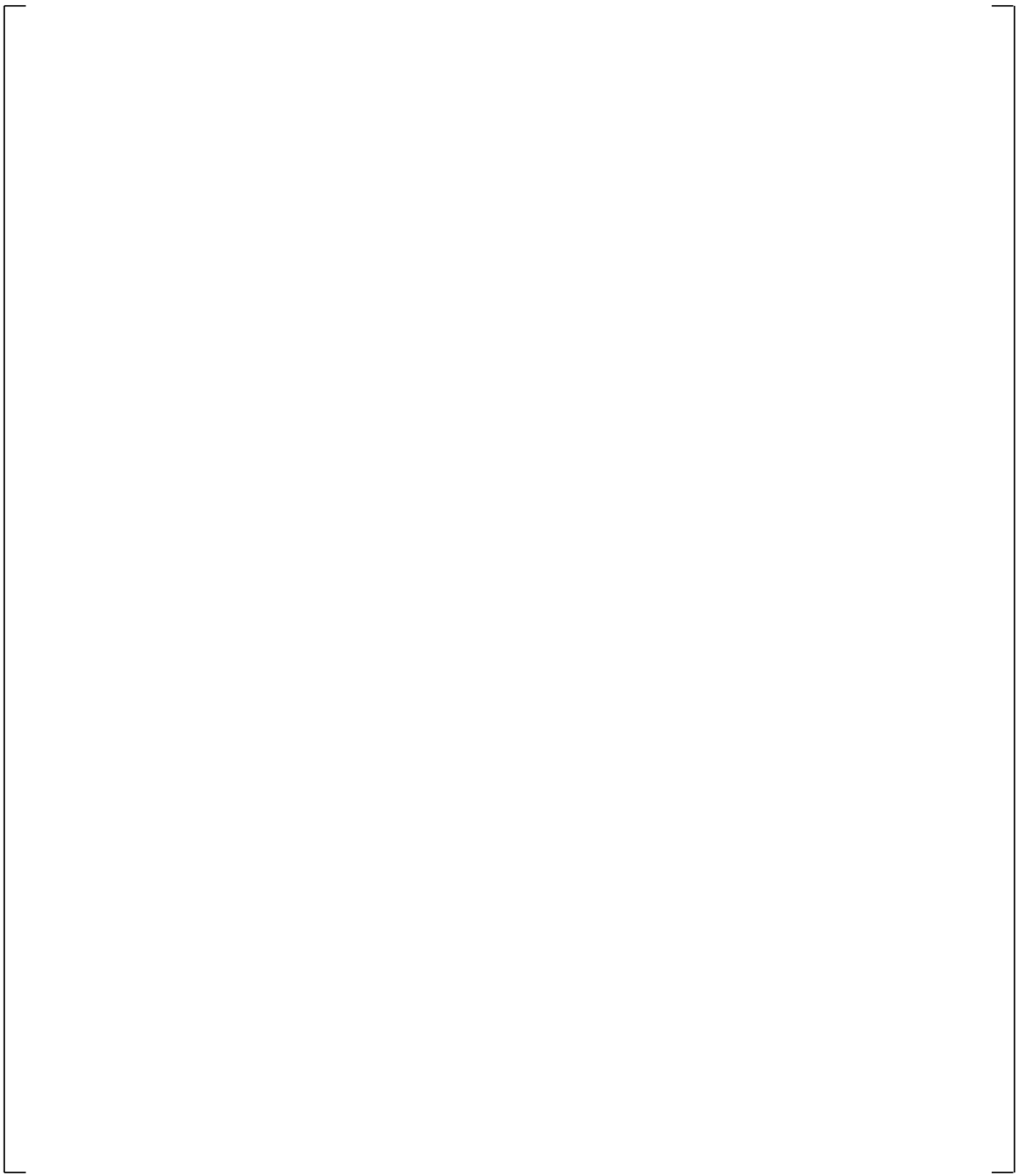

Figure 21.11.3-5 Lower Plenum Differential Pressures

a,c

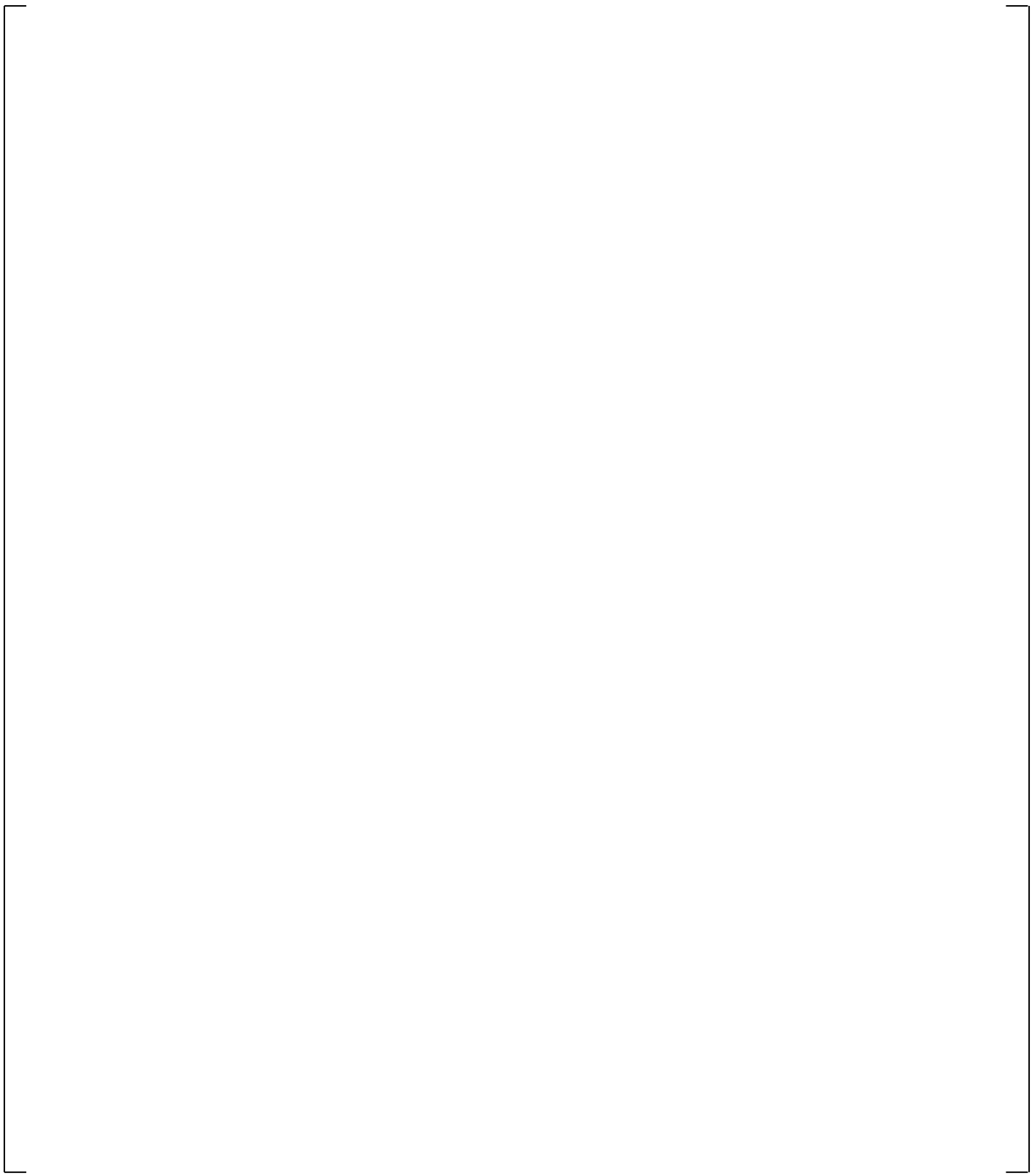

Figure 21.11.3-6 Upper Plenum Differential Pressures

a,c

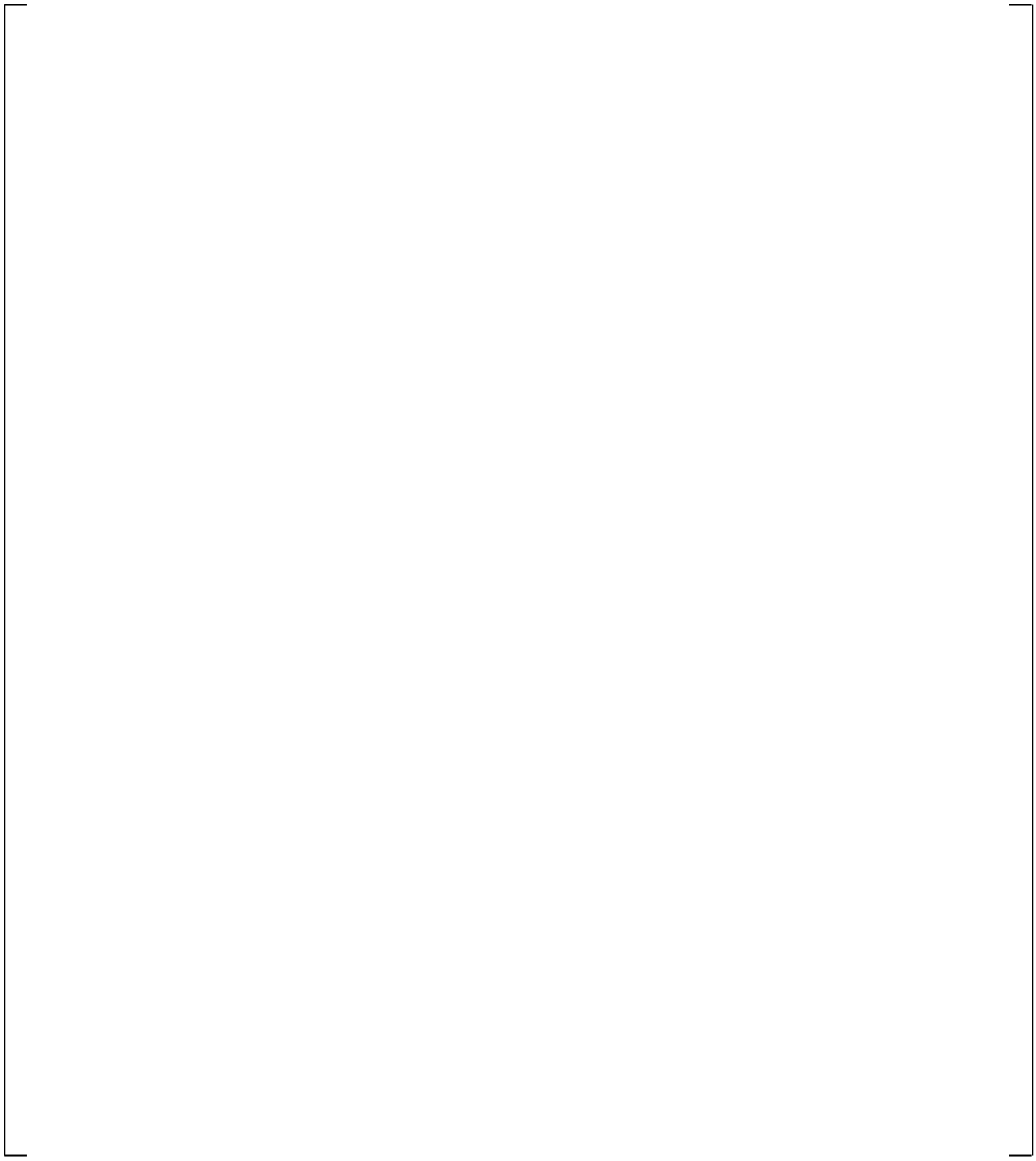

Figure 21.11.3-7 Peak Cladding Temperatures

21.12 SUB-COOLED BREAK DISCHARGE COEFFICIENT (CD1) SENSITIVITY

Two simulations of the SB-CL-18 test were performed implementing a sub-cooled break discharge coefficients (CD1) at high and low values. The extreme values of CD1 were set at **[**

][a,c]. It is acknowledged that the CD1 range considered in this sensitivity is different from the CD1 uncertainty range established from the validation of the critical flow model in Section 12. However, the range considered here is sufficient to provide sensitivity results to illustrate the importance of this parameter and support the decision on how to address it within the uncertainty treatment approach established for the FSLOCA methodology, Section 29, Volume 3.

Figures 21.12-1 through 21.12-19 show a comparison of the SB-CL-18 simulation results using the two extreme values of CD1. **[**

][a,c] For each of the simulations, the SB-CL-18 test measurements are presented in the figures as well.

Obviously, the effect of the extreme CD1 variation manifests from the very early stages of the transient. The higher CD1 coefficient results in a visibly higher peak of the break flow, Figure 21.12-1. The increased loss of inventory with the higher CD1 results in earlier transition to two-phase discharge, Figure 21.12-2, and earlier loop seal clearance, Figures 21.12-3 and 21.12-4. The system depressurization is visibly affected as well, Figure 21.12-5.

The draining of the uphill side of the steam generator tubes occurs visibly earlier in the simulation with the higher CD1 coefficient, Figures 21.12-6 to 21.12-9. With the higher CD1, the draining of the steam generator inlet plenums, Figures 21.12-10 and 21.12-11, and the hot legs, Figures 21.12-12 and 21.12-13, is predicted to occur relatively earlier as well. The calculated differential pressures in the different regions of the test facility is consistent with the expected effect of the inventory lost, which is dependent on the value of CD1, see Figures 21.12-14 through 21.12-17.

[

][a,c]

As a result of the greater inventory loss with the higher CD1, the accumulator injection is predicted to occur earlier than the case with low CD1, see Figure 21.12-19.

a,c

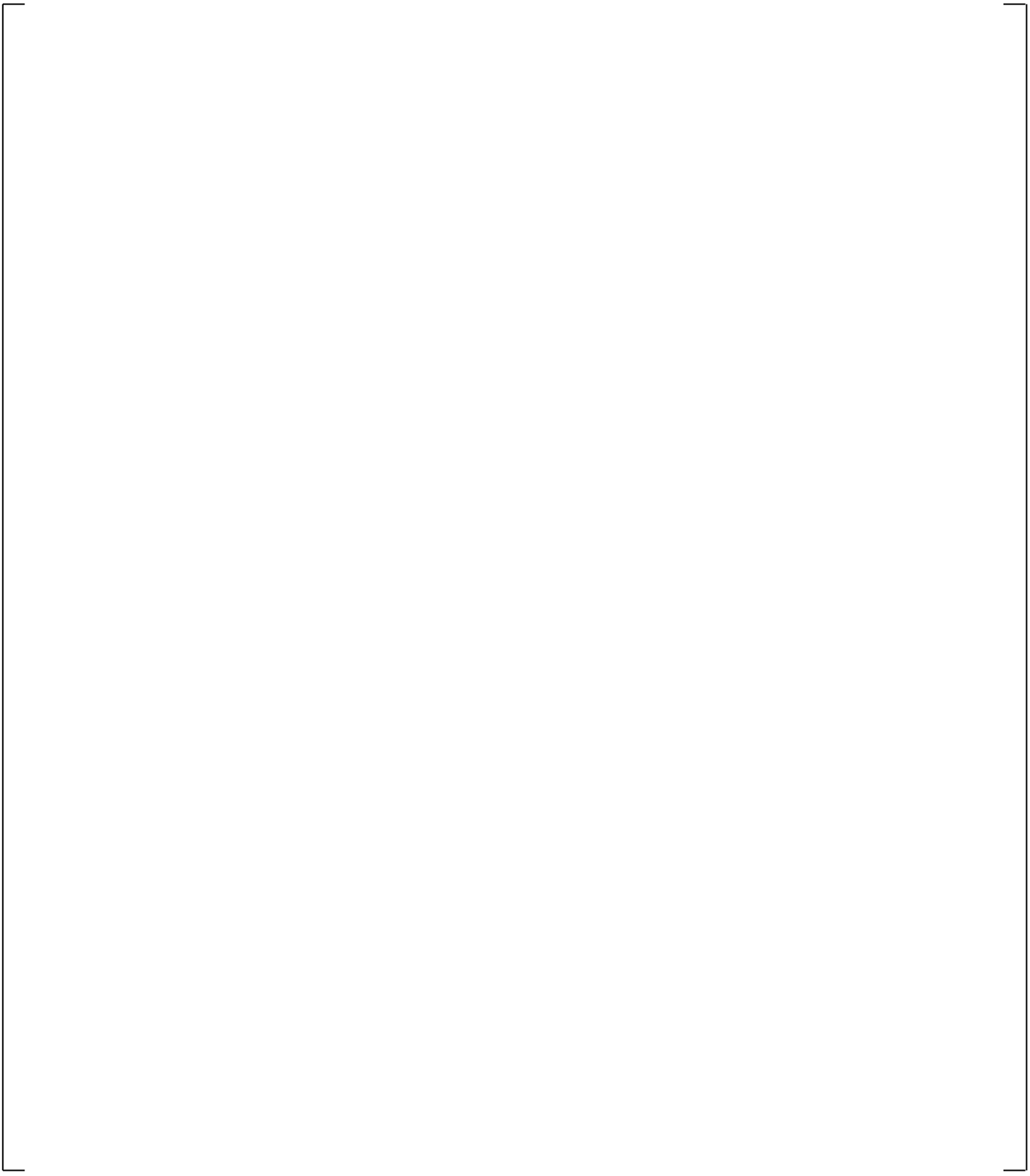

Figure 21.12-1 Break Flows

a,c

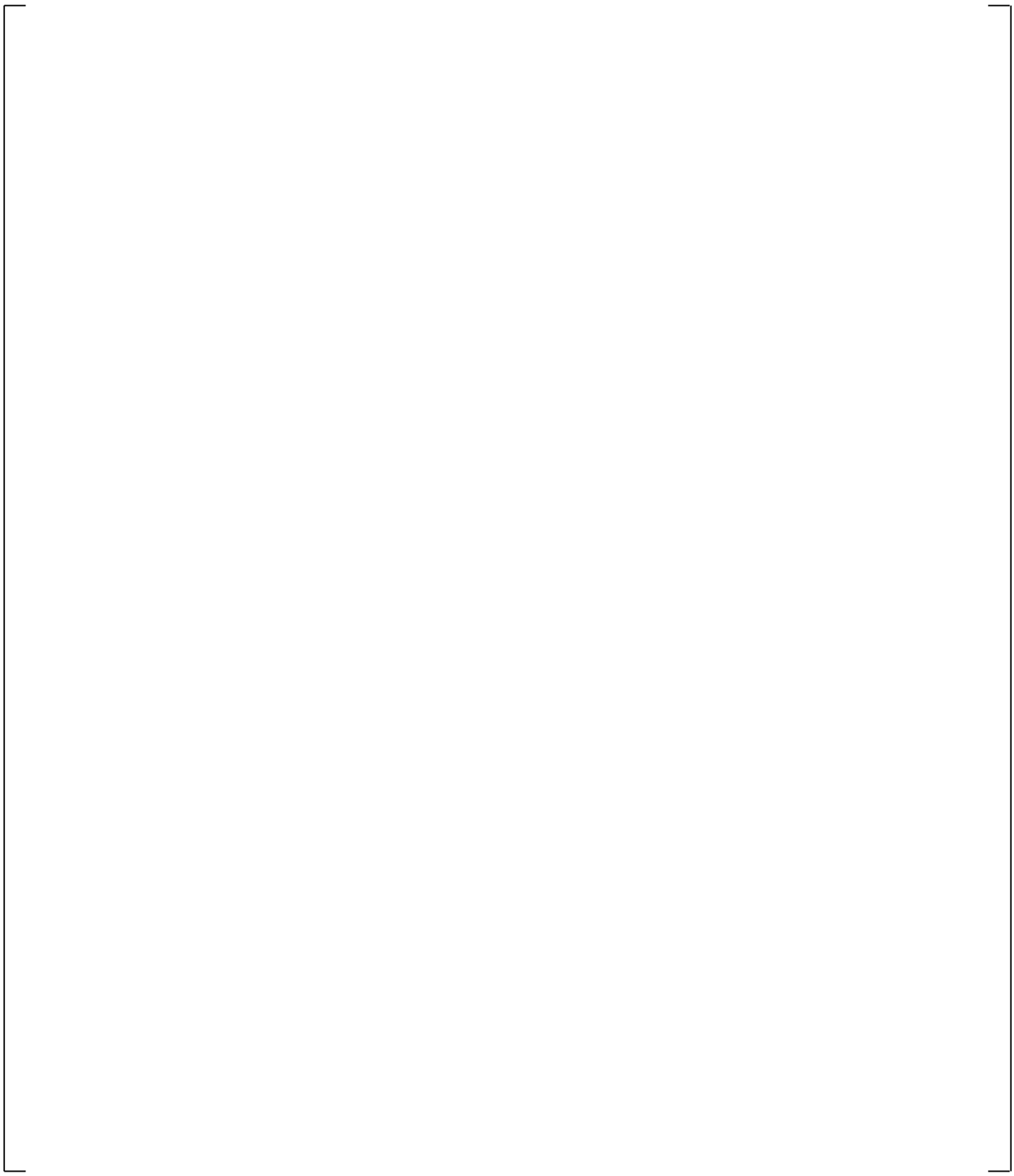

Figure 21.12-2 Calculated Break Void Fraction

a,c

Figure 21.12-3 Cross-Over Leg A Differential Pressures

a,c

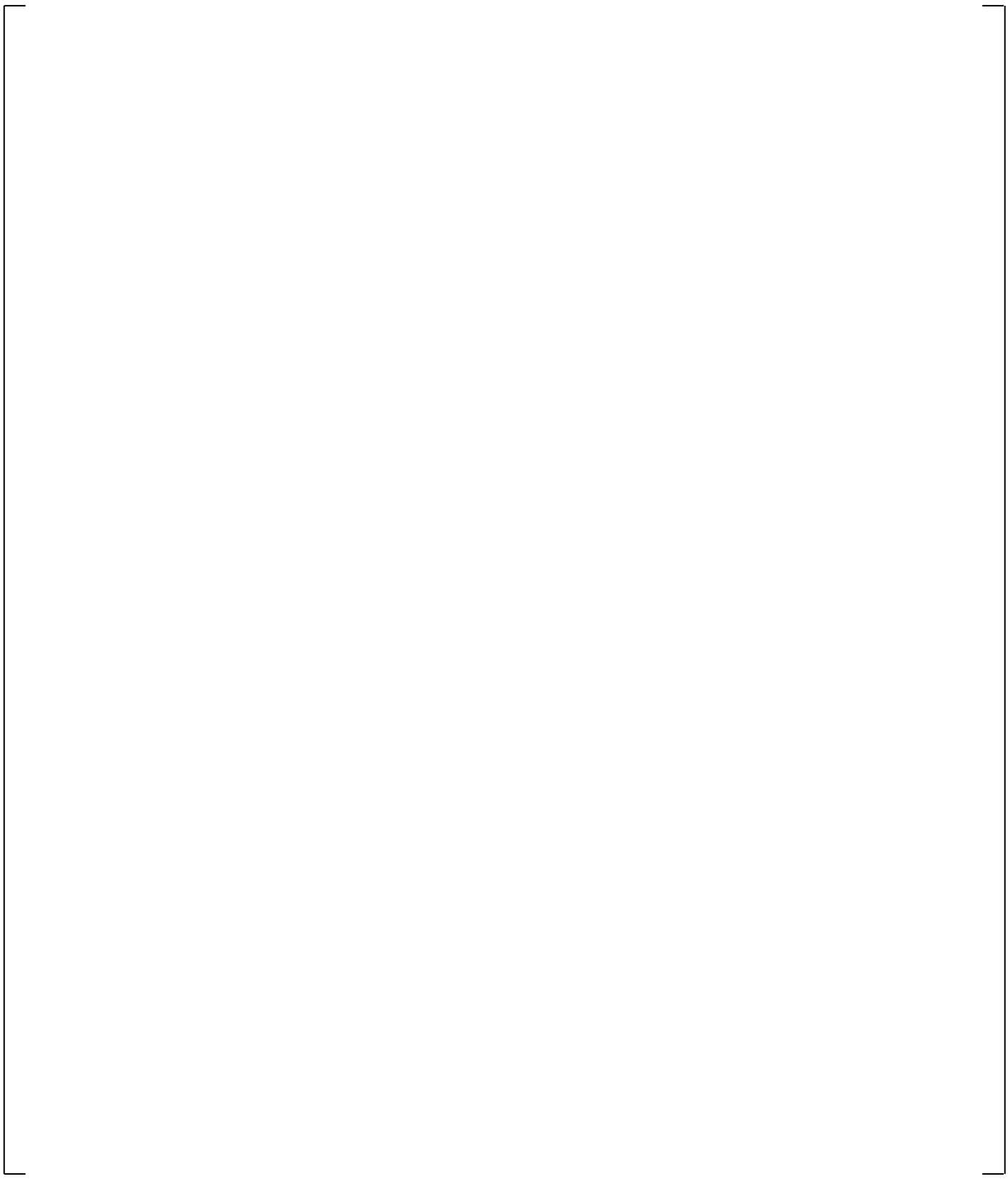

Figure 21.12-4 Cross-Over Leg B Differential Pressures

a,c

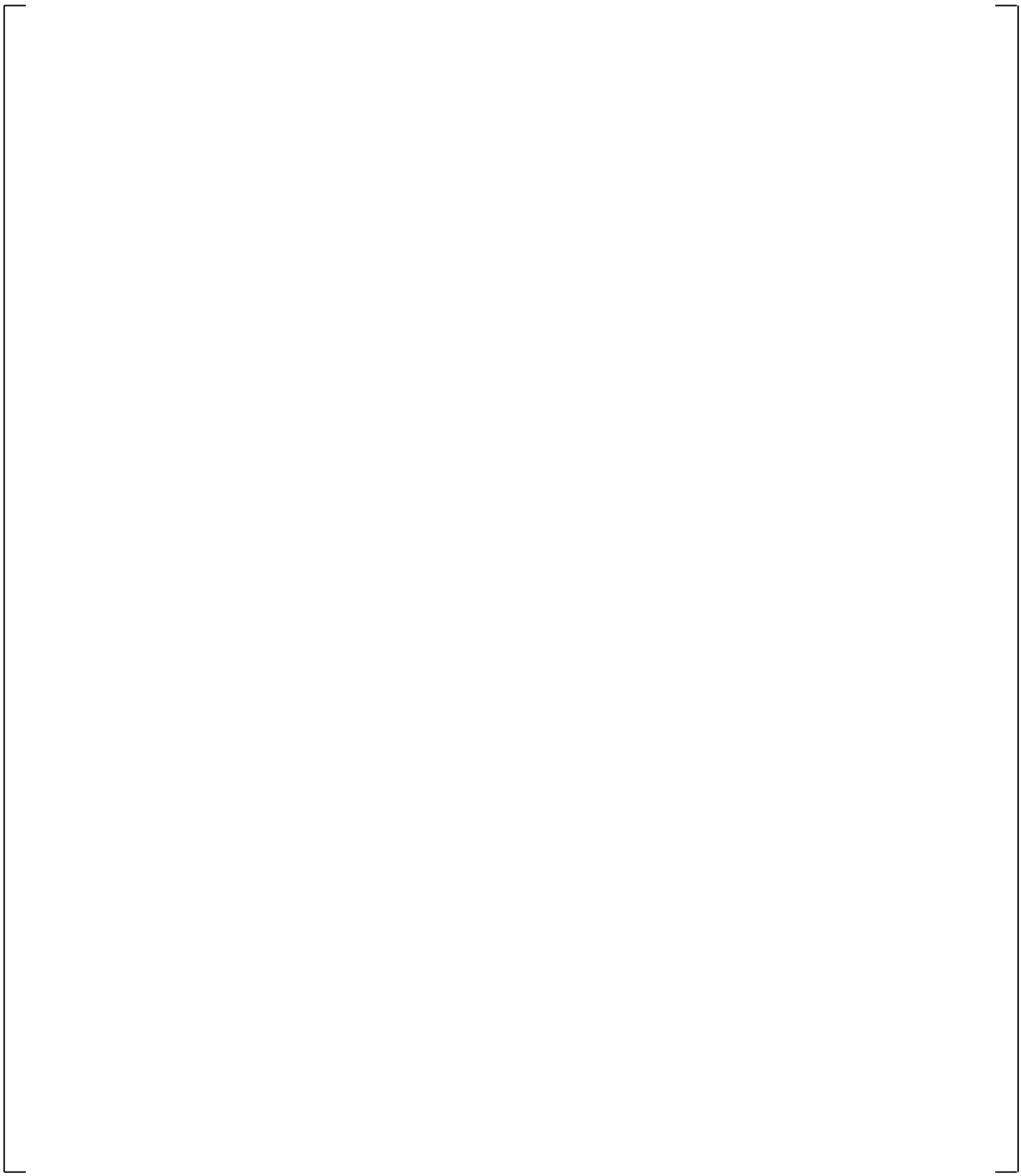

Figure 21.12-5 Pressurizer Pressures

a,c

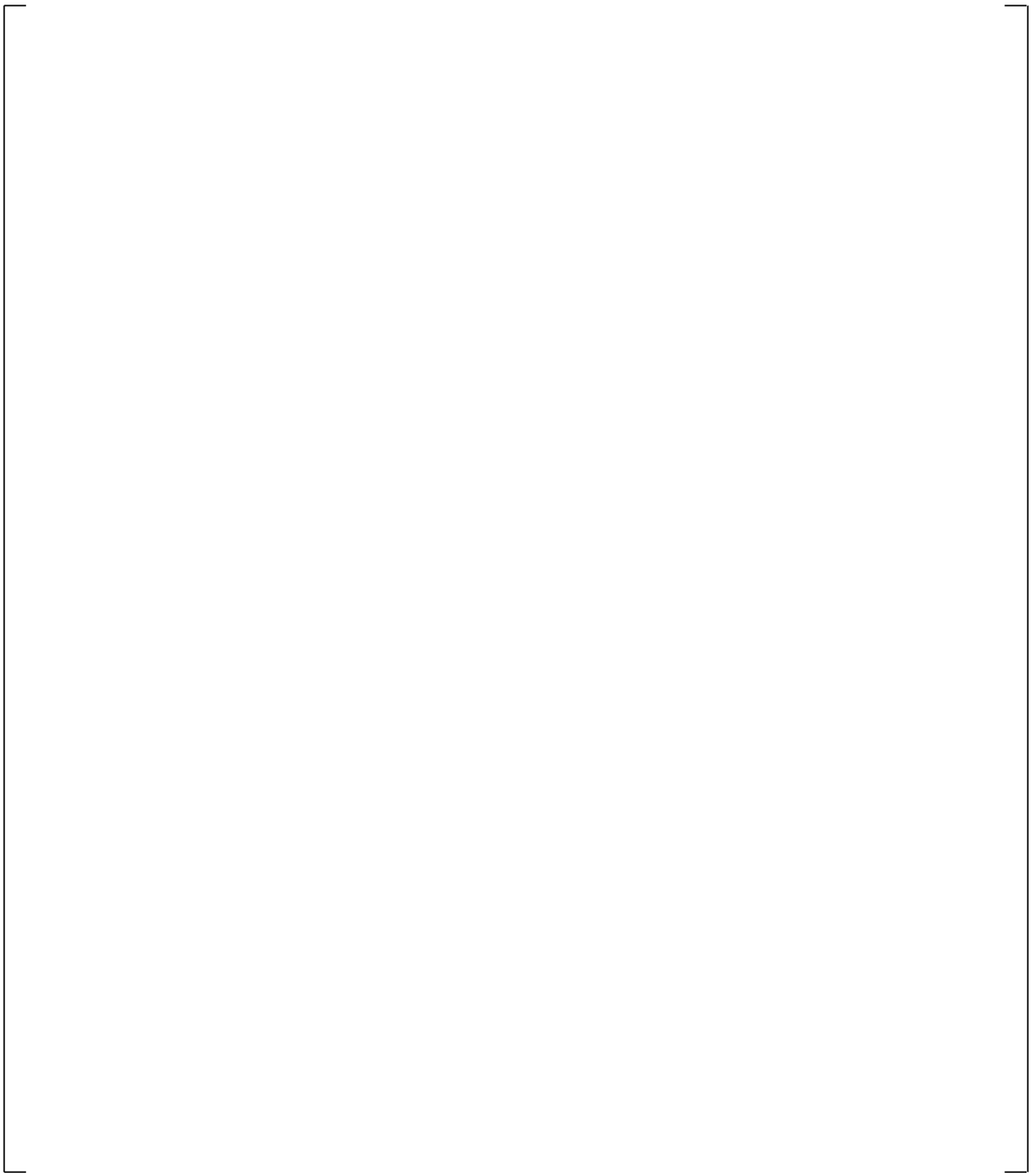

Figure 21.12-6 Steam Generator A U-tubes Inlet-to-Top Differential Pressure

a,c

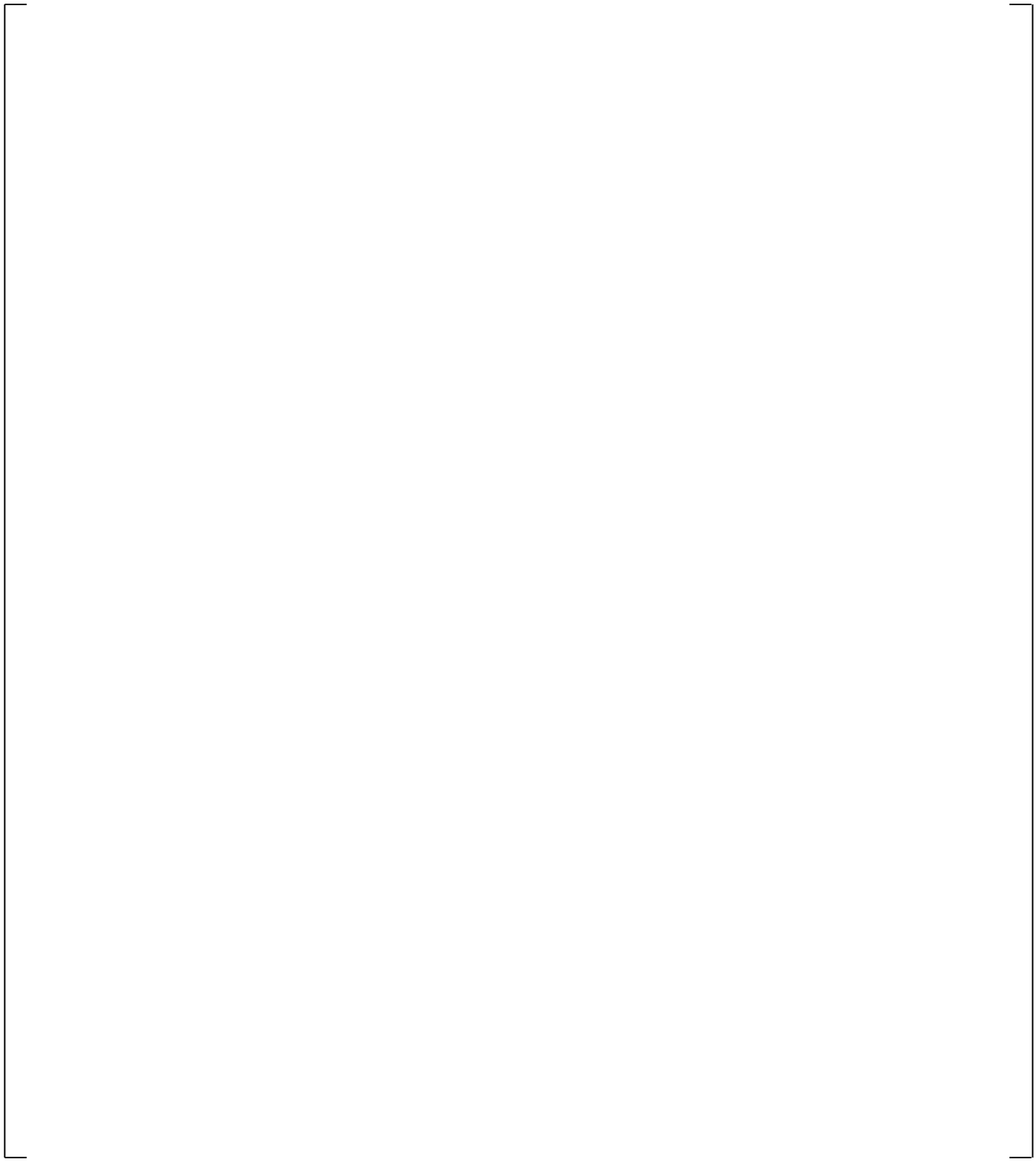

Figure 21.12-7 Steam Generator B U-tubes Inlet-to-Top Differential Pressures

a,c

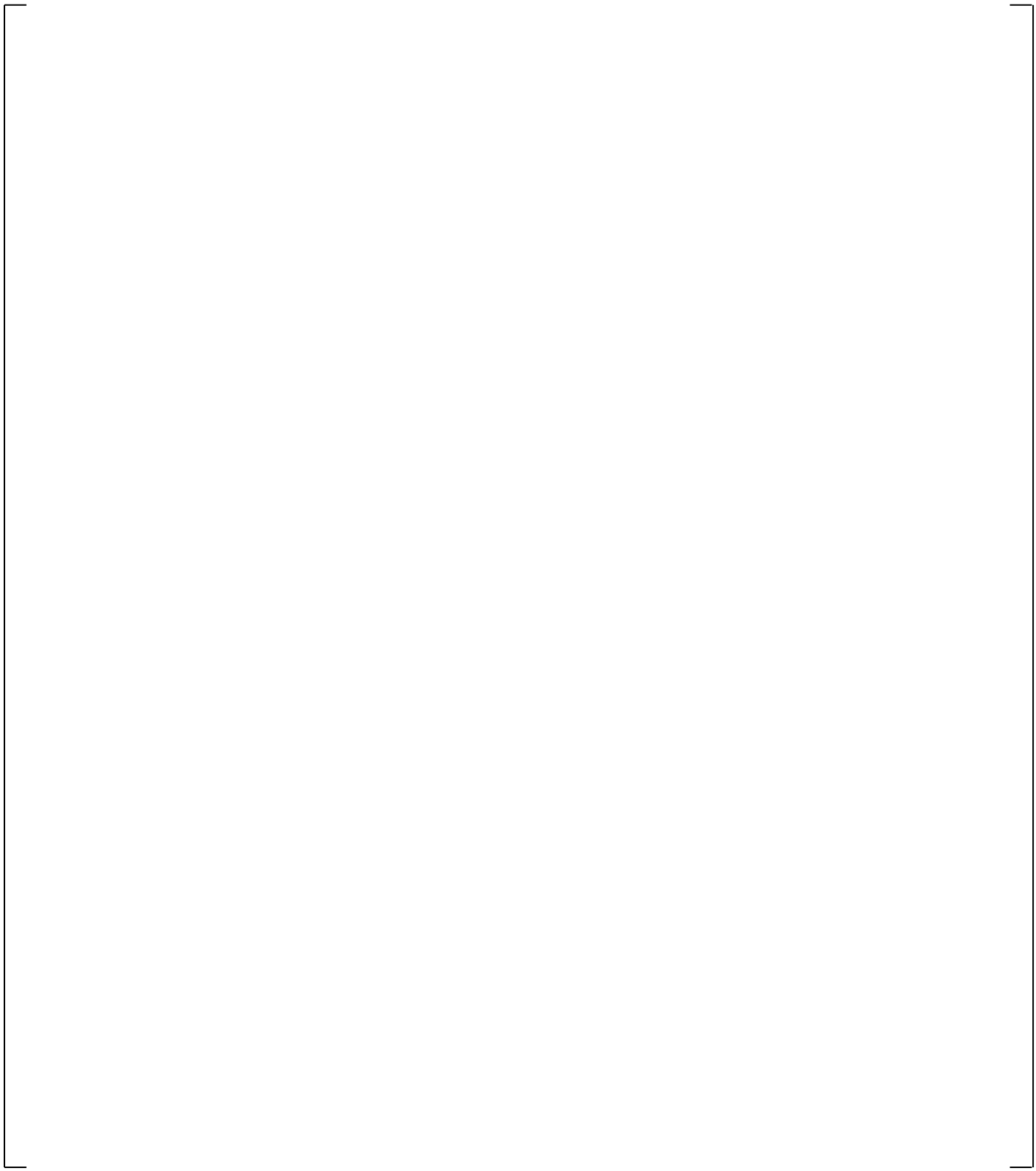

Figure 21.12-8 Steam Generator A U-tubes Outlet-to-Top Differential Pressures

a,c

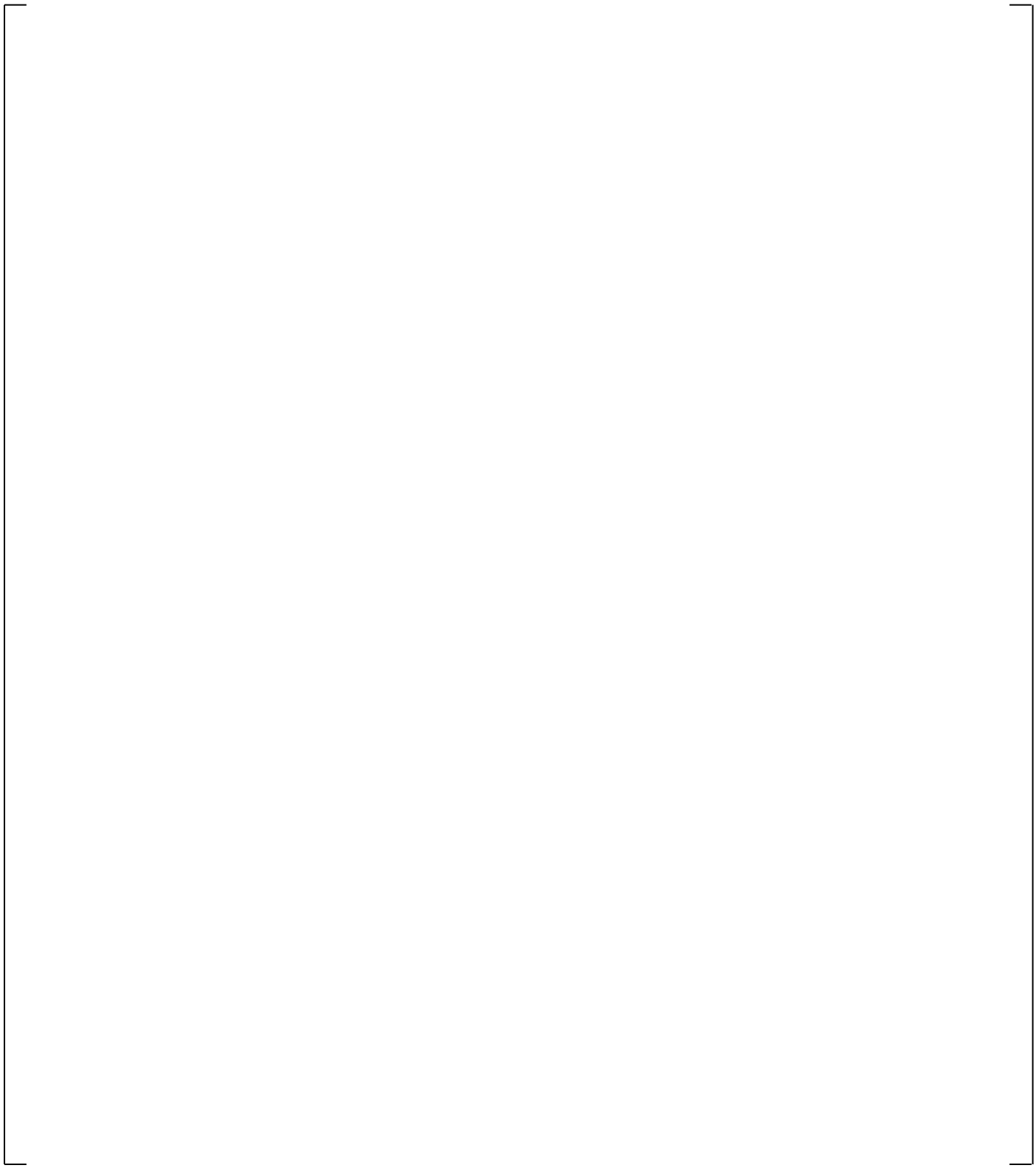

Figure 21.12-9 Steam Generator B U-tube Outlet-to-Top Differential Pressures

a,c

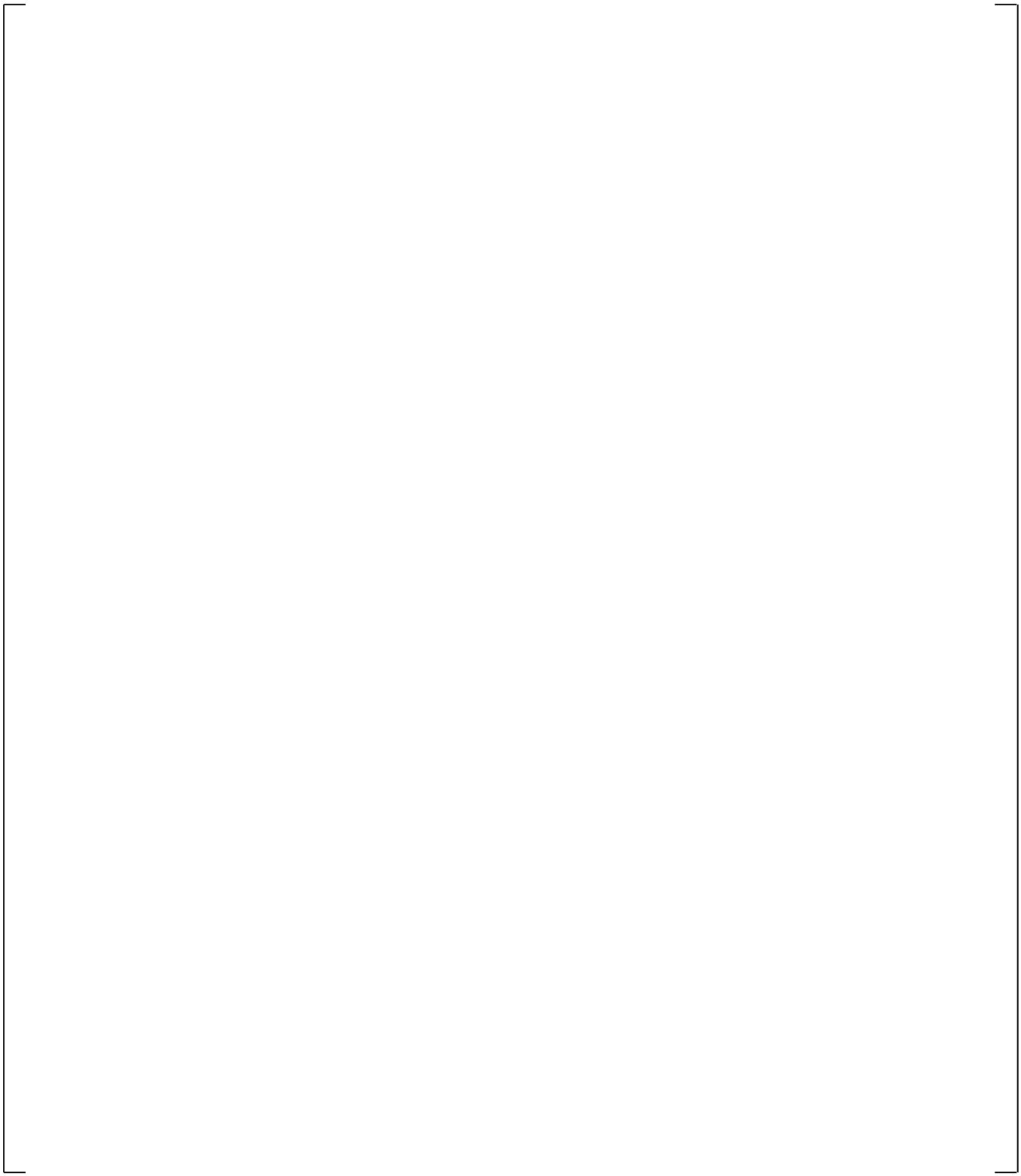

Figure 21.12-10 Steam Generator A Inlet Plenum Collapsed Liquid Levels

a,c

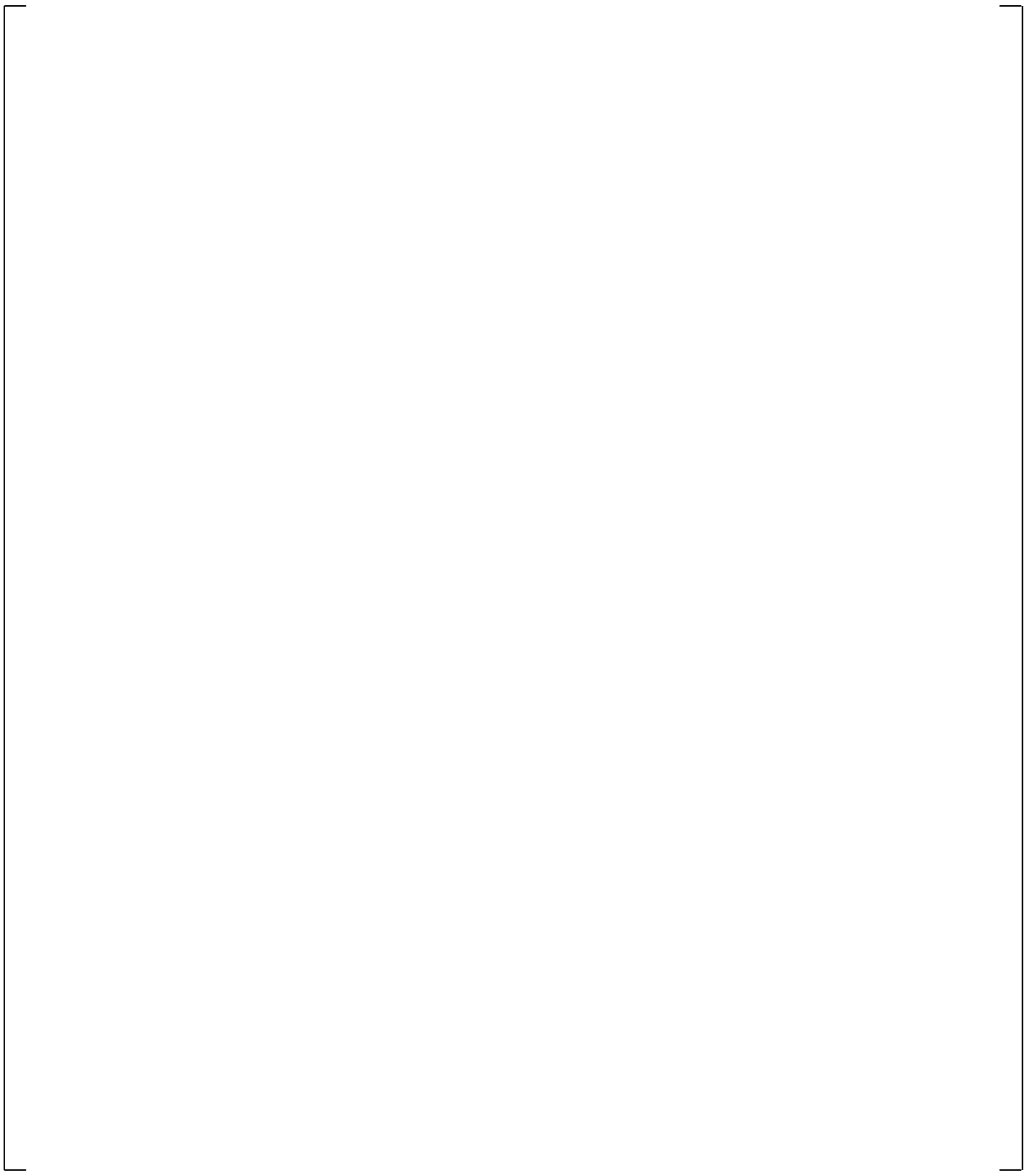

Figure 21.12-11 Steam Generator B Inlet Plenum Collapsed Liquid Levels

a,c

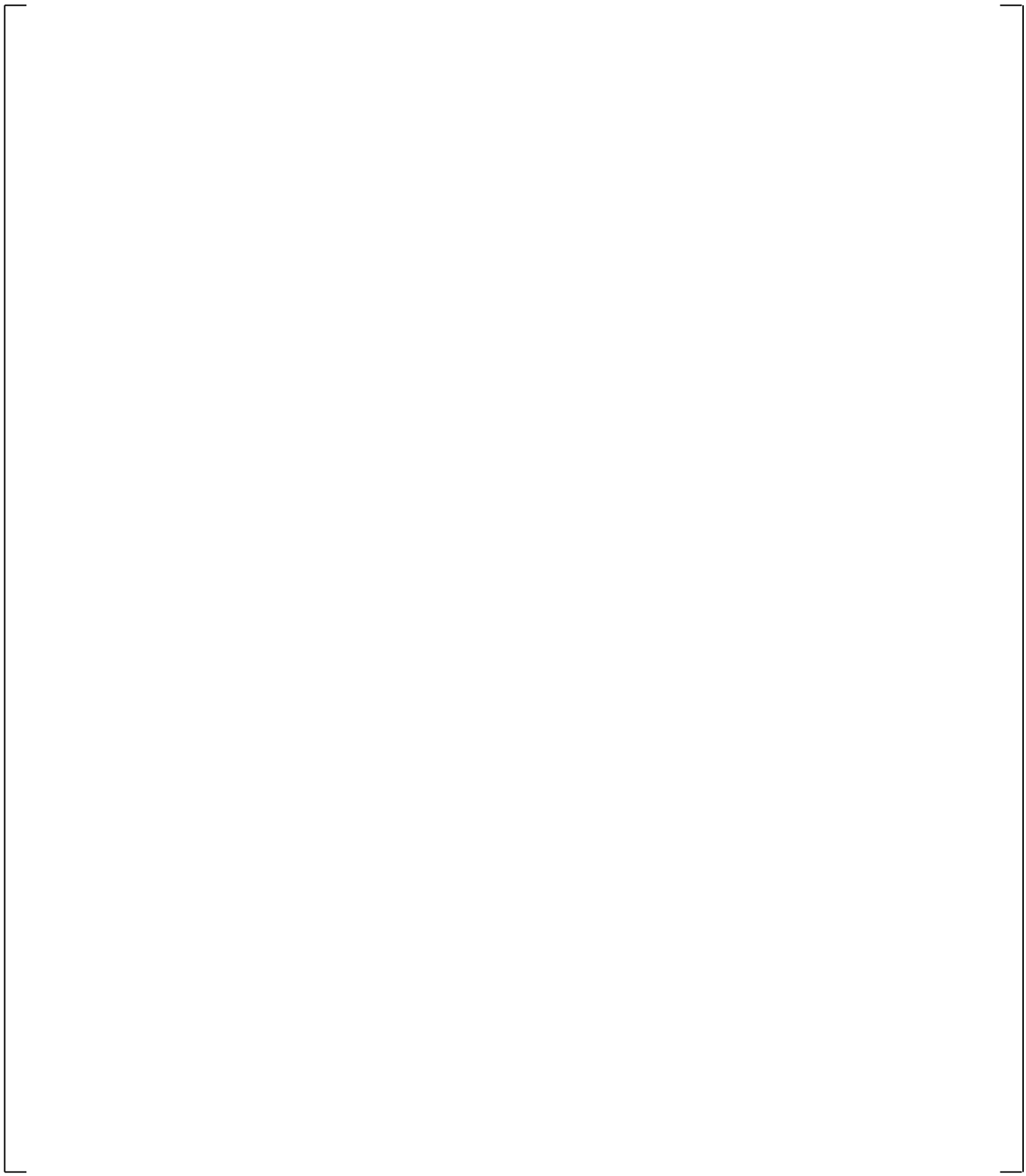

Figure 21.12-12 Upper Plenum to Steam Generator A Inlet Differential Pressures

a,c

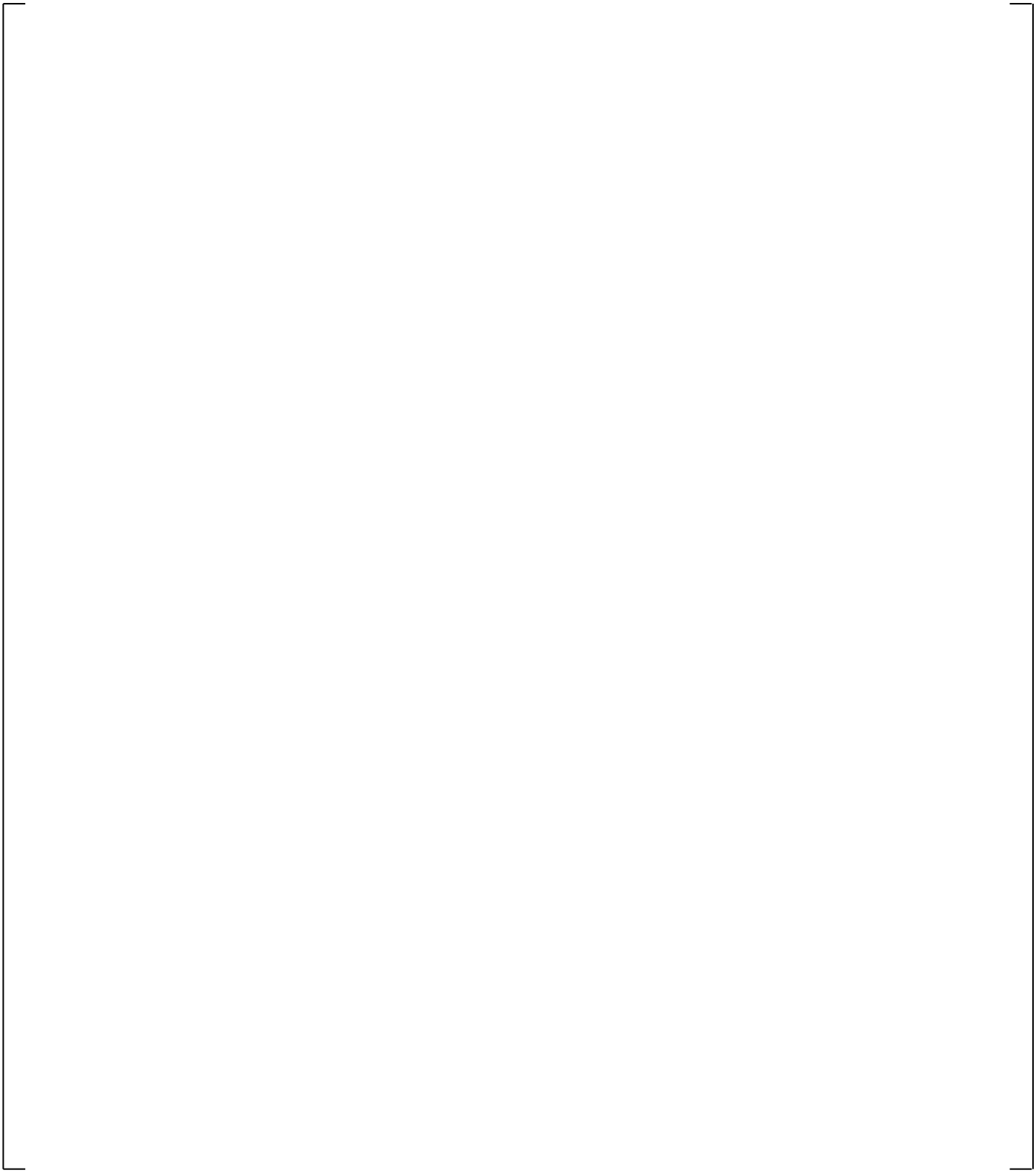

Figure 21.12-13 Upper Plenum to Steam Generator B Inlet Differential Pressures

a,c

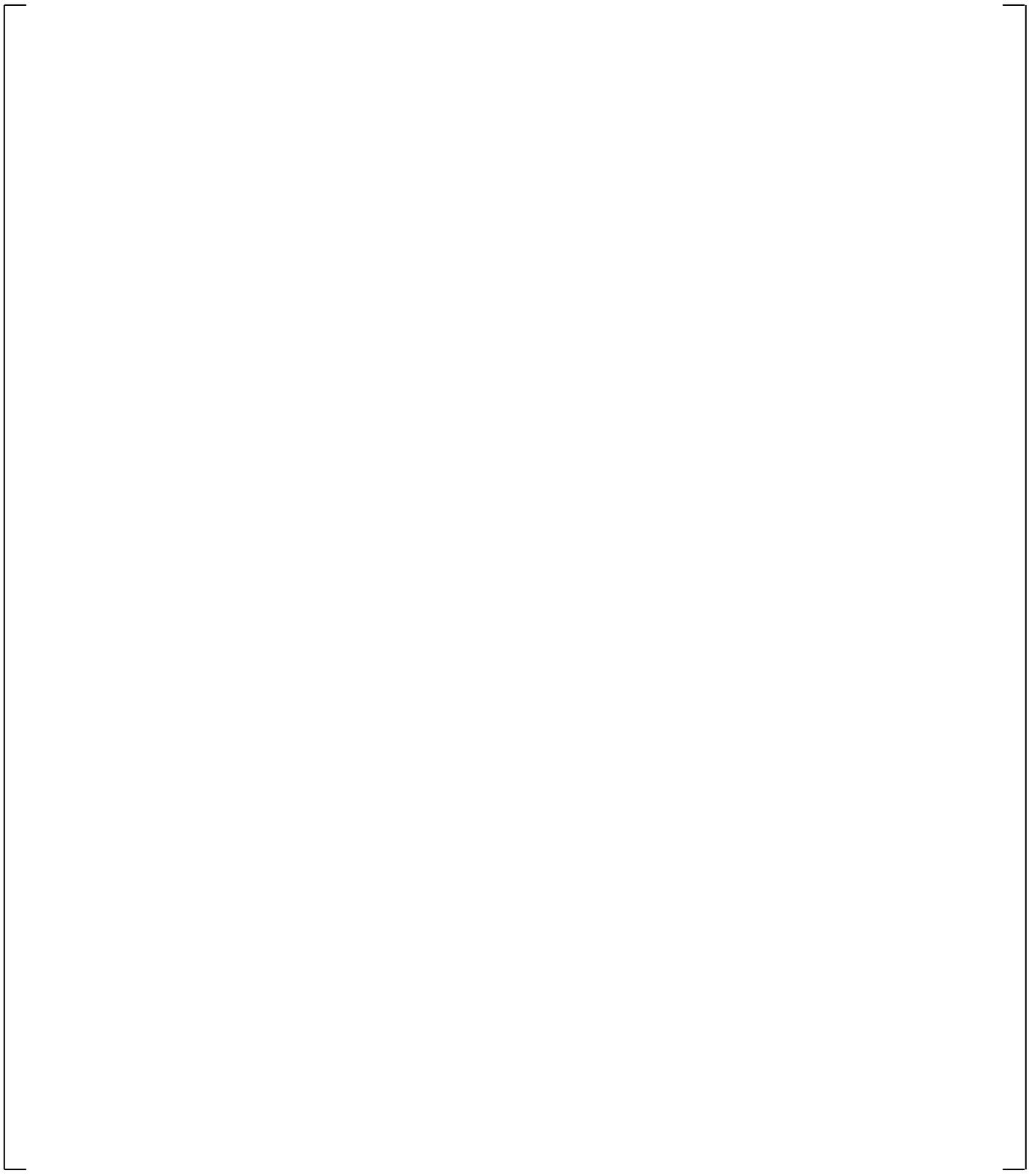

Figure 21.12-14 Downcomer Differential Pressures

a,c

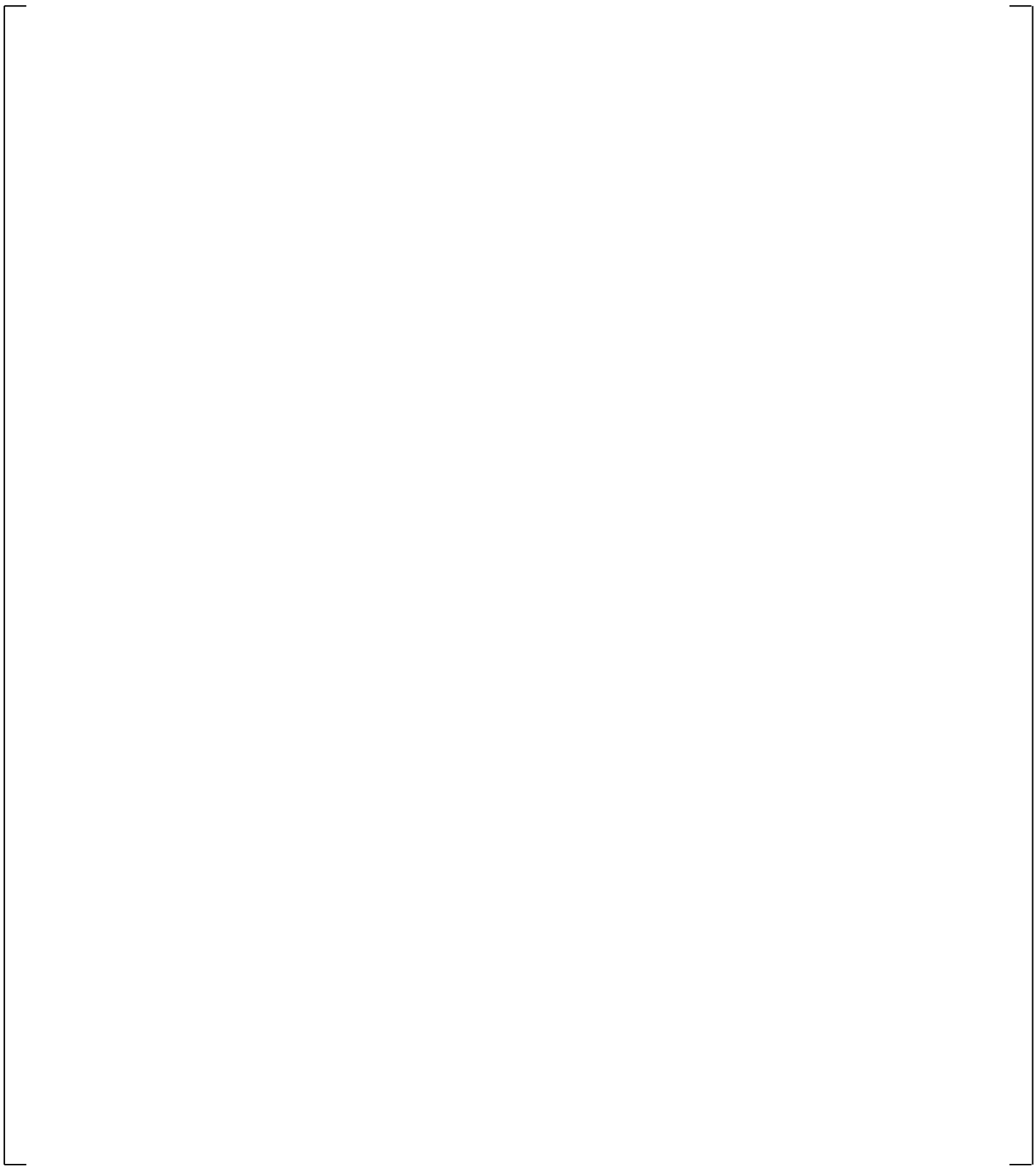

Figure 21.12-15 Upper Plenum Differential Pressures

a,c

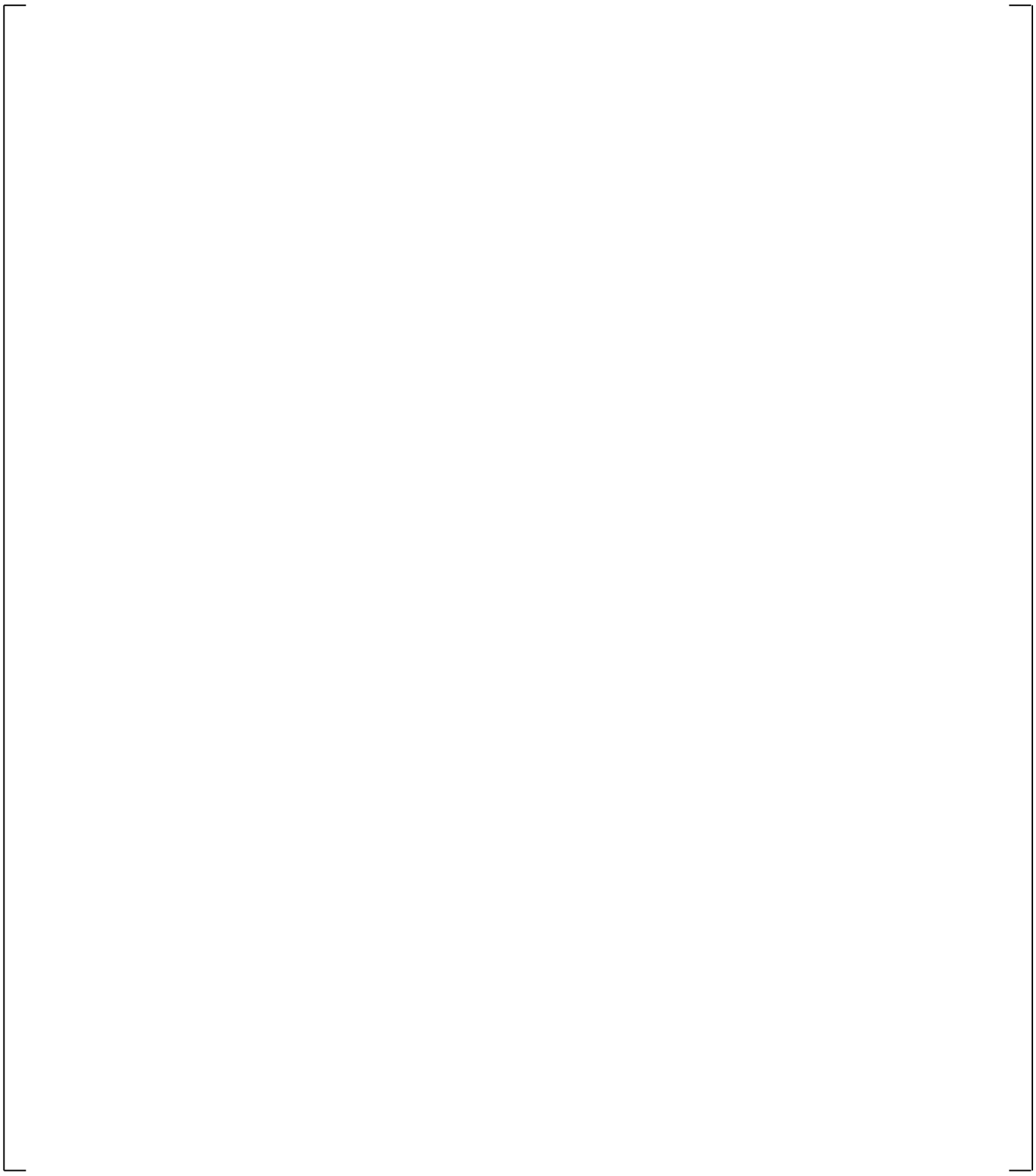

Figure 21.12-16 Inner Vessel (LP+Core+UP) Differential Pressures

a,c

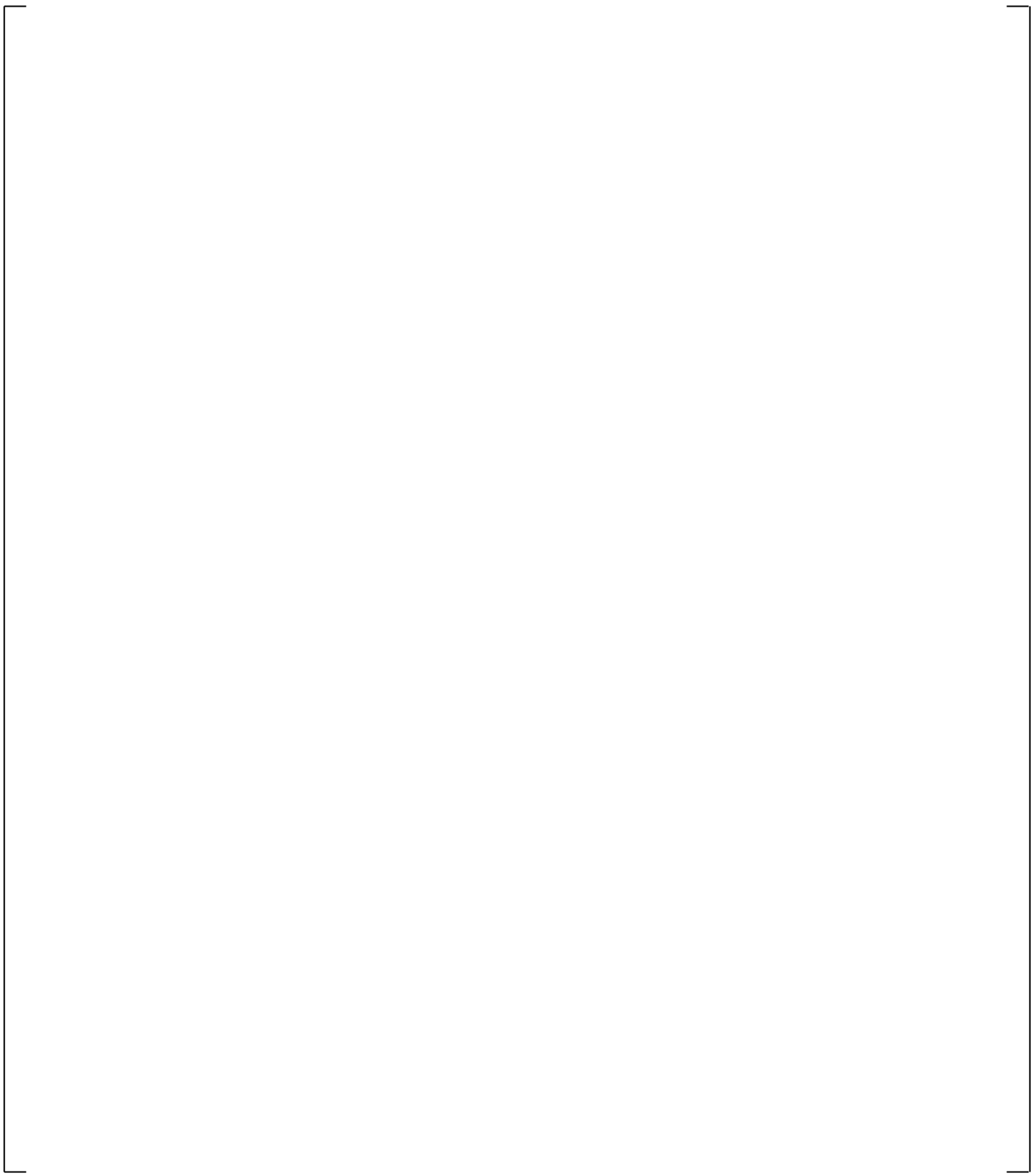

Figure 21.12-17 Lower Plenum Differential Pressures

a,c

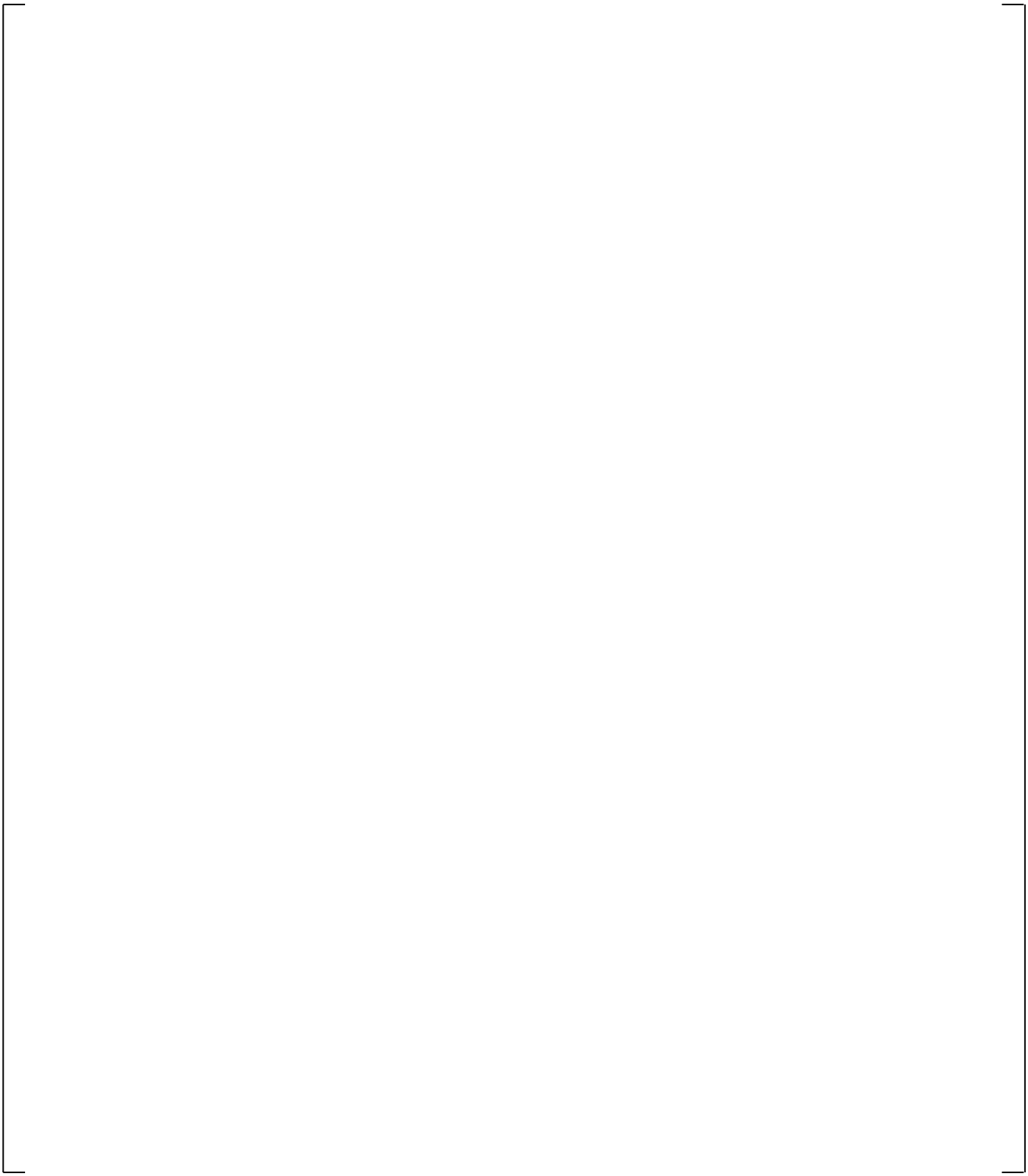

Figure 21.12-18 Peak Cladding Temperatures

a,c

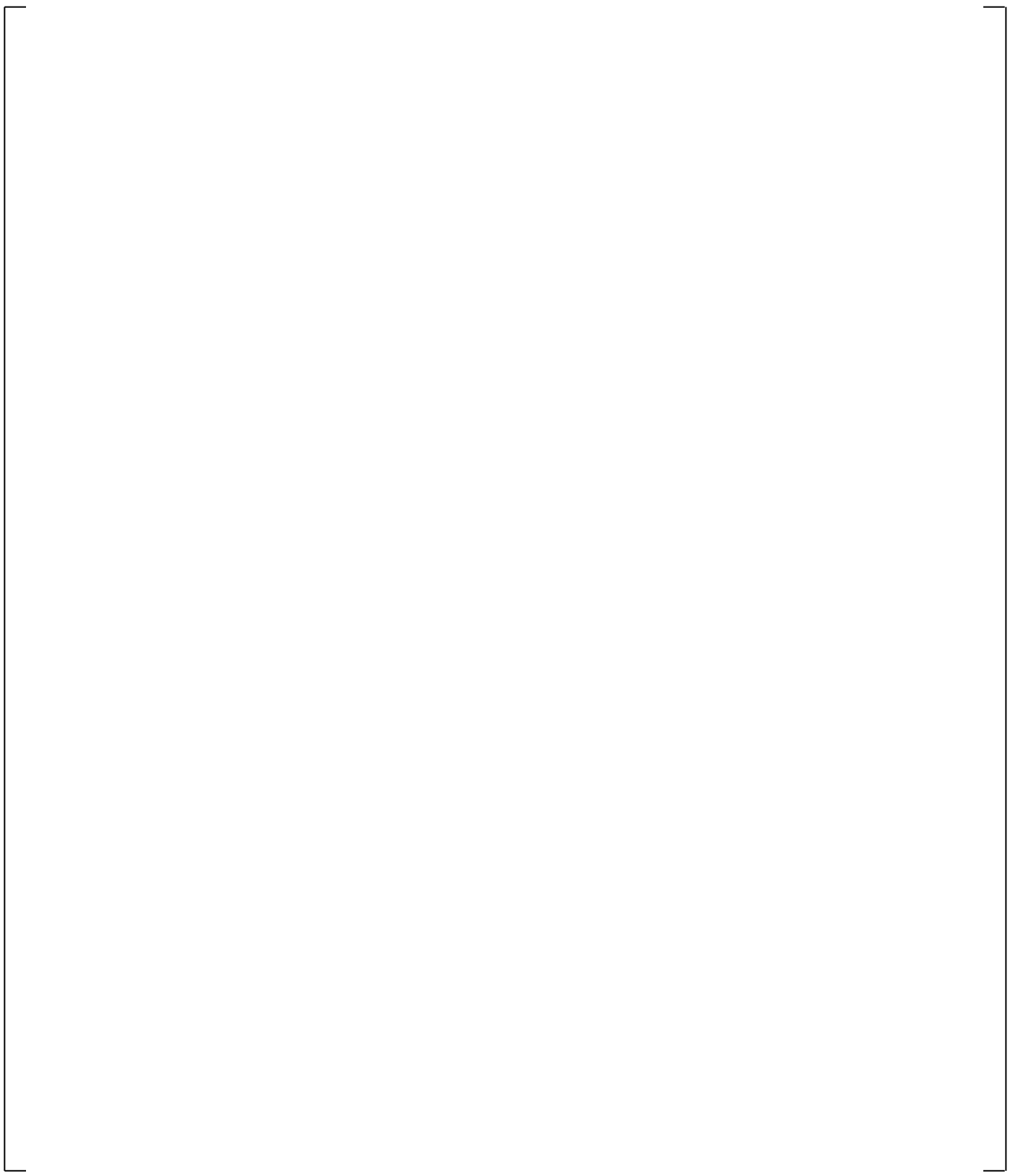

Figure 21.12-19 Accumulator A Injection Flows

21.13 TWO-PHASE BREAK DISCHARGE COEFFICIENT (CD2) SENSITIVITY

The effect of the two-phase break discharge coefficient (CD2) on the small break LOCA transient is shown by comparison of two simulations of the SB-CL-18 test. **[**

][a,c]

The results of the two simulations are presented in Figures 21.13-1 through 21.13-19. **[**

][a,c]

Since the sub-cooled discharge coefficient used in the two simulations was the same, the initial break flow until the time when transition to two-phase flow occurred was not affected, Figure 21.13-1. There is a small difference in the calculated break flow (Figure 21.13-1) during the transition from sub-cooled to two-phase, **[**

][a,c]

The system depressurization rate is visibly affected by the CD2 coefficient during the period of the transient following loop seal clearance, Figure 21.13-5. The case with higher CD2 resulted in faster system depressurization after the loop seals cleared. As a result, the earlier accumulator injection calculated in the simulation with higher CD2 coefficient, Figure 21.13-19.

The draining of the steam generator U-tubes and inlet and outlet plenums is not affected by CD2 as well, Figures 21.13-6 through 21.13-11.

[

][a,c]

[

][a,c]

a,c

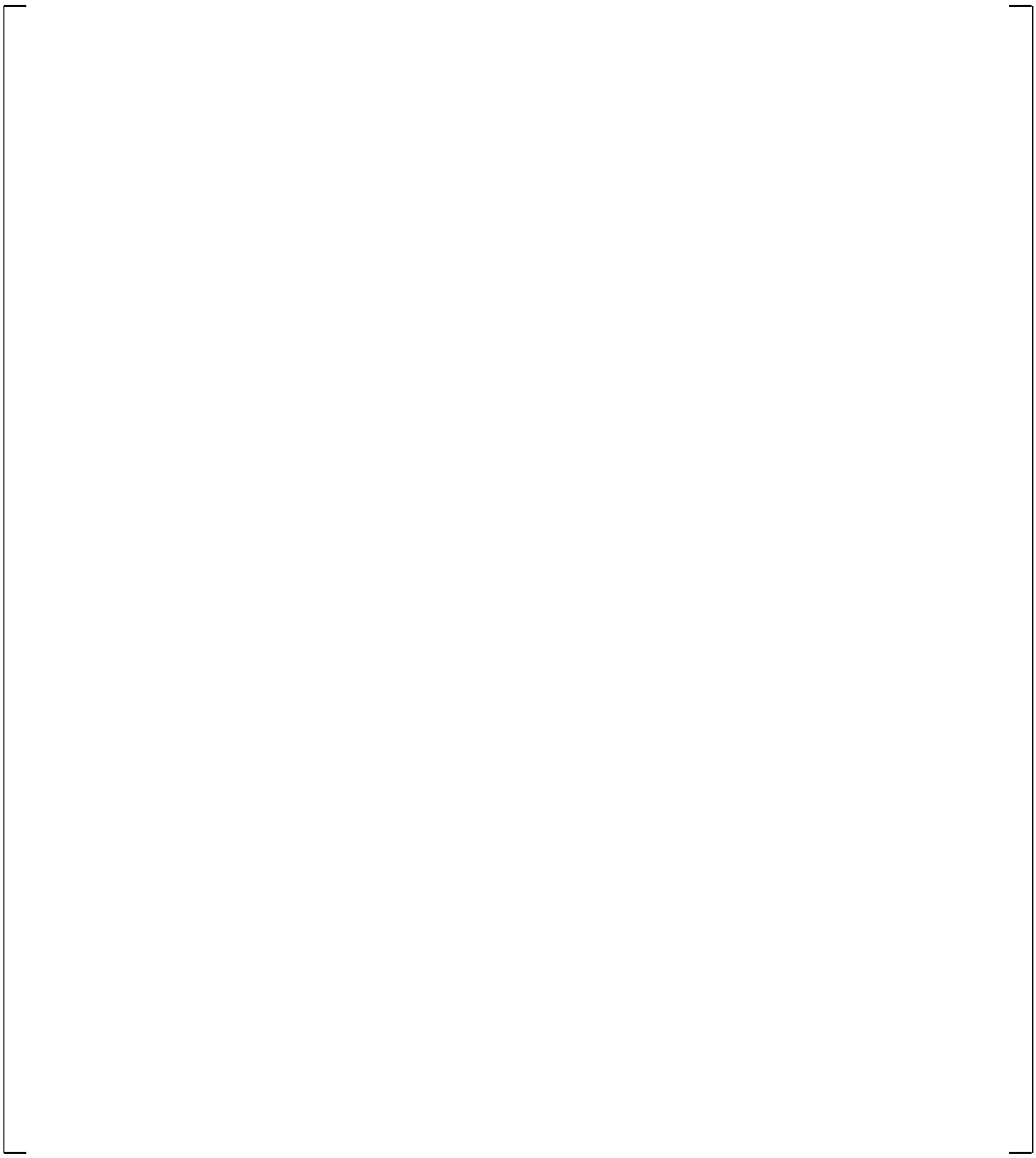

Figure 21.13-1 Break Flows

a,c

Figure 21.13-2 Calculated Break Void Fraction

a,c

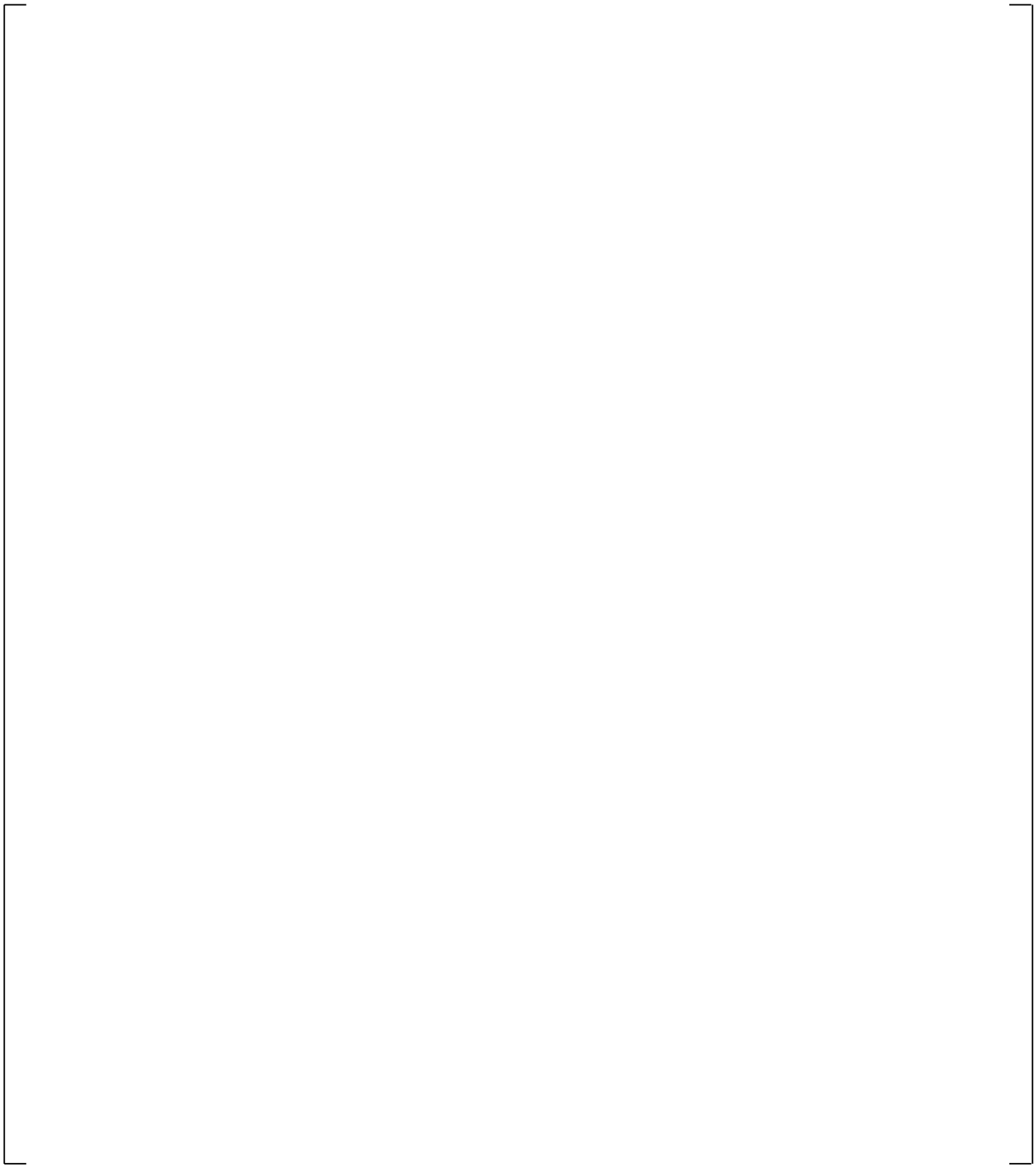

Figure 21.13-3 Cross-Over Leg A Differential Pressures

a,c

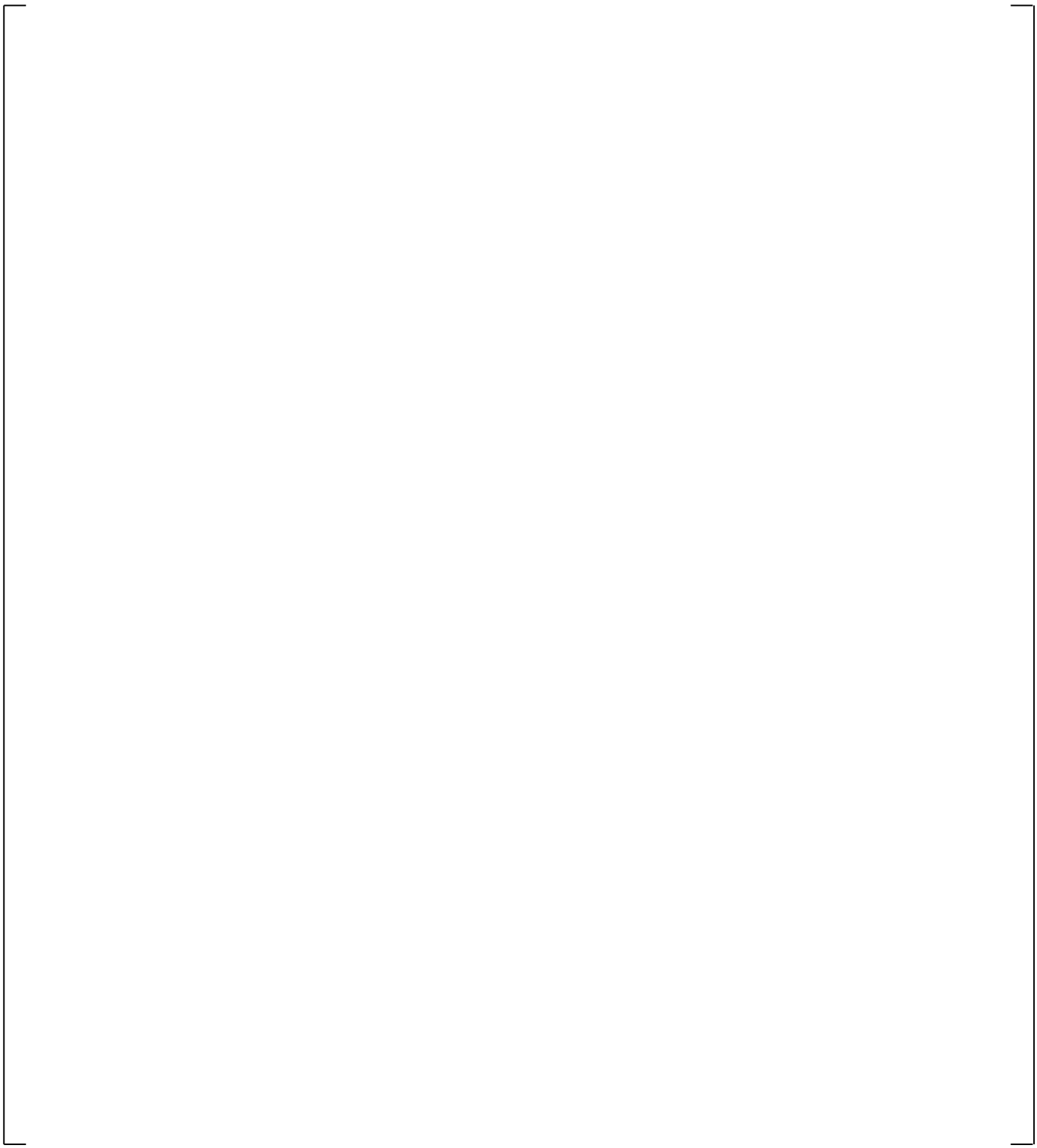

Figure 21.13-4 Cross-Over Leg B Differential Pressures

a,c

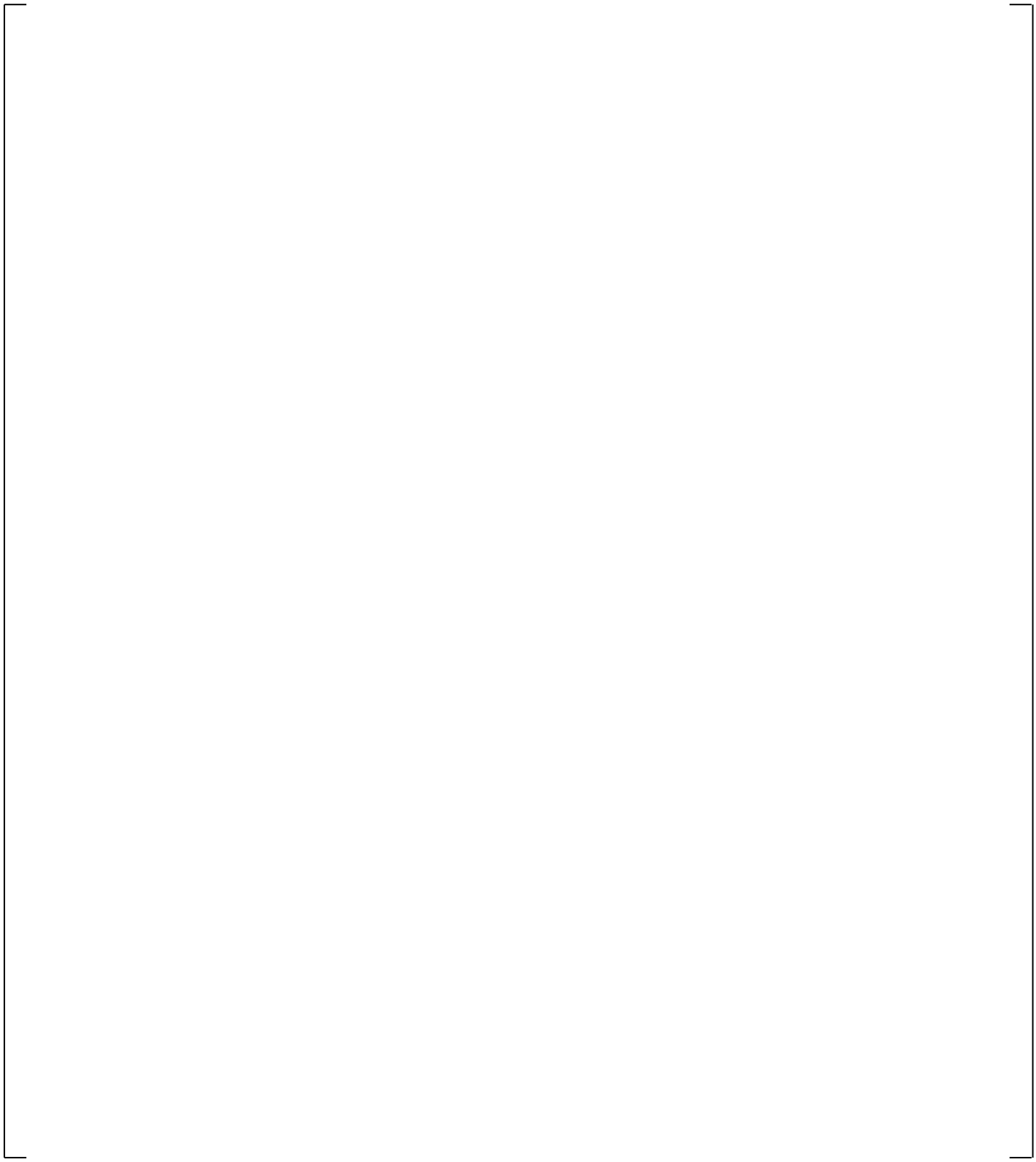

Figure 21.13-5 Pressurizer Pressures

a,c

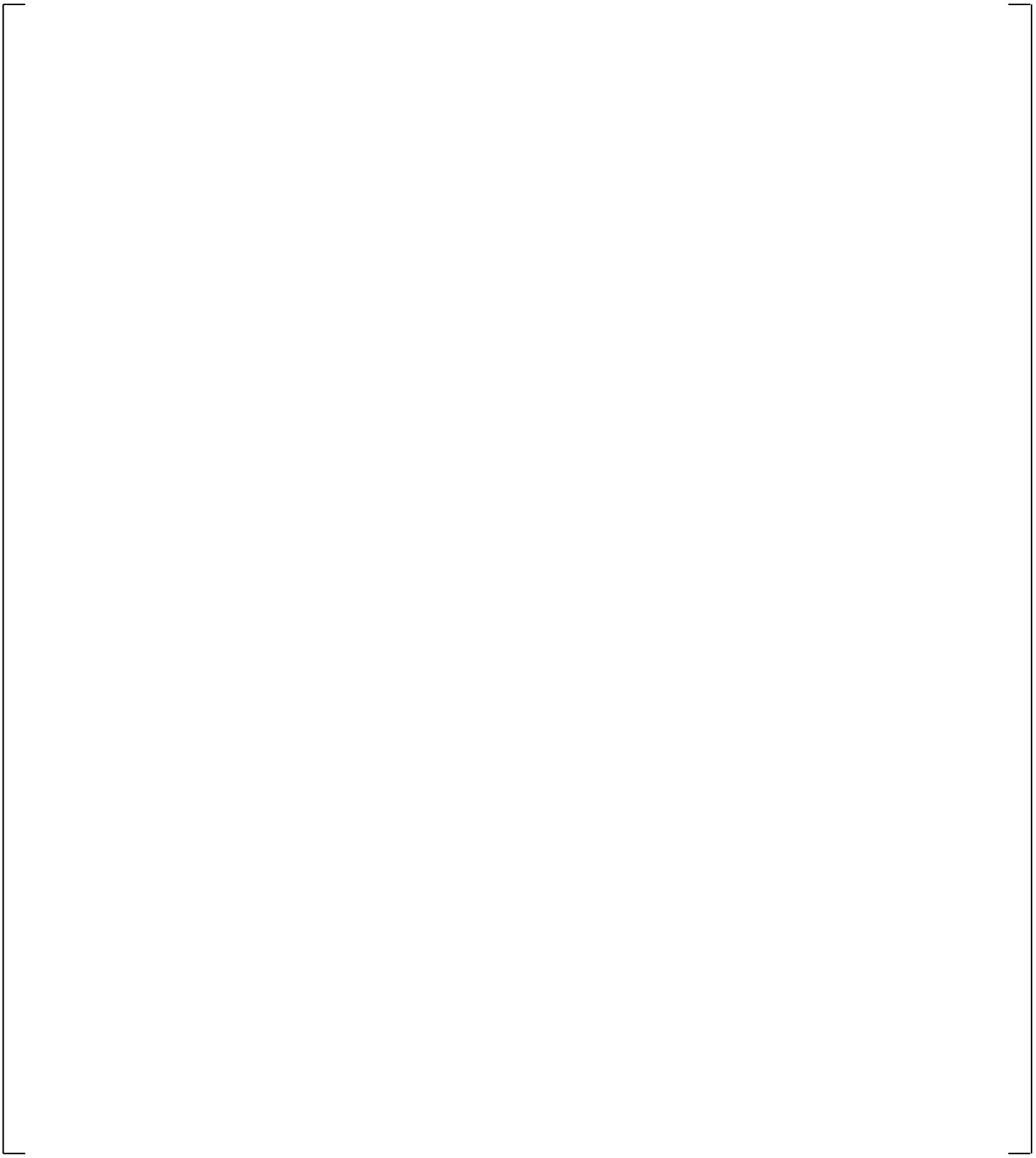

Figure 21.13-6 Steam Generator A U-tubes Inlet-to-Top Differential Pressure

a,c

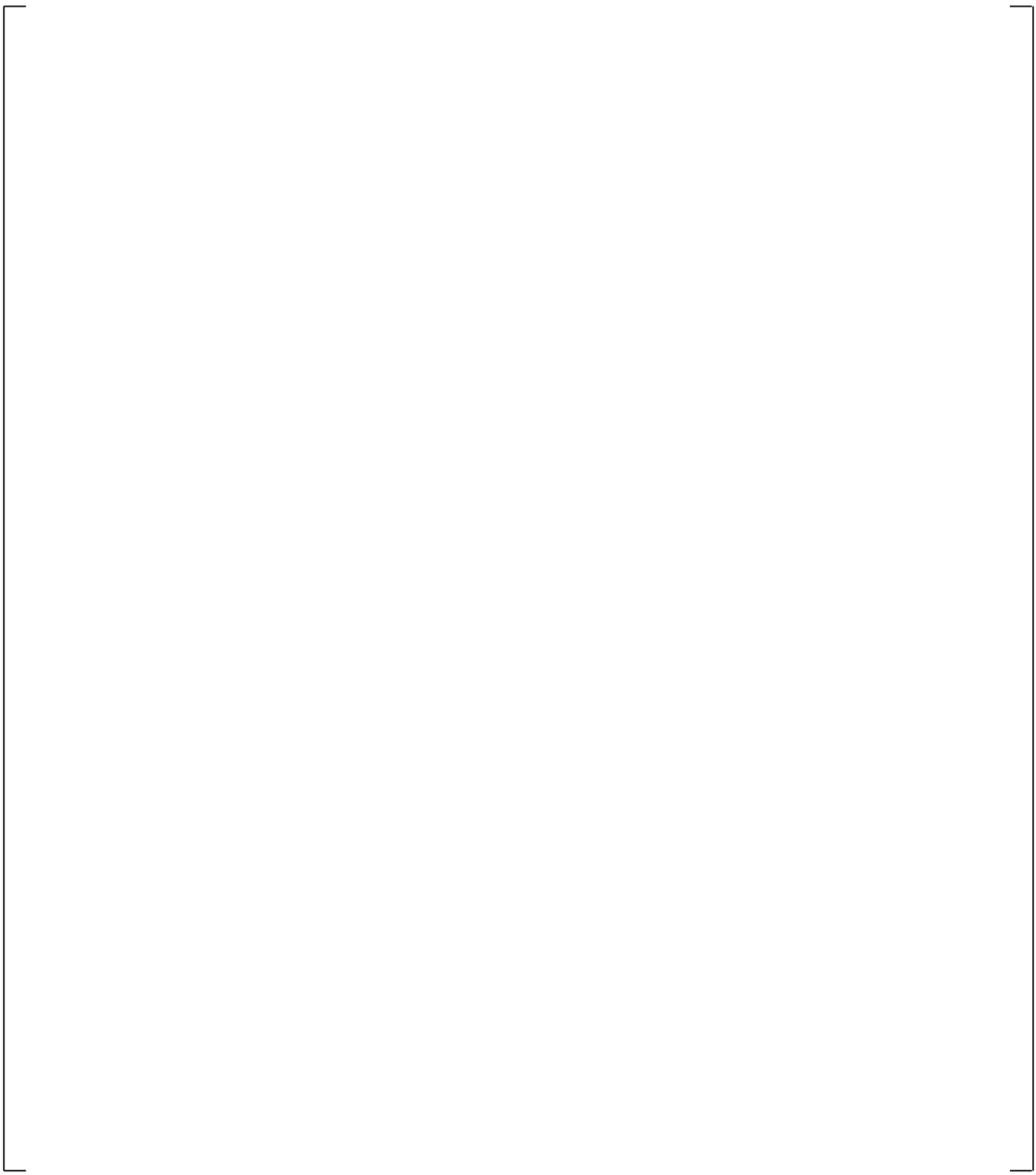

Figure 21.13-7 Steam Generator B U-tubes Inlet-to-Top Differential Pressures

a,c

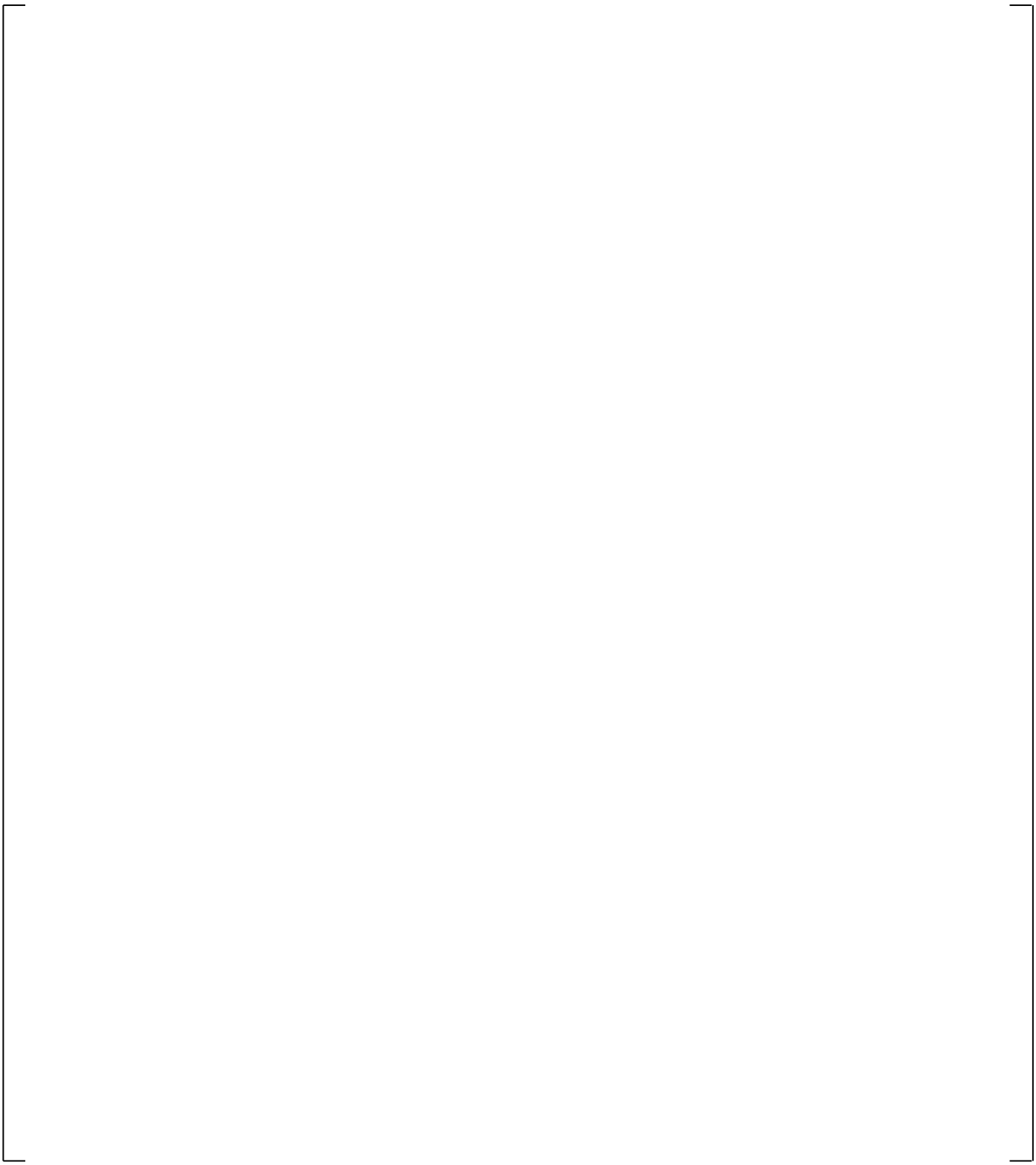

Figure 21.13-8 Steam Generator A U-tubes Outlet-to-Top Differential Pressures

a,c

Figure 21.13-9 Steam Generator B U-tube Outlet-to-Top Differential Pressures

a,c

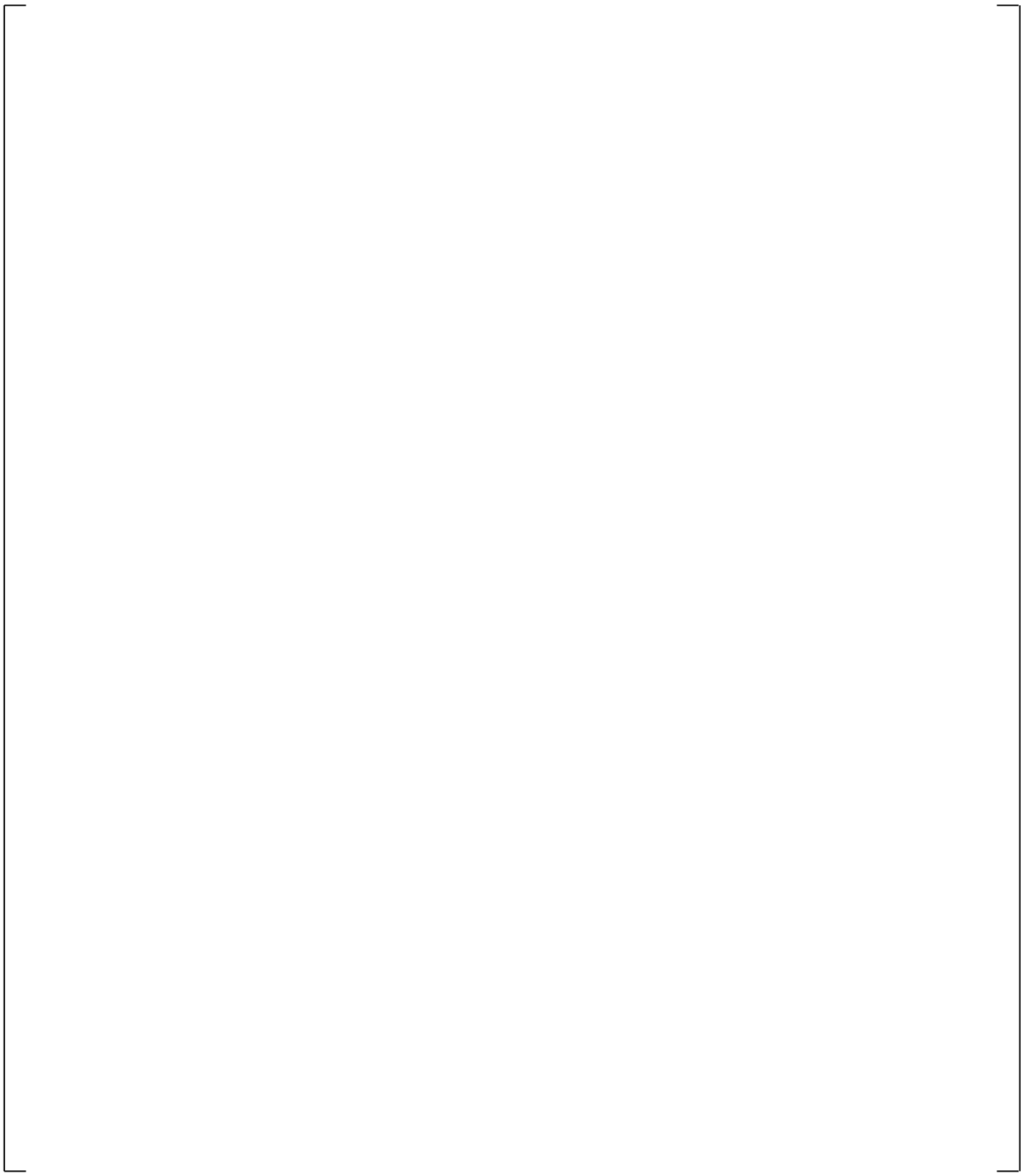

Figure 21.13-10 Steam Generator A Inlet Plenum Collapsed Liquid Levels

a,c

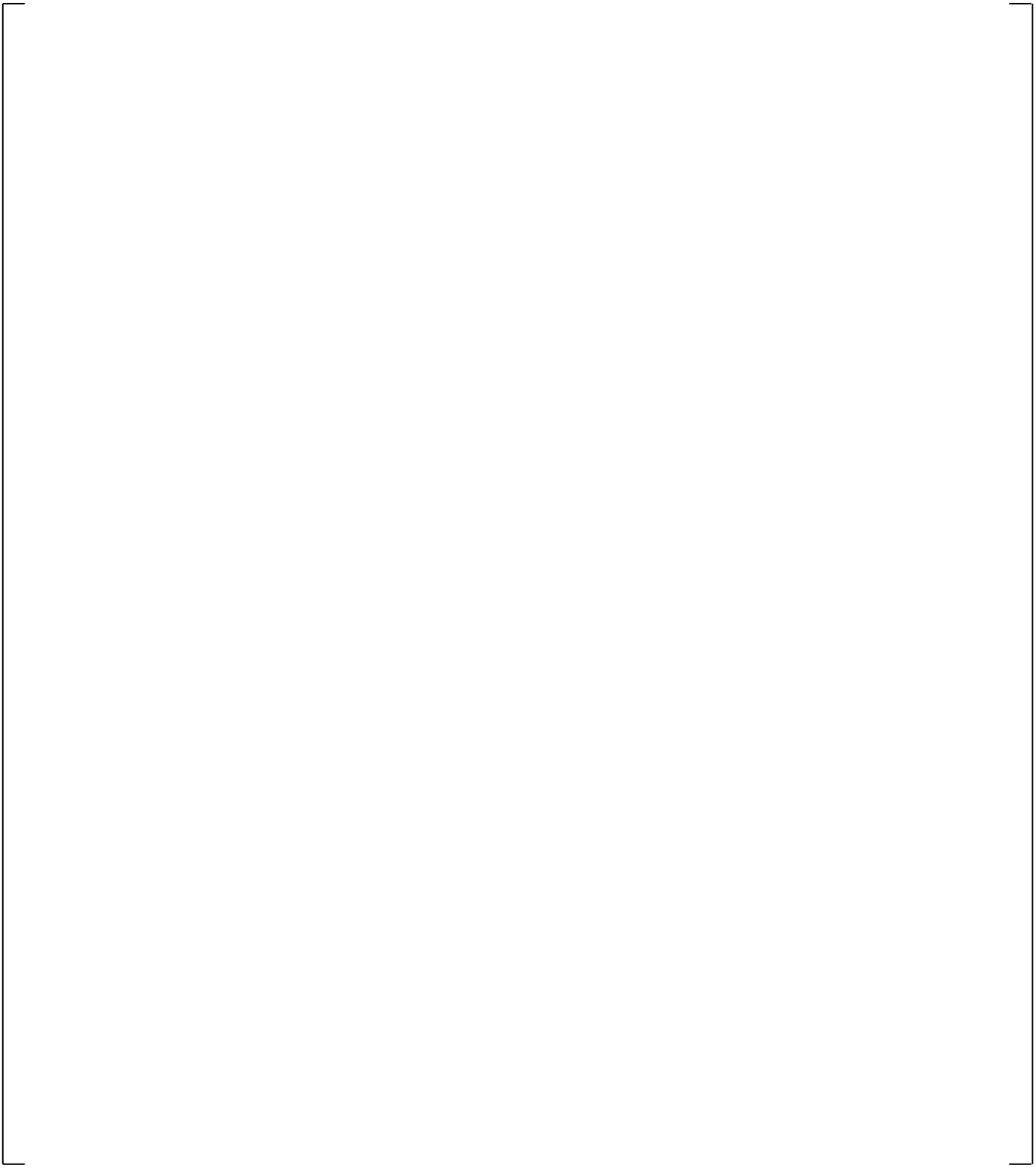

Figure 21.13-11 Steam Generator B Inlet Plenum Collapsed Liquid Levels

a,c

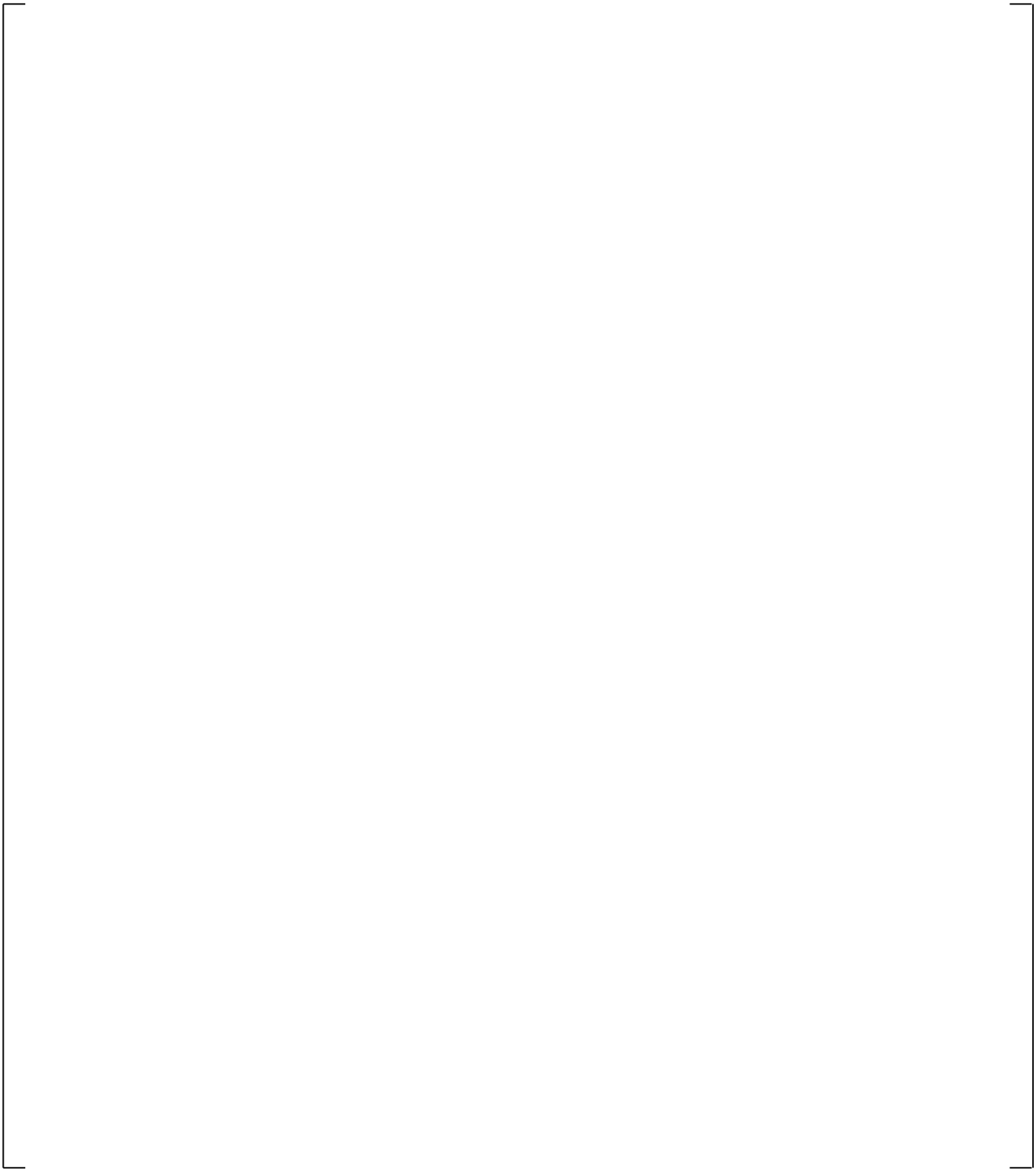

Figure 21.13-12 Upper Plenum to Steam Generator A Inlet Differential Pressures

a,c

Figure 21.13-13 Upper Plenum to Steam Generator B Inlet Differential Pressures

a,c

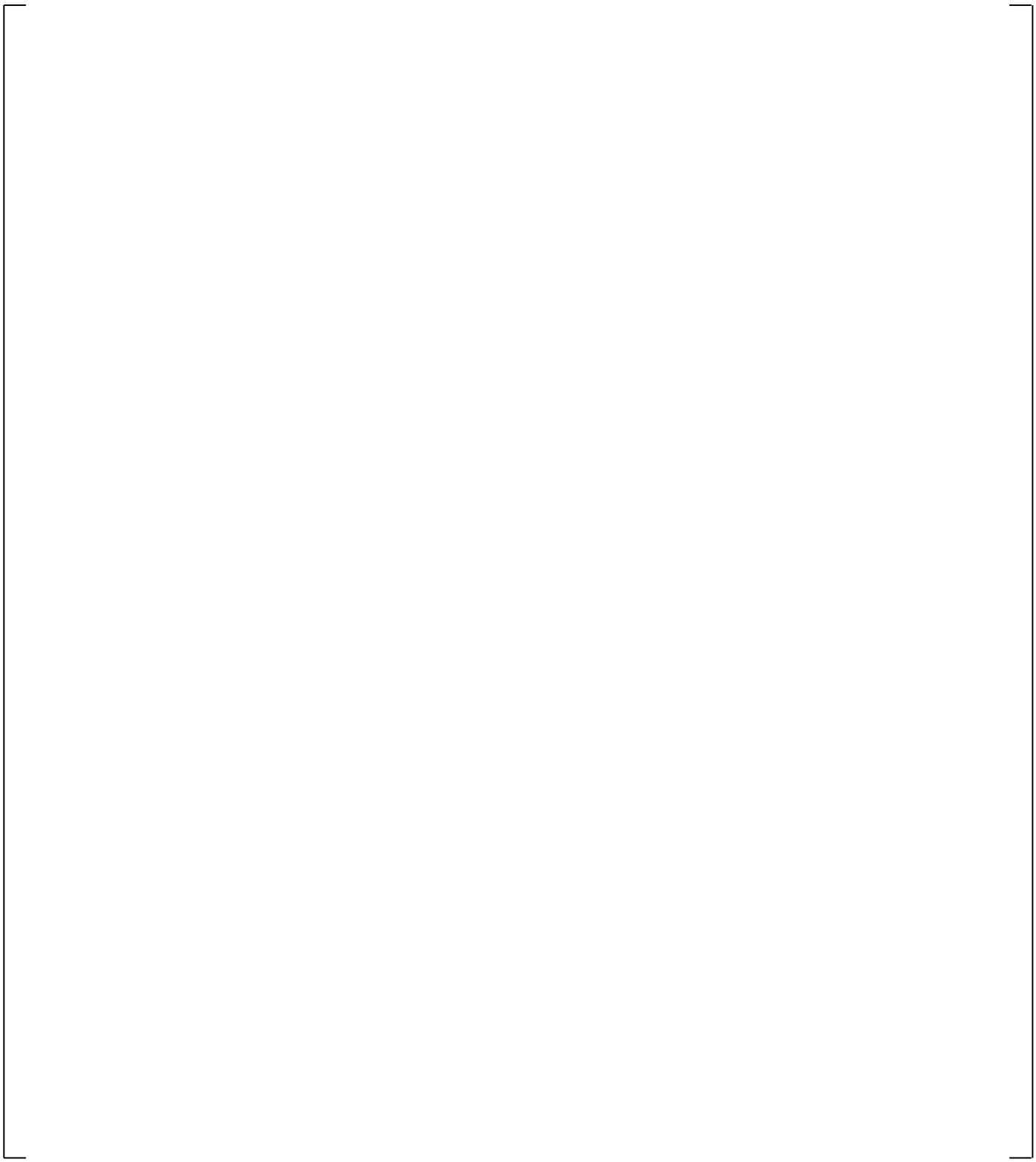

Figure 21.13-14 Downcomer Differential Pressures

a,c

Figure 21.13-15 Upper Plenum Differential Pressures

a,c

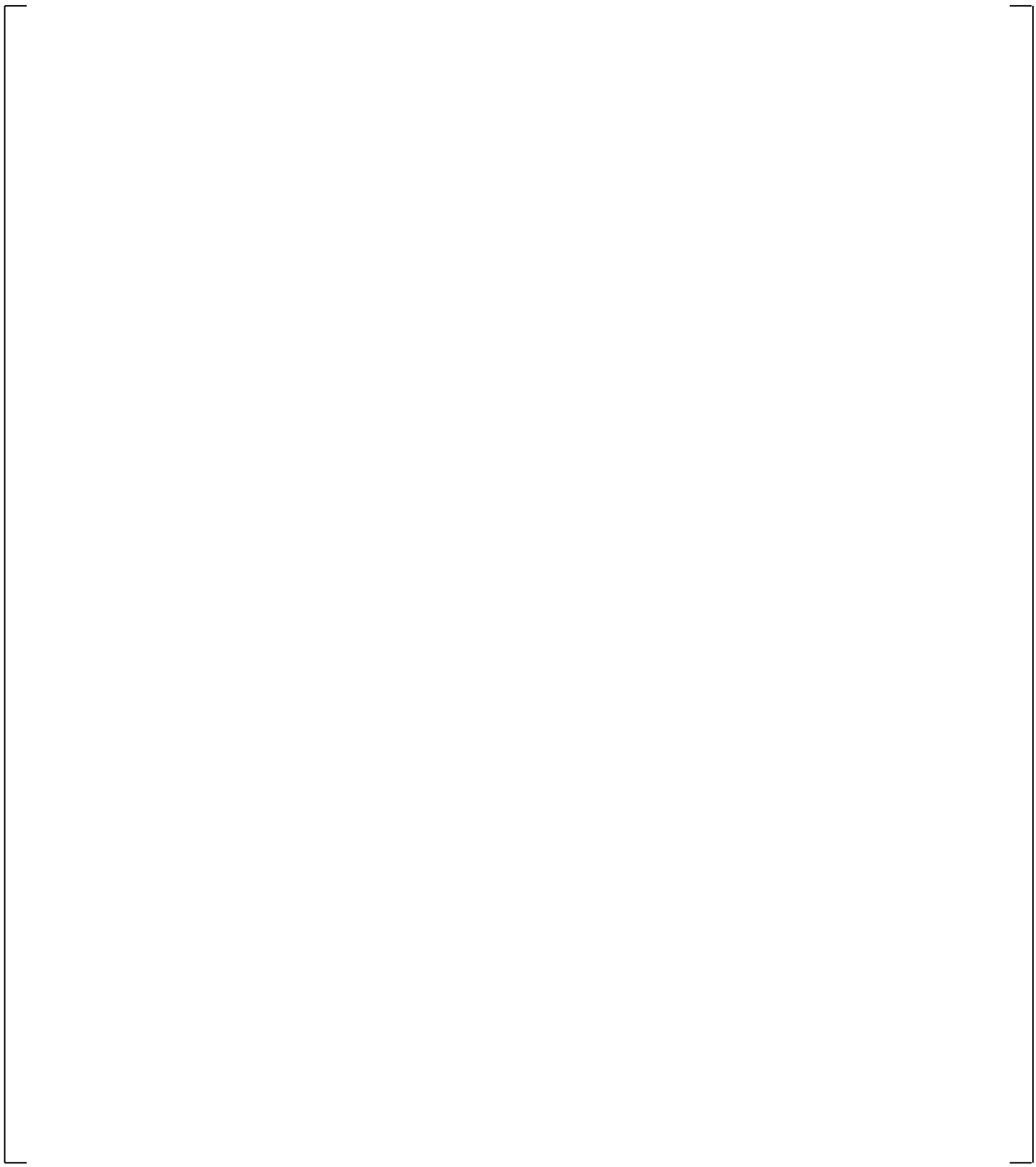

Figure 21.13-16 Inner Vessel (LP+Core+UP) Differential Pressures

a,c

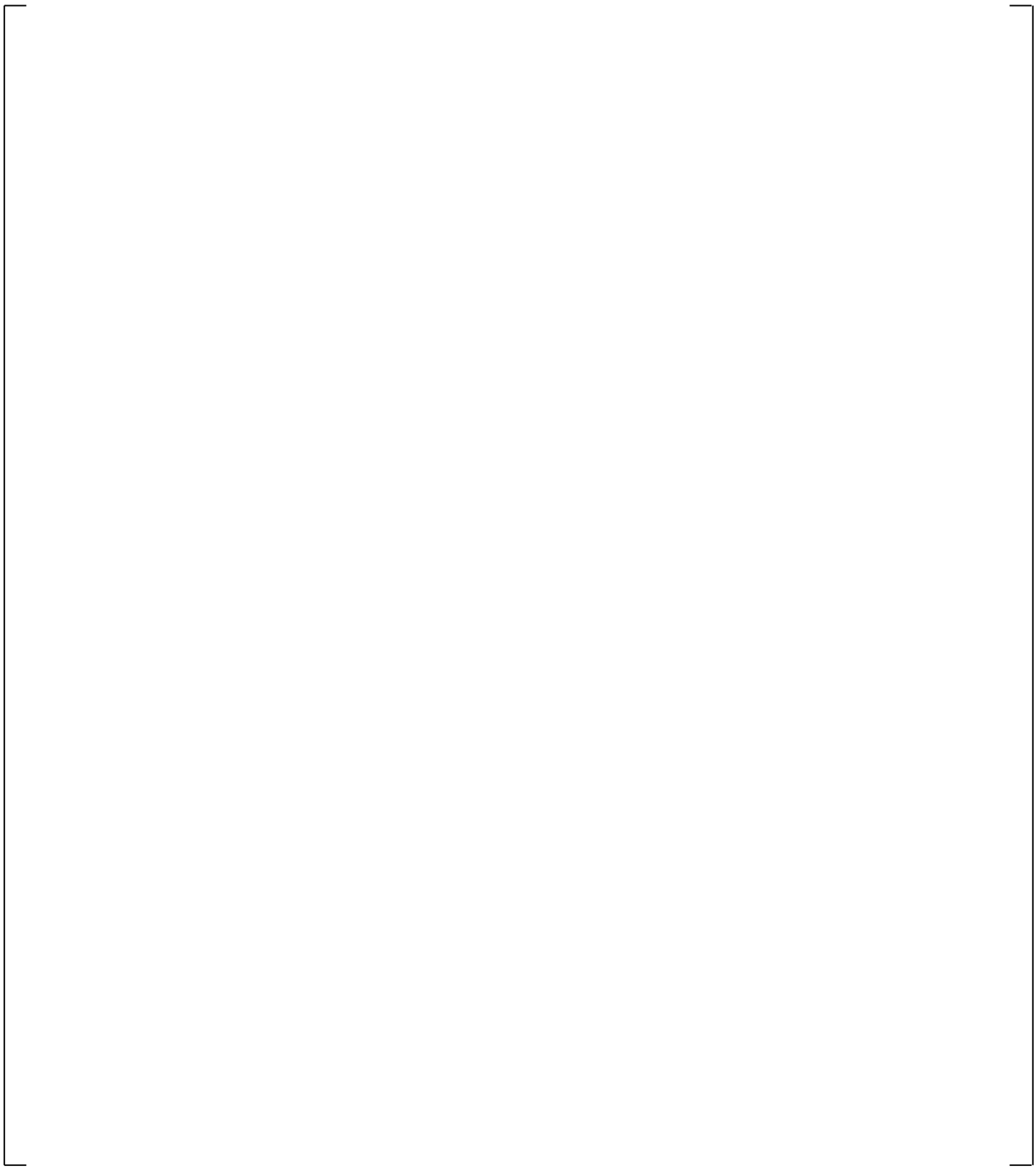

Figure 21.13-17 Lower Plenum Differential Pressures

a,c

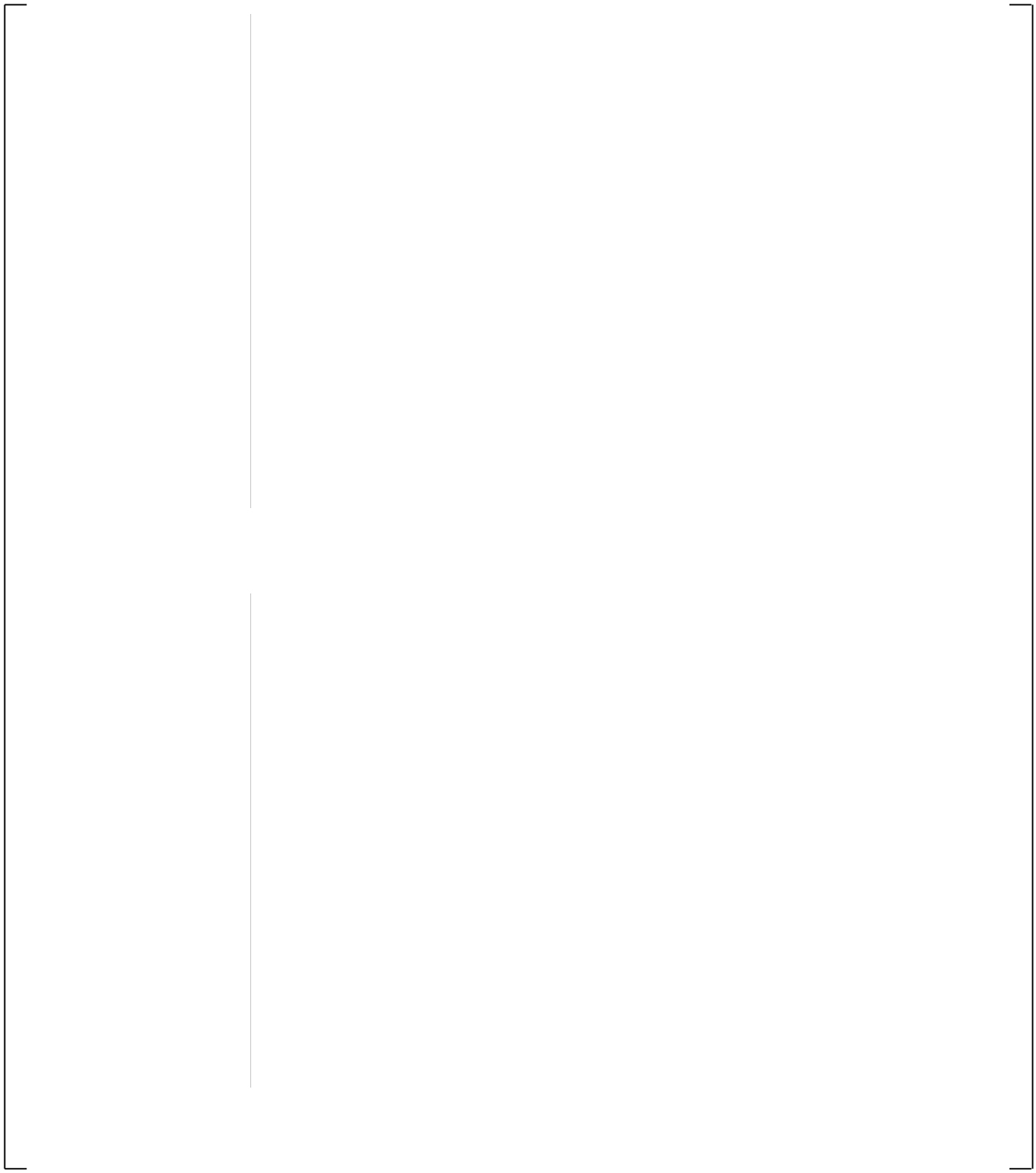

Figure 21.13-18 Peak Cladding Temperatures

a,c

Figure 21.13-19 Accumulator A Injection Flows

21.14 BROKEN LOOP PUMP RESISTANCE SENSITIVITY CALCULATION

This sensitivity calculation is performed to support a discussion in Section 29, Volume 3, which is related to the ranging of the broken loop pump resistance (KP). The approach on KP ranging is considered to be applicable to both small and large break LOCA scenarios. The sensitivity performed herein is not a sensitivity on KP; it simply looks at the effect on the simulation results when the resistance at zero pump velocity is shifted by a certain amount. In this case, the homologous curve point at zero pump speed is modified so that the resistance for both pumps is reduced by 50% from the one used in the SB-CL-18 simulation in Section 21.4.

Figures 21.14-1 through 21.14-10 show comparison of SB-CL-18 simulation with 50% reduced locked rotor resistance to the SB-CL-18 simulation in Section 21.4. The simulations with the 50% reduced locked rotor resistance are shown in the bottom figures on each page. Except for the slightly different pump differential pressure after the pumps are locked at about 260 seconds, Figure 21.14-1, no major differences are observed in the comparison of the rest of the simulation results.

a,c

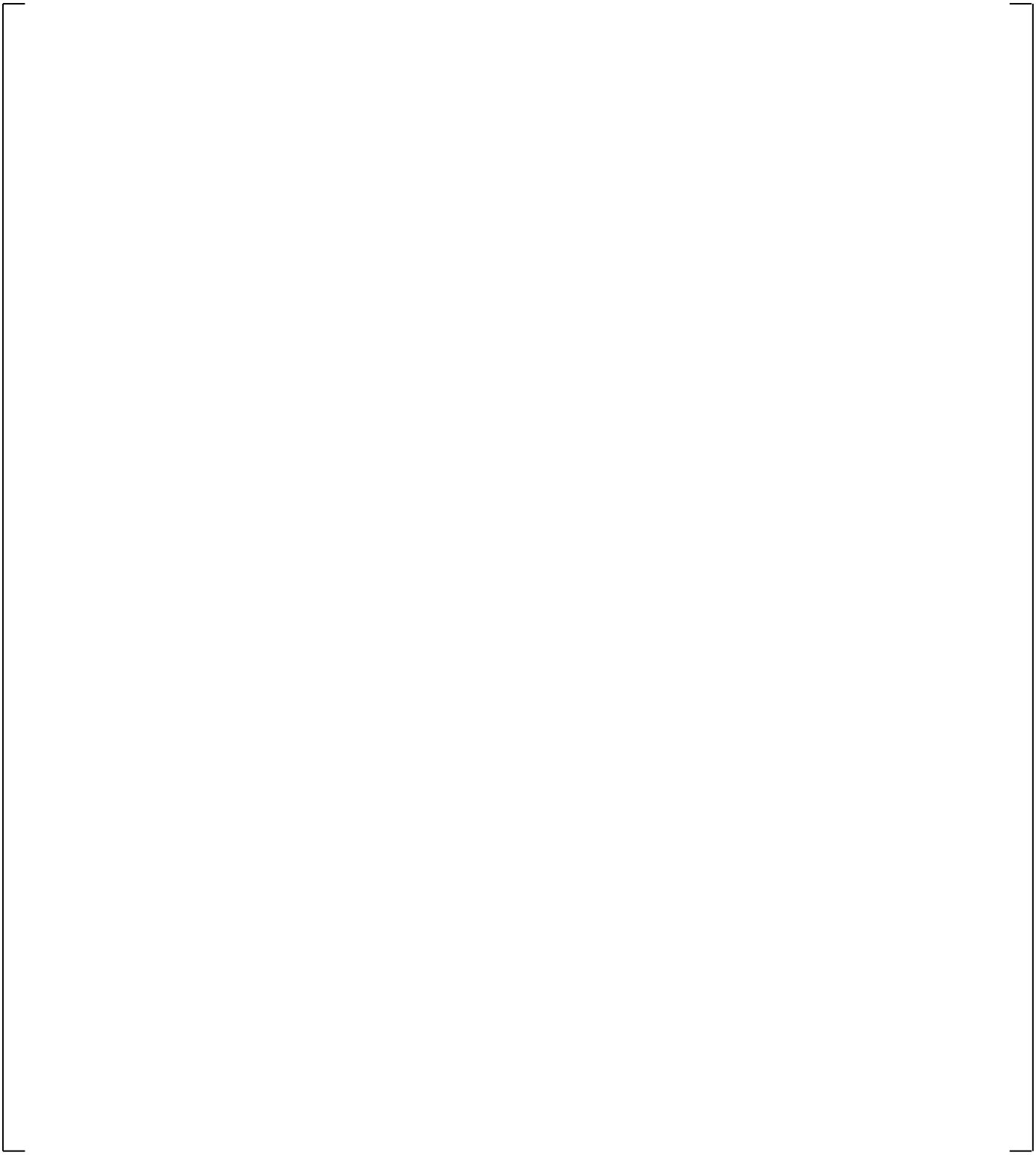

Figure 21.14-1 Pump A Differential Pressures

a,c

Figure 21.14-2 SB-CL-18 Cross-Over Leg A Differential Pressures

a,c

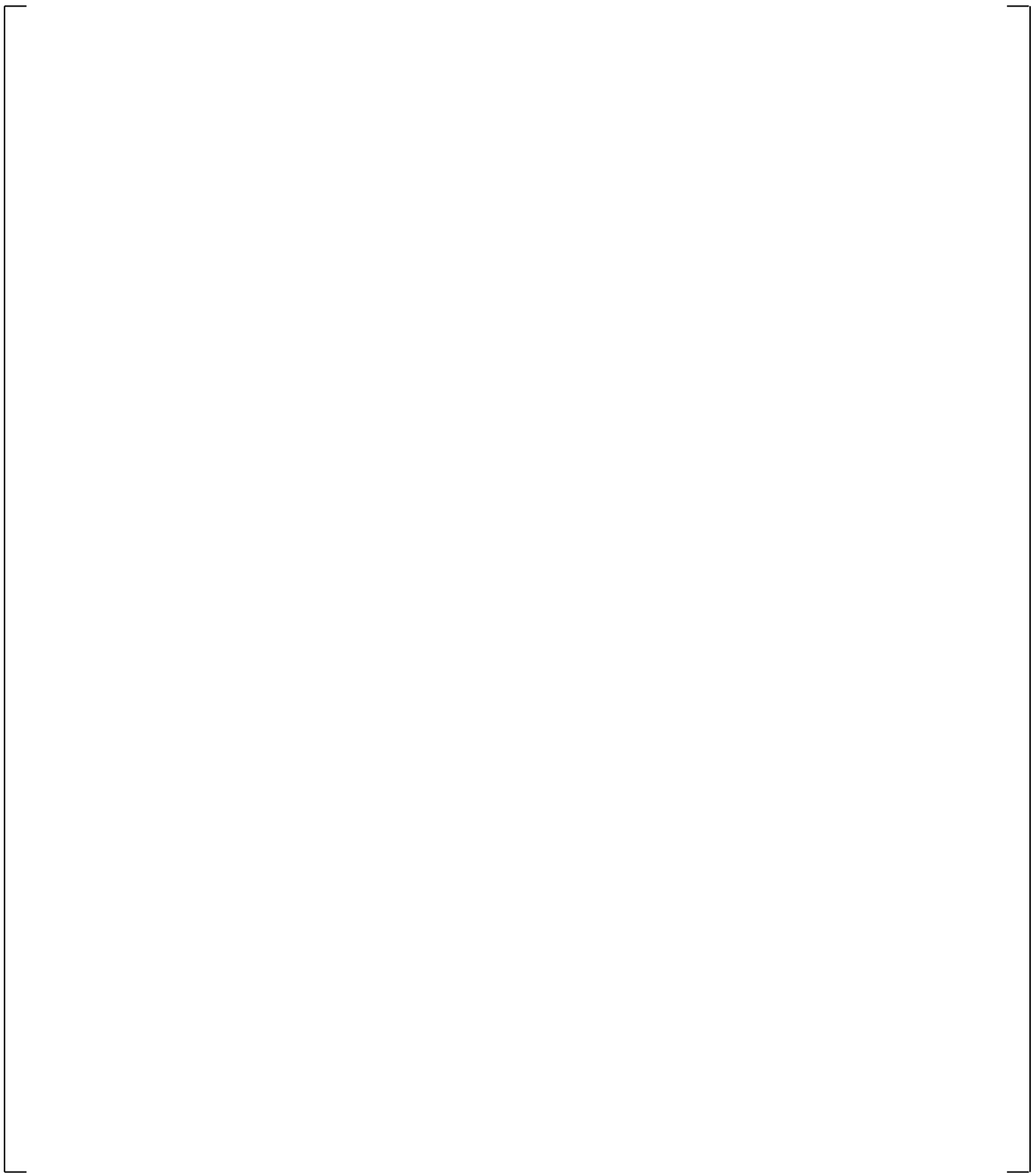

Figure 21.14-3 SB-CL-18 Cross-Over Leg B Differential Pressures

a,c

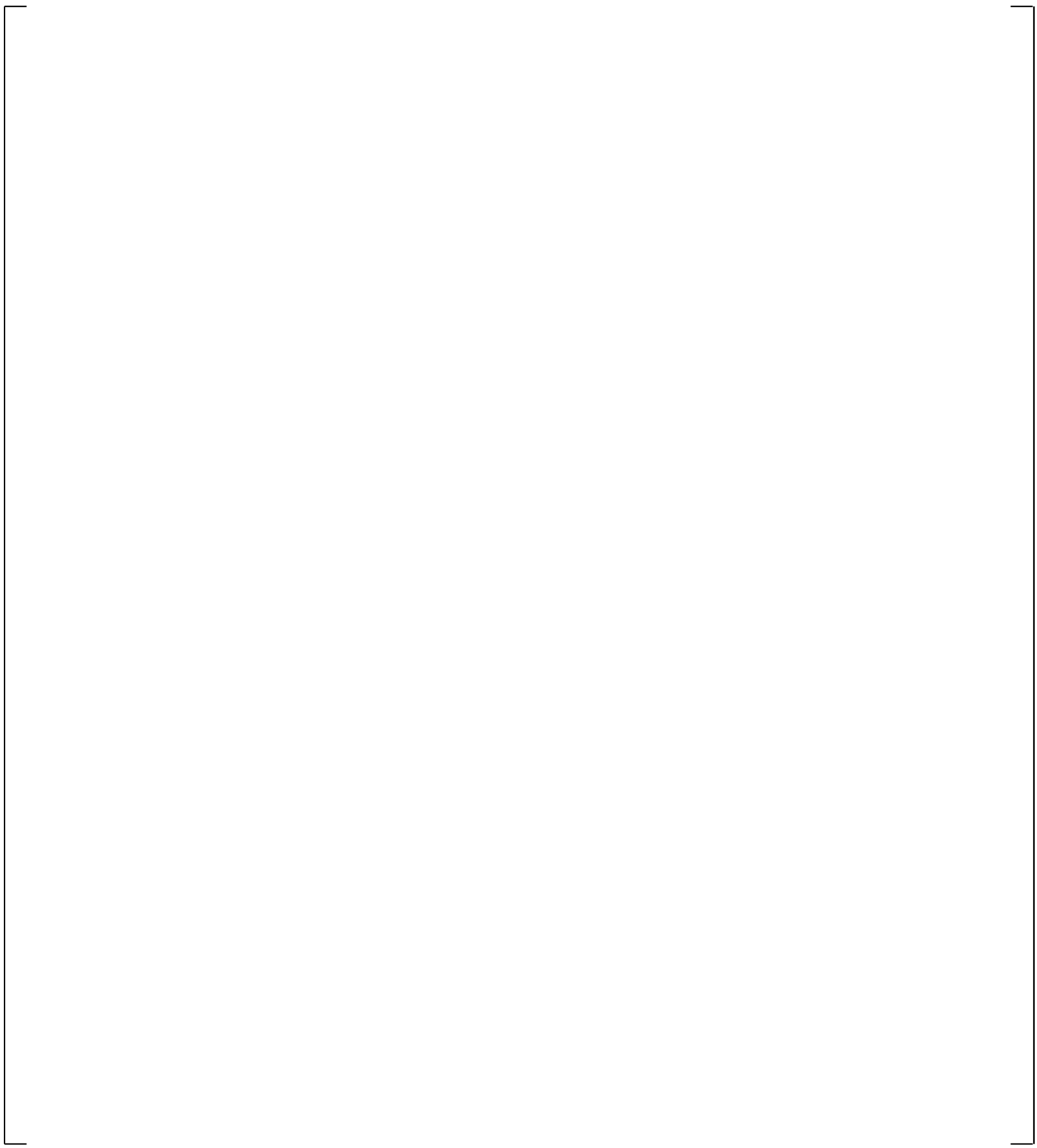

Figure 21.14-4 Inner Vessel Differential Pressures (LP+Core+UCP)

a,c

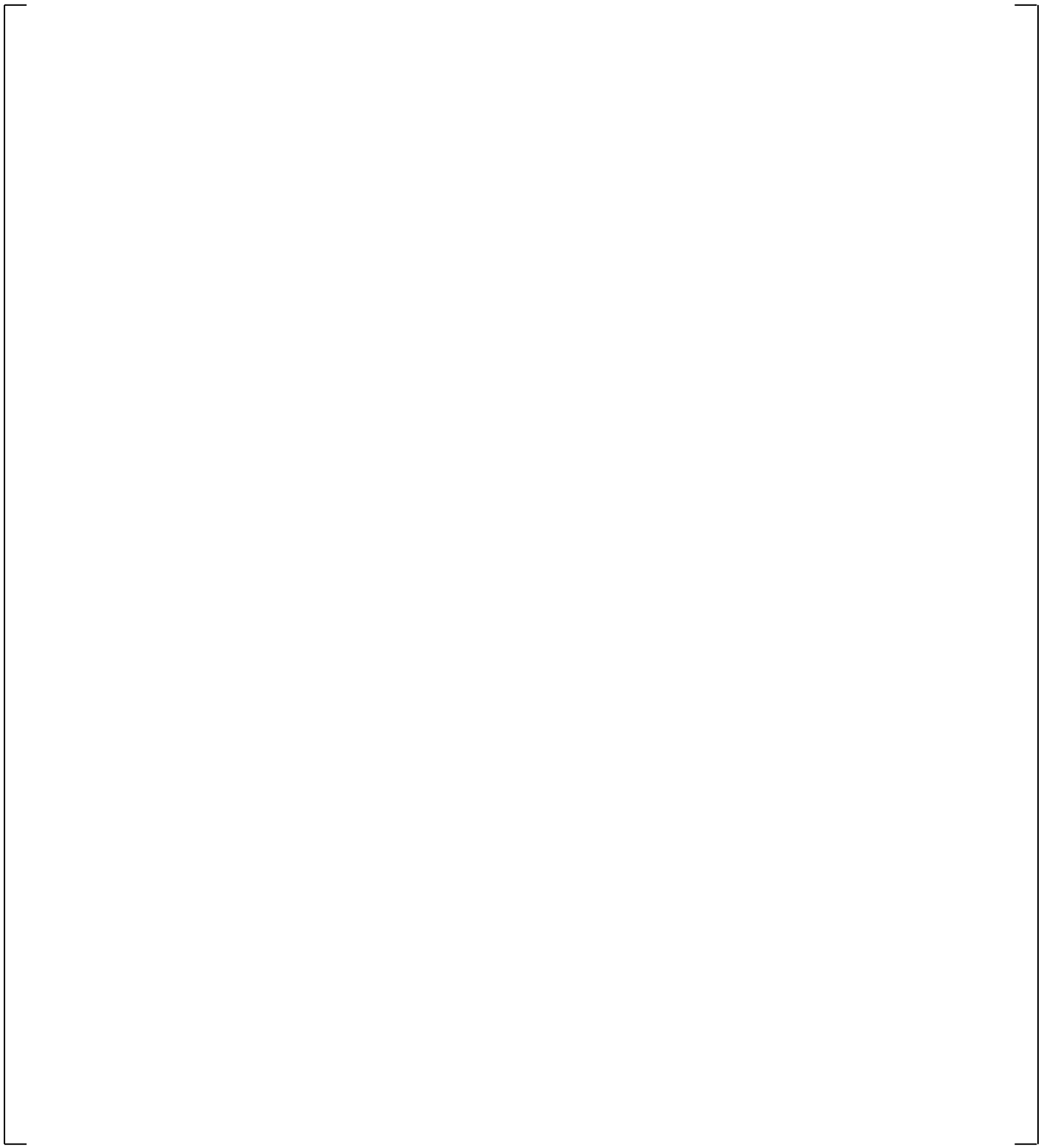

Figure 21.14-5 Downcomer Differential Pressures

a,c

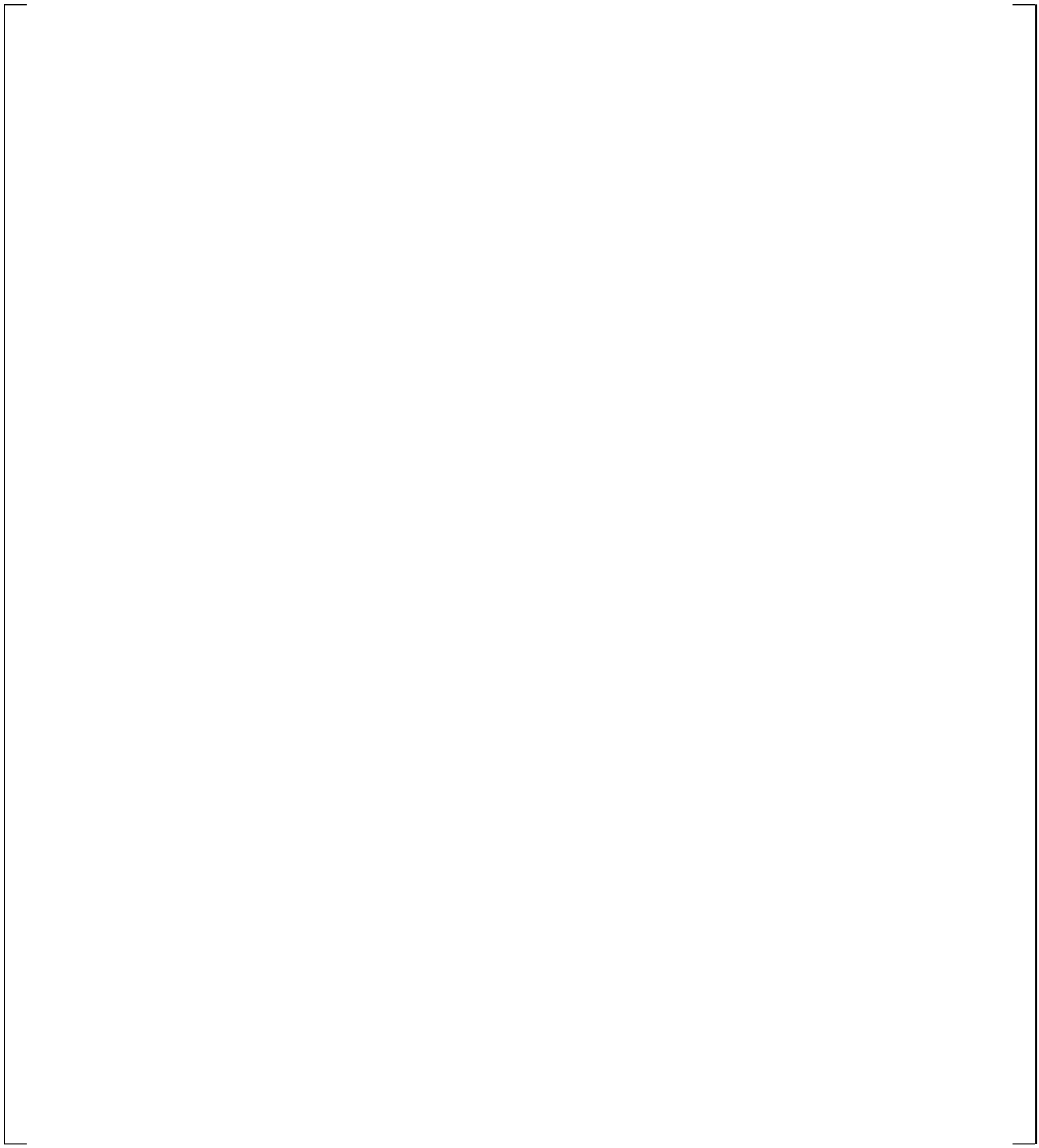

Figure 21.14-6 Lower Plenum Differential Pressures

a,c

Figure 21.14-7 Upper Plenum Differential Pressures

a,c

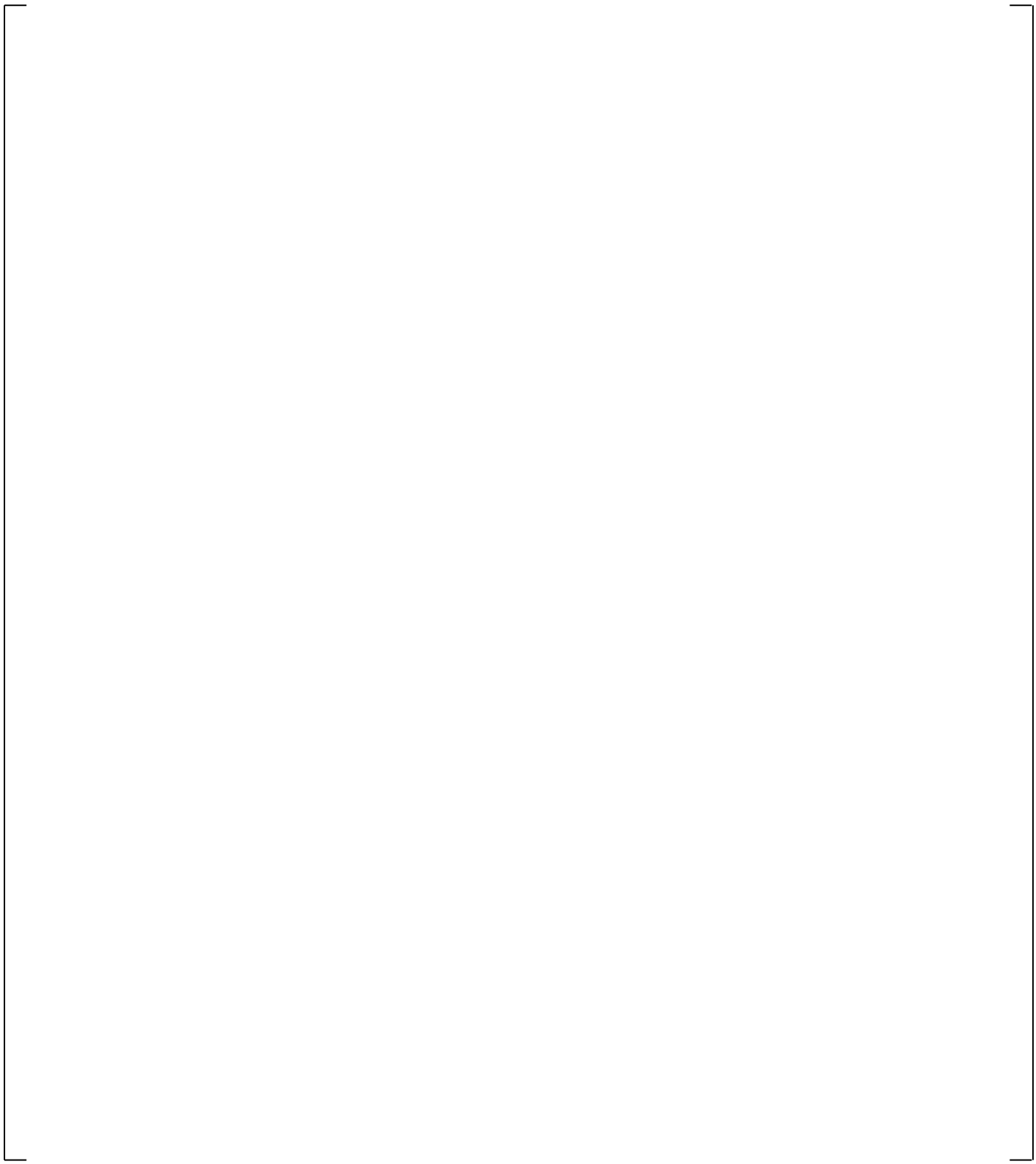

Figure 21.14-8 Hot Leg A Differential Pressures

a,c

Figure 21.14-9 Hot Leg B Differential Pressures

a,c

Figure 21.14-10 Peak Cladding Temperatures

21.15 YDRAG SENSITIVITY CALCULATIONS

This sensitivity is performed to investigate the effect of the variation of YDRAG in the core channels on the transient calculation results. The YDRAG multiplier in the core region is set at extreme minimum **[ ]**[a,c] and maximum **[ ]**[a,c] values.

The results of the YDRAG sensitivity are presented in Figures 21.15-1 through 21.15-6.

The loop seal clearance is not affected visibly by the variation of the core YDRAG parameter, Figures 21.15-1 and 21.15-2.

[

][a,c]

a,c

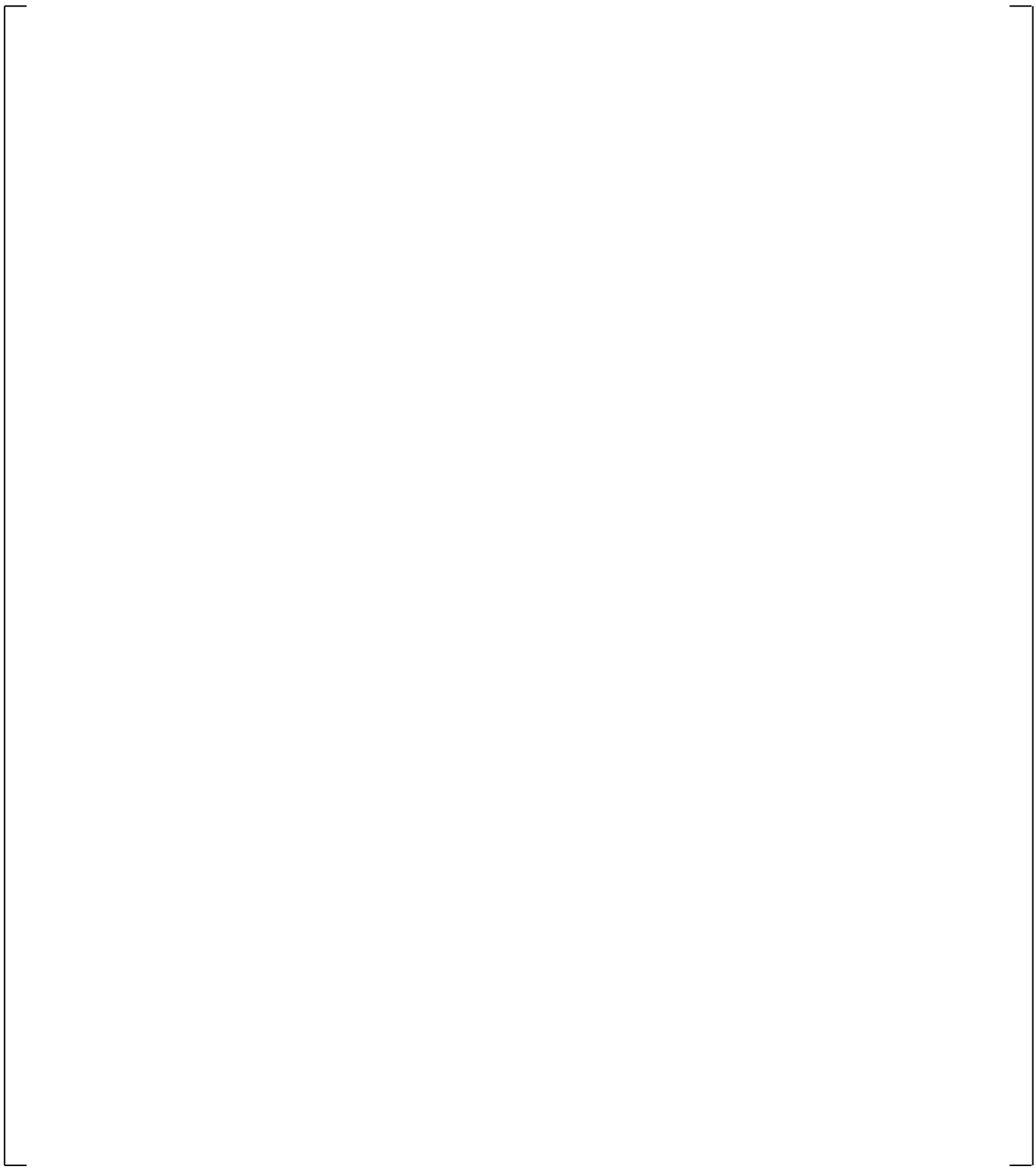

Figure 21.15-1 SB-CL-18 Cross-Over Leg A Differential Pressures

a,c

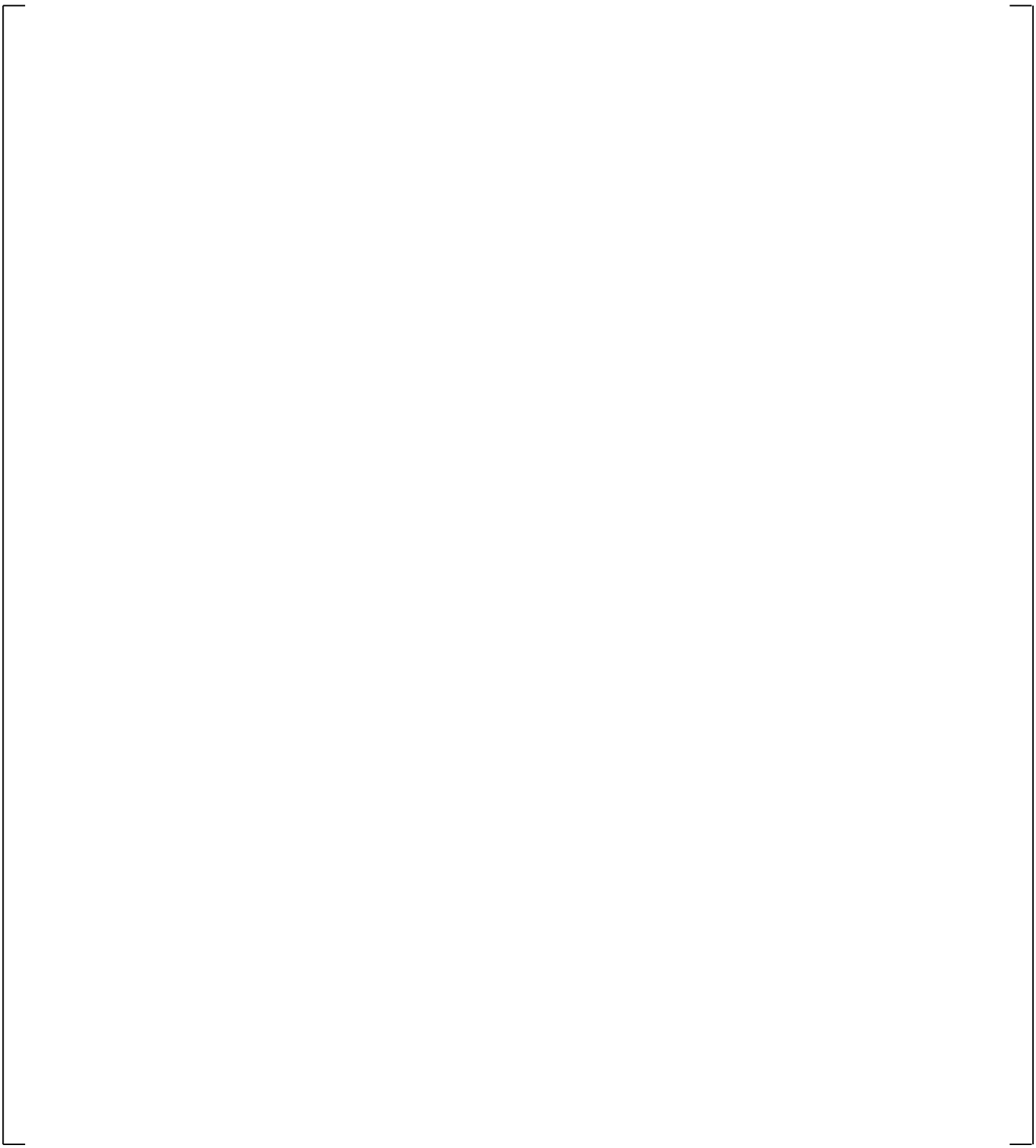

Figure 21.15-2 SB-CL-18 Cross-Over Leg B Differential Pressures

a,c

Figure 21.15-3 Inner Vessel Differential Pressures (LP+Core+UCP)

a,c

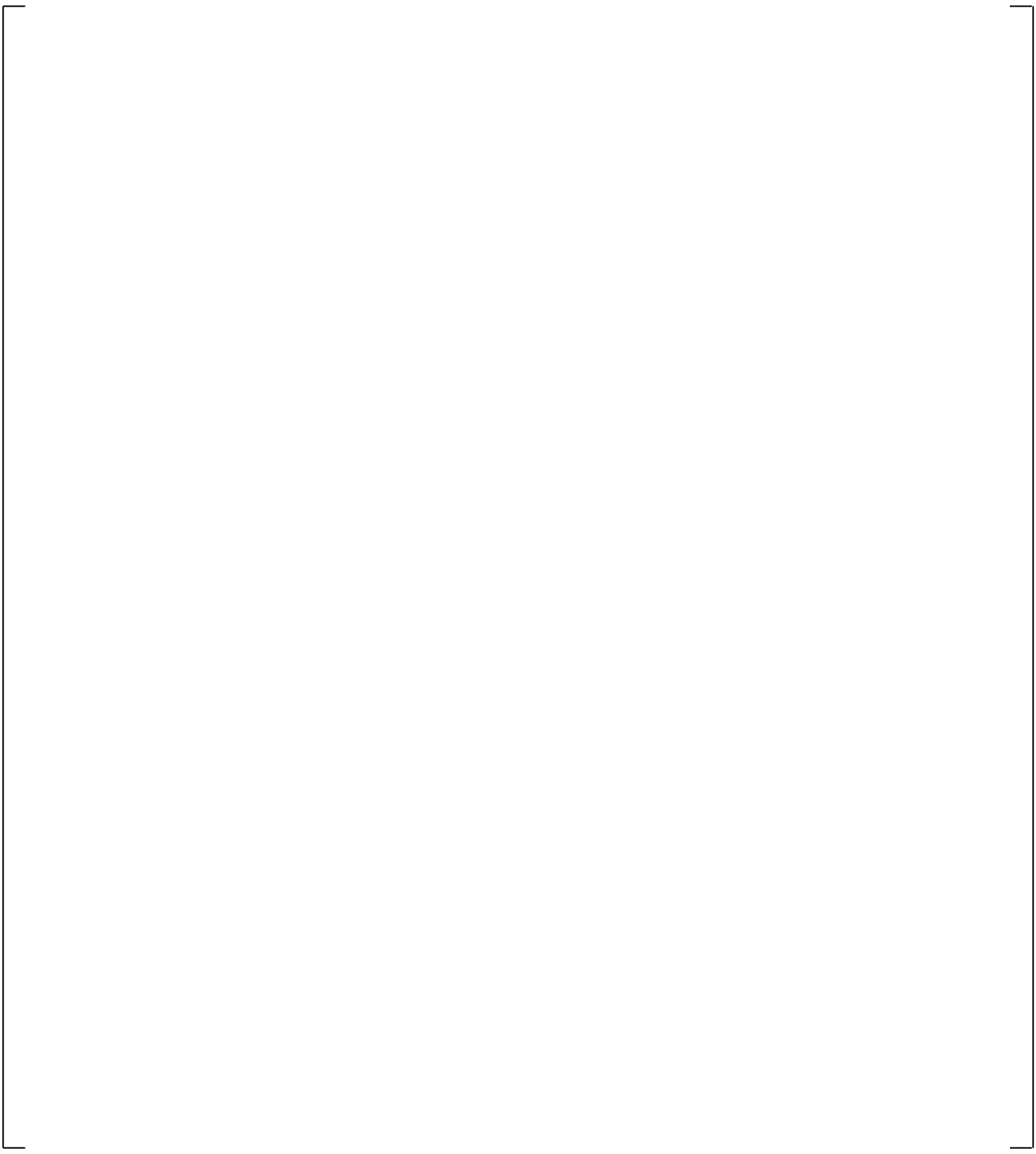

Figure 21.15-4 Upper Plenum Differential Pressures

a,c

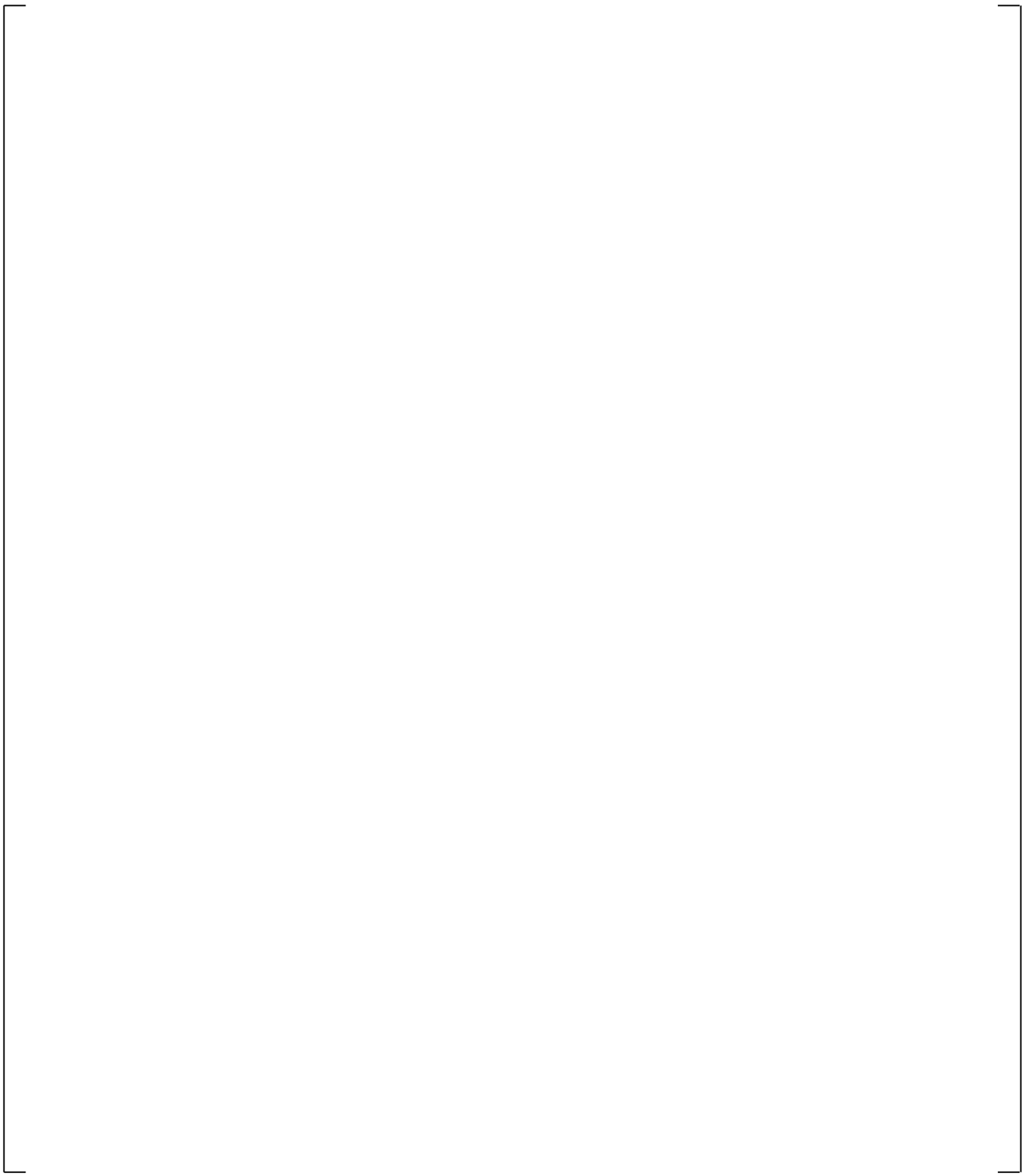

Figure 21.15-5 Downcomer Differential Pressures

a,c

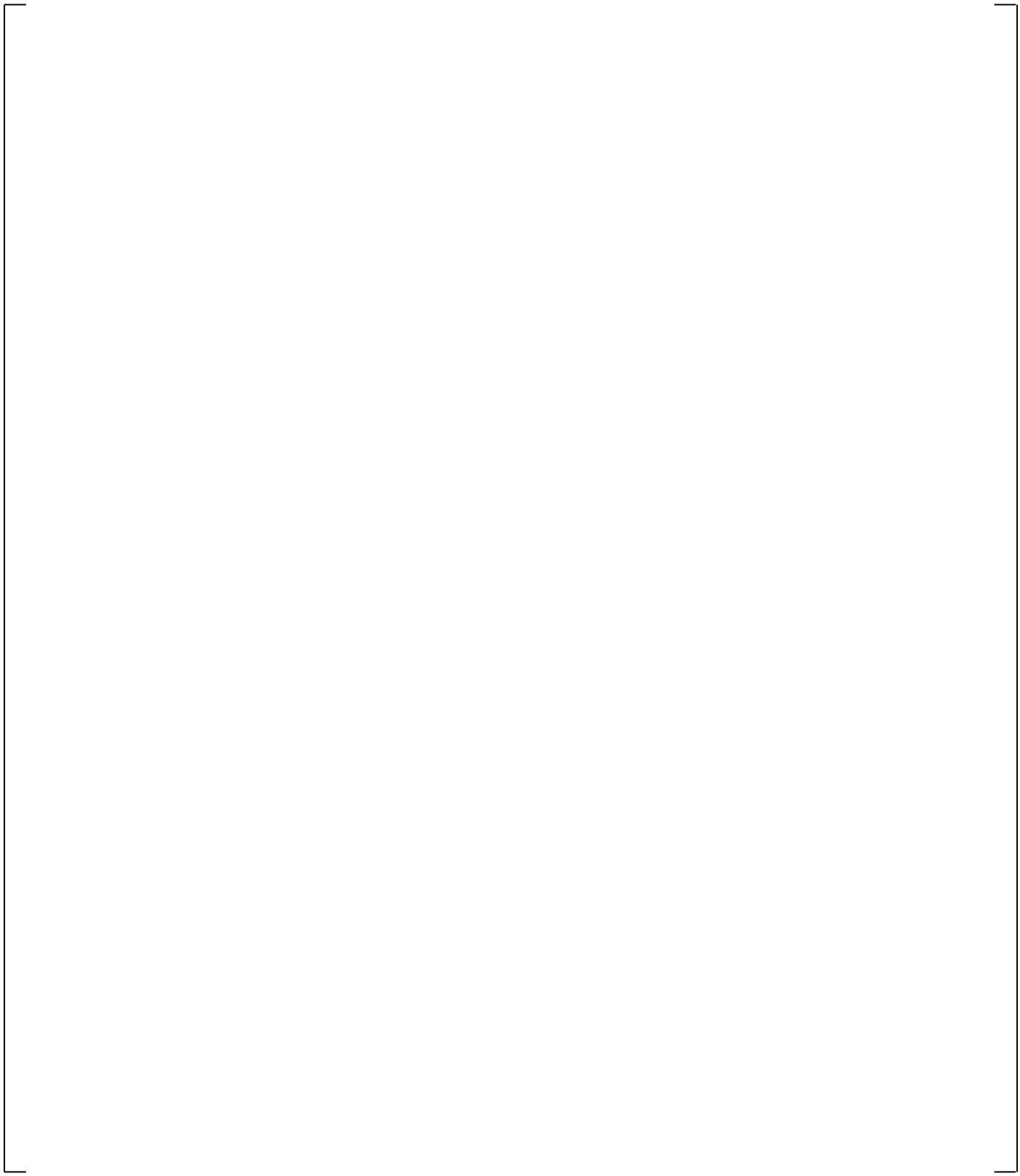

Figure 21.15-6 Peak Cladding Temperatures

21.16 HS_SLUG SENSITIVITY CALCULATIONS

21.16.1 HS_SLUG Sensitivity with 0.5% Side Break Test SB-CL-16

HS_SLUG sensitivity calculations were performed with the 0.5% side cold leg break test SB-CL-16. In these calculations, the HS_SLUG multiplier was set at the maximum **[ ]**[a,c] and minimum **[ ]**[a,c] values. The results of these calculations are shown in Figures 21.16.1-1 through 21.16.1-10.

As seen in Figure 21.16.1-1, the break discharge flow was not affected much by the HS_SLUG variation. The timing of the transition from sub-cooled to two-phase and later to pure steam break flow was not affected much as well. As a result, the predicted system pressure response remains unaffected, as seen in Figure 21.16.1-2.

An asymmetry is observed in the calculated draining of the steam generators, Figure 21.16.1-3. However, if we ignore the asymmetry, the timing when the individual steam generators are completely drained is similar.

The calculated loop seal clearance in the individual cross-over legs, Figures 21.16.1-4 and 21.16.1-5, shows that an asymmetry exists in the calculated differential pressures (SG outlet to bottom), Figures 21.16.1-4(a) and 21.16.1-5(a). This asymmetry can be related to the calculated asymmetry in the steam generator draining, mentioned above.

The HS_SLUG variation does appear to affect the loop seal clearance. With **[ ]**[a,c] loop A does not clear completely, Figure 21.16.1-4, but loop B is predicted to clear, Figure 21.16.1-5. With **[ ]**[a,c] loop A clears better, Figure 21.16-4, but loop B does not clear, Figure 21.16-5. A precursor of this asymmetry appears to be the steam generator draining asymmetry discussed above.

The calculated downcomer differential pressures, Figure 21.16.1-6, and upper plenum differential pressures, Figure 21.16.1-7, are not affected by the HS_SLUG variation as well.

Asymmetry is observed in the calculated hot leg differential pressures, Figure 21.16.1-8, which can be related to the calculated asymmetrical draining of the steam generators, Figure 21.16.1-3.

The asymmetrical steam generator and loop seal clearance behavior, caused by the HS_SLUG variation, does not however affect the calculated core uncovery, Figure 21.16.1-9, and the related rod heatup, Figure 21.16.1-10.

a,c

Figure 21.16.1-1 Calculated Break Flow Rates

a,c

Figure 21.16.1-2 Calculated Pressurizer and Steam Generator Secondary Pressures

a,c

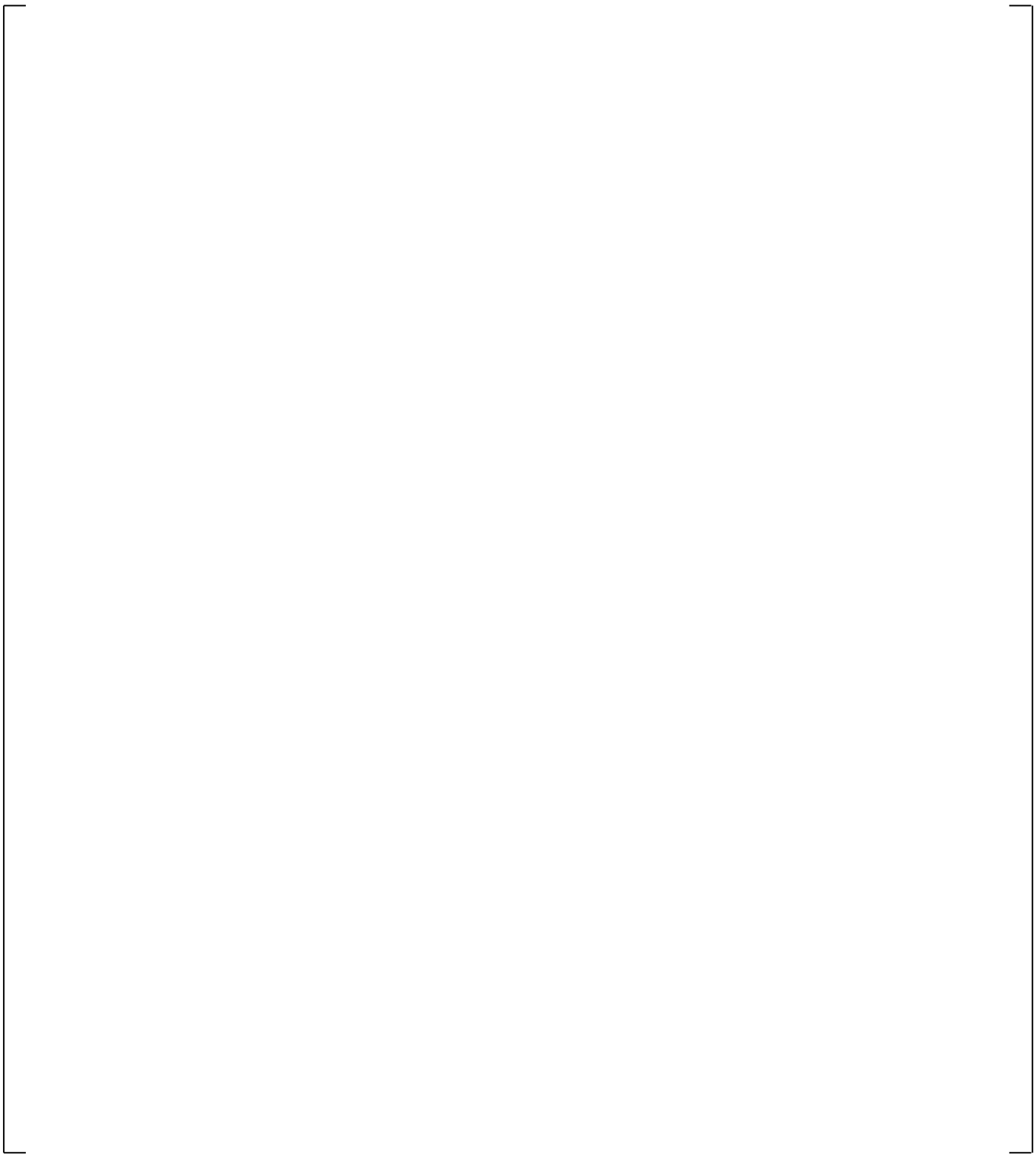

Figure 21.16.1-3 Calculated Steam Generator U-tube Uphill Side Differential Pressures

a,c

Figure 21.16.1-4 Calculated Cross-Over Leg A Differential Pressures

a,c

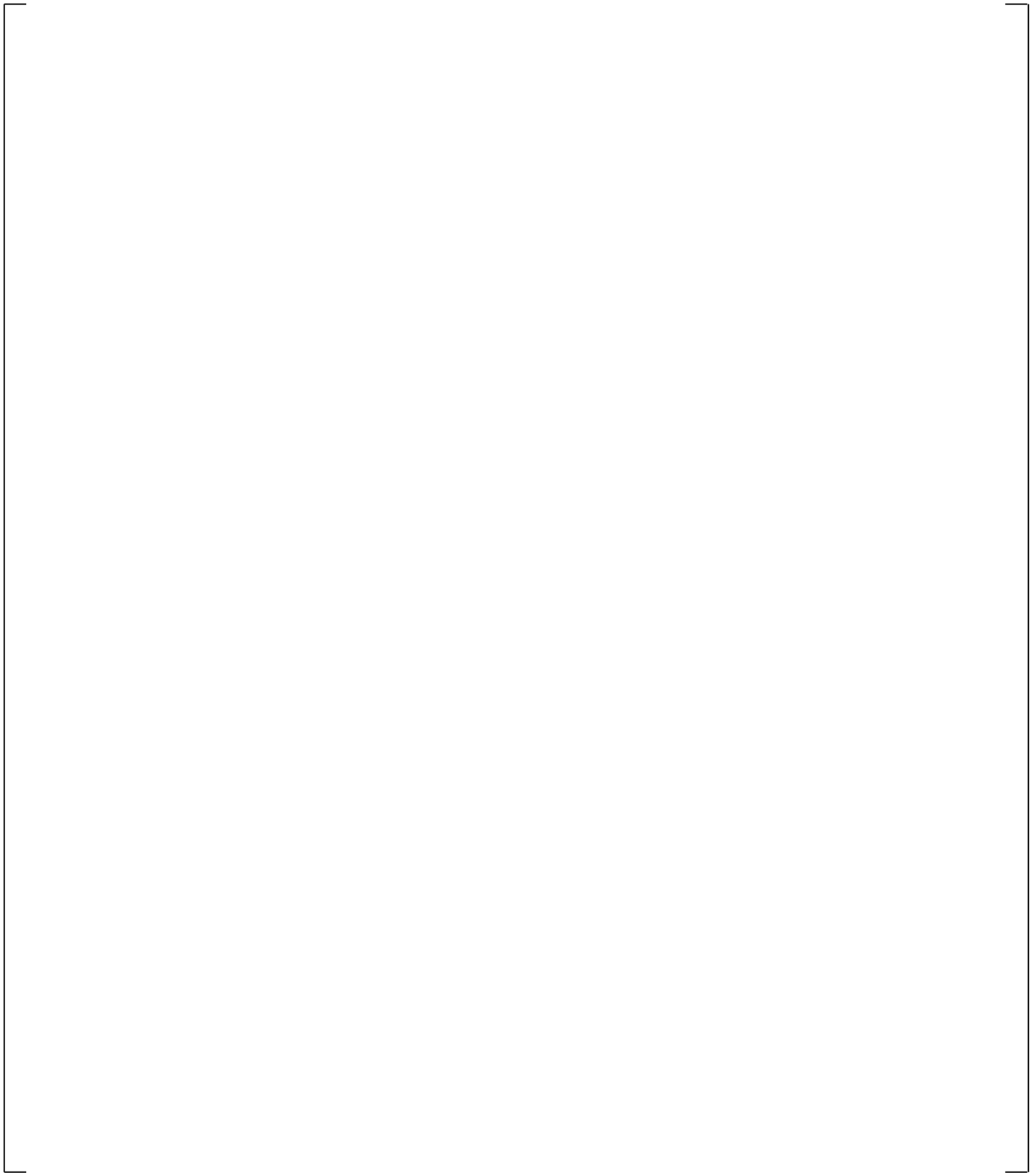

Figure 21.16.1-5 Calculated Cross-Over Leg B Differential Pressures

a,c

Figure 21.16.1-6 Calculated Downcomer Differential Pressures

a,c

Figure 21.16.1-7 Calculated Upper Plenum Differential Pressures

a,c

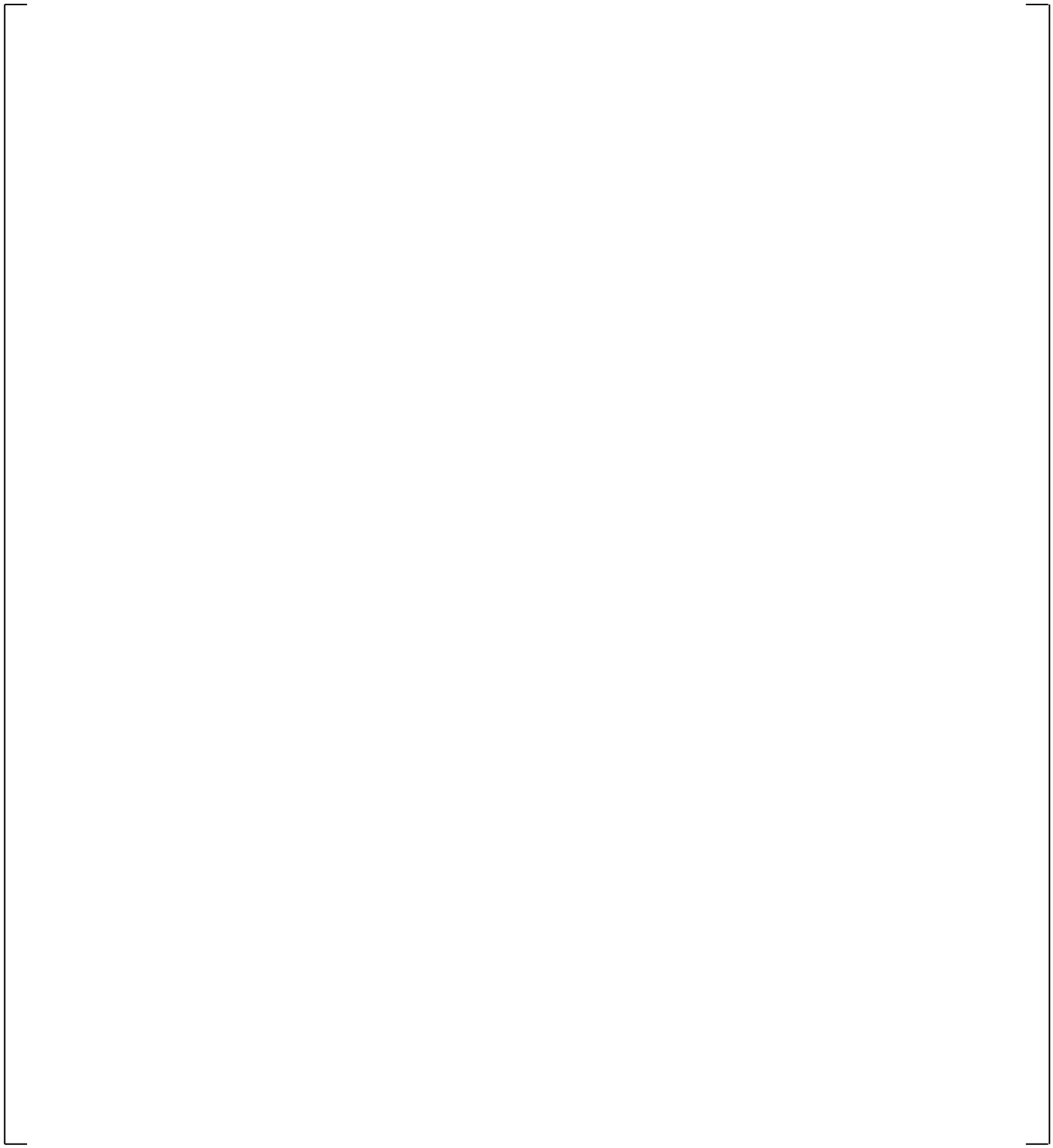

Figure 21.16.1-8 Calculated Hot Leg Differential Pressures

a,c

Figure 21.16.1-9 Calculated Core Differential Pressures

a,c

Figure 21.16.1-10 Calculated Peak Cladding Temperatures

21.16.2 HS_SLUG Sensitivity with the 5% Top Break test SB-CL-18

Two simulations of the 5% side break test SB-CL-18 test were performed with setting the HS_SLUG multiplier at its maximum **[ ]**[a,c] and minimum **[ ]**[a,c] values. The results of these simulations are shown in Figures 21.16.2-1 through 21.16.2-10.

With **[ ]**[a,c] the predicted break flow is mostly unaffected, but the transition to two-phase is predicted to occur slightly earlier, Figure 21.16.2-1. The system pressure response, Figure 21.16.2-2, is not significantly affected by the HS_SLUG variation.

The calculated steam generator draining is very similar as well, Figure 21.16.2-3.

The calculated differential pressures in the cross-over legs (bottom to pump inlet), Figures 21.16.2-4 and 21.16.2-5, do not appear to be affected by the HS_SLUG variation with the timing of the loop seal clearance predicted almost identical.

The calculated upper plenum differential pressures are not affected much by the HS_SLUG variation, Figure 21.16.2-7, as well as the predicted hot leg differential pressures, Figure 21.16.2-8.

The downcomer differential pressure appears to be affected by the HS_SLUG variation, Figure 21.16.2-6. The higher downcomer differential pressure (or level) calculated with **[ ]**[a,c] can be attributed to the predicted earlier transition to two-phase break flow; this is less loss of inventory, hence higher downcomer level. As a result, the effect of on the calculated core differential pressures, Figure 21.16.2-9, is a delayed onset of boiloff (due to the higher downcomer driving head) and, as a result, less boiloff heatup with **[ ]**[a,c], Figure 21.16.2-10.

The overall results, however, show that the effect of the HS_SLUG variation on the predicted system behavior in the SB-CL-18 simulation is **[ ]**[a,c]

a,c

Figure 21.16.2-1 Calculated Break Flow Rates

a,c

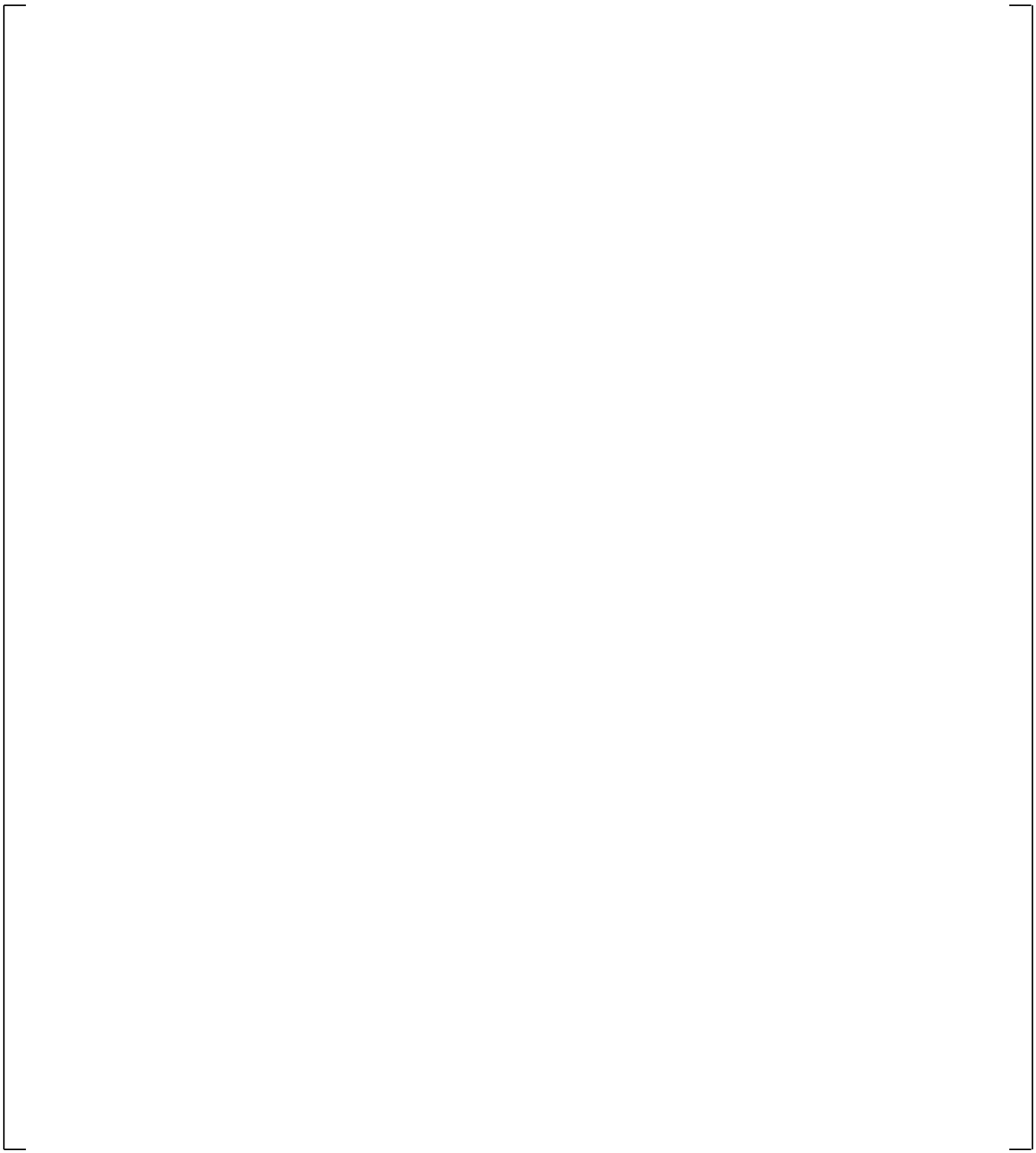

Figure 21.16.2-2 Calculated Pressurizer and Steam Generator Secondary Pressures

a,c

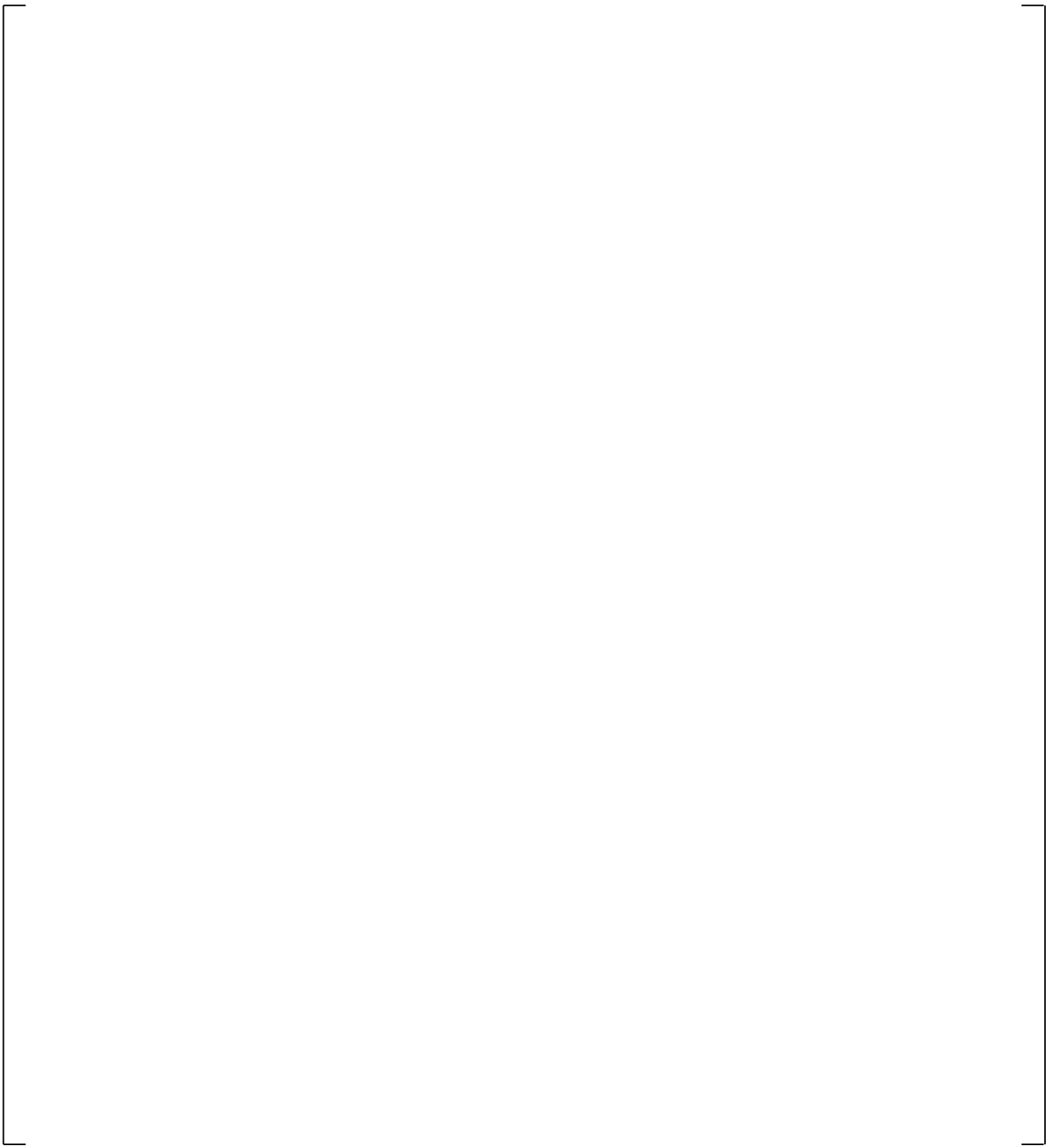

Figure 21.16.2-3 Calculated Steam Generator U-tube Uphill Side Differential Pressures

a,c

Figure 21.16.2-4 Calculated Cross-Over Leg A Differential Pressures

a,c

Figure 21.16.2-5 Calculated Cross-Over Leg B Differential Pressures

a,c

Figure 21.16.2-6 Calculated Downcomer Differential Pressures

a,c

Figure 21.16.2-7 Calculated Upper Plenum Differential Pressures

a,c

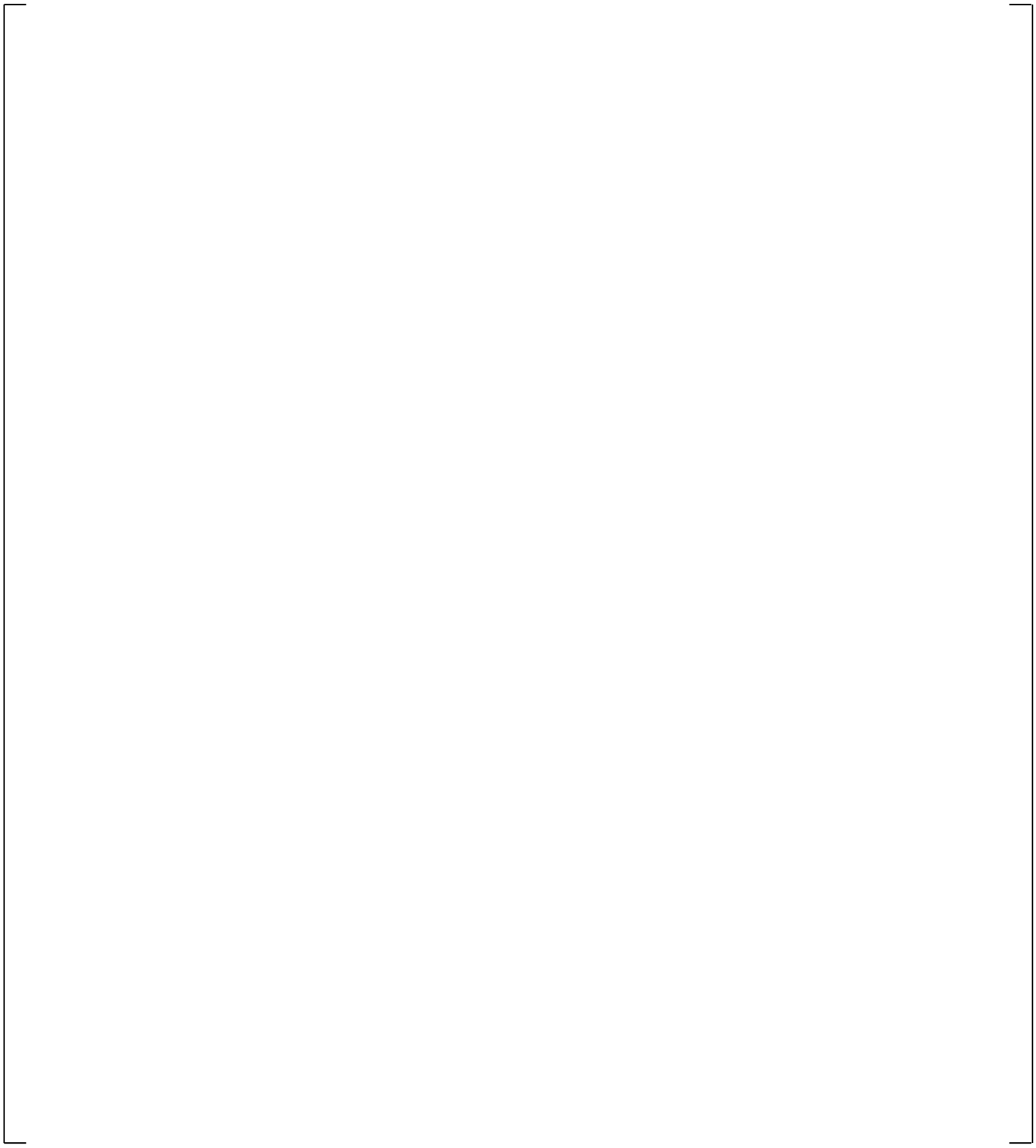

Figure 21.16.2-8 Calculated Hot Leg Differential Pressures

a,c

Figure 21.16.2-9 Calculated Core Differential Pressures

a,c

Figure 21.16.2-10 Calculated Peak Cladding Temperatures

21.16.3 HS_SLUG Sensitivity with 10% Side Break Test SB-CL-14

Two simulations of the 10% side break test SB-CL-14 test were performed with setting the HS_SLUG multiplier at its maximum **[ ]**[a,c] and minimum **[ ]**[a,c] values. The results of these simulations are shown in Figures 21.16.3-1 through 21.16.3-10.

The break flow, Figure 21.16.3-1, and system pressure response, Figure 21.16.3-2, are not affected by the HS_SLUG variation. The calculated steam generator draining is almost identical, Figure 21.16.3-3.

The calculated downcomer, upper plenum and hot leg differential pressures are not affected much by the HS_SLUG variation, as shown in Figures 21.16.3-6 through 21.16.3-8.

For the 10% break size the calculated timing of the loop seal clearance is almost identical, Figures 21.16.3-4 and 21.16.3-5. **[**

][a,c]

a,c

Figure 21.16.3-1 Calculated Break Flow Rates

a,c

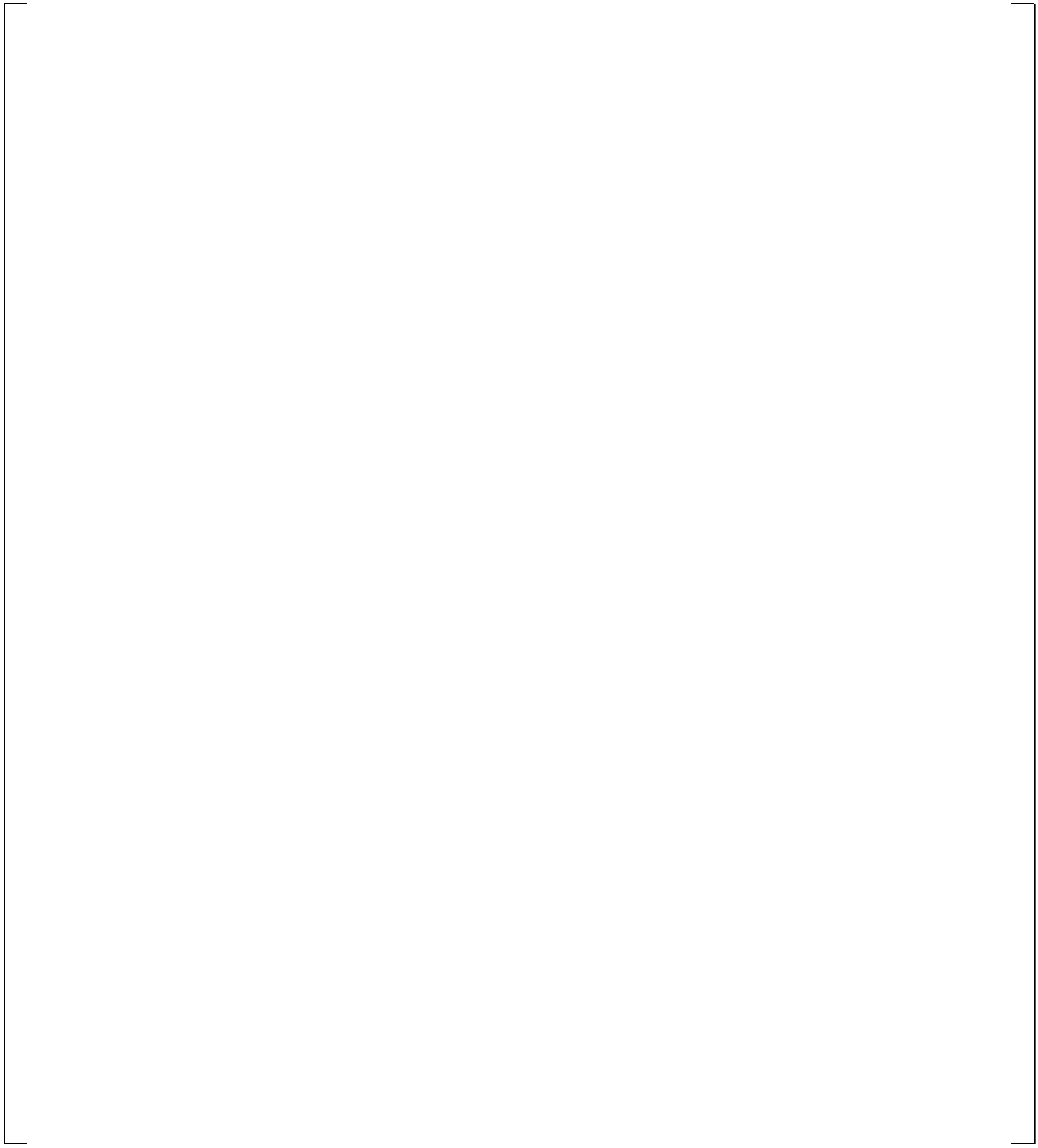

Figure 21.16.3-2 Calculated Pressurizer and Steam Generator Secondary Pressures

a,c

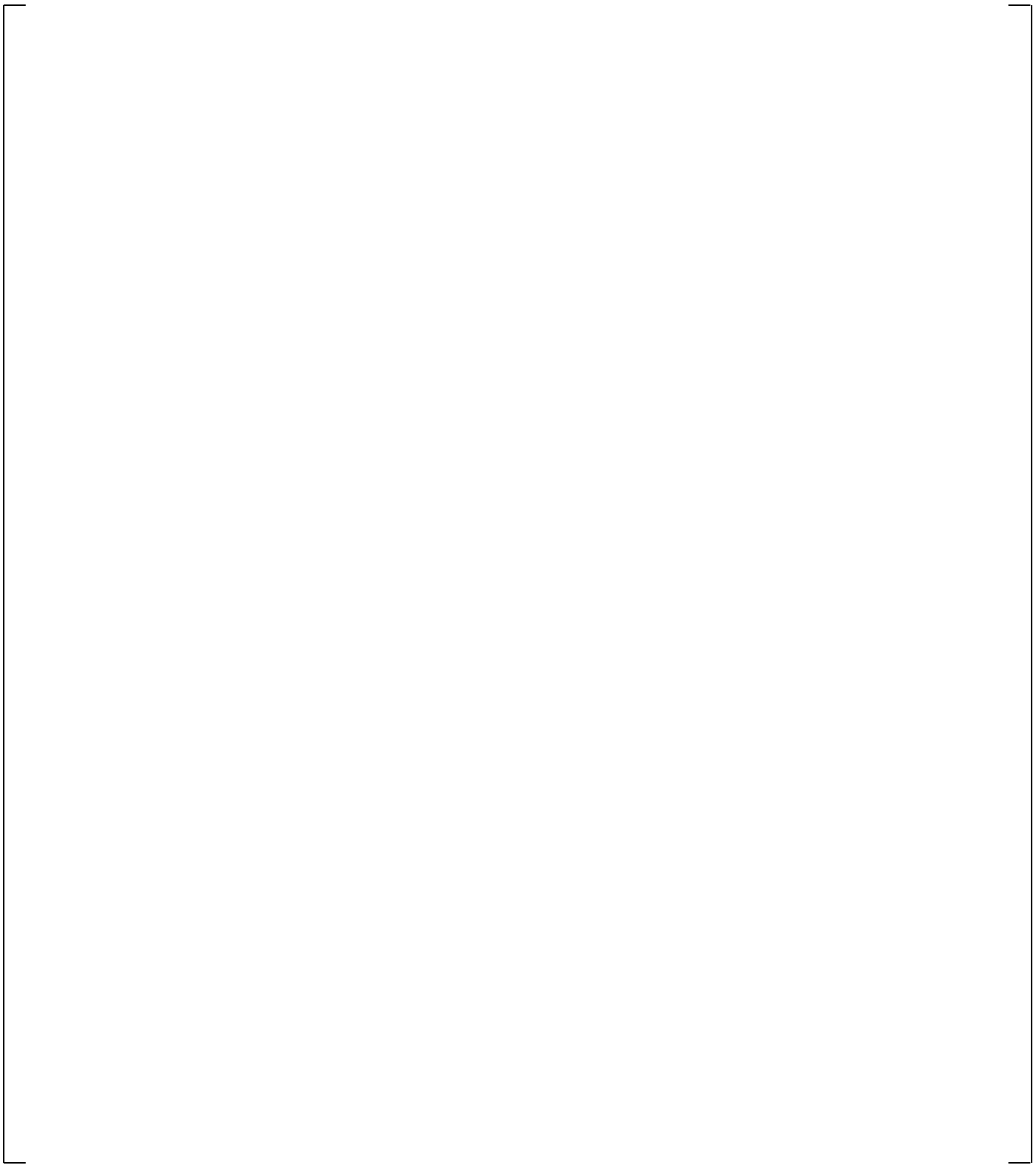

Figure 21.16.3-3 Calculated Steam Generator U-tube Uphill Side Differential Pressures

a,c

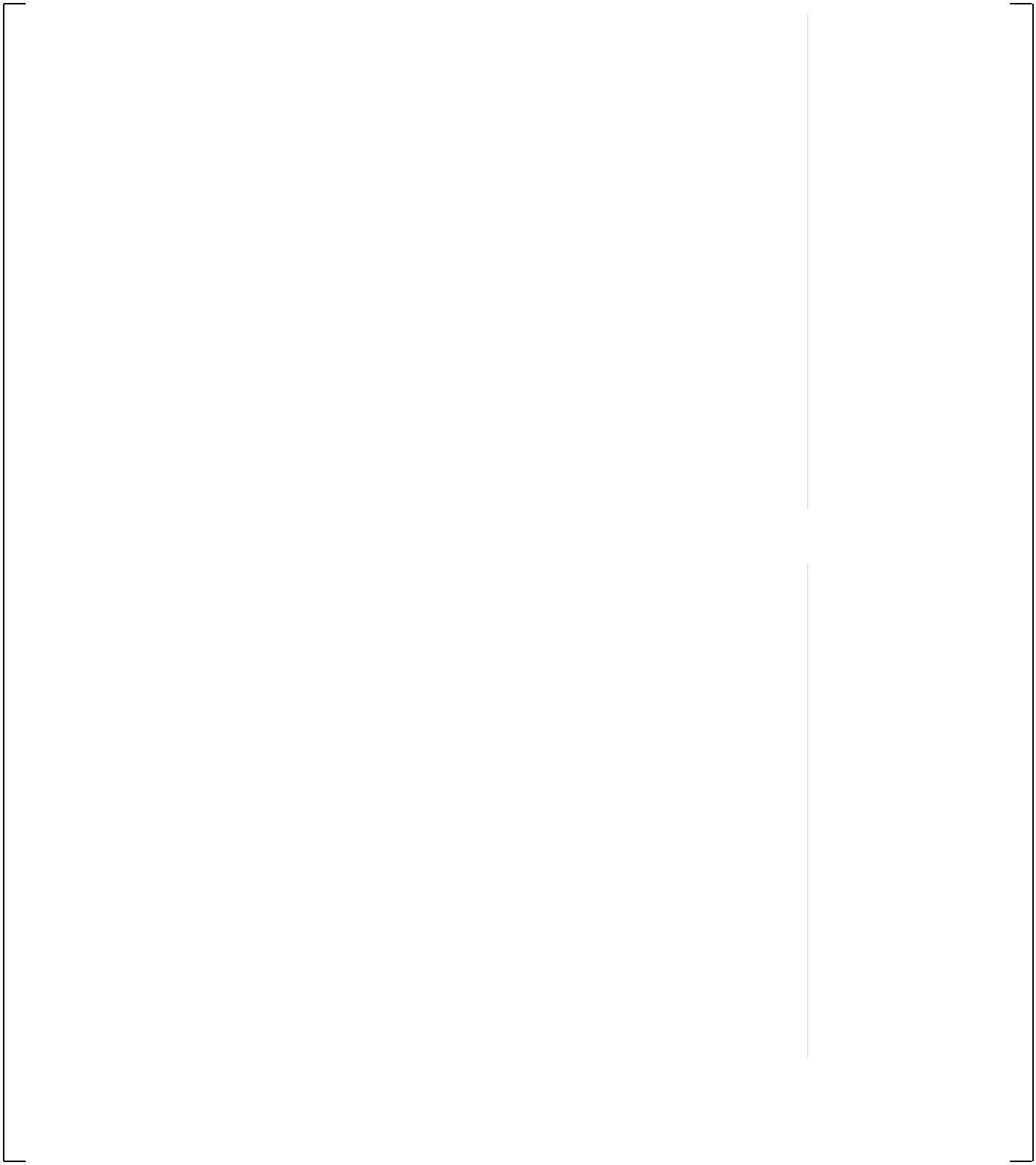

Figure 21.16.3-4 Calculated Cross-Over Leg A Differential Pressures

a,c

Figure 21.16.3-5 Calculated Cross-Over Leg B Differential Pressures

a,c

Figure 21.16.3-6 Calculated Downcomer Differential Pressures

a,c

Figure 21.16.3-7 Calculated Upper Plenum Differential Pressures

a,c

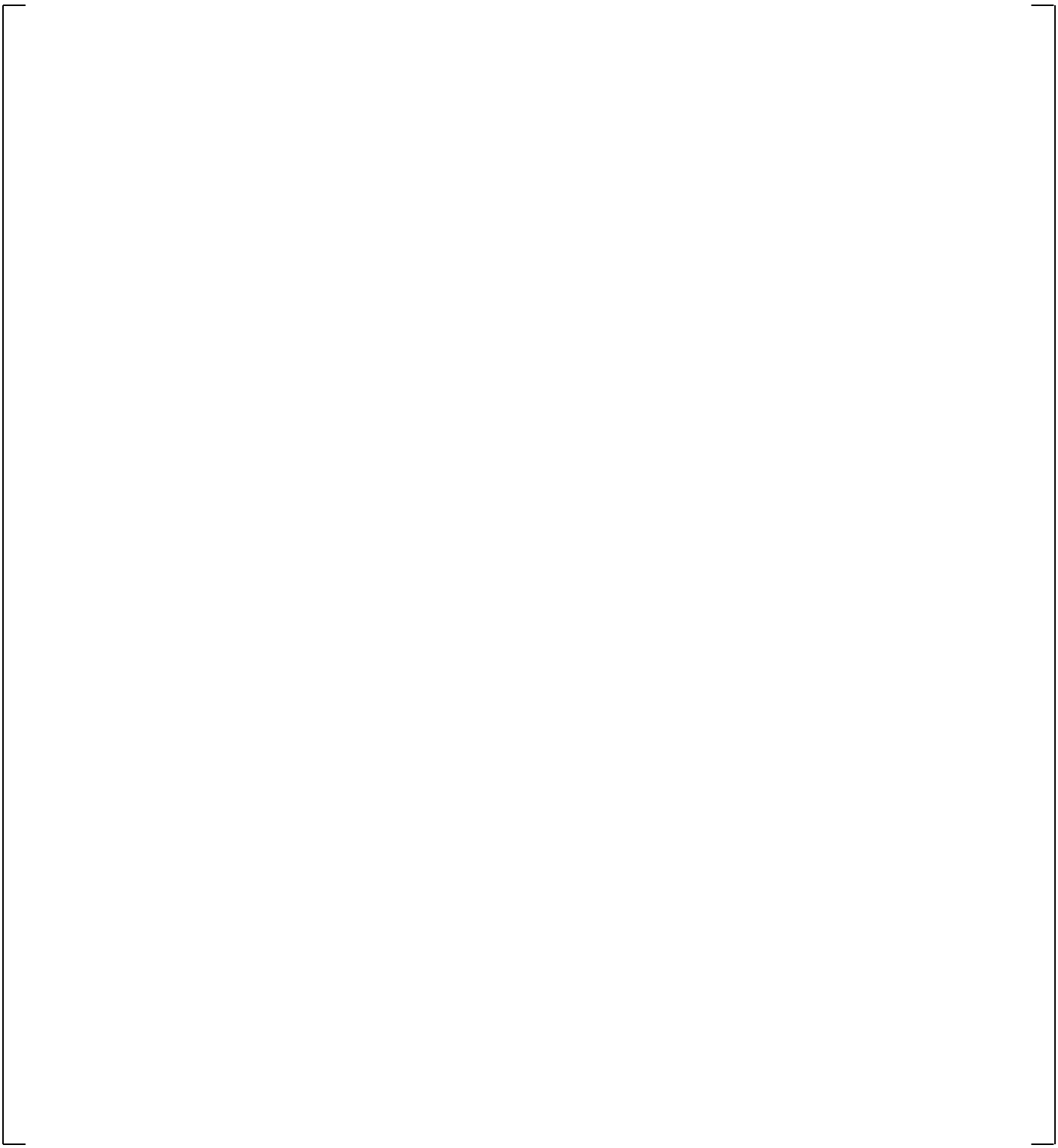

Figure 21.16.3-8 Calculated Hot Leg Differential Pressures

a,c

Figure 21.16.3-9 Calculated Core Differential Pressures

a,c

Figure 21.16.3-10 Calculated Peak Cladding Temperatures

21.16.4 Conclusion Regarding the HS_SLUG Sensitivity Simulations

Based on the results from the HS_SLUG sensitivity calculations presented herein, it can be concluded that the effect of the HS_SLUG ranging would have minimal effect on the Small Break LOCA transient.

21.17 KCOSI SENSITIVITY CALCULATIONS

This section presents the results of two simulations of the 5% side break test SB-CL-05 (reference case documented in Section 21.5), performed with setting the cold leg condensation multiplier KCOSI at high [ ]^{a,c} and low [ ]^{a,c} values. The results of the sensitivity are presented in Figures 21.17-1 through 21.17-12.

With the KCOSI multiplier set at maximum, the code calculates increased liquid present at the SI injection node of the intact cold leg, Figure 21.17-1(a). At the broken cold leg SI injection node the liquid content does not seem to be affected by the KCOSI variation in the intact cold leg, Figure 21.17-1(b). This is explained by the fact that, in this sensitivity, the cold leg condensation model is turned off in the broken cold leg to be consistent with the modeling approach adopted for the PWR simulations, Section 26, Volume 3.

[

]^{a,c}

a,c

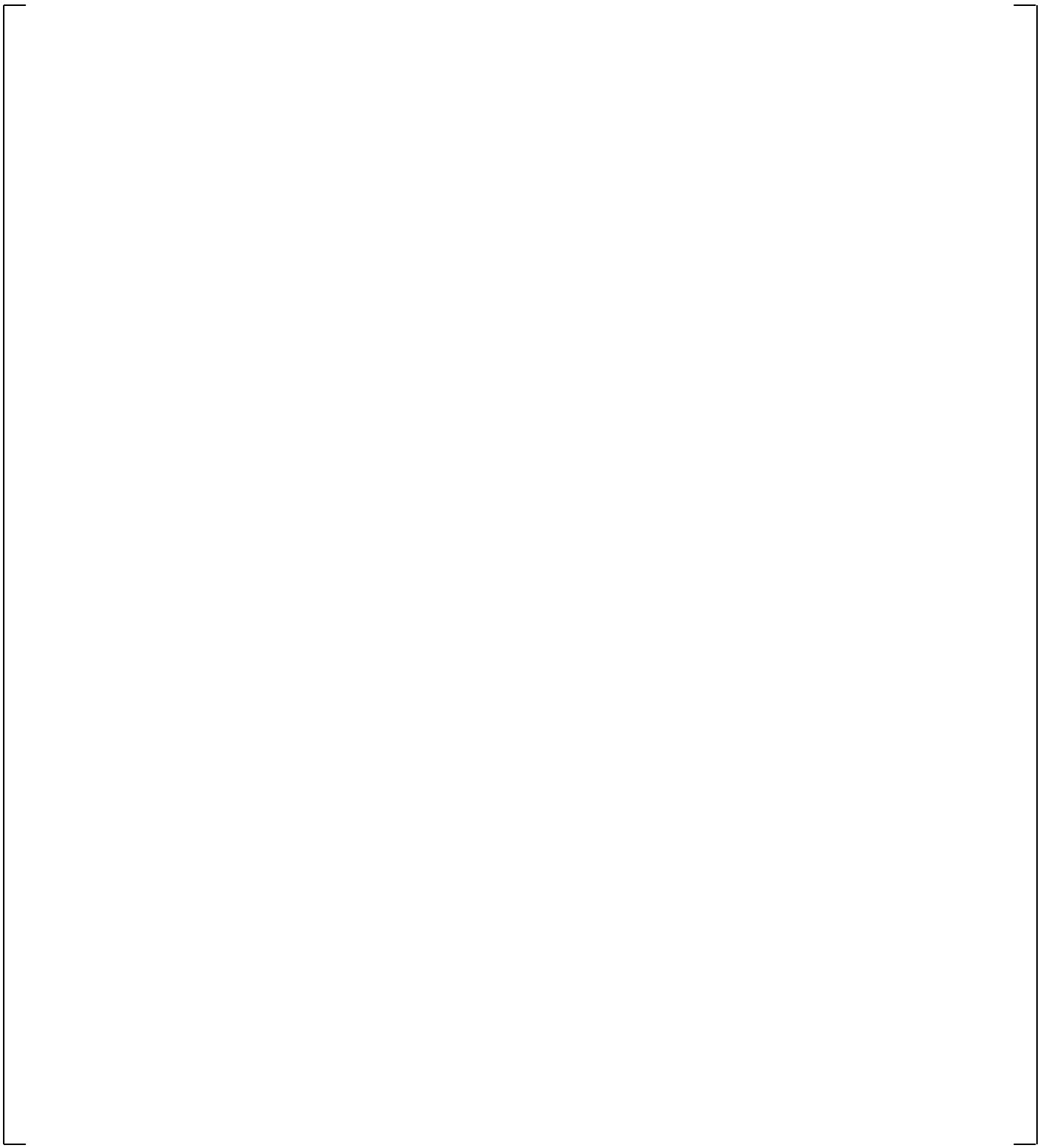

Figure 21.17-1 Cold Leg Void Fractions at the SI Injection Nodes

a,c

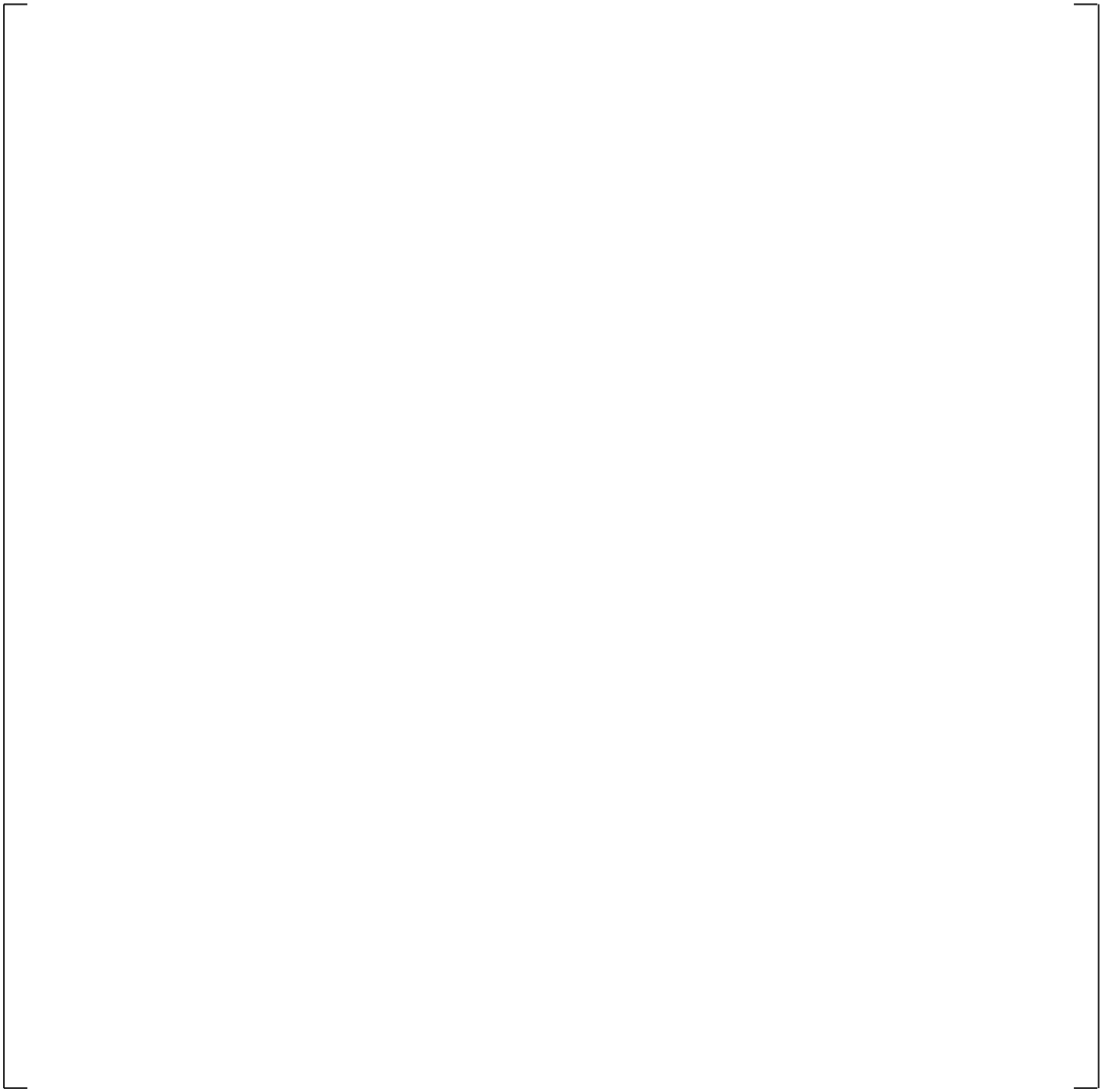

Figure 21.17-2 Mixture Flow at the Broken Cold Leg Nozzle (interface with the vessel)

Note: Negative is flow from the vessel into the cold leg.

a,c

Figure 21.17-3 Total SI Condensation Heat Rate at Cold Leg Injection Node in Cold Leg A

Note: With the cold leg condensation model turned off, CSIQTOT is not calculated in the SI injection node of the broken cold leg.

a,c

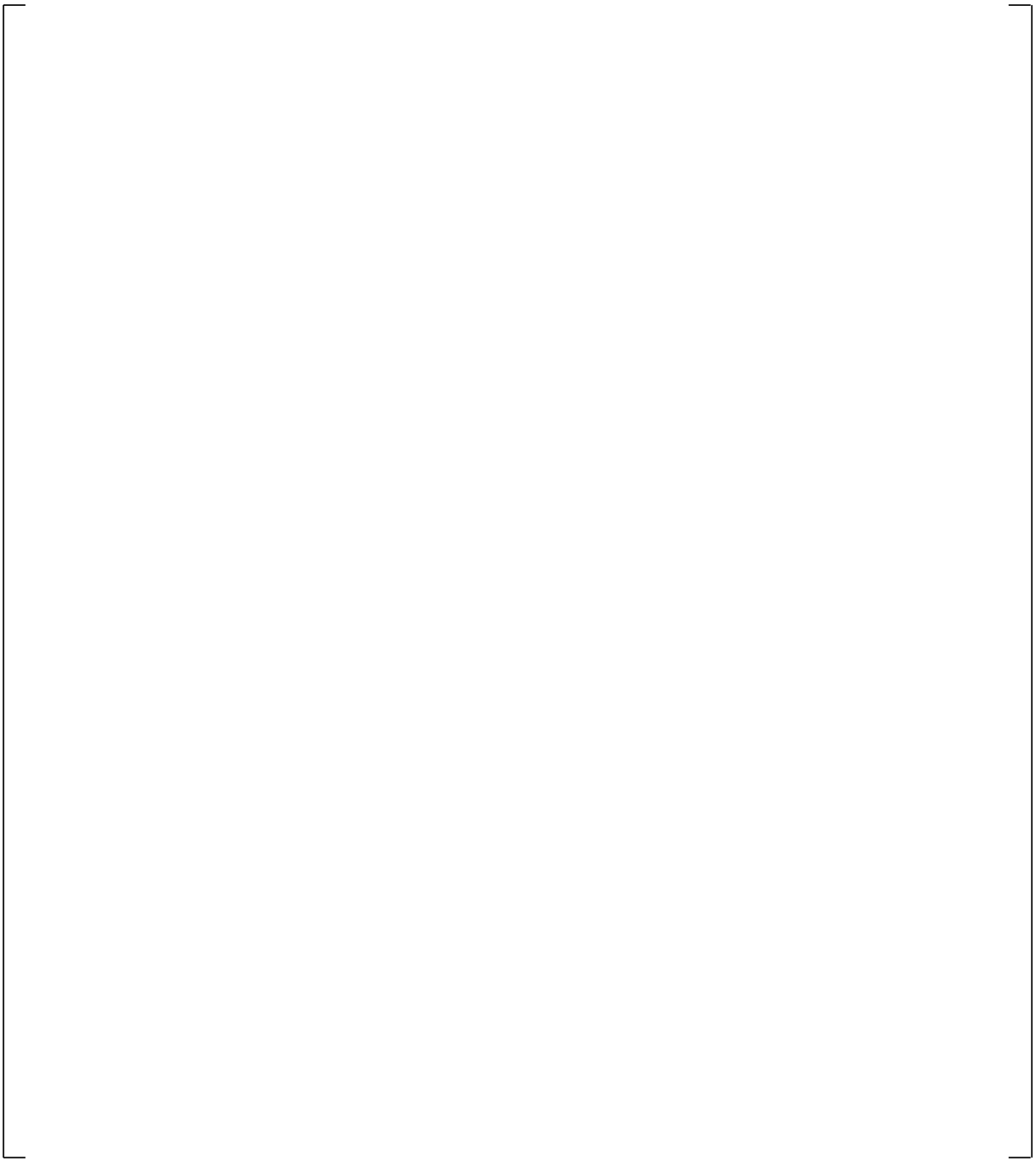

Figure 21.17-4 Cold Leg Fluid Temperatures at SI Injection Nodes

Note: The temperature of the pumped SI delivered into the cold legs is ~310K (98 F)

a,c

Figure 21.17-5 Cold Leg Pressures at SI Injection Nodes

a,c

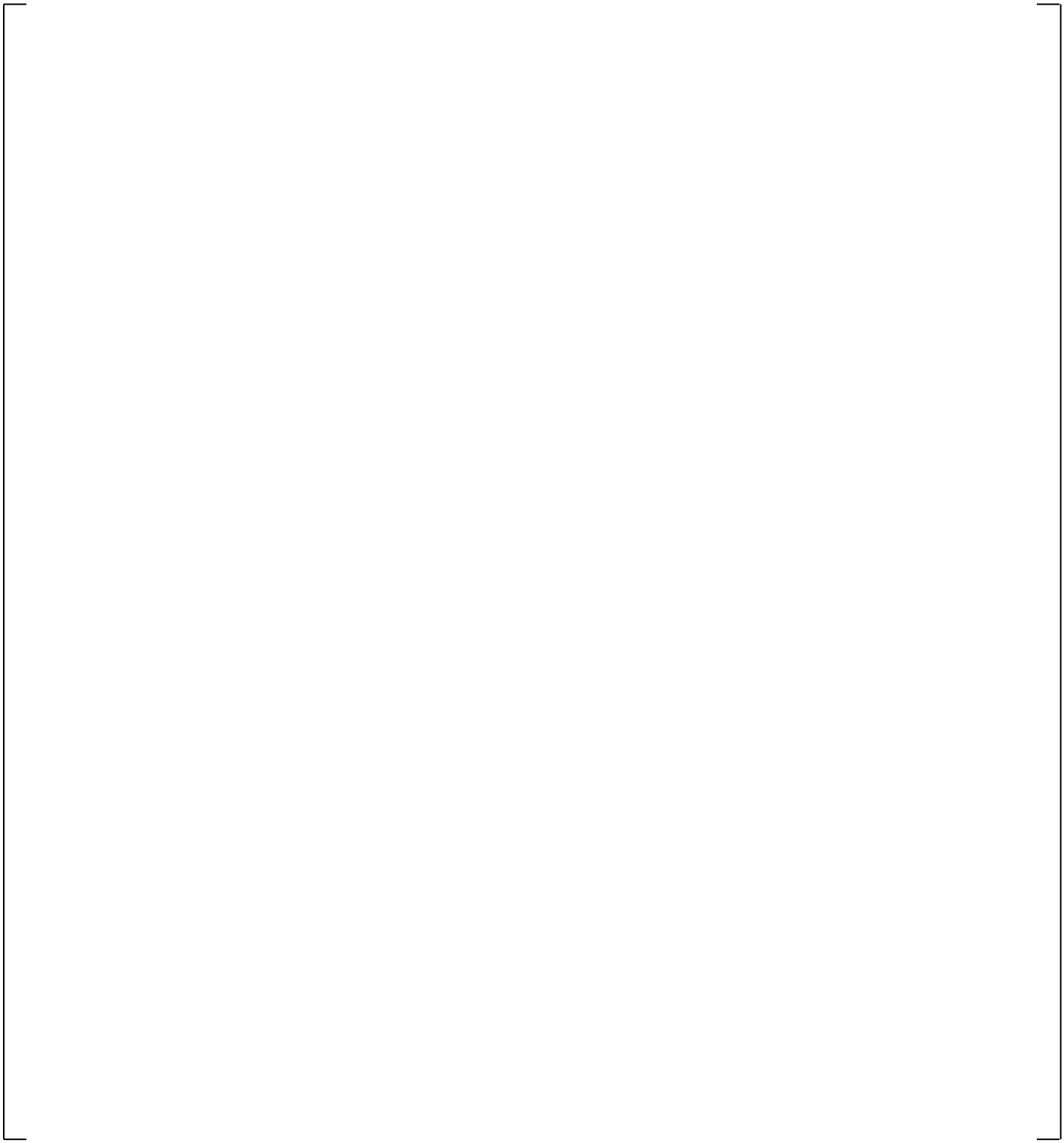

Figure 21.17-6 Accumulator Injection Flows

a,c

Figure 21.17-7 Broken Cold Leg Void at Break Off-take Node

a,c

Figure 21.17-8 Break Void Fractions

a,c

Figure 21.17-9 Fluid Temperatures at the Break

a,c

Figure 21.17-10 Break Flow Rates

a,c

Figure 21.17-11 Integrated Break Flows

a,c

Figure 21.17-12 Integrated Break Flow Difference (KCOSI_low-KCOSI_high)

21.18 MAIN STEAM SAFETY VALVE SETPOINT SENSITIVITY CALCULATION

A sensitivity calculation is performed with the 0.5% side break test SB-CL-15 to provide a basis for assessing the effect of increased main steam safety valve setpoint on the SBLOCA transient. The 0.5% break was selected for this sensitivity since with this break size the loss of inventory is the lowest, the holdup of the primary system pressure above the secondary side pressure is for a longer period of time, and the effect of the increase of the MSSV setpoint would be greater.

For the purpose of the sensitivity study, the steam generator MSSV pressure setpoints were increased arbitrarily, as follows.

MSSV Open @ 9.37 MPa (old value 8.0 MPa)
MSSV Close @ 8.5 MPa (old value 7.8 MPa)

With the setpoints selected above, the average MSSV setpoint is increased by 1.035 MPa (150 psi).

The calculation results from this sensitivity are compared to the results of the SB-CL-15 simulation, performed for the break orientation studies in Section 21.7.

Figure 21.18-1 compares the calculated pressurizer and steam generator secondary side pressures from the two simulations. As seen, the increase of the MSSV setpoint results in an increased primary system pressure during the prolonged period when the steam generator acts as a heat sink. The cyclical behavior of the secondary side pressure affects the primary side pressure in a similar way, through the primary-to-secondary side heat transfer feedback mechanism. The greater amplitude of the calculated pressure oscillations in the high MSSV setpoint case is due to the greater difference between the Open and Close pressure setpoints of the MSSV, implemented for that case.

The comparison of the calculated break flows, Figure 21.18-2, shows a minor effect on the calculated inventory loss through the break.

With the MSSV setpoint increased, the calculated steam generator draining is asymmetrical, but the steam generators drain at about the same time, Figure 21.18-3. Increased loss of inventory through the break might be the reason for the predicted somewhat earlier draining of the upper plenum, Figure 21.18-4, and the hot legs as well, Figure 21.18-5.

Figure 21.18-6, shows a comparison of the calculated differential pressures from the bottom of the cross-over leg to the pump inlet for the two loops. As seen in that figure, with the increase of the MSSV the loop seal clearance in loop A is predicted to occur a little earlier. The calculated loop flows, Figure 21.18-7, are very similar.

As a result of the calculated greater inventory loss with increased MSSV setpoint, the loop seal clearance uncovery of the core occurs a little earlier, as well as the boiloff, Figure 21.18-8. Consequently, in the case of increased MSSV setpoint the calculated rod heatup is higher, as seen in Figure 21.18-9. The overall effect of the MSSV setpoint, however, does not appear to be significant.

a,c

Figure 21.18-1 Calculated Primary and Steam Generator Secondary Pressures

a,c

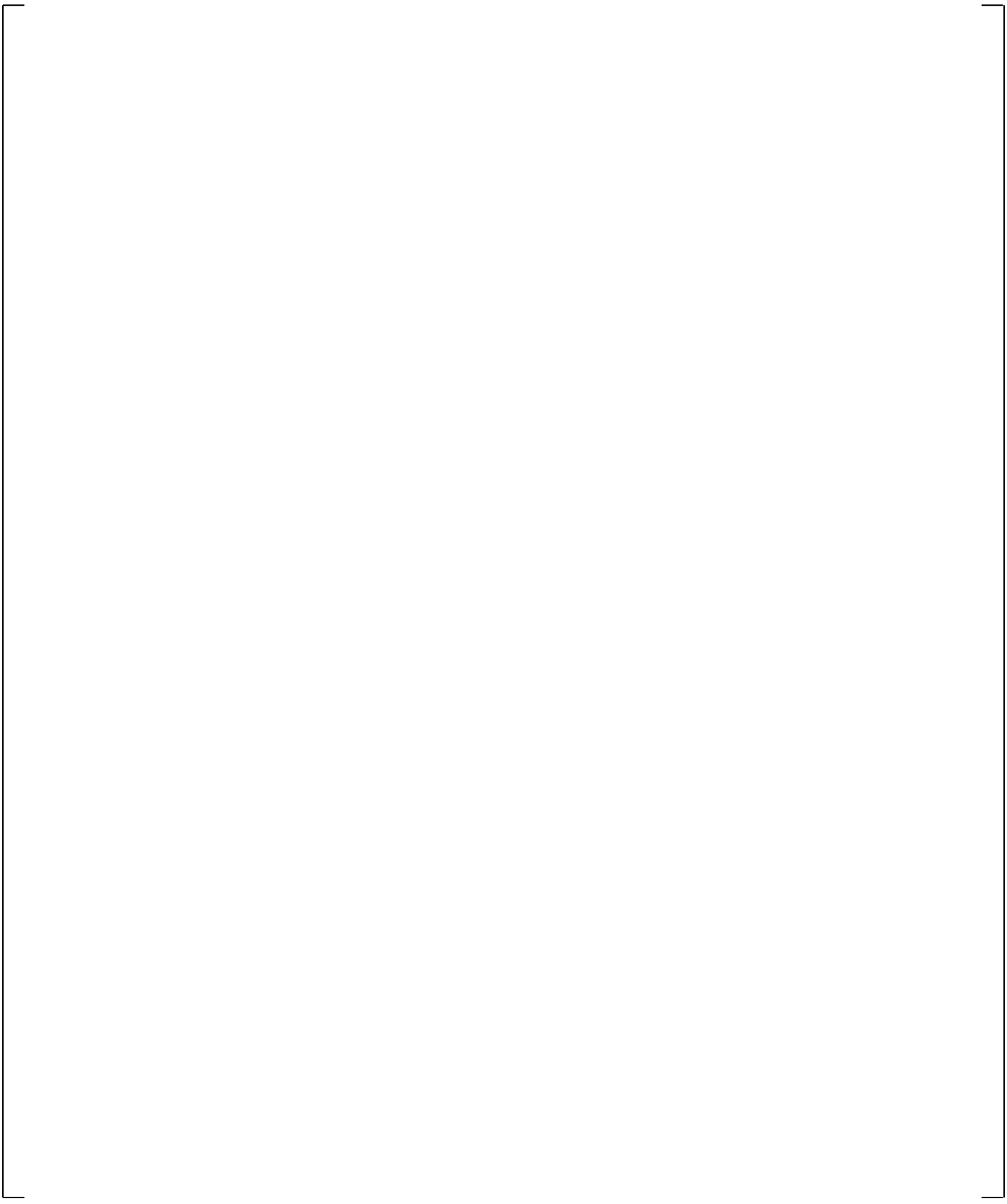

Figure 21.18-2 Calculated Break Flows

a,c

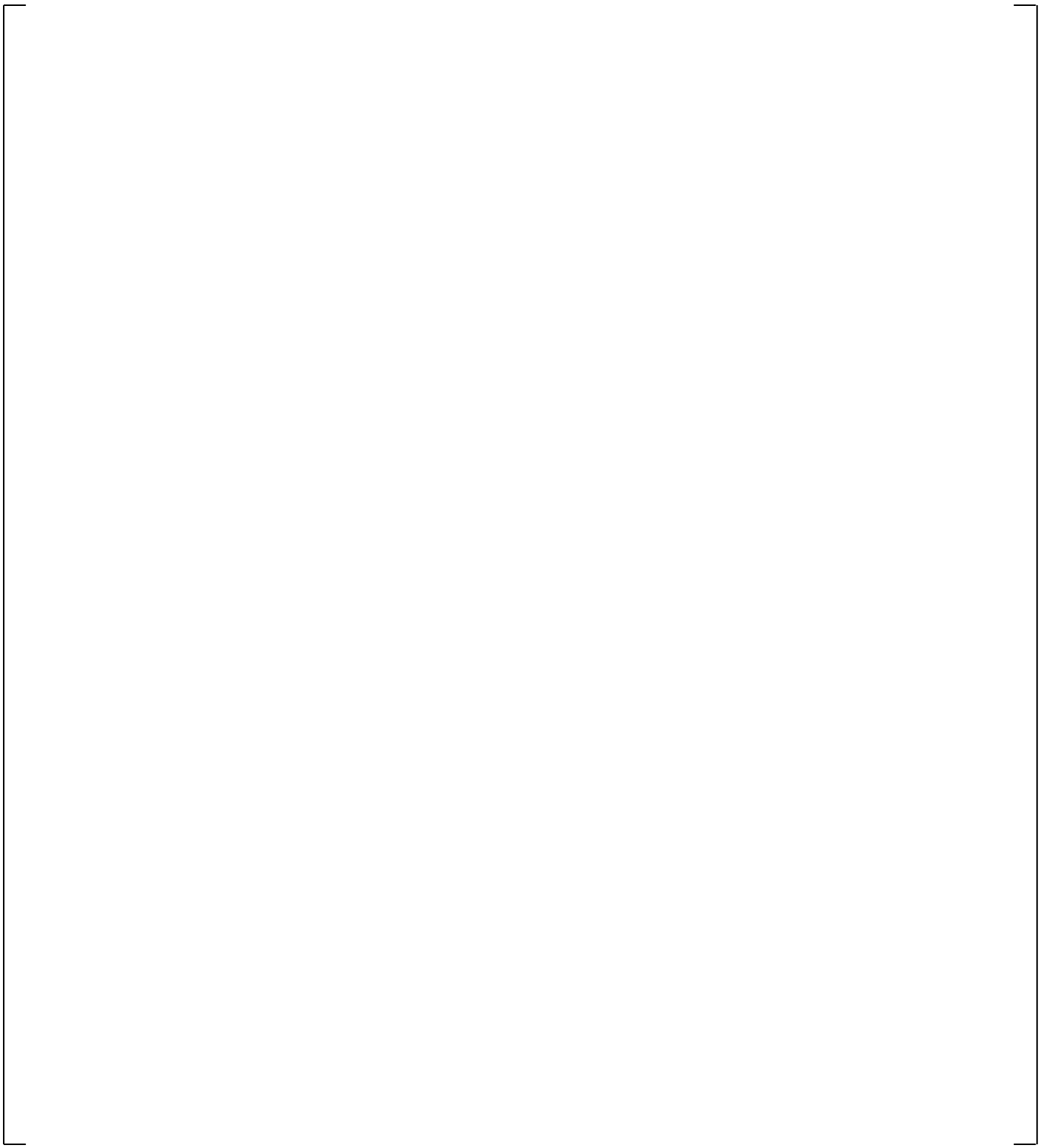

Figure 21.18-3 Calculated Draining of Steam Generator U-tubes Uphill Side

a,c

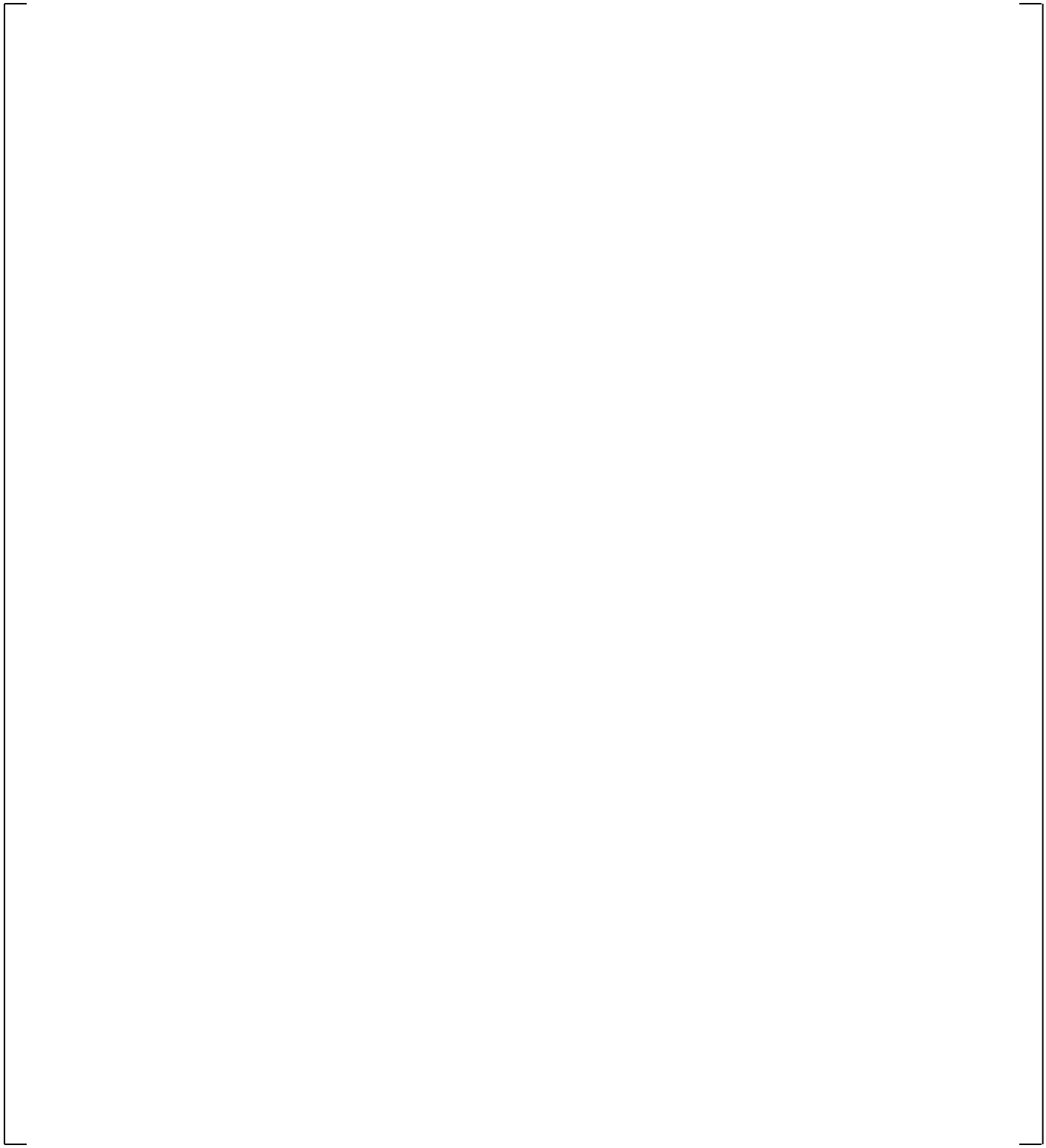

Figure 21.18-4 Calculated Upper Plenum Differential Pressures

a,c

Figure 21.18-5 Calculated Upper Plenum to Steam Generator Inlet Differential Pressures

a,c

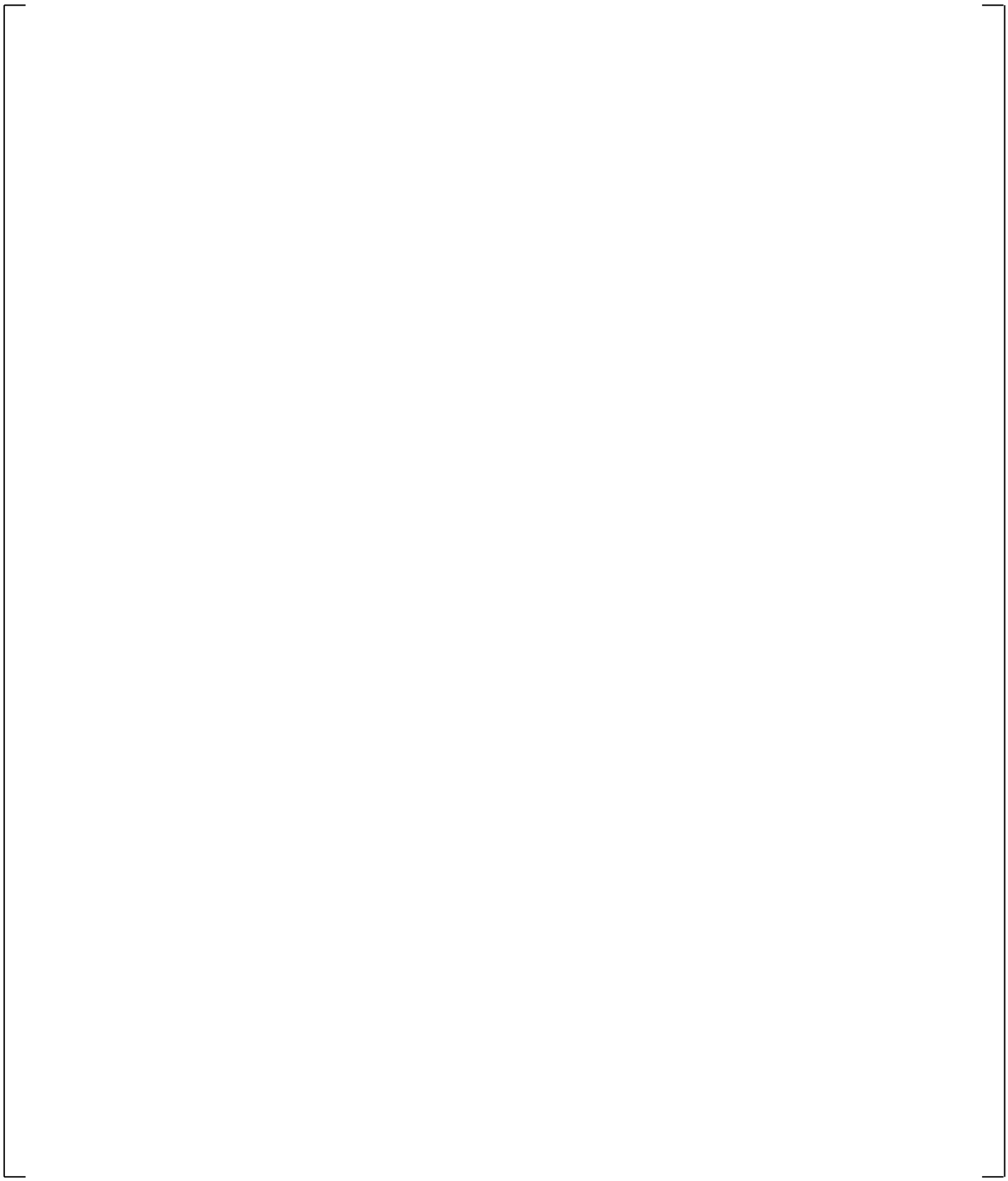

Figure 21.18-6 Calculated Cross-Over Leg Differential Pressures (Bottom-to-Pump Inlet)

a,c

Figure 21.18-7 Calculated Loop Flow Rates

a,c

Figure 21.18-8 Calculated Core Differential Pressures

a,c

Figure 21.18-9 Calculated Peak Cladding Temperatures

21.19 CONCLUSIONS

The analysis of the results of the various ROSA-IV LSTF test simulations presented in this section demonstrates that WCOBRA-TRAC-TF2 is capable of simulating with sufficient accuracy the key thermal-hydraulic phenomena that might occur during a PWR small break LOCA accident. The major conclusions from the analysis of the test simulations with the ROSA-IV LSTF model presented in this section are summarized below.

- [

]^{a,c}

- The simulation of the ST-NC-02 test shows that the code calculates natural circulation phenomena in a manner consistent with the test observations. The transition to reflux condensation is calculated to occur at system inventory consistent with that observed in the test. [

]^{a,c}

- The break orientation studies in Section 21.7 show results which are consistent with those observed in the tests. [

]^{a,c}

- The various sensitivity studies show results that are consistent with the expected effect of the parameter being ranged in these small break LOCA test simulations.

21.20 REFERENCES

1. Asaka, et al., 1990, "Results of 0.5% Cold-Leg Small-Break LOCA Experiments at ROSA-IV/LSTF: Effect of Break Orientation," *Experimental Thermal and Fluid Science*, 3, 588-596.

2. Chauliac, C., et al., 1988, "Post-Test Analysis with RELAP5/MOD2 of ROSA-IV/LSTF Natural Circulation Test ST-NC-02," JAERI-M 88-215.

3. Glaeser, H., et al., 1993, "The Contribution of UPPTF Experiments to Resolve Some Scale-up Uncertainties in Countercurrent Two Phase Flow," *Nuclear Engineering and Design*, 145 (63-84).

4. Glaeser, H., et al., 2000, "OECD/CSNI Uncertainty Methods Study for "Best Estimate" Analysis," International Meeting on "Best-Estimate" Methods in Nuclear Installation Safety Analysis (BE-2000), Washington, DC.

5. Hsieh, C., et al., 1980, "Countercurrent Air/Water and Steam/Water Flow above a Perforated Plate," NUREG/CR-1808.

6. Kawaji, M., et al., 1986, "ROSA-IV/LSTF 5% Cold Leg Break LOCA Experiment Data Report, Run SB-CL-05," JAERI-memo 61-056.

7. Koizumi, Y., et al., 1987, "ROSA-IV/LSTF 2.5% Cold Leg Break LOCA Experiment Data Report for Runs SB-CL-01, 02 and 03," JAERI-memo 62-399.

8. Koizumi, Y., et al., 1988, "Investigation of Break Orientation Effect During Cold Leg Small-Break LOCA at ROSA-IV LSTF," *Journal of Nuclear Science and Technology*, 25.

9. Koizumi, Y. and Tasaka, K., 1988a, "Quick Look Report for ROSA-IV/LSTF 10% Cold Leg Break LOCA Test, SB-CL-14," **[ ]**[b]

10. Koizumi, Y. and Tasaka, K., 1988b, "Quick Look Report for ROSA-IV/LSTF 0.5% Cold Leg Break LOCA Tests, SB-CL-15 and SB-CL-16," **[ ]**[b]

11. Kukita, Y., et al., 1988, "Nonuniform Steam Generator U-Tube Flow Distribution During Natural Circulation Tests in ROSA-IV Large Scale Test Facility," *Nuclear Science and Engineering*, Vol. 99.

12. Kukita, Y., et al., 1989, "Hot Leg Flow Characteristics during Two-phase Natural Circulation in Pressurized Water Reactor," *Proceedings/Fourth International Topical Meeting on Nuclear Reactor Thermal Hydraulics*, NURETH-4, page 465-470.

13. Kukita, Y., et al., 1990a, "Loop Seal Clearing and Refilling During a PWR Small-Break LOCA," *Nuclear Engineering and Design*, 121, pp. 431-440.

14. Kukita, Y., et al., 1990b, "The effect of break location on PWR small break LOCA: Experimental study at the ROSA-IV LSTF," *Nuclear Engineering and Design*, 122, pp. 255-262.

15. Kukita, Y., et al., 1991, "Summary of ROSA-IV LSTF First-phase Test Program – Integral Simulation of PWR Small-break LOCAs and Transients," *Nuclear Engineering and Design*, 131 101-111.

16. Kukita, Y., et al., 1992, "OECD/NEA/CSNI International Standard Problem No. 26 (ISP-26) ROSA-IV LSTF Cold-Leg Small-Break LOCA Experiment – Comparison Report."

17. Kumamaru, et al., 1989, "ROSA-IV/LSTF 5% Cold Leg Break LOCA Experiment, Run SB-CL-18 Data Report," JAERI-M 89-027.

18. Leonard, M. T., 1982a, "Vessel Coolant Mass Depletion During a Small Break LOCA," EGG-SEMI-6010.

19. Leonard, M. T., 1982b, "An Analytical Study of a Small Break Loss-Of-Coolant Accident with Upper Head Injection," *Nuclear Technology*, Vol. 62.

20. Loomis, G. G. and Streit, J. E., 1985, "Quick Look Report for Semiscale Mod-2C Experiments S-LH-1 and S-LH-2," EGG-SEMI-6884.

21. Osakabe, M., et al., 1987, "Core Liquid Level Depression due to Manometric Effect during PWR Small Break LOCA – Effect of Break Area," *Journal of Nuclear Science and Technology*, 24, pp. 103-110.

22. Osakabe, M., et al., 1988, "Core Liquid Level Depression due to Manometric Effect during PWR Small Break LOCA – Effect of Core Bypass," *Journal of Nuclear Science and Technology*, 25, pp. 274-282.

23. The ROSA IV Group, 1985, "ROSA-IV Large Scale Test Facility (LSTF) System Description," JAERI-M 84-237.

24. The ROSA-IV Group, 1989, "Supplemental Description of ROSA-IV/LSTF with No.1 Simulated Fuel-Rod Assembly," JAERI-M 89-113.

25. Stumpf, H. et al., 1987, "Reverse Primary-Side Flow in Steam Generators During Natural Circulation Cooling," *ASME Heat Transfer Division (HTD)*, Vol. 92.

26. Tasaka, K., et al., 1988, "The Results of 5% Small Break LOCA Tests and Natural Recirculation Tests at the ROSA-IV LSTF," *Nuclear Engineering and Design*, 108.

27. Yonomoto, T., 2005, "ROSA/LSTF Experiments of PWR Natural Circulation and Validation of RELAP5/MOD3.3," IAEA's 2nd Research Coordination Meeting on the CRP on Natural Circulation Phenomena, Modeling and Reliability of Passive Safety Systems that Utilize Natural Circulation, Corvallis, Oregon (USA).

22 LOSS-OF-FLUID INTEGRAL TEST SIMULATIONS

22.1 INTRODUCTION

The Loss-of-Fluid Test (LOFT) experiments have been widely used for validation of pressurized water reactor (PWR) computer models due to the relatively large scale of the facility (1:60 volume scaling of a commercial four-loop PWR) and the use of a nuclear core designed to have the same physical, chemical, and metallurgical properties as a PWR core (Reeder, 1978). The large scale of the facility enables multidimensional effects, which allow assessment of the ability of the code to predict these effects. Also, because LOFT is the only integral facility to use a nuclear core, the experiments are considered to be an essential part of the validation package for any PWR computer model.

The LOFT facility is designed to provide thermal-hydraulic data representative of a large rupture of a main coolant pipe. A large amount of thermal and hydraulic data is available from the tests performed on the LOFT facility, which allow the assessment of the key processes in a postulated loss-of-coolant accident (LOCA) event covering a full spectrum (or range) of break sizes from small to large breaks. As such, LOFT represents a unique set of tests, which can be used to assess the performance of WCOBRA/TRAC-TF2 in a simulation of LOCA over a wide spectrum of pipe break sizes.

The LOFT facility contains a number of atypicalities relative to a large-scale PWR for large and small break LOCA simulations. Nevertheless, the facility remains a valuable benchmark for model assessment, provided the atypicalities are recognized and do not overshadow the thermal-hydraulic behavior of interest. In general, LOFT fluid volumes were scaled according to the ratio of LOFT core power to PWR core power of a large plant. If practical, flow areas were scaled by the same ratio. A more detailed LOFT scaling discussion is provided in Section 22.2.2.

Four LOFT large break (LB) tests were simulated with WCOBRA/TRAC-TF2: L2-2, L2-3, L2-5, and LB-1. Tests L2-2 (McCormick-Barger, 1979) and L2-3 (Prassinos et al., 1979) were low and intermediate power tests in which the reactor coolant pumps were allowed to continue operating under the inertia of the flywheels. Tests L2-5 (Bayless and Divine, 1982) and LB-1 (Adams and Birchley, 1984) were intermediate and high power tests in which the pumps were tripped and the pump flywheels disconnected. These four experiments are used to assess the code's ability to predict the following quantities:

1. Reactor power decay
2. Emergency core cooling (ECC) bypass
3. Reactor coolant pump behavior
4. Break flow rate
5. Fuel rod cladding temperature
6. Core and loop flow distribution

To complete the assessment across the break spectrum, the WCOBRA/TRAC-TF2 simulations of one LOFT small break (SB) test L3-1 (Adams, 1979, Bayless et al, 1980, and Condie et al., 1981) and one LOFT intermediate break (IB) test L5-1 (Jarrell and Divine, 1981) are performed. LOFT L3-1 simulates a 4-inch equivalent diameter pipe break, while L5-1 is a 14-inch accumulator line break. The breaks are located at the centerline of the inactive loop cold leg. The L3-1 and L5-1 experiments are of interest for model validation due to the influence of accumulator injection on the primary system response in both tests.

The LOFT facility and the tests chosen for simulation are described in Section 22.2 and Section 22.3, respectively. The WCOBRA/TRAC-TF2 models of the facility used for the analysis of the chosen tests are presented subsequently in Section 22.4. Sections 22.5, 22.6 and 22.7 provide a brief description of the calculated results in comparison to the available test data for simulated large, small and intermediate break tests, respectively. Particularly for the LOFT large break simulations, a more detailed analysis of the simulation results including the assessment of compensating error is further provided in Section 24.

22.2 LOFT FACILITY AND SCALING

22.2.1 LOFT Facility Description

The following text describing the LOFT facility is summarized from NUREG/CR-1145 (Bayless, et al., 1980) and NUREG/CR-2398 (Jarrell and Divine, 1981) with additional information from NUREG/CR-0247 (Reeder, 1978).

The LOFT facility (operated by EG&G Idaho Inc. for the Department of Energy) was designed to represent a 1/60 scale (by volume) of a four loop PWR. Figure 22-1 (Bayless, et al., 1980) illustrates the layout of the LOFT facility. LOFT consists of five major components: the reactor vessel, the active loop, the inactive loop, the blowdown suppression system, and the emergency core cooling system (ECCS). A reflood assist bypass line (RABL) was also included in the inactive loop to provide additional safeguards capability in an emergency.

The LOFT reactor vessel is similar to a PWR reactor vessel in that it includes a nuclear core and an integral annular downcomer. However, the LOFT downcomer contains large metal filler blocks not found in a standard PWR downcomer to maintain volume scaling. Also, the LOFT vessel does not have an upper head typical of a PWR vessel. Figure 22-2 (Reeder, 1978) illustrates the LOFT reactor vessel and shows the various flow paths that are available for coolant that enters through the vessel inlet nozzle. The main flow path is around the distributor annulus, down the downcomer, through the core, and out the outlet nozzles. There are alternate paths that do not direct the coolant through the core, particularly through the thimble tubes and the inactive loop; these are termed core bypass paths and amount to approximately 5 percent of the total initial reactor vessel flow.

The 5.5-foot core used in LOFT is designed to have the same physical, chemical, and metallurgical properties as those in a PWR. It is also designed to provide thermal-hydraulic relationships, mechanical responses, and fission product releases that are representative of a PWR during the LOCA and ECC recovery. Figure 22-3 (Bayless, et al., 1980) shows a cross-sectional layout of the LOFT core.

The LOFT nuclear core consists of nine fuel assemblies designed for a thermal output of 50 MW. Two basic fuel assembly configurations are used in LOFT. As shown in Figure 22-3 (Bayless, et al., 1980), five assemblies have a 15×15 square cross section with fuel pins and guide tubes in locations typical of those in PWR fuel assembly structures. The remaining four assemblies have a triangular cross section with 12 fuel pins along each side that represents a portion of the square cross-sectional design. The square assemblies have 225 pin locations, 21 of which are occupied by guide tubes except for the center assembly; the center guide tube is not installed to allow for additional instrumentation. The triangular assemblies have 78 pin locations, 8 of which are occupied by guide tubes. In all, the nine LOFT fuel assemblies contain 1,300 fuel rods, 136 guide tubes, and 1 open hole for instrumentation.

The LOFT facility has one active loop that is similar to a PWR main coolant loop in that it includes a hot leg, an active steam generator (inverted U-tube and shell design), pump suction piping, and a cold leg. However, the LOFT active loop uses two coolant pumps in parallel, rather than a single coolant pump typical of a PWR loop, and the LOFT steam generator tubes are not full height. The steam generator simulates the response of three out of four steam generators in the unbroken loops of a PWR during a large break LOCA. The steam flow control valve motion is electronically controlled as a function of secondary pressure after reactor trip. The LOFT secondary side steam flow is controlled on a pressure hysteresis following steam generator trip; since the secondary side steam flow control valve is not positioned in the same way each time it closes, the secondary side steam leakage varies from test to test.

The LOFT inactive loop contains a hot leg, a steam generator simulator to represent the steam generator resistance, a reactor coolant pump (RCP) simulator to represent the pump resistance, and a cold leg. The hot and cold legs are connected on one side to the reactor vessel and on the other side to the quick-opening blowdown valves of the blowdown suppression system. The hot and cold legs are also connected to each other by the RABL, normally closed during the simulated LOCA event. This provides additional safeguards capability by allowing steam generated in the core to be vented directly to the break in an emergency.

The LOFT blowdown suppression system consists of header pipes from the quick-opening blowdown valves in the inactive loop, connected to a blowdown suppression tank with a spray system for steam condensation. This system provides the backpressure to the reactor coolant system (RCS) for the simulated LOCA event and, therefore, approximates the containment response during a postulated LOCA.

The LOFT ECCS consists of two accumulators; a high-pressure injection system (HPIS), consisting of two high-pressure injection pumps and a low-pressure injection system (LPIS), consisting of two low-pressure injection pumps. Generally, only one of each is active during a given experiment.

22.2.2 LOFT Scaling Consideration

The scaling discussion of the LOFT test facility in this section is summarized from NUREG/CR-3005 (Nalezny, 1985) and McPherson (1979).

The 55 MW LOFT was scaled to simulate the behavior of a 1000 MWe commercial PWR at reduced size but full pressure. It was designed with the power-volume scaling to ensure that the important features of the PWR during the postulated LOCA be properly simulated, e.g., the energy distribution process during the saturated blowdown, the primary concern during a PWR LOCA, is distorted at minimum. The similar thermal-hydraulic phenomena are expected to occur in both the LOFT and PWR systems in the same time scale as the power-volume scaling preserves the time scale.

The LOFT nuclear core is 5.5 ft (1.68 m) long and 2 ft (0.61 m) in diameter. It provides reasonable axial and radial power profiles with fuel assemblies that are geometric and full-scaled (except length) replicas of their commercial PWR counterparts, and allows extensive instrumentation and radial flow effects. The core height of LOFT is reduced by a factor of about 2 compared to the full length of a typical PWR.

Based on the scaling method, each component volume in the LOFT system was designed to be proportional to its counterpart in a PWR to the extent that is practical.

Table 22-1 shows the comparison of the subsystem volume, power, core length and core surface area per unit primary coolant system volume of the LOFT to a commercial PWR.

22.3 LOFT TEST DESCRIPTION

LOFT L2-2, L2-3, L2-5 and LB-1 were designed to represent double-ended cold leg pipe breaks (200%) in a full-scale PWR. LOFT L3-1 was configured to simulate a PWR LOCA caused by a cold leg small break equivalent to a 4-inch pipe rupture (2.5%), and LOFT 5-1 represents an intermediate break PWR LOCA caused by a 14-inch accumulator injection line rupture (25%).

The configuration and size of the breaks were modeled following the layout and the diameter of the break orifices located at the inactive/broken loop in the test facility, as shown in Figure 22-11(a), Figure 22-11(b) and Figure 22-11(c). In the four large break tests simulated, two break orifices, one at the broken cold leg and one at the broken hot leg, were connected to the blowdown suppression tank that simulated the condition of a PWR containment in the test through two Quick Opening Blowdown Valves (QOBV). In the LOFT L3-1 and L5-1 tests, the broken loop hot leg was blocked during the break transient and only one break orifice located at the broken cold leg was connected to the suppression tank through the QOBV.

Besides the different break sizes, the six LOFT tests feature different operating conditions in their steady states and transients, and the detail of which will be discussed in Sections 22.5.1, 22.6.1 and 22.7.1 for the large, small and intermediate break tests, respectively.

Each test began when the quick-opening blowdown valve connecting the inactive cold leg to the blowdown suppression system was opened (or in tests simulating the double-ended cold leg break, both quick-opening blowdown valves connecting the inactive cold leg and hot leg, respectively, to the blowdown suppression system were opened), simulating a pipe break.

The thermal-hydraulic responses of the reactor coolant system and the reactor core following a large break event are inertially dominated, whereas small break transients are hydrostatically controlled. For the intermediate break sizes, the transient process after the break could be similar to a prolonged transient process typical of a large break transient without severe ECCS bypass, or to a quicker small break transient process without an extended natural circulation phase.

The LOFT L2 series and LB-1 tests simulated the postulated large break LOCA events of a PWR. During the blowdown period of the transient, the initial reversed core flow occurred before the break flows became two-phase and the vessel fluid in the lower plenum and downcomer started to flash. This reversed core flow resulted in departure from the nuclear boiling (DNB) and rapid heatup of the core. At the end of the subcooled blowdown period, the core was rewetted in the L2-2 and L2-3 tests. As the decay heat in the core is large enough to keep drying out the core before the ECCS water entered the core from the bottom, the cladding temperature rose again during the reflood period of the transient before the bottom-up quenching due to ECCS water occurred.

The LOFT small break test L3-1 exhibited the typical small break transient phases of the rapid initial blowdown, the quasi-equilibrium natural circulation, the loop seal clearance and the boiloff. L3-1 did not experience any core dryout and fuel rod heatup. The primary system pressure fell rapidly until the subcooled break flow ends. At this time, the primary system pressure was still higher than the steam generator secondary side pressure and natural circulation occurred. The measured pressure then decreased more slowly until the loop seal cleared resulting in an increased depressurization rate. The scaled HPIS and LPIS safety injection were initiated by the low primary system pressure. The test was terminated once the accumulator water was injected.

The transient processes observed in the LOFT intermediate break test L5-1 are similar to the L3-1 test, but occur in a shorter time period and with a different depressurization rate. However, the L5-1 experiment shows core dryout and fuel rod heatup during the boiloff portion of the transient from the high to low elevations of the core. Initially, the depressurization rate was the highest due to the high single-phase break flow. As the flow to the break became two-phase, the depressurization rate decreased with the decreased break flow. A relatively stable RCS pressure was still noticed before the primary pressure 'crosses' the steam generator secondary side pressure, similar to the small break quasi-equilibrium natural circulation period. Finally, the RCS pressure decreased at a higher rate again until the end of the transient marked by the quenched core due to accumulator injection.

22.4 WCOBRA/TRAC-TF2 LOFT MODEL

22.4.1 General Modeling Considerations

A WCOBRA/TRAC-TF2 model of the LOFT test facility consists of three major regions: the vessel, the active loop, and the inactive loop.

Section 26.1.1, Volume 3 describes the general noding guidelines, hereafter referred to as guidelines, in order to set a specific relationship between the noding used for the PWR, and that used for the validation experiments. The application of these guidelines is explained below for LOFT:

1. Vessel

    a. Lower Plenum – The LOFT lower plenum region (bottom of vessel to bottom of core) is shorter than the PWR (Table 22-3). However, the noding guidelines in Section 26.1.1 of Volume 3 require cell boundaries at the bottom of the barrel and at the core inlet, and axial and lateral cells where the flow changes direction at the bottom of the lower plenum. Therefore in this region, there are **[ ]**[a,c] axial levels and lateral channels interior and exterior to the core barrel, similar to the PWR. This results in cell axial dimensions approximately **[ ]**[a,c].

b. Core – The guidelines, as well as the need to properly simulate grid locations, result in cell boundaries at each grid location, with a cell boundary in between. This results in **[ ]**[a,c] axial cells in the shorter LOFT core, as opposed to **[ ]**[a,c] in the PWR core. **[ ]**[a,c] In the lateral direction, the guidelines have been applied in a manner similar to the PWR; **[**

][a,c]

In LOFT, the basic structures described above also exist. Consequently, channels in the core representing fuel channels below each specific upper plenum structure type are defined, similar to the PWR.

In addition, the guidelines have been applied to simulate the hot assembly in the center of the core.

c. Downcomer – In the axial direction, the noding in the downcomer is controlled by noding requirements in the core and upper plenum. Recall that in WCOBRA/TRAC-TF2, cell axial dimensions are laterally uniform at each axial location. This results in several additional cells in the downcomer beyond what is required by a simple application of the noding guidelines. This additional detail is probably desirable in view of the complex processes occurring in the downcomer during blowdown. The downcomer is divided into **[ ]**[a,c] azimuthal channels. This is consistent with the number of loops involved and the noding philosophy of **[ ]**[a,c] downcomer channels per cold leg entrance nozzle.

d. Counter Current Flow Limitation (CCFL) Region – **[**

][a,c]

e. Upper Plenum – The noding guidelines require at least [ ]^{a,c} axial cells between the bottom of the upper plenum, and the elevation of the hot legs (a change in flow direction), and an additional [ ]^{a,c} from the hot leg elevation to the top of the upper plenum. Since the LOFT axial dimension from the bottom of the upper plenum to the hot leg is roughly twice that of the PWR, [ ]^{a,c}. This results in [ ]^{a,c} axial cells in LOFT, as opposed to [ ]^{a,c} used in the PWR. [ ]^{a,c}

2. Intact Loop

a. Hot Leg – The LOFT hot leg is approximately the same length as the PWR (Table 22-3). Consequently, application of the guidelines should result in the same number of cells, and due to other WCOBRA/TRAC-TF2 modeling restrictions, a total of [ ]^{a,c} cells is specified.

b. Steam Generator – The LOFT steam generator plena and tubes are substantially shorter than the PWR. Consistency with the guidelines would require short cells to be employed to represent the inlet and outlet plena. [ ]^{a,c}

c. Crossover Leg – The special nature of the LOFT crossover legs with the dual RCS pumps requires [ ]^{a,c} noding in this region, compared with the PWR. In general, the LOFT crossover leg cell lengths are about half the PWR value.

d. Pump – The LOFT pumps are approximately the same length as the PWR. Applying the guidelines, the LOFT pump model contains the same number of cells as the PWR model.

e. Cold Leg – The LOFT cold leg is shorter than the PWR cold leg. Application of the guidelines results in a compromise to preserve the cell length to the extent possible.

f. Pressurizer – The LOFT pressurizer is substantially shorter than the PWR. Application of the guidelines controls the choice of noding size here, with the number of cells in LOFT chosen to be the same as that of PWR.

22.4.2 WCOBRA/TRAC-TF2 Vessel Model of the LOFT Facility

A diagram of the vessel model is shown in Figure 22-4 and the section views are shown in Figure 22-5, Figure 22-6 and Figure 22-7. The arrangement of the core channels is shown in Figure 22-8.

The vessel model contains [ ]^{a,c} azimuthal channels at each elevation of the downcomer. The downcomer annulus extends to the bottom of the lower plenum. The cylinder inside the downcomer annulus represents the inner part of the lower plenum, core region, and the upper plenum. Channel numbers are enclosed by squares in the figure. Channels are laterally connected to one another

by gaps represented by circles in each figure. **[**

][a,c]

The hydraulic loss at the inlet nozzle/downcomer junction is modeled at the last cell of the cold leg pipe component (using the same calibrated value specific to the LOFT facility geometry). The friction and hydraulic losses inside the vessel are modeled so that the losses for the vertical flow are divided and distributed at appropriate cell locations. For lateral flow, hydraulic loss is applied by wall-friction factors applied to gaps between the cells. **[**

][a,c] Hydraulic losses between core channels are similarly taken into account.

The metal structures in the vessel are composed of lower and upper support plates plus many other structures. The metal structures are divided into sections in accordance with the interfacing hydraulic channels. Unheated conductors are used to model the metal structures by conserving the metal mass and heat transfer area associated with each fluid channel.

[

][a,c]

Normalized axial distributions of the power generation rates in the HA, GT, and SC channels are assumed approximately equal, and are represented by a single table describing the axial profile with the data pairs of power and elevation.

The fine mesh rezoning option of the fuel rod model is used, allowing for finer resolution of heat transfer in the region of a quench front.

For the calculation of gap conductance, the same dynamic gap-conductance model as used in the PWR is employed. This model accounts for thermal and elastic expansion of the fuel and cladding. Fuel relocation, conductivity degradation, and other factors affecting the gap conductance are taken into account by specifying the size of the gap width to attain the desired initial fuel temperature, using data obtained from the same fuel design codes used in the PWR calculations.

The WCOBRA/TRAC-TF2 point kinetics and decay heat models are used to predict the LOFT reactor power during the transient. The gamma redistribution model used for the PWR was not used, since it assumes a PWR core geometry. A constant value of **[ ]**[a,c] percent was used as the fraction of the local power in both the hot rod and hot assembly rod redistributed to the average channel. Detailed PWR calculations indicate redistribution values slightly higher for the hot rod (about 4 percent) and lower for the hot assembly rod (about 2 percent). It is noted that for the simulation of the smaller break tests (L3-1 and L5-1), the core power as a function of time for the LOFT small break LOCAs is supplied as a boundary condition to WCOBRA/TRAC-TF2, based on Figure 21 of NUREG/CR-1145 (Bayless, et al., 1980) for L3-1 and for L5-1. Use of these best-estimate curves in place of the WCOBRA/TRAC-TF2 kinetics and decay heat models ensures that the thermal-hydraulic predictions are not influenced by known differences in core power behavior between the code modeling and the experiments.

The experimenters identified that about 5% leakage occurred between the upper plenum and downcomer in the LOFT reactor vessel hot leg nozzle region. This leakage is modeled in the gaps 68 through 71 as shown in Figure 22-4.

22.4.3 WCOBRA/TRAC-TF2 Loop Model of the LOFT Facility

22.4.3.1 Active Loop Model

The active loop is modeled with TEE, PUMP, VALVE and PIPE components, as shown in Figure 22-9. The hot leg is modeled by **[**

][a,c]. The crossover leg is modeled by

[

][a,c]. The cold leg is modeled by **[**

][a,c]

The pressurizer is modeled with **[ ]**[a,c] cells; **[**

][a,c]

In the LOFT model, the active loop steam generator is modeled **[**

][a,c]

The heat transfer between the primary side of the U-tubes **[** **]**[a,c] and the secondary side **[** **]**[a,c] is modeled through the **[**

][a,c]

Figure 22-10 illustrates the active loop steam generator modeling for the WCOBRA/TRAC-TF2 simulations of the LOFT tests.

It is noted that the LOFT steam control valve operates on a pressure hysteresis following steam generator trip and is, therefore, different from the PWR. For L3-1 a non-trivial amount of leakage through this valve affected the experimental results. **[**

][a,c]

In the LOFT model, the active loop pump suction piping is modeled **[**

][a,c]. The pump volume is 3.5 cubic feet and is represented by **[** **]**[a,c]. The pumps are modeled using single- and two-phase hydraulic characteristics obtained from the Semiscale pump (Reeder, 1978). This data is compared with PWR data in Section 20.2. Pump rated characteristics are: the rated torque (T_R = 369 ft-lbf), the rated density (ρ_R = 38.31 lbm/ft^3), the rated speed (N_R = 3530 rpm), the rated flow rate (QR = 5117 gpm), and the rated pump head (H_R = 315 lb$_f$-ft/lbm). The pump coastdown for all LOFT tests is supplied to WCOBRA/TRAC-TF2 as a boundary condition, based on the test information (for example, Figures 59 and 60 of NUREG/CR-1145 (Bayless, et al., 1980) for L3-1). Use of these experimentally obtained curves in place of the WCOBRA/TRAC-TF2 pump coastdown calculations ensures that the thermal-hydraulic predictions are not influenced by the known differences in RCP behavior among the various LOFT experiments.

The piping layout of the crossover leg from the steam generator outlet to the RCP inlets in the LOFT facility is very unique and different from the PWR loop seal piping. The crossover leg is modeled by **[** **]**[a,c] as shown in Figure 22-9.

In the LOFT model, the active loop cold leg was modeled **[**

][a,c]. Figure 22-9 illustrates the active loop cold leg modeling for the WCOBRA/TRAC-TF2 LOFT simulations.

The LOFT pumped injection enters the cold leg at a location near the reactor vessel, while the PWR injection point is typically further upstream. This results in distortion between the flow regimes observed in the LOFT cold leg and the flow regimes observed in a PWR cold leg and must be considered before using LOFT cold leg behavior to draw conclusions regarding the PWR small break model.

In the LOFT model, the accumulator and ECCSs were modeled using: **[**

][a,c] Water injection rates and timing from HPIS and LPIS are determined by the test procedure, so these injection systems are jointly modeled by one flow rate boundary condition. In all LOFT simulations, the accumulators were active and injected when the predicted RCS pressure achieved the accumulator pressure value. The non-condensable nitrogen was expelled when the tank emptied of liquid in all the simulations reported herein.

The heat losses occurred in the LOFT coolant loops during the test are neglected in the LOFT LOCA simulations.

22.4.3.2 Broken Loop Model

[

][a,c]

The broken cold leg hydraulic losses are calculated **[**

][a,c]. Modeled also are the approximate liquid temperature distributions measured during steady-state operation.

The broken hot leg is composed of piping, and steam generator and pump simulators. The steam generator and pump simulator hydraulic resistances are calculated by the code using the natural geometry input of these components. The pipeline (RABL) connecting the broken hot leg and cold leg is modeled (Figure 22-12).

For small breaks (L3-1 and L5-1), the inactive loop modeling as illustrated in Figure 22-12 includes a zero FILL, whereas for the large break tests (L2-2, L2-3, L2-5 and LB1) a BREAK is instead used for Component #10. This difference is due to the different test procedure for large and small breaks. For the large breaks, both ends of the broken loop (Components # 10 and #30) were opened, simulating a 'double-ended' rupture. However, for small break tests, the valves connected to the hot leg in the broken loop were kept closed; to be consistent with the actual test configuration, BREAK 10 is therefore replaced with a zero FILL component.

The RABL connecting the inactive loop hot and cold legs was designed to remain closed during the experiments. During testing, although possible leakage through the RABL was reported, the information available was not sufficient to quantify the RABL line model in the input for specific test simulations, and thus the RABL line was modeled to **[**

][a,c]

22.5 LARGE BREAK LOFT SIMULATIONS USING WCOBRA/TRAC-TF2

22.5.1 Large Break LOFT Tests Description

The LOFT experiments L2-2, L2-3, L2-5, and LB-1 were designed to represent double-ended pipe breaks of the cold leg in a full-scale PWR. The differences between the three L2 series tests were in their power levels and whether the reactor coolant pumps were tripped or not, as shown in Table 22-2. In addition to the differences listed in Table 22-2, LB-1 was run with a much lower accumulator water volume than the other three large break tests.

The tests began when the quick-opening blowdown valves connecting the inactive hot leg and cold leg to the blowdown suppression system were opened, simulating a pipe break.

After the break occurred, the primary system in each of the four experiments depressurized and mass depletion caused the core to uncover. ECCS flow was injected into the intact loop cold leg at low RCS pressure. During the blowdown portion of the transient, the cladding temperature increased due to DNB. Later, some of the fuel rods cooled as rewet occurred in the two tests L2-2 and L2-3 where the primary coolant pumps coasted down and their flywheels were not disconnected instantly after the break. Near the end of the blowdown transient, decay heat in the core was large enough to dry out the core and consequently, the cladding temperature rose during the reflood portion of the transient until the fuel rods again quenched as ECCS water entered the core from the bottom. Figure 22-13 shows a typical time history of the cladding temperature.

22.5.2 Steady-State Calculations

The methods for setting up the LOFT model initial conditions were similar to those used in the PWR. In particular, the hot assembly power and fuel stored energy were input as best-estimate representations of actual core conditions (radial power distribution). Measured data (axial power distribution) were used to obtain estimates of peak and average linear heat rates for each region. The initial fuel stored energy (fuel temperature) was obtained from the same fuel design code used for the PWR, using LOFT specific burnup conditions and core power. Table 22-4 summarizes input hot assembly conditions for Test L2-5, as an example. Prior to simulating any of the transients, WCOBRA/TRAC-TF2 steady-state simulations were performed. The steady-state simulations resulted in favorable comparisons with the initial conditions as can be seen in Table 22-5, and the reactor vessel and active loop pressure drops were calibrated to approximate values published for the four large break tests, as available. The steady-states achieved are considered acceptable for simulation of the LOFT large break transients, as stable thermal-hydraulic states of the system are asymptotically achieved and match the initial test conditions within their measurement uncertainties.

22.5.3 Transient Calculations

The simulation of the break transients were initiated by restarting the calculation from the steady-state simulation and opening the break. In the WCOBRA/TRAC-TF2 model, the valve opening time of 30 milliseconds is simulated by linearly reducing the break pressure over 30 milliseconds to the suppression tank header pressure, which is available from test data.

The sequences of events for these analyses are compared to the sequences of events observed in the experiments in Tables 22-6 through 22-9. The measured end of bypass time (also referred to as reflood initiated time) was estimated from the core level plots, if available from the data reports, as shown in Figure 22-30c, Figure 22-31c and Figure 22-32c for Tests L2-2, L2-3 and L2-5, respectively. The measured end of bypass time for Test LB-1 was estimated from the lower plenum liquid temperature per Figure 22-33e. The predicted end of bypass time was estimated from the predicted levels shown in Figures 22-30d, 22-31d, 22-32d, and 22-33d.

The transient results of the calculation are compared to the measured test data in Figures 22-14 through 22-42 (in the figures, the instrument used for comparison is indicated; if data was extracted from the data reports, the figures used are indicated). The system pressure transient is shown in Figure 22-14 through Figure 22-17. **[**

][a,c]

The broken hot leg flow rates for each test are shown in Figure 22-18 to Figure 22-21. The broken cold leg flow rates are shown in Figure 22-22 to Figure 22-25. **[**

][a,c]

The flow rate in the intact hot leg is shown in Figure 22-26 and Figure 22-27 for Tests L2-2 and L2-3, respectively **[**

][a,c]

Figure 22-30a, Figure 22-31a, Figure 22-32a and Figure 22-33a compare measured and predicted volumetric flow rate from the accumulator in Tests L2-2, L2-3, L2-5 and LB-1, respectively. **[**

][a,c]

The comparisons in Figure 22-30a, Figure 22-31a, Figure 22-32a and Figure 22-33a are intended for the accumulator liquid injections (from 0 to about 40 seconds) before the nitrogen starts to flow through the test flow meters, since there was unknown uncertainties associated with the flow meter reading when it measured two-phase flow. The time when nitrogen starts to be discharged from the accumulator tank can be estimated based on the void fraction at the exit of the accumulator tank (void fraction of the discharge line adjoining the bottom of the accumulator tank is co-plotted in Figure 22-30a, Figure 22-31a, Figure 22-32a and Figure 22-33a for Tests L2-2, L2-3, L2-5 and LB-1, respectively).

[

][a,c] Figure 22-30e, Figure 22-31e and Figure 22-32e show the predicted and measured core liquid levels of L2-2, L2-3 and L2-5, respectively. **[**

][a,c]

Figure 22-30b, Figure 22-31b, Figure 22-32b and Figure 22-33b present the measured and predicted accumulator water levels during L2-2, L2-3, L2-5 and LB-1 tests, respectively. **[**

][a,c]

Figure 22-34 through Figure 22-37 show the measured and predicted peak cladding temperatures in the hot assembly region. **[**

][a,c]

The occurrence of critical heat flux (CHF) due to the reversed core flow **[**

][a,c], as shown in Tables 22-6 through 22-9 for tests L2-2, L2-3, L2-5 and LB-1, respectively.

[

]a,c

Figure 22-41 shows that the predicted fluid temperature for Test L2-5 [

]a,c

Figure 22-43 compares the predicted pressure difference across the intact loop pump for Test L2-5.
[

]a,c

Figure 22-44 compares the fuel temperature for Test L2-5. [

]a,c

Figure 22-45 compares the measured nuclear power with the predicted value, normalized to the initial power. **[**

][a,c]

22.5.4 Conclusions

The WCOBRA/TRAC-TF2 computer code **[**

][a,c]

22.6 SMALL BREAK LOFT SIMULATION USING WCOBRA/TRAC-TF2

22.6.1 Small Break LOFT Test Description

The LOFT L3-1 test is a simulated small break LOCA test that has a 4-inch equivalent break in the inactive loop cold leg. The reactor was tripped 2 seconds prior to opening the blowdown valve to initiate the break when the control rods were signaled to reach the bottom of the core. In the test, only the blowdown valve in the inactive loop cold leg was opened, with the one in the inactive loop hot leg remaining closed throughout the test transient. This unique physical arrangement of the inactive loop means that L3-1 is atypical of a full-scale PWR layout in a postulated small break accident scenario.

The initial conditions prior to the break transient in test L3-1 are detailed in Table 22-10. After the blowdown, the reactor coolant pumps were tripped and the pumps began to coast down under the influence of a flywheel system. Upon receipt of the reactor trip signal, the feed water pump tripped off and the main feed water isolation valve shut. The electronically controlled steam generator steam control valve started ramping shut after the blowdown at 5% position/second. The scaled emergency core coolant injection was directed to the intact loop cold leg through the use of a high pressure safety injection (HPSI) pump, accumulator and a low pressure safety injection (LPSI) pump. The accumulator initiated injection at about 634 seconds, and HPSI flow and LPSI flow were initiated at about 5 and 4240 seconds after the rupture, respectively. The secondary coolant system (SCS) auxiliary feed pump was operated from about 75 to 1875 seconds to deliver cold water at 70°F to the steam generator (SG). The simulation transient was terminated approximately at the end of the accumulator liquid injection, which is 2000 seconds after the break occurs.

There was no observed core dryout and heatup in test L3-1 before the termination of the test and simulation transients.

22.6.2 Steady-State Calculations

Prior to the transient simulations, a 200-second steady-state was run to ensure stable system states that match what were reported prior to break initiation in the test. As in the test, the break valves are closed during the steady state with trivial leakage through the RABL connecting the inactive loop cold and hot leg [ ]^{a,c}. Consequently, the inactive loop initial temperatures at the components close to the break orifice are barely changed from their initial values during the steady-state run due to the limited amount of circulation in the dead ends before the break valve.

The pressurizer component sets the primary system pressure. Pump speed is varied to obtain the desired primary system flow. Secondary system pressure is varied to obtain active loop hot and cold leg temperatures within specified limits. The average linear heat generation rate is set to obtain the correct core power.

The initial conditions prior to the break transient are listed in Table 22-10, which shows the comparison of the measured conditions in the test (Bayless, et al., 1980) and the conditions achieved at the end of the WCOBRA/TRAC-TF2 steady-state calculation. The steady-state results are deemed as acceptable initial conditions to the subsequent transient simulation of test L3-1.

22.6.3 Transient Calculations

The L3-1 sequence of events is compared in Table 22-11 between the test (Bayless, et al., 1980) and the prediction. [

]^{a,c}

The comparisons of the important system parameters representative of the thermal-hydraulic responses of the system during the test transient are generated between the calculation and the measurement in Figure 22-46 through Figure 22-50, with Figure 22-51 presenting additional test data. As there were no core dryout and rod heatup observed and predicted in this test, the key parameters to compare are primary system pressure, break flows, steam generator secondary side pressure, and accumulator injection and its influence on the primary system pressure.

A comparison of the calculated and measured primary coolant system pressure, as seen in Figure 22-46, shows that [

]^{a,c}

[

]a,c

The comparison of the SG secondary side pressure is shown in Figure 22-47. [

]a,c

A comparison of the measured inactive loop mass flow rate and the calculated break mass flow rate is shown in Figure 22-48. [

]a,c

In Figure 22-53 and Figure 22-54, the comparisons of the two WCOBRA/TRAC-TF2 simulation runs and the test data are made. **[**

][a,c]

The accumulator liquid level and pressure are shown in Figure 22-49 and Figure 22-50, respectively. **[**

][a,c]

22.6.4 Conclusions

The WCOBRA/TRAC-TF2 computer code **[**

][a,c]

22.7 INTERMEDIATE BREAK LOFT SIMULATIONS USING WCOBRA/TRAC-TF2

22.7.1 Intermediate Break LOFT Tests Description

The LOFT L5-1 test is a simulated intermediate break LOCA test that has a 14-inch equivalent break in the inactive loop cold leg. The size of the break simulates a single 14-in accumulator injection line in a commercial PWR.

Similar to test L3-1, the quick-opening blowdown valve in the inactive loop hot leg remained closed throughout the test L5-1, and the one in the inactive loop cold leg was opened to initiate the break transient. A low-pressure scram followed at 0.17 seconds, and the emergency core cooling system HPIS started at 0.4 seconds. Power to the PCS pumps motor-generator sets was manually tripped at 4.0 seconds; coastdown was complete at 19.3 seconds. The secondary coolant system main feed pump was tripped on reactor scram coincident with the steam generator control valve beginning to ramp close; the valve was fully closed at 12.1 seconds.

The L5-1 break transient started from the initial conditions that are detailed in Table 22-12. Saturation pressure was reached in the upper plenum at 0.2 seconds and in the broken loop cold leg at 10.5 seconds. Fuel cladding thermal excursion began at about 110 seconds as the PCS continued to blowdown. A maximum fuel cladding temperature of 833°F (718 K) was reached at 198 seconds before the reactor core was recovered by scaled flow from the accumulator (commencing at 186 seconds) and LPIS (commencing at 201 seconds). The transient was terminated at 213 seconds following its initiation when all monitored core thermocouples indicated at or below saturation temperature.

22.7.2 Steady-State Calculations

Prior to the transient simulations, a 200-second steady-state was run to ensure stable system states that match what were reported prior to break initiation in the test. The same as in the test, both break valves are closed during the steady state with trivial leakage through the RABL connecting the inactive loop cold and hot leg **[ ]**[a,c]. Consequently, the inactive loop initial temperatures of the components close to the break orifice are barely changed from their initial guesses during the steady-state run due to the limited amount of circulation in the dead ends before the break valve.

The initial conditions prior to the break transient are listed in Table 22-12, which shows the comparison of the measured conditions in the test (Jarrell and Divine, 1981) and the asymptotically achieved conditions at the end of the WCOBRA/TRAC-TF2 steady-state run. The steady-state results are deemed as acceptable initial conditions to the subsequent transient simulation of test L5-1.

22.7.3 Transient Calculations

The sequence of events in test L5-1 is compared in Table 22-13 between the test (Jarrell and Divine, 1981) and the prediction. **[**

][a,c]

Figure 22-55 through Figure 22-59 show the comparisons of the test to the simulation transient results resulting from the input model in which the models are set at their nominal values. **[**

][a,c]

The steam generator secondary side pressure and RCS pressure are shown in Figure 22-57. **[**

][a,c]

The comparison of the predicted hot assembly fuel rod cladding temperatures against the data is shown in Figure 22-58. **[**

][a,c]

[

]^{a,c}

[

]a,c

22.7.4 Conclusions

The WCOBRA/TRAC-TF2 input model of the LOFT Test L5-1 is consistent with those used for the LOFT LB and SB test simulations, except for the test-specific components, such as break orifice in the broken (inactive) loop, the HPIS and LPIS, Pump coastdown tables, etc. [

]a,c

22.8 REFERENCES

1. Adams, J. P., 1979, "Quick-Look Report on LOFT Nuclear Experiment L3-1," EGG-LOFT-5057.

2. Adams, J. P. and Birchley, J. C., 1984, "Quick-Look Report on OECD LOFT Experiment LP-LB-1," OECD LOFT-T-3504.

3. Bayless, P. D., et al., 1980, "Experiment Data Report for LOFT Nuclear Small Break Experiment L3-1," NUREG/CR-1145, EGG-2007.

4. Bayless, P. D. and Divine, J. M., 1982, "Experiment Data Report for LOFT Large-Break Loss-of-Coolant Experiment L2-5," NUREG/CR-2826.

5. Condie, K. G., et al., 1981, "Four-Inch Equivalent Break Loss-of-Coolant Experiments: Posttest Analysis of LOFT Experiments L3-1, L3-5 (Pumps Off), and L3-6 (Pumps On)," EGG-LOFT-5480.

6. Gillas, D. L. and Carpenter, J. M., 1980, "Experiment Data Report for LOFT Nuclear Small Break Experiment L3-7," NUREG/CR-1570, EGG-2049.

7. Jarrell, Donald B. and Divine, Janice M., 1981, "Experiment Data Report for LOFT Intermediate Break Experiment L5-1 and Severe Core Transient Experiment L8-2," NUREG/CR-2398.

8. McCormick-Barger, M., 1979, "Experiment Data Report for LOFT Power Ascension Test L2-2," NUREG/CR-0492.

9. McPherson, G. D., 1979, "The LOFT Facility and Test Program," Presentation at GRS-Fachgespräch, Munich, Germany.

10. Nalezny, C. L., 1985, "Summary of the Nuclear Regulatory Commission's LOFT Program Research Findings," NUREG/CR-3005.

11. Prassinos, P. G. et al., 1979, “Experiment Data Report for LOFT Power Ascension Experiment L2-3,” NUREG/CR-0792.

12. Reeder, D. L., 1978, “LOFT System and Test Description (5.5-ft. Nuclear Core 1 LOCEs),” NUREG/CR-0247, TREE-1208.

13. Tolman, E. L., Driskell, W. E. and Carboneau, M. L., 1981, “Comparison of Nuclear and Electric Heater Rod Responses for Large Break PWR LOCA Conditions,” EGG-LOFT-5529.

Table 22-1 Comparison of LOFT and PWR

	LOFT	PWR
Volumes (ft^3)		
Total PCS	272	12240
Reactor Vessel (% of Primary Coolant Volume)	34	38
Intact Loop (% of Primary Coolant Volume, including pressurizer)	48	51
Broken Loop (% of Primary Coolant Volume)	18	11
Power (MWt)	55	3400
Length of Active Core (ft)	5.5	12
Ratios		
Volume/Power (ft^3/MWt)	5.0	3.6
Break Area/Primary Coolant Volume ($ft^{-1} \times 10^4$)	6.6	6.7
Core Surface Area/Primary Coolant Volume (ft^{-1})	3.5	4.5
PWR Volume/Volume	47	1

Table 22-2 Differences among LOFT Experiments

Test	Peak Power	Reactor Coolant Pump	Equivalent Pipe Break Size
	(kW/ft)		
L2-2	8.04	Coastdown	Double-ended Cold Leg (200%)
L2-3	11.89	Coastdown	Double-ended Cold Leg (200%)
L2-5	12.20	Tripped at Reactor Scram (Flywheel disconnected)	Double-ended Cold Leg (200%)
LB-1	15.80	Same as L2-5	Double-ended Cold Leg (200%)
L3-1	15.76	Coastdown	4.0-inch Cold Leg (2.5%)
L5-1	14.02	Coastdown(1)	14.0-inch Accumulator Line (25%)
PWR	13-17	Both Conditions Analyzed	All Break Sizes Analyzed

Note:
1. The pumps began to coast down after being manually tripped at 4 s after the break.

Table 22-3 LOFT/PWR Axial Noding Ratio Comparison

a,c

Table 22-4 LOFT L2-5 Hot Assembly Fuel Initial Conditions

a,c

Parameter	Value	Comments

Table 22-5 LOFT Large Break Tests WCOBRA/TRAC-TF2 Steady-State Simulation Results

	L2-2		L2-3		L2-5		LB-1	
Parameter	**Measured Data[1]**	**Analysis Result**	**Measured Data**	**Analysis Result**	**Measured Data**	**Analysis Result**	**Measured Data**	**Analysis Result**
Active loop Pressure (psia)[2]	2265.5	2265.7	2184.0 ±4.4	2184.2	2166.9 ±8.7	2167.2	2152.0 ±16.0	2151.9
SG Secondary Pressure (psia)	921.0	887.3	896.3 ±11.6	897.8	848.4 ±9.0	835.9	–	779.8
Active Loop Flow (lbm/s)	428.1	427.4	438.7 ±13.9	440.3	424.2 ±17.2	424.0	674.2 ±5.7	674.0
SG Secondary Flow (lbm/s)	27.9	27.9	43.0 ±0.9	41.4	42.1 ±0.88	42.1	–	54
Vessel Bypass Flow (% of loop flow)	5.0	4.9	5.0	4.8	5	4.8	–	1.9
Pressurizer Level (ft)	3.573	3.54	3.90 ±0.03	3.90	3.74 ±0.1	3.74	–	3.42
Active Loop Hot Leg Temperature (°F)	585.1	586.9	607.6 ±3.2	609.3	601.8 ±7.2	603.1	595.3 ±1.8	595.1
Active Loop Cold Leg Temperature (°F)	544.2	543.6	549.6 ±3.2	550.6	542.2 ±7.2	541.8	542.2 ±1.8	541.6
Inactive Loop Hot Leg Temperature (°F)	550.5	549.9	558.2 ±3.2	556.8	556 ±7.7	551.4	–	546.8
Inactive Loop Cold Leg Temperature (°F)	539.3	542.0	538.7 ±3.2	538.7	538.1 ±7.6	538.0	–	541.9

Notes:
1. Measurement uncertainties were not given in the test report (McCormick-Barger, 1979); the steady state is considered acceptable referring to the measurement uncertainties in L2-3 test.
2. Pressurizer pressures were given in L2-2, L2-3 and LB-1 test reports (McCormick-Barger, 1979; Prassinos et al., 1979; and Adams and Birchley, 1984); hot leg pressures were given in L2-5 test report (Bayless and Divine, 1982).

Table 22-6 [ ]a,c

a,c

Table 22-7 [ ]a,c

a,c

[

Table 22-8 [ ]a,c

]a,c

[

Table 22-9 [ ]a,c

]a,c

Table 22-10 LOFT L3-1 Steady State Comparison		
Parameter	**Measured Data and Uncertainty Range**	**Analysis Result**
Core Power (MW)	48.9 ±1.0	48.9
Active Loop Hot Leg Pressure (psia)	2153.25 ±5.8	2150.7
Pressurizer Pressure (psia)	2148.0 ±5.8	2148.4
Steam Generator Secondary Pressure (psia)	787.4 ±16.0	761.3
Active Loop Flow (lbm/s)	1067.0 ±13.9	1056.7
Steam Generator Secondary Flow (lbm/s)	55.1	54.0
Pressurizer Level (ft)	3.61 ±0.03	3.61
Active Loop Hot Leg Temperature (°F)	573.5 ±5.4	575.9
Active Loop Cold Leg Temperature (°F)	537.5 ±5.4	541.2

a,c

Table 22-11 [ ]a,c		

a,c

Table 22-12 LOFT L5-1 Steady State Comparison

Parameter	Measured Data and Uncertainty Range	Analysis Result
Core Power (MW)	45.9 ±1.2	45.99
Active Loop Hot Leg Pressure (psia)	2165.4 ±11.6	2167.8
Steam Generator Secondary Pressure (psia)	732.4 ±8.7	734.0
Active Loop Flow (lbm/s)	679.5 ±8.8	679.1
Steam Generator Secondary Flow (lbm/s)	55.8	54.7
Pressurizer Level (ft)	3.71 ±0.1	3.69
Active Loop Hot Leg Temperature (°F)	582.7 ±1.6	584.5
Active Loop Cold Leg Temperature (°F)	534.5 ±1.6	533.6

Table 22-13 [ ][a,c] a,c

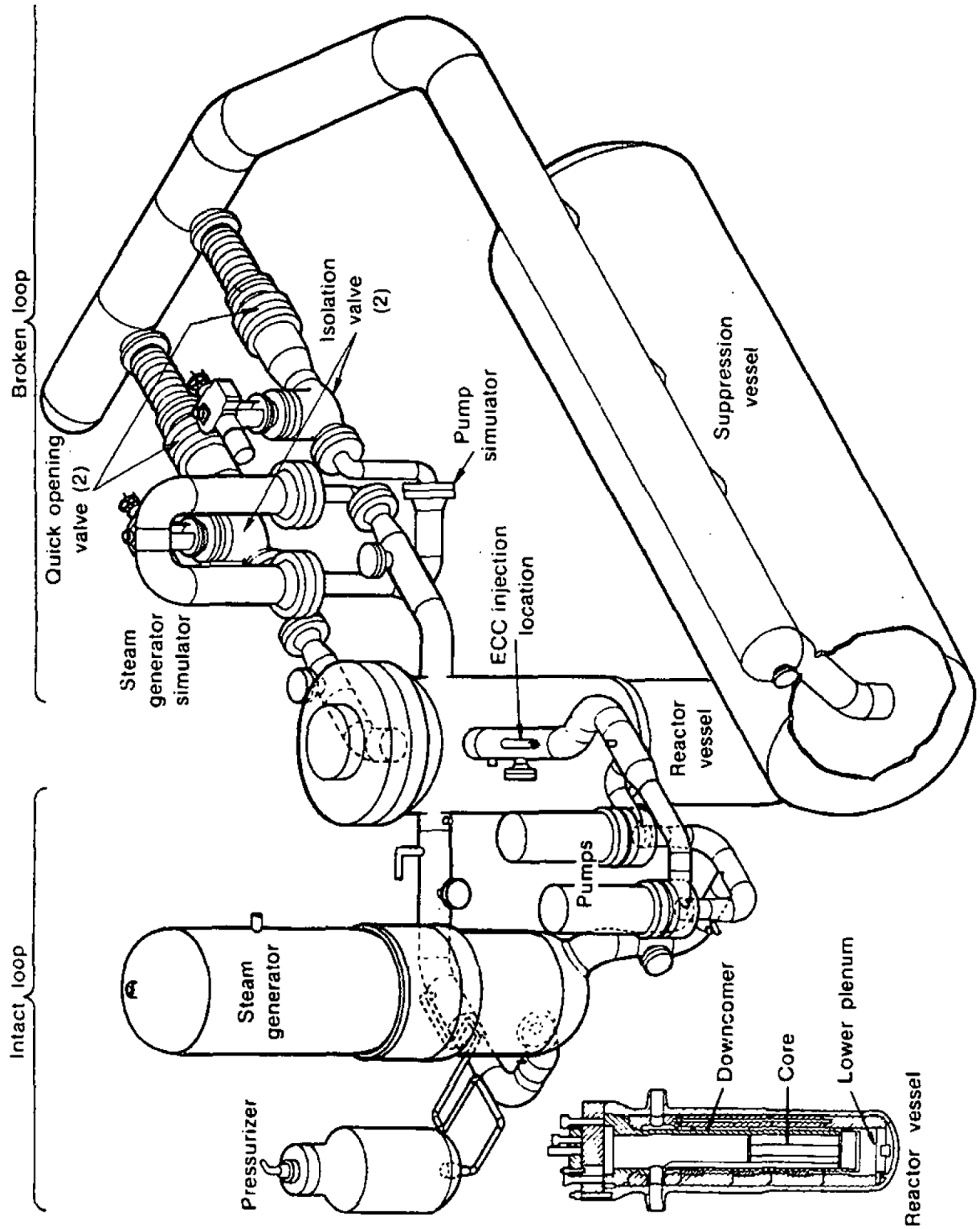

Figure 22-1 Schematic of LOFT Facility

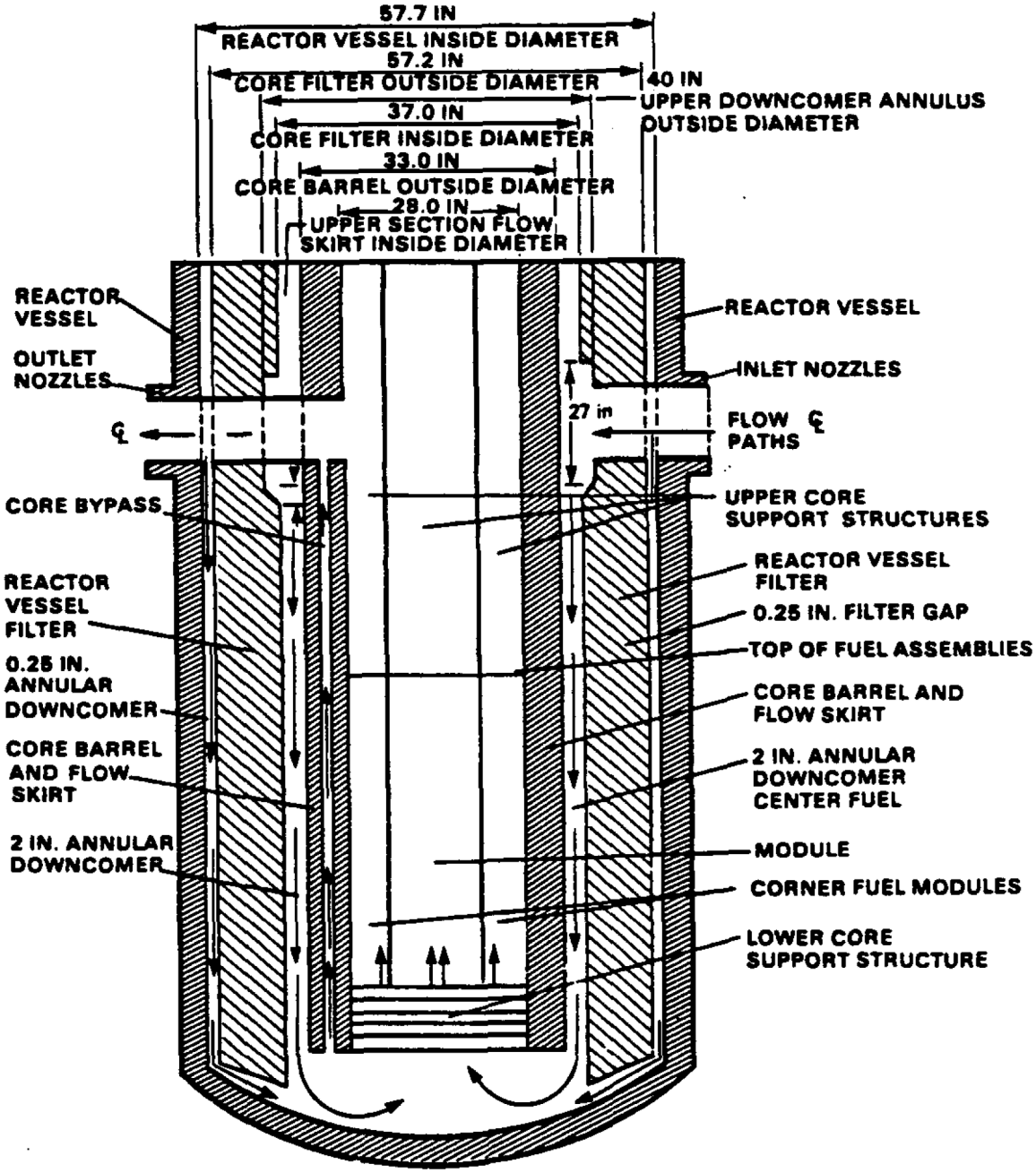

Figure 22-2 LOFT Reactor Vessel Diagram with Flow Paths

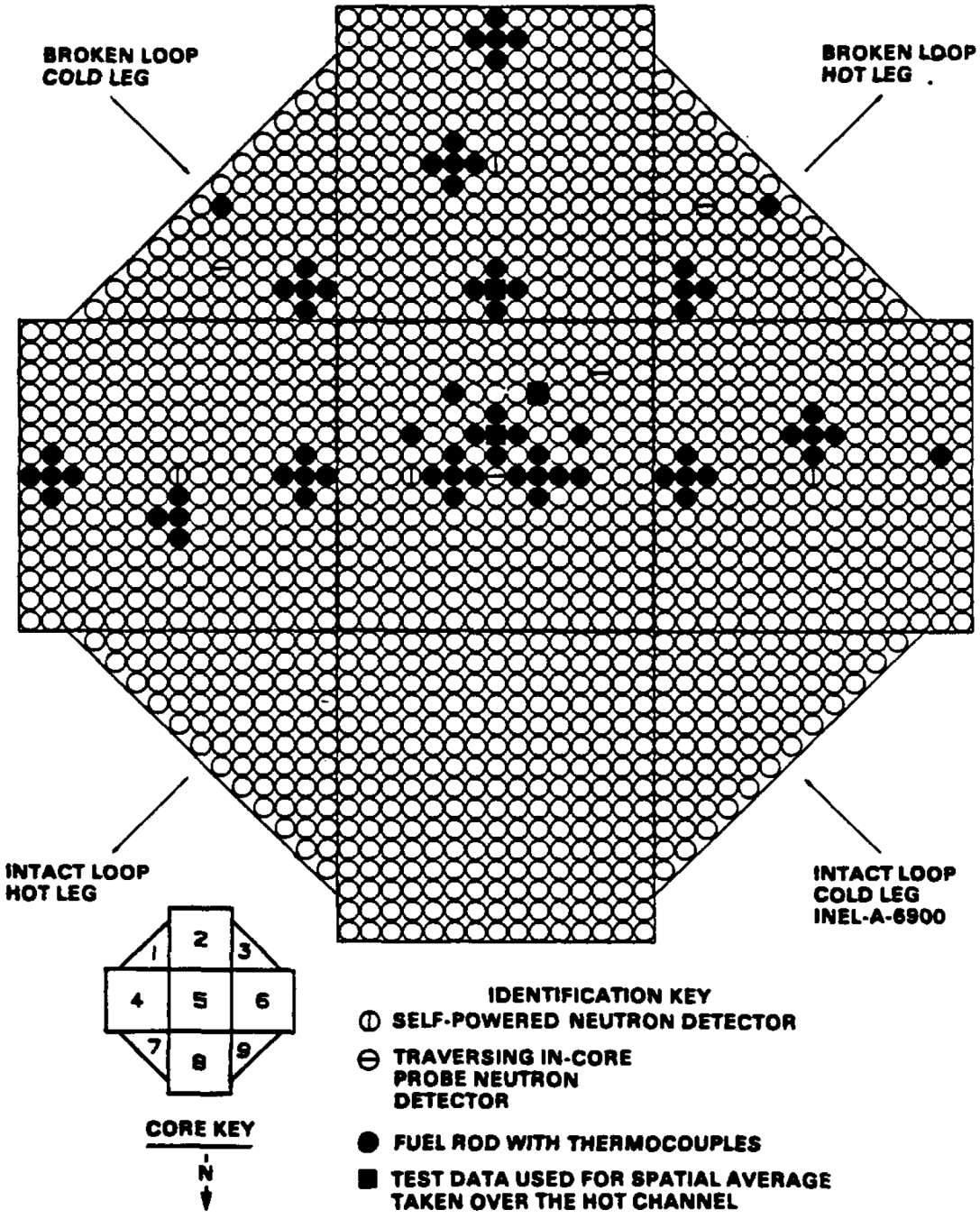

Figure 22-3 LOFT Reactor Core and Arrangement of Incore Instrumentation

a,c

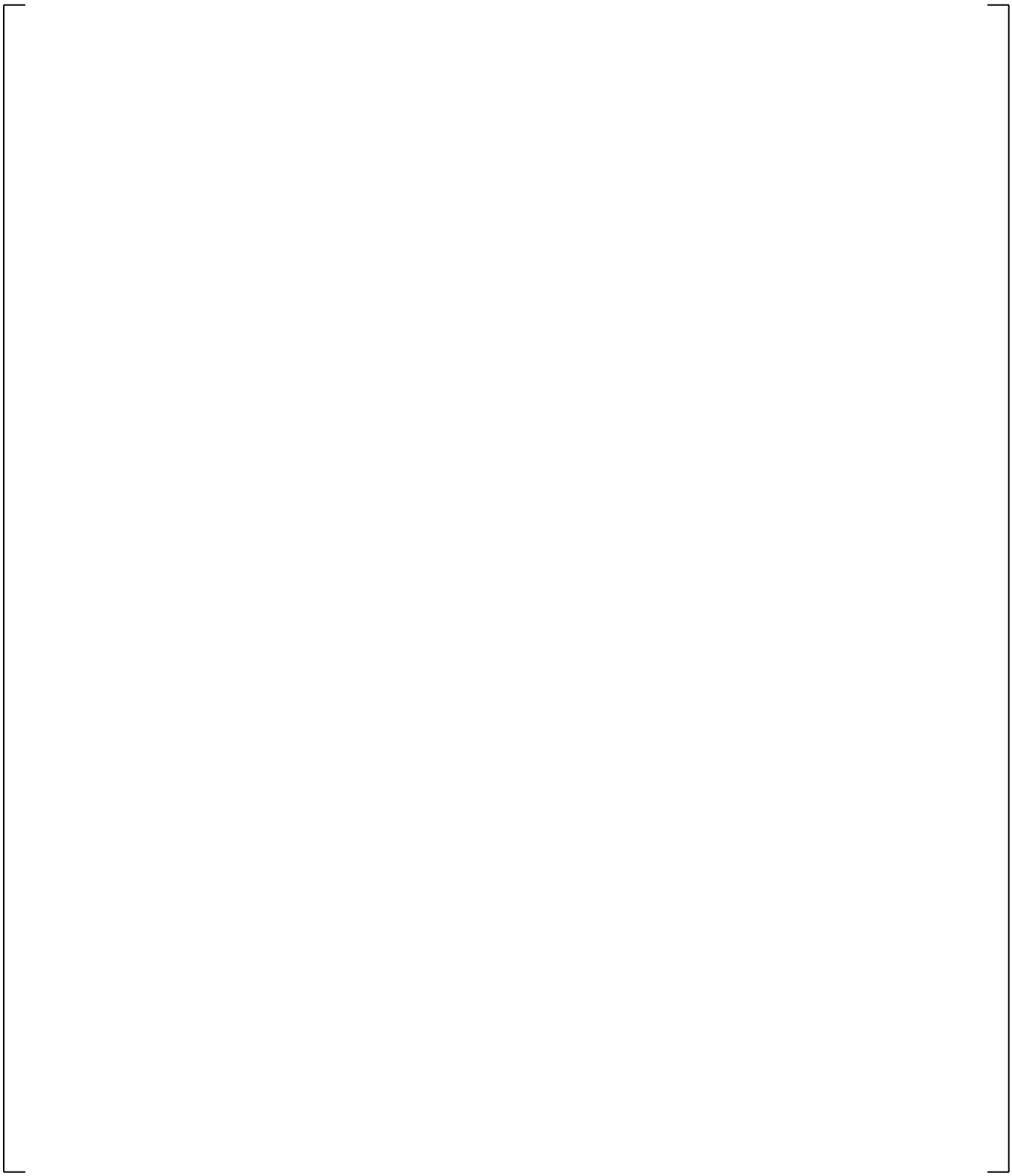

Figure 22-4 LOFT WCOBRA/TRAC-TF2 Vessel Model

a,c

Figure 22-5 Section Views of LOFT WCOBRA/TRAC-TF2 Vessel Model

a,c

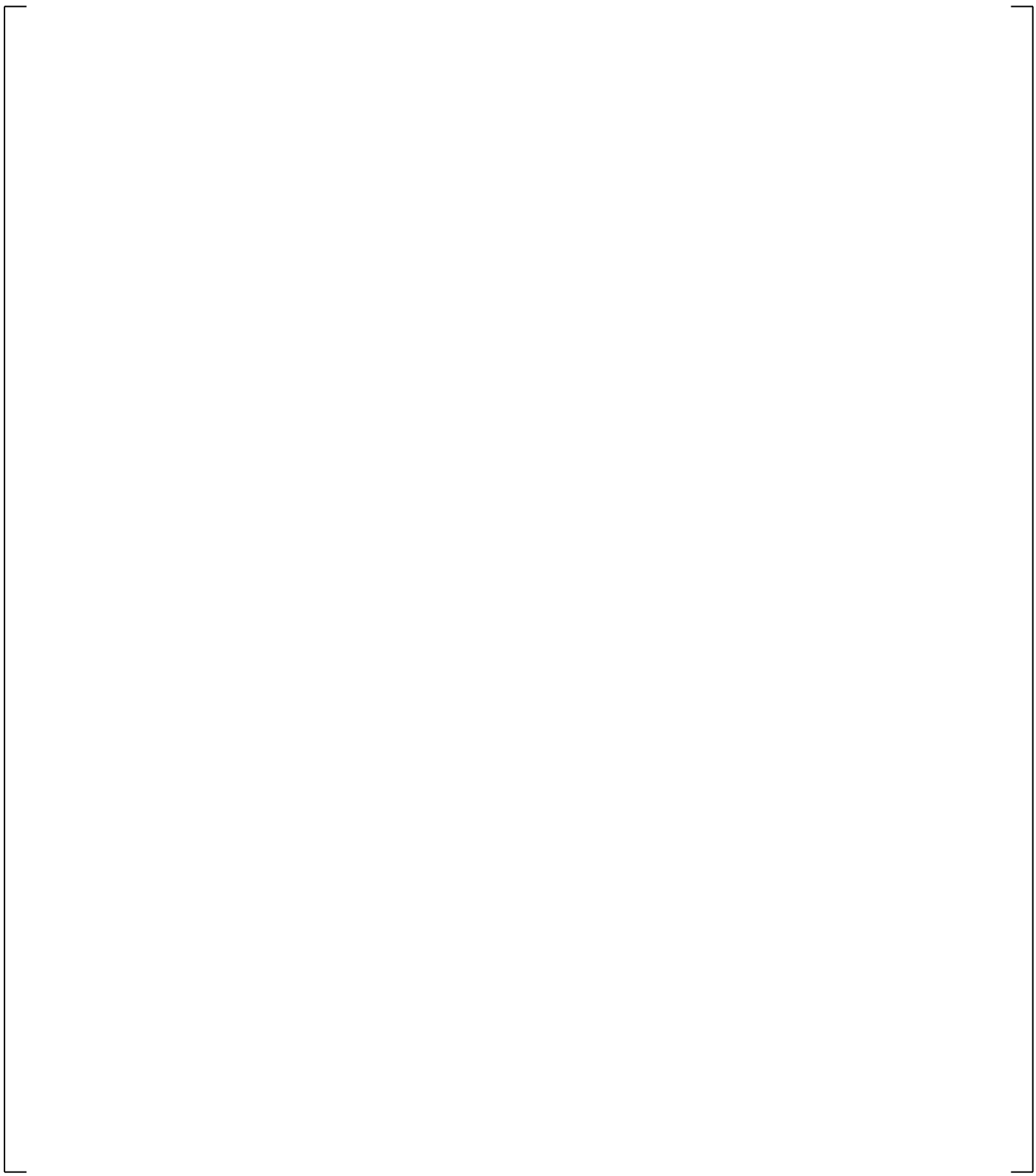

Figure 22-6 Section Views of LOFT WCOBRA/TRAC-TF2 Vessel Model

a,c

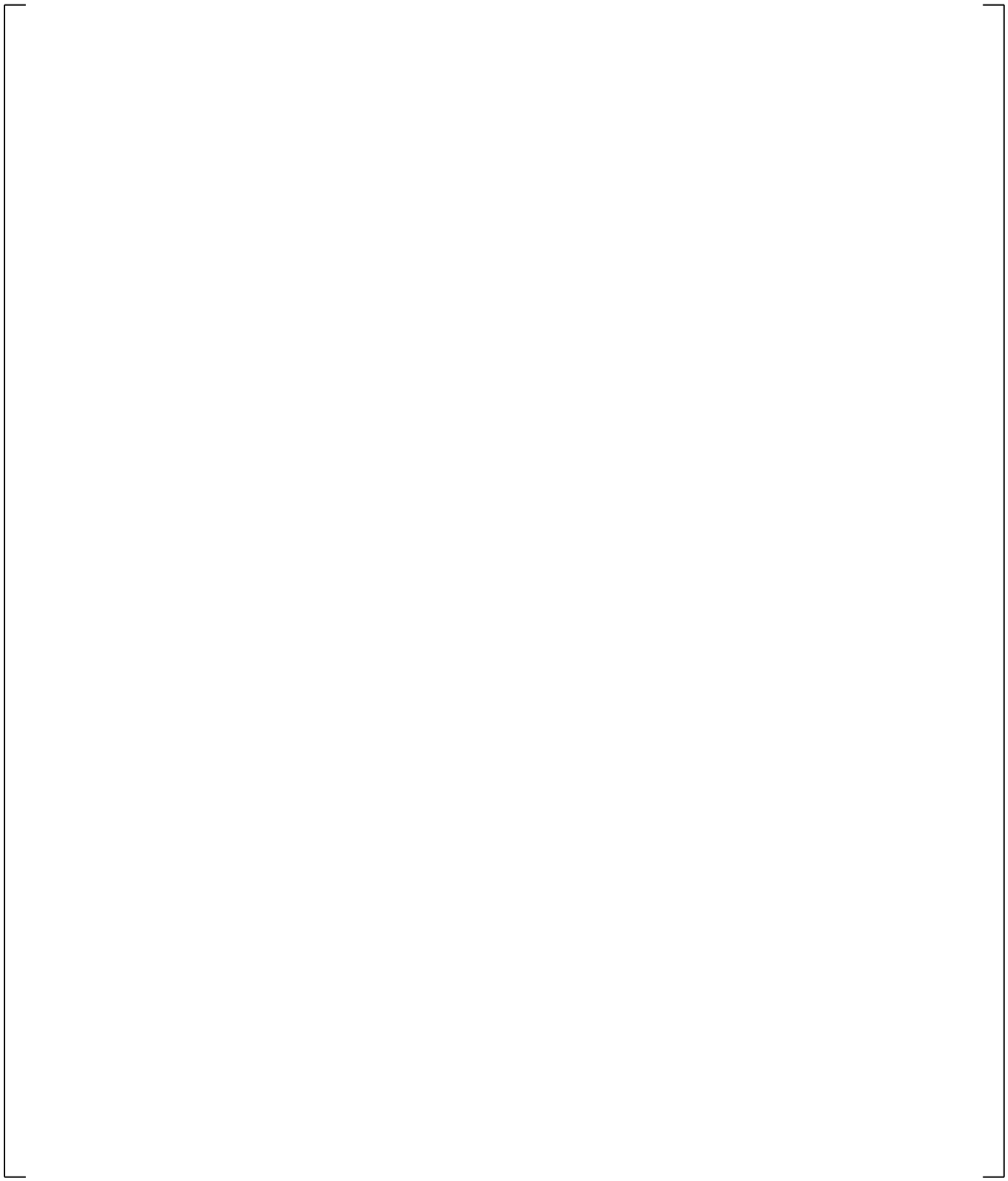

Figure 22-7 Section Views of LOFT WCOBRA/TRAC-TF2 Vessel Model

a,c

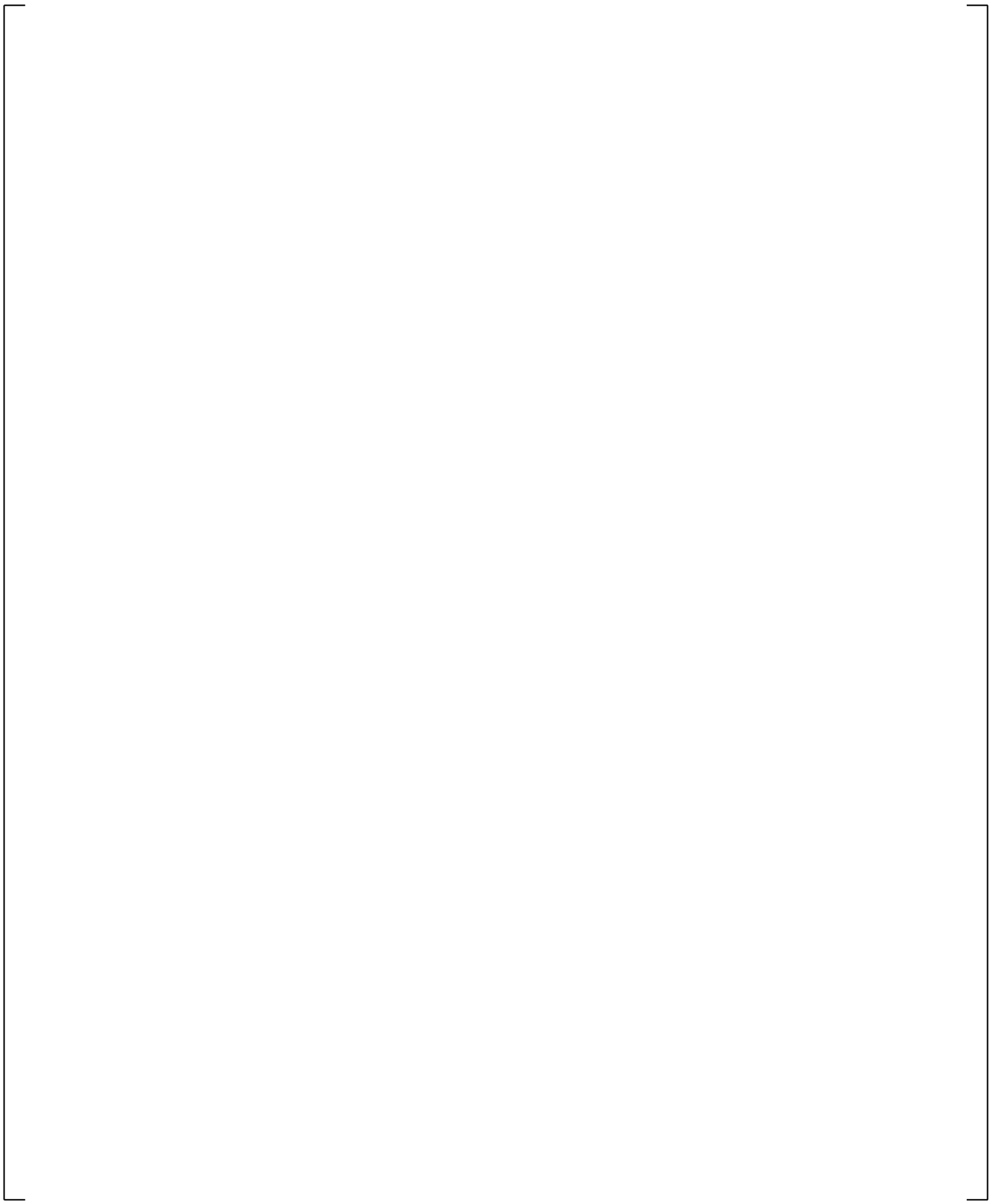

Figure 22-8 Arrangement of WCOBRA/TRAC Core Channels

a,c

Figure 22-9 LOFT Intact Loop WCOBRA/TRAC-TF2 Model

a,c

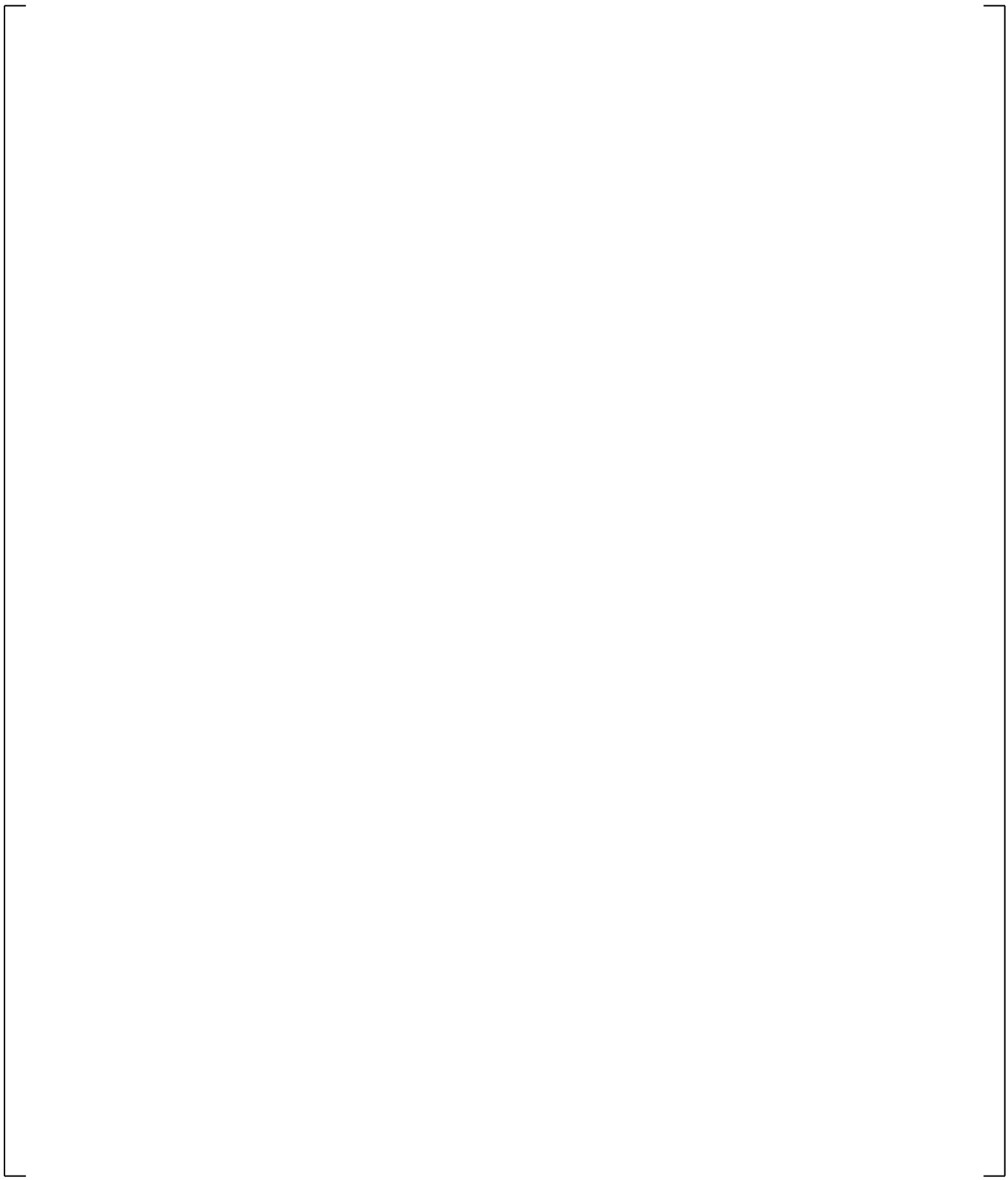

Figure 22-10 LOFT Active Loop Steam Generator WCOBRA/TRAC-TF2 Model

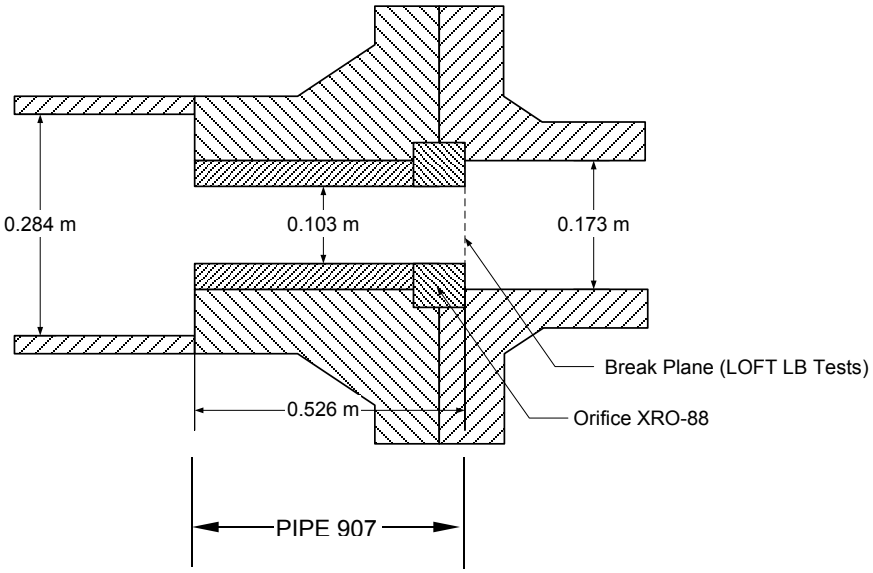

a,c

[

]

Figure 22-11a Inactive (Broken) Loop Break Orifice and Cold Leg Modeling – LOFT Large Break

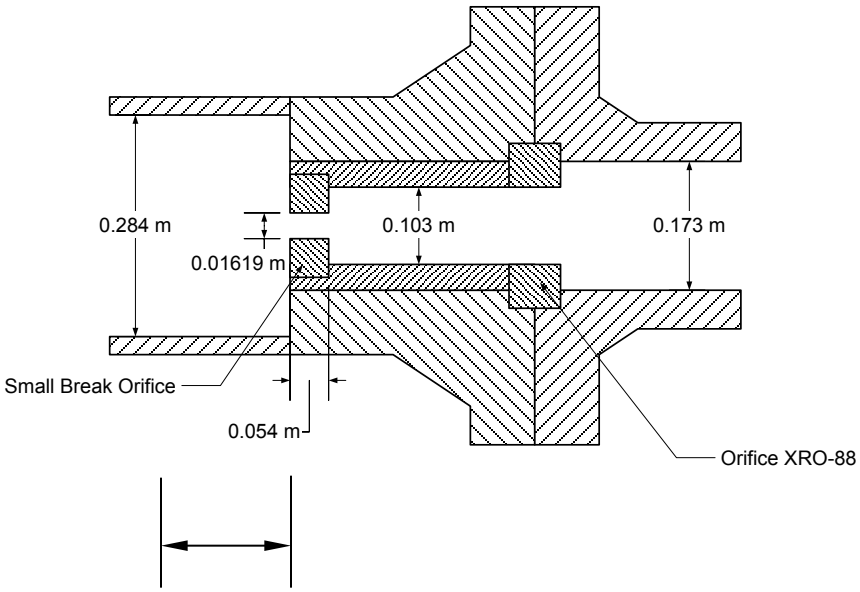

a,c

[

]

Figure 22-11b Inactive (Broken) Loop Break Orifice and Cold Leg Modeling – LOFT Small Break

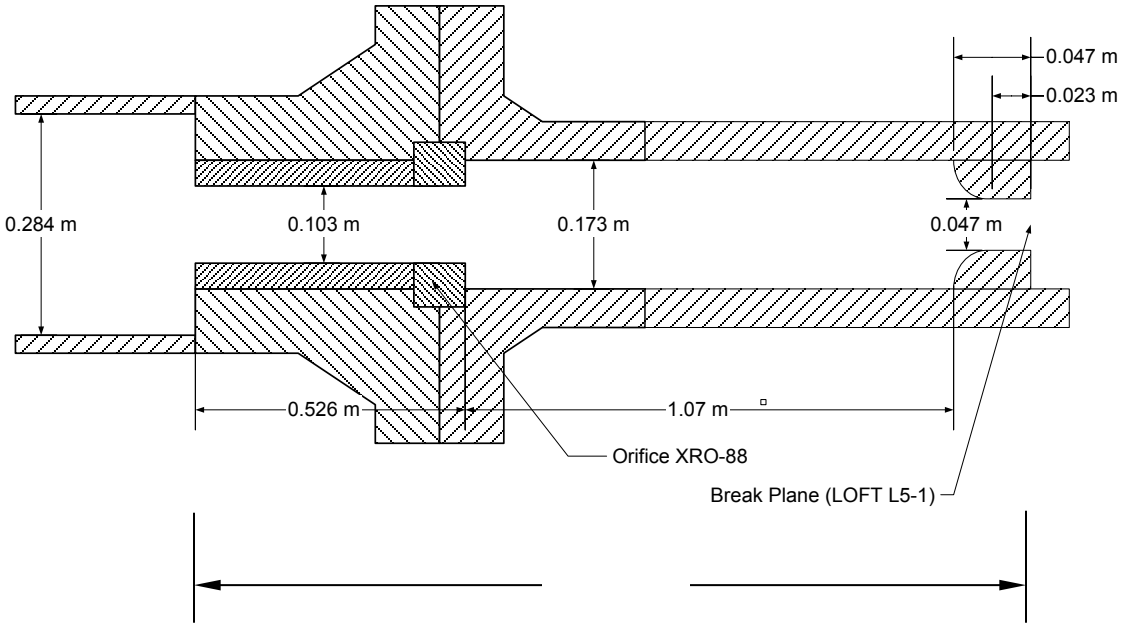

a,c

Figure 22-11c Inactive (Broken) Loop Break Orifice (Gillas and Carpenter, 1980) and Cold Leg Modeling – LOFT Intermediate Break

a,c

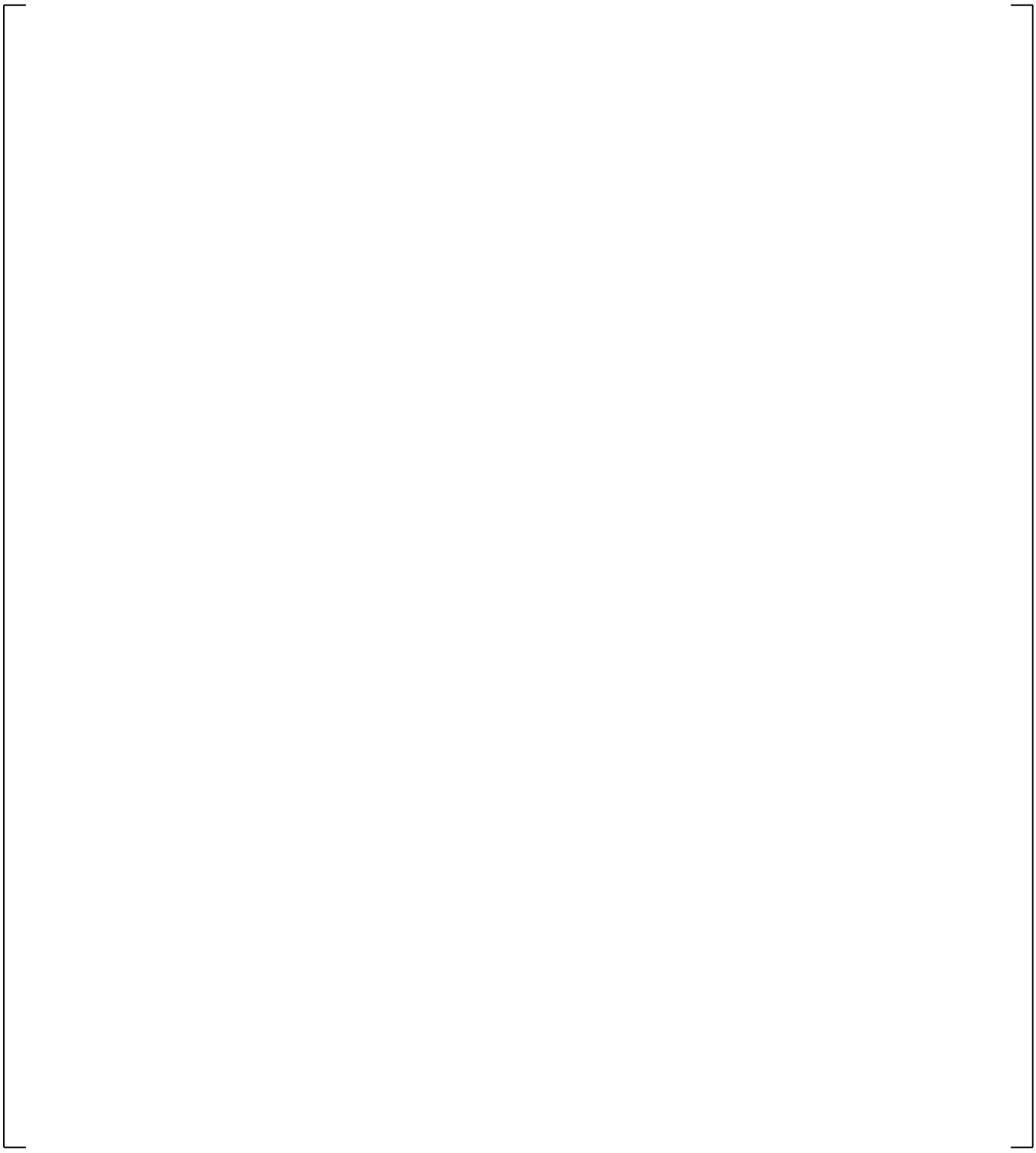

Figure 22-12 LOFT Inactive (Broken) Loop Hot Leg WCOBRA/TRAC-TF2 Model

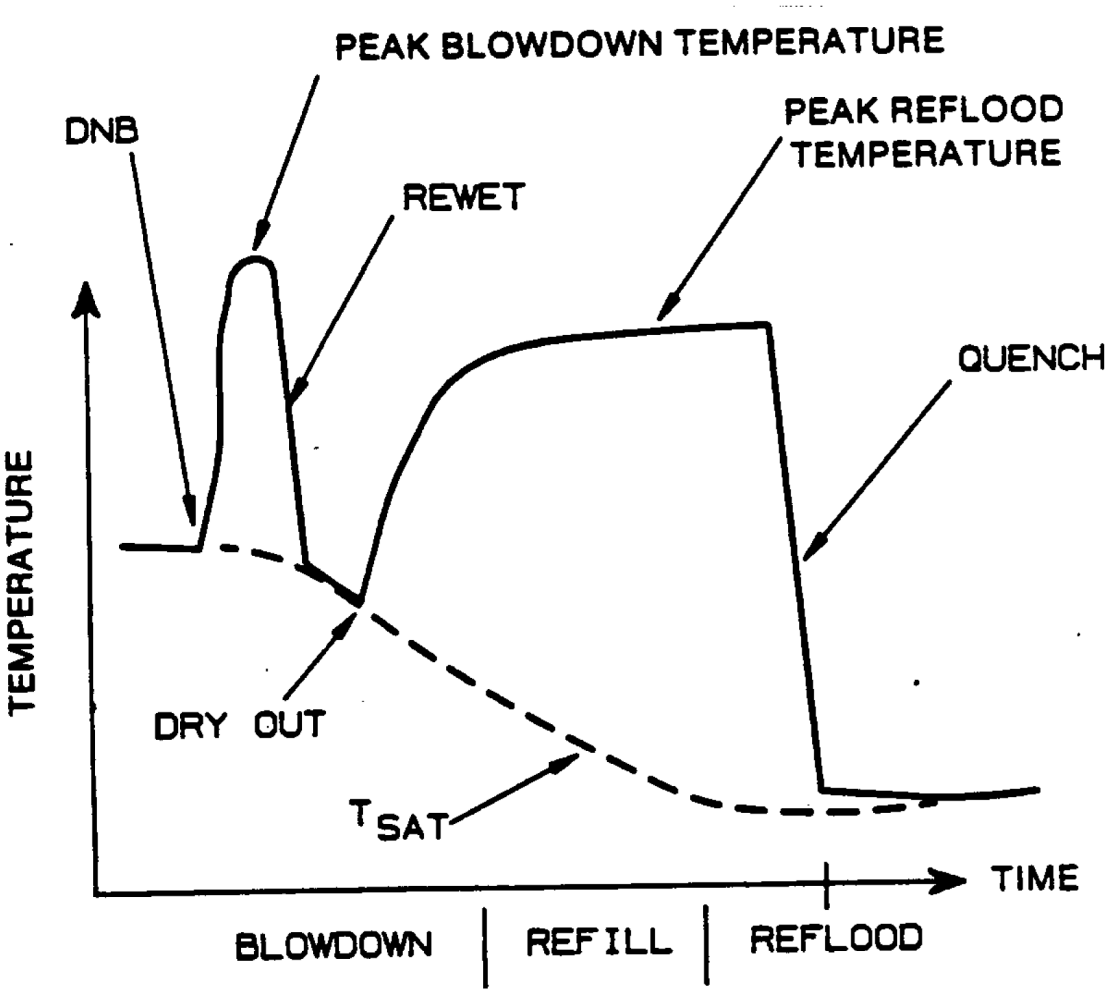

Figure 22-13 Typical Time History of Cladding Temperature during a LOFT Large Break Test Transient

a,c

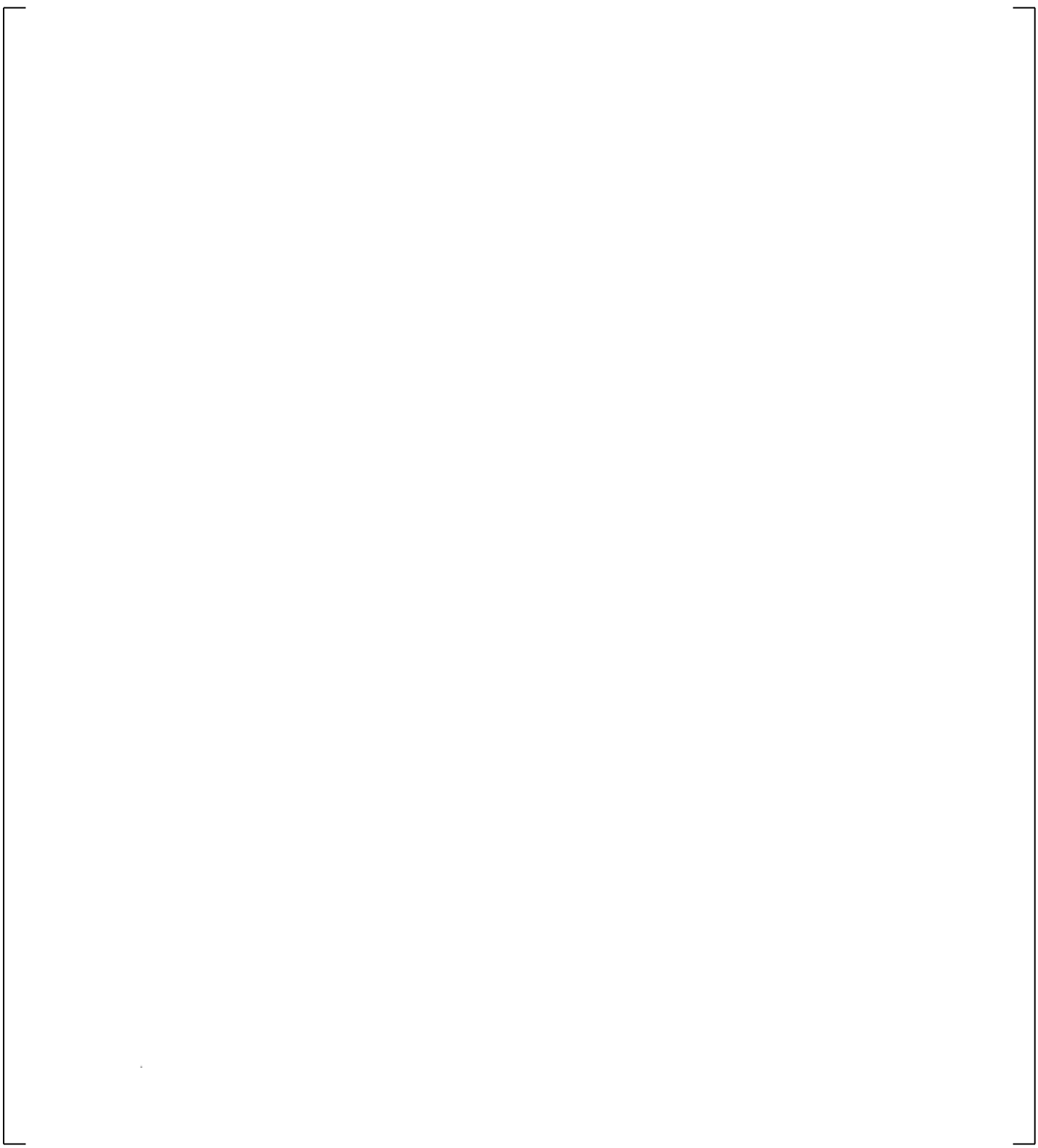

Figure 22-14 Predicted (Component 500) and Measured (PE-PC-005) Pressure, Test L2-2

a,c

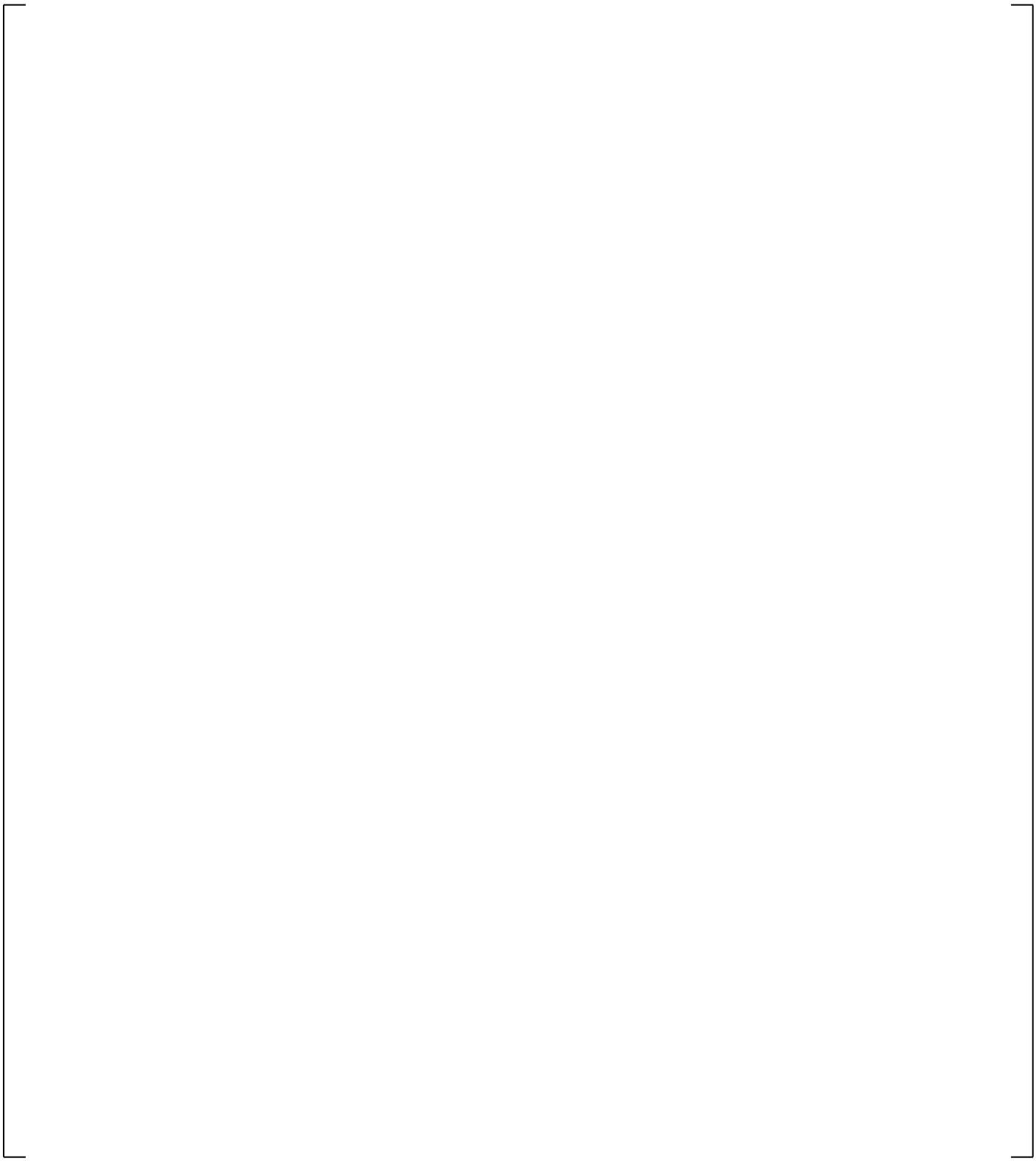

Figure 22-15 Predicted (Component 500) and Measured (PE-PC-005) Pressure, Test L2-3

a,c

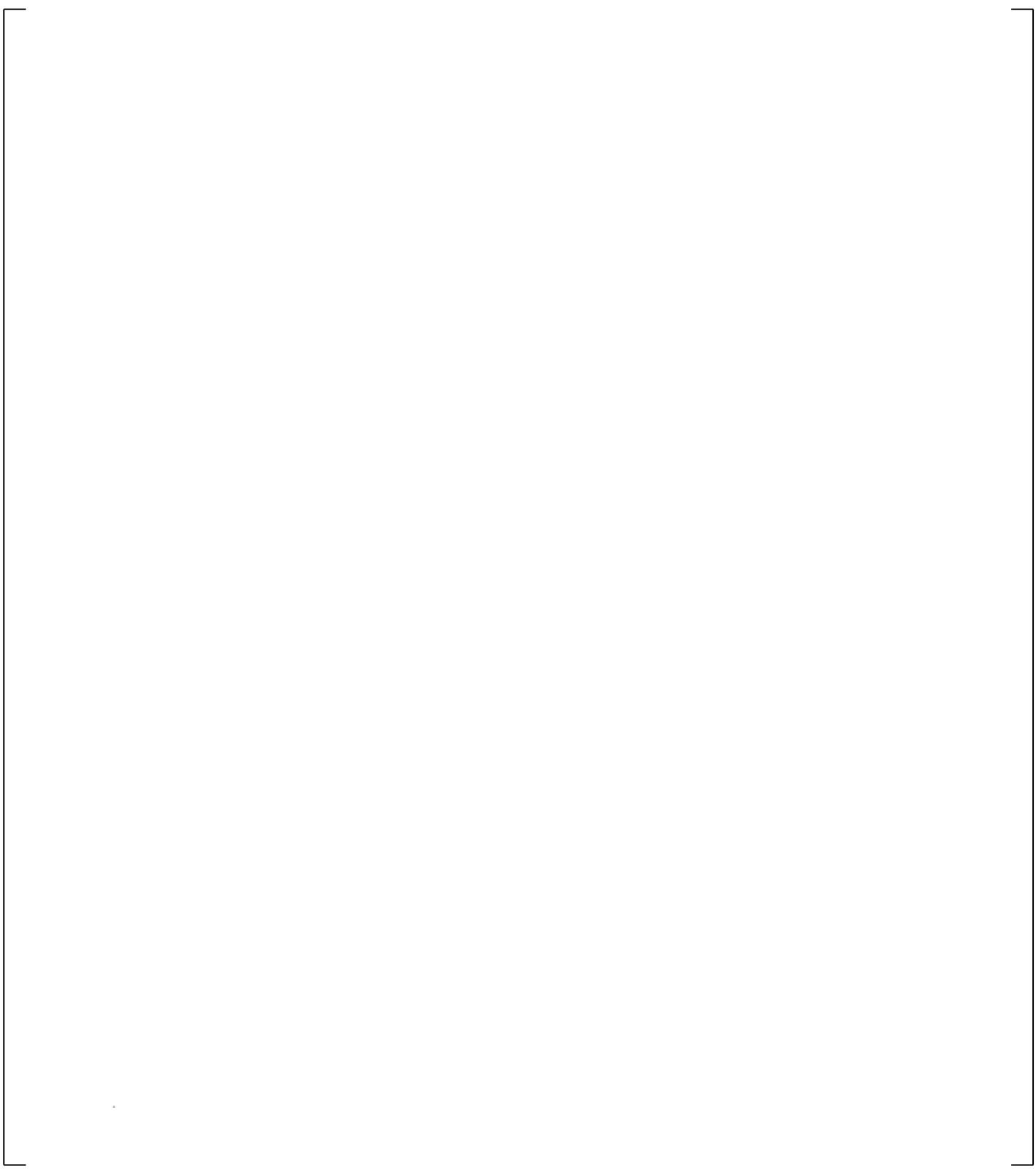

Figure 22-16 Predicted (Component 500) and Measured (PE-PC-005) Pressure, Test L2-5

a,c

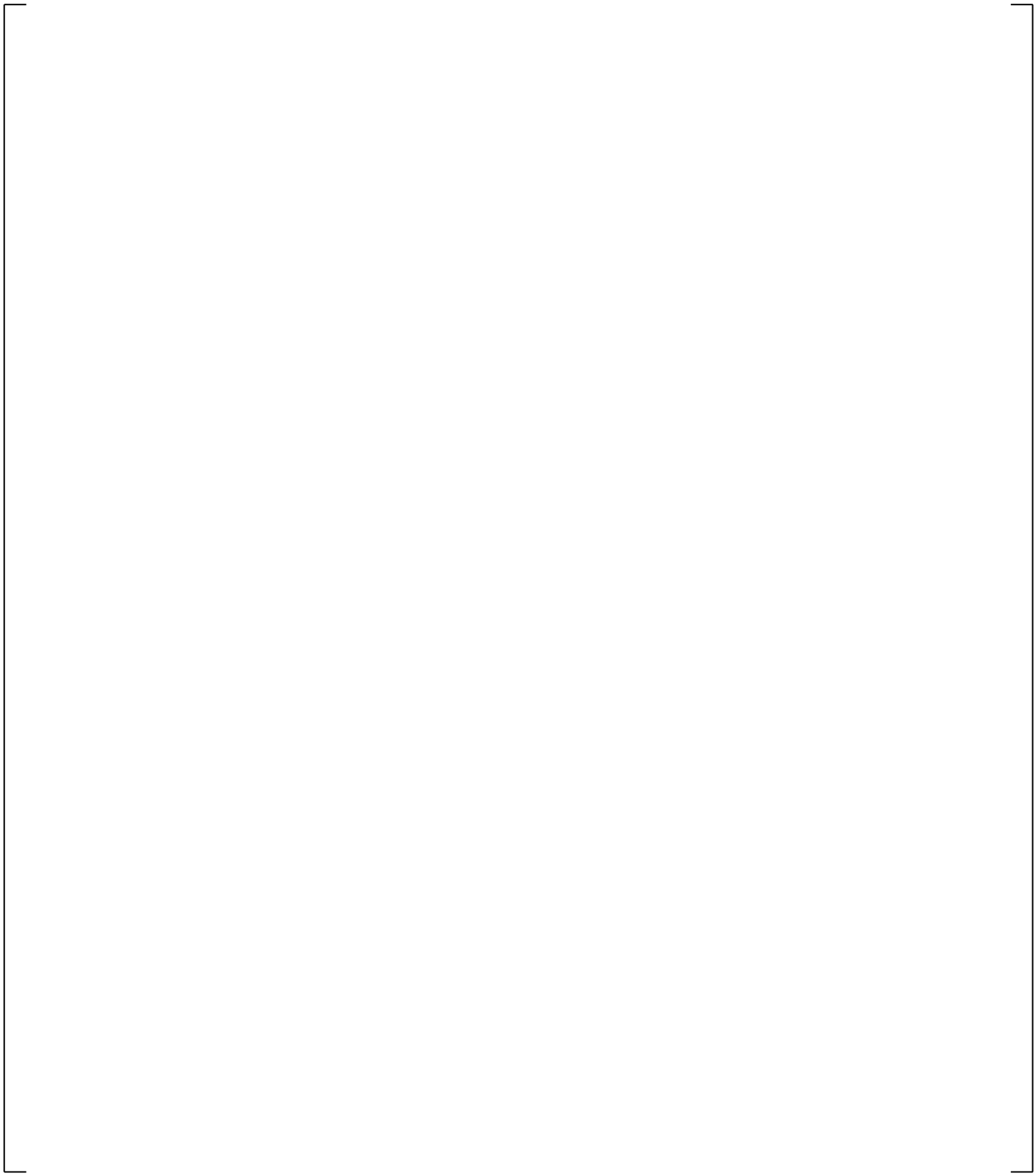

Figure 22-17 Predicted (Component 500) and Measured (PE-PC-005) Pressure, Test LB-1

a,c

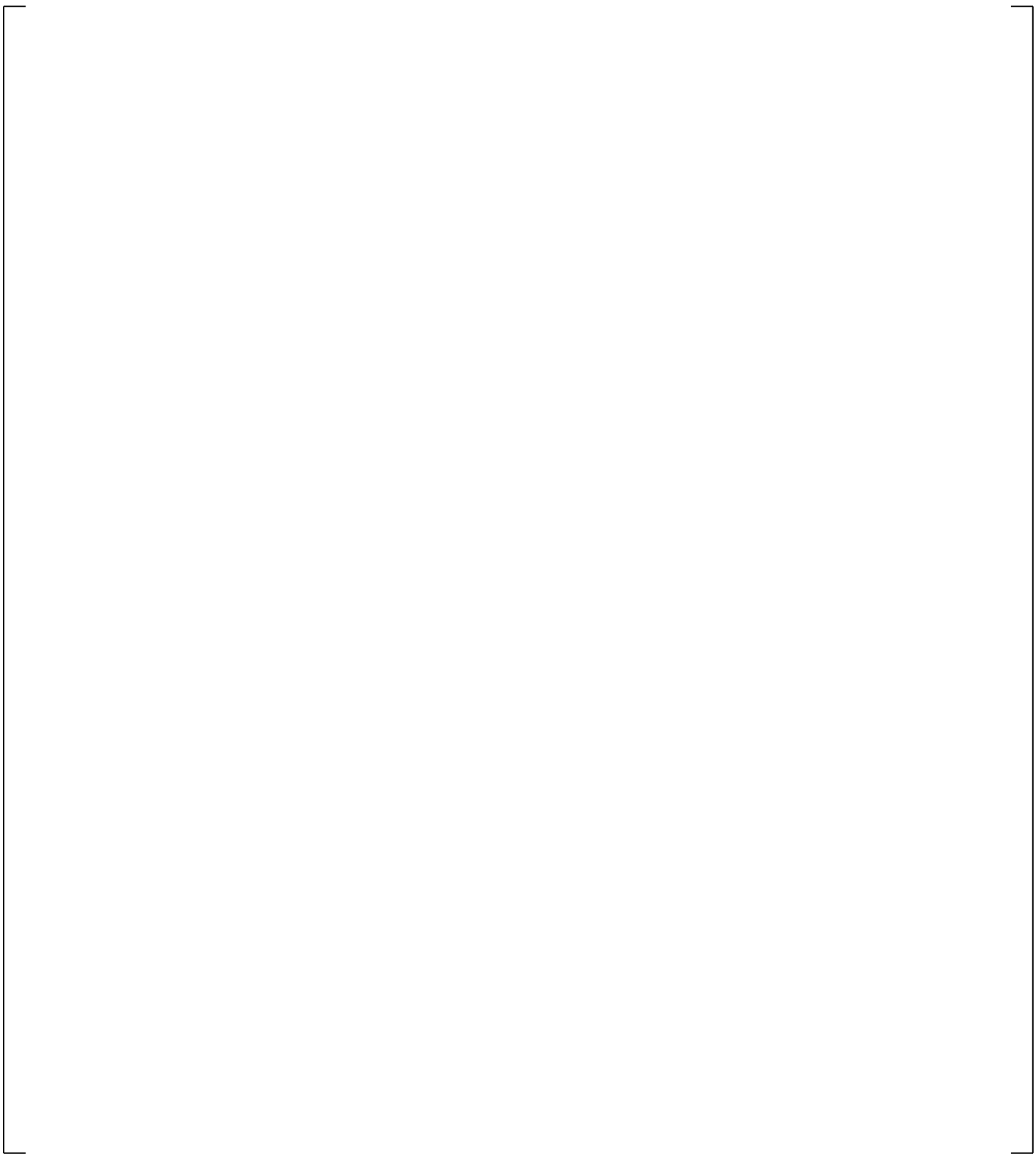

Figure 22-18 Predicted (Component 900) and Measured (FR-BL-216) Mass Flow Rate in Broken Hot Leg, Test L2-2

a,c

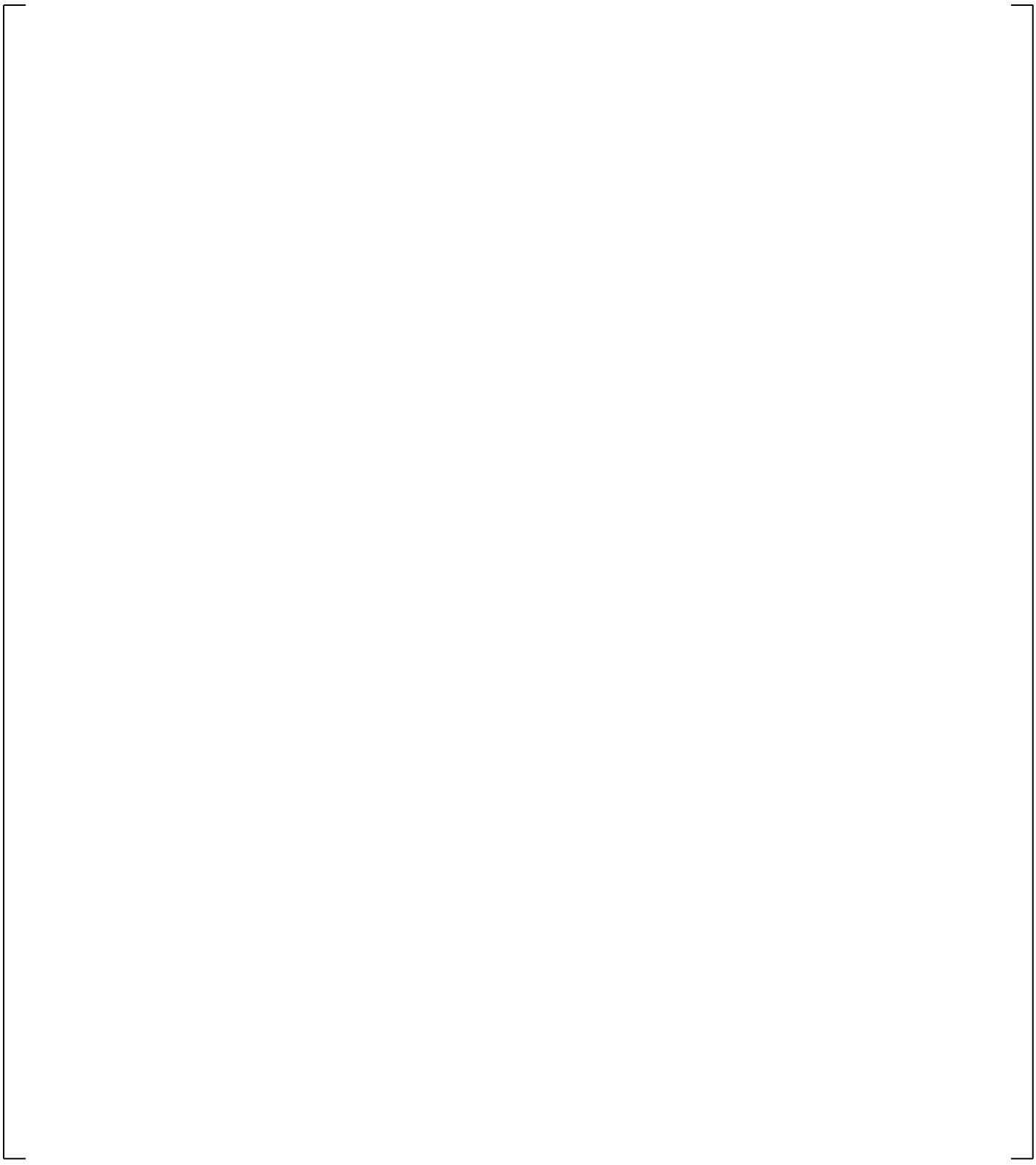

Figure 22-19 Predicted (Component 900) and Measured (FR-BL-116) Mass Flow Rate in Broken Hot Leg, Test L2-3

a,c

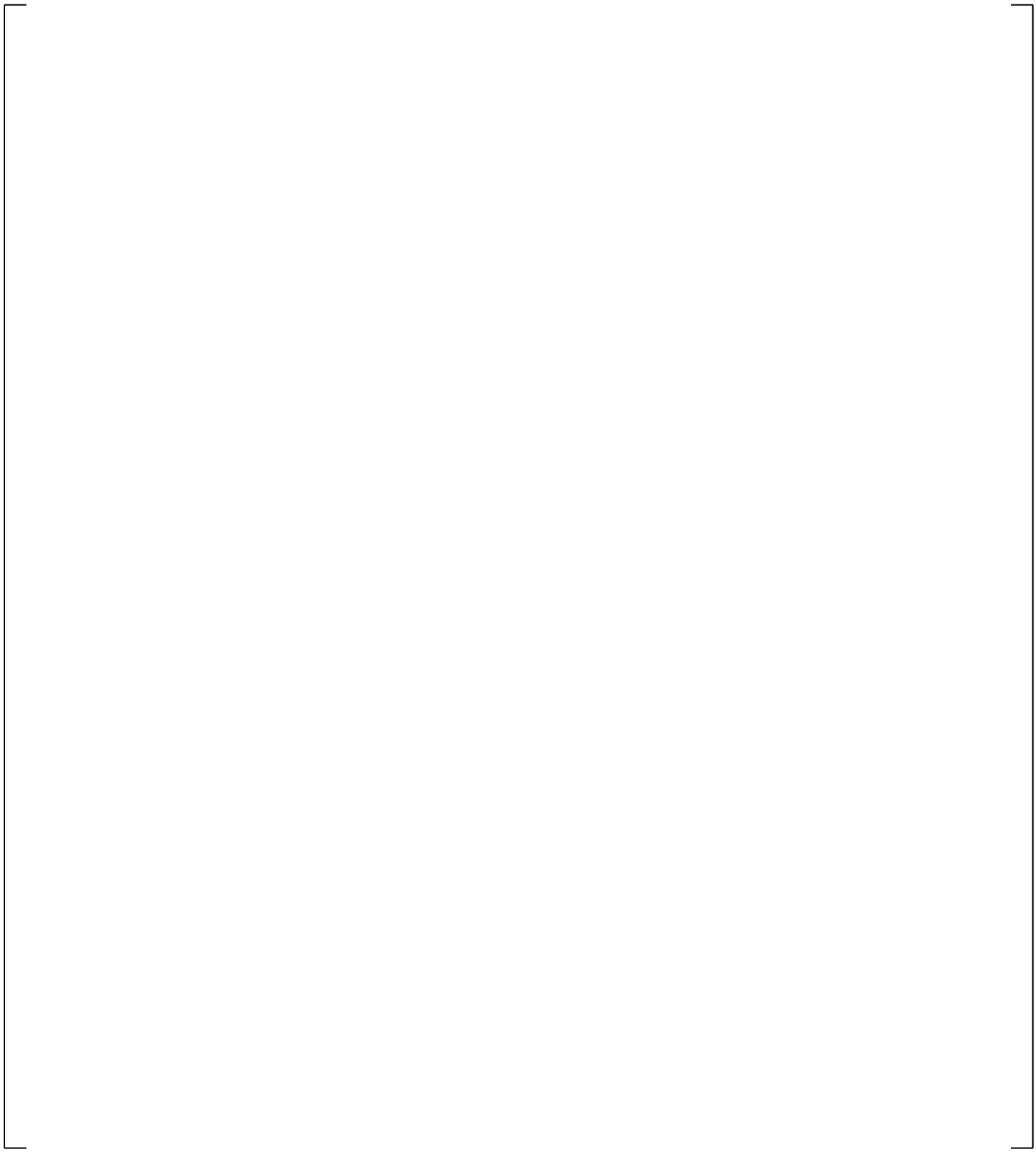

Figure 22-20 Predicted (Component 900) and Measured (FR-BL-002) Mass Flow Rate in Broken Hot Leg, Test L2-5

a,c

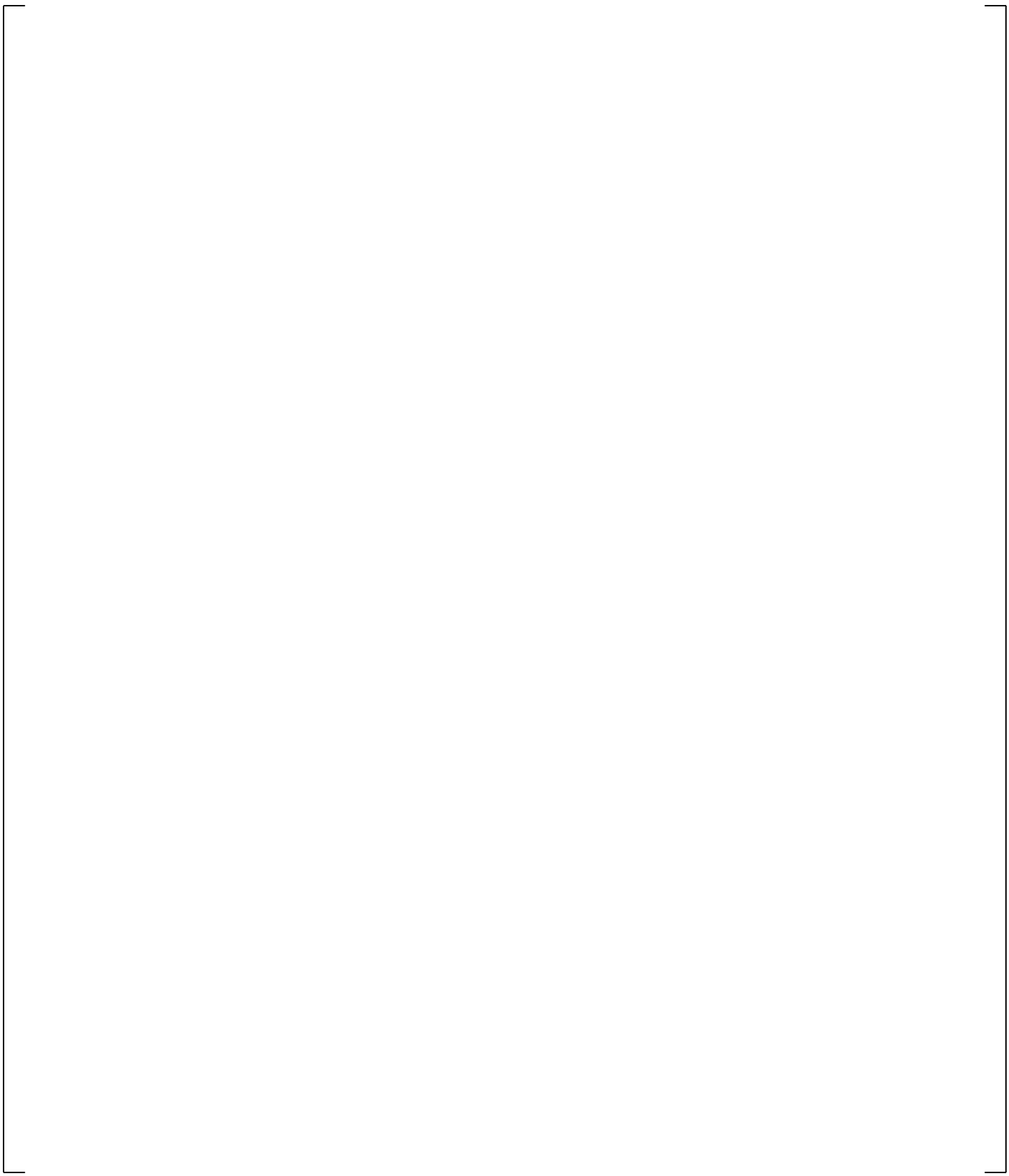

Figure 22-21 Predicted (Component 900) and Measured (FR-BL-205) Mass Flow Rate in Broken Hot Leg, Test LB-1

a,c

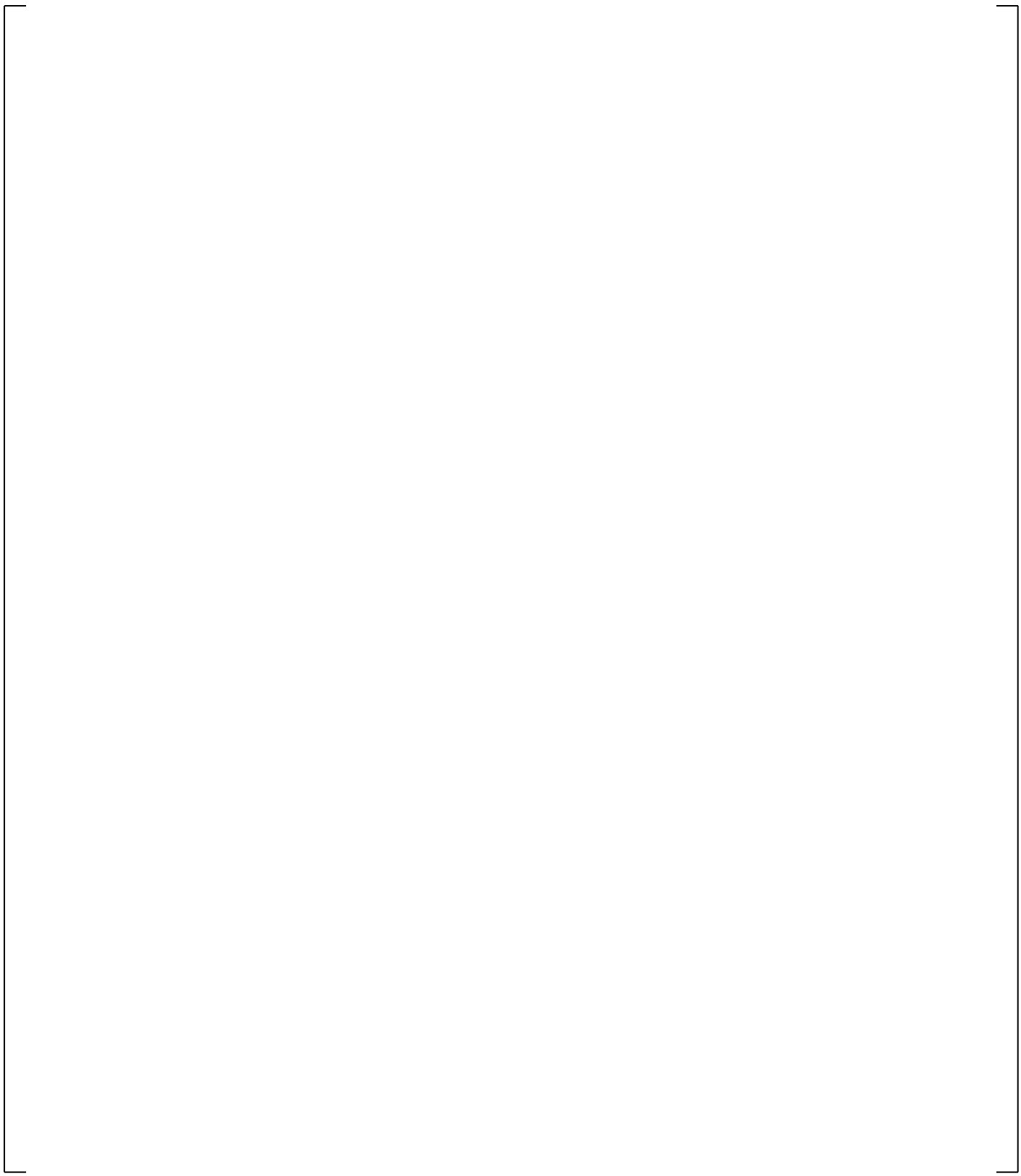

Figure 22-22 Predicted (Component 905) and Measured (FR-BL-116) Mass Flow Rate in Broken Cold Leg, Test L2-2

a,c

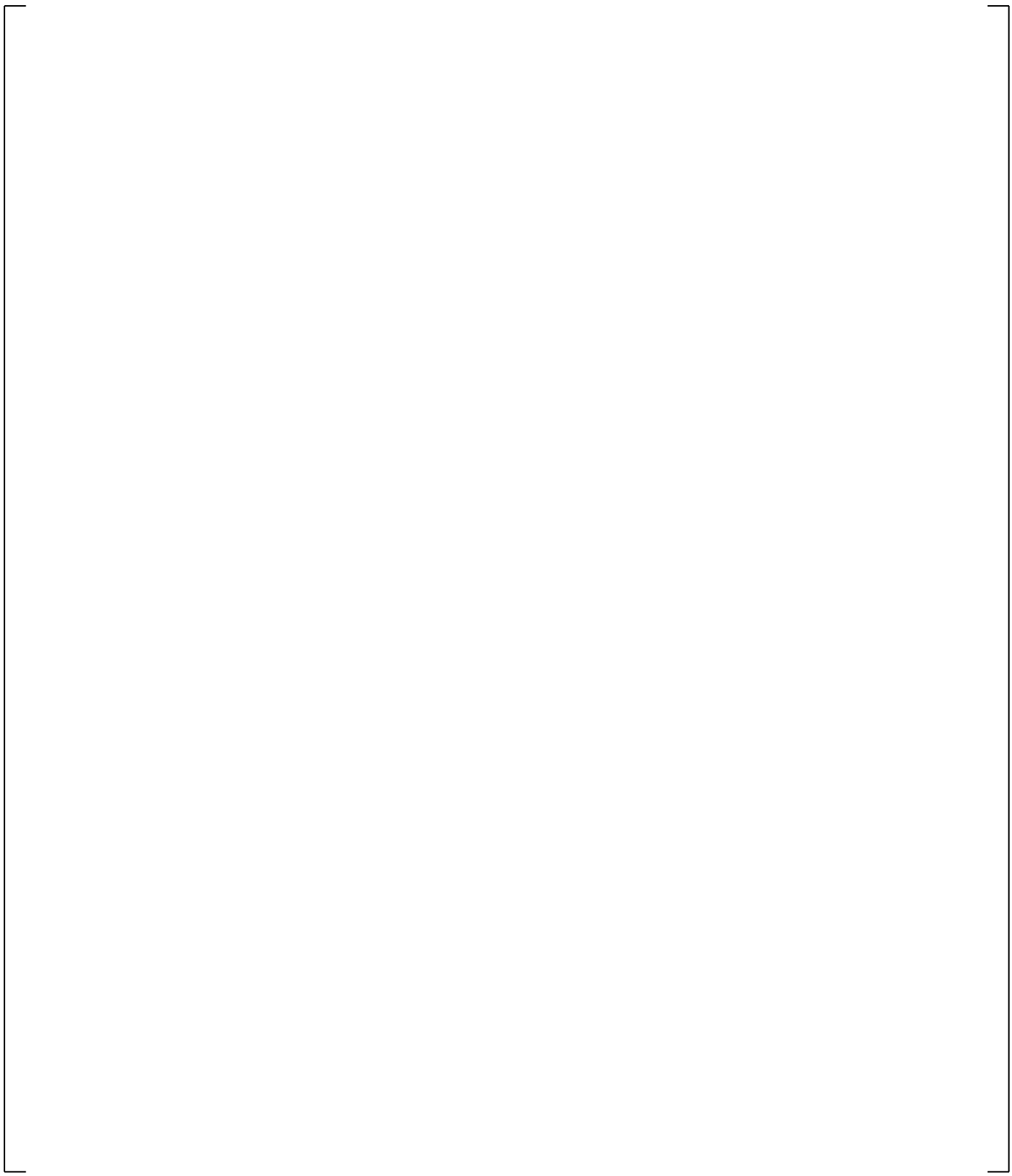

Figure 22-23 Predicted (Component 905) and Measured (FR-BL-216) Mass Flow Rate in Broken Cold Leg, Test L2-3

a,c

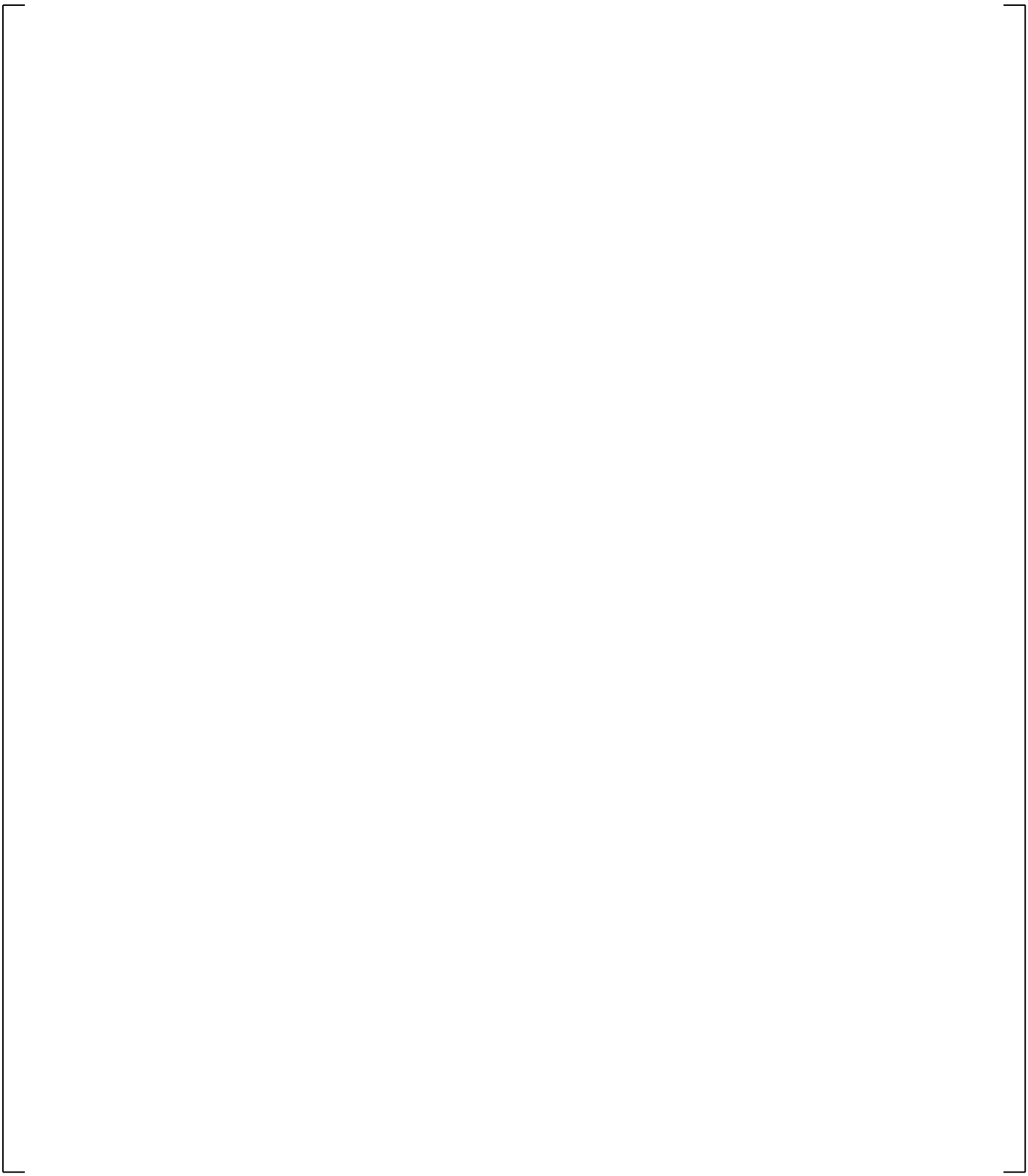

Figure 22-24 Predicted (Component 905) and Measured (FR-BL-001) Mass Flow Rate in Broken Cold Leg, Test L2-5

a,c

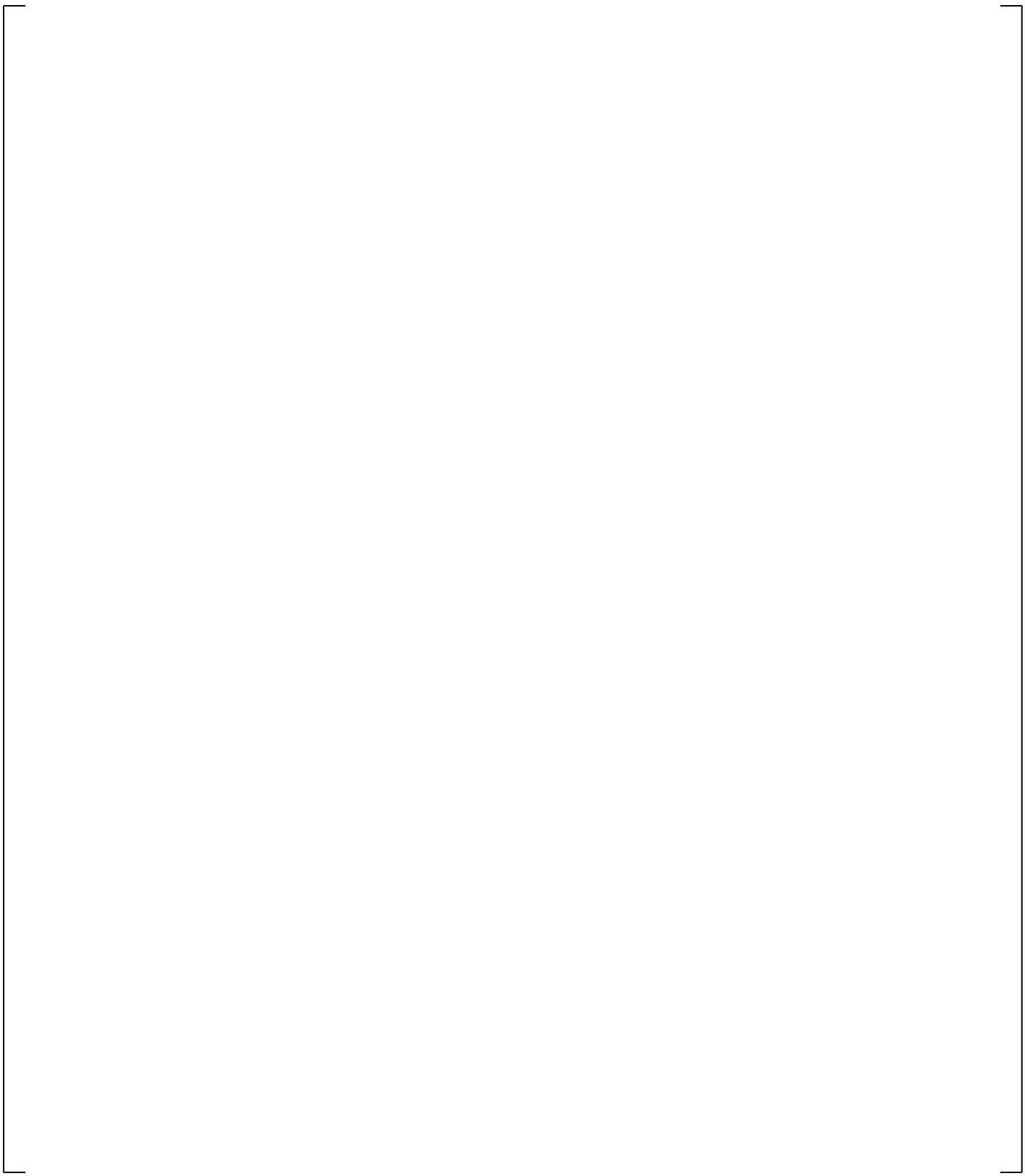

Figure 22-25 Predicted (Component 905) and Measured (FR-BL-105) Mass Flow Rate in Broken Cold Leg, Test LB-1

a,c

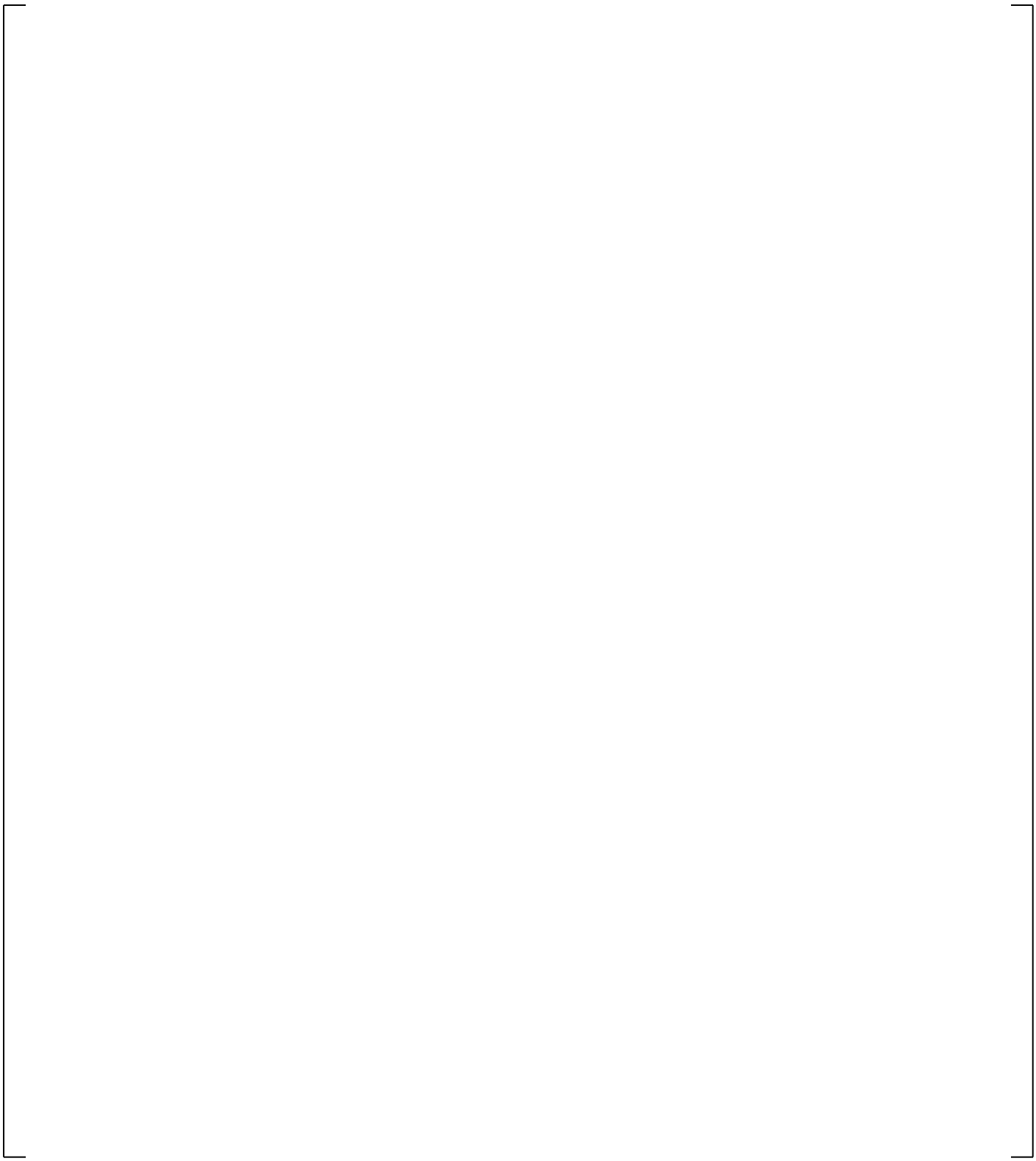

Figure 22-26 Predicted (Component 300) and Measured (FT-P139-27) Mass Flow Rate in Intact Hot Leg, Test L2-2

a,c

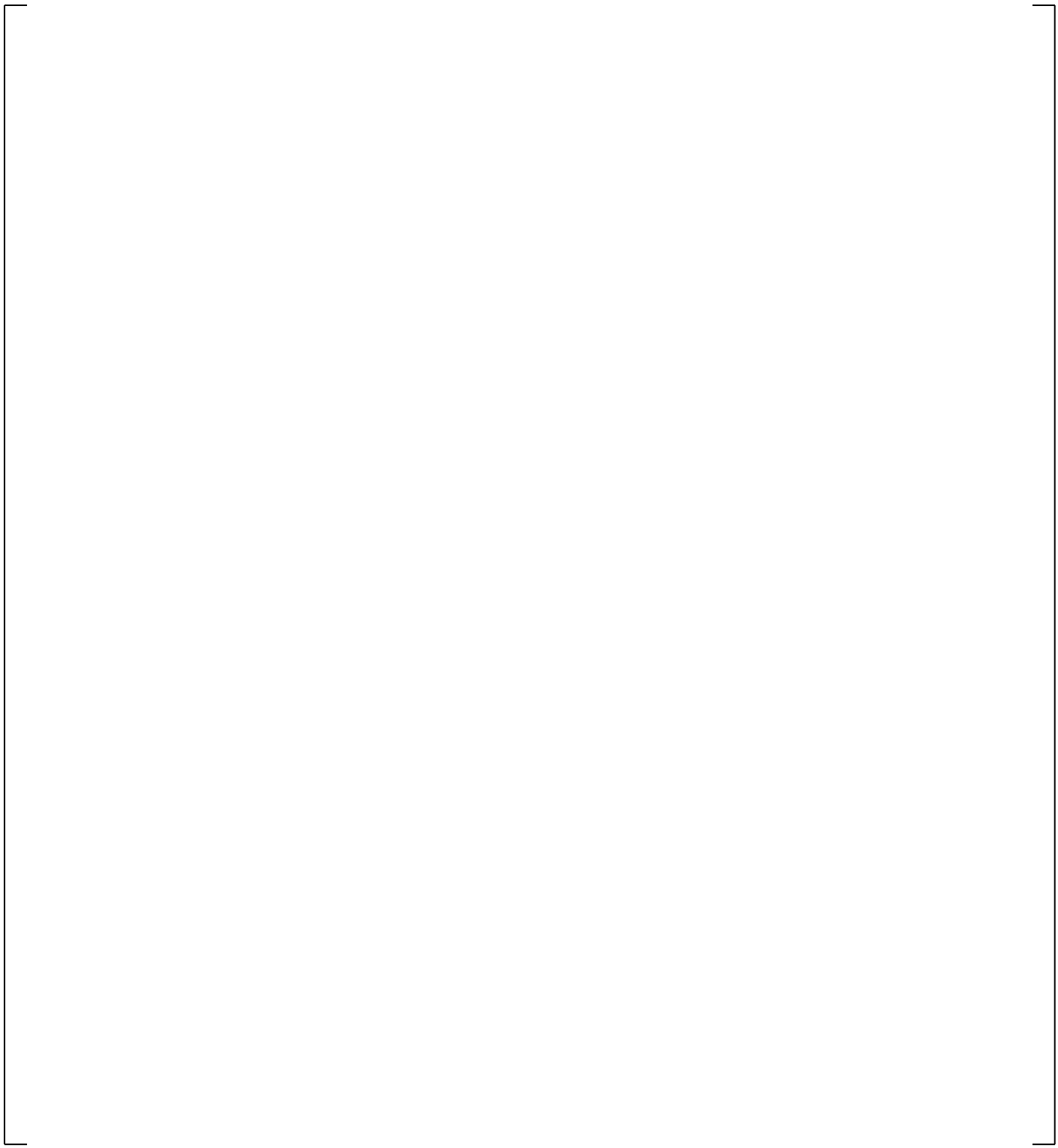

Figure 22-27 Predicted (Component 300) and Measured (Figures 69, 78, Prassinos, et. al, 1979) Mass Flow Rate in Intact Hot Leg, Test L2-3

a,c

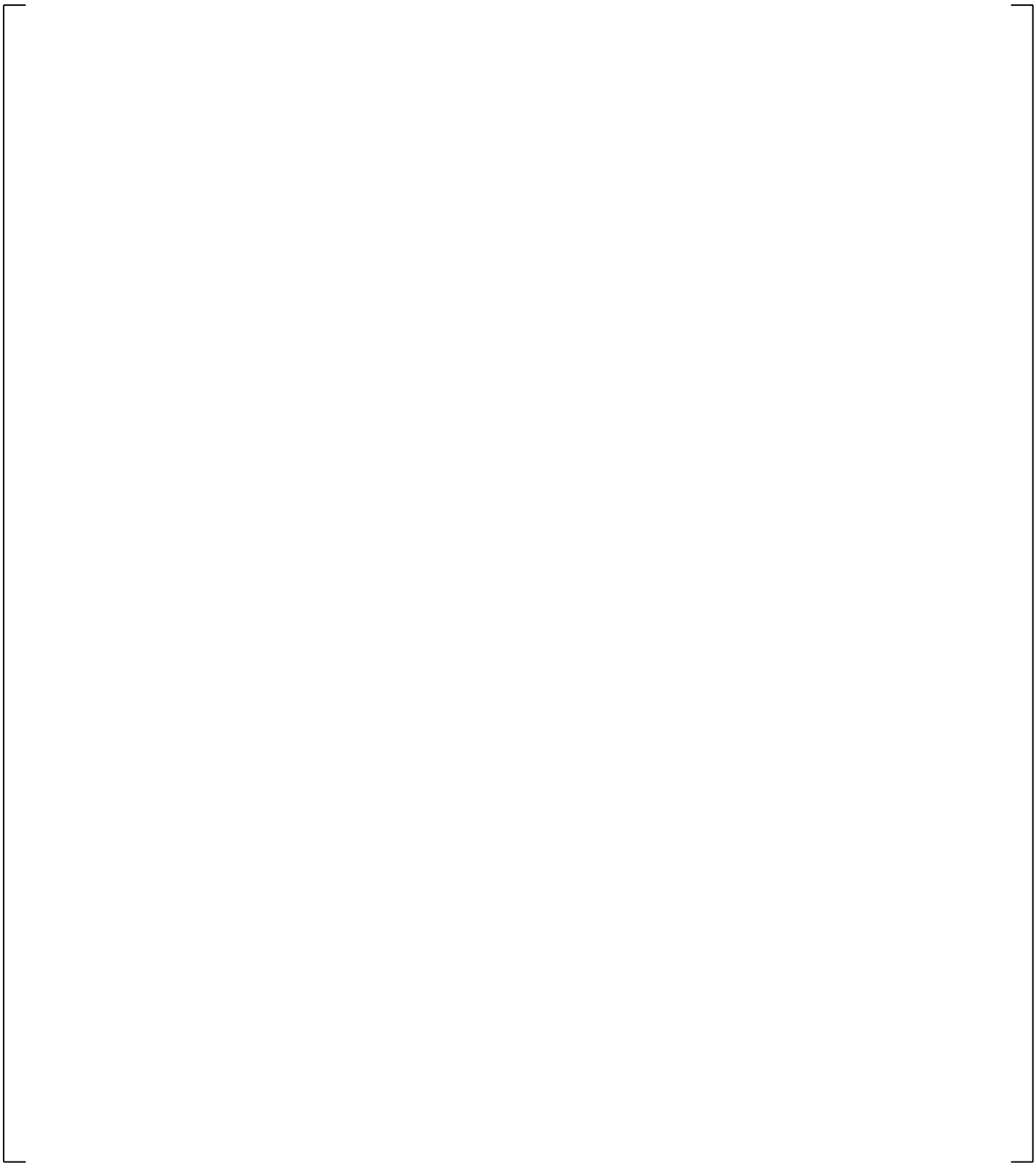

Figure 22-28 Predicted (Component 300) and Measured (FR-PC-201) Mass Flow Rate in Intact Hot Leg, Test L2-5

a,c

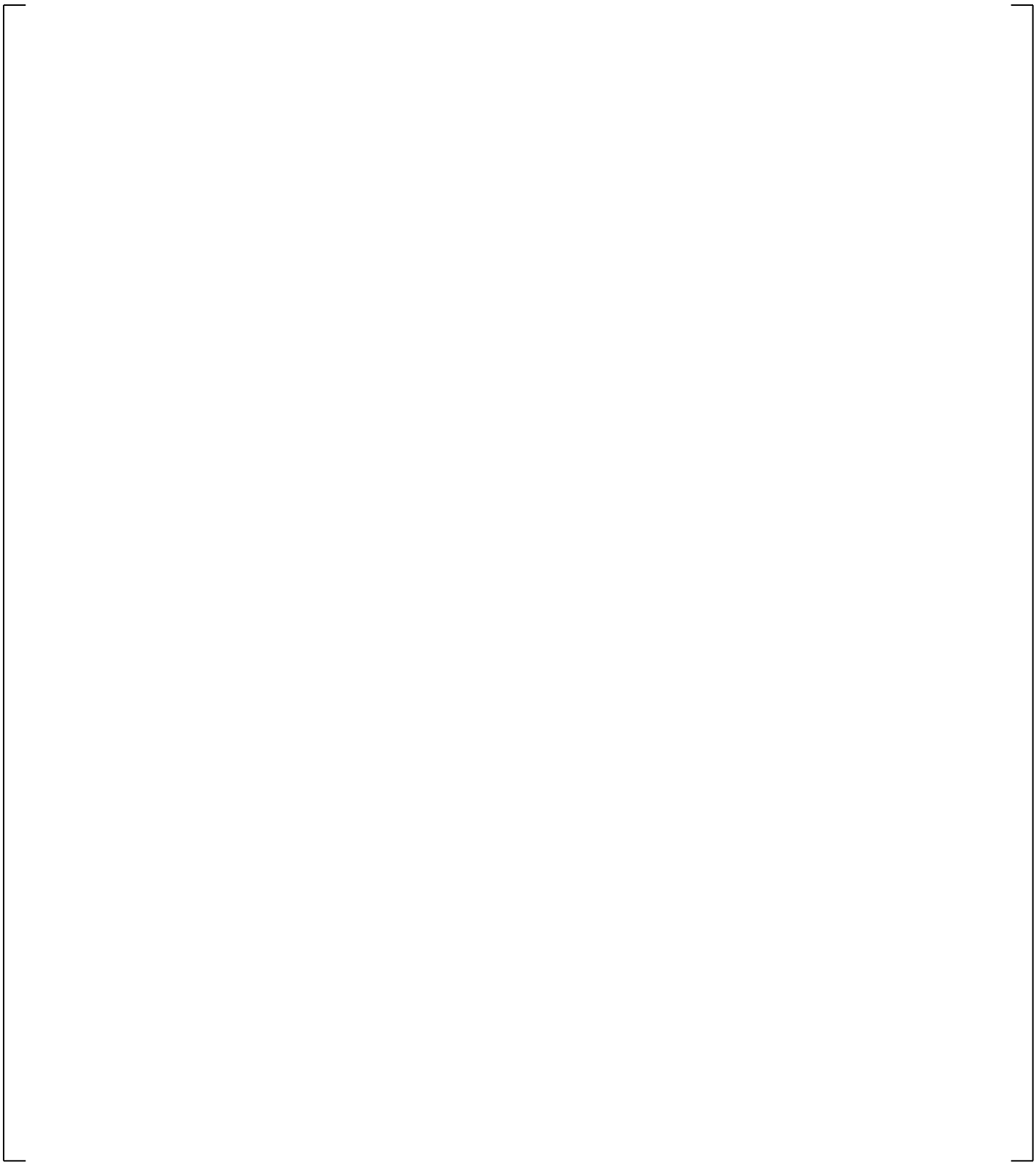

Figure 22-29 Predicted (Component 810) and Measured (FR-PC-105) Mass Flow Rate in Intact Cold Leg, Test LB-1

a,c

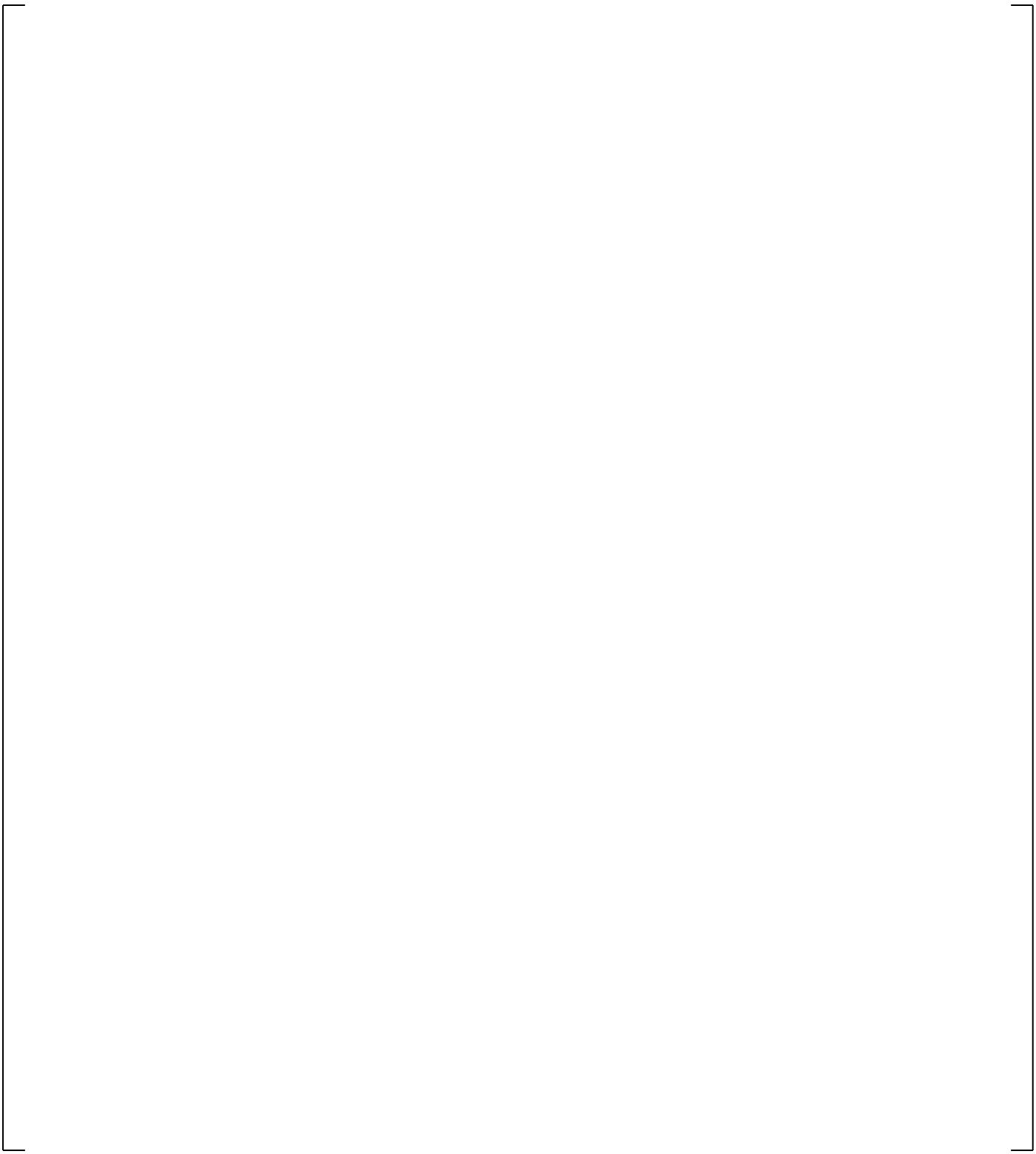

Figure 22-30a Predicted (Component 840) and Measured (FT-P120-36) Volumetric Flow Rate and Predicted (Component 840) Void Fraction from Accumulator, Test L2-2

a,c

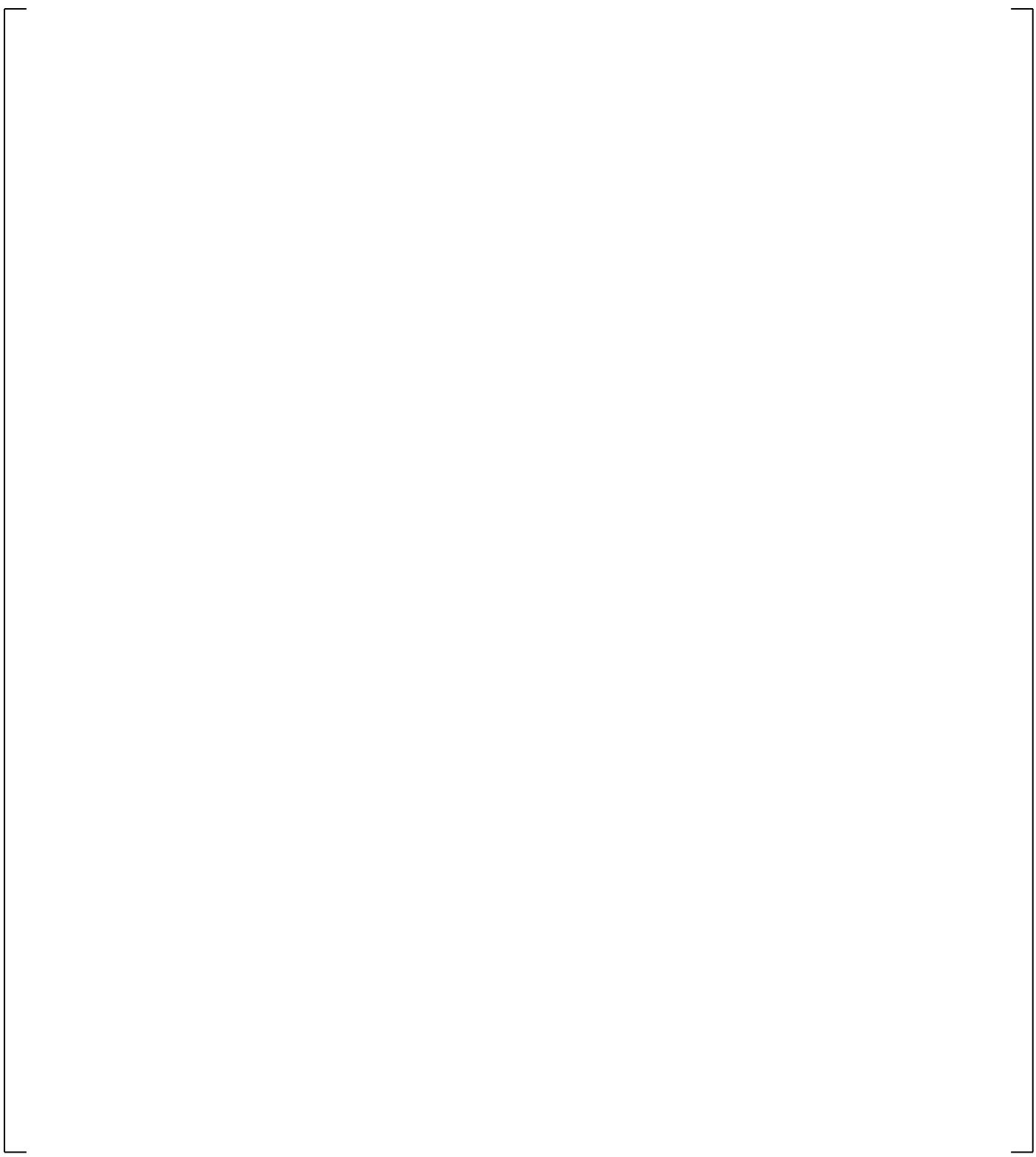

Figure 22-30b Predicted (Component 850) and Measured (LIT-P120-087) Liquid Level in Accumulator, Test L2-2

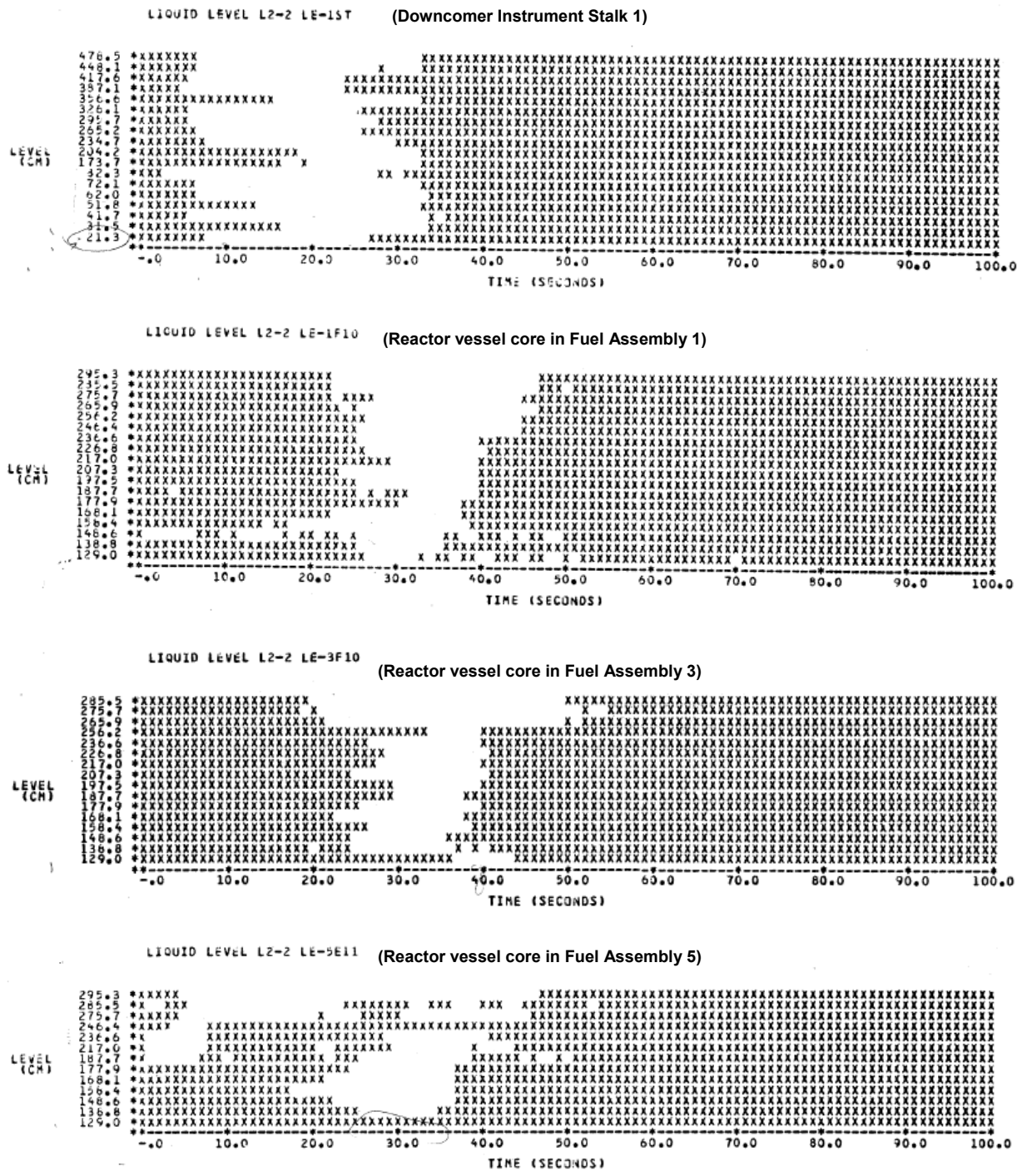

Figure 22-30c Measured Liquid Levels in Downcomer and Core Regions, Test L2-2

a,c

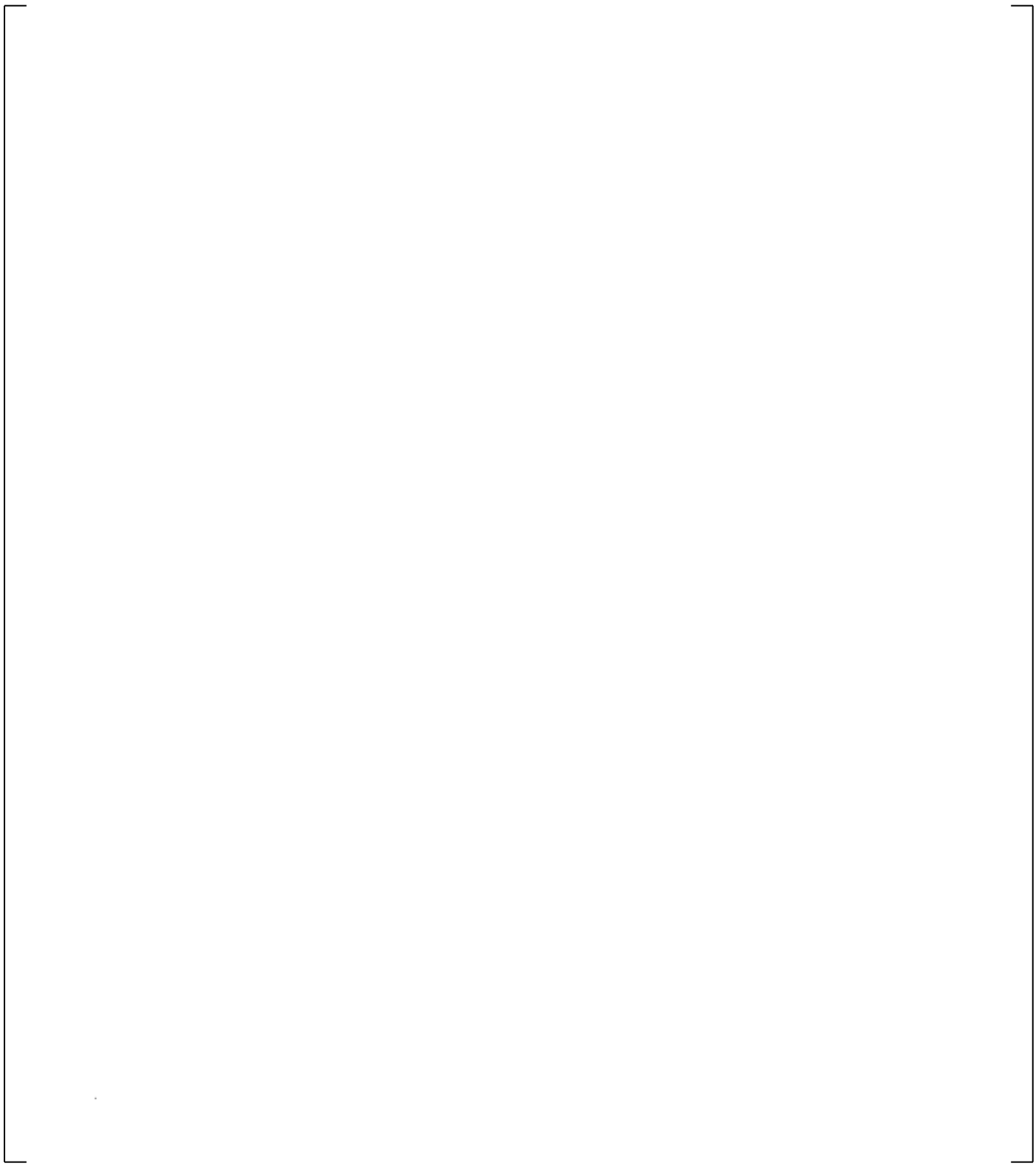

Figure 22-30d Predicted Liquid Levels in Downcomer and Core Region, Test L2-2

a,c

Figure 22-30e Predicted and Measured Liquid Levels in Vessel Core Regions, Test L2-2

a,c

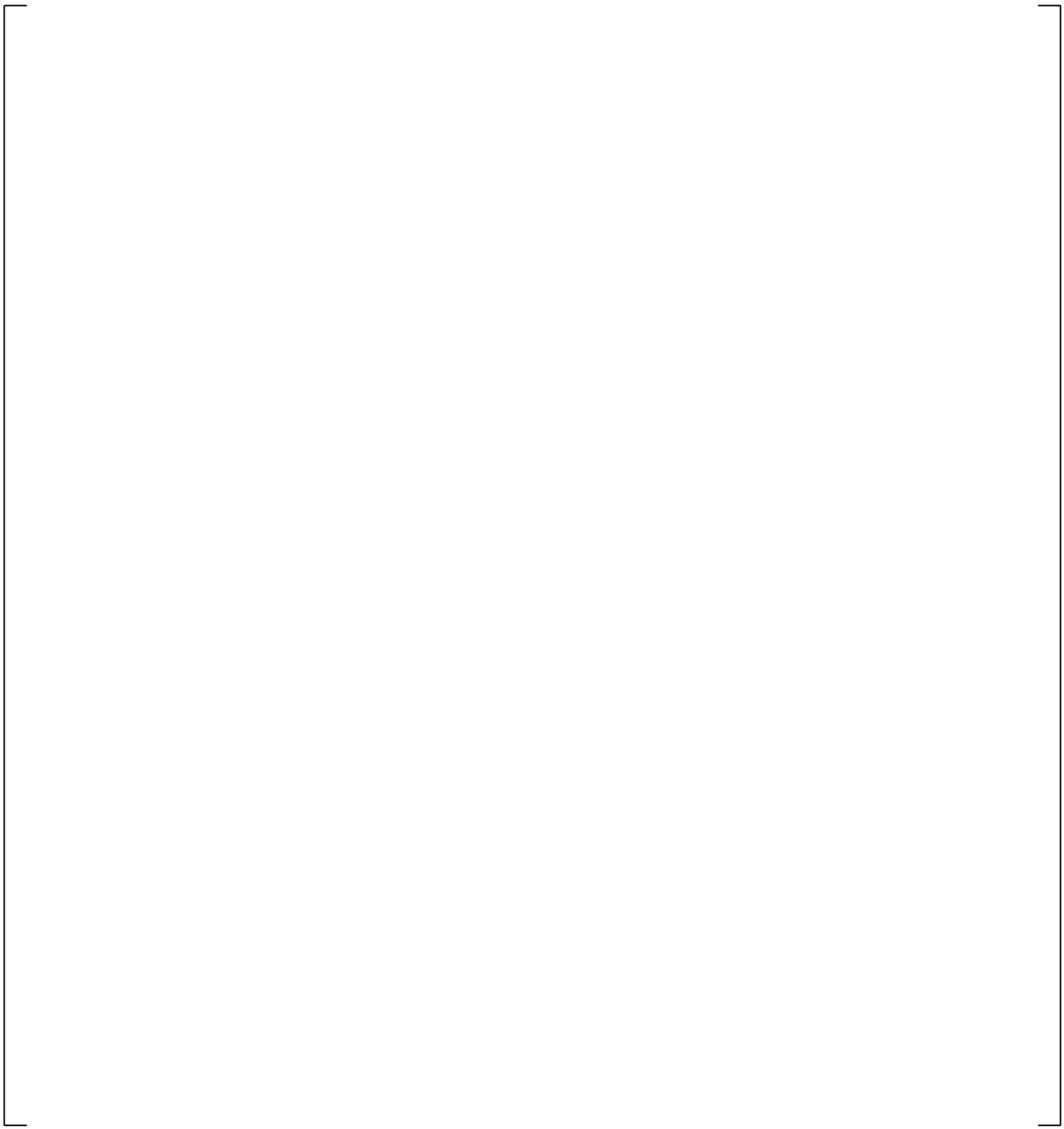

Figure 22-31a Predicted (Component 840) and Measured (FT-P120-36) Volumetric Flow Rate and Predicted (Component 840) Void Fraction from Accumulator, Test L2-3

a,c

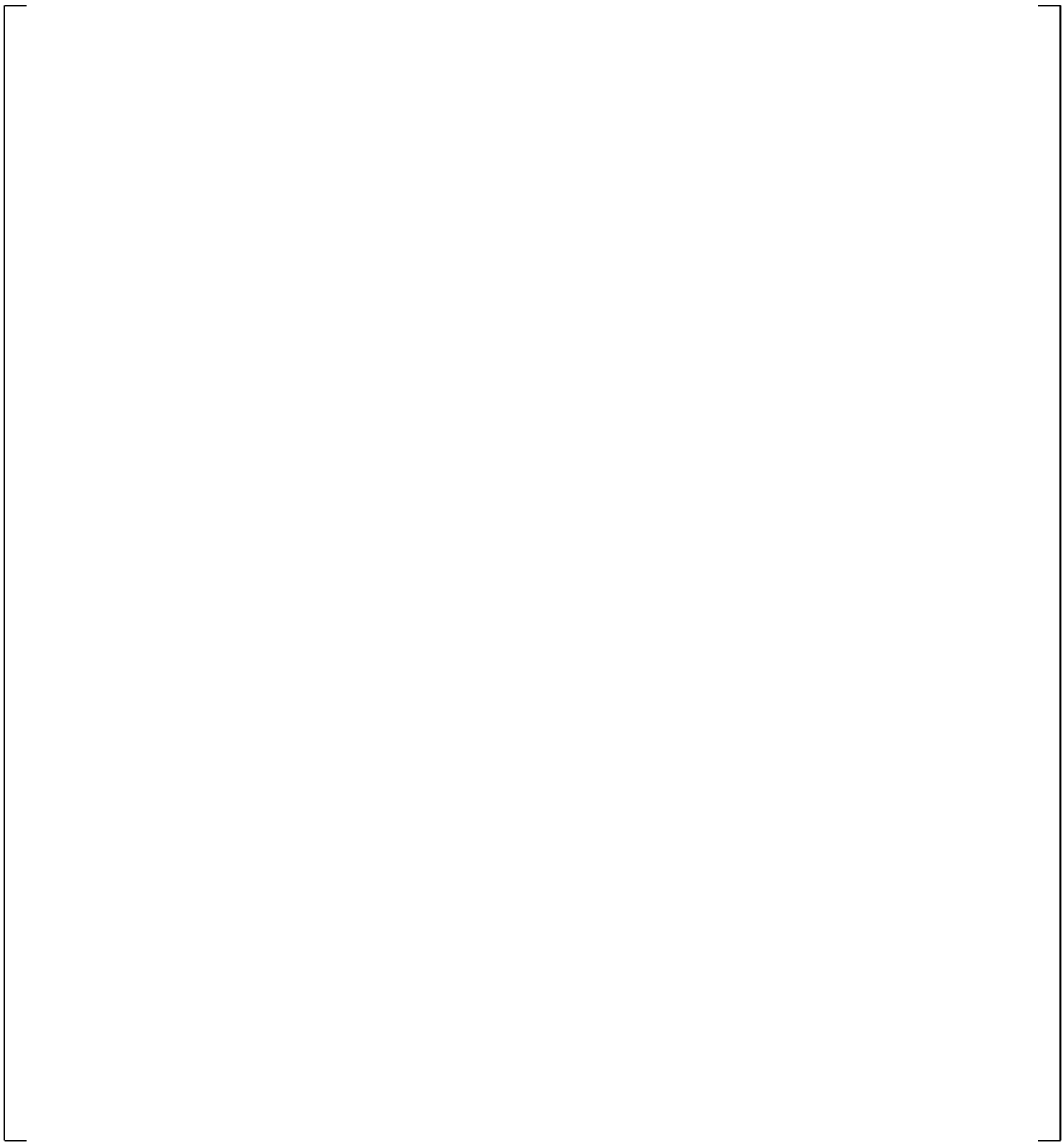

Figure 22-31b Predicted (Component 850) and Measured (LIT-P120-044) Liquid Level in Accumulator, Test L2-3

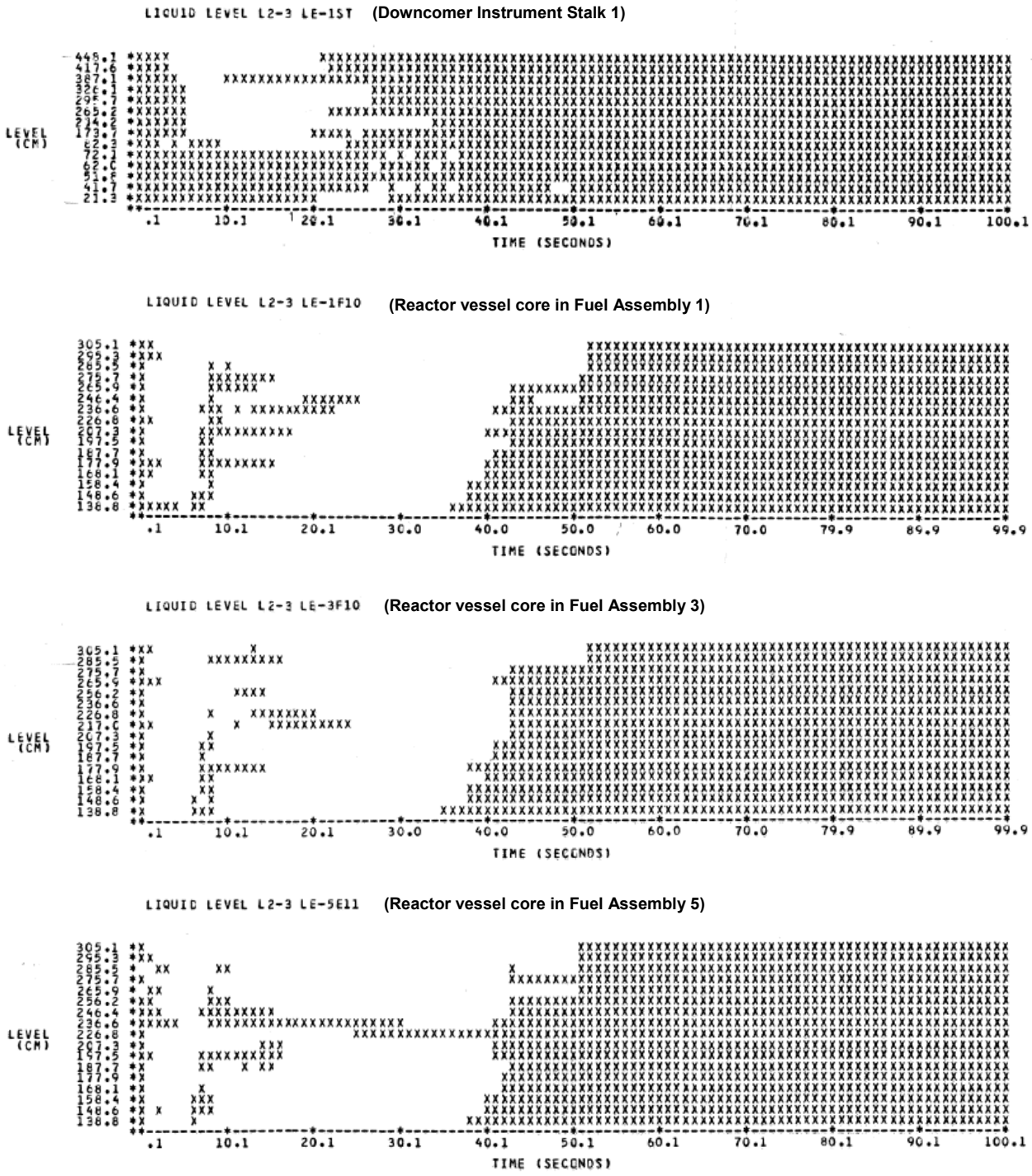

Figure 22-31c Measured Liquid Levels in Downcomer and Core Regions, Test L2-3

a,c

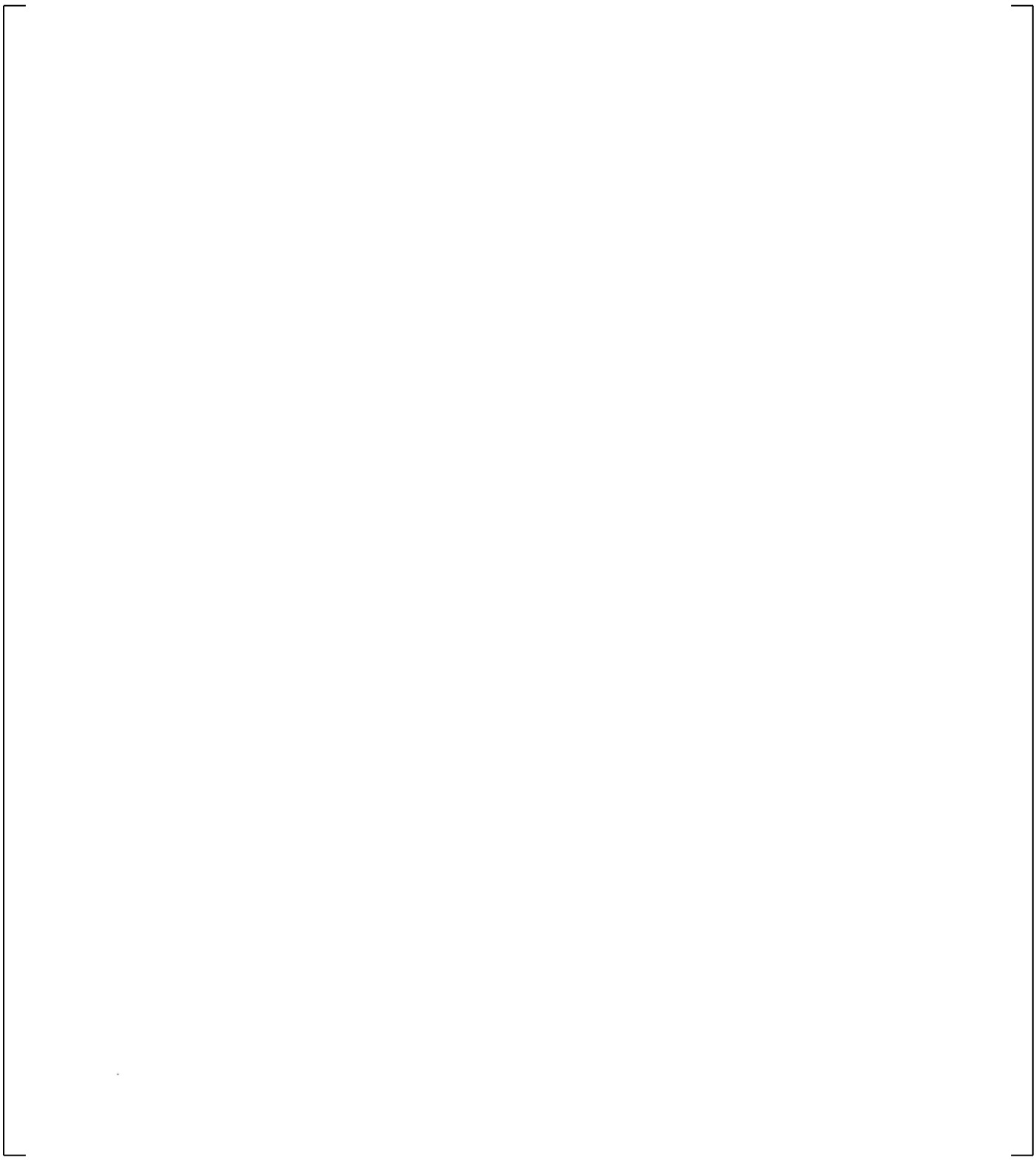

Figure 22-31d Predicted Liquid Levels in Downcomer and Vessel Core Regions, Test L2-3

a,c

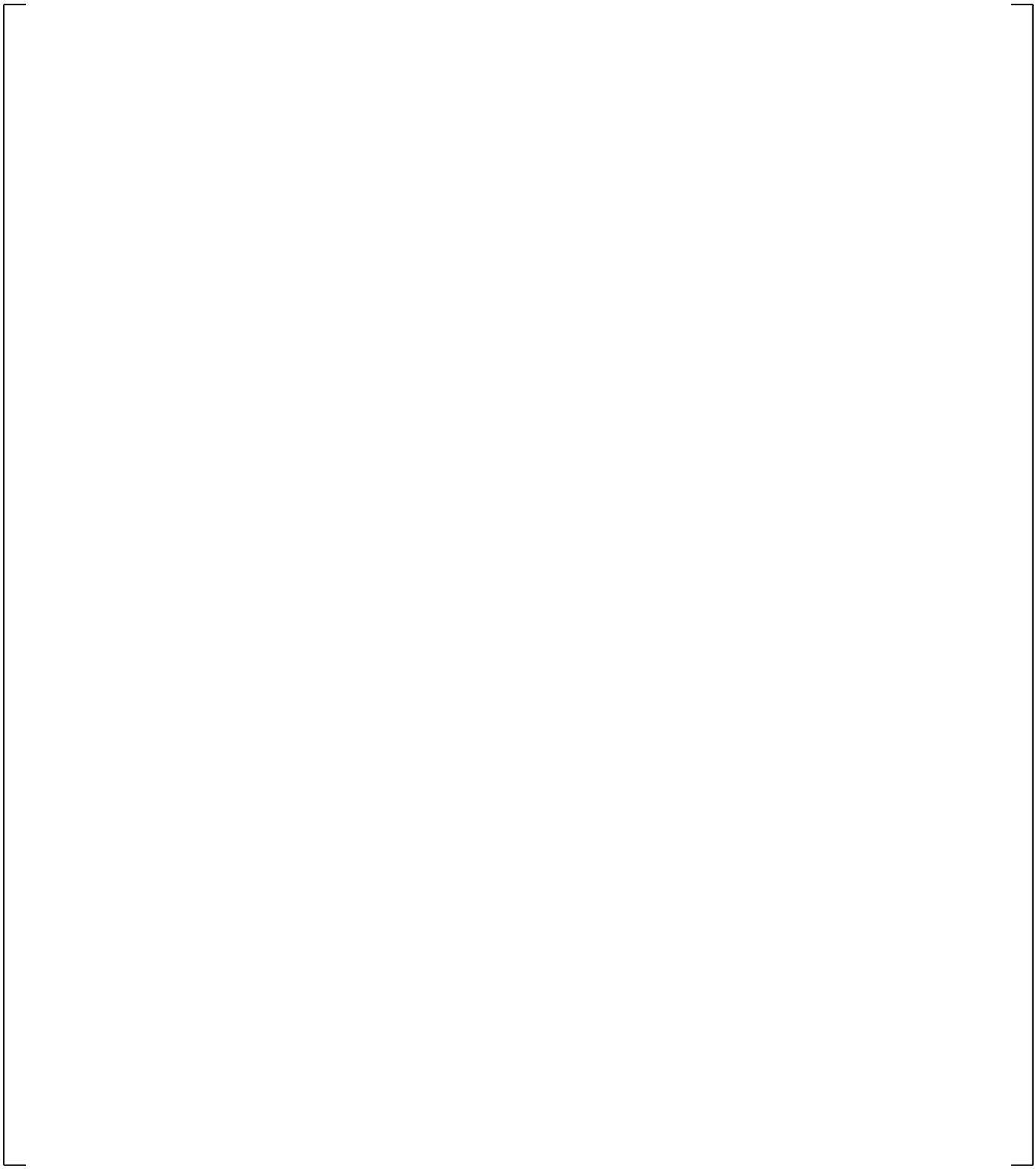

Figure 22-31e Predicted and Measured Liquid Levels in Vessel Core Regions, Test L2-3

a,c

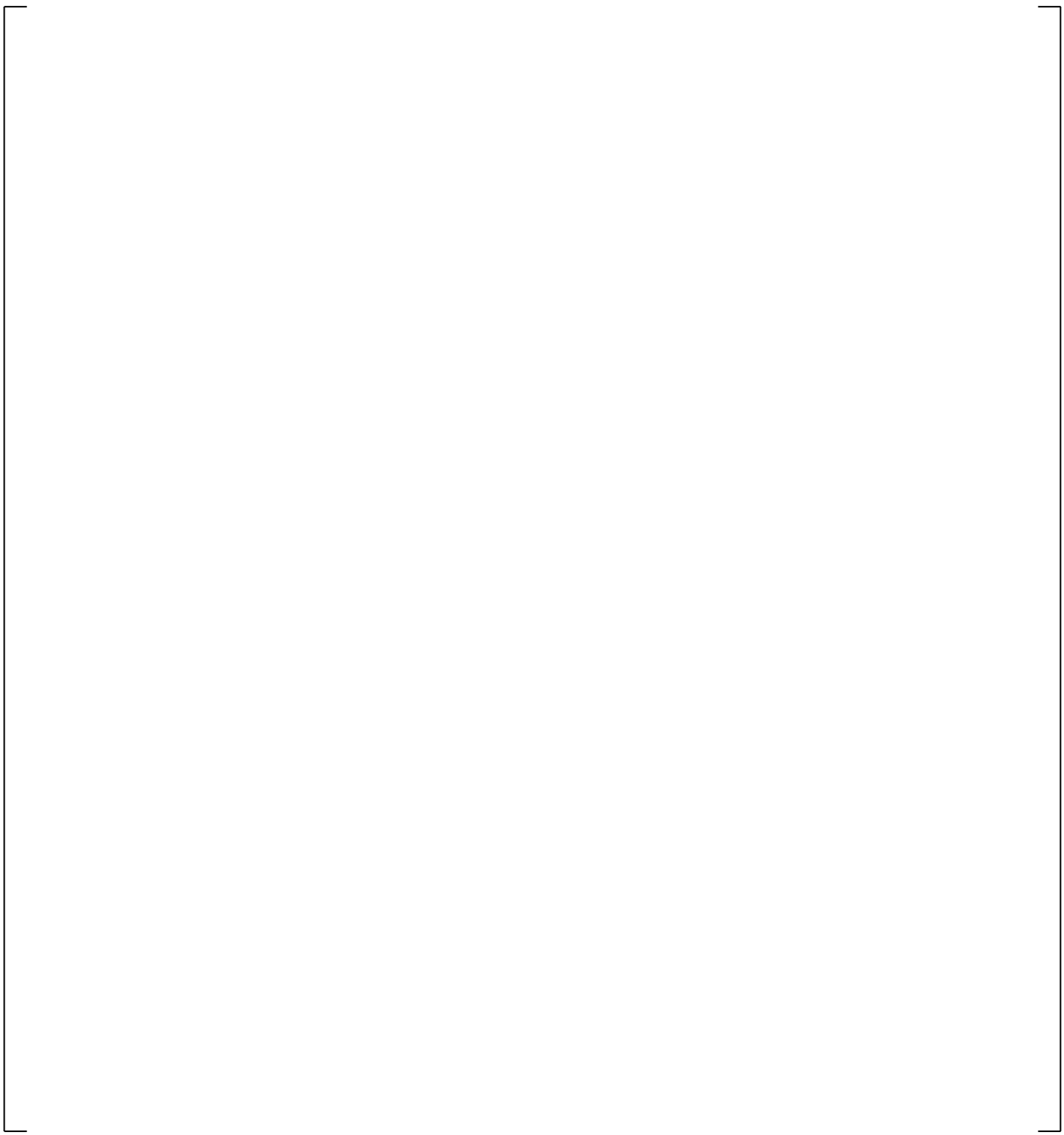

Figure 22-32a Predicted (Component 840) Accumulator Volumetric Flow Rate and Void Fraction[1], Test L2-5

1. Measured data are not available from test report (Bayless and Divine, 1982).

a,c

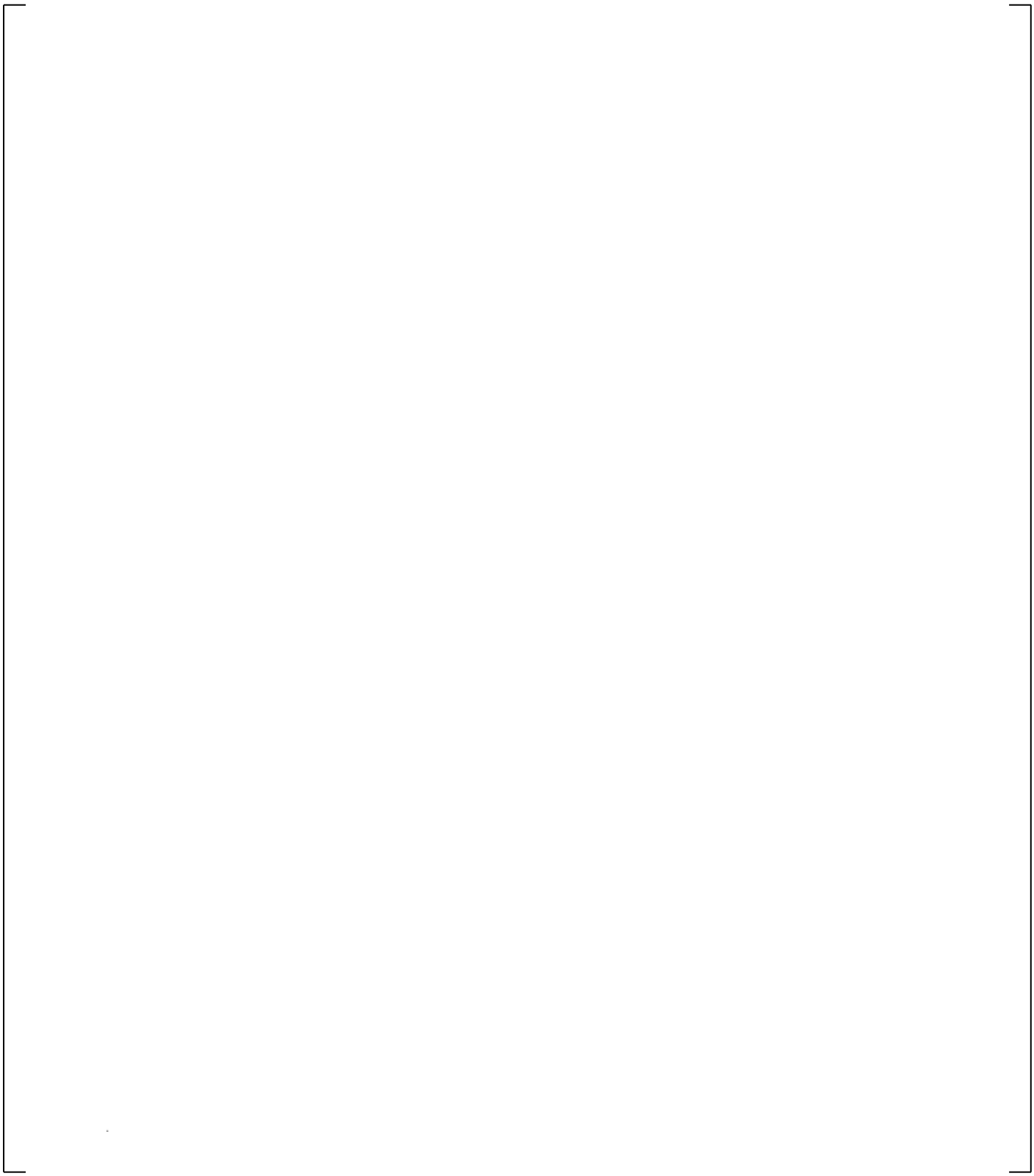

Figure 22-32b Predicted (Component 850) and Measured Accumulator Water Level, Test L2-5

(Downcomer Instrument Stalk 1)

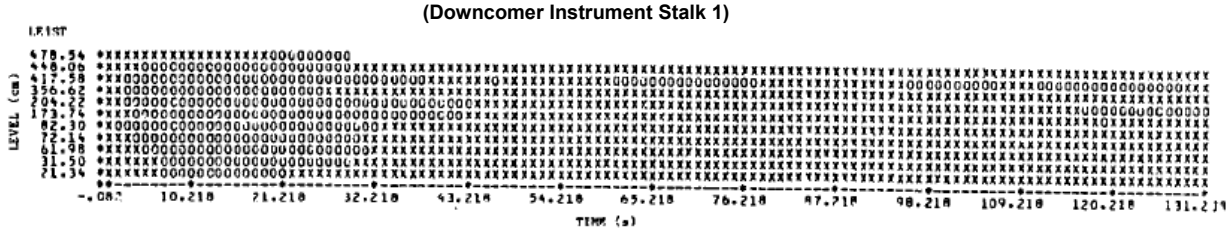

(Reactor vessel core in Fuel Assembly 3)

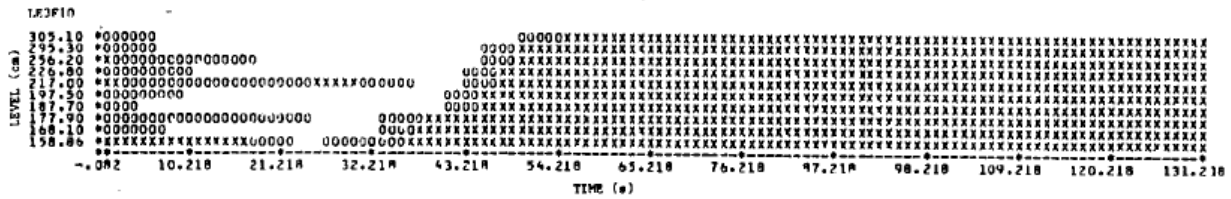

(Reactor vessel core in Fuel Assembly 5)

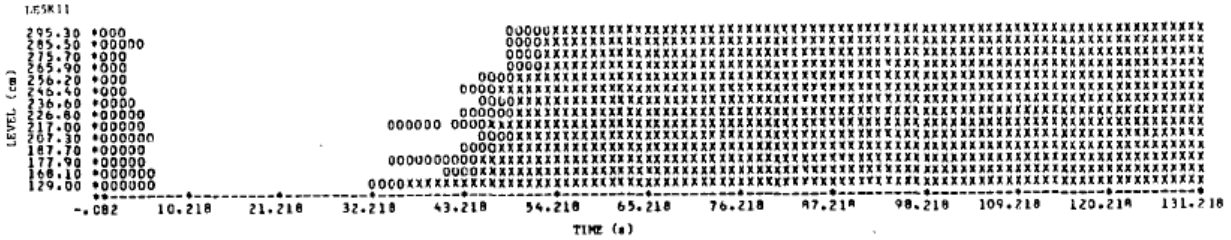

Figure 22-32c Measured Liquid Levels in Downcomer and Core Regions, Test L2-5

a,c

Figure 22-32d Predicted Liquid Levels in Downcomer and Vessel Core Regions, Test L2-5

a,c

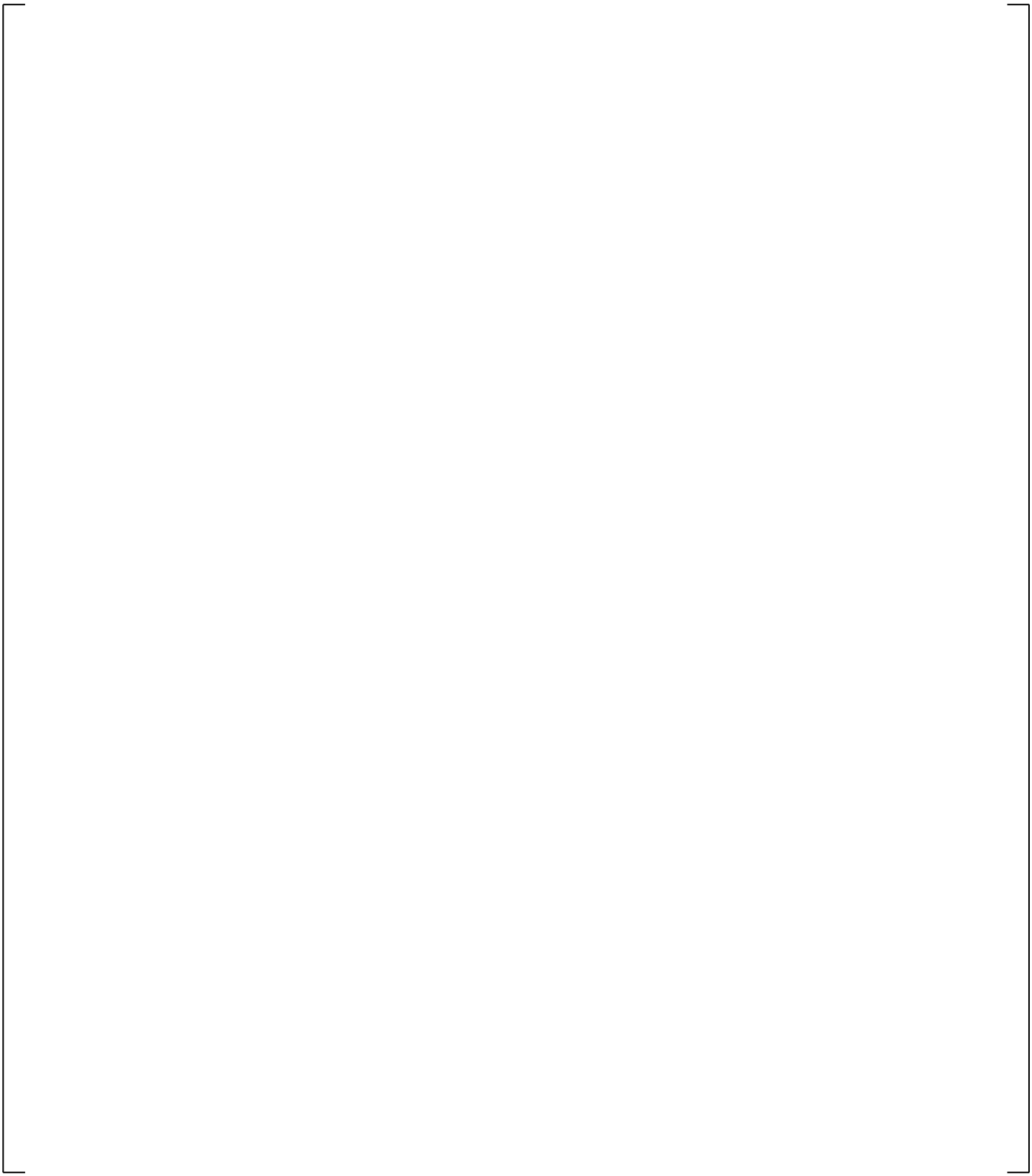

Figure 22-32e Predicted and Measured Liquid Levels in Vessel Core Regions, Test L2-5

a,c

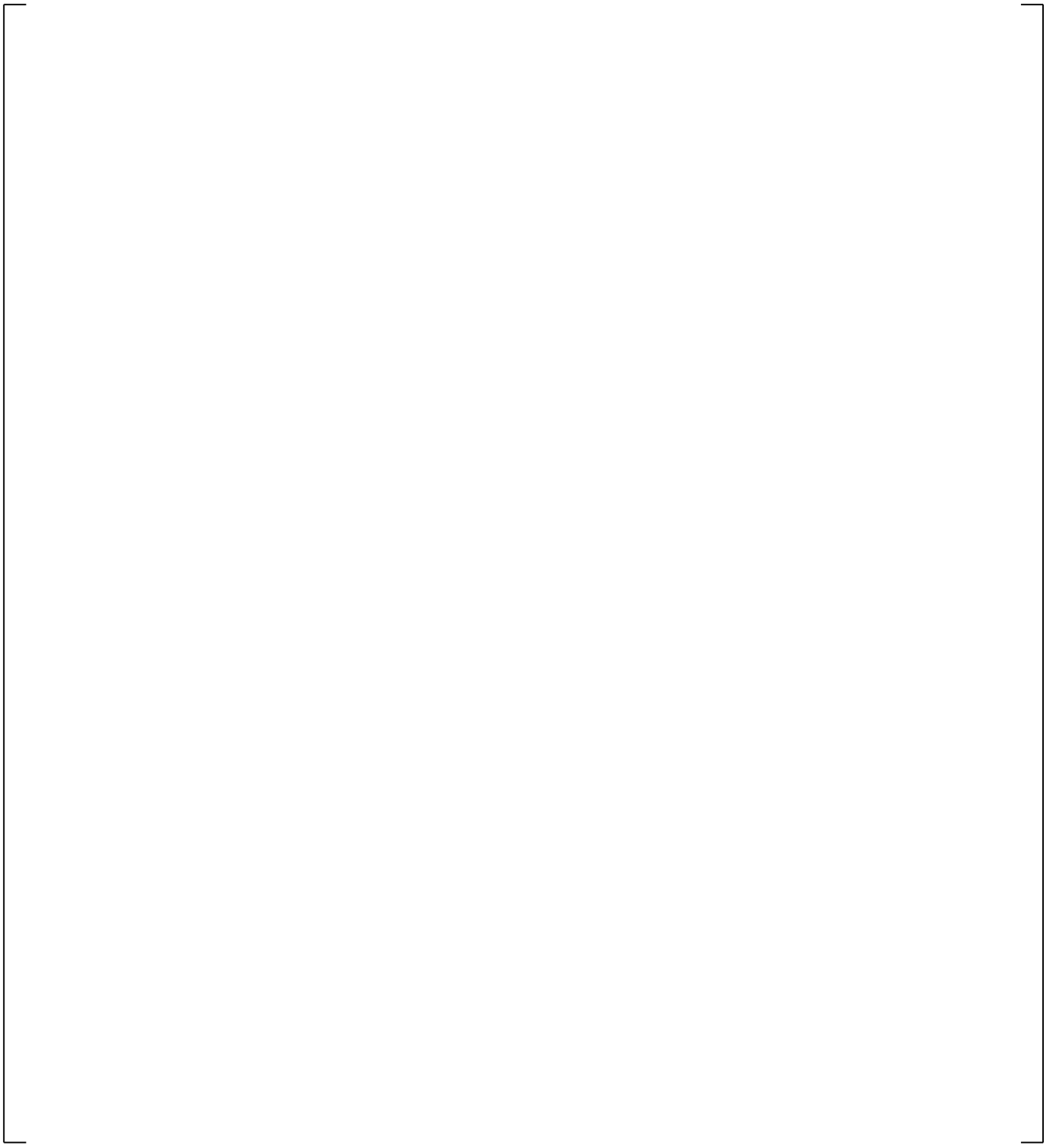

Figure 22-33a Predicted (Component 840) and Measured (FT-P120-36-1) Volumetric Flow Rate and Predicted (Component 840) Void Fraction from Accumulator, Test LB-1

a,c

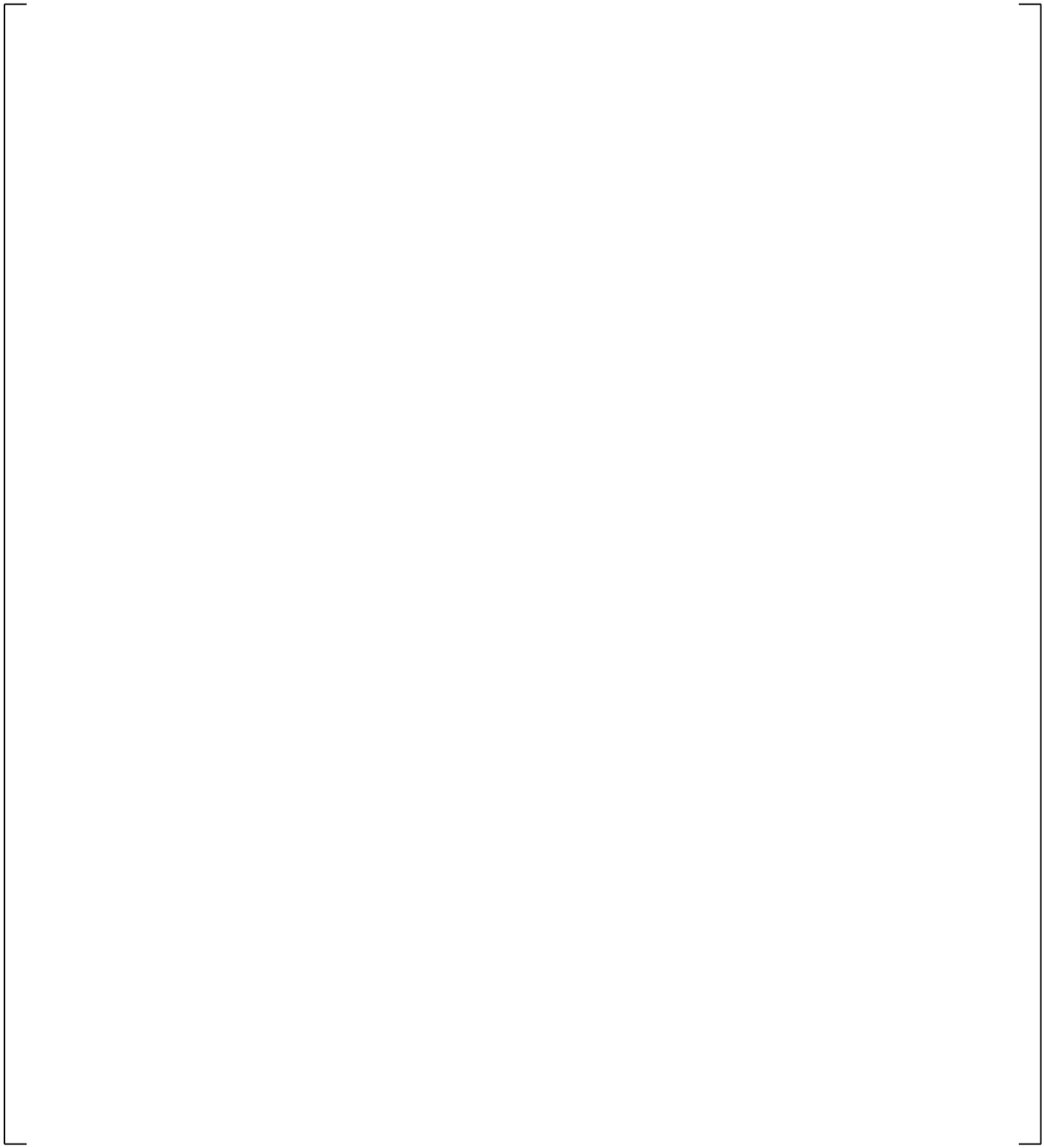

Figure 22-33b Predicted (Component 850) and Measured (LIT-P120-044, LIT-P120-087) Accumulator Water Level, Test LB-1

a,c

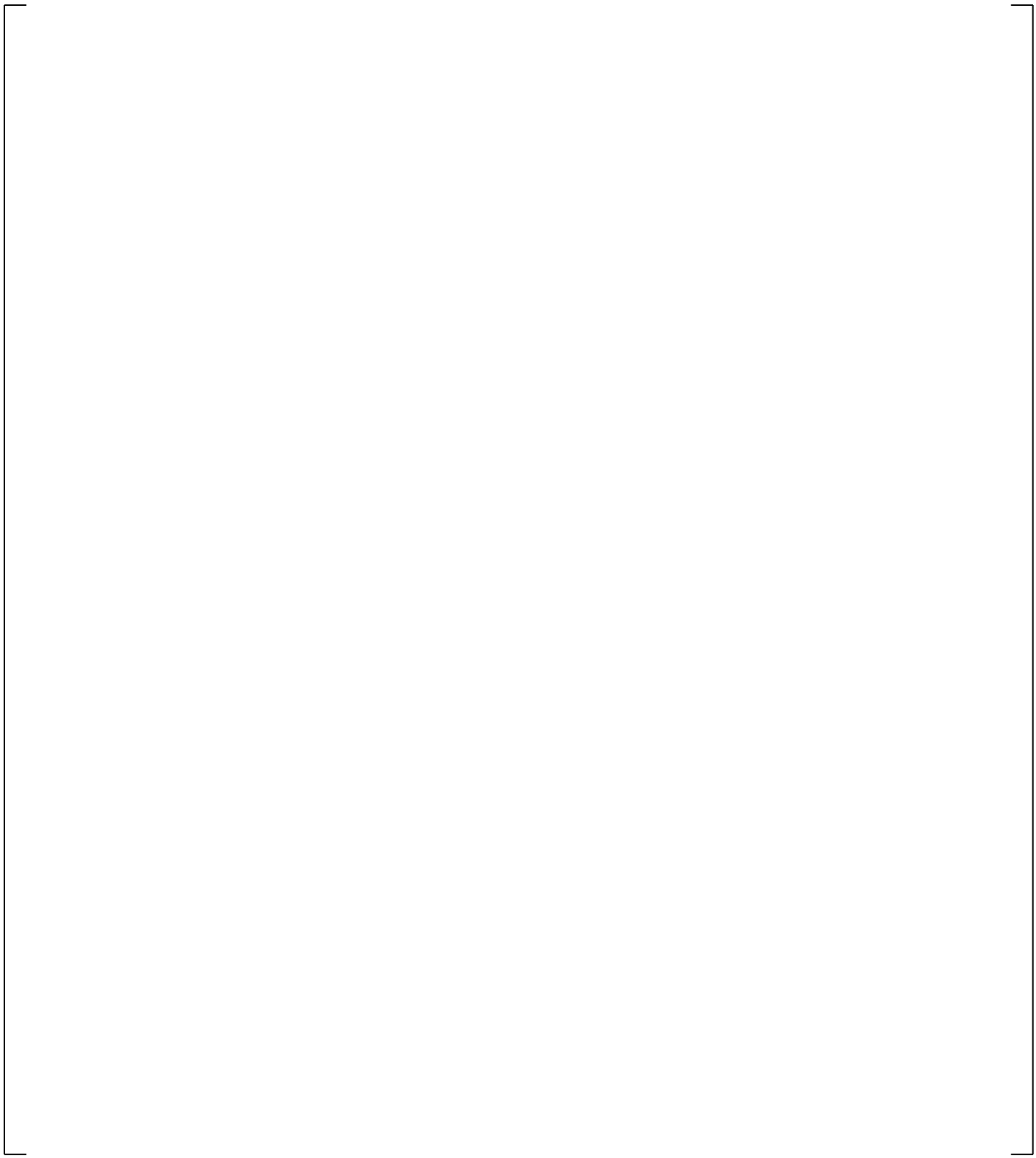

Figure 22-33d Predicted Liquid Levels in Downcomer and Vessel Core Regions, Test LB-1

a,c

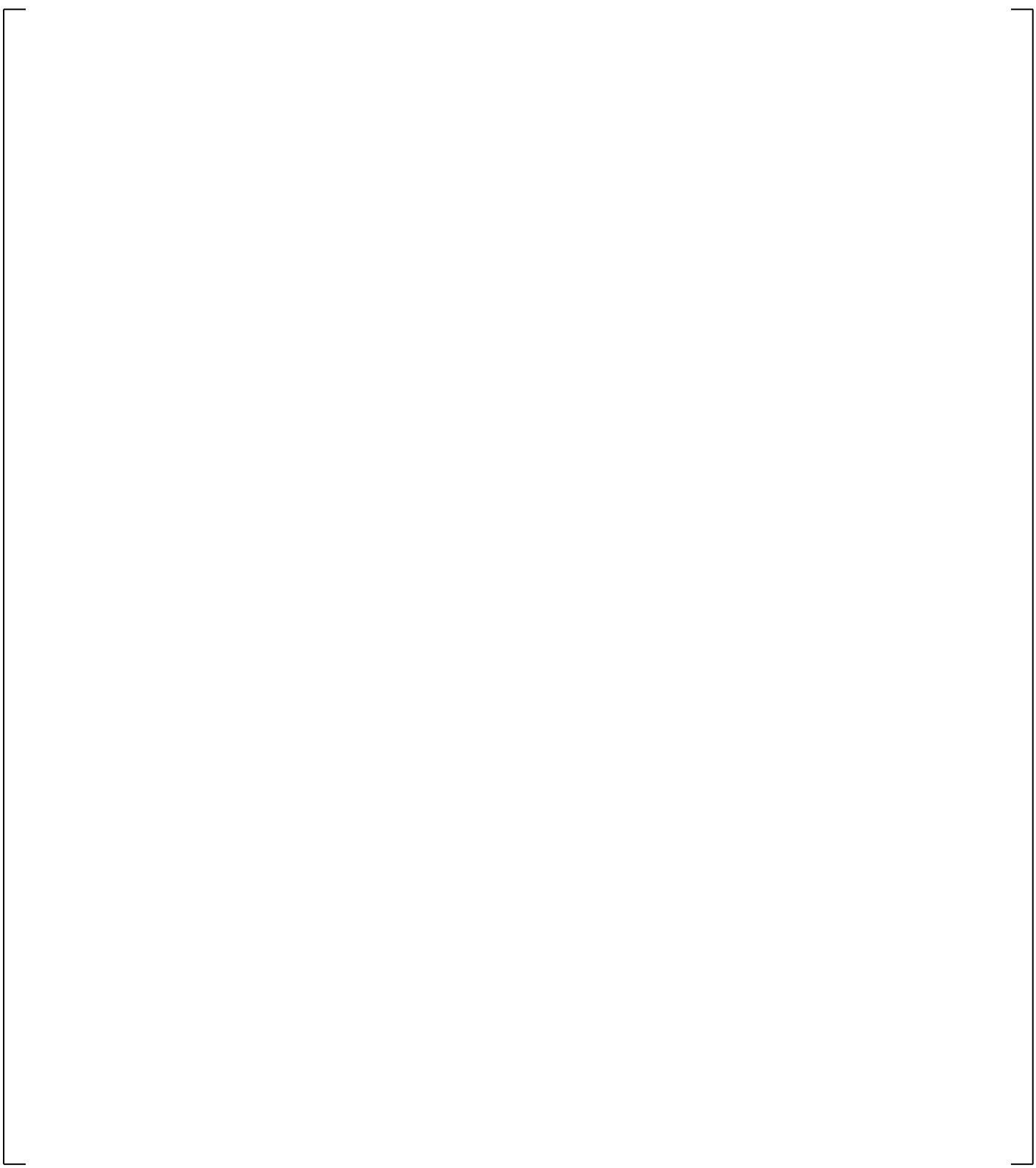

Figure 22-33e Predicted Liquid Level in Vessel Core Regions and Measured Vessel Lower Plenum Fluid Temperature, Test LB-1

a,c

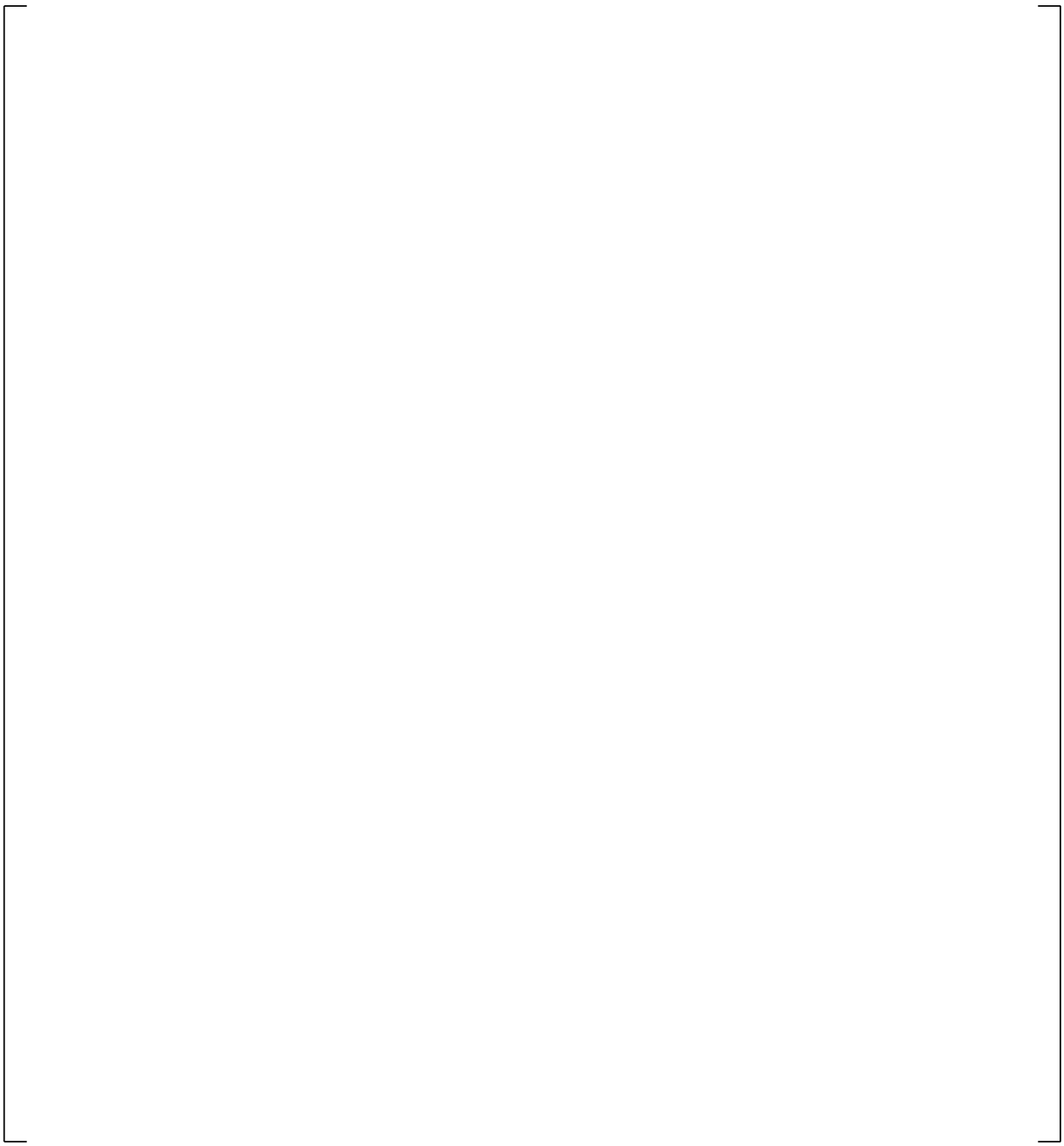

Figure 22-34 Predicted (2.72 ft) and Measured Cladding Temperature in the Hot Channel, Test L2-2

a,c

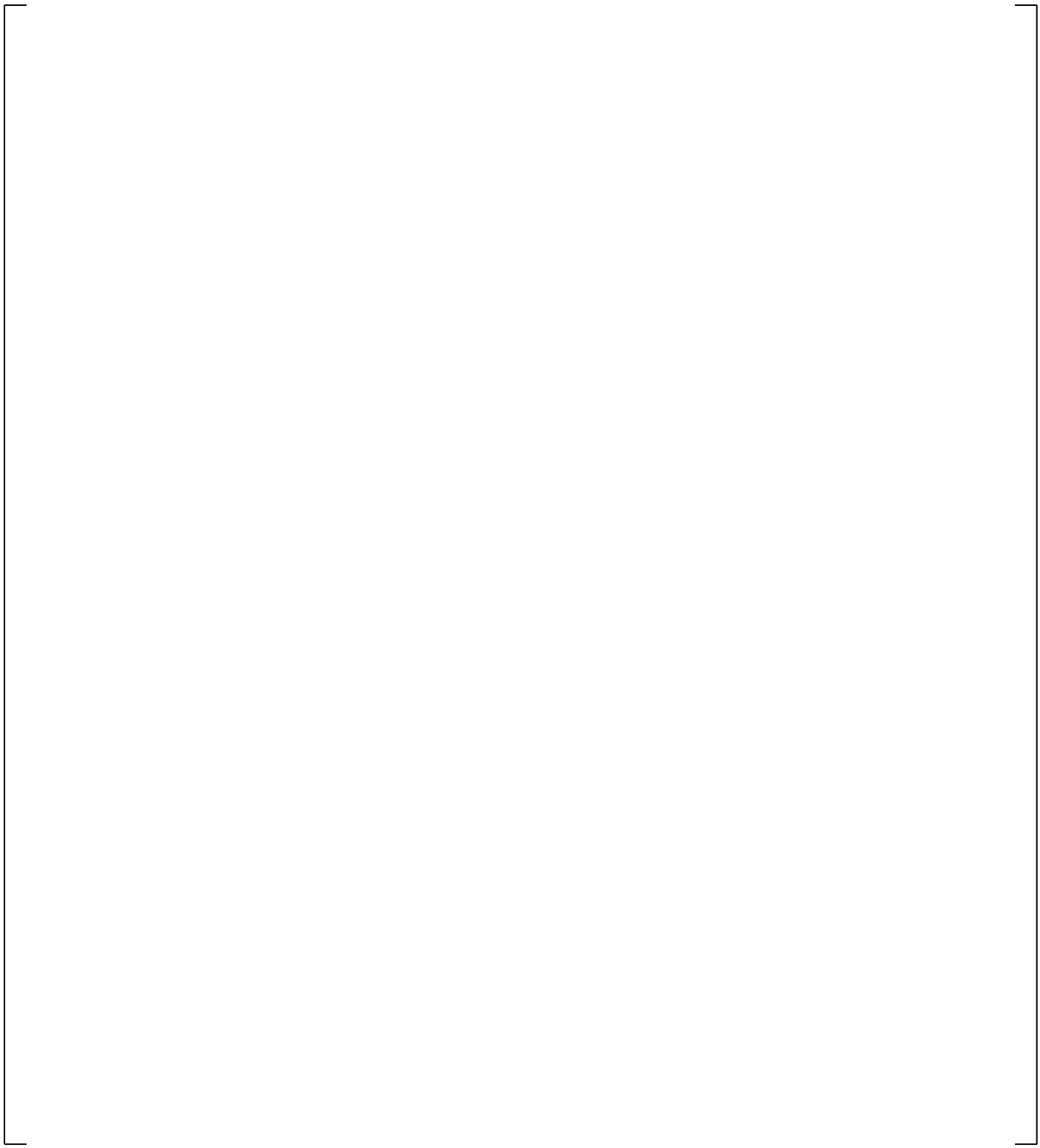

Figure 22-35 Predicted (2.79 ft) and Measured Cladding Temperature in the Hot Channel, Test L2-3

a,c

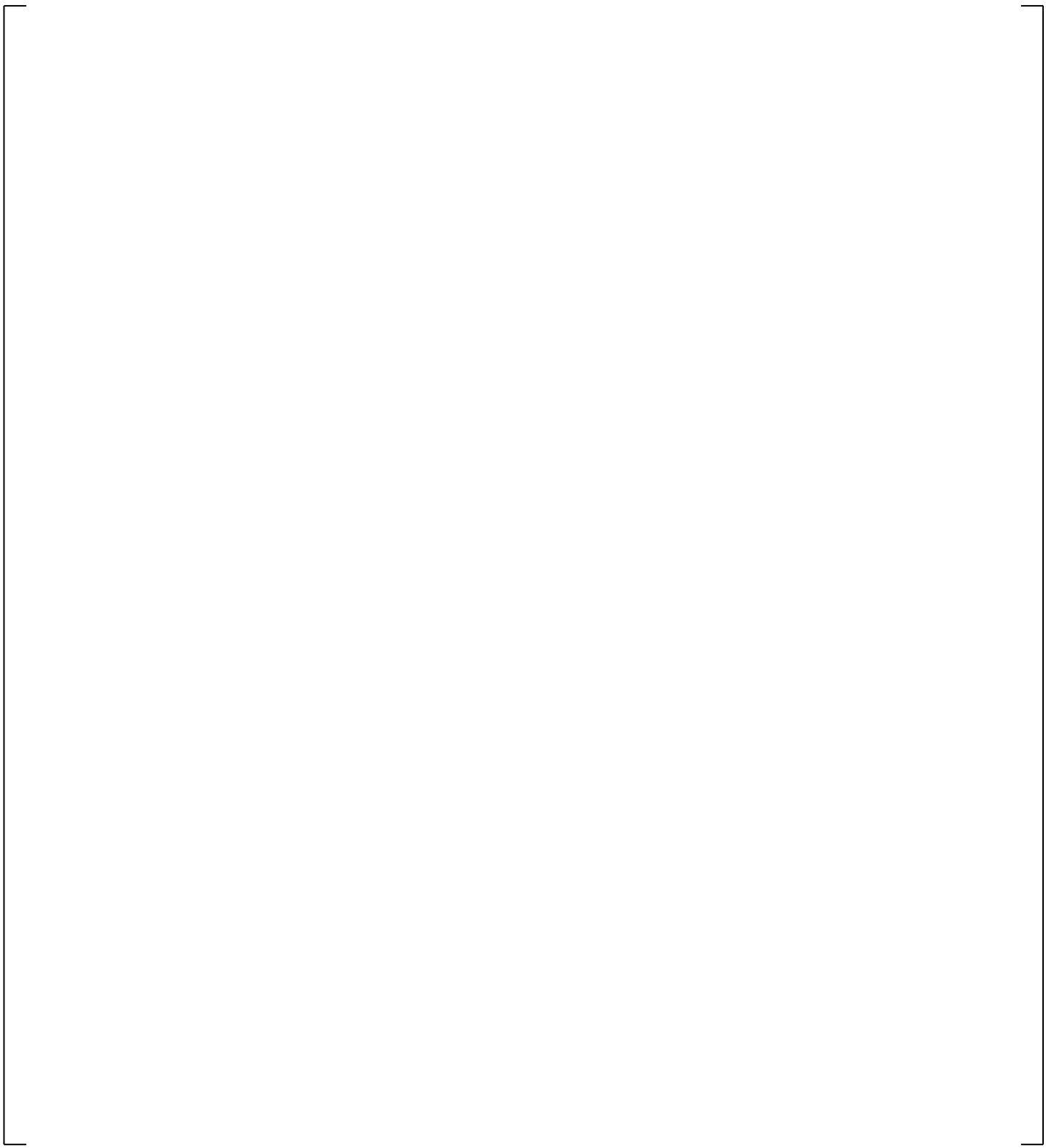

Figure 22-36 Predicted (1.54 ft) and Measured Cladding Temperature in the Hot Channel, Test L2-5

a,c

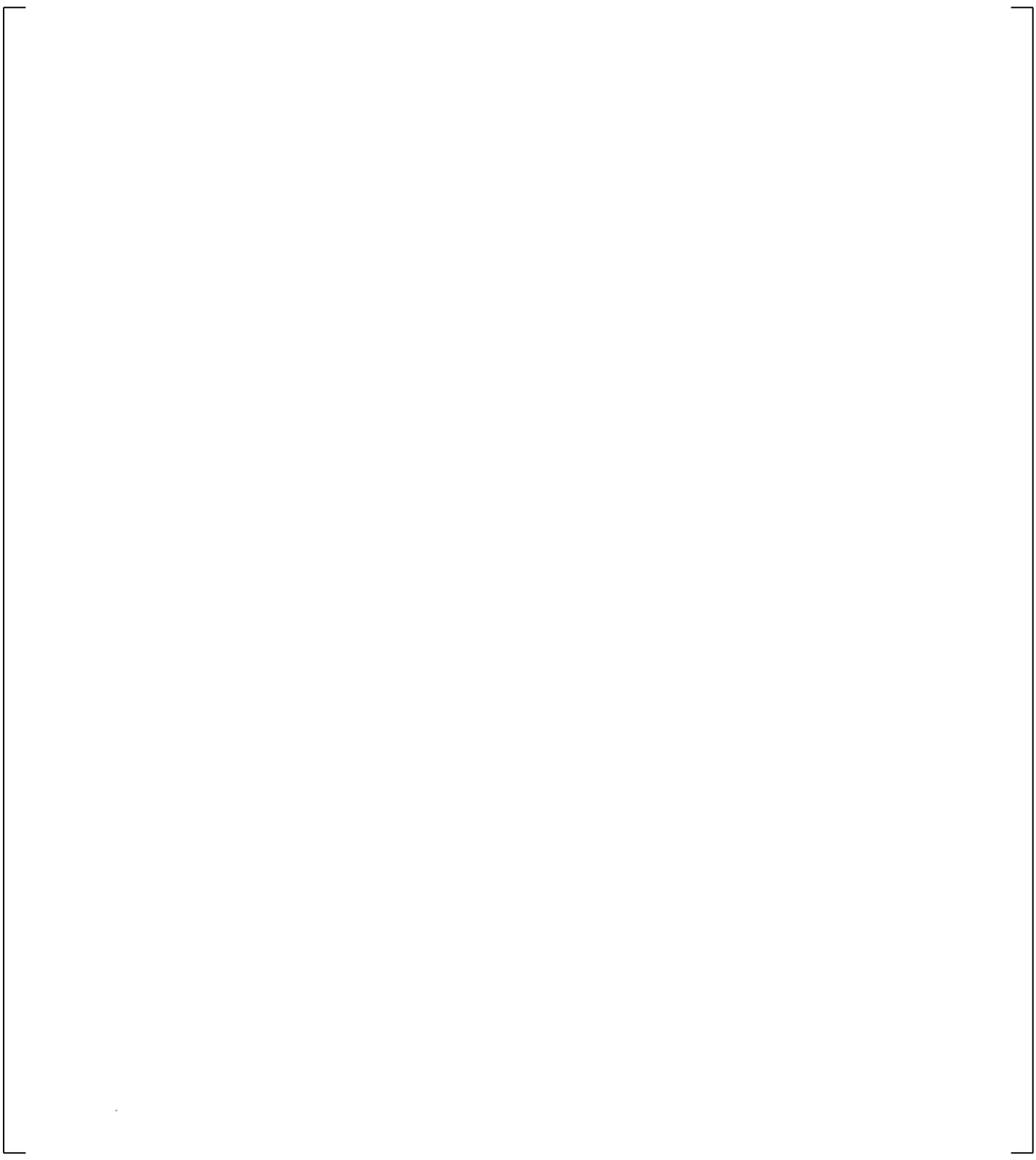

Figure 22-37 Predicted (2.06 and 2.28 ft) and Measured Cladding Temperature in Hot Channel, Test LB-1

a,c

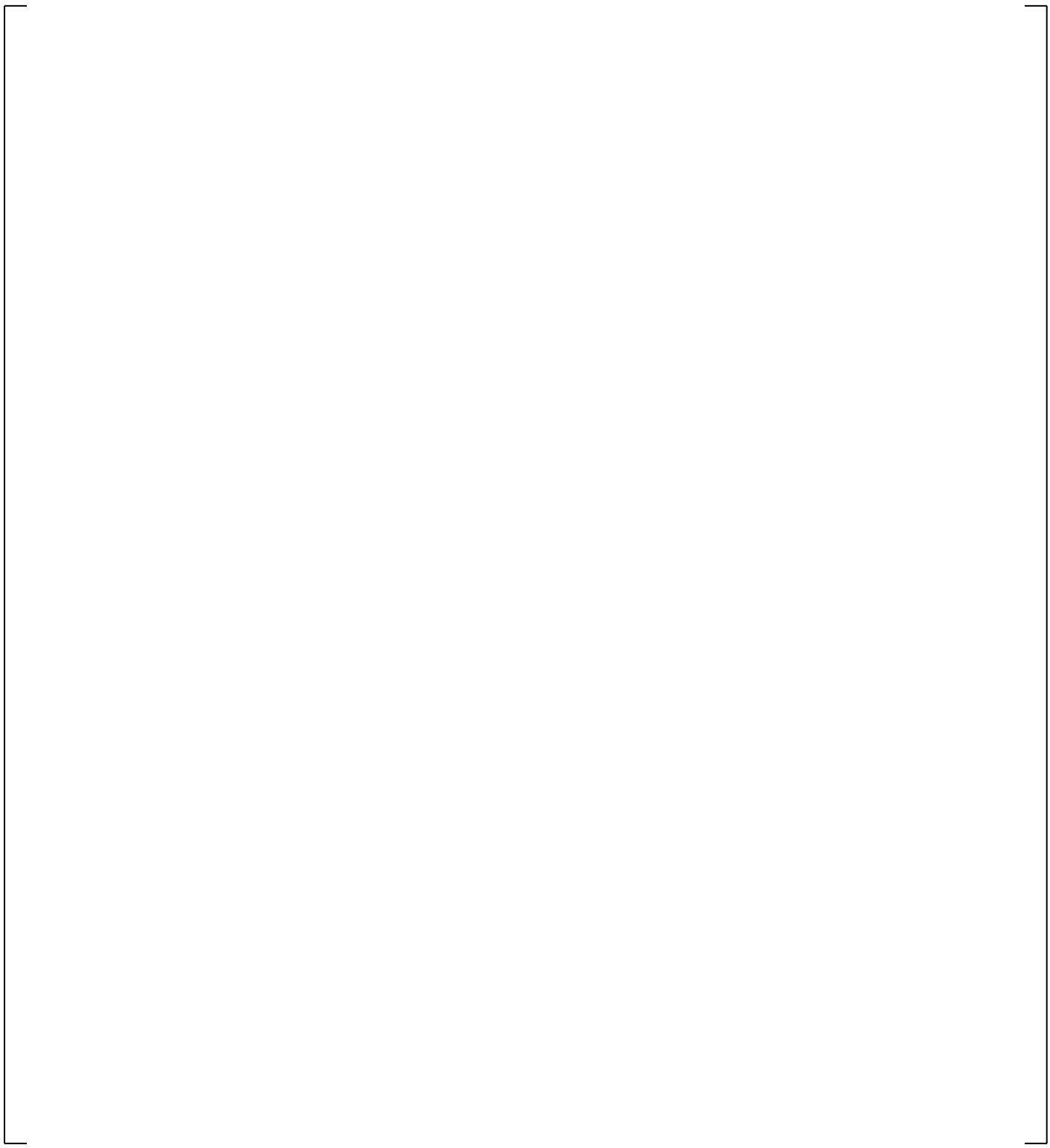

Figure 22-38 Impact of Critical Flow Model Uncertainties on PCS Pressure, Test L2-3

a,c

Figure 22-39 Impact of Critical Flow Model Uncertainties on Cold Leg Break Flow, Test L2-3

a,c

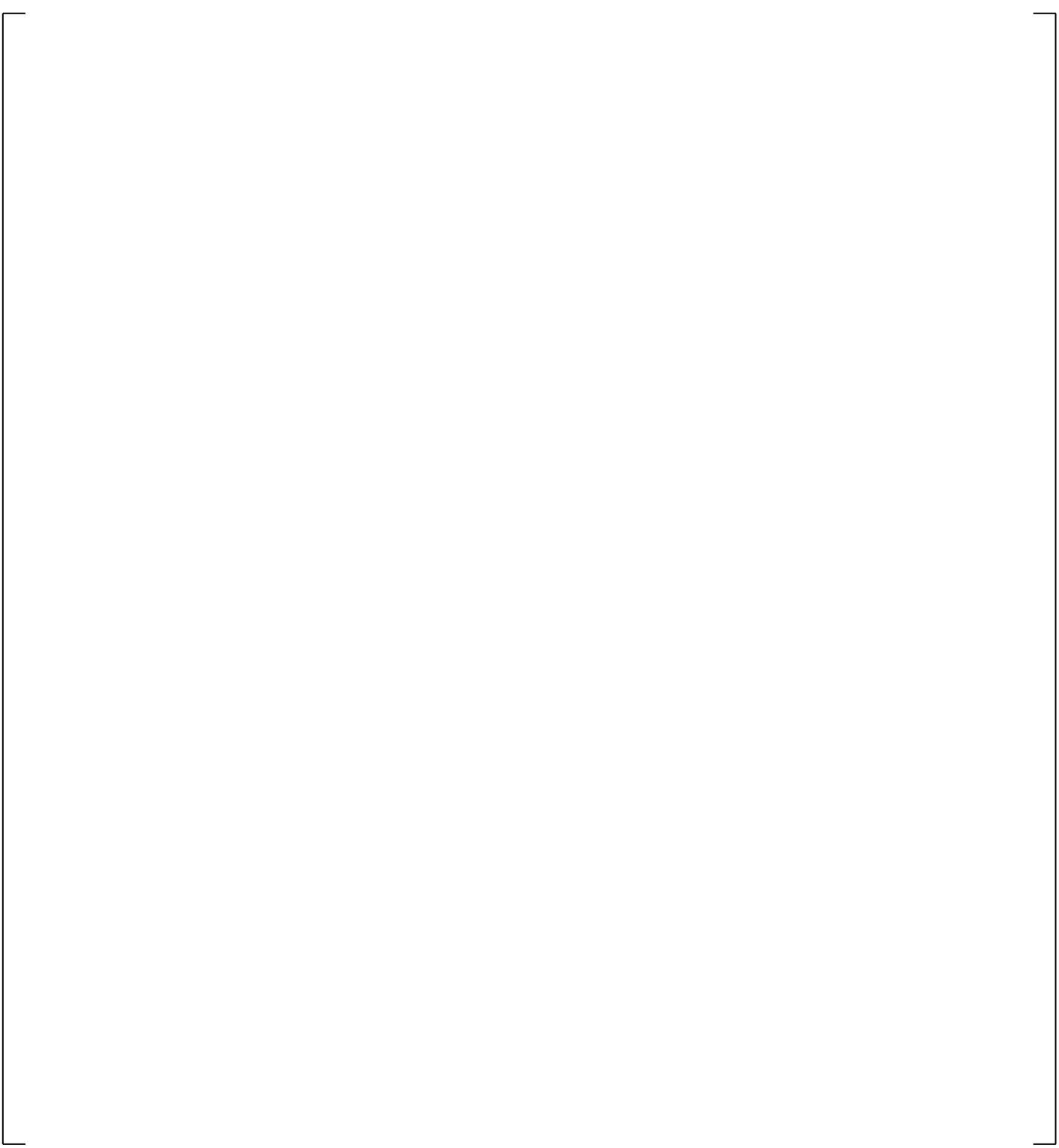

Figure 22-40 Impact of Critical Flow Model Uncertainties on Cladding Temperature, Test L2-3

a,c

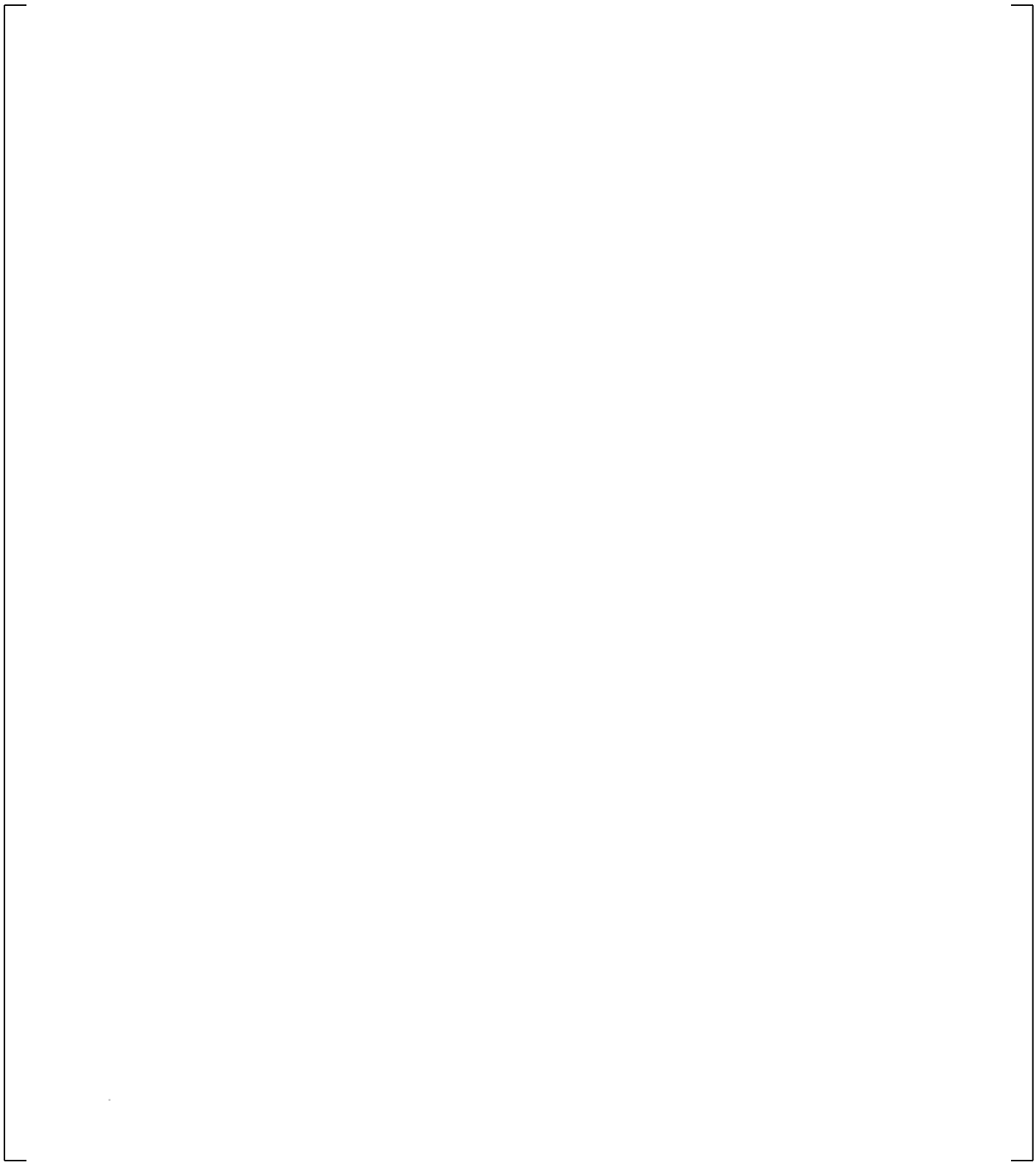

Figure 22-41 Predicted (Component 810) and Measured Fluid Temperatures in Intact Cold Leg, Test L2-5

a,c

Figure 22-42 Predicted and Measured Inlet and Outlet Fluid Temperature in Intact Loop Steam Generator, Test L2-5

a,c

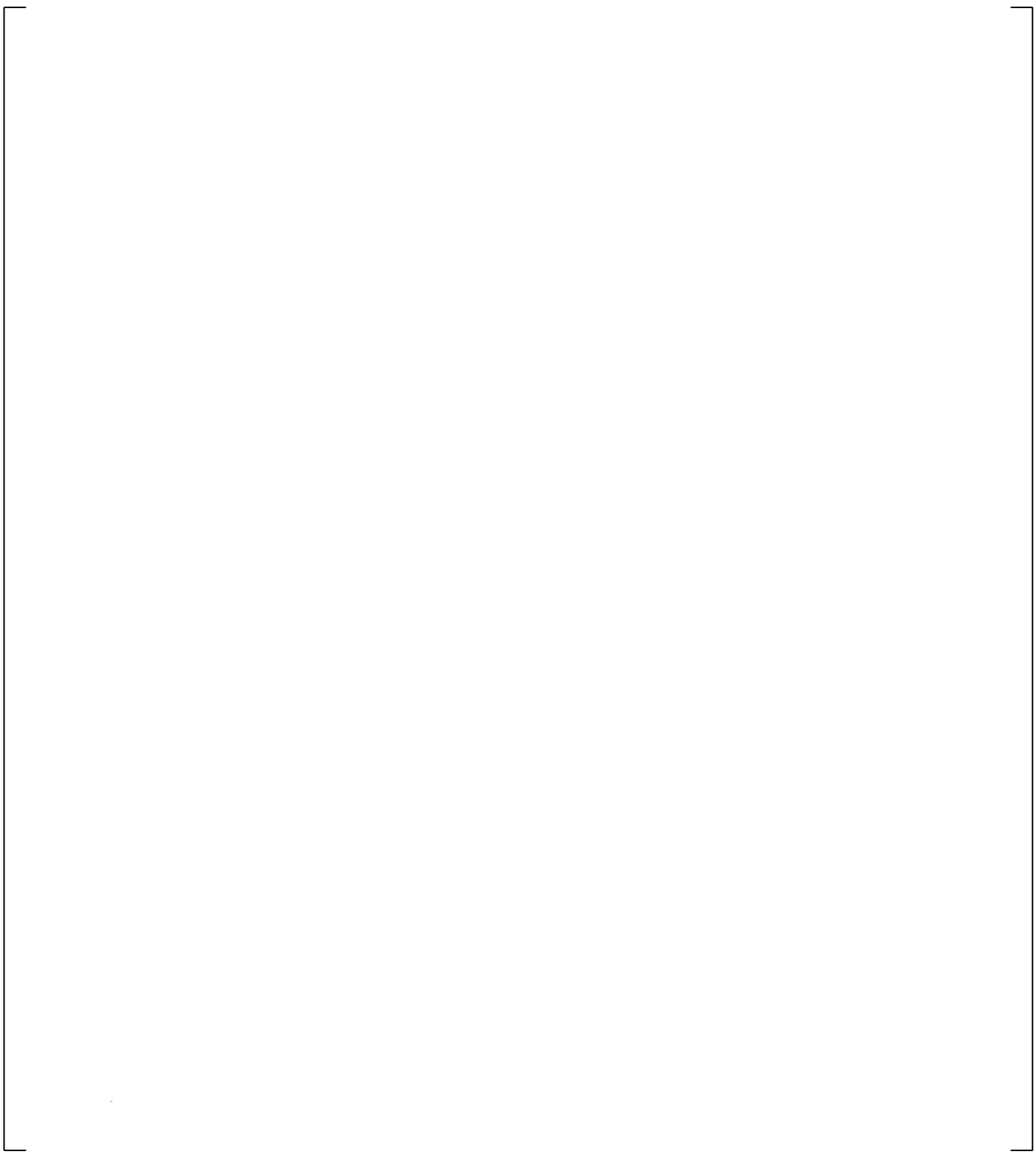

Figure 22-43 Predicted (Component 600) and Measured Pressure Difference Across Intact Loop Pump, Test L2-5

a,c

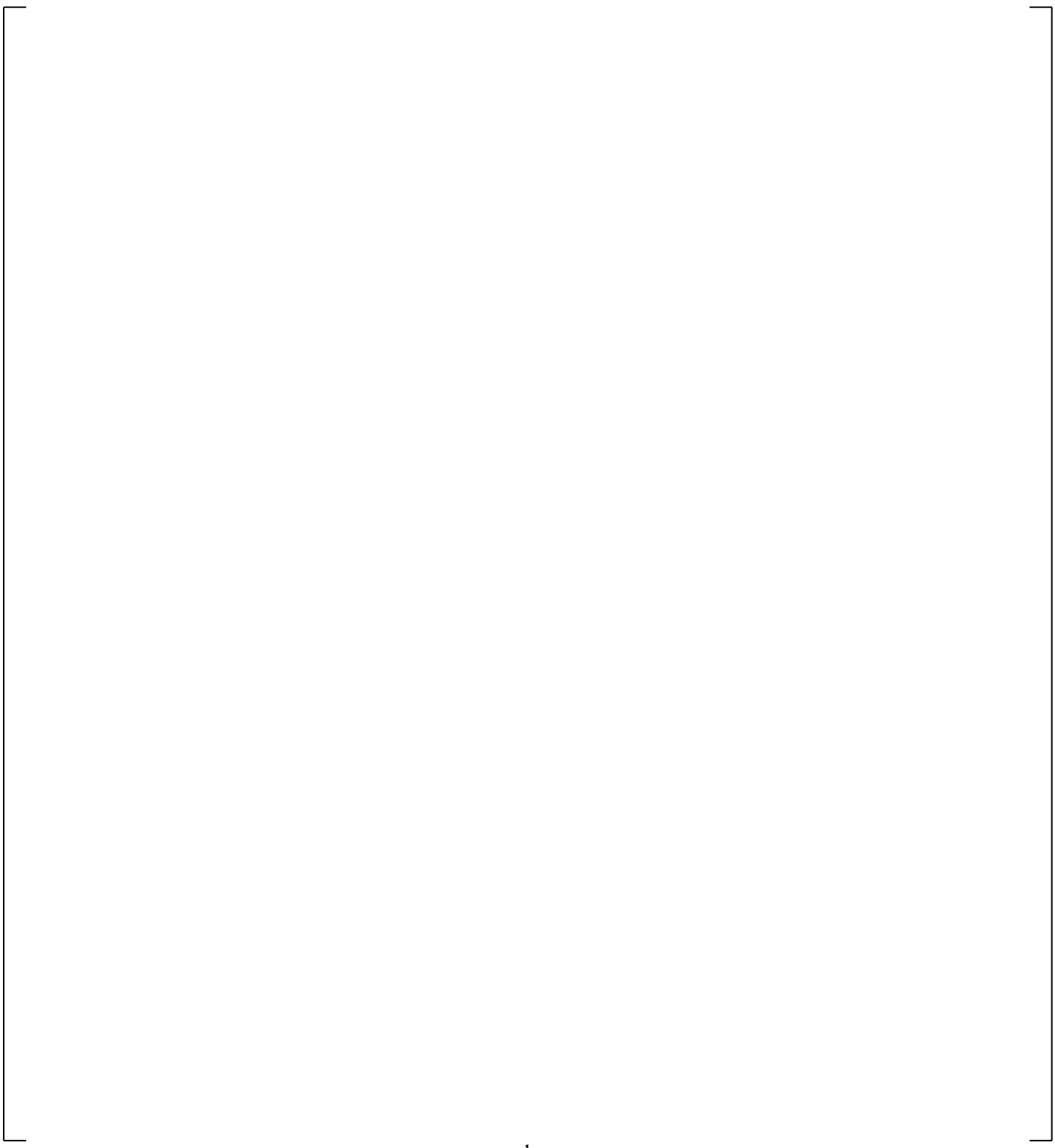

Figure 22-44 Predicted (Rod 1 at 2.18 ft.[1]) and Measured Fuel Temperatures, Test L2-5

1. 2.18 ft. from the bottom of the fuel rod.

a,c

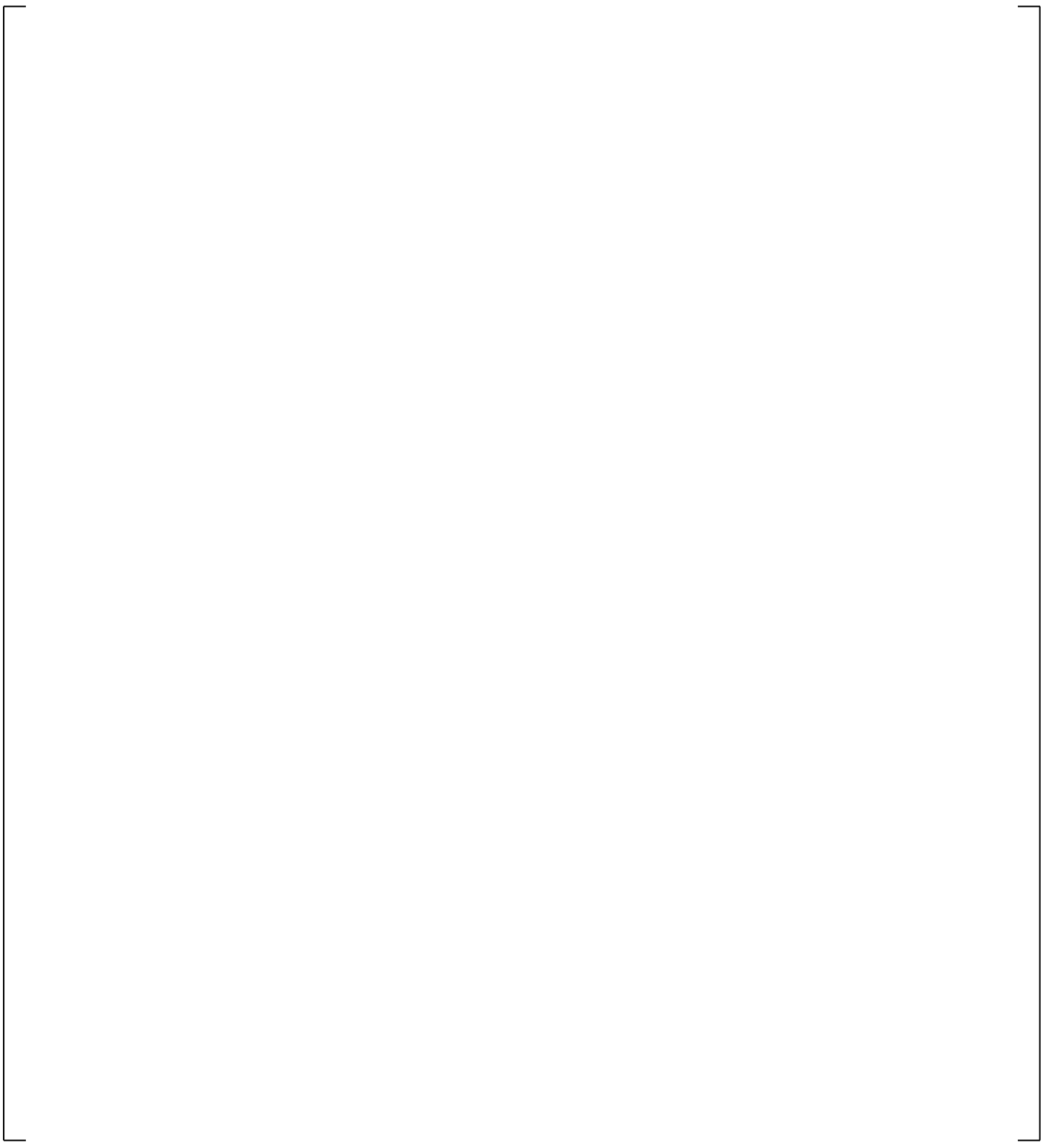

Figure 22-45 Predicted and Measured Core Power, Test L2-5

a,c

Figure 22-46 Predicted and Measured Primary System Pressure, Test L3-1

a,c

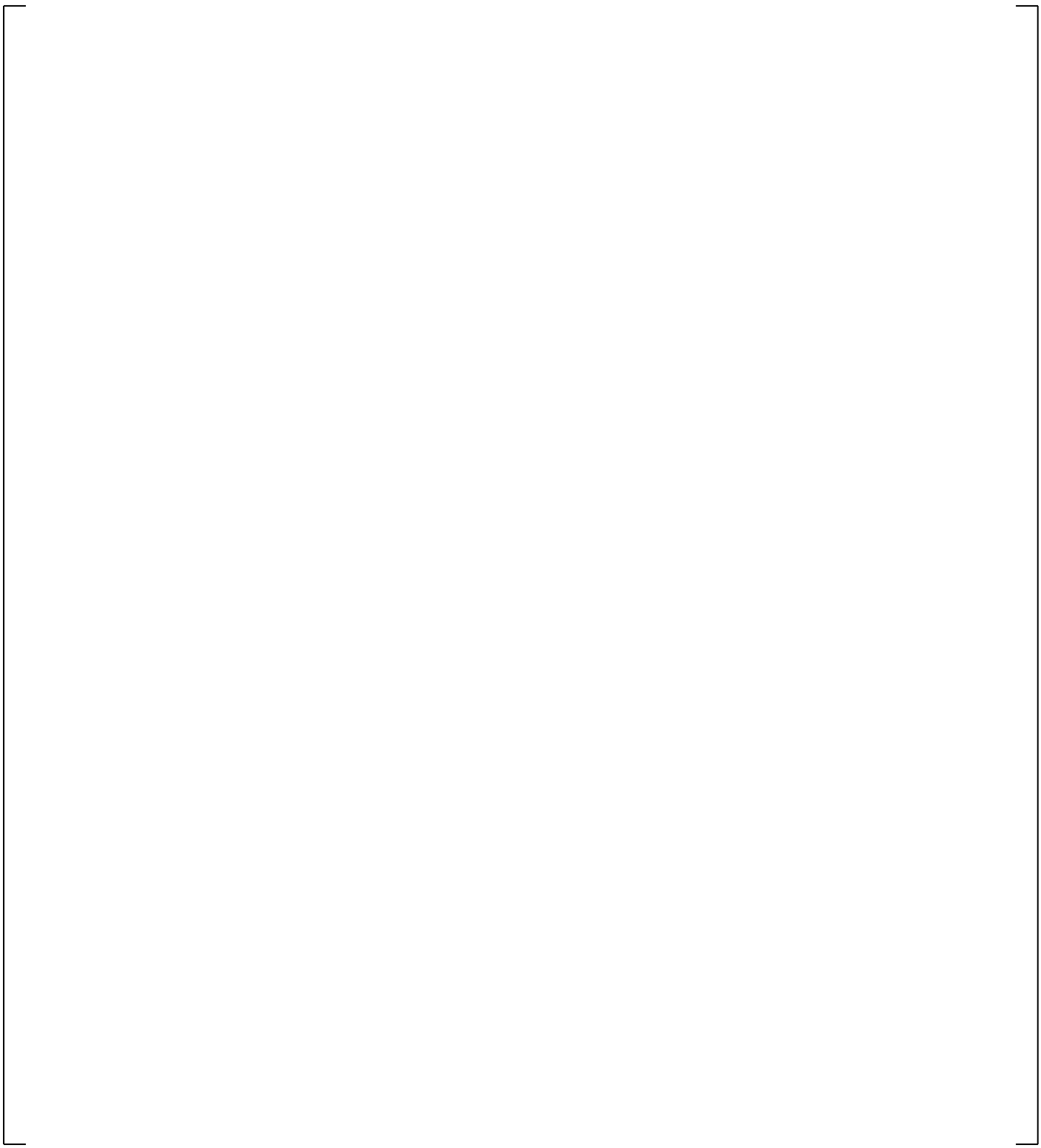

Figure 22-47 Predicted and Measured Steam Generator Secondary Side Pressure, Test L3-1

a,c

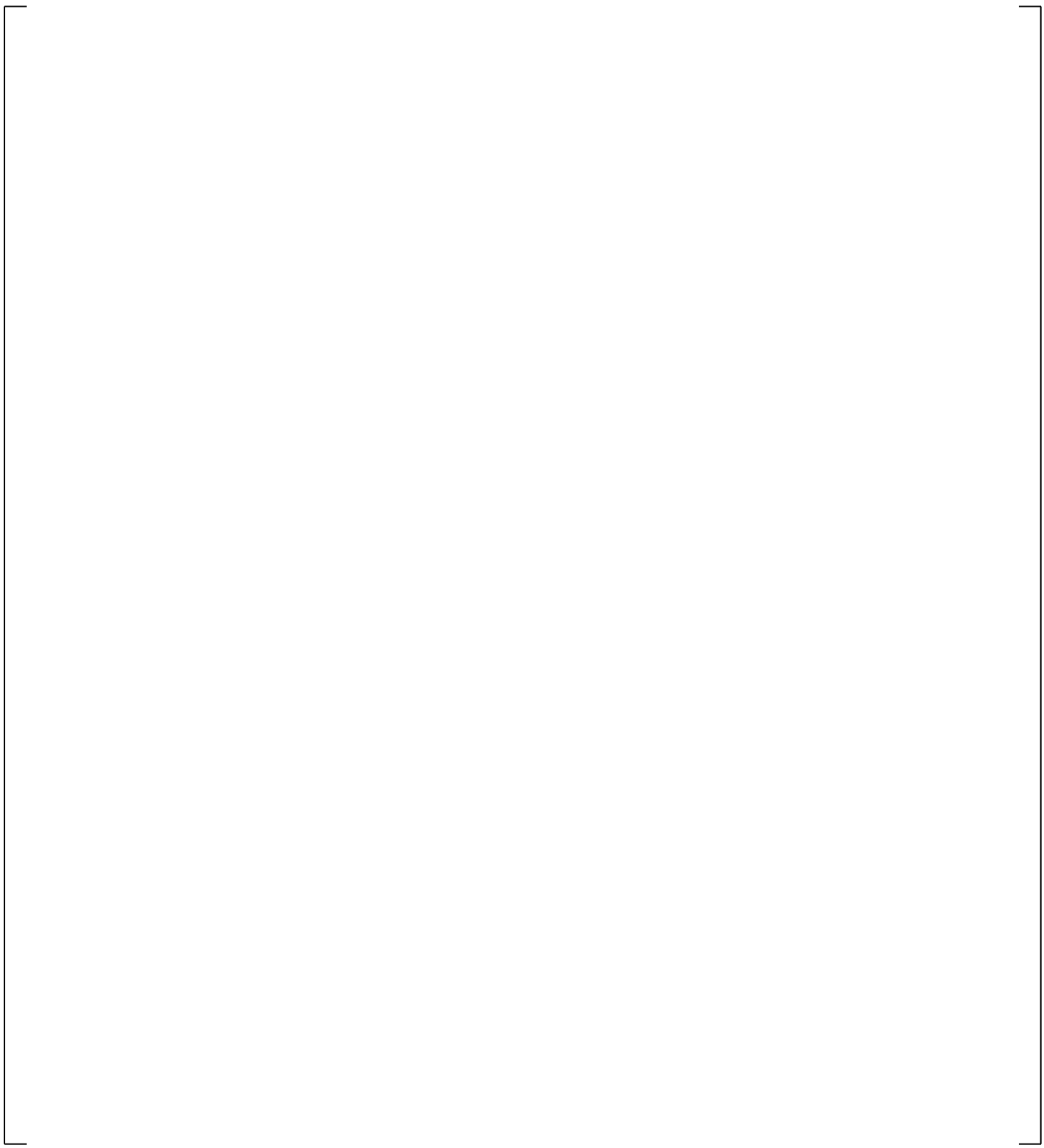

Figure 22-48 Predicted and Measured Cold Leg Break Flow and Void Fraction Before the Break, Test L3-1

a,c

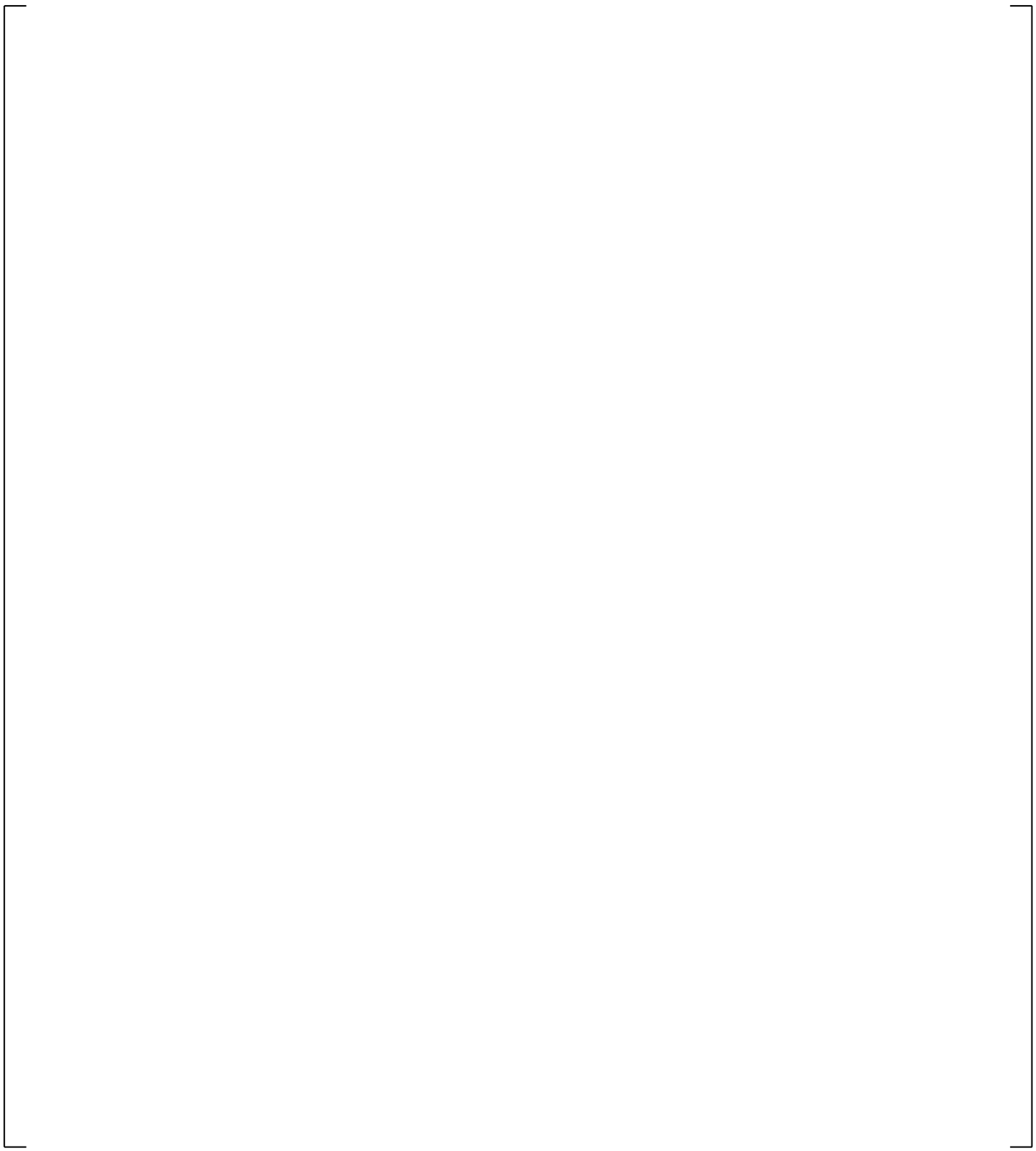

Figure 22-49 Predicted and Measured Accumulator Liquid Level, Test L3-1

a,c

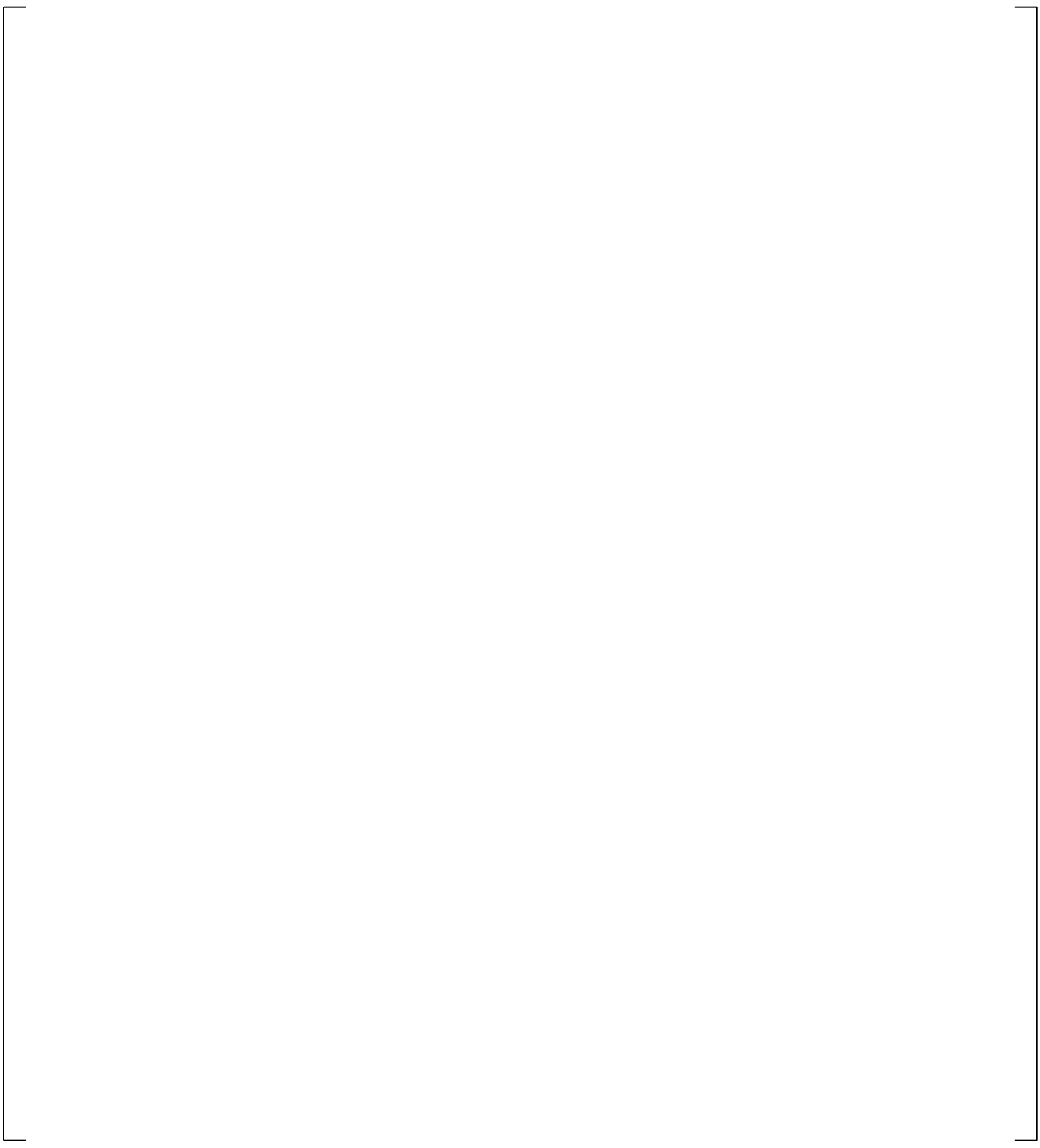

Figure 22-50 Predicted and Measured Accumulator Pressure, Test L3-1

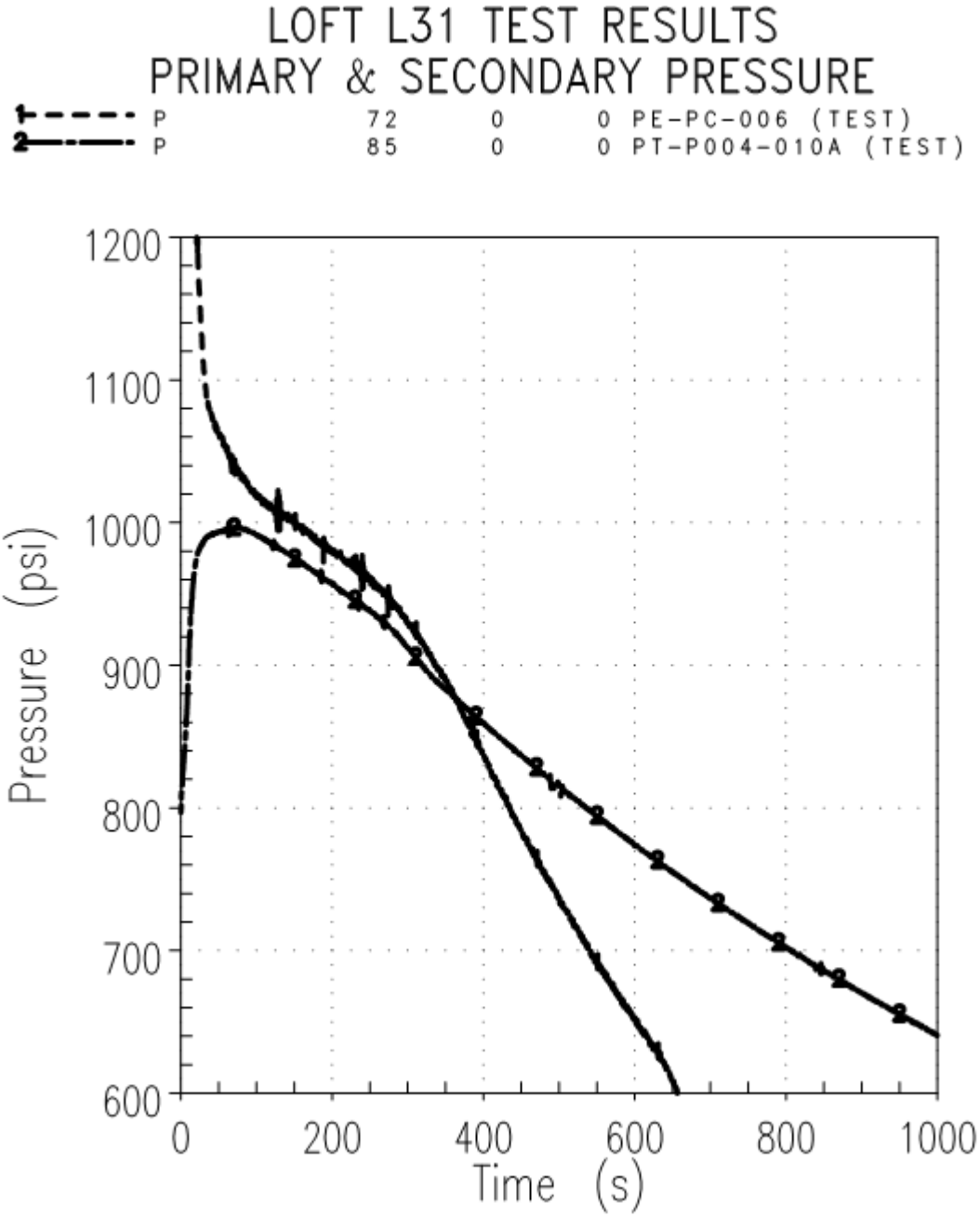

Figure 22-51 Measured Primary and SG Secondary Pressure, Test L3-1

a,c

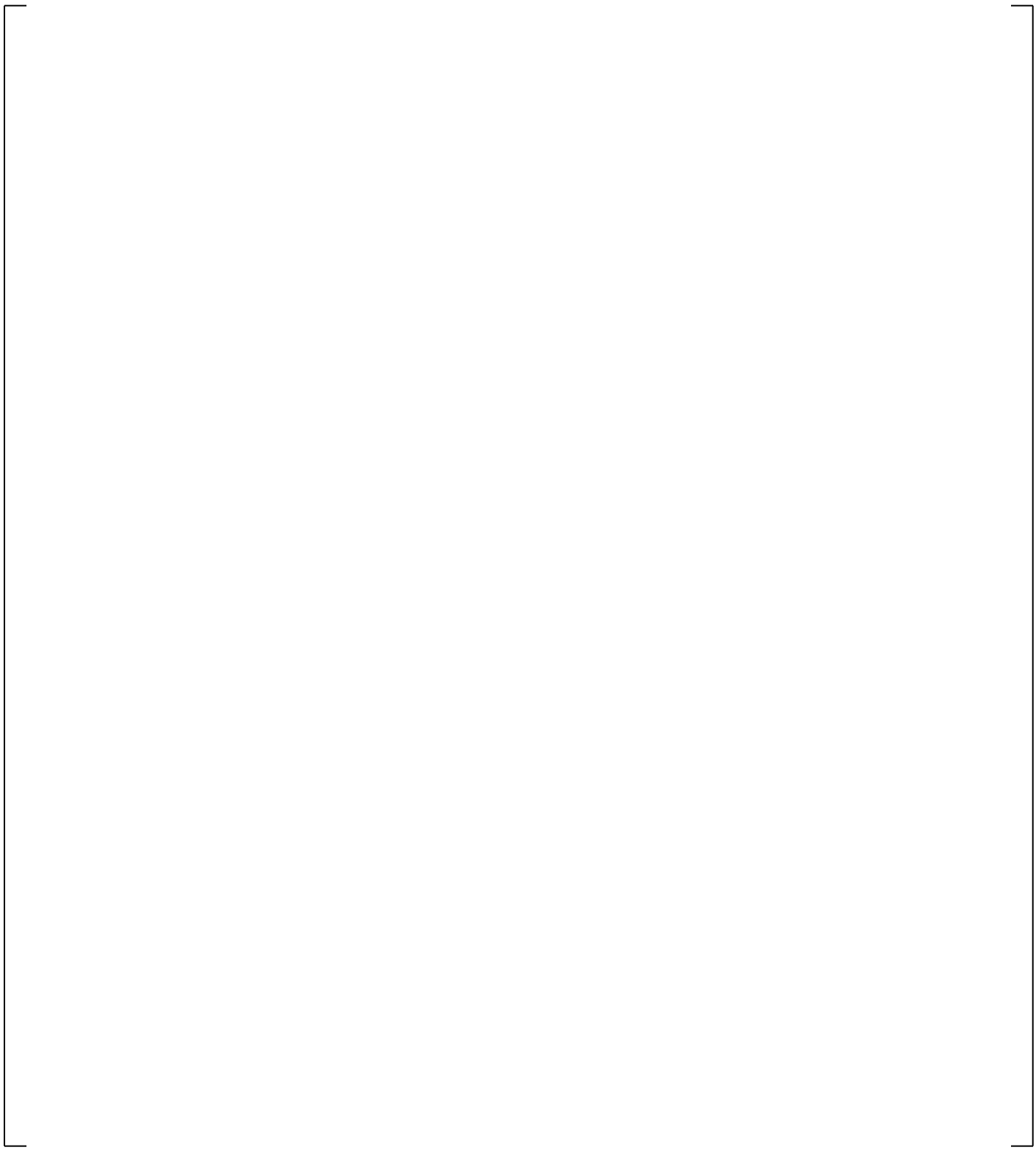

Figure 22-52 Impact of SG Secondary Side Pressure on Primary Pressure, Test L3-1

a,c

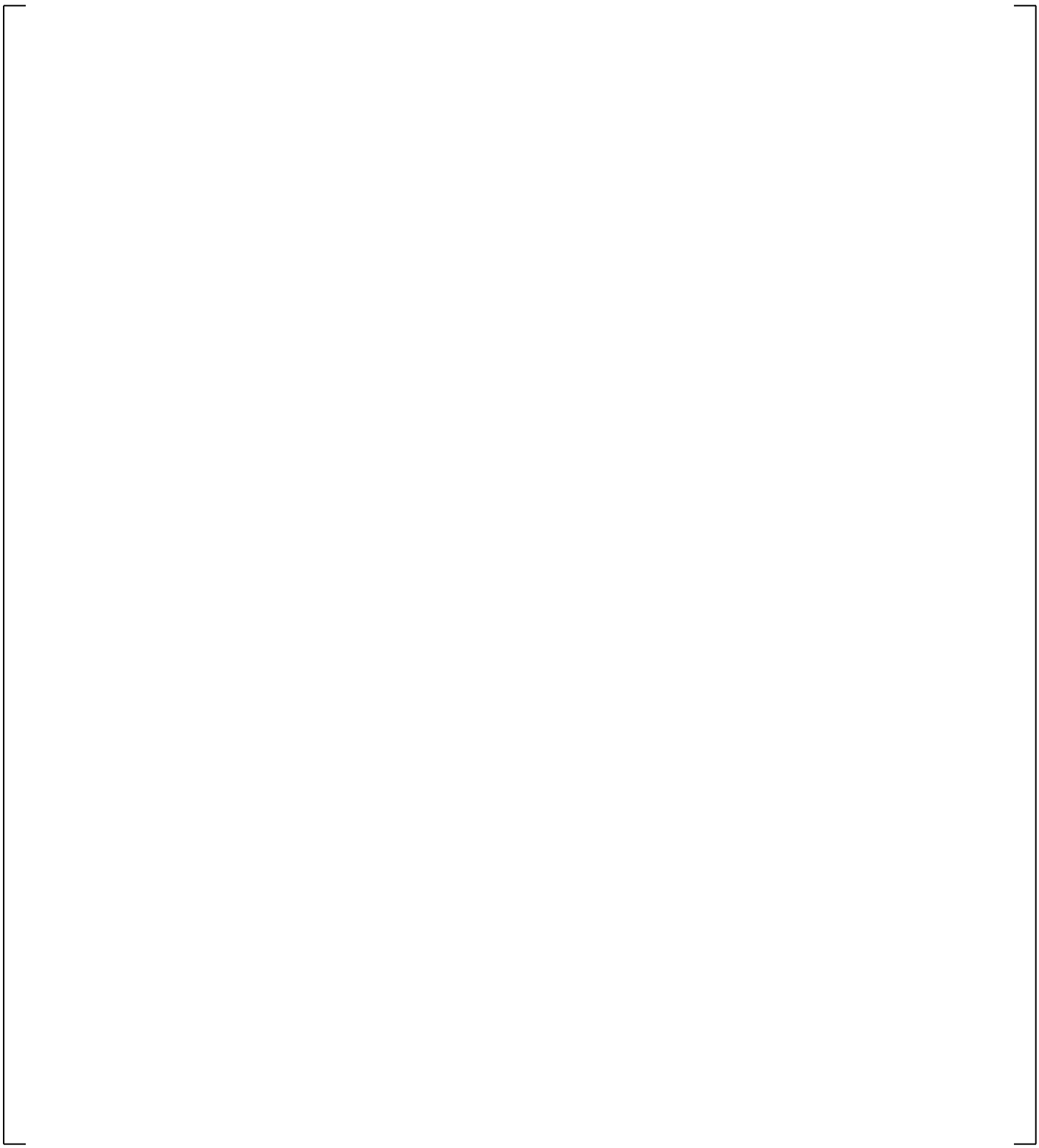

Figure 22-53 Impact of Critical Flow Model Uncertainties on Primary Pressure, Test L3-1

a,c

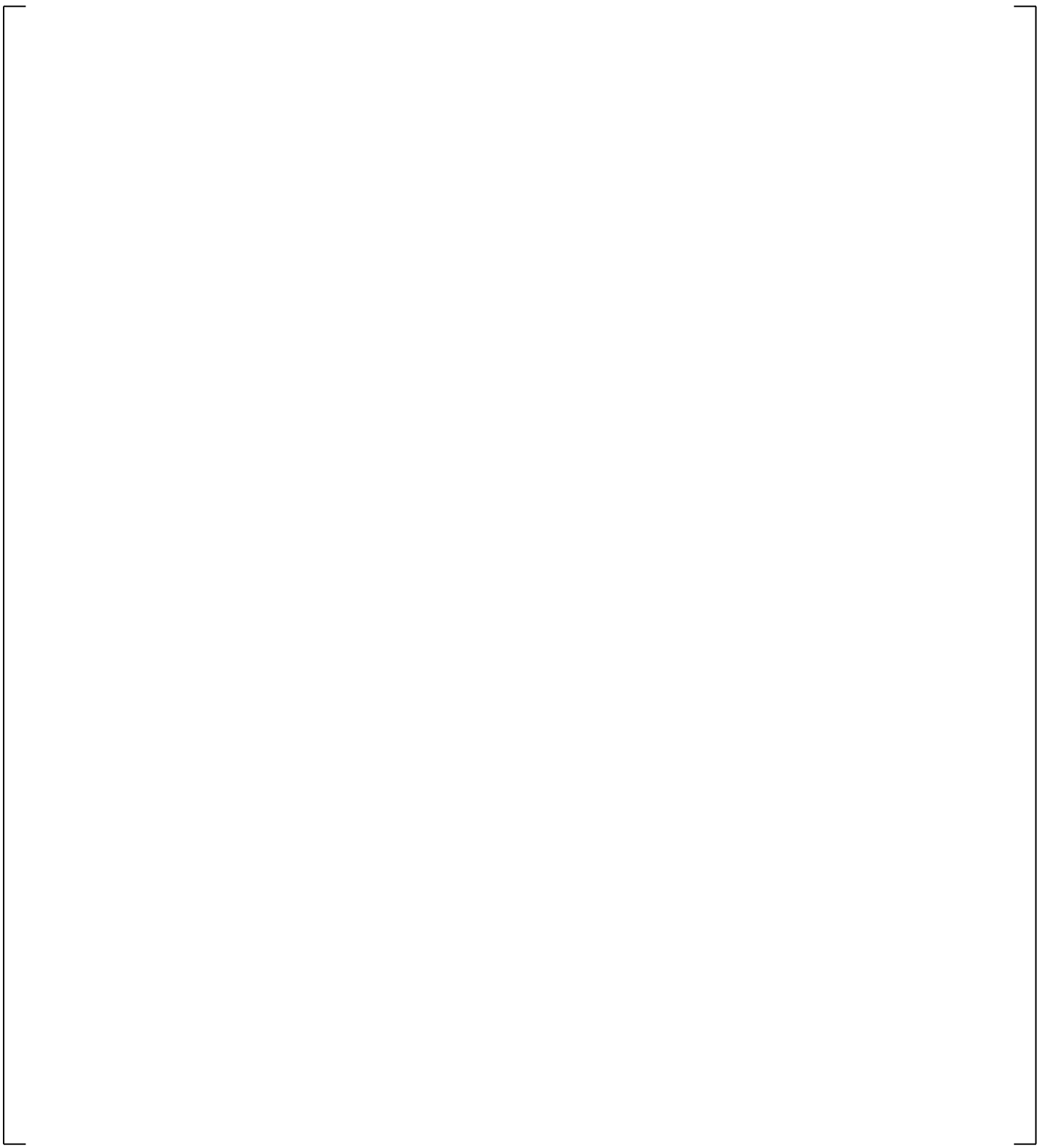

Figure 22-54 Impact of Critical Flow Model Uncertainties on Break Flow, Test L3-1

a,c

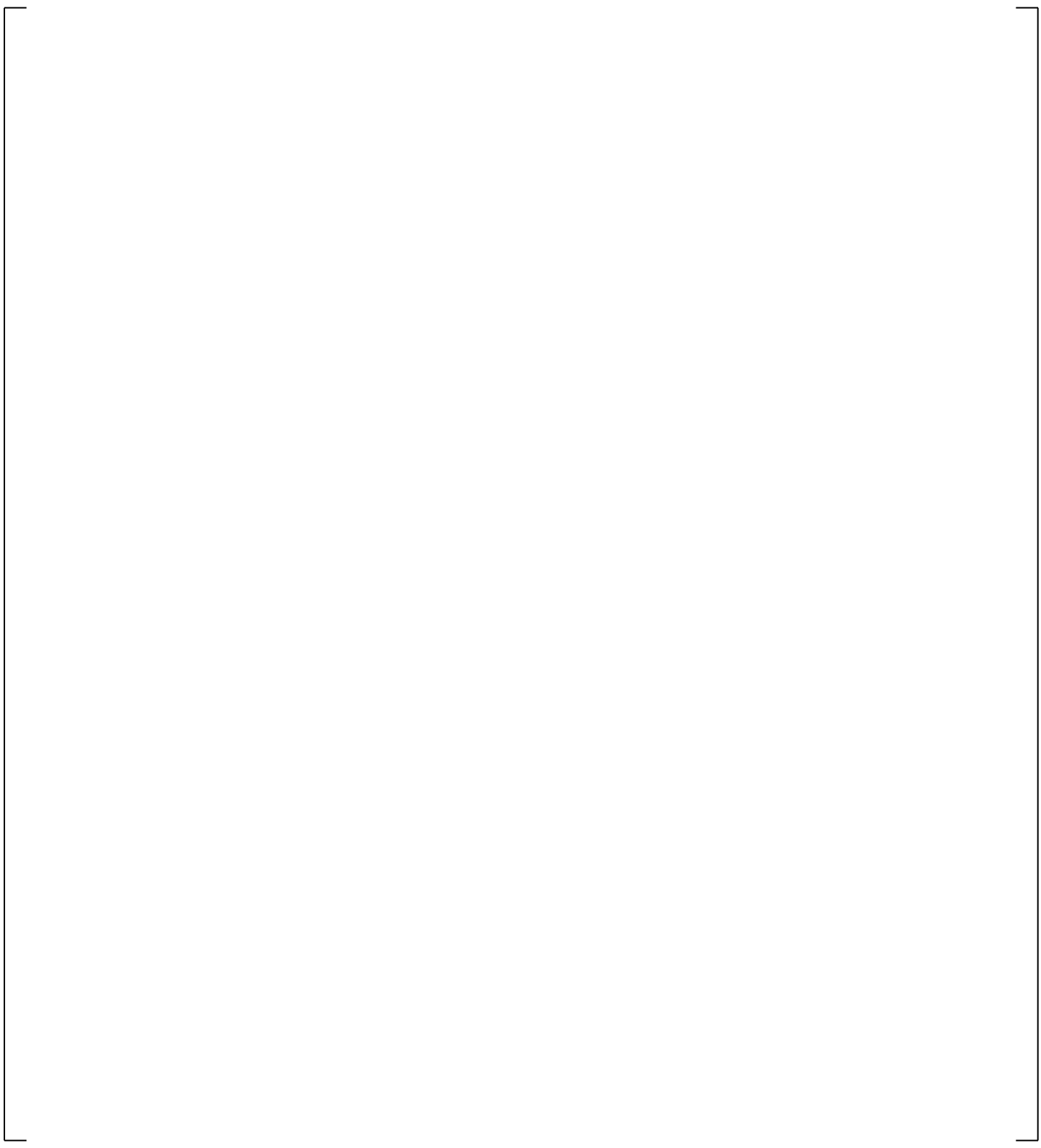

Figure 22-55 Predicted and Measured Primary System Pressure, Test L5-1

a,c

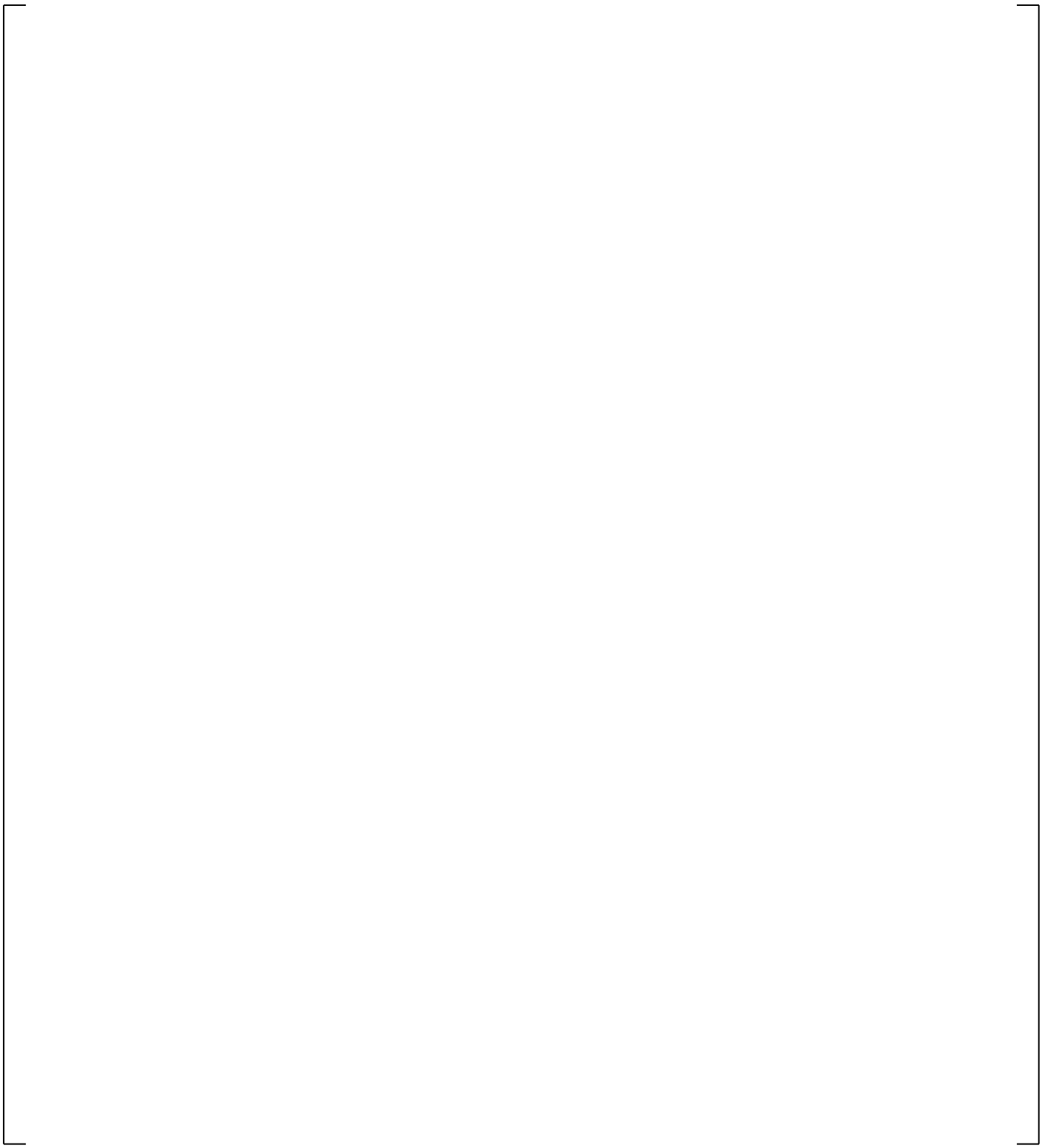

Figure 22-56 Predicted and Measured Cold Leg Break Flow and Predicted Break Upstream Void Fraction, Test L5-1

a,c

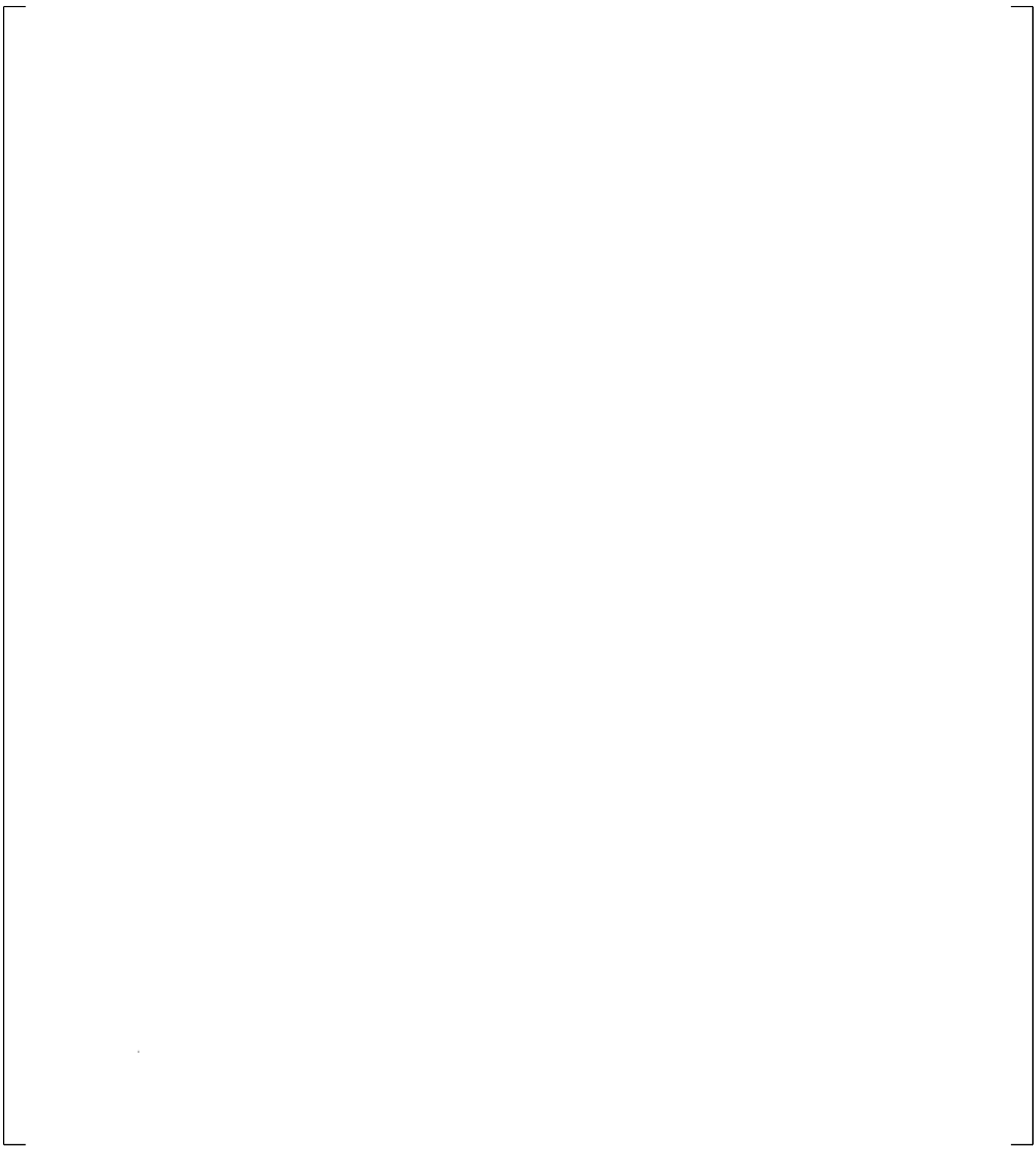

Figure 22-57 Predicted and Measured Primary and Steam Generator Secondary Side Pressure, Test L5-1

a,c

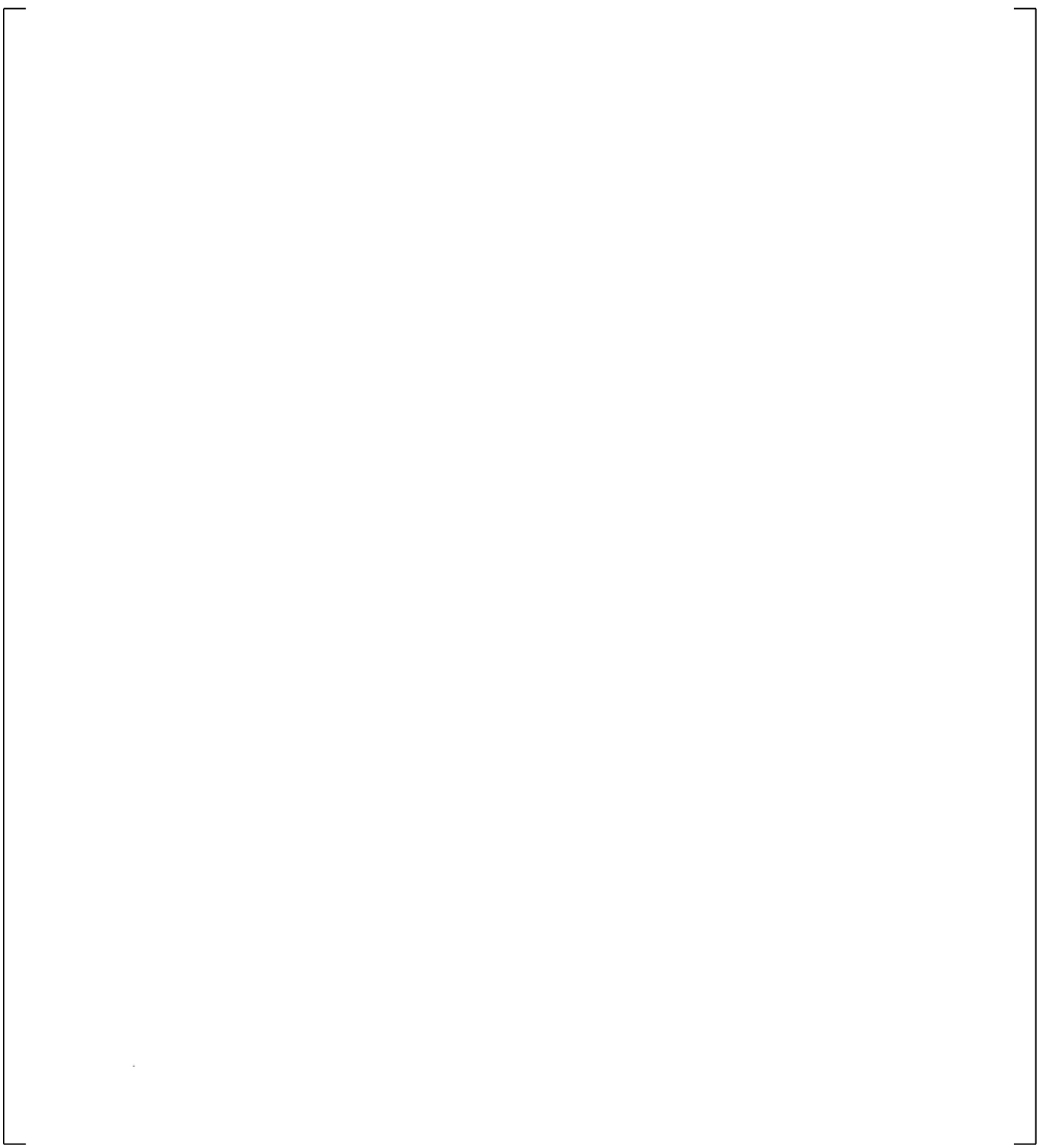

Figure 22-58 Predicted and Measured Hot Assembly Cladding Temperature, Test L5-1

a,c

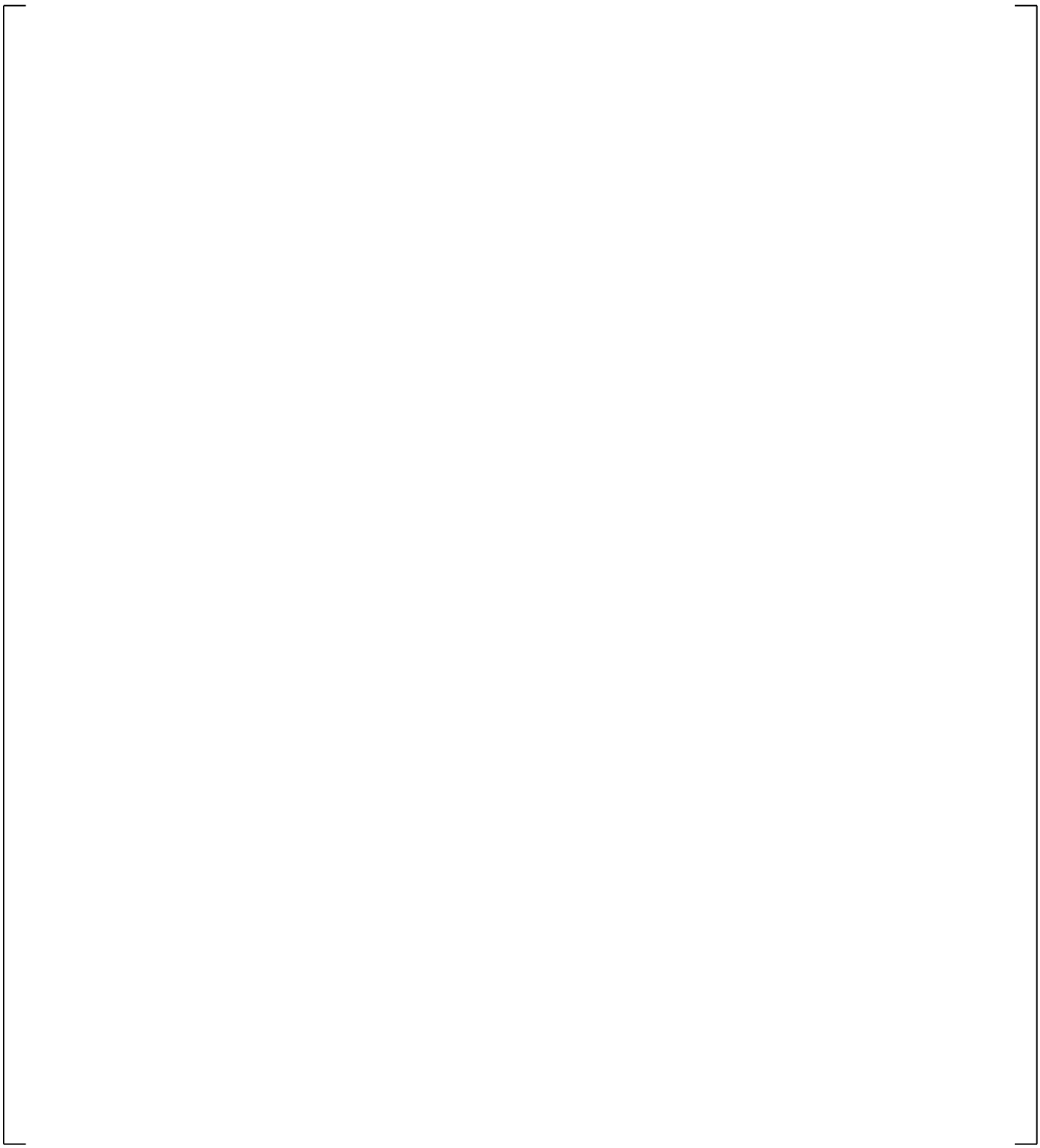

Figure 22-59 Predicted and Measured Accumulator Liquid Level, Test L5-1

a,c

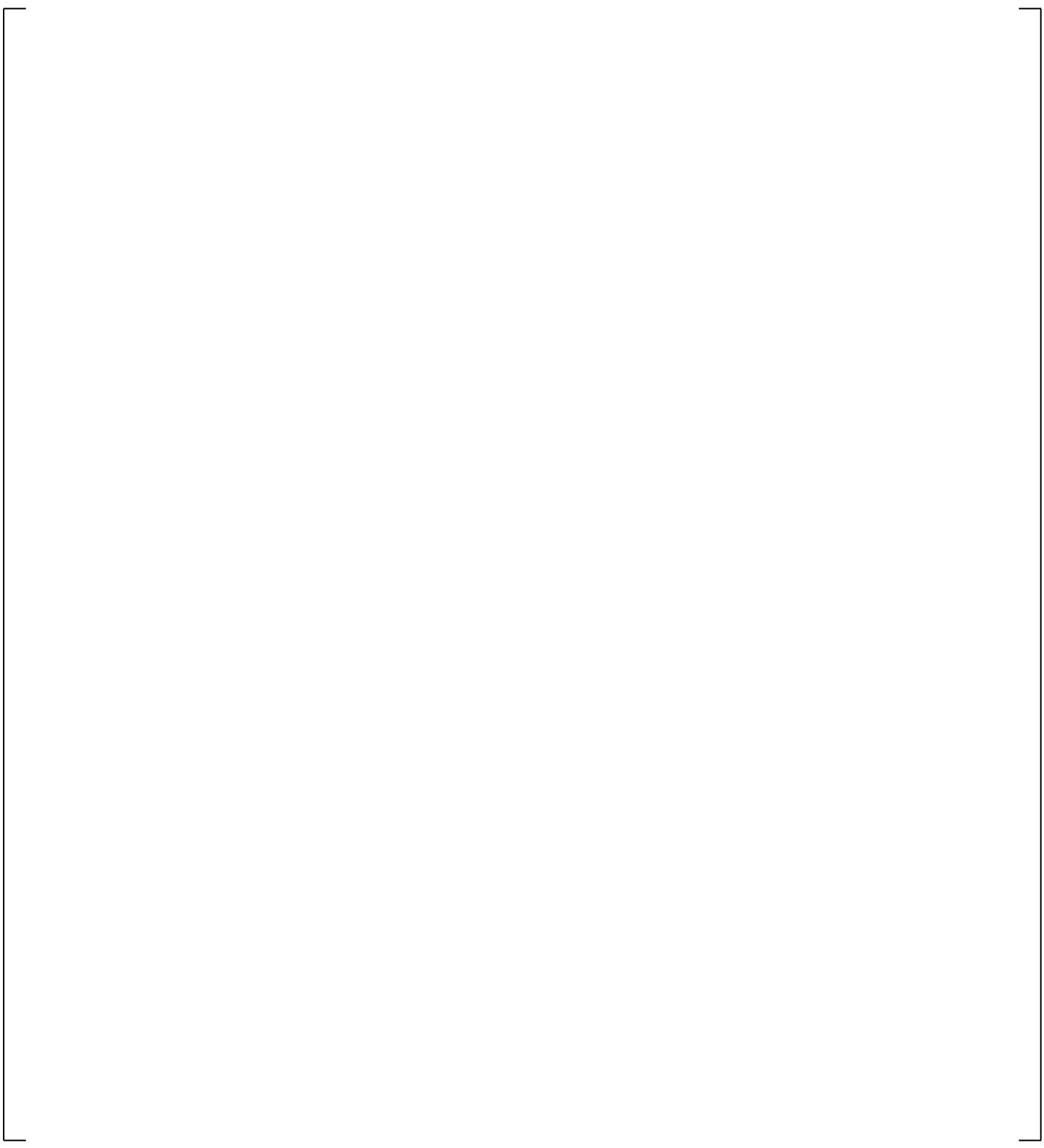

Figure 22-60 Impact of Critical Flow Model Uncertainties on Primary Pressure, Test L5-1

a,c

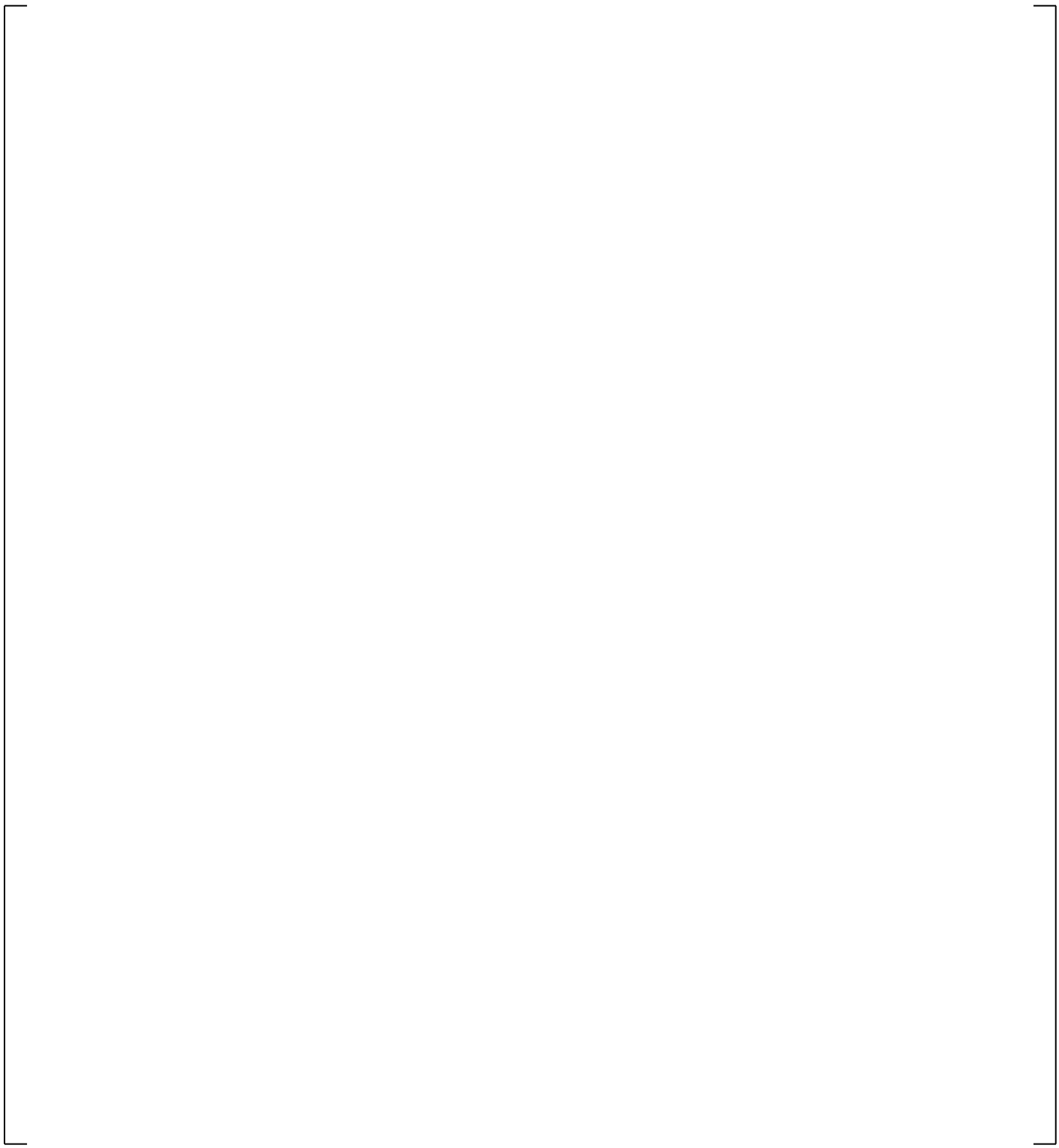

Figure 22-61 Impact of Critical Flow Model Uncertainties on Break Flow, Test L5-1

a,c

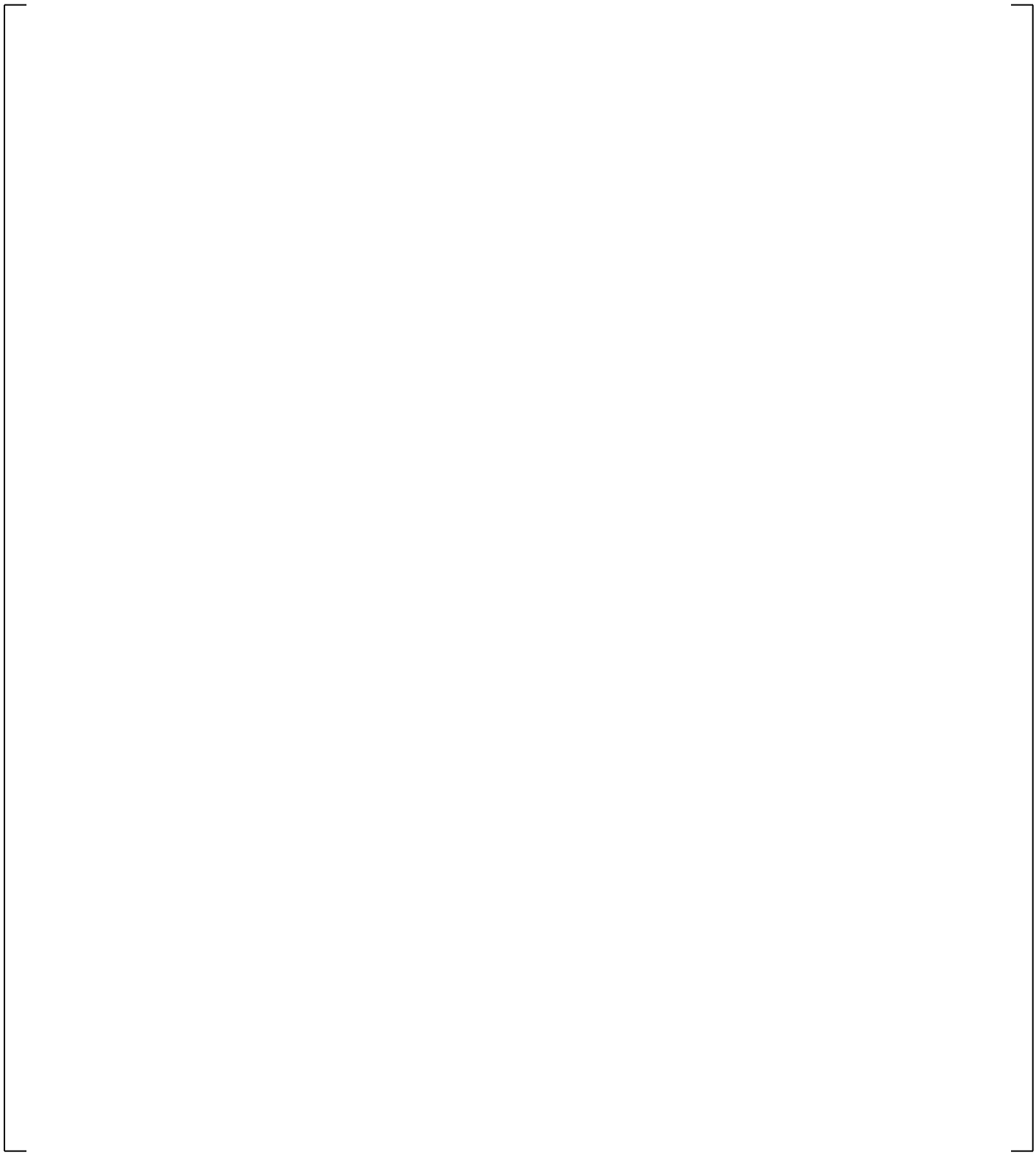

Figure 22-62 Impact of Critical Flow Model Uncertainties on Cladding Temperature, Test L5-1

a,c

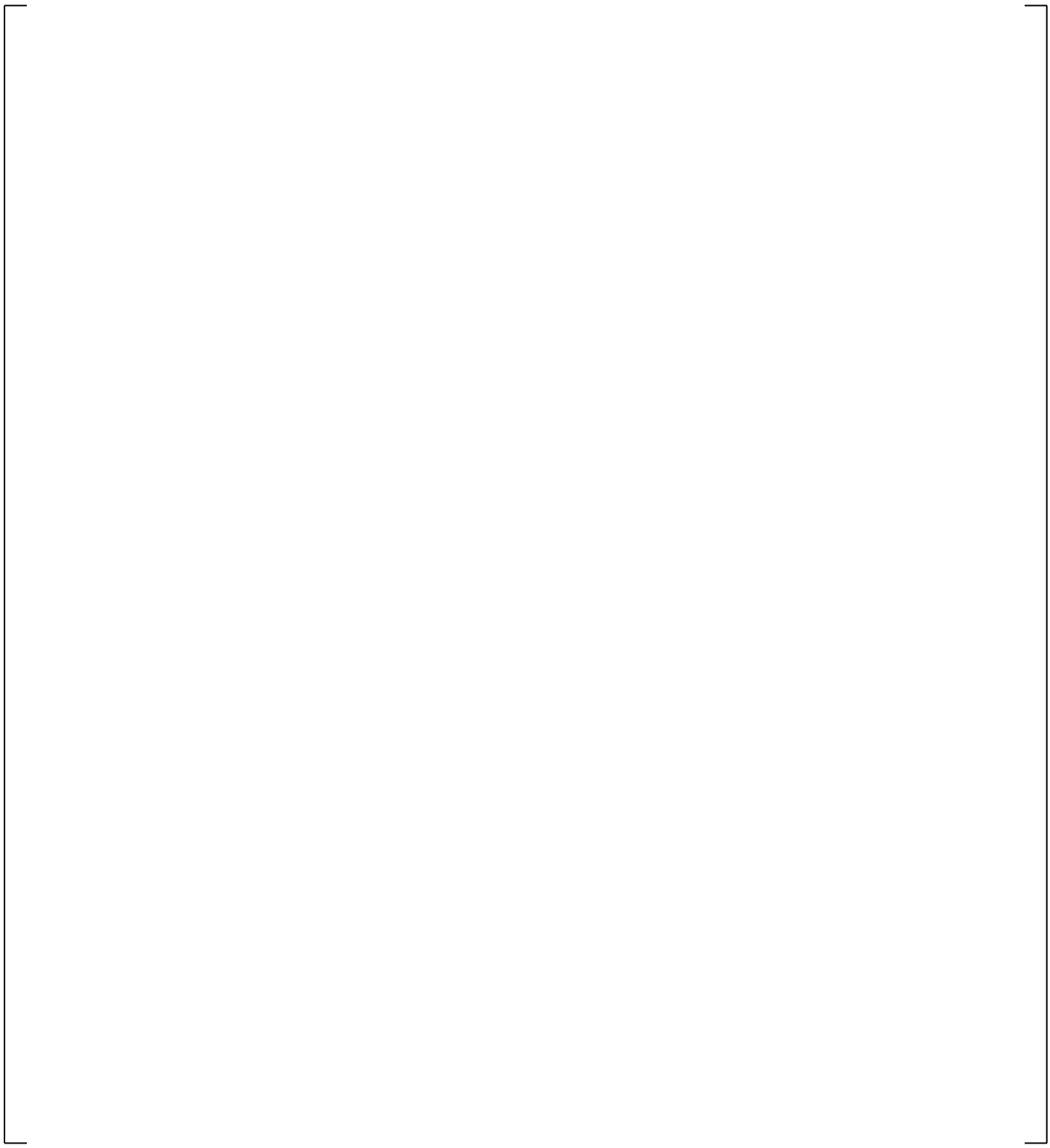

Figure 22-63 Impact of Horizontal Stratification in the Intact Hot Leg on Pressure, Test L5-1

a,c

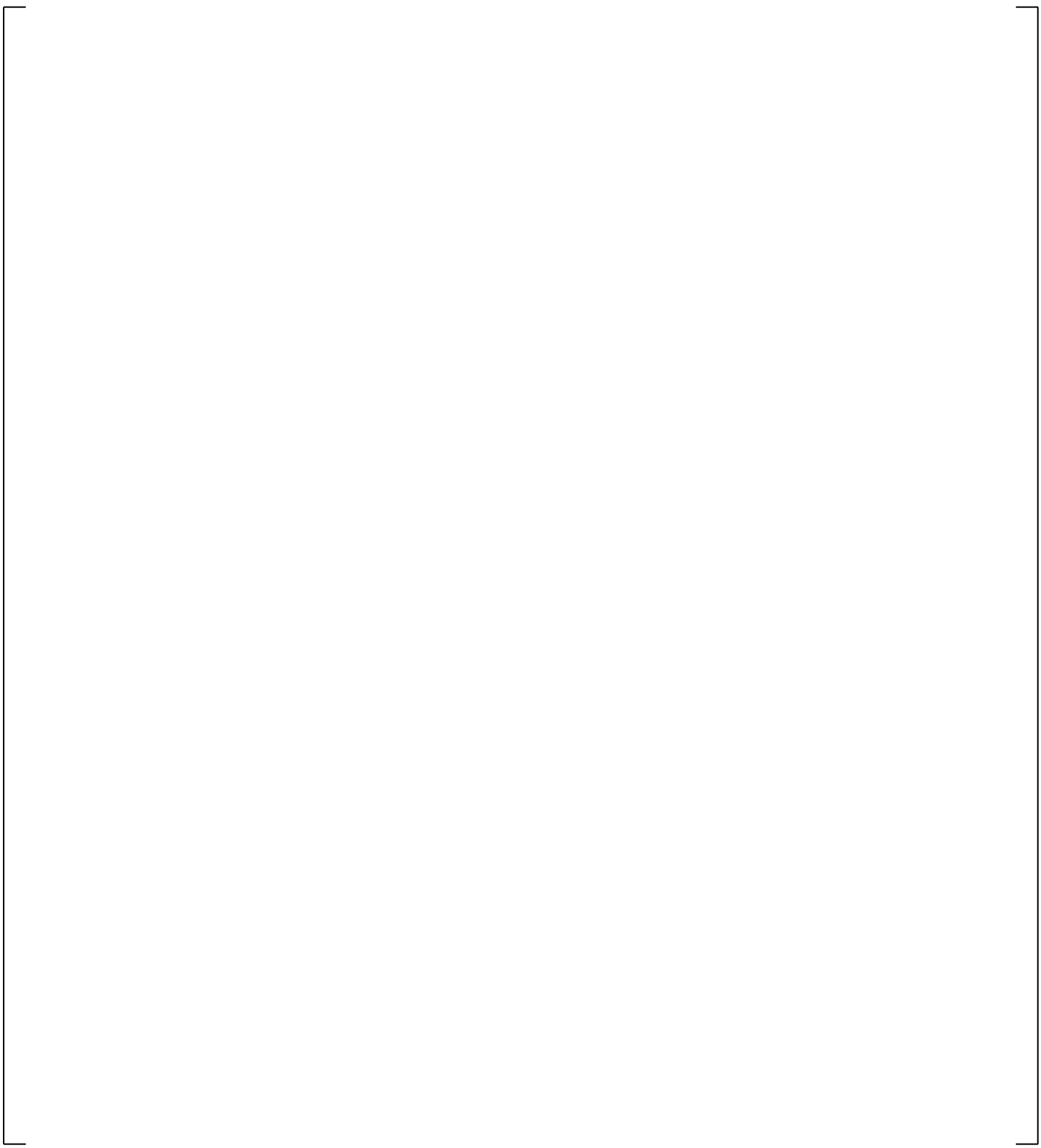

Figure 22-64 Impact of Horizontal Stratification in the Intact Hot Leg on Break Flow, Test L5-1

a,c

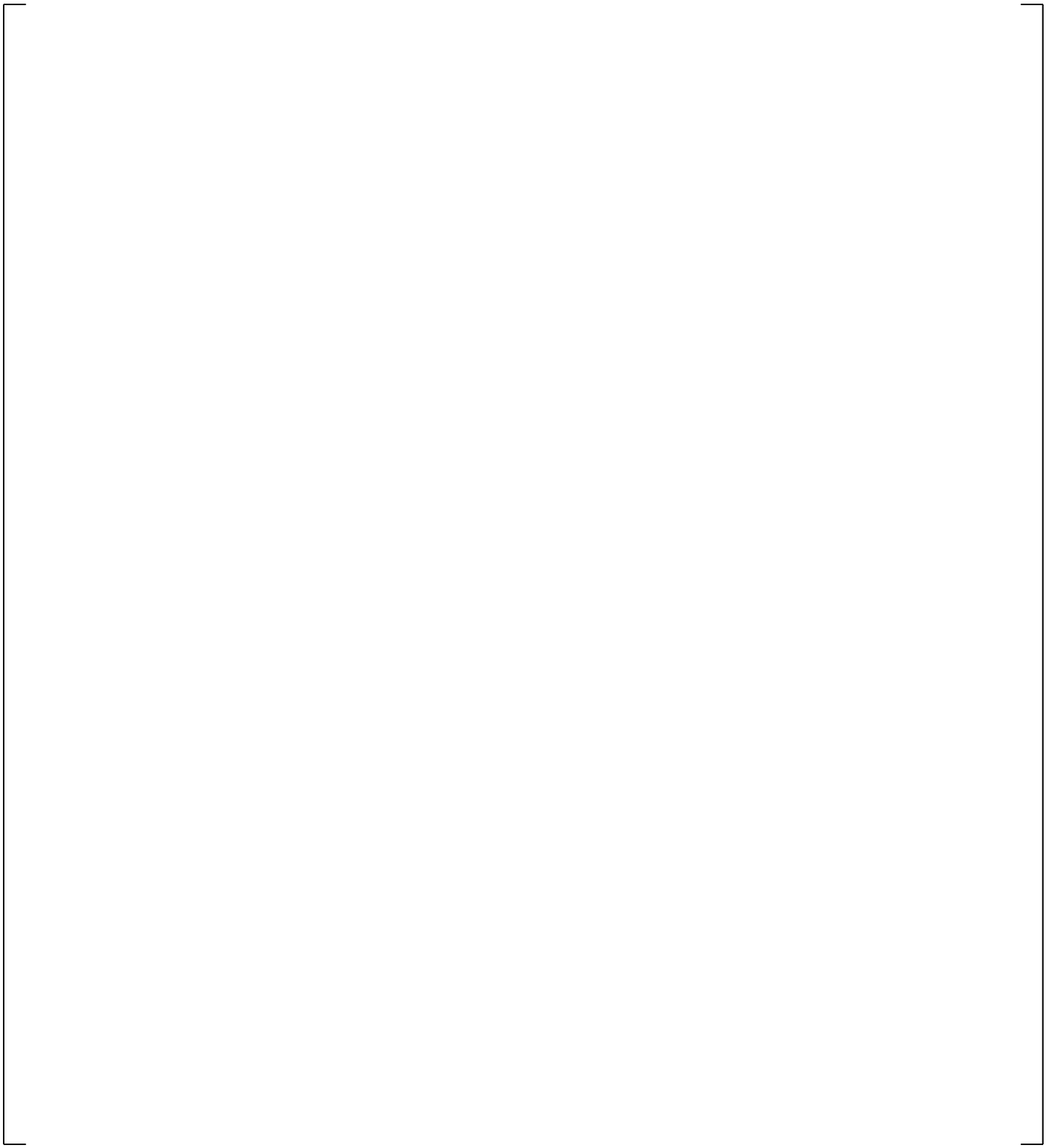

Figure 22-65 Impact of Horizontal Stratification in the Intact Hot Leg on Cladding Temperature, Test L5-1

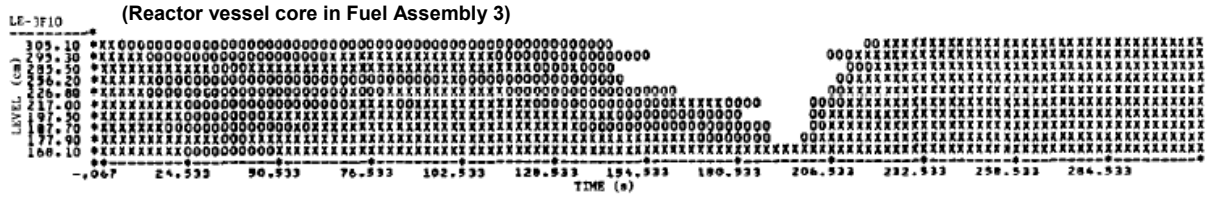

Figure 22-66 Measured Liquid Levels in Reactor Vessel Core Region, Test L5-1

a,c

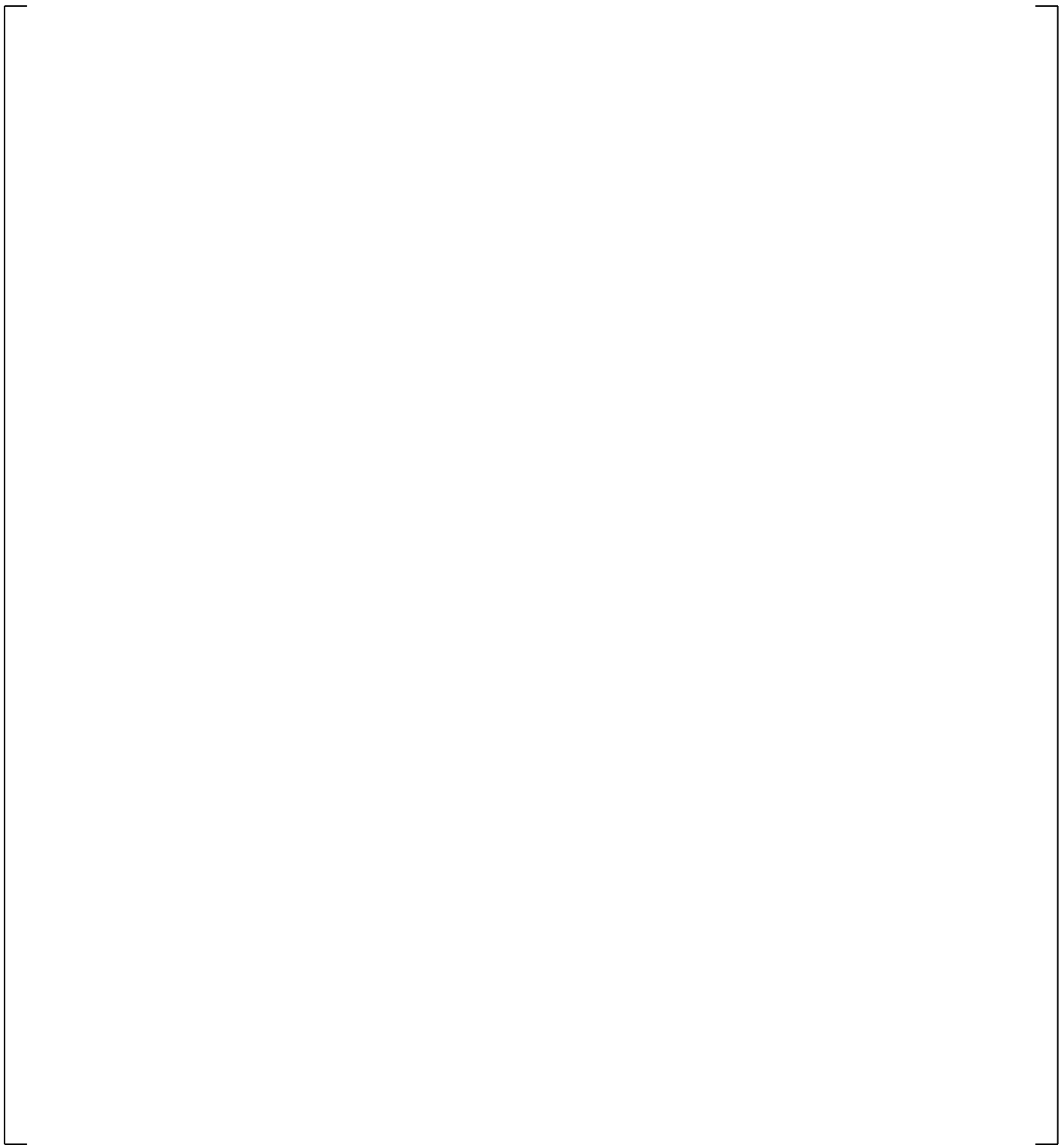

Figure 22-67 Predicted Liquid Levels in Upper Plenum and Vessel Core Regions (Base Case), Test L5-1

a,c

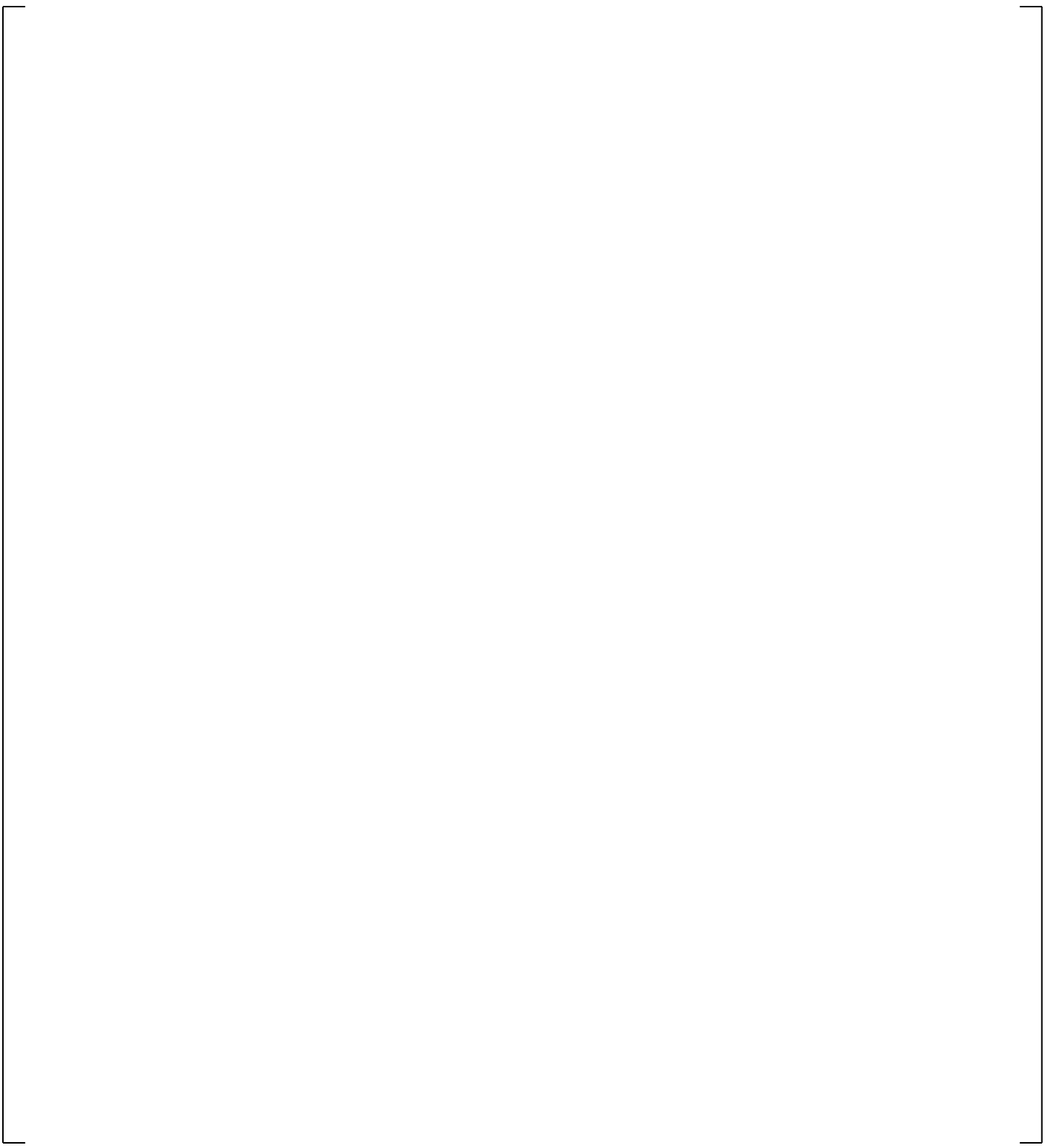

Figure 22-68 Predicted Liquid Levels in Upper Plenum and Vessel Core Regions (with HS_SLUG=0.1) for Test L5-1

a,c

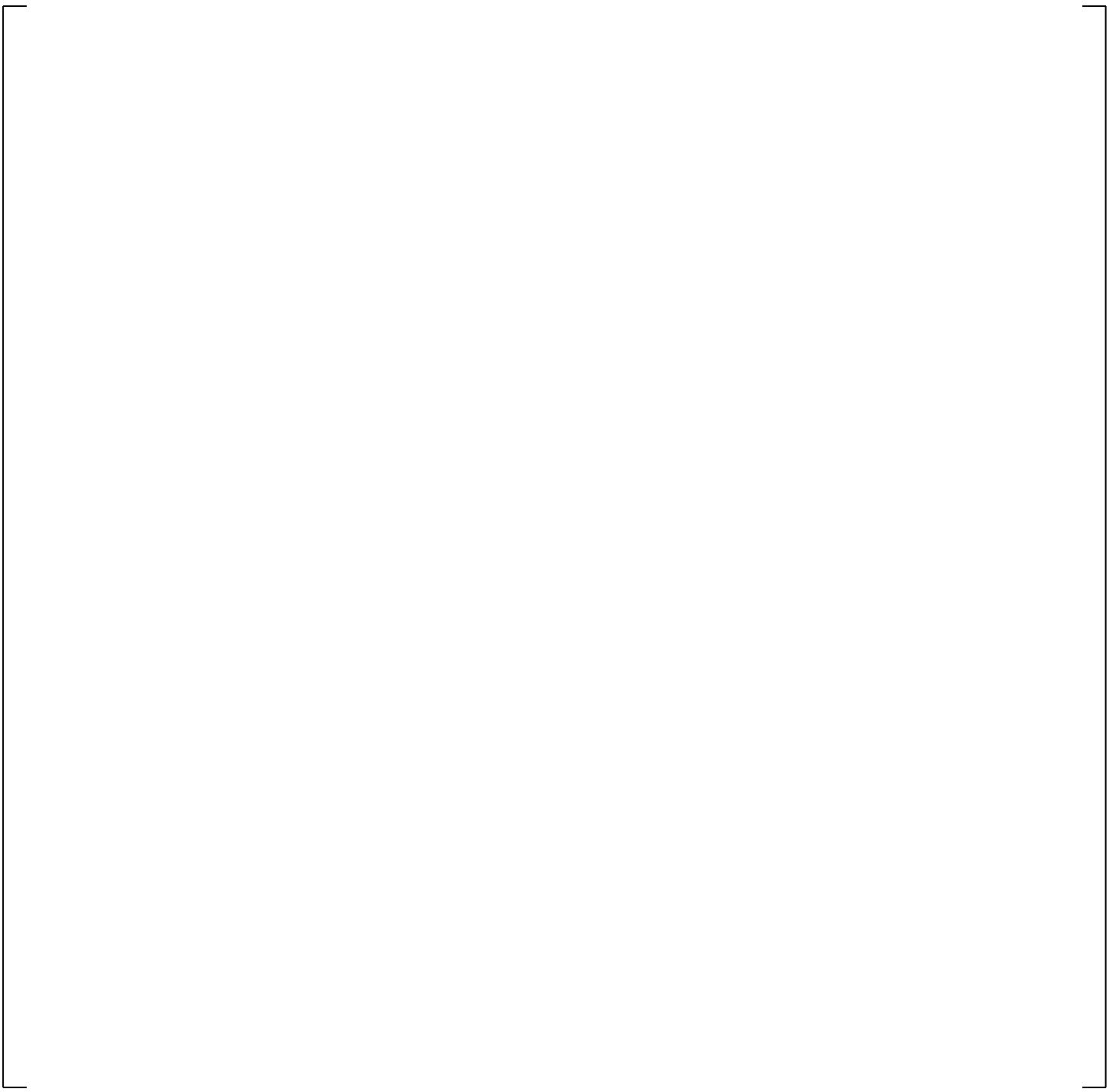

Figure 22-69 Predicted Flow Regime and Liquid Flow Rate in the Hot Leg for both the Base case and Sensitivity case (with HS_SLUG=0.1) for Test L5-1

23 ADDITIONAL VALIDATION AND NUMERICAL PROBLEMS

Sections 12 through 20 provide the validation basis of WCOBRA/TRAC-TF2 against the critical phenomena identified in the Phenomena Identification and Ranking Table (PIRT) documented in Section 2, Volume 1. Sections 21 and 22 provide information on the analysis of two series of integral effect tests, Rig-of-Safety Assessment (ROSA) and Loss-of-Fluid Test (LOFT), covering the whole spectrum of postulated break sizes. This final assessment Section documents additional validation, and in particular some numerical thought problems, and has two key objectives:

1. Complete the validation basis documented in Sections 12 through 22, with the evaluation of critical issues that have not been addressed in previous Sections. In essence, some specific limitations of the previous validation are analyzed and completed herein.

2. Use a series of numerical problems, for which an analytical solution can be developed, to verify that not only WCOBRA/TRAC-TF2 correctly predicts the complex physical phenomena analyzed in previous sections, but is also capable of providing physically sound solutions to some standard problems, thus verifying the overall code robustness and quality. Consistent with Regulatory Guide 1.203, these numerical problems are performed "to illustrate fundamental calculational device capability."

To achieve these objectives, the following analyses are documented in this Section.

- Section 23.1 Additional Validation

  - — Section 23.1.1 General Electric (GE) Blowdown – The level swell analysis documented in Section 13 relies mostly on steady state or boiloff tests. The objective of the GE Blowdown analysis is to assess WCOBRA/TRAC-TF2 in a dynamic, blowdown transient. This section will demonstrate that the WCOBRA/TRAC-TF2 level swell prediction remains adequate in these conditions.

  - — Section 23.1.2 Semiscale – The Level Swell and Boiloff analyses documented in Section 13 are all characterized by relatively low clad temperature. Selected Semiscale boiloff tests are analyzed herein to verify the WCOBRA/TRAC-TF2 prediction of level swell and post-critical heat flux (CHF) heat transfer when clad temperatures are high.

- Section 23.2 Numerical Test Problems

  - — Section 23.2.1 1D PIPE Manometer Problem with Non-Condensable Gases
  - — Section 23.2.2 3D VESSEL Manometer Problem with Non-Condensable Gases
  - — Section 23.2.3 1D PIPE Steam Expulsion Test
  - — Section 23.2.4 3D VESSEL Steam Expulsion Test
  - — Section 23.2.5 1D PIPE Fill and Drain Test
  - — Section 23.2.6 3D VESSEL Fill and Drain Test
  - — Section 23.2.7 Condensation Test

23.1 ADDITIONAL VALIDATION

23.1.1 GE Vessel Blowdown Tests

23.1.1.1 Introduction

Early in a loss-of-coolant accident (LOCA), voids are generated in the primary reactor coolant system (RCS) by flashing and boiling in the core. During the blowdown phase, depressurization is rapid and flashing can play an important role. Flashing in the core and upper plenum can re-distribute fluid in the RCS, which can lead to uncertainty in loop seal clearing time (for smaller break sizes) and analysis results. **[**

][a,c]

The void distribution in the reactor vessel during the blowdown phase depends on several processes; the interfacial drag between the vapor and liquid (film), wall drag, the bubble rise velocity and bubble size, the entrainment of droplets at the two-phase interface, the transition point between bubbly and other vertical flow regimes, and the rate of system depressurization. The rate of depressurization depends on the break flow rate.

The GE Vessel Blowdown Facility is designed to study basic phenomena such as void fraction distribution and transient liquid-vapor level swell during blowdown. Several top-break blowdown tests were conducted using different-sized orifice plates to vary the blowdown transient. The tests also varied the open area of the resistance plate at the vessel mid-plane. **[**

][a,c]

A description of all the tests performed is given in NUREG/CR-1899 (Findlay and Sozzi, 1981).

23.1.1.2 GE Blowdown Test Facility Description

The blowdown tests were performed in a cylindrical carbon steel vessel. The vessel was a two-piece unit that could be separated at a pair of flanges located near the center of the vessel. The cylindrical portion of the vessel was constructed from Schedule 80 pipe, 12 feet long with an inside diameter of 1 foot. Elliptical heads were welded onto the ends of the pipe to create the vessel. The total vessel volume was 10 cubic feet, and the total height was 14 feet. There were five calorimetric heater rods, 1 inch in diameter and 2 feet high, in the bottom of the vessel to heat the water. The steam exhaust was located at the 13-foot elevation with an orifice that was captured in a flange. The orifices used to control the tank blowdown rate were plates with the prescribed hole machined without a chamfer. The orifice was located close to the vessel in a 2-inch Schedule 80 pipe. Figure 23.1.1-1 is a scaled drawing that shows the vessel, its penetrations, the blowdown line, and a suppression pool where the blowdown effluent was discharged.

A 3/4-inch thick perforated plate (containing 109 holes, 9/16-inch diameter), designed to provide an internal flow restriction, was installed between the main vessel flanges at the mid-elevation during some of the tests. The resistance of the plate was varied by plugging a selected number of holes. Orifice plates with different flow areas were used in the blowdown line to limit the blowdown flow rate and vary the vessel depressurization rate.

Figure 23.1.1-2 shows the instrumentation arrangement used to measure three basic parameters: pressures, pressure differences, and temperatures. Vessel pressure and differential pressures were measured using strain-gauge pressure transducers, and temperatures were measured using Iron-Constantan thermocouples. The transient void fraction and the mixture level were calculated from differential pressure measurements.

23.1.1.3 Test Matrix for GE Blowdown Simulations

Table 23.1.1-1 lists the seven experiments in the test series. All seven of the tests were simulated with WCOBRA/TRAC-TF2, and none were excluded. These tests span a range of orifice diameters from 3/8 of an inch to 2 inch, and a variety of different flow restrictions at the midpoint of the vessel.

23.1.1.4 Test Procedure for GE Blowdown Simulations

The vessel was initially filled with demineralized water and boiled at atmospheric pressure for approximately 30 minutes to liberate any dissolved gas in the supply water. A vent at the top of the vessel was then closed, and the water was heated to establish the initial conditions (which were a nominal pressure of 1000 psia and 545°F). Actual initial conditions for each test are given in the test matrix in Table 23.1.1-1. With the facility initially heated and pressurized, several top-break blowdown tests were conducted.

23.1.1.5 WCOBRA/TRAC-TF2 Model for GE Vessel Blowdown Tests

The WCOBRA/TRAC-TF2 model of the GE Vessel Blowdown Facility is shown in Figure 23.1.1-3.
[

]^{a,c}

23.1.1.6 Simulation of GE Vessel Blowdown Tests

The primary figure of merit for these simulations is the ability of the WCOBRA/TRAC-TF2 code to predict the void distribution in the vessel for these simulations. The results of the WCOBRA/TRAC-TF2 simulations of the Vessel Blowdown Tests are summarized and compared to the experimental data in Table 23.1.1-2. The ability of the code to predict the void fraction trends in each of the simulations was assessed in the first column of the table. The specific void fraction prediction at six elevations (see Figure 23.1.1-3) in the vessel was then assessed against the test data in the remaining table columns.

[

][a,c]

23.1.1.7 Effect of Interfacial Drag Multiplier

The simulations of the GE Vessel Blowdown Tests were also run with WCOBRA/TRAC-TF2 to investigate the impact of the interfacial drag multiplier (YDRAG) on the prediction of the two-phase level and void distribution. **[**

][a,c]

Figures 23.1.1-4 through 23.1.1-45 compare the code-predicted void distributions **[**
][a,c] to the experimental data for each of the GE blowdown tests. **[**

][a,c] The experimental data is presented as dashed black lines, with both the nominal and upper/lower bound uncertainties presented. It can be seen from these plots that **[**

][a,c]

23.1.1.8 Summary and Conclusions

The results of the GE Vessel Blowdown Test simulations confirmed that the **[**

][a,c]

23.1.1.9 References

1. Findlay, J. A. and Sozzi, G. L., 1981, "BWR Refill-Reflood Program B Model Qualification Task Plan," NUREG/CR-1899.

Table 23.1.1-1 Summary of Test Parameters for Small Blowdown Vessel Steam Blowdown Tests				
			Initial Conditions	
Test No.	Orifice Size (in.)	Restriction Plate (9/16 in. Diameter Holes)	Pressure (psia)	Level (ft)
8-21-1	3/8	109 holes	1015	8.89
8-25-1	2	109 holes	1020	8.82
8-28-1	1	109 holes	1015	8.76
9-1-1	3/8	77 holes	1014	8.75
9-15-1	3/8	55 holes	1015	8.74
1004-3	3/8	No plate	1011	10.4
1004-2	7/8	No plate	1011	10.5

Table 23.1.1-2 Characterization of WCOBRA/TRAC-TF2 Results Versus Test Data

a,c

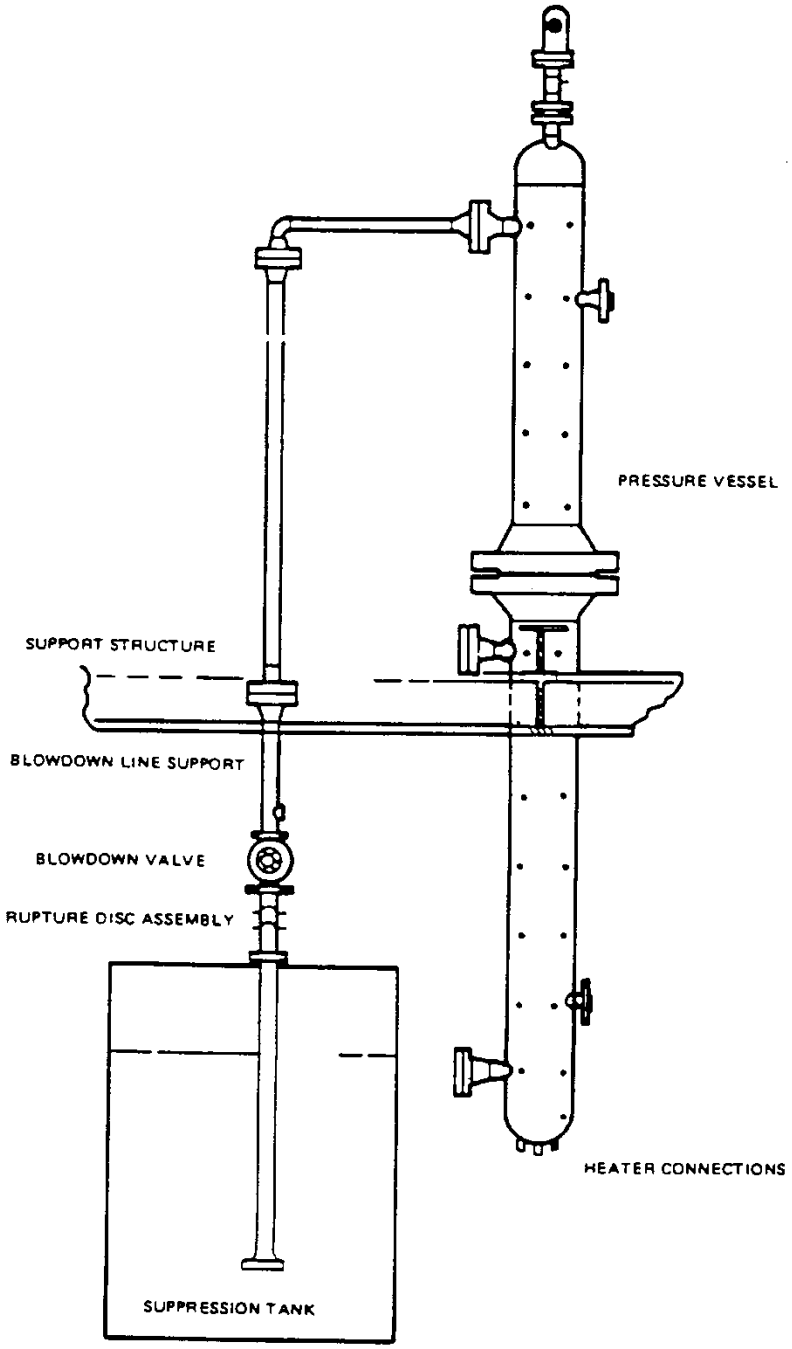

Figure 23.1.1-1 Small Blowdown Vessel

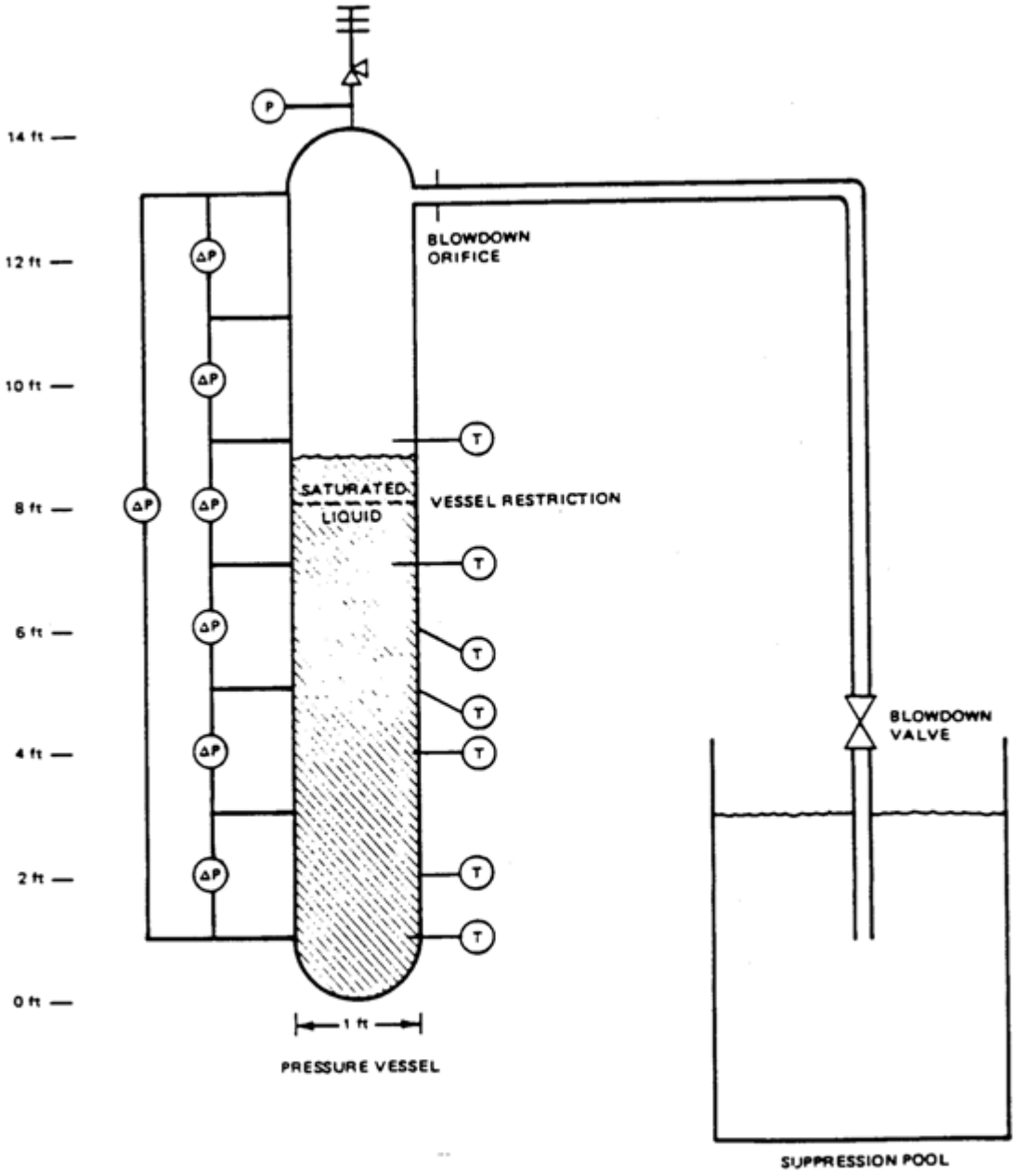

Figure 23.1.1-2 Small Blowdown Vessel Instrumentation

a,c

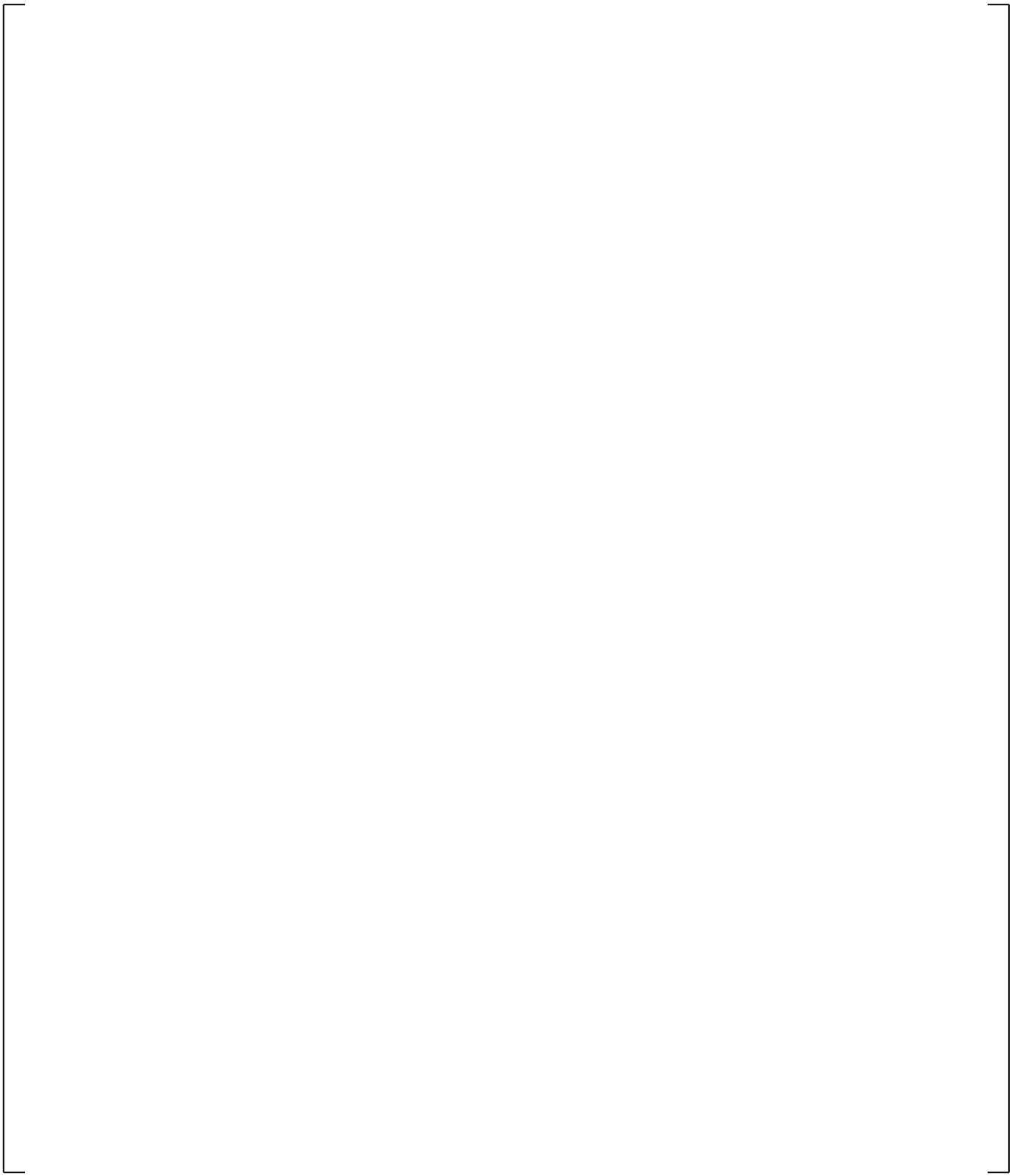

Figure 23.1.1-3 WCOBRA/TRAC-TF2 Model of the GE Vessel Blowdown Facility

a,c

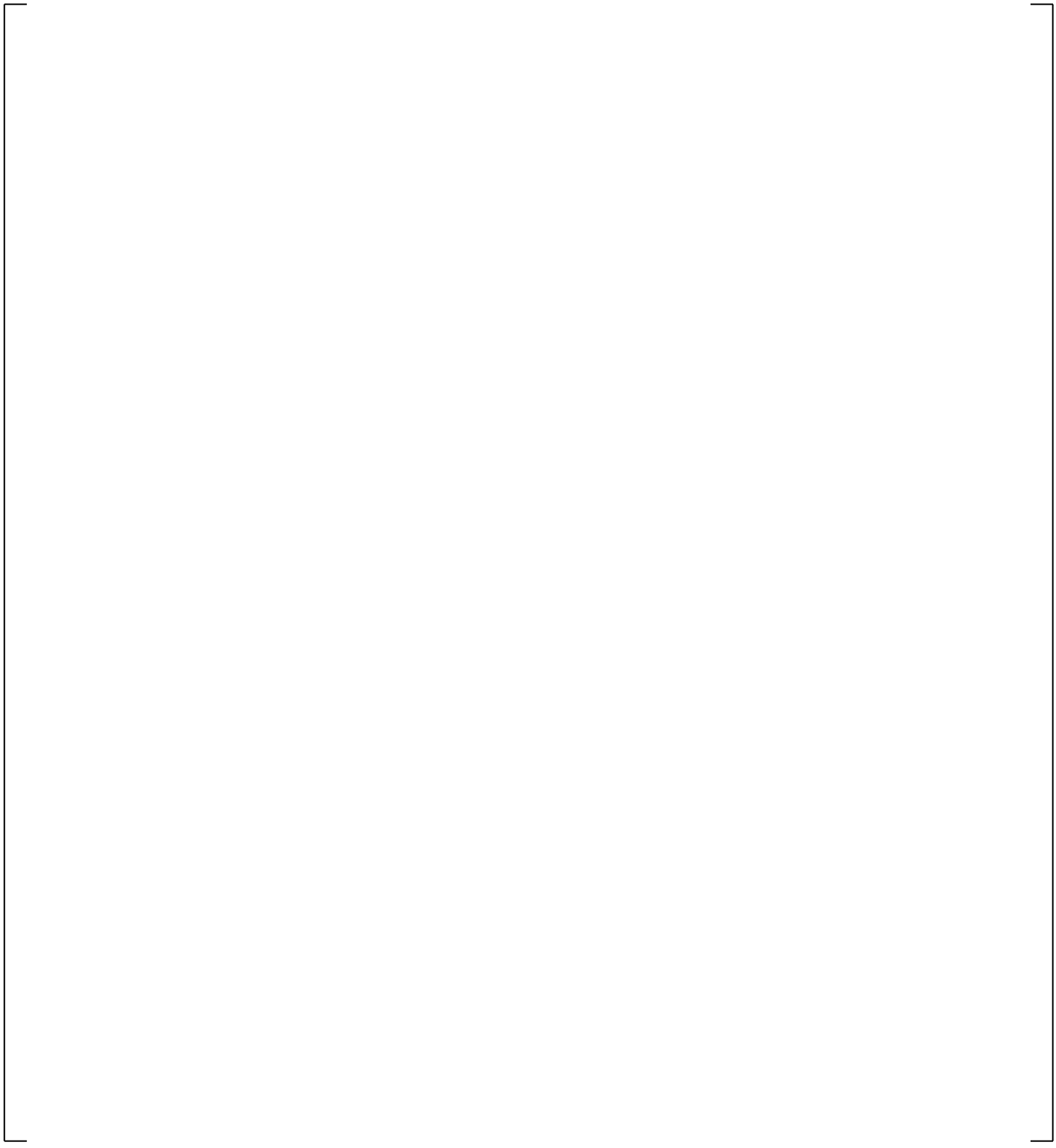

Figure 23.1.1-4 Comparison of Predicted and Measured Void Fraction at Level 1, Test 8-21-1

a,c

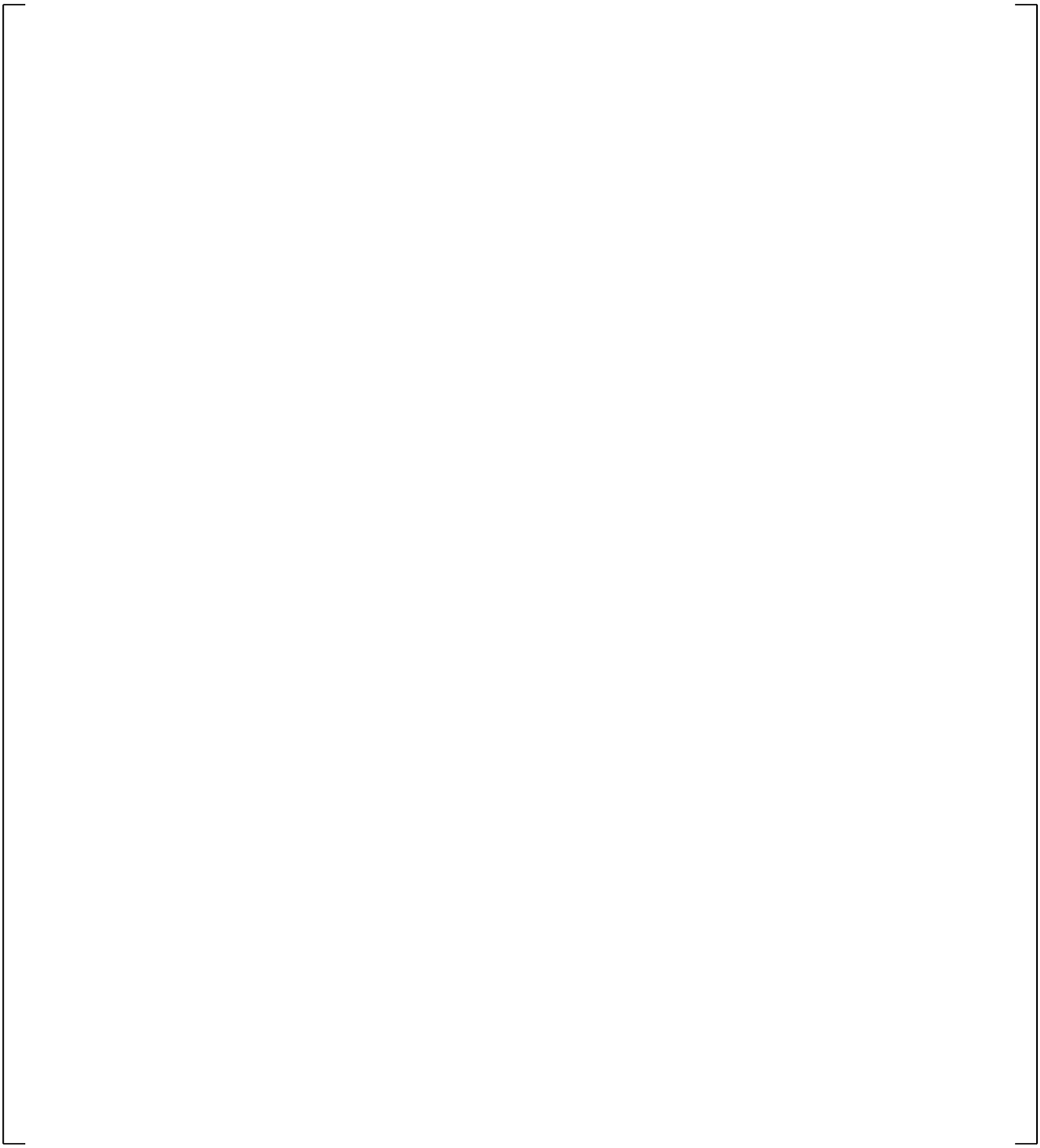

Figure 23.1.1-5 Comparison of Predicted and Measured Void Fraction at Level 2, Test 8-21-1

a,c

Figure 23.1.1-6 Comparison of Predicted and Measured Void Fraction at Level 3, Test 8-21-1

a,c

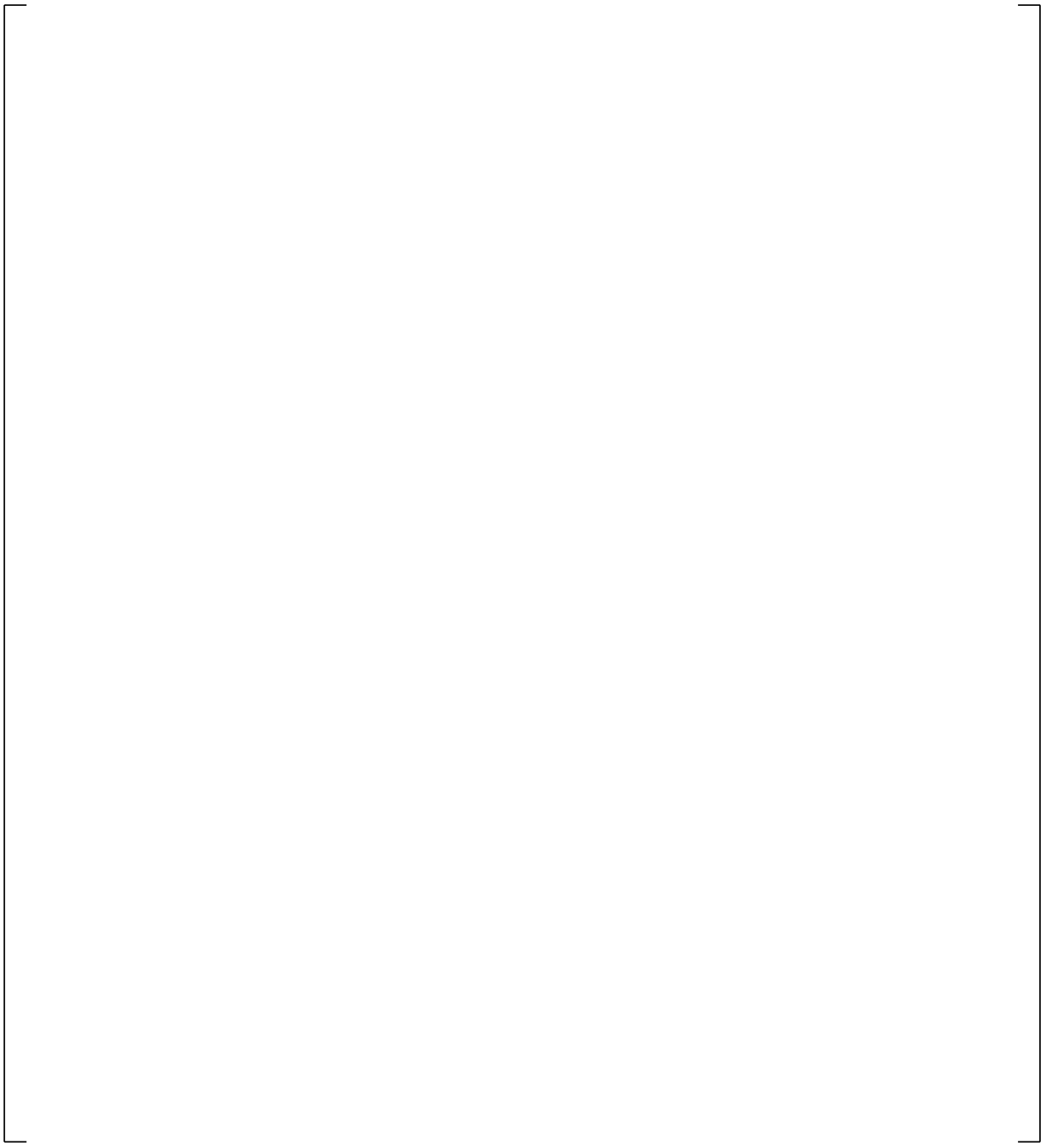

Figure 23.1.1-7 Comparison of Predicted and Measured Void Fraction at Level 4, Test 8-21-1

a,c

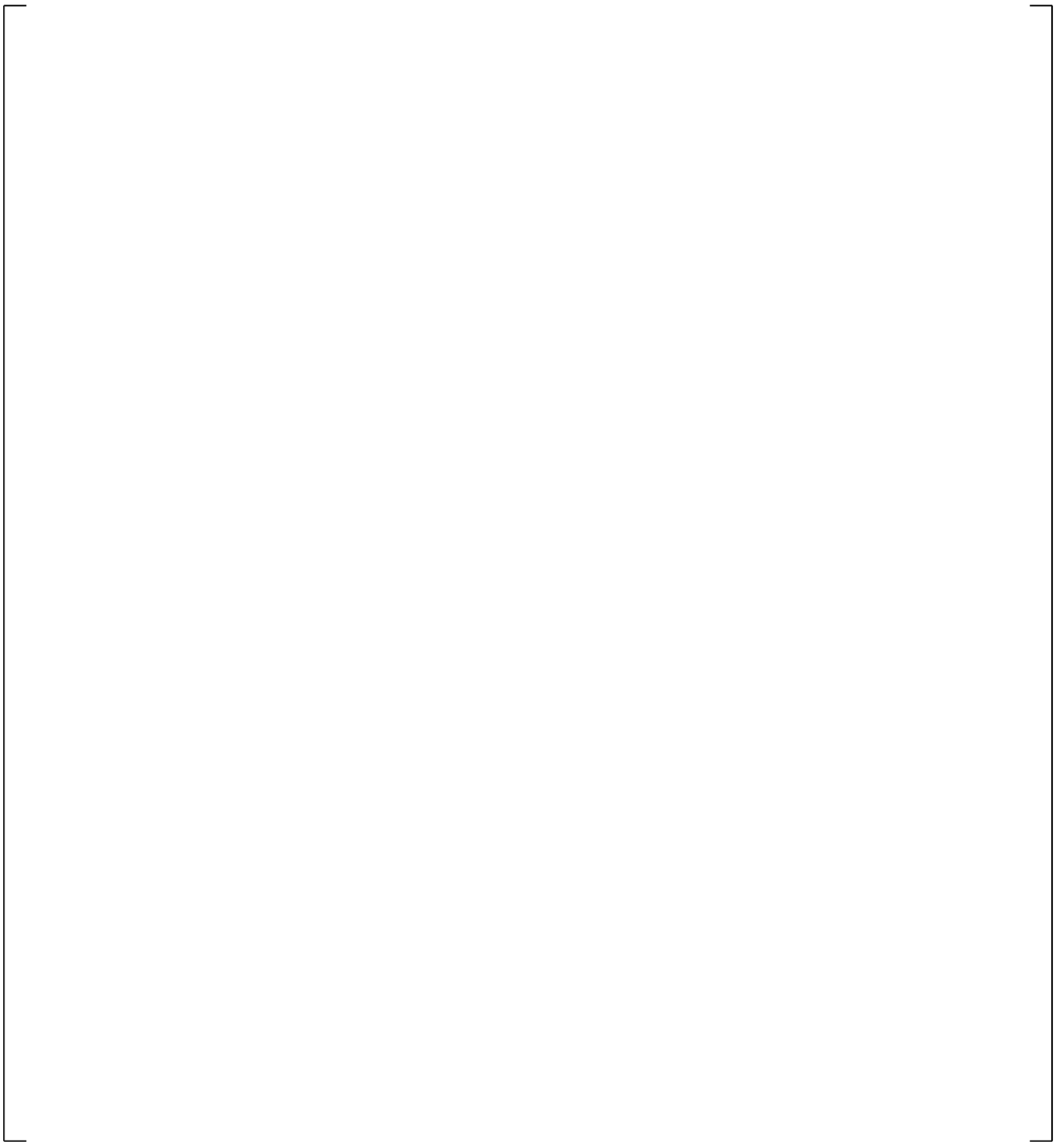

Figure 23.1.1-8 Comparison of Predicted and Measured Void Fraction at Level 5, Test 8-21-1

a,c

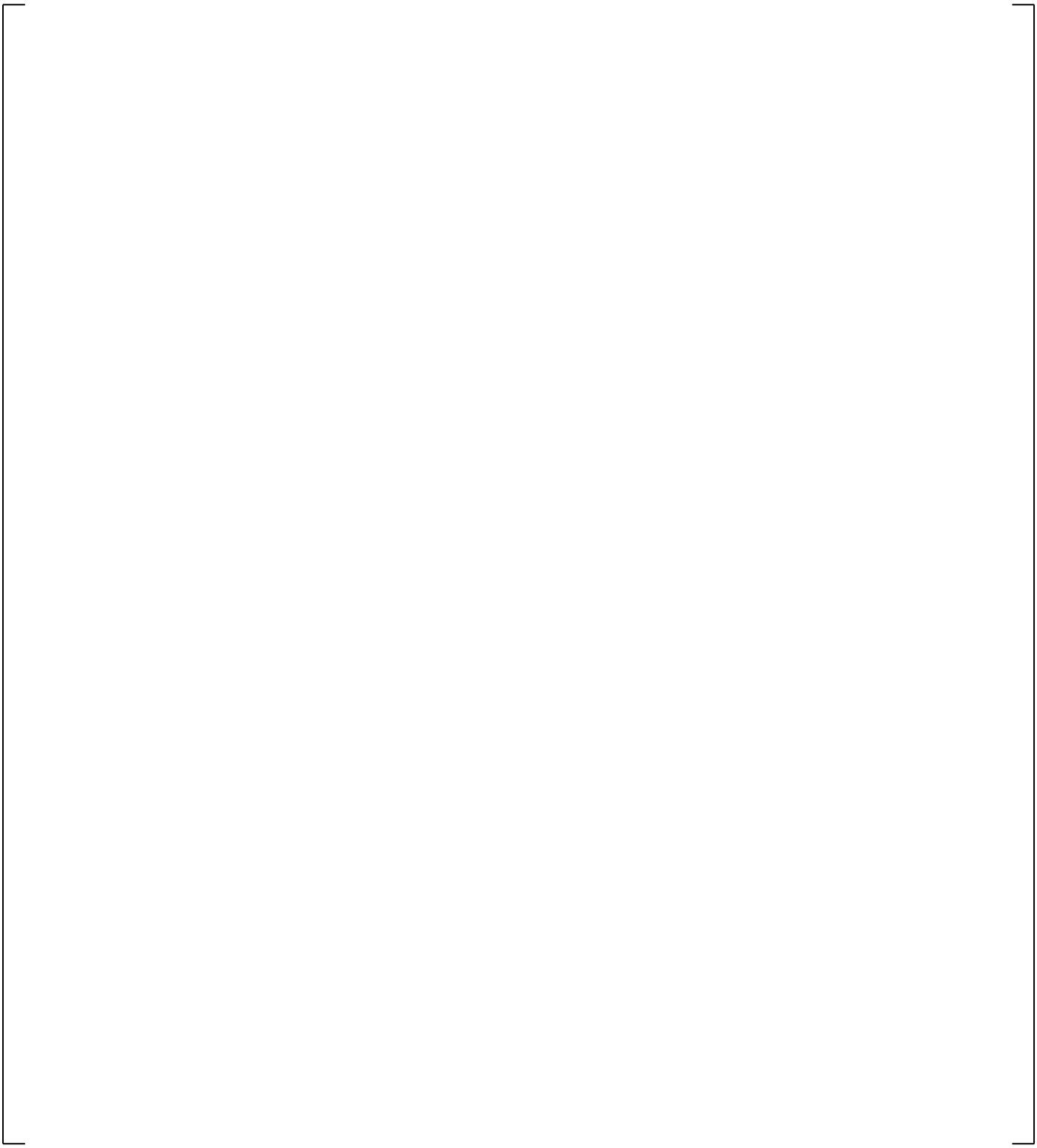

Figure 23.1.1-9 Comparison of Predicted and Measured Void Fraction at Level 6, Test 8-21-1

a,c

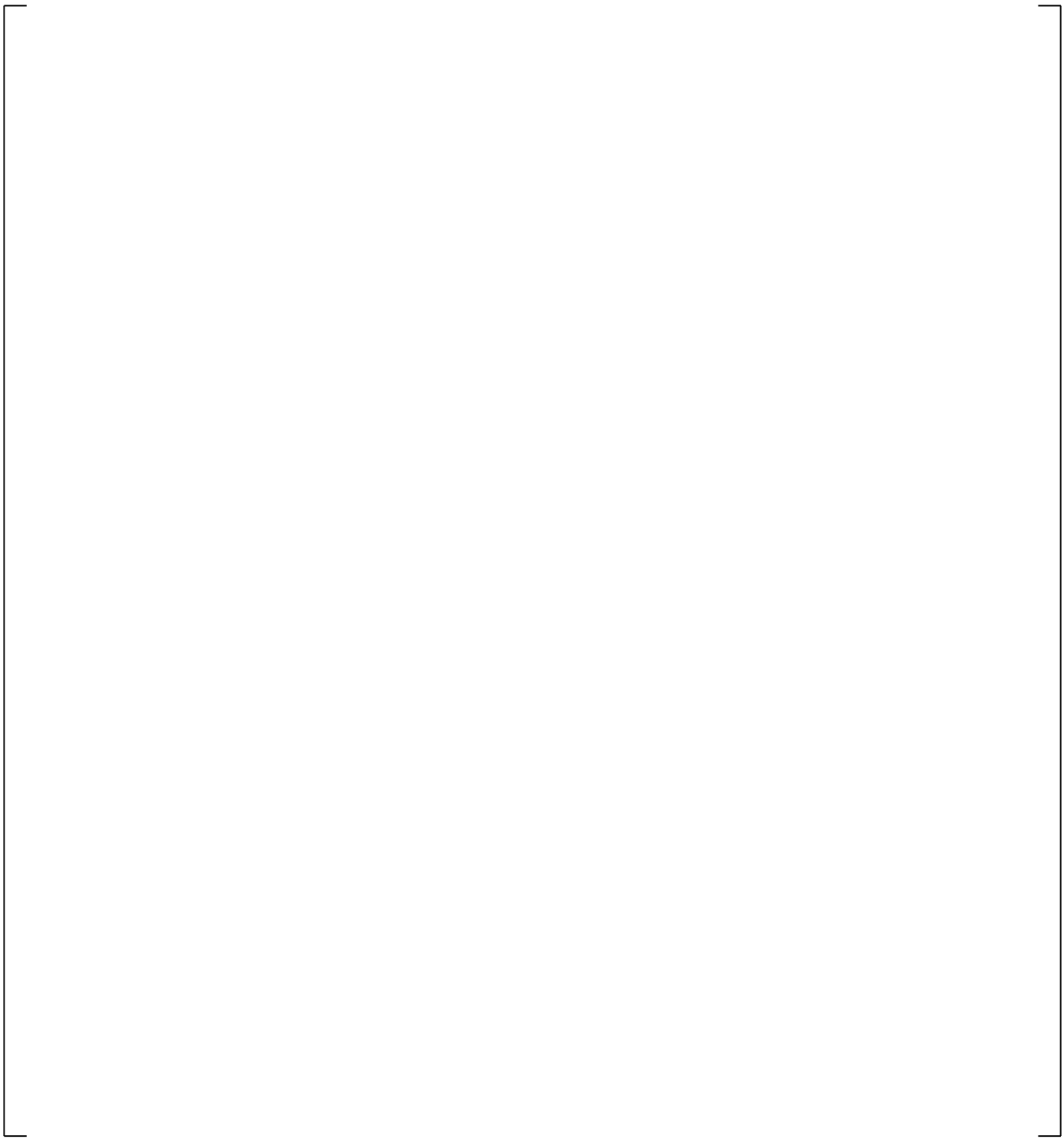

Figure 23.1.1-10 Comparison of Predicted and Measured Void Fraction at Level 1, Test 8-25-1

a,c

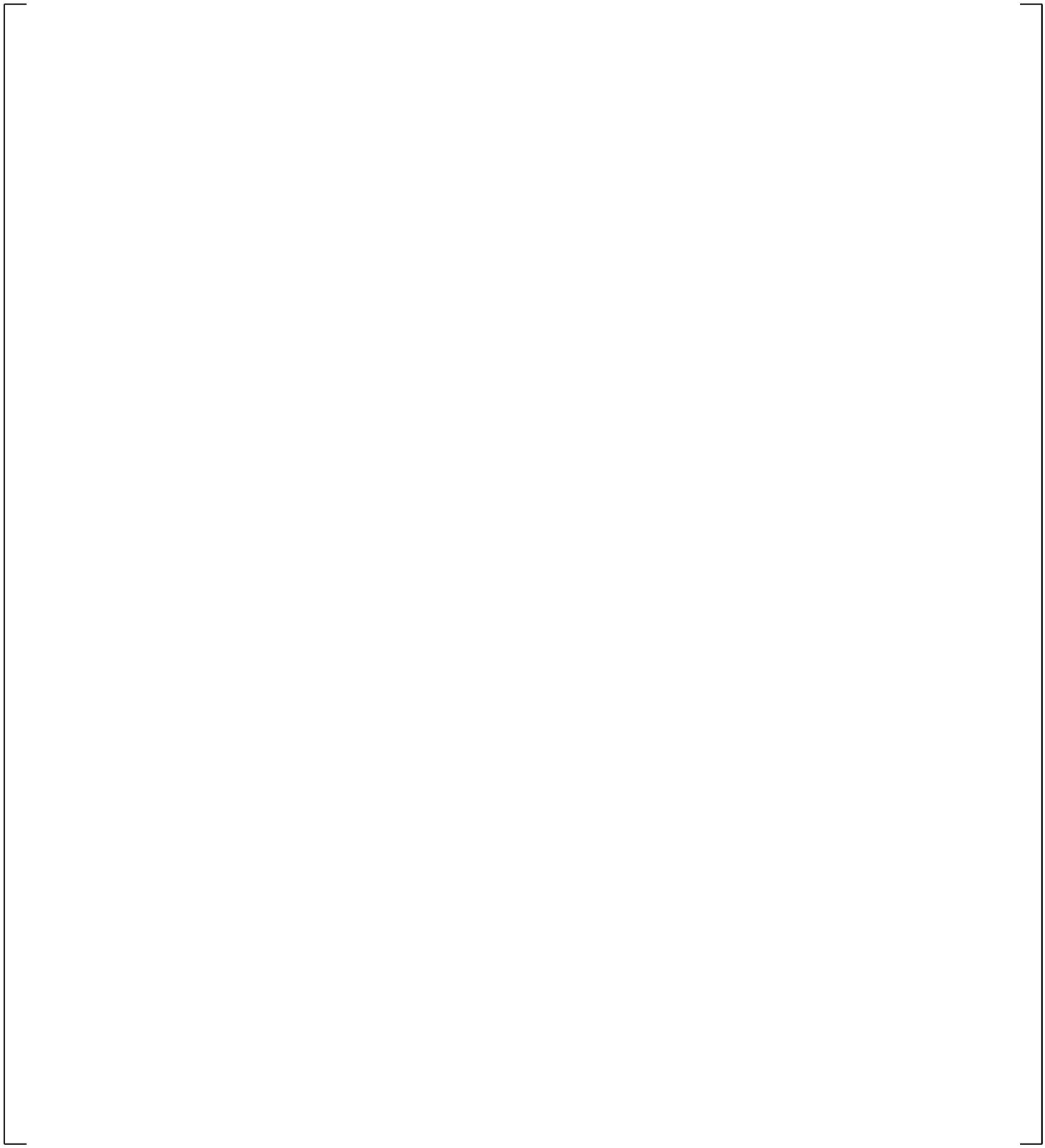

Figure 23.1.1-11 Comparison of Predicted and Measured Void Fraction at Level 2, Test 8-25-1

a,c

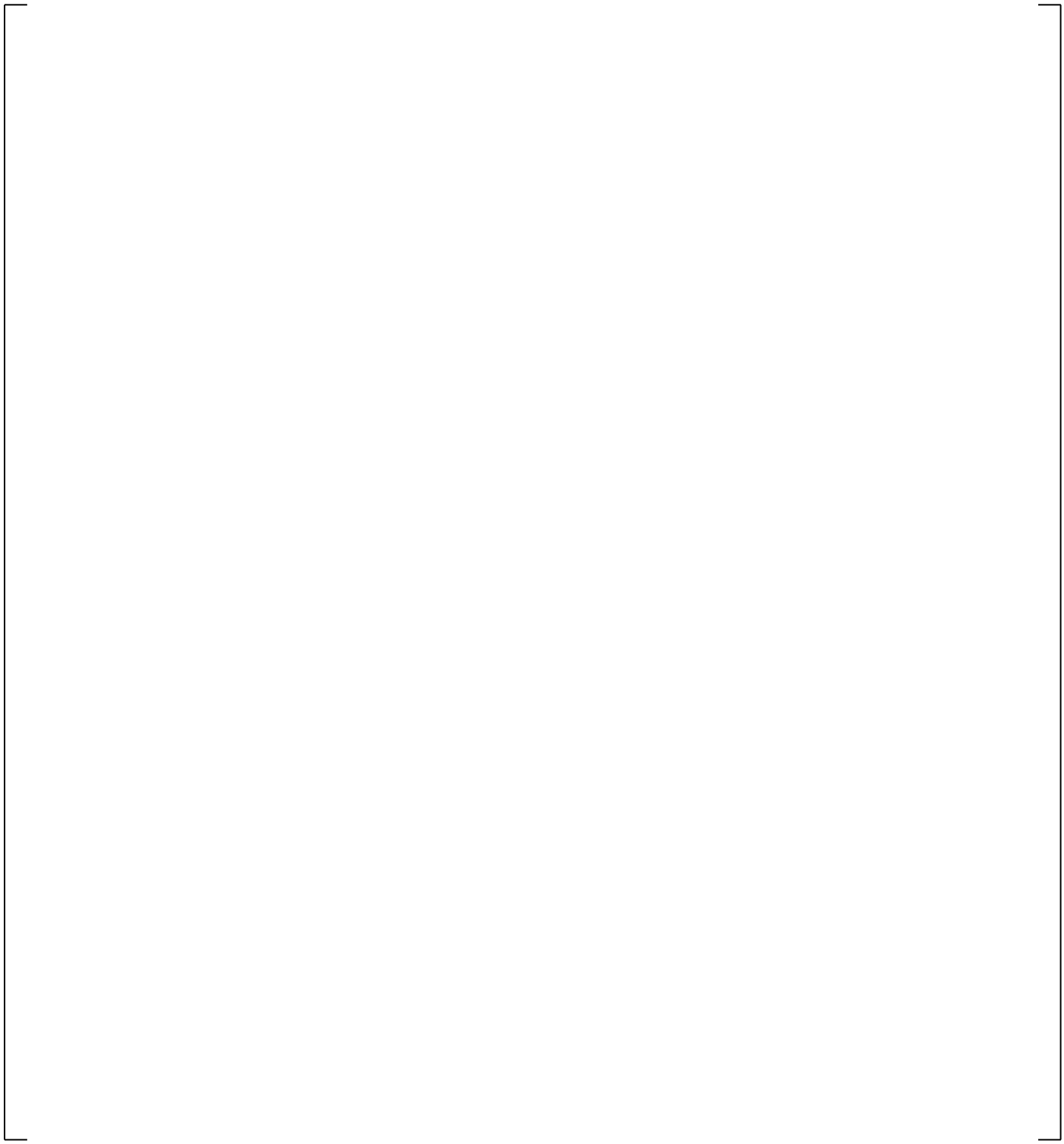

Figure 23.1.1-12 Comparison of Predicted and Measured Void Fraction at Level 3, Test 8-25-1

a,c

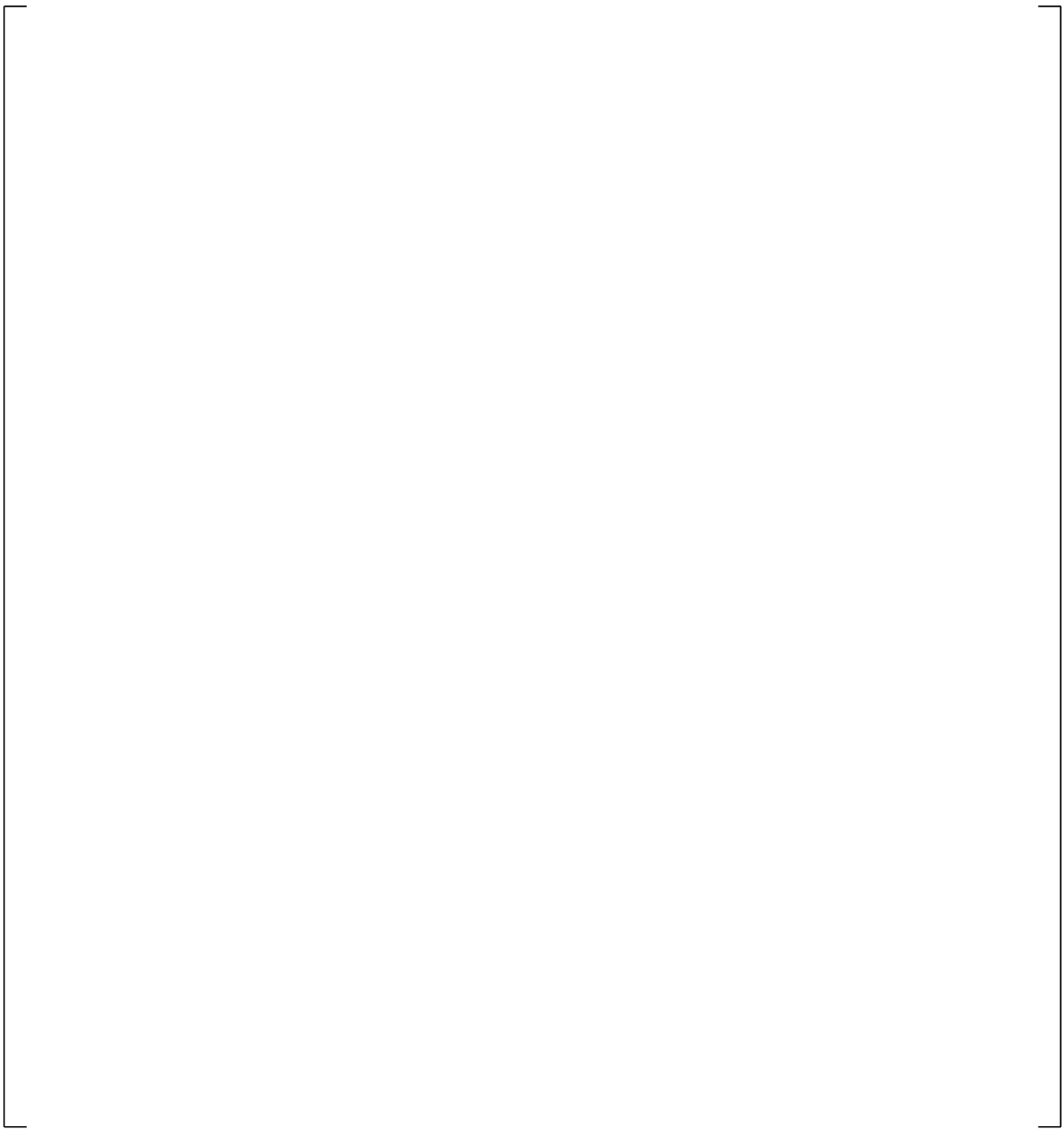

Figure 23.1.1-13 Comparison of Predicted and Measured Void Fraction at Level 4, Test 8-25-1

a,c

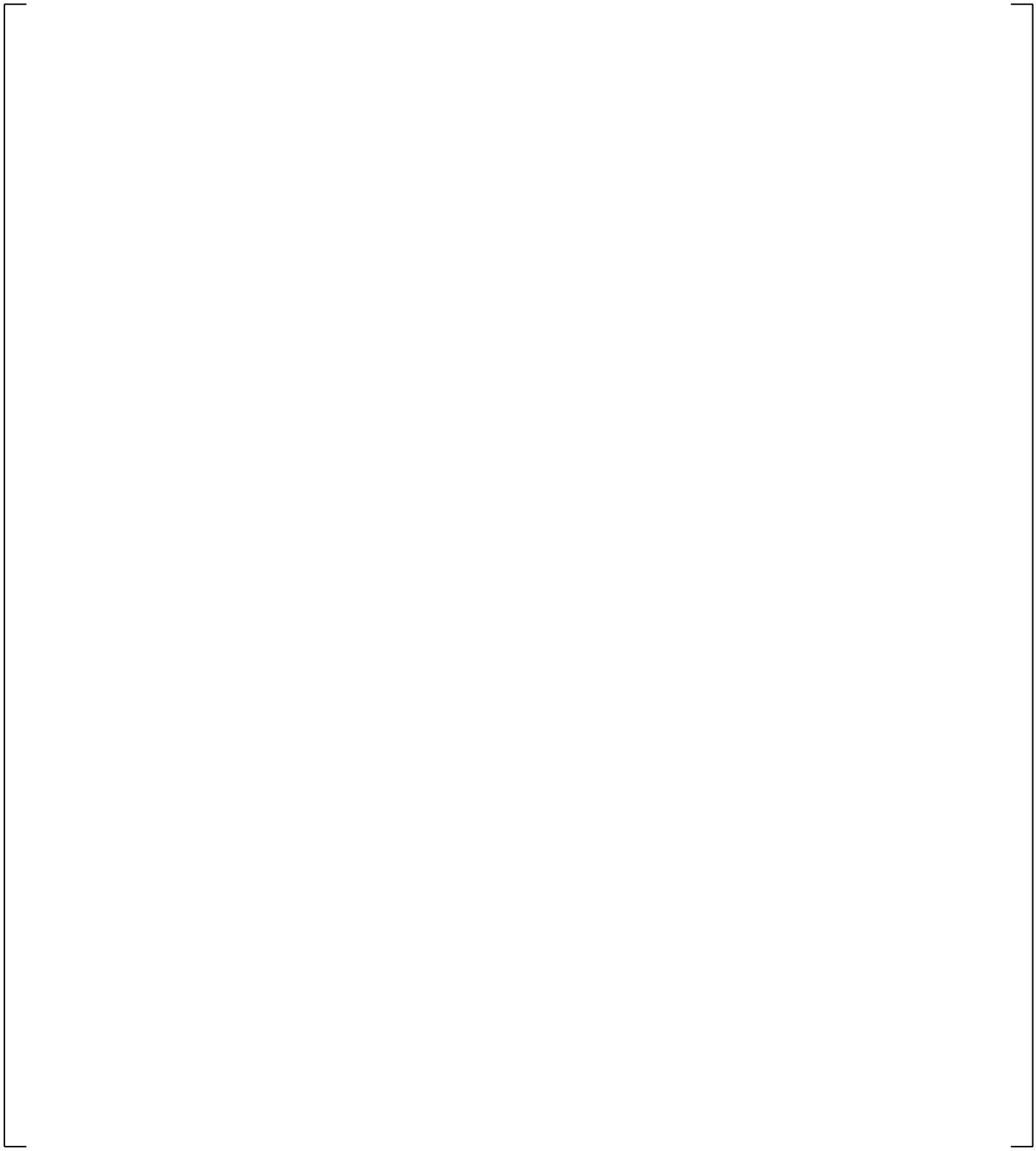

Figure 23.1.1-14 Comparison of Predicted and Measured Void Fraction at Level 5, Test 8-25-1

a,c

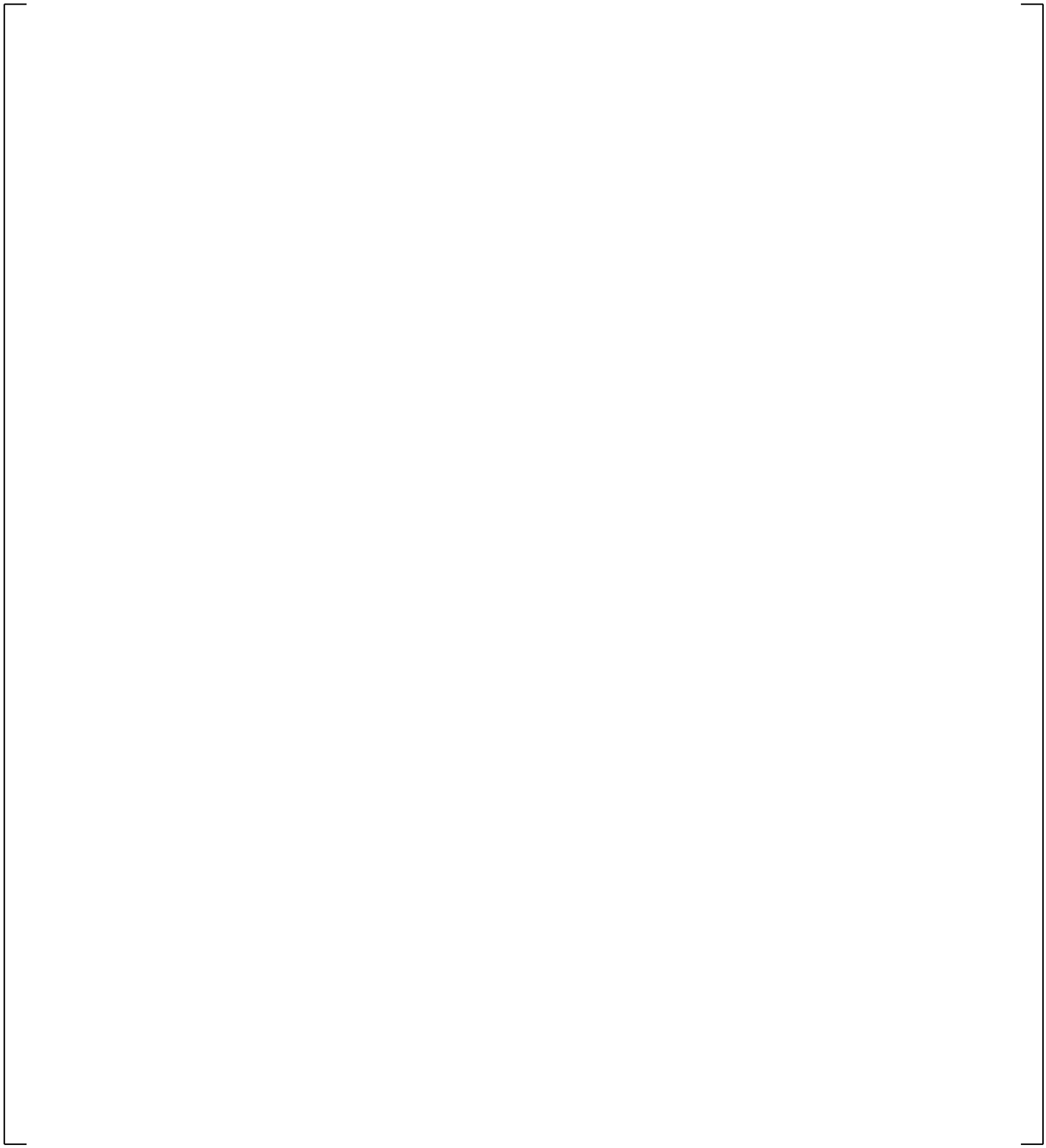

Figure 23.1.1-15 Comparison of Predicted and Measured Void Fraction at Level 6, Test 8-25-1

a,c

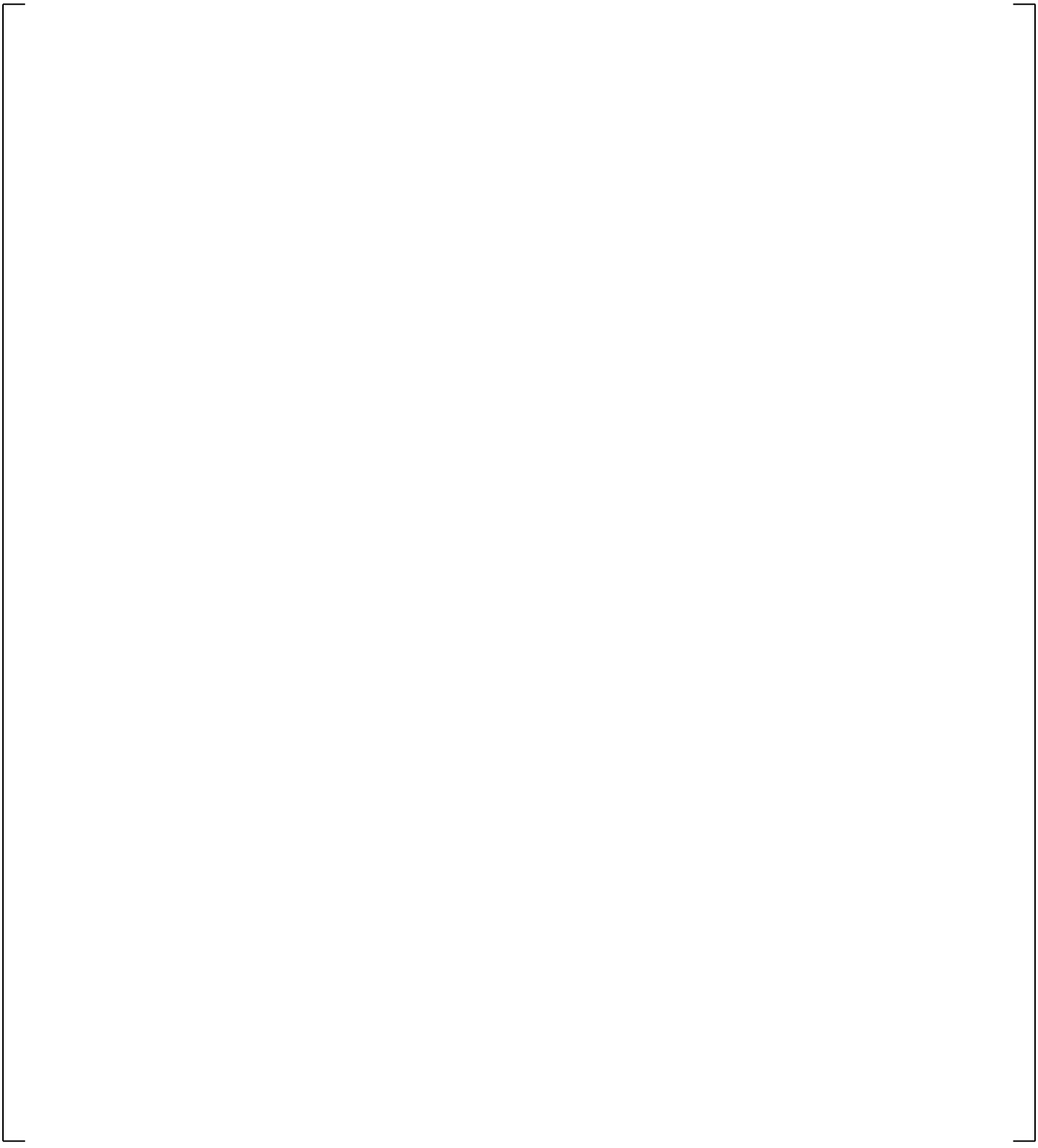

Figure 23.1.1-16 Comparison of Predicted and Measured Void Fraction at Level 1, Test 8-28-1

a,c

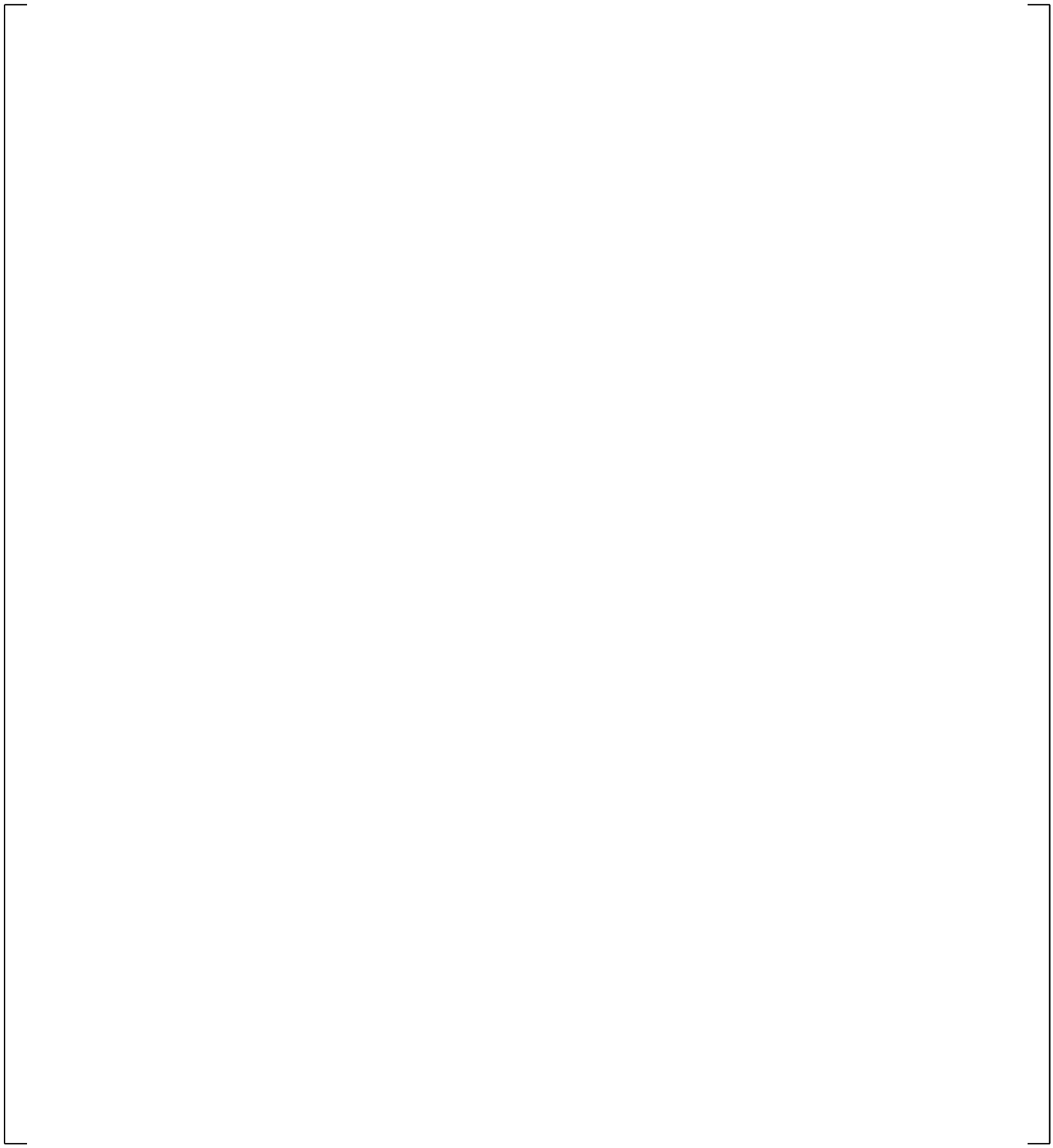

Figure 23.1.1-17 Comparison of Predicted and Measured Void Fraction at Level 2, Test 8-28-1

a,c

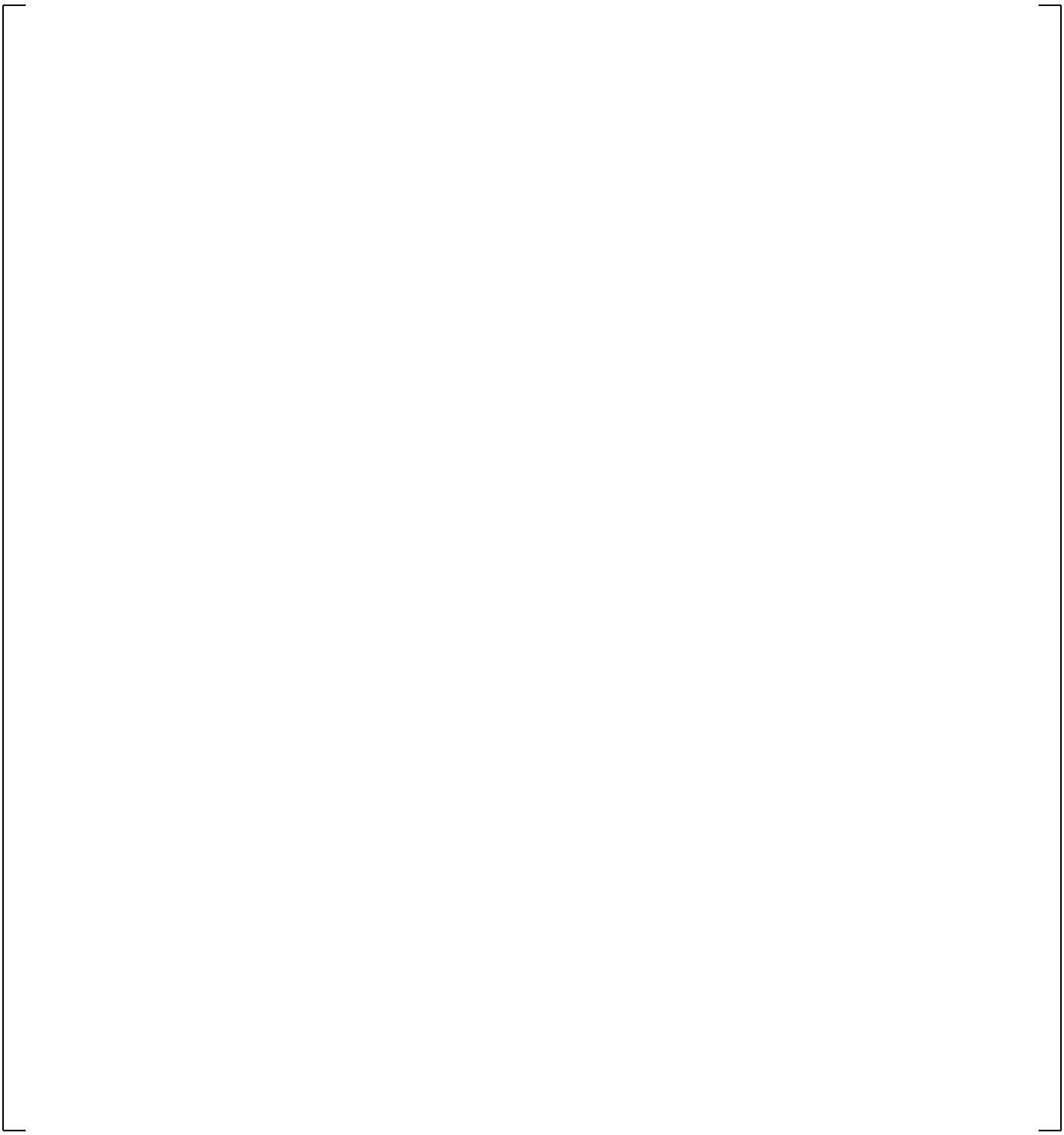

Figure 23.1.1-18 Comparison of Predicted and Measured Void Fraction at Level 3, Test 8-28-1

a,c

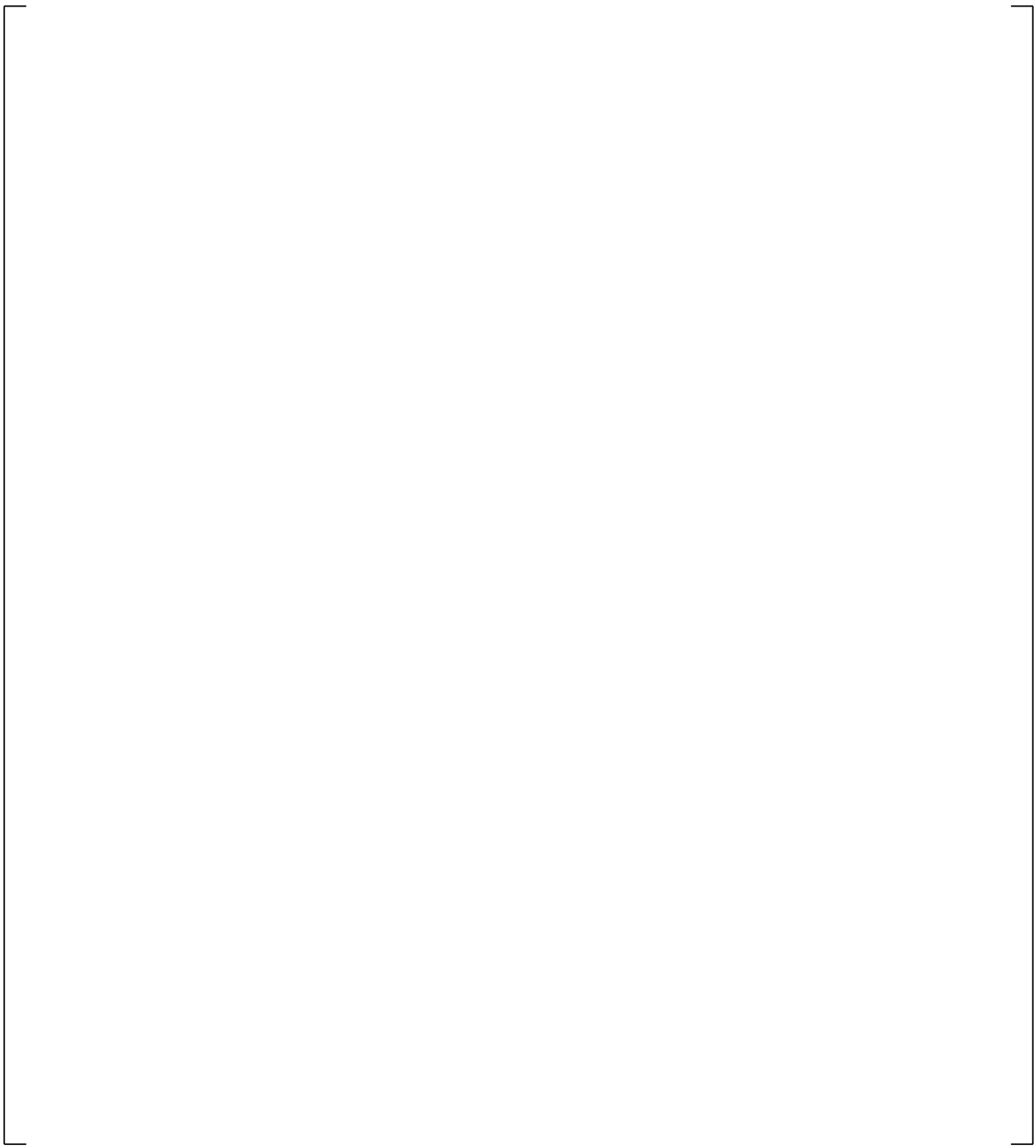

Figure 23.1.1-19 Comparison of Predicted and Measured Void Fraction at Level 4, Test 8-28-1

a,c

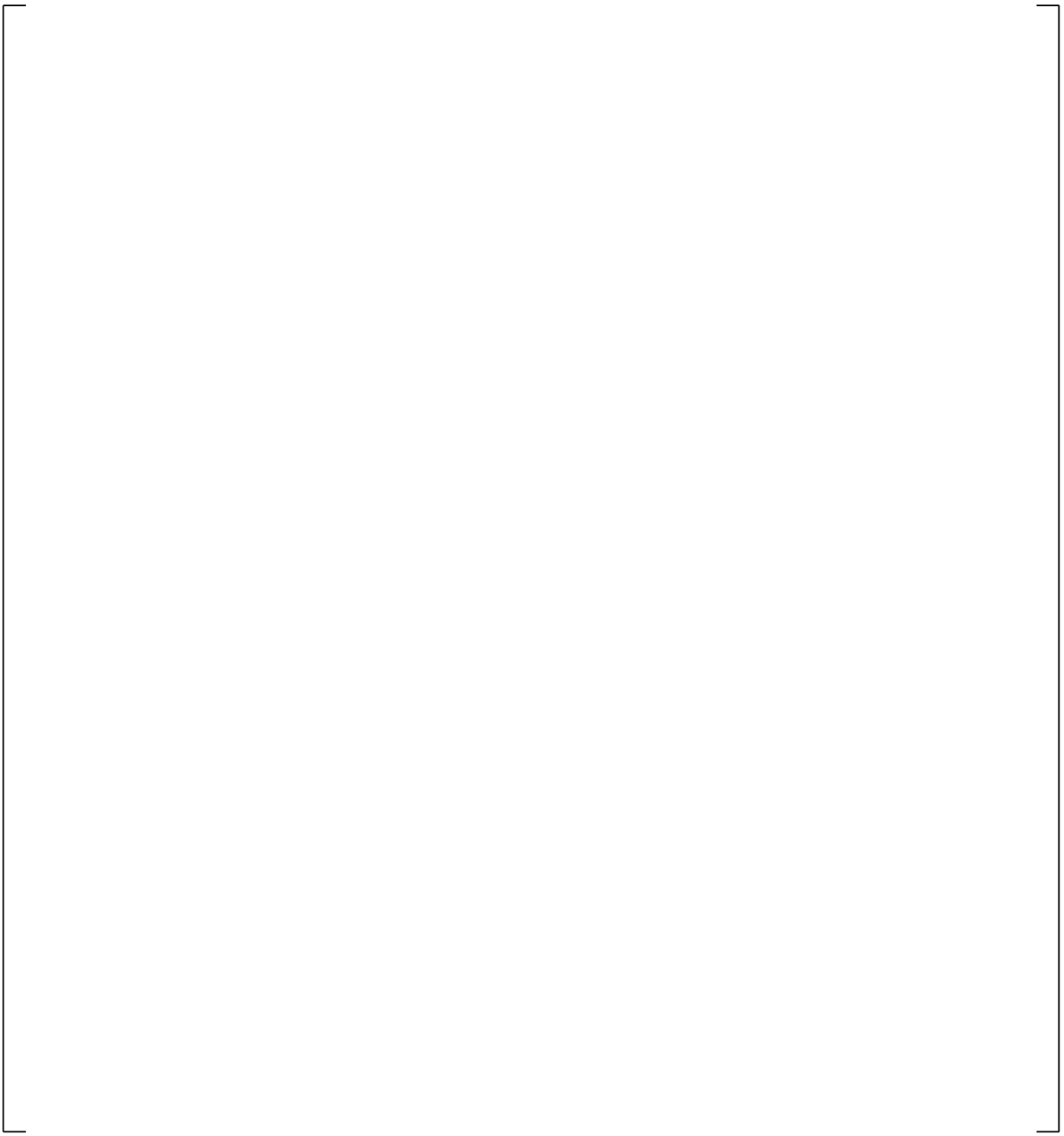

Figure 23.1.1-20 Comparison of Predicted and Measured Void Fraction at Level 5, Test 8-28-1

a,c

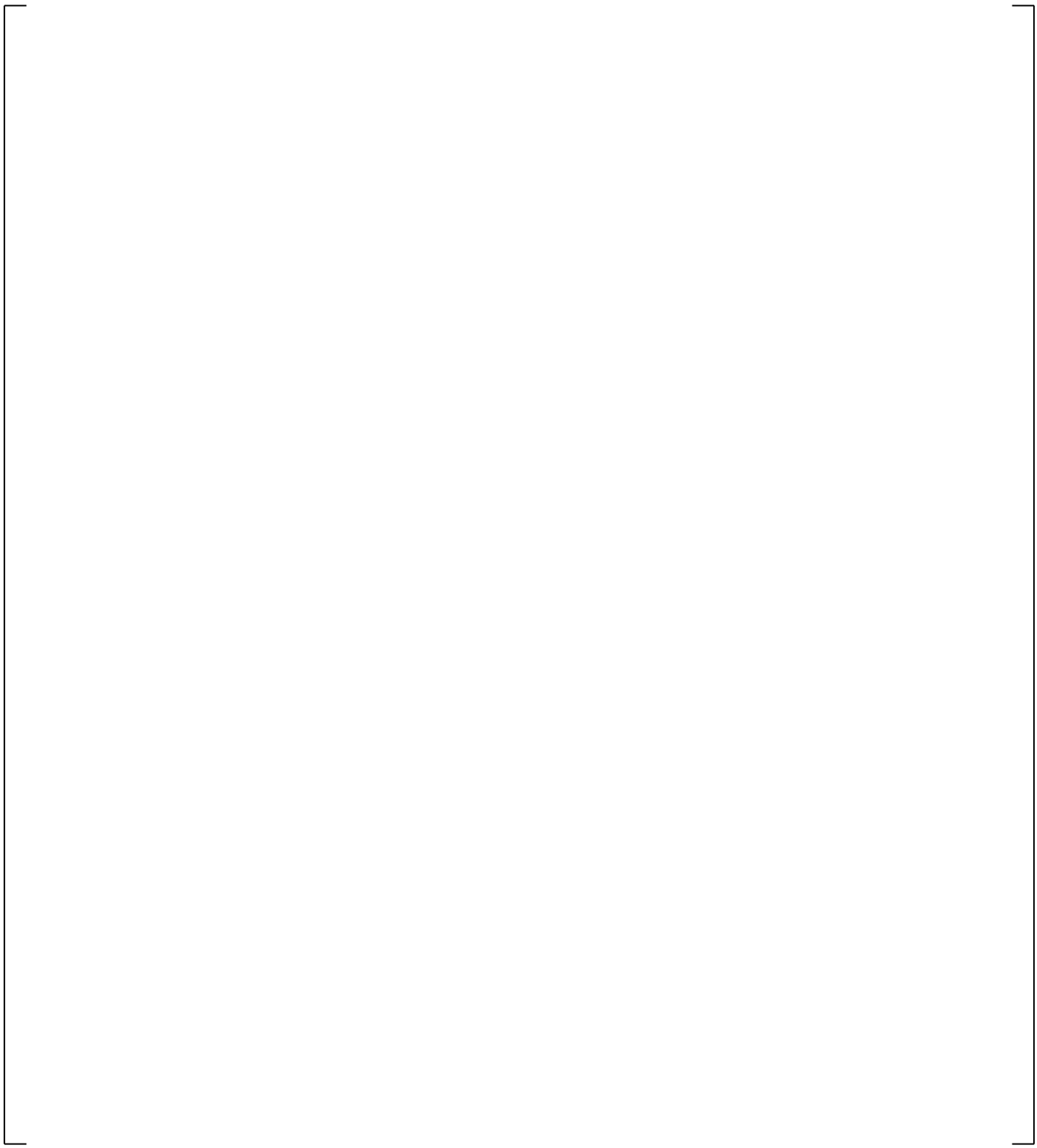

Figure 23.1.1-21 Comparison of Predicted and Measured Void Fraction at Level 6, Test 8-28-1

a,c

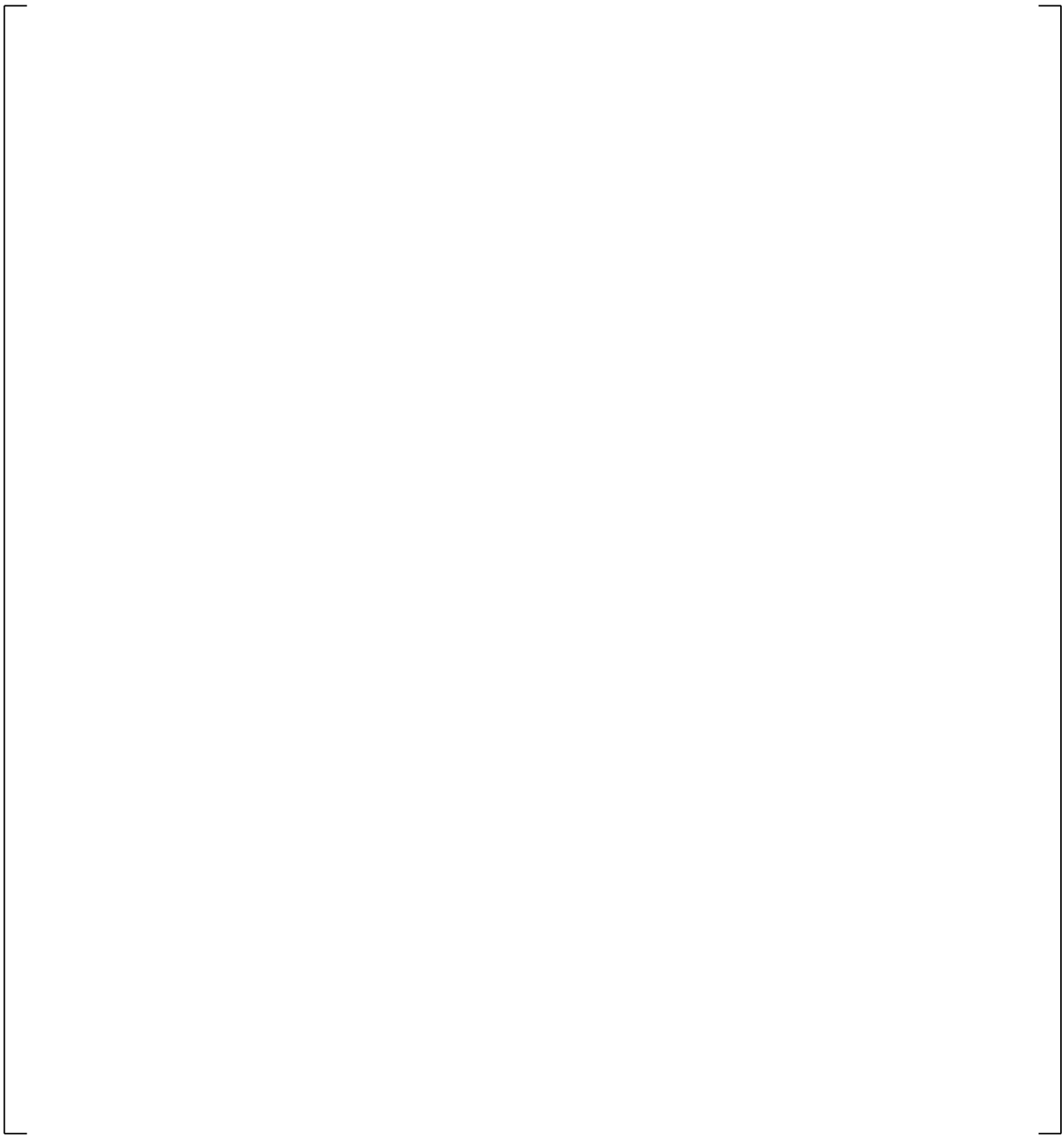

Figure 23.1.1-22 Comparison of Predicted and Measured Void Fraction at Level 1, Test 9-1-1

a,c

Figure 23.1.1-23 Comparison of Predicted and Measured Void Fraction at Level 2, Test 9-1-1

a,c

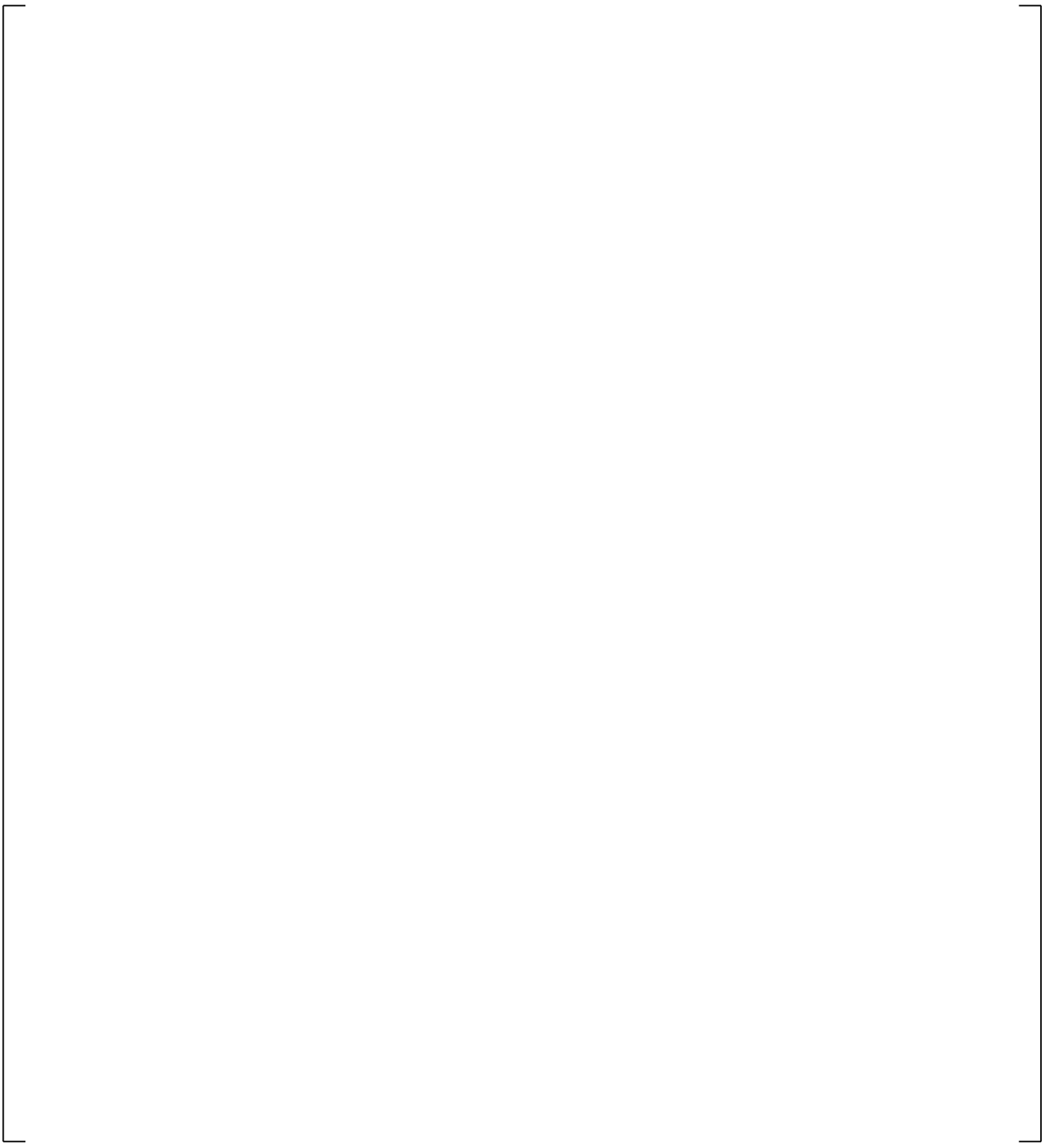

Figure 23.1.1-24 Comparison of Predicted and Measured Void Fraction at Level 3, Test 9-1-1

a,c

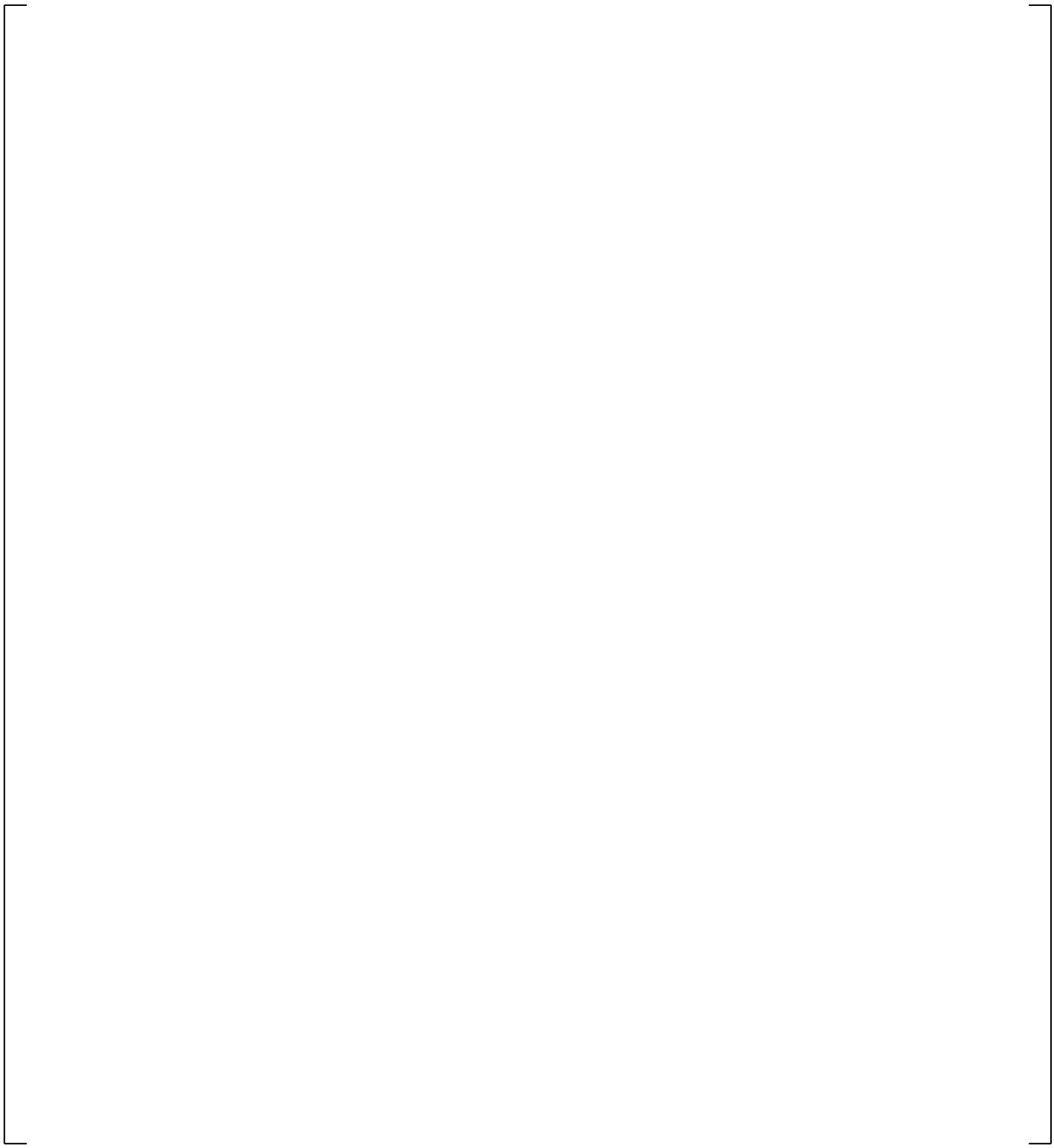

Figure 23.1.1-25 Comparison of Predicted and Measured Void Fraction at Level 4, Test 9-1-1

a,c

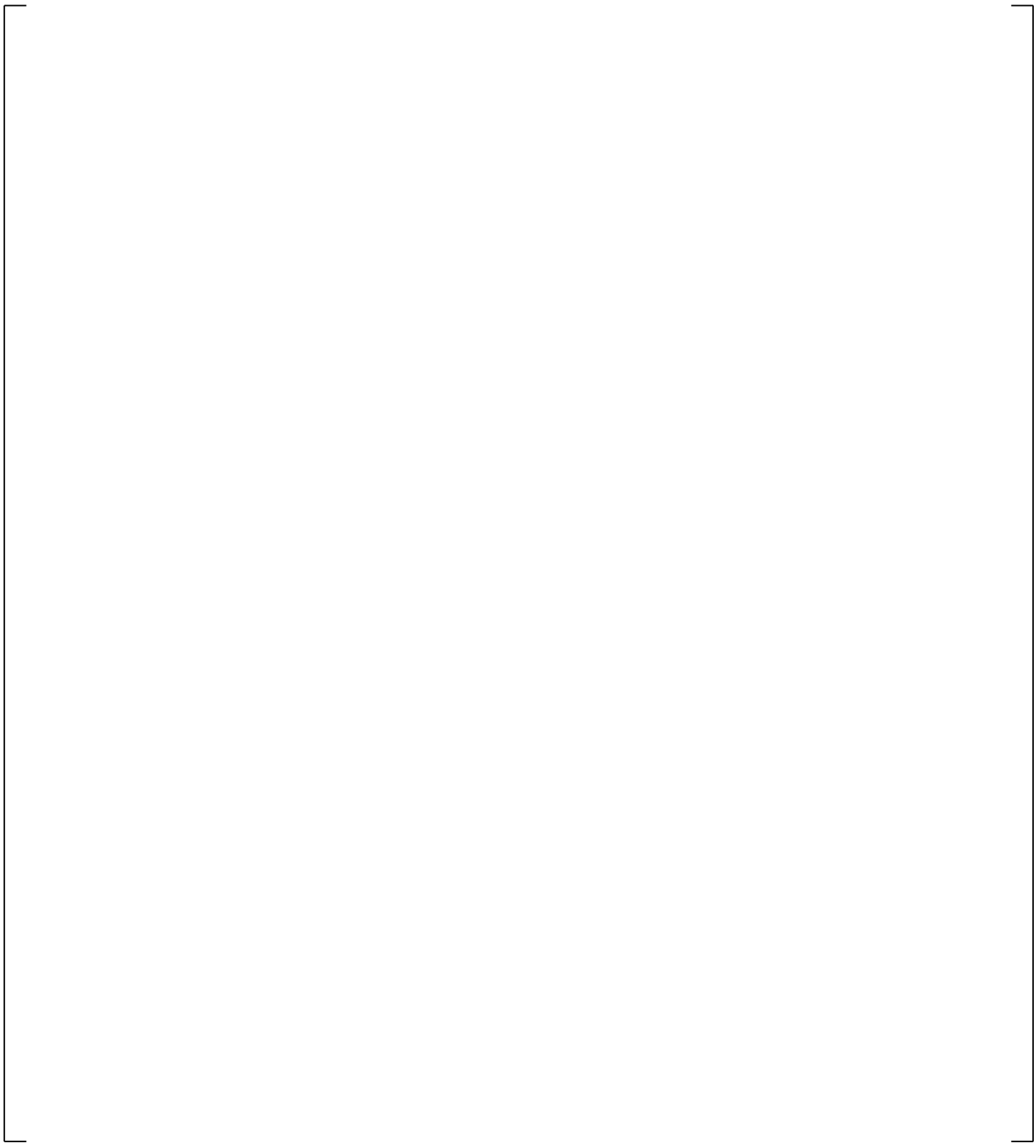

Figure 23.1.1-26 Comparison of Predicted and Measured Void Fraction at Level 5, Test 9-1-1

a,c

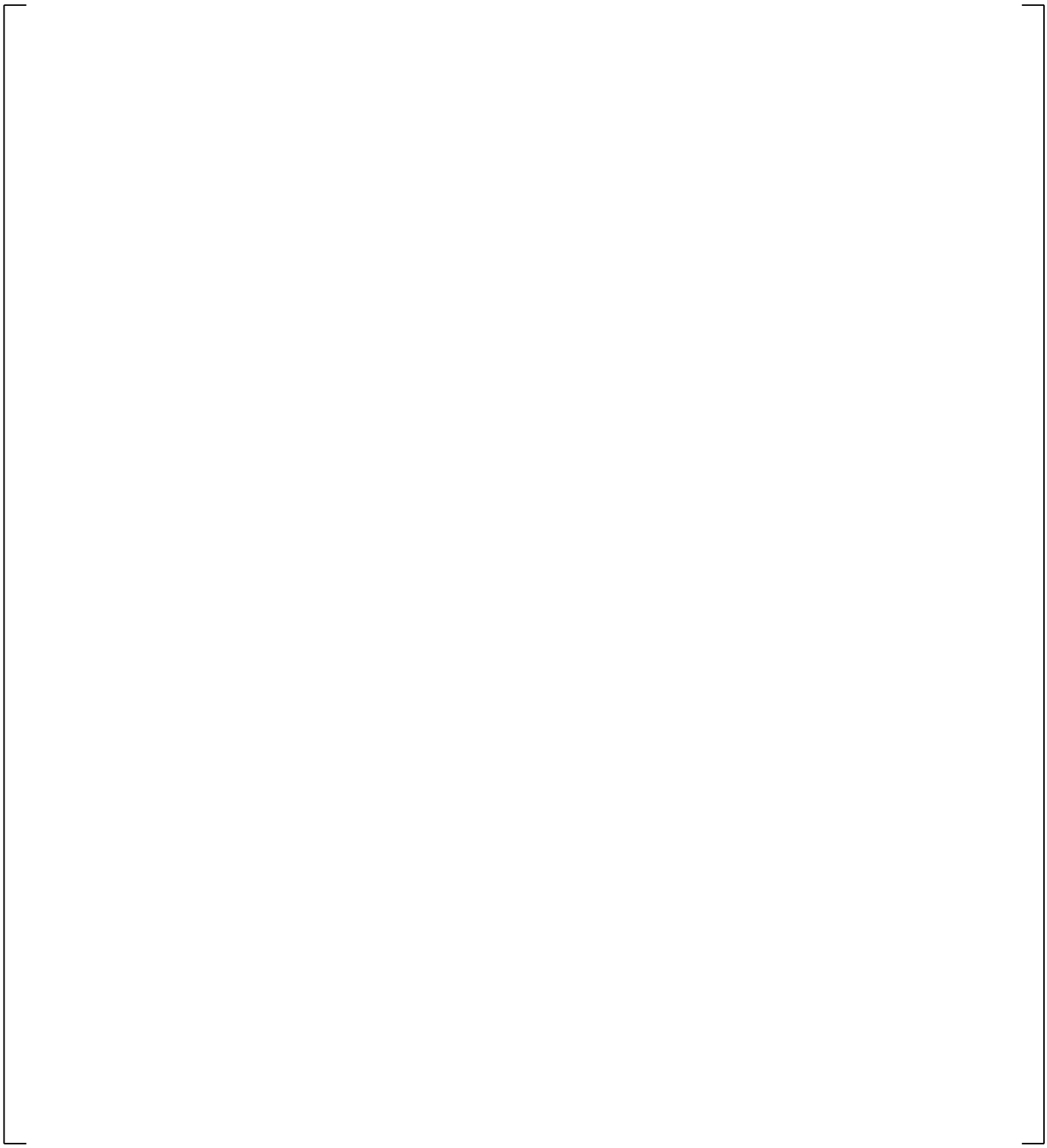

Figure 23.1.1-27 Comparison of Predicted and Measured Void Fraction at Level 6, Test 9-1-1

a,c

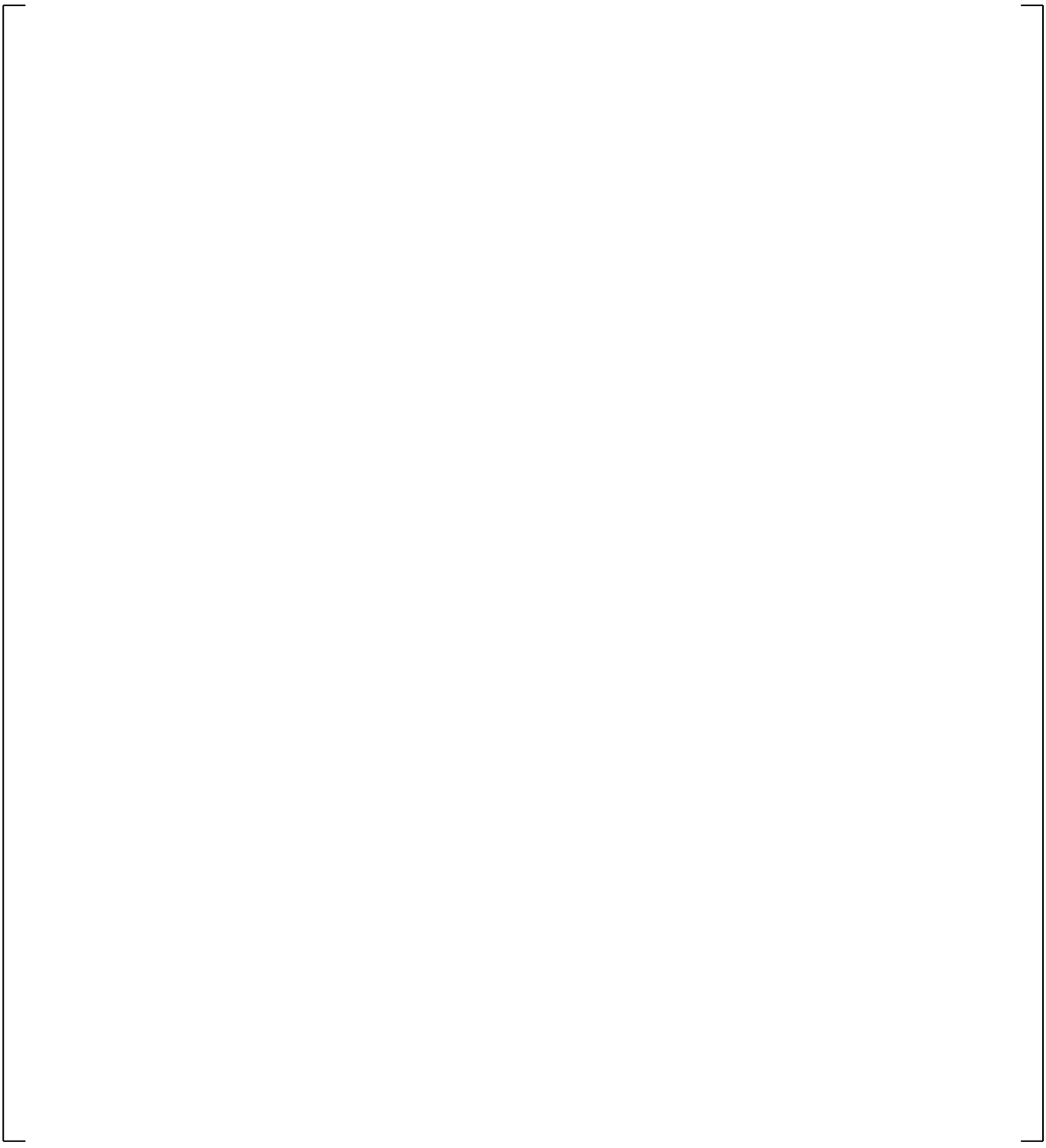

Figure 23.1.1-28 Comparison of Predicted and Measured Void Fraction at Level 1, Test 9-15-1

a,c

Figure 23.1.1-29 Comparison of Predicted and Measured Void Fraction at Level 2, Test 9-15-1

a,c

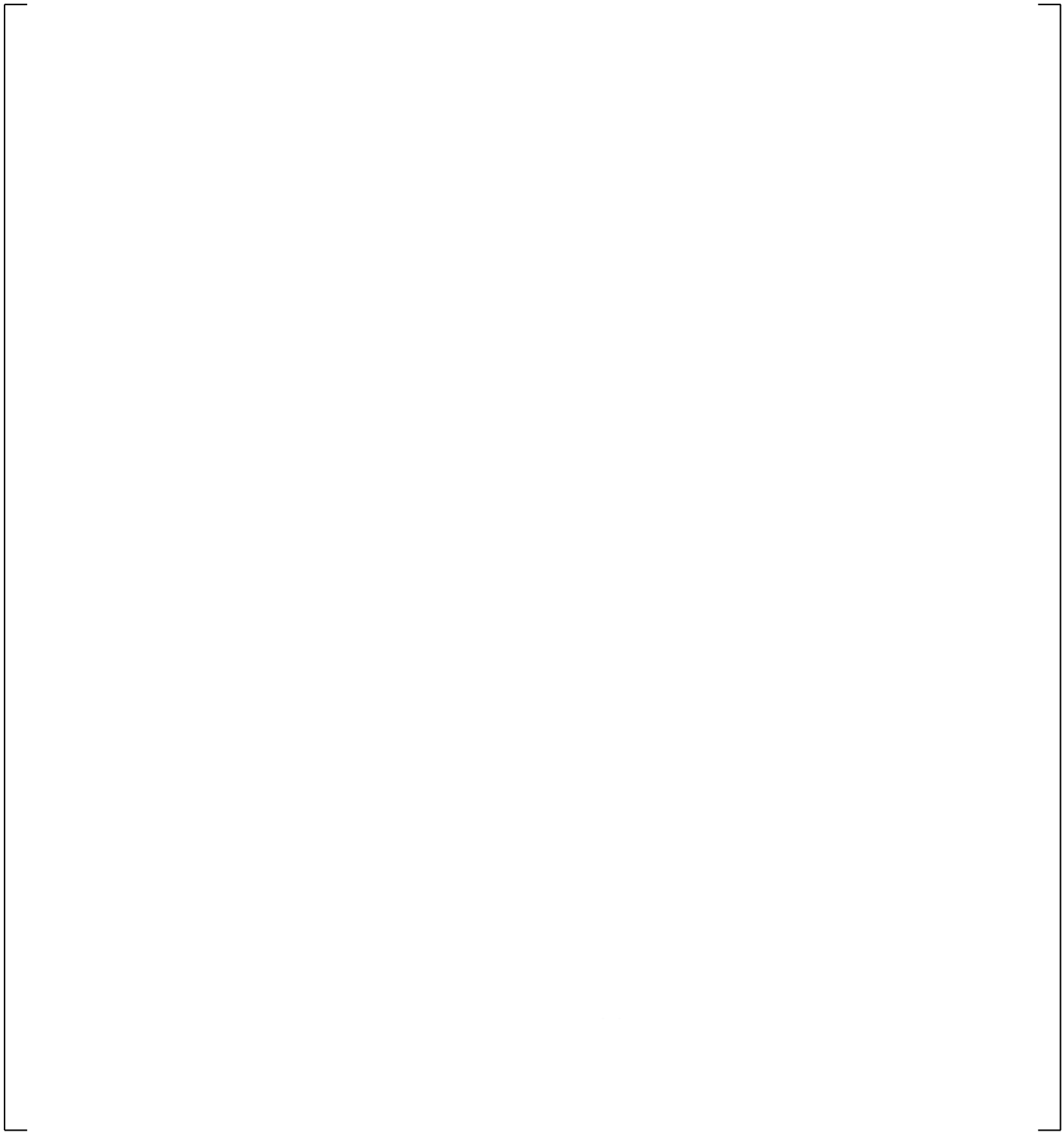

Figure 23.1.1-30 Comparison of Predicted and Measured Void Fraction at Level 3, Test 9-15-1

a,c

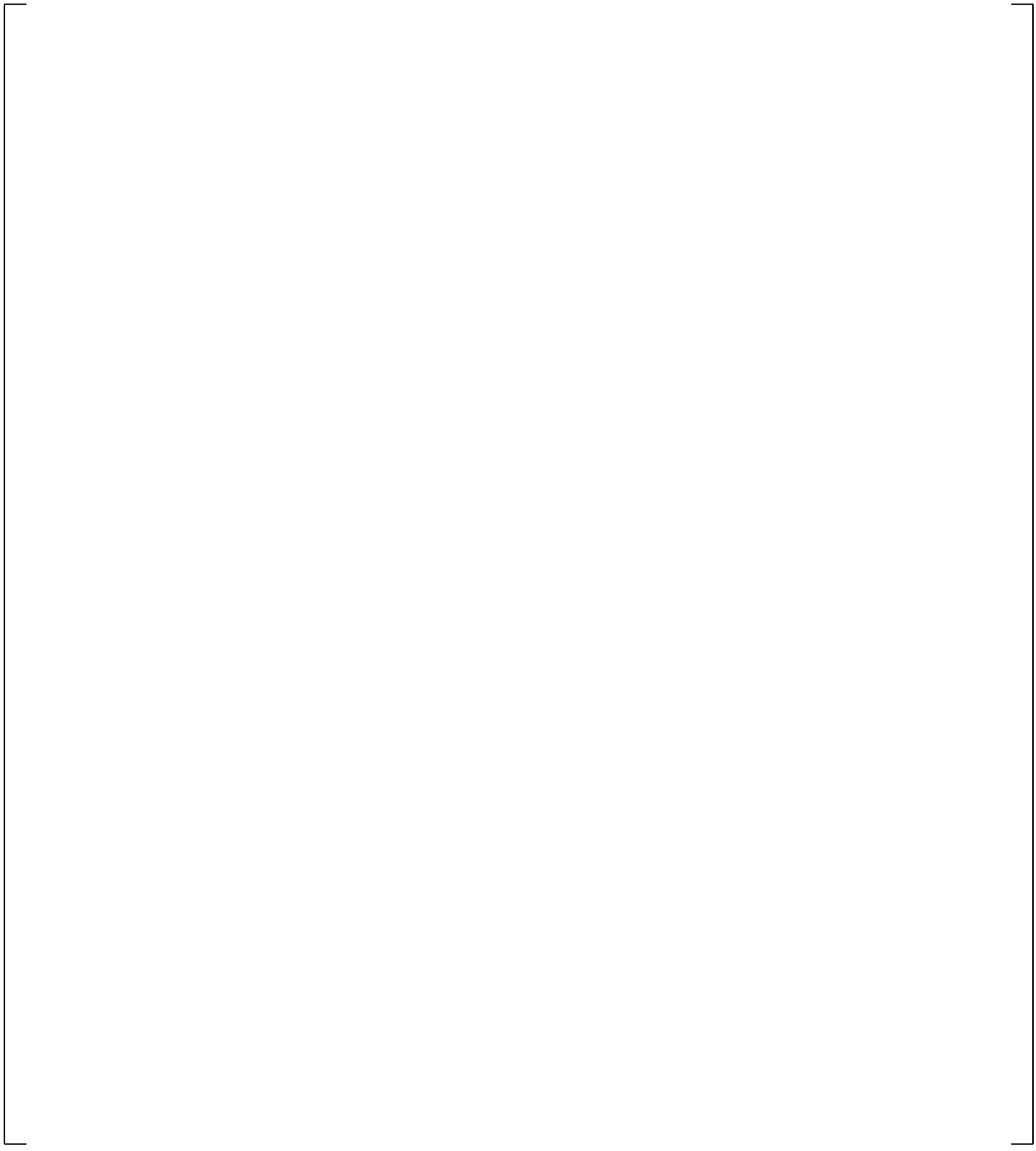

Figure 23.1.1-31 Comparison of Predicted and Measured Void Fraction at Level 4, Test 9-15-1

a,c

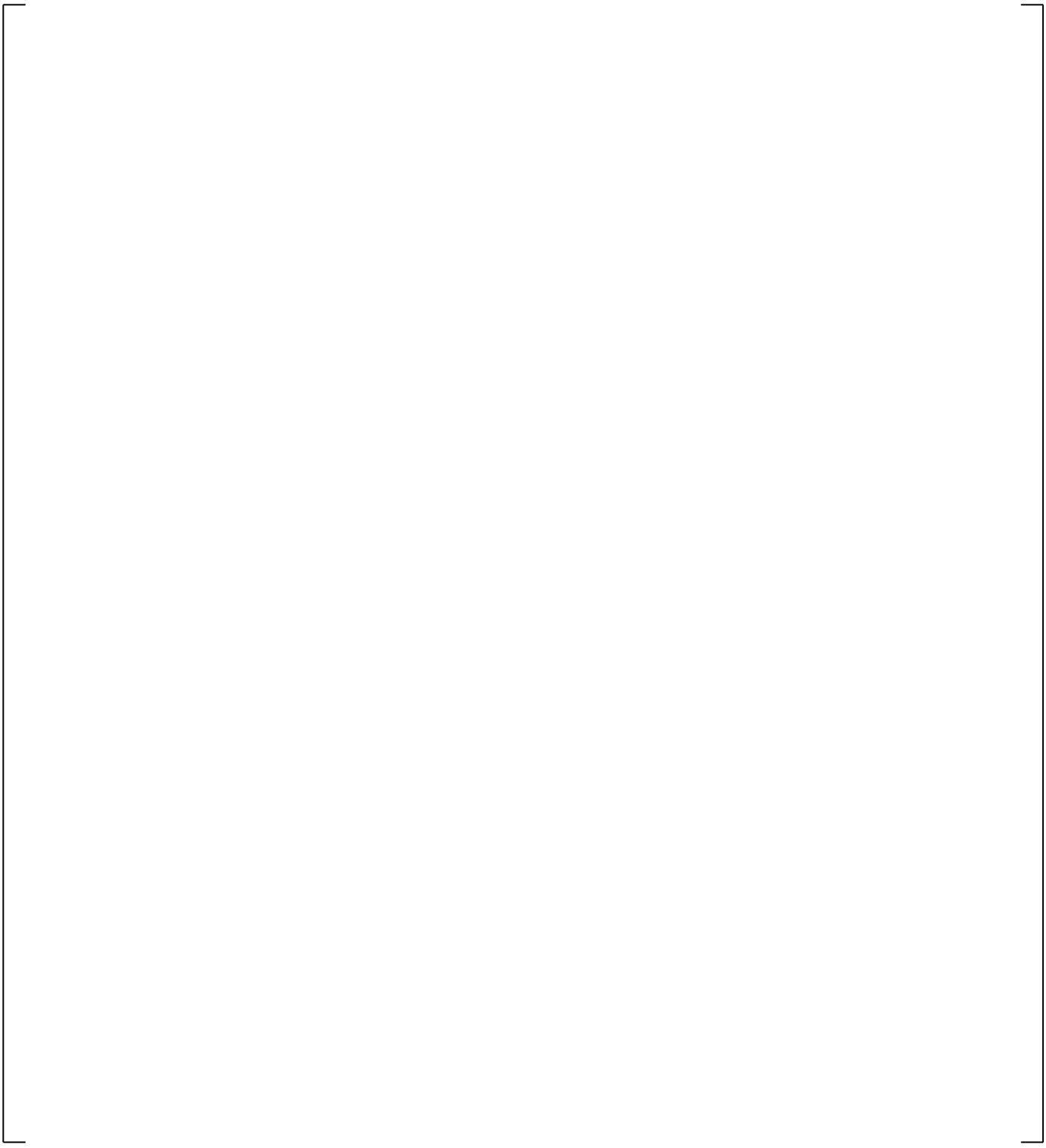

Figure 23.1.1-32 Comparison of Predicted and Measured Void Fraction at Level 5, Test 9-15-1

a,c

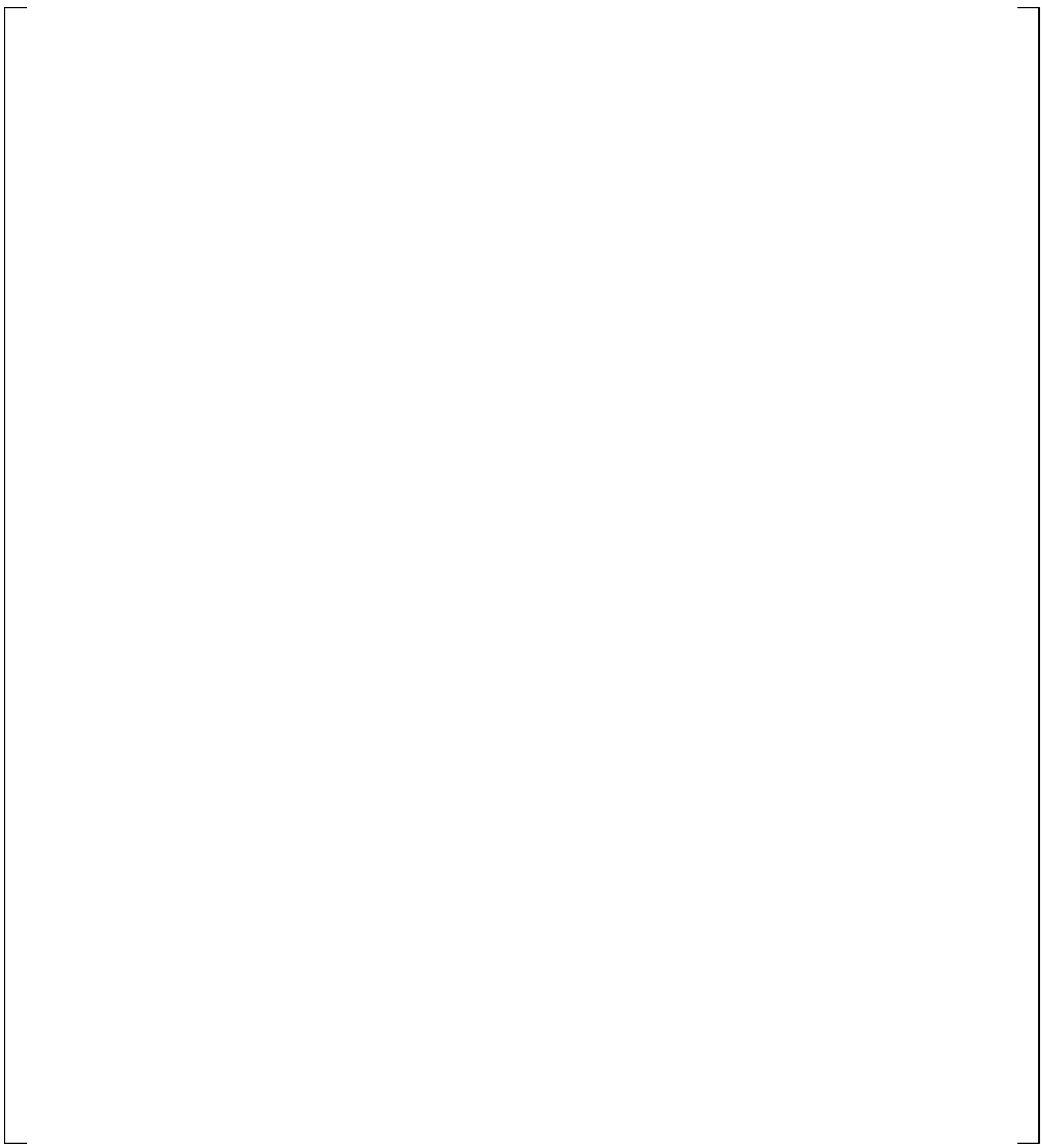

Figure 23.1.1-33 Comparison of Predicted and Measured Void Fraction at Level 6, Test 9-15-1

a,c

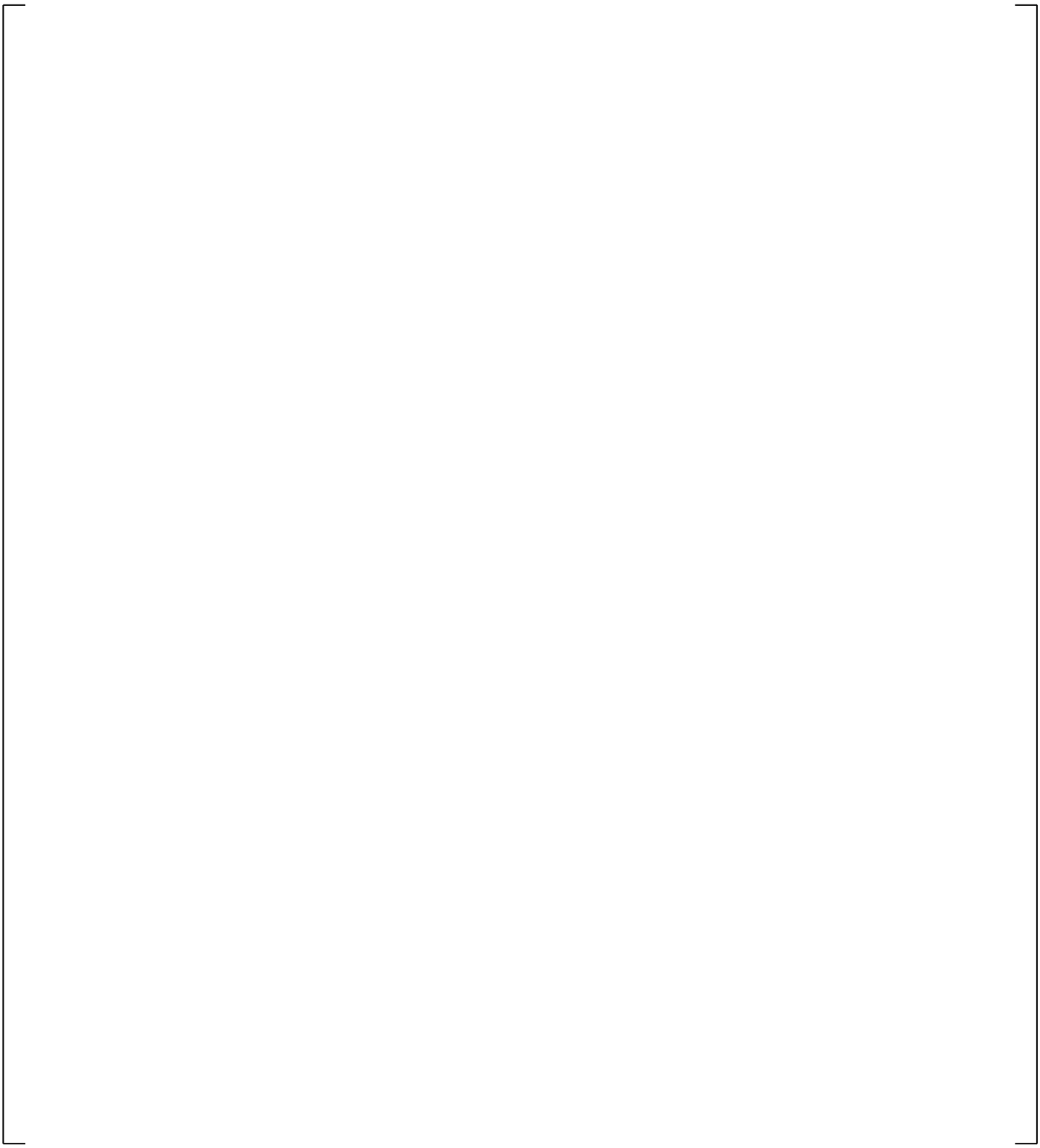

Figure 23.1.1-34 Comparison of Predicted and Measured Void Fraction at Level 1, Test 1004-3

a,c

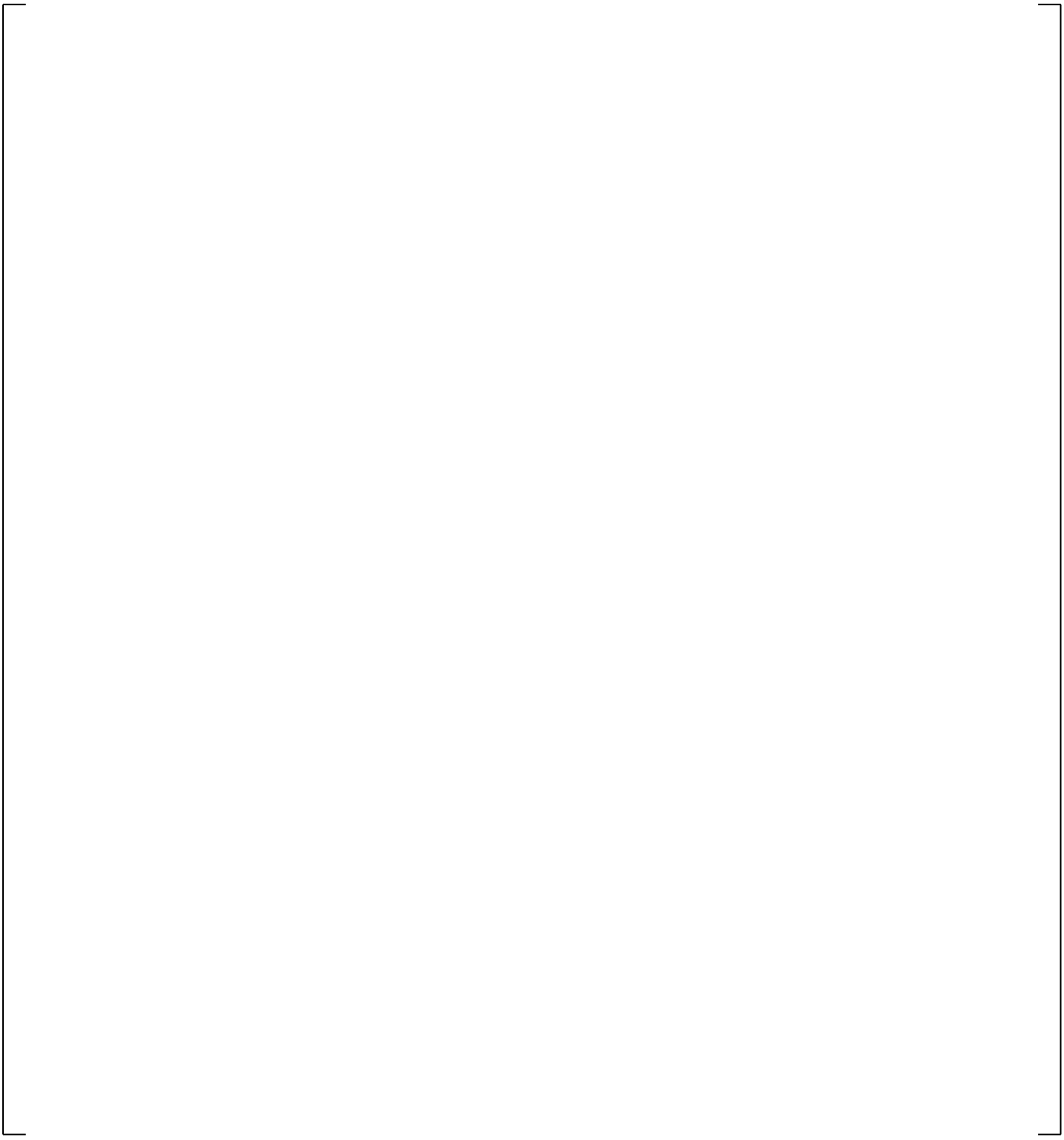

Figure 23.1.1-35 Comparison of Predicted and Measured Void Fraction at Level 2, Test 1004-3

a,c

Figure 23.1.1-36 Comparison of Predicted and Measured Void Fraction at Level 3, Test 1004-3

a,c

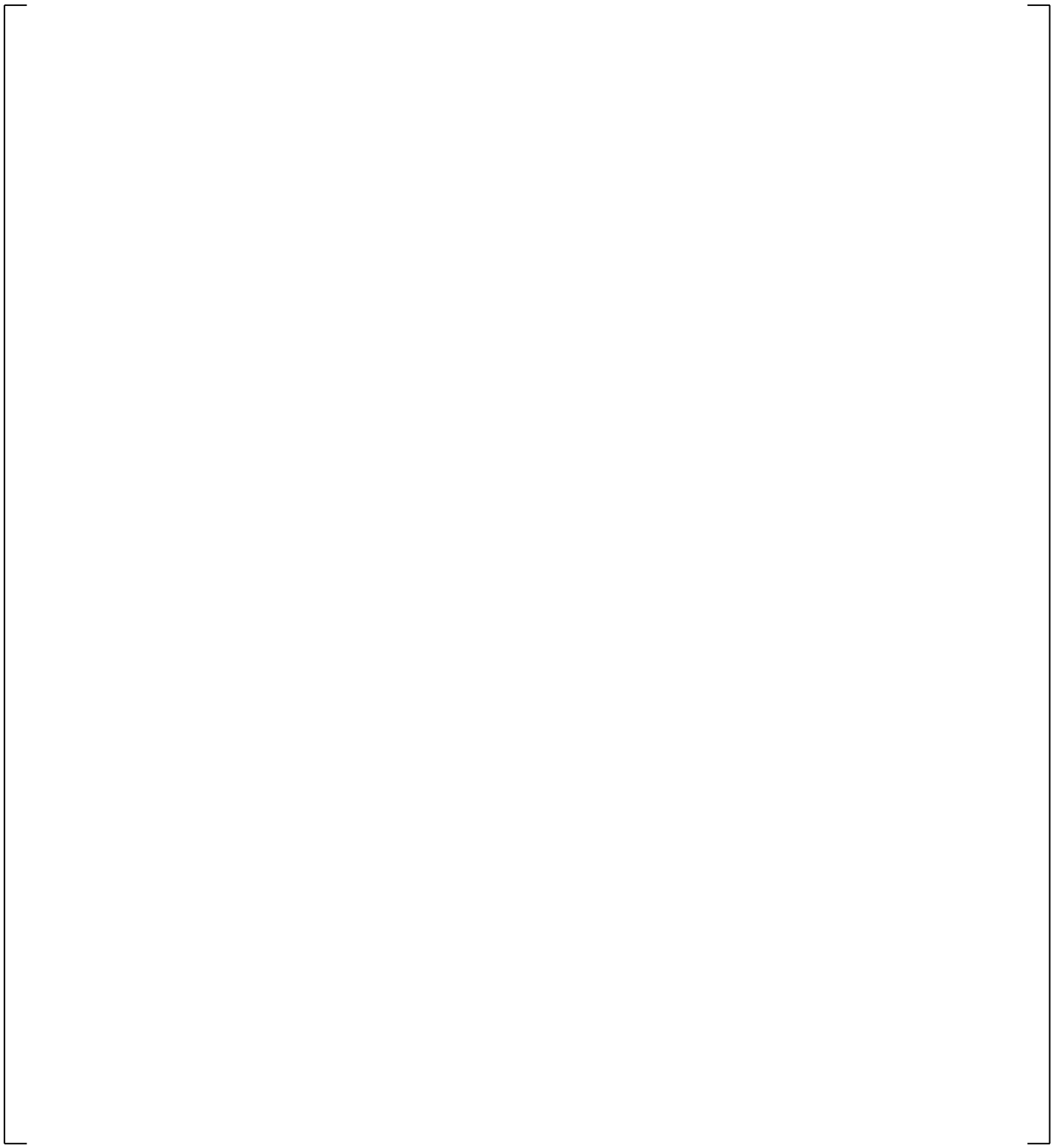

Figure 23.1.1-37 Comparison of Predicted and Measured Void Fraction at Level 4, Test 1004-3

a,c

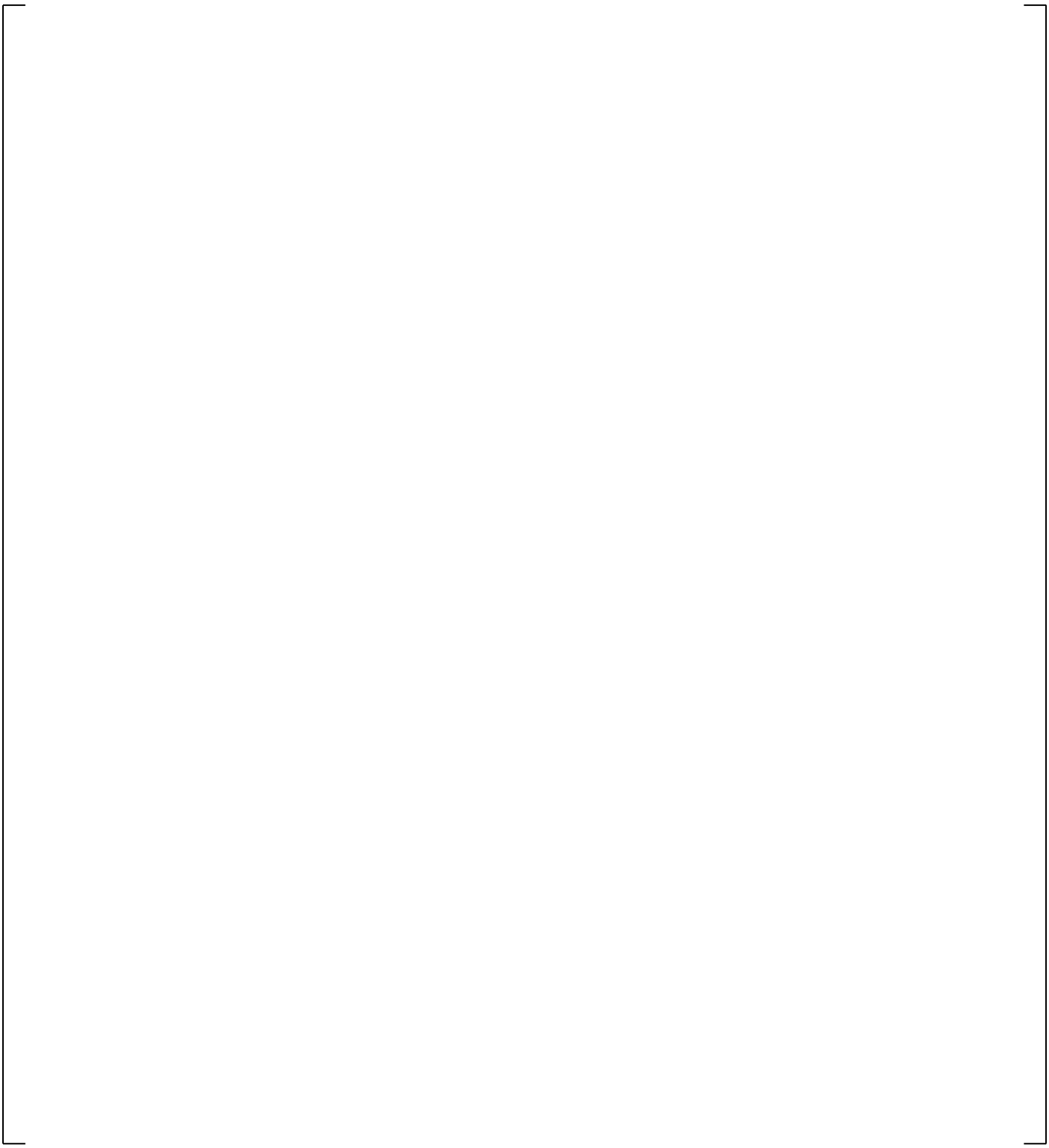

Figure 23.1.1-38 Comparison of Predicted and Measured Void Fraction at Level 5, Test 1004-3

a,c

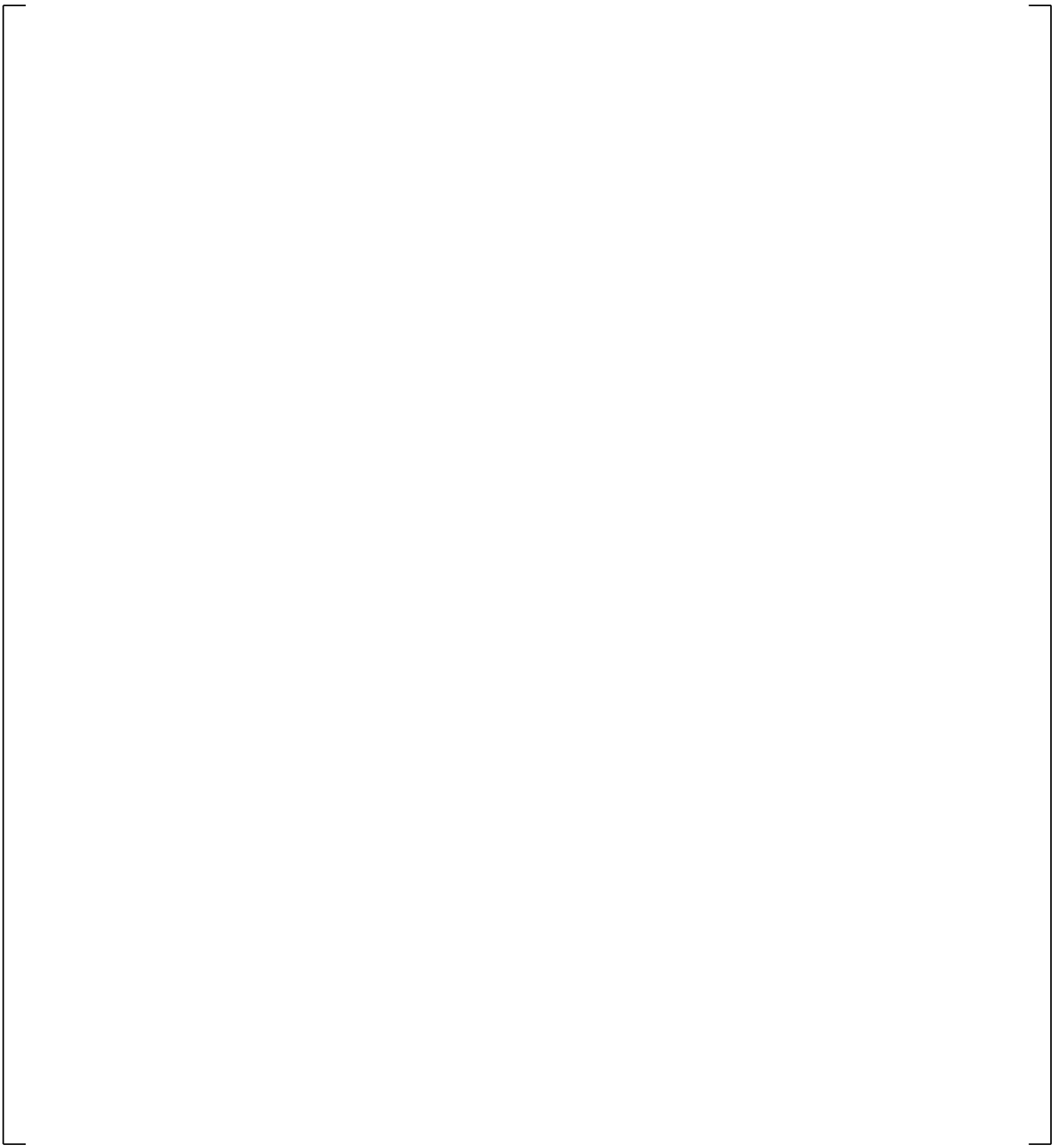

Figure 23.1.1-39 Comparison of Predicted and Measured Void Fraction at Level 6, Test 1004-3

a,c

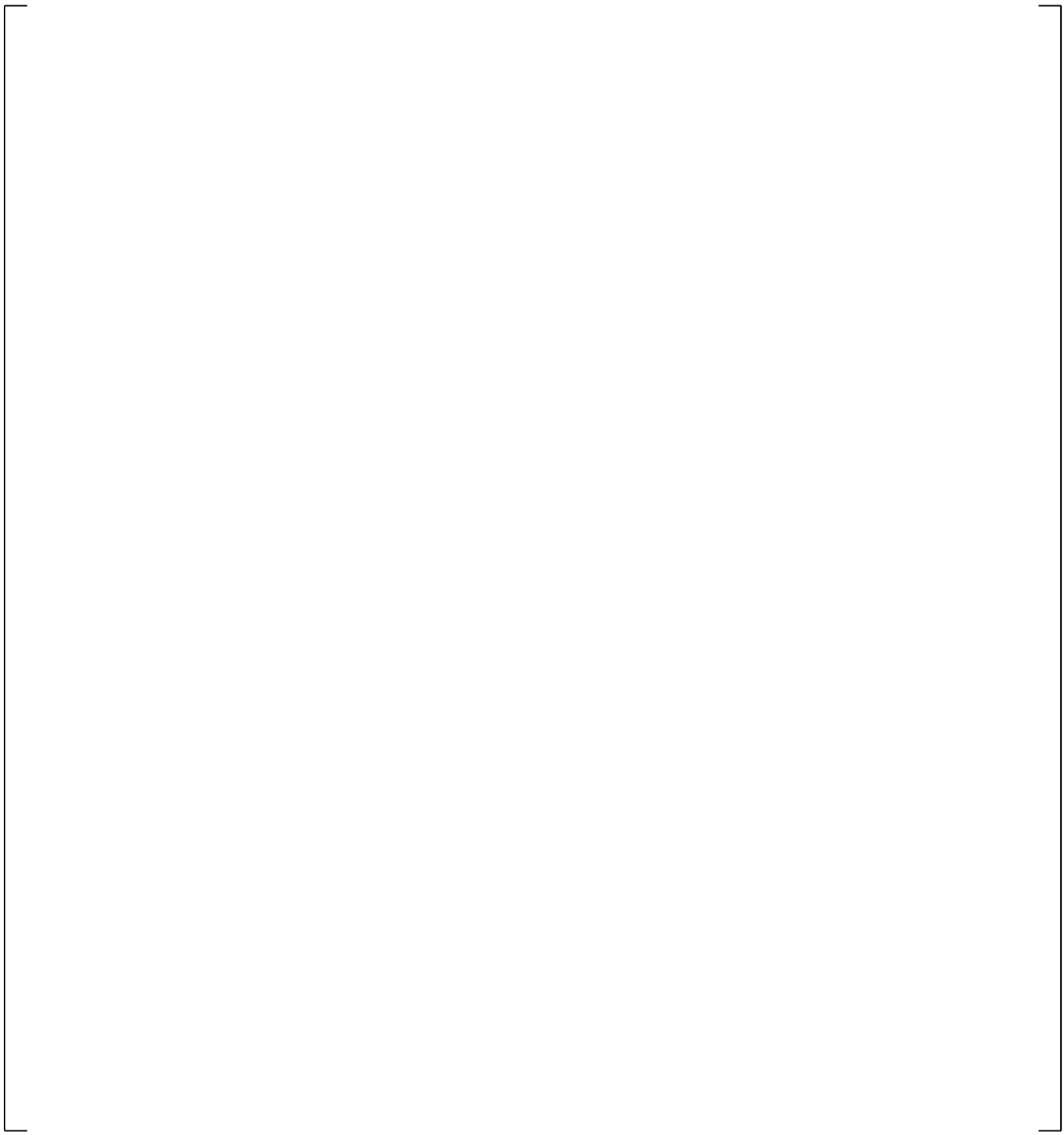

Figure 23.1.1-40 Comparison of Predicted and Measured Void Fraction at Level 1, Test 1004-2

a,c

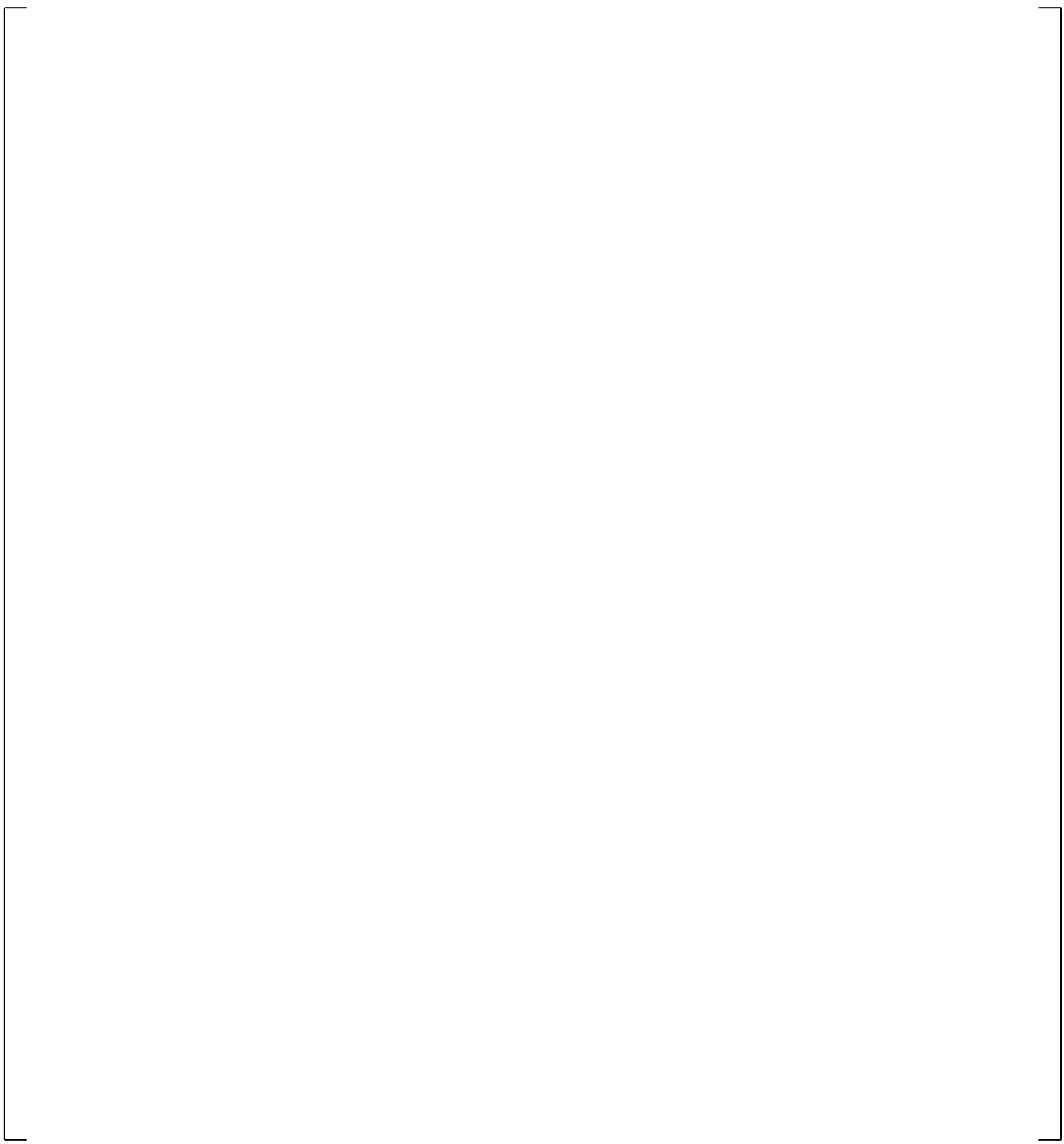

Figure 23.1.1-41 Comparison of Predicted and Measured Void Fraction at Level 2, Test 1004-2

a,c

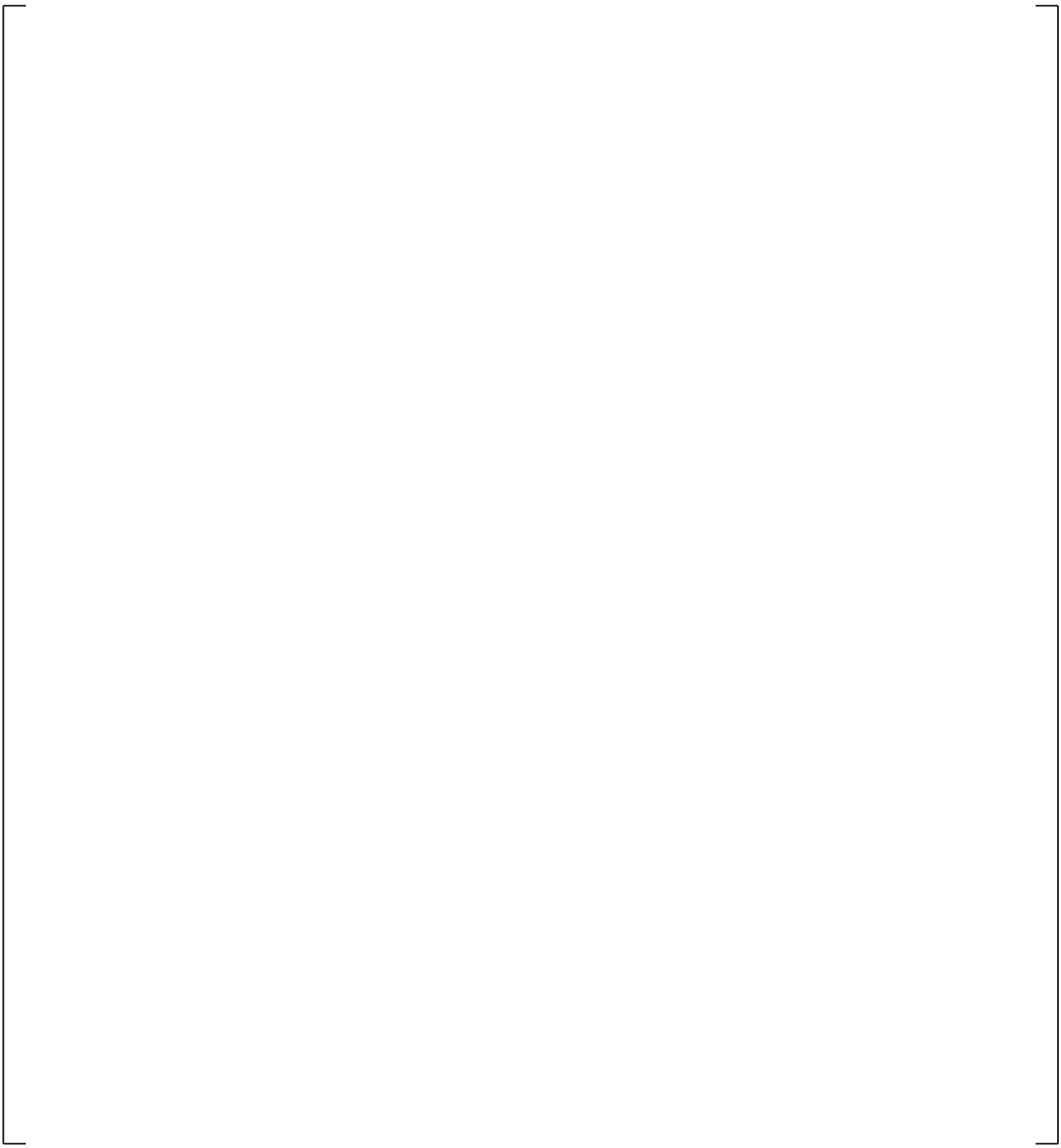

Figure 23.1.1-42 Comparison of Predicted and Measured Void Fraction at Level 3, Test 1004-2

a,c

Figure 23.1.1-43 Comparison of Predicted and Measured Void Fraction at Level 4, Test 1004-2

a,c

Figure 23.1.1-44 Comparison of Predicted and Measured Void Fraction at Level 5, Test 1004-2

a,c

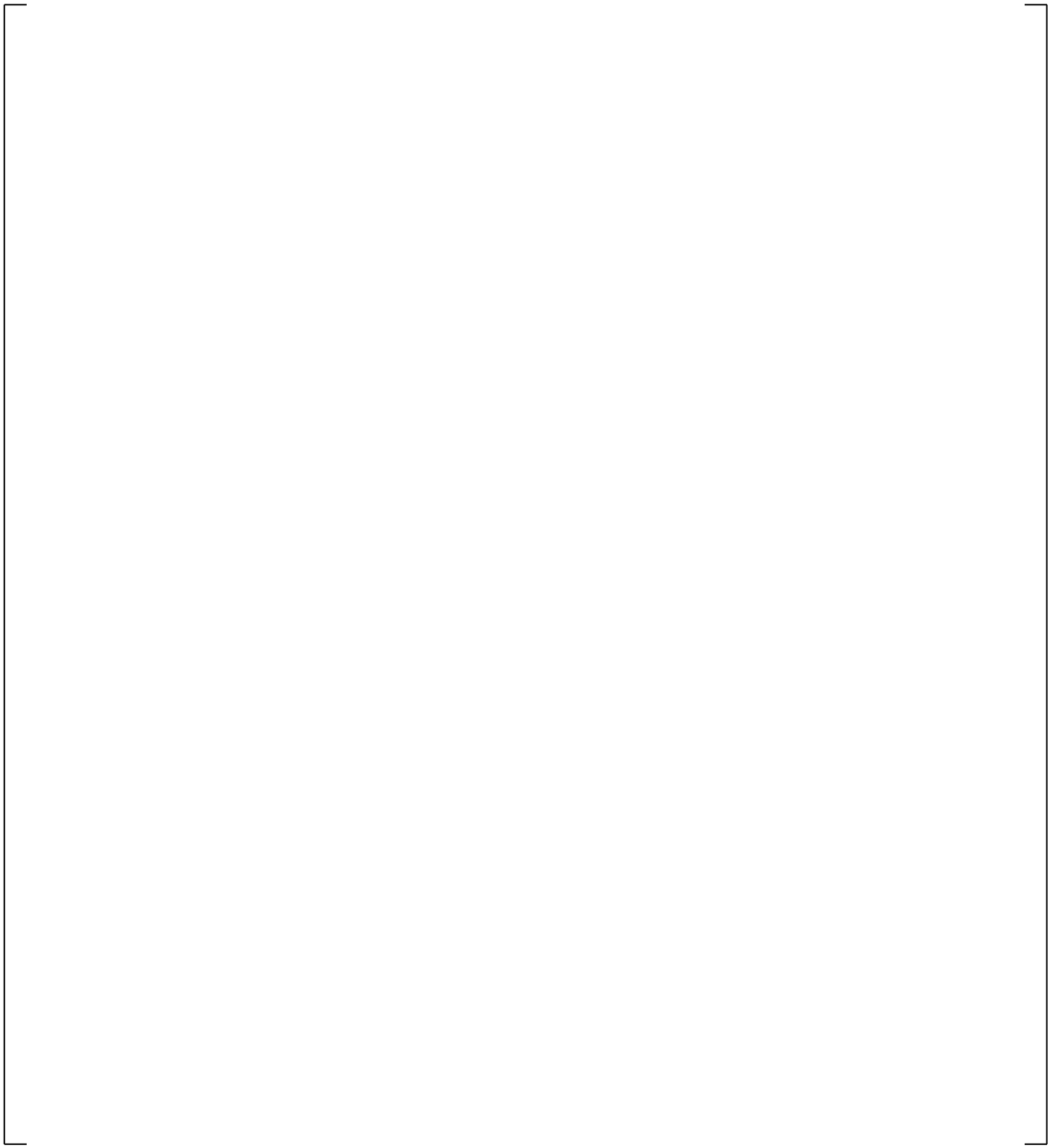

Figure 23.1.1-45 Comparison of Predicted and Measured Void Fraction at Level 6, Test 1004-2

23.1.2 Semiscale Tests

23.1.2.1 Introduction

The FULL SPECTRUM LOCA (FSLOCA) methodology PIRT in Section 2, Volume 1 [

]^{a,c} The Semiscale simulation study in this section provides further assessment of the code's capability in predicting the void distribution and the post-CHF heater rod temperature excursion in a prolonged boiloff transient with unusually high cladding temperature attained.

As a portion of the Semiscale Mod-3 experimental program conducted by EG&G Inc. under the sponsorship of the United States Nuclear Regulatory Commission (US NRC), Semiscale Tests S-07-10 and S-07-10D (Sackett and Clegg, 1980) feature deep core uncovery and high heater rod temperature due to manually delayed ECCS injection. In these two tests, the core was almost completely uncovered and the peak heater rod temperature was as high as 1145 K before the emergency core cooling system (ECCS) injection, providing a valuable database in assessing the WCOBRA/TRAC-TF2 code covering extreme conditions, and complementing the validation documented in Sections 13 and 15.

Semiscale test S-07-10D is a repeat of S-07-10, which was designated as a United States Standard Problem Small Break Experiment (SBE) (Shimeck, 1980). Both tests simulated a 10% cold leg break. The difference between them is that the steam generator in S-07-10 was isolated at 17 s into the transient, while it was allowed to blowdown throughout the transient in S-07-10D.

This section assesses the important phenomena occurring in the Semiscale S-07-10D test and the performance of WCOBRA/TRAC-TF2 in predicting two-phase mixture level swell and post-CHF heat transfer.

23.1.2.2 Semiscale Test Facility Description

The Semiscale Mod-3 facility is a small-scale model of the primary system of a four loop PWR. The system includes equivalent elevations and component layout (including steam generators, vessel, pumps, pressurizer, and loop piping) at 1:1705.5 volumetric scaling. One intact loop is scaled to simulate the three intact loops, while a broken loop simulates the single loop in which a break is postulated to occur. Geometric similarity is maintained between a PWR and Mod-3, most notably in the design of a 25 rod, full-length (3.66 m), electrically heated core, full length upper head and upper plenum, component layout, and relative elevations of various components. The scaling philosophy followed in the design of the Mod-3 system (modified volume scaling) is intended to preserve the most important first order effects for small break LOCA transients.

The Semiscale Mod-3 system consists of a pressure vessel with simulated reactor internals, including a 25 rod core with electrically heated rods and an external downcomer assembly; an intact loop with a pressurizer, steam generator, and pump; and a broken loop with a steam generator, pump, and rupture assembly. The system has an ECCS with the high and low pressure coolant injection pumps for each loop, an accumulator for the intact loop and a pressure suppression system with header and suppression tank.

Figure 23.1.2-1 provides an isometric of the Semiscale Mod-3 facility, as configured for Tests S-07-10 and S-07-10D. The tests had a communicative break simulator configuration with the break nozzle located in the broken loop cold leg between the pump and the vessel. The break size was 0.223 cm^2, which is volumetrically scaled to represent 10% of the area of a cold leg pipe in a PWR. For the broken loop, a sharp edged pipe orifice with a length-to-diameter ratio of 0.27 was used to represent an orifice-like break.

Figure 23.1.2-2 is a plan view of the 25-rod Mod-3 core for Test S-07-10D which shows the location of the unpowered rods, their orientation with respect to the remainder of the system, and the distribution of the internal cladding thermocouples monitored during each test. Internally heated electric rods with a heated length of 3.66 m and an outside diameter of 1.072 cm were used to geometrically simulate PWR nuclear rods. Figure 23.1.2-3 shows the step cosine axial power profile for the rods with a 1.55 peak to average power factor. The relative location of in-core instrumentation (gamma dosimeters and core inlet drag screen) and grid spacers are provided in Figure 23.1.2-4.

For the S-07-10D test, the 5x5 core was configured with the 9 center rods operating at an initial maximum linear heat generation rate (MLHGR) of 46.7 kW/m and the 13 peripheral rods at an initial MLHGR of 30.9 kW/m with A1, A3, and A4 unpowered. The total core power for the test was 1.94 ±0.1 MW.

23.1.2.3 Semiscale Test S-07-10D Description

The Semiscale Mod-3 small break test S-07-10D was conducted to assist the US NRC licensing staff in evaluating the acceptability of small break licensing models used by pressurized water reactor vendors. The test simulated a 10% cold leg break in which no emergency core coolant was injected until elevated core heater rod temperatures were achieved. The broken loop steam generator secondary side was allowed to blow down to investigate the effect of secondary side conditions on primary behavior.

Test S-07-10D was conducted from initial conditions of 15.73 MPa (2281.5 psia) pressurizer pressure, and core inlet temperature of 556 K (541.1°F), with a core power level of 1.94 MW. The simulated small break with a break area of 0.223 cm^2 (0.0346 $in.^2$) was located on the centerline of the broken loop cold leg between the pump and the vessel and was scaled to represent 10% of the area of a cold leg pipe in a PWR.

After initiation of the blowdown, power to the electrically heated core was reduced to simulate the predicted heat flux response of nuclear fuel rods during a LOCA. The intact and broken loop circulation pumps continued to operate until 1 s after the pressurizer pressure reached 12.41 MPa (1800 psia) approximately 10 s after initiation of blowdown. At this time, and for the next 60 s, the pumps followed a predetermined profile after which power was tripped and pumps were allowed to coast down.

Table 23.1.2-1 provides the conditions in the Semiscale Mod-3 system for S-07-10D test at initiation of blowdown. Tables 23.1.2-2 and 23.1.2-3 provide the sequence of operational procedures and events relative to rupture.

In Test S-07-10D, the coolant injection systems were arranged to discharge into the cold leg of the intact loop. The high pressure and low pressure injection pumps were started at 460 seconds and 560 seconds after blowdown initiation at a flow rate of 0.059 L/s and 0.135 L/s, respectively, and continued for the duration of the test. Intact loop accumulator coolant injection started 458 seconds after blowdown initiation and continued for 23 seconds. The total volume of coolant injected into the system was 0.028 m^3. Nitrogen was not discharged into the system.

The Semiscale S-07-10D was well equipped with sufficient instruments to measure the test system thermal hydraulic response in a simulated small break LOCA transient of a PWR. The performance of the system during the test was monitored by 268 detectors. A digital data acquisition system recorded data for Test S-07-10D at an effective sample rate of 28.75 points per second per channel for the first 100 seconds and then 9.58 points per second per channel for the remainder of the test.

23.1.2.4 WCOBRA/TRAC-TF2 Model for Semiscale Boiloff Tests

The WCOBRA/TRAC-TF2 simulation of the Semiscale test documented herein focuses only on the boiloff transient period after the loop seals are cleared in both loops and therefore consists of a simplified model with just a VESSEL component with the boundary conditions defining the mass flow between the downcomer and vessel, and BREAK components connected to the hot legs to simulate the depressurization based on the test measurement.

The Semiscale vessel noding diagram is provided in Figure 23.1.2-5 **[**

][a,c] the hot leg back pressure, lower plenum feed temperature, core collapsed liquid level, and heater rod power decay, provided in Figures 23.1.2-6 through 23.1.2-9, respectively.

Figure 23.1.2-10 provides the Density Measurement recorded over time for the S-07-10D test, which shows complete core uncovery – vapor density at the core entrance.

23.1.2.5 Simulation of Semiscale Boiloff Tests

The objective of the Semiscale S-07-10D simulation with WCOBRA/TRAC-TF2 is to assess the two-phase mixture level swell and post-CHF heat transfer models in the code. To assess these two phenomena, the heater rod temperature response and core void fraction calculated by WCOBRA/TRAC-TF2 during the boiloff transient are compared with the test data at elevations where test measurements are available.

Figures 23.1.2-11 through 23.1.2-24 provide the comparison of the predicted and measured clad temperature at various elevations, from top to bottom of the core. **[**

][a,c]

Also, the heatup transient above the dryout point shows that the WCOBRA/TRAC-TF2 predicted **[**

][a,c]

Figures 23.1.2-26 to 23.1.2-32 provide the predicted and measured void fraction at different elevations; **[**

][a,c]

The overall results of the simulation are summarized in Figure 23.1.2-33 which provides the heater rod dryout history (two-phase mixture level) during the boiloff transient compared with the test, for both the high and low power rods. **[**

][a,c]

23.1.2.6 Summary and Conclusions

As discussed in Section 23.1.2.5, the Semiscale S-7-10D test has been evaluated in this section **[**

][a,c]

The simulation with WCOBRA/TRAC-TF2 of the S-07-10D test has shown that:
[

]^{a,c}

As such, it is concluded that the WCOBRA/TRAC-TF2 is capable of predicting the level swell and post-CHF heat transfer satisfactorily.

23.1.2.7 References

1. Sackett, Kenneth E. and Clegg, L. Bruce, 1980, "Experiment Data Report for Semiscale MOD-3 Small Break Test S-07-10D (Baseline Test Series)," prepared for the U.S. Nuclear Regulatory Commission under Department of Energy Contract No. DE-AC07-76IDO1570.

2. Shimeck, D.J., 1980, "Analysis of Semiscale MOD-3 Small Break Test S-07-10 and S-07-10D," prepared for the U.S. Nuclear Regulatory Commission under Department of Energy Contract No. DE-AC07-761DO1570.

Table 23.1.2-1 Initial Conditions and ECC Requirements S-07-10D Test		
Configuration	**Specified**	**S-07-10D Actual[(1)]**
Break Size	0.223 cm^2 (10%)	0.223 cm^2 (10%)
Break Type	Communicative	Communicative
Break Location	Cold Leg	Cold Leg
Break Orientation	Side of pipe	Side of pipe
Pressurizer Location	Intact loop	Intact loop
Initial Conditions	**Specified**	**S-07-10D Actual**
Core Power	1.94 MW	1.925 MW
Nominal System Pressure	15.7 MPa	15.73 MPa
Intact Loop Cold Leg Fluid Temperature	556 K	556 K
Broken Loop Cold Leg Fluid Temperature	556 K	558 K
Intact Loop Core Delta T	35 K	37 K
Broken Loop Core Delta T	35 K	33 K
Core Inlet Flow	9.77 kg/s	9.7 kg/s
Intact Loop Cold Leg Flow	Note 2	10 L/s
Broken Loop Cold Leg Flow	Note 2	3.2 L/s
Intact Loop Steam Generator Liquid Level (above top of tube sheets)	295 ±5 cm	Note 3
Broken Loop Steam Generator Liquid Level (above top of tube sheets)	998 ±5 cm	978 cm
ECC Parameters		
Intact Loop Accumulator		
Location	Cold Leg	Cold Leg
System Pressure at actuation	None	1600 kPa
Tank Pressure at actuation	None	3100 kPa
Liquid Volume	0.045 m^3	0.045 m^3
Gas Volume	0.025 m^3	0.025 m^3
Line resistance	10675 s^2/m^3-cm^2	Same
Temperature	300 K	300 K
Intact Loop High Pressure Injection (HPI)		
Location	Cold Leg	
Actuation Pressure	None	1600 kPa

Table 23.1.2-1 Initial Conditions and ECC Requirements S-07-10D Test (cont.)		
Injection Rate (average)	0.062 kg/s	0.075 kg/s
Temperature	300 K	300 K
Intact Loop Low Pressure Injection (LPI)		
Location	Cold Leg	
Actuation Pressure	none	2100 kPa
Injection Rate (average)	0.16 kg/s	0.11 kg/s
Temperature	300 K	300 K
PSS Tank Pressure	Pressure range over time	

Notes:
1. Measured initial conditions are taken from digital acquisition system read just prior to blowdown initiation.
2. Flow is not specified since it must be adjusted to achieve the required differential pressure across the core.
3. Level detector erratic prior to blowdown initiation. Liquid level not available.

Table 23.1.2-2 Sequence of Operational Procedures for Test S-07-10D		
Event	**Specified Time (s)**	**Actual Time (s)**
Rupture	0.0	0.0
Initiate PSS tank pressure reduction	50	50
Enable accumulator and high pressure injection system (HPIS) injection	When on-line monitors indicate high core temperatures	460
Enable low pressure injection system (LPIS) injection	When on-line monitors indicate high core temperatures	560
Terminate Test		748

Table 23.1.2-3 Sequence of Events for Test S-07-10D	
	S-07-10D Time in Seconds
Blowdown Initiated	0
Pressurizer Pressure = 12.41 MPa	6.9
Begin core power decay	7.7
Intact loop steam generator feedwater closed	
Broken loop steam generator feedwater closed	
Upper plenum fluid saturates	8.0
Intact loop steam generator steam valve closed	21
Broken loop steam generator steam valve closed	
Pressurizer empties	20
Entire system saturated, system pressure = 7.1 MPa	27
Upper plenum liquid level reaches intact loop hot leg	42
Pressure suppression system pressure reduction begins	52
Intact loop pump suction blows out	85
Liquid from cold legs drains to vessel and pump suctions resulting in two-phase mixture at break	65 to 90
Power to pumps terminated	69.7
Pumps stop	79
Top of support tubes uncovered in upper head	80
Pressure suppression system tank pressure reduction finished	160
Broken loop pump suction swept out	N/A
First dryouts indicated in upper regions of the core	268 – 300
Dryout of core peak power zone from top down	268 – 300
Core completely void	435
Fallback turns over and/or rewets thermocouples progressively from upper to mid core	N/A
Accumulator Injection begins	460
HPIS injection begins	
ECC water reaches bottom of core	467
Accumulator flow falls to zero as accumulator “floats” on the system	482
System repressurized due to steam generation	
Core peak power zone quenched	488 to 498
LPIS injection initiated	560
Entire core quenched	525
Test terminated	748

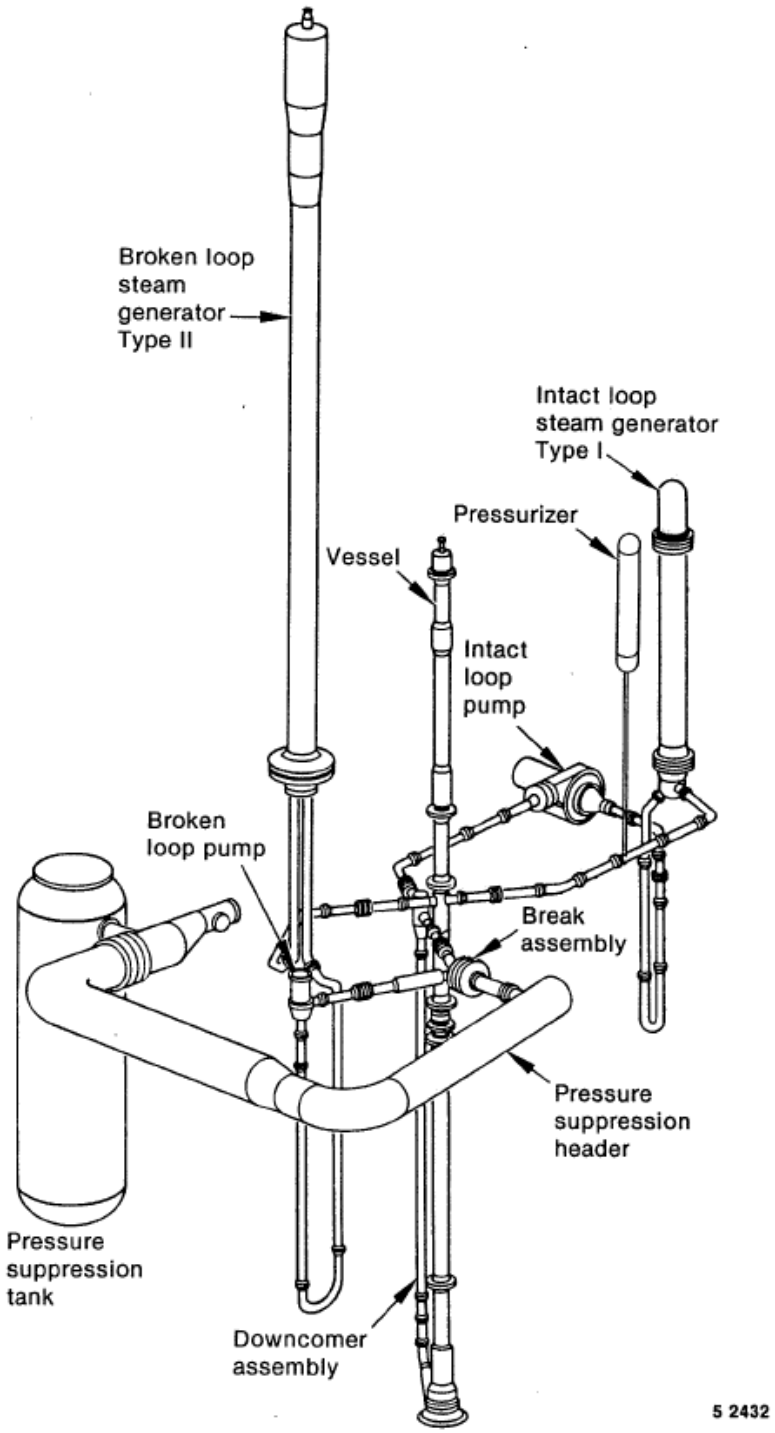

Figure 23.1.2-1 Semiscale Mod-3 Facility Overview

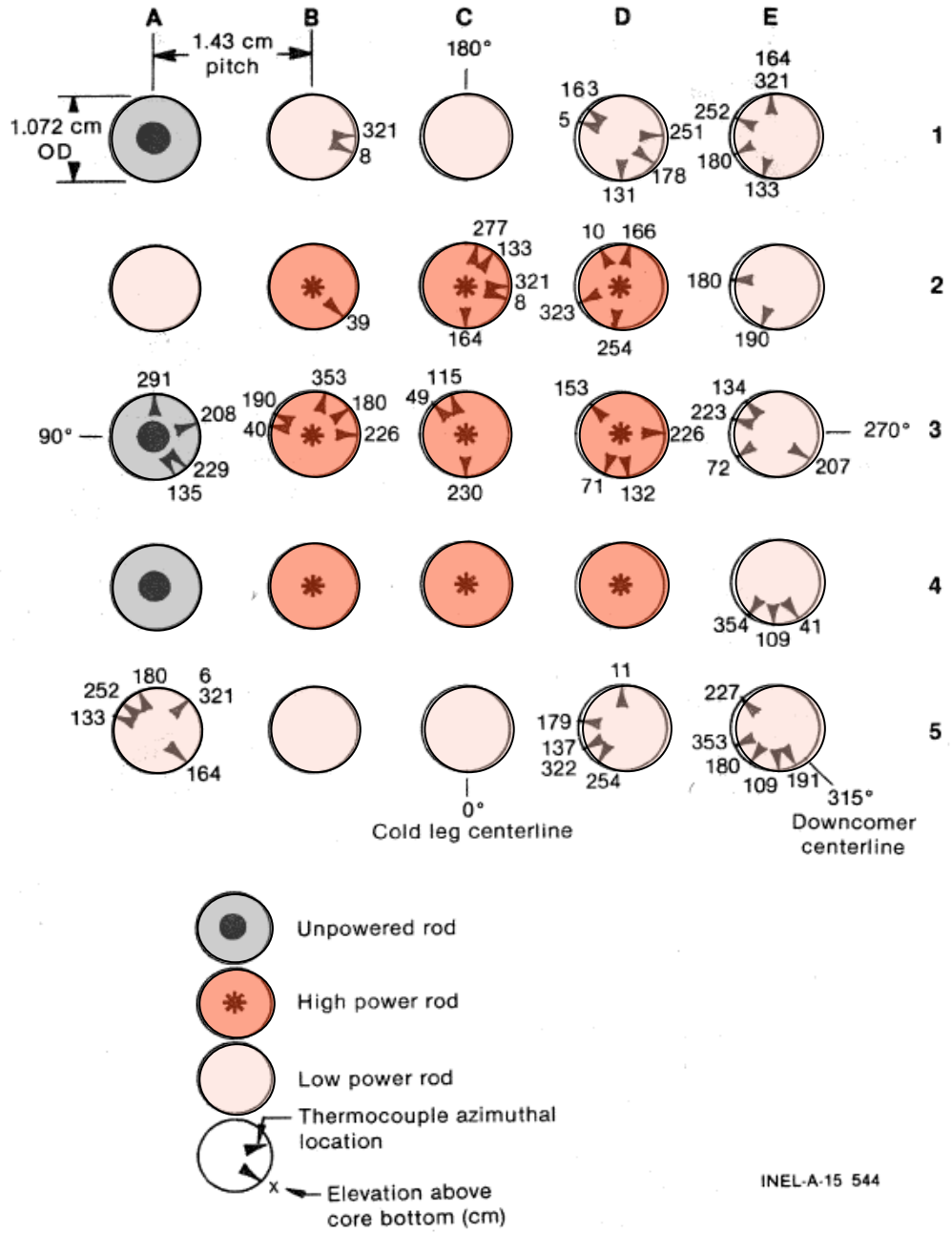

Figure 23.1.2-2 Plan View of Semiscale Mod-3 Core for S-07-10D Test

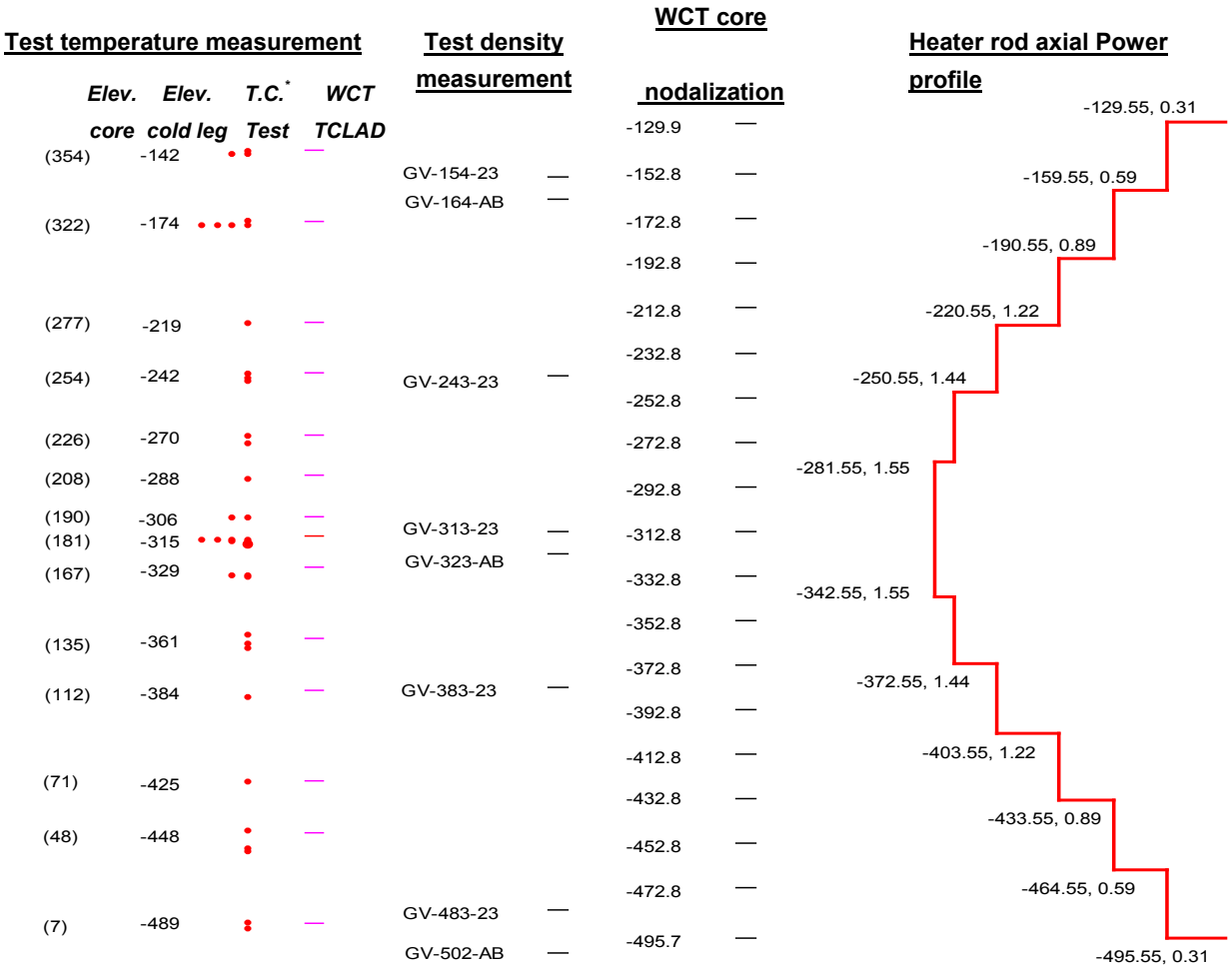

Figure 23.1.2-3 Semiscale S-07-10D Test Axial Power Profile in Relation to Vessel Instrumentation

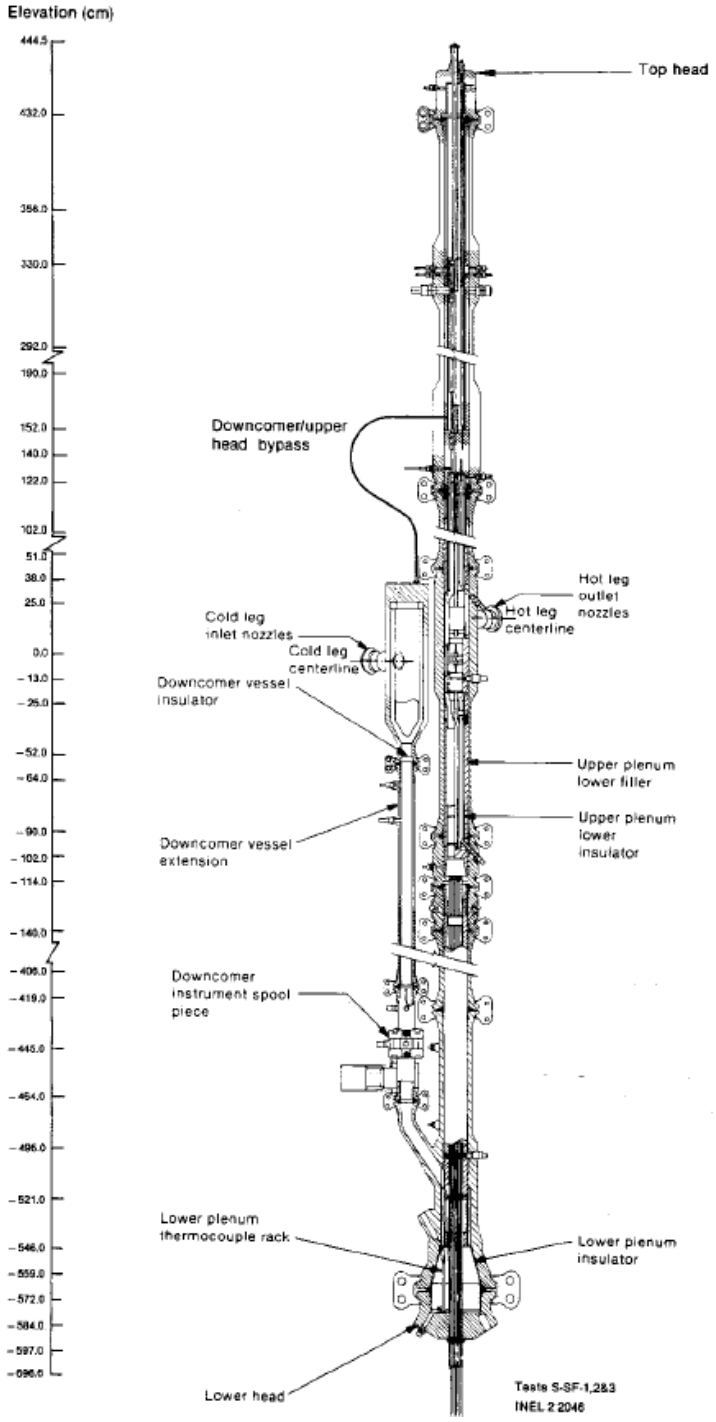

Figure 23.1.2-4 Semiscale Mod-3 Pressure Vessel and Downcomer – Cross Section Showing Instrumentation

a,c

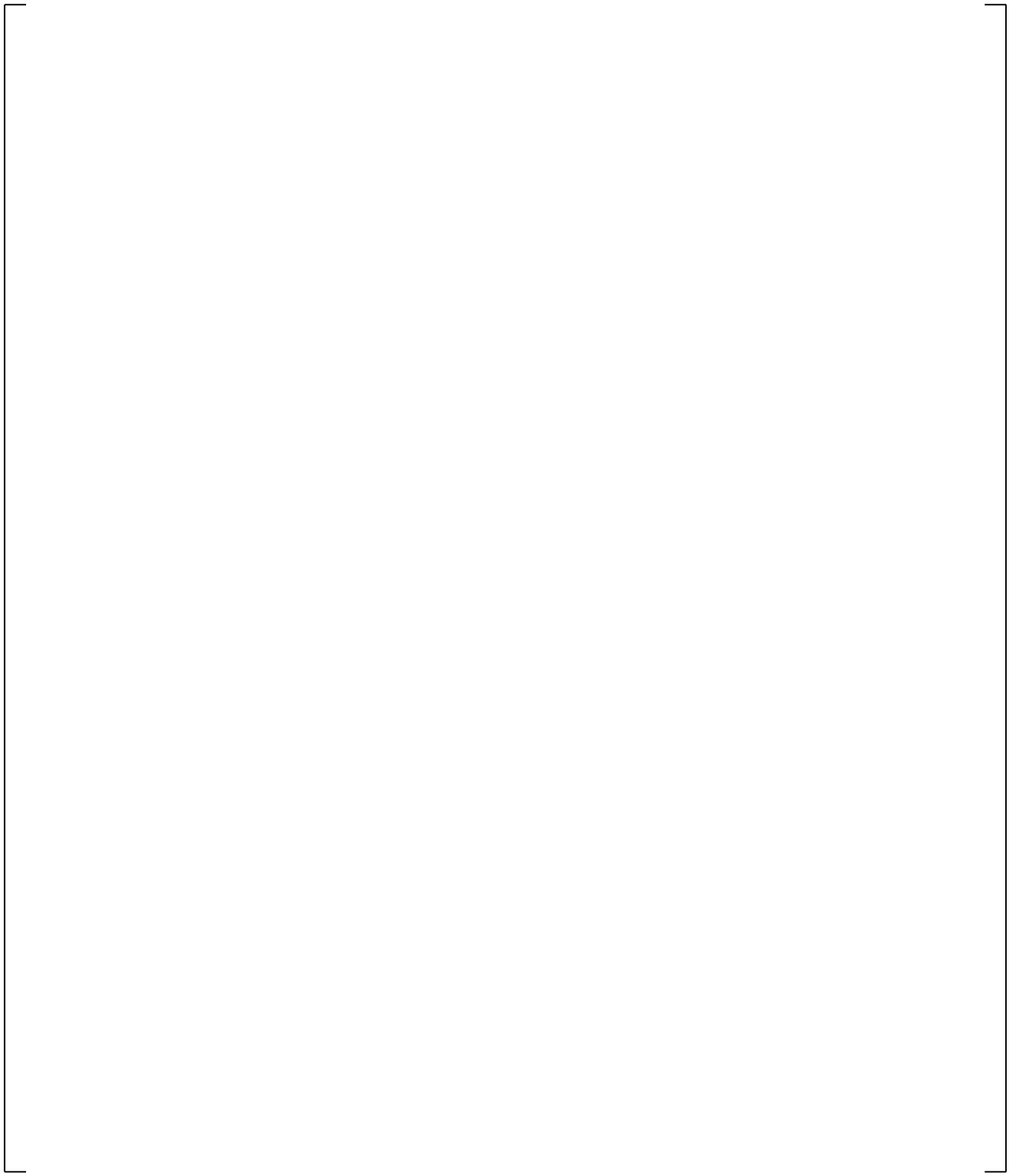

Figure 23.1.2-5 WCOBRA/TRAC-TF2 Semiscale Mod 3 Vessel Model

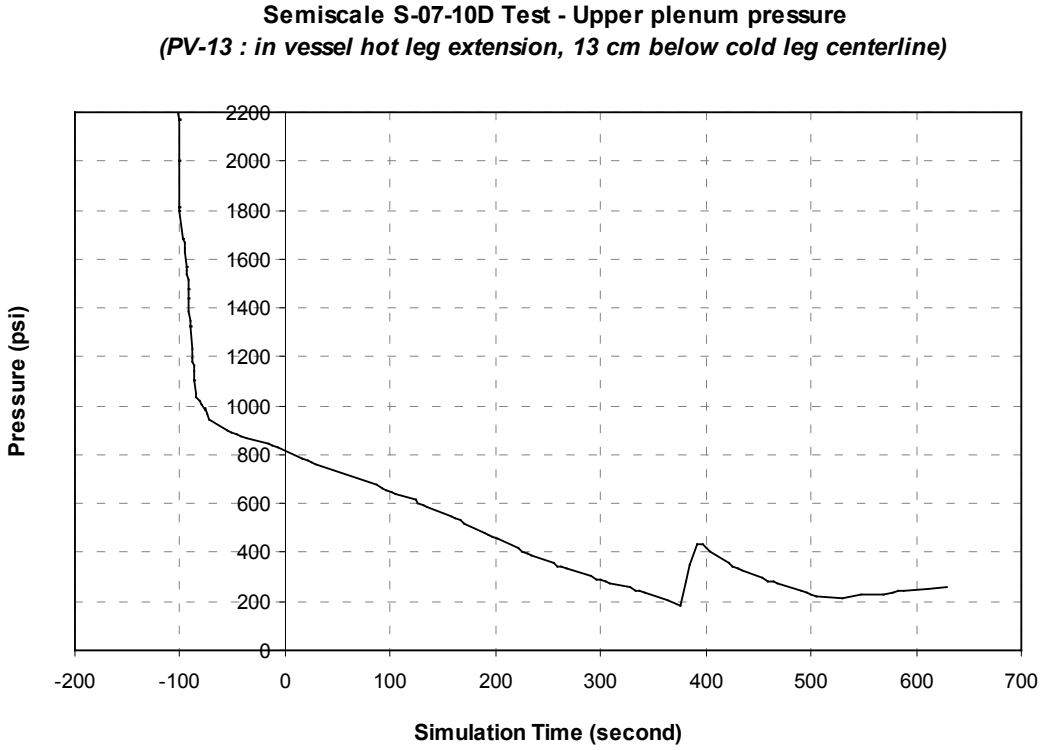

Figure 23.1.2-6 Semiscale S-07-10D Test Upper Plenum Pressure (Hot Leg Backpressure)

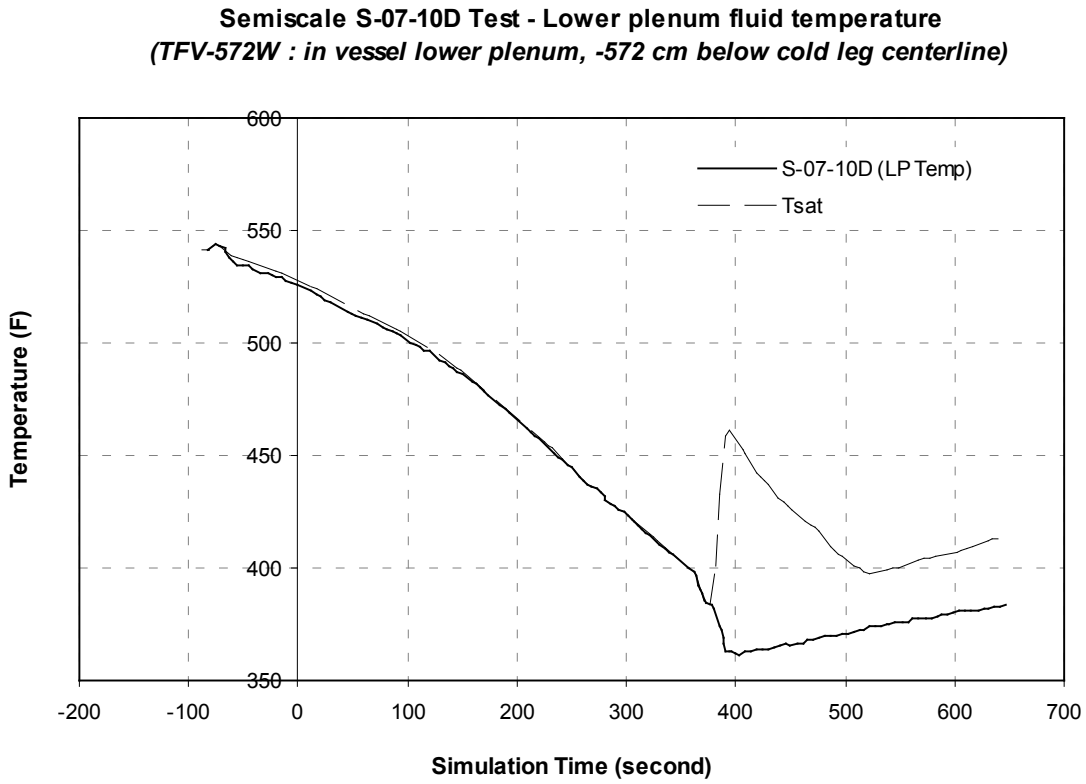

Figure 23.1.2-7 Semiscale S-07-10D Test Lower Plenum Fluid Temperature

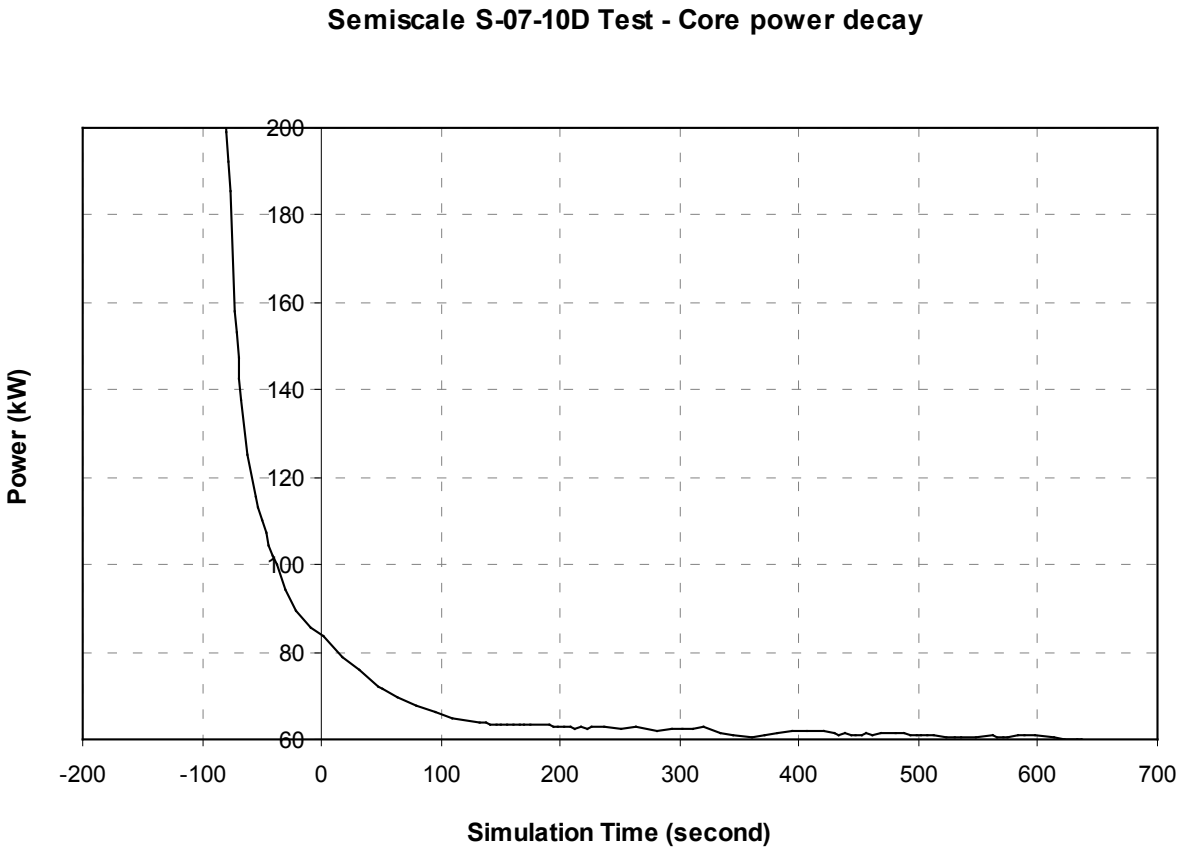

Figure 23.1.2-8 Semiscale S-07-10D Test Core Power Decay

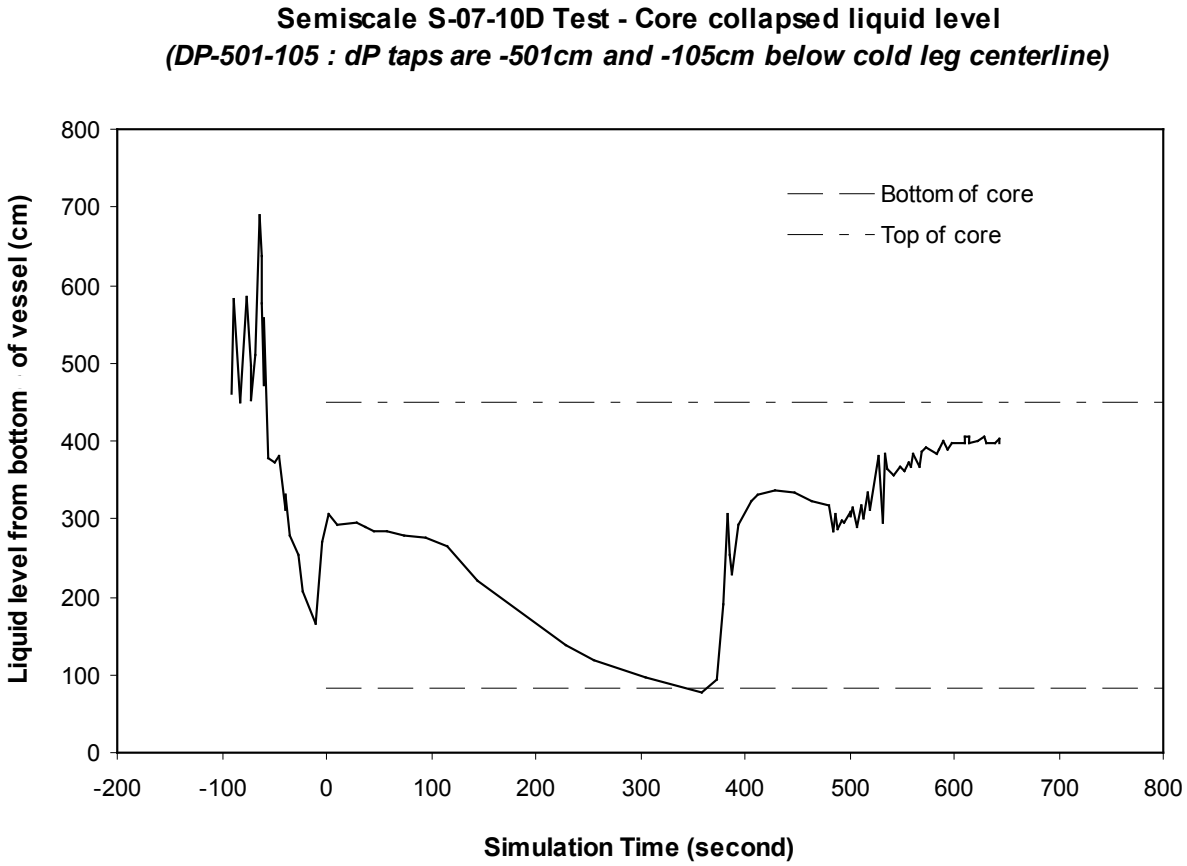

Figure 23.1.2-9 Semiscale S-07-10D Test Core Collapsed Liquid Level

a,c

Figure 23.1.2-10 Density Measurement Recorded During Semiscale S-07-10D Test

a,c

Figure 23.1.2-11 Semiscale S-07-10D Clad Temperature at Elevation = 354 cm (from the Bottom of the Core)

a,c

Figure 23.1.2-12 Semiscale S-07-10D Clad Temperature at Elevation = 322 cm (from the Bottom of the Core)

a,c

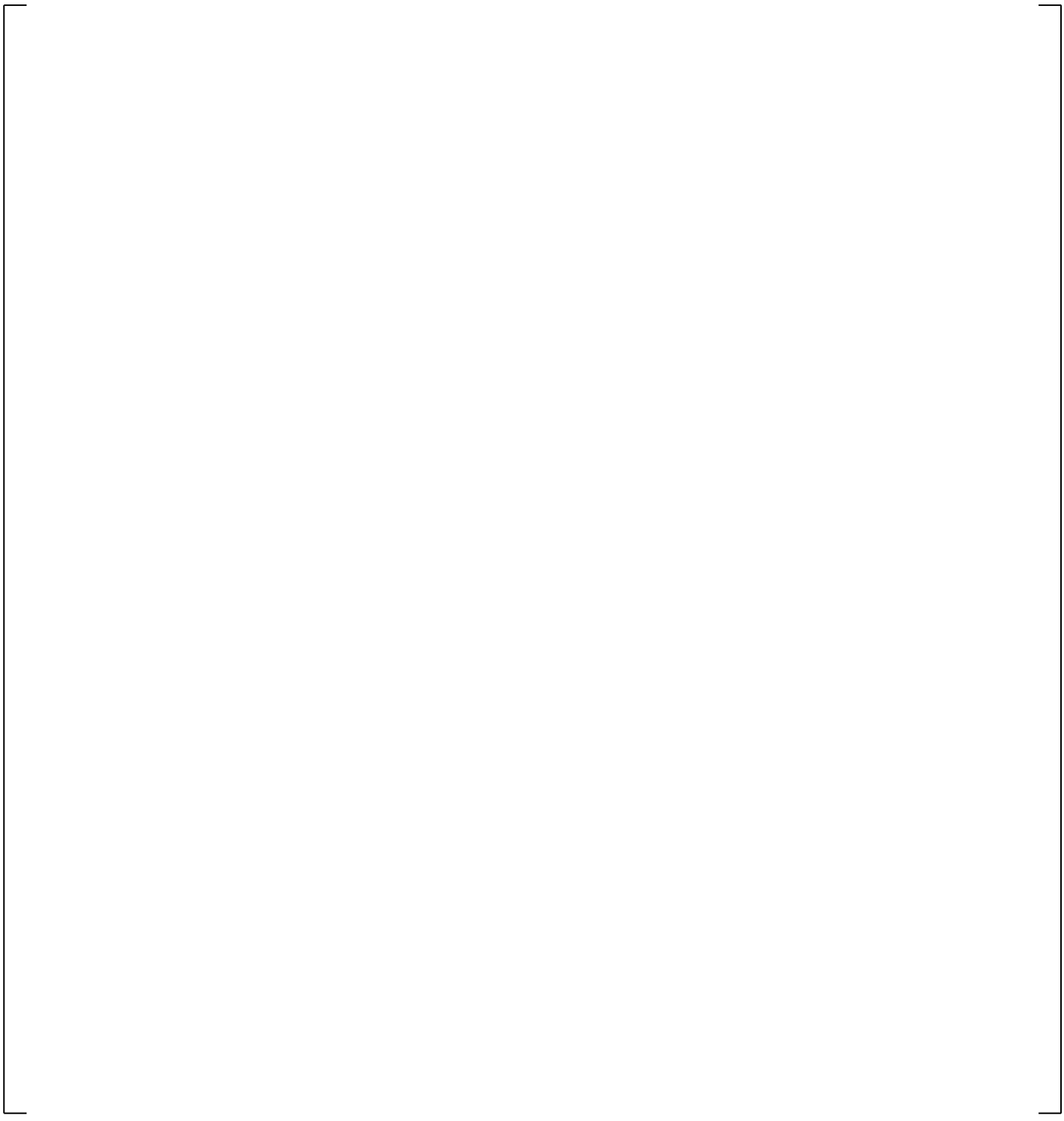

Figure 23.1.2-13 Semiscale S-07-10D Clad Temperature at Elevation = 277 cm (from the Bottom of the Core)

a,c

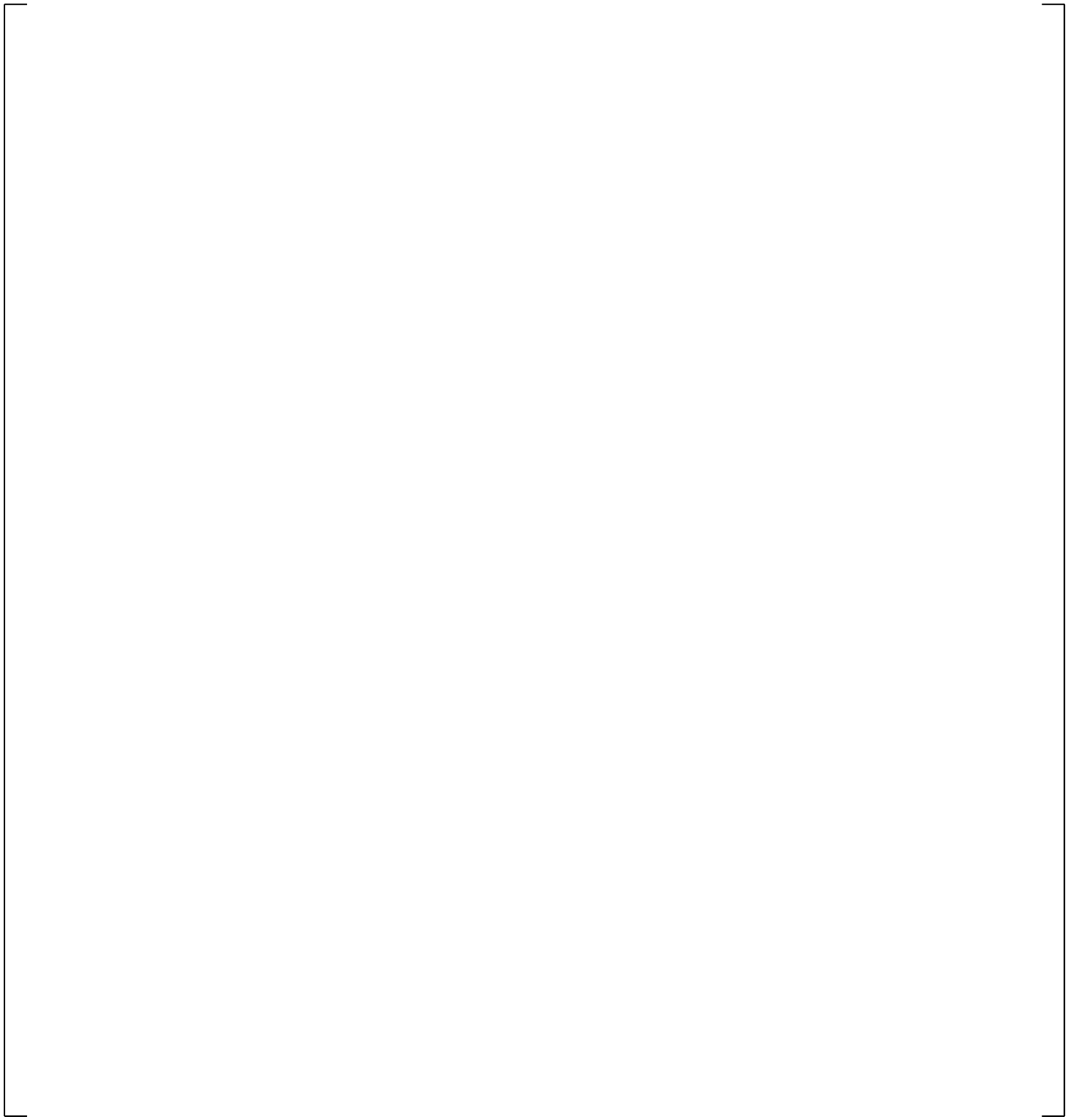

Figure 23.1.2-14 Semiscale S-07-10D Clad Temperature at Elevation = 254 cm (from the Bottom of the Core)

a,c

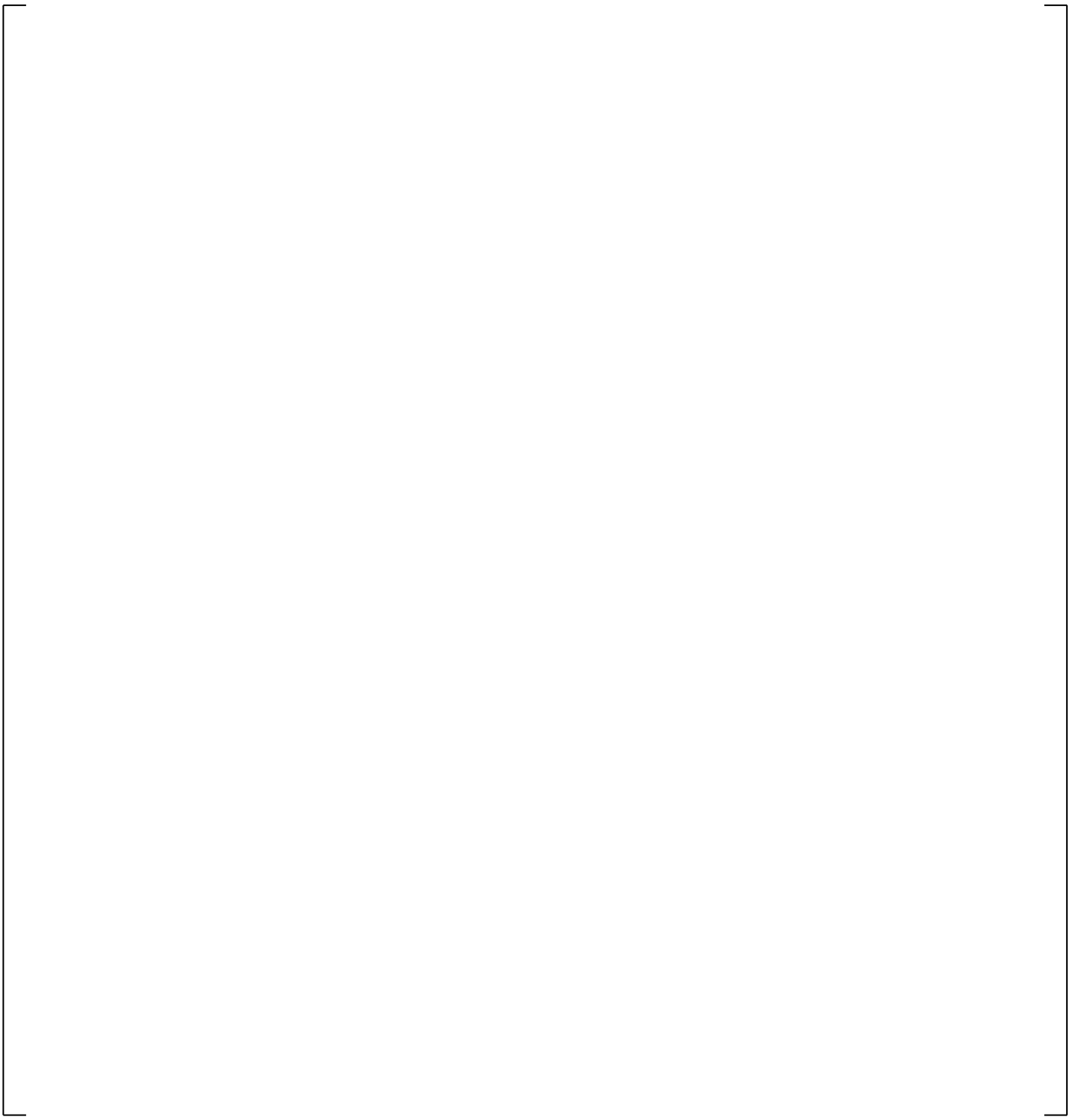

Figure 23.1.2-15 Semiscale S-07-10D Clad Temperature at Elevation = 226 cm (from the Bottom of the Core)

a,c

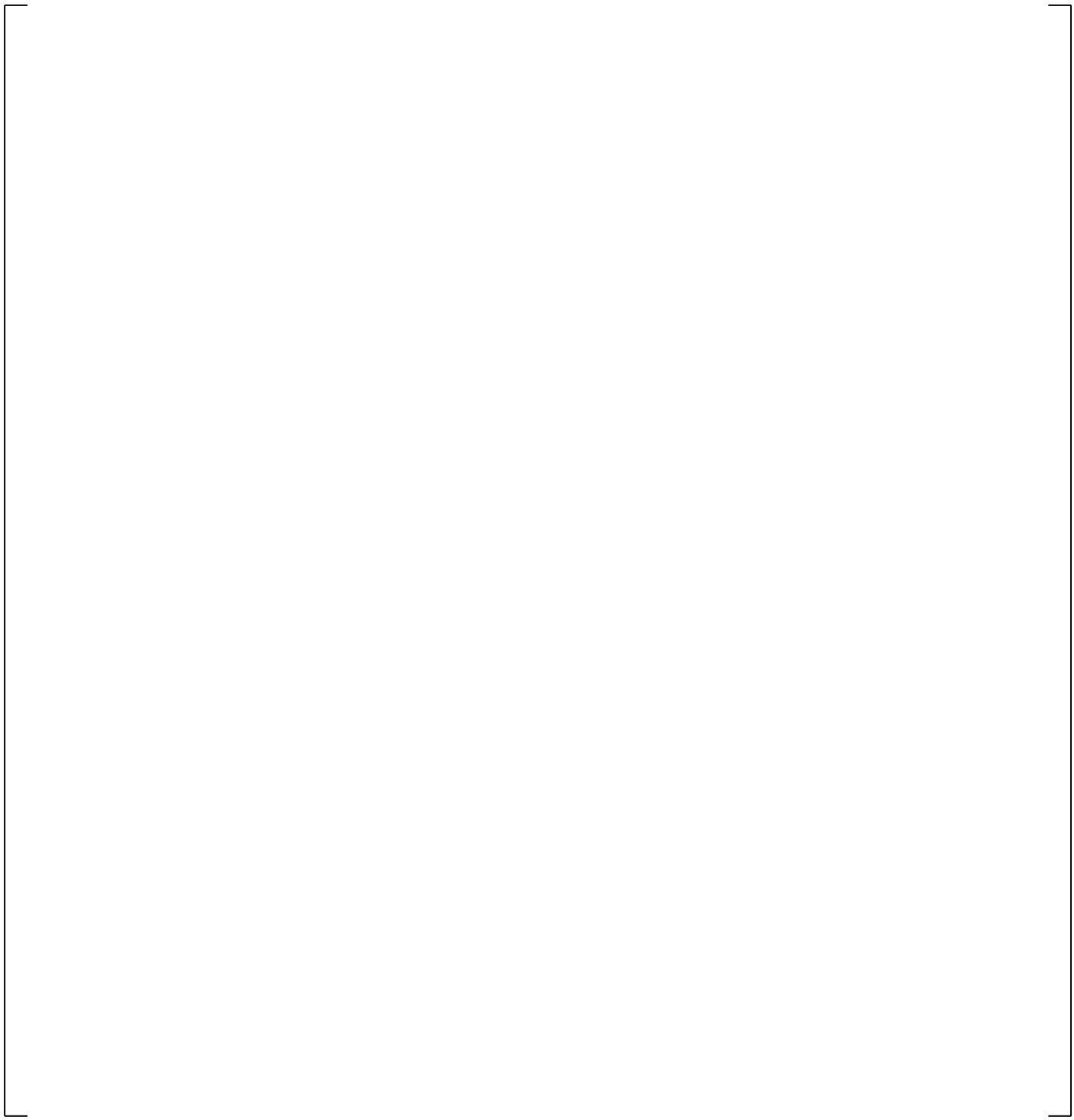

Figure 23.1.2-16 Semiscale S-07-10D Clad Temperature at Elevation = 208 cm (from the Bottom of the Core)

a,c

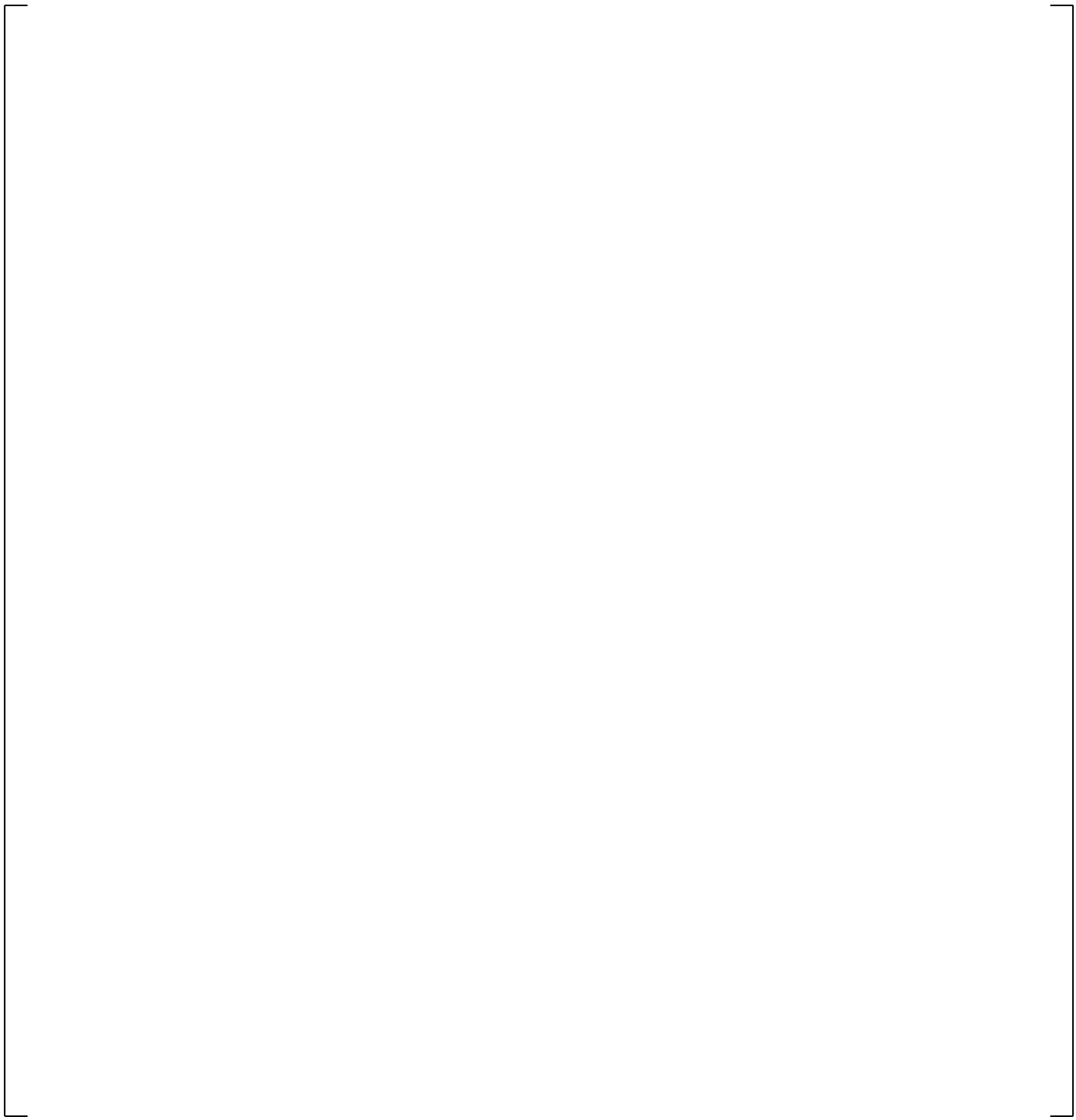

Figure 23.1.2-17 Semiscale S-07-10D Clad Temperature at Elevation = 190 cm (from the Bottom of the Core)

a,c

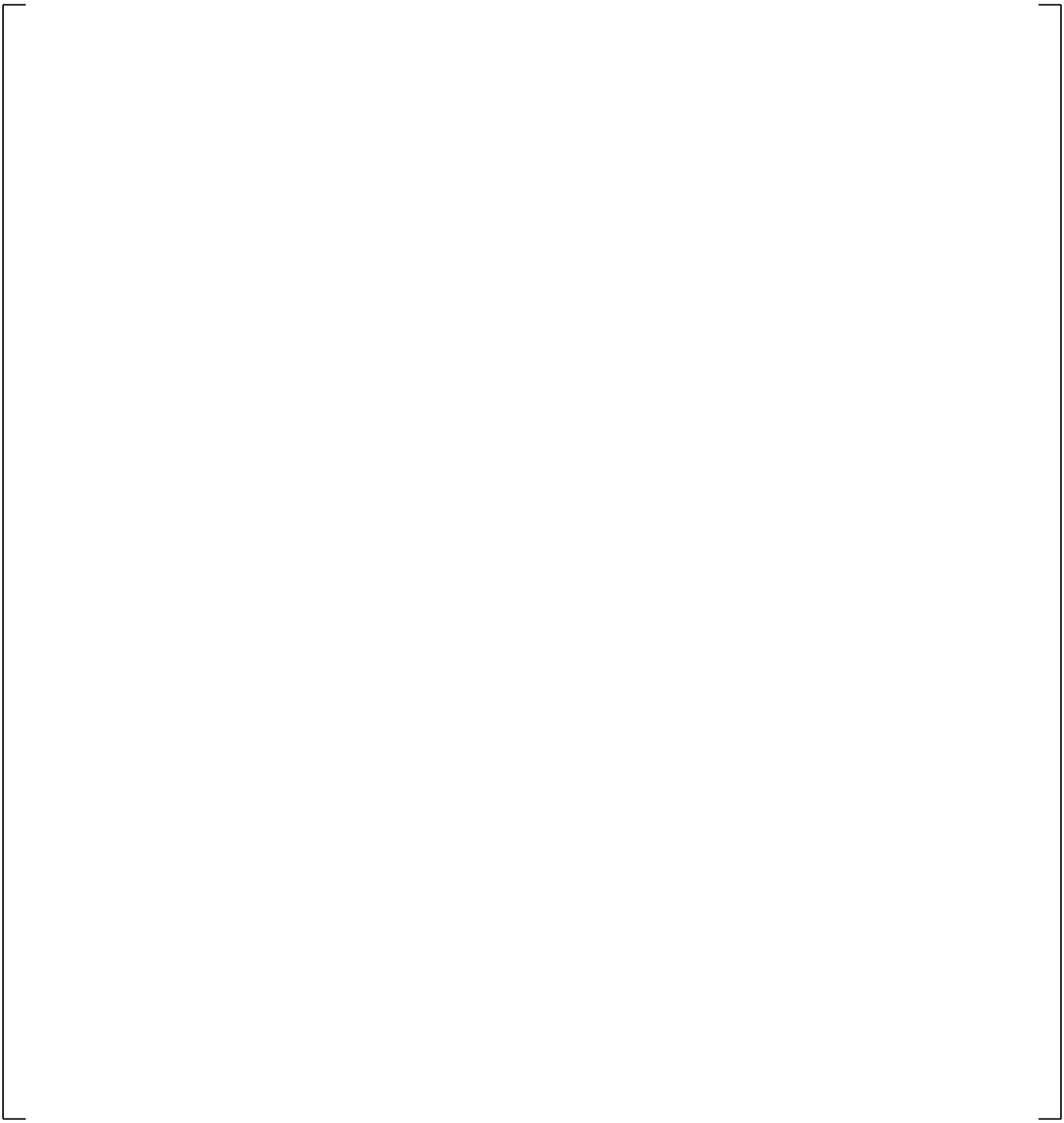

Figure 23.1.2-18 Semiscale S-07-10D Clad Temperature at Elevation = 181 cm (from the Bottom of the Core)

a,c

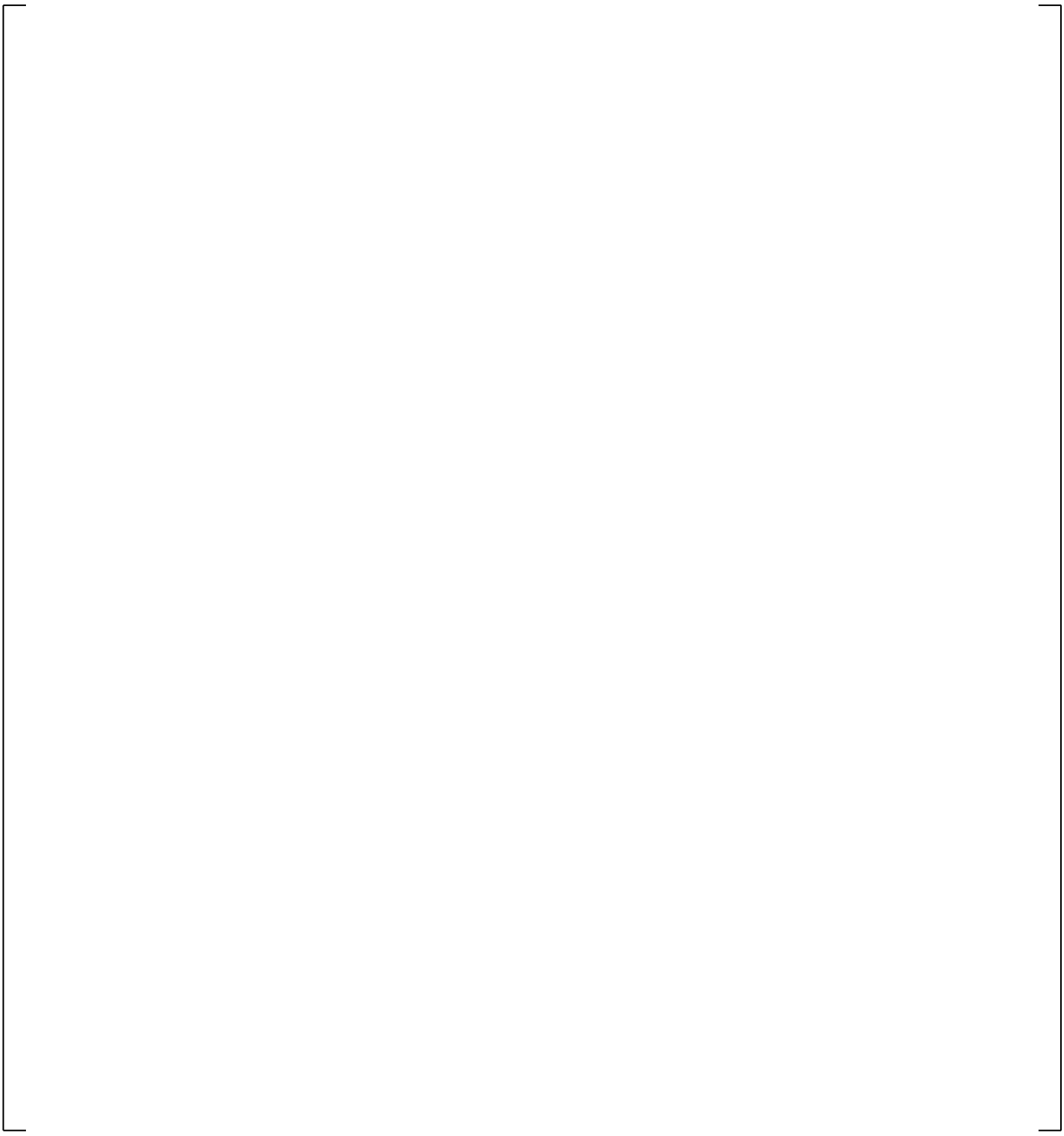

Figure 23.1.2-19 Semiscale S-07-10D Clad Temperature at Elevation = 167 cm (from the Bottom of the Core)

a,c

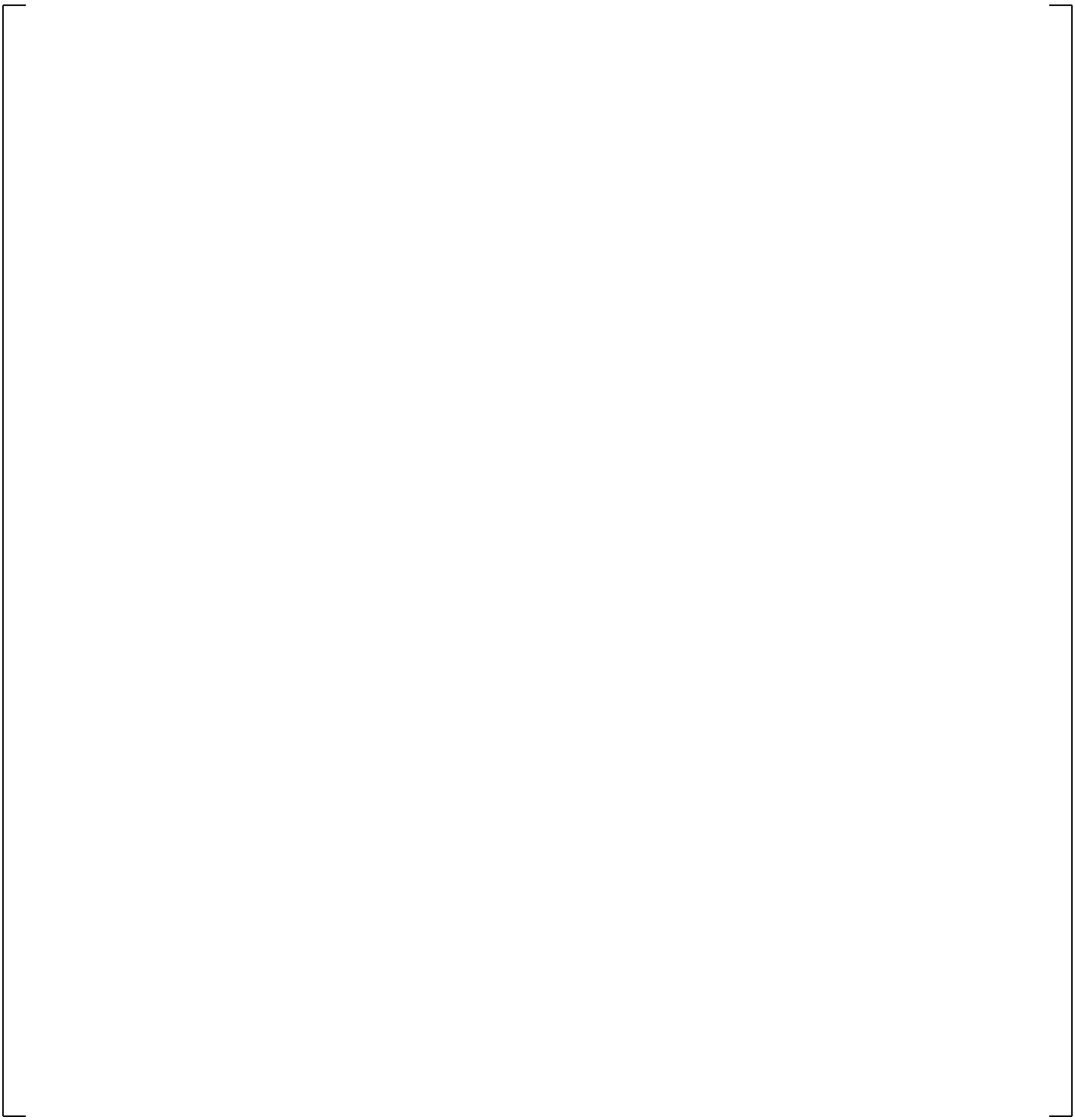

Figure 23.1.2-20 Semiscale S-07-10D Clad Temperature Elevation = 135 cm (from the Bottom of the Core)

a,c

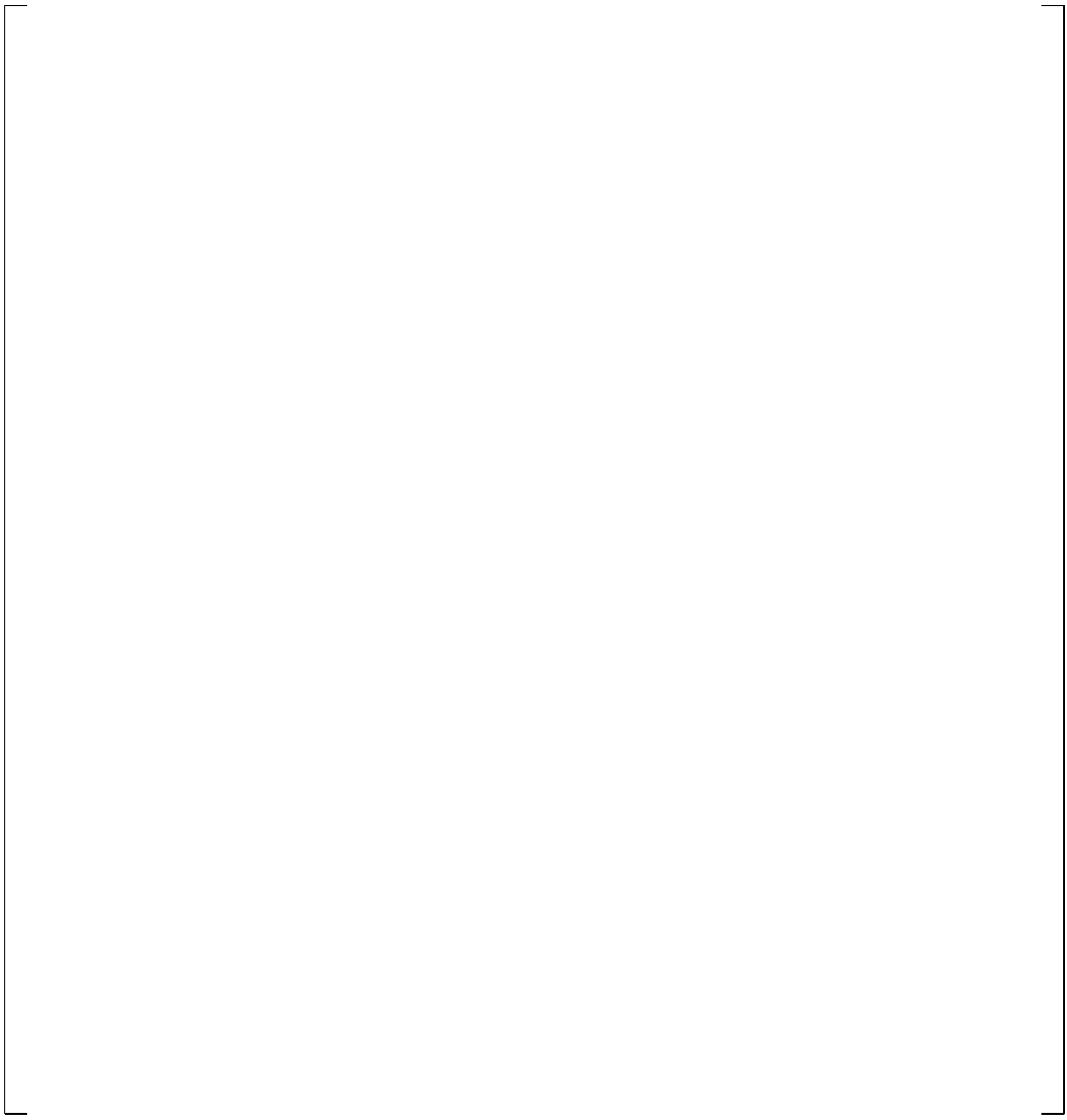

Figure 23.1.2-21 Semiscale S-07-10D Clad Temperature at Elevation = 112 cm (from the Bottom of the Core)

a,c

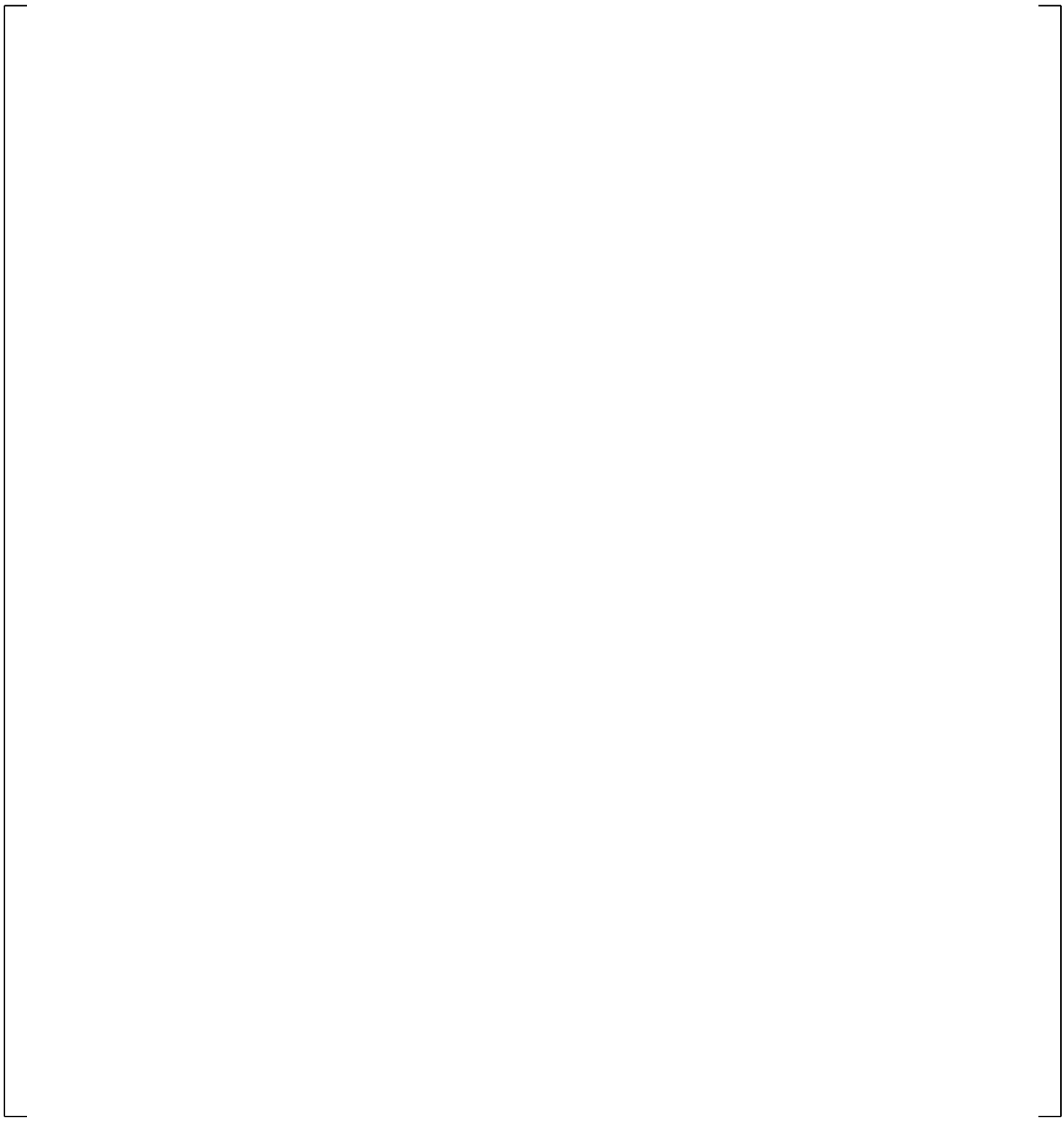

Figure 23.1.2-22 Semiscale S-07-10D Clad Temperature at Elevation = 71 cm (from the Bottom of the Core)

a,c

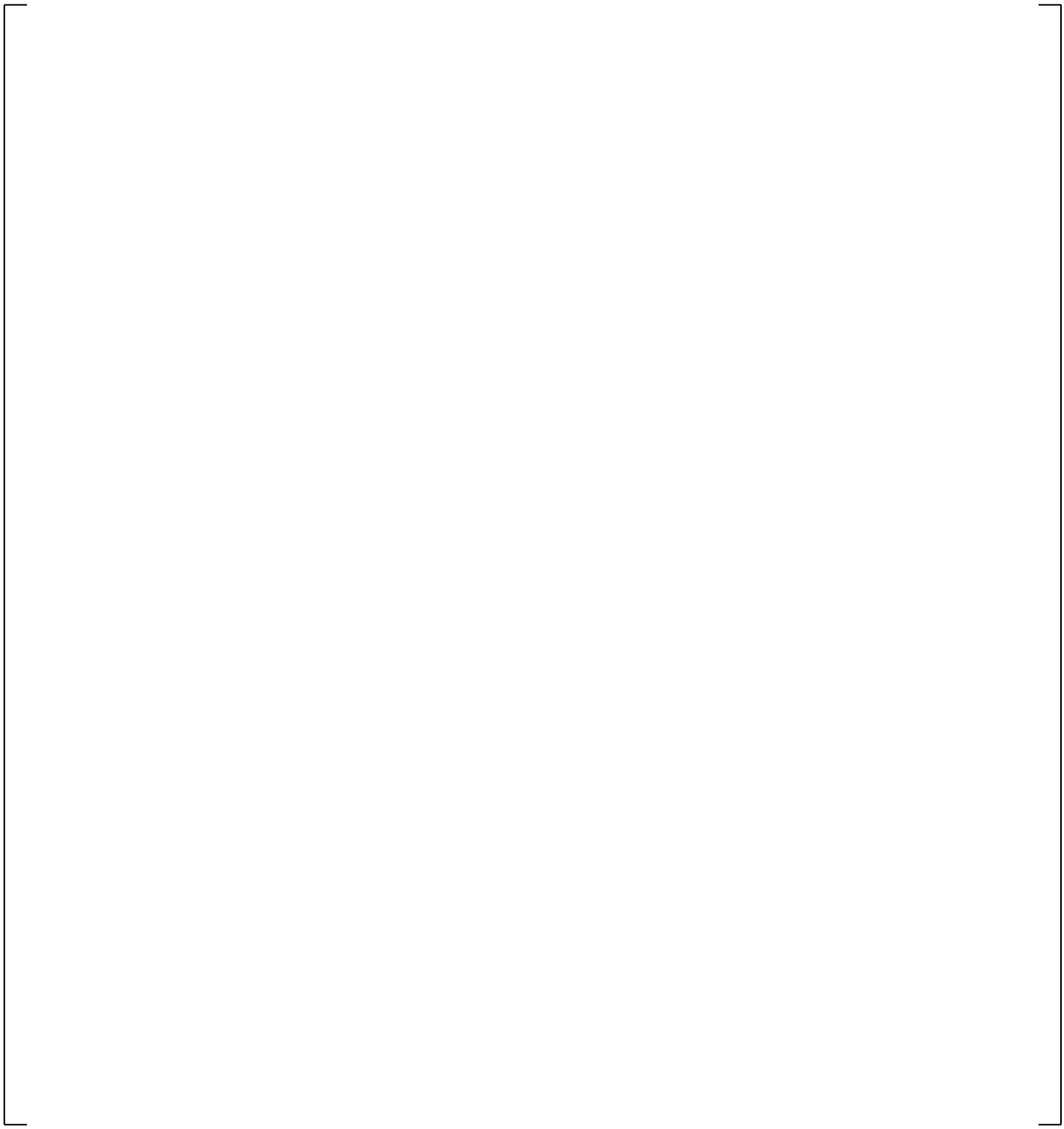

Figure 23.1.2-23 Semiscale S-07-10D Clad Temperature at Elevation = 48 cm (from the Bottom of the Core)

a,c

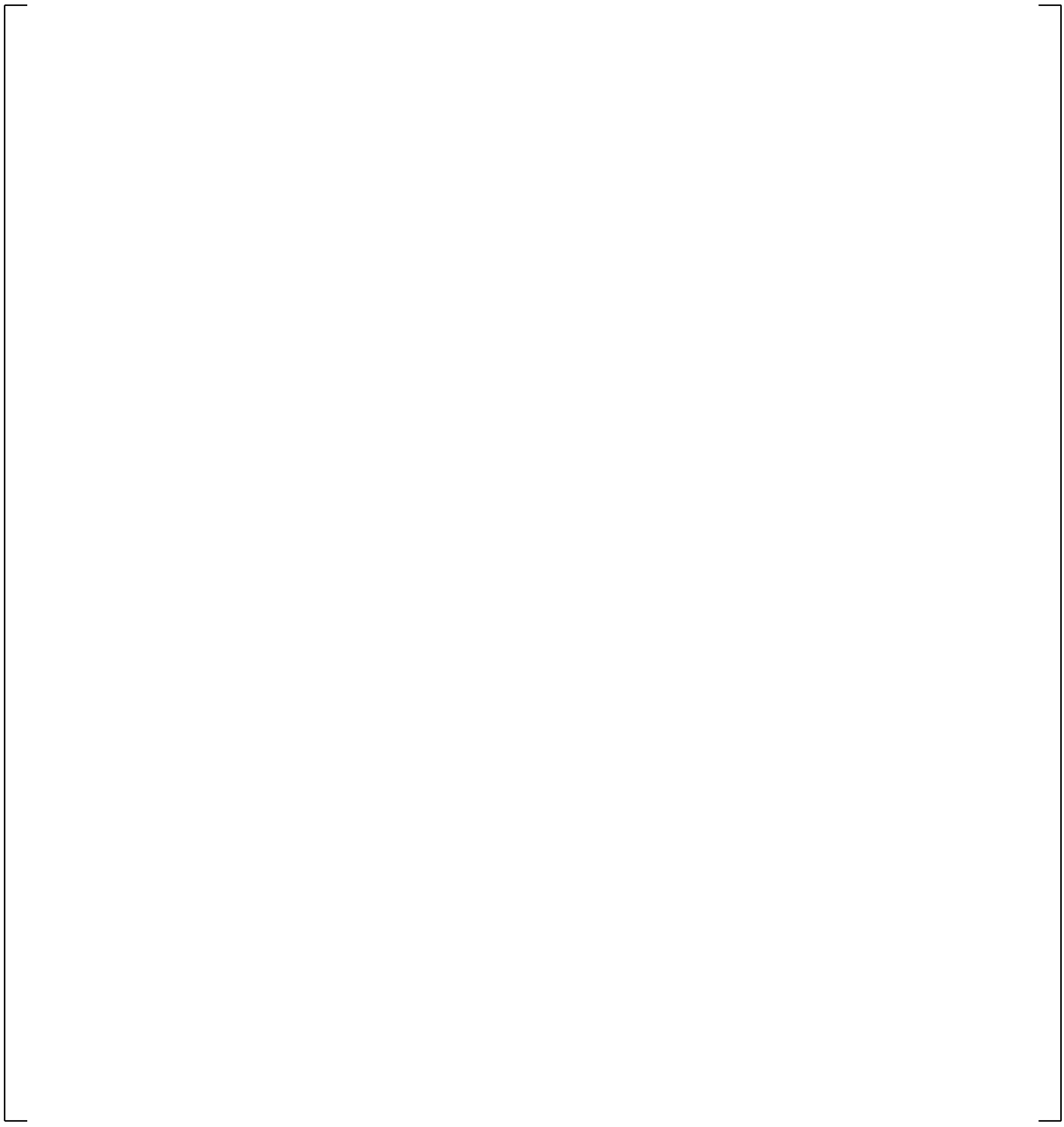

Figure 23.1.2-24 Semiscale S-07-10D Clad Temperature at Elevation = 7 cm (from the Bottom of the Core)

a,c

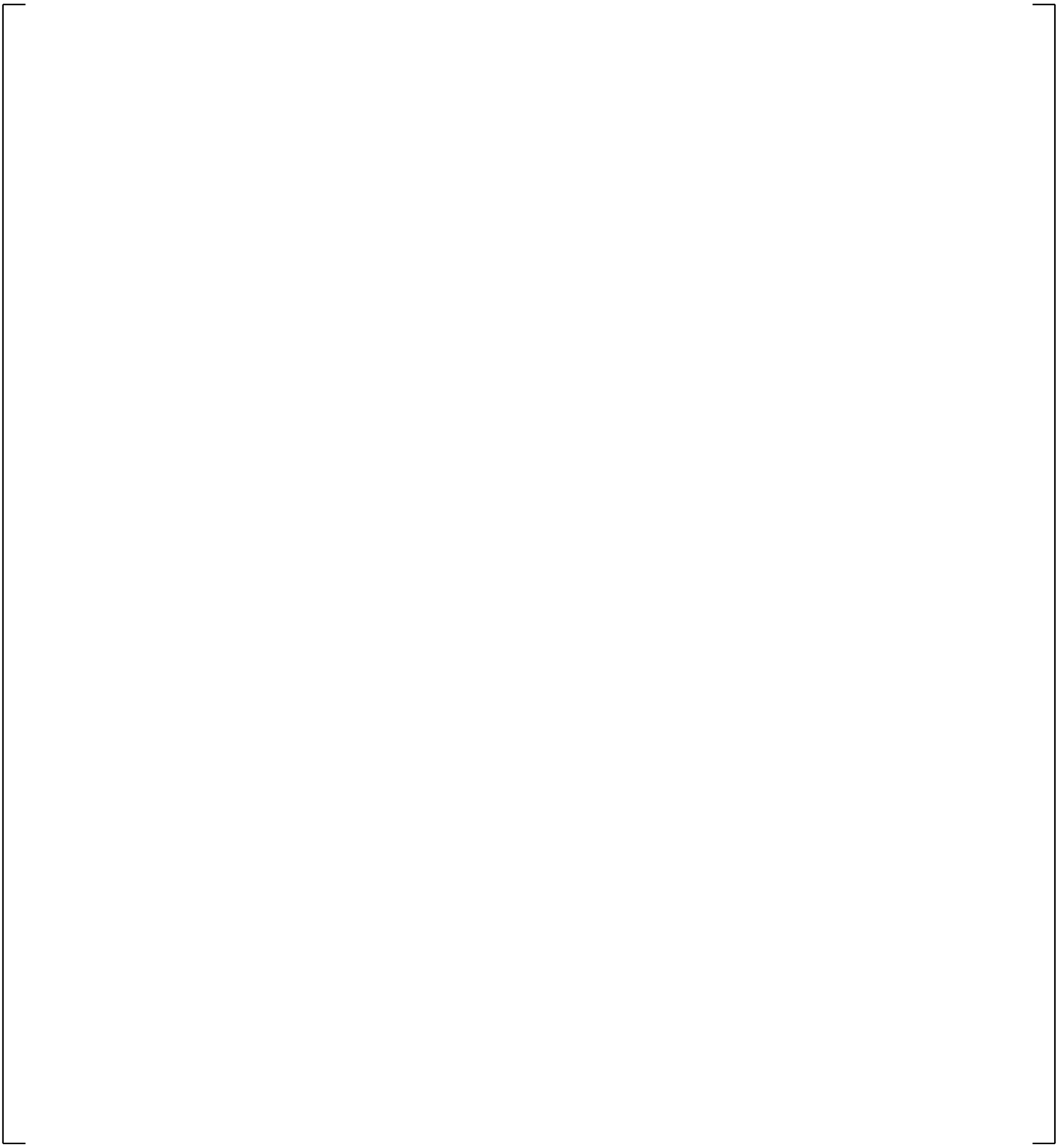

Figure 23.1.2-25 Semiscale S-07-10D Collapsed Liquid Level

a,c

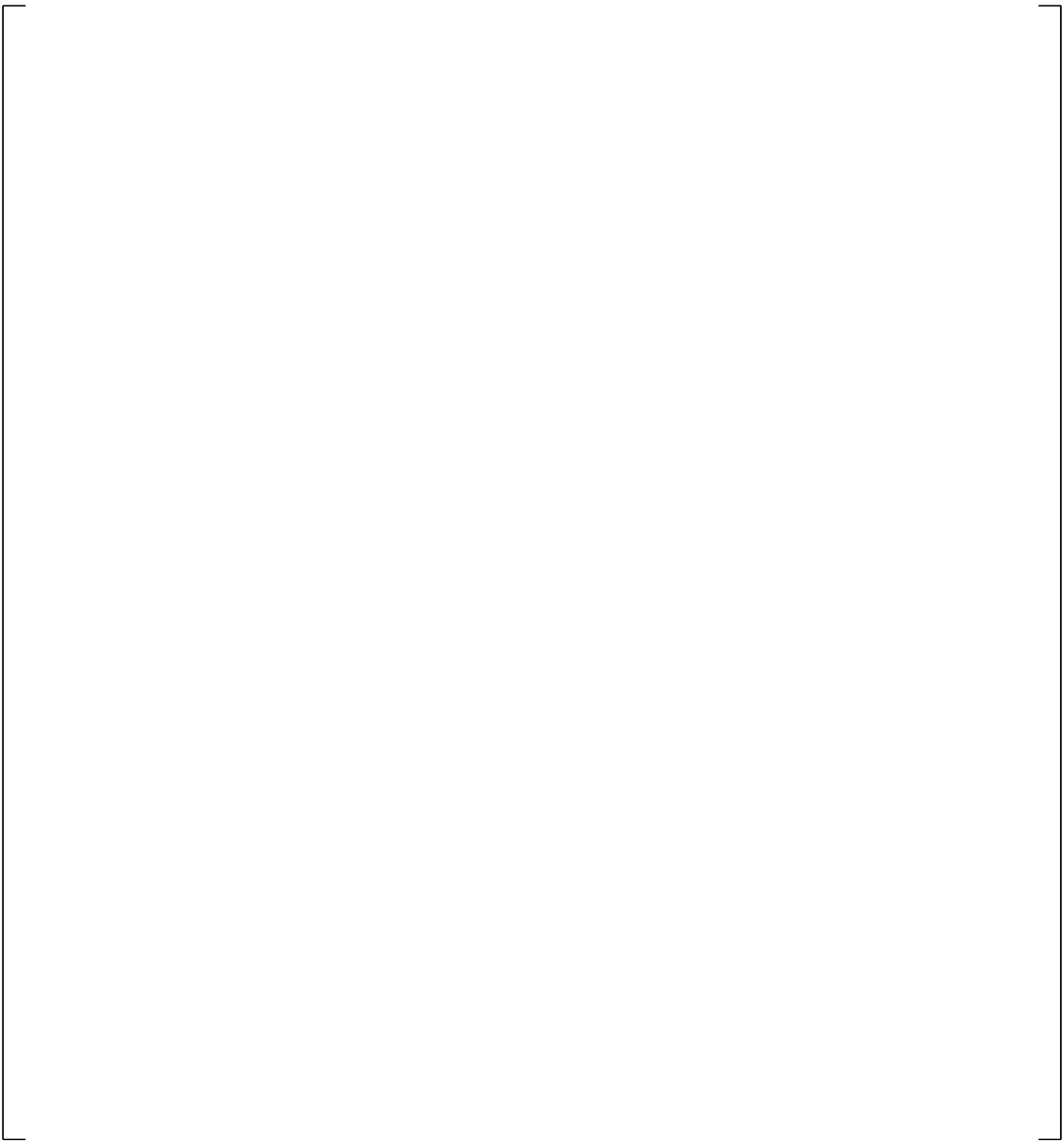

Figure 23.1.2-26 Semiscale S-07-10D Void Fraction at Inlet of the Core (502 cm below Cold Leg (CL) Centerline)

a,c

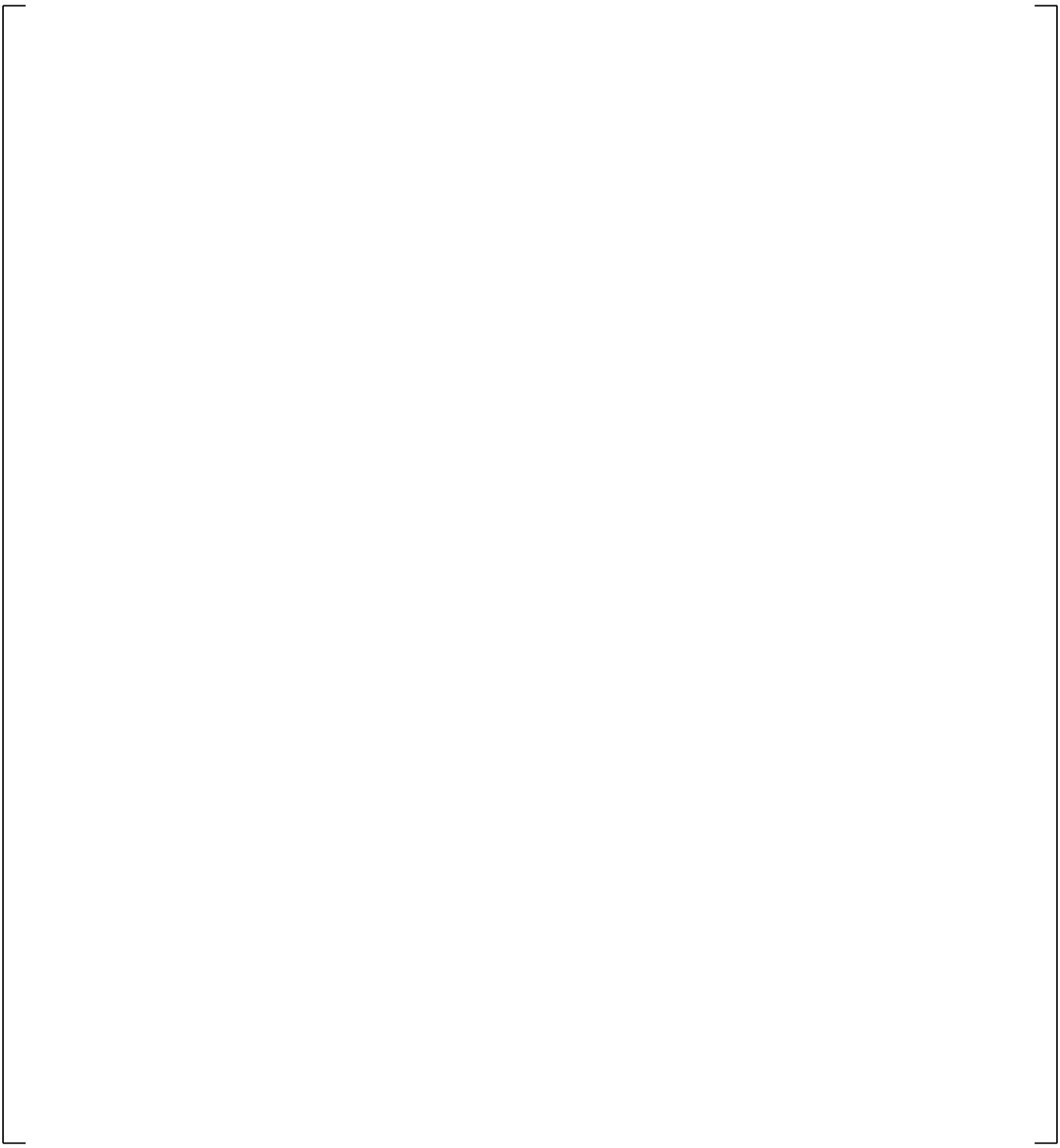

Figure 23.1.2-27 Semiscale S-07-10D Void Fraction at 483 cm below CL Centerline

a,c

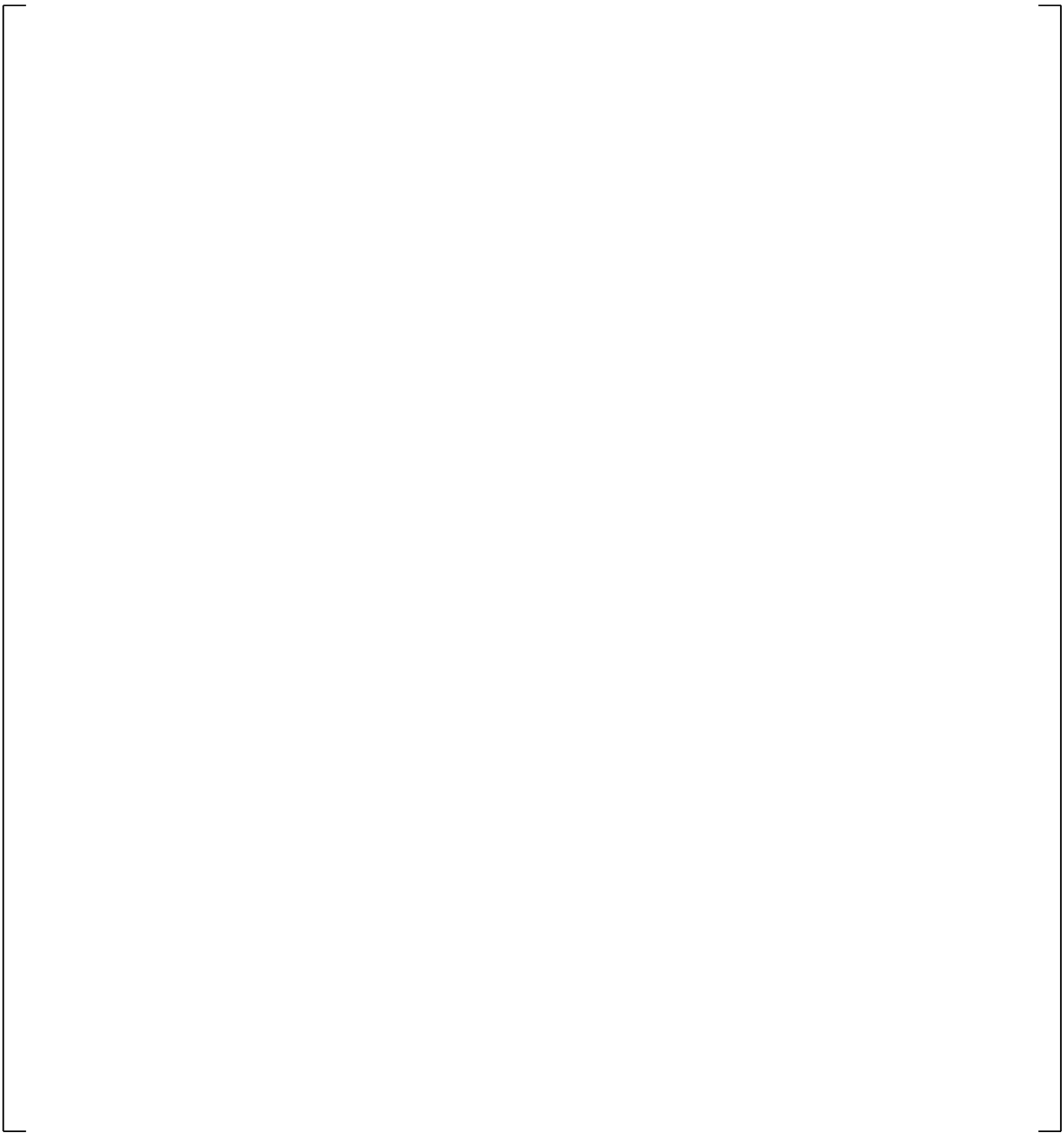

Figure 23.1.2-28 Semiscale S-07-10D Void Fraction at 323 cm below CL Centerline

a,c

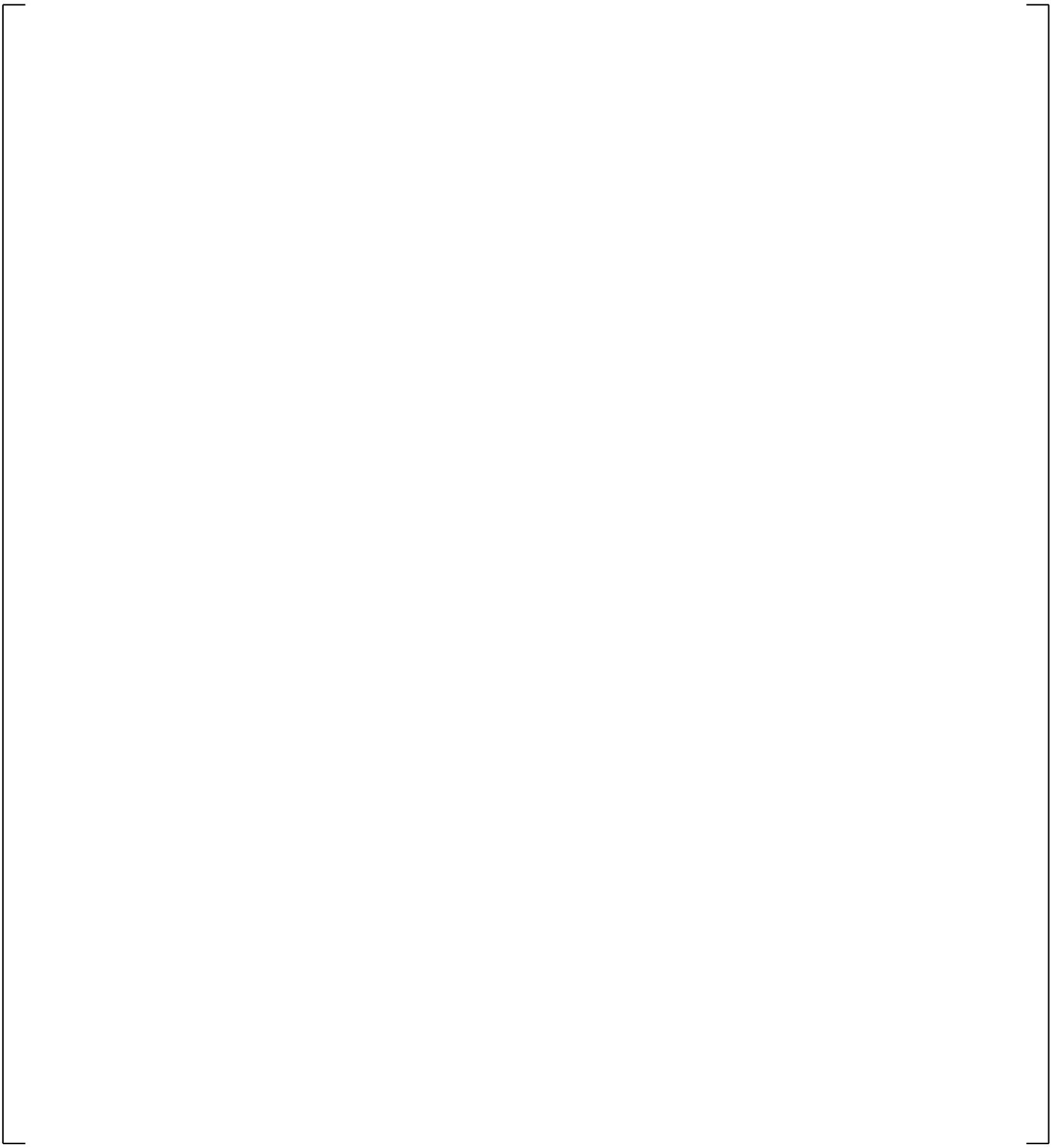

Figure 23.1.2-29 Semiscale S-07-10D Void Fraction at 313 cm below CL Centerline

a,c

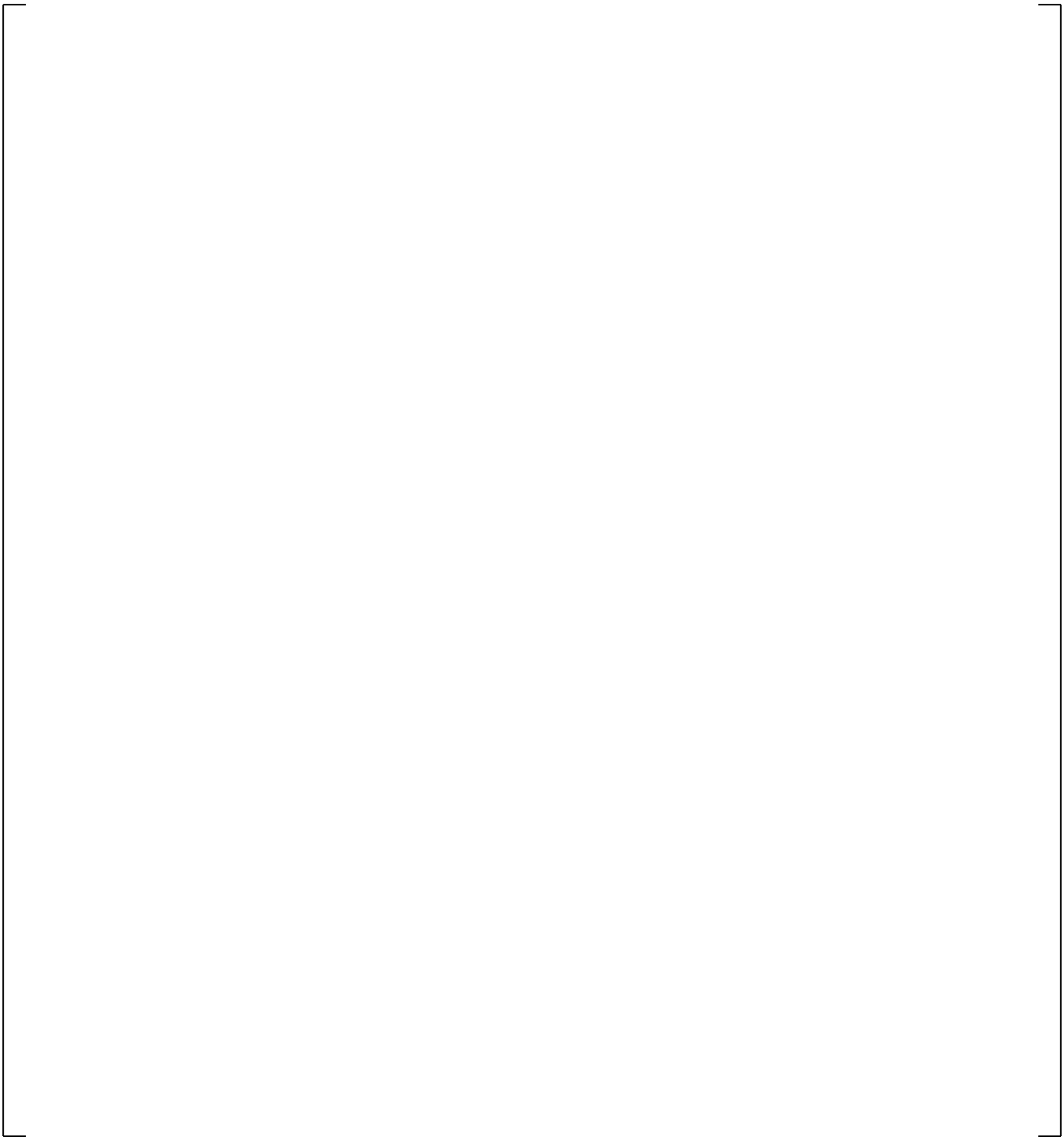

Figure 23.1.2-30 Semiscale S-07-10D Void Fraction at 243 cm below CL Centerline

a,c

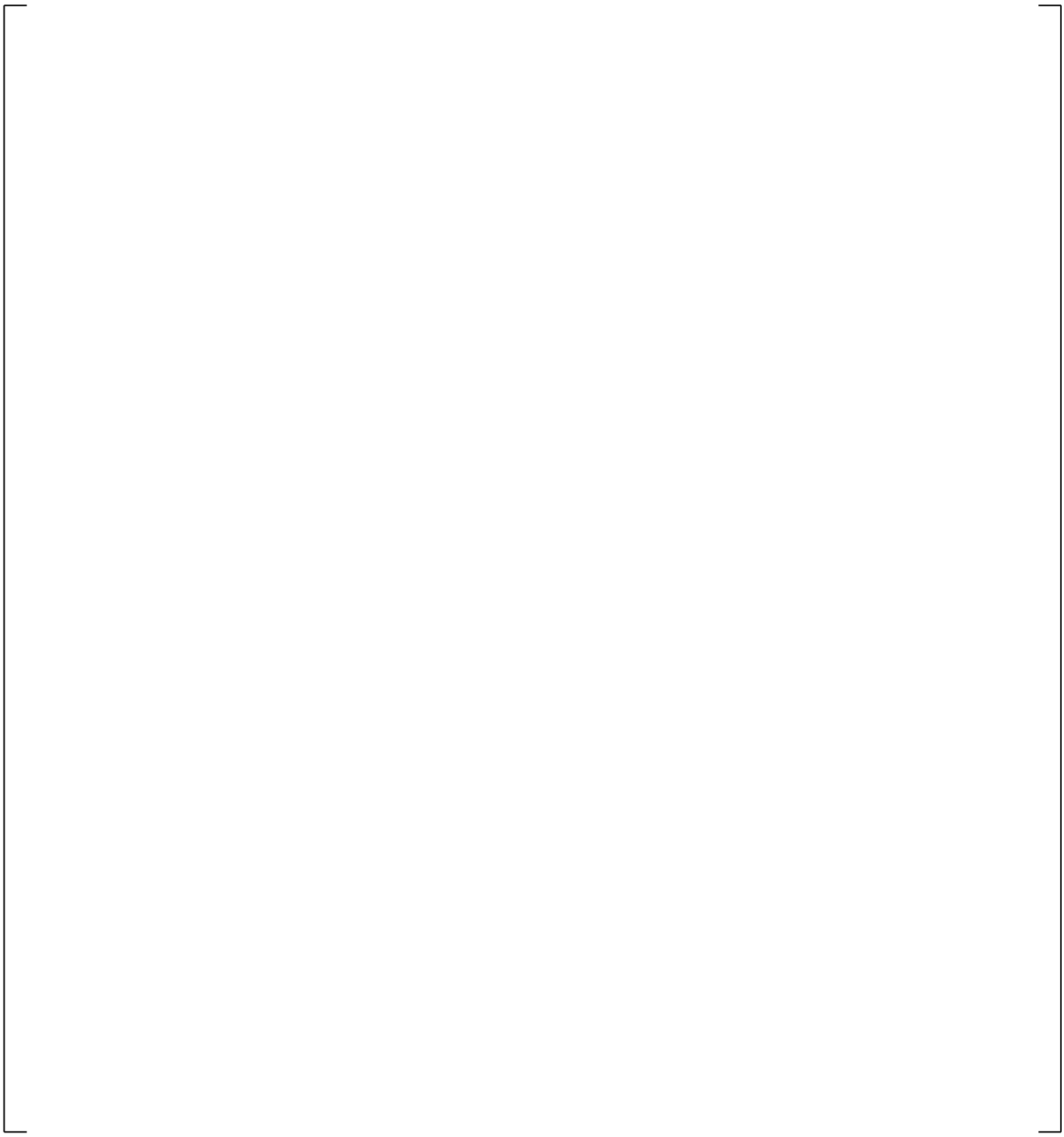

Figure 23.1.2-31 Semiscale S-07-10D Void Fraction at 164 cm below CL Centerline

a,c

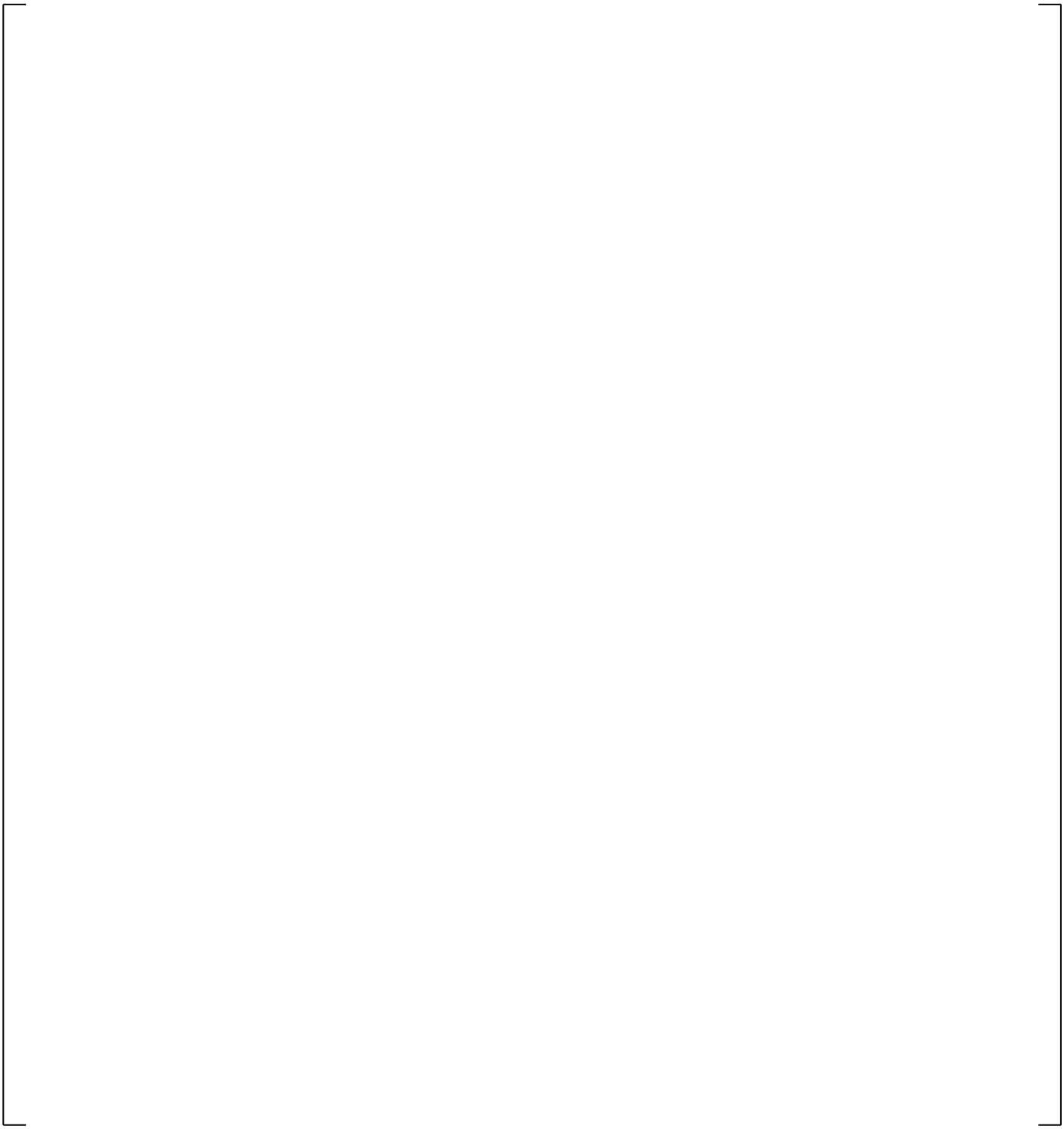

Figure 23.1.2-32 Semiscale S-07-10D Void Fraction at Core Outlet (11 cm below CL Centerline)

a,c

Figure 23.1.2-33 Semiscale S-07-10D Mixture Level

23.2 NUMERICAL PROBLEMS

23.2.1 1D PIPE Manometer Problem with Non-Condensable Gases

23.2.1.1 Introduction

The objective of this problem is to test the ability of the numerical solution method to preserve system mass, which is a constant; to model the period of oscillation, which is analytically known; and to evaluate the capability of the numerical discretization scheme to retain the gas-liquid interface. The problem is established as Numerical Benchmark Test No. 2.2 (NBT2.2) in (Hewitt et al., 1992).

23.2.1.2 Problem Description

The apparatus consists of a 'U' tube manometer which is connected at the top, so that a closed system is formed. The system initially contains gas and liquid with the liquid forming equal collapsed liquid levels in each arm of the manometer. Further, all parts of the fluid system have a uniform velocity of 2.1 m/s but zero acceleration. Under these initial conditions, a hydrostatic pressure profile exists throughout the system. Figure 23.2.1-1 is an illustration of the initial state of the manometer system with a superimposed fixed nodalization schematic.

23.2.1.3 WCOBRA/TRAC-TF2 Model

The U-tube manometer is modeled in WCOBRA/TRAC-TF2 as a 1D pipe consisting of 20 cells. The pipe junctions are connected at the top via a secondary pipe to form a closed loop. Ten of the cell interface boundaries are oriented downward, one horizontal at the bottom and the remaining 10 as upward. Each cell has a length of 1.0 m and a hydraulic diameter of 1.0 m. The initial liquid velocity in the pipe is set to 2.1 m/s as prescribed in (Hewitt et al., 1992). The top 5 cells of each leg of the pipe are initially void (vapor), whereas the remaining part is filled with subcooled liquid at 323.15K (50°C). The gas volume is filled with non-condensable gas to eliminate the complication of interfacial heat and mass transfer. The problem is assumed to be frictionless. The lower and upper limits to time step size are set to 1.0×10^{-6} s and 5.0×10^{-3} s, respectively.

23.2.1.4 Numerical/Analytical Solution

In the absence of friction, the oscillating motion of a liquid in a 'U' tube obeys the following equation:

$$\frac{d^2x}{dt^2} + 2gx/L = 0$$

The problem has a solution for the velocity at the bottom of the manometer as an un-damped cosine wave with amplitude equal to the initial perturbation velocity (from Hewitt et al., 1992).

$$v = \frac{dx}{dt} + v_o \cdot \cos\left(2g/L\right)^{1/2}$$

$$\text{Period} = 2\pi\sqrt{\frac{L}{2g}} = 4.255\text{s}$$

where,

x = elevation (position) of water level.
L = length of the water column.
v = velocity of the water column.
g = acceleration due to gravity.

23.2.1.5 WCOBRA/TRAC-TF2 Assessment

Figure 23.2.1-2 shows the liquid velocity at the bottom of the U-tubes and Figure 23.2.1-3 shows the liquid mass in the left and right legs and the system total. The period of oscillations shows good agreement with the analytical solution ([ ]^{a,c} compared with 4.255 seconds) and the total mass in the system is preserved. The results show that numerical viscosity has some impact, albeit small, as evidenced by the slight damping; a reduction in amplitude is observed over time.

As discussed in Section 2.2 of NBT2.2 in (Hewitt, et al., 1992), truncation errors due to finite difference equations are not necessarily zero for this problem, depending on the degree of implicitness in the mass and momentum solution. "Too implicit" schemes will cause false (numerical) damping, "too explicit" schemes will amplify the oscillations over time, and time-centered solution schemes will show no damping. Figure 23.2.1-2 shows that the 1-D module of WCOBRA/TRAC-TF2 exhibits behavior typical of a semi-implicit code, less damped than a fully implicit scheme (see Figure 3 in Section 2.2 of NBT2.2) and more damped than the undamped solution from a time-centered scheme (see Figure 5 in Section 2.2 of NBT2.2).

23.2.1.6 Summary and Conclusions

The U-tube manometer problem has been modeled with a 1D pipe component. Results show slight damping, indicating the presence of a small numerical viscosity (diffusion) as a result of the semi-implicit numerical scheme. However the code is in general able to resolve this problem well and good agreement is seen relative to the analytical solution, comparable to other semi-implicit codes presented in (Hewitt et al., 1992).

23.2.1.7 References

1. Hewitt, G. F., Delhaye, J. M. and Zuber, N., 1992, Multiphase Science and Technology, Vol.6.

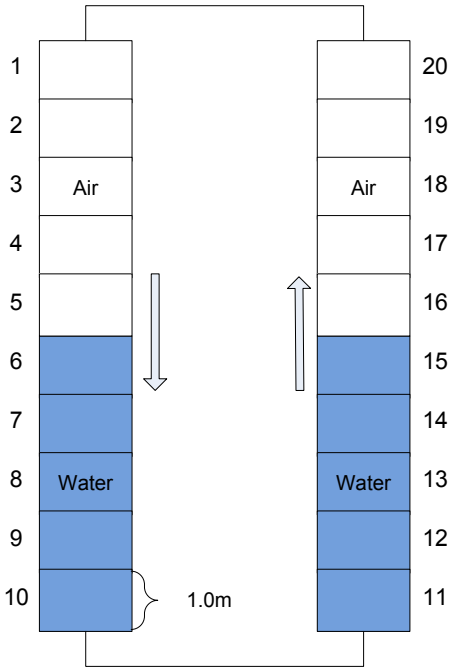

Figure 23.2.1-1 Schematic and Nodalization Diagram for the Oscillating Manometer (Note that Nodes 1 and 20 are each Connected to a PIPE Component not Depicted in the Diagram)

a,c

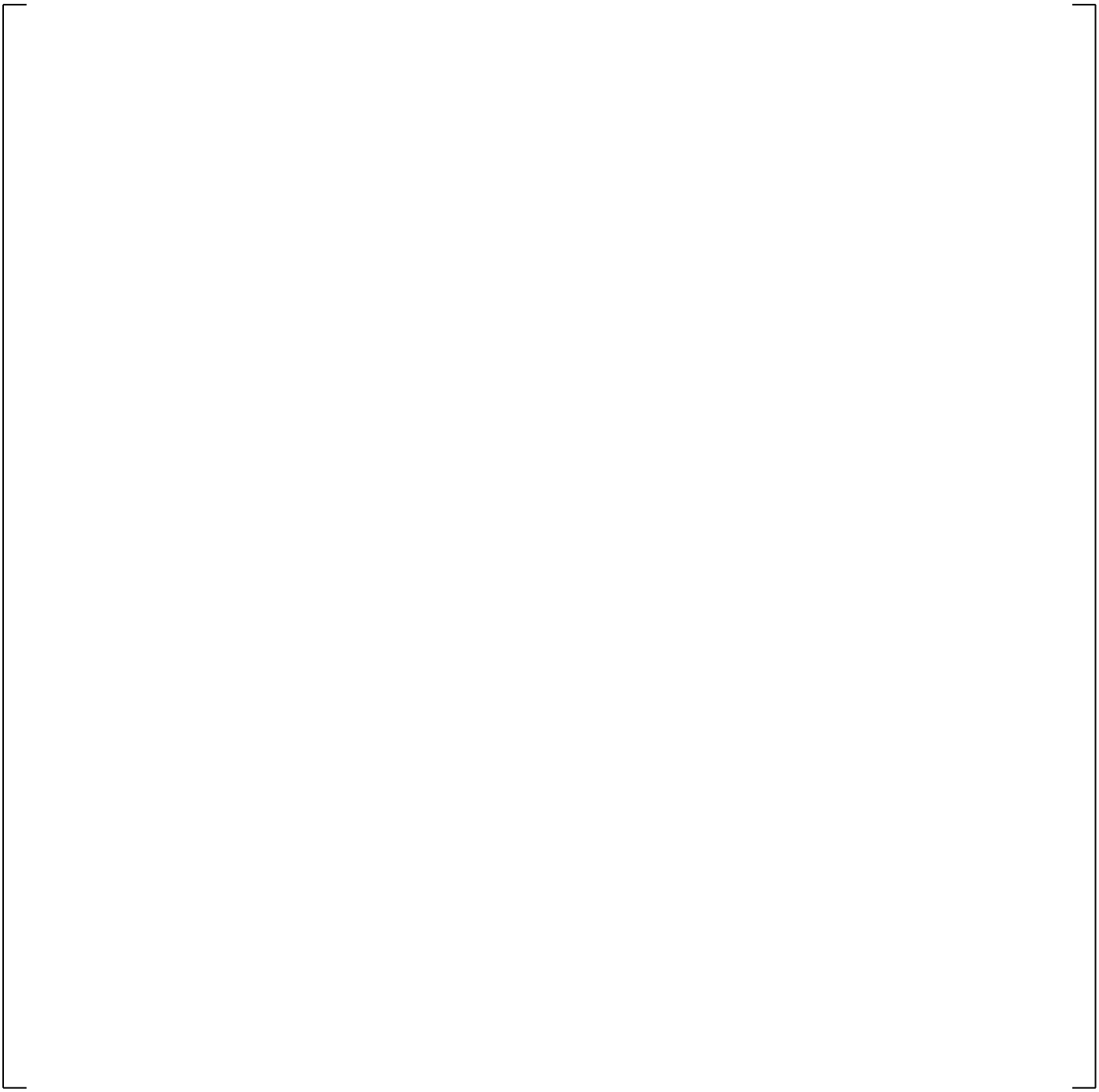

Figure 23.2.1-2 WCOBRA/TRAC-TF2 Results for Liquid Velocity at the Bottom of the Tube

a,c

Figure 23.2.1-3 WCOBRA/TRAC-TF2 Results for Total Fluid Mass

23.2.2 3D VESSEL Manometer Problem with Non-Condensable Gases

23.2.2.1 Introduction

The objective of this problem is identical to that discussed in Section 23.2.1.1, with the only difference that the 3D VESSEL is tested here.

23.2.2.2 Problem Description

See Section 23.2.1.2. Here, since the VESSEL component cannot be initialized with liquid velocities, an elevation difference between the two sides of the manometer is applied at the beginning of the transient.

23.2.2.3 WCOBRA/TRAC-TF2 Model

The U-tube manometer is modeled in WCOBRA/TRAC-TF2 using a 2 channel VESSEL component. The channels have 10 axial nodes each, with 1.0m height and 1.0m hydraulic diameter. The channels are connected via a 1.0m long gap at the bottom. Initially, one leg of the manometer is filled with subcooled liquid up to the 7th axial node, and the other leg to the 5th. A 1D pipe is attached to the vessel component at the top of the channels providing a closed loop system. A zero velocity boundary condition is prescribed at the channel top and bottom faces. The gas volume is filled with non-condensable gas to eliminate the complication of interfacial heat and mass transfer. Figure 23.2.2-1 is an illustration of the initial state of the manometer system with a superimposed fixed nodalization schematic.

23.2.2.4 Numerical/Analytical Solution

See Section 23.2.1.4; the analytical solution is applicable here as well. See Section 23.2.1.5 for a discussion of the effects of the numerical solution scheme on the observed damping.

23.2.2.5 WCOBRA/TRAC-TF2 Assessment

Figure 23.2.2-2 shows the velocity at the bottom of 3D Vessel manometer, while Figure 23.2.2-3 shows the collapsed liquid levels in the two legs as well as the total system fluid mass. **[**

][a,c]

As a result of the noding, shown in Figure 23.2.2-1, the flowpath of a liquid particle through the bottom of the manometer consists of a downward flow within a channel (1) to a dead-end cell, purely horizontal flow through a gap to a second channel (2), and then upward flow from a dead-end cell in the new channel (2). The deceleration of downward flow results in a calculated irreversible loss equal to the dynamic pressure, as does the acceleration to create upward flow. The implied loss coefficient is then

$$K = \frac{\Delta P}{\frac{1}{2}\rho V^2} = \frac{2 \cdot \left[\frac{1}{2}\rho V^2\right]}{\frac{1}{2}\rho V^2} = 2 \qquad (23\text{-}1)$$

[**]**[a,c]

23.2.2.6 Summary and Conclusions

Manometric oscillations in the downcomer and core are evident during early reflood following a large break LOCA. Such is observed in integral effects tests (Cylindrical Core Test Facility (CCTF), see Section 19.6). Downcomer and lower plenum noding for the plants and integral effects tests are similar to the 3-D manometer noding in that downcomer channels are connected to the lower plenum through gaps in the lower cell(s). In the plant, external pressure forces act in addition to gravity as the liquid accumulation in the downcomer is opposed by vapor generation in the core and the consequent pressurization of the upper plenum and upper head regions. Evidenced by the CCTF simulations in Section 19.6, the oscillatory behavior in the plant case is captured adequately.

The oscillatory core injection on the reflood is expected to cause increased cooling (Oh et al., 1983). The expected improvement in cooling is **[**

][a,c]

23.2.2.7 References

1. Oh, S., Banerjee, S. and Yadigaroglu, G., 1983, "The Effect of Inlet Flow Oscillations on Reflooding of a Tubular Test Section," *Thermal Hydraulics of Nuclear Reactors*, Volume 1, pp. 674-680. Presented at The Second International Topical Meeting on Nuclear Reactor Thermal-Hydraulics, Santa Barbara CA, USA.

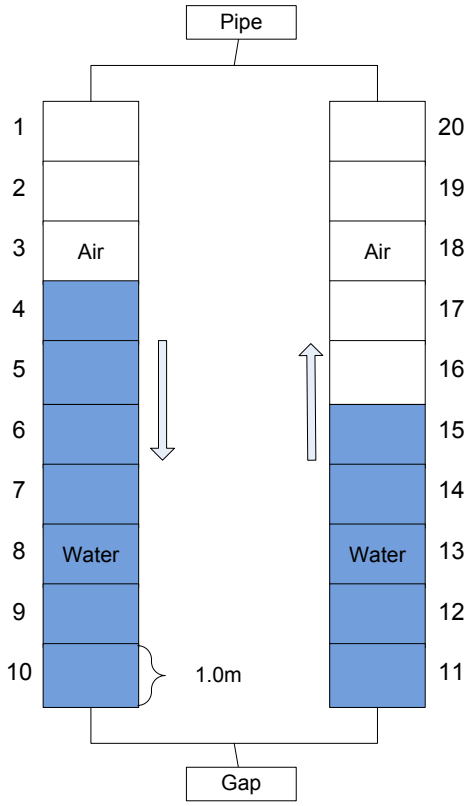

Figure 23.2.2-1 WCOBRA/TRAC-TF2 Model of the Manometer Test Problem using the VESSEL Component

a,c

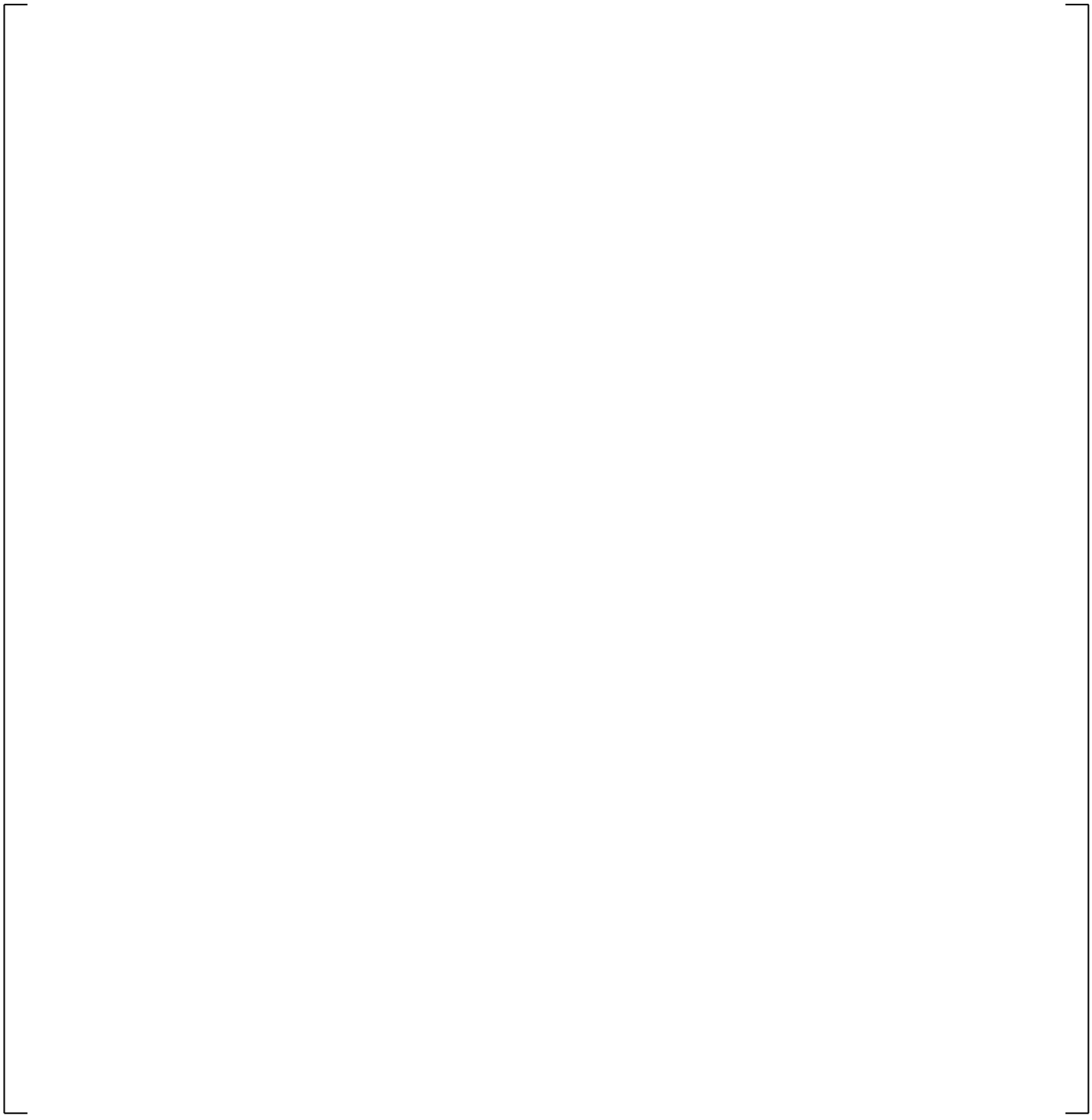

Figure 23.2.2-2 Velocity at the Bottom Gap of the 3D Manometer

a,c

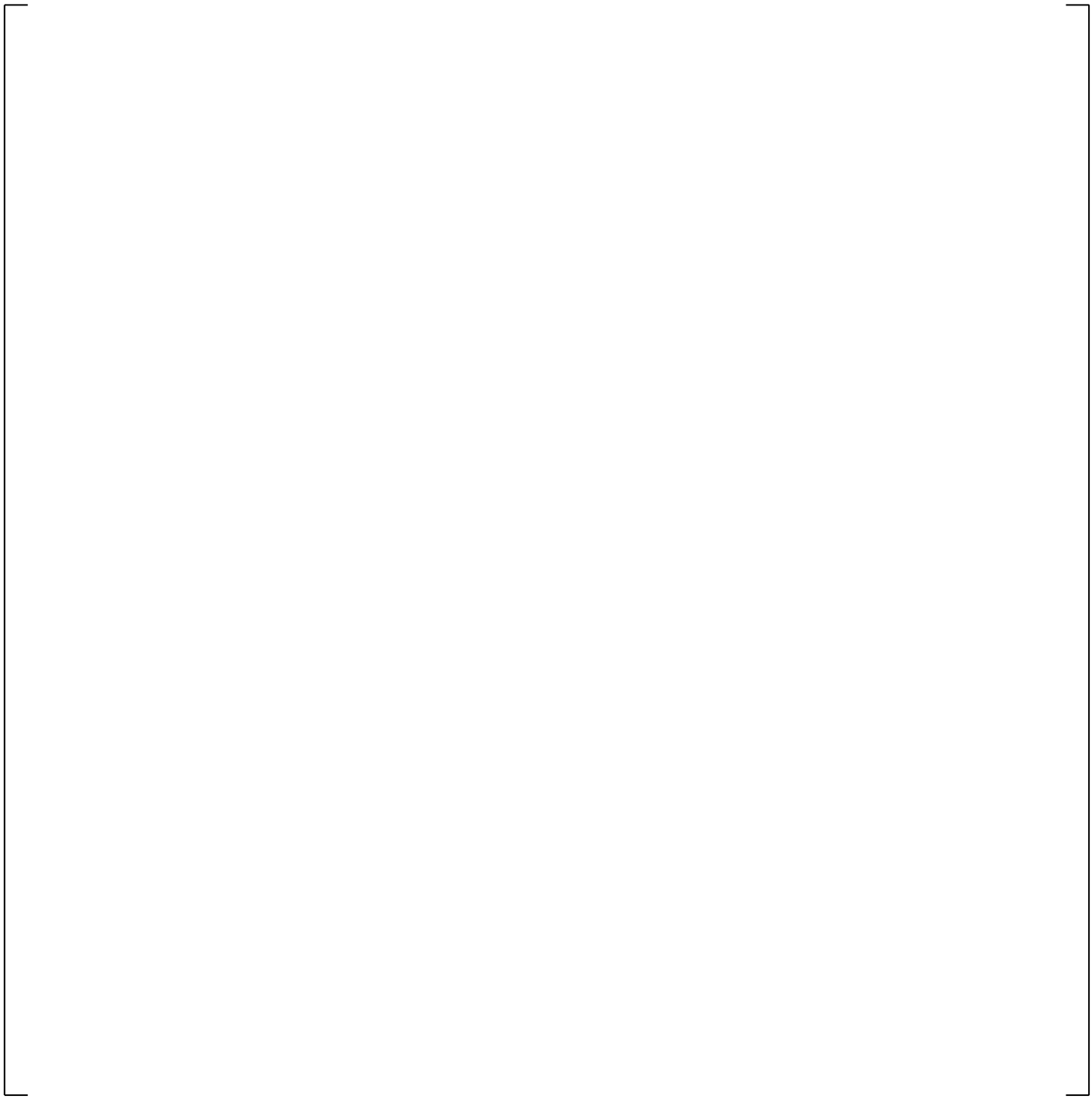

Figure 23.2.2-3 Collapsed Liquid Levels and Total System Mass in the 3D Manometer

23.2.3 1D PIPE Steam Expulsion Test

23.2.3.1 Introduction

This problem is established as Numerical Benchmark Test No. 2.3 (NBT2.3) in (Hewitt et al., 1992).

23.2.3.2 Problem Description

From (Hewitt et al., 1992):

"The problem is formulated to test the numerical solution methods for anomalous numerical behavior associated with the mass transfer modeling that is characteristic of fixed node discretization schemes. The problem consists of, in a physical sense, a constant volume injection rate of subcooled water into a vertical tube initially filled with superheated steam and connected at the top to a constant pressure source of superheated steam."

"As the subcooled water is injected, condensation begins and the superheated steam is drawn into the tube. The condensation process adds energy to the injected liquid raising its temperature. In the usual fixed-mesh discretization scheme, the spacial grid spacing is too coarse to permit accurate modeling of the temperature gradient near the interface. This results in over-prediction of the condensation rate. In addition, when a node exactly fills with liquid, the condensation rate must become zero for at least one time step. This momentary numerical cessation of condensation results in a compression wave (water hammer) that propagates up the tube. The magnitude of compression depends upon the magnitude of the time step in which the condensation rate is zero."

23.2.3.3 WCOBRA/TRAC-TF2 Model

In this test problem, a vertical tube is connected to a constant pressure source of steam at superheated and saturated conditions. Initially, the tube is filled with steam, but subcooled water is then injected from the bottom of the tube at a constant velocity of 0.5 m/s. The vertical tube is 1.0 m in diameter and 3.0 m tall. The steam reservoir is held at a constant pressure of 4.0E+5 Pa and temperature of 163°C, respectively.

The steam expulsion test is modeled in WCOBRA/TRAC-TF2 as a single vertical 1D pipe, consisting of 10 cells. Each cell has a height of 0.3 m and a hydraulic diameter of 1.0 m. A BREAK component is connected at the top providing a pressure boundary condition of 4.0E+5 Pa. Two cases are modeled. In the first case, the initial pressure and temperature in the pipe is 4.0E+5 Pa and 163.0°C, representing superheated steam. In the second case, the temperature is decreased to the saturation temperature of 143.6°C. A FILL component is attached to the pipe at the bottom. Subcooled liquid injection is started at the FILL with a ramp, reaching a constant 0.5 m/s steady flow in 1.0 s. This model is illustrated in Figure 23.2.3-1.

23.2.3.4 Numerical/Analytical Solution

As described in (Hewitt et al., 1992), an exact analytical solution would require resolving the interfacial heat and mass transfer between the top of the liquid column and the vapor. This will depend on the rate of heat conduction in the liquid phase and the rate of convective heating of the interface by the steam.

However, for a low filling rate of the pipe, the fill time can be estimated as slightly less than 6 sec., as a result of liquid injection at a rate of 0.5 m/s and condensation of steam. Also the process should be continuous. The condensation rate should be very small because a layer of saturated liquid would develop at the top of the liquid column limiting the condensation.

The objective of this study is therefore to assess the fill time and analyze the effects of the spatial discretization associated with the noding scheme discussed in Section 23.2.3.3.

23.2.3.5 WCOBRA/TRAC-TF2 Assessment

23.2.3.5.1 Superheated Steam Case

Figure 23.2.3-2 (Figure 23.2.3-3 with adjusted scale) and Figure 23.2.3-4 show the pressure and void fraction, respectively, in every two cells in the pipe, during the steam expulsion simulation. As seen in the pressure profile, [

]^{a,c}

Other relevant plots, including liquid and vapor velocities and temperatures, are shown in Figure 23.2.3-5 through Figure 23.2.3-8. [

]^{a,c}

The liquid temperature (Figure 23.2.3-7) is near saturation when the cell is gas filled, and drops to the liquid temperature of the cell upstream when the liquid front crosses the bottom cell boundary. The vapor in a cell is initially superheated (Figure 23.2.3-8) and quickly de-superheats as a result of the interfacial heat transfer until it reaches saturation when the cell is water-packed.

23.2.3.5.2 Saturated Steam Case

Figure 23.2.3-9 and Figure 23.2.3-10 show the pressure and void fraction, respectively, in every two cells in the pipe, during the steam expulsion simulation with saturated steam. As seen in the pressure profile, [

]^{a,c} Other relevant plots, including liquid and vapor velocities and temperatures are shown in Figure 23.2.3-11 through Figure 23.2.3-14. It can be seen that the results are quite similar to the superheated steam case, [

]^{a,c}

23.2.3.6 Summary and Conclusions

The steam expulsion problem is a standard numerical benchmark problem that was exercised with different codes (Hewitt et al., 1992, Pryor et al., 1978). As described in Section 3 of NBT2.3 of (Hewitt et al., 1992), the qualitative analytic solution is absent of any "spikes," although it is known that a discretized noding scheme will result in some spikes or ripples as described in Section 23.2.3.2.
[

]^{a,c}

23.2.3.7 References

1. Hewitt, G. F., Delhaye, J. M. and Zuber, N., 1992, Multiphase Science and Technology, Vol. 6.

2. Pryor, R. J., Liles, D. R. and Mahaffy, J. H., 1978, "Treatment of Water Packing Effects," *Trans. ANS* 30, pp. 208-209.

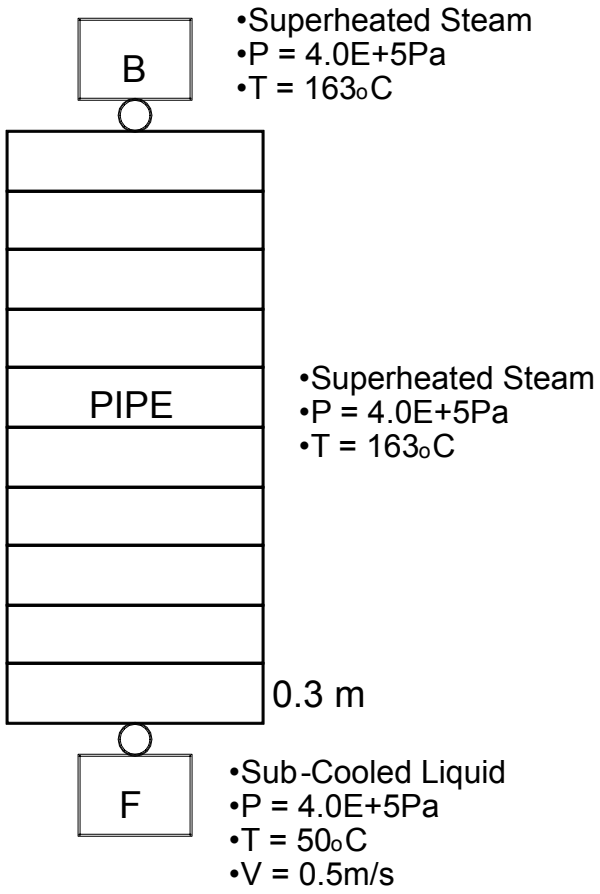

Figure 23.2.3-1 Nodalization and Schematic for Steam Expulsion Test using 1D Pipe

a,c

Figure 23.2.3-2 Pressure Profile in the 1D Pipe for the Steam Expulsion Test, Superheated Steam Case

a,c

Figure 23.2.3-3 Pressure Profile in the 1D Pipe for the Steam Expulsion Test, Superheated Steam Case

a,c

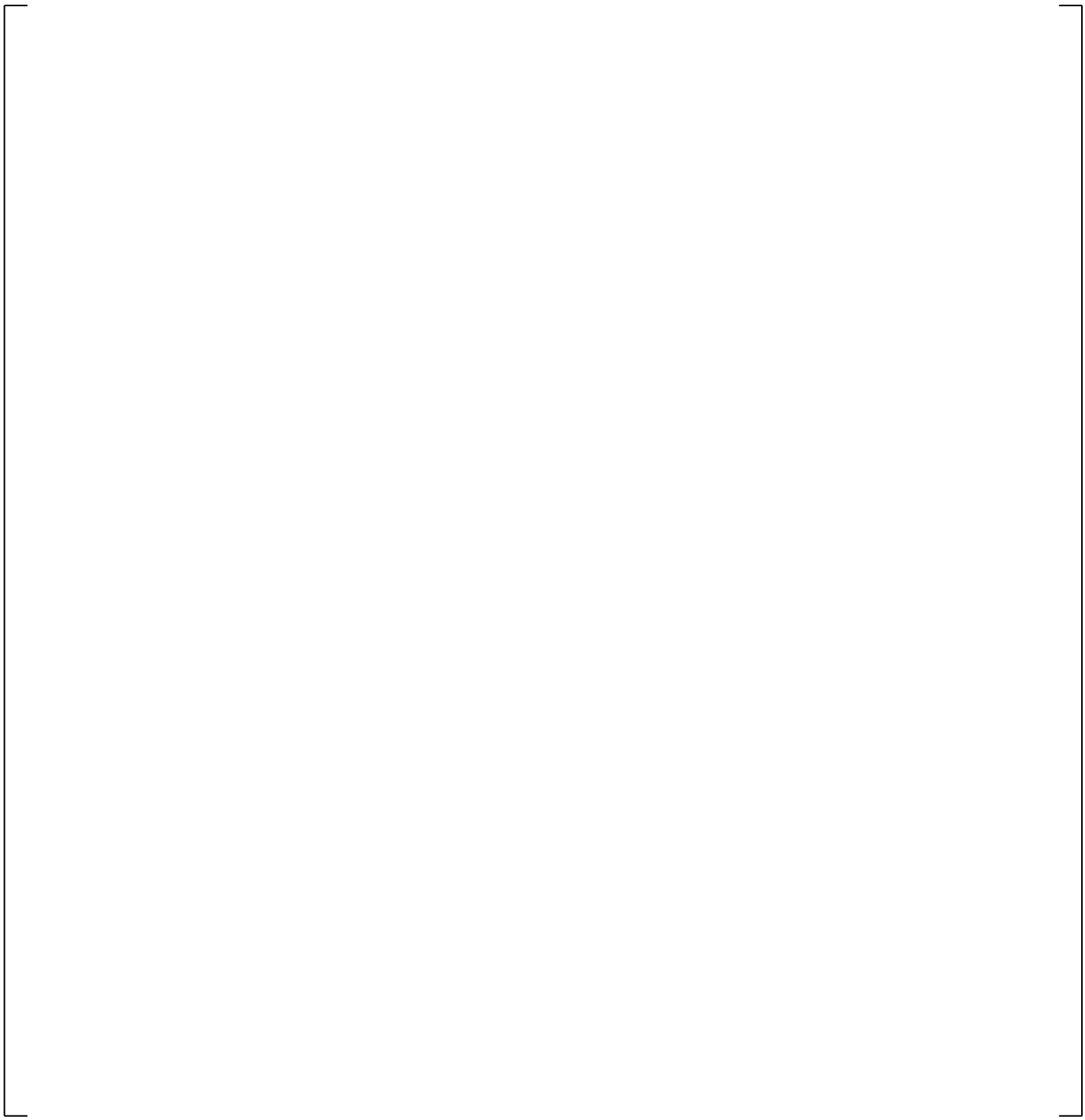

Figure 23.2.3-4 Void Fraction Profile in the 1D Pipe for the Steam Expulsion Test, Superheated Steam Case

a,c

Figure 23.2.3-5 Liquid Velocity Profile in the 1D Pipe for the Steam Expulsion Test, Superheated Steam Case

a,c

Figure 23.2.3-6 Steam Velocity Profile in the 1D Pipe for the Steam Expulsion Test, Superheated Steam Case

a,c

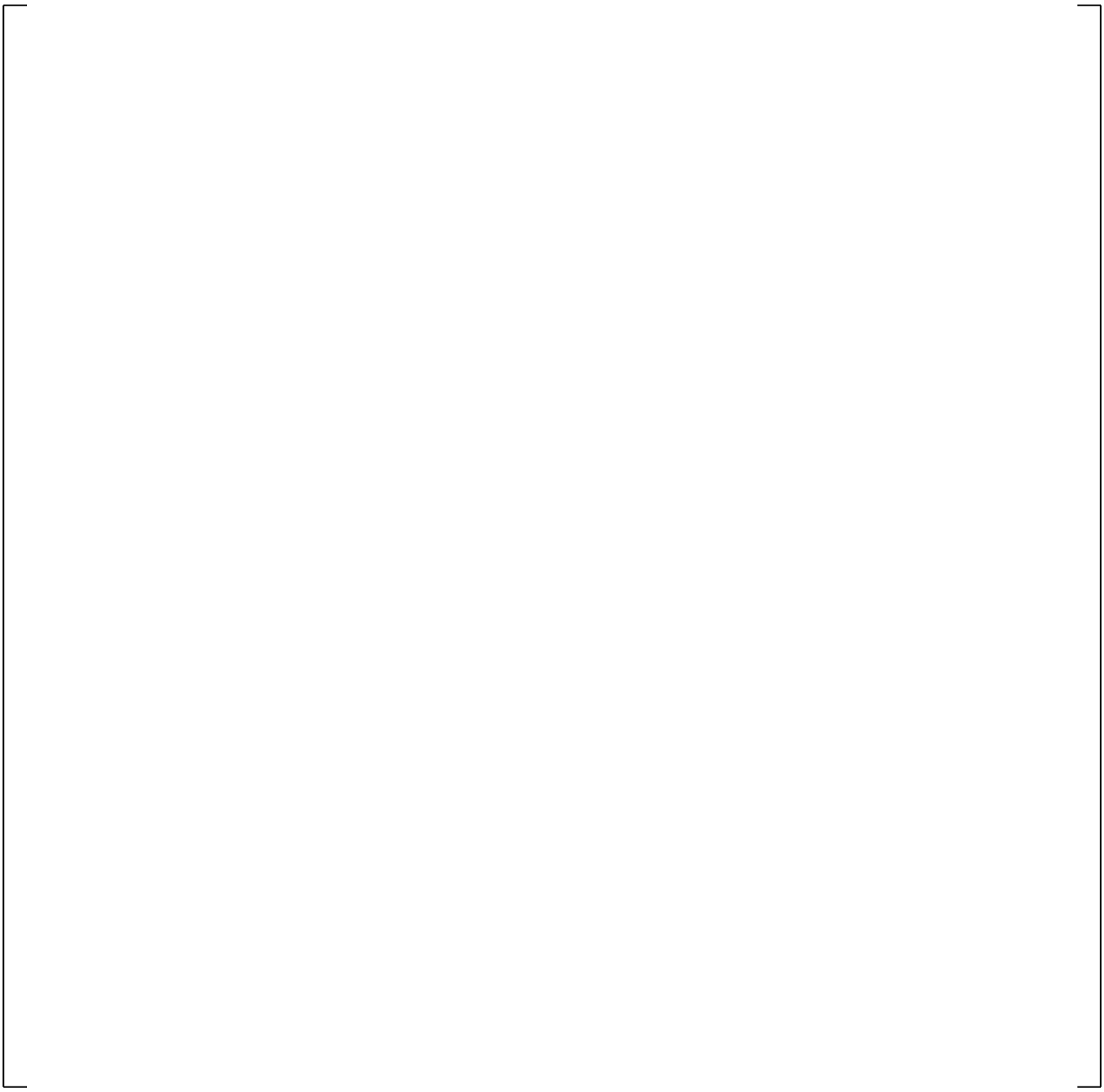

Figure 23.2.3-7 Liquid Temperature Profile in the 1D Pipe for the Steam Expulsion Test, Superheated Steam Case

a,c

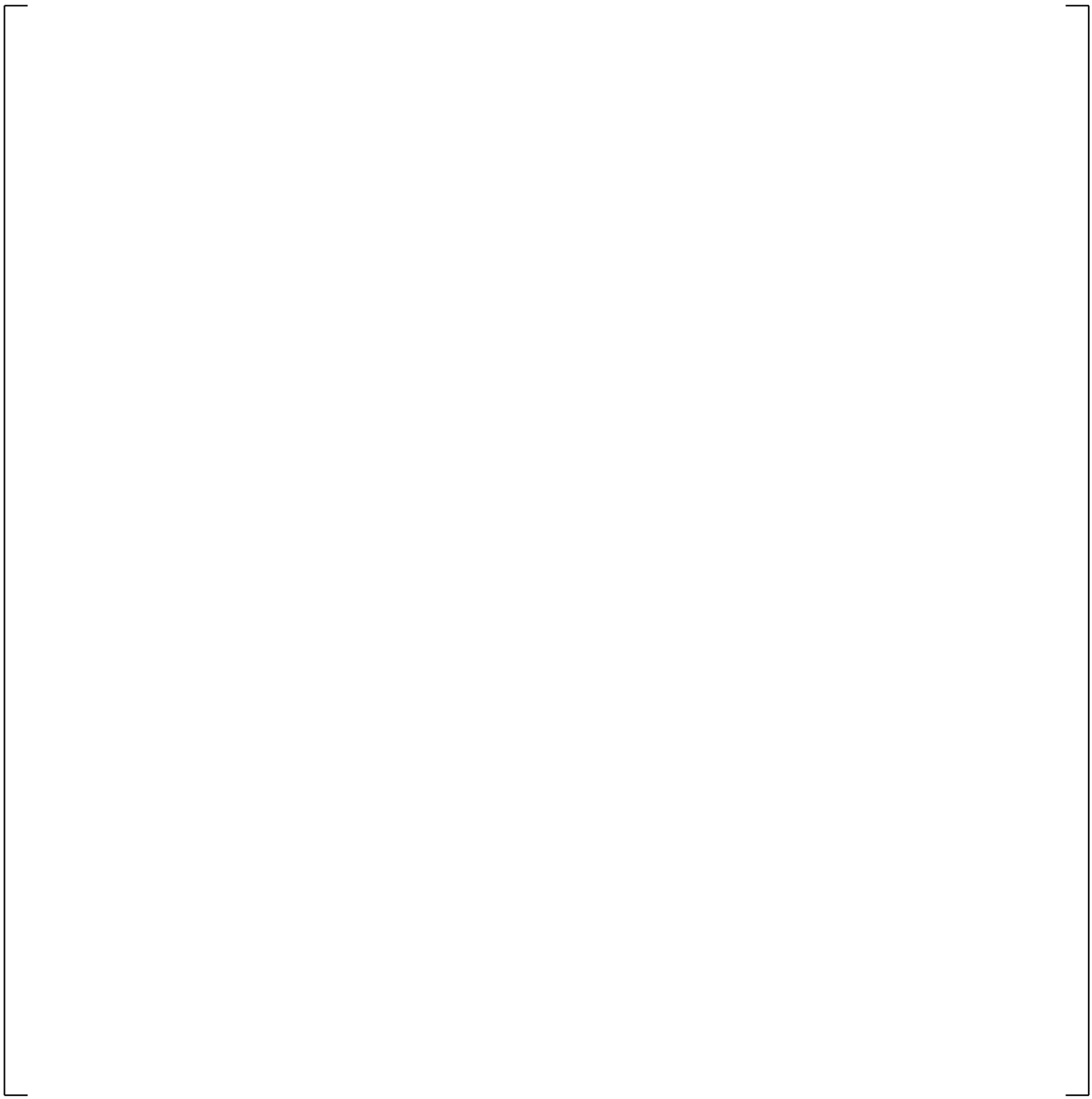

Figure 23.2.3-8 Vapor Temperature Profile in the 1D Pipe for the Steam Expulsion Test, Superheated Steam Case

a,c

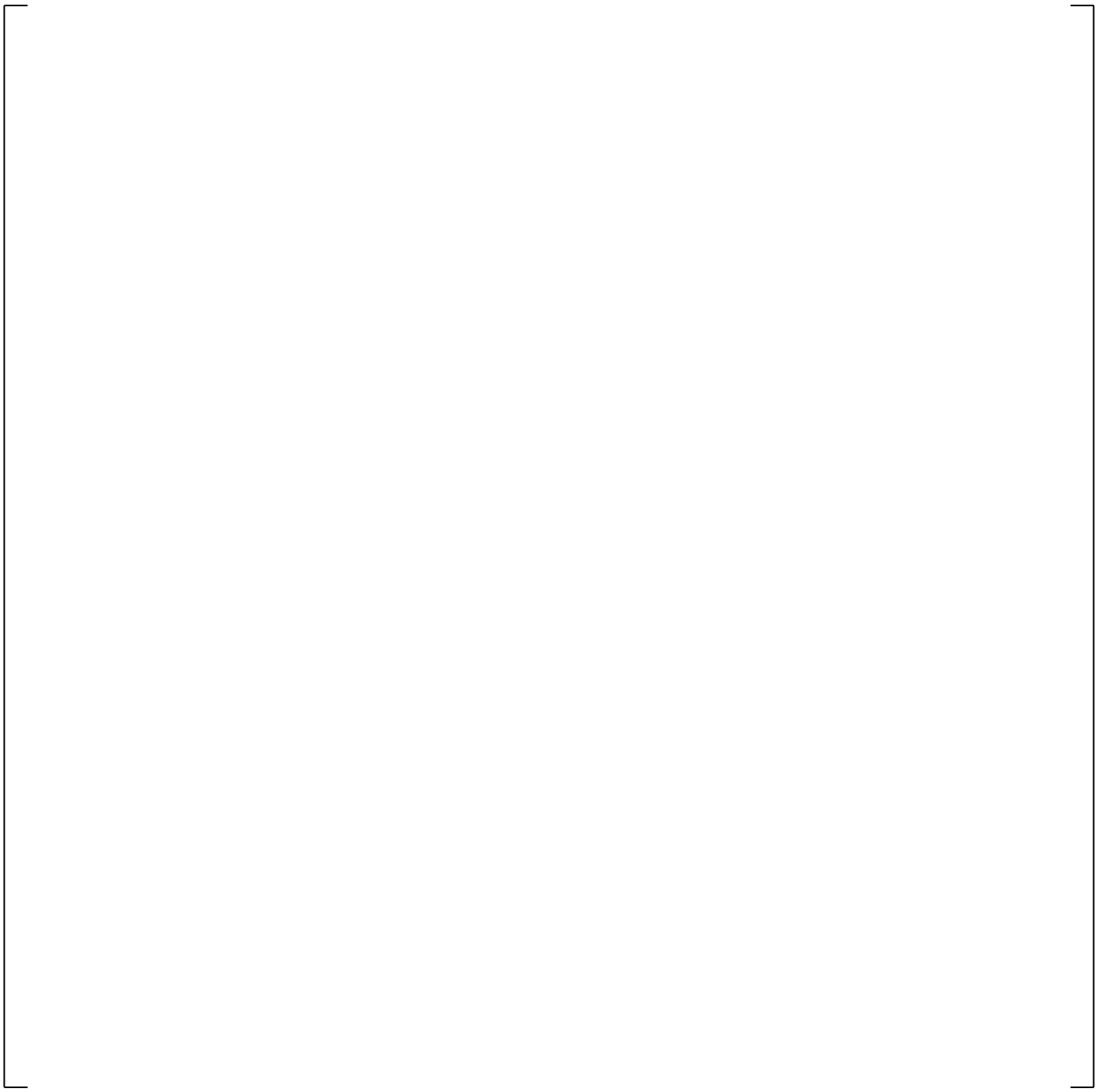

Figure 23.2.3-9 Pressure Profile in the 1D Pipe for the Steam Expulsion Test, Saturated Steam Case

a,c

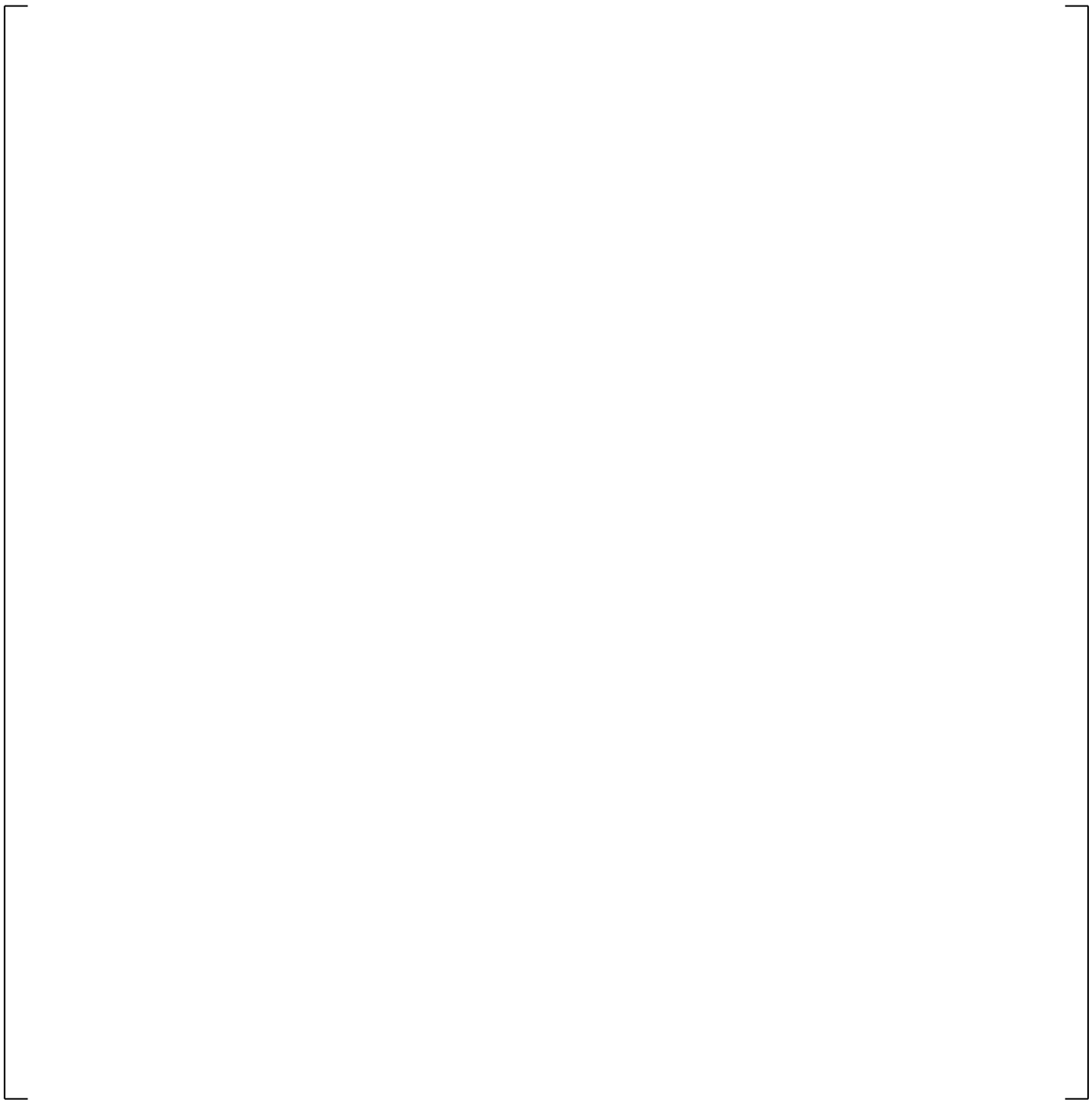

Figure 23.2.3-10 Void Fraction Profile in the 1D Pipe for the Steam Expulsion Test, Saturated Steam Case

a,c

Figure 23.2.3-11 Liquid Velocity Profile in the 1D Pipe for the Steam Expulsion Test, Saturated Steam Case

a,c

Figure 23.2.3-12 Steam Velocity Profile in the 1D Pipe for the Steam Expulsion Test, Saturated Steam Case

a,c

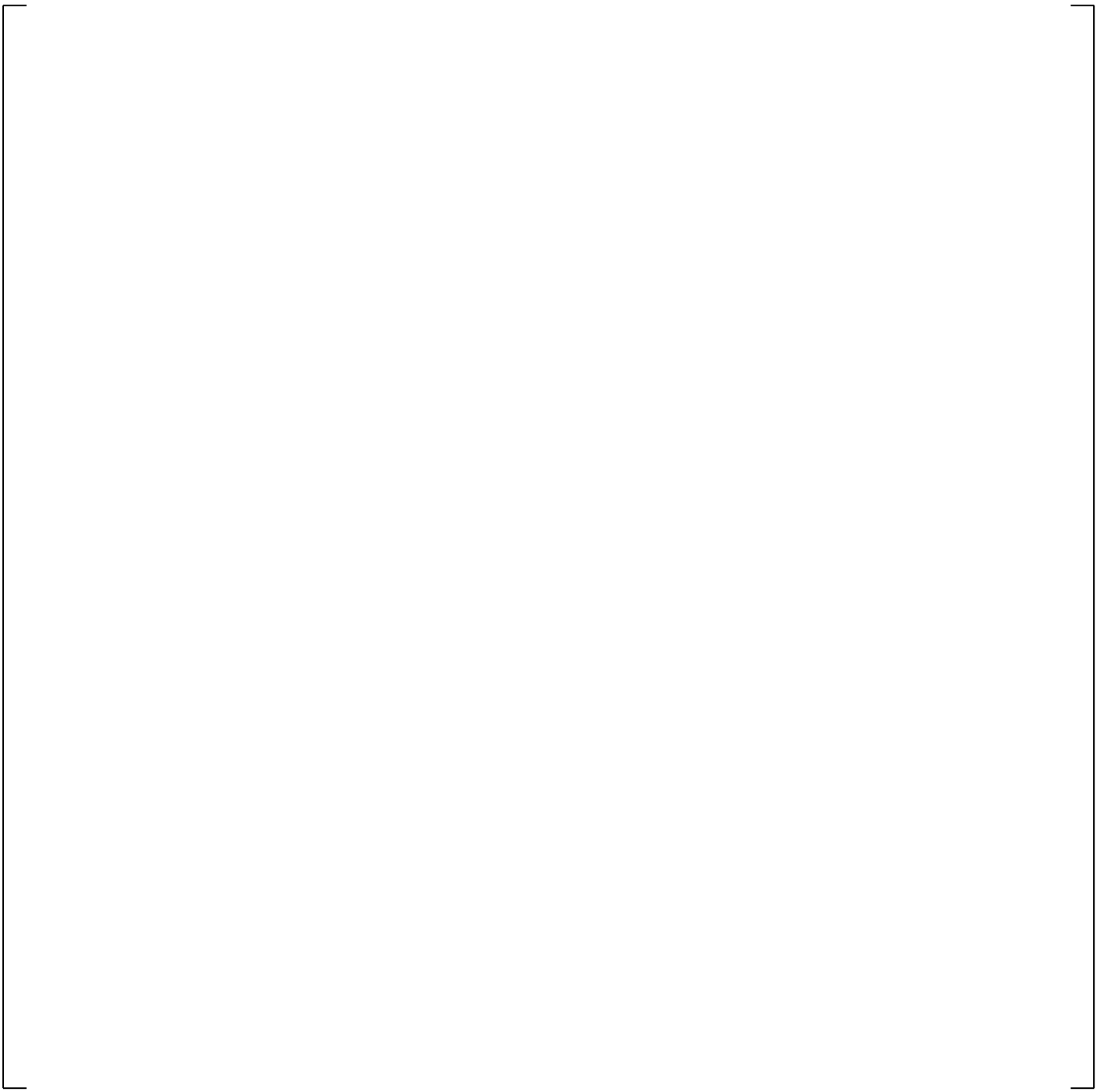

Figure 23.2.3-13 Liquid Temperature Profile in the 1D Pipe for the Steam Expulsion Test, Saturated Steam Case

a,c

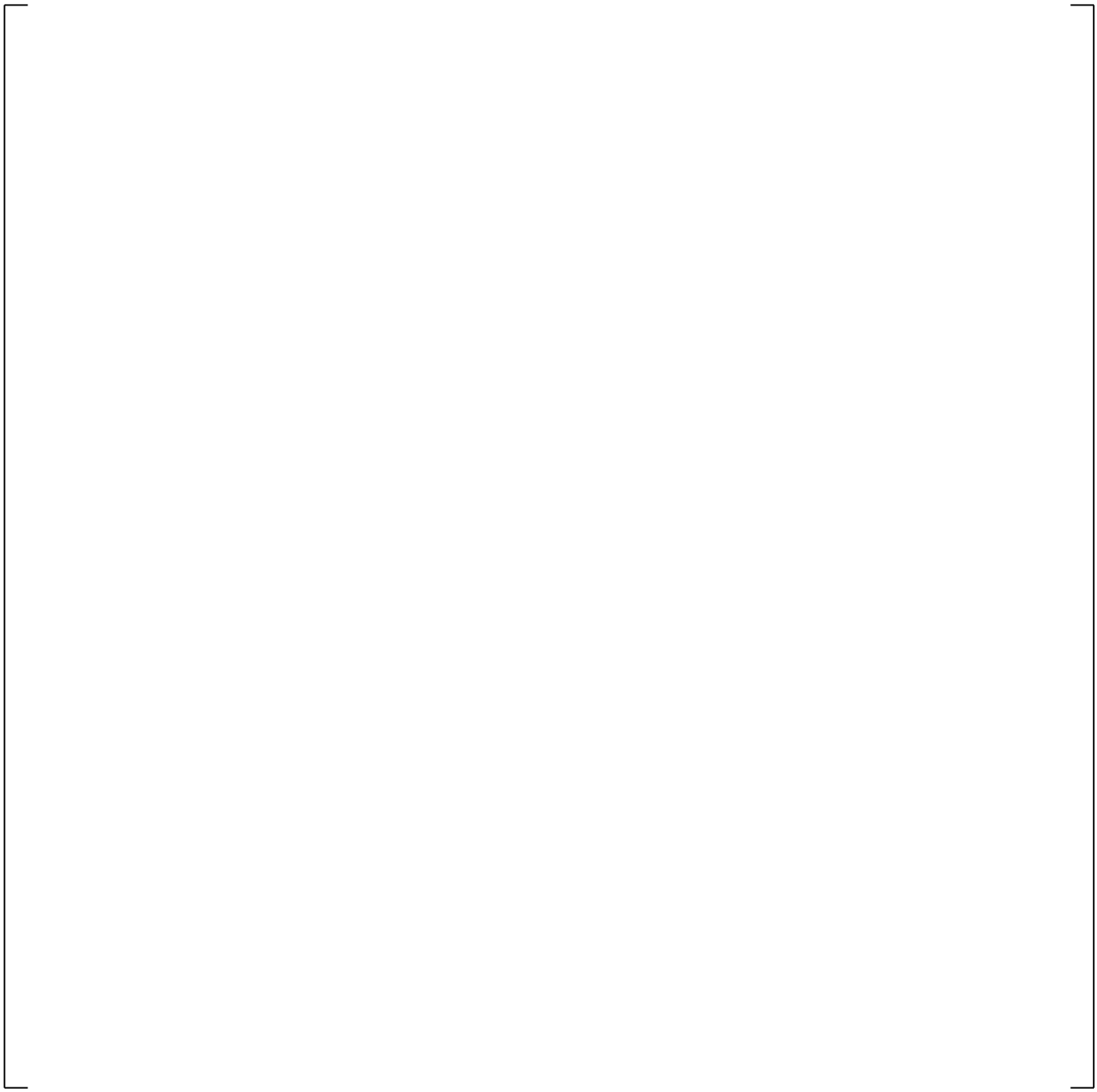

Figure 23.2.3-14 Vapor Temperature Profile in the 1D Pipe for the Steam Expulsion Test, Saturated Steam Case

23.2.4 3D VESSEL Steam Expulsion Test

23.2.4.1 Introduction

The steam expulsion test presented in Section 23.2.3 with a 1-D pipe is repeated here with the 3D Vessel component.

23.2.4.2 Problem Description

See Section 23.2.3.2.

23.2.4.3 WCOBRA/TRAC-TF2 Model

The steam expulsion test is modeled in WCOBRA/TRAC-TF2 as a single channel VESSEL (Figure 23.2.4-1) consisting of 10 axial nodes. Each node has a height of 0.3m and a hydraulic diameter of 1.0 m. A single cell PIPE is connected to the VESSEL at the top. A BREAK component is attached to the PIPE providing a pressure boundary condition at 4.0E+5 Pa. The initial pressure and enthalpy in the vessel are 4.0E+5 Pa and 2.782E+6 J/kg, respectively for the superheated steam case and 4.0E+5 Pa and 2.738E+6 J/kg in the saturated steam case. An inlet flow boundary condition is specified at the bottom of the vessel, ramping from 0.0 to 0.5 m/s in 1 s. The inlet flow is sub-cooled liquid at 50°C.

23.2.4.4 Numerical/Analytical Solution

See Section 23.2.3.4.

23.2.4.5 WCOBRA/TRAC-TF2 Assessment

23.2.4.5.1 Superheated Steam Results

The collapsed liquid level in the vessel is shown in Figure 23.2.4-2. As indicated in the plot, liquid fills the vessel entirely, displacing the steam, by combination of expulsion and condensation, in about **[ ]**[a,c]. This is consistent with the expectation. Figure 23.2.4-3 and Figure 23.2.4-4 show the pressure and void fraction, respectively, in every other cell in the vessel. **[ ]**[a,c] Other relevant plots, including liquid and vapor velocities and temperatures are shown in Figures 23.2.4-5 through 23.2.4-8.

The liquid temperature (Figure 23.2.4-5) is near saturation when the cell is gas filled, and gradually drops to the liquid temperature of the cell upstream when the liquid front crosses the bottom cell boundary. The vapor in a cell is initially superheated (Figure 23.2.4-5) and gradually de-superheats as a result of the interfacial heat transfer until it reaches saturation when the cell is water-solid. The filling of each cell results in a vapor velocity increase (Figure 23.2.4-8), forcing the vapor upward as the cell fills with liquid.

23.2.4.5.2 Saturated Steam Results

The collapsed liquid level in the vessel is shown in 23.2.4-9. As indicated in the plot, liquid fills the vessel entirely, displacing the steam, by combination of expulsion and condensation, in about **[ ]**[a,c] This is consistent with the expectation.

Figure 23.2.4-10 and Figure 23.2.4-11 show the pressure and void fraction, respectively, in every two cells in the vessel. Other relevant plots, including liquid and vapor velocities and temperatures are shown in Figure 23.2.4-12 through Figure 23.2.4-15.

The only discernible difference between the case with saturated steam and that with superheated steam (Section 23.2.4.5.1) is the prediction of vapor temperature, due to the initially lower temperature of the saturated steam.

23.2.4.6 Summary and Conclusions

The steam expulsion problem is a standard numerical benchmark problem that was exercised with different codes (Hewitt et al., 1992, Pryor et al., 1978). As described in Section 3 of NBT2.3 of (Hewitt et al., 1992), the qualitative analytic solution is absent of any "spikes" or "ripples," although it is known that a discretized noding scheme will result in some spikes or ripples as described in Section 23.2.3.2. **[ ]**[a,c] The fill rate is comparable to the qualitative analytic expectation, as is the general behavior regarding temperatures and pressures.

23.2.4.7 References

1. Hewitt, G. F., Delhaye, J. M. and Zuber, N., 1992, Multiphase Science and Technology, Vol.6.

2. Pryor, R. J., Liles, D. R. and Mahaffy, J. H., 1978, "Treatment of Water Packing Effects," *Trans. ANS* 30, pp. 208-209.

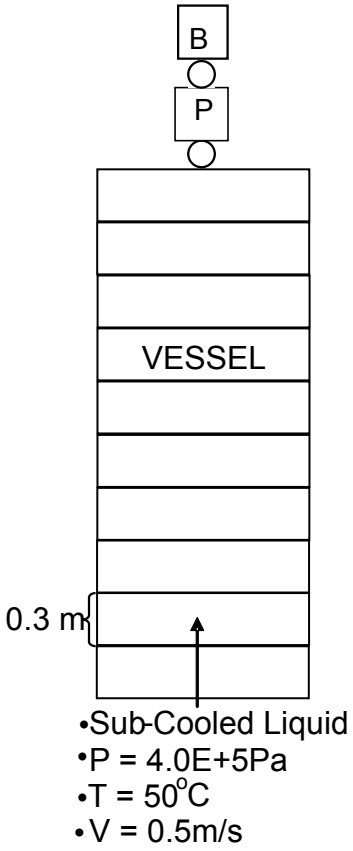

Figure 23.2.4-1 Steam Expulsion Test using 3D Vessel

a,c

Figure 23.2.4-2 Collapsed Liquid Level in the Vessel for the Steam Expulsion Test, Superheated Steam Case

a,c

Figure 23.2.4-3 Pressure Profile in the 3D Vessel for Steam Expulsion Test, Superheated Steam Case

a,c

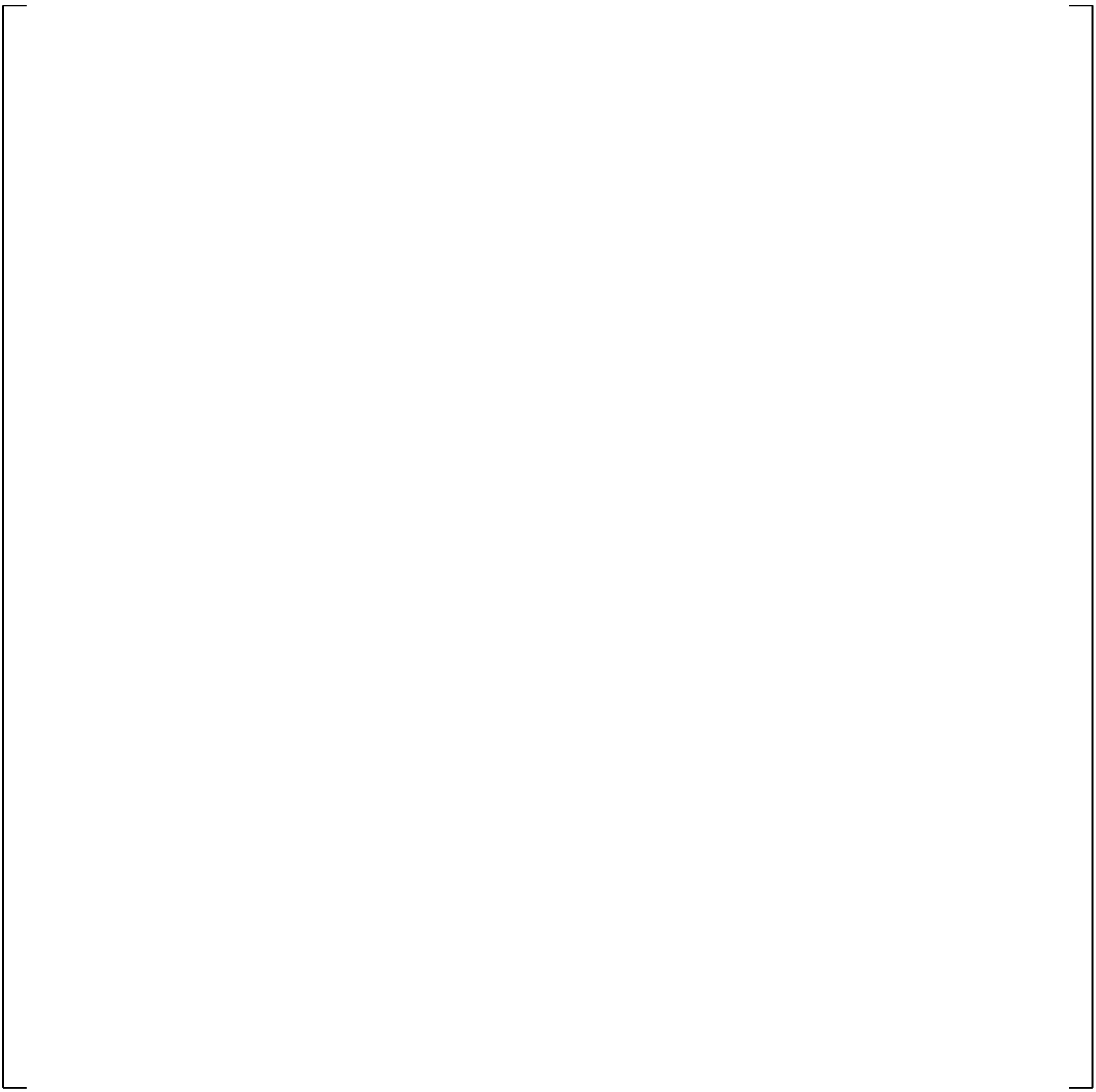

Figure 23.2.4-4 Void Fraction Profile in the 3D Vessel for the Steam Expulsion Test, Superheated Steam Case

a,c

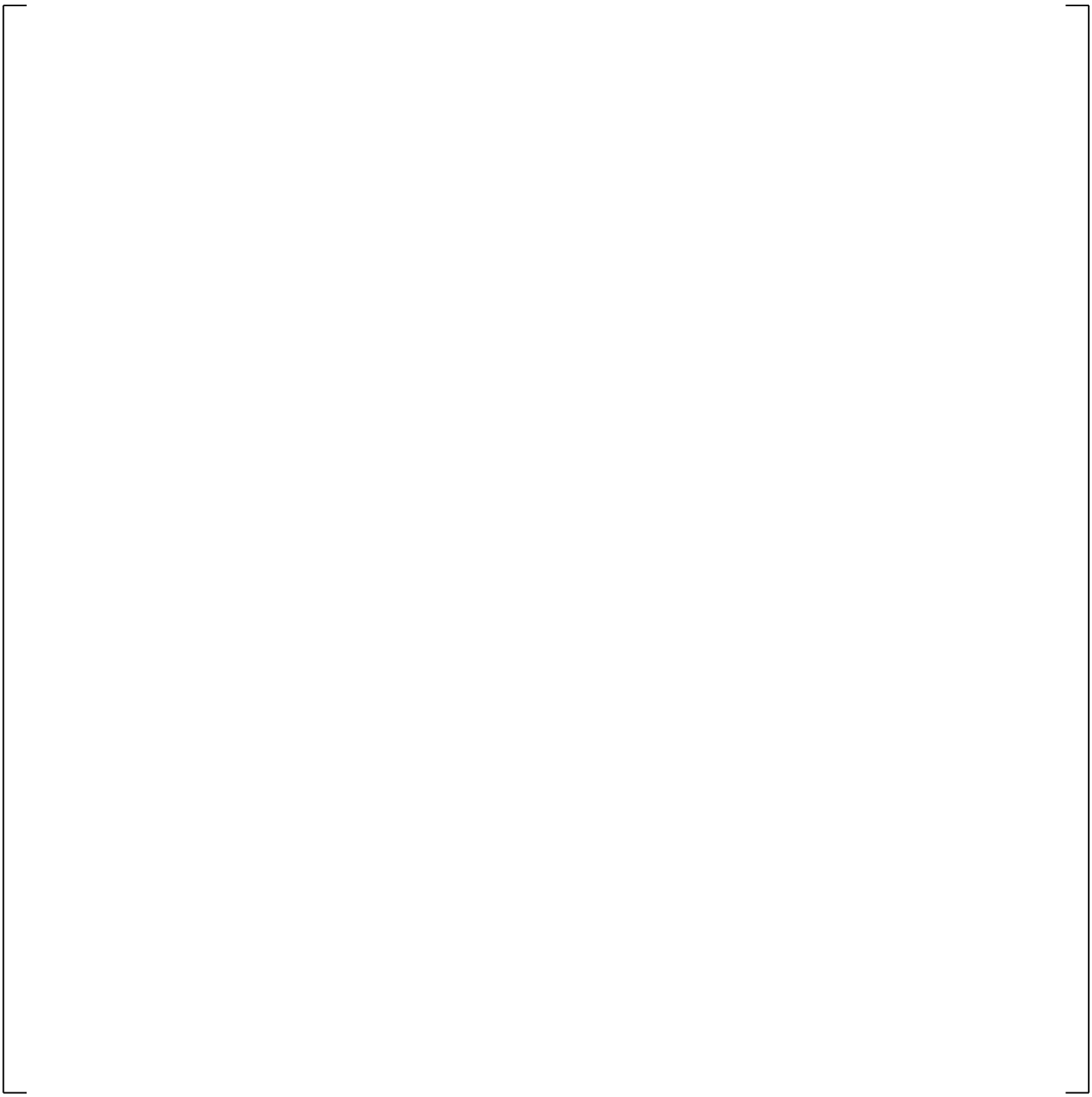

Figure 23.2.4-5 Liquid Temperature Profile in the 3D Pipe for the Steam Expulsion Test, Superheated Steam Case

a,c

Figure 23.2.4-6 Vapor Temperature Profile in the 3D Vessel for the Steam Expulsion Test, Superheated Steam Case

a,c

Figure 23.2.4-7 Liquid Velocity Profile in the 3D Vessel for the Steam Expulsion Test, Superheated Steam Case

a,c

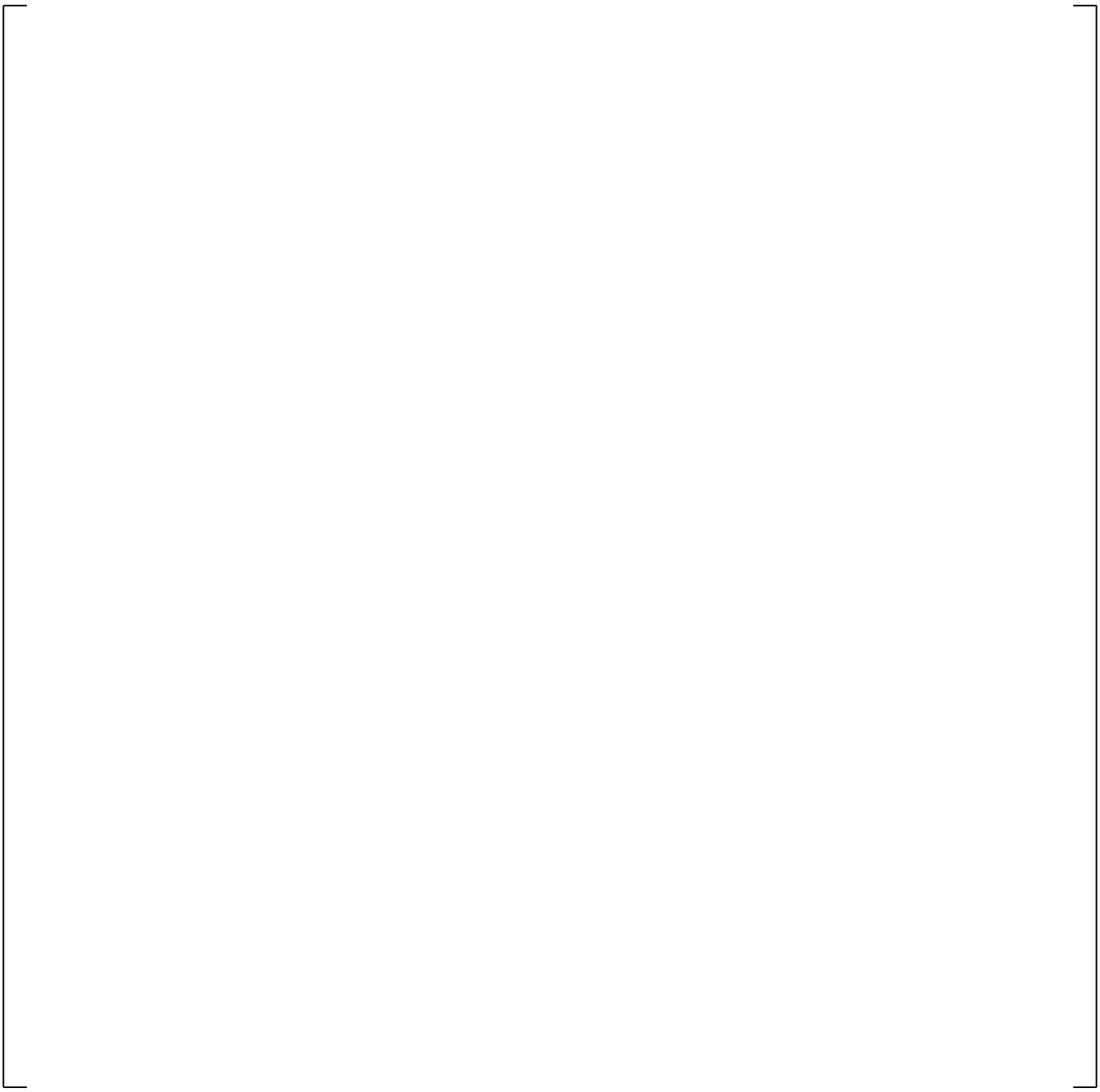

Figure 23.2.4-8 Vapor Velocity Profile in the 3D Vessel for the Steam Expulsion Test, Superheated Steam Case

a,c

Figure 23.2.4-9 Collapsed Liquid Level in the Vessel for the Steam Expulsion Test, Saturated Steam Case

a,c

Figure 23.2.4-10 Pressure Profile in the 3D Vessel for the Steam Expulsion Test, Saturated Steam Case

a,c

Figure 23.2.4-11 Void Fraction Profile in the 3D Vessel for the Steam Expulsion Test, Saturated Steam Case

a,c

Figure 23.2.4-12 Liquid Temperature Profile in the 3D Pipe for the Steam Expulsion Test, Saturated Steam Case

a,c

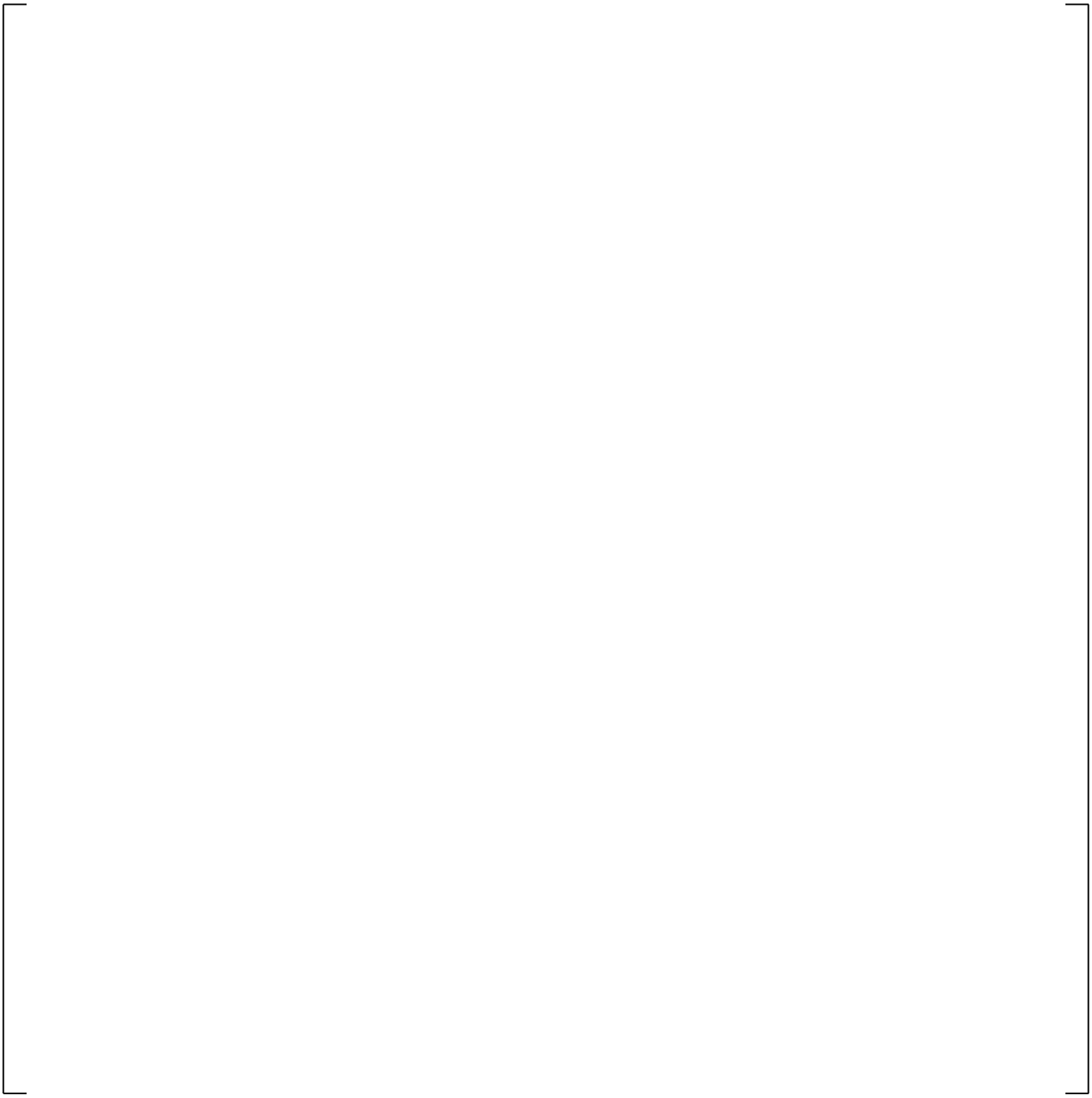

Figure 23.2.4-13 Vapor Temperature Profile in the 3D Vessel for the Steam Expulsion Test, Saturated Steam Case

a,c

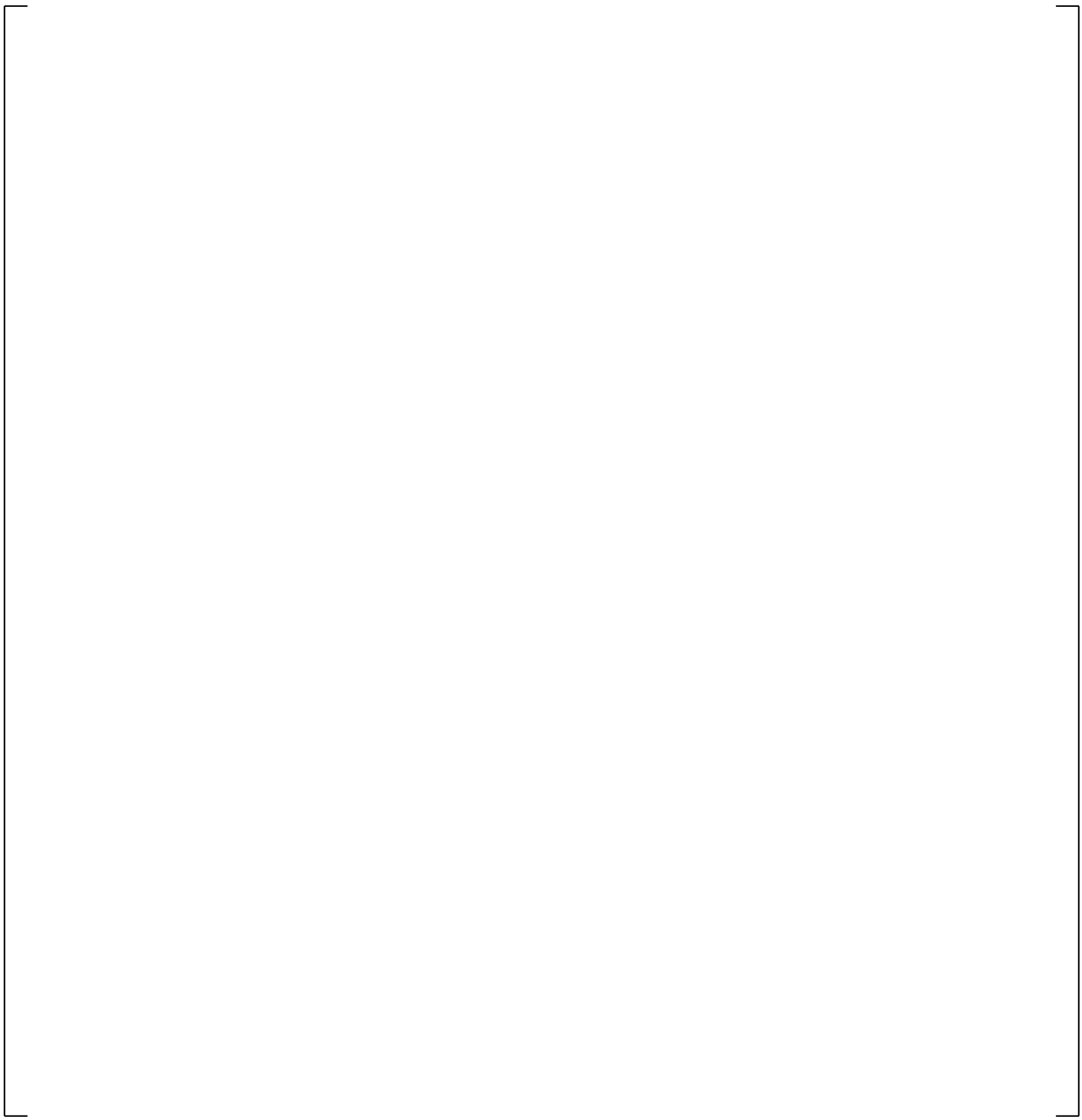

Figure 23.2.4-14 Liquid Velocity Profile in the 3D Vessel for the Steam Expulsion Test, Saturated Steam Case

a,c

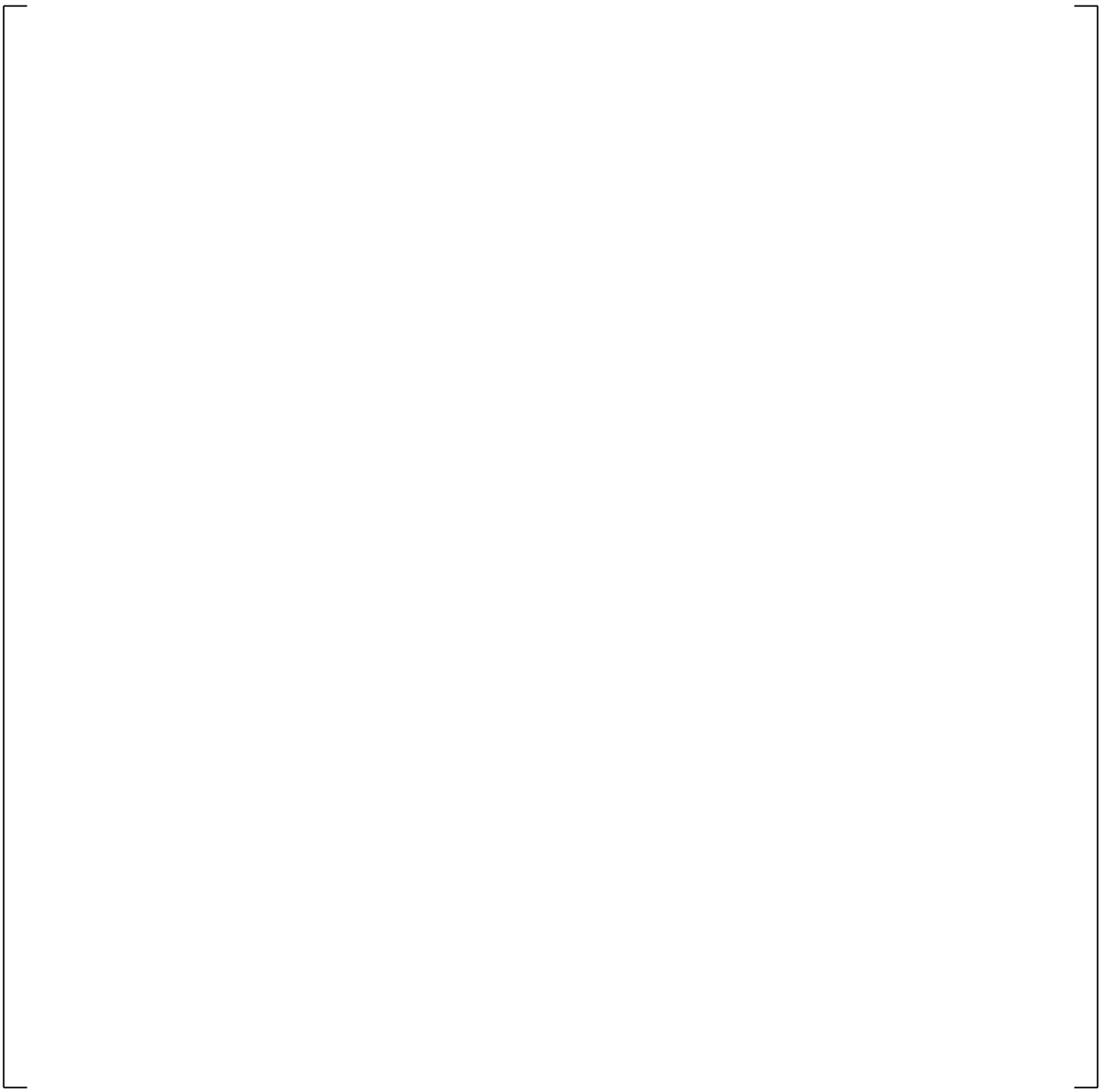

Figure 23.2.4-15 Vapor Velocity Profile in the 3D Vessel for the Steam Expulsion Test, Saturated Steam Case

23.2.5 1D PIPE Fill and Drain Test

23.2.5.1 Introduction

The objective of this test is to study the capability of WCOBRA/TRAC-TF2 (1D Module) of tracking a two-phase mixture level in a vertical pipe as it crosses cell boundaries. The problem is similar to the steam expulsion test, with the difference that the interfacial heat transfer is turned off, gas is injected in the liquid column and the level crosses the cell boundary in both the upward and downward direction.

The problem was first presented by Aktas and Mahaffy (1996) to evaluate a two-phase level tracking method implemented in TRAC-BWR. WCOBRA/TRAC-TF2 has no level tracking capability, however the problem provides some insights on the interfacial drag model and how it behaves in situations where a sharp void fraction gradient exists across cell boundaries. The problem was also studied in (Frepoli et al., 2003).

23.2.5.2 Problem Description

In this test problem, a 1D pipe is first filled and then drained to observe the mixture level crossing cell boundaries. During the first 10 seconds of the transient, a steady-state mixture level is established in the vertical pipe by injecting a constant flow of steam (0.5 m/s) at the bottom of a quiescent column of water. At 10 s, water starts to be injected at the velocity of 2.0 m/s for 5 s. At 15 s the liquid flow rate is reversed and the inlet liquid velocity is set to -2.0 m/s for another 5 s. As a result, between 10 s and 20 s, the mixture level crosses two cell boundaries in both directions. The interfacial heat transfer is turned off to focus the attention to the hydraulic behavior of the two-phase mixture. Two cases are studied:

1. Single-phase liquid column (steam flow from the bottom of the pipe is set to zero)
2. Two-phase mixture column (steam flow from the bottom of the pipe is set to 0.5 m/s)

23.2.5.3 WCOBRA/TRAC-TF2 (1D Module) Model

The model consists of a vertical pipe with 1.0 m^2 axial flow area and 10.0 m height. A TEE branch with 0.5 m^2 axial flow area and 3.0 m height is connected to the bottom of the pipe. Liquid water is injected, at the branch pipe of the TEE, to raise the liquid column and then withdrawn to let the level drop back to its starting point. The injection and withdrawal rate of liquid water is 2.0 m/s, subcooled at 300K, provided by the FILL attached to the branch pipe of the TEE. A second zero velocity FILL is attached to the TEE main pipe for the case without steam injection. For the steam injection case, a constant 0.5 m/s steam flow is prescribed at the FILL component. A BREAK component is attached to the top of the PIPE to maintain the system pressure at 1.0E+5 Pa. The noding diagram is shown in Figure 23.2.5-1.

23.2.5.4 Numerical/Analytical Solution

The solution to the problem is simply a linear increase of the water level starting as soon as liquid is injected (10 seconds). The level rises for 5 seconds, reaches the maximum elevation at 15 seconds, and then decreases for another 5 seconds returning to its starting elevation.

23.2.5.5 WCOBRA/TRAC-TF2 (1D Module) Assessment

23.2.5.5.1 Case 1 Without Steam Injection

Figure 23.2.5-2 and Figure 23.2.5-3 show the predicted transient void fraction and pressure, respectively, in cells 5 through 8 during the time window when the level is rising and dropping (from 10 to 20 seconds). The void fraction plot shows that the liquid front moves to the next cell above, before the cell is liquid solid, therefore not resolving a perfect sharp level but diffusing the void gradient across the two cells. The liquid front is smeared over several cells. The behavior is similar during both the upward and downward movement. The predicted pressure change (Figure 23.2.5-3) **[**

][a,c]

23.2.5.5.2 Case 2 With Steam Injection

Figure 23.2.5-4 and Figure 23.2.5-5 show a similar smearing effect on the void fraction profile. This is reflected on the pressure response which **[**

][a,c]

23.2.5.6 Summary and Conclusions

The 1D Module (Loop) of WCOBRA/TRAC-TF2, although incapable of resolving a precise sharp two-phase mixture level, adequately calculates the movement of a two-phase front in a vertical pipe with pressure and void fraction effects consistent with semi-implicit numerical schemes.

23.2.5.7 References

1. Aktas and Mahaffy, 1996, "A two-phase level tracking method," *Nuclear Engineering and Design*, 162, pp. 271-280.

2. Frepoli, Mahaffy and Ohkawa, 2003, "Notes on implementation of a fully-implicit numerical scheme for a two-phase three-field flow model," *Nuclear Engineering and Design*, 225, pp.191-217.

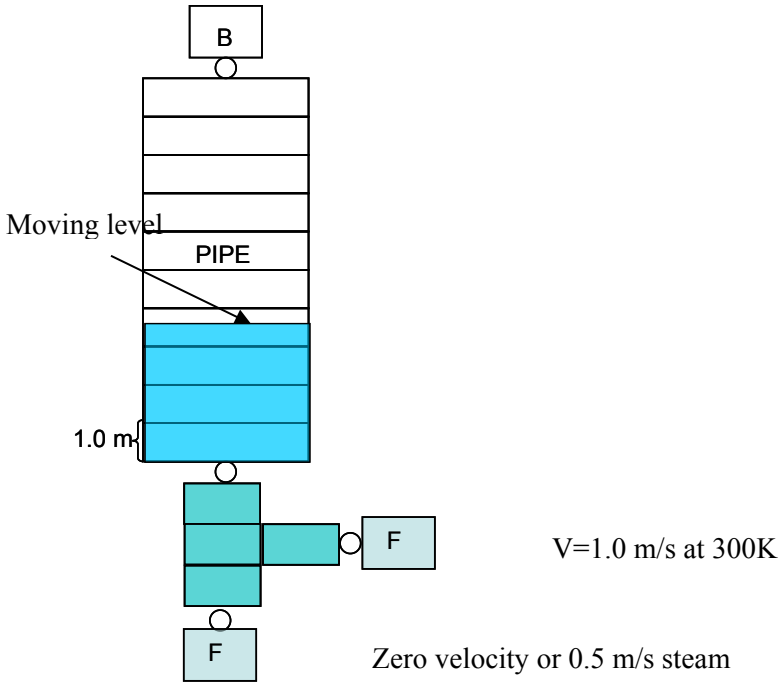

Figure 23.2.5-1 Fill and Drain Model using 1D Pipe

a,c

Figure 23.2.5-2 Predicted Void Fraction between 10 s and 20 s in the 1D Fill and Drain Problem without Steam Injection

a,c

Figure 23.2.5-3 Predicted Pressure between 10 s and 20 s in the 1D Fill and Drain Problem without Steam Injection

a,c

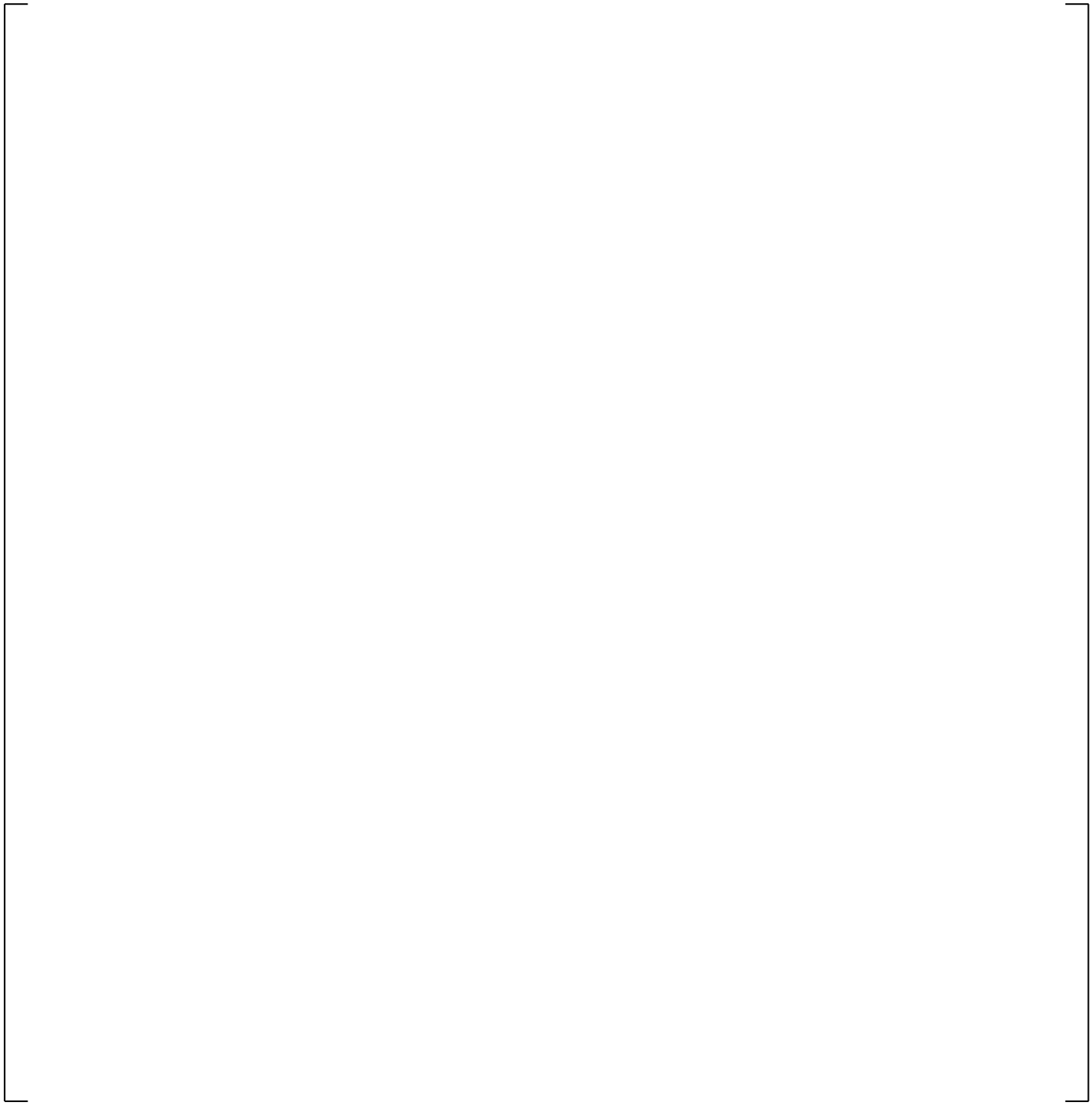

Figure 23.2.5-4 Predicted Void Fraction between 10 s and 20 s in the 1D Fill and Drain Problem with Steam Injection

a,c

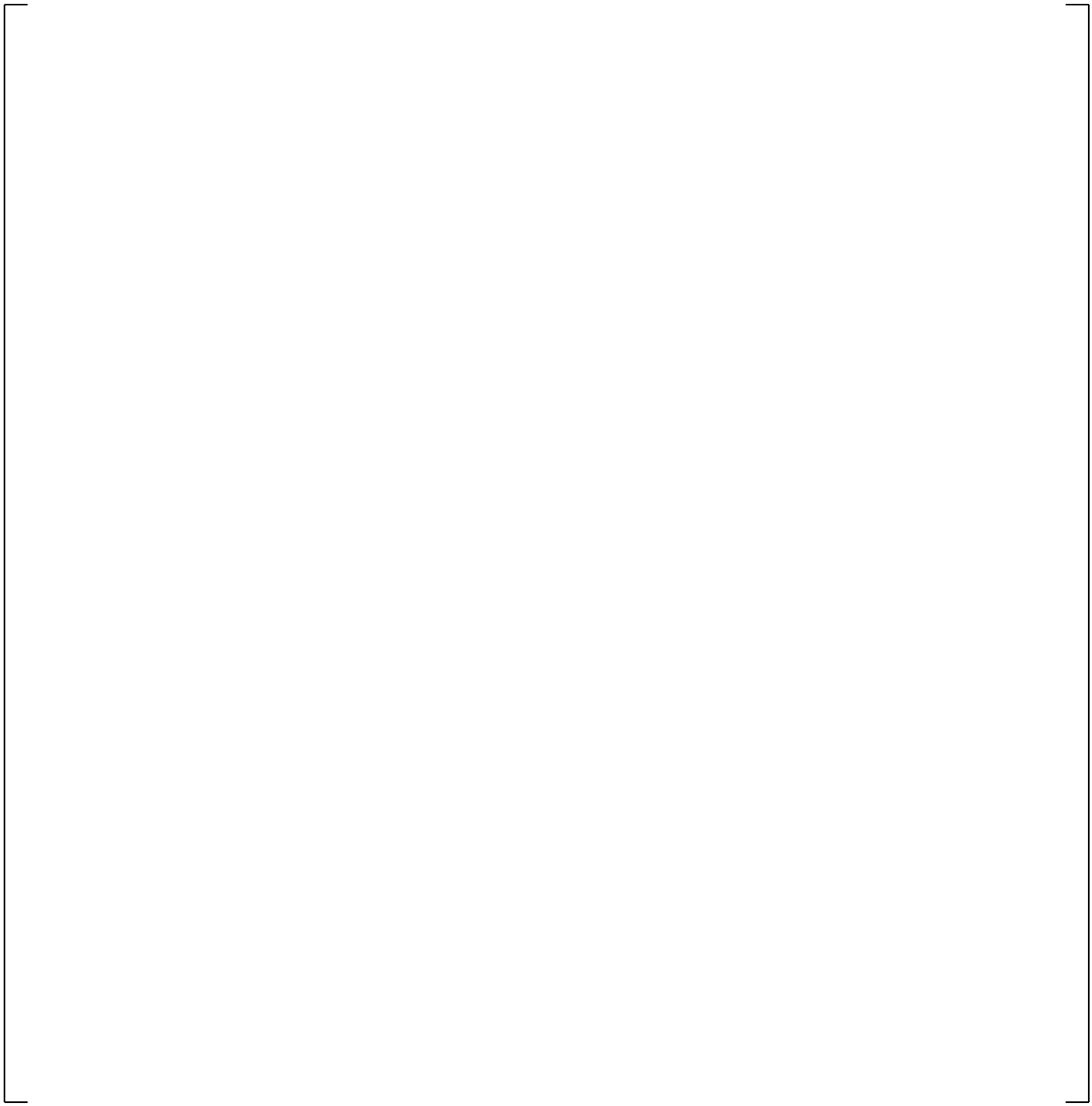

Figure 23.2.5-5 Predicted Pressure between 10 s and 20 s in the 1D Fill and Drain Problem with Steam Injection

23.2.6 3D VESSEL Fill and Drain Test

23.2.6.1 Introduction

The objective of this test is to study the capability of WCOBRA/TRAC-TF2 (3D Module) of tracking a two-phase mixture level in a vertical pipe as it crosses cell boundaries. The problem is identical to what was presented for the corresponding 1D case (Section 23.2.5).

23.2.6.2 Problem Description

See Section 23.2.5.2.

23.2.6.3 WCOBRA/TRAC-TF2 Model

The model consists of a single channel vessel with 1.0 m^2 axial flow area and 10.0 m height. A TEE branch with 0.5 m^2 axial flow area and 3.0 m height is connected to the bottom of the vessel. Liquid water is injected, at the branch pipe of the TEE, to raise the liquid column and then withdrawn to let the level drop back to its starting point. The injection and withdrawal rate of liquid water is 2.0 m/s, subcooled at 300K, provided by the FILL attached to the branch pipe of the TEE. A second zero velocity FILL is attached to the TEE main pipe for the case without steam injection. For the steam injection case, a constant 0.5 m/s steam flow is prescribed at the FILL component. A short pipe and a BREAK component are attached to the top of the vessel to maintain the system pressure at 1.0E+5 Pa. The noding diagram is shown in Figure 23.2.6-1.

23.2.6.4 Numerical/Analytical Solution

See Section 23.2.5.4.

23.2.6.5 WCOBRA/TRAC-TF2 Assessment

23.2.6.5.1 Case 1 Without Steam Injection

Figure 23.2.6-2 shows the predicted collapsed liquid level in the vessel. In the first 10 s, the problem reaches a steady-state. The transient starts at 10.0 s, when the liquid water starts injecting at a rate of 2.0 m/s for 5.0 s. At 15.0 s, the collapsed liquid level reaches approximately 9 m, at which point the flow is reversed, and the vessel starts draining. Similar to the 1D pipe results, the liquid front moves to the next cell before the cell is fully liquid water, as seen in the void fraction plot in Figure 23.2.6-3. **[**

][a,c]

Behavior is in general similar to the corresponding 1D case with a smaller diffusion of the void front in this case as indicated by the void fraction results in Figure 23.2.6-3.

23.2.6.5.2 Case 2 With Steam Injection

Figure 23.2.6-6 shows the predicted collapsed liquid level in the vessel. In the first 10 s, the problem reaches a steady-state. The transient starts at 10.0 s, when the liquid water starts injecting at a rate of 2.0 m/s for 5.0 s. At 15.0 s, the collapsed liquid level reaches approximately 9 m, at which point the flow is reversed, and the vessel starts draining.

Results from the 3D simulation (Figure 23.2.6-7 and Figure 23.2.6-8) are similar to the corresponding 1D pipe results. There is a diffusion of the void front, possibly to a lesser extent in this case.

23.2.6.6 Summary and Conclusions

Similar to the 1D case, the 3D Module (Vessel) of WCOBRA/TRAC-TF2, although not capable of resolving a precise sharp two-phase mixture level, calculates adequately the movement of a two-phase front in a vertical pipe with pressure and void fraction effects consistent with semi-implicit numerical schemes.

23.2.6.7 References

1. Aktas and Mahaffy, 1996, “A two-phase level tracking method,” *Nuclear Engineering and Design*, 162, pp. 271-280.

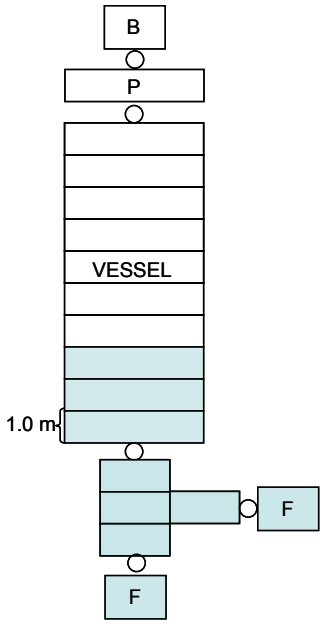

Figure 23.2.6-1 Fill and Drain Model using 3D Vessel

a,c

Figure 23.2.6-2 Predicted Collapsed Liquid Level in the 3D Fill and Drain Problem without Steam Injection

a,c

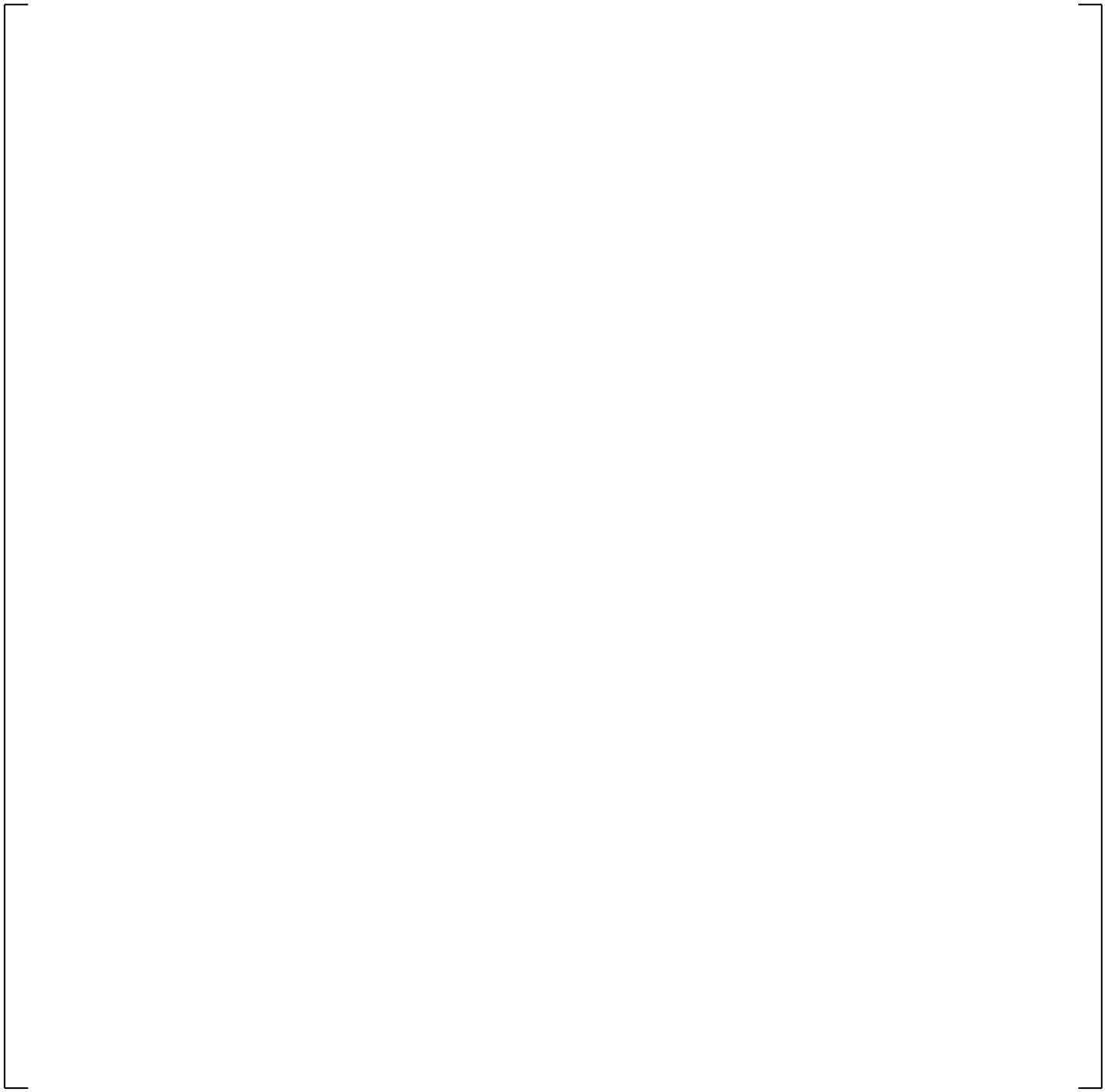

Figure 23.2.6-3 Predicted Void Fraction between 10 s and 20 s in the 3D Fill and Drain Problem without Steam Injection

a,c

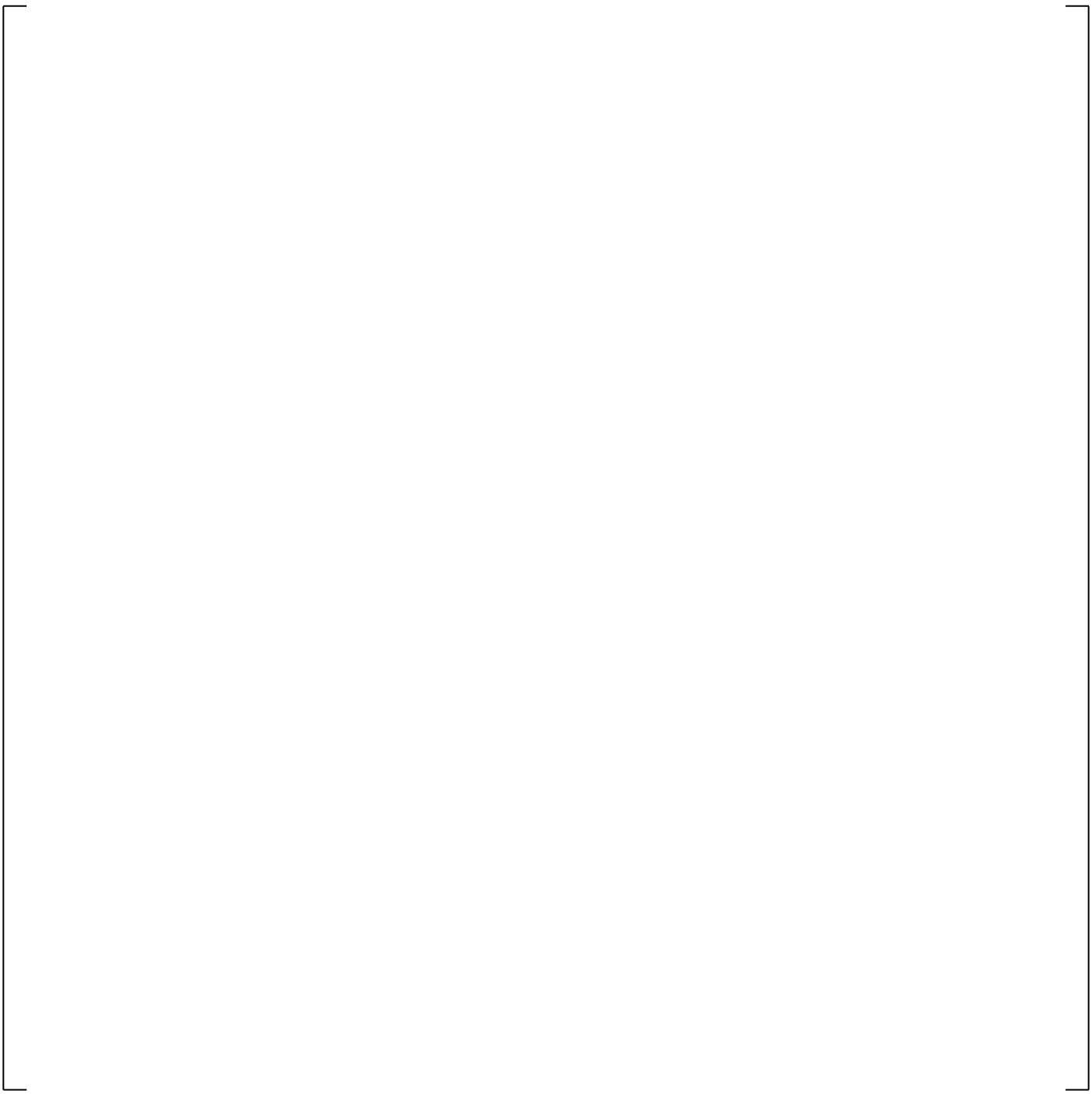

Figure 23.2.6-4 Predicted Pressure between 10 s and 20 s in the 3D Fill and Drain Problem without Steam Injection

a,c

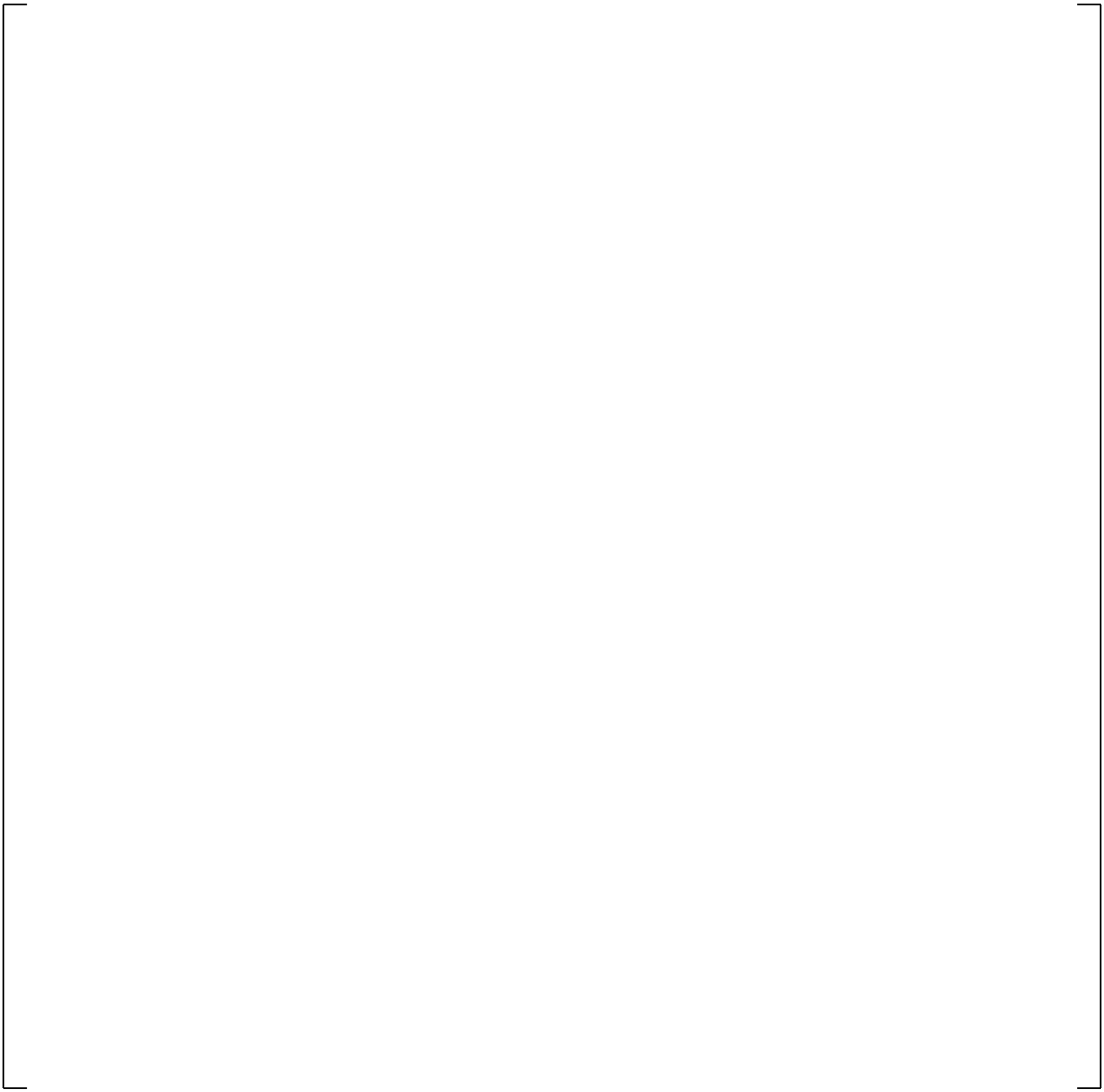

Figure 23.2.6-5 Predicted Pressure between 10 s and 20 s in the 3D Fill and Drain Problem without Steam Injection

a,c

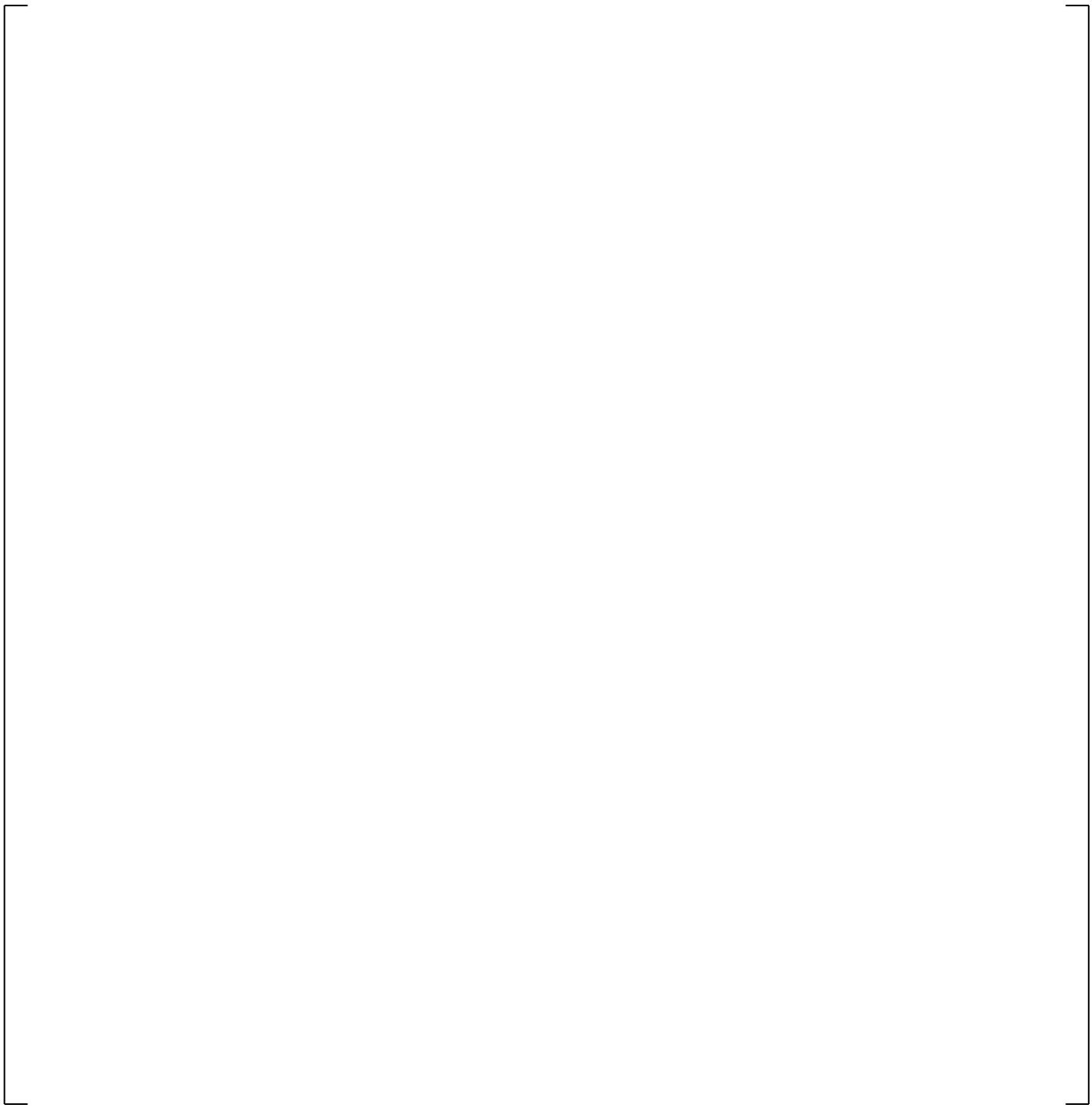

Figure 23.2.6-6 Predicted Collapsed Liquid Level in the 3D Fill and Drain Problem with Steam Injection

a,c

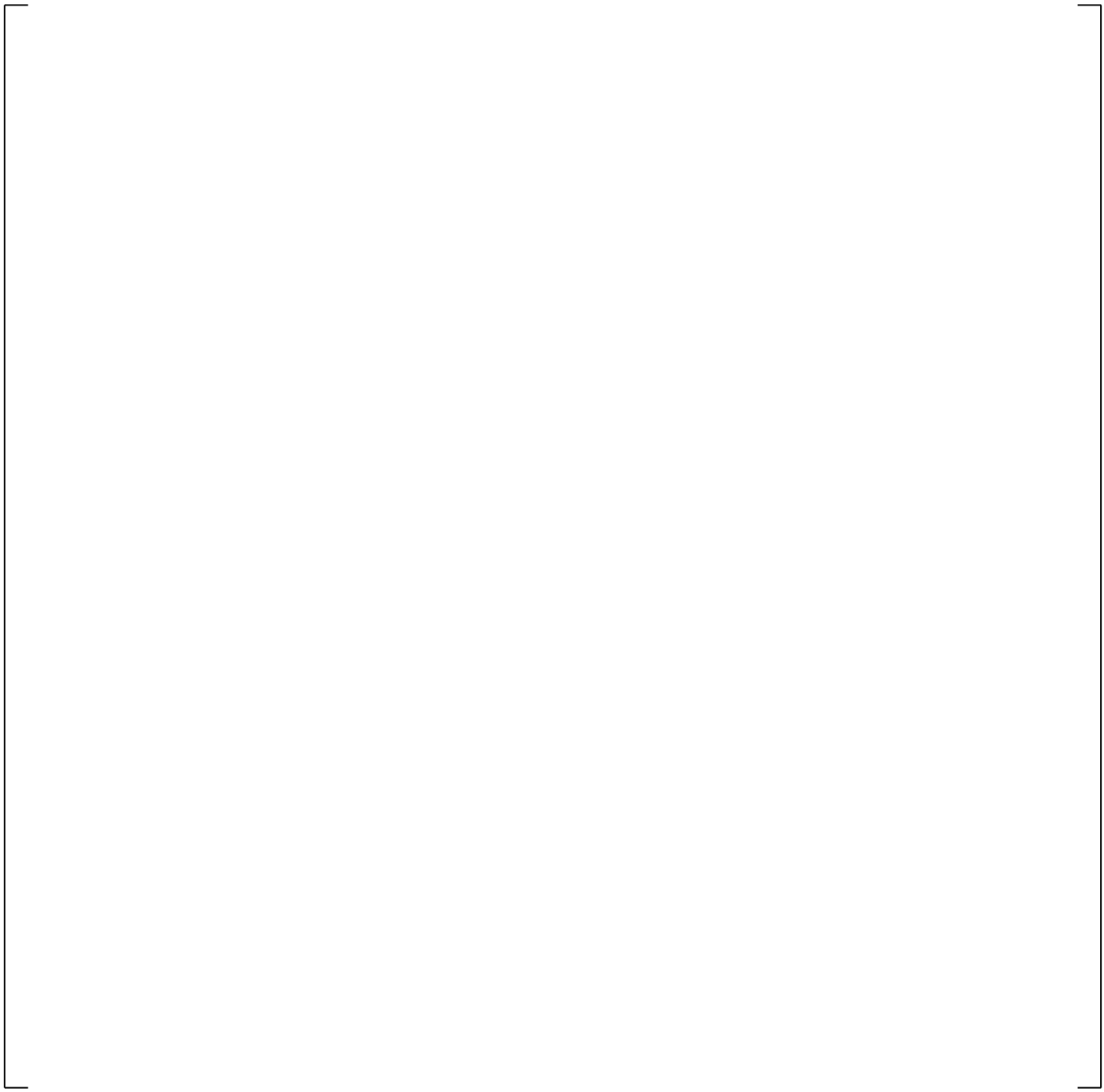

Figure 23.2.6-7 Predicted Void Fraction between 10 s and 20 s in the 3D Fill and Drain Problem with Steam Injection

a,c

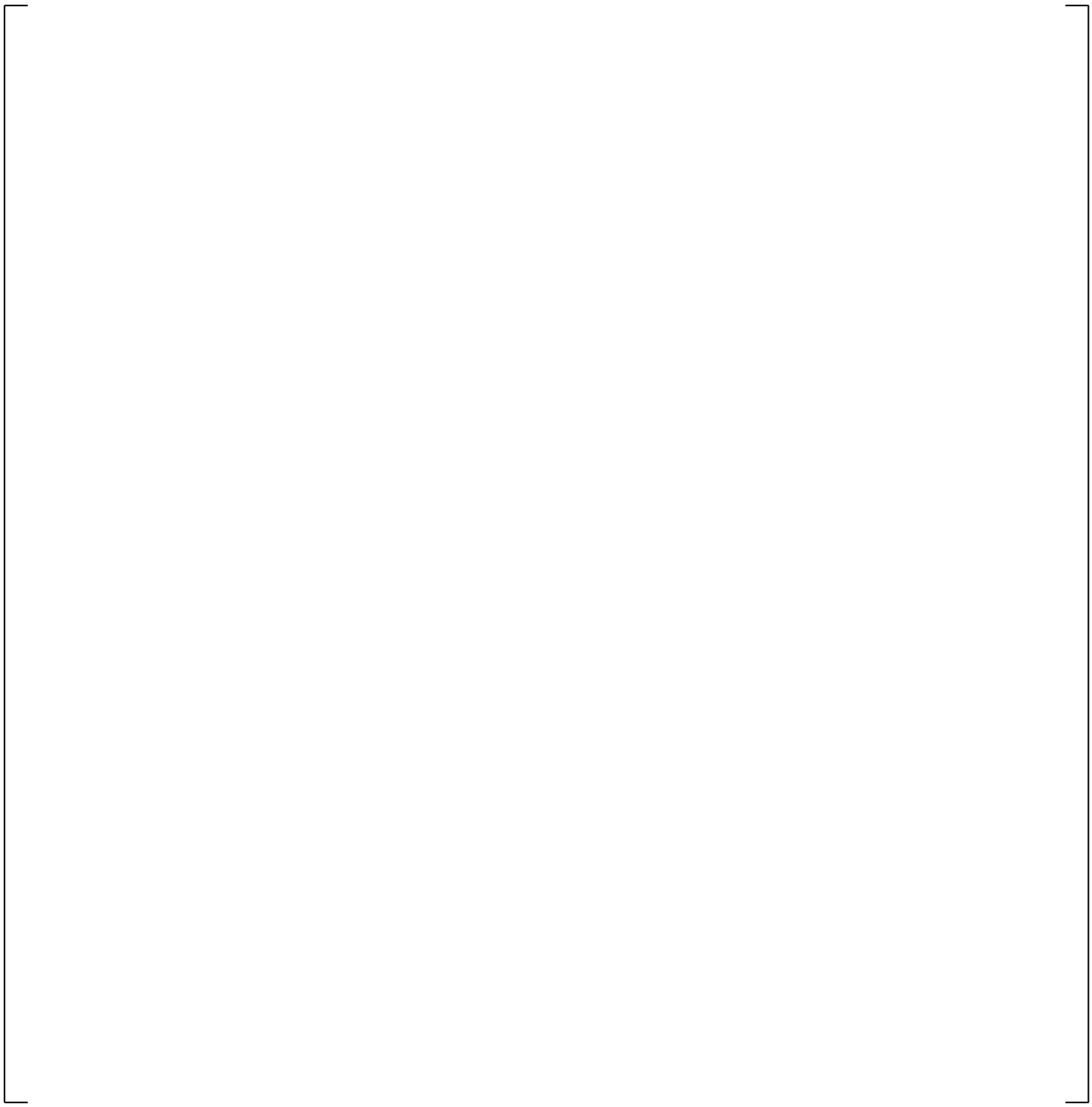

Figure 23.2.6-8 Predicted Pressure between 10 s and 20 s in the 3D Fill and Drain Problem with Steam Injection

23.2.7 Condensation Test

23.2.7.1 Introduction

The condensation model used in WCOBRA/TRAC-TF2 is described in Section 6 of Volume 1. The objective of this Section is to assess the performance of the WCOBRA/TRAC-TF2 condensation model on simple problems, to verify that the code results are in agreement with expectations.

23.2.7.2 Problem Description

A vessel (1.0 ft^2 flow area and 1.0 ft height) is initially filled with saturated steam at 1000 psia. A heat slab is included in the vessel, which is kept at 80°F wall temperature, providing a medium for condensation. The top of the vessel is connected to a pipe, and a constant pressure of 1000 psia is maintained at the other end of the pipe. The first case analyzed does not have non-condensable gas present. In the second case, the partial pressure of non-condensable gas is set to 1000 psia at the outlet of the pipe. The objective is to evaluate the condensation within the vessel with and without non-condensable gas present.

23.2.7.3 WCOBRA/TRAC-TF2 Model

The vessel is modeled via a single channel with a 1.0 ft^2 flow area and 2 axial nodes, each with 1.0 ft height. The pressure boundary is maintained by a BREAK component at 1000 psia attached to the outlet pipe. A schematic of the test problem is shown in Figure 23.2.7-1.

23.2.7.4 Numerical/Analytical Solution

No attempt is made to develop an analytical solution of the transient for the purpose of this assessment. Results are checked against the equilibrium condition reached as a steady-state is reached. The equilibrium condition is known and is reached when all of the vapor will condense on the cold wall surface filling up the cell. Introduction of any non-condensable gases is expected to suppress the condensation.

23.2.7.5 WCOBRA/TRAC-TF2 Assessment

23.2.7.5.1 Vapor Only Case

Saturated vapor condenses on the cold wall at the top and bottom cells and quickly forms a liquid film.
[

]^{a,c}

The early part of the transient is characterized by a small downward gas and liquid velocity in the bottom cell as the condensation of gas pulls saturated vapor downward. As the flow regime in the bottom cell switches to bubbly flow, the heat transfer coefficient to vapor in the top cell (Figure 23.2.7-4) and to liquid in both the bottom and top cells (Figure 23.2.7-5) increases such that the bottom cell becomes fully liquid and the top cell undergoes condensation resulting in a void fraction near **[ ]**[a,c] Once the bottom cell is filled with liquid, the phasic velocities become zero, resulting in negligibly small wall-fluid heat transfer and a cessation of condensation in the top cell.

23.2.7.5.2 Non-Condensable Gas Case

In this test, as the saturated vapor condenses, non-condensable gas is pulled into the vessel. As the non-condensable gas enters the cell and its partial pressure increases, the relative humidity and the dew point temperature decrease, as seen in Figures 23.2.7-6, 23.2.7-7, and 23.2.7-8. Once the cell is entirely filled with liquid and non-condensables, no vapor remains for condensation and the void fraction reaches equilibrium. Since the pressure is held constant, the equilibrium solution is that the partial pressure of steam is equal to the saturation pressure at the vapor temperature. For this test, WCOBRA/TRAC-TF2 predicts a steam partial pressure of **[ ]**[a,c], appropriate for the equilibrium vapor temperature of **[ ]**[a,c]

23.2.7.6 Summary and Conclusions

The expected outcome is achieved by the WCOBRA/TRAC-TF2 test problems: the vapor condenses on the cold wall surface filling up the cells and the introduction of non-condensable gases suppresses the condensation.

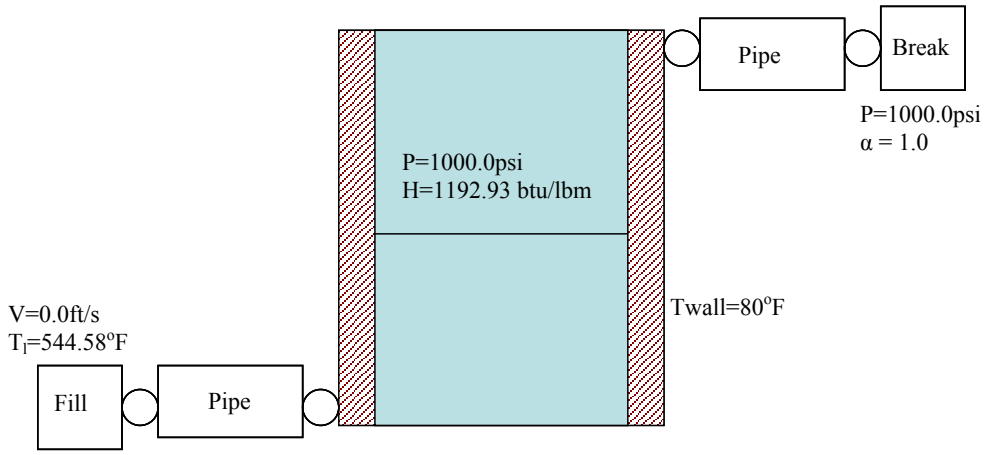

Figure 23.2.7-1 3D Vessel Model used in the Condensation Test Problem

a,c

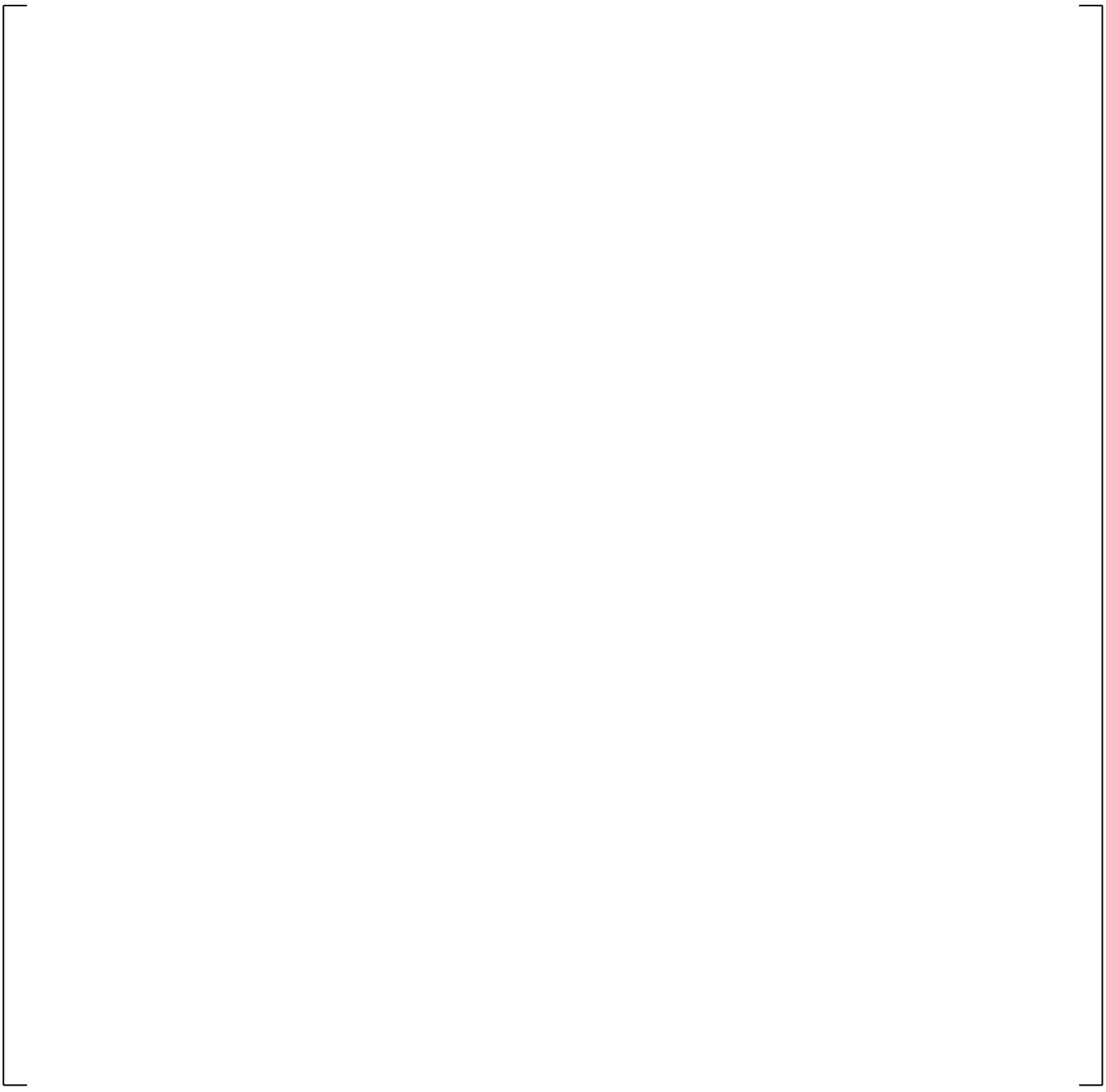

Figure 23.2.7-2 Void Fraction in the Condensation Test Problem, Vapor only Case

a,c

Figure 23.2.7-3 Flow Regime in the Condensation Test Problem, Vapor Only Case

a,c

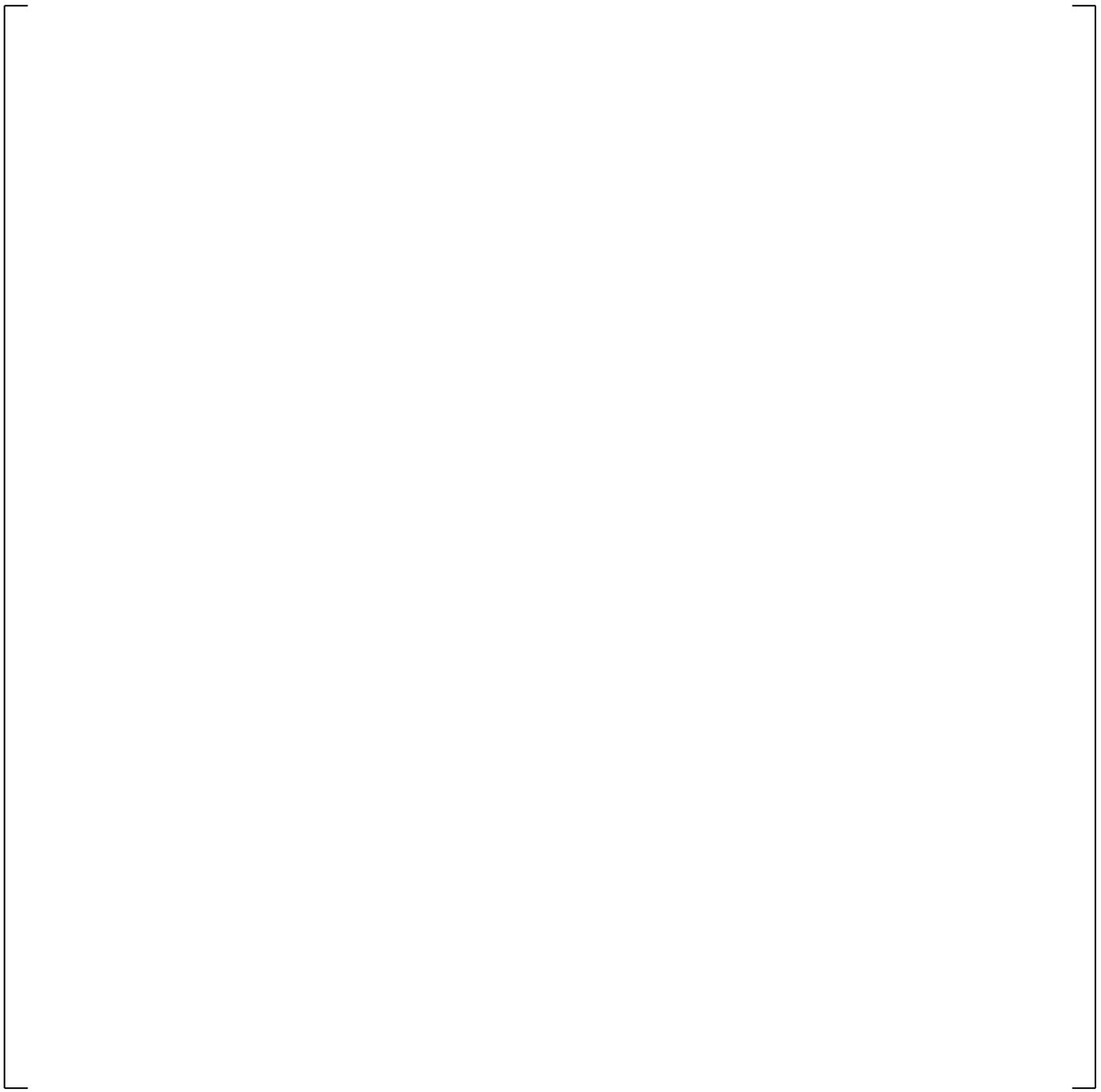

Figure 23.2.7-4 Heat Transfer to Vapor and Vapor Velocity in the Condensation Test Problem, Vapor Only Case

a,c

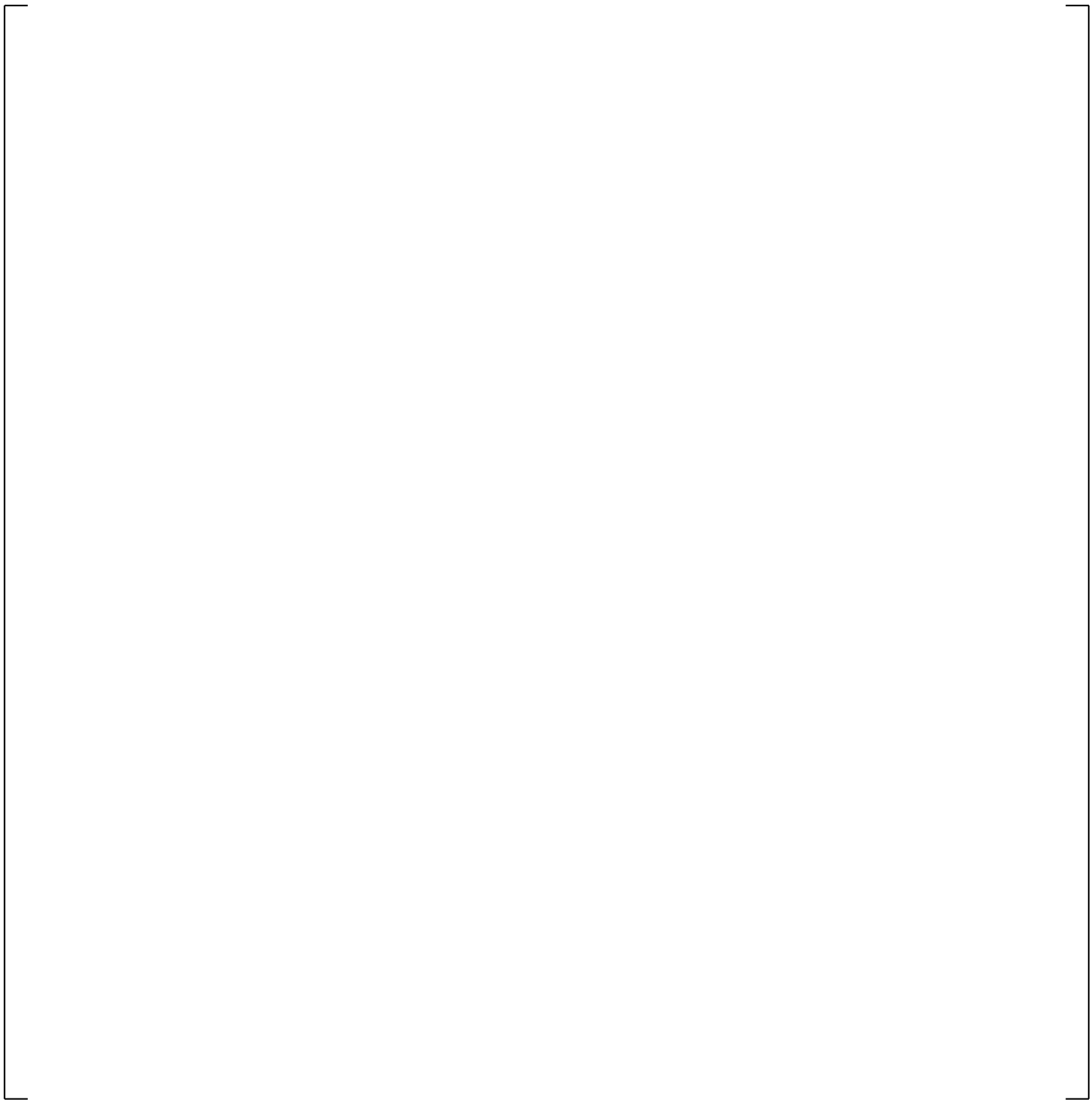

Figure 23.2.7-5 Heat Transfer to Liquid and Liquid Velocity in the Condensation Test Problem, Vapor Only Case

a,c

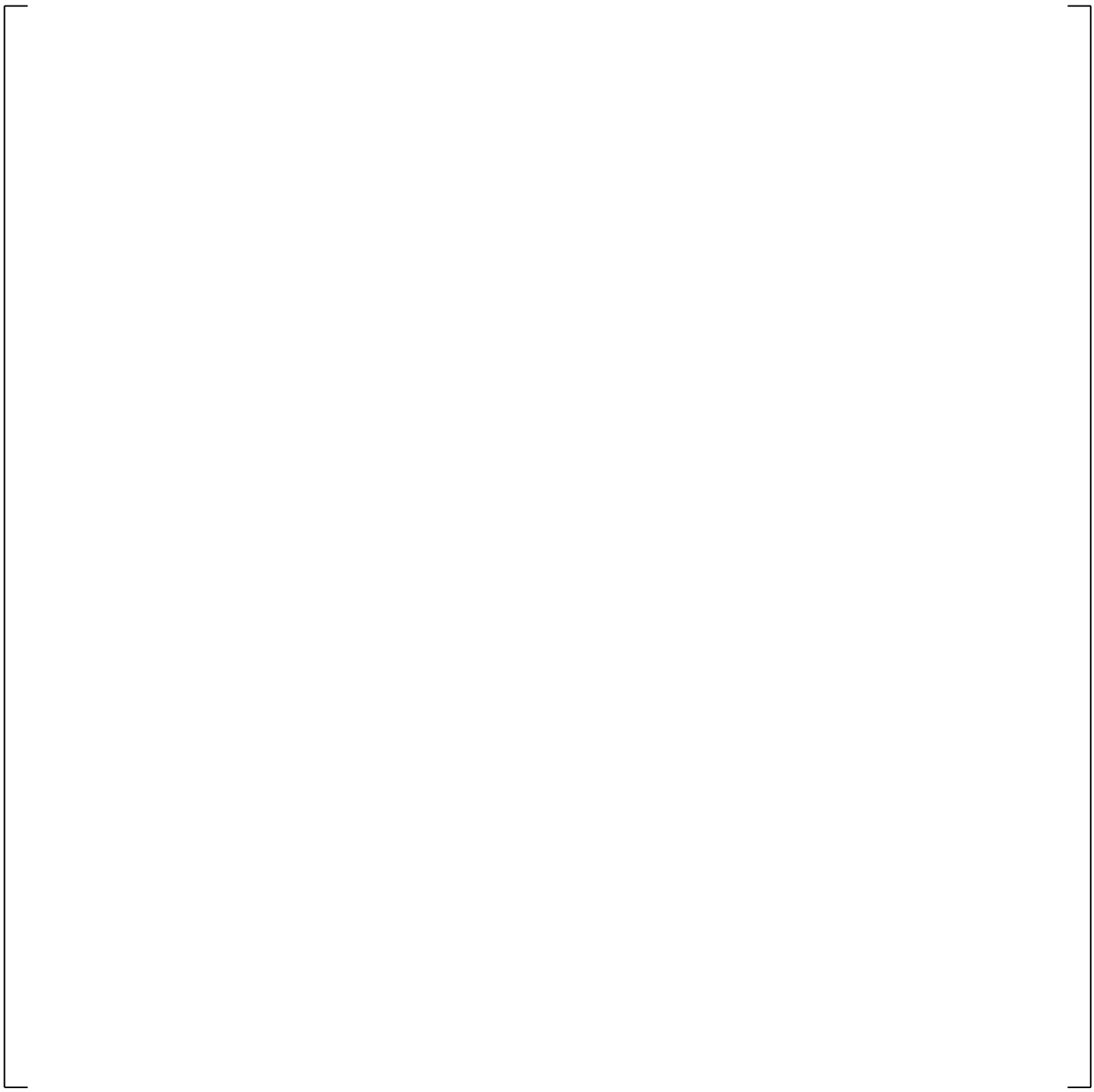

Figure 23.2.7-6 Void Fraction and Relative Humidity in the Condensation Test Problem, Vapor and Non-Condensable Gas Case

a,c

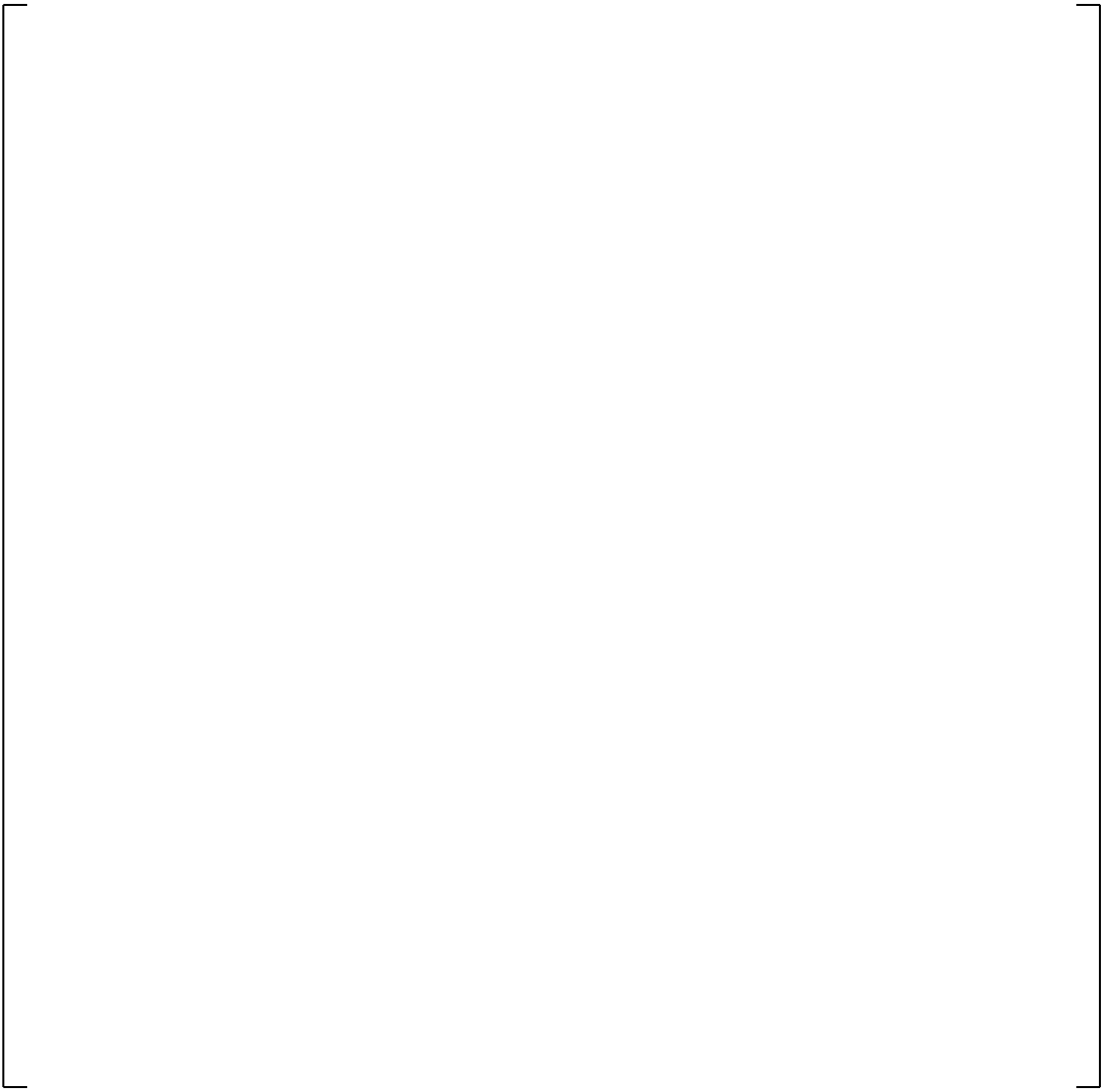

Figure 23.2.7-7 Total, Steam, and Non-Condensable Gas Partial Pressures in the Condensation Test Problem, Vapor and Non-Condensable Gas Case

a,c

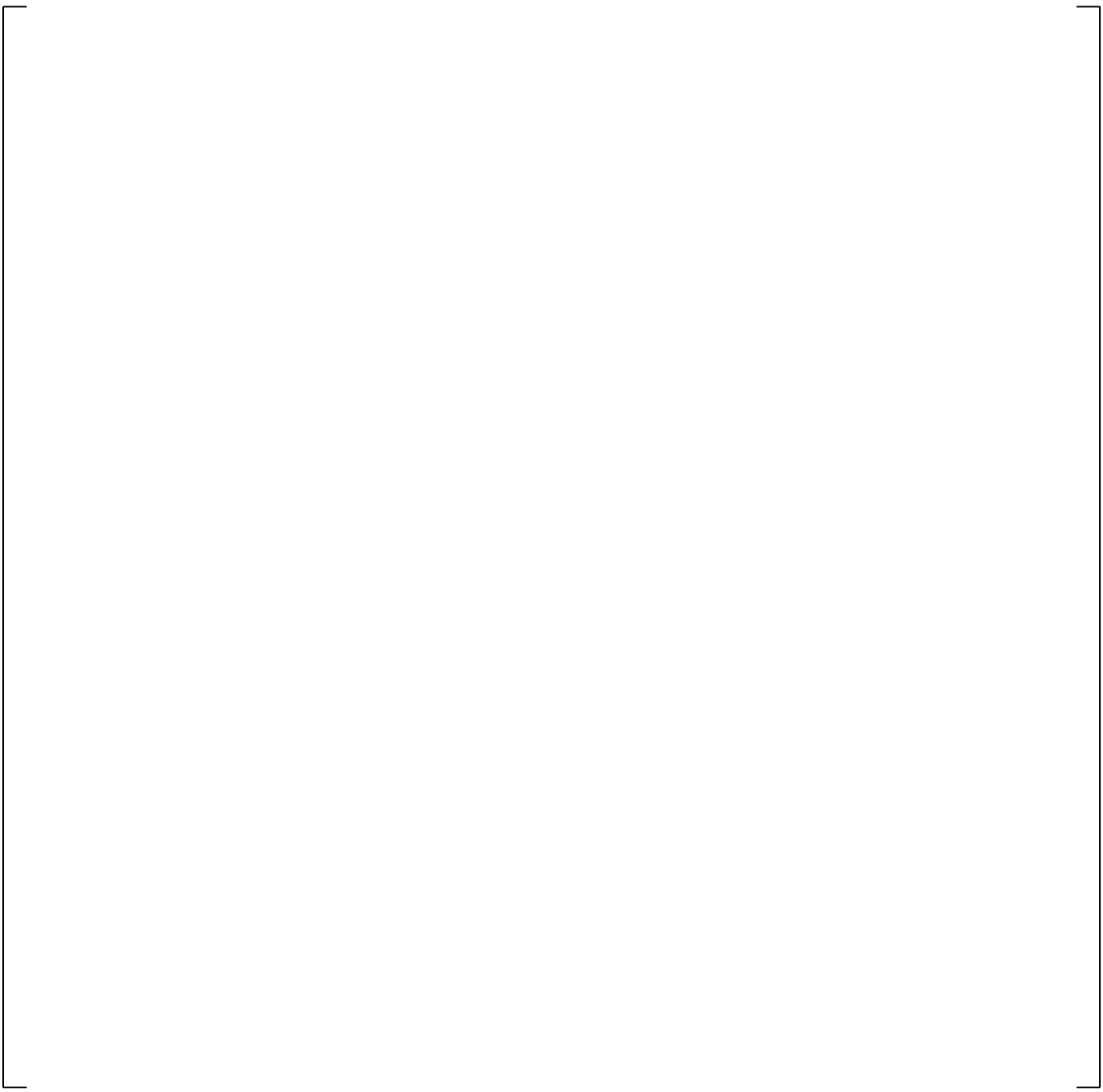

Figure 23.2.7-8 Gas, Liquid, Saturation, and Dew point Temperatures in the Condensation Test Problem, Vapor and Non-Condensable Gas Case

24 ASSESSMENT OF COMPENSATING ERROR IN EVALUATION MODEL USING WCOBRA/TRAC-TF2

24.1 INTRODUCTION

Compensating Errors in Simulations

In Section 1.1.2 of RG 1.203, Step 2 discusses "Figure of Merit" for the assessment, and also describes the need to consider "compensating errors" when assessing the adequacy of the code models. Section 1.1.2 states,

> *"In line with the surrogate figure of merit, it is also important to consider other related performance measures in conjunction with the principle objectives. Because compensating errors in the code can unintentionally lead to correct answers, additional performance measures serve as physical tracking points and additional proof of accuracy. While the code may calculate the correct peak cladding temperature (PCT), for example, incorrect or physically impossible parameter values could evolve in other areas of the calculation."*

Compensating errors are those model errors which, when acting in combination, could result in good but misleading prediction of the phenomena or the parameter of interest for which the code is being assessed. This is especially important because most of the validation tests use small scale tests, and scale impacts could magnify the code model errors of this kind. If the code contains significant compensating errors and scale test simulations appear well predicted because of the compensating errors, the accuracy of full scale transient simulations such as loss-of-coolant accident (LOCA) analysis of a pressurized water reactor (PWR) could be suspect.

An evaluation of the potential for the existence of compensating error in the predicted results of selected integral and separate effects tests from WCOBRA/TRAC-TF2 is performed in this section. Compensating errors are those model errors which, when operating in combination, could result in good prediction of a key parameter only as a result of inaccurate prediction of factors contributing to the calculation of that parameter. This is a concern particularly for integral effects tests, where there are few fixed boundary conditions. For example, the prediction of apparently correct cladding temperature response in the Loss-of-Fluid Test (LOFT) experiments could occur because the core flow rate was under predicted, while the heat transfer model over predicts the local heat transfer coefficient.

Not all model errors are compensating. For example, over predicting the core flow may result in over-estimating the core heat transfer. This effect would be expected if the heat transfer model was physically correct, and therefore does not point to a significant deficiency in the heat transfer model. The process of evaluation for compensating errors is briefly outlined below.

Identification of Possible Compensating Errors

The process of evaluation starts with the review of Highly Ranked Phenomena tabulated in Table 2-2, and WCOBRA/TRAC-TF2 Model Assessments validation matrix using Separate Effects Tests (SETs) given in Tables 2-3, 2-4 and 2-5. For each model assessment, possible compensating errors involving sub-models (or constituent models) are sought and identified. For example some models such as Post Critical Heat Flux (CHF) Heat Transfer Model, are constructed from multiple sub-models such as the single phase vapor heat transfer, vapor-droplet evaporation heat transfer, and the heat transfer due to droplet-wall impaction, all of which work in combination to form a heat transfer value which determines the cladding temperature which is the primary figure of merit. Because a good cladding temperature prediction requires only that the sum of three models to be reasonable, there is a possibility of compensating errors where individual values may be unreasonable but the sum of three is reasonable. For all highly ranked phenomena in SETs, the possibility of errors of a kind described above is examined and identified.

In Integral Effects Tests (IETs) by design, multiple physical models and components are often in competition as the transient evolves. Thus there are possible compensating errors which involve interaction of multiple models/phenomena. For example, the peak cladding temperature (PCT) in a Small Break LOCA (SBLOCA) is strongly impacted by the mixture level and the heat transfer prediction. A reasonable prediction of PCT may be obtained even when the mixture level is biased too low but the heat transfer is biased too high. For IETs of SBLOCA, Intermediate Break LOCA (IBLOCA), and Large Break LOCA (LBLOCA) sub-scenarios, possible occurrences of this type of compensating errors are sought and identified.

Evaluation of Compensating Errors in Simulations

For selected simulations in which potential of compensating errors is identified, the simulation fidelity of parameters in addition to the main parameters of interest is evaluated for additional proof of accuracy. For example, the primary figure of merit for LOFT simulations is the PCT. But the assessment will be performed utilizing comparisons to other measured quantities such as vapor temperatures in the vicinity of core, flow, void fraction, and loop flow so that the existence or absence of significant compensating errors could be evaluated. With additional proof of accuracy, the confidence that the adequacy of the evaluation model using WCOBRA/TRAC-TF2 at the PWR scale would be increased.

24.2 IDENTIFICATION OF HIGHLY RANKED PHENOMENA AND MODEL ASSESSMENT

Section 2 in Volume 1 of this document discusses Phenomena Identification and Ranking Table (PIRT) for the FULL SPECTRUM LOCA methodology. A validation test matrix for highly ranked phenomena was developed based on the high and medium ranked phenomena from the PIRT and available separate effects and integral effects tests. Tables 24.2-1 through 24.2-4 represent the validation matrix for WCOBRA/TRAC-TF2 which lists highly ranked phenomena, and SETs and IETs for LBLOCAs, SBLOCAs and IBLOCAs. The table format is altered from Tables 2-3 through 2-6 to emphasize the phenomena and supporting validation tests. For each of the phenomena listed in these tables, possible compensating errors which may be present in the assessment simulations are sought and results are summarized in the subsequent sections.

Table 24.2-1 V&V Matrix for Large Break LOCA Processes, Blowdown Phase SETs & IETs		
Phenomena	**Test**	**Comments**
Critical Flow	Marviken, LOFT	High/full pressure in a full/sub scale facility
Break Resistance	LOFT, UPTF Test 6	Loop Piping may not be prototypic, Broken cold leg nozzle.
Fuel Rod	LOFT	Blowdown heat-up
Heat Transfer	ORNL-THTF (Film Boiling Tests), Westinghouse G-1 (Blowdown), LOFT	Steady State and transient dispersed flow film boiling tests
ECC Bypass	UPTF Test 6, LOFT	Full scale low pressure/sub scale full pressure
SI & DC Condensation	UPTF Test 6, UPTF Test 8, LOFT	Full scale low pressure/sub scale full pressure

Table 24.2-2 V&V Matrix for Large Break LOCA Processes, Refill/Reflood Phase SETs & IETs		
Phenomena	**Test**	**Comments**
Heat Transfer	Westinghouse G-2 Refill/Reflood, FLECHT-LFR, FLECHT-SEASET (Reflood and Steam Cooling), FLECHT-Skewed, FEBA, Achilles, CCTF, LOFT (part length)	Full height refill/reflood bundle tests, simulated and nuclear rods (LOFT)
SI & DC Condensation	UPTF Test 25A, LOFT	Full/sub scale tests
N_2 Injection	Achilles, LOFT	Test L2-5 showed some impact due to N_2 injection. The simulation was compared to the observation in the test.
Fuel Rod	LOFT	Not simulated. Models and correlations are judged to not contain competing effects to cause compensating errors.
Entrainment/ De-entrainment	Westinghouse G-2 Reflood, FLECHT-LFR, FLECHT-SEASET, FLECHT-Skewed, FEBA, Achilles, UPTF Test 29B, UPTF Test 25A, CCTF, LOFT	Full height refill/reflood bundle entrainment, upper plenum and downcomer entrainment

Table 24.2-3 V&V Matrix for Small Break LOCA Processes, Separate Effect Tests		
Small Break Process	**Test**	**Comments**
Critical Flow	EPRI-NP-4556 + additional Marviken Dataset represents approximately 3200 points from 53 geometries, and 10 facilities, containing data from 13 to 2500 psia. The geometrical range: 0 < L < 2300mm, 0.464 < DH < 500mm.	Available data appears to span PWR ranges of conditions for break area, upstream subcooling, and flow quality. (V. Ilic, S. Banerjee and S. Behling, "A Qualified Database for the Critical Flow of Water," EPRI-NP-4556, May, 1986.)
Mixture Level	ORNL, Westinghouse G-1& G-2 Boiloff, TPTF, GE Blowdown, Semiscale S-7-10D (SET Mode)	Data covers PWR expected range of pressure and bundle power.
Horizontal Flow Regimes	JAERI-TPTF Horizontal Flow Tests	Horizontal stratified regime transitions predicted according to modified Taitel-Dukler/Wallis-Dobson map.
Loop Seal Clearance	UPTF Loop Seal Tests	Full scale geometry, provides information for range of Jg* that covers PWRs.
Fuel Rod Models: Nuclear Rod Models Heat Transfer	Various sets of test data from LBLOCA, Single Phase Vapor Heat Transfer: ORNL-THTF (Uncovered Bundle Tests)	Fuel rod models were assessed and quantified for large break. Data representative of SBLOCA conditions.
Pump Performance	Pump Specific Data from LBLOCA	Empirical pump data; assessed for large break LOCA.
SI Condensation	COSI Tests, ROSA-IV SB-CL-05 (SET Mode)	High pressure SI condensation.
Break Flow, entrainment at Break/Offtake	TPFL	Single and two-phase critical break flow measurements available. Orientation effect.

Table 24.2-4 V&V Matrix for Small Break LOCA Processes, Integral Effect Tests		
Small Break Process	**Test**	**Comments**
Break Flow, entrainment at Break	LOFT Test L3-1, ROSA-IV cold leg (CL) break tests: 10% (side), 5% (side), 2.5% (side, top, and bottom), 0.5% (top, side, and bottom)	Single and two-phase critical break flow measurements available. Orientation effect.
Mixture Level	ROSA-IV CL break tests: 10%, 5%, 2.5%, and 0.5%, LOFT test L5-1	Range of break sizes. Vessel inventories and system wide mass distributions.
Steam Generator Hydraulics	ROSA-IV natural circulation test ST-NC-02, SB-CL series	Provides information on system wide phase separation, primary-secondary heat transfer.
Loop Seal Clearance	ROSA-IV CL break tests: 10%, 5%, 2.5%, 0.5%, and additional 5% CL break with higher Core Bypass and high-head safety injection SB-CL-05	Provides information on loop seal clearing phenomena.
Fuel Rod Models: Nuclear Rod Models Heat Transfer	LOFT ROSA-IV SB-CL series	Nuclear rods. Cladding heatup & peak cladding temperatures.
IBLOCAs	ROSA-IV 10% CL break test, LOFT L5-1	A 10% cold leg break and a 14in accumulator line break

24.3 IDENTIFICATION OF POSSIBLE COMPENSATING ERRORS IN MODEL ASSESSMENT

24.3.1 Possible Compensating Errors in Separate Effects Test Simulations

24.3.1.1 Delivery and Bypassing of ECC and Condensation in the Downcomer

The validation of the ECC bypass model is documented in Section 19.3.5. The delivery of emergency core cooling (ECC) liquid into the lower downcomer is impacted by the counter current limit in the downcomer due to high vapor flow from the core. The Counter Current Flow Limitation (CCFL) is affected by interfacial drag and also by condensation. CCFL conditions could be predicted well, even though under-estimating the interfacial drag (too little liquid holdup for a given steam flowrate), by under-estimating the condensation rate (too much steam flow). Therefore condensation and interfacial drag are potential source of compensating error relative to the prediction of delivery and bypass of ECC liquid.

24.3.1.2 Post-CHF Heat Transfer

A specific area of concern is the way in which the film boiling models are constructed in WCOBRA/TRAC-TF2. The heat transfer models are constructed as a combination of several heat transfer mechanisms. This construction is described in Section 7.2.11, Volume 1 of this document. In the Code Scaling, Applicability, and Uncertainty (CSAU) development (Boyack et al., 1989), it was concluded that the TRAC code with the similar film boiling model with several superimposed mechanisms, could have resulted in compensating errors (i.e., too much heat transfer at moderately high liquid fractions), such that the heat transfer in some integral tests was predicted correctly because the predicted vapor fraction was too high.

Another potential compensating error is the mis-prediction of vapor temperature. The identification of evidence of non-equilibrium conditions in the core is important for post-CHF heat transfer, since the heat transfer models in WCOBRA/TRAC-TF2 rely on the local vapor temperature as the heat sink. It is well known that vapor superheating significantly reduces post-CHF heat transfer from high temperature fuel rods. An example of a compensating error is where the overall heat transfer is “correctly” calculated because the local heat transfer coefficient is under-predicted (due to an inappropriate model) but the temperature difference between the fuel rod and the fluid is over-predicted. Most measurements of non-equilibrium conditions, usually by thermocouples exposed to the fluid, are affected by rewet by liquid impact. However, it is believed one can safely assume that a measurement of any level of superheat above saturation temperature is a sure sign of significant non-equilibrium in the fluid, which should also be predicted by the code.

In post blowdown heat transfer, the core entrainment rate, droplet size, and interfacial drag models act in combination to predict the corresponding relative velocities, vapor fraction, and interfacial heat transfers which ultimately determine the vapor temperature and wall heat flux. Evidence of compensating error among these quantities is therefore important.

24.3.1.3 Blowdown and Post Blowdown Thermal-Hydraulics/Entrainment

During blowdown, the correct prediction of mass flowrates in the broken and intact loops is important, since the core flowrate is driven by the break flowrate in the broken loop, and by the pumps in the intact loops. An example of a compensating error would be a "correct" prediction of core flow resulting from a lucky combination of incorrect loop flows.

During reflood, the pertinent question to ask in terms of compensating errors is whether the mass flow into and out of the core is calculated correctly, and is the result of a proper balance between the driving force caused by the difference in water level between the core and the downcomer, and the pressure drop in the loops. An example of a compensating error is the situation where the core inlet flowrate is calculated "correctly" because the core level is too high (leading to a low driving force), but is compensated by a loop pressure drop which is too low.

A key aspect of the post blowdown thermal-hydraulics prediction pertaining to core cooling is the entrainment calculation; the inlet flow is controlled by the steam generation rate and liquid entrainment from the core, and by the amount of liquid which is predicted to collect in the upper plenum (UP) and hot legs.

24.3.1.4 Fuel Rod Models (Oxidation, Swelling/Burst)

Models and correlations used to calculate the oxidation and swelling/burst effects are documented in Section 8, Volume 1. The bias and uncertainty of the model will be accounted for in the uncertainty treatment.

24.3.1.5 Break Flow

The validation and assessment of the critical flow model, Homogeneous Relaxation Model (HRM) option, is documented in Section 12 of this document. **[**

][a,c]

24.3.1.6 Mixture Level/Level Swell in Simulated Core

Prediction of mixture level inferred by the heat up location is impacted by the accuracy of interfacial drag, CHF models, noding sizes, thermocouple (T/C) elevations, and presence/absence of grids.

The energy equation discretization, the coarse hydraulic node size and donoring scheme in the core leads to a limiting resolution of enthalpy prediction which may result in biased cladding temperature prediction.

The use of relatively coarse hydraulic noding in the core limits the accuracy of the prediction because the node average enthalpy is computed based on the heat flow in and out of the control volume. The enthalpy is computed accounting for the heat flow up to the top of the control volume. Thus in an upflow situation, the predicted enthalpy of the node corresponds to the fluid enthalpy at the top of the cell and not at the cell center point. In a downflow situation on the other hand, the predicted cell enthalpy corresponds to the fluid enthalpy at the bottom of the cell. **[**

][a,c]

In addition to the resolution limit, in a boiloff test, a potential compensating error exists because of the process of evaporation. If the level swell is predicted high, the mixture level is high, thus more heat from the heater rods is absorbed by the liquid resulting in the higher evaporation rate which reduces the liquid inventory and subsequently the level. So the mixture level comparison may appear reasonable.

24.3.1.7 Horizontally Stratified Flow Regime Transition Boundary

Prediction of horizontal stratified regime transition is impacted by the accuracy of phasic velocities, thus by the liquid level (if the total phasic flow rates are given), interfacial drag/wall drag models, also by the boundary conditions to the pipe section of interest such as the liquid level imposed at the ends.

When the level is imposed on the downstream end of pipe, and if the liquid flow is supercritical, the level is more likely determined by the wall and interfacial drag for a given J_G-J_L, and if the liquid flow is subcritical, the level is determined by the downstream liquid level set by the boundary such as the downcomer liquid level. Therefore a potential compensating error exists for horizontal stratified flow test simulations. The transition to slug may be correctly predicted if the liquid level prediction is biased high and the transition criteria model is biased to high vapor flows.

24.3.1.8 Steam Generator Thermal-Hydraulics

WCOBRA/TRAC-TF2's predictive capability of steam generator (SG) hydraulic behavior such as the reflux condensation heat transfer and the CCFL in the tubes during and at the end of natural circulation period in SBLOCA is **[**

][a,c]

There are multiple locations in the region between the hot leg nozzle and the steam generator where CCFL is possible and thus limits liquid down flow from the intact steam generator prior to clearing the loop seal. Steam Generator tube inlet is one such location. **[**

][a,c]

24.3.1.9 Loop Seal Clearance

The loop seal starts to clear when the liquid level formed in the downhill side of pump suction piping reaches the top of the horizontal pipe. The onset of loop seal clearing timing is determined by the break flow, vapor generation rate in the core, the condensation rate in the SG tubes, and the core bypass flow rate. Once the clearing commences, because of the significant volume of vapor accumulated in the inner vessel, a relatively high vapor flow is maintained for a significant time such that significant fraction or all of the liquid in the loop seal is swept out of the cross-over leg and to the cold leg. At a larger break size, the vapor volumetric flow is high enough to clear loop seal in multiple loops.

The number of cleared loops is determined by the available vapor flow due to flashing from depressurization which increases with the break size, in addition to already accumulated vapor in the inner vessel, loop resistance, and the broken cold leg pressure which decreases faster as the break size increases. For a stable loop seal clearing which may include a partially cleared loop, the remaining liquid in the horizontal leg of the pump suction piping and the pressure loss through an intact loop become a factor.

The Upper Plenum Test Facility (UPTF) loop seal test (Liebert and Emmerling, 1998) while it is quasi-steady state, provides important full scale single loop seal clearing data in a prototypic PWR geometry, and provides ΔP and liquid level information for a range of J_g^* that covers conditions expected in SBLOCA in PWRs. The phenomena of loop seal clearing involves several physical models, namely the onset of slugging, entrainment in the horizontal section, the CCFL in the uphill pipe and entrainment in the vertical upflow as described in Section 18, thus there is a possibility of compensating errors.

24.3.1.10 Pump Performance

There is no compensating error within the pump model. However, immediately after the break, the intact flow is still controlled by the pump which then competes against the break flow, thus impacting the core inlet flow. The interaction between the broken cold leg flow and pump creates a possibility for compensating error where the core inlet flow may be reasonably predicted when the sum total of break flow and intact pump is correct but both break flow and the pump flow may be incorrect.

24.3.1.11 Safety Injection Direct Condensation in the Cold Leg

The direct condensation due to safety injection in cold legs is calculated by the use of a model which was constructed based on the 1/100 scaled condensation on safety injection (COSI) test. Because the operation of the cold leg, direct injection condensation model requires the horizontally stratified or the separated flow (wavy dispersed or annular mist) in the cold leg, the model performance may be impacted by the stratified flow to slug transition criteria.

For LBLOCA application, UPTF Test 8 (2D/3D, 1988) was used to assess the cold leg, direct injection condensation model for the low pressure, high steam flow conditions typical for LBLOCA conditions (Section 19). **[**

][a,c]

24.3.2 Possible Compensating Errors in Integral Effects Test Simulations

In IETs, multiple physical models and components are interacting as the transient evolves which give rise to opportunities for compensating errors. Rather than identifying possible compensating errors, phenomena will be listed under the relevant sub-scenario simulations which will be used for the assessment of compensating errors.

24.3.2.1 SBLOCA

The cladding temperature could be calculated correctly if the heat transfer and the core level swell are biased in the opposite direction (higher heat-transfer coefficient (HTC) and low mixture level). Additionally, the correct core mixture level could be the result of mis-prediction in the liquid inventory in the core and the level swell (e.g., low inventory in the core and high swell). ROSA series will be used to help assess compensating errors in the areas mentioned above.

24.3.2.2 IBLOCA

Though the behavior of IBLOCA may be a combination of small break (SB) and LBLOCAs, the relative importance of observed SB and LB phenomena are different and thus the different biases in the predicted behavior are expected. SB-CL-14 (Koizumi and Tasaka, 1988) from ROSA series is a simulation of 10% cold leg break of a PWR. Minor cladding heat up was observed in this test. The test is well instrumented to allow assessing of compensating errors in WCOBRA/TRAC-TF2's simulation. Additionally LOFT intermediate break test L5-1 (Jarrell and Divine, 1981) which simulated a guillotine break of a 14 in dia. accumulator line of a 4 loop PWR, may be available to investigate the possible compensating errors, although the test was conducted in a non-prototypic arrangement where there was no break in the hot leg of a "broken loop." Minor cladding heatup was observed which would enable one

to assess the core mixture level prediction. In addition to a set of global parameters such as the vessel pressure and the break flow rate, there are some local measurements (for example hot leg density and flow rates) which allow one to evaluate the reasonableness of the flow regime prediction around the loops.

24.3.2.3 LBLOCA

One possible compensating error would be associated with the blowdown cladding temperature prediction. During blowdown, the core inlet flow prediction may be impacted by compensating errors in the PUMP performance and the break flow prediction. Additionally, compensating error may be present in the cladding temperature prediction due to an interaction of the post-CHF heat transfer prediction and the core flow prediction. The cladding temperature may appear reasonable when the heat transfer coefficient is biased high and the lower core flow is predicted.

24.4 COMPENSATING ERROR ASSESSMENT OF SELECTED HIGHLY RANKED PHENOMENA IN SETS AND IETS

The compensating error analysis of selected highly ranked phenomena is presented in the Sections 24.5 through 24.8, where in addition to the main parameters of interest, i.e., PCT, additional parameters such as core flow and the heat transfer coefficient, which impact the computation of main parameters of interest, will be compared with measurement or assessed in terms of consistency with secondary figures of merit. For example, PCT or total heat transfer from the rod to the coolant is predicted with reasonable accuracy, but is impacted by the heat transfer coefficient and the flowrate. This exercise attempts to determine if the heat transfer is correct because both the heat transfer coefficient and the flow rate are predicted reasonably well, or the heat transfer is predicted well because these two main parameters are predicted with bias of opposite direction.

In previous sections of this document, highly ranked phenomena and models were validated for use in the LOCA analysis. Though the aspect of compensating errors in these assessments were not explicitly examined, relevant conclusions could be drawn from the assessments because of additional parametric sensitivity studies and scaling analyses that were performed, and they are summarized below.

In Section 12 the break flow model was validated, and the examination of parameter impact on the prediction was conducted. The conclusion from Section 12 is that **[**

][a,c]

Along with the heat transfer calculation, the prediction of Mixture Level/Level Swell in the Core Region was assessed in Section 13. **[**

][a,c]

The prediction of Transition to Horizontal Stratified Flow was validated in Section 16 where the focus was the model performance in typical SBLOCA conditions. It was concluded that the model performed as expected. **[**

][a,c]

The predicted Steam Generator Thermal-Hydraulics was examined as part of ROSA test simulations in Section 21. Section 21 confirmed that the code predicted reflux condensation heat transfer was **[**
][a,c] determined for the LSTF post-natural circulation test ST-SG-02 (Tasaka et al., 1988). **[**

][a,c]

The prediction of Loop Seal Clearance was the focus of Section 18 where the analysis of scaled loop seal test was presented, and the full scale test simulation was used to assess the code prediction. **[**

][a,c]

The model prediction for the Safety Injection Direct Condensation in Cold Leg was assessed in Section 17, and the model performance in the multi-component tests were assessed in Sections 19.3.8 and 19.3.11. **[**
][a,c]

In Sections 24.5 through 24.7, the compensating errors in phenomena associated with LBLOCA, namely the ECC bypass, post-CHF Heat Transfer, Blowdown/Post Blowdown Thermal-hydraulics, are examined. The SBLOCA related phenomena are examined in Section 24.8.

24.5 DELIVERY AND BYPASSING OF ECC

Summary Conclusion

Cold leg ECC injection tests, **[**

][a,c]

Analysis

The ECC bypass and condensation prediction in UPTF Test 6 and UPTF Test 25A test simulations were examined. The results of these simulations are documented in Section 19.3. **[**

][a,c]

[

]a,c

a,c

Figure 24.5-1 Comparison of Vessel Condensation Efficiency versus Nominal Steam Flow Rate, UPTF Test 6; The Experimental Condensation Efficiency is Estimated by MPR (MPR-1163, 1990)

a,c

Figure 24.5-2 ECC Liquid Temperature Comparison near Vessel Inlet

a,c

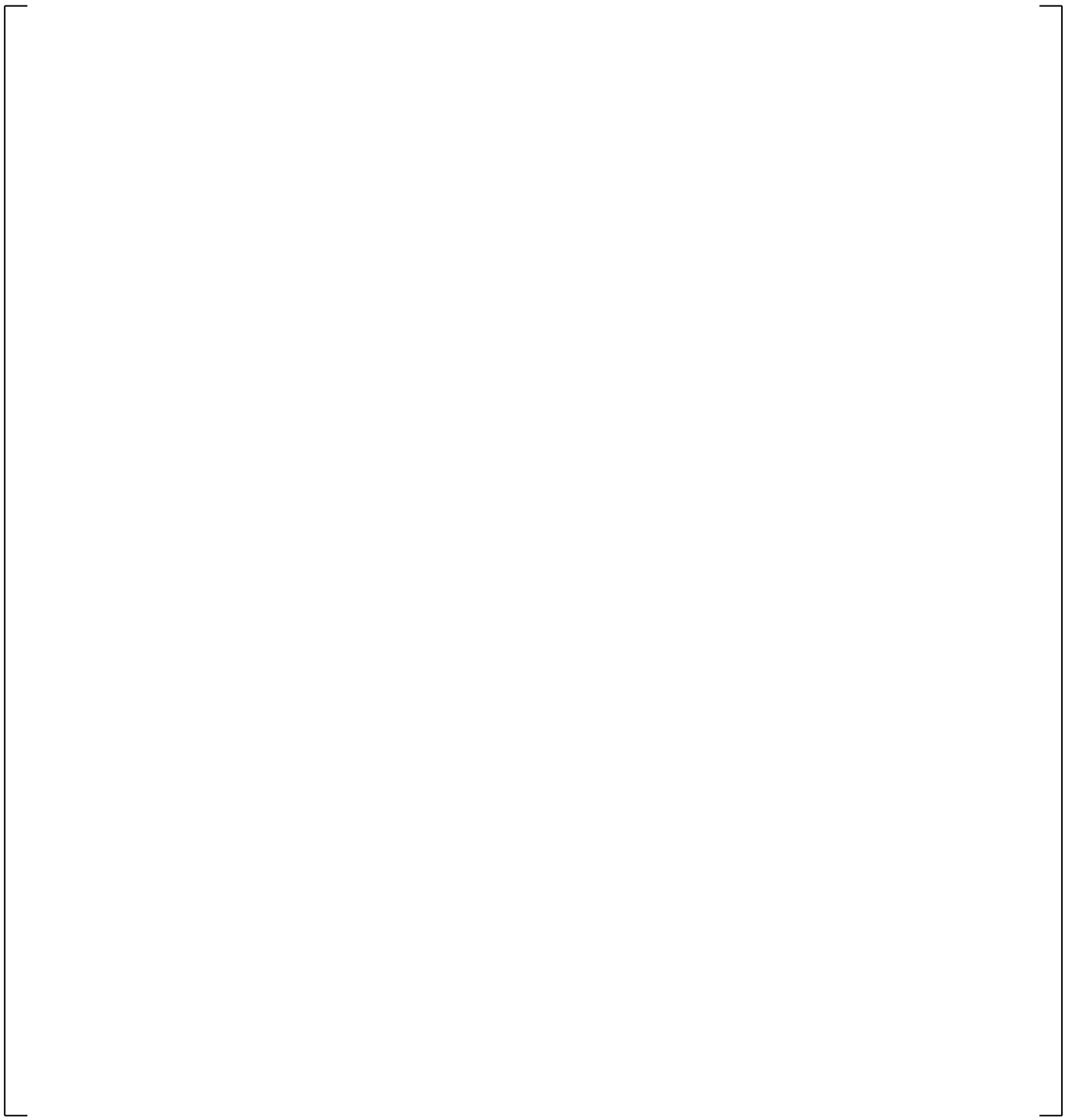

Figure 24.5-3 Downcomer Void Height Comparison in UPTF Test 25A

a,c

Figure 24.5-4 Broken Loop Steam Flow Rate in UPTF Test 25A

a,c

Figure 24.5-5 Cold Leg Temperature at Exit of Cold Leg for UPTF Test 25A

24.6 POST-CHF HEAT TRANSFER

Potential compensating errors in the post-CHF heat transfer models are investigated by first reviewing the assessment using the stand-alone heat transfer package, COBRAHT-TF2 and by examining WCOBRA/TRAC-TF2's simulation of the following test simulations:

- ORNL Uncovered Bundle Tests for Single Phase Vapor (SPV) Data (COBRAHT-TF2) (Anklam et al., 1982)
- Full-Length Emergency Core Heat Transfer (FLECHT) Steam Cooling Tests for SPV Data (COBRAHT-TF2) (Wong and Hochreiter, 1981)
- ORNL high pressure Film Boiling Tests (COBRAHT-TF2 and WCOBRA/TRAC-TF2) (Mullins et al., 1982)
- G-1 Blowdown Heat Transfer Tests (WCOBRA/TRAC-TF2) (Cunningham et al., 1974)
- FLECHT- Separate-Effects and System-Effects Tests (SEASET) forced flooding reflood tests (WCOBRA/TRAC-TF2) (Loftus et al., 1981)

24.6.1 Summary of Assessment with Stand-alone COBRAHT-TF2

Several tests included measurements of wall temperature, mass flux, inlet quality, and local vapor temperature. The test measurements were used to compare directly to the WCOBRA/TRAC-TF2 heat transfer package since all the required fluid parameters are available or can be estimated.

SPV HTC Assessment Results

The single phase vapor heat transfer was assessed in Section 15. Figures 15.4.1-1a and 15.4.1-1b in Section 15 (repeated here as Figures 24.6.1-1 and 24.6.1-2) show a comparison of the predicted heat transfer coefficient by the stand-alone WCOBRA/TRAC-TF2's heat transfer package against the high pressure measurement from ORNL-THTF uncovered bundle tests. The vapor Reynolds numbers and pressure range are appropriate to cover a range representative of blowdown period in LBLOCA, and the boiloff period in SBLOCA. Single phase vapor heat transfer in refill/reflood condition was assessed against low pressure FLECHT-SEASET Steam Cooling Test Data, **[**

][a,c]

Reynolds number dependency for the single phase vapor in the higher pressure is shown in Figure 24.6.1-2. The figure indicates that **[**

][a,c]

[

]^{a,c}

DFFB Assessment Results

The ORNL steady state tests (Yoder et al., 1982) were used to assess the Dispersed Flow Film Boiling (DFFB) model in Section 15.5. As with the assessment of SPV using the ORNL tests, the DFFB model assessment was conducted with the use of a stand-alone heat transfer package extracted from WCOBRA/TRAC-TF2. Figure 24.6.1-5 shows the comparison with the ORNL steady state tests.

[

]^{a,c}

a,c

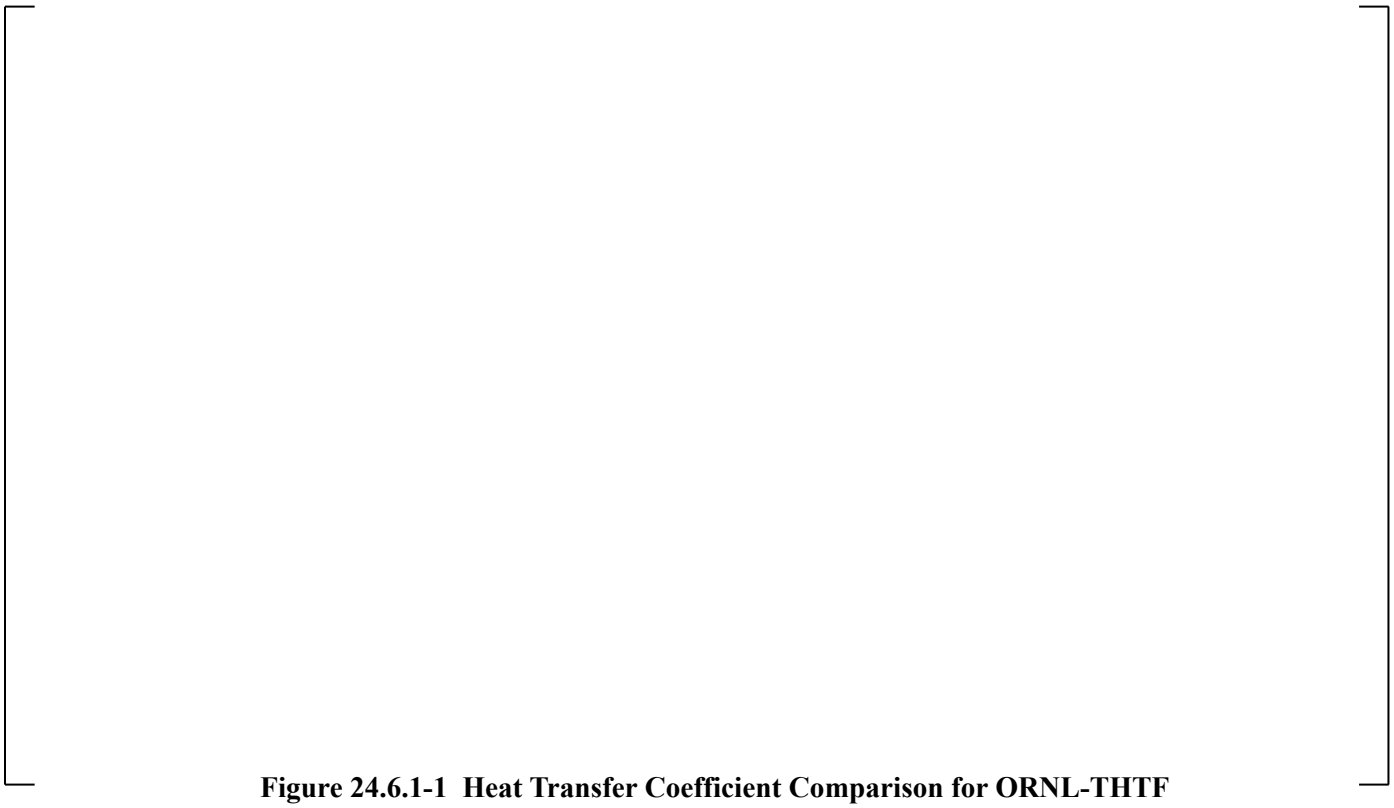

Figure 24.6.1-1 Heat Transfer Coefficient Comparison for ORNL-THTF

a,c

Figure 24.6.1-2 Prediction Error as a Function of Vapor Reynolds Number

a,c

Figure 24.6.1-3 Heat Transfer Coefficient Comparison for FLECHT SPV Tests

a,c

Figure 24.6.1-4 Ratio of Measured to Predicted Heat Transfer Coefficient vs. Vapor Film Reynolds Number for FLECHT SPV Tests (from COBRAHT-TF2)

a,c

Figure 24.6.1-5 Average Heat Transfer Coefficient Comparison for ORNL Steady-State Film Boiling Tests

a,c

Figure 24.6.1-6 Predicted Heat Flux Bias vs. Rev for ORNL Data

a,c

Figure 24.6.1-7 Predicted Heat Flux Bias vs. Void Fraction for DFFB Data

24.6.2 ORNL Film Boiling Test Simulation

[

]^{a,c}

Table 24.6.2-1 Bundle Exit Temperatures for ORNL Tests

a,c

a,c

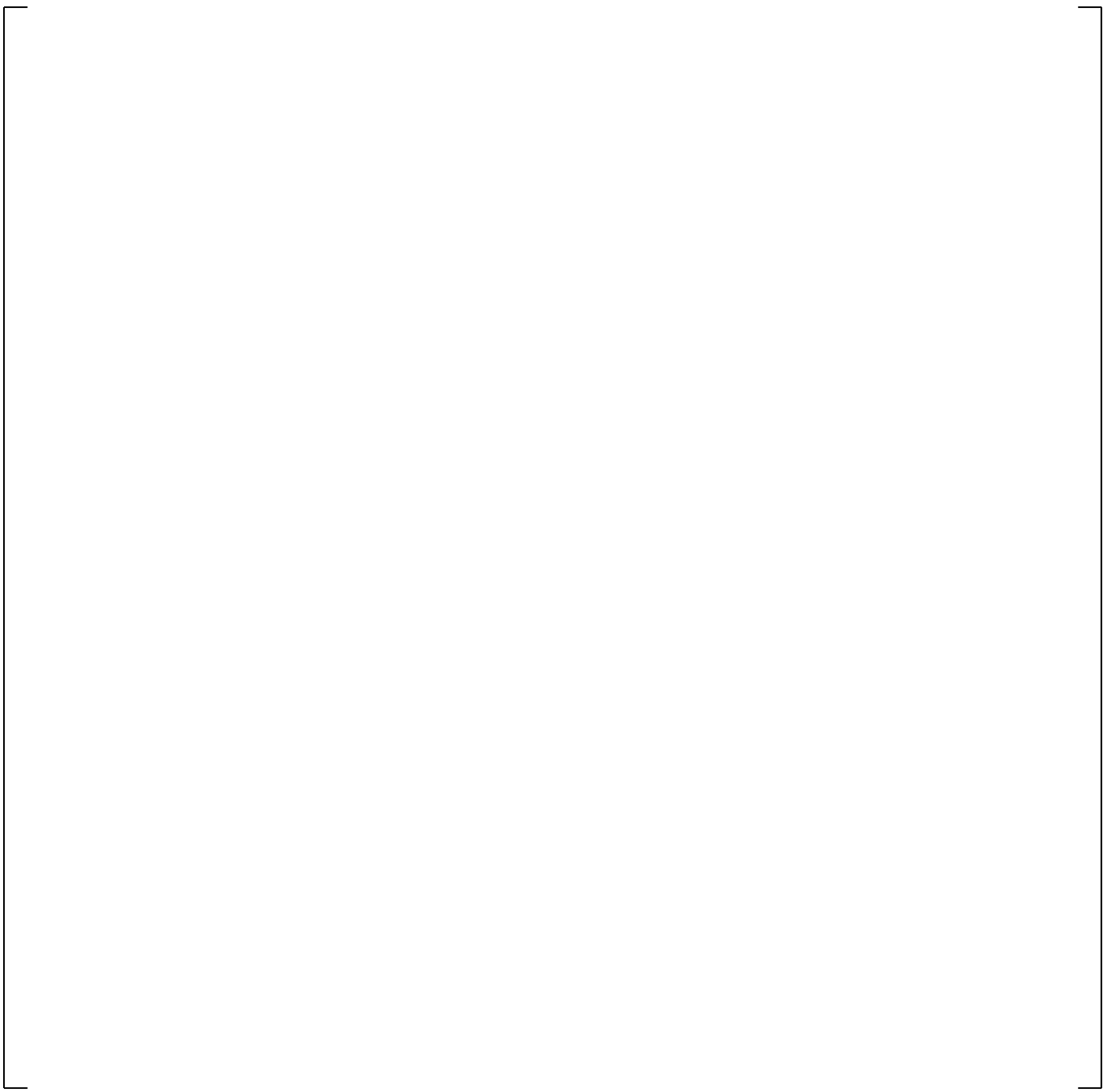

Figure 24.6.2-1 ORNL Test 3.03.36AR – Vapor Temperature and TLIQ (=Tsat) at Bundle Exit Calculated by WCOBRA/TRAC-TF2

a,c

Figure 24.6.2-2 ORNL Test 3.08.6C – Vapor Temperature and TLIQ (=Tsat) at Bundle Exit Calculated by WCOBRA/TRAC-TF2

24.6.3 G-1 Blowdown Test Simulation

Figures 24.6.3-1 to 24.6.3-5 show the transient cladding temperature, mass flux, and vapor fraction at the hot spot, and axial temperature distribution at various times, for a typical three-loop plant under a LBLOCA as calculated using WCOBRA/TRAC-TF2. Three-loop plants typically have a relatively high blowdown cooling period under nominal break flow conditions. The cladding experiences substantial cooling shortly after the transient has begun (about ~10.5 seconds after the break in Figure 24.6.3-1) due to reverse (downward) core flow (Figure 24.6.3-2). As the Reactor Coolant System depressurizes and refills, the core flow is reduced and the cladding once again heats up beginning at about 35 seconds, until it reaches a maximum during reflood. The core cooling due to the reverse flow during blowdown is a very important process since the highest PCT often occurs in cases with poor blowdown cooling where the core remains in high temperature at the end of the blowdown period.

The G-1 Blowdown film boiling tests were performed in a 12-foot long, 480-heater rod test bundle (Section 14.2.2.2). These tests were initiated from high temperature (1500 to 1700°F) and high pressure (800 psia). A simultaneous depressurization and downward flow of steam and water were imposed on the test section, simulating the core cooling phase of the blowdown transient. In some tests, the injected water was subcooled. These tests were chosen because they include all the basic features of a blowdown transient: downward flow into a hot dry bundle, two-phase inlet conditions, and depressurization.

Cladding temperatures were measured and heat transfer coefficients were inferred, using the saturation temperature as the sink temperature. No vapor temperature measurements were available. Six of these tests were modeled with WCOBRA/TRAC-TF2, ranging initial cladding temperature and inlet flowrate as shown in Table 24.6.3-1. **[**

][a,c]

The predicted cooling rates for these tests are compared to the measured bundle average values at several elevations in Figure 24.6.3-6. **[**

][a,c]

Figures 24.6.3-7 to 24.6.3-12 show the axial cladding temperature distribution at various times for each test. The predicted values are the solid lines, and the measured average bundle temperatures are represented by the squares. As the inlet flow is increased, the following trends are evident.

[

][a,c]

[

]a,c

There are two energy flows to the vapor which affect its temperature as it flows towards the hot spot; heat transfer to the vapor from the wall (heating the vapor), and evaporation of droplets (adding saturated vapor and cooling the vapor). The evaporation is from two sources: heat transfer from vapor to liquid, and evaporation of liquid from heat transfer directly partitioned to the liquid from the wall. Figures 24.6.4-14 to 24.6.3-19 show the WCOBRA/TRAC-TF2 calculated vapor fraction and heat flux to the vapor and liquid for Test 148 (low flow) and Test 146 (high flow). The heat transfer regime map used by WCOBRA/TRAC-TF2 is shown in Figure 24.6.3-13. The calculated heat transfer regime is also shown on the figures. [

]a,c

Sensitivity studies were performed on Test Cases 148 and 146, [

]a,c

[ ]a,c
The results are shown in Figures 24.6.3-20 to 24.6.3-27 for Tests 148 and 146. These results indicate that:
[

]a,c

There are several models in WCOBRA/TRAC-TF2 designed to produce a reasonable drop size for blowdown conditions; the models account for the possibility of droplet break up as the liquid flows through the constricted area of the top fuel nozzle and the grids, and (through a critical Weber number), the possibility of droplet break up due to acceleration. [

]a,c

Compensating Errors Found in G-1 Blowdown Tests
[

]a,c

Table 24.6.3-1 G-1 Blowdown Test Conditions

[

] a,c

a,c

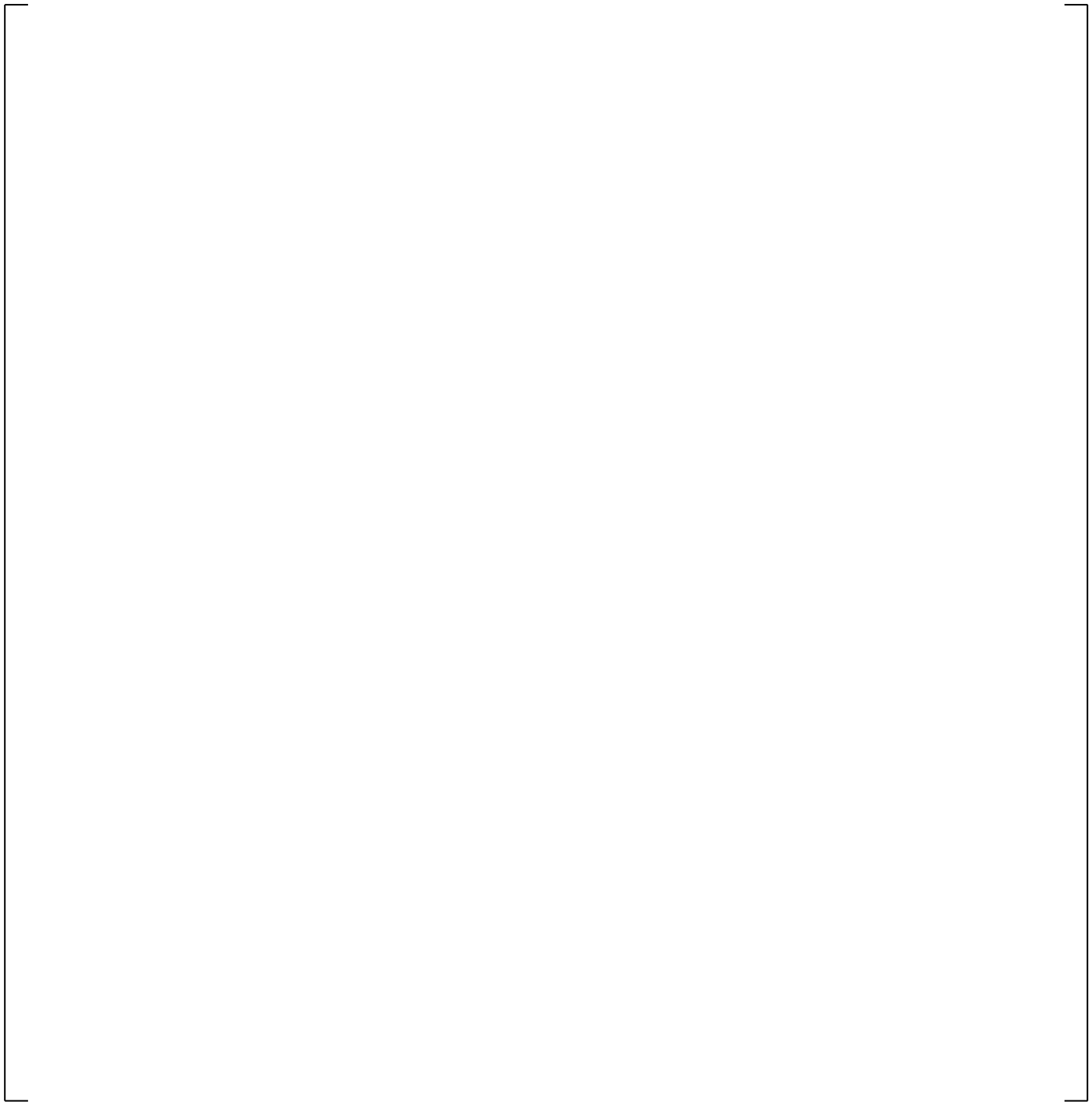

Figure 24.6.3-1 Cladding Temperature During LBLOCA for Three-Loop Plant

a,c

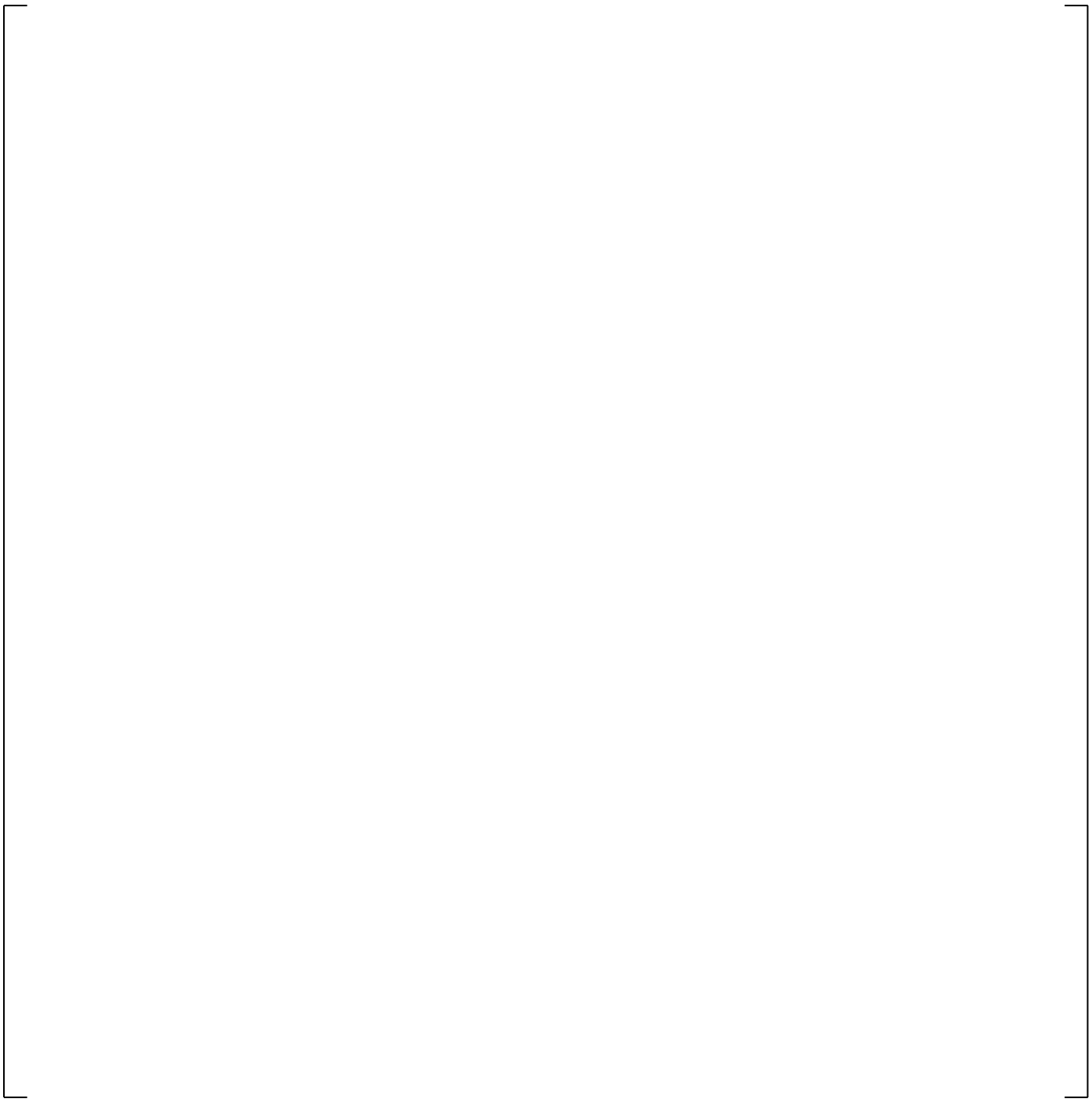

Figure 24.6.3-2 Mass Flux at PCT Location During Blowdown (0-30 Seconds)

a,c

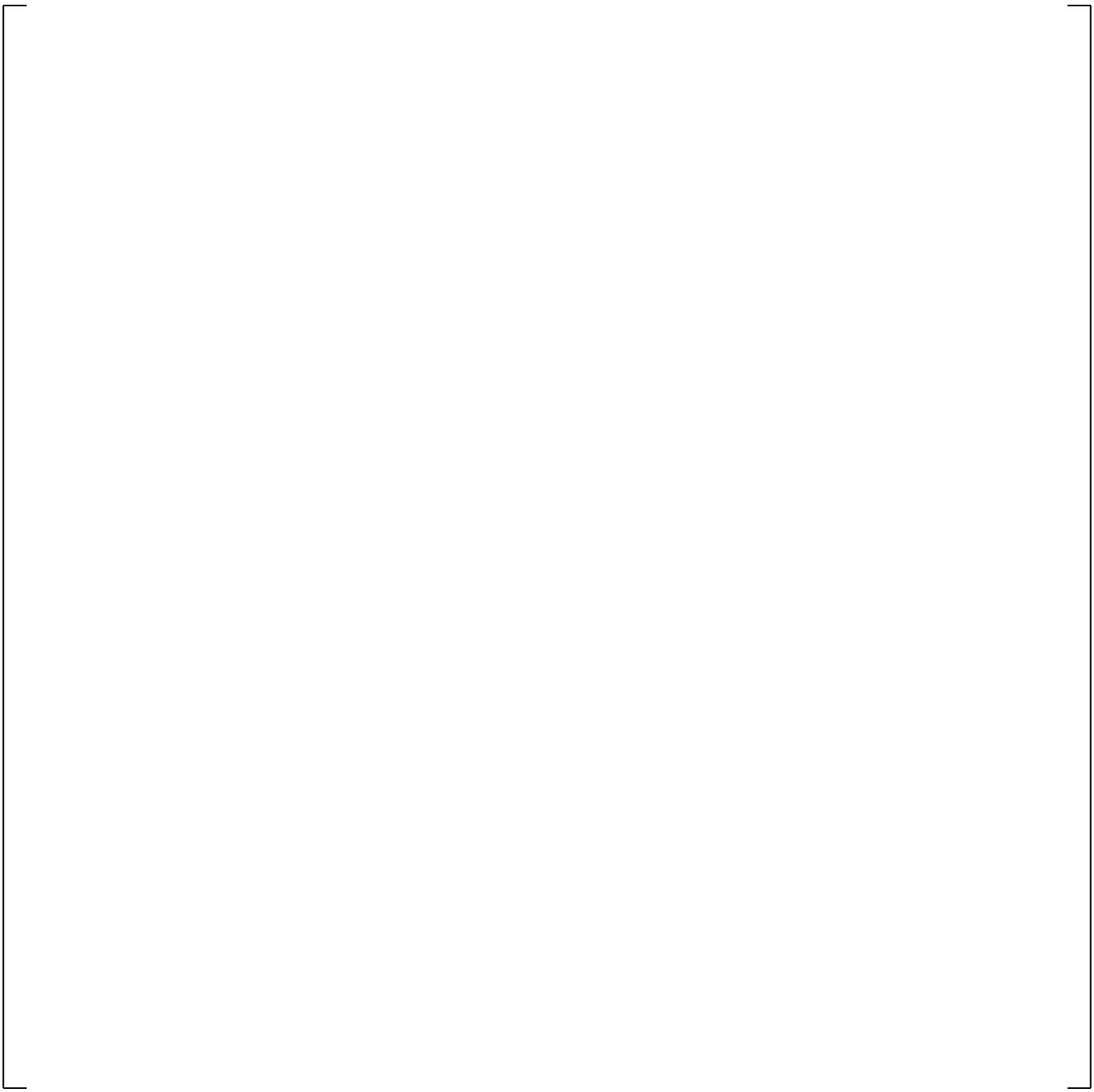

Figure 24.6.3-3 Void Fraction at PCT Location During Blowdown (0-30 Seconds)

a,c

Figure 24.6.3-4 Axial Cladding Temperature Distribution at Blowdown PCT Time (10.5 Seconds after Break)

a,c

Figure 24.6.3-5 Axial Cladding Temperature Profile at End of Blowdown Cooling Time (13.5 Seconds after Break)

a,c

Figure 24.6.3-6 Blowdown Cooling Rates for the G 1 Blowdown Heat Transfer Tests

a,c

Figure 24.6.3-7 Cladding Axial Temperature at Start of Test (6 Seconds), 15, 20, 30 Seconds for Test 148

a,c

Figure 24.6.3-8 Cladding Axial Temperature at Start of Test (6 Seconds), 15, 20, 30 Seconds for Test 143

a,c

Figure 24.6.3-9 Cladding Axial Temperature at Start of Test (6 Seconds), 15, 20, 30 Seconds for Test 152

a,c

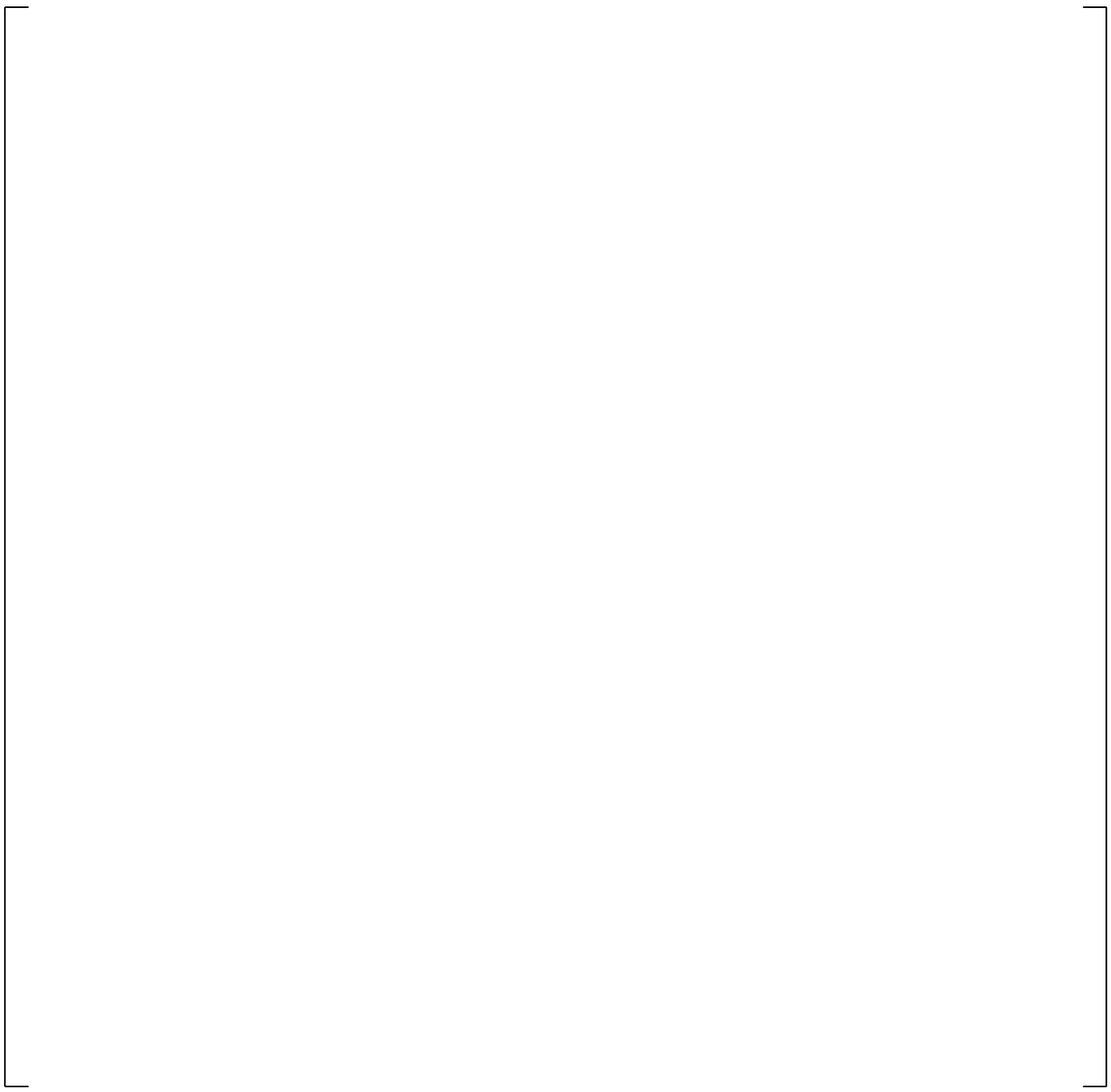

Figure 24.6.3-10 Cladding Axial Temperature at Start of Test (6 Seconds), 15, 20, 30 Seconds for Test 146

a,c

Figure 24.6.3-11 Cladding Axial Temperature at Start of Test (6 Seconds), 15, 20, 30 Seconds for Test 154

a,c

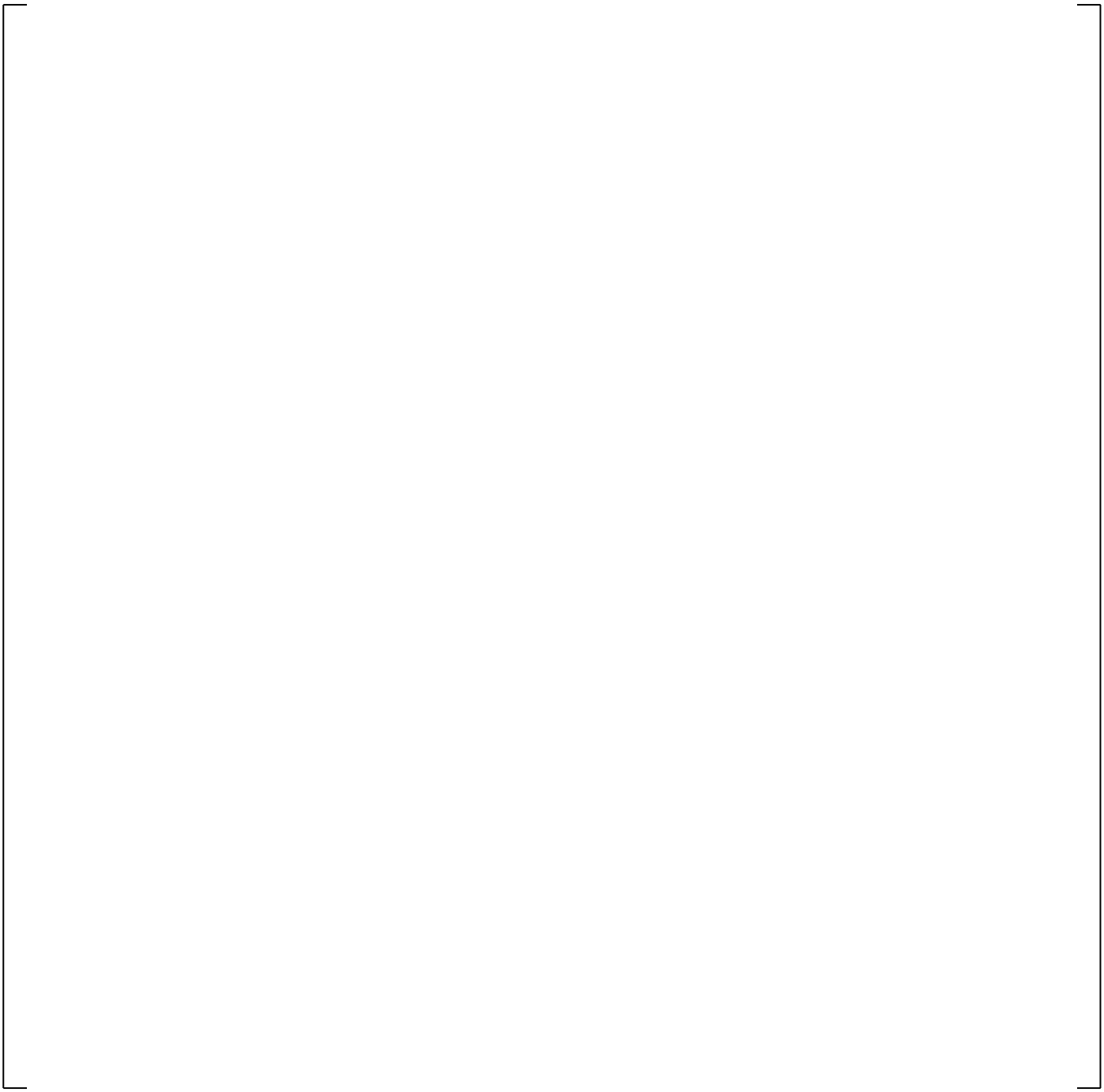

Figure 24.6.3-12 Cladding Axial Temperature at Start of Test (6 Seconds), 15, 20, 30 Seconds for Test 153

a,c

Figure 24.6.3-13 WCOBRA/TRAC-TF2 Heat Transfer Regime Map

a,c

Figure 24.6.3-14 Vapor Fraction at 72-inch Elevation for Test 148

a,c

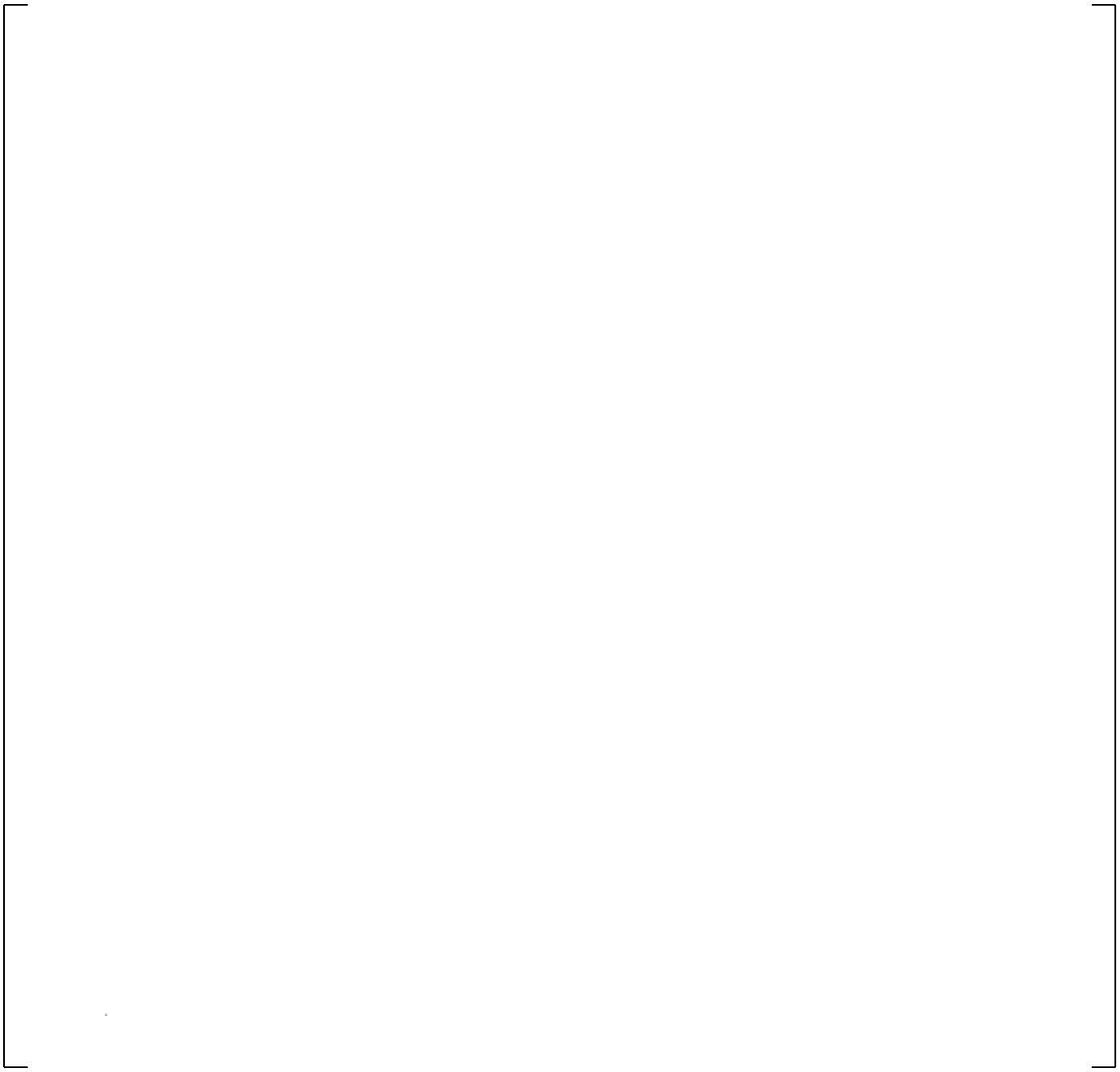

Figure 24.6.3-15 Heat Flux to Vapor at 72-inch Elevation for Test 148

a,c

Figure 24.6.3-16 Heat Flux to Liquid at 72-inch Elevation for Test 148

a,c

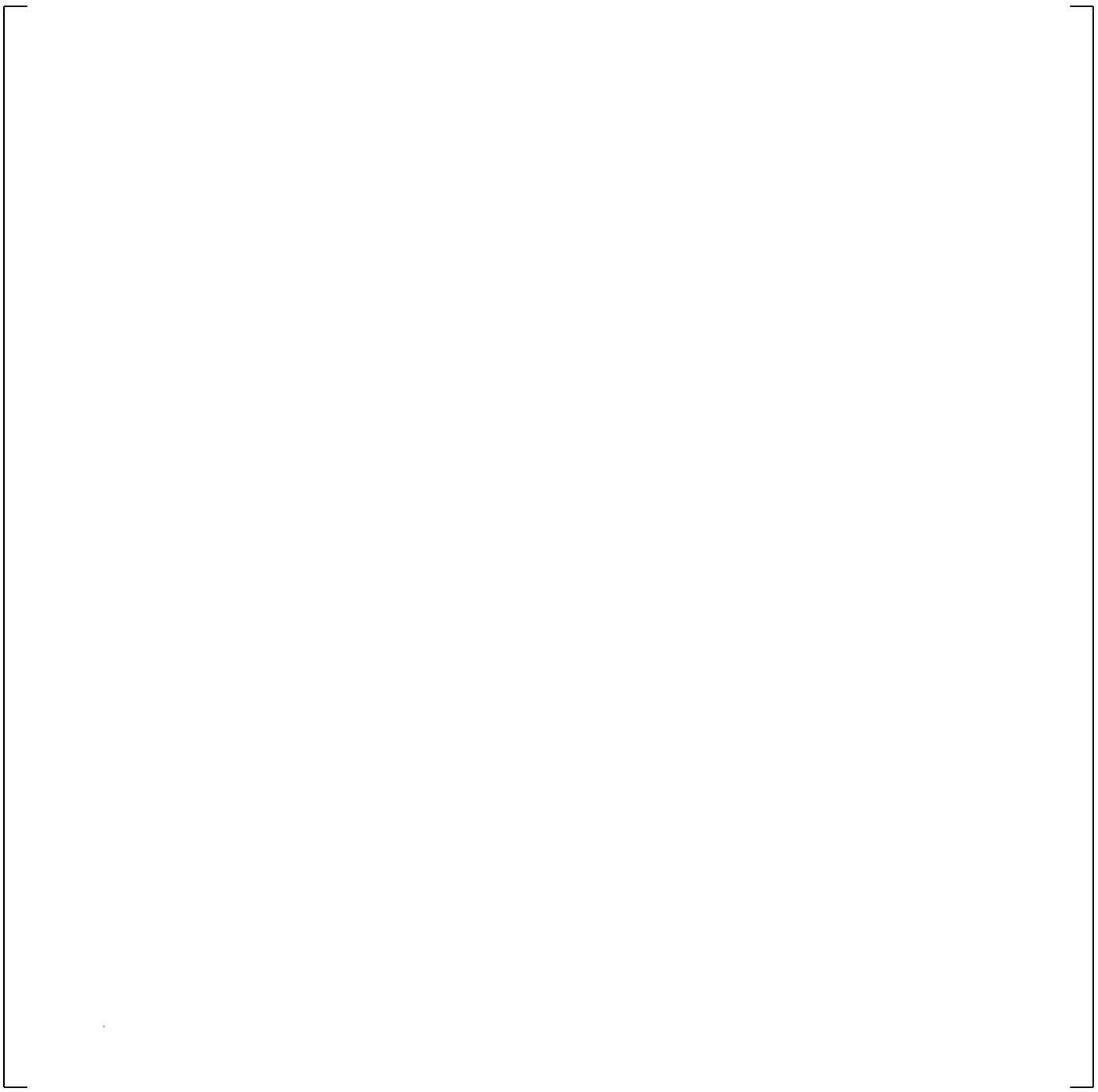

Figure 24.6.3-17 Vapor Fraction at 72-inch Elevation for Test 146

a,c

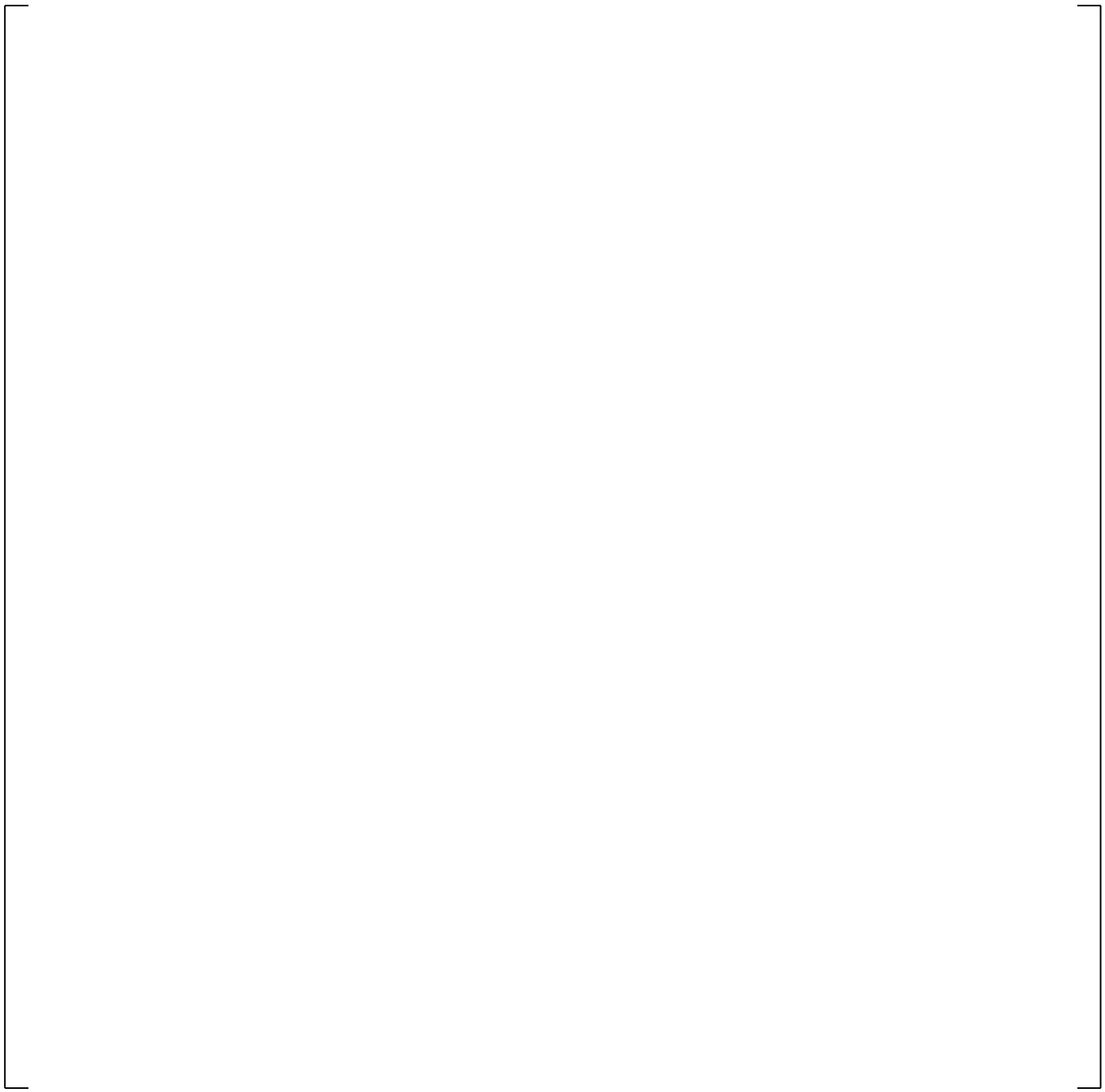

Figure 24.6.3-18 Heat Flux to Vapor at 72-inch Elevation for Test 146

a,c

Figure 24.6.3-19 Heat Flux to Liquid at 72-inch Elevation for Test 146

a,c

Figure 24.6.3-20 Effect of Reduced T_{min} on Cladding Axial Temperature at 26 Seconds for Test 148

a,c

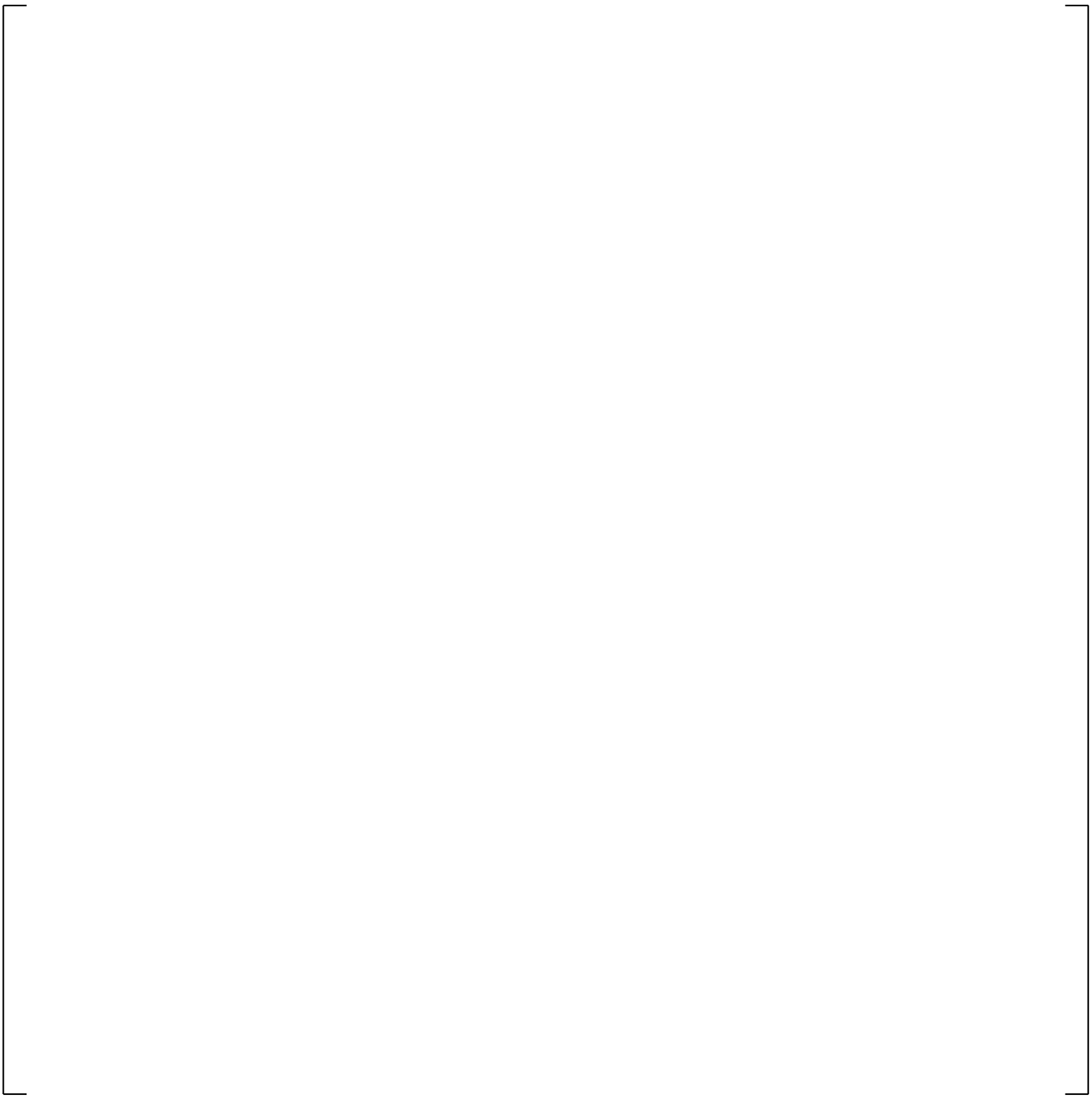

Figure 24.6.3-21 Effect of Reduced T_{min} on Axial Vapor Temperature at 26 Seconds for Test 148

a,c

Figure 24.6.3-22 Effect of Reduced D_{DROP} on Cladding Axial Temperature at 26 Seconds for Test 148

a,c

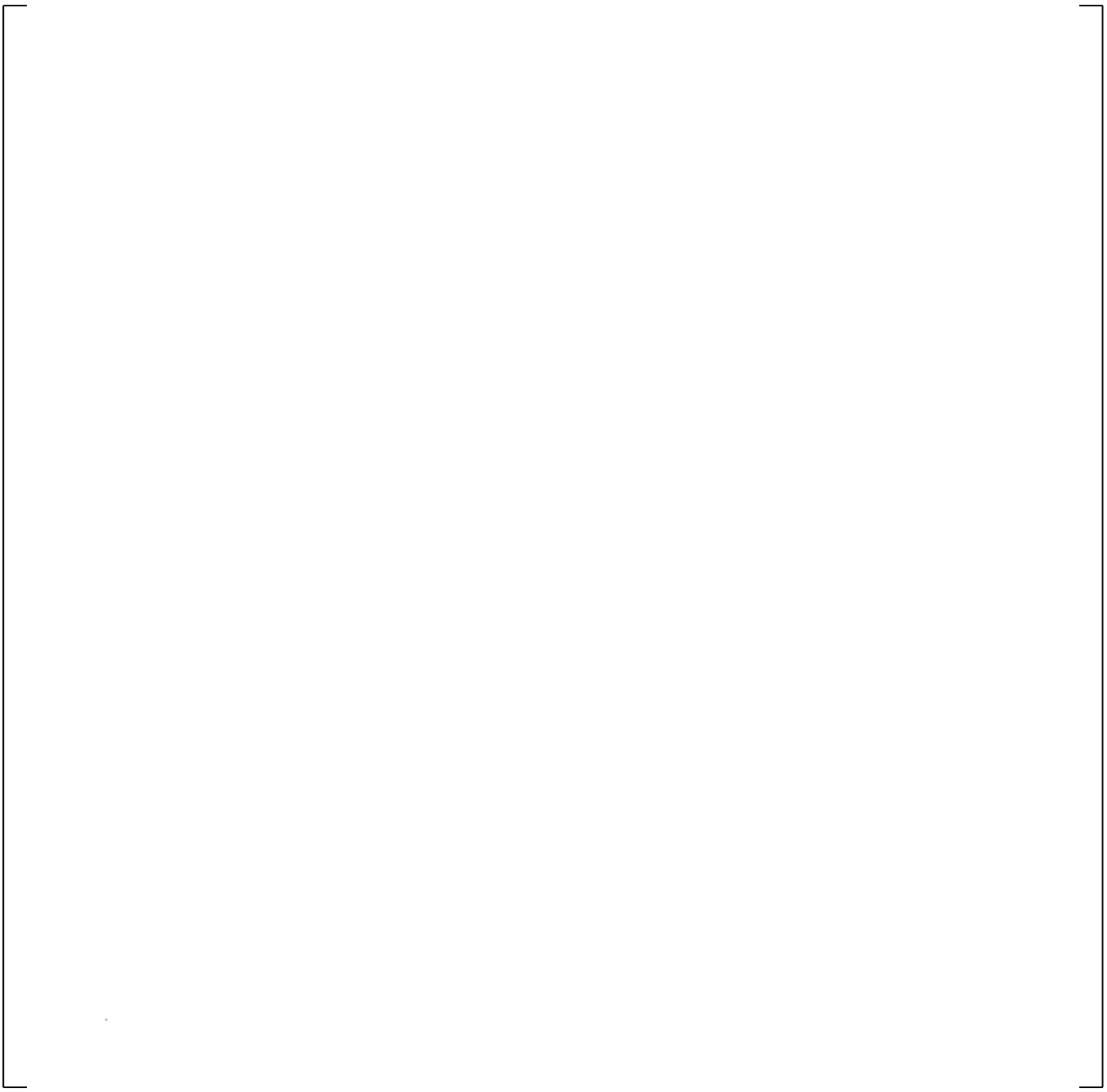

Figure 24.6.3-23 Effect of Reduced D_{DROP} on Axial Vapor Temperature at 26 Seconds for Test 148

a,c

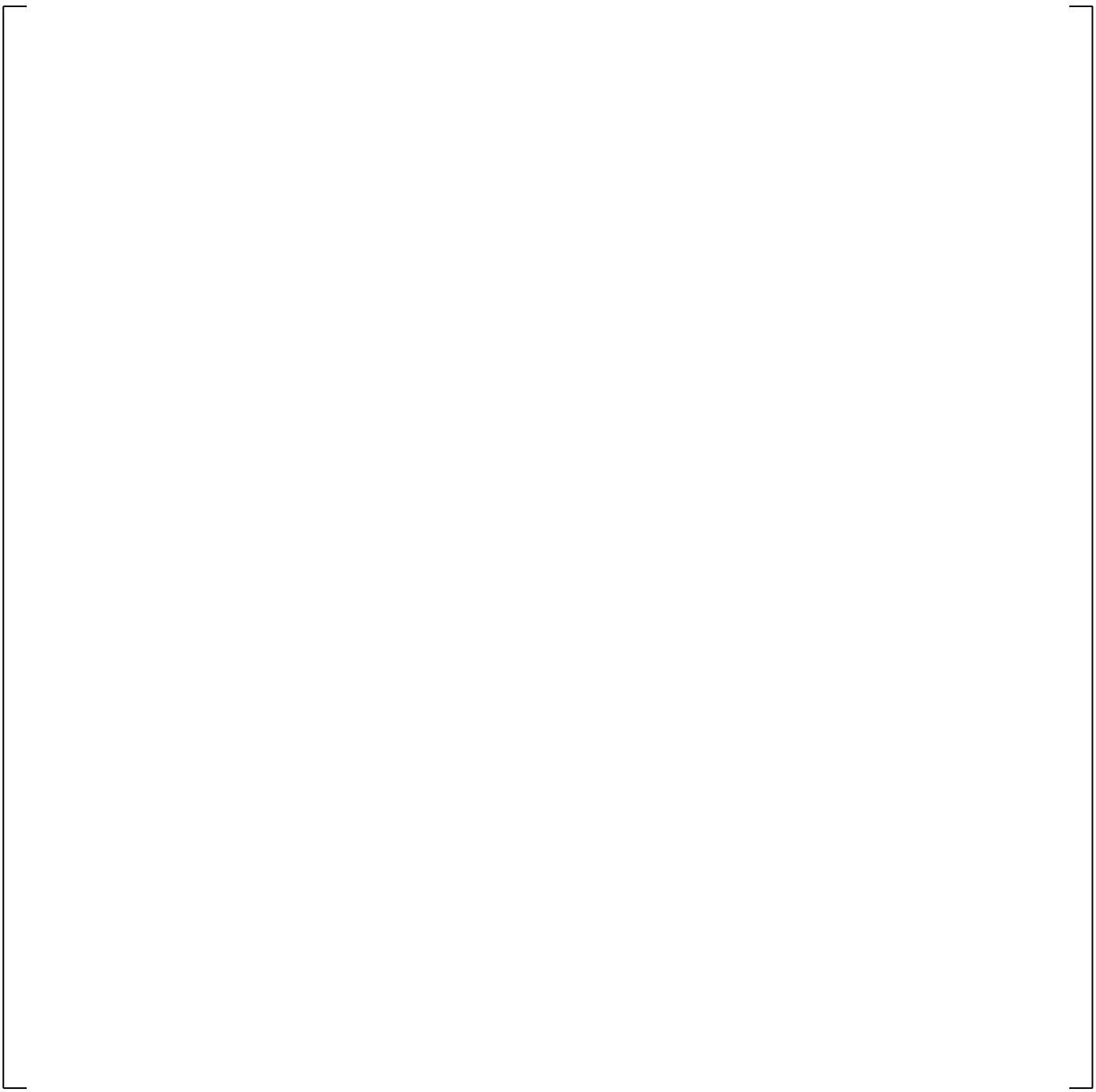

Figure 24.6.3-24 Effect of Reduced T_{min} on Cladding Axial Temperature at 22 Seconds for Test 146

a,c

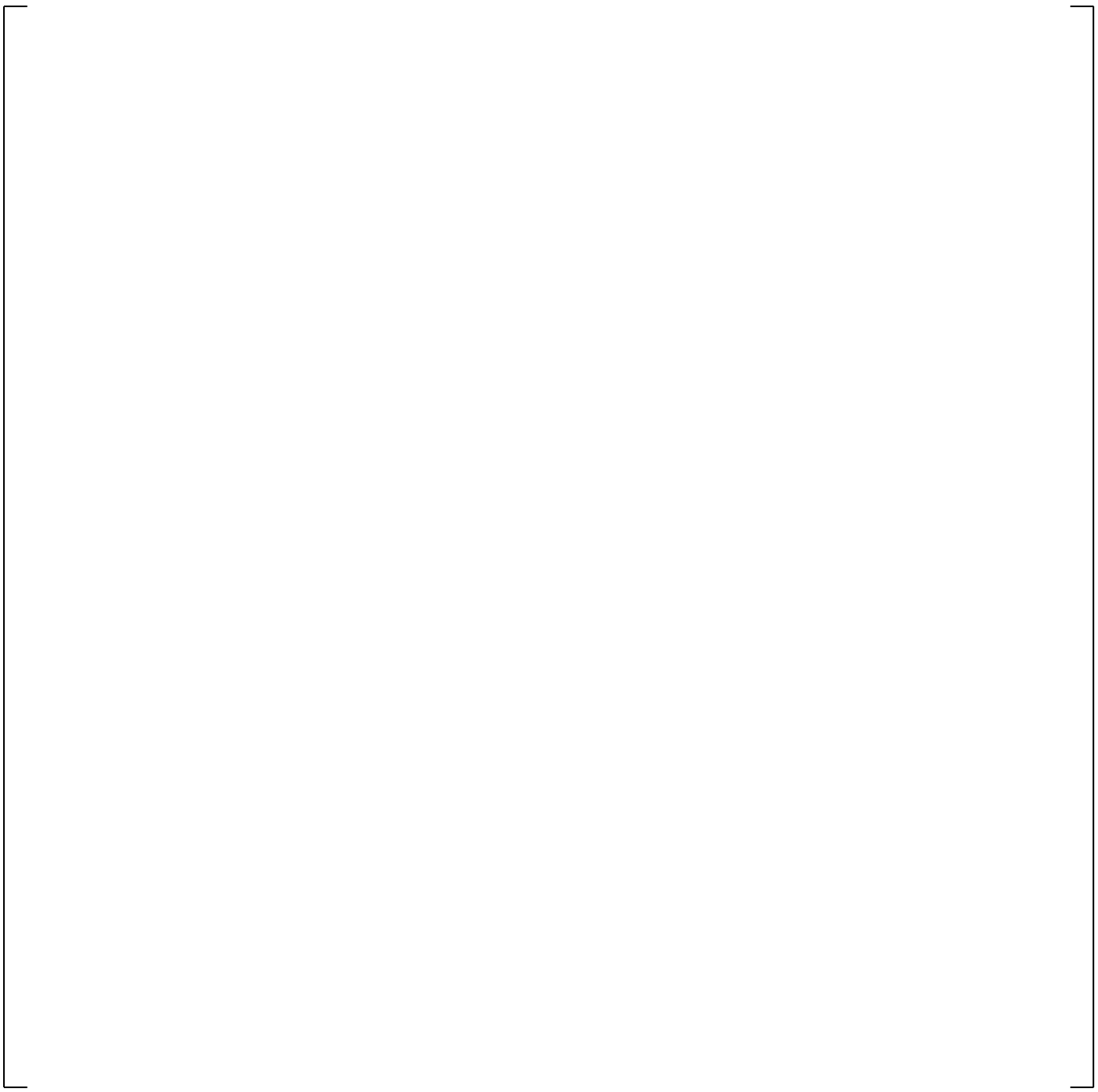

Figure 24.6.3-25 Effect of Reduced T_{min} on Axial Vapor Temperature at 22 Seconds for Test 146

a,c

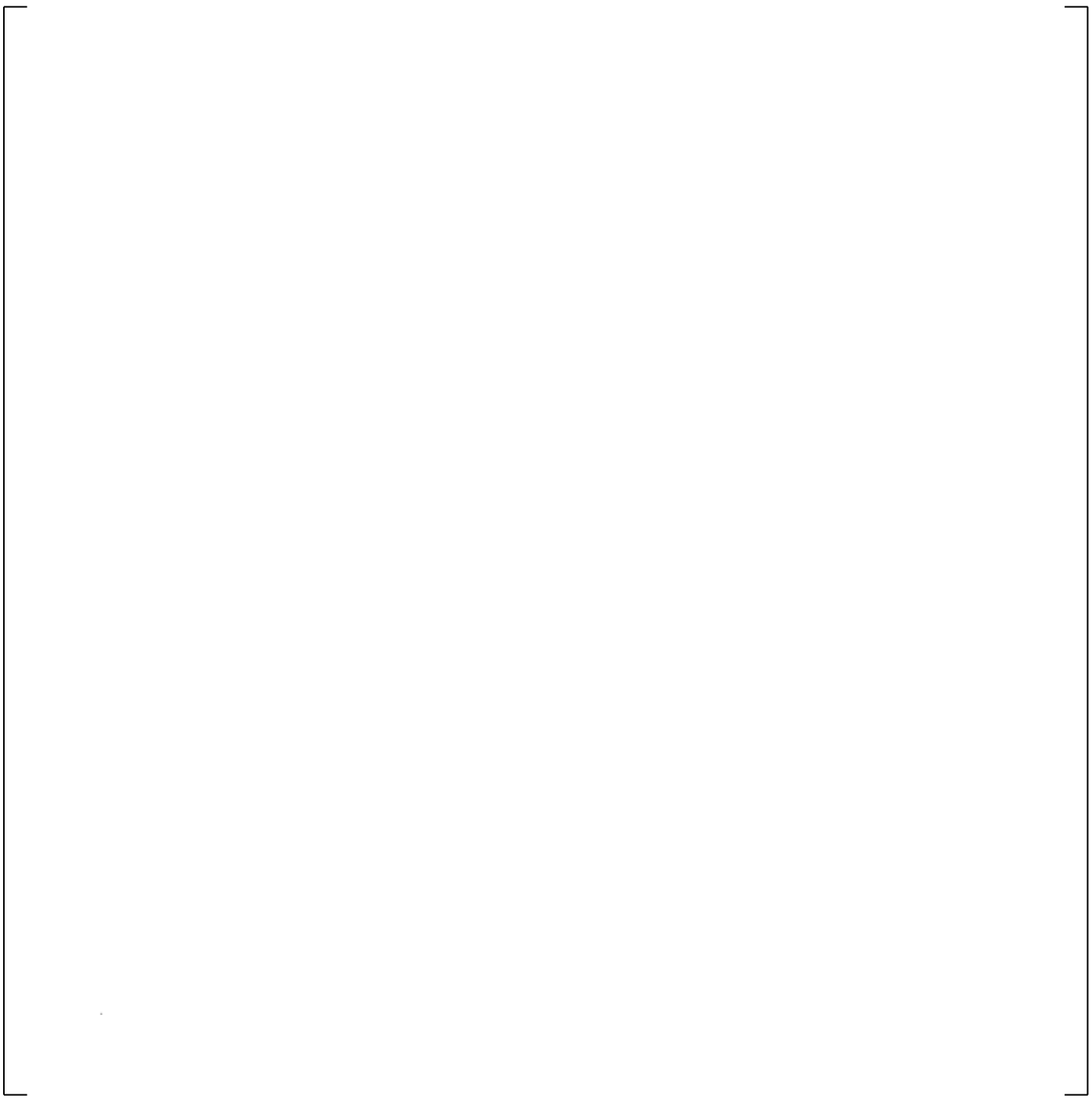

Figure 24.6.3-26 Effect of Reduced D_{DROP} on Cladding Axial Temperature at 22 Seconds for Test 146

a,c

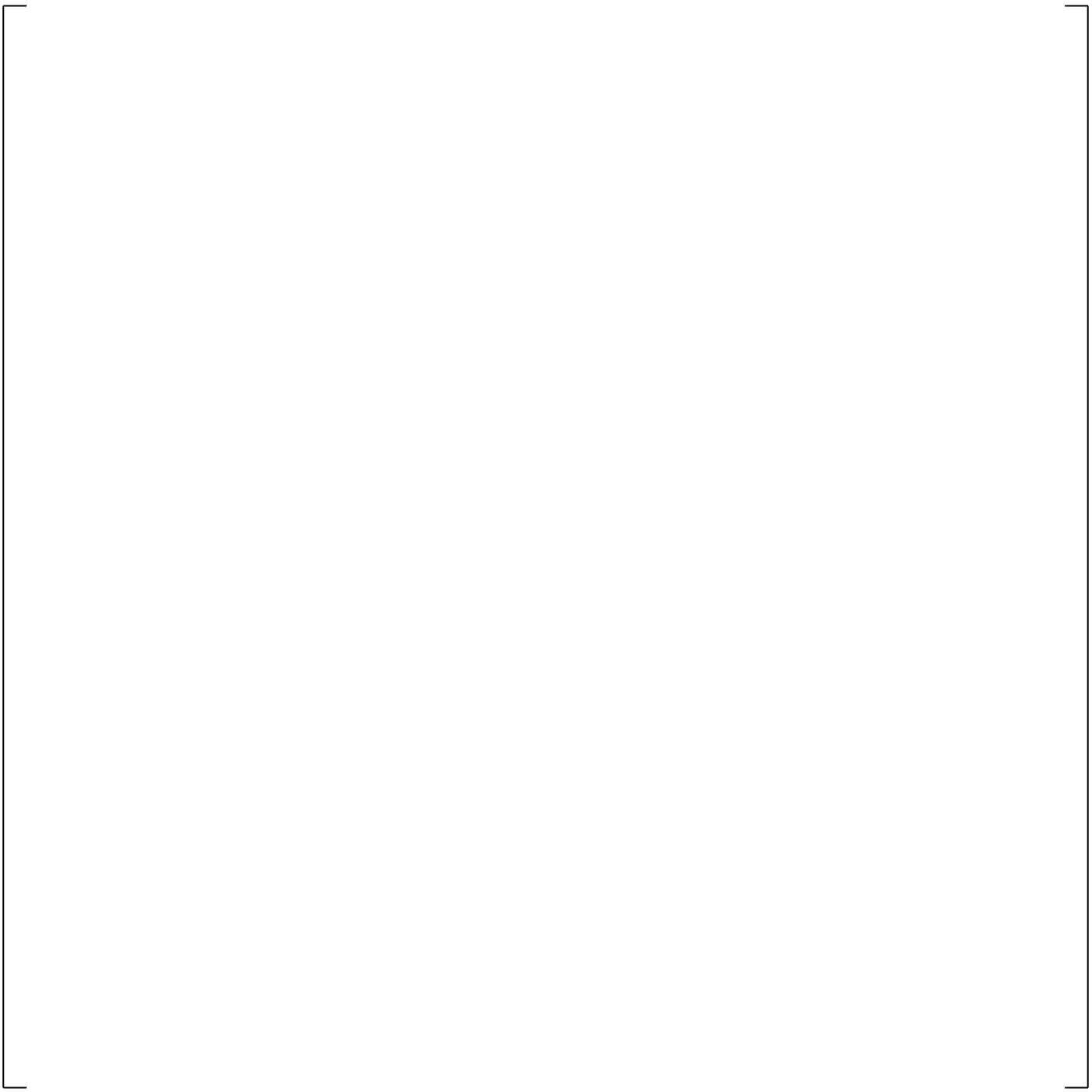

Figure 24.6.3-27 Effect of Reduced D_{DROP} on Axial Vapor Temperature at 22 Seconds for Test 146

24.6.4 FLECHT-SEASET 31504 Reflood Test Simulation

FLECHT-SEASET Test 31504 was evaluated for compensating error. **[**

][a,c]

Axial profiles at **[**

][a,c]

[

]a,c

The evaluation of FLECHT-SEASET Test 31504 showed that [

]a,c

a,c

Figure 24.6.4-1 Cladding Temperature (TCLAD) vs. Time at 6 ft for FLECHT-31504

a,c

Figure 24.6.4-2 TCLAD vs. Time at 9.3 ft for FLECHT-31504

a,c

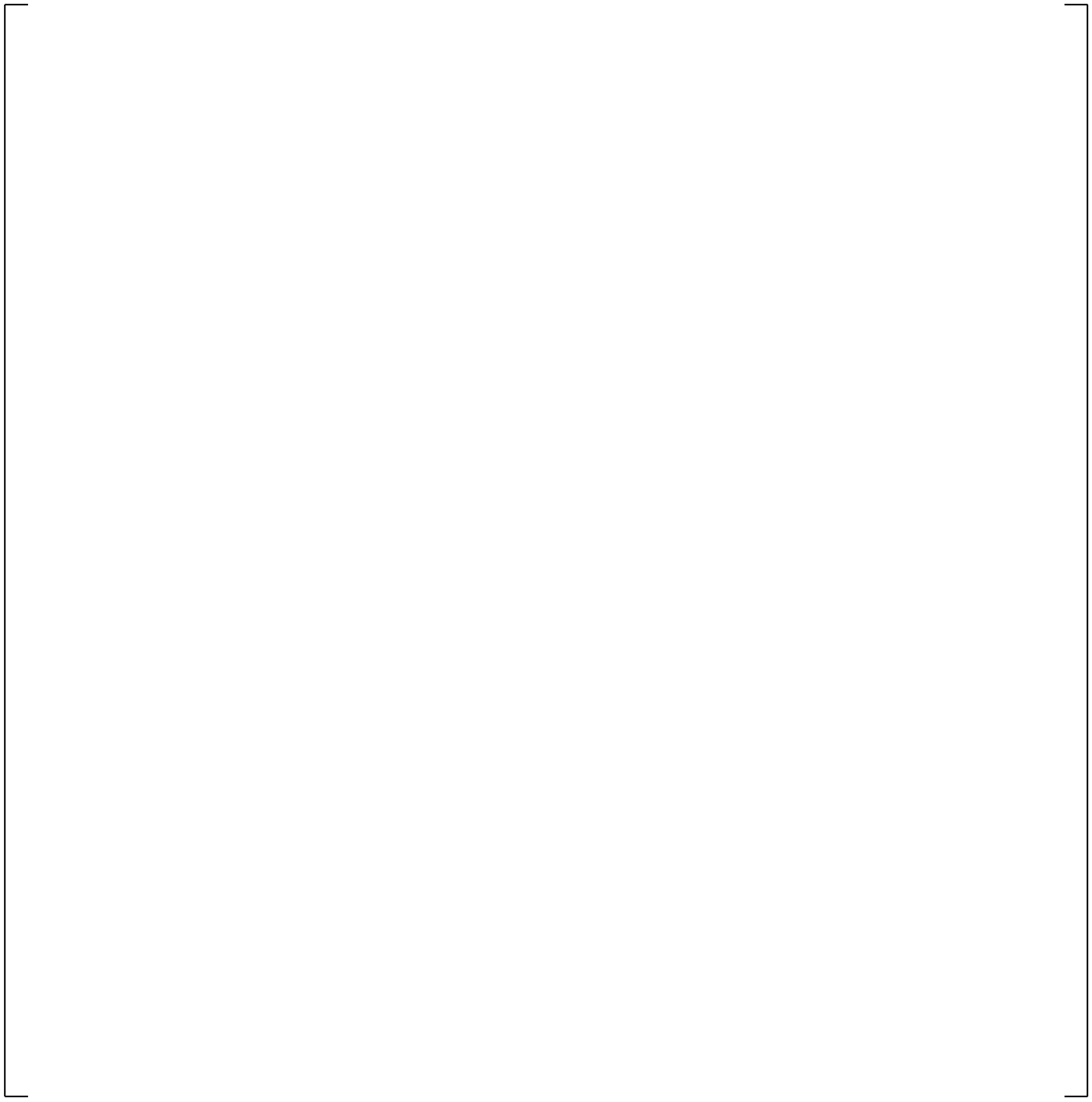

Figure 24.6.4-3 Lower DP vs. Time for FLECHT-31504

a,c

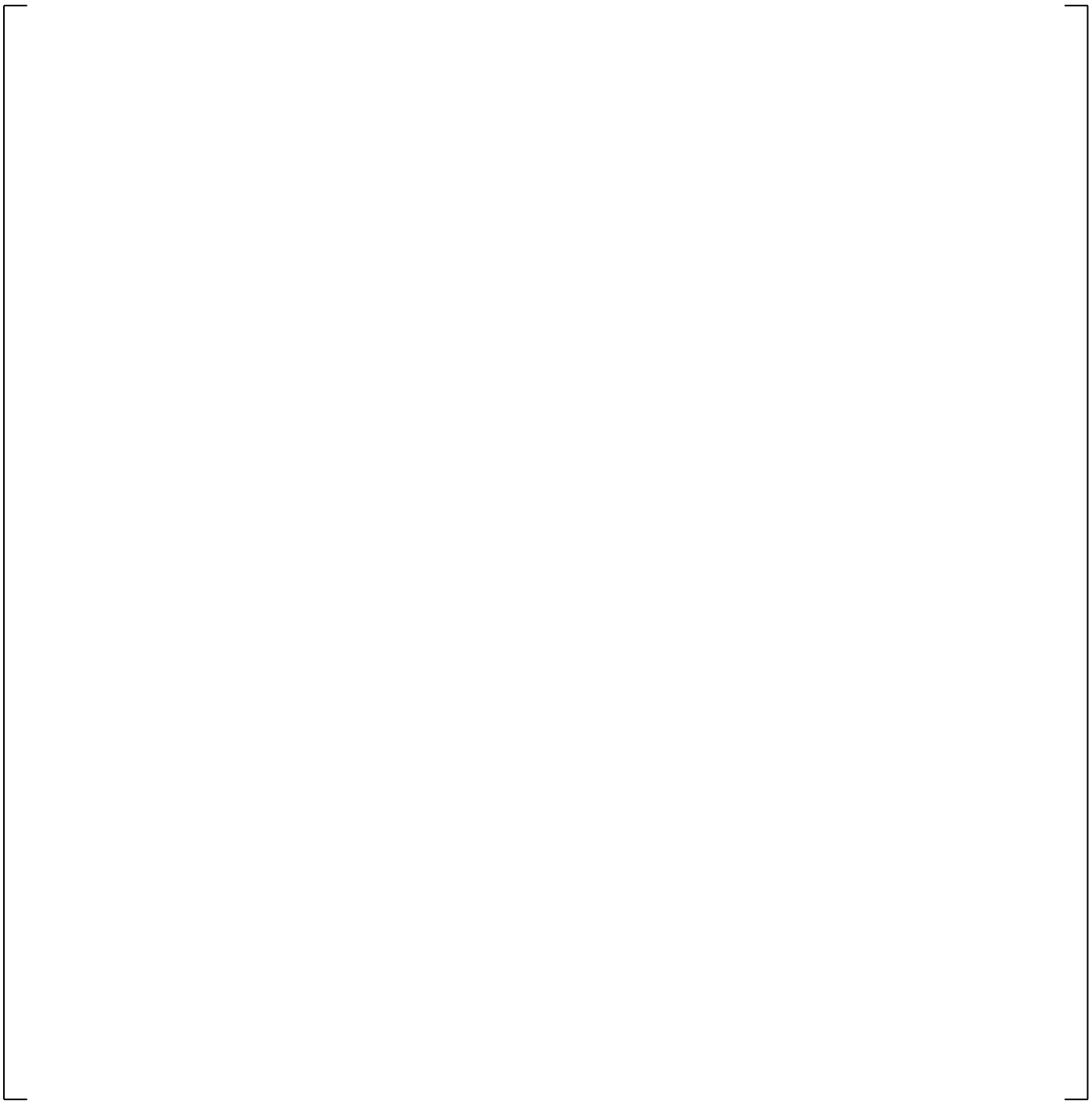

Figure 24.6.4-4 Upper DP vs. Time for FLECHT-31504

a,c

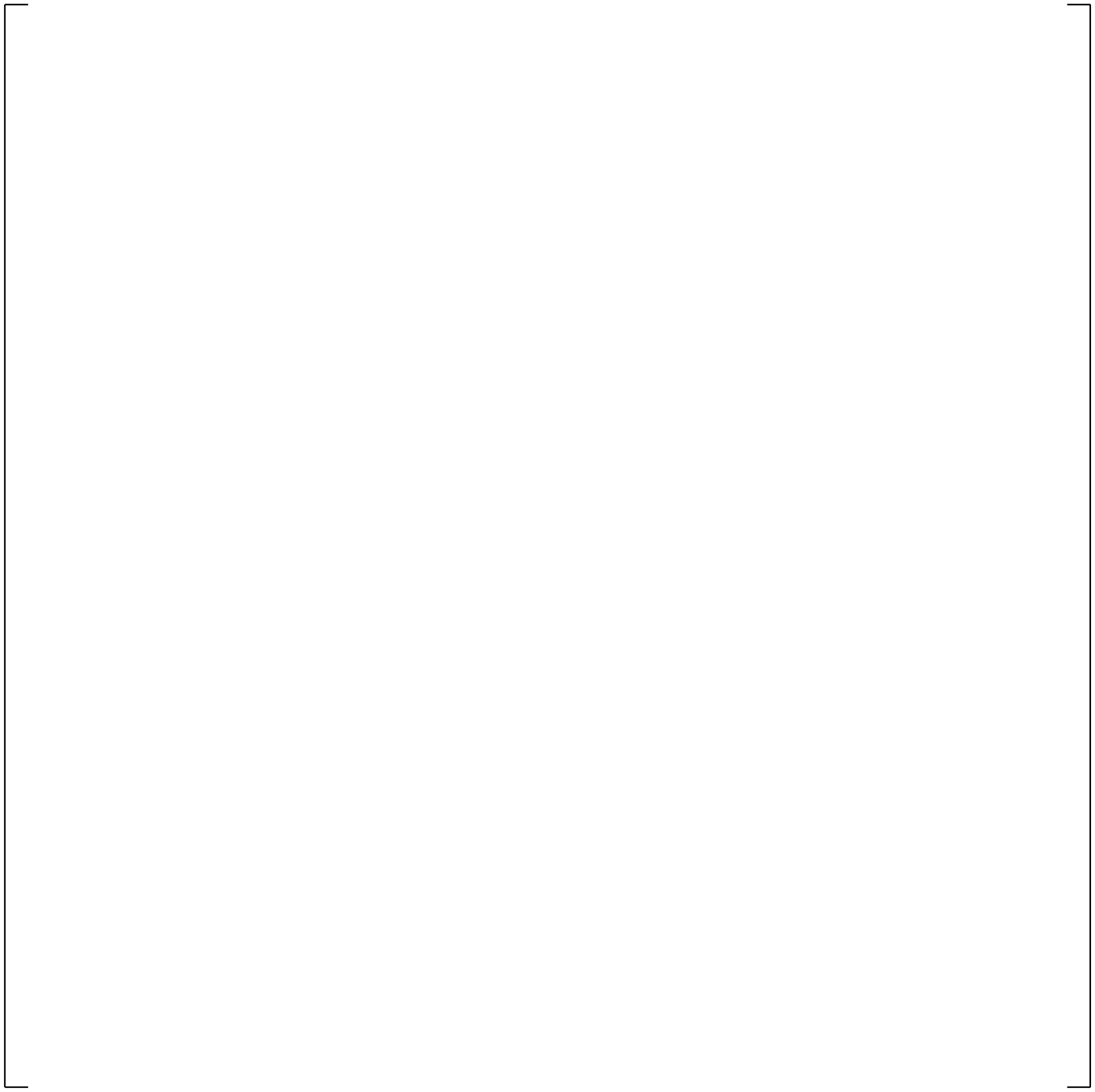

Figure 24.6.4-5 Quench Front Elevation vs. Time for FLECHT-31504

a,c

Figure 24.6.4-6a Vapor Temperature Profile Prediction at 200 Seconds in FLECHT-31504

a,c

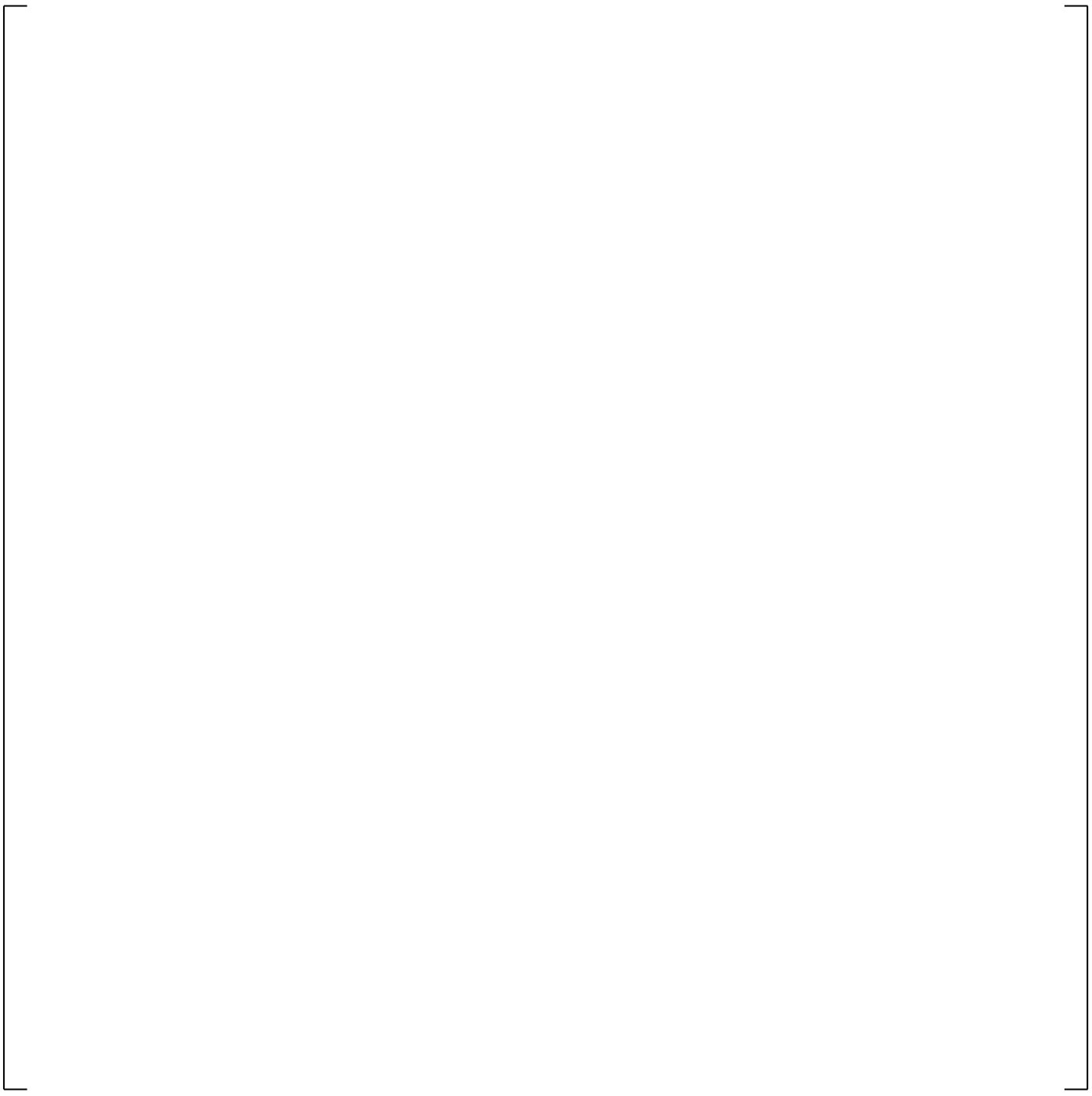

Figure 24.6.4-6b Vapor Temperature Profile Prediction at 290 Seconds Compared against Data taken at 200 Seconds

a,c

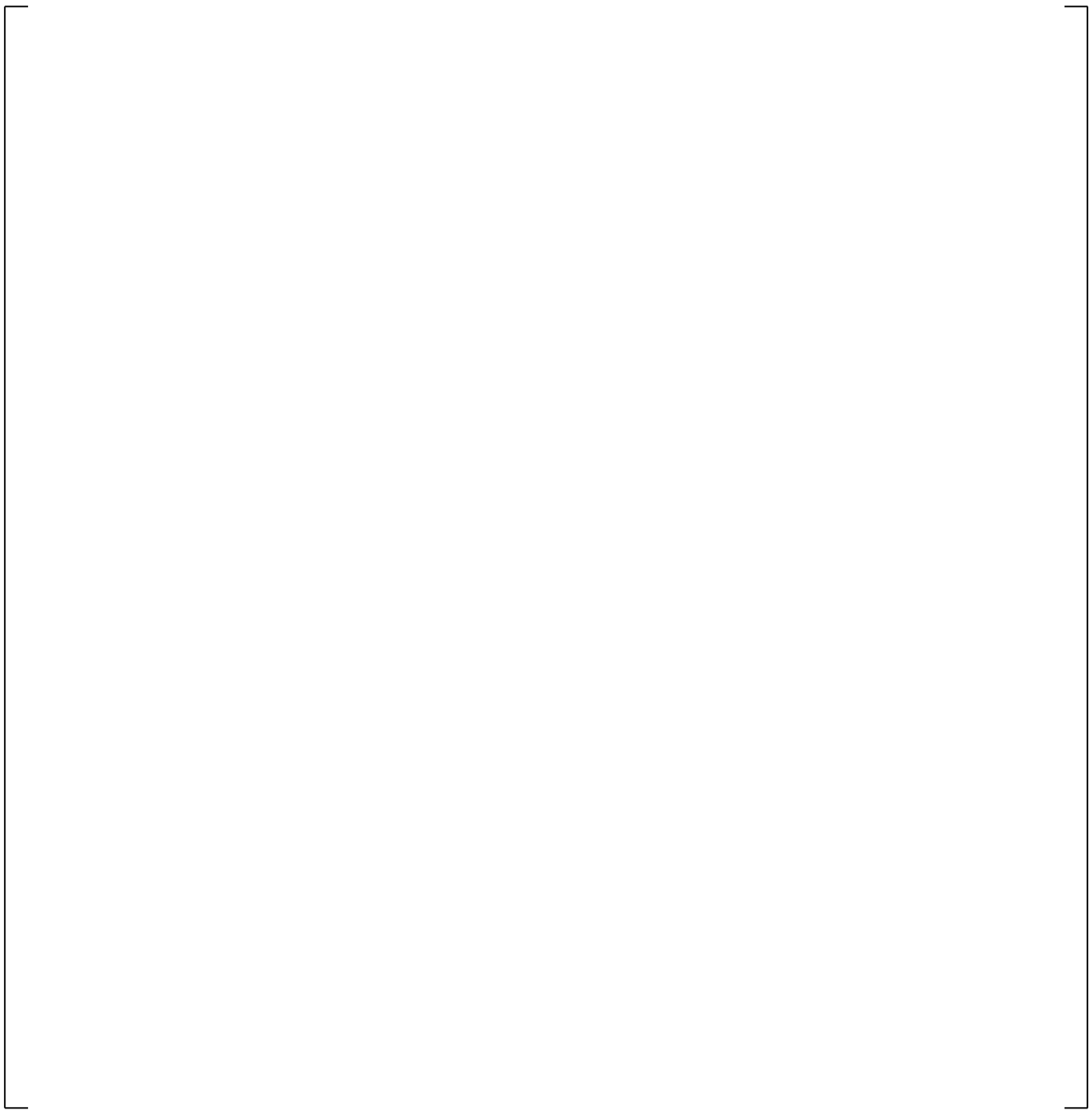

Figure 24.6.4-7 Void Fraction Profile Comparison when the Quench Front is at 60 inches (Prediction at 290 and Data at 200 Seconds) in FLECHT-31504

a,c

Figure 24.6.4-8 Drop Velocity vs. Diameter Comparison at ~1ft above Quench Front (Prediction at 290 and Data at 200~206 Seconds) in FLECHT-31504

a,c

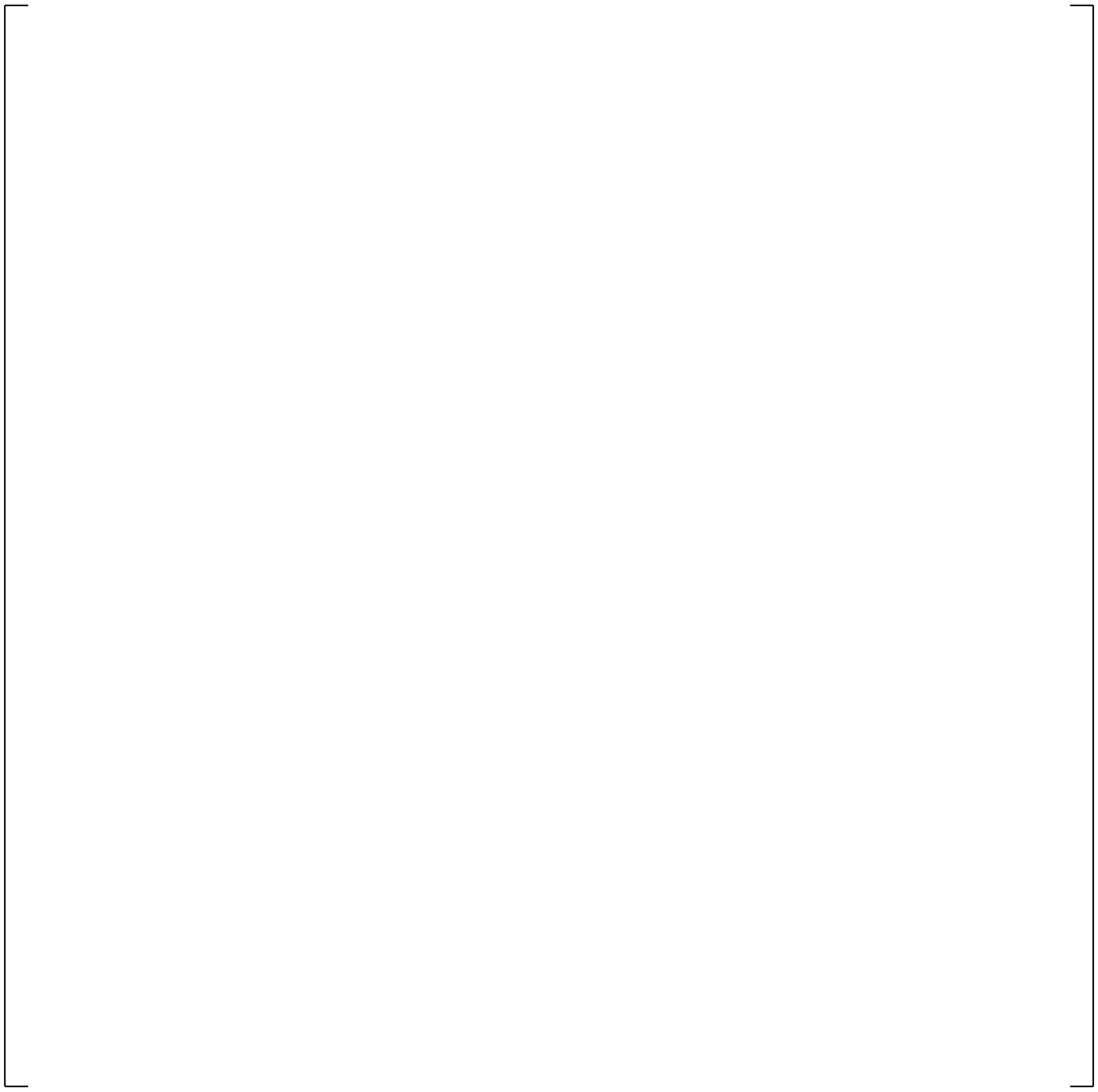

Figure 24.6.4-9 Bundle Vapor Flow Comparison (Prediction at 290 and Data at 200 Seconds) in FLECHT-31504

a,c

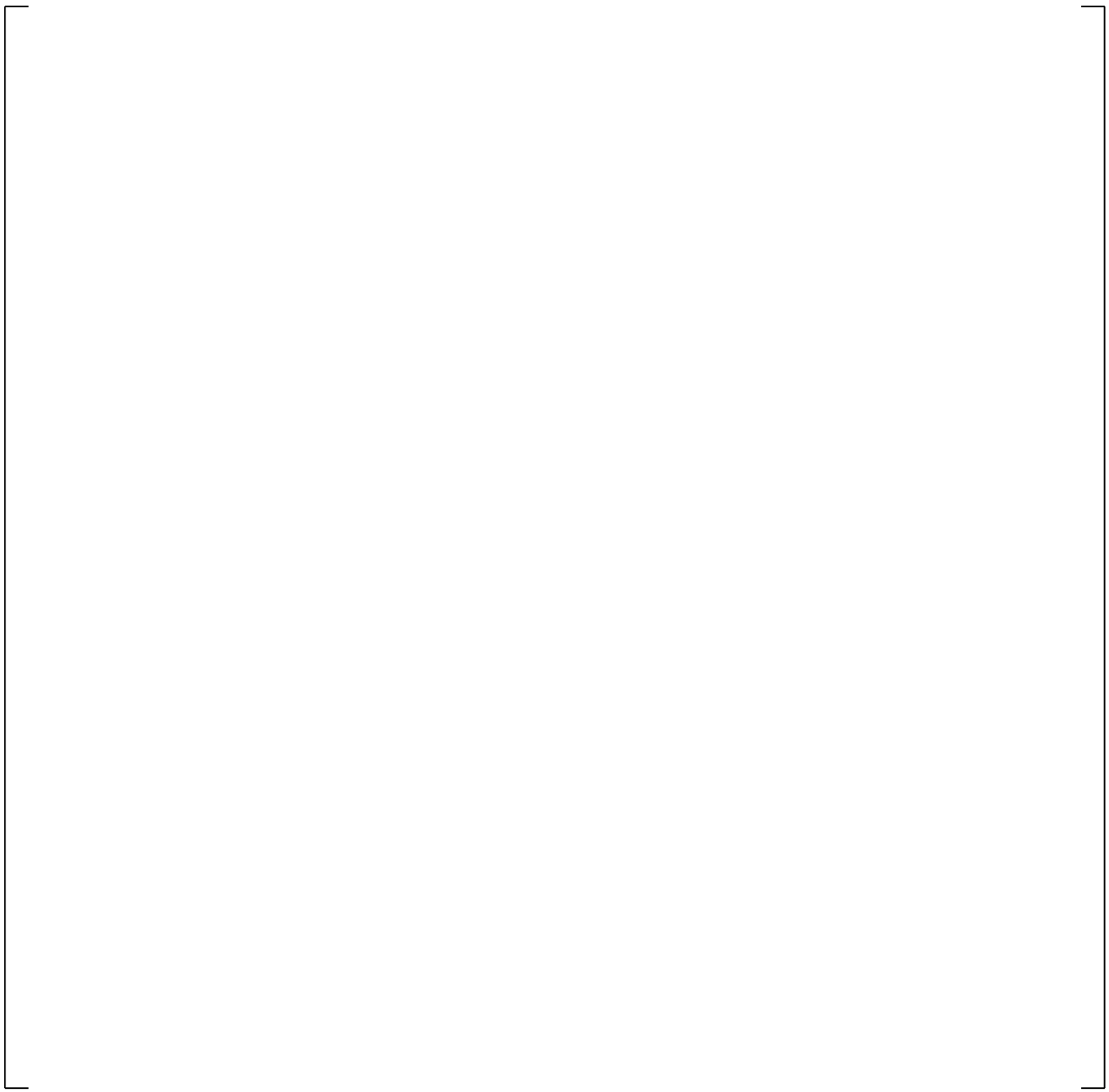

Figure 24.6.4-10 Heat Transfer to Vapor Comparison (Prediction at 290 and Data at 200 Seconds) in FLECHT-31504

a,c

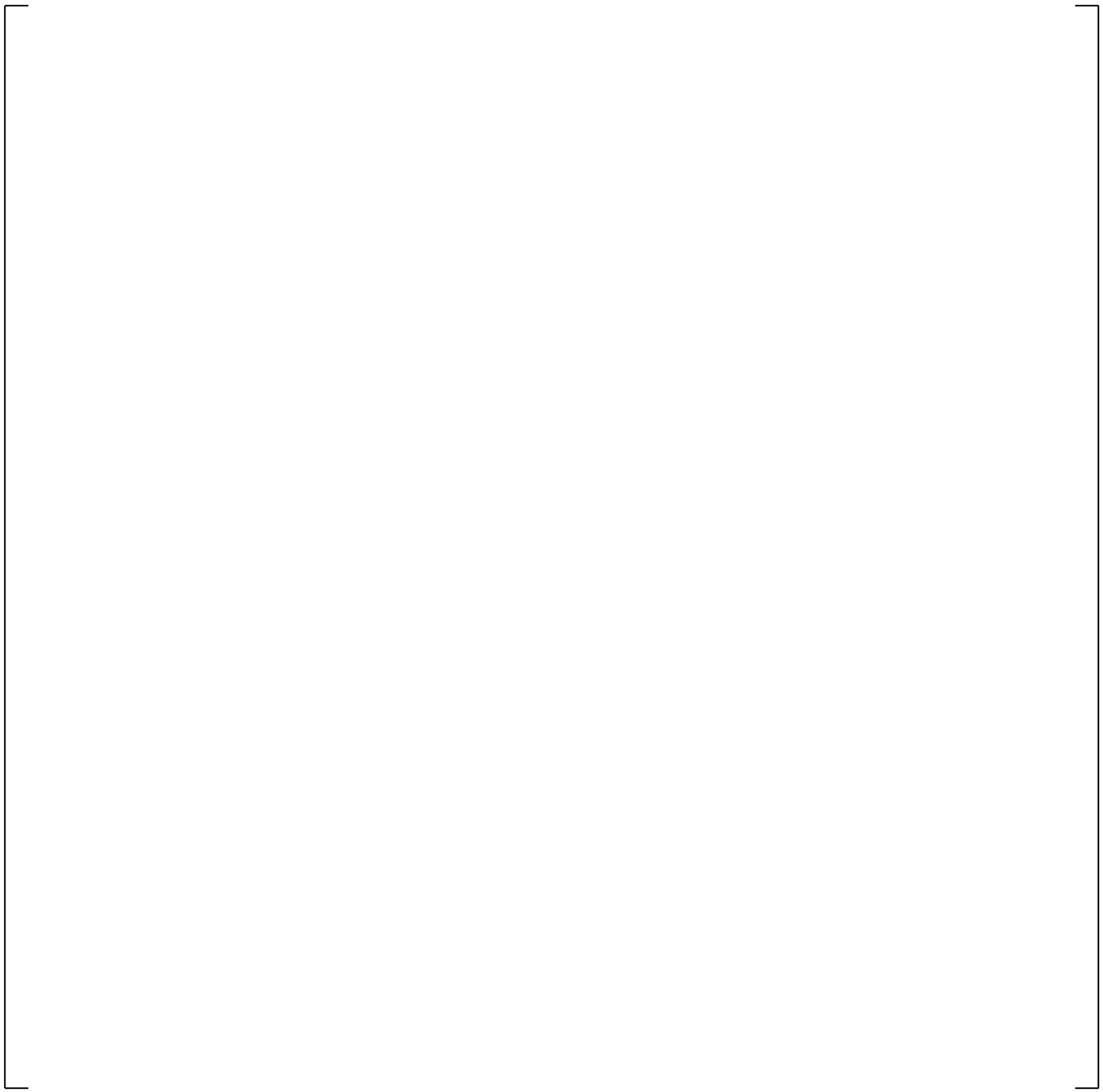

Figure 24.6.4-11 Heat Transfer to Liquid Comparison (Prediction at 290 and Data at 200 Seconds) in FLECHT-31504

a,c

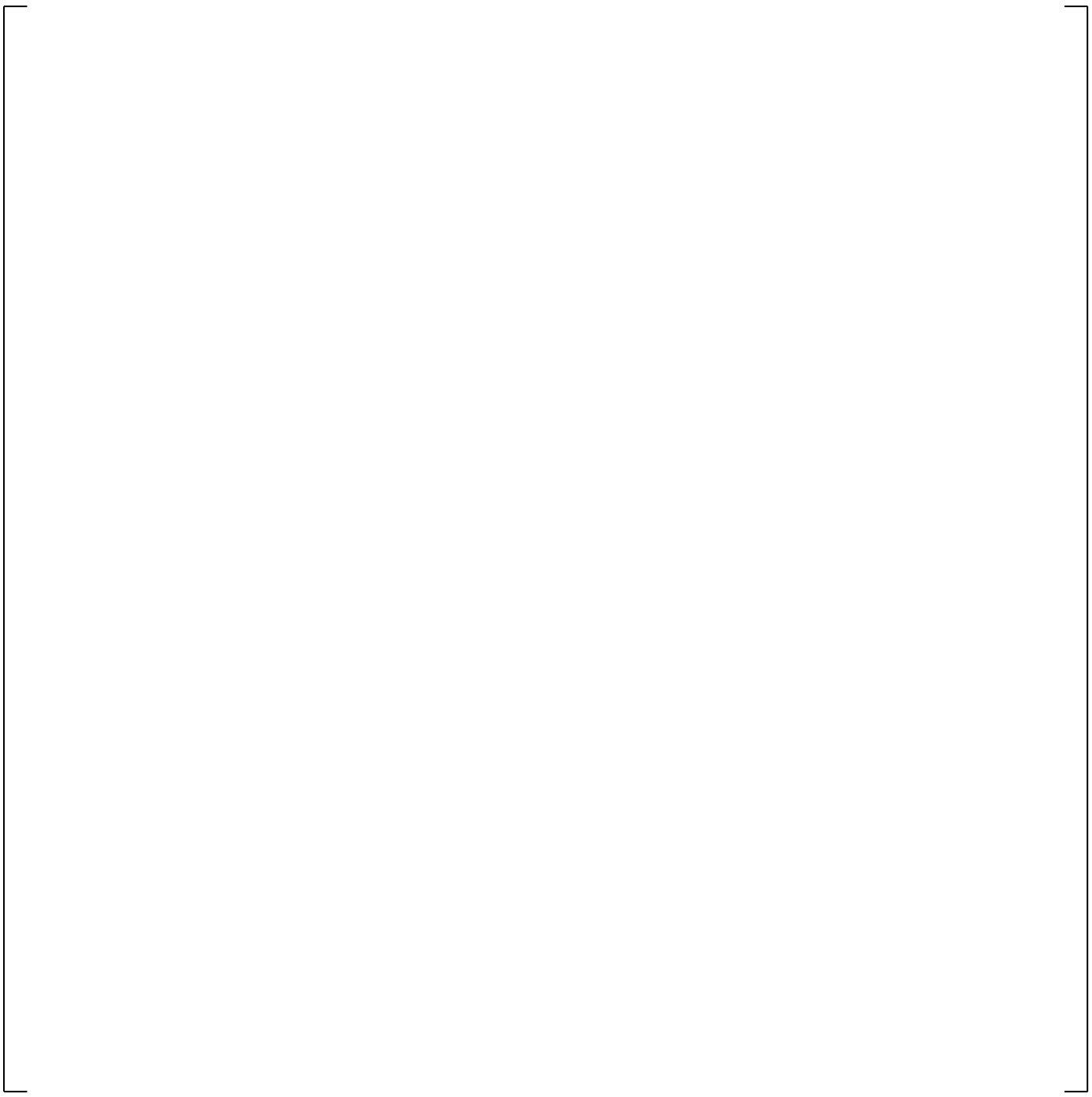

Figure 24.6.4-12 Predicted Fraction of Heat Transfer to Liquid in FLECHT-31504

a,c

Figure 24.6.4-13 Vapor Reynolds Number Comparison (Prediction at 290 and Data at 200 Seconds) in FLECHT-31504

a,c

Figure 24.6.4-14 Vapor Nusselt Number Comparison (Prediction at 290 and Data at 200 Seconds) in FLECHT-31504

24.6.5 FLECHT-SEASET Test 31805

Two forced reflood tests, 31805 and 31701 are examined for the investigation of Void Fraction-Heat Transfer relation. The examination of Test 31805 is presented first. Test 31805 had a very low flooding rate (0.81 in/sec), and Test 31701 had a very high flooding rate (6.1 in/sec). Figure 24.6.5-1 shows the comparison of measured void fraction profile at the PCT time. In terms of the void distribution, the tests are considerably different. Because of the low flooding rate in Test 31805, the axial void profile has a sharp gradient near the quench front, while in Test 31701 there is a significant amount of liquid at all elevations. Note that in Test 31701, only 5 seconds had elapsed since the start of the reflood.

Figure 24.6.5-2 shows a comparison of the predicted and measured axial temperature profile at 100 seconds, which just precedes the PCT time of 108 seconds for the 72-inch elevation for Test 31805. [

]^{a,c}

The predicted and measured axial void fraction profiles at 100 seconds are compared in Figure 24.6.5-5. The agreement is good, although the prediction shows near single phase vapor condition above 6 ft while the measurement indicates some drops at high elevations.

Next, consider the variation of cladding temperatures, heat transfer coefficients, and void fraction in the vicinity of the quench front. Figure 24.6.5-6 shows the measured void fraction at the 5- to 6-ft and 6- to 7-ft elevations. [

]^{a,c}

Figure 24.6.5-7 shows the variation of cladding temperature and void fraction with time at the 6 ft elevation based on the test data. The void fraction is the 6- to 7-ft measurement. Figure 24.6.5-8 shows the variation in heat transfer coefficient and void fraction with time at the same elevation. The individual T/Cs quench over a span of about 40 seconds. The heat transfer coefficients are seen to increase to values typical of nucleate boiling following the quench. Figures 24.6.5-9 and 24.6.5-10 expand the period near the quench times.

[

]^{a,c}

Figures 24.6.5-11 and 24.6.5-12 show the corresponding behavior of cladding temperature and heat transfer coefficient with void fraction based on WCOBRA/TRAC-TF2 prediction. **[**

][a,c]

Figure 24.6.5-13 compares the predicted and measured void fraction for the 6- to 7-ft region of the bundle. **[**

][a,c]

Figures 24.6.5-14 through 24.6.5-17 show the variation of cladding temperature and heat transfer coefficient with void fraction at the 10 ft elevation. **[**

][a,c] Figure 24.6.5-18 compares the predicted and measured void fraction at the 10- to 11-ft region. **[**

][a,c]

Level Swell Considerations

Data recording was continued in the FLECHT-SEASET tests well after bundle quench. Bundle power remained on, and although the power became low late in time, it was sufficient to maintain boiling in much of the bundle. The WCOBRA/TRAC-TF2 simulations were run past the bundle quench time (based on data), and thus simulated part of this post-quench period. A comparison of the predicted and measured void fraction distribution for this period is useful, in that it is not complicated by the entrainment process that accompanies quench.

Figure 24.6.5-19 shows a comparison of the predicted and measured **[**

][a,c]

a,c

Figure 24.6.5-1 Comparison of Measured Void Fraction Distribution Reported for FLECHT-SEASET Tests 31805 and 31701

a,c

Figure 24.6.5-2 TCLAD Profile at 100 Seconds in FLECHT-31805

a,c

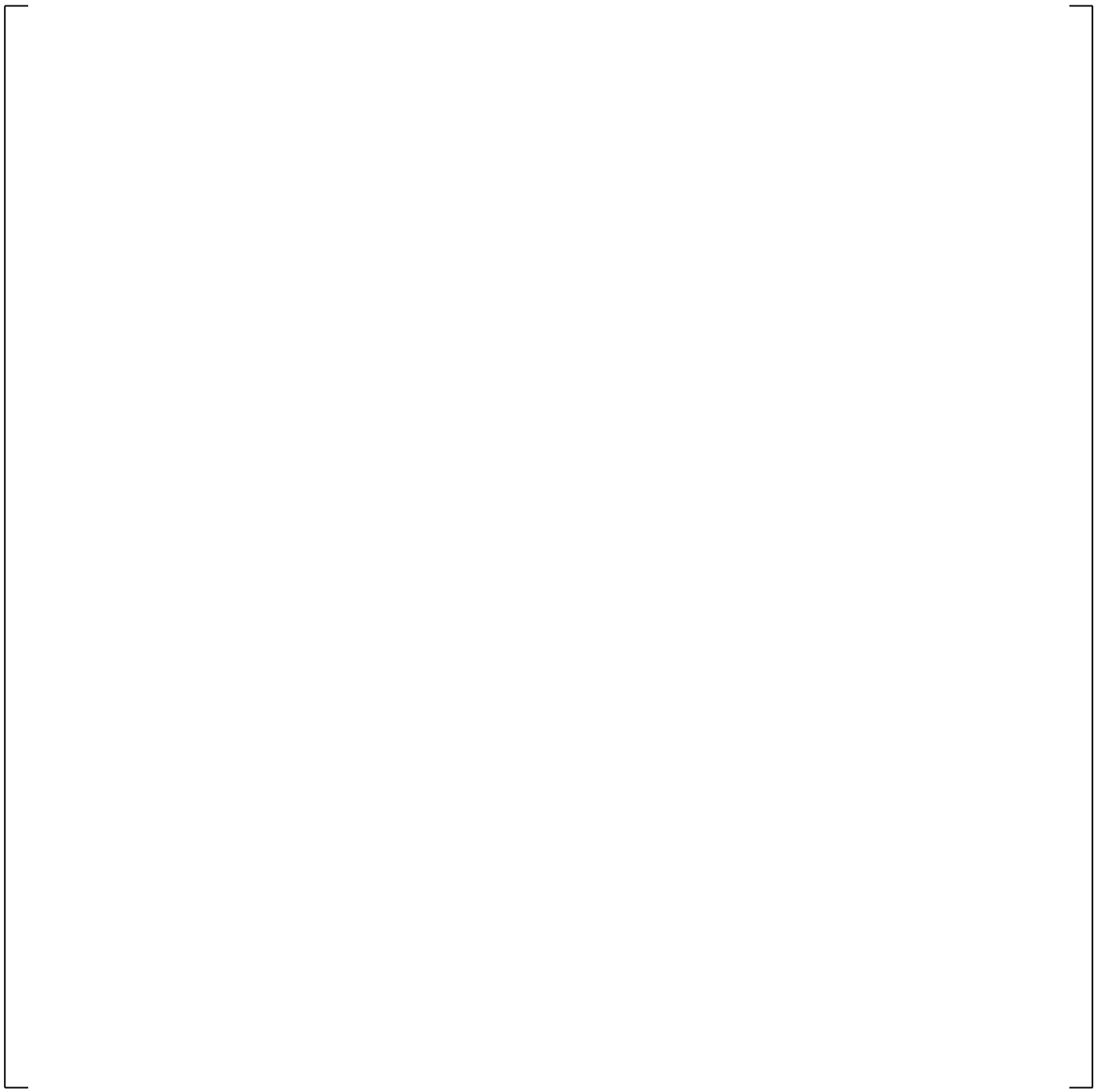

Figure 24.6.5-3 Heat Transfer Coefficient vs. Time at ~6 ft in FLECHT-31805

a,c

Figure 24.6.5-4 Axial Comparison of Predicted and Measured HTC in FLECHT-SEASET 31805

a,c

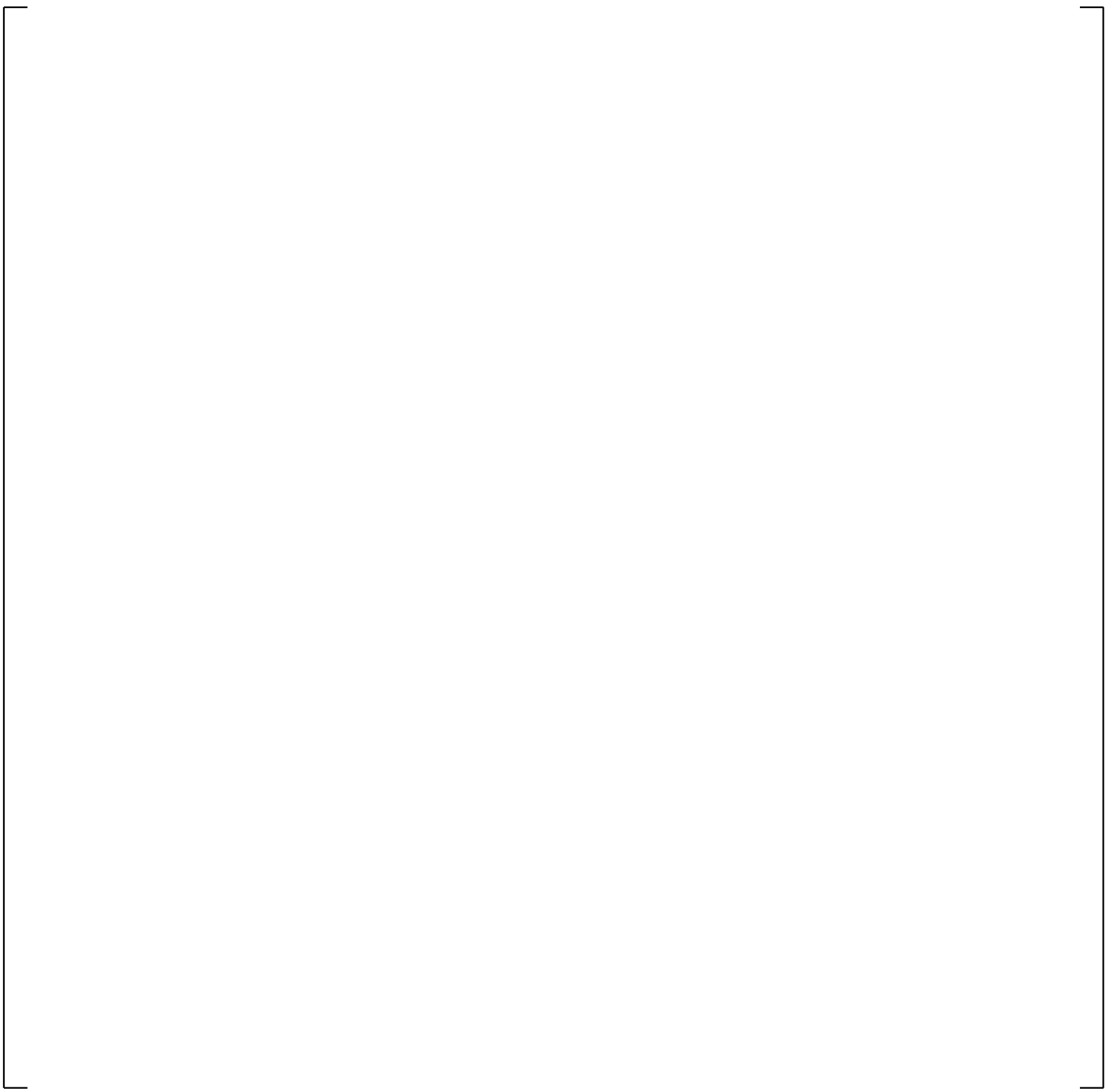

Figure 24.6.5-5 Void Fraction Profile in FLECHT-SEASET 31805

a,c

Figure 24.6.5-6 Measured Void Fraction near 6 ft in FLECHT-SEASET 31805

a,c

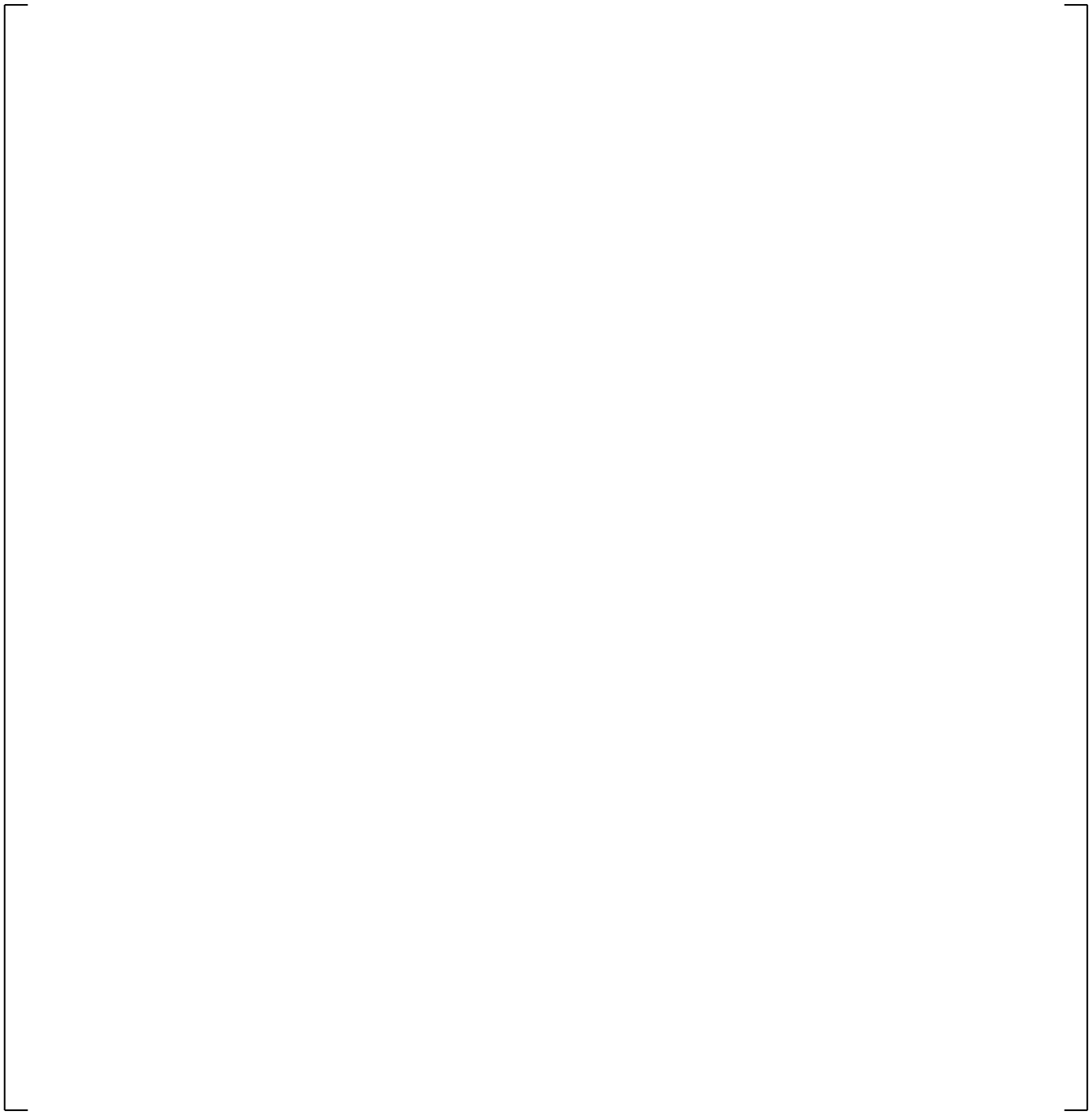

Figure 24.6.5-7 Measured Cladding Temperature, Void Fraction at 6 ft in FLECHT-SEASET 31805 (Only one Legend is shown but all Available Thermocouples are Plotted)

a,c

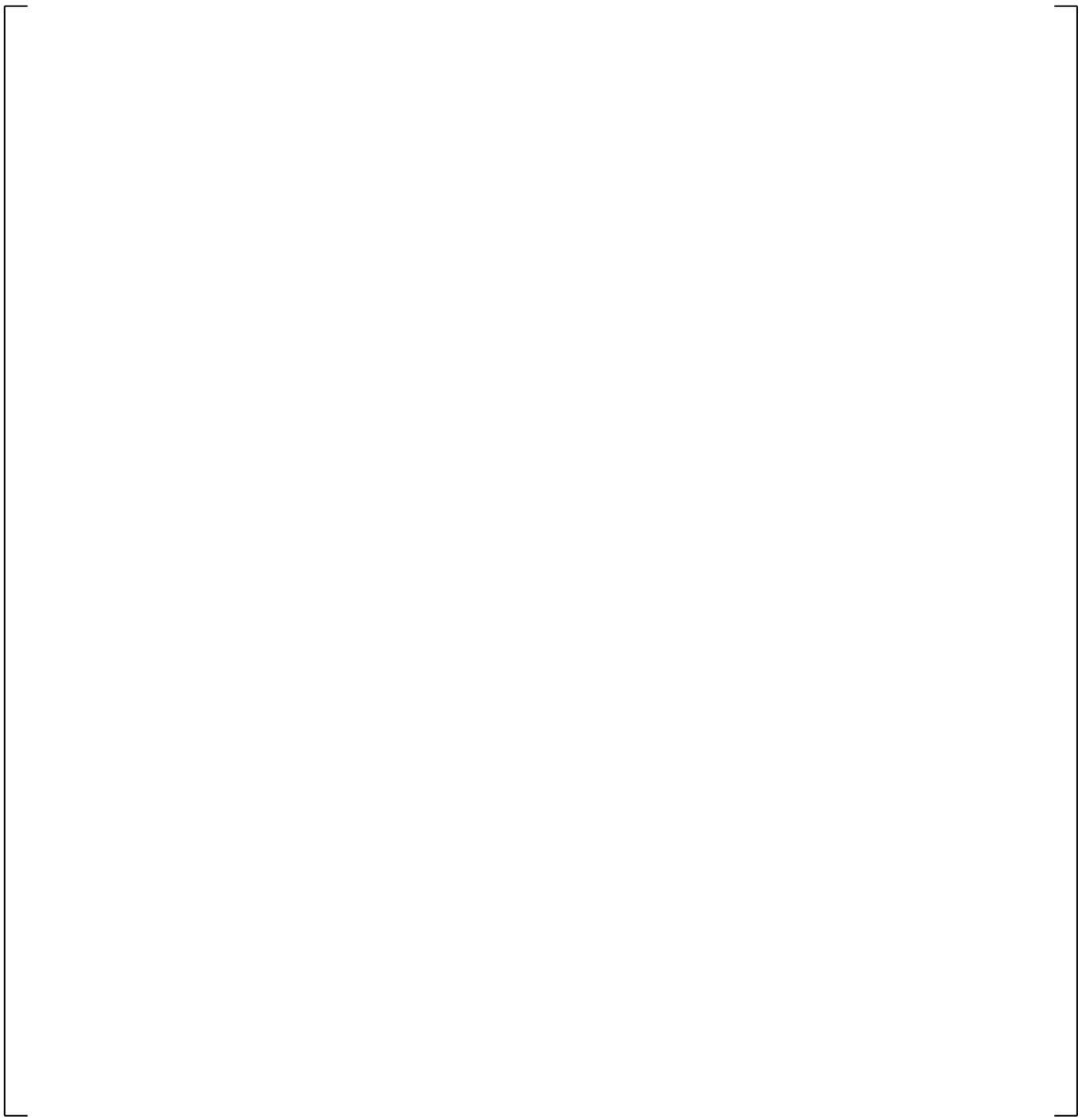

Figure 24.6.5-8 Measured HTC, Void Fraction at 6 ft in FLECHT-SEASET 31805 (Only one Legend is shown but all Available Thermocouples are Plotted)

a,c

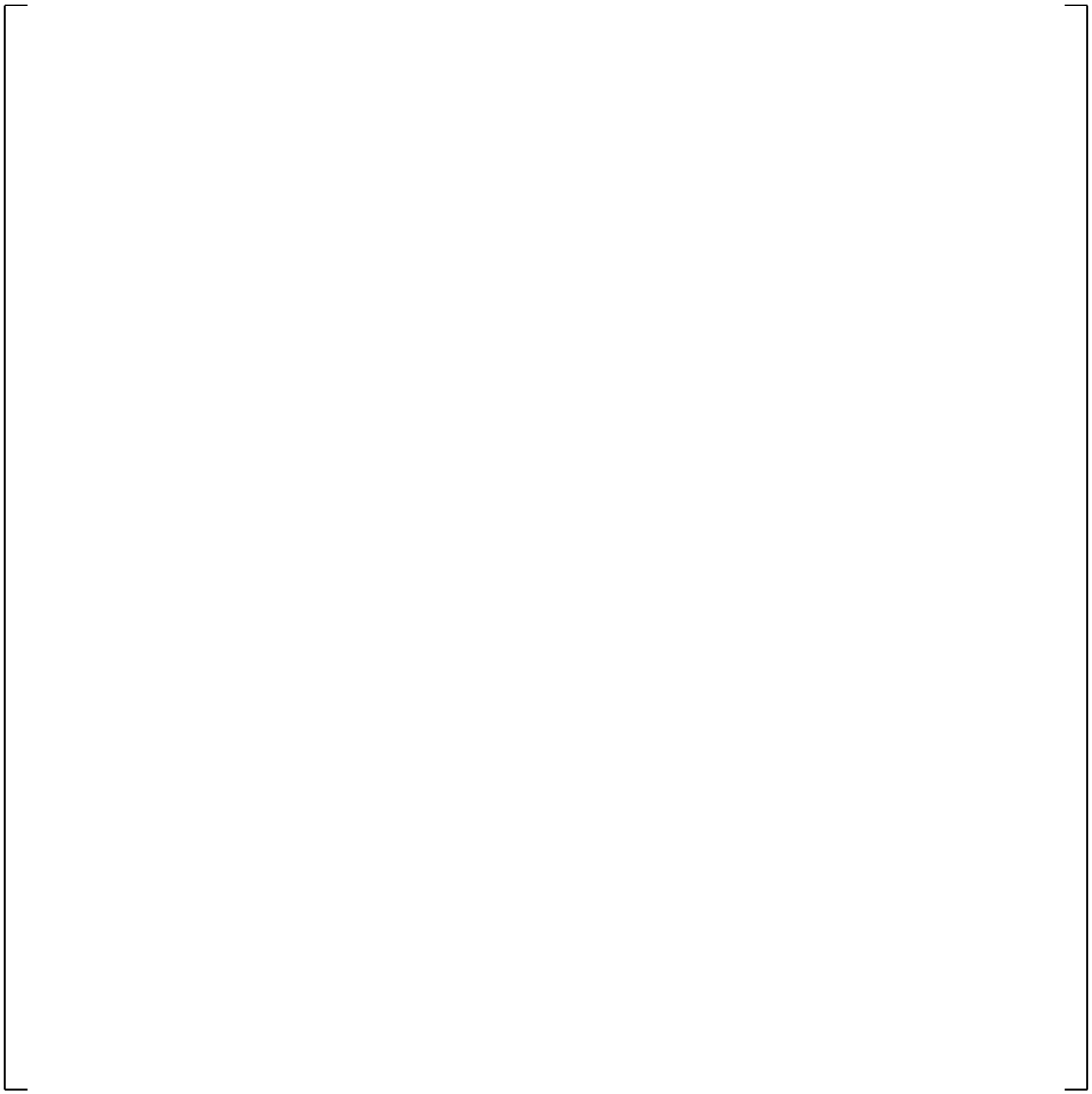

Figure 24.6.5-9 Expanded View of Measured Cladding Temperature, Void Fraction at 6 ft in FLECHT-SEASET 31805 (Only one Legend is shown but all Available Thermocouples are Plotted)

a,c

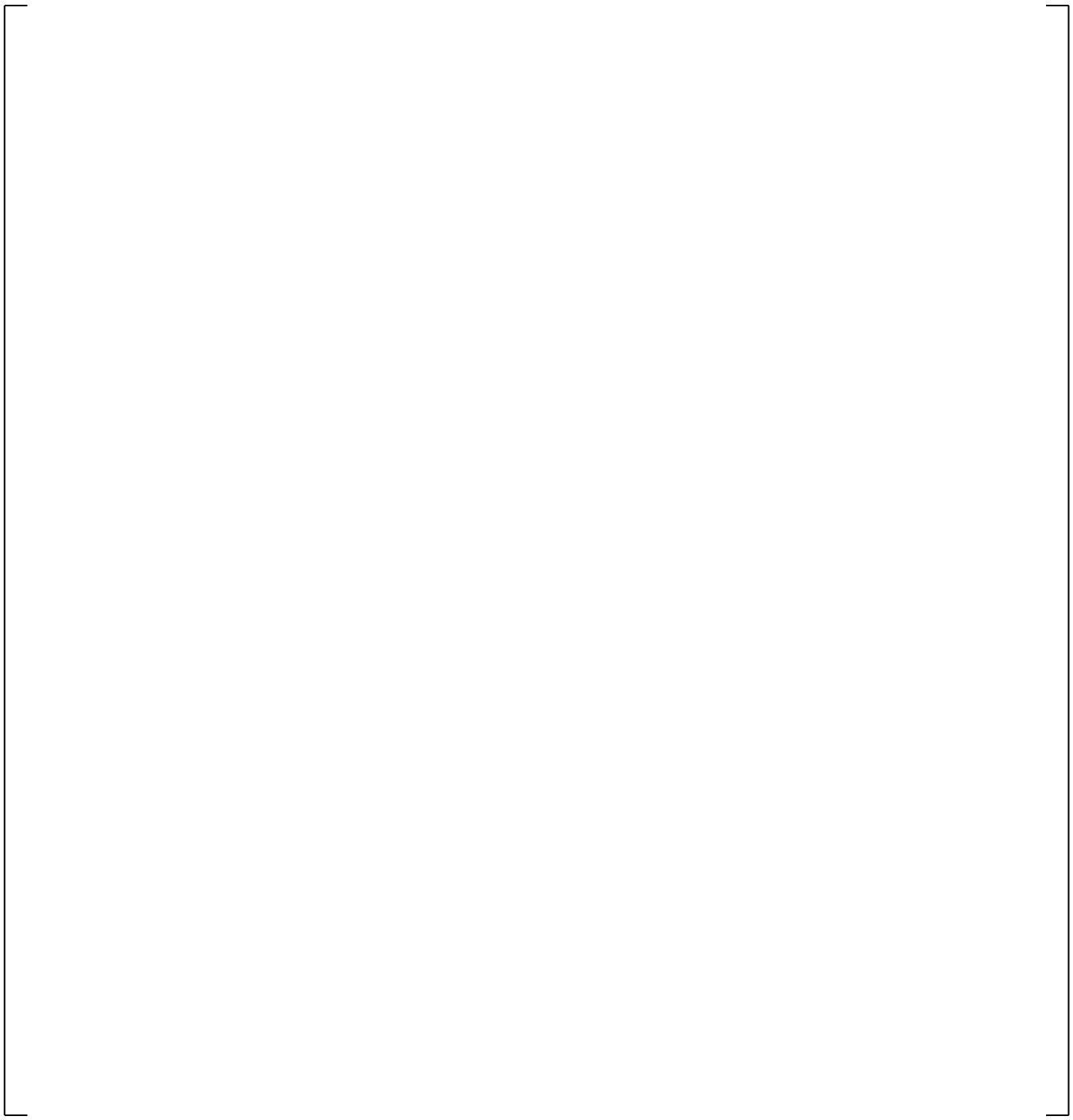

Figure 24.6.5-10 Expanded View of Measured HTC, Void Fraction at 6 ft in FLECHT-SEASET 31805 (Only one Legend is shown but all Available Thermocouples are Plotted)

a,c

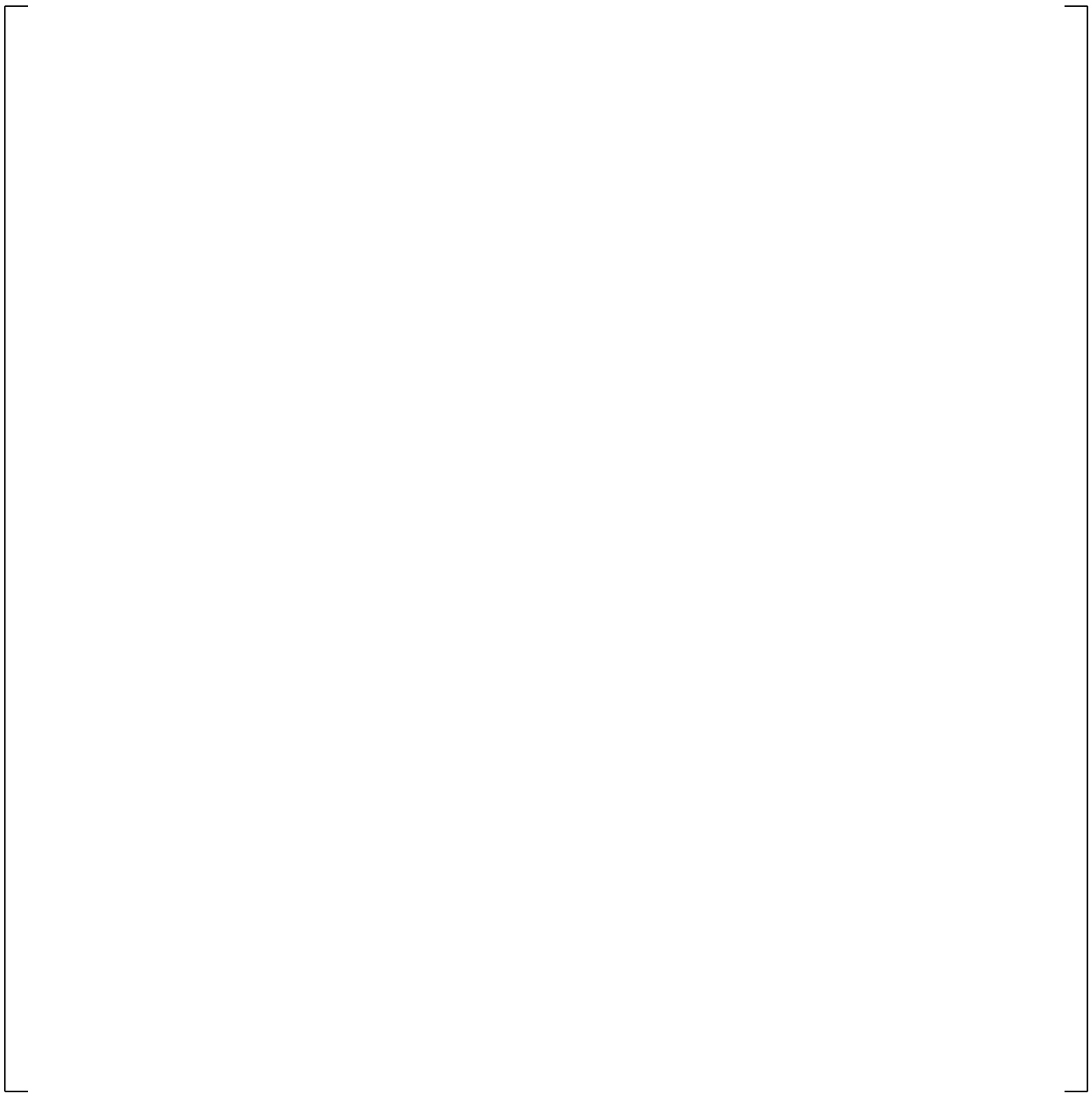

Figure 24.6.5-11 Predicted Cladding Temperature, Void Fraction at 6 ft in FLECHT-SEASET 31805

a,c

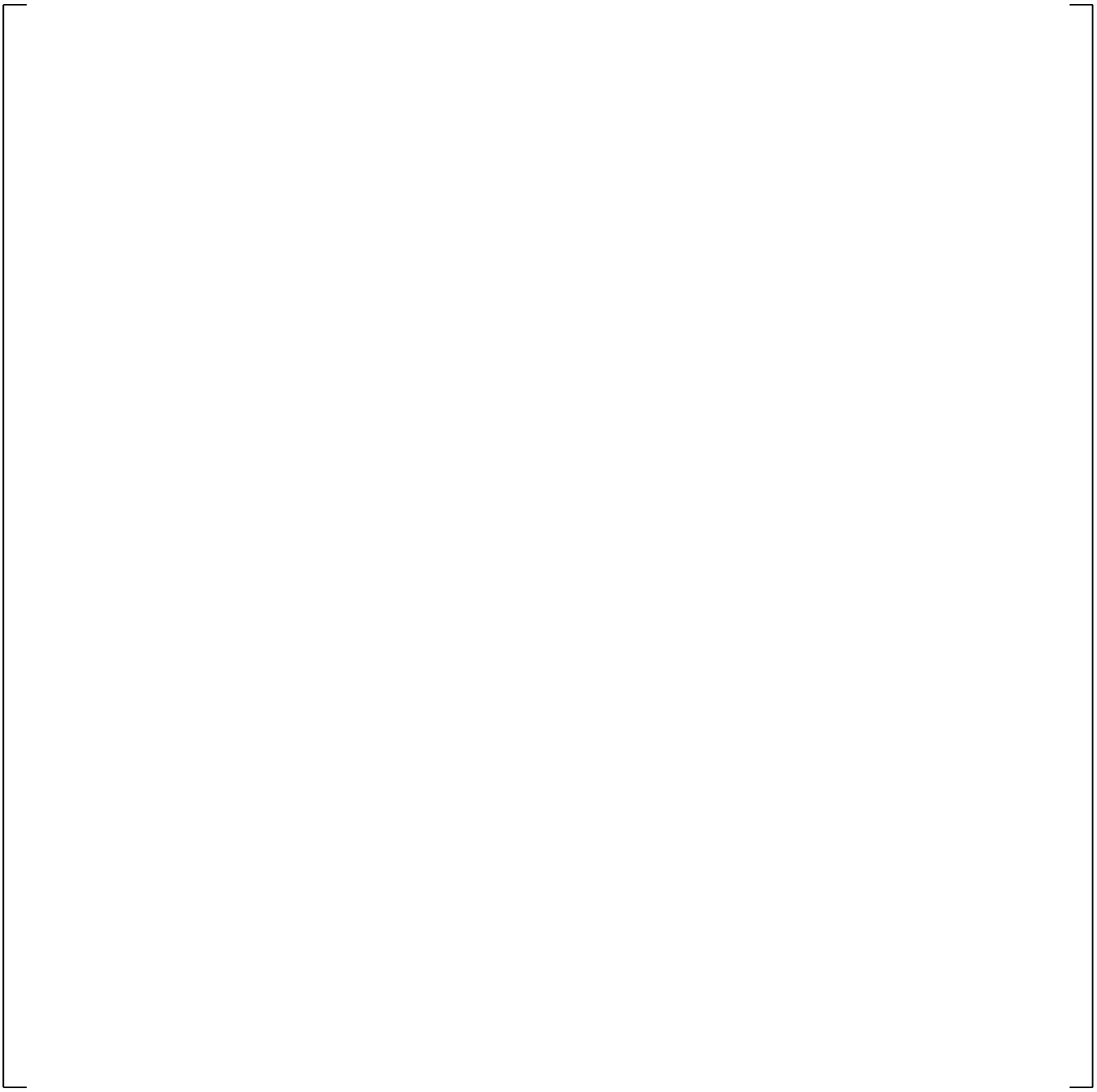

Figure 24.6.5-12 Predicted HTC, Void Fraction at 6 ft in FLECHT-SEASET 31805

a,c

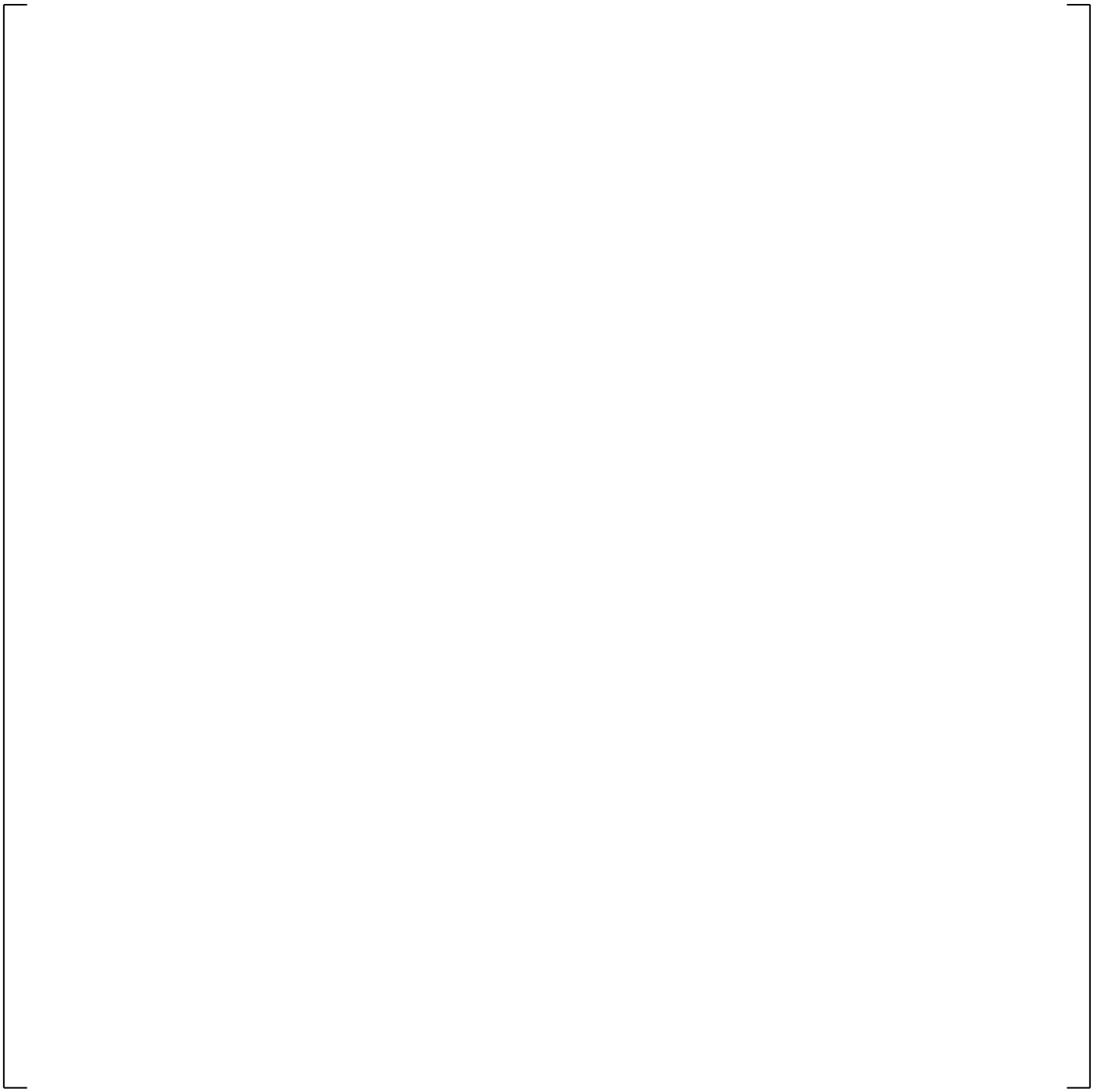

Figure 24.6.5-13 Void Fraction Comparison at 6 ft in FLECHT-SEASET 31805

a,c

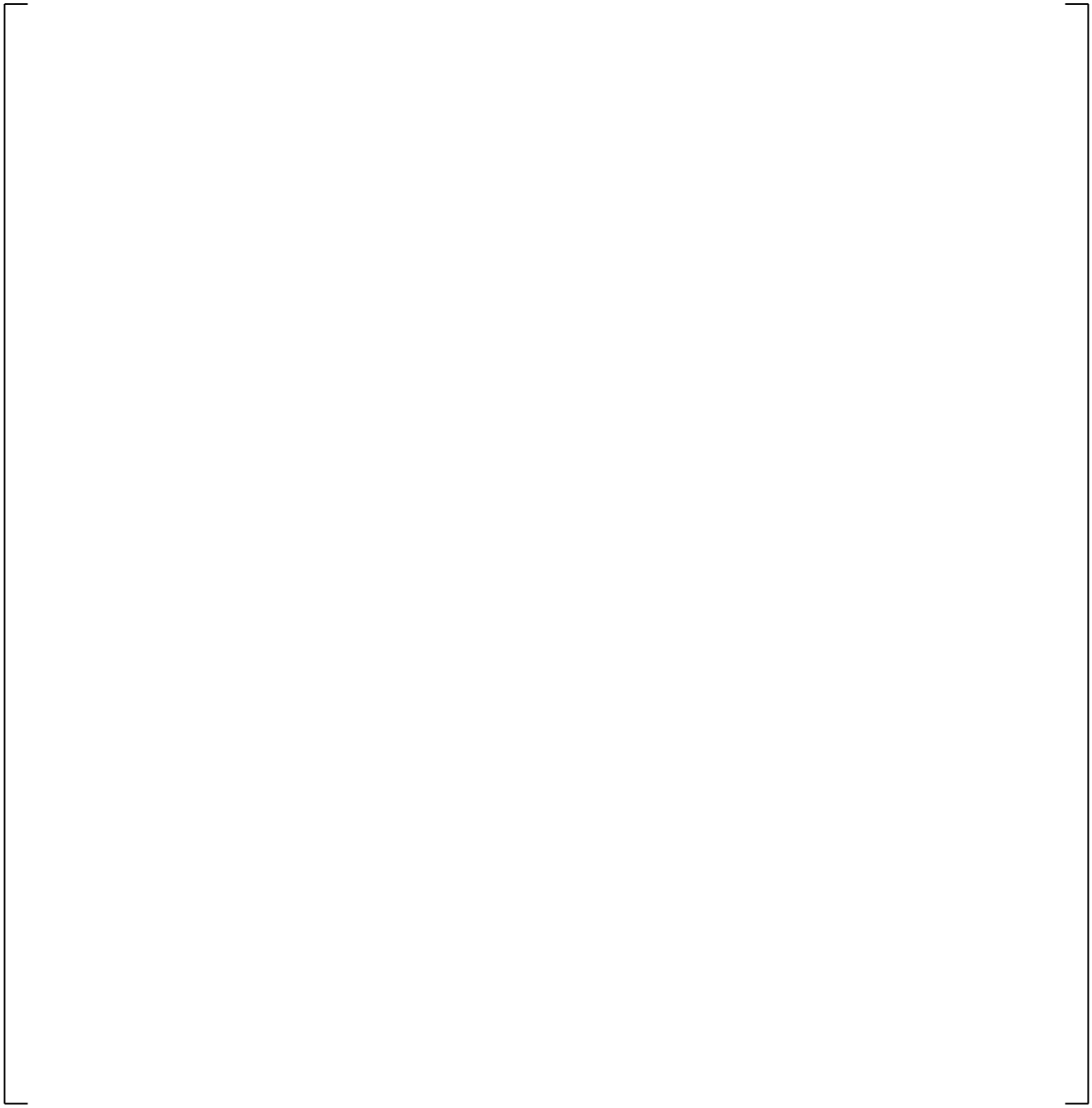

Figure 24.6.5-14 Measured Cladding Temperature, Void Fraction at 10 ft in FLECHT-31805 (Only one Legend is shown but all Available Thermocouples are Plotted)

a,c

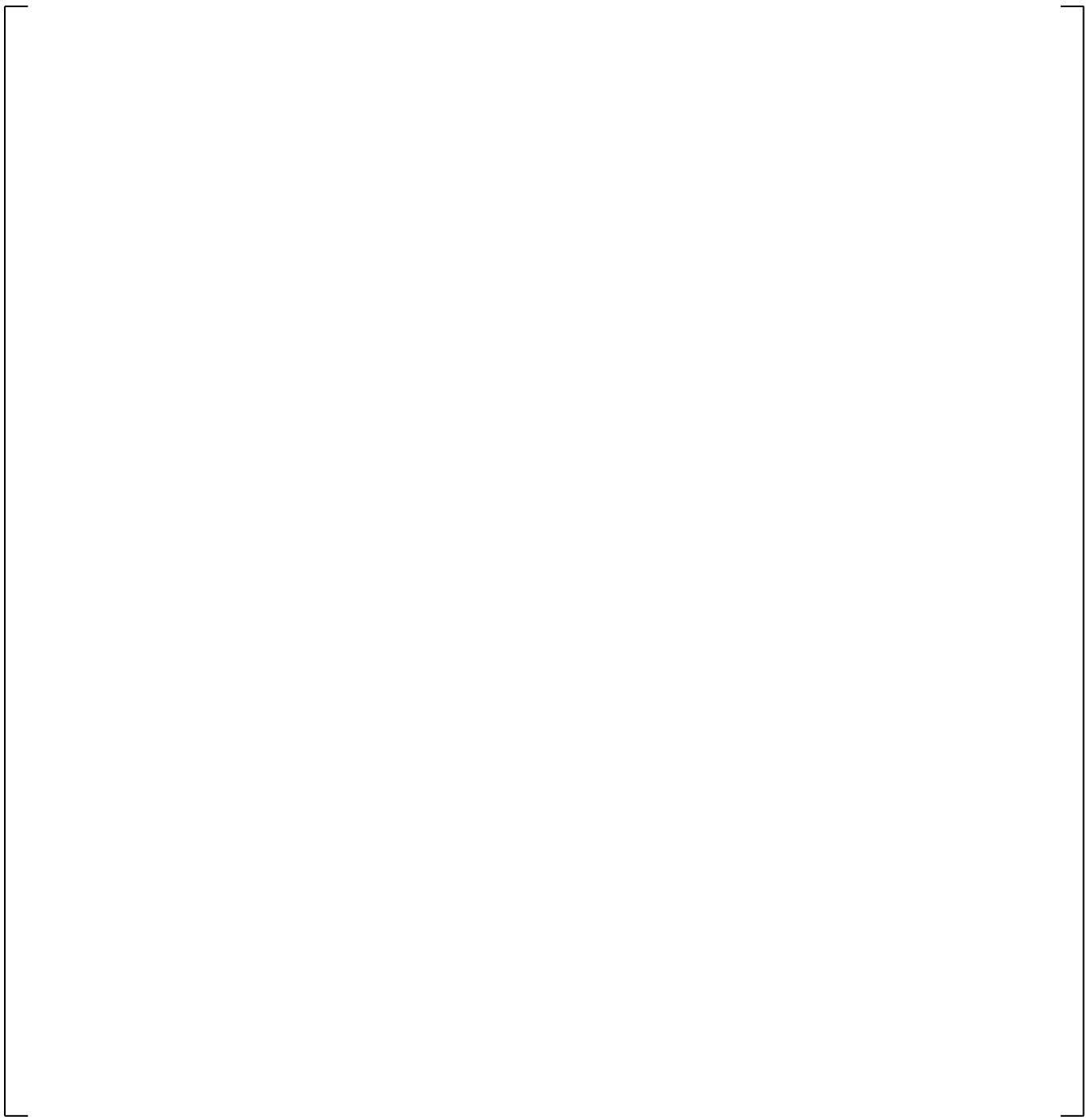

Figure 24.6.5-15 Measured HTC, Void Fraction at 10 ft in FLECHT-SEASET 31805 (Only one Legend is shown but all Available Thermocouples are Plotted)

a,c

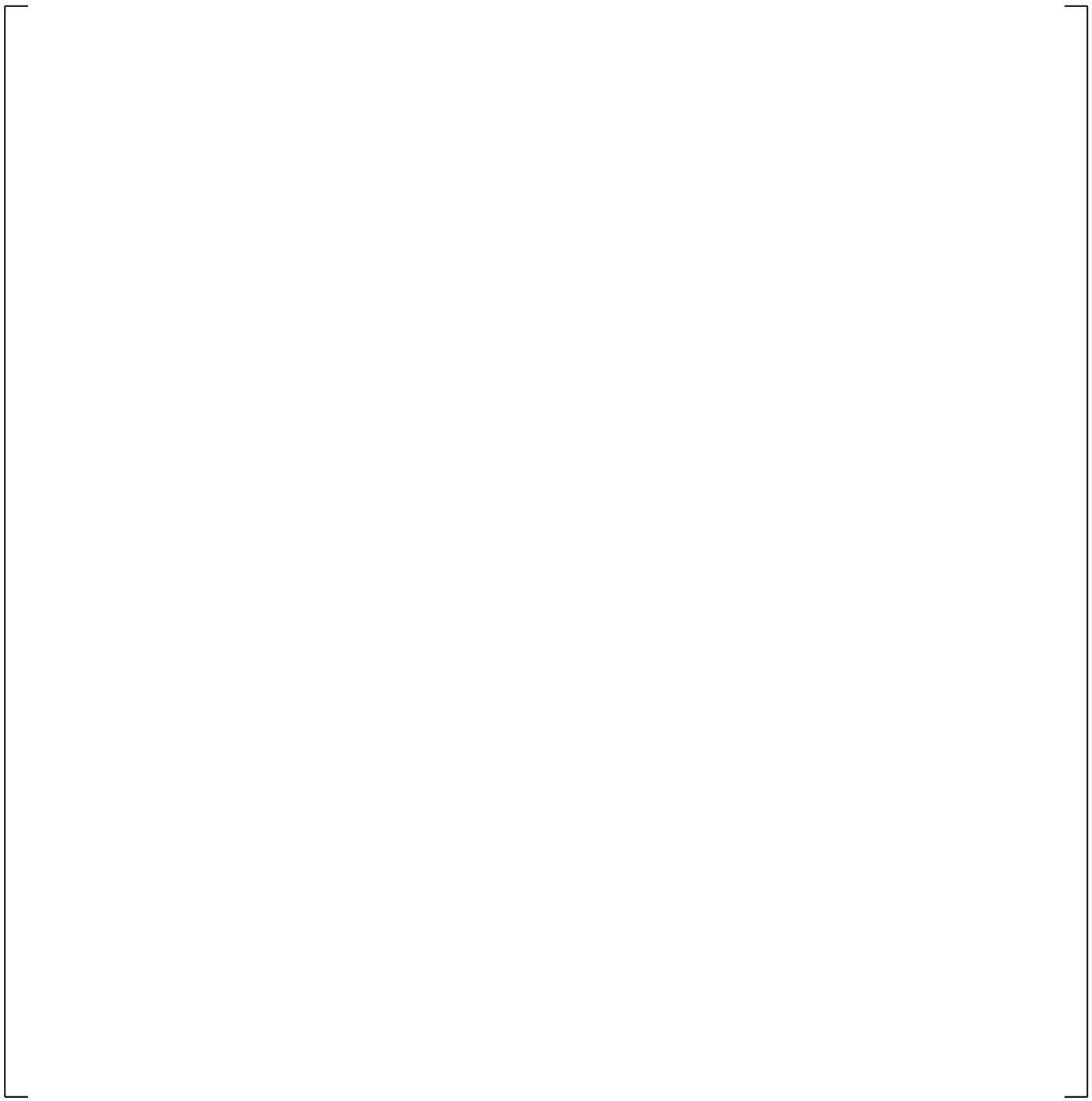

Figure 24.6.5-16 Predicted Cladding Temperature, Void Fraction at 10 ft in FLECHT-SEASET 31805

a,c

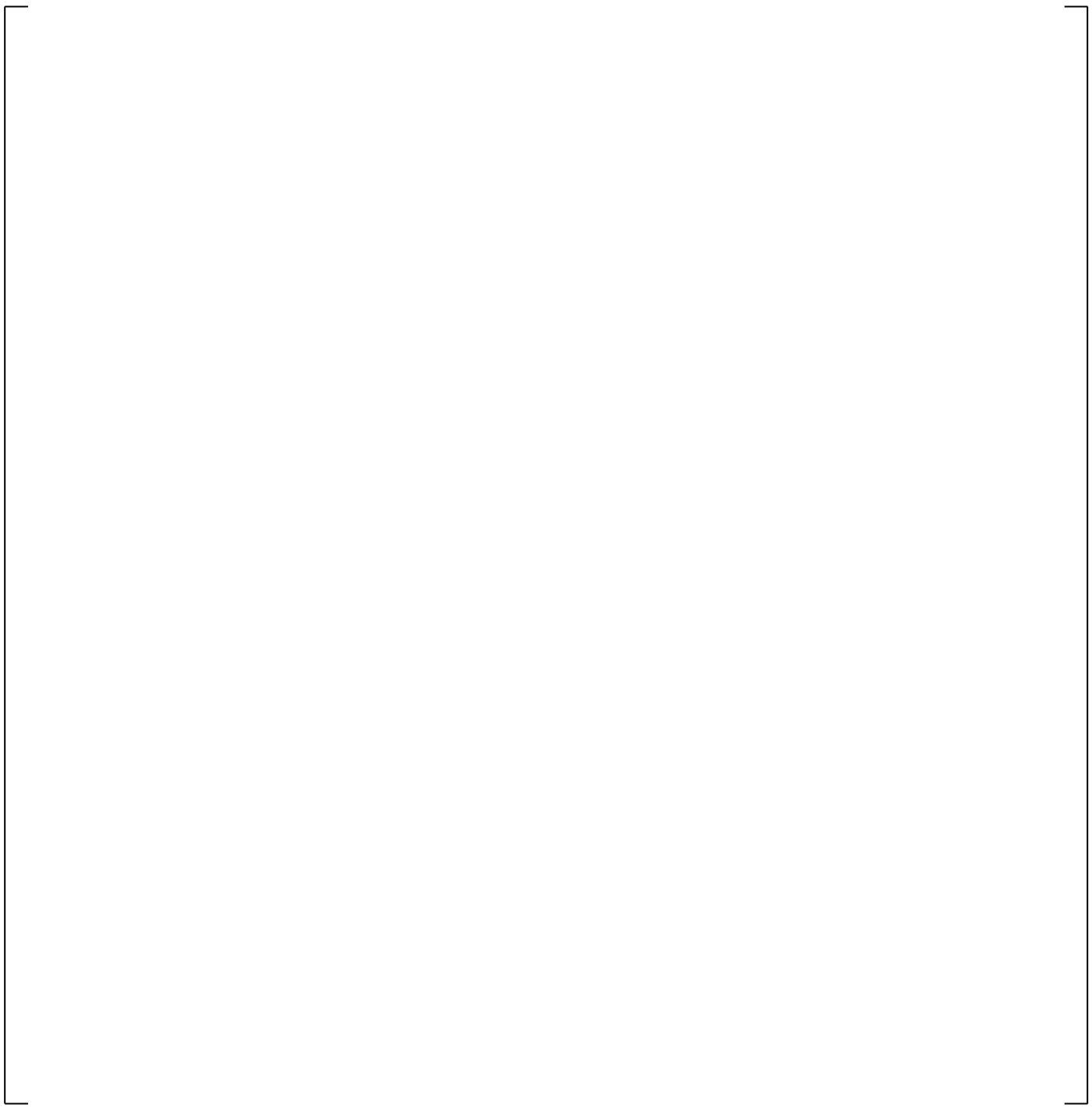

Figure 24.6.5-17 Predicted HTC, Void Fraction at 10 ft in FLECHT-SEASET 31805

a,c

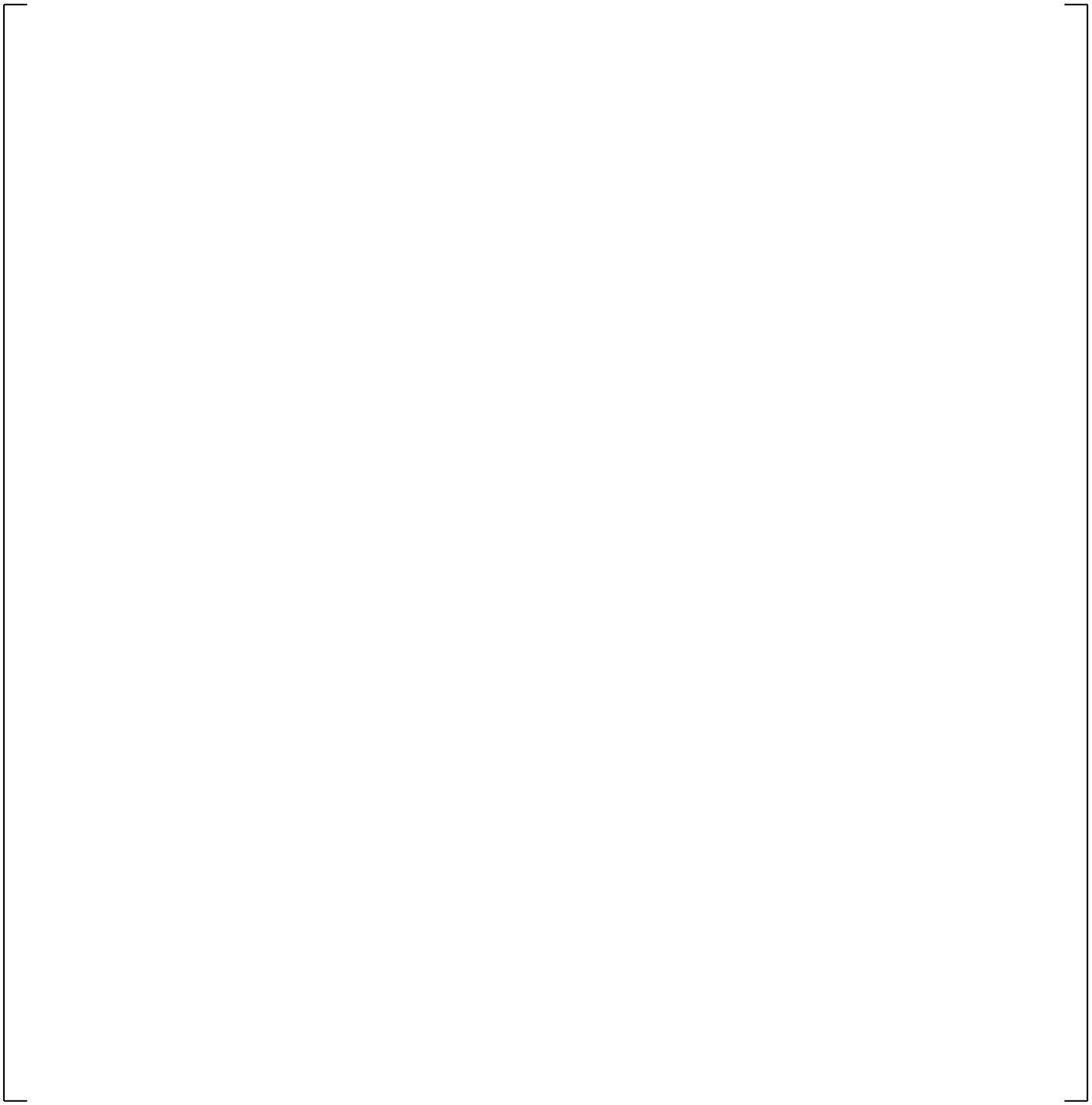

Figure 24.6.5-18 Void Fraction Comparison at 10-11 ft in FLECHT-SEASET 31805

a,c

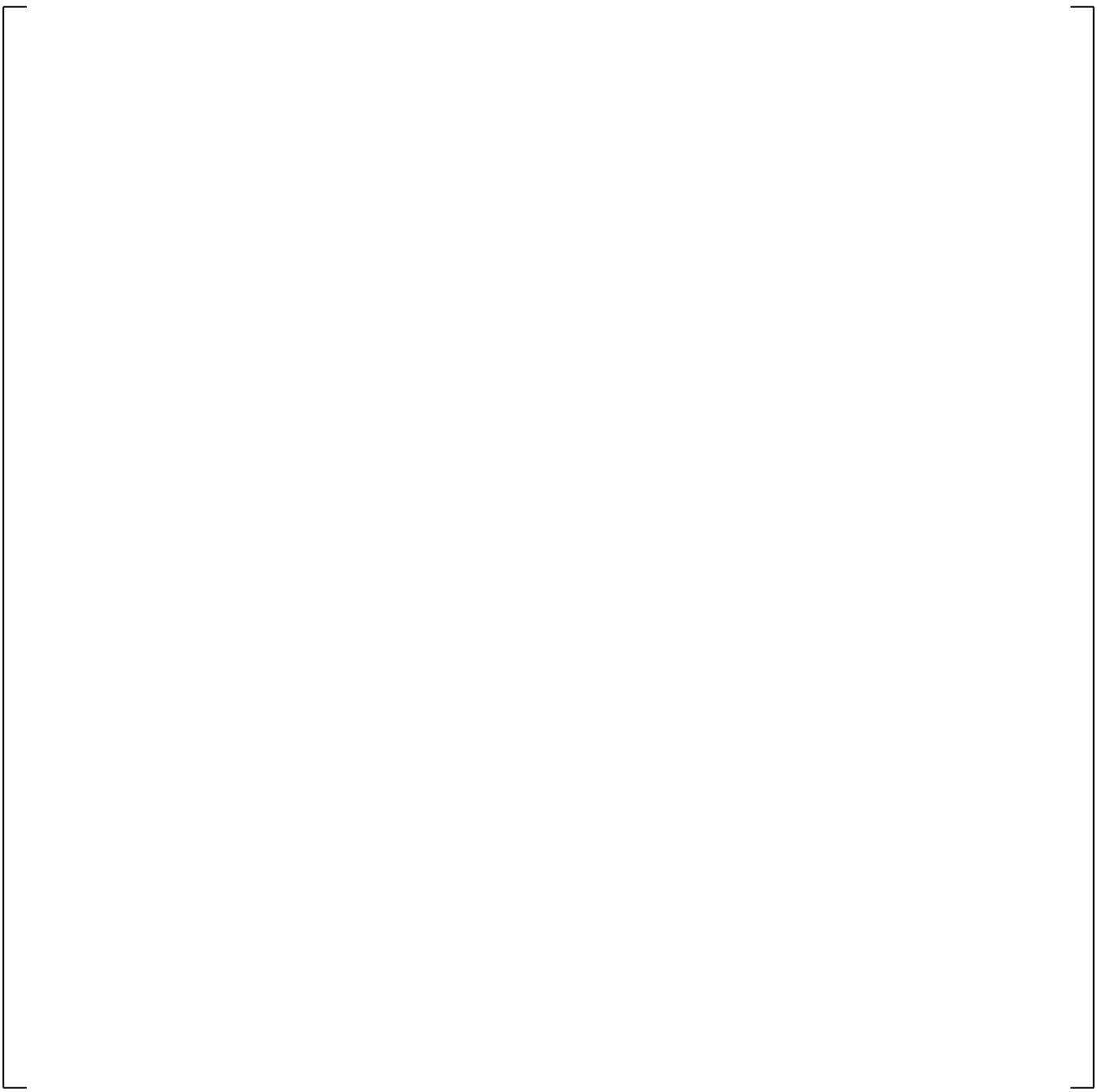

Figure 24.6.5-19 Void Fraction Axial Profile Comparison [ ]^{a,c} in FLECHT-SEASET 31805

24.6.6 FLECHT-SEASET Test 31701

Test 31701, because of its very high reflood rate of 6.1 in/sec, is a test that should be expected to produce an inverted annular flow over a significant region of the bundle. This is a rate sufficient to cold fill the bundle within only 24 seconds.

Figure 24.6.6-1 shows the void fractions reported for this test from the 5- to 6-ft and the 6- to 7-ft DP cells. **[**

][a,c]

Figures 24.6.6-2 and 24.6.6-3 show the relation of cladding temperature and heat transfer coefficient with void fraction, based on the test data. **[**

][a,c]

Figures 24.6.6-4 and 24.6.6-5 show the cladding temperature and heat transfer coefficient relationship with void fraction as predicted by WCOBRA/TRAC-TF2 for Test 31701. **[**

][a,c]

The vertical line which appears in Figure 24.6.6-5 at **[**

][a,c]

Figure 24.6.6-6 compares the predicted and measured void fraction for the 6- and 7-ft region.
[

][a,c]

Because of the high reflood rate and rapid entrainment in Test 31701, the liquid was quickly present at the 10 ft elevation also. As at the 6-ft elevation, the void fraction measurements at the 9- to 10-ft and 10- to 11-ft elevations showed an inverse void gradient. Figure 24.6.6-7 shows the reported void fraction measurements, and an average that will be used in later plots for the 10-ft elevation. **[**

][a,c]

The 10-ft elevation in Test 31701 was found to have conditions typical of an inverted annular post-CHF flow for a significant period of time. Figures 24.6.6-8 and 24.6.6-9 show the experimental relation of cladding temperature and heat transfer coefficient with void fraction. **[** **]**[a,c]

[

]a,c

The predicted relations of cladding temperature and heat transfer coefficient with void fraction are shown in Figures 24.6.6-10 and 24.6.6-11. [

]a,c

The predicted and measured void fraction for the 10- to 11-ft region is shown in Figure 24.6.6-12.
[

]a,c

a,c

Figure 24.6.6-1 Void Fraction Measurement at 5-7 ft for FLECHT-SEASET 31701

a,c

Figure 24.6.6-2 Measured Cladding Temperature, Void Fraction for FLECHT-SEASET 31701

a,c

Figure 24.6.6-3 Measured HTC, Void Fraction Relation for FLECHT-SEASET 31701

a,c

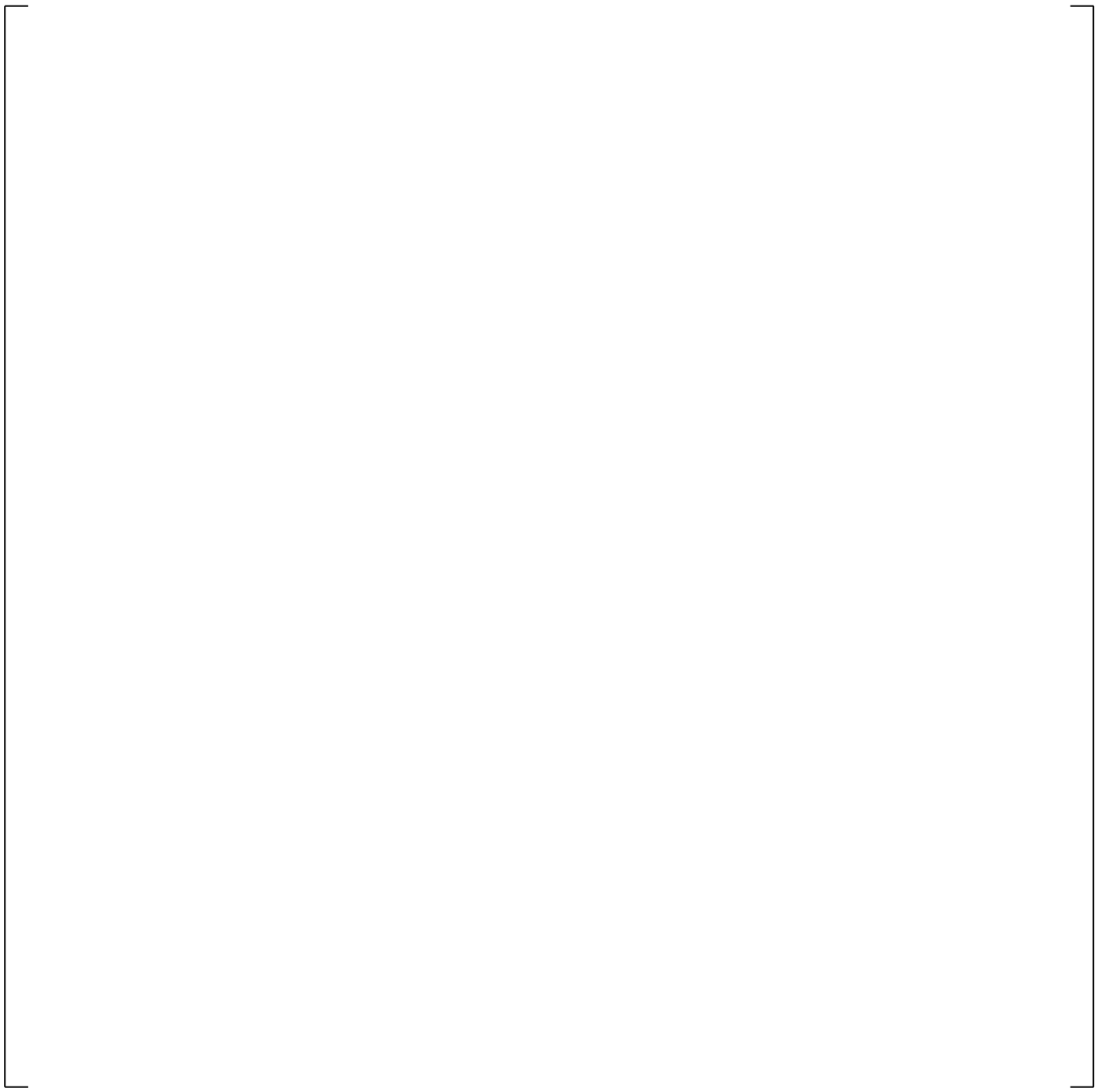

Figure 24.6.6-4 Predicted Cladding Temperature, Void Fraction Relation at 6 ft for FLECHT-SEASET 31701

a,c

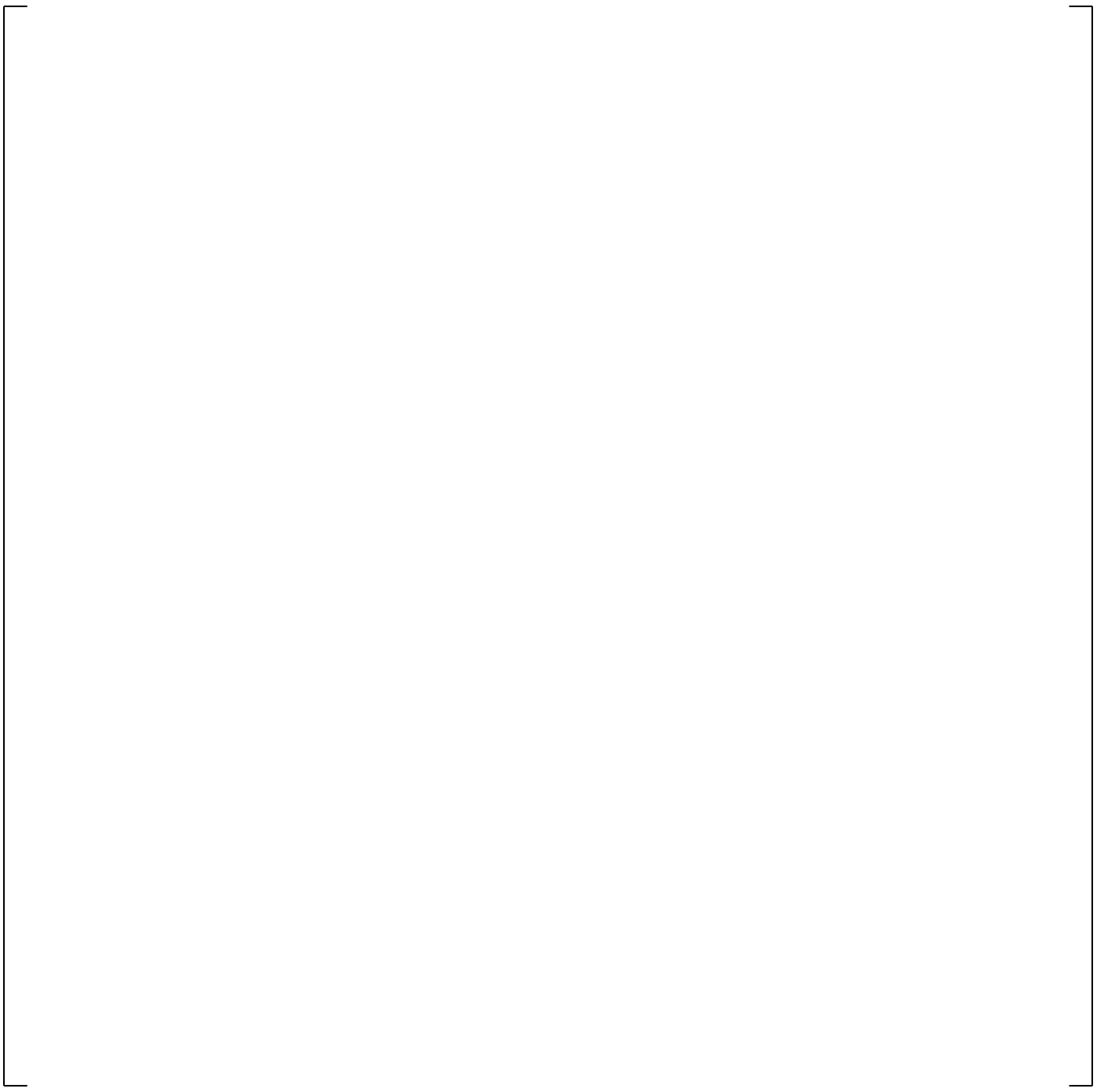

Figure 24.6.6-5 Predicted HTC, Void Fraction Relation at 6 ft for FLECHT-SEASET 31701

a,c

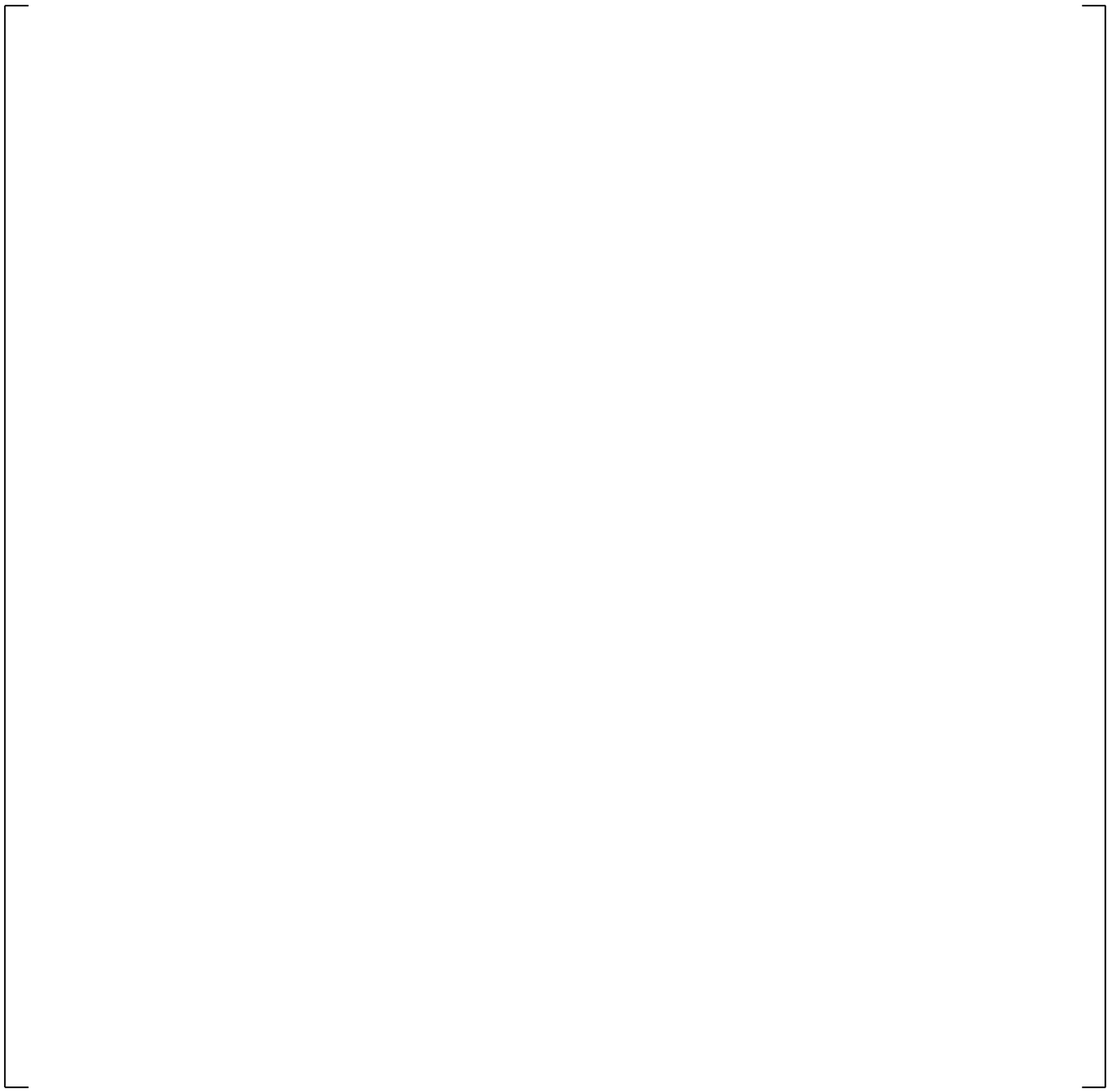

Figure 24.6.6-6 Comparison of Predicted and Measured Void Fraction Relation at 6-7 ft for FLECHT-SEASET 31701

a,c

Figure 24.6.6-7 Void Fraction Measurement at 9-11 ft for FLECHT-SEASET 31701

a,c

Figure 24.6.6-8 Measured Cladding Temperature, Void Fraction Relation at 10 ft for FLECHT-SEASET 31701

a,c

Figure 24.6.6-9 Measured HTC, Void Fraction Relation at 10 ft for FLECHT-SEASET 31701

a,c

Figure 24.6.6-10 Predicted Cladding Temperature, Void Fraction Relation at 10 ft for FLECHT-SEASET 31701

a,c

Figure 24.6.6-11 Predicted HTC, Void Fraction Relation at 10 ft for FLECHT-SEASET 31701

a,c

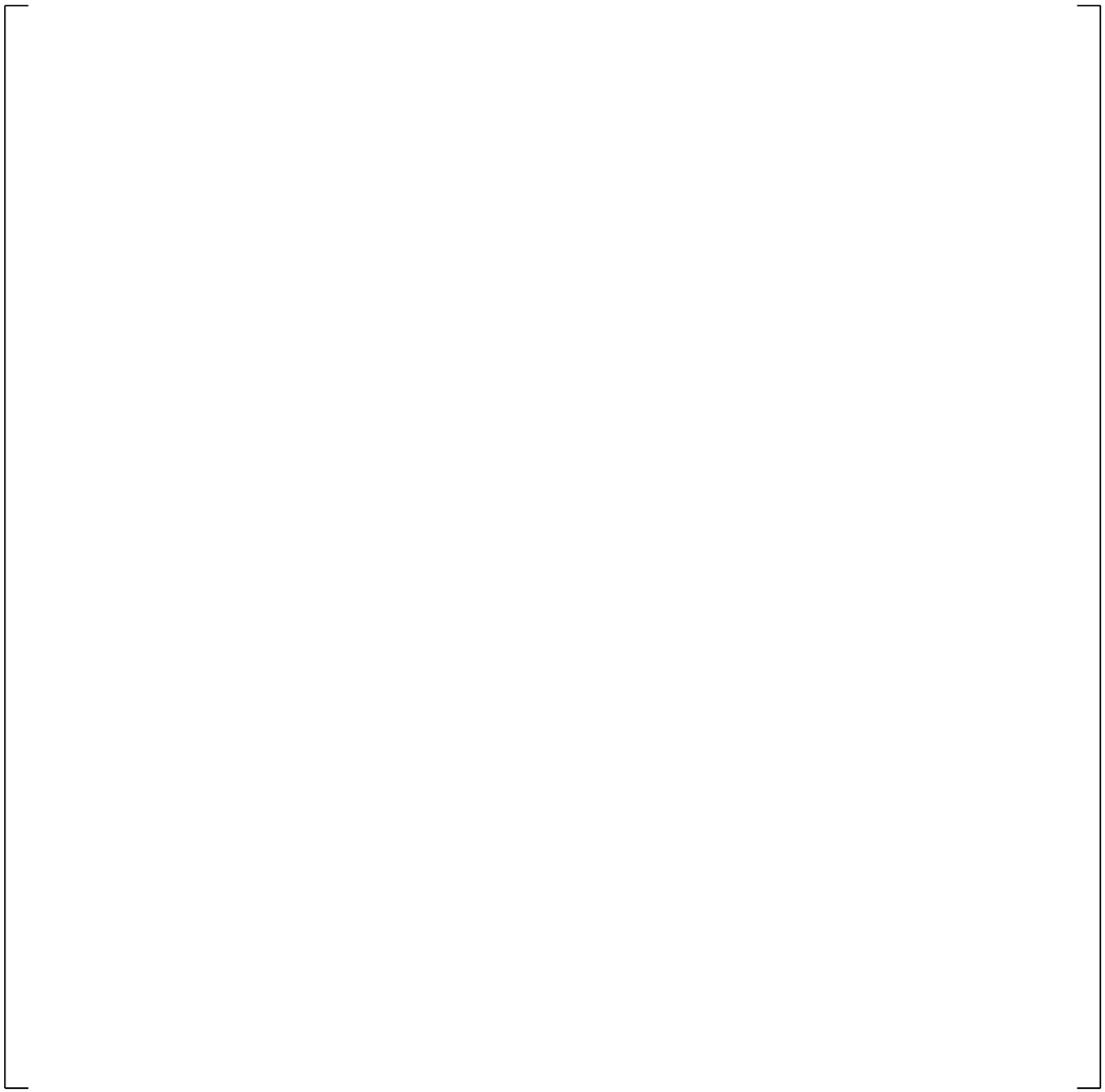

Figure 24.6.6-12 Comparison of Measured and Predicted Void Fraction at 10 ft for FLECHT-SEASET 31701

24.6.7 Conclusions

Two different FLECHT-SEASET tests were reviewed in order to identify compensating errors due to an improper coupling between heat transfer coefficient and void fraction. Both Tests 31805 and 31701 showed that [

]^{a,c}

24.7 BLOWDOWN AND POST BLOWDOWN THERMAL-HYDRAULICS/ ENTRAINMENT

24.7.1 LOFT Test L2-3

The plots for this section are designated Figures 24.7.1-1 through 24.7.1-33. In all figures, Data legend uses the same system detector identification as in the test Data report (Prassinos et al., 1979) where possible (e.g., Figure 24.7.1-19 refers to DE-PC-001B). These references are to the corresponding figures in the LOFT test reports. The LOFT system is shown in Figure 24.7.1-1. LOFT Test L2-3 (Prassinos et al., 1979) was a pump-on, intermediate power test. A summary of measured event times is given below:

Event	Time (s)
Blowdown begins	0
Accumulator begins injecting	17
End of Blowdown/beginning of reflood	40
Accumulator empty (N_2 injection)	50-60
Core quench	55

End of blowdown is defined above as the time where system pressure levels off to a constant value, and a liquid level is detected in the core.

In addition to cladding temperature, fluid conditions at several locations in the LOFT system (Figure 24.7.1-1) were examined for compensating error.

Core Thermal-Hydraulics

Initial blowdown heat-up and cooldown of the cladding temperatures for LOFT Test L2-3 were predicted [

]^{a,c}

[

][a,c]

System Behavior

The system pressure was **[**

][a,c]

Loop Behavior: Intact loop

Figures 24.7.1-13 to 24.7.1-15 compared **[**

][a,c]

[

]a,c

Figures 24.7.1-16 through 24.7.1-21 show predicted and measured trends in the [

]a,c

Loop Behavior: Broken loop

[

]a,c

[

]a,c

Sensitivity Studies

Several studies were performed to examine what factors contribute most to the mis-prediction of core flow. [

]a,c

a,c

Figure 24.7.1-1 LOFT Measurement/Prediction Locations

a,c

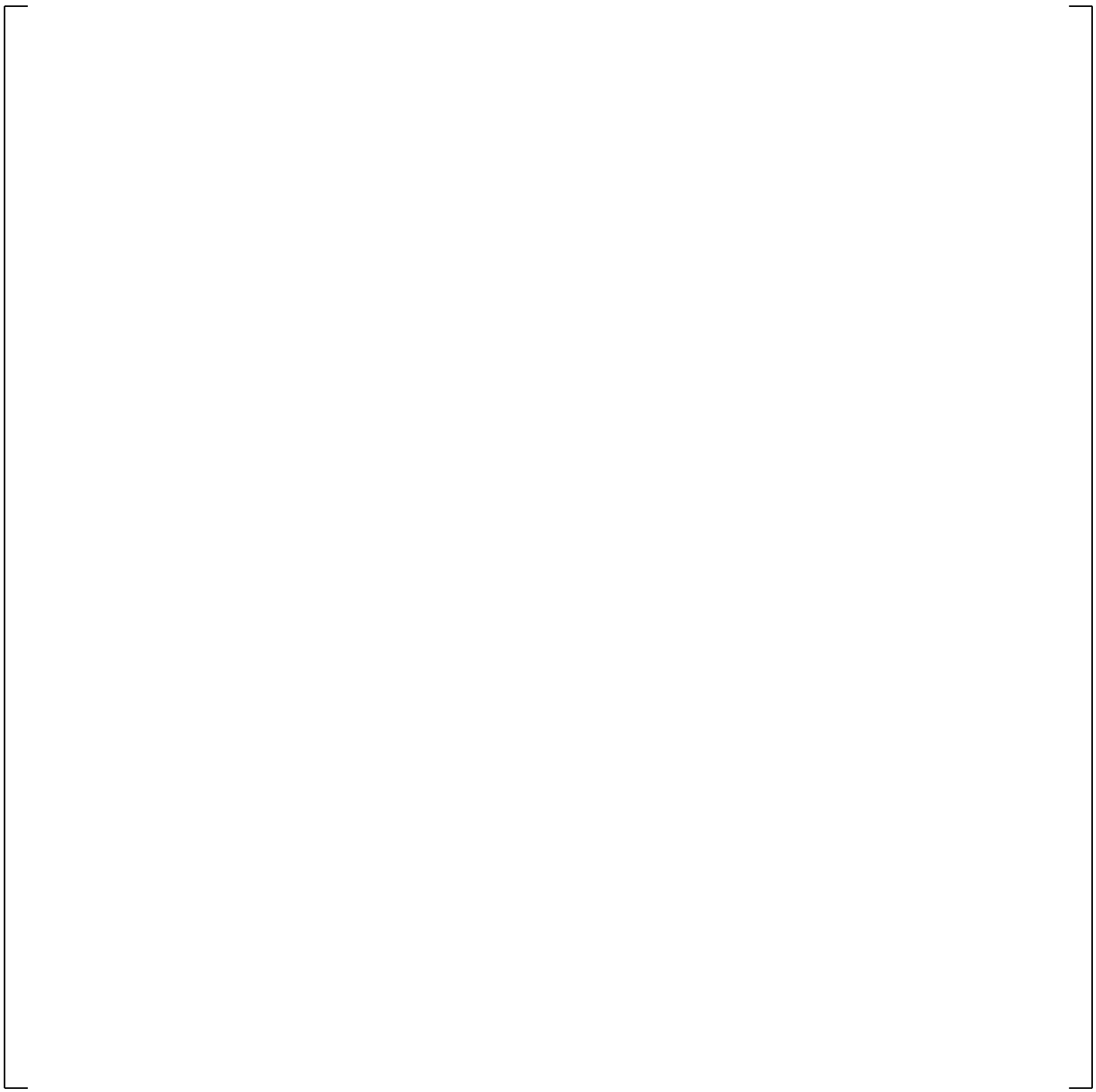

Figure 24.7.1-2 LOFT L2-3 Data vs. Predicted Hot Rod Cladding Temperature

a,c

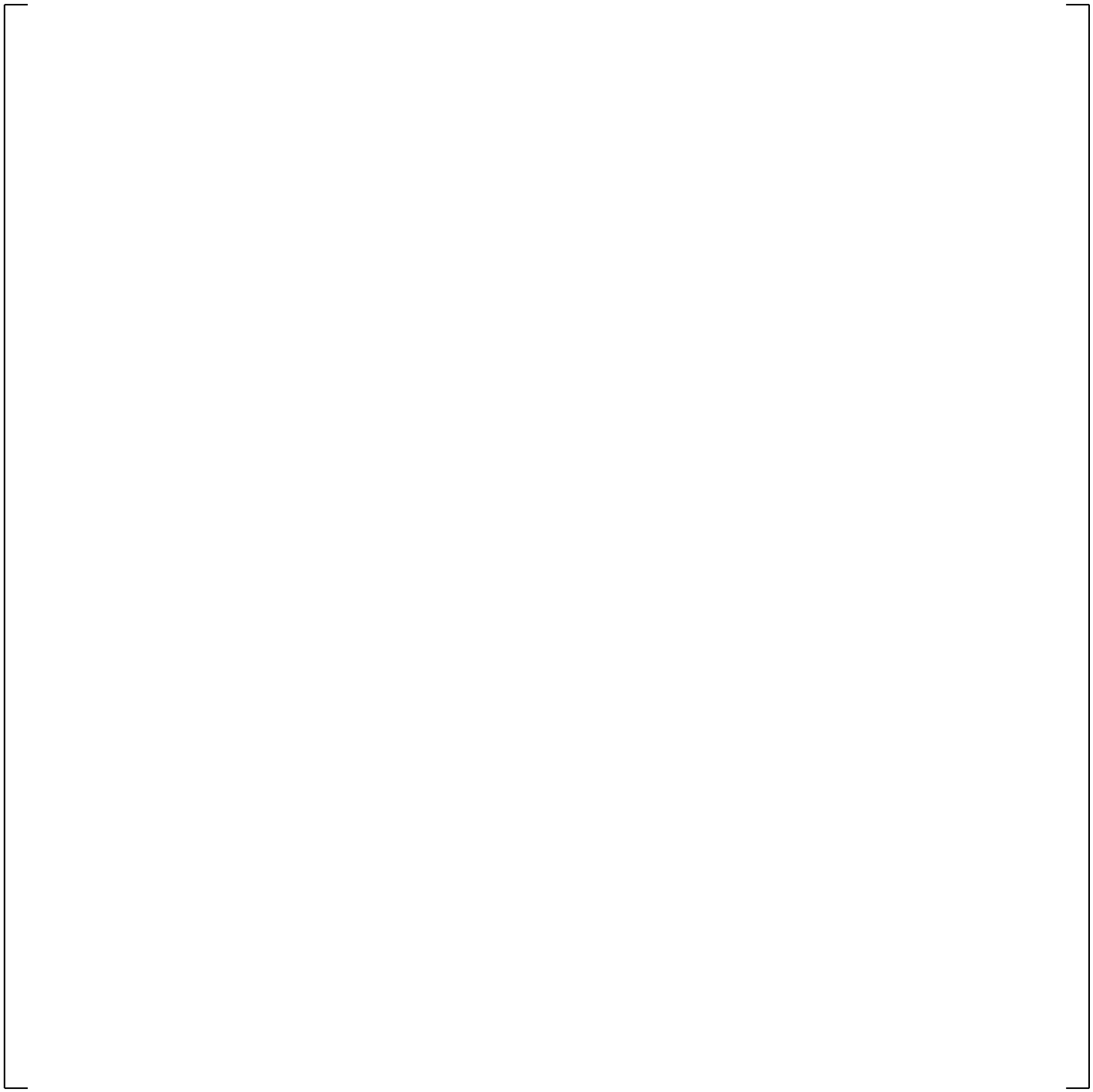

Figure 24.7.1-3 Predicted Vapor Flowrate at Top and Bottom of Hot Assembly

a,c

Figure 24.7.1-4 Predicted Entrained Drop Flowrate at Top and Bottom of Hot Assembly

a,c

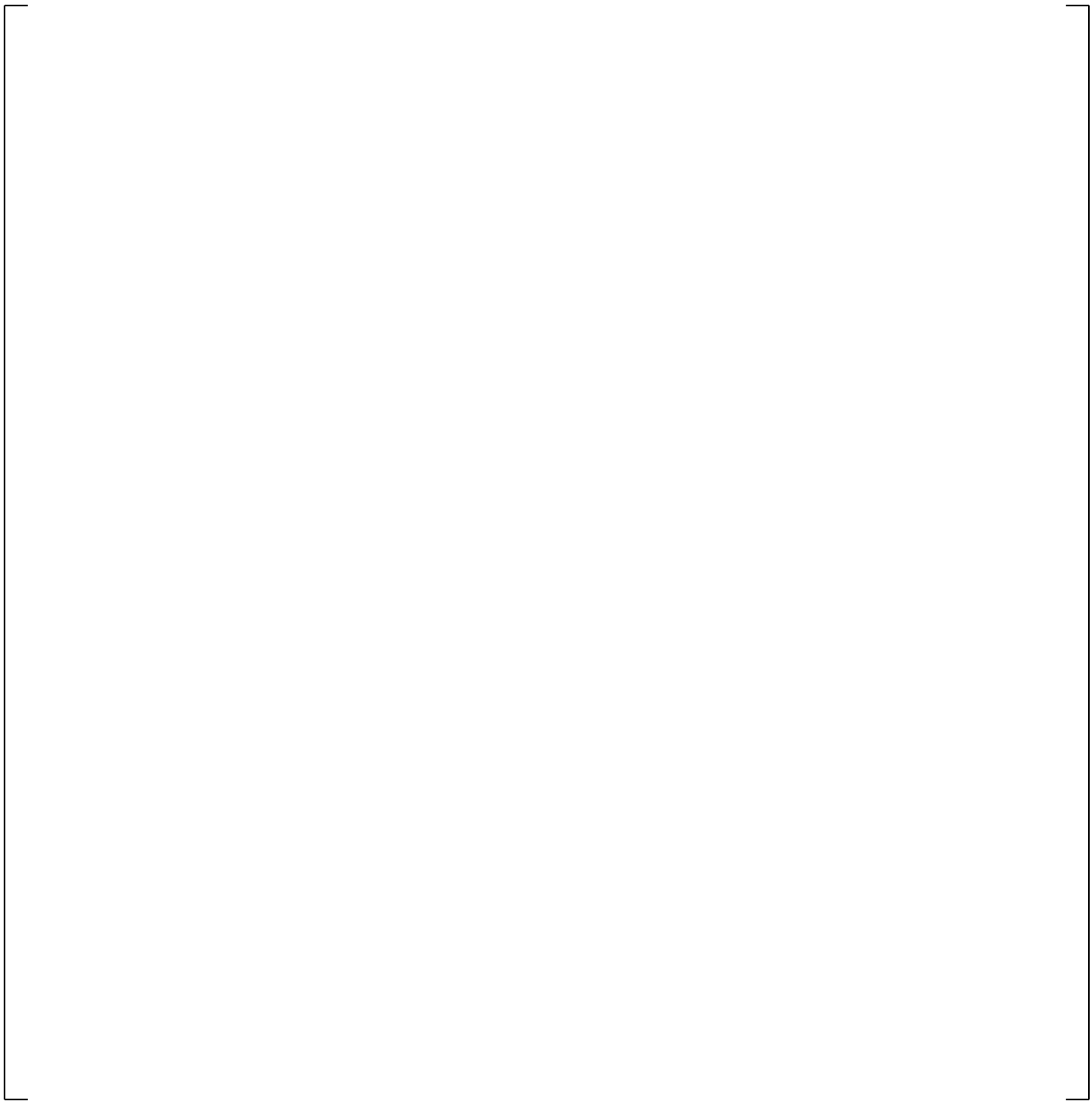

Figure 24.7.1-5 LOFT L2-3 Data vs. Predicted Steam Temperature at Top of Hot Assembly

a,c

Figure 24.7.1-6 LOFT L2-3 Data vs. Predicted Steam Temperature at Bottom of Hot Assembly

a,c

Figure 24.7.1-7 Predicted Hot Rod Vapor Heat Transfer Coefficient at PCT Elevation

a,c

Figure 24.7.1-8 Predicted Hot Rod Liquid Heat Transfer Coefficient at PCT Elevation

a,c

Figure 24.7.1-8a Predicted Hot Rod Liquid Heat Transfer Coefficient at PCT Elevation (Narrowed Ordinate Scale)

a,c

Figure 24.7.1-9 Measured and Predicted Intact Loop Pressure

a,c

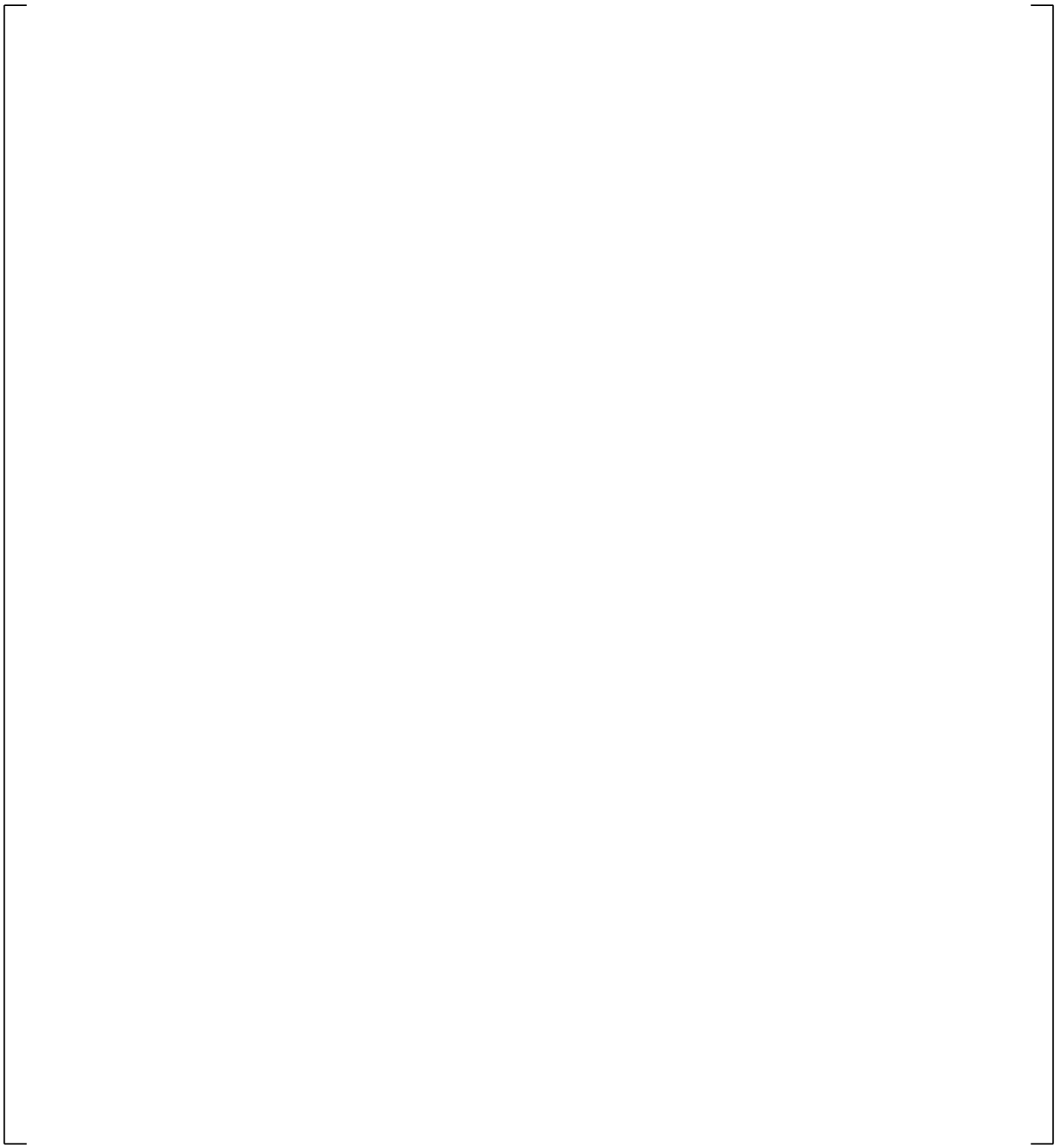

Figure 24.7.1-10 Predicted Downcomer Collapsed Liquid Level (1- Intact, 2-Broken Side)

a,c

Figure 24.7.1-11 Predicted and Measured Core Collapsed Liquid Level (Line 5-Estimated from the Liquid Detector)

a,c

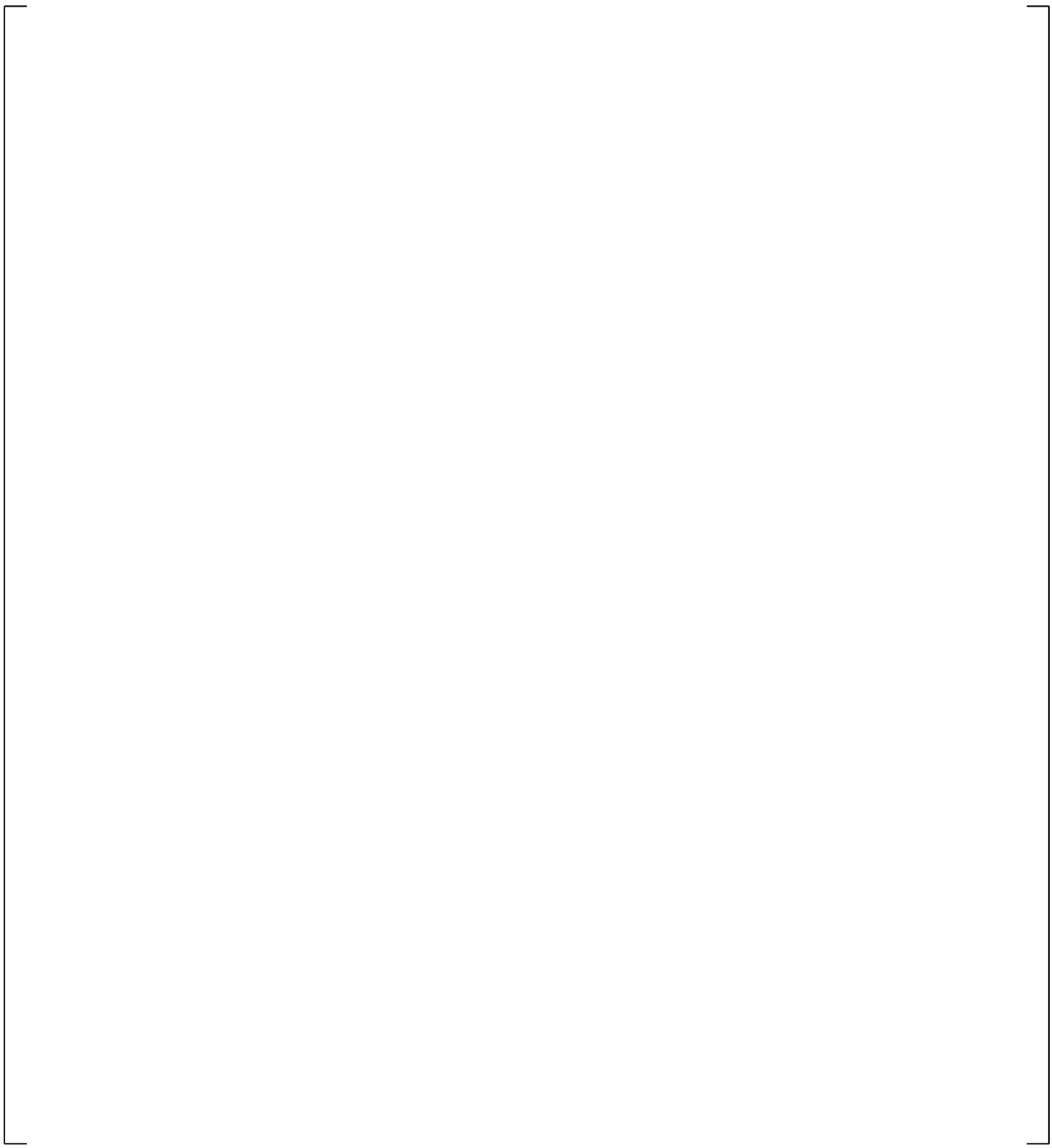

Figure 24.7.1-12 Predicted Upper Plenum Collapsed Liquid Level

a,c

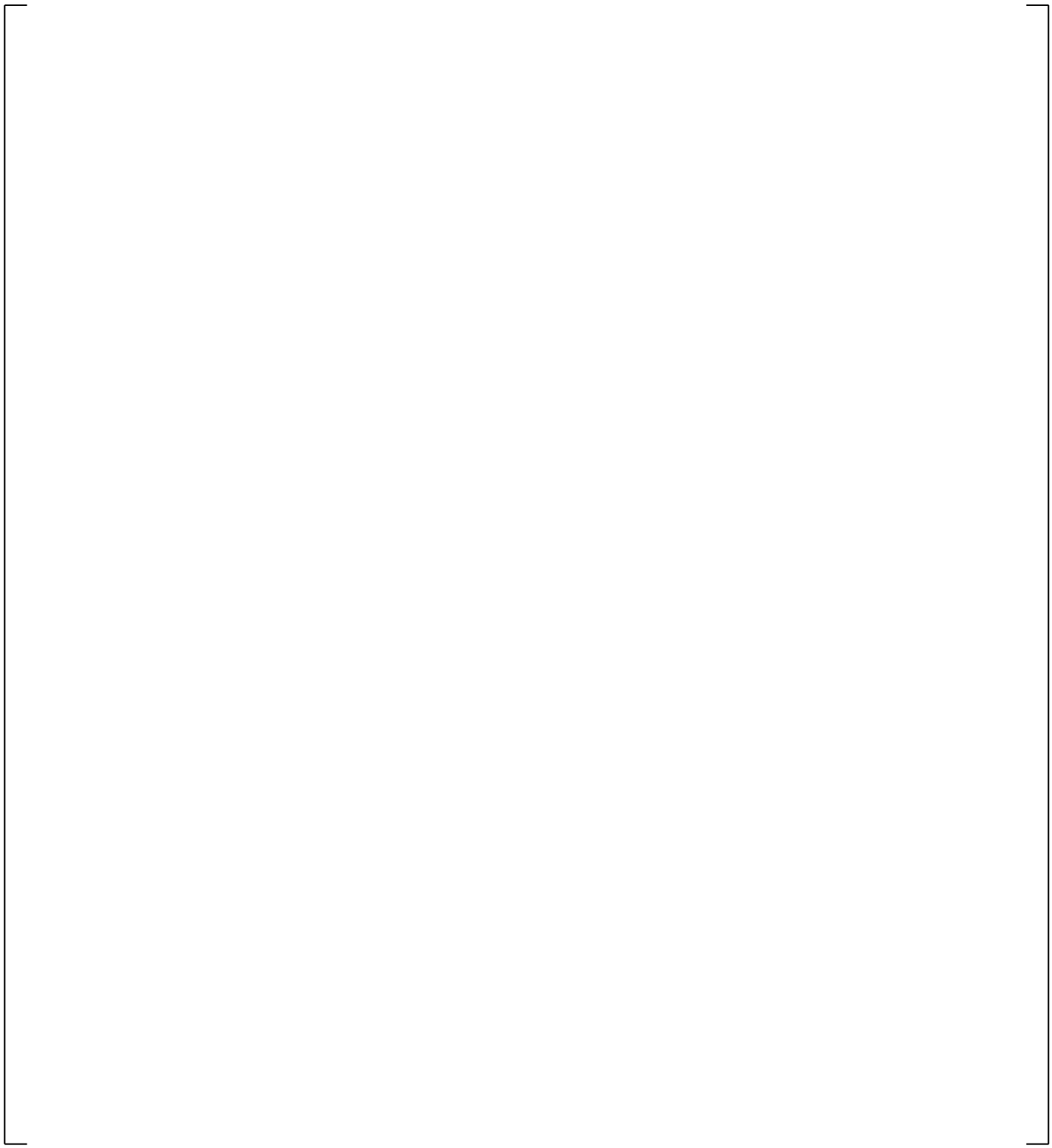

Figure 24.7.1-13 Measured and Predicted Intact Loop Hot Leg Flowrate

a,c

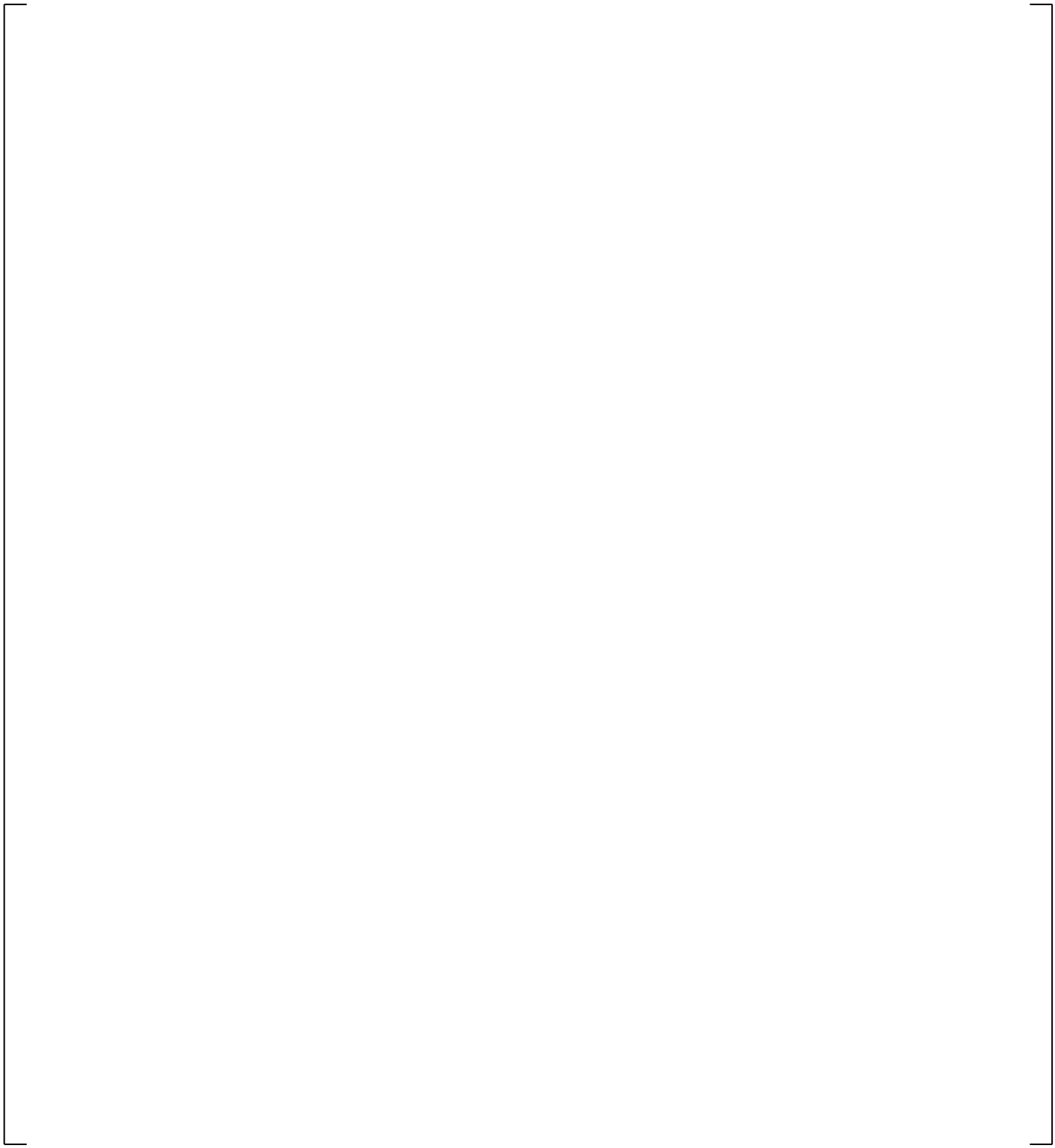

Figure 24.7.1-14 Measured and Predicted Intact Loop Hot Leg Mixture Density

a,c

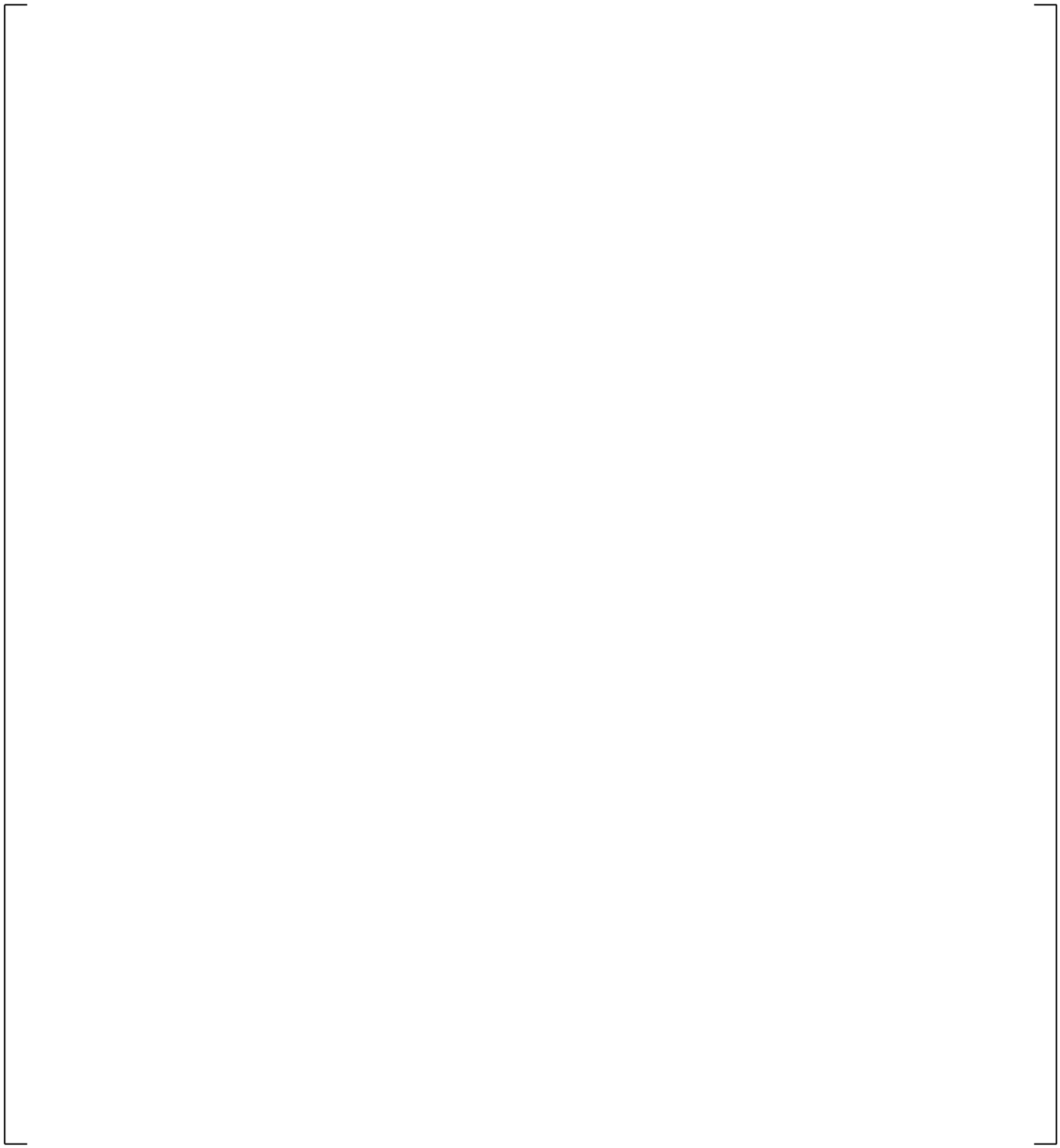

Figure 24.7.1-15 Measured and Predicted Intact Loop Hot Leg Mixture Velocity

a,c

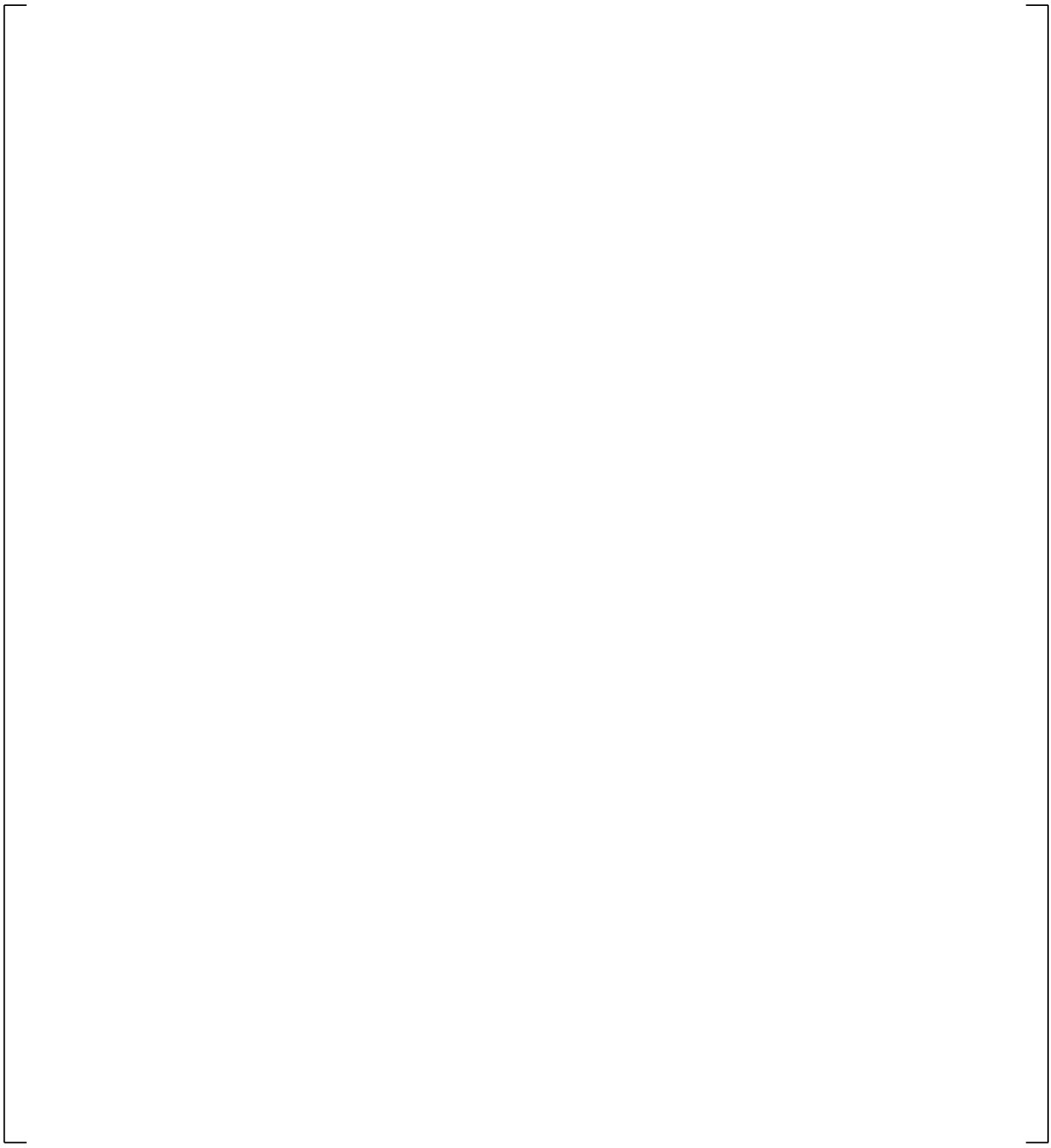

Figure 24.7.1-15a Measured and Predicted Intact Loop Pressure Comparison

a,c

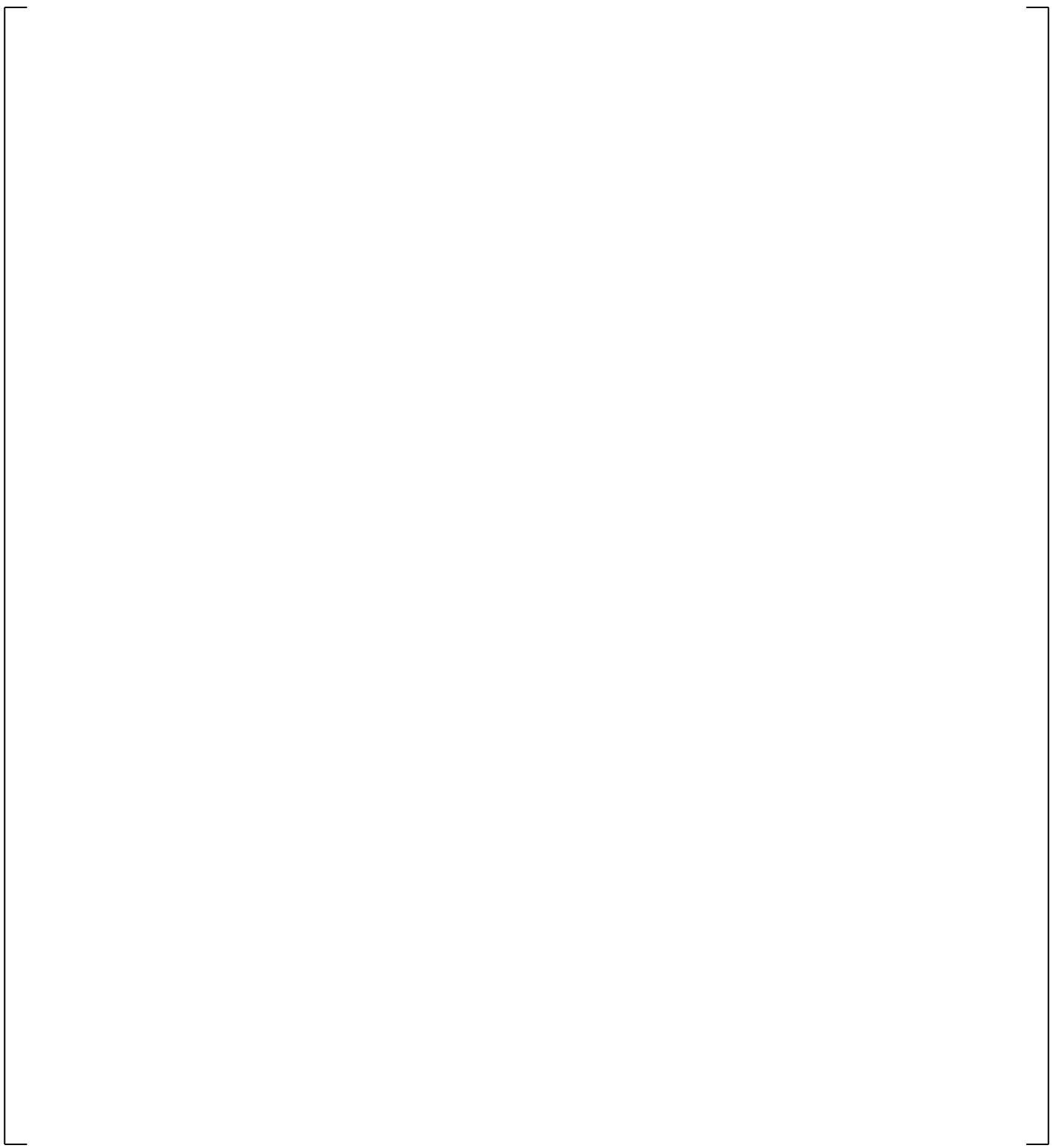

Figure 24.7.1-16 Measured and Predicted Intact Loop Cold Leg Flowrate

a,c

Figure 24.7.1-17 Measured and Predicted Intact Loop Cold Leg Flowrate

a,c

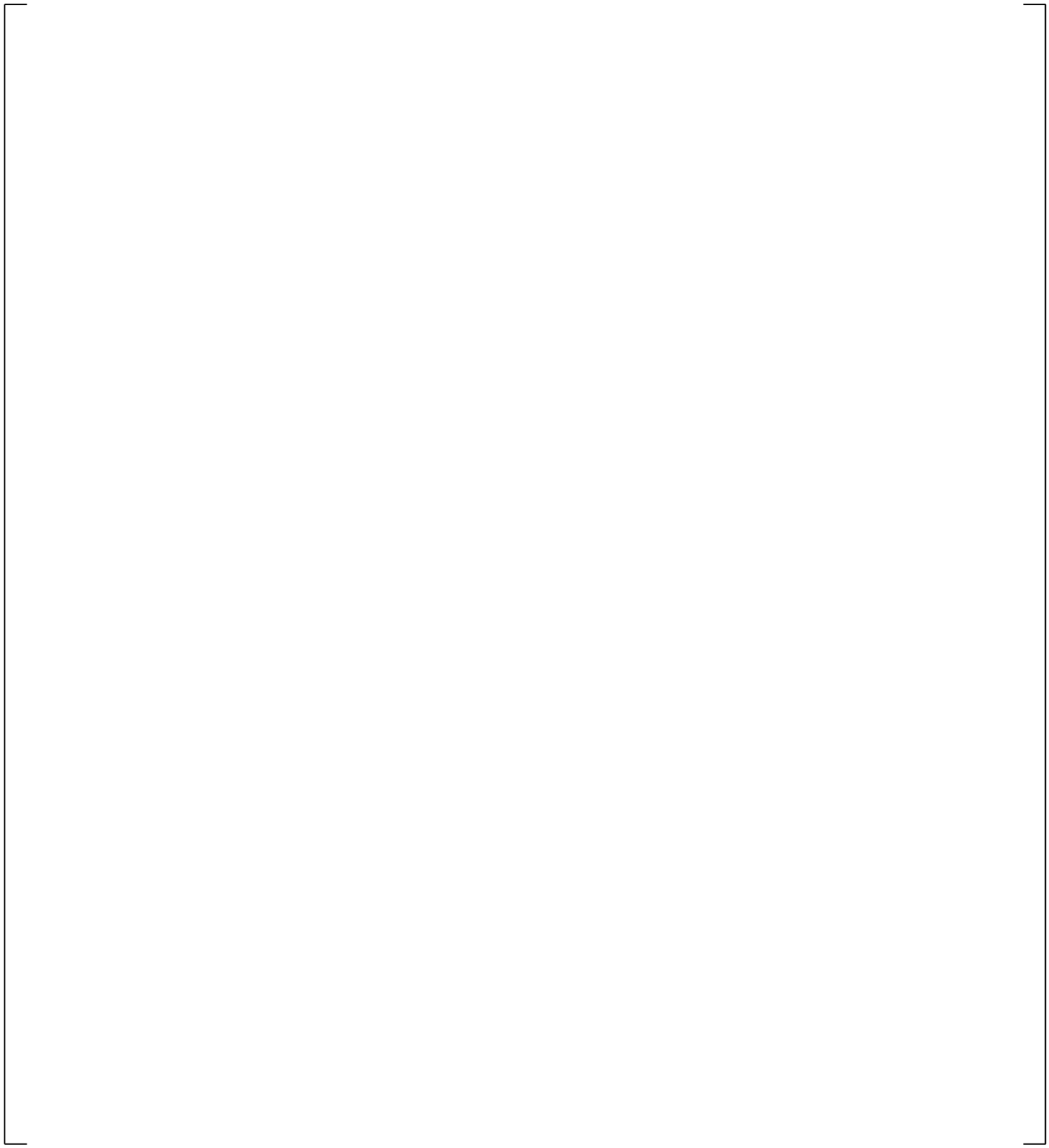

Figure 24.7.1-18 Measured and Predicted Intact Loop Cold Leg Mixture Density

a,c

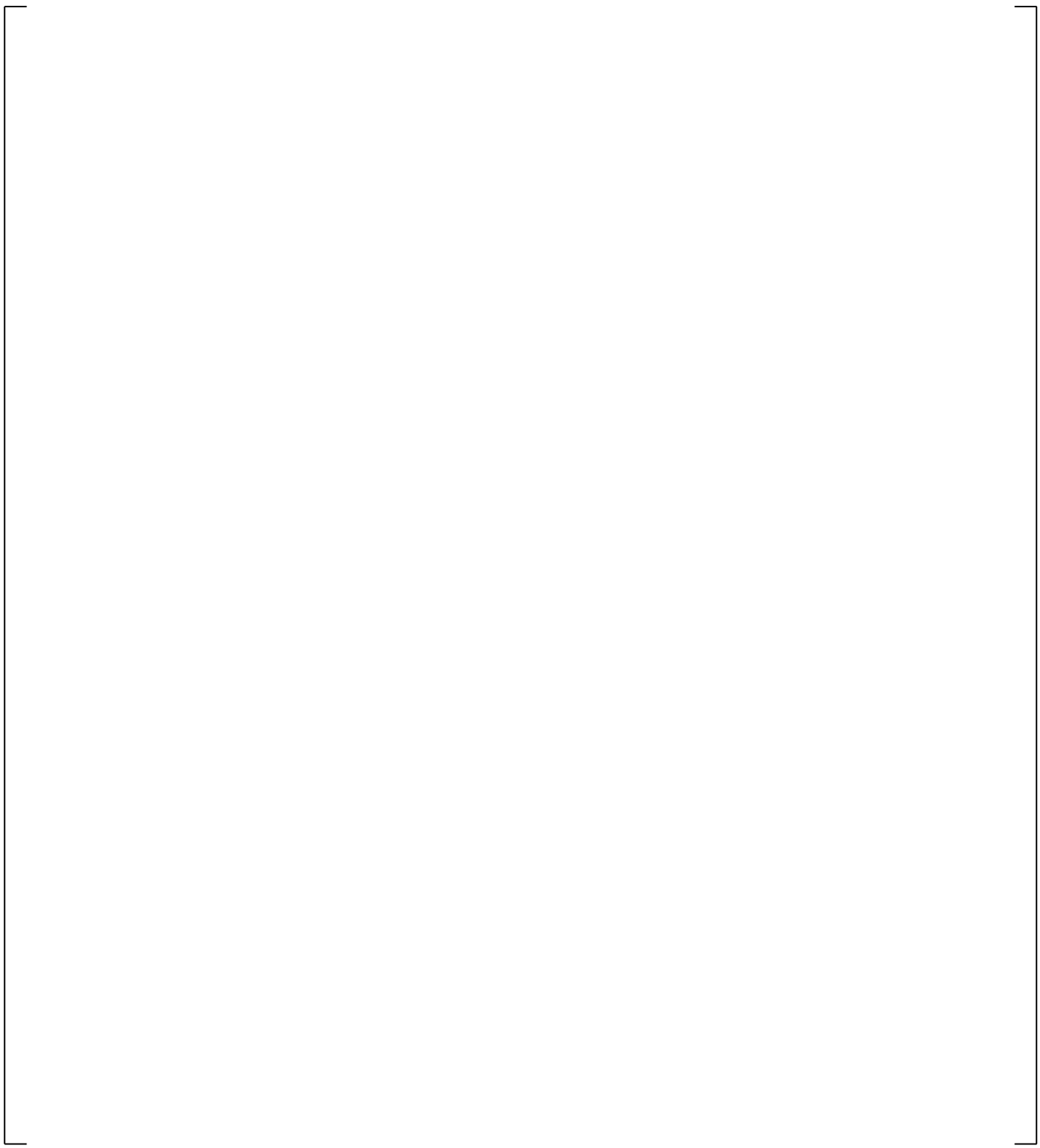

Figure 24.7.1-19 Measured and Predicted Intact Loop Cold Leg Mixture Density

a,c

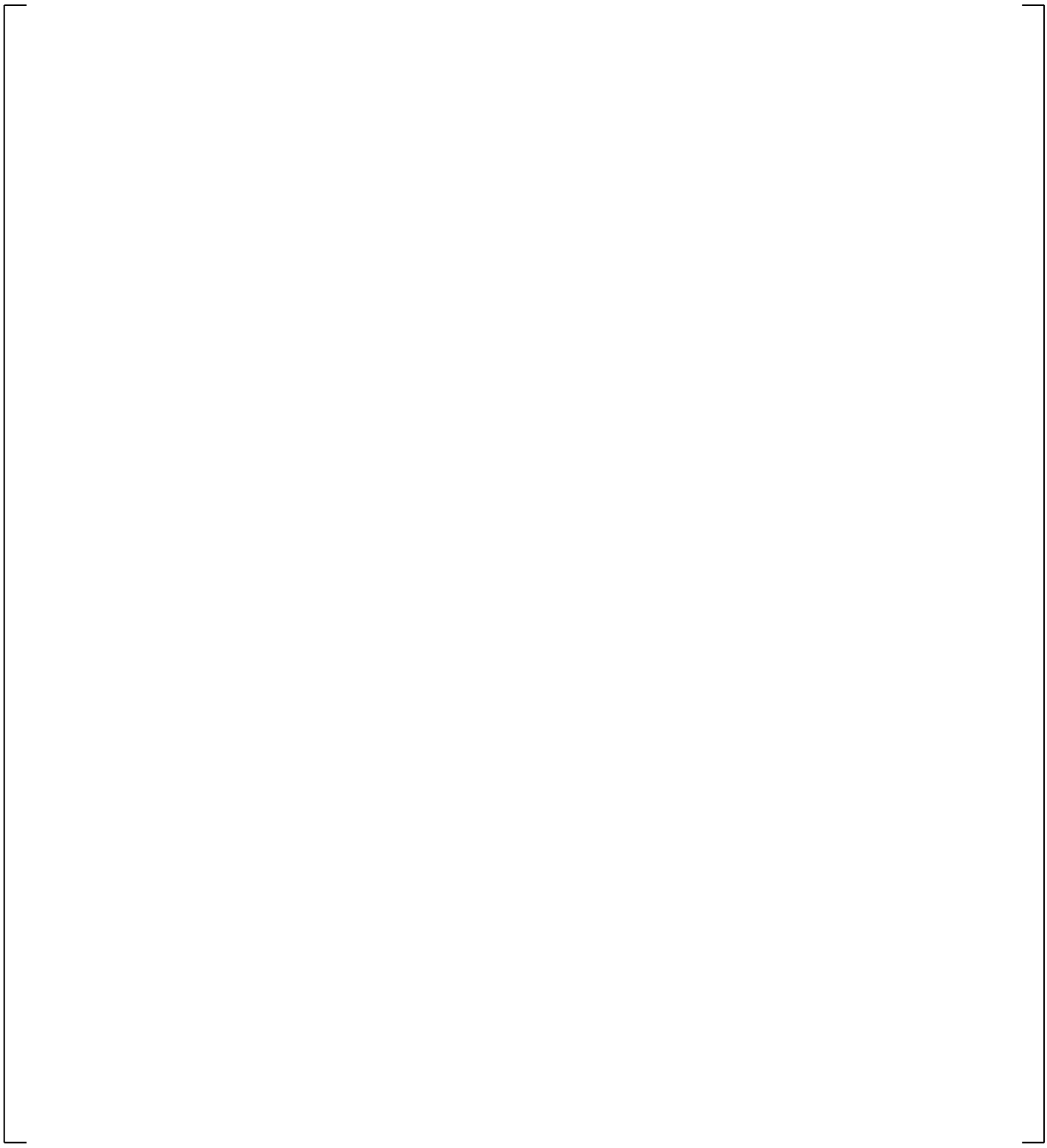

Figure 24.7.1-20 Measured and Predicted Intact Loop Cold Leg Mixture Velocity

a,c

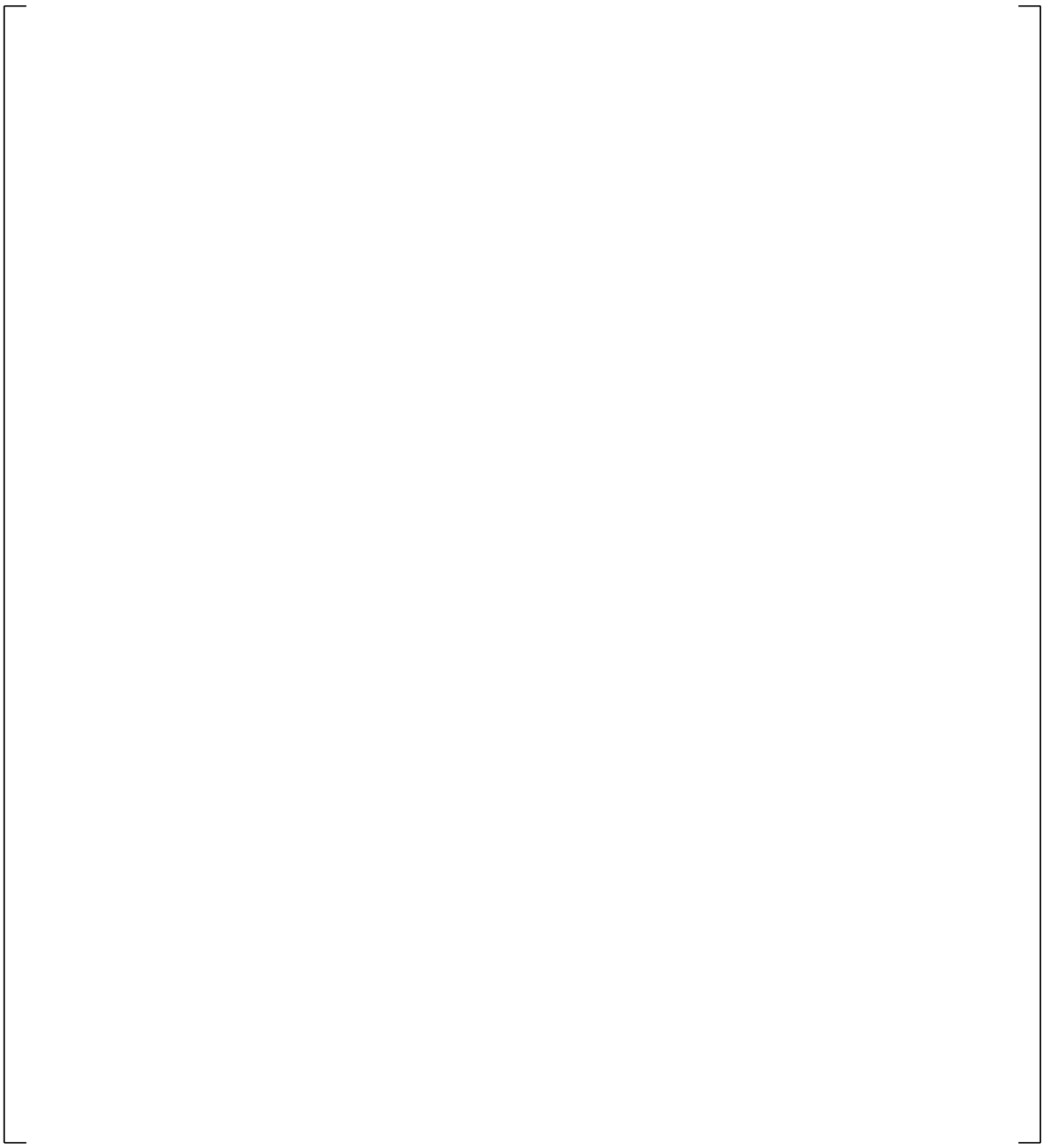

Figure 24.7.1-21 Measured and Predicted Intact Loop Cold Leg Mixture Velocity

a,c

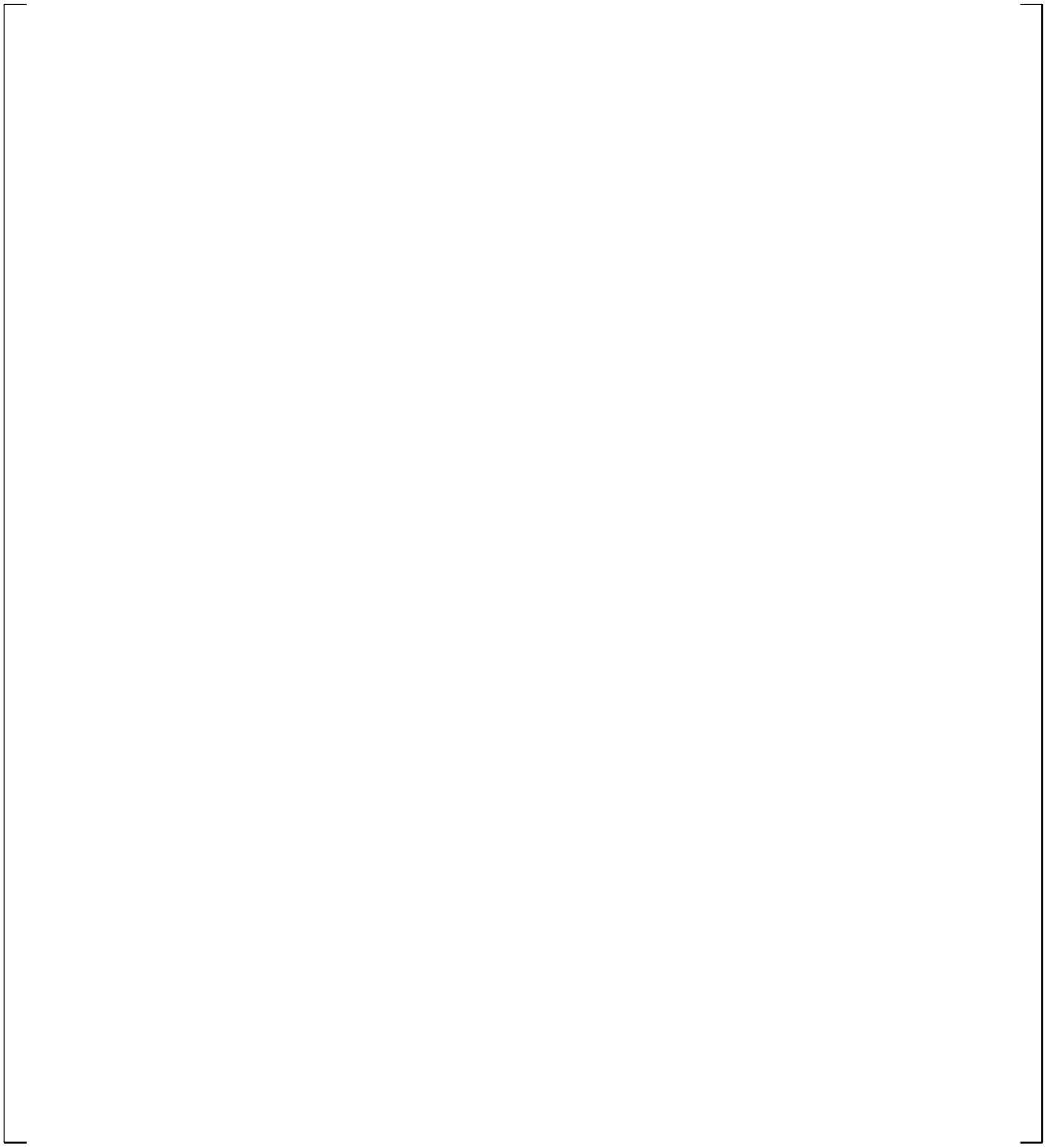

Figure 24.7.1-22 Measured and Predicted Hot Leg Break Flowrate

a,c

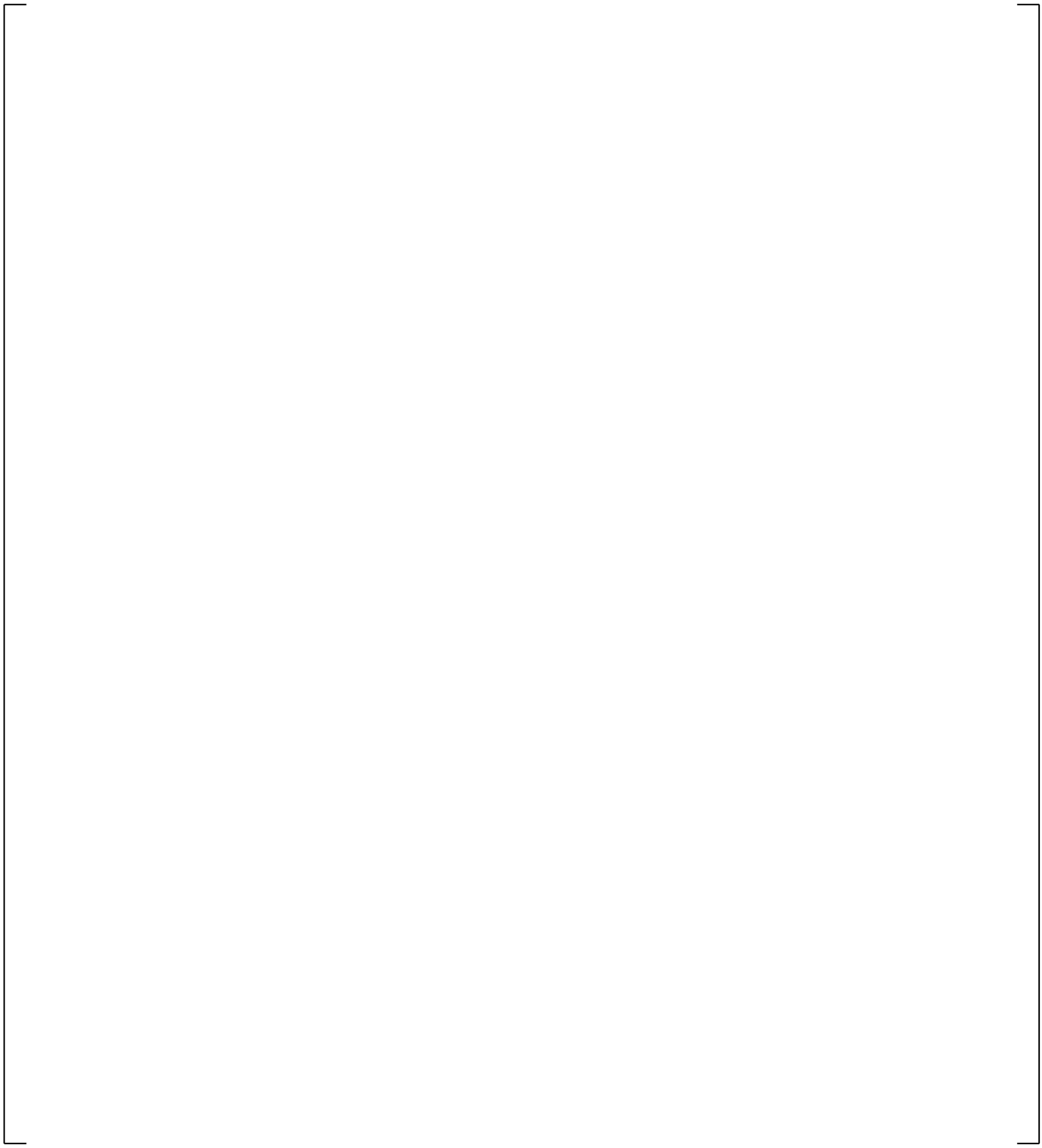

Figure 24.7.1-23 Measured and Predicted Broken Loop Hot Leg Mixture Density

a,c

Figure 24.7.1-24 Measured and Predicted Broken Loop Hot Leg Mixture Velocity

a,c

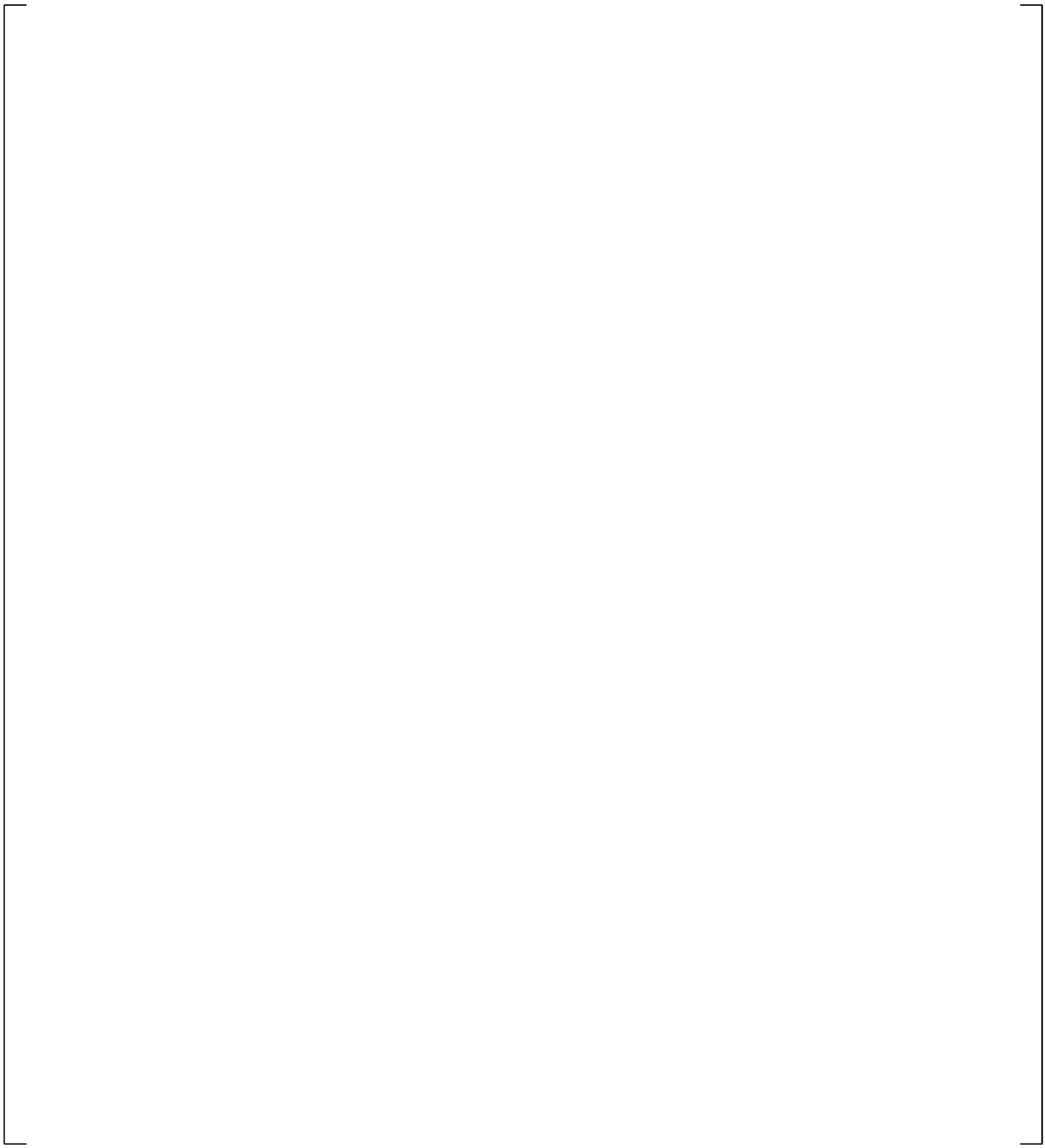

Figure 24.7.1-25 Predicted Void Fraction in Upper Plenum at Loop Level

a,c

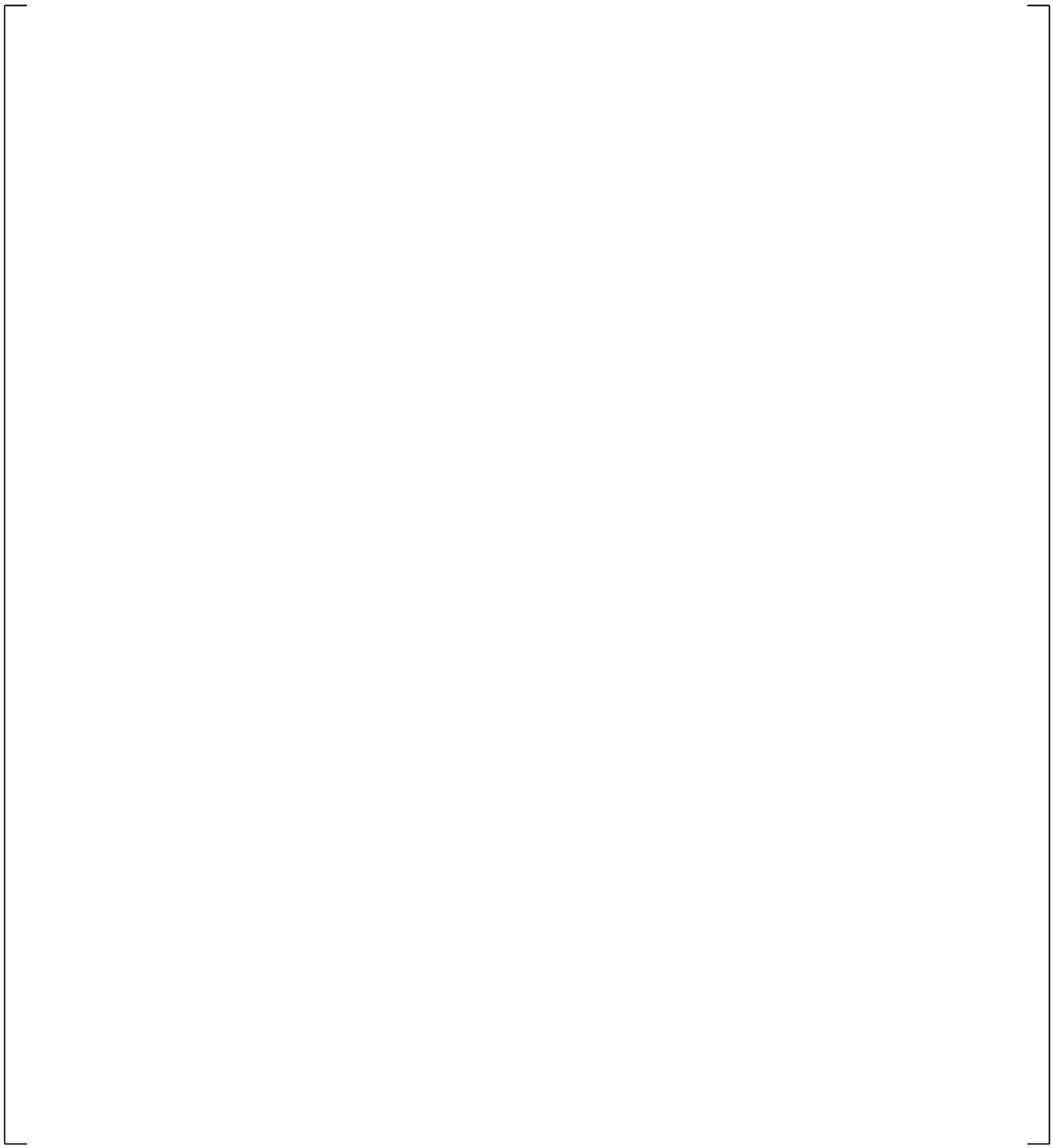

Figure 24.7.1-26 Predicted Void Fraction in Upper Plenum above Upper Core Plate

a,c

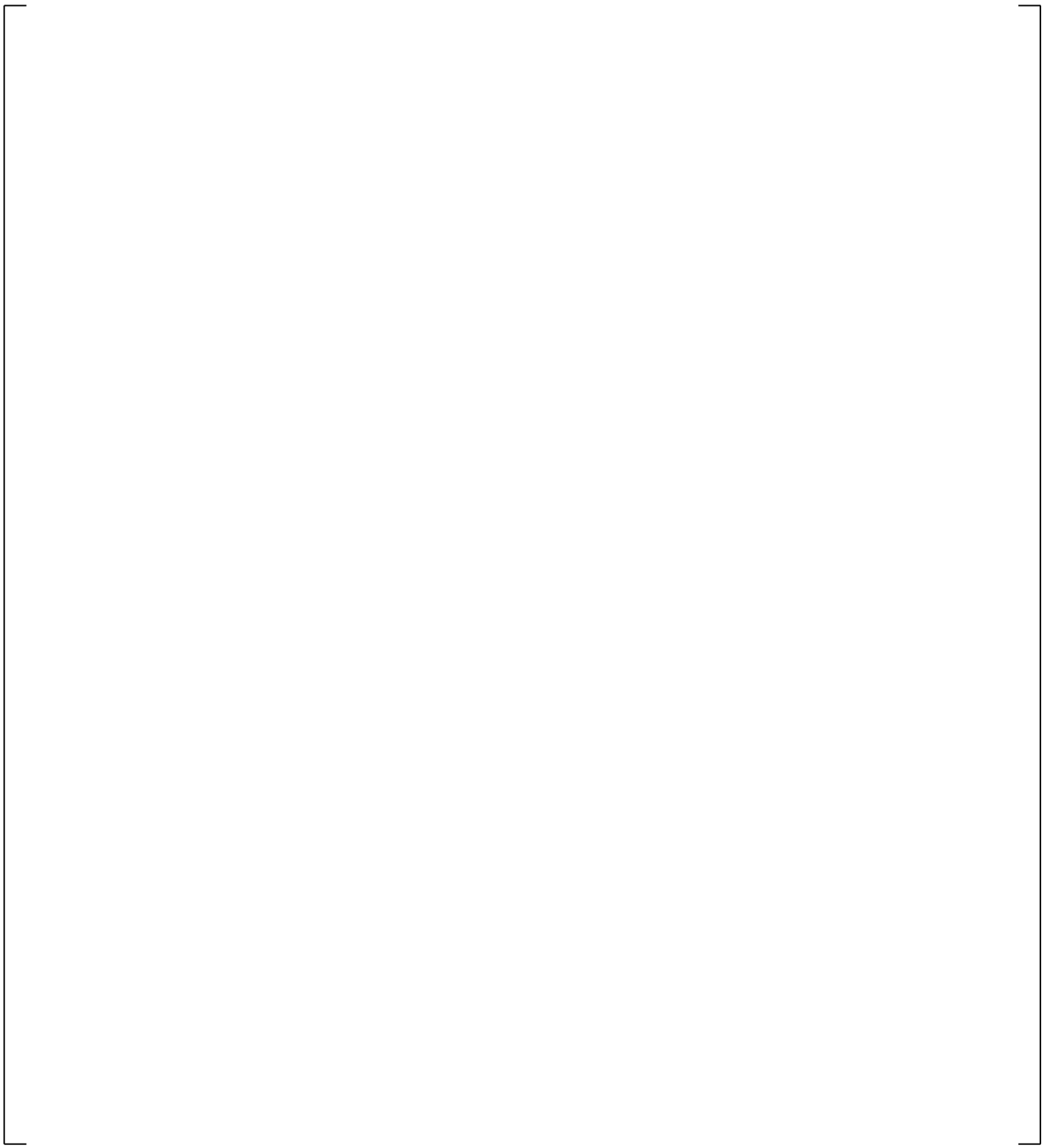

Figure 24.7.1-27 Measured and Predicted Cold Leg Break Flowrate

a,c

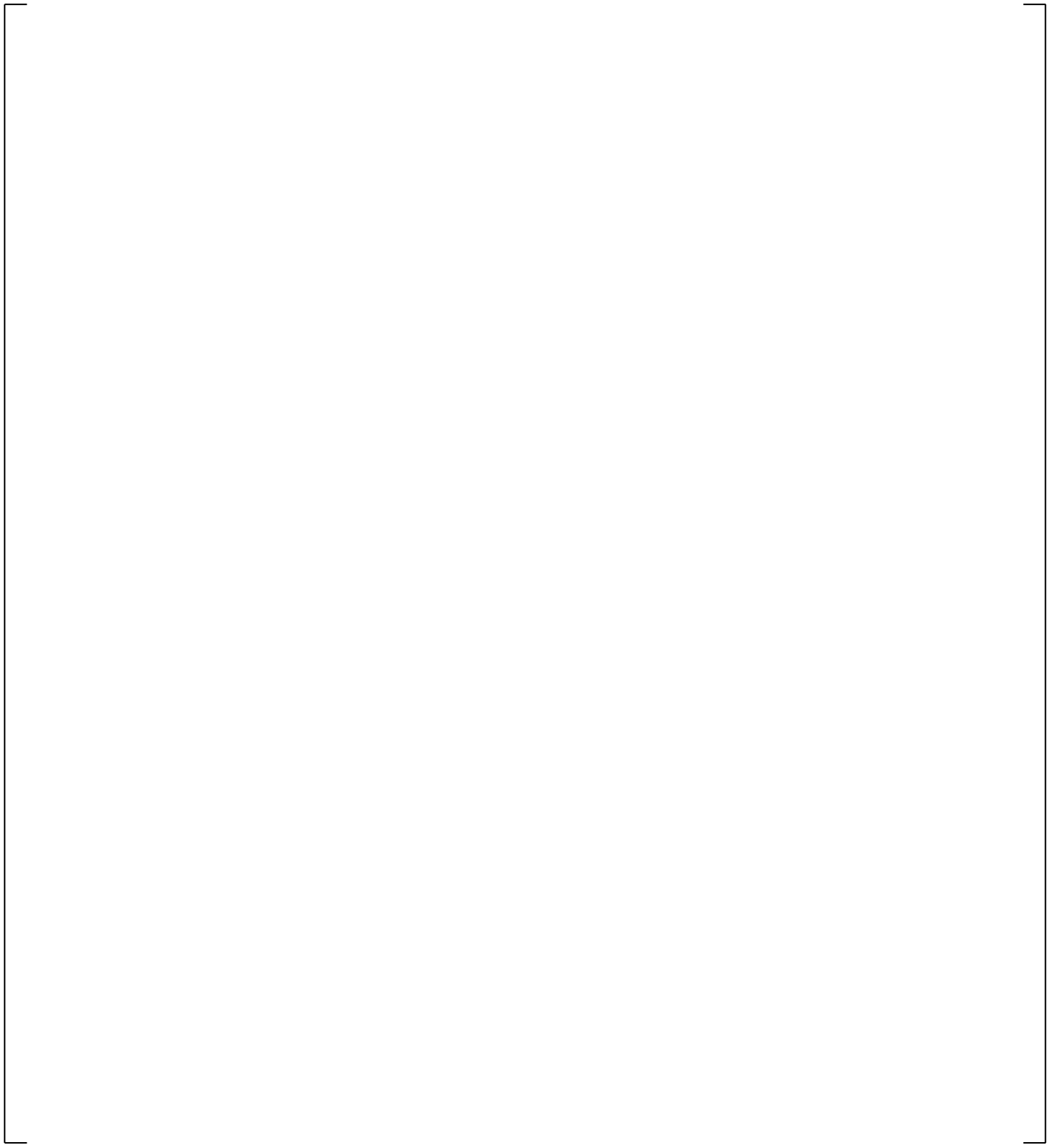

Figure 24.7.1-28 Measured and Predicted Broken Cold Leg Mixture Density

a,c

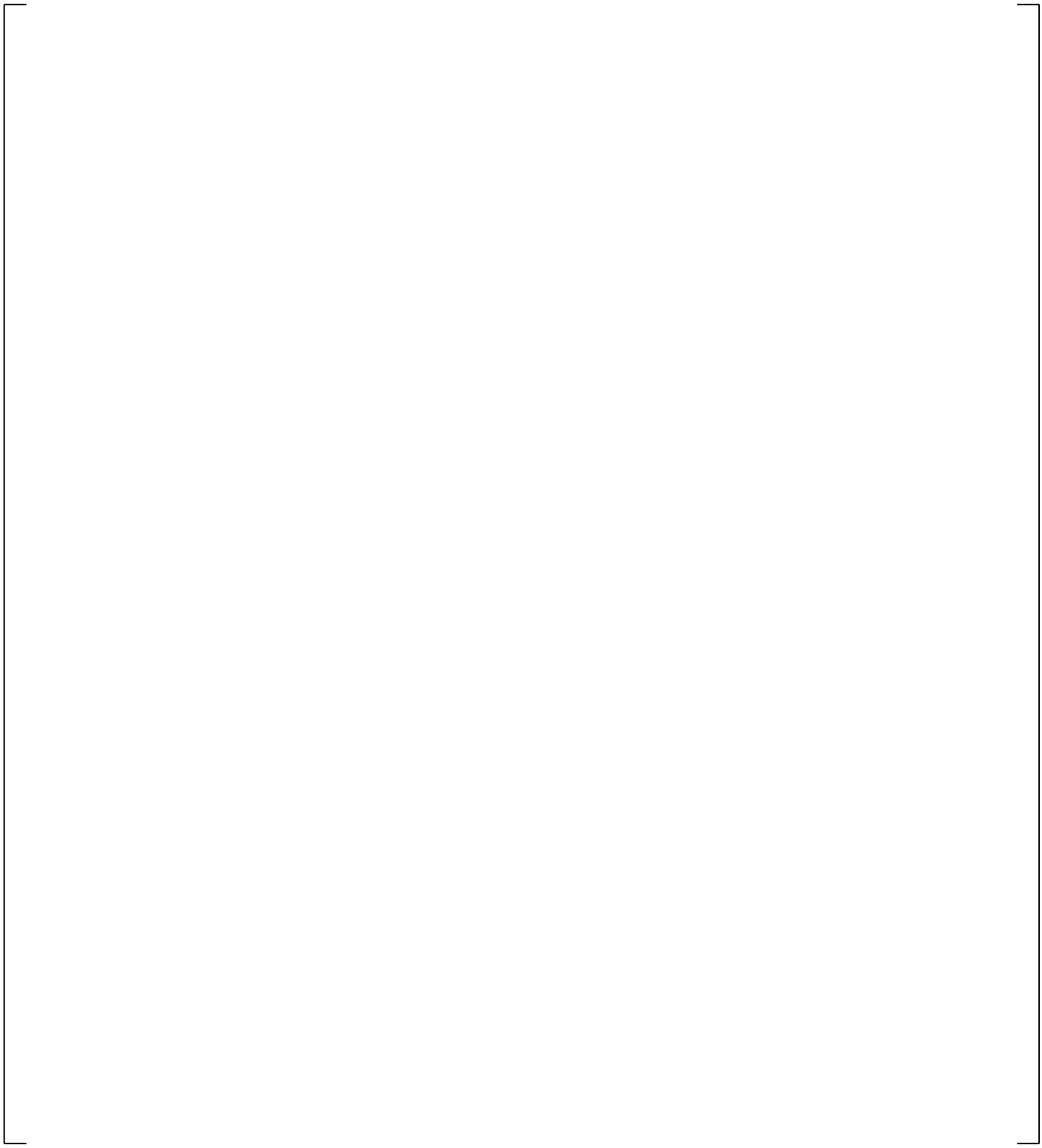

Figure 24.7.1-29 Measured and Predicted Broken Cold Leg Mixture Velocity

a,c

Figure 24.7.1-30 Mid-Elevation Cladding Temperature Comparison in Sensitivity Run with CD2=1.05

a,c

Figure 24.7.1-31 Predicted Vapor Flowrate at Top and Bottom of Hot Assembly in Sensitivity Run with CD2=1.05

a,c

Figure 24.7.1-32 Predicted Entrained Drop Flowrate at Top and Bottom of Hot Assembly in Sensitivity Run with CD2=1.05

a,c

Figure 24.7.1-33 Predicted Hot Rod Liquid Heat Transfer Coefficient at PCT Elevation in Sensitivity Run with CD2=1.05

24.7.2 LOFT Test L2-5

The plots for this section are designated Figures 24.7.2-1 through 24.7.2-30. LOFT Test L2-5 (Bayless and Divine, 1982) was a pumps "off," intermediate power test. A summary of event times is given below, where end of blowdown is defined as the time when the system pressure reaches a minimum:

Event	Time (s)
Blowdown begins	0
Accumulator begins injecting	17
End of Blowdown/beginning of reflood	40
Accumulator empty (N_2 injection)	50-60
Core quench	65

The prediction and data assessment will follow the same format as in LOFT Test L2-3.

Core Thermal-Hydraulics

The cladding temperature for LOFT Test L2-5 was **[**

][a,c]

System Behavior

[

]a,c

Loop Behavior: Intact loop

[

]a,c

Loop Behavior: Broken loop

[

]^{a,c}

Sensitivity Studies

Several studies were performed to examine what factors contribute most to the mis-prediction of core flow. **[**

][a,c]

a,c

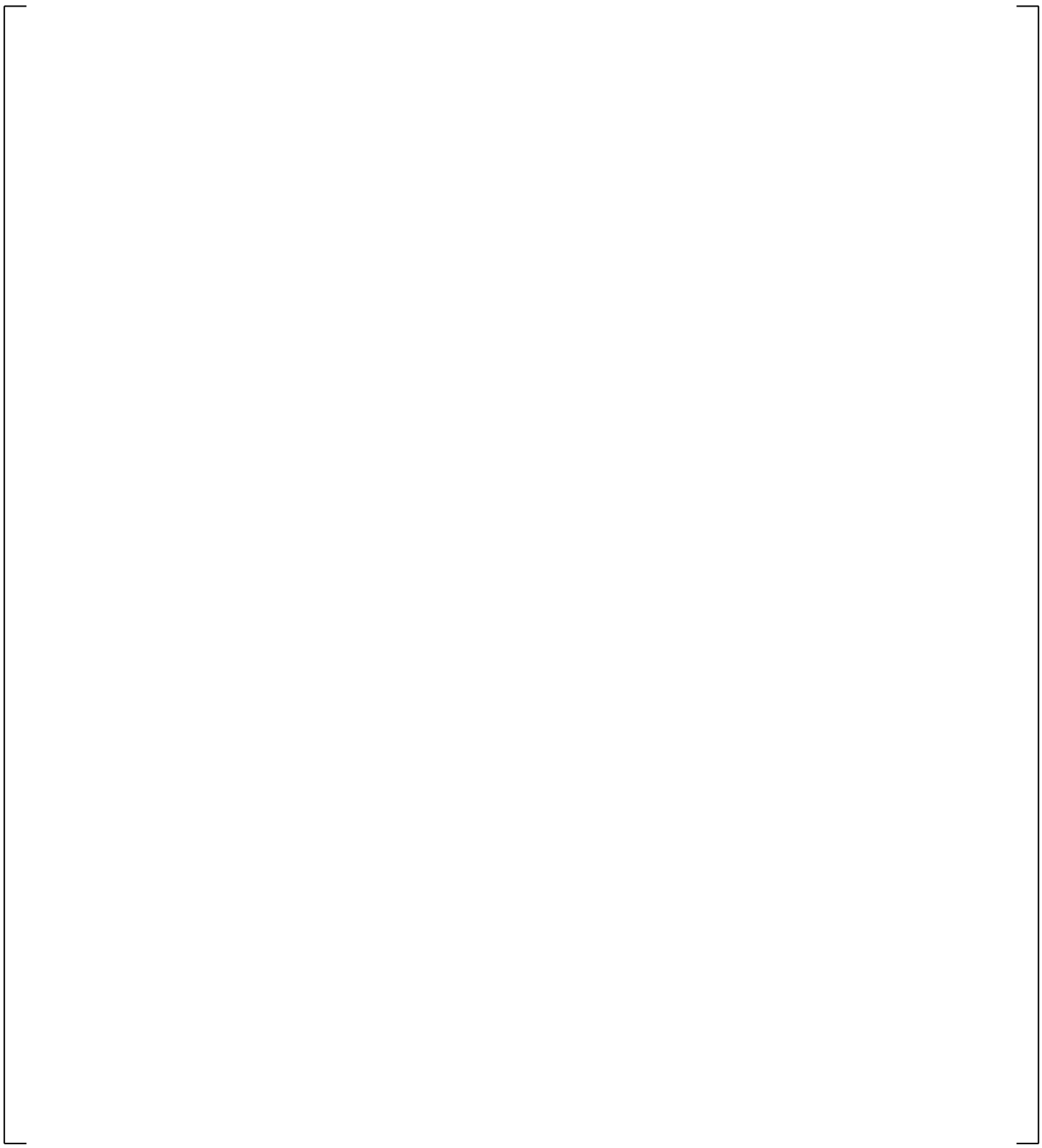

Figure 24.7.2-1 Measured vs. Predicted Hot Rod Cladding Temperature

a,c

Figure 24.7.2-2 Predicted Vapor Flowrate at Top and Bottom of Hot Assembly

a,c

Figure 24.7.2-3 Predicted Entrained Drop Flowrate at Top and Bottom of Hot Assembly

a,c

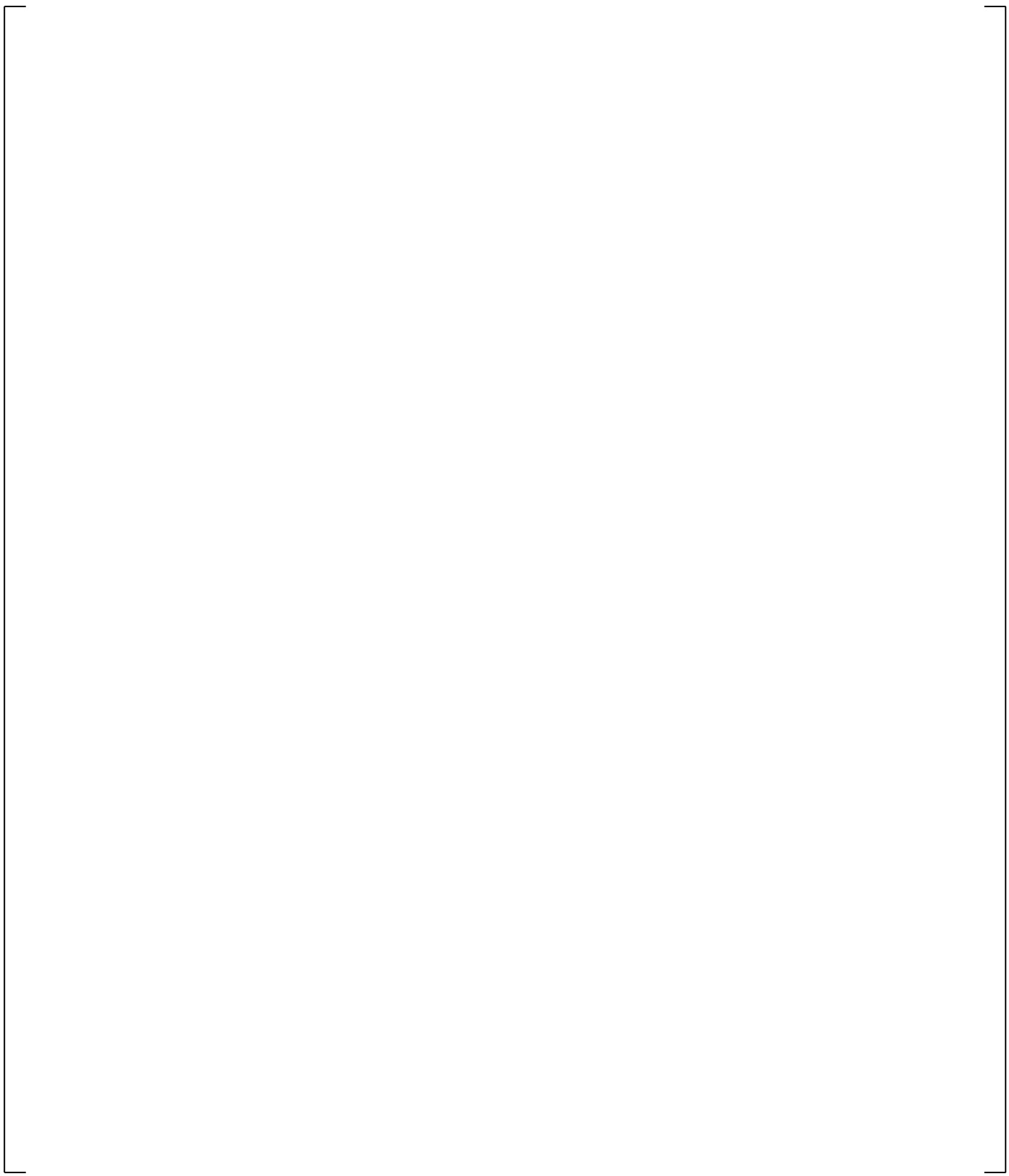

Figure 24.7.2-4 LOFT L2-5 Data vs. Predicted Steam Temperature at Top of Hot Assembly

a,c

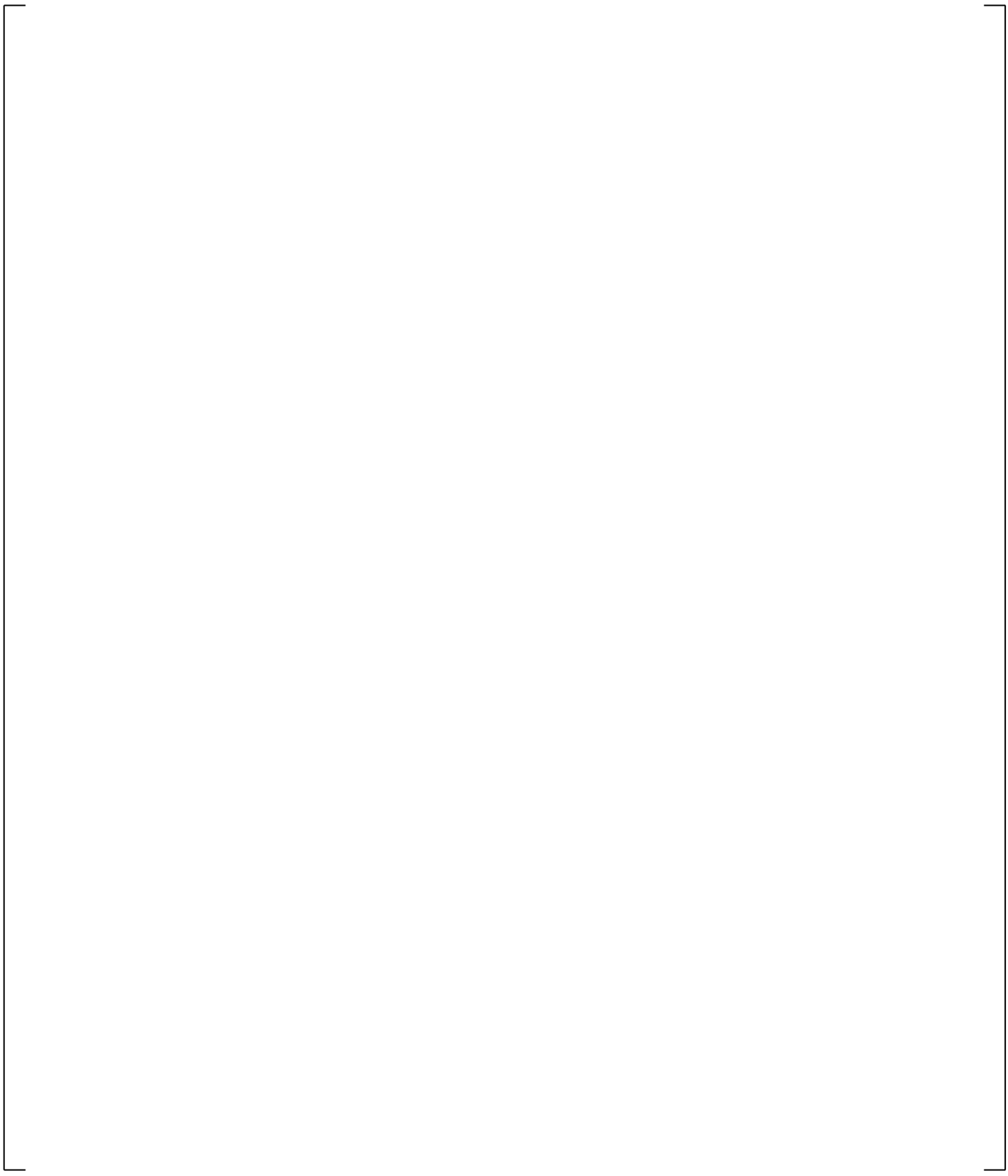

Figure 24.7.2-5 LOFT L2-5 Data vs. Predicted Steam Temperature at Bottom of Hot Assembly

a,c

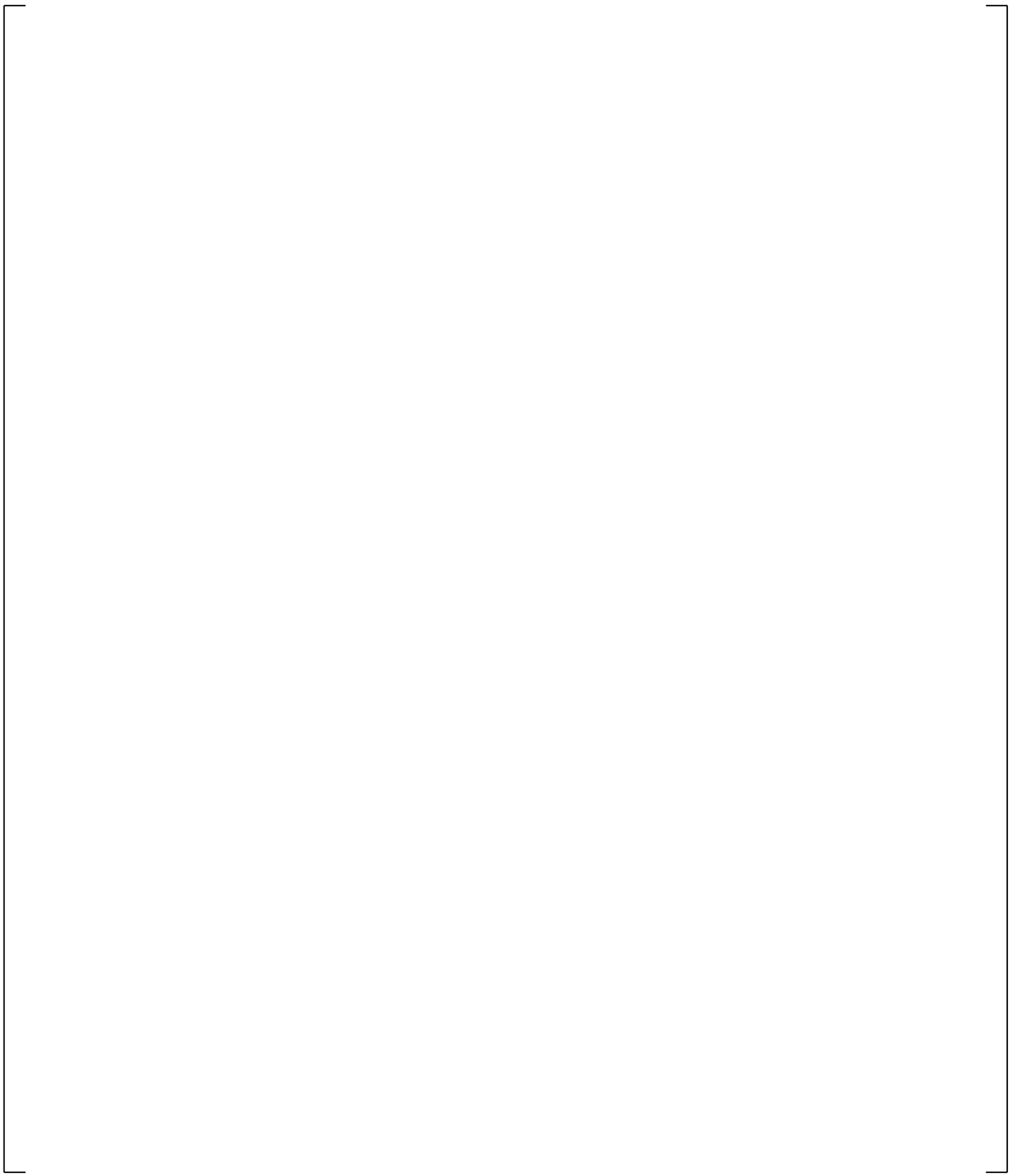

Figure 24.7.2-6 Predicted Hot Rod Vapor Heat Transfer Coefficient at PCT Elevation

a,c

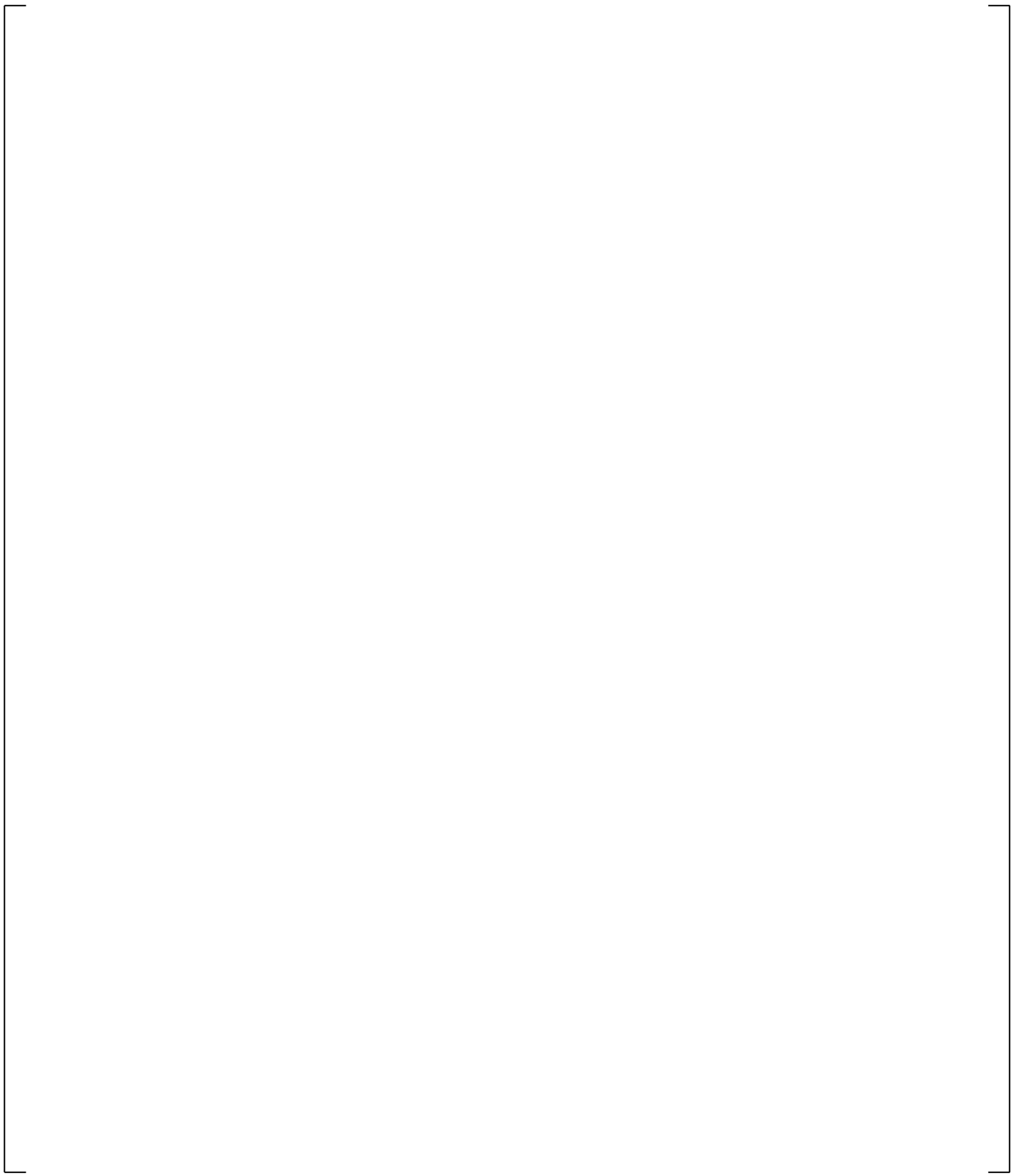

Figure 24.7.2-7 Predicted Hot Rod Liquid Heat Transfer Coefficient at PCT Elevation

a,c

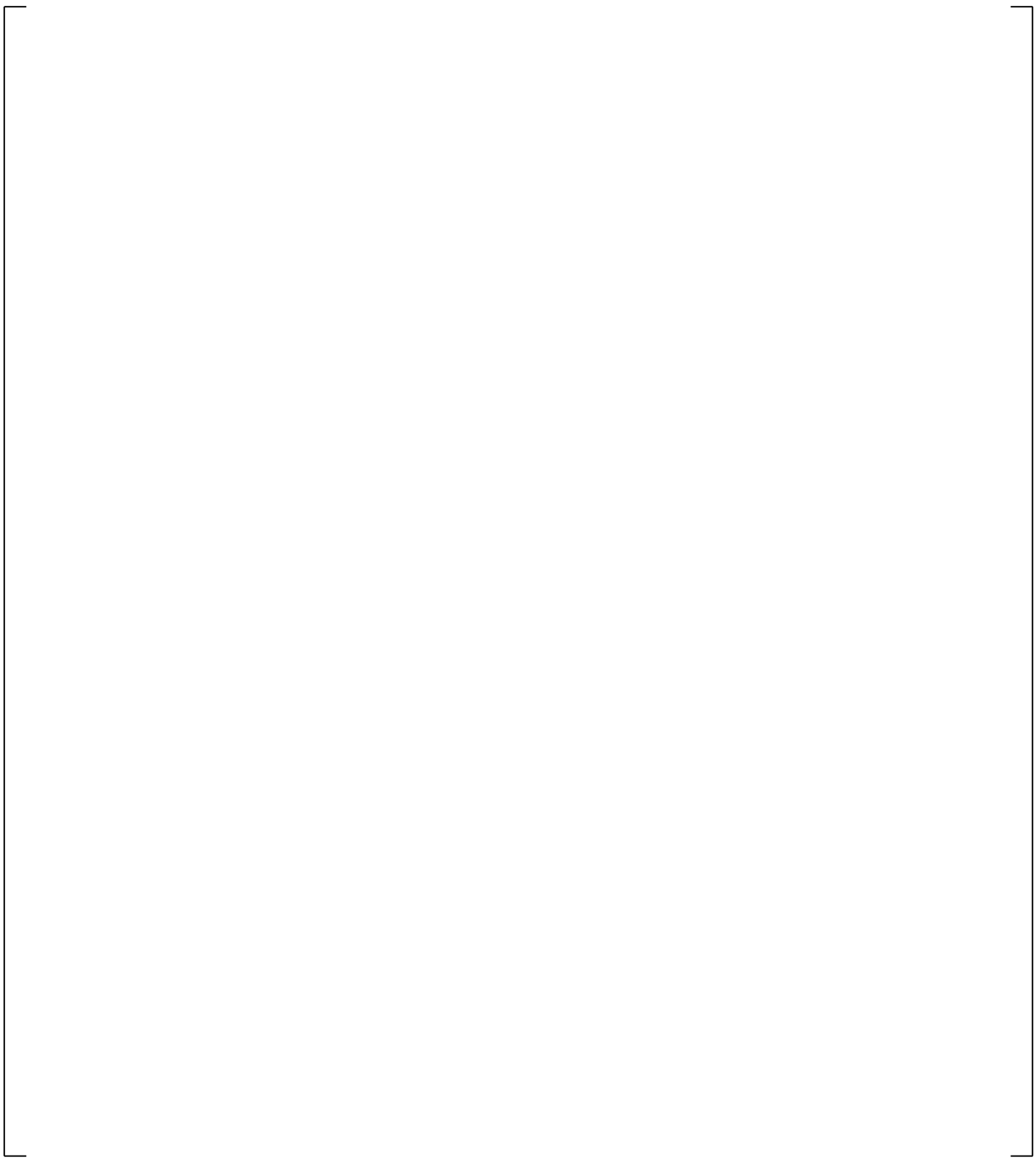

Figure 24.7.2-7a Predicted Hot Rod Liquid Heat Transfer Coefficient at PCT Elevation (with Expanded Scale)

a,c

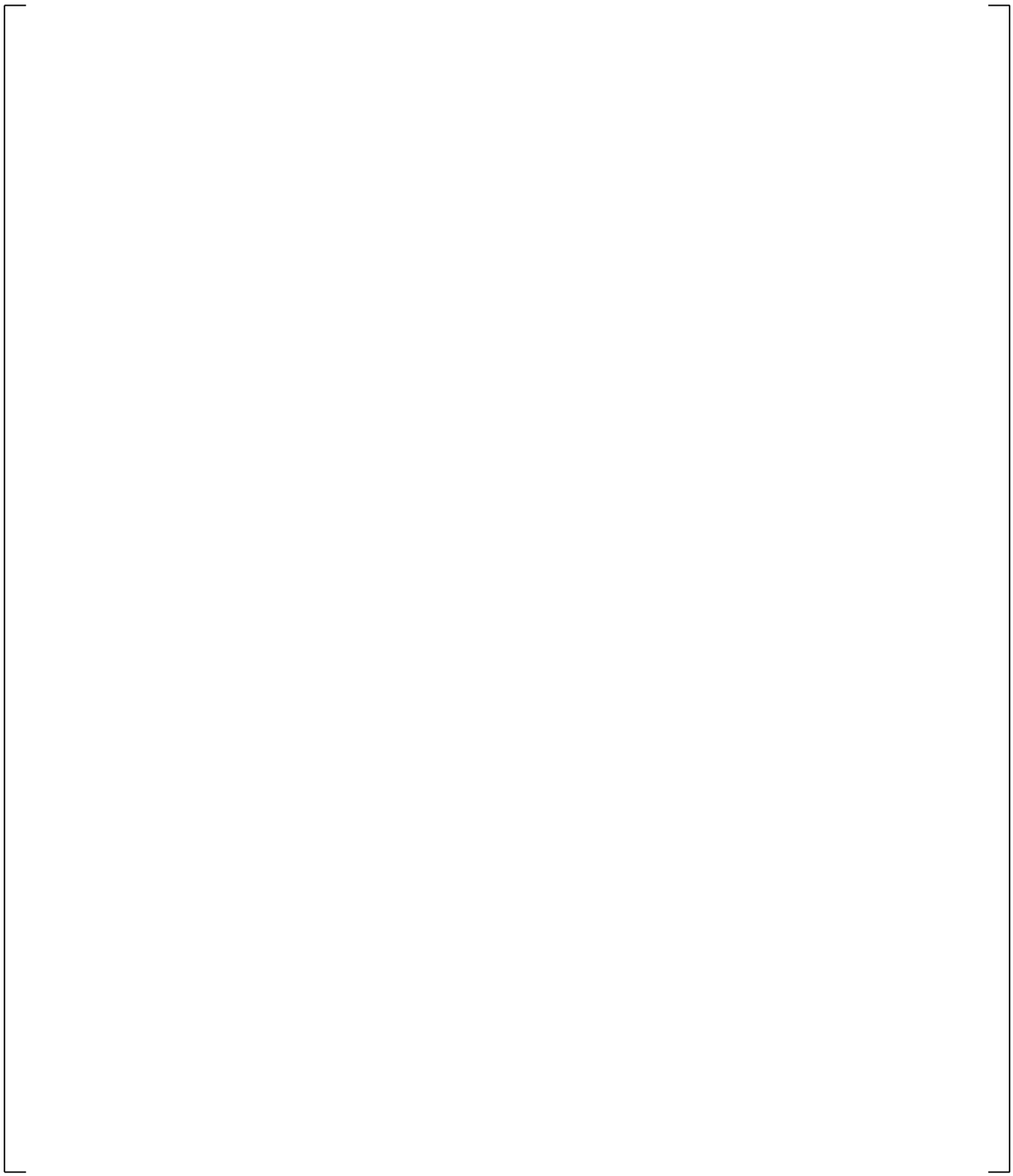

Figure 24.7.2-8 Measured and Predicted Intact Loop Pressure

a,c

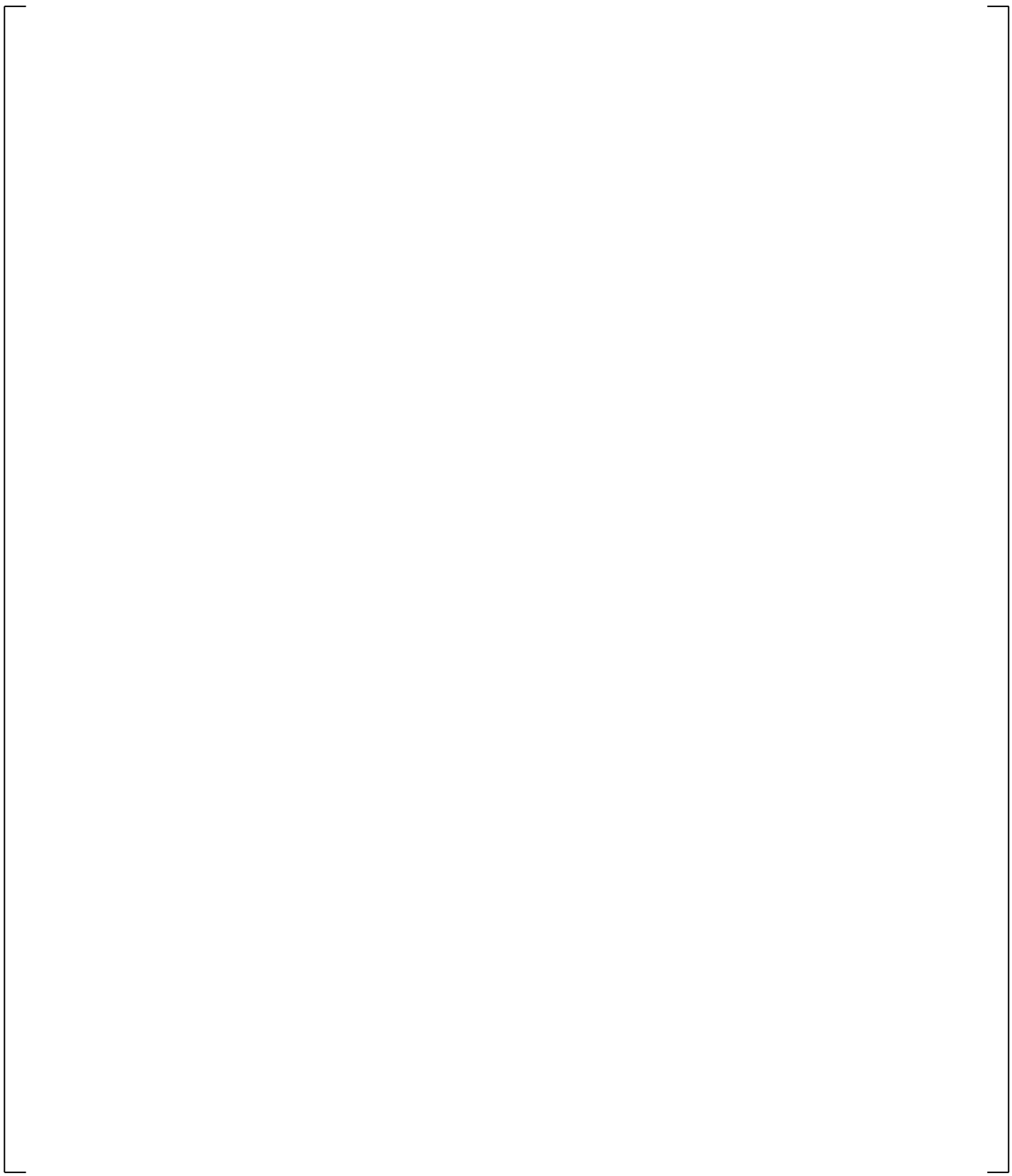

Figure 24.7.2-9 Predicted Downcomer Collapsed Liquid Level (1- Intact, 2-Broken side)

a,c

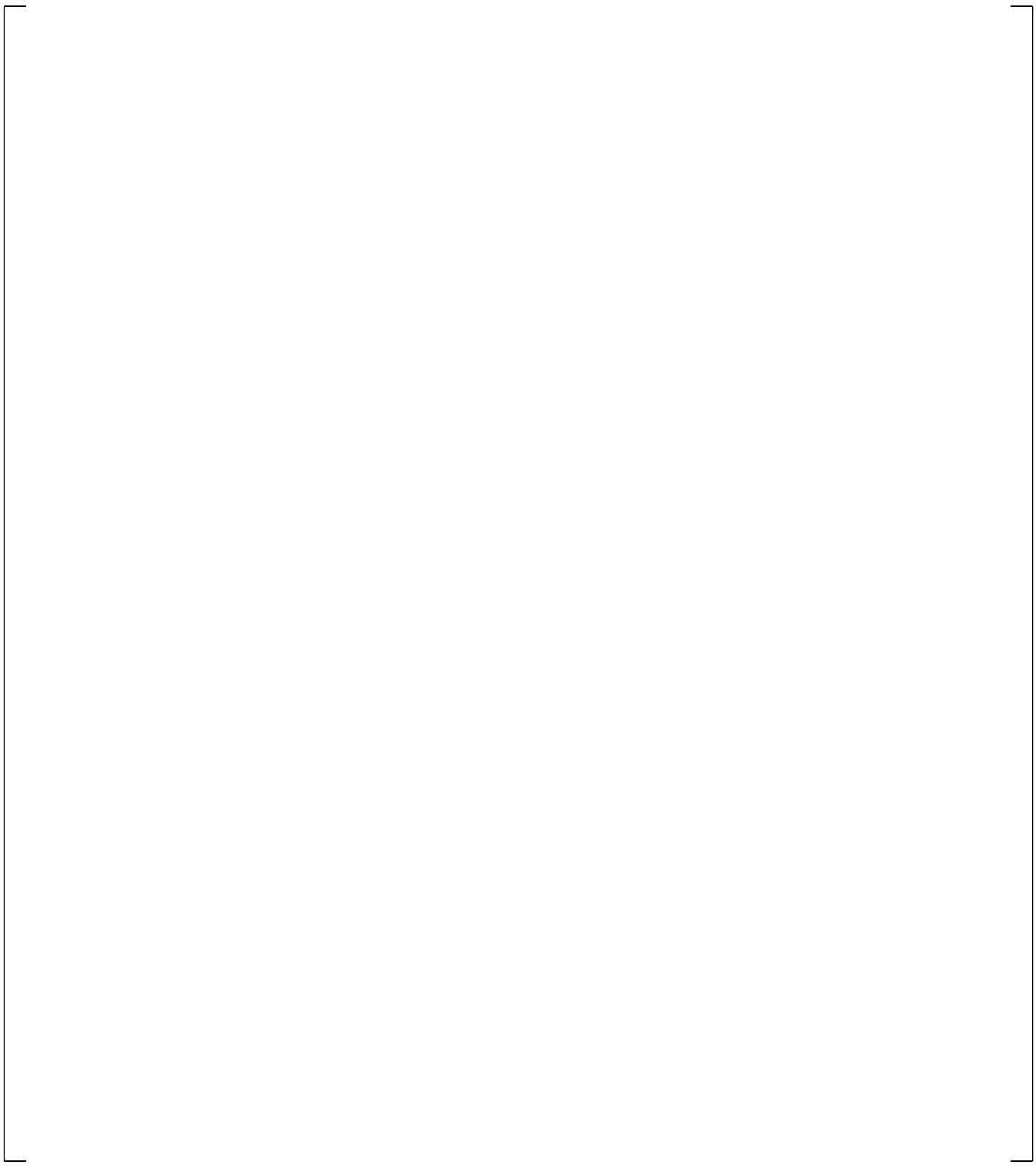

Figure 24.7.2-10 Predicted and Measured Core Collapsed Liquid Level (Line 2-Estimated from the Liquid Detector)

a,c

Figure 24.7.2-11 Predicted Upper Plenum Collapsed Liquid Level

a,c

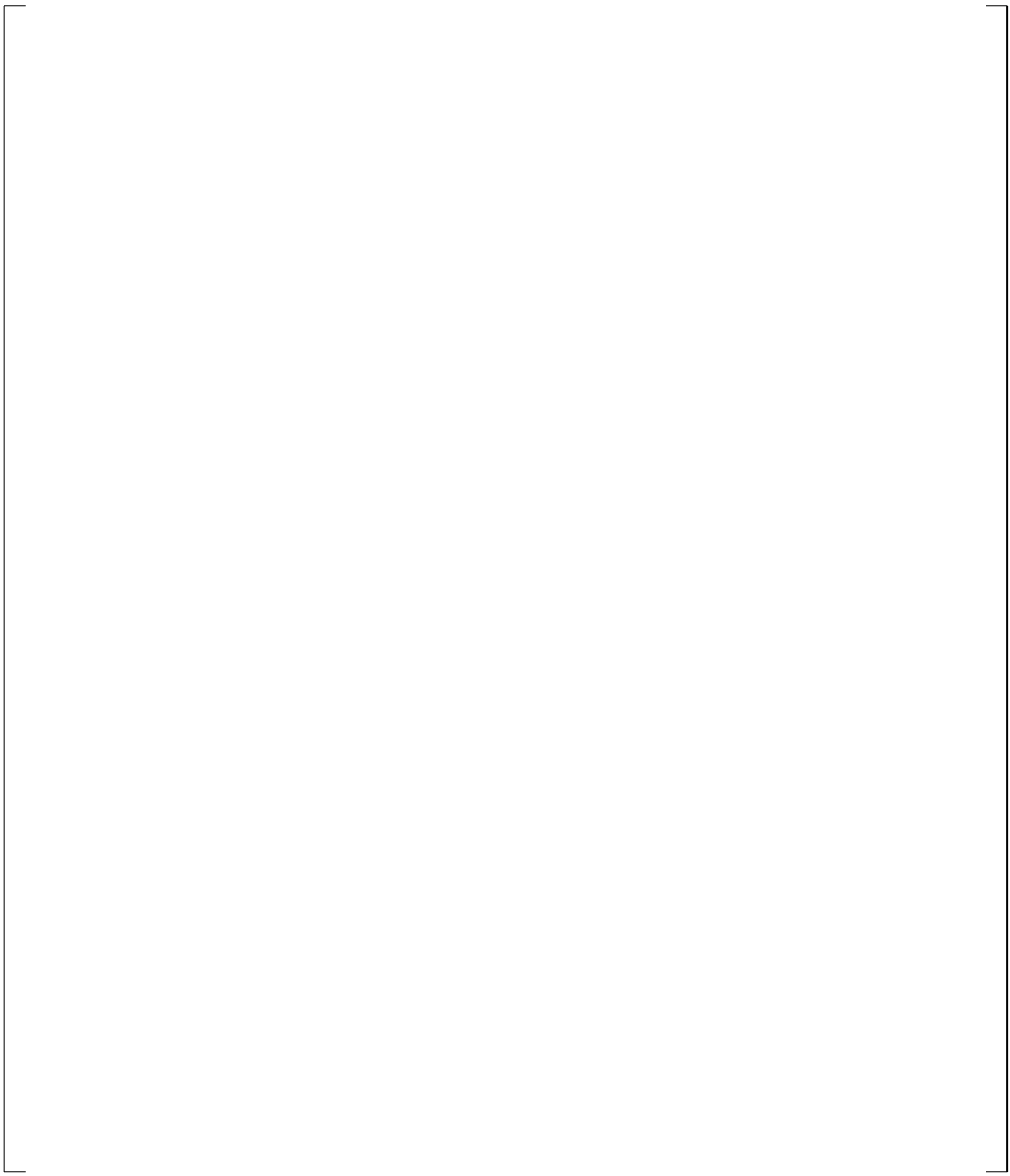

Figure 24.7.2-12 Measured and Predicted Intact Loop Hot Leg Flowrate

a,c

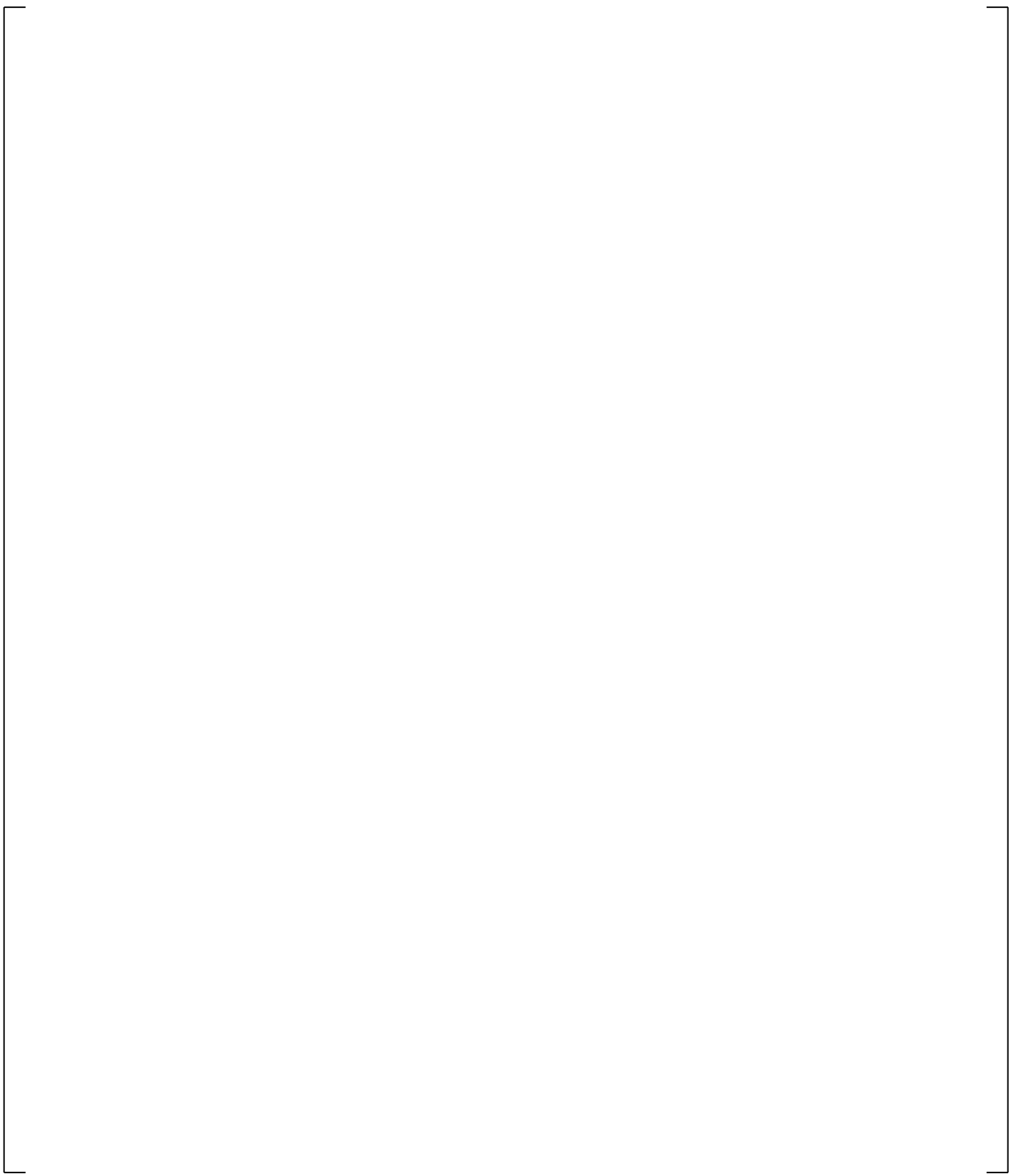

Figure 24.7.2-13 Measured and Predicted Intact Loop Hot Leg Mixture Density

a,c

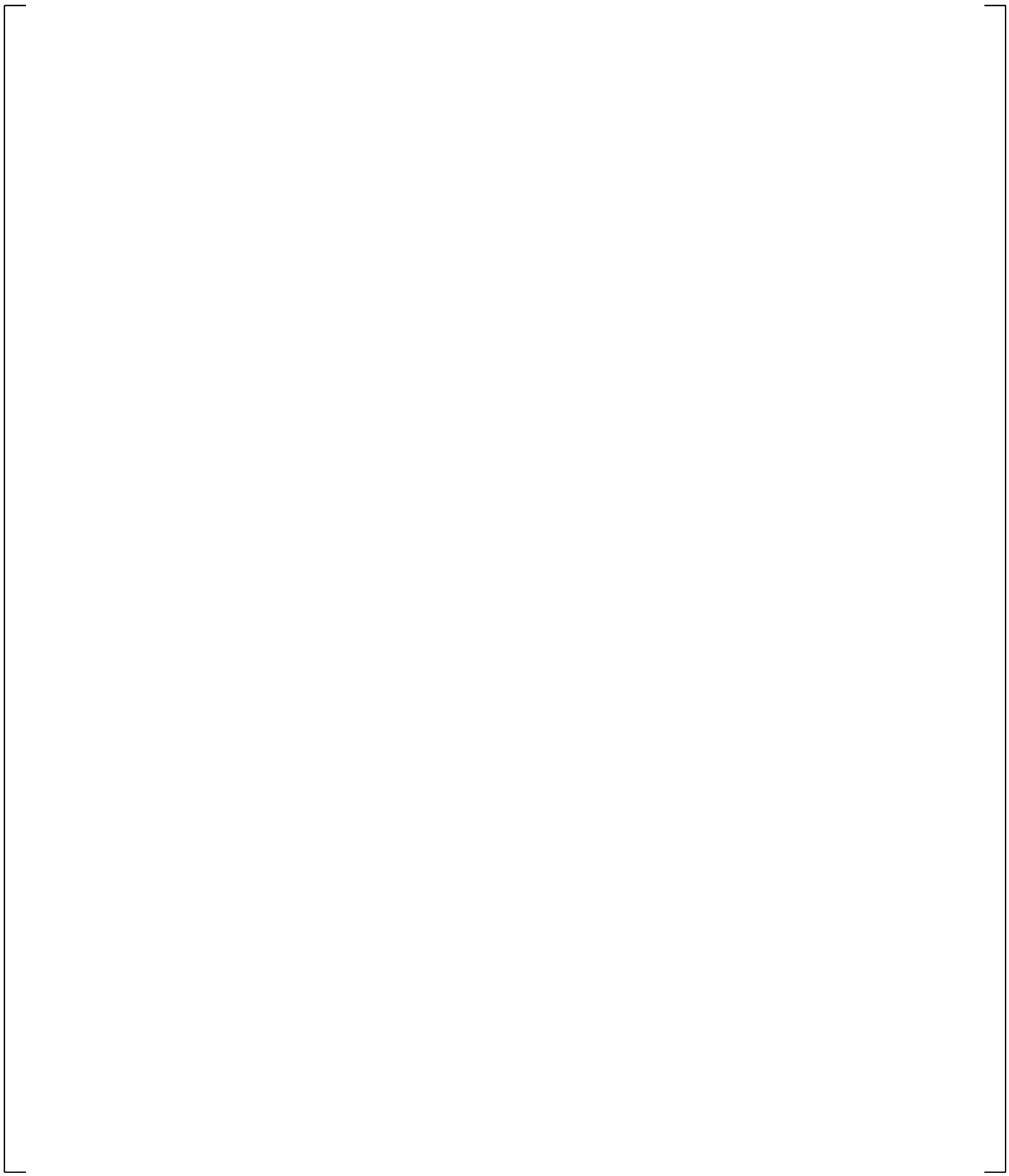

Figure 24.7.2-14 Measured and Predicted Intact Loop Hot Leg Mixture Velocity

a,c

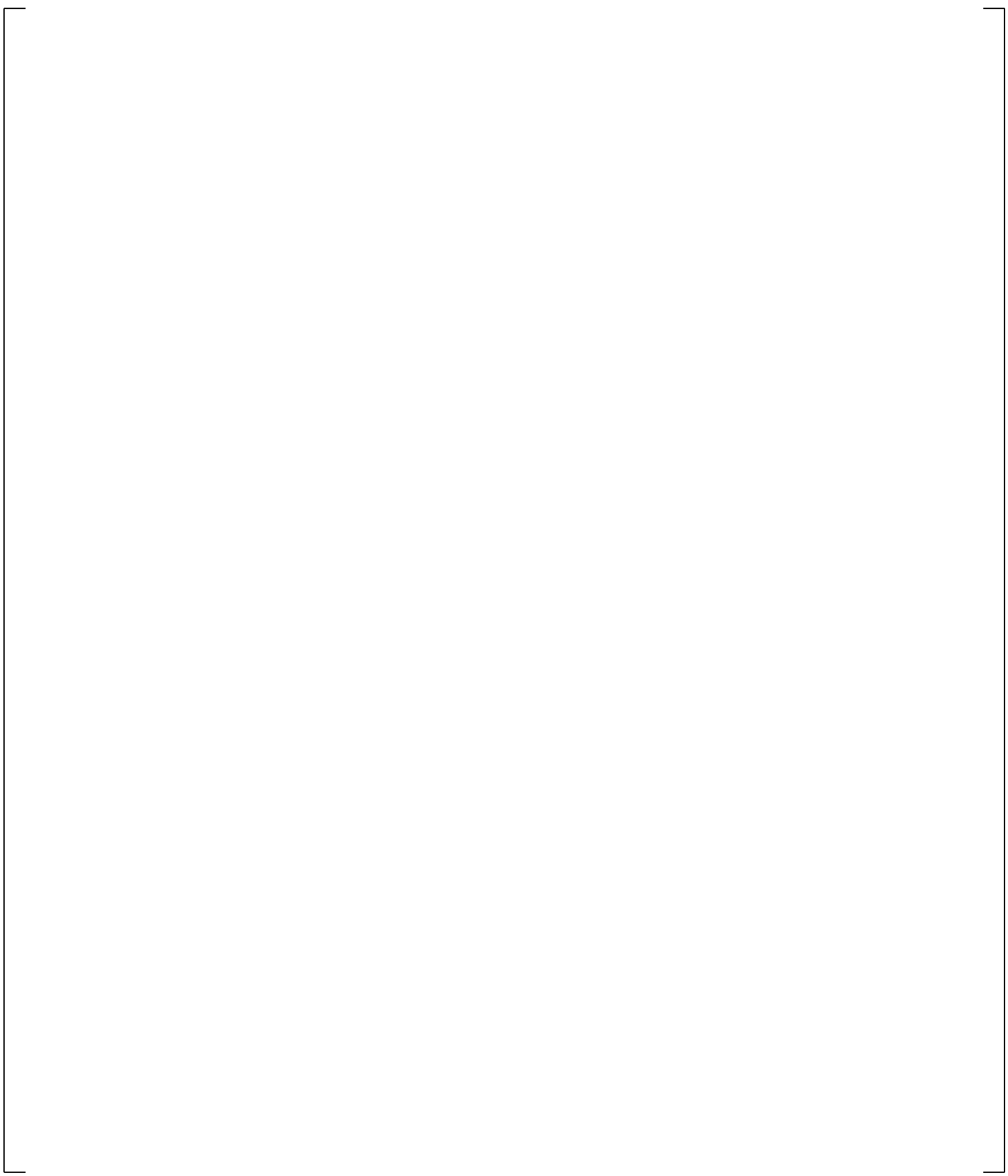

Figure 24.7.2-15 Measured and Predicted Intact Loop Cold Leg Flowrate

a,c

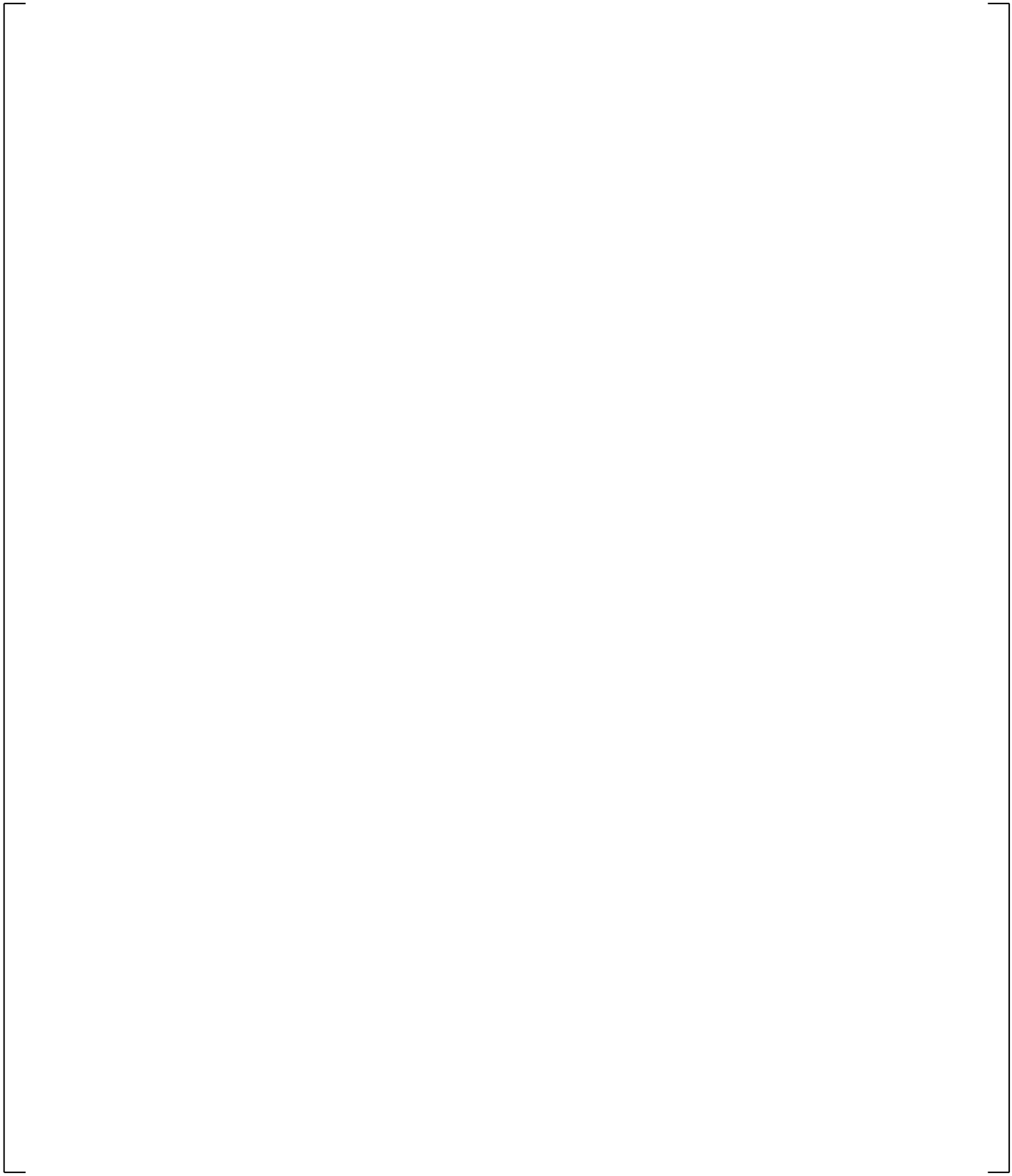

Figure 24.7.2-16 Measured and Predicted Intact Loop Cold Leg Flowrate

a,c

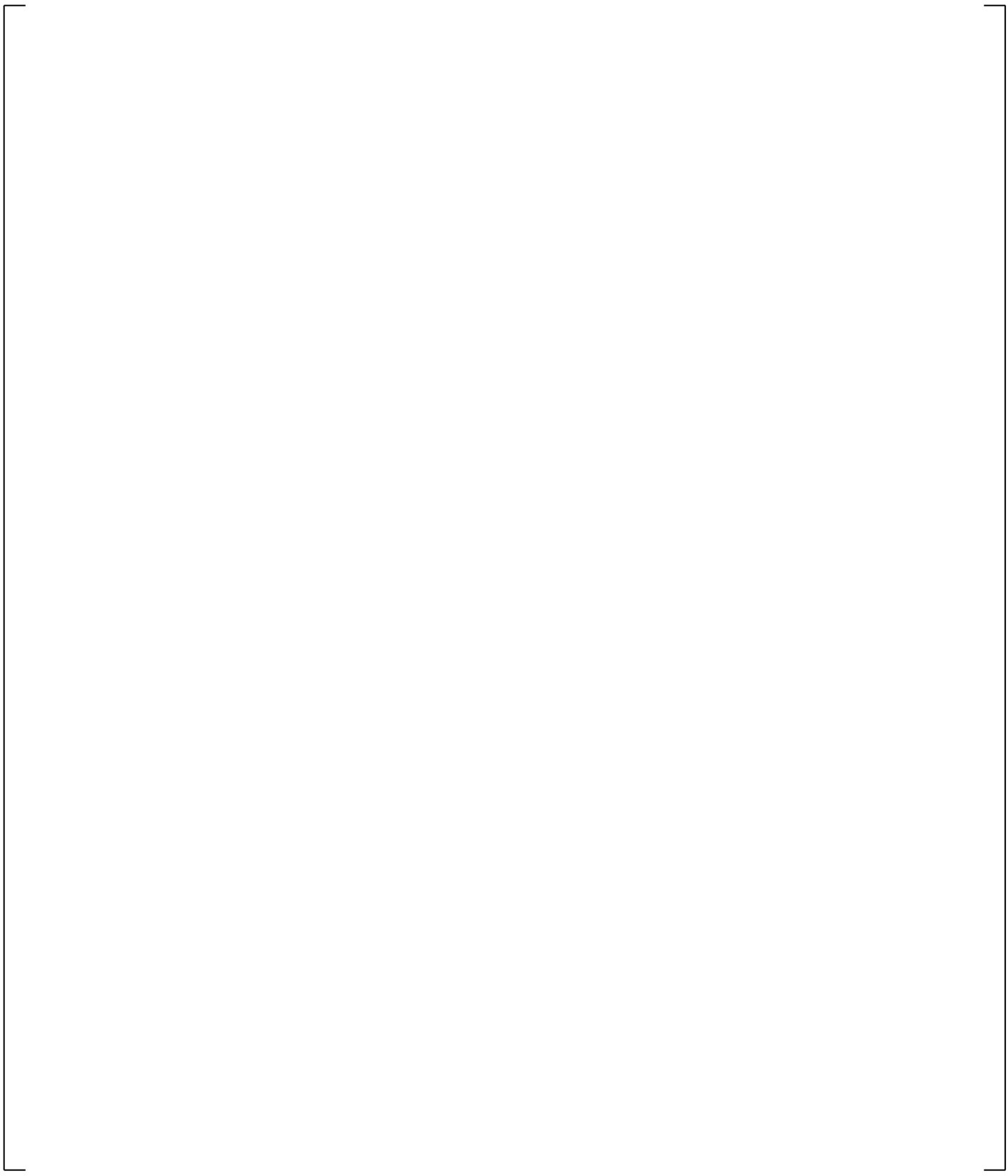

Figure 24.7.2-17 Measured and Predicted Intact Loop Cold Leg Mixture Density

a,c

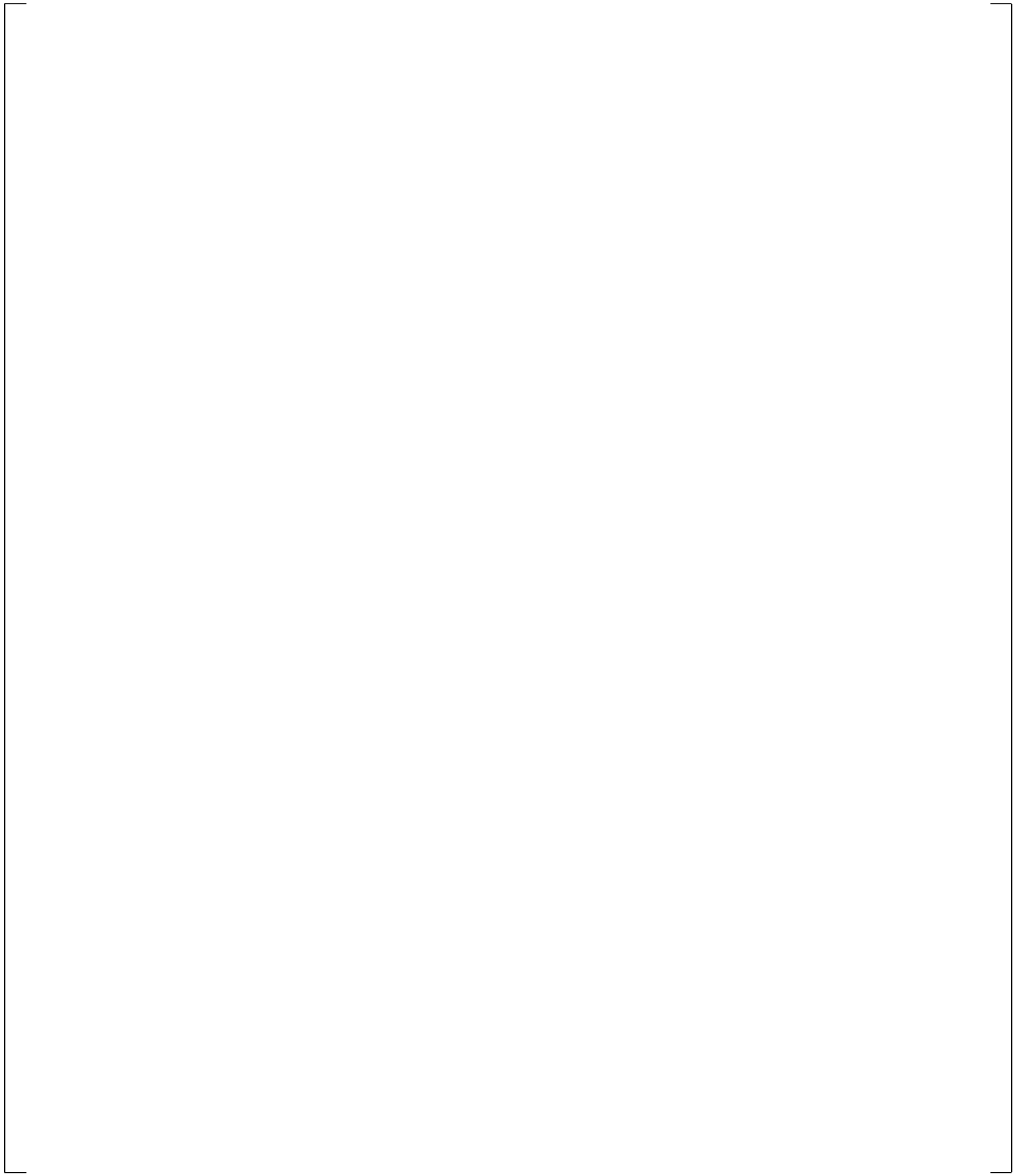

Figure 24.7.2-18 Measured and Predicted Intact Loop Cold Leg Mixture Density

a,c

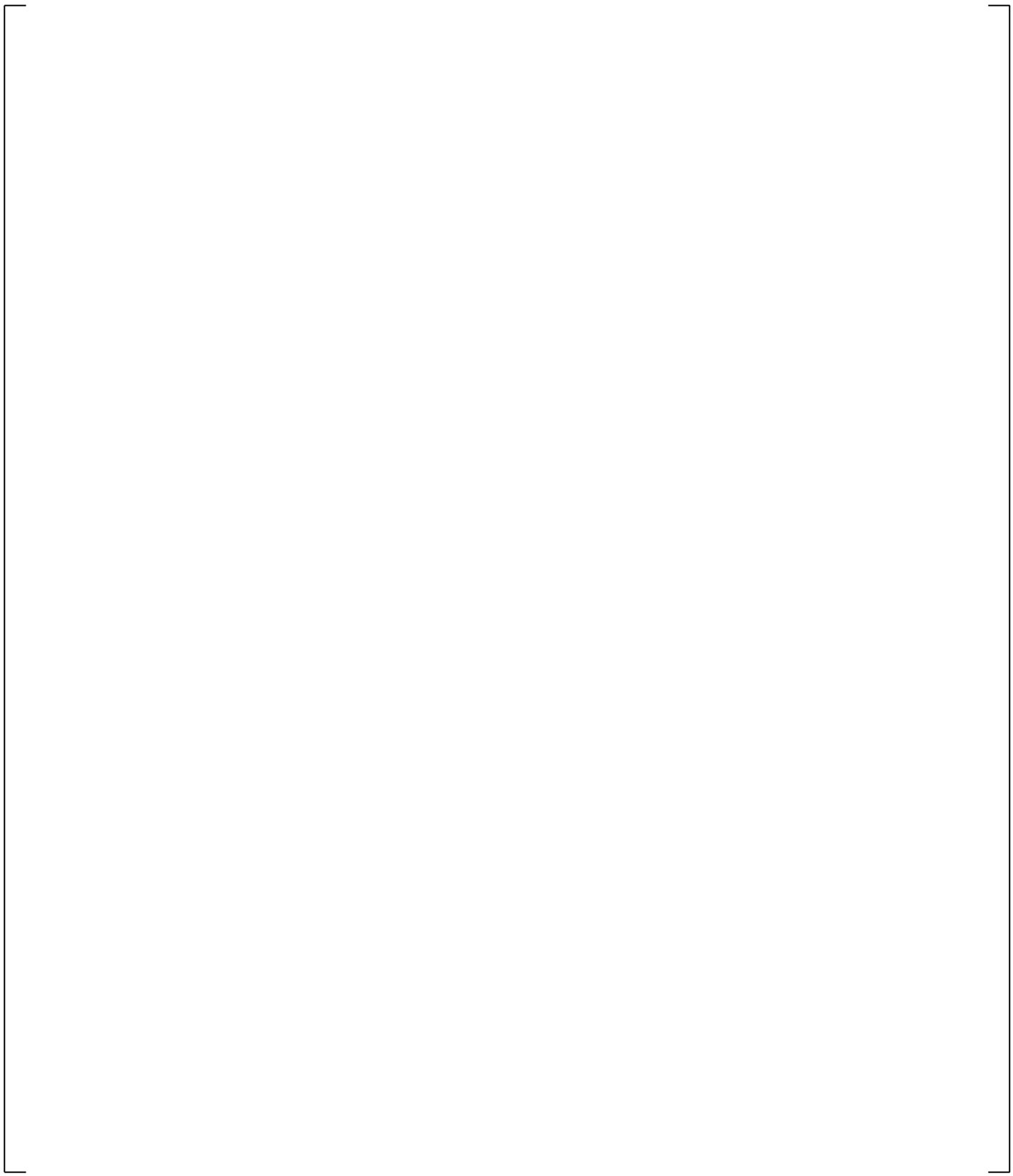

Figure 24.7.2-19 Measured and Predicted Intact Loop Cold Leg Mixture Velocity

a,c

Figure 24.7.2-20 Measured and Predicted Intact Loop Cold Leg Mixture Velocity

a,c

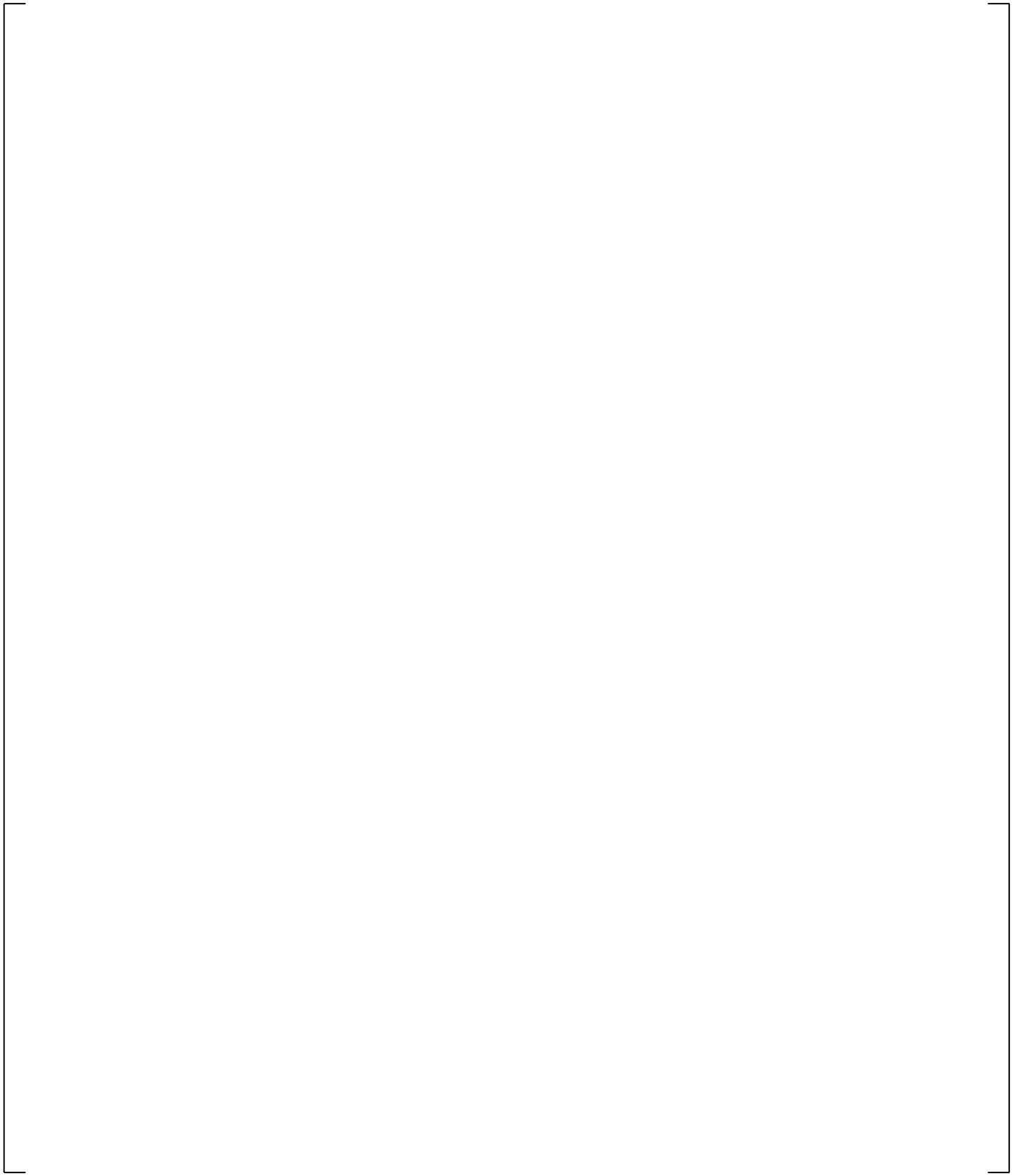

Figure 24.7.2-21 Measured and Predicted Hot Leg Break Flowrate

a,c

Figure 24.7.2-22 Measured and Predicted Hot Leg Mixture Density

a,c

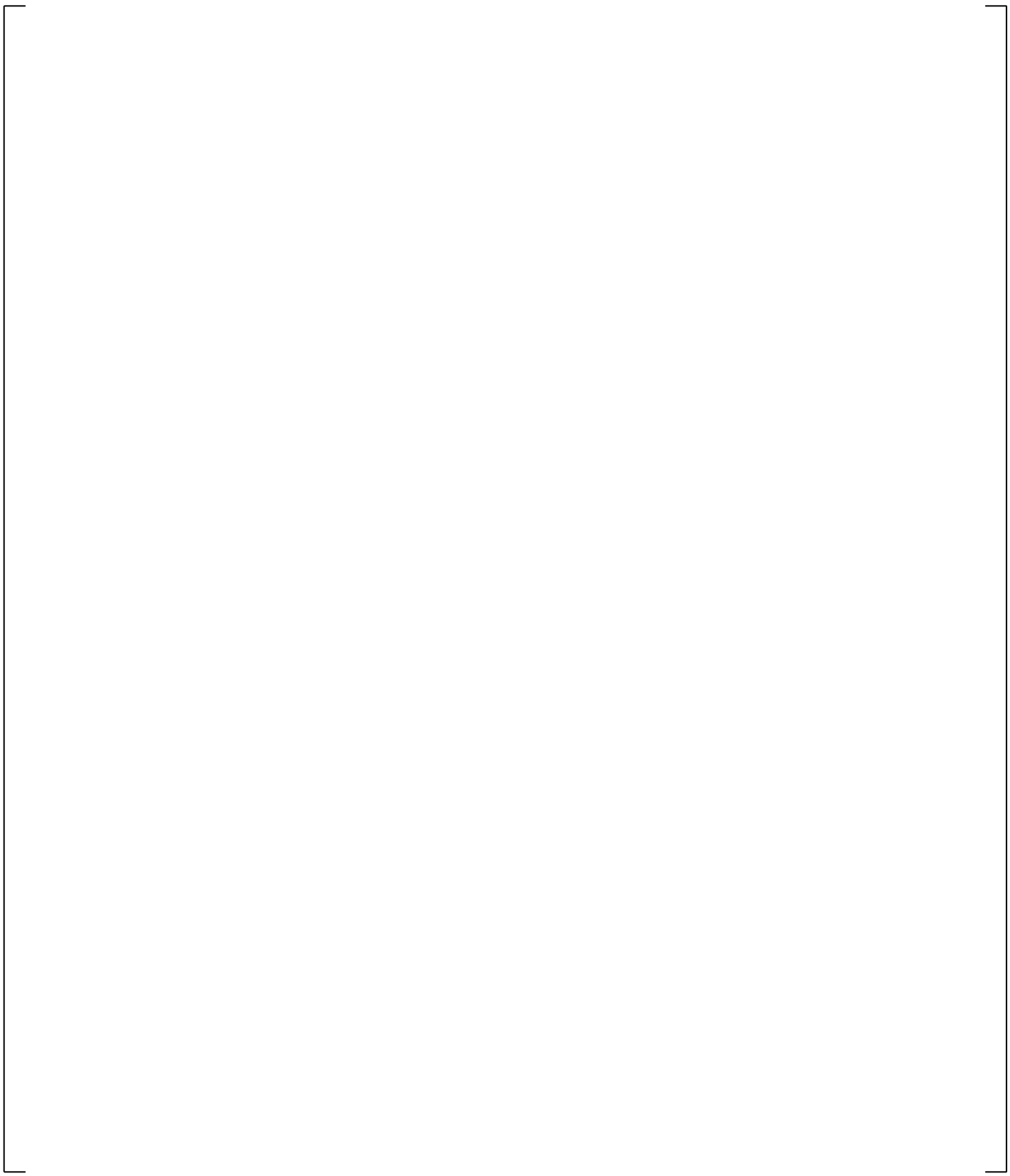

Figure 24.7.2-23 Measured and Predicted Broken Loop Hot Leg Mixture Velocity

a,c

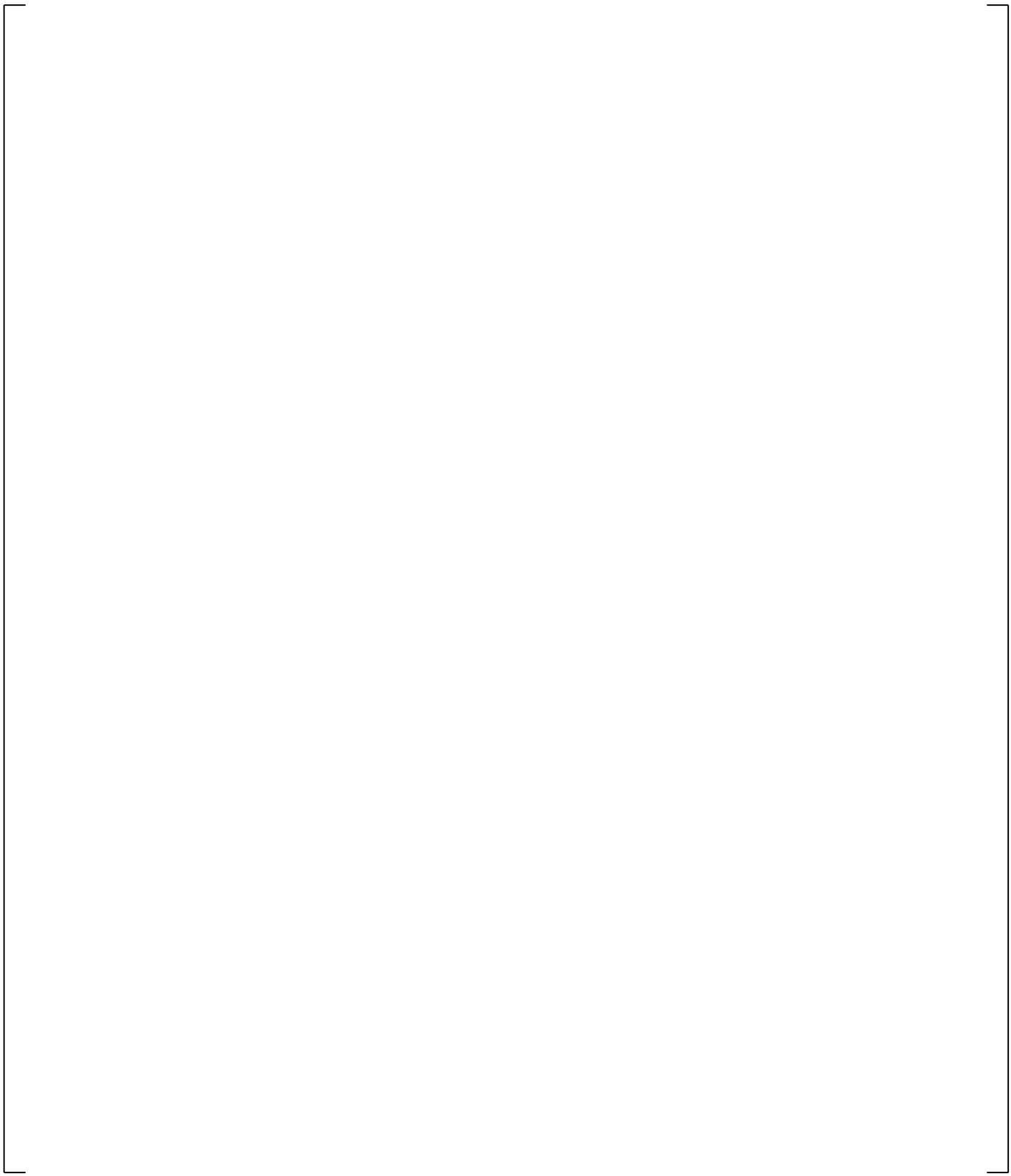

Figure 24.7.2-24 Predicted Void Fraction in Upper Plenum at Loop Level

a,c

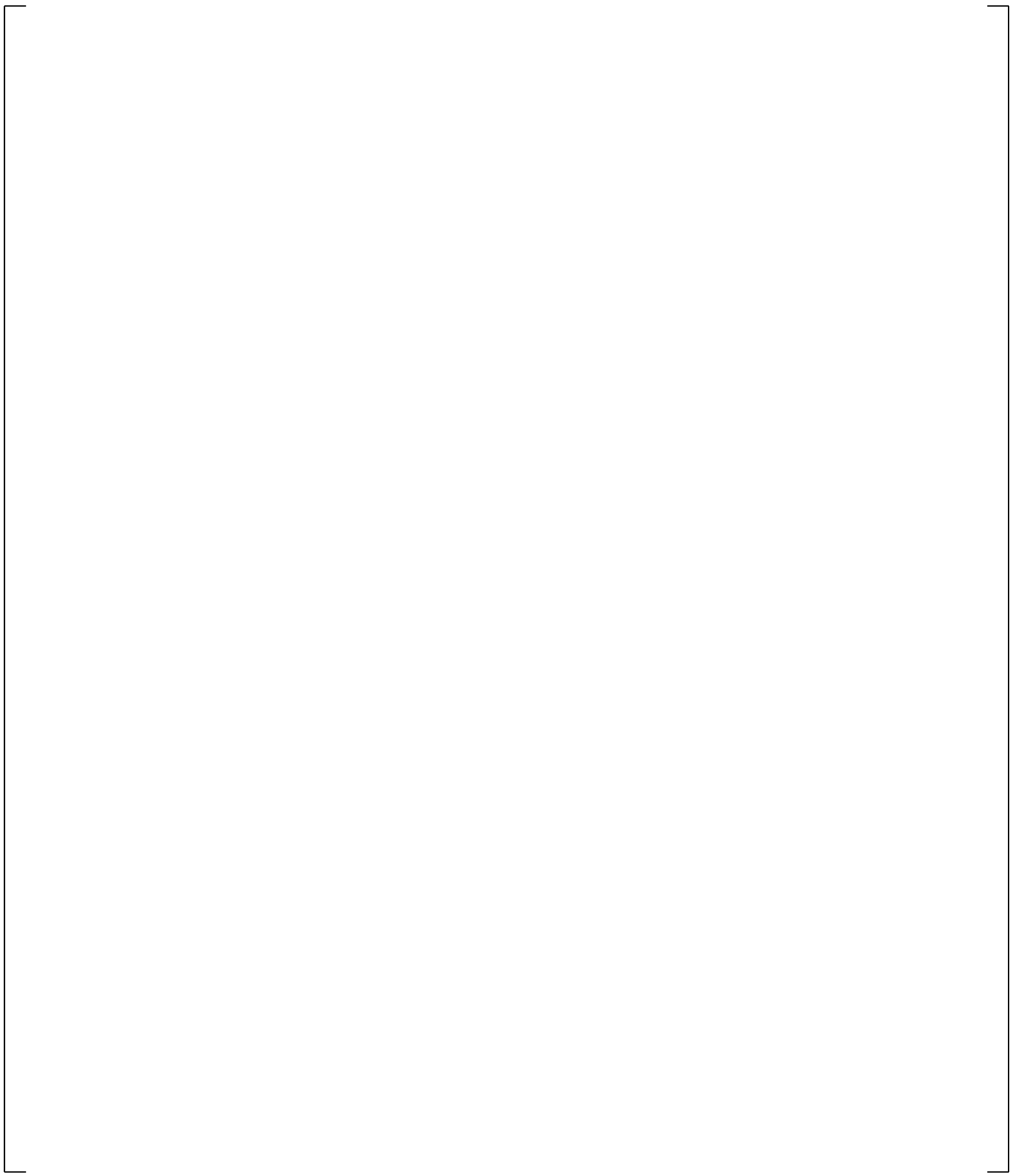

Figure 24.7.2-25 Predicted Void Fraction in Upper Plenum at Exit of CCFL Region

a,c

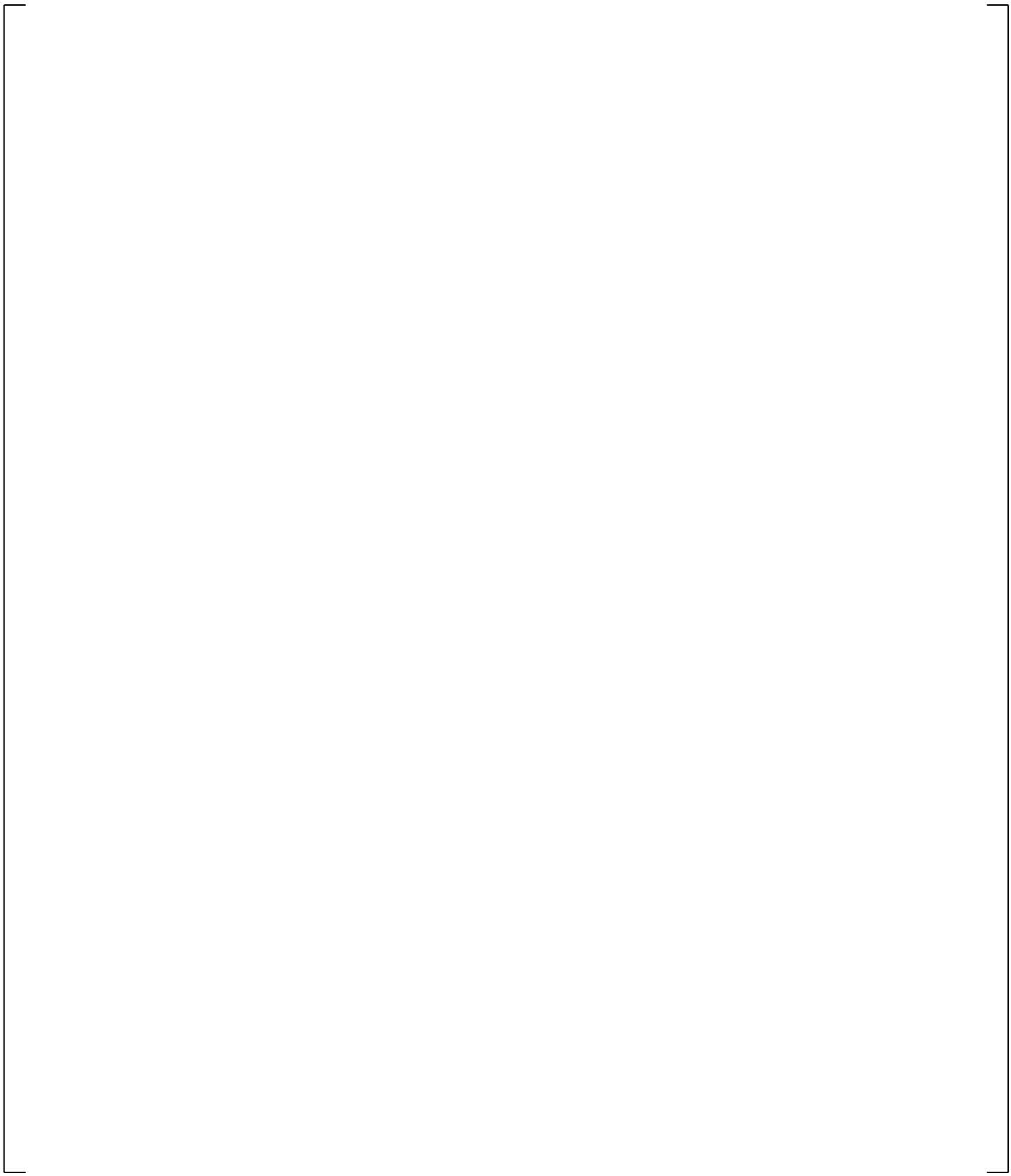

Figure 24.7.2-26 Measured and Predicted Cold Leg Break Flowrate

a,c

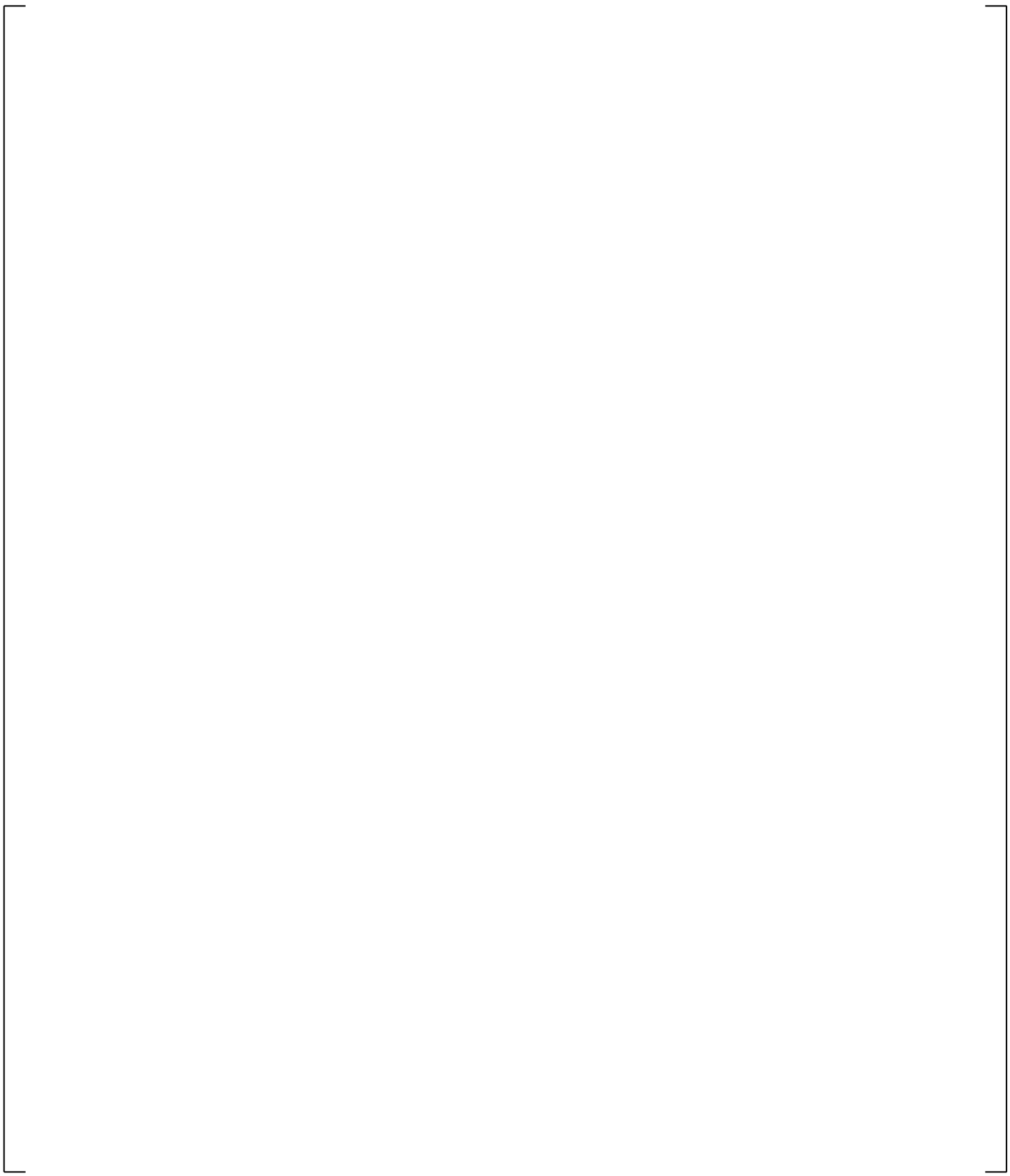

Figure 24.7.2-27 Measured and Predicted Broken Cold Leg Mixture Density

a,c

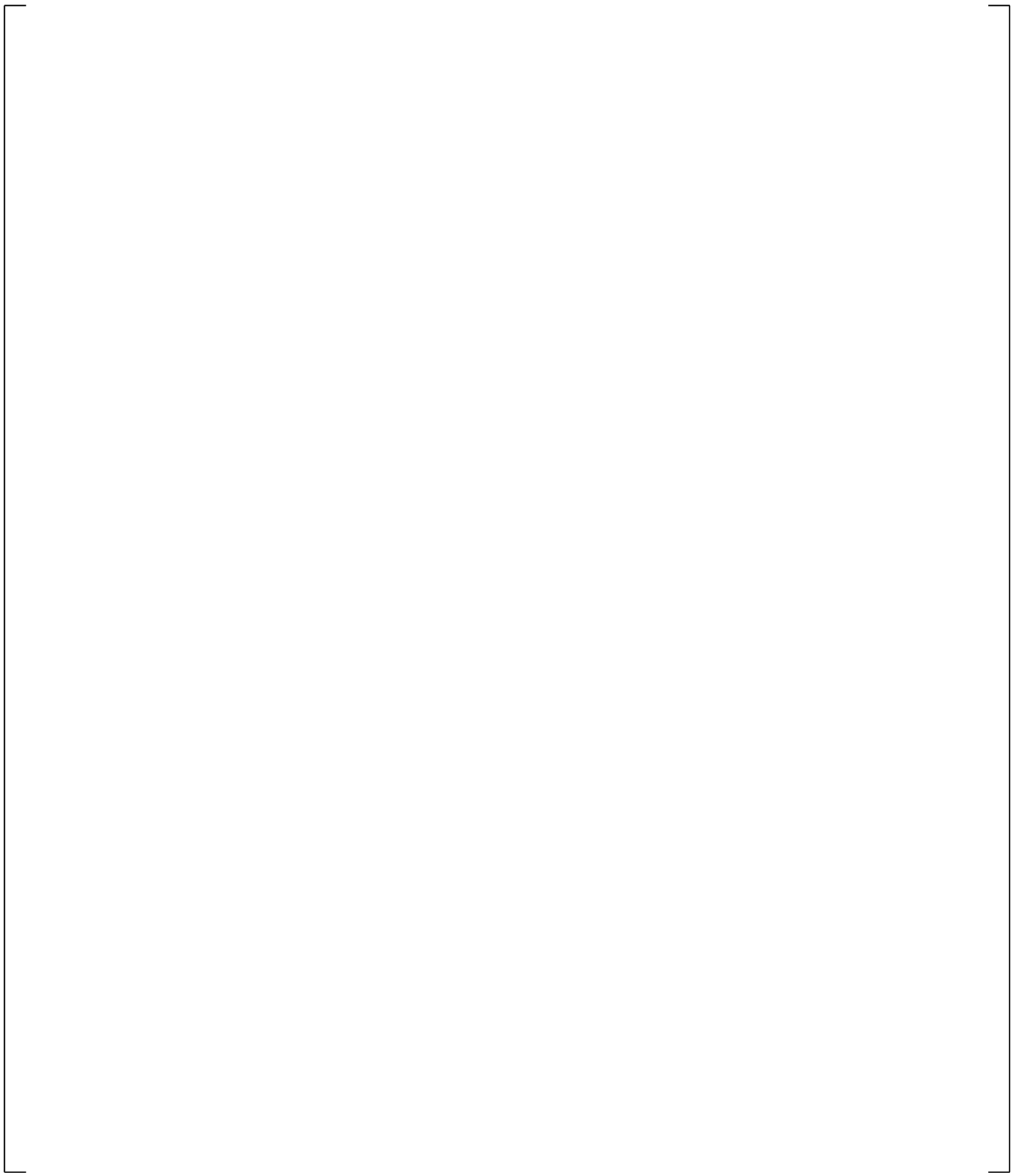

Figure 24.7.2-28 Measured and Predicted Broken Cold Leg Mixture Velocity

a,c

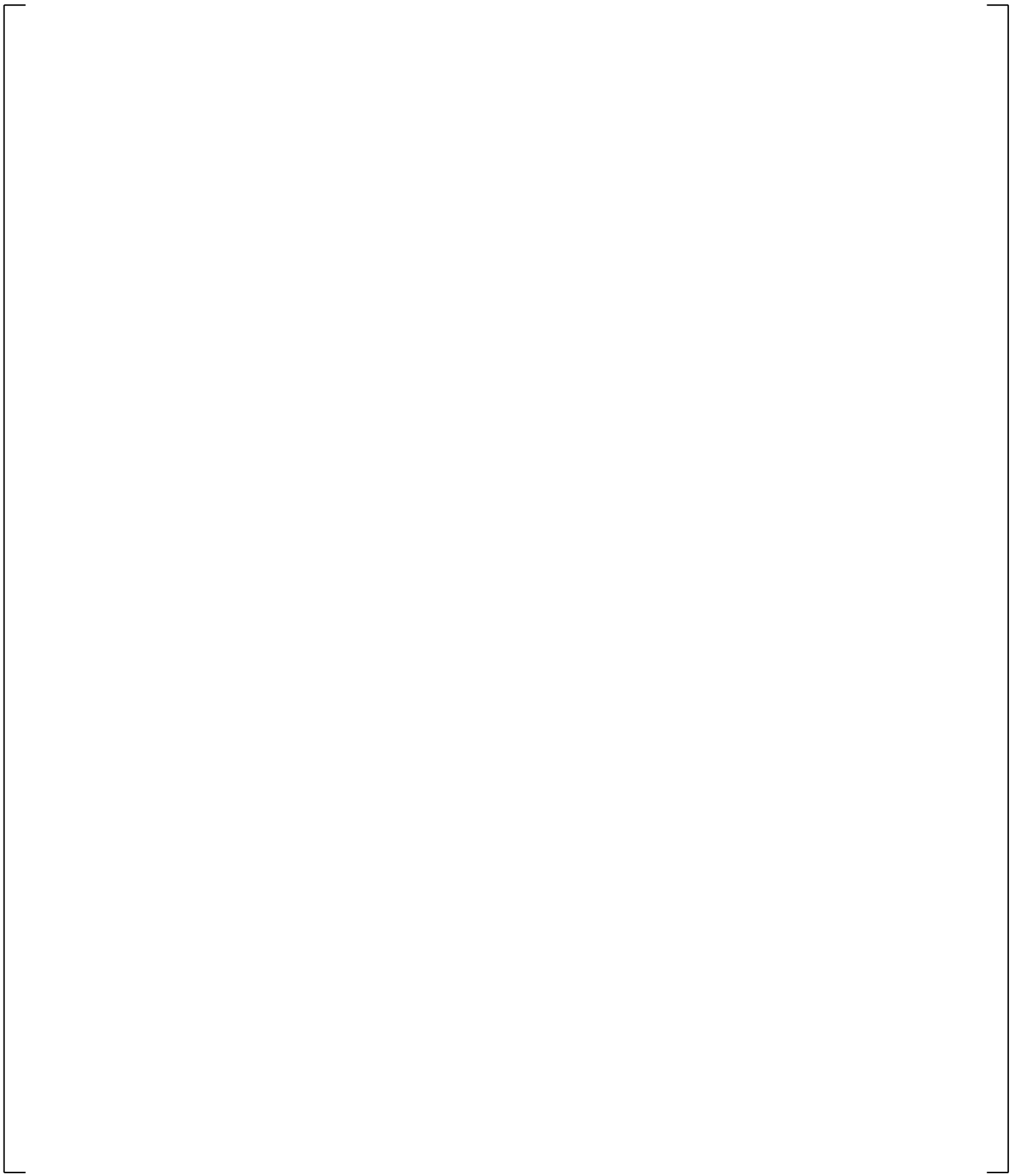

Figure 24.7.2-29 Predicted Broken Cold Leg Nozzle DP

a,c

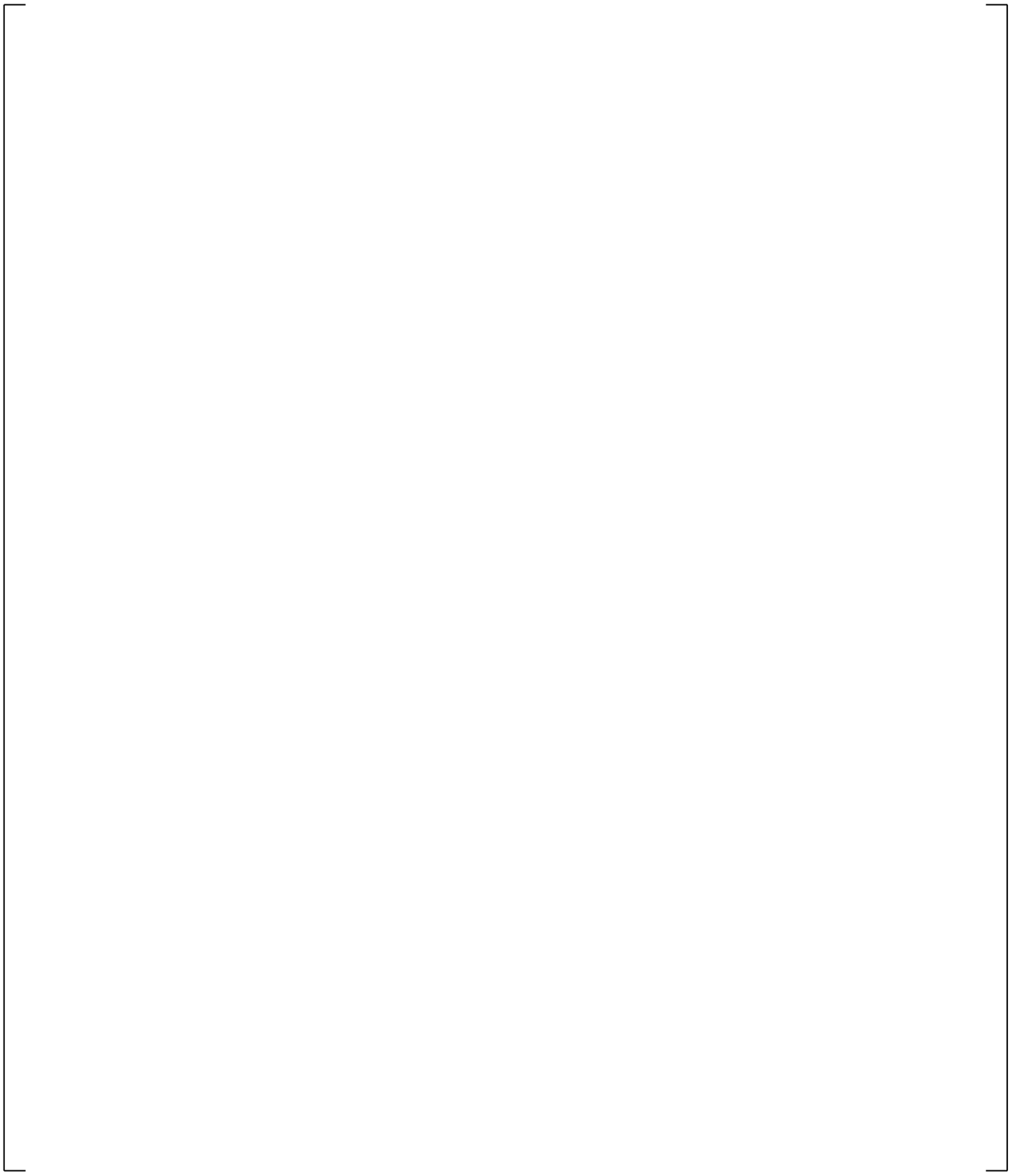

Figure 24.7.2-30 Predicted Broken Cold Leg Pressure Drop to the Break Plane

24.7.3 CCTF Run 62

CCTF Test 62 (Okubo et al., 1985) is a gravity-reflood test with initial system pressure at 29 psia. In this type of test, the predicted flow through the core depends on the prediction of hydrostatic pressure in the core and downcomer, and pressure drops through the loops. Comparisons will be made between predicted and measured cladding temperatures at the locations marked by "x" in Figure 24.7.3-1a. The pressure differences are a measure of the hydrostatic head due to liquid, as well as frictional losses. In components containing significant liquid, the pressure difference is usually a reliable indicator of collapsed liquid level or liquid fraction. **[**

][a,c]

Core Thermal-Hydraulics

[

][a,c]

Figures 24.7.3-10 to 24.7.3-15 compare measured and predicted average vapor fraction within the spans indicated in Figure 24.7.3-1a. **[**

][a,c]

[

][a,c]

The average vapor fraction in the end box and in the upper plenum is compared in Figures 24.7.3-16a and 24.7.3-16b. **[**

][a,c]

Loop Thermal-Hydraulics

Figure 24.7.3-19 compares the upper plenum pressure which is under-predicted. **[**

][a,c]

Figures 24.7.3-22 to 24.7.3-26 compare the pressure difference across the intact loop **[**

][a,c]

[

][a,c]

Sensitivity Run

Figure 24.7.3-19 (UP Pressure) indicates **[**

][a,c]

Figure 24.7.3-46 shows the UP pressure **[**

][a,c]

In summary, the total mass flows into the core and through the loops are predicted **[**

][a,c]

a,c

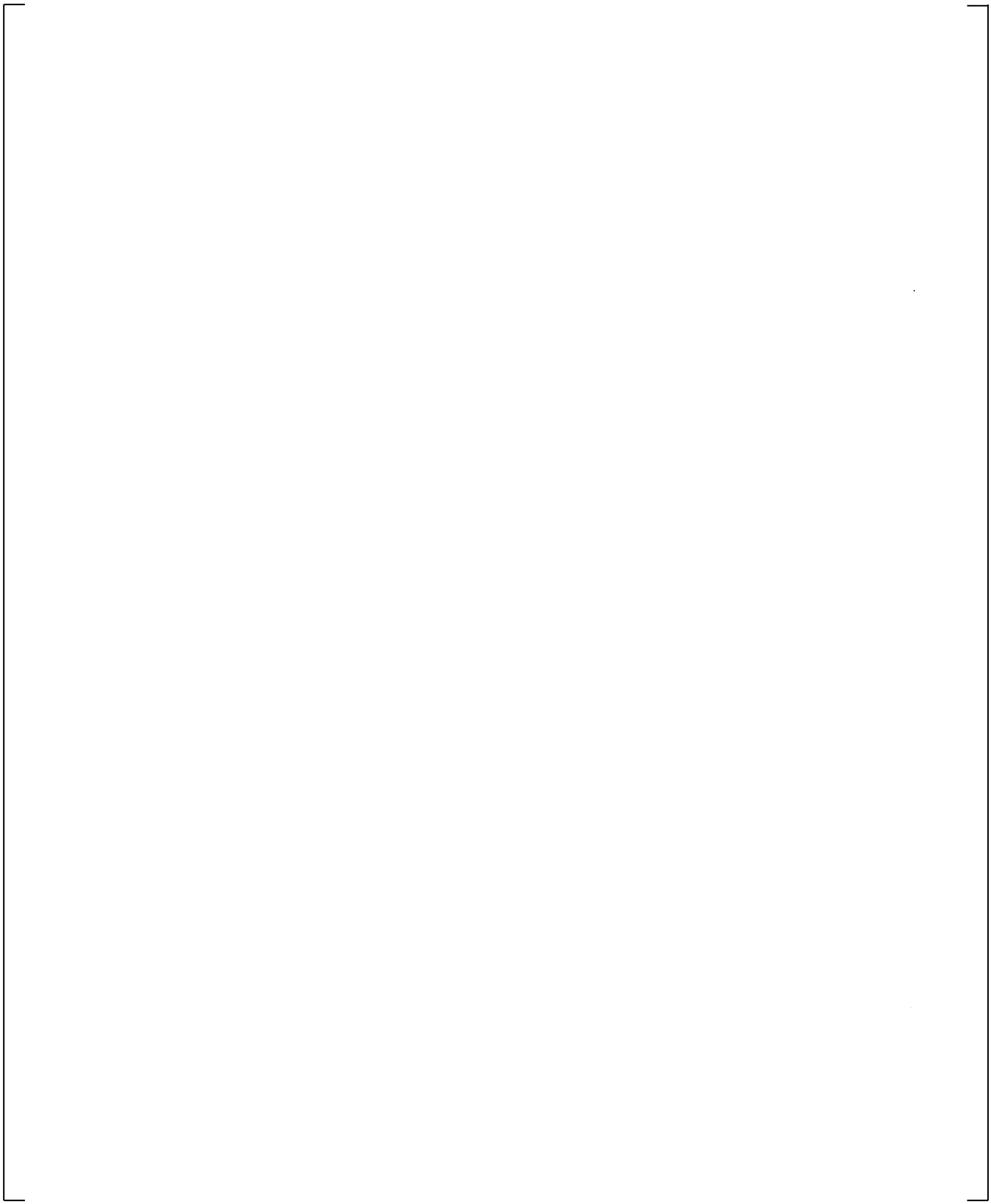

Figure 24.7.3-1a Pressure, Differential Pressure, Liquid Level and Mass Flowrate Instrumentation Location in Pressure Vessel

a,c

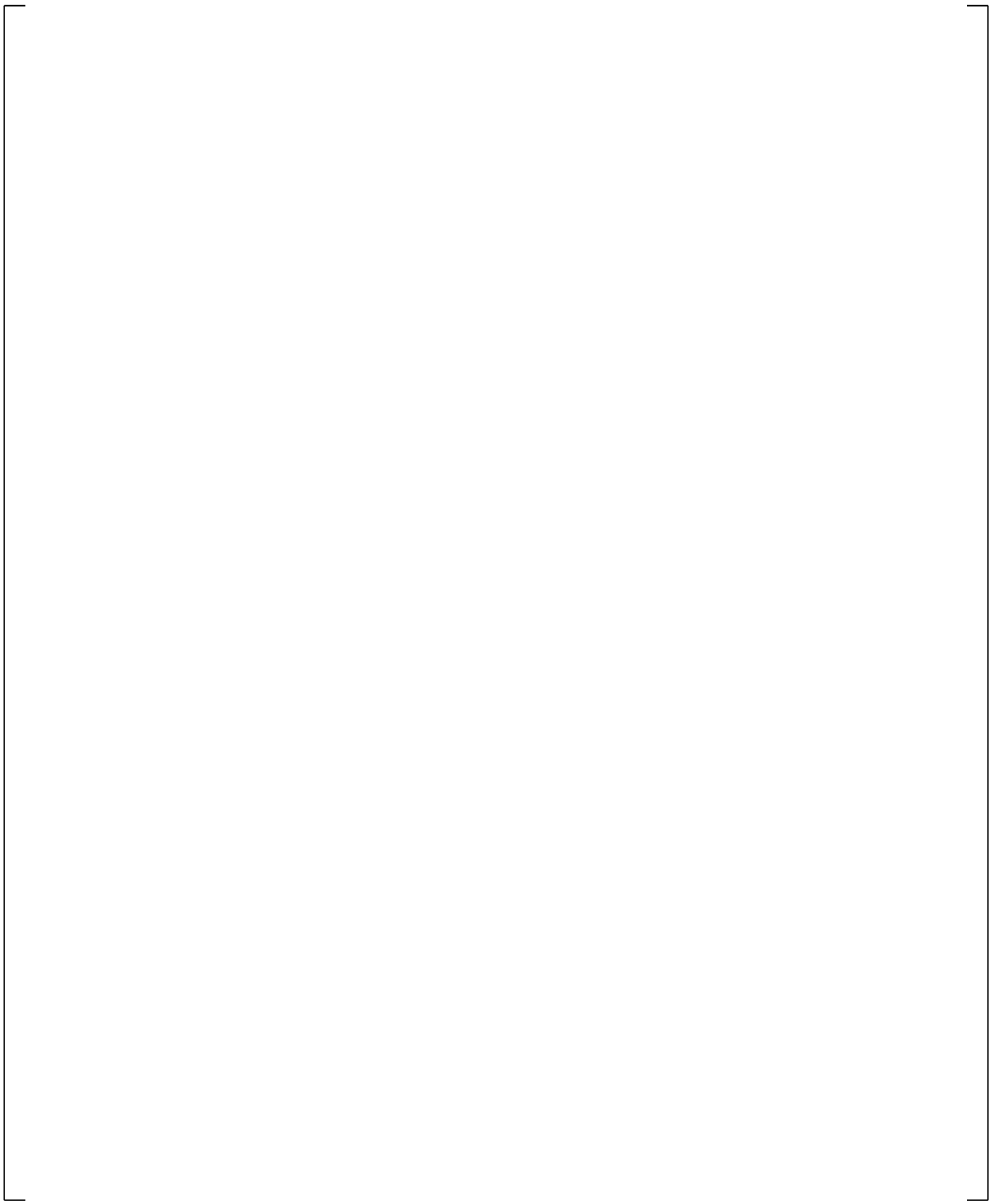

Figure 24.7.3-1b Top View of Primary Loop Piping

a,c

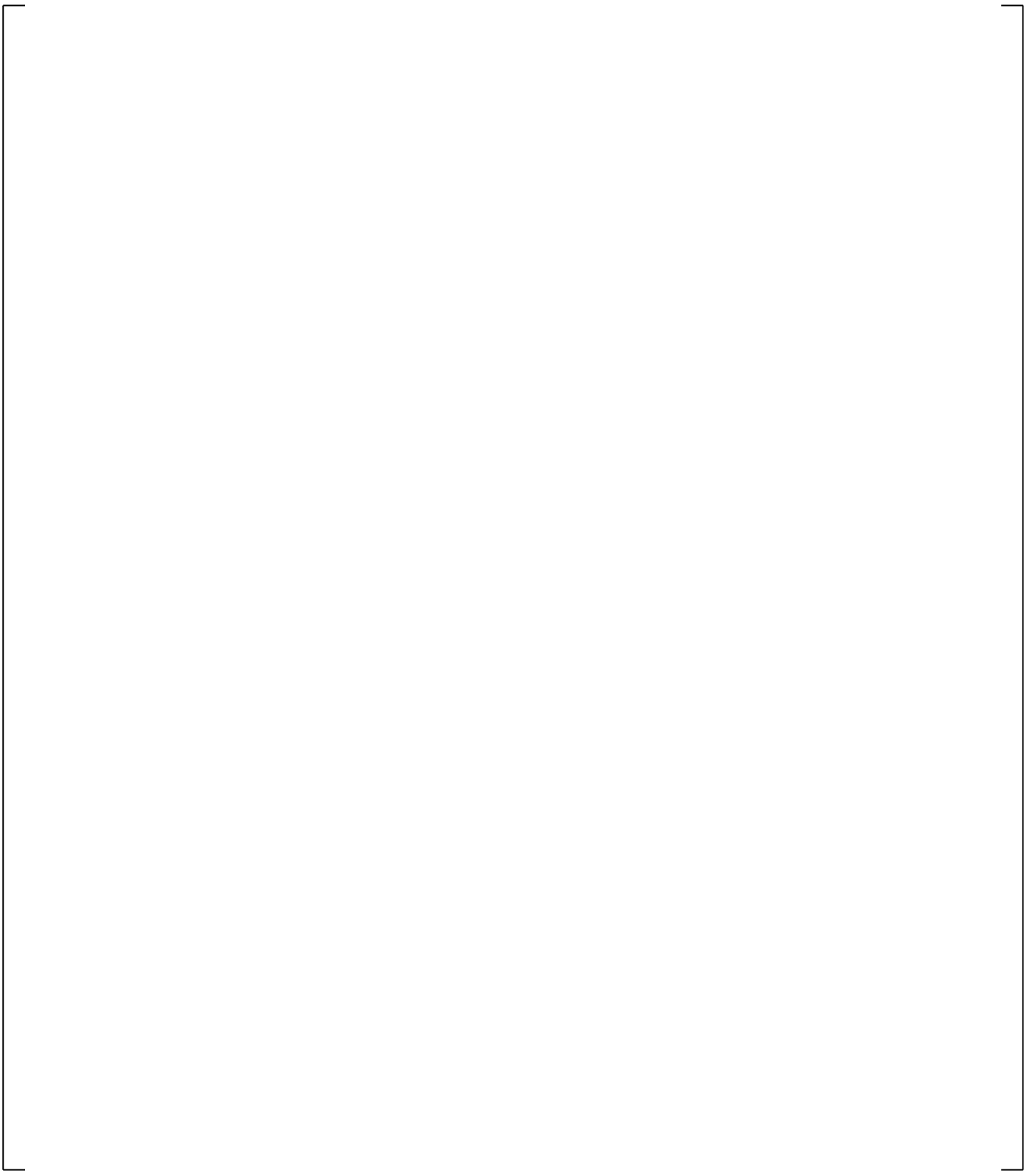

Figure 24.7.3-2 Core Inlet Flow Comparison

a,c

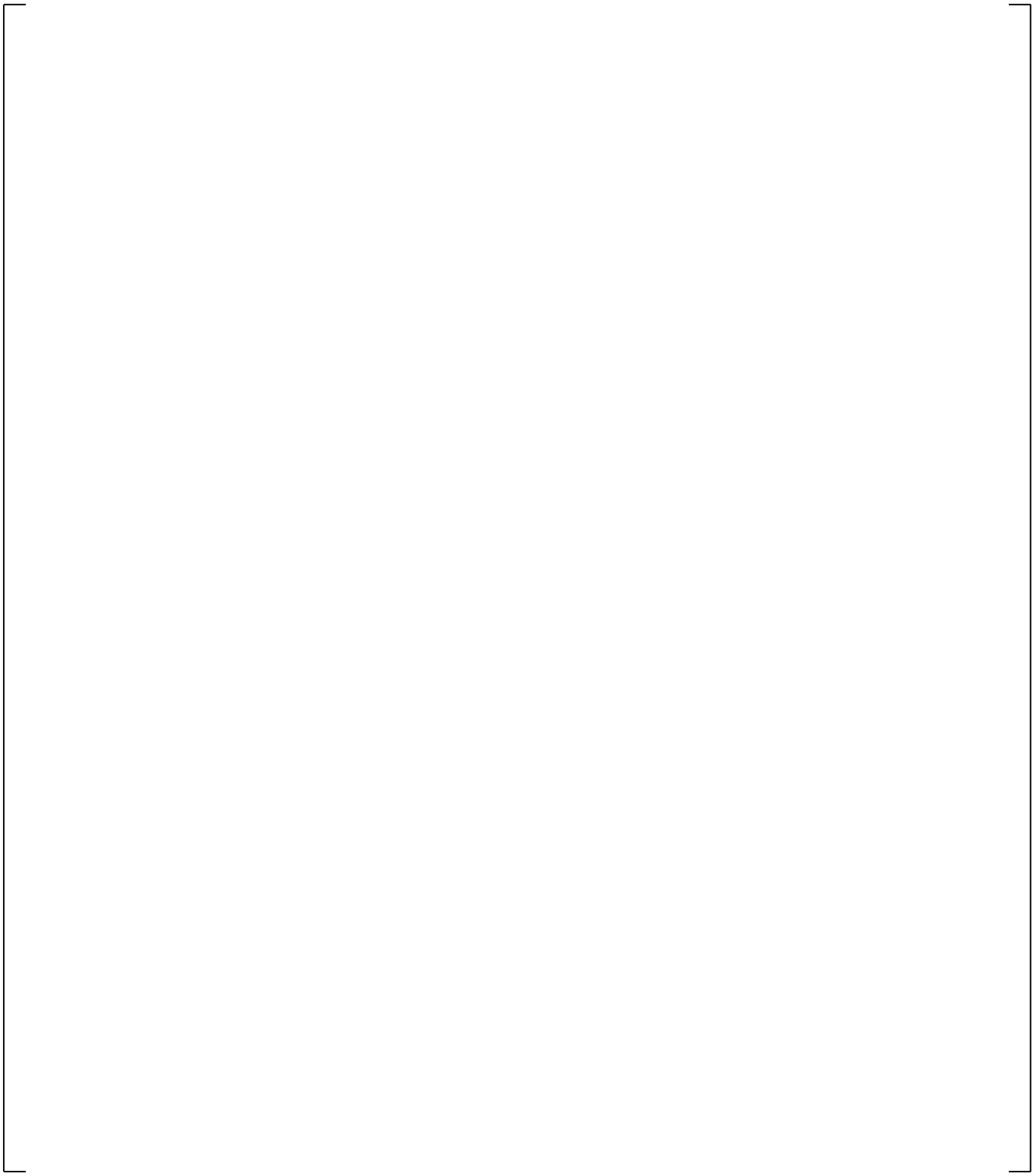

Figure 24.7.3-3 CCTF Run 62 WCOBRA/TRAC-TF2 vs. Data – Cladding Temperature Comparison at 3.33 ft

a,c

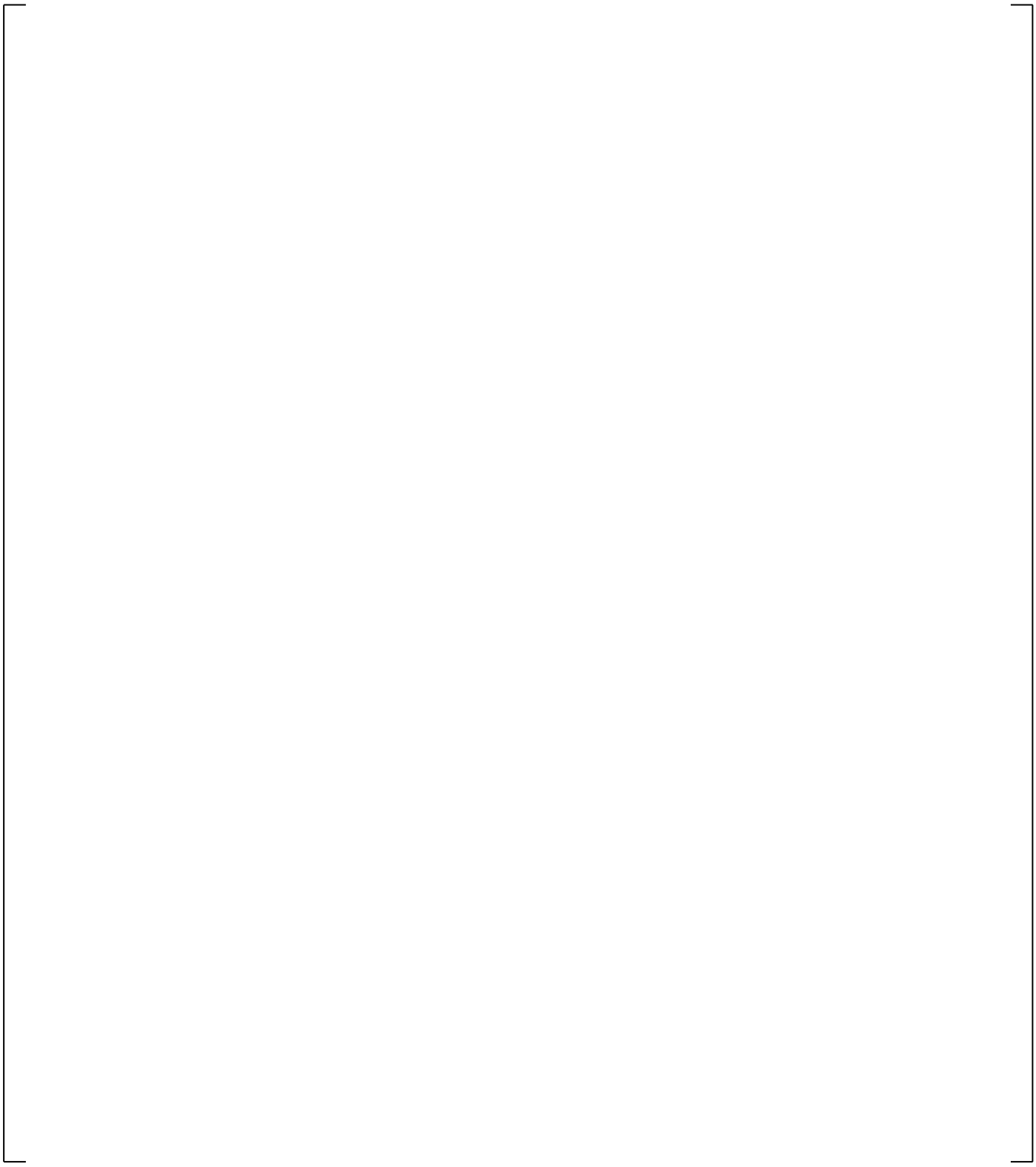

Figure 24.7.3-4 CCTF Run 62 WCOBRA/TRAC-TF2 vs. Data Cladding Temperature Comparison at 6 ft

a,c

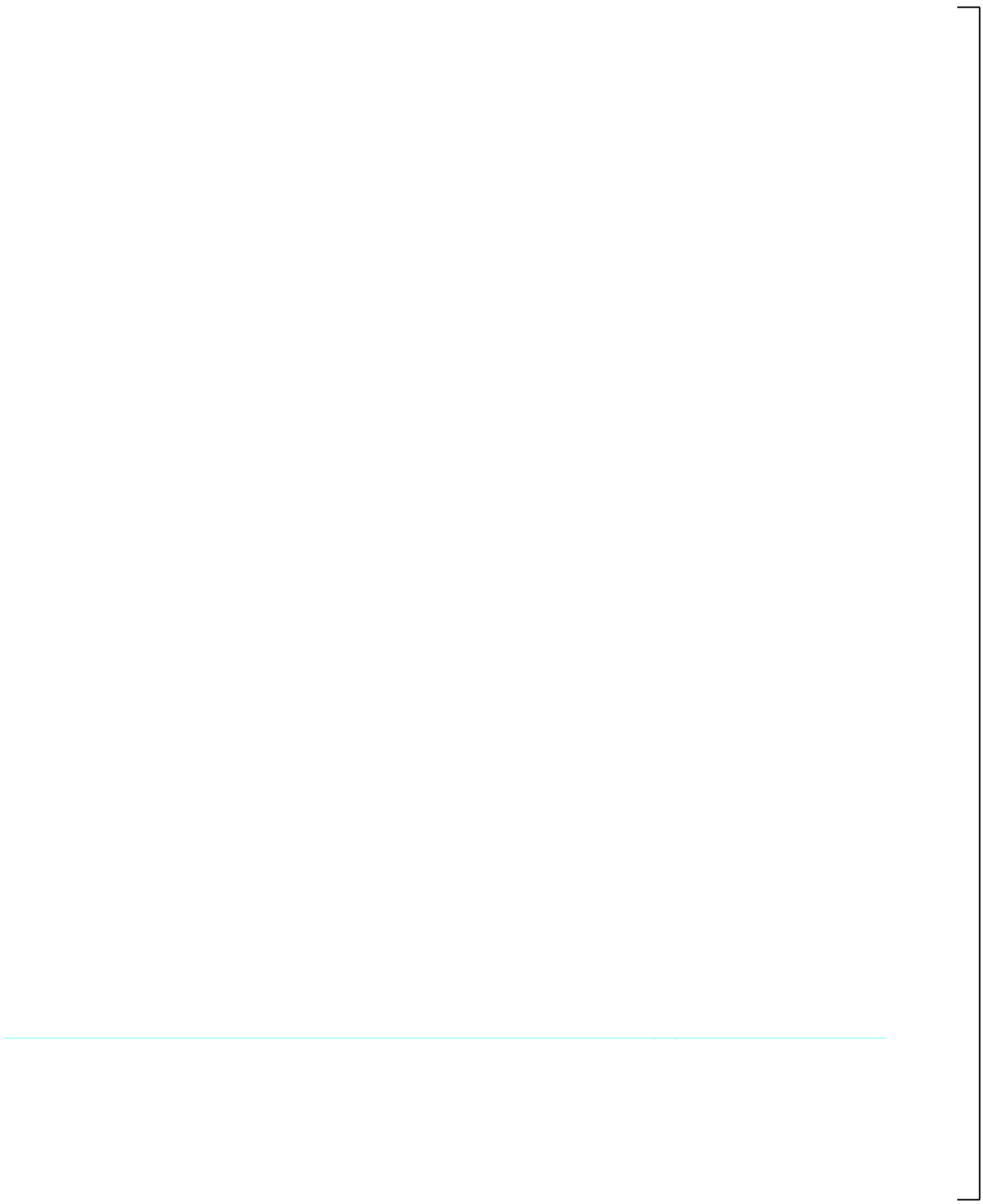

Figure 24.7.3-5 CCTF Run 62 WCOBRA/TRAC-TF2 vs. Data Cladding Temperature Comparison at 6.68 ft

a,c

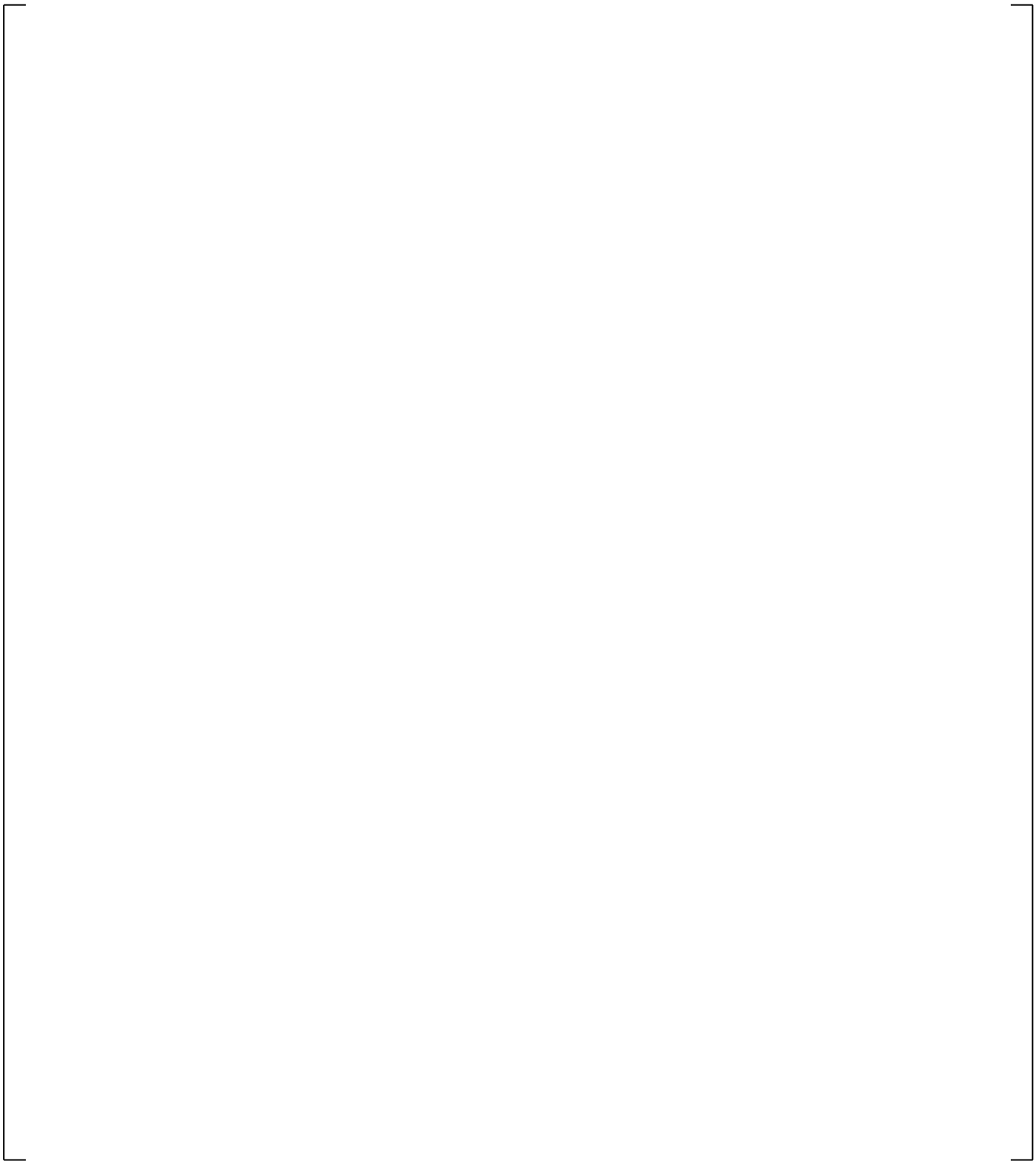

Figure 24.7.3-6 CCTF Run 62 WCOBRA/TRAC-TF2 vs. Data Cladding Temperature Comparison at 8 ft

a,c

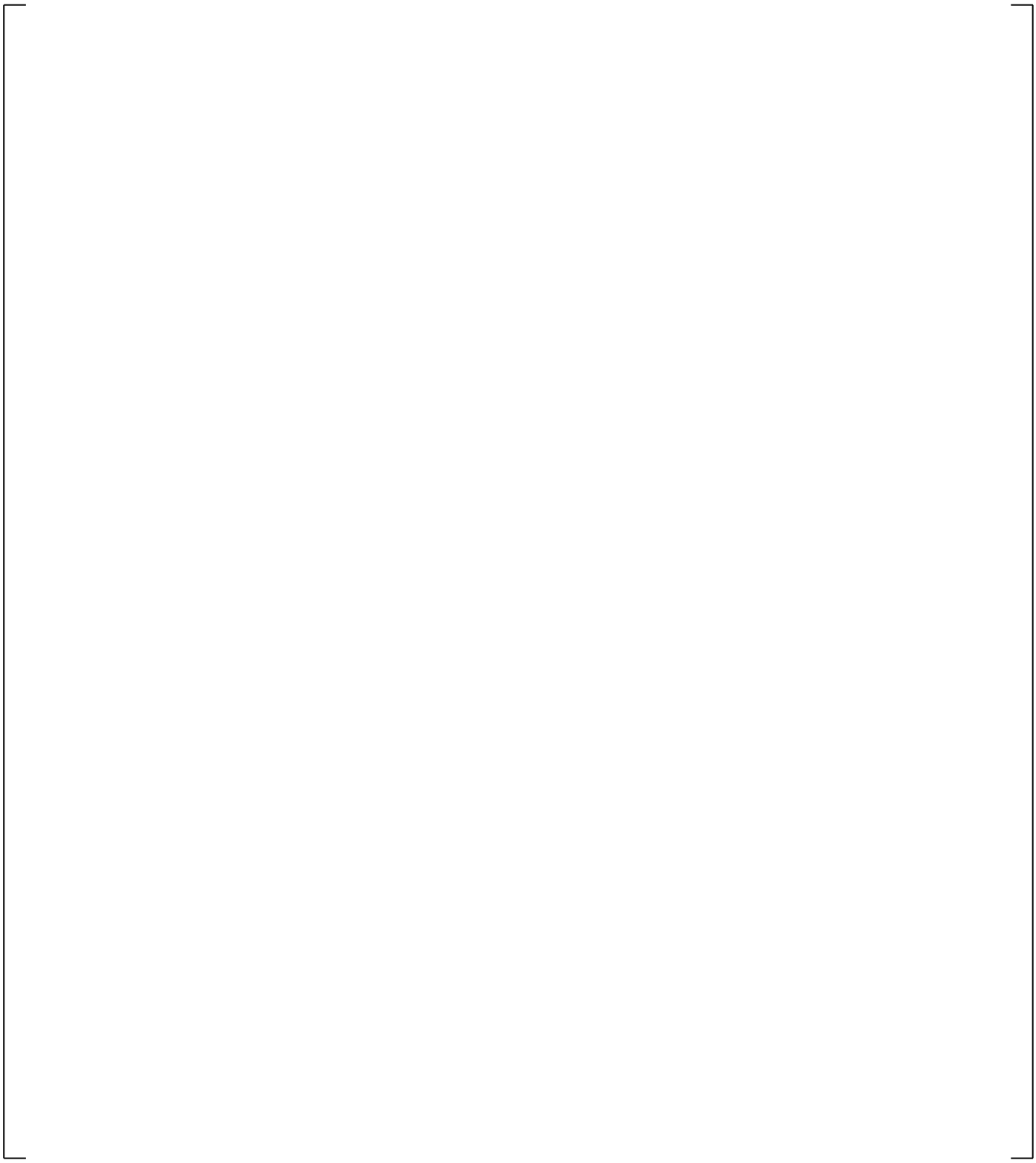

Figure 24.7.3-7 CCTF Run 62 WCOBRA/TRAC-TF2 vs. Data Cladding Temperature Comparison at 10 ft

a,c

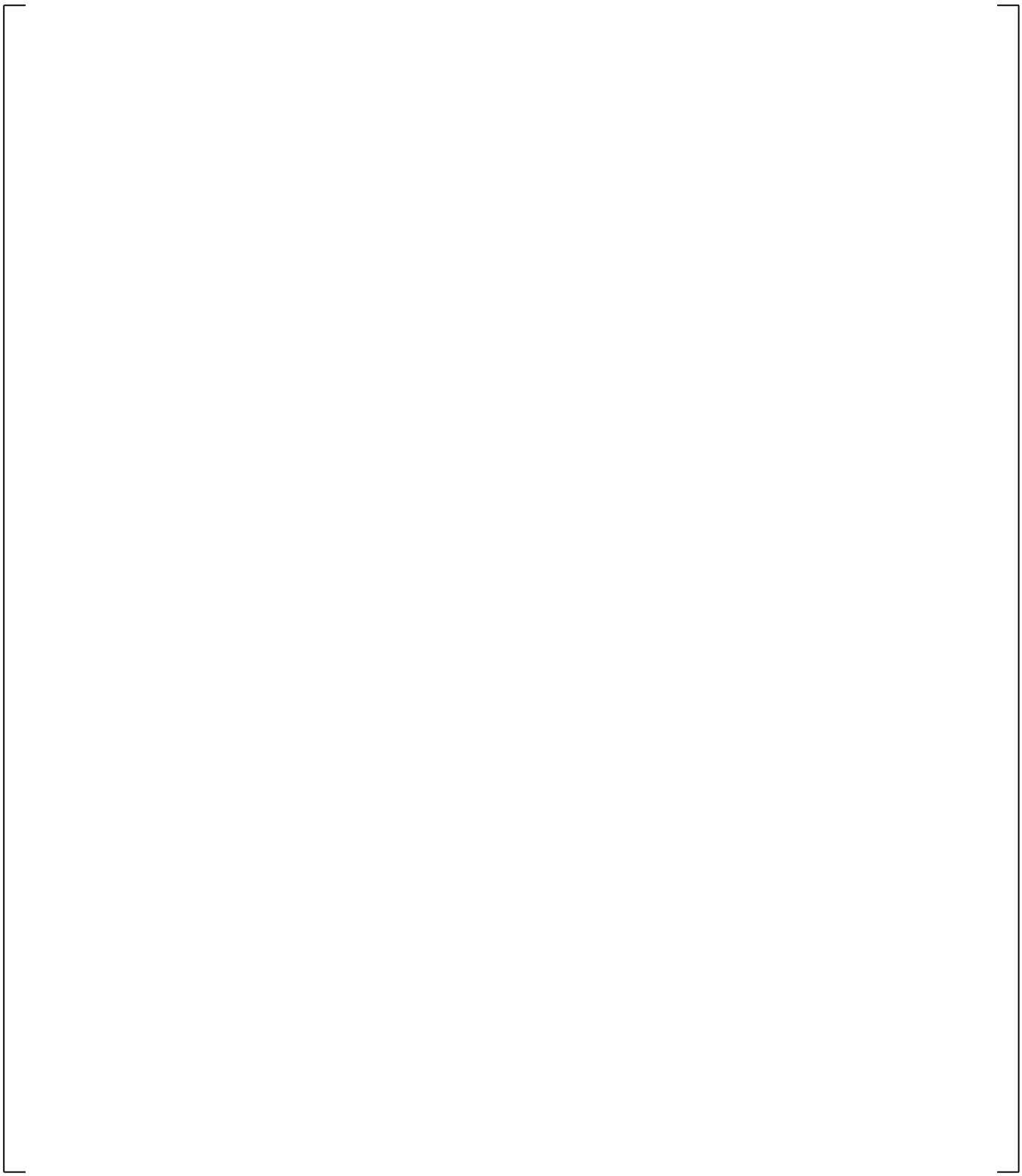

Figure 24.7.3-8 CCTF Run 62 WCOBRA/TRAC-TF2 vs. Data Vapor Temperature Comparison at 6 ft

a,c

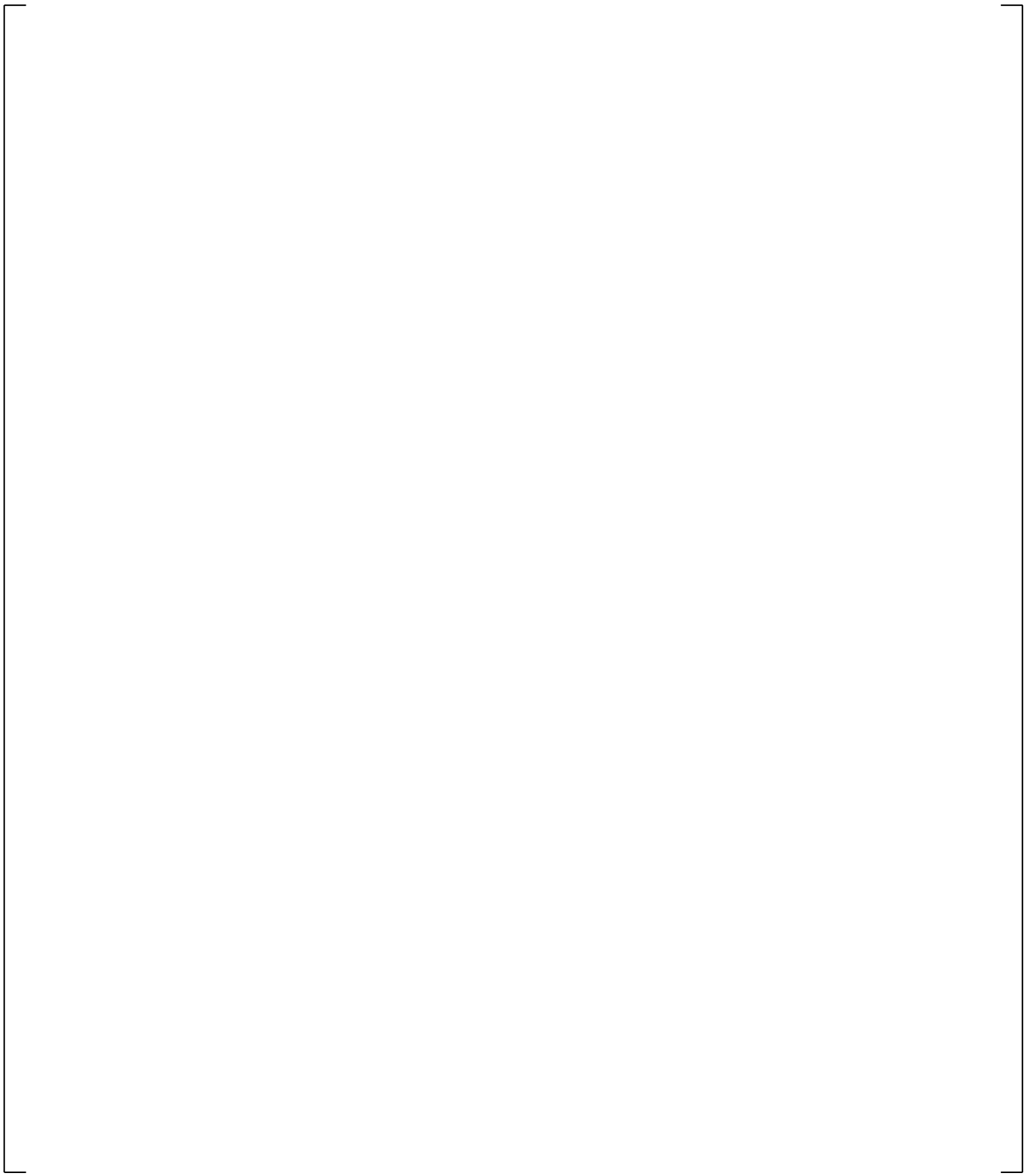

Figure 24.7.3-9 CCTF Run 62 WCOBRA/TRAC-TF2 vs. Data Vapor Temperature Comparison at 8 ft

a,c

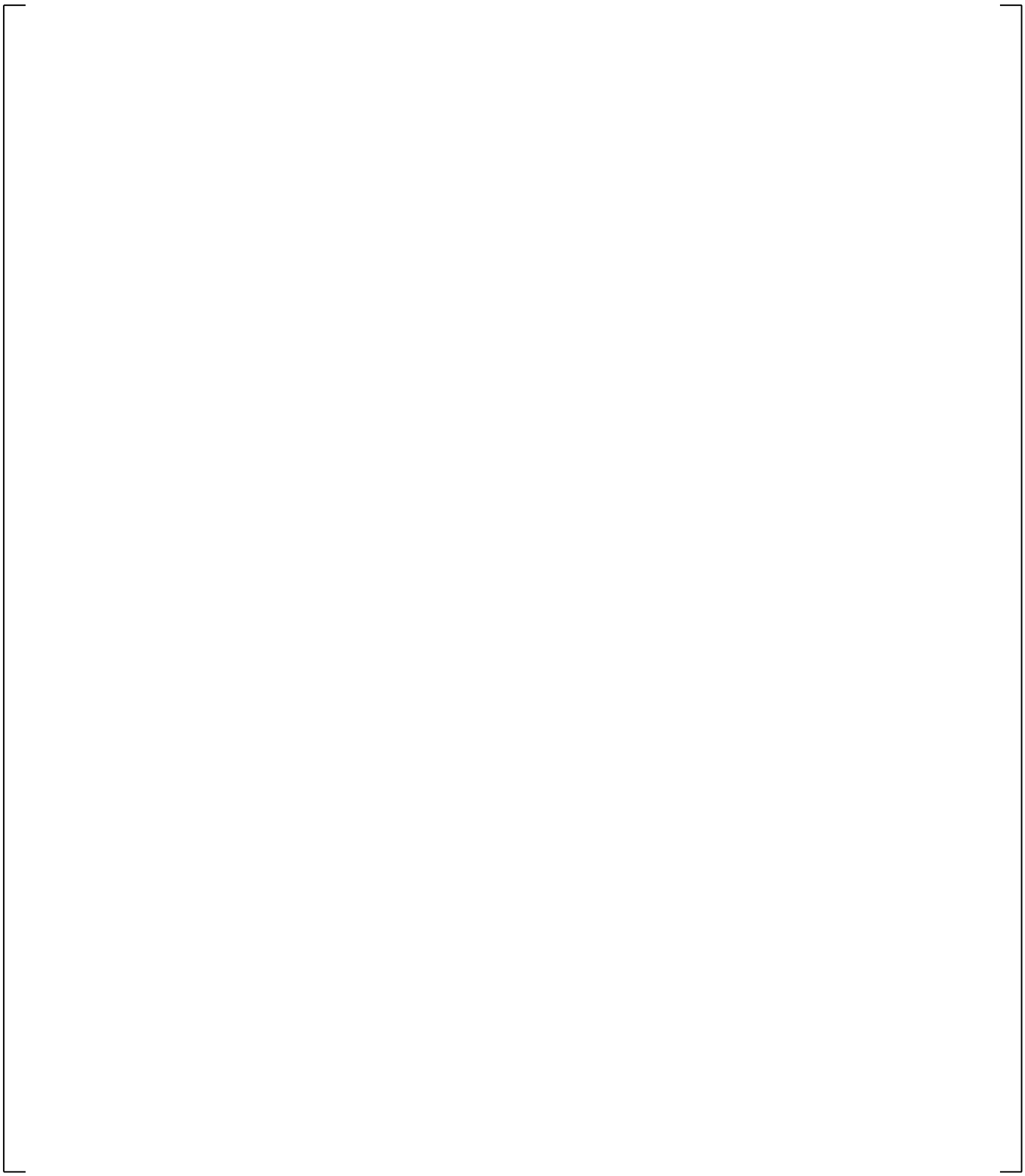

Figure 24.7.3-10 CCTF Run 62 WCOBRA/TRAC-TF2 vs. Data Comparison Void Fraction from 2.1 to 2.71 m (0-to-2 ft)

a,c

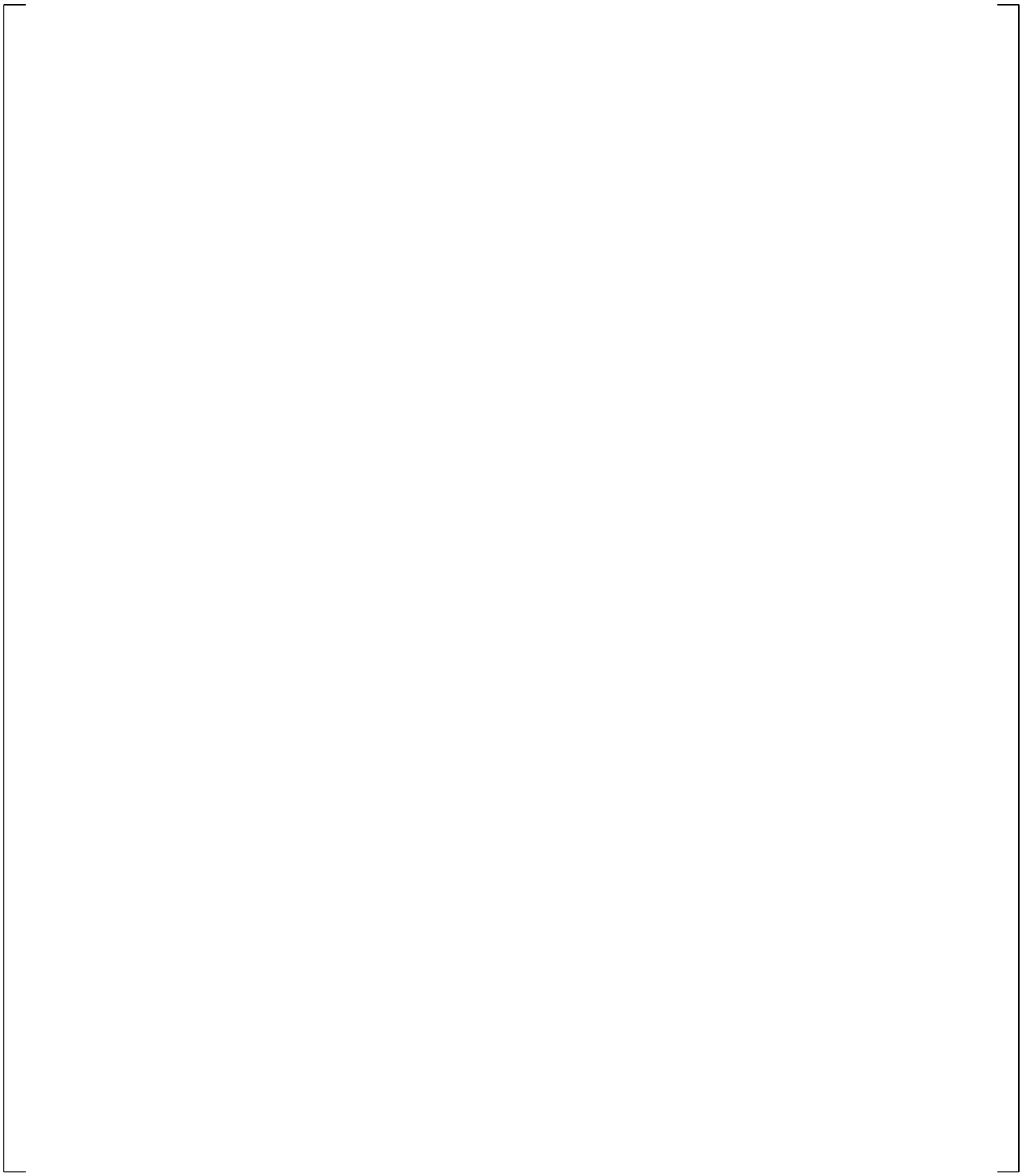

Figure 24.7.3-11 CCTF Run 62 WCOBRA/TRAC-TF2 vs. Data Comparison Void Fraction from 2.71 to 3.32 m (2-to-4 ft)

a,c

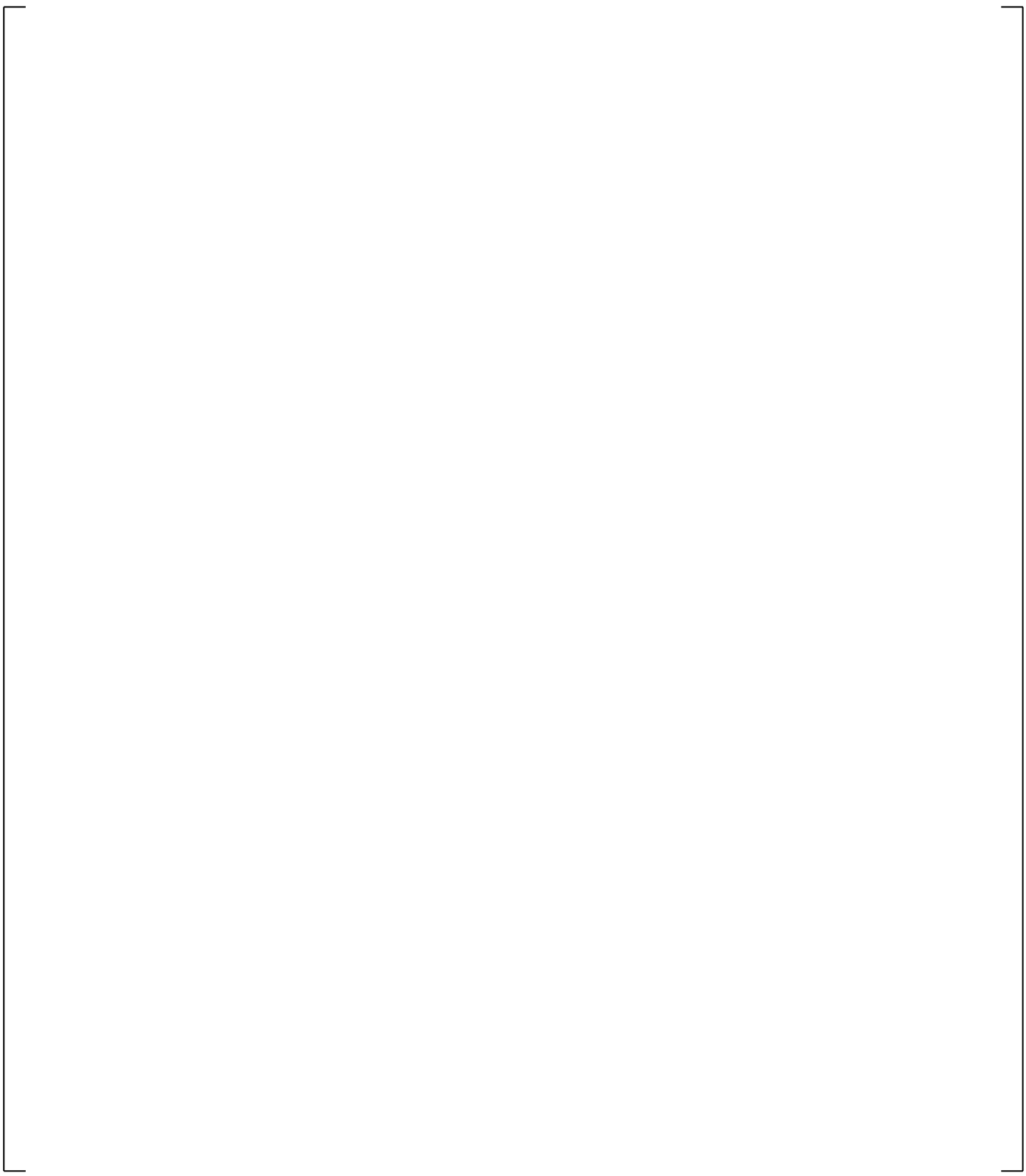

Figure 24.7.3-12 CCTF Run 62 WCOBRA/TRAC-TF2 vs. Data Comparison Void Fraction from 3.32 to 3.93 m (4-to-6 ft)

a,c

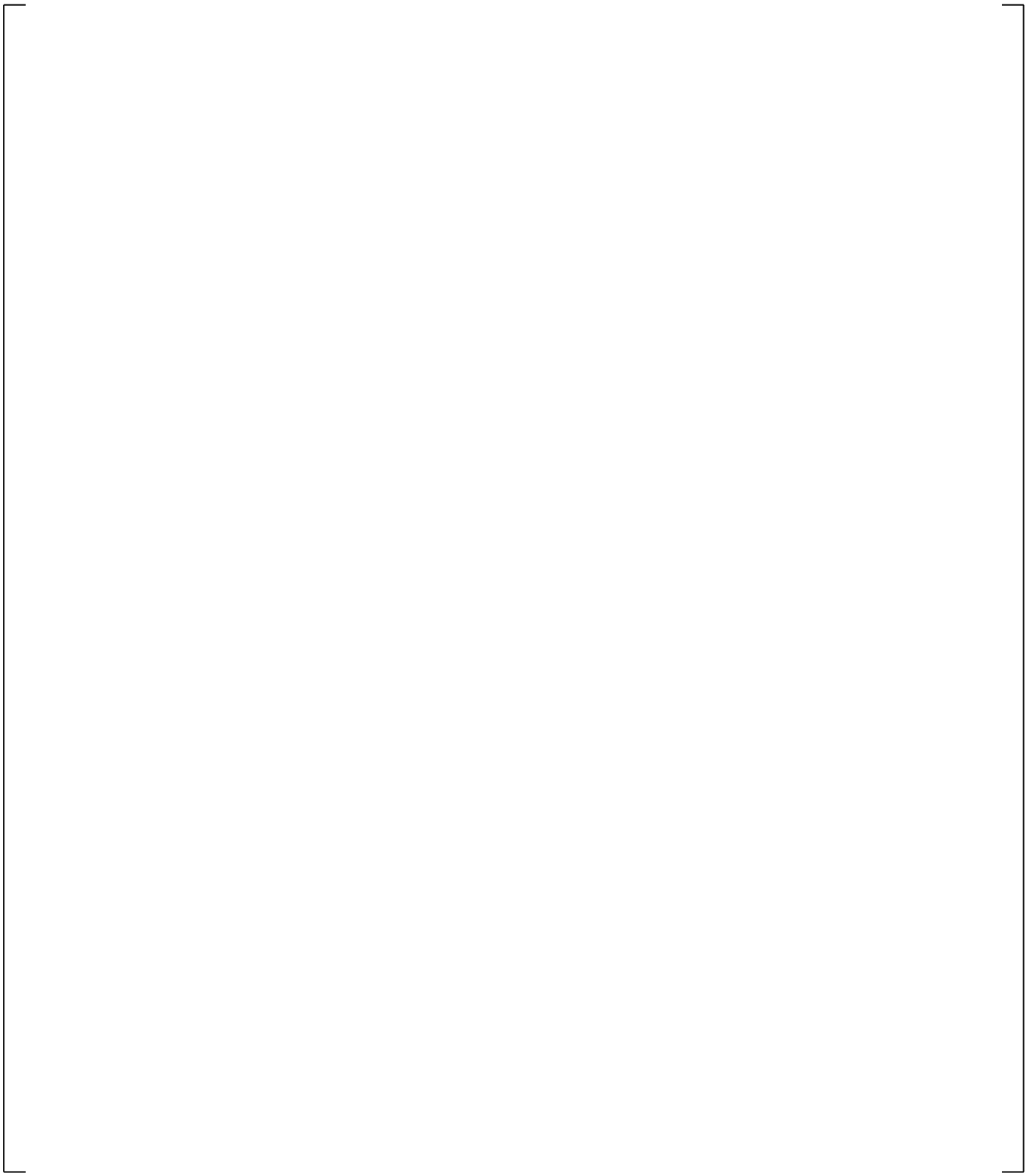

Figure 24.7.3-13 CCTF Run 62 WCOBRA/TRAC-TF2 vs. Data Comparison Void Fraction from 3.93 to 4.54 m (6-to-8 ft)

a,c

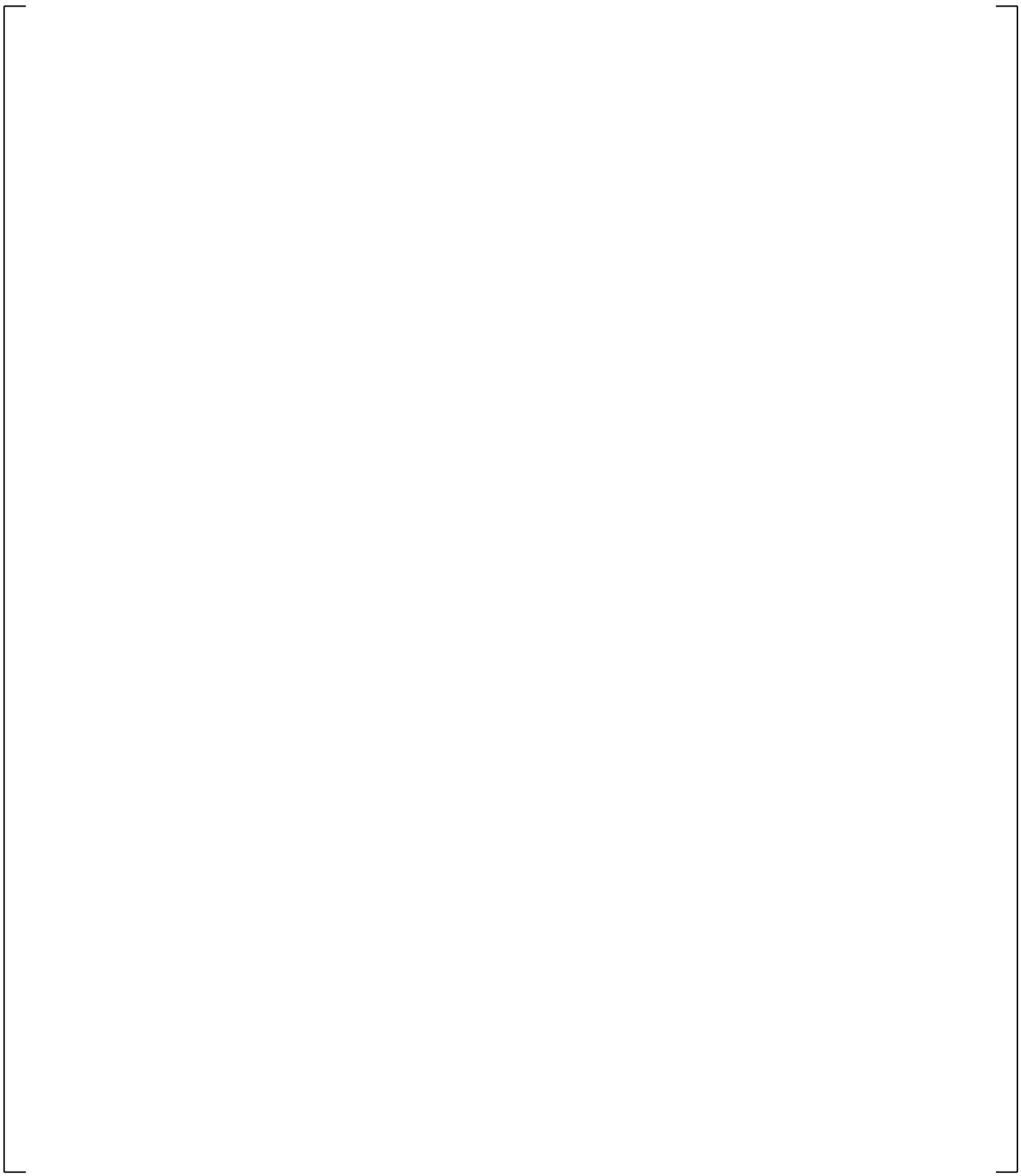

Figure 24.7.3-14 CCTF Run 62 WCOBRA/TRAC-TF2 vs. Data Comparison Void Fraction from 4.54 to 5.15 m (8-to-10 ft)

a,c

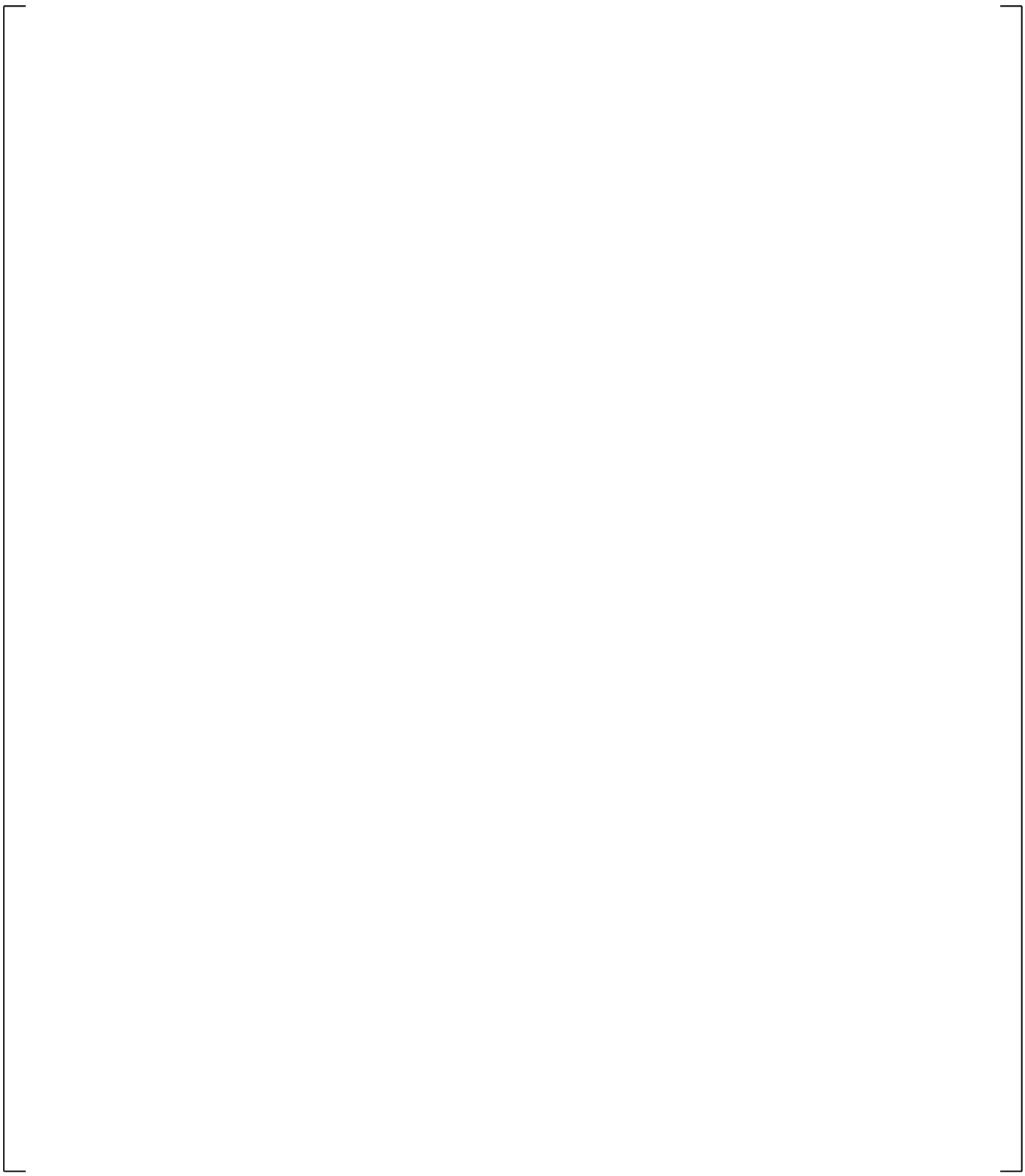

Figure 24.7.3-15 CCTF Run 62 WCOBRA/TRAC-TF2 vs. Data Comparison Void Fraction from 5.15 to 5.76 m (10-to-12 ft)

a,c

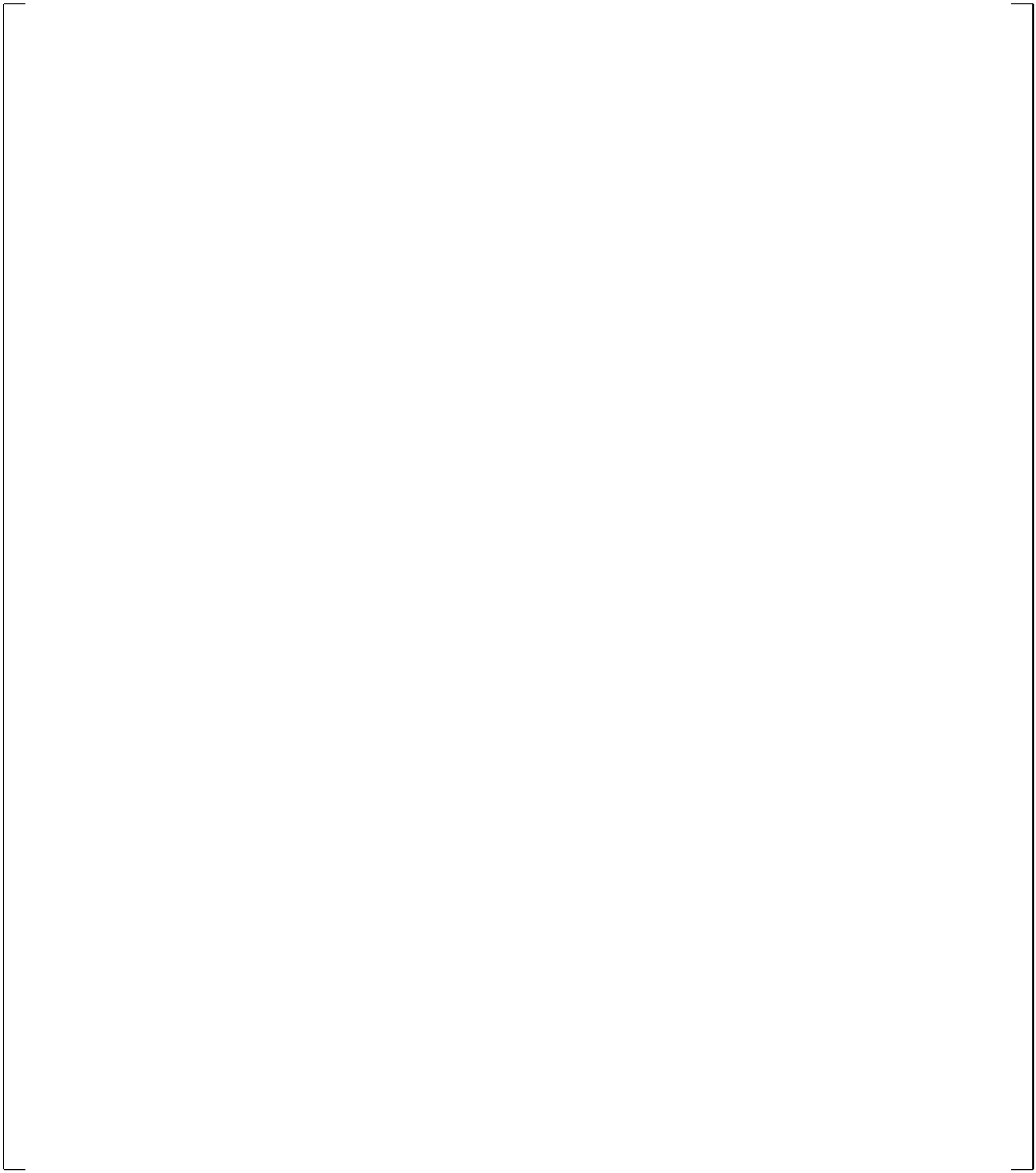

Figure 24.7.3-16a CCTF Run 62 WCOBRA/TRAC-TF2 vs. Data Comparison Vapor Fraction in End Box

a,c

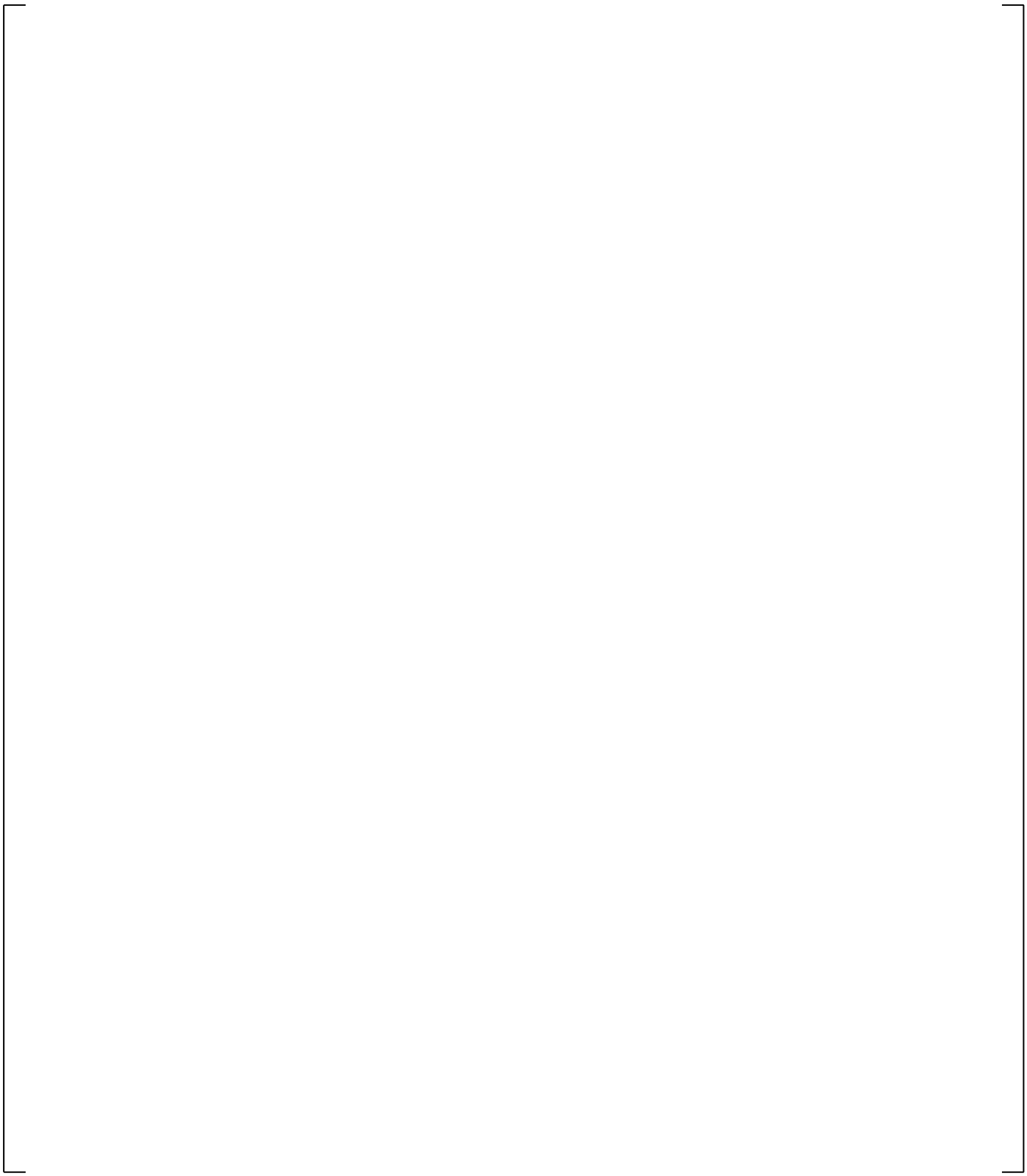

Figure 24.7.3-16b CCTF Run 62 WCOBRA/TRAC-TF2 vs. Data Comparison Void Fraction from Top of Upper Core Plate to Bottom of Upper Support Plate

a,c

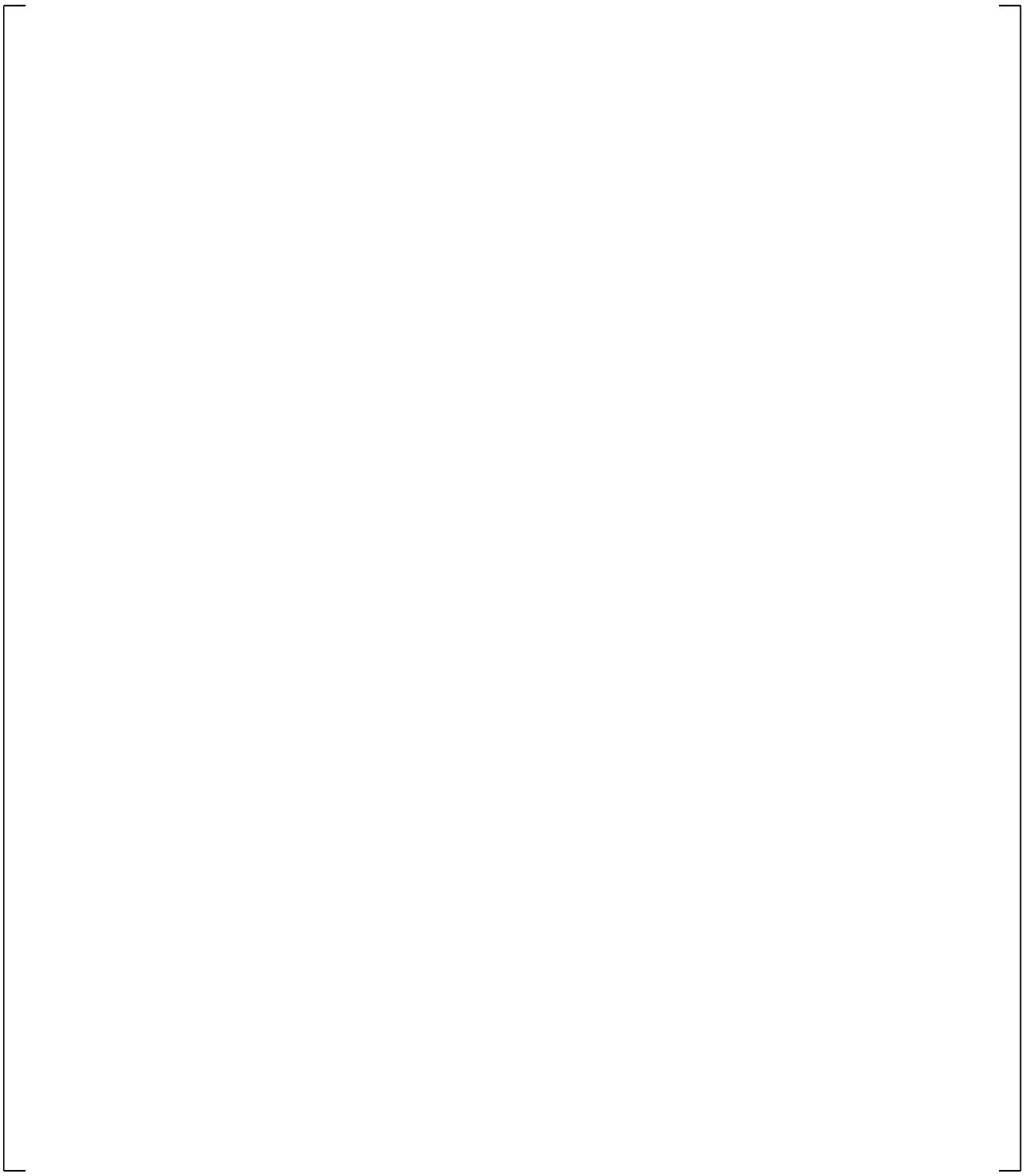

Figure 24.7.3-17 CCTF Run 62 WCOBRA/TRAC-TF2 vs. Data Collapsed Liquid Level in Core

a,c

Figure 24.7.3-18 CCTF Run 62 WCOBRA/TRAC-TF2 vs. Data Collapsed Liquid Level in Upper Plenum

a,c

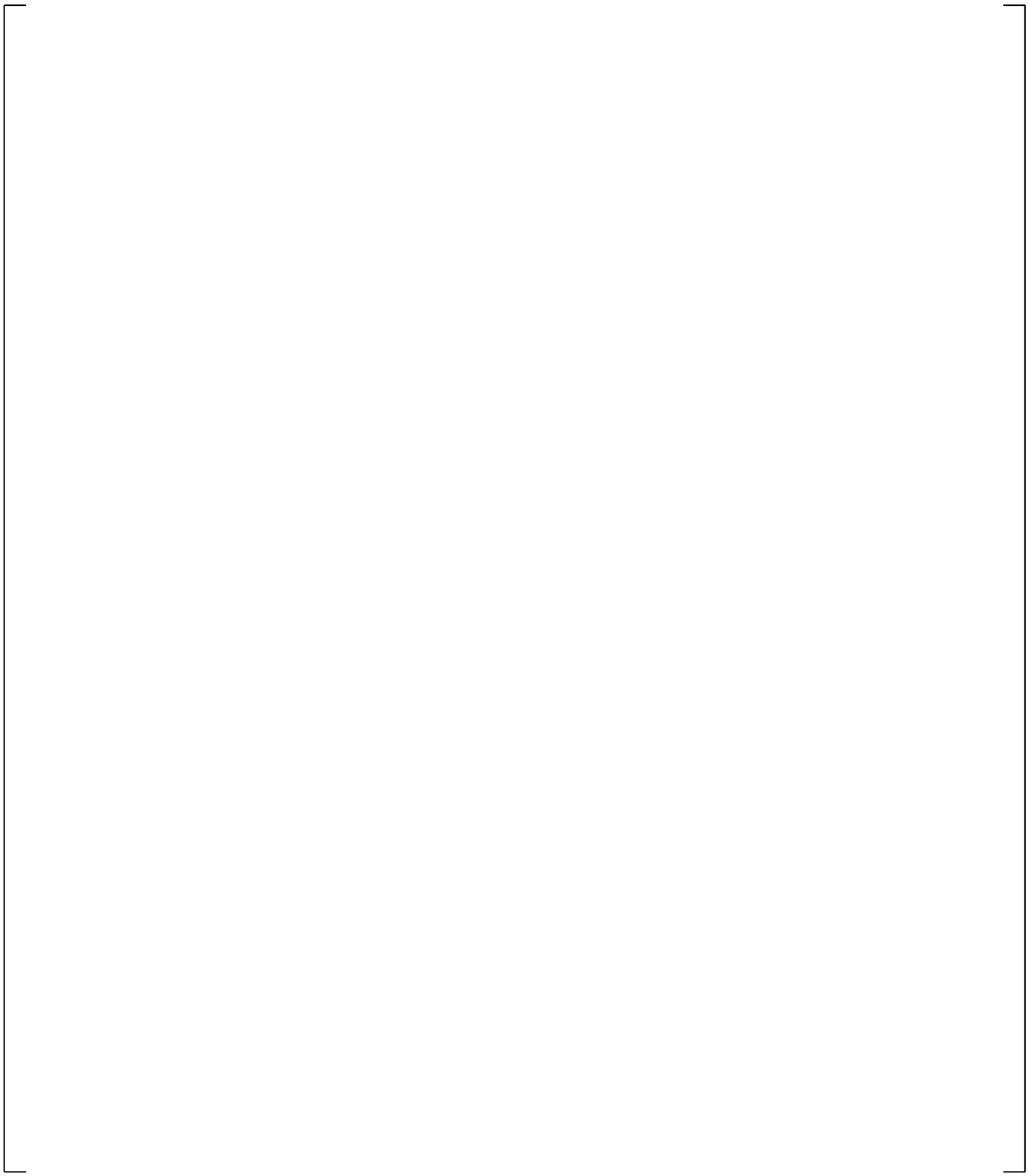

Figure 24.7.3-19 CCTF Run 62 WCOBRA/TRAC-TF2 vs. Data Pressure in Upper Plenum

a,c

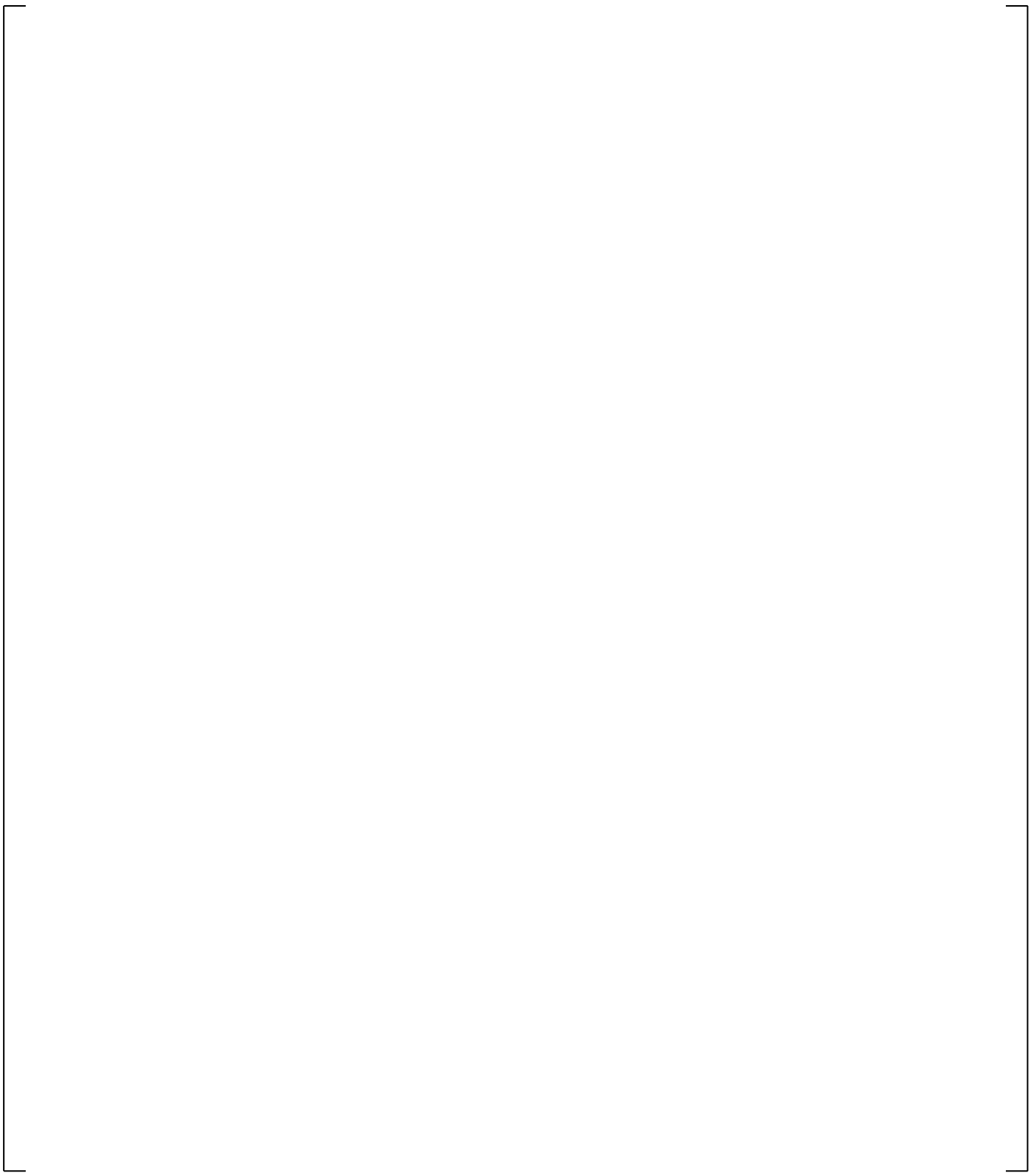

Figure 24.7.3-20 CCTF Run 62 WCOBRA/TRAC-TF2 vs. Data Pressure Difference from Lower Plenum to Upper Plenum

a,c

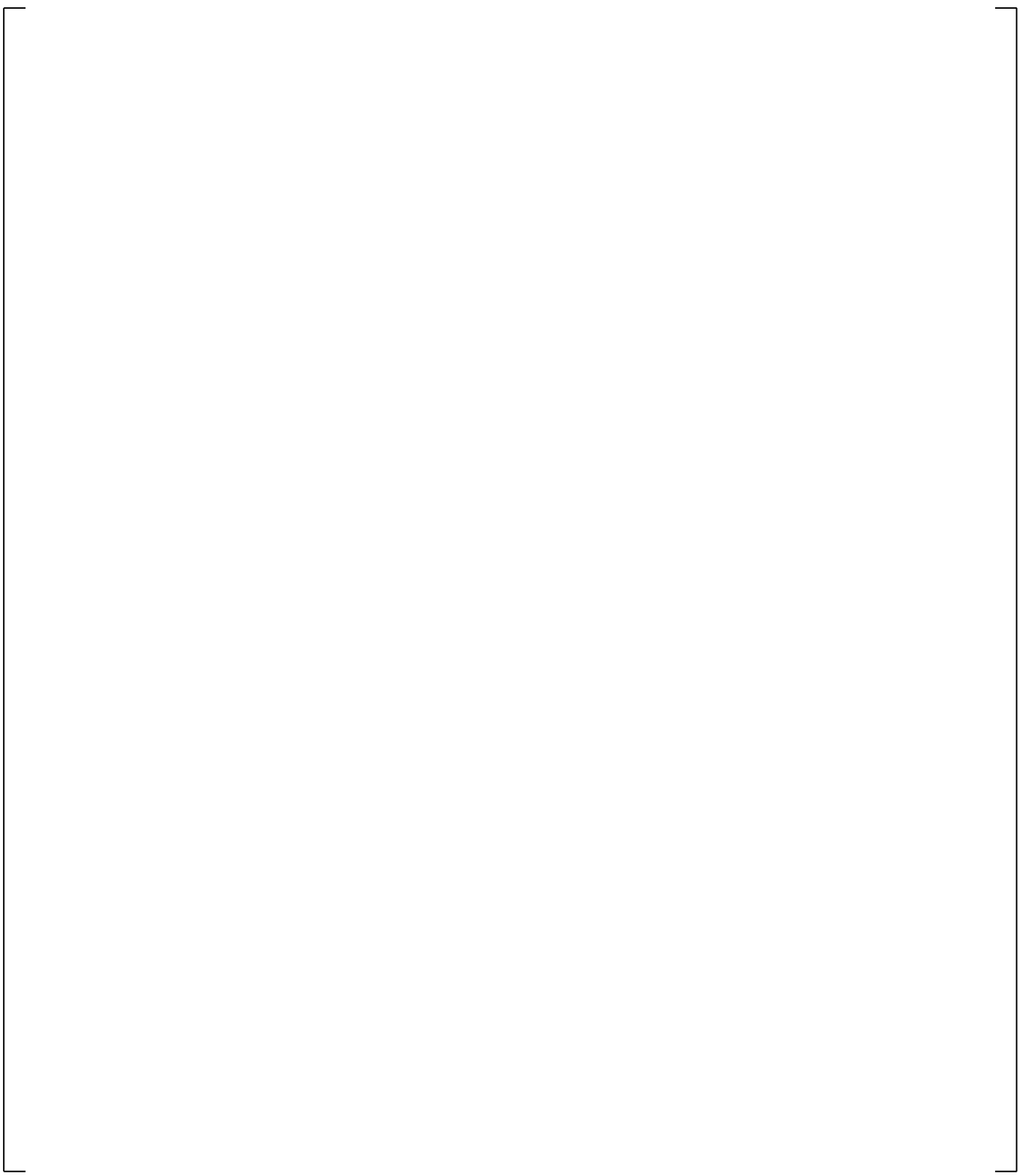

Figure 24.7.3-21 CCTF Run 62 WCOBRA/TRAC-TF2 vs. Data Pressure Difference from Lower Plenum to Top of Downcomer

a,c

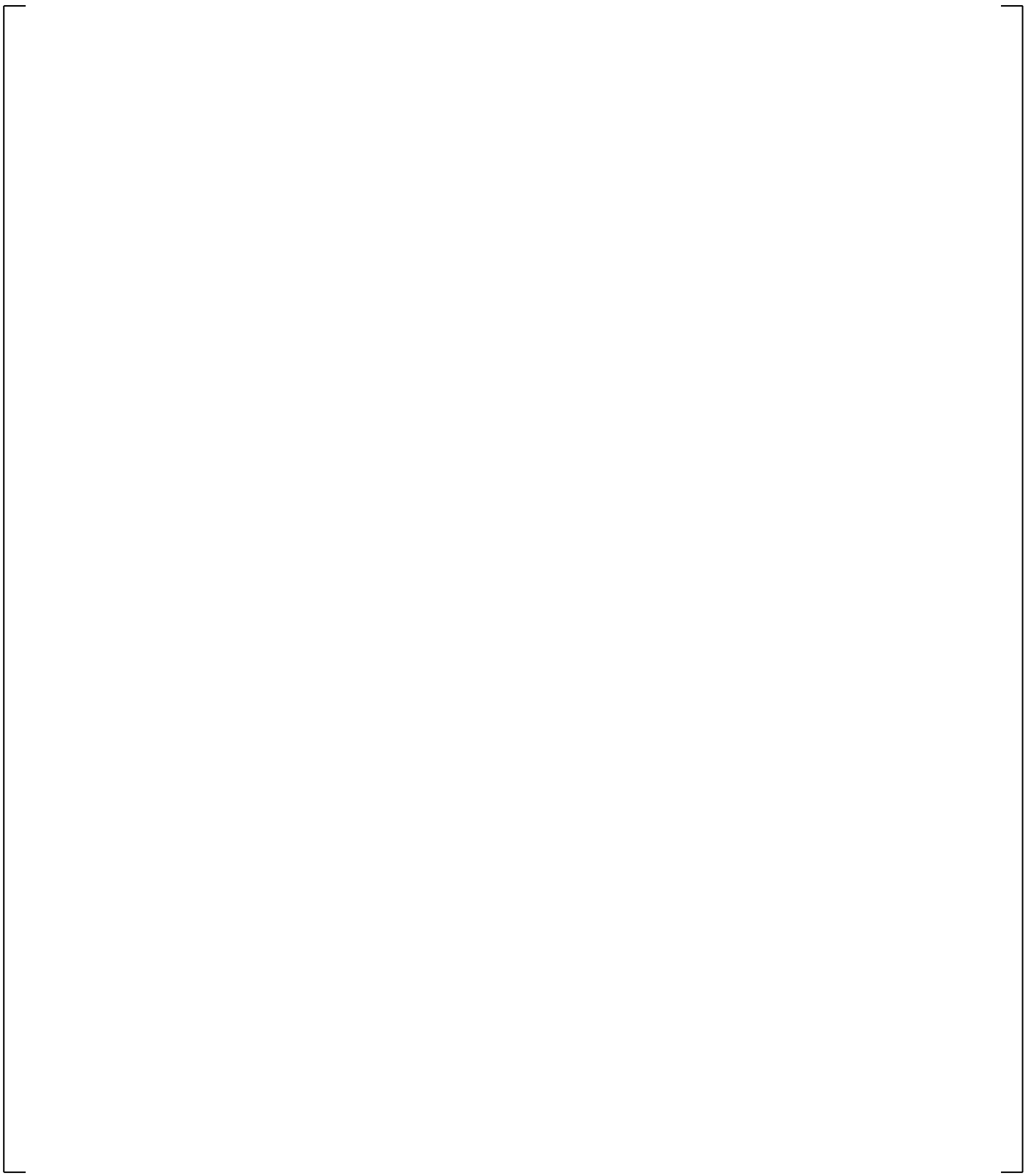

Figure 24.7.3-22 CCTF Run 62 WCOBRA/TRAC-TF2 vs. Data Pressure Difference from Upper Plenum to Intact Cold Leg Nozzle (Intact Loop ΔP)

a,c

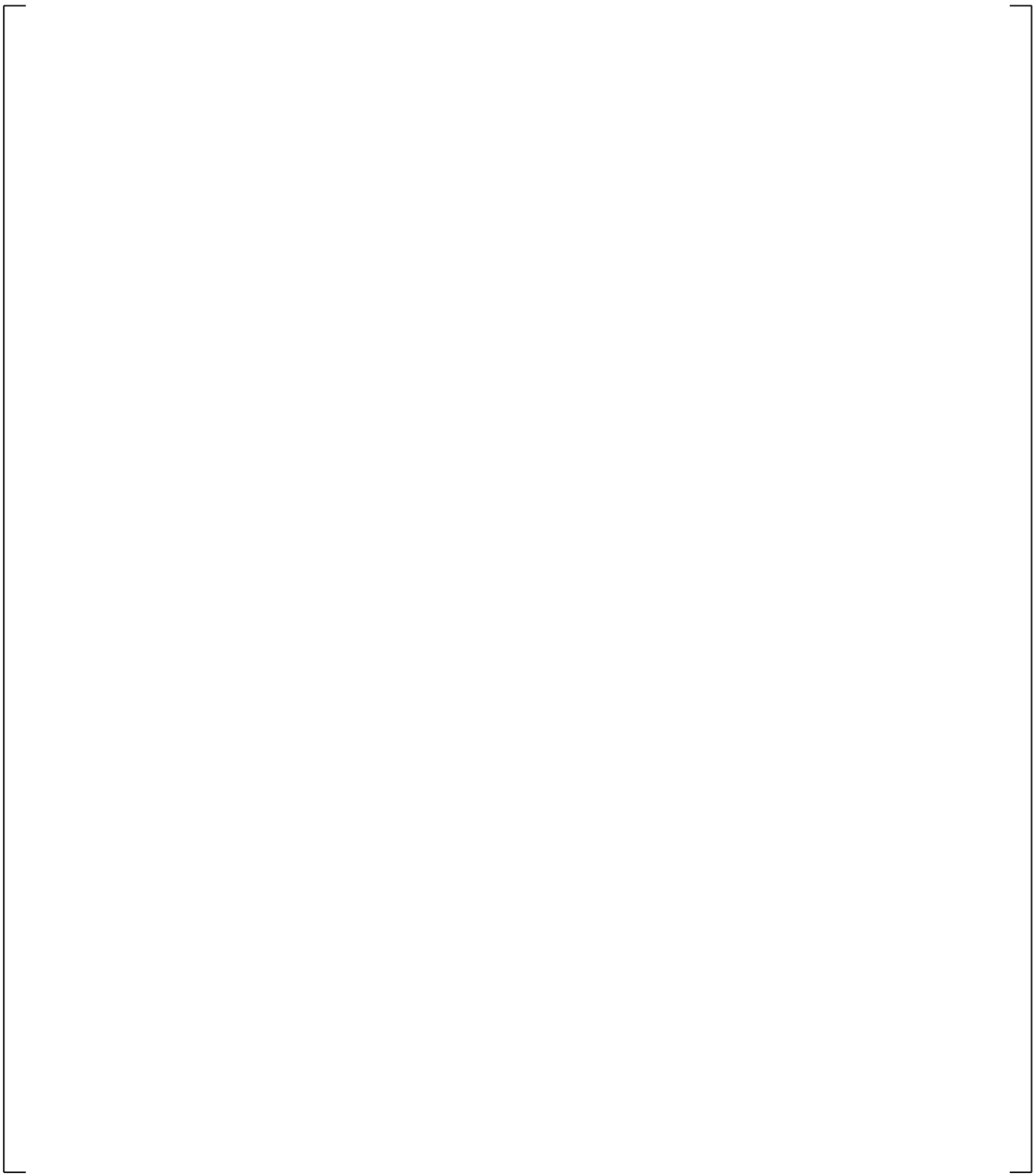

Figure 24.7.3-23 CCTF Run 62 WCOBRA/TRAC-TF2 vs. Data Pressure Difference from Upper Plenum to Steam Generator (Intact Loop ΔP)

a,c

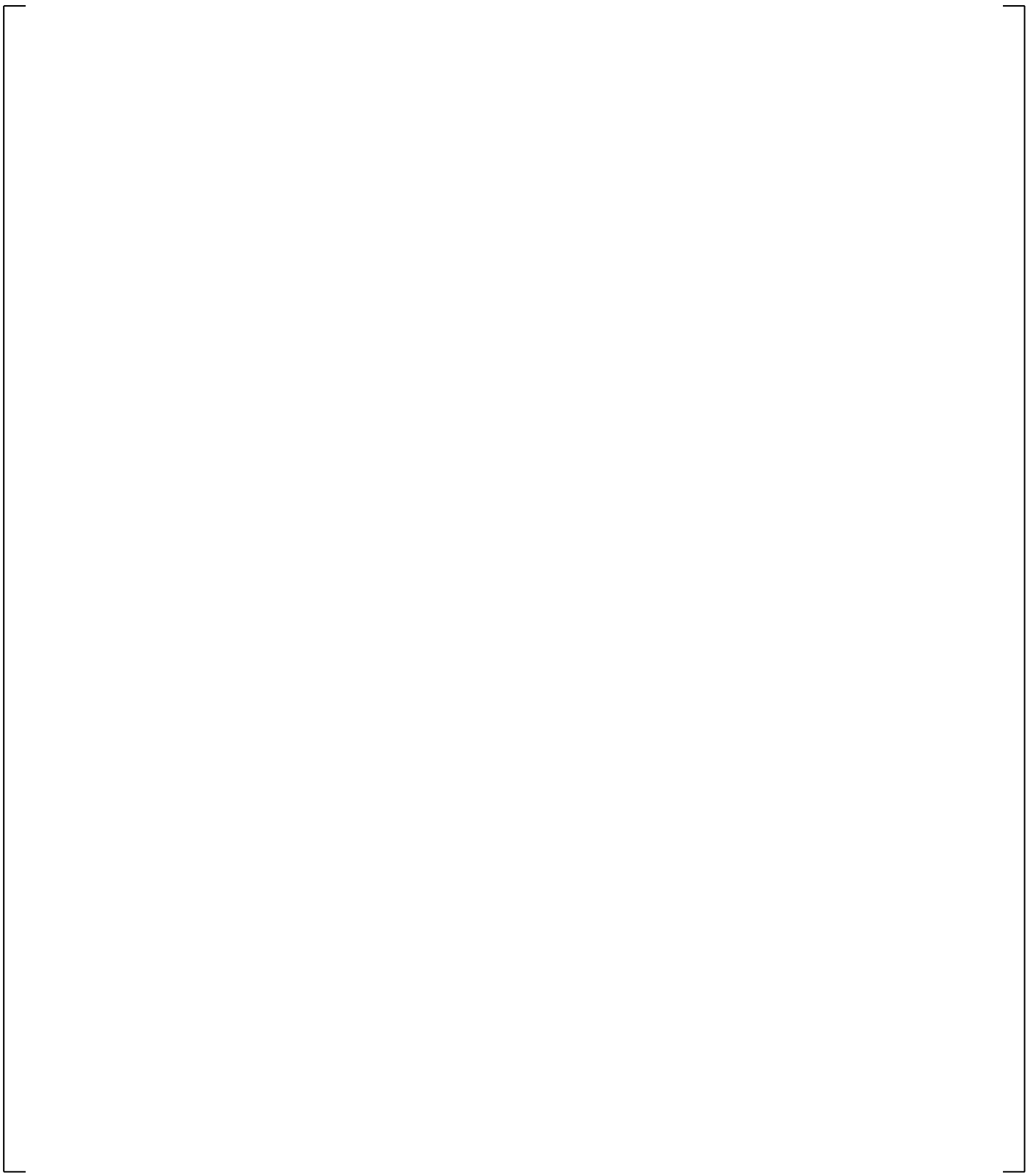

Figure 24.7.3-24 CCTF Run 62 WCOBRA/TRAC-TF2 vs. Data Pressure Difference from Inlet to Outlet Plenum of Steam Generator (Intact Loop ΔP)

a,c

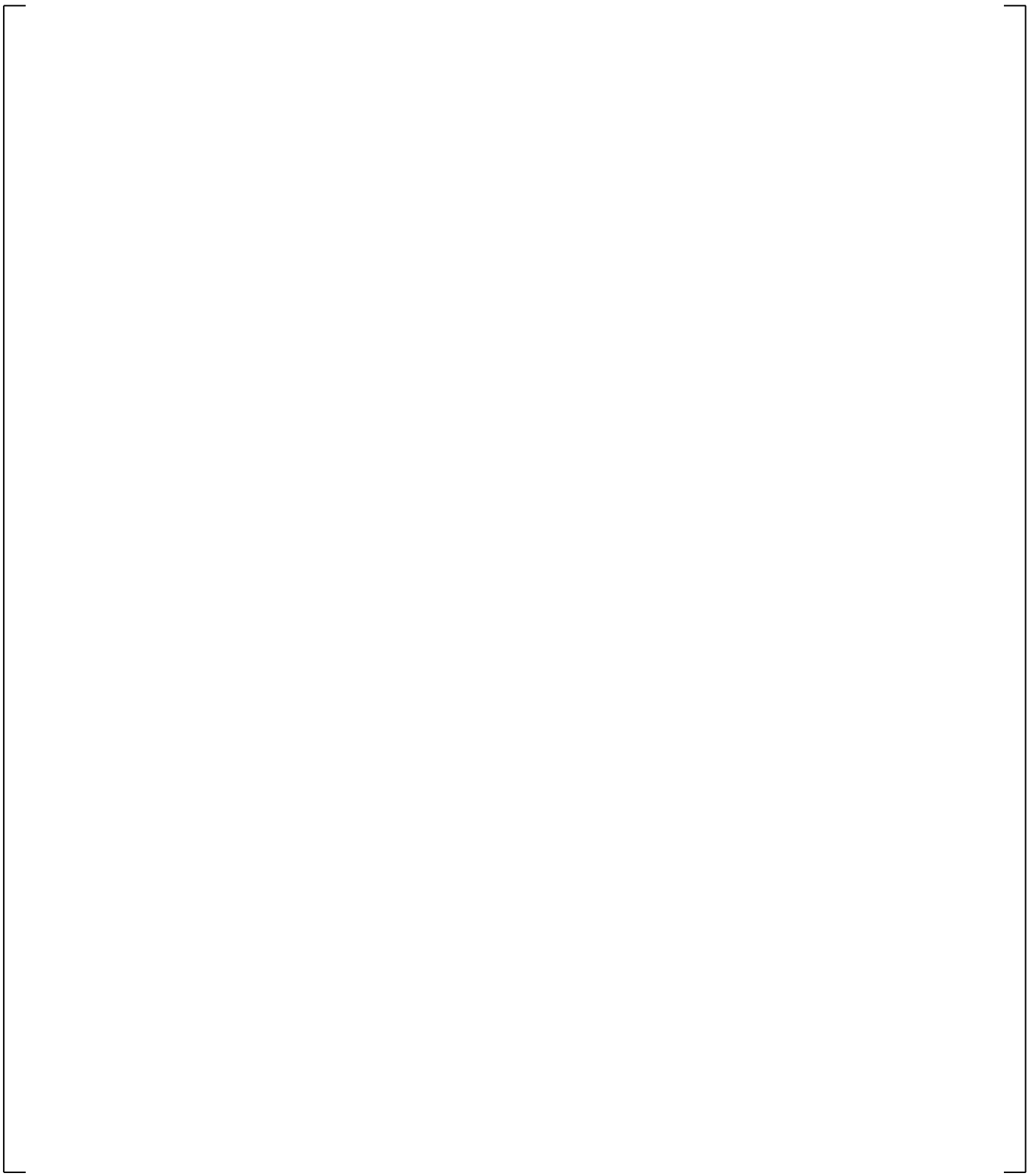

Figure 24.7.3-25 CCTF Run 62 WCOBRA/TRAC-TF2 vs. Data Pressure Difference across RCP (Intact Loop ΔP)

a,c

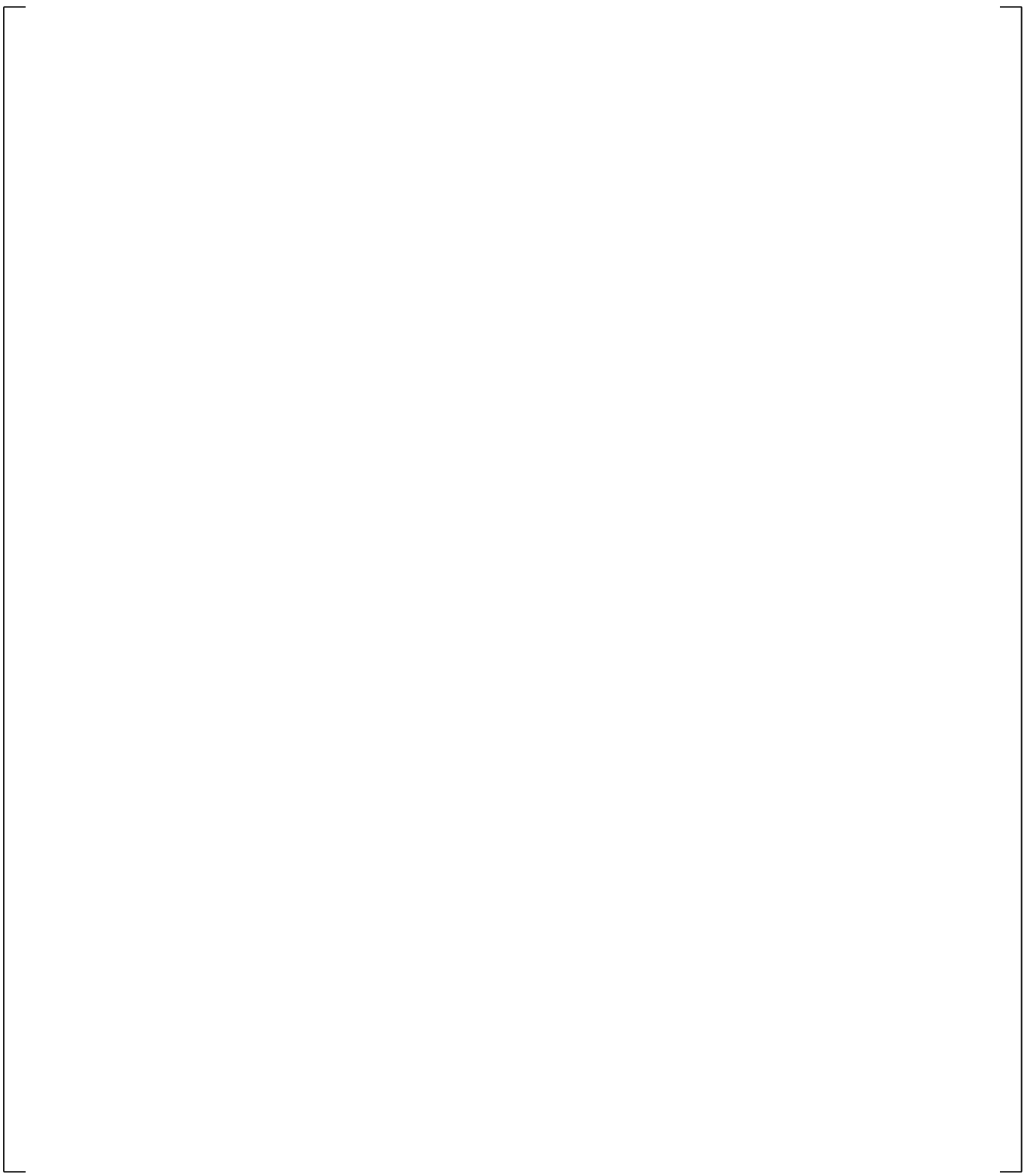

Figure 24.7.3-26 CCTF Run 62 WCOBRA/TRAC-TF2 vs. Data Pressure Difference from RCP to Downcomer (Intact Loop ΔP)

a,c

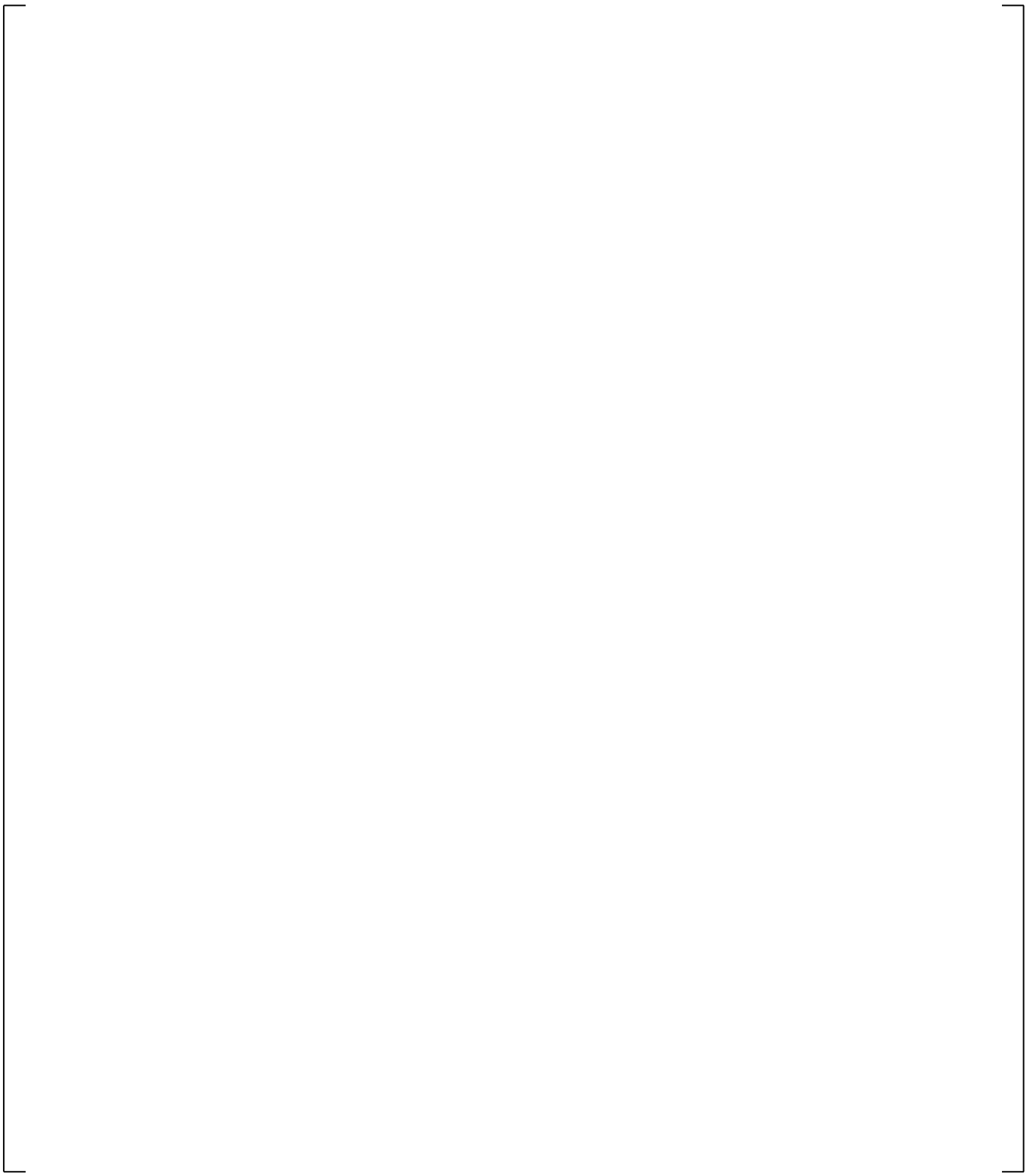

Figure 24.7.3-27 CCTF Run 62 Pressure Difference from UP to SG

a,c

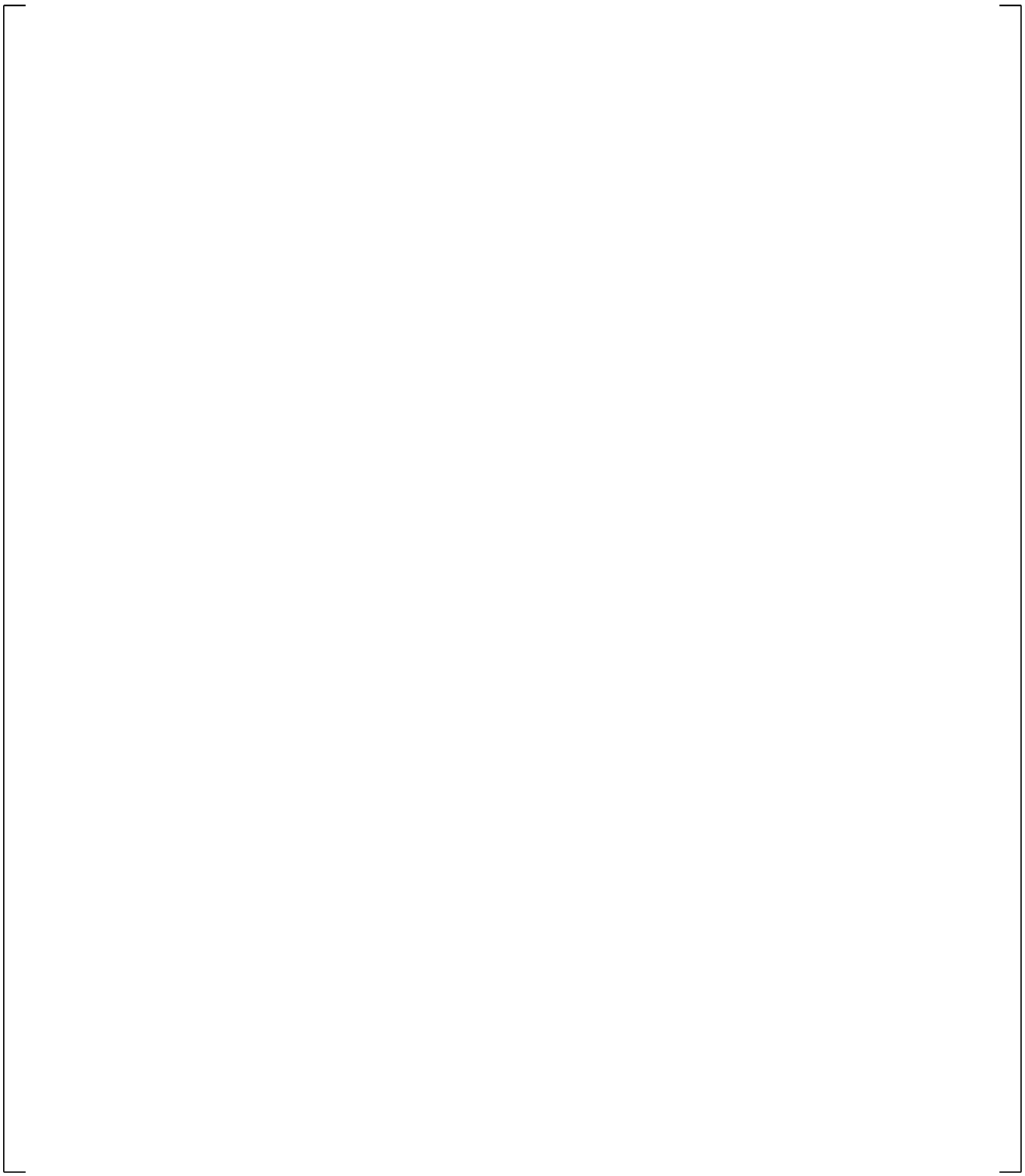

Figure 24.7.3-28 CCTF Run 62 Pressure Difference from UP to PUMP

a,c

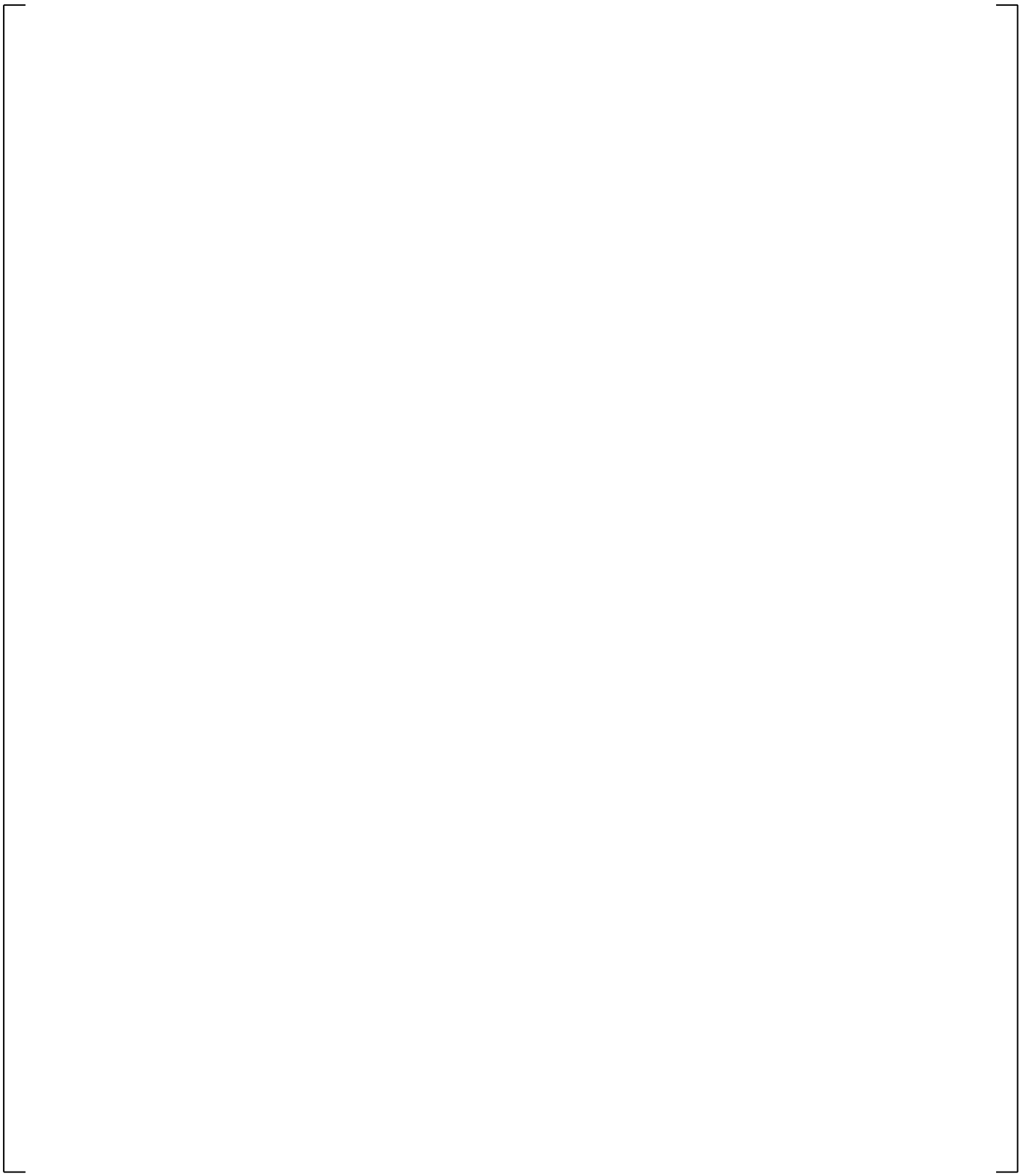

Figure 24.7.3-29 CCTF Run 62 WCOBRA/TRAC-TF2 vs. Data Pressure Difference in Broken Loop Hot Leg (Broken Loop ΔP)

a,c

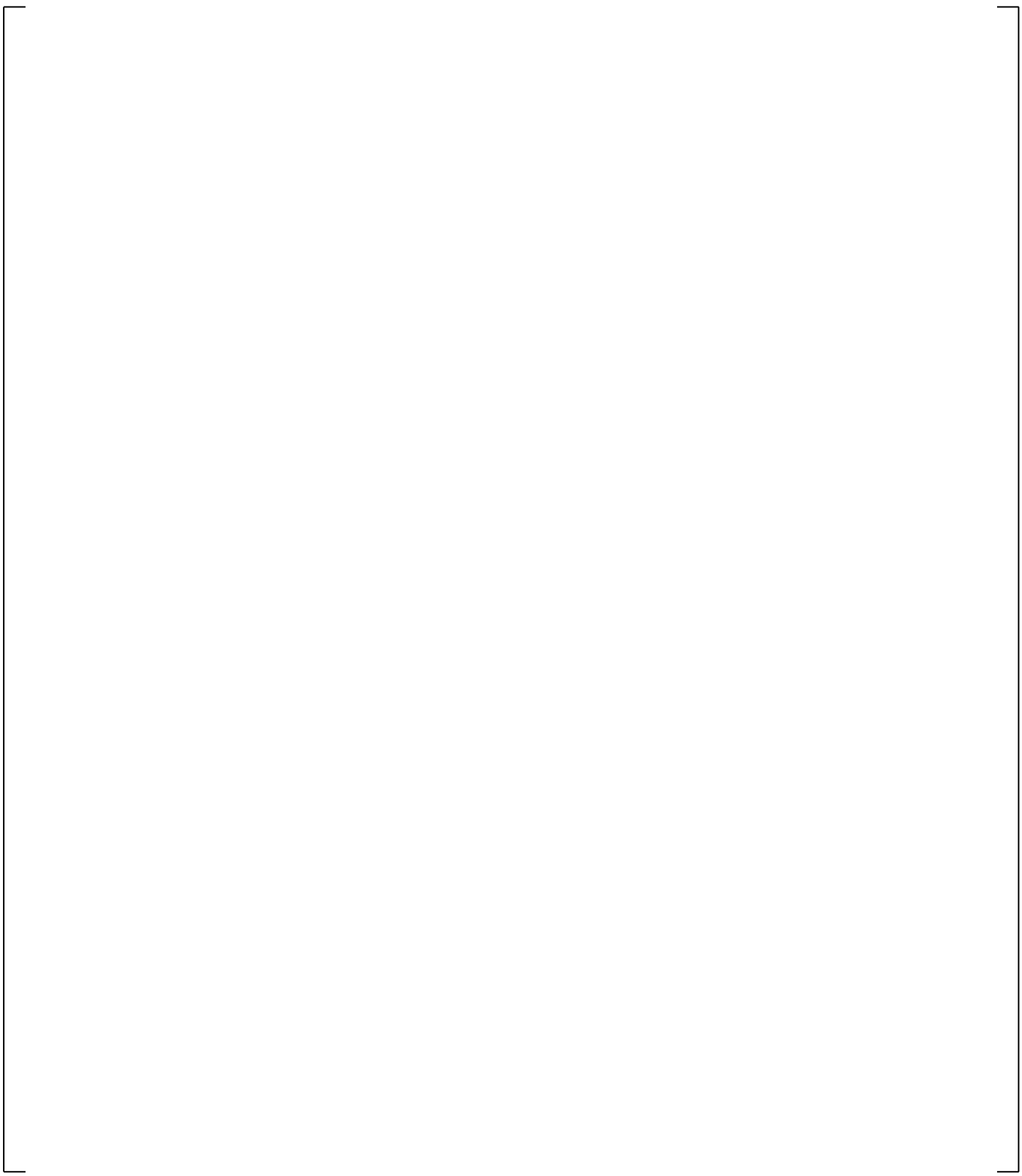

Figure 24.7.3-30 CCTF Run 62 WCOBRA/TRAC-TF2 vs. Data Pressure Difference from Upper Plenum to Steam Generator in Broken Loop (Broken Loop ΔP)

a,c

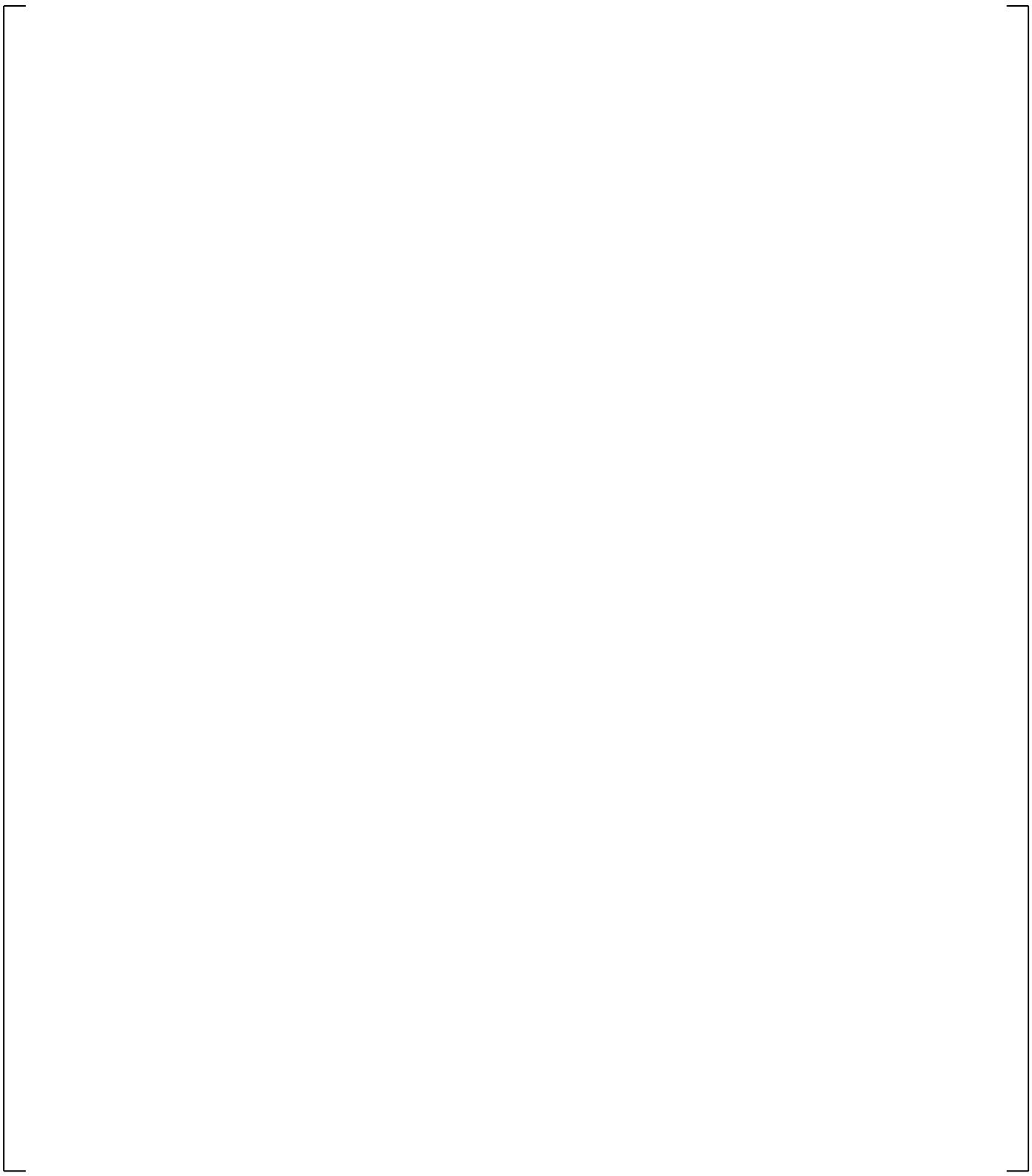

Figure 24.7.3-31 CCTF Run 62 WCOBRA/TRAC-TF2 vs. Data Pressure Difference from Inlet to Outlet Plenum of Steam Generator in Broken Loop (Broken Loop ΔP)

a,c

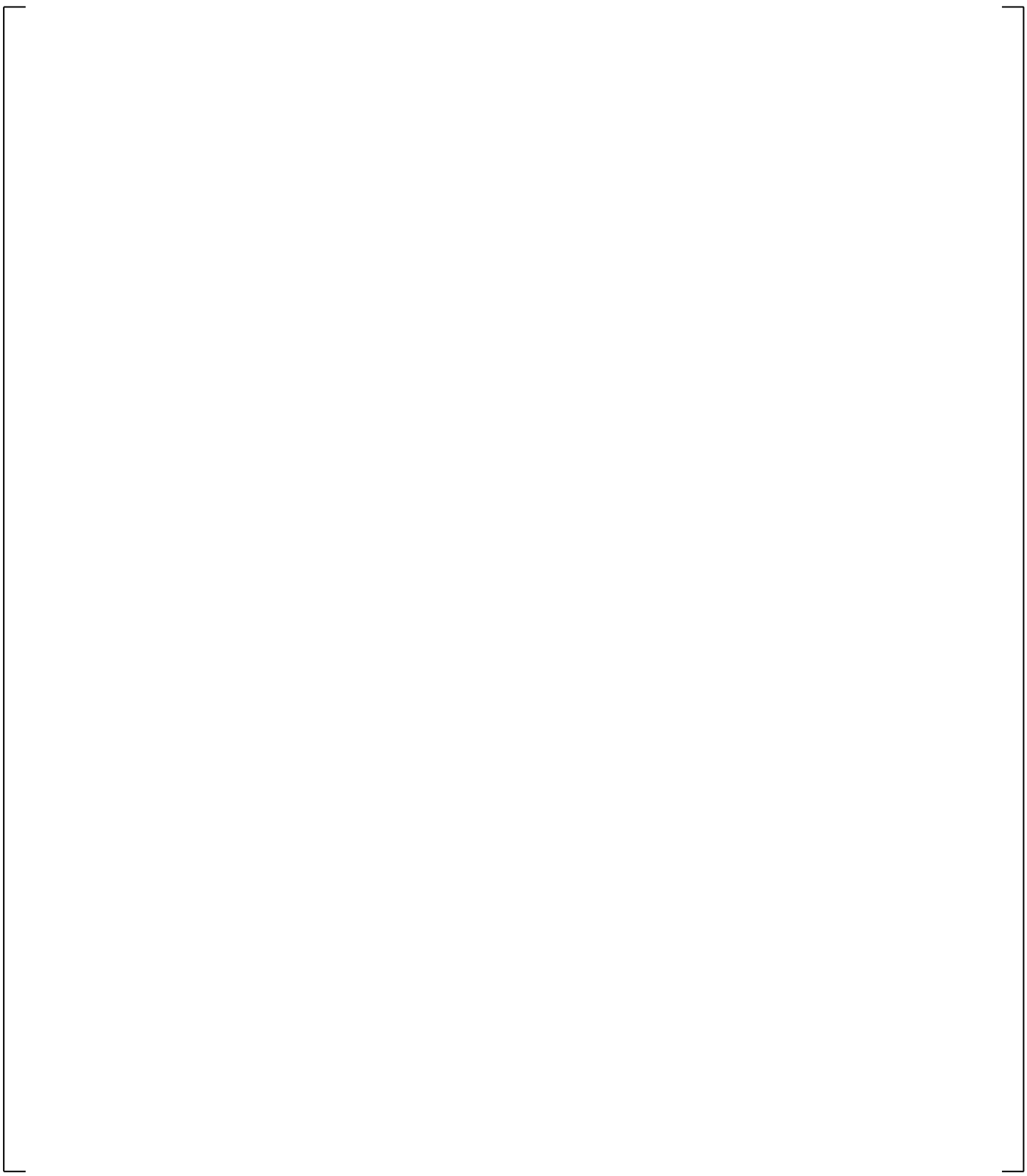

Figure 24.7.3-32 CCTF Run 62 WCOBRA/TRAC-TF2 vs. Data Pressure Difference across RCP in Broken Loop (Broken Loop ΔP)

a,c

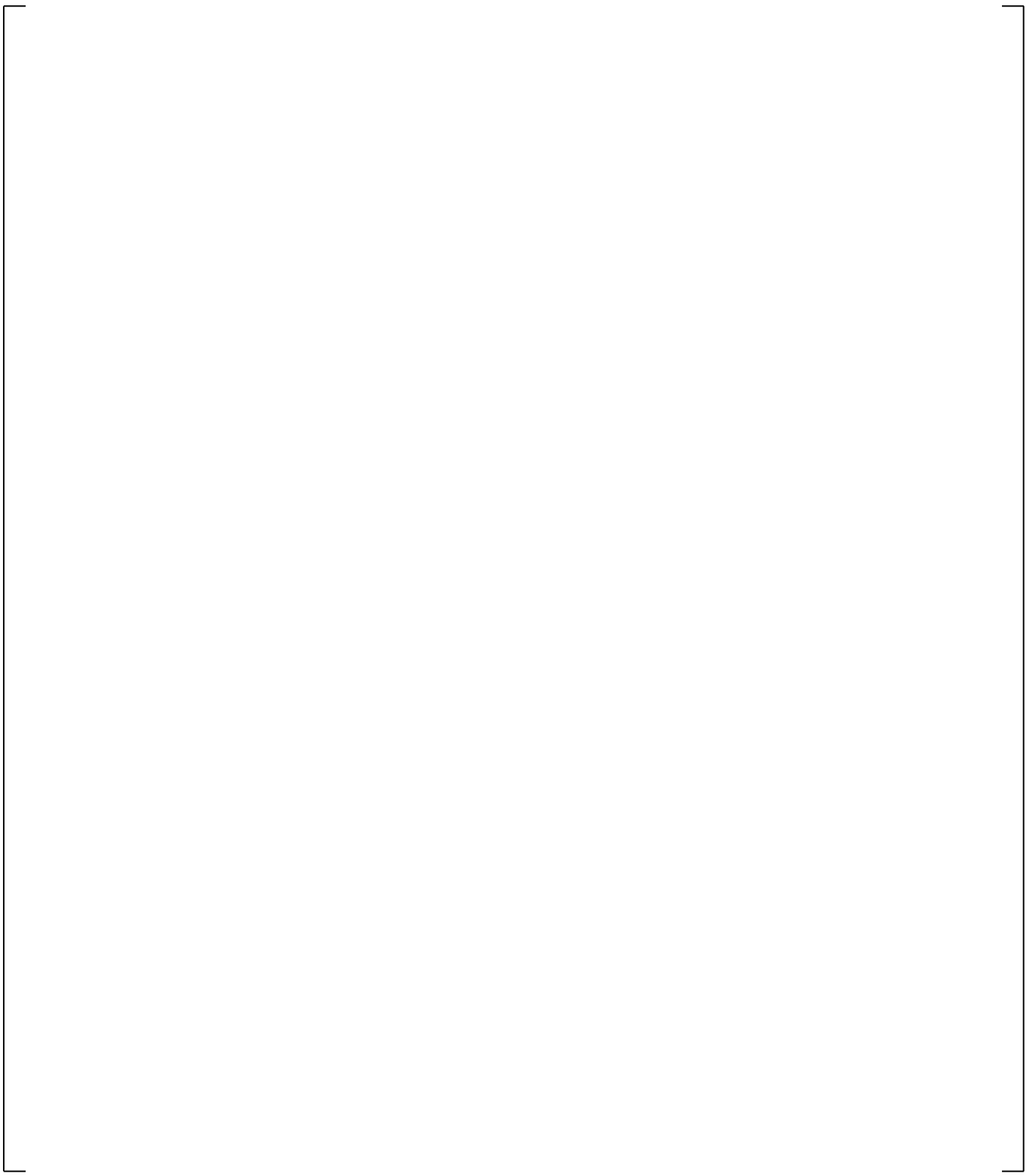

Figure 24.7.3-33 CCTF Run 62 WCOBRA/TRAC-TF2 vs. Data Pressure Difference from RCP to CV (Broken Loop ΔP)

a,c

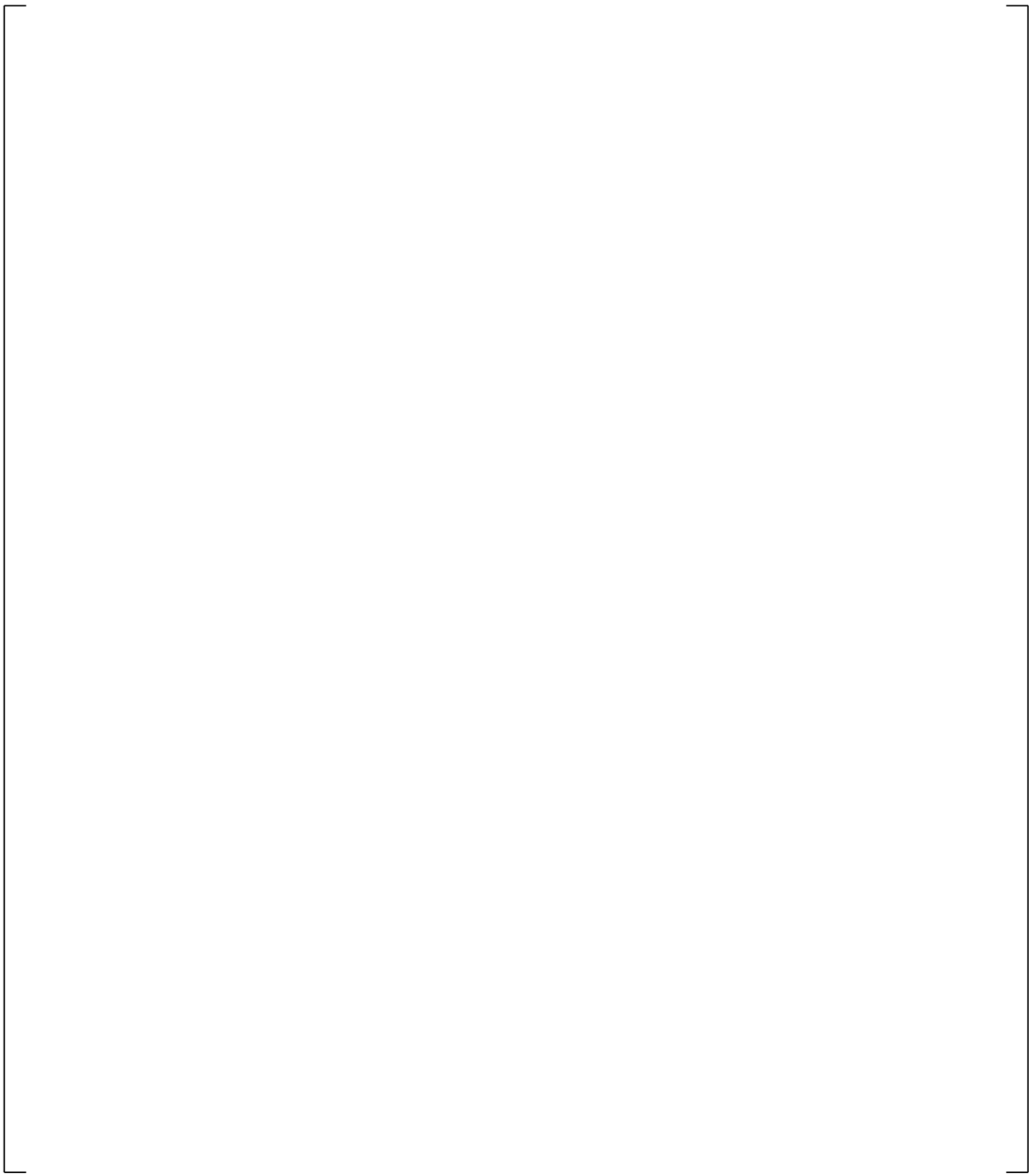

Figure 24.7.3-34 CCTF Run 62 WCOBRA/TRAC-TF2 vs. Data Vapor Mass Flowrate in Intact Hot Leg

a,c

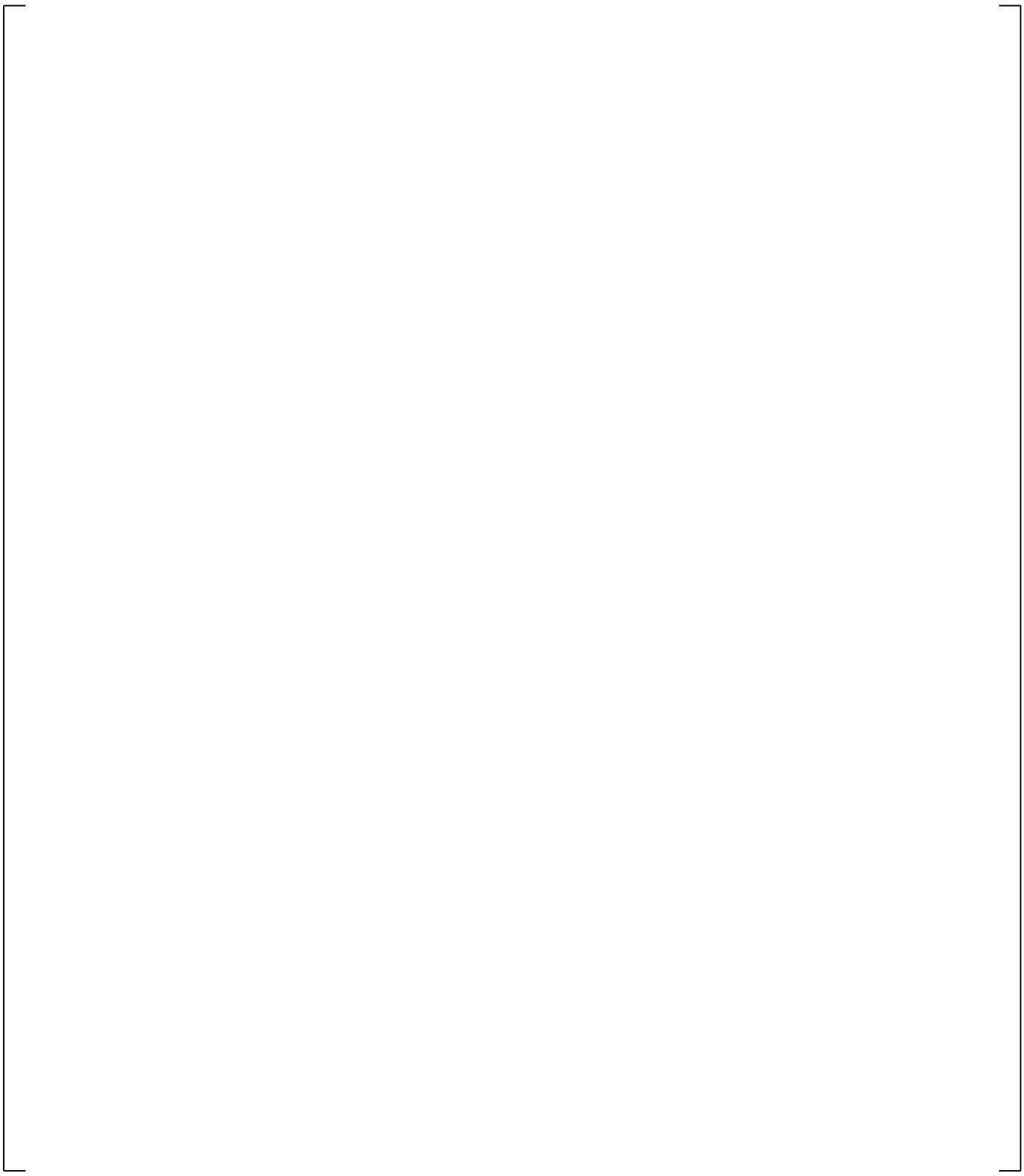

Figure 24.7.3-35 CCTF Run 62 WCOBRA/TRAC-TF2 vs. Data Vapor Velocity in Intact Hot Leg

a,c

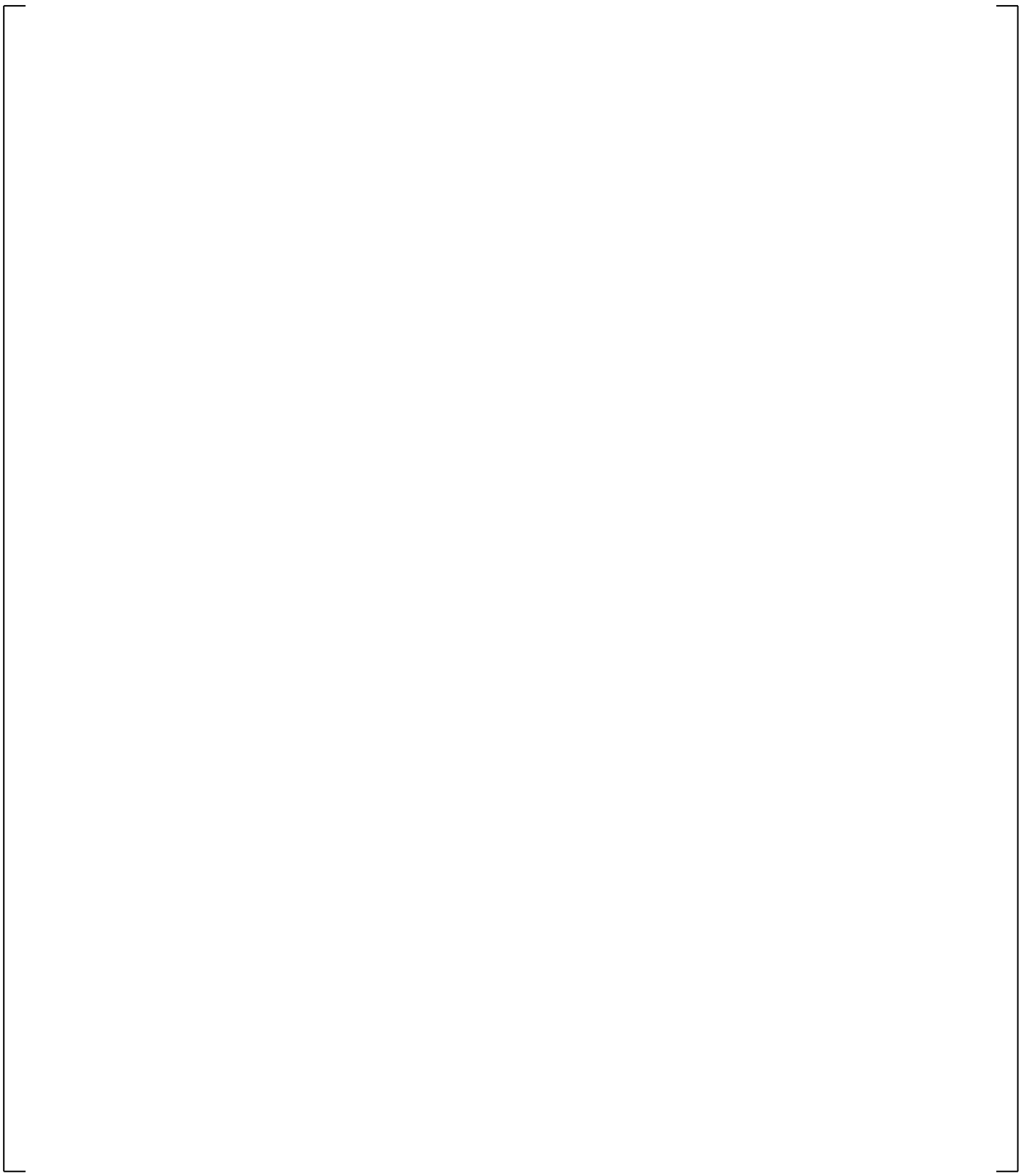

Figure 24.7.3-36 CCTF Run 62 WCOBRA/TRAC-TF2 vs. Data Vapor Density in Intact Hot Leg

a,c

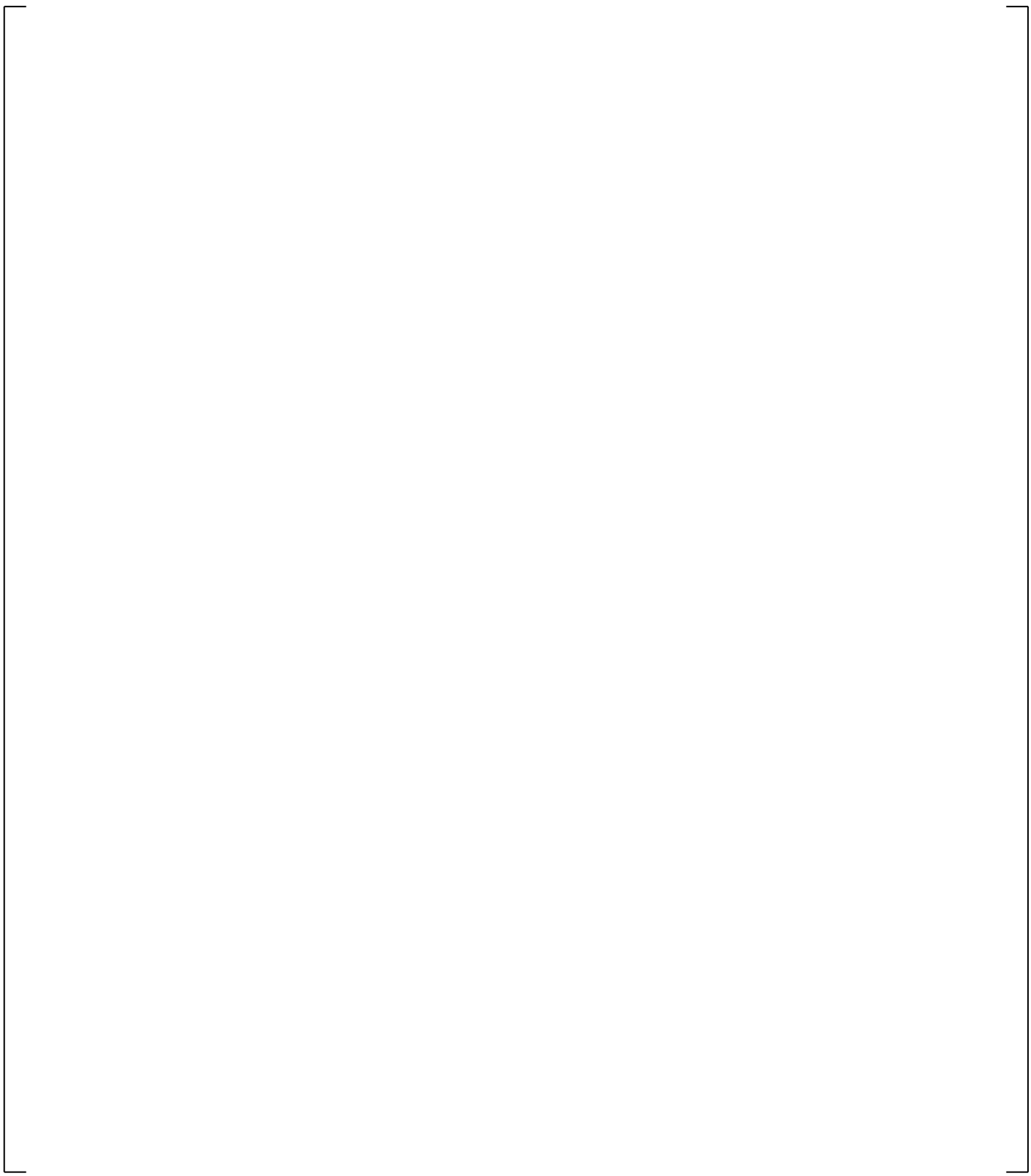

Figure 24.7.3-37 CCTF Run 62 WCOBRA/TRAC-TF2 vs. Data Liquid Mass Flowrate in Intact Hot Leg

a,c

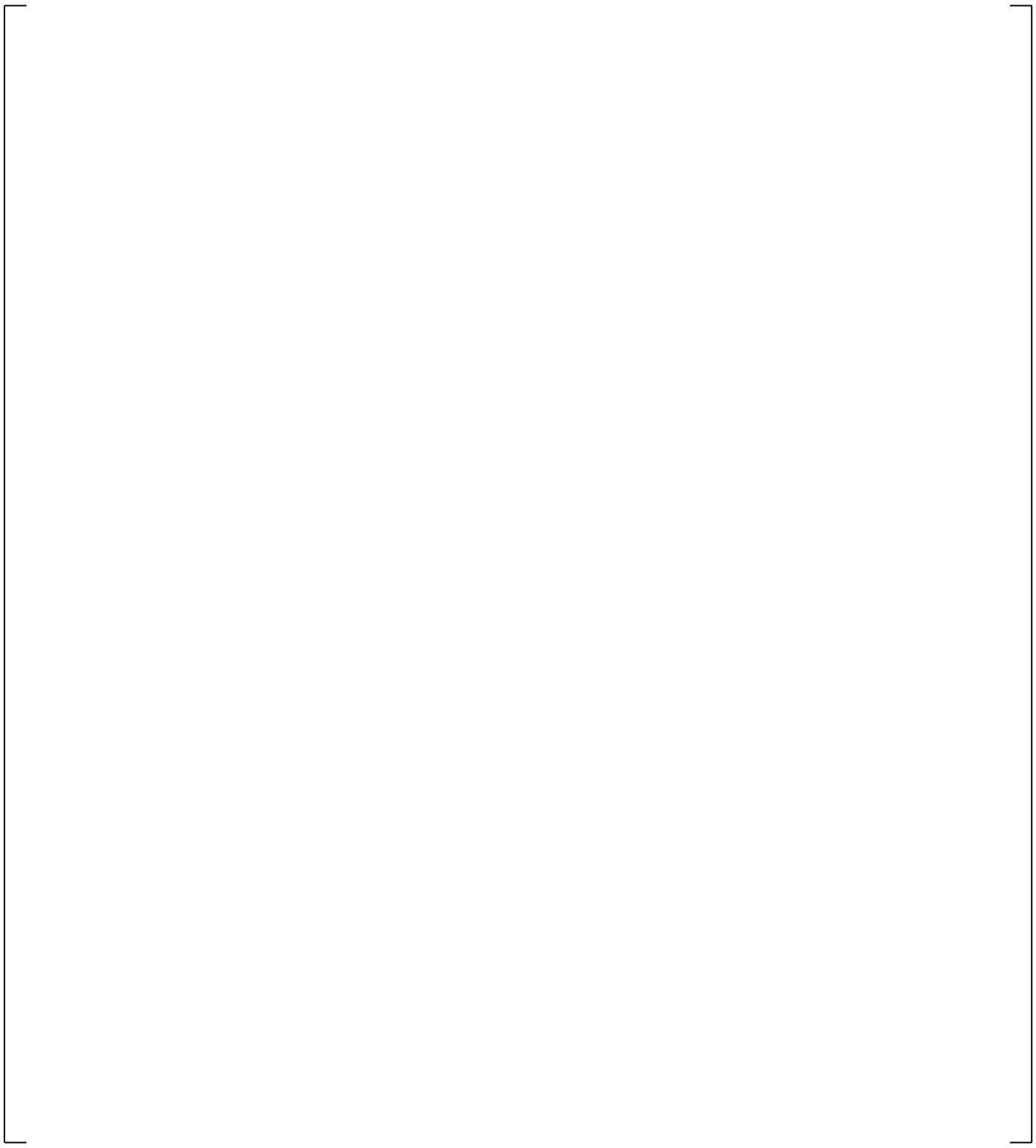

Figure 24.7.3-38 CCTF Run 62 WCOBRA/TRAC-TF2 vs. Data Total Mass Flowrate in Intact Hot Leg

a,c

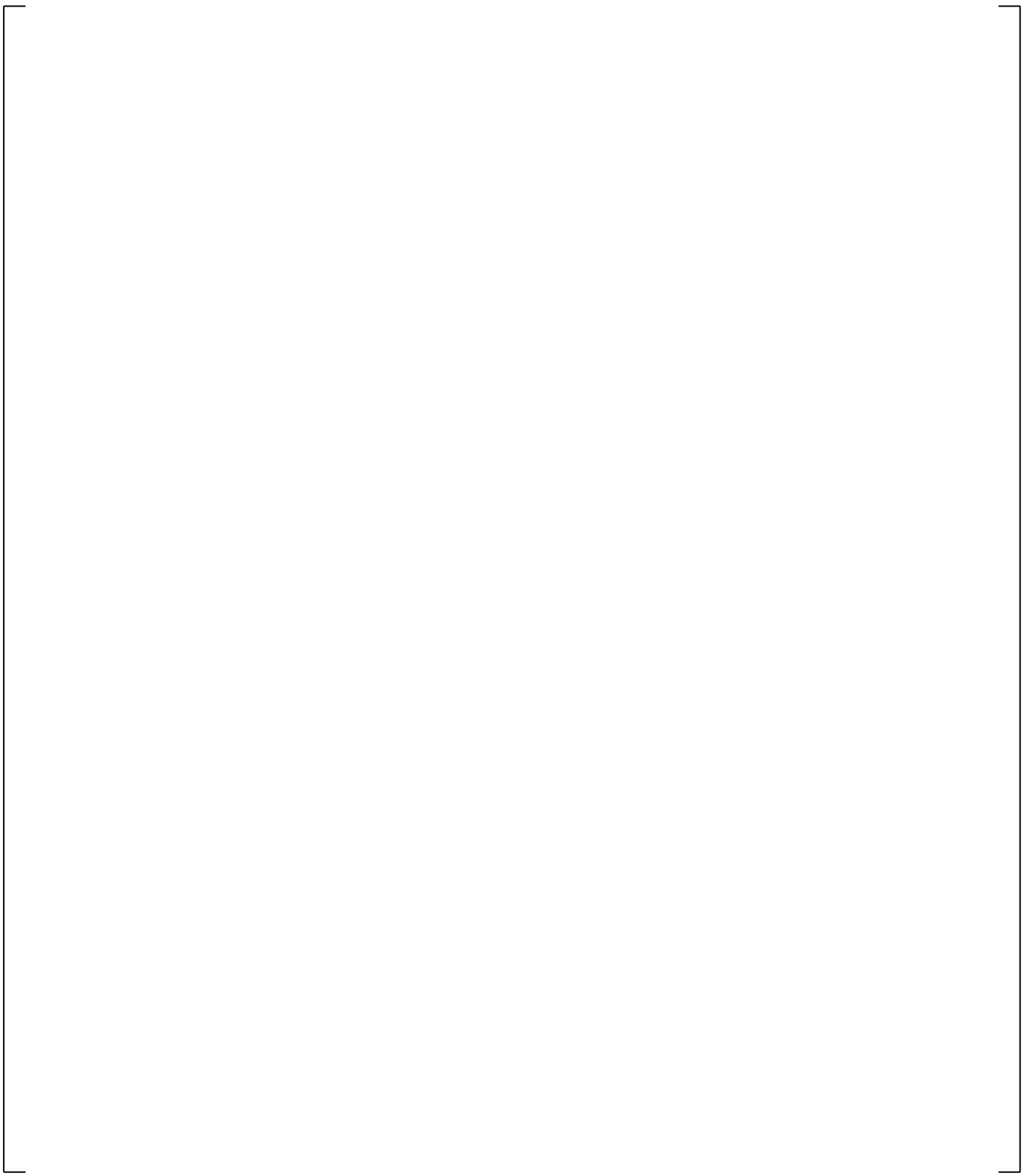

Figure 24.7.3-39 CCTF Run 62 WCOBRA/TRAC-TF2 vs. Data Vapor Mass Flowrate in Intact Cold Leg

a,c

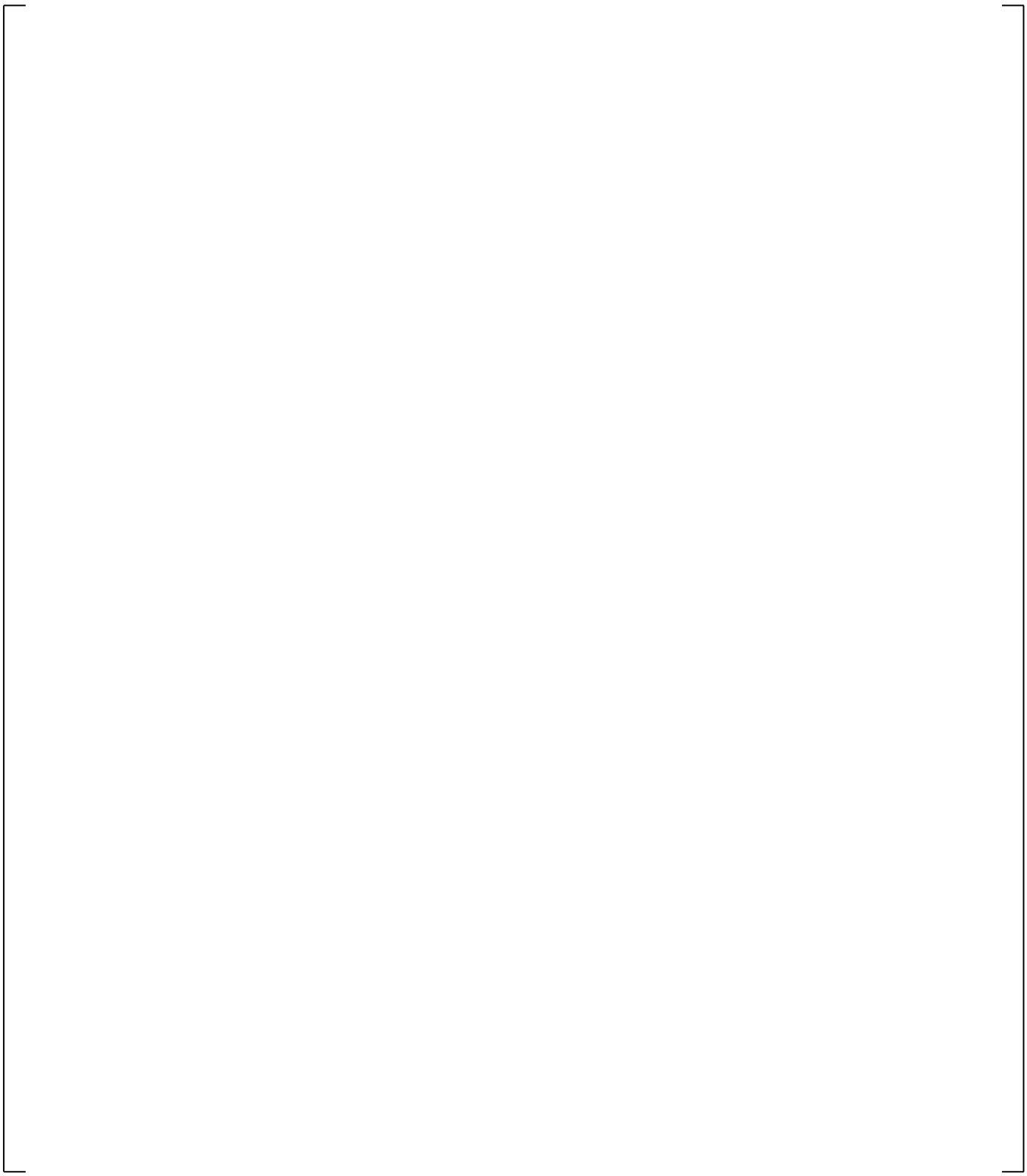

Figure 24.7.3-40 CCTF Run 62 WCOBRA/TRAC-TF2 vs. Data Liquid Mass Flowrate in Intact Cold Leg

a,c

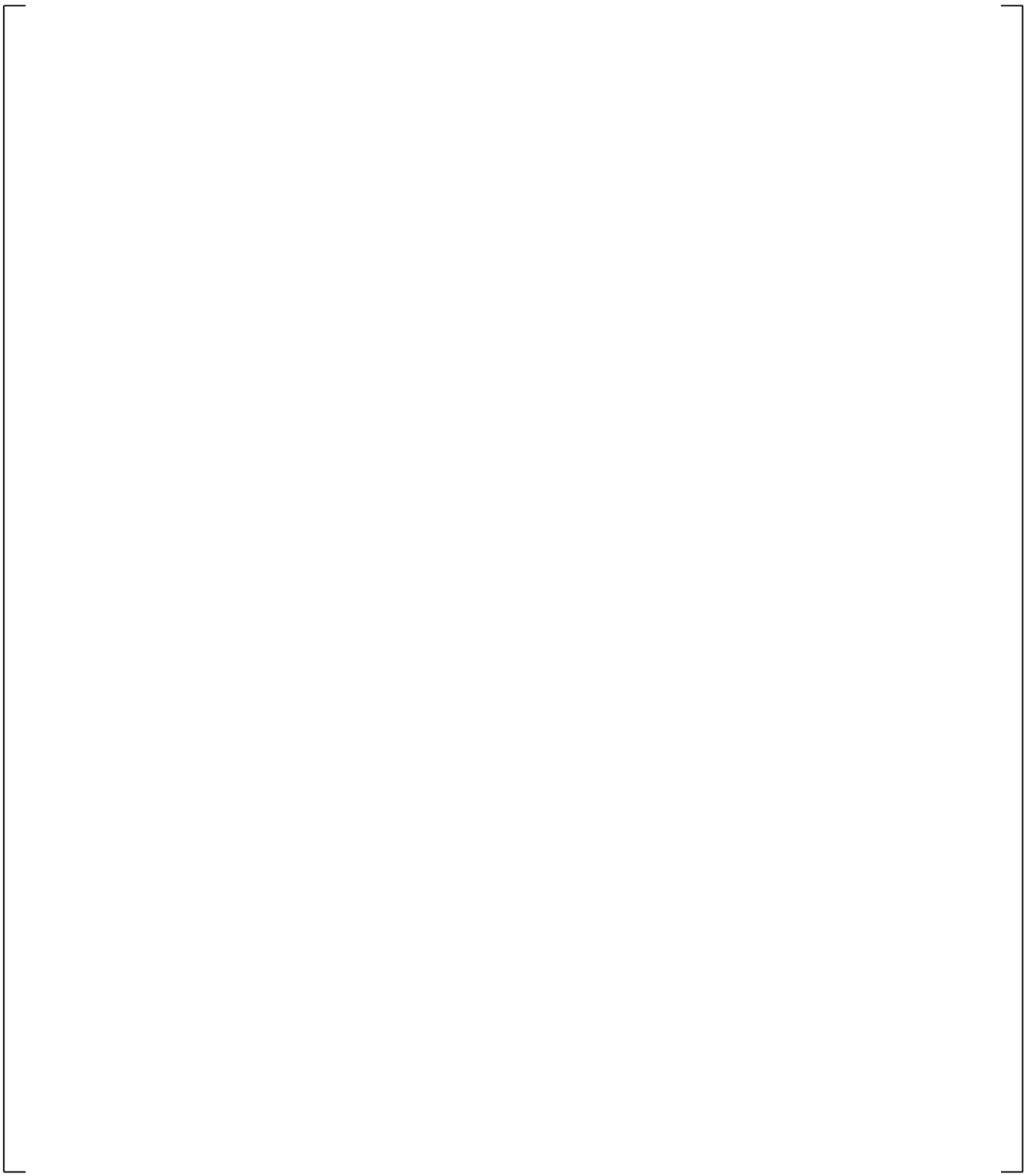

Figure 24.7.3-41 CCTF Run 62 WCOBRA/TRAC-TF2 vs. Data Total Mass Flowrate in Intact Cold Leg

a,c

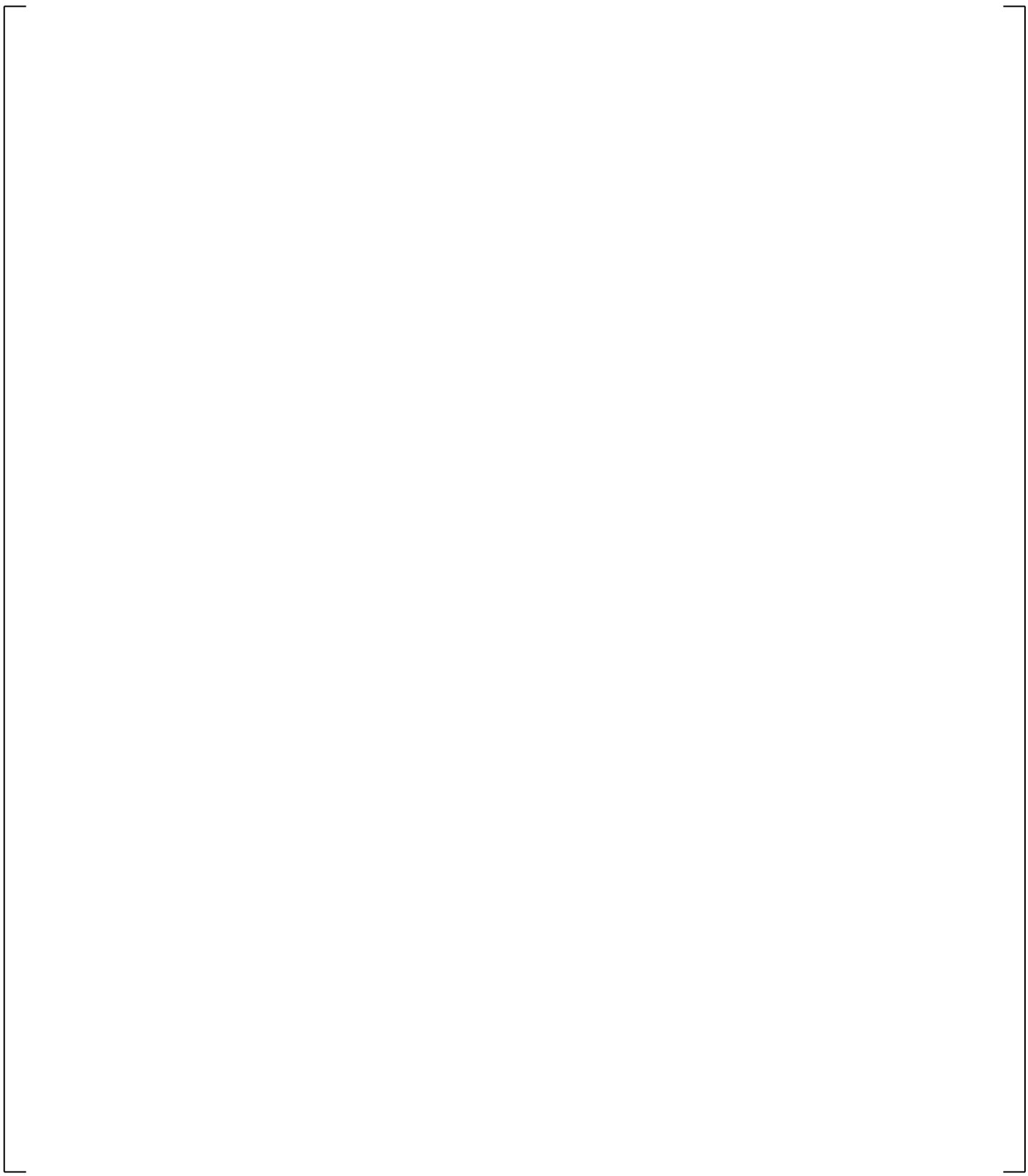

Figure 24.7.3-42 CCTF Run 62 WCOBRA/TRAC-TF2 vs. Data Liquid Mass Flowrate in Broken Hot Leg

a,c

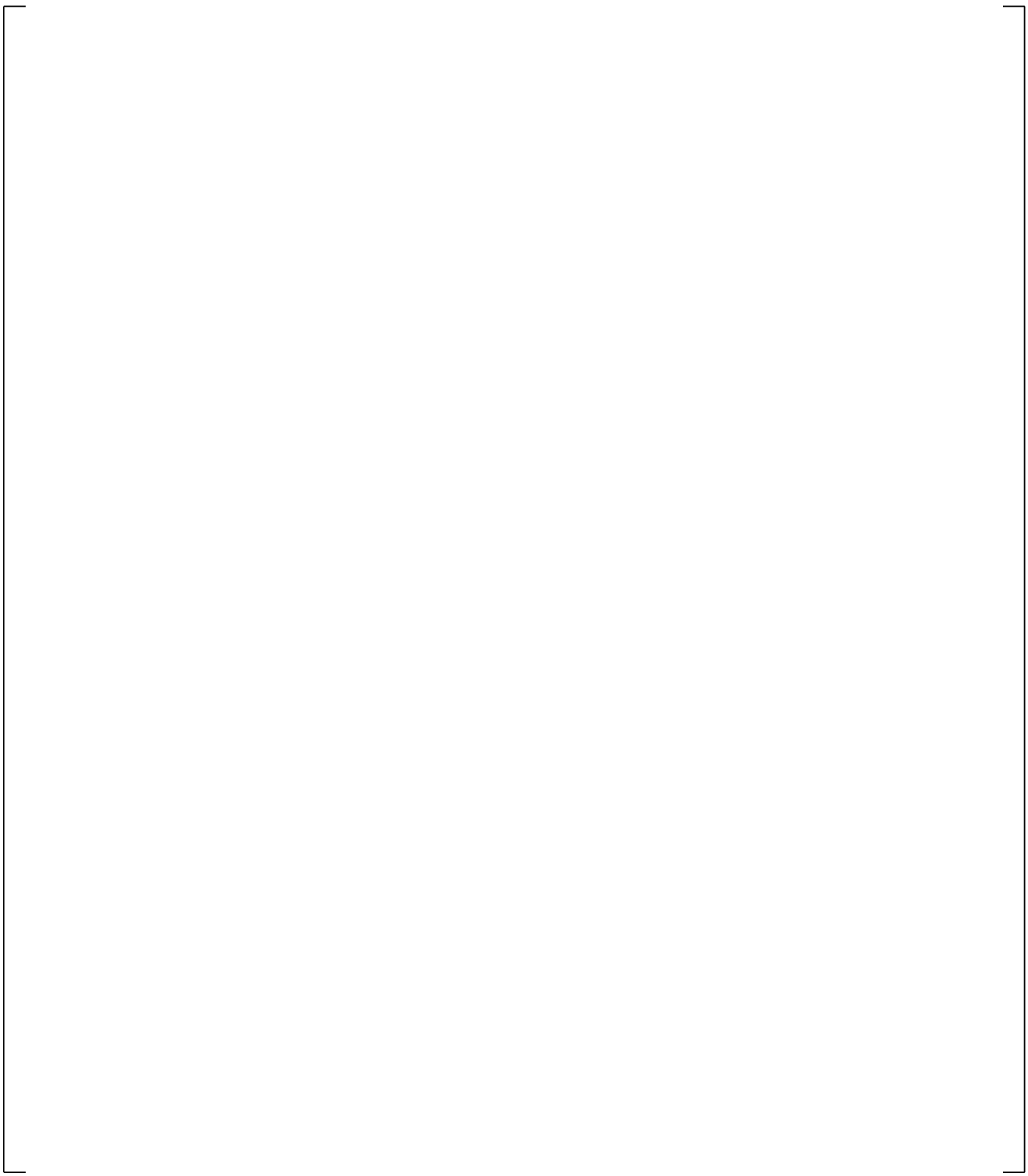

Figure 24.7.3-43 CCTF Run 62 WCOBRA/TRAC-TF2 vs. Data Vapor Mass Flowrate in Broken Hot Leg

a,c

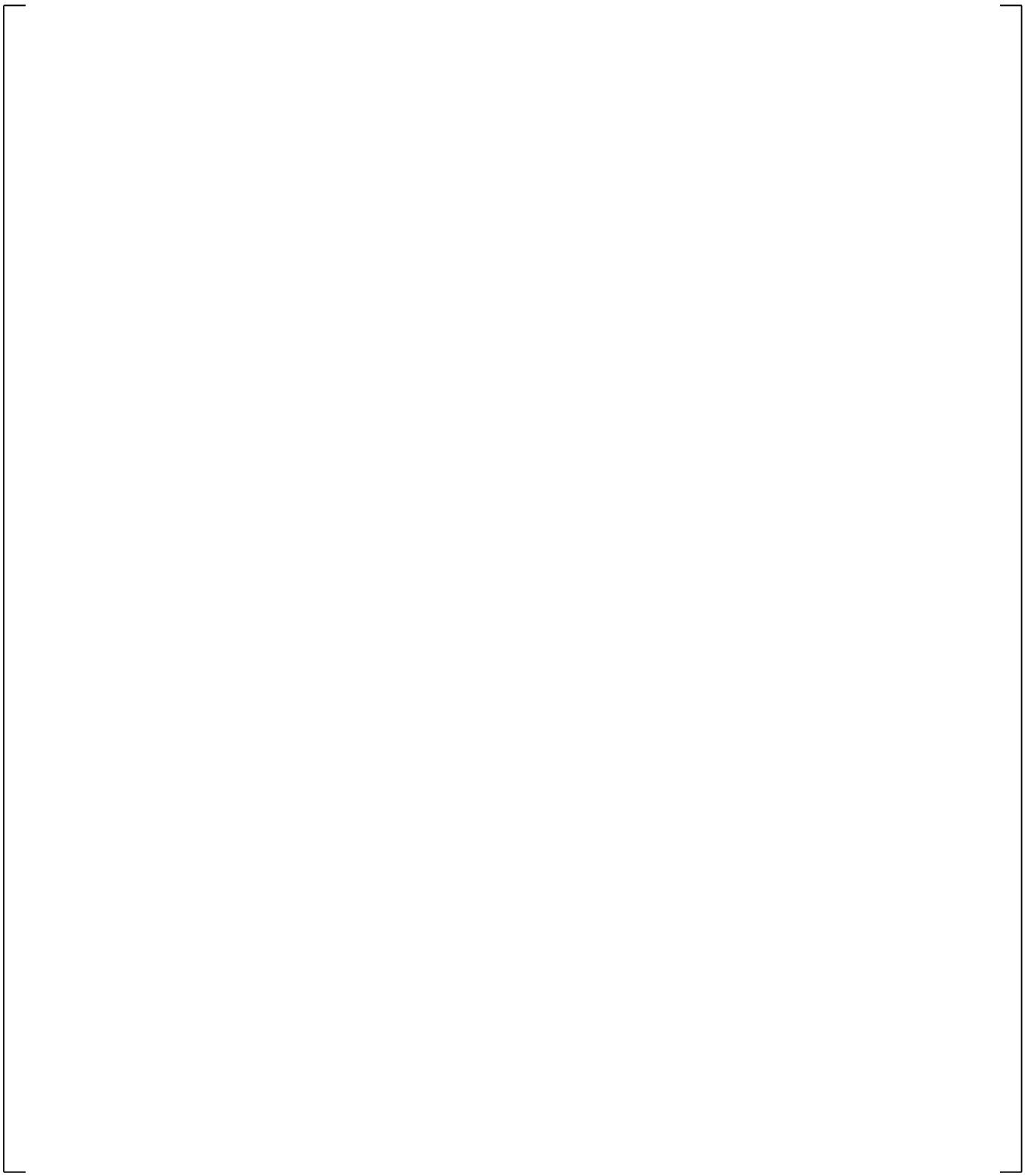

Figure 24.7.3-44 CCTF Run 62 WCOBRA/TRAC-TF2 vs. Data Total Mass Flowrate in Broken Hot Leg

a,c

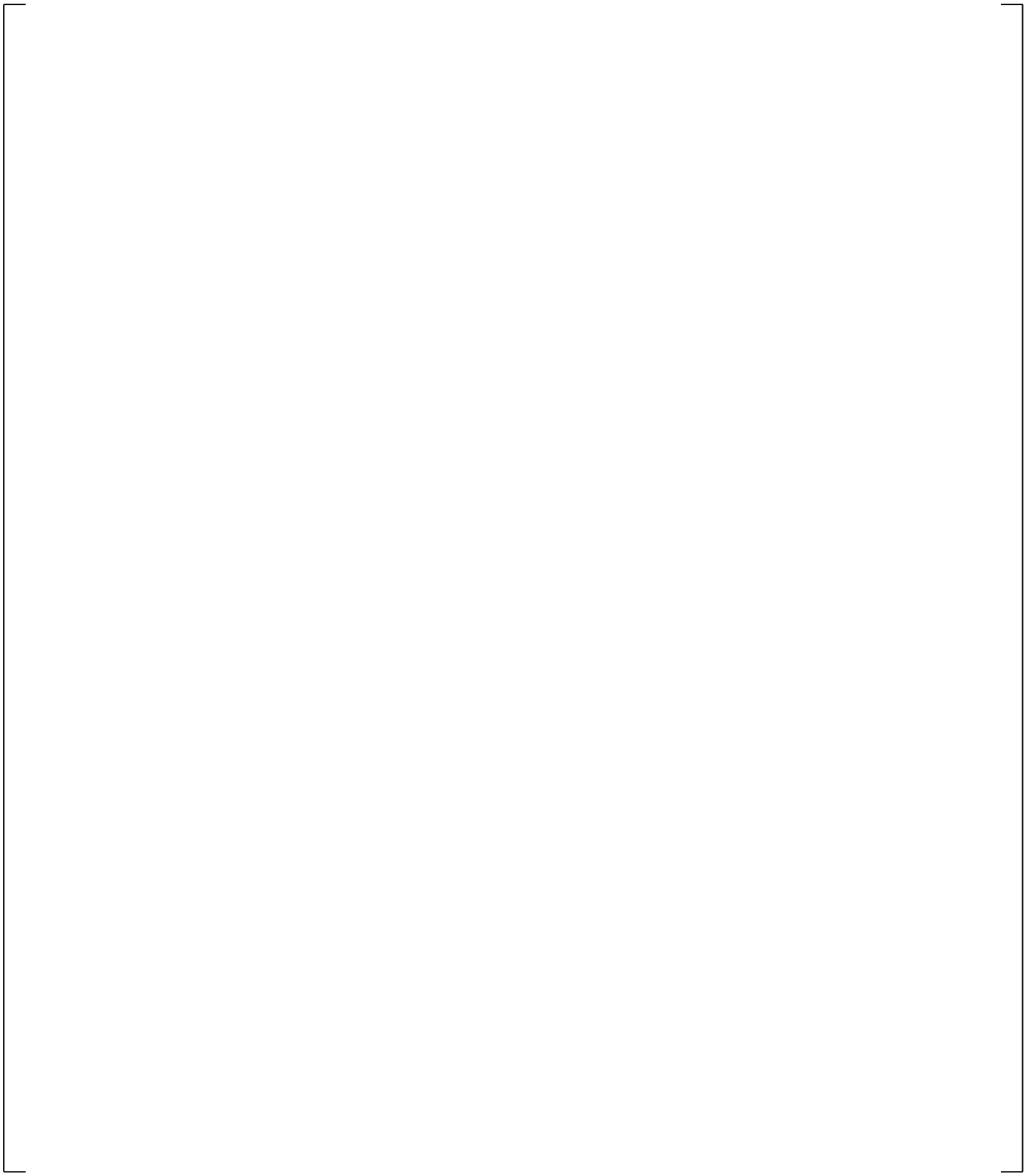

Figure 24.7.3-45 CCTF Run 62 WCOBRA/TRAC-TF2 vs. Data Vapor Mass Flowrate in Broken Cold Leg

a,c

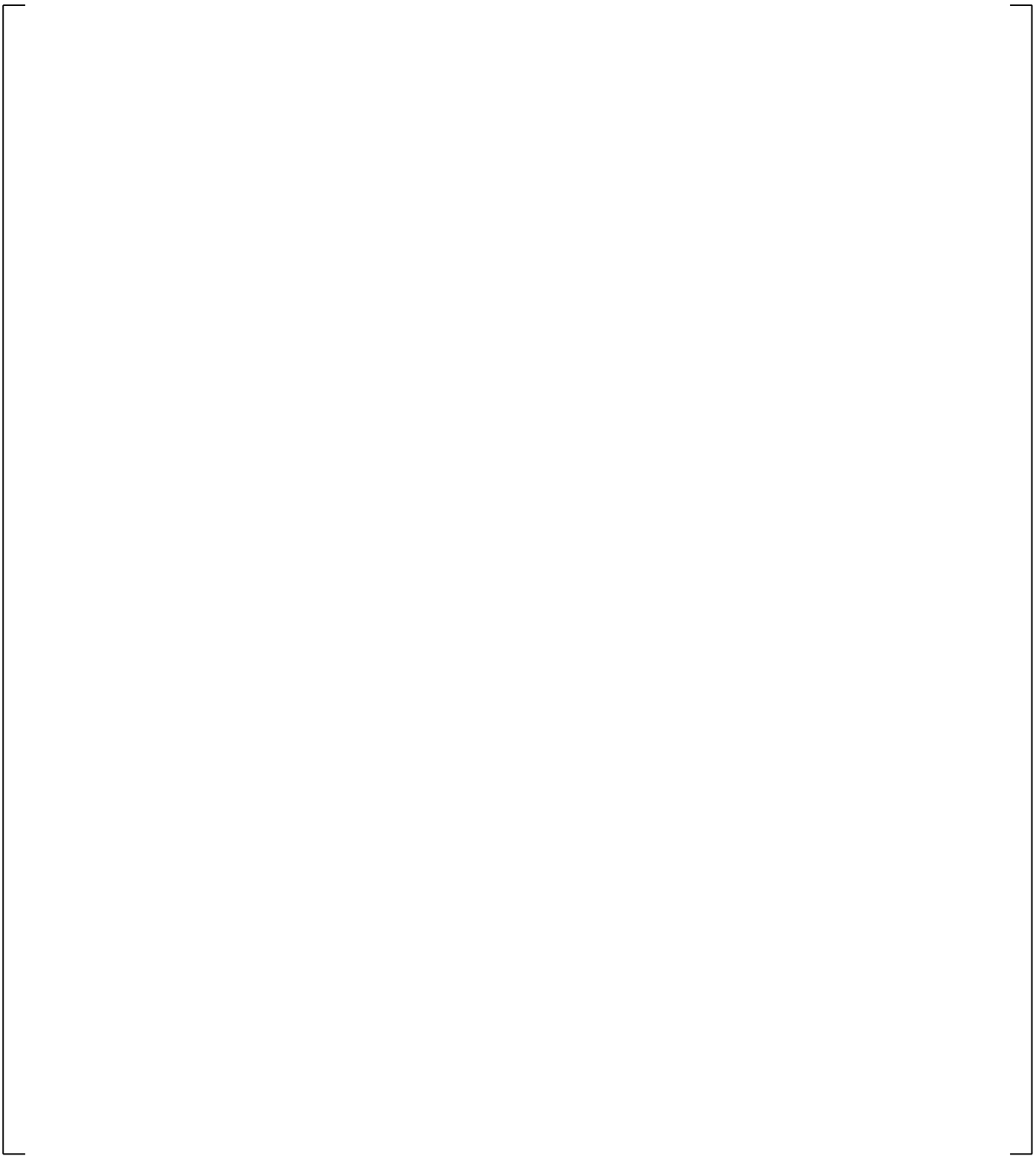

Figure 24.7.3-46 CCTF Run 62 WCOBRA/TRAC-TF2 vs. Data Pressure in Upper Plenum in Higher Containment Pressure Case

a,c

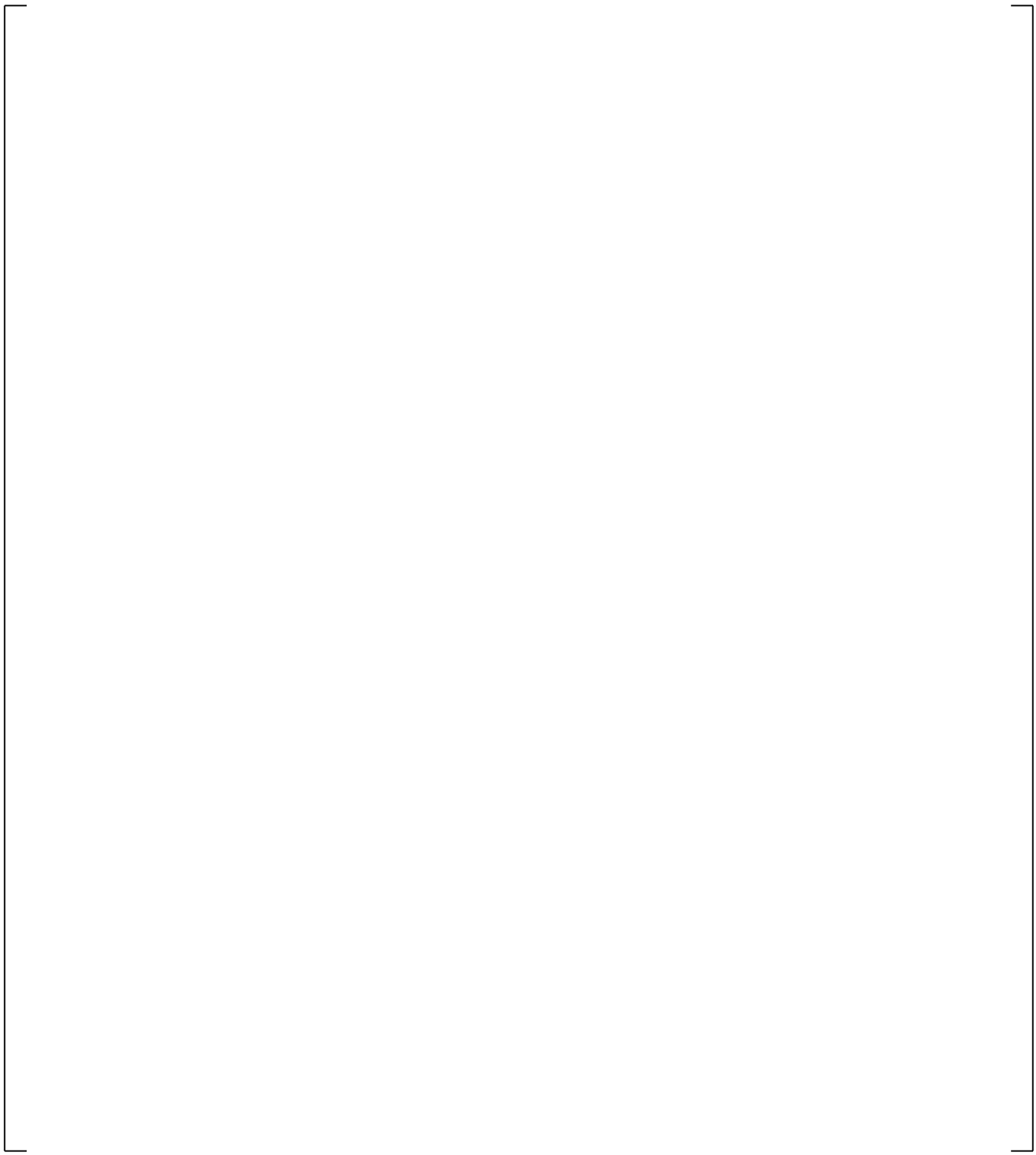

Figure 24.7.3-47 CCTF Run 62 WCOBRA/TRAC-TF2 vs. Data Cladding Temperature Comparison at 6 ft in Higher Containment Pressure Case

a,c

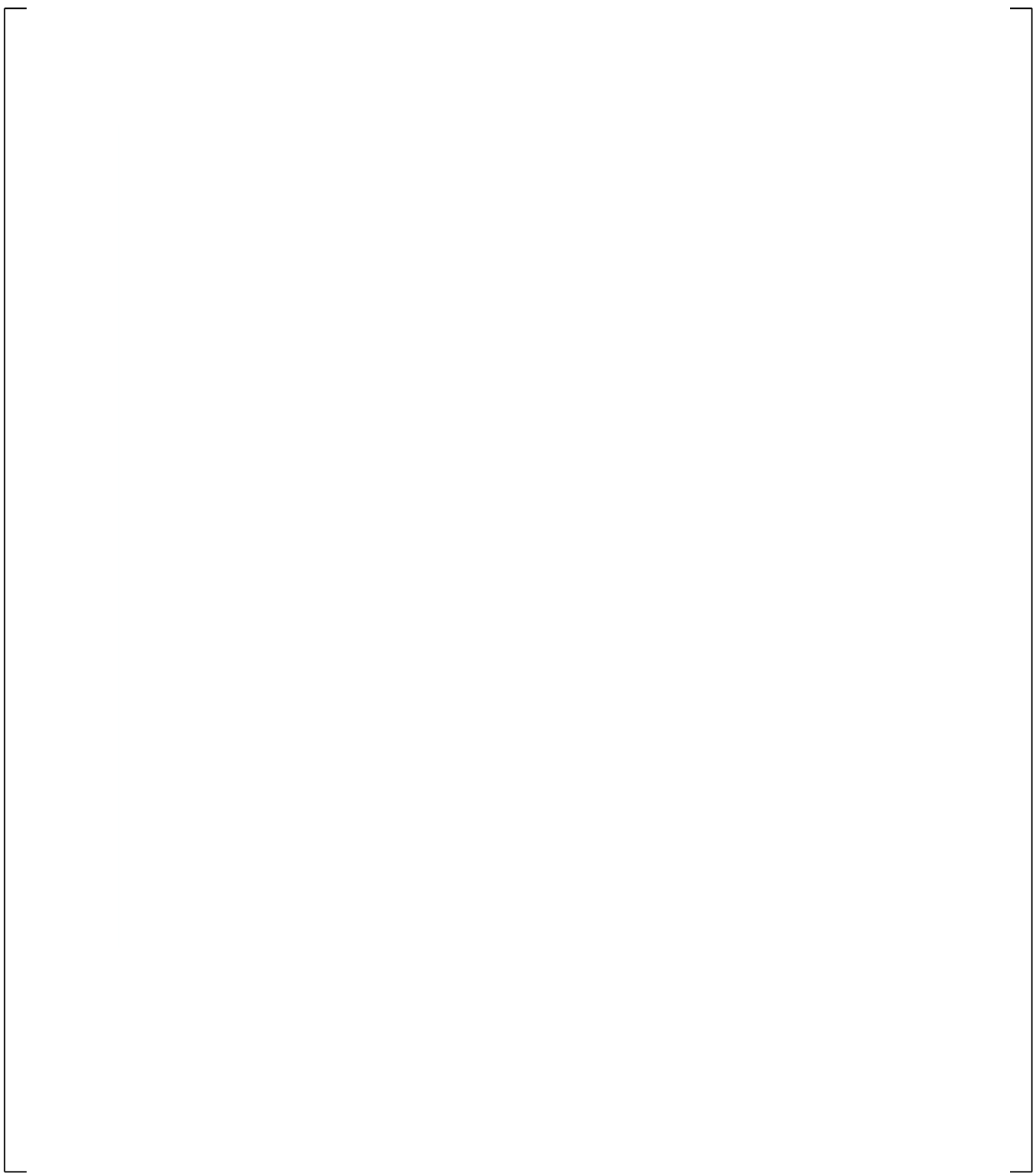

Figure 24.7.3-48 CCTF Run 62 WCOBRA/TRAC-TF2 vs. Data Cladding Temperature Comparison at 6.68 ft in Higher Containment Pressure Case

a,c

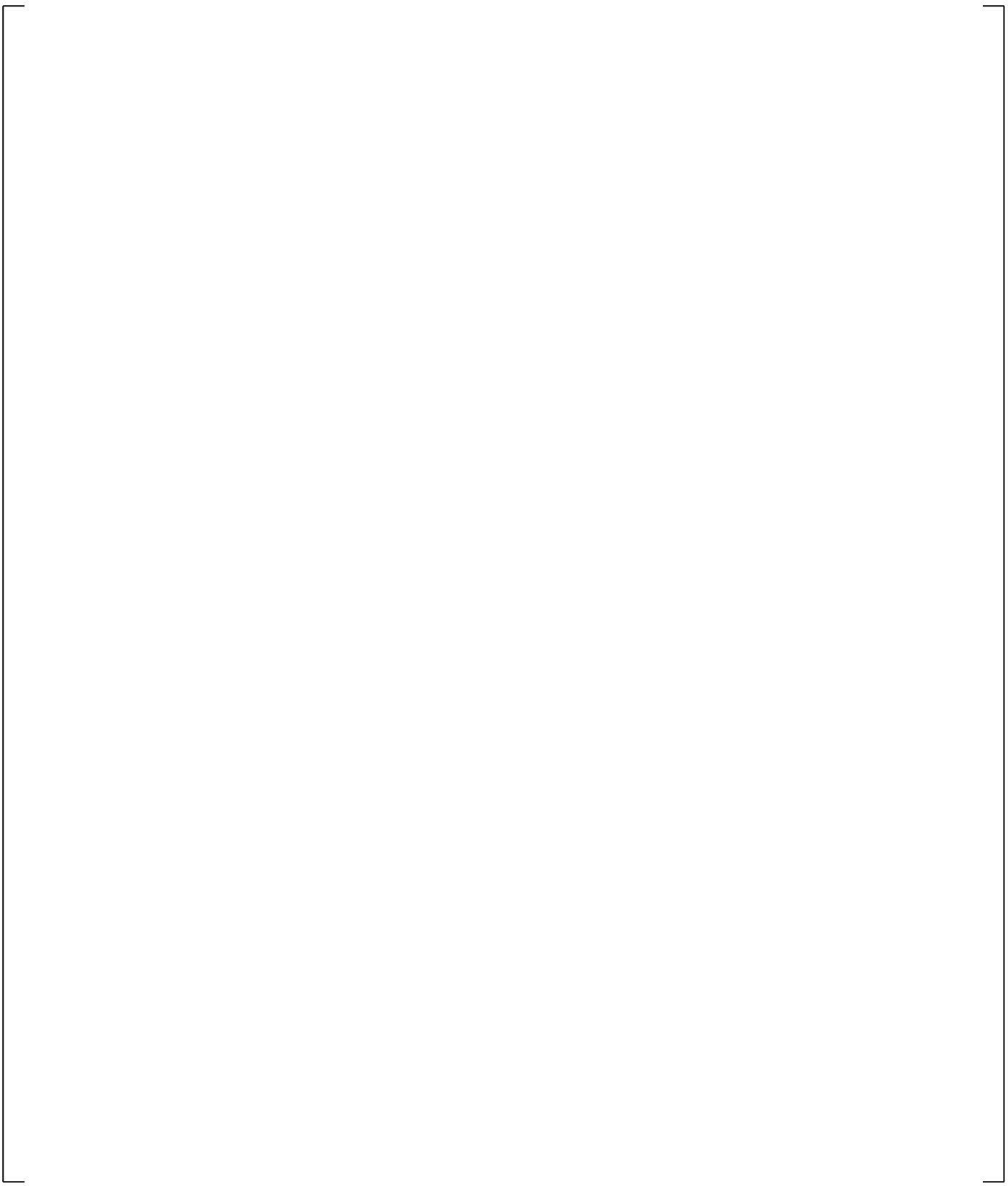

Figure 24.7.3-49 Core Inlet Flow Comparison in Higher Containment Pressure Case

a,c

Figure 24.7.3-50 CCTF Run 62 WCOBRA/TRAC-TF2 vs. Data Collapsed Liquid Level in Core in Higher Containment Pressure Case

a,c

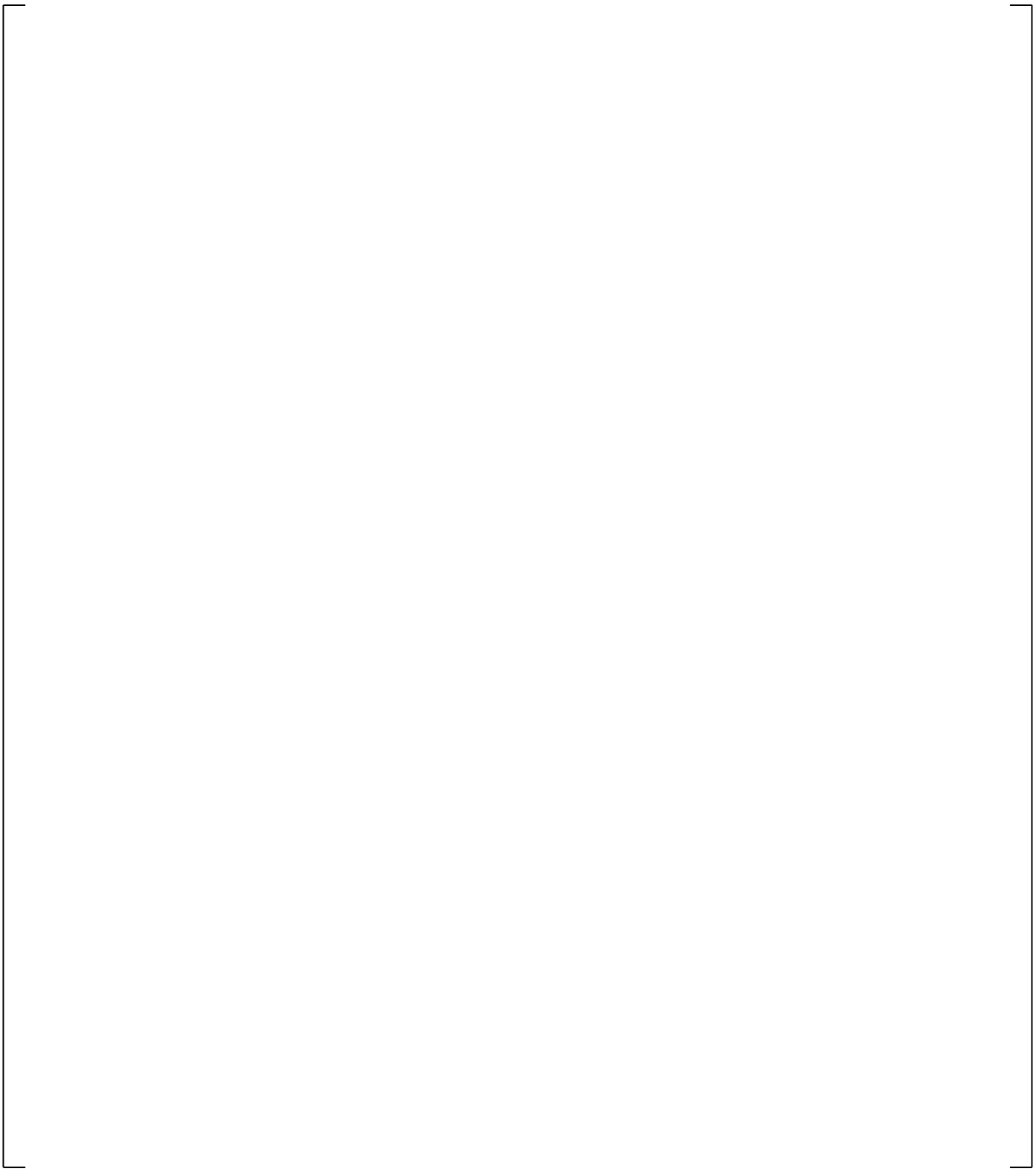

Figure 24.7.3-51 CCTF Run 62 WCOBRA/TRAC-TF2 vs. Data Collapsed Liquid Level in Upper Plenum in Higher Containment Pressure Case

24.8 CORE LEVEL PREDICTION IN SB-CL-18 TEST

In a small break LOCA, the mixture level in the core directly impacts the peak cladding temperature. This section examines the predictions of mixture level seen in the SB-CL-18 (Kumamaru et al., 1989) simulation presented in Section 21.

This section discusses the results of the SB-CL-18 simulation performed without enforcing CCFL limits. The simulation without CCFL is chosen since it was shown in Section 21.4 that enforcing CCFL, at the steam generator U-tube inlet in particular, results in a transient simulation which is skewed too much in a conservative direction with respect to the predicted core mixture level and is therefore unsuitable for the mixture level and level swell discussion presented in this section. Simulation of the 10% break test SB-CL-14 without CCFL enforcement is selected for the discussion herein for the same reason.

The predicted core differential pressure from the ROSA-IV SB-CL-18, a 5% cold leg (CL) break simulation is compared against the measurement in Figure 24.8.1-1. The figure shows **[**

][a,c] prediction is examined in detail.

24.8.1 Core Collapsed Liquid Level

The comparison in Figure 24.8.1-1 shows **[**

][a,c]

Observed Core DP General Trend

The core DP increases initially and peaks at about 20 seconds followed by a constant decrease which slows down at t~50 seconds. Then core DP continues to decrease at a relatively constant rate until t=100 seconds. The rate of DP decrease increases due to the loop seal clearance depression which according to the measurement bottoms out at t=140 seconds followed by a quick recovery due to the venting of trapped steam in the inner vessel. The core level recovers to a constant level which lasted until t=400 seconds, followed by the boiloff during which the cladding temperature increased significantly above saturation signifying the dryout condition which was terminated by the level increase at t=460 seconds due to accumulator injection.

Predicted Core DP General Trend

The predicted core DP, Figure 24.8.1-1, **[**

][a,c]

The details of the transient in terms of core DP are examined next.

Core DP Increase at 20 Seconds

Since the facility's power capability is 10 MW which is 14% of power required to match the scaled (1/48th) PWR's full power, the steady state loop flow is reduced to 14% of the rated flow to match the hot and cold leg temperatures of the PWR steady state. After the break at t=0 second, the pump speed is accelerated from the steady state level in order to match the expected coastdown curve from the rated pump speed (Figure 24.8.1-2), **[**

][a,c]

Core DP Increase at ~50 Seconds

After the initial acceleration, the pump coasts down rapidly and the pump becomes **[**

][a,c]

Core DP Decrease until Loop Seal Clearance

After the natural circulation driving force peaks at **[**

][a,c] Figures 24.8.1-9 and 24.8.1-10 show the pressure drop

from the upper plenum to the Steam Generator inlet plenum, and from Steam Generator inlet to outlet plenum. **[**

][a,c]

Level Recovery after Loop Seal Clearing

Figure 24.8.1-11 shows that the **[**

][a,c]

Boil-off Core Level and PCT

The predicted boiloff begins **[**

][a,c]

Core Level Prediction at Simulations of Other Break Sizes

Core DP comparison for SB-CL-01 (2.5% Cold Leg Break) (Koizumi et al., 1987) simulation is shown in Figure 24.8.1-14. The simulation of SB-CL-01 is described in Section 21. In this transient, Steam Generators drained prior to the loop seal clearance at about 320 seconds, Figures 21.7-8 and 21.7-9 **[**

][a,c]

The core collapsed liquid level comparison for the SB-CL-14 (10% Cold Leg Break) (Koizumi and Tasaka, 1988) simulation is shown in Figure 24.8.1-18. The simulation of SB-CL-14 is described in Section 21.6. **[**

][a,c]

24.8.2 Prediction of Core Mixture Level and Cladding Heat-up

The mixture level in the core region directly determines the heat-up elevation during a small break LOCA because the CHF takes place at or near where the equilibrium quality approaches unity for the heat flux range typical of a small break LOCA (Guo, Kumamaru, and Kukita, 1993). In this section, **[**

][a,c]

24.8.3 Level Swell Prediction

The cladding heat-up is a result of the mixture level dropping into the core and uncovering the rod. Since at low heat flux which is the case for boiloff in SBLOCAs, **[**

][a,c]

[a,c]

[

]a,c

a,c

Figure 24.8.1-1 Core DP Comparison in SB-CL-18 Simulation

a,c

Figure 24.8.1-2 Pump Speed used in Test and in Simulation

a,c

Figure 24.8.1-3 SB-CL-18 Core DP Comparison with Core Inlet Liquid Velocity

a,c

Figure 24.8.1-4 SB-CL-18 Core DP Comparison with Pump DP in Loop A and B

a,c

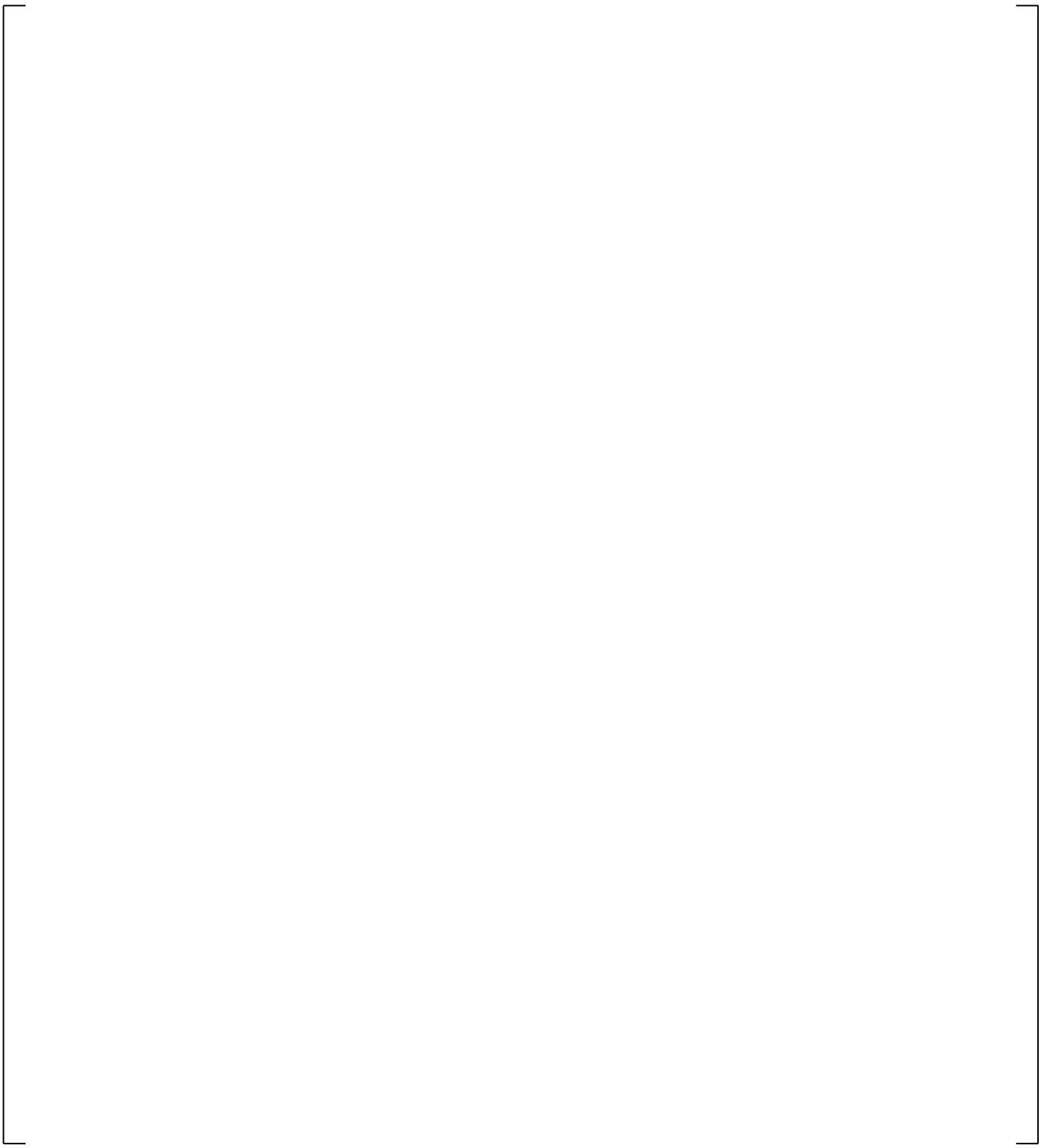

Figure 24.8.1-5 Primary Side Circulation Flow as a Function of Primary Side Inventory

a,c

Figure 24.8.1-6 Core DP Comparison with the Void Fraction in Downhill side on Steam Generator and Cross-over Leg

a,c

Figure 24.8.1-7 Calculated Liquid Flows at the Top of Core Channels (Curve-1 = Outer Low Power Assembly, Curve-2 = Inner Average Assembly, Curve-3 = Hot Assembly)

Note: Liquid flows shown in Figure 24.8.1-7 are normalized (kg/sec per assembly)

a,c

Figure 24.8.1-8 Core DP Comparison with the Hot Leg Nozzle Liquid Flowrates

a,c

Figure 24.8.1-9 DP Comparison from Upper Plenum to Steam Generator Inlet

a,c

Figure 24.8.1-10 DP Comparison from Steam Generator Inlet to Outlet Plenum

a,c

Figure 24.8.1-11 Core DP Comparison with Void Fraction in Cross-over Leg Piping

a,c

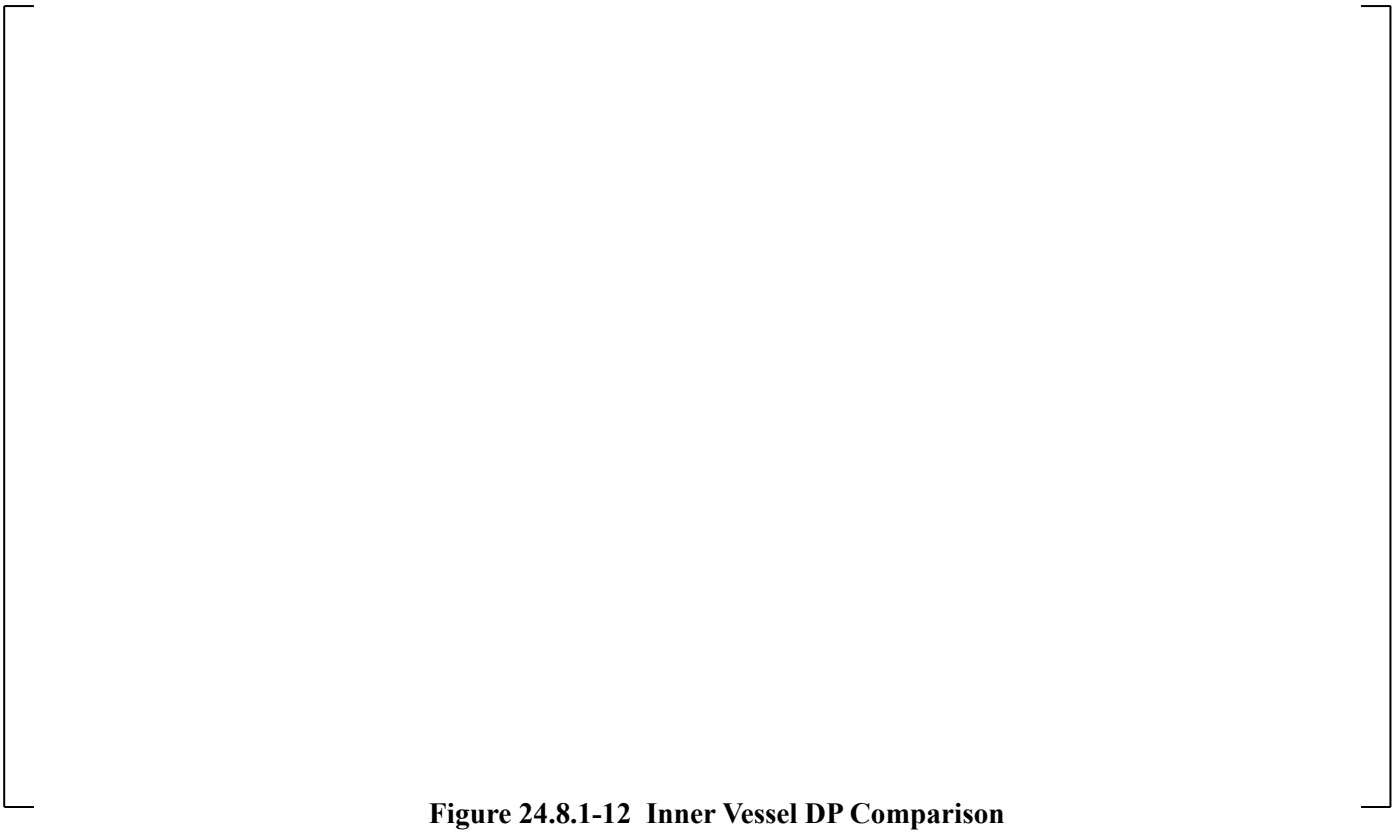

Figure 24.8.1-12 Inner Vessel DP Comparison

a,c

Figure 24.8.1-13 Downcomer to Upper Plenum Pressure Difference

a,c

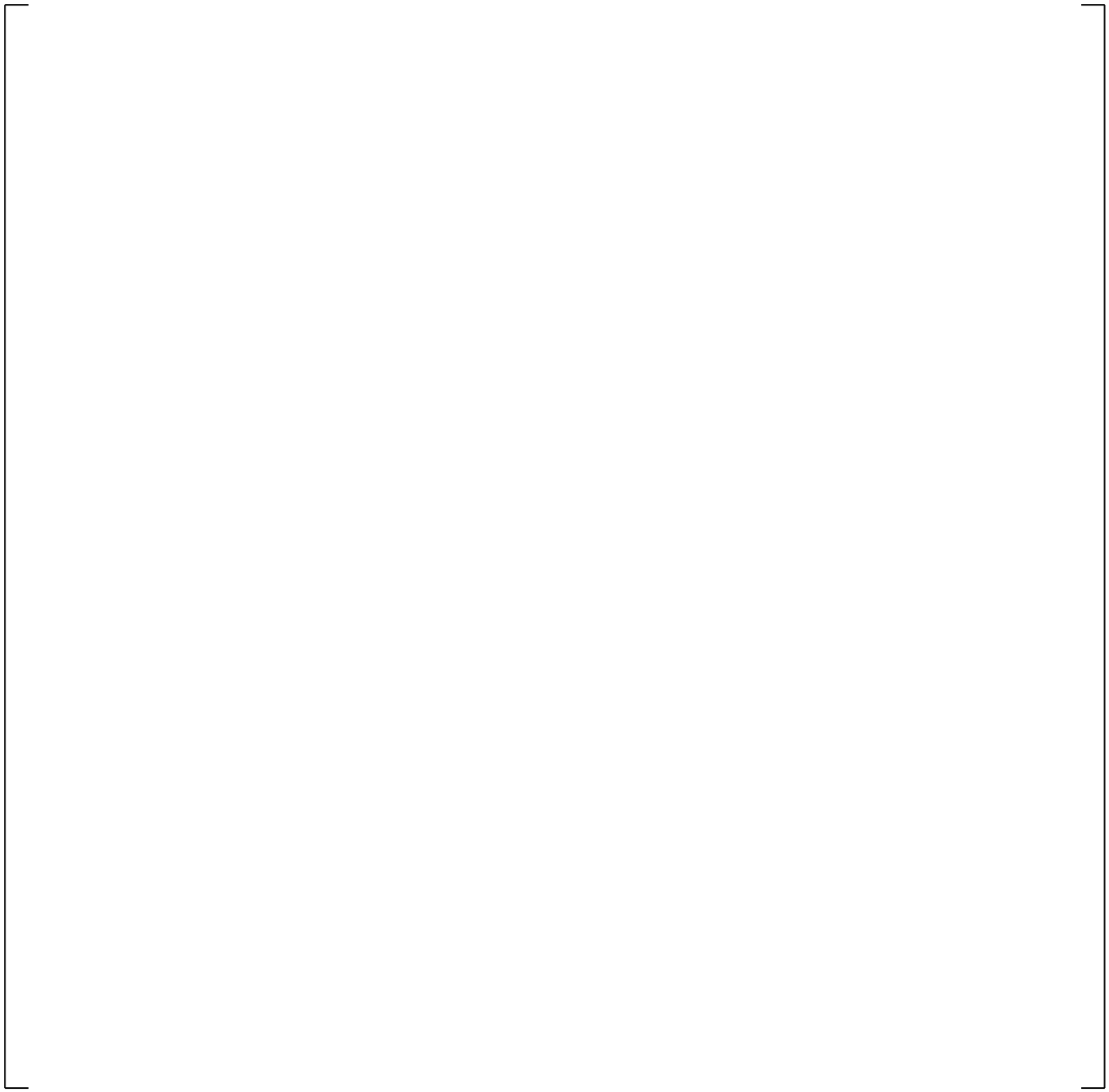

Figure 24.8.1-14 Core DP Comparison for SB-CL-01 (2.5%)

a,c

Figure 24.8.1-15 Loop-A Loop Seal Bottom to Pump DP Comparison for SB-CL-01 (2.5%)

a,c

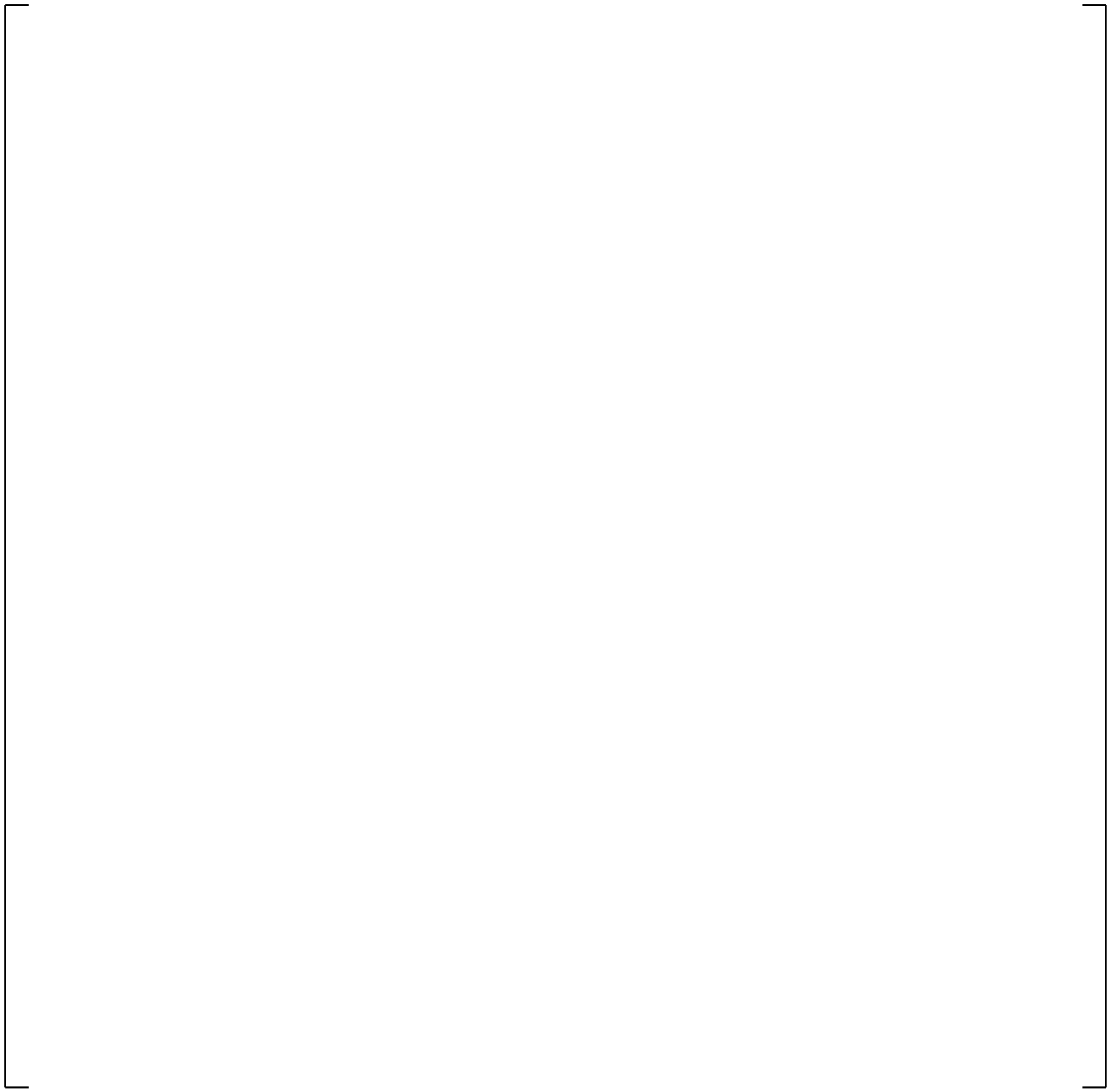

Figure 24.8.1-16 Loop-B Loop Seal Bottom to Pump DP Comparison for SB-CL-01 (2.5%)

a,c

Figure 24.8.1-17 Downcomer to Upper Plenum Pressure Difference in SB-CL-01 (2.5%)

a,c

Figure 24.8.1-18 Core Collapsed Liquid Level Comparison for SB-CL-14 (10%)

a,c

Figure 24.8.1-19 Steam Generator Inlet to Top of Tube DP Comparison for SB-CL-14 (10%)

a,c

Figure 24.8.1-20 Comparison of Loop-A Cross-Over Leg Differential Pressures

a,c

Figure 24.8.1-21 Comparison of Loop-B Cross-Over Leg Differential Pressures

a,c

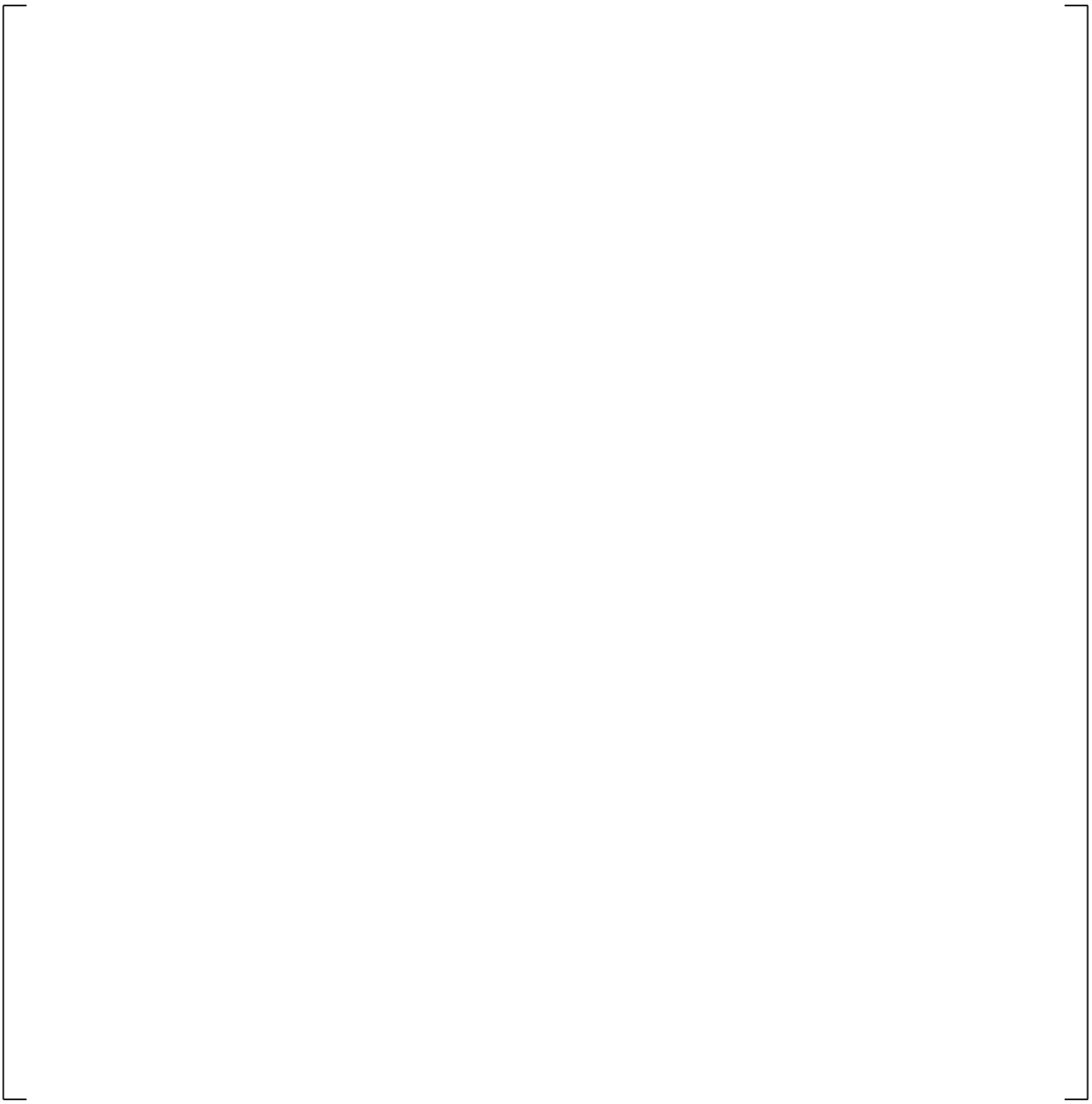

Figure 24.8.2-1 Comparison of Predicted Mixture Level and Test Data

a,c

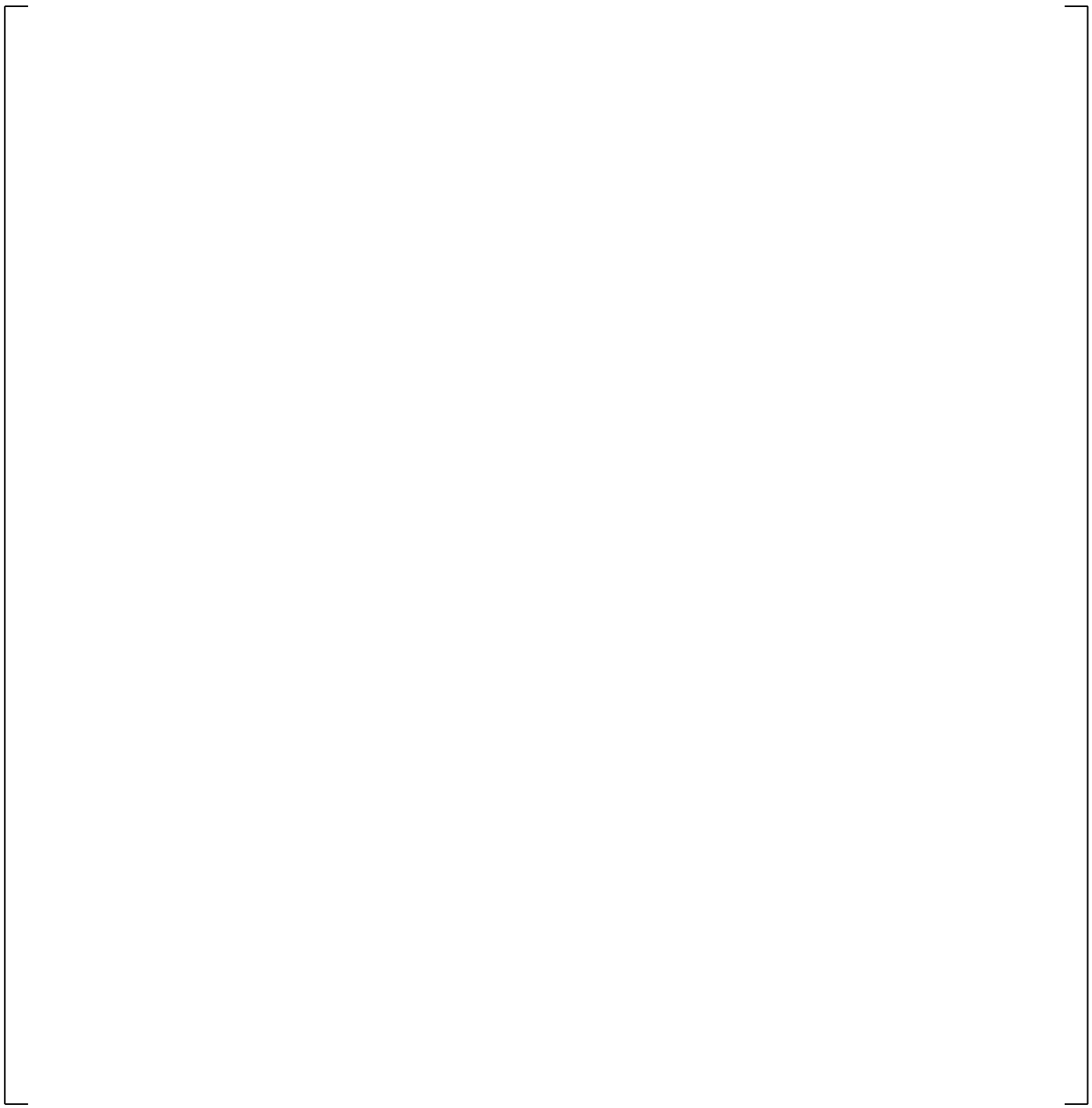

Figure 24.8.2-2A Comparison of Predicted Mixture Level and Test Data, and YDRAG Sensitivity

a,c

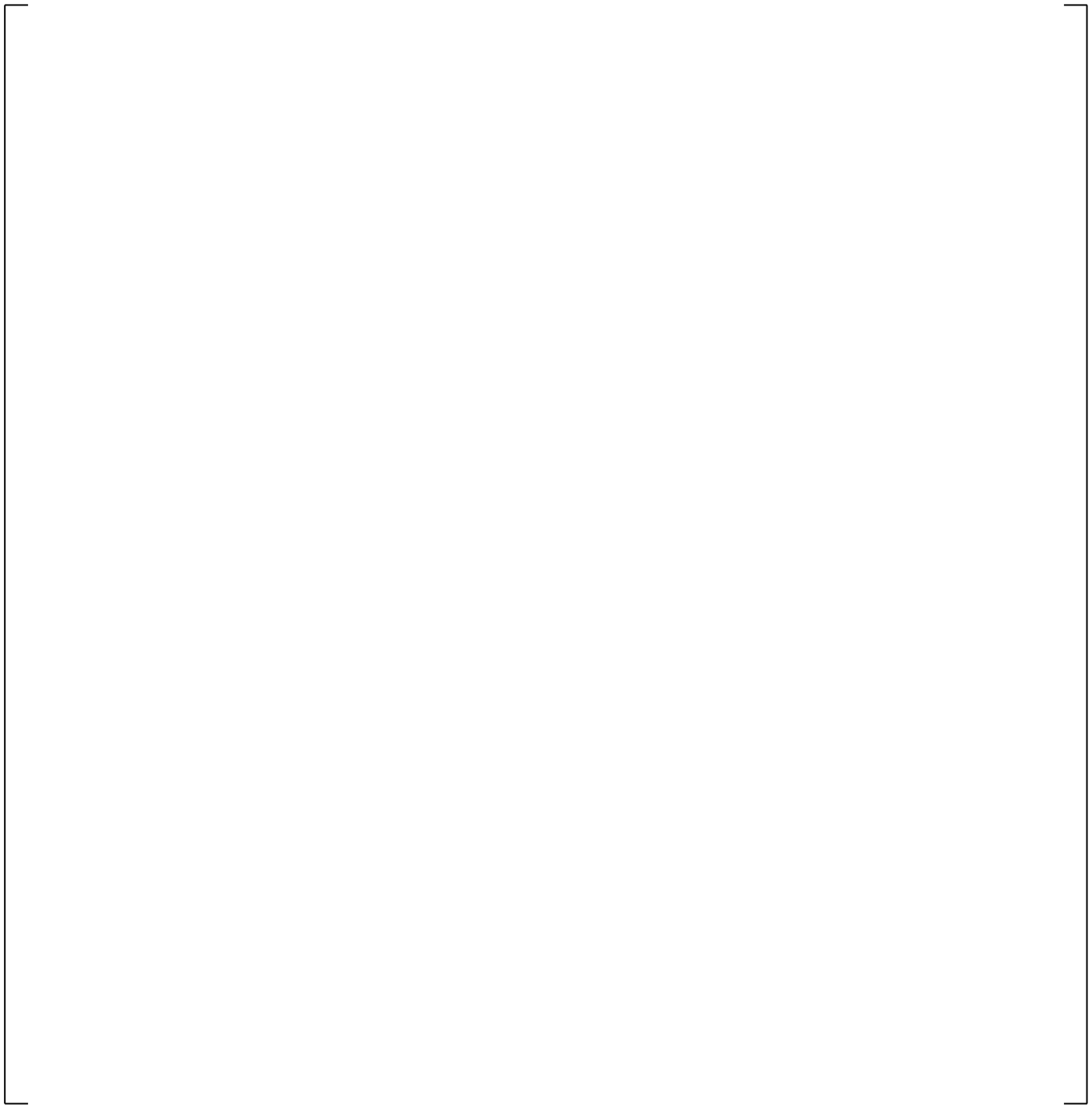

Figure 24.8.2-2B Comparison of Predicted Mixture Level and Test Data, and YDRAG Sensitivity

a,c

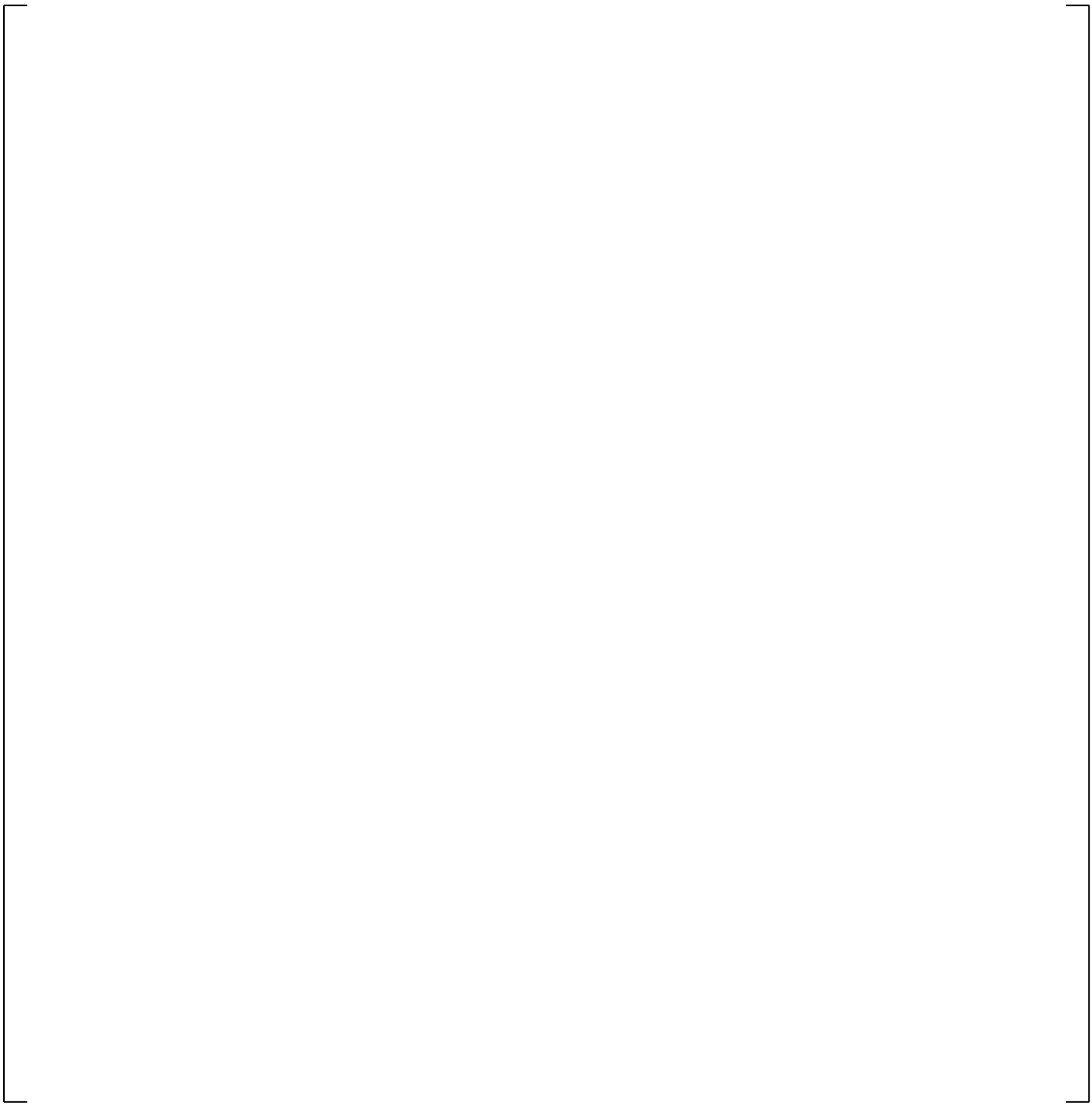

Figure 24.8.3-1 Comparison of Predicted Level Swell against Measured

a,c

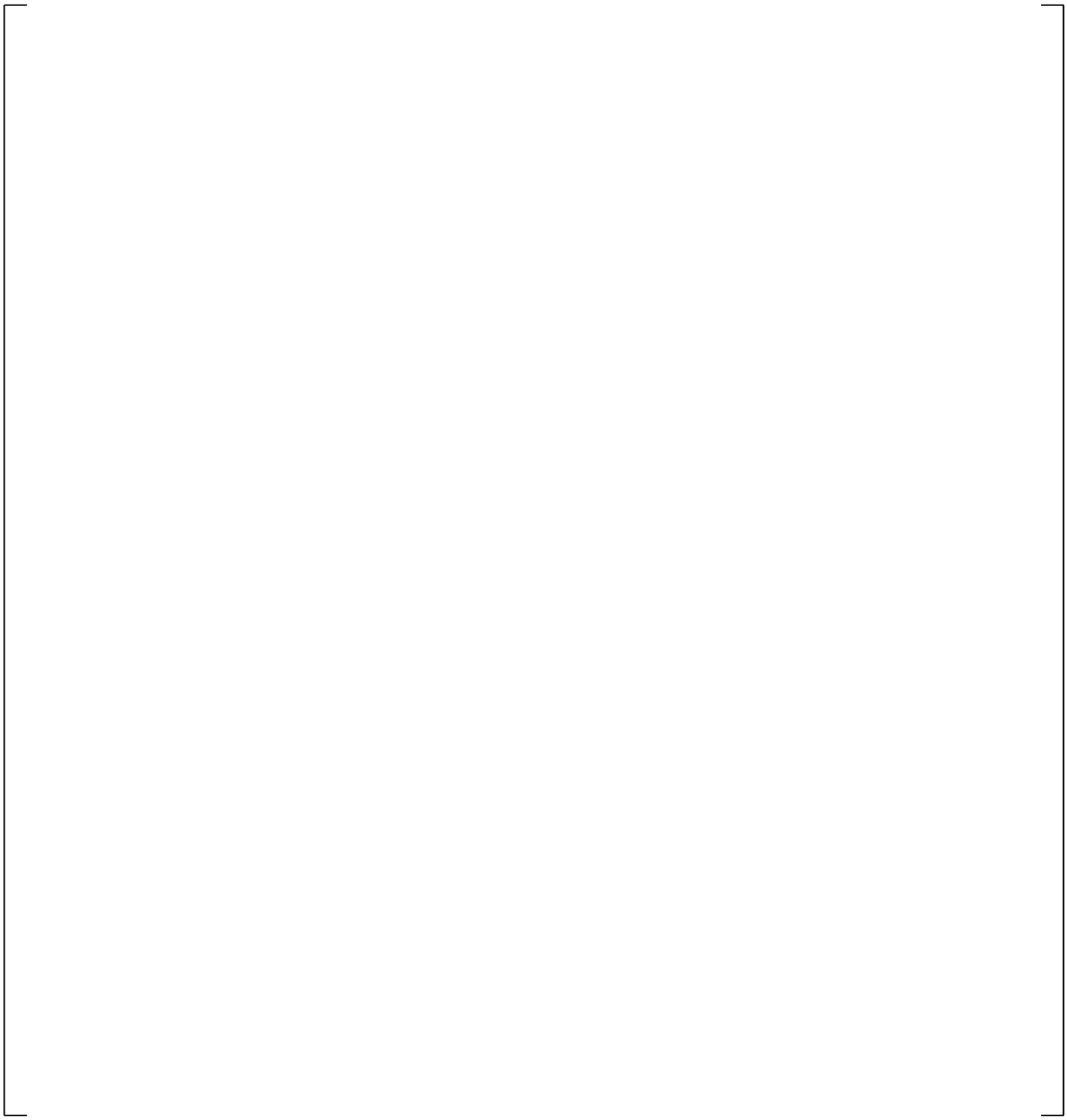

Figure 24.8.3-2 Impact of YDRAG Variation on Predicted Level Swell

24.9 SUMMARY OF COMPENSATING ERROR ASSESSMENT

The evaluations provided in this section as well as those previously performed in the model validation sections of this document give confidence that compensating errors of a nature which seriously compromise the ability of WCOBRA/TRAC-TF2 to predict conditions during a LOCA of a PWR do not exist and that the **[**

][a,c] The major finding from the analysis is tabulated below:

[

][a,c]

24.10 REFERENCES

1. 2D/3D Program Upper Plenum Test Facility Experimental Data Report, 1988, "Test No. 8, Cold/Hot Leg Flow Pattern Test," U9 316/88/12, KWU.

2. 2D/3D Program Upper Plenum Test Facility Quick Look Report, 1989, "Test No. 6; Downcomer Countercurrent Flow Test," Siemens/KWU U9 316/89/2.

3. 2D/3D Program Upper Plenum Test Facility Experimental Data Report, 1990, "Test No. 25, Downcomer/Cold Leg Steam/Water Interaction Test," E314/90/11, KWU.

4. Anklam, T. M., et al., 1982, "Experimental Investigations of Uncovered Bundle Heat Transfer and Two-Phase Mixture Level Swell Under High Pressure Low Heat Flux Conditions," NUREG/CR-2456.

5. Bayless, P. D. and Divine, J. M., 1982, "Experiment Data Report for LOFT Large-Break Loss-of-Coolant Experiment L2-5," NUREG/CR-2826.

6. Boyack, B., et al., 1989, "Quantifying Reactor Safety Margins," NUREG/CR-5249.

7. Chauliac, C., et al., 1988, "Post-Test Analysis with RELAP5/MOD2 of ROSA-IV/LSTF Natural Circulation Test ST-NC-02," JAERI-M 88-215.

8. Cunningham, J. P., Fayfich, R. R., Mendler, D. J. and Steer, R. W., 1974, "ECCS HEAT TRANSFER EXPERIMENTS WITH UPPER HEAD INJECTION, TEST FACILITY, PROCEDURE AND DATA," WCAP-8400, Volume 1.

9. Guo, Z., Kumamaru, H. and Kukita, Y., 1993, "CRITICAL HEAT FLUX FLOW ROD BUNDLE UNDER HIGH-PRESSURE BOIL-OFF CONDITIONS," JAERI-M 93-238.

10. Ilic, V., Banerjee, S. and Behling, S., 1986, "A Qualified Database for the Critical Flow of Water," EPRI-NP-4556.

11. Jarrell, Donald B. and Divine, Janice M., 1981, "Experiment Data Report for LOFT Intermediate Break Experiment L5-1 and Severe Core Transient Experiment L8-2," NUREG/CR-2398.

12. Koizumi, Y., et al., 1987, "ROSA-IV/LSTF 2.5% Cold Leg Break LOCA Experiment Data Report for Runs SB-CL-01, 02 and 03," JAERI-memo 62-399.

13. Koizumi, Y. and Tasaka, K., 1988, "Quick Look Report for ROSA-IV/LSTF 10% Cold Leg Break LOCA Test, SB-CL-14," **[ ]**[b]

14. Kumamaru, et al., 1989, "ROSA-IV/LSTF 5% Cold Leg Break LOCA Experiment, Run SB-CL-18 Data Report," JAERI-M 89-027.

15. Lee, N., Wong, S., Yeh, H. C., and Hochreiter, L. E., 1981, "PWR FLECHT SEASET UNBLOCKED BUNDLE, FORCED AND GRAVITY REFLOOD TASK, DATA EVALUATION AND ANALYSIS REPORT," WCAP-9891.

16. Liebert, J. and Emmerling, R., 1998, "UPTF Experiment Flow Phenomena During Full-Scale Loop Seal Clearing of a PWR," *Nuclear Engineering and Design*, Vol. 179, pp. 51-64.

17. Loftus, M. J. et al., 1981, "PWR FLECHT-SEASET Unblocked Bundle, Forced and Gravity Reflood Task Data Report," Volumes 1 and 2, NUREG/CR-1532, WCAP-9699.

18. Morris, D. G., Mullins, C. B. and Yoder, G. L., 1982, "An Analysis of Transient Film Boiling of High-Pressure Water in a Rod Bundle," NUREG/CR-2469.

19. MPR Associates, 1990, "Summary of Results from the UPTF Downcomer Separate Effects Tests, Comparison to Previous Scaled Tests, and Application to U.S. PWRs," MPR-1163.

20. Mullins, C. B., et al., 1982, “Thermal-Hydraulic Test Facility Experimental Data Report for Test 3.03.6AR and Test 308.6C – Transient Film Boiling in Upflow,” NUREG/CR-2525, Volumes 2 and 5.

21. Okubo, T., Iguchi, T., Okabe, K., Sugimoto, J., Akimoto, H., and Murao, Y., 1985, “Evaluation Report on CCTF Core-II Reflood Test C2-4 (Run 62),” JAERI-M 85-026.

22. Prassinos, P. G., et al., 1979, “Experiment Data Report for LOFT Power Ascension Experiment L2-3,” NUREG/CR-0792.

23. Sackett, Kenneth E. and Clegg, L. Bruce, 1980, “Experiment Data Report For Semiscale MOD-3 Small Break Test S-07-10D (Baseline Test Series),” prepared for the U.S. Nuclear Regulatory Commission under Department of Energy Contract No. DE-AC07-76IDO1570.

24. Tasaka, K., et al., 1988, “The Results of 5% Small Break LOCA Tests and Natural Recirculation Tests at the ROSA-IV LSTF,” Nuclear Engineering and Design, 108.

25. Tolman, E. L. and Coryell, E. W., 1980, “REVIEW OF LOFT CLADDING TEMPERATURE RESPONSE FOR L2-2 & L2-3: RECOMMENDATIONS FOR IMPROVED LOFT FUEL ROD MEASUREMENTS (SYSTEMS 14 & 87),” EGG-LOFT-5244.

26. Wong, S. and Hochreiter, L. E., 1981, “Analysis of the FLECHT SEASET Unblocked Bundle Steam Cooling and Boiloff Tests,” WCAP-9729.

27. Yoder, et al., 1982, “Dispersed Flow Film Boiling in Rod Bundle Geometry-Steady State Heat Transfer Data and Correlation Comparisons,” NUREG/CR-2435, ORNL-5822.